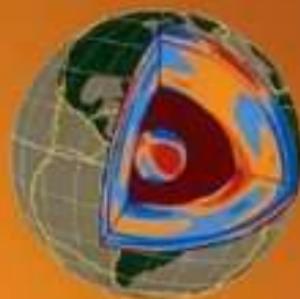




VOLUME 1

TREATISE ON GEOPHYSICS

SEISMOLOGY AND STRUCTURE OF THE EARTH



Volume Editors

Adam M. Dziewonski

Barbara A. Romanowicz

Editor-in-Chief Gerald Schubert

Editor-in-Chief

Professor Gerald Schubert

*Department of Earth and Space Sciences and Institute of Geophysics and Planetary Physics,
University of California Los Angeles, Los Angeles, CA, USA*

Volume Editors

Volume 1 Seismology and the Structure of the Earth

Dr. Barbara Romanowicz

University of California at Berkeley, CA, USA

Dr. Adam Dziewonski

Harvard University, Cambridge, MA, USA

Volume 2 Mineral Physics

Dr. G. David Price

University College London, London, UK

Volume 3 Geodesy

Dr. Tom Herring

Massachusetts Institute of Technology, Cambridge, MA, USA

Volume 4 Earthquake Seismology

Dr. Hiroo Kanamori

California Institute of Technology, Pasadena, CA, USA

Volume 5 Geomagnetism

Dr. Masaru Kono

Tokyo Institute of Technology, Tokyo, Japan

Volume 6 Crust and Lithosphere Dynamics

Professor Anthony B. Watts

University of Oxford, Oxford, UK

Volume 7 Mantle Dynamics

Dr. David Bercovici

Yale University, New Haven, CT, USA

Volume 8 Core Dynamics

Dr. Peter Olson

Johns Hopkins University, Baltimore, MD, USA

Volume 9 Evolution of the Earth

Dr. David Stevenson

California Institute of Technology, Pasadena, CA, USA

Volume 10 Planets and Moons

Dr. Tilman Spohn

Deutsches Zentrum für Luft- und Raumfahrt, Berlin, Germany

Preface

Geophysics is the physics of the Earth, the science that studies the Earth by measuring the physical consequences of its presence and activity. It is a science of extraordinary breadth, requiring 10 volumes of this treatise for its description. Only a treatise can present a science with the breadth of geophysics if, in addition to completeness of the subject matter, it is intended to discuss the material in great depth. Thus, while there are many books on geophysics dealing with its many subdivisions, a single book cannot give more than an introductory flavor of each topic. At the other extreme, a single book can cover one aspect of geophysics in great detail, as is done in each of the volumes of this treatise, but the treatise has the unique advantage of having been designed as an integrated series, an important feature of an interdisciplinary science such as geophysics. From the outset, the treatise was planned to cover each area of geophysics from the basics to the cutting edge so that the beginning student could learn the subject and the advanced researcher could have an up-to-date and thorough exposition of the state of the field. The planning of the contents of each volume was carried out with the active participation of the editors of all the volumes to insure that each subject area of the treatise benefited from the multitude of connections to other areas.

Geophysics includes the study of the Earth's fluid envelope and its near-space environment. However, in this treatise, the subject has been narrowed to the solid Earth. The *Treatise on Geophysics* discusses the atmosphere, ocean, and plasmasphere of the Earth only in connection with how these parts of the Earth affect the solid planet. While the realm of geophysics has here been narrowed to the solid Earth, it is broadened to include other planets of our solar system and the planets of other stars. Accordingly, the treatise includes a volume on the planets, although that volume deals mostly with the terrestrial planets of our own solar system. The gas and ice giant planets of the outer solar system and similar extra-solar planets are discussed in only one chapter of the treatise. Even the *Treatise on Geophysics* must be circumscribed to some extent. One could envision a future treatise on Planetary and Space Physics or a treatise on Atmospheric and Oceanic Physics.

Geophysics is fundamentally an interdisciplinary endeavor, built on the foundations of physics, mathematics, geology, astronomy, and other disciplines. Its roots therefore go far back in history, but the science has blossomed only in the last century with the explosive increase in our ability to measure the properties of the Earth and the processes going on inside the Earth and on and above its surface. The technological advances of the last century in laboratory and field instrumentation, computing, and satellite-based remote sensing are largely responsible for the explosive growth of geophysics. In addition to the enhanced ability to make crucial measurements and collect and analyze enormous amounts of data, progress in geophysics was facilitated by the acceptance of the paradigm of plate tectonics and mantle convection in the 1960s. This new view of how the Earth works enabled an understanding of earthquakes, volcanoes, mountain building, indeed all of geology, at a fundamental level. The exploration of the planets and moons of our solar system, beginning with the Apollo missions to the Moon, has invigorated geophysics and further extended its purview beyond the Earth. Today geophysics is a vital and thriving enterprise involving many thousands of scientists throughout the world. The interdisciplinarity and global nature of geophysics identifies it as one of the great unifying endeavors of humanity.

The keys to the success of an enterprise such as the *Treatise on Geophysics* are the editors of the individual volumes and the authors who have contributed chapters. The editors are leaders in their fields of expertise, as distinguished a group of geophysicists as could be assembled on the planet. They know well the topics that had to be covered to achieve the breadth and depth required by the treatise, and they know who were the best of

their colleagues to write on each subject. The list of chapter authors is an impressive one, consisting of geophysicists who have made major contributions to their fields of study. The quality and coverage achieved by this group of editors and authors has insured that the treatise will be the definitive major reference work and textbook in geophysics.

Each volume of the treatise begins with an ‘Overview’ chapter by the volume editor. The Overviews provide the editors’ perspectives of their fields, views of the past, present, and future. They also summarize the contents of their volumes and discuss important topics not addressed elsewhere in the chapters. The Overview chapters are excellent introductions to their volumes and should not be missed in the rush to read a particular chapter. The title and editors of the 10 volumes of the treatise are:

Volume 1: Seismology and Structure of the Earth

Barbara Romanowicz
University of California, Berkeley, CA, USA
Adam Dziewonski
Harvard University, Cambridge, MA, USA

Volume 2: Mineral Physics

G. David Price
University College London, UK

Volume 3: Geodesy

Thomas Herring
Massachusetts Institute of Technology, Cambridge, MA, USA

Volume 4: Earthquake Seismology

Hiroo Kanamori
California Institute of Technology, Pasadena, CA, USA

Volume 5: Geomagnetism

Masaru Kono
Okayama University, Misasa, Japan

Volume 6: Crustal and Lithosphere Dynamics

Anthony B. Watts
University of Oxford, Oxford, UK

Volume 7: Mantle Dynamics

David Bercovici
Yale University, New Haven, CT, USA

Volume 8: Core Dynamics

Peter Olson
Johns Hopkins University, Baltimore, MD, USA

Volume 9: Evolution of the Earth

David Stevenson
California Institute of Technology, Pasadena, CA, USA

Volume 10: Planets and Moons

Tilman Spohn
Deutsches Zentrum für Luft-und Raumfahrt, GER

In addition, an eleventh volume of the treatise provides a comprehensive index.

The *Treatise on Geophysics* has the advantage of a role model to emulate, the highly successful *Treatise on Geochemistry*. Indeed, the name *Treatise on Geophysics* was decided on by the editors in analogy with the geochemistry compendium. The *Concise Oxford English Dictionary* defines treatise as “a written work dealing formally and systematically with a subject.” Treatise aptly describes both the geochemistry and geophysics collections.

The *Treatise on Geophysics* was initially promoted by Casper van Dijk (Publisher at Elsevier) who persuaded the Editor-in-Chief to take on the project. Initial meetings between the two defined the scope of the treatise and led to invitations to the editors of the individual volumes to participate. Once the editors were on board, the details of the volume contents were decided and the invitations to individual chapter authors were issued. There followed a period of hard work by the editors and authors to bring the treatise to completion. Thanks are due to a number of members of the Elsevier team, Brian Ronan (Developmental Editor), Tirza Van Daalen (Books Publisher), Zoe Kruze (Senior Development Editor), Gareth Steed (Production Project Manager), and Kate Newell (Editorial Assistant).

G. Schubert

Editor-in-Chief

1.01 Overview

A. M. Dziewonski, Harvard University, Cambridge, MA, USA

B. A. Romanowicz, University of California at Berkeley, Berkeley, CA, USA

© 2007 Elsevier B.V. All rights reserved.

1.01.1	Developments from the Late Nineteenth Century until the Early 1950s	2
1.01.2	Developments from 1950s through the Early 1980s	6
1.01.3	From 1980 to Present: The Era of Tomography and Broadband Digital Seismic Networks	12
1.01.4	Current Issues in Global Tomography	18
References		25

Applications of seismology to the study of the Earth's interior are only about 100 years old. Its tools in determining the properties of inaccessible Earth are the most powerful among all geophysical methods. The principal reasons are the availability of natural (earthquakes) or controlled (explosions, vibrators) sources of elastic waves and their relatively low attenuation with distance. Seismological methods span some six orders of magnitude in frequency and the depth of an investigated structure may range from a few meters in engineering applications to the center of the Earth. Progress in seismology has been achieved through developments on several fronts: theory, instrumentation and its deployment, as well as computational resources.

Even though the studies of earthquakes and Earth's structure are closely related, the two subjects are often discussed separately. This volume is devoted to the Earth's structure, and Volume 4 to studies of earthquakes. Nevertheless, the relationship is intimate. For example, it is possible to formulate an inverse problem in which earthquake locations are sought simultaneously with the parameters of the Earth's structure, including three-dimensional (3-D) models (*see* Chapter 1.10).

In the last 25 years, important progress has been made on several fronts: (1) the development of broadband digital instrumentation, which has allowed the construction of digital seismic databases of unprecedented quality at both the global and regional scales; (2) the development of powerful data analysis tools, made possible by ever more efficient computer technology; and (3) theoretical progress in the forward and inverse computation of the effects of strong lateral heterogeneity on seismic-wave propagation. The combination of these factors has led to much improved

images of structure at the global and regional scale, often helped by the inclusion of constraints from other types of data, primarily from the fields of mineral physics and geodynamics. This volume is thus divided into four parts. The first part principally covers theoretical developments and seismic data analysis techniques. Chapter 1.02 discusses the state of the art in the computation of the Earth's normal modes, while Chapter 1.03 describes progress in the measurements of normal-mode and long-period surface waves. Two chapters are devoted to the computation of synthetic seismograms in the presence of lateral heterogeneity, suitable for the case of body waves (*see* Chapters 1.04, 1.05). Significant progress has recently been made in the computation of synthetic seismograms in a 3-D Earth using numerical methods. A review is given in Chapter 1.06. With the deployment of dense regional arrays of broadband seismometers, another area of rapid progress has been that of the adaptation of methodologies first developed in exploration seismology to the case of fine structure imaging of the crust and upper mantle at larger scale. These approaches are described in Chapter 1.07 for passive-source applications, and in Chapter 1.08, for the case of active sources. The realization of the importance of anisotropy in the Earth has led to theoretical and methodological developments (*see* Chapter 1.09). Note that the issue of anisotropy is also discussed in Chapter 1.16 in the context of inversion of surface-wave data. Inverse methods, in particular in the context of global and regional tomography, are discussed in Chapter 1.10.

In the second part of Volume 1, reviews of the status of our knowledge on the structure of the Earth's shallow layers are presented, starting with a global review of the Earth's crustal structure (*see* Chapter 1.11). Two chapters discuss regional structure in the oceans:

Chapter 1.12 for mid-ocean ridges and Chapter 1.13 for hot-spot swells. Finally, two chapters are devoted to the results of regional experiments: upper-mantle studies using data from portable broadband experiments (*see* Chapter 1.14) and crustal studies, specifically in Europe, from high-resolution long-range active-source experiments (*see* Chapter 1.15).

The third part of this volume concerns the Earth's deep structure, divided into its main units: the upper mantle (*see* Chapter 1.16), the transition zone and upper-mantle discontinuities (*see* Chapter 1.17), the D'' region at the base of the mantle (*see* Chapter 1.18) as well as the Earth's core (*see* Chapter 1.19). Chapter 1.20 is devoted to the subject of scattering in the Earth and Chapter 1.21 to that of attenuation. Finally, the third part of this volume comprises two chapters, in which constraints on Earth structure from fields other than seismology: mineral physics (*see* Chapter 1.22) as well as geodynamics (*see* Chapter 1.23) are discussed.

This volume addresses various aspects of 'structural seismology' and its applications to other fields of Earth sciences. Not all the subjects are covered in comparable detail, even though the completeness of the coverage was the initial objective of the editors. In particular, there is no chapter on instrumentation, and we have tried to partially make up for it by discussing this subject in this overview; portable instrumentation is discussed to some extent in Chapter 1.14. We also present our point of view on current issues in global tomography not discussed in any of the chapters.

We thus proceed to describe briefly the developments in seismology from the end of the nineteenth century until the present, with the main emphasis on the development of instrumentation and its deployment, because seismology is a data-driven science. An account of the history of seismology can be found, among others, in Agnew (2002).

1.01.1 Developments from the Late Nineteenth Century until the Early 1950s

The theoretical beginnings of seismology may be traced to the eighteenth and nineteenth century studies of elasticity and propagation of elastic waves in solids. Lord Kelvin provided the first numerical estimate of the period of the fundamental vibrational mode (${}_0S_2$) in 1863, but the development of the proper theory for a homogeneous sphere had to wait nearly 50 years (Love, 1911). Lord Rayleigh solved the problem of propagation of surface waves in an elastic half-space in 1877.

This preceded the first mechanical seismographs, which were developed in the 1880s. Originally, the seismographs had very low sensitivity and were used for the recording of local earthquakes. The history of global seismology begins with the recording of an earthquake in Japan on 19 April 1889 by von Rebeur-Paschwitz. He associated a disturbance recorded on a tiltmeter, used to study the Earth's tides, with the reports of a great earthquake in Japan. **Figure 1** shows a copy of this recording as published in *Nature* (1889) (von Rebeur-Paschwitz, 1895).

The early seismographs were mechanical pendulums with no damping, other than friction. Their magnifications (the ratio of the amplitude on a seismogram to the actual ground motion) were very low, and because of the lack of damping, the records were very oscillatory and it was difficult to distinguish the arrivals of different phases. An improved mechanical seismograph with controlled damping was built by Wiechert in 1904. Soon afterward Galitzin (1914) developed an electromagnetic seismograph system, where the motion of the seismometer's pendulum generated an electric current by motion of a coil in the magnetic field. This current was, in turn, carried to a galvanometer; the rotation of the galvanometer's coil in a magnetic field was recorded on photographic paper by a beam of light reflected from a mirror attached to the coil. The response of the system depended on the sensitivity and free period of the seismometer and of the galvanometer and their damping. While the system was more complex, it allowed for much more flexibility in selecting a desired

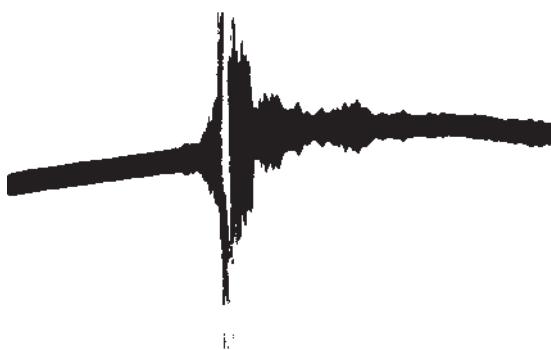


Figure 1 The historical first recording of a teleseismic event: an earthquake in Japan recorded in Potsdam on a tiltmeter designed by von Rubeur-Paschwitz. The early seismograms had difficulty with damping the pendulum motion and made phase identification difficult. From von Rebeur-Paschwitz E (1895) *Horizontalpendal-Beobachtungen auf der Kaiserlichen Universitäts-Sternwarte zu Strassburg 1892–1894. Gerland Beitr. Zur Geophys.* 2: 211–536.

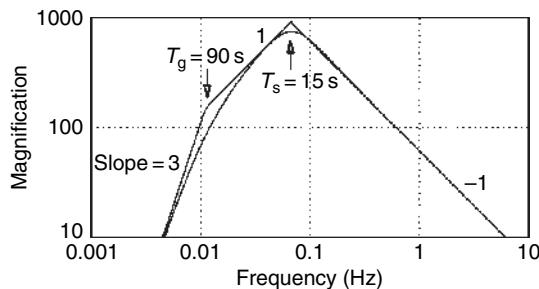


Figure 2 Plot of the ground-motion (amplitude) response of a WWSSN station with a seismograph free period (T_s) of 15 s and galvanometer with a free period (T_g) of 90 s. The segment between these two periods has a flat velocity response, characteristic of broadband seismometers. The response in modern instruments is shaped electronically; a typical FDSN station has a flat velocity response from 5 Hz to 360 seconds. From Wielandt E (2002) Seismic sensors and their calibration. In: Bormann IP (ed.) IASPEI New Manual of Seismological Observatory Practice, vol. I, Ch. 5, pp. 1–46. Potsdam: GeoForschungsZentrum Potsdam.

response. **Figure 2** shows the response of the seismograph–galvanometer system and gives an idea of the way it could be shaped by the choice of different free periods of the system's components. With gradual improvements, the seismometer–galvanometer system and recording on photographic paper was commonly used during the following 60–70 years, when it was gradually replaced by digital systems.

With the improvement of the recording systems technology, phase identification became easier, and it was possible to identify P-arrivals (primary) corresponding to compressional waves, S-arrivals (secondary) corresponding to shear waves, and L-arrivals, sometimes called ‘the main phase’, corresponding to surface waves. The surface waves caused some confusion because there was also a transverse motion, not predicted by Rayleigh. It was not until 1911 that Love showed that transversely polarized surface waves can propagate in a layered Earth.

Progress in the first decade of the twentieth century was rapid. Some classical problems such as computation and inversion of traveltimes for the velocity structure were solved by Benndorf (1905, 1906), Herglotz (1907), and Wiechert (1907); Knott (1899) and Zöppritz (1907) independently developed equations for the amplitude of reflected and transmitted waves at the boundary between two elastic media.

As regards Earth's structure, there was a paper by Schweitzer (2007), in which he proposed the existence of the Earth's core, although there has been some confusion in identification of phases: what he thought to be a delayed S-wave was actually an SS.

Gutenberg (1913) properly identified reflections from the core–mantle boundary and determined the radius of the core quite accurately, and Jeffreys (1926) showed that the core is liquid. Mohorovičić (1910) discovered the boundary between the crust and upper mantle, thus beginning the era of studies of the crust and lithosphere, which greatly accelerated after World War II.

The first global seismographic networks were established in the early years of the twentieth century. The first one was deployed by John Milne in various countries of the British Commonwealth with the support of the British Association for the Advancement of Science and eventually consisted of 30 stations (Adams, 2002). The Jesuit Network was established soon afterward, with a particularly large number of instruments in the United States, but also including stations on all continents (Udias and Stauder, 2002). With a global coverage sufficient to locate large earthquakes, informal bulletins were published using the location method developed by Geiger (1910, 1912), which (with many modifications) is still used today. In 1922, the International Seismological Summary (ISS), with international governance, was established under Professor Turner of Oxford University with the charge to produce ‘definitive global catalogs’ from 1918 onward.

The slow progress in unraveling the Earth structure culminated in the 1930s with the discovery of the inner core by Inge Lehmann (1936) and the compressional velocity, shear velocity and density models by Gutenberg (1913), Jeffreys (1926), and Bullen (1940). The Gutenberg and Jeffreys velocity models are shown in **Figure 3**; except for the details of the upper-mantle structure, these models are very similar to the modern ones. The low-velocity zone above the inner–outer core boundary in the model of Jeffreys illustrates the sometimes unfortunate tendency of seismologists to introduce physically implausible features in the model in order to match the data; Jeffreys needed to add a 2 s delay to match the inner-core traveltimes and accomplished it by inserting this feature, which is impossible to reconcile with the chemical and physical properties of materials in this depth range. The other important difference between the models of Jeffreys and Gutenberg was the existence of a low-velocity zone in the depth range 100–200 km in the upper mantle. There were very hot debates on this issue; it now can be explained by the fact that they used data from tectonically different regions; there is a pronounced low-velocity zone in the Western US, but not under the Eurasian Shield regions.

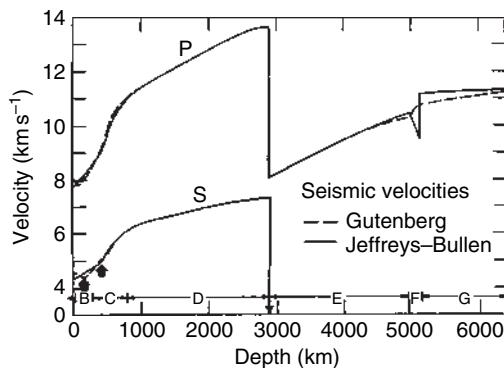


Figure 3 Comparison of the seismic velocity models of Gutenberg and Jeffreys, both built in the 1930s. The principal difference between the models is the presence of the low-velocity zone in Gutenberg's model and the structure near the inner–outer core boundary; the low-velocity zone in Jeffreys's model is erroneous and the velocity increase in the inner core is larger than in Gutenberg's model. With the exception of the transition zone (400–650 km depth) the modern models are not very different. From Anderson DL (1963) Recent evidence concerning the structure and composition of the Earth's mantle. *Physics and Chemistry of the Earth* 6: 1–129.

With internal reflections and conversions of waves at the boundaries, seismologists developed a system of phase identification that reflects a combination of the types of waves (P or S), the region in which they propagate (K and I for the P waves in the outer and inner core, respectively; PKIKP designates a phase that travels as P in the mantle, P in the outer core, and P in the inner core), the boundary at which they were reflected (c for core–mantle boundary, i for the inner–outer core boundary). A shear wave reflected once from the free surface at the mid-point of its path is designated by SS; higher multiple reflections, like SSS or SSSSS, can be observed by sampling a large volume of the Earth along their paths. For earthquakes with a finite focal depth, the P and S waves traveling upward from the source have designation of p or s; following reflection at the surface they represent the so-called ‘depth phases’ (e.g., pP, sP); the traveltime difference between the arrival of pP and P strongly depends on focal depth.

Figure 4 shows examples of various seismic phases, and **Figure 5** is the graphic representation

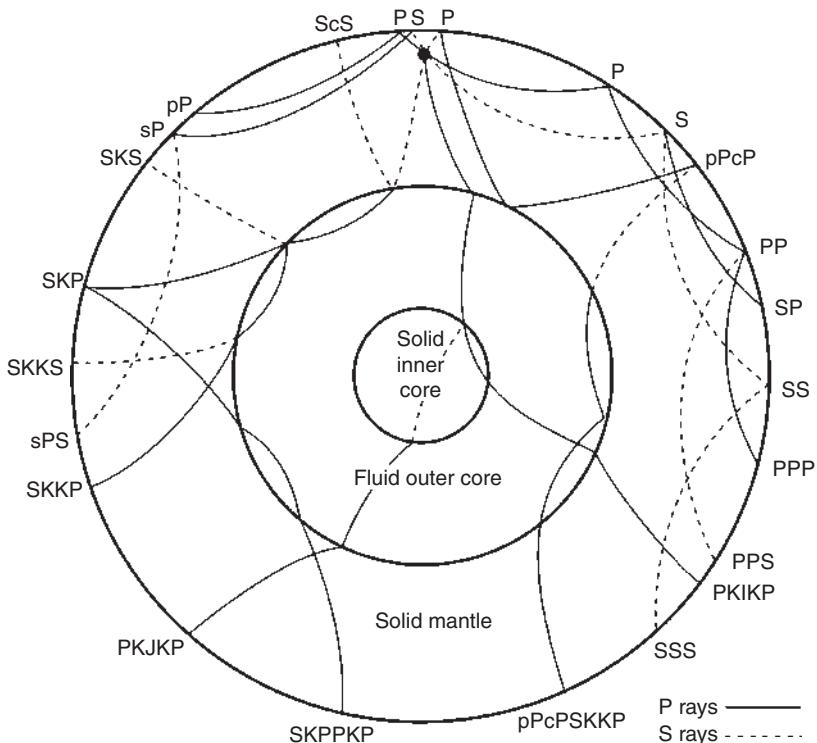


Figure 4 Examples of seismic rays and their nomenclature. The most commonly identified phases used in earthquake location are the first arriving phases: P and PKIKP. From Stein S and Wysession M (2003) *An Introduction to Seismology, Earthquakes and Earth Structure*. Oxford: Blackwell (isbn 0865420785).

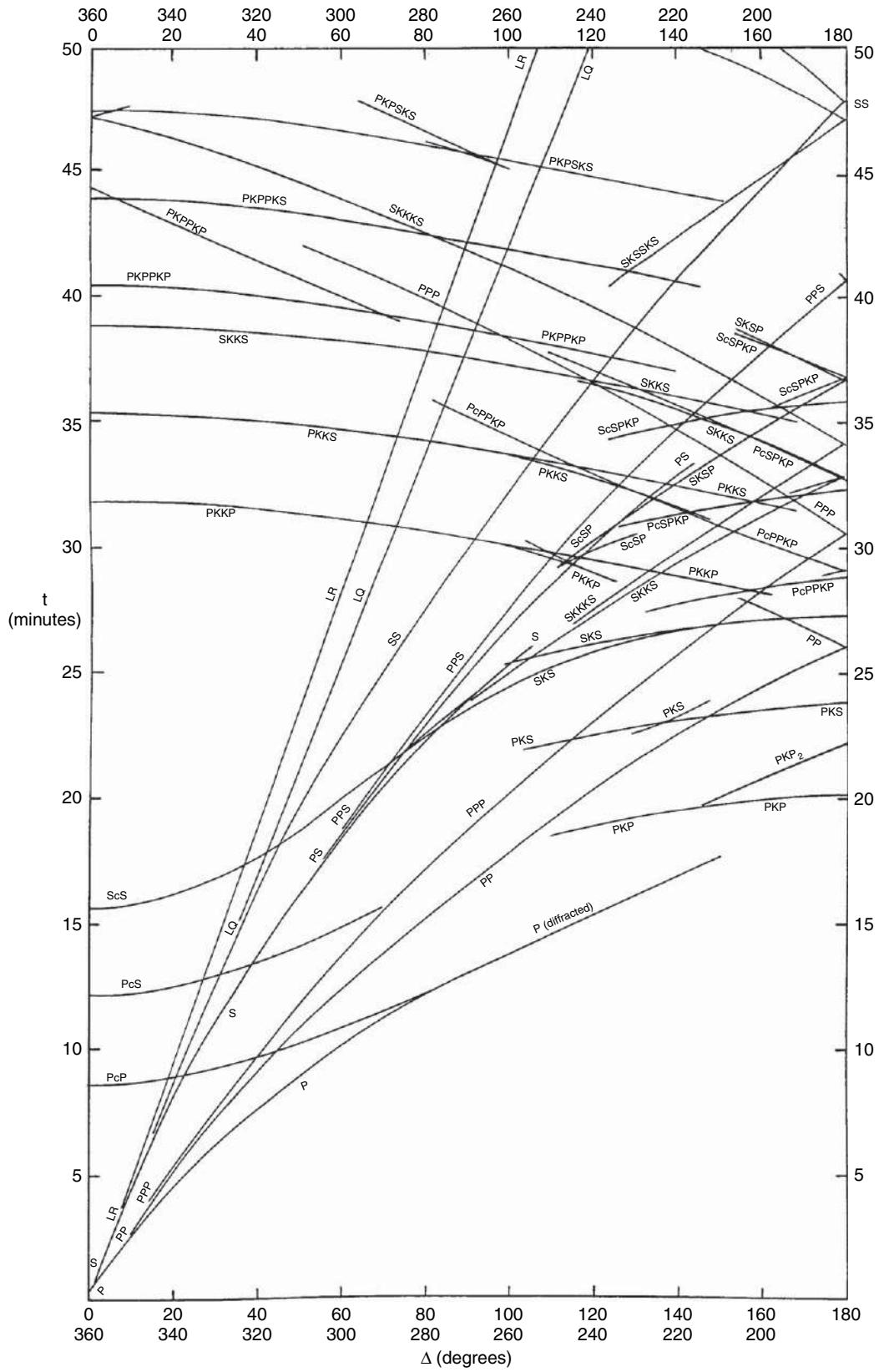


Figure 5 Traveltimes of seismic phases for the surface focus as computed by Jeffreys and Bullen (1940). From Jeffreys H and Bullen KE (1940) *Seismological Tables*, 50pp. London: British Association for the Advancement of Science.

of the traveltimes as a function of distance computed by [Jeffreys and Bullen \(1940\)](#) for the model of [Jeffreys \(1926\)](#). It is remarkable that this set of tables, including predictions for different focal depths, was calculated using a mechanical calculator! The data used by Jeffreys were extracted from the ISS, the precursor of the International Seismological Centre (ISC), which (with international financial support and governance) resumed the ISS role in 1964 and continues until today.

[Bullen \(1949\)](#) divided the Earth into a number of concentric shells, designated by letters from A through F; in this division, the lower mantle was designated by the letter D; when Bullen recognized that the deepest 150 km of the lower mantle had an anomalously flat velocity gradient, he divided the region D into D' and D''. More recently, and not entirely correctly, D'' came to signify the structure in the deepest 300 km, or so, of the lower mantle, which is characterized by a still-growing collection of structural and compositional complexities.

It was recognized relatively early that the dispersion of surface waves was different in the continents than in the oceans; with an indication that the oceanic crust was significantly thinner. Computing the dispersion of surface waves was algebraically and numerically difficult; the correct formulas for dispersion of Rayleigh waves in a layer over a half-space was correctly formulated by Stoneley in 1928, and the case of two layers over a half-space could be solved only for a very specific set of parameters.

1.01.2 Developments from 1950s through the Early 1980s

It must have been frustrating for seismologists not to be able to use information about the Earth's structure contained in the most prominent features of the seismograms: the dispersed surface waves. This changed when [Haskell \(1953\)](#) adapted to the case of elastic media the method first proposed by [Thomson \(1950\)](#) in the acoustics case. The approach made it possible to compute dispersion of surface waves (Rayleigh and Love) in a layered medium with an arbitrary number of layers over a half-space. It involved multiplication of matrices, one for each layer, changing the wave number for a fixed frequency such as to match the boundary conditions (vanishing of stresses) at the free surface. Because of the enormous amount of calculations to be performed, it required application of an electronic computer, and its application opened yet a

new era in seismology. The Haskell's matrix method has been adapted to other problems in seismology, such as calculation of synthetic seismograms using the 'reflectivity method' ([Fuchs and Müller, 1971](#)). Electronic computers were at first very expensive and rare, and it was not until the 1960s that they became generally available at universities (Haskell worked at the Air Force Cambridge Laboratories).

Surface-wave dispersion began to be studied intensively in the 1950s principally at the Lamont Geological Observatory of Columbia University, primarily by Ewing and Press, who observed mantle waves in the 1952 Kamchatka earthquake, identifying arrivals from R6 to R15 and measuring their group velocities up to a period of 500 seconds ([Ewing and Press, 1954](#)). Regional measurements of surface-wave dispersion were initiated by [Press \(1956\)](#). A monograph by [Ewing et al. \(1957\)](#) summarizes the state of the knowledge on seismic-wave propagation in layered media at that time. Ewing and Press also developed a true long-period seismograph, which was capable of recording mantle waves even for moderately sized earthquakes. This instrument was deployed at 10 globally distributed International Geophysical Year network stations operated by Lamont.

It is not often that a mistake leads to favorable results, but this was the case with the free oscillations of the Earth. [Benioff \(1958\)](#) reported an oscillation with a period of 57 min seen in the record of the 1952 Kamchatka earthquake. Even though this observation was eventually attributed to an artifact in the functioning of the instrument, it stimulated the theoretical and computational research needed to calculate eigenfrequencies for a realistic Earth model. Some of the calculations preceded Benioff's report ([Jobert, 1956, 1957](#)), but the efforts of [Pekeris and Jarosch \(1958\)](#) and [Takeuchi \(1959\)](#) were clearly motivated to explain the observed period. These calculations, using the variational approach and the Jeffreys–Bullen Earth model, predicted the period of ${}_0S_2$ to be 52 min and that of ${}_0T_2$, 43.5 min; neither was close enough to Benioff's 'observation'. The modern approach was developed by [Alterman et al. \(1959\)](#), who recast the system of three second-order partial differential equations into a system of six first-order differential equations, thus removing the need for differentiation of the elastic constants and allowed the use of standard numerical methods to obtain the solution. Tests using Gutenberg's and Jeffreys–Bullen models showed that they predict very similar free oscillation periods for the gravest modes, but differ at shorter periods by 1–2%.

When the greatest instrumentally recorded earthquake of 20 May 1960 occurred in Chile, seismologists had all the tools (theory, computers, and instrumentation) needed to measure and interpret its recordings. Three back-to-back papers in a 1961 issue of the *Journal of Geophysical Research* reported the first correct measurements of free oscillation periods: Benioff *et al.*, Ness *et al.*, and Alsop *et al.* The observations were made on strainmeters in Isabella, Ñaña, and Ogdensburg, seismographs at Pasadena, and a gravimeter at University of California, Los Angeles (UCLA). All three studies agreed in mode identification and found that their periods were very close to those predicted by the existing Earth models (Pekeris *et al.*, 1961a). More detailed studies of the spectra revealed that they are split; the effect of the Earth's rotation was shown to explain this effect (Backus and Gilbert, 1961; Pekeris *et al.*, 1961b). Thus normal-mode seismology was born. Progress in the theory, particularly considering the effect of lateral heterogeneities and mode coupling would extend over decades to come. First attempts at inversion of normal-mode data were not particularly successful; the density model of Landisman *et al.* (1965) was flat throughout the lower mantle, implying either a strong radial heterogeneity or an immensely superadiabatic gradient.

Backus and Gilbert (1967, 1968, 1970) provided the formal background for consideration of geophysical inverse problems, and even though their own experiments with inversion of normal-mode periods for the velocities and density, using a subset of normal-mode data, were discouraging (two very different models were found fitting the data nearly exactly; Backus and Gilbert, 1968), the idea of resolving kernels and tradeoffs became part of the geophysical terminology.

Seismic methods were considered essential in discriminating between earthquakes and nuclear explosions (Berkner *et al.*, 1959), and an intensive observational program, called VELA Uniform, was initiated. One of its components of great significance to studies of the Earth's interior was the World-Wide Standard Seismograph Network (WWSSN), consisting of a set of three-component short-period and three-component long-period seismographs, with identical responses, except for magnification, which depended on local noise levels. At its peak, the WWSSN consisted of 125 stations (Figure 6), with distribution limited by geography and politics: there were no stations in the Soviet Union, China, and poorly developed areas in Africa and South America. The novel aspect of WWSSN was its standardized

response and centralized system of distribution of copies of seismograms. Individual stations were sending the original seismograms to a central location, where they were microfilmed, using a very high-resolution camera, and then returned to the stations. A seismologist could request copies of seismograms for a particular date and receive them either as microfilm chips or photographic enlargements to the original size. Several larger institutions had a blanket order on all the records. This data accessibility represented major progress with respect to the earlier procedures, where one had to request copies of seismograms from individual stations, which greatly limited and delayed the research. WWSSN functioned for 20–25 years, slowly declining in the quality and number of stations; it ceased functioning in the late 1980s when data from new digital stations became available.

Another development of the 1960s was the introduction to seismology of digital recording, greatly facilitating research and the development of massive, computerized data-processing methods. One such facility, the Large Aperture Seismic Array (LASA), was built in the mid-1960s in Montana, shown in Figure 7. It contained six 'rings', for a total of 21 subarrays, each with 25 short-period seismometers emplaced in boreholes, to improve the signal-to-noise ratio. The data were telemetered in real time to a central location in Billings, Montana, where they were processed for detection of a signal. Major scientific discoveries were made with this tool, particularly when weak signals were involved; for example, observations of reflections from the inner core. In practical terms, the array did not meet the expectations; the site response across this 200 km aperture array varied so much that the signals had limited coherency and signal enhancement by stacking was not as effective as planned. A somewhat smaller array was installed a few years later in Norway (NORSAR); elements of this array are still active. Modern arrays used for seismic discrimination purposes have an aperture of only several kilometers, because on that scale, the coherency at 1 Hz frequency can be achieved. One of the important results obtained from the analysis of array data was the detection of upper-mantle discontinuities (Johnson, 1967), confirming the result predicted by experimental petrology that there should be two discontinuities at pressures and temperatures corresponding to depths of about 400 and 650 km, respectively (Birch, 1952).

Surface-wave studies blossomed in the 1960s. At first, measurements of dispersion involved rather simple 'analog' methods, such as the peak-and-trough

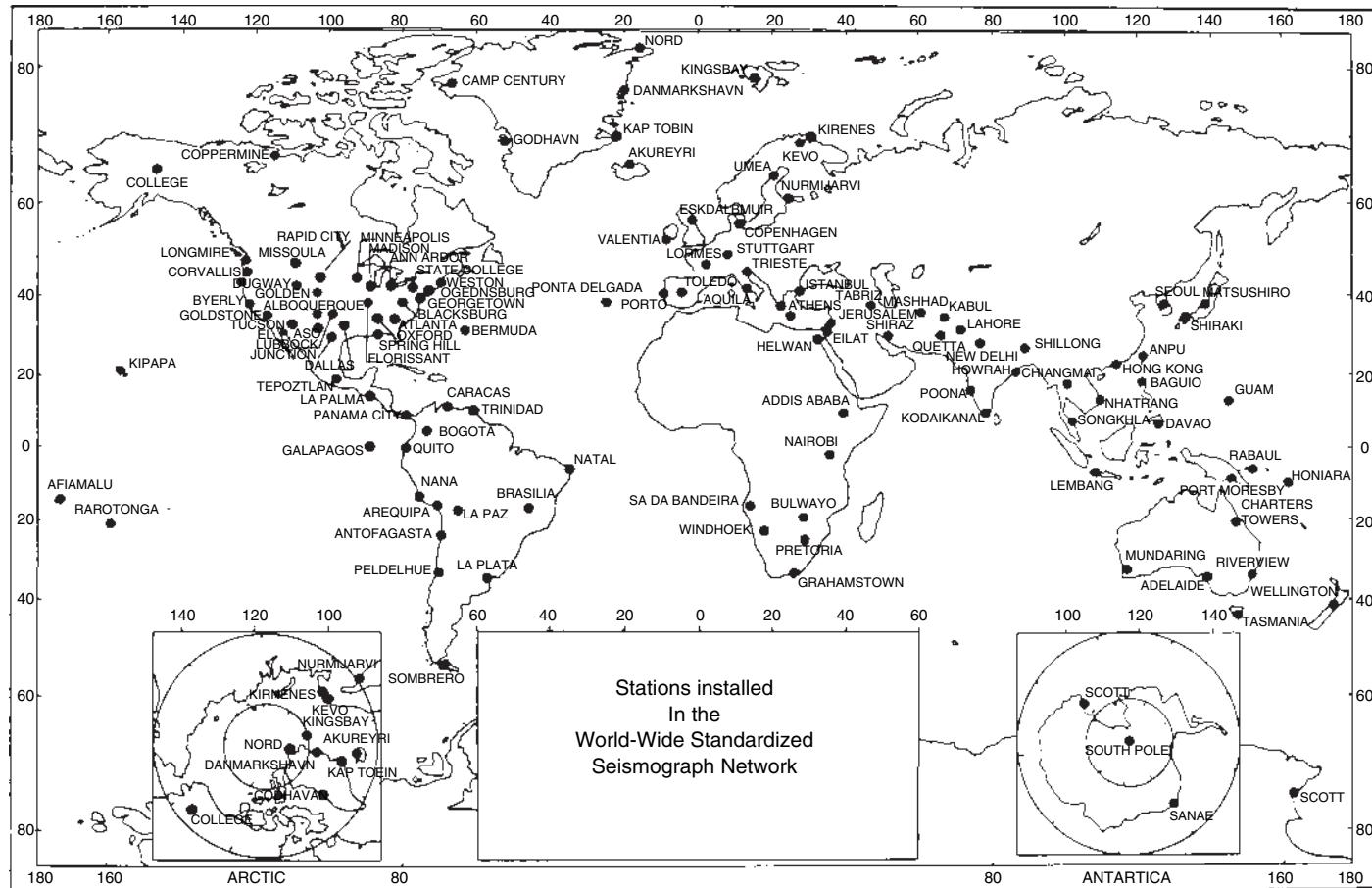


Figure 6 Map of the stations of World-Wide Standard Seismograph Network (WWSSN) established in the early 1960s, following recommendations of Berkner *et al.* (1959). Courtesy of US Geological Survey.

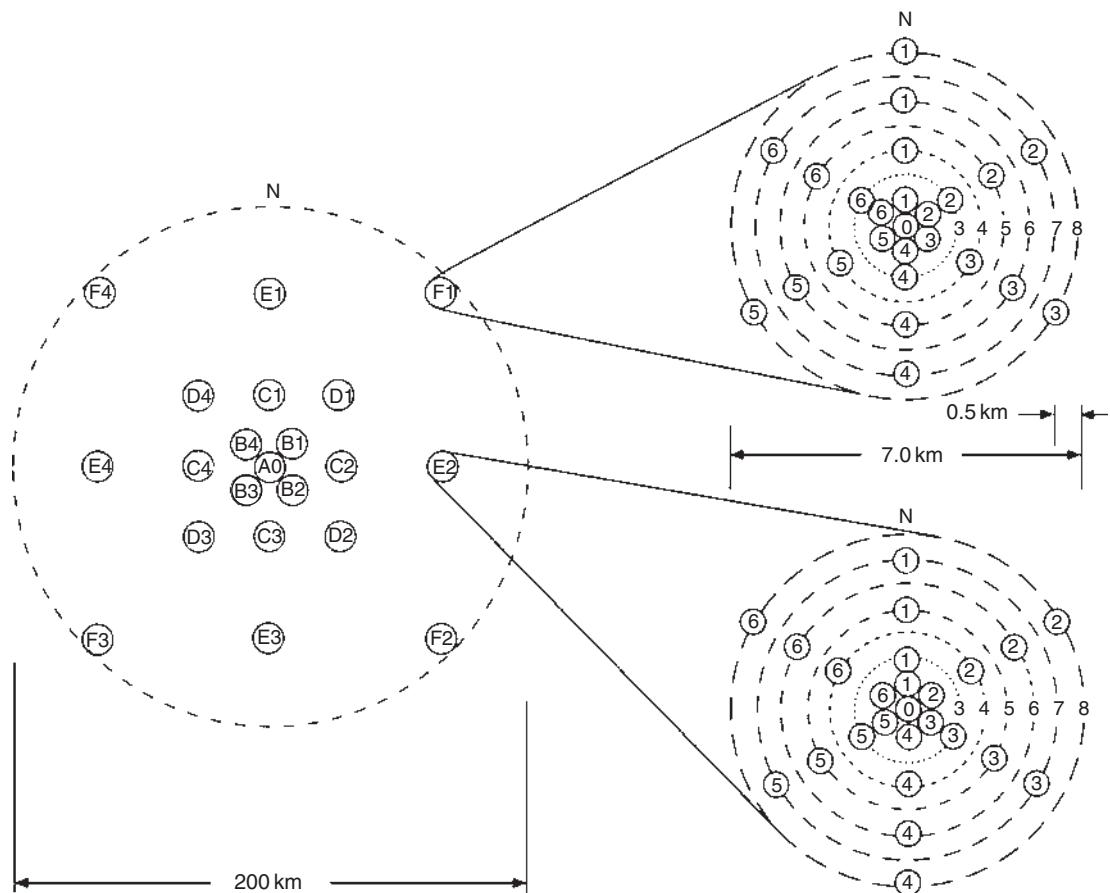


Figure 7 Configuration of the Long-Aperture Seismic Array (LASA) and an expanded view of two of its subarrays. From Stein S and Wyssession M (2003) *An Introduction to Seismology, Earthquakes and Earth Structure*. Oxford: Blackwell (isbn 0865420785).

approach to measuring phase and group velocities. Some very important results were obtained in this way, such as the Canadian Shield study of Brune and Dorman (1963). Digital analysis, however, was soon to take over. Manual digitization of analog recordings, WWSSN data in particular, became easier, and with increasing availability of computers and decreasing cost of computations various techniques were developed, for the most part involving applications of the Fourier-transform technique. With the development of the fast Fourier transform (FFT) algorithm (Cooley and Tukey, 1965), the cost of time-series analysis declined dramatically; a review by Dziewonski and Hales (1972) summarizes the state of the art at the beginning of the 1970s. Some of these methods, such as the multiple filtration technique to measure group velocity dispersion, residual dispersion measurements, and time-variable filtration, are still in use today. The 1960s have also seen the first studies of intrinsic attenuation (Anderson

and Archambeau, 1964), who developed partial derivatives for Q from mantle-wave attenuation. Also, the first studies of lateral heterogeneity were conducted using the ‘pure path’ approach (Toksoz and Anderson, 1966). Seismic experiments with controlled sources were conducted in a multi-institutional mode. One of the largest experiments was Early Rise, with up to 5 ton explosions in Lake Superior, with hundreds of seismometers spreading radially in all directions. Signals were recorded as far as 2500 km, reaching teleseismic distances and providing a detailed profile of P velocity under a continental upper mantle (Green and Hales, 1968); a detailed review of crustal and upper-mantle studies with controlled sources is provided in Chapter 1.11.

With a large new data set, particularly measurements of previously unreported periods of long-period overtones provided by the analysis of free oscillations generated by the 1964 Alaskan earthquake and recorded at WWSSN stations

(Dziewonski and Gilbert, 1972, 1973), studies of 1-D structure entered a new era. The resolution of this data set was sufficient to constrain the density profile in the mantle and the core; this turned out to be quite consistent with the behavior, in the lower mantle and outer core, of a homogeneous material under adiabatic compression. Jordan and Anderson (1974) were the first to combine the normal-mode and traveltimes data, including differential traveltimes.

Numerous additional overtone data were obtained by Mendiguren (1973) and Gilbert and Dziewonski (1975) by introducing phase equalization techniques, such as ‘stacking’ and ‘stripping’. These methods require the knowledge of the source mechanism to predict the proper phase for each seismogram to be considered; this in itself turned out to be a challenging inverse problem. Dziewonski and Gilbert (1974) derived the spectrum of all six components of the moment-rate tensor as a function of time for two deep earthquakes (Brazil, 1963; Colombia, 1970). For both events, they detected a precursive isotropic component. Eventually, this turned out to be an artifact of coupling between toroidal and spheroidal (Russakoff *et al.*, 1998) modes, but the requisite theory to consider this effect was not available until 1984. Gilbert and Dziewonski (1975) presented two models based on measurements of eigenfrequencies of 1064 modes and mass and moment of inertia for a total of 1066 data. They derived two models 1066A and 1066B, with the first being smooth through the transition zone and the latter including the 400 and 660 km discontinuities.

At the 1971 General Assembly of the International Union of Geodesy and Geophysics (IUGG) in Moscow, the need for a reference Earth model was stated, and a Standard Earth Model Committee formed under the chairmanship of Keith Bullen. The Committee appointed several subcommittees, including one for the radius of the core–mantle boundary: there were discrepancies on the order of 10 km at the time. The value recommended by the subcommittee was 3484 km (Dziewonski and Haddon, 1974), which withstood the trial of time, within 1 km. Hales *et al.* (1974) proposed that the seismic velocities and density in the Standard Earth Model should be described by a low-order polynomial, with discontinuities at the appropriate depths. Dziewonski *et al.* (1975) constructed such a model, named Parametric Earth Model (PEM), which satisfied the normal-mode, traveltimes, and surface-wave data. The novelty of this model was that, in a single inversion, different

structures were obtained for the continental and oceanic crust and upper mantle. The normal-mode periods predicted by these two models (PEM-O and PEM-C) averaged in 2/3 and 1/3 proportion were constrained to match the observed periods and teleseismic traveltimes, but separate data sets for continental and oceanic surface-wave dispersion. The differences between these two models ceased at the 400 km discontinuity, at which depth they became identical with the average Earth model, PEM-A.

The drawback of the PEM and all the previous models was that they did not consider the physical dispersion due to anelastic attenuation. For a signal propagating in an attenuating medium to be causal, the wave with higher frequencies must propagate with higher velocities. Thus waves with a frequency of 1 Hz will propagate more rapidly than waves at a frequency of 1 mHz. In order to reconcile the seismic data that span 3.5 orders of magnitude, it is necessary to consider the frequency dependence of elastic parameters. This was pointed out by Liu *et al.* (1976). The Preliminary Reference Earth Model (PREM) constructed by Dziewonski and Anderson (1981), following the idea of parametric representation, considered the frequency dependence using the assumption that Q is constant in the band from 0.3 mHz to 1 Hz.

This necessitated obtaining the radial profiles of Q_μ and Q_δ ; fortunately, there were new measurements available of normal-mode and surface-wave Q (Sailor and Dziewonski, 1978) such that a formal inversion for Q could be conducted simultaneously with the inversion for the velocities and density. It was recognized earlier that to explain the observed attenuation of radial modes, which contain a very high percentage of compressional energy (97.5% for ${}_0S_0$), it was necessary to introduce a finite bulk attenuation; Anderson and Hart (1978) preferred to place it in the inner core, Sailor and Dziewonski (1978) thought that Q_δ is finite in the upper mantle; unfortunately, the radial modes do not have the requisite depth resolution. Figure 8 shows the seismic velocities and density as a function of radius; the attenuation in PREM is discussed in Chapter 1.21. Another novel aspect of PREM was its radial anisotropy between the Moho and 220 km depth. This feature, at first suspected to be an artifact of the nonlinearity of the inverse problem, has been confirmed by global tomographic studies (e.g., Ekström and Dziewonski, 1998).

The 1970s have also seen the beginning of seismic tomography; two studies published simultaneously (Aki *et al.*, 1977; Dziewonski *et al.*, 1977) addressed

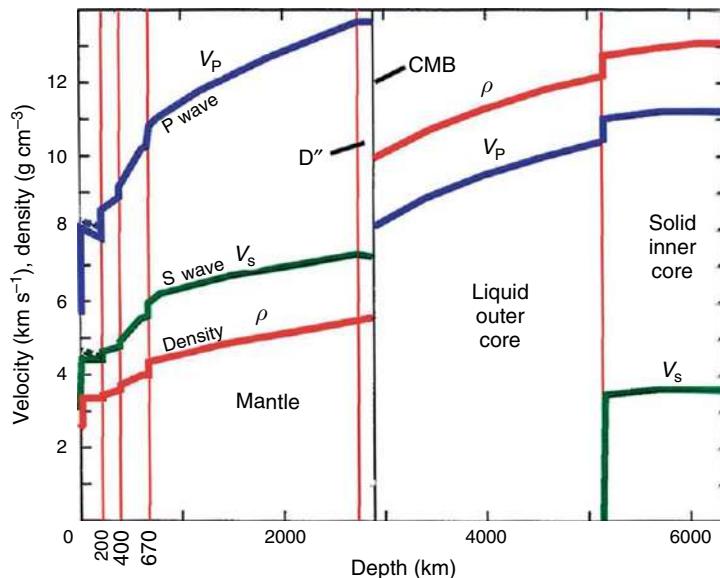


Figure 8 The Preliminary Reference Earth Model (PREM) of Dziewonski and Anderson (1981). In addition to the distribution of seismic velocities and density, PREM contains also the distribution of attenuation of the shear and compressional energy. From the web site of Ed Garnero.

the problem on different scales: regional and global. Aki *et al.* solved for 3-D velocity structure under the NORSAR array, while Dziewonski *et al.* obtained a very low resolution model of 3-D velocity perturbations in the entire mantle and showed significant correlation between velocity anomalies in the lower-most mantle and the gravest harmonics of the gravity field. The study of Dziewonski *et al.* (1977) was motivated by a paper by Julian and Sengupta (1973) who noticed that traveltimes for rays bottoming in the same region of the mantle tend to show similar residuals; they interpreted this result qualitatively as the evidence of lateral velocity variations; no modeling was presented in that paper. The first continental-scale 3-D model of the upper mantle, under North America, was published by Romanowicz (1979).

Two digital seismographic networks were established in the mid-1970s. One was the International Deployment of Accelerometers (IDA; Agnew *et al.*, 1976, 1986), consisting of some 18 globally distributed Lacoste–Romberg gravimeters with a feedback system that allowed digitization of the signal. It was designed to record very long-period waves, including the gravest modes of free oscillations of the Earth: one sample was taken every 20 s (later changed to 10 s). Only the vertical component of acceleration was recorded and the word length was 12 bits; the dynamic range was, therefore, rather limited, but still considerably greater than that of analog recordings. The sensitivity was set such

that the scale was saturated for the first surface-wave arrivals for events with magnitude 7.0, or so, depending on the station's distance from the source and radiation pattern. The IDA network was operated by the Scripps Institution of Oceanography and the centrally collected data were freely distributed to the academic community; this later became the future standard in global seismology. An early illustration of the power of such a global array was the analysis of splitting of the gravest modes of free oscillations generated by the 1977 Sumbawa earthquake (Buland *et al.*, 1979; M_w only 8.4).

The other network consisted originally of nine installations called Seismic Research Observatories (SRO) and five Abbreviated Seismic Research Observatories (ASRO). The SROs were borehole instruments, with significantly suppressed wind-generated noise levels particularly on horizontal components. The ASROs were placed in underground tunnels or mine shafts and the seismographs were protected from the effects of changing pressure and temperature. The instrumentation is described by Peterson *et al.* (1976). This network was designed for monitoring the Nuclear Test Ban Treaty and high sensitivity was the main objective. In order to increase the dynamic range, the signal was sharply band-pass-filtered, so that at very long periods (>200 s) the response to acceleration was falling as ω^{-3} , while it was flat for the IDA instruments. Even so, the SRO and ASRO stations were able to produce

useful mantle-wave records for events with magnitude greater than about 6.5. Later, the network was augmented by 10 WWSSN stations, with the analog output amplified and digitized using 16-bit digitizers. The entire system was called Global Digital Seismographic Network (GDSN). There was no general data distribution system, but data for selected dates were available upon request from the Albuquerque Seismological Laboratory.

Until then, a seismic station typically comprised a set of seismometers with either ‘long-period’ or ‘short-period’ responses, or sometimes, as was the case for the WWSSN, one of each. This setup was designed at the time of analog recording to avoid the microseismic noise peak around 6–7 s period, which would have made it impossible to digitize all but the largest earthquake signals. With digital recording, and the possibility of filtering out the microseismic noise by postprocessing, this traditional instrument design became unnecessary.

A very important development in seismic instrumentation thus took place in Germany in the mid-1970s. An array of a new kind of instruments with digital recording was deployed near Gräfenberg (Harjes and Seidl, 1978). It used a novel feedback seismograph (Wielandt and Streckeisen, 1982). The system was rapidly recognized for its linearity and large dynamic range within a wide band of frequencies – hence the name ‘broadband’. The Gräfenberg array’s central station had been co-located with the SRO bore-hole station GRFO, and the comparisons were very favorable for the broadband instruments, which were capable of reproducing different narrow-band responses using a single data stream. This type of instrumentation became the pattern for future developments.

In addition to the developments in instrumentation, the late 1970s saw important theoretical developments, related to the asymptotic properties and coupling of the normal modes. Examples of such developments are papers by Woodhouse and Dahlen (1978), Jordan (1978), and Woodhouse and Girnius (1982).

1.01.3 From 1980 to Present: The Era of Tomography and Broadband Digital Seismic Networks

The data from both global networks of the 1970s led to results that demonstrated the need for development of a global network that would better satisfy the needs of basic research in seismology; three studies are noteworthy. A robust method, which uses entire segments of (digital) seismograms, was

developed to obtain reliable mechanisms of earthquakes with magnitude 5.0 and above (Dziewonski *et al.*, 1981; Ekström *et al.*, 2005). In addition, the method refines the location of the source, which for an event of finite size need not be identical with the hypocenter determined from the first arrivals of the P waves. This topic is discussed at length in Chapter 4.16. The reason that the subject is brought up here is that in most aspects of using waveform analysis for the purpose of drawing inferences about the Earth’s structure, it is necessary to know the source mechanism. The so called ‘centroid-moment tensor’ method has now been applied to over 25 000 earthquakes from 1976 till present, and this catalog is available online.

Masters *et al.* (1982) measured center frequencies of spectral peaks of the fundamental spheroidal mode from hundreds of IDA records and discovered that there are spatially distinct patterns in the frequency shifts when plotted at locations of the poles of the great circles corresponding to the paths between the source and receiver. By fitting spherical harmonics (even degrees only, because of the symmetry) these authors realized that the pattern is dominated by spherical harmonics of degree 2, an observation also made from great-circling surface waves by Souriau and Souriau (1983). Figure 9 shows the pattern of the shifts of spectral peaks and zero line of the best-fitting spherical harmonics of degree 2 for four groups of ${}_0S_\ell$ modes with different ranges of degree ℓ . Note that the modes with the lowest ℓ show a different pattern than the remaining three groups. Our current understanding of this fact is that the low- ℓ modes sample deeper structure (lower mantle) than the higher- ℓ groups which predominantly sample the upper mantle. The authors performed a parameter search, in which they changed the radii of a shell in which the anomaly is located. The best variance reduction was for the anomaly placed in the transition zone. The lasting importance of this paper is that it demonstrated that heterogeneity of very large wavelength and sizeable amplitude ($\pm 1.5\%$) exists in the Earth’s interior.

Following the development of a waveform-fitting technique that allowed the simultaneous measurement of phase velocity and attenuation along a great-circle path (Dziewonski and Stein, 1982), Woodhouse and Dziewonski (1984) developed an approach to interpretation of waveforms that could extract both the even- and odd-harmonic coefficients of lateral heterogeneity as a function of depth. Their method involves the ‘path average approximation’, sometimes called PAVA. The seismograms are represented as a sum of all normal modes (spheroidal and

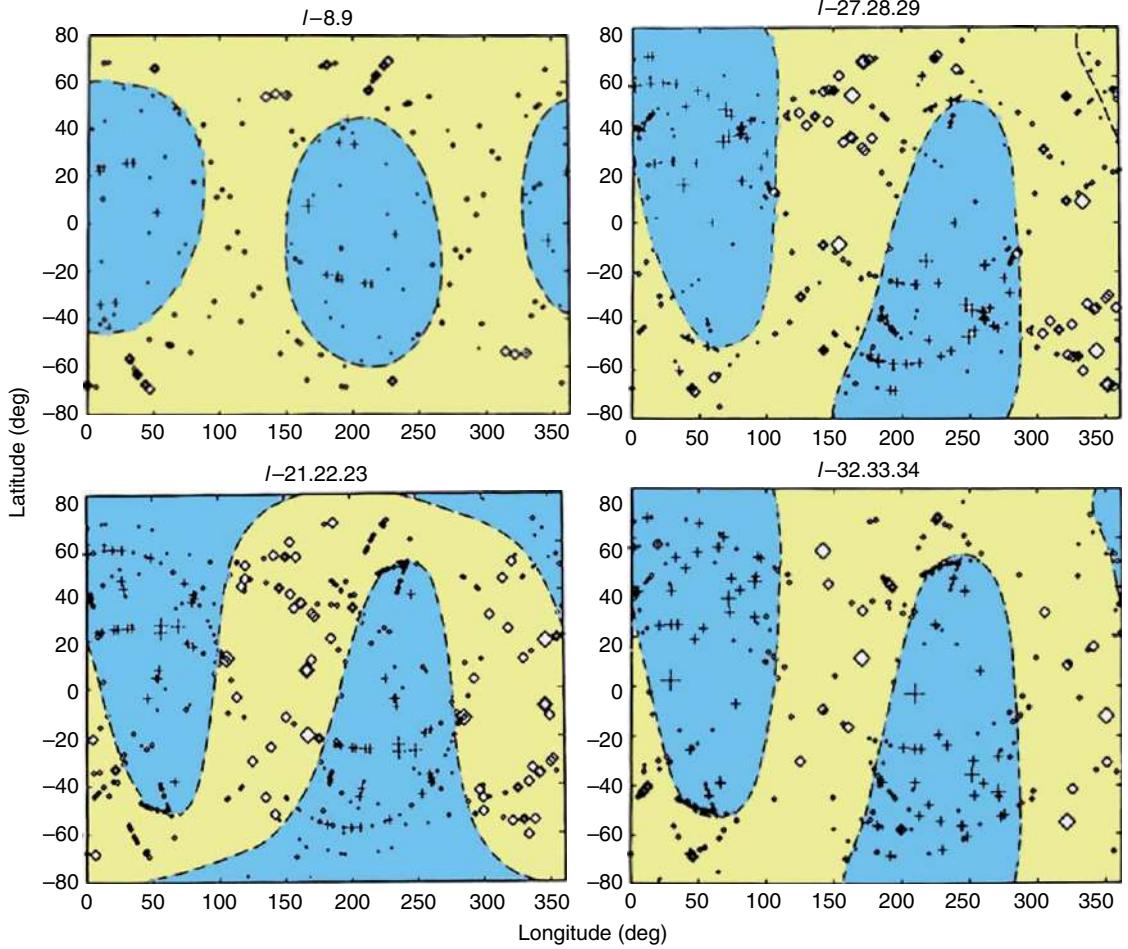


Figure 9 Maps of the observed frequency shifts of the fundamental spheroidal modes for four ranges of the order numbers as reported by Masters *et al.* (1982). The frequency shifts are plotted at the poles of the individual great-circle paths. It indicates the presence of very large wavelength-velocity anomalies in the Earth's interior; the preferred location of the source of the anomaly shown in the figure is the transition zone. Modified from Masters G, Jordan TH, Silver PG, and Gilbert F (1982) Aspherical Earth structure from fundamental spheroidal mode data. *Nature* 298: 609–613.

toroidal) up to a certain frequency ω_{\max} . For a given great circle, each mode is assumed to be affected by the average deviation from reference structure along the great-circle path (which is sensitive only to even-order harmonics), and along the minor-circle path (sensitive to both even- and odd-harmonics). The effect of the great-circle path can be modeled by a shift in eigenfrequency of the mode; the effect of the minor-arc structure is modeled by a fictitious shift of the epicentral distance for that mode; this shift depends on both even and odd parts of the structure. Woodhouse and Dziewonski (1984) processed about 2000 mantle-wave seismograms from the GDSN and IDA networks and obtained a model of the upper mantle (Moho – 670 km), M84C, using as basis functions spherical harmonics up to degree 8 for

horizontal variations, and Legendre polynomials as a function of radius up to degree 3. Figure 10 shows a map of shear-velocity anomalies at a depth of 100 km; there was no *a priori* information used on the location of the plate boundaries. Corrections were made for crustal thickness, recognizing only the continental and oceanic structure. An experimental model, M84A, obtained without applying crustal corrections, showed that not taking crustal thickness into account may result in mapping artificial anomalies at depths as large as 300 km. Model M84C had a strong degree-2 anomaly in the transition zone, confirming the results of Masters *et al.* (1982).

Another result also affected future developments, even though this study was not based on waveform analysis, but on the ISC bulletin data. With greater

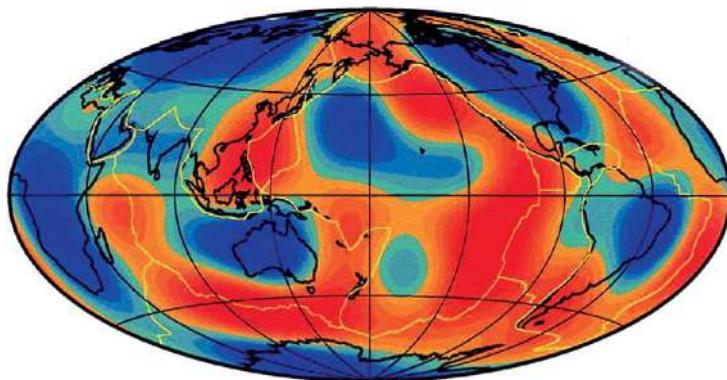


Figure 10 Shear-velocity anomalies at a depth of 100 km in the model M84C of Woodhouse and Dziewonski (1984). The scale range is $\pm 5\%$ and the resolving half-wavelength is 2500 km. Except for the correction for crustal thickness, there was no additional *a priori* included in the inversion, so the result demonstrates that the waveform inversion approach is able to distinguish the slow velocities under the mid-ocean ridges and ancient cratons, for example.

computational resources, it was possible to cast the inverse problem for lateral heterogeneities in the lower mantle on a larger scale using a substantially greater body of data than in Dziewonski *et al.* (1977). Unlike in this earlier study, in which blocks were used, Dziewonski (1984) used global functions: spherical harmonics representing horizontal variations and Legendre polynomials for radial variations. The degree of expansion was modest: only degree 6 in harmonics and degree 4 in radius, with the inversion limited to lower-mantle structure. In many ways, this new study confirmed the earlier one – including the correlation of lower-mantle structure with the gravity field – but it allowed resolution of a truly remarkable concentration of the power of heterogeneity in low-order harmonics. **Figure 11** shows a

map of P-velocity anomalies at a depth of 2500 km. The structure, dominated by degree 2 (and, to a lesser extent, degree 3) shows two large slow regions, which came to be known as the African and Pacific ‘superplumes’, and a ring of fast velocities around the Pacific.

Thus seismology demonstrated that it can resolve 3-D structure within the Earth interior, giving the promise of an unprecedented ability to look at a present-day snapshot of mantle dynamics. Yet, the observing networks were in decline, with the support for the GDSN likely to be discontinued altogether, and the original IDA network (limited to recording of vertical-component mantle waves and free oscillations) not meeting the needs of the broader community. In 1983, a plan was put forward to create

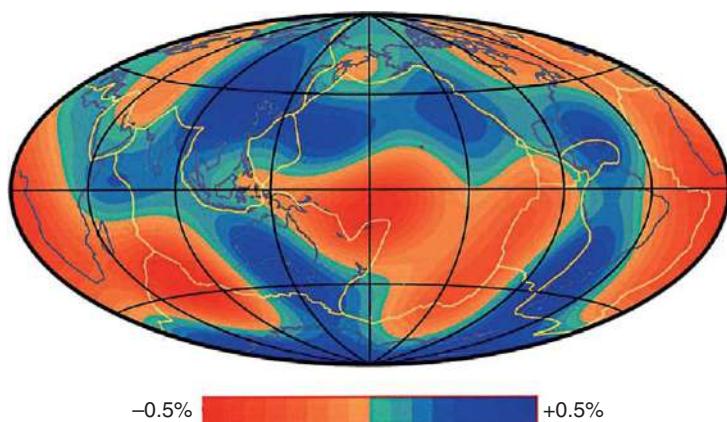


Figure 11 Map of P-velocity anomalies at a depth of 2500 km in model of Dziewonski (1984) derived from inversion of traveltimes from ISC Bulletins. The resolving half-wavelength of the model is about 3500 km (at the surface). The model, dominated by the harmonics 2 and 3, clearly shows two large superplumes (African and Pacific) and the ring of fast velocities circumscribing the Pacific rim. The scale is $\pm 0.5\%$.

a Global Seismographic Network (GSN) of some 100 broadband, three-component seismographic stations sending the data in nearly real time to a central collection facility. The expectation was that this network would be supported by the National Science Foundation (NSF), in analogy to NSF supporting astronomy facilities. At the same time, seismologists using portable instrumentation came to the realization that they needed a centralized and standardized instrument pool. This led to formation of a project called Portable Array for Seismological Studies of Continental Lithosphere – PASSCAL. The GSN and PASSCAL groups merged and formed a consortium known as Incorporated Research Institutions for Seismology (IRIS), which incorporated in 1984.

At the same time, Steim (1986) was developing at Harvard his very-broadband (VBB) instrument, based on the STS-1 broadband seismograph (Wielandt and Steim, 1986), and a very high-resolution (24-bit) digitizer. The response of a VBB instrument is designed to have a flat response to ground velocity between 5 Hz and 3 mHz, that is,

over more than three orders of magnitude. Such an instrument had to have a very large dynamic range, of about 140 dB to span the range of ground velocities from the minimum Earth noise to a magnitude 9.4 earthquake at 30° epicentral distance. All these requirements were met, and Steim's VBB system became the design goal for the GSN and other networks. Figure 12 shows the operating range of the system and Figure 13 illustrates the dynamic range of the GSN station in Albuquerque. The high-pass-filtered (75 s) record of the Sumatra-Andaman $M_w = 9.3$ earthquake shows surface waves with an amplitude of several millimeters and a record of a local microearthquake ($M < 1$) extracted from the same record; the ratio of the amplitudes is about 10 000 000!

Meanwhile, as the US seismologists were organizing themselves, a French effort named Geoscope had already begun taking shape; the objective being the establishment of a global network of some 20–25 broadband digital seismographic stations utilizing the STS-1 seismometer, and destined in priority for

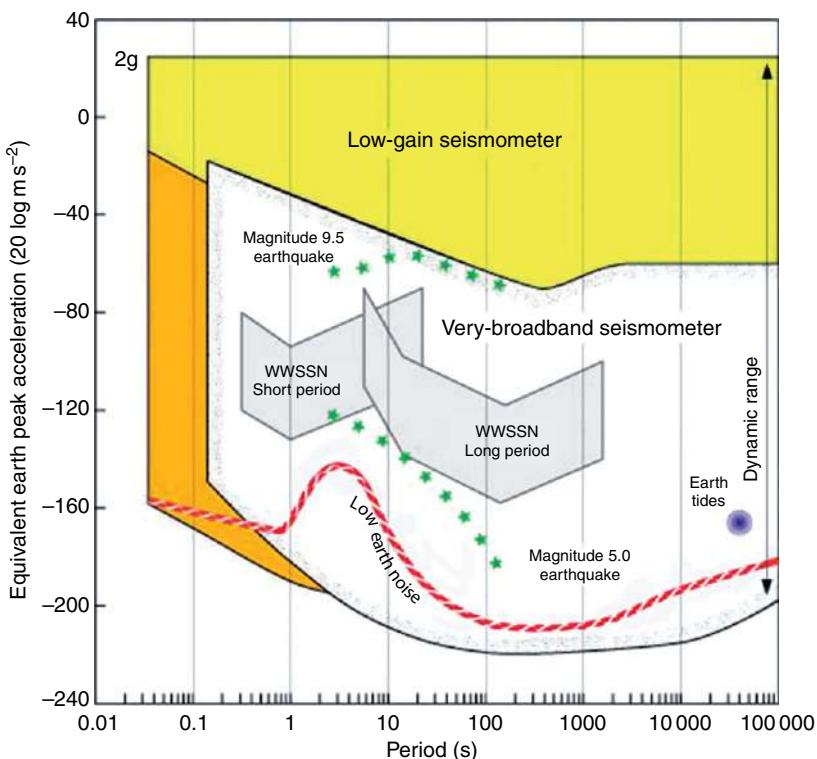


Figure 12 The dynamic range of the VBB channels of a Global Seismographic Network station. The range of the WWSSN short- and long-period channels are shown for comparison. At some GSN stations the VBB channels are augmented by very short-period channels and accelerometers. The response was designed to resolve the ground noise from 5 Hz to tidal frequencies and to record on scale a magnitude-9 earthquake at a distance of 30°. Courtesy of Rhett Butler.

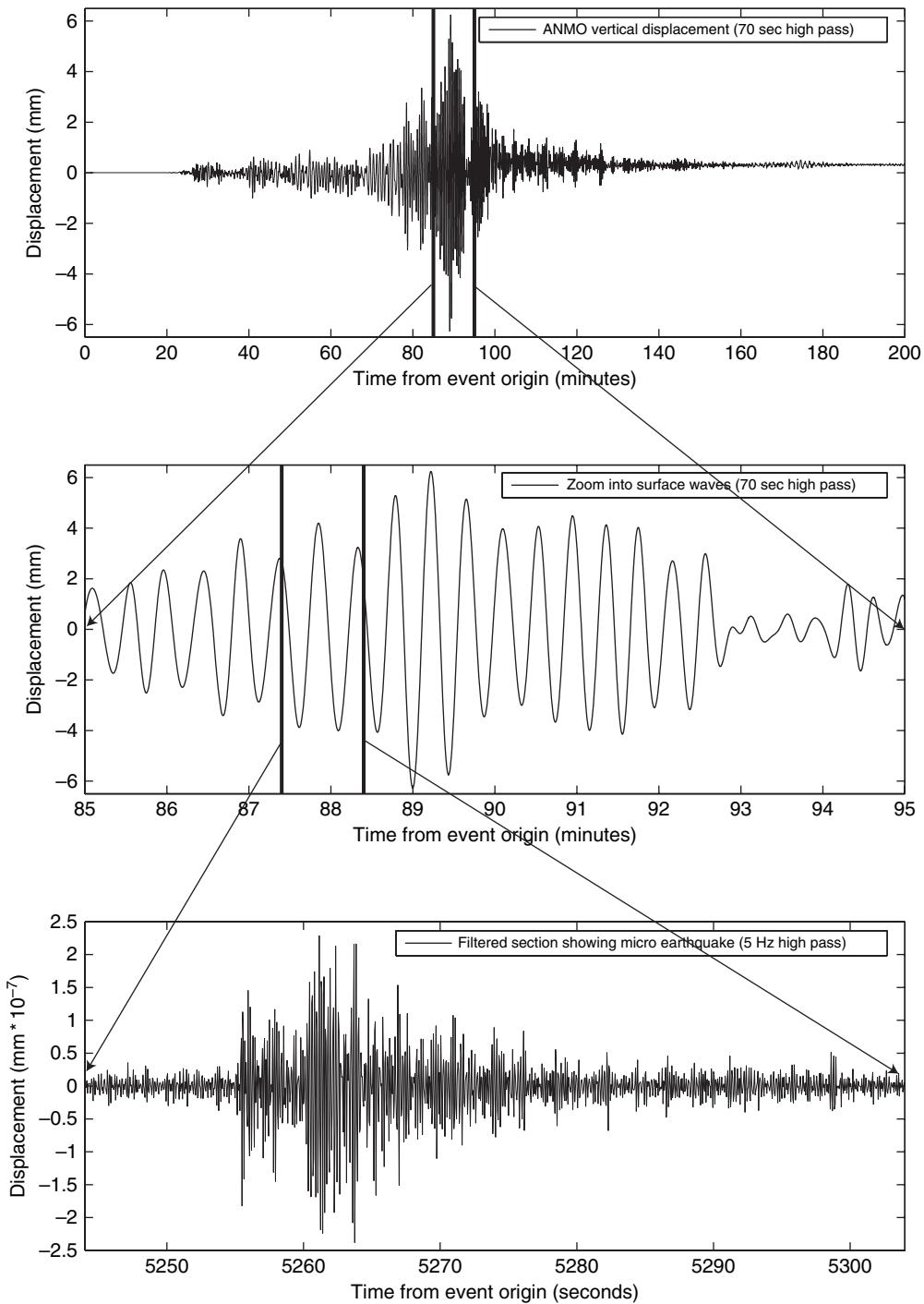


Figure 13 Illustration of the dynamic range of a VBB station (ANMO). A recording of a local microearthquake with magnitude below 1 is extracted from the record dominated by the minor-arc surface waves generated by the Sumatra-Andaman magnitude-9.3 event. Reproduced from Park *et al.* (2005).

locations around the world that filled gaps in the distribution of seismic stations. The project had officially begun in 1982 and in 1984 there were already

five operational stations (Romanowicz *et al.*, 1984), and 13 in 1986. While telemetry of the data was established later (in 1987), from early on, state of

health of the remote stations was monitored using the satellite system Argos, which greatly facilitated their maintenance. As it was clear that it was inefficient to have two competing global networks, the need for a framework for international cooperation arose. Also, many countries were interested in deploying broadband instrumentation for their national or regional purposes, and were agreeable to share these data. A Federation of Digital Seismographic Networks (FDSN) was formed in 1986 (Romanowicz and Dziewonski, 1986), with the purpose of coordinating site selection, data exchange, and standardizing instrument responses. The FDSN has been very successful in achieving these goals, despite the fact that it is a purely voluntary, zero-budget organization. **Figure 14** shows a map of the FDSN network as of January 2007 (after some 25 years of development); there are over 200 participating VBB stations, most of which now send data in nearly real time.

Similarly impressive progress was made in the area of field seismology, where progress in electronics led to overall improvement of the portability of the equipment and, in particular, reduction of power requirements, which makes operations much easier. In parallel with the development of the PASSCAL program of IRIS in the US (see Chapter 1.14), other portable arrays were developed in other countries in

the last 20 years, such as the Lithoscope program in France (Poupinet *et al.*, 1989) or the SKIPPY array in Australia (van der Hilst *et al.*, 1994). Most recently, an ambitious program, USArray, was launched in the US as part of the Earthscope project. USArray is aimed at a systematic, investigation of the structure under the contiguous United States with uniform resolution. It consists of three parts: a Permanent Array of 100 stations (the ‘backbone’ or ‘reference array’), a Transportable Array (TA), and a Flexible Array (FA). The FA will provide some 300 broadband seismographs and over 1000 active-source instruments, for experiments proposed by individual research groups, aimed at elaborating detailed local structure. The TA is the largest component of the program and it consists of 400 broadband seismograph systems, that will move gradually across the continental US over a 7-year period, to cover the entire area with, roughly, 2000 deployments for up to 2 years in a given location; the average instrument spacing is 70 km. The ‘reference array’ will provide the means to relate the waveforms recorded at different stages of TA deployment. Many other portable networks for regional studies of the crust and lithosphere using passive and active sources have been developed and deployed in the last 20 years (see Chapters 1.11, 1.14, 1.15).

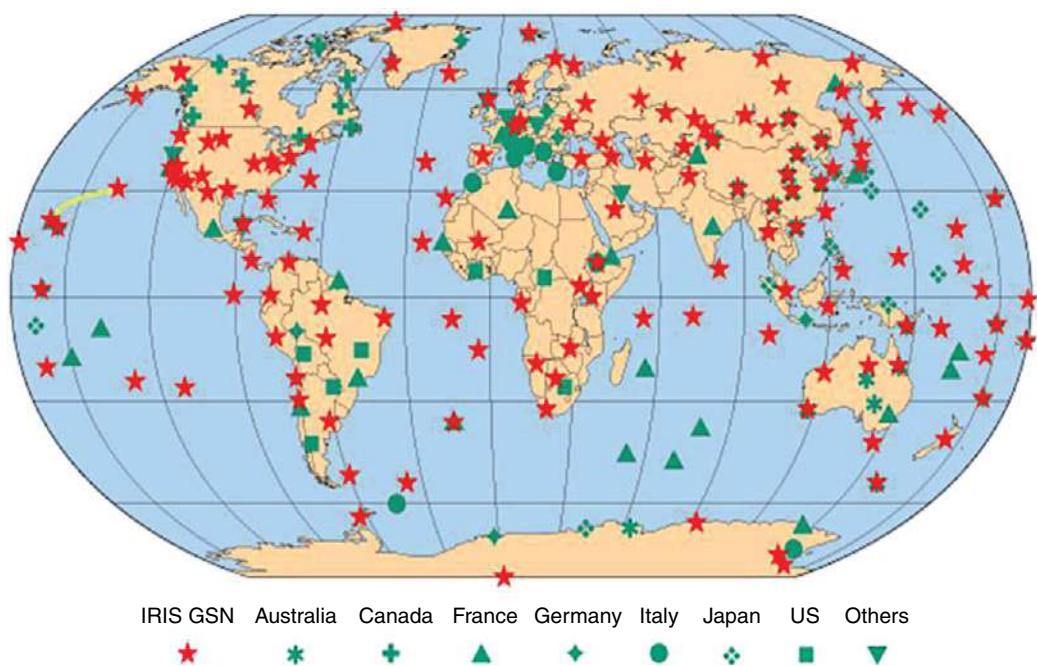


Figure 14 Current (January 2007) map of the stations of the Federation of Digital Seismographic Networks. Stations of different member networks are identified by symbols shown at the bottom. Courtesy of Rhett Butler.

1.01.4 Current Issues in Global Tomography

In parallel with instrument development, scientific progress in seismic tomography has been rapid during the last 20 years, and most of the accomplishments are summarized in two reviews by Romanowicz (1991, 2003), as well as in Chapters 1.10 and 1.16. However, there are still issues that remain unresolved or controversial. Certainly, there are confusing observations related, for example, to anisotropic properties or differential rotation of the inner core, the core–mantle topography, anti-correlation of density and shear velocity near the bottom of the mantle, the strength and depth distribution of anisotropy in the Earth’s mantle, and the role of the post-perovskite phase change in mantle dynamics.

But the foremost issue in our view relates to the derivation and interpretation of 3-D Earth models. Ever since it was discovered that inversion of ill-

conditioned matrices can be dealt with by requiring minimization of the norm or roughness of the model, we have been obtaining models whose reliability is difficult to assess. **Figure 15** illustrates an example of how the results can be altered with the change of parametrization. A set of about 40 000 phase-delay data for Rayleigh wave with 75 s period (Ekström *et al.*, 1997) is inverted for ‘local’ phase velocities. The top panel of **Figure 15** shows the result in which the data were inverted for a set of basis functions represented by spherical harmonics up to degree 16; this requires solving for 289 unknown coefficients. Because the data set is so large and the global coverage is good, the solution was obtained by an exact matrix inversion. The results look reasonable, without any indication of instability. The lower panel of **Figure 15** shows the result obtained using a $2^\circ \times 2^\circ$ block expansion, which requires solving for approximately 10 000 unknown values. Matrix conditioning was required in this case, and it was accomplished by

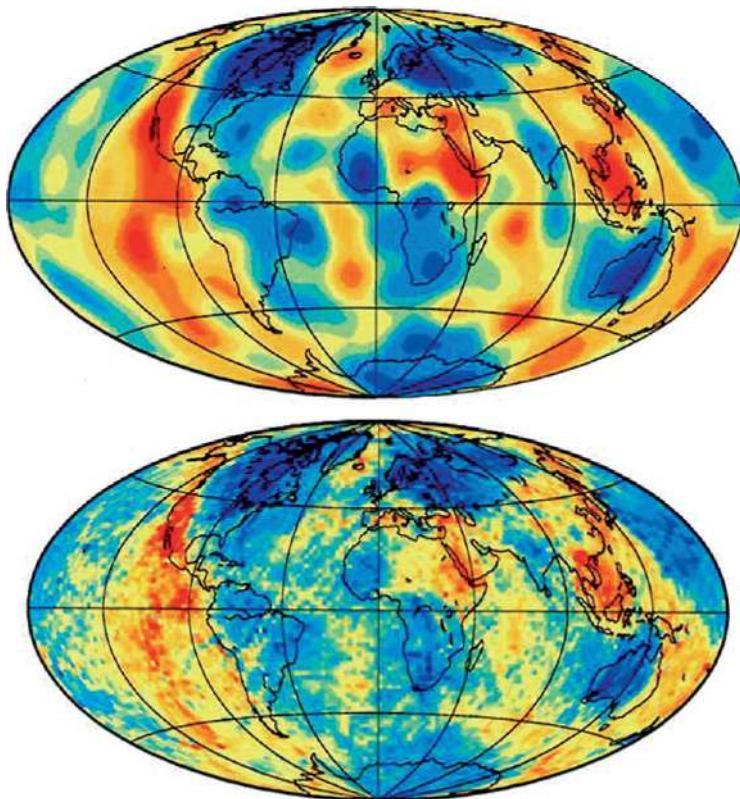


Figure 15 Demonstration of the results of inversion of the same data set (40 000 phase delay data for 75-s Rayleigh waves measured by Ekström *et al.*, 1997) for different numbers of parameters. The top map shows inversion for spherical harmonic coefficients up to degree 16 (289 parameters). The bottom map shows the results of inversion for about 10 000 equal-area blocks; in this case matrix conditioning is necessary. The amplitude of the anomalies is lower, artifacts of an uneven path distribution are visible (e.g., across the central Atlantic) and it is difficult to find features that have not been resolved by the top map. The conclusion is that there is a price for unduly increasing the number of unknowns. Courtesy of L. Boschi.

applying combined norm and roughness damping. What is clear from the ‘high-resolution’ solution, is that the amplitudes are generally lower and there are ‘streaks’ indicating artifacts caused by uneven sampling of the area. What is difficult to find, however, are any features that appear to be significant that are not present in the solution with 30 times fewer parameters.

Thus, sometimes, less is better. There is no absolute rule; the answer depends on the character of power spectra of a particular function. **Figure 16** shows results from Su and Dziewonski (1992) which indicate that spectra of several global functions, such

as free-air gravity, continent–ocean function, or SS-S traveltimes residuals, have a power spectrum that is relatively flat up to degrees from 6 to 8, after which it begins to decrease as ℓ^{-2} . This seems typical of the spectra of 2-D functions that are characterized by a set of large ‘patches’, such as the large land masses in the continent–ocean function. If the spherical harmonic expansion is truncated at an order number beyond the corner wave number, the synthesis of such truncated series retains the main character of the original function (see figure 5 in Woodhouse and Dziewonski (1984), for an example of the continent–ocean function truncated at degree 8). Similarly, an inversion for a

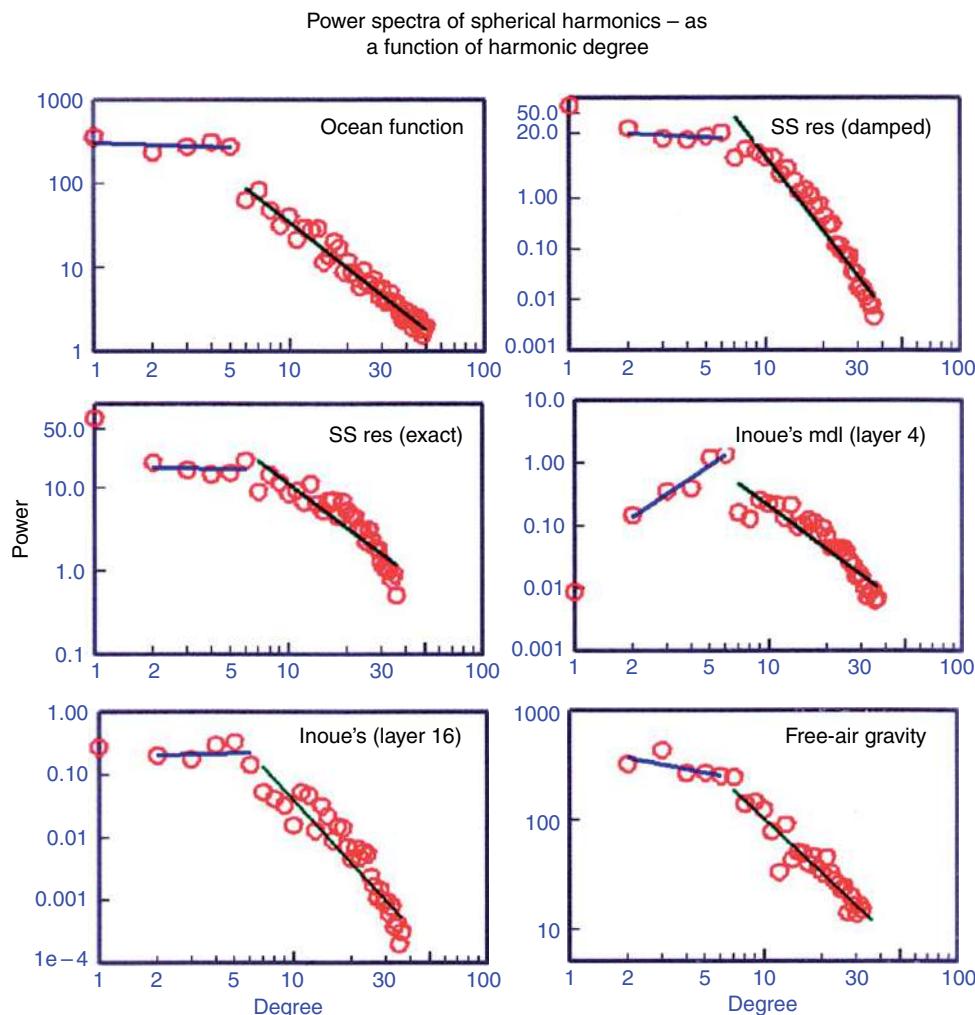


Figure 16 Illustration of the power spectra for several global functions, including two layers from a P-velocity model of Inoue *et al.* (1990). Most of the functions shown have a flat power spectrum at low-order numbers and rapidly decreasing power above degrees 6–8. The practical result of such a property of the spectra is that truncation of the expansion at an order number corresponding to the steeply decaying power does not alias inversion results at low-order numbers (Su and Dziewonski, 1991, 1992). Modified from Su W-J and Dziewonski AM (1992) On the scale of mantle heterogeneity. *Physics of the Earth and Planetary Interiors* 74: 29–54.

truncated series of spherical harmonic coefficients does not introduce aliasing if truncation occurs in the steeply decreasing part of the power spectrum. There are some geophysically important functions whose spectra have distinctly different characters; for example, linear features (slabs) have power spectra that are flat with harmonic order, point-like features (plumes?) have power spectra whose values increase with ℓ . In these cases, truncation would result in significantly lower amplitudes in the low-pass-filtered image.

The issue of parametrization is an important one, particularly if the global behavior of the solution is to be preserved. **Figure 17** illustrates cross sections of four global P-velocity models – derived from the

same data source (ISC Bulletins) – that span 3 orders of magnitude in the number of parameters. Clearly, there is not a simple relationship between the number of parameters and information contained in the model. It is so, partly, because the lower-mantle spectrum is dominated by the very low degrees that are fully recovered by the degree-6 model.

Another important issue in assessing global, as well as regional, tomographic models is the data set (or subsets) and the resolving properties that were used to derive them. The mantle models derived using only teleseismic traveltimes, for example, have very little radial resolution in the upper mantle, because the ray paths do not bottom there. The

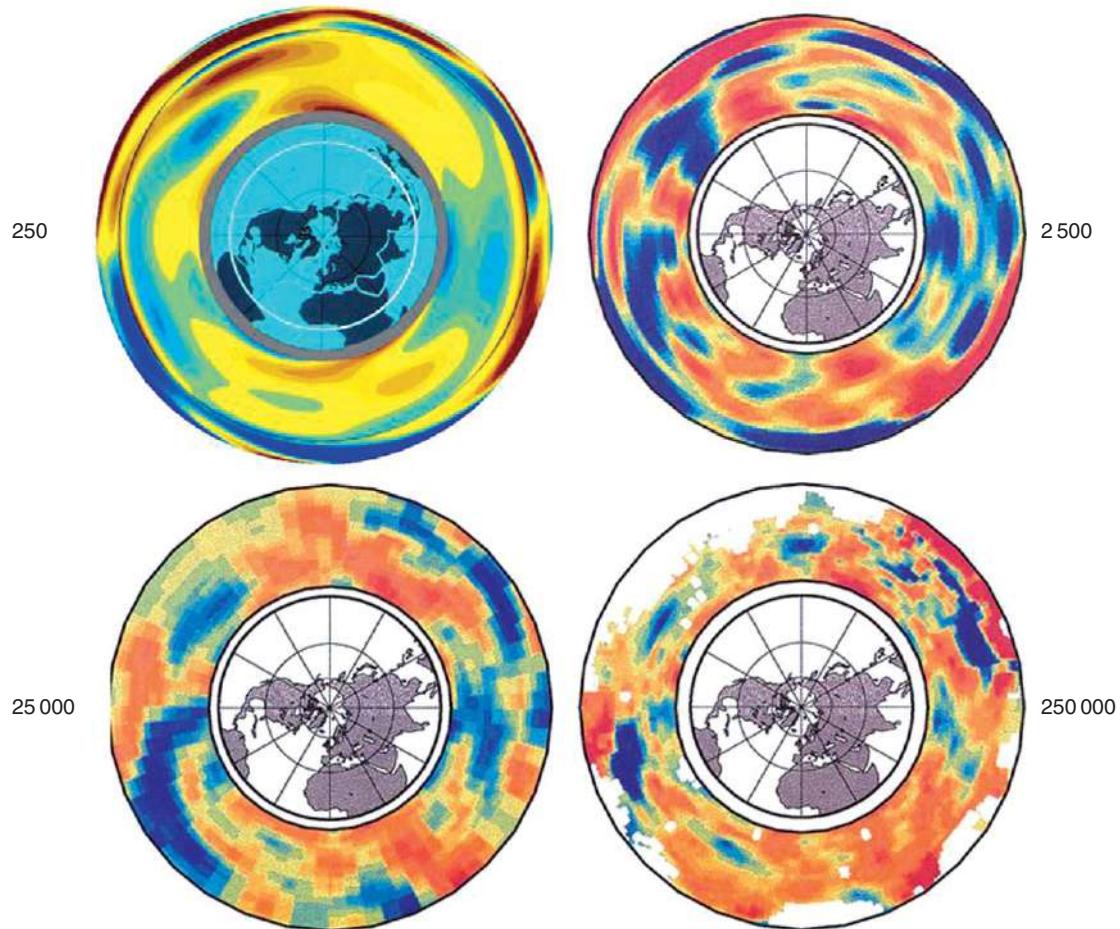


Figure 17 Comparison of the equatorial cross-sections of four P-velocity models obtained by inversion of traveltime residuals from ISC Bulletins using a number of unknown parameters that cover three orders of magnitude. The image of the African and Pacific superplumes is clearly seen in the model derived by using 250 parameters, while it could not be readily inferred from the model that used 250 000 parameters. The models obtained using 2500 and 25 000 parameters support the conclusion drawn in **Figure 16**. Modified from Boschi L and Dziewonski AM (1999) ‘High’ and ‘low’ resolution images of the Earth’s mantle – Implications of different approaches to tomographic modeling. *Journal of Geophysical Research* 104: 25567–25594.

teleseismic traveltimes are sensitive to velocity perturbations in the upper mantle, but the variations with radius cannot be resolved above the lower mantle. For example, all maps of upper-mantle velocity anomalies in [Figure 18](#) show that a model derived using only teleseismic traveltimes have slow velocities under the mid-ocean ridges at all upper-mantle depths, simply from the smearing with depth of the large slow anomalies occurring near the surface.

Models built using teleseismic traveltimes and fundamental-mode dispersion data do not have sufficient resolution in the transition zone to distinguish its unique properties. Only three research groups involved in whole-mantle modeling (Caltech/Oxford, Berkeley, and Harvard) use data allowing sufficient resolution in this region; it is interesting that they derive this information differently, therefore adding to the credibility to the

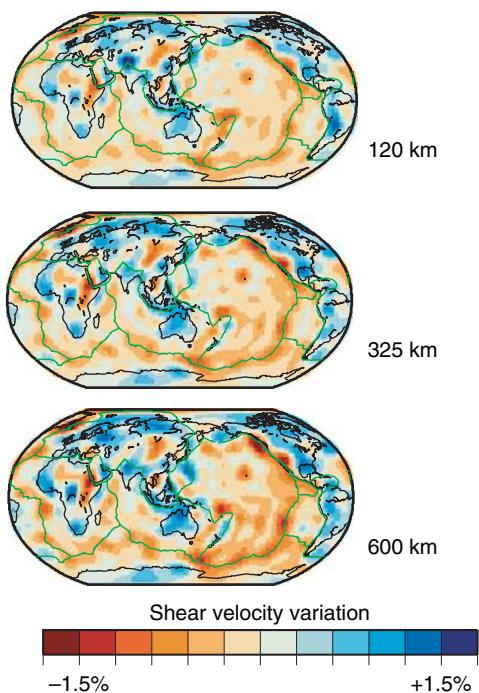


Figure 18 A fragment of a figure from [Ritsema et al. \(2004\)](#) illustrating a typical result of an upper-mantle structure obtained using teleseismic traveltimes, whose rays do not bottom in the upper mantle. The three maps show smeared-out structure from near the top of the mantle (mid-ocean ridge anomalies). The conclusion drawn from the full figure (see Chapter 1.10) is that, to obtain a whole-mantle model, one should use diverse types of data. Modified from [Ritsema J, van Heijst HJ, and Woodhouse JH \(2004\) Global transition zone tomography. Journal of Geophysical Research 109: B02302 \(doi:10.1029/2003JB002610\).](#)

results. The use of waveforms in deriving 3-D models was pioneered by [Woodhouse and Dziewonski \(1984\)](#), but in the original paper only data with periods longer than 135 s were used. Long-period body waves were used in inversion by [Woodhouse and Dziewonski \(1986, 1989\)](#). [Dziewonski and Woodward \(1992\)](#) combined waveforms and teleseismic traveltimes measured by [Woodward and Masters \(1991\)](#). The immediate result was that the two models they derived showed a sudden change in the pattern of heterogeneities across the 670 km boundary, and this was pointed out and discussed by [Woodward et al. \(1994\)](#). Later inversions by the Harvard group included also surface-wave dispersion data reported by [Ekström et al. \(1997\)](#). This increased resolution near the surface but did not alter the behavior across the upper-lower mantle boundary ([Gu et al., 2001, 2003; Kustowski et al., 2006](#)). All these models were obtained using the PAVA, which assumes constant average structure along the raypath. The Berkeley group pioneered use of a more advanced theory called nonlinear asymptotic coupling theory (NACT) first described by [Li and Romanowicz \(1995\)](#) and based on the across-branch coupling asymptotic development of [Li and Tanimoto \(1993\)](#). This theory allows to construct kernels that give good representation of the sensitivity along and around the raypath as shown in [Figure 19](#). In applying NACT to the development of several generations of global mantle models ([Li and Romanowicz, 1996; Mégnin and Romanowicz, 1999](#)), most recently including attenuation ([Gung and Romanowicz, 2004](#)) and radial anisotropy ([Panning and Romanowicz, 2006](#)), the Berkeley group divided the seismograms into wave packets containing one or several body waves or surface-wave overtones, which allowed them to weigh different phases differently in order to obtain uniform sensitivity with depth. The Berkeley group does not use traveltimes explicitly, but information on structure is included in the phase of a waveform of, for example, an SS arrival. Thus, a large collection of waveforms containing images of phases such as S, SKS, S_{diff}, Love, and Rayleigh fundamental and overtone waves will represent similar information as the combination of teleseismic traveltimes and surface-wave phase velocities in Caltech/Oxford or Harvard models. In addition, unlike traveltimes analysis, wave packets containing several phases with close arrival times but different sampling of mantle structure, can be included, improving resolution. An important element of the data set used by [Ritsema](#)

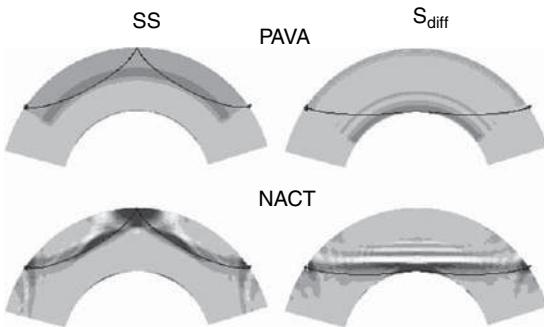


Figure 19 Comparison of sensitivity kernels in the vertical plane containing the source and the receiver for SS waves (left) and S_{diff} waves (right), using the Path Average approximation (PAVA, top) and the non-linear asymptotic coupling theory (NACT, bottom). PAVA produces 1D kernels, which do not represent well the ray character of body waves. NACT, which includes across-branch mode coupling, produces 2D finite frequency kernels that more accurately represent the sensitivity along and around the ray path as well as its variations with position along the ray. The NACT kernels are time dependent and are here represented at a particular point in the waveform, with positive maxima in black and negative ones in white. Shadows beyond the source and receiver are due to the truncation in the coupling series. Adapted from Li XD and Romanowicz B (1995) Comparison of global waveform inversions with and without considering cross branch coupling. *Geophysical Journal International* 121: 695–709.

et al. (1999) is a set of maps of Rayleigh wave overtone dispersion from the first through fifth overtones. These were obtained by ‘stripping’ the seismograms of subsequent overtones, thus providing the data on the average phase velocity of a particular overtone between the source and receiver (van Heijst and Woodhouse, 1997). Since body waves represent superposition of overtones, use of complete waveforms is, to a large extent, equivalent; however, the separation of data for individual overtones allows assignment of different weights to different overtones, while direct waveform methods use them with the weight that is determined by their excitation; generally, the amplitude of overtones decreases with the overtone number. On the other hand, waveforms contain information about all the overtones. The importance of the overtones (body-wave waveforms) was shown implicitly by Gu *et al.* (2001) and explicitly by Ritsema *et al.* (2004). The importance of using adequate kernels for overtone and body waveforms was illustrated by Mégnin and Romanowicz (1999) in a comparison of the PAVA and NACT inversion approaches.

Figure 20 shows maps of shear-velocity anomalies at depths of 600 and 800 km, spanning the 650 km

discontinuity for the three models discussed above; it also shows the power spectra for those models at both depths. All models show strong degree-2 in the transition zone and significantly weaker, whiter spectrum in the lower mantle. This is similar to the result obtained by Gu *et al.* (2001), which pointed out the abrupt change in the pattern of lateral heterogeneity above and below the 650 km discontinuity.

Figure 21 compares the power spectra of the three models as a function of depth. The increase in degree-2 power is limited to the transition zone and does not extend either above or below; this indicates that the transition zone is a boundary layer (Dziewonski *et al.*, 2006), and the flux between the upper and lower mantle is likely to be significantly impeded. The similarity of the models indicates robustness of the results and that the differences caused by using different theories and data sets are not sufficient to overwhelm convergence of the modeling effort. Favorable comparisons of features in models obtained by different research groups is probably the most practical approach to assessing credibility of tomographic models or their specific features.

The question of using ‘better theory’ has been brought to focus by the work of Montelli *et al.* (2004a, 2004b) who adapted the ‘banana–doughnut’ (finite-frequency) algorithm (Dahlen *et al.*, 2000) to inversion of teleseismic P-wave data set for a 3-D model of the mantle. These authors suggested that it was the application of this theory which allowed them to map plumes in the mantle. However, comparison of the velocity anomaly maps of models obtained using both ray theory and finite-frequency kernels reveals that maps are essentially identical, except for a constant scaling factor of 1.13 (van der Hilst and de Hoop, 2005). A pair of maps (from figure 8 of Montelli *et al.*, 2004b) at a depth of 2750 km is shown in **Figure 22**. All the same features are present in both maps (including the alleged plumes); only a slight scaling effect can be seen, with amplitudes being higher in the ‘finite-frequency’ map. One way to interpret this picture is that, in this particular case, the ‘ray theory’ and ‘finite-frequency’ approaches lead to nearly identical results. The important point is that this negates the implication of the papers by Montelli *et al.* that results obtained using ray theory cannot be trusted, possibly invalidating much of tomographic research during the previous quarter of the century.

A number of papers have been published on the question of using first-order scattering (Born) theory in inversion of seismic data (cf. Boschi *et al.*, 2006); in

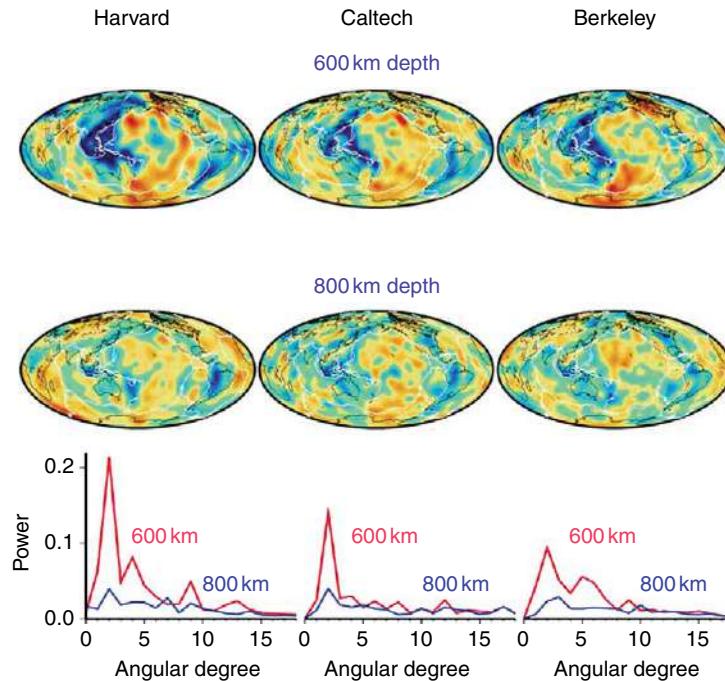


Figure 20 Maps from the three models that use data sets (overtones/waveforms) that control the structure in the transition zone (Ritsema *et al.*, 1999; Panning and Romanowicz, 2006; Kustowski *et al.*, 2006). The difference between the maps at 600 and 800 km depth is large both in the space and wave-number domains, leading to the conclusion that the transition zone represents a boundary layer that may impede the flow between the upper and lower mantle. The strong degree-2 signal in the transition zone correlates with the location of subduction in the western Pacific and to a lesser extent, under South America.

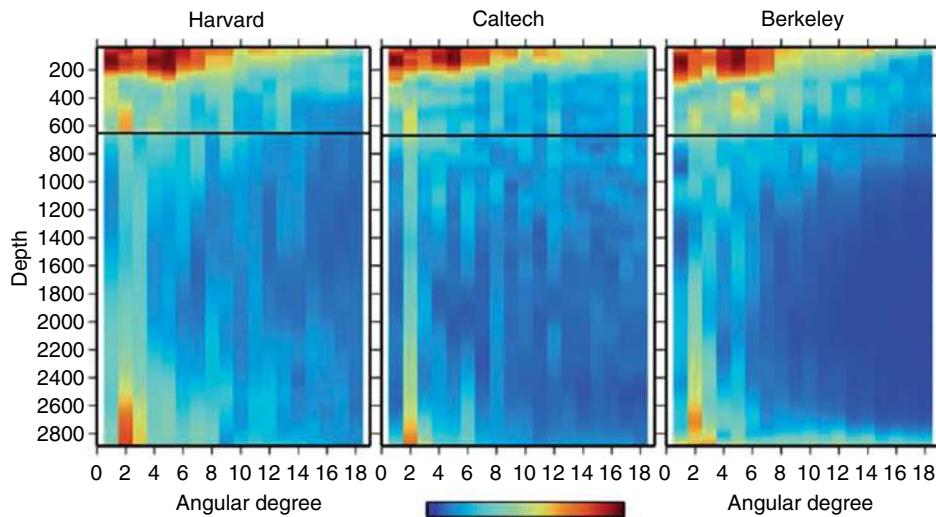


Figure 21 Comparison of the power spectra as a function of depth for the three models discussed in **Figure 20**. All models show a surface boundary layer dominated by degree 5; a boundary layer near the core–mantle boundary, dominated by degrees 2 and 3; and an additional boundary layer – the third most prominent feature in the Earth models – in the transition zone.

general, conclusions were that the difference was not substantial and in some cases Born theory gave even worse results. It should be realized that the way that

ray theory is applied in practice, with finite area or volume parametrization and matrix conditioning (smoothness, in particular), it really does not involve

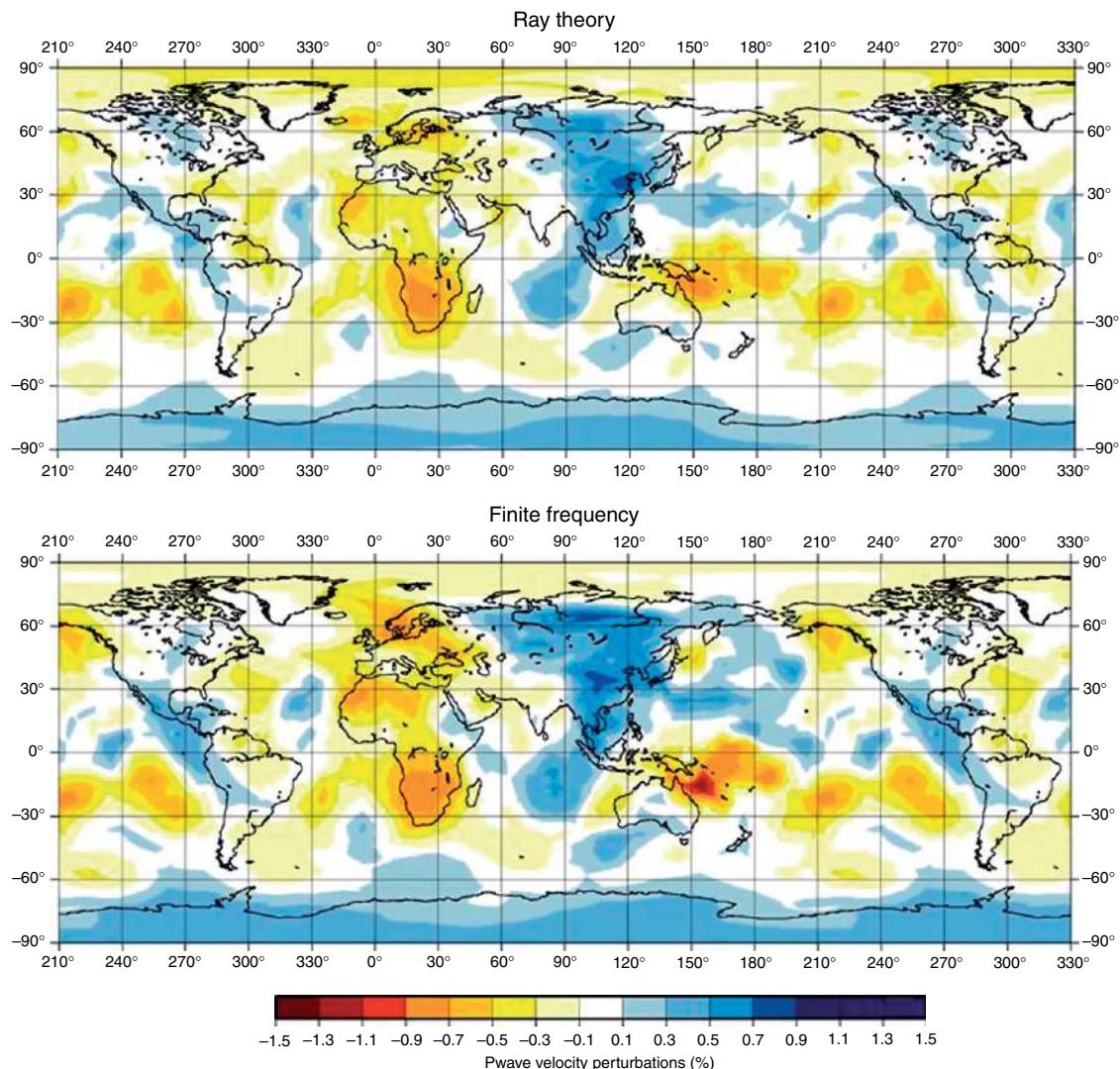


Figure 22 Comparison of two maps of P-wave velocity anomalies at 2770 km depth from the models of Montelli *et al.* (2004b). It is very difficult to identify a feature that is different in the ‘ray theory’ model (left) and ‘finite frequency’ model (right); there is a constant scaling factor between the two results (van der Hilst and de Hoop, 2005), which does not change the conclusion that the difference between the two models does not have a geophysical significance. Modified from Montelli R, Nolet G, Dahlen F, Masters G, Engdahl E, and Hung SH (2004b) Finite-frequency tomography reveals a variety of plumes in the mantle. *Science* 303: 338–343.

an infinitely thin ray, but rather a finite area or volume, which will also be sampled by nearby rays, thus introducing smoothing of the structure. This is illustrated in Figure 23 (from Nettles, 2005) comparing the best representation of a ‘ray’ in the local basis expansion using 362 spherical splines; these ‘fat rays’ are compared with the ‘influence zone’ computed for 40-s and 150-s Love waves using the method developed by Yoshizawa and Kennett (2002); the ‘fat rays’ are broader than the ‘influence zones’, indicating that, from the point of finite-frequency theory,

spherical splines with a smaller radius could be adopted to resolve finer details of the structure. It may be that, when the wavelength of a seismic wave and the distance between the source and receiver are comparable, the finite-frequency approach can be important. Clearly, improvements in theory are needed; development of accurate numerical methods for the computation of ‘exact’ synthetic seismograms for 3-D Earth models (see Chapter 1.06) already provides the means for comparison of various approximations used in inverse problems.

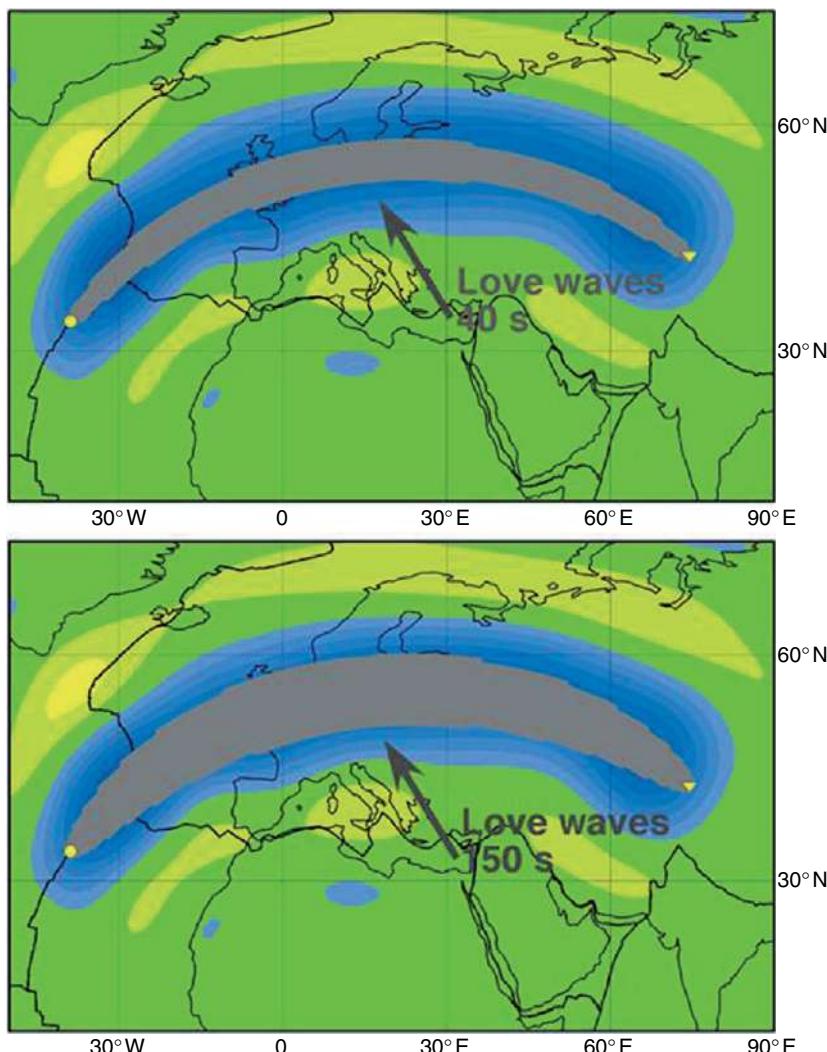


Figure 23 Basis function (spherical caps) expansion of a minor-arc raypath, which illustrates that the ‘infinitely thin’ rays become quite substantial when parametrized, in this case, using 362 caps (blue area). The ‘area of influence’ of Yoshizawa and Kennett (2002, shown in gray) for 40-s (top) and 150-s (bottom) Love waves is shown for comparison. From Nettles M (2005) Anisotropic velocity structure of the mantle beneath North America. PhD Thesis, Harvard University.

References

- Adams RD, et al. (2002) International seismology. In: Lee WHK, Kanamori H, Jennings PC, and Kisslinger C (eds.) *International Handbook of Earthquake and Engineering Seismology Part A*, pp. 29–37. San Diego, CA: Academic Press.
- Agnew DC, et al. (2002) History of seismology. In: Lee WHK, Kanamori H, Jennings PC, and Kisslinger C (eds.) *International Handbook of Earthquake and Engineering Seismology*, pp. 3–12. San Diego, CA: Academic Press.
- Agnew D, Berger J, Buland R, Farrell W, and Gilbert F (1976) International deployment of accelerometers: A network for very long period seismology. *EOS, Transactions of American Geophysical Union* 57: 180–188.
- Agnew DC, Berger J, Farrell WE, Gilbert JF, Masters G, and Miller D (1986) Project IDA; a decade in review. *EOS, Transactions of American Geophysical Union* 67: 203–212.
- Aki K, Christofferson A, and Husebye E (1977) Determination of the three-dimensional structure of the lithosphere. *Journal of Geophysical Research* 82: 277–296.
- Alsop LE, Sutton GH, and Ewing M (1961) Free oscillations of the Earth observed on strain and pendulum seismographs. *Journal of Geophysical Research* 66: 631–641.
- Alterman Z, Jarosch H, and Pekeris CL (1959) Oscillations of the Earth. *Proceedings of the Royal Society of London, Series A* 259: 80–95.
- Anderson DL (1963) Recent evidence concerning the structure and composition of the Earth’s mantle. *Physics and Chemistry of the Earth* 6: 1–129.
- Anderson DL and Hart RS (1978) Q of the Earth. *Journal of Geophysical Research* 83: 5869–5882.
- Anderson DL and Archambeau CB (1964) The anelasticity of the Earth. *Journal of Geophysical Research* 69: 2071–2084.

- Backus GE and Gilbert F (1961) The rotational splitting of free oscillations of the Earth. *Proceedings of the National Academy of Sciences of the United States of America* 47: 362–371.
- Backus GE and Gilbert F (1967) Numerical applications of formalism for geophysical inverse problems. *Geophysical Journal of the Royal Astronomical Society* 13: 247–276.
- Backus GE and Gilbert F (1968) The resolving power of gross Earth data. *Geophysical Journal of the Royal Astronomical Society* 16: 169–205.
- Backus GE and Gilbert F (1970) Uniqueness in the inversion of gross Earth data. *Philosophical Transactions of the Royal Society of London, Series A* 266: 169–205.
- Benioff H (1958) Long waves observed in the Kamchatka earthquake of November 2, 1952. *Journal of Geophysical Research* 63: 589–593.
- Benndorf H (1905) Über die Art der Fortpflanzung der Erdbebenwellen im Erdinneren. 1. Mitteilung. *Sitzungsberichte der Kaiserlichen Akademie in Wien. Mathematisch-Naturwissenschaftliche Klasse* 114, *Mitteilungen der Erdbebenkommission*, Neue Folge 29, 1–42.
- Benndorf H (1906) Über die Art der Fortpflanzung der Erdbebenwellen im Erdinneren. 2. Mitteilung. *Sitzungsberichte der Kaiserlichen Akademie in Wien. Mathematisch-Naturwissenschaftliche Klasse* 115, *Mitteilungen der Erdbebenkommission*, Neue Folge 31, 1–24.
- Berkner LV and members of the panel (1959) *Report of the Panel on Seismic Improvement. The Need for Fundamental Research in Seismology*, 212pp. Washington, DC: Department of State.
- Boschi L and Dziewonski AM (1999) 'High' and 'low' resolution images of the Earth's mantle – Implications of different approaches to tomographic modeling. *Journal of Geophysical Research* 104: 25567–25594.
- Boschi L, Becker TW, Soldati G, and Dziewonski AM (2006) On the relevance of Born theory in global seismic tomography. *Geophysical Research Letters* 33: L06302 (doi:10.1029/2005GL025063).
- Birch AF (1952) Elasticity and constitution of the Earth's interior. *Journal of Geophysical Research* 57: 227–286.
- Brune J and Dorman J (1963) Seismic waves and the structure of the crust and mantle in the Canadian Shield. *Special Paper – Geological Society of America*, pp. 28–29.
- Buland R, Berger J, and Gilbert F (1979) Observations from the IDA network of attenuation and splitting during a recent earthquake. *Nature* 277: 358–362.
- Bullen KE (1940) The problem of the Earth's density variation. *Bulletin of the Seismological Society of America* 30: 235–250.
- Bullen KE (1949) Compressibility-pressure hypothesis and the Earth's interior. *Geophysical Journal of the Royal Astronomical Society* 5: 355–368.
- Cooley JW and Tukey JW (1965) An algorithm for machine computation of complex Fourier series. *Mathematics of Computation* 19: 297–301.
- Dahlen F, Hung S-H, and Nolet G (2000) Fréchet kernels for finite-frequency traveltimes – I. Theory. *Geophysical Journal International* 141: 157–174.
- Dziewonski AM (1984) Mapping the lower mantle: Determination of lateral heterogeneity in \$P\$-velocity up to degree and order \$6\delta\$. *Journal of Geophysical Research* 89: 5929–5952.
- Dziewonski AM and Anderson DL (1981) Preliminary Earth model (PREM). *Physics of the Earth and Planetary Interiors* 25: 297–356.
- Dziewonski AM, Chou T-A, and Woodhouse JH (1981) Determination of earthquake source parameters from waveform data for studies of global and regional seismicity. *Journal of Geophysical Research* 86: 2825–2852.
- Dziewonski AM and Gilbert F (1971) Solidity of the inner core of the Earth inferred from normal mode observations. *Nature* 234: 465–466.
- Dziewonski AM and Gilbert F (1972) Observations of normal modes from 84 recordings of the Alaskan earthquake of 28 March 1964. *Geophysical Journal of Royal Astronomical Society* 27: 393–446.
- Dziewonski AM and Gilbert F (1973) Observations of normal modes from 84 recordings of the Alaskan earthquake of 28 March 1964, Part II: Spheroidal overtones from 285–100 seconds. *Geophysical Journal of the Royal Astronomical Society* 35: 401–437.
- Dziewonski AM and Gilbert F (1974) Temporal variation of the seismic moment tensor and the evidence of precursive compression for two deep earthquakes. *Nature* 247: 185–188.
- Dziewonski AM and Haddon RAW (1974) The radius of the core–mantle boundary inferred from travel time and free oscillation data: A critical review. *Physics of the Earth and Planetary Interiors* 9: 28–35.
- Dziewonski AM, Hager BH, and O'Connell RJ (1977) Large scale heterogeneities in the lower mantle. *Journal of Geophysical Research* 82: 239–255.
- Dziewonski AM and Hales AL (1972) Numerical analysis of dispersed seismic waves. In: Adler B, Fernbach S, and Bolt BA (eds.) *Methods in Computational Physics*, vol. 11, pp. 39–85. New York: Academic Press.
- Dziewonski AM, Hales AL, and Lapwood ER (1975) Parametrically simple Earth models consistent with geophysical data. *Physics of the Earth and Planetary Interiors* 10: 12–48.
- Dziewonski AM, Lekic V, Kustowski B, and Romanowicz BA (2006) Transition zone as a boundary layer. *EOS, Transactions of the American Geophysical Union, Fall Meeting Supplement*, 87: Abstract U11A-03.
- Dziewonski AM and Stein JM (1982) Dispersion and attenuation of mantle waves through waveform inversion. *Geophysical Journal of the Royal Astronomical Society* 70: 503–527.
- Dziewonski AM and Woodward RL (1992) Acoustic imaging at the planetary scale. In: Ermert H and Harjes H-P (eds.) *Acoustical Imaging*, vol. 19, pp. 785–797. New York: Plenum Press.
- Ekström G and Dziewonski AM (1998) The unique anisotropy of the Pacific upper mantle. *Nature* 394: 168–172.
- Ekström G, Dziewonski AM, Maternovskaya NN, and Nettles M (2005) Global seismicity of 2003: Centroid-moment-tensor solutions for 1087 earthquakes. *Physics of the Earth and Planetary Interiors* 148: 327–351.
- Ekström G, Tromp J, and Larson EW (1997) Measurements and models of global surface wave propagation. *Journal of Geophysical Research* 102: 8137–8157.
- Ewing M, Jaretzky WS, and Press F (1957) *Elastic Waves in Layered Media*. New York: McGraw-Hill.
- Ewing M and Press F (1954) An investigation of mantle Rayleigh waves. *Bulletin of the Seismological Society of America* 44: 127–148.
- Fuchs K and Müller G (1971) Computation of synthetic seismograms and comparison with observations. *Geophysical Journal of the Royal Astronomical Society* 23: 417–433.
- Galitzin (also Golycin) BB (1914) *Vorlesungen über Seismometrie*, deutsche Bearbeitung unter Mitwirkung von Clara Reinfeldt, herausgegeben von Oskar Hecker, vol. VIII, 538pp. Berlin: Verlag Teubner.
- Geiger L (1910) Herdbestimmung bei Erdbeben aus den Ankunftszeiten. Nachrichten von der Königlichen Gesellschaft der Wissenschaften zu Göttingen. *Mathematisch-physikalische Klasse* 331–349. (Translated into English by Peebles FWL, Anthony H, Corey SJ)

- Geiger L (1912) Probability method for the determination of earthquake epicenters from the arrival time only. *Bulletin of St. Louis University* 8: 60–71.
- Gilbert F and Dziewonski AM (1975) An application of normal mode theory to the retrieval of structural parameters and source mechanisms from seismic spectra. *Philosophical Transactions of the Royal Society of London, Series A* 278: 187–269.
- Green RWE and Hales AL (1968) Travel times of P waves to 30 degrees in central United States and upper mantle structure. *Bulletin of the Seismological Society of America* 58: 267–289.
- Gu YJ, Dziewonski AM, and Ekström G (2003) Simultaneous inversion for mantle shear velocity and topography of transition zone discontinuities. *Geophysical Journal International* 154: 559–583.
- Gu JY, Dziewonski AM, Su W-J, and Ekström G (2001) Shear velocity model of the mantle and discontinuities in the pattern of lateral heterogeneities. *Journal of Geophysical Research* 106: 11169–11199.
- Gung Y and Romanowicz B (2004) Q tomography of the upper mantle using three component long period waveforms. *Geophysical Journal International* 157: 813–830.
- Gutenberg B (1913) Über die Konstitution des Erdinnern, erschlossen aus Erdbebenbeobachtungen. *Physikalische Zeitschrift* 14: 1217–1218.
- Gutenberg B and Richter CF (1934) On seismic waves (first paper). *Gerlands Beiträge Zur Geophysik* 43: 56–133.
- Gutenberg B and Richter CF (1936) On seismic waves (third paper). *Gerlands Beiträge Zur Geophysik* 47: 73–131.
- Hales AL, Lapwood ER, and Dziewonski AM (1974) Parameterization of a spherically symmetrical Earth model with special references to the upper mantle. *Physics of the Earth and Planetary Interiors* 9: 9–12.
- Harjes H-P and Seidl D (1978) Digital recording and analysis of broad-band seismic data at the Gräfenberg (GRF) array. *Journal of Geophysics* 44: 511–523.
- Haskell NA (1953) The dispersion of surface waves on multilayered media. *Bulletin of the Seismological Society of America* 43: 17–43.
- Herglotz G (1907) Über das Benndorfsche Problem der Fortpflanzungsgeschwindigkeit der Erdbebenwellen. *Physikalische Zeitschrift* 8: 145–147.
- Inoue H, Fukao Y, Tanabe K, and Ogata Y (1990) Whole mantle P-wave travel time tomography. *Physics of the Earth and Planetary Interiors* 59: 294–328.
- Jeffreys H (1926) The rigidity of the Earth's central core. *Monthly Notices of the Royal Astronomical Society, Geophysical Supplement* 1: 371–383.
- Jeffreys H and Bullen KE (1940) *Seismological Tables*, 50pp. London: British Association for the Advancement of Science.
- Jobert N (1956) Évaluation de la période d'oscillation d'une sphère hétérogène, par application du principe de Rayleigh. *Comptes Rendus De L Académie Des Sciences, Paris* 243: 1230–1232.
- Jobert N (1957) Sur la période propre des oscillations sphéroïdales de la Terre. *Comptes Rendus De L Académie Des Sciences, Paris* 244: 242–258.
- Jobert N (1961) Calcul approché de la période des oscillations sphéroïdales de la Terre. *Geophysical Journal of the Royal Astronomical Society* 4: 242–258.
- Jordan TH (1978) A procedure for estimating lateral variations from low-frequency eigenspectra data. *Geophysical Journal of the Royal Astronomical Society* 52: 441–455.
- Jordan TH and Anderson DL (1974) Earth structure from free oscillations and travel times. *Geophysical Journal of the Royal Astronomical Society* 36: 411–459.
- Julian BR and Sengupta MK (1973) Seismic travel time evidence for lateral inhomogeneity in the deep mantle. *Nature* 242: 443–447.
- Kennett BLN, Engdahl ER, and Buland R (1995) Constraints on seismic velocities in the Earth from traveltimes. *Geophysical Journal International* 122: 108–124.
- Knott CG (1899) Reflection and refraction of elastic waves, with seismological applications. *The London, Edinburgh, and Dublin Philosophical Magazine and Journal of Science, Series 5* 48: 64–97/ 567–569.
- Kustowski B, Dziewonski AM, and Ekström G (2006) Modeling the anisotropic shear-wave velocity structure in the Earth's mantle on global and regional scales. *EOS, Transactions of the American Geophysical Union, Fall Meeting Supplement*, 87: Abstract S41E-02.
- Landisman M, Sato Y, and Nafe JE (1965) Free vibrations of the Earth and the properties of its deep interior regions: Part 1. Density. *Geophysical Journal of the Royal Astronomical Society* 9: 439–502.
- Lehmann I (1936) P'. *Publ. Bureau Cent. Séism. Inter., Série A, Trav. Scient* 14: 87–115.
- Li XD and Tanimoto T (1993) Waveforms of long-period body waves in a slightly aspherical Earth model. *Geophysical Journal International* 112: 92–102.
- Li XD and Romanowicz B (1995) Comparison of global waveform inversions with and without considering cross branch coupling. *Geophysical Journal International* 121: 695–709.
- Li X-D and Romanowicz B (1996) Global mantle shear velocity model developed using nonlinear asymptotic coupling theory. *Journal of Geophysical Research* 101: 22245–22272.
- Liu H-P, Anderson DL, and Kanamori H (1976) Velocity dispersion due to anelasticity: Implications for seismology and mantle composition. *Geophysical Journal of the Royal Astronomical Society* 47: 41–58.
- Love AEH (1911) *Some Problems of Geodynamics*. Cambridge: Cambridge University Press.
- Masters G, Jordan TH, Silver PG, and Gilbert F (1982) Aspherical earth structure from fundamental spheroidal mode data. *Nature* 298: 609–613.
- Mégnin C and Romanowicz B (1999) The effects of the theoretical formalism and data selection on mantle models derived from waveform tomography. *Geophysical Journal International* 138: 366–380.
- Mendiguren J (1973) Identification of free oscillation spectral peaks for 1970 July 31, Colombian deep shock using the excitation criterion. *Geophysical Journal of the Royal Astronomical Society* 33: 281–321.
- Mohorovičić A (1910) Potres od 8. X 1909. God. Izvješće Zagr. met. Ops. Zag. 1909, Zagreb (Das Beben vom 8. X 1909. *Jahrbuch des meteorologischen Observatoriums in Zagreb für das Jahr 1909*), 9, Part 4, 1–63.
- Montelli R, Nolet G, Dahlen F, Masters G, Engdahl E, and Hung SH (2004a) Global P and PP travel time tomography: Rays vs. waves. *Geophysical Journal International* 158: 637–654.
- Montelli R, Nolet G, Dahlen F, Masters G, Engdahl E, and Hung SH (2004b) Finite-frequency tomography reveals a variety of plumes in the mantle. *Science* 303: 338–343.
- Ness NF, Harrison JC, and Slichter LB (1961) Observations of the free oscillations of the Earth. *Journal of Geophysical Research* 66: 621–629.
- Nettles M (2005) *Anisotropic velocity structure of the mantle beneath North America*. PhD Thesis, Harvard University.
- Panning M and Romanowicz B (2006) A three dimensional radially anisotropic model of shear velocity in the whole mantle. *Geophysical Journal International* 167: 361–379.
- Park J, Butler R, Anderson K, et al. (2005) Performance review of the global seismographic network for the Sumatra–Andaman megathrust earthquake. *Seismological Research Letters* 76(3): 331–343.
- Pekeris CL, Alterman Z, and Jarosch H (1961a) Comparison of theoretical with observed values of the periods of the free

- oscillations of the Earth. *Proceedings of the National Academy of Sciences of the United States of America* 47: 91–98.
- Pekeris CL, Alterman Z, and Jarosch H (1961b) Rotational multiplets in the spectrum of the Earth. *Physical Review* 122: 1692–1700.
- Pekeris CL and Jarosch H (1958) The free oscillations of the Earth. In: Benioff H, Ewing M, Howell jun BF, and Press K (eds.) *Contributions in Geophysics in Honor of Beno Gutenberg et al.*, pp. 171–192. New York: Pergamon.
- Peterson J, Butler HM, Holcomb LT, and Hutt C (1976) The seismic research observatory. *Bulletin of the Seismological Society of America* 66: 2049–2068.
- Poupinet G, Frechet J, and Thouvenot F (1989) Portable short period vertical seismic stations transmitting via telephone or satellite. In: Cassinis R and Nolet G (eds.) *Digital Seismology and Fine Modelling of the Lithosphere*, pp. 9–26. London: Plenum.
- Press F (1956) Determination of crustal structure from phase velocity of Rayleigh waves – Part I. Southern California. *Bulletin of Geological Society of America* 67: 1647–1658.
- Rayleigh JWS (1885) On waves propagated along plane surface of an elastic solid. *Proceedings of the London Mathematical Society* 17: 4–11.
- Rebeur-Paschwitz E v (1889) The earthquake of Tokyo, April 18, 1889. *Nature* 40: 294–295.
- Ritsema J, van Heijst HH, and Woodhouse JH (1999) Complex shear wave velocity structure imaged beneath Africa and Iceland. *Science* 286: 1925–1928.
- Ritsema J, van Heijst HJ, and Woodhouse JH (2004) Global transition zone tomography. *Journal of Geophysical Research* 109: B02302 (doi:10.1029/2003JB002610).
- Romanowicz B (1979) Seismic structure of the upper mantle beneath the United States by three-dimensional inversion of body wave arrival times. *Geophysical Journal of the Royal Astronomical Society* 57: 479–506.
- Romanowicz B (1991) Seismic tomography of the Earth's mantle. *Annual Review of Earth and Planetary Science* 19: 77–99.
- Romanowicz B (2003) Global mantle tomography: Progress status in the last 10 years. *Annual Review of Geophysics and Space Physics* 31: 303–328.
- Romanowicz BA, Cara M, Fels JF, and Rouland D (1984) Geoscope: A French initiative in long-period three-component seismic networks. *EOS Transactions of American Geophysical Union* 65: 753–754.
- Romanowicz BA and Dziewonski AM (1986) Towards a federation of broadband seismic networks. *EOS Transactions of American Geophysical Union* 67: 541–542.
- Russakoff D, Ekström G, and Tromp J (1998) A new analysis of the great 1970 Colombia earthquake and its isotropic component. *Journal of Geophysical Research* 102: 20423–20434.
- Sailor RV and Dziewonski AM (1978) Observations and interpretation of attenuation of normal modes. *Geophysical Journal of the Royal Astronomical Society* 53: 559–581.
- Schweitzer J (2007) Oldham RD (1858–1936). In: D Gubbins and EHerrero-Bervera (eds.) *Encyclopedia of Geomagnetism and Paleomagnetism* ISBN 1-4020-3992-1 Kluwer-Springer, (in print).
- Souriau A and Souriau M (1983) Test of tectonic models by great-circle Rayleigh waves. *Geophysical Journal of the Royal Astronomical Society* 73: 533–551.
- Steim JM (1986) *The very-broad-band seismograph*, 184pp. Doctoral Thesis, Department of Geological Sciences, Harvard University, Cambridge, MA.
- Stoneley R (1928) A Rayleigh wave problem. *Proceedings of the Leeds Philosophical and Literary Society (Science Section)* 1: 217–225.
- Stein S and Wysession M (2003) *An Introduction to Seismology, Earthquakes and Earth Structure*. Oxford: Blackwell (isbn 0865420785).
- Su W-J and Dziewonski AM (1991) Predominance of long-wavelength heterogeneity in the mantle. *Nature* 352: 121–126.
- Su W-J and Dziewonski AM (1992) On the scale of mantle heterogeneity. *Physics of the Earth and Planetary Interiors* 74: 29–54.
- Takeyuchi H (1959) Torsional oscillations of the Earth and some related problems. *Geophysical Journal of the Royal Astronomical Society* 2: 89–100.
- Thomson ST (1950) Transmission of elastic waves through a stratified solid medium. *Journal of Applied Physics* 21: 89–93.
- Toksoz MN and Anderson DL (1966) Phase velocities of long-period surface waves and structure of the upper mantle. *Journal of Geophysical Research* 71: 1649–1658.
- Udias A and Stauder W (2002) The Jesuit contribution to seismology. In: Lee WHK, Kanamori H, Jennings PC, and Kisslinger C (eds.) *International Handbook of Earthquake and Engineering Seismology et al.*, pp. 19–27. San Diego, CA: Academic Press.
- van der Hilst RD and deHoop MV (2005) Banana-doughnut kernels and mantle tomography. *Geophysical Journal International* 163: 956–961.
- van der Hilst R, Kennett B, Christie D, and Grant J (1994) Project Skippy explores the lithosphere and upper mantle below Australia. *EOS Transactions of the American Geophysical Union* 75 177/ 180–181.
- van Heijst HJ and Woodhouse JH (1997) Measuring surface-wave overtone phase velocities using a mode-branch stripping technique. *Geophysical Journal International* 131: 209–230.
- von Rebeur-Paschwitz E (1895) Horizontalpendal-Beobachtungen auf der Kaiserlichen Universitäts-Sternwarte zu Strassburg 1892–1894. *Gerland Beitr. Zur Geophys.* 2: 211–536.
- Wiechert E (1907) Über Erdbebenwellen. Theoretisches über die Ausbreitung der Erdbebenwellen. *Nachrichten von der Königlichen Gesellschaft der Wissenschaften zu Göttingen, Mathematisch-physikalische Klasse* 413–529.
- Wielandt E (2002) Seismic sensors and their calibration. In: Bormann IP (ed.) *IASPEI New Manual of Seismological Observatory Practice*, vol. 1, Ch. 5, pp. 1–46. Potsdam: GeoForschungsZentrum Potsdam.
- Wielandt E and Streckeisen G (1982) The leaf-spring seismometer: Design and performance. *Bulletin of the Seismological Society of America* 72: 2349–2367.
- Wielandt E and Stein JM (1986) A digital very-broad-band seismograph. *Annales Geophysicae* 4: 227–232.
- Woodhouse JH (1980) The coupling and attenuation of nearly resonant multiplets in the Earth's free oscillation spectrum. *Geophysical Journal of the Royal Astronomical Society* 61: 261–283.
- Woodhouse JH and Dahlen FA (1978) The effect of a general aspherical perturbation on the free oscillations of the Earth. *Geophysical Journal of the Royal Astronomical Society* 53: 335–354.
- Woodhouse JH and Dziewonski AM (1984) Mapping the upper mantle: Three dimensional modeling of earth structure by inversion of seismic waveforms. *Journal of Geophysical Research* 89: 5953–5986.
- Woodhouse J and Dziewonski A (1986) Three dimensional mantle models based on mantle wave and long period body wave data. *EOS Transactions of the American Geophysical Union* 67: 307.
- Woodhouse JH and Dziewonski AM (1989) Seismic modelling of the Earth's large-scale three dimensional structure. *Philosophical Transactions of the Royal Society of London, Series A* 328: 291–308.

- Woodhouse JH and Girnius TP (1982) Surface waves and free oscillations in a regionalized Earth model. *Geophysical Journal International* 68: 653–673.
- Woodward RL, Dziewonski AM, and Peltier WR (1994) Comparisons of seismic heterogeneity models and convective flow calculations. *Geophysical Research Letters* 21: 325–328.
- Woodward RL and Masters G (1991) Lower-mantle structure from ScS-S differential travel times. *Nature* 352: 231–233.
- Yoshizawa K and Kennett BLN (2002) Determination of the influence zone for surface waves. *Geophysical Journal International* 149: 440–453.
- Zöppritz K (1907) Über Erdbebenwellen. II: Laufzeitkurven. *Nachrichten von der Königlichen Gesellschaft der Wissenschaften zu Göttingen, Mathematisch-physikalische Klasse* 529–549.

Relevant Website

<http://www.globalcmt.org>—Global CMT Web Page.

1.02 Theory and Observations – Earth’s Free Oscillations

J. H. Woodhouse, University of Oxford, Oxford, UK

A. Deuss, University of Cambridge, Cambridge, UK

© 2007 Elsevier B.V. All rights reserved.

1.02.1	Introduction	31
1.02.2	Hamilton’s Principle and the Equations of Motion	32
1.02.3	The Generalized Spherical Harmonics	37
1.02.4	The Green’s Function for the Spherically Symmetric Earth	40
1.02.5	Numerical Solution	45
1.02.6	Elastic Displacement as a Sum over Modes	52
1.02.7	The Normal Mode Spectrum	53
1.02.8	Normal Modes and Theoretical Seismograms in Three-Dimensional Earth Models	58
1.02.9	Concluding Discussion	63
	References	64

1.02.1 Introduction

The study of the Earth’s free oscillations is fundamental to seismology, as it is a key part of the theory of the Earth’s dynamic response to external or internal forces. Essentially, the same theory is applicable to phenomena as diverse as postseismic relaxation, analysis of seismic surface waves and body waves. The study of free oscillations *per se* is concerned with analyzing and extracting information at very long periods ($\sim 3000\text{--}200\text{s}$ period) since in this range of periods the intrinsic standing wave modes of oscillation are evident in seismic spectra. Such spectra contain important information about the large-scale structure of the Earth. For example, the strongest evidence that the inner core is solid (Dziewonski and Gilbert, 1971) and anisotropic (Woodhouse *et al.*, 1986; Tromp, 1993; Romanowicz and Breger, 2000) comes from the study of free oscillations. Free oscillations provide essential constraints on both the spherically symmetric ‘average’ Earth, and also on lateral variations in Earth structure due to heterogeneity in temperature, composition, and anisotropy. Modal data are particularly valuable in this regard because, unlike other kinds of seismic data, modal observables depend upon broad averages of the Earth’s structural parameters, and are not nearly so affected by limitations of data coverage due to the uneven distribution of seismic events and stations. There is an enormous wealth of information yet to be extracted from long period spectra; one has

only to examine almost any portion of a seismic spectrum in detail to realize that current models often do not come close to providing adequate predictions. It is only from such very long period data that it may be possible to obtain direct information on the three-dimensional distribution of density. Even very large scale information on lateral variations in density has the potential to bring unique information to the study of convection and thermal and compositional evolution.

Very long period spectra are also an essential element in the study of earthquakes, as it is only by using data at the longest periods that it is possible to determine the overall moment of very large events. For example, estimates of the moment of the great Sumatra earthquake based on mantle waves, even at periods of several hundred seconds, significantly underestimate the true moment, as the length and duration of the rupture make it possible to gauge the true, integrated moment only by using data at the longest seismic periods (e.g. Park *et al.*, 2005).

Figure 1 shows an example of data and theoretical amplitude spectra computed for the spherically symmetric PREM model (Dziewonski and Anderson, 1981). Modes appear as distinct peaks in the frequency domain. For higher frequencies, the modes are more closely spaced and begin to overlap. The theoretical peaks appear at frequencies very close to the observed peaks. However, the observed peaks are distorted in shape and amplitude due to three-dimensional effects. For example, mode $_{1S_4}$ is split

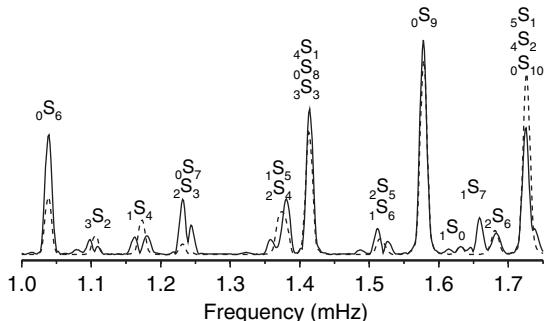


Figure 1 Data (solid line) and PREM synthetic spectrum (dashed line) computed using normal mode summation, for the vertical component recording at station ANMO following the great Sumatra event of 26 December 2004.

into two peaks in the data spectrum, which is not seen in the theoretical spectrum. Not shown here, but equally important in studying both Earth structure and earthquakes, is the ‘phase spectrum’. Examples illustrating this are shown in later sections.

Normal mode studies represent the quest to reveal and understand the Earth’s intrinsic vibrational spectrum. However, this is a difficult quest, because it is only at the very longest periods (≥ 500 s, say) that there is the possibility of obtaining data of sufficient duration to make it possible to achieve the necessary spectral resolution. Essentially, the modes attenuate before the many cycles necessary to establish a standing wave pattern have elapsed. Thus, in many observational studies, over a wide range of frequencies, the normal mode representation has the role, primarily, of providing a method for the calculation of theoretical seismograms. Although observed spectra contain spectral peaks, the peaks are broadened by the effects of attenuation in a path-dependent way. Thus, rather than making direct measurements on observed spectra, the analysis needs to be based on comparisons between data and synthetic spectra, in order to derive models able to give improved agreement between data and synthetics.

The use of normal mode theory as a method of synthesis extends well beyond the realm normally thought of as normal mode studies. For example, it has become commonplace to calculate global body wave theoretical seismograms by mode summation in a spherical model, to frequencies higher than 100 mHz (10 s period). Typically, such calculations can be done in seconds on an ordinary workstation, the time, of course, depending strongly upon the upper limit in frequency and on the number of samples in the time series. The advantage of the method

is that all seismic phases are automatically included, with realistic time and amplitude relationships. Although the technique is limited (probably for the foreseeable future) to spherically symmetric models, the comparison of such synthetics with data provides a valuable tool for understanding the nature and potential of the observations and for making measurements such as differences in timing between data and synthetics, for use in tomography. Thus, the period range of applications of the normal mode representation extends from several thousand seconds to ~ 5 s. In between these ends of the spectrum is an enormous range of applications: studies of modes *per se*, surface wave studies, analysis of overtones, and long period body waves, each having relevance to areas such as source parameter estimation and tomography. **Figure 2** shows an example of synthetic and data traces, illustrating this.

There are a number of excellent sources of information on normal modes theory and applications. The comprehensive monograph by [Dahlen and Tromp \(1998\)](#) provides in-depth coverage of the material and an extensive bibliography. An earlier monograph by [Lapwood and Usami \(1981\)](#) contains much interesting and useful information, treated from a fundamental point of view, as well as historical material about early theoretical work and early observations. A review by [Takeuchi and Saito \(1972\)](#) is a good source for the ordinary differential equations for spherical Earth models and methods of solution. Other reviews are by [Gilbert \(1980\)](#), [Dziewonski and Woodhouse \(1983\)](#), and [Woodhouse \(1996\)](#). A review of normal mode observations can be found in Chapter 1.03. Because of this extensive literature we tend in this chapter to expand on some topics that have not found their way into earlier reviews but are nevertheless of fundamental interest and utility.

1.02.2 Hamilton’s Principle and the Equations of Motion

To a good approximation, except in the vicinity of an earthquake or explosion, seismic displacements are governed by the equations of elasticity. At long periods self-gravitation also plays an important role. Here we show how the equations of motion arise from Hamilton’s principle.

Consider a material which is initially in equilibrium under self-gravitation. Each particle of the material is labeled by Cartesian coordinates x_i ($i = 1, 2, 3$), representing its initial position. The

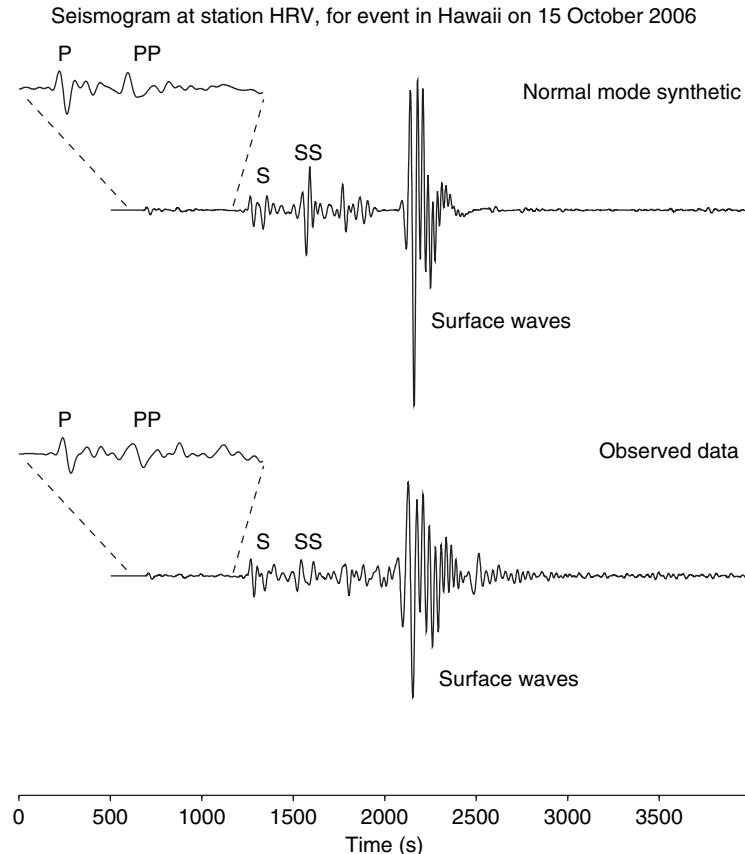


Figure 2 Data and synthetic for a vertical component record at station HRV following the recent event in Hawaii on 15 October 2006. The epicentral distance is 73° . For the calculation of the synthetic seismogram the Harvard/Lamont quick-CMT centroid location and moment tensor parameters were used (G. Ekström, www.globalcmt.org).

material undergoes time-dependent deformation in which the particle initially at x_i moves to $r_i = r_i(\mathbf{x}, t)$ where t is time. A 'hyperelastic' material is defined as one in which there exists an internal energy density function which is a function of the Green strain tensor

$$e_{ij} = \frac{1}{2} (r_{k,i} r_{k,j} - \delta_{ij}) \quad [1]$$

where $r_{k,i} \equiv \partial r_k / \partial x_i$, δ_{ij} is the Kronecker delta; summation over repeated indices is assumed. Thus, we introduce the internal elastic energy function, per unit mass, $E(\mathbf{x}, \mathbf{e}, s)$, where s is specific entropy. We shall be concerned only with isentropic deformations, and can henceforth omit the dependence on s . Note that E is represented as a function of the coordinates x_i which label a specific material particle. $E(\mathbf{x}, \mathbf{e})$ is regarded as a given function characterizing the elastic properties of the material. This form of the internal energy function, which forms the basis of finite theories of elasticity, as well as the theory of linear

elasticity which we need here, arises from the very general consideration that elastic internal energy should not change as a result of rigid rotations of the material.

The gravitational field is characterized by a potential field $\phi(\mathbf{r})$, which satisfies Poisson's equation

$$\frac{\partial^2 \phi}{\partial r_k \partial r_k} = 4\pi G \rho(\mathbf{r}) \quad [2]$$

where ρ is the density. We state this equation in terms of the coordinates r_k , as it represents an equation valid in the current configuration of the material.

The Lagrangian governing motion of the elastic-gravitational system (total kinetic energy minus total potential energy) is

$$L = \int \int \left(\frac{1}{2} \rho \dot{r}_k \dot{r}_k - \rho E(\mathbf{x}, \mathbf{e}) - \frac{1}{2} \rho \phi \right) d^3 r dt \quad [3]$$

where 'overdot' represents the material time derivative (i.e., the derivative with respect to t at constant \mathbf{x}).

The three terms of the integrand represent the kinetic energy, (minus) the elastic energy, and (minus) the gravitational energy, respectively, making use of the fact that the gravitational energy released by assembling a body from material dispersed at infinity is $-\int \frac{1}{2} \rho \phi d^3 r$. The integral in [3] is over the volume occupied by the Earth, which is taken to consist of a number of subregions with internal interfaces and an external free surface. Hamilton's principle requires that L be stationary with respect to variations $\delta r_i(\mathbf{x}, t)$, subject to the constraint that ϕ is determined by [2], and also to the requirement of mass conservation:

$$\rho d^3 r = \rho^0 d^3 x \quad [4]$$

where $\rho^0 = \rho^0(\mathbf{x})$ is the initial density, that is,

$$\rho = \rho^0 / \mathcal{J} \quad [5]$$

where \mathcal{J} is the Jacobian,

$$\mathcal{J} = \frac{\partial(r_1, r_2, r_3)}{\partial(x_1, x_2, x_3)} \quad [6]$$

The constraint [2] can be incorporated into the variational principle by introducing a field η which acts as a Lagrange multiplier (e.g., Seliger and Whitham, 1968):

$$\begin{aligned} L' = & \iint \left\{ \frac{1}{2} \rho \dot{r}_k \dot{r}_k - \rho E(\mathbf{x}, \mathbf{e}) - \frac{1}{2} \rho \phi \right. \\ & \left. + \eta \left(\frac{\partial^2 \phi}{\partial r_k \partial r_k} - 4\pi G \rho \right) \right\} d^3 r dt \end{aligned} \quad [7]$$

the term involving η vanishes by [2], and therefore, L' is stationary with respect to variations in η . If we also require that L' be stationary under variations $\delta\phi$, we obtain the Euler–Lagrange equation for η :

$$\frac{\partial^2 \eta}{\partial r_k \partial r_k} = \frac{1}{2} \rho \quad [8]$$

which can be satisfied by setting $\eta = \phi/8\pi G$. Thus, we obtain

$$L' = \iint \left\{ \frac{1}{2} \rho \dot{r}_k \dot{r}_k - \rho E(\mathbf{x}, \mathbf{e}) - \rho \phi - \frac{1}{8\pi G} \frac{\partial \phi}{\partial r_k} \frac{\partial \phi}{\partial r_k} \right\} d^3 r dt \quad [9]$$

Changing the spatial integration variables, making use of [4], we may also write

$$\begin{aligned} L' = & \iint \left\{ \frac{1}{2} \rho^0 \dot{r}_k \dot{r}_k - \rho^0 E(\mathbf{x}, \mathbf{e}) - \rho^0 \phi \right. \\ & \left. - \frac{1}{8\pi G} \phi'_{,k} \phi'_{,k} \right\} d^3 x dt \end{aligned} \quad [10]$$

where ϕ' represents the gravitational potential at the fixed coordinate point \mathbf{x} . Notice that the first three

terms of the integrand have been transformed by regarding \mathbf{r} to be a function of \mathbf{x} (at each fixed t) through the function $\mathbf{r}(\mathbf{x}, t)$ which defines the deformation. However, the fourth term (which ‘could’ be treated in the same way) has been transformed by renaming the dummy integration variables r_i to x_i . Hence, the need to introduce ϕ' since ϕ represents $\phi(\mathbf{r}(\mathbf{x}, t))$, which is different from $\phi(\mathbf{x}, t)$. The requirement that L' be stationary with respect to variations $\delta\mathbf{r}(\mathbf{x}, t)$, $\delta\phi(\mathbf{r}, t)$ provides a very succinct, complete statement of the elasto-gravitational dynamical equations.

To obtain the partial differential equations for infinitesimal deformations, we approximate L' in the case that $r_k = x_k + \epsilon u_k(\mathbf{x}, t)$ and $\phi' = \phi^0 + \epsilon \phi^1(\mathbf{x}, t)$, where ϵ is a small parameter. We seek to express the Lagrangian L' in terms of the fields u_b , ϕ^1 , to second order in ϵ . We have, to second order in ϵ ,

$$\phi = \phi^0 + \epsilon u_i \phi_{,i}^0 + \frac{1}{2} \epsilon^2 u_i u_j \phi_{,ij}^0 + \epsilon \phi^1 + \epsilon^2 u_i \phi_{,i}^1 \quad [11]$$

We expand $\rho^0 E[\mathbf{x}, \mathbf{e}]$ to second order in strain

$$\rho^0(\mathbf{x}) E(\mathbf{x}, \mathbf{e}) = a + t_{ij}^0 e_{ij} + \frac{1}{2} c_{ijkl} e_{ij} e_{kl} \quad [12]$$

As a result of their definitions, as first and second derivatives of $\rho^0(\mathbf{x}) E(\mathbf{x}, \mathbf{e})$ with respect to strain, at zero strain, t_{ij}^0 and c_{ijkl} possess the symmetries:

$$t_{ij}^0 = t_{ji}^0 \quad [13]$$

$$c_{ijkl} = c_{jikl} = c_{ijlk} = c_{klji} \quad [14]$$

We use the notation t_{ij}^0 since these expansion coefficients represent the initial stress field. The strain tensor [1] is

$$e_{ij} = \frac{1}{2} \epsilon(u_{i,j} + u_{j,i}) + \frac{1}{2} \epsilon^2 u_{k,i} u_{k,j} \quad [15]$$

Thus, the second-order expansion of L' becomes

$$\begin{aligned} L' = & \iint \left\{ -a - \rho_0 \phi^0 - \frac{1}{8\pi G} \phi_{,i}^0 \phi_{,i}^0 \right. \\ & - \epsilon \left(t_{ij}^0 u_{i,j} + \rho_0 u_i \phi_{,i}^0 + \rho_0 \phi^1 + \frac{1}{4\pi G} \phi_{,i}^0 \phi_{,i}^1 \right) \\ & + \frac{1}{2} \epsilon^2 \left[\rho^0 \dot{u}_k \dot{u}_k - \Lambda_{jilk} u_{i,j} u_{k,l} - \rho^0 u_i u_j \phi_{,ij}^0 \right. \\ & \left. - 2\rho^0 u_j \phi_{,j}^1 - \frac{1}{4\pi G} \phi_{,i}^1 \phi_{,i}^1 \right] \right\} d^3 x dt \end{aligned} \quad [16]$$

where we have introduced

$$\Lambda_{jilk} \equiv \delta_{ik} t_{jl}^0 + c_{ijkl} \quad [17]$$

The Euler–Lagrange equations arising from the requirement that L' be stationary with respect to variations $\delta\mathbf{u}$, $\delta\phi^1$ must hold for each power of ϵ . Thus, the first-order terms give the following equations, which represent the requirement that the initial configuration be in equilibrium under self-gravitation:

$$t_{ij,j}^0 = \rho^0 \phi_{,i}^0 \quad [18]$$

$$\phi_{,ii}^0 = 4\pi G \rho^0 \quad [19]$$

The terms in L' that are independent of ϵ do not contribute to the variation, and thus can be omitted. When [18], [19] are satisfied, there remain only the second-order terms:

$$L'' = \iint \frac{1}{2} \left[\rho^0 \dot{u}_k \dot{u}_k - \Lambda_{jilk} u_{i,j} u_{k,l} - \rho^0 u_i u_j \phi_{,ij}^0 - 2\rho^0 u_i \phi_{,i}^1 - \frac{1}{4\pi G} \phi_{,i}^1 \phi_{,i}^1 \right] d^3 x \, dt \quad [20]$$

In [20] we omit the factor ϵ^2 , absorbing the small parameter into the definitions of the fields \mathbf{u} , ϕ^1 .

The Euler–Lagrange equations corresponding to variations $\delta\mathbf{u}$, $\delta\phi^1$ give the equations of motion

$$\rho^0 (\ddot{u}_i + \phi_{,i}^1 + \phi_{,ij}^0 u_j) = (\Lambda_{jilk} u_{k,l})_j \quad [21]$$

$$\phi_{,jj}^1 = -4\pi G (\rho^0 u_i)_i \quad [22]$$

Welded:	$[t_{ij}^0 n_j]_-^+ = 0$	$[u_i]_-^+ = 0$	$[t_i]_-^+ = 0$		
Frictionless:	$[t_{ij}^0 n_j]_-^+ = 0$	$t_{ij}^0 n_j = n_i \pi^0$	$[u_k n_k]_-^+ = 0$	$[t_i]_-^+ = 0$	$t_i = n_i t_k n_k$
Free:	$t_{ij}^0 n_j = 0$		$t_i = 0$		
All:	$[\phi^0]_-^+ = 0$	$[\phi_{,i}^0]_-^+ = 0$	$[\phi^1]_-^+ = 0$	$[\phi_i^1 + 4\pi G \rho^0 u_i]_-^+ = 0$	
Infinity:	$\phi^0 \rightarrow 0$		$\phi^1 \rightarrow 0$		

where $[]_-^+$ represents the discontinuity of the enclosed quantity accross the boundary.

In the presence of an applied force distribution $f_i = f_i(\mathbf{x}, t)$, per unit volume, the equation of motion [21] becomes

$$\rho^0 (\ddot{u}_i + \phi_{,i}^1 + \phi_{,ij}^0 u_j) - (\Lambda_{jilk} u_{k,l})_j = f_i \quad [25]$$

Taking the Fourier transform in time, we shall also write

$$\rho^0 (-\omega^2 u_i + \phi_{,i}^1 + \phi_{,ij}^0 u_j) - (\Lambda_{jilk} u_{k,l})_j = f_i \quad [26]$$

The variational principle also leads to certain natural boundary conditions at the free surface and at internal boundaries in the case that $\mathbf{r}(\mathbf{x}, t)$ is required to be continuous at such boundaries – so-called ‘welded’ boundaries. These are as given below. We also wish to include the case that the model contains fluid regions, having free-slip, boundary conditions at their interfaces with solid regions – so-called ‘frictionless’ boundaries. The correct treatment of such boundaries introduces complications that, in the interests of giving a concise account, we do not analyze in detail here. [Woodhouse and Dahlen \(1978\)](#) show that it is necessary to include additional terms in the Lagrangian to account for the additional degrees of freedom corresponding to slip (i.e., discontinuous u_i) at such boundaries. The stress boundary conditions are most conveniently stated in terms of the vector t_i defined on the boundary by

$$t_i = \Lambda_{jilk} u_{k,l} n_j - n_i (\pi^0 u_k)_{;k} + \pi^0 u_{k;i} n_k \text{ with } \pi^0 = t_{jk}^0 n_j n_k \quad [23]$$

where n_i is the Unit normal to the boundary, and where the semicolon notation, for example, $u_{k;i}$, is used to indicate differentiation in the surface: $u_{k;i} = u_{k,i} - n_i n_j u_{k,j}$. The complete set of boundary conditions is

where ω is the frequency. We shall employ the transform pair:

$$u_i(\mathbf{x}, \omega) = \int_{-\infty}^{\infty} u_i(\mathbf{x}, t) e^{-i\omega t} dt$$

$$u_i(\mathbf{x}, t) = \frac{1}{2\pi} \int_{-\infty}^{\infty} u_i(\mathbf{x}, \omega) e^{i\omega t} dt \quad [27]$$

Here, and in subsequent equations we rely on the context to distinguish between time-domain and frequency-domain quantities, adopting the convention that if ω appears in an equation then all functions appearing are the Fourier transforms of the original, time-dependent functions.

Earthquake sources can be modeled by choosing particular force distributions f_i . The problem of determining the ‘equivalent body force distribution’ to represent (prescribed) slip on an earthquake fault was originally solved by [Burridge and Knopoff \(1964\)](#) using the elastodynamic representation theorem. A very general and, at the same time, simple approach to the problem of determining body force equivalents is that of [Backus and Mulcahy \(1976\)](#). They argue that an earthquake occurs as a result of the failure of the assumed constitutive law, in the linear case Hooke’s law, relating stress and strain. This leads them to introduce a symmetric tensor quantity $\Gamma_{ij} = \Gamma_{ij}(\mathbf{x}, t)$, called the ‘stress glut’, which represents the failure of Hooke’s law to be satisfied. Importantly, Γ_{ij} (1) will be zero outside the fault zone; (2) will be zero at times before the earthquake, and (3) will have vanishing time derivative at times after slip has ceased. Thus the ‘glut rate’, $\dot{\Gamma}_{ij}$, is compact in space and time. The earlier concept of ‘stress-free strain’, due to [Eshelby \(1957\)](#) is a closely related one. The strain, for slip on a fault, contains δ -function terms at the fault, because the displacement is discontinuous. The stress, on the other hand, is finite on the fault. Thus, there exists a stress-glut – a failure of the stress to satisfy Hooke’s law, and a stress-free strain, that is, a component of the strain field that is not reflected in the stress. The existence of a nonvanishing stress-glut, Γ_{ij} , leads us to replace [21] by

$$\rho^0 \left(\ddot{u}_i + \phi_{,i}^1 + \phi_{,ij}^0 u_j \right) = (\Lambda_{jilk} u_{k,l} - \Gamma_{ij})_j \quad [28]$$

that is,

$$\rho^0 \left(\ddot{u}_i + \phi_{,i}^1 + \phi_{,ij}^0 u_j \right) - (\Lambda_{jilk} u_{k,l})_j = -\Gamma_{ij,j} \quad [29]$$

and thus comparing [25] with [29], the equivalent body force distribution is found to be $f_i = -\Gamma_{ij,j}$. Because $\dot{\Gamma}_{ij}(\mathbf{x}, t)$ is compact in space and time, it is appropriate for calculations at long period and long wavelength to replace it by a δ -function in space and time. Defining the ‘moment tensor’

$$M_{ij} = \int_V \Gamma_{ij}(\mathbf{x}, \infty) d^3x = \int_{-\infty}^{\infty} \int_V \dot{\Gamma}_{ij}(\mathbf{x}, t) d^3x dt \quad [30]$$

where V is the source volume – the region over which Γ_{ij} is nonzero – a suitable form for Γ_{ij} is $\Gamma_{ij}(\mathbf{x}, t) \approx M_{ij} \delta^3(\mathbf{x} - \mathbf{x}_s) H(t - t_s)$, where $H(t)$ is the Heaviside step function, and where \mathbf{x}_s, t_s are the source coordinates. Thus, $f_i \approx -M_{ij} \partial_j \delta^3(\mathbf{x} - \mathbf{x}_s)$

$H(t - t_s)$. In what follows, we shall consider the more general point source

$$f_i = (F_i - M_{ij} \partial_j) \delta^3(\mathbf{x} - \mathbf{x}_s) H(t - t_s) \quad [31]$$

in which M_{ij} is not necessarily symmetric, recognizing that for sources not involving the action of forces external to the Earth, so-called indigenous sources, M_{ij} must be symmetric and F_i must be zero. The solution for a point force F_i is of fundamental theoretical interest since the solution in this case is the Green’s function for the problem, which can be used to construct solutions for any force distribution f_i . Nonsymmetric M_{ij} corresponds to a source which exerts a net torque or couple on the Earth.

The hyperelastic constitutive law based on the internal energy function $E(\mathbf{x}, \mathbf{e})$ needs to be modified to include the effects of energy loss due to such effects as grain boundary sliding and creep. Such ‘anelastic’ effects lead to dissipation of energy (i.e., conversion of elastic stored energy into heat) and thus to the decay, or ‘attenuation’ of seismic waves. In addition, they are responsible for such effects as postseismic relaxation, and the theory developed here is in large part applicable to this problem also. A generalization of the constitutive law which retains linearity is the viscoelastic law, which supposes that stress depends not only on the strain at a given instant, but also on the strain history. This can be written as

$$t_{ij}(t) = \int_{-\infty}^{\infty} c_{ijkl}(t - t') u_{k,l}(t') dt' \quad [32]$$

where t_{ij} is incremental stress. (In fact, it can be shown that the true increment in stress, at a material particle, includes terms in the initial stress: $t_{ij}^1 = c_{ijkl} u_{k,l} + t_{ik}^0 u_{j,k} + t_{jk}^0 u_{i,k} - t_{ij}^0 u_{k,k}$, but this makes no difference to the discussion here.) Thus, the elastic constants become functions of time, relative to a given time t at which the stress is evaluated. Importantly, since stress can depend only upon *past* times, $c_{ijkl}(t)$ must vanish for negative values of t ; that is, it must be a ‘causal’ function of time. In order to recover the strict Hooke’s law, $t_{ij} = c_{ijkl} u_{k,l}$ we need $c_{ijkl}(t) = c_{ijkl} \delta(t)$ (we are distinguishing here between c_{ijkl} unadorned, which has the units of stress, and $c_{ijkl}(t)$, which has the units of stress/time). In the frequency domain, using the convolution theorem,

$$t_{ij}(\omega) = c_{ijkl}(\omega) u_{i,j}(\omega) \quad [33]$$

Because $c_{ijkl}(t)$ is a causal function, its Fourier transform

$$c_{ijkl}(\omega) = \int_0^\infty c_{ijkl}(t)e^{-i\omega t} dt \quad [34]$$

will be analytic, that is, will have no singularities, in the lower half of the complex ω -plane, as the integral (34) will converge unconditionally in the case that ω possesses a negative imaginary part. From [34] $c_{ijkl}(\omega)^* = c_{ijkl}(-\omega^*)$. For our purposes here, the key conclusion is that 'in the frequency domain', it makes virtually no difference to the theory whether the material is hyperelastic, or viscoelastic, as we have simply everywhere to substitute $c_{ijkl}(\omega)$ for c_{ijkl} . In fact, there is even no need to introduce a new notation, but only to remember that now c_{ijkl} can represent a complex quantity depending on ω and analytic in the lower half of the complex ω -plane. When writing equations in the time domain, we have to remember that c_{ijkl} can be a convolution 'operator', acting on the strain. (It may be remarked that the above derivation of the equations of motion, based on Hamilton's principle, is in need of modification if $E(\mathbf{x}, \mathbf{e})$ does not exist. We do not quite know how to do this, but a monograph by Biot (1965) discusses the use of variational principles in the presence of anelastic effects.) Kanamori and Anderson (1977), and references cited therein, is a good source for further information on this topic.

It is often useful to summarize the equations and the boundary conditions by a single simple equation:

$$(\mathcal{H} + \rho^0 \partial_t^2) \mathbf{u} = \mathbf{f} \quad [35]$$

where \mathcal{H} represents the integro-differential operator corresponding to the left side of [25], omitting the term in $\rho^0 \ddot{\mathbf{u}}$, in which ϕ^1 is thought of as a functional of \mathbf{u} that is, as the solution of Poisson's equation [22] corresponding to a given $\mathbf{u}(\mathbf{x}, t)$, together with the boundary conditions relating to ϕ^1 in [24]. Thus, $\mathcal{H}\mathbf{u}$ incorporates the solution of [22]. In the attenuating case, \mathcal{H} also includes the time-domain convolutions arising from the viscoelastic rheology.

1.02.3 The Generalized Spherical Harmonics

The reduction of these equations in spherical coordinates is most easily accomplished through the use of the generalized spherical harmonic formalism (Phinney and Burridge, 1973). Here we describe how this formalism is used, giving some key results

without derivation. We shall use a standard set of Cartesian coordinates (x, y, z) and spherical coordinates (r, θ, ϕ) related by

$$\begin{aligned} x_1 &= x = r \sin \theta \cos \phi \\ x_2 &= y = r \sin \theta \sin \phi \\ x_3 &= z = r \cos \theta \end{aligned} \quad [36]$$

Unit vectors in the coordinate directions are given by

$$\begin{aligned} \hat{\mathbf{r}} &= [\sin \theta \cos \phi, \sin \theta \sin \phi, \cos \theta] \\ \hat{\boldsymbol{\theta}} &= [\cos \theta \cos \phi, \cos \theta \sin \phi, -\sin \theta] \\ \hat{\boldsymbol{\phi}} &= [-\sin \phi, \cos \phi, 0] \end{aligned} \quad [37]$$

Spherical components of vectors and tensors will be written, for example, as $u_\theta = u_k \hat{\theta}_{k,r\phi} = t_{ij}^0 \hat{r}_i \hat{\phi}_j$.

The prescription provided by the generalized spherical harmonic formalism is first to define the 'spherical contravariant components' of the vectors and tenors that appear, and then to expand their dependence on (θ, ϕ) in terms of complete sets of functions appropriate to the particular component. For a tensor of rank p , having spherical components $s_{i_1 i_2 \dots i_p}$, spherical contravariant components are defined by

$$s^{\alpha_1 \alpha_2 \dots \alpha_p} = C^{\dagger \alpha_1 i_1} C^{\dagger \alpha_2 i_2} \times \dots \times C^{\dagger \alpha_p i_p} s_{i_1 i_2 \dots i_p} \quad [38]$$

where indices i_k label the spherical components $i_k \in \{r, \theta, \phi\}$ and where indices α_k take values $\alpha_k \in \{-1, 0, +1\}$; the nonvanishing coefficients $C^{\dagger \alpha i}$ are $C^{\dagger 0r} = 1$, $C^{\dagger \pm 1\theta} = \mp 2^{-1/2}$, $C^{\dagger \pm 1\phi} = 2^{-1/2} i$. The inverse transformation, from spherical contravariant components to spherical components, is

$$s_{i_1 i_2 \dots i_p} = C_{i_1 \alpha_1} C_{i_2 \alpha_2} \times \dots \times C_{i_p \alpha_p} s^{\alpha_1 \alpha_2 \dots \alpha_p} \quad [39]$$

with $C_{i\alpha} = (C^{\dagger \alpha i})^*$. The spherical harmonic basis, $Y_l^{Nm}(\theta, \phi)$ appropriate for each contravariant component is determined by the sum $N = \alpha_1 + \alpha_2 + \dots + \alpha_p$ of its indices. Thus, we expand

$$\begin{aligned} s^{\alpha_1 \alpha_2 \dots \alpha_p} &= \sum_{lm} s_{lm}^{\alpha_1 \alpha_2 \dots \alpha_p}(r) Y_l^{Nm}(\theta, \phi) \quad \text{with} \\ N &= \alpha_1 + \alpha_2 + \dots + \alpha_p \end{aligned} \quad [40]$$

$Y_l^{Nm}(\theta, \phi)$ are the generalized spherical harmonics:

$$Y_l^{Nm}(\theta, \phi) = P_l^{Nm}(\cos \theta) e^{im\phi} = d_{Nm}^{(l)}(\theta) e^{im\phi} \quad [41]$$

where the 'real' quantities $d_{Nm}^{(l)}(\theta) = P_l^{Nm}(\cos \theta)$ are rotation matrix elements employed in the quantum mechanical theory of angular momentum (Edmonds, 1960); thus, Y_l^{Nm} vanish for N or m outside the range $-l$ to l . In [40] summations over l and m are for

integers $l=0, 1, \dots, \infty, m=-l, -l+1, \dots, l$. The spherical harmonic degree l characterizes a group representation of the rotation group; as a consequence, tensor fields that are spherically symmetric have only the term with $l=0, N=0, m=0$. The property of the rotation matrix elements

$$d_{Nm}^{(l)}(0) = \begin{cases} 1, & \text{if } m=N \text{ and } l \geq |N| \\ 0, & \text{otherwise} \end{cases} \quad [42]$$

is a very useful one, for example, for calculations of source excitation coefficients when it is required to evaluate spherical harmonic expressions for $\theta=0$ (see below). Equation [42] says that regarded as $(2l+1) \times (2l+1)$ matrix, having row index N and column index m , $d_{Nm}^{(l)}(0)$ is the unit matrix. Matrices $d_{Nm}^{(l)}(\theta)$ have symmetries $d_{-N-m}^{(l)}(\theta) = d_{mN}^{(l)}(\theta) = (-1)^{m-N} d_{Nm}^{(l)}(\theta)$, from which follows the relation $Y_l^{Nm}(\theta, \phi)^* = (-1)^{m-N} Y_l^{-N-m}(\theta, \phi)$ where asterick denotes the complex conjugate.

Y_l^{Nm} satisfy the orthogonality relation

$$\int_{-\pi}^{\pi} \int_0^{\pi} Y_l^{Nm'}(\theta, \phi)^* Y_l^{Nm}(\theta, \phi) \times \sin \theta d\theta d\phi = \frac{4\pi}{2l+1} \delta_{l'l} \delta_{m'm} \quad [43]$$

Thus, the expansion coefficients in [40] can be written as

$$\begin{aligned} s_{lm}^{\alpha_1 \alpha_2 \dots \alpha_p}(r) &= \frac{2l+1}{4\pi} \int_{-\pi}^{\pi} \int_0^{\pi} Y_l^{Nm}(\theta, \phi)^* s^{\alpha_1 \alpha_2 \dots \alpha_p} \\ &\quad \times \sin \theta d\theta d\phi \quad \text{with} \\ N &= \alpha_1 + \alpha_2 + \dots + \alpha_p \end{aligned} \quad [44]$$

Other normalizations for the spherical harmonics have frequently been used in the literature.

Completely normalized spherical harmonics can be written as $Y_l^m(\theta, \phi) = \nu_l Y_l^{0m}$, where $\nu_l \equiv \sqrt{(2l+1)/4\pi}$. In this chapter we shall adopt the same conventions as in the paper by [Phinney and Burridge \(1973\)](#) for the generalized spherical harmonics, using the explicit form $\nu_l Y_l^{0m}$ when completely normalized spherical harmonics are needed.

The following is the key property of the generalized spherical harmonics under differentiation:

$$(\pm \partial_\theta + i \csc \theta \partial_\phi) Y_l^{Nm} = \sqrt{2} \Omega_{\pm N}^l Y_l^{N \mp 1m} - N \cot \theta Y_l^{Nm} \quad [45]$$

which leads to the following rule for the expansion coefficients of the gradient of a tensor:

$$\begin{aligned} s_{lm}^{\alpha_1 \alpha_2 \dots \alpha_p | 0} &= \frac{d}{dr} s_{lm}^{\alpha_1 \alpha_2 \dots \alpha_p} \\ s_{lm}^{\alpha_1 \alpha_2 \dots \alpha_p | \pm} &= r^{-1} \Omega_{\mp N}^l s_{lm}^{\alpha_1 \alpha_2 \dots \alpha_p} \\ - r^{-1} \left(\begin{array}{l} \text{the sum of the terms obtained} \\ \text{from } s_{lm}^{\alpha_1 \alpha_2 \dots \alpha_p} \text{ by adding } \pm 1 \text{ to each} \\ \text{of } \alpha_1 \alpha_2 \dots \alpha_p \text{ in turn, omitting any} \\ \text{terms for which the resulting} \\ \text{index } \alpha_k \pm 1 \notin \{-1, 0, 1\} \end{array} \right) \end{aligned} \quad [46]$$

where $\Omega_N^l \equiv [(l+N)(l-N+1)/2]^{1/2}$ and $N \equiv \alpha_1 + \alpha_2 + \dots + \alpha_p$. The notation $s_{lm}^{\alpha_1 \alpha_2 \dots \alpha_p | \alpha_{p+1}}$ is used to denote the expansion coefficients of the spherical contravariant components of the tensor having Cartesian components $s_{i_1 i_2 \dots i_p i_{p+1}}$. Contraction over contravariant indices is carried out using the metric tensor $g_{\alpha_1 \alpha_2} = C_{i\alpha_1} C_{i\alpha_2}$, which has nonvanishing entries $g_{00} = 1, g_{+-} = g_{-+} = -1$. Thus, for example, the expansion coefficients of the divergence of a tensor $t_i = s_{ij,j}$, say, are given by

$$\begin{aligned} t_{lm}^\alpha &= -s_{lm}^{\alpha+|-} + s_{lm}^{\alpha|0|0} - s_{lm}^{\alpha-|+} = \begin{cases} -s_{lm}^{-+|-} + s_{lm}^{-0|0} - s_{lm}^{-|-+}, & \alpha = -1 \\ -s_{lm}^{0+|-} + s_{lm}^{00|0} - s_{lm}^{0-|+}, & \alpha = 0 \\ -s_{lm}^{++|-} + s_{lm}^{+0|0} - s_{lm}^{+-|+}, & \alpha = 1 \end{cases} \\ &= \begin{cases} -\frac{1}{r} (\Omega_0^l s_{lm}^{-+} - s_{lm}^{-0}) + \frac{d}{dr} s_{lm}^{-0} - \frac{1}{r} (\Omega_2^l s_{lm}^{-}- - s_{lm}^{0-} - s_{lm}^{-0}), & \alpha = -1 \\ -\frac{1}{r} (\Omega_1^l s_{lm}^{0+} - s_{lm}^{-+} - s_{lm}^{00}) + \frac{d}{dr} s_{lm}^{00} - \frac{1}{r} (\Omega_1^l s_{lm}^{0-} - s_{lm}^{+-} - s_{lm}^{00}), & \alpha = 0 \\ -\frac{1}{r} (\Omega_2^l s_{lm}^{++} - s_{lm}^{0+} - s_{lm}^{+0}) + \frac{d}{dr} s_{lm}^{+0} - \frac{1}{r} (\Omega_0^l s_{lm}^{+-} - s_{lm}^{+0}), & \alpha = 1 \end{cases} \end{aligned} \quad [47]$$

The major advantage of this formalism is that, in a spherically symmetric system, it enables vector and tensor relations to be transformed into relations for

spherical harmonic coefficients, by the application of a straightforward set of rules. Importantly, the resulting relations (1) are true for each value of l and m

separately, and (2) are the same for each spherical harmonic order m .

The treatment of aspherical systems requires results for the products of spherical harmonic expansions. It can be shown that

$$\begin{aligned} Y_l^{N_1 m_1} Y_{l_2}^{N_2 m_2} &= (-1)^{N_1 + N_2 - m_1 - m_2} \sum_{l=|l_1-l_2|}^{l_1+l_2} (2l+1) \\ &\times \begin{pmatrix} l & l_1 & l_2 \\ -N_1 - N_2 & N_1 & N_2 \end{pmatrix} \\ &\times \begin{pmatrix} l & l_1 & l_2 \\ -m_1 - m_2 & m_1 & m_2 \end{pmatrix} Y_l^{N_1 + N_2 m_1 + m_2} \quad [48] \end{aligned}$$

Where the so-called ‘Wigner 3-j symbols’ are the (real) quantities arising in the theory of the coupling of angular momentum in quantum mechanics (see Edmonds (1960)). These satisfy

unless:

$$\begin{aligned} |l_2 - l_3| &\leq l_1, |l_3 - l_1| \leq l_2, |l_1 - l_2| \leq l_3, \\ \begin{pmatrix} l_1 & l_2 & l_3 \\ m_1 & m_2 & m_3 \end{pmatrix} &= 0 \quad \text{any one of which implies the other two} \\ |m_1| &\leq l_1, |m_2| \leq l_2, |m_3| \leq l_3 \\ m_1 + m_2 + m_3 &= 0 \end{aligned} \quad [49]$$

The 3-j symbol is symmetric under even permutations of its columns, and either symmetric or antisymmetric under odd permutations, depending upon whether $l_1 + l_2 + l_3$ is even or odd. This has the consequence that if the sum of the l s is odd and if the m s are zero, the 3-j symbol is 0. Equation [48] leads to the following result for the spherical harmonic coefficients of the product of two tensor fields; suppose that $c_{i_1 i_2 \dots i_p j_1 j_2 \dots j_q} = a_{i_1 i_2 \dots i_p} b_{j_1 j_2 \dots j_q}$; then

$$\begin{aligned} c_{lm}^{\alpha_1 \alpha_2 \dots \alpha_p \beta_1 \beta_2 \dots \beta_q} &= (-1)^{N_1 + N_2 - m} \\ &\times \sum_{l_1 l_2 m_1} \begin{pmatrix} l & l_1 & l_2 \\ -N_1 - N_2 & N_1 & N_2 \end{pmatrix} \\ &\times \begin{pmatrix} l & l_1 & l_2 \\ -m & m_1 & m - m_1 \end{pmatrix} a_{l_1 m_1}^{\alpha_1 \alpha_2 \dots \alpha_p} b_{l_2 m - m_1}^{\beta_1 \beta_2 \dots \beta_q} \quad [50] \end{aligned}$$

The summations here are over all values of l, l_1, m_1 ; however, it is a ‘finite’ sum by virtue of the fact that the terms vanish for values outside the ranges specified in [49].

As an application of the spherical harmonic formalism, here we consider the expansion of the point force distribution [31] in spherical harmonics. It will be sufficient to locate the source at time $t_s = 0$ and at a point on the positive z-axis, that is, at $x = 0, y = 0, z = r_s$, where r_s is the source radius. Because $\theta = 0$ is a singular point in the spherical coordinate system, we

shall consider the limit as the source approaches the ‘pole’, $\theta_s = 0$, along the ‘meridian’, $\phi_s = 0$. In the frequency domain, [31] becomes

$$f_i = \frac{1}{i\omega} (F_i - M_{ij} \hat{\partial}_j) r^{-2} \csc \theta \delta(\theta - \theta_s) \delta(\phi) \delta(r - r_s) \quad [51]$$

In the limiting process, $\theta_s \rightarrow 0$, we shall take F_i, M_{ij} to have constant spherical components $F_\phi, M_m, M_{r\theta}$, etc. As $\theta_s \rightarrow 0$, the $\hat{\theta}, \hat{\phi}$, and \hat{r} directions end up pointing along the x, y, z directions, respectively, of the global Cartesian coordinate system (e.g, see eqn [37]), and thus although $\hat{\theta}, \hat{\phi}$ are undefined at $\theta = 0$, we can nevertheless interpret the spherical components $F_\phi, M_{r\theta}$, etc., as representing the components F_y, M_{zx} , etc., of the point force and moment tensor in the global Cartesian system. Let χ represent the expression $\chi = (i\omega)^{-1} r^{-2} \csc \theta \delta(\theta - \theta_s) \delta(\phi) \delta(r - r_s)$, so that [51] can be written as $f_i = F_i \chi - \partial_i M_{ij} \chi$. The spherical contravariant components of F_i and M_{ij} using a matrix representation of [39], are given by

$$\begin{aligned} \begin{bmatrix} F^- \\ F^0 \\ F^+ \end{bmatrix} &= \begin{pmatrix} \frac{1}{\sqrt{2}} & \frac{i}{\sqrt{2}} & 0 \\ 0 & 0 & 1 \\ -\frac{1}{\sqrt{2}} & \frac{i}{\sqrt{2}} & 0 \end{pmatrix} \begin{bmatrix} F_\theta \\ F_\phi \\ F_r \end{bmatrix} \\ \begin{pmatrix} M^{-} & M^{0-} & M^{-+} \\ M^{0-} & M^{00} & M^{0+} \\ M^{+-} & M^{+0} & M^{++} \end{pmatrix} &= \begin{pmatrix} \frac{1}{\sqrt{2}} & \frac{i}{\sqrt{2}} & 0 \\ 0 & 0 & 1 \\ -\frac{1}{\sqrt{2}} & \frac{i}{\sqrt{2}} & 0 \end{pmatrix} \quad [52] \\ \times \begin{pmatrix} M_{\theta\theta} & M_{\theta\phi} & M_{\theta r} \\ M_{\phi\theta} & M_{\phi\phi} & M_{\phi r} \\ M_{r\theta} & M_{r\phi} & M_{rr} \end{pmatrix} &\begin{pmatrix} \frac{1}{\sqrt{2}} & 0 & -\frac{1}{\sqrt{2}} \\ \frac{i}{\sqrt{2}} & 0 & \frac{i}{\sqrt{2}} \\ 0 & 1 & 0 \end{pmatrix} \end{aligned}$$

The spherical harmonic expansion coefficients of $F^\alpha \chi$ and $M^{\alpha_1 \alpha_2} \chi$, for which we use the notation $(F^\alpha \chi)_{lm}, (M^{\alpha_1 \alpha_2} \chi)_{lm}$, are immediate using [44], integrating out the δ -functions contained in χ . We obtain

$$\begin{aligned} (F^\alpha \chi)_{lm} &= \frac{2l+1}{4\pi i\omega} \frac{\delta(r-r_s)}{r^2} Y_l^{\alpha m}(\theta_s, 0)^* F^\alpha \\ &= \frac{2l+1}{4\pi i\omega} \frac{\delta(r-r_s)}{r^2} d_{\alpha m}^{(l)}(\theta_s) F^\alpha \\ &= \begin{cases} \frac{2l+1}{4\pi i\omega} \frac{\delta(r-r_s)}{r^2} F^\alpha, & \text{if } m = \alpha \text{ and } l \geq |\alpha| \\ 0, & \text{otherwise} \end{cases} \quad [53] \end{aligned}$$

where θ_s has been set to 0 in the second line, using [42]. Similarly,

$$\begin{aligned} & (M^{\alpha_1 \alpha_2} \chi)_{lm} \\ &= \frac{2l+1}{4\pi i \omega} \frac{\delta(r-r_s)}{r^2} Y_l^{\alpha_1 + \alpha_2 m}(\theta_s, 0)^* M^{\alpha_1 \alpha_2} \\ &= \frac{2l+1}{4\pi i \omega} \frac{\delta(r-r_s)}{r^2} d_{\alpha_1 + \alpha_2 m}^{(l)}(\theta_s) M^{\alpha_1 \alpha_2} \\ &= \begin{cases} \frac{2l+1}{4\pi i \omega} \frac{\delta(r-r_s)}{r^2} M^{\alpha_1 \alpha_2}, & \text{if } m = \alpha_1 + \alpha_2 \\ 0, & \text{otherwise} \end{cases} \quad [54] \end{aligned}$$

To complete the evaluation of the coefficients f_{lm}^{α} corresponding to [51], we need to find the spherical

harmonic coefficients of the divergence of the field represented in [54], for which we can employ [47]; we find

$$\begin{bmatrix} f_{lm}^- \\ f_{lm}^0 \\ f_{lm}^+ \end{bmatrix} = \begin{bmatrix} (F^- \chi)_{lm} + (M^{-+} \chi)_{lm}^{|-} - (M^{-0} \chi)_{lm}^{|0} \\ +(M^{--} \chi)_{lm}^{|+} \\ (F^0 \chi)_{lm} + (M^{0+} \chi)_{lm}^{|-} - (M^{00} \chi)_{lm}^{|0} \\ +(M^{0-} \chi)_{lm}^{|+} \\ (F^+ \chi)_{lm} + (M^{++} \chi)_{lm}^{|-} - (M^{+0} \chi)_{lm}^{|0} \\ +(M^{+-} \chi)_{lm}^{|+} \end{bmatrix} \quad [55]$$

$$\begin{aligned} & \left(\begin{bmatrix} M^{--} \Omega_2^l r^{-1} \\ 0 \\ 0 \end{bmatrix} \frac{\delta(r-r_s)}{r^2}, \quad m = -2, l \geq 2 \right. \\ & \left. \begin{bmatrix} F^- - M^{-0} \partial_r - 2M^{-0} r^{-1} - M^{0-} r^{-1} \\ M^{0-} \Omega_1^l r^{-1} \\ 0 \end{bmatrix} \frac{\delta(r-r_s)}{r^2}, \quad m = -1, l \geq 1 \right. \\ & \left. \begin{bmatrix} M^{-+} \Omega_0^l r^{-1} \\ F_0 - M^{00} \partial_r - 2M^{00} r^{-1} - M^{-+} r^{-1} - M^{+-} r^{-1} \\ M^{+-} \Omega_0^l r^{-1} \end{bmatrix} \frac{\delta(r-r_s)}{r^2}, \quad m = 0 \right. \\ & \left. \begin{bmatrix} 0 \\ M^{0+} \Omega_1^l r^{-1} \\ F^+ - M^{+0} \partial_r - 2M^{+0} r^{-1} - M^{0+} r^{-1} \end{bmatrix} \frac{\delta(r-r_s)}{r^2}, \quad m = 1, l \geq 1 \right. \\ & \left. \begin{bmatrix} 0 \\ 0 \\ M^{++} \Omega_2^l r^{-1} \end{bmatrix} \frac{\delta(r-r_s)}{r^2}, \quad m = 2, l \geq 2 \right) \\ & = \frac{2l+1}{4\pi i \omega} \times \end{aligned} \quad [56]$$

These are the spherical harmonic coefficients of the force distribution (31) which will be needed in the following sections. The coefficients are zero for $|m| > 2$.

1.02.4 The Green's Function for the Spherically Symmetric Earth

We consider here the case in which the Earth model is spherically symmetric. In this case the equations of

motion are separable in spherical coordinates, and thus can be solved by reduction to ordinary differential equations. Since deviations from spherical symmetry are relatively small in the Earth, they can subsequently be treated by perturbation theory. We assume that in the initial equilibrium configuration the stress is hydrostatic, that is,

$$\tau_{ij}^0 = -p^0 \delta_{ij} \quad [57]$$

Spherical symmetry requires that ρ^0, ϕ^0, p^0 are functions only of r . The gravitational acceleration is

$g_i^0 = \phi_{,i}^0 = g^0(r)\hat{r}_i$, and the equilibrium equations [18], [19], and the boundary conditions in [24] have the solutions:

$$\begin{aligned} g^0(r) &= \frac{4\pi G}{r^2} \int_0^r \rho^0(r) dr \\ \phi^0(r) &= - \int_r^\infty g^0(r) dr \\ \rho^0(r) &= \int_r^a \rho^0(r) g^0(r) dr \end{aligned} \quad [58]$$

where a is the radius of the Earth. The equations of motion [25] with [17] and [19] can be put into the form

$$\rho \left[-\omega^2 u_i - u_{k,k} g_i + \varphi_{,i} + (u_k g_k)_{,i} \right] - (C_{ijkl} u_{k,l})_{,j} = f_i \quad [59]$$

$$(\varphi_{,k} + 4\pi G\rho u_k)_{,k} = 0 \quad [60]$$

where we have introduced the effective stiffness tensor

$$C_{ijkl} = c_{ijkl} + p^0 (\delta_{ij}\delta_{kl} - \delta_{il}\delta_{jk} - \delta_{ik}\delta_{jl}) \quad [61]$$

which has the same symmetries (eqn [14]) as does c_{ijkl} . In [59], [60], and in subsequent equations, we drop the superscripts in ρ^0, g^0 , using simply ρ, g for these quantities. We also use the notation φ in place of ϕ^1 . The applied force distribution f_i will be taken to be that given in [31] and [51], having the spherical harmonic coefficients [56].

In a spherically symmetric model, the tensor field C_{ijkl} must be a spherically symmetric tensor field, and therefore its spherical harmonic expansion will have terms only of degree $l=0$. Its spherical contravariant components $C^{\alpha_1\alpha_2\alpha_3\alpha_3} = C_{00}^{\alpha_1\alpha_2\alpha_3\alpha_3}$ must have indices that sum to zero, and must also satisfy the usual elastic tensor symmetries [14]. It is easily seen that there are only five independent components that satisfy these requirements: $C^{0000}, C^{+-00}, C^{+0-0}, C^{++--}, C^{+-+-}$, which must be real (in the nonattenuating case) in order that the spherical components C_{ijkl} are real. Conventionally, these are designated (Love, 1927; Takeuchi and Saito, 1972) as

$$\begin{aligned} C^{0000} &= C(r), \quad C^{+-00} = -F(r), \quad C^{+0-0} = -L(r) \\ C^{++--} &= 2N(r), \quad C^{+-+-} = A(r) - N(r) \end{aligned} \quad [62]$$

the independent spherical components being (using [39])

$$\begin{aligned} C_{rrr} &= C(r), \quad C_{rr\theta\theta} = C_{rr\phi\phi} = F(r) \\ C_{r\theta r\theta} &= C_{r\phi r\phi} = L(r), \quad C_{\theta\phi\theta\phi} = N(r) \\ C_{\theta\theta\phi\phi} &= A(r) - 2N(r), \quad C_{\theta\theta\theta\theta} = C_{\phi\phi\phi\phi} = A(r) \end{aligned} \quad [63]$$

The mean ‘bulk modulus’ κ and ‘shear modulus’ μ can be defined by

$$\begin{aligned} \kappa &= \frac{1}{9} C_{i\bar{i}\bar{j}\bar{j}} = \frac{1}{9} (4A + C - 4N + 4F) \\ \mu &= \frac{1}{10} C_{i\bar{i}\bar{j}\bar{j}} - \frac{1}{30} C_{i\bar{i}\bar{i}\bar{j}} = \frac{1}{15} (A + C + 6L + 5N - 2F) \end{aligned} \quad [64]$$

Other conventional notations are

$$\begin{aligned} \lambda &= \kappa - \frac{2}{3}\mu, \quad v_{PV}^2 = C/\rho, \quad v_{PH}^2 = A/\rho, \quad v_{SV}^2 = L/\rho \\ v_{SH}^2 &= N/\rho, \quad \eta = F/(A-2L) \end{aligned} \quad [65]$$

In the case that the material is ‘isotropic’, $A = C = \lambda + 2\mu = \kappa + \frac{4}{3}\mu$, $N = L = \mu$, and $\eta = 1$.

Now we seek solutions u_i, φ [59], [60] in terms of spherical harmonic expansions. It is convenient to write

$$u_{lm}^- = \nu_l \Omega_0^l [V_{lm}(r) - iW_{lm}(r)] \quad [66]$$

$$u_{lm}^0 = \nu_l U_{lm}(r) \quad [67]$$

$$u_{lm}^+ = \nu_l \Omega_0^l [V_{lm}(r) + iW_{lm}(r)] \quad [68]$$

where $\nu_l = \sqrt{(2l+1/4\pi)}$, as the ‘ U, V, W ’ notation is almost universally used in the literature on long period seismology. The expansion corresponding to [40] is then equivalent to the vector spherical harmonic representation (e.g., Morse and Feshbach, 1953):

$$\begin{aligned} u_r &= \sum_{lm} U_{lm}(r) \nu_l Y_l^{0m}(\theta, \phi) \\ u_\theta &= \sum_{lm} [V_{lm}(r) \partial_\theta + W_{lm}(r) \csc \theta \partial_\phi] \nu_l Y_l^{0m}(\theta, \phi) \\ u_\phi &= \sum_{lm} [V_{lm}(r) \csc \theta \partial_\phi - W_{lm}(r) \partial_\theta] \nu_l Y_l^{0m}(\theta, \phi) \end{aligned} \quad [69]$$

We shall abbreviate such vector spherical harmonic expansions using the shorthand

$$u_i \rightarrow \begin{bmatrix} U_{lm}(r) \\ V_{lm}(r) \\ W_{lm}(r) \end{bmatrix} \quad [70]$$

meaning that the vector field having Cartesian components u_i is expressible in vector spherical harmonics as in [69]. We shall also suppress the suffices l, m and the explicit dependence upon r , writing simply U, V, W .

The spherical harmonic expansion of f_i can also be converted into this vector spherical harmonic notation. Using [56] with [52], we obtain

$$f_i \rightarrow \frac{\nu_l}{i\omega} \left\{ \begin{array}{l} \left[\begin{array}{c} (rF_r + M_{\theta\theta} + M_{\phi\phi})\delta^{(0)}(r) - M_{rr}\delta^{(1)}(r) \\ \frac{1}{2}(-M_{\theta\theta} - M_{\phi\phi})\delta^{(0)}(r) \\ \frac{1}{2}(-M_{\theta\phi} + M_{\phi\theta})\delta^{(0)}(r) \end{array} \right], \quad m = 0 \\ \left[\begin{array}{c} \frac{\zeta}{2}(\mp M_{r\theta} + iM_{r\phi})\delta^{(0)}(r) \\ \frac{1}{2\zeta}[(\mp rF_\theta + irF_\phi \pm M_{r\theta} - iM_{r\phi})\delta^{(0)}(r) + (\pm M_{\theta r} - iM_{\phi r})\delta^{(1)}(r)] \\ \mp \frac{i}{2\zeta}[(\mp rF_\theta + irF_\phi \pm M_{r\theta} - iM_{r\phi})\delta^{(0)}(r) + (\pm M_{\theta r} - iM_{\phi r})\delta^{(1)}(r)] \end{array} \right], \quad m = \pm 1 \\ \left[\begin{array}{c} 0 \\ \frac{1}{4\zeta}\sqrt{\zeta^2 - 2}(M_{\theta\theta} - M_{\phi\phi} \mp iM_{\theta\phi} \mp iM_{\phi\theta})\delta^{(0)}(r) \\ \mp \frac{i}{4\zeta}\sqrt{\zeta^2 - 2}(M_{\theta\theta} - M_{\phi\phi} \mp iM_{\theta\phi} \mp iM_{\phi\theta})\delta^{(0)}(r) \end{array} \right], \quad m = \pm 2 \end{array} \right. \quad [71]$$

where $\delta^{(0)}(r) = r^{-3}\delta(r-r_s)$ and $\delta^{(1)}(r) = r^{-2}\delta'(r-r_s)$ and where $\zeta = \sqrt{l(l+1)}$.

Using the spherical harmonic formalism, the vector spherical harmonic representation of the ‘radial tractions’ is given by

$$C_{ijkl}u_{k,l}\hat{r_j} \rightarrow \begin{cases} P = Fr^{-1}(2U - \zeta^2 V) + C\partial_r U \\ S = L(\partial_r V - r^{-1}V + r^{-1}U) \\ T = L(\partial_r W - r^{-1}W) \end{cases} \quad [72]$$

where we have introduced traction scalars $P = P_{lm}(r)$, $S = S_{lm}(r)$, $T = T_{lm}(r)$. Because the

radial tractions are required to be continuous at interfaces between different regions of the model (from [24]), it is usual to treat them as new dependent variables, and to express the derivatives $\partial_r U$, $\partial_r V$, $\partial_r W$ in terms of them:

$$\begin{aligned} \partial_r U &= -r^{-1}FC^{-1}(2U - \zeta^2 V) + C^{-1}P \\ \partial_r V &= r^{-1}(V - U) + L^{-1}S \\ \partial_r W &= r^{-1}W + L^{-1}T \end{aligned} \quad [73]$$

The vector spherical harmonic expansion of the left side of [59] becomes

$$f_i \rightarrow \begin{cases} -\rho\omega^2 U + 2r^{-2}(A - N)(2U - \zeta^2 V) + \rho(\partial_r g - 2r^{-1}g)U + \zeta^2 r^{-1}\rho g V - \partial_r P + 2r^{-1}F\partial_r U - 2r^{-1}P + r^{-1}\zeta^2 S + \rho\partial_r \varphi \\ -\rho\omega^2 V - r^{-2}A(2U - \zeta^2 V + 2r^{-2}N(U - V)) + r^{-1}\rho(gU + \varphi) - \partial_r S - 3r^{-1}S - r^{-1}\partial_r U \\ -\rho\omega^2 W + r^{-2}N(\zeta^2 - 2)W - \partial_r T - 3r^{-1}T \end{cases} \quad [74]$$

Thus, ordinary differential equations in r for U, V, W, P, S, T are obtained by equating these to the forcing terms in [71]. In addition, the expansion coefficients of the perturbation in gravitational potential, $\varphi = \varphi_{lm}(r)$, are subject to equations derived from (60). The boundary conditions [24] require that φ and $\partial_r \varphi + 4\pi G\rho U$ are continuous throughout the model, and that φ vanishes at infinity. For a given spherical harmonic degree l the solutions of Laplace’s equation tending to zero at infinity are proportional to r^{-l-1} , and for this reason it is useful to define the new dependent variable

$\psi = \partial_r \varphi + (l+1)r^{-1}\varphi + 4\pi G\rho U$, so that ψ is continuous throughout the model and vanishes at the surface. This leads to the following coupled equations for $\varphi_{lm}(r)$, $\psi_{lm}(r)$:

$$\begin{aligned} \partial_r \varphi &= \psi - (l+1)r^{-1}\varphi - 4\pi G\rho U \\ \partial_r \psi &= 4\pi G\rho r^{-1}(\zeta^2 V - (l+1)U) + r^{-1}(l-1)\psi \end{aligned} \quad [75]$$

Thus, the complete boundary-value problem for $\mathbf{u}(\mathbf{x}, \omega)$ is to find, for each l, m , solutions $U_{lm}(r)$, $V_{lm}(r)$, $W_{lm}(r)$, $\phi_{lm}(r)$, $P_{lm}(r)$, $S_{lm}(r)$, $T_{lm}(r)$, $\psi_{lm}(r)$, satisfying (1) equality of the expressions in [71] and [74], (2) eqns [73] – in essence definitions of P , S ,

$T -$ and (3) eqns [75] governing the self-gravitation. The equations governing W and T are independent of the others, and so the problem naturally separates into the problems for the six functions U, V, ϕ, P, S, ψ , relating to 'spheroidal' motion, and for the two functions W, T , relating to 'toroidal' motion. In a fluid region, shear stresses are required to vanish, resulting in $S = 0$ and $L = N = 0, A = C = F$; the second equation in [72] drops out and the equation arising from the second of [74] can be solved for $V, V = (gU - P/\rho + \varphi)/r\omega^2$,

$$\text{Spheroidal solid: } \mathbf{y}^{Ss} = \begin{bmatrix} rU \\ r\zeta V \\ r\phi \\ rP \\ r\zeta S \\ r\psi/4\pi G \end{bmatrix}, \quad \text{Spheroidal fluid: } \mathbf{y}^{Sf} = \begin{bmatrix} rU \\ r\phi \\ rP \\ r\psi/4\pi G \end{bmatrix}, \quad \text{Radial: } \mathbf{y}^R = \begin{bmatrix} rU \\ rP \end{bmatrix} \quad [76]$$

$$\text{Toroidal solid: } \mathbf{y}^{Ts} = \begin{bmatrix} r\zeta W \\ r\zeta T \end{bmatrix}$$

In each case, the resulting equations take the form

$$\frac{d\mathbf{y}}{dr} = \mathbf{A}\mathbf{y} + \mathbf{a}\delta(r - r_s) + \mathbf{b}\delta'(r - r_s) \quad [77]$$

where the vectors $\mathbf{a} = \mathbf{a}(r, \omega, l, m)$, $\mathbf{b} = \mathbf{b}(r, \omega, l, m)$ can be readily derived from [71], and where the matrices $\mathbf{A} = \mathbf{A}(r, \omega, l)$ can be written in terms of submatrices in the form

$$\mathbf{A} = \begin{pmatrix} \mathbf{T} & \mathbf{K} \\ \mathbf{S} & -\mathbf{T}' \end{pmatrix} \quad [78]$$

where \mathbf{K} and \mathbf{S} are symmetric and where \mathbf{T}' is the transpose of \mathbf{T} . The fact that the equations have this special form stems from the fact that they arise from a variational principle, and in fact are a case of Hamilton's canonical equations (Woodhouse, 1974; Chapman and Woodhouse, 1981). However, the usual variational derivations of the equations of motion neglect attenuation, and so it is interesting that this symmetry of the equations remains valid in the attenuating case. It plays an important part in methods of calculation of normal

and thus S and V can be eliminated from the equations, resulting in equations for the four remaining variables U, ϕ, P, ψ . The case $l=0$ leads to purely radial motion, $V=0$ with $\psi = \varphi/r$, $d\varphi/dr = -4\pi G\rho U$, and the effective equations involve only U, P . The equations are most conveniently stated as matrix differential equations, by rearranging them to give the radial derivatives of either the six, four or two functions to be determined in terms of the functions themselves. Here we define 'stress displacement vectors' as follows:

modes (see below), and also enables a complex version of the theory in attenuating media to be developed along the same lines (AL-Attar, 2007). It will later be useful to introduce the partitioned matrix

$$\Sigma = \begin{pmatrix} 0 & 1 \\ -1 & 0 \end{pmatrix}$$

where 1 is the unit matrix of appropriate dimension, so that the matrix

$$\Sigma\mathbf{A} = \begin{pmatrix} \mathbf{S} & -\mathbf{T}' \\ -\mathbf{T} & -\mathbf{K} \end{pmatrix}$$

is symmetric. We shall also make use of the fact (Woodhouse, 1988) that in the non-attenuating case, $-\Sigma\mathbf{A}_\lambda$, by which we shall mean the partial derivative of \mathbf{A} with respect to $\lambda = \omega^2$, is positive semidefinite, i.e. that $\mathbf{y}'(-\Sigma\mathbf{A}_\lambda)\mathbf{y} \geq 0$ for any real column \mathbf{y} , as can be verified using the following forms for the submatrices of \mathbf{A} . The specific forms of matrices $\mathbf{T}, \mathbf{K}, \mathbf{S}$ are:

$$\mathbf{T}^{Ss} = \begin{pmatrix} (1-2F/C)/r & \zeta F/Cr & 0 \\ -\zeta/r & 2/r & 0 \\ -4\pi G\rho & 0 & -l/r \end{pmatrix}, \quad \mathbf{K}^{Ss} = \begin{pmatrix} 1/C & 0 & 0 \\ 0 & 1/L & 0 \\ 0 & 0 & 4\pi G \end{pmatrix}$$

$$\mathbf{S}^{Ss} = \begin{pmatrix} -\rho\omega^2 + 4(\gamma - \rho gr)/r^2 & \zeta(\rho gr - 2\gamma)/r^2 & -\rho(l+1)/r \\ \zeta(\rho gr - 2\gamma)/r^2 & -\rho\omega^2 + [\zeta^2(\gamma + N) - 2N]/r^2 & \rho\zeta/r \\ -\rho(l+1)/r & \rho\zeta/r & 0 \end{pmatrix} \quad [79]$$

$$\mathbf{T}^{\text{sf}} = \begin{pmatrix} (g\zeta^2/\omega^2 r - 1)/r & \zeta^2/\omega^2 r^2 \\ -4\pi G\rho & -l/r \end{pmatrix}$$

$$\mathbf{K}^{\text{sf}} = \begin{pmatrix} 1/C - \zeta^2/\rho\omega^2 r^2 & 0 \\ 0 & 4\pi G \end{pmatrix} \quad [80]$$

$$\mathbf{S}^{\text{sf}} = \begin{pmatrix} -\rho\omega^2 + \rho g & \rho(g\zeta^2/r\omega^2 - l - 1)/r \\ \times(g\zeta^2/r\omega^2 - 4)/r & \rho(g\zeta^2/r\omega^2 - l - 1)/r \end{pmatrix}$$

$$\mathbf{T}^{\text{R}} = ((1 - 2F/C)/r), \quad \mathbf{K}^{\text{R}} = (1/C) \quad [81]$$

$$\mathbf{S}^{\text{R}} = (-\rho\omega^2 + 4(\gamma - \rho gr)/r^2)$$

$$\mathbf{T}^{\text{Ts}} = (2/r), \quad \mathbf{K}^{\text{Ts}} = (1/L) \quad [82]$$

$$\mathbf{S}^{\text{Ts}} = (-\rho\omega^2 + (\zeta^2 - 2)N/r^2)$$

where $\gamma = A - N - F^2/C$.

Equation [77] leads to solutions $\mathbf{y}(l, m, r)$ which are discontinuous at the source radius r_s . It can be shown that the discontinuity at r_s is given by (Hudson, 1969; Ward, 1980)

$$[\mathbf{y}]_{r=r_s^-}^{r=r_s^+} = \mathbf{s} = \mathbf{a} + \mathbf{Ab} - \frac{d\mathbf{b}}{dr} \quad [83]$$

and thus the boundary-value problem for \mathbf{y} requires the solution of the homogeneous equation $d\mathbf{y}/dr = \mathbf{Ay}$ above and below the source, subject to the conditions that the solution (1) is nonsingular at the center of the Earth, (2) has vanishing traction components at the surface, and (3) has the prescribed discontinuity \mathbf{s} at the source radius r_s . The specific forms for the discontinuity vector \mathbf{s} , using [71] and [83], are

$$\mathbf{s}^{\text{ss}} = \frac{\nu_l}{i\omega r_s^2} \times \begin{cases} \begin{bmatrix} r_s M_{rr}/C \\ 0 \\ 0 \\ -r_s F_r - M_{\theta\theta} - M_{\phi\phi} + 2M_{rr}F/C \\ \zeta(M_{\theta\theta} + M_{\phi\phi})/2 - \zeta M_{rr}F/C \\ 0 \end{bmatrix}, & l \geq 1, m = 0 \\ \begin{bmatrix} 0 \\ r_s(\mp M_{\theta r} + iM_{\phi r})/2L \\ 0 \\ \zeta(\mp M_{\theta r} + iM_{\phi r} \pm M_{r\theta} - iM_{r\phi})/2 \\ r_s(\pm F_\theta - iF_\phi)/2 - (\mp M_{\theta r} + iM_{\phi r} \pm M_{r\theta} - iM_{r\phi})/2 \\ 0 \end{bmatrix}, & l \geq 1, m = \pm 1 \\ \begin{bmatrix} 0 \\ 0 \\ 0 \\ 0 \\ 0 \\ 0 \end{bmatrix}, & l \geq 2, m = \pm 2 \\ \begin{bmatrix} \sqrt{\zeta^2 - 2}(-M_{\theta\theta} + M_{\phi\phi} \pm iM_{\theta\phi} \pm iM_{\phi\theta})/4 \\ 0 \end{bmatrix} \end{cases} \quad [84]$$

$$\mathbf{s}^R = \frac{\nu_0}{i\omega r_s^2} \times \begin{bmatrix} r_s M_{rr}/C \\ -r_s F_r - M_{\theta\theta} - M_{\phi\phi} + 2M_{rr}F/C \end{bmatrix}, \quad l = m = 0 \quad [85]$$

$$\mathbf{s}^{Ts} = \frac{\nu l}{i\omega r_s^2} \times \begin{cases} \begin{bmatrix} 0 \\ \zeta(M_{\theta\phi} - M_{\phi\theta})/2 \end{bmatrix}, & l \geq 1, m = 0 \\ \begin{bmatrix} r_s(\pm M_{\phi r} + iM_{\theta r})/2L \\ r_s(\mp F_\phi - iF_\theta)/2 + (\mp M_{\phi r} - iM_{\theta r} \pm M_{r\phi} + iM_{r\theta})/2 \end{bmatrix}, & l \geq 1, m = \pm 1 \\ \begin{bmatrix} 0 \\ \sqrt{\zeta^2 - 2}(\pm iM_{\theta\theta} \mp iM_{\phi\phi} + M_{\theta\phi} + M_{\phi\theta})/4 \end{bmatrix}, & l \geq 2, m = \pm 2 \end{cases} \quad [86]$$

where the elastic parameters are those evaluated at the source radius r_s . We consider here only the case that the source is located in a continuous, solid region of the model. Equivalent results (in the case that the moment tensor is symmetric and the material is isotropic) are given by Ward (1980). (As described earlier we are here considering the source to be located at $(\theta = \varepsilon, \phi = 0)$, for some infinitesimal, positive ε ; thus, (F_θ, F_ϕ, F_r) coincide with (F_x, F_y, F_z) in the global Cartesian frame defined in [36]. Similarly, $(M_{\theta\theta}, M_{\theta\phi}, \text{etc.})$ coincide with $(M_{xx}, M_{xy}, \text{etc.})$) If the source is located at a general colatitude θ_s and longitude ϕ_s , the results can be applied in a rotated frame in which the (θ, ϕ, r) components map into (South, East, Up), coordinate θ is epicentral distance and coordinate ϕ is azimuth of the receiver at the source, measured anticlockwise from South.)

In the case that there is no forcing f_i , the equations reduce to the homogeneous system $d\mathbf{y}/dr = \mathbf{A}\mathbf{y}$, together with the usual boundary conditions at the center of the Earth and at the surface. This is an eigenvalue problem for ω having solutions corresponding to the modes of 'free oscillation'. The eigenvalues will be denoted by ω_k , where k is an index that incorporates the angular order l , the 'overtone number' n , and the mode type: spheroidal or toroidal. Overtone number is an index labeling the eigenfrequencies for a given l and for a given mode type, in increasing order. Since the spherical harmonic order m does not enter into the equations, the modes are 'degenerate', meaning that there are $2l+1$ different eigenfunctions, $m = -l, -l+1, \dots, l$ corresponding to a given eigenvalue ω_k . The eigenfunctions will be denoted by $\mathbf{s}^{(km)}(\mathbf{x})$. These are the solutions $\mathbf{u}(\mathbf{x})$ given by [69], for different

values of m , but with the 'same' scalar eigenfunctions $U(r)$, $V(r)$, $W(r)$, $\varphi(r)$. The set of eigenfunctions, $\mathbf{s}^{(km)}(\mathbf{x})$, for a given eigenfrequency ω_k is said to constitute a 'multiplet'. The eigenfunctions represent the spatial shape of a mode of free oscillation at frequency ω_k , because $\mathbf{s}^{(km)}(\mathbf{x})e^{i\omega_k t}$ is a solution of the complete dynamical equations in the absence of any forcing. Of course the eigenfunction is defined only up to an overall factor. If the medium is attenuating, the eigenfrequencies will be complex, their (positive) imaginary parts determining the rate of decay of the mode with time. It is conventional to quantify this decay rate in terms of the ' Q ' of the multiplet, Q_k , which is defined in such a way that the mode decays in amplitude by a factor $e^{-\pi/Q_k}$ per cycle. Therefore, $Q_k = \text{Re}\omega_k/2\text{Im}\omega_k$ is typically a large number, indicating that the modes decay by a relatively small fraction in each cycle. The modal multiplets are conventionally given the names $_nS_l$ for spheroidals and $_nT_l$ for toroidals.

1.02.5 Numerical Solution

The inhomogeneous (i.e., with forcing term f_i) boundary-value problem as formulated above gives a unique solution for each value of ω . The solution in the time domain can then be obtained in the form of an integral in ω , using the inverse Fourier transform [27]. This, in essence, is the basis of several practical methods for calculating theoretical seismogram, for example, the 'reflectivity method' (Fuchs and Muller, 1971) and the direct solution method of Friederich and Dalkolmo (1995). Alternatively, the inverse transform can be evaluated by completing the

integration contour in the upper half of the complex ω plane. Then it is found that the solution can be reduced to a sum over residues, each pole of the integrand corresponding to a particular mode of ‘free oscillation’ of the model. A more usual approach to the normal mode problem is to consider first the free (i.e., unforced) modal solutions of the equations, and then to make use of the orthogonality and completeness properties of the eigenfunctions to obtain solutions of the inhomogeneous (i.e., forced) problem. Here, we have examined first the inhomogenous problem because the demonstration of orthogonality and completeness in the general (attenuating) case is a nontrivial issue, and it is only by virtue of the analysis of the inhomogeneous problem, and the resulting analytic structure of the integrand in the complex ω -plane, that orthogonality and completeness can be demonstrated. It is necessary to show (in the nonattenuating case) that the only singularities of the integrand are simple poles on the real ω -axis. Then the modal sum emerges and completeness is demonstrated by the solution itself. In the attenuating case the situation is more complex, and there are other singularities located on the positive imaginary ω -axis – let us call them the relaxation singularities, as they are associated with decaying exponential functions in the time domain. Thus, while the solution developed here for the inhomogeneous problem remains valid in this case, arguments based on orthogonality and completeness cannot be made. The solution can nevertheless be derived in the form of a sum over residues, and other singularities. While the contribution from relaxation singularities is the main focus of attention in the analysis of postseismic relaxation, they are expected to make negligible contributions for the typical seismic application. However, even in the seismic domain it is necessary to know modal excitations in the attenuating case, and these are difficult to determine, other than by a rather complex application of mode-coupling theory (Tromp and Dahlen, 1990; Lognonne, 1991), which will be difficult to carry out to high frequencies. Using the inhomogenous solution, on the other hand, the ‘seismic’ modes and their excitations emerge naturally as the contributions from the residues of poles near the real axis, and can be calculated exactly and economically.

In both the attenuating and nonattenuating cases and for both the homogenous and inhomogeneous problems, the integration of the ordinary differential equation presents severe numerical difficulties. One problem is that the equations are such that

evanescent – exponentially increasing and decreasing – solutions exist on more than one spatial scale. At moderately high frequencies, when the equations are integrated numerically, the solutions are effectively projected onto the solution having the most rapid exponential increase, and thus even though a linearly independent set of solutions is guaranteed, theoretically, to remain a linearly independent set, it becomes, numerically, a one-dimensional projection. The general solution of this difficulty is to reformulate the equations in terms of minors (i.e., subdeterminants) of sets of solutions (Gilbert and Backus, 1966). The standard method for normal mode calculations (Woodhouse, 1988) is based on the minor formulation of the equations, and uses a novel generalization of Sturm–Liouville theory to bracket modal frequencies, itself a nontrivial issue for the spheroidal modes, as the modes are irregularly and sometimes very closely spaced in frequency, making an exhaustive search difficult and computationally expensive. The program MINOS of Guy Masters, developed from earlier programs of Gilbert, and of Woodhouse (also a development of Gilbert’s earlier programs), implements this method, and has been generously made available to the community. The direct solution method for the inhomogeneous problem of Friederich and Dalkolmo (1995) is based on the minor formulation in the non-self-gravitating case, developed for the flat-earth problem by Woodhouse (1980b).

Here we outline some of the key features of the minor approach. Let us be specific by assuming that the model has a solid inner core, a fluid outer core, and a solid mantle. It may, or may not have an ocean. Let us also consider the case of spheroidal oscillations, for which the solution vector is six dimensional in solid regions (\mathbf{y}^{ss}) and 4-dimensional in fluid regions (\mathbf{y}^{sf}). Toroidal and radial modes are much simpler. The basic method of solution is to start at the center of the Earth, and to specify that the solution should be nonsingular there. By assuming that the medium is homogeneous and isotropic within a small sphere at the center, it is possible to make use of known analytical solutions in terms of the spherical Bessel functions (Love, 1911; Pekeris and Jarosch, 1958; Takeuchi and Saito, 1972). Thus (in the spheroidal case that we are considering), there is a three-dimensional set of solutions to be regarded as candidates for components of the solution at the center. Using these three solutions as starting solutions, the equations can be integrated toward the surface, for example, using Runge–Kutta techniques. We introduce a 6×3 matrix $\mathbf{Y} = \mathbf{Y}^{ss}(r)$ having

columns equal to these three solutions, which has 3×3 subpartitions $\mathbf{Q} = \mathbf{Q}^{Ss}(r)$ and $\mathbf{P} = \mathbf{P}^{Ss}(r)$, that is,

$$\mathbf{Y} = \begin{bmatrix} \mathbf{Q} \\ \mathbf{P} \end{bmatrix}$$

What is important about \mathbf{Y} is the subspace of six-dimensional space that is spanned by its three columns, a property that is left unchanged if \mathbf{Y} is postmultiplied by any nonsingular 3×3 matrix. Assuming, for the moment, that \mathbf{Q} and \mathbf{P} are nonsingular, and postmultiplying by \mathbf{Q}^{-1} and by \mathbf{P}^{-1} we conclude that both $\begin{bmatrix} 1 \\ \mathbf{U} \end{bmatrix}$ and $\begin{bmatrix} \mathbf{V} \\ 1 \end{bmatrix}$, where \mathbf{V} and \mathbf{U} are the mutually inverse matrices $\mathbf{V} = \mathbf{Q}\mathbf{P}^{-1}$, $\mathbf{U} = \mathbf{P}\mathbf{Q}^{-1}$ and where $\mathbf{1}$ is the unit matrix, have columns spanning the same three dimensional space as is spanned by the columns of \mathbf{Y} . An unexpected property of \mathbf{U} , \mathbf{V} , stemming from the self-adjointness property of the equations and boundary conditions, is that they are 'symmetric'. It is not difficult to show that by virtue of the particular structure of the differential equations noted in [78] that if \mathbf{U} , and (therefore) \mathbf{V} are symmetric at a given radius, then they remain symmetric as the equations are integrated to other radii. To demonstrate this, consider

$$\begin{aligned} \frac{d}{dr}(\mathbf{Q}'\mathbf{P} - \mathbf{P}'\mathbf{Q}) &= \frac{d}{dr}(\mathbf{Y}'\Sigma\mathbf{Y}) \\ &= \mathbf{Y}'\mathbf{A}'\Sigma\mathbf{Y} + \mathbf{Y}'\Sigma\mathbf{A}\mathbf{Y} = 0 \end{aligned} \quad [87]$$

where we have used the fact that $\Sigma\mathbf{A}$ is symmetric and Σ is antisymmetric (see discussion following eqn [78]). Thus, if $\mathbf{Q}'\mathbf{P} - \mathbf{P}'\mathbf{Q}$ vanishes at a given radius, it vanishes everywhere in the interval over which the equations are being integrated. But we can write $\mathbf{Q}'\mathbf{P} - \mathbf{P}'\mathbf{Q} = \mathbf{Q}'(\mathbf{P}\mathbf{Q}^{-1} - \mathbf{Q}'^{-1}\mathbf{P}')\mathbf{Q}$, which shows that $\mathbf{P}\mathbf{Q}^{-1}$ is symmetric if $\mathbf{Q}'\mathbf{P} - \mathbf{P}'\mathbf{Q}$ vanishes. It is interesting to note that this argument does not rely on \mathbf{Q} and \mathbf{P} being nonsingular throughout the interval of integration, since $\mathbf{Q}'\mathbf{P} - \mathbf{P}'\mathbf{Q}$ remains finite and continuous. It is a lengthy algebraic exercise to show that \mathbf{U} and \mathbf{V} are symmetric at the centre of the Earth (i.e., when the analytic solutions are used), but nevertheless this can be verified (it can be easily checked numerically).

To continue the narrative, the equations for \mathbf{Y}^{IC} are being integrated in the inner core, and we arrive at the inner-core boundary. Here, the component of the solution corresponding to the shear traction on the boundary (the fifth element in our notation) is required to vanish. Thus, at the boundary we need to select from the three-dimensional space spanned by

the columns of \mathbf{Y} the (in general) two-dimensional subspace of stress-displacement vectors having vanishing fifth elements. This subspace is most easily identified by considering the basis constituted by $\begin{bmatrix} \mathbf{V} \\ 1 \end{bmatrix}$, since its first and third columns have vanishing fifth elements, and thus by deleting the middle column, together with the second and fifth rows, as they correspond to variables not needed on the fluid side, we obtain the following rule for transmitting the basis of allowable solutions from the solid to the fluid side of the boundary:

$$\begin{pmatrix} v_{11} & v_{12} & v_{13} \\ v_{12} & v_{22} & v_{23} \\ v_{13} & v_{23} & v_{33} \\ 1 & 0 & 0 \\ 0 & 1 & 0 \\ 0 & 0 & 1 \end{pmatrix} \rightarrow \begin{pmatrix} v_{11} & v_{13} \\ v_{13} & v_{33} \\ 1 & 0 \\ 0 & 1 \end{pmatrix} \quad [88]$$

We can now continue the integration, using the 4×2 matrix \mathbf{Y}^{OC} in the fluid outer core. We can define \mathbf{Q} , \mathbf{P} , \mathbf{V} , \mathbf{U} similarly, now 2×2 , rather than 3×3 matrices, and again \mathbf{V} , \mathbf{U} , are symmetric. Continuing the integration, we arrive at the outer-core boundary, and again need to consider how to transmit the solution space across the boundary. Elements in rows 1, 2, 3, 4 on the fluid side need to be continuous with elements in rows 1, 3, 4, 6 on the solid side. The fifth element on the solid side, the shear traction component $r\zeta S$, has to vanish. Since the horizontal displacement can be anything on the solid side we have to add to the basis to represent solutions having nonvanishing horizontal displacements on the solid side. The easiest way to satisfy these requirements is to consider the basis represented by $\begin{bmatrix} 1 \\ \mathbf{U} \end{bmatrix}$. It can be easily verified that the following rule satisfies the requirements:

$$\begin{pmatrix} 1 & 0 \\ 0 & 1 \\ u_{11} & u_{12} \\ u_{12} & u_{22} \end{pmatrix} \rightarrow \begin{pmatrix} 1 & 0 & 0 \\ 0 & 1 & 0 \\ 0 & 0 & 1 \\ u_{11} & 0 & u_{12} \\ 0 & 0 & 0 \\ u_{12} & 0 & u_{22} \end{pmatrix} \quad [89]$$

The middle column has been inserted to represent the fact that the solution space has to contain vectors with nonvanishing horizontal displacement scalar ($r\zeta V$) at the base of the mantle.

We can now continue the integration through the mantle. In the inhomogenous problem, the next interesting event is when we arrive at the source radius r_s . In the homogeneous problem, on the other hand we can continue the integrations to the ocean floor, applying the same rule as at the inner-core boundary to transmit the solution space into the ocean, and then continue to the surface, where the free surface condition needs to be satisfied. The requirement, of course, is that there be a linear combination of the columns of the 4×2 matrix

$$\mathbf{Y}^O = \begin{bmatrix} \mathbf{Q}^O \\ \mathbf{P}^O \end{bmatrix}$$

(where superscript 'O' is for ocean) that have vanishing surface traction scalar rP and vanishing gravity scalar $r\psi/4\pi G$, that is, vanishing elements 3 and 4. This requires $\det(\mathbf{P}^O) = 0$ at the free surface. In the absence of an ocean, we similarly need $\det(\mathbf{P}^C) = 0$ where \mathbf{P}^C is the 3×3 matrix in the crust.

In the inhomogeneous case, we need to arrange for there to be a prescribed discontinuity \mathbf{s}^{ss} at the source depth. Thus, we need to characterize the solution space above, as well as below the source. At the surface of the ocean the solution must have vanishing elements 3 and 4, and thus we choose \mathbf{Y}^O at the free surface to be, simply

$$\mathbf{Y}^O = \begin{bmatrix} 1 \\ 0 \end{bmatrix}$$

Now we can integrate the solution downwards, using the same fluid–solid rule at the ocean floor as was employed at the core–mantle boundary, until we reach the source radius r_s from above. If $\begin{bmatrix} 1 \\ \mathbf{U}_1^s \end{bmatrix}$ spans the solution space below the source and $\begin{bmatrix} 1 \\ \mathbf{U}_2^s \end{bmatrix}$ spans the solution space above the source, we need to solve

$$\begin{bmatrix} 1 \\ \mathbf{U}_2^s \end{bmatrix} \mathbf{x}_2 - \begin{bmatrix} 1 \\ \mathbf{U}_1^s \end{bmatrix} \mathbf{x}_1 = \mathbf{s}^{ss} \quad [90]$$

for the two 3-vectors $\mathbf{x}_1, \mathbf{x}_2$ which represent the multipliers for the columns of each matrix that are needed to satisfy the condition that the solution has the prescribed discontinuity. The solution is easily found to be

$$\begin{aligned} \mathbf{x}_1 &= (\mathbf{U}_2 - \mathbf{U}_1)^{-1} (\mathbf{s}_p^{ss} - \mathbf{U}_2 \mathbf{s}_Q^{ss}) \\ \mathbf{x}_2 &= (\mathbf{U}_2 - \mathbf{U}_1)^{-1} (\mathbf{s}_p^{ss} - \mathbf{U}_1 \mathbf{s}_Q^{ss}) \end{aligned} \quad [91]$$

where $\mathbf{s}_Q^{ss}, \mathbf{s}_p^{ss}$ are the upper and lower halves of \mathbf{s}^{ss} , and the solution vectors below and above the source are given by

$$\mathbf{y}_1^{ss} = \begin{bmatrix} \mathbf{x}_1 \\ \mathbf{U}_1 \mathbf{x}_1 \end{bmatrix}, \quad \mathbf{y}_2^{ss} = \begin{bmatrix} \mathbf{x}_2 \\ \mathbf{U}_2 \mathbf{x}_2 \end{bmatrix} \quad [92]$$

This determines the linear combination of the basis vectors that are needed to satisfy the source discontinuity condition, and hence to determine the solution at any point of the medium and, in particular, at the surface, where it may be required to calculate some seismograms.

There will be singularities in the integrand of the inverse Fourier transform when $\mathbf{U}_2 - \mathbf{U}_1$ is singular. This will occur for frequencies ω for which a solution exists to the homogenous (i.e., unforced) problem, that is, at the frequencies of free oscillation. If $\mathbf{U}_2 - \mathbf{U}_1$ is singular at a particular source radius, it is, therefore, necessarily singular at all radii. To evaluate the inverse transform as a sum over residues, we can write

$$\frac{1}{2\pi} \int_{-\infty}^{\infty} I(\omega) e^{i\omega r} d\omega \rightarrow \sum_k i \frac{\lim_{\omega \rightarrow \omega_k} \Delta(\omega) I(\omega)}{\Delta'(\omega_k)} \quad [93]$$

where ω_k is a mode frequency and $\Delta(\omega)$ is that factor in the denominator of the integrand $I(\omega)$ that vanishes at ω_k , assuming that it has a simple zero at ω_k . Thus, we can replace the inverse transform by a sum over residues provided that the singular part of the integrand is replaced by the expression corresponding to it on the right-hand side of [93]. From [91] we find that the necessary replacement is

$$(\mathbf{U}_2 - \mathbf{U}_1)^{-1} \rightarrow i \frac{\text{adj}(\mathbf{U}_2 - \mathbf{U}_1)}{\partial_\omega \det(\mathbf{U}_2 - \mathbf{U}_1)} \Big|_{\omega=\omega_k} = \frac{1}{2i\omega_k} \mathbf{z}_k \mathbf{z}'_k \quad [94]$$

where adj represents matrix adjoint – the matrix of cofactors. The second equality defines the column \mathbf{z}_k and its transpose \mathbf{z}'_k , and arises from the fact that the adjoint of a singular matrix, assuming that the rank defect is 1, is expressible as a dyad; the factor $-1/2\omega_k$ is included in the definition for convenience, as with this definition of \mathbf{z}_k , it can be shown that the column

$$\mathbf{y}_k = \begin{bmatrix} \mathbf{z}_k \\ \mathbf{U}_1 \mathbf{z}_k \end{bmatrix} = \begin{bmatrix} \mathbf{z}_k \\ \mathbf{U}_2 \mathbf{z}_k \end{bmatrix}$$

is an eigenfunction (i.e., a solution of $d\mathbf{y}/dr = \mathbf{A}\mathbf{y}$) and has normalization

$$\int_0^a \mathbf{y}'_k(-\Sigma \mathbf{A}_\lambda) \mathbf{y}_k dr = 1 \quad [95]$$

where the notation $-\Sigma \mathbf{A}_\lambda$ is that introduced in the discussion following [78]. The eigenfunctions can be found without needing to calculate the derivatives of solutions with respect to ω , as it can be shown that $\det \mathbf{Q}_1 \det \mathbf{Q}_2 \partial_\omega \det(\mathbf{U}_2 - \mathbf{U}_1)$ is independent of r .

This is the basis for the construction of the eigenfunctions from solutions of the minor equations, although it was arrived at differently in Woodhouse (1988). We see that it is necessary to integrate both upwards and downwards in order to obtain \mathbf{U}_1 and \mathbf{U}_2 (or, rather, the minors from which they can be constructed, see below) at all radii r .

In the nonattenuating case, the eigenfunctions \mathbf{y}_k are real, and [95] reduces to the standard normalization conditions for the scalar eigenfunctions U_k, V_k, W_k (defined in terms of \mathbf{y}_k as in eqn [76],

$$\begin{aligned} \text{spheroidal: } & \int_0^a \rho(U_k^2 + \zeta^2 V_k^2) r^2 dr = 1 \\ \text{toroidal: } & \int_0^a \rho \zeta^2 W_k^2 r^2 dr \end{aligned} \quad [96]$$

$$\begin{aligned} E_{km} = & \left\{ \begin{array}{l} \mathbf{y}'_k \sum \mathbf{s}^{Ss} \text{spheroidal} \\ \mathbf{y}_k \sum \mathbf{s}^{Ts} \text{toroidal} \end{array} \right. \\ = & \frac{\nu_l}{r_s} \left\{ \begin{array}{ll} -r_s U_k F_r - r_s \partial_r U_k M_{rr} - U_k (M_{\theta\theta} + M_{\phi\phi}) + \frac{1}{2} \zeta^2 V_k (M_{\theta\theta} + M_{\phi\phi}) \\ \quad + \frac{1}{2} \zeta^2 W_k (M_{\theta\phi} - M_{\phi\theta}) & m = 0 \\ \frac{1}{2} \zeta r_s (V_k \mp iW_k) (\pm F_\theta - iF_\phi) + \frac{1}{2} \zeta r_s (\partial_r V_k \mp i\partial_r W_k) (\pm M_{\theta r} - iM_{\phi r}) \\ \quad + \frac{1}{2} \zeta (U_k - V_k \pm iW_k) (\pm M_{r\theta} - iM_{r\phi}) & l \geq 1, m = \pm 1 \\ \frac{1}{4} \zeta \sqrt{\zeta^2 - 2} (V_k \mp iW_k) (M_{\phi\phi} - M_{\theta\theta} \pm iM_{\theta\phi} \pm iM_{\phi\theta}) & l \geq 2, m = \pm 2 \end{array} \right. \end{aligned} \quad [98]$$

where [72] has been used to express the radial traction components P_k, S_k, T_k in \mathbf{y}_k in terms of U_k, V_k, W_k and their derivatives. The eigenfunctions are those evaluated at the source radius r_s . In [98] we have combined the results for toroidal and spheroidal modes; of course, for spheroidal modes $W_k = 0$ and for toroidal modes $U_k = V_k = 0$. This result for the modal excitations is equivalent, in the case of a symmetric moment tensor to the forms given in table 1 of Woodhouse and Girnius (1982).

The sum over residues [97] needs to be carried out over all simple poles in the upper half of the complex ω -plane. It will include the oscillatory ‘seismic modes’ having $\operatorname{Re} \omega_k \neq 0$, and also, possibly, ‘relaxation modes’ having $\operatorname{Re} \omega_k = 0, \operatorname{Im} \omega_k > 0$. The seismic modes will occur in pairs, $\omega_k, -\omega_k^*$ because the equations are symmetric under replacement of ω_k by $-\omega_k^*$ followed by complex conjugation (see discussion following eqn [34]). Thus, each seismic mode having $\operatorname{Re} \omega_k > 0$ will have a partner, obtained by reflection in the imaginary axis, at $-\omega_k^*$. It is not necessary to consider the modes for

In the attenuating case, on the other hand, the eigenfunctions are complex and the normalization condition [95] includes terms arising from the derivatives of the elastic parameters with respect to ω . In this case [95] determines both the phase and the amplitude of the eigenfunction. Using the replacement [94] in [91], and making use of the definitions of \mathbf{s}^{Ss} , and similarly \mathbf{s}^{Ts} , from [84]–[86] it can be shown that the inhomogeneous solution, now in the time domain, can be written as a sum over residues:

$$\mathbf{y}_{lm}(r, t) = \sum_k -\frac{1}{2\omega_k^2} E_{km} \mathbf{y}_k(r) e^{i\omega_k t} \quad [97]$$

where ‘modal excitations’ E_{km} are given by

which $\operatorname{Re} \omega_k < 0$ explicitly, as when the final result for the displacement in the time domain is calculated, it is possible to include them automatically by adding the complex conjugate, in order that the final result should be real. In the attenuating case, the solution is still not necessarily complete, as the constitutive law may introduce a branch cut along the positive imaginary axis, corresponding to a continuous distribution of relaxation mechanisms. In this case, the sum over residues needs to be augmented by an integral around any branch-cut singularities on the positive imaginary axis. In order to include the ‘static’ response of the medium, it is necessary to analyze the behavior of the integrand at $\omega = 0$. We do not pursue this in detail here but make some general observations. Because the source that is being considered has, in general, nonvanishing net force and net moment, we would obtain secular terms corresponding to translational and rotational rigid motions (degree $l=1$ spheroidal and toroidal modes having zero frequency). If the force is set to zero and the moment tensor is taken to be symmetric, these modes would

not be excited. In this case, the final displacement field, after all seismic modes and relaxation modes have died away, can be found from the residue at zero frequency, and will correspond to the static ($\omega=0$) solution of the equations in which the elastic parameters are replaced by their values at zero frequency – their so-called ‘relaxed’ values. Alternatively, the final displacement can be found by considering the fact that if the static terms are omitted the final displacement is zero, because all modes attenuate with time, whereas, in fact, it is the ‘initial’ displacement that should be zero. Thus, the static terms must be such as to cancel the dynamic terms at zero time. It is not obvious that these two different ways of evaluating the static response will agree (i.e., using the static solution for relaxed values of the moduli, or using the fact that the initial displacement must be zero). We conjecture, but do not claim to prove that these two methods will give the same result. If this is so, it means that, provided all modes are included in the sum, we can include the static response by substituting $e^{i\omega_k t} - 1$ for $e^{i\omega_k t}$ in [97] – that is, by subtracting the value at zero time.

A central role is played in the foregoing theory by the symmetric matrices \mathbf{U} and \mathbf{V} , notwithstanding that they possess singularities within the domain of integration. From their definitions $\mathbf{V} = \mathbf{Q}\mathbf{P}^{-1}$, $\mathbf{U} = \mathbf{P}\mathbf{Q}^{-1}$, using the following standard formula for the inverse of a matrix in terms of its cofactors and its determinant, they can be expressed in terms of the various 3×3 or (in the fluid case) or 2×2 subdeterminants of \mathbf{Y} . Explicitly, we have

$$\mathbf{U} = \frac{m_2}{m_1}, \quad \mathbf{V} = \frac{m_1}{m_2} \quad (n=1) \quad [99]$$

$$\mathbf{U} = \frac{1}{m_1} \begin{pmatrix} -m_4 & m_2 \\ m_2 & m_3 \end{pmatrix}, \quad \mathbf{V} = \frac{1}{m_6} \begin{pmatrix} m_3 & -m_2 \\ -m_2 & -m_4 \end{pmatrix}$$

$$m_1 = \det \mathbf{Q}, \quad m_6 = \det \mathbf{P} \quad (n=2) \quad [100]$$

$$\mathbf{U} = \frac{1}{m_1} \begin{pmatrix} m_{11} & -m_5 & m_2 \\ -m_5 & -m_6 & m_3 \\ m_2 & m_3 & m_4 \end{pmatrix}, \quad \mathbf{V} = \frac{1}{m_{20}} \begin{pmatrix} m_{10} & -m_9 & m_8 \\ -m_9 & -m_{15} & m_{14} \\ m_8 & m_{14} & m_{17} \end{pmatrix}$$

$$m_1 = \det \mathbf{Q}, \quad m_{20} = \det \mathbf{P} \quad (n=3) \quad [101]$$

where m_k are the minors of the relevant 2×1 , 4×2 , 3×6 ($n=1, 2$ or 3) solution matrices \mathbf{Y} . We are using a standard way of enumerating these (see Woodhouse, (1988) and Gilbert and Backus, (1966)). We include the $n=1$ case here, which is relevant to

the case of toroidal and radial oscillations, for the sake of completeness. The results still hold in this case, although the matrices \mathbf{Q} , \mathbf{P} , \mathbf{V} , \mathbf{U} reduce in this case to simple numbers, and the minors reduce to the elements of the solution vector itself (the 1×1 subdeterminants of a 2×1 matrix \mathbf{Y}). It is well known (Gilbert and Backus, 1966) that differential equations can be derived that are satisfied by the minors, and thus they can be calculated directly, without the need to integrate the equations for particular solution sets \mathbf{Y} . Thus, formulas and results involving \mathbf{V} , \mathbf{U} can be readily transcribed into formulas involving the minors. Essentially, any one of \mathbf{U} , \mathbf{V} , \mathbf{m} provides a way of characterizing a subspace of the $2n$ -dimensional space of interest ($n=1, 2$, or 3), in a way that is independent of any specific basis. However, the minors have the practical advantage that they do not become infinite in the domain of integration.

The matrices \mathbf{U} and \mathbf{V} possess another remarkable property which results from the positive semidefiniteness of $-\Sigma \mathbf{A}_\lambda$ in the nonattenuating case. Using this property, it is possible to show that the derivatives \mathbf{U}_λ and \mathbf{V}_λ also have definiteness properties. For upward integration $\mathbf{U}_\lambda \leq 0$ and $\mathbf{V}_\lambda \geq 0$ where ≥ 0 and ≤ 0 is used as a shorthand for the relevant semidefiniteness property. To prove this, consider the matrix $\mathbf{P}'\mathbf{Q}_\lambda - \mathbf{Q}'\mathbf{P}_\lambda = -\mathbf{Y}'\Sigma\mathbf{Y}_\lambda$. The radial derivative of this matrix is given by

$$\begin{aligned} \frac{d}{dr}(\mathbf{P}'\mathbf{Q}_\lambda - \mathbf{Q}'\mathbf{P}_\lambda) &= -\frac{d}{dr}(\mathbf{Y}'\Sigma\mathbf{Y}_\lambda) \\ &= -\mathbf{Y}'\mathbf{A}'\Sigma\mathbf{Y}_\lambda - \mathbf{Y}'\Sigma(\mathbf{A}_\lambda\mathbf{Y} + \mathbf{A}\mathbf{Y}_\lambda) \\ &= -\mathbf{Y}'\Sigma\mathbf{A}_\lambda\mathbf{Y} \geq 0 \end{aligned} \quad [102]$$

where we have used $d\mathbf{Y}/dr = \mathbf{AY}$, together with its transpose and its derivative with respect to λ . The cancellation of the terms not involving \mathbf{A}_λ is due to the symmetry of $\Sigma\mathbf{A}$ and the antisymmetry of Σ . We also have

$$\begin{aligned} \mathbf{V}_\lambda &= (\mathbf{Q}\mathbf{P}^{-1})_\lambda = \mathbf{Q}_\lambda\mathbf{P}^{-1} - \mathbf{Q}\mathbf{P}^{-1}\mathbf{P}_\lambda\mathbf{P}^{-1} \\ &= \mathbf{Q}_\lambda\mathbf{P}^{-1} - \mathbf{P}'^{-1}\mathbf{Q}'\mathbf{P}_\lambda\mathbf{P}^{-1} \\ &= \mathbf{P}'^{-1}(\mathbf{P}'\mathbf{Q}_\lambda - \mathbf{Q}'\mathbf{P}_\lambda)\mathbf{P}^{-1} \end{aligned} \quad [103]$$

Thus, [102] shows that if $\mathbf{P}'\mathbf{Q}_\lambda - \mathbf{Q}'\mathbf{P}_\lambda \geq 0$ at some initial point, then it remains positive semidefinite during upward integration. Then, from [103], $\mathbf{V}_\lambda \geq 0$, as we wished to show. Using the analytic solutions at the center of the Earth, it can be shown that \mathbf{V}_λ does have the required properties at the

starting point of integration, being independent of frequency at the center of the Earth. Also, its semidefiniteness property is preserved on passing from solid to fluid and vice versa. Similarly, it can be shown that for upward integration $\mathbf{U}_\lambda \leq 0$.

The diagonal elements of \mathbf{V}_λ and \mathbf{U}_λ , which necessarily share the semidefiniteness properties of the matrices themselves, require, for upward integration, that the diagonal elements of \mathbf{V} and \mathbf{U} are nondecreasing and nonincreasing functions of frequency, respectively. As a function of frequency these diagonal elements behave like the familiar tangent and cotangent functions, having monotonic increase or decrease between their singularities. The singularities in \mathbf{V} at the surface are of particular interest, since the frequencies for which \mathbf{V} is singular (i.e., infinite) at the surface are precisely the frequencies of the normal modes. One particular diagonal element, namely v_{11} in the notation used here, has the additional property, using [88], [89], that it is continuous at solid–fluid and fluid–solid boundaries. In the case of fluid–solid boundaries, this is not so obvious, as both m_{10} and m_{20} vanish on the solid side ($v_{11} = m_{10}/m_{20}$, eqn [101]), but it can be shown that the limit as the boundary is approached from the solid side is, in fact, equal to v_{11} on the fluid side.

The function $\theta_R(r, \lambda) = -\frac{1}{\pi} \cot^{-1}(v_{11})$, which can be made continuous (as a function of r and as a function of λ) through singularities of v_{11} , has the properties that (1) it is independent of frequency at the center of the Earth, (2) it is nondecreasing as a function of λ , and (3) it takes on integer values at the surface at the frequencies $\omega^2 = \lambda$ corresponding the normal modes. This makes it an ideal mode counter, since two integrations of the equations, at frequencies ω_1, ω_2 say, can determine the values $\theta_R(a, \omega_1^2), \theta_R(a, \omega_2^2)$ at the Earth's surface and it is necessary only to find how many integers lie between these values to determine how many modal frequencies lie between ω_1 and ω_2 . There is a complication associated with fluid–solid boundaries. As discussed above, both m_{10} and m_{20} vanish on the solid side, even though v_{11} remains continuous. This circumstance leads to singular behavior of θ_R as a function of λ , and we find that it is necessary to increment θ_R by 1 at a fluid solid boundary when the (2, 2) element of \mathbf{s}^{ss} (eqn [79]) is negative on the solid side, that is, for $\omega^2 > [\zeta^2(A - F^2/C) - 2N]/\rho r^2$, in which the elastic constants are those evaluated at the boundary, on the solid side and r is the radius of the boundary. For upward integration (the usual case) this occurs at the core–mantle boundary.

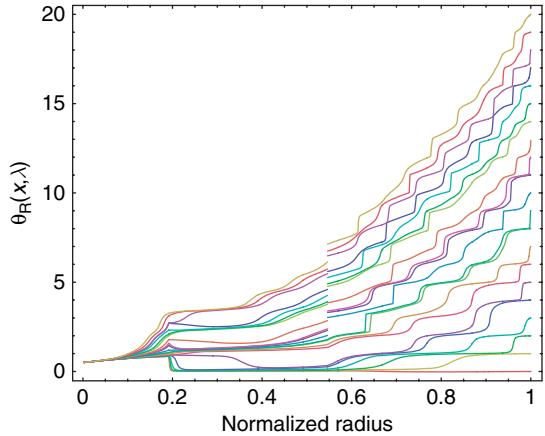


Figure 3 An example of the behavior of $\theta_R(x, \lambda)$ for the spheroidal oscillations of degree $l = 10$. It has been calculated for the true modal frequencies up to ${}_{20}S_{10}$, and thus the surface value of $\theta_R(x, \lambda)$, at normalized radius $x = 1$, takes on successive integer values equal to the overtone number. θ_R can be seen to be independent of frequency at the center of the Earth ($x = 0$), where $\theta_R(x, \lambda) = 1/2$. The nondecreasing property of θ_R as a function of $\lambda = \omega^2$ means that successive curves never cross. Notice that θ_R is not a monotonic function of r . The discontinuity in θ_R at the core–mantle boundary, discussed in the text, affects the mode count for modes higher than ${}_{9}S_{10}$. In a sense the values of $\theta_R(x, \lambda) = -(1/\pi) \cot^{-1} v_{11}$ are not of physical significance, since v_{11} is a dimensional quantity, and thus the value of $\theta_R(x, \lambda)$ depends on the units employed. In any system of units, however, θ_R takes on integer values at the same values of its arguments. In other words, it is the ‘zero crossings’ of v_{11} , for which θ_R acts as a counter, that are of primary significance. The results shown here are for $\theta_R(x, \lambda) = -(1/\pi) \cot^{-1} \alpha v_{11}$, with $\alpha = 4 \times 10^4 \text{ N m}^{-3}$.

Figure 3 shows an example of the behavior of $\theta_R(x, \lambda)$ for spheroidal oscillations of degree $l=10$. The θ_R mode counter can be used to bracket the modal frequencies by a bisection method that seeks values of frequency such that $\theta_R(a, \omega^2)$ takes on values lying between any pair of successive integers in an interval $[\theta_R(a, \omega_{\min}^2), \theta_R(a, \omega_{\max}^2)]$.

Having bracketed the modal frequencies (for a given l), it is necessary to converge on the zeros of $\det[\mathbf{P}]|_{r=a}$. This can be done in a variety of standard ways, bisection being the ultimately safe method if all else fails. **Figure 4** shows the resulting ‘dispersion diagram’ for spheroidal modes up to 30 mHz. The crowding and irregularity of the distribution in the left side of the diagram demonstrate the need for the mode-counting scheme. For the toroidal modes, the dispersion diagram is much simpler (**Figure 5**), and so the mode-counting scheme is less critical.

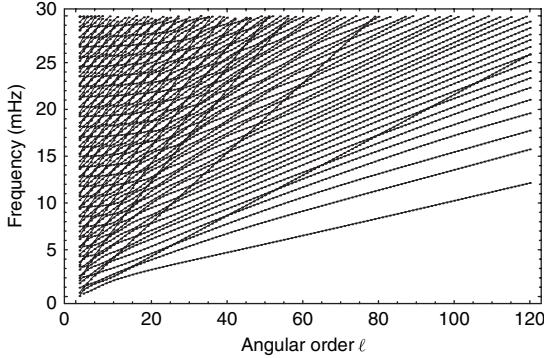


Figure 4 The dispersion diagram for spheroidal modes to 30 mHz.

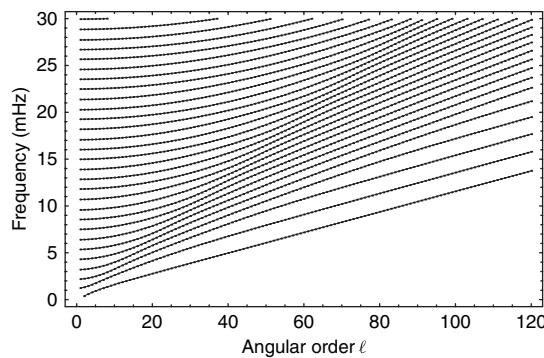


Figure 5 The dispersion diagram for toroidal modes to 30 mHz.

1.02.6 Elastic Displacement as a Sum over Modes

We shall here assume that a catalog of normal mode eigenfrequencies and scalar eigenfunctions has been calculated. Rather than pursuing the inhomogenous problem outlined in earlier sections we shall now adopt the more classical approach, making use of the orthogonality properties of the eigenfunctions to expand the applied force distribution and to find the modal excitations. The argument is strictly valid only in the nonattenuating case. Attenuation is subsequently included by introducing decay constants associated with each mode. Recall that the eigenfrequencies ω_k and the eigenfunctions $s^{(km)}$ are solutions of the eigenvalue problem

$$\mathcal{H}s^{(km)} = \rho\omega_k^2 s^{(km)} \quad [104]$$

It can be shown that the operator \mathcal{H} is self adjoint in the sense

$$\int_V s' \cdot \mathcal{H} s d^3x = \int_V s \cdot \mathcal{H} s' d^3x \quad [105]$$

for any differentiable $s(x)$, $s'(x)$ satisfying the boundary conditions for \mathbf{u} in [24], where the volume integration is over the entire Earth model. From this it follows that the eigenfunctions $s^{(km)}(x)$ form a complete set and that the eigenvalues ω_k^2 are real. We can also assume that they are positive, on the grounds that the model should initially be in stable equilibrium. It is not difficult to show that eigenfunctions belonging to different eigenvalues are orthogonal or, in the case of degeneracy, can be orthogonalized, in the sense

$$\int_V \rho s^{(k'm')*} \cdot s^{(km)} d^3x = 0, \text{ when } k \neq k' \text{ or } m \neq m' \quad [106]$$

It is straightforward to obtain a formal solution of the equations of motion [35] in terms of a sum of eigenfunctions $s^{(km)}$. We expand the displacement field $\mathbf{u}(x, t)$

$$\mathbf{u}(\mathbf{x}, t) = \sum_{km} a_{km}(t) s^{(km)}(\mathbf{x}) \quad [107]$$

where $a_{km}(t)$ are to be found. On substituting into [35], multiplying by $s^{(k'm')*}$ and integrating, making use of the orthogonality relation (106), we obtain

$$\ddot{a}_{km}(t) + \omega_k^2 a_{km}(t) = \omega_k^2 f_{km}(t) \quad [108]$$

with

$$f_{km}(t) \equiv \frac{1}{\omega_k^2} \frac{\int_V s^{(km)*}(\mathbf{x}) \cdot \mathbf{f}(\mathbf{x}, t) d^3x}{\int_V \rho s^{(km)*}(\mathbf{x}) \cdot s^{(km)}(\mathbf{x}) d^3x} \quad [109]$$

The ordinary differential equations [108] for each $a_{km}(t)$ may be solved (e.g., using the method of ‘variation of parameters’ or Laplace transformation) to give

$$a_{km}(t) = \int_{-\infty}^t b_k(t-t') \dot{f}_{km}(t') dt' \quad [110]$$

with

$$b_k(t) = 1 - \cos \omega_k t \quad [111]$$

a result due to Gilbert (1971). As pointed out by Gilbert, this result needs to be modified to account for attenuation by incorporating a decay factor $\exp(-\alpha_k t)$ into the cosine term, and thus in place of [111] we write

$$b_k(t) = 1 - e^{-\alpha_k t} \cos \omega_k t \quad [112]$$

where α_k is given in terms of the Q of the mode by $\alpha_k = \omega_k / 2Q_k$.

Inserting the point source defined in [31], we obtain

$$\alpha_{km}(t) = \frac{1}{\omega_k^2} \left(F_i s_i^{(km)}(\mathbf{x}_s)^* + M_{ij} s_{i,j}^{(km)}(\mathbf{x}_s)^* \right) b_k(t) \quad [113]$$

assuming that eigenfunctions are normalized such that $\int_V \rho \mathbf{s}^{(km)*}(\mathbf{x}) \cdot \mathbf{s}^{(km)}(\mathbf{x}) d^3x = 1$. The eigenfunctions are of the form [69] and thus it is a further exercise in spherical harmonic analysis to reduce the excitation coefficients, $E_{km} = (F_i s_i^{(km)}(\mathbf{x}_s)^* + M_{ij} s_{i,j}^{(km)}(\mathbf{x}_s)^*)$, to forms involving the scalar eigenfunctions U_k, V_k, W_k and their derivatives. The result has already been derived in [98], by a different route. Similar formulas are also to be found in Gilbert and Dziewonski (1975), Woodhouse and Girnius (1982), and Dziewonski and Woodhouse (1983). Using [113] in [107], we obtain the following expression for a theoretical seismogram:

$$\mathbf{u}(\mathbf{x}, t) = \sum_{km} \frac{1}{\omega_k^2} E_{km} \mathbf{s}^{(km)}(\mathbf{x}) (1 - e^{-\alpha_k t} \cos \omega_k t) \quad [114]$$

The argument of the previous section shows that the correct form of this expression in the attenuating case is

$$\mathbf{u}(\mathbf{x}, t) = \sum_{\substack{km \\ \operatorname{Re} \omega_k > 0}} \operatorname{Re} \left\{ \frac{1}{\omega_k^2} E_{km} \mathbf{s}^{(km)}(\mathbf{x}) (1 - e^{i\omega_k t}) \right\} \quad [115]$$

where ω_k is now the complex frequency, and $\mathbf{s}^{(km)}$ is the complex eigenfunction, having normalization [95]. Additional terms need to be added to [115] if it is desired to include relaxation effects.

This rather simple formula is the key ingredient of many seismological studies, as outlined in the introduction. Mode catalogs for PREM (Dziewonski and Anderson, 1981) exist up to 170 mHz (6 s period). Figure 2 shows an example of such a synthetic seismogram. For comparison, the observed seismogram is also shown. The direct P and S surface reflected PP and SS body waves are visible in both the synthetic and data seismograms. At later times, the surface waves can be observed. Differences between the synthetic and data seismogram can be attributed to three-dimensional structure, which is not included in the calculation.

1.02.7 The Normal Mode Spectrum

Here we illustrate some of the properties of different multiplets in the normal mode spectrum. One way to

gain understanding of the physical properties is through the use of ‘differential kernels’ $K(r)$. These are, in essence, the derivatives of the eigenfrequency of a given mode with respect to a structural change at any radius. This takes the form of an integral (cf. the chain rule applied to an infinite number of independent variables). Differential kernels can be defined, for example, corresponding to perturbations in shear modulus and bulk modulus, at fixed density, and these are related to the distribution of elastic shear energy and compressional energy with radius. Similarly, kernels can be defined corresponding to anisotropic perturbations (see Chapter 1.16). Theoretical formulas for such kernels can be found in, for example, Backus and Gilbert (1967), and for anisotropic elastic parameters A, C, L, N, F in Dziewonski and Anderson (1981). Such kernels are a special case, in which the perturbation is spherically symmetric, of the kernels that arise when a general aspherical perturbation of the model is considered. This will be further discussed in a later section. Here we shall take relative perturbations in (isotropic) P-velocity, v_p , S-velocity, v_s and density ρ (at constant v_p and v_s) as the independent perturbations, and write

$$\delta\omega_k = \int_0^a \left(K_\rho(r) \frac{\delta\rho(r)}{\rho(r)} + K_P(r) \frac{\delta v_p(r)}{v_p(r)} + K_S(r) \frac{\delta v_s(r)}{v_s(r)} \right) dr \quad [116]$$

Our aim here is to use the kernels $K_P(r), K_S(r)$ to give insight into the nature of the mode in terms of its traveling-wave content, and into how the P- and S-velocity distributions can be constrained by making observations of a given mode. The kernel $K_\rho(r)$ (for constant v_p and v_s) gives information about how the mode probes the density structure, adding to information about v_p and v_s available from modes but also from travel times.

Another way to gain insight into the physical character of modes is by relating them to traveling body waves and surface waves. The essential quantitative connection between modes and traveling waves is made by equating the horizontal wavelength (or wave number) of the mode with the corresponding horizontal wavelength (or wave number) of a traveling wave. For modes, this wavelength can be derived from the asymptotic properties of the spherical harmonics for large l . A point source at the pole

$\theta = 0$ excites only the modes having low azimuthal order $|m| \leq 2$, as we have seen. For fixed m and large l , we have (e.g., Abramowitz and Stegun, 1965)

$$Y_l^{0m}(\theta, \phi) \sim \frac{1}{\pi} \sqrt{\frac{2l+1}{4\pi}} (\sin \theta)^{-1/2} \cos \left[\left(l + \frac{1}{2} \right) \theta \right. \\ \left. + \frac{1}{2} m\pi - \frac{1}{4}\pi \right] e^{im\phi} \quad [117]$$

where θ plays the role of epicentral distance. Thus, we can identify the horizontal wave number $k (= 2\pi/\text{wavelength})$ to be

$$k = \left(l + \frac{1}{2} \right) / a \quad [118]$$

The angular order l , therefore, is a proxy for wave number k and dispersion diagrams such as those shown in Figures 4 and 5 can be interpreted, for large l , in the same way as are dispersion relations $\omega(k)$ for surface waves. In particular, we can define phase velocity

$$c(\omega) = \frac{\omega}{k} \quad [119]$$

and group velocity

$$U(\omega) = \frac{d\omega}{dk} \quad [120]$$

This defines the relationship between the $\omega - l$ plane and the dispersion properties of Love and Rayleigh waves and their overtones, Love waves corresponding to toroidal modes, and Rayleigh waves to spheroidal modes.

In the case of body waves we may, similarly, identify the horizontal wave number in terms of frequency and ‘ray parameter’ p (Brune, 1964, 1966). From classical ray theory in the spherical Earth, the horizontal wave number at the Earth’s surface for a monochromatic signal traveling along a ray with given ray parameter $p = dT/d\Delta$ is

$$k = \frac{\omega p}{a} \quad [121]$$

Therefore, using [118],

$$p = \frac{l + \frac{1}{2}}{\omega} \quad [122]$$

Thus, a mode of angular order l and angular frequency ω is associated with rays having the ray parameter given by [122]. For toroidal modes, these are S-rays, and for spheroidal modes they are both P- and S-rays. It is well known that rays exist only for ranges of depth for which

$$\frac{r}{v_p(r)} \geq p, \quad \text{for P-waves} \quad [123]$$

$$\frac{r}{v_s(r)} \geq p, \quad \text{for S-waves} \quad [124]$$

In the diagrams of Figures 7 and 8 the ranges of depth for which these inequalities are satisfied are indicated in two columns on the right-hand side of each panel. The left column is for P-waves (relevant only for spheroidal multiplets) and the right column for S-waves.

Figure 6 shows the combined dispersion diagrams for spheroidal and toroidal modes at low frequencies ($f \leq 3$ MHz), an expanded version of the lower left corner of the dispersion diagrams in Figures 4 and 5. Lines connect modes of the same type (spheroidal or toroidal) and the same overtone number n , and define different branches of the dispersion curves. The ‘fundamental mode branch’ ($n=0$) contains the modes with the lowest frequency for each l . Modes with $n > 1$ are called ‘overtones’. We will make a tour of $\omega - l$ space and use the eigenfunctions and differential kernels defined above to gain insight into the nature of the different types of mode.

Figures 7–9 show eigenfunctions and differential kernels for a number of toroidal and spheroidal modes. By inspecting these diagrams, a few general observations can be made. Moving up along a mode branch (horizontal rows in Figures 7–9) will result in eigenfunctions and kernels which are more concentrated toward the surface. This reflects the fact that, for high l , the modes may be interpreted as surface waves. Moving up in overtone number n , for constant l (vertical columns in Figures 8 and 9), leads to eigenfunctions that are more oscillatory and to sensitivity kernels that penetrate more deeply.

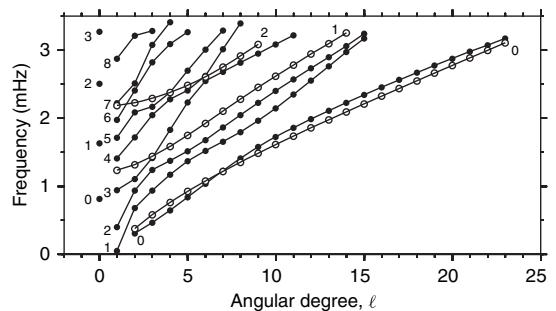


Figure 6 Eigenfrequencies of spheroidal (black circles) and toroidal multiples (white circles) below 3 mHz for the Preliminary Reference Model (PREM, Dziewonski and Anderson, 1981). A multiplet with angular order l consists of $2l+1$ singlets with azimuthal order $m = -l, -l+1, \dots, l-1, l$. The branches are labeled by their overtone number n (left spheroidal, right toroidal), the fundamental mode branch is $n = 0$.

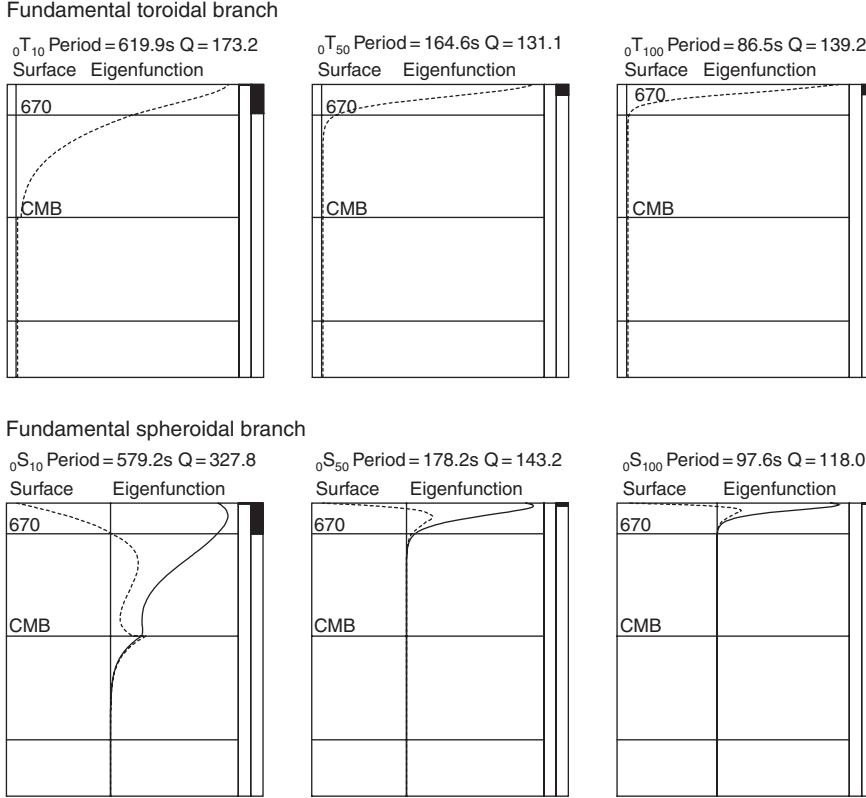


Figure 7 Eigenfunctions of selected toroidal and spheroidal fundamental modes ($n = 0$). For the toroidal modes, the dashed lines show $W(r)$, and for spheroidal modes the dashed lines denote $V(r)$ and the solid lines $U(r)$. At high angular order l the toroidal modes correspond to Love waves and the spheroidal modes to Rayleigh waves.

The wave motion of toroidal modes is purely horizontal (see [Figure 7](#)), and thus these modes are sensitive only to perturbations in S-velocity and density and have no sensitivity to the core ([Figure 8](#)). The differential kernels tell us how the frequency of the mode will change if we increase the spherical velocity or density at a certain depth. When inspecting [Figure 8](#), we find that increasing the shear wave velocity at any depth in the mantle, will always lead to an increase in toroidal mode frequency as the $K_S(r)$ sensitivity kernel is always positive. For density, however, we find that it depends on the depth of the perturbation. For mode $_0T_2$, for example, an increase in density in the upper mantle will lead to a decrease in frequency, while an increase in the lower mantle will increase the frequency. When we move from the fundamental to the overtones, we find that the density kernel $K_\rho(r)$ becomes oscillatory around zero (see, e.g., the $n=5$ overtones). These modes are almost insensitive to smooth variations in density, as the kernels will average to zero. The sensitivity

to desity also becomes smaller for larger l along the same branch, which can clearly be seen when progressing from $_0T_2$ to $_0T_{10}$ along the fundamental mode branch. This agrees well with the interpretation of shorter period toroidal modes in terms of Love waves, which are also dominated by sensitivity to shear wave velocity.

[Figure 9](#) shows examples of sensitivity kernels for the spheroidal modes. The spheroidal modes involve wave motion in both horizontal and vertical directions, and so are sensitive to perturbations in density and to both v_P and v_S . Again, moving to the right along the fundamental mode branch shows that sensitivities become progressively concentrated closer to the surface. Spheroidal modes correspond to Rayleigh waves and at higher l the largest sensitivity is to shear wave velocity, similar to the toroidal modes, except that peak sensitivity is reached at subcrustal depths, making them less sensitive to large variations in shear velocity in the crust than is the case for toroidal modes. The overtones sample

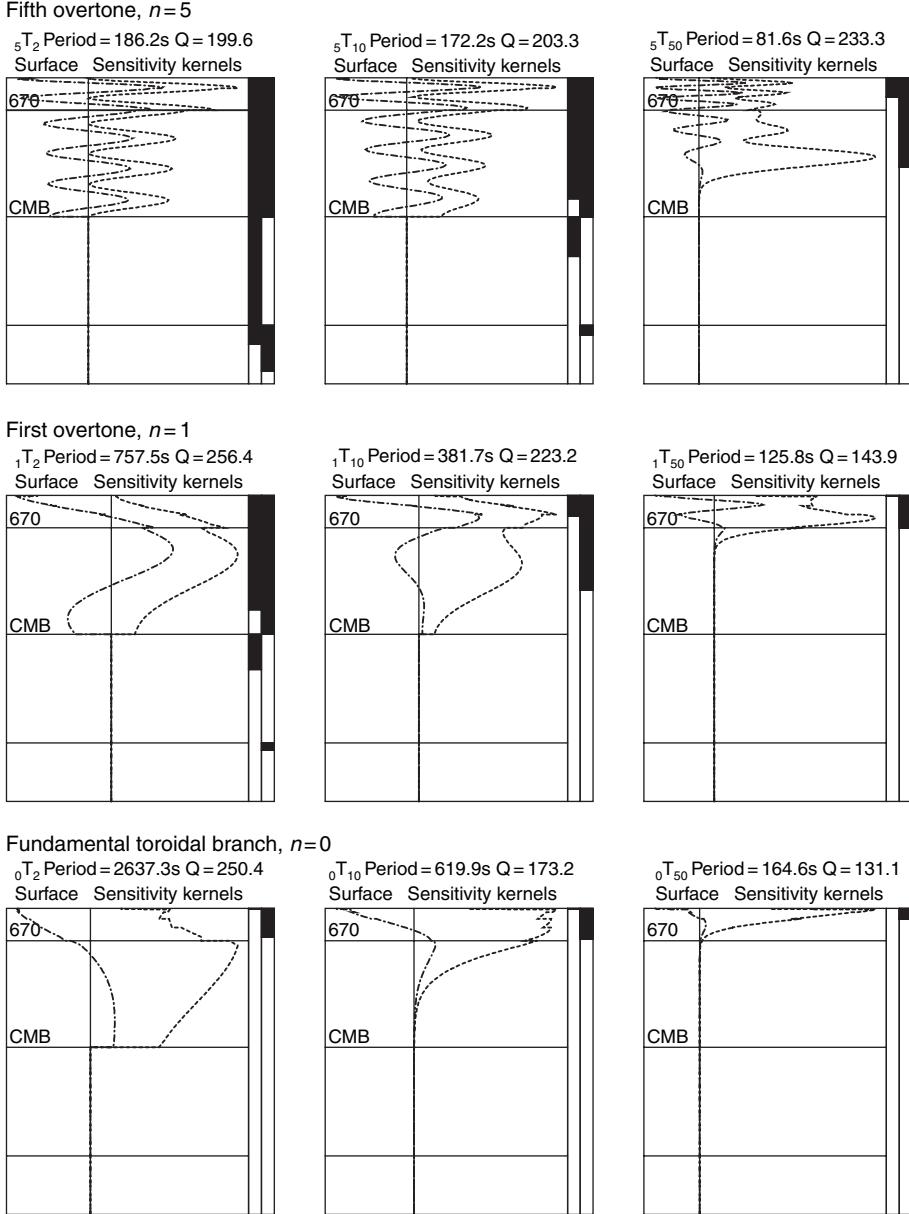


Figure 8 Sensitivity kernels $K_S(r)$ (dashed lines) and $K_p(r)$ (dot-dashed lines) of selected toroidal modes.

different families of modes. The mode ${}_5S_{10}$ corresponds to a Stoneley wave (the analog of a Rayleigh wave, but at a fluid–solid interface, rather than at a free surface), traveling along the inner-core boundary. ${}_1S_{10}$ is a mixture of a mantle mode and a Stoneley wave at the core–mantle boundary. The other modes in Figure 9 show a behavior similar to the toroidal modes. Notice that for ${}_5S_{50}$ the v_p sensitivity decays below the P-wave ray-theoretic turning point (the point at which the shading terminates in the left vertical stripe at the right of the plot), and the v_S

sensitivity decays below the S-wave turning point. The fact that, for a given ray parameter, S-waves turn at greater depth than P-waves means that in modeling there is some potential for shallow P-velocity structure to trade off with deep S-velocity structure.

Figure 10 shows another family of spheroidal modes, which are characterised by low l and high overtone number n . These modes are the PKIKP equivalent modes which have strong sensitivity to core structure.

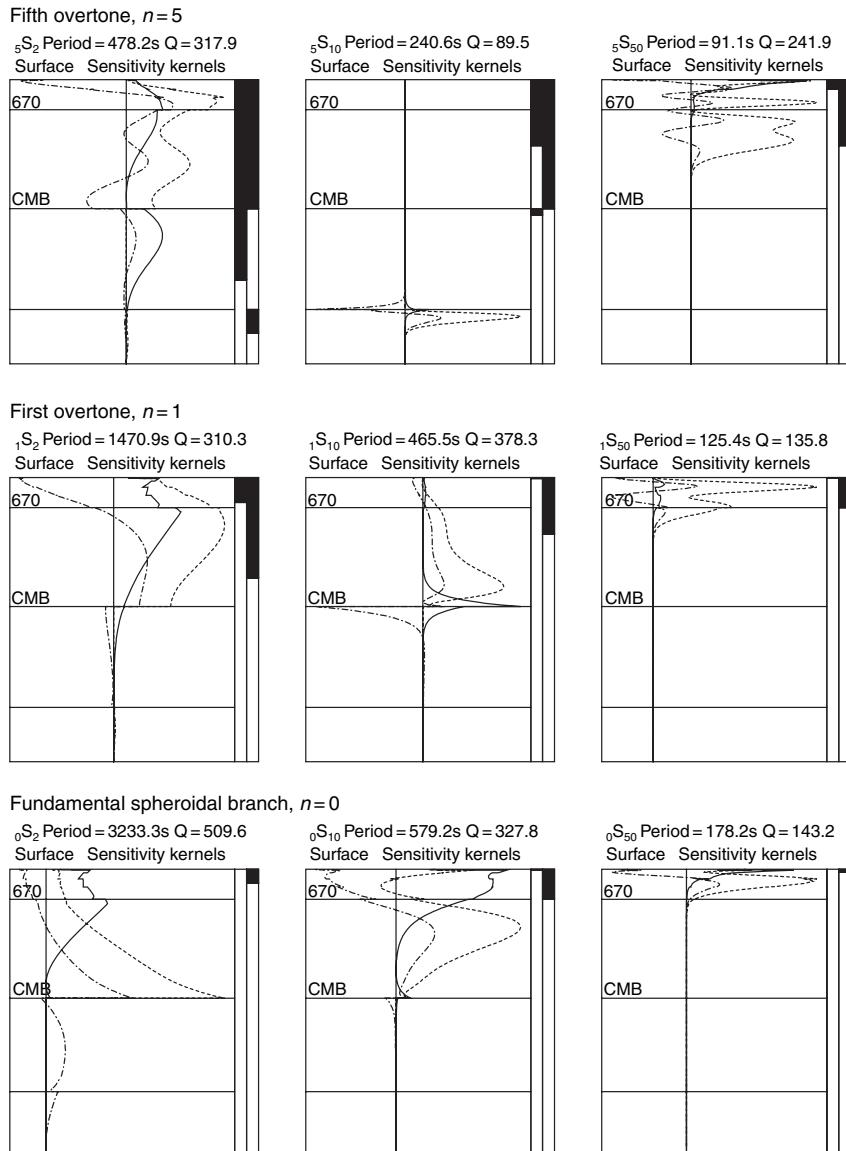


Figure 9 Sensitivity kernels of selected spheroidal modes. $K_S(r)$ dashed, $K_P(r)$ solid, $K_\rho(r)$ dot-dash.

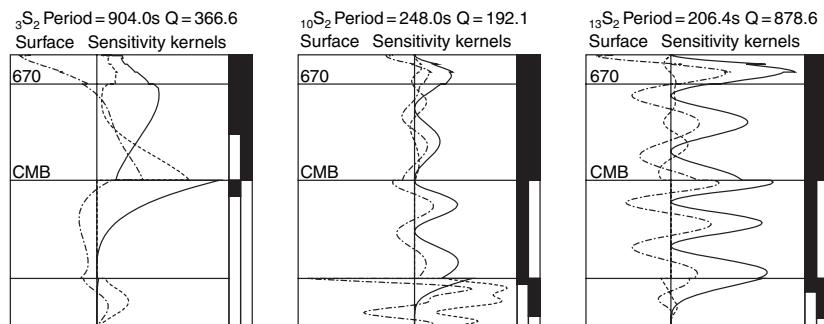


Figure 10 Sensitivity kernels of selected PKIKP equivalent spheroidal modes.

1.02.8 Normal Modes and Theoretical Seismograms in Three-Dimensional Earth Models

The problem of calculating theoretical seismograms and spectra for three-dimensional models is a challenging one. A theoretically straightforward formalism exists for such calculations, based on expanding the wave field in terms of a complete set of (vector) functions. The equations that arise from requiring that the equations of motion be satisfied can be regarded as exact matrix equations. However, they are of infinite dimension, and even when truncated to give a practicable method of solution, the calculations require the manipulation and diagonalization of extremely large matrices. If the expansion is carried out in terms of the eigenfunctions of a spherical model (that is close to reality), the process is simplified, as the off-diagonal terms in the resulting matrices are small, allowing some approximate schemes that are much less cumbersome to be developed.

Let us take as our starting point in considering the form that this theory takes the equation of motion in operator form given in [35]. In the frequency domain

$$(\mathcal{H} - \rho\omega^2)\mathbf{u} = \mathbf{f} \quad [125]$$

The Earth will be considered to be in a state of steady rotation with angular velocity $\boldsymbol{\Omega}$ about its center of mass, so that the expression for \mathcal{H} acquires additional terms representing the Coriolis force and the centrifugal potential (Dahlen, 1968):

$$\begin{aligned} (\mathcal{H}\mathbf{u})_i = & \rho \left(\phi_{,i}^1 + \left[\phi^0 - \frac{1}{2} (\Omega_k \Omega_k x_l x_l - \Omega_k \Omega_l x_k x_l) \right]_{ij} u_j \right. \\ & \left. + 2i\epsilon_{ijk} \Omega_j u_k \right) - (\Lambda_{jilk} u_{k,l})_j \end{aligned} \quad [126]$$

where, as previously, ϕ^1 is regarded as a functional of \mathbf{u} , by virtue of Poisson's equation [22]. Let $\mathbf{s}^{(km)}$ represent the eigenfunctions of a spherical, nonrotating, nonattenuating reference model, with eigenfrequencies ω_k so that

$$\mathcal{H}_0 \mathbf{s}^{(km)} = \rho_0 \omega_k^2 \mathbf{s}^{(km)} \quad [127]$$

satisfying the orthogonality relation

$$\int_V \rho_0 \mathbf{s}^{(km)*} \cdot \mathbf{s}^{(km)} dV = \delta_{k'k} \delta_{m'm} \quad [128]$$

Where \mathcal{H}_0 and ρ_0 are for the reference model, and let us seek a solution of [125] in terms of an expansion

$$\mathbf{u}(\mathbf{x}, \omega) = \sum_{km} a_{km} \mathbf{s}^{(km)}(\mathbf{x}) \quad [129]$$

with coefficients a_{km} to be found. Substituting into [125], and then taking the dot product with $\mathbf{s}^{(k'm')*}$ and integrating, we find

$$\begin{aligned} \sum_{km} [(k'm'|\mathcal{H}_1 - \rho_1 \omega^2|km) - (\omega^2 - \omega_k^2) \delta_{k'k} \delta_{m'm}] a_{km} \\ = (k'm'|\mathbf{f}) \end{aligned} \quad [130]$$

where $\mathcal{H}_1 = \mathcal{H} - \mathcal{H}_0$, $\rho_1 = \rho - \rho_0$, and where we have introduced the notations $(k'm'|\mathbf{f}) = \int_V \mathbf{s}^{(k'm')*} \cdot \mathbf{f} dV$, $(k'm'|\mathcal{H}_1 - \rho_1 \omega^2|km) = \int_V \mathbf{s}^{(k'm')*} (\mathcal{H}_1 - \rho_1 \omega^2) \mathbf{s}^{(km)} dV$. Equation [130] can be regarded as a matrix equation, albeit of infinite dimension, in which rows and columns of the matrix on the left side are labeled by (k', m') , (k, m) , respectively and in which the rows of the column on the right side are labeled by (k', m') . We can write

$$\mathbf{C}(\omega) \mathbf{a} = \frac{1}{i\omega} \mathbf{E} \quad [131]$$

where \mathbf{C} is the matrix having matrix elements $(k'm'|\mathcal{C}(\omega)|km) = (k'm'|\mathcal{H}_1 - \rho_1 \omega^2|km) - (\omega^2 - \omega_k^2) \delta_{k'k} \delta_{m'm}$ and where $\mathbf{E}/i\omega$ is the column vector having elements $(k'm'|\mathbf{f})$, the factor $1/i\omega$ being inserted to reflect the assumed step-function time dependence of the source, so that \mathbf{E} , which has elements E_{km} given in [98], is independent of frequency. Hence the formal solution is given by

$$\mathbf{a} = \frac{1}{i\omega} \mathbf{C}(\omega)^{-1} \mathbf{E} \quad [132]$$

Recalling that we are thinking of the index k as incorporating angular order l , overtone number n , and the mode type (spheroidal or toroidal), the matrix $\mathbf{C}(\omega)$ consists of blocks of dimension $(2l+1) \times (2l+1)$, as row index m' takes on values $-l$ to l and column index m takes on values $-l$ to l . Thus, each block within $\mathbf{C}(\omega)$ relates two particular multiplets k, k' of the spherical reference model. Because the deviation from the spherical reference model is regarded as small, the matrix elements in \mathbf{C} are small, except for the elements on the diagonal proportional to $\omega^2 - \omega_k^2$. These diagonal terms are small for values of ω close to ω_k , for a given multiplet k , but for other diagonal blocks, corresponding to multiplets not close in frequency to multiplet k , they are not small; thus, the matrix is, mostly, diagonally dominant, except for diagonal blocks corresponding to multiplets close in frequency to ω . Of course, the complete solution is to be obtained by substituting [132] into [129] and then evaluating the inverse Fourier transform; thus, we need to consider the behavior of the solution as a function of complex variable ω . In

particular, we are interested in the singularities that occur in the complex ω plane, as these will correspond to the modes of the aspherical model, in much the same way as the modes of the spherical model correspond to singularities, in the frequency domain, of the solution of the inhomogenous problem (eqn, [93] and the related discussion). The singularities in the solution [132] will be at the frequencies $\omega = \omega_b$, say, for which there exists a non-trivial solution to the homogeneous problem

$$\mathbf{C}(\omega_b)\mathbf{r}_b = 0 \quad [133]$$

This is an eigenvalue problem for ω_b and the corresponding right eigenvector \mathbf{r}_b . The eigenvalue problem is of a nonstandard form, since the dependence of \mathbf{C} on the eigenvalue parameter $\lambda = \omega^2$ say, is not of the usual form $\mathbf{C}_0 - \lambda\mathbf{I}$. This is because, (1) perturbations in density ρ_1 introduce a more general dependence on ω^2 , (2) by virtue of attenuation, the perturbations in the elastic parameters entering into \mathcal{H}_1 are dependent upon ω , (3) the terms arising from rotation depend upon ω , rather than on ω^2 . The form of the solution as a sum over residues arising from singularities at $\omega = \omega_b$ can be obtained by replacing the inverse Fourier transform by a summation over singularities b , and within the integrand carrying out the replacement (Deuss and Woodhouse, 2004; AL-Attar, 2007; cf. eqn [94]):

$$\mathbf{C}(\omega)^{-1} \rightarrow i \frac{\mathbf{r}_b \mathbf{l}_b}{\mathbf{l}_b \partial_\omega \mathbf{C}(\omega_b) \mathbf{r}_b} \quad [134]$$

where \mathbf{l}_b is the left-eigenvector (a ‘row’ rather than a column), the solution of

$$\mathbf{l}_b \mathbf{C}(\omega_b) = 0 \quad [135]$$

We are assuming here that [133] and [135] determine the right and left eigenvectors $\mathbf{r}_b, \mathbf{l}_b$ uniquely, up to multiplying factors, such factors being immaterial for the evaluation of the residue contribution [134]. Thus, from [129] the solution in the time domain can be written as

$$\begin{aligned} \mathbf{u}(\mathbf{x}, t) &= 2\operatorname{Re} \sum_{bkm} \frac{1}{\omega_b} \frac{\mathbf{l}_b \cdot \mathbf{E}}{\mathbf{l}_b \partial_\omega \mathbf{C}(\omega_b) \mathbf{r}_b} \\ &\times (km|\mathbf{r}_b) s^{(km)}(\mathbf{x}) e^{i\omega_b t} \end{aligned} \quad [136]$$

where the notation $(km|\mathbf{r}_b)$ represents individual elements of the column \mathbf{r}_b . As previously, the contribution from singularities in the left half of the complex ω -plane is incorporated by taking twice the real part, the summation in [136] being taken only for ω_b in the right half-plane.

In order to make use of this theory, it is necessary to obtain expressions for the matrix elements $(k'm'|\mathbf{C}(\omega)|km)$ in terms of the perturbations in elastic parameters, density, etc., and deviations of surfaces of discontinuity from the spherically symmetric reference model. Fairly complete forms for these are given by Woodhouse (1980a), omitting terms in anisotropic parameters and in initial stress. For anisotropic perturbations, see Chapter 1.16. The basic method is to expand the perturbations in spherical harmonics, and then to evaluate the integrals of triples of spherical harmonics using the formula, derivable from [43] and [48]:

$$\begin{aligned} &\frac{1}{4\pi} \int_{-\pi}^{\pi} \int_0^{\pi} (Y_l^{N'm'})^* Y_l^{N''m''} Y_l^{Nm} \sin \theta d\theta d\phi \\ &= (-1)^{N'-m'} \begin{pmatrix} l' & l'' & l \\ -N' & N'' & N \end{pmatrix} \begin{pmatrix} l' & l' & l \\ -m' & m'' & m \end{pmatrix} \\ &(N' = N'' + N) \end{aligned} \quad [137]$$

The resulting form for the matrix elements can then be written in the form

$$\begin{aligned} (k'm'|\mathbf{C}(\omega)|km) &= \sum_{l'm''} (-1)^{-m'} \begin{pmatrix} l' & l'' & l \\ -m' & m'' & m \end{pmatrix} \\ &\times (k'|\mathbf{C}(l''m'')(\omega)||k) \end{aligned} \quad [138]$$

where the so-called ‘reduced matrix element’ appearing in the right side, itself defined by this equation, is independent of m and m' . This particular form for the dependence of the matrix elements on m and m' is a consequence of the Wigner–Eckart theorem (see Edmonds (1960)). The expressions for the reduced matrix elements take the form of radial integrals involving pairs of scalar eigenfunctions, for multiplets k' and k , and on the $(l''m'')$ component of the spherical harmonic expansion of heterogeneity, together with terms evaluated at boundaries corresponding to the $(l''m'')$ components of the deflections of the boundaries.

This is a fairly complete theory for the oscillations of a general Earth model. Apart from the treatment of aspherical boundary perturbations, which involves a linearization of the boundary conditions, it is in principle an exact theory (Woodhouse, 1983), provided that coupling between all multiplets is taken into account – that is, provided that the eigenvalue problem for ω_b includes all the blocks of the full matrix $\mathbf{C}(\omega)$. Of course, the theory cannot be applied in its full form, owing to the need to manipulate infinite-dimensional matrices, and so a number of approximate schemes have been developed. The

simplest, and up to now most widely applied method is to reduce the eigenvalue problem for ω_b to that for a single diagonal block – the so-called ‘self-coupling’ approximation. In this case we focus on a single multiplet, k , and reduce $\mathbf{C}(\omega)$ to the $(2l+1) \times (2l+1)$ block corresponding to multiplet k . This is a justifiable approximation for the calculation of $\mathbf{u}(\mathbf{x}, \omega)$ for frequencies near ω_k if the mode can be considered ‘isolated’, which is to say that there are no other modes nearby having significant coupling terms. A precise statement of the conditions that need to be satisfied for a mode to be considered isolated has not, to our knowledge, been worked out but, roughly speaking, it is necessary for the ratio $(k'm'|\mathbf{C}(\omega)|km)/(\omega_k^2 - \omega_k'^2)$ for all other multiplets k' to be small, for ω near the frequency ω_k of the target multiplet. In the self-coupling approximation the dependence of $\mathbf{C}(\omega)$ can be linearized for frequencies near ω_k : $\mathbf{C}(\omega) \approx \mathbf{C}(\omega_k) + \mathbf{C}'(\omega_k)\delta\omega$, and a $(2l+1) \times (2l+1)$ matrix eigenvalue problem is obtained for $\delta\omega$:

$$[\mathbf{C}(\omega_k) + \mathbf{C}'(\omega_k)\delta\omega]\mathbf{r} = 0 \quad [139]$$

having eigenvalues $\delta\omega_b$, say. This can also be written, to zeroth order, as

$$\mathbf{H}^{(k)}\mathbf{r} = \delta\omega\mathbf{r} \quad [140]$$

where the $(2l+1) \times (2l+1)$ matrix $\mathbf{H}^{(k)}$, called the ‘splitting matrix’ of the target multiplet, k , has elements $(km'|\mathbf{H}^{(k)}|km) = (km'|\mathbf{C}(\omega_k)|km)/2\omega_k$. The contribution to the right-hand side of [136] can be written (Woodhouse and Girnius, 1982) as

$$\begin{aligned} \mathbf{u}_k(\mathbf{x}, t) &= \mathbf{Re} \sum_{m'm} -\frac{1}{\omega_k^2} \left(\exp(i\mathbf{H}^{(k)}t) \right)_{mm'} \\ &\times E_{km'} \mathbf{s}^{(km)}(\mathbf{x}) e^{i\omega_k t} \end{aligned} \quad [141]$$

the matrix exponential arising from the identity

$$\sum_{b=1}^{2l+1} \frac{\mathbf{r}_b \mathbf{l}_b}{\mathbf{l}_b \cdot \mathbf{r}_b} \exp(i\delta\omega_b t) = \exp(i\mathbf{H}t) \quad [142]$$

Equation [141], which is directly comparable to the result for the spherical reference model in [115], has the simple interpretation that at time $t=0$ the modes are excited as they would be in the reference model, as the matrix exponential is initially equal to the unit matrix. (The static, time-independent terms are not included, as we are considering an approximation valid only in the spectral neighborhood of ω_k , the frequency of the target multiplet.) With time, the effective excitation $\exp(i\mathbf{H}^{(k)}t)\mathbf{E}_k$ evolves on a slow

timescale characterized by the incremental eigenfrequencies $\delta\omega_b$, the eigenvalues of $\mathbf{H}^{(k)}$. In the frequency domain, this leads to ‘splitting’ of the degenerate eigenfrequency ω_k into $2l+1$ ‘singlets’ – hence the name ‘splitting matrix’ for $\mathbf{H}^{(k)}$.

It is straightforward to set up the inverse problem of estimating the splitting matrix for isolated multiplets using data spectra for many events. This is simplified by recognizing that the $(2l+1) \times (2l+1)$ matrix $\mathbf{H}^{(k)}$ is equivalent to a certain function on the sphere, known as the ‘splitting function’ (Woodhouse and Giardini, 1985). It can be shown that for scalar perturbations from the reference model, such as ρ_1 , κ_1 , μ_1 , $\mathbf{H}^{(k)}$ is expressible in terms of coefficients $c_{l'm''}$ which represent the spherical harmonic expansion coefficients of even degree l'' , and up to finite spherical harmonic degree $l'' \leq 2l$ by the expression

$$\begin{aligned} (km'|\mathbf{H}^{(k)}|km) &= \Omega \beta_k m \delta_{m'm} + \omega_k \sum_{\substack{l''=0 \\ l'' \text{ even}}}^{2l} \sum_{m''=-l''}^{l''} (-1)^{m'} \\ &\times \left(\frac{2l''+1}{4\pi} \right)^{1/2} (2l+1) \begin{pmatrix} l & l'' & l \\ 0 & 0 & 0 \end{pmatrix} \\ &\times \begin{pmatrix} l & l'' & l \\ -m' & m'' & m \end{pmatrix} c_{l'm''}^{(k)} \end{aligned} \quad [143]$$

where the first term is the effect of Coriolis forces (Dahlen, 1968), β_k being the (known) rotational splitting parameter for the multiplet. Thus, the inverse problem for $\mathbf{H}^{(k)}$ is equivalent to the estimation of $c_{l'm''}$. The function on the sphere

$$\eta(\theta, \phi) = \sum_{\substack{l''=0 \\ l'' \text{ even}}}^{2l} \sum_{m''=-l''}^{l''} c_{l'm''}^{(k)} \nu_l Y_l^{0m''}(\theta, \phi) \quad [144]$$

can be interpreted, at least for high- l modes, as the even degree expansion of $\delta\omega_{\text{local}}/\omega_k$, in which $\delta\omega_{\text{local}}$ is the eigenfrequency that a spherically symmetric model would possess if its radial structure were the same as the structure beneath the point (θ, ϕ) (Jordan, 1978). Only even degrees are present by virtue of the fact that the first $3-j$ symbol in [143] vanishes for odd values of l'' . The splitting function leads to a two-stage inversion for three-dimensional structure in which stage 1 is to find the structure coefficients $c_{l'm''}^{(k)}$ that bring data and theoretical spectra into agreement, using as many events and stations as are available, and the stage 2 is to determine the structural perturbations needed to match the inferred values of $c_{l'm''}^{(k)}$. Stage 1 of the procedure is nonlinear, owing to the fact that the relation between the synthetics and $c_{l'm''}^{(k)}$ involves the exponential $\exp i\mathbf{H}^{(k)}t$.

Stage 2, on the other hand, is linear; $c_{r'm'}^{(k)}$ is related to three-dimensional structural perturbations by integrals involving known differential kernels. This is a similar procedure to that commonly employed in surface wave studies, in which one first determines two-dimensional maps of phase velocity, over a range of frequencies, and then uses these to infer the three-dimensional structure perturbations needed to explain the inferred phase velocity maps. The spectral fitting approach using splitting function coefficients $c_{r'm'}^{(k)}$ has been widely applied (e.g., Giardini *et al.*, 1987, 1988; Ritzwoller *et al.*, 1988; He and Tromp, 1996; Resovsky and Ritzwoller, 1995, 1998; Romanowicz and Breger, 2000; Masters *et al.*, 2000).

Figure 11 shows an example of data and theoretical spectra using the self-coupling approximation, and splitting function coefficients estimated from a large collection of data. In the left panel the splitting effects only of rotation and ellipticity are taken into account, whereas in the right panel the estimated splitting function has been used to calculate the synthetic spectra. The distribution of singlets and their excitations is known only by virtue of the inversion itself. There is no possibility here of resolving the singlets in individual spectra, but by modeling a large collection of spectra, for many events and stations, the underlying singlet distribution is unmasked. This example illustrates the fact that there are large differences between data and synthetics prior to modeling,

indicating that long period spectra represent a rich source of information about the Earth's three-dimensional structure.

The fact that in the self-coupling approximation seismic spectra depend only upon the 'even' spherical harmonic degrees of heterogeneity points to a shortcoming of the theory. Since spherical harmonics of even degree are symmetric under point reflection in the center of the Earth, self-coupling theory predicts that the seismic spectra depend only upon the average structure between pairs of antipodal points. Thus, the interaction, or coupling, of modes must be a key effect for understanding wave phenomena that do not have this symmetry property. The theory can be straightforwardly extended to include the coupling of groups of modes. The resulting method is known as 'quasi-degenerate perturbation theory' (Dahlen, 1969; Luh, 1973, 1974; Woodhouse, 1980a), or 'group coupling'. A small group of multiplets $\{k_1, k_2, k_3, \dots\}$, close in frequency, is selected, and the eigenvalue problem is reduced to that for the matrix obtained from $C(\omega)$ by selecting only the blocks corresponding to the chosen multiplets. This problem can then be linearized in $\delta\omega$, relative to a fiducial frequency in the chosen band, in much the same way as in the case of self-coupling, outlined above, the resulting matrix eigenvalue problem being of dimension $(2l_1 + 1) + (2l_2 + 1) + (2l_3 + 1) + \dots$. The selected group of modes is said to form a 'super-multiplet'. Resovsky and Ritzwoller (1995)

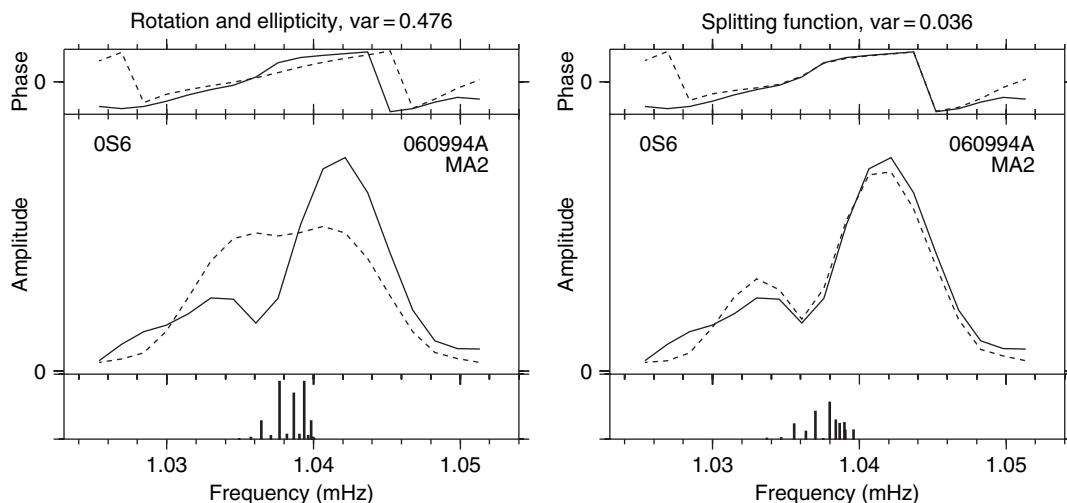


Figure 11 Data and synthetic spectra for oS_6 for an earthquake in Bolivia. The time window is 5–70 h. The solid lines are the observed phase (top) and amplitude spectrum (middle), and dashed lines are for the synthetic spectra. In the left diagram only splitting due to rotation and ellipticity is taken into account, in the right diagram the estimated splitting function is used, reducing the misfit variance ratio for this record from 0.476 to 0.036. The distribution of singlets contributing to the synthetic spectra and their relative excitation amplitudes are indicated at the bottom of each panel. Phase is in the interval $(-\pi, \pi]$.

have generalized the notion of the splitting function and structure coefficients to include coupling between pairs of multiplets, so that $c_{l'm''}^{(k)}$ becomes $c_{l'm''}^{(k_1, k_2)}$, and have made estimates of such coefficients from seismic spectra (see, e.g., Resovsky and Pestana (2003)).

The splitting function approach has been used in inversions for tomographic velocity models (Li *et al.*, 1991; Resovsky and Ritzwoller, 1999; Ishii and Tromp, 1999). Some recent tomographic shear wave velocity models such as S20RTS (Ritsema *et al.*, 1999), make use of splitting functions in addition to body wave, surface wave, and overtone data to provide improved constraints on the low degree structure. Splitting functions have also been used in the discovery of inner-core anisotropy (Woodhouse *et al.*, 1986) and have provided constraints on the possible rotation of the inner core (Sharrock and Woodhouse, 1998; Laske and Masters, 1999).

The ‘self-coupling’ and ‘group coupling’ techniques depend upon the assumption that further cross-coupling is not needed to approximate the complete solution, which as we have shown includes coupling between all multiplets. Of course, full coupling calculations cannot be done for a truly infinite set of modes, but it is feasible at low frequencies to include coupling between all multiplets below a specified frequency. We shall call this ‘full coupling’. Deuss and Woodhouse (2001) have compared the different approximations used in computing normal mode spectra, and have found that ‘self-coupling’ and

‘group coupling’ can be a poor approximation to ‘full coupling’, indicating that a more complete version of the theory will need to be used in the future as it is desired to constrain the three-dimensional distribution of parameters, such as density, attenuation, and mantle anisotropy, on which the spectra depend more subtly.

Figure 12 shows a comparison between data and spectra calculated using the ‘self-coupling’ with those resulting from a ‘full coupling’ calculation in which the coupling of all 140 modes up to 3 mHz has been included (see Deuss and Woodhouse, (2001) for details of the calculation). The spheroidal modes are clearly seen, and there is also signal for toroidal mode ${}_0T_{10}$ on the vertical component, which is due to Coriolis coupling. There is reasonable agreement between the data and full coupling synthetics, but the differences between data and synthetics are comparable to the difference between the ‘self-coupling’ and ‘full coupling’ synthetics. It may be expected that ‘group coupling’ would be justified, and that coupling among wide bands of modes can be ignored. However, coupling on groups still shows significant differences compared to ‘full coupling’ (see **Figure 13**).

In principle, normal mode spectra can be inverted directly to derive tomographic models, avoiding the intermediate step of estimating the splitting function coefficients (Li *et al.*, 1991; Hara and Geller, 2000; Kuo and Romanowicz, 2002). This leads to a one-step inversion procedure in which model parameter

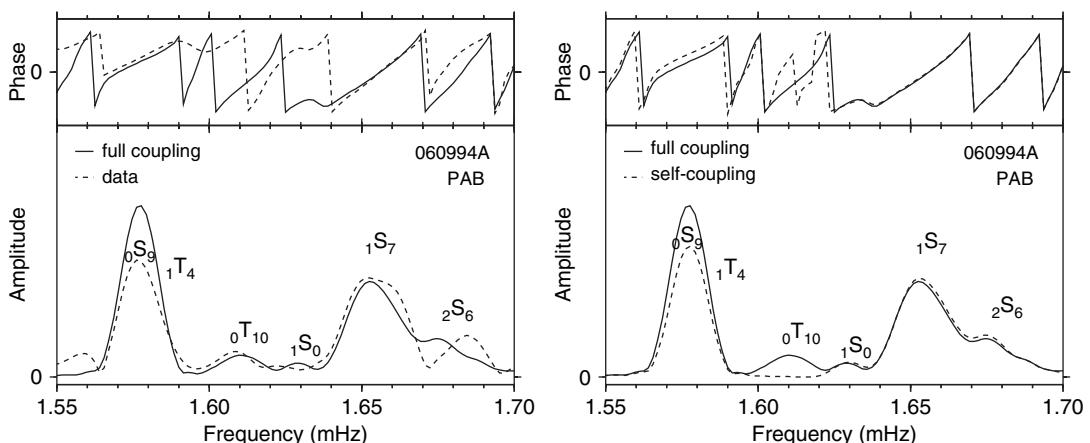


Figure 12 Data and synthetics for modes ${}_0S_9$, ${}_1T_4$, ${}_0T_{10}$, ${}_1S_0$, ${}_1S_7$ and ${}_2S_6$ at station PAB for an earthquake in Bolivia. The time window is 5–45 h. The differences between full coupling and self-coupling are similar to the differences between the data and full coupling and are of the same order as the differences that one would attempt to model. This indicates that full coupling is essential in future attempts to model inhomogeneous structure. From Deuss A and Woodhouse JH (2001) Theoretical free oscillation spectra: The importance of wide band coupling. *Geophysical Journal International* 146: 833–842.

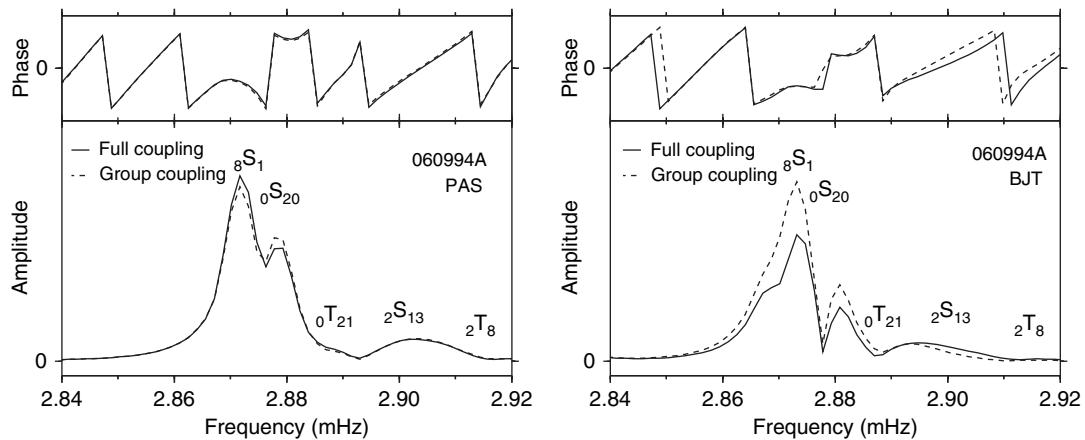


Figure 13 Synthetics for modes $_{2}S_{13}$, $_{0}T_{21}$, $_{0}S_{20}$, $_{8}S_1$, $_{2}T_8$ for stations PAS and BJT of the Bolivia event of 9 June 1994, from Deuss and Woodhouse (2001). The time window is 5–80 h. All modes in the frequency interval shown were allowed to couple for the group coupling calculations; the full coupling calculation includes all modes up to 3 mHz.

adjustments that enable the data and theoretical spectra to be brought into agreement are sought directly. This scheme has the advantage that the full coupling approach can be used for the solution of the forward problem and for calculations of the derivatives needed for formulating the inverse problem. Of course, it has the disadvantage that a nonlinear inverse problem needs to be solved within a large model space, rather than being able to restrict the nonlinear stage of inversion to the much smaller number of parameters represented by splitting functions. The calculations are also much more burdensome in terms of computer time and memory. This means that the splitting function technique is still largely the preferred method in spectral fitting studies; however, to investigate the large regions of the spectrum where wide-band coupling is expected to be significant, a final stage inversion involving full coupling will be needed.

Significant theoretical work has been directed toward developing methods able to give accurate splitting and coupling results using a practicable amount of computer time and memory (e.g., Lognonne and Romanowicz, 1990; Park, 1990; Lognonne, 1991). Deuss and Woodhouse (2004) have developed a technique for solving the full coupling generalized eigenvalue problem [133], [135] by an iterative technique, not requiring the eigenvalue decomposition of very large matrices, which is well suited to the accurate modeling of small spectral segments. The first iteration of this technique is similar to the ‘subspace projection method’ of Park (1990), which similarly aims to

approximate full coupling effects while avoiding the need to find the eigenvectors and eigenvalues of very large matrices.

1.02.9 Concluding Discussion

The normal mode formalism provides a well-developed theoretical framework for the calculation of theoretical seismograms in both spherically symmetric and three-dimensional Earth models. For spherically symmetric models, the ability to simply and quickly calculate complete theoretical seismograms plays an important role in the formulation and solution of many seismological problems involving both surface waves and long period body waves. In the three-dimensional case, the theory of mode coupling is too cumbersome to be applied in full, but it enables a number of useful approximations to be developed and tested. The increasing capacity in high-performance computing means that it becomes possible to develop and test increasingly more complete implementations of the fully coupled theory. Progress on fully numerical solutions for seismic wave fields in realistic three-dimensional spherical models (Komatitsch and Tromp, 2002a, 2002b), while it is providing a new and invaluable tool in many areas of global seismology, has not yet made it possible to calculate accurate very long period spectra. In part, this is because a way has not (yet?) been found to fully implement self-gravitation in the spectral element method, and in part because the small time step needed in finite difference and spectral

element calculations leads to very long execution times; also, there are very stringent limits on the tolerable amount of numerical dispersion in the solution.

Long period modal spectra constitute a rich source of information on long wavelength heterogeneity, studies to date, we believe, having only scratched the surface. To realize the potential of this information will require large-scale coupling calculations or, possibly, other methods for calculating very long period wave fields yet to be developed. This will make it possible to bring modal spectral data increasingly to bear on furthering our understanding of the Earth's three-dimensional structure.

References

- Abramowitz M and Stegun IA (1965) *Handbook of Mathematical Functions*. New York: Dover.
- Backus GE and Gilbert F (1967) Numerical applications of a formalism for geophysical inverse problems. *Geophysical Journal of the Royal Astronomical Society* 13: 247–276.
- Backus GE and Mulcahy M (1976) Moment tensors and other phenomenological descriptions of seismic sources, i. continuous displacements. *Geophysical Journal of the Royal Astronomical Society* 46: 341–362.
- Biot MA (1965) *Mechanics of Incremental Deformation*. New York: Wiley.
- Brune JN (1964) Travel times, body waves and normal modes of the earth. *Bulletin of the Seismological Society of America* 54: 2099–2128.
- Brune JN (1966) *p* and *s* wave travel times and spheroidal normal modes of a homogeneous sphere. *Journal of Geophysical Research* 71: 2959–2965.
- Burridge R and Knopoff L (1964) Body force equivalents for seismic dislocations. *Bulletin of the Seismological Society of America* 54: 1875–1888.
- Chapman CH and Woodhouse JH (1981) Symmetry of the wave equation and excitation of body waves. *Geophysical Journal of the Royal Astronomical Society* 65: 777–782.
- Dahlen FA (1968) The normal modes of a rotating, elliptical earth. *Geophysical Journal of the Royal Astronomical Society* 16: 329–367.
- Dahlen FA (1969) The normal modes of a rotating, elliptical earth, II, Near resonant multiplet coupling. *Geophysical Journal of the Royal Astronomical Society* 18: 397–436.
- Dahlen FA and Tromp J (1998) *Theoretical Global Seismology*. Princeton, New Jersey: Princeton University Press.
- Deuss A and Woodhouse JH (2001) Theoretical free oscillation spectra: The importance of wide band coupling. *Geophysical Journal International* 146: 833–842.
- Deuss A and Woodhouse JH (2004) Iteration method to determine the eigenvalues and eigenvectors of a target multiplet including full mode coupling. *Geophysical Journal International* 159: 326–332.
- Dziewonski A and Anderson D (1981) Preliminary reference earth model. *Physics of the Earth and Planetary Interiors* 25: 297–356.
- Dziewonski AM and Gilbert F (1971) Solidity of the inner core of the earth inferred from normal mode observations. *Nature* 234: 465–466.
- Dziewonski AM and Woodhouse JH (1983) Studies of the seismic source using normal mode theory. In: Kanamori H and Boschi E (eds.) *Earthquakes: Observation, Theory and Interpretation, Proc. 'Enrico Fermi' International School of Physics*, vol. LXXXV, pp. 45–137. Amsterdam: North Holland Publ. Co.
- Edmonds AR (1960) *Angular Momentum and Quantum Mechanics*. Princeton, New Jersey: Princeton University Press.
- Eshelby JD (1957) The determination of the elastic field of an ellipsoidal inclusion, and related problems. *Proceedings of the Royal Society of London Series A* 241: 376–396.
- Friederich W and Dalkolmo J (1995) Complete synthetic seismograms for a spherically symmetric earth by numerical computation of the green's function in the frequency domain. *Geophysical Journal International* 122: 537–550.
- Fuchs K and Müller G (1971) Computation of synthetic seismograms by the reflectivity method and comparison with observations. *Geophysical Journal of the Royal Astronomical Society* 23: 417–433.
- Giardini D, Li XD, and Woodhouse JH (1987) Three dimensional structure of the Earth from splitting in free oscillation spectra. *Nature* 325: 405–411.
- Giardini D, Li XD, and Woodhouse JH (1988) Splitting functions of long-period normal modes of the earth. *Journal of Geophysical Research* 93: 13716–13742.
- Gilbert F (1971) Excitation of normal modes of the earth by earthquake sources. *Geophysical Journal of the Royal Astronomical Society* 22: 223–226.
- Gilbert F (1980) An introduction to low frequency seismology. In: Dziewonski AM and Boschi E (eds.) *Physics of the Earth's Interior, Proc. 'Enrico Fermi' International School of Physics*, vol. LXXVIII, pp. 41–81. Amsterdam: North Holland Publ. Co.
- Gilbert F and Backus GE (1966) Propagator matrices in elastic wave and vibration problems. *Geophysics* 31: 326–333.
- Gilbert F and Dziewonski AM (1975) An application of normal mode theory to the retrieval of structural parameters and source mechanisms from seismic spectra. *Philosophical Transactions of the Royal Society of London Series A* 278: 187–269.
- Hara T and Geller R (2000) Simultaneous waveform inversion for three-dimensional earth structure and earthquake source parameters considering a wide range of modal coupling. *Geophysical Journal International* 142: 539–550.
- He X and Tromp J (1996) Normal-mode constraints on the structure of the earth. *Journal of Geophysical Research* 101: 20053–20082.
- Hudson JA (1969) A quantitative evaluation of seismic signals at teleseismic distances, i: Radiation from point sources. *Geophysical Journal of the Royal Astronomical Society* 18: 233–249.
- Ishii M and Tromp J (1999) Normal-mode and free-air gravity constraints on lateral variations in velocity and density of the earth's mantle. *Science* 285: 1231–1236.
- Jordan TH (1978) A procedure for estimating lateral variations from low-frequency eigenspectra data. *Geophysical Journal of the Royal Astronomical Society* 52: 441–455.
- Kanamori H and Anderson DL (1977) Importance of physical dispersion in surface wave and free oscillation problems: Review. *Reviews of Geophysics and Space Physics* 15: 105–112.
- Komatitsch D and Tromp J (2002a) Spectral-element simulations of global seismic wave propagation-I. Validation. *Geophysical Journal International* 149: 390–412.
- Komatitsch D and Tromp J (2002b) Spectral-element simulations of global seismic wave propagation-II. 3-D models, oceans, rotation, and self-gravitation. *Geophysical Journal International* 150: 303–318.

- Kuo C and Romanowicz B (2002) On the resolution of density anomalies in the earth's mantle using spectral fitting of normal-mode data. *Geophysical Journal International* 150: 162–179.
- Lapwood ER and Usami T (1981) *Free Oscillations of the Earth*. Cambridge: Cambridge University Press.
- Laske G and Masters G (1999) Limits on differential rotation of the inner core from an analysis of the earth's free oscillations. *Nature* 402: 66–69.
- Li X-D, Giardini D, and Woodhouse JH (1991) Large scale three dimensional even degree structure of the earth from splitting of long period normal modes. *Journal of Geophysical Research* 96: 551–577.
- Lognonné P (1991) Normal modes and seismograms in an anelastic rotating Earth. *Journal of Geophysical Research* 96: 20309–20319.
- Lognonné P and Romanowicz B (1990) Modelling of coupled normal modes of the Earth – the spectral method. *Geophysical Journal International* 102: 365–395.
- Love AEH (1911) *Some problems in Geodynamics*. Cambridge and New York: Cambridge University Press.
- Love AEH (1927) *A Treatise on the Theory of Elasticity*. Cambridge and New York: Cambridge University Press.
- Luh PC (1973) Free oscillations of the laterally inhomogeneous earth: Quasi-degenerate multiplet coupling. *Geophysical Journal of the Royal Astronomical Society* 32: 187–202.
- Luh PC (1974) Normal modes of a rotating, self gravitating inhomogeneous earth. *Geophysical Journal of the Royal Astronomical Society* 38: 187–224.
- Masters G, Laske G, and Gilbert F (2000) Matrix autoregressive analysis of free-oscillation coupling and splitting. *Geophysical Journal International* 143: 478–489.
- Morse PM and Feshbach H (1953) *Methods of Theoretical Physics*. New York: McGraw Hill.
- Park J (1990) The subspace projection method for constructing coupled-mode synthetic seismograms. *Geophysical Journal International* 101: 111–123.
- Park J, Song TA, Tromp J, et al. (2005) Earth's free oscillations excited by the 26 December 2004 Sumatra–Andaman earthquake. *Science* 308: 1139–1144.
- Pekeris CL and Jarosch H (1958) The free oscillations of the earth. In: Ewing M, Howell BF, Jr., and Press F (eds.) *Contributions in Geophysics in Honor of Beno Gutenberg*, pp. 171–192. New York: Pergamon.
- Phinney RA and Burridge R (1973) Representation of the elastic-gravitational excitation of a spherical earth model by generalized spherical harmonics. *Geophysical Journal of the Royal Astronomical Society* 34: 451–487.
- Resovsky JS and Pestana R (2003) Improved normal mode constraints on lower mantle v_p from generalized spectral fitting. *Geophysical Research Letters* 30: Art.No.1383.
- Resovsky JS and Ritzwoller MH (1995) Constraining odd-degree earth structure with coupled free-oscillations. *Geophysical Research Letters* 22: 2301–2304.
- Resovsky JS and Ritzwoller MH (1998) New and refined constraints on three-dimensional earth structure from normal modes below 3 mhz. *Journal of Geophysical Research* 103: 783–810.
- Resovsky JS and Ritzwoller MH (1999) A degree 8 shear velocity model from normal mode observations below 3 mhz. *Journal of Geophysical Research* 104: 993–1014.
- Ritsema J, van Heijst H, and Woodhouse JH (1999) Complex shear wave velocity structure imaged beneath Africa and Iceland. *Science* 286: 1925–1928.
- Ritzwoller M, Masters G, and Gilbert F (1988) Constraining aspherical structure with low-degree interaction coefficients: Application to uncoupled multiplets. *Journal of Geophysical Research* 93: 6369–6396.
- Romanowicz B and Breger L (2000) Anomalous splitting of free oscillations: A reevaluation of possible interpretations. *Journal of Geophysical Research* 105: 21559–21578.
- Seliger RL and Whitham GB (1968) Variational principles in continuum mechanics. *Proceedings of the Royal Society of London Series A* 305: 1–25.
- Shaddock DS and Woodhouse JH (1998) Investigation of time dependent inner core structure by analysis of free oscillation spectra. *Earth Planets Space* 50: 1013–1018.
- Takeuchi H and Saito M (1972) Seismic surface waves. *Methods in Computational Physics* 11: 217–295.
- Tromp J (1993) Support for anisotropy of the earth's inner core from free oscillations. *Nature* 366: 678–681.
- Tromp J and Dahlen FA (1990) Free oscillations of a spherical anelastic earth. *Geophysical Journal International* 103: 707–723.
- Ward SN (1980) Body wave calculations using moment tensor sources in spherically symmetric, inhomogeneous media. *Geophysical Journal of the Royal Astronomical Society* 60: 53–66.
- Woodhouse JH (1974) Surface waves in a laterally varying layered structure. *Geophysical Journal of the Royal Astronomical Society* 37: 461–490.
- Woodhouse JH (1980a) The coupling and attenuation of nearly resonant multiplets in the Earth's free oscillation spectrum. *Geophysical Journal of the Royal Astronomical Society* 61: 261–283.
- Woodhouse JH (1980b) Efficient and stable methods for performing seismic calculations in stratified media. In: Dziewonski AM and Boschi E (eds.) *Physics of the Earth's Interior, Proc. 'Enrico Fermi' International School of Physics*, vol. LXXVIII, pp. 127–151. Amsterdam: North Holland Publ. Co.
- Woodhouse JH (1983) The joint inversion of seismic waveforms for lateral variations in earth structure and earthquake source parameters. In: Kanamori H and Boschi E (eds.) *Earthquakes: Observation, Theory and Interpretation, Proc. 'Enrico Fermi' International School of Physics*, vol. LXXXV, pp. 366–397. Amsterdam: North Holland Publ. Co.
- Woodhouse JH (1988) The calculation of the eigenfrequencies and eigenfunctions of the free oscillations of the earth and the sun. In: Doornbos DJ (ed.) *Seismological Algorithms*, pp. 321–370. London: Academic Press.
- Woodhouse JH (1996) Long period seismology and the earth's free oscillations. In: Boschi E, Ekström G, and Morelli A (eds.) *Seismic Modelling of Earth Structure*, pp. 31–80. Rome: Istituto Nazionale di Geofisica.
- Woodhouse JH and Dahlen FA (1978) The effect of a general aspherical perturbation on the free oscillations of the earth. *Geophysical Journal of the Royal Astronomical Society* 53: 335–354.
- Woodhouse JH and Giardini D (1985) Inversion for the splitting function of isolated low order normal mode multiplets. *EOS, Transaction American Geophysical Union* 66: 300.
- Woodhouse JH, Giardini D, and Li XD (1986) Evidence for inner core anisotropy from free oscillations. *Geophysical Research Letters* 13: 1549–1552.
- Woodhouse JH and Gurni TP (1982) Surface waves and free oscillations in a regionalized earth model. *Geophysical Journal of the Royal Astronomical Society* 68: 653–673.

1.03 Theory and Observations – Normal Modes and Surface Wave Measurements

R. Widmer-Schnidrig, Black Forest Observatory, Wolfach, Germany

G. Laske, University of California San Diego, LaJolla, CA, USA

© 2007 Elsevier B.V. All rights reserved.

1.03.1	Introduction	67
1.03.1.1	Free Oscillations	67
1.03.1.2	Surface Waves	69
1.03.1.3	What We See in Seismograms – The Basics	69
1.03.2	Free Oscillations	71
1.03.2.1	Modes of a Spherically Symmetric Earth	71
1.03.2.2	Modes of a Heterogeneous Earth	73
1.03.2.2.1	Mode splitting	73
1.03.2.2.2	Mode coupling	77
1.03.2.3	Measuring Mode Observables	81
1.03.2.3.1	Multiplet stripping and degenerate mode frequencies	82
1.03.2.3.2	Singlet and receiver stripping	85
1.03.2.3.3	Retrieving the splitting matrix with the matrix autoregressive technique	86
1.03.2.3.4	Retrieving the splitting matrix with iterative spectral fitting	86
1.03.2.3.5	Observed mode coupling	88
1.03.2.4	Example of a Mode Application: IC Rotation	91
1.03.2.5	Example of a Mode Application: Earth's Hum	92
1.03.3	Surface Waves	94
1.03.3.1	Standing Waves and Traveling Waves	94
1.03.3.2	The Measurement of Fundamental Mode Dispersion	98
1.03.3.2.1	Group velocity	101
1.03.3.2.2	Phase velocity	103
1.03.3.2.3	Time variable filtering	106
1.03.3.3	Other Surface Wave Observables	107
1.03.3.4	Higher Modes	109
1.03.3.4.1	Higher mode dispersion and waveform modeling	109
1.03.3.4.2	Love waves and overtones	113
1.03.3.5	Surface Waves and Structure at Depth	114
1.03.3.6	The Validity of the Great Circle Approximation and Data Accuracy	117
1.03.4	Concluding Remarks	117
References		118

1.03.1 Introduction

1.03.1.1 Free Oscillations

In order to observe Earth's free oscillations, one often has to wait many years for a great, preferably deep earthquake to occur. It is therefore not surprising that free oscillation studies started relatively late last century, after the great 22 May 1960 Chilean earthquake. It was not until 1975 – after the analysis of digitized records of the deep 31 July 1970 Colombian

earthquake – that enough mode measurements were available to construct the first one-dimensional (1-D) Earth model from mode data that could withstand decades of testing as a reference Earth model (1066A by [Gilbert and Dziewonski, 1975](#)). Not much later, great progress was achieved to facilitate the collection of high-quality mode data by installing the global digital seismic network IDA (International Deployment of Accelerometers), a LaCoste–Romberg gravimeter network that was specifically designed to

observe Earth's free oscillations (Agnew *et al.*, 1976, 1986). In the meantime, permanent stations of several other global seismic networks have been upgraded with very broadband seismic sensors – typically Wielandt–Streckeisen STS-1 vault seismometers or Teledyne–Geotech KS54000 borehole seismometers – and digital recording units. This includes early networks that were designed to monitor global seismicity and the Comprehensive Test Ban Treaty (CTBT) such as the High-Gain Long-Period Network (HGLP, first digitally recording network; Savino *et al.*, 1972), the Seismic Research Observatory (SRO, Peterson *et al.*, 1980), the World-Wide Standardized Seismograph Network (WWSSN, Oliver and Murphy, 1971) and the China Digital Seismograph Network (CDSN, Peterson and Tilgner, 1985). Many of these stations as well as the upgraded IDA network are now part of the US American Global Seismic Network (GSN) operated by IRIS (Incorporated Research Institution For Seismology) but other global networks exist such as the French GEOSCOPE (Romanowicz *et al.*, 1984) and the German GEOFON (Hanka and Kind, 1994). All these and more operate under the umbrella of the international Federation of Digital Seismograph Networks (FDSN; Romanowicz and Dziewonski, 1986). Roughly 25 years into very broadband seismic networks, a normal mode seismologist now can enjoy a more than 10 fold increase in high-quality vertical-component long-period seismic records for a given earthquake. But even in the late 1990s – a few years after the deep 09 June 1994 Bolivia earthquake provided spectacular spectra – great effort was invested to digitize the legendary 1970 Colombia records. Since ‘Bolivia’ there have been a handful of other great earthquakes but even the great 23 June 2001 Arequipa/Peru earthquake, the largest digitally recorded earthquake until the 26 December 2004 Andaman–Sumatra event, did not excite the relatively few normal mode observers whose interest lies in unraveling the deep secrets of the inner core (IC). ‘Peru’ was simply not deep (or great) enough to make some of the modes ring that the observers are interested in. On the other hand, since normal modes involve the vibration of the whole planet, mode observations at a single station readily reveal a wealth of information about Earth structure that no other seismic technique can provide. Modes are intrinsic low-pass filters of Earth structure. It is relatively easy to collect unbiased estimates of mode observables that constrain the spherical average of Earth as well as long-wavelength perturbations to it. It is therefore not surprising that in the current efforts to remove the more than two

and half decade old ‘preliminary’ from PREM (Preliminary Reference Earth Model, Dziewonski and Anderson, 1981) – the currently still most widely accepted Reference Earth Model of the spherical average – a suitable mode data set for an updated model exists, while we still struggle to obtain an unbiased body wave data set.

Normal mode seismology has facilitated other great achievements that we can proudly look back to. For example, the analysis of modes provided the ultimate proof that the IC is solid (Dziewonski and Gilbert, 1971). Normal mode studies were at the forefront to assess Earth's attenuation (Smith, 1972) and to retrieve earthquake moment tensors (Gilbert and Dziewonski, 1975), which has been continued in the faithful delivery of the Harvard centroid moment tensors (CMTs) (Dziewonski *et al.*, 1981) that many colleagues depend on for their own studies. Normal mode studies also were at the forefront to assess Earth's 3-D structure. For example, Jobert and Roult (1978) found early evidence for large-scale lateral variations from free oscillations and surface waves and Masters *et al.* (1982) discovered harmonic degree 2 variations in the transition zone that are associated with subducting slabs. The first widely used 3-D models of Earth's upper mantle, M84A and M84C (Woodhouse and Dziewonski, 1984) were obtained using mode theory. Still today, careful analysis of high-precision mode measurements provides crucial clues to answer some of the most fundamental geodynamical questions that remain elusive to other seismic techniques. For example, the analysis of Masters and Gubbins (2003) provides new estimates of the density jump across the IC boundary which is relevant to the discussion of the growth rate and the age of the IC. They also argue against a significant overall excess density in the lowermost mantle that was proposed by Kellogg *et al.* (1999) for locally varying hot abyssal layers for which seismic evidence was presented by Ishii and Tromp (1999). Earth's density structure and the solidity of the IC are best constrained by mode data. Similarly, modes help determine Earth's internal anelastic and anisotropic structure. There are many more aspects where mode data can help out to understand how our planet works. One example is the differential rotation of the IC. Evidence for this was first observed using body wave data and was initially reported to be between 1° and 3° per year (Song and Richards, 1996; Su *et al.*, 1996) but hotly debated (e.g., Souriau, 1998). As subsequent studies accumulated, this number decreased dramatically

and is currently estimated at 1/10 of the initial rate. It was not lastly the mode observations (Sharrock and Woodhouse, 1998; Laske and Masters, 1999, 2003) that provided the conclusive constraints to correct the rotation estimates downward.

In the first part of this chapter, the reader gets acquainted with the jargon used in normal mode seismology some of which requires to summarize the theoretical background that is described by Chapter 1.02. We then introduce some of the most commonly used measurement techniques that we have been involved in. Mode analysis involves more than simply reading the peak frequency and amplitudes from a spectrum. In fact, in most cases, such an approach leads to biased estimates. One also has to bear in mind that the most basic analysis techniques treat modes as being isolated from their neighbors in which case only Earth structure of even-degree symmetry can be retrieved. Earth's rotation and lateral variations cause modes to couple which complicates mode analysis but facilitates the assessment of odd-degree structure. This is briefly described.

1.03.1.2 Surface Waves

Surface waves can be understood as a superposition of free oscillations. It is therefore not surprising that many long-period surface wave seismologists analyzed normal modes at some time in their career. With a few exceptions, including very deep earthquakes, fundamental mode surface waves are the largest signal in a seismogram. Surface wave packets are relatively short and do not require the consistently high signal levels, over several days, as normal modes do. Nor do they require the wait for very large earthquakes. The analysis of surface waves essentially involves the analysis of fundamental modes and the first few overtones, at high frequencies. Surface waves are therefore a natural choice to explore Earth's crust, upper mantle, and transition zone. Much like in a body wave study, the analyst collects traveltimes but the complication is that these depend on frequency. Rather than a sharp onset, a wave packet is observed that is often likened to a Gaussian packet. The two traveltimes-equivalent observables of dispersed surface waves are phase velocity, the speed at which a certain point in the waveform travels, and group velocity, the speed at which wave energy or a point on the envelope of the waveform travels. Though both observables constrain structure at depth, they have different dependencies and ideally one would want to measure both. Group

velocity tends to change more significantly with structure at depth but its measurement errors are also larger than those of phase velocity. On the other hand, source effects on group velocity are relatively small and are usually ignored. Details on earthquake source processes therefore do not have to be known to measure group velocity.

The analysis of surface waves has a major advantage over that of body waves. In the upper mantle, imaging capabilities using body waves are dictated by the distribution of earthquakes and seismic stations. Surface waves travel along the surface between sources and receivers, crossing remote areas and thereby picking up invaluable information about along-path upper-mantle structure that remains elusive to body waves. Like a body wave arrival, group velocity can be measured on a single wave train recorded at a single station without having to resort to calculating synthetic seismograms that are necessary to measure phase traveltimes. For this reason, group velocity analysis has seen a wide range of applications in regional seismology, especially in the CTBT community, even before the advent of sophisticated signal processing.

In the second part of this chapter, we first summarize the relationship between normal modes and surface waves. Some of the surface wave observables are described and how they are measured. We touch on the observation of higher modes and discuss the relationship between dispersion and structure at depth but the reader interested in Earth structure is referred to other contributions in this volume.

1.03.1.3 What We See in Seismograms – The Basics

For moderately large earthquakes, seismograms exhibit a number of wave trains some of which circled the globe completely before arriving at a station. [Figure 1](#) shows the nomenclature for these wave trains. We distinguish between minor and major arc wave trains that arrive at a station from the source directly or took the long path in the opposite direction. [Figure 2](#) shows an example of a vertical seismic record collected at a station of the GEOSCOPE network. Rayleigh wave trains are usually labeled R, while overtones are often labeled X (e.g., [Roult et al., 1986](#)). Love wave trains carry the label G and are observed on the transverse component only, unless Earth's rotation and/or heterogeneity causes strong lateral refraction or, to use the mode analogy, toroidal–spheroidal mode

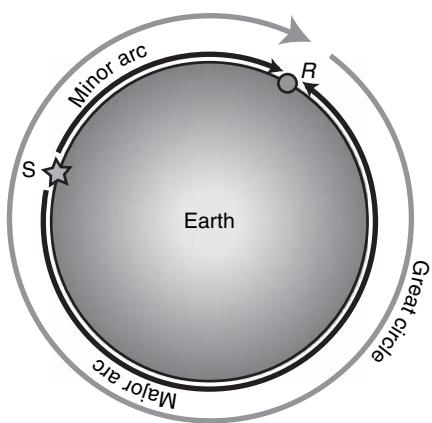


Figure 1 Surface wave paths from source S to receiver R. Paths with distance less than 180° are minor arc paths (R_1), paths with larger distances are major arc paths (R_2). The number following R is the wave orbit number. The wave orbit number advances by two when successive wave trains include a complete great circle (e.g., R_3 and R_5 for the minor arc).

coupling. For large earthquakes with magnitudes typically larger than $M_S = 6.5$, surface waves may be observed as they circle the globe multiple times. At group velocities of about 3.7 km s^{-1} , long-period Rayleigh waves take about 3 h to complete one orbit.

Very large earthquakes can be observed at many global seismic stations with fidelity high enough to discern many wave trains in a record section. **Figure 3** shows the tsunami-generating 2001 Arequipa, Peru earthquake. We can follow R_1 across the globe from the source toward its antipode where the wave train merges with R_2 . Near the source, R_2 and R_3 overlap. A similar collapse of waveforms can be observed for later wave trains. Gray lines mark some of the body wave phases that combine to form the overtones X wave trains as shown in **Figure 2**. For earthquakes as large as the Arequipa event, multiple body wave reflections off the surface, or globe-circling overtones, are also discernible. Very nicely displayed for the Arequipa event, we can follow these overtones at significant signal levels between the fundamental modes and later overtone packages also merge near the source and its antipode. If we consider these overtone packets as modes, some of them have very low attenuation rates and can persist well after the fundamental modes have decayed into the noise. To observe these modes with high fidelity, the collected records typically have to be at least 5 days long.

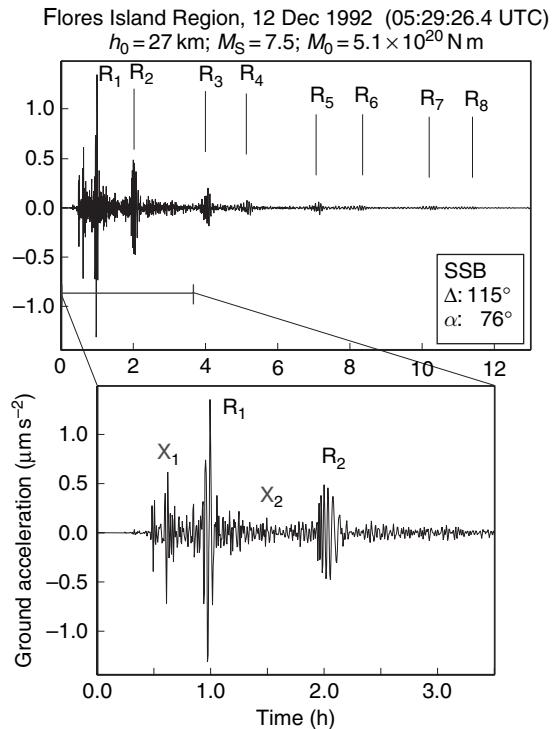


Figure 2 The 1992 Flores Island earthquake, recorded at GEOSCOPE station SSB (Saint Sauveur Badole, France). Marked are eight fundamental mode Rayleigh wavetrains (R_n) and the first two overtone groups (X_n). Δ and α are the epicentral distance and the back azimuth to the event. Since the earthquake was more than 90° away, R_1 and R_2 are closer together than R_2 and R_3 . At group velocities of about 3.7 km s^{-1} , it takes 3 h for Rayleigh waves to circle the globe. Hence R_3 arrives at a station 3 h after R_1 . The seismogram was low-pass filtered with a convolution filter to suppress signal above 20 mHz.

Figure 4 shows the spectrum of a large earthquake observed at the Black Forest Observatory (BFO) in Germany. Since Earth is a finite body, transient waves propagating away from a localized source eventually interfere. For paths whose orbital length is an integer multiple of the wavelength, the two signals interfere constructively while destructive interference occurs otherwise. The spectrum of the several-day long coda therefore yields discrete lines that correspond to Earth's normal modes, while destructive interference is responsible for the gaps separating the peaks.

We distinguish between observably split and not observably split modes. A spectral line of the former type has more than one peak in a typical spectrum (**Figure 5**). This ‘splitting’ of a mode is caused by the fact that individual singlets, the different ‘vibrational

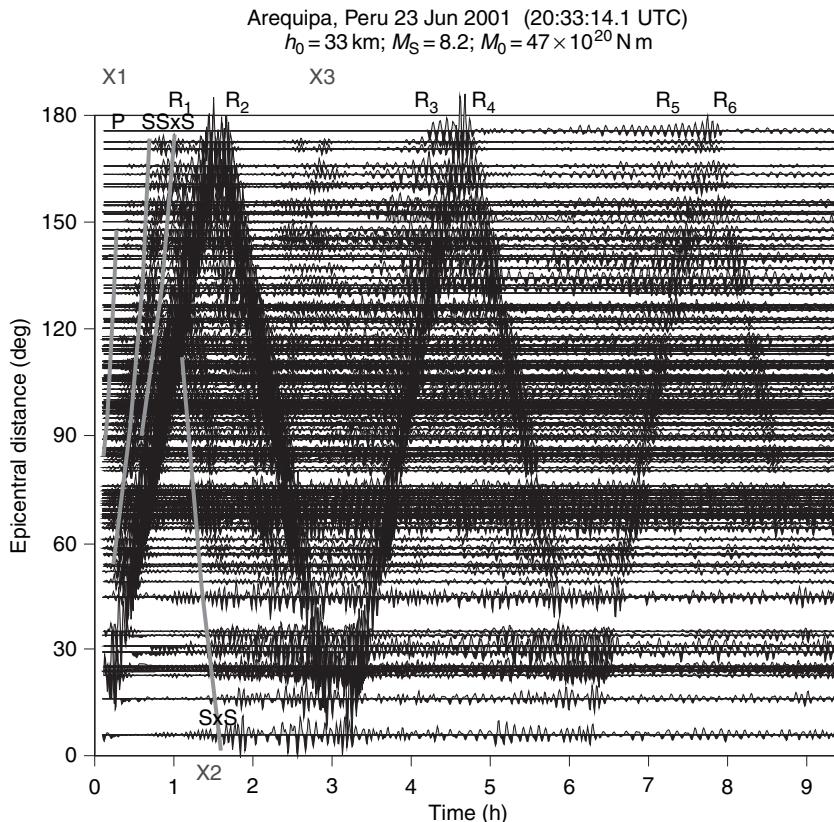


Figure 3 Record section of the 2001 Arequipa, Peru earthquake, the largest digitally recorded earthquake before the 2004 Sumatra–Andaman earthquake. Marked are six fundamental mode Rayleigh wave trains (R_n) and early compressional (P) and shear (S) body wave arrivals. Also marked are S multiples that bounced off the surface (SxS). Such phases are contributors to the major arc overtone phases X_n . At 90° epicentral distance, surface wave trains traveling in opposite directions arrive at a station at equidistant time intervals, while wave trains overlap at the antipode and near the source.

states' of a certain mode (multiplet), are no longer degenerate in a nonspherical Earth. Observably split modes are typically of low angular order, that is, the geographical pattern of surface displacement is simple and the mode has few singlets. In the case of not observably split modes (Figure 4), there are so many singlets of a mode or the singlets are so close together that a standard spectral analysis is not able to resolve them. Another limiting factor to resolve a mode's splitting is its attenuation rate. The rather complex superposition of all the singlets causes an 'apparent frequency shift' of an otherwise ordinary-looking spectral peak where the shift depends on lateral variations in Earth's structure (Jordan, 1978).

Having long wavelengths compared to transient seismic waves, free oscillations inherently average over large volumes which leads to comparatively poor resolution of Earth's heterogeneous structure. On the other hand, free oscillation studies are much less likely biased by the uneven distribution of

earthquake sources and seismic receivers. Mode observables are relatively weakly sensitive to structure with odd-degree symmetry because waves traveling on a sphere lose their sensitivity to this structure as time goes on. We will revisit this problem in the surface wave section.

1.03.2 Free Oscillations

1.03.2.1 Modes of a Spherically Symmetric Earth

The elastic-gravitational response of Earth to localized, transient excitations consists of impulsive disturbances followed by dispersed wave trains and long-lasting standing waves, as seen in Figures 2–4. As long as an earthquake rupture is ongoing, the Earth responds with forced vibrations. Once the rupture has ceased, Earth undergoes free oscillations around its new equilibrium state. The rupture

duration of the largest earthquakes are on the order of a few minutes and thus very much shorter than the typical decay time of modes of a few tens of hours. A study of the source based on low-frequency seismic records reduces to the estimation of the initial amplitude and phase of the modes, while studies of Earth's internal mechanical structure concentrates on the frequency and attenuation of the modes.

The deviations of Earth structure from a spherically symmetric reference state are quite small. It is

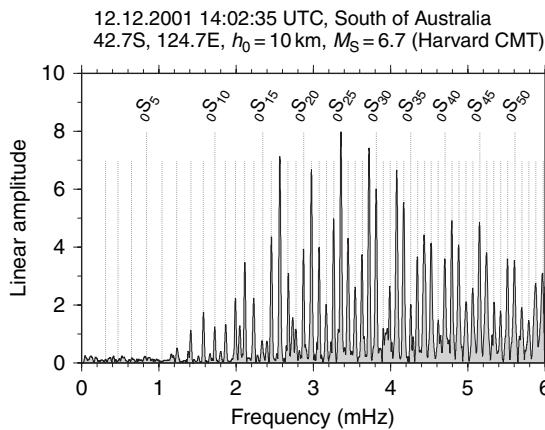


Figure 4 Spectrum of a magnitude $M_S = 6.7$ earthquake south of Australia that was recorded at station BFO (Black Forest Observatory, Germany). The succession of globe-circling Rayleigh wave packets in roughly 3-h intervals manifests itself in the spectrum through the regular spacing between adjacent fundamental spheroidal modes $_0S_\ell$ of about $(3\text{h})^{-1} = 0.1 \text{ mHz}$. The underlying time series is 18 h long.

therefore convenient to discuss free oscillations of a spherically averaged Earth and treat any deviation away from this state with perturbation theory. On a spherically symmetric Earth three integer quantum numbers, n , ℓ , and m , fully specify the set of normal modes. The azimuthal order, $|m|$, counts the number of nodal surfaces in the longitudinal direction $\hat{\phi}$. The number of nodal surfaces in the colatitudinal direction, $\hat{\theta}$, is $|\ell - m|$, where ℓ is the angular order. For fixed ℓ and m the overtone number n indexes the modes with increasing frequency.

Solutions of the linearized, homogeneous equations of motion for a self-gravitating elastic Earth can be written as (Backus, 1967; Aki and Richards, 1980, 2002; Dahlen and Tromp, 1988; Chapter 1.02)

$${}_n u_\ell^m(\mathbf{r}, t) = \text{Re} \left[(\hat{\mathbf{r}} {}_n U_\ell(r) Y_\ell^m(\theta, \phi) + {}_n V_\ell(r) \nabla_1 Y_\ell^m(\theta, \phi) - {}_n W_\ell(r) \hat{\mathbf{r}} \times \nabla_1 Y_\ell^m(\theta, \phi)) e^{i n \omega_\ell^m t} \right] \quad [1]$$

where ${}_n u_\ell^m$ is the displacement eigenfunction of the mode singlet identified by the (n, ℓ, m) -triplet and ${}_n \omega_\ell^m$ is its eigenfrequency. Y_ℓ^m are surface spherical harmonics functions and ∇_1 is the surface gradient operator. While n and ℓ can be any non-negative number ($n \geq 0, \ell \geq 0$), the azimuthal order is limited to the interval $-\ell \leq m \leq \ell$. The spherical harmonics describe the angular shape of the eigenfunction. An example for some low-order spherical harmonics is shown in **Figure 6**.

The three scalar radial eigenfunctions, ${}_n U_\ell(r)$, ${}_n V_\ell(r)$, and ${}_n W_\ell(r)$, describe the way the mode samples Earth with depth. As n increases they become more oscillatory with depth leading to an increased number of nodal

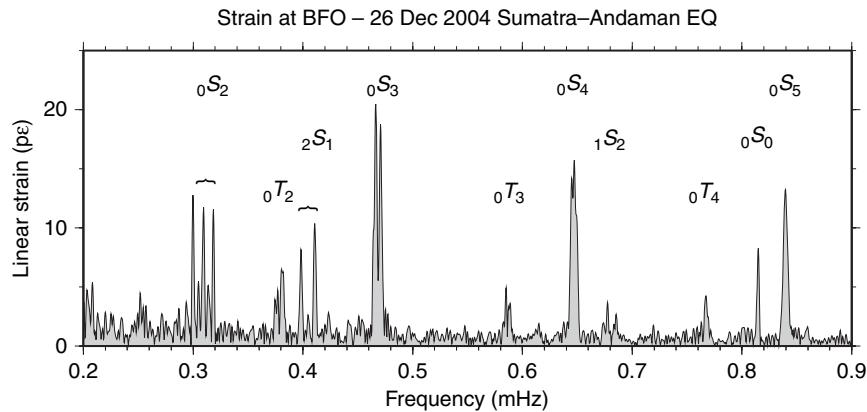


Figure 5 Linear Fourier amplitude spectrum of strain from the 2004 Sumatra-Andaman earthquake recorded by the invar wire strainmeter at station BFO with azimuth N2° E. The time domain amplitude of $_0S_0$ at 0.814 mHz is $8 \times 10^{-12} \epsilon$. This is a rare spectrum showing evidence of Zeeman splitting of the two lowest order toroidal modes $_0T_2$ and $_0T_3$. The strainmeter array at BFO is described in Widmer et al. (1992). A barometric correction similar to that of Zürn and Widmer (1995) has been applied to this spectrum. With an empirically determined strain pressure compliance of $0.8 \text{ n}\epsilon \text{ hPa}^{-1}$ a lowering of the noise floor by a factor 4 was achieved. The first 240 h after the event were used for the spectrum.

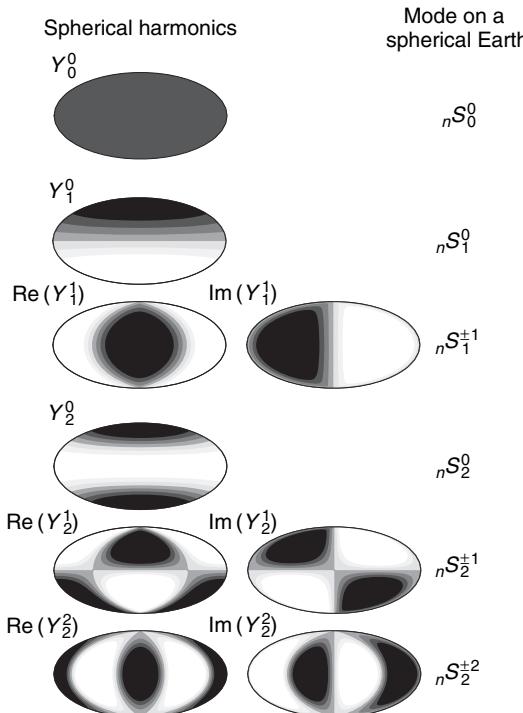


Figure 6 Surface spherical harmonics $Y_\ell^m = X_\ell^m(\theta)e^{im\phi}$ that compose the basis set for $\ell = 0, 1$, and 2 spheroidal modes (e.g., ${}_0S_1$, ${}_2S_1$, ${}_0S_2$, ${}_3S_2$), plotted in Hammer–Aitoff projection. The singlets of modes have these shapes on the \hat{r} component of recordings on a spherical, nonrotating Earth. Modified from Masters TG, Laske G, and Gilbert F (2000d) Large-scale Earth structure from analyses of free oscillation splitting and coupling. In: Boschi E, Ekström G, and Morelli A (eds.) *Problems in Geophysics for the New Millennium*, pp. 255–288. Bologna: Editrice Compositori.

spheres. For toroidal modes n is the number of nodes in W while for radial modes n is the number of nodes in U . The radial eigenfunctions do not depend on the azimuthal order m and are thus identical for all singlets within a multiplet. Eigenfunctions for some mode examples are shown in **Figures 7 and 8**. The relevant quantity for the sensitivity of a mode to structure with depth is actually not the eigenfunction but the energy density. This is because the modes are stationary solutions to the Lagrangian energy functional (Gilbert, 1980). A mode can store elastic energy in shear and in compression and it can store gravitational potential energy. Significant amounts of the latter can be stored only by spheroidal modes below 1 mHz. For most other modes, their sensitivity to structure can be discussed based solely on their shear and compressional energy densities.

For the spherically symmetric reference state, the structure of the spectrum of a mode (fixed n and ℓ)

exhibits a high degree of degeneracy in that all of its $2\ell + 1$ singlets have the same frequency. This degeneracy in m is a consequence of the fact that the singlet eigenfrequencies cannot depend on the choice of the coordinate system. The ensemble of $2\ell + 1$ singlets comprise the mode multiplet. Further classification into spheroidal and toroidal modes is possible in the spherically symmetric case. The displacement field of toroidal modes, “ T_ℓ^m ”, is purely horizontal and divergence free with ${}_nU_\ell(r) = {}_nV_\ell(r) = 0$. Thus, it involves only shearing and does not lead to any deformation of the radial interfaces. Spheroidal modes, “ S_ℓ^m ”, for which ${}_nW_\ell(r) = 0$, involve volumetric changes as they are composed of both horizontal and vertical displacements. They deform interfaces and also perturb the gravity field. A third subclass of modes are the radial modes, ${}_nS_0$, for which $\ell = 0$ and also ${}_nV_\ell(r) = {}_nW_\ell(r) = 0$.

Freeman Gilbert first wrote computer program EOS to solve the ordinary differential equations governing free oscillations, and various descendants of this code have been circulating informally since the early 1970s. We mention two versions here: OBANI by John Woodhouse and MINOS by Guy Masters. Woodhouse advanced the code by allowing to compute the eigenfunctions through the method of minors. He also introduced a mode counter for spheroidal modes, while Masters added one for toroidal and radial, Stoneley and IC modes. A description of OBANI can be found in Woodhouse (1988). MINOS can be downloaded from the REM web site.

1.03.2.2 Modes of a Heterogeneous Earth

1.03.2.2.1 Mode splitting

As an Earth model becomes successively more realistic and complex, the spherical symmetry is broken and a mode spectrum becomes more complex. The principal deviations from the spherically symmetric reference state are Earth’s daily rotation, its hydrostatic ellipticity in response to the rotation and general aspherical structure. The latter includes the topography of interfaces and lateral variations in isotropic and anisotropic volumetric parameters. The distribution of singlets within a multiplet on a rotating Earth in hydrostatic equilibrium is given by Dahlen (1968). If the (n, ℓ) -tuple denotes the k th spheroidal or toroidal multiplet, then the eigenfrequency of the m th singlet of an isolated multiplet is

$$\omega_k^m = \bar{\omega}_k(1 + a + mb + m^2c) \text{ with } -\ell \leq m \leq \ell \quad [2]$$

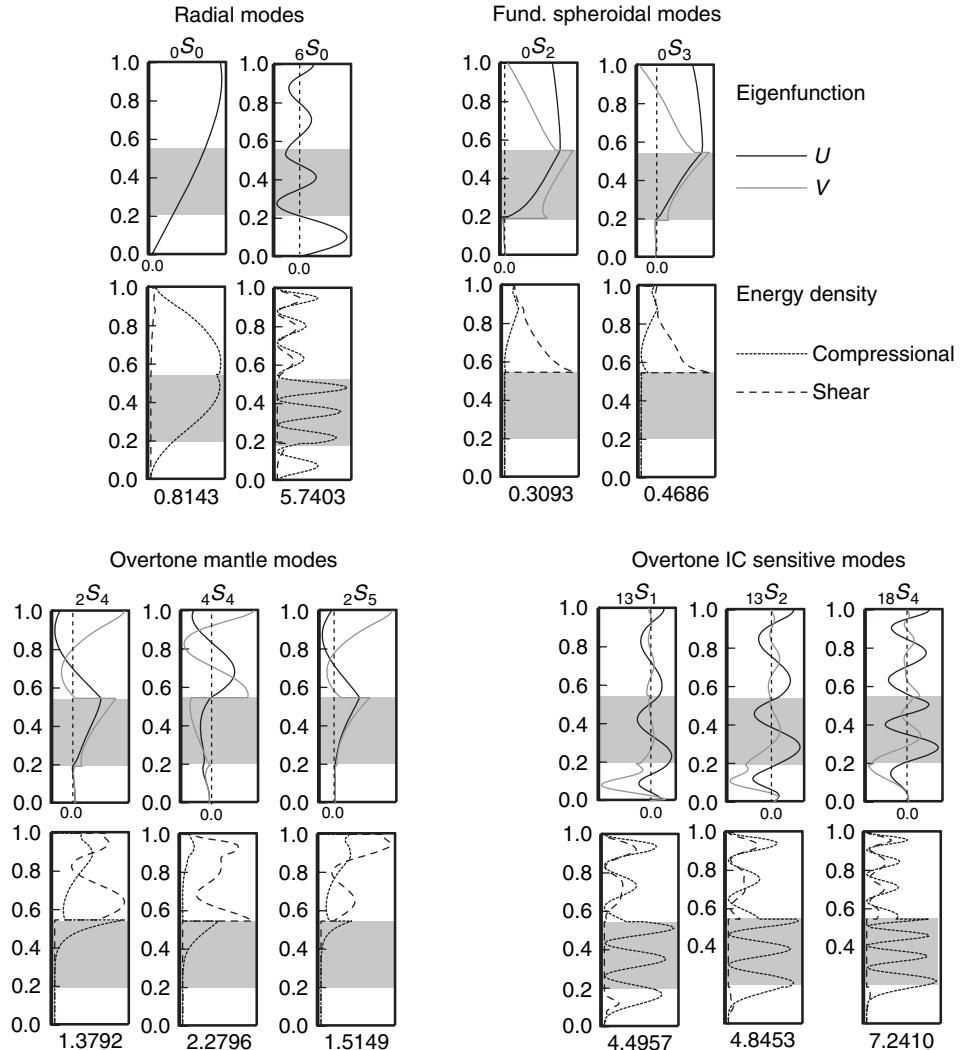


Figure 7 Eigenfunctions U and V and compressional and shear energy densities for some modes described in this chapter, displayed as function of normalized radius (0 is at the center, 1 is at the surface). Gray areas mark the outer core. Numbers at the bottom of the panels are PREM mode frequencies in mHz (Dziewonski and Anderson, 1981). Radial modes are very sensitive to core structure, while spheroidal fundamental modes are not very sensitive to κ and μ in the core. On the other hand, overtone mantle modes that are primarily sensitive to mantle structure are also influenced by κ in the core. IC sensitive modes that can be observed at the Earth's surface are typically quite sensitive to mantle structure.

where $\bar{\omega}_k$ is the multiplet degenerate frequency, a and c the ellipticity splitting coefficient (to first order) and b the rotational splitting coefficient (Dahlen, 1968). The ellipticity of figure removes the degeneracy of a mode only partly, with ${}_{\mu}\omega_k^m = {}_{\mu}\omega_k^{-m}$. This splitting is asymmetric with respect to the degenerate frequency. On the other hand, the rotational splitting is symmetric, or of Zeeman type, and removes the degeneracy completely. Splitting due to rotation dominates at low frequencies ($b \gg c$) so that the spacing between adjacent singlets is nearly constant

(see Figures 9 and 5). Other examples of modes whose splitting is dominated by rotation are modes ${}_0S_5$ and ${}_1S_4$ (Figure 10). At higher frequencies, ellipticity and heterogeneous structure become the dominant cause and frequencies become partially degenerate when $b \ll c$. Examples of such modes are ${}_{13}S_2$ and ${}_{18}S_4$. IC sensitive modes ${}_{3}S_2$, ${}_{13}S_2$, and ${}_{18}S_4$ are anomalously split, as first observed by Masters and Gilbert (1981). The splitting width, the range of singlet frequencies, in these cases is significantly larger than that predicted by rotation and ellipticity.

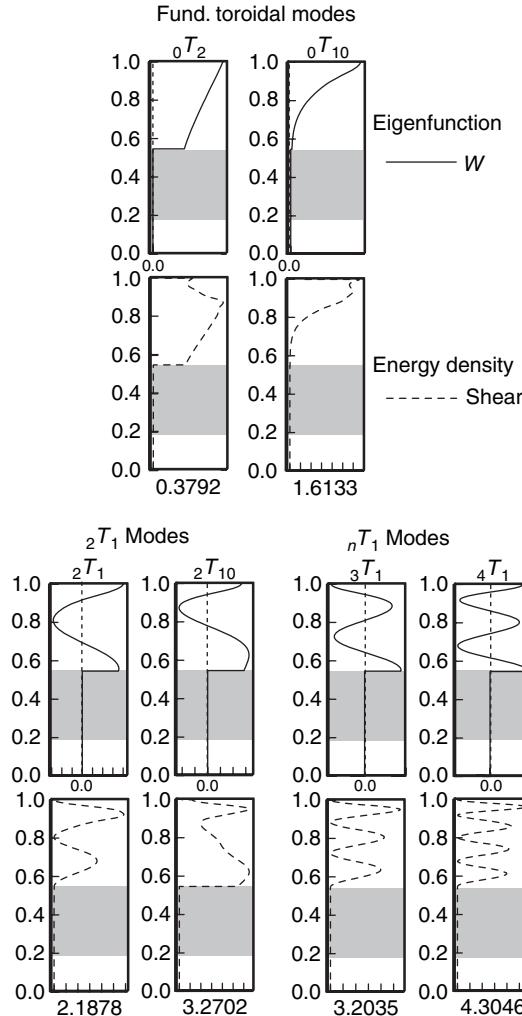


Figure 8 Eigenfunctions W and shear energy densities for some toroidal modes. Toroidal modes are sensitive only to μ . For details see [Figure 7](#).

In fact, the extreme splitting of ${}_{10}S_2$ led [Gilbert and Dziewonski \(1975\)](#) to misidentify the $m=0$ line of ${}_{10}S_2$ as mode ${}_{11}S_2$. Based on their observations, [Masters and Gilbert \(1981\)](#) argued for high Q in the IC but did not interpret the anomalous splitting. [Ritzwoller et al. \(1986\)](#) speculated that the anomalous splitting is due to axisymmetric structure in the outer core (see also [Romanowicz and Breger \(2000\)](#)). [Woodhouse et al. \(1986\)](#) were the first to attribute this splitting to the anisotropic IC which now appears to be widely accepted (see, e.g., [Tramp \(1993\)](#)).

[Gilbert \(1971\)](#) investigated how small structural perturbations to a spherically symmetric Earth affect the spectrum of a multiplet. He formulated the

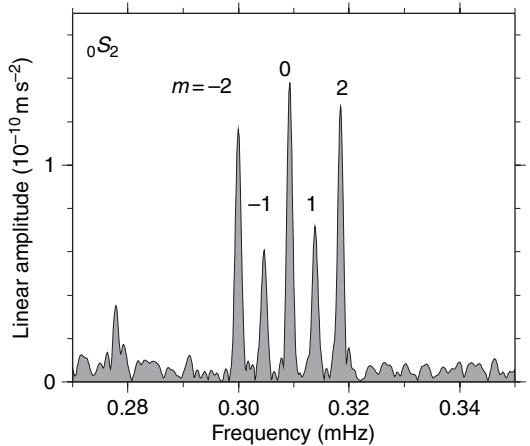


Figure 9 Zeeman splitting of the ‘football mode’ ${}_0S_2$. This is a Fourier spectrum of a 500 h long record of the 2004 Sumatra event by the superconducting gravimeter at Strasbourg, France ([Rosat et al., 2005](#)). A scaled version of the locally recorded barometric pressure was subtracted from the gravity record to achieve a noise reduction by a factor 2. The time-domain acceleration amplitude of the singlets is close to $10^{-10} \text{ m s}^{-2}$. Zeeman-type splitting of a mode is caused by Earth’s rotation.

‘diagonal sum rule’ which states that, to first order, the arithmetic mean of the $2\ell + 1$ singlet frequencies is the multiplet’s degenerate frequency $\bar{\omega}_k$

$$\bar{\omega}_k = \frac{1}{2\ell + 1} \sum_{m=-\ell}^{\ell} \omega_k^m \quad [3]$$

Any first-order perturbation in structure leaves the degenerate frequencies of the spherical Earth unchanged. On the other hand, second-order effects of the Coriolis force may cause a frequency shift. [Dahlen \(1968\)](#) showed that the singlet distribution within a multiplet still follows the parabolic distribution of eqn [2] but second-order terms contribute to factors a and c and the diagonal sum rule is no longer valid. [Dahlen \(1968\)](#) and [Dahlen and Sailor \(1979\)](#) provide the splitting parameters for modes below 2 mHz for a variety of Earth models. Since the splitting parameters caused by rotation and Earth’s hydrostatic ellipticity are well understood, their effect are usually corrected for before mode parameters are interpreted in terms of Earth structure.

Once the eigenfrequencies and eigenfunctions of a 1-D Earth model have been computed, the synthesis of seismograms based on free oscillations is rather straightforward as it only involves the summation over all multiplets in a desired frequency band. The representation of the time series of an

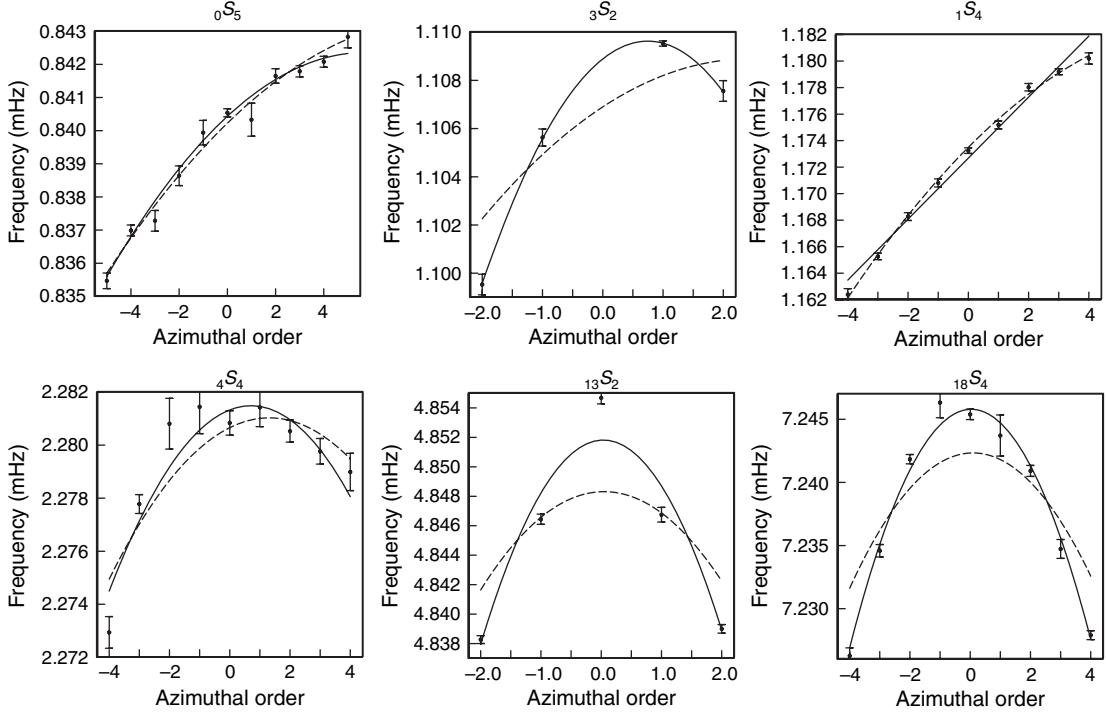


Figure 10 Observed singlet frequencies as a function of azimuthal order, m , for six modes. The dashed lines mark the splitting predicted for Earth's rotation and hydrostatic ellipticity. Solid lines mark best-fitting parabolas. The splitting of low-frequency modes ${}_0S_5$ and ${}_1S_4$ is dominated by rotation, while that of IC sensitive modes ${}_{13}S_2$ and ${}_{18}S_4$ is dominated by ellipticity. The splitting of mantle mode ${}_4S_4$ and low-frequency IC sensitive mode ${}_3S_2$ is mixed. The $m = 0$ singlet of ${}_3S_2$ has not yet been observed reliably. IC sensitive modes are anomalously split, that is, the observed splitting is significantly larger than that predicted for rotation and ellipticity alone.

isolated split multiplet with degenerate frequency $\bar{\omega}_k$ at station j is given by

$$u_j(t) = \sum_{m=1}^{2\ell+1} R_{jm} a_m(t) e^{i\bar{\omega}_k t} \quad \text{or} \quad \mathbf{u}(t) = \mathbf{R} \cdot \mathbf{a}(t) e^{i\bar{\omega}_k t} \quad [4]$$

where the real part is understood (e.g., Woodhouse and Girnius, 1982; Landau and Lifshitz, 1958, section 40; Woodhouse, 1983). The j th row of \mathbf{R} is a $2\ell + 1$ vector of spherical harmonics which describe the motion of the spherical-earth singlets at the j th receiver and is readily calculated. $\mathbf{a}(t)$ is a slowly varying function of time given by

$$\mathbf{a}(t) = \exp(i\mathbf{H}t) \cdot \mathbf{a}(0) \quad [5]$$

where $\mathbf{a}(0)$ is a $2\ell + 1$ vector of spherical-Earth singlet excitation coefficients which can be computed if the source mechanism of the event is known. \mathbf{H} is the complex ‘splitting matrix’ of the multiplet and incorporates all the information about elastic and anelastic 3-D structure to which the mode is sensitive, that is,

$$H_{mm'} = \bar{\omega}_k \left[(a + mb + m^2 c) \delta_{mm'} + \sum \gamma_s^{mm'} c_s^t + i \sum \gamma_s^{mm'} d_s^t \right] \quad [6]$$

where $-\ell \leq m \leq \ell$; $-\ell \leq m' \leq \ell$ and $t = m - m'$. The first term describes the splitting due to Earth's rotation and ellipticity (eqn [2]) and the second and third terms describe the effects from elastic and anelastic structure through the ‘structure coefficients’, c_s^t and d_s^t (e.g., Ritzwoller *et al.*, 1986; Smith and Masters, 1989b). Equation [6] changes to equation (14.84) of Dahlen and Tromp (1998) if real instead of complex basis eigen functions and spherical harmonics are considered in eqn [1]. \mathbf{H} , and consequently $\exp(i\mathbf{H}t)$, are $(2\ell + 1) \times (2\ell + 1)$ -dimensional square matrices. The $\gamma_s^{mm'}$ are integrals over three spherical harmonics (e.g., Dahlen and Tromp, 1998). These integrals are often zero, and the ‘selection rules’ summarize the nonzero conditions:

1. $m - m' = t$
2. $\ell + s + \ell$ must be even; i.e., s must be even
3. $0 \leq s \leq 2\ell$ (triangle rule)

Rule (1) implies that axisymmetric structure ($t=0$) gives nonzero contributions to the splitting matrix only if $m=m'$, so that \mathbf{H} is diagonal. Rule (2) implies that an isolated mode is sensitive only to structure of even degree. The rule can be expanded to two coupling modes in which case $\ell+s+\ell'$ must be even (for same-type coupling; see section ‘mode coupling’ for details). In order to retrieve structure of odd harmonic degree, $\ell+\ell'$ must therefore be odd. Rule (3) implies that a mode cannot be sensitive to structure of arbitrarily high degree. It can also be expanded for two coupling modes where $|\ell-\ell'| \leq s \leq \ell+\ell'$. The structure coefficients for elastic structure, c_s^t , are given by

$$c_s^t = \int_0^a \mathbf{M}_s(r) \cdot \delta\mathbf{m}_s^t(r) r^2 dr \quad [8]$$

and a similar expression exists for the anelastic structure coefficients, d_s^t . The coefficients $\delta\mathbf{m}_s^t$ are the expansion coefficients of the 3-D aspherical Earth structure: $\delta\mathbf{m}(r, \theta, \phi) = \sum \delta\mathbf{m}_s^t(r) Y_s^t(\theta, \phi)$ and \mathbf{M}_s are integral kernels which can be computed (Woodhouse and Dahlen, 1978; Woodhouse, 1980; Henson, 1989, Li *et al.*, 1991a). Equation [8] and its counterpart for the d_s^t s can be regarded as a pair of linear inverse problems for \mathbf{c} and \mathbf{d} . Strictly speaking, eqn [4] is not quite correct since both \mathbf{R} and $\mathbf{a}(0)$ should include small renormalization terms (see Dahlen and Tromp (1998) and equations 14.87 and 14.88). The renormalization requires the knowledge of the splitting matrix which we ultimately want to determine in a mode analysis. While the renormalization terms are expected to be small for isolated modes, we may have to iterate the retrieval of the splitting matrix for coupled modes.

It is convenient to visualize the geographic distribution of structure as sensed by a mode by forming the elastic and anelastic ‘splitting functions’ (Woodhouse and Giardini, 1985):

$$\begin{aligned} f_E(\theta, \phi) &= \sum_{s,t} c_s^t Y_s^t(\theta, \phi) \\ f_A(\theta, \phi) &= \sum_{s,t} d_s^t Y_s^t(\theta, \phi) \end{aligned} \quad [9]$$

The $Y_s^t = X_s^t(\theta)e^{it\phi}$ is a spherical harmonic of harmonic degree s and azimuthal order number t . An example is shown in **Figure 11**. The elastic splitting function shows local peak shift variations caused by the local structure beneath a geographic location, as ‘seen’ by an isolated mode. Recall that isolated modes are not sensitive to odd-degree structure.

In a similar way, the anelastic splitting function shows attenuation. Bearing this restriction in mind, a splitting function can be understood as the mode equivalent of a surface wave phase velocity map.

To summarize, an isolated mode of harmonic degree ℓ is sensitive to even-degree structure only, up to harmonic degree $s=2\ell$. If the structure within the Earth is axisymmetric, then the splitting matrix is diagonal, the individual singlets can be identified by the index m and the only singlet visible at a station at the Earth’s poles is the $m=0$ singlet.

1.03.2.2.2 Mode coupling

While the treatment of isolated modes is appealing because of its simplicity, it is insufficient to describe free oscillations of the real Earth. The coupling between modes has two fundamental effects: (1) varying coupling effects on individual singlets causes a shift of the mode’s degenerate frequency and \mathcal{Q} ; (2) coupling to certain other modes gives a mode sensitivity to odd-degree structure. We distinguish between along-branch (same mode type and n but different ℓ) and cross-branch coupling (any other mode combination). The coupling between two modes is particularly strong if their frequencies are close and the radial and geographical shape of their displacement field is similar. Numerically, the complex frequencies must be close but in fact the real part (frequency) is more dominant than the imaginary part (attenuation). As in the case of isolated modes, selection rules dictate through which mechanism and in which way two modes couple:

- Coriolis force causes spheroidal–toroidal mode coupling for mode pairs of the form ${}_nS_\ell - {}_{n'}T_{\ell \pm 1}$, that is, between multiplets that differ by a single angular degree ($|\ell - \ell'| = 1$), for example, ${}_0S_4 - {}_0T_3, {}_0S_8 - {}_0T_9, {}_1S_4 - {}_0T_3$.
- Earth’s ellipticity also causes spheroidal–toroidal mode coupling for $|\ell - \ell'| = 1$.
- Earth’s ellipticity causes same-type (spheroidal or toroidal) mode coupling for $|\ell - \ell'| = 0$ and for $|\ell - \ell'| = 2$, for example, ${}_0S_4 - {}_1S_4, {}_0S_3 - {}_0S_5$.
- Rotation causes spheroidal–spheroidal mode coupling for $|\ell - \ell'| = 0$, for example, ${}_0S_4 - {}_1S_4$.
- Lateral heterogeneity of degree s causes spheroidal–toroidal mode coupling under the condition that $|\ell - \ell'| + 1 \leq s \leq \ell' + \ell - 1$ and $\ell' + \ell + s$ is odd, for example, ${}_0S_4 - {}_0T_3$ are coupled through structure of degrees 2,4,6; as a consequence, if $|\ell - \ell'|$ is even, then modes can couple through odd-harmonic degree structure, for example, ${}_0S_5 - {}_0T_3$ are coupled through structure of degrees 3,5,7.

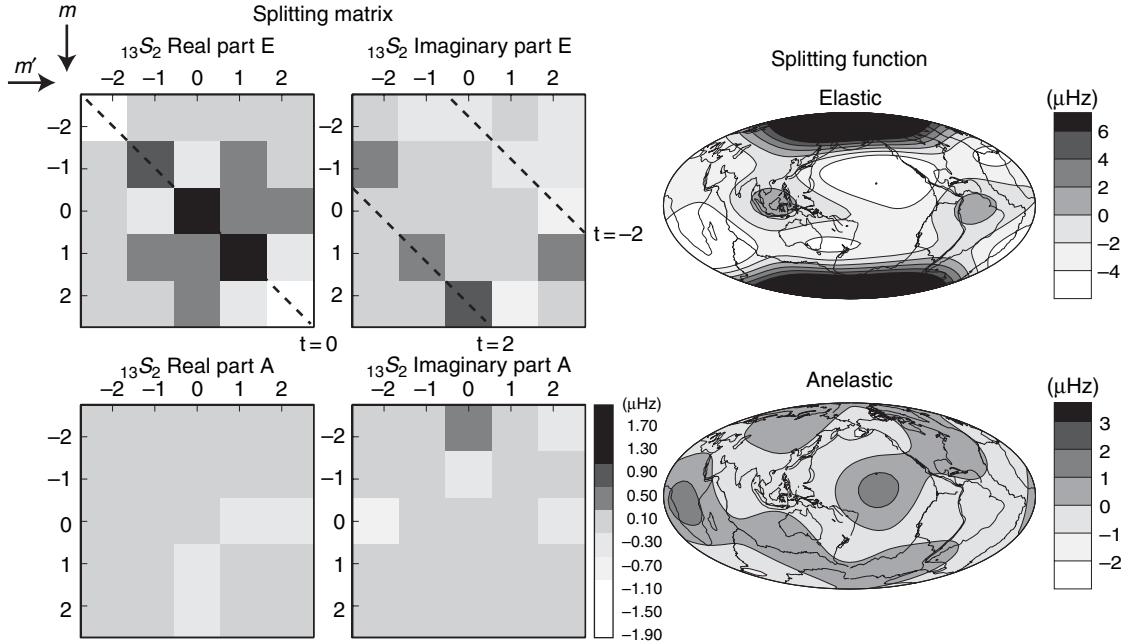


Figure 11 Left: Observed complete splitting matrix for mode $^{13}S_2$, decomposed into its elastic (E) and anelastic (A) parts, both of which are Hermitian. The data from 13 earthquakes were used to determine this matrix. The signal down the diagonal of the matrices is caused by zonal (axisymmetric) structure ($t=0$), as constrained by the selection rules for a mode. Also indicated are the contributions from $t=\pm 2$ -structure (which is sectoral for $s=2$). Right: Splitting functions obtained from the splitting matrix on the left. The signal from anelastic structure is typically much smaller than that from elastic structure.

- Lateral heterogeneity of degree s causes same-type mode coupling under the conditions that (1) $m + t - m' = 0$; (2) $\ell' + \ell + s$ is even; (3) $|\ell - \ell'| \leq s \leq \ell' + \ell$, for example, ${}_0S_2 - {}_0S_3$ are coupled through structure of degrees 1,3,5.

Coriolis coupling between fundamental spheroidal and toroidal modes was first observed and modeled by Masters *et al.* (1983). Coupling spheroidal–toroidal mode pairs form hybrid modes that share some of the characteristics of both modes. Toroidal modes can then be observed on vertical-component seismic spectra in the form of additional peaks, which Masters *et al.* nicely showed. For angular orders $7 \leq \ell \leq 26$, ${}_0T_{\ell+1}$ modes are closer neighbors to ${}_0S_\ell$ modes than ${}_0T_{\ell-1}$ modes are. The strongest coupling occurs between pairs ${}_0S_{11} - {}_0T_{12}$ whose PREM degenerate frequencies are about 4.5 μHz apart (1 μHz for 1066A) and ${}_0S_{19} - {}_0T_{20}$ whose PREM frequencies are within 0.5 μHz of each other (2.5 μHz apart in 1066A). Figure 12 shows that predicted frequency shifts for Coriolis-coupled modes can be up to 5 μHz , which is significant with respect to measurement errors (see Figure 24; regard a ‘strip’ as a spectral

line of a mode for now). Figure 12 also indicates that coupling modes ‘repel’ each other. For example, while the frequency of ${}_0S_{10}$ gets pulled downward, the frequency of ${}_0T_{11}$ get pushed upward. The coupling between two multiplets actually has a different effect on each singlet of the modes, as is shown in Figure 13. As discussed above, for uncoupled modes, rotation and Earth’s hydrostatic ellipticity remove the frequency degeneracy. The coupling of the mode pairs causes the sets of mode singlets to rearrange. Strongly coupled modes form a hybrid pair in which the sets of singlet frequencies repel each other but the attenuation is ‘shared’. As shown by Masters *et al.* (1983), Earth’s aspherical structure causes further rearrangement of the singlets.

Coupling between two modes also manifests itself in the splitting matrix. Instead of two matrices with ranks $2\ell + 1$ and $2\ell' + 1$ that describe the effects of rotation, ellipticity, and structure for two modes, we now deal with a larger matrix with rank $2(\ell + \ell' + 1)$ that has four subblocks: the two original matrices that are now the two self-coupling blocks in the upper-left and lower-right corner; two cross-coupling

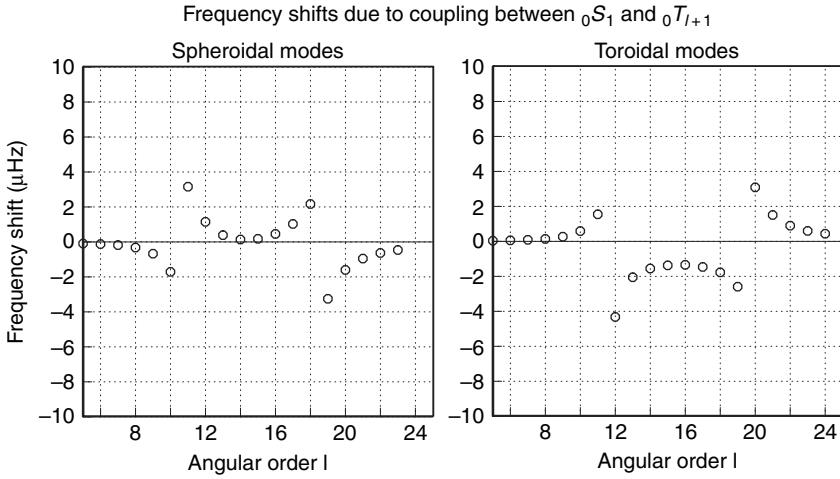


Figure 12 Predicted frequency shifts for mode pairs ${}_0S_\ell - {}_0T_{\ell+1}$ caused by Coriolis coupling. Predictions are for Earth model 1066A (Gilbert and Dziewonski, 1975). The strongest coupling occurs between pairs ${}_0S_{11} - {}_0T_{12}$ and ${}_0S_{19} - {}_0T_{20}$.

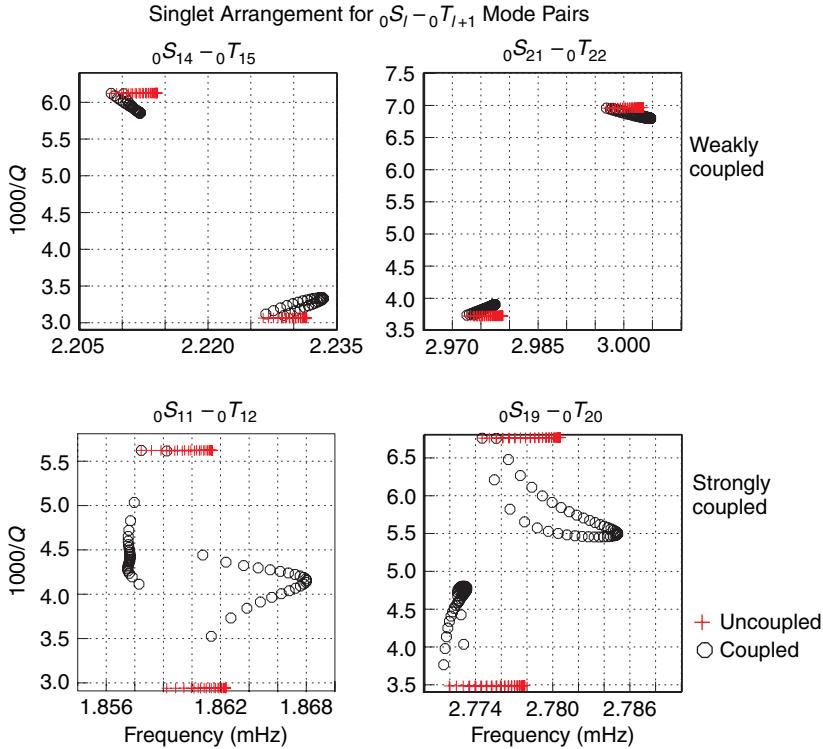


Figure 13 Predicted rearrangement of singlet frequencies and Q's for weakly coupled mode pairs ${}_0S_{14} - {}_0T_{15}$ and ${}_0S_{11} - {}_0T_{12}$, and for strongly coupled pairs ${}_0S_{21} - {}_0T_{22}$ and ${}_0S_{19} - {}_0T_{20}$. The coupling calculations included effects from both rotation and ellipticity but for the modes discussed here, Coriolis coupling is the dominant cause. Strongly coupled modes form a hybrid pair in which the sets of singlet frequencies repel each other but the attenuation is 'shared'.

blocks of dimensions $(2\ell + 1) \times (2\ell' + 1)$ and $(2\ell' + 1) \times (2\ell + 1)$. As an example of spheroidal-toroidal mode coupling, **Figure 14** shows how Earth's rotation and ellipticity affect the four

coupling blocks in the splitting matrix for modes ${}_0S_4$ and ${}_0T_3$.

Earth's structure can complicate the splitting matrix substantially, which we show in a schematic example

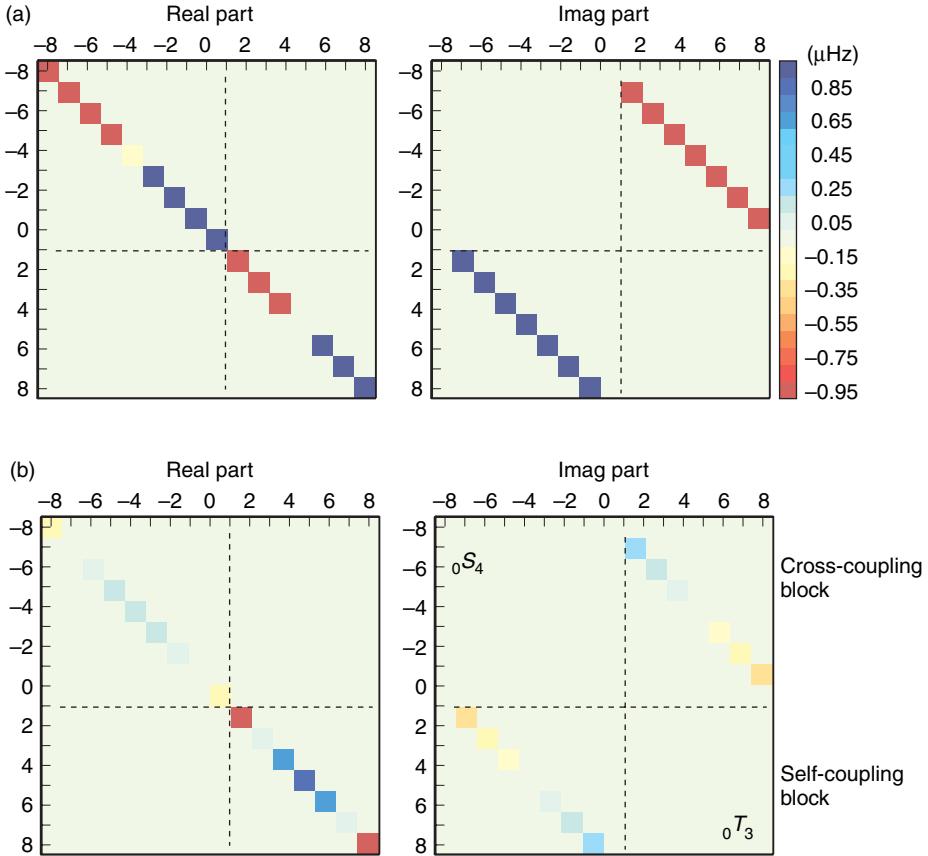


Figure 14 Synthetic splitting matrices to illustrate the coupling effect of Earth's (a) rotation and (b) ellipticity on the mode pair ${}_0S_4 - {}_0T_3$. Self-coupling fills the diagonals of the self-coupling blocks, while multiplet–multiplet coupling fills the cross-coupling blocks. For this pair, the effect of rotation is 10 times larger than that of ellipticity.

for a $\ell = 2$ mode coupling with a $\ell' = 3$ mode of the same type (i.e., either spheroidal or toroidal). **Figure 15** compares the structure of the splitting matrix in the case of the self-coupling of an isolated $\ell = 2$ mode and the upper-right cross-coupling block with a $\ell' = 3$ mode. According to the selection rules, structure of certain symmetries affects certain elements in the splitting matrix. As already discussed, the effects from axisymmetric structure are found down the diagonal, while nonaxisymmetric, even-degree structure affects off-diagonal elements (cf. **Figure 11**). Depending on ℓ and ℓ' of the coupling modes, some elements in the cross-coupling blocks are now affected by structure of odd harmonic degree. An example of an observed splitting matrix is discussed in the ‘observations’ section.

We should mention that the coupling calculations presented here were done with a code based on the work of Jeff Park (Park and Gilbert, 1986). His method uses a Galerkin procedure that allows the assessment of mode coupling in a dissipating Earth. To reduce the computational burden, the

method applies a trick. The exact representation of interaction on a rotating Earth requires a matrix equation that is quadratic in eigenfrequency ω . Coriolis interaction terms are grouped in a matrix linear in ω . This linear dependence is removed by replacing ω with a fixed fiducial frequency (reference frequency) $\hat{\omega}_0$. Park’s numerical experiments showed that this approximation is adequate for modes above 1 mHz as long as the relative frequency spread, $\Delta\omega/\hat{\omega}_0$, is not large. Modes in a certain frequency band all couple through various mechanisms. When modeling the interaction in a group of modes, all these have to be taken into account simultaneously. The examples of coupling mode pairs shown here are only to illustrate how mode coupling works and where Park and Gilbert’s method is appropriate. A treatment of coupling modes in a wider frequency band requires more general procedures. Some are discussed in the ‘observations’ section but the interested reader is also referred to Chapter 1.02.

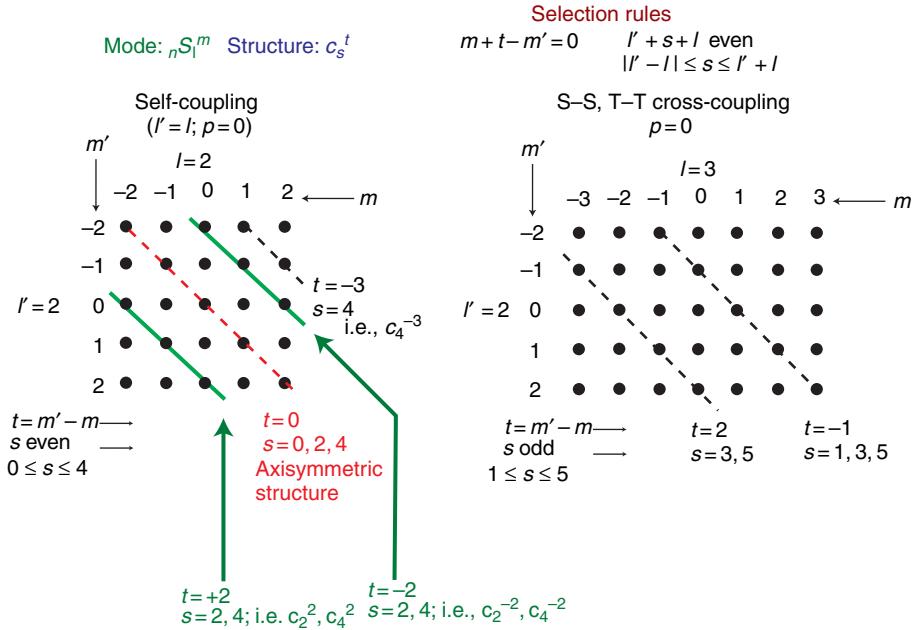


Figure 15 Elements in the splitting matrix that are affected by coupling. Left panel: An isolated $\ell = 2$ mode experiences self-coupling through Earth's rotation and ellipticity. Together with axisymmetric structure this manifests itself in the diagonal. Other even-degree structure (s even) affects off-diagonal elements. When two modes couple, the splitting matrix has four blocks: two self-coupling blocks (one for each mode) and two cross-coupling blocks. The right panel shows how elements in a cross-coupling block with an $\ell' = 3$ mode are affected for same-type coupling ($p = 0$). Some of the elements are now affected by odd-degree structure (s odd).

1.03.2.3 Measuring Mode Observables

The most basic approach to extract mode observables from a seismogram is to calculate the spectrum of a tapered seismogram. The finiteness of the underlying time series prohibits a parameter estimation with arbitrary precision, for example, see Jenkins (1961) for an early assessment of the Blackman and Tukey (1958) approach. Modal decay rates, the vicinity of other modes, and the presence of noise necessitates the application of spectral optimization procedures which involve the choice of a proper set of time windows. Harris (1978) presents a comprehensive overview on the use of windows in discrete Fourier analysis. Based on this, Dahlen (1982) first provided formal expressions for the variances and covariances of free oscillation parameters when using arbitrary data windows. He also showed that the optimum- or minimum-variance record lengths for measuring frequencies and decay rates (to determine Earth structure) using a Hanning taper is 1.1 Q -cycles but only 0.5 Q -cycles for measuring amplitudes and phases (to determine the earthquake source). Park *et al.* (1987b) and Lindberg and Park (1987) adapted and applied Thomson's (1982) multitaper technique

to optimize the bias from ambient noise and spectral leakage of decaying sinusoids in the free oscillation spectrum. Though we have not used this technique ourselves, they found that their approach provides a much improved detector for modes in a time series contaminated by white noise. Properly tapering free oscillation spectra is particularly important for measuring attenuation rates which is discussed in Masters and Gilbert (1983). Complicating direct spectral estimation is the fact that, even today, it is not as trivial as it may appear to find continuous undisturbed seismic records that stretch over more than a week or so. A proper analysis of Earth's breathing mode ${}_0S_0$ requires records of more than two and half months! A somewhat disturbing fact is also that some continuous records that were available at the IRIS data management center (DMC) or other DMCs less than 10 years ago now have data gaps due to data storage failures. It is therefore essential to understand how data gaps cause additional distortions in a complex spectrum. The best way to address this is by comparing a real data spectrum with a synthetic one that uses the same windowing and data gap structure, provided the source mechanism is known.

An obvious approach to assess Earth's 1-D and 3-D structure is to measure the apparent frequency of a certain mode for many stations and many earthquakes. Each of these 'peak shift data' can be plotted at the two poles of its source–receiver great circle. We make use of [Backus' \(1964\)](#) discovery that such data represent the great-circle integrals over surface spherical harmonics

$$P_s(0) Y_s^t(\Theta, \Phi) = \frac{1}{2\pi} \oint_C Y_s^t(\theta, \phi) d\Delta \quad [10]$$

where (Θ, Φ) is the positive pole of the source–receiver great circle C and $P_s(0)$ is a Legendre polynomial. This representation can be used for peak shift data as long as the structural wavelength along the great circle is much longer than the modal wavelength ([Jordan, 1978](#)). Thus, we can extract the effects of Earth structure on a particular mode in an inversion for the structure coefficients of a splitting function (see eqns [9]). Examples of using this technique are the work of [Masters et al. \(1982\)](#), who found evidence for subducting slabs in the transition zone and [Romanowicz's et al. \(1987\)](#) discussion of the degree-2 pattern of structure in the upper mantle. In principle, the c_0^0 term in the splitting function gives the degenerate mode frequency. In practice, an unbiased estimation of c_0^0 requires a large data set of peak shift measurements. More efficient tools to measure degenerate mode frequencies are based on mode stripping which is laid out in the next section. Peak shift measurements to extract effects of 3-D structure are only possible in spectra with high signal levels which is typically the case only for fundamental modes. For other modes, this technique has been superseded by the regionalized stripping technique. The use of the different methods is summarized in [Figure 16](#) that includes only methods that we have used ourselves. Other methods include the time lapse spectra approach used by [Dratler et al. \(1971\)](#) to measure attenuation rates of high- Q overtone modes. This method was also used by [Roult \(1974\)](#) and [Jobert and Roult \(1976\)](#) and others to determine attenuation rates for fundamental spheroidal and toroidal modes and the first few overtones. In this method, a sliding window of several hours (e.g., 6 h) is moved over a time series. An attenuation rate is then fit to the collected amplitude values of a certain mode in a least-squares procedure. Our own (limited) experiments have shown that this technique gives accurate estimates as long as the spectral peaks are large and the frequency picked for the estimation is close to the observed peak shift frequency.

Otherwise, oscillating amplitudes hamper the least-squares fitting procedure. For a discussion on mode attenuation rates, the interested reader is referred to Chapter 1.21 in this volume. Roult and colleagues made use of the time variable filtering (TVF) technique to extract individual mode branches from a seismogram prior to analysis. The TVF technique is laid out in the surface wave section. [Romanowicz and Roult \(1986\)](#) showed in a later intriguing study that information on lateral heterogeneity can be obtained from records of a single station by modeling the fluctuations of frequency shifts along a mode branch, for different earthquakes.

1.03.2.3.1 Multiplet stripping and degenerate mode frequencies

In the multiplet stripping procedure, we 'strip' an overtone from a 'stack' of spectra. This process requires a large set of recordings from different stations and events. The average location of a multiplet coincides with the multiplet degenerate frequency as long as the set of seismograms samples the globe evenly (condition 1) and as long as the distribution of singlets within a multiplet is relatively even (condition 2). Spectral stacking using a phase equalization procedure to extract free oscillation parameters was first used by [Mendiguren \(1973\)](#). Mode or multiplet 'stripping' was first introduced in the seminal paper of [Gilbert and Dziewonski \(1975\)](#) who used hand digitized WWSSN recordings of the 1970 Colombian event and the 15 August 1963 Peru–Bolivia event. The set of mode frequencies they obtained constituted the bulk information in the construction of spherical Earth models 1066A and PREM ([Dziewonski and Anderson, 1981](#)).

In the multiplet stripping approach, we measure mode degenerate frequencies by linearly estimating multiplet resonance functions. In a second nonlinear step a complex synthetic resonance function is fit to the estimated resonance function to obtain the mode frequency and attenuation rate. With given starting models for the 1-D Earth and the earthquake source, the acceleration spectrum at the j th station, $u_j(\omega)$, can be computed as a weighted sum of multiplet resonance functions $c_k(\omega)$, the multiplet strips, (see eqn [4])

$$u_j(\omega) = A_{jk} c_k(\omega) \quad [11]$$

Within narrow frequency bands the multiplet excitation, A , can be considered constant and

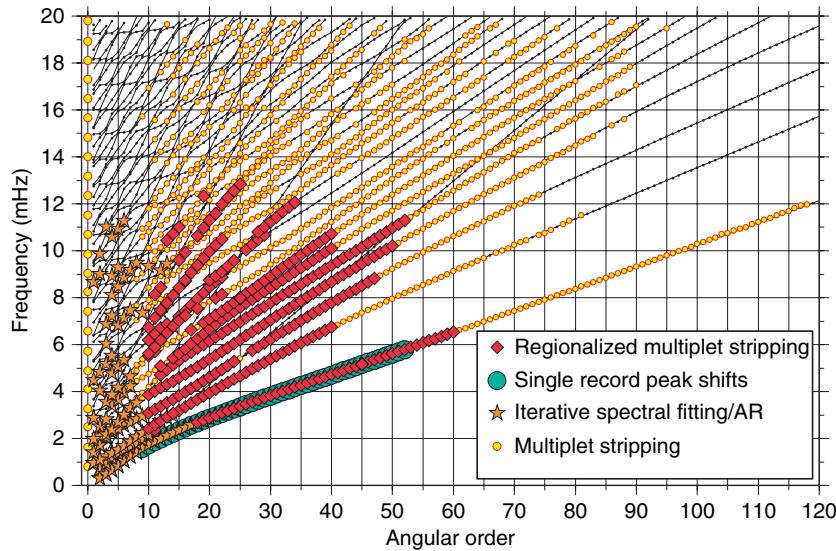


Figure 16 Spheroidal mode dispersion diagram (ω - ℓ plot) for spherical Earth model PREM. Different symbols indicate by which method a particular mode has been observed. Black dots are predicted modes that still await observation. The mode frequencies are published on the REM web site except for the multiplet stripping results. Single record peak shifts refer primarily to the work of Smith and Masters (1989b). The first comprehensive ω - ℓ diagram showing observed modes was presented by Dziewonski and Gilbert (1972).

frequency independent. Multiplet stripping consists in estimating the ‘strips’ $\hat{c}_k(\omega) = A_{jk}^{-1} u_j(\omega)$ in a least-squares sense, given observed spectra $u_j(\omega)$ and given the predicted multiplet excitations A_{jk} .

By applying multiplet stripping to large sets of seismograms we can isolate individual multiplets even at frequencies where the spectrum of modes is dense compared to the line width. [Figures 17 and 18](#) show the result of multiplet stripping for the two spheroidal mode branches ${}_7S_\ell$ and ${}_{23}S_\ell$. The frequency band covered by the strips is 0.5 mHz and contains as many as 200 toroidal and 300 spheroidal modes. Nevertheless, the good sampling of the globe provided by 12 000 seismograms of 260 different events allows us to separate one mode from the others based solely on the shape of its eigenfunction and its excitation. The along-branch consistency such as exhibited by the mode group ${}_{23}S_{39}-{}_{23}S_{44}$ is a strong indication of the success of the method.

With the same large data set we have tried to extract the radial modes ${}_nS_0$ which consist of only one singlet and hence cannot get split by aspherical structure. They are of particular interest because of their high sensitivity to density structure and to structure of the IC. [Figure 19](#) shows the multiplet strips that we obtain for modes ${}_{10}S_0$ at 9 mHz through ${}_{23}S_0$ at 19.8 mHz. While for the two branches shown in [Figures 17 and](#)

[18](#) the prediction of MEMO0 (Valette and Lesage, 1992) are in good agreement with the stripping results. The data set used for the construction of MEMO0 (Mean Earth MOdel) consisted of 617 mode degenerate frequencies in the period band 185–3230 s and included 198 toroidal, 10 radial, and 409 spheroidal modes from Masters and Widmer (1995). Neither PREM nor MEMO0 provides a satisfactory fit to our radial mode observations. Whether this discrepancy requires new structure in the IC or whether it is due to coupling with nearby high-Q modes is still an open question.

As stated above, one of the conditions for unbiased results is an even data coverage. In the long-wavelength limit of Jordan (1978), the sampling of the globe can be quantified by the density of great circle poles. A scheme to optimize the selection of high signal-to-noise spectra that provide best possible sampling could minimize a possible bias. Unfortunately, large-size earthquakes and high-quality stations are very unevenly distributed. These issues have been addressed with regionalized multiplet stripping by Widmer-Schnidrig (2002), where regular multiplet stripping is carried out for subsets of seismograms which sample only a particular great circle. While there is no substitute for missing data, regionalized multiplet stripping has at

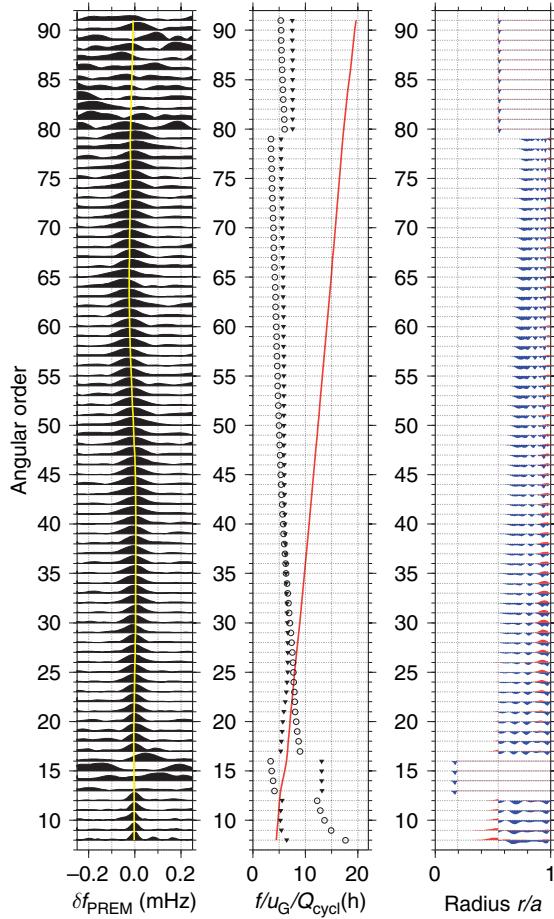


Figure 17 Multiplet strips for mode branch ${}^7S_\ell$, obtained from a data set of 12 000 records of 260 events between 1991 and 1998. The left panel shows the strips for the individual modes centered on the predicted PREM frequencies. The middle panel shows the predicted degenerate frequencies (red line, mHz), group velocity (triangles, km s^{-1}) and Q -cycles (circles, h). The right panel shows compressional (red) and shear (blue) energy densities. Multiplet stripping works well up to 17 mHz where the ${}^7S_\ell$ modes become Stoneley modes. Systematic deviations from PREM are evident in the left panel. The yellow line in that panel shows the predicted frequencies of MEMO0 (Valette and Lesage, 1992). This model seems to go a long way to explaining the new observations even though it was constructed from a data set of modes below 5.4 mHz.

least allowed us to minimize the bias from long wavelength structure. To date, about 30 years of high-quality digital seismic data enable us to successfully isolate individual modes to frequencies as high as 20 mHz. However, only the regionalized multiplet stripping results presented by Widmer-Schnidrig (2002), which stop at 12 mHz, are largely free of

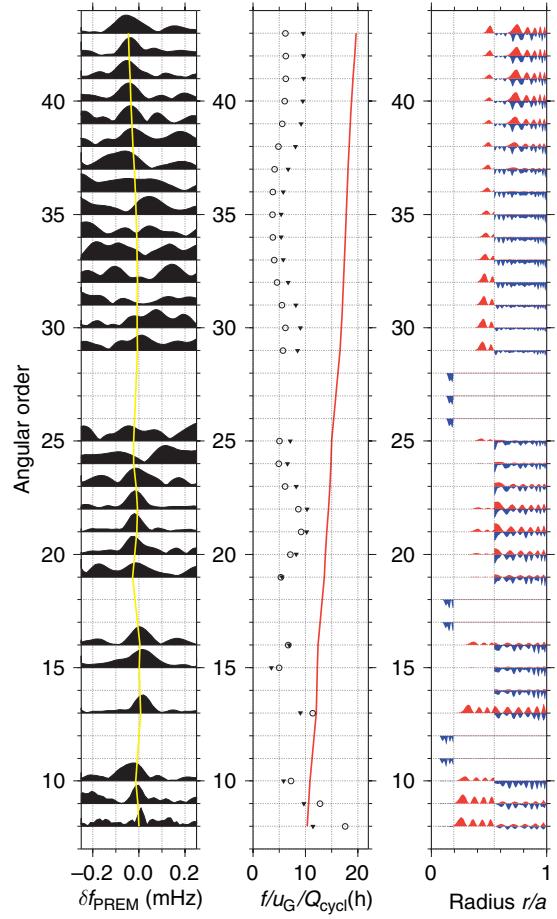


Figure 18 Multiplet strips for mode branch ${}^{23}S_\ell$, obtained from a data set of 12 000 records of 260 events between 1991 and 1998. For well-excited multiplets with intermediate to high-quality factors, Q , and sensitivity to lower mantle and core structure, multiplet stripping works well up to 20 mHz. Systematic deviations from PREM are evident in the left panel, particularly between ${}^{23}S_{39}$ and ${}^{23}S_{43}$. For details, see Figure 17.

bias from 3-D structure because the data were selected and weighted to specifically minimize this bias. The multiplet strips presented here maximize the signal-to-noise ratio at the expense of some geographic bias (i.e., some source-receiver great circles may dominate the coverage).

Condition 2 at the beginning of this section addresses pathological cases when one or more singlets are located far away from their neighbors. Isolated singlets with low spectral amplitudes are likely missed and omitted from the stripping. Examples are anomalously split IC sensitive modes such as ${}^{13}S_2$ for which the $m=0$ singlet lies

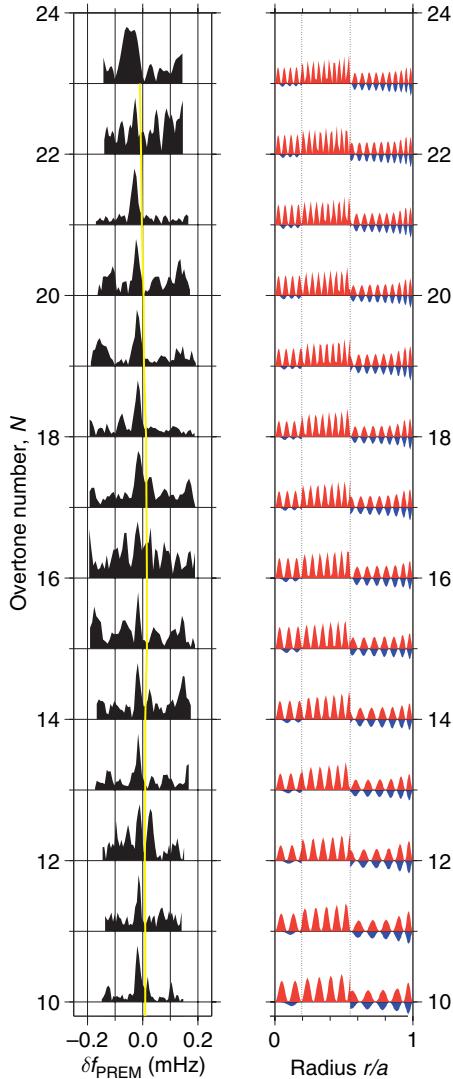


Figure 19 Multiplet stripping results for radial modes between 10 and 20 mHz. Strips with multiple peaks are likely due to coupling to nearby high-Q spheroidal overtones (Laske *et al.*, 2001). The yellow line shows the predictions of MEMO0. Neither PREM nor MEMO0 gives a satisfactory fit to these modes. While a model with an additional first-order discontinuity in the IC can explain the new radial mode frequencies, such a model leads to degradation of the fit of other IC sensitive modes (B. Valette, personal communication, 2002). For details see Figure 17.

anomalously far away from the mode's degenerate frequency (see Figure 10). Multiplet stripping for such a mode can produce strips with two peaks: a large peak near the four singlets $m = \pm 1, 2$ and a small peak near the $m = 0$ singlet. Estimating the multiplet frequency by fitting only a single resonance function to the large peak produces a biased

degenerate frequency estimate. A still elusive mode is ${}_3S_2$ for which no reliable observations of the $m = 0$ line exist, not even after the Andaman–Sumatra event. The reason for this is not fully understood but possible causes include weak excitation, peculiar anelastic structure, and coupling to other modes. Fortunately, the splitting of many low- ℓ modes can be resolved fully so that its degenerate frequency can be estimated using other techniques. For high- ℓ overtones, which are analyzed exclusively with the multiplet stripping technique, this kind of extreme singlet distribution does not appear to be a problem.

1.03.2.3.2 Singlet and receiver stripping

Historically, singlet stripping was the first method to dissect a multiplet into its singlets (Buland *et al.*, 1979). While it is a robust technique, it has been superseded by the AR receiver stripping technique (Masters *et al.*, 2000b). This is because the latter makes less assumptions about the shape of Earth's heterogeneity and also needs no accurate earthquake source model. Singlet stripping assumes that the dominant structure leading to splitting is axisymmetric. In this case, the splitting matrix \mathbf{H} (eqn [6]) remains diagonal. For the vertical component, one singlet frequency is then associated with a single Y_ℓ^m , as on the spherically symmetric Earth. The spectrum of a multiplet with angular order ℓ at the j th station, $u_j(\omega)$, can then be written as a weighted sum of singlet resonance functions $c_m(\omega)$,

$$u_j(\omega) = A_{jm}c_m(\omega) \quad \text{with} \quad -\ell \leq m \leq \ell \quad [12]$$

where the singlet excitations, A_{jm} , have been computed based on eqn [4]. Equation [12] is an overdetermined system that can be solved for the 'singlet strips', $\hat{c}_m(\omega) = A_{jm}^{-1}u_j(\omega)$. This procedure typically includes the records of many earthquakes.

In the receiver stripping approach, we treat each earthquake individually. Using eqns [4] and [5], we 'collapse' the set of spectra into a set of $2\ell + 1$ 'receiver strips', for each earthquake and each mode:

$$\mathbf{b}(t) = \mathbf{R}^{-1} \cdot \mathbf{u}(t) = \exp[i(\mathbf{H} + \mathbf{I}\bar{\omega})t] \cdot \mathbf{a}(0) \quad [13]$$

We actually work in the frequency domain using spectra of Hanning-tapered records in a small frequency band about a multiplet of interest. Examples are found in Figure 20. The spectral lines in these diagrams are proportional to the spectra of individual singlets, if axisymmetric structure dominates the

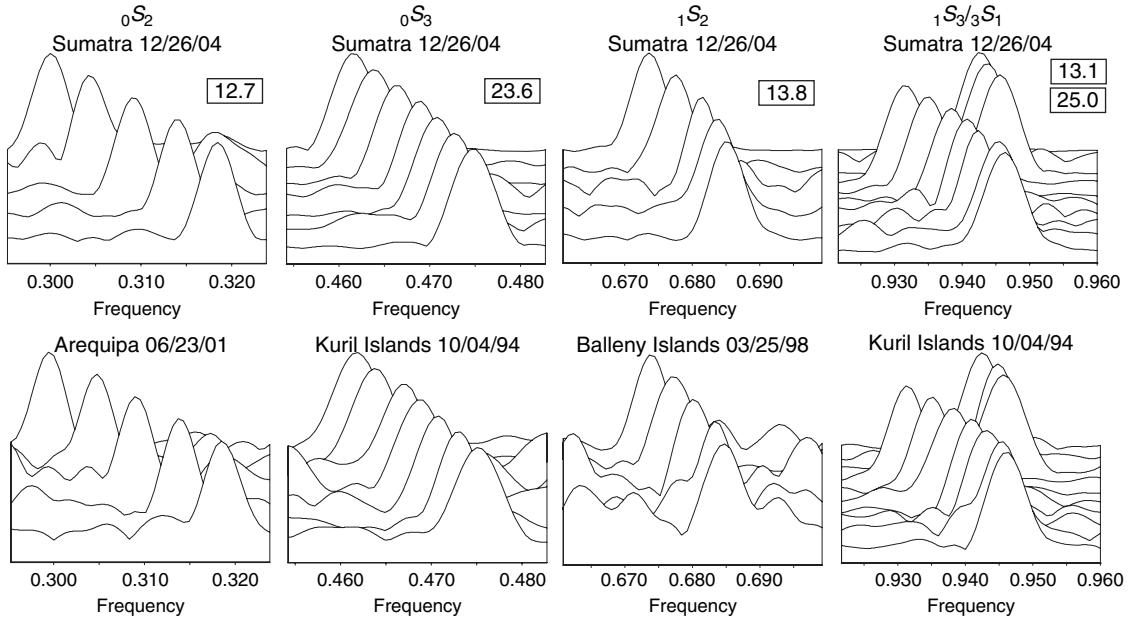


Figure 20 Normalized receiver strips for very low-frequency modes. For these modes, the splitting is dominated by axisymmetric structure and the $2\ell + 1$ strips closely resemble the spectral lines of each singlet. The upper row shows the strips for the 2004 Sumatra–Andaman earthquake, while the lower row shows the best set of strips that we have had so far. The boxed numbers indicate how much larger the amplitudes of the Andaman strips are with respect to the best other earthquake.

splitting matrix. Modes ${}_1S_3$ and ${}_3S_1$ are so close together in frequency that their receiver strips overlap. A joint analysis prevents bias introduced when ignoring one of the modes.

1.03.2.3.3 Retrieving the splitting matrix with the matrix autoregressive technique

Figure 21 shows typical examples of spectra for IC sensitive mode ${}_{13}S_2$ and the steps involved going from seismograms (or spectra) to retrieve Earth's internal structure. We use the autoregressive nature of the receiver strips to make our analysis technique for the splitting matrix independent of earthquake location and source mechanism. The receiver strips satisfy a recurrence in time. Using eqn [13], we obtain $\mathbf{b}(t)$ after the time increment δt :

$$\begin{aligned}\mathbf{b}(t + \delta t) &= \mathbf{R}^{-1} \cdot \mathbf{u}(t + \delta t) \\ &= \exp[i(\mathbf{H} + \mathbf{I}\bar{\omega})(t + \delta t)] \cdot \mathbf{a}(0) \\ &= \mathbf{P}(\delta t)\mathbf{b}(t)\end{aligned}$$

so

$$\mathbf{b}(t + \delta t) = \mathbf{P}(\delta t)\mathbf{b}(t), \quad \mathbf{P}(\delta t) = \exp[i\delta t(\mathbf{H} + \mathbf{I}\bar{\omega})] \quad [14]$$

which describes the autoregressive nature of $\mathbf{b}(t)$. Equation [14] has no term that depends on the seismic source. An inverse problem is set up for the propagator matrix \mathbf{P} , using the strips of many events

simultaneously. The splitting matrix \mathbf{H} is determined from \mathbf{P} using the eigenvalue decomposition of \mathbf{P} (Masters *et al.*, 2000b). The complex matrix \mathbf{H} we retrieve in this process is non-Hermitian (no symmetry) and includes elastic and anelastic structure. We use the unique representation

$$\mathbf{H} = \mathbf{E} + i\mathbf{A} \quad [15]$$

to decompose \mathbf{H} into its elastic, $\mathbf{E} = \frac{1}{2}(\mathbf{H} + \mathbf{H}^H)$, and anelastic, $i\mathbf{A} = \frac{1}{2}(\mathbf{H} - \mathbf{H}^H)$, components where superscript H indicates Hermitian transpose. Both \mathbf{E} and \mathbf{A} are Hermitian and are the matrices for eqn [6] (where the effects of rotation and ellipticity are included in \mathbf{E}). Examples of splitting matrices retrieved with this technique are shown in Figure 11 and Figure 25 in the observed mode coupling section. A discussion on retrieving Earth's density from splitting functions that were obtained using this method can be found in Masters *et al.* (2000c). An application to investigate the IC differential rotation is described in a later section.

1.03.2.3.4 Retrieving the splitting matrix with iterative spectral fitting

The first technique to retrieve all elements of the splitting matrix of an isolated multiplet was iterative spectral fitting (ISF) introduced by Ritzwoller *et al.*

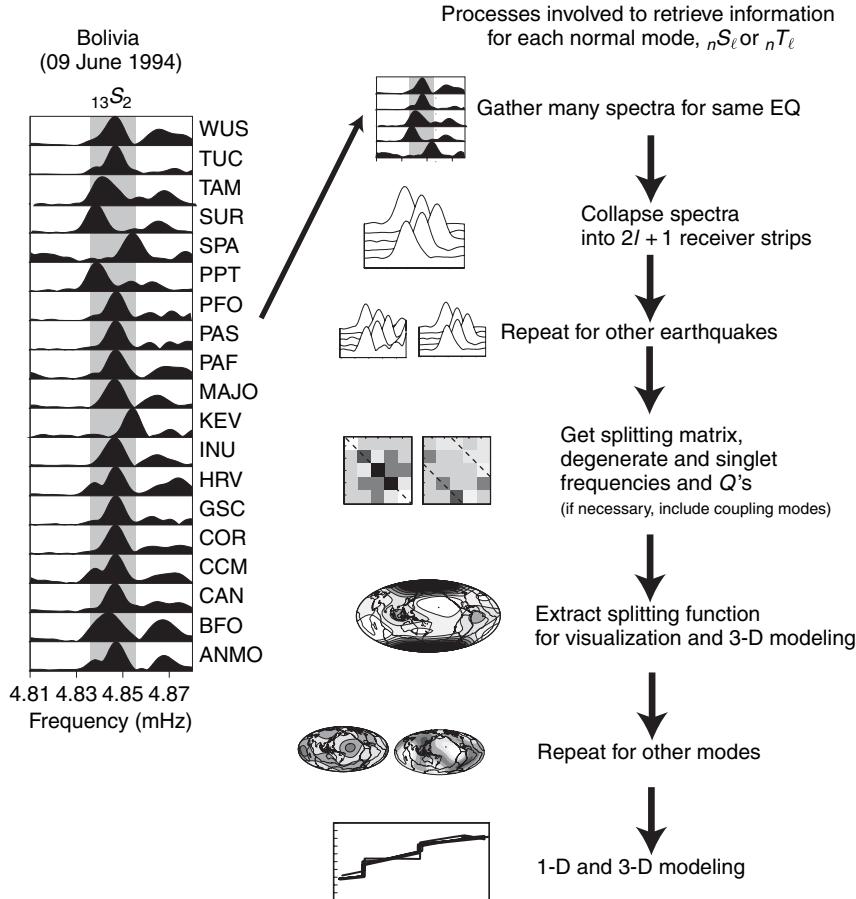


Figure 21 Left: Selected spectra for mode $_{13}S_2$, for the 1994 Bolivia earthquake. Right: Simplified flowchart of our approach to extract mode information from seismograms of large earthquakes.

(1986, 1988) and Giardini *et al.* (1987). It has been refined and applied in a number of studies, including Li *et al.* (1991a, 1991b), Widmer *et al.* (1992), He and Tromp (1996), and Resovsky and Ritzwoller (1998). ISF considers the Fourier transform of eqns [4]–[6]. In this coupled set of equations, the $\ell-1$ real and $\ell(\ell+1)$ complex structure coefficients c_s^ℓ are nonlinearly related to the observed spectra $u(\omega)$. The problem of finding the structure coefficients from a set of observed spectra is then formulated as a nonlinear parameter estimation problem. Figure 22 shows an example of how ISF allows detailed modeling of a split mode spectrum. The prediction from a model including only Earth's rotation and hydrostatic ellipticity provides a poor fit to the observed spectrum. If ISF is implemented with a local search algorithm, this prediction can serve as starting solution. Spectral fitting is then iterated and converges to a new solution that fits the observation much better. The splitting of the mode shown here,

$_{1}S_8$, reflects lower mantle V_S heterogeneity. A crucial aspect of ISF is the need of a source model so that the vector of singlet excitations $a(0)$ in eqn [5] can be computed. Matters are further complicated, if local rather than the computationally more expensive global algorithms are used to search for the set of best-fitting structure coefficients. Nevertheless, for well-excited multiplets for which records from many events can be used simultaneously it was possible with the data coverage of the 1980s to obtain robust estimates of degree $s=2$ and perhaps also $s=4$ structure coefficients.

ISF was also applied to high- Q , low-order modes up to 9 mHz (Widmer *et al.*, 1992). These modes sample the outer and IC and many of them are anomalously split. The large majority of other modes attenuates so rapidly that the spectra are dominated by the relatively sparse class of high- Q modes, if the first 6–8 h of data after an earthquake are discarded. The set of structure coefficients of

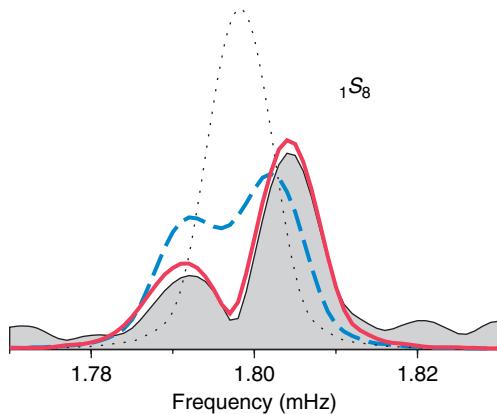


Figure 22 Modeling of the spectrum of multiplet 1S_8 with the ISF procedure, for a recording of the 9 June 1994 Bolivia earthquake at station MAJO (Matsushiro Observatory, Japan). Black line: observed linear amplitude spectrum; dotted line: prediction for PREM; dashed blue line: splitting caused by Earth's rotation and hydrostatic ellipticity; red line: final solution for the spectrum after ISF. Spectra courtesy of Joe Resovsky, personal comm. 1998. Vertical ground displacement due to this mode at MAJO measured $10\text{ }\mu\text{m}$.

these high- Q modes analyzed by Widmer *et al.* (1992) with both ISF and singlet stripping were used primarily by Tromp (1993) to corroborate the hypothesis of Giardini *et al.* (1987) that axisymmetric IC anisotropy can explain the anomalous splitting of IC sensitive modes. The most comprehensive set of structure coefficients based on ISF was compiled by Resovsky and Ritzwoller (1998). Restricting their analysis to modes below 3 mHz, they obtained 3100 structure coefficients for 90 multiplets. These authors also generalized the ISF procedure to coupled modes and obtained, for the first time, constraints on odd-degree structure using normal modes (Resovsky and Ritzwoller, 1995).

1.03.2.3.5 Observed mode coupling

As mentioned above, we observe toroidal-mode energy on vertical components because Coriolis coupling causes the formation of hybrid mode pairs in which mode energy is exchanged between modes. While this has been well observed for modes above 2 mHz, Zürn *et al.* (2000) recently also observed this for the gravest modes below 1 mHz (Figure 23). In gravimeter spectra of the great 1998 Balleny Island earthquake, they identified spectral lines at the toroidal mode frequencies of ${}_0T_3$ through ${}_0T_6$. A correction of the LaCoste Romberg gravimeter ET-19 record at station BFO for local atmospheric pressure variations (Zürn and Widmer, 1995) helped raise mode ${}_0T_3$ above the noise floor, while the spectrum of the

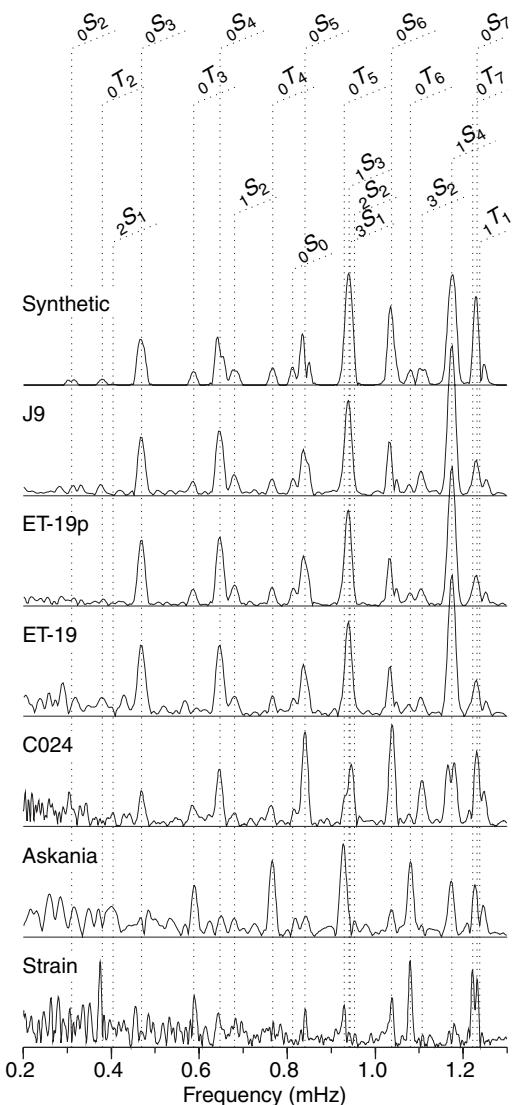


Figure 23 Coriolis coupling below 1 mHz, observed for the 25 March 1998 Balleny Islands earthquake. Spectral peaks appear in vertical component spectra at the frequencies of toroidal modes ${}_0T_3$ through ${}_0T_6$. Shown are spectra of the LaCoste Romberg spring gravimeter ET-19p at station BFO, the superconducting gravimeters GWR-C026 at station J9 near Strasbourg, 60 km from BFO, and GMR-C024 at Table Mountain Observatory near Boulder, CO (USA). To reduce noise, the gravimeter records were corrected for variations in local atmospheric pressure (Zürn and Widmer, 1995). For comparison, the uncorrected spectrum at BFO is also shown (ET-19). The synthetic spectrum was obtained from a coupled-mode synthetic for BFO, using Park and Gilbert's (1986) method to account for effects from rotation, hydrostatic ellipticity and aspherical structure. ‘Askania’ and ‘strain’ refer to data from the Askania borehole tiltmeter and the invar wire strainmeter array at BFO and show that the low order fundamental toroidal modes were efficiently excited by the event. Reproduced from Zürn W, Laske G, Widmer-Schnidrig R, and Gilbert F (2000) Observation of Coriolis coupled modes below 1 mHz. *Geophysical Journal International* 143: 113–118.

superconducting gravimeter GWR-C026 at station J9 near Strasbourg also may have shown this peak. After the Sumatra event, Hu *et al.* (2006) observed the gravest toroidal mode ${}_0T_2$ and overtones ${}_1T_2$ and ${}_1T_3$ in gravimeter spectra. Using the method of Park and Gilbert (1986), Zürn *et al.* (2000) compared the effects of rotation, hydrostatic ellipticity, and aspherical Earth structure on coupled-modes synthetic spectra. They identified Coriolis coupling as the most effective mechanism responsible for toroidal mode energy to appear in the vertical component spectra.

Above we have described how the coupling of modes can lead to a frequency shift of the entire multiplet. An example is the Coriolis coupling between spheroidal and toroidal fundamental modes. The observation of Coriolis coupling is well documented for fundamental modes between 2 and 4 mHz (Masters *et al.*, 1983; Smith and Masters, 1989a) and we recall that it is particularly strong for the two pairs ${}_0S_{11}-{}_0T_{12}$ and ${}_0S_{19}-{}_0T_{20}$. Figure 24 shows this mode coupling in an analysis where we applied the multiplet stripping technique. In general,

the effect of multiplet–multiplet coupling on the degenerate frequency cannot be corrected for using this technique, except for the case shown here (e.g., Smith and Masters, 1989a). For multiplet–multiplet coupling caused by aspherical structure, it has to be assumed that the induced shift of the degenerate frequency can be treated as a source of random noise. This may be justified as the frequency separation to the nearest coupling partners is different for every multiplet so the cross-branch coupling is different for every multiplet. For along-branch coupling systematic effects may be significant, since the frequency separation for modes belonging to the same branch is nearly the same.

Coupling through Earth's structure manifests itself in the cross-coupling blocks of the splitting matrix. We have recently started to apply the matrix AR technique to coupled modes and an example for weakly coupled modes ${}_1S_5$ and ${}_2S_4$ is shown in Figure 25. Since the selection rules state that $\ell + \ell' + s$ must be even, these two modes couple through structure of odd harmonic degree. Coupling through Earth's structure makes the

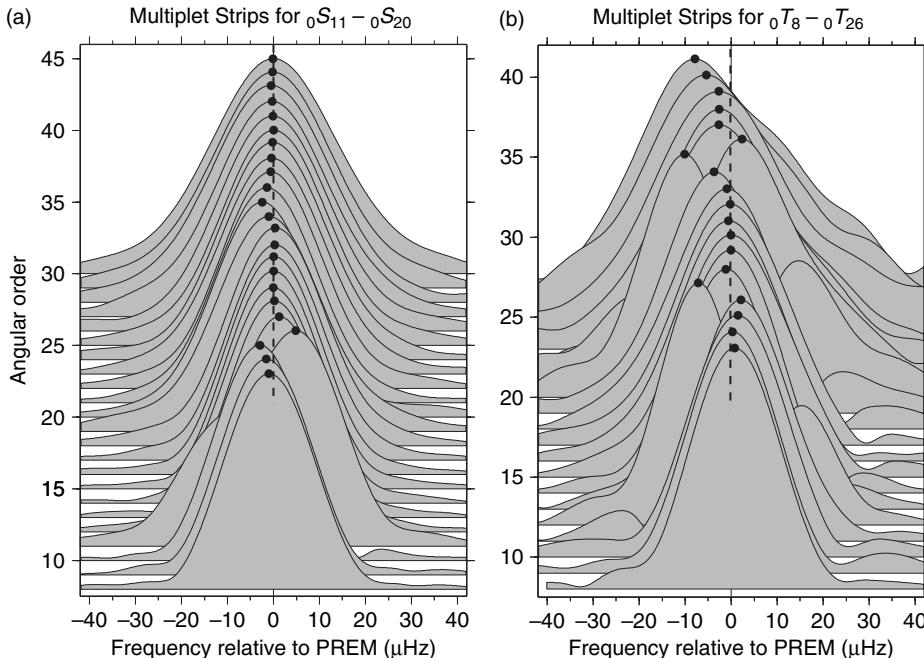


Figure 24 Observed effects of Coriolis coupling above 1 mHz. (a) multiplet strips of fundamental spheroidal modes ${}_0S_8$ through ${}_0S_{30}$, aligned relative to PREM (Dziewonski and Anderson, 1981). (b) Multiplet strips of fundamental toroidal modes ${}_0T_8$ through ${}_0T_{26}$. Coupling effects are different for each singlet, resulting in a shift of the entire multiplet. Modes ${}_0S_{11}$ and ${}_0S_{20}$ are within a few μHz of neighboring ${}_0T_{\ell+1}$ modes so coupling effects are particularly large. Coriolis coupling effects are significant for ${}_0S_9$ through ${}_0S_{22}$, relative to the observational uncertainties of less than 0.3 μHz . Modified from Widmer R (1991) *The Large-Scale Structure of the Deep Earth as Constrained by Free Oscillation Observations*. PhD Thesis, University of California San Diego, La Jolla, CA.

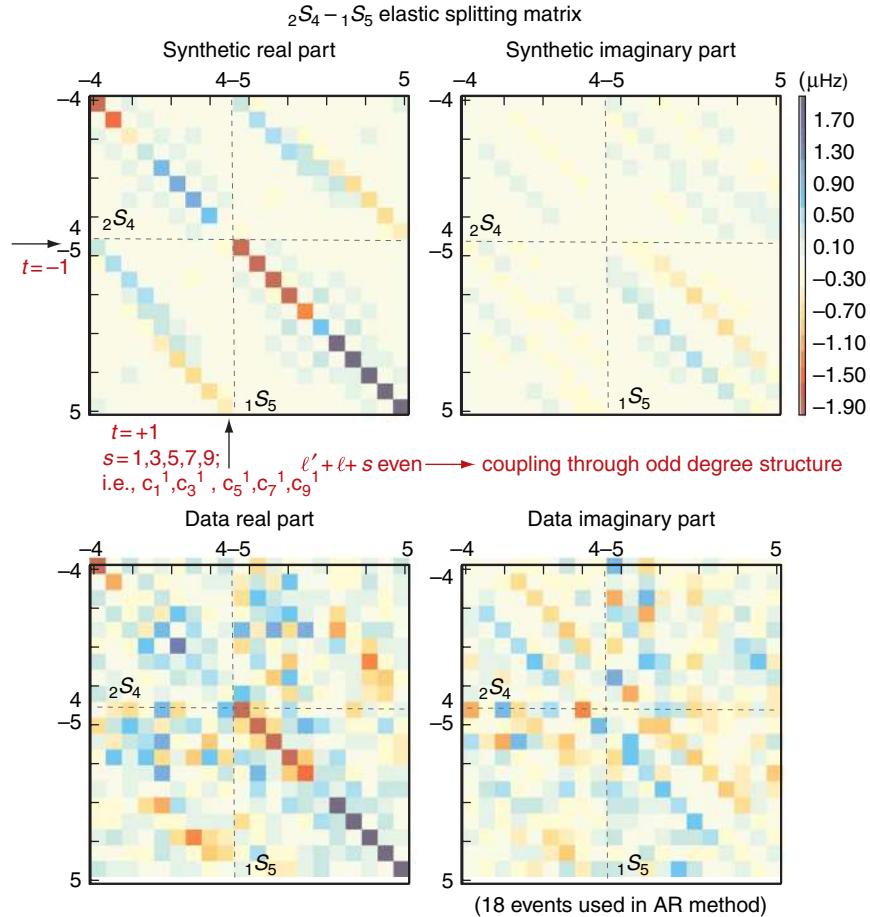


Figure 25 Predicted and measured elastic splitting matrix \mathbf{E} of the coupled mode pair ${}_1S_5 - {}_2S_4$. The signal in the diagonal self-coupling blocks is generally somewhat larger in the observations than in the predictions (e.g., imaginary part for mode ${}_2S_4$). Some predicted features show up in the measured off-diagonal cross-coupling blocks (e.g., blue in upper left corner, red toward the lower right in the real part) but noise probably inhibits a reliable extraction of odd-degree structure from these blocks at this time. The 3-D model used for the synthetic splitting matrix is S16B30 (Masters *et al.* 1996). Reproduced from Masters TG, Laske G, and Gilbert F (2000d) Large-scale Earth structure from analyses of free oscillation splitting and coupling. In: Boschi E, Ekström G, and Morelli A (eds.) *Problems in Geophysics for the New Millennium* pp. 255–288. Bologna: Editrice Compositori.

splitting matrix quite complex and the cross-coupling blocks we determine with our technique may yet be too noisy to extract odd degree structure. This should be improved in the future by including more earthquakes in the analysis. Resovsky and Ritzwoller (1995) successfully determined odd-degree structure implied in the cross-coupling blocks by using the iterative spectral fitting method. In the example shown here, only a mode pair was considered and Resovsky and Ritzwoller (1995) considered relatively small groups of modes below 3 mHz. Deuss and Woodhouse (2001) showed that wide-band coupling can significantly alter the shape of spectral lines

though it is not immediately clear if this effect is significant with respect to measurement errors of mode observables.

Since the coupling strength scales with the inverse of the frequency separation of coupling modes, splitting matrices above 3 mHz become so large that their decomposition turns into a numerically formidable task. Several different strategies have been suggested to reduce the computational burden. Lognonné and Romanowicz (1990) and Lognonné (1991) introduced the efficient spectral method to compute coupled modes and seismograms for an anelastic rotating Earth. More recently, Millot-Langet *et al.*

(2003) used third-order perturbation theory to calculate coupled-mode synthetics on an anelastic 3-D Earth. Deuss and Woodhouse (2004) introduced a method that is similar to subspace projection methods but can be iterated several times to completely represent the exact solution. They found that only one iteration usually brings the solution sufficiently close to the exact solution.

Alternatives to the approach based on mode summation other approaches include the direct solution method DSM (Geller and Takeuchi, 1995) for which an application to 3-D heterogeneity can be found in Takeuchi *et al.* (2000). The spectral element method (SEM) of Komatitsch and Vilotte (1998) also has been shown to provide an efficient tool to study wave propagation, diffraction, and body-wave conversion in a 3-D Earth. Applications of this method can be found in Komatitsch and Tromp (2002), Komatitsch *et al.* (2002), Capdeville *et al.* (2003), and Chaljub and Valette (2004). Gilbert (2001) suggested that a Vandermonde matrix analysis allows the independent determination of earthquake mechanisms and Earth structure. The method also allows the analysis of ‘latent’ modes that are not observed but coupled to observed modes (e.g., modes with extremely little energy density near the surface). For a detailed discussion of numerical methods, the reader is referred to Chapter 1.06.

1.03.2.4 Example of a Mode Application: IC Rotation

Differential rotation of the IC has been inferred by several body-wave studies with most agreeing that a superrotation may exist with a rate between 0.2° and 3° per year (e.g., Song and Richards, 1996; Creager, 2000). The wide range of inferred rotation rates is caused by the sensitivity of such studies to local complexities in structure which have been demonstrated to exist. Free oscillations, on the other hand, are natural low-pass filters of 3-D structure, so that long-wavelength phenomena, such as IC rotation, are prime study targets. Free oscillations ‘see’ the Earth as a whole, so the observation of how a free oscillation splitting pattern changes with time and any inference on IC rotation is not biased by effects of localized structures. It is also not necessary to know the physical cause of the patterns (anisotropy or heterogeneity). All that needs to be observed is if and how they change with time. Free-oscillation splitting functions are therefore better candidates for estimating differential IC rotation accurately.

The most obvious approach to do this analysis is to compare splitting functions obtained with earlier earthquakes to those obtained with recent events. A problem with this approach is that the sparsity of early data does not allow us to construct early splitting functions with the required accuracy. Sharrock and Woodhouse (1998) therefore studied the time dependence of the fit of splitting functions to spectra of earthquakes over time for some IC-sensitive modes. Their estimates of a westward rotation of the IC with respect to the mantle appear to be inconsistent with the results from body wave studies. We prefer to use our autoregressive technique for this analysis.

In a hypothesis test, we seek the optimal IC rotation rate that matches our splitting functions for recent earthquakes with receiver strips over time. Our initial finding was that the IC rotation is essentially zero over the last 20 years (0.01 ± 0.21 ; Laske and Masters, 1999). A complication in this analysis – that also plays a role in many body wave studies – is that IC-sensitive modes are also very sensitive to mantle structure. Prior to applying the assumed IC rotation rate in the test, we therefore have to correct for the contributions from the heterogeneous mantle. In a detailed and updated analysis (Laske and Masters, 2003), we applied mantle corrections using a variety of published mantle models (Figure 26). Our preferred model is SB10L18 (Masters *et al.*, 2000a), a 10-degree equal area block model that was derived simultaneously for shear velocity and bulk sound speed, $V_C = \sqrt{\kappa/\rho}$, and our mode data were included in the inversions. The majority of models in the literature are shear velocity models that were derived using only shear sensitive modes (e.g., SAW24B16 by Mégnin and Romanowicz (2000) or using established scaling relationship for V_P and ρ (or ignoring sensitivity to the latter entirely) to include spheroidal modes (e.g., S20RTS by Ritsema and van Heijst (2000)). Our comparison also includes our older model S16B30 (Masters *et al.*, 1996) that was the result of a direct matrix inversion for a model described by spherical harmonics. As can be seen from Figure 26, inferred rotation rates vary with different mantle models but most results lie within our error bars for SB10L18. Our current best estimate is a barely significant superrotation of $0.13 \pm 0.11^\circ \text{ yr}^{-1}$, which is still consistent with the idea that the IC is gravitationally locked to the mantle. Our value is consistent with many body wave results (e.g., Creager, 1997, 2000) though the discrepancy to the more recent estimate of

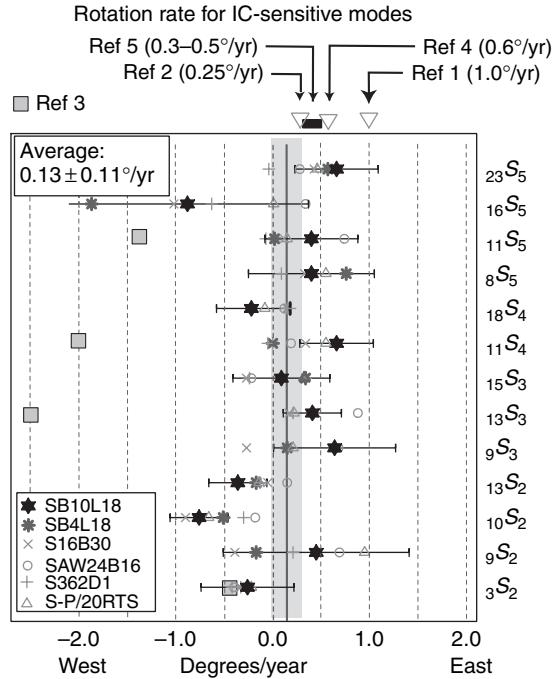


Figure 26 IC rotation rates obtained for 13 IC-sensitive modes, using our preferred $V_S/V_C/V_P$ mantle model SB10L18 (Masters *et al.*, 2000a). Also shown are the results obtained using other mantle models: shear velocity models SB4L18 (Masters *et al.*, 2000a), S16B30 (Masters *et al.*, 1996), SAW24B16 (Mignot and Romanowicz, 2000), S362D1 (Gu and Dziewonski, 1999) and V_S/V_P models S-P/20RTS (Ritsema and van Heijst, 2000). Other symbols and lines mark results from other publications: Song and Richards (1996) (Ref.1), Creager (1997) (Ref.2), Sharrock and Woodhouse (1998) (Ref.3), Song (2000) (Ref.4), Zhang *et al.* (2005) (Ref.5).

$0.3\text{--}0.5^\circ \text{ yr}^{-1}$ by (e.g., Zhang *et al.*, 2005) is marginal but still significant.

There are limitations to this type of analysis and not all IC-sensitive modes can be utilized. For example, although $\ell = 1$ modes (e.g., ${}_8S_1$, ${}_{13}S_1$) are quite sensitive to IC structure, they can constrain IC rotation only poorly because the mantle-corrected splitting functions are dominated by a large zonal (axisymmetric) component. Also, so far, we have ignored mode coupling in our analysis. Some IC sensitive modes significantly overlap in frequency with other modes of high angular order ℓ , thereby hampering an analysis using the receiver strip method. For example, with a degenerate frequency in PREM (Dziewonski and Anderson, 1981) of 1.242 mHz, mode ${}_2S_3$ is very sensitive to IC shear velocity but overlaps with ${}_0T_7$, ${}_0S_7$, and ${}_1T_1$ which couple through Earth's 3-D structure. For a given mode pair ${}_0S_\ell/{}_0T_\ell$ we need at least $2 \times (\ell' + \ell + 1)$ high-quality records to

construct receiver strips. These many records are often not available for earlier earthquakes. Many $\ell = 2$ modes that are very sensitive to IC structure are strongly coupled to radial modes. We can analyze such mode pairs with our AR technique but the IC rotation hypothesis test becomes more cumbersome and was not done in our 2003 study. We notice that mode ${}_{13}S_2$, which couples with ${}_5S_0$, and mode ${}_{10}S_2$, which couples with ${}_4S_0$, systematically suggest a westward IC rotation, regardless of the mantle model chosen for the corrections. The analysis of ${}_3S_2$, whose coupling properties with neighboring modes is quite complex (see also Zürn *et al.* (2000)), also gives westward rotation rates. Mode ${}_{9}S_2$ is difficult to observe and errors are quite large. When not taking these modes into account, we obtain an eastward IC rotation rate of $0.34 \pm 0.13^\circ \text{ yr}^{-1}$. This marginally agrees with the estimate of (Zhang *et al.*, 2005).

A caveat when analyzing modes using the isolated-mode assumption is that only even degree structure can be determined. It is known from body wave studies that the heterogeneity at the top of the IC has a strong $s=1$ signal that is roughly divided into a Western and an Eastern Hemisphere (Tanaka and Hamaguchi, 1997; Creager, 2000). The fact that isolated modes are insensitive to such structure does not invalidate our IC rotation results, provided the IC rotates as a rigid body. Structure of uneven harmonic degree can potentially be determined by analyzing coupled modes but the coupling effects for the modes considered here is rather weak. Core structure and IC differential rotation is discussed in Chapter 1.19.

1.03.2.5 Example of a Mode Application: Earth's Hum

It took as long as 38 years after the first observation of the Earth's free oscillations of the 1960 Great Chilean earthquake before convincing evidence was found that the Earth's normal modes never cease to vibrate but instead remain excited at a low but constant level (Suda *et al.*, 1998; Tanimoto *et al.*, 1998; Ekström, 2001). This normal mode background signal is now often termed Earth's 'hum'. Early on, Benioff *et al.* (1959) looked for modal signals in noise spectra of LaCoste–Romberg gravimeters but the sensitivity of these instruments (which at the time were operated with a mechanical feedback) was too low by three orders of magnitude for a positive hum detection. It was not until Nawa *et al.* (1998) first inspected data from the superconducting gravimeter at Syowa

(Antarctica) and subsequently from seismic stations of the global network (Suda *et al.*, 1998) that evidence for the incessant excitation of seismic free oscillations was presented.

Fundamental spheroidal modes ${}_0S_\ell$ are observed to be permanently excited in the frequency band 2–7 mHz, with an RMS acceleration amplitude of ~ 1 ngal ($= 10^{-11} \text{ m s}^{-2}$) over a 100 μHz bandwidth (Figure 27). Additional characteristic hum features are a slight semiannual modulation of the amplitude and a resonant enhancement near 3.7 mHz (Nishida *et al.*, 2000; Ekström, 2001). At frequencies below 2 mHz, vertical seismic noise is primarily of local barometric origin and some of this noise can be removed by regression with the locally recorded pressure fluctuations (Zürn and Widmer, 1995). However, this crude correction does not allow to remove all of the barometric noise, making a hum detection below

2 mHz nearly impossible. At frequencies near 7 mHz the splitting of the fundamental spheroidal modes due to heterogeneous upper mantle structure is as wide as the frequency separation between adjacent fundamental modes. Modes then overlap and cause an overall rise of the noise base level into which peaks disappear. Nishida *et al.* (2002) showed that the vertical component seismic noise consists of globe circling Rayleigh waves all the way up to 20 mHz, and it seems likely that the same mechanism is responsible for the generation of Rayleigh wave background noise as for the hum at lower frequency. The detection of the hum is an instrumental challenge because of its exceptionally small amplitude. The self-noise of all instruments that have so far been able to detect the hum is at or very near the amplitude of the hum itself. These include superconducting gravimeters, LaCoste–Romberg spring gravimeters, Streckeisen STS-1 and STS-2 seismometers. Widmer-Schnidrig (2002) computed coherences for pairs of colocated sensors and in the hum band obtained values not exceeding 0.5. The low signal-to-noise ratio necessitates much averaging in time or array techniques to enhance the hum signal.

The physical cause for the excitation of the hum remains somewhat of a puzzle. Considering that wave motion in the oceans is responsible for the marine microseisms at periods shorter than ~ 25 s and that below 2 mHz atmospheric phenomena dominate the seismic noise, one can speculate that the signals in between are also generated by atmospheric and/or hydrospheric processes. The semiannual modulation supports this hypothesis, while the resonant enhancement near 3.7 mHz is evidence for at least partial involvement of the atmosphere (e.g., Widmer and Zürn, 1992). The lack of overtones in the hum favors near-surface excitation and also speaks for the atmosphere and/or hydrosphere excitation hypothesis. From the observation that individual mode excitations do not correlate between pairs of stations Nishida and Kobayashi (1999) have drawn the conclusion that the source of the hum cannot be localized but must be of global origin: they hypothesize that pressure exerted on the solid Earth by global atmospheric turbulence is responsible for the hum excitation. This conclusion however is not compelling because of the low signal-to-noise ratio mentioned above.

Trying to elucidate the hum excitation mechanism, Rhie and Romanowicz (2004) used the BDSN (Berkeley Digital Seismic Network) in California and the F-Net in Japan to estimate the back azimuth of the Rayleigh wave background signal. They located

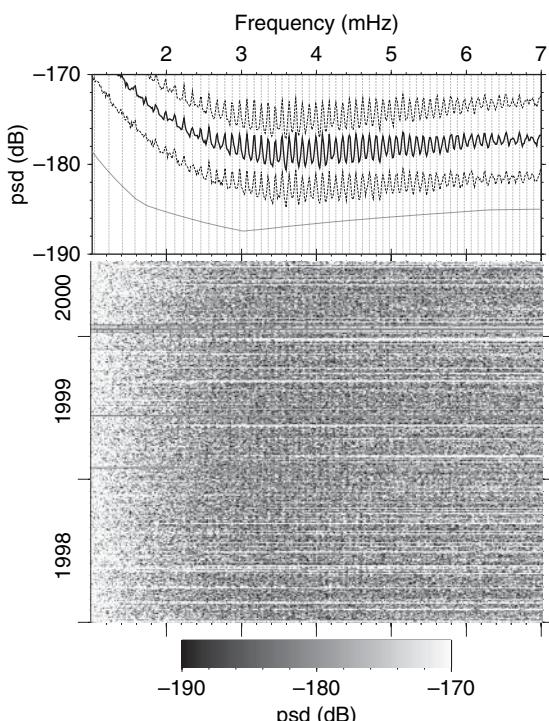


Figure 27 Time–frequency plot covering 2.5 years of data from the STS-2 seismometer of the German Regional Seismic Network (GRSN) at BFO. The range of the gray scale is chosen to emphasize structure in the noise during seismically quiet times. The upper panel shows median psd levels (black) together with the first and third quartile (dashed). The New Low Noise Model of Peterson (1993) (gray) is shown for reference. The vertical dashed lines indicate the predicted frequencies of the fundamental spheroidal modes ${}_0S_\ell$ and coincide with light-gray vertical bands in the lower panel.

hum sources in the north Pacific during Northern Hemisphere winter and in the southern oceans during summer. A subsequent analysis of 5 years of data from the GRSN (German Regional Seismic Network) in Germany found back azimuths consistent with these source regions (Kurle and Widmer-Schnidrig, 2006). **Figure 28** shows that the back azimuths of Rayleigh waves at GRSN also have a very pronounced seasonality. Prevalent winter back azimuths around 30° point toward the North Pacific while summer back azimuths of 210° and 120° point to the southern Pacific and southern Indian ocean, both in accordance with Rhie and Romanowicz (2004). More recently, Rhie and Romanowicz (2006) studied two winter storms off the west coast of N-America during 4 seismically quiet, consecutive days. As the storms hit the coast, the amplitude of both the marine microseisms and the low-frequency Rayleigh waves increased and both wave types could be traced back to the same coastal segment where the storms hit the shore.

While the generation of microseisms by ocean waves is well understood, it is not entirely clear how the band-limited storm-generated surf can be related to infragravity waves and the generation of

low-frequency Rayleigh waves. Infragravity wave generation involves nonlinear wave–wave interactions on the shelf (e.g., Galagher, 1971; Webb, 1998; Tanimoto, 2005). Rhie and Romanowicz not only observed hum excitations along the West coast of North America where the infragravity waves were originally generated but also along the North Pacific rim after the waves apparently traveled there and dissipated. The timing was found to be consistent with the propagation speed of $\sim 200 \text{ m s}^{-1}$ for infragravity waves in the open ocean. Whether the processes invoked to explain the observations from two large winter storms are representative for everyday hum excitation remains to be seen. If infragravity waves are capable of exciting the hum to observable levels after crossing entire ocean basins, that may explain why previous attempts at locating the source regions of the hum produced only very diffuse maps.

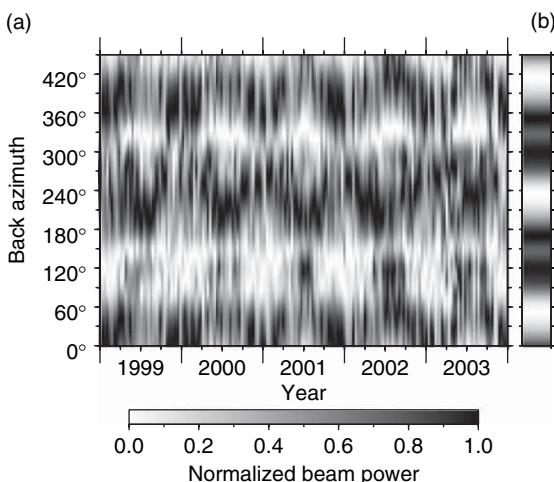


Figure 28 (a) Beam power distribution of Rayleigh wave background between 5 and 8 mHz estimated from vertical component recordings of a nine station array in central Europe. (b) Back azimuths of an incident plane wave field cannot be recovered perfectly from a sparse 9 station array. This is evident from the array response shown here. Reproduced from Kurle D and Widmer-Schnidrig R (2006) Spatiotemporal features of the Earth's background oscillations observed in central Europe. *Geophysical Research Letters* 33: L24304, doi:10.1029/2006GL028429.

1.03.3 Surface Waves

1.03.3.1 Standing Waves and Traveling Waves

Many papers document that there is no real boundary between free oscillation and surface wave measurements. For example, early free oscillation papers that discuss great-circle surface wave dispersion actually discuss free oscillation peak shifts (e.g., Roult and Romanowicz, 1984). Studying long-period surface waves, Souriau and Souriau (1983) found a plate-subduction-related degree 2 anomaly in the transition zone that was similar to that of Masters *et al.* (1982) using their mode approach. In fact, surface wave theory on the spherical Earth can be understood as a high-frequency approximation of mode theory. As mentioned in the mode section, the motion of standing waves on a sphere is expressed in spherical harmonics. At epicentral distance Δ , standing waves along a source–receiver great circle are described by zonal harmonics where the Legendre polynomials $P_\ell(\cos \Delta)$ are the relevant terms (**Figure 29**). In the high-frequency or high- ℓ asymptotic expansion, this term is approximated by cosines which are the relevant terms of traveling waves (e.g., Jordan, 1978; Aki and Richards, 1980, 2002; Romanowicz and Roult, 1986):

$$P_\ell(\cos \Delta) \approx \left(\frac{2}{\pi \ell \sin \Delta} \right)^{1/2} \cos \left[\left(\ell + \frac{1}{2} \right) \Delta - \frac{\pi}{4} \right] \quad [16]$$

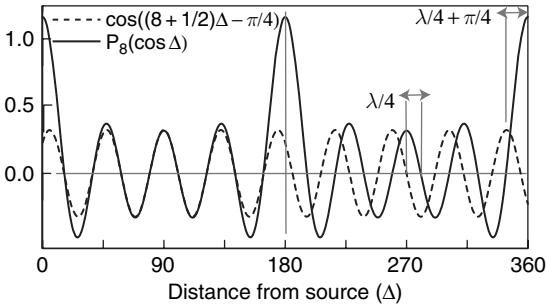


Figure 29 A comparison of the degree 8 Legendre polynomial with its asymptotic representative. The scaling factor of eqn [16] was omitted but a constant factor was applied for optimal illustration. The graph also illustrates the validity of Jeans' formula. The asymptotic representation is applicable strictly only near $\Delta = 90^\circ$. After passing a pole, the asymptotic leads by $\pi/2$ or approximately a quarter wavelength where $\lambda = 2\pi/(\ell + 1/2)$. Entering and exiting a pole each adds $\pi/4$.

Away from the poles, Jeans' formula (Jeans, 1923) gives the approximate wave number, k , of such a cosine:

$$k = (\ell + 1/2)/a \quad [17]$$

where a is Earth's radius.

Dahlen and Tromp (1998) describe the conversion from the standing wave to the traveling wave representation through the Watson transformation

$$\sum_{\ell=0}^{\infty} f\left(\ell + \frac{1}{2}\right) = \frac{1}{2} \int_C f(k) e^{-ik\pi} \cos(k\pi)^{-1} dk \quad [18]$$

where f is any function that is analytic near the real k -axis and C is a closed contour along the positive real k -axis (see also box 9.7 in Aki and Richards (2002) and box 9.3 in Aki and Richards (1980)). This demonstrates how a sum over discrete modes (standing waves) is expressed as an integral over continuous wavenumber (traveling waves).

Approaching the problem from the other end, to observe a free oscillation spectrum, the time series has to include at least a pair of wave trains traveling in opposite directions as well as a third wave train that circled the Earth, that is, the time window has to be at least roughly 5 h long (Figure 30; see also Figure 3). The synthetic seismograms that Figure 30 is based on were calculated for an epicentral distance of nearly 90° . In this case, the fundamental mode spectra are modulated such that often every other mode has a significantly reduced amplitude though this modulation also depends on the source. For the examples

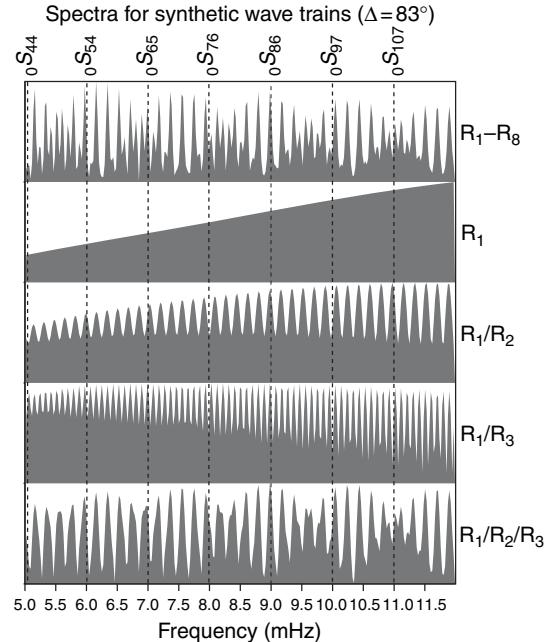


Figure 30 Spectra of synthetic acceleration seismograms at an epicentral distance of 83° , with a variety of wave-trains as indicated on the right. All time series are 12 h long. Only the top spectrum contains all wavetrains that arrive at a station within 12h. Wave trains in the other records were zeroed out. A Hanning taper was applied before calculating the spectra. The full amplitude modulation is apparent only after 3 wavetrains are recorded at a station. The combination R_1/R_3 is an unrealistic case but demonstrates that wave trains separated by a full great circle carry mode information (see also the caption to Figure 4). The seismograms were calculation with a mode summation code based on MINOS (see section on Modes of a Spherically Symmetric Earth).

shown here, we assume a double-couple point source. A seismogram including only one wave train carries no information on the finite body Earth; hence, we do not observe normal modes. As soon as a major and a minor arc wave train are recorded, an amplitude modulation pattern emerges that depends on the epicentral distance and the source mechanism. If two wave trains are recorded that are separated by a complete great circle, modes can be observed though without this amplitude modulation. This peculiar behavior becomes clear when we discuss the representation of a surface wave seismogram on the spherical Earth.

Away from the poles, surface waves traveling on the spherical Earth can be expressed by

$$s(t) = \frac{1}{2\pi} \int_{-\infty}^{\infty} A_s(\omega) e^{-\alpha(\omega)t} \times e^{i(\omega t - k(\omega)x + (N-1)\pi/2 + \Phi_s(\omega))} d\omega \quad [19]$$

where A_s is the source amplitude, $\exp(-\alpha(\omega)t)$ describes the attenuation along the path, Φ_s is the source phase, and $i(\omega t - kx)$ describes the evolution of the phase along the travel path. Brune *et al.* (1961) first described and experimentally verified that surface waves traveling on a sphere experience a $\pi/2$ phase shift each time the wave passes a pole. This is accounted for by the term $(N-1)\pi/2$, where N is the wave orbit number. The polar phase shift can be explained by the fact that eqn [16] is a good approximation only for distances less than 180° where the $P_\ell(\cos \Delta)$ are in phase with the cosines (Figure 29). For distances $180^\circ < \Delta < 360^\circ$, this representation lags by a quarter of a wavelength, or $\pi/2$. Note that we ignore the scaling factor of Equation 16 in Figure 29. Including this factor provides a better match in amplitudes for a wider distance range away from 90° but the factor is singular near the poles. From a traveling wave perspective, the poles are locations of caustics where an approaching surface wave from one direction is not defined (e.g., Schwab and Kausel, 1976b; Wielandt, 1980; Romanowicz and Roult, 1986). Using eqn [19] we can also understand how two wave trains that are separated by a complete great circle interfere to form standing waves. The contributions of the two wave trains to the seismogram are largest (constructive interference), when the phase difference between the two, $\delta\Psi(\omega) = -2\pi ak(\omega) + \pi$, is an integer multiple of 2π , that is, $\ell 2\pi$. This results in Jeans' Formula.

The surface wave analog to measuring mode frequency shifts is the measurement of phase velocity, $c(\omega) = \omega/k$, which is achieved by measuring the phase, $\Psi = -kx$. Two principal hurdles impede a straightforward analysis. The first hurdle has to do with the time series in general. Surface wave packets are nonstationary and the phase changes rapidly with frequency. It is therefore not practical to extract accurate phase estimates using a simple periodogram technique. The second hurdle comes from the fact that we use the approximation in eqn [16], which is a high- ℓ asymptotic. Wielandt (1980) pointed out that, at a given frequency, Jeans' formula gives only an average wave number on a sphere which changes with travel distance, so the phase velocity also changes. The measured phase velocity, which he termed 'dynamic phase velocity' (Wielandt, 1993), is the asymptotic one only at distance $\Delta = 90^\circ$, but slower at shorter distances and faster at longer ones. The 'dynamic phase velocity' is attached to the wavefield (which includes the nonuniform amplitude

on a spherical Earth, see Figure 29) and is not to be confused with the 'structural phase velocity' that we seek which, in the case of a 1-D Earth, is the asymptotic phase velocity. Wielandt (1980) suggested to apply correction factors for waves that do not cross a pole. He estimated that ignoring such factors can amount to errors of 1% which is of the same order of magnitude as phase perturbations caused by structure. This consideration is relevant only at extremely long periods beyond 300 s ($\ell \approx 25$) where these factors become significant, given modern measurement errors. Schwab and Kausel (1976b) provided graphs of correction factors for Love waves for certain travel distances and earthquake source mechanisms. We prefer to measure phase perturbations with respect to a reference model by determining the transfer function between an observed and a mode synthetic seismogram. This implicitly reduces the variation of phase with frequency (hurdle 1). It accounts for the polar phase shift and source phase automatically and fully accounts for the approximation of eqn [16] (hurdle 2). A phase perturbation $\delta\Psi(\omega)/\Psi(\omega)$, caused by lateral heterogeneity, is then

$$\frac{\delta\Psi(\omega)}{\Psi(\omega)} = -\frac{1}{\Delta} \int_0^\Delta \frac{\delta c(\omega)}{c_0(\omega)} dx \quad [20]$$

where $\Psi(\omega)$ is the frequency-dependent phase accumulated along the perturbed travel path, Δ is the travel distance, and $c_0(\omega)$ is the frequency-dependent reference phase velocity. Equation [20] is correct to first order in lateral heterogeneity. Pollitz (1994) calculated the second-order contribution which arises from gradients perpendicular to the great circle path. Pollitz concluded that the second-order effect is insignificant in the determination of long-wavelength structure up to harmonic degree 12 (anomalies of scale 1500 km and larger). Ignoring this contribution may cause a bias in phase velocity maps for structure significantly beyond harmonic degree 16 (anomalies smaller than 1200 km) though the impact of this on models obtained with large global datasets requires further investigation.

On a sphere, it is convenient to expand lateral heterogeneity in terms of surface spherical harmonics $Y_l^m(\theta, \phi)$ as function of geographic coordinates θ and ϕ , so that $\delta c/c_0$ is

$$\frac{\delta c(\omega)}{c_0(\omega)} = \sum_{l=0}^{L_M} \sum_{m=-l}^l c_l^m(\omega) Y_l^m(\theta, \phi) \quad [21]$$

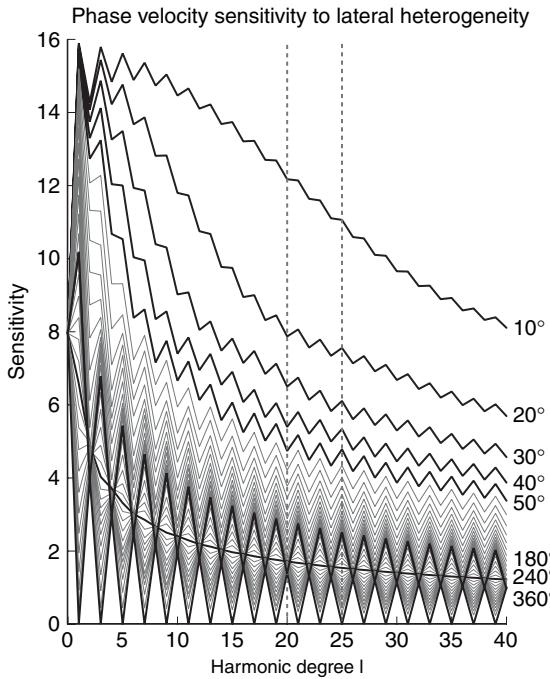


Figure 31 Phase sensitivity to lateral heterogeneity (integral kernel of eqn [20]), as function of harmonic degree in structure. Curves are shown for travel distances between 10° and 360°. Paths with distance less than 180° are for minor arc paths (R_1), larger distances are for major arc paths (R_2).

where the c_l^m are complex coefficients and L_M is the maximum harmonic degree to which lateral phase velocity variation (a ‘phase velocity map’) is expanded. Note that l and m here describe structure while the ℓ and m in the modes section describe a normal mode.

Considering the parametrization of eqn [21], it is interesting to plot the integral kernels in eqn [20] to examine how phase perturbations depend on lateral heterogeneity. In Figure 31 we notice that sensitivity falls off with harmonic degree in structure though it is initially relatively high, for short travel distances. The sensitivity to even degree structure decreases relative to odd harmonic degrees, up to a travel distance of 180°, at the antipode of the source. Then sensitivity evens out up to 240° travel distance, which corresponds to R_2 , the major arc wave train for an epicentral distance of 120°. After that, the relative sensitivity to odd harmonics falls below the sensitivity to even harmonic degrees, until it is zero at 360°, when a wave train completed a great circle. Recall that we had mentioned in the mode section that waves lose sensitivity to odd-degree structure as time goes on and that eqn [10] (Backus, 1964)

shows that a complete great circle integral over Y_l^m s has no sensitivity to odd-degree structure.

Phase velocity maps derived exclusively from great-circle data are equivalent to the mode splitting functions in eqn [9], except that phase velocity maps are measured at fixed frequency, ω , and splitting functions at fixed wave number, k (or ℓ). From the cyclic relation for partial differentiation (e.g., Riley *et al.*, 2002),

$$\left(\frac{\partial\omega}{\partial m}\right)_k \cdot \left(\frac{\partial m}{\partial k}\right)_\omega \cdot \left(\frac{\partial k}{\partial\omega}\right)_m = -1$$

where m is a model parameter, we can derive a conversion factor between splitting functions and phase velocity maps,

$$\left(\frac{\delta\omega}{\omega}\right)_k = \frac{u}{c} \cdot \left(\frac{\delta c}{c}\right)_\omega \quad [22]$$

where $c = \omega/k$ and $u = \partial\omega/\partial k$ are phase and group velocity (see next paragraph). An example of this relationship is shown in Figure 32 where both maps were obtained by inverting our standing and traveling wave observations. The patterns in the maps, caused by lateral heterogeneity within the Earth, are quite similar visually and the correlation between the maps is above the 99% confidence level (Laske and Masters, 1996). Small variations that are numerically barely significant may result from differences in the data sets and inversion schemes used. We can therefore convince ourselves that analyzing standing and traveling waves result in the same models of even-degree Earth structure.

The phase velocity is the speed at which a certain point in the wave train travels, while a certain point of the envelope (or the energy) travels with the group velocity (see Figure 36b for concept). Both together define the dispersion of surface waves and a last comparison with modes is done here. In the mode section, we introduced the ω - ℓ dispersion diagram (Figure 16) that shows mode frequencies as a function of mode identifiers n and ℓ . Using Jeans’ formula (eqn [17]), which is valid for $\ell \gg n$, this diagram implicitly summarizes the dispersion of surface waves (Figure 33). For most Rayleigh wave frequencies, we observe normal dispersion with $c > u$, or $dc/dk < 0$. An exception is the range below 2 mHz, where we observe anomalous dispersion, $u > c$, or $dc/dk > 0$. In the range of low-frequency modes below $\ell = 25$, c/u increases until c is roughly 42% larger than u , then it decreases. At frequencies above about 6 mHz, c/u approaches 1 and variations in local peak shift can be related directly to phase velocity variations.

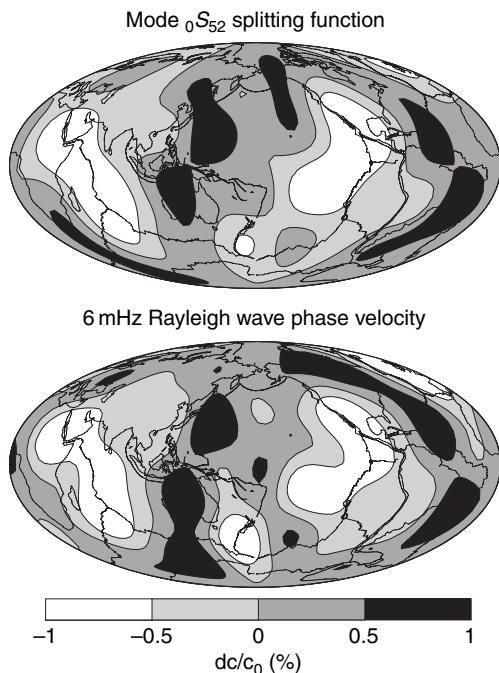


Figure 32 Comparison of effects of 3D structure on standing waves (splitting function) and traveling waves (phase velocity map). The splitting function was converted to phase velocity perturbation using the conversion factor given by Equation 22. Only even harmonic degrees are shown for the Rayleigh wave map to make it compatible with the splitting function of an isolated mode that is not sensitive to odd harmonics. Both maps are truncated at harmonic degree 8. Adapted from Laske and Masters (1996).

Group and phase velocities for Love waves are typically larger than those for Rayleigh waves at the same frequency, except above roughly 50 mHz when the Love wave group velocity drops off significantly for oceanic structure (see next section). Also, c/u starts to approach 1 at much lower frequencies than for Rayleigh waves.

1.03.3.2 The Measurement of Fundamental Mode Dispersion

For surface waves, dispersion is usually presented in frequency–velocity (or period–velocity) diagrams (Figure 34 and 35). Before we elaborate on measurement techniques, we briefly summarize some early observations of surface wave dispersion. Probably one of the most well-known and subsequently cited summaries of early observed dispersion curves for both group and phase velocities is that of Oliver (1962). He published curves for both Love and

Rayleigh wave fundamental modes and the first two overtones, for oceanic and continental paths. He summarized results in a wide frequency range (1 h–1 s). At the time, overtone phase velocities remained largely unobserved. The summary was mainly based on observations by Maurice Ewing and his group at LDEO, then the Lamont Geological Observatory, but the observation of Rayleigh wave dispersion goes back to at least the 1930s (e.g., Carder, 1934 for oceanic paths, and Röhrbach, 1932, Gutenberg and Richter, 1936 for continental paths). Ewing and Press (1954, 1956) collected long-period Rayleigh wave group velocities between 10 and 500 s. They observed a significant difference in dispersion for continental and oceanic paths at periods shorter than roughly 75 s and attributed dispersion at longer periods to be influenced primarily by structure in the mantle. Subsequently, surface waves at periods 75 s and longer were called mantle waves which is still used today (e.g., Ekström *et al.*, 1997). Ewing and Press remarked that the dispersion of oceanic paths is strongly influenced by the presence of a water layer (e.g., Ewing and Press, 1952, but also Berckhemer, 1956). It was observed that, due to the steep dispersion at periods shorter than 20 s, oceanic Rayleigh wave packets are far more stretched out than continental Rayleigh waves. The latter required long travel paths to resolve details in the dispersion curve. Short-period dispersion of the first ‘shear mode’ (overtone) was first observed by Oliver and Ewing (1958), for paths traversing the deep ocean after a nuclear explosion in 1955, about 700 km off the coast of Southern California (Operation Wigwam). The wave trains appeared unusually complicated but also gave seismologists a chance to observe oceanic dispersion for the first time at periods shorter than 15 s. Oceanic short-period overtone signals are usually hard to observe in teleseismic records due to the dominance of swell-generated microseism noise. The Wigwam records also revealed, for the first time, the slow Airy phase (waves with stationary group velocities; Pekeris, 1946) at around 7 s for oceanic paths.

Love wave dispersion is usually more difficult to measure than that of Rayleigh waves because the process involves the analysis of the typically noisier horizontal seismometer components. Also, long-period Love waves have similar group velocities over a wide frequency band, especially in the oceans (see Figure 35). This often makes Love waves to appear pulse-like which hampered early dispersion

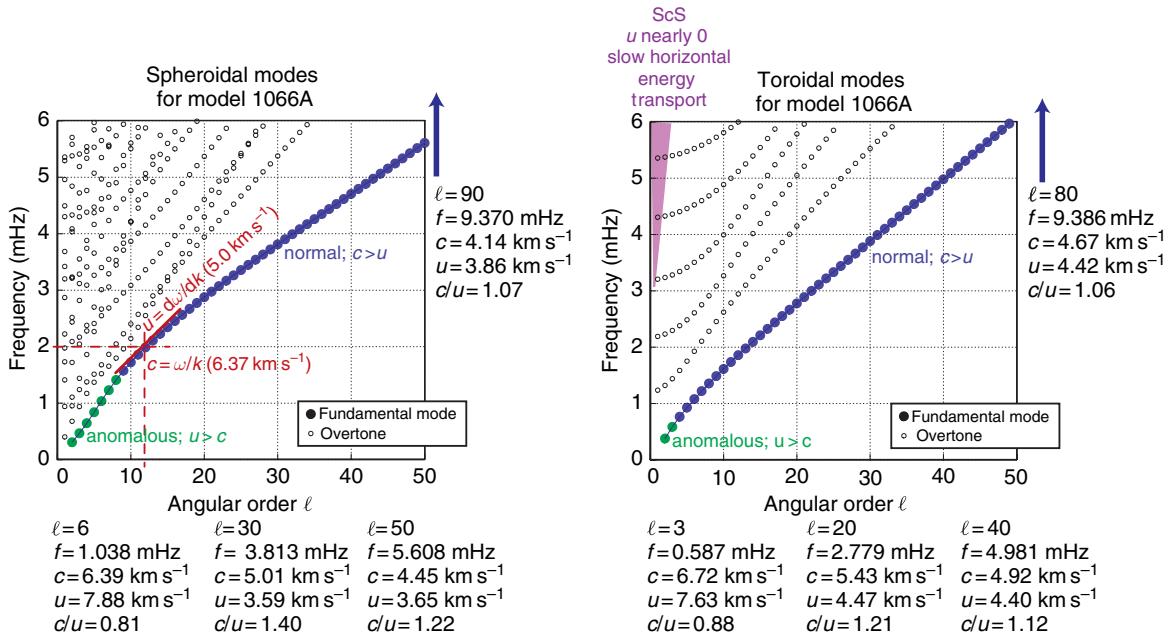


Figure 33 Dispersion diagram (ω - ℓ plot) for spheroidal and toroidal modes for model 1066A of (Gilbert and Dziewonski, 1975). Red lettering describes the concept of phase (c) and group (u) velocity for mode ${}_0S_{12}$. Blue symbols mark fundamental modes with normal dispersion ($u < c$), while green symbols mark modes with anomalous dispersion ($u > c$). The purple area marks the location of ScS equivalent modes whose group velocity is nearly zero. The scalar c/u is used to convert splitting functions to phase velocity maps (see Figure 32; eqn [22]).

measurements before the computer era. Nevertheless, Love wave dispersion measurements go back to at least the 1940s (e.g., Wilson, 1940). Figures 34 and 35 give a summary of the expected dispersion curves for fundamental mode Rayleigh and Love waves and their first five overtones. The curves are shown for isotropic PREM and both continental and oceanic crust. At frequencies above 10 mHz, variations in crustal structure have a significant effect on dispersion. Throughout a wide range in frequency, Rayleigh wave fundamental mode group velocity curves are fairly isolated from overtones which allows easy dispersion measurement. This is not the case for overtones which overlap at frequencies above 15 mHz. Sophisticated ‘tuning’ techniques, such as array stacking, are then necessary to assess individual overtone dispersion (see Section 1.03.3.4). Also note that the first overtone branch overlaps with the Love wave fundamental mode branch between 10 and 30 mHz, for oceanic paths. Ignoring possible interference effects may lead to biased Love wave dispersion data, which is revisited in a later section.

For Rayleigh waves, we observe two Airy phases for which group velocity does not change much with frequency (Figures 34 and 35). One is near 4 mHz,

the other one is near 20 mHz. Between 4 and 20 mHz, the group velocity dispersion is inverse. The condition $du/dk < 0$ implies that modes with higher ℓ , hence higher frequency, are faster than modes with lower ℓ (compare also with Figure 33). This can be seen in the low-pass filtered seismogram of Figure 2. Below 4 mHz and above 20 mHz, we observe regular dispersion with $du/dk > 0$ (low- ℓ modes are faster). This can be seen in Figure 36 that shows Rayleigh wave seismograms between 20 and 50 mHz in an oceanic setting. The figure also emphasizes that modern ocean bottom seismic instrumentation allows us to observe long-period surface waves on the ocean floor to an unprecedented signal level. Depending on crustal structure, a third Airy phase may be observed for Rayleigh waves near 50 mHz. For Love waves, group velocities are very similar over a large range in frequency. In oceanic settings in particular, the dispersion is very weak between 4 and 20 mHz, so that Love wave trains usually appear quite pulse like.

First attempts to take a general regionalization of surface wave dispersion beyond a distinction between continents and oceans go back to Toksöz and Anderson (1966) who decomposed composite-path great-circle data into those of ‘pure-path’

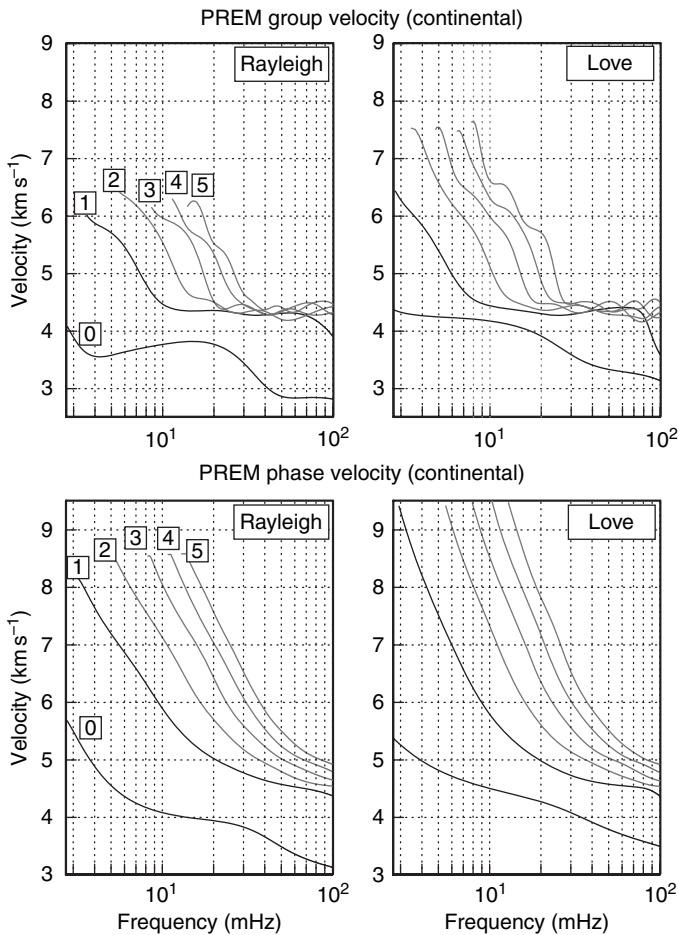


Figure 34 Group and phase velocity curves for isotropic PREM (Dziewonski and Anderson, 1981) with a 39 km thick continental crust. Shown are the fundamental modes (label 0) and the first five overtones (labels 1–5). Phase velocities span a greater range than group velocities. Overtones have nearly the same group velocities above 30 mHz (periods shorter than 33 s). For clarity of the diagrams, dispersion for IC modes and ScS equivalent modes at long periods are not shown.

oceanic, shield and mountain-tectonic regions. They analyzed records of the great Good Friday 1964 Alaska Earthquake (28 Mar 1964) at stations Isabella, California (later station ISA of the TerraScope Network), Kipapa, Hawaii (later station KIP of the IDA, GSN and GEOSCOPE networks) and Stuttgart, Germany (later station STU of the GEOFON network). Kanamori (1970) analyzed many more records of this event ($M=8.5$ as reported by Kanamori), another great earthquake in the Kuril Islands Region 13 Oct 1963; $M=8.3$) and a supplement of earlier published data. Apart from phase and group velocity, he also measured great-circle attenuation but did not interpret the latter further. Dziewonski (1970) analyzed phase and group velocity for the 15 Aug 1963 Peru earthquake (the same earthquake that provided

mode data for Earth model 1066A by Gilbert and Dziewonski (1975) though phase velocities were derived from mode observations. This paper also showed, for the first time, that world-circling measured phase and group velocities are mutually consistent. Knopoff (1972) first provided a more detailed discussion of surface wave dispersion in different tectonic regions.

Early measurements of surface wave dispersion was extended to frequencies much below 4 mHz, for example, the analysis of Ewing and Press (1956) extended to 2 mHz and that of Toksöz and Anderson (1966) extended even to 1.5 mHz. At such long periods, Coriolis coupling between Rayleigh and Love waves becomes considerable (see Figure 13). Backus (1962) discussed the effects of a rotating Earth on the propagation path of very

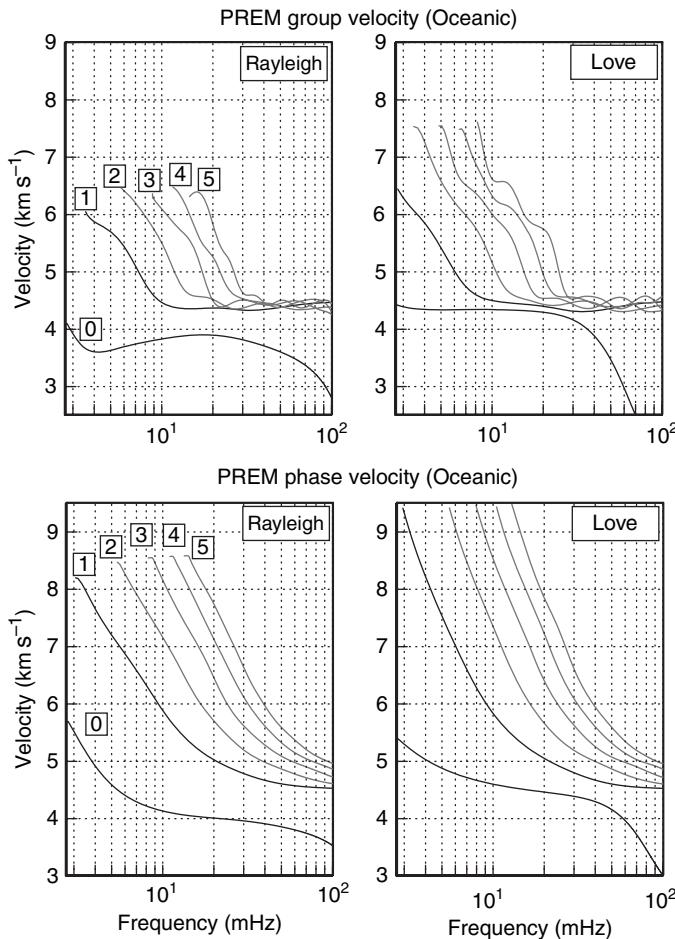


Figure 35 Group and phase velocity curves for isotropic PREM with a 7 km thick crystalline oceanic crust, overlain by 5 km of sediments (no water layer). Shown are the fundamental modes (label 0) and the first five overtones (labels 1–5). Phase velocities span a greater range than group velocities. Overtones have nearly the same group velocities above 30 mHz (periods shorter than 33 s). Love wave fundamental modes have similar group velocities as overtones between 10 and 20 mHz. For clarity of the diagrams, dispersion for IC modes and ScS equivalent modes at long periods are not shown.

long-period surface waves. While Love wave paths remain largely unaffected, Rayleigh wave great-circle paths precess about Earth's axis of rotation, effectively lengthening the travel path. Dispersion estimation that assume the direct great-circle path are then biased. While early measurements were not precise enough for this effect to be significant, modern observations probably need to be corrected for this effect, which depends on Earth's 1-D structure much like the spheroidal-toroidal mode coupling does.

1.03.3.2.1 Group velocity

In the precomputer era, surface wave group velocity was measured using the peak-and-trough method (e.g., Ewing and Press, 1954; Ewing *et al.*, 1957). In a

paper record, each peak, trough and zero was numbered and plotted against recorded time. The slope of this curve gives the period as function of travel time, from which the group velocity can be computed. This technique can be applied on well-dispersed signals but fails near Airy phases and for most Love waves because the waveforms are compressed. Even for the well-dispersed case, measurement errors are rarely better than 0.2 km s^{-1} , or about 6.5%. Since the late 1960s, when computers and the fast Fourier transform by Cooley and Tukey (1965) facilitated quick and comprehensive harmonic analyses, group velocity has been measured in the time–frequency domain. The most basic approach is the ‘moving window analysis’ (Landisman *et al.*, 1969). A sliding window is applied to a time series and the spectrum

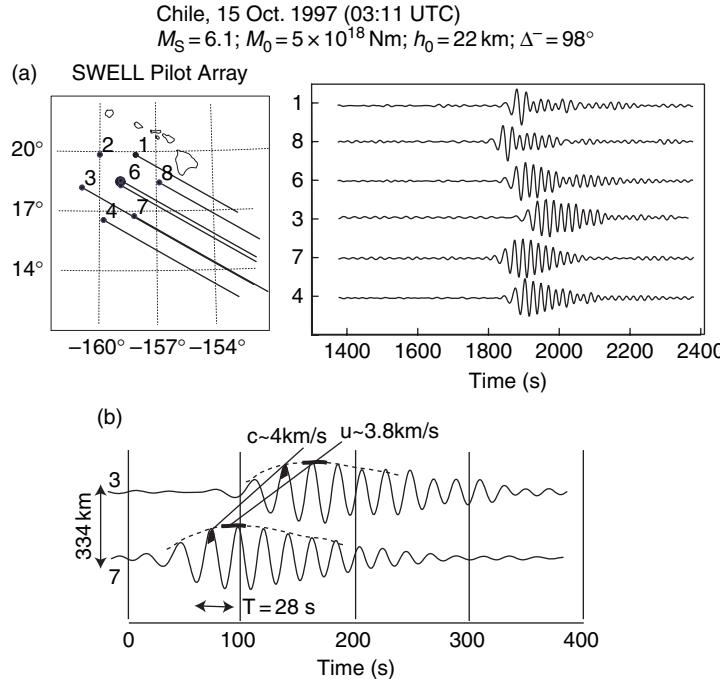


Figure 36 (a) Seismograms recorded on ocean bottom differential pressure sensors during the 97/98 SWELL Pilot Deployment southwest of Hawaii (Laske *et al.*, 1998). The recorded frequencies range from 20 to 50 mHz. The waveforms exhibit regular dispersion, that is, low frequencies arrive earlier than higher frequencies. (b) Schematic concept of phase (c) and group (u) velocities along two-station leg 7-3.

for each increment is tabulated in a time–frequency matrix, often called a Gabor matrix after Hungarian physicist Dennis Gabor (Gabor, 1947). Such a diagram is also called energy diagram (when amplitude squared is plotted) or, when the travel time is converted to velocity, a vespagram. Figure 37 shows the Gabor matrix for the 1992 Flores Island Region record at station SSB (see Figure 2). The group velocity is then determined by tracing the ridge with the highest amplitudes in the 2-D plot. This approach has seen wide use in a number of applications that deal with nonstationary signals and is still used today, for example, in the study of ocean swell generated signal in the microseism band (between 20 and 4 s) that is caused by approaching large storm systems (e.g., Bromirski and Duennebier, 2002).

When measuring dispersion, one has to be aware of the resolution limits in the Gabor matrix imposed by the Schwarz inequality (Gabor, 1947), where the smallest frequency separation, Δf , and the length of the sliding window, T , must satisfy $\Delta f \cdot T \geq 1$. For example, if the moving window is 1000 s long, the frequency resolution is not better than 1 mHz. To obtain the same relative resolution $\Delta f/f$ in the Gabor matrix, the sliding window can be made proportional

to the period investigated where the window is usually 4–8 times the period. Since this entails the separate calculation of a certain harmonic coefficient for each element in the Gabor matrix, this was sometimes prohibitively inefficient in the early days of computing. A quicker method is the multiple filtering technique (described in Dziewonski *et al.* (1969)) that starts with the spectrum of a complete time series. A Gaussian filter is centered on a certain target frequency. The analytic signal, which provides the envelope function of the corresponding time series, is then determined for this frequency using the spectrum for positive frequencies only. Instead of just one element in the Gabor matrix, the envelope function now composes a whole column.

Measuring group velocity requires either interactive picking or a sophisticated routine that recognizes which ridge to pick. A widely used application in regional studies is the FTAN (frequency time analysis) package by Levshin *et al.* (1972) (see also Levshin *et al.* (1989)). FTAN is similar to earlier multiple filtering methods except that FTAN uses an efficient folding algorithm to determine the complex time–frequency array from which the Gabor matrix is estimated. This allows the extraction of phase

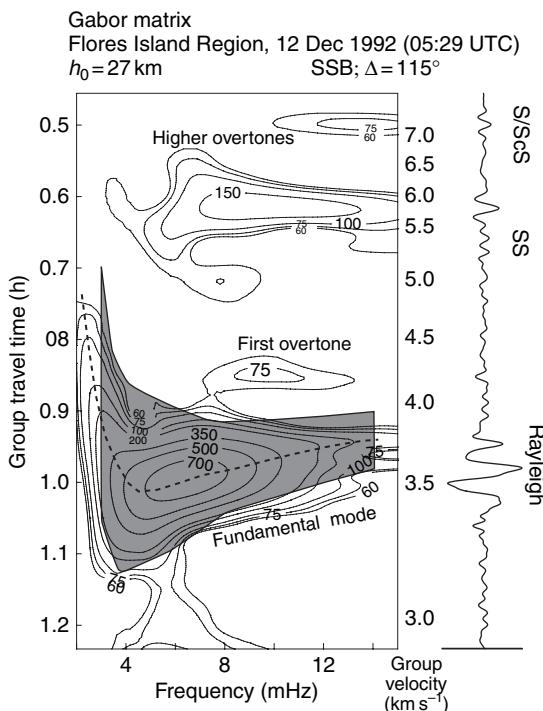


Figure 37 Visualization of a Gabor matrix for the seismogram in Figure 2. Amplitudes in the matrix are normalized to optimize the display. The largest signal is the fundamental mode that exhibits dispersion (cf. Figure 34) where the dashed line marks the group velocity an analyst would choose. A combination of overtones arrives before the Rayleigh wave. The gray area marks the time–frequency range used in a time-variable filtering approach to isolate the fundamental mode.

velocity as well. Signal enhancement in the Gabor matrix can also be achieved by the logarithmic stacking of several events in the period-group velocity domain (Shapiro *et al.*, 1997). Modern techniques allow us to measure group velocity with an error that is usually much less than 0.1 km s^{-1} , or about 3.2%. The measurement of group velocity is advantageous over that of phase because many phase measurement applications require the knowledge of the source process (see eqn [19]). Group velocity observations are largely unaffected by source processes which makes this approach very attractive in regional studies where earthquakes are typically small. For events deeper than about 25 km, the source may affect group travel times at long periods beyond 100 s though the bias is usually not significant, that is, smaller than the measurement error (Levshin *et al.*, 1999).

Group velocities picked from the Gabor matrix can be biased, as first discussed by Dziewonski *et al.*

(1972). As seen in Figure 30, the spectral amplitude for the first wave train increases with frequency. In this case, group velocity estimates from periodograms are biased toward high-frequency values. Changes in the spectral amplitude may be particularly large when dispersion is strong, which is the case for frequencies below 4 mHz. A similar bias occurs when phase velocities are estimated from the phase of the complex analysis of the Gabor matrix. Dziewonski *et al.* (1972) suggested to deconvolve the time series with a synthetic seismogram before measuring the much less pronounced ‘residual dispersion’. There have also been developments to improve the multiple filtering technique itself. Wielandt and Schenk (1983) provided a formalism to correct the bias in phase-velocity estimates to within 0.1%. A more recent reference is that of Shapiro and Singh (1999) who suggest to use a centroid frequency of the filtered spectrum rather than the center frequency of the Gaussian filter to tabulate the Gabor matrix.

At short periods between 15 and 5 s, the study of microseismic noise has recently experienced great interest among investigators. Though such studies are quite band-limited, they may provide valuable dispersion data where inadequate earthquake distribution does not allow an analysis otherwise. Microseisms are generated by the interaction of ocean swell with the coast. The resulting Rayleigh waves which are generated continuously but incoherently can be observed in continental interiors. With the aid of a network, the dispersion of such microseisms can be extracted to constrain local crustal structure (e.g., Sabra *et al.*, 2005a; Shapiro *et al.*, 2005). In essence, a cross-correlation technique is applied to station pairs in an array to extract empirical Green’s functions (e.g., Shapiro and Campillo, 2004; Sabra *et al.*, 2005b). A precondition of this method to yield unbiased dispersion data is that the microseisms have to approach the array from all directions which may not be the case. For example, Schulte-Pelkum *et al.* (2004) found preferential directions of approach at the ANZA network in Southern California and strong directivity was also found in Europe (Essen *et al.*, 2003). Clearly, the technique is still in its infancy but delivers promising initial results.

1.03.3.2.2 Phase velocity

Unlike group travel times, the phase explicitly includes a source term (see eqn [19]). Measuring phase between a source and receiver therefore requires accurate knowledge of the seismic source.

The measurement of phase velocities without spectral analysis requires the comparison of at least two waveforms, for example, from seismograms of neighboring stations that form a great circle with the source (two-station method, for example, Brune and Dorman, 1963). Using a one-station approach, Nafe and Brune (1960) first measured complete great-circle phase velocity for the 15 August 1960 Assam earthquake at station PAS (Pasadena, California) with errors less than 1%. Ten years later, the observation of phase velocity on a global scale was still in its infancy when Kanamori (1970) reported surface wave great-circle phase velocity observations for surface wave packets separated by a complete great-circle orbit, while others preferred to derive phase velocities from mode observations (Dziewonski, 1970; Dziewonski and Landisman, 1970).

The phase of a surface wave packet changes very rapidly with frequency and its 2π -ambiguity almost never allows us to measure phase between source and receiver directly from a single waveform. Early works suggested that in the two-station approach phase estimated from a cross correlogram of the two seismograms yields more stable estimates than from phases differences (Landisman *et al.*, 1969). Before we elaborate on our own measurement technique on the global scale, we briefly review advances in regional studies. For dense arrays where the station spacing is on the order of the signal wavelength, individual peaks or troughs can be followed across the array and phase velocities can be measured as function of period. Some of the earliest such measurements of phase velocity, for periods less than 1 s, can be found in the oil exploration literature, (e.g., Dobrin *et al.*, 1951). For crustal or mantle studies, seismic arrays are typically sparse. Press (1956, 1957) used the triangulation or tripartite method to determine crustal structure in California from average phase velocities but the use of the method goes back further (e.g., Evernden, 1953, 1954) and was also used to retrace hurricane tracks with seismic data (e.g., Donn and Blaik, 1953). In fact, the tripartite method was first used by Milne and the interested reader is referred to Evernden (1953) for a brief review of early applications. In the studies of the 1950s, only few earthquakes were used for a particular station triangle and measurement errors were on the order of 0.1 km s^{-1} (3%) or less. The technique assumes that plane waves approach a station triangle, whose aperture could reach several 100 km (e.g., Knopoff *et al.*, 1966). These authors found that even though the method allows for an arbitrary arrival

angle of the approaching wave, it yields biased results unless the wave propagation direction is aligned with one of the network legs. Knopoff *et al.* (1967) later found the two-station method to be superior to the tripartite method to minimize errors in phase shifts in the presence of lateral heterogeneity. Schwab and Kausel (1976a) suggested to expand the recording array to at least four stations and allow the consideration of curved wavefronts. In essence, in an optimization process waveforms are matched to be in phase to form a single beam (beam forming). This is an approach that can still be found in the literature to determine the average structure beneath a recording array (e.g., Alsina and Snieder, 1993; Stange and Friederich, 1993). The preposition here is that incoming wavefronts are uniform and distortion of the wavefronts within the array due to heterogeneous structure is insignificant though this may not be the case (Wielandt, 1993).

Numerous studies followed, and the two-station method is still used today to retrieve regional and local structure, often along only one particular two-station path. A recent example of using the multiple-filtering technique on a cross-correlogram in the two-station case (between two real seismograms) is that of Meier *et al.* (2004) who studied Rayleigh wave phase velocity in the Eastern Mediterranean. It can be argued that phase velocities estimated with the two-station technique are systematically biased high when waves do not approach a station along the great circle, which is to be expected particularly in the analysis of teleseismic events. In our global studies, we have found that lateral refraction caused by heterogeneity in the mantle can change the direction of approach at a station by as much as 20° . The deviation of an arriving wave packet away from the great circle direction effectively shortens the travel path. For a regional study that uses teleseismic earthquakes the bias in the estimated phase velocity for a single travel path can therefore be as large 6.4%. The bias on local or regional phase velocity can be reduced when many crossing paths are considered, but the estimates will remain biased high, unless the phase estimates are corrected for off-great circle approach.

Another problem arises from multipathing when wave packets get refracted away from the great circle and then travel along multiple paths and interfere at the recording station upon arrival. Multipathing was detected in the early study of Evernden (1953) for surface waves traveling along the west coast of North America. Wavefronts get bent in complex structures

and the plane wave approach is no longer valid. For example, waves get bent around an enclosed low velocity anomaly so that the sides of a plane wave advance. In the extreme case, wavefront healing occurs when the wave travels long enough and ‘forgets’ that it passed this structure (Wielandt, 1987). To illustrate the gravity of the problem, one of the most remarkable examples of the controversy over the two-station method is probably that of Woods *et al.* (1991) along the Hawaiian Island Chain. They could not find a low-velocity anomaly associated with the proposed reheating of the Pacific Plate by the Hawaiian hot spot and therefore argued against the plate reheating concept. On the other hand, Maupin (1992) argued that complex wave propagation along a relatively narrow low-velocity anomaly inhibits the application of the two-station approach. Pedersen (2006) recently estimated that bias from ignoring the nonplane geometry of the incoming wavefield can be reduced to 1% in the two-station method for 200 km profiles, if at least 10 earthquakes with different hypocenters are analyzed. This may be achieved for permanent station installations but is often difficult to achieve for temporary deployments of typically less than 2 years. The recovery of structure within an array in the case of nonplane waves approaching the array requires the analysis of both phase and amplitude (Wielandt, 1993; Friederich *et al.*, 1994). Of course, such an approach is only possible for dense arrays. Forsyth and Li (2005) recently proposed a technique that fits two approaching plane waves to the observed phase measurements of an array.

For our global studies, we measure phase relative to a synthetic seismogram. In the simplest case, this can be a synthetic computed for a spherical Earth (e.g., Laske and Masters, 1996). We measure the transfer function between the observed and a synthetic fundamental mode waveform that is calculated for Earth model 1066A (Gilbert and Dziewonski, 1975). An early example of the transfer function technique measuring great-circle dispersion and attenuation can be found in Dziewonski and Stein (1982). A multitaper approach provides an optimal compromise between frequency resolution and resistance to bias from ambient noise. The multitaper approach also allows us to assign measurement errors in a statistical sense. The analysis is done interactively on the computer screen where we choose the optimal time window to isolate the fundamental mode. An example is shown in Figure 38. Other workers choose automated approaches (e.g.,

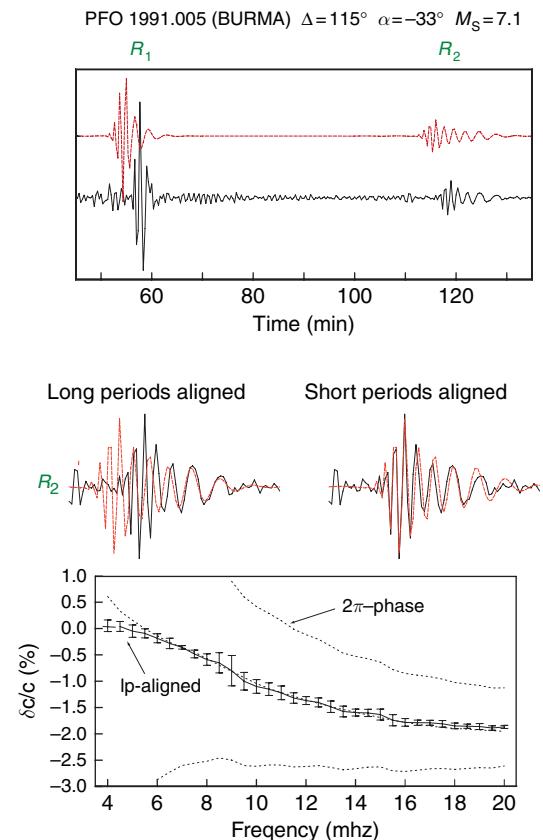


Figure 38 Example of our interactive phase measurement procedure in which the transfer function between an observed seismogram and a synthetic is retrieved. A seismogram at station PFO (Piñon Flat, California) is compared to a fundamental mode synthetic. The example is extreme in that the transfer function has to be determined iteratively, due to the large difference between observed and synthetic waveform. The bottom panel shows the resulting path-averaged phase velocity perturbation. The dashed line marks the results when the waveforms are aligned on the short periods. Also shown in the results when 2π are subtracted or added to the phase.

Trampert and Woodhouse, 1995). These approaches take significantly less time but may either produce a noisy dataset or quality control restrictions yield a significantly reduced dataset, compared to our hand-picked one. Measured phase perturbations typically amount to a few percent and measurement errors are 0.15% on average for R_1 , while measurement errors in R_2 and great circle data are somewhat smaller. Even though we measure phase with respect to a synthetic, some of our short-period data are 2π -phase ambiguous. At short periods, the phase ambiguity is enhanced by the fact that small perturbations to a model may cause many 2π -phase wraps. The phase ambiguity can be removed by the

condition that the phase has to vary smoothly with frequency. Since we observe no phase ambiguity at 4 mHz, our phase data set is unique, for the frequency range chosen in our global study (4–17 mHz). We usually need only one iteration to determine the transfer function but occasionally the great difference between data and synthetic requires one or two additional iterations (see [Figure 38](#)). Nevertheless, our ‘one-step’ spectral approach does not allow us to go much beyond 20 mHz. An alternative approach to obtain unbiased estimates in a wider frequency range is that of [Ekström et al. \(1997\)](#) who determine phase perturbation in several pass-bands rather than just one. As in our approach, they use synthetic seismograms in a phase-matched filtering procedure. The process is iterated to minimize residual dispersion and to suppress interference from overtones. They succeeded to collect an impressive global data set between 150 and 35 s. With 50 000 high-quality dispersion curves their data set was the largest at the time, and their phase velocity maps are still used today by other workers to calibrate regional crustal models (e.g., [Yang et al., 2004](#)).

1.03.3.2.3 Time variable filtering

Time variable filtering (TVF) was proposed to stabilize fundamental mode surface wave dispersion estimation when waveforms appear contaminated. Interference effects from other mode branches, multipathing or other concurrent signals are the most likely cause. Arguably, one should probably refrain entirely from analyzing such contaminated waveforms. This may be feasible in global long-period seismology below 20 mHz, where large waveform collections are available. However, in regional studies, in monitoring efforts of the CTBT or to study the dispersion at shorter periods this may not be possible. Aside from TVF, various techniques are available to extract a primary signal from a time series. [Herrin and Goforth \(1977\)](#) applied phase-matched filters (PMFs) to Rayleigh waves of an earthquake and a nuclear explosion. In this process, a time series is matched to a synthetic by iteratively windowing a narrow-band filtered correlation function between the two or eliminate interfering signals. PMF makes no assumptions about the time–frequency structure of the interfering signals in a seismogram. TVF takes into account the dispersion. The idea behind TVF is that different signals may arrive at the recording station at the same time but the frequency content and group velocities are sufficiently different that the signal to be studied can be

isolated by time-frequency filtering. For example, the Gabor matrix in [Figure 37](#) shows the fundamental mode as the largest signal but at the same time as the very low-frequency fundamental mode reaches the station, the first overtone, with frequencies around 10 mHz also comes in. A time–frequency filter that enhances the signal below 3 mHz at this time but then enhances 6 mHz signal at a later time significantly reduces the biasing effects of a single window covering the whole time series for analysis. [Pilant and Knopoff \(1964\)](#) first applied TVF to separate the seismic signal from two different earthquakes that arrived at a station nearly at the same time and therefore created a beating pattern in the waveform. Since then, the method has been applied to investigate structure of the crust and upper mantle (e.g., [Knopoff et al., 1966](#)). TVF is also included in the FTAN package of [Levshin et al. \(1989\)](#) in a second iteration to improve measurement precision. A technique that combines PMF with TVF is the frequency variable filtering of [Russell et al. \(1998\)](#) to reduce spectral amplitude biasing introduced by frequency domain filtering.

Technical details of the time variable filtering approach are described in [Landisman et al. \(1969\)](#). The filtering can be done either in the time or the frequency domain. In the latter, the starting point is the spectrum of the original time series. Each harmonic coefficient is multiplied by a function that has a certain shape in the time domain. [Landisman et al. \(1969\)](#) suggest a cosine taper with

$$w(t) = \begin{cases} \cos\left(\frac{\pi(t-t_n(\omega))}{2L(\omega)}\right), & \text{for } t_n-L \leq t \leq t_n + L \\ 0 & \text{else} \end{cases}$$

where

$$L(\omega) = T(\alpha + \beta|du(T)/dT|).$$

$L(\omega)$ is the window length in the time domain, $T=2\pi/\omega$ and $t_n(\omega)$ is the center group traveltime. Other workers refined the filtering to optimize the tradeoff between interference from unwanted signals and loss of energy for the signal analyzed (e.g., [Cara, 1973](#); [Roult, 1974](#)). In the frequency range with strong dispersion, TVF should probably be applied with caution to avoid biased estimates, if $t_n(\omega)$ are the predictions of a model. The technique has also found application in normal mode studies (e.g., [Jobert and Roult, 1976](#); [Roult et al., 1990](#); [Roult and Romanowicz, 1984](#)). Our own experience is that the

technique works best for seismograms with epicentral distances far away from 90° (Koitschalitsch, 1988). For epicentral distances near 90° , the close temporal succession of overtones and fundamental modes does not allow an effective suppression of overtones without significantly affecting fundamental mode frequencies by several μHz and Q by up to 20%. A topic of research still is why mean attenuation estimates for surface waves below 5 mHz often disagree significantly with those obtained from mode studies. Durek and Ekström (1996) suggested that noise contamination in the much longer normal mode seismograms can bias Q estimates high. Roult and Clévéde (2000) have recently improved their time lapse technique to obtain more accurate mode Q data that are in agreement with those of others though the discrepancy to surface wave Q remains. We speculate that overtone interference contributes significantly to the discrepancy (Masters and Laske, 1997) and that some of this can be removed by time variable filtering. Figures can be found on the REM web page. For a more detailed discussion see also Chapter 1.01.

1.03.3.3 Other Surface Wave Observables

Surface waves can be deflected significantly from the source-receiver great circle by lateral refraction in a heterogeneous medium. Evernden (1953, 1954) was among the first to observe this phenomenon at long periods. Capon (1970) observed off-great circle propagation also at short periods (20–40 s) and found that refraction and reflection of wave packets at continental margins was responsible for this. Lateral refraction has also been observed by a large group of other workers and array techniques, such as the tripartite method of Press (1956) or comprehensive modifications thereof (e.g., Stange and Friederich, 1993), have been used to obtain unbiased dispersion estimates. In essence, incoming wavefronts are fit simultaneously to the phase data of all stations in an array, where phase velocity and angle of approach are free parameters to search for. In regional studies that search for structure within an array, these arrival angles are discarded but they can serve as additional constraint on structure along the travel path. Woodhouse and Wong (1986) developed the elegant linearized path integral approximation (PIA) to relate arrival angles to lateral heterogeneity. Similar to the integral in eqn [20], we can relate the tangent of the observed arrival angle, $\nu = \tan \Theta$, to the phase

velocity anomalies along the source–receiver great circle

$$\nu(\Delta) \approx -\operatorname{cosec}(\Delta) \int_0^\Delta \sin \phi \frac{\partial}{\partial \theta} \left[\frac{\delta c(\pi/2, \phi)}{c_0} \right] d\phi \quad [23]$$

where the great circle has been rotated onto the equator, the source is at $\phi = 0$, the receiver at distance Δ , and θ is the colatitude. A similar expression exists for the amplitude

$$\ln A \approx \frac{1}{2} \operatorname{cosec}(\Delta) \int_0^\Delta \sin(\Delta - \phi) \left[\sin \phi \hat{\partial}_\theta^2 - \cos \phi \hat{\partial}_\phi \right] \times \left[\frac{\delta c(\pi/2, \phi)}{c_0} \right] d\phi \quad [24]$$

where $\hat{\partial}_\theta$ and $\hat{\partial}_\phi$ are derivatives with respect to θ and ϕ . Dahlen and Tromp (1998) slightly modified this to include a term with sensitivity to phase velocity at the receiver. Both ν and A depend on frequency because phase velocity does.

Both arrival angles and amplitudes depend on gradients of structure rather than structure itself which gives them sensitivity to shorter wavelengths than the corresponding phase data (see also Romanowicz (1987)). Wong (1989) applied this theory to include amplitude data to obtain frequency-dependent phase velocity maps at very long periods (modes up to angular order $\ell = 59$ at about 6.5 mHz). We developed an interactive technique to measure arrival angles using the multitaper approach of Park *et al.* (1987a). In the most general case, this method models elliptical particle motion in 3-D space. In a singular value decomposition (SVD) of the three component seismogram, we seek the frequency-dependent complex eigenvector that spans the plane of particle motion. From the eigenvectors, we can derive polarization parameter, such as the eccentricity of the ellipse and three angles that define the orientation of the ellipse and the eccentricity of the ellipse. The eigenvalues give us an idea of how well-defined the particle motion is, that is, how well it can be explained by a single ellipse. As in the case of phase data, the multitaper approach provides statistical error bars as well as resistance to bias from ambient noise error bars. Lerner-Lam and Park (1989) first used this technique to investigate lateral refraction and multipathing of long-periods surface waves in the Western Pacific.

Other methods to analyze particle motion exist, for example, the method by Jurkevics (1988) that works in real space. In the interactive analysis of Plešinger *et al.* (1986) one seeks the local coordinate

system for which certain component products are zero. These products, as function of time, can be used to either discriminate between wave types or measure arrival angles. Paulssen *et al.* (1990) expanded the basic time–frequency analysis for three-component seismograms and presented the time and frequency-dependent polarization of anomalous surface waves observed at stations on the Iberian peninsula. They constructed a quality factor that depends on the largest eigenvalue of the SVD to assess the likeness of the signal to a Rayleigh or Love wave. Lilly and Park (1995) applied the time–frequency analysis using a wavelet algorithm and the multitaper technique to investigate the evolution of the frequency-dependent polarization in a time series. The methods described here all involve the analysis of single three-component seismograms. As discussed in the last section, assuming a simple incoming wavefield, arrival angles can also be determined from array analyses (e.g., beam forming). A recent example of this is the study of Cotte *et al.* (2000) who investigated off-great circle propagation in Southern France caused by lateral refraction of surface waves by the French Alps. Using the beam-forming technique, Friedrich *et al.* (1998) and Essen *et al.* (2003) observed a strong directivity of ocean-generated microseism noise in Europe. Similar observations exist for Southern California (e.g., Schulte-Pelkum *et al.*, 2004).

Arrival angle data have been included successfully in inversions for global structure (e.g., Laske and Masters, 1996; Yoshizawa *et al.*, 1999). It is interesting

to compare the sensitivity of arrival angles and phase to lateral heterogeneity. Figure 39 shows the integral kernels of eqn [23] in a similar way as those for the phase integral in Figure 31. Sensitivity to short-wavelength structure increases with harmonic degree which is the opposite of the behavior for the phase. This is due to the fact that arrival angles depend on the gradient of structure, not structure itself as phase does (see eqn [20]). We also notice that sensitivity to high- l structure, relative to low- l structure, increases with travel distance and not decreases as the sensitivity of phase does. Except for very short paths of less than 20°, sensitivity to even harmonic degrees is always higher than to odd harmonic degrees. Near the antipode, sensitivity in the path integral approximation becomes extremely large. At the same time, the antipode is a caustic with severe multipathing effects where asymptotic theories tend to break down (e.g., Romanowicz and Roult, 1986). We therefore discard data for epicentral distances larger than 160°. Relatively speaking, arrival angle data also have larger measurement errors than phase data. In principle, sensitivity to short-wavelength structure can be enhanced by including large data sets of phase data for very short travel paths (i.e., less than 30°) though the separation of the fundamental mode to obtain uncontaminated phase estimates at long periods becomes problematic. The collection of a global data set of arrival angle data, and its subsequent usage in the modeling of global structure, also has a useful byproduct. Arrival angle data are sensitive to the misalignment of the horizontal seismometer

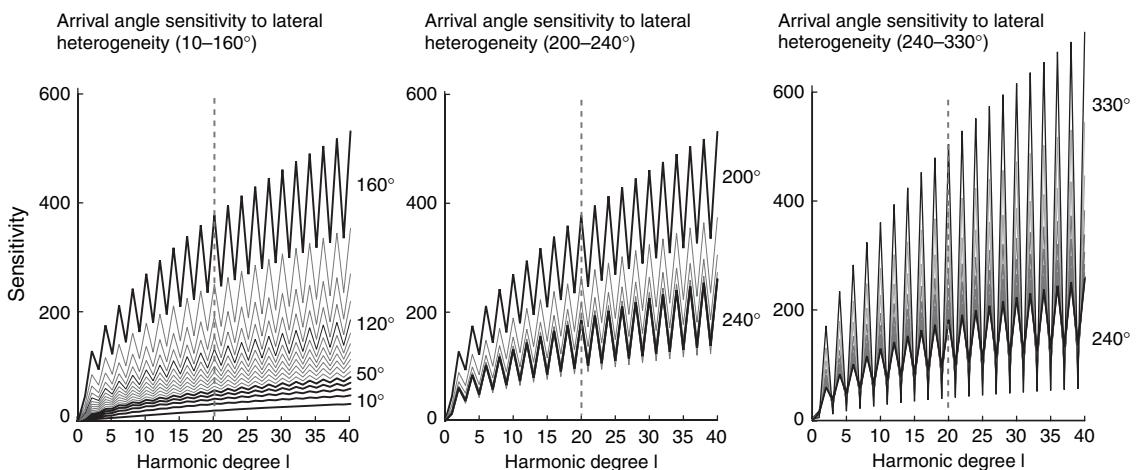


Figure 39 Arrival angle sensitivity to lateral heterogeneity, as function of harmonic degree in structure. Curves are shown for travel distances between 10° and 330°. Paths with distance less than 180° are for minor arc paths (R_1), larger distances are for major arc paths (R_2). We do not analyze data within 20° of the antipode so the kernels were omitted.

components from East and North and such information was not available when we first started our investigation. The joint inversion of arrival angles for structure and component misalignment can be linearized but the inversion requires several iterations for misalignments of more than 5°. The Harvard group has also observed station misalignment though they use a different approach (Larson and Ekström, 2002): arrival angle information is extracted from smoothed amplitude estimates using a phase-matched filter technique and synthetic seismograms computed with the dispersion measured for each waveform. Their station misalignment data agree quite well with our own. Some of the misalignments that we published (Laske, 1995) have been confirmed by station operators and this information is now routinely available at the data management centers, together with the instrument responses.

As mentioned above, amplitude data are also very useful to constrain lateral heterogeneity. In fact, due to the second derivative in eqn [24], amplitudes are even more sensitive to short-wavelength structure than arrival angles are. Amplitude information has been used as additional constraints to investigate elastic structure. Some of the earliest work is that of Yomogida and Aki (1987) who used the Gaussian beam method to obtain 30–80 s Rayleigh wave phase velocity structure in the Pacific Ocean. Wong (1989) used their linear theory to include amplitudes in the retrieval of elastic structure at very long periods beyond 150 s. Dalton and Ekström (2006) have recently shown that it is possible to retrieve elastic structure using surface wave amplitudes alone but the primary purpose to study surface wave amplitudes has been to retrieve Earth's attenuation structure (e.g., Durek *et al.*, 1993; Billien *et al.*, 2000). The problem with analyzing surface wave amplitudes is that the effects of lateral heterogeneity may be an order of magnitude larger than those of attenuation. Selby and Woodhouse (2000) found that amplitude variations are dominated by anelastic structure for long wavelengths, and by elastic structure at short wavelengths. If the linear approximation of eqn [24] holds, then this would perhaps be expected because the amplitude great circle integral over anelastic structure is linear and does not involve any gradients as that over elastic structure does. The first to successfully address this problem in the retrieval of attenuation structure was Romanowicz (1994) who took focusing/defocusing effects into account before constructing the first attenuation maps for long-period

Rayleigh waves. More recent work to retrieve attenuation includes that of Gung and Romanowicz (2004) who provide a 3-D attenuation model for the upper mantle. Using the nonlinear asymptotic coupling theory (NACT), they first derive an elastic model for V_{SH} and V_{SV} using long-period surface and body waveforms. The surface waveforms are then aligned using this model and inverted for 3-D attenuation.

Here we have only discussed the horizontal arrival angles as observables to assess Earth structure but the particle motion of surface waves is characterized by two additional angles: the sloping angle which describes the deviation of a Rayleigh wave orbit from the vertical and the tilting angle of the elliptical orbit with respect to the horizontal. Vig and Mitchell (1990) attempted to relate arrival angles (which they call inclination) and the sloping angles observed at station HON (Honolulu, Hawaii) of the DWWSSN to the anisotropic mantle around Hawaii. The shape of the Rayleigh wave ellipse, that is, the ratio between major and minor axis of particle motion (HZ ratio) depends on shallow structure. Tanimoto and Alvizuri (2006) have recently used the HZ ratio of microseisms to infer shallow crustal structure above 5 km in Southern California.

1.03.3.4 Higher Modes

The analysis of overtones, or higher modes, is attractive because it yields independent constraints on structure at depth. Overtones are also more sensitive to deep structure than fundamental modes of the same frequency (see Figure 43 in the next section). At long periods, overtones would significantly enhance resolution in the transition zone and uppermost lower mantle. At shorter periods, overtones carry better constraints on the low-velocity zone in the upper mantle than fundamental modes do. The analysis of overtones, however, faces several problems which are outlined in this section.

1.03.3.4.1 Higher mode dispersion and waveform modeling

From Figures 34, 35 and 37, we have seen that the fundamental mode is fairly isolated in time and frequency because its group velocities are significantly lower than those of overtones. Overtone velocities, on the other hand, overlap significantly, except at low frequencies. Figure 37 suggests that we could analyze the first overtone, if we were able to isolate it, for example, using time variable filtering or a phase-matched filtering operation (e.g., Jobert and Roult,

1976). Note, however, that for this particular earthquake the mode contains relatively little energy. For the other modes, extraction appears very uncertain. To illustrate the problem, **Figure 40** shows the Gabor matrix for a synthetic calculated for isotropic

PREM with a 39 km thick crust. For the seismogram in the top panel, all modes were included in the calculations and we can discern the same body wave phases, composed of interfering overtones, that we observe in the real seismogram. The other

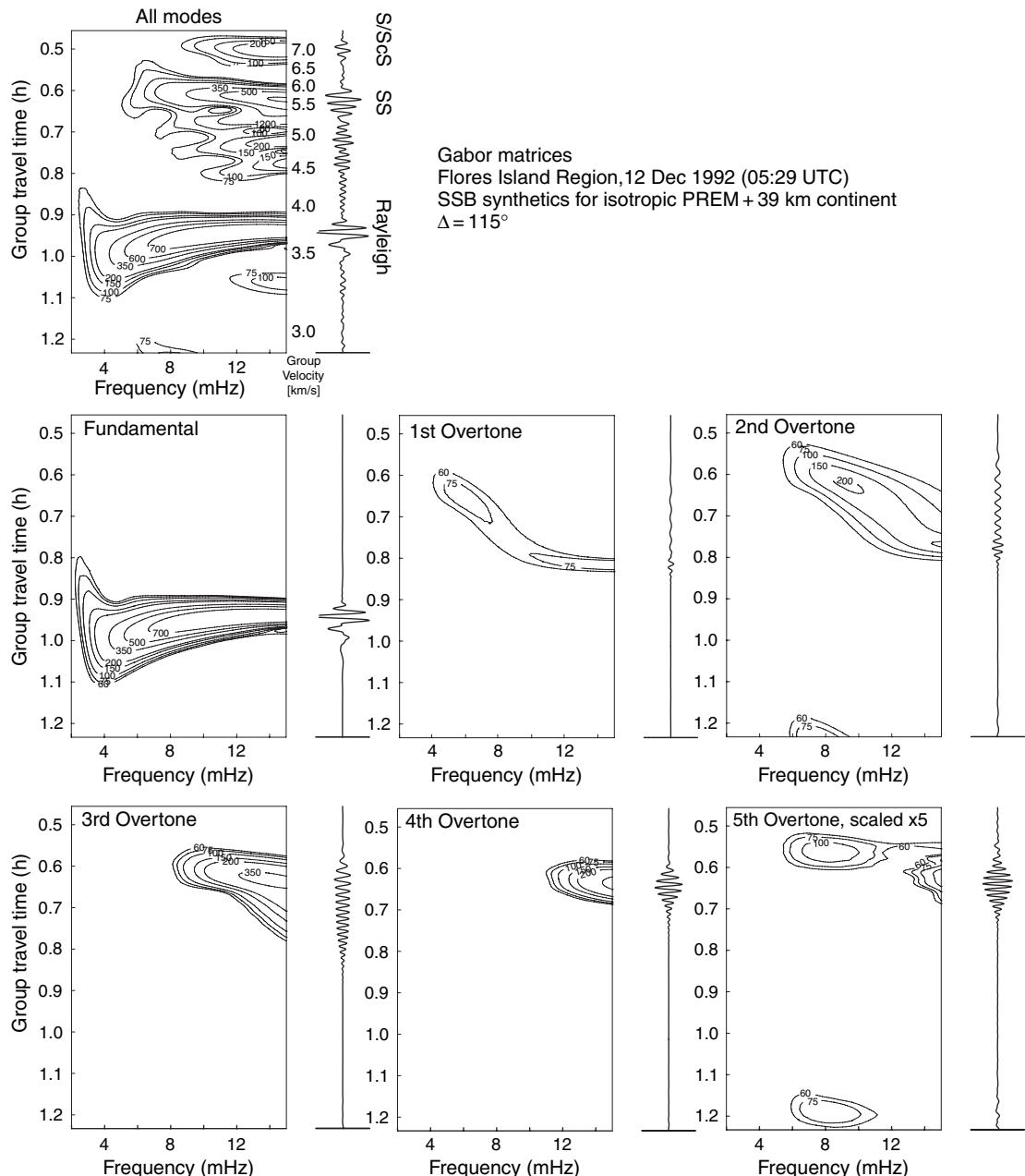


Figure 40 Visualization of a Gabor matrix for the synthetic seismogram of **Figure 37**. The top panel shows the complete synthetic, including all modes computed for isotropic PREM with a 39 km thick continental crust. The bottom panels show the Gabor matrices for the fundamental mode and first five overtones. While the fundamental mode is well isolated, the interference between overtones is rather complex. Note that the amplitudes for the fifth overtone are rather small. Also note that overtones beyond order 7 are required to compose the overlapping body wave phases S and ScS (see also **Figure 33**).

panels show the contribution from each mode, up to the fifth overtone. As just mentioned, the first overtone appears quite isolated in time–frequency space but its energy is so little that it is not discernible in the composite Gabor matrix. The other overtones overlap significantly though extraction of the second higher mode may be possible at frequencies higher than 10 mHz, because group velocities are relatively low. At lower frequencies, there is significant overlap between the second and third overtones. At frequencies above 12 mHz, the third and fourth overtone overlap. Time variable filtering may provide only limited success in this case.

The first convincing observation of overtone dispersion was probably that of [Oliver and Ewing \(1957\)](#) for a path across eastern North America but utilizing overtone dispersion to study Earth's interior obviously requires a different approach than fundamental modes do. The first breakthrough was achieved by [Nolet \(1975\)](#) and [Cara \(1978\)](#) who used an array stacking technique to separate different overtone branches using a $\omega-k$ transform, for studies of structure in Western Europe and across North America. This approach has also been used in other studies (e.g., [Cara et al. \(1981\)](#) for the Western US). At fixed frequency, different overtone branches then appear separated in phase-group velocity space. This approach works well to obtain average structure within an array but does not allow us to assess variations within an array. The problem with this approach is also that it needs an array.

Using individual source-receiver data on a global scale, a successful separation of overtones up to order 8 was achieved by [van Heijst and Woodhouse \(1999\)](#). They used their mode branch stripping technique ([van Heijst and Woodhouse, 1997](#)) to isolate the overtone branches and make global phase velocity maps (termed Oxford approach hereafter). This technique makes use of branch cross-correlation functions (bccf's) that increase sensitivity to a certain overtone signal. The signal with the most energy is analyzed first and subtracted from the seismogram before successive branches are analyzed in a similar fashion. The technique works well for Rayleigh waves but appears to fail for Love waves due to strong interference effects. This is one of few studies that extract dispersion. The vast majority of publications utilizes waveform modeling to retrieve structure at depth directly, without involving the intermediate step of determining dispersion. One may argue about which approach is superior but a useful byproduct of the Oxford approach is the

ability to check for consistencies in the data. For example, they were able to compare their fundamental mode Rayleigh wave maps at 40 s with that of the fourth overtone at 62 s. Since their dependence on structure at depth is quite similar, the phase velocity maps should highly correlate.

The bccf's have been used by others as well who choose the waveform modeling approach (e.g., [Cara and Lévéque, 1987](#); [Debayle and Lévéque, 1997](#)). Other advances to study overtone branches include the hybrid technique by [Stutzmann and Montagner \(1993\)](#). This waveform fitting technique retrieves path-averaged overtone phase velocities and path-averaged velocity structure in successive steps. An attempt to determine global structure was discussed by [Stutzmann and Montagner \(1994\)](#) though data coverage was quite sparse. Similar to Nolet's array technique, they utilized several earthquakes along similar paths to retrieve phase velocities. They recently developed the ‘roller-coaster technique’ ([Beucler et al., 2003](#)) which is named after the shape of the misfit function in their method. Their method can be applied to a cluster of events to retrieve structure along a single source-receiver great circle in a nonlinear scheme. Another recent development is that of [Yoshizawa and Kennett \(2002, 2004\)](#) who used [Sambridge's \(1999\)](#) neighborhood algorithm to efficiently search the model space for multimode dispersion in a nonlinear waveform inversion.

Most of the other techniques involve full waveform modeling and the retrieval of structure at depth directly, without determining dispersion first. The first study on a global scale was that of [Woodhouse and Dziewonski \(1984\)](#) whose global upper-mantle shear velocity models, M84A and M84C, were regarded as reference 3-D model upper-mantle models for the following decade. The technique is still used by the Harvard group and has led to a series of updated whole mantle models such as S12/WM13 ([Su et al., 1994](#)) and S362D1 ([Gu and Dziewonski, 1999](#)). Though Woodhouse and Dziewonski used normal mode summation to calculate synthetic seismograms, they used a clever trick to account for sensitivity to odd-degree structure by introducing a fictitious epicentral distance shift in the minor and major arc great circle integrals. This was later justified theoretically by [Mochizuki \(1986a, 1986b\)](#) and [Romanowicz \(1987\)](#). Woodhouse and Dziewonski argued that individual waveforms are probably too noisy for direct inversions for structure so they projected their measurements onto a set of global basis functions in a two-step procedure. Another global

waveform modeling approach is that of the Berkeley group called nonlinear asymptotic coupling theory (NACT; Li and Romanowicz, 1995). This technique accounts for cross-branch coupling that is ignored in conventional path average approximations. While this is less of an issue for fundamental modes surface waves, it becomes relevant for overtones that involve deep-turning body waves. The application of this technique led to the first ‘Berkeley model’, SAW12D (Li and Romanowicz, 1996) as well as more recent models (e.g., SAW24B16 by Mégny and Romanowicz (2000)). In contrast to other mantle models, the Berkeley models have traditionally been V_{SH} models. A recent discussion of asymptotic and nonasymptotic waveform modeling approaches can be found in Clévédé *et al.* (2000).

With his nonlinear partitioned waveform inversion, Nolet (1990) provided a tool that is widely used in regional-scale studies. The technique is similar to step 1 in the Woodhouse and Dziewonski approach. Publications are too numerous to list here but examples include work in western Europe (e.g., Zielhuis and Nolet, 1994), in North America (e.g., van der Lee and Nolet, 1997) and on the Skippy array in Australia (e.g., Simons *et al.*, 2002). Nolet argued that full waveform inversions directly for 3-D structure are computationally expensive and do not allow for a proper assessment of resolution capabilities. Rather, one can ‘partition’ the process and search for multi-parameter, path-averaged structure first, for each source-receiver path, before conducting a computationally efficient inversion of a sparse matrix to retrieve 3-D structure. A recent advancement of this technique is its automation by Lebedev *et al.* (2005) which allows the processing of large data sets such as is expected for the USArray.

A few concluding words of caution are in order. We have seen that overtones have the potential to constrain deep Earth structure much better than fundamental modes do and numerous studies emphasize that resolution is ‘significantly’ enhanced over fundamental-mode only studies. A reader has to bear in mind though that in the parametric approach, due to the massive interference with other overtone branches, errors in the fit to overtone data are probably much larger than to fundamental mode data. Another important point is the relative weight of overtone data in an inversion. We have seen in Figure 37 that recorded amplitudes of overtones were much smaller than those of the fundamental mode. Overtone experts may argue that the choice of the seismogram to demonstrate this point is poor

because this earthquake was shallow. Such earthquakes excite fundamental modes particularly well and usually leave overtones with much reduced amplitudes in the seismogram. A proper choice of earthquakes for overtone studies therefore focuses on deep events. Unfortunately, such events are relatively rare and even more unevenly distributed than shallow events. Figure 41 shows that earthquakes with source depths greater than 75 km account for only 21% of all earthquakes, while the rest is shallower. Even with source depths of about 150 km, the fundamental modes still dominate the seismogram. Only when source depths become significantly greater than that, overtones above 4 mHz have larger spectral amplitudes than fundamental modes, which implies further reduction in the number of suitable earthquakes. A careful assessment of the resolution capabilities of a certain data set therefore entails more than just comparing the sensitivity kernels of fundamental modes and overtones. A 3-D surface wave tomographer essentially faces a tradeoff problem. One can use all earthquakes to obtain best lateral resolution but bearing in mind that the vertical resolution is dominated by the limitations that fundamental modes dictate. Or one can chose mostly deep events to obtain optimal depth resolution, at the expense of decreased lateral resolution dictated by the sparser source distribution. The Berkeley and

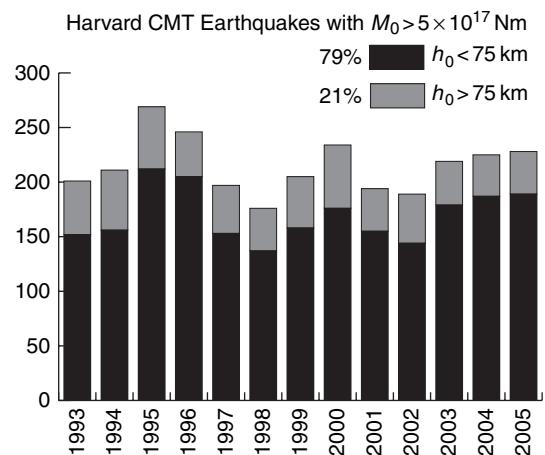


Figure 41 Events from the Harvard CMT catalog, for each year since 1993. Shown are all event with scalar seismic moment $M_0 \geq 5 \times 10^{17} \text{ N m}$. For shallow events, this corresponds approximately to $M_S \geq 5.4$. Shown are ‘shallow’ events with source depths less than 75 km which comprise 79% of all earthquakes. Events deeper than 75 km, which are potentially better earthquakes to study overtones, account for only 21% of all earthquakes.

Oxford approaches appear to account for this by giving different weights to overtones but the issue appears somewhat unresolved.

1.03.3.4.2 Love waves and overtones

With increasing amounts of data and the sophistication of measurement techniques, measurement errors have become ever smaller. Systematic biases introduced by unmodeled effects then become significant. We have already pointed out in [Figures 34 and 35](#) that Love wave overtone group velocity curves are quite close to that of the fundamental mode between 8 and 12 mHz (125–85 s). In a seismogram, short-period Love wave overtones therefore appear at the same times as long-period fundamental modes. Using sophisticated time-frequency analyses, such as the multiple filtering technique, one may be able to separate the different mode branches. However, it appears that even advanced techniques such as the branch stripping technique are not able to properly separate Love wave overtone branches, possibly because cross-branch coupling is significant ([Mégnin and Romanowicz, 1999](#)). The question now is whether even the fundamental modes can be analyzed without taking interference effects into account. For oceanic paths in particular, overtones and fundamental mode group velocities are nearly the same for similar frequencies and separation is no longer trivial. It was discovered early that Rayleigh and Love waves are often incompatible, that is, that no realistic isotropic model fits the dispersion of both wave types simultaneously (e.g., [McEvilly, 1964](#)). Often, such models exhibit low-velocity zones overlain by thin lids with nearly unrealistically high shear velocities.

Some argued that at least some of this discrepancy can be explained by Love wave overtone contamination (e.g., [Thatcher and Brune, 1969](#)). Others suggested that no uniform bias can be found in a large data set that includes several earthquakes, for a given path and model (e.g., [Boore, 1969](#)). Due to this unsatisfying problem, initial collections of regionalized models resulting from inversions of dispersion curves did not include Love waves ([Knopoff, 1972](#)). The vast majority of publications addresses this problem by allowing transverse isotropy in the model, also called polarization anisotropy or radial anisotropy. More recently, [Polet and Kanamori \(1997\)](#) revisited this problem by studying the biasing effects for an upper-mantle model in Southern California. They found that after correcting for the biasing effect on Love waves from overtone

contamination, the models obtained from Love and from Rayleigh waves were much more compatible than before. They also found that after the correction, the isotropic model that fit both wave types was much more realistic than before though the model had an unusually fast thin lid beneath the Moho and a low-velocity zone near 100 km depth, both not obtained when inverting for each wave type alone. On the other hand, [Ekström and Dziewonski \(1998\)](#) argued that anomalies found in V_{SV} , deduced from uncontaminated Rayleigh waves, and not in V_{SH} led to their discovery of anomalous azimuthal anisotropy in the Pacific ocean, while V_{SH} basically follows the lithospheric age progression.

With two-thirds of Earth covered by oceans, a possible contamination of Love wave data by overtones would pose a serious problem to find a proper reference Earth model (REM). Our REM website compares the spherical averages of various published Love wave phase velocity maps with toroidal fundamental mode frequencies. Mode frequencies should not be biased by overtone contamination because an entirely different measurement technique is applied. A discrepancy between Love waves and toroidal modes is not apparent, which could indicate that, at least on average, overtone interference does not affect global estimates of Love wave phase velocity. A Rayleigh–Love incompatibility therefore can only be due to transverse isotropy. Nevertheless, a test with synthetic seismograms could help to illuminate how large a possible bias could be. We calculated 1200 mode synthetic seismograms for model 1066A that included the complete set of overtones. Using the same technique that we used in [Laske and Masters \(1996\)](#), we then measured phase relative to 1066A fundamental mode synthetics. [Figure 42](#) shows the median of our measured phase velocity anomalies. Rayleigh waves are essentially not affected by overtone contamination. Love wave data, on the other hand, show a bias that becomes significant at higher frequencies and can reach 0.06%, a result which could potentially raise concern. However, when comparing these discrepancies with the medians in the real data, we find that this bias is an order of magnitude smaller than what we observe. Potentially, Rayleigh wave overtone contamination could play a role if significant lateral refraction rotates some of the signal from the radial onto the transverse component. We have not tested how much this affects our data set but we suspect that this effect is much smaller than Love wave overtone contamination. It appears therefore that a possible

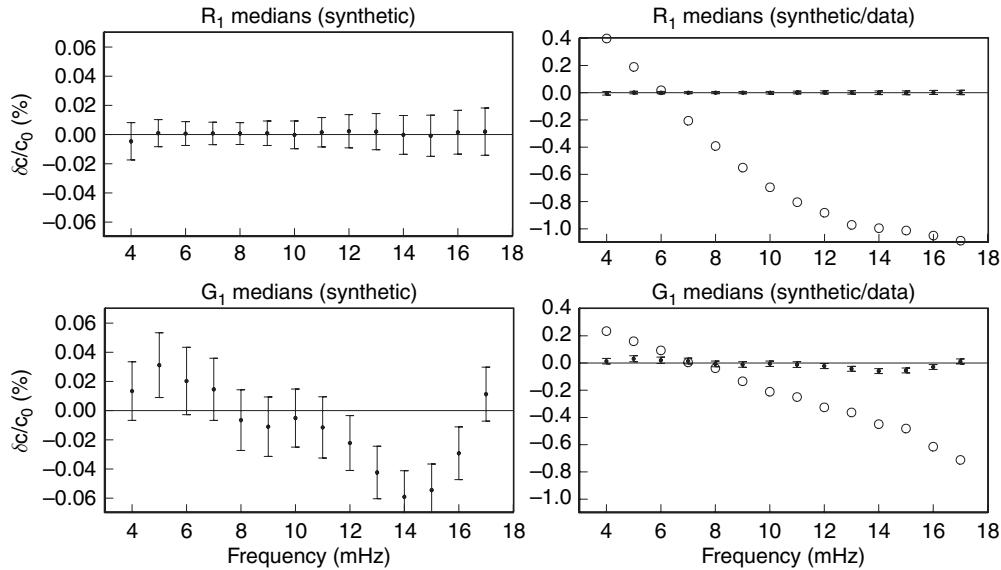


Figure 42 Estimation of the bias on fundamental mode phase velocity estimates introduced by overtone interference. Measurements are with respect to fundamental mode synthetics computed for model 1066A of [Gilbert and Dziewonski \(1975\)](#). The left panels show the bias on about 1200 synthetic waveforms that include the complete set of overtones, for Rayleigh (R_1) and Love (G_1) waves. The right panels show the same synthetic results but now together with the anomalies that we measured in our [Laske and Masters \(1996\)](#) data set (open circles). The synthetic test shows that the bias on Love waves is much greater than on Rayleigh waves, and the bias is significant. On the other hand, the anomalies that we measure on real data are an order of magnitude larger.

Rayleigh–Love incompatibility requires a transversely isotropic REM. Note that the medians shown here are averages in the data set and not true spherical averages, which are obtained only after an inversion for phase velocity maps. The small changes this would entail are irrelevant and do not at all affect the discussion here.

1.03.3.5 Surface Waves and Structure at Depth

The first inversion of surface wave dispersion to obtain mantle structure was carried out for the Canadian Shield by [Brune and Dorman \(1963\)](#) along a two-station pair though forward modeling attempts go back at least 10 years (e.g., [Ewing and Press, 1954](#)). A vast amount of modeling attempts has followed since then and the interested reader finds a detailed description of the quest for structure in the mantle in other contributions in this volume, for example Chapter 1.16 which also discusses azimuthal anisotropy or that of Chapter 1.21 which discusses attenuation. A comprehensive review on the inversion of surface waves can be found in [Romanowicz \(2002\)](#). Here we would like to close the discussion on surface wave data and their inversion for structure at

depth with just a few remarks. Surface wave phase velocity is sensitive to all three elastic parameters, V_S (or β), V_P (or α), as well as density ρ :

$$\frac{\delta c}{c} = \int_0^a r^2 dr (\tilde{A} \cdot \delta\alpha + \tilde{B} \cdot \delta\beta + \tilde{R} \cdot \delta\rho) \quad [25]$$

For uncoupled modes in transversely isotropic media, phase velocity sensitivity is expressed in terms of even more parameters where the two velocities are replaced by the five elastic parameters A , C , N , L , and F (e.g., [Dziewonski and Anderson, 1981](#)) where

$$V_{PH} = \sqrt{A/\rho}, \quad V_{SH} = \sqrt{N/\rho}$$

$$V_{PV} = \sqrt{C/\rho}, \quad V_{SV} = \sqrt{L/\rho}$$

$$\eta = F/(A-2L)$$

where $A=C$, $N=L$, $\eta=1$ for isotropic media. [Montagner and Nataf \(1986\)](#) devised an elegant technique to generalize this representation to model azimuthal anisotropy in the so-called vectorial tomography ([Montagner and Nataf, 1988](#)). In transversely isotropic media, Rayleigh waves are sensitive to all four velocities: V_{PV} , V_{PH} , V_{SV} , and V_{SH} where sensitivity to the latter is practically negligible. On the other hand, Love waves are

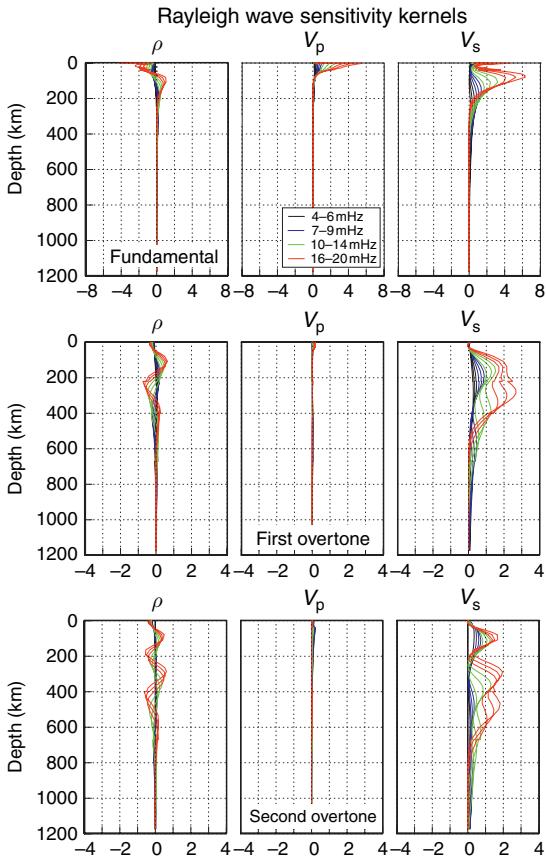


Figure 43 Sensitivity kernels for phase velocity to isotropic structure at depth, for Rayleigh wave fundamental modes and the first two overtones. Rayleigh waves depend on all three parameters but sensitivity to V_s dominates. Overtone sensitivity to V_p is weak and fundamental modes are affected only by V_p shallower than 50 km, when sensitivity to V_s decreases. Overtone sensitivity to structure below about 300 km is larger than that of fundamental modes though note that the scale is different by a factor 2. The model used to calculate the kernels is PREM.

sensitive to V_{SH} and V_{SV} where sensitivity to the latter is significantly smaller and usually ignored. We have no space to discuss the effects of anisotropy in greater detail but the interested reader is referred to Chapter 1.16.

As mentioned above, investigators strive to include overtones in our modeling because they have enhanced sensitivity to structure at greater depth than fundamental modes do. Figures 43 and 44 show the sensitivity of Rayleigh and Love wave fundamental modes and their first two overtones to isotropic structure at depth. In the frequency range considered here (4–20 mHz), fundamental modes do not reach much beyond 300 km, though some sensitivity exists down to 500 km for 4 mHz Rayleigh

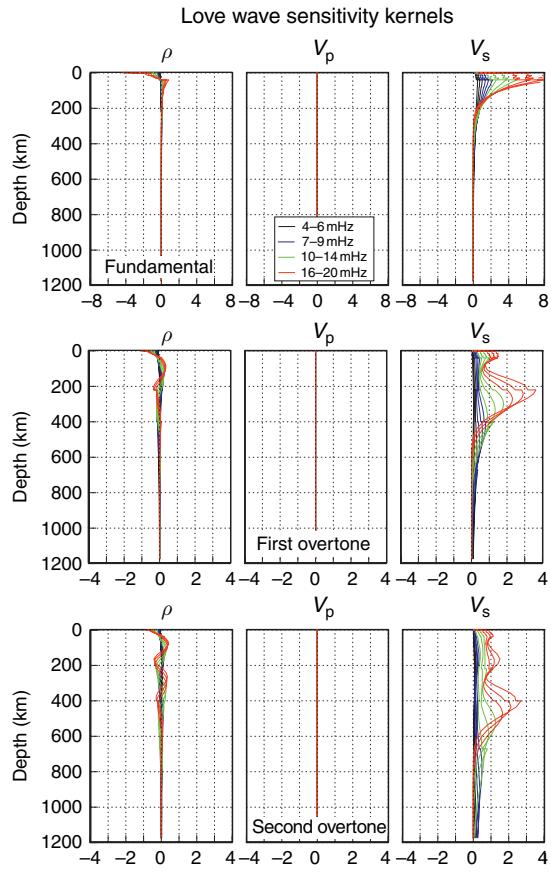


Figure 44 Sensitivity kernels for phase velocity to isotropic structure at depth, for Love wave fundamental modes and the first two overtones. Love wave fundamental modes are primarily sensitive to V_s only, but some sensitivity for density exists, especially for overtones. For details see Figure 43. Second overtones are particularly useful to constrain structure in the transition zone.

waves. Overtones, on the other hand, reach well into the lower mantle. This fact has been utilized by numerous surface wave studies that concentrate on the transition zone and subducting slabs (e.g., Stutzmann and Montagner, 1994; van der Lee and Nolet, 1997; Trampert and van Heijst, 2002). In the isotropic case, Rayleigh waves are not very sensitive to V_p deeper than 50 km but sensitivity is significant at shallower depths where sensitivity to V_s is very low. A comprehensive inversion for structure at depth would include the search for all three elastic parameters. In practice, this is usually not feasible, because the frequency range covered by the measurements does not provide enough independent information to make an inversion well constrained. To simplify an inversion, scaling relationships are often used that are consistent with mineral physics

constraints and include the kernels for V_p and ρ in the kernels for V_s . We then invert only for V_s . For mantle structure, we commonly use

$$\begin{aligned}\tilde{A} \cdot \delta\alpha &= (1/1.7)\tilde{B} \cdot \delta\beta \\ \tilde{R} \cdot \delta\rho &= (1/2.5)\tilde{B} \cdot \delta\beta\end{aligned}$$

This assumption is basically valid if observed seismic anomalies are caused by thermal effects. In the crust, above 50 km depth, compositional variations may dominate and the scaling relationships no longer hold (e.g., in thick sedimentary basins). It is somewhat fortunate that sensitivity to shallow V_s is greatly diminished. Consequently, if we invert for a model, the shallow structure should probably be attributed to variations in V_p , not V_s as is commonly done. Note however, that sensitivity to shallow density is also significant and a detailed discussion of tectonic implications should take this into account. A point that has not been treated here is that group velocities provide additional independent constraints, not in the physical sense but from a measurement technique point of view. A combination of the two is particularly useful to reduce ambiguities resulting from data uncertainties and to enhance the modeling of crustal structure (e.g., [Shapiro and Ritzwoller, 2002](#)).

We should mention that all examples shown in this chapter use a spherical Earth approach. On regional scale, investigators may choose to use a flat Earth approach. Surface wave applications overlap sufficiently that data or models may be compared that did not use the same approach. In this case an Earth-flattening transformation has to be applied to facilitate this comparison (e.g., [Biswas and Knopoff, 1970](#); [Ben-Menahem and Singh, 1981](#)). In the case of a velocity model comparison, a conversion can be done through

$$v_f(z_f) = (a/r)v_s(r) \quad [26]$$

where the subscripts f and s denote ‘flat’ and ‘spherical’, z is the depth, r is the radius, and a is Earth’s radius ([Shearer, 1999](#)). Near the surface, the differences between v_f and v_s are insignificant but they become larger with depth. To use Shearer’s example, with $v_s = 8.6 \text{ km s}^{-1}$ at 150 km depth, the velocity in the flat-Earth model would be 2.4% larger and the impact on velocity becomes relevant when discussing geodynamical implications.

A major issue not covered in this paper is the model parametrization and the regularization during an inversion. Both influence the outcome of the modeling effort. The two basic classes of

parametrizations include ‘global’ and ‘local’ ones. In a ‘global’ parametrization, each contributor to a set of basis functions covers the entire model space but represents different wavelengths (e.g., Chebyshev polynomials or spherical harmonics). In a ‘local’ parametrization, each contributor covers only part of the model (e.g., layers or local B-splines). Comprehensive techniques also search for perturbations in boundaries, not only perturbations in elastic parameters. Regularizations or damping try to account for the fact that some parts of the model space remain poorly constrained by the available data. For example, Rayleigh waves at periods shorter than 50 s have only marginal sensitivity to structure below 150 km. An undamped inversion could falsely place structure at these depths after a least-squares procedure dictated that this is the minimum norm solution. From a data perspective, this solution is not justifiable because there were no data to reliably constrain this. A careful analyst therefore conducts thorough *a posteriori* hypothesis testing (e.g., spike, checker board, or other tests with hypothetical input structures) on which structures of the model are reliably imaged and which are likely not. Other issues include how the inversion is done. Depending on the inversion algorithm, the modeling can end up in a local minimum of the misfit function in which case the model does not represent the best model consistent with our data. The Monte Carlo technique is used in forward modeling to explore larger areas in the model space (e.g., [Shapiro and Ritzwoller, 2002](#)). To make the search computationally more economical, [Knopoff \(1972\)](#) employed a hedgehog algorithm that he and Keilis-Borok developed (see also [Keilis-Borok and Yanovskaja, 1967](#)). The search starts out in a Monte Carlo fashion but then refines it once a minimum is found. Neighboring model parameters are tried out but discarded if the predictions move the value in the misfit function outside of a certain boundary around the minimum. Recently, [Beghein and Trampert \(2004\)](#) provide a novel approach using the neighborhood algorithm of [Sambridge \(1999\)](#). They define probability density functions to explore the range of possible models. Such forward approaches are attractive but one should carefully evaluate the coverage of the null space. Last but not least, the [Backus and Gilbert \(1968\)](#) approach is still used today ([Masters and Gubbins, 2003](#)) when specific targets are investigated. In the B&G approach, specific linear combinations of data are selected that illuminate a certain model parameter (e.g., density near the core–mantle

boundary). This method is attractive in that it provides an elegant way to assess the resolution capabilities of the data.

1.03.3.6 The Validity of the Great Circle Approximation and Data Accuracy

Much of the discussion presented here is based on the use of Fermat's principle. Anomalies are assumed to accumulate along the great circle arc between source and receiver. Concerns about the validity of the great circle approximation and suggestions to improve the interpretation of observables may go back as far as the great circle approximation itself and we need to be aware to which limit approximate theories are applicable. For example, [Woodhouse and Girnius \(1982\)](#) presented surface kernels for normal modes that show a rather broad corridor of sensitivity to structure along the source–receiver great circle. On the other hand, [Jordan \(1978\)](#) made a good argument that modes are essentially sensitive to structure in the immediate vicinity of the source-receiver great circle. This is true if structure is smooth and the structural wavelength remains much larger than the signal wavelength. This applies not only to normal modes but to surface waves as well. Advances in parametric surface wave modeling have been made through Gaussian beam ray-tracing techniques (e.g., [Yomogida, 1985](#)), Born single and multiple scattering (e.g., [Snieder and Nolet, 1987](#); [Friederich et al., 1993](#)) or diffraction tomography (e.g., [Meier et al., 1997](#); [Ritzwoller et al., 2002](#)). Recently, finite-frequency theory (e.g., [Zhou et al., 2005](#), [Yoshizawa and Kennett, 2005](#)) has been added to the tools in the quest to resolve ever smaller details in Earth structure using surface waves. While each of these techniques promises vast improvement over simple approximations, they almost always also have their own limitations. Equally if not more importantly, we must not forget that the resulting models can only be as good as the data which the modeling is based on (see, e.g., [Trampert and Spetzler \(2006\)](#)). Measurement uncertainties can be large due to noise in the time series that may often be accepted too readily as being Gaussian because the theory requires it. Often, noise is produced systematically, for example, through coupling or interference effects or by inappropriate measurement techniques or by not accounting for them properly. Noise may simply be introduced by unknown effects such as a failing instrument, a faulty installation or unknown coupling of the instrument to the ground. It

is probably not unheard of that a spurious resonance in an installation (e.g., a process turning on every few minutes) nearly coincided with a normal mode frequency of Earth and the data analyst was not aware of the problem. We hope that this chapter has contributed to raise awareness of how important it is to understand how data are collected, how one's favorite measurement technique works and to judge its strengths and pitfalls objectively. Only then is one able to discuss the validity of small details in a model.

1.03.4 Concluding Remarks

As mentioned in Section 1.03.1, the seismograms we analyze are typically collected within the FDSN that includes the GSN, GEOSCOPE, and the GEOFON global seismic networks but also regional networks of permanent seismometer installations such as the German GRSN, the Canadian Digital Seismic Network, the Italian MEDNET, the Japanese F-NET and the Californian TERRAscope and BDSN. Some of these have been recording continuously for nearly 20 years or longer or have replaced earlier networks, such as the DWWSSN and SRO. The observation of normal modes, with periods up to 54 min, requires a very long-period sensor and some of the best early digital observations were collected on LaCoste Romberg gravimeters (e.g., IDA; [Agnew et al., 1976](#)) that have been used primarily to observe tides. The disadvantage of recording with gravimeters is that we collect only the vertical ground movement. Also, the first few wave trains in earlier recordings of large earthquakes were typically saturated. More modern equipment therefore includes a very broadband three-component seismometer, such as the Wielandt–Streckeisen STS-1 vault seismometer or the Teledyne KS54000 bore-hole seismometer. Though some individual installations of the broadband STS-2s deliver spectacular low-frequency spectra, more often the signal of the gravest modes are buried in the noise. STS-1 and KS54000 are no longer produced. As sensors age and start to fail, we are losing some of the best and quietest stations that collected records of memorable quality. For example, at the old IDA/UCLA station SPA at the south pole, the gravimeter recorded the deep 09 June 1994 Bolivia earthquake which is, to this day and after the 2004 Andaman–Sumatra earthquake, the best digitally recorded deep earthquake to study many overtone modes, including IC-sensitive modes. The station was closed soon after 'Bolivia',

and the site was equipped with seismometers and operated under the GSN umbrella. Though the installation included an STS-1, the 1994 Bolivia spectrum was the last, and one of very few noteworthy normal mode spectra collected at SPA. Spectra collected at Earth's poles are invaluable to us because they provide the unique opportunity to study in detail the $m=0$ singlet of a mode. To this day, some $m=0$ singlets, such as that of IC-sensitive mode ${}_3S_2$ have not yet been observed and we have yet to understand whether this is caused by Earth structure, low excitation by the seismic source, or high noise levels at SPA. The low signal quality at SPA has been known for many years but such a station is extremely difficult to operate, not lastly for environmental reasons. It is therefore not surprising that it took almost 10 years before new equipment was installed at the new site QSPA, not too far away. The 2004 Sumatra–Andaman EQ did produce a nice spectrum at QSPA but this earthquake was exceptionally large. It remains to be seen, if the 1994 Bolivia SPA spectrum can be reproduced in the future. The GSN has now reached its design goals (Butler *et al.*, 2004). No new stations will come online and the networks are in transition from a R&D (research and development) to an O&M (operation and maintenance) modus of operandi. To guarantee the data flow that we enjoy today requires the continued commitment of network operators to maintain stations at observatory-quality level, preferably at remote, low-noise locations. Amazingly enough, some network operators have run these networks on budgets that have not increased or, at the least, kept up with inflation rates. In today's world of high-resolution tomography and squeezed in between large projects such as the US EARTHSCOPE and other high-visibility endeavors, it is becoming increasingly difficult to make the case for running, and funding, a very long-period global seismic network. There are many yet unresolved problems in Earth science to which normal modes seismology may hold the crucial clues, if not the only ones. Our greatest commitment therefore must be to ensure that we have not yet passed the golden age of normal mode observational seismology.

Acknowledgments

We wish to thank the network and station operators for their unselfish long-term commitment to continuously and consistently collect high-quality long-period

seismic data. Foremost among these are GEOSCOPE (IPGP, Paris, France), IRIS-IDA (UC San Diego, USA), IRIS-USGS (ASL Albuquerque), GEOFON (GFZ, Potsdam, Germany), TERRASCOPE/TRINET (Caltech, USA), BDSN (UC Berkeley, California), GRSN (SZGRF, Erlangen, Germany), BFO (Black Forest Observatory, Germany), and the operators of superconducting gravimeters. Thanks also go to IRIS, FDSN, the global geodynamics project (GGP; Crossley *et al.*, 1999) and all data management centers for freely and readily making the data available to us. This research was funded by grant EAR03-36864 of the US National Science Foundation.

References

- Agnew DC, Berger J, Buland R, Farrell WE, and Gilbert JF (1976) International deployment of accelerometers: A network for very long period seismology. *EOS Transactions of the American Geophysical Union* 77: 180–188.
- Agnew DC, Berger J, Farrell WE, Gilbert JF, Masters G, and Miller D (1986) Project IDA: A decade in review. *EOS Transactions of the American Geophysical Union* 67: 203–212.
- Aki K and Richards PG (1980) *Quantitative Seismology, Theory and Methods*. San Francisco, FL: W.H. Freeman.
- Aki K and Richards PG (2002) *Quantitative Seismology, Theory and Methods*. San Francisco, FL: University Science Books.
- Alsina D and Snieder R (1993) A test of the great circle approximation in the analysis of surface waves. *Geophysical Research Letters* 20: 915–928.
- Backus G (1962) The propagation of short elastic surface waves on a slowly rotating Earth. *Bulletin of the Seismological Society of America* 52: 823–846.
- Backus G (1964) Geographical interpretation of measurements of average phase velocities of surface waves over great circular and great semi-circular paths. *Bulletin of the Seismological Society of America* 54: 571–610.
- Backus G (1967) Converting vector and tensor equations to scalar equations in spherical coordinates. *Geophysical Journal of the Royal Astronomical Society* 13: 71–101.
- Backus G and Gilbert F (1968) The resolving power of gross Earth data. *Geophysical Journal of the Royal Astronomical Society* 16: 169–205.
- Beghein C and Trampert J (2004) Probability density functions for radial anisotropy from fundamental mode surface wave data and the neighbourhood algorithm. *Geophysical Journal International* 157: 1163–1174.
- Ben-Menahem A and Singh SJ (1981) *Seismic Waves and Sources*. New York: Springer-Verlag.
- Benioff H, Harrison JC, LaCoste L, Munk WH, and Slichter LB (1959) Searching for the Earth's free oscillations. *Journal of Geophysical Research* 64: 1334.
- Berckhemer H (1956) Rayleigh-wave dispersion and crustal structure in the East Atlantic Ocean Basin. *Bulletin of the Seismological Society of America* 46: 83–86.
- Beucler É, Stutzmann É, and Montagner J-P (2003) Surface wave higher-mode phase velocity measurements using a roller-coaster-type algorithm. *Geophysical Journal International* 155: 289–307.
- Billien M, Lévéque J-J, and Trampert J (2000) Global maps of Rayleigh wave attenuation for periods between 40 and 150 seconds. *Geophysical Research Letters* 27: 3619–3622.

- Biswas NN and Knopoff L (1970) Exact Earth-flattening calculation for Love waves. *Bulletin of the Seismological Society of America* 60: 1123–1137.
- Blackman RB and Tukey JW (1958) *The Measurement of Power Spectra*. New York: Dover.
- Boore DM (1969) Effect of higher mode contamination on measured Love wave phase velocities. *Journal of Geophysical Research* 74: 6612–6616.
- Bromirski PD and Duennebier FK (2002) The near-coastal microseism spectrum: Spatial and temporal wave climate relationships. *Journal of Geophysical Research* 107B: 2166–2185.
- Brune J and Dorman J (1963) Seismic seismic waves and Earth structure in the Canadian shield. *Bulletin of the Seismological Society of America* 53: 167–209.
- Brune JN, Nafe JE, and Alsop LE (1961) The polar phase shift of surface waves on a sphere. *Bulletin of the Seismological Society of America* 51: 247–257.
- Buland R, Berger J, and Gilbert F (1979) Observations from the IDA network of attenuation and splitting during a recent earthquake. *Nature* 277: 358–362.
- Butler R, Lay T, Creager K, et al. (2004) The global seismographic network surpasses its design goal. *EOS Transactions of the American Geophysical Union* 85: 225–229.
- Capdeville Y, Chaljub E, Villette JP, and Montagner JP (2003) Coupling the spectral element method with a modal solution for elastic wave propagation in global Earth models. *Geophysical Journal International* 152: 34–67.
- Capon J (1970) Analysis of Rayleigh-wave multipath propagation at LASA. *Bulletin of the Seismological Society of America* 60: 1701–1731.
- Cara M (1973) Filtering of dispersed wavetrains. *Geophysical Journal of the Royal Astronomical Society* 33: 65–80.
- Cara M (1978) Regional variations of higher Rayleigh-mode phase velocities: A spatial-filtering method. *Geophysical Journal of the Royal Astronomical Society* 54: 439–460.
- Cara M and Lévêque J-J (1987) Waveform inversion using secondary observables. *Geophysical Research Letters* 14: 1046–1049.
- Cara M, Minster J-B, and Le Bras R (1981) Multi-mode analysis of Rayleigh-type L_g . Part 2: Application to Southern California and the Northwestern Sierra Nevada. *Bulletin of the Seismological Society of America* 71: 985–1002.
- Carder DS (1934) Seismic surface waves and the crustal structure of the Pacific region. *Bulletin of the Seismological Society of America* 24: 231–302.
- Chaljub E and Valette B (2004) Spectral element modelling of three-dimensional wave propagation in a self-gravitating Earth with an arbitrarily stratified outer core. *Geophysical Journal International* 158: 131–141.
- Clévétré É, Mégnin C, Romanowicz B, and Lognonné P (2000) Seismic waveform modeling and surface wave tomography in a three-dimensional Earth: Asymptotic and non-asymptotic approaches. *Physics of the Earth and Planetary Interiors* 119: 37–56.
- Cooley JW and Tukey JW (1965) An algorithm for the machine computation of complex Fourier series. *Mathematics of Computation* 19: 297–301.
- Cotte N, Pedersen HA, Campillo M, Farra V, and Cansi Y (2000) Off-great-circle propagation of intermediate-period surface waves observed on a dense array in the French Alps. *Geophysical Journal International* 142: 825–840.
- Creager KC (1997) Inner core rotation rate from small-scale heterogeneity and time-varying travel times. *Science* 278: 1248–1288.
- Creager KC (2000) Inner core anisotropy and rotation. In: Karato S-I, Forte AM, Libermann RC, Masters G, and Stixrude L (eds.) *AGU Monograph 117: Earth's Deep Interior: Mineral Physics and Tomography*, pp. 89–114. Washington, DC: American Geophysical Union.
- Crossley D, Hinderer J, Casula G, et al. (1999) Network of superconducting gravimeters benefit a number of disciplines. *EOS Transactions of the American Geophysical Union* 80: 125–126.
- Dahlen FA (1968) The normal modes of a rotating, elliptical Earth. *Geophysical Journal of the Royal Astronomical Society* 16: 329–367.
- Dahlen FA (1982) The effect of data windows on the estimation of free oscillation parameters. *Geophysical Journal of the Royal Astronomical Society* 69: 537–549.
- Dahlen FA and Sailor RV (1979) Rotational and elliptical splitting of the free oscillations of the Earth. *Geophysical Journal of the Royal Astronomical Society* 58: 609–623.
- Dahlen FA and Tromp J (1998) *Theoretical Global Seismology*, 1025 pp. Princeton, NJ: Princeton University Press.
- Dalton C and Ekström G (2006) Constraints on global maps of phase velocity from surface-wave amplitudes. *Geophysical Journal International* 161: 820–826.
- Debayle E and Lévêque J-J (1997) Upper mantle heterogeneities in the Indian ocean from waveform inversion. *Geophysical Research Letters* 24: 245–248.
- Deuss A and Woodhouse J (2001) Theoretical free-oscillation spectra; the importance of wide band coupling. *Geophysical Journal International* 146: 833–842.
- Deuss A and Woodhouse J (2004) Iteration method to determine the eigenvalues and eigenvectors of a target multiplet including full mode coupling. *Geophysical Journal International* 159: 326–332.
- Doorn MB, Simon RF, and Lawrence PL (1951) Rayleigh waves from small explosions. *Transactions of the American Geophysical Union* 32: 822–832.
- Donn WL and Blaik M (1953) A study and evaluation of the tripartite seismic method of locating hurricanes. *Bulletin of the Seismological Society of America* 43: 311–329.
- Dratler J, Farrell W, Block B, and Gilbert F (1971) High-Q overtone modes of the Earth. *Geophysical Journal of the Royal Astronomical Society* 23: 399–410.
- Durek JJ and Ekström G (1996) A model of radial anelasticity consistent with observed surface wave attenuation. *Bulletin of the Seismological Society of America* 86: 144–158.
- Durek JJ, Ritzwoller MH, and Woodhouse JH (1993) Constraining upper mantle anelasticity using surface wave amplitude anomalies. *Geophysical Journal International* 114: 249–272.
- Dziewonski AM (1970) On regional differences in dispersion of mantle Rayleigh waves. *Geophysical Journal of the Royal Astronomical Society* 22: 289–325.
- Dziewonski AM and Anderson DL (1981) Preliminary reference Earth model. *Physics of the Earth and Planetary Interiors* 25: 297–356.
- Dziewonski AM, Bloch S, and Landisman M (1969) A technique for the analysis of transient seismic signals. *Bulletin of the Seismological Society of America* 59: 427–444.
- Dziewonski AM, Chou TA, and Woodhouse JH (1981) Determination of earthquake source parameters from waveform data for studies of global and regional seismicity. *Journal of Geophysical Research* 86: 2825–2852.
- Dziewonski AM and Gilbert F (1971) Solidity of the inner core of the Earth inferred from normal mode observations. *Nature* 234: 465–466.
- Dziewonski AM and Gilbert F (1972) Observations of normal modes from 84 recordings of the Alaskan earthquake of 1964 March 28. *Geophysical Journal of the Royal Astronomical Society* 27: 393–446.

- Dziewonski AM and Landisman M (1970) Great circle Rayleigh and Love wave dispersion from 100 to 900 seconds. *Geophysical Journal of the Royal Astronomical Society* 19: 37–91.
- Dziewonski AM, Mills J, and Bloch S (1972) Residual dispersion measurement – A new method of surface-wave analysis. *Bulletin of the Seismological Society of America* 62: 129–139.
- Dziewonski AM and Stein J (1982) Dispersion and attenuation of mantle waves through wave-form inversion. *Geophysical Journal of the Royal Astronomical Society* 70: 503–527.
- Ekström G (2001) Time domain analysis of the Earth's long-period background seismic radiation. *Journal of Geophysical Research* 106: 26483–26494.
- Ekström G and Dziewonski AM (1998) The unique anisotropy of the Pacific upper mantle. *Nature* 394: 168–172.
- Ekström G, Tromp J, and Larson EW (1997) Measurements and models of global surface wave propagation. *Journal of Geophysical Research* 102: 8137–8157.
- Essen H-H, Krüger F, Dahm T, and Grevermeyer I (2003) On the generation of secondary microseisms observed in northern and central Europe. *Journal of Geophysical Research* 108: 2506 (doi:10.1029/2002JB002338).
- Evernden JE (1953) Direction of approach of Rayleigh waves and related problems. Part I. *Bulletin of the Seismological Society of America* 43: 335–357.
- Evernden JE (1954) Direction of approach of Rayleigh waves and related problems. Part II. *Bulletin of the Seismological Society of America* 44: 159–184.
- Ewing M and Press F (1952) Crustal structure and surface wave dispersion. Part 2. *Bulletin of the Seismological Society of America* 42: 315–325.
- Ewing M and Press F (1954) An investigation of mantle Rayleigh waves. *Bulletin of the Seismological Society of America* 44: 127–147.
- Ewing M and Press F (1956) Rayleigh wave dispersion in the period range 10 to 500 seconds. *Transactions of the American Geophysical Union* 37: 213–215.
- Ewing M, Jaretzky WS, and Press F (1957) *Elastic Waves in Layered Media*, 380 pp. New York: McGraw-Hill Book Company.
- Forsyth D and Li A (2005) Array-analysis of two-dimensional variations in surface wave phase velocity and azimuthal anisotropy in the presence of multi-pathing interference. In: Levander A and Nolet G (eds.) *Geophysical Monograph 157: Seismic Earth: Array Analysis of Broadband Seismograms*, pp. 81–97. Washington, DC: American Geophysical Union.
- Friedrich A, Krüger F, and Klinge K (1998) Ocean generated microseismic noise located with the Gräfenberg array. *Journal of Seismology* 2: 47–64.
- Friederich W, Wielandt E, and Stange S (1993) Multiple forward scattering of surface waves; comparison with an exact solution and Born single-scattering methods. *Geophysical Journal International* 112: 264–275.
- Friederich W, Wielandt E, and Stange S (1994) Non-plane geometries of seismic surface wavefields and their implications for regional surface-wave tomography. *Geophysical Journal International* 119: 931–948.
- Gabor D (1947) Acoustical quanta and the theory of hearing. *Nature* 159: 591–594.
- Galagher B (1971) Generation of surf beat by non-linear wave interactions. *Journal of Fluid Mechanics* 49: 1–20.
- Geller RJ and Takeuchi N (1995) A new method for computing highly accurate DSM synthetic seismograms. *Geophysical Journal International* 123: 449–470.
- Giardini D, Li X-D, and Woodhouse JH (1987) Three-dimensional structure of the Earth from splitting in free oscillation spectra. *Nature* 325: 405–411.
- Gilbert F (1971) The diagonal sum rule and averaged eigenfrequencies. *Geophysical Journal of the Royal Astronomical Society* 23: 119–123.
- Gilbert F (1980) An introduction to low-frequency seismology. *Proceedings of the Enrico Fermi Summer School of 1979* 41–81.
- Gilbert F (2001) Vandermonde matrix analysis of long-period seismograms. *Geophysical Journal International* 146: 843–849.
- Gilbert F and Dziewonski AM (1975) An application of normal mode theory to the retrieval of structural parameters and source mechanisms from seismic spectra. *Philosophical Transactions of the Royal Society A* 278: 187–269.
- Gu YJ and Dziewonski AM (1999) Mantle discontinuities and 3-D tomographic models. *EOS Transactions of the American Geophysical Union* 80: F717.
- Gung Y and Romanowicz B (2004) Q tomography of the upper mantle using three-component long-period waveforms. *Geophysical Journal International* 157: 813–830.
- Gutenberg B and Richter CF (1936) On seismic waves, 3rd paper. *Geologische Beiträge Zur Geophysik* 47: 73–131.
- Hanka W and Kind R (1994) The GEOFON Program. *IRIS Newsletter* XIII: 1–4.
- Harris F (1978) On the use of windows for harmonic analysis with the discrete Fourier transform. *Proceedings of the IEEE* 66: 51–83.
- He X and Tromp J (1996) Normal-mode constraints on the structure of the Earth. *Journal of Geophysical Research* 87: 7772–7778.
- Henson IH (1989) Multiplet coupling of the normal modes of an elliptical, transversely isotropic Earth. *Geophysical Journal International* 98: 457–459.
- Herrin E and Goforth T (1977) Phase-matched filters: Application to the study of Rayleigh waves. *Bulletin of the Seismological Society of America* 67: 1259–1275.
- Hu X-G, Liu L-T, Hinderer J, Hsu HT, and Sun H-P (2006) Wavelet filter analysis of atmospheric pressure effects in the long-period seismic mode band. *Physics of the Earth and Planetary Interiors* 154: 70–84.
- Ishii M and Tromp J (1999) Normal-mode and free-air gravity constraints on lateral variations in velocity and density of Earth's mantle. *Science* 285: 1231–1236.
- Jeans JH (1923) The propagation of earthquake waves. *Geologische Beiträge Zur Geophysik A* 102: 554–574.
- Jenkins GM (1961) General considerations in the analysis of spectra. *Techometrics* 3: 133–166.
- Jobert N and Roult G (1976) Periods and damping of free oscillations observed in France after sixteen earthquakes. *Geophysical Journal of the Royal Astronomical Society* 45: 155–176.
- Jobert N and Roult G (1978) Evidence of lateral variations from free oscillations and surface waves. *Geophysical Research Letters* 5: 569–572.
- Jordan T (1978) A procedure for estimating lateral variations from low-frequency eigenspectra data. *Geophysical Journal of the Royal Astronomical Society* 52: 441–455.
- Jurkevics A (1988) Polarization analysis of three-component array data. *Seismological Society of America* 78: 1725–1743.
- Kanamori H (1970) Velocity and Q of the mantle waves. *Physics of the Earth and Planetary Interiors* 2: 259–275.
- Keilis-Borok VI and Yanovskaja TB (1967) Inverse problems of seismology (Structural Review). *Geophysical Journal of the Royal Astronomical Society* 13: 223–234.
- Kellogg LH, Hager BH, and van der Hilst RD (1999) Compositional stratification in the deep mantle. *Science* 283: 1881–1884.
- Knopoff L (1972) Observation and inversion of surface-wave dispersion. *Tectonophysics* 13: 497–519.

- Knopoff L, Berry MJ, and Schwab FA (1967) Tripartite phase velocity observations in laterally heterogeneous regions. *Journal of Geophysical Research* 72: 2595–2601.
- Knopoff L, Mueller S, and Pilant WL (1966) Structure of the crust and upper mantle in the Alps from the phase velocity of Rayleigh waves. *Bulletin of the Seismological Society of America* 56: 1009–1044.
- Komatitsch D, Ritsema J, and Tromp J (2002) The spectral-element method, Beowulf computing, and global seismology. *Science* 298: 1737–1742.
- Komatitsch D and Tromp J (2002) Spectral-element simulations of global seismic wave propagation. Part II: Three-dimensional models, oceans, rotation and self-gravitation. *Geophysical Journal International* 150: 303–318.
- Komatitsch D and Vilotte J-P (1998) The spectral element method: An efficient tool to simulate the seismic response of 2D and 3D geological structure. *Bulletin of the Seismological Society of America* 88: 368–392.
- Kopitschalitsch G (1988) *Die Anwendung der zeitvariablen Filterung bei der Eigenschwingungs-analyse*. Masters Thesis Universität Karlsruhe, Germany.
- Kurrale D and Widmer-Schnidrig R (2006) Spatiotemporal features of the Earth's background oscillations observed in central Europe. *Geophysical Research Letters* 33: L24304 (doi:10.1029/2006GL028429).
- Landau LD and Lifshitz EM (1958) *Quantum Mechanics*, 515 pp. Reading, MA: Addison Wesley.
- Landisman M, Dziewonski A, and Satô Y (1969) Recent improvements in the analysis of surface wave observations. *Geophysical Journal of the Royal Astronomical Society* 17: 369–403.
- Larson EWF and Ekström G (2002) Determining surface wave arrival angle anomalies. *Journal of Geophysical Research* 107: doi:10.1029/2000JB000048.
- Laske G (1995) Global observation of off-great-circle propagation of long-period surface waves. *Geophysical Journal International* 123: 245–259.
- Laske G, Masters G, and Dziewonski AM (2001) New measurements of radial mode eigenfrequencies. *EOS Transactions AGU* 82: F873.
- Laske G and Masters G (1996) Constraints on global phase velocity maps from long-period polarization data. *Journal of Geophysical Research* 101: 16059–16075.
- Laske G and Masters G (1999) Limits on the rotation of the inner core from a new analysis of free oscillations. *Nature* 402: 66–69.
- Laske G and Masters G (2003) The Earth's free oscillations and the differential rotation of the inner core. In: Dehant V, Creager K, Zatman S, and Karato S-I (eds.) *Geodynamics Series 31 Earth's Core: Dynamics, Structure, Rotation*, pp. 5–21. Washington, DC: AGU.
- Laske G, Phipps Morgan J, and Orcutt J (1998) First results from the Hawaiian SWELL Pilot Experiment. *Geophysical Research Letters* 26: 3397–3400.
- Lebedev S, Nolet G, Meier T, and van der Hilst RD (2005) Automated multimode inversion of surface and S waveforms. *Geophysical Journal International* 162: 951–964.
- Lerner-Lam AL and Park JJ (1989) Frequency-dependent refraction and multipathing of 10–100 second surface waves in the Western Pacific. *Geophysical Research Letters* 16: 527–530.
- Levshin AL, Pisarenko VF, and Pogrebinsky GA (1972) On a frequency-time analysis of oscillations. *Annales Geophysicae* 28: 211–218.
- Levshin AL, Ritzwoller MH, and Resovsky J (1999) Source effects on surface wave group travel times and group velocity maps. *Physics of the Earth and Planetary Interiors* 115: 293–312.
- Levshin AL, Yanovskaya TB, Lander AV, et al. (1989) Recording identification and measurements of surface wave parameters. In: Keilis-Borok VI (ed.) *Seismic Surface Waves in a Laterally Inhomogeneous Earth*, pp. 131–182. Dordrecht: Kluwer.
- Li X-D, Giardini D, and Woodhouse JH (1991a) Large-scale three-dimensional even-degree structure of the Earth from splitting of long-period normal modes. *Journal of Geophysical Research* 96: 551–557.
- Li X-D, Giardini D, and Woodhouse JH (1991b) The relative amplitudes of mantle heterogeneity in P velocity, S velocity, and density from free oscillation data. *Geophysical Journal International* 105: 649–657.
- Li X-D and Romanowicz B (1995) Comparison of global waveform inversions with and without considering cross-branch modal coupling. *Geophysical Journal International* 121: 695–709.
- Li X-D and Romanowicz B (1996) Global mantle shear velocity model developed using non-linear asymptotic coupling theory. *Journal of Geophysical Research* 101: 22245–22272.
- Lilly JM and Park J (1995) Multiwavelet spectral and polarization analyses of seismic records. *Geophysical Journal International* 122: 1001–1021.
- Lindberg CR and Park J (1987) Multiple-taper spectral analysis of terrestrial free oscillations. Part II. *Geophysical Journal of the Royal Astronomical Society* 91: 795–836.
- Lognonné P (1991) Normal modes and seismograms in an anelastic rotating Earth. *Journal of Geophysical Research* 96: 20309–20319.
- Lognonné P and Romanowicz B (1990) Modelling of coupled normal modes of the Earth: The spectral method. *Geophysical Journal International* 102: 365–395.
- Masters G and Gilbert F (1981) Structure of the inner core inferred from observations of its spheroidal shear modes. *Geophysical Research Letters* 8: 569–571.
- Masters G and Gilbert F (1983) Attenuation in the Earth at low frequencies. *Philosophical Transactions of the Royal Society of London A* 308: 479–522.
- Masters TG and Gubbins D (2003) On the resolution of density within the Earth. *Physics of the Earth and Planetary Interiors* 140: 159–167.
- Masters G, Johnson S, Laske G, and Bolton H (1996) A shear velocity model of the mantle. *Philosophical Transactions of the Royal Society of London* 354A: 1385–1411.
- Masters G, Jordan TH, Silver PG, and Gilbert F (1982) Aspherical Earth structure from fundamental spheroidal-mode data. *Nature* 298: 609–613.
- Masters G and Laske G (1997) On bias in surface wave and free oscillation attenuation measurements. *EOS Transactions of the American Geophysical Union* 78: F485.
- Masters G, Laske G, Bolton H, and Dziewonski A (2000a) The relative behavior of shear velocity, bulk sound speed, and compressional velocity in the mantle: Implications for chemical and thermal structure. In: Karato S-I, Forte AM, Libermann RC, Masters G, and Stixrude L (eds.) *AGU Monograph 117: Earth's Deep Interior: Mineral Physics and Tomography*, pp. 63–87. Washington, DC: American Geophysical Union.
- Masters TG, Laske G, and Gilbert F (2000b) Autoregressive estimation of the splitting matrix of free-oscillation multiplets. *Geophysical Journal International* 141: 25–42.
- Masters TG, Laske G, and Gilbert F (2000c) Matrix autoregressive analysis of free-oscillation coupling and splitting. *Geophysical Journal International* 143: 478–489.
- Masters TG, Laske G, and Gilbert F (2000d) Large-scale Earth structure from analyses of free oscillation splitting and coupling. In: Boschi E, Ekström G, and Morelli A (eds.) *Problems in Geophysics for the New Millennium*, pp. 255–288. Bologna: Editrice Compositori.

- Masters G, Park J, and Gilbert F (1983) Observations of coupled spheroidal and toroidal modes. *Journal of Geophysical Research* 88: 10285–10298.
- Masters TG and Widmer R (1995) Free-oscillations: frequencies and attenuations. In: Ahrens Th J (ed.) *Global Earth Physics: A Handbook of Physical Constants*, pp. 104–125. Washington, DC: American Geophysical Union.
- Maupin V (1992) Modelling of laterally trapped surface waves with application to Rayleigh waves in the Hawaiian swell. *Geophysical Journal International* 110: 533–570.
- McEvilly TV (1964) Central US crust–upper mantle structure from Love and Rayleigh wave phase velocity inversion. *Bulletin of the Seismological Society of America* 54: 1997–2015.
- Mégnin C and Romanowicz B (1999) The effects of the theoretical formalism and data selection on mantle models derived from waveform tomography. *Geophysical Journal International* 138: 366–380.
- Mégnin C and Romanowicz B (2000) The 3D shear velocity of the mantle from the inversion of body, surface, and higher mode waveforms. *Geophysical Journal International* 143: 709–728.
- Meier T, Dietrich K, Stöckhert B, and Harjes H-P (2004) One-dimensional models of shear wave velocity for the eastern Mediterranean obtained from the inversion of Rayleigh wave phase velocities and tectonic implications. *Geophysical Journal International* 156: 45–58.
- Meier T, Lebedev S, Nolet G, and Dahlen FA (1997) Diffraction tomography using multimode surface waves. *Journal of Geophysical Research* 102: 8255–8267.
- Mendiguren JA (1973) Identification of free oscillation spectral peaks for 1970 July 31, Colombian deep shock using the excitation criterion. *Geophysical Journal of the Royal Astronomical Society* 33: 281–321.
- Millot-Langet R, Clévédi E, and Lognonné P (2003) Normal modes and long period seismograms in a 3D anelastic elliptical rotating Earth. *Geophysical Research Letters* 30: doi:10.1029/2002GL016257.
- Mochizuki E (1986a) Free oscillations and surface waves in an aspherical Earth. *Geophysical Research Letters* 13: 1478–1481.
- Mochizuki E (1986b) The free oscillations of an anisotropic and heterogeneous Earth. *Geophysical Journal of the Royal Astronomical Society* 86: 167–176.
- Montagner J-P and Nataf H-C (1986) A simple method for inverting the azimuthal anisotropy of surface waves. *Journal of Geophysical Research* 91: 511–520.
- Montagner J-P and Nataf H-C (1988) Vectorial tomography. Part I: Theory. *Journal of Geophysical Research* 94: 295–307.
- Nafe JE and Brune JN (1960) Observations of phase velocity for Rayleigh waves in the period range 100–400 s. *Bulletin of the Seismological Society of America* 50: 427–439.
- Nawa K, Suda N, Fukao Y, Sato T, Aoyama Y, and Shibuya K (1998) Incessant excitation of the Earth's free oscillations. *Earth Planets and Space* 50: 3–8.
- Nishida K and Kobayashi N (1999) Statistical features of the Earth's continuous free oscillations. *Journal of Geophysical Research* 104: 28741–28750.
- Nishida K, Kobayashi N, and Fukao Y (2000) Resonant oscillations between the solid Earth and the Atmosphere. *Science* 287: 2244–2246.
- Nishida K, Kobayashi N, and Fukao Y (2002) Origin of Earth's ground noise from 2 to 20 mHz. *Geophysical Research Letters* 29(52): 1–4.
- Nolet G (1975) Higher Rayleigh modes in western Europe. *Geophysical Research Letters* 2: 60–62.
- Nolet G (1990) Partitioned waveform inversion and two-dimensional structure under the network of autonomously recording seismographs. *Journal of Geophysical Research* 95: 8499–8512.
- Oliver J (1962) A Summary of observed seismic surface wave dispersion. *Bulletin of the Seismological Society of America* 52: 49–52.
- Oliver J and Ewing M (1957) Higher modes of continental Rayleigh waves. *Bulletin of the Seismological Society of America* 47: 187–204.
- Oliver J and Ewing M (1958) Short-period oceanic surface waves of the Rayleigh and first shear modes. *Transactions of the American Geophysical Union* 39: 483–485.
- Oliver J and Murphy L (1971) WWNSS: Seismology's global network of observing stations. *Science* 174: 254–261.
- Park J and Gilbert F (1986) Coupled free oscillations of an aspherical, dissipative, rotation Earth: Galerkin theory. *Journal of Geophysical Research* 91: 7241–7260.
- Park J, Lindberg CR, and Vernon FL, III (1987a) Multitaper spectral analysis of high-frequency seismograms. *Journal of Geophysical Research* 92: 12675–12684.
- Park J, Lindberg CR, and Thomson DJ (1987b) Multiple-taper spectral analysis of terrestrial free oscillations. Part I. *Geophysical Journal of the Royal Astronomical Society* 91: 755–794.
- Paulsen H, Levshin AL, Lander AV, and Snieder R (1990) Time- and frequency-dependent polarization analysis: Anomalous surface wave observations in Iberia. *Geophysical Journal International* 103: 483–496.
- Pedersen HA (2006) Impacts of non-plane waves on two-station measurements of phase velocities. *Geophysical Journal International* 165: 279–287.
- Pekeris CL (1946) The theory of propagation of sound in a half space of variable sound velocity under conditions of formation of a shadow zone. *Journal of the Acoustical Society of America* 18: 295–315.
- Peterson J (1993) Observations and modeling of seismic background noise. *US Geological Survey, Open-file Report* 93–322: 1–45.
- Peterson J, Hutt CR, and Holcomb LG (1980) Test and calibration of the seismic research observatory. *US Geological Survey, Open-file Report* 80–187: 1–86.
- Peterson J and Tilgner EE (1985) Description and preliminary testing of the DCSN seismic sensor systems. *US Geological Survey, Open-file Report* 85–288: 1–60.
- Pilant WL and Knopoff L (1964) Observations of multiple seismic events. *Bulletin of the Seismological Society of America* 54: 19–39.
- Plešinger A, Hellweg M, and Seidl D (1986) Interactive high-resolution polarization analysis of broad-band seismograms. *Journal of Geophysics* 59: 129–139.
- Polet J and Kanamori H (1997) Upper-mantle shear velocities beneath Southern California determined from long-period surface waves. *Bulletin of the Seismological Society of America* 87: 200–209.
- Pollitz F (1994) Global tomography from Rayleigh and Love wave dispersion: Effect of raypath bending. *Geophysical Journal International* 118: 730–758.
- Press F (1956) Determination of crustal structure from phase velocity of Rayleigh waves. Part I: Southern California. *Bulletin of the Seismological Society of America* 46: 1647–1658.
- Press F (1957) Determination of crustal structure from phase velocity of Rayleigh waves. Part II: San Francisco Bay region. *Bulletin of the Seismological Society of America* 47: 87–88.
- Resovsky J and Ritzwoller M (1995) Constraining odd-degree mantle structure with normal modes. *Geophysical Research Letters* 22: 2301–2304.
- Resovsky J and Ritzwoller M (1998) New and refined constraints on the three-dimensional Earth structure from

- normal modes below 3 mHz. *Journal of Geophysical Research* 103: 783–810.
- Riley KF, Hobson MP, and Bence SJ (2002) *Mathematical Methods for Physics and Engineering*, 1232 pp. Cambridge: Cambridge University Press.
- Ritsema J and Van Heijst H (2000) Seismic imaging of structural heterogeneity in Earth's mantle: Evidence for large-scale mantle flow. *Science Progress* 83: 243–259.
- Ritzwoller M, Masters G, and Gilbert F (1986) Observations of anomalous splitting and their interpretation in terms of aspherical structure. *Journal of Geophysical Research* 91: 10203–10228.
- Ritzwoller M, Masters G, and Gilbert F (1988) Constraining aspherical structure with low frequency interaction coefficients: Application to uncoupled multiplets. *Journal of Geophysical Research* 93: 6369–6396.
- Ritzwoller MH, Shapiro NM, Barmin MP, and Levshin AL (2002) Global surface wave diffraction tomography. *Journal of Geophysical Research* 107: doi:10.1029/2002JB001777.
- Rhie J and Romanowicz B (2004) Excitation of Earth's continuous free oscillations by atmosphere-ocean-seafloor coupling. *Nature* 431: 552–556.
- Rhie J and Romanowicz B (2006) A study of the relation between ocean storms and the Earth's hum. *Geochemistry Geophysics Geosystems* 7: doi:10.1029/2006GC001274.
- Romanowicz B (1994) On the measurement of anelastic attenuation using amplitudes of low-frequency surface waves. *Physics of the Earth and Planetary Interiors* 84: 179–191.
- Romanowicz B (1987) Multiplet-multiplet coupling due to lateral heterogeneity: Asymptotic effects on the amplitude and frequency of the Earth's normal modes. *Geophysical Journal of the Royal Astronomical Society* 90: 75–100.
- Romanowicz B (2002) Inversion of surface waves: A review. In: Jennings PC, Kisslinger C, Kanamori H, and Lee WHK (eds.) *International Handbook of Earthquake and Engineering Seismology*. vol. 81A, pp. 149–173. International Association of Seismology and Physics of the Earth's Interior Committee on Education. Amsterdam: Academic Press.
- Romanowicz B and Bréger L (2000) Anomalous splitting of free oscillations; a reevaluation of possible interpretations. *Journal of Geophysical Research* 105: 21559–21578.
- Romanowicz BA and Dziewonski AM (1986) Toward a federation of broadband seismic networks. *Eos Transactions of the American Geophysical Union* 67: 541–542.
- Romanowicz B, Cara M, Fels JF, and Roult G (1984) GEOSCOPE: A French initiative in long period three component global seismic networks. *Eos Transactions of the American Geophysical Union* 65: 753–756.
- Romanowicz B and Roult G (1986) First-order asymptotics for the eigenfrequencies of the Earth and application to the retrieval of large-scale lateral variations of structures. *Geophysical Journal of the Royal Astronomical Society* 87: 209–239.
- Romanowicz B, Roult G, and Kohl T (1987) The upper mantle degree two pattern: Constraints from GEOSCOPE fundamental spheroidal mode eigenfrequency and attenuation measurements. *Geophysical Research Letters* 14: 1219–1222.
- Rosat S, Sato T, Imanishi Y, et al. (2005) High resolution analysis of the gravest seismic normal modes after the 2004 Mw = 9 Sumatra earthquake using superconducting gravimeter data. *Geophysical Research Letters* 32: L13304 (doi:10.1029/2005GL023128).
- Roult G (1974) Atténuation des ondes sismiques de très sasse fréquence. *Annales Geophysicae* 30: 141–167.
- Roult G and Clévédé E (2000) New refinements in attenuation measurements from free-oscillation and surface-wave observations. *Physics of the Earth and Planetary Interiors* 121: 1–37.
- Roult G and Romanowicz B (1984) Very long-period data from the GEOSCOPE network: Preliminary results on great circle averages of fundamental and higher Rayleigh and Love modes. *Bulletin of the Seismological Society of America* 74: 2221–2243.
- Roult G, Romanowicz B, and Jobert N (1986) Observations of departures from classical approximations on very long period GEOSCOPE records. *Annales Geophysicae* 4: 241–249.
- Roult G, Romanowicz B, and Montagner JP (1990) 3-D upper mantle shear velocity and attenuation from fundamental mode free oscillation data. *Geophysical Journal International* 101: 61–80.
- Russell DR, Herrmann RB, and Hwang H-J (1988) Application of frequency variable filters to surface-wave amplitude analysis. *Bulletin of the Seismological Society of America* 78: 339–354.
- Röhrbach W (1932) Über die dispersion seismischer Oberflächenwellen. *Zeitschrift für Geophysik* 8: 113–129.
- Sabra KG, Gerstoft P, Roux P, Kuperman WA, and Fehler MC (2005a) Surface wave tomography from microseisms in Southern California. *Geophysical Research Letters* 32: L14311 (doi:10.1029/2005GL023155).
- Sabre KG, Gerstoft P, Roux P, Kuperman WA, and Fehler MC (2005b) Extracting time-domain Greens function estimates from ambient seismic noise. *Geophysical Research Letters* 32: L03310 (doi:10.1029/2004GL021862).
- Sambridge M (1999) Geophysical inversion with a neighborhood algorithm. Part I: Searching a parameter space. *Geophysical Journal International* 138: 479–494.
- Savino J, Murphy A, Rynn JM, et al. (1972) Results from the high-gain long-period seismograph experiment. *Geophysical Journal of the Royal Astronomical Society* 31: 179–204.
- Schulte-Pelkum V, Earle PS, and Vernon FL (2004) Strong directivity of ocean-generated seismic noise. *Geochemistry Geophysics Geosystems* 5: Q03004 (doi:10.1029/2003GC000520).
- Schwab F and Kausel E (1976a) Quadripartite surface wave method: Development. *Geophysical Journal of the Royal Astronomical Society* 45: 231–244.
- Schwab F and Kausel E (1976b) Long-period surface wave seismology: Love wave phase velocity and polar phase shift. *Geophysical Journal of the Royal Astronomical Society* 45: 407–435.
- Shapiro NM and Campillo M (2004) Emergence of broadband Rayleigh waves from correlations of the ambient seismic noise. *Geophysical Research Letters* 31: doi:10.1029/2004GL019491.
- Shapiro NM, Campillo M, Paul A, Singh SK, Jongmans D, and Sanchez-Sesma J (1997) Surface-wave propagation across the Mexican volcanic belt and origin of the long-period seismic-wave amplification in the Valley of Mexico. *Geophysical Journal International* 128: 151–166.
- Shapiro NM, Campillo M, Stehly L, and Ritzwoller MH (2005) High-resolution surface-wave tomography from ambient seismic noise. *Science* 29: 1615–1617.
- Shapiro NM and Singh SK (1999) A systematic error in estimating surface-wave group-velocity dispersion curves and a procedure for its correction. *Bulletin of the Seismological Society of America* 89: 1138–1142.
- Shapiro NM and Ritzwoller MH (2002) Monte-Carlo inversion for a global shear-velocity model of the crust and upper mantle. *Geophysical Journal International* 151: 88–105.
- Selby ND and Woodhouse JH (2000) Controls on Rayleigh wave amplitudes: Attenuation and focusing. *Geophysical Journal International* 142: 933–940.

- Sharrock DS and Woodhouse JH (1998) Investigation of time dependent inner core structure by the analysis of free oscillation spectra. *Earth, Planets, and Space* 50: 1013–1018.
- Shearer P (1999) *Introduction to Seismology*, 260 pp. New York: Cambridge University Press.
- Simons FJ, van der Hilst RD, Montagner J-P, and Zielhuis A (2002) Multimode Rayleigh wave inversion for heterogeneity and azimuthal anisotropy of the Australian upper mantle. *Geophysical Journal International* 151: 738–754.
- Smith SW (1972) The anelasticity of the mantle. *Tectonophysics* 13: 601–622.
- Smith MF and Masters G (1989a) The effect of Coriolis coupling of free oscillation multiplets on the determination of aspherical Earth structure. *Geophysical Research Letters* 16: 263–266.
- Smith MF and Masters G (1989b) Aspherical structure constraints from free oscillation frequency and attenuation measurements. *Journal of Geophysical Research* 94: 1953–1976.
- Snieder R and Nolet G (1987) Linearized scattering of surface waves on a spherical Earth. *Journal of Geophysics* 61: 55–63.
- Song X (2000) Joint inversion for inner core rotation, inner core anisotropy, and mantle heterogeneity. *Journal of Geophysical Research* 105: 7931–7943.
- Song X and Richards PG (1996) Seismological evidence for differential rotation of the Earth's inner core. *Nature* 382: 221–224.
- Souriau A (1998) Earth's inner core – Is the rotation real? *Science* 281: 55–56.
- Souriau A and Souriau M (1983) Test of tectonic models by great circle Rayleigh waves. *Geophysical Journal of the Royal Astronomical Society* 73: 533–551.
- Stange S and Friederich W (1993) Surface wave dispersion and upper mantle structure beneath southern Germany from joint inversion of network recorded teleseismic events. *Geophysical Research Letters* 20: 2375–2378.
- Stutzmann É and Montagner JP (1993) An inverse technique for retrieving higher mode phase velocity and mantle structure. *Geophysical Journal International* 113: 663–683.
- Stutzmann É and Montagner JP (1994) Tomography of the transition zone from the inversion of higher-mode surface waves. *Physics of the Earth and Planetary Interiors* 86: 99–115.
- Su W-J, Dziewonski AM, and Jeanloz R (1996) Planet within a planet: Rotation of the inner core of Earth. *Science* 274: 1883–1887.
- Su W-J, Woodward RL, and Dziewonski AM (1994) Degree 12 model of shear velocity heterogeneity in the mantle. *Journal of Geophysical Research* 99: 6945–6980.
- Suda N, Nawa K, and Fukao Y (1998) Earth's background free oscillations. *Science* 279: 2089–2091.
- Takeuchi N, Geller RJ, and Cummins PR (2000) Complete synthetic seismograms for 3D heterogeneous Earth models computed using modified DMS operators and their applicability to inversion for Earth structure. *Physics of the Earth and Planetary Interiors* 119: 25–36.
- Tanaka S and Hamaguchi H (1997) Degree one heterogeneity and hemispherical variation of anisotropy in the inner core from PKPBC–PKPDF times. *Journal of Geophysical Research* 102: 2925–2938.
- Tanimoto T (2005) The ocean excitation hypothesis for the continuous oscillations of the Earth. *Geophysical Journal International* 160: 276–288.
- Tanimoto T and Alvizuri C (2006) Inversion of the HZ ratio of microseisms for S-wave velocity in the crust. *Geophysical Journal International* 165: 323–335.
- Tanimoto T, Um J, Nishida K, and Kobayashi N (1998) Earth's continuous oscillations observed on seismically quiet days. *Geophysical Research Letters* 25: 1553–1556.
- Thatcher W and Brune J (1969) Higher mode interference and observed anomalous apparent Love wave phase velocities. *Journal of Geophysical Research* 74: 6603–6611.
- Thomson DJ Spectrum estimation and harmonic analysis. *Proceedings of the IEEE* 70: 1055–1096.
- Toksoz MN and Anderson DL (1966) Phase velocity of long-period surface waves and structure of the upper mantle. *Journal of Geophysical Research* 71: 1649–1658.
- Trampert J and Spetzler J (2006) Surface wave tomography: Finite-frequency effects lost in the null space. *Geophysical Journal International* 164: 394–400.
- Trampert J and van Heijst H-J (2002) Global azimuthal anisotropy in the transition zone. *Science* 296: 1297–1299.
- Trampert J and Woodhouse JH (1995) Global phase velocity maps of Love and Rayleigh waves between 40 and 150 seconds. *Geophysical Journal International* 122: 675–690.
- Tromp J (1993) Support for anisotropy of the Earth's inner core from free oscillations. *Nature* 366: 678–681.
- Valette B and Lesage P (1992) Retrieving mean Earth models. *Conference on Mathematical Geophysics*, Taxco, Mexico.
- van der Lee S and Nolet G (1997) Upper mantle S velocity structure of North America. *Journal of Geophysical Research* 102: 22815–22838.
- van Heijst H and Woodhouse JH (1997) Measuring surface-wave overtone phase velocities using a mode branch stripping technique. *Geophysical Journal International* 131: 209–230.
- van Heijst H and Woodhouse JH (1999) Global high-resolution phase velocity distribution of overtone and fundamental-mode surface waves determined by mode-branch stripping. *Geophysical Journal International* 137: 601–620.
- Vig PK and Mitchell BJ (1990) Anisotropy beneath Hawaii from surface wave particle motion observations. *Pure and Applied Geophysics* 133: 1–22.
- Webb SC (1998) Broadband seismology and noise under the ocean. *Reviews of Geophysics* 36: 105–142.
- Widmer R (1991) *The Large-Scale Structure of the Deep Earth as Constrained by Free Oscillation Observations*. PhD Thesis, University of California San Diego, La Jolla, CA.
- Widmer R and Zürn W (1992) Bichromatic excitation of long-period Rayleigh and air waves by the Mount Pinatubo and El Chichón volcanic eruptions. *Geophysical Research Letters* 19: 765–768.
- Widmer R, Masters G, and Gilbert F (1992) Observably split multiplets – data analysis and interpretation in terms of large-scale aspherical structure. *Geophysical Journal International* 111: 559–576.
- Widmer-Schnidrig R (2002) Application of regionalized multiplet stripping to retrieval of aspherical structure constraints. *Geophysical Journal International* 148: 201–213.
- Wielandt E (1980) First-order asymptotic theory of the polar phase shift of Rayleigh waves. *Pure and Applied Geophysics* 118: 1214–1227.
- Wielandt E (1987) On the validity of the ray approximation for interpreting delay times. In: Nolet G (ed.) *Seismic Tomography*, pp. 85–98. Dordrecht: D. Reidel Publishing Company.
- Wielandt E (1993) Propagation and structural interpretation of non-plane waves. *Geophysical Journal International* 113: 45–53.
- Wielandt E and Schenk H (1983) On systematic errors in phase-velocity analysis. *Journal of Geophysics* 52: 1–6.
- Wilson T (1940) The Love waves of the South Atlantic earthquake of August 28, 1933. *Bulletin of the Seismological Society of America* 30: 273–301.
- Wong YK (1989) *Upper Mantle Heterogeneity From Phase and Amplitude Data of Mantle Waves*. PhD Thesis, Harvard University Cambridge, MA.

- Woodhouse JH (1980) The coupling and attenuation of nearly resonant multiplets in the Earth's free oscillation spectrum. *Geophysical Journal of the Royal Astronomical Society* 61: 261–283.
- Woodhouse JH (1983) The joint inversion of seismic wave forms for lateral variations in Earth structure and earthquake source parameters. In: Kanamori H and Boschi E (eds.) *Proceedings of the Enrico Fermi International School of Physics LXXXV*, pp. 336–397. Amsterdam: North Holland.
- Woodhouse JH (1988) The calculation of Eigenfrequencies and Eigenfunctions of the free oscillations of the Earth and the Sun. In: Doornbos DJ (ed.) *Seismological Algorithms, Computational Methods and Computer Programs*, pp. 321–370. London: Academic Press.
- Woodhouse JH and Dahlen FA (1978) The effect of a general aspherical perturbation on the free oscillations of the Earth. *Geophysical Journal of the Royal Astronomical Society* 53: 335–354.
- Woodhouse JH and Dziewonski AM (1984) Mapping the upper mantle-3-dimensional modeling of Earth structure by inversion of seismic waveforms. *Journal of Geophysical Research* 89: 5953–5986.
- Woodhouse JH and Giardini D (1985) Inversion for the splitting function of isolated low order normal mode multiplets. *Eos Transactions of the American Geophysical Union* 66: 300.
- Woodhouse JH, Giardini D, and Li X-D (1986) Evidence for inner core anisotropy from splitting in free oscillations data. *Geophysical Research Letters* 13: 1549–1552.
- Woodhouse JH and Girnius TP (1982) Surface waves and free oscillations in a regionalized earth model. *Geophysical Journal of the Royal Astronomical Society* 68: 653–673.
- Woodhouse JH and Wong YK (1986) Amplitude, phase and path anomalies of mantle waves. *Geophysical Journal of the Royal Astronomical Society* 87: 753–773.
- Woods MT, Lévéque J-J, Okal EA, and Cara M (1991) Two-station measurements of Rayleigh wave group velocity along the Hawaiian Swell. *Geophysical Research Letters* 18: 105–108.
- Yang X, Bondar I, Bhattacharyya J, et al. (2004) Validation of regional and teleseismic travel-time models by relocating ground-truth events. *Bulletin of the Seismological Society of America* 94: 897–919.
- Yomogida K (1985) Gaussian beams for surface waves in laterally slowly varying media. *Geophysical Journal of the Royal Astronomical Society* 82: 511–533.
- Yomogida K and Aki K (1987) Amplitude and phase data inversions for phase velocity anomalies in the Pacific ocean basin. *Geophysical Journal of the Royal Astronomical Society* 88: 161–204.
- Yoshizawa K and Kennett BLN (2002) Non-linear waveform inversion for surface waves with a neighbourhood algorithm; application to multimode dispersion measurements. *Geophysical Journal International* 149: 118–133.
- Yoshizawa K and Kennett BLN (2004) Multimode surface wave tomography for the Australian region using a three-stage approach incorporating finite frequency effects. *Journal of Geophysical Research* 109: doi:10.1029/2002JB002254.
- Yoshizawa K and Kennett BLN (2005) Sensitivity kernels for finite-frequency surface waves. *Geophysical Journal International* 162: 910–926.
- Yoshizawa K, Yomogida K, and Tsuboi S (1999) Resolving power of surface wave polarization data for higher order heterogeneities. *Geophysical Journal International* 138: 205–220.
- Zhang J, Song X, Li Y, Richards PG, Sun X, and Waldhauser F (2005) Inner core differential motion confirmed by earthquake waveform doublets. *Science* 309: 1357–1361.
- Zhou Y, Dahlen FA, Nolet G, and Laske G (2005) Finite-frequency effects in global surface-wave tomography. *Geophysical Journal International* 163: 1087–1111.
- Zielhuis A and Nolet G (1994) Shear wave velocity variations in the upper mantle. *Geophysical Journal International* 117: 695–715.
- Zürn W, Laske G, Widmer-Schnidrig R, and Gilbert F (2000) Observation of Coriolis coupled modes below 1 mHz. *Geophysical Journal International* 143: 113–118.
- Zürn W and Widmer R (1995) On noise reduction in vertical seismic records below 2 mHz using local barometric pressure. *Geophysical Research Letters* 22: 3537–3540.

Relevant Website

<http://mahi.ucsd.edu> – The Reference Earth Model Website (accessed Mar 2007).

1.04 Theory and Observations – Body Waves: Ray Methods and Finite Frequency Effects

J. Virieux, Université de Nice – Sophia Antipolis, Nice, France

G. Lambaré, École des Mines de Paris, Paris, France

© 2007 Elsevier B.V. All rights reserved.

1.04.1	Introduction	127
1.04.2	Ray Theory	130
1.04.2.1	Intuitive Approach	130
1.04.2.2	Elastodynamic Equations and Wave Equations	131
1.04.2.3	Asymptotic Ray Theory	132
1.04.2.4	Rays and Wave Fronts	132
1.04.2.5	Variational Approaches of Ray Tracing	133
1.04.2.6	Transport Equation	134
1.04.2.7	Acoustic and Elastic Ray Theory	135
1.04.2.8	Paraxial Ray Theory	136
1.04.2.9	Ray Tracing Tools	137
1.04.3	Rays at Interfaces	138
1.04.3.1	Boundary Conditions, Continuity, Reflection/Transmission Coefficients	138
1.04.3.2	Paraxial Conditions	139
1.04.4	Ray Seismograms	139
1.04.4.1	Classical Ray Seismograms	139
1.04.4.2	Seismograms by Summation on the Ray Field	139
1.04.4.2.1	WKBJ summation	139
1.04.4.2.2	Maslov summation	141
1.04.4.2.3	Gaussian beam summation	141
1.04.4.2.4	Coherent-state transformation technique	142
1.04.4.3	Geometrical Theory of Diffraction	143
1.04.5	Finite Frequency Effects	144
1.04.5.1	Ray + Born/Rytov Formulation	144
1.04.5.2	Ray + Kirchhoff Approximation	145
1.04.5.3	Finite Frequency Effects on Ray Functions	147
1.04.6	Conclusion	148
	References	150

1.04.1 Introduction

Since the first seismic signal (Figure 1) recorded at Potsdam (Germany) from an earthquake in Japan, accumulation of seismic data (as shown by the stack of thousand of records (Figure 2); Astiz *et al.*, 1996) illustrates the very special well-structured way waves propagate inside an Earth which is mainly stratified with depth. Various energy packets can be identified and tracked from one station to the other one. Where in depth these waves have been converted is always a difficult question to which seismologists are required to provide more and more precise answers.

Each seismic event generates several wavetrains well-identified on station records. In those traces, we may distinguish three characteristic timescales associated with three typical length scales. The source duration related to the duration of each wavelet comes from the seismic source extension from less than 1 km to more than 1000 km length. Time shifts between wavetrains are not only related to the velocity difference between P and S waves but also to distances between interfaces inside the Earth, which may range from tens of meters to thousands of kilometers. Finally, the recorded time window related to the volume investigated by waves which may range



Figure 1 First instrumental recording of seismic waves from a distant earthquake obtained by an horizontal pendulum, installed by von Reben Paschwitz in Potsdam (Germany), 15 min after the earthquake faulting occurred in Japan.

from the whole Earth (Figure 3) to the shallower layers in applied seismology. Systematic feature of seismograms comes from the relatively smooth variations of rheological parameters almost everywhere inside the Earth. This has been an important discovery and a great motivation for the development of instrumental seismology on the Earth. For comparison, when considering moonquakes (Latham *et al.*, 1971), no wavelets (except the first arrival signal) can be identified (Figure 4). If global seismology had been developed on a celestial body like the Moon, it would not have been so successful, and it would certainly not have known such a development as on the Earth, where the structure of seismic records is

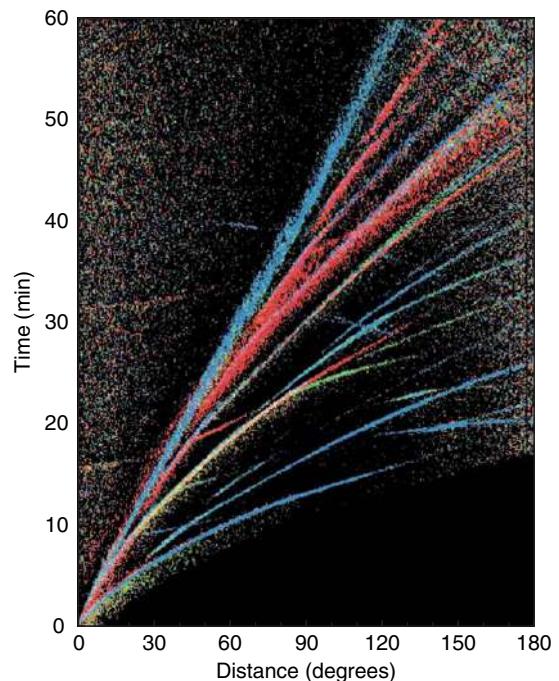


Figure 2 Stack of 30 000 seismograms over the global Earth. Color scale is for normalized energy amplitude and shows the temporal organization of seismograms (Astiz *et al.*, 1996). Courtesy of P. Shearer.

also intensively used at local scales for hydrocarbon reservoir exploration and characterization (Figure 5). From the theoretical point of view, the very special feature of seismograms on the Earth must be associated to the general relevance in the Earth of the asymptotic high-frequency approximations of seismic wave propagation, that is, seismic ray theory (Červený, 2001).

As geometrical optics, seismic ray theory is based on a rather intuitive physical notion but requires a quite sophisticated mathematical framework for consistent analysis. Behind this powerful interpretation tool are important practical consequences for our exploitation of the Earth's resources and for the mitigation of seismic risks, making worthwhile the effort for understanding ray approaches.

Ray theory has been thoroughly used for the analysis of seismic signals: for example, Lehman (1936) has discovered the solid core by using straight rays inside the Earth. Most of the present interpretation of body waves for structure analysis has involved essentially picked traveltimes on traces, although now we consider curved rays either in a vertically varying Earth (Bullen and Bolt, 1985; Aki and Richards, 1980) and more often in a laterally varying

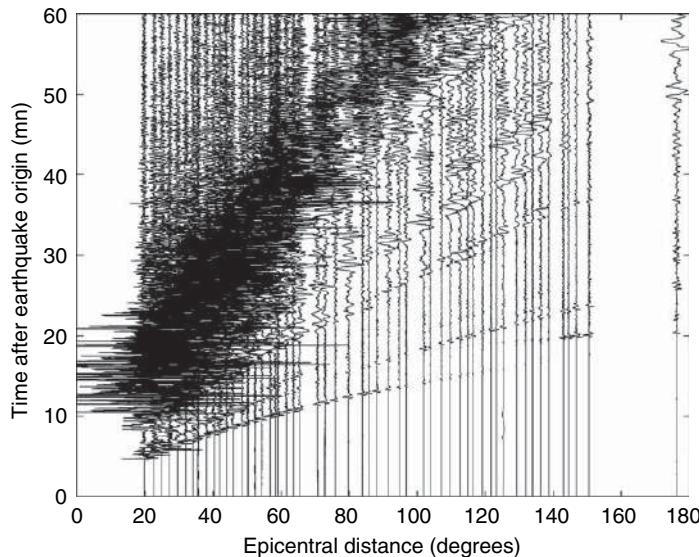


Figure 3 Records of the Indian earthquake ($M_m = 7.6$, 26 Jan. 2001) on the worldwide seismic network. For displacement, horizontal scale is 1 mm for 10° . Different phases as P , P_{diff} , PKIKP , PP , S , PS , PPS and SS are easily seen before the high-amplitude surface wavetrains. Courtesy of M. Vallée, IRD.

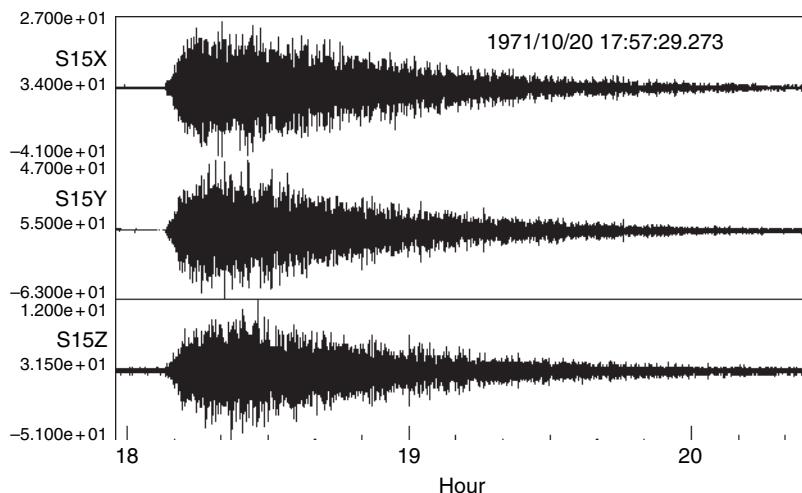


Figure 4 Seismograms produced by the impact of a meteorite on the station S15 of the seismic moon network installed by the Apollo 14 mission. The short-period three-component instrument records ground motion for more than 2 h and half with waves being scattered from the highly heterogeneous region near the Moon's surface. The coda is spindle shaped and analysis of the particle motions indicates that the energy is arriving from all the directions. These records differ from typical Earth ones for which coda is weaker than direct arrivals. The attenuation is much smaller on the Moon while diffraction is stronger, allowing strongly scattered waves to propagate in any direction during a quite significant time (Lay and Wallace, 1995, p. 107). Courtesy of J. Gagnepain-Beyneix, IPGP.

medium as our knowledge of the Earth's interior has increased from core–mantle boundary (Richards, 1973; Chapman and Orcutt, 1985; Kendall and Nangini, 1996; Lay and Garnero, 2004), mantle plumes (Montelli *et al.*, 2004a), and slab geometries (Biggaard *et al.*, 1998).

Meanwhile ray theory has been improved theoretically and numerically leading to a great variety of methods and algorithms considering various media (Červený, 2001; Chapman, 2004). Polarizations and even amplitudes have been estimated in more and more complex structures, and the addition of

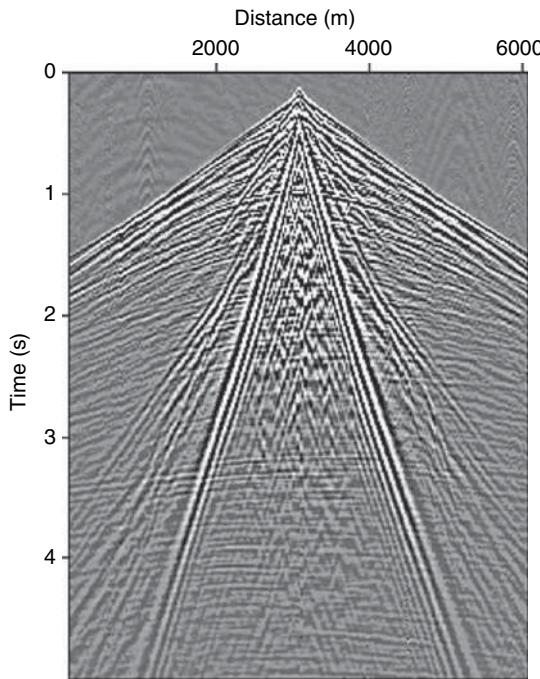


Figure 5 Common shot gather on land seismic acquisition: body wave and surface wave have been recorded on these vertical components. Reflection hyperbolae are visible as well and illustrate again the time organization of seismic traces. Courtesy of D. LeMeur, CGG.

anisotropic and attenuation effects has led to full waveform interpretation (Weber, 1988; Zhu and Chun, 1994b).

This chapter will present the seismic ray theory and its extensions. We will describe basic concepts of high-frequency approximations of seismic waves as well as limitations and features related to the practical finite frequency contents of seismic waves. Ray theory still appears as a very powerful interpretative tool and will remain a necessary and elegant alternative to brute force tools such as numerical wave propagation (Virieux, 1984, 1986), another necessary tool for seismogram interpretation.

1.04.2 Ray Theory

As has been said by Chapman (2004, p. 134), “Ray theory is the cornerstone of high-frequency, body-wave seismology.” This theory has also been applied to surface waves by considering evanescent waves along a given direction which is often the vertical axis for the Earth (Woodhouse, 1974; Burridge and

Weinberg, 1977). Excellent description of these approaches of horizontal rays and vertical modes may be found in Keilis-Borok (1989) or Dahlen and Tromp (1998). A compact review has been performed by Červený (2001, p. 229). Ray theory has been applied as well for moving media, especially fluids inside a waveguide (Abdullaev, 1993; Virieux *et al.*, 2004), giving the illustration of the broad application of this method.

1.04.2.1 Intuitive Approach

Let us assume an isotropic medium with smooth velocity heterogeneities with respect to the wavelength of the signal we want to propagate. Let us attach a Cartesian reference frame $(0, x, y, z)$ to this medium. Consider, at a given time t , a set of particles, at position $\mathbf{x} = (x, y, z)$, vibrating in phase on a smooth surface. We call this surface a wavefront. Particles on this wavefront have the same traveltimes, $T(\mathbf{x}) = T_0$. As time increases, the wavefront moves locally at speed $c(\mathbf{x})$ and the gradient $\nabla T(\mathbf{x})$ is orthogonal to the wavefront (Figure 6). Although the wavefront moves in one direction, local properties do not allow us to detect what is the direction which must be known from the previous position of the wavefront. Therefore, we must consider the square of the gradient which gives us the eikonal equation

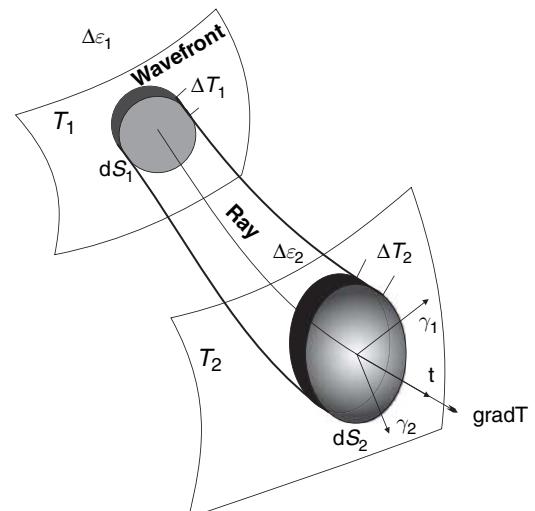


Figure 6 Ray tube geometry: rays are orthogonal to wavefronts in isotropic medium. Energy flows along rays. The local energy is preserved over an infinitesimal volume controlled by the local velocity. Polarizations of particle displacement are shown for both P and S waves.

$$(\nabla T)^2(\mathbf{x}) = \frac{1}{c^2(\mathbf{x})} \quad [1]$$

The gradient is called the slowness vector. In isotropic media, curves orthogonal to the wavefronts, that is, parallel to the slowness vector field, can be defined. We call them rays. Rays are very useful trajectories for calculating not only traveltime but also amplitude variations. Indeed, the vibration energy moves along the ray tube without any energy leaking (**Figure 6**). The energy over a small volume of length ΔT_1 crossing the wavefront T_1 through the surface dS_1 is related to the square of the amplitude A_1 through the expression: $d\varepsilon_1 = A_1^2 dS_1 / \Delta T_1$. The energy should be preserved at the wavefront T_2 which gives the following conservation of flux:

$$A^2(\mathbf{x}_1) \frac{dS(\mathbf{x}_1)}{c(\mathbf{x}_1)} = A^2(\mathbf{x}_2) \frac{dS(\mathbf{x}_2)}{c(\mathbf{x}_2)} \quad [2]$$

where two different points along the ray tube are denoted by \mathbf{x}_1 and \mathbf{x}_2 , and dS denotes the surface of the elementary orthogonal cross-sections of the ray tube. From this equation, applying the divergence theorem over an infinitesimal volume, we can obtain the local transport equation

$$2\nabla A(\mathbf{x}) \cdot \nabla T(\mathbf{x}) + A(\mathbf{x}) \nabla^2 T(\mathbf{x}) = 0 \quad [3]$$

The eikonal and transport equations are fundamental ingredients of ray theory and highlight required properties such as wavefront smooth spatial continuity as well as amplitude conservation along ray tubes. Unfortunately, failures of such properties exist quite often in the Earth (interfaces with sharp discontinuity of media properties, shadow zones where no rays are entering, caustics where rays cross each other, strong velocity gradients, etc.). We shall describe efforts to overcome these difficulties by introducing a more rigorous framework behind this intuitive ray concept.

1.04.2.2 Elastodynamic Equations and Wave Equations

Let us first consider wave propagation in elastic solid media without attenuation. For the vector displacement field $\mathbf{u}(\mathbf{x}, t)$ at the position \mathbf{x} for the time t , the linear elastodynamic equation can be expressed as

$$(c_{ijkl}(\mathbf{x}) u_{k,l}(\mathbf{x}, t))_j + f_i(\mathbf{x}, t) = \rho(\mathbf{x}) u_{i,n}(\mathbf{x}, t) \quad [4]$$

where $\mathbf{f}(\mathbf{x}, t)$ denotes the vector source field; $c_{ijkl}(\mathbf{x})$ the components of the stiffness tensor; and $\rho(\mathbf{x})$

the density. We use the Einstein convention for summation, boldface symbols for vector and tensor fields, and a comma between subscripts for spatial derivatives (e.g., $u_{i,j} = \partial u_i / \partial x_j$). For the pressure field $P(\mathbf{x}, t)$, the acoustic wave equation can be expressed as

$$(\rho^{-1}(\mathbf{x}) P_{,i}(\mathbf{x}))_i + f^p(\mathbf{x}, t) = \kappa(\mathbf{x}) P_{,nn}(\mathbf{x}, t) \quad [5]$$

where $f^p(\mathbf{x}, t)$ is the volumetric distribution of pressure source and the compressibility $\kappa(\mathbf{x})$ is the inverse of the bulk modulus $k(\mathbf{x})$. The particle displacement \mathbf{u} is deduced from $P = -k \nabla \cdot \mathbf{u}$, where the sign \cdot denotes the scalar product. When the density is constant, this so-called acoustic wave equation reduces to the scalar wave equation for the pressure field $w(\mathbf{x}, t)$ written as

$$\frac{1}{c^2(\mathbf{x})} w_{,nn}(\mathbf{x}, t) - w_{,ii}(\mathbf{x}, t) = f^w(\mathbf{x}, t) \quad [6]$$

where the speed is denoted by $c(\mathbf{x})$ and where the specific distribution of pressure source $f^w(\mathbf{x}, t)$ is equal to $f^p(\mathbf{x}, t) / \kappa(\mathbf{x})$. Some authors introduce first-order hyperbolic systems keeping both displacements/velocities and stresses/pressure as variables describing the motion (Chapman, 2004, p. 100).

Solving one of these equations in heterogeneous media could not be performed analytically and we either rely on numerical methods or on a specific description of approximate solutions. We shall consider a high-frequency asymptotic solution involving a traveltime function, an amplitude factor, and a source wavelet. Demonstrations could be performed either in the time or in the frequency domain: we select the second domain for easier notations.

The acoustic case is directly connected to our intuitive introduction of the eikonal and transport equations. For the isotropic elastic case, the elastic wavefield can be approximately separated into individual elementary waves. These individual waves, P and S waves, propagate independently in a smoothly varying structure, but their traveltimes are still controlled by eikonal equations, and their amplitudes by transport equations. Because construction of solutions in the elastic case is quite cumbersome, we shall rather consider from now on the scalar wave equation which captures numerous aspects of the acoustic and elastic cases. We shall mention a few specific considerations for the elastic isotropic and anisotropic cases, and few words will be said when considering attenuating media.

1.04.2.3 Asymptotic Ray Theory

For specific configurations known as canonical problems, one can get exact solutions of the wave equation. For an homogeneous medium with one speed, canonical solutions can be found as plane waves through separations of variables, or as Green's functions for a point source (Morse and Feshbach, 1953). The form of these exact solutions should also be valid at high frequency in other media when wavelengths are small compared with the propagation distances and medium heterogeneities. We can then guess probable forms of the solution, known mathematically as an ansatz and, then, find conditions for them in order to satisfy wave equations.

Fundamental discussions have occurred on ansatz structures with very sophisticated arguments for one form or the other, depending on the problem to be solved (Buldyrev and Molotkov, 1985; Kravtsov and Orlov, 1990; Červený, 2001). The simplest is the ray ansatz we shall introduce. One must be aware that the ansatz will only fit high-frequency contents of some specific canonical solutions. For example, the Green's function for a point source in a 2D medium exhibits low-frequency content that the high-frequency approximation will not reproduce (Virieux, 1996).

The ray ansatz we shall consider expresses the scalar wave in the frequency domain (Chapman, 2004, p. 137; Babić, 1956; Karal and Keller, 1959):

$$w(\mathbf{x}, \omega) = S(\omega) e^{i\omega T(\mathbf{x})} A_0(\mathbf{x}) \quad [7]$$

where the angular frequency is denoted ω and the source wavelet $S(\omega)$. The subscript zero in the amplitude $A_0(\mathbf{x})$ is related to this so-called zero-order approximation solution. Our conventions for the direct and inverse Fourier transforms of a time function $f(t)$ are $f(\omega) = \int_{-\infty}^{+\infty} dt f(t) e^{i\omega t}$ and $f(t) = 1/(2\pi) \int_{-\infty}^{+\infty} d\omega f(\omega) e^{-i\omega t}$. Smooth functions, traveltimes $T(\mathbf{x})$ and amplitude coefficient $A_0(\mathbf{x})$, are assumed to be independent of the frequency for the construction of an unique solution. We allow the amplitude coefficients to be complex but the traveltimes should be real. Specific extensions towards complex values of traveltimes may lead to new ways of computing seismograms (Felsen, 1984). Let us underline that this estimation should be summed up on the different wavefronts arriving at the position \mathbf{x} . The automatic determination of relevant wavefronts at a given receiver has been solved in a combinatorial exercise for multilayered media (Hron, 1972; Hron *et al.*, 1986) but remains a difficult task for an arbitrary inhomogeneous medium as discussed by Clarke (1993a, 1993b).

When introducing this ansatz in the scalar wave equation in the frequency domain away from the source zone, we obtain the following equation organized in simple frequency powers:

$$\omega^2 A_0(\mathbf{x}) \left[(\nabla T)^2(\mathbf{x}) - \frac{1}{c^2(\mathbf{x})} \right] + i\omega [2\nabla A_0(\mathbf{x}) \cdot \nabla T(\mathbf{x}) + A_0(\mathbf{x}) \nabla^2 T(\mathbf{x})] + \nabla^2 A_0(\mathbf{x}) = 0 \quad [8]$$

Because we are interested in high-frequency solutions, we may neglect the term in ω^0 and set to zero the two other terms in ω^2 and ω^1 , leading to eikonal [1] and transport [3] equations.

Further approximations may consider the influence of the neglected term when frequency is finite. Among these alternatives, we must quote the definition of the hypereikonal equation (Zhu, 1988; Biondi, 1992; Zhu and Chun, 1994a) where the eikonal is frequency dependent as are ray trajectories. A more formal description of the solution in negative power series of $-i\omega$ gives a solution with amplitude terms $A_k(\mathbf{x})$ verifying new transport equations (Červený, 2001, p. 549). As far as we know, only the A_1 term has been used practically for head waves modeling along interfaces (Červený and Ravindra, 1971; Hill, 1973; Thomson, 1990).

1.04.2.4 Rays and Wave Fronts

The eikonal equation is a nonlinear, partial differential equation of the first order belonging to the Hamilton–Jacobi variety (Kravtsov and Orlov, 1990), usually solved in terms of characteristics (Courant and Hilbert, 1966). The characteristics are 3D trajectories $\mathbf{x} = \mathbf{x}(\tau)$ verifying a set of ordinary differential equations (ODEs). If needed, traveltimes is integrated through quadratures along these trajectories called rays. For isotropic media, these rays are orthogonal to wavefronts, sometimes called isochrones. A nice tutorial on characteristics has been given by Bleistein (1984, chapter 1) in relation with differential geometry.

Techniques exist to compute directly wavefronts mainly based either on the Huygens principle (the new wavefront is the envelope of spheres drawn from an initial wavefront with local velocity) or on ray tracing (short ray elements from an initial wavefront allow the construction of the new wavefront) (Figure 7). Solving directly the eikonal equation for the first-arrival traveltimes turns out to be performed quite efficiently: finite difference (FD) method has been proposed by Vidale (1988, 1990) and numerous more or less precise algorithms have been designed for

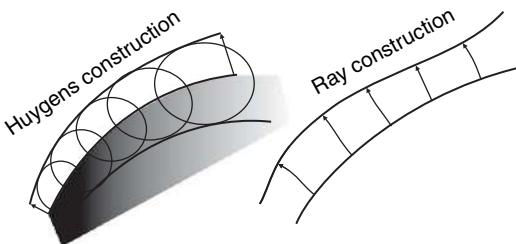


Figure 7 Computation of wavefronts. On the left panel, the construction is based on the Huygens principle, where the new wavefront is the envelope of spheres drawn from an initial wavefront with local velocity. The direction is unknown locally. On the right panel, the construction is based on ray tracing equation, where short ray segments are drawn from an initial wavefront to the new one. The local direction is known by the ray orientation.

both isotropic and anisotropic media (Podvin and Lecomte, 1991; Lecomte, 1993; Eaton, 1993). FD techniques such as the fast marching method (Sethian and Popovici, 1999) may also account for large velocity gradients. Techniques for solving these types of Hamilton–Jacobi equations have been developed by Fatemi *et al.* (1995) and Sethian (1999) for various problems. Combining ray tracing and FD methods may lead to multivalued traveltimes estimations as suggested by Benamou (1996) or Abgrall and Benamou (1999). These techniques have been very attractive in many applications such as first-arrival traveltimes delay seismic tomography because they always provide a trajectory connecting the source and the receiver and, therefore, a synthetic traveltimes whatever is the precision on it. When inverting a huge amount of data, a few miscomputed traveltimes will not affect the tomographic inversion (Benz *et al.*, 1996; Le Meur *et al.*, 1997). These techniques have also been thoroughly used for 3-D reflection seismic imaging (Gray and May, 1994).

The characteristic system of nonlinear first-order partial differential equations (eqn [1]) consists of seven equations in a 3-D medium connecting the position \mathbf{x} , the slowness vector \mathbf{p} , and the travel time T , which are very similar to dynamic particle equations of classical mechanics (Goldstein, 1980):

$$\begin{aligned} \frac{dx_i}{d\tau} &= \frac{\partial \mathcal{H}}{\partial p_i} \\ \frac{dp_i}{d\tau} &= -\frac{\partial \mathcal{H}}{\partial x_i}, \quad i = 1, 2, 3 \\ \frac{dT}{d\tau} &= p_k \frac{\partial \mathcal{H}}{\partial p_k} \end{aligned} \quad [9]$$

where the variable τ defined as $d\tau = dT / (p_k \partial \mathcal{H} / \partial p_k)$ depends on the selected form of the function $\mathcal{H}(\mathbf{x}, \mathbf{p})$. The independent variables are position \mathbf{x} and slowness vector \mathbf{p} , defining a 6-D space, called phase space, on which the constant Hamiltonian defines an hypersurface, also called a Lagrangian manifold (Lambaré *et al.*, 1996).

1.04.2.5 Variational Approaches of Ray Tracing

The ray equations can also be considered in the framework of variational approaches where Lagrangian and Hamiltonian formulations reveal their fruitfulness. The choice of the following Hamiltonian $\mathcal{H}(\mathbf{x}, \mathbf{p}) = 1/2[\mathbf{p}^2 - 1/c^2(\mathbf{x})]$ leads to the simplest differential system to be solved with a sampling variable equal to $d\tau = dT/c^2(\mathbf{x})$ while the Hamiltonian $\mathcal{H}(\mathbf{x}, \mathbf{p}) = 1/2c^2(\mathbf{x})\mathbf{p}^2$ has the traveltimes for sampling variable τ along rays, making the third equation of the system [9] automatically verified. These choices seem to be quite natural ones especially for anisotropic media because, only if the Hamiltonian is of second degree in slowness, Lagrangian and Hamiltonian may be related by the Legendre transform defined as

$$\mathcal{L}(\mathbf{x}, \dot{\mathbf{x}}) = \mathbf{p} \cdot \dot{\mathbf{x}} - \mathcal{H}(\mathbf{x}, \mathbf{p}) \quad [10]$$

where $\dot{\mathbf{x}}$ denotes $d\mathbf{x}/d\tau$. The Lagrangian, defined in the 3-D space of position \mathbf{x} , verifies the Euler–Lagrange equations which are of second order:

$$\frac{d}{dT} \left(\frac{\partial \mathcal{L}}{\partial \dot{x}_i} \right) - \frac{\mathcal{L}}{\partial x_i} = 0 \quad [11]$$

Its integral over the ray path is stationary (Hamilton's principle). The traveltimes is given by the integral

$$\begin{aligned} T(\mathbf{x}) - T_0(\mathbf{x}) &= \int_{\tau_0}^{\tau} (\mathcal{L}(\mathbf{x}, \dot{\mathbf{x}}) + \mathcal{H}(\mathbf{x}, \mathbf{p})) d\tau = \int_{\mathbf{x}_0}^{\mathbf{x}} \mathbf{p} \cdot d\mathbf{x} \\ &= \int_{\mathbf{x}_0}^{\mathbf{x}} \frac{1}{c(\mathbf{x})} ds \end{aligned} \quad [12]$$

where s denotes the curvilinear abscissa. This last integral is stationary for fixed \mathbf{x}_0 and \mathbf{x} trajectories, which is the reduced least action principle of mechanics, often called Maupertuis–Euler–Lagrange–Jacobi principle (Goldstein, 1980; Arnold, 1976), or equivalently the Fermat principle in optics.

When the Hamiltonian depends explicitly on the sampling parameter, we may consider the least action principle related to the Poincaré–Cartan invariant. This is the case for the atmosphere where the speed is

time dependent (Abdullaev, 1993). The augmented time-space phase space $2n+1$ where the space dimension is denoted by n is always an odd space which has been investigated by many mathematicians as famous as H. Poincaré or H Cartan using differential geometry techniques. When the Hamiltonian $\mathcal{H}(\mathbf{x}, \mathbf{p})$ does not depend explicitly on time, the dimension of the chosen phase space may be reduced by two (Arnold, 1976, p. 240); as an example, only four ODEs have to be solved in a 3-D medium (Červený, 2001, p. 107).

Although one might not find these identifications between different theoretical formulations necessary, we shall borrow, from mechanics and optics, well-designed tools for performing ray tracing: as an example, mechanics of small vibrations or equivalently Gauss optics will open a road for performing efficiently ray tracing in the vicinity of an already traced ray, on which topic we shall focus in the next paragraph. This example illustrates the usefulness of this excursion into differential geometry, which has deep roots in physics (Goldstein, 1980, p. 489).

The Fermat principle, its minimum time aspect, plays an important role for the computations of traveltimes when considering first arrival times only. Finding the shortest path between the source and the receiver leads to network ray tracing. It may be based on graph theory applied to a grid of points with connections between them making a network and related to the well-known travel man problem. The connection between two grid points is the traveltime between these two points. A very efficient algorithm has been proposed by Dijkstra (1959), and various implementations and modifications have been performed in seismology (Moser *et al.*, 1992a). One must be aware that this technique leads to rays, while solving first-arrival times through FD eikonal approaches leads to traveltimes. Klímeš and Kvaskička (1994) have shown that actual algorithms give smaller errors in time estimation for the network approach than for eikonal discrete solvers previously considered. Drawing rays from the time grid in the eikonal approach is possible and will certainly allow accurate recomputation of traveltimes (Latorre *et al.*, 2004) as bending rays between source and receiver will improve precision for network approach. Very active algorithmic designing (Pica, 1997, 1998; Zhang *et al.*, 2005) with a high degree of precision of both trajectories and traveltimes may replace, in the near future, fast but less precise tools for locating earthquakes (Moser *et al.*, 1992b; Lomax *et al.*, 2000; Font *et al.*, 2004) or for seismic travelttime tomography (Benz *et al.*, 1996; Le Meur *et al.*, 1997).

1.04.2.6 Transport Equation

When we consider the transport equation, we see that the amplitude estimation is linked to the traveltime field. Multiplying the transport equation by the complex conjugate of the assumed nonzero amplitude $A_0^*(\mathbf{x})$, we obtain the local property $\nabla \cdot (A_0^*(\mathbf{x})A_0(\mathbf{x})\nabla T(\mathbf{x})) = 0$. By following backwards our intuitive presentation, we end up with the description of the amplitude evolution expressed as

$$A_0(\mathbf{x}_2) = A_0(\mathbf{x}_1)\sqrt{\frac{c^2(\mathbf{x}_2)\mathcal{J}_T(\mathbf{x}_1)}{c^2(\mathbf{x}_1)\mathcal{J}_T(\mathbf{x}_2)}} \quad [13]$$

where the position \mathbf{x}_1 (resp. \mathbf{x}_2) is implicitly defined by the sampling parameter time T_1 (resp. T_2), and where the elementary surface dS is estimated through geometrical spreading \mathcal{J}_T . This geometrical spreading factor is obtained by looking at the wavefront evolving inside a ray tube defined by neighboring rays with slightly different initial conditions. By noting two variables γ_1 and γ_2 related to the ray position at time T_1 parametrizing the wavefront and orthogonal to the wavefront normal (Figure 6), the geometrical spreading is defined as the Jacobian

$$\mathcal{J}_T = \left| \frac{\partial(x, y, z)}{\partial(T, \gamma_1, \gamma_2)} \right| \quad [14]$$

from which one can see the dependence of the geometrical spreading on the sampling parameter (Červený, 2001, p. 215).

The scalar wave field $w(\mathbf{x}, \omega)$ may then be written as

$$w(\mathbf{x}, \omega) \approx S(\omega)\phi_w(\gamma_1, \gamma_2)\sqrt{\frac{c^2(\mathbf{x})}{\mathcal{J}_T(\mathbf{x})}}e^{i\omega T(\mathbf{x})} \quad [15]$$

where the expression $S(\omega)$ denotes the signature of the source. The radiation pattern $\phi_w(\gamma_1, \gamma_2)$ must be found by matching this asymptotic solution and a canonical solution as the exact solution for a local homogeneous medium around the source (γ_1 and γ_2 depend on \mathbf{x}). We shall postpone this estimation for the computation of seismograms.

Points along the ray where the Jacobian vanishes are called caustic points. Caustic points of first order, when the rank of the Jacobian matrix [14] is equal to two, make the ray tube shrink into a line. These points create caustic surfaces that are envelopes of rays classified into folds, cusps, and swallowtails using a terminology related to catastrophic theory (Gilmore, 1981; Brown and Tappert, 1987). Caustic points of second order, when the rank is equal to one,

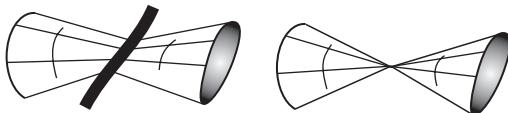


Figure 8 Points along the ray where the Jacobian [14] vanishes are called caustic points. For caustic points of first order (left), the rank of the Jacobian matrix [14] is two and the ray tube shink into a line. For caustic points of second order (right), the rank of the Jacobian matrix [14] is one and the point is called a focus point.

are often called focus points (Figure 8). As the ray crosses a caustic, the Jacobian changes its sign and the phase suffers a negative shift $-\pi/2$ for a first-order caustic and $-\pi$ for a second-order caustic. This shift is estimated through matching different asymptotic solutions (Ludwig, 1966). The phase shift is cumulative along the ray as we cross caustics. The associated index, called KMAH index as proposed by Ziolkowski and Deschamps (1984) for acknowledging contributions of JB Keller, VP Maslov, V Arnold, and L Hörmander, may jump by one or two depending on the change of rank of the Jacobian. The scalar wavefield expression is now

$$w(\mathbf{x}, \omega) \approx S(\omega)\phi_w(\gamma_1, \gamma_2) \times \sqrt{\frac{c^2(\mathbf{x})}{|\mathcal{J}_T(\mathbf{x})|}} e^{i\omega T(\mathbf{x})} e^{-i(\frac{\pi}{2})\text{KMAH}(\mathbf{x})} \quad [16]$$

1.04.2.7 Acoustic and Elastic Ray Theory

When considering the isotropic acoustic and elastic cases, very similar eikonal and transport equations can be derived. Let us first consider the acoustic equation where the density may vary. The eikonal equation is the same as for the scalar wave while the transport equation is

$$2\nabla T \cdot \nabla \left(\frac{A_0^{\text{acous}}}{\sqrt{\rho}} \right) + \frac{A_0^{\text{acous}}}{\sqrt{\rho}} \nabla^2 T = 0 \quad [17]$$

which is essentially the same equation as for the scalar wave when considering $A_0^{\text{acous}}(\mathbf{x})/\sqrt{\rho(\mathbf{x})}$. Therefore, we can write the pressure as

$$P_0(\mathbf{x}, \omega) \approx S(\omega)\phi_P(\gamma_1, \gamma_2) \times \sqrt{\frac{\rho(\mathbf{x})c^2(\mathbf{x})}{|\mathcal{J}_T(\mathbf{x})|}} e^{i\omega T(\mathbf{x})} e^{-i(\frac{\pi}{2})\text{KMAH}(\mathbf{x})} \quad [18]$$

from which one can deduce the asymptotic form of the particle displacement in the acoustic case:

$$\mathbf{u}_0(\mathbf{x}, \omega) \approx S_u(\omega)\mathbf{e}(\mathbf{x})\phi_P(\gamma_1, \gamma_2) \times \sqrt{\frac{1}{\rho(\mathbf{x})|\mathcal{J}_T(\mathbf{x})|}} e^{i\omega T(\mathbf{x})} e^{-i(\frac{\pi}{2})\text{KMAH}} \quad [19]$$

where the vector \mathbf{e} denotes the normalized polarization of the wave (orthogonal to wavefront), and where S_u is the displacement signature, which can be directly obtained from the pressure signature S .

Without increasing the complexity of notation, we may consider the general anisotropic case for elastic wave propagation. The wavefield is now a vector field and the polarization has to be considered (Červený, 2001). Eikonal equations are defined by

$$G_m(\mathbf{x}, \mathbf{p}) = 1, m = 1, 2, 3 \quad [20]$$

where G_m are the eigenvalues of the 3×3 Christoffel matrix defined by

$$\Gamma_{ik}(\mathbf{x}, \mathbf{p}) = \frac{c_{ijkl}}{\rho}(\mathbf{x})p_j p_l \quad [21]$$

The polarization vectors are the corresponding eigenvectors and it can be shown that associated amplitudes still satisfy some scalar transport equation involving the geometrical spreading along the rays (Červený, 2001, p. 60).

For the isotropic case, two identical eigenvalues $G_1(\mathbf{x}, \mathbf{p}) = G_2(\mathbf{x}, \mathbf{p}) = \beta^2(\mathbf{x})\mathbf{p}^2$ give two polarizations for the shear wave speed $\beta(\mathbf{x})$ of S waves, while the third eigenvalue $G_3(\mathbf{x}, \mathbf{p}) = \alpha^2(\mathbf{x})\mathbf{p}^2$ is related to the compressional wave speed $\alpha(\mathbf{x})$ of P waves. The corresponding eigenvector $\mathbf{g}_3(\mathbf{x}, \mathbf{p})$ is simply orthogonal to the wavefront. Orthogonal eigenvectors $\mathbf{g}_1(\mathbf{x}, \mathbf{p})$ and $\mathbf{g}_2(\mathbf{x}, \mathbf{p})$, corresponding to shear waves, may be estimated through the differential equation

$$\frac{dg_i}{dT} = (\mathbf{g}_i(\mathbf{x}, \mathbf{p}) \cdot \nabla \beta(\mathbf{x}))\mathbf{g}_3(\mathbf{x}, \mathbf{p}) \quad [22]$$

where $i = 1, 2$ (Chapman, 2004, p. 181).

For the anisotropic case, we must consider qS_1 and qS_2 on one side and qP on the other side. We are often unable to obtain explicitly eigenvalues for the anisotropic case while we can achieve that for the elastic case (Červený, 2001, p. 62). Moreover, propagations of qS_1 and qS_2 must be considered together because of possible shear singularities (Červený, 2001, p. 512). The anisotropic elastic case follows the same general scheme but also exhibits some important particularities. For example, rays are not orthogonal to isochrones. Amplitude still satisfies some scalar transport equation involving estimation of geometrical spreading along rays (Červený, 2001).

1.04.2.8 Paraxial Ray Theory

The ray tube can be estimated by tracing neighboring rays which must be kept near the studied ray. Therefore, small perturbation approach known as paraxial ray tracing should be preferred. One must consider that the paraxial ray is only sensitive to velocity/slowness variations (as well as spatial derivatives) on the central ray: it may deviate from a neighboring ray which samples velocity variations differently (Figure 9). Around a given central ray, the perturbation $\delta\mathbf{y}' = (\delta\mathbf{x}, \delta\mathbf{p})$ of both the position and the slowness vector follows, to the first order, the linear ordinary differential system:

$$\frac{d\delta\mathbf{y}}{dT} = \begin{pmatrix} \nabla_{\mathbf{p}} \nabla_{\mathbf{x}} \mathcal{H}_0 & \nabla_{\mathbf{p}} \nabla_{\mathbf{p}} \mathcal{H}_0 \\ -\nabla_{\mathbf{x}} \nabla_{\mathbf{x}} \mathcal{H}_0 & -\nabla_{\mathbf{x}} \nabla_{\mathbf{p}} \mathcal{H}_0 \end{pmatrix} \delta\mathbf{y} \quad [23]$$

where the Hamiltonian \mathcal{H} has a subscript zero because it is evaluated on the central ray regardless of the perturbation vector $\delta\mathbf{y}$ (Figure 9). This linear system could be solved following the standard propagator formulation introduced by Gilbert and Backus (1966) in seismology, while Farra and Madariaga (1987) emphasized the Hamiltonian formulation initially introduced by Backus (1964) and Burridge (1976). In this approach, the propagator $P(T, T_0)$ links $\delta\mathbf{y}$ at times T and T_0 through

$$\delta\mathbf{y}(T) = P(T, T_0)\delta\mathbf{y}(T_0) = \begin{pmatrix} P_{xx} & P_{xp} \\ P_{px} & P_{pp} \end{pmatrix} \delta\mathbf{y}(T_0) \quad [24]$$

For example, the sub-matrix P_{xp} contains partial derivatives of the position \mathbf{x} with respect to the slowness vector $\mathbf{p}_0 = \mathbf{p}(T_0)$, which describes the geometrical spreading from a point source and will give us an easy way for computing the cross-sectional area or for caustics detection. In practice, the 6×6 propagator could be reduced to a 4×4 propagator depending on the problem at hand (Červený, 2001; Farra and Madariaga, 1987; Virieux and Farra, 1991). Symplectic symmetries are very important both from the theoretical point of view and from the practical point of view because rays can be traced in either direction without the need for inverting a 6×6 matrix (Luneberg, 1964; Červený, 2001; Chapman, 2004). We have the following relation:

$$P^{-1}(T, T_0) = P(T_0, T) \quad [25]$$

from which one can deduce the so-called Luneberg relations in optics or Poisson and Lagrange brackets of classical mechanics (Goldstein, 1980). Initial values are defined by

$$P(T_0, T_0) = I_d \quad [26]$$

where I_d is the identity matrix. For further discussions, the reader is referred to Červený (2001) and Chapman (2004). One must remember that the traveltime function is expanded to the second-order terms when considering this paraxial theory. In the

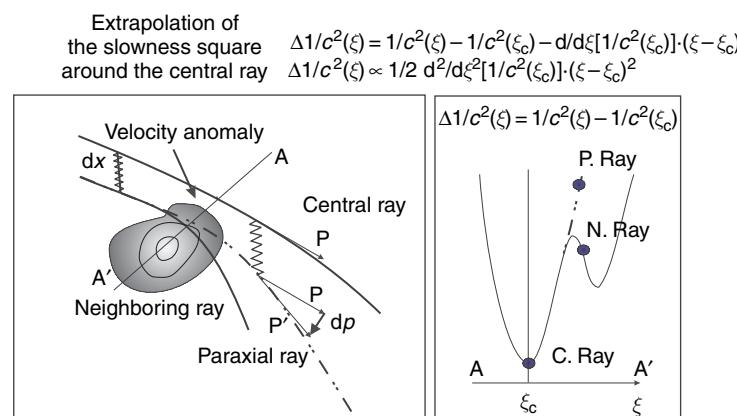


Figure 9 Paraxial ray tracing. The left panel shows the central ray as well as the paraxial ray deduced from the velocity anomaly felt by the central ray as symbolized by a spring. Therefore, the paraxial ray is different from a neighboring ray. The right panel shows the difference between the square of the slowness $1/c^2$ in the medium and the parabolic extrapolation of the square of the slowness from the central ray across the section AA'. The true profile shown as a continuous line is felt by the neighboring ray while the approximate parabolic profile, expanded from the central ray and shown by a dotted line when away from the true profile, controls the paraxial ray.

configuration space, around a given ray position $(\mathbf{x}_0, \mathbf{p}_0)$, this leads to the general expression:

$$\begin{aligned} T(\mathbf{x}, \mathbf{p}_0) = & T(\mathbf{x}_0, \mathbf{p}_0) + \frac{\partial T}{\partial \mathbf{x}}(\mathbf{x}_0, \mathbf{p}_0) \delta \mathbf{x} \\ & + \frac{1}{2} \delta \mathbf{x}' \mathcal{M}(\mathbf{x}_0, \mathbf{p}_0) \delta \mathbf{x} \end{aligned} \quad [27]$$

where the curvature matrix \mathcal{M} , a real matrix in classical ray theory, can be constructed from paraxial quantities, since we have

$$\begin{aligned} \mathcal{M}(\mathbf{x}_0, \mathbf{p}_0) = & \left(P_{xx} \frac{\partial \mathbf{x}}{\partial \gamma_1 \gamma_2 T} + P_{xp} \frac{\partial \mathbf{p}}{\partial \gamma_1 \gamma_2 T} \right) \\ & \times \left(P_{px} \frac{\partial \mathbf{x}}{\partial \gamma_1 \gamma_2 T} + P_{pp} \frac{\partial \mathbf{p}}{\partial \gamma_1 \gamma_2 T} \right)^{-1} \end{aligned} \quad [28]$$

where γ_1 and γ_2 are two ray parameters describing a two orthonormal system of rays, that is, a fan of rays (Červený, 2001, p. 235). This overcomplete expansion may be carried out on a subset of perturbations and in different coordinate systems as we shall see later on. The ray-centered one is often used in practice. We must emphasize that solutions of paraxial equations are coordinate-dependent while solutions of ray equations are coordinate independent but, as we move towards the central ray, paraxial quantities have similar infinitesimal behavior. Ray coordinates and paraxial ray quantities must verify the eikonal equations and perturbed eikonal equations if we want to consider them as rays or paraxial rays (Farra and Madariaga, 1987).

In seismology, we have not yet tackled theories beyond the paraxial one as already performed in optics as the geometrical theory of aberrations (Born and Wolf, 1980, chapter 5) where third-order terms around a given ray are considered. These approaches were often developed for homogeneous media, and have strong relations with finite-frequency effects and diffraction phenomena we shall consider latter on. Note that paraxial ray theory is also very useful for introducing perturbations of the velocity field. Applications in fast ray tracing (Virieux, 1991; Farra, 1990, 2005; Pšenčík and Farra, 2005) and Fréchet derivatives estimations in tomographic applications (Billette and Lambaré, 1998) have been proposed.

1.04.2.9 Ray Tracing Tools

Both ray and paraxial ray equations, which are ODEs, can be solved by numerical tools using Runge–Kutta (RK) of specified order or Predictor–Corrector (PC) schemes (Press *et al.*, 1994, chapter 16). Initial boundary problems, where both initial position and initial

slowness (i.e., six initial values) are specified, can be efficiently solved. Because we have a first integral of these equations, which is the Hamiltonian/Eikonal value, we may efficiently avoid Gear-like methods (Press *et al.*, 1994, p. 739) and check accuracy at each integration step by estimating the eikonal constant (Virieux and Farra, 1991). Of course, if we use the reduced Hamiltonian system, we lose this first integral at the benefit of fewer variables to be integrated. Although PC schemes are far more superior than RK schemes (only one spatial derivative to be estimated at each integration step whatever the order of precision), we rely essentially on the latter in seismology because it is easy to implement considering its self-starting property. Paraxial equations are linear equations and could be solved with quite significantly coarser integration steps than ray equations. They may be solved in a second step once rays have been found and may well compete with integral formulations of propagator matrices. Other strategies based on analytical solutions inside each cell of a mesh have been considered although efficiency is effective only when simple coarse discretization is performed (Červený, 1985; Chapman, 1985; Farra, 1990; Virieux, 1991; Körnig, 1995).

An order of magnitude more difficult is the two-point ray tracing problem where rays between a couple (source/receiver) have to be estimated (Červený *et al.*, 1977; Sambridge and Kennett, 1990; Virieux and Farra, 1991; Červený, 2001). In the frame of ray tracing by rays, we may consider three kinds of methods for making the ray converge to the receiver. The shooting method corrects an initial value problem until the ray hits the receiver. How to estimate the new initial slowness relies on many different numerical strategies linked to root solvers (Press *et al.*, 1994): the paraxial ray turns out to be the Newton procedure (Virieux *et al.*, 1988). The bending method deforms an already-specified curve connecting the source and the receiver: the search is essentially performed in the spatial domain (Pereyra *et al.*, 1980; Um and Thurber, 1987; Pereyra, 1992; Farra, 1992) where each node along the trajectory is perturbed until we may consider it as a ray. The continuation method is based on rays connecting the source and the receiver for rather simple velocity structures for which one may find easily the connecting ray. The velocity field is then deformed until it matches the true velocity field (Keller and Perozzi, 1983; Snieder and Spencer, 1993).

We may find these tracing techniques quite inefficient if one has to span the entire medium

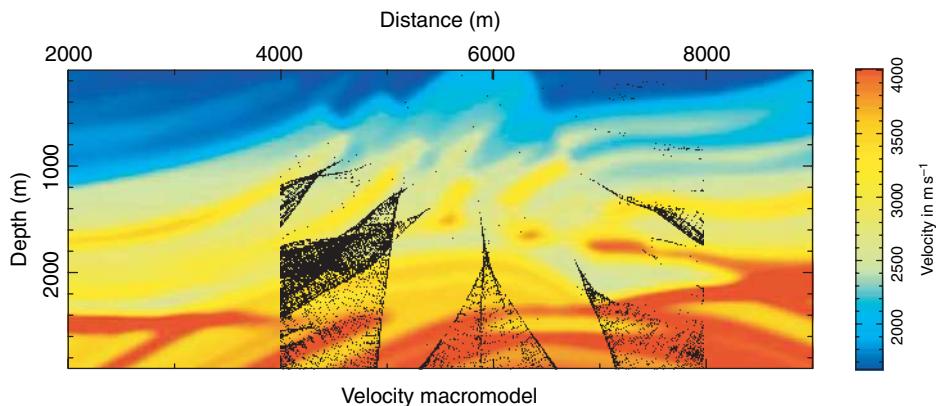


Figure 10 Wavefront construction with a uniform ray density criterion in the smooth Marmousi model (Thierry *et al.*, 1999b). Upgoing rays have been eliminated.

with many receivers. Another strategy is the ray tracing by wavefronts where we perform ray tracing from an already evaluated wavefront (Figure 7) (Vinje *et al.*, 1993, 1996a, 1996b). When ray density becomes too high, we may decimate rays; when ray density becomes too low, we may increase the number. Adaptative techniques have been developed and paraxial information may help such strategy of fixing ray density according to ray curvature in the phase space (Lambaré *et al.*, 1996; Lucio *et al.*, 1996) (Figure 10). Of course, the entire medium is sampled which may be a quite intensive task compared to the 1-D sampling performed by a single ray. Unfortunately, for multivalued estimations of time and amplitude, this is up to now the unique solution while, for first-arrival computations, we may have other efficient numerical techniques (see the previous section).

1.04.3 Rays at Interfaces

Up to now, we have considered media without any abrupt change of properties. If there is a sharp contrast, ray theory fails. All that we have seen until now was described for media without discontinuities. “If the medium contains interfaces, i.e. discontinuities in the material properties, density or elastic parameters, then the ray theory solution breaks down due to discontinuities in the solution or its derivatives. It is then necessary to impose the boundary conditions on the solution at the interface before continuing the ray solution.” (Chapman, 2004, p. 198).

In the context of the high-frequency approximation wavetrains arriving on an interface can be

viewed as plane waves hitting a flat interface. Consequently, many features of plane waves can be generalized to ray theory when dealing with interfaces. Because many textbooks (Aki and Richards, 1980; Kennett, 1983; Červený *et al.*, 1977; Červený, 2001; Chapman, 2004) have described these features in great details, we shall only outline specific features important for rays.

1.04.3.1 Boundary Conditions, Continuity, Reflection/Transmission Coefficients

As soon as the ray hits an interface, we must estimate quantities as times, slowness vectors, amplitudes and consider possible converted rays as reflected or transmitted rays. Continuity of traveltimes leads to the Snell–Descartes law, which states that the tangent slowness component is preserved at the interface. This means that the transmitted wavefront is moving locally at the same speed as the incident and reflected wavefronts along the interface.

Energy conservation goes through continuity of stresses and displacements at the hit point on the interface. “In the seismic ray method, the reflection/transmission coefficients can be locally applied even to a nonplanar wave, incident at a curved interface separating two inhomogeneous anisotropic media.” (Červený, 2001). Although these coefficients, called Zoeppritz coefficients, are quite well known (Aki and Richards, 1980; Červený, 2001), let us mention recent results for viscoelastic anisotropic media (Červený and Pšenčík, 2005a, 2005b).

Whatever the formulas to be used, we must stress that slowness components play a key role and that one should avoid headaches related to multivalued

trigonometric functions when implementing numerical tools related to interface conversions.

A very complementary point of view has been proposed for first-arrival Eikonal solvers. As the wavefront computed by any eikonal solver hits the interface, one may evaluate traveltimes onto the interface and restart the eikonal solver for either reflection or transmission (Rawlinson and Sambridge, 2004). Of course, only single-valued traveltime computations may be considered.

1.04.3.2 Paraxial Conditions

When dealing with paraxial rays at interfaces, one must consider continuity of traveltimes up to second-order derivatives. This continuity is necessary for starting the transmitted or reflected paraxial rays. This second-order continuity requires estimations of curvature of the incident wave, of the interface, and of the converted wave. Pure differential geometry tools have been used by Popov and Pšenčík (1978) while Farra *et al.* (1989) have explicated a more tractable deduction of this second-order continuity, thanks to the Hamiltonian formulation.

1.04.4 Ray Seismograms

When properties of the medium vary smoothly with respect to the characteristic wavelengths of the propagating wavetrain, source signature $S(t)$ is transported everywhere with time shift related to traveltime. It is scaled by an amplitude factor and, eventually for the elastic case, polarized toward a specific direction through a polarization vector. Hilbert transformation of the source signature is expected when crossing a caustic. Therefore, source signature (with a negative sign) is recovered after the second caustic crossed. The Hilbert transform $\mathcal{S}(t)$ of the function $S(t)$ is defined as

$$\mathcal{S}(t) = \frac{1}{\pi} \int \frac{S(\xi)}{(t-\xi)} d\xi \quad [29]$$

and has as Fourier transform $-i\text{sgn}(\omega)S(\omega)$, which introduces the $-i = \exp(-i\pi/2)$ phase shift required by the caustic crossing (Chapman, 1978).

For such computation of seismograms, we need all the rays connecting source and receiver. By summing over these rays, we may estimate seismograms as long as receivers stand away from caustic zones. Unfortunately, we may find difficult the computation

of these problematic rays. Techniques have been suggested for turning this problem around, techniques based on different integral wave decompositions (plane waves, Snell waves, beams, etc.), which somehow smooth out very local instable variations of the amplitude.

1.04.4.1 Classical Ray Seismograms

Following Chapman (1978), we may write, in a very compact form ray seismograms, at a receiver \mathbf{x} for an elastic wave emitted by a source \mathbf{x}_0 using the frequency domain expression [19]. We end up with a sum over rays which gives the following asymptotic displacement:

$$\mathbf{u}(\mathbf{x}, t) \approx \sum_{\text{rays}} \text{Real} \left[\phi_P(\gamma_1, \gamma_2)(\mathbf{x}, \mathbf{x}_0) \sqrt{\frac{1}{\rho(\mathbf{x})|\mathcal{J}_T(\mathbf{x}, \mathbf{x}_0)|}} e^{-i\left(\frac{\pi}{2}\right)\text{KMAH}(\mathbf{x}, \mathbf{x}_0)} \right. \\ \left. + \mathbf{e}(\mathbf{x}, \mathbf{x}_0) \tilde{\mathcal{S}}(t - T(\mathbf{x}, \mathbf{x}_0)) \right] \quad [30]$$

where $\tilde{\mathcal{S}}$ is the analytical function associated with the source signature \mathcal{S} which is simply a complex function with the function for the real part and its Hilbert transform for the imaginary part.

There is *a priori* no difficulty in using this asymptotic formula, except for a few configurations. There is failure of the expression when the receiver is exactly located at a position where geometrical spreading is equal to zero. From eqn [30], we see that the amplitude then grows to infinity providing an erroneous expression for the seismogram amplitude. This failure of asymptotic ray theory at caustics is a well-known artifact of the method. Other pathological cases exist as shadow zones where no rays enter while vibrations still exist (Chapman, 1985). Several solutions have been proposed for solving this problem: the high-frequency singular wave field is expressed as a summation of regular high-frequency asymptotic elementary solutions. Several types of waves can be used as plane waves or Gaussian beams.

1.04.4.2 Seismograms by Summation on the Ray Field

1.04.4.2.1 WKBJ summation

This approach is based on the introduction of high-frequency asymptotics into the 1D wave equation resulting from the spatial horizontal Fourier

transform of the scalar wave equation (eqn [6]) in a laterally invariant velocity model, $c(z)$. In the time frequency domain, we obtain an ODE for $w(z) = w(\omega p_x, \omega p_y, z, \omega) = w(k_x, k_y, z, \omega)$:

$$-\omega^2 p_z^2(z) w(z) - \frac{d^2}{dz^2} w(z) = f^w(z) \quad [31]$$

with $p_z^2(z) = (1/c^2(z)) - p_x^2 - p_y^2$ and $f^w(z) = f^w(\omega p_x, \omega p_y, z, \omega) = f^w(k_x, k_y, z, \omega)$ where we introduce slowness vector \mathbf{p} rather than wave number \mathbf{k} . As in the case of ray theory, we can introduce a WKBJ ansatz (Chapman, 2004, p. 278):

$$w(z) = S(\omega) \left(\sum_{n=0}^{\infty} \frac{W_n(z)}{(-i\omega)} \right) e^{i\omega\tau(z)} \quad [32]$$

where expansion is done at constant p_x and p_y . We find, equivalently to the eikonal and transport equations, two equations

$$\frac{d\tau(z)}{dz} = \pm p_z(z) \quad [33]$$

and

$$\frac{d^2\tau}{dz^2}(z) W_0(z) + 2 \frac{d\tau}{dz}(z) \frac{dW_0}{dz}(z) = 0 \quad [34]$$

These equations are ODEs that can be easily integrated using analytical or numerical solutions. The sign in eqn [33] determines the up- or down-going behavior of the wave. Asymptotic WKBJ solutions appear as an extension of plane waves from homogeneous to general 1-D models. They fit with plane waves when the velocity model does not depend on depth. Equations [33] and [34] are only valid when the velocity model is continuous and derivable in z up to the second order. When there are interfaces, similarly to the ray solution, high-frequency asymptotic continuity conditions have to be introduced. They reduce to the application of Snell–Descartes law and introduction of standard reflection/transmission coefficients.

The WKBJ expansion [32] also breaks down when a turning point exists, that is, when the vertical slowness is zero (Chapman, 2004, p. 286). Another asymptotic expansion can then be proposed: the Langer asymptotic expansion (Langer, 1937; Wasow, 1965; Chapman, 1974; Woodhouse, 1974) involving Airy functions (Abramowitz and Stegun, 1972) with finite amplitudes on caustics.

An alternative to the WKBJ expansion [32] has also been proposed as the WKBJ iterative solution or Bremmer series. This approach allows us to solve the

WKBJ paradox (Gray, 1982), that is, whatever the vertical gradient of the velocity, it will never generate a reflected wave. We would expect to observe such a phenomenon at low frequency but since up- and down-going waves are fully decoupled in the WKBJ expansion it will never happen using this approximation. In the WKBJ iterative formulation, we assume that the wavefield can be represented as a combination of up- and down-going first-order WKBJ solutions. This combination involves a function coupling the amplitudes of the up- and down-going waves. This coupling function satisfies an ODE in z called the ‘coupling equation’, which can be solved iteratively leading to a series of solutions (Scholte, 1962; Richards and Frasier, 1976; Gray, 1983; Verweij and de Hoop, 1990; de Hoop, 1990).

Once the 1-D wave equation [31] has been integrated using some high-frequency approximation, it may be necessary to perform the inverse Fourier transform in order to come back to the (x, t) domain. Several methods can be used as the exact technique of ‘Cagniard–de Hoop–Pekeris method’ (Cagniard, 1939; Pekeris, 1955a, 1955b; de Hoop, 1960), the ‘WKBJ approach’, where the slowness summation is truncated to real values of traveltimes (Chapman, 1978), or spectral methods such as the ‘reflectivity method’ (Fuchs and Müller, 1971) or ‘full wave theory’ (Aki and Richards, 1980, chapter 9). A complete review has been performed by Chapman and Orcutt (1985) using both a WKBJ and Langer approximation with applications to realistic profiles in the global Earth.

Truncation errors in the solution (Yedlin *et al.*, 1990) especially in the presence of strong velocity gradients as well as numerical effects coming from smoothing boxcar windows or convolution operator (Dey-Sarkar and Chapman, 1978) require specific attention when one wants to reconstruct velocity structure. Reverberations on a stack of layered structures, which can be observed in the ‘reflectivity method’, are well separated as WKBJ contributions (Shaw, 1986).

Finally, if WKBJ appears limited to 1-D media, it also exhibits interesting properties when compared to classical ray theory. WKBJ provides high-frequency asymptotic solutions in the (x, t) domain as summations of high-frequency asymptotic plane waves. Indeed, it appears that these summations may be regular at caustics, providing an interesting opportunity for computing high-frequency asymptotic solutions in those locations where classical ray theory fails. Moreover, as we will see now, extension

of WKBJ summations exists which allow one to consider fully heterogeneous velocity models.

1.04.4.2.2 Maslov summation

The WKBJ approach is limited to 1-D media. Extension to laterally varying velocities is not straightforward. Approximative solutions considering small lateral variations of velocity have been introduced recently by Ni *et al.* (2003), but a more systematic formulation can be based on Maslov approach using the Legendre transformation (Kravtsov, 1968; Maslov and Fedoriuk, 1981). Maslov summation has been introduced by Chapman and Drummond (1982) in seismology and by Ziolkowski and Deschamps (1984) in electromagnetism. The Maslov approach, which reduces to the WKBJ approach for laterally homogeneous media, involves summation of high-frequency asymptotic local plane waves. In fact, high-frequency asymptotic solutions can be obtained in any of the 3-D dimensional subspaces of the phase space, that is, (x, y, p_z) , (x, p_y, z) , (p_x, y, z) , ... or even (p_x, p_y, p_z) . These solutions can be obtained by applying the stationary phase approximation (Chapman, 2004) to some Fourier transforms of high-frequency asymptotic approximations in the (x, y, z) space. For example, we obtain from expression [15]

$$w(p_x, y, z, \omega) \approx \sqrt{i\pi \operatorname{sign}\left(\frac{\partial^2 T}{\partial x^2}\right)} S(\omega) \phi_w(\gamma_1, \gamma_2) \\ \times \sqrt{\frac{c^2(x_{\text{spec}}, y, z)}{G_T(x_{\text{spec}}, y, z)}} e^{i\omega T(x_{\text{spec}}, y, z) - ip_x x_{\text{spec}}} \quad [35]$$

where $x_{\text{spec}}(p_x, y, z)$ denotes the specular position (we assume a single specular point), for which $(\partial T/\partial x) = p_x$, that is, where the Fourier parameter $p_x = k_x/\omega$ fits with the ray field parameter $p_x^{\text{spec}} = (\partial T/\partial x)$, and the Jacobian G_T is defined by

$$G_T = \left| \frac{\partial(p_x, y, z)}{\partial(T, \gamma_1, \gamma_2)} \right| \quad [36]$$

Once we have these high-frequency asymptotic approximations, we can express the solution in the configuration space as an inverse Fourier transform, or equivalently as a p_x slowness integral as in WKBJ summation. This expression is called the Maslov summation. At high frequency this integral expression agrees with the classical ray solution, when it exists. When the classical ray solution is singular (caustic point), it can be shown from Liouville's theorem (Goldstein, 1980) that there exists at least one

alternate projection where the Maslov summation involves regular asymptotic plane waves. Regular high-frequency asymptotic solutions of the wave equation can then be found by blending both the ray solution and the Maslov summations using weighting functions (Chapman and Drummond, 1982; Huang and West, 1997; Chapman, 2004).

Note that equivalently to caustics in classical ray theory, singularities may appear in the elementary high-frequency solutions obtained in the other subspaces. They are called pseudocaustics and correspond to zeroes of the Jacobian [36] (we follow the terminology of Klauder (1987a) as suggested by Kendall and Thomson (1993)).

A more general approach known as phase partitioning (Kendall and Thomson, 1993) may be used in practical situations where caustics and pseudocaustics could not be separated (the frequency could be considered high enough to make them separable, making these strategies unnecessary from the theoretical point of view).

1.04.4.2.3 Gaussian beam summation

Another technique of summation will be through local Gaussian beams which are used in the boundary-layer approach and which originally were applied to the computation of seismograms (see Popov (1982) for original references in Russian). It has been popularized by Červený *et al.* (1982) and co-workers. One advantage is that individual Gaussian beams have no singularities either at caustics or at pseudocaustics. Moreover, two-point ray tracing is unnecessary and the summation is less sensitive to model parametrizations. A nice review has been performed by Nowack (2003).

A Gaussian beam can be defined around a central ray $(\mathbf{x}_0, \mathbf{p}_0)$ from the paraxial approximation [27]:

$$W_{\text{GB}}(\mathbf{x}_0 + \delta\mathbf{x}, \mathbf{p}_0, \omega) \\ = W_{\text{GB}}(\mathbf{x}_0, \mathbf{p}_0, \omega) \exp^{i\omega}(T(\mathbf{x}_0, \mathbf{p}_0) \\ + \mathbf{p}_0 \delta\mathbf{x} + \frac{1}{2} \delta\mathbf{x}' \mathcal{M}(\mathbf{x}_0, \mathbf{p}_0) \delta\mathbf{x}) \quad [37]$$

where \mathcal{M} is now complex with $\operatorname{Im}(\mathcal{M}(\mathbf{x}_0, \mathbf{p}_0))$ being positive definite. Note that, although this method has been presented mainly in the ray-centered system of coordinates, it can be constructed in any global coordinate system; such as here using general Cartesian coordinates. The value of the Gaussian beam along the central ray is given from paraxial quantities [23] and initial curvature matrix [28] by the relation

$$W_{\text{GB}}(T, \omega) = \frac{W_{\text{GB}}(T_0, \omega) e^{i\omega(T-T_0)}}{\sqrt{\det(\mathcal{P}_{xx}(T, T_0) + \mathcal{P}_{xp}(T, T_0)\mathcal{M}(T_0))}} \quad [38]$$

This expression remains finite as long as the term $\mathcal{M}(T_0)$ is symmetrical, the term $\text{Im}(\mathcal{M}(T_0))$ is positive definite and the term $\partial \mathbf{x}/\partial(\gamma_1, \gamma_2, T)(T_0)$ is regular. The width of the Gaussian beam depends on the imaginary part of \mathcal{M} , which insures a Gaussian decay of amplitude away from the central ray. The width of the beam varies according to variations of \mathcal{M} and may be chosen according to various strategies. For example, Hill (1990) has proposed to choose an initial complex \mathcal{M} related to an initial beam width w_i at frequency ω_i . This has been applied efficiently in pre-stack depth migration (Hill, 2001) using Gaussian beam summation (GBS) with a ray sampling compatible with the beam width. Numerical comparisons have been investigated by many authors (Madariaga, 1984; White *et al.*, 1987; Weber, 1988; Nowack and Stacy, 2002) in seismology (Figure 11).

The Gaussian beam solution represents an approximate solution of the wave equation, and their superposition integral represents an asymptotic approximation of the wavefield. In practice, once the complex curvature matrix has been chosen at some T_0 , the weighting of the various Gaussian beams in the superposition integral has to be defined in such a way as to fit with asymptotic ray theory, where it is regular. By construction, Gaussian beams are always regular and they consequently provide regular high-frequency solutions.

GBS may be shown to be equivalent to Maslov summation under the hypothesis of plane wave with infinitely wide Gaussian decay (Madariaga, 1984). This equivalence shows the larger possibilities offered by GBS with, for example, the advantage of limited truncation artifacts.

1.04.4.2.4 Coherent-state transformation technique

Formulations based on the coherent-state transformation technique (Klauder, 1987a, 1987b) fill the gap between local plane waves decomposition of WKB/Maslov approaches and overcomplete beam decomposition with a simple parabolic approximation of the phase function (Thomson, 2001, 2004). This allows us to preserve tracing tools for real rays.

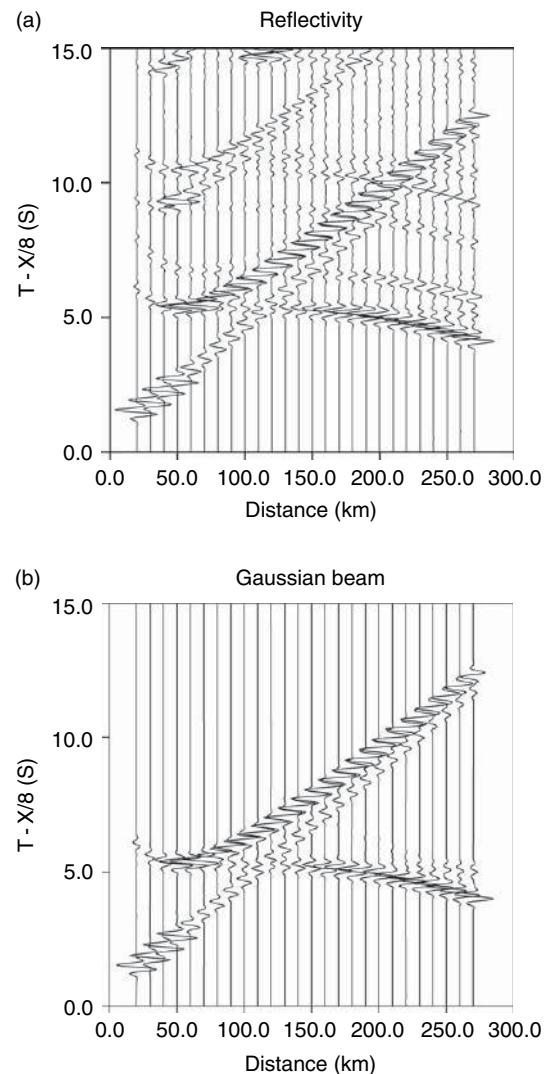


Figure 11 Comparison between Gaussian beam summation (b) and reflectivity method (a). For rays included in the GBS, amplitudes are quantitatively modeled. Courtesy of R. Nowack.

Few attempts have been performed for moving toward complex rays where both amplitudes and traveltimes are complex functions, because analytical continuation of velocity variations is easily possible for simple analytic functions (Keller, 1971; Deschamps, 1971; Felsen, 1976, 1984; Wu, 1985; Zhu and Chun, 1994b). Extensions to arbitrary numerical velocity variations are still a challenging problem, although recent work (Amodei *et al.*, 2006) seems to solve analytical continuation for numerical velocity variations, opening the road to complex ray theory for heterogeneous media.

1.04.4.3 Geometrical Theory of Diffraction

In addition to previous strategies, which can be used to avoid caustic singularities or to estimate fields inside shadow zones in smooth media, other uniform ray expansions are also possible when considering caustics (Kravtsov, 1964; Ludwig, 1966) using Airy functions or at discontinuities, where the wave field creates a shadow zone. Although rather sophisticated tools of Riemannian geometry are required, we may adopt a phenomenological point of view and illustrate this geometrical theory of diffraction introduced by Keller (1962). Justification of Keller's formula from the mathematical point of view, especially when media have variable velocity, have generated an impressive list of references and one may quote fruitful monographs such as Babič and Kirpičnikova (1979), Babič and Buldyrev (1991), and Klem-Musatov (1995). Nice reviews by Kravtsov (1968), Babič (1986), and Hron and Chan (1995) may help the reader in understanding various methods for the construction of asymptotic solutions.

The method of canonical problems transforms the problem at hand into a simpler problem. By matching asymptotically field expansions for the simpler problem, expansion coefficients are estimated (Keller, 1962). The best example is the diffraction of an

arbitrary field on a body with a rib which can be transformed into the diffraction of a plane wave by a wedge.

Boundary-layer formulation will develop the solution in the transition zone the width of which should go to zero when frequency goes to infinity (Buchal and Keller, 1960; Babič, 1975). This approach related to the method of parabolic equations (see reference works in Fock, 1965) does not require any analytical solutions as for the canonical matching approach.

On a linear edge an incident plane wave is reflected creating illuminated and shadow zones for the reflection wavefront (Figure 12). Energy will flow into the shadow zone and, asymptotically, this diffraction may be well modeled by diffraction rays following an eikonal equation with a source at point D. Therefore, we must consider both reflected waves and edge waves. Their wavefronts must coincide along the shadow boundary. The boundary ray separating illuminated and shadow zones does not follow the usual transport equation and dedicated theory. Comprehensive analysis based on previous works has been addressed by Klem-Musatov (1995) to compute scalar diffraction amplitudes (see the review by Hron and Chan (1995)).

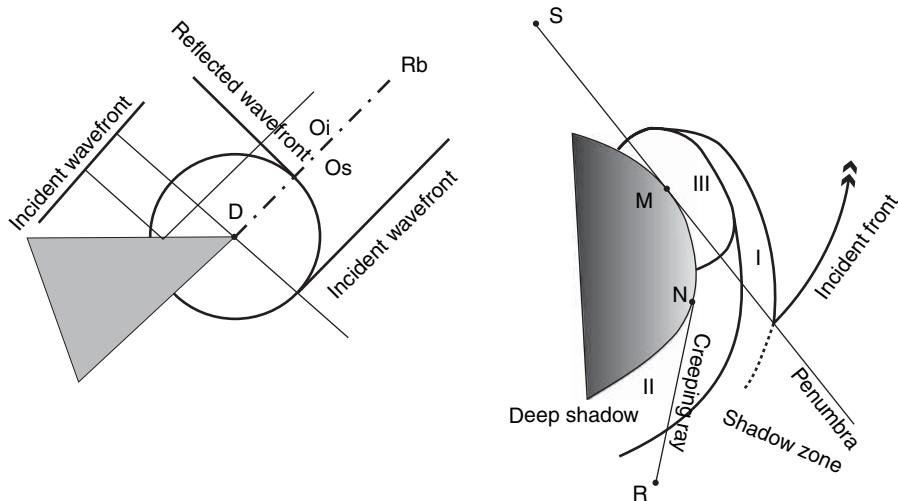


Figure 12 Geometrical interpretation of diffraction. On the left panel, the gray diffracting object does not allow wave penetration. The reflection wavefront is connected to the diffraction front emitting from point D. This wavefront is connected to the incident wavefront. Ray Rb separates reflection zone and diffraction zone. On the right panel, waves may penetrate the diffracting body. The line SM separates the penumbra zone and the lighted zone. Because the creeping ray leaves the obstacle at the point N (which is defined both by front and interface curvatures for a specific ray), we shall distinguish the deep shadow zone (II) from the standard shadow zone. The diffraction zone (III) will move into the lighted zone behind the converted front related to the first diffraction at the point M (I). These limits will be very sensitive to the frequency content of waves and *ad hoc* corrections are necessary to keep the ray approximation as an useful interpretation tool.

The surface limiting the illuminated and shadow zones may have a complex geometry (Borovikov and Kinber, 1974). For a convex body limited by a discontinuous surface, three zones in the shadow may be distinguished: the neighborhood of the shadow zone (I), the neighborhood of the body surface (II), and the intersection of these two zones (III), related to the point M of the body surface hit by the grazing ray (see Figure 12).

In seismology, diffractions by the core–mantle or inner core boundaries of the Earth require deep understanding of these approaches (see the interesting presentation by Thomson (1989)). Because seismology deals with elastic propagation, Thomson (1989) stresses that the boundary layer method could be applied when considering P and S wavefields as long as P and S grazing rays do not hit the boundary at the same point. A canonical solution with detailed elastic diffraction coefficient estimation has been constructed in 3-D for a crack diffraction by Achenbach and Gautesen (1977). Improvements could be performed in this direction for elastic diffraction in the future.

1.04.5 Finite Frequency Effects

The ray path connecting a source S and a receiver R is a trajectory along which the high-frequency part of the energy is propagating. Because the frequency we consider is always finite, the wavefield at the receiver is also modified by the velocity distribution in the vicinity of the ray. This volume, called Fresnel volume, may be defined in a very simple way for a wave with frequency content f : any point F of this volume should verify the inequality (Kravtsov and Orlov, 1990):

$$|T(S, F) + T(F, R) - T(S, R)| \leq \frac{1}{2}f^{-1} \quad [39]$$

Basically, this means that only points verifying inequality [39] will contribute significantly to the seismogram at the receiver around time $T(S, R)$. Often, we call the Fresnel volume a physical ray (Červený, 2001, p. 115). This volume plays a key role for resolution estimation of seismic imaging methods in relation with the validity domain of ray theory (Kvasnička and Janský, 1999). We will now consider a procedure linking model perturbations and seismogram perturbations, which allows us to quantitatively introduce the contribution of this volume to seismogram computation.

Before going to these linearized approximations, we must emphasize the path integral approach where any trajectory connecting the source and the receiver may contribute to seismogram estimation (Lomax, 1999; Schlottmann, 1999; Thomson, 2001). Although we have not yet found a practical way of assessing convergence toward the true solution of these integrals, these methods exhibit nonlocal behaviors which make them completely different from approaches we consider now.

1.04.5.1 Ray + Born/Rytov Formulation

The resolution of the seismic inverse problem (recovering the elastic parameter field from the seismic data) is one of the major challenges of seismology. The problem is a huge ill-constrained nonlinear inverse problem (Tarantola, 1987), which has to be addressed in some appropriate ways. For example, as soon as we have some reasonable initial model for the elastic parameters, one may build linearization of the relation connecting data perturbation to model perturbation. This is the Born approximation, which has been widely used as a basis for seismic linearized inversion (Tarantola, 1984b, 1986; Beylkin, 1985; Beylkin and Burridge, 1990). In fact, the Born approximation is only the first-order term of a recursive relation connecting seismic wavefield perturbation $\delta w(\mathbf{r}, \omega)$ to model perturbation $\delta m(\mathbf{x})$ (Hudson and Heritage, 1981). We may write, for the squared slowness perturbation $\delta m(\mathbf{x}) = 1/c^2(\mathbf{x}) - 1/c_0^2(\mathbf{x})$ (where $c_0(\mathbf{x})$ denotes the velocity in the reference model), the set of relations

$$\begin{aligned} \delta w_{n+1}(\mathbf{r}, \omega) &= \omega^2 \int_V d\mathbf{x} \delta m(\mathbf{x}) G_0(\mathbf{r}, \omega; \mathbf{x}) (\delta w_n(\mathbf{x}, \omega) \\ &\quad + w_0(\mathbf{x}, \omega)) \end{aligned} \quad [40]$$

where n denotes the order of the Born approximation, V denotes the full space volume, and $G_0(\mathbf{r}, \omega; \mathbf{x})$ denotes the Green's function for a point source at position \mathbf{x} and a receiver at position \mathbf{r} in the reference velocity model. We have for the first order $\delta w_0(\mathbf{x}, \omega) = 0$, which provides the classical Born approximation, that is, a linearized approximation. Born approximation can be extended to acoustic and elastic media (Ben Menahem and Gibson, 1990; Gibson and Ben Menahem, 1991).

The reference model can be chosen to be homogeneous in order to take advantage of exact and explicit expression of Green's function. For realistic problems, inhomogeneous reference models are

necessary and lead us to the distorted Born approximation (Chapman, 2004). In this case, it is possible to use an approximative expression of the Green's function as it can be obtained by ray theory, for example. We obtain then the WKB + Born (Clayton and Stolt, 1981; Ikelle *et al.*, 1988) or ray + Born approximations (Bleistein, 1984; Beylkin, 1985; Cohen *et al.*, 1986; Bleistein *et al.*, 1987; Beydoun and Mendes, 1989; Beylkin and Burridge, 1990; Jin *et al.*, 1992; Thierry *et al.*, 1999a, 1999b; Operto *et al.*, 2000; Xu *et al.*, 2001, 2004; Xu and Lambaré, 2004) so widely used for seismic imaging. From the expression [40], the ray + Born approximation can be expressed for the perturbation of the Green's function as

$$\delta G(\mathbf{r}, \omega; \mathbf{s}) = \omega^2 \int_V d\mathbf{x} \delta m(\mathbf{x}) \mathcal{A}(\mathbf{r}, \mathbf{x}, \mathbf{s}) e^{i\omega T(\mathbf{r}, \mathbf{x}, \mathbf{s})} \quad [41]$$

where $\mathcal{A}(\mathbf{r}, \mathbf{x}, \mathbf{s}) = A(\mathbf{r}, \mathbf{x}) A(\mathbf{s}, \mathbf{x})$ is the product of the amplitude of asymptotic Green's functions for the rays $\mathbf{x} \rightarrow \mathbf{s}$ and $\mathbf{x} \rightarrow \mathbf{r}$ in the reference velocity model, and $T(\mathbf{r}, \mathbf{x}, \mathbf{s}) = T(\mathbf{r}, \mathbf{x}) + T(\mathbf{s}, \mathbf{x})$ is the sum of the corresponding traveltimes. **Figure 13** shows some seismograms obtained using the ray + Born approximation.

Since we use, in the ray + Born approximation, high-frequency approximations of the Green's function in eqn [40], there may be difficulties iterating these equations even if generally smooth reference velocity models are used. For remedying this, Coates and Chapman (1990) and Chapman and Coates (1994) proposed a generalization of the Born approximation which takes into account approximate Green's functions. This generalization emphasizes a difficult aspect of the use of the ray + Born approximation, the definition of limits of perturbation approach related to the reference velocity model selection. These limits are related to limitations of ray theory and to first-order Born approximation. Practically, the reference velocity model should be valid for ray theory, but should also be sufficiently heterogeneous for reproducing main features of the forward seismic wave propagation in the perturbed velocity model. In terms of ray tracing, it means that the reference velocity model should preserve, within the precision of propagated wavelengths, the traveltime of the forward propagation. In practice ray + Born approximation essentially works for small-sized heterogeneities and for short angles of reflection or diffraction (Keller, 1969; Beydoun and Tarantola, 1988; Wu, 1989). This is the context of reflection seismic exploration, where linearization has been proposed (Lailly, 1983; Tarantola, 1984a, 1984b), and even nonlinear seismic inversions (Tarantola, 1986; Pica

et al., 1990) based on local iterative optimization schemes. In fact, limitations of the standard local optimization methods have rapidly been recognized (Gauthier *et al.*, 1986; Kolb *et al.*, 1986; Jannane *et al.*, 1989) and credited to the strong nonlinearity of the problem, when considering long wavelength components of the velocity model.

Several solutions have been proposed to overcome this difficulty by using global optimization schemes (Snieder *et al.*, 1989; Cao *et al.*, 1990), by changing the optimized cost function (Symes and Carazzone, 1991; Symes, 1993; Symes and Kern, 1994; Plessix *et al.*, 1995; Chauris and Noble, 2001), by changing the optimization strategy (Pratt *et al.*, 1996), or even by definitely changing the data set from traces to picked traveltimes, which have a much more linear relation with the long wavelength components of the velocity model (Bishop *et al.*, 1985; Farra and Madariaga, 1988; Billette and Lambaré, 1998). In fact, this interesting property of traveltimes can also be used in the framework of a full waveform inversion. It is possible indeed to develop in the frequency domain a polynomial series for the relation connecting the perturbation of the phase of the wavefields to the velocity model perturbation. $\delta\Phi = \ln(w/w_0)$. This is the Rytov approximation (Keller, 1969; Rytov *et al.*, 1987; Beydoun and Tarantola, 1988; Samuelides, 1998), which provides to the first order

$$\delta\Phi(\mathbf{r}, \omega) \approx \omega^2 \int_V d\mathbf{x} \delta m(\mathbf{x}) \frac{G_0(\mathbf{r}, \omega; \mathbf{x}) w_0(\mathbf{x}, \omega)}{w_0(\mathbf{r}, \omega)} \quad [42]$$

which fits much better the perturbed transmitted wavefield than the Born approximation. It is also unfortunately penalized by some spurious artifacts, and until now it has not been really applied to seismic inversion (Devaney, 1981; Nahamoo *et al.*, 1984) in spite of recent work (Gélis *et al.*, 2006).

1.04.5.2 Ray + Kirchhoff Approximation

Born approximation is not the only linearized approximation used for seismic modeling and therefore for inversion. In the context of reflection seismic exploration, the first-order Kirchhoff approximation is certainly the most preferred. This approximation provides a relation between the primary reflected wavefield and a distribution of reflectivity in the model. This approximation is derived from the representation theorem (Aki and Richards, 1980), which allows us to express any causal wavefield, $w(\mathbf{x}, \omega)$, associated to the source distribution, $f(\mathbf{x}, \omega)$, as a volume

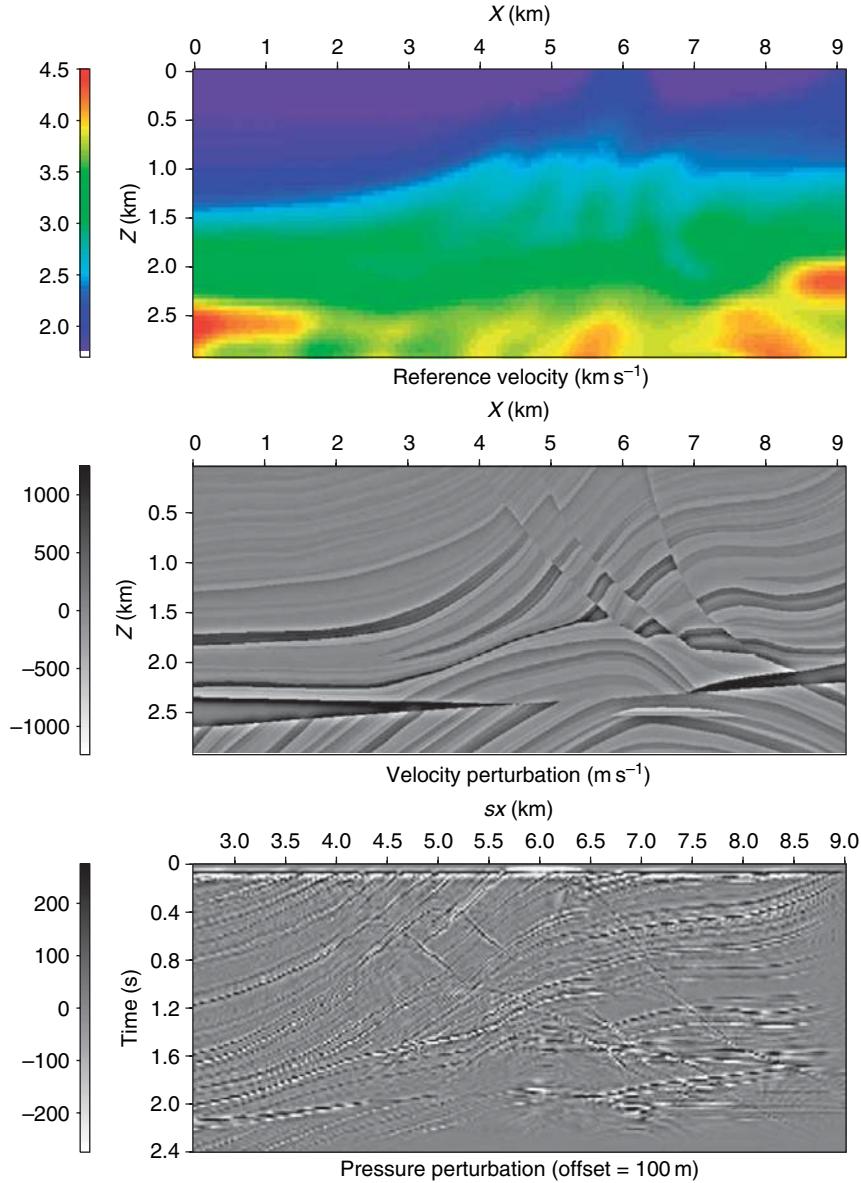


Figure 13 The ray + Born approximation: the Marmousoft model and data set (Billette et al., 2003). On top panel, the smooth reference velocity model; middle panel, the velocity perturbation; and bottom panel, the common offset section (offset is 100 m) profile.

integral over the volume V of source distribution and a surface integral over the volume boundary δV

$$\begin{aligned} w(\mathbf{r}, \omega) &= \int \int \int_V d\mathbf{x} G(\mathbf{r}, \omega; \mathbf{x}) f(\mathbf{x}, \omega) \\ &+ \int \int_{\delta V} d\mathbf{x} \left(\frac{\partial G}{\partial n}(\mathbf{r}, \omega; \mathbf{x}) \omega(\mathbf{x}, \omega) \right. \\ &\quad \left. - G(\mathbf{r}, \omega; \mathbf{x}) \frac{\partial w}{\partial n}(\mathbf{x}, \omega) \right) \end{aligned} \quad [43]$$

where $\partial/\partial n$ denotes the spatial derivative along the outer normal to the surface. Let us assume now

that we consider Green's function, that is, $w(\mathbf{x}, \omega) = G(\mathbf{x}, \omega; \mathbf{s})$ or equivalently $f(\mathbf{x}, \omega) = \delta(\mathbf{x} - \mathbf{s})$, and that the volume V leans on a reflecting surface. We can express the reflected wavefield as

$$\begin{aligned} G_{\text{refl}}(\mathbf{r}, \omega; \mathbf{s}) &= \int \int_{\delta V} d\mathbf{x} \left(\frac{\partial G}{\partial n}(\mathbf{r}, \omega; \mathbf{x}) G_{\text{refl}}(\mathbf{x}, \omega; \mathbf{s}) \right. \\ &\quad \left. - G(\mathbf{r}, \omega; \mathbf{x}) \frac{\partial G_{\text{refl}}}{\partial n}(\mathbf{x}, \omega; \mathbf{s}) \right) \end{aligned} \quad [44]$$

where G is now the free-space Green's function (Bleistein, 1984; Chapman, 2004) (i.e., the direct

wave from the source that do not interact with the scatterer). The reflected field is expressed as a summation over the unknown reflected wavefield. In the frame of high-frequency asymptotics, it is possible to approximate the reflected wavefield on the reflecting interface from the incident wavefield and the reflection coefficient. This provides the Kirchhoff approximation (Bleistein, 1984; Frazer and Sen, 1985)

$$G_{\text{refl.}}(\mathbf{r}, \omega; \mathbf{s}) = i\omega \int \int_{\delta V} d\mathbf{x} \mathcal{R}(\mathbf{r}, \mathbf{x}, \mathbf{s}) A(\mathbf{r}, \mathbf{x}, \mathbf{s}) e^{i\omega T(\mathbf{r}, \mathbf{x}, \mathbf{s})} \quad [45]$$

where

$$\mathcal{R}(\mathbf{r}, \mathbf{x}, \mathbf{s}) = q(\mathbf{x}, \theta(\mathbf{r}, \mathbf{x}, \mathbf{s})) R(\mathbf{x}, \theta(\mathbf{r}, \mathbf{x}, \mathbf{s})) \quad [46]$$

denotes the product of the reflection coefficient $R(\mathbf{x}, \theta)$ and of the stretching factor, $q(\mathbf{x}, \theta) = |\nabla_{\mathbf{x}} T| = 2 \cos \theta / c(\mathbf{x})$, where θ denotes the half aperture angle between rays $\mathbf{x} \rightarrow \mathbf{s}$ and $\mathbf{x} \rightarrow \mathbf{r}$ (see Figure 14 for an illustration). The expression [46] is reciprocal for the source and receiver positions (Ursin and Tygel, 1997). Kirchhoff approximation can be easily extended to the acoustic and elastic cases (Ursin and Tygel, 1997; Chapman, 2004), where a summation is done for any interface and any mode conversion.

We see when comparing expressions [41] and [45] that ray + Born and ray + Kirchhoff expressions are very similar. This similarity can still be enhanced if we extend the summation from a surface to a volume, assuming that the whole reflected wavefield can be build by stacking contributions of individual reflectors. In this case, we consider a volumetric distribution of specular reflectivity $R(\mathbf{x}, \theta(\mathbf{r}, \mathbf{x}, \mathbf{s}))$

$$G_{\text{refl.}}(\mathbf{r}, \omega; \mathbf{s}) = i\omega \int \int \int d\mathbf{x} q(\mathbf{x}, \theta(\mathbf{r}, \mathbf{x}, \mathbf{s})) R(\mathbf{x}, \theta(\mathbf{r}, \mathbf{x}, \mathbf{s})) G(\mathbf{s}, \omega, \mathbf{x}) = G(\mathbf{r}, \omega, \mathbf{x}) \quad [47]$$

where the Green's function, $G(\mathbf{s}, \omega, \mathbf{x}) = A(\mathbf{s}, \mathbf{x}) e^{i\omega T(\mathbf{s}, \mathbf{x})}$ and $G(\mathbf{r}, \omega, \mathbf{x}) = A(\mathbf{r}, \mathbf{x}) e^{i\omega T(\mathbf{r}, \mathbf{x})}$, has to be calculated in some reference velocity model.

The Born and Kirchhoff approximations, in an even more widespread use, are at the basis of numerous seismic imaging methods. In practice, even if the derivation of the formulas relies on high-frequency asymptotics, the asymptotic Green's functions in expression [47] are sometimes replaced by other types of numerical Green's functions like one-way paraxial approximations of the wave equation

(Claerbout, 1970). Most depth migration methods consider these Green's functions in order to recover the reflectivity function at any point of the medium, knowing some reference velocity model. When ray-based Green's functions are used, this type of migration is called Kirchhoff migration (French, 1974, 1975; Bleistein, 1987). It is widely used in industry for 3-D depth migration (Xu and Lambaré, 2004; Xu et al., 2004) while applications at crustal and mantle scales may be possible.

1.04.5.3 Finite Frequency Effects on Ray Functions

Away from waveform estimation and fitting, can we introduce the finite-frequency features on traveltimes and/or amplitudes analysis? Filling the gap between, on the one side, travelttime inversion, and on the other, full-wave inversion has gathered the attention of many workers since the pioneering work of Luo and Schuster (1991) and Woodward (1992). The concept of wavepath (Woodward, 1992) as the product of the incident wavefield from the source and the retropropagated wavefield from the receiver displays nicely the Fresnel volume (Figure 15) and how contributions of points moving away from the first Fresnel zone bring higher-frequency contents in the image reconstruction, especially for waveform fitting (Pratt et al., 1996; Operto et al., 2004).

Linear kernels, often called Fréchet kernels, have been introduced for traveltimes: a recent impressive literature on surface waves (Marquering et al., 1998, 1999; Zhou et al., 2004), normal modes (Li and Tanimoto, 1993; Li and Romanowicz, 1995; Tanimoto, 1995; Katzman et al., 1998; Zhao et al., 2000), and rays (Dahlen et al., 2000; Hung et al., 2000; Montelli et al., 2004a, 2004b) shows the vitality of such a concept. For example, the time delay δT at a given receiver r coming from a scattering point x for a given source s is associated with the time difference $\Delta T(s, r, x, \omega) = T_{sr} - T_{sx} - T_{xr}$ through the equation

$$\delta T(s, r) = \int_D K_r(x, \omega) dV \quad [48]$$

where the integration domain D is over diffracting points x . This domain must be defined carefully. The Fréchet kernel or sensitivity kernel $K_r(x, \omega)$ has an expression depending on frequency ω and time difference $\Delta T(s, r, x, \omega)$ (Dahlen et al., 2000) and the use of paraxial theory will speed up significantly its estimation. Applications to amplitudes (Dahlen and Baig,

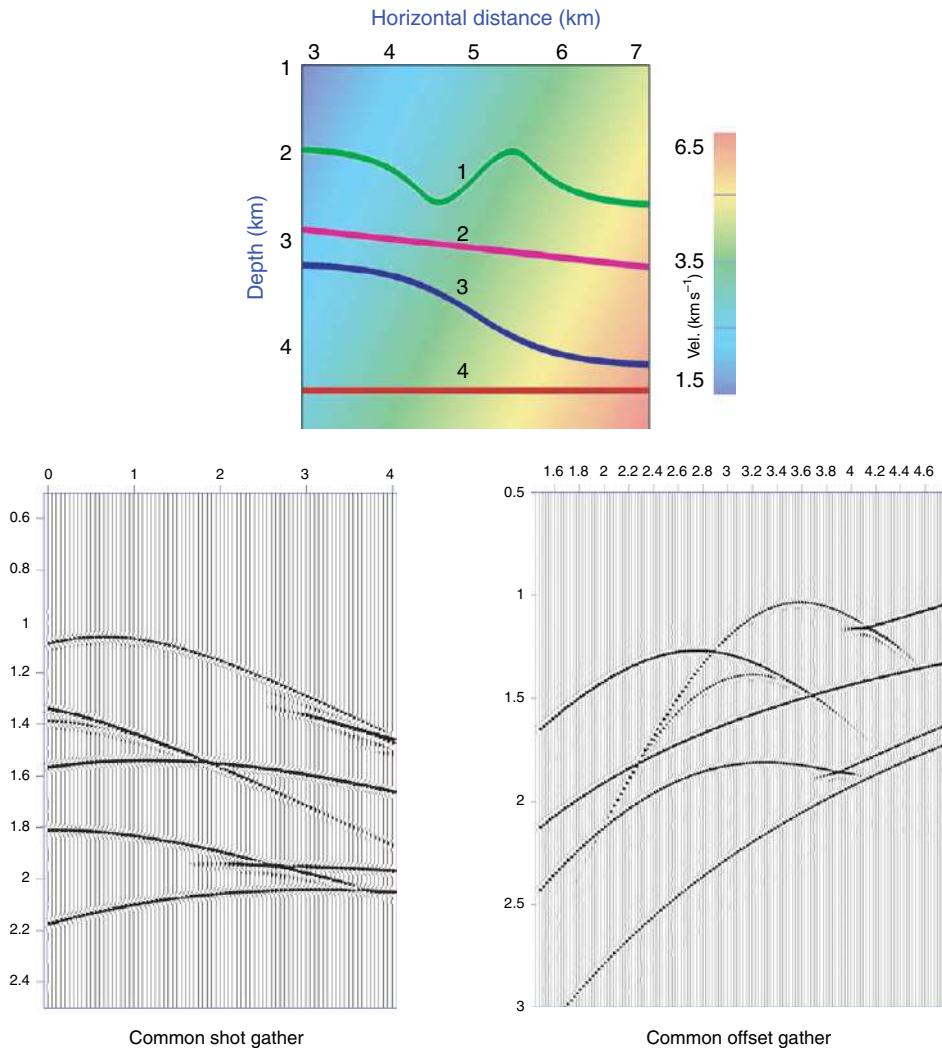


Figure 14 Synthetic seismograms using Kirchhoff summation. On top panel, the smooth velocity model (tilted gradient of the velocity) with the three superimposed reflectors. On bottom panel, the left figure shows the common shot gather modeled by ray + Kirchhoff summation while the right figure shows common offset gather modeled by ray + Kirchhoff summation. Courtesy of R. Baina (OPERA, France).

2002), to anisotropy (Favier and Chevrot, 2003) (with the splitting intensity related to polarization of the incoming wave (Chevrot, 2000)), introduce new sensitivity kernels and will extend applicability in the near future. Contribution of points increases when we move away from the ray, making the so-called banana–doughnut shape for traveltimes which has been questioned by de Hoop and van der Hilst (2005) while maximal contribution is found on the ray for amplitudes (Figure 16). Near-field influence has been discussed by Favier *et al.* (2004). Further improvements will certainly close up the loop and will bring us back to waveform fitting, an important challenge for global seismology in the next 10 years.

1.04.6 Conclusion

Until now the growth of seismology as an investigation tool for the Earth's interior have essentially relied on the use of ray theory. During this time, significant progress has been made in ray theory, which is definitely not a “discipline from the XIXth century.” This constant progress (not only in terms of numerical developments) has, for example, considerably extended the application domain of these techniques, which still remain essential for the analysis of seismic traces.

Although numerical methods for solving wave equations (FD methods (e.g., Virieux, 1986; Moczo

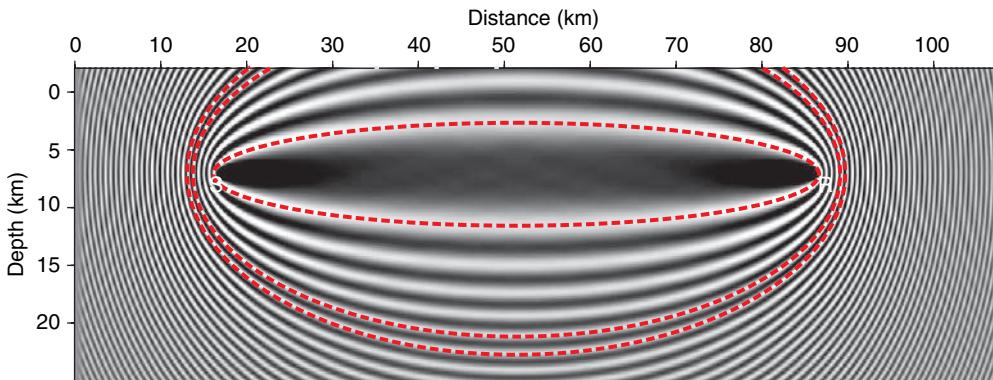


Figure 15 A simple description of wavepath: the first Fresnel zone is the zone of main contribution for diffraction while considering finite-frequency effects. As we introduce other Fresnel zones, smaller features are considered on both medium description and seismogram estimation. Courtesy of S. Operto, CNRS.

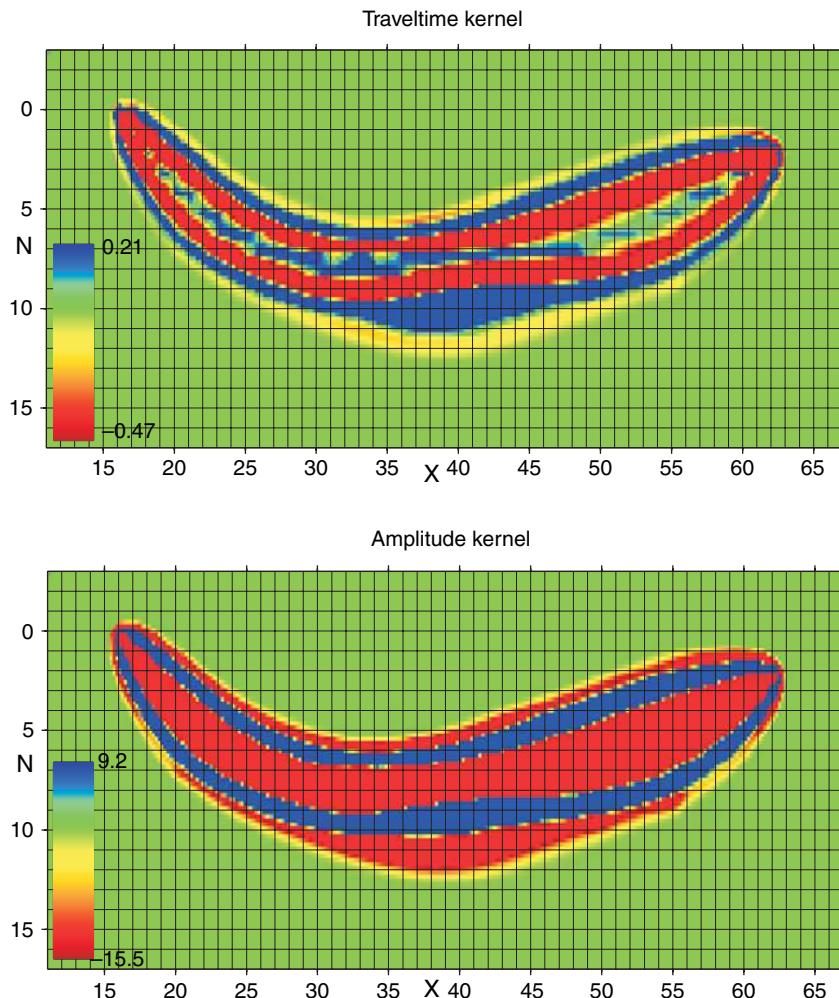


Figure 16 Travelttime and amplitude sensitivity kernels in a local heterogeneous medium. The weak contribution in the central part of the kernel for traveltimes associated with Fermat principle (top panel) while the contribution is maximal for amplitude (bottom panel). Courtesy of S. Gautier and G. Nolet.

et al., 2006), finite element methods with fast convergence such as spectral element methods (e.g., Chaljub *et al.*, 2003)) may open new strategies for both forward and inverse problems because of the increasing performance of computers, understanding of seismograms (and often numerical ones) will still require the interpretation in terms of high-frequency asymptotic approximations. Many observables which can be deduced from ray theory are still not strongly investigated. For example, differential informations, as the slope (Yanovskaya, 1996; Billette and Lambaré, 1998) or the polarization of the events (Le Bégat and Farra, 1997), are rapidly developed. Even the use of amplitudes starts to be exploited in the asymptotic hypothesis. In this context, the present development of dense data acquisition will be a real challenge, where the assets of ray theory will certainly open roads to interesting opportunities for describing complex media.

Finally, the efforts for the adaptation of ray theory to more complex rheologies involving complex geometries, anisotropy, viscoelasticity (Ribodetti *et al.*, 2000), or multiphase media have to be pursued. These new developments will certainly also offer important opportunities for the analysis of seismograms in the future.

Acknowledgments

We gratefully thank Reda Baina, Jeannine Gagnepain-Beyneix, Stéphanie Gautier, David Le Meur, Guust Nolet, Bob Nowack, Stéphane Operto, Peter Shearer, Martin Vallée for kindly providing us with figures. This is contribution no. 843 of Géosciences Azur.

References

- Abdullaev S (1993) *Chaos and Dynamics of Rays in Waveguide Media*. Amsterdam: Gordon and Breach.
- Abgrall R and Benamou J (1999) Big ray tracing and eikonal solver on unstructured grids: An application to the computation of a multivalued traveltime field in the marmousi model. *Geophysics* 64: 230–239.
- Abramowitz M and Stegun I (1972) *Handbook of Mathematical Functions with Formulas, Graphs, and Mathematical Tables*. New York: Dover.
- Achenbach J and Gautesen A (1977) Geometrical theory of diffraction for three-D elastodynamics. *Journal of Acoustics Society of America* 61: 413–421.
- Aki K and Richards P (1980) *Quantitative Seismology: Theory and Methods*. San Francisco: W. H. Freeman.
- Amodei D, Keers H, Vasco D, and Johnson L (2006) Computation of uniform waveforms using complex rays. *Physical Review E* 73: 036704–1–13.
- Arnold V (1976) *Les Méthodes Mathématiques De La Mécanique Classique*. Moscou: Mir Editions.
- Astiz L, Earle P, and Shearer P (1996) Global stacking of broadband seismograms. *Seismological Research Letters* 67: 4.8–4.18.
- Babić V (1956) Ray method of the computation of the intensity of wave fronts (in Russian). *Doklady Akademii Nauk SSSR* 110: 355–357.
- Babić V (1975) Ludwig's method and the boundary layer method in the problem of diffraction on a smooth body. *Journal of Soviet Mathematics* 3: 395–407.
- Babić V (1986) The mathematical theory of diffraction (a survey of some investigations carried out in the laboratory of mathematical problems of geophysics, leningrad branch of the mathematical institute), translated in English 1988. *Proceedings of the Steklov Institute of Mathematics* 2: 47–63.
- Babić V and Buldyrev V (1991) *Short-Wavelength Diffraction Theory – Asymptotic Methods*, vol. 4. Berlin: Springer.
- Babić V and Kirpičnikova NY (1979) *The Boundary-Layer Method in Diffraction Problems*, vol. 3. Berlin: Springer.
- Backus G (1964) Geographical interpretation of measurements of average phase velocities of surface waves over great circular and great semi-circular paths. *Bulletin of the Seismological Society of America* 54: 571–610.
- Ben Menahem A and Gibson RL (1990) Scattering of elastic waves by localized anisotropic inclusions. *Journal of Acoustics Society of America* 87: 2300–2309.
- Benamou J (1996) Big ray tracing: Multivalued traveltime computation using viscosity solutions of the eikonal equation. *Journal of Computational Physics* 128: 463–474.
- Benz HM, Chouet SA, Dawson PB, Lahr JC, Page RA, and Hole JA (1996) Three-dimensional P and S wave velocity structure of Redoubt Volcano, Alaska. *Journal of Geophysical Research* 101: 8111–8128.
- Beydoun WB and Mendes M (1989) Elastic ray-Born ℓ^2 – migration/inversion. *Geophysical Journal* 97: 151–160.
- Beydoun WB and Tarantola A (1988) First Born and Rytov approximation: Modeling and inversion conditions in a canonical example. *Journal of Acoustics Society of America* 83: 1045–1055.
- Beylkin G (1985) Imaging of discontinuities in the inverse scattering problem by inversion of a causal generalized Radon transform. *Journal of Mathematical Physics* 26: 99–108.
- Beylkin G and Burridge R (1990) Linearized inverse scattering problems in acoustics and elasticity. *Wave Motion* 12: 15–52.
- Biggaard H, Spakman W, and Engdahl E (1998) Closing the gap between regional and global travel time tomography. *Journal of Geophysical Research* 103: 30055–30078.
- Billette F and Lambaré G (1998) Velocity macro-model estimation from seismic reflection data by stereotomography. *Geophysical Journal International* 135: 671–680.
- Billette F, Le Bégat S, Podvin P, and Lambaré G (2003) Practical aspects and applications of 2D stereotomography. *Geophysics* 68: 1008–1021.
- Biondi B (1992) Solving the frequency dependent eikonal equation. *62th Annual International Meeting, SEG, Expanded Abstracts* 1315–1319.
- Bishop TN, Bube KP, Cutler RT, *et al.* (1985) Tomographic determination of velocity and depth in laterally varying media. *Geophysics* 50: 903–923.
- Bleistein N (1984) *Mathematical Methods for Wave Phenomena*. London: Academic Press.
- Bleistein N (1987) On the imaging of reflectors in the Earth. *Geophysics* 52: 931–942.

- Bleistein N, Cohen J, and Hagin F (1987) Two and one half dimensional Born inversion with an arbitrary reference. *Geophysics* 52: 26–36.
- Born M and Wolf E (1980) *Principles of Optics*, 6th edn. Oxford: Pergamon.
- Borovikov V and Kinber BY (1974) Some problems in the asymptotic theory of diffraction. *Proceedings of the IEEE* 62: 1416–1437.
- Brown M and Tappert F (1987) Catastrophe theory, caustics and traveltime diagrams in seismology. *Geophysical Journal of the Royal Astronomical Society* 88: 217–229.
- Buchal RN and Keller JB (1960) Boundary layer problems in diffraction theory. *Communications on Pure and Applied Mathematics* 13: 85–114.
- Buldyrev VBV and Molotkov I (1985) *Space-Time Ray Method. Linear and Non-Linear Waves* (in Russian). Leningrad: Leningrad University Press.
- Bullen K and Bolt B (1985) *An Introduction to the Theory of Seismology*. Berlin, Heidelberg: Cambridge University Press.
- Burridge R (1976) *Some Mathematical Topics in Seismology*. New York University, New York: Courant Institute of Mathematics and Science.
- Burridge R and Weinberg H (1977) Horizontal rays and vertical modes. In: Keller J and Papadakis J (eds.) *Wave Propagation and Underwater Acoustics*, vol. 70, pp. 86–152. Berlin: Springer.
- Cagniard L (1939) *Réflexion Et Réfraction Des Ondes Séismiques Progressives*. Paris: Gauthier-Villars.
- Cao D, Beydoun WB, Singh S, and Tarantola A (1990) A simultaneous inversion for back-ground velocity and impedance maps. *Geophysics* 55: 458–469.
- Červený V (1985) The application of ray tracing to the numerical modeling of seismic wavefields in complex structures. In: Helbig K and Treitel S (eds.) *Handbook of Geophysical Exploration, Section I: Seismic Exploration*, vol. 15, pp. 1–124. London: G. Dohr, Geophysical Press.
- Červený V (2001) *Seismic Ray Theory*. Cambridge: Cambridge University Press.
- Červený V, Molotkov IA, and Pšenčík I (1977) *Ray Theory in Seismology*. Praha: Charles University Press.
- Červený V, Popov M, and Pšenčík I (1982) Computation of wave fields in inhomogeneous media – gaussian beam approach. *Geophysical Journal of the Royal Astronomical Society* 70: 109–128.
- Červený V and Pšenčík I (2005) Plane waves in viscoelastic anisotropic media – I. Theory. *Geophysical Journal International* 161: 197–212.
- Červený V and Pšenčík I (2005) Plane waves in viscoelastic anisotropic media – II. Numerical examples. *Geophysical Journal International* 161: 197–212.
- Červený V and Ravindra R (1971) *Theory of Seismic Head Waves*. Toronto: Toronto University Press.
- Chaljub E, Capdeville Y, and Villette J-P (2003) Solving elastodynamics in a fluid-solid heterogeneous sphere: A parallel spectral element approximation on non-conforming grids. *Journal of Computational Physics* 187: 457–491.
- Chapman C (1974) The turning point of elastodynamic waves. *Geophysical Journal of the Royal Astronomical Society* 39: 673–704.
- Chapman C (1978) A new method of computing synthetic seismograms. *Geophysical Journal of the Royal Astronomical Society* 54: 481–518.
- Chapman C (1985) Ray theory and its extension: WKBJ and Maslov seismograms. *Journal of Geophysics* 58: 27–43.
- Chapman C and Coates R (1994) Generalized Born scattering in anisotropic media. *Wave Motion* 19: 309–341.
- Chapman C and Drummond R (1982) Body-wave seismograms in inhomogeneous media using Maslov asymptotic theory. *Bulletin of the Seismological Society of America* 72: S277–S317.
- Chapman C and Orcutt J (1985) The computation of body wave synthetic seismograms in laterally homogeneous media. *Reviews of Geophysics* 23: 105–163.
- Chapman CH (2004) *Fundamentals of Seismic Wave Propagation*. Cambridge: Cambridge University Press.
- Chauris H and Noble M (2001) 2D velocity macro model estimation from seismic reflection data by local Differential Semblance Optimization: Applications on synthetic and real data. *Geophysical Journal International* 144: 14–26.
- Chevrot S (2000) Multichannel analysis of shear wave splitting. *Journal of Geophysical Research* 105: 21579–21590.
- Claerbout JF (1970) Coarse grid calculations of wave in inhomogeneous media with application to delineation of complicated seismic structure. *Geophysics* 35: 407–418.
- Clarke TJ (1993) The complete ordered ray expansion – I. Calculation of synthetic seismograms. *Geophysical Journal International* 115: 421–434.
- Clarke TJ (1993) The complete ordered ray expansion – II. Multiphase body wave tomography. *Geophysical Journal International* 115: 435–444.
- Clayton RW and Stolt R (1981) A Born-WKBJ inversion method for acoustic reflection data. *Geophysics* 46: 1558–1565.
- Coates RT and Chapman CH (1990) Ray perturbation theory and the Born approximation. *Geophysical Journal International* 100: 379–392.
- Cohen JK, Hagin F, and Bleistein N (1986) Three-dimensional Born inversion with an arbitrary reference. *Geophysics* 51: 1552–1558.
- Courant R and Hilbert D (1966) *Methods of Mathematical Physics*. New York: Wiley.
- Dahlen F and Baig A (2002) Fréchet kernels for body-wave amplitudes. *Geophysical Journal International* 150: 440–466.
- Dahlen F, Hung S-H, and Nolet G (2000) Fréchet kernels for finite-frequency traveltimes – I. Theory. *Geophysical Journal International* 141: 157–174.
- Dahlen F and Tromp J (1998) *Theoretical Global Seismology*. Princeton: Princeton University Press.
- de Hoop AT (1960) A modification of Cagniard's method for solving seismic pulse problems. *Applied Scientific Research* B8: 349–356.
- de Hoop AT (1990) Acoustic radiation from an impulsive point source in a continuously layered fluid – an analysis based on the Cagniard method. *Journal of Acoustics Society of America* 88: 2376–2388.
- de Hoop M and van der Hilst R (2005) On sensitivity kernels for ‘wave-equation’ transmission tomography. *Geophysical Journal International* 160: 621–633.
- Deschamps GA (1971) Gaussian beams as a bundle of complex rays. *Electronics Letters* 7: 684–685.
- Devaney A (1981) Inverse scattering theory within the Rytov approximation. *Optics Letters* 6: 374–376.
- Dey-Sarkar S and Chapman C (1978) A simple method for the computation of body-wave seismograms. *Bulletin of the Seismological Society of America* 68: 1577–1593.
- Dijkstra E (1959) A note on two problems in connection with graphs. *Numerische Mathematik* 1: 269–271.
- Eaton D (1993) Finite difference traveltime calculation for anisotropic media. *Geophysical Journal International* 114: 273–280.
- Farra V (1990) Amplitude computation in heterogeneous media by ray perturbation theory: A finite element approach. *Geophysical Journal International* 103: 341–354.
- Farra V (1992) Bending method revisited: A hamiltonian approach. *Geophysical Journal International* 109: 138–150.
- Farra V (2005) First-order ray tracing for qS waves in inhomogeneous weakly anisotropic media. *Geophysical Journal International* 161: 309–324.

- Farra V and Madariaga R (1987) Seismic waveform modeling in heterogeneous media by ray perturbation theory. *Journal of Geophysical Research* 92: 2697–2712.
- Farra V and Madariaga R (1988) Non-linear reflection tomography. *Geophysical Journal* 95: 135–147.
- Farra V, Virieux J, and Madariaga R (1989) Ray perturbation theory for interfaces. *Geophysical Journal International* 99: 377–390.
- Fatemi E, Engquist B, and Osher S (1995) Numerical solution of the high frequency asymptotic expansion for the scalar wave equation. *Journal of Computational Physics* 120: 145–155.
- Favier N and Chevrot S (2003) Sensitivity kernels for shear wave splitting in transverse isotropic media. *Geophysical Journal International* 153: 213–228.
- Favier N, Chevrot S, and Komatitsch D (2004) Near-field influence on shear wave splitting and traveltimes sensitivity kernels. *Geophysical Journal International* 156: 467–482.
- Felsen L (1976) Evanescent waves. *Journal of the Optical Society of America* 66: 751–760.
- Felsen L (1984) Geometrical theory of diffraction, evanescent waves, complex rays and gaussians beams. *Geophysical Journal of the Royal Astronomical Society* 79: 77–88.
- Fock V (1965) *Electromagnetic Diffraction and Propagation Problems*. Oxford: Pergamon.
- Font Y, Kao H, Lallemand S, Liu C-S, and Chiao J-Y (2004) Hypocentral determination offshore Eastern Taiwan using the Maximum Intersection method. *Geophysical Journal International* 158: 655–675.
- Frazer L and Sen M (1985) Kirchhoff-Helmholtz reflection seismograms in a laterally inhomogeneous multi-layered elastic medium – I. Theory. *Geophysical Journal of the Royal Astronomical Society* 80: 121–147.
- French W (1974) Two-dimensional and three dimensional migration of model-experiment reflection profiles. *Geophysics* 39: 265–277.
- French WS (1975) Computer migration of oblique seismic reflection profiles. *Geophysics* 40: 961–980.
- Fuchs K and Müller G (1971) Computation of synthetic seismograms with the reflectivity method and comparison of observations. *Geophysical Journal of the Royal Astronomical Society* 23: 417–433.
- Gauthier O, Virieux J, and Tarantola A (1986) Two-dimensional nonlinear inversion of seismic waveforms: Numerical results. *Geophysics* 51: 1387–1403.
- Gélis C, Virieux J, and Grandjean G (2007) 2D elastic full waveform inversion using Born and Rytov formulations in the frequency domain. *Geophysical Journal International* 168: 605–633.
- Gibson RL and Ben Menahem A (1991) Elastic wave scattering by anisotropic obstacles: Application to fractured volumes. *Journal of Geophysical Research* 96: 19905–19924.
- Gilbert F and Backus G (1966) Propagator matrices in elastic wave and vibration problems. *Geophysics* 31: 326–332.
- Gilmore R (1981) *Catastrophe Theory for Scientists and Engineers*. New York: Wiley-Interscience.
- Goldstein H (1980) *Classical Mechanics*. Addison-Wesley Reading: Publishing Compagny.
- Gray S (1982) A geometric-optic serie and a WKB paradox. *Quarterly of Applied Mathematics* 40: 73–81.
- Gray S (1983) On the convergence of the time-domain Bremmer series. *Wave Motion* 5: 249–255.
- Gray SH and May WP (1994) Kirchhoff migration using eikonal equation traveltimes. *Geophysics* 54: 810–817.
- Hill D (1973) Critical refracted waves in a spherically symmetric radially heterogeneous Earth model. *Geophysical Journal of the Royal Astronomical Society* 34: 149–179.
- Hill N (1990) Gaussian beam migration. *Geophysics* 55: 1416–1428.
- Hill N (2001) Prestack Gaussian-beam depth migration. *Geophysics* 66: 1240–1250.
- Hron F (1972) Numerical methods of ray generation in multi-layered media. In: Bolt B, Alder B, Fernbach S, and Rotenberg M (eds.) *Methods in Computational Physics*, vol. 12, pp. 1–34. New York: Academic Press.
- Hron F and Chan G (1995) Tutorial on the numerical modeling of edge diffracted waves by the ray method. *Studia Geophysica Et Geodaetica* 39: 103–137.
- Hron F, May B, Covey J, and Daley P (1986) Synthetic seismic sections for acoustic, elastic, anisotropic and inhomogeneous layered media. *Geophysics* 51: 710–735.
- Huang X and West G (1997) Effects of weighting functions on Maslov uniform seismograms: A robust weighting method. *Bulletin of the Seismological Society of America* 87: 164–173.
- Hudson J and Heritage J (1981) *Use of the Born Approximation in Seismic Scattering Problems*. Cambridge: Cambridge University Press.
- Hung S-H, Dahlen F, and Nolet G (2000) Fréchet kernels for finite-frequency traveltimes – II. Examples. *Geophysical Journal International* 141: 175–203.
- Ikelle L, Diet JP, and Tarantola A (1988) Linearized inversion of multioffset seismic reflection data in the $\omega - k$ domain: Depth-dependent reference medium. *Geophysics* 53: 50–64.
- Jannane M, Beydoun W, Crase E, et al. (1989) Wavelengths of Earth structures that can be resolved from seismic reflection data. *Geophysics* 54: 906–910.
- Jin S, Madariaga R, Virieux J, and Lambaré G (1992) Two-dimensional asymptotic iterative elastic inversion. *Geophysical Journal International* 108: 575–588.
- Karal F and Keller J (1959) Elastic wave propagation in homogeneous and inhomogeneous media. *Journal of the Optical Society of America* 31: 694–705.
- Katzman R, Zhao L, and Jordan T (1998) High-resolution, two-dimensional vertical tomography of the central Pacific mantle using SCS reverberations and frequency-dependent travel times. *Journal of Geophysical Research* 103: 17933–17971.
- Keilis-Borok V (1989) *Seismic Surface Waves in a Laterally Inhomogeneous Earth*. Dordrecht: Kluwer.
- Keller H and Perozzi P (1983) Fast seismic ray tracing. *Siam Journal of Applied Mathematics* 43: 981–992.
- Keller J (1962) A geometrical theory of diffraction. *Journal of the Optical Society of America* 52: 116–130.
- Keller J (1969) Accuracy and validity of the Born and Rytov approximations. *Journal of the Optical Society of America* 59: 1003–1004.
- Keller J (1971) Complex rays with an application to Gaussian beams. *Journal of the Optical Society of America* 61: 40–43.
- Kendall J-M and Nangini C (1996) Lateral variations in D below the Caribbean. *Geophysical Research Letters* 23: 399–402.
- Kendall J-M and Thomson C (1993) Maslov ray summation, pseudo-caustics, lagrangian equivalence and transient seismic waveforms. *Geophysical Journal International* 113: 186–214.
- Kennett B (1983) *Seismic Wave Propagation in Stratified Media*. Cambridge: Cambridge University Press.
- Klauder J (1987a) Global uniform asymptotic wave-equation solutions for large wavenumbers. *Annals of Physics* 180: 108–151.
- Klauder J (1987b) New asymptotics for old wave equations. *Science* 239: 760–762.
- Klem-Musatov K (1995) *Theory of Seismic Diffraction*. Tulsa: Society of Exploration Geophysicists.
- Klimeš L and Kvaskička M (1994) 3-D network ray tracing. *Geophysical Journal International* 116: 726–738.
- Kolb P, Collino F, and Lailly P (1986) Prestack inversion of 1D medium. *Proceedings of the IEEE* 74: 498–508.

- Körnig M (1995) Cell ray tracing for smooth, isotropic media: A new concept based on a generalized analytic solution. *Geophysical Journal International* 123: 391–408.
- Kravtsov Y (1964) On a modification of the method of geometrical optics. *Radiotekhnika* 7: 664–673.
- Kravtsov Y (1968) Two new asymptotic methods in the theory of wave propagation in inhomogeneous media (review). *Soviet Physics Acoustics* 14: 1–17.
- Kravtsov Y and Orlov Y (1990) *Geometrical Optics of Inhomogeneous Media*. Berlin: Springer.
- Kvasnička M and Janský J (1999) Fresnel volumes corresponding to PKP waves in the IASP91 model. *Journal of Seismology* 3: 375–391.
- Lailly P (1983) The seismic inverse problem as a sequence of before stack migrations. In: Bednar R and Weglein (eds.) *Conference on Inverse Scattering, Theory and Application, SIAM*, pp. 206–220. Philadelphia, PA: Society for Industrial and Applied Mathematics.
- Lambaré G, Lucio PS, and Hanyga A (1996) Two-dimensional multivalued traveltime and amplitude maps by uniform sampling of ray field. *Geophysical Journal International* 125: 584–598.
- Langer R (1937) On the connection formulas and the solution of the wave equation. *Physical Reviews* 51: 669–676.
- Latham G, Ewing M, Dorman J, et al. (1971) Moonquakes. *Science* 174: 687–692.
- Latorre D, Virieux J, Monfret T, et al. (2004) A new seismic tomography of Aigion area (Gulf of Corinth, Greece) from the 1991 data set. *Geophysical Journal International* 159: 1013–1031.
- Lay T and Garnero E (2004) Core mantle boundary structure and processes. In: Sparks R and Hawkesworth C (eds.) *The State of the Planet: Frontiers and Challenges in Geophysics*, vol. 150, pp. 25–41. Washington, DC: Geophysical Monograph Series, AGU.
- Lay T and Wallace T (1995) *Modern Global Seismology*. New York: Academic Press.
- Le Bégat S and Farra V (1997) P-wave travel time polarization tomography of VSP data. *Geophysical Journal International* 131: 100–114.
- Le Meur H, Virieux J, and Podvin P (1997) Seismic tomography of the gulf of Corinth: A comparison of methods. *Annali Di Geofisica XL*: 1–24.
- Lecomte I (1993) Finite difference calculation of first traveltimes in anisotropic media. *Geophysical Journal International* 113: 318–342.
- Li X and Romanowicz B (1995) Comparison of global waveform inversions with and without considering cross branch coupling. *Geophysical Journal International* 121: 695–709.
- Li X and Tanimoto T (1993) Waveforms of long period body waves in a slightly aspherical earth. *Geophysical Journal International* 112: 92–112.
- Lomax A (1999) Path-summation waveforms. *Geophysical Journal International* 138: 702–716.
- Lomax A, Virieux J, Volant P, and Berge C (2000) Probabilistic earthquake location in 3D and layered models: Introduction of a Metropolis-Gibbs method and comparison with linear locations. In: Thurber C and Rabinowitz N (eds.) *Advances in Seismic Event Location*, vol. 281, pp. 101–134. Amsterdam: Kluwer.
- Lucio P, Lambaré G, and Hanyga A (1996) 3D multivalued travel time and amplitude maps. *Pure and Applied Geophysics* 148: 113–136.
- Ludwig D (1966) Uniform asymptotic expansions at a caustic. *Communications on Pure and Applied Mathematics* 19: 215–250.
- Luneberg R (1964) *Mathematical Theory of Optics*. Berkeley: University of California Press.
- Luo Y and Schuster G (1991) Wave-equation travel time tomography. *Geophysics* 56: 645–653.
- Madariaga R (1984) Gaussian beam synthetic seismograms in a vertically varying medium. *Geophysical Journal of the Royal Astronomical Society* 79: 589–612.
- Marquering H, Dahlen F, and Nolet G (1999) Three-dimensional sensitivity kernels for finite-frequency traveltimes: The banana-doughnut paradox. *Geophysical Journal International* 137: 805–815.
- Marquering H, Nolet G, and Dahlen F (1998) Three-dimensional waveform sensitivity kernels. *Geophysical Journal International* 132: 521–534.
- Maslov V and Fedoriuk M (1981) *Semi-Classical Approximation in Quantum Mechanics*. Dordrecht: D. Reidel Publication Company.
- Moczo P, Robertsson J, and Eisner L (2007) The finite-difference time-domain method for modelling of seismic wave propagation. In: Wu R-S and Maupin V (eds.) *Advances in Wave Propagation in Heterogeneous Earth*, Vol. 48, p. 96. Elsevier-Pergamon.
- Montelli R, Nolet G, Dahlen F, Masters G, Engdahl E, and Hung S (2004) Finite-frequency tomography reveals a variety of plumes in the mantle. *Science* 303: 338–343.
- Montelli R, Nolet G, Masters G, Dahlen F, and Hung S (2004) P and PP global travel time tomography. *Geophysical Journal International* 158: 637–654.
- Morse P and Feshbach H (1953) *Methods of Theoretical Physics*. New York: McGraw-Hill.
- Moser T, Nolet G, and Snieder R (1992) Ray bending revisited. *Bulletin of the Seismological Society of America* 82: 259–288.
- Moser T, van Eck T, and Nolet G (1992) Hypocenter determination in strongly heterogeneous earth models using the shortest path method. *Journal of Geophysical Research* 97: 6563–6572.
- Nahamoo D, Pan S, and Kak A (1984) Synthetic aperture diffraction tomography and its interpolation-free computer implementation. *IEE Transactions on Sonics and Ultrasonics* 4(SU31): 218–228.
- Ni S, Cormier V, and Helmberger D (2003) A comparison of synthetic seismograms for 2D structures: Semianalytical versus numerical. *Bulletin of the Seismological Society of America* 93: 2752–2757.
- Nowack R (2003) Calculating of synthetic seismograms with Gaussian beams. *Pure and Applied Geophysics* 160: 487–507.
- Nowack R and Stacy S (2002) Synthetic seismograms and wide-angle seismic attributes for the Gaussian beam and reflectivity methods for models with interfaces and velocity gradients. *Pure and Applied Geophysics* 159: 1447–1464.
- Operto S, Ravaut C, Imrota L, Virieux J, Herrero A, and Dell'Aversana P (2004) Quantitative imaging of complex structures from dense wide-aperture seismic data by multi-scale traveltime and waveform inversions: A case study. *Geophysical Prospecting* 52: 625–651.
- Operto S, Xu S, and Lambaré G (2000) Can we quantitatively image complex models with rays? *Geophysics* 65: 1223–1238.
- Pekeris C (1955) The seismic surface pulse. *Proceedings of the National Academy of Sciences of United States of America* 41: 469–480.
- Pekeris C (1955) The seismic buried pulse. *Proceedings of the National Academy of Sciences of United States of America* 41: 629–639.
- Pereyra V (1992) Two-point ray tracing in a general 3D media. *Geophysical Prospecting* 40: 267–287.
- Pereyra V, Lee W, and Keller H (1980) Solving two-point seismic-ray tracing problems in a heterogeneous medium. Part 1: A general adaptive finite difference method. *Bulletin of the Seismological Society of America* 70: 79–99.

- Pica A (1997) Fast and accurate finite-difference solutions of the 3-D eikonal equation parameterized in celerity. *67th Annual International Meeting, SEG, Expanded Abstracts* 1774–1777.
- Pica A (1998) Resolution of the 3-D eikonal equation parameterized in celerity in weak TI media. *68th Annual International Meeting, SEG, Expanded Abstracts* 1–23.
- Pica A, Diet J, and Tarantola A (1990) Nonlinear inversion of seismic reflection data in laterally invariant medium. *Geophysics* 55: 284–292.
- Plessix RE, Chavent G, and De Roeck Y (1995) Automatic and simultaneous migration velocity analysis and waveform inversion of real data using a MBTT/WKBJ formulation. *65th Annual Meeting, SEG, Expanded Abstracts* 1099–1101.
- Podvin P and Lecomte I (1991) Finite difference computation of traveltimes in very contrasted velocity models: A massively parallel approach and its associated tools. *Geophysical Journal International* 105: 271–284.
- Popov M (1982) A new method of computation of wave fields using Gaussian beams. *Wave Motion* 4: 85–95.
- Popov M and Pšenčík I (1978) Computation of ray amplitudes in inhomogeneous media with curved interfaces. *Studia Geophysica Et Geodaetica* 22: 248–258.
- Pratt RG, Song Z, and Warner M (1996) Two-dimensional velocity models from wide-angle seismic data by wavefield inversion. *Geophysical Journal International* 124: 323–340.
- Press WH, Vetterling WT, Teukolsky SA, and Flannery BP (1994) *Numerical Recipies in Fortran*, 2nd edn. Cambridge: Cambridge University Press.
- Pšenčík I and Farra V (2005) First-order ray tracing for qP waves in inhomogeneous weakly anisotropic media. *Geophysics* 70: D65–D67.
- Rawlinson N and Sambridge M (2004) Wave front evolution in strongly heterogeneous layered media using the fast marching. *Geophysical Journal International* 156: 631–647.
- Ribodetti A, Operto S, Virieux J, Lambaré G, Valéro H-P, and Gibert D (2000) Asymptotic viscoacoustic diffraction tomography of ultrasonic laboratory data: A tool for rock properties analysis. *Geophysical Journal International* 140: 324–340.
- Richards P (1973) Calculation of body waves for caustics and tunnelling core phases. *Geophysical Journal of the Royal Astronomical Society* 66: 701–718.
- Richards PG and Frasier CW (1976) Scattering of elastic waves from depth-dependent inhomogeneities. *Geophysics* 41: 441–458.
- Rytov S, Kravtsov Y, and Tatarskii V (1987) *Principles of Statistical Radiophysics*. Berlin: Springer.
- Sambridge M and Kennett B (1990) Boundary value ray tracing in a heterogeneous medium: A simple and versatile algorithm. *Geophysical Journal International* 101: 157–168.
- Samuelides Y (1998) Velocity shift using the Rytov approximation. *Journal of Acoustics Society of America* 104: 2596–2603.
- Schlottmann R (1999) A path integral formulation of acoustic wave propagation. *Geophysical Journal International* 137: 353–363.
- Scholte J (1962) Oblique propagation of waves in inhomogeneous media. *Geophysical Journal of the Royal Astronomical Society* 7: 244–261.
- Sethian J (1999) *Level Set Methods and Fast Marching Methods*. Cambridge: Cambridge University Press.
- Sethian J and Popovici A (1999) 3-D travelttime computation using the fast marching method. *Geophysics* 64: 516–523.
- Shaw P (1986) The accuracy of models derived by WKBJ waveform inversion. *Geophysical Journal of the Royal Astronomical Society* 85: 291–313.
- Snieler R and Spencer C (1993) A unified approach to ray bending, ray perturbation and paraxial ray theory. *Geophysical Journal International* 115: 456–470.
- Snieler R, Xie M, Pica A, and Tarantola A (1989) Retrieving both the impedance contrast and background velocity: A global strategy for the seismic reflection problem. *Geophysics* 54: 991–1000.
- Symes W and Kern M (1994) Inversion of reflection seismograms by differential semblance analysis: Algorithm structure and synthetic examples. *Geophysical Prospecting* 42: 565–614.
- Symes WW (1993) A differential semblance criterion for inversion of multioffset seismic reflection data. *Journal of Geophysical Research* 98: 2061–2073.
- Symes WW and Carazzone J (1991) Velocity inversion by differential semblance optimization. *Geophysics* 56: 654–663.
- Tanimoto T (1995) Formalism for travelttime inversion with finite frequency effects. *Geophysical Journal International* 121: 103–110.
- Tarantola A (1984a) Inversion of seismic reflection data in the acoustic approximation. *Geophysics* 49: 1259–1266.
- Tarantola A (1984b) Linearized inversion of seismic reflection data. *Geophysical Prospecting* 32: 998–1015.
- Tarantola A (1986) A strategy for non linear inversion of seismic reflection data. *Geophysics* 51: 1893–1903.
- Tarantola A (1987) *Inverse Problem Theory: Methods for Data Fitting and Model Parameter Estimation*. Netherlands: Elsevier.
- Thierry P, Lambaré G, Podvin P, and Noble M (1999a) 3-D preserved amplitude prestack depth migration on a workstation. *Geophysics* 64: 222–229.
- Thierry P, Operto S, and Lambaré G (1999b) Fast 2D ray-Born inversion/migration in complex media. *Geophysics* 64: 162–181.
- Thomson C (1989) Corrections for grazing rays in 2-D seismic modelling. *Geophysical Journal* 96: 415–446.
- Thomson C (1990) Corrections for critical rays in 2-D seismic modelling. *Geophysical Journal International* 103: 171–210.
- Thomson C (2001) Seismic coherent states and geometrical spreading. *Geophysical Journal International* 144: 320–342.
- Thomson C (2004) Coherent-state analysis of the seismic head wave problem: An overcomplete representation and its relationship to rays and beams. *Geophysical Journal International* 157: 1189–1205.
- Um J and Thurber C (1987) A fast algorithm for two-point seismic ray tracing. *Bulletin of the Seismological Society of America* 77: 972–986.
- Ursin B and Tygel M (1997) Reciprocal volume and surface scattering integrals for anisotropic elastic media. *Wave Motion* 26: 31–42.
- Verweij M and de Hoop AT (1990) Determination of seismic wavefields in arbitrarily continuous layered media using the modified Cagniard method. *Geophysical Journal International* 103: 731–754.
- Vidale D (1988) Finite-difference calculation of travel time. *Bulletin of the Seismological Society of America* 78: 2062–2076.
- Vidale D (1990) Finite-difference calculation of traveltimes in three dimensions. *Geophysics* 55: 521–526.
- Vinje V, Iversen E, Astebøl K, and Gjøystdal H (1996a) Estimation of multivalued arrivals in 3D models using wavefront construction-part I. *Geophysical Prospecting* 44: 819–842.
- Vinje V, Iversen E, Astebøl K, and Gjøystdal H (1996b) Estimation of multivalued arrivals in 3D models using wavefront construction-part II: Tracing and interpolation. *Geophysical Prospecting* 44: 843–858.
- Vinje V, Iversen E, and Gjøystdal H (1993) Travelttime and amplitude estimation using wavefront construction. *Geophysics* 58: 1157–1166.
- Virieux J (1984) SH wave propagation in heterogeneous media, velocity-stress finite difference method. *Geophysics* 49: 1259–1266.

- Virieux J (1986) P-SV wave propagation in heterogeneous media, velocity-stress finite difference method. *Geophysics* 51: 889–901.
- Virieux J (1991) Fast and accurate ray tracing by Hamiltonian perturbation. *Journal of Geophysical Research* 96: 579–594.
- Virieux J (1996) Seismic ray tracing. In: Boschi E, Ekström G, and Morelli A (eds.) *Seismic Modelling of Earth Structure*. pp. 223–304. Bologna: Editrice Compositori.
- Virieux J and Farra V (1991) Ray tracing in 3-D complex isotropic media: An analysis of the problem. *Geophysics* 56: 2057–2069.
- Virieux J, Farra V, and Madariaga R (1988) Ray tracing for earthquake location in laterally heterogeneous media. *Journal of Geophysical Research* 93: 1116–1120.
- Virieux J, Garnier N, Blanc E, and Dessa J-X (2004) Paraxial ray tracing for atmospheric wave propagation. *Geophysical Research Letters* 31: L20106 (doi:10.1029/2004GL020514).
- Wasow W (1965) *Asymptotic Expansions of Ordinary Differential Equations*, vol. 14. New York: Interscience Publishers, Wiley.
- Weber M (1988) Computation of body-wave seismograms in absorbing 2-D media using the Gaussian beam method: Comparison and exact methods. *Geophysical Journal* 92: 9–24.
- White B, Norris A, Bayliss A, and Burridge R (1987) Some remarks on the Gaussian beam summation method. *Geophysical Journal of the Royal Astronomical Society* 89: 579–636.
- Woodhouse J (1974) Asymptotic results for elastodynamic propagator matrices in plane stratified and spherically stratified Earth models. *Geophysical Journal of the Royal Astronomical Society* 37: 263–280.
- Woodward M (1992) Wave-equation tomography. *Geophysics* 57: 15–26.
- Wu R (1989) The perturbation method in elastic wave scattering. *Pure and Applied Geophysics* 131: 605–638.
- Wu R-S (1985) Gaussian beams, complex rays, and analytic extension of the Green's function in smoothly inhomogeneous media. *Geophysical Journal of the Royal Astronomical Society* 83: 93–110.
- Xu S, Chauris H, Lambaré G, and Noble M (2001) Common angle image gather: A strategy for imaging complex media. *Geophysics* 66: 1877–1894.
- Xu S and Lambaré G (2004) Fast migration/inversion with multiarrival ray fields. Part I: Method, validation test and application in 2D to Marmousi. *Geophysics* 69: 1311–1319.
- Xu S, Lambaré G, and Calandra H (2004) Fast migration/inversion with multiarrival ray fields. Part II: Application to the 3D SEG/EAGE Salt model. *Geophysics* 69: 1320–1328.
- Yanovskaya TB (1996) Ray tomography based on azimuthal anomalies. *Pure and Applied Geophysics* 148: 319–336.
- Yedlin M, Seymour B, and Zelt B (1990) Comparison of the WKBJ and truncated asymptotic methods for an acoustic medium. *Geophysical Journal International* 101: 49–60.
- Zhang L, Rector JW, III, and Hoversten G (2005) Eikonal solver in the celerity domain. *Geophysical Journal International* 162: 1–8.
- Zhao L, Jordan T, and Chapman C (2000) Three-dimensional Fréchet differential kernels for seismic delay times. *Geophysical Journal International* 141: 558–576.
- Zhou Y, Dahlen F, and Nolet G (2004) Three-dimensional sensitivity kernels for surface wave observables. *Geophysical Journal International* 158: 142–168.
- Zhu T (1988) A ray-Kirchhoff method for body-wave calculations in inhomogeneous media: Theory. *Geophysical Journal* 92: 181–193.
- Zhu T and Chun K-Y (1994a) Understanding finite-frequency wave phenomena: Phase-ray formulation and inhomogeneity scattering. *Geophysical Journal International* 119: 78–90.
- Zhu T and Chun K-Y (1994b) Complex rays in elastic and anelastic media. *Geophysical Journal International* 119: 269–276.
- Ziolkowski R and Deschamps G (1984) Asymptotic evaluation of high-frequency fields near a caustic: An introduction to Maslov's method. *Radio Science* 19: 1001–1025.

1.05 Theory and Observations – Forward Modeling/Synthetic Body Wave Seismograms

V. F. Cormier, University of Connecticut, Storrs, CT, USA

© 2007 Elsevier B.V. All rights reserved.

1.05.1	Introduction	157
1.05.2	Plane-Wave Modeling	159
1.05.2.1	Elastic Velocities and Polarizations	159
1.05.2.2	Superposition of Plane Waves	161
1.05.3	Structural Effects	161
1.05.3.1	Common Structural Effects on Waveforms	161
1.05.3.2	Deep-Earth Structural Problems	164
1.05.4	Modeling Algorithms and Codes	165
1.05.4.1	Reflectivity	166
1.05.4.2	Generalized Ray	168
1.05.4.3	WKB-J-Maslov	168
1.05.4.4	Full-Wave Theory and Integration in Complex p Plane	170
1.05.4.5	DRT and Gaussian Beams	171
1.05.4.6	Modal Methods	172
1.05.4.7	Numerical Methods	173
1.05.5	Parametrization of the Earth Model	176
1.05.5.1	Homogeneous Layers Separated by Curved or Tilted Boundaries	176
1.05.5.2	Vertically Inhomogeneous Layers	177
1.05.5.3	General 3-D Models	177
1.05.6	Instrument and Source	178
1.05.6.1	Instrument Responses and Deconvolution	179
1.05.6.2	Far-Field Source Time Function	179
1.05.7	Extensions	181
1.05.7.1	Adapting 1-D Codes to 2-D and 3-D	181
1.05.7.2	Hybrid Methods	181
1.05.7.3	Frequency-Dependent Ray Theory	181
1.05.7.4	Attenuation	182
1.05.7.5	Anisotropy	183
1.05.7.6	Scattering	184
1.05.8	Conclusions	185
References		185

1.05.1 Introduction

Body waves are solutions of the elastic equation of motion that propagate outward from a seismic source in expanding, quasi-spherical wave fronts, much like the rings seen when a rock is thrown in a pond. The normals to the wave fronts, called rays, are useful in illustrating body waves' interactions with gradients and discontinuities in elastic velocities and as well as their sense of polarization of particle motion. Except for the special cases of grazing incidence to discontinuities,

body-wave solutions to the equations of motion are nearly nondispersive. All frequencies propagate at nearly the same phase and group velocities. Hence the body wave excited by an impulsive, delta-like, seismic source-time function will retain its delta-like shape with propagation to great distances ([Figure 1](#)).

Surface waves are solutions of the elastic equations of motion that exponentially decay with depth beneath the surface of the Earth for a boundary condition of vanishing stress at the surface (*see* Chapter 1.02). Unlike body waves, surface waves are strongly

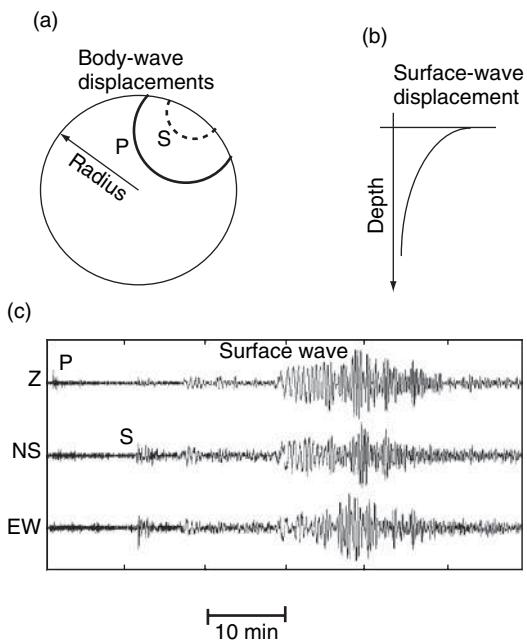


Figure 1 (a) Displacement of body waves is concentrated in propagating quasi-spherical wave fronts. (b) The displacement of surface waves exponentially decays away from the surface of the Earth. (c) Example seismogram showing impulsive, pulse-like, body waves and dispersive surface waves.

dispersed in the Earth, having phase and group velocities that depend on frequency. Observations of surface waves in the 0.001–0.1 Hz band of frequencies can constrain structure of the crust and upper mantle of the Earth, but only body waves provide information on the elastic velocities of the deeper interior of the Earth, all the way to its center. Summing modes of free oscillation of the Earth can represent both body and surface waves. The most efficient representation of the highest frequency content body waves, however, is given by propagating wave front or ray-type solutions of the elastic equations.

In a homogeneous Earth, the wave fronts of body waves are spherical, with radii equal to the distance from the source to an observation point on the wave front. Since the density of kinetic energy at a point in time is simply the surface area of the wave front, the particle velocity of a body wave is inversely proportional to the distance to the source. This inverse scaling of amplitude with increasing distance is termed the geometric spreading factor, R . Even in an inhomogeneous Earth, the inverse-distance scaling of body-wave amplitude can be used to make a rough estimate of the behavior of amplitude versus distance.

Rays follow paths of least or extremal time, representing a stationary phase approximation to a solution of a wave equation, Fourier-transformed in space and time. The least-time principle is expressed by Snell's law. In spherical geometry and radially varying velocity, Snell's law is equivalent to the constancy of a ray parameter or horizontal slowness p . The ray parameter is defined by $p = r \sin(i)/v(r)$, where i is the acute angle between the intersection of a ray path and a surface of radius r , and v is the body-wave velocity. Snell's law is obeyed by ray paths in regions of continuously varying velocity as well as by the ray paths of reflected and transmitted/converted waves excited at discontinuities. Since velocities usually increase with depth (decrease with radius) in the Earth, ray paths of body waves are usually concave upward (**Figure 2**). The least-time principle can also be exploited in linearized tomography to find perturbations to reference Earth models by assuming that ray paths are stationary with respect to small perturbations in velocities.

Complementing the information contained in travel times are the shapes (waveforms) of the body waves. Complexities and subtle shape changes observed in waveforms can be used to image elastic properties of the Earth at spatial scales down to a quarter wavelength from its surface to its center. The velocities of body waves in the Earth range from 1.5 km s^{-1} to greater than 13 km s^{-1} . Since waves that penetrate the deep interior of the Earth are commonly observed at frequencies at least up to 2 Hz, structure having spatial scales as small as 1 km can be potentially imaged from a densely sampled wavefield. Body waveforms also contain information about the spatial and temporal history of earthquake, explosion, or impact seismic sources.

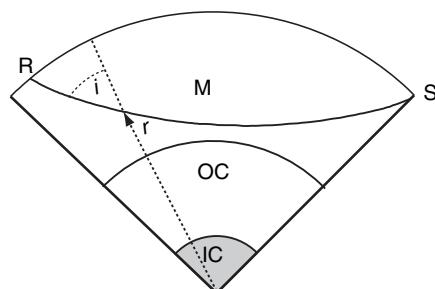


Figure 2 Following Snell's law in spherical geometry ($r \sin(i)/v = \text{constant}$), the ray paths of body waves in the Earth are mostly concave upward because elastic velocities mostly increase with depth.

This chapter reviews algorithms for modeling the effects of structure and source on teleseismic waveforms (see Chapter 1.22). It will point to references for the theoretical background of each algorithm and currently existing software. It will also make suggestions for the model parametrization appropriate to each algorithm, and the treatment of source-time functions, instrument responses, attenuation, and scattering. Mathematical development of each algorithm can be found in textbooks in advanced and computational seismology (Dahlen and Tromp, 1998; Aki and Richards, 1980, 2002; Kennett, 1983, 2001; Cerveny, 2001; Chapman, 2004). A thorough understanding of the derivation of each algorithm requires a background that includes solution of partial differential equations by separation of variables, special functions, integral transforms, complex variables and contour integration, and linear algebra. Practical use of each algorithm, however, often requires no more than a background in simple calculus and an intuitive understanding how a wavefield can be represented by superposing either wave fronts or modes at different frequencies.

1.05.2 Plane-Wave Modeling

1.05.2.1 Elastic Velocities and Polarizations

Two types of body waves were identified in early observational seismology, P, or primary, for the first arriving impulsive wave and S, or secondary, for a second slower impulsive wave (Bullen and Bolt, 1985). These are the elastic-wave types that propagate in an isotropic solid. In most regions of the Earth, elasticity can be well approximated by isotropy, in which only two elastic constants are required to describe a stress-strain relation that is independent of the choice of the coordinate system. In the case of anisotropy, additional elastic constants are required to describe the stress-strain relation. In a general anisotropic solid, there are three possible body-wave types, P, and two quasi-S waves, each having a different velocity.

The velocities of propagation and polarizations of motion of P and S waves can be derived from elastic equation of motion for an infinitesimal volume in a continuum:

$$\rho \frac{\partial^2 u_i}{\partial t^2} = +\sigma_{ij,j} = -f_i \quad [1]$$

where ρ is density, u_i is the i th component of the particle displacement vector \mathbf{U} , σ_{ij} is the stress tensor, and f_i is the i th component of body force that excites elastic motion. The elastic contact force in the i th direction is represented by the j th spatial derivative of the stress tensor, $\sigma_{ij,j}$. The stress tensor elements are related to spatial derivatives of displacement components (strains) by Hooke's law, which for general anisotropy takes the form

$$\sigma_{ij} = c_{ijkl} u_{k,l} \quad [2]$$

and for isotropy the form

$$\sigma_{ij} = \lambda \frac{\partial u_i}{\partial x_j} + \mu \left(\frac{\partial u_i}{\partial x_j} + \frac{\partial u_j}{\partial x_i} \right) \quad [3]$$

where c_{ijkl} , λ , and μ are elastic constants. The summation convention is assumed in [1]–[3], that is, quantities are summed over repeated indices.

Elastic-wave equations for P and S waves can be derived by respectively taking the divergence and curl of the equation of motion [1], demonstrating that volumetric strain, $\nabla \cdot \mathbf{U}$, propagates with a P-wave velocity,

$$V_p = \sqrt{\frac{\lambda + 2\mu}{\rho}} = \sqrt{\frac{K + 4/3\mu}{\rho}} \quad [4a]$$

and rotational strain, $\nabla \times \mathbf{U}$, propagates with the S-wave velocity,

$$V_s = \sqrt{\frac{\mu}{\rho}} \quad [4b]$$

Note that the P-wave velocity can be represented in terms of either the Lame parameter λ and shear modulus μ or the bulk modulus K and shear modulus μ .

Alternatively, the phase velocities and polarizations of body waves can be derived by assuming propagation of a plane wave having frequency ω and a normal \mathbf{k} of the form

$$\mathbf{U}(\mathbf{x}, t) = \mathbf{A} e^{i\omega t - \mathbf{k} \cdot \mathbf{x}} \quad [5]$$

and substituting this form into [1]. This substitution leads to an eigenvalue/eigenvector problem, in which the eigenvalues represent the magnitudes of the wavenumber vector \mathbf{k} , and hence phase velocities from $v = \omega/|\mathbf{k}|$. The associated eigenvectors represent the possible orientations of particle motion (e.g., Keith and Crampin, 1977). For propagation in three dimensions (3-D), there are three possible eigenvalues/eigenvectors, two of which are equal or degenerate in an isotropic medium. The eigenvalue

with the fastest phase velocity is the P wave. It has an eigenvector or polarization that is in the direction of the P ray, normal to the wave front. In an isotropic medium, the two degenerate eigenvalues and their eigenvectors are associated with the S wave. Their eigenvectors of polarization are perpendicular to the S ray, tangent to the wave front.

To facilitate the solution and understanding of the interactions of the P- and S-wave types with discontinuities in elastic moduli and/or density, it is convenient to define a ray (sagittal) plane containing the source, receiver, and center of the Earth. In an isotropic medium, the S polarization, which depends on the details of source excitation and receiver azimuth, is decomposed into an SV component, lying in the sagittal plane, and an SH component, perpendicular to the sagittal plane (Figure 3). At a discontinuity in elastic velocity, SV waves can excite converted-transmitted and reflected P waves and vice versa, but SH waves can only excite transmitted and reflected SH waves. The effects of body-wave-type conversions on polarizations have contributed to fundamental discoveries in deep Earth structure. The most famous example of these discoveries is the SV polarization of the SKS wave, which confirms that the outer core of the Earth is liquid. In this example, the SV component of an S wave incident on the boundary of the solid mantle excites a converted-transmitted P wave in the liquid outer core (K wave), which can convert back to an SV wave in the solid mantle. The SH component of the incident S wave cannot excite a K wave in the liquid

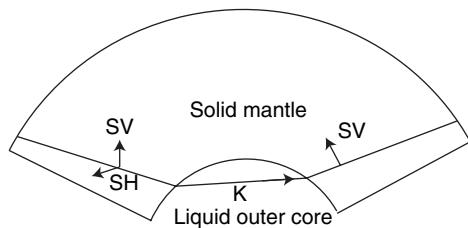


Figure 4 The SV component of the S wave on core–mantle boundary excites a compressional (K) wave in the outer core, which has its particle motion along its ray. The K wave exits the outer core as a transmitted SV wave in the mantle, which has its particle motion perpendicular to its ray, lying in the sagittal plane.

outer core, and hence the received SKS wave is purely SV polarized in an isotropic Earth (Figure 4).

Solutions of the elastic equations of motions can also be developed in terms of potentials, showing that the existence of fully decoupled P- and S-wave equations exist only in homogeneous regions where elastic moduli and density are constant in space (e.g., Aki and Richards, 2001). The use of potentials, however, leads to needless mathematical complexity when the quantities of modeling interest are displacements and stresses. This is especially true when solutions are continued across discontinuities in elastic moduli and density. At discontinuities, boundary conditions must be imposed on components u_i of the particle displacement vector \mathbf{U} and stress tensor elements σ_{ij} . Three fundamental types of boundary conditions occur in seismic wave propagation in the Earth: (1) the surface of the Earth, where all elements σ_{ij} vanish; (2) welded, slip-free, discontinuities between two solid discontinuities, where both particle displacements and stress tensor elements are continuous; and (3) liquid–solid discontinuities such as the ocean/ocean crust, mantle/outer core, and outer core/inner core, where only the displacements and stresses perpendicular to the discontinuity are continuous (see Chapter 1.19). These boundary conditions and the associated changes in the eigenvectors and eigenvalues of plane-wave solutions can be compactly handled by a fundamental matrix and propagator formalism (Gilbert and Backus, 1966). In this approach, the vertically separated component for the solution to the equations of motion is written as a linear system of the type:

$$\frac{df}{dz} = Af \quad [6]$$

where f is a 2-vector for the components of displacement and stress associated with SH waves or a

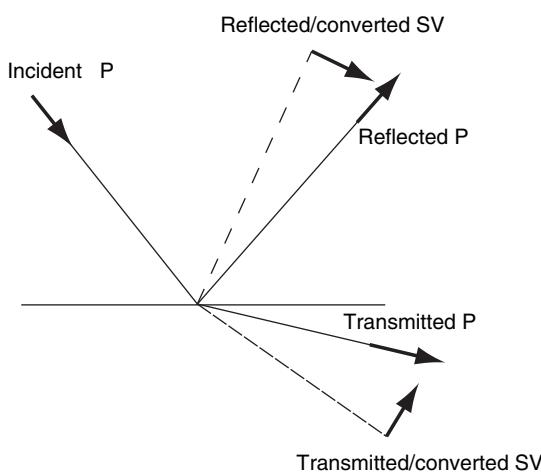


Figure 3 The interaction of a P wave incident on a discontinuity in P and S velocity, showing reflected and converted P and SV waves and their polarizations (arrows).

4-vector for the components of stress and displacement associated with P and SV waves; \mathbf{A} is either a 2×2 matrix for SH waves or a 4×4 matrix for P and SV waves; and derivative d/dz is with respect to depth or radius. The possibility of both up- and down-going waves allows the most general solution of the linear system in eqn [6] to be written as a solution for a fundamental matrix \mathbf{F} , where the rows of \mathbf{F} are the components of displacement and stress and the columns correspond to up- and down-going P and S waves. For P and SV waves, \mathbf{F} is a 4×4 matrix; for SH waves, \mathbf{F} is a 2×2 matrix. An example of the fundamental matrix for SH waves in a homogeneous layer is

$$\mathbf{F} = \begin{pmatrix} e^{i\omega k_z(z-z_0)} & e^{-i\omega k_z(z-z_0)} \\ ik_z \mu e^{i\omega k_z(z-z_0)} & -ik_z \mu e^{-i\omega k_z(z-z_0)} \end{pmatrix} \quad [7]$$

where z_0 is the reference depth, and the sign of the complex phasors represents propagation with or against the z -axis to describe down- or up-going waves.

The solution of [6] can be continued across discontinuities, with all boundary conditions satisfied, by use of a propagator matrix \mathbf{P} , where \mathbf{P} also satisfies [6]. The fundamental matrix in layer 0 at depth z_1 , $\mathbf{F}_0(z_1)$, is related to the fundamental matrix in layer N at z_N , $\mathbf{F}_N(z_N)$, through a propagator matrix $\mathbf{P}(z_1, z_N)$ such that

$$\mathbf{F}_0(z_1) = \mathbf{P}(z_1, z_N) \mathbf{F}_N(z_N) \quad [8a]$$

where

$$\mathbf{P}(z_1, z_N) = (\mathbf{F}_1(z_1) \mathbf{F}_1^{-1}(z_2))(\mathbf{F}_2(z_2) \mathbf{F}_2^{-1}(z_3)) \cdots \times (\mathbf{F}_{N-1}(z_{N-1}) \mathbf{F}_{N-1}^{-1}(z_N)) \quad [8b]$$

In an isotropic Earth model, once the relative source excitation of S waves has been resolved into separate SH and SV components of polarization, the treatment of boundary conditions on P and SV waves can be separated from that needed for SH waves by the use of the either the 4×4 fundamental matrices for P and SV waves or the 2×2 fundamental matrices for SH waves.

1.05.2.2 Superposition of Plane Waves

Superposition of plane waves of the form in [5] along with techniques of satisfying boundary conditions at discontinuities using fundamental and propagator matrix solutions of [8a] and [8b] allow calculation of all possible body-wave solutions of the elastic equations of motion as well as the dispersive-wave

interactions with the free surface (surface waves) and deeper discontinuities (diffractions and head waves). This process of superposition in space and frequency is equivalent to solution of the equations of motion by the integral transform methods of Fourier, Laplace, Bessel, or spherical harmonics. Fourier and Laplace transforms can always be applied in a Cartesian coordinate system, but analytic solutions of the equation of motion in terms of Bessel/Hankel and spherical harmonics is limited to Earth models whose layers and discontinuities are either spherically symmetric or plane-layered, having cylindrical symmetry about the source point. Some well-tested extensions and perturbation methods, however, allow their application to models in which the symmetry is broken by lateral heterogeneity, aspherical or non-planar boundaries, and anisotropy.

Transform-based methods, ray-based methods, and their extensions are reviewed in Section 1.05.4. Before beginning this review, however, it is important to have an intuitive feel for the effects of the Earth structure on the propagation of body waves, how structure can induce complexity in body waveforms, and what outstanding problems can be investigated by the synthesis of waveforms.

1.05.3 Structural Effects

1.05.3.1 Common Structural Effects on Waveforms

Body waves are commonly synthesized to study the effects of waveform complexity or multipathing due to rapid or discontinuous changes in elastic velocity. Two common structures inducing waveform complexity are a rapid or discontinuous velocity decrease and a rapid or discontinuous velocity increase (Figure 5). A rapid or discontinuous decrease is characterized by a shadow zone, followed by a caustic and two multipaths in the lit zone, each having opposite sign of curvature in their associated traveltime curves. A caustic is a surface, line, or point where body waves are strongly focused, frequency-independent ray theory breaks down, and geometric spreading vanishes. A rapid or discontinuous velocity increase produces a triplication of the traveltime curve, with a region of distances in which three different ray paths, one of which has an opposite sign of curvature in its traveltime curve compared to those of the other two paths. The two points where the curvature of traveltime versus distance changes

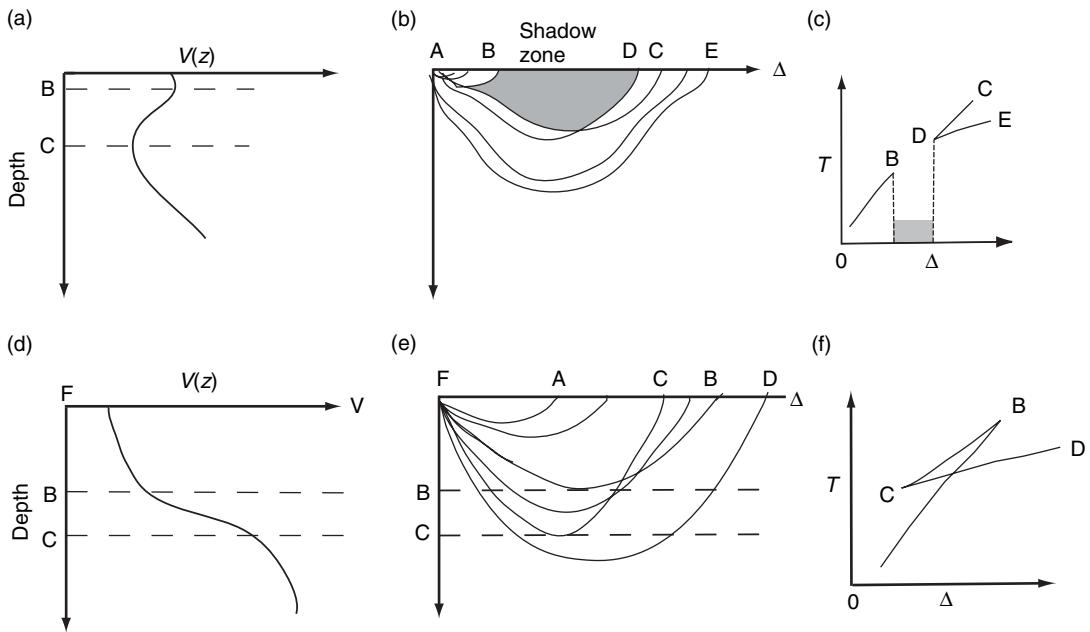


Figure 5 Ray multipathing and traveltime complexity induced by regions of either rapid velocity decrease with depth ((a)–(c)) or rapid increase ((d)–(f)) with depth.

denote the distance at which the caustics intersect the Earth's surface.

P waves interacting with the Earth's inner and outer core boundaries provide an example of both the waveform complexity induced by a discontinuous velocity increase and a discontinuous velocity decrease. A shadow zone and caustic are induced by a discontinuous velocity decrease at the core–mantle

boundary, and a triplication is induced by a discontinuous velocity increase at the inner core boundary (Figure 6). The velocity decrease at the core–mantle boundary generates a reversal of the traveltime–distance curve and strong focusing of waves at the caustic distance B. The discontinuous increase in velocity at the outer core–inner core boundary generates the triplication C–D–F.

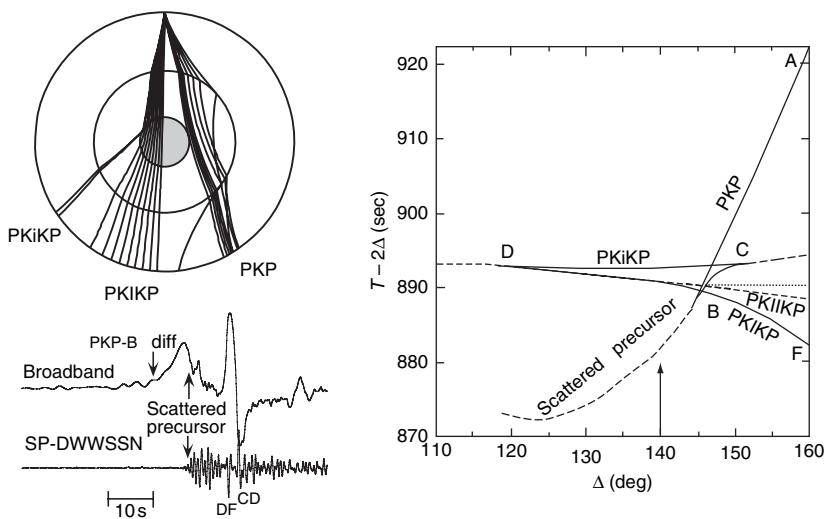


Figure 6 Rays and traveltime curves of P waves interacting with the Earth's inner and outer cores. Bottom left: Observed broadband displacement and narrow band-passed velocity (SP-DWWSSN) seismograms from a deep earthquake recorded near 140° .

Frequency-dependent diffraction occurs along the extension of BC to shorter distance. A lower-amplitude partial reflection along the dashed segment extends from D to shorter distances. In addition to the effects induced by radially symmetric structure, lateral heterogeneity near the core–mantle boundary can scatter body waves in all directions. The curved dashed line extended to shorter distances from point B in **Figure 6** represents the minimum arrival time of high-frequency energy scattered from either heterogeneity near or topography on the core–mantle boundary.

Changes in the curvature of traveltimes for waves also induce changes in the shapes of the waves associated with each multipath. These waveform distortions can be understood from geometric spreading effects. In an inhomogeneous medium, geometric spreading R is proportional to the square root of the product of the principal radii of curvature of the wave front,

$$R \propto \sqrt{r_1 r_2} \quad [9]$$

In a homogeneous medium, where wave fronts are spherical, $r_1 = r_2$, and geometric spreading reduces simply to the distance to the source. A wave front is described by a 3-D surface $\tau(\mathbf{x})$ over which traveltime is constant. Hence, the principal radii of curvature of the wave front are determined by the second spatial derivatives of the traveltime surface τ . From [9], a change in the sign of either of the two principal wave front curvatures (r_1 or r_2) produces a change in the sign of the argument of the square root in [9] and hence a $\pi/2$ phase change in the waveform associated with that wave front. A consequence of this relation is that any two waveforms having traveltimes branches with a difference in the sign of the second derivative with respect to great circle distance, will differ by $\pi/2$ in phase. This $\pi/2$ phase change is called a Hilbert transform. A Hilbert transform of a delta function has a gradual positive onset, sharp downswing to negative values, and a gradual negative return to zero (**Figure 7**). The traveltime curve of the PKP waves along the AB branch in **Figure 6** has a concave upward curvature, while traveltimes curvatures of the PKP waves along the BC branch and the PKIKP waves along the DF branch are concave downward. Hence, waveforms of PKP-AB are Hilbert transformed with respect to those of the PKP-BC and PKP-DF (**Figure 8**).

These changes in pulse shape are correct in the limit of infinite frequency, but at finite frequency pulse shapes near the cusps B, C, and D are neither

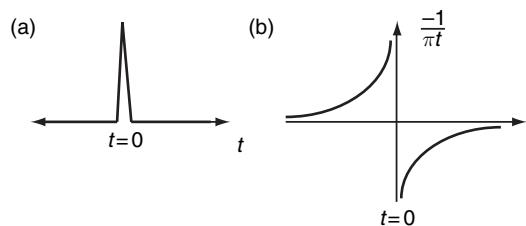


Figure 7 (a) Delta function and (b) its Hilbert transform.

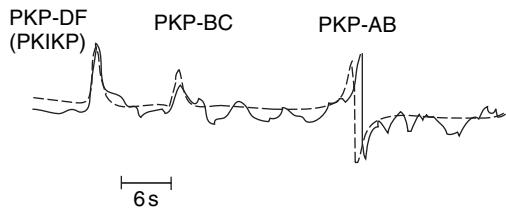


Figure 8 Observed and synthesized PKP waveforms from Choy and Cormier (1993). PKP-AB is Hilbert-transformed with respect to PKP-DF.

delta-like nor Hilbert-transformed-like. Near these points, the shapes exhibit frequency dependence and appear as some kind of average of the two fundamental shapes. This type of pulse shape can also exist in cases where a reflection/transmission/conversion coefficient of a plane wave becomes complex, as in certain distance ranges of the SKS phase. In these cases, the pulse shape can be represented by a linear combination of a delta function and Hilbert-transformed delta function (Aki and Richards, 1980, pp. 157–158). In the shadows of cusps and caustics, diffracted waves exist, which decay with increasing frequency and increasing distance from the cusp or caustic (e.g., the diffracted PKP-B in the broadband seismogram in **Figure 6**).

Waves having rays with multiple turning points also exhibit $\pi/2$ phase shifts for each turning point. Examples are PP waves and SS waves that are Hilbert-transformed with respect to the waveforms of the direct P and S waves, and waves multiply reflected along the underside of the core–mantle boundary, such as PKKP, SKKS, PKnKP, SKnKS, etc. (Choy and Richards, 1975). In three-dimensionally varying media and for body waves having multiple turning points in waveguide-like structures, it is possible to have N multiple $\pi/2$ phase shifts for N turning points or N points of tangency to a caustic. N is termed the KMAH index (named after wave theorists Keller, Maslov, Arnold, and Hormander). The KMAH index is an important parameter to inventory

as rays are shot or traced in dynamic ray tracing (DRT). In DRT (Section 1.05.4.5), the KMAH index can be determined by tracking accumulated sign changes in the determinant of Cerveny's (2001) \mathbf{Q} matrix, where geometric spreading R is proportional to the square root of the determinant of \mathbf{Q} :

$$R \propto \sqrt{\det(\mathbf{Q})} \quad [10]$$

In vertically varying, flat-layered models, $\det(\mathbf{Q})$ takes the form

$$\det(\mathbf{Q}) = \frac{\cos(i)}{V} \frac{\cos(i_o)}{V_o} \frac{X}{p} \frac{dX}{dp} \quad [11a]$$

and in spherically symmetric Earth models,

$$\det(\mathbf{Q}) = (r r_o)^2 \cos(i) \cos(i_o) \frac{\sin(\Delta)}{p} \frac{d\Delta}{dp} \quad [11b]$$

In [11a] and [11b], vertical takeoff angle i , velocity V , and radius r having the subscript 'o' are evaluated at a ray origin or source point, and unsubscripted quantities are evaluated at a ray end point or receiver. X is the distance measured from source to receiver along the surface of the Earth model, and Δ is the great circle distance of the source to the receiver measured in radians. In [11a] the ray parameter p is that for rays in plane-layered models ($p = \sin(i)/V = \text{constant} = dT/dX$), but in [11b] p is that for rays in spherically layered models ($p = r \sin(i)/V = \text{constant} = dT/d\Delta$).

Head waves are another effect of a discontinuous velocity increase with depth that can induce frequency-dependent effects and waveform complexity. Head waves travel along the underside of a boundary in the higher-velocity medium. Depending on vertical gradient of the medium below the discontinuity, a head wave can either have an amplitude inversely proportional to frequency (no gradient) or be represented by an interference or a whispering gallery of waves multiply reflected along the underside of the discontinuity (e.g., Cerveny and Ravindra, 1971; Menke and Richards, 1980).

In some distance ranges, surface waves, and phases best described by modal representations interfere with body waves. Examples include late arriving body waves having multiple interactions with the core–mantle boundary and/or the free surface that interfere with fundamental mode Love and Rayleigh waves. Another example is shear-coupled PL waves that are generated by SV waves that turn in the mantle and excite converted P waves trapped in

the crust (Baag and Langston, 1985). Shear-coupled PL waves can arrive as a dispersive wavetrain immediately following an SV wave in some distance ranges. The interference of shear-coupled PL waves with the direct SV phase has made it difficult to simultaneously model SH and SV phases to obtain mantle models from S waveforms (e.g., Helmberger and Engen, 1974). In this situation, it is important to choose an algorithm that includes a sufficiently complete set of rays or modes to represent both the direct body wave as well as the dispersed waves interacting with the crust and surface of the Earth.

1.05.3.2 Deep-Earth Structural Problems

The modeling problems of greatest research interest are structures in depth zones that introduce waveform complexity in the form of triplications, caustics, shadow zones, diffractions, head waves, and multipaths. For teleseismic observations, the zones of rapid spatial variation that are most often studied are the crust–mantle discontinuity (Moho), a regionally varying low-velocity zone in the upper mantle, narrow zones or discontinuities in velocity and density at or near 400 km, 500 km, and 660 km depth, a zone of regionally varying velocities between 100 and 300 km above the core–mantle boundary, and a 100–300 km region on both sides of the inner core boundary.

Key to the interpretation of these zones of rapid spatial variation is the relative changes in P velocity, S velocity, and density. From body-wave modeling, it is often only possible to make an estimate of velocity changes, either P or S velocity, but neither simultaneously, with little or no constraint on the associated density change. A common example of this is the estimate of the velocity increase required to reproduce the spacing of traveltimes in the ranges of the triplicated portion of a traveltime curve due to a rapid increase in velocity with depth (e.g., Figures 5 and 6). The amplitudes of the body waves in the triplicated range, where one travelttime branch corresponds to a wave totally reflected from the discontinuity, have little or no sensitivity to any density change associated with the velocity change. The amplitude of a reflected body wave at more vertical incidence, however, is much more sensitive to the product of density and velocity changes (Figure 9). By combining observations of narrow angle and grazing incidence waves to a discontinuity, it is possible to remove or reduce the tradeoffs between velocity and density change. Combined

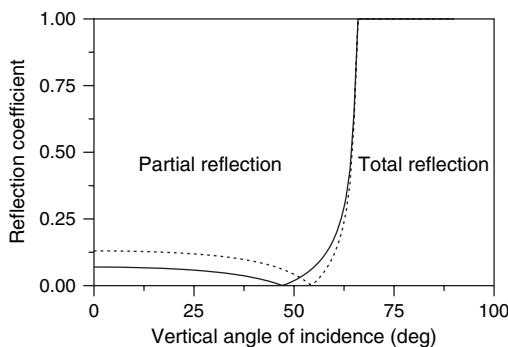


Figure 9 Example of a reflection coefficient showing total and partial reflection for a discontinuity for two cases: (1) velocity and density increase (solid) and (2) velocity increase identical but a different density increase (dashed). Note insensitivity of total reflection region to the size of the density increase.

modeling of P and S waveforms for both narrow- and wide-angle incidence then makes it possible to separately estimate P, S, and density changes at a discontinuity. From these estimates, it is possible to distinguish the nature of the discontinuity, for example, whether it is chemical change or a solid–solid mineral phase change.

When P- and S-wave waveform analyses are available, an additional diagnostic tool can be the calculation of the change in bulk sound velocity V_K , where

$$V_K^2 = V_p^2 - 4/3 V_S^2 \quad [12]$$

and V_p and V_S are the P and S velocities, respectively (Su and Dziewonki, 1997). Bulk sound velocities are more directly observed in high-pressure mineral physics experiments and theory, and can be directly compared against known mineralogy (Zhao and Anderson, 1994). Other constraints in interpreting 3-D variations in velocity are provided in comparing theoretical and observed estimates of the relative fractional changes in P velocity, S velocity, and density, $d\ln V_p/d\ln V_S$ and $d\ln V_S/d\ln \rho$ (e.g., Trampert *et al.*, 2001). Care, however, might be needed in comparing the frequency band of an observation with that of theoretical predictions due to the dispersive effects of viscoelasticity (Section 1.05.7.4; Karato, 1993).

The effect of temperature on velocity is known from experimental and theoretical predictions. Known temperature derivatives, or even practical bounds on the temperature derivative, can be used to determine whether a rapid velocity change is due to either a spatially sharp temperature, chemical, or

phase change. In this analysis, it is also important to consider the effects of thermal diffusivity. For example, given an estimate of the thermal diffusivity, the spatial extent of a thermally induced velocity anomaly cannot persist at a scale smaller than a certain size. Thermally induced anomalies below this size diffuse away over time periods shorter than the timescale at which they are created by mantle circulation.

Estimating whether a region of velocity change is a true discontinuity or a transition spread out in space requires careful study of the frequency content of reflected and converted waves interacting with the region of rapid velocity change (see Chapter 1.17). This has been an enduring challenge in interpreting rapid changes in velocity in the upper mantle as solid–solid phase changes. Waves reflected at wavelengths much longer than the depth range of a gradient transition cannot distinguish a transition from a discontinuity. Shorter-wavelength waves, however, will not be reflected at narrow incidence angles. Reflected and converted waves at grazing incidence to a depth zone of rapid transition are relatively insensitive to the width of the transition even for a relatively broad frequency band of recording (e.g., Ward, 1978). Taking these sensitivities together, the frequency-dependent behavior of the amplitudes of body waves partially reflected at narrow angles of incidence to regions of rapid transition in depth can help diagnose whether a structure is a true discontinuity or transition zone. In practice, only a lower bound on the width of a depth transition can be safely diagnosed (e.g., Richards and Frasier, 1976), since there is typically an upper bound on the frequency (lower bound on wavelength) on observable teleseismic body waves (usually 2–3 Hz).

1.05.4 Modeling Algorithms and Codes

Modeling of body waves can be broadly classified into four approaches: (1) transform methods for spherically symmetric or plane-layered media, with some extensions for weak heterogeneity and anisotropy; (2) ray summation methods for regions in which frequency-independent ray theory is a good approximate solution; (3) mode summation methods; and (4) full or partial numerical solutions to elastic equations of motion that can treat the cases of strong heterogeneity, anisotropy, and small spatial scales of heterogeneity. A summary of these modeling methods follows. Published applications of each method are extensive,

and an attempt is made to primarily cite material in which the theory of each method is most completely developed. In many cases, this will be a textbook rather than a journal paper. Good starting points to obtain software for many approaches are the ORFEUS software library, codes deposited with the World Data Center as part of the *Seismological Algorithms* text, codes and tutorials by R. Hermann, example synthetics and codes distributed by the COSY Project, codes distributed on a CD supplied with the *International Handbook for Earthquake and Engineering Seismology* (Lee *et al.*, 2001), and computational seismology software available from the Computational Infrastructure in Geodynamics (CIG) web page.

1.05.4.1 Reflectivity

Reflectivity (Fuchs and Müller, 1971; Müller, 1985; Kind, 1985; Kennett, 1983, 2001) is perhaps the most general and popular transform method of modeling seismograms in radially symmetric or plane-layered Earth models. Planar homogeneous layers parameterize the Earth model, after an Earth-flattening approximation (EFA) is applied. Plane-wave solutions of the wave equation are found in the frequency domain, with boundary conditions handled by propagator matrix techniques. This approach is used to derive a transformed solution at great circle distance Δ_o for displacement, $u(\omega, p, \Delta_o)$, in ray parameter and frequency space, where p is related to the horizontal component of the wave-number vector by $k_z = \frac{\omega p}{r_e}$, with r_e the mean spherical radius of the Earth. The solution $U(t, \Delta_o)$ is then found by inverting Fourier transforms represented by

$$U(\omega, \Delta_o) = \frac{1}{2\pi} \int_{-\infty}^{\infty} d\omega e^{-i\omega t} \int_{\Gamma} dp u(\omega, p, \Delta_o) \quad [13]$$

Transform inversion is commonly accomplished by integrating $u(\omega, p, \Delta_o)$ along a contour Γ confined to a finite segment of the real p or k_x axis for the series of discrete 2^N frequencies required to invert the complex frequency spectrum by a fast Fourier transform (FFT).

Depending on the needs of the modeler, the integrand of [13] can be constructed to contain either one or several body-wave arrivals interacting with major discontinuities, fundamental or higher-mode surface waves, or a complete seismogram. In the most common applications, the integrand is constructed to represent the reflection of a body wave incident on a stack of layers in a reflection zone (**Figure 10**). Above the reflection zone, the incident wave is

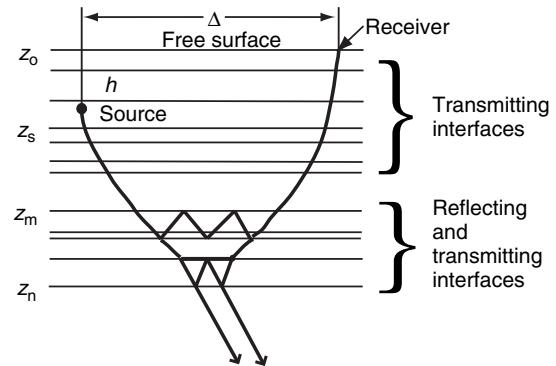


Figure 10 A typical layered model used in reflectivity synthesis, showing a transmission zone and rays reverberating in a reflection zone.

assumed to be transmitted down through and back up the layers overlying the reflection zone. Neglecting details of the source excitation, the factors making up $u(\omega, p, \Delta)$ include transmission coefficients T_D down and T_U up through the layers above the reflection zone, the reflection R_U from the reflection zone, and phase factor $\exp(i\omega p \Delta)$ accumulated through horizontal propagation to the great circle distance Δ , or

$$u(\omega, p, \Delta) \propto T_D R_U T_D \frac{\exp[i(\omega p \Delta - \pi/4)]}{\sqrt{\omega p \sin(\Delta)}} \quad [14]$$

The reflectivity response R_U can include all internal multiples and P-to-SV conversions within the thin homogeneous layers of the reflection zone. The reflectivity can be calculated from fundamental and propagator matrices. For example, R_U for SH waves can be calculated by solving the system

$$\mathbf{F}_o(z_1) \begin{pmatrix} 1 \\ R_U^o \end{pmatrix} = \mathbf{P}(z_1, z_N) \mathbf{F}_N(z_N) (T_D^N) \quad [15]$$

where R_U^o is the total wavefield reflected upward at the top of the boundary of the layered reflection zone and T_D^N is the total wavefield transmitted through the bottom of the reflection zone. A similar system can be set up for P and SV reflectivity, but care must be taken to rearrange the system to exploit algebraic cancellation of some exponentially growing terms for certain domains of ray parameter (Abo-Zena, 1979). Elimination of these troublesome terms can also be accomplished by rearranging the multiplication of fundamental matrices in such a way that also enables identification of infinite series of internal layer multiples. These interlayer multiples can be neglected after a small finite number of

reverberations (Kennett, 1983, 2001). Truncation of these internal multiples helps eliminate later-arriving energy that folds back into the finite time window required given by finite-length Fourier transforms. An alternative approach to eliminate the acausal arrival of the late-arriving interlayer multiples is to add a small imaginary part to each frequency $-i/\tau$ in the evaluation of the reflectivity response before inverting the Fourier transform (Kennett, 1979; Chapman, 2004, p. 361). Using the damping theorem of Fourier transforms, at each time point the inverted signal is then multiplied by the exponential $\exp(t/\tau)$.

After choosing a method to eliminate acausal late-arriving multiples, one must still decide on how to best suppress the numerical noise of the all of the causal internal layer multiples of the thin layers used to approximate a continuously varying model. This numerical noise can be minimized by either low-pass-filtering the response before inverting the Fourier transform or by making layer thicknesses smaller than 1/4 the shortest wavelength corresponding to the highest frequency of interest to model (**Figure 11**).

Parametrization of the spherical Earth by plane homogeneous layers with depth z first requires an EFA of velocities $v(r)$ of the type (Müller, 1977)

$$v_f(z) = \frac{r_e}{r} v(r) \quad [16a]$$

$$z = r_e \ln\left(\frac{r}{r_e}\right) \quad [16b]$$

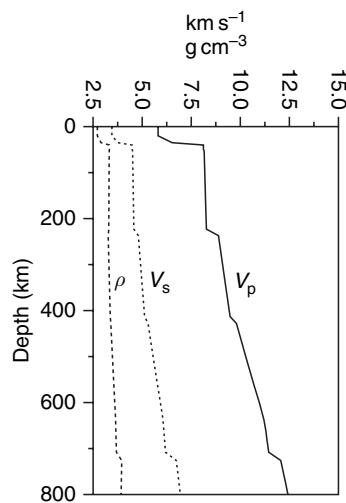
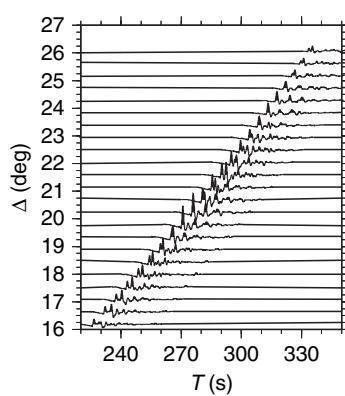


Figure 11 P waves synthesized by the reflectivity method using the program and example input provided by Kennett in the Orfeus web pages. Note the increase in amplitude around 20° associated with overlapping triplications induced by an upper-mantle model having rapid velocity increases near 400 and 700 km depth.

Errors on the order of $1/\omega$ are introduced in synthetic seismograms in this process, and include problems associated with the decoupling of P and S wave potentials and the lack of an ideal density transformation (Chapman, 1973). The EFA will also breakdown at the center of the Earth ($r = 0$), limiting accurate modeling to body waves that penetrate only the upper 500 km of the inner core. With this limitation and unless applied to a region in which velocity gradients are anomalously high at very low (<0.01 Hz) frequencies, the EFA combined with thin homogeneous layering can usually be applied without introducing significant error in the modeling.

Another variant of the reflectivity method is the discrete wave number method, in which the integral over ray parameter p is replaced by a sum over discrete horizontal wave numbers, k_x (Bouchon and Aki, 1977; Bouchon, 1979). One advantage of this method is that it can include the zero wave number, which provides a solution for the static displacement near an earthquake source (Honda and Yomogida, 2003). The need for fictitious image sources to treat the surface boundary conditions introduces some complexity in the formulation of the discrete wave number method, but both SH and P-SV codes are available and well developed.

Because its input parameters are simple to understand, the reflectivity method is probably the most popular forward modeling technique. Input consists of an Earth model specified by velocities and densities in a stack of homogeneous layers, starting and



ending points of integration along a real ray parameter axis, a time window and sampling rate, and a simple source description. Some 2-D extensions are now available, allowing separate models to be specified in the source and receiver regions (see Section 1.05.7.1). Aside from simplicity of the input parameters, an advantage of reflectivity is that it easily allows the investigation of vertical transition zones in properties modeled by arbitrarily thin layers. This advantage, in common with all methods that allow for the insertion of thin layers, can lead to the neglect of physical constraints on radial derivatives of elastic moduli and density. Compared to ray-based methods that assume asymptotic approximations to vertical wave functions discussed in following sections, reflectivity can be numerically expensive for problems requiring thousands of thin layers.

1.05.4.2 Generalized Ray

The method commonly dubbed the generalized ray technique (GRT) originated from a technique of handling the integral transform inversions from ray parameter and frequency to time and space by the Cagniard–de Hoop method. It was recognized that most important teleseismic arrivals can be calculated by a first-motion approximation, allowing the time domain solution for ray interactions in each layer, both reflected and head waves, to be solved analytically (Helmerger 1974; Helmerger and Harkrider, 1978). Ray solutions within each layer are summed, usually just the first multiples. The volume of published applications using the GRT method is probably the largest of any other method, but its available computer codes are less widely circulated than those employing reflectivity methods. An

application of GRT synthetics (Burdick and Helmberger, 1978) was instrumental in the first major revision of standard Earth models originating from the pioneering work of Jeffreys and Bullen, namely the replacement of a zone of strong velocity gradient in the upper mantle (Jeffreys, 1936) with two first-order discontinuities at 400 and 660 km depth (Figure 12).

The GRT commonly assumes an EFA and ignores higher than first-order internal multiples in each layer. It has been tested against other methods in many standard, vertically varying, Earth models and usually produces seismograms that are indistinguishable from those calculated by other common methods discussed in this chapter.

1.05.4.3 WKBJ-Maslov

A key difference in this technique is that thin homogeneous layers no longer parametrize the Earth model. Vertical gradients in depth or radius are allowed in velocity, and asymptotically approximate, WKBJ, solutions of the vertically separated part of the wave equation are assumed. In contrast to vertically homogeneous layers, where the up- and down-going vertical wave functions are simply $\exp[\pm ik_z(z - z_{ref})]$, the WKBJ solution approximates the vertical wave functions by

$$g^{(1)}(r, p, \omega) = \frac{e^{\pm i\pi/4}}{\omega r} \sqrt{\frac{V}{\xi(r)}} \exp(\pm i\omega\tau) \quad [17a]$$

where the superscripts (1) and (2) refer to up- and down-going waves, respectively. $\xi(r)$ is the vertical slowness and is related to the cosine of the angle of incidence of a ray at any level r by

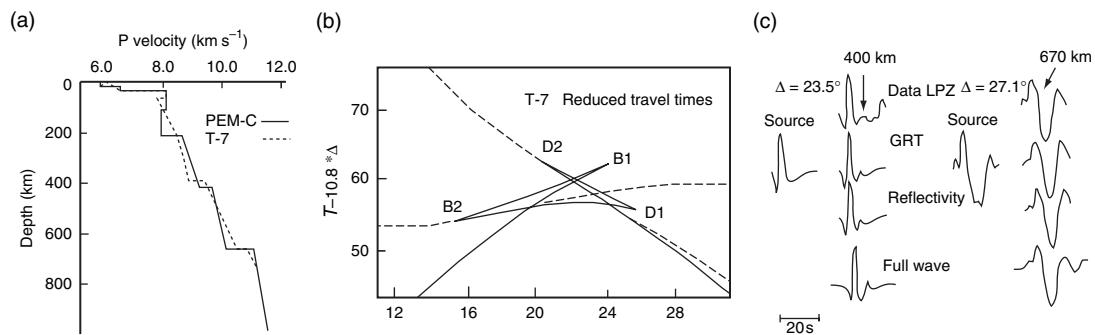


Figure 12 (a) Two models of P velocity in the upper 1000 km of the Earth. (b) Discontinuities at 400 and 650 km depth create two overlapping triplications in the traveltime curve and multiple phase arrivals in the great circle range 10–30°. (c) A comparison of observed and synthesized seismograms in the T-7 model for three different methods of synthesis that include diffraction effects (Burdick and Orcutt, 1978; Cormier and Choy, 1981).

$\xi(r) = \cos(i)/V = \sqrt{1/V^2 - p^2/r^2}$. τ is the delay time obtained by integrating the vertical slowness from the radius turning point radius r_p , where $\cos(i) = 0$, to r :

$$\tau = \int_{r_p}^r \sqrt{1/V^2 - p^2/r^2} \quad [17b]$$

The accuracy of these high-frequency approximations increases as the ratio λ/s decreases, where λ is the wavelength and s is the scale length of the medium. The scale length s is defined by

$$s = \min\left(\frac{V_S}{|\nabla V_S|}, \frac{V_P}{|\nabla V_P|}, \frac{\rho}{|\nabla \rho|}, r_b\right) \quad [18]$$

where r_b is the radius of curvature of a first-order discontinuity in density or elastic velocity (Beydoun and Ben-Menahem, 1985). Separability of P and S wave potentials is assumed in each inhomogeneous layer, and frequency-dependent reflections and P-to-S conversions by regions of strong gradients are ignored. Hence, transition zones, which may be of interest to mantle solid-solid phase changes, should be handled by thin layers of weaker gradient where the asymptotic approximations remain valid. For problems consisting of a body wave reflected by or bottoming above a discontinuity, the integrand $u(\omega, p, \Delta_o)$ in [5] is replaced by

$$u(\omega, p) = \omega^{1/2} \Pi(p) e^{i\omega\theta(p)} \quad [19a]$$

where

$$\theta(p) = \int_{r_p}^r \sqrt{1/v^2 - p^2/r^2} + \int_{r_p}^{r_o} \sqrt{1/v^2 - p^2/r^2} + p\Delta_o \quad [19b]$$

$\Pi(p)$ is a product of the plane-wave reflection coefficient of the discontinuity and the plane-wave transmission coefficients through layers above the discontinuity. The factor $\theta(p)$ in the phase originates from the phases associated with the WKBJ solutions to vertical wave functions in the transmission region above the discontinuity and the horizontal wave function for propagation to great circle distance, Δ_o . Hence, the name WKBJ is applied to this method. In this method, body waves are synthesized by summing a series of representations of the type given by [19a]. Each body wave in this sum is assumed to be associated with rays that are either reflected by or turn just above the first inhomogeneous layer above each discontinuity (Figure 13).

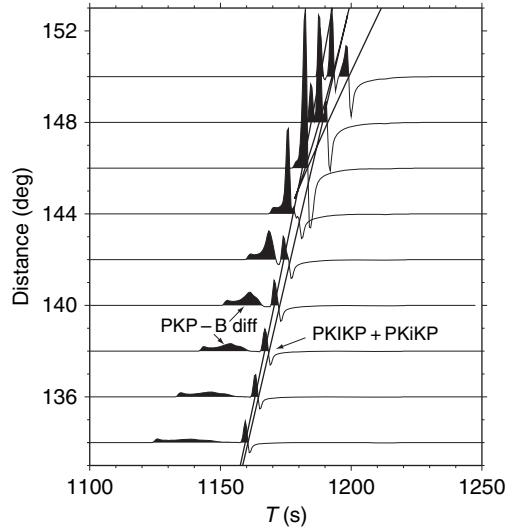


Figure 13 Seismograms synthesized by the WKBJ method for P waves interacting with the Earth's core using the program and example input by Chapman et al., (1988) distributed with *Seismological Algorithms*.

Inversion to the time and space domain of the transformed solution $u(\omega, p, \Delta_o)$ of [13] is performed by a slowness method rather than by a spectral method as commonly done in reflectivity methods. In slowness methods, the inversion to the time domain is performed analytically, recognizing that separate frequency-dependent factors in the integrand can be written as convolutions in the time domain. The final inversion to the space domain is performed by numerical integration over horizontal slowness p by a method in which the combined phase factor $\theta(p) - t$ is sampled in slowness intervals corresponding to a fixed sampling rate in time t (Figure 14). This key step is contained in the phase-sampling subroutine

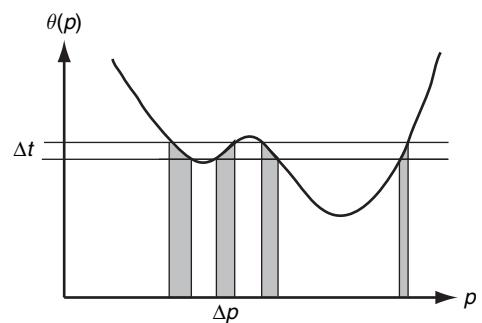


Figure 14 The ray parameter integrand in the WKBJ method is performed numerically by taking ray parameter intervals Δp equal to the desired sampling rate in time Δt as mapped by the total WKBJ phase function $\theta(p)$.

THETAC of Chapman's WKBJ original codes. The integration over horizontal slowness is truncated at points along the real p -axis, which introduces truncation phases in the synthetic. These can be removed by approximating the phase function's dependence on ray parameter from the truncation slownesses to $\pm\infty$, assuming a linear dependence on p , and analytically integrating the approximation (Chapman, 1978). A well-documented package of the WKBJ algorithm by A.R. Gorman, tailored toward continental-scale reflection and refraction, exists in the PLOTSEC package. A code for teleseismic applications and example inputs can be obtained from Chapman's contribution to the *Seismological Algorithm* text. Software for the evaluation of the delay time $\tau(p)$ in many standard Earth models can be obtained from the TauP Toolkit (Crotwell et al., 1999). Due to the need of separately describing ray interactions with discontinuities, the input to WKBJ codes is less black box-like than the input to typical reflectivity codes.

The Maslov technique (Chapman and Drummond, 1982) generalizes the WKBJ seismogram technique to 2- and 3-D velocity variations. The restrictions of the asymptotic approximations still apply, that is, the medium scale length in any inhomogeneous region must be greater than the wavelength. Full implementation of the technique sometimes requires an artful averaging of solutions in slowness p space with those in the physical x space. Each of these spaces can contain caustics where a weight factor or geometric spreading factor becomes singular. Regions of models having strong spatial gradients, where the asymptotic approximations are failing, are often characterized by closely spaced caustics in slowness space and physical space for waves at grazing incidence to the strong gradient regions. In these regions, the weight factors averaging the solutions in phase and physical space can be difficult to design. This situation can exist if high gradient zones define the boundaries of a thin high- or low-velocity zone (e.g., subducting slab or a fault zone). In these situations, it is better to define the anomalous structures by first-order discontinuities and apply boundary conditions for multiply reflected and refracted body waves.

Compared to the reflectivity method, the WKBJ and its related Maslov extensions are computationally much faster and, hence, better suited to problems in waveform inversion that may require many repeated syntheses to evaluate a misfit or object function. The speed of these methods is due to the use of an asymptotically approximate solution in spatially varying

layers. Therein, however, lies the limitation of these methods. The vertical variation must be sufficiently weak so as not to exceed the errors associated with the approximation. When there is a need to sum ray interactions with more than two or three first-order discontinuities in a distance range, the input parameters describing the separate ray interactions in some WKBJ codes can become complex unless a user-friendly input interface is provided.

1.05.4.4 Full-Wave Theory and Integration in Complex p Plane

The term full-wave theory can be applied to any technique that incorporates frequency-dependent effects of wave interactions with boundaries, including diffraction and tunneling. Any transform approach that includes a broad enough domain in frequency and wave number to simulate these frequency-dependent effects, often due to poles or branch cuts in the response function, can be called a full-wave theory. This term was specifically applied by Cormier and Richards (1977) to an asymptotic spectral technique that inverts the slowness integral by paths Γ in the complex p plane and substitutes a Langer approximation for the WKBJ approximation to the vertical wave functions. The vertical wave function in the Langer approximation is given by

$$g^{(2)}(r, p, \omega) = \frac{\pi \rho_s V_s}{2\rho V} \frac{V_s e^{\pm i\pi/6}}{\omega \xi} \sqrt{\frac{\omega \tau}{V \xi}} H_{1/3}^{(2)}(\omega \tau) \quad [20]$$

The Langer approximation remains regular at grazing incidence to boundaries where ξ and τ vanish but returns the WKBJ approximation where it is accurate. The integration over the contour Γ is carried out numerically, with Γ extended into regions off the real p -axis where the integrand in [13] exponentially decays. For portions of Γ along the real p -axis, the integrand can be very oscillatory, and integration can be handled efficiently by Filon's method (Frazer and Gettrust, 1985). Full-wave theory includes tunneling, diffraction, and other phenomena related to frequency dependence of reflection-transmission coefficients at grazing incidence to boundaries. An example of the importance of these phenomena includes the very strong frequency dependence of the P wave that bottoms just above the core-mantle boundary and tunnels across the core-mantle boundary, exciting compressional (K) waves in the liquid outer core that multiply reflect along the underside of the core-mantle boundary

(PKnKP waves; e.g., Richards (1973). Applying attention to the validity of asymptotic approximations to the Legendre function representing the phase effects of propagating in the horizontal or Δ direction, full-wave theory has been extended to synthesize body waves that are strongly focused at the antipode by diffraction around spherical boundaries from all azimuths (Rial and Cormier, 1980).

The theory is most completely developed in chapter 9 of Aki and Richards (1981) and in *Seismological Algorithms* (Cormier and Richards, 1988), where example codes and inputs are distributed. As an asymptotic theory, full-wave theory shares the limitations of WKBJ codes, in that care must be taken not to assume too strong a velocity and density gradient in each inhomogeneous layer. Added to the complexity in the description of ray interactions shared with WKBJ code input, the construction of full-wave theory integrands and complex integration paths can be challenging, particularly for interference head wave and antipodal problems. Often it is best to start with example input files specifying ray descriptions and integration paths for these problems, which are distributed with *Seismological Algorithms*.

1.05.4.5 DRT and Gaussian Beams

DRT is simply a ray theory solution to the elastic equations of motion, consisting of a pulse arriving at the least or stationary phase time, scaled by the amplitude factors due to plane-wave reflection and transmission and geometric spreading. In an inhomogeneous region, DRT solutions in the frequency domain start from a trial solution in the form of factors multiplying inverse powers of radian frequency ω :

$$u(\omega) = \sum_n \frac{A_n}{\omega^n} \exp(i\omega T) \quad [21]$$

The errors in the approximation given by $n = 0$ remain small for wavelengths much smaller than the scale length of the medium given by [18]. In practice, no more than the $n=0$ term is ever calculated, because higher-order terms are expensive to calculate and can never properly include the frequency-dependent effects of waves reflected and converted by regions of high spatial gradients in velocity and density. The review by Lambare and Virieux (this volume) provides further details on the derivation, accuracy, and frequency-dependent corrections to asymptotic ray theory and also reviews the relations between DRT, WKBJ/Maslov, and Gaussian beam summation.

Superposition of Gaussian beams is an extension of DRT and is closely related to the WKJB/Maslov techniques. It amounts to a superposition of approximated wave fronts, weighted by a Gaussian-shaped window in space centered about each ray. The shape of the wave front is estimated from the first and second spatial derivatives of the wave front at the end point of each ray. This is referred to as a paraxial (close to the axis of the ray) approximation of the wave front. To calculate the first- and second-order spatial derivatives of the wave front, a system of linear equations must be integrated. These equations, also required by DRT, consist of the kinematic equations that describe the evolution of ray trajectory, its vector slowness \mathbf{p} , and traveltime, an equation to describe the rotation of ray-centered coordinates in which S-wave polarization remains fixed, and a system of equations for matrices \mathbf{P} and \mathbf{Q} needed to describe the evolution of wave front curvature and geometric spreading. The vector slowness \mathbf{p} is simply the spatial gradient of traveltime, and the geometric spreading is related to the wave front curvature or second spatial derivatives of traveltime. When a receiver is not near a caustic, the quantities determined from integrating the DRT system can be used to determine the frequency-dependent ray theory solution, consisting of geometric spreading, traveltime, and products of reflection/transmission coefficients. The paraxially estimated phase from the \mathbf{P} and \mathbf{Q} matrices of the DRT system can be used to either avoid two-point ray tracing by spatially extrapolating the traveltime near a ray or to iteratively solve the two-point ray-tracing problem. The traveltime at a point \mathbf{x} in the vicinity of a ray end point at \mathbf{x}_o can be estimated by:

$$T(\mathbf{x}) = T(\mathbf{x}_o) + \mathbf{p} \cdot \Delta \mathbf{x} + \frac{1}{2} \Delta \mathbf{x}' \mathbf{H}' \mathbf{M} \mathbf{H} \Delta \mathbf{x} \quad [22]$$

where

$$\mathbf{M} = \mathbf{P} \mathbf{Q}^{-1} \text{ and} \\ \Delta \mathbf{x} = \mathbf{x} - \mathbf{x}_o$$

The 2×2 matrices \mathbf{P} and \mathbf{Q} are determined by integrating the systems

$$\frac{d\mathbf{P}}{ds} = \mathbf{V}\mathbf{Q} \quad [23] \\ \frac{d\mathbf{Q}}{ds} = v\mathbf{P}$$

along the ray paths. In [22], \mathbf{H} is the transformation between ray-centered coordinates to Cartesian

coordinates. The columns of \mathbf{H} are the vector basis of the ray-centered coordinate system at the ray end point. \mathbf{V} is a matrix of second spatial derivatives of velocity in the ray-centered coordinate system. The matrix \mathbf{Q} can also be used to calculate geometric spreading [10]. The system in [23] can be generalized using a propagator, fundamental matrix formulism, similar to that used for propagating the solution to vertically separated equations of motion, except that in this system the solutions are quantities related to wave front curvature and ray density rather than components of displacement and stress.

Gaussian beams are defined by adding a small imaginary part to the matrix \mathbf{M} in the paraxially extrapolated phase in [22], which gives an exponential decay of a beam in space away from the central ray. The amplitude of each beam is proportional to real part of $\exp(i\omega T)$, where T is made complex in [22] by the inclusion of a complex \mathbf{M} . Beam summation remains regular in the vicinity of ray caustics, where geometric spreading vanishes and ray theory solutions become singular. It supplies estimates of frequency-dependent diffraction in the shadow of caustics and grazing incidence to boundaries.

To properly model classical head waves, some care must be used in the design of beam weighting and beam widths. Weight factors of beams are determined such that a superposition of beams returns a ray theory solution for the complex spectrum, that is, $U(\omega, x) = \exp(i\omega T)/\sqrt{\det(\mathbf{Q})}$, under a stationary phase approximation to an integral over ray parameter or take-off angles. Like the WKB/Maslov solution, Gaussian beams give a nonsingular approximation to the solution of the wavefield near a caustic. Restrictions on the validity of the method tend to be similar to that of the WKB/Maslov method. The scale length of the medium needs to be much larger than the wavelength and also larger than the beam widths (Ben-Menahem and Beydoun, 1985).

Compared to the Maslov technique, superposition of Gaussian beams has less mathematical support unless formulated in terms of complex rays as in some electromagnetic wave applications (Felsen, 1984). For grazing incidence to regions of strong velocity gradient, the paraxial approximation quickly fails and caustics become closely spaced, making it difficult to design optimal beam widths such that the paraxial approximation has small error in regions off the central ray where some beams may still have large amplitude.

The notational framework of the \mathbf{P} and \mathbf{Q} matrices and the propagator matrix of the dynamic

ray-tracing system developed by Cerveny and his co-workers are powerful tools that can simplify the coding and understanding of any problem requiring the use of ray theory. The DRT notation can be exploited to calculate the integrand for Kirchhoff integrals and the banana-shaped kernels needed for frequency-dependent tomography.

Computer codes for superposition of Gaussian beams and DRT can be obtained from Cerveny's group at Charles University as well as the World Data Center. The best-developed codes are tailored to continental scale reflection-refraction problems. One version (ANRAY) is one of the rare codes that combines general anisotropy with 3-D variations. A teleseismic-oriented version of DRT and beam summation was written by Davis and Henson (1993), with a user-friendly graphical interface.

1.05.4.6 Modal Methods

Solutions of the elastic-wave equations can be obtained from either a superposition of ray/wave front solutions or from superposition modes (Figure 15). Rays and mode representations are fully equivalent in accuracy if properly applied to a specific Earth model and frequency domain. In a modal approach, the eigenfunctions of free oscillation of a sphere have a characteristic frequency, and are classified by the position of nodes at the surface and at depth where displacements go through a zero and change sign (e.g., Lapwood and Usami, 1981). For a modal solution to be accurate at the lowest frequencies of free oscillation, restoring forces due to gravity and rotation of the Earth must be included as additional forces in [1]. In a spherically symmetric, nonrotating, isotropic (SNREI) Earth, modes can be separated into either spheroidal or toroidal modes of oscillation. The motions of spheroidal modes are analogous to those of P and SV body waves and Rayleigh surface waves; those of toroidal modes to those of SH body waves and Love surface waves. Summation of normal modes of the Earth can provide a complete image of the wavefield at the surface and at every depth (Dahlen and Tromp, 1998). Every body wave observed at the surface can be represented by a subset of normal modes (Figure 15). The frequency-dependent effects of diffraction at ray-grazing incidence to boundaries are also included in mode sums. The normal modes of a SNREI Earth can be efficiently computed on a single processor for frequencies up to 0.1 Hz. A code by G. Masters for synthesizing seismograms from sums of normal mode

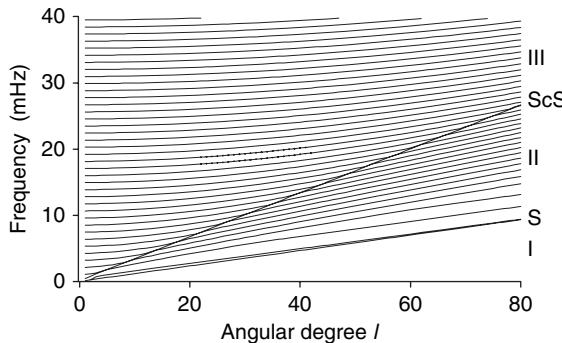


Figure 15 Toroidal modes in frequency and angular order number space, which, when summed, correspond to specific SH waves in the frequency and angular order number regions I, II, and III bounded by the two linear solid lines (Dahlen and Tromp, 1998).

is included on the CD supplied with the *International Handbook for Earthquake and Engineering Seismology* (Lee, et al., 2001).

An advantage of mode summation is that input parameters are especially simple, basically just an Earth model parametrization, a frequency band, and desired number of modes. Mode summation is routinely used in the inversion of complete seismograms to retrieve moment-tensor representations of earthquake sources (Dziewonski et al., 1981). A disadvantage is that it is limited to lower frequencies for practical computation on a single workstation. Effects of gravity, Earth rotation, anisotropy, and lateral heterogeneity remove degeneracy from SNREI modes and couple spheroidal with toroidal modes. Extensive literature exists on incorporation of the mode coupling induced by lateral heterogeneity by applying perturbation techniques to SNREI modes (e.g., Dahlen, 1987; Li and Tanimoto, 1993).

Another modal-type approach is that of locked modes (Figure 16). Here the modes are not whole-Earth modes of free oscillation, but rather the surface-wave modal energy that exponentially decays with increasing depth from the surface. Modes are numbered by sign changes in displacement with depth, the zeroth mode corresponding to either the fundamental mode Love or Rayleigh surface wave. The integrand $u(\omega, p)$ in [13] must first be constructed to include all interactions with the surface. The locked-mode approach then evaluates the ray parameter or wave number integral of [13] in the frequency domain by deforming the integration contour in the complex plane and applying the residue theorem to the integrand. A high-velocity capping layer is placed at depth, which locks plate-like modes into layers

above the capping layer. The capping layer is placed deep enough such that mode sums representing waves of interest in a particular time window all turn or refract above the capping layer. Since all body waves, multiply reflected in the layers above the capping layer, are included, the locked-mode technique has a problem shared with the conventional reflectivity technique in which late-arriving waves are folded back into a finite-length time window. Similar to reflectivity, this problem can be handled by adding a small complex part to frequency. Harvey (1981) describes derivation of the technique in models described by plane homogeneous layers and available codes. An extension to vertically inhomogeneous layers using the Langer approximation is given by Cormier et al. (1991).

1.05.4.7 Numerical Methods

Fully numerical solutions of the elastic equations of motion can treat wave propagation in an arbitrarily complex 3-D Earth, having velocity variations over a broad range of scale lengths. A full solution is obtained, containing body waves, surface waves, and all diffraction, head-wave and leaky mode effects. Chapter 1.06 reviews numerical techniques, concentrating on current methods that can handle fully 3-D models and complete seismograms. This subsection is a brief summary of some of the techniques that occur in the expanded discussions in Chapter 1.06, including both 2-D and 3-D techniques and those that are applied to primarily the highest-frequency body waves and shorter time windows.

The principal numerical techniques are finite difference and finite element. For accuracy up to ranges

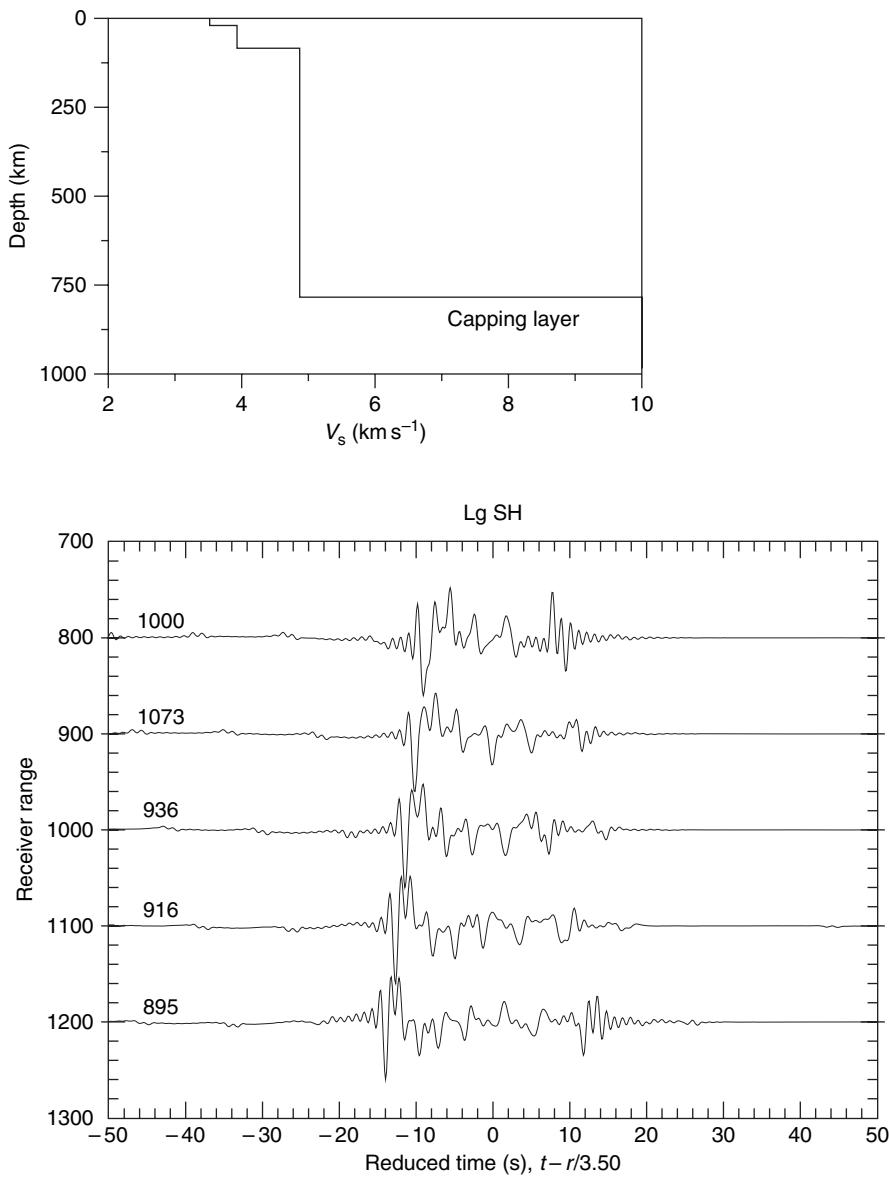


Figure 16 A crustal model and transverse component seismograms synthesized by the locked-mode method using programs by Harvey (1981). The Lg modes have a ray analog in multiple, Moho critically reflected, S waves reverberating in the Earth's crust. A high-velocity capping traps Love modes in the layers above the capping layers.

of 100 to 1000 wavelengths, conventional finite difference solutions typically are performed with fourth- to eighth-order difference approximations to spatial derivatives. The equations of motion are most commonly solved for particle velocity and stress on a staggered grid (Virieux, 1985, 1986). The pseudospectral method (e.g., Figure 17) calculates spatial derivatives in the wavenumber domain, multiplying by ik and inverse Fourier transforming back to space. It is computationally more expensive than higher-order differences but achieves much higher

accuracy at long ranges, typically having little grid dispersion in applications to ranges of 10 000 wavelengths or higher. For this reason, the pseudospectral method can be an ideal choice for teleseismic applications, where high accuracy is desirable at both regional and teleseismic range. Kosloff and Kessler (1990) and Fornberg (1998) review both conventional finite difference and pseudospectral numerical approaches, estimating error and stability conditions.

The spectral element method (SEM) formulated with the SPECFEM code (Komatitsch and Vilotte,

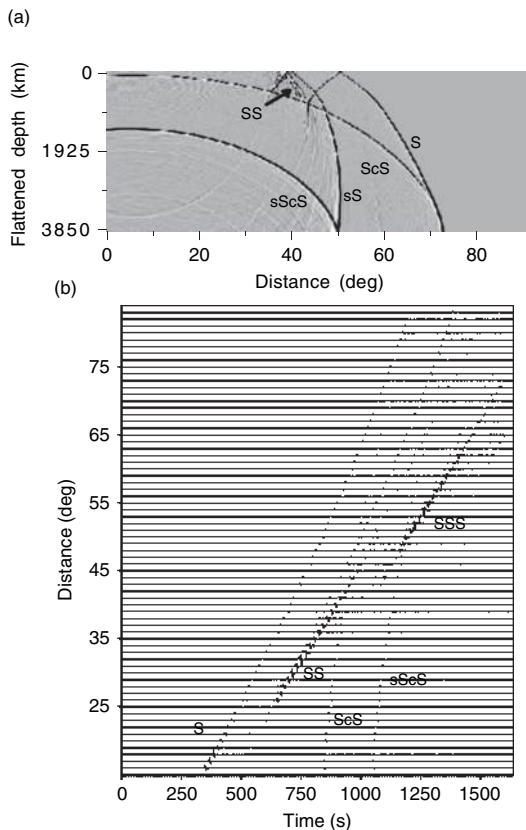


Figure 17 Wave fronts (a) and complete transverse (SH) component seismograms (b) synthesized by the pseudospectral method from Cormier (2000). Note the increase in amplitudes occurring at roughly 20° intervals in S, SS, and SSS due to rapid increases in velocity at upper-mantle solid-solid phase transitions.

1998; Komatitsch and Tromp, 1999, 2002) is currently one of the few numeric methods designed to handle a fully 3-D Earth model. SPECFEM has a well-developed interface to grid the elements needed for arbitrarily complex 3-D models. Versions of SPECFEM are available for both local/regional-scale problems for ranges on the order of 0–100 km, and for global- or teleseismic-scale problems. Another popular regional scale code is the elastic finite difference program by Larsen and Schultz (1995), which has been applied to the effects of 3-D basins and extended fault slip (e.g., Hartzell *et al.*, 1999).

The direct solution method (DSM) is a numerical technique that numerically solves the equations of motion for a series of frequencies required for inversion to the time domain by an FFT (Cummins *et al.*, 1994a, 1994b). The particular numerical technique consists in expanding displacements in the frequency domain by a series of basis functions consisting of a

product of splines in the vertical direction and spherical harmonics in the angular direction. In some respects, the use of basis functions is similar to pseudospectral methods that represent the spatial spectrum of model variations by Fourier or spherical harmonic series. In DSM, the coefficients for the basis functions are found by the method of weighted residuals (Geller and Ohminato, 1994). The SH and P-SV seismograms be computed by DSM are complete, in that they contain all possible body and surface waves. Hence, DSM is a viable alternative to summing modes of free oscillation. Weak 3-D perturbations to a radially symmetric background model are possible in DSM at a computational cost not much higher than that required for the background model (Takeuchi *et al.*, 2000).

Computational time is a practical limitation to numerical modeling. Since most numerical techniques require Earth models specified on a spatial grid or elements, it is straightforward to parallelize the computation by decomposing the spatial grid or elements over multiple processors. Practical computations can be defined by time required to compute a problem. Depending on the algorithm and frequency band, common computer resources in most labs allow a complete teleseismic wavefield to be synthesized in 1 or 2 days using 10–100 processors in parallel. Typical body waves having a high signal-to-noise ratio in the teleseismic range ($10\text{--}180^{\circ}$) exist up to 2 Hz. Practical 2-D modeling can be currently performed at teleseismic range up to 1 Hz with finite difference and pseudospectral methods; 3-D problems with the SPECFEM finite element method can be done up to 0.1 Hz in this time period with a similar number of processors. At ranges less than 100 km, 3-D problems can be practically performed at frequencies up to 1 or 2 Hz (order of 200 wavelengths). This range and frequency band just starts to cover the frequencies of interest to strong ground motion. Frequencies up to 10 Hz at 2000 km range (>5000 wavelengths) in complex 3-D structure are of interest to the problem of discriminating earthquake sources from underground nuclear tests. This is a research problem that is still inaccessible with small to moderate size clusters (less than 100 nodes) and numerical methods.

A large body of literature exists in the application of finite difference and pseudospectral solutions for local-scale problems up to 100 km for exploration applications and strong ground motion applications (e.g., Harzell *et al.*, 1999; Olsen, 2000). Significantly smaller amounts of published work exists for

applications at regional distances (100–2000 km), in which waves are primarily trapped in the crust and the uppermost mantle, and a much smaller amount exists for teleseismic propagation (e.g., Furumura *et al.*, 1998; Igel, 1999; Cormier, 2000).

1.05.5 Parametrization of the Earth Model

An important choice in modeling a seismogram will be the parametrization of the Earth model, or how to describe the spatial variation of its elastic moduli and density (**Figure 18**). The choice of parametrization can have important geodynamic and geochemical implications and is often tightly coupled to the choice made for the modeling algorithm (*see* Chapter 1.23).

1.05.5.1 Homogeneous Layers Separated by Curved or Tilted Boundaries

Certain parametrizations allow seismograms to be synthesized by simple analytic formulas. For example, if the Earth is isotropic and homogeneous, then ray paths are straight lines. The amplitude of body waves are inversely proportional to distance between source and receiver, $1/|\mathbf{x}_o - \mathbf{x}|$. A received waveform is simply the far-field approximation of the source-time function $S(t)$ evaluated at the retarded time, $S(t - |\mathbf{x}_o - \mathbf{x}/v|)$. This simple solution can be extended to models described by sequences of homogeneous layers bounded by planes of varying dip by incorporating elastic boundary conditions at each boundary to calculate reflection/transmission/conversion coefficients. Snell's law is applied in an

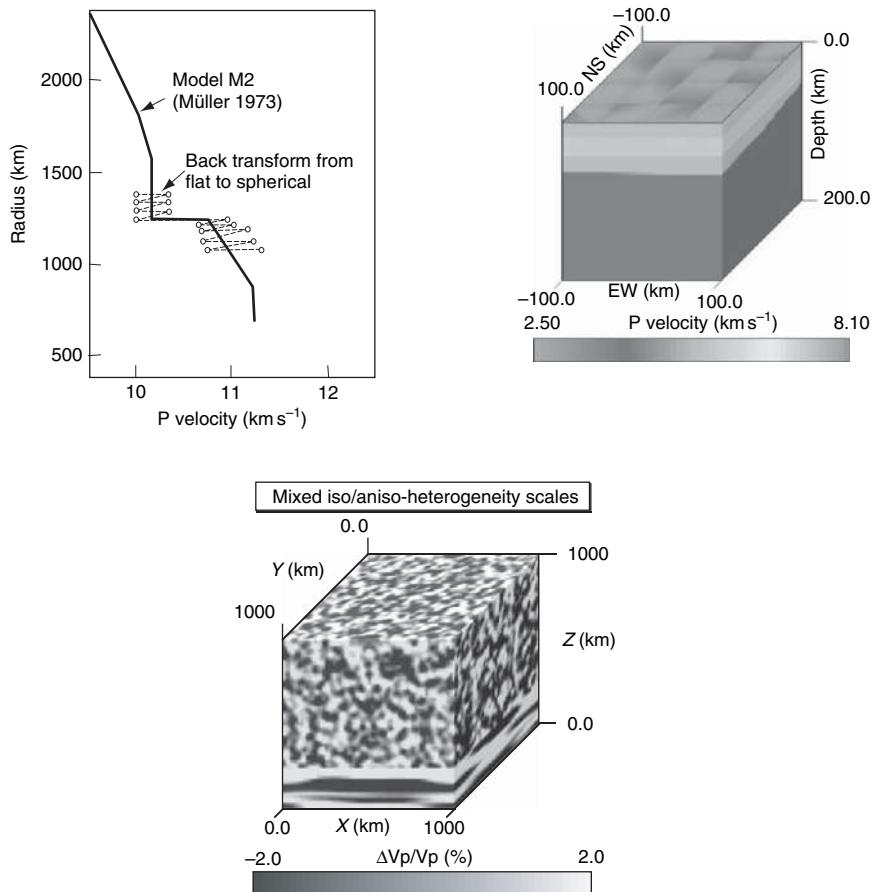


Figure 18 A comparison of the PREM model parametrized by continuous polynomials in radius vs the EFA and discrete homogeneous layers and discrete parametrization back-transformed to a spherical model (Müller, 1973; Aki and Richards, 1980). Bottom left: A 3-D model of the crust and uppermost mantle beneath Nilore, Pakistan, parametrized by Delaunay tetrahedra constructed from codes by Sambridge and Gudmundsson (1998). Bottom right: A 3-D model for testing the effects of possible structure near the core–mantle boundary having P velocity perturbations with both isotropic and anisotropic spatial distributions, constructed using the techniques described by Frankel and Clayton (1986).

incidence plane defined by ray direction and interface normal. Geometric spreading can be calculated from a simple function of ray length in each layer. This algorithm is just DRT applied to homogeneous layers.

Stacks of homogeneous layers can accurately describe continuous spatial variations, provided that the discretization of the model is much finer than the shortest wavelength of interest. The accuracy of the ray solution depends on the ratio of wavelength to boundary curvature. The frequency dependence of reflection by curved boundaries can be treated by the Kirchhoff integral technique.

1.05.5.2 Vertically Inhomogeneous Layers

Except for the case of back-of-the envelope calculations and the limiting case of layering much finer than wavelength, the Earth cannot often be well approximated by either homogenous planar or radially symmetric layers. Velocities and densities vary in all three coordinate directions, but the next most important approximation of the Earth is to make this variation occur in the vertical direction. If this vertical variation is approximated by thin homogeneous plane layers and an EFA (Section 1.05.4.1), then simple plane wave or analytic solutions to the wave equation can still be effectively employed in each layer. In addition to errors associated with the EFA, this discretization should consider physical constraints of finite-strain and buoyancy neutrality to be realistic, or at least the consequences of those constraints need to be evaluated. Except at near-vertical incidence, body waves are notoriously insensitive to density variations and it is especially easy to ignore unphysical effects of any constraints on the velocity–density relations of known materials or the geodynamic effects of buoyancy. The parametrization of the Earth by polynomials analytic in depth was proposed in Preliminary Reference Earth Model (PREM; [Dziewonski and Anderson, 1981](#)) in part to obey the constraints of stable stratification. Modifications to PREM and other reference earths should attempt to take similar care in obeying such constraints. Methods using asymptotic-ray approximations to vertical wave functions (e.g., WKBJ, full wave, GRT) are readily adaptable to this parametrization simply by extending the calculation of delay time $\tau(p)$ to numerical integration over radius or depth. Alternative parametrizations in radius ($V = ar^b$ and $V = a + br$) are computationally more efficient, but little penalty is involved with

current-generation processors by calculating $\tau(p)$ by numerical integration over radius.

1.05.5.3 General 3-D Models

Tomographic models are often the starting point of synthetic modeling. The two most common parametrizations of these 3-D models are either by spherical harmonics (e.g., [Gu et al., 2001](#); [Masters et al., 2000](#); [Ritsema and van Heijst, 2000](#); Chapter 1.10) or by block volumetric elements (e.g., [Grand et al., 1997](#)). Except in fully 3-D modeling methods such as SPECFEM, a choice made in all 2-D modeling methods is to assume that body-wave propagation remains in the sagittal plane and to compute motions in a 2-D model derived by taking a cross section of the 3-D model. If velocity perturbations are assumed to be the same as the typically small (<3%) perturbations of the original tomographic model, the assumption of propagation remaining within or close to the sagittal plane is quite accurate. Indeed, to be consistent with the assumptions of linearized tomographic inversion, it is appropriate to even assume that paths are unperturbed from those in a reference model in the computation of traveltimes in ray-based methods. In this case, the results of the forward modeling can be disappointing, in that the only change in synthetic seismograms from those computed in a reference model will be small changes in relative traveltimes with little or no waveform perturbations. Larger variations in amplitudes and waveforms can be achieved with higher perturbations that violate the assumptions of linearized tomographic inversions.

Since tomographic imaging can smear a more intensely perturbed anomaly over its sampled ray paths into a smoother, less intense anomaly, one approach that has been used in forward waveform modeling is to multiply the perturbations of the tomographic starting model by a scale factor. Some success in matching waveforms by this technique has been achieved using factors of 2–3 to multiply the images of tomographically estimated perturbations to shear velocity ([Ni et al., 2000](#)). Some adjustments in the boundaries of anomalies were also necessary to obtain good matches with observed waveforms. Starting with a tomographic model parametrized by spherical harmonics, Breger and Romanowicz (1998) and [To et al. \(2005\)](#) achieve a good match to S waves interacting with the core–mantle boundary by preserving the boundaries between the largest-scale positive and negative velocity anomalies but

increasing the maximum and minimum values of velocity perturbation.

A simple parametrization allowing for fast analytic computation of amplitudes and ray paths is that used by the code Raytrace3D by Menke (2005), which can be downloaded from the IRIS web site. The Earth model is parametrized by tetrahedra constructed from a grid specified in Cartesian coordinates. Linear interpolation of velocities between knots ($v = a + bx + cy + dz$) is assumed in each tetrahedral element, allowing ray paths to be computed analytically as summed segments of circles. Although geometric spreading is also analytically calculated, this code is primarily intended for calculating traveltimes rather than synthetic seismograms at local and regional ranges. The fast analytic computation of traveltimes and ray paths of this code are ideal for nonlinear tomographic inversions, where it is necessary to assume large perturbations from a background model.

Sophisticated and user-friendly tools for gridding 3-D models have existed in exploration and engineering applications for some time, but are often available only as expensive commercial packages. One public domain package is distributed with the finite element SPECFEM code. Another set of tools are those that employ irregular cells specified by Voronoi tetrahedra, which use a nearest neighbor interpolation to calculate velocities and their first spatial derivatives on irregularly spaced 3-D grids (Sambridge and Gudmundsson, 1998). This can be used in conjunction with the convex hull grid mapping software from University of Minnesota to retrieve a physical quantity and its spatial derivatives at any coordinate point. One example where this approach can be examined are the 3-D slab models shown in Sambridge's web pages, where velocity perturbations have been centered on Benioff zone seismicity.

Some computational difficulties can arise in the parametrization of general 2-D and 3-D models due to the handling of first- and higher-order spatial derivatives of velocity. Ray and asymptotically approximate methods of solving elastic propagation are strictly valid for relatively slow spatial variation of velocity, where medium-scale lengths are much larger than wavelength. Some parametrizations that interpolate velocities in space can introduce high gradients in velocity that lead to false caustics where geometric spreading fails. Spatially continuous interpolations like spherical harmonics and cubic splines can introduce large first- and second-order spatial derivatives of velocity as perturbations

increase. Some DRT codes use a spline-under-tension routine (Cline, 1974) to interpolate between velocities specified at grid points to reduce the size of spurious gradients introduced by the interpolation. In cases of high perturbations, the wave interactions with anomalies must be treated by solving boundary conditions on discrete scatterers (e.g., Korneev and Johnson, 1993; Imhof and Toksoz, 2001).

Rapid advances in computation have made it possible to more routinely include the effects of heterogeneity on the scale of wavelengths using numerical finite difference and finite element methods. It is usually impossible to deterministically know fine-scale structure except in a statistical sense as a spatial spectrum of heterogeneity. The most common way of constructing these types of models is to impose a random number generator at finite difference or element grid points, Fourier transform the grid from physical space to wavenumber space, filter by an assumed spatial spectrum of heterogeneity, and inverse Fourier transform to physical space (Frankel and Clayton, 1986). This idea has been extended to media that may be composed of 2 or n types of specific rocks or medium phases (Holliger *et al.*, 1993).

1.05.6 Instrument and Source

Assuming an Earth model and one of the algorithms previously described, a model response $M(t, \Delta_o)$ can be computed for a source consisting of a delta function in time and space. $M(t, \Delta_o)$ is termed the Green's function. The remaining task in synthesizing a body-wave seismogram consists in either incorporating or removing the effects of the seismograph response and source-time function. This task can be simplified using the ideas of superposition and linear systems. The seismogram can be thought of as a series of convolutions of a model response $M(t, \Delta_o)$, an instrument operator $I(t)$, a source time function $S(t)$, a receiver crustal response $C(t, \Delta_o)$, and an attenuation operator $A(t, \Delta_o)$:

$$U(t, \Delta_o) = I(t)^* S(t)^* C(t, \Delta_o)^* A(t, \Delta_o)^* M(t, \Delta_o) \quad [24]$$

The two common modeling choices to infer Earth structure are either to (1) convolve all of the operators in [24] and compare the resultant synthetic seismogram with an observed synthetic seismogram or to (2) deconvolve as many operators as possible to retrieve the model response. The first choice has

been the more common, but as the density of receiver and source arrays has approached that common in exploration seismology, the deconvolution choice has become increasingly popular. Deconvolution can increase the frequency content of the wavefield, and hence its spatial sensitivity. It allows different sources, receivers, and instruments to be combined to invert an observed wavefield to an image of reflectors and scatterers (e.g., [Rost and Thomas, 2002](#)).

1.05.6.1 Instrument Responses and Deconvolution

The Fourier transform of $I(t)$, or $I(\omega)$, is a filter that is typically a narrow band pass of particle velocity. Most instrument responses are now reported by complex poles, ω_p^i , and complex zeros, ω_o^i , from which the complex frequency response $I(\omega)$ of the seismograph can be represented by

$$I(\omega) = \frac{(\omega - \omega_o^1)(\omega - \omega_o^2)\cdots(\omega - \omega_o^n)}{(\omega - \omega_p^1)(\omega - \omega_p^2)\cdots(\omega - \omega_p^m)} \quad [25]$$

The effect of the instrument can then be included by filtering the synthetic spectrum by multiplying by $I(\omega)$ and inverse Fourier transforming the result to the time domain. Alternatively, the instrument can be deconvolved by spectral division, but $I(\omega)$ must be modified by adding a constant term (water level) to avoid division by zero as the response goes to zero outside the pass band of the instrument. The instrument response can be deconvolved to displacement, velocity, or acceleration ([Figure 19](#)). The deconvolved particle velocity in the pass band of 0.01–2 Hz usually offers the best compromise between useful information content and high signal-to-noise ratio for teleseismic body waves. Deconvolved displacement, however, offers nearly a direct observation of the far-field source time function, given by shape of the P or S wave displacements in the range of 35–90°. In this range, the waveform of the observed displacement is primarily affected by the pulse broadening due to viscoelastic attenuation.

1.05.6.2 Far-Field Source Time Function

Detailed and accurate representation of the forcing function of the elastic equation of motion, or source-time function, requires the input of both theory and experiment for brittle failure and stick-slip friction. Chapter 4.02 provides a review of source representations and the physical assumptions behind them. For

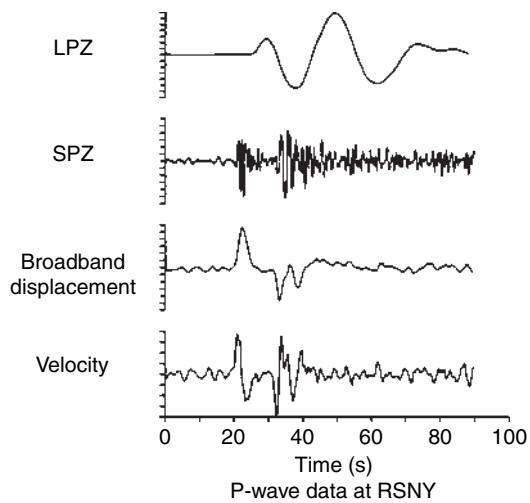


Figure 19 Instrument deconvolution showing a short- and long-period seismogram response and the deconvolved particle velocity and displacement from [Choy and Engdahl \(1987\)](#).

most modeling applications, a simple far-field representation and a judicious choice of earthquakes are all that is needed to begin to separate the effects of source from the effects of structure.

The far-field displacement is proportional to the time derivative of a moment-rate tensor $d\mathbf{M}(t)/dt$. A common scalar moment M_o can be factored out of $d\mathbf{M}(t)/dt$, leaving a far-field time source-time function $S(t)$. In the case of an earthquake faulting source, $S(t)$ is proportional to the time derivative of its slip history (e.g., [Shearer, 1999](#), chapter 9). An operator combining the convolution of $S(t)$, $A(t, \Delta_o)$, and $C(t, \Delta_o)$ can be derived from either inversion or empirical observations of instrument-deconvolved P-wave displacements at all distances between 30° and 90°.

The $S(t)$ of many earthquakes having body-wave magnitudes less than 6.5 often can be adequately represented by a simple triangle-shaped pulse, where the triangle width is related to the corner frequency and fault length in a [Brune \(1970\)](#) model of the source spectrum. A body wave magnitude of 5.5 is often the practical lower limit to modeling, because earthquakes smaller than this size rarely generate sufficient teleseismic recordings of body waves having a high signal-to-noise ratio. After factoring out the time-dependent factor $S(t)$ and scalar moment M_o from the moment-rate tensor, a radiation pattern $R(\phi, p)$ can be constructed from weighted elements of the moment-rate tensor where ϕ is the azimuth and p is the ray parameter of a body wave ray

connecting source and receiver. This weighting is equivalent to representing general faulting by three fundamental types of faulting or source types (e.g., Aki and Richards, 1980, chapter 4).

The process of factoring out a slip-time history from a point-source radiation pattern should be avoided for earthquakes having body-wave magnitude greater than 6.5 or fault lengths greater than 50 km. For these larger earthquakes, a simple point-source representation fails, and the time history and the slip distribution become too complex to be easily separated from the waveform complexities due to structure.

If it were not for the fact that the majority of earthquakes are at depths of 20 km or less, incorporating a radiation factor $R(\phi, p)$ in the integrand of [13] would be all that is needed to include an earthquake source at teleseismic range. Since most earthquakes are shallow, the effects of surface reflections near the source (pP , sP) generally need to be included in modeling a 5–10 s time window surrounding an observed body wave. The effect of different radiation patterns for the near-source reflections is helpful in inversion of teleseismic P waves for the far-field moment-rate tensor (Langston and Helmberger, 1975). The inverted source depth and point-source representation (centroid moment-rate tensor) can be used to construct a predicted equivalent source-time function and radiation pattern containing P + pP + sP waves (Figure 20). Alternatively, the effect of the surface reflections can be handled by incorporating

the moment-rate representation at the appropriate depth in reflectivity or mode summation techniques or be included by separately adding predicted pP and sP waveforms to P waveforms synthesized by ray-based or other transform methods.

At local and regional ranges, surface interactions as well as a more detailed source description can often still be handled by superposing far-field point-source representations. These point-source representations can be distributed at discrete points along fault plane, delayed by the time slip initiates and stops at each discrete point. This type of source representation is said to be kinematic rather than dynamic because the slip history is prescribed rather than resulting from a slip initiation condition related to either crack failure or friction on the fault surface. At very close range, the wavefield can be well approximated by a few simple directly arriving body waves, and the far-field Green's function for each body wave can be calculated by ray theory. The synthesis problem can then be reduced to an integral over the fault plane in which the integral is carried out over lines of equal arrival time of energy (isochrones) corresponding to the sum of the rupture time to a point on the fault and the traveltimes of a body wave to a receiver (Spudich and Frazer, 1994). The effects of 3-D structure and frequency-dependent diffraction can be incorporated in this technique by substituting the ray-theoretical Green's functions with Green's functions calculated by Gaussian beam summation (e.g., Cerveny *et al.*, 1987) or WKBJ/

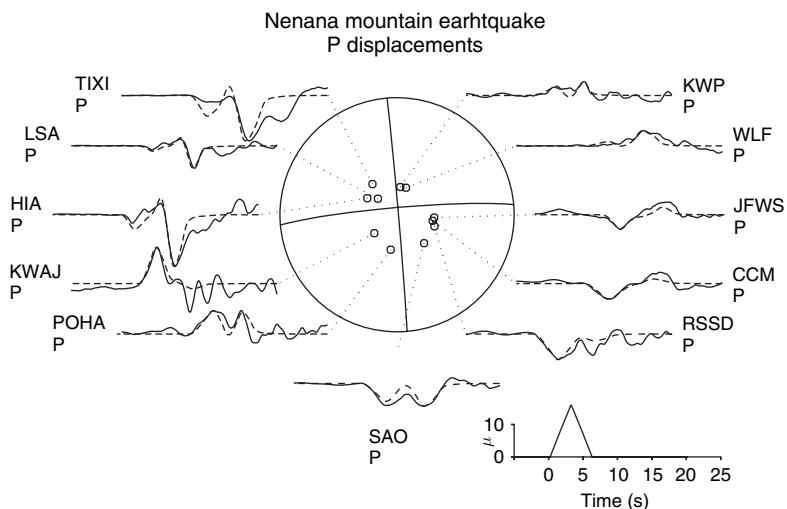


Figure 20 Teleseismic P-wave displacements for the Nenana earthquake of 23 October 2002. The broadband data are plotted as solid lines; the synthetic displacements are plotted as dashed lines. The far-field source-time function is plotted on the time axis, determined from modeling the P waves as a combination of P, pP , and sP waves (Choy and Boatwright, 2004).

Maslov superposition of plane waves. See Chapter 4.18 for a complete review of algorithms for synthesis at local ranges in which spatially extended slip models are required for earthquake slip inversions and simulation of strong ground motions.

1.05.7 Extensions

1.05.7.1 Adapting 1-D Codes to 2-D and 3-D

Since the delay time $\tau(p)$ in the WKBJ, GRT, and full-wave methods can be calculated from integrals of vertical slowness up to ray turning points, it is simple to consider different Earth models on either side of the turning points. For example, to calculate the effect of the upper mantle in the eastern US to a station in the western US, one might use two different models, keeping track of where rays enter and leave the two models (Helmberger *et al.*, 1996). In reflectivity methods, it is a little more difficult, but not impossible, to incorporate different receiver- and source-side models. One would need to separately consider a receiver- and source-side transmission response. Control of ray expansions within thin layers as in Kennett's formulation of the reflectivity method makes it possible to consider the effects of more general 2-D models.

Purely ray-based methods, such as DRT and/or superposition of Gaussian beams or Maslov plane waves, can consider continuously varying models in 2-D or 3-D space. Modal methods, including the locked-mode method, can be adapted to 2-D, 3-D, and anisotropic models by calculating the coupling between modes, including interactions between Love and Rayleigh modes. Maupin (1987), Maupin and Kennett (1989), and Kennett (1998) describe schemes for calculating modal coupling and show seismograms synthesized for rapid lateral transitions in crustal thickness.

1.05.7.2 Hybrid Methods

To save computation, it is sometimes necessary to combine two methods, a computationally cheaper method in a large region, and a computationally more expensive method in a small region to study structural complexity near a boundary or region of rapid velocity or density transition. Usually the computationally more expensive method is a numerical method, such as finite difference or spectral element. The usual way in which the two methods are connected is to compute a Kirchhoff integral. The integral

is carried out on a surface or boundary that separates the structurally complex region from the simple region, employing Huygens principle to connect the wavefields in the two regions by allowing each point on a wave front to propagate as a new point source. Kirchhoff integrals can also be used to calculate the effects of scattering by inclusions or the frequency-dependent reflection or transmission across a curved interface when the radius of curvature is on the order of a wavelength. A hybrid method of this type was used by Wen *et al.* (1998) to study heterogeneity in the lowermost mantle using a finite difference method, connecting it to GRT in a radially symmetric overlying mantle. The most detailed treatment of fully elastic integrands for P, SV, and SH waves can be found in Frazer and Sen (1985). Probably due to the need for intense customization for specific problems, codes for Kirchhoff integrals are not generally distributed. A good starting point for any application are the acoustic problems described in Shearer (1999, pp. 138–140), which can then be generalized using the elastic formulas in Frazer and Sen (1985).

Capdeville *et al.* (2003a) developed a hybrid method that allows modal solutions in large homogeneous or weakly heterogeneous regions to be coupled to the numerical SEM solutions in strongly heterogeneous regions. This hybrid method has been applied to a thin, strongly heterogeneous, D'' region at the base of the mantle sandwiched between a homogeneous core and mantle (Capdeville *et al.*, 2003b; To *et al.*, 2005; see Chapter 1.18). A similar approach might also be feasible at higher frequencies and local and regional ranges by coupling locked surface-wave modes to SEM solutions.

1.05.7.3 Frequency-Dependent Ray Theory

Recognizing that ray theory is an approximation applicable at infinite frequency, corrections to ray theoretical approximation can be based on a Born approximation that corrects amplitude and traveltimes in such a way that a finite region in space determines the amplitude and traveltimes of a body wave, making both depend on frequency (Dahlen *et al.* 2000). Chapter 1.04 provides a review and additional references on the calculation of these frequency-dependent corrections. One way in which the banana-doughnut sensitivity kernels needed to calculate the frequency dependence of traveltimes and amplitudes is to use the a paraxial approximation around a central ray using DRT. This approach can exploit the strong notational framework developed by Cerveny and colleagues

(e.g., Dahlen *et al.*, 2000). Sensitivity kernels derived from the Born approximation show that traveltime is most sensitive to velocity along the boundaries of the banana or rim of the doughnut away from the central ray, whereas amplitude is most sensitive to velocity in the center of the banana in the doughnut hole. The traveltime sensitivity is closely related to the behavior of the stationary-phase approximation, in which the path is assumed to be invariant for variations in velocity along the central ray. It is important to recognize that an accurate measurement of the frequency-dependent effects on traveltime depends on waveform measurements in which the effects on amplitude and phase are combined. To properly incorporate these combined effects in a tomographic inversion, a synthetic waveform must be cross-correlated with an observed waveform to obtain a traveltime residual. Except in tomographic inversion, these frequency-dependent corrections to ray theory using the Born approximation have not yet been used or tested as a general forward modeling technique. It is as yet unknown how the weak dispersion due to velocity variation tradeoffs with the weak dispersion due to viscoelasticity (Section 1.05.7.4), or how accurate the amplitude correction due to a simple Born approximation is compared to that predicted by the generalized Born approximation of Coates and Chapman (1991).

The frequency-dependent, banana-shaped, sensitivity kernels of seismic rays can also be calculated from a modal approach using a nonlinear perturbation theory (Li and Romanowicz, 1995). In this case, the forward modeling approach is mode summation. The approximations and behavior of errors due to asymptotic approximations of the effects of heterogeneous structure are better understood in this method but are practically limited to frequencies on the order of 0.1 Hz and lower.

1.05.7.4 Attenuation

Chapter 1.21 reviews the physical mechanisms and global models of seismic attenuation. Thus subsection reviews common procedures for incorporating attenuation into the synthesis of body waves.

Viscoelasticity is the term that best describes the type of seismic attenuation resulting from the dissipation of elastic energy into heat. This heat dissipation is analogous to the heat dissipated in electric circuits, where stress is analogous to current, voltage is analogous to strain, and complex impedance is analogous to a complex compliance (reciprocal of a complex elastic modulus). For

ray-based and integral transform-based methods, viscoelastic attenuation is most directly treated by making velocity complex through the square root of a complex modulus divided by density. The effect of attenuation on the spectrum of a propagating body wave can be written as

$$A(\omega) = e^{i\omega T(\omega)} \quad [26]$$

where $A(\omega)$ is just the Fourier transform of the attenuation operator $A(t)$ in [24]. The complex traveltime $T(\omega)$ is determined by integrating a ray over a path in which velocity is complex and frequency dependent, or $T(\omega) = \int_{\text{path}} ds/V(\omega)$.

The frequency dispersion of velocity in a viscoelastic medium is similar to the dispersion of a complex index of refraction in electromagnetic propagation, in which absorption is always associated with dispersion. In body waves, this dispersion is small and difficult to detect with narrow-band instrumentation. In sufficiently broadband recordings, viscoelastic dispersion is detectable as an asymmetry in the propagation of delta function time pulse. High frequencies travel faster than low frequencies, making a steeper rise time than fall time as the pulse propagates (Figure 21). Velocity dispersion was first recognized to be important in global seismology when the elastic moduli derived from the study of low-frequency free oscillations were found to be smaller than those derived from the traveltimes of high-frequency body waves (Dziewonski and Anderson, 1981).

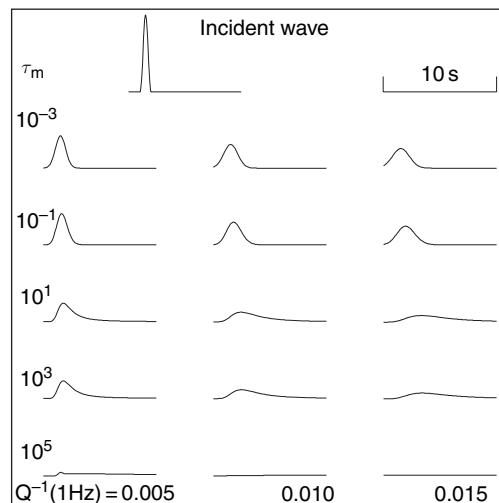


Figure 21 Attenuation operators convolved with a given wavelet for varying parameters of a viscoelastic relaxation spectrum from Li and Cormier (2002).

There is a consensus that the quality factor, Q , in the attenuation of teleseismic body waves is nearly independent of or slowly varying with frequency from 0.001 to 0.1 Hz, with possibly some stronger frequency dependence beginning between 0.1 and 1 Hz. For frequencies close to neither the low- or high-frequency corner of a relaxation spectrum (absorption band) of constant Q , this assumption leads to an approximate formula for complex velocity of the type

$$V(\omega) \cong V(\omega_r) \left(1 + \left(\frac{1}{\pi Q} \right) \ln \left(\frac{\omega}{\omega_r} \right) - i \left(\frac{1}{2Q} \right) \right) \quad [27]$$

where $V(\omega_r)$ is the real velocity at a reference frequency. Substitution of $V(\omega)$ into the ray path integral for complex time $T(\omega)$ in [26] and inverting the complex spectrum defines a time domain attenuation operator that is commonly termed the [Futterman \(1962\)](#) or [Carpenter \(1967\)](#) Q operator. This operator is valid in regions of the relaxation spectrum where attenuation ($1/Q$) is constant. It is not valid near the corners of the true relaxation spectrum, where $1/Q$ decays as ω^{-1} . It is relatively simple, however, to derive a formula for complex velocity that is valid across the entire relaxation spectrum (e.g., [Cormier and Richards, 1988](#)). An example of the effect of attenuation operators constructed with this formula is shown in [Figure 21](#).

The width of relaxation spectra in which attenuation $1/Q$ is nearly constant or slowly varying (often observed to be $\omega^{1/3}$) is typically 5 decades in frequency ([Anderson and Given, 1981](#)). A problem often not considered in modeling the effects of viscoelasticity are the limitations viscoelastic theory imposes on the difference between the static (relaxed) elastic modulus and the infinite frequency (unrelaxed) modulus. There are limits on the band over which viscoelastic Q can be constant given by this modulus difference or defect. In practice, this means that any Q inferred from a body-wave pulse width or spectrum that has an exceptionally low value, for example, 10 or lower, is probably the result of scattering rather than viscoelasticity.

Slowness or ray-based methods often treat attenuation by solving the equations of motion with real velocities defined at the reference frequency (often chosen to be 1 Hz) and then convolving the result with the time domain attenuation operator of [26] appropriate for each ray path. Since the units of this ray-path integrand are time, a parameter often

cited in the literature of teleseismic body waves is t^* . Considering only the real part of [26] and assuming [27] for $V(\omega)$, each frequency is exponentially attenuated by the factor $\exp(-\omega t^*)$, where

$$t^* = \int_{\text{path}} \frac{1}{V(\omega_r)Q} ds \quad [28]$$

The parameter t^* is found to vary relatively slowly with range and path length of P waves in the mantle, and is on the order of 1 s for frequencies between 0.01 and 0.2 Hz in the distance range 30–90°.

Spectral methods that first compute the complex spectrum of the solution of the equation of motion (e.g., reflectivity, discrete wave number, full wave, the DSM, mode summation) can treat attenuation simply by substituting a complex velocity and analytically continuing all formulas in propagator matrices and phase factors that contain wave numbers and elastic moduli to complex numbers. To include the dispersive effect of attenuation in DRT and beam summation, a Futterman-type Q operator can be convolved with the computed amplitude of each ray or beam calculated in a model specified at a reference frequency. Another more general approach would be to compute amplitudes by DRT at the real velocities, $Re(V(\omega))$, defined at each frequency and then multiply each spectral component by an exponential scale factor

$$\exp \left(-\omega \int \text{Im} \left(\frac{1}{V(\omega)} \right) ds \right)^{-1}$$

In finite difference methods that integrate the equation of motion in the time domain, it is not practical to handle viscoelastic attenuation by a convolution. Instead, it is possible to design a system of stress-strain memory functions that can be simultaneously integrated in the time domain with the equations of motion ([Robertsson et al., 1994](#)). Using a memory function for only three specific relaxation times, it is usually possible to reproduce the effects of a relaxation spectrum of nearly constant attenuation in a frequency band of interest.

1.05.7.5 Anisotropy

Chapter 1.09 reviews the elastic anisotropy and computational approaches for its effects. Summarized here are considerations primarily related to ray- and transform-based methods of body-wave synthesis.

Elastic anisotropy removes the degeneracy of the S-wave eigenvalue/eigenvector solutions to the wave numbers of propagating plane waves. The SH

and SV definitions defined by source and receiver geometry are no longer useful for formulating boundary conditions needed for calculating reflection and refraction. S polarization is best resolved into components of motion along two orthogonal quasi-S-wave eigenvectors, with motion on both the SH and SV components of motion generally consisting of a combination of two quasi-S waves. A pure SV polarized wave incident on a weakly anisotropic region excites two transmitted quasi-S waves such that the SH component of the transmitted wave has the approximate shape of the time derivative of the SV component (Silver and Chan, 1991).

A special case of anisotropic propagation is that of transverse isotropy with a vertical axis of symmetry. In this case, the two-quasi S-waves are exactly polarized in the SH and SV directions defined by source–receiver geometry but with two different velocities. Transverse isotropy can be an accurate representation for Earth models consisting of thin planar or radially symmetric layers, having alternating or randomly fluctuation velocities and layer thicknesses much smaller than the smallest wavelength of interest (Backus, 1962). Transverse isotropy can be easily incorporated in all layered 1-D body-wave codes by modifying the calculations of reflection–transmission coefficients and the $\tau(p)$ function in the phase factor of WKBJ, GRT, or full-wave techniques (e.g., Chapman, 2004).

General anisotropy breaks the symmetry upon which some integral transforms and spherical harmonic analysis are based. Body waves can propagate in and out of the sagittal plane. This makes the problem of synthesizing body waves in a generally anisotropic model automatically a 3-D problem. In plane-layered models and Cartesian coordinates, the generalized wave number superposition leads to reflectivity formulations that require integration over two horizontal wave numbers to invert wave number transforms to the spatial domain (Fryer and Frazer, 1984, 1987). Similarly, the WKBJ/Maslov methods can be generalized by integrals over two horizontal slownesses (Garmany, 1989; Chapman, 2001). Some approximations for weak general anisotropy and expansion of the phase near its stationary point can be employed to simplify the problem to integration over a single wave number corresponding to waves propagating in and near the sagittal plane. For seismograms synthesized by DRT or Gaussian beam summation, the kinematic system needed for ray trajectory and traveltimes is easily extended to the case of general anisotropy, where

an eigenvector–eigenvalue problem for the wave types is solved for each spatial or time increment used in numerical integration. A system for dynamic quantities corresponding to the \mathbf{P} and \mathbf{Q} matrices can be formulated for summation of Gaussian beams (Hanyga, 1986), but a more tractable approach is to take difference derivatives of ray positions and slownesses (Gajewski and Psencik, 1987) to determine geometric spreading and wave front curvature.

1.05.7.6 Scattering

Chapter 1.20 reviews seismic scattering. A few fundamental effects important to consider in the synthesis of body waves are reviewed here, some of which are computationally simple to include.

Single scattering by small-scale heterogeneity can be incorporated by a Born approximation (e.g., Chapman, 2004, chapter 10). The Born approximation effectively treats small perturbations in velocity and density from a background medium as seismic sources by moving terms due to the difference in perturbed velocity from the background velocity to the source side of the wave equation. The strength of these scattering sources that re-radiate energy are proportional to the energy of the wave incident on the heterogeneity and the size of its perturbations. For wavelengths much greater than the heterogeneity, each heterogeneity can be treated by a point-source representation similar to the moment-rate tensor representation of earthquake sources (Wu and Aki, 1985). The effects of many small-scale heterogeneities can be obtained by summing the radiated body waves of each small scatterer. The Green’s function solutions of the equations of motion must be known from the source to the position of each scatterer and from the scatterer to the receiver. These Green’s functions can be calculated by any of the methods described in Section 1.05.4. The volume of the region of scatterers contributing to a specific time window surrounding a body wave is the banana-shaped region surrounding a least-time ray described in Section 1.05.7.3. An example of this approach is the synthesis of the precursor coda of PKIKP from scatterers near the core–mantle boundary (Cormier, 1999).

Forward scattering in the direction close to the direction of the least-time ray can affect the pulse shape of broadband body waves. A finite frequency band of observation can blur the effects of many scatterers, whose arrivals can occur over time spacings much shorter than the shortest period in the

pass band of observation. This broadening and multi-pathing can be mistaken for the effects of viscoelastic attenuation. Unlike viscoelastic attenuation, where energy is lost to heat, scattering attenuation simply redistributes high-frequency energy in time and space out of a finite time window surrounding the pulse observed at a particular location. One recent approximate method of including this effect is the theory of dynamic composite elastic moduli (DYCEM) of [Kaelin and Johnson \(1998\)](#). This technique can be formulated in terms of a complex wave number, allowing it to be treated in much the same way as complex velocities in viscoelasticity (e.g., Cormier and Li, 2002).

1.05.8 Conclusions

Most of the algorithms for synthesizing body waves in radially symmetric (1-D) structure have been successfully tested and verified against each other (e.g., Choy *et al.*, 1980; [Figure 12](#)). Factors to consider in choosing an algorithm include the accuracy in a required frequency band and distance range, the width of the time window and number and types of seismic phases, speed of computation, the completeness of documentation, and the existence and accessibility of software.

The frequency band of calculation is probably the foremost important factor. If working in the frequency band less than several one-tenths of a hertz, then modal summation or the DSM are good choices because they easily include all possible body waves, surface waves, and frequency-dependent interactions with discontinuities in an arbitrarily wide time window at an acceptable computational cost on a single workstation. Using a perturbation approach, they can also handle weak lateral heterogeneity (several percent perturbation in velocity and density) with little additional computational overhead. At higher frequencies, reflectivity/GRT or locked-mode approaches in thin homogeneous layers or asymptotically approximate ray-based methods (WKBJ/full wave/Maslov/DRT and Gaussian beams) in homogeneous layers are efficient and produce identical results if carefully used.

In either low- or high-frequency bands, the most important limitations of each algorithm are related to its accurate reproduction of the waveform effects of the broad spatial spectrum of Earth structure. In all algorithms, it is important to consider the effects of neglecting small-scale structure on the order of a

wavelength or smaller. In high-frequency algorithms, limitations are related to either the validity of the EFA, the physicality of thin-layer representations, or the validity of asymptotic approximations of wave functions in layers having continuous and large spatial gradients. Understanding these limitations is also key to the problems of separating the effects of anisotropy from heterogeneity and viscoelasticity from scattering.

Computational hardware now makes it possible to routinely model seismic waveforms to invert for both radially symmetric (1-D) Earth structure and simple point-source representations of earthquake faulting. Recent advances in digital recording and network telemetry have now made these inversions possible in near real-time. The remaining advance needed to fully exploit the real-time capabilities of 1-D modeling lies in making user-friendly software interfaces.

Three-dimensional modeling is still strongly limited by current computational hardware. Ray-based 3-D modeling is feasible on single workstations in smooth models having a relatively large ratio of scale length of heterogeneity to wavelength and for relatively mild velocity and density perturbations (less than several percent). Similarly, perturbation approaches based on mode summation or the DSM can be performed with modest computational overhead for relatively weak velocity perturbations (several percent) and at large scale lengths (thousands of kilometers). Investigation of effects of very small-scale heterogeneity (10 km or less) at high frequencies (>1 Hz) can be done in 3-D but is currently only practical for ranges on the order of hundreds of wavelengths using clusters of processors. An effort to test and verify 3-D modeling algorithms against each other has just begun in the last several years ([Igel *et al.*, 2000](#)).

Acknowledgments

The author thanks the National Science Foundation for continued support on problem in wave propagation and Earth structure, most recently under grant EAR 02-29586.

References

- Abo-Zena A (1979) Dispersion function computations for unlimited frequency values. *Geophysical Journal of the Royal Astronomical Society* 58: 91–105.

- Aki K and Richards PG (1980) *Quantitative Seismology: Theory and Methods*. San Francisco, CA: W.H. Freeman.
- Aki K and Richards PG (2002) *Quantitative Seismology*, 2nd edn. Sausalito, CA: University Science Books.
- Anderson DL and Given JW (1982) Absorption band Q model for the Earth. *Journal of Geophysical Research* 87: 3893–3904.
- Baag C and Langston CA (1985) Shear-coupled PL. *Geophysical Journal of the Royal Astronomical Society* 80: 363–385.
- Backus GE (1962) Long-wave elastic anisotropy produced by horizontal layering. *Journal of Geophysical Research* 67: 4427–4440.
- Ben-Menahem A and Beydoun WB (1985) Range of validity of seismic ray and beam methods in general inhomogeneous media, Part I: General theory. *Geophysical Journal of the Royal Astronomical Society* 82: 207–234.
- Bouchon M and Aki K (1977) Discrete wave-number representation of seismic wave source fields. *Bulletin of the Seismological Society of America* 67: 259–277.
- Bouchon M (1979) Discrete wave number representation of elastic wave fields in three-space dimensions. *Journal of Geophysical Research* 84: 3609–3614.
- Bréger L and Romanowicz B (1998) Three dimensional structure at the base of the mantle beneath the central Pacific. *Science* 382: 244–248.
- Brune JN (1970) Tectonic stress and the spectra of seismic shear waves from earthquakes. *Journal of Geophysical Research* 75: 4997–5009.
- Bullen KE and Bolt BA (1985) *Introduction to the Theory of Seismology*, pp. 499. Cambridge, UK: Cambridge University Press.
- Burdick LJ and Helmberger DV (1978) The upper mantle P velocity structure of the Western United States. *Journal of Geophysical Research* 83: 1699–1712.
- Burdick LJ and Orcutt JA (1979) A comparison of the generalized ray and reflectivity methods of waveform synthesis. *Geophysical Journal of the Royal Astronomical Society* 58: 261–278.
- Capdeville Y, Chaljub E, Villette JP, and Montagner JP (2003a) Coupling the spectral element method with a modal solution for elastic wave propagation in global Earth models. *Geophysical Journal International* 153: 34–66.
- Capdeville Y, Romanowicz B, and To A (2003b) Coupling spectral elements and modes in a spherical Earth: An extension to the ‘sandwich’ case. *Geophysical Journal International* 154: 44–57.
- Carpenter EW (1967) Teleseismic signal calculated for underground, underwater, and atmospheric explosions. *Geophysics* 32: 17–32.
- Cerveny V and Ravindra R (1971) *Theory of Seismic Head Waves*. Toronto, ON: University of Toronto Press.
- Cerveny V (1985) The application of ray tracing to the numerical modeling of the seismic wave field in complex structures. In: Helbig K and Treitel S (eds.) *Seismic Shear Waves: Handbook of Geophysical Exploration, Section I: Seismic Exploration*, vol. 15A, pp. 1–124. London: Geophysical Press.
- Cerveny V, Pleinerová J, Klimes L, and Psencík I (1987) High frequency radiation from earthquake sources in laterally varying structures. *Geophysical Journal of the Royal Astronomical Society* 88: 43–80.
- Cerveny V (2001) *Seismic Ray Theory*. New York: Cambridge University Press.
- Chapman CH (1973) The Earth flattening transformation in body wave theory. *Geophysical Journal of the Royal Astronomical Society* 35: 55–70.
- Chapman CH (1978) A new method for computing synthetic seismograms. *Geophysical Journal of the Royal Astronomical Society* 54: 481–518.
- Chapman CH and Drummond R (1982) Body-wave seismograms in inhomogeneous media using Maslov asymptotic theory. *Bulletin of the Seismological Society of America* 72: S277–S317.
- Chapman CH, Chu J-Y, and Lyness DG (1988) The WKBJ seismogram algorithm. In: Doornbos DJ (ed.) *Seismological Algorithms*, pp. 47–74. London: Academic Press.
- Chapman CH (2004) *Fundamentals of Seismic Wave Propagation*. Cambridge, UK: Cambridge University Press.
- Choy GL and Richards PG (1975) Pulse distortion and Hilbert transformation in multiply reflected and refracted body waves. *Bulletin of the Seismological Society of America* 65: 55–70.
- Choy GL, Cormier VF, Kind R, Müller G, and Richards PG (1980) A comparison of synthetic seismograms of phases generated by the full wave theory and by the reflectivity method. *Geophysical Journal of the Royal Astronomical Society* 61: 21–39.
- Choy GL and Cormier VF (1983) The structure of the inner core inferred from short-period and broad-band GDSN data. *Geophysical Journal of the Royal Astronomical Society* 72: 1–21.
- Choy GL and Engdahl ER (1987) Analysis of broadband seismograms from selected IASPEI events. *Physics of Earth and Planetary Interiors* 44: 80–92.
- Choy GL and Boatwright J (2004) Radiated energy and the rupture process of the Denali Fault earthquake sequence of 2002 from broadband teleseismic body waves. *Bulletin of the Seismological Society of America* 94: S269–S277.
- Cline AK (1874) Six subprograms for curve fitting using splines under tension. *Communications of the ACM* 17: 220–223.
- Coates RT and Chapman CH (1991) Generalized Born scattering of elastic waves in 3D media. *Geophysical Journal International* 107: 231–263.
- Cormier VF (1999) Anisotropy of heterogeneity scale lengths in the lowermost mantle from PKIKP precursors. *Geophysical Journal International* 136: 373–384.
- Cormier VF (2000) D'' as a transition in the heterogeneity spectrum of the lowermost mantle. *Journal of Geophysical Research* 105: 16193–16205.
- Cormier VF and Choy GL (1981) Theoretical body wave interactions with upper mantle structure. *Journal of Geophysical Research* 86: 1673–1678.
- Cormier VF and Li X (2002) Frequency dependent attenuation in the inner core: Part II. A scattering and fabric interpretation. *Journal of Geophysical Research* 107(B12): 2362 (doi:10.1029/2002JB1796).
- Cormier VF, Mandal B, and Harvey D (1991) Incorporation of velocity gradients in the synthesis of complete seismograms by the locked mode method. *Bulletin of the Seismological Society of America* 81: 897–930.
- Cormier VF and Richards PG (1977) Full wave theory applied to a discontinuous velocity increase: The inner core boundary. *Journal of Geophysics* 43: 3–31.
- Cormier VF and Richards PG (1988) Spectral synthesis of body waves in Earth models specified by vertically varying layers. In: Doornbos D (ed.) *Seismological Algorithms*, pp. 3–45. London: Academic Press.
- Crotwell HP, Owens TJ, and Ritsema J (1999) The TauP Toolkit: Flexible seismic travel-time and raypath utilities. *Seismological Research Letters* 70: 154–170.
- Cummins PR, Geller RJ, Hatori T, and Takeuchi N (1994a) DSM complete synthetic seismograms: SH, spherically symmetric, case. *Geophysical Research Letters* 21: 533–536.
- Cummins PR, Geller RJ, and Takeuchi N (1994b) DSM complete synthetic seismograms: P-SV, spherically symmetric, case. *Geophysical Research Letters* 21: 1663–1666.

- Dahlen FA (1987) Multiplet coupling and the calculation of synthetic long-period seismograms. *Geophysical Journal of the Royal Astronomical Society* 91: 241–254.
- Dahlen FA and Tromp J (1998) *Theoretical Global Seismology*, P. 944. Princeton, NJ: Princeton University.
- Dahlen FA, Hung S-H, and Nolet G (2000) Frechet kernels for finite-frequency traveltimes-I. Theory. *Geophysical Journal International* 141: 157–174.
- Davis JP and Henson IH (1993) Users Guide to Xgbm: An X-Windows System to Compute Gaussian Beam Synthetic Seismograms, Rept TGAL-93-02. Alexandria, VA: Teledyne-Geotech.
- Doornbos DJ (ed.) (1988) *Seismological Algorithms: Computational Methods and Computer Programs*, P. 469. New York: Academic Press.
- Dziewonski AM, Chou T-A, and Woodhouse JH (1981) Determination of earthquake source parameters from waveform data for studies of global and regional seismicity. *Journal of Geophysical Research* 86: 2825–2852.
- Dziewonski AM and Anderson DL (1981) Preliminary reference Earth model. *Physics of the Earth and Planetary Interiors* 25: 297–356.
- Felsen LB (1984) Geometrical theory of diffraction, evanescent waves, complex rays and Gaussian beams. *Geophysical Journal of the Royal Astronomical Society* 79: 77–88.
- Fornberg B (1998) *A Practical Guide to Pseudospectral Methods*. Cambridge, UK: Cambridge University Press.
- Frankel A and Clayton RW (1986) Finite-difference simulations of seismic scattering: Implications for the propagation of short-period seismic waves in the crust and models of crustal heterogeneity. *Journal of Geophysical Research* 91: 6465–6489.
- Frazer LN and Gettrustur JF (1984) On a generalization of Filon's method and the computation of the oscillatory integrals of seismology. *Geophysical Journal of the Royal Astronomical Society* 76: 461–481.
- Frazer LN and Sen M (1985) Kirchhoff–Helmholtz reflection seismograms in a laterally variable multi-layered elastic medium. Part I. Theory. *Geophysical Journal of the Royal Astronomical Society* 80: 121–147.
- Fryer GJ and Frazer LN (1984) Seismic waves in stratified anisotropic media. *Geophysical Journal of the Royal Astronomical Society* 78: 691–710.
- Fryer GJ and Frazer LN (1987) Seismic waves in stratified anisotropic media – II. Elastodynamic eigensolutions for some anisotropic systems. *Geophysical Journal of the Royal Astronomical Society* 91: 73–101.
- Fuchs K and Müller G (1971) Computation of synthetic seismograms with the reflectivity method and comparison with observations. *Geophysical Journal of the Royal Astronomical Society* 23(4): 417–433.
- Furumura T, Kennett BLN, and Furumura M (1998) Seismic wavefield calculation for laterally heterogeneous spherical Earth models using the pseudospectral method. *Geophysical Journal International* 135: 845–860.
- Futterman WI (1962) Dispersive body waves. *Journal of Geophysical Research* 67: 5279–5291.
- Gajewski D and Psencík I (1987) Computation of high-frequency seismic wavefields in 3-D laterally inhomogeneous anisotropic media. *Geophysical Journal of the Royal Astronomical Society* 91: 383–411.
- Garmany J (1989) A student's grader of anisotropy. *Annual Review of Earth and Planetary Sciences* 17: 285–308.
- Geller RJ and Ohminato T (1994) Computation of synthetic seismograms and their partial derivatives for heterogeneous media with arbitrary natural boundary conditions using the direct solution method (DSM). *Geophysical Journal International* 116: 421–446.
- Gilbert F and Backus GE (1966) Propagator matrices in elastic wave and vibration problems. *Geophysics* 31: 326–332.
- Grand SP, van der Hilst RD, and Widjiantoro S (1997) Global seismic tomography; a snapshot of convection in the Earth. *GSA Today* 7: 1–7.
- Gu YJ, Dziewonski AM, Su W-J, and Ekström G (2001) Models of the mantle shear velocity and discontinuities in the pattern of lateral heterogeneities. *Journal of Geophysical Research* 106: 11169–11199.
- Hanyga H (1986) Gaussian beams in anisotropic elastic media. *Geophysical Journal of the Royal Astronomical Society* 85: 473–503.
- Harvey DJ (1981) Seismogram synthesis using normal mode superposition: The locked mode approximation. *Geophysical Journal of the Royal Astronomical Society* 66: 37–69.
- Harvey D and Choy GL (1982) Broadband deconvolution of GDSN data. *Geophysical Journal of the Royal Astronomical Society* 69: 659–668.
- Hartzell S, Harmsen S, Frankel A, and Larsen S (1999) Calculation of broadband time histories of ground motion: Comparison of methods and validation using strong-ground motion from the 1994 Northridge earthquake. *Bulletin of the Seismological Society of America* 89: 1484–1504.
- Helmburger DV (1974) Generalized ray theory for shear dislocations. *Bulletin of the Seismological Society of America* 64: 45–64.
- Helmburger DV and Engen, GR (1974) Upper mantle shear structure. *Journal of Geophysical Research* 79: 4017–4028.
- Helmburger DV and Harkrider D (1978) Modeling earthquakes with generalized ray theory. In: Miklowitz J and Achenbach JD (eds.) *Modern Problems in Elastic Wave Propagation*. New York: Wiley.
- Helmburger DV, Zhao LS, and Garnero EJ (1996) Construction of synthetics for 2D structures, core phases. In: Boschi E and Ekstrom G (eds.) *Proceedings of International School of Solid Earth Geophysics: Seismic Modeling of the Earth's Structure*, pp. 183–222. Bologna, Italy: Società Italiana di Fisica.
- Honda R and Yomogida K (2003) Static and dynamic displacement near a fault with the discrete wavenumber method. *Physics of the Earth and Planetary Interiors* 137: 107–127.
- Holliger K, Levander A, and Goff JA (1993) Stochastic modeling of the reflective lower crust: Petrophysical and geological evidence from the Ivrea Zone (northern Italy). *Journal of Geophysical Research* 98: 11967–11980.
- Igel H (1999) Modeling wave propagation in 3-D spherical sections by the Chebyshev spectral method. *Geophysical Journal International* 136: 559–567.
- Igel H, Takeuchi N, Geller RJ, et al. (2000) The COSY Project: Verification of global seismic modeling algorithms. *Physics of the Earth and Planetary Interiors* 119: 3–23.
- Imhof MG and Toksoz MN (2000) Multiple multipole expansions for elastic scattering. *Journal of the Acoustic Society of America* 100: 2969–2979.
- Jeffreys H (1936) The structure of the Earth down to the 20 discontinuity. *Monthly Notices of the Royal Astronomical Society Geophysical Supplement* 3: 401–422.
- Kaelin B and Johnson LR (1998) Dynamic composite elastic medium theory. Part II. Three-dimensional media. *Journal of Applied Physics* 84: 5488–5468.
- Karato S-I (1993) Importance of anelasticity in the interpretation of seismic tomography. *Geophysical Research Letters* 20: 1623–1626.
- Keith M and Crampin S (1977) Seismic body waves in anisotropic media: Reflection and refraction at a plane interface. *Geophysical Journal of the Royal Astronomical Society* 49: 181–208.

- Kind R (1985) The reflectivity method for different source and receiver structures and comparison with GRF data. *Journal of Geophysics* 58: 146–152.
- Kennett BLN (1983) *Seismic Wave Propagation in Stratified Media*. New York: Cambridge University Press.
- Kennett BLN (1998) Guided-waves in three-dimensional structures. *Geophysical Journal International* 133: 159–174.
- Kennett BLN (2001) *The Seismic Wavefield*, vols. I and II. New York: Cambridge University Press.
- Komatitsch D and Vilotte J-P (1998) The spectral element method: An efficient tool to simulate the seismic response of 2D and 3D geological structures. *Bulletin of the Seismological Society of America* 88: 368–392.
- Komatitsch D and Tromp J (1999) Introduction to the spectral-element method for 3-D seismic wave propagation. *Geophysical Journal International* 139: 806–822.
- Komatitsch D and Tromp J (2002) Spectral-element simulations of global seismic wave propagation-II. 3-D models, oceans, rotation, and self gravitation. *Geophysical Journal International* 149: 390–412.
- Korneev VA and Johnson LR (1993) Scattering of elastic waves by a spherical inclusion – I. Theory and numerical results. *Geophysical Journal International* 115: 230–250.
- Kosloff D and Kessler D (1990) *Seismic Numerical Modeling: Oceanographic and Geophysical Tomography*, pp. 251–312. Amsterdam: Elsevier Science Publishers.
- Langston CA and Helmberger DV (1975) A procedure for modeling dislocation sources. *Geophysical Journal* 42: 112–130.
- Lapwood ER and Usami T (1981) *Free Oscillations of the Earth*. Cambridge, UK: Cambridge University Press.
- Larsen S and Schultz CA (1995) ELAS3D: 2D/3D elastic finite difference propagation code, *Technical Report No. UCRL-MA-121792*, p. 19 Livermore, CA: Lawrence Livermore National Laboratory.
- Li X-D and Tanimoto T (1993) Waveforms of long period body waves in a slightly aspherical earth model. *Geophysical Journal International* 112: 92–102.
- Li X-D and Romanowicz B (1995) Comparison of global waveform inversions with and without considering cross branch coupling. *Geophysical Journal International* 121: 695–709.
- Li X and Cormier VF (2002) Frequency dependent attenuation in the inner core: Part I. A viscoelastic interpretation. *Journal of Geophysical Research* 107, doi:10.1029/2002JB001795.
- Masters G, Laske G, Bolton H, and Dziewonski A (2000) The relative behavior of shear velocity, bulk sound speed, and compressional velocity in the mantle: Implications for chemical and thermal structure. In: Karato S, Forte AM, Liebermann RC, Masters G, and Stixrude L (eds.) *AGU Monograph 117: Earth's Deep Interior*, pp. 63–86. Washington, DC: AGU.
- Maupin V and Kennett BLN (1987) On the use of truncated model expansion in laterally varying media. *Geophysical Journal of the Royal Astronomical Society* 91: 837–851.
- Maupin V (1989) Numerical modeling of Lg wave propagation across the North Sea Central Graben. *Geophysical Journal International* 99: 273–283.
- Menke W and Richards PG (1980) Crust–mantle whispering gallery phases: A deterministic model of teleseismic Pn wave propagation. *Journal of Geophysical Research* 85: 5416–5422.
- Menke W (2005) Case studies of seismic tomography and earthquake location in a regional context. In: Levander A and Nolet G (eds.) *Geophysical Monograph Series 157: Seismic Earth: Array Analysis of Broadband Seismograms*, pp. 7–36. Washington, DC: American Geophysical Union.
- Müller G (1973) Amplitude studies of core phases. *Journal of Geophysical Research* 78: 3469–3490.
- Müller G (1977) Earth-flattening approximation for body waves derived from geometric ray theory; improvements, corrections and range of applicability. *Journal of Geophysics* 42: 429–436.
- Müller G (1985) The reflectivity method: A tutorial. *Journal of Geophysics* 58: 153–174.
- Ni SD, Ding X, and Helmberger DV (2000) Constructing synthetics from deep Earth tomographic models. *Geophysical Journal International* 140: 71–82.
- Olsen KB (2000) Site amplification in the Los Angeles basin from three-dimensional modeling of ground motion. *Bulletin of the Seismological Society of America* 90: S77–S94.
- Rial JA and Cormier VF (1980) Seismic waves at the epicenter's antipode. *Journal of Geophysical Research* 85: 2661–2668.
- Richards PG (1973) Calculation of body waves, for caustics and tunnelling in core phases. *Geophysical Journal of the Royal Astronomical Society* 35: 243–264.
- Richards PG and Frasier CW (1976) Scattering of elastic waves from depth dependent inhomogeneities. *Geophysics* 41: 441–458.
- Ritsema J and van Heijst HJ (2000) Seismic imaging of structural heterogeneity in Earth's mantle: Evidence for large-scale mantle flow. *Science Progress* 83: 243–259.
- Robertsson JOA, Blanch JO, and Symes WW (1994) Viscoelastic finite-difference modeling. *Geophysics* 59: 1444–1456.
- Rost S and Thomas C (2002) Array seismology: Methods and applications. *Reviews of Geophysics* 40, doi:10.1029/2000RG000100.
- Sambridge M and Gudmundsson O (1998) Tomography with irregular cells. *Journal of Geophysical Research* 103: 773–781.
- Shearer PM (1999) *Introduction to Seismology*. Cambridge, UK: Cambridge University Press.
- Spudich P and Frazer LN (1984) Use of ray theory to calculate high-frequency radiation from earthquake sources having spatially variable rupture velocity and stress drop. *Bulletin of the Seismological Society of America* 74: 2061–2082.
- Su W-J and Dziewonski AM (1997) Simultaneous inversions for 3-D variations in shear and bulk velocity in the mantle. *Physics of the Earth and Planetary Interiors* 100: 135–156.
- Takeuchi N, Geller RJ, and Cummins PR (2000) Complete synthetic seismograms for 3-D heterogeneous Earth models computed using modified DSM operators and their applicability to inversion for Earth structure. *Physics of the Earth and Planetary Interiors* 119: 25–36.
- To A, Romanowicz B, Capdeville Y, and Takeuchi N (2005) 3D effects of sharp boundaries at the borders of the African and Pacific superplumes: Observation and modeling. *Earth and Planetary Science Letters* 233: 137–153.
- Trampert J, Vacher P, and Vilar N (2001) Sensitivities of seismic velocities to temperature, pressure and composition in the lower mantle. *Physics of the Earth and Planetary Interiors* 124: 255–267.
- Virieux J (1985) SH-wave propagation in heterogeneous media: Velocity stress finite difference method. *Geophysics* 49: 1933–1957.
- Virieux J (1986) P–SV wave propagation in heterogeneous media: Velocity–stress finite-difference method. *Geophysics* 51: 889–901.
- Ward SN (1978) Long period reflected and converted upper mantle phases. *Bulletin of the Seismological Society of America* 68: 133–153.
- Wen L and Helmberger DV (1998) A two-dimensional P–SV hybrid method and its application to modeling localized structures near the core–mantle boundary. *Journal of Geophysical Research* 103: 17901–17918.
- Wu RS and Aki K (1985) Scattering characteristics of waves by an elastic heterogeneity. *Geophysics* 50: 582–595.

Zhao Y and Anderson DL (1994) Mineral physics constraints on the chemical composition of Earth's lower mantle. *Physics of the Earth and Planetary Interiors* 85: 273–292.

Relevant Websites

<http://www.geodynamics.org> – CIG, Computational Infrastructure for Geodynamics

<http://www.eas.slu.edu> – Computer Programs in Seismology, Department of Earth & Atmospheric Sciences, Saint Louis University.

<http://www.geophysik.uni-muenchen.de> – Geophysics, Department of Earth and Environmental Sciences, Ludwig-Maximilians, University.

<http://www.iris.edu> – IRIS, Incorporated Research Institutions for Seismology.

<http://www.ngdc.noaa.gov> – NGDC Seismological Algorithms, USDOC/NOAA/NESDIS/National Geophysical Data Center (NGDC) Home Page.

<http://www.orfeus-eu.org> – Seismological Software Library, ORFEUS.

<http://www.rses.anu.edu.au> – Perspective Images of Slab Models by Oli Gudmundsson and Malcolm Cambridge, The RUM, ANU Research School of Earth Sciences.

<http://sw3d.mff.cuni.cz> – Seismic Waves in Complex 3-D Structures (SW3D), Charles University of Prague.

<http://www.geom.uiuc.edu> – The Geometry Center.

1.06 Theory and Observations – Forward Modeling and Synthetic Seismograms: 3-D Numerical Methods

J. Tromp, California Institute of Technology, Pasadena, CA, USA

© 2007 Elsevier B.V. All rights reserved.

1.06.1	Introduction	191
1.06.2	The Challenge	192
1.06.2.1	Benchmarking	194
1.06.3	Equation of Motion	194
1.06.4	Strong Implementations	196
1.06.4.1	Finite Difference Method	196
1.06.4.2	Pseudospectral Method	197
1.06.5	Weak Implementations	199
1.06.5.1	Rayleigh–Ritz Method	200
1.06.5.1.1	Coupled mode method	201
1.06.5.1.2	Direct solution method	202
1.06.5.2	Finite Element Method	203
1.06.5.3	Spectral Element Method	206
1.06.6	Discussion and Conclusions	210
	References	213

1.06.1 Introduction

Synthetic seismograms are at the heart of modern global seismology. For spherically symmetric, that is, one-dimensional (1-D), Earth models, normal mode summation is the preferred method for the calculation of broadband seismograms (e.g., Gilbert, 1970; Dahlen and Tromp, 1998). Normal mode synthetics incorporate effects due to fluid–solid boundaries, transverse isotropy with a radial symmetry axis, and attenuation. Mode synthetics are frequently used as reference seismograms, for example, to make cross-correlation body-wave traveltimes measurements, or to characterize fundamental Love and Rayleigh surface-wave dispersion.

Before fully 3-D numerical techniques became available and practical, one had to resort to asymptotic methods for the calculation of synthetic seismograms. Over the years, numerous asymptotic methods have been – and are continuing to be – developed. For example, in the path-average or great-circle approximation (e.g., Woodhouse and Dziewonski, 1984; Nolet, 1990), one assumes that a seismogram may be calculated based upon a spherically symmetric Earth model that is characteristic of a particular source–receiver combination. From an inverse theory perspective, in this approximation a

change in the waveform is related to a change in the Earth model via a 1-D Fréchet or sensitivity kernel. By asymptotically accounting for mode coupling, Li and Tanimoto (1993) extended the path-average method to gain 2-D sensitivity to structure in the source–receiver plane. In this approach, changes in the waveform are related to model changes through a 2-D sensitivity kernel (Marquering and Snieder, 1995; Li and Romanowicz, 1995, 1996; Marquering and Snieder, 1996). Nowadays, seismologists are calculating fully 3-D synthetic seismograms at the scale of the globe, and the relationship between waveforms and Earth structure is expressed in terms of 3-D sensitivity kernels. The calculation of such kernels for spherically symmetric reference models may be accomplished based upon mode summation (Marquering *et al.*, 1998; Zhao *et al.*, 2000) or ray theory (Dahlen *et al.*, 2000; Hung *et al.*, 2000; Montelli *et al.*, 2004), but for 3-D reference models such calculations involve the use of so-called adjoint simulations (e.g., Tarantola, 1984; Talagrand and Courtier, 1987; Akçelik *et al.*, 2002, 2003; Tromp *et al.*, 2005).

The number of numerical techniques that can handle seismic wave propagation in 3-D Earth models accurately is rather limited. All the classical numerical methods have been employed, for example, finite

difference and pseudospectral methods, but thus far these techniques have either been restricted to portions of the globe, that is, limited in terms of the dimensions of the modeling domain (e.g., Furumura *et al.*, 1998, 1999; Igel, 1999; Wang *et al.*, 2001), or to purely shear/acoustic problems, that is, incorporating only shear/compressional waves (e.g., Igel and Weber, 1995; Thomas *et al.*, 2000).

Numerical simulations based upon integral or weak implementations of the equation of motion have been most successful in terms of capturing the full complexity of global Earth models. Coupled mode methods (CMMs), in which the modes of a 3-D Earth model are expressed as a sum over the modes of a spherically symmetric reference Earth model (e.g., Park, 1986; Park and Yu, 1992; Lognonné and Romanowicz, 1990; Capdeville *et al.*, 2000), or direct solution methods (DSMs), which use more general basis functions (e.g., Hara *et al.*, 1991; Geller and Ohminato, 1994; Takeuchi *et al.*, 2000), are capable of calculating synthetic seismograms in 3-D Earth model at relatively long periods.

To date, the most successful numerical technique for simulating global seismic wave propagation has been the spectral element method (SEM) (Chaljub, 2000; Komatitsch and Tromp, 2002a, 2002b; Komatitsch *et al.*, 2002, 2003; Chaljub *et al.*, 2003). See Komatitsch *et al.* (2005) and Chaljub *et al.* (2007) for detailed recent reviews of the method. Like coupled mode, direct solution, and finite element methods, the SEM is based upon an integral or weak implementation of the equation of motion. It combines the accuracy of the global pseudospectral method (PM) with the flexibility of the finite element method (FEM). The wavefield is typically represented in terms of high-degree Lagrange interpolants, and integrals are computed based upon Gauss–Lobatto–Legendre (GLL) quadrature, which leads to a simple explicit time scheme that lends itself very well to calculations on parallel computers. Capdeville *et al.* (2003a) and Capdeville *et al.* (2003b) demonstrate how the computational burden associated with the SEM may be reduced by coupling it to a normal mode solution. This allows one to reduce the cost of the method by assuming a spherically symmetric solution in a portion of the Earth, for example, the core, using spectral elements only in the remaining parts of the model, for example, the mantle.

The purpose of this chapter is to introduce and review various numerical methods used in global seismology to generate synthetic seismograms in

3-D Earth models. We begin by posing the challenges associated with simulating global seismic wave propagation. We then introduce the elastic wave equation, which forms the basis of all numerical simulations of seismic wave propagation. We discuss the basic boundary conditions which arise in Earth models with a free surface and a variety of internal solid–solid and fluid–solid discontinuities. Complications due to anisotropy, attenuation, and self-gravitation are important in the context of seismic wave propagation, but for the sake of simplicity these effects are only discussed peripherally. We distinguish between numerical methods based upon the equation of motion in its differential form subject to certain boundary conditions, referred to as differential or strong implementations, for example, finite difference and pseudospectral methods, and numerical methods based upon an integral or weak implementation of the equation of motion that contains the boundary conditions implicitly, for example, coupled mode, direct solution, finite element, and spectral element methods. We conclude by discussing the potential for using 3-D numerical simulation to address the inverse problem. We will assume basic knowledge of tensor notation and algebra.

1.06.2 The Challenge

The calculation of accurate synthetic seismograms for 3-D global Earth models poses a significant computational challenge, both in terms of the demands on the numerical algorithm and with regards to computer hardware (i.e., memory and CPU requirements). This section enumerates the main algorithmic issues that need to be addressed and resolved in the context of simulating global seismic wave propagation. Few numerical techniques can currently accommodate all the demands imposed by this daunting problem.

Gridding. Any numerical technique involves a grid on which the wavefield is evaluated, be it a finite difference stencil or the GLL points of a hexahedral spectral element. Gridding – or meshing – the globe is challenging for two key reasons, both related to spherical geometry. First, to grid the entire surface of the globe one has to design a scheme that covers the unit sphere evenly. A simple grid in terms of latitude and longitude, frequently used in strong implementations, leads to an uneven grid spacing with an undesired concentration of points near the poles.

The second difficulty is associated with the fact that the spherical geometry tends to lead to a concentration of grid points with depth and a singularity at the center of the Earth. Thus, one needs to design a gridding scheme that increases the grid spacing with depth to reduce the computational burden and improve numerical stability. The fact that wave speeds generally increase with depth further enhances the need for coarsening the grid with depth for reasons of numerical stability and efficiency.

Surface waves. At the scale of the globe, surface waves are an important source of information for two main reasons. One, they help constrain shallow upper mantle structure beneath ocean basins, which are difficult to image with body waves. Two, they are widely used to constrain the source characteristics of earthquakes. Any numerical technique aimed at simulating global seismic wave propagation must therefore be able to accurately simulate the propagation of surface waves. The numerical challenges lie in the implementation of the stress-free surface boundary condition and in the fact that surface waves travel at relatively slow phase speeds requiring a fine grid spacing of more than five grid points per wavelength.

Diffracted waves. At greater epicentral distances, a number of body waves diffract at the core–mantle boundary (CMB), for example, P_{diff} and S_{diff} . These waves contain important information about the lowermost mantle, in particular the intensely studied D'' region, and it is important that 3-D simulations accurately capture these diffraction effects. Part of the difficulty involves the implementation of the fluid–solid boundary condition mentioned next.

Fluid–solid boundaries. Typical Earth models have three main fluid solid boundaries: the ocean floor, the CMB, and the inner core boundary (ICB). These boundaries need special attention in the sense that the traction is normal to the boundary and continuous across it, the normal component of displacement is also continuous, but the tangential component of displacement is discontinuous, that is, there may be slip across the boundary. The implementation of fluid–solid boundaries typically involves domain decomposition between the fluid and the solid, such that one solves an (an)elastic wave equation in the solid crust, mantle, and inner core, and an acoustic wave equation in the liquid outer core and ocean, matching the two solutions at the fluid–solid boundary.

Attenuation. The shear quality factor is observed to be fairly small in the upper mantle and, in particular,

in the inner core. Surface waves and waves that turn or reflect in the upper mantle are significantly attenuated, an effect that needs to be accommodated in numerical simulations. Observational global seismologists routinely use data over a broad frequency range, from short-period PKP waves in the 1–2 Hz range to long-period surface waves in the 5 mHz range. Because we are dealing with such broadband signals, we must take into account the fact that in an anelastic Earth model the wave speeds become frequency dependent. Such physical dispersion can have a dramatic effect on both body and surface waveforms.

Anisotropy. Global Earth models frequently exhibit anisotropy, that is, a directional dependence of the wave speed. Even 1-D models are generally transversely isotropic (e.g., PREM) to accommodate the observed dispersion of Love and Rayleigh waves. Thus, suitable numerical techniques should incorporate the effects of an anisotropic constitutive relationship on seismic wave propagation. The related additional model parameters increase the memory requirements and the CPU time.

Rotation and self-gravitation. At periods longer than about 150 s, surface waves are affected by the Earth's rotation, and Rayleigh wave propagation needs to accommodate the effects of self-gravitation, that is, the perturbations in the gravitational field induced by the seismic motions. Normal mode summation codes routinely incorporate the effects of self-gravitation, and this provides an excellent benchmark for more general, 3-D codes.

Ellipticity, topography, and bathymetry. The Earth is to a close approximation elliptical in shape, and the numerical grid should reflect this. Furthermore, there is significant topography and bathymetry associated with mountain ranges and the ocean basins. The grid should be adjusted to reflect these topographic variations, and the numerical implementation of the free surface boundary conditions should account for the undulations. Free surface boundary conditions are notoriously difficult to implement, in particular in the context of strong formulations of the equations of motion.

Crustal thickness. The Earth's crust varies in thickness by an order of magnitude, with depths of approximately 8 km underneath the oceans to depths of more than 70 km underneath the Andes and Tibet. These crustal thickness variations have a profound effect on the dispersion of short- and intermediate-period surface waves. They also affect the traveltimes and amplitude of surface-reflected phases, for example,

PP and SS. Various asymptotic techniques attempt to accommodate lateral variations in crustal thickness by making a ‘crustal correction’, but in particular for surface waves such ‘corrections’ quickly become inadequate.

Oceans. Some 1-D models incorporate an ocean layer. Such a layer gives rise to complications associated with fluid–solid interfaces, as discussed in a previous item. The presence of oceans is mostly relevant for the dispersion of Rayleigh waves, as well as for surface-reflected phases, such as pP, PP, SS, and SP. Normal mode summation codes routinely incorporate the effects of a water layer, thus providing a good benchmark. For 3-D Earth models, the oceans pose a much more significant challenge related to their highly variable depth.

Core. The fact that the Earth has a liquid outer core and a solid inner core poses significant computational challenges. In addition to the fluid–solid boundary conditions mentioned in an earlier item, we need to solve an (an)elastic wave equation in the inner core, which is coupled across the ICB to an acoustic wave equation in the outer core, which is coupled across the CMB to an (an)elastic wave equation in the mantle and crust. Thus the need arises for two distinct solvers for the fluid and solid regions of the model, which are coupled across the fluid–solid boundaries. Meshing the inner core is another non-trivial issue that requires the use of highly uneven grids, in particular with depth.

In what follows we will discuss the merits and demerits of the various numerical techniques in the context of the challenges laid out in this section.

1.06.2.1 Benchmarking

Any numerical method aimed at simulating global seismic wave propagation must be carefully benchmarked against semi-analytical methods, for example, normal mode summation, as well as other 3-D techniques. At the scale of the globe, such benchmarks are difficult and must be carefully executed. In this section, we briefly enumerate some of the main challenges associated with benchmarking.

First, rather obviously, the Earth model must be exactly the same in all techniques competing in the benchmark, which means among other things that all first- and second-order discontinuities must be honored. At a first-order discontinuity, a function – and possibly its first derivative – are discontinuous, whereas at a second-order discontinuity a function is

continuous but its first derivative is not. Most 1-D Earth models, for example, PREM, have both types of discontinuities. Special attention must be paid to the implementation of the crust. Seemingly subtle model differences, for example, in crustal thickness or a division in terms of upper and lower crust, can have a profound effect on surface-wave dispersion and surface-reflected body-wave amplitudes. The presence of an ocean layer has a profound effect on the dispersion of Rayleigh waves and can affect the amplitudes of surface-reflected P–SV body waves. Most 1-D Earth models incorporate radial models of attenuation, and one must ensure that the associated effects are properly implemented. As mentioned among the challenges, in an anelastic medium the shear and compressional wave speeds become frequency dependent, an effect that most normal mode codes incorporate. So, besides reducing wave amplitudes, attenuation can have a strong effect on the phase of a broadband signal. The fact that we need to simulate seismograms over more than three decades in frequency, that is, periods from shorter than 1 s to longer than 1000 s, makes the implementation of such physical dispersion in numerical algorithms a necessity. Finally one needs to decide whether or not effects due to self-gravitation and transverse isotropy, both readily accommodated in normal mode algorithms, will form part of the benchmark.

The COSY project (Igel *et al.*, 2000) brought together several research groups in an attempt to benchmark numerical algorithms for spherically symmetric and 3-D Earth models. The results are summarized in a special issue of *Physics of the Earth and Planetary Interiors* (volume 119, 2000). Even for 1-D models, the COSY benchmarks are disappointing in terms of their relatively low level of agreement, in particular for surface waves. This serves as an illustration of the great difficulties associated with developing, implementing, and benchmarking numerical techniques for the simulation of global seismic wave propagation.

1.06.3 Equation of Motion

An isotropic, elastic Earth model may be characterized in terms of three parameters: the distribution of mass density ρ , the compressional wave speed α , and the shear wave speed β . Rather than the compressional and shear wave speeds one may also use the bulk modulus or incompressibility κ and the shear

modulus or rigidity μ . The two sets of model parameters are related by $\alpha = [(\kappa + (4/3)\mu)/\rho]^{1/2}$ and $\beta = (\mu/\rho)^{1/2}$. In a spherically symmetric (1-D) Earth model, such as PREM (Dziewonski and Anderson, 1981), IASP91 (Kennett and Engdahl, 1991), or AK135 (Kennett *et al.*, 1995), the model parameters vary only as a function of the radius, whereas in a general 3-D Earth model the model parameters also vary laterally. The model parameters may exhibit a number of discontinuities as a function of depth, for example, at the ocean floor, the Moho, across the upper mantle phase transitions, at the CMB, and at the ICB. The most general spherically symmetric Earth model is not isotropic but rather transversely isotropic. Such an Earth model is characterized by five elastic parameters: A , C , L , N , and F (Love, 1911). Alternatively, one may use a representation in terms of the speeds of horizontally and vertically propagating compressional waves $\alpha_v = (C/\rho)^{1/2}$ and $\alpha_h = (A/\rho)^{1/2}$, the speeds of vertically and horizontally propagating horizontally polarized shear waves $\beta_v = (L/\rho)^{1/2}$ and $\beta_h = (N/\rho)^{1/2}$, and the dimensionless parameter $\eta = F/(A - 2L)$. Because the widely used PREM is a transversely isotropic Earth model, numerical simulations of global seismic wave propagation should facilitate the use of such models. The parameters that characterize an isotropic or transversely isotropic Earth model need to be specified at all grid points used by the numerical method.

Let \mathbf{s} denote the displacement field induced by an earthquake. In an isotropic, elastic Earth model, the stress tensor \mathbf{T} is determined in terms of the elastic moduli κ and μ and the strain tensor $\boldsymbol{\epsilon} = \frac{1}{2}[\nabla\mathbf{s} + (\nabla\mathbf{s})^T]$ by Hooke's law:

$$\mathbf{T} = (\kappa - \frac{2}{3}\mu)\text{tr}(\boldsymbol{\epsilon})\mathbf{I} + 2\mu\boldsymbol{\epsilon} \quad [1]$$

Here, \mathbf{I} denotes the 3×3 identity tensor and a superscript T denotes the transpose. Note that the strain and stress tensors are both symmetric tensors, $\boldsymbol{\epsilon}^T = \boldsymbol{\epsilon}$ and $\mathbf{T}^T = \mathbf{T}$. In the fluid regions of the Earth model, for example, in the oceans and in the outer core, the shear modulus vanishes, and Hooke's law [1] reduces to $\mathbf{T} = \kappa \text{tr}(\boldsymbol{\epsilon})\mathbf{I}$. Hooke's law [1] is an example of a constitutive relationship between stress and strain. The most general linear relationship between stress \mathbf{T} and strain $\boldsymbol{\epsilon}$ involves the fourth-order elastic tensor $\mathbf{c}: \mathbf{T} = \mathbf{c}:\boldsymbol{\epsilon}$. Because both the stress and the strain tensor are symmetric and due to certain thermodynamic considerations (Aki and Richards, 1980; Dahlen and Tromp, 1998), the elastic tensor

exhibits the following symmetries: $c_{ijkl} = c_{jikl} = c_{ijlk} = c_{klji}$. These symmetries reduce the number of independent elastic parameters from 81 to 21. For mathematical and notational convenience, we will sometimes use the anisotropic constitutive relationship, rather than the more practical isotropic version [1].

The Earth is not a perfectly elastic body, and effects due to attenuation should be incorporated. In an anelastic medium, the stress \mathbf{T} at time t is determined by the entire strain history $\boldsymbol{\epsilon}(t)$, and in its most general anisotropic form Hooke's law becomes (e.g., Aki and Richards, 1980; Dahlen and Tromp, 1998)

$$\mathbf{T}(t) = \int_{-\infty}^t \partial_t \mathbf{c}(t-t') : \mathbf{Vs}(t') dt' \quad [2]$$

Attenuation is well represented by an absorption-band solid, which may be approximated by using a series of standard linear solids (Liu *et al.*, 1976). Numerically, the behavior of the standard linear solids is modeled by tracking so-called memory variables (e.g., Emmerich and Korn, 1987; Carcione *et al.*, 1988; Robertsson *et al.*, 1994; Moczo *et al.*, 1997; Komatitsch and Tromp, 1999). In the Earth, bulk attenuation is several hundred times less significant than shear attenuation. Therefore, as far as attenuation is concerned, one can safely assume that it is sufficient to model the time evolution of the shear modulus. In this chapter we will avoid the mathematical and numerical complications associated with attenuation, but suffice it to say that these effects can be readily accommodated in most numerical simulations. The main difficulty is the increase in computer memory requirements.

Having introduced various possibilities for the constitutive relationship, the displacement field \mathbf{s} generated by an earthquake is governed by the elastic wave equation, which may be written in the form (e.g., Aki and Richards, 1980)

$$\rho \partial_t^2 \mathbf{s} = \nabla \cdot \mathbf{T} + \mathbf{f} \quad [3]$$

For earthquakes that are small enough such that they can be treated as a point source, the force \mathbf{f} in [3] may be expressed in terms of the moment tensor \mathbf{M} as (e.g., Aki and Richards, 1980; Dahlen and Tromp, 1998)

$$\mathbf{f} = -\mathbf{M} \cdot \nabla \delta(\mathbf{x} - \mathbf{x}_s) S(t) \quad [4]$$

The location of the point source is denoted by \mathbf{x}_s , $\delta(\mathbf{x} - \mathbf{x}_s)$ is the Dirac delta distribution located at \mathbf{x}_s , and $S(t)$ is the source-time function. For a source of finite size, such as a fault plane Σ_s , the force \mathbf{f} in [3]

may be written in terms of the moment-density tensor \mathbf{m} as

$$\mathbf{f} = -\mathbf{m}(\mathbf{x}_s, t) \cdot \nabla \delta(\mathbf{x} - \mathbf{x}_s) \quad \mathbf{r} \in \Sigma_s \quad [5]$$

For simplicity, we work with the point source representation [4] in the rest of this chapter.

The equation of motion [3] must be solved subject to a number of boundary conditions. On the Earth's surface, the traction $\hat{\mathbf{n}} \cdot \mathbf{T}$, where $\hat{\mathbf{n}}$ denotes the unit outward normal to the free surface, should vanish, that is, $\hat{\mathbf{n}} \cdot \mathbf{T} = 0$. On solid–solid boundaries, such as the Moho or the upper-mantle discontinuities, both the traction $\hat{\mathbf{n}} \cdot \mathbf{T}$ and the displacement \mathbf{s} need to be continuous, whereas on fluid–solid boundaries, such as the ocean floor, the CMB, and the ICB, both the traction $\hat{\mathbf{n}} \cdot \mathbf{T}$ and the normal component of displacement $\hat{\mathbf{n}} \cdot \mathbf{s}$ need to be continuous.

When our modeling domain is not the entire Earth, seismic energy needs to be absorbed on the fictitious boundaries of the domain. To accomplish this, one generally uses a paraxial equation to damp the wavefield on the edges (Clayton and Engquist, 1977; Quarteroni *et al.*, 1998). In recent years, a significantly more efficient absorbing condition called the perfectly matched layer (PML) has been introduced (Bérenger, 1994), which is now being used in regional numerical simulations (e.g., Collino and Tsogka, 2001; Basu and Chopra, 2003; Komatitsch and Tromp, 2003; Festa and Vilotte, 2005). In this chapter, we largely ignore the numerical complications associated with absorbing boundary conditions.

At periods longer than about 150 s, self-gravitation and rotation start to play a role in global seismic wave propagation. The equation of motion for a rotating, self-gravitating Earth model is significantly more complicated than [3] (e.g., Dahlen and Tromp, 1998). Nevertheless, numerical simulations based upon a weak implementation of the equation of motion frequently do take these complications into account. In this chapter, we do not incorporate these long-period complications for the sake of simplicity.

Numerical solutions to the elastic wave equation may be subdivided into two categories: strong and weak implementations. Strong implementations use the differential form of the wave equation subject to certain explicit boundary conditions, whereas weak implementations are based upon an integral form that contains the free surface boundary conditions implicitly. Both implementations are popular in global seismology, and for each category we discuss a number of numerical applications.

1.06.4 Strong Implementations

Strong implementations of the equation of motion typically involve rewriting [3] and the constitutive relationship as a system of coupled first-order differential equations in space and time, known as the velocity–stress formulation:

$$\partial_t \mathbf{v} = \rho^{-1} (\nabla \cdot \mathbf{T} + \mathbf{f}), \quad \partial_t \mathbf{T} = \mathbf{c} : \nabla \mathbf{v} \quad [6]$$

where $\mathbf{v} = \partial_t \mathbf{s}$. For brevity, we have used the general anisotropic constitutive relationship and one of the symmetries of the elastic tensor. The system of eqn [6] must be solved for the three components of velocity \mathbf{v} and the six independent components of the stress tensor \mathbf{T} subject to the appropriate boundary conditions, that is, a total of nine unknown parameters. Finite difference and pseudospectral methods, which are discussed in the next two sections, are frequently based upon the velocity–stress formulation [6].

1.06.4.1 Finite Difference Method

Perhaps the most intuitively appealing numerical technique is the finite difference method (FDM) (e.g., Madariaga, 1976; Virieux, 1984, 1986). In this approach, the first-order spatial and temporal derivatives in [6] are approximated by taking differences between neighboring grid points. To limit numerical grid dispersion and anisotropy, one typically uses a fourth-order scheme on a staggered grid in space, and a second-order scheme in time (e.g., Levander, 1988). For example, consider a function f sampled at N grid points with a grid spacing Δx : $f_n = f(n\Delta x)$, $n = 0, \dots, N-1$. The derivative of f on this grid may be approximated accurate to second-order in Δx by the centered-difference expression (often called a stencil)

$$\frac{d}{dx} f(n\Delta x) = (f_{n+1} - f_{n-1}) / (2\Delta x), \quad n = 1, \dots, N-2 \quad [7]$$

and accurate to fourth-order by the centered-difference stencil

$$\frac{d}{dx} f(n\Delta x) = (-f_{n+2} + 8f_{n+1} - 8f_{n-1} + f_{n-2}) / (12\Delta x), \quad n = 2, \dots, N-3 \quad [8]$$

These results are valid in the interior of the domain. Near the domain boundaries, less accurate one-sided difference operators come into play, and for this reason the implementation of free surface boundary conditions is often problematic, and in particular surface waves are poorly simulated (e.g., Robertsson, 1996;

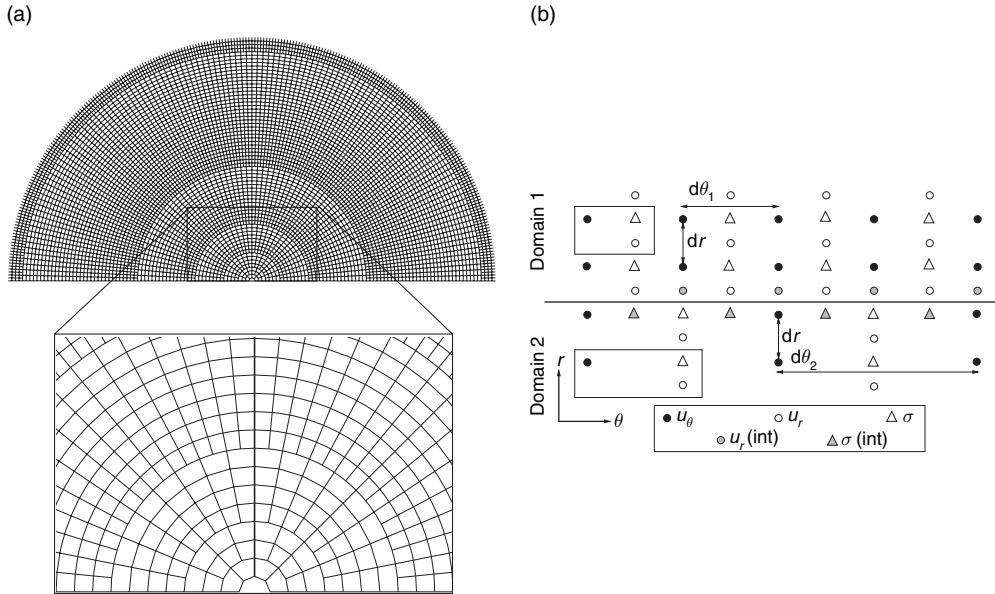


Figure 1 (a) Two-dimensional finite difference grid used in the axisymmetric simulations of Thomas et al. (2000). The lateral grid spacing is increased each time the arc length is halved. (b) Staggered grid and domain decomposition. The vertical (u_r) and lateral (u_θ) components of the velocity and the pressure (σ) are evaluated based upon a fourth-order accurate scheme on different, staggered grids. At the domain boundaries, where the lateral grid spacing is increased from $d\theta_1$ to $d\theta_2$, some fields have to be interpolated (dashed symbols) to connect the domains, and a second-order accurate approach for the derivatives and the interpolation is used. The radial grid spacing (dr) remains unchanged across the boundary. Courtesy of Thomas C, Igel H, Weber M, and Scherbaum F (2000) Acoustic simulation of P-wave propagation in a heterogeneous spherical Earth: Numerical method and application to precursor waves to PKP_{df}. *Geophysical Journal International* 141: 6441–6464.

Graves, 1996; Ohminato and Chouet, 1997). Recently developed optimal or compact finite difference operators will perhaps improve this situation (e.g., Zingg et al., 1996; Zingg, 2000); see also the optimal finite difference operators introduced by Geller and Takeuchi (1995) in the context of weak applications.

An example of a 2-D (axisymmetric) staggered finite difference grid used to simulate acoustic (purely compressional) wave propagation by Thomas et al. (2000) is shown in Figure 1. Snapshots of such a simulation are shown in Figure 2. The FDM is widely used to calculate the wavefield in 3-D local and regional models (e.g., Graves, 1996; Ohminato and Chouet, 1997), most recently for finite rupture scenarios, and has a long and distinguished record in exploration seismology. On the scale of the globe it has only been used to a limited extend (e.g., Igel and Weber, 1995, 1996; Igel and Gudmundsson, 1997; Chaljub and Tarantola, 1997; Thomas et al., 2000), and never at the scale of the entire globe.

The main advantage of the FDM is its relative ease of implementation. Still, at the scale of the globe, designing a good grid with an even number of grid points per wavelength and a relatively constant stability condition is difficult because one needs to resort to

unevenly spaced stencils. In particular the poles and the Earth's center pose challenges. Perhaps the main disadvantage of the FDM is its poor representation of surface waves due to the difficulty of implementing accurate free surface boundary conditions.

1.06.4.2 Pseudospectral Method

The motivation behind the PM is a desire for more accurate spatial derivative operators. Such operators are obtained by expanding the components of the velocity–stress wavefield in terms of known global basis functions, for example, sines and cosines or Chebyshev polynomials, and calculating derivatives based upon fast transforms. For example, consider a function f sampled at N grid points with a grid spacing Δx : $f(n \Delta x)$, $n = 0, \dots, N - 1$. This function may be transformed to the wave number domain based upon the 1-D fast Fourier transform (FFT) to obtain

$$F(l \Delta k) = \Delta x \sum_{n=0}^{N-1} f(n \Delta x) \exp(-2\pi i nl/N),$$

$$l = 0, \dots, N - 1$$
[9]

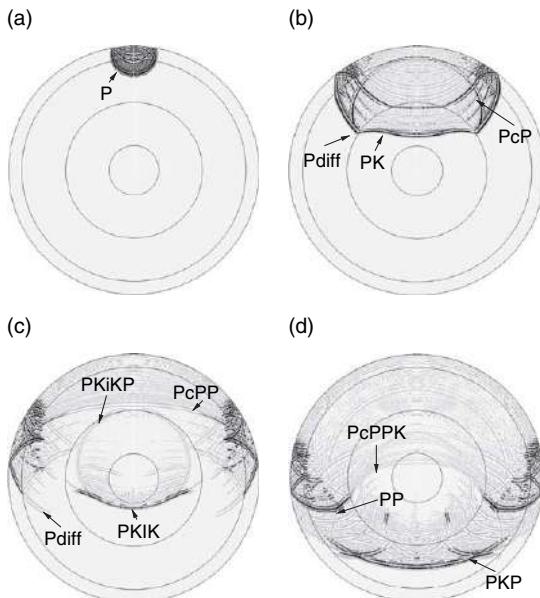


Figure 2 Finite difference snapshots of P wave propagation through PREM for a source at the surface. The 2-D simulations are based upon the acoustic wave equation involving the grid shown in [Figure 1](#). The dominant period is 20 s. (a) P wavefield after 150 s; (b) 450 s; (c) 750 s; (d) 1050 s. The 670 km discontinuity, the CMB, and the ICB are shown by the concentric circles, and some of the main phases have been labeled. Courtesy of Thomas C, Igel H, Weber M, and Scherbaum F (2000) Acoustic simulation of P-wave propagation in a heterogeneous spherical Earth: Numerical method and application to precursor waves to PKPdf. *Geophysical Journal International* 141: 6441–6464.

where $\Delta k = 2\pi/(N \Delta x)$. The derivative of the function may now be calculated in the wave number domain by simply multiplying by $i(l \Delta k)$ and using an inverse FFT to go back to the spatial domain:

$$\frac{d}{dx} f(n \Delta x) = \frac{1}{N \Delta x} \sum_{l=0}^{N-1} i(l \Delta k) F(l \Delta k) \exp(2\pi i n l / N), \\ n = 0, \dots, N-1 \quad [10]$$

This derivative operation is based upon information from all available N grid points, and is therefore much more accurate than a derivative operator based upon first and second neighbors, as in the finite difference expressions [7] and [8].

The PM has been used to address regional (e.g., Carcione, 1994) as well as global (e.g., Tessmer *et al.*, 1992; Hung and Forsyth, 1998) seismic wave propagation problems. Fourier basis functions (e.g., Kosloff and Baysal, 1982; Kosloff *et al.*, 1984; Furumura *et al.*, 1998, 1999; Wang *et al.*, 2001; Wang and Takenaka, 2001), Chebyshev basis functions (e.g., Kosloff *et al.*, 1990;

Kosloff and Tal-Ezer, 1993; Carcione and Wang, 1993; Tessmer and Kosloff, 1994; Tessmer, 1995; Igel, 1999; Igel *et al.*, 2002), and combinations of Fourier and Chebyshev basis functions (e.g., Tessmer *et al.*, 1992) have all been used. Because the Fourier basis is periodic, one often introduces periodic boundary conditions. At the free surface this is not an option, and less accurate approximations need to be invoked. The advantage of the Chebyshev basis over the Fourier basis is that it is nonperiodic and uses unevenly spaced grid points with a concentration of points near the edges of the domain, which leads to more accurate surface waves due to a more precise implementation of the free surface boundary conditions. An implementation based upon wavelets, which does not use the velocity–stress formulation [6], was introduced by Hong and Kennett (2002). Like FDMs, one typically uses a second-order accurate time scheme in a PM.

Because of the use of global basis functions, the pseudospectral technique is limited to smooth media, and numerical noise appears in the presence of sharp discontinuities in the model, such as first-order solid–solid upper-mantle discontinuities. Such ringing can be avoided by using a domain decomposition approach (e.g., Hung and Forsyth, 1998; Wang and Takenaka, 2001).

An example of a 2-D axisymmetric elastic pseudospectral simulation by Wang *et al.* (2001) for model IASP91 is shown in [Figure 3](#). The implementation is based upon a Fourier basis. Unlike the acoustic FDM simulation shown in [Figure 2](#), one can see both compressional and shear waves in this simulation. Igel (1999) used a PM based upon a Chebyshev implementation for the simulation of 3-D seismic wave propagation in a section of the globe, as illustrated in [Figure 4](#). Snapshots from a simulation for PREM are shown in [Figure 5](#). The 3D simulation is restricted to a section of the globe to save memory and to avoid problems associated with diminishing grid spacing and related numerical instabilities toward the Earth's center.

The main advantage of the PM is its precision for smooth isotropic and anisotropic models. Its main demerits are related to the difficulties of designing effective fast transforms for the sphere, and the generally poor representation of surface waves. Transform methods frequently impose an undesirable grid spacing that reflects geometry rather than material properties. Large simulations on parallel machines with distributed memory are challenging because subsequent FFTs in the x -, y -, and z -directions require repeated gather–scatter operations that are computationally expensive.

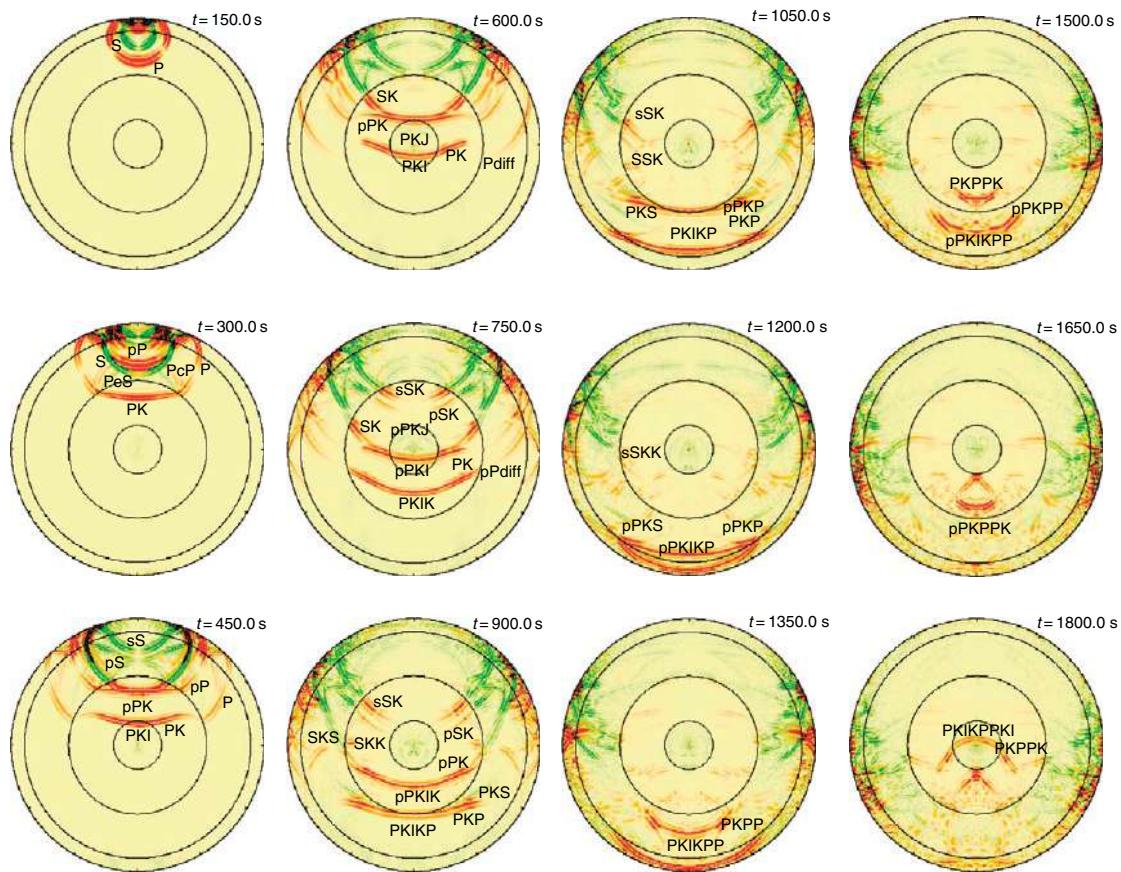


Figure 3 Snapshots of an axisymmetric pseudospectral simulation in the IASP91 model for a source at a depth of 600 km. The 2-D simulations solve the elastic wave equation in cylindrical coordinates. The red and green colors represent P and S waves, respectively. Concentric circles denote the 660 km discontinuity, the CMB, and the ICB. It is instructive to compare these elastic pseudospectral snapshots with the purely acoustic finite difference snapshots shown in [Figure 2](#). (Note, however, the difference in source depth.) The shortest period in the synthetics is 30 s. Courtesy of Wang Y, Takenaka H, and Furumura T (2001) Modelling seismic wave propagation in a two-dimensional cylindrical whole-Earth model using the pseudospectral method. *Geophysical Journal International* 145: 689–708.

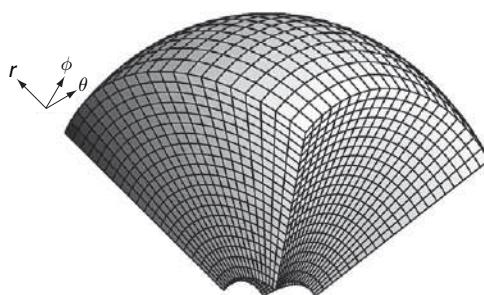


Figure 4 Physical domain for a 3-D pseudospectral simulation based upon Chebyshev polynomials. The chunk of the globe spans $80^\circ \times 80^\circ$ on the Earth's surface, ranges in radius from 1371 to 6371 km, and is centered around the equator. Courtesy of Igel H (1999) Wave propagation in three-dimensional spherical sections by the Chebyshev spectral method. *Geophysical Journal International* 136: 559–566.

1.06.5 Weak Implementations

For a number of numerical techniques one works with a modified version of the equation of motion called the integral or weak formulation of the problem. It is obtained by taking the dot product of the momentum eqn [3] with an arbitrary test vector \mathbf{w} , and integrating by parts over the volume V of the Earth:

$$\int_V \rho \mathbf{w} \cdot \partial_t^2 \mathbf{s} \, d^3x = - \int_V \nabla \mathbf{w} : \mathbf{T} d^3x + \mathbf{M} : \nabla \mathbf{w}(\mathbf{x}_s) S(t) \quad [11]$$

Equation [11] is equivalent to the strong formulation [6] because it holds for any test vector \mathbf{w} . The term on the left-hand side is related to the mass matrix in finite element parlance, and the first term on the right

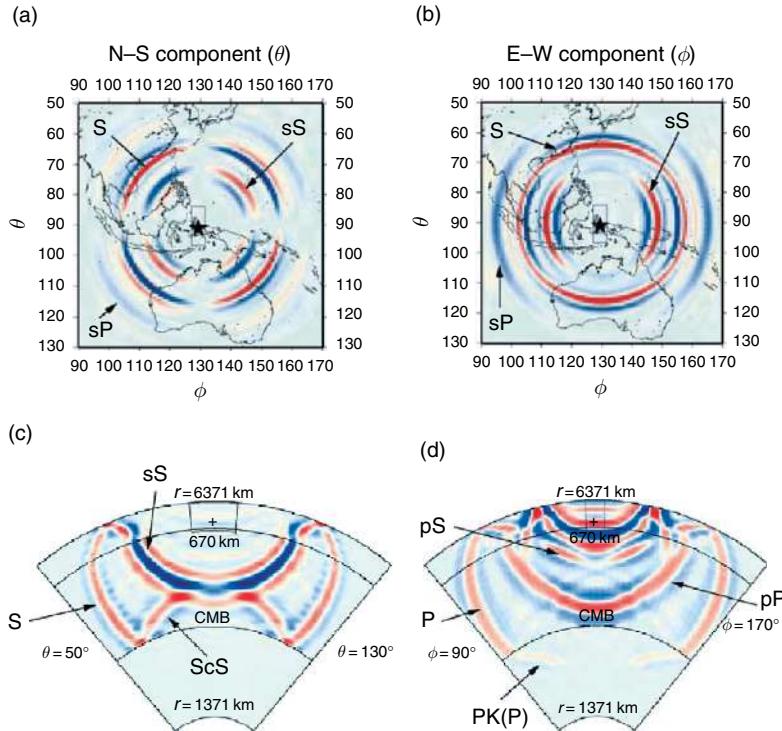


Figure 5 Top: pseudospectral snapshots of the north-south (left) and east-west (right) components of the velocity field at the Earth's surface at 550 s. Red and blue colors denote positive and negative velocities, respectively. The epicenter is indicated by the star, and the hypocenter is located at a depth of 600 km. The dominant period is 50 s, and the spherically symmetric Earth model is PREM. We clearly see the S and sS arrivals; at this stage in the simulation, the compressional waves P and pP have already been absorbed by the boundaries. Bottom: snapshots of the velocity field in a longitudinal cross section through the hypocenter. Left: transverse component of motion at 550 s. Notice that, as expected, there are no shear waves in the core. Right: radial component of motion at 300 s. Notice how compressional waves are entering the core. Courtesy of Igel H (1999) Wave propagation in three-dimensional spherical sections by the Chebyshev spectral method. *Geophysical Journal International* 136: 559–566.

leads to the stiffness matrix. The second term on the right is the source term [4], which has been integrated explicitly by using the properties of the Dirac delta distribution. Note that, like the velocity-stress strong form [6], only first-order spatial derivatives of the displacement field and the test vector are involved in the weak form [11], but that, unlike the velocity-stress formulation, the temporal derivatives are of second order.

It is important to appreciate that the traction-free surface condition $\hat{\mathbf{n}} \cdot \mathbf{T} = 0$ is imposed naturally and automatically during the integration by parts, because the contour integral over the free surface simply vanishes. In other words, the free-surface condition is a natural condition of the problem. In the context of regional simulations, an additional term appears in [11] which represents the absorption of energy on the artificial boundaries of the domain (e.g., Komatitsch and Tromp, 1999).

In the next section, we introduce Rayleigh-Ritz methods, of which coupled mode and direct solution methods are examples. Other numerical methods based upon the weak formulation [11] that are discussed in subsequent sections are finite element and spectral element methods.

1.06.5.1 Rayleigh-Ritz Method

The idea behind a Rayleigh-Ritz method is to expand the unknown displacement field \mathbf{s} in terms of a set of known trial or basis functions \mathbf{s}_k (Dahlen and Tromp, 1998):

$$\mathbf{s} = \sum_k q_k \mathbf{s}_k \quad [12]$$

In this approach, one seeks to determine the expansion coefficients q_k . Notice that at this stage we need

not be specific about the exact choice of the basis functions. Rayleigh–Ritz methods are generally implemented in the frequency domain. It is readily shown that the weak form of the frequency domain version of the equation of motion [3] is (Geller and Ohminato, 1994; Dahlen and Tromp, 1998)

$$-\omega^2 \int_V \rho \mathbf{w} \cdot \mathbf{s} d^3x = - \int_V \nabla \mathbf{w} : \mathbf{T} d^3x + \mathbf{M} : \nabla \mathbf{w}(\mathbf{x}_s) S(\omega) \quad [13]$$

Upon substituting the expansion [12] in [13] and choosing the test vector $\mathbf{w} = \mathbf{s}_{k'}$ we obtain the matrix equation

$$\sum_k (V_{k'k} - \omega^2 T_{k'k}) q_k(\omega) = S_{k'}(\omega) \quad [14]$$

where we have defined the matrix and vector elements

$$\begin{aligned} V_{k'k} &= \int_{\Omega} \nabla \mathbf{s}_{k'} : \mathbf{c} : \nabla \mathbf{s}_k d^3x, & T_{k'k} &= \int_{\Omega} \rho \mathbf{s}_{k'} \cdot \mathbf{s}_k d^3x, \\ S_{k'}(\omega) &= \mathbf{M} : \nabla \mathbf{s}_{k'}(\mathbf{x}_s) S(\omega) \end{aligned} \quad [15]$$

For brevity, we use the full anisotropic elastic tensor in the definition of the matrix elements $V_{k'k}$. Because the test vector \mathbf{w} and the basis functions \mathbf{s}_k are the same, the Rayleigh–Ritz method is also referred to as a Galerkin method. By introducing the $(\infty \times \infty)$ -dimensional kinetic and potential energy matrices

$$\mathbf{T} = \begin{pmatrix} & \vdots & \\ \cdots & T_{k'k} & \cdots \\ & \vdots & \end{pmatrix}, \quad \mathbf{V} = \begin{pmatrix} & \vdots & \\ \cdots & V_{k'k} & \cdots \\ & \vdots & \end{pmatrix} \quad [16]$$

and the ∞ -dimensional source vector

$$\mathbf{S} = \begin{pmatrix} \vdots \\ S_{k'} \\ \vdots \end{pmatrix} \quad [17]$$

the solution to [14] may be formally expressed as

$$\mathbf{q}(\omega) = (\mathbf{V} - \omega^2 \mathbf{T})^{-1} \mathbf{S}(\omega) \quad [18]$$

In an anelastic Earth model, the potential energy matrix also depends on frequency, $\mathbf{V} = \mathbf{V}(\omega)$, because in that case the elastic tensor \mathbf{c} becomes frequency dependent (see [2]). Of course, in practice one uses a finite-dimensional set of basis functions \mathbf{s}_k , leading to a finite-dimensional matrix solution [18]. This truncation of the eigenvalue problem leads to

inaccuracies in the synthetics. Such truncation errors are most pronounced in models with sharp heterogeneities, which induce a wide coupling band.

Let us denote the $\hat{\mathbf{v}}$ component of the displacement by $\mathbf{s} = \hat{\mathbf{v}} \cdot \mathbf{s}$, and let us define the receiver vector elements $R_k = \hat{\mathbf{v}} \cdot \mathbf{s}_k$. Upon introducing the ∞ -dimensional receiver vector

$$\mathbf{R} = \begin{pmatrix} \vdots \\ R_k \\ \vdots \end{pmatrix} \quad [19]$$

and using [12] and [18] it may be shown that the spectrum of the $\hat{\mathbf{v}}$ component of the displacement is given by

$$\mathbf{s}(\omega) = \mathbf{R}^T (\mathbf{V} - \omega^2 \mathbf{T})^{-1} \mathbf{S}(\omega) \quad [20]$$

This expression gives the response of a 3-D Earth model to an earthquake and forms the basis of the CMM discussed in Section 1.06.5.1.1 as well as the DSM discussed in Section 1.06.5.1.2.

Finally, we note that the eigenfrequencies of the 3-D Earth model are determined by (Dahlen and Tromp, 1998)

$$\det(\mathbf{V} - \omega^2 \mathbf{T}) = 0 \quad [21]$$

1.06.5.1.1 Coupled mode method

The CMM for calculating 3-D synthetic seismograms was pioneered by Park (1986) and gained significant interest (e.g., Lognonné and Romanowicz, 1990; Tromp and Dahlen, 1990; Park and Yu, 1992; Capdeville *et al.*, 2000). In this approach, the basis functions \mathbf{s}_k in [12] are chosen to be the eigenfunctions of a spherically symmetric Earth model. These eigenfunctions have a radial dependence that is dictated by the radial structure of the spherically symmetric reference Earth model, for example, PREM, and a lateral dependence that involves (vector) spherical harmonics. Expressions for the coupling matrices [16] based upon these eigenfunctions were first derived by Woodhouse (1980) and are summarized in Dahlen and Tromp (1998).

There are two main problems with the CMM. The first problem is that the basis functions are spherically symmetric whereas the 3-D Earth is elliptical and has topography and bathymetry. Typically, first-order perturbation theory is used to linearize these boundary undulations, which leads to errors in the forward calculation. A more serious problem has to do with the size of the matrices [16] involved in the coupled mode calculations. As the frequency

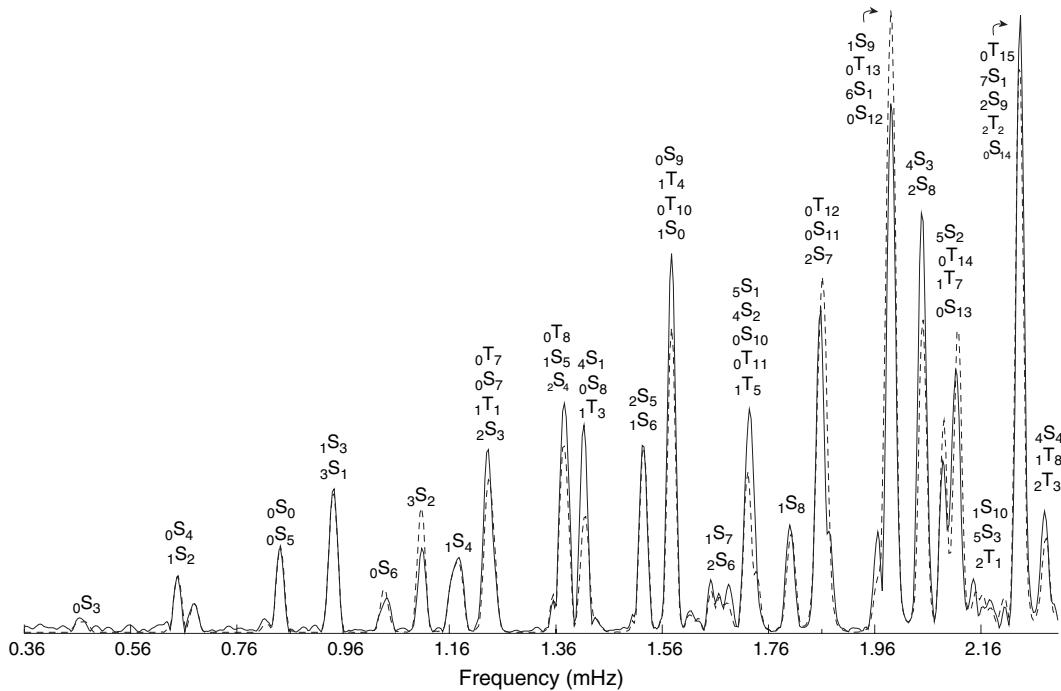


Figure 6 Vertical-component amplitude spectra of the 9 Jun. 1994, Bolivia deep-focus earthquake recorded at station PAS in Pasadena, CA. The solid line shows the observed spectrum; the dashed line shows the synthetic coupled mode spectrum. Rotation, ellipticity, and the lateral variations in shear wave speed of model SKS12WM13 ([Dziewonski et al., 1997](#)) have been accounted for in the calculations. The vertical arrays of mode labels identify the 22 super-multiplets considered. A Hann taper has been applied to both 35 h time series prior to Fourier transformation.

content of the synthetics is increased, the size of the matrices grows very rapidly, leading to large matrix-vector operations. Such operations are computationally very expensive, in particular on computers with distributed memory. Therefore, coupled mode calculations do not scale well on parallel machines, and in recent years they have largely gone out of favor. Only when one wants to calculate the very long-period response of the Earth, say at periods of 500 s and longer, is the coupled mode approach the method of choice (e.g., [Deuss and Woodhouse, 2001](#)). **Figure 6** shows an example of a coupled mode calculation for the 9 June 1994, deep Bolivia earthquake. In this calculation, neighboring modes are grouped in super-multiplets, in which the singlets that constitute the multiplets that define the group are coupled through a matrix expression of the form [20].

1.06.5.1.2 Direct solution method

In the DSM pioneered by Geller (e.g., [Hara et al., 1991](#); [Geller and Ohminato, 1994](#); [Geller and Hatori, 1995](#); [Geller and Takeuchi, 1995](#); [Takeuchi et al., 2000](#)), the basis functions in [12] are low-order polynomials, for example, splines, or analytic functions.

Complications due to the representation of the source term, which may not be representable in terms of these basis functions, are discussed in [Takeuchi and Geller \(2003\)](#). For spherically symmetric Earth models, the DSM may be used to calculate high-frequency synthetic seismograms, as illustrated in **Figure 7**. At 2 Hz, these synthetics are detailed enough to show the weak ICB-reflected PKiKP arrival. [Geller and Takeuchi \(1995\)](#) have designed finite difference operators that optimize the accuracy of the DSM synthetics.

DSM synthetics may be used to benchmark other numerical techniques. A comparison between a 2-D axisymmetric PS simulation, such as the one shown in 3, and 3-D DSM for spherically symmetric Earth model IASP91 is shown in **Figure 8**. To facilitate this comparison, the 2-D PS synthetics are mapped to approximate 3-D synthetics ([Wang et al., 2001](#)). This mapping produces approximately the right 3-D geometrical spreading and dispersion and produces adequate fits to the body-wave arrivals.

Like coupled mode synthetics, the DSM generally uses a linearized treatment of boundary undulations, which diminishes the accuracy of the 3-D synthetics.

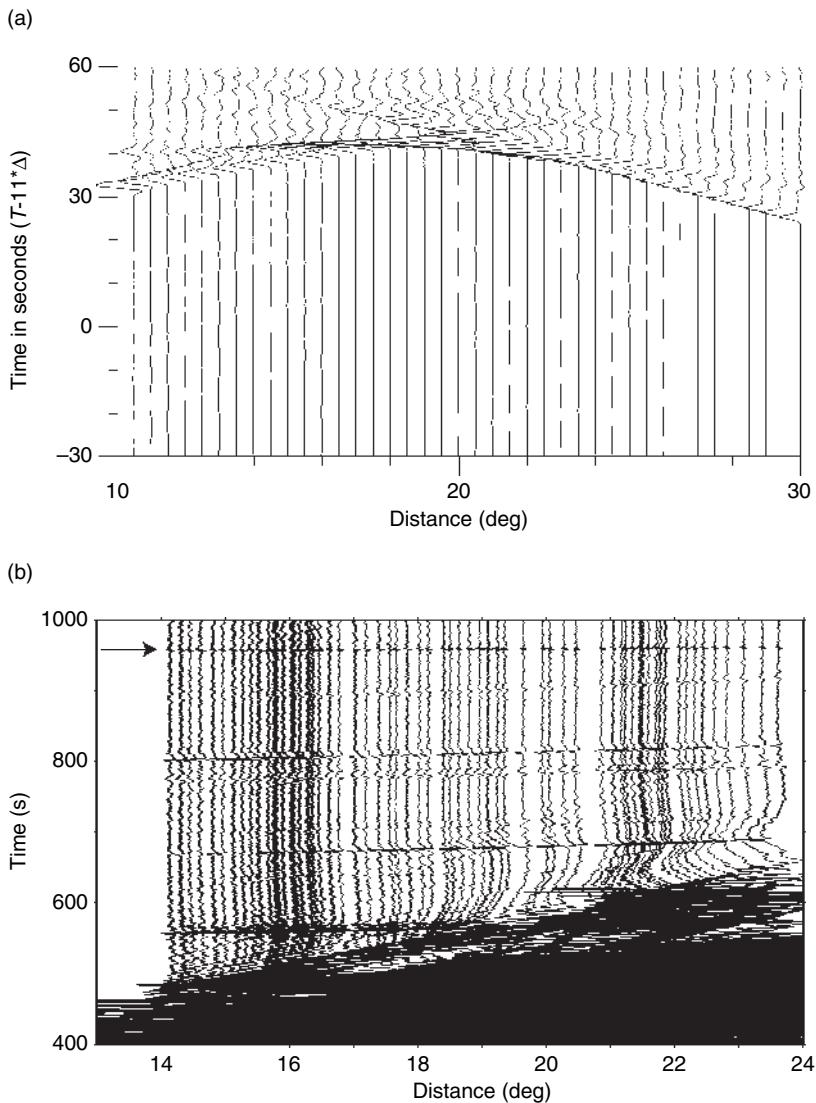


Figure 7 Examples of high-frequency DSM synthetics for isotropic PREM. (a) Displacement synthetic seismograms for upper-mantle triplication phases. The maximum frequency is 1 Hz. (b) Displacement synthetic seismograms for the PKiKP phase (indicated by the arrow). The maximum frequency is 2 Hz. Courtesy of Nozomu Takeuchi.

Takeuchi (2005) has recently extended the method to include arbitrary perturbations in boundary locations, as illustrated in Figure 9. Probably the main restriction for the DSM, like the CMM, is the need for significant amount of shared memory to perform the necessary matrix-vector manipulations for fully 3-D Earth models. Some of the main advantages of the DSM are that it addresses broadband wave propagation at the scale of the entire globe, and that it agrees closely with normal mode algorithms for spherically symmetric Earth model. For relatively smooth 3-D models at longer periods, the method is precise and effective.

1.06.5.2 Finite Element Method

The FEM is very popular in science and engineering (e.g., Zienkiewicz, 1977; Hughes, 1987), but has found limited application in seismology in general, and is currently not used for simulations at the scale of the globe. In the context of regional simulations, for the purpose of seismic hazard assessment, the method is actively being used (e.g., Bao *et al.*, 1998; Bielak *et al.*, 1999; Garatani *et al.*, 2000; Aagaard *et al.*, 2001). The method accommodates previously mentioned difficulties related to the presence of topography on

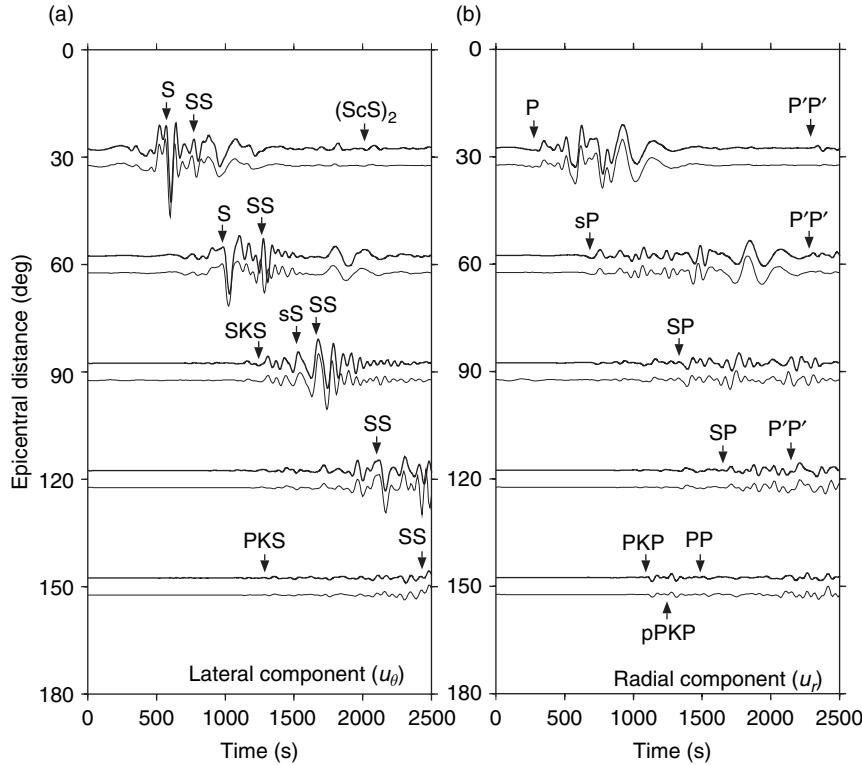


Figure 8 Comparison of axisymmetric pseudospectral (thin line) and DSM (thick line) synthetics at five epicentral distances. (a) lateral component; (b) vertical component. Both sets of seismograms are bandpass-filtered between 40 and 300 s. The spherically symmetric Earth model is IASP91. Courtesy of Wang Y, Takenaka H, and Furumura T (2001) Modelling seismic wave propagation in a two-dimensional cylindrical whole-Earth model using the pseudospectral method. *Geophysical Journal International* 145: 689–708.

major interfaces by allowing the grid boundaries to follow the local topography. Despite the fact that the FEM is presently not used for simulations in global seismology we discuss the method in some detail, because the SEM, which is extensively used in global seismology, has many common features.

In an FEM, the model domain is subdivided into a large number of small elements, which may take a variety of forms, for example, tetrahedra, hexahedra, pyramids, and prisms. Cartesian points $\mathbf{x} = (x, y, z)$ within a given deformed element Ω are mapped to points $\xi = (\xi, \eta, \zeta)$ in the reference element based upon the transformation

$$\mathbf{x}(\xi) = \sum_{a=1}^{n_a} N_a(\xi) \mathbf{x}_a \quad [22]$$

The control points or anchors \mathbf{x}_a define the geometry of the element, and the shape functions N_a provide a means for mapping and interpolation. For example, the geometry of hexahedral elements (deformed

cubes) may be controlled by $n_a = 8, 20$, or 27 anchors, as illustrated in Figure 10.

As an example, hexahedral shape functions are typically products of degree 1 or 2 Lagrange polynomials. The $n+1$ Lagrange polynomials of degree n are defined in terms of $n+1$ control points $-1 \leq \xi_\alpha \leq 1$, $\alpha = 0, \dots, n$, by

$$\ell_\alpha(\xi) = \frac{(\xi - \xi_0) \cdots (\xi - \xi_{\alpha-1})(\xi - \xi_{\alpha+1}) \cdots (\xi - \xi_n)}{(\xi_\alpha - \xi_0) \cdots (\xi_\alpha - \xi_{\alpha-1})(\xi_\alpha - \xi_{\alpha+1}) \cdots (\xi_\alpha - \xi_n)} \quad [23]$$

As a result of this definition, the Lagrange polynomials are equal to either 0 or 1 at any given control point: $\ell_\alpha(\xi_\beta) = \delta_{\alpha\beta}$, where δ denotes the Kronecker delta. The two Lagrange polynomials of degree 1 with two control points $\xi = -1$ and $\xi = 1$ are $\ell_0(\xi) = \frac{1}{2}(1-\xi)$ and $\ell_1(\xi) = \frac{1}{2}(1+\xi)$, and the three Lagrange polynomials of degree 2 with three control points $\xi = -1$, $\xi = 0$, and $\xi = 1$ are $\ell_0(\xi) = \frac{1}{2}\xi(\xi-1)$, $\ell_1(\xi) = 1-\xi^2$, and $\ell_2(\xi) = \frac{1}{2}\xi(\xi+1)$.

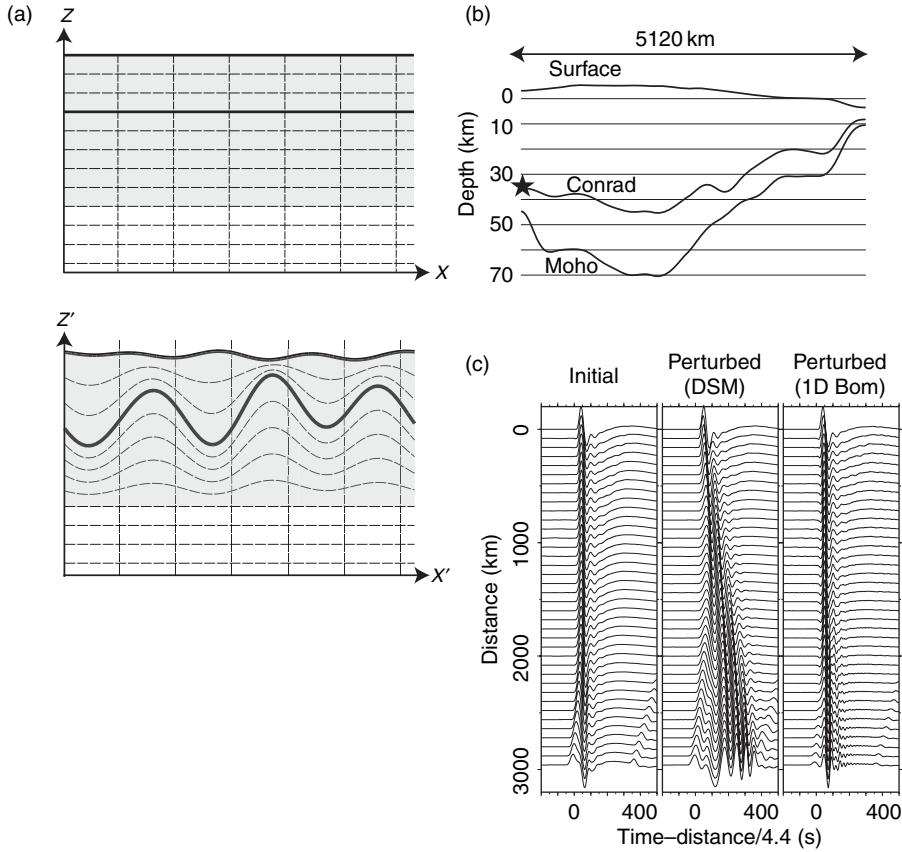


Figure 9 Illustration of the inclusion of topographic effects in the DSM. The basis functions are defined by using a one-to-one mapping of the boundaries in the initial model to those in the perturbed model. (a) Schematic illustration of the one-to-one mapping between the initial, laterally homogeneous model (top) and the perturbed model (bottom). Solid thick lines show the external and internal boundaries, and the shaded area shows the region deformed by the mapping. (b) Two-dimensional model which mimics crustal thickening in the Tibet region. The star shows the location of the source. (c) Example of synthetic seismograms computed for the model shown in (b). Synthetic seismograms for the initial (PREM) model are shown on the left, DSM synthetics for the perturbed model are shown in the middle, and synthetics based upon the conventional first-order Born approximation are shown on the right. Courtesy of Takeuchi N (2005) Finite boundary perturbation theory for the elastic equation of motion. *Geophysical Journal International* 160: 1044–1058.

Functions f , for example, components of the displacement field \mathbf{s} or the test vector \mathbf{w} , are expanded in the n_a shape functions N_a :

$$f(\mathbf{x}(\xi)) = \sum_{a=1}^{n_a} f_a N_a(\xi) \quad [24]$$

where f_a denotes the value of the function f at anchor \mathbf{x}_a . The weak implementation [11] involves gradients of the displacement \mathbf{s} and the test vector \mathbf{w} . Thus, the need arises to determine the gradient of functions

$$\begin{aligned} \nabla f &= \sum_{i=1}^3 \hat{\mathbf{x}}_i \partial_i f \\ &= \sum_{i=1}^3 \hat{\mathbf{x}}_i \sum_{a=1}^{n_a} f_a [\partial_\xi N_a(\xi) (\partial_i \xi) + \partial_\eta N_a(\xi) (\partial_i \eta) \\ &\quad + \partial_\zeta N_a(\xi) (\partial_i \zeta)] \end{aligned} \quad [25]$$

where $\hat{\mathbf{x}}_i$, $i = 1, 2, 3$, denote unit vectors in the direction of increasing x , y , and z , respectively, and ∂_i , $i = 1, 2, 3$, denote partial derivatives in those directions. The matrix $\partial\xi/\partial\mathbf{x}$ is obtained by inverting the matrix $\partial\mathbf{x}/\partial\xi$, whose elements may be determined by differentiating [22]. The existence of this matrix is a requirement that is imposed during the design of the mesh, that is, the Jacobian of the mapping [22] should never vanish. Notice how in an FEM the accuracy of the gradient [25] is controlled by the polynomial degree of the shape functions. Typically, one uses low-degree polynomials for the shape functions, which leads to relatively inaccurate derivatives, as in a low-degree FDM based upon [7]. Numerically, this leads to grid dispersion and anisotropy. There are so-called b - p FEMs which use higher-degree

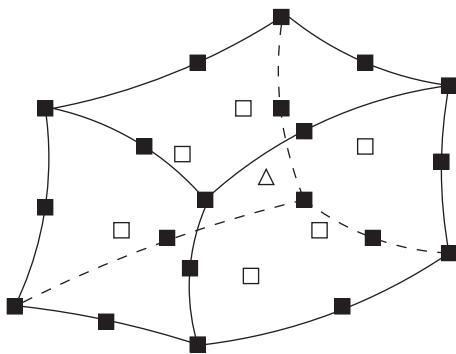


Figure 10 The geometry of a hexahedral finite element may be defined in terms of its eight corners, the eight corners plus the 12 edge centers (the 20 black squares), or the eight corners plus the 12 edge centers plus the six face centers (the six open squares) plus the center (the open triangle). In a classical FEM these 8, 20, or 27 anchors are used to define the shape of the element as well for the interpolation of functions. Courtesy of Komatitsch D and Tromp J (1999) Introduction to the spectral-element method for 3-D seismic wave propagation. *Geophysical Journal International* 139: 806–822.

polynomials for the shape functions to combat this problem (e.g., Guo and Babuška, 1986). A drawback for b - p FEMs is that they lead to large systems of linear equations which are difficult to solve, in particular on parallel machines.

The weak form [11] involves numerical integration of functions over the elements. In an FEM, this is generally accomplished based upon Gauss quadrature, such that integrations over elements Ω may be approximated as

$$\int_{\Omega} f(\mathbf{x}) d^3x = \sum_{\alpha=0}^n \sum_{\beta=0}^n \sum_{\gamma=0}^n \omega_{\alpha} \omega_{\beta} \omega_{\gamma} \times f(\xi_{\alpha}, \eta_{\beta}, \zeta_{\gamma}) \mathcal{J}(\xi_{\alpha}, \eta_{\beta}, \zeta_{\gamma}) \quad [26]$$

where ω_{α} , $\alpha=0, \dots, n$, denote the $n+1$ weights associated with the Gauss quadrature, the $(n+1)^3$ points $(\xi_{\alpha}, \eta_{\beta}, \zeta_{\gamma})$ denote the associated Gauss integration points, and \mathcal{J} denotes the Jacobian of the mapping [22]. The Gauss weights and integration points are chosen such that in 1-D they exactly integrate a polynomial of degree $2n$. To facilitate the integration of functions and their partial derivatives over the elements, the values of the inverse Jacobian matrix $\partial\xi/\partial\mathbf{x}$ need to be stored at the Gauss integration points for each element.

In a finite element mesh, grid points that lie on the sides, edges, or corners of an element are shared among neighboring elements. Therefore one needs to distinguish between the grid points that define an

element, the local mesh, and all the grid points in the model, many of which are shared among several finite elements, the global mesh. One needs to determine a mapping between grid points in the local mesh and grid points in the global mesh; efficient finite element routines are available for this purpose. Before the system can be marched forward in time, the contributions from all the elements that share a common global grid point need to be summed. This is referred to as the assembly of the system.

The implementation of an FEM on parallel computers involves partitioning the mesh in slices of elements, such that each processor in the parallel machine is only responsible for the elements in one particular slice. At the edges of a slice, results need to be communicated to its neighbors. Therefore, a parallel computer assembly involves communication between adjacent mesh slices. Because the mass matrix in an FEM is nondiagonal, one needs to use an implicit time scheme, that is, one needs to resolve a system of linear equations. On a parallel machine, this too requires communication between distinct compute nodes. We discuss mesh partitioning in more detail in the context of spectral element simulations, which we introduce in the next section.

Like a low-order FDM, the FEM tends to suffer from numerical grid dispersion and anisotropy, which is highly undesirable for seismic wave propagation problems which involve real dispersion and anisotropy. Its main attribute is its flexibility, which allows one to design complicated meshes capturing realistic 3-D Earth models.

1.06.5.3 Spectral Element Method

The SEM has been used for two decades in computational fluid dynamics (e.g., Patera, 1984). It has more recently been applied to problems related to 2-D (Cohen *et al.*, 1993; Priolo *et al.*, 1994) and 3-D local or regional (Komatitsch, 1997; Faccioli *et al.*, 1997; Komatitsch and Vilotte, 1998; Seriani, 1998; Komatitsch and Tromp, 1999; Komatitsch *et al.*, 2004) and global (Chaljub, 2000; Komatitsch and Tromp, 2002a, 2002b; Komatitsch *et al.*, 2002, 2003; Chaljub *et al.*, 2003; Chaljub and Valette, 2004) seismic wave propagation. As in the classical FEM discussed in the previous section, the first step in the SEM is to subdivide the model volume into a number of nonoverlapping elements. In an FEM, one can choose from a variety of elements, for example, tetrahedra, hexahedra, or prisms, but in the classical SEM one uses only hexahedra. In 2-D, the SEM has

been extended to include triangles (e.g., Sherwin and Karniadakis, 1995; Taylor and Wingate, 2000; Komatitsch *et al.*, 2001), but this leads to complications that are beyond the scope of this chapter. The mesh of elements needs to be geometrically conforming, that is, the six sides of each hexahedral element must match up exactly with the sides of neighboring elements. The SEM can be adapted to geometrically nonconforming meshes based on what is known as the mortar-matching method (e.g., Chaljub, 2000; Chaljub *et al.*, 2003), but this is also beyond the scope of the present chapter. Recent reviews of the SEM in seismology are given by Komatitsch *et al.* (2005) and Chaljub *et al.* (2007).

Figure 11 shows an example of a hexahedral SEM mesh for the globe. The mesh is designed based upon an analytical mapping between the cube and the sphere called the cubed sphere (Sadourny, 1972; Ronchi *et al.*, 1996; Chaljub, 2000). Each of the six chunks that constitute the cubed sphere is meshed in such a way that they match perfectly at their common interfaces. Following Chaljub (2000), the singularity of coordinates at the Earth's center is avoided by placing a small cube around the center of the inner core. The mesh within this cube matches up with the cubed sphere mesh at the ICB. This mesh honors all first- and second-order

discontinuities in PREM (Dziewonski and Anderson, 1981). Any typical 3-D mantle and/or crustal model may now be superimposed on the mesh.

In an SEM, one generally uses hexahedral elements, which may be mapped back to the reference cube based upon shape functions expressed in terms of low-degree Lagrange polynomials. After meshing the model, we need to define basis functions to represent the unknown displacement vector \mathbf{s} and the test vector \mathbf{w} on an element. In most FEMs, both the geometry of the problem and the vector fields are expressed using shape functions defined in terms of low-degree polynomials, as in [24]. In the SEM, the geometry of the curved elements is also defined using low-degree polynomials, but the displacement field and the test vector are defined using higher-degree polynomials. This is the major difference between SEMs and FEMs. In this regard, SEMs are related to $b\text{-}p$ FEMs, which also use polynomials of higher degree (but result in a nondiagonal mass matrix) (e.g., Guo and Babuška, 1986).

An SEM typically uses Lagrange polynomials [23] of degree 4–10 for the interpolation of functions. In an SEM, the control points ξ_α , $\alpha = 0, \dots, n$, needed in the definition [23] are chosen to be the $n + 1$ GLL points, which are the roots of $(1 - \xi^2)P'_n(\xi) = 0$, where P'_n denotes the derivative of the Legendre polynomial

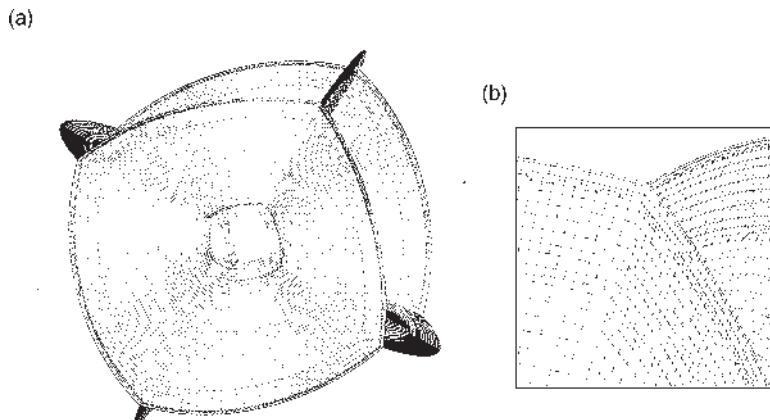


Figure 11 (a) Example of a spectral element mesh in the mantle. (b) Close-up of the mesh doublings in the upper mantle. The spectral element mesh is conforming, that is, every side of every element matches up perfectly with the side of a neighboring element, but nonstructured, that is, the number of elements that share a given point can vary and take any value. The mesh honors first-order discontinuities in PREM at depths of 24.4 km, 220 km, 400 km, and 670 km, the CMB, and the ICB; it also honors second-order discontinuities in PREM at 600 km, 771 km, and at the top of D''. The mesh is doubled in size once below the Moho, a second time below the 670 km discontinuity, and a third time just above the ICB. Each of the six chunks that constitute the cubed sphere has 240×240 elements at the free surface and 30×30 elements at the ICB. The central cube in the inner core has been removed for clarity of viewing. For a later experiment shown in **Figure 15**, the triangle indicates the location of the source, situated on the equator and the Greenwich meridian. Rings of receivers with a 2° spacing along the equator and the Greenwich meridian are shown by the dashes. Courtesy of Komatitsch D and Tromp J (2002a) Spectral-element simulations of global seismic wave propagation. I: Validation. *Geophysical Journal International* 149: 390–412.

of degree n (Canuto *et al.*, 1988). As an example, the five Lagrange polynomials of degree 4 are shown in **Figure 12(a)**, and **Figure 12(b)** illustrates the distribution of associated GLL points on the face of a hexahedral element. As we will see, the combination of Lagrange interpolants with a particular integration rule leads to an exactly diagonal mass matrix, and a diagonal mass matrix leads to a simple explicit time scheme that lends itself very well to numerical simulations on parallel computers.

We note that there are implementations of the SEM based upon Chebyshev basis functions that do not lead to a diagonal mass matrix (e.g., Patera, 1984; Priolo *et al.*, 1994; Seriani, 1998). The main advantages are that the related Gauss–Lobatto–Chebyshev integration rule is exact for the chosen polynomial basis, while it is only approximate in the case of GLL quadrature, and that the Gauss–Lobatto–Chebyshev points and weights are known analytically (in the GLL version, they are computed numerically). The main disadvantage of the Chebyshev approach is that an iterative solver for large matrix systems needs to be implemented, and implicit time-marching schemes are frequently used. This implementation is technically difficult but has been used successfully (Seriani, 1997, 1998).

In the weak form of the wave eqn [11], we expand functions f , for example, a component of the displacement field \mathbf{s} or the test vector \mathbf{w} , in terms of degree- n Lagrange polynomials:

$$f(\mathbf{x}(\xi, \eta, \zeta)) = \sum_{\alpha=0}^n \sum_{\beta=0}^n \sum_{\gamma=0}^n f^{\alpha\beta\gamma} \ell_\alpha(\xi) \ell_\beta(\eta) \ell_\gamma(\zeta) \quad [27]$$

where $f^{\alpha\beta\gamma} = f(\mathbf{x}(\xi_\alpha, \eta_\beta, \zeta_\gamma))$ denotes the value of the function f at the GLL point $\mathbf{x}(\xi_\alpha, \eta_\beta, \zeta_\gamma)$. Using the polynomial representation [27], the gradient of a function can be expressed as

$$\begin{aligned} \nabla f(\mathbf{x}(\xi, \eta, \zeta)) &= \sum_{i=1}^3 \hat{\mathbf{x}}_i \sum_{\alpha=0}^n \sum_{\beta=0}^n \sum_{\gamma=0}^n f^{\alpha\beta\gamma} [\ell'_\alpha(\xi) \ell_\beta(\eta) \\ &\quad \times \ell_\gamma(\zeta) \partial_i \xi + \ell_\alpha(\xi) \ell'_\beta(\eta) \ell_\gamma(\zeta) \partial_i \eta \\ &\quad + \ell_\alpha(\xi) \ell_\beta(\eta) \ell'_\gamma(\zeta) \partial_i \zeta] \end{aligned} \quad [28]$$

where a prime denotes the derivative of a Lagrange polynomials. As in the FEM, the matrix $\partial \mathbf{x} / \partial \boldsymbol{\xi}$ is obtained by inverting the matrix $\partial \mathbf{x} / \partial \boldsymbol{\xi}$. Because one typically uses polynomials of degree 4–10, the derivatives calculated based upon [28] tend to be more accurate than those used in an FEM or FDM.

The next step is to evaluate the integrals in the weak form [11] at the elemental level. In the context of classical FEMs, we saw in the previous section that one frequently uses Gauss quadrature [26] for this purpose. In an SEM, a GLL integration rule is used instead, because, as we will see, it leads to a diagonal mass matrix when used in conjunction with GLL interpolation points. Under this approach, integrations over elements Ω may be approximated as

$$\begin{aligned} \int_{\Omega} f(\mathbf{x}) d^3 \mathbf{x} &= \int_{-1}^1 \int_{-1}^1 \int_{-1}^1 f(\mathbf{x}(\xi, \eta, \zeta)) J(\xi, \eta, \zeta) d\xi d\eta d\zeta \\ &= \sum_{\alpha=0}^n \sum_{\beta=0}^n \sum_{\gamma=0}^n \omega_\alpha \omega_\beta \omega_\gamma f^{\alpha\beta\gamma} J^{\alpha\beta\gamma} \end{aligned} \quad [29]$$

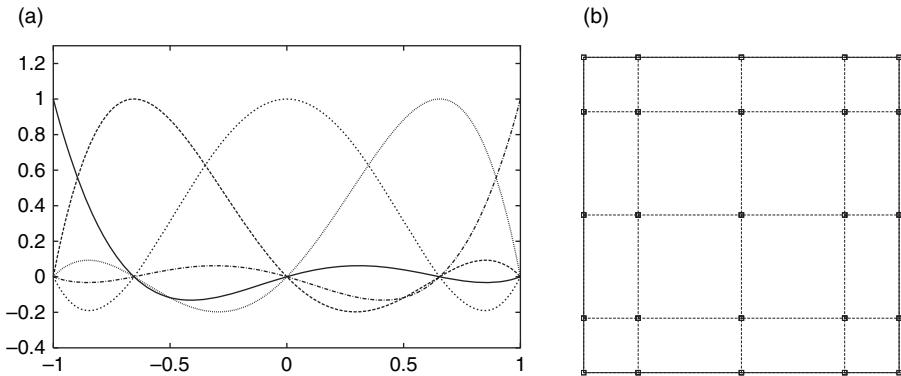


Figure 12 (a) The five Lagrange interpolants of degree $N=4$ on the reference segment $[-1, 1]$. The $N+1=5$ GLL points can be distinguished along the horizontal axis. All Lagrange polynomials are, by definition, equal to 1 or 0 at each of these points. Note that the first and last points are exactly -1 and 1 . (b) When Lagrange polynomials of degree n are used to discretize the wavefield, each 3-D spectral element contains a grid of $(n+1)^3$ GLL points, and each 2-D face of an element contains a grid of $(n+1)^2$ GLL points, as illustrated here for the degree 4 polynomials shown on the left. Courtesy of Komatitsch D, Tsuboi S, and Tromp J (2005) The spectral-element method in seismology. In: Levander A and Nolet G (eds.) *The Seismic Earth: Array Analysis of Broadband Seismograms*, pp. 205–227. Washington DC: AGU.

where ω_α , $\alpha=0,\dots,n$, denote the $n+1$ weights associated with the GLL points of integration, and $\mathcal{J}^{\alpha\beta\gamma}=\mathcal{J}(\xi_\alpha, \eta_\beta, \zeta_\gamma)$ denotes the value of the Jacobian \mathcal{J} of the mapping at a GLL point. To facilitate the integration of functions and their partial derivatives over the elements, the values of the inverse Jacobian matrix $\partial\xi/\partial x$ need to be stored at the $(n+1)^3$ GLL integration points for each element.

We illustrate the reasons for using GLL quadrature by explicitly calculating the SEM mass matrix, that is, the integral on the left-hand side of [11]. First, we expand the displacement field s and the test vector w in terms of Lagrange polynomials:

$$\begin{aligned} s(x(\xi, \eta, \zeta), t) &= \sum_{i=1}^3 \hat{x}_i \sum_{\sigma=0}^n \sum_{\tau=0}^n \sum_{\nu=0}^n s_i^{\sigma\tau\nu}(t) \ell_\sigma(\xi) \ell_\tau(\eta) \\ &\quad \times \ell_\nu(\zeta) \end{aligned} \quad [30]$$

$$w(x(\xi, \eta, \zeta)) = \sum_{i=1}^3 \hat{x}_i \sum_{\sigma=0}^n \sum_{\tau=0}^n \sum_{\nu=0}^n w_i^{\alpha\beta\gamma} \ell_\alpha(\xi) \ell_\beta(\eta) \ell_\gamma(\zeta) \quad [31]$$

Because we use the same basis functions to express the displacement and test vectors, the SEM is another example of a Galerkin method. Next, we substitute the interpolations [30] and [31] in the mass matrix at the elemental level, using GLL quadrature [29], to obtain

$$\begin{aligned} \int_{\Omega} \rho w \cdot \partial_i^2 s d^3x &= \int_{-1}^1 \int_{-1}^1 \int_{-1}^1 \rho(x(\xi)) w(x(\xi)) \cdot \partial_i^2 s(x(\xi), t) \\ &\quad \times \mathcal{J}(\xi) d^3\xi \\ &= \sum_{\alpha=0}^n \sum_{\beta=0}^n \sum_{\gamma=0}^n \omega_\alpha \omega_\beta \omega_\gamma \mathcal{J}^{\alpha\beta\gamma} \rho^{\alpha\beta\gamma} \\ &\quad \times \sum_{i=1}^3 w_i^{\alpha\beta\gamma} \dot{s}_i^{\alpha\beta\gamma} \end{aligned} \quad [32]$$

where $\rho^{\alpha\beta\gamma} = \rho(x(\xi_\alpha, \eta_\beta, \zeta_\gamma))$, and where a dot denotes differentiation with respect to time. By independently setting factors of $w_1^{\alpha\beta\gamma}$, $w_2^{\alpha\beta\gamma}$, and $w_3^{\alpha\beta\gamma}$ equal to zero, since the weak formulation [11] must hold for any test vector w , we obtain independent equations for each component of acceleration $\ddot{s}_i^{\alpha\beta\gamma}(t)$ at grid point $(\xi_\alpha, \eta_\beta, \zeta_\gamma)$. One can see that the value of acceleration at each point of a given element $\ddot{s}_i^{\alpha\beta\gamma}(t)$ is simply multiplied by the factor $\omega_\alpha \omega_\beta \omega_\gamma \rho^{\alpha\beta\gamma} \mathcal{J}^{\alpha\beta\gamma}$, which means that the elemental mass matrix is exactly diagonal. This is one of the key ideas behind the SEM, and the main motivation behind the choice of Lagrange interpolation at the GLL points used in conjunction with GLL numerical integration.

In summary, the main differences between FEM and SEM are the polynomial degree of the basis

functions, the choice of integration rule, and, as a consequence, the nature of the time-marching scheme. In an FEM, one tends to use low-degree basis functions and Gauss quadrature. In an SEM, one uses higher-degree basis functions and GLL quadrature to obtain better resolution as well as a diagonal mass matrix. For the SEM, this leads to simple explicit time schemes, as opposed to the numerically more expensive implicit time schemes used in FEMs. It is important to note that even under ideal circumstances the GLL rule is exact only for integrands that are polynomials of degree $2n-1$. Since integrations in the SEM involve the product of two polynomials of degree n – the displacement and the test function – the integration of the resulting polynomial of degree $2n$ is never exact. As in an FEM, for deformed elements there are additional errors related to curvature (Maday and Rønquist, 1990); the same is true for elements with heterogeneous material properties. Thus in an SEM a diagonal mass matrix is obtained by a process of subintegration. In this respect, the SEM is related to FEMs in which mass lumping is used to avoid the costly resolution of the nondiagonal system resulting from the use of Gauss quadrature (Cohen *et al.*, 1993). Evaluating the stiffness matrix and the source term in [11] is a bit more complicated (e.g., Komatitsch and Vilotte, 1998; Komatitsch and Tromp, 1999), because this involves taking first-order spatial derivatives of the displacement field and the test vector. These derivatives may be expressed in terms of Lagrange polynomials and their derivatives.

The SEM uses domain decomposition between the fluid and solid regions of the Earth model. In the inner core, mantle, and crust, one solves the anelastic wave equation, and in the liquid outer core one solves the acoustic wave equation. At the fluid–solid boundaries, that is, at the ICB and CMB, the continuity in traction and the normal component of displacement may be imposed exactly (Komatitsch and Tromp, 2002b; Chaljub and Valette, 2004; Komatitsch *et al.*, 2005), which leads to a very accurate representation of waves that interact with the fluid–solid boundary, in particular diffracted phases.

FEM and SEM meshes, for example, the mesh shown in [Figure 11](#), are generally too large to fit in memory on a single computer. Modern parallel computers, such as clusters or grids of computers, have a distributed memory architecture. A standard, portable approach for programming parallel machines with distributed memory is to use a message-passing methodology, usually based upon the

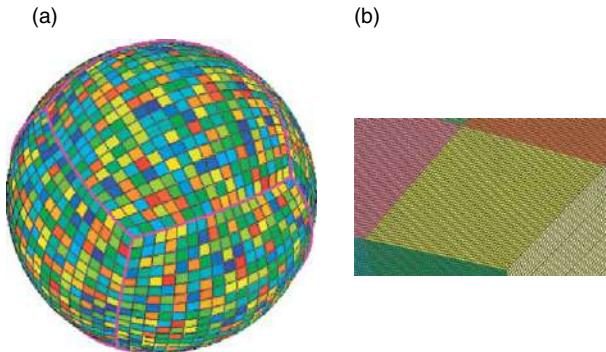


Figure 13 The SEM uses a mesh of hexahedral finite elements on which the wavefield is interpolated by high-degree Lagrange polynomials on GLL integration points. In order to perform the calculations on a parallel computer with distributed memory, the mesh is split into slices based upon a regular domain-decomposition topology. Each slice is handled by a separate processor. Adjacent slices located on different processors exchange information about common faces and edges based upon a message-passing methodology. (a) A global view of the mesh at the surface, illustrating that each of the six sides of the cubed sphere mesh is divided into 18×18 slices, shown here with different colors, for a total of 1944 slices. The elements within each slice reside in memory on a single processor of the parallel machine. (b) A close-up of the mesh of 48×48 spectral elements at the surface of each slice. Within each surface spectral element, we use $5 \times 5 = 25$ GLL grid points, which translates into an average grid spacing of 2.9 km (i.e., 0.026°) on the surface of the Earth. Courtesy of Komatitsch D, Tsuboi S, Chen J and Tromp J (2003) A 14.6 billion degrees of freedom, 5 teraflops, 2.5 terabyte earthquake simulation on the Earth Simulator. In: *Proceedings of the ACM/IEEE Supercomputing SC'2003 Conference*.

Message Passing Interface (MPI) library (e.g., [Gropp et al., 1994](#)). On such parallel machines we need to split the mesh into as many slices as the available number of processors. [Figure 13](#) illustrates how an SEM mesh may be split into 1944 slices for a parallel calculation on 1944 processors.

Time marching in an SEM is frequently accomplished based upon an explicit second-order Newmark scheme (e.g., [Komatitsch, 1997](#)). Therefore, the main numerical cost associated with the SEM is in small local matrix-vector products within each spectral element and not in the time scheme. This implies that the processors spend most of their time doing actual calculations, and only a small amount of time on communications.

The SEM has been extensively benchmarked against normal mode synthetics for spherically symmetric Earth model PREM (e.g., [Komatitsch and Tromp, 2002a, 2002b](#)). [Figure 14](#) shows an example of such a benchmark for the 9 June 1994, Bolivia earthquake recorded at station PAS in Pasadena, CA. The match between the SEM and mode synthetics on all three components is perfect. An even more difficult benchmark between modes and the SEM for PKP arrivals at near-antipodal distances is shown in [Figure 15](#). Notice how one can see a weak P_{diff} arrival prior to the arrival of PKIKP in both the SEM and the normal mode synthetics. This benchmark favorably tests the domain decomposition

between the fluid and solid regions, as well as the quality of the mesh, in particular near the CMB and in the inner core.

A snapshot of a global SEM simulation for the November 3, 2002, Denali Fault, AK, earthquake is shown in [Figure 16](#) ([Tsuboi et al., 2003; Chen et al., 2005](#)). Because the rupture propagates in a southeast-erly direction along the Denali Fault, the waves that propagate along the west coast of the United States have large amplitudes. This directivity effect due to the finite size of the earthquake fault is clearly visible in the SEM simulations. [Figure 17](#) shows waveform comparisons between SEM synthetics and data recorded by the Global Seismographic Network. Note that the SEM synthetic seismograms for mantle model S20RTS ([Ritsema et al., 1999](#)), accurate at periods of 5 s and longer, capture the dispersion of the Rayleigh waves reasonably well.

1.06.6 Discussion and Conclusions

We have provided an overview of the various numerical methods used in global seismology. Of these methods, currently only coupled mode, direct solution, and the spectral element methods are capable of simulating 3-D seismic wave propagation throughout the entire globe. CMMs are quite useful for calculating the very long period (>500 s) response of a

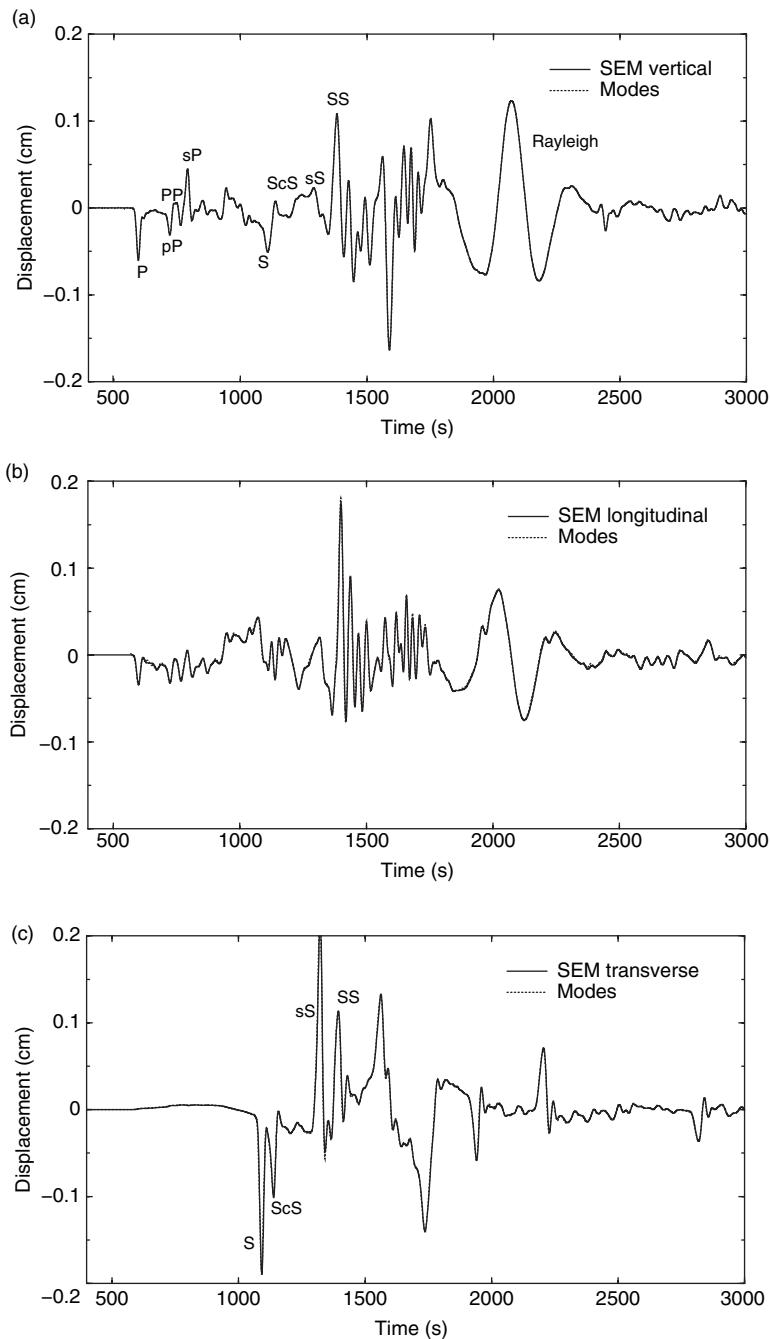


Figure 14 SEM (solid line) and mode (dotted line) synthetic seismograms in PREM for the great magnitude 8.2 Bolivia earthquake of 9 Jun. 1994, recorded at SCSN station PAS in Pasadena, CA. The depth of the event is 647 km. Anisotropy and attenuation are both included in this simulation. (a) Vertical component; (b) longitudinal component; (c) transverse component. The synthetics are accurate at periods of 18 s and longer. Courtesy of Komatitsch D and Tromp J (2002a) Spectral-element simulations of global seismic wave propagation. I: Validation. *Geophysical Journal International* 149: 390–412.

laterally heterogeneous, rotating, self-gravitating Earth model, and DSMs accomplish the same at somewhat shorter periods. The main difficulties with both CMM and DSM have to do with a linearized

treatment of boundary perturbations and, more severely, practical limitations associated with large matrix-vector operations that do not lend themselves well to calculations on parallel computers.

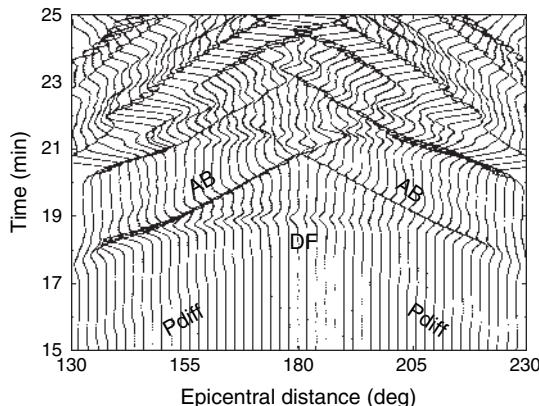


Figure 15 Record section comparison of PKP phases calculated for anelastic, anisotropic PREM based upon the SEM (solid lines) and modes (dotted lines) between 130° and 230° along the Greenwich meridian (see Figure 11 for the source–receiver geometry). At each epicentral distance, we plot both the SEM and the mode solution. All PKP arrivals, including PKIKP, which has traveled through the central cube in the mesh, are well reproduced. Note also a very weak P_{diff} arrival in both synthetics between 130° and 170° and between 190° and 230°. The correct representation of this diffracted signal in the SEM illustrates the accuracy of the domain decomposition between the fluid outer core and the solid mantle and the effective implementation of the related fluid–solid boundary conditions. The synthetics are accurate at periods of 18 s and longer. Courtesy of Komatitsch D and Tromp J (2002a) Spectral-element simulations of global seismic wave propagation. I: Validation. *Geophysical Journal International* 149: 390–412.

The only method capable of generating fully 3-D synthetic seismograms at the scale of the entire globe at short periods is the SEM. On a modest PC cluster, one can now calculate global synthetics at periods of 20 s and longer that account for heterogeneity in the crust and mantle, topography, anisotropy, attenuation, fluid–solid interactions, self-gravitation, rotation, and the oceans. At the present time, on 150 processors, a 1 h long seismogram may be calculated in about 5 h. On the Earth Simulator at the Japan Agency for Marine-Earth Science and Technology, one can reach a shortest period of 3.5 s. Such a calculation involves more than 4000 processors and requires about 18 h of compute time. Interestingly, broadband normal mode synthetics for spherically symmetric (1-D) Earth models are typically restricted to periods of 6 s and longer, so seismologists can now calculate 3-D synthetics accurate at periods shorter than 1-D mode synthetics.

In the context of inverse problems, the challenge now lies in harnessing these new-found forward capabilities to enhance the quality of models of Earth's

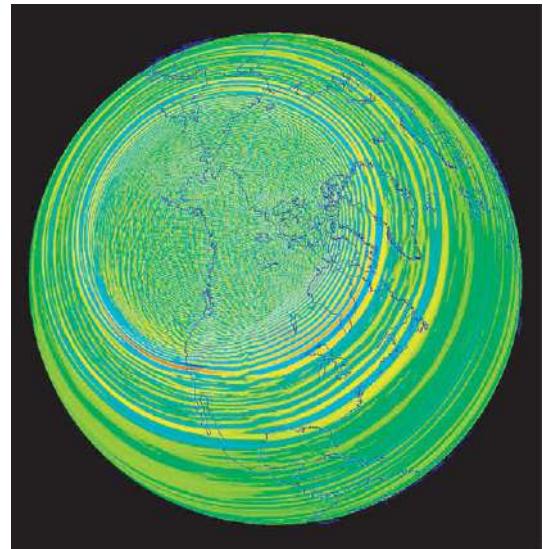


Figure 16 Spectral element snapshot of the propagation of seismic waves in the Earth generated by the $M_w = 7.9$ (3 Nov. 2002) Denali Fault, AK, earthquake. Note the large amplification of the waves along the western coast of the United States due to the directivity associated with the finite rupture. Note also the difference in dispersion between the oceanic and continental Rayleigh waves. The Airy phase has just reached Hudson Bay. The 3-D model includes mantle model S20RTS (Ritsema et al., 1999) and crustal model crust 2.0 (Bassin et al., 2000). Courtesy of Chen J, Tsuboi S, Komatitsch D, and Tromp J (2005) Rayleigh-wave multi-pathing along the west coast of North America. *Bulletin of the Seismological Society of America* 95(6): 2115–2124.

interior, in conjunction with improving models of the rupture process during an earthquake. On the face of it, this seems like a Herculean task because hundreds or even thousands of model parameters are involved in such inversions. In principle, the sensitivity of a seismogram with respect to the model parameters may be calculated numerically, but this would require a number of forward calculations equal to the number of model parameters (typically thousands). Tarantola (1984) demonstrated that one iteration in tomographic and source inversions may be performed based upon just two calculations for each earthquake: one calculation for the current model and a second ‘adjoint’ calculation that uses time-reversed signals at the receivers as simultaneous, fictitious sources. This approach has been used in global seismology based upon the DSM (e.g., Geller and Hara, 1993; Hara and Geller, 2000; Hara, 2004). Adjoint methods (e.g., Talagrand and Courtier, 1987) have opened the door to solving the full 3-D inverse problem, that is, the problem of using

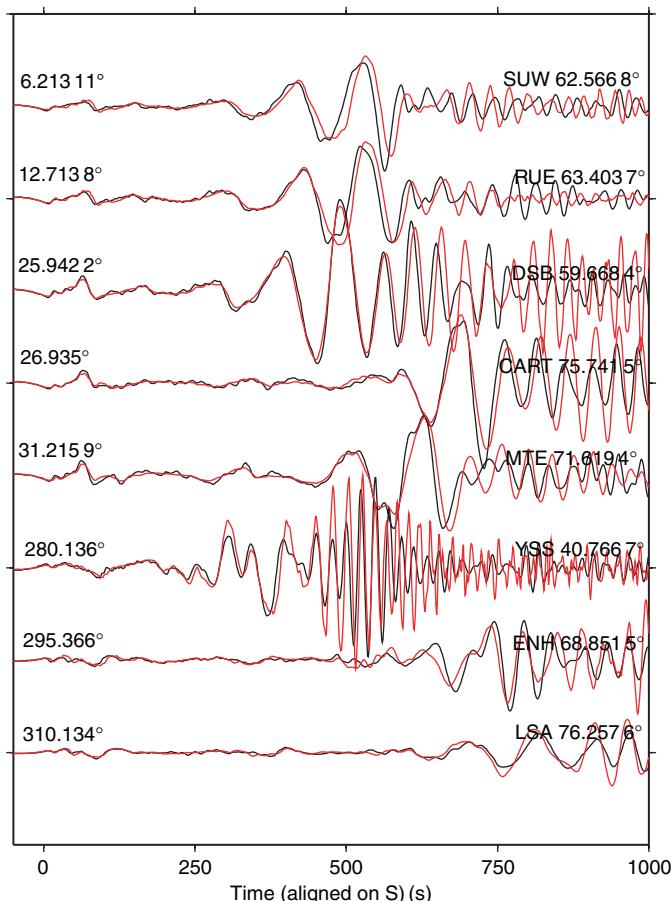


Figure 17 Comparison of transverse component data (black line) and spectral element synthetic seismograms (red line) for the 3 Nov. 2002, Denali Fault, AK, earthquake. Both the synthetic seismograms and the data are lowpass-filtered at 5 s. The source azimuth measured clockwise from due North is indicated on the left of each trace, and the station name and epicentral distance are on the right. Records are aligned on the S wave. The 3-D model includes mantle model S20RTS (Ritsema *et al.*, 1999) and crustal model crust 2.0 (Basson *et al.*, 2000). Courtesy of Tsuboi S, Komatitsch D, Chen J, and Tromp J (2003) Spectral-element simulations of the November 3, 2002, Denali, Alaska earthquake on the Earth Simulator. *Physics of the Earth and Planetary Interiors* 139: 305–312.

the remaining differences between the data and the synthetics to improve source and Earth models (e.g., Akçelik *et al.*, 2002, 2003; Tromp *et al.*, 2005). Recently, Capdeville *et al.* (2005) have proposed a spectral element approach to the inverse problem based upon a source-stacking technique that may further reduce the numerical burden.

Acknowledgments

The author would like to thank Heiner Igel, Dimitri Komatitsch, Nozomu Takeuchi, Christine Thomas, Seiji Tsuboi, and Yanbin Wang for contributing figures to this chapter. The SEM synthetics were calculated by Seiji Tsuboi on the Earth Simulator computer at the

Japan Agency for Marine-Earth Science and Technology. Broadband data were obtained from the IRIS Data Management Center. This material is based in part upon work supported by the National Science Foundation under grant EAR-0309576. This is contribution No. 9124 of the Division of Geological & Planetary Sciences, California Institute of Technology.

References

- Aagaard BT, Hall JF, and Heaton TH (2001) Characterization of near-source ground motions with earthquake simulations. *Earthquake Spectra* 17(2): 177–207.
- Akçelik V, Bielak J, Biros G, *et al.* (2003) High resolution forward and inverse earthquake modeling on terascale computers. In: *Proceedings of the ACM/IEEE Supercomputing SC'2003*

- Conference. www.sc-conference.org/sc2003 (published on CD-ROM).
- Akçelik V, Biros G, and Ghattas O (2002) Parallel multiscale Gauss–Newton–Krylov methods for inverse wave propagation. In: *Proceedings of the ACM/IEEE Supercomputing SC'2002 Conference*. www.sc-conference.org/sc2002 (published on CD-ROM).
- Aki K and Richards PG (1980) *Quantitative Seismology, Theory and Methods*. San Francisco: W.H. Freeman.
- Bao H, Bielak J, Ghattas O, et al. (1998) Large-scale simulation of elastic wave propagation in heterogeneous media on parallel computers. *Computer Methods in Applied Mechanics and Engineering* 152: 85–102.
- Bassin C, Laske G, and Masters G (2000) The current limits of resolution for surface wave tomography in North America. *EOS*, 81: F897.
- Basu U and Chopra AK (2003) Perfectly matched layers for time-harmonic elastodynamics of unbounded domains: Theory and finite-element implementation. *Computer Methods in Applied Mechanics and Engineering* 192: 1337–1375.
- Bérenger JP (1994) A perfectly matched layer for the absorption of electromagnetic waves. *Journal of Computational Physics* 114: 185–200.
- Bielak J, Xu J, and Ghattas O (1999) Earthquake ground motion and structural response in alluvial valleys. *Journal of Geotechnical and Geoenvironmental Engineering* 125: 413–423.
- Canuto C, Hussaini MY, Quarteroni A, and Zang TA (1988) *Spectral Methods in Fluid Dynamics*. New York: Springer-Verlag.
- Capdeville Y, Chaljub E, Villette JP, and Montagner JP (2003a) Coupling the spectral element method with a modal solution for elastic wave propagation in global Earth models. *Geophysical Journal International* 152: 34–67.
- Capdeville Y, Gung Y, and Romanowicz B (2005) Towards global Earth tomography using the spectral element method: A technique based on source stacking. *Geophysical Journal International* 162: 541–554.
- Capdeville Y, Romanowicz B, and To A (2003b) Coupling spectral elements and modes in a spherical Earth: An extension to the ‘sandwich’ case. *Geophysical Journal International* 154: 44–57.
- Capdeville Y, Stutzmann E, and Montagner J (2000) Effect of a plume on long-period surface waves computed with normal-mode coupling. *Physics of the Earth and Planetary Interiors* 119: 54–71.
- Carcione JM (1994) The wave equation in generalized coordinates. *Geophysics* 59: 1911–1919.
- Carcione JM, Kosloff D, and Kosloff R (1988) Wave propagation simulation in a linear viscoelastic medium. *Geophysical Journal International* 95: 597–611.
- Carcione JM and Wang PJ (1993) A Chebyshev collocation method for the wave equation in generalized coordinates. *Computational Fluid Dynamics Journal* 2: 269–290.
- Chaljub E (2000) *Modélisation numérique de la propagation d’ondes sismiques en géométrie sphérique: Application à la sismologie globale (Numerical modeling of the propagation of seismic waves in spherical geometry: Applications to global seismology)*. Ph.D. Thesis, Université Paris VII Denis Diderot, Paris, France.
- Chaljub E, Capdeville Y, and Villette JP (2003) Solving elastodynamics in a fluid-solid heterogeneous sphere: A parallel spectral element approximation on non-conforming grids. *Journal of Computational Physics* 187(2): 457–491.
- Chaljub E, Komatitsch D, Villette J-P, Capdeville Y, Valette B, and Festa G (2007) Spectral element analysis in seismology. In: Wu R-S and Maupin V (eds.) *IASPEI Monograph on Advances in Wave Propagation in Heterogeneous Media*, Vol. 48, pp. 365–419. Elsevier.
- Chaljub E and Tarantola A (1997) Sensitivity of SS precursors to topography on the upper-mantle 660-km discontinuity. *Geophysical Research Letters* 24(21): 2613–2616.
- Chaljub E and Valette B (2004) Spectral-element modeling of three-dimensional wave propagation in a self-gravitating Earth with an arbitrarily stratified outer core. *Geophysical Journal International* 158: 131–141.
- Chen J, Tsuboi S, Komatitsch D, and Tromp J (2005) Rayleigh-wave multi-pathing along the west coast of North America. *Bulletin of the Seismological Society of America* 95(6): 2115–2124.
- Clayton R and Engquist B (1977) Absorbing boundary conditions for acoustic and elastic wave equations. *Bulletin of the Seismological Society of America* 67: 1529–1540.
- Cohen G, Joly P, and Tordjman N (1993) Construction and analysis of higher-order finite elements with mass lumping for the wave equation. In: Kleinman R (ed.) *Proceedings of the Second International Conference on Mathematical and Numerical Aspects of Wave Propagation*, pp. 152–160. Philadelphia, PA: SIAM.
- Collino F and Tsogka C (2001) Application of the PML absorbing layer model to the linear elastodynamic problem in anisotropic heterogeneous media. *Geophysics* 66(1): 294–307.
- Dahlen FA, Nolet G, and Hung S-H (2000) Fréchet kernels for finite-frequency traveltimes – I. Theory. *Geophysical Journal International* 141: 157–174.
- Dahlen FA and Tromp J (1998) *Theoretical Global Seismology*. Princeton: Princeton University Press.
- Deuss A and Woodhouse JH (2001) Theoretical free-oscillation spectra: The importance of wide band coupling. *Geophysical Journal International* 155: 193–199.
- Dziewonski AM and Anderson DL (1981) Preliminary reference Earth model. *Physics of the Earth and Planetary Interiors* 25: 297–356.
- Dziewonski AM, Liu X-F, and Su W-J (1997) Lateral heterogeneity in the lowermost mantle. In: Crossley D (ed.) *Earth’s Deep Interior*, pp. 11–50. Amsterdam: Gordon and Breach.
- Emmerich H and Korn M (1987) Incorporation of attenuation into time-domain computations of seismic wave fields. *Geophysics* 52: 1252–1264.
- Faccioli E, Maggio F, Paolucci R, and Quarteroni A (1997) 2D and 3D elastic wave propagation by a pseudo-spectral domain decomposition method. *Journal of Seismology* 1: 237–251.
- Festa G and Villette JP (2005) The Newmark scheme as velocity-stress time-staggering and efficient pml implementation for spectral element simulations of elastodynamics. *Geophysical Journal International* 161: 789–812.
- Furumura T, Kennett BLN, and Furumura M (1998) Seismic wavefield calculation for laterally heterogeneous whole Earth models using the pseudospectral method. *Geophysical Journal International* 135(3): 845–860.
- Furumura T, Kennett BLN, and Furumura M (1999) Seismic wavefield calculation for laterally heterogeneous whole Earth models-II. The influence of upper mantle heterogeneity. *Geophysical Journal International* 139(3): 623–644.
- Garatani K, Nakamura H, Okuda H, and Yagawa G (2000) Large-scale parallel wave propagation analysis by GeoFEM. *Lecture Notes in Computer Science* 1823: 445–453.
- Geller RJ and Hara T (1993) Two efficient algorithms for iterative linearized inversion of seismic waveform data. *Geophysical Journal International* 115: 699–710.
- Geller RJ and Hatori T (1995) Dsm synthetic seismograms using analytic trial functions: Plane-layered, isotropic case. *Geophysical Journal International* 120: 163–172.
- Geller RJ and Ohminato T (1994) Computation of synthetic seismograms and their partial derivatives for heterogeneous media with arbitrary natural boundary conditions using the

- Direct Solution Method. *Geophysical Journal International* 116: 421–446.
- Geller RJ and Takeuchi N (1995) A new method for computing highly accurate dsm synthetic seismograms. *Geophysical Journal International* 123: 449–470.
- Gilbert F (1970) Excitation of the normal modes of the Earth by earthquake sources. *Geophysical Journal of the Royal Astronomical Society* 22: 223–226.
- Graves RW (1996) Simulating seismic wave propagation in 3D elastic media using staggered-grid finite differences. *Bulletin of the Seismological Society of America* 86(4): 1091–1106.
- Gropp W, Lusk E, and Skjellum A (1994) *Using MPI, Portable Parallel Programming with the Message-Passing Interface*. Cambridge: MIT Press.
- Guo B and Babuška I (1986) The $h-p$ version of the finite element method. *Computational Mechanics* 1: 21–41.
- Hara T (2004) Waveform inversion for 3-D Earth structure using the direct solution method implemented on vector-parallel supercomputer. *Physics of the Earth and Planetary Interiors* 146: 65–74.
- Hara T and Geller RJ (2000) Simultaneous waveform inversion for three-dimensional earth structure and earthquake source parameters considering a wide range of modal coupling. *Geophysical Journal International* 142: 539–550.
- Hara T, Tsuboi S, and Geller R (1991) Inversion for laterally heterogeneous Earth structure using a laterally heterogeneous starting model: Preliminary results. *Geophysical Journal International* 104: 523–540.
- Hong T-K and Kennett B (2002) A wavelet-based method for simulation of two-dimensional elastic wave propagation. *Geophysical Journal International* 150: 610–638.
- Hughes TJR (1987) *The Finite Element Method, Linear Static and Dynamic Finite Element Analysis*. Englewood Cliffs, NJ: Prentice-Hall International.
- Hung S-H, Dahlen FA, and Nolet G (2000) Fréchet kernels for finite-frequency traveltimes. II: Examples. *Geophysical Journal International* 141: 175–203.
- Hung SH and Forsyth D (1998) Modelling anisotropic wave propagation in oceanic inhomogeneous structures using the parallel multidomain pseudo-spectral method. *Geophysical Journal International* 133(3): 726–740.
- Igel H (1999) Wave propagation in three-dimensional spherical sections by the Chebyshev spectral method. *Geophysical Journal International* 136: 559–566.
- Igel H and Gudmundsson O (1997) Frequency-dependent effects on travel times and waveforms of long-period S and SS waves. *Physics of the Earth and Planetary Interiors* 104: 229–246.
- Igel H, Nissen-Meyer T, and Jahnke G (2002) Wave propagation in 3d spherical sections: Effects of subduction zones. *Physics of the Earth and Planetary Interiors* 132: 219–234.
- Igel H, Takeuchi N, Geller R, et al. (2000) The COSY Project: Verification of global seismic modeling algorithms. *Physics of the Earth and Planetary Interiors* 119: 3–24.
- Igel H and Weber M (1995) SH-wave propagation in the whole mantle using high-order finite differences. *Geophysical Research Letters* 22: 731–734.
- Igel H and Weber M (1996) P–SV wave propagation in the whole mantle using high-order finite differences: Application to lowermost mantle structure. *Geophysical Research Letters* 23: 415–418.
- Kennett BLN and Engdahl ER (1991) Traveltimes for global earthquake location and phase identification. *Geophysical Journal International* 105: 429–465.
- Kennett BLN, Engdahl ER, and Buland R (1995) Constraints on seismic velocities in the Earth from traveltimes. *Geophysical Journal International* 122: 108–124.
- Komatitsch D (1997) *Méthodes spectrales et éléments spectraux pour l'équation de l'élastodynamique 2D et 3D en milieu hétérogène (Spectral and Spectral-element Methods for the 2D and 3D Elastodynamics Equations in Heterogeneous Media)*. Ph.D. Thesis, Institut de Physique du Globe, Paris, France.
- Komatitsch D, Liu Q, Tromp J, Süss P, Stidham C, and Shaw JH (2004) Simulations of ground motion in the Los Angeles Basin based upon the spectral-element method. *Bulletin of the Seismological Society of America* 94: 187–206.
- Komatitsch D, Martin R, Tromp J, Taylor MA, and Wingate BA (2001) Wave propagation in 2-D elastic media using a spectral element method with triangles and quadrangles. *Journal of Computational Acoustics* 9(2): 703–718.
- Komatitsch D, Ritsema J, and Tromp J (2002) The spectral-element method, Beowulf computing, and global seismology. *Science* 298: 1737–1742.
- Komatitsch D and Tromp J (1999) Introduction to the spectral-element method for 3-D seismic wave propagation. *Geophysical Journal International* 139: 806–822.
- Komatitsch D and Tromp J (2002a) Spectral-element simulations of global seismic wave propagation. I: Validation. *Geophysical Journal International* 149: 390–412.
- Komatitsch D and Tromp J (2002b) Spectral-element simulations of global seismic wave propagation. II: 3-D models, oceans, rotation, and self-gravitation. *Geophysical Journal International* 150: 303–318.
- Komatitsch D and Tromp J (2003) A perfectly matched layer absorbing boundary condition for the second-order seismic wave equation. *Geophysical Journal International* 154: 146–153.
- Komatitsch D, Tsuboi S, Chen J, and Tromp J (2003) A 14.6 billion degrees of freedom, 5 teraflops, 2.5 terabyte earthquake simulation on the Earth Simulator. In: *Proceedings of the ACM/IEEE Supercomputing SC'2003 Conference*.
- Komatitsch D, Tsuboi S, and Tromp J (2005) The spectral-element method in seismology. In: Levander A and Nolet G (eds.) *The Seismic Earth: Array Analysis of Broadband Seismograms*, pp. 205–227. Washington DC: AGU.
- Komatitsch D and Vilotte JP (1998) The spectral-element method: An efficient tool to simulate the seismic response of 2D and 3D geological structures. *Bulletin of the Seismological Society of America* 88(2): 368–392.
- Kosloff D and Baysal E (1982) Forward modeling by the Fourier method. *Geophysics* 47: 1402–1412.
- Kosloff D, Kessler D, Filho AQ, Tessmer E, Behle A, and Strahilevitz R (1990) Solution of the equations of dynamics elasticity by a Chebyshev spectral method. *Geophysics* 55: 748–754.
- Kosloff D, Reshef M, and Loewenthal D (1984) Elastic wave calculations by the Fourier method. *Bulletin of the Seismological Society of America* 74: 875–891.
- Kosloff D and Tal-Ezer H (1993) A modified Chebyshev pseudospectral method with an $O(N^{-1})$ time step restriction. *Journal of Computational Physics* 104: 457–469.
- Levander AR (1988) Fourth-order finite-difference P–SV seismograms. *Geophysics* 53: 1425–1436.
- Li X-D and Romanowicz B (1995) Comparison of global waveform inversions with and without considering cross-branch modal coupling. *Geophysical Journal International* 121: 695–709.
- Li X-D and Romanowicz B (1996) Global mantle shear-velocity model developed using nonlinear asymptotic coupling theory. *Journal of Geophysical Research* 101: 22245–22272.
- Li XD and Tanimoto T (1993) Waveforms of long-period body waves in a slightly aspherical Earth model. *Geophysical Journal International* 112: 92–102.
- Li HP, Anderson DL, and Kanamori H (1976) Velocity dispersion due to anelasticity: Implications for seismology and

- mantle composition. *Geophysical Journal of the Royal Astronomical Society* 47: 41–58.
- Lognonné P and Romanowicz B (1990) Modeling of coupled normal modes of the Earth: The spectral method. *Geophysical Journal International* 102: 365–395.
- Love AEH (1911) *Some Problems of Geodynamics*. Cambridge: Cambridge University Press.
- Madariaga R (1976) Dynamics of an expanding circular fault. *Bulletin of the Seismological Society of America* 65: 163–182.
- Maday Y and Rønquist EM (1990) Optimal error analysis of spectral methods with emphasis on non-constant coefficients and deformed geometries. *Computer Methods in Applied Mechanics and Engineering* 80: 91–115.
- Marquering H, Nolet G, and Dahlen FA (1998) Three-dimensional waveform sensitivity kernels. *Geophysical Journal International* 132: 521–534.
- Marquering H and Snieder R (1995) Surface-wave mode coupling for efficient forward modelling and inversion of body-wave phases. *Geophysical Journal International* 120: 186–208.
- Marquering H and Snieder R (1996) Shear-wave velocity structure beneath europe, the northeastern atlantic and western asia from waveform inversions including surface-wave mode coupling. *Geophysical Journal International* 127: 283–304.
- Moczo P, Bystrický E, Kristek J, Carcione JM, and Bouchon M (1997) Hybrid modeling of P–SV seismic motion at inhomogeneous viscoelastic topographic structures. *Bulletin of the Seismological Society of America* 87: 1305–1323.
- Montelli R, Nolet G, Dahlen F, Masters G, Engdahl ER, and Hung S-H (2004) Finite-frequency tomography reveals a variety of plumes in the mantle. *Science* 303: 338–343.
- Nolet G (1990) Partitioned waveform inversion and two-dimensional structure under the network of autonomously recording seismographs. *Journal of Geophysical Research* 95: 8499–8512.
- Ohminato T and Chouet BA (1997) A free-surface boundary condition for including 3D topography in the finite difference method. *Bulletin of the Seismological Society of America* 87: 494–515.
- Park J (1986) Synthetic seismograms from coupled free oscillations: The effects of lateral structure and rotation. *Journal of Geophysical Research* 91: 6441–6464.
- Park J and Yu Y (1992) Anisotropy and coupled free oscillations: Simplified models and surface wave observations. *Geophysical Journal International* 110: 401–420.
- Patera AT (1984) A spectral element method for fluid dynamics: Laminar flow in a channel expansion. *Journal of Computational Physics* 54: 468–488.
- Priolo E, Carcione JM, and Seriani G (1994) Numerical simulation of interface waves by high-order spectral modeling techniques. *Journal of the Acoustical Society of America* 95(2): 681–693.
- Quarteroni A, Tagliani A, and Zampieri E (1998) Generalized Galerkin approximations of elastic waves with absorbing boundary conditions. *Computer Methods in Applied Mechanics and Engineering* 163: 323–341.
- Ritsema J, Van Heijst HJ, and Woodhouse JH (1999) Complex shear velocity structure imaged beneath Africa and Iceland. *Science* 286: 1925–1928.
- Robertsson JOA (1996) A numerical free-surface condition for elastic-viscoelastic finite-difference modeling in the presence of topography. *Geophysics* 61: 1921–1934.
- Robertsson JOA, Blanch JO, and Symes WW (1994) Viscoelastic finite-difference modeling. *Geophysics* 59: 1444–1456.
- Ronchi C, Iancocca R, and Paolucci PS (1996) The ‘cubed sphere’: A new method for the solution of partial differential equations in spherical geometry. *Journal of Computational Physics* 124: 93–114.
- Sadourny R (1972) Conservative finite-difference approximations of the primitive equations on quasi-uniform spherical grids. *Monthly Weather Review* 100: 136–144.
- Seriani G (1997) A parallel spectral element method for acoustic wave modeling. *Journal of Computational Acoustics* 5: 53–69.
- Seriani G (1998) 3-D large-scale wave propagation modeling by a spectral element method on a Cray T3E multiprocessor. *Computer Methods in Applied Mechanics and Engineering* 164: 235–247.
- Sherwin SJ and Karniadakis GE (1995) A triangular spectral element method: Applications to the incompressible Navier–Stokes equations. *Computer Methods in Applied Mechanics and Engineering* 123: 189–229.
- Takeuchi N (2005) Finite boundary perturbation theory for the elastic equation of motion. *Geophysical Journal International* 160: 1044–1058.
- Takeuchi N and Geller R (2003) Accurate numerical methods for solving the elastic equation of motion for arbitrary source locations. *Geophysical Journal International* 154: 852–866.
- Takeuchi N, Geller R, and Cummins P (2000) Complete synthetic seismograms for 3-D heterogeneous Earth models computed using modified DSM operators and their applicability to inversion for Earth structure. *Physics of the Earth and Planetary Interiors* 119: 25–36.
- Talagrand O and Courtier P (1987) Variational assimilation of meteorological observations with the adjoint vorticity equation. I: Theory. *Quarterly Journal of the Royal Meteorological Society* 113: 1311–1328.
- Tarantola A (1984) Inversion of seismic reflection data in the acoustic approximation. *Geophysics* 49: 1259–1266.
- Taylor MA and Wingate BA (2000) A generalized diagonal mass matrix spectral element method for non-quadrilateral elements. *Applied Numerical Mathematics* 33: 259–265.
- Tessmer E (1995) 3-D seismic modelling of general material anisotropy in the presence of the free surface by a Chebyshev spectral method. *Geophysical Journal International* 121: 557–575.
- Tessmer E, Kessler D, Kosloff D, and Behle A (1992) Multi-domain Chebyshev–Fourier method for the solution of the equations of motion of dynamic elasticity. *Journal of Computational Physics* 100: 355–363.
- Tessmer E and Kosloff D (1994) 3-D elastic modeling with surface topography by a Chebyshev spectral method. *Geophysics* 59(3): 464–473.
- Thomas C, Igel H, Weber M, and Scherbaum F (2000) Acoustic simulation of P-wave propagation in a heterogeneous spherical Earth: Numerical method and application to precursor waves to PKPdf. *Geophysical Journal International* 141: 6441–6464.
- Tromp J and Dahlen F (1990) Summation of the Born series for the normal modes of the Earth. *Geophysical Journal International* 100: 527–533.
- Tromp J, Tape CH, and Liu Q (2005) Seismic tomography, adjoint methods, time reversal, and banana–doughnut kernels. *Geophysical Journal International* 160: 195–216.
- Tsuboi S, Komatsitsch D, Chen J, and Tromp J (2003) Spectral-element simulations of the November 3, 2002, Denali, Alaska earthquake on the Earth Simulator. *Physics of the Earth and Planetary Interiors* 139: 305–312.
- Virieux J (1984) SH wave propagation in heterogeneous media: Velocity–stress finite-difference method. *Geophysics* 49: 1933–1942.
- Virieux J (1986) P–SV wave propagation in heterogeneous media: Velocity–stress finite-difference method. *Geophysics* 51: 889–901.
- Wang Y and Takenaka H (2001) A multidomain approach of the Fourier pseudospectral method using discontinuous

- grid for elastic wave modeling. *Earth Planets Space* 53: 149–158.
- Wang Y, Takenaka H, and Furumura T (2001) Modelling seismic wave propagation in a two-dimensional cylindrical whole-Earth model using the pseudospectral method. *Geophysical Journal International* 145: 689–708.
- Woodhouse JH (1980) The coupling and attenuation of nearly resonant multiplets in the Earth's free oscillation spectrum. *Geophysical Journal of the Royal Astronomical Society* 61: 261–283.
- Woodhouse JH and Dziewonski AM (1984) Mapping the upper mantle: Three-dimensional modeling of earth structure by inversion of seismic waveforms. *Journal of Geophysical Research* 89: 5953–5986.
- Zhao L, Jordan TH, and Chapman CH (2000) Three-dimensional Fréchet differential kernels for seismic delay times. *Geophysical Journal International* 141: 558–576.
- Zienkiewicz OC (1977) *The Finite Element Method in Engineering Science*, 3rd edn. New York: McGraw-Hill.
- Zingg DW (2000) Comparison of high-accuracy finite-difference methods for linear wave propagation. *SIAM Journal on Scientific Computing* 22(2): 476–502 (doi:10.1137/S106482759350320).
- Zingg DW, Lomax H, and Jurgens H (1996) High-accuracy finite-difference schemes for linear wave propagation. *SIAM Journal on Scientific Computing* 17(2): 328–346 (doi:10.1137/S1064827594267173).

1.07 Theory and Observations – Teleseismic Body-Wave Scattering and Receiver-Side Structure

M. G. Bostock, The University of British Columbia, Vancouver, BC, Canada

© 2007 Elsevier B.V. All rights reserved.

1.07.1	Introduction	219
1.07.2	Geometrical Preliminaries	220
1.07.3	Source Removal	222
1.07.3.1	Modal Decomposition	222
1.07.3.2	Receiver Functions and the Property of Minimum Phase	224
1.07.3.3	Improved Teleseismic P Green's Functions	225
1.07.3.4	Teleseismic S Green's Functions	227
1.07.3.5	Deconvolution, Stacking, and Array Processing	228
1.07.4	1-D Inversion	229
1.07.4.1	Least-Squares Optimization	229
1.07.4.2	Monte Carlo Inversion	230
1.07.4.3	Born Inversion and Classic (Delay-and-Sum) Studies	231
1.07.5	Multidimensional Inversion	235
1.07.6	Beyond the Born Approximation	238
1.07.6.1	Shortcomings of the Born Approximation	239
1.07.6.2	The Inverse-Scattering Series	239
1.07.6.3	Transmission to Reflection	240
1.07.7	Conclusions	242
	References	243

1.07.1 Introduction

The analysis of scattered, teleseismic body waves to characterize the receiver-side lithosphere and upper mantle spans over four decades, and it is now among the most widely used means of resolving fine-scale structure in these outer layers of the Earth. The first studies to harness converted teleseismic waves for investigation of deep Earth structure were undertaken in the former Soviet Block (Rainer Kind, personal communication; see, e.g., Hoffmann *et al.*, 1989). Most early studies involved single-station analyses, and the work of Phinney (1964) represents an important milestone. He recognized that one could remove the effect of the earthquake source by examining spectral ratios of radial and vertical component P seismograms measured at a surface receiver, and thereby gain insight into the bulk properties of the Earth's crust. His work was formulated in the frequency domain (see also Kurita, 1973) and constitutes the first application of the so-called 'receiver function' technique. Soon thereafter, Båth and Stefánson (1966) examined recordings of

teleseismic S , and identified S -to- P precursors scattered from the crust–mantle boundary as a viable means once again of characterizing crustal structure. A full decade was to elapse before the next major development. Working independently on transition zone and crustal structure, respectively, Vinnik (1977) and Langston (1979) introduced the time-domain, P receiver function to characterize receiver-side P -to- S conversions present within the coda of teleseismic P . The time-domain receiver function, which contains information on phase, has intuitive appeal as a leading-order approximation to the Earth's Green's function at early times (i.e., up until the arrival of the next major phase PP). In addition, Vinnik (1977) enhanced the weak scattered signals present in the receiver function by stacking multiple receiver functions from different epicentral distance ranges along theoretical move-out curves for a radial Earth model, thereby effectively approximating a 1-D, single-scattering inversion. By the mid-1980s, an increasing number of researchers had come to recognize the potential of the approach in general applications (e.g., Owens *et al.* 1984, Zandt and

Owens, 1986; Kind and Vinnik, 1988). This recognition combined with the growing availability of three-component, broadband seismometers and high-capacity, digital acquisition systems has led to the popularity that teleseismic receiver function analysis enjoys today in regional studies of lithospheric and upper mantle structure.

In the last decade, there has been a major focus on placing the empirical ‘receiver function’ technique on a firmer theoretical foundation and extending its application to multichannel data sets. In both respects, much has been (and may still be) learned from the vast, accumulated experience in exploration seismology. Although geometries in the global and exploration contexts are at first glance quite different (plane wave excitation from below versus point source excitation from above), both disciplines share an important common element, namely, the interaction of near-vertically propagating waves with near-horizontal and, often, modest-contrast stratification. The recorded wavefields are thus free of postcritical interactions that lead to dispersive, guided waves, and can be inverted to extract highly resolved information on subsurface material property contrasts within a single-scattering (or ‘Born approximation’) framework. Nonetheless, there are important distinctions between the two disciplines. Exploration seismology has, for practical reasons (source generation and recording), largely ignored elastic phenomena by focusing on pure P -mode scattering and modeling data with acoustic theory. Global seismology, in contrast, relies primarily on conversions to resolve subsurface structure, and pure mode reflections have, to date, played a far lesser role. It is interesting to note that the two communities have begun to forge closer links (e.g., Marfurt *et al.*, 2003), due in part to the growing interest in exploration for the use of local, passive seismicity to monitor changes in hydrocarbon reservoirs.

In this chapter, we provide an overview of the theory that underlies the processing of scattered teleseismic wavefields and thereby facilitates interpretation for regional lithospheric and upper mantle structure. Section 1.07.2 begins with a description of the geometrical attributes of different teleseismic phases that can be considered for use in studies of the lithosphere and upper mantle, along with their merits and shortcomings. The canonical problem of structural response/source signature separation is then addressed in the teleseismic context. This discussion centers on the relationship between the classic receiver function and the more fundamental

Green’s function that is required in formal inverse-scattering approaches. Sections 1.07.4 and 1.07.5 examine the inverse problem for one- and multi-dimensional heterogeneity. The focus here is on formal inverse-scattering techniques because of the insight they afford into physics of the scattering process and because they provide a framework through which more empirical schemes can be understood. In the final section, we discuss several shortcomings arising from the single scattering or Born approximation that has, to this point, underlain most attempts to invert scattered teleseismic body waves for receiver-side structure. We then sketch out a means through which nonlinear inverse scattering could, in principle, be applied to teleseismic wavefields, based on recent theoretical developments in exploration seismology. Before proceeding, we mention two additional review sources that the reader may wish to consult in gaining a broader appreciation for the field, namely, Pavlis (2005), which discusses outstanding issues in the inversion of teleseismic P wavefields for receiver-side structure, and Kennett (2002), a more general treatise of observational seismology at regional scales that includes a chapter on teleseismic body wavefields.

1.07.2 Geometrical Preliminaries

In this section, we sketch out the general scattering geometry to be considered for the remainder of the chapter. We shall restrict our attention to incident wavefields representing sources located at teleseismic distances (that is epicentral distance $\Delta > 30^\circ$) from one or more receivers located at the Earth’s surface. The term ‘incident wavefield’ will be defined more precisely in later sections, but for the present it can be considered to be the signal associated with a primary body-wave phase that has reflected/converted, if at all, only at the Earth’s surface and/or core–mantle boundary, for example, P , pP , PP , S , pS , PKP , SKS , and ScS (see Figure 1). This definition serves to distinguish the incident wavefield from the scattered waves generated through reflection or mode conversion at receiver-side heterogeneity, and which we are ultimately interested in exploiting (Burdick and Langston, 1977). Signals originating through source-side scattering will, in contrast, be most conveniently treated as part of the source signature.

For much of what follows we shall focus our attention on teleseismic P as it is the most practically

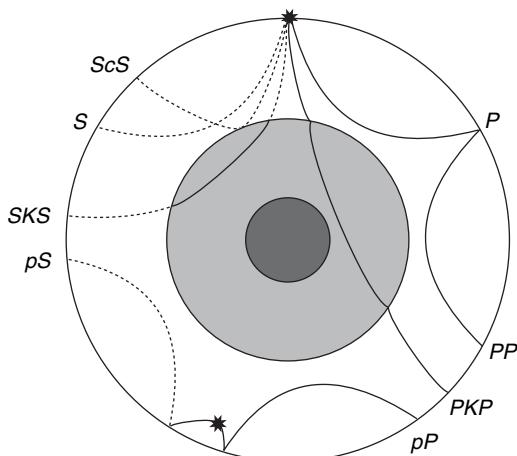


Figure 1 Ray paths of some major phases referred to in text that may serve as incident wavefields for study of near-receiver scattering from subsurface structure (P -wave legs, solid; S -wave legs, dashed).

useful of the candidate incident wavefields, and ignore, for the moment, associated depth phases created by deep earthquakes. At lesser distances ($14^\circ < \Delta < 30^\circ$), P (and S) waves traveling through the mantle experience triplications at strong velocity gradients defining the Earth's transition zone (between approximately 400 and 670 km depth) and, consequently, the incident wavefield will comprise several superposed arrivals characterized by different horizontal slownesses that are difficult to distinguish and separate (see **Figure 2**; Kennett 2002). In the distance range $30^\circ < \Delta < 100^\circ$, teleseismic P bottoms within the lower mantle which is generally characterized by a smoothly varying and dominantly radial velocity profile. Consequently, propagation is simple and the wavefield is accurately modeled by a single surface

slowness that decreases monotonically from approximately 0.08 to 0.04 s km^{-1} (or, equivalently, through ray parameters of 8.8 to 4.4 s deg^{-1}) over this distance range. Moreover, wavefront curvature is small because we are well into the far field, and it is frequently convenient in both single- and multistation applications to approximate the incident teleseismic wavefield as planar in horizontal aspect (see, e.g., Section 1.07.3.1). The small values of horizontal slowness also manifest steep angles of propagation which are, again, advantageous in that the likelihood of postcritical interactions is reduced. Complications due to depth phases can be dealt with in two ways, depending on source depth. As depth decreases, the slowness (and timing) of the depth phases approach that of the incident wavefield such that they can be considered one and the same. At greater depths, the difference in slowness may be significant but, in this case, the short duration of time functions that characterize Wadati–Benioff sources combined with greater time separation between the incident wavefield and depth phases will usually permit the depth phases to be temporally windowed and analyzed independently. The source depth at which one draws the line between inclusion versus separation of depth phases will depend on the application but will generally be taken to lie between 100 and 200 km.

The treatment of teleseismic S is rather more difficult than teleseismic P for a number of reasons. First, the distance range over which useful recordings can be procured is more limited. This is due in part to the development of postcritical S -to- P conversion from deeper (e.g., transition zone) discontinuities at larger slowness. In addition, conversion and triplication at the core–mantle boundary lead to close coincidence and interference of S , SKS , and ScS over the distance range $70. Depending on source mechanism, all the three S phases may possess comparable amplitudes and their separation (and that of associated scattered fields) is difficult, especially where 3-D heterogeneity is expected. SKS extends the usable distance range well beyond 100° , but the number of high signal-to-noise ratio recordings diminishes rapidly with distance. Second, because teleseismic S is characterized by larger slowness than teleseismic P at any given epicentral distance, postcritical phenomena within the receiver-side crust occur at smaller epicentral distances (Spdp, Zandt and Randall (1985); shear-coupled PL, Frazer (1977); Baag and Langston (1985), Owens and Zandt (1997)) that can complicate interpretation and$

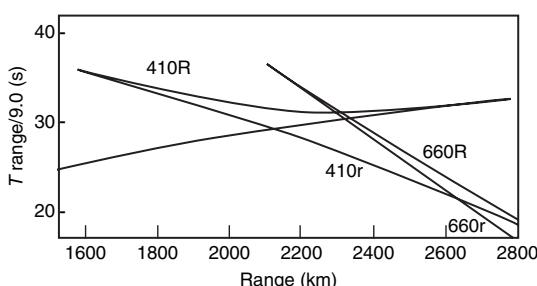


Figure 2 Traveltime curves at regional distances displaying triplications due to transition zone (410 km and 660 km) discontinuities that complicate analysis of scattering from more shallow discontinuities. Individual traveltime branches are labeled by the associated discontinuity (r, refraction; R, reflection).

inversion. Third, the receiver-side response to an incident S wavefield will generally depend on the wavefield polarization as imparted by the source and modified by source-side heterogeneity/anisotropy. The incident polarization is not generally known (with the exception of SKS which is radially polarized due to receiver-side conversion from P to S at the core–mantle boundary), though its influence can under certain assumptions be removed (e.g., Farra and Vinnik, 2000; Section 1.07.3.4). Fourth, higher frequencies in teleseismic S (and hence its resolving power) are attenuated more severely than those in teleseismic P due to lower Q , especially in the shallow upper mantle. Finally, signal-generated noise levels are generally higher in teleseismic S due to energy that has propagated some large portion of its path as P (Vinnik and Romanowicz, 1991; Bock, 1994). Although it might be argued that free-surface multiples arriving as S waves in the coda of teleseismic P represent a comparable form of signal-generated noise exacerbating interpretation of direct P -to- S conversions, these multiples are generated by receiver-side heterogeneity and can be exploited to leverage additional and complementary constraint on structure (see Sections 1.07.4.3 and 1.07.5). Despite these complications, there has been renewed interest in recent years in S -to- P conversions as means of characterizing the transition from lithosphere to asthenosphere (e.g., Oreshin *et al.*, 2002; Li *et al.*, 2004; Kumar *et al.*, 2005; Vinnik *et al.*, 2005; Yuan *et al.*, 2006).

The utility of most other phases is still more limited due either to interference or to low signal-to-noise levels, although PP is often used to augment teleseismic P data (e.g., Gurrola *et al.*, 1994). Useful structural information has on occasion also been extracted from regional P (e.g., Park and Levin, 2001) and PKP (e.g., Park and Levin, 2000) using ‘receiver-function’ style approaches.

1.07.3 Source Removal

With the geometrical framework just described in mind, the first task in most structural studies employing teleseismic wavefields is to characterize and remove the source. The standard model is a linear convolution of the form:

$$u_{in}(\mathbf{x}, t) = S(t) \otimes G_{in}(\mathbf{x}, t; \mathbf{p}_\perp) \quad [1]$$

where u_{in} is the observed particle displacement/velocity in direction i at location \mathbf{x} as a function of time t , $S(t)$ is an effective source time function, \otimes signifies temporal convolution, and $G_{in}(\mathbf{x}, t; \mathbf{p}_\perp)$ is a ‘Green’s function’ or, more precisely, receiver-side response to an impulsive quasi-plane wave incident from below which is characterized, for example, by horizontal slowness \mathbf{p}_\perp . Index n denotes the incident wave polarization and will be omitted (or, rather, implicitly assumed) in the discussions that follow; however it is important to acknowledge, in particular, in dealing with incident S wavefields. Note that eqn [1] is a farfield approximation that ignores finite source directivity. Early applications of receiver functions (e.g., Phinney, 1964; Langston, 1979) implicitly approximated $S(t)$ on a teleseismic P recording by the vertical component of motion, $u_z(t)$. In the following sections, we will describe procedures whereby this approximation can be improved leading to more accurate estimates of the Green’s function. We begin by discussing means by which incident and scattered wave energy can be more effectively separated on different components. We will then proceed to review the minimum phase nature of teleseismic wavefields that will allow us to simplify characterization and removal of the source. Our focus throughout this analysis will be on teleseismic P but reference to teleseismic S is made toward the end of the section.

1.07.3.1 Modal Decomposition

The combination of transmission geometry, precritical incidence, and modest material property gradients within the crust and upper mantle generally results in the incident wave arrival (i.e., teleseismic P) being the most energetic feature on a seismogram windowed to exclude other principal phases, usually by at least an order of magnitude. **Figure 3** demonstrates this property with synthetic seismograms for P wavefield incident upon an idealized, layer-over-a-half-space crustal model. Because the incident wavefield comprises a single mode type, that is either P or S , it is useful to decompose the observed wavefield into separate modes in order to aid in source deconvolution and characterization of the scattered wavefield. In early studies, ‘modal decomposition’ was crudely accomplished through the identification of the vertical/radial components of displacement with dominantly P/S energy, respectively. A better isolation of energy into modes can be achieved in a number of ways. In principle, one could isolate P and S waves exactly in laterally

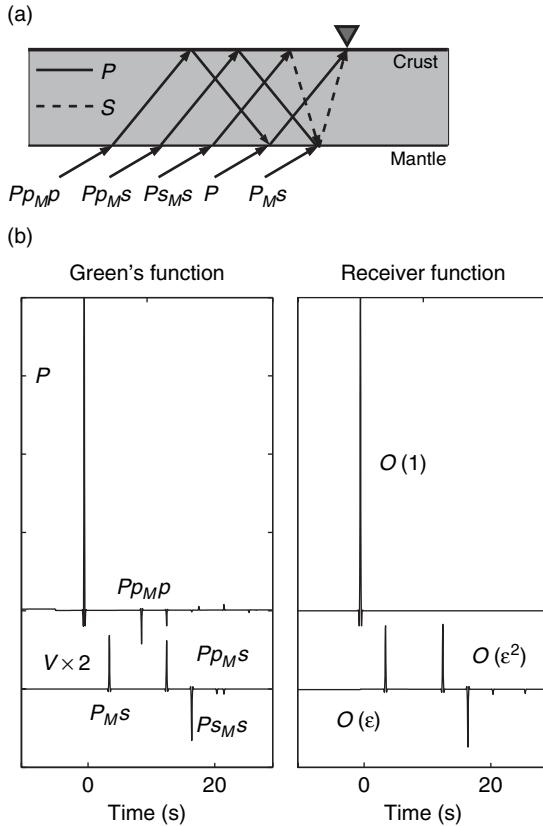


Figure 3 Synthetic seismograms for a layer-over-a-half-space crustal model. (a) Ray paths of largest amplitude phases (P_M^s , Pp_{MP} , Pp_{MS} , Ps_{MS}) scattered crustal phases from the crust–mantle boundary resulting from an incident P wavefield (P wave legs, solid; S wave legs, dashed). See **Figure 4** for examples of these phases on observed seismograms. (b) Left panel shows Green’s function P and (SV) seismograms with phases labeled and right panel comprises the corresponding time series in the receiver-function approximation. Note that the direct P arrival dominates the Green’s function and that the receiver function is a leading-order approximation to the Green’s function correct to $O(1)$ on the P component and to $O(\epsilon)$ on the SV component where $\epsilon \ll 1$ measures the amplitude of the first-order scattered field relative to the incident wave.

heterogeneous, isotropic media by identifying the respective modes as the curl- and divergence-free components of displacement. The density of recording instrumentation is rarely, if ever, sufficient, however, to accurately estimate the necessary spatial derivatives. As a practical alternative and as justified in Section 1.07.2, we may assume that the incident wavefield is dominated by a single horizontal slowness $p = |\mathbf{p}_\perp|$. By further assuming that near-surface P and S velocities α and β are known, an approximate, 1-D, up-going wavefield separation can be

used to isolate P and S modes (Kennett, 1991; Bostock, 1998; Reading *et al.*, 2003), specifically,

$$\begin{pmatrix} P \\ V \\ H \end{pmatrix} = \begin{pmatrix} \frac{p\beta^2}{\alpha} & 0 & \frac{\beta^2 p^2 - 1/2}{\alpha q_\alpha} \\ \frac{1/2 - \beta^2 p^2}{\beta^2 q_\beta} & 0 & p\beta \\ 0 & 1/2 & 0 \end{pmatrix} \begin{pmatrix} u_r \\ u_t \\ u_z \end{pmatrix} \quad [2]$$

where P, V, H are estimates of the upgoing P, SV , and SH component seismograms; u_r, u_t, u_z are the radial, transverse, and vertical displacement seismograms; and q_α, q_β , and p are the vertical P , vertical S , and horizontal components of slowness at the surface. The modal field $[P, V, H]^T$, deconvolved of source and transformed back to upgoing (Cartesian) displacement $[\hat{u}_r, \hat{u}_t, \hat{u}_z]^T$ as

$$\begin{pmatrix} \hat{u}_r \\ \hat{u}_t \\ \hat{u}_z \end{pmatrix} = \begin{pmatrix} \alpha p & \beta q_\beta & 0 \\ 0 & 0 & 1 \\ \alpha q_\alpha & -\beta p & 0 \end{pmatrix} \begin{pmatrix} P \\ V \\ H \end{pmatrix} \quad [3]$$

(versus the original displacement field $[u_r, u_t, u_z]^T$ that contains both up- and down-going waves), is generally the quantity that will be required in the inverse-scattering analysis of subsequent sections. Note that the near-surface velocities α and β can be determined from the data (assuming known slowness) from measurements of first-motion amplitudes on seismograms representing individual, incident P and S waves (Helmberger, 1968; Bostock and Rondenay, 1999) or, equivalently, from the zero-lag amplitudes of radial/vertical receiver functions (Ammon, 1991).

An alternative approach involves rotation of the particle displacement field to a coordinate system where maximum energy is transferred to a single component. The angle of rotation can be determined by diagonalizing the displacement covariance matrix \mathbf{C} (Vinnik, 1977) defined as

$$\mathbf{C} = \begin{pmatrix} \int_{t_1}^{t_2} dt u_r^2(t) & \int_{t_1}^{t_2} dt u_r(t) u_z(t) \\ \int_{t_1}^{t_2} dt u_r(t) u_z(t) & \int_{t_1}^{t_2} dt u_z^2(t) \end{pmatrix} \quad [4]$$

where $[t_1, t_2]$ is a time window that encompasses the energy associated with the primary phase. The latter approach fails to acknowledge the presence of the free surface (and more specifically, the generation of down-going waves therefrom) but may be used where the incident slowness is unknown or the wavefield is distorted by strong, laterally heterogeneous

structure. A more detailed comparison of the two approaches is made by [Svennsgen and Jacobsen \(2004\)](#).

1.07.3.2 Receiver Functions and the Property of Minimum Phase

Once modal decomposition has been accomplished, we shall (either implicitly or explicitly) draw upon an important property of teleseismic body wavefields to remove the effects of the source, namely that the underlying Green's function component in the incident mode (i.e., the P component of teleseismic P) is minimum phase. To provide intuitive justification for the minimum-phase assertion, we consider the seismograms in [Figure 3\(b\)](#) and note that the incident P wave at $t=0$ clearly dominates other arrivals in amplitude. In particular, let us normalize the amplitude of this arrival to unity, such that the amplitudes of the first-order scattered phases (i.e., those phases that have reflected/converted once from heterogeneity, not including the free surface) are of order ϵ . Because material property contrasts are small and scattering interactions occur at near-normal incidence, we have in general that $\epsilon \ll 1$. Multiply scattered wavefields (i.e., two or more reflection/conversion interactions with subsurface heterogeneity) attenuate as ϵ^n where n is the order of scattering and can be safely neglected in most applications. Accordingly, we may characterize the modal component of the Green's function in the incident mode as $G^P(t) \sim \delta(t) + s(t)$, where $\delta(t)$ is the delta-function direct arrival and $s(t)$ represents the scattered field and is $O(\epsilon)$ in amplitude. Following [Claerbout \(1976\)](#), we shall examine the properties of

the $G^P(t)$ in the frequency domain, that is $G^P(\omega)$. As shown in [Figure 4](#), the delta function makes a purely real contribution to the spectrum that is constant, say 1, for all frequencies. Moreover, if the amplitude spectrum of $s(t)$, that is, $s(\omega)$, is less than 1 for all frequencies, we note that it is impossible for the phase of $G^P(\omega) = 1 + s(\omega)$ to wrap around the origin. This scenario thus constitutes a sufficient condition for $G^P(t)$ to be minimum phase. If a signal is minimum phase, it is by definition that signal, among all signals sharing the same amplitude spectrum, which possesses maximum possible energy concentrated near its onset ([Robinson and Treitel, 1980](#)). [Bostock \(2004\)](#) provides a more detailed justification and examination of the conditions under which the minimum-phase assumption is likely to apply to teleseismic wavefields (see also [Sherwood and Trrorey, 1965](#); [Li and Nabelek, 1999](#)). We note at this juncture that an effective modal decomposition, as outlined in the previous section, is important in this regard as it improves the likelihood that the estimated P component impulse response is minimum phase by ensuring that the delta function $\delta(t)$ in the definition of $G^P(t)$ is of maximum possible amplitude relative to the scattered waves $s(t)$.

The minimum-phase property is important in at least two respects. First, it implies that energy is strongly concentrated at early times within the time series. In particular, the P -component, teleseismic P Green's function is to leading order $O(1)$ a delta function. Consequently, an observed P -component seismogram can be taken to be an estimate of the earthquake source time function that is accurate to leading order. Moreover, deconvolution of the corresponding S -component with the P -component will

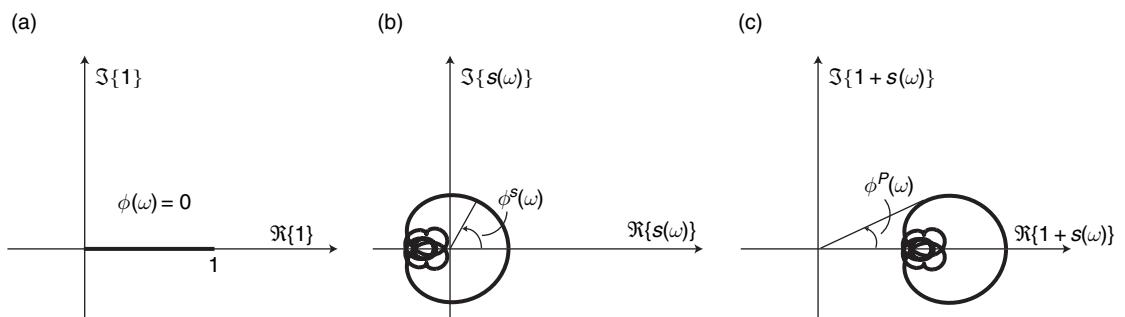


Figure 4 Frequency domain description of $G^P(t) = \delta(t) + s(t)$. (a) Direct wave. The direct wave is represented by a delta function at time 0 and is thus pure real, constant (amplitude 1) with phase $\phi(\omega) = 0$ for all frequencies ω . (b) Scattered waves. The scattered wave spectrum $s(\omega)$ is characterized by an amplitude spectrum $|s(\omega)| < 1$ and a more general phase spectrum $\phi^s(\omega)$. (c) $G^P(\omega)$. The total spectrum is characterized by a real component that is positive for all ω thereby ensuring that $G^P(t)$ is minimum phase ([Claerbout, 1976](#)).

result in an estimate of the S -component Green's function that is correct to leading order, that is, $O(\epsilon)$, since the S -component of teleseismic P comprises only scattered (converted) waves. The foregoing argument provides justification for the validity of the classic receiver function as a leading-order estimate of the S -component of the teleseismic P Green's function. Indeed, interpretation of the receiver function as a series of discretely scattered arrivals from subsurface discontinuities relies intrinsically on this observation. In situations where the minimum phase assumption is questionable, as for example at regional distances where several incident arrivals with comparable magnitudes and different slownesses originate from triplication at transition zone discontinuities (cf. Park and Levin, 2001), interpretation must proceed with caution. In such cases, the receiver function (i.e., spectral ratio of different modal components) can no longer be considered as good an approximation to the Green's function, although it may still possess utility as a source-independent transfer function.

A second point of importance is that the minimum-phase property affords insight into how more accurate estimates of the Earth's true Green's function can be recovered. Improved knowledge of the P -component Green's function is particularly desirable because this component is a simple delta function (i.e., the direct wave) within the receiver function approximation. That is, it contains no information on pure P (i.e., P -to- P) scattering whatsoever. The P -to- P scattering mode is important because it alone provides constraints on short-wavelength variations in subsurface compressional moduli (e.g., P impedance, P velocity, bulk modulus). Conversions and pure S reflections, in contrast, have first-order sensitivity only to shear properties (e.g., S impedance, S velocity; see, e.g., Aki and Richards, 2002). Numerous authors (e.g., Clayton and Wiggins, 1976; Paulssen *et al.*, 1993; Revenaugh, 1995; Bostock and Sacchi, 1997; Bostock and Rondenay, 1999; Li and Nabelek, 1999; Zhu and Kanamori, 2000; Langston and Hammer, 2001) have exploited the minimum-phase property within a multichannel context to procure better estimates of the teleseismic P Green's function. In these studies, P -component time series from a number of stations recording the same earthquake are time-normalized and averaged in some fashion to approximate the source. Weaker ($O(\epsilon)$ in amplitude) scattered wave contributions at different stations are assumed to be incoherent in time and thus sum destructively,

whereas the incident wave, $O(1)$ in amplitude and fixed at time 0 on all traces, adds constructively to produce a scaled estimate of the true source time function. The teleseismic P Green's function is then recovered by deconvolving this source estimate from both P - and S -component seismograms recorded at all stations. The main drawback to this approach is that the signal from structure that exhibits little or no lateral variation (e.g., the continental Moho in many instances) is identified with the source and, consequently, is not represented in the deconvolved Green's function estimates. An alternative to this approach that also relies on the minimum-phase property but does not suffer from this last shortcoming is described below.

1.07.3.3 Improved Teleseismic P Green's Functions

The minimum phase property implies that knowledge of the P -component amplitude spectrum alone is sufficient to define the time domain function, since its phase, ϕ^P , is simply related to amplitude A^P through (e.g., Claerbout 1976)

$$\phi^P(\omega) = \mathcal{H}\{\log(A^P)\} \quad [5]$$

In fact, the phase of all the three components of motion (or, more specifically, upgoing P , SV , and SH), as well as the source, need not be considered until their respective amplitude spectra have been recovered. As explained by Baig *et al.* (2005) and Mercier *et al.* (2006), estimation of, for example, the source amplitude spectrum can be accomplished by considering the cross-spectrum of two seismograms sharing that source. As an example, consider two components P and SV of the same three-component recording represented in the frequency domain as $P(\omega)$ and $V(\omega)$. Their cross-spectrum can be written as

$$P(\omega)V^*(\omega) = |S(\omega)|^2 |G^P(\omega)| |G^V(\omega)| e^{i(\phi^P - \phi^V)} \quad [6]$$

where $|G^P(\omega)|$, $|G^V(\omega)|$, and $|S(\omega)|$ are amplitude spectra of the Green's function components and the source, respectively, and asterisk denotes complex conjugate. Note that the source enters the cross-spectrum as a common convolutional element and that, accordingly, it does not contribute to the cross-spectrum phase, $\phi^P - \phi^V$. We can say, therefore, that the source makes a zero-phase contribution to the cross-spectrum $P(\omega)V^*(\omega)$. There are several algorithms that can, in principle, be utilized to isolate the

zero-phase component of a signal (Hayes *et al.*, 1980) and thus to form an estimate of $|S(\omega)|$ under the assumption that the cross-spectrum of the two Green's function components, that is, $G^P(\omega)G^{V*}(\omega)$, contains no zero-phase component. Moreover, by appealing to causality and a model of propagation that includes a dominantly 1-D lower mantle, the duration of the two components $P(t)$ and $V(t)$ in the time domain will determine the maximum depth to which scattered energy is mapped to the Green's function cross-spectrum. All scattered signals generated in advance of this depth will either arrive outside the recording interval (in the case of conversions), or be mapped to $|S(\omega)|$ (in the case of same mode interactions). The latter result is a beneficial consequence for studies of receiver-side structure.

The procedures for zero-phase signal extraction tend, unfortunately, to be highly sensitive to noise, and Baig *et al.* (2005) discuss modifications based on spectral smoothing that tend to improve recovery on synthetic examples. Nonetheless, it is advantageous, when possible, to further improve upon estimates by making use of multichannel measurements. Even a single, three-component seismogram will afford three independent estimates of a common source, and when multiple stations and events are available this number can increase dramatically. Consider, for example, a data set comprising \mathcal{J} stations recording I three-component seismograms. By casting the

convolution relation in the log-spectral domain such that a single recording representing source i and impulse response j is represented as, for example,

$$\log(|P_{ij}(\omega)|) = \log(|S_i(\omega)|) + \left(|G_j^P(\omega)| \right) \quad [7]$$

we may generate a large linear system of equations (see Andrews, 1986) that includes $3I\mathcal{J}$ equations in $I+3\mathcal{J}$ unknowns. This system, when augmented with equations that include source estimates $|S_i(\omega)| \approx |\tilde{S}_i(\omega)|$ determined as outlined above, becomes highly redundant and can be solved via least squares to recover the improved amplitude spectra $|G_j^P(\omega)|$, $|G_j^V(\omega)|$, $|G_j^H(\omega)|$, and $|S_i(\omega)|$. The phase of $G_j^P(\omega)$ is readily determined directly through eqn [5], whereas the phase of the two remaining quantities can be recovered through a slightly more involved procedure described by Mercier *et al.* (2006). An example showing teleseismic P Green's function estimates as a function of horizontal slowness for station HYB at Hyderabad, India, is shown in Figure 5. The P image clearly reveals the pure P -surface Moho reflection that cannot be recovered through conventional receiver function analysis.

The approach outlined in this section can in principle be applied to P phases other than teleseismic P (e.g., PP and PKP), provided that these recordings are free of other primary phases. We consider its relevance and application to S phases below.

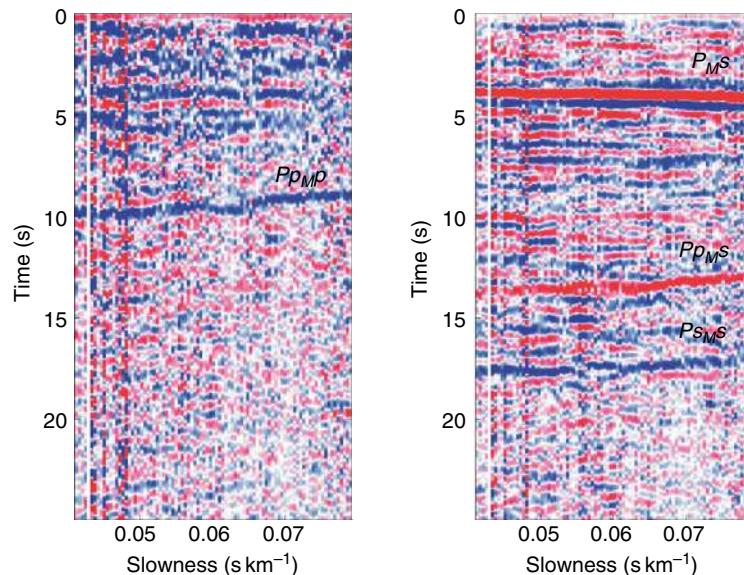


Figure 5 Teleseismic P and SV Green's function estimates for station HYB, India, as a function of horizontal slowness $\sqrt{\rho_\alpha \rho_\alpha'}$. Note the clear definition of the main first-order scattered phases from the continental Moho on both components, as defined in Figure 3.

1.07.3.4 Teleseismic S Green's Functions

There are two principal complications that arise when seeking to extend the approach of the previous section to *S* phases, both of which concern the applicability of the minimum-phase assumption. The first complication is primarily theoretical in nature and is easily qualified. The second issue pertains to the polarization of *S* waves and poses more practical difficulty. We discuss each in turn.

We have already alluded to the increased tendency for multiply interfering phases (e.g., teleseismic *S*, *ScS*, *SKS*) within the teleseismic *S* wavefield in some circumstances, but will assume that these complications have been dealt with and that our observations represent a single, direct phase with known slowness. Strictly speaking, the *S* component of the impulse response (i.e., the *S* component of the teleseismic *S* Green's function) cannot be minimum phase in the presence of heterogeneity owing to the generation of acausal, for example, *S*-to-*P*-to-*S* scattering interactions that arrive as *S* waves in advance of the incident *S* wavefield. These early arrivals are, however, of order $O(\epsilon^2)$ in amplitude and so can be ignored within the single scattering formulations that dominate inversion practice (see Sections 1.07.4 and 1.07.5).

The next issue, then, is to determine to which component of *S* the minimum phase assumption should apply. In 1-D, isotropic (or transversely isotropic) media, this question is easily addressed since *P/SV* and *SH* interactions are decoupled and the minimum-phase assumption can be made independently for both the *SV* and *SH* components of motion. A number of earlier studies (Båth and Stefansson, 1966; Jordan and Frazer, 1975; Sacks *et al.*, 1979; Faber and Müller, 1980; Baumgardt and Alexander, 1984; Bock, 1991) have avoided source deconvolution by employing deep focus events to examine *SV*-to-*P* conversions. More recently, teleseismic *SV* Green's/receiver functions have been generated in a manner directly analogous to teleseismic *P* by simply interchanging the roles of the *P* and *SV* components (e.g., Li *et al.*, 2004; Kumar *et al.*, 2005; Vinnik *et al.*, 2005) or by using teleseismic *P* as a source estimate (Zhou *et al.*, 2000). Considerably less attention has been paid to *SH* due to the lack of conversions in isotropic, 1-D media, although multichannel stacking has been used in at least one study to recover *SH* reflections from dipping structures (Li, 1996).

In more realistic circumstances, particularly those involving azimuthal anisotropy, we recognize, however, that *S* waves with different polarizations will couple such that the impulse response becomes

a more complex function of the incident *S* polarization (Farra *et al.*, 1991). Our objective in this class of study is thus to extract an azimuth- and polarization-dependent impulse response (Farra and Vinnik, 2000; Frederiksen and Bostock, 2000). Because (quasi-) *S* modes propagate at different velocities in anisotropic media, situations will frequently arise where at least one component of *S* motion recorded at the surface is decidedly nonminimum phase.

To address this issue, we write the up-going wavefield (which contains both direct and scattered wave contributions) recorded at the surface $[P, V, H]^T$ in terms of a purely *S* wave field $[0, V_0, H_0]^T$ incident at the base of laterally homogeneous, generally anisotropic, receiver-side stratification,

$$\begin{pmatrix} P \\ V \\ H \end{pmatrix} = \begin{pmatrix} U^{PP} & U^{PV} & U^{PH} \\ U^{VP} & U^{VV} & U^{VH} \\ U^{HP} & U^{HV} & U^{HH} \end{pmatrix} \begin{pmatrix} 0 \\ V_0 \\ H_0 \end{pmatrix} \quad [8]$$

where the various elements of the transmission matrix for upgoing waves $\mathbf{U} = \mathbf{U}(\omega, \mathbf{p}_\perp)$ are functions of frequency and horizontal slowness p_α , $\alpha = 1, 2$. Note that the matrix \mathbf{U} can be related to the transmission matrix \mathbf{T}_U for upward incidence in the absence of a free surface as $\mathbf{U} = (\mathbf{I} - \mathbf{R}_D \tilde{\mathbf{R}})^{-1} \mathbf{T}_U$ (Kennett, 1983), where the effects of reverberation are expressed through the free-surface reflection matrix $\tilde{\mathbf{R}}$ and reflection matrix \mathbf{R}_D for the stratification in the absence of free surface. We will further assume that the incident wave-field $[0, V_0, H_0]^T$ is linearly polarized as would be the case for a simple, for example, double-couple, point source within an isotropic source-side structure. Upon arrival at the surface, the *V*, *H* components can combine to produce an elliptically polarized wavefield characterized by low eccentricity that is the manifestation of shear-wave splitting (e.g., Vinnik *et al.*, 1989; Silver and Chan, 1991). This observation indicates that the elements U^{HV} and U^{VH} can be comparable in magnitude to the diagonal elements of \mathbf{U} for structures representing the real Earth.

An obvious way to proceed is thus to follow standard practice for shear-wave splitting analysis and search for the combination of fast-polarization direction and delay time that most nearly corrects for shear-wave splitting to produce a linearly polarized estimate of V_0 , H_0 . Although this downward continuation (i.e., simulation of \mathbf{U}^{-1}) is only approximate in that internal reverberations/reflections are neglected, our main concern is with the dominant, incident *S* arrival. In particular, the component of the

resulting time series in the polarization direction, say s_0 , will then be minimum phase under the condition that the incident wave has been reduced to a single impulse on one component and is more energetic than all remaining signals. Accordingly, the source can be removed following the approach taken in Section 1.07.3.3 for P waves. Once the source is removed, we may reverse the downward continuation (including errors therein) by applying the forward splitting operator to produce the corresponding source-deconvolved surface wavefield $[P, V, H]^T$. To create the Green's function, it remains to distinguish between the impulse responses produced by individual V_0, H_0 . We may exploit multichannel measurements taken at the same horizontal slowness $\mathbf{p}_\perp = [p_1, p_2]$ (i.e., seismograms representing different source mechanisms but the same geographical source–receiver combinations) to this end, by taking appropriate linear combinations of the deconvolved $[P, V, H]^T$ as dictated by independent values of s_0 .

The approach outlined above may break down where source-side anisotropy has contributed to splitting or where a single fast-polarization direction and delay time do not adequately characterize the transmission response. This latter situation may arise where multiple, strongly anisotropic layers exist. In these cases, a single measured s_0 may not accurately represent the polarization state of the wavefield incident on receiver-side heterogeneity (e.g., Silver and Savage, 1994). Farra and Vinnik (2000) describe an alternate procedure, also using multichannel measurements, for computing the S-receiver function by deconvolving the P -component with the projection of the S wave in the direction of strongest polarization. The interpretation of this quantity faces the same restrictions identified above and is based on a linearization which limits allowable relative magnitudes of off-diagonal elements in \mathbf{U} .

1.07.3.5 Deconvolution, Stacking, and Array Processing

Our focus throughout the majority of this section has been to establish the physical basis for the classical receiver function and extensions that allow us to recover a more fundamental quantity, namely the Green's function, which is required in the inverse scattering approaches to be described in Sections 1.07.4.3 and 1.07.5. In so doing, we have paid little attention to a significant body of work that has been devoted to a more general topic of signal processing as applied to teleseismic wavefields, specifically, deconvolution. For

the most part, this work is concerned with estimating a transfer function (i.e., either receiver function or Green's function) such that the effect of noise is mitigated, usually under the assumption that the source wavelet is perfectly known. We provide, below, a brief overview of deconvolution applications to receiver-side scattering of teleseismic wavefields.

Among the first attempts to extract an impulse response from teleseismic body waves, Ulrych and co-workers (Ulrych, 1971; Ulrych *et al.*, 1972) employed filtering in the cepstral domain to separate source from structural signal. The cepstrum of a signal is computed by inverse Fourier transformation of the logarithm of its Fourier transform. It and [7] are therefore termed homomorphic decompositions since they transform the convolutional operation to an additive one (see, e.g., Oppenheim and Schafer, 1975). The difficulty in applying such homomorphic decompositions to non-zero-phase signals (versus autocorrelations) resides in the necessity for phase unwrapping, which effectively renders the approach intractable for many practical purposes. This shortcoming was noted by Clayton and Wiggins (1976), who proposed an alternative ‘water-level’ method that has subsequently found widespread use. The receiver function $R(t)$ is thereby computed as

$$R(t) = \mathcal{F}^{-1} \left\{ \frac{P^*(\omega)S(\omega)}{\max(P^*(\omega)P(\omega), cP_{\max}^*P_{\max})} \right\} \quad [9]$$

where $\mathcal{F}^{-1}\{\}$ denotes inverse Fourier transformation, P_{\max} is the spectral value for which $P(\omega)$ achieves maximum absolute value, and c is a user-specified water-level parameter that regularizes the deconvolution by damping contributions at frequencies where signal levels are low and thus more likely to be corrupted by noise. Note that when $c=0$, eqn [9] reduces to simple spectral division, whereas large values of c produce a receiver function that is a scaled cross-correlation of the P and S components. In the latter case, the P -component acts as a matched filter (Kind and Vinnik, 1988). Variations on this same theme include the standard damped least-squares deconvolution solution

$$R(t) = \mathcal{F}^{-1} \left\{ \frac{P^*(\omega)S(\omega)}{P^*(\omega)P(\omega) + \delta} \right\} \quad [10]$$

where δ is a constant Tichonov regularization parameter determined by standard (e.g., L-curve, generalized cross-validation (Golub *et al.*, 1979)) means, and Wiener deconvolution (e.g., Press *et al.*, 1992) where δ in [10] becomes frequency dependent

and proportional to the pre-event noise spectrum. When multichannel measurements representing the same $R(t)$ are available, it is advisable to compute a simultaneous estimate (Gurrola *et al.*, 1995) as

$$R(t) = \mathcal{F}^{-1} \left\{ \frac{\sum_i P_i^*(\omega) S_i(\omega)}{\sum_i P_i^*(\omega) P_i(\omega) + \delta} \right\} \quad [11]$$

rather than stacking individual estimates computed by, for example, [10], because only one value of δ needs to be chosen and that value is likely to be small since different seismograms will, in general, exhibit spectra with different signal-to-noise characteristics. Park and Levin (2000) advocate using multi-taper spectral estimates (Thomson, 1982) to help stabilize receiver-function deconvolution, where the individual multichannel recordings within the sums in [11] are replaced by the tapered spectral estimates for a single seismogram.

While quadratic misfit and model norms are being considered, Parseval's theorem ensures that results of deconvolution in the time domain and frequency domain will be equivalent, and it is therefore expedient to perform computations in the frequency domain to take advantage of the fast Fourier transform. Time domain deconvolution may be desirable, however, where time-domain-specific regularization of $R(t)$ such as sparseness is required (Gurrola *et al.*, 1995; Ligorria and Ammon, 1999).

In addition to deconvolution, nonlinear stacking and array-processing methods are often used to improve signal-to-noise levels on teleseismic body-wave recordings and, in particular, for emphasizing discrete, weak arrivals. Popular nonlinear stacking techniques include the Nth root stack (Muirhead and Datt, 1976) and the phase-weighted stack (Schimmel and Paulsen, 1997); Kennett (2000) discusses the application of these approaches to multicomponent teleseismic wavefields. In the next two sections, we examine the multichannel processing of scattered teleseismic wavefields in the context of structural inversion for which (weighted but linear) stacking enters naturally through surface integration. For a summary of more general array-processing techniques applied to teleseismic wavefields, the reader is referred to Rost and Thomas (2002).

1.07.4 1-D Inversion

The use of single-station data in early receiver function studies forced practitioners to focus attention on

delineation of strictly 1-D structures. In fact, this practice is still commonplace today because, in many circumstances, the target discontinuities are expected to be locally horizontal or to vary slowly in lateral coordinates. Thus, for example, in studies of the continental crust (e.g., Owens *et al.*, 1984; Zandt and Ammon, 1995) and transition-zone discontinuities (e.g., Vinnik, 1977; Kind and Vinnik, 1988; Chevrot *et al.*, 1999), the 1-D analysis has proved to be quite adequate and has yielded valuable information on the characteristics of these structures in different tectonic regimes. The more recent documentation of near-horizontal, anisotropic discontinuities within the continental lithosphere (Bostock, 1997, 1998; Levin and Park, 1997, 1998; Saul *et al.*, 2000; Asencio *et al.*, 2003; Leidig and Zandt, 2003) has opened new avenues for study with regard to both inverse modeling and complementary new information that anisotropy can potentially deliver on subsurface structures and dynamics.

Methods employed to invert receiver functions for 1-D variations in material properties can be classified into three categories: optimization based on least squares, Monte Carlo methods, and inverse scattering. We discuss each category in turn, but pay special attention to the last method because it is most closely tied to the physics of scattering and provides formal justification for the ‘delay-and-sum’ and ‘squeezing-and-stretching’ approaches that have dominated 1-D studies of lithospheric and upper-mantle discontinuities to date.

1.07.4.1 Least-Squares Optimization

Optimization by least squares is the most widely used and generic method for solving geophysical inverse problems (Menke, 1984; Parker, 1994). It is less expensive than Monte Carlo inversion and, in the context of teleseismic body waveforms, makes less stringent demands on data than inverse-scattering methods. More specifically to the latter point, data insufficiency (in the form, say, of limited frequency and/or slowness content) can be readily compensated for through model regularization and there is no formal requirement that data be supplied in the form of Green’s functions. This means that model matching by least-squares techniques can be directly undertaken using transfer functions, for example, the receiver function, without concern for the proximity of this quantity to the true Green’s function. All that

is required is a means of performing receiver-function forward modeling.

Implementation is straightforward; see, for example, Ammon *et al.* (1990) for a more detailed account. A receiver function or series of receiver functions strung end to end and represented in either the time or frequency domains is assembled within a vector \mathbf{d} , with individual elements d_i . For consistency with later notation, we shall define \mathbf{c} to be a vector containing the elasticity and densities of a sequence of horizontal layers bounded by a free surface above and half-space below, thereby representing a 1-D Earth model. The forward modeling operator is represented by a (nonlinear) functional \mathcal{D} that operates on \mathbf{c} to produce synthetic data, that is,

$$\mathbf{d} = \mathcal{D}\{\mathbf{c}\} \quad [12]$$

In the 1-D context, both exact layer-matrix methods (Haskell, 1962; Kennett, 1983; Ammon *et al.*, 1990; Kosarev *et al.*, 1993; Kind *et al.*, 1995) and approximate ray methods (e.g., Langston, 1977; Owens *et al.*, 1984) are feasible means of representing \mathcal{D} . Ray methods are more economical in time domain implementations where only a limited number of low-order scattering interactions are to be modeled, whereas layer matrix methods provide a complete representation wherein economies may be gained by restricting computation to the range of frequencies and slowness that characterize the data.

Nonlinearity is addressed in the inverse problem by expanding the receiver-function vector as a Taylor series about a starting model \mathbf{c}_0 , such that

$$d_i = \mathcal{D}_i(\mathbf{c}) = \mathcal{D}_i\{\mathbf{c}_0\} + \frac{\partial \mathcal{D}_i}{\partial c_j}\{\mathbf{c}_0\} \Delta c_j + O(||\Delta \mathbf{c}||^2) \quad [13]$$

Rearranging [13], discarding nonlinear terms, and writing in matrix form yields

$$\mathbf{W} \Delta \mathbf{c} = \mathbf{f} \quad [14]$$

where the data residual vector is $\mathbf{f} = \mathbf{d} - \mathcal{D}(\mathbf{c}_0)$, and the elements of the sensitivity matrix \mathbf{N} are defined by $W_{ij} = (\partial \mathcal{D}_i / \partial c_j)$. Randall (1989) describes a particularly economical means to compute W_{ij} for receiver-function inversions that exploits Kennett's (1983) reflection/transmission layer matrix formalism. Alternatively, this quantity can be determined numerically. Since receiver functions are sensitive primarily to short-wavelength structure, \mathbf{c}_0 is generally taken to represent a slowly varying

velocity model on which the unknown short-wavelength perturbation $\Delta \mathbf{c}$ is superposed.

Solution of the linear system [14] can be accomplished in a number of ways, although minimization of the quadratic norm of \mathbf{f} leading to solution of the normal equations is the standard approach. Depending on the form of model parametrization (e.g., layer thicknesses), the system in [14] may be rank deficient in which case regularization via, for example, damping can be implemented. Further accommodation of nonlinearity can, in principle, be accomplished by Newton iteration on [13].

1.07.4.2 Monte Carlo Inversion

The advent of high-performance computing and the relatively few model parameters that characterize 1-D problems have led to the investigation of Monte Carlo methods for performing receiver-function inversions. These methods require only a forward modeling engine without need for calculation of derivatives (i.e., W_{ij}), since the sole criterion for model selection is an arbitrary measure of fit. They hold the distinct advantage over least-squares optimization that they are global in nature and less apt to identify incorrect, local misfit minima as solutions. Although the number of unknowns is relatively small, a purely random sampling of the model space is still computationally demanding and, at best, inefficient. Consequently, preference has been given to ‘directed search’ algorithms that exploit information from past computations to guide future sampling. Two examples of directed-search algorithms that have been applied to receiver function inversion are the genetic algorithm (Goldberg, 1989; Shibutani *et al.*, 1996; Clitheroe *et al.*, 2000; Lawrence and Wiens, 2004) and the recently introduced nearest-neighbor algorithm (Sambridge, 1999a; Frederiksen *et al.*, 2004; Lucente *et al.*, 2005; Nicholson *et al.*, 2005). Both algorithms begin with a population of models generated through an initial (uniform or random) sampling of model space. Genetic algorithms employ an evolutionary analogy wherein model parameters are encoded within binary strings or ‘chromosomes’. The model population is allowed to evolve through iterations (or ‘generations’) by stochastic selection of models based on goodness of fit, by recombination of models (through chromosomal splicing), and by random ‘mutation’. The natural neighborhood algorithm employs an adaptive Voronoi cellular network to drive the parameter search, where each successive iteration randomly samples the model space within cells occupied by the

fittest models of the previous iteration. The algorithm thereby focuses increasingly on regions in model space that produce models which come closer to satisfying the data. Another important advantage of these directed-search approaches lies in the output of model populations that afford the opportunity for either qualitative or quantitative (Sambridge, 1999b) appraisal of the model space.

1.07.4.3 Born Inversion and Classic (Delay-and-Sum) Studies

Unlike the two methods just described, inverse-scattering approaches to the receiver-function inversion problem rely fundamentally on an explicit description of the scattering process. Accordingly, the starting point is the Lippman–Schwinger equation which we shall write in the frequency domain as (see Hudson and Heritage, 1981)

$$\Delta u_n(\mathbf{x}', \omega) = \int_V d\mathbf{x} (-\Delta c_{ijkl}(\mathbf{x}) \partial_k u_l(\mathbf{x}, \omega) \\ \times \partial_j G_{in}^0(\mathbf{x}, \mathbf{x}', \omega) + \Delta \rho(\mathbf{x}) \omega^2 u_i(\mathbf{x}, \omega) \\ \times G_{in}^0(\mathbf{x}, \mathbf{x}', \omega)) \quad [15]$$

This equation is cast in terms of field quantities and perturbations in material properties whose support is the volume V . The material properties of the medium are described by the stiffness tensor c_{ijkl} and density ρ through

$$c_{ijkl}(\mathbf{x}) = c_{ijkl}^0(\mathbf{x}) + \Delta c_{ijkl}(\mathbf{x}), \rho(\mathbf{x}) = \rho^0(\mathbf{x}) + \Delta \rho(\mathbf{x}) \quad [16]$$

where quantities with superscript zero denote those of a background reference medium and the ‘ Δ ’ quantities are perturbations. Although not strictly required at this stage, we shall assume that short-wavelength heterogeneity is represented within $\Delta c_{ijkl}(\mathbf{x})$, $\Delta \rho(\mathbf{x})$ and ascribe the smoothly varying component of the material property perturbations to $c_{ijkl}^0(\mathbf{x})$, $\rho^0(\mathbf{x})$. The total wavefield u_i is defined as

$$u_i(\mathbf{x}, \omega) = u_i^0(\mathbf{x}, \omega) + \Delta u_i(\mathbf{x}, \omega) \quad [17]$$

where $u_i^0(\mathbf{x}, \omega)$ is the incident (or ‘reference’) wavefield, created by a source with $\delta(t)$ time dependence, that would propagate independently in a medium with properties $c_{ijkl}^0(\mathbf{x})$, $\rho^0(\mathbf{x})$. Note that this definition is consistent with our earlier designation of the incident wavefield as a primary phase such as teleseismic P or S propagating through a smoothly varying mantle. The scattered (or ‘perturbed’) wavefield $\Delta u_i(\mathbf{x}, \omega)$ arises through the interaction of $u_i^0(\mathbf{x}, \omega)$ with short-wave-length structure $\Delta c_{ijkl}(\mathbf{x})$, $\Delta \rho(\mathbf{x})$. We will assume that

an accurate representation of $\Delta u_i(\mathbf{x}', \omega)$ has been secured using methods described in Section 1.07.3, where $\mathbf{x}' = [x'_1, x'_2, 0]^T$ shall be taken in this and the following sections to parameterize the Earth’s surface. The quantity $G_{in}^0(\mathbf{x}, \mathbf{x}', \omega)$ represents the Green’s function for the reference medium and will be determined analytically. We now make the customary ‘single-scattering’ or ‘Born’ approximation by assuming that $\Delta u_i(\mathbf{x})$ is small relative to $u_i^0(\mathbf{x}, \omega)$ such that we may rewrite [15] as

$$\Delta u_n(\mathbf{x}', \omega) \approx \int_V d\mathbf{x} (-\Delta c_{ijkl}(\mathbf{x}) \partial_k u_l^0(\mathbf{x}, \omega) \partial_j \\ \times G_{in}^0(\mathbf{x}, \mathbf{x}', \omega) + \Delta \rho(\mathbf{x}) \omega^2 u_i^0(\mathbf{x}, \omega) \\ \times G_{in}^0(\mathbf{x}, \mathbf{x}', \omega)) \quad [18]$$

(see section 5 in Chapter 1.04 for an account of the Born approximation in an acoustic context). Note that this step is analogous to the linearization of [13], where the forward modeling operator (or, more specifically, $\mathcal{D}_i\{\mathbf{c}\} - \mathcal{D}_i\{\{\mathbf{c}_0\}\}$) is given by [15].

To set the problem in a form that is appropriate for plane-wave propagation in a 1-D Earth, we recognize that plane waves (or, more precisely, wavefields with constant horizontal slowness p_α , $\alpha = 1, 2$) propagate independently in media exhibiting strictly vertical variations in material properties, that is, $\Delta c_{ijkl}(x_3)$, $\Delta \rho(x_3)$. Since propagation takes place in the reference medium, we will make use of plane wave, model expansions for $u_i^0(\mathbf{x}, \omega)$ and $G_{in}^0(\mathbf{x}, \mathbf{x}', \omega)$ that also employ the high-frequency or Wentzel, Kramers, Brillouin, and Jeffreys (WKBJ) approximation. Following Bostock (2003) (and correcting an error in equation (32) therein), we write

$$u_i^0(\mathbf{x}, \omega) = \sum_r A^r(x_3) s_i^r(x_3) e^{i\omega(\tau^r(x_3) + p_\alpha x_\alpha)} \quad [19]$$

$$G_{in}^0(\mathbf{x}, \mathbf{x}', \omega) = \sum_s \frac{-is_n^s(0)s_i^s(x_3)}{2\omega\sqrt{\rho^0(0)\rho^0(x_3)|U_3^s(0)||U_3^s(x_3)|}} e^{i\omega(\tau^s(x_3, 0) + p_\alpha(x'_\alpha - x_\alpha))} \quad [20]$$

where the subscript α follows the repeated index summation convention, the superscripts r and s index the incident and scattered wave modes (that is P , SV , SH , or their analogs in anisotropic media), s_i^r and s_n^s are corresponding depth-dependent, unit polarization vectors, $A^r(x_3)$ is the source amplitude, $U_3^r(x_3)$ and $U_3^s(x_3)$ are the vertical components of group velocity, and $\tau^r(x_3)$ and $\tau^s(x_3)$ are delay times of the incident and scattered modes, respectively.

The modal expansion allows us to isolate and describe individual scattering interactions; for

example, we set $A^r(x_3) = 1/\sqrt{\rho(x_3)|U_3^r(x_3)|}$ for direct P -to- S scattering (say, $r=1$, $s=2$), and the corresponding delay-time functions are written as

$$\begin{aligned}\tau^r(x_3) &= - \int_0^{x_3} dy_3 p_3^P(y_3) \\ \tau^r(x_3, 0) &= \int_0^{x_3} dy_3 p_3^S(y_3)\end{aligned}\quad [21]$$

where $p_3^P(y_3)$ and $p_3^S(y_3)$ are the vertical components of phase slowness for P and S waves, respectively. The choice of $\tau^r(x_3)$ above implies a time normalization where the direct P wave ($r=1$) arrives at the Earth's surface at $\tau^r=0$ consistent with the output of most deconvolution schemes described in Sections 1.07.3.3–1.07.3.5. Back-scattering that involves free-surface reflection of the up-going incident wave can be described through an alternate set of amplitude and delay-time functions. For example, pure P mode reflection (say, $r=2$, $s=1$) is characterized by $A^r(x_3) = \tilde{R}^{PP}/\sqrt{\rho(x_3)|U_3^r(x_3)|}$, where \tilde{R}^{PP} is the free surface P -to- P reflection coefficient and the delay-time functions are

$$\begin{aligned}\tau^r(x_3) &= \int_0^{x_3} dy_3 p_3^P(y_3) \\ \tau^r(x_3, 0) &= \int_0^{x_3} dy_3 p_3^P(y_3)\end{aligned}\quad [22]$$

(note that for an anisotropic reference medium that does not exhibit mirror symmetry, we would have to employ different values for up- and down-going phase slowness in eqns [22]).

Inserting expressions [19] and [20] into [18] and retaining only the leading-order terms in frequency, one obtains

$$\begin{aligned}\Delta u_n(\mathbf{x}', \omega) &\approx \sum_r \sum_s s_n^s(0) e^{i\omega p_\alpha x'_\alpha} \\ &\times \int dx_3 B^{rs}(x_3, \omega) \\ &\times \left[\frac{\Delta c_{ijkl}}{\rho^0} s_i^r p_k^r s_i^s p_j^s + \frac{\Delta \rho}{\rho^0} s_i^r s_i^s \right] \\ &\times e^{i\omega(\tau^r(x_3) + \tau^r(x_3, 0))}\end{aligned}\quad [23]$$

where, for brevity, we have suppressed the x_3 dependence in all quantities within the square brackets, p_i^r and p_i^s are the phase slowness vectors of the incident and scattered wavefields at depth x_3 , and the factor $B^{rs}(x_3, \omega)$ is defined by

$$B^{rs}(x_3, \omega) = - \frac{i\omega A^r(x_3) \sqrt{\rho^0(x_3)}}{2\sqrt{\rho^0(0)|U_3^r(0)||U_3^r(x_3)|}} \quad [24]$$

Equation [23] represents an asymptotic, linearized relation between the scattered field $\Delta u_n(0)$ measured

at the Earth's surface and the unknown material parameters $\Delta c_{ijkl}(x_3)$, $\Delta \rho(x_3)$. To simplify the extraction of these parameters, we follow Burridge *et al.* (1998) and define a fourth-rank tensor a_{ijkl} that possesses the same symmetry properties as Δc_{ijkl} and satisfies

$$\frac{\Delta c_{ijkl}}{V^r V^s} a_{ijkl} = \Delta c_{ijkl} s_i^r p_k^r s_i^s p_j^s \quad [25]$$

where V^r and V^s represent the phase velocities of incident and scattered modes, respectively, averaged over all angles, that is,

$$\begin{aligned}a_{ijkl} &= \frac{V^r V^s}{8} \left[\left(s_i^s p_j^s + s_j^s p_i^s \right) \left(s_k^r p_l^r + s_l^r p_k^r \right) \right. \\ &\quad \left. + \left(s_k^s p_l^s + s_l^s p_k^s \right) \left(s_i^r p_j^r + s_j^r p_i^r \right) \right]\end{aligned}\quad [26]$$

This construction allows us to adopt a more compact notation and rewrite eqn [23] as

$$\begin{aligned}\Delta u_n(0, \omega) &\approx \sum_r \sum_s s_n^s(0) e^{i\omega p_\alpha x'_\alpha} \\ &\times \int dx_3 B^{rs}(x_3, \omega) \\ &\times e^{i\omega(\tau^r(x_3) + \tau^r(x_3, 0))} \mathbf{w}^\text{T} \Delta \mathbf{c}\end{aligned}\quad [27]$$

The radiation patterns and material property perturbations are now contained within 22-element vectors, \mathbf{w} and $\Delta \mathbf{c}$, whose entries correspond to the 21 independent elastic constants and density as

$$\mathbf{w} \leftrightarrow [a_{ijkl}, s_i^s s_i^r], \quad \Delta \mathbf{c} \leftrightarrow \left[\frac{\Delta c_{ijkl}}{\rho^0}, \frac{\Delta \rho}{\rho^0} \right] \quad [28]$$

Equation [27] takes a form that may be readily discretized and solved for $\Delta \mathbf{c}$. It is common practice, however, to consider the contribution of each scattering mode $\Delta u_i^{rs}(0, \omega)$ (where $\Delta u_i(\mathbf{x}, \omega) = \sum_r \sum_s \Delta u_i^{rs}(\mathbf{x}, \omega)$), independently. Assuming that the individual $\Delta u_i^{rs}(\mathbf{x}, \omega)$ can be approximately isolated (see Section 1.07.6 for further discussion on this assumption), we define the scalar, time domain quantity

$$\begin{aligned}f^{rs}(t) &= \mathcal{F}^{-1} \left\{ \frac{\Delta u_i^{rs}(0, \omega) s_i^s(0) e^{-i\omega p_\alpha x'_\alpha}}{B^{rs}(x_3, \omega)} \right\} \\ &\times [p_3^s(x_3) + p_3^r(x_3)]\end{aligned}\quad [29]$$

where \mathcal{F}^{-1} denotes, as before, inverse Fourier transformation. Note that contraction with $s_i^s(0)$ rotates the data into the anticipated polarization direction of the up-going scattered mode s . In practice, we accomplish this operation using eqn [2], since the effect of the free surface on polarization of the

recorded wavefield is not explicitly accounted for in the treatment of this section. Multiplication by $e^{-i\omega p_0 x_0}$ in eqn [29] removes the time shift associated with horizontal coordinate such that the arrival of the direct wave (P for $r=1$, S for $r=2, 3$) corresponds to time 0. By inserting the expression for $\Delta u_i^{rs}(0, \omega)$ in [27] into [29] and evaluating both integrals in ω and x_3 (with the aid of Leibniz' rule), we arrive at

$$f^{rs}(t = \tau^r(x_3) + \tau^s(x_3, 0)) = \mathbf{w}^T(x_3) \Delta \mathbf{c}(x_3) \quad [30]$$

that is, a one-to-one relation between material property perturbations at depth x_3 and the value of $f^{rs}(t)$ evaluated at time $t = \tau^r(x_3) + \tau^s(x_3, 0)$. If we now assemble a large number of data $u_i^{rs}(0, \omega)$ representing different scattering interactions r, s and geometries (as reflected in p_i^r, p_i^s), normalize as in [29], and arrange these data in a column vector \mathbf{f} , a system of equations can be written as

$$\mathbf{f}(x_3) = \mathbf{W}(x_3) \Delta \mathbf{c}(x_3) \quad [31]$$

where the transposed vectors \mathbf{w}^T form the rows of \mathbf{W} . The solution to this system of equations amounts to an amplitude-versus-slowness analysis of the scattering coefficient corresponding to depth x_3 . Normalization of the up-going wavefield by $[p_3^r + p_3^s]/B^r(x_3, \omega)$ in [29] ensures that it is appropriately scaled and filtered such that the perturbation profile $\Delta \mathbf{c}(x_3)$ is, within the single-scattering and high-frequency approximations, correctly recovered. If, instead, we wish to recover a profile of reflectivity (or, more precisely, the singular function of the discontinuity surface scaled to the amplitude of the perturbation; e.g., Bleistein, 1987), we must remove the factor $i\omega$ in [24]. In so doing, solution of [31] is seen to be simply a weighted diffraction stack of the data along move-out curves corresponding to the various scattering interactions r, s within the 1-D reference medium.

In the case of isotropic stratification, the reflectivity inversion affords a formal justification for the delay-and-sum approach introduced by Vinnik in his analysis of P -to- S conversions from the mantle transition zone in 1977, and adopted subsequently by numerous workers (e.g., Kind and Vinnik, 1988; Stammmer *et al.*, 1992; Bostock, 1996; Chevrot *et al.*, 1999; Dueker and Sheehan, 1998). In these studies, data are stacked along move-out curves computed for a 1-D Earth model and corresponding to a range of trial depths, to produce a map of stacked amplitude as a function of delay time and discontinuity depth. If amplitude extrema are observed at delay times

consistent with a trial depth, a discontinuity is tentatively identified (see Figure 6). An approximate reflectivity (or ‘convertibility’) depth profile can be recovered by slicing through the amplitude map along the appropriate traveltime curve (see Figure 7). This empirical approach is equivalent to migrating (or ‘squeezing and stretching’) traces to depth prior to stacking (e.g., Gilbert *et al.*, 2003; Fee and Dueker, 2004). It handles kinematics in precisely the same way as solution of [31]. The dynamics are of secondary importance and their neglect in empirical migration approaches only means that the stacked waveforms are less directly interpretable in terms of

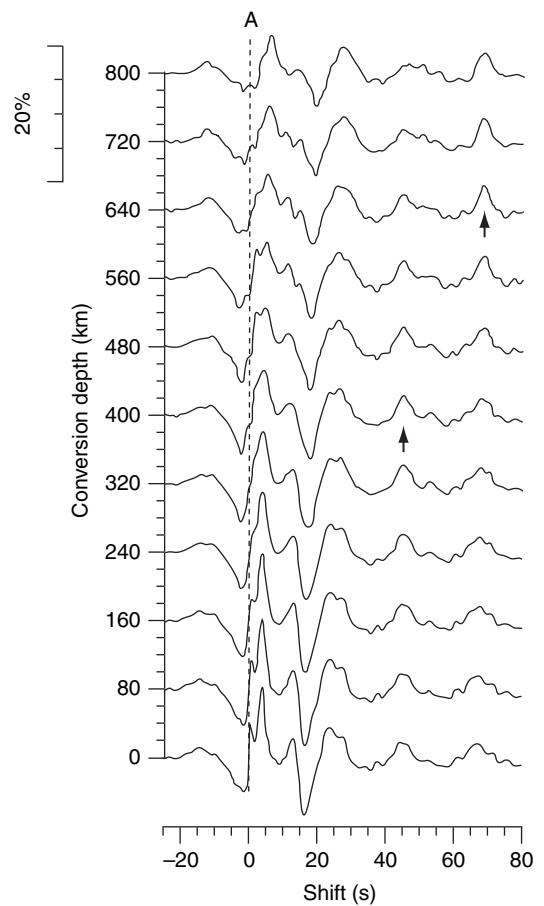


Figure 6 Delayed and summed SV components of source-normalized teleseismic P recorded at the Gräfenberg array, Germany, from Kind and Vinnik (1988). Each trace represents a sum of seismograms, from events at different epicentral distances, delayed by a time interval corresponding to the expected arrival of a conversion from a given trial depth. Arrows point to amplitude maxima that occur for trial depths of 400 and 640 km and are therefore consistent with the origin of P -to- S conversions from the two major transition zone discontinuities.

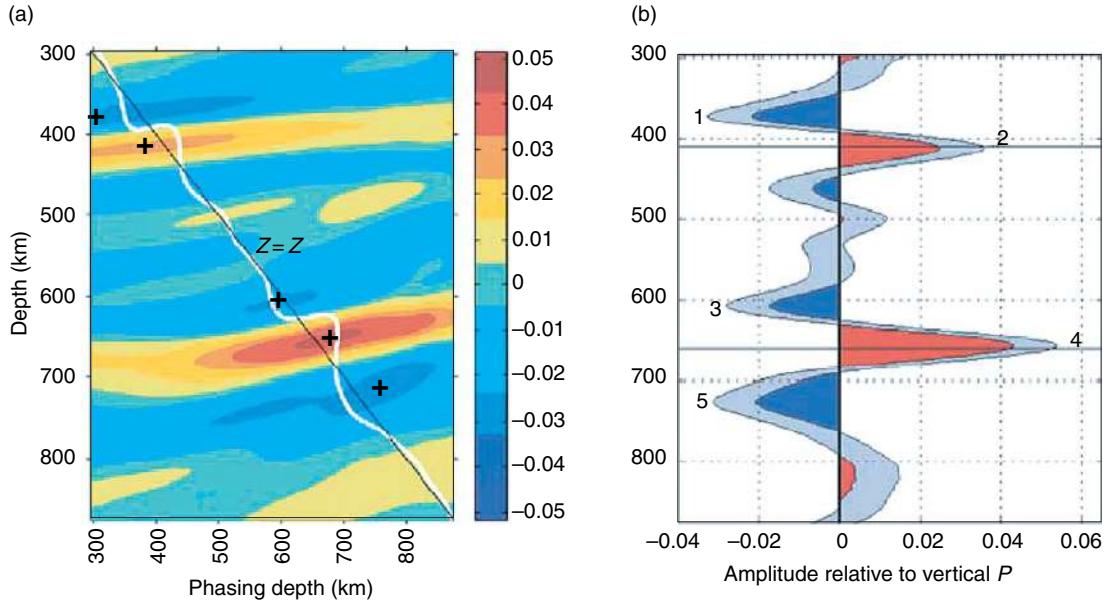


Figure 7 One-dimensional migration from Fee and Dueker (2004). (a) Left panel shows amplitude map that results from stacking data along move-out curves corresponding to a range of conversion (phasing) depths. The vertical depth axis is proportional to time as mapped through a 1-D velocity model. (b) Right panel plots a slice through the 45° line shown in (a) and accomplishes a 1-D migrated depth profile of ‘convertibility’ below the Yellowstone hotspot.

perturbations in Earth’s material properties. The creation of an amplitude map has the advantage of permitting visual assessment of the veracity of a potential structural signal on the basis of whether its amplitude maximum occurs at or near the expected travelttime. In this sense, Vinnik’s approach has much in common with the velocity spectrum stack developed for exploration applications, and also applied to teleseismic wavefields by Gurrola *et al.* (1994). In this case, amplitude maxima of delayed and stacked waveforms are used to provide improved velocity (or in the case of teleseismic P -to- S conversions, Poisson’s ratio) model information for structural imaging. The more recent work of Zhu and Kanamori (2000; following Zandt and Ammon, 1995) follows along this same theme but involves stacking of multiple scattering modes r , s (consistent with the formulation in [31]) to more tightly constrain depth of Moho and crustal Poisson’s ratio.

Previous empirical studies of anisotropic stratification using scattered teleseismic wavefields can also be related to the linearized, 1-D inverse-scattering solution in [31]. In this case, the Earth’s response is not simply a function of epicentral distance (or, more precisely, the magnitude of horizontal slowness, $|\mathbf{p}_\perp| = \sqrt{p_\alpha p_\alpha}$) but also depends on back azimuth. Various authors (Kosarev *et al.*, 1984; Vinnik and

Montagner, 1996; Bostock, 1997, 1998; Levin and Park, 1997, 1998; Farra *et al.*, 1991; Farra and Vinnik, 2000; Wilson *et al.*, 2004) have noted that the back-azimuthal response of a stratified medium exhibiting different classes of anisotropic symmetry and orientation can be represented in simple trigonometric terms. Consequently, several schemes involving stacking with trigonometric weights have been proposed to investigate anisotropic stratigraphy. These schemes can be related to [31] by noting that the linear system, for general $\Delta\mathbf{c}$ and typical teleseismic data sets, will be rank deficient. It will thus be necessary to solve [31] pseudo-inversely (e.g., Bank and Bostock, 2003) with singular value decomposition being an obvious and tractable choice. These latter authors noted that only five to seven parameter combinations of $\Delta\mathbf{c}$ are likely to be resolvable using teleseismic P and that these parameter combinations can be identified with different harmonic orders of response in back azimuth θ , notably 1θ , 2θ , and 3θ . Recovery of $\Delta\mathbf{c}$ through [31] thus amounts once more to a weighted diffraction stack and holds the advantage over more empirical schemes that the full data sensitivity to the elastic stiffness tensor is exploited without having to resort to simplified *a priori* model representations (e.g., hexagonal symmetry).

Finally, we remark that, in practice, it is difficult to isolate the individual scattering mode contributions, $\Delta u^{\text{rx}}(\mathbf{x}, \omega)$, and in general we will approximate these quantities by the observed wavefield, $\Delta u(\mathbf{x}, \omega)$, for each scattering mode interaction. The main drawback with this course of action is that we interpret a superposition of several different styles of scattering interaction r, s as that due to a single one with the result that artificial structures appear in the solution. The most commonplace example is the misinterpretation of the free-surface-reflected, back-scattered waves from shallow interfaces for direct, forward scattered conversions from deeper interfaces. This shortcoming afflicts both 1-D and multidimensional analyses of teleseismic waves and we shall comment on a potential remedy in Section 1.07.6.

1.07.5 Multidimensional Inversion

There are several approaches to consider in moving from 1-D to multiple dimensions. The first and simplest strategy is to assume that the Earth structure varies slowly in the horizontal coordinates, in which case a 2-D or 3-D profile can be assembled as a cascade of local 1-D models determined from individual, adjacent stations (e.g., Kumar *et al.*, 2005). If stations are sufficiently closely spaced that the (1-D) ray paths of scattered phases intersect below the profile, it becomes advantageous to consider a 2-D model where scattered energy on seismogram is mapped to common conversion points (CCPs)

assuming a locally horizontal, plane-layer scattering geometry (e.g., Dueker and Sheehan, 1998; Kosarev *et al.*, 1999; Simmons and Gurrola, 2000; Ferris *et al.*, 2003; Zandt *et al.*, 2004; Niu *et al.*, 2005; Schulte-Pelkum *et al.*, 2005). The so-called CCP stack is commonly employed because it places less stringent requirements on spatial sampling than formal multi-dimensional inversion schemes but, of course, its accuracy deteriorates as departures from one-dimensionalality become more pronounced (Figure 8).

Unlike the strictly 1-D case, the multidimensional inverse problem has not lent itself so readily to treatment using optimization via least squares because of the large increase in model parameters and concomitant rise in computations. It is likely, however, that in the near future computational tractability will become less of a concern. Indeed, two recent studies (Frederiksen and Revenaugh, 2004; Wilson and Aster, 2005) have explored different least-squares formulations for solving multidimensional receiver-function inversions, a trend which is likely to continue. Much of the essential machinery for this task has already been developed for exploration applications; we note, in particular, the work of Tarantola (1984, 1986).

The 1-D, high-frequency, Born-approximate inverse solution described in the previous section can, however, be efficiently extended to multiple dimensions so as to be computationally tractable on standard desktop computers. In this extension, there are no conceptual difficulties in dealing with 2-D versus 3-D problems, although there are practical

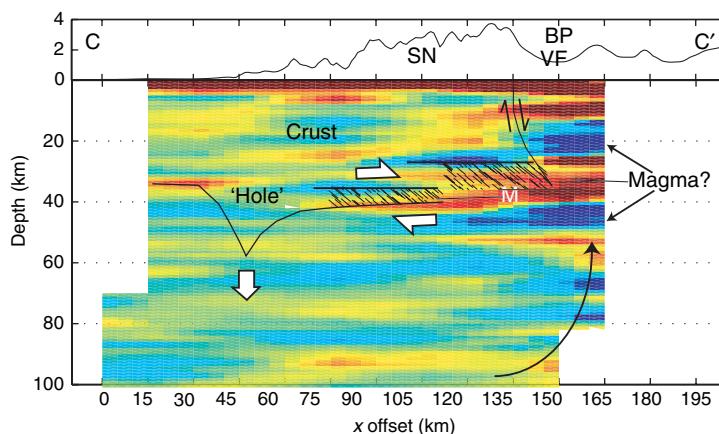


Figure 8 CCP image below the Sierra Nevada, California, from Zandt *et al.* (2004). Image was formed by back-projecting receiver-function amplitude along ray path for a 1-D Earth model for a given recording, then summing results for all available (source-receiver pair) recordings. In this image, presence of a Moho hole near 50 km offset is interpreted to manifest the development of lithospheric detachment.

limitations, in particular, for data from temporary, portable deployments. More specifically, it is difficult at the current time to assemble numbers of instruments sufficient to ensure that the teleseismic wavefield is sampled with sufficient areal density (and aperture) to avoid aliasing most of its useful spectrum. Two approaches may be taken to remedy this difficulty. One may seek to interpolate data to a finer spacing over an areal grid followed by 3-D inversion (Neal and Pavlis, 1999, 2001; Poppeliers and Pavlis, 2003a, 2003b), or follow the lead of early exploration practice and adopt a 2-D inverse strategy under the assumption that a dominant geologic strike direction can be identified (Bostock *et al.*, 2001). In the following, we summarize the approach taken by the latter authors which can be regarded as a 2-D, isotropic extension of the 1-D treatment outlined in Section 1.07.4.3.

We begin with linearized integral equation [18]. In the 1-D case, the invariance of material properties in horizontal coordinates together with the far-field (quasi-planar) nature of the incident wavefield $u_i^0(\mathbf{x}, \omega)$ allowed us to adopt plane-wave expansions for the incident and scattered modes as in [19] and [20]. This choice is effectively equivalent to Fourier-transforming over the horizontal plane. Accordingly, for a 2-D inversion where there is only one coordinate of spatial invariance, say the strike coordinate x_2 , we Fourier-transform over this coordinate. We thereby assume that, for an incident (e.g., planar) wavefield characterized by a single value of slowness p_2 in the strike direction, all resulting scattering interactions will be characterized by this same component of horizontal slowness, and so we may parametrize the wavefields by this variable. Although not required, it will be computationally and practically expedient to assume that the reference medium is both 1-D and isotropic, so that the reference medium description is reduced from $c_{ijk}^0(x_1, x_3)$, $\rho^0(x_1, x_3)$ to, for example, $\alpha^0(x_3)$, $\beta^0(x_3)$, $\rho^0(x_3)$. Consequently, we may adopt the same 1-D form for the incident wavefield $u_i^0(\mathbf{x}, \omega)$, that is, [19], whereas for the Green's function we adopt a form that allows for interaction with 2-D (i.e., line) scatterers,

$$\begin{aligned} G_m^0(\mathbf{x}, 0, \omega) = & \sum_s \frac{1}{\sqrt{-i\omega}} A^s(\mathbf{x}_\perp, \mathbf{x}'_\perp, p_2) \\ & \times e^{i\omega[p_1^s|x_1 - x'_1| - p_2 x_2 + \tau^s(\mathbf{x}_\perp, \mathbf{x}'_\perp)]} \\ & \times s_i^s(\mathbf{x}_\perp) s_n^s(\mathbf{x}'_\perp) \end{aligned} \quad [32]$$

where, as before, $s=1, 2$, and 3 correspond to P , SV , and SH waves, respectively, and the 2-D amplitude functions A^s are defined, for example, for $s=1$ as

$$\begin{aligned} A^s(\mathbf{x}_\perp, \mathbf{x}'_\perp, p_2) = & \frac{1}{4\alpha^0(0)} \\ & \times \sqrt{\frac{2}{\pi\rho^0(x_3)\alpha^0(x_3)\rho^0(0)[\mathcal{J}^P(\mathbf{x}_\perp, \mathbf{x}'_\perp, p_2)]^2\sqrt{1-p_2^2[\alpha^0(0)]^2}}} \end{aligned} \quad [33]$$

with a comparable expression holding for the S modes (i.e., $s=2, 3$). We employ $\mathbf{x}_\perp=(x_1, x_3)$ to represent observation coordinates within the plane of 2-D spatial variations, and evaluate source coordinates (\mathbf{x}'_\perp) along the Earth's surface, that is, $\mathbf{x}'_\perp=(x'_1, 0)$. The traveltimes functions $\tau^s(\mathbf{x}_\perp, \mathbf{x}'_\perp)$ are computed as in [21], but now we recognize that p_1^s is no longer constant but depends on $x_1 - x'_1$. A similar consideration also applies in the definition of the unit polarization vectors $s_n^s(\mathbf{x}_\perp)$. The 2-D geometrical spreading functions $\mathcal{J}^s(\mathbf{x}_\perp, \mathbf{x}'_\perp, p_2) (= \mathcal{J}^P(\mathbf{x}_\perp, \mathbf{x}'_\perp, p_2))$, for $s=1$; see, e.g., Hudson, 1980) depend on the divergence of the rays in the x_1, x_3 plane. Note that we have permitted an oblique component of incidence through dependence on x_2, p_2 which bears important practical implications as it will allow us to employ a full range of earthquake sources that need not align with the 2-D model geometry. If forms [19] and [32] are inserted within the isotropic equivalent of [18], we may construct 2-D, high-frequency, single-scattering, forward modeling equations for various incident/scattering mode combinations r, s of the form

$$\begin{aligned} \Delta u_n(\mathbf{x}'_\perp, p_2, \omega) = & \sum_r \sum_s s_n^s(\mathbf{x}'_\perp) \\ & \times \int d\mathbf{x}_\perp F^{rs}(\mathbf{x}_\perp, \theta) A^r(x_3) \\ & \times A^s(\mathbf{x}_\perp, \mathbf{x}'_\perp, p_2) \\ & \times e^{i\omega(\tau^r(x_3) + \tau^s(\mathbf{x}_\perp, \mathbf{x}'_\perp))} \end{aligned} \quad [34]$$

The 2-D ‘scattering potential’, $F^{rs}(\mathbf{x}_\perp, \theta)$, is derived from contractions of the stiffness tensor (expressed in terms of, e.g., velocities and density) and the local polarization and slowness vectors of the incident and scattered waves. It is expressed as a function of the scattering angle, $\theta = \theta^{rs}(\mathbf{x}_\perp, \mathbf{x}'_\perp)$, between the slowness vectors of these two wavefields (see Figure 9), and the material property perturbations such that for forward P -to- S conversions ($r=1, s=2$)

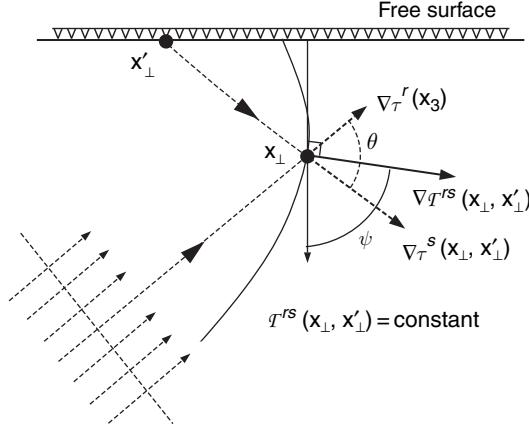


Figure 9 Geometrical quantities relevant to high-frequency, inverse scattering of teleseismic wavefields for 2-D structure. The vector $\nabla\tau^r$ and $\nabla\tau^s$ are the slowness vectors for the incident and scattered waves, respectively, whereas θ is the ‘scattering’ angle between them. The total slowness vector $\nabla\mathcal{T}^{rs} = \nabla\tau^r + \nabla\tau^s$, characterized by angle ψ , plays an important role in controlling spatial resolution within the generalized Radon transform.

$$F^{rs}(\mathbf{x}_\perp, \theta) = \rho^0 \left[\frac{\Delta\beta}{\beta^0} \left(2 \frac{\beta^0}{\alpha^0} \sin 2\theta \right) + \frac{\Delta\rho}{\rho^0} \left(\sin \theta + \frac{\beta^0}{\alpha^0} \sin 2\theta \right) \right] \quad [35]$$

where the dependence of the material property perturbations is, for example, $\Delta\beta = \Delta\beta(\mathbf{x}_\perp)$. Similar relations can be written for other combinations of scattering interaction r, s (see, e.g., Bostock *et al.*, 2001).

The inverse problem can be tackled by applying an inverse Fourier transform to [34], that is,

$$\begin{aligned} \Delta u_n(\mathbf{x}'_\perp, p_2, t) &= \frac{1}{2\pi} \sum_r \sum_s s_n^s(\mathbf{x}'_\perp) \\ &\times \int d\mathbf{x}_\perp F^{rs}(\mathbf{x}_\perp, \theta) \mathcal{A}^r(x_3) \mathcal{A}^s(\mathbf{x}_\perp, \mathbf{x}'_\perp, p_2) \\ &\times \delta(t - \tau^r(x_3) - \tau^s(\mathbf{x}_\perp, \mathbf{x}'_\perp)) \end{aligned} \quad [36]$$

and noting that the result bears a close resemblance to the definition of the 2-D Radon transform $F(\mathbf{n}, t)$ of a function $f(\mathbf{x}_\perp)$ (Deans, 1983; Miller *et al.*, 1987)

$$F(\mathbf{n}, t) = \int d\mathbf{x}_\perp f(\mathbf{x}_\perp) \delta(t - \mathbf{n} \cdot \mathbf{x}_\perp) \quad [37]$$

where \mathbf{n} is a unit vector in the 2-D plane defined by \mathbf{x}_\perp , especially if we restrict attention to a single scattering mode $\Delta u_n^{rs}(\mathbf{x}'_\perp, p_2, t)$. Here, we identify the scattered field $\Delta u_n(\mathbf{x}'_\perp, p_2, t)$ with $F(\mathbf{n}, t)$ and the scattering potential $F^{rs}(\mathbf{x}_\perp, \theta)$ with $f(\mathbf{x}_\perp)$. The

primary differences between the two equations are that the integrand in [36] contains additional factors in the form $\mathcal{A}^r(x_3)\mathcal{A}^s(\mathbf{x}_\perp, \mathbf{x}'_\perp, p_2)$ and that the arguments of the delta function are not straight lines but, rather, isochronal curves along which the sum $\tau^r(x_3) + \tau^s(\mathbf{x}_\perp, \mathbf{x}'_\perp)$ is constant. The correspondence can be made closer still by recognizing that the product of geometrical amplitudes will, in general, be slowly varying and that, in keeping with the asymptotic forms adopted in [19] and [32], the isochronal curves can be approximated locally as planar. We may then draw upon the formal inverse Radon transform (Deans, 1983; Beylkin, 1985; Miller *et al.*, 1987; Beylkin and Burridge, 1990):

$$\begin{aligned} f(\mathbf{x}'_\perp) &= -\frac{1}{4\pi} \int d\mathbf{n} \mathcal{H} \left\{ \frac{\partial}{\partial t} F(\mathbf{n}, t) \right\} \Big|_{t=\mathbf{n} \cdot \mathbf{x}'} \\ &= -\frac{1}{4\pi} \int d\mathbf{n} \int d\mathbf{x}_\perp f(\mathbf{x}) \mathcal{H} \{ \delta'(\mathbf{n} \cdot (\mathbf{x}'_\perp - \mathbf{x}_\perp)) \} \\ &= -\frac{1}{4\pi} \int d\psi \int d\mathbf{x}_\perp f(\mathbf{x}) \mathcal{H} \{ \delta'(\mathbf{n} \cdot (\mathbf{x}'_\perp - \mathbf{x}_\perp)) \} \end{aligned} \quad [38]$$

where ψ is the angle of \mathbf{n} , $\mathcal{H}\{\cdot\}$ denotes Hilbert transform, and $\delta'(x)$ is the derivative of $\delta(x)$, to devise a back-projection operator for the recovery of $F^{rs}(\mathbf{x}_\perp, \theta)$, namely,

$$\begin{aligned} F^{rs}(\mathbf{x}_\perp, \theta) &\approx \frac{1}{4\pi} \int d\psi \frac{|\nabla\mathcal{T}^{rs}|^2}{\sum_n \mathcal{A}_n^{rs} \mathcal{A}_n^{rs}} \\ &\times \sum_n \mathcal{A}_n^{rs} v_n^{rs}(\mathbf{x}'_\perp, p_2, t = \mathcal{T}^{rs}(\mathbf{x}_\perp, \mathbf{x}'_\perp)) \end{aligned} \quad [39]$$

Here we have, for brevity, defined the composite quantities

$$\begin{aligned} \mathcal{T}^{rs}(\mathbf{x}_\perp, \mathbf{x}'_\perp) &= \tau^r(x_3) + \tau^s(\mathbf{x}_\perp, \mathbf{x}'_\perp) \\ \mathcal{A}_n^{rs} &= \mathcal{A}^r(x_3) \mathcal{A}^s(\mathbf{x}_\perp, \mathbf{x}'_\perp, p_2) s_n^s(\mathbf{x}'_\perp) \end{aligned} \quad [40]$$

and have identified $\nabla\mathcal{T}^{rs}(\mathbf{x}_\perp, \mathbf{x}'_\perp)/|\nabla\mathcal{T}^{rs}(\mathbf{x}_\perp, \mathbf{x}'_\perp)|$ with \mathbf{n} . Thus, the integration variable ψ is the angle of $\nabla\mathcal{T}^{rs}(\mathbf{x}_\perp, \mathbf{x}'_\perp)$, that is,

$$\psi = \text{atan} \frac{\partial_3 \mathcal{T}^{rs}(\mathbf{x}_\perp, \mathbf{x}'_\perp)}{\partial_1 \mathcal{T}^{rs}(\mathbf{x}_\perp, \mathbf{x}'_\perp)} \quad [41]$$

and the scattered wavefield is represented through the time series

$$\nu_n^{rs}(\mathbf{x}'_\perp, p_2, t) = \mathcal{F}^{-1} \left\{ \frac{\Delta u_n^{rs}(\mathbf{x}'_\perp, p_2, \omega) - i \text{sgn}(\omega)}{\sqrt{-i\omega}} \right\} \quad [42]$$

The geometrical relationships among the various quantities defined above are illustrated in Figure 9. As for the 1-D case, we have assumed that we are able to separate the recorded wavefield into its individual

scattering mode (r, s) contributions $\Delta u_n^{rs}(\mathbf{x}'_\perp, p_2, \omega)$. From [39], we note that the scattering potential can be approximately recovered as a weighted diffraction stack of filtered data $v_n^{rs}(\mathbf{x}'_\perp, p_2, t)$ over the isochronal traveltime curves. The form of filter $-i \operatorname{sgn}(\omega)/\sqrt{-i\omega}$ applied to the scattered wavefield data in [42] stems from the plane-wave/2-D geometry and ensures that, for example, a step function perturbation is recovered in the case of a discontinuity in material properties. Recovery of $F^{rs}(\mathbf{x}_\perp, \theta)$ is, of course, an intermediate result from which we wish to resolve the individual material property perturbations $\Delta \mathbf{c}(\mathbf{x}_\perp) = [\Delta\alpha/\alpha', \Delta\beta/\beta^0, \Delta\rho/\rho^0]^T$. Exploiting the linear relation in [35], this task is readily accomplished by assembling measurements of $F^{rs}(\mathbf{x}_\perp, \theta)$ for all available scattering interactions at a given model point within a column vector $\mathbf{f}(\mathbf{x}_\perp, \theta)$ and solving the trivial 3×3 system

$$\mathbf{f}(\mathbf{x}_\perp, \theta) = \mathbf{W}(\theta) \Delta \mathbf{c}(\mathbf{x}_\perp) \quad [43]$$

where, as in [31], the row vectors constituting the matrix \mathbf{W} represent radiation patterns for the various scattering mode combinations r, s .

The main computational effort in this approach is expended in computing the weighted diffraction stack in [39]. The appearance of $|\nabla T^{rs}|^2$ as a weight in that equation corresponds to the factor $[p_3^r(x_3) + p_3^s(x_3)]$ in [29] for the 1-D case. It represents the sensitivity of traveltime to scatterer position and, as a product with frequency ω , governs the scale of resolution. For example, back-scattered modes, for which $|\nabla T^{rs}|^2$ is in general large, possess better resolving capability than forward-scattered waves, since a given change in scatterer position has a larger effect on timing of the scattered arrival (see, e.g., Rondenay *et al.*, 2005). The direction of ∇T^{rs} , as quantified by dip angle ψ , controls the degree to which different structural dips can be resolved at a given model point. In contrast, material property resolution depends on the range of scattering angle θ afforded by the data and the different modal scattering sensitivities as represented through the radiation patterns, for example, [35]. Material property resolution may be analyzed through eigenvector decomposition of the matrix $\mathbf{W}^T \mathbf{W}$, for example, Forgues and Lambaré (1992) and Bostock and Rondenay (1999). Since teleseismic data are characterized by a limited range of θ , the simultaneous inversion of different scattering modes r and s affords the best prospects for discrimination of material properties.

In addition to the plane-wave, isotropic, 2-D oblique incidence geometry described above, the generalized

Radon transform treatment of the inverse-scattering problem has also been developed with point sources for acoustic waves (Miller *et al.*, 1987), elastic waves in 3-D isotropic (Beylkin and Burridge, 1990), and anisotropic (Burridge *et al.*, 1998) media. Like the 1-D case, these algorithms can be recast to recover singular functions of discontinuity surfaces (versus Born-approximate perturbations), thereby accomplishing Kirchhoff-approximate inversion (Bleistein, 1987; Beylkin and Burridge, 1990; de Hoop and Bleistein, 1997; Bostock, 2002). In the teleseismic context, generalized Radon transform inversions have been strictly applied in a limited number of studies on subduction zones (Rondenay *et al.*, 2001; Nicholson *et al.*, 2005) and Precambrian mobile belts (Poppeliers and Pavlis, 2003b; Rondenay *et al.*, 2005).

If the weights in [39] are ignored and otherwise normalized seismograms are simply stacked along move-out curves $t = T^{rs}(\mathbf{x}_\perp, \mathbf{x}'_\perp)$, the formal parameter inversion is reduced to migration. Variants include migration via the Kirchhoff scattering integral (French, 1974; Schneider, 1978), which has been applied to receiver (versus Green's) functions with the aim of imaging (rather than inverting for) structure (e.g., Revenaugh, 1995; Sheehan *et al.*, 2000; Kind *et al.*, 2002; Levander *et al.*, 2005; Niu *et al.*, 2005; Wilson *et al.*, 2005). All of the approaches mentioned above can be classified as ‘prestack’ in that they deal directly with the individual Green’s function or receiver function data. Ryberg and Weber (2000) have described a teleseismic analogy to active source ‘poststack’ migration. This procedure involves normalizing teleseismic data to vertical incidence and stacking to produce a reduced data set which can be readily processed using seismic reflection algorithms. Chen *et al.* (2005a) have built upon this poststack framework to develop a wave-equation migration method that back-propagates CCP-stacked receiver functions into structural models, and it has been applied to image the Japanese subduction zones (Chen *et al.*, 2005b).

1.07.6 Beyond the Born Approximation

As argued in Sections 1.07.4 and 1.07.5, the tools of inverse scattering provide a framework for understanding many of the empirical approaches developed and employed over the past four decades to analyze scattered teleseismic wavefields in terms of lithospheric and upper-mantle structure. In addition, the application of

these techniques in recent years to multichannel data sets collected over, for example, plate boundaries, have led to new insights into the structures and dynamics of these complex regions, which would have been difficult to achieve through a less complete analysis. As access to a large number of instruments improves, it is possible that sampling of teleseismic wavefields may begin to approach that in exploration practice, allowing and prompting still more ambitious and complete treatments. We shall conclude this chapter by sketching out a formulation, based on recent theoretical developments in reflection seismology, that would permit a nonlinear treatment of inverse scattering for teleseismic wavefields.

1.07.6.1 Shortcomings of the Born Approximation

Perhaps the most serious shortcomings of the methodologies heretofore described in Sections 1.07.4 and 1.07.5 lie in the linearization or ‘Born approximation’ made in [18]. There are several negative consequences that follow from the Born approximation. First, as is widely appreciated, the reference medium must be sufficiently close to the real Earth to ensure that the phase of the wavefields is accurately represented. If not, images may become seriously distorted, usually through blurring, leading to reduced resolution, and worse, misinterpretation (see, e.g., Yilmaz, 2001). As researchers attempt to exploit higher frequencies in the teleseismic wavefield (up to 10 Hz for teleseismic P generated by deep earthquakes), there will be increased need to improve reference velocity estimates.

A second drawback of the Born approximation is its failure to account for higher-order scattering in the form of multiple reflection/conversion. In reflection seismology, the most serious manifestation of multiple scattering is present in the form of free-surface multiples which are order $O(\epsilon^2)$ in amplitude. In the teleseismic context, the free-surface multiples are still larger ($O(\epsilon)$) due to the transmission geometry, as explained in Section 1.07.3.2, and have presented a major impediment to lithospheric imaging due to the arrival of multiple signals from the Moho during the same time interval that direct conversions from the shallow mantle (say, 100–250 km depth) would be expected. Using formal inversion approaches, the multiples can be accommodated to varying degrees through the simultaneous inclusion of both direct and free-surface reflected waves within the incident wavefield $u_i^0(\mathbf{x}, \omega)$ as in [19]. If, however, as we have

advocated in coming to solutions for [31] and [43], the approximation $\Delta u^{rs}(\mathbf{x}, \omega) \approx \Delta u(\mathbf{x}, \omega)$ is made for each mode combination r,s , this accommodation is incomplete and artificial structures resulting from misidentification of one scattering mode for another will occur (e.g., Shragge *et al.*, 2001). Most studies based on diffraction stacking have implicitly adopted the $\Delta u^{rs}(\mathbf{x}, \omega) \approx \Delta u(\mathbf{x}, \omega)$ assumption for computational expedience. The advantage, as exemplified in the generalized Radon transform approach of the previous section (cf. eqn [43]), is that the matrix $\mathbf{W}^T \mathbf{W}$ is block diagonal in structure, leading to solution of a small (rank equivalent to number of material parameters considered) linear system for each spatial location within the model. If we choose, instead, to include both forward- and back-scattered (multiples) waves simultaneously and avoid the latter approximation, this matrix becomes block-band diagonal and computational expense increases dramatically. This latter approach is feasible using sparse matrix techniques, especially in 2-D, but to our knowledge is yet to be applied.

Notwithstanding the viability of simultaneously including the direct wave and free-surface reflections within the definition of $u_i^0(\mathbf{x}, \omega)$, there is reason to consider a formal decomposition of the observed field, $\Delta u(\mathbf{x}, \omega)$, into individual scattering modes, $\Delta u_i^{rs}(\mathbf{x}, \omega)$. Motivation for this line of thought stems from recent progress in reflection seismology by Weglein and co-workers (Matson, 1997; Weglein *et al.*, 1997; Weglein *et al.*, 2003) and Wapenaar *et al.* (2004). Weglein’s group has demonstrated that a sequential, task-driven approach, which includes isolation and removal of free-surface reflections, results in a better posed, nonlinear treatment of the inverse-scattering problem within the seismic reflection context. Moreover, Wapenaar *et al.* have developed a theoretical framework based on correlational reciprocity (Bojarski, 1983) that allows the transformation of transmission (earthquake) data into reflection data, thereby effectively accomplishing the scattering mode decomposition and allowing, in principle, the inversion of transmission data with reflection algorithms. In the following two subsections, we shall outline these procedures in more detail.

1.07.6.2 The Inverse-Scattering Series

Weglein and co-workers adopt operator-series representations to address both the forward- and inverse-scattering problems. The operator notation is convenient because it is largely independent of geometry and model type, and affords a succinct summary

of the main arguments. For further detail and background, the reader is referred to [Weglein et al. \(2003\)](#).

We begin with the operator form of the Lippman–Schwinger equation [15],

$$\mathcal{U} = \mathcal{G} - \mathcal{G}^0 = \mathcal{G}^0 \mathcal{V} \mathcal{G}$$
 [44]

where we define \mathcal{U} to be the data generation operator, and \mathcal{G} and \mathcal{G}^0 are Green's operators for the true Earth and reference medium, respectively, that act on a given force distribution $f_i(\mathbf{x}, \omega)$ to produce a vector wavefield. For example, in the teleseismic context, the scattered wavefield (cf. [15]) can be written as

$$\begin{aligned} \Delta u_i(\mathbf{x}, \omega) &= \mathcal{U}\{f_i\} \\ &= \mathcal{G}\{f_i\} - \mathcal{G}^0\{f_i\} \\ &= \int dy \left[G_{ij}(\mathbf{x}, \mathbf{y}, \omega) - G_{ij}^0(\mathbf{x}, \mathbf{y}, \omega) \right] f_j(\mathbf{y}, \omega) \end{aligned}$$
 [45]

where, as before, $G_{ij}^0(\mathbf{x}, \mathbf{y}, \omega)$ is the Green's function for the reference medium (e.g., [20] and [32] for laterally homogeneous reference media with 1-D and 2-D source geometries, respectively, in the high-frequency approximation), $G_{ij}(\mathbf{x}, \mathbf{y}, \omega)$ is the unknown Green's function of the true Earth, and f_i then represents the force distribution that gives rise to up-going, planar P or S wavefields in the absence of heterogeneity. The differential operator \mathcal{V} includes the action of the material property perturbations and can be written as

$$\mathcal{V} = \partial_j \Delta c_{ijkl} \partial_k + \Delta \rho \omega^2 \delta_{il}$$
 [46]

Note that [44] implies $\mathcal{G} = \mathcal{G}^0 + \mathcal{G}^0 \mathcal{V} \mathcal{G}$ and so, by successive insertion, we recover the forward-scattering series

$$\mathcal{U} = \mathcal{G}^0 \mathcal{V} \mathcal{G}^0 + \mathcal{G}^0 \mathcal{V} \mathcal{G}^0 \mathcal{V} \mathcal{G}^0 + \mathcal{G}^0 \mathcal{V} \mathcal{G}^0 \mathcal{V} \mathcal{G}^0 \mathcal{V} \mathcal{G}^0 + \dots$$
 [47]

From the right-hand side of eqn [47], we note that \mathcal{G} is not required to solve the forward problem; that is, knowledge of $\mathcal{G}^0\{f_i\}$ is sufficient to recover $\mathcal{U}\{f_i\}$, if \mathcal{V} is given.

The goal of the inverse problem is to isolate the scattering operator \mathcal{V} (and from it Δc_{ijkl} , $\Delta \rho$) from the data generation operator \mathcal{U} as represented by the data $\Delta u_i(\mathbf{x}, \omega)$ in [45] using, again, knowledge of \mathcal{G}^0 alone. The inverse scattering series solution represents \mathcal{V} in series form as

$$\mathcal{V} = \mathcal{V}_1 + \mathcal{V}_2 + \mathcal{V}_3 + \mathcal{V}_4 + \dots$$
 [48]

where the individual terms are organized in orders of the data \mathcal{U} . Inserting [48] within [47] allows one to solve for these terms explicitly. For example, the first three equations are

$$\begin{aligned} \mathcal{U} &= \mathcal{G}^0 \mathcal{V}_1 \mathcal{G}^0 \mathcal{G}^0 + \mathcal{G}^0 \mathcal{V}_1 \mathcal{G}^0 \mathcal{V}_1 \mathcal{G}^0 \mathcal{G}^0 \mathcal{G}^0 \\ 0 &= \mathcal{G}^0 \mathcal{V}_2 \\ &= \mathcal{G}^0 \mathcal{V}_3 \mathcal{G}^0 + \mathcal{G}^0 \mathcal{V}_2 \mathcal{G}^0 \mathcal{V}_1 \mathcal{G}^0 + \mathcal{G}^0 \mathcal{V}_1 \mathcal{G}^0 \mathcal{V}_2 \mathcal{G}^0 \\ &\quad + \mathcal{G}^0 \mathcal{V}_1 \mathcal{G}^0 \mathcal{V}_1 \mathcal{G}^0 \mathcal{V}_1 \mathcal{G}^0 \end{aligned}$$
 [49]

where we have used the fact that \mathcal{U} is, by definition, first order in itself. In principle, these equations can be solved sequentially, first for \mathcal{V}_1 , then for \mathcal{V}_2 , and so on. Note that \mathcal{V}_1 is just the Born-approximate solution to the inverse problem, which may or may not accurately represent the true Earth (i.e., \mathcal{V}) depending on the proximity of \mathcal{G}^0 to \mathcal{G} .

Blind application of the series solution to raw data is marred by poor convergence properties and thus does not afford a practical solution to the inverse-scattering problem. Rather, Weglein *et al.* advocate that a ‘subseries’ approach be taken whereby sets of terms in the inverse series are identified with specific tasks and a sequential application is performed. This sequence of tasks is (1) removal of free-surface multiples, (2) removal of internal multiples, (3) imaging of scatterer location, and (4) material property recovery. It has been noted that tasks (1) and (2) can be effectively performed with absolutely no knowledge of the underlying velocity structure and with excellent convergence properties. Tasks (3) and (4) are the topics of current research and early results show promise ([Weglein et al., 2002](#)).

The relevance of the latter work to the teleseismic problem is twofold. First, it indicates that a sequential treatment which proceeds from multiple removal through material property inversion is likely to be better posed than simultaneous solution. Second, as we sketch out below, it is possible, at least in principle, to transform the teleseismic transmission problem directly into a reflection problem such that the inverse-scattering series, as developed for exploration purposes, is then directly applicable.

1.07.6.3 Transmission to Reflection

Perhaps the most direct way of isolating individual scattering modes $\Delta u_i^{rs}(\mathbf{x}, \omega)$ is to consider reformulating the transmission problem as a reflection problem. Motivation for this concept stems from early work of [Claerbout \(1968\)](#), who demonstrated a relationship between the transmission response of a layered acoustic half-space and its reflection response. For precritical, energy flux-normalized elastic waves in 1-D media, this relation can be written as

$$\mathbf{U}^* \mathbf{U}^T = \mathbf{I} + \tilde{\mathbf{R}} \mathbf{V} + \mathbf{V}^H \tilde{\mathbf{R}}^H \quad [50]$$

where $\mathbf{U} = \mathbf{U}(\omega, \mathbf{p}_\perp)$ is the 3×3 matrix of [8] containing the transmission response for different modes incident upon the base of a stratified half-space bounded above by free surface; $\mathbf{V} = \mathbf{V}(\omega, \mathbf{p}_\perp)$ represents the corresponding reflection response for the same medium to different modes incident from above; $\tilde{\mathbf{R}} = \tilde{\mathbf{R}}(\mathbf{p}_\perp)$ is the free-surface reflection matrix; \mathbf{I} is the identity matrix; and superscript H denotes conjugate transpose. The two geometrical configurations are illustrated in [Figure 10](#).

Recall that complex conjugation in the frequency domain is equivalent to time reversal, and that the inverse Fourier transforms of the elements of \mathbf{U} and \mathbf{V} are causal functions. Accordingly, each element on

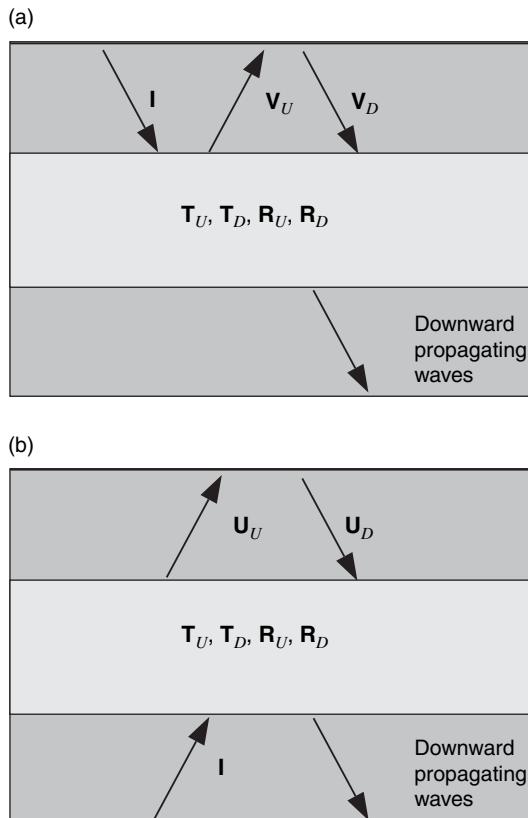


Figure 10 Geometrical definition of quantities relevant to the transformation of transmission wavefields to reflection wavefields. (a) Reflection experiment. An incident wavefield (\mathbf{I}) interacts with stratification from above to produce an up-going wavefield \mathbf{V}_U and a down-going wavefield \mathbf{V}_D at the Earth's free surface. (b) Transmission experiment. In this case, direct wave (\mathbf{I}) is incident on stratification from below and produces up- (\mathbf{U}_U) and down-going (\mathbf{U}_D) wavefields at the free surface.

the left-hand side of [50] represents, in the time domain, a sum of cross-correlations and equates to the sum of a causal function ($\mathcal{F}^{-1}\{\tilde{\mathbf{R}}\mathbf{V}\}$), an acausal function ($\mathcal{F}^{-1}\{\mathbf{V}^H \tilde{\mathbf{R}}^H\}$), and, for diagonal elements, an impulse ($\mathcal{F}^{-1}\{\mathbf{I}\}$) at zero-lag. The time-domain reflection response $\mathcal{F}^{-1}\{\mathbf{V}\}$ can therefore be recovered by applying $\tilde{\mathbf{R}}^{-1}$ to $\mathcal{F}^{-1}\{\mathbf{U}^* \mathbf{U}^T\}$ upon zeroing negative lags, where, as in [2], we have assumed that the near-surface material properties (and hence $\tilde{\mathbf{R}}$) are known. Since the individual elements of $\mathcal{F}^{-1}\{\mathbf{V}\}$ represent the reflection response of the stratified half-space to a separate incident mode, an isolation of different, first-order ($O(\epsilon)$) modal interactions to individual components has therefore been achieved. [Figure 11](#) shows the result of this procedure applied to data from station HYB by [Kumar and Bostock \(2006\)](#) who outline a practical recipe for its implementation.

Note that the effect of the free surface is still included within \mathbf{V} insofar as $O(\epsilon^2)$ and higher-order, free-surface-related multiples are contained therein. The first step of the inverse-scattering series scheme involves removing these multiples. For 1-D, we accomplish this task by writing

$$\mathbf{V} = \mathbf{R}_D (\mathbf{I} - \tilde{\mathbf{R}} \mathbf{R}_D)^{-1} \quad [51]$$

where we have, once more, employed the notation of [Kennett \(1983\)](#) and used \mathbf{R}_D to denote the reflection matrix for the stratification alone (no free surface included). Reorganizing, and solving for \mathbf{R}_D using successive insertion, leads to the series solution

$$\mathbf{R}_D = \mathbf{V} - \tilde{\mathbf{R}} \mathbf{V} + \mathbf{V} \tilde{\mathbf{R}} \mathbf{V} \tilde{\mathbf{R}} - \mathbf{V} \tilde{\mathbf{R}} \mathbf{V} \tilde{\mathbf{R}} \mathbf{V} \tilde{\mathbf{R}} + \dots \quad [52]$$

Subsequent steps, including multiple elimination, spatial imaging, and material property recovery are more involved, and the reader is referred to [Weglein et al. \(2003\)](#) for details and discussion.

The theory describing extension of the transmission-to-reflection transformation to multiple dimensions has recently been developed by [Wapenaar et al. \(2004\)](#) by exploiting correlational and convolutional reciprocity. Accordingly, the 3-D extension to [50] expressed in the spatial (versus slowness) domain becomes

$$\begin{aligned} & \int_z dx \mathbf{U}^*(x'_A, x, \omega) \mathbf{U}^T(x'_B, x, \omega) \\ &= \mathbf{I} \delta(x'_A - x'_B) + \tilde{\mathbf{R}} \mathbf{V}(x'_A, x'_B, \omega) + \mathbf{V}^H(x'_A, x'_B, \omega) \tilde{\mathbf{R}}^H \end{aligned} \quad [53]$$

where, as before, the primed coordinates are located at the free surface, the surface integral over horizontal coordinate x is evaluated at some depth z below

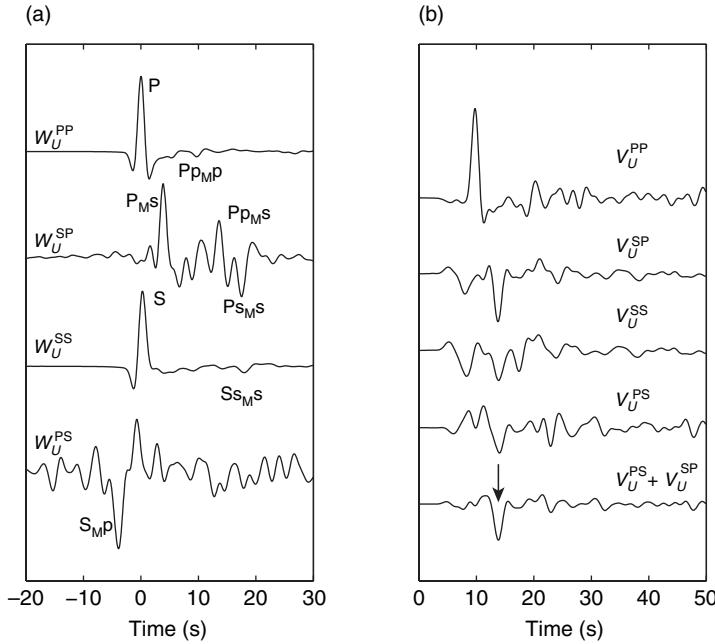


Figure 11 Transmission-to-reflection transformation of data from HYB. (a) Input transmission data. Components W_U^{PP} and W_U^{SP} were computed from telesismic P data shown in [Figure 5](#) over the slowness range $0.04\text{--}0.0575\text{ s km}^{-1}$, whereas components W_U^{PS} and W_U^{SS} were computed from SKS recordings over the same range. (b) Transformed reflection response. Note that bottom trace is computed as sum of $V_U^{PS} + V_U^{SP}$ since these two traces should, by reciprocity, be equivalent. Arrow indicates the reflection conversion from the continental Moho.

the heterogeneity, and the dependencies indicate that, for example, $\mathbf{V}(\mathbf{x}'_A, \mathbf{x}'_B, \omega)$ is the up-going wavefield recorded at surface location \mathbf{x}'_A due to a source at surface location \mathbf{x}'_B , at frequency ω . Similarly, the multidimensional equivalent of [51] can be written as

$$\mathbf{V}(\mathbf{x}'_A, \mathbf{x}'_B, \omega) = \mathbf{R}_D(\mathbf{x}'_A, \mathbf{x}'_B, \omega) + \int d\mathbf{x}' \mathbf{R}_D(\mathbf{x}'_A, \mathbf{x}', \omega) \tilde{\mathbf{R}} \mathbf{V}(\mathbf{x}', \mathbf{x}'_B, \omega) \quad [54]$$

The extension to multiple dimensions thus places greater demands on data by requiring the evaluation of surface integrals within certain depth ranges. It remains to be seen whether these demands can be accommodated through data interpolation/extrapolation in the telesismic context where seismicity is sparse and irregularly distributed.

1.07.7 Conclusions

Over the past few decades, scattered telesismic body waves have contributed greatly to our understanding of crust and mantle structure (*see*, for example, Chapters 1.14, 1.17, 1.20). They possess higher

resolving capability of small-scale structure than other elements of the global seismic wave train and do not suffer from the shallow depth sampling that limits active source seismic surveys. In this chapter, we have provided an overview of methodologies used to extract receiver-side structural information from the scattered telesismic wavefields. These methodologies address two fundamental issues: (1) the isolation of structural signal from earthquake source signature and (2) the translation of structural signals into Earth models. The identification, in early practice, of source-free transfer functions formed by simple ratios of vector component waveforms, has gradually given way in more recent work to better approximations to the true Earth ‘Green’s function’, thereby extending sensitivity to Earth’s material parameters. In like manner, the processing of these structural signals using empirical delay-and-sum approaches has progressed in the last few years to formal inversion where quantitative material property separation is, at least in principle, possible. These technological advances have brought analysis of scattered telesismic waveforms in line with modern reflection seismic signal processing. In fact, as we have attempted to illustrate in the previous section, it

is now possible to contemplate unified reflection/transmission approaches to the inverse-scattering problem. An important future challenge in application to global seismology will be to overcome the sparse sampling imposed by earthquake source distributions and current inventories of instrumentation.

References

- Aki K and Richards PG (2002) *Quantitative Seismology*. Sausalito, CA: University Science Books.
- Ammon CJ (1991) The isolation of receiver effects from teleseismic P waveforms. *Bulletin of the Seismological Society of America* 81: 2504–2510.
- Ammon CJ, Randall GE, and Zandt G (1990) On the nonuniqueness of receiver function inversions. *Journal of Geophysical Research* 95: 15303–15318.
- Andrews DJ (1986) Objective determination of source parameters and similarity of earthquakes of different size. In: Das S, Boatwright J, and Scholz CH (eds.) *Earthquake Source Mechanics*, vol. 37, pp. 259–267. Washington, DC: American Geophysical Union.
- Asencio E, Knapp JH, Owens TJ, and Helffrich G (2003) Mapping fine-scale heterogeneities within the continental mantle lithosphere beneath Scotland: Combining active- and passive-source seismology. *Geology* 31: 477–480.
- Baag CE and Langston CA (1985) Shear-coupled PL. *Geophysical Journal of the Royal Astronomical Society* 80: 363–385.
- Baig AM, Bostock MG, and Mercier J-P (2005) Spectral reconstruction of teleseismic P Green's Functions. *Journal of Geophysical Research* 110, doi:10.1029/2003JB003625.
- Bank C-G and Bostock M (2003) Linearized inverse scattering of teleseismic waves for anisotropic crust and mantle structure. 2: Numerical examples and application to data from Canadian stations. *Journal of Geophysical Research* 108, doi: 10.1029/2002JB001951.
- Báth M and Stefánson R (1966) S-P conversion at the base of the crust. *Annales de Géophysique* 19: 119–130.
- Baumgardt DR and Alexander SS (1984) Structure of the mantle beneath Montana Lasa from analysis of long-period, mode-converted phases. *Bulletin of the Seismological Society of America* 74: 1683–1703.
- Beylkin G (1985) Imaging of discontinuities in the inverse scattering problems by inversion of causal generalized Radon transform. *Journal of Mathematical Physics* 26: 99–108.
- Beylkin G and Burridge R (1990) Linearized inverse scattering problems in acoustics and elasticity. *Wave Motion* 11: 15–52.
- Bleistein N (1987) On the imaging of reflectors in the Earth. *Geophysics* 52: 931–942.
- Bock G (1991) Long-period S to P converted waves and the onset of partial melting beneath Oahu, Hawaii. *Geophysical Research Letters* 18: 869–872.
- Bock G (1994) Multiples as precursors to S, SKS and ScS. *Geophysical Journal International* 119: 421–427.
- Bojarski NN (1983) Generalized reaction principles and reciprocity theorems for the wave equations, and the relationship between the time-advanced and time-retarded fields. *Journal of the Acoustical Society of America* 74: 281–285.
- Bostock MG (1996) Ps conversions from the upper mantle transition zone beneath the Canadian landmass. *Journal of Geophysical Research* 101: 8393–8402.
- Bostock MG (1997) Anisotropic upper mantle stratigraphy and architecture of the Slave craton. *Nature* 390: 392–395.
- Bostock MG (1998) Mantle stratigraphy and evolution of the Slave province. *Journal of Geophysical Research* 103: 21183–21200.
- Bostock MG (2002) Kirchhoff-approximate inversion of teleseismic wavefields. *Geophysical Journal International* 149: 787–795.
- Bostock MG (2003) Linearized inverse scattering of teleseismic waves for anisotropic crust and mantle structure. 1: Theory. *Journal of Geophysical Research* 108, doi:10.1029/2002JB001950.
- Bostock MG (2004) Green's functions, source signatures, and the normalization of teleseismic wave fields. *Journal of Geophysical Research* B03303: doi:10.1029/2003B002783.
- Bostock MG and Rondenay S (1999) Migration of scattered teleseismic body waves. *Geophysical Journal International* 137: 732–746.
- Bostock MG, Rondenay S, and Shrager J (2001) Multiparameter two-dimensional inversion of scattered teleseismic body waves. 1: Theory for oblique incidence. *Journal of Geophysical Research* 106: 30771–30782.
- Bostock M and Sacchi MD (1997) Deconvolution of teleseismic recordings for mantle structure. *Geophysical Journal International* 129: 143–152.
- Burdick LJ and Langston CA (1977) Modeling crustal structure through the use of converted phases in teleseismic body waveforms. *Bulletin of the Seismological Society of America* 67: 677–692.
- Burridge R, de Hoop MV, Miller D, and Spencer C (1998) Multiparameter inversion in anisotropic elastic media. *Geophysical Journal International* 134: 757–777.
- Chen L, Wen L, and Zheng T (2005a) A wave equation migration method for receiver function imaging. 1: Theory. *Journal of Geophysical Research* 110: B11309 (doi:10.1029/2005JB003665).
- Chen L, Wen L, and Zheng T (2005b) A wave equation migration method for receiver function imaging. 2: Application to the Japan subduction zone. *Journal of Geophysical Research* 110: B11310 (doi:10.1029/2005JB003666).
- Chevrot S, Vinnik LP, and Montagner J-P (1999) Global-scale analysis of mantle Ps phases. *Journal of Geophysical Research* 104: 20203–20219.
- Claerbout JF (1968) Synthesis of a layered medium from its acoustic transmission response. *Geophysics* 33: 264–269.
- Claerbout JF (1976) *Fundamentals of Geophysical Data Processing*. New York: McGraw-Hill.
- Clayton RW and Wiggins RA (1976) Source shape estimation and deconvolution of teleseismic body waves. *Geophysical Journal International* 103: 301–320.
- Clitheroe G, Gudmundsson O, and Kennett BLN (2000) The crustal thickness of Australia. *Journal of Geophysical Research* 105: 13697–13713.
- de Hoop MV and Bleistein N (1997) Generalized Radon transform inversions for reflectivity in anisotropic elastic media. *Inverse Problems* 13: 669–690.
- Deans SR (1983) *The Radon Transform and Some of Its Applications*. New York: John Wiley.
- Dueker KG and Sheehan AF (1998) Mantle discontinuity structure beneath the Colorado Rocky Mountains and High Plains. *Journal of Geophysical Research* 103: 7153–7169.
- Faber S and Müller G (1980) Sp phases from the transition zone between the upper and lower mantle. *Bulletin of the Seismological Society of America* 70: 487–508.

- Farra V and Vinnik L (2000) Upper mantle stratification by P and S receiver functions. *Geophysical Journal International* 141: 699–712.
- Farra V, Vinnik L, Romanowicz B, Kosarev GL, and Kind R (1991) Inversion of teleseismic S particle motion for azimuthal anisotropy in the upper mantle: A feasibility study. *Geophysical Journal International* 106: 421–431.
- Fee D and Dueker K (2004) Mantle transition zone topography and structure beneath the Yellowstone hotspot. *Geophysical Research Letters* 31: L18603 (doi:10.1029/2004GL020636).
- Ferris A, Abers GA, Christensen DH, and Veenstra E (2003) High resolution image of the subducted Pacific (?) plate beneath central Alaska, 50–150 km depth. *Earth and Planetary Science Letters* 214: 575–588.
- Forgues E and Lambaré G (1992) Parameterization study for acoustic and elastic ray-Born inversion. *Journal of Seismic Exploration* 6: 253–277.
- Frazer LN (1977) *Synthesis of Shear Coupled PL Waves* PhD thesis, Princeton University.
- Frederiksen AW and Bostock MG (2000) Modelling teleseismic waves in dipping anisotropic structures. *Geophysical Journal International* 141: 401–412.
- Frederiksen AW, Folsom H, and Zandt G (2004) Neighbourhood inversion of teleseismic Ps conversions for anisotropy and layer dip. *Geophysical Journal International* 155: 200–212.
- Frederiksen AW and Revenaugh J (2004) Lithospheric imaging via teleseismic scattering tomography. *Geophysical Journal International* 159: 978–990.
- French WS (1974) Two-dimensional and three-dimensional migration of model-experiment reflection profiles. *Geophysics* 39: 265–277.
- Gilbert HJ, Sheehan AF, Dueker KG, and Molnar P (2003) Receiver functions in the western United States, with implications for upper mantle structure and dynamics. *Journal of Geophysical Research* 108, doi:10.1029/2001JB001194.
- Goldberg DE (1989) *Genetic Algorithms in Search, Optimization, and Machine Learning*. Reading, MA: Addison-Wesley.
- Golub G, Heath M, and Wahba G (1979) Generalized cross-validation as a method for choosing a good ridge parameter. *Technometrics* 21: 215–223.
- Gurrola H, Baker GE, and Minster JB (1995) Simultaneous time domain deconvolution with application to the computation of receiver functions. *Geophysical Journal International* 120: 537–543.
- Gurrola H, Minster JB, and Owens T (1994) The use of velocity spectrum for stacking receiver functions and imaging upper mantle discontinuities. *Geophysical Journal International* 117: 427–440.
- Haskell NA (1962) Crustal reflection of plane P and SV waves. *Journal of Geophysical Research* 67: 4751–4767.
- Hayes MH, Lim JS, and Oppenheim AV (1980) Signal reconstruction from phase or magnitude. *IEEE Transactions on Acoustics Speech and Signal Processing ASSP-28(6)*: 672–680.
- Helmerger DV (1968) The crust–mantle transition in the Bering Sea. *Bulletin of the Seismological Society of America* 58: 179–214.
- Hoffmann H, Boelsche J, Horst W, et al. (1989) Tiefenseismische untersuchungen in der DDR durch den VEB geophysik – Stand und ergebnisse. *Zeitschrift für angewandte Geologie* 35: 308–314.
- Hudson JA (1980) *The Excitation and Propagation of Elastic Waves*. New York, NY: Cambridge University Press.
- Hudson JA and Heritage JR (1981) The use of the Born approximation in seismic scattering problems. *Geophysical Journal of the Royal Astronomical Society* 66: 221–240.
- Jordan TH and Frazer LN (1975) Crustal and upper mantle structure from Sp phases. *Journal of Geophysical Research* 80: 1504–1518.
- Kennett BLN (1991) The removal of free surface interactions from three-component seismograms. *Geophysical Journal International* 104: 153–163.
- Kennett BLN (1983) *Seismic Wave Propagation in Stratified Media*. Cambridge: Cambridge University Press.
- Kennett BLN (2000) Stacking three-component seismograms. *Geophysical Journal International* 141: 263–269.
- Kennett BLN (2002) *The Seismic Wavefield Volume II: Interpretation of Seismograms on Regional and Global Scales*. New York: Cambridge University Press.
- Kind R, Kosarev GL, and Petersen NV (1995) Receiver functions at the stations of the German Regional Seismic Network (GRSN). *Geophysical Journal International* 121: 191–202.
- Kind R and Vinnik LP (1988) The upper-mantle discontinuities underneath the GRF array from P-to-SV converted phases. *Journal of Geophysics* 62: 138–147.
- Kind R, Yuan X, Saul J, et al. (2002) Seismic images of crust and upper mantle beneath Tibet: Evidence for Eurasian plate subduction. *Science* 298: 1219–1221.
- Kosarev G, Kind R, Sobolev SV, Yuan X, Hanka W, and Oreshin S (1999) Seismic evidence for a detached Indian lithospheric mantle beneath Tibet. *Science* 283: 1306–1309.
- Kosarev GL, Makeyeva LI, and Vinnik LP (1984) Anisotropy of the mantle inferred from observations of P to S converted waves. *Geophysical Journal of the Royal Astronomical Society* 76: 209–220.
- Kosarev GL, Petersen NV, Vinnik LP, and Roecker SW (1993) Receiver functions for the Tien Shan analog broadband network: Contrasts in the evolution of structures across the Talasso–Fergana Fault. *Journal of Geophysical Research* 98: 4437–4448.
- Kumar MR and Bostock MG (2006) Transmission to reflection transformation of teleseismic wavefields. *Journal of Geophysical Research* 111, doi:10.1029/2005JB004104.
- Kumar P, Kind R, Hanka W, et al. (2005) The lithosphere–asthenosphere boundary in the North-West Atlantic region. *Earth and Planetary Science Letters* 1–2: 249–257.
- Kurita T (1973) A procedure for elucidating fine structure of the crust and upper mantle from seismological data. *Bulletin of the Seismological Society of America* 63: 189–204.
- Langston CA (1977) The effect of planar dipping structure on source and receiver responses for constant ray parameter. *Bulletin of the Seismological Society of America* 67: 1029–1050.
- Langston CA (1979) Structure under Mt Rainier, Washington, inferred from teleseismic body waves. *Journal of Geophysical Research* 94: 1935–1951.
- Langston CA and Hammer JK (2001) The vertical component P-wave receiver function. *Bulletin of the Seismological Society of America* 91: 1805–1819.
- Lawrence JF and Wiens DA (2004) Combined receiver-function and surface wave phase-velocity inversion using a niching genetic algorithm: Application to Patagonia. *Bulletin of the Seismological Society of America* 94: 977–987.
- Leidig M and Zandt G (2003) Highly anisotropic crust in the Altiplano–Puna volcanic complex of the central Andes. *Journal of Geophysical Research* 108: doi:10.1029/2001JB00649.
- Levander A, Niu F, and Symes WW (2005) Imaging teleseismic P to S scattered waves using the Kirchhoff integral. In: Levander A and Nolet G (eds.) *Seismic Earth: Array Analysis of Broadband Seismograms*, vol. 157, pp. 149–169. Washington: American Geophysical Union.
- Levin V and Park J (1997) P–SH conversions in a flat-layered medium with anisotropy of arbitrary orientation. *Geophysical Journal International* 131: 253–266.
- Levin V and Park J (1998) P–SH Conversions in layered media with hexagonally symmetric anisotropy. A Cookbook. *Pure and Applied Geophysics* 151: 669–697.

- Li X, Kind R, Yuan X, Wolbern I, and Hanka W (2004) Rejuvenation of the lithosphere by the Hawaiian plume. *Nature* 427: 827–829.
- Li X-Q (1996) *Deconvolving Orbital Surface Waves for the Source Duration of Large Earthquakes and Modeling the Receiver Functions for the Earth Structure Beneath a Broadband Seismometer Array in the Cascadia Subduction Zone*. PhD Thesis, Oregon State University, Corvallis.
- Li X-Q and Nabelek JL (1999) Deconvolution of teleseismic body waves for enhancing structure beneath a seismometer array. *Bulletin of the Seismological Society of America* 89: 190–201.
- Ligorio JP and Ammon CJ (1999) Iterative deconvolution and receiver-function estimation. *Bulletin of the Seismological Society of America* 89: 1395–1400.
- Lucente FP, Agostinetti NP, Moro M, Selvaggi G, and Di Bona M (2005) Possible fault plane in a seismic gap area of the southern Apennines (Italy) revealed by receiver function analysis. *Journal of Geophysical Research* 110, doi:10.1029/2004JB003187.
- Marfurt KJ, Johnson RA, and Pennington WD (2003) An introduction – Solid-Earth seismology: Initiatives from IRIS. *The Leading Edge* 22: 218–219.
- Matson KH (1997) *An Inverse-Scattering Series Method for Attenuating Elastic Multiples from Multicomponent Land and Ocean Bottom Seismic Data*. PhD Thesis, University of British Columbia, Vancouver.
- Menke W (1984) *Geophysical Data Analysis: Discrete Inverse Theory*. Orlando, FL: Academic Press.
- Mercier J-P, Bostock MG, and Baig A (2006) Improved Green's functions for passive source structural studies. *Geophysics* 71: SI95–SI102.
- Miller DM, Oristaglio M, and Beylkin G (1987) A new slant on seismic imaging: Migration and integral geometry. *Geophysics* 52: 943–964.
- Muirhead KJ and Datt R (1976) The N-th root process applied to seismic array data. *Geophysical Journal of the Royal Astronomical Society* 47: 197–210.
- Neal SL and Pavlis GL (1999) Imaging P to S conversions with multichannel receiver functions. *Geophysical and Research Letters* 26: 2581–2584.
- Neal SL and Pavlis GL (2001) Imaging P to S conversions with broadband seismic arrays using multichannel time-domain deconvolution. *Geophysical Journal International* 147: 57–67.
- Nicholson T, Bostock M, and Cassidy JF (2005) New constraints on subduction zone structure in northern Cascadia. *Geophysical Journal International* 161: 849–859.
- Niu F, Levander A, Ham S, and Obayashi M (2005) Mapping the subducting Pacific slab beneath southwest Japan with Hinet receiver functions. *Earth and Planetary Science Letters* 239: 9–17.
- Oppenheim AV and Schafer RW (1975) *Digital Signal Processing*. Englewood Cliffs, NJ: Prentice-Hall.
- Oreshin S, Vinnik L, Peregoudov D, and Roecker S (2002) Lithosphere and asthenosphere of the Tien Shan imaged by S receiver functions. *Geophysical Research Letters* 29, doi:10.1029/2001GL014441.
- Owens TJ, Nyblade AA, Gurrola H, and Langston CA (2000) Mantle transition zone structure beneath Tanzania, east Africa. *Geophysical Research Letters* 27: 827–830.
- Owens TJ and Zandt G (1997) The implications of crustal property variations on models of Tibetan Plateau evolution. *Nature* 387: 37–43.
- Owens TJ, Zandt G, and Taylor SR (1984) Seismic evidence for an ancient rift beneath the Cumberland Plateau, Tennessee: A detailed analysis of broadband teleseismic P waveforms. *Journal of Geophysical Research* 89: 7783–7795.
- Park J and Levin V (2000) Receiver functions from multiple-taper spectral correlation estimates. *Bulletin of the Seismological Society of America* 90: 1507–1520.
- Park J and Levin V (2001) Receiver functions from regional P waves. *Geophysical Journal International* 147: 1–11.
- Parker RL (1994) *Geophysical Inverse Theory*. Princeton, NJ: Princeton University Press.
- Paulssen H, Visser J, and Nolet G (1993) The crustal structure from teleseismic, P-wave coda-l. method. *Geophysical Journal International* 112: 15–25.
- Pavlis GL (2005) Direct imaging of the Coda of teleseismic P waves. In: Levander A and Nolet G (eds.) *Seismic Earth: Array Analysis of Broadband Seismograms*, vol. 157, pp. 171–185. Washington: American Geophysical Union.
- Phinney RA (1964) Structure of the Earth's crust from spectral behaviour of long-period body waves. *Journal of Geophysical Research* 69: 2997–3017.
- Poppeliers C and Pavlis GL (2003a) Three-dimensional, pre-stack, plane wave migration of teleseismic P-to-S converted phases. 1: Theory. *Journal of Geophysical Research* 108: doi:10.1029/2001JB000216.
- Poppeliers C and Pavlis GL (2003b) Three-dimensional, pre-stack, plane wave migration of teleseismic P-to-S converted phases. 2: Stacking multiple events. *Journal of Geophysical Research* 108, doi:10.1029/2001JB001583.
- Press WH, Flannery BP, Teukolsky SA, and Vetterling WT (1992) *Numerical Recipes: The Art of Scientific Computing*. Cambridge: Cambridge University Press.
- Randall GE (1989) Efficient calculation of differential seismograms for lithospheric receiver functions. *Geophysical Journal International* 99: 469–481.
- Reading A, Kennett B, and Sambridge M (2003) Improved inversion for seismic structure using transformed S-wave vector receiver functions: Removing the effect of the free surface. *Geophysical Research Letters* 30, doi:10.1029/2003GL018090.
- Revenaugh J (1995) A scattered-wave image of subduction beneath the Transverse Ranges, California. *Science* 268: 1888–1892.
- Robinson E and Treitel S (1980) *Geophysical Signal Analysis*. Englewood Cliffs, NJ: Prentice-Hall.
- Rondenay S, Bostock MG, and Fischer KM (2005) Multichannel inversion of scattered teleseismic body waves: Practical considerations and applicability. In: Levander A and Nolet G (eds.) *Seismic Earth: Array Analysis of Broadband Seismograms*, vol. 157, pp. 187–203. Washington: American Geophysical Union.
- Rondenay S, Bostock MG, and Shragge J (2001) Multiparameter two-dimensional inversion of scattered teleseismic body waves, 3. Application to the Cascadia 1993 data set. *Journal of Geophysical Research* 106: 30795–30808.
- Rost S and Thomas C (2002) Array seismology: Methods and applications. *Review of Geophysics* 40: 10.1029/2000RG000100.
- Ryberg T and Weber M (2000) Receiver function arrays: A reflection seismic approach. *Geophysical Journal International* 141: 1–11.
- Sacks IS, Snoker JA, and Husebye ES (1979) Lithosphere thickness beneath the Baltic shield. *Tectonophysics* 56: 101–110.
- Saul J, Kumar MR, and Sarkar D (2000) Lithospheric and upper mantle structure of the Indian Shield, from teleseismic receiver functions. *Geophysical Research Letters* 27: 2357–2360.
- Sambridge M (1999a) Geophysical inversion with a neighbourhood algorithm. I: Search a parameter space. *Geophysical Journal International* 138: 479–494.

- Sambridge M (1999b) Geophysical inversion with a neighbourhood algorithm. II: Appraising the ensemble. *Geophysical Journal International* 138: 727–746.
- Schimmel M and Paulsen H (1997) Noise reduction and the detection of weak, coherent signals through phase-weighted stacks. *Geophysical Journal International* 130: 497–505.
- Schneider WS (1978) Integral formulation for migration in two and three dimensions. *Geophysics* 43: 49–76.
- Schlüter-Pelkum V, Monsalve G, Sheehan A, et al. (2005) Imaging the Indian subcontinent beneath the Himalaya. *Nature* 435: 1222–1225.
- Sheehan AF, Shearer PM, Gilbert HJ, and Dueker KG (2000) Seismic migration processing of P–SV converted phases for mantle discontinuity structure beneath the Snake River Plain, western United States. *Journal of Geophysics Research* 105: 19055–19065.
- Sherwood JWC and Trörey AW (1965) Minimum-phase and related properties of a horizontally stratified absorptive Earth to plane acoustic waves. *Geophysics* 30: 191–197.
- Shibutani T, Sambridge M, and Kennett BLN (1996) Genetic algorithm inversion for receiver functions with application to crust and uppermost mantle structure beneath eastern Australia. *Geophysical Research Letters* 23: 1829–1832.
- Shragge J, Bostock MG, and Rondenay S (2001) Multiparameter two-dimensional inversion of scattered teleseismic body waves, 2. Numerical examples. *Journal of Geophysical Research* 106: 30783–30794.
- Silver PG and Chan WW (1991) Shear-wave splitting and subcontinental mantle deformation. *Journal of Geophysical Research* 96: 16429–16454.
- Silver PG and Savage M (1994) The interpretation of shear-wave splitting parameters in the presence of two anisotropic layers. *Geophysical Journal International* 119: 949–963.
- Simmons NA and Gurrola H (2000) Multiple seismic discontinuities near the base of the transition zone in the Earth's mantle. *Nature* 405: 559–562.
- Stammer K, Kind R, Petersen N, Kosarev G, Vinnik LP, and Qiuyan L (1992) The upper mantle discontinuities: Correlated or anticorrelated? *Geophysical Research Letters* 19: 1563–1566.
- Svenningsen L and Jacobsen BH (2004) Comment on 'Improved inversion for seismic structure using transformed, S-wavevector receiver functions: Removing the effect of the free surface' by Anya Reading, Brian Kennett, and Malcolm Sambridge. *Geophysical Research Letters* 31: 10.1029/2004GL021413.
- Tarantola A (1984) Inversion of seismic reflection data in the acoustic approximation. *Geophysics* 49: 1259–1266.
- Tarantola A (1986) A strategy for nonlinear elastic inversion of seismic reflection data. *Geophysics* 51: 1893–1903.
- Thomson DJ (1982) Spectrum estimation and harmonic analysis. *Proceedings of the IEEE*, 70: 1055–1096.
- Ulrych TJ (1971) Application of homomorphic deconvolution to seismology. *Geophysics* 36: 650–660.
- Ulrych TJ, Jensen OG, Ellis RM, and Somerville PG (1972) Homomorphic deconvolution of some teleseismic events. *Bulletin of the Seismological Society of America* 62: 1269–1281.
- Vinnik LP (1977) Detection of waves converted from P to SV in the mantle. *Physics of the Earth and Planetary Interiors* 15: 39–45.
- Vinnik LP, Farra V, and Romanowicz B (1989) Azimuthal anisotropy in the Earth from observations of SKS at GEOSCOPE and NARS broad band stations. *Bulletin of the Seismological Society of America* 79: 1542–1558.
- Vinnik LP, Foulger GR, and Du Z (2005) Seismic boundaries in the mantle beneath Iceland: A new constraint on temperature. *Geophysical Journal International* 160: 533–538.
- Vinnik LP and Montagner J-P (1996) Shear-wave splitting in the mantle Ps phases. *Geophysical Research Letters* 23: 2449–2452.
- Vinnik L and Romanowicz B (1991) Origin of precursors to teleseismic S waves. *Bulletin of the Seismological Society of America* 81: 1216–1230.
- Wapenaar K, Thorbecke J, and Draganov D (2004) Relations between reflection and transmission responses of three-dimensional inhomogeneous media. *Geophysical Journal International* 156: 179–194.
- Weglein AB, Araújo FV, Carvalho PM, et al. (2003) Inverse scattering series and seismic exploration. *Inverse Problems* 19: R27–R83.
- Weglein AB, Foster DJ, Matson KH, Shaw SA, Carvalho PM, and Corrigan D (2002) Predicting the correct spatial location of reflectors without knowing or determining the precise medium and wave velocity: Initial concept, algorithm and analytic and numerical example. *Journal of Seismic Exploration*. 10: 367–382.
- Weglein AB, Gasparotto FA, Carvalho PM, and Stolt RH (1997) An inverse scattering series method for attenuating multiples in seismic reflection data. *Geophysics* 62: 1975–1989.
- Wilson CK, Jones CH, Molnar P, Sheehan AF, and Boyd OS (2004) Distributed deformation in the lower crust and upper mantle beneath a continental strike-slip fault zone: Marlborough fault system, South Island, New Zealand. *Geology* 32: 837–840.
- Wilson D and Aster R (2005) Seismic imaging of the crust and upper mantle using regularized joint receiver functions, frequency P-wave number filtering, and multimode Kirchhoff migration. *Journal of Geophysical Research* 110: doi:10.1029/2004JB003430.
- Wilson D, Aster R, Ni J, et al. (2005) Imaging the seismic structure of the crust and upper mantle beneath the Great Plains, Rio Grande Rift, and Colorado Plateau using receiver functions. *Journal of Geophysical Research* 110: doi:10.1029/2004JB003492.
- Yilmaz O (2001) *Seismic Data Analysis: Processing, Inversion, and Interpretation of Seismic Data*. Tulsa: Society of Exploration Geophysicists.
- Yuan X, Kind R, Li X, and Wang R (2006) The S receiver functions: Synthetics and data examples. *Geophysical Journal International* 165: 555–564.
- Zandt G and Ammon C (1995) Continental crust composition constrained by measurements of crustal Poisson's ratio. *Nature* 374: 152–154.
- Zandt G, Gilbert H, Owens TJ, Ducea M, Saleeby J, and Jones CH (2004) Active foundering of a continental arc root beneath the southern Sierra Nevada in California. *Nature* 431: 41–46.
- Zandt G and Owens TJ (1986) Comparison of crustal velocity profiles determined by seismic refraction and teleseismic methods. *Tectonophysics* 128: 155–161.
- Zandt G and Randall GE (1985) Observations of shear-coupled P waves. *Geophysical Research Letters* 12: 565–568.
- Zhou L, Chen W-P, and Özalaybey S (2000) Seismic properties of the central Indian Shield. *Bulletin of the Seismological Society of America* 90: 1295–1304.
- Zhu L and Kanamori H (2000) Moho depth variation in southern California from teleseismic receiver functions. *Journal of Geophysical Research* 105: 2969–2980.

1.08 Crust and Lithospheric Structure – Active Source Studies of Crust and Lithospheric Structure

A. Levander, C. A. Zelt and W. W. Symes, Rice University, Houston, TX, USA

© 2007 Elsevier B.V. All rights reserved.

1.08.1	Introduction	247
1.08.2	Vertical-Incidence and Wide-Angle Seismology	248
1.08.3	Background	250
1.08.4	Reflection Seismology	250
1.08.5	The CMP Method in Reflection Seismology	253
1.08.6	Migration	255
1.08.6.1	Imaging Condition	256
1.08.6.2	Back-Propagation Operators	256
1.08.7	Reflection Seismology Examples	258
1.08.8	Refraction/Wide-Angle Seismology	260
1.08.9	Wide-Angle Seismology Experiments	261
1.08.10	Data Processing	263
1.08.11	Model Dimension	263
1.08.12	Forward Modeling	264
1.08.13	Traveltime Inversion and Tomography: Theory and Practical Issues	265
1.08.14	Traveltime Inversion and Tomography: Algorithms	270
1.08.15	Amplitude Modeling	272
1.08.16	S-Waves, Density, Attenuation, and Anisotropy	272
1.08.17	Fine-Scale Heterogeneities	273
1.08.18	Joint Inversion	274
1.08.19	Model Assessment	274
1.08.20	Wide-Angle Migration	276
1.08.21	Wavefield Inversion	277
1.08.22	Wavefield Inversion Examples	279
1.08.23	Future Directions	280
	References	283

1.08.1 Introduction

Controlled-source seismic methods are used widely at small, medium, and large scales for investigating the Earth from the shallow subsurface (upper tens of meters) to structures in and below the continental lithosphere (a few to a few hundred kilometers depth). Also called active-source seismology, controlled-source seismology requires the timed release of mechanical energy to generate elastic wavefields. For investigation as deep as the upper mantle the mechanical energy is generated by release and conversion of chemical energy (occasional use has been made of nuclear explosions, particularly in the Former Soviet Union). Marine investigations of the crust and top of the mantle commonly utilize the

release of pressurized air, whereas on land oscillating masses at the surface are used. For shallow investigations (tens to hundreds of meters depth) the sources include gunshots, weight drops, hammer blows, oscillating masses, or small explosives. Generally the seismic data are recorded on fairly dense arrays of portable seismic instruments, also referred to as seismic channels, numbering in the hundreds to thousands or even tens of thousands.

The most widely used application of controlled-source seismology is the reflection seismic method employed in the exploration for petroleum. Seismic surveys, processing, and interpretation account for the bulk of petroleum exploration budgets prior to drilling. Recently the mining industry has employed seismic reflection and refraction methods for investigating the

extent of known ore bodies, and for identifying fault zones along which economically viable mineralization has occurred. At smaller scales both reflection imaging and refraction velocity analysis are used in geotechnical and engineering applications, groundwater resource assessment, and environmental investigations.

In this chapter we confine our attention to controlled-source investigations used primarily to determine structure of the crust and upper mantle. There is considerable overlap between experimental methods used in academic investigations and those used in the various industries.

1.08.2 Vertical-Incidence and Wide-Angle Seismology

Controlled-source imaging of the lithosphere can be divided into two main areas: (1) near-vertical reflection methods and (2) refraction/wide-angle reflection methods. We assume that the reader is familiar with Snell's law of reflection and refraction at an interface separating two materials with different seismic velocities, and the reflection and transmission coefficients that describe the partition of motion during the interaction. Reflection and transmission coefficients depend on contrasts in seismic impedances, the product of seismic velocity, c , and density, ρ , as well as the incidence angle, θ . An important point in the behavior of a reflected and refracted wave occurs at the critical angle, θ_c , the incidence and reflection angle in the slower medium at which the wave in the faster medium refracts parallel to the interface with a refraction angle of $\pi/2$ taken from the normal to the interface. In the Earth velocity generally increases with depth, producing critical refraction at different angles depending on depth. Reflection coefficients in the 'precritical' regime, $\theta < \theta_c$, are typically small and real ($R(\theta < \theta_c) < 0.1$), whereas those in the 'post-critical' regime are of order 1 and can be complex ($R(\theta > \theta_c) = |R(\theta)|\exp(i\phi(\theta))$, $|R(\theta)| \sim 1$, $\phi \neq 0$) producing large reflections and distorting the waveform (see Aki and Richards, 2002, chapter 5). There are a number of important distinctions between the two methods that include data-acquisition geometry, and hence the completeness of the wavefield recorded and analyzed, the approach used to make an image of the Earth, and the meaning and resolution of the final image. The first concerns the maximum distance between source location, x_s , and receiver location, x_r , during recording compared to the maximum experiment target depth, z_{\max} . The distance between source and receiver,

$x_s - x_r$, is referred to as the source-receiver offset or just the offset; in the coordinate system we are using x is the location in 3-space, z is the vertical coordinate, positive down, and x_s and x_r are the positions of the source and receiver, usually at or near the Earth's surface. Reflection seismology normally uses waves that travel further vertically than horizontally:

$$\max|(x_s - x_r)/z_{\max}| \leq 1 \quad [1]$$

and directly uses the reflected or back-scattered wavefield to form an image of the 'reflectivity structure'. Reflectivity structure is the vertical derivative of seismic impedance normalized by its average value. For a layered medium this is proportional to the reflection coefficient at normal incidence calculated as a continuous function of depth. Seismic waves arrive at subhorizontal interfaces with small, precritical incidence angles, giving small real reflection coefficients ($0.1 \leq R$). The data to be analyzed are the precritical back-scattered wavefield (Figure 1). Reflection processing is based on the common midpoint (CMP) method, combined with an image formation step based on one of various formulations of the wave equation to yield a reflectivity map that ideally corresponds to the earth's 'impedance structure'. For whole-crust studies the customary frequency band of interest is 8–60 Hz.

In contrast the wide-angle method relies on identification of first-arriving refracted waves and large-amplitude postcritical reflections where

$$\max|(x_s - x_r)/z_{\max}| \gg 1 \quad [2a]$$

and usually,

$$\max|(x_s - x_r)/z_{\max}| > 5 \quad [2b]$$

In very densely recorded wide-aperture surveys pre-critical reflections can be identified and used as well. Data analysis typically employs a model-based approach, such as traveltime inversion, to yield a spatial map of 'seismic velocity'. For lithospheric studies the typical frequency band of interest is 1–20 Hz. This approach is variously referred to as the refraction method, wide-angle method, or refraction/wide-angle reflection method. For brevity we use the terms wide-angle data and wide-angle method (a more precise term would be wide aperture).

The two conventional controlled-source methods are essentially end members: reflection data provide a high-resolution structural image, the wide-angle data provides a lower-resolution velocity model. The difference in resolution scales between the two methods is

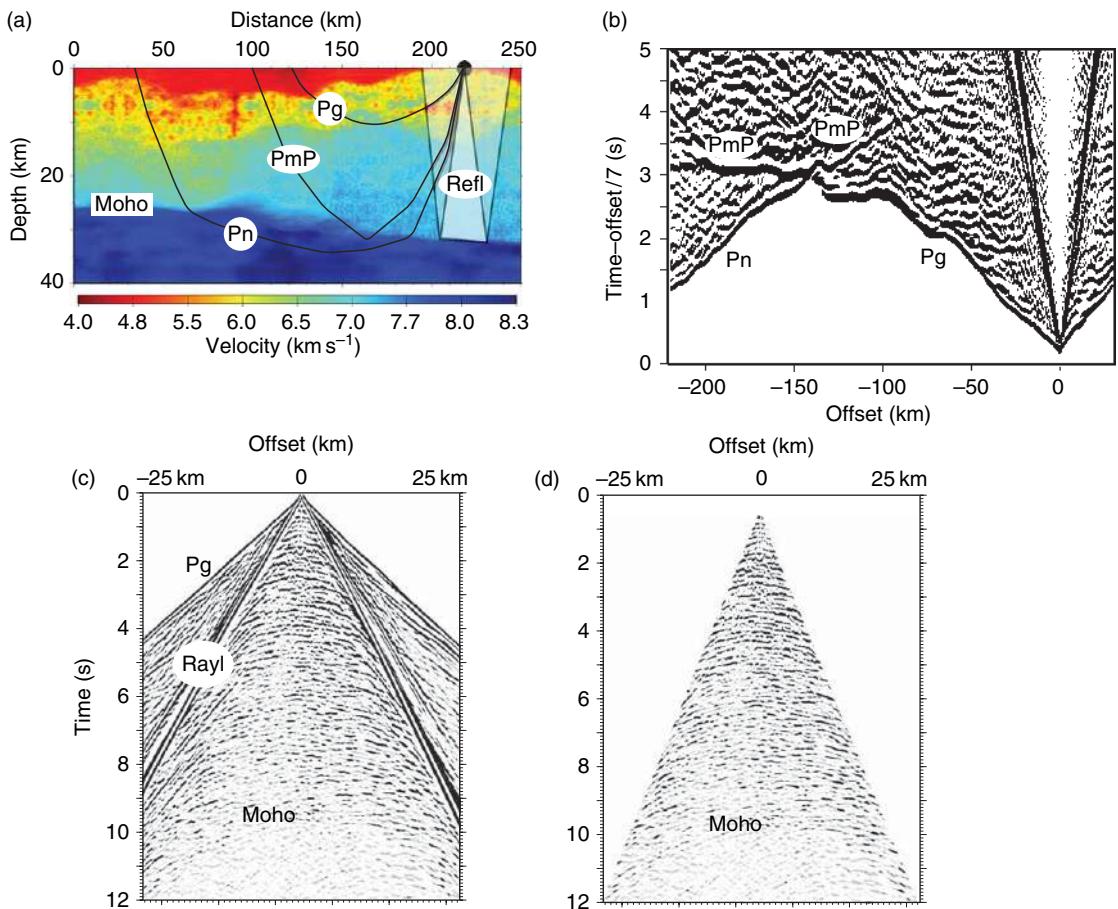


Figure 1 Example of phases used in crustal reflection and wide-angle studies. (a) Synthetic crustal P-wave velocity model from Hole *et al.* (2005) and representative ray paths for main phases: Pg – crustal refraction; PmP – Moho reflection; Pn – upper-mantle refraction. Refl – the area sampled by reflection data from this shot. Source location indicated by black dot. (b) Vertical component, viscoelastic full wavefield data for source location indicated in (a). Phases are labeled corresponding to those in (a); both pre- and postcritical PmP is visible. Time is reduced by 7 km s⁻¹ which means a correction equal to offset/7 km s⁻¹ is applied. Phases with velocity of 7 km s⁻¹ will appear horizontal. (c) The same shot record showing 25 km offset around the shotpoint. The Pg phase and Rayleigh waves are visible in the record, as well as converted shear waves. All of this energy is considered noise in the reflection model. A series of reflection events appear with hyperbolic shape inside the Rayleigh wave cone. (d) The same shot record with the noise field zeroed out. This is the part of the wavefield used for reflection imaging. In conventional reflection acquisition, each receiver point has a small array of geophones which is used to suppress the Rayleigh waves, increasing the size of the region from which reflection data can be recovered.

generally more than an order of magnitude. Hybrid methods which combine the reflection and wide-angle approaches are gradually evolving, as we describe later.

Figure 1(a) shows a two-dimensional (2-D) model of crustal P-wave velocity structure (Hole *et al.*, 2005) used to generate viscoelastic synthetic seismograms for testing various analysis methods. **Figure 1(b)** is a vertical-component synthetic shot gather illustrating the main arrival types (phases or events) used in traveltime and amplitude modeling of wide-angle data. Often only the first arrival times are modeled; these correspond to the Pg and Pn arrivals before and after the Pg/Pn

crossover point (~140 km in **Figure 1(b)**). Although the wide-angle wavefield can be complicated, as in this synthetic example, identifying and modeling the arrival times of first arrivals and prominent reflections, such as from the Moho (PmP), is a much more robust and less-demanding problem than modeling the full wavefield (described in Section 1.08.21). **Figures 1(c)** and **1(d)** shows the same shot but at offsets to ±25 km with and without the Pg and Rayleigh waves. **Figure 1(d)** shows the wavefield that would be processed to form a reflection image. Numerous reflections are visible from within the crust and as deep as the Moho.

1.08.3 Background

We begin with a few background equations relevant to both reflection and refraction seismology. We consider a wave operator, L , for the 3-D inhomogeneous wave equation:

$$LG(x, x_s, t) = \delta(t)\delta(x - x_s) \quad [3]$$

where G is the Green's function for either the acoustic wave equation, or one of the elastic wave potentials (see Aki and Richards (2002, p. 64)). For a constant coefficient equation, that is, a constant velocity medium, the solution is

$$G(x, x_s, t) = \frac{1}{4\pi c^2} \frac{\delta(t - |x - x_s|/c)}{|x - x_s|} \quad [4]$$

where c is the material velocity. Here the spreading is the reciprocal distance between the observation point and the source point, x_s , and the delta function is delayed by that distance divided by the medium velocity. For a variable velocity medium one of the commonly employed solutions is to introduce a high-frequency approximation with a similar form as the constant velocity solution:

$$G(x, x_s, t) \approx a(x, x_s)\delta(t - \tau(x, x_s)) \quad [5]$$

Here $a(x, x_s)$ is the geometrical optics amplitude resulting from spreading, and again the delta function carries the time dependence. Equation [5] is valid only in the absence of caustics. The traveltimes obeys the ‘eikonal’ equation:

$$|\nabla \tau| = \frac{1}{c(x)} \quad [6]$$

The eikonal equation can be integrated along the path of the wave through the medium:

$$\tau(x, x_s) = \int_{x_s}^x \frac{dl(x, x_s)}{c(l)} \quad [7]$$

The distance l is the ray connecting x_s to x . Much of reflection and refraction seismology are based on numerical implementations of these equations. We develop [5] and [6] for the acoustic equation in the section on reflection seismology. Equation [7] is the starting point for the discussion on wide-angle analysis methods.

1.08.4 Reflection Seismology

The goal of this section is to provide an understanding of the theoretical basis of reflection seismology, rather

than a comprehensive literature review. Because reflection seismology is the principal petroleum exploration tool and is now also an important tool in oil field management, the reflection seismology literature is extremely large, highly specialized, and heavily laden with commercial jargon. We have tried to minimize the jargon but still introduce enough common terminology so that the reader can consult the journals of the Society of Exploration Geophysicists, *Geophysics*, and the European Association of Exploration Geophysicists, *Geophysical Prospecting*, and understand much of the seismic literature.

Reflection experiment geometries are designed to produce as regular a sampling of the subsurface as possible. The receiver geometry is usually fixed relative to and moves with the source point. In the marine environment this is accomplished by towing an airgun source array and one or multiple linear arrays of pressure sensors behind the acquisition vessel. On land vertical-component geophones are deployed in linear or areal arrays to record signals from accelerated weight drops, explosive charges, or vibrating masses on trucks, a source known as Vibroseis™. For efficiency on land the acquisition requires that about twice as many geophones are deployed on the ground as are recording at a given time. As the source point moves, different parts of the seismic array are turned on and off to maintain a constant recording aperture, a practice called ‘roll-along’ recording.

For a variety of pragmatic reasons, wave propagation and imaging in reflection seismology are normally based on a scalar, acoustic wave equation. For the forward and inverse problems we follow a development for solution of the wave equation from a set of course notes by Symes, as this development illustrates imaging with the back-scattered wavefield, as well as allows us to describe traditional reflection seismology. For a 3-D medium having laterally and vertically variable density and sound speed

$$\frac{1}{\rho(x)c^2(x)} \frac{\partial^2 p(x, t)}{\partial t^2} - \nabla \cdot \left[\frac{1}{\rho(x)} \nabla p(x, t) \right] = f(t)\delta(x) \\ c(x) = \sqrt{\kappa(x)/\rho(x)} \quad [8]$$

where $p(x, t)$ is the pressure field, $\rho(x)$ is mass density, $c(x)$ is the sound speed, $\kappa(x)$ is the bulk modulus, and $f(t)$ is a temporally dependent, but spatially localized source field.

We assume that the sound speed can be decomposed into a low wave number, smoothly varying

term $c_0(x)$, and a rapidly varying component $\delta c(x)$. Similarly, we can separate the density field and the pressure fields into background and perturbed fields:

$$\begin{aligned} c(x) &= c_0(x) + \delta c(x) \\ \rho(x) &= \rho_0(x) + \delta \rho(x) \\ p(x, t) &= p_0(x, t) + \delta p(x, t) \end{aligned} \quad [9]$$

The scale separation is designed to produce kinematically correct traveltimes and approximately correct geometrical optics amplitudes by solving for a solution to the smooth background field, but is also designed so that the detailed dynamics (amplitudes) result from terms scaled by perturbed material properties. We term the former field the smooth velocity model, and the latter, with velocity scaled by density, the acoustic impedance, $i(x)$. Estimating the smooth velocity field from seismic data is one of the principal challenges in seismic reflection imaging, and for the imaging problem this field is termed the ‘migration velocity model’. The spatial variation of the impedance normalized by the average impedance is the reflectivity, $r(x)$, which provides the most basic high-frequency image of the subsurface (i.e., the details in $r(x)$ are considerably higher resolution than the details in $c_0(x)$):

$$\begin{aligned} i(x) &= c(x)\rho(x) \\ i(x) &\approx c_0(x)\rho_0(x) + \delta c(x)\rho_0(x) + \delta \rho(x)c_0(x) \\ r(x) &= \frac{\delta i(x)}{i_0(x)} = \left[\frac{\delta c}{c_0} + \frac{\delta \rho}{\rho_0} \right] \end{aligned} \quad [10]$$

There are few analytical guidelines quantifying what constitutes smooth and rapidly varying in the scale separation. Numerical experiments on the Marmousi synthetic model (see Versteeg (1994)) suggest that the migration velocity model needs to be specified at about three times the dominant wavelength in the illuminating wavefield to provide an accurate migration model. This is restrictive in a complicated model. For many places in sedimentary basins, a quasi-linear velocity increase with depth is a reasonable estimate of $c_0(x)$. A reasonable approximation for the crystalline crust is the velocity field determined by a refraction profile that has been interpreted using the regularized inversion methods discussed in the following section.

Substituting the perturbed quantities into [8], and solving for $\delta p(x, t)$ to first order gives

$$\frac{1}{\rho c^2} \frac{\partial^2 \delta p}{\partial t^2} - \nabla \cdot \frac{1}{\rho} \nabla \delta p = \frac{2\delta c}{\rho c^3} \frac{\partial^2 p}{\partial t^2} - \frac{1}{\rho} \nabla \cdot \left[\frac{\delta \rho}{\rho} \nabla p \right] \quad [11]$$

We can develop a solution for $\delta p(x, t)$ from solutions for $p(x, t)$. Let $G(x_s, x, t)$ be the Green’s function for the solution of the inhomogenous equation

$$\begin{aligned} \frac{1}{\rho(x)c^2(x)} \frac{\partial^2 G(x_s, x, t)}{\partial t^2} - \nabla \cdot \frac{1}{\rho(x)} \nabla G(x_s, x, t) \\ = \delta(t)\delta(x-x_s) \end{aligned} \quad [12]$$

where x_s is the source position and x the observation position. The solution $p_0(x_s, x, t)$ is given by integrating G against the extended time source:

$$p_0(x_s, x, t) = \int dt' f(t-t')G(x_s, x, t) \quad [13]$$

Estimating $f(t)$, termed the source wavelet, has a long history in exploration geophysics and is still a research topic. Early developments in statistical communication theory are the most widely used methods for reshaping the source pulse to a spike or relatively flat band-limited function. The reader is referred to landmark books by Robinson and Treitel (1980) and Claerbout (1976), and the practical processing text by Yilmaz (2001). These pulse estimation and reshaping methods are termed statistical, spiking, and predictive deconvolution. They have been applied very successfully to receiver-function processing in teleseismic seismology.

For constant velocity the solution to [12] is given by eqn [4]. For a smoothly variable velocity we develop an asymptotic solution by assuming a progressive wave expansion of the form

$$u(x_s, x, t) = a(x, x_s)S(t-\tau(x_s, x)) + R(x_s, x, t) \quad [14]$$

where $S(x_s, x, t)$ is assumed to have the same order of singularity as the constant velocity Green’s function, and the remainder, R , is smoother than S . Substituting [14] into [12] gives

$$\begin{aligned} \left[\frac{1}{\rho c^2} \frac{\partial^2}{\partial t^2} - \nabla \cdot \frac{1}{\rho} \nabla \right] u &= \frac{a}{\rho} \left[\frac{1}{c^2} - |\nabla \tau|^2 \right] S''(t-\tau) \\ &+ \frac{1}{\rho} \left[2\nabla \tau \cdot \nabla a - \left(\nabla \tau \cdot \frac{\nabla \rho}{\rho} + \nabla^2 \tau \right) a \right] S''(t-\tau) \\ &+ \left[\nabla \cdot \frac{1}{\rho} \nabla a \right] S(t-\tau) + \left[\frac{1}{\rho c^2} \frac{\partial^2 R}{\partial t^2} - \nabla \cdot \frac{1}{\rho} \nabla R \right] \end{aligned} \quad [15]$$

If the coefficients of the four terms on the right vanish then u satisfies the acoustic wave equation. The order of singularity decreases term by term on the right-hand side, so that if

$$\frac{1}{c^2} - |\nabla \tau|^2 = 0 \quad [16]$$

and

$$2\nabla\tau \cdot \nabla a - \left(\nabla\tau \cdot \frac{\nabla\rho}{\rho} + \nabla^2\tau \right) a = 0 \quad [17]$$

the solution is approximately correct in high-frequency components. Equation [16] is the eikonal equation of geometrical optics, with $\tau(x, x_s)$ the traveltimes field, and eqn [17] is the transport equation, with $a(x, x_s)$ the geometrical optics amplitude field. Both of these quantities can be solved numerically for laterally and vertically variable media of some complexity either by ray tracing or finite differences (e.g., Cerveny *et al.*, 1977; Vidale, 1988, 1990; Van Trier and Symes, 1991). In analogy to the constant coefficient Green's functions solution we can write the approximate Green's function solution as

$$G(x_s, x, t) \cong a(x, x_s)\delta(t - \tau(x_s, x)) \quad [18]$$

This suffices for the ‘incident’ field and the direct wave when applied against the source function $f(t)$. To solve for the back-scattered field, that is, the field of interest in reflection seismology, we find the perturbed field $\delta p = f^* \delta G(x_s, x, t)$ by solving

$$\frac{1}{\rho_0 c_0^2} \frac{\partial \delta G}{\partial t^2} - \nabla \cdot \frac{1}{\rho_0} \nabla \delta G = \frac{\delta c}{\rho_0 c_0^3} \frac{\partial^2 G}{\partial t^2} - \frac{1}{\rho_0} \left(\nabla \frac{\delta \rho}{\rho_0} \right) \cdot \nabla G \quad [19]$$

Let the acoustic wave operator be denoted L , and apply Green's formula

$$\int_V dx \int dt [(Lu)v] = \int_V dx \int dt [u(Lv)] \quad [20]$$

with $u = G$, and $v = \delta G$. At this point we want to specify the observation point, x_r , measure time with respect to the observation coordinate, t_r , and so make use of the identity

$$\begin{aligned} \delta G(x_s, x_r, t_r) &= \int_V dx \int dt [\delta G(x_s, x_r, t) \\ &\times \delta(x - x_r)\delta(t - t_r)] \end{aligned} \quad [21]$$

Substituting and rearranging [20] gives

$$\begin{aligned} \delta G(x_s, x_r, t_r) &= \int_V dx \left[\frac{2\delta c(x)}{\rho_0(x)c_0^3(x)} \frac{\partial^2 G(x_s, x, t)}{\partial t^2} \right. \\ &\quad \left. - \frac{1}{\rho_0(x)} \left(\nabla \frac{\delta \rho(x)}{\rho_0(x)} \right) \cdot \nabla G(x_s, x, t) \right] \\ &\quad \times G(x_s, x_r, t_r) \end{aligned} \quad [22]$$

This is a very general expression for the perturbation field, which is referenced to the shot and receiver coordinates, and the receiver time scale. For

calculations, we substitute the approximate 3-D Green's function [18]

$$\begin{aligned} \delta G(x_s, x_r, t_r) &\sim \frac{\partial^2}{\partial t_r^2} \int_V \frac{dx}{\rho_0(x)} \left[a(x_r, x)a(x_s, x) \right. \\ &\quad \times \left. \left\{ \frac{2\delta c(x)}{c_0^3(x)} \right\} \delta(t_r - \tau(x_r, x) - \tau(x_s, x)) \right] \\ &\quad + \frac{\partial}{\partial t_r} \int_V \frac{dx}{\rho_0(x)} \left[a(x_r, x)a(x_s, x) \right. \\ &\quad \times \left. \left\{ \nabla \frac{\delta \rho(x)}{\rho_0(x)} \cdot \nabla_x \tau(x_s, x) \right\} \delta(t_r - \tau(x_r, x) - \tau(x_s, x)) \right] \\ &\quad - \int_V \frac{dx}{\rho_0(x)} \left[a(x_r, x)a(x_s, x) \left\{ \nabla_x a(x_s, x) \cdot \nabla \frac{\delta \rho(x)}{\rho_0(x)} \right\} \right. \\ &\quad \left. \times \delta(t_r - \tau(x_r, x) - \tau(x_s, x)) \right] \end{aligned} \quad [23]$$

Note that the terms in braces, containing material property fluctuations, are coefficients in integral equations having the same basic form. This expression can be used for Kirchhoff forward modeling of the back-scattered field. If density is a constant, the expression reduces to

$$\begin{aligned} \delta p(x_s, x_r, t_r) &= \frac{\partial^2}{\partial t_r^2} \int_V \frac{dx}{\rho} \left[a(x_r, x)a(x_s, x) \left\{ \frac{2\delta c(x)}{c_0^3(x)} \right\} \right. \\ &\quad \left. \times f(t_r - \tau(x_r, x) - \tau(x_s, x)) \right] \\ \delta p(x_s, x_r, t_r) &= \int d\omega (-\omega^2) \exp(-i\omega t_r) \\ &\quad \times \int_V \frac{dx}{\rho_0} \left[a(x_r, x)a(x_s, x) \left\{ \frac{2\delta c(x)}{c_0^3(x)} \right\} \right] \\ &\quad \times f(\omega) \exp(i\omega(\tau(x_r, x) + \tau(x_s, x))) \end{aligned} \quad [24]$$

The coefficient scaling the amplitude and phase terms contains the reflectivity function $r(x) \sim \delta c(x)/c_0(x)$. Both integrals show the two phase factors corresponding to traveltimes to and from the scattering point.

For illustration, we can simplify the equations by assuming that $c = \text{constant}$ everywhere, that δc is nonzero at $x = (x_1, y_1, z_1)$ within the integration volume, and that $\rho = \text{constant}$ everywhere. The perturbation Green's function is

$$\begin{aligned} \delta G(x_s, x_r, x, t) &= \frac{2\delta c}{c_0^3 \rho_0} \frac{\delta''(t - (R_s + R_r)/c)}{16\pi^2 R_s R_r} \\ R_s &= \sqrt{(x_{s1} - x_1)^2 + (x_{s2} - y_1)^2 + (z_s - z_1)^2} \\ R_r &= \sqrt{(x_{r1} - x_1)^2 + (x_{r2} - y_1)^2 + (z_r - z_1)^2} \end{aligned} \quad [25]$$

Applying the source wavelet against [25] gives

$$\delta p(x_s, x_r, x, t) = \frac{2\delta c f''(t - (R_s + R_r)/c)}{c^3 \rho} \frac{1}{16\pi^2 R_s R_r} \quad [26]$$

1.08.5 The CMP Method in Reflection Seismology

Traditional reflection seismology is based on the coordinate transformation:

$$\begin{aligned} m &= (x_s + x_r)/2 \\ b &= (x_s - x_r)/2 \end{aligned} \quad [27]$$

where m is the midpoint coordinate, the average position of the source and receiver, and b is the half-offset, which measures the source and receiver distance away from the midpoint. This methodology was patented in 1950 by W.H. Mayne who called it the common depth point method. Reflection data acquisition is designed so that all the midpoints have an equal number of seismograms with a nearly identical and full range of offsets and azimuths. Populating the midpoint locations uniformly requires very regular data-acquisition geometries.

Traditional reflection seismology makes use of properties of the midpoint-offset domain to form the simplest form of backscattered image (**Figure 2**). The outstanding properties of this coordinate system are that (1) for any plane interface and scattering point the traveltime curves are symmetric in offset around any midpoint, with the minimum at $b = 0$ (**Figure 2(c)**); (2) for constant velocity, the traveltime curve for a flat reflector is a hyperbola expressed in offset and the ‘two-way zero-offset travelttime’ $t_0 = 2z_0/c_0$; and (3) many types of multiple reflections are strongly attenuated relative to primary reflections.

The symmetry of the traveltime curve allows us to estimate $t_0(m = \text{constant})$, and the hyperbolic form of the traveltime curve allows us to estimate the medium velocity using multiple $b(m = \text{constant})$ values. This is the most rudimentary form of velocity analysis to find c_0 . Expressing [26] in midpoint and offsets gives

$$\begin{aligned} \delta p(m, b, t_r) &= \frac{2\delta c f''(t - 2R/c)}{c^3 \rho} \frac{1}{16\pi^2 R^2} \\ \delta p(m, b, t_r) &= \frac{2\delta c f''(t - (t_0(z_0) + \Delta t_{\text{NMO}}(z_0, b)))}{c^3 \rho} \frac{1}{16\pi^2 R^2} \end{aligned} \quad [28]$$

where

$$R = \sqrt{(b^2 + z_0^2)}, \quad t_0 = 2z_0/c, \quad \Delta t_{\text{NMO}} = 2R/c - t_0$$

where Δt_{NMO} is called the ‘normal moveout (NMO) time’. For fixed m the travelttime curves are symmetric in b around $b = 0$. For any horizontal reflector in

a background velocity dependent only on depth, $c_0(z)$, the travelttime curve can be approximated as a hyperbola that is parametrized by the zero-offset time and a time (depth)-dependent velocity to second order in the ratio b/z . This velocity is called the ‘root mean square (rms) velocity’ ([Dix, 1955](#)). The rms velocity is interpreted as the velocity that gives the set of straight ray, approximate, traveltimes closest to the actual curved ray path traveltimes for a given depth. The rms velocity at a given depth is always less than the true velocity above that depth. Characterization of the travelttime curve as a hyperbola expressed in two-way travelttime and offset coordinates is true for any reflecting plane regardless of dip and azimuth, but the physical meaning of the derived velocities becomes increasingly obscure.

Correcting the travelttime by the difference between the hyperbolic time at offset b to that at t_0 , termed the ‘normal moveout’ correction (**Figure 2(d)**), gives a vertical focusing principle. This aligns the arrivals on all the seismograms at a CMP allowing them to be summed, or ‘stacked’, to enhance signal to noise. If each midpoint has N individual seismograms at different b ($m = \text{constant}$) and if the noise field is random in time and space, the theoretical signal to noise improvement by stacking is $N^{1/2}$. N is referred to as the ‘fold’, or redundancy of the data. The collection of seismograms at a CMP is termed a ‘gather’. The seismograms can be sorted, or ‘gathered’, into any common coordinate. The original seismic record of all seismograms for one shot is referred to as a shot gather. All the shots recorded by one receiver is a receiver gather, and all seismograms from all shots and receivers at a single offset is called a common offset gather.

The ‘CMP stacked section’ is an approximation to a zero-offset section. The ‘zero-offset’ section would be the image formed by making measurements along the surface with a coincident source and receiver. One of the most important steps in making the CMP stacked section is estimating $c(z)$, or $c_{\text{rms}}(z)$, known as ‘velocity analysis’. [Taner and Koehler \(1969\)](#) introduced the velocity spectrum, in which CMP data are summed using a ‘spectrum’ of different trial velocities for NMO correction at each depth. The velocity giving the maximum power in the stack at a given depth is chosen as correct.

The CMP stacked section was the first widespread imaging technique for the subsurface that made direct use of the recorded seismograms (**Figure 3(a)**). For a quasi-layered medium it provides a very accurate representation of the

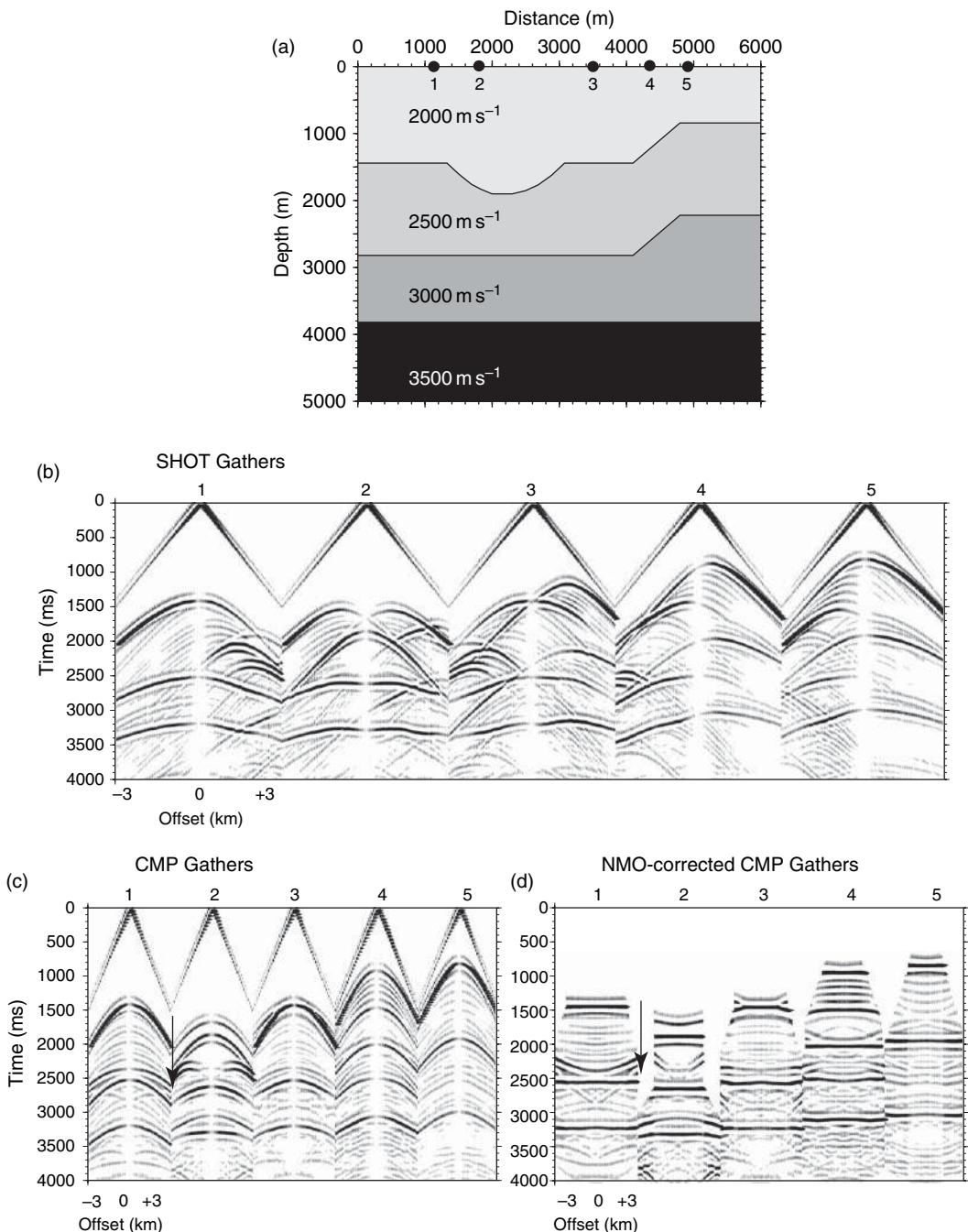


Figure 2 Synthetic reflection data set calculated with an acoustic finite-difference wave equation code. (a) The finite-difference velocity model with locations of the shot and CMP gathers that are shown in the following panels (locations 1–5). (b) Five of several hundred shot records showing the complex reflection patterns originating from laterally variable layering. (c) CMP gathers from five locations along the velocity model. In the midpoint-offset domain the traveltimes are symmetric about $h = 0$. (d) Vertical focus provided by normal moveout correction to the CMP gathers with the direct wave zeroed. The NMO correction was made using the local rms velocities. Note that the NMO correction fails to flatten events arriving at the same zero-offset time, but having different phase velocities, i.e., conflicting dips (arrows in (c) and (d)).

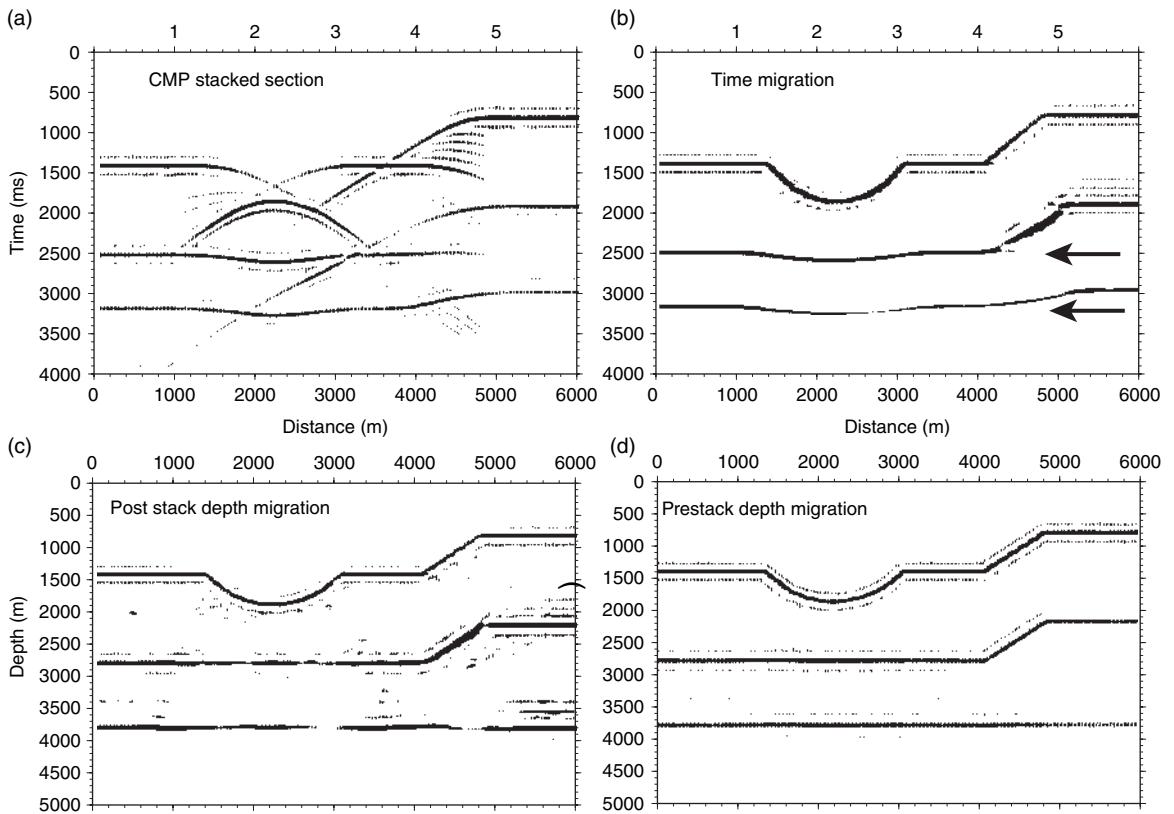


Figure 3 Processed synthetic data from the model in Figure 2. (a) The CMP stacked section shows distortions resulting from the lack of a lateral focus. Note particularly the caustic from the bowl-shaped feature in the shallowest interface at location 2, and the large diffractions from locations 2 to 4 from the dipping portions of the two shallowest interfaces. (b) Time migrating the CMP stacked section removes the distortion of the caustic, but fails to flatten the two deeper horizons (arrows). (c) Poststack depth migration flattens the deeper reflectors but fails to illuminate them uniformly. (d) Prestack depth migration produces the clearest image, note the lack of amplitude fluctuation in the deepest horizon. Prestack migration operates on the original data without the intermediate step of NMO correction and stacking, and provides both horizontal and vertical focusing simultaneously. All the migrations were done with Kirchhoff algorithms similar to those described in the text.

subsurface, but as it lacks a horizontal focus, the images of laterally variable structures are distorted in a number of predictable ways.

1.08.6 Migration

The true power of imaging with reflection data emerged when computationally efficient expressions for the back projection and horizontal focusing of the field δp were developed, allowing highly detailed images of geologic structures to be made in media with laterally variable velocity, $c_0 = c_0(x_1, x_2, z)$. Migration, most simply, increases lateral resolution by collapsing diffractions from points and edges, and restores continuous reflections from dipping structures to their ‘true’ dips and positions, the fidelity

of ‘true’ depending on the approximations used (see Yilmaz (2001)). ‘Time migration’ makes use of constant or fairly smoothly varying velocity and back-propagates along straight rays (Figure 3(b)), whereas ‘depth migration’ attempts to reposition energy along estimates of the true travel paths, and provides a mapping from time to depth (Figures 3(c) and 3(d)). The former is much less expensive computationally than the latter. These methods require a propagation operator and an imaging condition. The literature on the former is large, while the development of the imaging condition, as well as a class of back-propagation operators, is largely attributed to Claerbout (1970, 1971, 1976, 1985).

To start, let us expand what we mean by an image of the subsurface. The CMP section is an image that provides only a vertical focus. Scales (1995) provides

a useful definition of an image that is a frequency sum at a point, x , in the subsurface:

$$I(x) = S_{\text{PP}}(x) = \int_{-\infty}^{\infty} d\omega \left[F_1(\omega) \frac{\delta p_{\text{ref}}(x, x_r, \omega)}{p_{\text{inc}}(x_s, x, \omega)} \right] \quad [29]$$

With this definition, the image is the acoustic scattering coefficient formed by dividing the field recorded at x_r back-propagated to x , by the field incident on x from x_s . The position x is now called a common image point, or a common reflection point. The collection of data migrated to that point for a variety of (x_r, x_s) is a common image gather (CIG; Al-Yahya, 1989).

$F_1(\omega)$ is a shaping filter that takes into account the finite bandwidth of the source. This is a particularly easy image to form, as it makes direct use of the recorded data $\delta p(x_s, x_r, t)$, requiring only that we back-propagate it to the scattering point, x , to form $\delta p(x, x_r, t)$. For $p(x_s, x, t)$ we can either estimate the incident field, or propagate the source field; if we choose the latter note that both δp and p contain $f(t) \Rightarrow F(\omega)$, and the source wavelet is theoretically removed automatically. In this case $F_1(\omega)$ is used to stabilize the division, but in practice filtering and deconvolution processing is employed prior to migration. Back-propagating both source and receiver wavefields is termed ‘shot–geophone pre-stack migration’. In this case the scattering coefficient is implicitly dependent on the incidence–reflection angle. Data compression, summing the redundant data reflected from x , is done as the last step. The scattering coefficient as a function of incidence angle can be extracted prior to summation by examining CIGs. We can also pre-stack migrate the data in the midpoint-offset domain, termed ‘constant offset prestack migration’, by fixing b and migrating the data at different offsets independently. This has a number of desirable qualities that make it a common form of prestack migration.

In the CMP stacked section, $b = 0$, and midpoint is the migration coordinate. This is termed ‘poststack migration’, and is much less expensive than prestack migration because the data are compressed by the CMP fold prior to migration. However, poststack migration loses the angular dependence of the scattering coefficient, and has other problems as well.

1.08.6.1 Imaging Condition

The imaging condition takes a form appropriate to the numerical implementation of the back-propagation

operator, but in its simplest form it is the negative of the time that back-scattered energy on the seismic record took to get there, that is, it is equal to the time that the scattered field takes to propagate back to the scattering object plus the time the incident field takes to propagate from the source to the scattering point. This is termed time reversal.

1.08.6.2 Back-Propagation Operators

We will continue with the asymptotic form for the back-scattered field to describe seismic migration, but we note that entirely numerical approaches, that is, finite-difference methods, mixed finite-difference Fourier transform, and Fourier transform methods using the full-wave equation and various approximations to the one-way wave equation are also widely used (e.g., Claerbout, 1970, 1985; Gazdag, 1978; Stolt, 1978).

Here we develop an intuitive approach to migration of the precritical field $\delta p(x_s, x_r, t)$ using the Kirchhoff integral (e.g., Gardner *et al.*, 1974; Schneider, 1978) and the high-frequency formulation described above. We write the wave equation in the frequency domain for the smooth model, and for simplicity consider constant density:

$$\begin{aligned} \left[\frac{-\omega^2}{\rho_0 c_0^2(x)} - \frac{1}{\rho_0} \nabla^2 \right] u(x, \omega) &= 0 \\ \left[\frac{-\omega^2}{\rho_0 c_0^2(x)} - \frac{1}{\rho_0} \nabla^2 \right] G(x_s, x, \omega) &= -4\pi\delta(x-x') \end{aligned} \quad [30]$$

These are Helmholtz equations which can be substituted into a form of Green’s theorem to isolate u , the field at x' :

$$\begin{aligned} \int_V dx [u \nabla^2 G - G \nabla^2 u] &= \int_S ds(x_0) \left[u \frac{dG}{dn} - G \frac{du}{dn} \right] \\ u(x', \omega) &= \frac{-1}{4\pi\rho_0} \int_S ds(x_0) \left[u(x_0, \omega) \frac{dG(x_0, x', \omega)}{dn} \right. \\ &\quad \left. - G(x_0, x', \omega) \frac{du(x_0, \omega)}{dn} \right] \end{aligned} \quad [31]$$

This integral has a simple interpretation: the field anywhere in a volume can be described by measurements of the field and its derivative on the surface bounding it. This forms the basis for several migration operators and is widely used in diffraction theory (e.g., Sommerfeld, 1954; Goodman, 1996). Generally, we have only a recording of the field or its derivative, so we choose a kinematically correct Green’s function that makes one of the two terms in

[31] vanish on S . The Green's function is then an auxiliary field; it does not necessarily solve the physical problem for u . Let the surface S be defined by $z=0$, and choose a Green's function that vanishes on S by introducing a mirror source in the region $z<0$. We can combine the asymptotic form of the free-space Green's function with a copy of its mirror source. Since the normal n is positive outward, at $z=0$ the two sources cancel:

$$\begin{aligned} G_f(x, x', t) &\cong a(x', x)\delta(t-\tau(x, x')) \\ G_f(x, x', \omega) &= a(x', x)\exp(i\omega\tau(x, x')) \\ G(x_0, x', \omega) &= a(x', x^+)\exp(i\omega\tau(x^+, x')) \\ &\quad - a(x', x^-)\exp(i\omega\tau(x^-, x')) \\ G(x_0(z=0), x', \omega) &= 0 \end{aligned} \quad [32]$$

where x^+ and x^- refer to fields approaching $z=0$ from below and above. The normal derivative of the Green's function becomes

$$\frac{dG}{dn} = 2 \frac{dG_f}{dn} \Big|_{z=0} \quad [33]$$

Substituting this into the diffraction integral

$$u(x', \omega) = \frac{-1}{2\pi} \int_S ds(x_0) \times \left[u(x_0, \omega) \frac{dG_f(x_0(z=0), x', \omega)}{dn} \right] \quad [34]$$

Evaluating the normal derivative of G gives

$$\begin{aligned} \frac{dG_f}{dn} &= \frac{da(x_0, x')}{dn} \exp(i\omega\tau(x_0, x')) \\ &\quad + a(x_0, x') i\omega \frac{d\tau}{dn} \exp(i\omega\tau(x_0, x')) \\ \frac{d\tau}{dn} &= |\nabla_{x_0} \tau(x_0, x')| \cdot n \\ \frac{d\tau}{dn} &= \frac{1}{c_0(x_0)} \cos(\theta(x_0)) \end{aligned} \quad [35]$$

We can further simplify the diffraction integral by assuming that the derivative of amplitude is much smaller than that of phase, and neglect the first term. This gives the Rayleigh–Sommerfeld diffraction integral

$$u(x', \omega) \cong \frac{-1}{2\pi\rho_0} \int_S ds(x_0) \left[u(x_0, \omega) a(x', x_0) \frac{(i\omega)\cos\theta(x_0)}{c_0(x_0)} \times \exp(i\omega\tau(x_0, x')) \right] \quad [36]$$

The integral [36] was developed for a flat surface, but is approximately true for a surface that undulates around $z=0$ with spatial frequency small compared

to that of the wavefield. The latter is known as Kirchhoff's approximation (Beckman and Spizzichino, 1963). If we let $u(x_0, \omega) = \delta p(x_0, \omega)$, the back-scattered field recorded at the surface, we can inverse Fourier transform to get

$$\begin{aligned} &\frac{1}{2\pi} \int d\omega [\delta p(x, \omega) \exp(-i\omega t)] \\ &\cong \frac{-1}{4\pi^2\rho_0} \int_S ds(x_0) \int d\omega(i\omega) \left[\delta p(x_0, \omega) a(x_0, x') \right. \\ &\quad \left. \times \frac{\cos\theta(x_0)}{c_0(x_0)} \exp(-i\omega(t-\tau(x', x_0))) \right] \end{aligned} \quad [37]$$

The integrand consists of known quantities, with the traveltime and amplitude field of the Green's function determined from the smooth velocity field. The diffraction integral looks very much like Scale's definition of a seismic image [29]. The differences from the image definition are that the spreading function is reversed in sense (i.e., this formulation is for forward, not reverse propagation), and the integrand is not scaled by the incident field and the pulse shaping filter. Let $x' = x$, and let $x_0 = m$ be the midpoint coordinate for $b=0$. We can modify the integral for poststack imaging, using the Green's function to estimate the amplitude of the incident field at x :

$$p(x; m, b=0) = a(x; m, b=0) \quad [38]$$

Dividing both integrands gives

$$\begin{aligned} &\frac{1}{2\pi} \int d\omega \left[F_1(\omega) \frac{\delta p(x, \omega)}{p(x; m)} \exp(-i\omega t) \right] \\ &\cong \frac{-1}{4\pi^2\rho_0} \int_S ds(m) \int d\omega(i\omega) \left[\delta p(m, \omega) B(x, m, \omega) \right. \\ &\quad \left. \times \frac{\cos\theta(m)}{c_0(m)} \exp(-i\omega(t-2\tau(x, m))) \right] \end{aligned} \quad [39]$$

where we have doubled the traveltime field to account for downward propagation, and B restores the spreading from the surface midpoint coordinate to the scattering point and contains the pulse shaping filter:

$$B(x, m, \omega) = \frac{F_1(\omega)}{a^2(x, m)} \quad [40]$$

This integral can be used for poststack migration of the CMP stacked section, or a zero-offset section. By invoking the imaging condition in the Fourier integral, $(t-2\tau(x, m)=0)$, the field δp is back-propagated

and focused when its time is equivalent to the zero-offset two-way traveltime:

$$I(x) = \frac{-1}{4\pi^2 \rho_0} \int_S ds(m) \int d\omega(i\omega) \left[\delta p(m, \omega) B(x, m, \omega) \times \frac{\cos \theta(m)}{c_0(m)} \exp(-i\omega(t - 2\tau(x, m))) \right] \Big|_{t=2\tau} \quad [41]$$

The imaging condition makes the frequency integral just a sum over frequency. The integral can be interpreted in two ways. If we fix x , a single point in the image space, the integral sums all $\delta p(m, t = 2\tau(x = \text{constant}, m))$ values in the data space along the two-way traveltime curve from x to all midpoints. For constant velocity this is a sum over a hyperboloid. If we fix m , the single point in data space $\delta p(m = \text{constant}, t = 2\tau(x, m) = \text{fixed})$ is spread over a surface in x at the distance corresponding to traveltime $2\tau(x, m)$. For constant velocity this is a spherical shell in image space. This is termed post-stack Kirchhoff migration (**Figure 3(c)**), and can be in time or depth, depending on whether we assume straight or curved rays.

For prestack depth migration we can apply the integral [39] twice and invoke the reciprocity principle, with one surface integral over the shot coordinate, and the other over a common receiver coordinate (e.g., Wiggins, 1984; **Figure 3(d)**), to give

$$I(x) = \frac{-1}{8\pi^3 \rho_0^2} \int_S ds(x_s) \int_S ds(x_r) \int d\omega(-\omega^2) \times \delta p(x_s, x_r, \omega) B_1(x, x_s, \omega) B_2(x, x_r, \omega) \times \left[\frac{\cos \theta(x_s) \cos \theta(x_r)}{c_0(x_s) c_0(x_r)} \times \exp(-i\omega(t - \tau(x, x_s) - \tau(x, x_r))) \right] \Big|_{t=\tau(x, x_s)+\tau(x, x_r)} \quad [42]$$

Integrating over the shot surface may seem counter-intuitive; however, it is a simple matter to sort the data into receiver gathers. This integral also can be simply rewritten in the midpoint-offset coordinates by substituting [27]. Data manipulations are somewhat easier in midpoint-offset coordinates, and more importantly, the edge effects introduced from the finite apertures in the receiver- and shot-spaces are mitigated.

1.08.7 Reflection Seismology Examples

Interesting reflection seismology examples abound in a literature that now spans more than four decades.

Readers are referred to the *American Association of Petroleum Geologists Bulletin*, and the *Bulletin of the Geological Society of America* for general applications in geology, and to *Geophysics* and *Exploration Geophysics* for methodology. The development of deep crustal reflection seismology is documented in the volumes from the proceedings of the International Symposia on Deep Crustal Reflection Profiling, published by the American Geophysical Union and *Tectonophysics*.

We conclude this section by presenting some academic applications of active-source seismic investigations. Many of the Earth's great Cenozoic mountain belts now have one or more deep crustal seismology profiles across them, as do paleo-mountain belts, and modern and ancient extensional terranes. The different types of plate boundary zones have now been studied using reflection and refraction seismology. The few examples we show here, we find particularly interesting for either their experimental method, or broader Earth science significance.

In northern Canada the Canadian Lithoprobe program has imaged a Proterozoic thrust belt to an unusually great depth that shows subducting slab(s) of ocean lithosphere frozen into the Precambrian lithosphere (**Figure 4**; Cook *et al.*, 1999; Bostock, 1998). The seismic data were acquired with Vibroseis™ sources using standard industry reflection equipment and a total recording spread of about 24 km.

This image is extraordinary for a number of reasons. It suggests that thrust stacking of oceanic lithosphere can be a means to stabilize and grow the continents, a long-standing problem in early Earth development. This and similar images also suggest that some mountain belts are formed by a process termed wedge tectonics in which some or all crustal layers are thrust upwards over a strong crustal wedge and are then eroded. Mantle layers subduct beneath the crustal wedge and can be accreted to the lithosphere inboard of the subduction zone. Another interesting aspect of this image is the appearance of numerous thrust faults extending to the Moho, implying that brittle behavior extended to Moho depths, requiring either very high strain rates, an unusually cold orogen, or unusual crustal rheology. Lastly, teleseismic signals from the Yellowknife array at the eastern edge of the profile have Pds-wave conversions correlated with the mantle reflections in the reflection section. The same structural features are observable over several decades of seismic bandwidth. This suggests that teleseismic-converted wave imaging and reflection seismology can be used jointly for high-resolution imaging of the entire lithosphere.

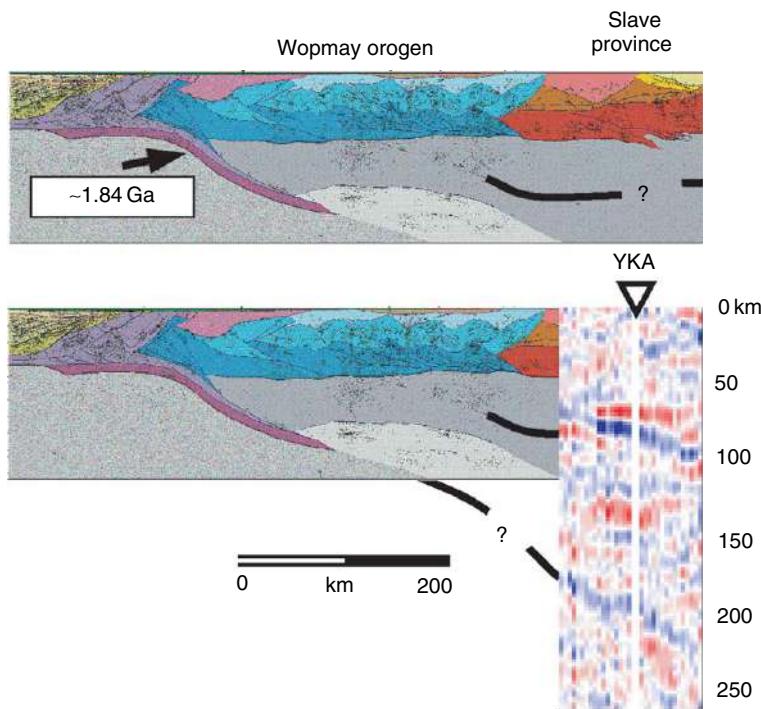


Figure 4 Lithoprobe's time-migrated SNORCLE deep-crustal and upper-mantle seismic reflection profile (top and bottom) and receiver functions (bottom) through the Proterozoic Wopmay orogen and Archean Slave Province. The receiver functions made at the Yellowknife (YKA) array show PdS-converted events at the same depths as the vertical incidence reflections (H, and possibly X and L). The profile shows an east dipping, 1.84 Ga subduction zone in which the subducting oceanic lithosphere appears to be tectonically accreted to the underside of the Wopmay orogen and the Slave craton. The Moho is relatively flat under the Wopmay orogen with thrust faults soling into the base of the crust. Crustal shortening is accommodated by a succession of west vergent crustal scale thrusts and duplexes, mantle shortening resulted from subduction with the apparent accretion of some of the subducted oceanic lithosphere to the periphery of the Slave craton. From Cook *et al.* (1999) and Bostock (1998).

In the 1990s the German–Chilean–Bolivian ANCORP program conducted reflection, refraction, and teleseismic experiments from the Pacific coast, across the Andes and the Altiplano to the Eastern Cordillera at about 21° S latitude. The reflection seismic data were acquired to image the deep crust, with relatively large source–receiver offsets (to ± 25 km), and widely spaced (~ 6.3 km), large explosive shots (ANCORP Working Group, 2003). The reflection section (Figure 5) and other geophysical data show a number of features that are interpreted as resulting from fluid-controlled processes. Three prominent bands of reflections appear in the section: (1) The Nazca reflector, (2) the Quebrada Blanca Bright Spot, and (3), bands of reflectors associated with the Altiplano low-velocity zone (LVZ). Most of the Nazca reflector, which extends from 40 to 80 km depth, and dips at about 20°, is associated with the interplate shear zone atop the subducting Nazca oceanic crust. Receiver-function imaging has identified the oceanic Moho beneath it. The Nazca reflector gains strength

and complexity as it deepens. It is interpreted as first a simple lithologic contrast that changes to a zone of dehydration as the subducting oceanic crust enters the amphibole stability field. The free fluids alter local mineralogy and weaken the overlying mantle. The reflections terminate where dehydration is complete, at about 80–90 km depth. Seismicity is low and somewhat diffuse in much of this part of the subducting plate, but resumes further downdip, assumed to result from dehydration embrittlement.

The Quebrada Blanca Bright Spot, which dips westward from the active volcanic front of the Andes toward the subduction zone, shows the strongest amplitude events in the section. These are interpreted as discrete lenses of melt which have migrated from deeper in the subduction system. Interestingly there is no electrical conductivity anomaly associated with the bright spot, suggesting that the melt lenses are not connected. In contrast the Altiplano reflectors, although weaker in amplitude, are associated with both a conductivity high and a

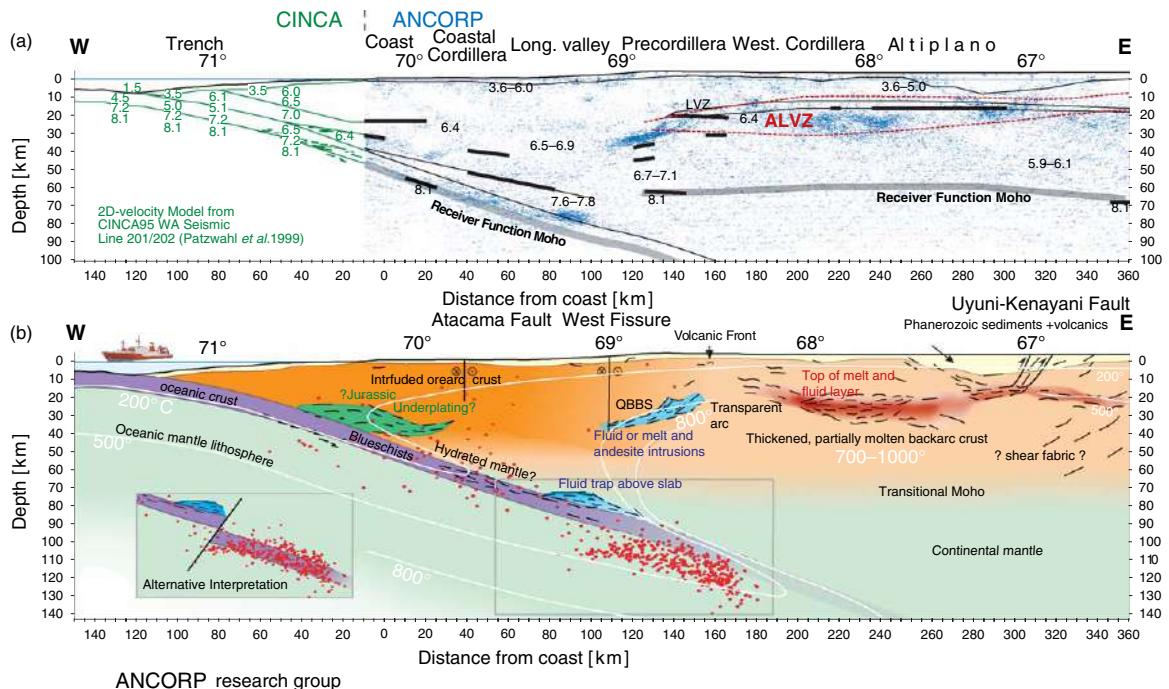


Figure 5 Summary figures showing results from ANCORP (2003) and related experiments across the Andean trench, the Andes, and Altiplano. (a) The depth migrated reflection data with seismic refraction and receiver-function results superimposed. The NAZCA reflection coincides to the shear zone separating South America from Nazca and is generally aseismic; it is interpreted as a zone of dehydration of the Nazca crust and lithosphere. Seismicity is concentrated deeper and to the east of this reflection and is distributed throughout the upper part of the Nazca Plate as a result of dehydration embrittlement. The Quebrada Blanca bright spot (QBBS) reflectors are interpreted as unconnected fluid or possibly melt lenses migrating from the lower crust to the Andean volcanic front. The midcrustal reflectivity beneath the Altiplano is interpreted as the reflection signature from a zone of 20% well-connected partial melt occupying much of the middle crust, and corresponding to a zone of low shear wave velocity identified by receiver functions, and a low-conductivity zone from magnetotelluric measurements. (b) An interpretation of all geophysical results including estimated isotherms in the trench region.

zone producing large P-to-S conversions in receiver functions. They are interpreted as being from a zone of well-connected pockets of partial melt defining an extensive midcrustal LVZ.

In a surprising application of reflection seismology to physical oceanography, Holbrook *et al.* (2003) have demonstrated that the temperature–salinity structure of the ocean can be imaged over large areas using CMP reflection surveying (Figure 6). Their data were acquired with a 480 channel, 6-km seismic streamer recording signals from a 140 liter airgun array, towed by the *R/V Ewing*. Processing the part of the seismic records that had previously been considered water column noise, they identified mixing structures between the cold Labrador current and the warm North Atlantic current. This application of reflection seismology to physical oceanography can provide high-resolution details of mixing structures and internal waves, and can be used for time-lapse imaging to monitor current changes.

1.08.8 Refraction/Wide-Angle Seismology

There are a number of reviews of methods for wide-angle data analysis: Braile and Smith (1975) demonstrated the amplitude–distance response of 1-D velocity models, stressing the importance of secondary arrivals. Mooney (1983) reviewed methods for calculating synthetic seismograms. Nowack and Braile (1993) reviewed traveltime and amplitude tomography methods in 1-D and 2-D media. Zelt (1999) focused on 2-D traveltime modeling and inversion, as well as model assessment methods. Rawlinson and Sambridge (2003a) presented an overview of traveltime tomography for 2-D and 3-D structure. This set of papers illustrates the evolution in wide-angle data analysis over the past 30 years from an emphasis on forward modeling amplitudes, secondary arrivals, and 1-D and 2-D models, to a focus on 2-D and 3-D traveltime automated inversion methods, often using only the first arrivals. This

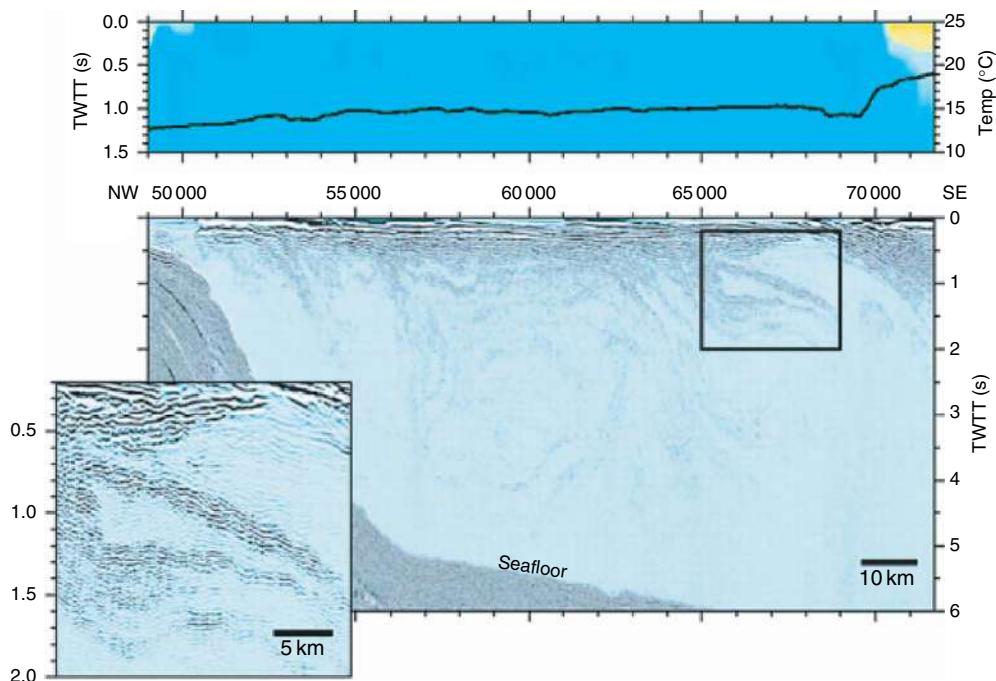


Figure 6 Middle: CMP stacked reflection image of the mixing of the Labrador and North Atlantic currents made by conventional CMP processing of water column reflections. Previously events in the water column had generally been considered to be random noise. Holbrook *et al.* (2003) imaged details of the structure of the mixing of the cold Labrador current (inset), and the warm North Atlantic current, with cold water masses descending beneath the warm. Top panel: CMP stacking velocities (color scale: blue, slow minimum 1440 m s^{-1} ; red, fast, maximum 1530 m s^{-1} ; blue–yellow transition 1503 m s^{-1}) indicating temperature variations in the ocean and intersection of the two currents at CMP 6950. The black line is sea-surface temperature measured by other means. Middle: From Holbrook WS, Páramo P, Pearse S, and Schmitt RW (2003) Thermohaline fine structure in an oceanographic front from seismic reflection profiling. *Science* 301: 821–824 (doi: 10.1126/science.1085116).

evolution was to a large extent driven by the increase in the typical size of the data set from a few seismograms, to hundreds of thousands of traces, combined with a massive increase in computational capability available to researchers. With a small amount of data, the intent was to try to extract as much information as possible. By comparison, the large data volumes today, coupled with a better understanding of wave propagation through realistic crustal models, tend to limit wide-angle analysis to the most robust features of the data: traveltimes, and often only first arrivals. Recently there has been a return to using more of the wavefield than traveltimes with 2-D full-waveform inverse methods discussed in Section 1.08.4.

1.08.9 Wide-Angle Seismology Experiments

Wide-angle seismic data have been used to constrain the lithospheric structure of continents, oceans, and their margins for over 40 years. For land experiments

the critical issue is usually the source, in terms of the type, cost, number, and location. Since the seismic waves must propagate $\sim 300 \text{ km}$ for crustal and uppermost mantle imaging using first arrivals, a chemical explosive is typically used. The chemicals are normally placed in single or multiple boreholes up to $\sim 100 \text{ m}$ deep, or at the bottom of moderately deep bodies of water (Jacob, 1975). The objective is to ensure a sufficient cap to avoid releasing energy into the atmosphere and to maximize ground coupling. The total amount of explosives for a single shot is usually in the $50\text{--}2000 \text{ kg}$ range, depending on the maximum offsets and depths to be investigated (e.g., Kohler and Fuis, 1992). The cost of drilling and explosives usually represents the largest part of the data acquisition budget, and thus the total number of sources is often small in comparison to the number of receivers, typically 5–100 shots are used today. Ideally, the sources should be placed at the ends of the 2-D line, and evenly spaced within, unless more resolution is required along a portion of the line. 3-D crustal wide-angle land surveys are relatively rare

since the number of sources required to achieve a spatial resolution comparable to a 2-D survey is very high. Typically, the number of sources used in a 3-D land survey means that only large-scale crustal structure will be resolved, and often 3-D data are a secondary component of an otherwise 2-D survey involving one or more lines (e.g., Kanasewich and Chiu 1985; Zelt *et al.*, 2006b).

For wide-angle land experiments, typically 100 to >1000 recorders are used, each one being a compact autonomous unit consisting of a digital acquisition system, an accurate clock, and a vertical-component geophone; three-component instruments are often embedded in surveys, but complete three-component surveys are still relatively rare. The sample rate is typically 2–16 ms and light-weight high-frequency geophones with a natural frequency of 4.5–40 Hz are used. Discrete recording windows can be programmed to capture land shots, or continuous recording of up to a few days can capture airgun shots in an onshore–offshore experiment (see below). The recorders are typically programmed at a central field location, and returned for download and clock check after recovery. One important difference between an active and passive geophone deployment is that many instruments are deployed in 1 or 2 days, and are left in the field for only a day to a week. As a result, there is less time available to ensure ideal geophone coupling, and the typical 100 m to 1 km receiver spacing along profiles means it is not possible to always chose ideal site conditions. Thus, modern active experiments rely on a large data volume with little or no site characterization, with a data loss of 5–10% expected due to instrument malfunction, deployer error, site noise, and theft in populated areas.

The experimental setup for a marine wide-angle survey is very different from a land survey. Airgun arrays are the most common source, often the same source being used for simultaneous acquisition of multichannel reflection data by towing a streamer from the same ship. Sometimes the airgun array will be tuned to a lower center frequency when deep crustal wide-angle data are being collected given that longer source-receiver offsets are sought. Typically 10–100 ocean-bottom seismometers (OBSs) or hydrophones (OBHs) are used to record marine wide-angle data, the former usually consisting of three components and one hydrophone. They may be deployed from the shooting ship or a second ship, and are normally programmed to record continuously for a few days, and are then recovered by the same ship using a timed release or acoustic signal. The internal workings of an

OBS or OBH are similar to a land recorder with respect to memory and an accurate clock. Since the sound source can cycle at a rate of 20 s or less (a common shooting rate for reflection data), previous shot noise generated within the water column can be a major noise source for wide-angle marine data. As a result, a longer shot interval of 60–120 s is used to record wide-angle data only. If both wide-angle and reflection data are sought, the lines will either be collected twice using the short and long shot intervals or a compromise shot interval of 30–45 s is used.

A combined vertical to wide-angle experiment known as an onshore–offshore survey has become quite popular in the past ~15 years. Land stations record marine shots and/or ocean-bottom receivers record land shots (e.g., BABEL Working Group 1993; Henstock *et al.*, 1997; Morgan *et al.*, 2000; Park *et al.* in press). As a result there is continuous data coverage across a land–water boundary, ideal for studying continental margins. Coincident but independent near-vertical reflection and wide-angle experiments are quite common (e.g., Mooney and Brocher 1987), but in some modern experiments both types of data are acquired simultaneously using densely spaced shots and receivers with sufficient offset that deep-penetrating first-arrival refractions are recorded (e.g., Levander *et al.*, 1994; Lafond and Levander, 1995; Fuis *et al.*, 2001). These types of data allow both conventional reflection and wide-angle analysis techniques, as well as wide-angle migration and waveform inversion (both discussed later). Similar experiments, known as deep seismic soundings (DSSs) were once common in Russia and India, but they usually did not use sufficient offsets to observe upper-mantle refractions, Pn (e.g., Kaila and Krishna, 1992). Wide-angle experiments with very long source–receiver offsets (>1000 km) have been used to image deep subcrustal lithospheric and asthenospheric structure (e.g., Gorman *et al.*, 2002), particularly in the former Soviet Union in which peaceful nuclear explosions were sometimes available as sources (e.g., Neves *et al.*, 1996; Morozova *et al.*, 1999 Thybo and Perchuc, 1997).

For upper-crustal and near-surface wide-angle studies, the experimental parameters mentioned previously for whole-crustal studies can be appropriately scaled, although the number of sources and receivers will remain roughly the same. The size of explosive near-surface sources ranges from tenths to tens of kilograms of explosives, and there are many viable nonexplosive sources, such as hammers, weight drops, rifles, shotguns, and minivibes (e.g.,

Jarchow *et al.*, 1994; Lanz *et al.*, 1998; Hughes *et al.*, 1998; Hole *et al.*, 2006; Zelt *et al.*, 2006a).

The modeling and inversion algorithms discussed later can be used to help design the optimum survey geometry given particular instrument resources and anticipated geologic structures (e.g., Peirce and Day 2002).

1.08.10 Data Processing

A major difference between conventional analyses of wide-angle data and reflection data is the use of a model-based approach versus a signal-processing approach for the latter. The reason for this is because it is possible to convert reflection data into a high-resolution, geologically interpretable form, ideally a representation of the primary reflectivity of the Earth. Much of this analysis is only weakly dependent on the velocity structure of the crust. However, for wide-angle data, the primary objective is to determine the velocity structure of the crust and uppermost mantle. Therefore, the analysis of wide-angle data typically includes only a minimal amount of data processing to ‘clean up’ the data to make it easier to pick arrival times from the seismograms. Bandpass filtering, velocity (frequency–wave number) filtering, trace summing, and deconvolution are sometimes used to remove incoherent and coherent noise and reduce complications from a ringy source, multiple reflections, or previous shot noise, particularly in marine data (Nakamura *et al.*, 1987; Christeson *et al.*, 1999). Except for 1-D modeling of wide-angle data, corrections for elevation and low surface velocities are neglected as they depend on the unknown velocity structure. Instead, most 2-D and 3-D modeling algorithms for wide-angle data allow the known surface topography and bathymetry to be incorporated into the model. If a 1-D velocity model is sought, either as a final result or as a starting model for subsequent 2-D or 3-D modeling, data processing/inversion techniques exist, such as tau- p inversion (e.g., Clayton and McMechan, 1981; Gorman and Clowes, 1999). In some cases, particularly with very laterally heterogeneous near-surface structure, phase identification and arrival picking may be difficult, and a processing technique such as wave equation datuming may prove effective (Hill and Wuenschel, 1985; Larkin and Levander, 1996). For marine data, applying corrections for rugged seafloor topography may be necessary (e.g., Spudich and Orcutt, 1980; Purdy, 1982).

Picking wide-angle arrival times is normally done from shot or receiver gathers, exploiting the lateral

coherence of closely spaced traces. Fully automated picking routines are usually not possible because of noise, lateral waveform changes, and onsets of later arrivals buried in the seismic coda. Interactive software is used to pick arrivals ‘manually’ by eye for each trace, or a representative subset of traces are picked and the intervening picks are determined automatically using a cross-correlation scheme (Zelt, 1999). Initially, only the most obvious arrivals are picked, typically the first arrivals. These initial arrivals are used to develop a preliminary model to help identify additional arrivals by overlaying predicted times on the data and then using the new set of picks to further develop the model in a bootstrap fashion. Interpolating traveltimes picks across significant gaps will provide an incorrect sense of model constraint and is to be avoided (Zelt, 1999).

Assigning prior uncertainties to the arrival picks avoids over- or underfitting the data, and allows the appropriate up- and downweighting of less noisy and more noisy data, respectively, when an inverse method is used (Zelt, 1999). Uncertainties are often assigned qualitatively by inspection, taking into account the data’s signal-to-noise ratio and frequency content. Zelt and Forsyth (1994) used an automated scheme involving an empirical relationship between signal-to-noise ratio and pick uncertainty. Another guideline for assigning pick uncertainties is the time differences of reciprocal pairs (Zelt *et al.*, 2006a) or where two profiles intersect (Park *et al.*, in press). Toomey *et al.*, (1994) estimated picking uncertainties as part of an automated picking routine.

1.08.11 Model Dimension

Up until about 1980, wide-angle data were generally modeled using a laterally homogeneous (1-D) representation of Earth structure (Mooney, 1983). This simplification allows for a number of efficient forward modeling and linear inversion techniques of the traveltimes and wavefield for velocity as a function of depth, such as the reflectivity method, Herglotz-Wiechert inversion, and tau- p inversion (Fuchs and Muller, 1971; Aki and Richards, 2002, pp. 413–29; Clayton and McMechan, 1981). These inversion techniques assume a monotonically increasing velocity–depth model, which in most tectonic settings is reasonable, but in some cases may be too restrictive, such as in high heat flow regions (Smith *et al.*, 1975; Wenzel and Sandmeier, 1992). If LVZs are involved, wide-angle reflections from the top and bottom of the LVZ can be used to constrain them (e.g., Sain and Kaila, 1996).

The 1-D ‘reflectivity’ method has been very popular because of its ability to provide elastic full-wavefield seismograms. The reflectivity method is also used where the velocity model is weakly 2-D so that a 1-D average for amplitude calculations is acceptable given that typically only the large-scale amplitude trends are modeled (e.g., Benz *et al.*, 1990; Zelt and White, 1995). 1-D modeling can also be used to construct a starting model for 2-D or 3-D analysis. In this case, the 1-D assumption is made for each shot or receiver gather, and the resulting velocity-depth profiles are interpolated to form an initial 2-D model. Alternatively, the traveltimes picks from all shots and receivers can be used to derive the best-fitting 1-D model which is then used as a starting model for 2-D or 3-D inversion (e.g., Zelt and Barton, 1998).

In the late 1970s, asymptotic (i.e., infinite-frequency) ray theory for laterally heterogeneous (2-D) media was adopted for interpretation of wide-angle data, including the calculation of synthetic seismograms (Cerveny *et al.*, 1977; McMechan and Mooney, 1980; Mooney, 1983). This was a significant step forward because it meant that Earth models of arbitrary lateral complexity could be considered, providing the tenants of ray theory were honored, that is, the velocity field varies slowly with respect to the seismic wavelengths involved. Sharp velocity changes are modeled using a velocity discontinuity, that is, a layer boundary, and the application of Snell’s law. As a result, 2-D ray theory models are typically composed of one or a few layers, bounded by smoothly varying interfaces, within which the velocity varies smoothly.

In the 1990s, acquisition of 3-D crustal wide-angle data became quite common, particularly in the oceans as 3-D marine surveys have simpler logistics, shallower targets requiring smaller offsets, and hence lower costs (e.g., Toomey *et al.*, 1994; Zelt and Barton, 1998), but also on land (e.g., Zelt *et al.*, 1996) and crossing ocean-continent boundaries in onshore–offshore experiments (Hole *et al.*, 2000a; Morgan *et al.*, 2000). The cost of most 3-D surveys is high, especially if the spatial resolution is to be comparable to a state-of-the-art 2-D survey, and so they are used when 2-D sampling of the target will be insufficient to address the research objectives. Sometimes relatively sparse 3-D crustal data sets are acquired as a result of a primarily 2-D survey that includes some broadside recordings, that is, shots from one profile recorded by receivers along another profile. The advantage of these types of surveys is that little or no compromise on the quality of the 2-D imaging is necessary, but the additional sparse 3-D coverage

may reveal structures not present in the 2-D models (e.g., Zelt *et al.*, 2006b).

For a 2-D survey in which the shot and receiver locations deviate significantly from a straight line, it may be necessary to consider 2.5-D modeling, that is, using a 3-D model and 3-D ray tracing, and the known topographic and bathymetric surfaces, but keeping the velocity model homogeneous in a direction perpendicular to the main trend of the profile (e.g., Van Avendonk *et al.*, 2004). Given the resolution of most wide-angle velocity models, the degree of profile ‘crookedness’ must be substantial to warrant 2.5-D modeling (Zelt and Zelt, 1998).

1.08.12 Forward Modeling

The late 1970s saw the introduction of various methods for calculating ray paths and traveltimes in laterally heterogeneous media (2-D and 3-D), and thereby establishing the basis of wide-angle data analysis used today. Two end-member approaches to ray tracing were put forward: numerical and analytical. In the former case the velocity field is specified by a regular (e.g., McMechan and Mooney, 1980) or irregular (e.g., Zelt and Ellis, 1988) grid of nodes, together with a scheme for interpolation between nodes, and a ray is traced by specifying a take-off angle from a point source and solving a set of ordinary differential equations, the ray-tracing equations (Cerveny *et al.*, 1977). In the analytic case, the velocity field can be specified by a regular (e.g., Chapman and Drummond, 1982; White, 1989; Rawlinson *et al.*, 2001) or irregular (e.g., Spence *et al.*, 1984) grid of nodes, but with a form of interpolation, typically linear, such that the ray paths can be calculated analytically. In practice, the analytic and numeric techniques are often about equally efficient if the analytic method uses a fine mesh of nodes to represent a sufficiently smooth velocity field as dictated by ray theory, and if the numeric scheme adjusts the step length according to the velocity gradients (Zelt and Ellis, 1988).

For an arbitrary 2-D velocity model, a nontrivial consideration is the determination of ray take-off angle from the source such that an arbitrary receiver point is reached, or such that a particular layer or interface in the model is sampled. In early algorithms it was left to the user to determine the necessary take-off angles through trial-and-error shooting of fans of rays (e.g., Spence *et al.*, 1984). Today, most 2-D ray tracing codes offer an automatic determination of take-off angles using a shooting approach and

a bisection algorithm to sufficiently refine the take-off angles so that the receiver points are hit (e.g., Zelt and Smith, 1992). The robustness of the shooting method is critical because the data from receivers for which it is not possible to find rays cannot be used in the forward or inverse modeling. Also, it is important to be sure that an inability to find rays is because of the model, for example, a shadow zone, as opposed to a shortcoming of the shooting algorithm.

To avoid the limitations of shooting, particularly for 3-D models, ray bending methods were developed (Julian and Gubbins, 1977; Um and Thurber, 1987). In this approach a ray path connecting a source and receiver is estimated, normally using a 1-D reference model, and the ray path is iteratively updated using Fermat's principle until the minimum-time path is determined. In practice, shooting methods are more efficient and sufficiently robust for 2-D models, whereas bending methods are favored for 3-D models. Zhao *et al.* (1997) and Chiu *et al.* (1986) applied bending methods to the inversion of 2-D and 3-D wide-angle data.

In the late 1980s a new forward modeling approach was introduced in which first-arrival traveltimes are calculated on a fine grid using a finite-difference solution of the eikonal equation (Vidale, 1988, 1990; Van Trier and Symes, 1991; Podvin and Lecomte, 1991). Ray paths are obtained in a second step by following the gradient of the traveltime field. These methods have become very popular and are collectively known as wavefront tracking methods (also known as eikonal solvers). Reflection ray paths can be calculated in a two-step procedure by calculating downgoing and upgoing wavefronts (Hole and Zelt, 1995). Hole and Zelt (1995) also presented a modification to Vidale's approach which otherwise breaks down for velocity contrasts of more than $\sim 40\%$. The advantage of finite-difference methods is that they find the fastest ray between any two points, including the diffracted path in the case of a geometrical shadow zone, and they can be very efficient, especially for 3-D models. The disadvantages are they are computationally cumbersome for calculating later arrivals, and they can be inaccurate and/or computationally intensive for high velocity contrast media. Another potential problem is that the calculated first arrival time may correspond to a very low-energy arrival, something that may not be recognized in real data. Another type of wavefront tracking scheme that solves the eikonal equation is the fast marching method, which is computationally efficient and unconditionally stable (Sethian and Popovici, 1999; Popovici and Sethian, 2002;

Rawlinson and Sambridge, 2004). Eaton (1993) developed a finite-difference method for anisotropic media.

Nakanishi and Yamaguchi (1986) and Moser (1991) introduced the shortest-path ray-tracing method based on Fermat's principle which uses a fine network of nodes and graph theory. It is capable of handling arbitrarily heterogeneous media and calculating first arrivals, reflections, and multiples easily. Its advantages over finite-difference methods are robustness and the grid does not have to be rectangular or regular. However, its memory and computation requirements are greater. Van Avendonk *et al.* (1998, 2001) developed a hybrid of the shortest-path and ray-bending methods building on the work of Moser (1991) and Moser *et al.* (1992). The hybrid method uses the shortest-path algorithm to find an initial ray path that is close to the minimum-traveltime path, and then refines it using a bending method. The result is an efficient and robust algorithm to calculate accurate traveltimes and ray paths for refractions and reflections in 2-D and 3-D media.

1.08.13 Traveltime Inversion and Tomography: Theory and Practical Issues

Today, 2-D and 3-D traveltime inversion and tomography are the central analysis methods applied to crustal wide-angle data. In this section we present an overview of the mathematical theory and practical considerations of the algorithms in use today. The distinction between inversion and tomography is not well defined in the seismology community. The latter usually implies a uniform, fine-grid model parametrization, in which a smooth model is sought (e.g., Toomey *et al.*, 1994; Zelt and Barton, 1998; Van Avendonk *et al.*, 1998). Any departure from this approach is usually referred to as traveltime inversion (e.g., Spence *et al.*, 1985; Zelt and Smith, 1992; Rawlinson *et al.*, 2001), although the distinction is an arbitrary one, as the mathematical description below shows. Here we caution the reader that some notation used in reflection seismology is also customarily used in wide-angle seismology, but with different meanings. In this section L is the ray path (as opposed to wave operator), and G is the matrix of Fréchet derivatives, rather than a Green's function.

The traveltime t between a source and receiver along a ray path L is given in integral form for a continuous or piecewise continuous velocity field $v(\mathbf{r})$ as

$$t = \int_L \frac{dL}{v(\mathbf{r})} \quad [43]$$

where \mathbf{r} is the position vector in 2-D or 3-D media. Finding $v(\mathbf{r})$ is a nonlinear inverse problem given the relationship between the measured data (traveltimes) and the unknown model parameters (the velocity field). However, by transforming variables to use slowness $s(\mathbf{r})$, the reciprocal of velocity, instead of velocity as the unknown, a linear inversion problem is created:

$$t = \int_L s(\mathbf{r}) d\ell \quad [44]$$

However, the ray path L is also dependent on the velocity (or slowness) model (**Figure 2**), thus making the inverse problem nonlinear regardless of what form of model variable or parametrization is used.

In global seismology, a 1-D (radially symmetric) earth model is often used to predict the ray paths given the relatively small velocity heterogeneities in

the mantle, and thereby converting the inverse problem into a linear one (e.g., Grand, 1994). In crustal seismology there is no concept of a reference model that is sufficiently accurate to predict the ray paths in advance given the relatively large velocity heterogeneities that are typically encountered in the crust and uppermost mantle (**Figure 7**). This means the wide-angle traveltime inverse problem is always treated as nonlinear, in which both the velocity field and ray paths are treated as unknowns to be solved for. This also means the model can be parametrized any number of ways using velocity or slowness, and nodes, cells, or splines, since the problem's nonlinearity must be dealt with regardless of the parametrization. Most often this means a linearized gradient approach is applied in which a starting model must be provided and both the model and ray paths are

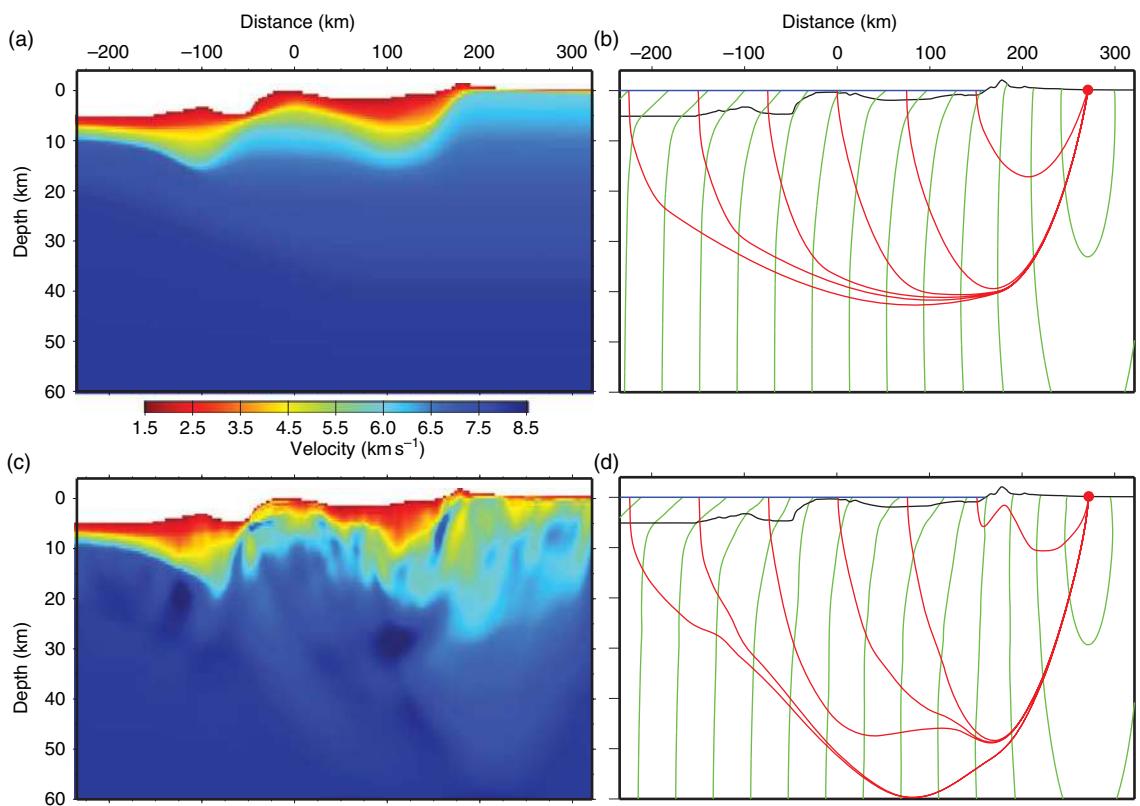


Figure 7 Example from an onshore–offshore study of the Venezuelan margin at 67.5 W (Zelt et al., 2004) to illustrate one aspect of nonlinearity in the inversion of wide-angle data. (a) Starting velocity model that provides an rms traveltime residual with respect to the picked times of ~ 1.0 s. (b) First-arrival ray paths between shots 75 km apart and receiver ~ 100 km inland (red) and isochrones (green) for the model in (a). Black line is bathymetry/topography; blue line is sea surface. (c) Final velocity model that provides an rms traveltime residual with respect to the picked times of about ~ 0.1 s. (d) First-arrival ray paths between the same shots and receiver as in (b) for the model in (c); details the same as in (b). Note the considerable difference between the ray paths in the two models as a result of the heterogeneity in the final model.

updated over a series of iterations with the hope that there will be convergence to an acceptable model.

For virtually all traveltime problems, the model is discretized using cells, nodes, splines, or other interpolating functions; in the latter two cases the discrete model parameters are the coefficients of the interpolating functions. In the simplest formulation of the tomography problem, the model is parametrized using constant-slowness cells, in which case the equation for the i th data becomes

$$t_i = \sum_j l_{ij} s_j \quad [45]$$

where l_{ij} is the length of the i th ray in the j th model cell and s_j is the slowness in the j th cell. In vector-matrix form this is

$$\mathbf{t} = \mathbf{Ls} \quad [46]$$

Applying a Taylor series expansion to this equation, assuming the ray paths are independent of slowness, and keeping only the linear term yields the perturbation equation

$$\delta\mathbf{t} = \mathbf{G}\delta\mathbf{s} \quad [47]$$

where $\delta\mathbf{t}$ is the data residual or misfit vector equal to the difference between the observed traveltimes and those predicted by a prior model, and $\delta\mathbf{s}$ is the difference between the unknown model and the prior model; the unknown model is also called the estimated model. The partial derivative matrix, \mathbf{G} , contains the elements $g_{ij} = \partial t_i / \partial s_j$, and for the constant-slowness cell parametrization, $g_{ij} = l_{ij}$ or $\mathbf{G} = \mathbf{L}$. In the general case, the elements of the partial derivative matrix are $g_{ij} = \delta t_i / \delta m_j$ where m_j is the j th model parameter, which could be the velocity at a node or the coefficient of an interpolating function, or the position of an interface within the velocity model (e.g., Zelt and Smith, 1992). In the general case, the perturbation equation becomes

$$\delta\mathbf{t} = \mathbf{G}\delta\mathbf{m} \quad [48]$$

The elements of the partial derivative matrix \mathbf{G} are usually calculated analytically, to avoid the potential inaccuracy of numerical differencing and the extra computation needed to trace additional rays. The approximations involved in the analytic partial derivatives, for example, the stationary ray-path assumption, are typically not a problem since the resultant gradient direction in model space can be improved with each iteration of the nonlinear process.

The perturbation equation is not solved directly because the unknown model parameters are typically under- or mix-determined (Menke, 1989), depending on the model parametrization; with relatively few model parameters it is possible for the problem to be overdetermined, but even in this case the perturbation equation is not solved directly because it is wise to constrain the magnitude of the model perturbation to avoid violating the linearization assumption. Thus, regardless of whether the problem is underdetermined or overdetermined, model constraints, in addition to the observed data, are included to stabilize the solution. Since all observed data contain noise, it makes no sense to overfit noisy data, so additional model constraints are required to select one model from an infinite number that will statistically predict the observed data at the equivalent desired misfit according to the estimated noise level. This issue points out the nonuniqueness of all inverse problems involving real data, regardless of whether the system of equations is overdetermined or underdetermined.

The additional model constraint is called regularization (e.g., Scales *et al.*, 1990), and in addition to stabilizing a solution, it is an effective way of steering the solution towards models with desirable predefined characteristics. The regularization is most often in the form of the zero-, first-, or second-order spatial derivatives of the estimated model parameters, or their perturbation from a reference model. This is because it is usually considered desirable to seek an estimated model that is as close as possible to a prior reference model, and/or a model that has minimum structure as measured by its spatial derivatives in keeping with Occam's principle (e.g., Constable *et al.*, 1987; Menke, 1989).

The most common forms of regularization in traveltime problems are the minimization of the model's perturbation from a prior model, and the minimization of the second-order spatial derivative of either the whole model or its perturbation from a prior model. These are called the smallest and smoothest models, respectively. Any combination of model constraints may be included as a part of the regularization to form the objective function, $\Phi(\mathbf{m})$, where \mathbf{m} is the vector containing the estimated model parameters. The objective function usually measures the square of the data residual vector and the square of the model constraints so that minimizing it leads to a linear system of equations that is amenable to efficient algorithms for their exact or

approximate solution. One example of a practical objective function for the traveltime problem is

$$\Phi(\mathbf{m}) = \delta\mathbf{t}^T \mathbf{C}_d^{-1} \delta\mathbf{t} + \lambda \left\{ \beta \left[\alpha (\mathbf{v}^T \mathbf{W}_h^T \mathbf{W}_h \mathbf{v} + s_z \mathbf{v}^T \mathbf{W}_v^T \mathbf{W}_v \mathbf{v}) \right. \right. \\ \left. \left. + (1-\alpha) \Delta\mathbf{v}^T \mathbf{W}_p^T \mathbf{W}_p \Delta\mathbf{v} \right] \right. \\ \left. + (1-\beta) [\mathbf{z}^T \mathbf{W}_z^T \mathbf{W}_z \mathbf{z}] \right\} \quad [49]$$

where $\mathbf{m} = \mathbf{v} + \mathbf{z}$; \mathbf{v} and \mathbf{z} are vectors containing the estimated model parameters defining the velocity (or slowness) field and the depth of interfaces; $\Delta\mathbf{v}$ is the velocity perturbation vector equal to $\mathbf{v} - \mathbf{v}_0$, and \mathbf{v}_0 is the reference velocity model vector. \mathbf{C}_d is the data covariance matrix containing the estimated pick uncertainties, providing the appropriate up-weighting and down-weighting of the low- and high-noise data, respectively. \mathbf{W}_h and \mathbf{W}_v are the horizontal and vertical roughness matrices containing the second-order spatial finite-difference operators that measure the roughness of the velocity field in the horizontal and vertical directions, respectively; \mathbf{W}_p is the velocity perturbation weighting matrix which is a diagonal matrix containing the weights applied to the perturbation between each estimated and reference velocity model parameter; \mathbf{W}_z is the interface roughness matrix containing the first-order spatial finite-difference operators that measure the variation of the interfaces.

When applying derivative operators to the velocity field, it is common to use different operators to measure the horizontal and vertical structure, and weight these differently, since one expects the Earth to contain more structure vertically than horizontally. Any or all of these operators may be normalized by the reference model values so that relative quantities are penalized as opposed to absolute values (e.g., Toomey *et al.*, 1994). In addition, the operators can be weighted according to their spatial position, for example, penalize structure more in the deep portion of the model versus the shallow portion since with wide-angle data one would generally expect decreasing resolution with depth. The relative weight of each term in the objective function is determined by the free parameters, λ , β , α , and s_z . The inversion is stabilized by systematic reduction of the overall amount of regularization, controlled by λ , allowing long-wavelength structure in the initial iterations and progressively finer model structure in later iterations (e.g., Zelt and Barton, 1998).

Minimizing the objective function with respect to the unknown model parameters (\mathbf{v} and \mathbf{z}) leads to a

system of linear equations that may be very large, depending on the number of data and model parameters. By today's standards, a small problem would involve on the order of 10^3 , or less, data and model parameters, and a large problem would involve 10^5 , or more, data and model parameters; the former will likely be 2-D problems, the latter will be 3-D.

The example objective function can be simplified or slightly modified to correspond to those used in most of the popular traveltime inversion and tomography algorithms. For example, the Zelt and Smith (1992) inverse method includes only perturbation constraint on the velocity and interface parameters with respect to the model from the previous iteration; this is the classical damped least-squares solution (Menke, 1989). The Zelt and Barton (1998) regularized tomographic method includes only smoothness constraints on the velocity field. Thus, these two algorithms can be viewed as end-members of the same regularized inverse approach we have presented, and most algorithms in use today fall somewhere in between. The main differences between the algorithms discussed in the next section lie not just in the details of the objective function, but more so in the form of model parametrization, forward calculation, and the types of arrivals considered.

If the linear system is large, it will typically be very sparse with 99.9% or more zero elements. In this case, it can be solved efficiently using an iterative, sparse linear-system solver, for example, the LSQR variant of the conjugate gradient algorithm (Paige and Saunders, 1982; Nolet, 1987). Another effective approach is the subspace method, particularly for mixed-parameter problems (Rawlinson *et al.*, 2001). If the linear system is relatively small, it can be solved directly using standard matrix inversion routines, such as LU decomposition (Press *et al.*, 1992).

Including both velocity and interface parameters in a single inversion scheme makes the problem significantly more complicated. There will be more model non-uniqueness because of tradeoffs between the two parameter types, and more subjective prior information will be required in order to deal with the increased ambiguity (Figure 8). Also, more testing will be required to ensure that the tradeoffs are fully understood.

When regularization is applied to the estimated model parameters or their perturbation from a fixed reference model, it is called a 'jumping' strategy (the former strategy is a special case of the latter in which

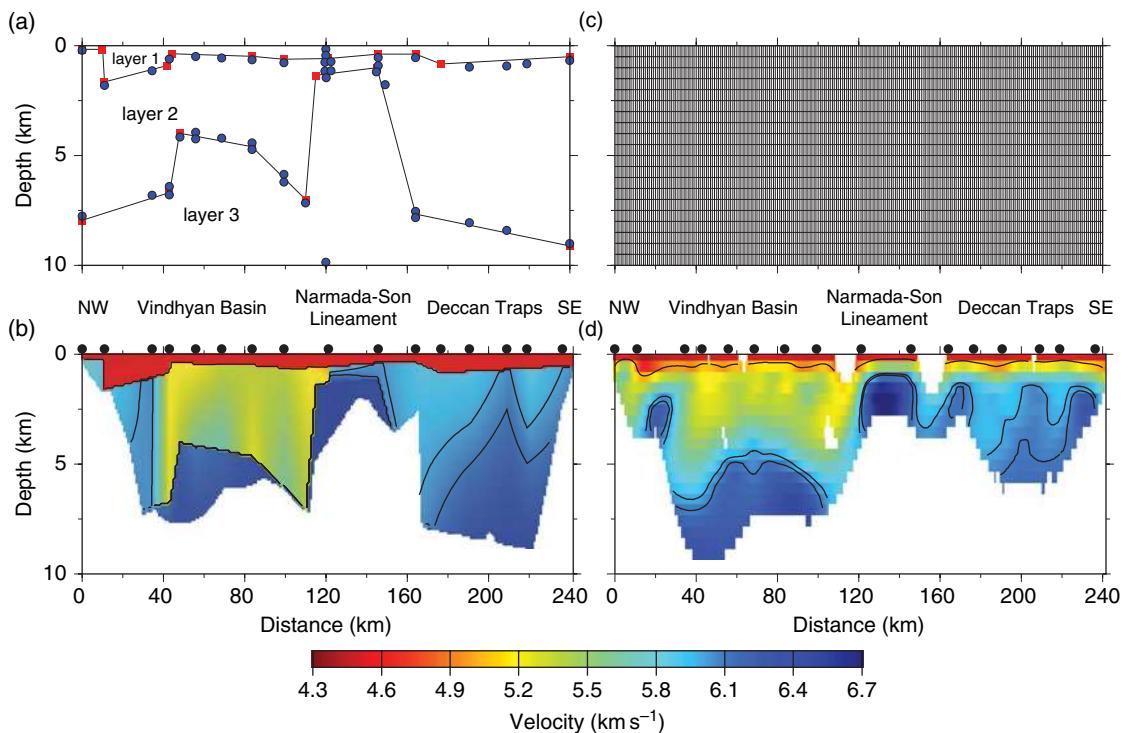


Figure 8 Example from Central India across the Narmada–Son lineament of applying two different traveltime inversion algorithms to the same wide-angle data (Zelt *et al.*, 2003). (a) Model parametrization using the Zelt and Smith (1992) algorithm; there are 43 velocity nodes (blue dots) and 21 interface nodes (red squares). (b) Velocity model corresponding to parametrization in (a). (c) Model parametrization using the Zelt and Barton (1998) algorithm; there are 7018 slowness cells. (d) Velocity model corresponding to parametrization in (c). Only those portions of the models sampled by ray paths are shown. Isovelocity contours of 5.0 km s^{-1} (black) and 6.0 and 6.1 km s^{-1} (white) indicated. Shot point locations (black dots) and geologic features labeled above the models.

the reference model is zero); when it is applied to the perturbation between the estimated model and the model from the previous iteration, it is called ‘creeping’. The rationale for jumping is that the final model will be less dependent on the starting model since the model constraints are relative to a fixed model at each iteration, and not an intermediate model encountered along the path in model space between the starting and final models. Creeping is used when the starting model and intermediate models are deemed to be significant and there is a desire for the final model to represent the end of a series of related models. The jumping strategy is more objective, whereas creeping allows the solution to be steered more easily to a desired result.

Almost all traveltime inversion and tomography algorithms today employ a jumping strategy (Shaw and Orcutt, 1985). The Zelt and Smith (1992) algorithm uses creeping to achieve what has been described as a method for automated forward modeling.

Assuming uncorrelated, Gaussian picking errors, and a model parametrization that does not limit the degree to which the observed data can be matched by the predicted data, a final model should be chosen that provides a normalized misfit, χ^2 (Bevington, 1969), of one:

$$\chi^2 = \frac{1}{N} [\delta \mathbf{t}^T \mathbf{C}_d^{-1} \delta \mathbf{t}] \quad [50]$$

where N is the number of data. A model that provides a χ^2 value less than 1 means the observed data are being overfit, and therefore, the noise in the data is also being fit. Although the χ^2 criterion is a good rule of thumb, there are several reasons why it should not always be followed strictly. First, traveltime picking errors of wide-angle data are likely never uncorrelated because each trace is usually picked from a shot or receiver gather by considering the correlation of waveforms adjacent to the trace being picked, either by eye or using a

cross-correlation picking algorithm (Zelt, 1999). Second, for relatively sparse wide-angle data from a region with strong lateral heterogeneities, it may be necessary to use so many independent model parameters in order to achieve $\chi^2 = 1$ that the constraint on some parameters is unacceptably small, in which case fewer parameters and a χ^2 value greater than one may be preferable (Zelt, 1999). An inability to reach $\chi^2 = 1$ may be because of picking inconsistencies of reciprocal pairs, or where two profiles intersect; in either case, the inconsistencies should either be corrected or used as the basis for assigning the pick uncertainties in the first place (e.g., Zelt *et al.* 2006a; Park *et al.*, in press).

Objective functions using L_p -norms with $p < 2$ may be desirable because the solutions will be less influenced by outliers. Iteratively reweighted least-squares (IRLS) is a method for approximating the use of an L_p -norm (Scales *et al.* 1988). Since it is an iterative approach, it can be incorporated into a non-linear traveltime algorithm with virtually no additional computation because there is already a need for an iterative solution. IRLS is not commonly used in wide-angle traveltime inversion probably because outliers are unlikely when picking traces within gathers, as opposed to individual seismograms as in earthquake seismology.

Global optimization (GO) methods are well suited to very nonlinear problems since their dependence on the starting model is small or none at all (Sen and Stoffa, 1995). However, they are computationally demanding and limited to problems in which the forward calculation is very quick and there are relatively few model parameters. This means GO is not commonly applied to fine-grid traveltime inversion problems, except to find a suitable starting model for a linearized gradient method. Pullammanappallil and Louie (1994) and Boschetti *et al.* (1996) applied GO schemes to small 2-D traveltime problems.

1.08.14 Travelttime Inversion and Tomography: Algorithms

Up until the 1990s, 2-D ray tracing and travelttime forward modeling through trial-and-error means, often supplemented by comparisons with synthetic seismograms, was the most common method for the analysis of wide-angle data. Popular algorithms were those of Cerveny *et al.* (1977) and McMechan and Mooney (1980). Trial-and-error forward modeling is still used today, at least in part because

of a sense that either high data quality, fine spatial sampling, or relatively simple geology is needed in order for inverse methods to work (e.g., Grad *et al.*, 2006).

The advantages of inversion over forward modeling include the ability to (1) explore model space more thoroughly to better understand what structure is required by the data and what structure is consistent with the data, that is, model nonuniqueness, (2) quantify model errors and resolution, (3) handle larger datasets, and (4) fit the data appropriately given the data uncertainties. The Zelt and Smith (1992) algorithm allows for a compromise approach, best described as automated forward modeling, given the ability to focus on selected model parameters, as opposed to the entire model, as would be the case in trial-and-error forward modeling. The algorithm's inverse mode can be used to quickly determine the selected model parameter values so as to best satisfy the data from all shots and receivers simultaneously, usually within a few iterations. Thus, this algorithm combines the parameter selective aspect of forward modeling with the speed of inversion. In the remainder of this section we briefly describe many of the algorithms available today, each with its own capabilities and limitations. There is likely a suitable travelttime inversion or tomography algorithm for just about every type of wide-angle data set.

Within the eastern European community, methods for the analysis of wide-angle travelttime data have been developed that have not been adopted worldwide (e.g., Pavlenkova, 1982; Ilchenko, 1985). They share some characteristics with the algorithms used primarily in the engineering and petroleum industry for near-surface studies and refraction statics, for example, the generalized reciprocal method (Palmer, 1981), but they are rarely applied to crustal data, and therefore will not be discussed here. Beginning in the 1980s, formal inverse theory was first applied to 2-D wide-angle travelttime inversion. About 10 years earlier it had been applied to earthquake travelttime data to derive 3-D velocity models using only first arrivals (Aki and Lee, 1976; Crosson, 1976). The delay in applying inversion to wide-angle data were the issues of data sparsity (e.g., typically only a few shots and/or receivers) and the desire to use both first and later arrivals (e.g., intra-crustal and crust–mantle reflections, and later refracted arrivals). Modeling later arrivals means having to include interfaces in the model parametrization, and the resultant complexity of dealing with a mixed inverse problem. Some of the earliest published 2-D

traveltime inversion algorithms were presented by Firbas (1981) and White (1989) which used a regular grid and only first arrivals, and Spence *et al.* (1985) and Huang *et al.* (1986) which allowed an irregular model grid and later arrivals.

In the 1990s, many 2-D and 3-D traveltimes inversion and tomography algorithms were developed. We briefly describe the key features of the more widely used and innovative algorithms. Lutter and Nowack (1990) and Lutter *et al.* (1990) developed a 2-D inversion algorithm using a regular grid of nodes and numerical ray tracing that allows for the independent inversion of first arrivals and reflections for velocity and interface geometry, respectively. The Zelt and Smith (1992) 2-D algorithm is the exact opposite in many respects. An irregular grid of velocity and interface nodes can be used, and any type of refracted or reflected arrival can be inverted simultaneously for velocity and interface geometry (Figure 8). As mentioned earlier, the inversion can be applied to any subset of the total model parameters, facilitating an automated forward modeling approach and making it straightforward to incorporate prior information. Zelt (1994) and Clowes *et al.* (1995) used the Zelt and Smith (1992) 2-D algorithm to simultaneously invert refraction and reflection times from a network of 2-D profiles such that the model parameters at the intersection points were linked to ensure consistency. This approach can be used to infer 3-D structure from 2-D data, and develop a starting model for the 3-D inversion of inline and offline data (e.g., Zelt *et al.*, 1999).

Hole (1992) developed a widely-used 3-D first-arrival tomography algorithm using the Vidale (1990) forward modeling scheme and back-projection to solve for a smooth velocity field. Hammer *et al.* (1994) developed a 3-D first-arrival tomography algorithm specially suited to sparse data using a spectral, continuous function model parametrization. Toomey *et al.* (1994) developed a 3-D first-arrival tomography algorithm to obtain a smooth velocity field in which the velocity grid is ‘draped’ from an irregular bathymetric surface by vertically shearing the columns of nodes to accurately model the sea-floor relief. Vertically sheared grids are particularly important for marine data, especially at mid-ocean ridges, where a large velocity discontinuity may exist. Forward modeling through this type of parametrization is straightforward using the shortest-path method (Toomey *et al.*, 1994). Similar algorithms with sheared grids have been developed by Van Avendonk *et al.* (1998) and Korenaga *et al.* (2000),

although they are limited to 2-D models, but include reflections, and use the hybrid shortest-path/bending scheme described earlier. The main difference between the Van Avendonk *et al.* (1998) and Korenaga *et al.* (2000) algorithms is the former uses first arrivals that can turn above or below a reflecting interface at which there is no velocity discontinuity, whereas the latter only uses first arrivals that turn above the reflecting interface.

Lailly and Sinoquet (1996) developed a 2-D algorithm for inverting reflection times for a smooth velocity and interface model using the wavefront-tracking method of Podvin and Lecomte (1991). Zelt and Barton (1998) developed a 3-D first-arrival tomography algorithm using smoothing regularization and compared the results with those from the back-projection method of Hole (1992). The results showed that for the same level of fit to the data, regularized inversion can provide a smoother model. Zelt *et al.* (1999) developed a 3-D simultaneous refraction and reflection tomography algorithm solving for smooth velocities and multiple interfaces. McCaughey and Singh (1997) and Hobro *et al.* (2003) developed related 2-D and 3-D simultaneous refraction and reflection tomography algorithms that solve for smooth velocities and interfaces with the allowance for discontinuities across the layer boundaries.

Most of the algorithms described above are fairly general purpose in nature and follow more or less from the objective function presented in the previous section. However, many more specialized algorithms have been developed. We describe a few of those here to give a sense of what is possible. Hole *et al.* (1992) developed an algorithm for determining a 3-D interface with known velocities above and below using first-arrivals. Zhang *et al.* (1998) used the shortest-path method to develop a 2-D algorithm for refraction and reflection tomography in which only refracted arrivals originating above the reflecting interface are considered. A novel aspect of their approach is the inversion of traveltimes instead of points, specifically average slowness and apparent slowness. They claim this balances the contribution from short and long ray paths, and enhances resolution and convergence speed (Zhang and Toksöz, 1998). Rawlinson *et al.* (2001) and Rawlinson and Sambridge (2003b) developed an algorithm for the inversion of refraction and reflection times using a 3-D multilayered model parametrization. Interfaces are defined by a nonuniform node distribution and velocities vary linearly with depth so ray paths are

calculated analytically as piecewise circular arcs using a shooting method. Trinks *et al.* (2005) present a method for simultaneous refraction and reflection inversion using a 2-D layered model parametrization which adapts to nonuniform ray coverage such that the cell size is inversely proportional to the local ray density.

1.08.15 Amplitude Modeling

The earliest analysis of crustal wide-angle data involved modeling the amplitudes, as well as the traveltimes, of the identifiable arrivals. In part this was because the numbers of shots and receivers typically were so few that amplitudes were used to extract more information from the data than just using the traveltimes alone. Two of the most common methods used for amplitude modeling have been the reflectivity method (Fuchs and Muller, 1971) and asymptotic ray theory (Cerveny *et al.*, 1977). The former has the advantage of including the complete elastic wavefield for a 1-D model. The latter has the advantage of being applicable to laterally inhomogeneous (2-D) models. The drawbacks of ray methods are their infinite frequency approximation and the need to specify the ray paths for each arrival type being modeled. These disadvantages are typically not a serious problem with crustal data, since it is usually only the large-scale amplitude trends of a few arrival types, such as the primary refractions and reflections, that are modeled.

To overcome some of the limitations of asymptotic ray theory, ray-based methods that incorporate finite-frequency effects were introduced, such as Gaussian beams (Cerveny *et al.*, 1982; Weber, 1988) and Maslov theory (Chapman and Drummond, 1982). These methods can accurately predict the frequency-dependent amplitudes associated with triclications, diffractions, and geometrical shadow zones. However, these methods have never experienced widespread use in crustal seismology because they lack the simplicity and predictability of asymptotic ray theory. Full-wavefield acoustic and elastic 2-D finite-difference algorithms (e.g., Levander, 1988; Robertsson *et al.*, 1994) have been applied in a few crustal studies. Their heavy computational demand has meant that only a few simulations are typically run for the purpose of visual comparison with the observed seismograms (e.g., Parsons *et al.*, 1996; Lendl *et al.*, 1997; Gorman *et al.*, 2006),

although in the future they will likely become more commonplace.

Although traveltime data are relatively insensitive to vertical velocity gradients and velocity discontinuities, such features may be well constrained by amplitude data (Braile and Smith, 1975). However, full-wavefield studies using models with fine-scale structure that is not resolved by traveltime data show that it can have a significant effect on wide-angle amplitudes (Levander and Holliger, 1992; Lendl *et al.*, 1997) as discussed later. Thus, only the large-scale amplitude trends of primary arrivals should be modeled (e.g., Zelt and Forsyth, 1994). Velocity gradients and discontinuities derived through amplitude modeling may be used as constraints during traveltime inversion (e.g., Zelt *et al.*, 1993). For amplitude modeling it is common to plot synthetic seismograms, in which case the same trace spacing and amplitude scaling should be used for the synthetic and real data (e.g., Grad *et al.*, 2006). A comparison of the observed and calculated amplitude-distance curves for individual phases allows a more quantitative comparison (e.g., Zelt and Forsyth, 1994; Zelt and White, 1995). As the number of shots and receivers used in typical wide-angle experiments has increased dramatically over the past 20 years, the resolution from traveltime data alone has also greatly improved. For this reason, and given the appreciation of the effects of fine-scale structure (Section 1.08.17), amplitude modeling is often ignored today.

1.08.16 S-Waves, Density, Attenuation, and Anisotropy

The majority of crustal wide-angle seismic studies today use only P-wave arrival times to constrain P-wave velocity structure. This is because P-wave arrival times are almost always the most reliable feature that can be extracted from crustal wide-angle data, and their constraint on P-wave velocity is probably the most robust data–model–parameter relationship. Second, there is a sense that P-wave velocity models are the most important in terms of addressing the key geologic and tectonic questions in most crustal studies, although this may be a perception driven by the first reason. Although rare today, studies that go beyond the determination of 2-D and 3-D P-wave velocity models will likely become more common in the future given the need to justify new data acquisition and analysis when so much good data already exist from many sites around the world.

S-waves and converted phases are sometimes recorded well in wide-angle experiments, even by vertical-component geophones. This allows S-wave velocity models to be developed, typically using the same traveltimes modeling and inversion algorithms described earlier. When combined with P-wave models, Poisson's ratio can also be estimated. Using S-wave velocities or Poisson's ratio in addition to P-wave velocities narrows the range of possible rock types in an interpretation (Christensen, 1996). Examples of using S-waves from wide-angle surveys include Gohl and Pedersen (1995), Carbonell *et al.* (1996), Musacchio *et al.* (1997), Darbyshire *et al.* (1998), Stoerzel and Smithson (1998), and Fernandez-Viejo *et al.* (2005).

In theory, rock densities could be inferred from amplitude modeling, but for reasons already discussed, amplitude modeling of wide-angle data is no longer common. Full-waveform modeling or inversion (discussed later) could be used to infer densities more reliably, but the typical procedure is to infer densities from P-wave velocities based on lab and field data compilations (Barton, 1986; Christensen and Mooney, 1995) in order to reduce the number of independent model parameters. It is fairly common to perform gravity modeling after obtaining a P-wave velocity model from wide-angle data, deriving the initial density model by converting the P-wave velocities to densities using an empirically derived velocity–density relationship (e.g., Zelt and White, 1995; Christeson *et al.*, 2001). Brocher (2005) presents an empirical velocity–density relationship based on extensive compilations of velocity–density data.

The attenuation of seismic waves through anelasticity is a poorly understood phenomenon. The dimensionless quantity Q is a measure of the anelasticity experienced by seismic waves, and as such its value can be spatially mapped using seismic data. The two methods commonly used to estimate Q from seismic data involve modeling amplitudes directly or using spectral ratios. Amplitude methods should be viewed with caution for the reasons already stated regarding amplitude modeling. Estimates of Q from wide-angle data are rare, but have been made by Braile (1977) and White and Clowes (1994) using amplitude methods, by Hashizume (1979), Zelt and Ellis (1990), and Wilcock *et al.* (1995) using spectral ratios, and by Li *et al.* (2006) using both methods on the same data.

Anisotropy estimates from wide-angle data are also rare, but are most common in oceanic-crust

and upper-mantle studies (e.g., Caress *et al.*, 1992; Dunn and Toomey, 2001). One problem is that multicomponent crustal data are rarely recorded. Stoerzel and Smithson (1998) estimate crustal anisotropy from shear-wave splitting using three-component wide-angle data. The isotropic assumption made in the vast majority of wide-angle lithospheric studies has rarely been questioned or tested, but it may be an important effect, particularly in the sedimentary section and upper mantle. Its importance in 2-D and 3-D studies will depend on the type of anisotropy involved. For example, the effect of anisotropy due to subhorizontal fabric or layering could be significant when modeling coincident wide-angle and near-vertical data (Jones *et al.*, 1999; Godfrey *et al.*, 2002). From lab studies, Christensen and Mooney (1995) show that anisotropy from preferred mineral orientation is likely to be most significant, as much as 10% or more, in upper and mid-crustal metamorphic rocks. Sroda (2006) reports 8–10% azimuthal anisotropy for P-wave velocity in the upper crust using profiles of different orientation.

1.08.17 Fine-Scale Heterogeneities

Full-wavefield studies using models with wavelength-or subwavelength-scale heterogeneities have shown that the traveltimes, amplitudes, and wavefield can be significantly effected (e.g., Muller *et al.*, 1992; Levander and Holliger, 1992), raising questions concerning the accuracy of results obtained using ray and wavefront tracking methods. For traveltimes, there may be a structural form of anisotropy if there is a preferred orientation of the heterogeneities. Even without a preferred orientation, the traveltimes will likely not correspond to the bulk velocity, but will be biased toward a higher velocity when using first-arrival times. Either way, traveltime methods will still constrain large-scale heterogeneities, at least in a relative sense, but the absolute velocities may be biased with respect to the bulk velocities depending on the nature of the fine-scale structure and the seismic wavelengths.

Even more so than the traveltimes, the amplitudes and wavefield can be significantly altered depending on the nature of the fine-scale structure (Levander and Holliger, 1992; Lendl *et al.*, 1997). For this reason, only the large-scale trend of amplitude-versus-offset variations or the overall relative amplitudes of different arrival types should be modeled when using

velocity models derived from infinite-frequency methods (e.g., Zelt and Forsyth, 1994; Zelt and White, 1995). Methods for estimating stochastic parameters that describe the fine-scale structure have been developed (Poppeliers and Levander, 2004). This information can be used to add a stochastic fine-scale structure to a long-wavelength model derived from traveltimes, and thereby allow a comparison between the observed and predicted seismograms using full-wavefield methods. Although usually limited by the computational requirements of full-wavefield methods, some trial-and-error forward modeling may be applied to refine the short- or long-wavelength model parameters (e.g., Lendl *et al.* 1997; Gorman *et al.*, 2006). Alternatively, it may be possible to estimate the fine-scale structure deterministically given sufficiently high-quality data using full-wavefield inversion techniques (Section 1.08.21).

1.08.18 Joint Inversion

Wide-angle data can be jointly inverted with other data that depend on P-wave velocity. Coincident near-vertical reflection data can be used in several ways (Zelt, 1999). From stacked data, the reflector geometries and interval velocities can be used as prior information in the regularization to constrain a layered velocity model (e.g., Bosch *et al.*, 2005). Alternatively, arrivals in prestack reflection data can be picked and inverted jointly with the wide-angle data. This approach will provide the most thorough use of the reflection data in terms of additional model constraint, but it is often difficult to pick weak events in prestack data. The most common approach is to pick reflections from a stacked reflection section and invert these data simultaneously with the wide-angle data by modeling zero-offset reflections (e.g., McCaughey and Singh, 1997; Zelt *et al.*, 2003). There are potential pitfalls when using coincident reflection data. First, incorrectly correlating the near-vertical reflection event with the corresponding wide-angle event or layer boundary; Jaiswal *et al.* (2006) present a way to avoid this problem. Second, as previously mentioned, errors and model distortion will occur if there is transverse isotropy, since wide-angle data are primarily sensitive to horizontal velocities and near-vertical reflection data are primarily sensitive to vertical velocities (Jones *et al.*, 1999; Godfrey *et al.*, 2002).

The second type of data that can be jointly inverted with wide-angle data in a straightforward manner is local and regional earthquake body-wave arrival times. An algorithm to jointly invert active and passive data needs to be 3-D and needs to be able to determine earthquake hypocenters in addition to velocities, either simultaneously or by iterating back and forth between locations and velocities. Benz *et al.* (1996), Symons and Crosson (1997), and Ramachandran *et al.* (2005) each developed similar algorithms to simultaneous invert active and passive data; the former uses the forward calculation method of Podvin and Lecomte (1991), the latter two use the Vidale (1990) scheme. Hole *et al.* (2000b) advocate a nonsimultaneous approach in their determination of 3-D velocity and hypocenters using active and passive data.

The close relationship between seismic velocity and density (Barton, 1986; Brocher, 2005) lends gravity data to a joint inversion with wide-angle data. Nielsen and Jacobsen (2000) used the Zelt and Smith (1992) algorithm as the basis for a simultaneous inversion of refraction and reflection times with gravity data to derive a layered 2-D crustal model. Korenaga *et al.* (2001) carried out a joint inversion of traveltime and gravity data in which error propagation from the velocity model to the predicted gravity anomalies was taken into account. Roy *et al.* (2005) jointly inverted first arrivals and gravity data using a global optimization scheme to derive a smooth 2-D layered model. 3-D velocity and density are jointly inverted by Parsons *et al.* (2001). One important issue in joint seismic-gravity inversion is whether the coefficients of the velocity-density relationship are fixed or determined as part of the inversion.

1.08.19 Model Assessment

Model assessment is used to explore nonuniqueness, resolution, and model errors. Different assessment techniques will be appropriate depending on the type of data and model parametrization. Linear methods assume it is valid to consider only a local neighborhood of the final model within which the model–data relationship is linear. Nonlinear methods involve additional nonlinear inversions of the real data and synthetic data using the true source–receiver geometry of the experiment. The former methods tend to be quick and easy to apply, although potentially less reliable depending on the nonlinearity of the problem. The latter methods tend to be

computationally intensive. Zelt (1999) and Rawlinson and Sambridge (2003a) describe many of the techniques in use today; we will highlight only the most popular. Zelt *et al.* (2006a) apply several different techniques to the same 3-D dataset.

The simplest form of model assessment is to examine the ray-path coverage, either through plots of ray paths or ‘hit counts’ (the number of rays sampling each model cell or node). These can be misleading since a nonuniform distribution of ray angles may provide less independent model constraint than expected from the number of rays alone. Toomey *et al.* (1994) use a measure called derivative weight sum (DWS) equal to the sum of the partial derivatives for each model parameter. This is more meaningful than hit count since it weights the contribution from each ray according to the parameter’s sensitivity to that ray. However, it also fails to account for the degree of independence within the ray-path set. Other common linear assessment measures include the diagonals of the posterior resolution and covariance matrices (e.g., Zelt and Smith, 1992). These are more precise measures since they account for the independence of the ray-path set, but they are best used in a relative sense as opposed to absolute sense, since they do not account for the nonlinearity of the problem. Rows of the resolution matrix, known as resolution kernels, provide a spatial sense of the averaging or smearing of the true structure by the model (e.g., White, 1989; Zelt, 1999). Probably the most precise linear assessment method uses singular-value decomposition (SVD) since it is able to quantify the nature and degree of model constraint through construction of an orthogonal set of basis vectors that span model space, each with a specified weight in the model reconstruction (e.g., White, 1989). However, SVD is generally limited to relatively small problems, although approximate methods for large problems have been developed (e.g., Scales, 1989).

A parameter-selective algorithm such as the Zelt and Smith (1992) approach allows for a nonlinear assessment of the error bounds and spatial resolution for a single model parameter, or set of parameters (Zelt, 1999). In these tests, the real data and synthetic data are inverted in the same way that the final model was derived, allowing the full nonlinearity of the problem to be accounted for, including tradeoffs between model parameters (e.g., Holbrook *et al.*, 1994; Zelt and White, 1995; Christeson *et al.*, 1999). These tests are time consuming and only representative parameters can be tested in this way. A fine-grid

tomographic approach can facilitate a similar type of test. For example, Zelt and Barton (1998) examined one region of a model where there was significant lateral structure even though the ray coverage was low in this area. They added regularization to the inversion to force that region to remain laterally homogeneous and thereby establish the required tradeoffs elsewhere in the model.

Other nonlinear assessment techniques include trying different starting models, different values of the free parameters in the objective function, and exclusion of subsets of the data considered less reliable (e.g., Zelt *et al.*, 2006a). Using different model parametrizations and different inversion algorithms can be particularly illuminating, especially when one algorithm seeks a model that satisfies all prior information and preconceived notions of what is geological reasonable, and one algorithm seeks the minimum-structure model (Zelt *et al.*, 2003; Figure 8). In this way it is possible to determine what model structure is consistent with the data to facilitate hypothesis testing, while at the same time establishing what model structure is required by the data. White and Boland (1992), Korenaga *et al.* (2000), Holbrook *et al.* (2001), Zelt *et al.* (2003), Levander *et al.* (2005) and Grad *et al.* (2006) (Figure 9) apply different forward and inversion algorithms to the same wide-angle data.

One of the most common forms of nonlinear model assessment for wide-angle data is the checkerboard test for estimating model resolution (e.g., Day *et al.*, 2001; Morgan *et al.*, 2002; Schlindwein *et al.*, 2003; Evangelidis *et al.*, 2004). In these tests an alternating pattern of high and low anomalies is superimposed on a reference model and synthetic data are calculated for the ‘checkerboard’ model. These data are inverted using the same starting model and source-receiver geometry as real the data inversions and the recovered model will closely resemble the checkerboard pattern in regions of good constraint. Results from anomaly patterns with different polarity, registration, and orientation should be averaged to reduce the effects of changing ray coverage due to the nonlinearity of the problem (Zelt, 1998). Anomaly patterns for velocity and depth nodes can be treated separately or simultaneously for mixed problems (e.g., Zelt *et al.*, 1999).

The most computationally intensive form of model assessment involves a Monte Carlo procedure. Many realizations are performed in which randomized data are inverted using randomized starting models. The resulting models are used to compute

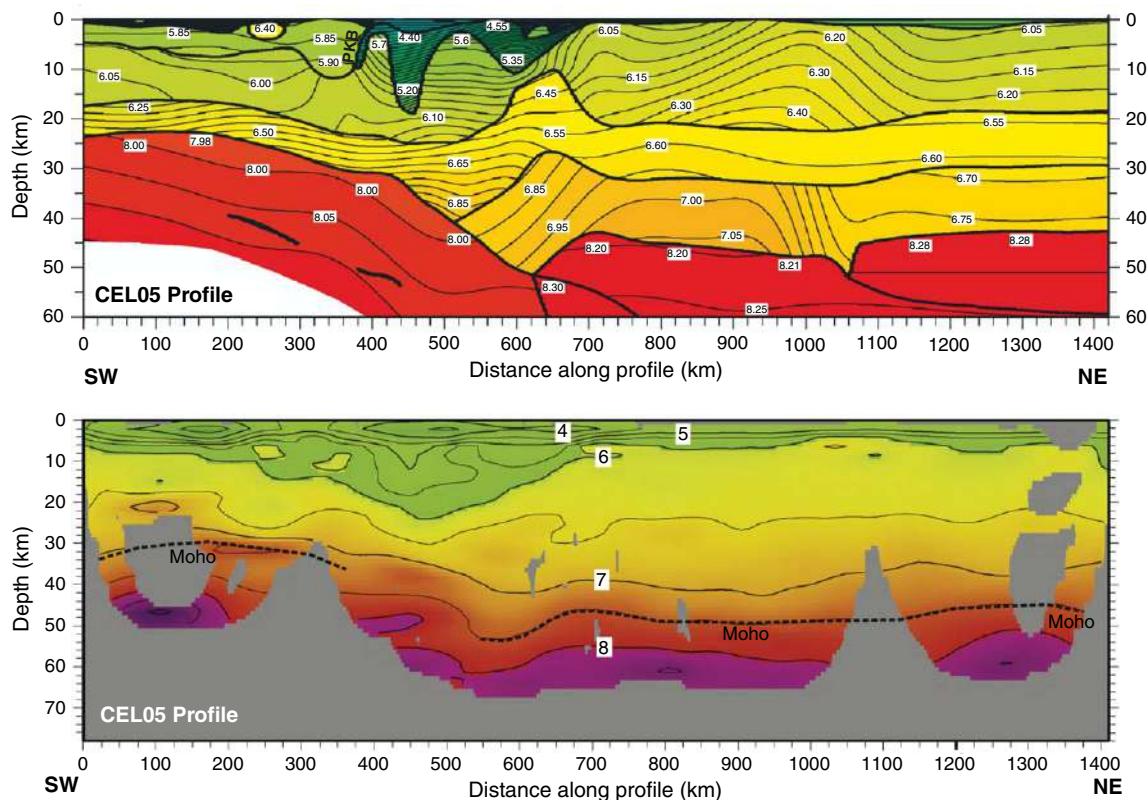


Figure 9 Example from the CELEBRATION 2000 experiment extending from Hungary to Russia in which two very different modeling approaches were applied to the same wide-angle data (Grad *et al.*, 2006). Data from 26 explosions were collected by 360 portable recorders along the profile. (a) P-wave model obtained by forward modeling of refraction and reflection traveltimes and amplitudes using a layered parametrization with a smooth velocity field between discontinuities using the method of Cerveny *et al.* (1977). (b) Model obtained by traveltime inversion using only first arrivals in which a smooth, minimum-structure was sought using the method of Zelt and Barton (1998). Velocity contours are labeled in km s⁻¹. The 7.5 km s⁻¹ contour was used as a guide to interpret the Moho in (b).

posterior model covariance and resolution estimates (Zhang and Toksöz, 1998; Zhang *et al.*, 1998; Korenaga *et al.*, 2000; Figure 10). This approach may not be feasible computationally for large problems.

1.08.20 Wide-Angle Migration

Conventional narrow-angle reflection and wide-angle seismology methods are beginning to merge in the academic community, as the number of shots and the station density in an average wide-angle survey has increased. Frequently intra-crustal, Moho, and sub-Moho reflections can be imaged using migration techniques applied to wide-angle data (McMechan and Fuis, 1987; Milkereit *et al.*, 1990; Holbrook *et al.*, 1992; Lafond and Levander, 1995; Henstock *et al.*, 1997; Henstock and

Levander, 2000; Morozov and Levander, 2002; Van Avendonk, 2004). However, the velocity model for wide-angle migration needs to be more accurate than for conventional migration, as minor lateral velocity errors are compounded for travel paths with large horizontal components. Typically, traveltime inversion and tomography provide velocity models suitable for wide-angle migrations (Zelt *et al.*, 1998). The greatest benefit from wide-angle migration, as with conventional reflection processing, is the ability to use the seismic wavefield to image wavelength-scale structure without having to explicitly identify, pick, and model individual arrivals within the wavefield, other than the primary phases already used in the traveltime modeling. Resolution reduces to about half of the vertical wavelength, which for waves traveling as far horizontally as vertically is significantly larger than for vertically incident waves only.

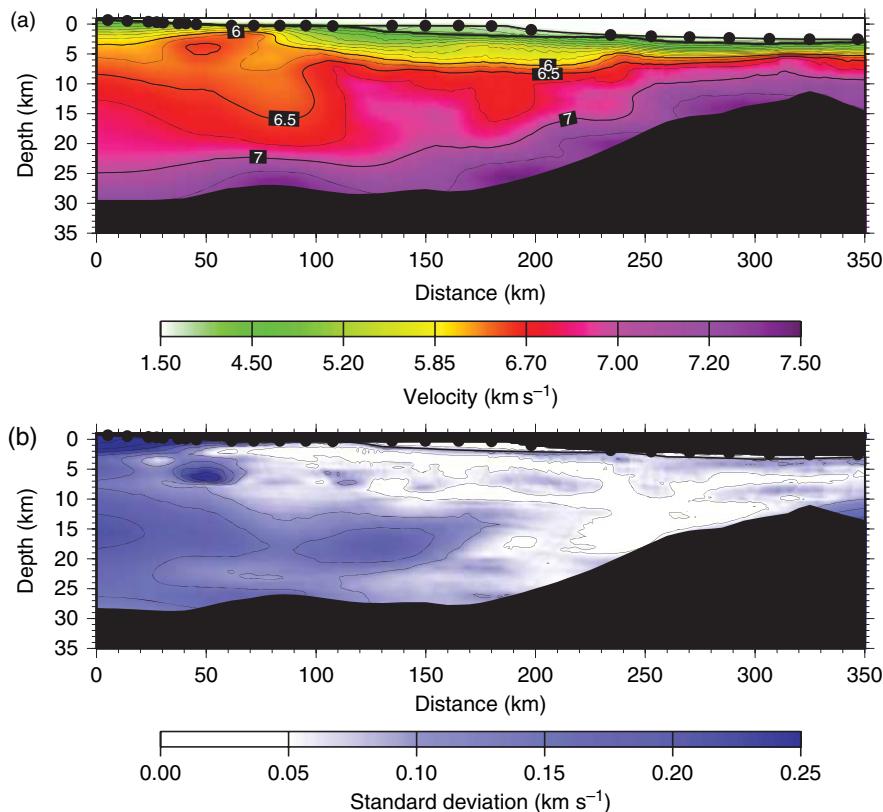


Figure 10 Example of model assessment using a nonlinear Monte Carlo procedure to estimate model variance (Korenaga *et al.*, 2000). (a) P-wave velocity model for the southeast Greenland continental Margin obtained by travelttime inversion of Pg and PmP arrivals recorded at 18 ocean-bottom instruments and eight land stations. This model was obtained by averaging 100 Monte Carlo ensembles. (b) Corresponding standard deviation for velocity and depth nodes; the standard deviation of the Moho is indicated by the width of the gray zone at the base of the crust.

A kinematic form of wide-angle migration can be carried out using a ray-tracing algorithm in which wide-angle reflection picks are modeled using floating reflecting surfaces (e.g., Holbrook *et al.*, 1994; Zelt and White, 1995; Wissinger *et al.*, 1997; Stoerzel and Smithson, 1998). These reflectors are typically relatively short interfaces with no associated velocity structure so that they ‘float’ within the velocity field of the model as defined by previous travelttime modeling of other phases. When a number of floating reflectors from different shots or receivers coalesce and align, then one can be confident that real structure is being imaged (e.g., Zelt and Forsyth, 1994).

1.08.21 Wavefield Inversion

Among others, Beylkin (1985), Beylkin and Burridge (1990), Tarantola (1984), Mora (1988), and Pratt *et al.* (1996, 1998) approach the active seismic imaging

problem as wavefield inversion, in which the image of the subsurface is defined as combinations of the perturbations of the material properties. For the constant density acoustic case this image is the field $\delta c(x)/c_0(x)$. Wavefield inversion, despite its computational costs, has several advantages over migration for image formation: (1) ideally one is calculating the correct amplitudes of the material perturbations; (2) the source time function, $f(t)$, can be determined as part of the solution rather than being estimated independently; (3) at least theoretically the development provides formal resolution estimates; and (4) perhaps most importantly, depending upon how one preconditions the data, both the background velocity field and the high-frequency fluctuation field can be estimated. The former is often referred to as waveform tomography and is applied to forward-scattered first arrivals with the backscattered field muted (e.g., Pratt *et al.*, 1998); the latter is reflection inversion and the data are preconditioned by

removing the first arrivals. As in the previous section, [Beylkin \(1985\)](#) and [Beylkin and Burridge \(1990\)](#) cast the inverse problem in terms of high-frequency asymptotics, and show that the inversion integrals are generalized inverse Radon transforms. This formalism was developed by [Bostock et al. \(2001\)](#) for inversion of teleseismic data. [Tarantola's \(1984\)](#) development relies on inverse theory, and being the most general, is repeated here. Letting G again be the Green's function and L the wave operator, we can write

$$p(x_r, t, x_s) = G(x_r, t, x_s, 0)^* f(t) \quad [51]$$

and

$$\begin{aligned} p &= q(c, f) \\ p &= q(m) \end{aligned} \quad [52]$$

with $m = (c, f)^T$ the vector of model parameters, and p the vector of predicted observations. We can define the covariance matrix of the observations as

$$C_p(x_r, t, x_s | x'_r, t', x'_s) = \sigma_{rs}^2 \delta_{rr'} \delta_{ss'} \delta_{tt'} \quad [53]$$

[Tarantola \(1984\)](#) defines the covariance matrix of the model as the expected variances in the solution based on prior information, and describes them with a Gaussian error model:

$$\begin{aligned} C_{cc}(x, x') &= \sigma_c^2 \exp\left(-\frac{1}{2} \left(\frac{(x_1 - x'_1)^2 + (x_2 - x'_2)^2}{a_H^2} + \frac{(z - z')^2}{a_z^2} \right)\right) \\ C_{ff}(t, t') &= \sigma_f^2 \exp\left(-\frac{1}{2} \left(\frac{(t - t')^2}{T_f^2} \right)\right) \end{aligned} \quad [54]$$

with crossvariances zero, and a_H , a_z , and T_f characteristic correlation lengths in the horizontal, vertical, and time coordinates. We note that many geologic structures have self-affine spatial covariance functions, and take the form of the von Kármán function (e.g., [Holliger and Levander, 1992](#)). The *a priori* covariance matrix is then

$$C_m = \begin{pmatrix} C_{cc} & 0 \\ 0 & C_{ff} \end{pmatrix} \quad [55]$$

Our initial guess of the model is

$$m_0 = \begin{pmatrix} c_0 \\ f_0 \end{pmatrix} \quad [56]$$

and note that the observations do not fit the initial model

$$p_0 \neq q(m_0) \quad [57]$$

We can define the data residual as the difference between the observations and the predictions

$$\delta d(m) = p_0 - q(m) \quad [58]$$

We wish to minimize

$$\begin{aligned} 2S(m) &= \|((p_0 - p), (m_0 - m))\|^2 \\ &= (p_0 - p)^* C_p (p_0 - p) + (m_0 - m)^* C_m (m_0 - m) \quad [59] \\ 2S(m) &= \delta d(m)^* C_p \delta d(m) + (m_0 - m)^* C_m (m_0 - m) \end{aligned}$$

where asterisk denotes complex conjugate. The minimum solution occurs where the gradient of S with respect to the model coordinates vanishes, giving

$$m - m_0 = C_m \nabla_m \delta d(m)^* C_p^{-1} \delta d(m) \quad [60]$$

[Tarantola \(1984\)](#) generalizes this expression by adding $C_m \nabla_m \delta d(m)^* C_p^{-1} \nabla_m (\delta d(m)(m_0 - m))$ to both sides, giving

$$\begin{aligned} m - m_0 &= (I + C_m \nabla_m \delta d(m)^* C_p^{-1} \nabla_m \delta d(m))^{-1} \\ &\quad \times C_m \nabla_m \delta d(m)^* C_p^{-1} (\delta d(m) \\ &\quad + \nabla_m \delta d(m)(m - m_0)) \quad [61] \\ m - m_0 &= W(C_m \nabla_m \delta d(m)^* C_p^{-1} \delta d(m) \\ &\quad + \nabla_m \delta d(m)(m - m_0))) \end{aligned}$$

which he describes as a ‘beautiful’ but ‘useless’ equation, as W is too large to compute for realistic problems. Of the various approximations to W , the simplest of these is a gradient algorithm for an iterative solution to the nonlinear seismic problem:

$$\begin{aligned} W_{app} &\approx \alpha I \\ m_{k+1} &= m_k + \alpha (C_m \nabla_m \delta d(m_k)^* C_p^{-1} \delta d(m_k) \\ &\quad - (m_k - m_0)) \end{aligned} \quad [62]$$

Other approximate iterative solutions include using the diagonal or banded diagonal forms of W . In these equations the forward model can be solved by any scheme capable of producing the field at any point, for instance, time- or frequency-domain finite-difference or finite-element methods.

In a series of papers Pratt and his colleagues develop a practical inversion scheme along similar lines based on 2-D frequency-domain finite-difference forward modeling. They assume that the *a priori*

covariance is infinite. The frequency-domain wave equation can be written as an operator:

$$\begin{aligned} \left[\nabla^2 + \frac{\omega^2}{c^2(x)} \right] p(x, x_s, \omega) &= f(x, x_s, \omega) \\ Lp(x, x_s, \omega) &= f(x, x_s, \omega) \\ p(x, x_s, \omega) &= L^{-1}f(x, x_s, \omega) \end{aligned} \quad [63]$$

where L is the discrete frequency-domain operator dependent upon the model parameters, and p is a function of the model parameters. Since L^{-1} generates p for a given source or collection of discrete sources f , the columns of L^{-1} are the Green's functions for the model. Restricting the model vector to material perturbations we can write eqn [59] in the more familiar form:

$$2S(\mathbf{m}) = \delta\mathbf{d}(\mathbf{m})^T \delta\mathbf{d}(\mathbf{m})^* \quad [64]$$

Minimizing this with respect to \mathbf{m} using a gradient method gives

$$\begin{aligned} \mathbf{m}^{(k+1)} &= \mathbf{m}^{(k)} - \alpha \nabla_m S(\mathbf{m}^{(k)}) \\ \mathbf{m}^{(k+1)} &= \mathbf{m}^{(k)} + \alpha \operatorname{Re} \left\{ \left[\frac{\partial \mathbf{p}}{\partial \mathbf{m}^{(k)}} \right]^T \delta\mathbf{d}(\mathbf{m}^{(k)})^* \right\} \\ \mathbf{m}^{(k+1)} &= \mathbf{m}^{(k)} + \alpha \operatorname{Re} \left\{ [\mathcal{J}^{(k)}]^T \delta\mathbf{d}(\mathbf{m}^{(k)})^* \right\} \end{aligned} \quad [65]$$

where \mathcal{J} is the Jacobian matrix of Fréchet derivatives of the calculated field, p_i with respect to the model parameters at the k th iteration, $m_j^{(k)}$. The last equation demonstrates several principles of imaging: the product of the frequency-domain data residuals with the derivatives of the estimated field constitutes a cross-correlation. The conjugate of the data residuals implies that the residuals are propagated in a time-reversed sense. The cross-correlation finds parts of the observed field that are missing from the predicted field. In particular, [Pratt et al. \(1998\)](#) show that the Jacobian finds those parts of the first-order scattered field that are present in the data but not in the model. Moreover noting that

$$\begin{aligned} \frac{\partial L}{\partial m_i} \mathbf{p} + L \frac{\partial \mathbf{p}}{\partial m_i} &= 0 \\ \frac{\partial \mathbf{p}}{\partial m_i} &= L^{-1} \left[\frac{\partial L}{\partial m_i} \mathbf{p} \right] = L^{-1} \mathbf{f}^{(i)} \\ \mathcal{J} &= L^{-1} [f^{(1)} \dots f^{(n)}] \\ \mathcal{J} &= L^{-1} F \end{aligned} \quad [66]$$

and comparing to eqn [65] we see that the Jacobian can be interpreted as a series of virtual sources

applied at the n parameter locations. The derivative of L with respect to the parameters turns eqn [65] to

$$\begin{aligned} \mathbf{m}^{(k+1)} &= \mathbf{m}^{(k)} + \alpha \operatorname{Re} \left\{ [L^{-1} F]^T \delta\mathbf{d}(\mathbf{m}^{(k)})^* \right\} \\ \mathbf{m}^{(k+1)} &= \mathbf{m}^{(k)} + \alpha \operatorname{Re} \left\{ [F^{(k)}]^T [L^{-1}]^T \delta\mathbf{d}(\mathbf{m}^{(k)})^* \right\} \end{aligned} \quad [67]$$

A number of authors have noted that the first iterate of [67] is equivalent to prestack migration: the data residual is calculated as the predictions between the smooth velocity-impedance field (i.e., there are no backscattered waves predicted), so the residual is just the back-projected set of observations

$$\begin{aligned} \delta\mathbf{m}^{(1)} &= \alpha \operatorname{Re} \left\{ [\mathcal{J}^{(0)}]^T \delta\mathbf{d}(\mathbf{m}^{(0)})^* \right\} \\ \delta\mathbf{m}^{(1)} &= \alpha \operatorname{Re} \left\{ [F^{(0)}]^T [L^{-1}]^T \delta\mathbf{d}(\mathbf{m}^{(0)})^* \right\} \end{aligned} \quad [68]$$

1.08.22 Wavefield Inversion Examples

We show three examples of wavefield inversion, one synthetic and two from field experiments. [Figure 11](#) shows an example of waveform tomography applied to a synthetic crustal data set using Pratt's method ([Brenders and Pratt, 2007](#)). The synthetic data set was developed using a viscoelastic finite-difference method for a blind test of traveltime and waveform tomography models for a Commission on Controlled Source Seismology Workshop ([Hole et al., 2005](#)). Long and short spatial wavelength structures were included using a variety of statistical descriptions of crustal rocks to make the model and data set as realistic as possible in terms of acquisition geometry, velocity heterogeneity, and wave propagation. Traveltime tomography recovers the large-scale structure quite well, and waveform tomography does a surprisingly good job of recovering the finer-scale structure.

[Figure 12](#) shows an example of waveform tomography applied to dense ocean-bottom seismometer data from the Nankai trough ([Operto et al. 2006](#)). Again, traveltime tomography defines the long-wavelength structure, and waveform tomography resolves the fine-scale structure by inverting frequencies up to 15 Hz.

Environmental geophysics is used to characterize the shallow subsurface to locate and map the underground flow of pollutants, or to estimate groundwater reserves. [Figure 13](#) is an example of traveltime and waveform tomography results using high-resolution

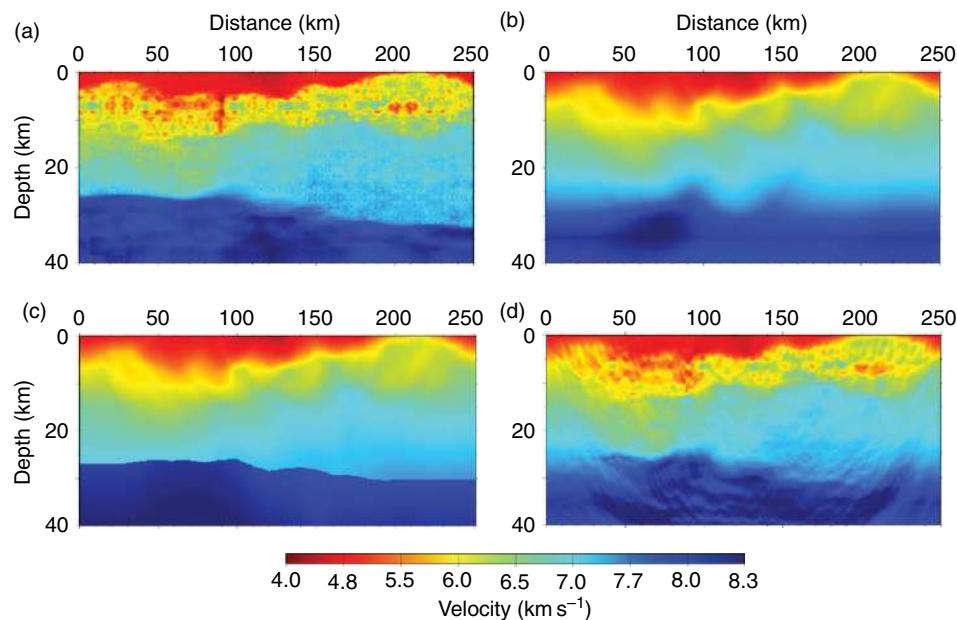


Figure 11 Blind test of traveltime and waveform inversion (Hole *et al.*, 2005). (a) True model used to compute 2-D visco-elastic full-wavefield data for a refraction/wide-angle reflection survey. (b) Model derived from traveltime tomography using only first arrivals. (c) Model derived from traveltime inversion using first arrivals and wide-angle reflections from the Moho. The traveltime models are smooth but robust versions of the true model. (d) Model derived from waveform tomography using (b) as the starting model (Brenders and Pratt, 2007). The waveform model significantly improves the spatial resolution over the traveltime result and matches many details of the true model in (a).

seismic data acquired at a groundwater contamination site in Ogden, Utah. The seismic target is a paleo-channel incised in a clay layer at a depth of a few to 15 m below the surface, and filled with low-velocity alluvium. The clay layer acts as an aquitard stopping descent of dense nonaqueous phase liquid (DNAPL) pollutants with the channel acting as a collection point for the pollutants. The geophysical problem was to identify the top of the clay layer and characterize the channel. Separate 3-D seismic reflection and refraction surveys as well as vertical seismic profiles were performed at the site. A 0.223 caliber rifle was used as the seismic source, geophones were spaced 30 cm apart. **Figure 13(b)** shows the image of the subsurface made using Pratt's method applied to surface and borehole seismic data collected along the axis of the channel (Gao *et al.*, 2006). The degree of lateral and vertical heterogeneity observed is surprising, velocities vary by a factor of 2–3 laterally and by an order of magnitude vertically. This poses a serious problem for conventional poststack seismic imaging methods.

1.08.23 Future Directions

The trends in data acquisition in both the industrial and academic communities are toward higher spatial

density recording using an ever-increasing number of instruments. Industrial acquisition now largely consists of 3-D surveys, whereas equipment and acquisition budgets restrict academia to 2-D and a small number of 3-D surveys. The US academic community now has ~ 3000 matched channel available for land-controlled source work (including three component instruments) through the IRIS PASSCAL facility. This is a factor of 5 greater than the total number of (unmatched) channels available from all North American academic sources in the early 1990s. The US marine community now has more than a hundred ocean-bottom seismographs for active-source work available from the national OBS Instrument Pool. The US academic fleet has just acquired its first seismic vessel designed for 3-D surveying. Similar instrument pools, of comparable size, exist or are in development in Europe and Asia. Data volumes are increasing rapidly in size, requiring more and more automation for preprocessing, and image formation and analysis. Combined with the Moore's law increase in computer speed, memory, and storage, the automatic inversion routines described in Section 1.08.21 are likely the path to the future.

Full-waveform inversion for 1-D models has been applied for many years to both reflection and

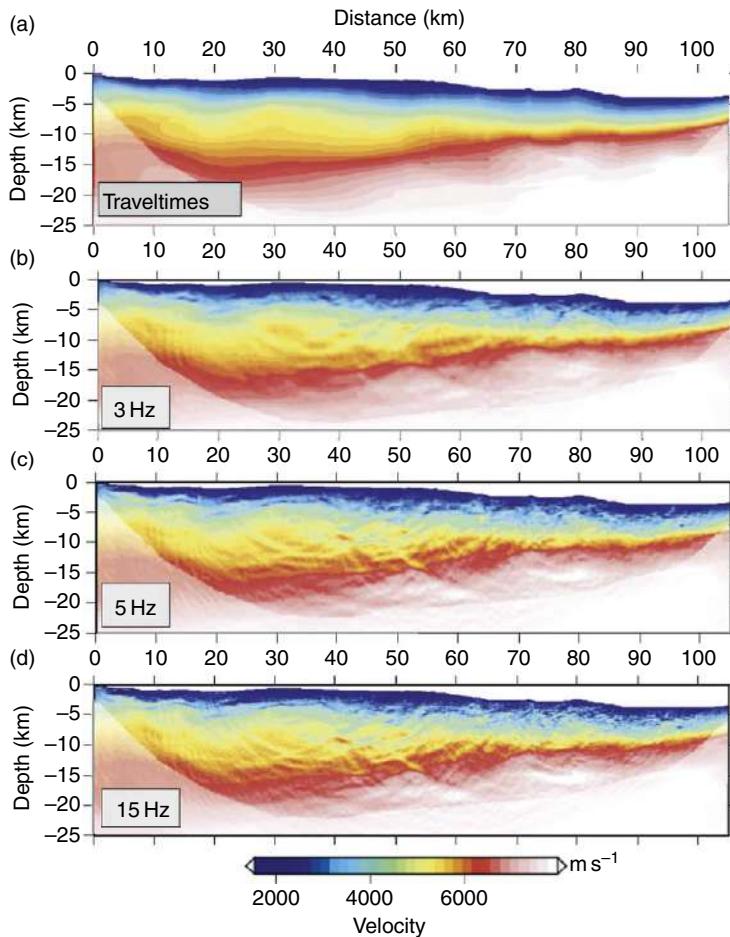


Figure 12 Example of waveform tomography applied to dense ocean-bottom seismometer data from the Nankai trough (Operto *et al.*, 2006). The vertical component seismograms of 93 instruments were used in the inversions, windowed to 1–3 s starting at the first arrival time, depending on the water depth. (a) P-wave model derived from traveltimes tomography used as the starting model for waveform tomography. (b)–(d) Models derived from waveform tomography at 3, 5, and 15 Hz, as labeled.

wide-angle data, the latter particularly in oceanic and gas hydrate studies (Shaw and Orcutt, 1985; Minshull *et al.*, 1994). Sun and McMechan (1992) and Pratt *et al.* (1996) applied 2-D elastic and acoustic full-waveform inversion to synthetic wide-angle data. Full-waveform inversion of real wide-angle data for 2-D models is just beginning to be applied (e.g., Shipp and Singh, 2002; Ravaud *et al.*, 2004; Chironi *et al.*, 2006; Operto *et al.*, 2006). These techniques are currently limited to 2-D acoustic models, primarily for computational reasons. They are nonlinear gradient methods that require a good starting model usually obtained through traveltime methods. Broadband, low-frequency data, like that collected by Spitzer and White (2005) for subbasalt imaging, are ideal for waveform inversion.

Brenders and Pratt (2007) present a comparison of velocity models derived from first-arrival traveltime tomography and waveform tomography for a realistic set of synthetic wide-angle data in a blind test; Hole *et al.* (2005) present a comparison of the same waveform-derived model with a velocity model derived from combined first-arrival and Moho-reflection traveltime inversion. These comparisons suggest that waveform methods have the potential to provide roughly an order-of-magnitude increase in spatial resolution over traveltime methods (Figure 11). Extending these methods to elastic models and 3-D, although not a major theoretical leap, will be a numerical analysis and computational challenge.

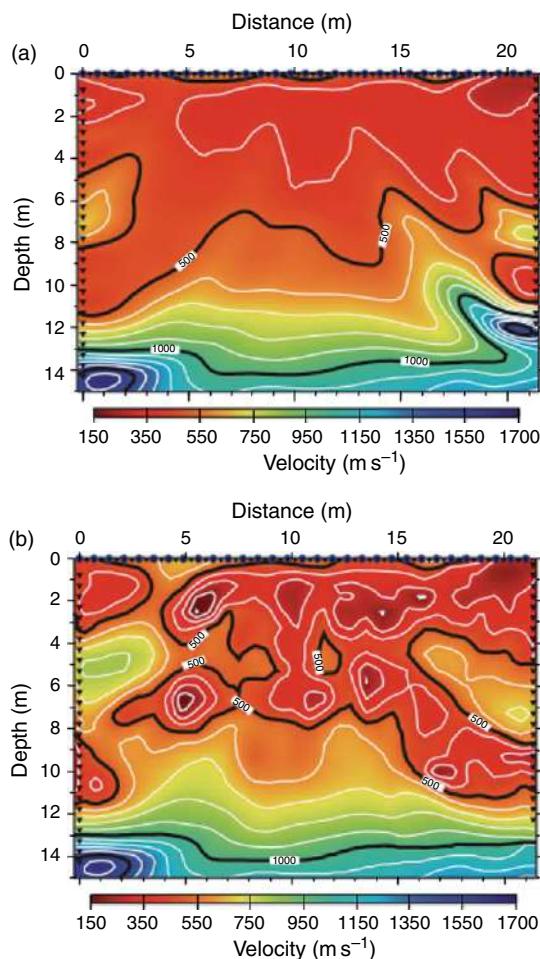


Figure 13 (a) Characterization of the shallow subsurface at a groundwater contamination site. Velocity model derived from first-arrival traveltome tomography from a VSP/surface seismic experiment along the axis of a buried paleochannel that acts as a trap for groundwater contaminants. A smoothed version of this model was used as the starting model for the waveform inversion. (b) Final velocity model derived from waveform tomography using the method of Pratt (1999) and Pratt and Shipp (1999). The velocity varies laterally by a factor of 2–3, and changes vertically by an order of magnitude over 15 m. The smallest features laterally are ~2–3 m, roughly the theoretical resolution obtainable. The sediments along the axis of the channel, above ~14 m depth, show a surprising degree of heterogeneity. Reproduced from Gao F, Levander A, Pratt RG, Zelt CA, and Fradelizio G-L (2006) Waveform tomography at a ground water contamination site: VSP-surface dataset. *Geophysics* 71: H1–H11, with permission from Society of Exploration Geophysics.

For lithospheric studies the need for flexible, general-purpose traveltome inversion and tomography algorithms will remain, both as primary modeling tools and to provide long-wavelength starting models

for higher-resolution wavefield techniques. We have already discussed the likelihood that S-waves, attenuation and anisotropy studies will become more commonplace in the future, although they have yet to be employed commonly in academic investigations.

For traveltome methods, formal treatment of Fresnel zones (Watanabe *et al.*, 1999), adaptation of frequency-dependent sensitivity kernels from global seismology (Dahlen *et al.*, 2000), and wave-equation-based modeling (Pyun *et al.*, 2005) will reduce the need for regularization, and improve the stability of gradient methods. The derived models will contain more structure and increased resolution as a result of more accurately honoring the physics of wave propagation. This will be particularly true for near-surface studies in which the length scales of heterogeneities are comparable or smaller than the seismic wavelengths (e.g., Zelt *et al.* 2006a).

Very efficient simulations of 2-D and 3-D viscoelastic wave propagation at realistic frequencies are needed for the forward modeling component of wavefield inversion schemes. The global seismology community also shares these needs. Advances have been made toward computing realistic global seismograms in laterally variable viscoelastic media (e.g., Komatitsch and Tromp, 1999, 2005). Simulating wave propagation using model parametrizations that incorporate mathematical descriptions of rock properties such as fractures, porosity, saturation, gas concentration, and partial melt (e.g., Aldridge *et al.*, 2004) will help ensure that seismic methods will continue to play a role in addressing the most relevant Earth science problems.

Many problems of interest to academic Earth scientists require relatively high-resolution imaging across a broad range of scales, from the surface geology through the crust and into the upper mantle. Highly detailed images of the crust and the top of the mantle are only available from controlled-source imaging, whereas much of the lithospheric mantle and deeper can only be imaged practically with earthquake sources. Perhaps one of the most interesting future research directions facing the academic community is the combined inversion of controlled-source data with teleseismic body-wave data. This poses a number of challenges, as the bandwidths recorded, the scales of spatial sampling and resolution, and the source and receiver configurations used in the various experiments are very different.

Acknowledgments

The author thanks Gian L. Fradelizio and Stephen Clark for assistance in making figures.

References

- Aki K and Lee WHK (1976) Determination of 3-dimensional velocity anomalies under a seismic array using 1st-P arrival times from local earthquakes. Part 1: A homogeneous initial model. *Journal of Geophysical Research* 81: 4381–4399.
- Aki K and Richards PG (2002) *Quantitative Seismology*, 2nd edn. Sausalito, CA: University Science Books.
- Aldridge DF, Bartel LC, and Symons NP (2004) Velocity-stress-pressure algorithm for 3D poroelastic wave propagation. In: *Society Exploration Geophysicists Technical Program Extended Abstracts* 23: 1917–1920.
- Al-Yahya K (1989) Velocity analysis by iterative profile migration. *Geophysics* 54: 718–729.
- ANCORP Working Group (2003) Seismic imaging of a convergent continental margin and plateau in the Central Andes (Andean Continental research Project 1996 (ANCORP96)). *Journal of Geophysical Research* 108: 2328 (doi: 10.1029/2002JB001771).
- BABEL Working Group (1993) Deep seismic reflection/refraction interpretation of crustal structure along BABEL profiles A and B in the southern Baltic Sea. *Geophysical Journal International* 112: 325–343.
- Barton PJ (1986) The relationship between seismic velocity and density in the continental-crust – A useful constraint. *Geophysical Journal of the Royal Astronomical Society* 87: 195–208.
- Beckman P and Spizzichino A (1963) *International Series of Monographs in Electromagnetic Waves*, 4: The Scattering of Electromagnetic Waves from Rough Surfaces. Oxford: Pergamon Press.
- Beylkin G (1985) Imaging of discontinuities in the inverse scattering problem by inversion of acusal generalized Radon transform. *Journal of Mathematical Physics* 26: 99–108.
- Beylkin G and Burridge R (1990) Linearized inverse scattering problems in acoustics and elasticity. *Wave Motion* 12: 15–52.
- Benz HM, Chouet BA, Dawson PB, Lahr JC, Page RA, and Hole JA (1996) Three-dimensional P and S wave velocity structure of Redoubt Volcano, Alaska. *Journal of Geophysical Research* 101: 8111–8128.
- Benz HM, Smith RB, and Mooney WD (1990) Crustal structure of the northwestern Basin and Range province from the 1985 Program for Array Seismic Studies of the Continental Lithosphere seismic Experiment. *Journal of Geophysical Research* 95: 21823–21842.
- Bevington PR (1969) *Data Reduction and Error Analysis for the Physical Sciences*. New York: McGraw-Hill.
- Bosch M, Barton P, Singh SC, and Trinks I (2005) Inversion of travelttime data under a statistical model for seismic velocities and layer interfaces. *Geophysics* 70: R33–R43.
- Boschetti F, Dentith MC, and List RD (1996) Inversion of seismic refraction data using genetic algorithms. *Geophysics* 61: 1715–1727.
- Bostock MG (1998) Mantle stratigraphy and evolution of the Slave province. *Journal of Geophysical Research* 103: 21193–21200.
- Bostock MG, Rondenay S, and Schragge DS (2001) Multiparameter two-dimensional version of scattered teleseismic body waves. Part 1: Theory for oblique incidence. *Journal of Geophysical Research* 106: 30771–30782.
- Braile LW (1977) Interpretation of crustal velocity gradients and Q structure using amplitude-corrected seismic refraction profiles. In: Heacock JG (ed.) *Geophysical Monograph Series 20: The Earth's Crust*, pp. 427–439. Washington, DC: American Geophysical Union.
- Braile LW and Smith RB (1975) Guide to the interpretation of crustal refraction profiles. *Journal of Geophysical Research* 40: 145–176.
- Brenders AJ and Pratt RG (2007) Full waveform tomography for lithospheric imaging: Results from a blind test in a realistic crustal model. *Geophysical Journal International* 168: 133–151.
- Brocher TM (2005) Empirical relations between elastic wavespeeds and density in the Earth's crust. *Bulletin of the Seismological Society of America* 95: 2081–2092.
- Carbonell R, Perez-Estaun P, Gallart J, et al. (1996) Crustal root beneath the Urals: Wide-angle seismic evidence. *Science* 274: 222–224.
- Carey DW, Burnett MS, and Orcutt JA (1992) Tomographic image of the axial low-velocity zone at 12-degrees–50°N on the East Pacific Rise. *Journal of Geophysical Research* 97: 9243–9263.
- Cerveny V, Molotkov I, and Psencik I (1977) *Ray Method in Seismology*. Prague, Czechoslovakia: University of Karlova.
- Cerveny V, Popov MM, and Psencik I (1982) Computation of wave fields in inhomogeneous-media–Gaussian-beam approach. *Geophysical Journal of the Royal Astronomical Society* 70: 109–128.
- Chapman CH and Drummond R (1982) Body-wave seismograms in inhomogeneous-media using Maslov asymptotic theory. *Bulletin of the Seismological Society of America* 72: S277–S317.
- Chironi C, Morgan JV, and Morgan MR (2006) Imaging of intrabasalt and subbasalt structure with full wavefield seismic tomography. *Journal of Geophysical Research* 111: B05313 (doi: 10.1029/2004JB003595).
- Chiu SKL, Kanasewich ER, and Phadke S (1986) Three-dimensional determination of structure and velocity by seismic tomography. *Geophysics* 51: 1559–1571.
- Christensen NI (1996) Poisson's ratio and crustal seismology. *Journal of Geophysical Research* 101: 3139–3156.
- Christensen NI and Mooney WD (1995) seismic velocity structure and composition of the continental-crust – A global view. *Journal of Geophysical Research* 100: 9761–9788.
- Christeson GL, McIntosh KD, Shipley TH, Flueh ER, and Goedde H (1999) Structure of the Costa Rica convergent margin, offshore Nicoya Peninsula. *Journal of Geophysical Research* 104: 25443–25468.
- Christeson GL, Nakamura Y, Buffler RT, Morgan J, and Warner M (2001) Deep crustal structure of the Chicxulub impact crater. *Journal of Geophysical Research* 106: 21751–21769.
- Claerbout JF (1970) Coarse grid calculations of waves in inhomogeneous media with applications to delineation of complicated seismic structure. *Geophysics* 35: 407–418.
- Claerbout JF (1971) Toward a unified theory of reflector mapping. *Geophysics* 36: 467–481.
- Claerbout JF (1976) *Fundamentals of Geophysical Data Processing*. New York: MacGraw-Hill.
- Claerbout JF (1985) *Imaging the Earth's Interior*, 412 pp. Cambridge, MA: Blackwell Science.
- Clayton RW and McMechan GA (1981) Inversion of refraction data by wave field continuation. *Geophysics* 46: 860–868.
- Clowes RM, Zelt CA, Amor JR, and Ellis RM (1995) Lithospheric structure in the southern Canadian Cordillera from a network of seismic refraction lines. *Canadian Journal of Earth Sciences* 32: 1485–1513.

- Constable SC, Parker RL, and Constable CG (1987) Occam's inversion: A practical algorithm for generating smooth models from electromagnetic sounding data. *Geophysics* 52: 289–300.
- Cook FA, van der Velden AJ, Hall KW, and Roberts BJ (1999) Frozen subduction in Canada's northwest territories; lithoprobe deep lithospheric reflection profiling of the western Canadian Shield. *Tectonics* 18: 1–24.
- Crosson RS (1976) Crustal structure modeling of earthquake data. Part 1: simultaneous least-squares estimation of hypocenter and velocity parameters. *Journal of Geophysical Research* 81: 3036–3046.
- Dahlen FA, Hung SH, and Nolet G (2000) Frechet kernels for finite-frequency traveltimes. Part I: Theory. *Geophysical Journal International* 141: 157–174.
- Darbyshire FA, Bjarnason I Th, White RS, and Flóvenz OG (1998) Crustal structure above the Iceland mantle plume imaged by the ICEMELT refraction profile. *Geophysical Journal International* 135: 1131–1149.
- Day AJ, Peirce C, and Sinha MC (2001) Three-dimensional crustal structure and magma chamber geometry at the intermediate-spreading, back-arc Valu Fa Ridge, Lau Basin—results of a wide-angle seismic tomographic inversion. *Geophysical Journal International* 146: 31–52.
- Dix CH (1955) Seismic velocities from surface measurements. *Geophysics* 20: 68–86.
- Dunn RA and Toomey DR (2001) Crack-induced seismic anisotropy in the oceanic crust across the East Pacific Rise (9 degrees 30'N). *Earth and Planetary Science Letters* 189: 9–17.
- Eaton DWS (1993) Finite difference traveltime calculation for anisotropic media. *Geophysical Journal International* 114: 273–280.
- Evangelidis CP, Minshull TA, and Henstock TJ (2004) Three-dimensional crustal structure of Ascension Island from active source seismic tomography. *Journal of Geophysical Research* 159: 311–325.
- Fernandez-Viejo G, Clowes RM, and Welford KM (2005) Constraints on the composition of the crust and uppermost mantle in northwestern Canada: Vp/Vs variations along Lithoprobe's SNorCLE transect. *Canadian Journal of Earth Sciences* 42: 1205–1222.
- Firbas P (1981) Inversion of travel-time data for laterally heterogeneous velocity structure-linearization approach. *Geophysical Journal of the Royal Astronomical Society* 67: 189–198.
- Fuchs K and Müller G (1971) Computation of synthetic seismograms with reflectivity method and comparison with observations. *Geophysical Journal of the Royal Astronomical Society* 23: 417–433.
- Fuis GS, Ryberg T, Godfrey NJ, Okaya DA, and Murphy JM (2001) Crustal structure and tectonics from the Los Angeles basin to the Mojave Desert, Southern California. *Geology* 29: 15–18.
- Gao F, Levander A, Pratt RG, Zelt CA, and Fradelizio G-L (2006) Waveform tomography at a ground water contamination site: VSP-surface dataset. *Geophysics* 71: H1–H11.
- Gardner GHF, French WS, and Matzuk T (1974) Elements of migration and velocity analysis. *Geophysics* 39: 811–825.
- Gazdag J (1978) Wave equation migration with the phase-shift method. *Geophysics* 43: 1342–1351.
- Godfrey NJ, Christensen NI, and Okaya DA (2002) The effect of crustal anisotropy on reflector depth and velocity determination from wide-angle seismic data: A synthetic example based on South Island, New Zealand. *Tectonophysics* 355: 145–161.
- Gohl K and Pedersen LB (1995) Collisional tectonics of the Baltic Shield in the northern Gulf of Bothnia from Seismic data of the BABEL project. *Geophysical Journal International* 120: 209–226.
- Goodman JW (1996) *Introduction to Fourier Optics*. New York: MacGraw-Hill.
- Gorman AR and Clowes RM (1999) Wave-field tau-p analysis for 2-D velocity models: Application to Western North American lithosphere. *Geophysical Research Letters* 26: 2323–2326.
- Gorman AR, Clowes RM, Ellis RM, et al. (2002) Deep probe: Imaging the roots of Western North America. *Canadian Journal of Earth Sciences* 39: 375–398.
- Gorman AR, Nemeth B, Clowes RM, and Hajnal Z (2006) An investigation of upper mantle heterogeneity beneath the Archaean and Proterozoic crust of western Canada from Lithoprobe controlled-source seismic experiments. *Tectonophysics* 416: 187–207.
- Grad M, Gutcher A, Keller GR, et al. (2006) Lithospheric structure beneath trans-Carpathian transect from Precambrian platform to Pannonian basin: CELEBRATION 2000 seismic profile CEL05. *Journal of Geophysical Research* 111: B03301 (doi: 10.1029/2005JB003647).
- Grand SP (1994) Mantle shear structure beneath the Americas and surrounding oceans. *Journal of Geophysical Research* 99: 11591–11622.
- Hammer PTC, Dorman LM, Hildebrand JA, and Cornuelle BD (1994) Jasper Seamount structure: Seafloor seismic refraction tomography. *Journal of Geophysical Research* 99: 6731–6752.
- Hashizume M (1979) Q of the crust beneath southwestern Honshu, Japan, derived from explosion seismic waves. *Physics of the Earth and Planetary Interiors* 20: 25–32.
- Henstock TJ and Levander A (2000) Lithospheric evolution in the wake of the Mendocino Triple Junction: Structure of the San Andreas Fault system at 2 Ma. *Geophysical Journal International* 140: 233–247.
- Henstock TJ, Levander A, and Hole JA (1997) Deformation in the lower crust of the San Andreas fault system in Northern California. *Science* 278: 650–653.
- Hill NR and Wuenschel PC (1985) Numerical modeling of refraction arrivals in complex areas. *Geophysics* 50: 90–98.
- Hobro JWD, Singh SC, and Minshull TA (2003) Three-dimensional tomographic inversion of combined reflection and refraction seismic traveltimes data. *Geophysical Journal International* 152: 79–93.
- Holbrook WS, Larsen HC, Korenaga J, et al. (2001) Mantle thermal structure and active upwelling during continental breakup in the North Atlantic. *Earth and Planetary Science Letters* 190: 251–262.
- Holbrook WS, Páramo P, Pearse S, and Schmitt RW (2003) Thermohaline fine structure in an oceanographic front from seismic reflection profiling. *Science* 301: 821–824 (doi: 10.1126/science.1085116).
- Holbrook WS, Reiter EC, Purdy GM, and Toksoz MN (1992) Image of the Moho across the continent-ocean transition, United-States east-coast. *Geology* 20: 203–206.
- Holbrook WS, Reiter EC, Purdy GM, et al. (1994) Deep structure of the US Atlantic continental margin, offshore South Carolina, from coincident ocean bottom and multichannel seismic data. *Journal of Geophysical Research* 99: 9155–9178.
- Hole JA (1992) Nonlinear high-resolution three-dimensional seismic travel time tomography. *Journal of Geophysical Research* 97: 6553–6562.
- Hole JA, Beaudoin BC, and Klemperer SL (2000a) Vertical extent of the newborn San Andreas fault at the Mendocino triple junction. *Geology* 28: 1111–1114.
- Hole JA, Brocher TM, Klemperer SL, Parsons T, Benz HM, and Furlong KP (2000b) Three-dimensional seismic velocity

- structure of the San Francisco Bay area. *Journal of Geophysical Research* 105: 13859–13873.
- Hole JA, Clowes RM, and Ellis RM (1992) Interface inversion using broadside seismic refraction data and 3-dimensional travel time calculations. *Journal of Geophysical Research* 97: 3417–3429.
- Hole JA, Ryberg T, Fuis GS, Bleibinhaus F, and Sharma AK (2006) Structure of the San Andreas fault zone at SAFOD from a seismic refraction survey. *Geophysical Research Letters* 33: L07312.
- Hole JA and Zelt BC (1995) Three-dimensional finite-difference reflection travel times. *Geophysical Journal International* 121: 427–434.
- Hole JA, Zelt CA, and Pratt RG (2005) Advances in controlled-source seismic imaging. *EOS Transactions of the American Geophysical Union* 86: 177–181.
- Holliger K and Levander AR (1992) A stochastic view of the lower crust based on the Ivrea Zone. *Geophysical Research Letters* 19: 111153–111156.
- Huang H, Spencer C, and Green A (1986) A method for the inversion of refraction and reflection travel times for laterally varying velocity structures. *Bulletin of the Seismological Society of America* 76: 837–846.
- Hughes S, Barton PJ, and Harrison D (1998) Exploration in the Shetland-Faeroe Basin using densely spaced arrays of ocean-bottom seismometers. *Geophysics* 63: 490–501.
- Ilchenko TV (1985) A technique for determining velocity structure from traveltimes along a system of DSS profiles. *Geophysical Journal* 7: 59–66.
- Jacob AWB (1975) Dispersed shots at optimum depth – An efficient seismic source for lithospheric studies. *Journal of Geophysics* 41: 63–70.
- Jaiswal P, Zelt CA, and Pecher IA (2006) Seismic characterization of a gas hydrate system in the Gulf of Mexico using wide-aperture data. *Geophysical Journal International* 165: 108–120.
- Jarchow CM, Catchings RD, and Lutter WJ (1994) Large-explosive source, wide-recording aperture, seismic profiling on the Columbia Plateau, Washington. *Geophysics* 59: 259–271.
- Jones K, Warner M, and Brittan J (1999) Anisotropy in multi-offset deep-crustal seismic experiments. *Geophysical Journal International* 264: 205–217.
- Julian BR and Gubbins D (1977) Three-dimensional seismic ray tracing. *Journal of Geophysics* 43: 95–113.
- Kaila KL and Krishna VG (1992) Deep seismic-sounding studies in India and major discoveries. *Current Science* 62: 117–154.
- Kanasewich ER and Chiu SKL (1985) Least-squares inversion of spatial seismic refraction data. *Bulletin of the Seismological Society of America* 75: 865–880.
- Kohler WM and Fuis GS (1992) Empirical dependence of seismic ground velocity on the weight of explosives, shotpoint site condition, and recording distance for seismic refraction data. *Bulletin of the Seismological Society of America* 82: 2032–2044.
- Komatitsch D and Tromp J (1999) Introduction to the spectral element method for three-dimensional seismic wave propagation. *Geophysical Journal International* 139: 806–822.
- Komatitsch D and Tromp J (2005) The spectral element method in seismology. In: Levander A and Nolet G (eds.) *Geophysical Monograph 157: Seismic Earth: Array Analysis of Broadband Seismograms*, pp. 205–228. Washington, DC: American Geophysical Union.
- Korenaga J, Holbrook WS, Detrick RS, and Kelemen PB (2001) Gravity anomalies and crustal structure at the southeast Greenland margin. *Journal of Geophysical Research* 106: 8853–8870.
- Korenaga J, Holbrook WS, Kent GM, et al. (2000) Crustal structure of the southeast Greenland margin from joint refraction and reflection seismic tomography. *Journal of Geophysical Research* 105: 21591–21614.
- Lafond CF and Levander A (1995) Migration of wide-aperture onshore-offshore seismic data, Central California: Seismic images of late-stage subduction. *Journal of Geophysical Research* 100: 22231–22243.
- Lailly P and Sinoquet D (1996) Smooth velocity models in reflection tomography for imaging complex geological structures. *Geophysical Journal International* 124: 349–362.
- Lanz E, Maurer H, and Green AG (1998) Refraction tomography over a buried waste disposal site. *Geophysics* 63: 1414–1433.
- Larkin SP and Levander A (1996) Wave-equation datuming for improving deep crustal seismic images. *Tectonophysics* 264: 371–379.
- Lendl C, Tréhu AM, Goff JA, Levander AR, and Beaudoin BC (1997) Synthetic seismograms through synthetic Franciscan: Insights into factors affecting large-aperture seismic data. *Geophysical Research Letters* 24: 3317–3320.
- Levander A (1988) Fourth-order finite-difference P-SV seismograms. *Geophysics* 53: 1425–1436.
- Levander A, Fuis GS, Wissinger ES, Lutter WJ, Oldow JS, and Moore TE (1994) Seismic images of the Brooks Range fold-and-thrust belt, arctic Alaska, from an integrated seismic-reflection refraction experiment. *Tectonophysics* 232: 13–30.
- Levander AR and Holliger K (1992) Small-scale heterogeneity and large-scale velocity structure of the continental crust. *Journal of Geophysical Research* 97: 8797–8804.
- Levander A, Zelt CA, and Magnani MB (2005) Crust and upper mantle velocity structure of the Southern Rocky Mountains from the Jemez Lineament to the Cheyenne belt. In: Karlstrom KE and Keller RG (eds.) *Geophysical Monograph Series 154: The Rocky Mountain Region: An Evolving Lithosphere*, pp. 293–308. Washington, DC: American Geophysical Union.
- Li Q, Wilcock WSD, Pratt TL, Snelson CM, and Brocher TM (2006) Seismic attenuation structure of the Seattle basin, Washington State, from explosive-source refraction data. *Bulletin of the Seismological Society of America* 96: 553–571.
- Lutter WJ and Nowack RL (1990) Inversion for crustal structure using reflections from the PASSCAL Ouachita experiment. *Journal of Geophysical Research* 95: 4633–4646.
- Lutter WJ, Nowack RL, and Braile LW (1990) Seismic imaging of upper crustal structure using travel times from the PASSCAL Ouachita experiment. *Journal of Geophysical Research* 95: 4621–4631.
- McCaughey M and Singh SC (1997) Simultaneous velocity and interface tomography of normal-incidence and wide-aperture traveltimes data. *Geophysical Journal International* 131: 87–99.
- McMechan GA and Fuis GS (1987) Ray equation migration of wide-angle reflections from southern Alaska. *Journal of Geophysical Research* 92: 407–420.
- McMechan GA and Mooney WD (1980) Asymptotic ray theory and synthetic seismograms for laterally varying structures: Theory and application to the Imperial Valley, California. *Bulletin of the Seismological Society of America* 70: 2021–2035.
- Menke W (1989) *Geophysical Data Analysis: Discrete Inverse Theory*. San Diego, CA: Academic Press.
- Milkerit B, Epili D, Green AG, Mereu RF, and Morel-à-I' Huissier P (1990) Migration of wide-angle seismic-reflection data from the Grenville Front in Lake Huron. *Journal of Geophysical Research* 95: 10987–10998.
- Minshull TA, Singh SC, and Westbrook GK (1994) Seismic velocity structure at a gas hydrate reflector, offshore western Colombia, from full-wave-form inversion. *Journal of Geophysical Research* 99: 4715–4734.

- Mooney HM (1983) Synthetic seismograms for body waves: An overview. *First Break* 1: 9–20.
- Mooney WD and Brocher TM (1987) Coincident seismic-reflection refraction studies of the continental lithosphere – A global review. *Reviews of Geophysics* 25: 723–743.
- Mora P (1987) Nonlinear two-dimensional elastic inversion of multi-offset seismic data. *Geophysics* 52: 1211–1228.
- Mora P (1988) Elastic wavefield inversion of reflection and transmission data. *Geophysics* 53: 750–759.
- Morgan JV, Christeson GL, and Zelt CA (2002) Testing the resolution of a 3D velocity tomogram across the Chicxulub crater. *Tectonophysics* 355: 215–226.
- Morgan JV, Warner MR, Collins GS, Melosh HJ, and Christeson GL (2000) Peak ring formation in large impact craters. *Earth and Planetary Science Letters* 183: 347–354.
- Morozova EA, Morozov IB, Smithson SB, and Solodilov LN (1999) Heterogeneity of the uppermost mantle beneath Russian Eurasia from the ultra-long-range profile QUARTZ. *Journal of Geophysical Research* 104: 20329–20348.
- Morozov IB and Levander A (2002) Depth image focusing in travel-time map based wide-angle migration. *Geophysics* 67: 1903–1912.
- Moser TJ (1991) Shortest path calculation of seismic rays. *Geophysics* 56: 59–67.
- Moser TJ, Nolet G, and Snieder R (1992) Ray bending revisited. *Bulletin of the Seismological Society of America* 82: 259–288.
- Muller G, Roth M, and Korn M (1992) Seismic-wave travel-times in random-media. *Geophysical Journal International* 110: 29–41.
- Musacchio G, Mooney WD, Luetgert JH, and Christensen NI (1997) Composition of the crust in the Grenville and Appalachian provinces of North America inferred from V_p/V_s ratios. *Journal of Geophysical Research* 102: 15225–15241.
- Nakamura Y, Donoho PL, Roper PH, and McPherson PM (1987) Large-offset seismic surveying using ocean-bottom seismographs and air guns – instrumentation and field technique. *Geophysics* 52: 1601–1611.
- Nakanishi I and Yamaguchi K (1986) A numerical experiment on nonlinear image reconstruction from first-arrival times for two-dimensional island arc structure. *Journal of Physics of the Earth* 34: 195–201.
- Neves FA, Singh SC, and Priestley KF (1996) Velocity structure of upper-mantle transition zones beneath central Eurasia from seismic inversion using genetic algorithms. *Geophysical Journal International* 125: 869–878.
- Nielsen L and Jacobsen BH (2000) Integrated gravity and wide-angle seismic inversion for 2-D crustal modelling. *Geophysical Journal International* 140: 222–232.
- Nolet G (1987) Seismic wave propagation and seismic tomography. In: Nolet G (ed.) *Seismic Tomography*, pp. 1–24. Dordrecht: Reidel.
- Nowack RL and Braile LW (1993) Refraction and wide-angle reflection tomography: Theory and results. In: Iyer HM and Hirahara K (eds.) *Seismic Tomography: Theory and Practice*, pp. 733–765. London: Chapman and Hall.
- Operto S, Virieux J, Dessa JX, and Pascal G (2006) Crustal seismic imaging from multifold ocean bottom seismometer data by frequency domain full waveform tomography: Application to the eastern Nankai trough. *Journal of Geophysical Research* 111: B09306 (doi: 10.1029/2005JB003835).
- Paige CC and Saunders MA (1982) LSQR: An algorithm for sparse linear equations and sparse least squares. *ACM Transactions on Mathematical Software* 8: 43–71.
- Palmer D (1981) An introduction to the generalized reciprocal method of seismic refraction interpretation. *Geophysics* 46: 1508–1518.
- Park J, Morgan JK, Zelt CA, Okubo PG, Peters L and Benesh N (in press) Comparative velocity structure of active Hawaiian volcanoes from 3-D onshore-offshore seismic tomography. *Earth and Planetary Science Letters*.
- Parsons T, Blakely RJ, and Brocher TM (2001) A simple algorithm for sequentially incorporating gravity observations in seismic traveltome tomography. *International Geology Review* 43: 1073–1086.
- Parsons T, McCarthy J, Kohler WM, et al. (1996) Crustal structure of the Colorado Plateau, Arizona: Application of new long-offset seismic data analysis techniques. *Journal of Geophysical Research* 101: 11173–11194.
- Palenková NI (1982) The intercept-time method – Possibilities and limitations. *Journal of Geophysics* 51: 85–95.
- Peirce C and Day AJ (2002) Ocean-bottom seismograph tomographic experiments – A consideration of acquisition geometries vs. resources. *Geophysical Journal International* 151: 543–565.
- Podvin P and Lecomte I (1991) Finite difference computation of traveltimes in very contrasted velocity models: A massively parallel approach and its associated tools. *Geophysical Journal International* 105: 271–284.
- Popovici AM and Sethian JA (2002) 3-D imaging using higher order fast marching traveltimes. *Geophysics* 67: 604–609.
- Poppeliers C and Levander A (2004) Estimation of vertical stochastic scale parameters in the Earth's crystalline crust from seismic reflection data. *Geophysical Research Letters* 31: L13607 (doi: 10.1029/2004GL019538).
- Pratt RG (1999) Seismic waveform inversion in the frequency domain. Part 1: Theory and verification in a physical scale model. *Geophysics* 64: 888–901.
- Pratt RG and Shipp RM (1999) Seismic waveform inversion in the frequency domain. Part 2: Fault delineation in sediments using crosshole data. *Geophysics* 64: 902–914.
- Pratt GR, Shin C, and Hicks GJ (1998) Gauss-Newton and full Newton methods in frequency-space seismic waveform inversion. *Geophysical Journal International* 133: 341–362.
- Pratt RG, Song Z-M, Williamson P, and Warner M (1996) Two-dimensional velocity models from wide-angle seismic data by wavefield inversion. *Geophysical Journal International* 124: 323–340.
- Press WH, Teukolsky SA, Vetterling WT, and Flannery BP (1992) *Numerical Recipes in Fortran: The Art of Scientific Computing*, 2nd edn. Cambridge, UK: Cambridge University Press.
- Pullammanappallil SK and Louie JN (1994) A generalized simulated-annealing optimization for inversion of first-arrival times. *Bulletin of the Seismological Society of America* 84: 1397–1409.
- Purdy GM (1982) The correction for the travel time effects of seafloor topography in the interpretation of marine seismic data. *Journal of Geophysical Research* 87: 8389–8396.
- Pyun S, Shin C, Min DJ, and Ha T (2005) Refraction traveltome tomography using damped monochromatic wavefield. *Geophysics* 70: U1–U7.
- Ramachandran K, Dosso SE, Spence GD, Hyndman RD, and Brocher TM (2005) Forearc structure beneath southwestern British Columbia: A three-dimensional tomographic velocity model. *Journal of Geophysical Research* 110: B02303 (doi: 10.1029/2004JB003258).
- Ravaut C, Operto S, Impronta L, Virieux J, Herrero A, and Dell'Aversana P (2004) Multiscale imaging of complex structures from multifold wide-aperture seismic data by frequency-domain full-waveform tomography: Application to a thrust belt. *Geophysical Journal International* 159: 1032–1056.
- Rawlinson N, Houseman GA, and Sambridge M (2001) Inversion of seismic refraction and wide-angle reflection traveltimes for 3-D layered crustal structure. *Geophysical Journal International* 145: 381–401.

- Rawlinson N and Sambridge M (2003a) Seismic traveltimes tomography of the crust and lithosphere. *Advances in Geophysics* 46: 181–198.
- Rawlinson N and Sambridge M (2003b) Irregular interface parametrization in 3-D wide-angle seismic traveltimes tomography. *Geophysical Journal International* 155: 79–92.
- Rawlinson N and Sambridge M (2004) Wave front evolution in strongly heterogeneous layered media using the fast marching method. *Geophysical Journal International* 156: 631–647.
- Robinson EA and Treitel S (1980) *Geophysical Signal Analysis*. Englewood Cliffs, NJ: Prentice-Hall.
- Robertsson JOA, Blanch JO, and Symes WW (1994) Viscoelastic finite-difference modeling. *Geophysics* 59: 1444–1456.
- Roy L, Sen MK, McIntosh K, Stoffa PL, and Nakamura Y (2005) Joint inversion of first arrival seismic travel-time and gravity data. *Journal of Geophysics and Engineering* 2: 277–289.
- Sain K and Kaila KL (1996) Ambiguity in the solution to the velocity inversion problem and a solution by joint inversion of seismic refraction and wide-angle reflection times. *Geophysical Journal International* 124: 215–227.
- Scales JA (1989) On the use of conjugate-gradient to calculate the eigenvalues and singular-values of large, sparse matrices. *Geophysical Journal* 97: 179–183.
- Scales JA (1995) *Theory of Seismic Imaging*, 291 pp. Berlin: Springer.
- Scales JA, Docherty P, and Gerszenkorn A (1990) Regularisation of nonlinear inverse problems: Imaging the near-surface weathering layer. *Inverse Problems* 6: 115–131.
- Scales JA, Gerszenkorn A, and Treitel S (1988) Fast Ip solution of large, sparse, linear-systems: Application to seismic travel time tomography. *Journal of Computational Physics* 75: 314–333.
- Schlindwein V, Bonnemann C, Reichert C, Grevermeyer I, and Flueh E (2003) Three-dimensional seismic refraction tomography of the crustal structure at the ION site on the Ninetyeast Ridge, Indian Ocean. *Geophysical Journal International* 152: 171–184.
- Schneider WA (1978) Integral formulation in two and three dimensions. *Geophysics* 43: 49–76.
- Sen M and Stoffa PL (1995) *Global Optimization Methods in Geophysical Inversion*. Amsterdam: Elsevier.
- Sethian JA and Popovici AM (1999) 3-D traveltimes computation using the fast marching method. *Geophysics* 64: 516–523.
- Shaw PR and Orcutt JA (1985) Waveform inversion of seismic refraction data and applications to young Pacific crust. *Geophysical Journal of the Royal Astronomical Society* 82: 375–414.
- Sheriff RA and Geldart LP (1995) *Exploration Seismology*, 624 pp. New York: Cambridge University Press.
- Shipp RM and Singh SC (2002) Two-dimensional full wavefield inversion of wide-aperture marine seismic streamer data. *Geophysical Journal International* 151: 325–344.
- Smith RB, Braile LW, and Keller GR (1975) Upper crustal low-velocity layers – possible effect of high-temperatures over a mantle upwarp at Basin Range Colorado Plateau transition. *Earth and Planetary Science Letters* 28: 197–204.
- Sommerfeld A (1954) Lectures on Theoretical Physics V: Optics V, 383 pp. New York: Academic Press.
- Spence GD, Clowes RM, and Ellis RM (1985) Seismic structure across the active subduction zone of western Canada. *Journal of Geophysical Research* 90: 6754–6772.
- Spence GD, Whittall KP, and Clowes RM (1984) Practical synthetic seismograms for laterally varying media calculated by asymptotic ray theory. *Bulletin of the Seismological Society of America* 74: 1209–1223.
- Spitzer R and White RS (2005) Advances in seismic imaging through basalts: A case study from the Faroe-Shetland Basin. *Petroleum Geoscience* 11: 147–156.
- Spudich P and Orcutt J (1980) Petrology and porosity of an oceanic crustal site: Results from wave form modeling of seismic refraction data. *Journal of Geophysical Research* 85: 1409–1433.
- Sroda P (2006) Seismic anisotropy of the upper crust in southeastern Poland – Effect of the compressional deformation at the EEC margin: Results of CELEBRATION 2000 seismic data inversion. *Geophysical Research Letters* 33: L22302 (doi: 10.1029/2006GL027701).
- Stoerzel A and Smithson SB (1998) Two-dimensional travel time inversion for the crustal P and S wave velocity structure of the Ruby Mountains metamorphic core complex, NE Nevada. *Journal of Geophysical Research* 103: 21121–21143.
- Stolt RH (1978) Migration by Fourier transform. *Geophysics* 43: 23–48.
- Sun R and McMechan GA (1992) 2-D full-wave-field inversion for wide-aperture, elastic, seismic data. *Geophysical Journal International* 111: 1–10.
- Symons NP and Crosson RS (1997) Seismic velocity structure of the Puget Sound region from 3-D non-linear tomography. *Geophysical Research Letters* 24: 2593–2596.
- Taner MT and Koehler F (1969) Velocity spectra – Digital computer derivation applications of velocity functions. *Geophysics* 34: 859.
- Tarantola A (1984) Inversion of seismic reflection data in the acoustic approximation. *Geophysics* 49: 1259–1266.
- Thybo H and Perchuc E (1997) The seismic 80 discontinuity and partial melting in the continental mantle. *Science* 275: 1626–1629.
- Toomey DR, Solomon SC, and Purdy GM (1994) Tomographic imaging of the shallow crustal structure of the East Pacific Rise at 9°30'N. *Journal of Geophysical Research* 99: 24135–24157.
- Trinks I, Singh SC, Chapman CH, Barton PJ, Bosch M, and Cherrett A (2005) Adaptive traveltimes tomography of densely sampled seismic data. *Geophysical Journal International* 160: 925–938.
- Um J and Thurber C (1987) A fast algorithm for two-point seismic ray tracing. *Bulletin of the Seismological Society of America* 77: 972–986.
- Van Avendonk HJA (2004) Slowness-weighted diffraction stack for migrating wide-angle seismic data in laterally varying media. *Geophysics* 69: 1046–1052.
- Van Avendonk HJA, Harding AJ, Orcutt JA, and Holbrook WS (2001) Hybrid shortest path and ray bending method for traveltimes and raypath calculations. *Geophysics* 66: 648–653.
- Van Avendonk HJA, Harding AJ, Orcutt JA, and McClain JS (1998) A two-dimensional tomographic study of the Clipperton transform, fault. *Journal of Geophysical Research* 103: 17885–17899.
- Van Avendonk HJA, Shillington DJ, Holbrook WS, and Hornbach MJ (2004) Inferring crustal structure in the Aleutian arc from a sparse wide-angle seismic data set. *Geochemistry Geophysics Geosystems* 5 (doi: 10.1029/2003GC000664).
- Van Trier J and Symes WW (1991) Upwind finite-difference calculation of traveltimes. *Geophysics* 56: 812–821.
- Versteeg R (1994) The Marmousi experience: Velocity model determination on a synthetic complex data set. *The Leading Edge* 13: 927–936.
- Vidale JE (1988) Finite-difference calculation of traveltimes. *Bulletin of the Seismological Society of America* 78: 2062–2076.
- Vidale JE (1990) Finite-difference calculation of traveltimes in three dimensions. *Geophysics* 55: 521–526.
- Watanabe T, Matsuoka T, and Ashida Y (1999) Seismic traveltimes tomography using Fresnel volume approach.

- Society of Exploration Geophysicists Technical Program Extended Abstracts, 18: 1402–1405.
- Weber M (1988) Computation of body-wave seismograms in absorbing 2-D media using the Gaussian-beam method: Comparison with exact methods. *Geophysical Journal* 92: 9–24.
- Wenzel F and Sandmeier KJ (1992) Geophysical evidence for fluids in the crust beneath the Black-Forest, SW Germany. *Earth-Science Reviews* 32: 61–75.
- White DJ (1989) Two-dimensional seismic refraction tomography. *Geophysical Journal International* 97: 223–245.
- White DJ and Boland AV (1992) A comparison of forward modeling and inversion of seismic first arrivals over the Kapuskasing Uplift. *Bulletin of the Seismological Society of America* 82: 304–322.
- White DJ and Clowes RM (1994) Seismic attenuation structure beneath the Juan-de-Fuca Ridge from tomographic inversion of amplitudes. *Journal of Geophysical Research* 99: 3043–3056.
- Wilcock WSD, Solomon SC, Purdy GM, and Toomey DR (1995) Seismic attenuation structure of the East Pacific Rise near 9 degrees 30'N. *Journal of Geophysical Research* 100: 24147–24165.
- Wiggins WJ (1984) Kirchhoff integral extrapolation and migration of nonplanar data. *Geophysics* 49: 1239–1248.
- Wissinger ES, Levander A, and Christensen NI (1997) Seismic images of crustal duplexing and continental subduction in the Brooks Range. *Journal of Geophysical Research* 102: 20847–20871.
- Yilmaz O (2001) *Seismic Data Analysis: Processing, Inversion and Interpretation of Seismic Data*, vols. I and II, 2024 pp. Tulsa, OK: Society of Exploration Geophysics.
- Zelt CA (1994) 3-D velocity structure from simultaneous traveltime inversion of in-line seismic data along intersecting profiles. *Geophysical Journal International* 118: 795–801.
- Zelt CA (1998) Lateral velocity resolution from three-dimensional seismic refraction data. *Geophysical Journal International* 135: 1101–1112.
- Zelt CA (1999) Modeling strategies and model assessment for wide-angle seismic traveltimes data. *Geophysical Journal International* 139: 183–204.
- Zelt CA, Azaria A, and Levander A (2006a) 3D seismic refraction traveltime tomography at a groundwater contamination site. *Geophysics* 71: H67–H78.
- Zelt CA and Barton PJ (1998) Three-dimensional seismic refraction tomography: A comparison of two methods applied to data from the Faeroe Basin. *Journal of Geophysical Research* 103: 7187–7210.
- Zelt CA and Ellis RM (1988) Practical and efficient ray tracing in two-dimensional media for rapid traveltimes and amplitude forward modeling. *Canadian Journal of Exploration Geophysics* 24: 16–31.
- Zelt CA and Ellis RM (1990) Crust and upper mantle Q from seismic refraction data – Peace River region. *Canadian Journal of Earth Sciences* 27: 1040–1047.
- Zelt BC, Ellis RM, and Clowes RM (1993) Crustal velocity structure in the eastern Insular and southernmost Coast belts, Canadian Cordillera. *Canadian Journal of Earth Sciences* 30: 1014–1027.
- Zelt BC, Ellis RM, Clowes RM, and Hole JA (1996) Inversion of three-dimensional wide-angle seismic data from the southwestern Canadian Cordillera. *Journal of Geophysical Research* 101: 8503–8529.
- Zelt CA, Ellis RM, and Zelt BC (2006b) 3-D structure across the Tintina strike-slip fault, northern Canadian Cordillera, from seismic refraction and reflection tomography. *Geophysical Journal International* 167: 1292–1308.
- Zelt CA and Forsyth DA (1994) Modeling wide-angle seismic data for crustal structure: Southeastern Grenville province. *Journal of Geophysical Research* 99: 11687–11704.
- Zelt CA, Hojka AM, Flueh ER, and McIntosh KD (1999) 3D simultaneous seismic refraction and reflection tomography of wide-angle data from the central Chilean margin. *Geophysical Research Letters* 26: 2577–2580.
- Zelt CA, Magnani MB, Levander A, et al. (2004) BOLIVAR: Crustal structure across the Caribbean-South American plate boundary at 67.5W: Results from wide-angle seismic data. In: Program with Abstracts, Fall Meeting, American Geophysical Union, San Francisco, CA.
- Zelt CA, Sain K, Naumenko JV, and Sawyer DS (2003) Assessment of crustal velocity models using seismic refraction and reflection tomography. *Geophysical Journal International* 153: 609–626.
- Zelt CA and Smith RB (1992) Seismic traveltimes inversion for 2-D crustal velocity structure. *Geophysical Journal International* 108: 16–34.
- Zelt BC, Talwani M, and Zelt CA (1998) Prestack depth migration of dense wide-angle seismic data. *Tectonophysics* 286: 193–208.
- Zelt CA and White DJ (1995) Crustal structure and tectonics of the southeastern Canadian Cordillera. *Journal of Geophysical Research* 100: 24255–24273.
- Zelt CA and Zelt BC (1998) Study of out-of-plane effects in the inversion of refraction/wide-angle reflection traveltimes. *Tectonophysics* 286: 209–221.
- Zhang J, ten Brink US, and Toksöz MN (1998) Nonlinear refraction and reflection traveltimes tomography. *Journal of Geophysical Research* 103: 29743–29757.
- Zhang J and Toksöz MN (1998) Nonlinear refraction traveltimes tomography. *Geophysics* 64: 1726–1737.
- Zhao Z, Kubota R, Fumio S, and Izuka S (1997) Crustal Structure in the southern Kanto-Tokai region derived from tomographic method for seismic explosion survey. *Journal of Physics of the Earth* 45: 433–453.

Relevant Website

<http://www.trip.caam.rice.edu> – The Rice Inversion Project.

1.09 Theory and Observations – Wave Propagation in Anisotropic Media

V. Maupin, University of Oslo, Oslo, Norway

J. Park, Yale University, New Haven, CT, USA

© 2007 Elsevier B.V. All rights reserved.

1.09.1	Introduction	289
1.09.2	Basic Theory of Seismic Anisotropy	290
1.09.2.1	Basic General Theory	290
1.09.2.2	Different Parametrizations of the Elastic Coefficients	292
1.09.2.3	Weak Anisotropy Approximation	294
1.09.2.4	Ray Theory	294
1.09.2.5	Reflection and Transmission Coefficients	296
1.09.2.6	Surface Waves and Normal Modes	296
1.09.3	Seismological Observations of Anisotropy	301
1.09.3.1	Crustal Anisotropy	301
1.09.3.2	Origin of Upper-Mantle Anisotropy	302
1.09.3.3	P Wave Velocities and Lithospheric Anisotropy	304
1.09.3.4	Traveltime Residuals and Lithospheric Anisotropy	304
1.09.3.5	Polarization of P Waves	306
1.09.3.6	SKS Waves and Upper-Mantle Anisotropy	306
1.09.3.7	P and S Waves and Subduction Zones	308
1.09.3.8	Surface Waves and Upper Mantle	309
1.09.3.9	Polarization of Surface Waves	311
1.09.3.10	Converted Waves and Lithospheric Anisotropy	312
1.09.3.11	ScS, S_{diff} , and the D'' Layer	314
1.09.3.12	PKP Waves and the Inner Core	314
1.09.4	Perspectives	315
References		315

1.09.1 Introduction

In order to understand what anisotropy is, it is important to realize the fundamental difference between anisotropy and heterogeneity, as well as their intimate relation. By definition, an anisotropic material has physical properties which depend on direction, whereas a heterogeneous material has properties which depend on location. But whether a material is heterogeneous or anisotropic is often a matter of the scale at which we analyze its properties. Alternating layers of stiff and soft material is a heterogeneous material at small scale. At large scale, it can be seen by seismic waves as a homogeneous anisotropic material, as was shown by [Backus \(1962\)](#). This can be easily understood by realizing that, exercising a unidirectional compression on such a stack, the deformation will be different if we exert the compression

perpendicularly to the layering or in the plane of the layering. A medium that responds differently in different directions is by definition an anisotropic medium.

The stack of layers is not the only case in which heterogeneity at one scale is seen as anisotropy at a larger scale. At the origin of any anisotropy, there is a form for heterogeneity. The most basic form of anisotropy, related to the regular pattern made by atoms in crystals, can also be seen as some form of heterogeneity at the atomic scale. Orientation of cracks is another example of how distributed heterogeneities express anisotropic behavior at large scale. A correct description at large scale of any heterogeneous structure which is not randomly heterogeneous in an isotropic way should include anisotropy ([Capdeville and Marigo, 2007](#)). What we see with seismology is large-scale anisotropy. A whole range of structures can, in principle and at first order, explain this anisotropy.

Layering and preferred directions as well as seismically anisotropic minerals are common in Earth's interior. Seismic anisotropy is therefore present at different scales and in many different settings. An excellent review of the significance of seismic anisotropy in exploration and reservoir seismics has been recently published by [Helbig and Thomsen \(2005\)](#), together with a nice historical perspective. Seismic waves from earthquakes have lower frequency and longer wavelengths than waves generated for resource exploration, and are more likely to respond to the effective anisotropy of fine-layering and similar heterogeneities. We review here the basic theoretical tools available in seismology to analyze wave propagation in anisotropic structures, earthquake-induced observations sensitive to anisotropy, and their geodynamical implications.

1.09.2 Basic Theory of Seismic Anisotropy

1.09.2.1 Basic General Theory

The fundamentals of seismic wave propagation in anisotropic media have been described in several papers and books, and we will only highlight them here. For more details, we refer to [Crampin \(1981\)](#), [Garmany \(1989\)](#), [Babuska and Cara \(1991\)](#), and [Chapman \(2004\)](#) for example.

The main characteristics of seismic wave propagation in anisotropic media compared to propagation in isotropic media is primarily that the waves velocities vary with propagation direction and that the *S* waves split into two waves with different velocities, also called *S*-wave birefringence. A more subtle behavior is that wave polarizations in anisotropic media do not lie parallel or perpendicular to the propagation direction, and that phase and group velocities are not parallel, aside from exceptional cases. Let us see briefly how these characteristics arise.

A linear elastic medium is characterized by its elastic tensor c_{ijkl} which relates linearly the stress tensor elements τ_{ij} to the strain tensor elements e_{kl} :

$$\tau_{ij} = c_{ijkl} e_{kl} \quad [1]$$

An alternative to the elastic tensor is the stiffness tensor s_{ijkl} which gives the strain tensor as a linear function of the stress tensor, but this entity is not commonly used in seismology.

The equation of motion for a plane wave $\mathbf{u}(\mathbf{x}, t) = \mathbf{a}f(\mathbf{n} \cdot \mathbf{x} - ct)$ propagating with velocity c in

direction \mathbf{n} in a uniform medium of density ρ can be written as

$$\frac{c_{ijkl}}{\rho} n_j n_k a_l = c^2 a_i \quad [2]$$

The term $(c_{ijkl}/\rho)n_j n_k$ on the LHS is a 3×3 matrix named the Christoffel matrix. It plays a fundamental and central role in anisotropic wave propagation. Solving eqn [2] for \mathbf{a} and c is equivalent to finding the three eigenvalues and eigenvectors of the Christoffel matrix. In the general case, the three eigenvalues are distinct, leading to three waves with three different velocities in the propagation direction \mathbf{n} . The polarizations of the three waves, given by the eigenvectors, are perpendicular to each other, but are in directions that, as opposed to the isotropic case, may deviate strongly from the propagation direction or the plane perpendicular to it. In strongly anisotropic media, the three waves' characteristics may hybridize so that one cannot label them unequivocally as P or S waves.

For weak anisotropy, the waves separate into one quasi-P wave, with the highest velocity and a polarization close to the propagation direction, and two quasi-S waves. The quasi-S waves have two different velocities (except in singular directions), and two polarization directions perpendicular to each other in a plane close to the plane perpendicular to the propagation direction. Shear-wave splitting occurs because any S-wave entering the anisotropic medium sees its particle motion projected onto the polarization directions of the two quasi S-waves which then propagate at different velocities ([Figure 1](#)). Let us note that once splitting has occurred, it is carried along by the S-wave even after leaving the anisotropic region.

Since the Christoffel matrix depends on the components of \mathbf{n} , the velocities and polarizations of the waves vary with propagation direction. Due to this angular dependence of the velocities, wavefronts are not spherical in homogeneous anisotropic media. The vector \mathbf{n} defines the direction of the phase propagation, and is perpendicular to the wavefront. Wave energy follows another direction, defined by the group velocity direction \mathbf{V} . In homogeneous media the group velocity follows a straight path from the wave's origin to the wavefront, as shown in [Figure 2](#). The difference between the phase and group velocity directions depends on the curvature of the wavefront through the relation

$$\mathbf{V} = \mathbf{C} + \partial \mathbf{C} / \partial \theta \quad [3]$$

where θ is the azimuth angle and $\mathbf{C} = c\mathbf{n}$.

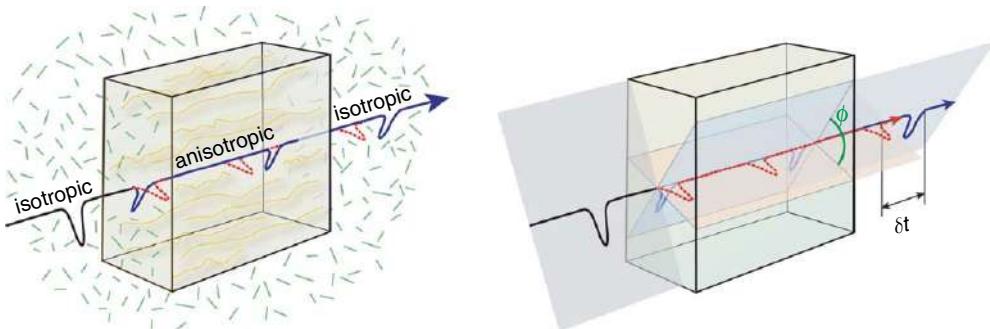


Figure 1 Principle of shear-wave birefringence. The leftmost figure shows the evolution with time of the polarization of an S wave (in black) which traverses a block of anisotropic medium. When the wave enters the anisotropic part, it splits into a fast S wave (in blue) and a slow one (in red). When the fast and slow waves leave the anisotropic region, they are separated by a time delay. The rightmost figure shows how the initial polarization of the S wave is projected onto the planes of the fast and slow waves in the anisotropic structure. Figure courtesy of Ed Garnero.

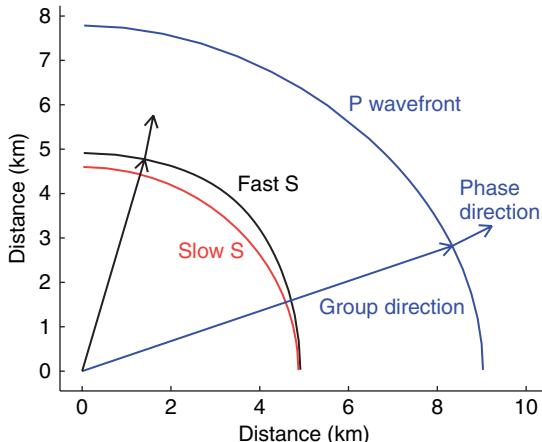


Figure 2 Wavefronts of the P wave (blue), the fast S wave (black), and the slow S wave (red) in pyrolytic material with 59% olivine (Estey and Douglas, 1986), after 1 s of propagation from a source located at the origin. The a -axis of the olivine is oriented along the horizontal direction and the c -axis along the vertical direction. The directions of the phase velocity (perpendicular to the wavefront) and of the group velocity (from the origin) are indicated at two locations of the wavefronts.

Depending on the elastic tensor and on the strength of the anisotropy, wavefronts can get quite complicated with folds and cusps, as shown in **Figure 3** which shows, at three different times, the wavefront of an acoustic (or P wave) propagating through a silicon crystal. Details about the experiment and other examples can be found in Wolfe (1998).

These characteristics of wave propagation in uniform anisotropic media also occur in more complex structures. All the classical modeling methods in

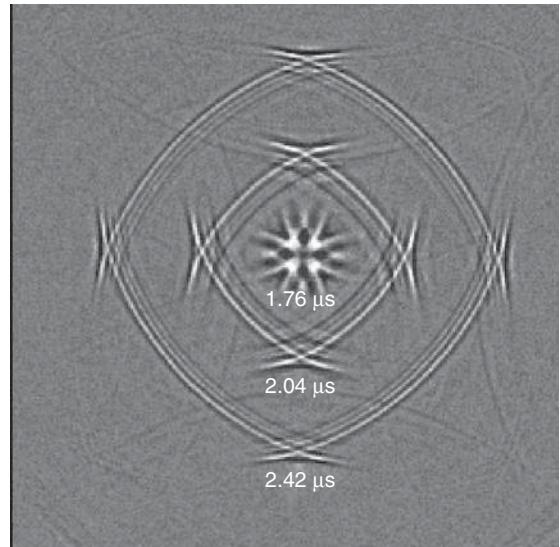


Figure 3 Snapshot of the acoustic wavefield that has propagated through a silicon crystal, recorded at three times after excitation on the other side of the crystal. Details can be found in Wolfe (1998). Photo is courtesy of J. P. Wolfe.

nonuniform structures like ray-theory, WKBJ, and reflectivity have been extended to account for anisotropy and its distinctive features (Cerveny, 1972; Garmany, 1988; Fryer and Fraser, 1984). Recent work focuses on improving the efficiency of the methods and their domains of applications, as we shall see later. The tensor of elastic coefficients is the key element which describes the anisotropic properties of any elastic material and we need first to analyze its form more in detail.

1.09.2.2 Different Parametrizations of the Elastic Coefficients

The elastic tensor has the following symmetries:

$$c_{ijkl} = c_{jikl} = c_{ijlk} = c_{klji} \quad [4]$$

resulting in 21 independent coefficients in the fully anisotropic case. These symmetries can be exploited to define a more convenient 6×6 matrix C_{mn} to describe the elasticity of the media. The so-called Voigt notation 6×6 matrix C_{mn} is symmetric and is derived from c_{ijkl} using the following correspondance conventions between ij and m and between kl and n :

$$(11) : 1 \quad (22) : 2 \quad (33) : 3 \quad (23) \text{ or } (32) : 4 \\ (13) \text{ or } (31) : 5 \quad (12) \text{ or } (21) : 6 \quad [5]$$

It should be noted that C_{mn} is not a tensor, but that, as nicely explained in Chapman (2004), it is possible to manipulate this matrix, in particular to rotate it to a different coordinate system, without having to go back to the physical c_{ijkl} tensor.

The resolution we have on Earth's anisotropy being limited, we do not usually have access to the 21 independent elastic coefficients, except on sample rocks where the elasticity can be measured in all directions. Symmetry in the anisotropy fortunately reduces the number of independent coefficients. Materials with orthorhombic symmetry, such as olivine, have nine independent coefficients, three of which define the positions of the principal coordinate axes of the material. A good approximation which is often used to reduce the number of free parameters is that the anisotropy has an axis of cylindrical symmetry (equivalent to hexagonal symmetry). Several realistic models for Earth anisotropy, such as fine layering and uniformly aligned penny-shaped or elongated cracks, show this kind of symmetry. In addition, olivine crystals, which are a dominant contributor to anisotropy in the mantle, orient with mechanisms that favor aggregate anisotropy with hexagonal symmetry, as we will see in a later section. Anisotropy with a cylindrical axis of symmetry is also called transverse isotropy (TI) because the solid is isotropic in directions transverse to the symmetry axis. A general TI medium can of course have the symmetry axis in any direction. In many applications, the axis is assumed to be either horizontal (HTI) or vertical (VTI).

There are unfortunately very many different notations used to characterize anisotropic solids, and the diversity can suggest that anisotropy is

more complicated than it actually is. It is impossible here to review all the notations, but we introduce the principal ones and their relations to each other.

The simplest notation for a TI medium is the so-called Love notation, where the five independent elastic coefficients are noted A, C, F, L, N , leading to the following C_{mn} when the symmetry axis is along axis 3:

$$\begin{pmatrix} A & (A-2N) & F & 0 & 0 & 0 \\ (A-2N) & A & F & 0 & 0 & 0 \\ F & F & C & 0 & 0 & 0 \\ 0 & 0 & 0 & L & 0 & 0 \\ 0 & 0 & 0 & 0 & L & 0 \\ 0 & 0 & 0 & 0 & 0 & N \end{pmatrix} \quad [6]$$

In the isotropic case, A and C reduce to $\lambda + 2\mu$, F reduces to λ , and L and N reduce to μ .

Instead of the elastic coefficients themselves, some authors use velocities, exploiting the simple expressions of the velocities of P and S waves along symmetry axes:

$$\alpha_{\perp} = \sqrt{A/\rho} \quad [7]$$

$$\alpha_{\parallel} = \sqrt{C/\rho} \quad [8]$$

$$\beta_{\parallel} = \sqrt{L/\rho} \quad [9]$$

$$\beta_{\perp} = \sqrt{N/\rho} \quad [10]$$

where \parallel and \perp refer to the propagation direction with respect to the symmetry axis for P waves, but has a slightly more complex meaning for S waves. β_{\parallel} is the velocity of waves that propagate along the symmetry axis or in the plane normal to it and polarized parallel to the symmetry axis. β_{\perp} is the velocity of waves propagating and polarized in the plane perpendicular to the symmetry axis. When the symmetry axis is vertical, \parallel reduces to v , for vertical, and \perp to h , for horizontal. F has no direct relation to a simple expression in terms of velocity and it is common to use as the fifth parameter $\eta = F/(A - 2L)$.

A more direct measure of anisotropic strength can be achieved by using A and L as references. The two reference velocities are then $\beta = \sqrt{L/\rho}$ and $\alpha = \sqrt{A/\rho}$. Note that β and α are not the mean velocities of the structure. The degree of anisotropy appears explicitly in the deviation from one of the three coefficients $\xi = N/L$, $\phi = C/A$, and $\eta = F/(A - 2L)$. This definition of the three coefficients is by far the most common one, but one should be aware of the fact that some authors use

other definitions of these parameters: for example, Beghein and Trampert (2003) define $\xi = 1 - N/L$ and similarly for ϕ and η .

Seismic exploration geophysicists use some variants of the coefficients as defined by Thomsen (1986). In seismic exploration, the dominant wave propagation direction is vertical. Assuming a vertical axis of symmetry, Thomsen (1986) defined the reference-wave velocities as those of vertically traveling waves: $\beta_0 = \sqrt{L/\rho}$ and $\alpha_o = \sqrt{C/\rho}$ and the three coefficients measuring anisotropy as

$$\epsilon = (1/\phi - 1)/2 \quad [11]$$

$$\gamma = (\xi - 1)/2 \quad [12]$$

$$\delta = (F + L)^2 - (F + L)^2/2C(C - L) \quad [13]$$

He shows that ϵ and γ , respectively, measure the difference in velocity between horizontally and vertically propagating P and SH waves respectively, whereas δ , a combination of basically ϕ and η in the previous notation, is the dominant factor controlling in weakly anisotropic media the deviation from sphericity of the P-wavefronts close to vertical propagation, an important element in exploration geophysics.

Rocks are aggregates of different crystals. How different anisotropic crystals combine to produce a large-scale anisotropic material is not simple, and the exact result depends in particular on the shape of the crystals and not only on their elastic coefficients. For practical purposes, one evaluates the elastic coefficients of composite materials without knowledge of their detailed geometry. The simplest algorithm is a linear average of the elastic coefficients of the material components. This is called the Voigt average. Alternatively, a linear average of the compliances is called the Reuss average. The mean of these two extreme averages is the Voigt–Reuss–Hill average, which is the closest to the physical real average usually.

Defining equivalent isotropic average properties of an anisotropic material, one faces the same difficulty as when trying to define the large-scale properties of an aggregate: the values depend on the way the averaging is done. Choosing the Voigt averaging method, that is, taking a linear average of the elastic coefficients when the sample is rotated in all space directions, a TI material has, for example, the following isotropic mean values:

$$\mu = (A + C - 2F + 6L + 5N)/15 \quad [14]$$

$$\lambda + 2\mu = (8A + 3C + 4F + 8L)/15 \quad [15]$$

This implies that the mean S-wave velocity depends partly on the parameters A and C , associated with P-wave velocities in the symmetry directions. Since the formulas above are based on the Voigt average, which is an approximation, it is as well to use simpler expressions for the mean velocities. The two common expressions for S waves are: $(V_{SH} + V_{SV})/2$ or $(V_{SH} + 2V_{SV})/3$. Which formula is used is not very important as long as one compares quantities that are comparable: Ekstrom and Dziewonski (1998) show how discrepancies between different global models can be partly explained by the fact that they are based on different data sets, basically SH versus SV waves. These provide information on different Earth properties, but bear the same name in most studies, that is, S-wave velocities.

In seismology, the term ‘transverse isotropy’ is sometimes restricted to models with a vertical axis of cylindrical symmetry, but the term applies to more general orientations of the symmetry axis. Any elastic tensor can be separated into a transverse vertical isotropic component, in the form of expression [6], corresponding to the azimuthal average of the model, plus deviations from this transverse isotropic mean, which are directly related to the azimuthal variations of the wave velocities. This notation is particularly useful for surface-wave analysis, where the vertical direction singles out quite naturally, or for body waves propagating in the horizontal plane. Crampin (1981) showed that, in structures with a horizontal plane of symmetry, the azimuthal velocity variations of body waves propagating in the horizontal plane depend on the following combinations of elastic coefficients:

$$B_c = (C_{11} - C_{22})/2 \quad [16]$$

$$B_s = C_{16} + C_{26} \quad [17]$$

$$G_c = (C_{55} - C_{44})/2 \quad [18]$$

$$G_s = C_{54} \quad [19]$$

$$H_c = (C_{13} - C_{23})/2 \quad [20]$$

$$H_s = C_{36} \quad [21]$$

$$C_c = (C_{11} + C_{22} - 2C_{12} - 4C_{66})/8 \quad [22]$$

$$C_s = (C_{16} - C_{26})/2 \quad [23]$$

with a c -index for the coefficients associated with $\cos 2\theta$ and $\cos 4\theta$ velocity variations, and those with an s -index for those associated with $\sin 2\theta$ and $\sin 4\theta$ variations. At first order in anisotropy, these combinations are also those which control the azimuthal

variations of the body waves propagating horizontally in anisotropic structures without horizontal symmetry (Leveque *et al.*, 1998), as well as the variations of the surface-wave phase velocities (Montagner and Nataf, 1986), as we will see later.

Data averaged over azimuth will give access only to the five coefficients of the vertical transverse isotropic average. Any global mean model, like PREM (Dziewonski and Anderson, 1981), cannot contain more elastic coefficients than these five. By contrast, if orthorhombic symmetry were prescribed with uniform orientation of its principal axes, six elastic coefficients would be necessary; the extra parameter breaks the symmetry between the horizontal directions.

1.09.2.3 Weak Anisotropy Approximation

Exact solution of eqn [2] is a nonlinear procedure. When averaging the volume of rock typically sampled by a seismic wave, linearized solutions are a good approximation, and illustrate the first-order influence of each elastic coefficient on the wavefield. A complete treatment by application of perturbation theory to the Christoffel equation at first order in anisotropy is presented in Jech and Psencik (1989), including perturbation of the polarization vectors.

For P-waves the perturbation in phase velocity has the simple form

$$\Delta V_P = \frac{1}{2V_P} \frac{\Delta c_{ijkl}}{\rho} n_i n_l g_j g_k \quad [24]$$

where \mathbf{g} is the unit vector in the direction of polarization in the unperturbed medium, that is equal to \mathbf{n} for P waves in isotropic structures. Summation should be made over repeated indexes. The azimuth angle θ appears in the vectors \mathbf{n} and \mathbf{g} , yielding an azimuthal dependence of the velocities with a maximum order of 4 and leading to the well-known expressions for the velocity variations of body waves at first order in anisotropy derived by Backus (1965), who showed that ΔV_P has an azimuthal dependence in 2θ and 4θ . The first-order perturbation of the P-wave polarization is normal to the unperturbed polarization. The work of Thomsen (1986), used extensively in seismic exploration and extended to more general anisotropy by Mensch and Rasolofosaon (1997), is also based on first-order approximations of the wave velocities.

The procedure to calculate the perturbations of the velocities and polarizations of S waves is more

complicated than the one for P waves due to the degeneracy of the Christoffel matrix for S waves in isotropic structures (Jech and Psencik, 1989). Results obtained from degenerate perturbation theory are valid even in strongly anisotropic structures with over 20% of anisotropy (Jech and Psencik, 1989). However, as opposed to the expression for P waves, the expressions for S waves are not linear in the perturbation of the elastic coefficients and one cannot derive analytically a simple expression for the azimuthal dependence of their velocities in the general case. In practice, the velocities of quasi-S waves also happen to show dominant azimuthal variations in 2θ and 4θ in many cases.

1.09.2.4 Ray Theory

Body waves are commonly interpreted in terms of single phases following ray paths, making ray theory a very important tool in seismology. Ray theory in anisotropic as well as in isotropic structures is summarized in the recent works of Cerveny (2001) and Chapman (2004). In anisotropic media, some of the simple intuitive aspects of ray theory in isotropic media are lost. This is especially true for quasi-S waves, for which ray theory cannot usually be employed without taking into account the frequency-dependent coupling of the two quasi-S waves.

Ray theory is a high-frequency approximation of the equation of motion in heterogeneous structures. Following Cerveny (1972, 2001), the basic system of equations which controls the tracing of the rays is

$$\frac{dx_i}{dt} = \frac{c_{ijkl}}{\rho} p_l g_j g_k = V_i \quad [25]$$

$$\frac{dp_i}{dt} = -\frac{1}{2} \frac{\partial}{\partial x_i} \frac{c_{jklm}}{\rho} p_j p_m g_k g_l \quad [26]$$

where \mathbf{x} is the location of the ray, \mathbf{p} its slowness, perpendicular to the wavefront and in the same direction as \mathbf{n} in the previous section. \mathbf{g} is one of the normalized eigenvectors of the Christoffel matrix, corresponding to the wave we want to follow along the ray. Let us note that the Christoffel matrix used in ray theory is usually normalized differently than in other studies: by replacing the components of propagation direction \mathbf{n} in eqn [2] by the components of the slowness \mathbf{p} , the expressions are better suited for the Hamiltonian formalism of ray theory (Cerveny, 2001).

Equation [25] also defines the group velocity V , which is by definition in the direction followed by the ray, and which is equivalent to the group velocity defined in eqn [3] for uniform media. This direction in general is not the same as the one of the phase slowness (or velocity) p , but the two vectors are related by the following relation:

$$Vp = 1 \quad [27]$$

As in isotropic structures, eqn [26] controls the deviation of the ray, which depends on the lateral derivatives of the density-normalized elastic coefficients. A significant difference with the isotropic case is that the polarization vectors g appear explicitly in the ray equation in anisotropic media, whereas they do not appear explicitly (but implicitly in the choice of the wave type) in the isotropic case. The equations can be rewritten without this explicit dependence by expressing the product of eigenvectors in eqns [25] and [26] as a function of selected elements of the Christoffel matrix and associated eigenvalues (Cerveny, 2001).

At leading order, the polarization of the wave motion along the ray follows the local direction of the polarization vector g , and the rays can be traced independently for the three waves. These results can be used readily for P waves in most cases. The situation is however more complex for S waves: In addition to ‘shear wave splitting’, we have ‘shear wave coupling’ in anisotropic media with lateral variations (Chapman and Shearer, 1989). In the same way as long-period P and S waves couple when they propagate through strong gradients in elastic properties (Richards and Frasier, 1976), split S waves couple to each other in gradient regions. The closer their velocities, the smaller the gradient that produces a significant coupling. Shear wave coupling is therefore a very important aspect of shear wave propagation in weakly anisotropic media (Coates and Chapman, 1990) and in strongly anisotropic media in the vicinity of singular points, where the velocities of the two quasi-S waves are close to each other and the polarizations of the two quasi-S waves rotate rapidly around the ray (Chapman and Shearer, 1989). The coupling is stronger at low frequencies and leads therefore to frequency-dependent polarizations. Coupling partly compensates for splitting, as illustrated in **Figure 4**, and makes quasi-S wave propagation converge toward the isotropic-media solution as the anisotropy goes to zero.

The nature of shear wave coupling can be understood intuitively by considering cases where the

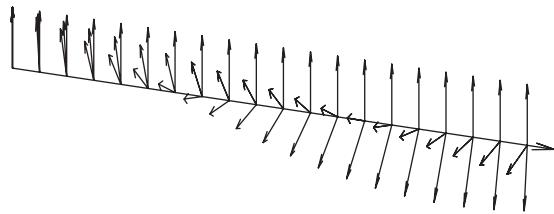


Figure 4 S-wave polarization vector along a ray: Isotropic-ray-theory polarization points upwards.

Anisotropic-ray-theory polarization points downwards on the right-hand side. Coupling-ray-theory polarization vector points between the two previous ones. At longer period, it would point closer to the isotropic-ray-theory polarization. At shorter period, it would point closer to the anisotropic-ray-theory polarization. Figure courtesy of Ludek Klimes.

theoretically determined polarization of a given quasi-S wave changes abruptly. The physical energy in the S wavefield will only partly follow the rotation of polarization, and will partly transfer onto the other quasi-S wave, leaving the overall particle motion weakly perturbed. Observable birefringence in the S wave as a result of this energy transfer develops as the wave propagates. Chapman and Shearer (1989) give an expression to connect the quasi-S rays across the gradient region where coupling occurs, which can be useful when coupling occurs only in a limited portion of the model. In cases of extended coupling through the whole model, such as with weakly anisotropic media, it is more appropriate to use approaches based on perturbation of the isotropic case. In the so-called quasi-isotropic approximation (Psencik, 1998) the quasi-S waves do not appear explicitly, and observed S waves are calculated through a system of two coupled frequency-dependent differential equations. For weak anisotropy or close to singularities, this gives a regular solution in which splitting and coupling are naturally taken into account together, and which naturally converges to the solution in the isotropic structure as anisotropy goes to zero. For strong anisotropy, the coupled equations transform to two decoupled equations for the two quasi-S waves.

An alternative approach based on higher-order perturbations and on an appropriate choice of coordinate system along the ray allows for separate ray tracing of the two quasi-S waves in weakly anisotropic media (Farra and Psencik, 2003; Farra, 2005). The expressions which can be used to analyze the errors in traveltimes related to different approaches of the shear-wave coupling problem can be found in Klimes and Bulant (2006). Similar to the one used in ray

theory, a quasi-isotropic perturbation approach of WKBJ and Langer approximation has been proposed by Maupin (1994) for layered structures.

1.09.2.5 Reflection and Transmission Coefficients

Anisotropy distorts the stress-strain relation for plane waves, and perturbs the orientations of particle motion and traction exerted at an interface between two layers. Because displacements and tractions must remain continuous across solid-solid interfaces, anisotropic distortions lead to a more complicated pattern of reflected and refracted waves than in isotropic media. Basically, anisotropy removes the decoupling between SH waves and P-SV waves which occurs in isotropic horizontally layered structures (Crampin, 1981; Fryer and Fraser, 1984). The coupling occurs also in the isotropic layer adjacent to the anisotropic one. This means, for example, that a P wave in an isotropic layer impinging on an anisotropic layer will yield a transmitted quasi-P wave, two transmitted quasi-S waves, reflected P and SV waves as well as a reflected SH wave. The conversion to an SH wave is a characteristic of anisotropy. The exact anisotropic reflection and transmission coefficients can be readily calculated (Keith and Crampin, 1977), but useful first-order expressions have also been derived for weak anisotropy (Vavrycuk, 1999), and for weak contrast across the interface (Klimes, 2003).

Seismic observations of wave conversions at buried interfaces, such as those retrieved from teleseismic receiver functions (Park and Levin, 2000; Farra and Vinnik, 2000), can inform us about the depth dependence of anisotropy. A primary indicator of anisotropy in receiver-function studies is the conversion of P- to SH-polarized shear waves. Levin and Park (1998a) show that, for hexagonal symmetry, P-to-SH converted waves follow a two-lobed or four-lobed radiation pattern with backazimuth, depending on the combination of symmetry-axis orientation and the relative strength of anisotropy in V_p and V_s . P-to-SV converted waves vary with backazimuth as well, perturbing the converted-wave amplitude associated with discontinuities in isotropic wavespeed. Anisotropy with a vertical axis of symmetry does not induce P-SH converted phases, and does not introduce backazimuth variation in the amplitude of P-SV converted waves. Four-lobed and two-lobed P-SH radiation are favored by a horizontal and a tilted symmetry axis, respectively. The scattered-wave amplitude vanishes for P waves

whose backazimuth parallels the strike of the anisotropic symmetry axis, and the SH wave has opposite polarity for impinging waves that approach from opposing sides of the symmetry axis. The P-SH scattered wave also vanishes for incoming P whose azimuth is normal to the strike of a horizontal symmetry axis.

A two-lobed P-SH radiation pattern is predicted to occur as a result of P-S conversion at a dipping interface in the absence of anisotropy (Savage, 1998; Levin and Park, 1997a), suggesting that anisotropy and deviations from layered structure can be confused. Moreover, at a dipping interface, there are P-SV amplitude variations (Figure 5), which are associated with the variation of the perturbed P incidence angle on the dipping interface: updip and downdip teleseismic P arrivals impinge at angles that differ by twice the dip angle, which leads to a variation in P-SV conversion amplitude. Discrimination between flat-layered anisotropic media and dipping isotropic media is difficult, because the mutual variation of the P-SH and P-SV converted waves with backazimuth is quite similar. Other information, such as an independent constraint on interface geometry, is useful. There can be a strong tradeoff when the dipping interface borders an anisotropic region with a tilted symmetry axis. The anisotropic effect on wave conversion also depends on the P incidence angle. Park *et al.* (2004) and Savage *et al.* (2006) found that the dip effect in the Cascadia (USA) and Hikurangi (New Zealand) subduction zones, respectively, enabled the P-SH conversion amplitudes to be fit with far less anisotropy (7% vs 10% in the case of Cascadia).

1.09.2.6 Surface Waves and Normal Modes

In strongly anisotropic layered media, the coupling between P, SV, and SH waves implies the loss of distinct Love and Rayleigh surface waves, to be replaced by generalized modes which are polarized in three directions. This is the essential difference between surface waves in isotropic and anisotropic media, together with azimuthal variation of their velocities and other characteristics, and that phase and group velocities are not aligned (Crampin, 1970). Anisotropy perturbs the frequencies and oscillation patterns of seismic free oscillations in a manner similar to isotropic lateral structure, especially for transversely isotropic media with a vertical axis of symmetry. However, anisotropy with a nonvertical symmetry axis, or with no symmetry axis, causes more extensive waveform perturbations.

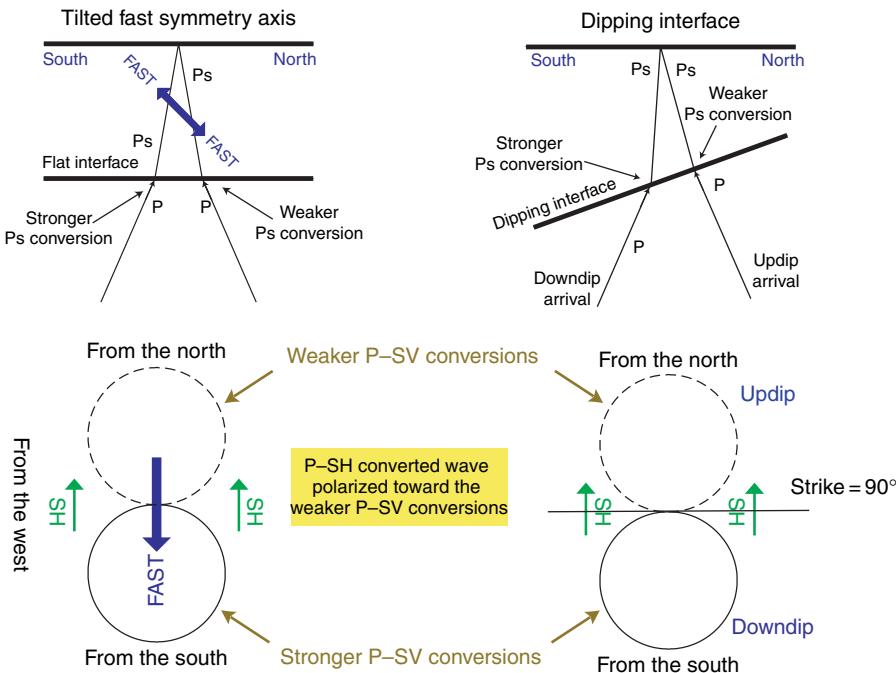


Figure 5 Schematic of S-to-P converted waves associated with anisotropy with a tilted fast symmetry axis (left) and a dipping interface between isotropic media (right). The back-azimuth variation of converted-wave amplitude follows a simple two-lobed harmonic pattern (to leading order) in both cases. The upper panels diagram the geometry of P-to-S conversion in side view. The lower panels indicate the amplitude and polarity patterns predicted for the two cases. The relationship of P-SV and P-SH conversions are similar for tilted-axis anisotropy and a dipping interface in isotropic media, suggesting that additional constraints are necessary to discriminate the two cases.

The distortion of vibrational polarization induced by an anisotropic stress-strain relation greatly encourages the coupling and hybridization of spheroidal (${}_nS_l$) and toroidal (${}_nT_l$) oscillation types. (The subscripts n and l refer to the overtone number and angular degree of the free oscillation, respectively. Each ${}_nS_l$ and ${}_nT_l$ is a ‘multiplet’, a collection of $2l+1$ distinct ‘singlet’ vibrations that share a common n , l , and oscillation frequency for a standard spherical Earth reference model.) Spheroidal and toroidal free oscillations with low overtone number combine to form Rayleigh and Love surface waves with particle motions that are mutually orthogonal. Smoothly varying isotropic velocity heterogeneity causes the spheroidal and toroidal oscillation types to interact weakly at best. Anisotropic structure induces mixed-type interaction far more effectively. Similar coupling efficiency arises from the deflection of seismic particle motion by Earth’s Coriolis force, but laterally variable anisotropy perturbs the seismic wavefield more extensively, facilitating many more coupling interactions.

As for body waves, first-order perturbations are used extensively to describe surface-wave propagation

in anisotropic Earth models. Smith and Dahlen (1973) showed that the phase velocities vary in 2θ and 4θ at first order in anisotropy, and depend on a set of 13 elastic coefficients. These expressions, rewritten by Montagner and Nataf (1986), are the basis for most of the tomographic inversions made with surface-wave phase velocities. For Love waves, perturbation in phase velocity depends on the elastic parameters through two kernels only:

$$\delta V_L = \frac{\partial V_L}{\partial L} (\delta L - G_C \cos 2\theta - G_S \sin 2\theta) + \frac{\partial V_L}{\partial N} (\delta N - C_C \cos 4\theta - C_S \sin 4\theta) \quad [28]$$

Similarly for Rayleigh waves, with four kernels

$$\begin{aligned} \delta V_R = & \frac{\partial V_R}{\partial A} (\delta A + B_C \cos 2\theta + B_S \sin 2\theta \\ & + C_C \cos 4\theta + C_S \sin 4\theta) + \frac{\partial V_R}{\partial C} \delta C \\ & + \frac{\partial V_R}{\partial F} (\delta F + H_C \cos 2\theta + H_S \sin 2\theta) \\ & + \frac{\partial V_R}{\partial L} (\delta L + G_C \cos 2\theta + G_S \sin 2\theta) \end{aligned} \quad [29]$$

All the sensitivity kernels $\partial V/\partial$ of these equations are plotted in **Figures 6 and 7** for Rayleigh and Love waves at different periods. $\partial V_L/\partial N$ dominates for Love waves and $\partial V_R/\partial L$ dominates for Rayleigh waves, at least for the deeper layers. As a result, Rayleigh phase velocities are more strongly influenced by the distribution with depth of L , G_C and

G_S , whereas Love phase velocities depend more strongly on N . C_C and C_S should also contribute significantly to Love phase velocities, but the difficulty in measuring 4θ variations in Love velocities makes it difficult to retrieve these parameters from Love-wave observations.

The dominance of the 2θ phase velocity azimuthal variation for Rayleigh waves and of the 4θ for Love waves can be seen in **Figure 8**. Peak-to-peak azimuthal variation is observed at 40 s period in this model with anisotropy in the form of 35% oriented olivine crystals in the upper 80 km of the mantle. The surface waves have been calculated exactly with the method of [Thomson \(1997\)](#). The olivine a -axis is either horizontal, dipping at 45° , or vertical. We see that Rayleigh waves have maximum velocity in the azimuth of the a -axis and minimum in the azimuth of the c -axis, and that a 45° dip of the a -axis modifies the average velocity but not the amplitude of the azimuthal variation. When the a -axis is close to the horizontal plane, the Rayleigh waves have average phase velocities that are lower than the isotropic reference. The average phase velocity is higher than the isotropic reference for large dips of the symmetry axis. The opposite is true for Love waves, which causes the apparent Love-Rayleigh discrepancy which is positive for horizontal a -axis and negative for vertical a -axis. The azimuthal variation is shown here for the fundamental mode at one period, but very similar curves are obtained at other periods and for the overtones ([Maupin, 1985](#)).

The three-dimensional (3-D) nature of the polarization of the surface waves in anisotropic media brings information on the nature of Earth's anisotropy that is complementary to the information we get from analysis of the seismic velocities. Coupling between fundamental Rayleigh and Love waves due to lateral gradients in anisotropy along the path of the surface waves produces wavetrains with arrival times between the direct Love and Rayleigh waves ([Park and Yu, 1993](#)). The timing can be understood in terms of the difference in group-velocity between Love and Rayleigh waves. If a fundamental Love wave scatters to fundamental Rayleigh, the scattered wave trails the Love wave because the scattered wave has lower group velocity, but arrives ahead of the direct Rayleigh wave because it gained a head start during its propagation as a Love wave. Similarly, a fundamental Rayleigh wave that scatters some energy to a fundamental Love wave is outpaced by the scattered phase, which is observed to arrive ahead of it. Overtone Love and Rayleigh waves have similar

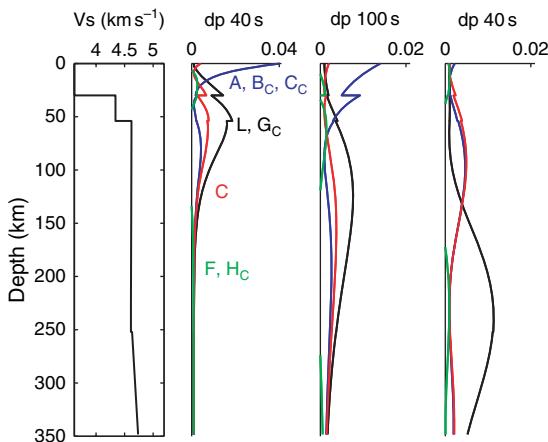


Figure 6 Sensitivity kernels of the Rayleigh wave phase velocities to different parameters as a function of depth. The S-wave velocity of the model in which the kernels have been calculated is shown to the left. The sensitivity kernels with respect to different elastic coefficients are shown in the subsequent plots for the fundamental mode at a period of 40 and 100 s, and for the first overtone at a period of 40 s.

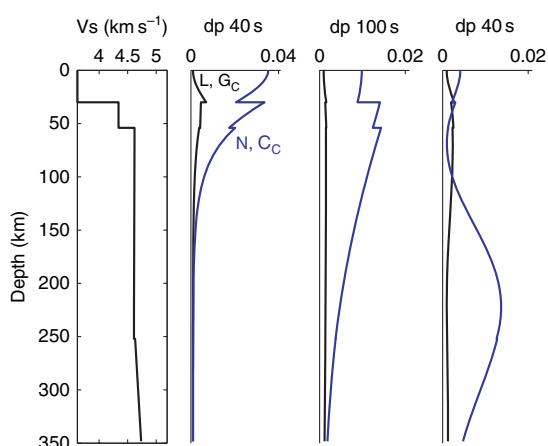


Figure 7 Sensitivity kernels of the Love-wave phase velocities to different parameters as a function of depth. The S-wave velocity of the model in which the kernels have been calculated is shown to the left. The sensitivity kernels with respect to different elastic coefficients are shown in the subsequent plots for the fundamental mode at a period of 40 and 100 s, and for the first overtone at a period of 40 s.

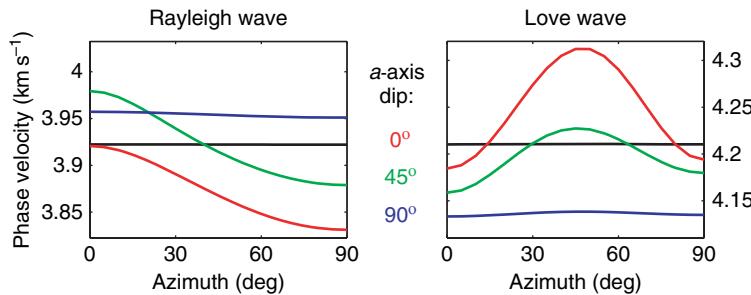


Figure 8 Azimuthal variation of the phase velocities of Rayleigh and Love wave fundamental modes at 40 s period in a model with 35% oriented olivine crystals (Kumazawa and Anderson, 1969) in the upper 80 km of the mantle. The olivine *a*-axis is in the vertical plane at azimuth 0°, and dipping either at 0° (in red), 45° (in green), or 90° (in blue), and the *c*-axis is in the azimuth 90°. The background isotropic Voigt average model is model iasp95, and the phase velocities in this model are shown as solid black lines.

group velocity at long period, leading to a near-simultaneous arrival of direct and scattered overtone waves. In addition, anisotropy close to the station distorts the polarizations of the direct waves.

Both scattered-wave and polarization effects have been called ‘quasi-Love’ waves or ‘quasi-Rayleigh’ waves in the literature. The effects have different manifestations, but are related. In the context of polarization distortion, a quasi-Rayleigh wave is mainly vertical/longitudinal with some transversal motion (Crampin, 1970), and a quasi-Love wave is mainly transversely polarized with some vertical/longitudinal motion. For fundamental surface wave scattering, the scattered wave is termed ‘quasi-Love’ or ‘quasi-Rayleigh’, even though scattered waves have vertical/longitudinal and transverse polarizations, respectively. This paradox is explained by the difference in dispersion between fundamental Love and Rayleigh waves. For instance, if a fundamental Love wave develops a polarization anomaly as it travels in anisotropic media, this anomaly has Rayleigh particle motion, cannot travel at the fundamental Love group velocity, and gradually separates from the direct Love wave to become a distinct wave.

The surface polarization of the Rayleigh waves whose phase velocities were shown in Figure 8 are presented in Figures 9 and 10. For a horizontal *a*-axis (Figure 9), the polarization remains linear, though deviated by up to 8° from the phase velocity direction. For an olivine *a*-axis dipping at 45°, the polarization anomaly is much more pronounced (Figure 10) with a distinctive elliptical motion. Generally speaking, coupling and polarization anomalies have maximum amplitude in propagation directions far from the symmetry axes and symmetry planes of the anisotropy. Polarization anomalies are

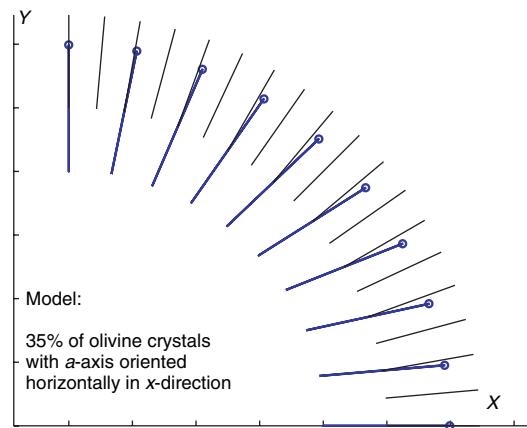


Figure 9 Polarization of a 40 s Rayleigh wave in the horizontal plane in different azimuths. The model is the same as in Figure 8. The olivine *a*-axis is in the *x*-direction and the *c*-axis is in the *y*-direction. Thin lines show the direction of the phase velocity and thicker blue ellipses (flat in the present case) show the surface polarizations.

therefore better suited than velocities to detect a plunge in the anisotropy symmetry axes (Maupin, 2001).

The polarization anomalies can be analyzed at first order in anisotropy using perturbation procedures (Park, 1997; Tanimoto, 2004). It should be noted that the computations for fundamental surface waves, based on nondegenerate perturbation theory, may need modifications for higher modes (Maupin, 2004). As for quasi-S waves, surface-wave modes have phase velocities which may be close to each other. Higher-mode Love and Rayleigh dispersion curves are roughly parallel over the broad frequency range where they can be identified with multiple SH and SV reverberations in the upper mantle.

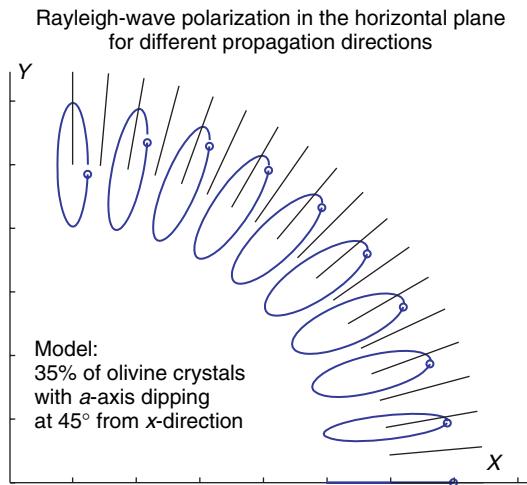


Figure 10 The same as **Figure 9** for an a -axis dipping at 45° in the vertical plane containing the x -direction. The prograde nature of the elliptic motion is shown with the small symbol at the start of the motion.

Fundamental Love and Rayleigh waves arise from dispersion branches that differ greatly, but which cross each other at specific free-oscillation multiplet pairs ${}_0S_l - {}_0T_{l'}$. At these crossing points, the nondegenerate perturbation theory is not valid anymore and one has to use degenerate or quasi-degenerate perturbation methods (Maupin, 1989).

The strength of coupling between two seismic free oscillations is inversely proportional to their frequency spacing. The largest coupling effects are seen for nearest-neighbor coupling pairs on similar dispersion branches, for example, the fundamental branch $n=0$. At frequencies $f < 2$ mHz (periods $T > 500$ s) most nearest-neighbor fundamental spheroidal–toroidal mode pairs differ by angular degree $s = |l - l'| = 1$ and are influenced strongly by Earth's Coriolis force (Masters *et al.*, 1983). At higher frequencies, the angular-degree difference $s = |l - l'|$ of these mode pairs increases as the Love and Rayleigh fundamental dispersion branches diverge (**Figure 11**). Coupling between spheroidal and toroidal free oscillations in these branches gives rise to the scattering of Love to Rayleigh and from Rayleigh to Love (**Figure 12**).

Park (1997) showed that, for a particular ${}_0S_l - {}_0T_{l'}$ coupling pair, the asymptotic effect of anisotropy is maximal for structure with wave number $s = |l - l'|$ along the source–receiver great circle. This leads to some unusual effects in hypothetical anisotropy models. For instance, anisotropy with a single angular degree s will influence a narrow frequency interval

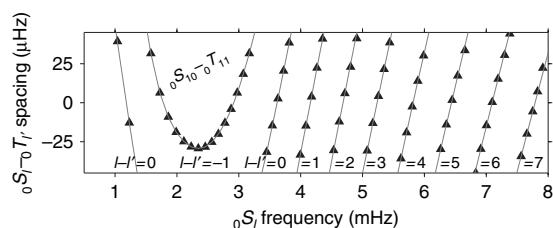


Figure 11 The relative placement of fundamental-mode branches of spheroidal (S) and toroidal (T) Earth free oscillations determines the coupling pairs ${}_0S_l - {}_0T_{l'}$ that are asymptotically sensitive to the wave number $s = |l - l'|$ of anisotropy along the great-circle path between source and receiver. At $f < 2$ mHz, $|l - l'| = 1$ for many nearest-neighbor mode pairs, so Earth's Coriolis force has a significant effect. At frequencies $f > 2$ mHz, $|l - l'|$ increases with frequency, increasing the influence of anisotropy.

where dispersion-branch crossings are auspicious for coupling, leading to a longer-duration scattered wave with narrowband frequency content. As the wave number s of the anisotropic structure along the great-circle path increases, the wave numbers and frequencies of the relevant modal coupling pairs increase. Because the fundamental-mode surface-wave perturbation kernels also vary with frequency, the depth of maximum sensitivity shallows as frequency increases. For free-oscillation overtone branches, nearest-neighbor toroidal and spheroidal coupling pairs differ little in angular degree (**Figure 13**), suggesting sensitivity to anisotropy that is near constant along the great-circle path. Coupling between mode branches will be sensitive to anisotropic gradients, for example, ${}_1T_{60} - {}_2S_{49}$ near $f = 9$ mHz will be sensitive to wave number $s = 11$, but will also be more difficult to isolate and interpret.

Anisotropic scattering effects on fundamental-mode surface waves depend therefore on the wave number of the structure along path. In contrast, a typical surface-wave phase delay is related to a simple path integral of seismic velocity, so that short-wavelength variations along the great-circle path have weak influence. Anisotropy with localized lateral gradients has a broad wave number spectrum along any source–receiver great circle that crosses it, leading to relatively impulsive scattered surface waves with broadband frequency content. The predictability of fundamental-branch surface-wave coupling relations suggests that a linearized inversion of Love–Rayleigh scattering for structure along path is possible (Oda, 2005).

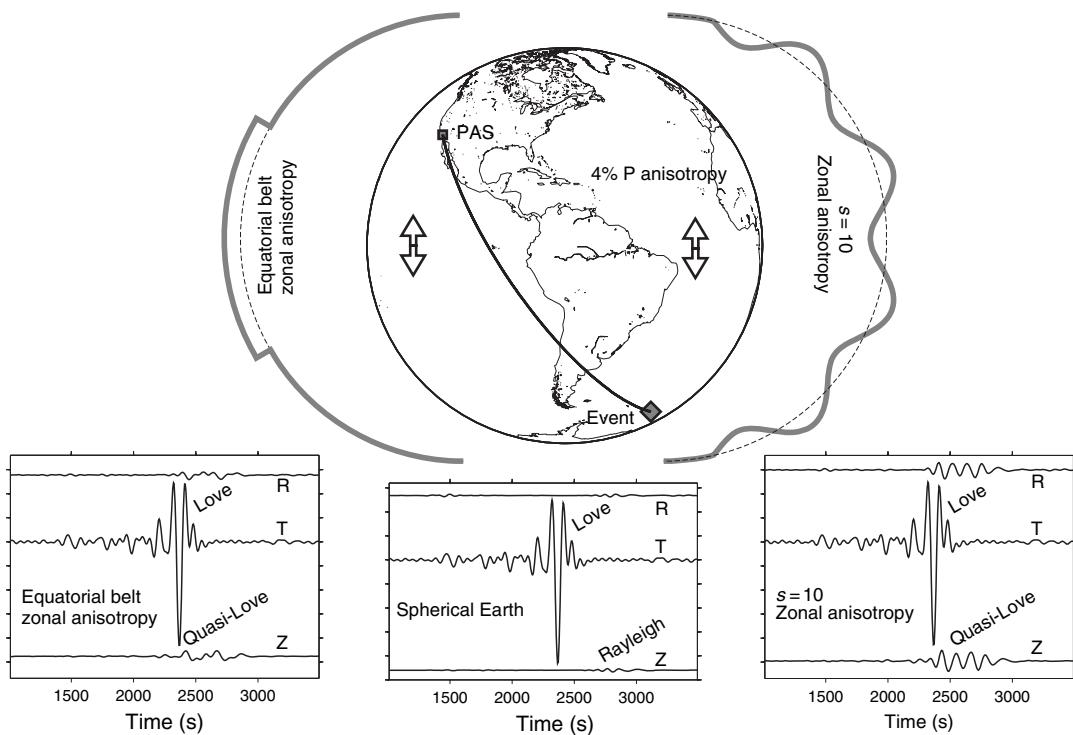


Figure 12 Examples of quasi-Love scattered waves computed for two simple anisotropic Earth models, compared with a synthetic seismogram for an unperturbed spherical Earth model. Coupled free oscillations are summed for all free oscillations with overtone number $n < 4$ and $f < 16 \text{ mHz}$ ($T > 62 \text{ s}$). Anisotropy with a north–south horizontal axis of symmetry is imposed between the Moho and 220 km depth, and the zonal symmetry to facilitate modal coupling computations. The earthquake source and station location are chosen to display a predominant Love wave, so that the quasi-Love scattered wave has larger amplitude than the Rayleigh wave. At left the synthetic seismograms for an equatorial belt of anisotropy display two pulses associated with lateral discontinuities at 30° S and 30° N. At right an anisotropic corrugation with wave number $s = 10$ generates a broader and more narrowband scattered wave, as a result of asymptotic selection rules in free-oscillation coupling.

1.09.3 Seismological Observations of Anisotropy

Considerable progress has been made in the last 20 years in mapping Earth's anisotropy. There is evidence at the present time for anisotropy in the inner core, in the D'' layer, and from the transition zone up to the surface. But the picture we have of Earth's anisotropy is indeed blurred and complex, and the mechanisms which create anisotropy are far from completely decyphered.

1.09.3.1 Crustal Anisotropy

Anisotropy in sedimentary layers is commonly observed in seismic exploration. As this subject is beyond the scope of this chapter, we refer to [Helbig and Thomsen \(2005\)](#) for a recent and excellent review of this. We focus here on crustal anisotropy

pertaining to crystalline basement rocks. The smaller volume and greater complexity of crustal rock relative to upper-mantle peridotites limits the crustal influence in many path-averaged observables, such as SKS birefringence, and the crust is usually considered as isotropic in global or large-scale models. However, local studies reveal that localized anisotropy is common in Earth's crust, dominantly in association with oceanic crustal structures, deformed regions of the lower continental crust in extensional regions ([Meissner et al., 2006](#)) and in the vicinity of fault zones ([Cochran et al., 2006; Peng and Ben-Zion, 2004](#)).

Many factors may contribute to crustal anisotropy ([Kern, 1993; Siegesmund et al., 1991a; Siegesmund et al., 1991b; Godfrey et al., 2000](#)), including lattice-preferred orientation (LPO) of mineral crystals, oriented cracks, and fine-layering of dissimilar lithologies. Crustal LPO can be substantial, owing to the

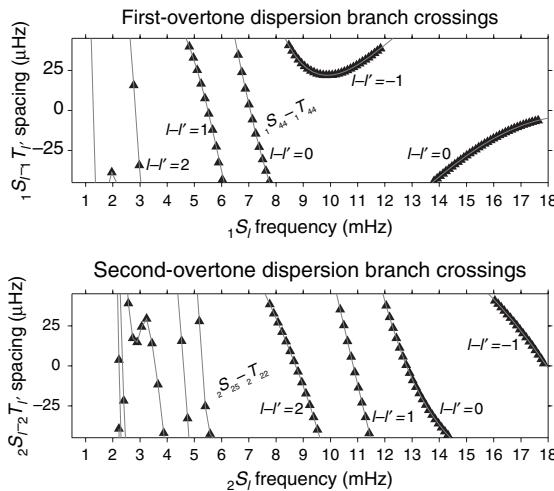


Figure 13 The relative placement of $n = 1, 2$ overtone branches of spheroidal (S) and toroidal (T) Earth free oscillations determines the coupling pairs that are asymptotically sensitive to the wave number $s = |l - l'|$ of anisotropy along the great-circle path between source and receiver. At $5 < f < 20$ mHz, $|l - l'| < 2$ for most nearest-neighbor mode pairs, in contrast to the behavior of the fundamental-mode branches. As a consequence, path-averaged anisotropy on the source–receiver great circle has a significant effect on ${}_1T_{l'} - {}_1S_l$ and ${}_2T_{l'} - {}_2S_l$ coupling pairs.

prevalence of hydrated minerals susceptible to slip on internal glide planes, commonly found in sedimentary and metamorphic rocks. The sheet-silicate structure of many metamorphic minerals typically induces the axis of symmetry to be slow rather than fast. The anisotropy of aligned planar cracks and of fine-layered dissimilar lithologies is also characterized by a slow axis of symmetry, and has much relevance in seismic exploration studies (Helbig, 1994) as well as in studies of the upper crust in general.

There is some indication that the seismic lamination which gives rise to high reflectivity features in the deep crust, as imaged in active-source seismic surveys, is associated with anisotropy (Godfrey *et al.*, 2000; Meissner *et al.*, 2006). This anisotropy, which is not precisely quantified, may have a component of azimuthal anisotropy or not. Since high reflectivity and associated anisotropy are characteristic of continental regions submitted to lateral extension, a possible interpretation is that the ductile lower crust reacts to extension by developing LPO in shear zones (Meissner *et al.*, 2006).

Another region where anisotropy is commonly observed is the upper 3–5 km of the crust, and this anisotropy is usually put in relation to the opening of

cracks by the tectonic stress of the area. In the oceanic crust, the structures associated with vertical dikes and cracks associated with hydrothermal cooling of young lithosphere near mid-ocean ridges lead to anisotropy. At large scale, crustal anisotropy affects Pg propagation, with, for example, 2% P-wave azimuthal anisotropy in the upper crust of Bohemia (Vavrycuk *et al.*, 2004), as well as Lg-waves, in the form of polarization anomalies (Maupin, 1990). Crack-induced anisotropy has a rich potential for determining stress directions in the shallow crust (Crampin and Chastin, 2003). Even a random distribution of cracks can develop an effective alignment, and elastic anisotropy, if cracks with favorable orientations open in response to the least compressive regional stress.

The orientation of cracks and anisotropy adjacent to fault zones can indicate whether the fault is too weak to sustain shear stresses and may be held open by fluid pressures in the cracks (Balfour *et al.*, 2005). The birefringence of high-frequency S waves from earthquakes at small epicentral distances has been used to monitor how anisotropy increases in the vicinity of major fault systems (Peng and Ben-Zion, 2004; Cochran *et al.*, 2006). Although the depth constraint is usually weak, there seems to be an indication that the fault-associated anisotropy is also confined to the upper few km of the crust. The anisotropy in S-velocity increases, for example, from 2% far from the North Anatolian Fault to 7% a few hundreds metres close to the fault (Peng and Ben-Zion, 2004). In the near-fault region, the fast directions rotate parallel to the fault plane, showing that the anisotropy is likely to originate from a combination of fabrics and shear-induced cracks. Very similar observations have been made in the San Andreas Fault zone (Cochran *et al.*, 2006). How anisotropy varies with time is however more uncertain. A lively debate continues over whether precursory loading of earthquake fault zones can be detected by temporal changes in crack anisotropy (Crampin and Chastin, 2003; Saiga *et al.*, 2003; Liu *et al.*, 2004; Peng and Ben-Zion, 2005).

1.09.3.2 Origin of Upper-Mantle Anisotropy

Most anisotropy studies in seismology pertain to upper-mantle anisotropy. Observations of ophiolites and deformation experiments show that mantle minerals, dominated by the strongly anisotropic olivine crystals, develop lattice-preferred orientation (LPO) in relation with the strain history. Seismic

anisotropy is therefore our most direct indicator of the mantle deformation associated with thermal convection and plate tectonics.

Single-crystal olivine suffers wavespeed variations of 24.6% and 22.3% in compressional (P) and shear (S) waves, respectively (Kumazawa and Anderson, 1969) (see also **Figure 2** for anisotropy in an olivine-rich material). Pyroxene crystals are similarly anisotropic, and contribute to bulk anisotropy in mantle peridotite. Garnet crystals exhibit a more isotropic elastic behavior. Olivine is roughly twice as abundant as pyroxene, and so its alignment is probably a dominant element in the bulk anisotropy of mantle peridotite (Babuška and Cara, 1991). The *a*-axis of olivine crystals corresponds to the direction in which P waves have highest velocities and, for *a*-axis close to the horizontal plane, to the polarization direction of the fast SKS-waves and to the direction in which Rayleigh phase velocities have a maximum. It is therefore commonly called ‘the fast axis’. There is less difference in velocities between the *b*- and *c*-axes and their directions are more difficult to infer from seismological data than the direction of the *a*-axis.

The direction of the *a*-axis is in many studies interpreted directly as being the direction of the mantle flow at the observation point. Such a simple interpretation must be made with caution since sample rock observations and numerical models show that the precise relation between deformation and mineral orientation depends on the type and strength of the deformation, pressure, temperature, and presence of melt, water, or other volatiles (Jung and Karato, 2001; Kaminski and Ribe, 2001; Holtzman *et al.*, 2003). Such behavior is reviewed in Chapter 1.22. Summarizing, we can say that the competing effects of intracrystalline slip on vulnerable glide planes within the crystal lattice, and of dynamic recrystallization associated with grain boundary migration leads to different LPO in different conditions at different stages of the deformation (Kaminski and Ribe, 2001). A good rule-of-thumb is that in dry unmolten regions the *a*-axis aligns within 10–20° of the major axis of the finite-strain ellipsoid (FSE), except where deformation varies rapidly along the flow lines. In shear and for large deformation, the fast axis aligns with the shear direction and slower axes in the plane perpendicular to it (**Figure 14**). In uniaxial compression, the slow *b*-axis tends to align with the compression direction and the *a*-axis to orient randomly in the plane normal to compression, leading to slow velocities in the compression direction and

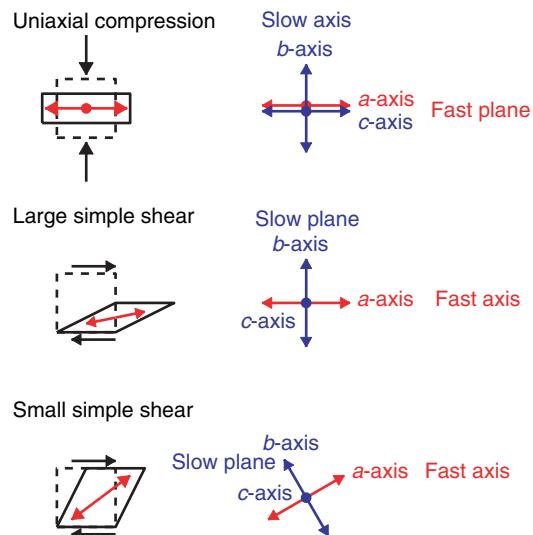


Figure 14 Long-term preferred orientation of dry olivine in simple shear and in uniaxial compressive deformation. The deformation style is depicted on the left side of the figure, with the direction of the major axis of the finite-strain-ellipsoid (FSE) as red arrows. Arrows pointing out of the figure plane are depicted by dots. Generally speaking, the *a*-axis follows the direction of the major axis of the FSE. In uniaxial compression, the *b*-axis orients in the compression direction, defining a slow axis, whereas the *a*- and *c*-axes orient randomly in the plane perpendicular to it, defining a fast plane. In large simple shear, the *a*-axis orients in the shear direction, defining a fast axis. The *b*-axis orients perpendicular to the shear plane and the *c*-axis along the neutral deformation direction. The *b*- and *c*-axis define a slow plane. In small simple shear, the pattern is similar, but tilted away from the shear direction due to the difference in direction between the major axis of the FSE and the shear.

faster velocities in the plane normal to it (Kaminski and Ribe, 2001).

The presence of water influences the relative strength of mineral slip systems and modifies thereby the relation between strain and orientation. In wet conditions, olivine may develop a B-type LPO (Jung and Karato, 2001), in which the *a*-axis orients at 90° from the strain direction. This yields fast directions perpendicular to what they would have been in the same strain field for the classical A-type dry olivine LPO described above! Strain partitioning in partially molten regions has a similar effect (Holtzman *et al.*, 2003), and this may be observed in a significant part of, for example, mid-ocean ridges (Kaminski, 2006). If A- and B-type fabrics coexist at regional scale, even a simple strain field may lead to complex anisotropy patterns. A diversity of fabrics may explain part of the complexity and diversity of anisotropy style found in subduction zones and at mid-ocean ridges.

It is important to realize that anisotropy maps the deformation, which is not related to the flow itself but to the flow gradient. The major axis of the finite strain ellipse, and thereby the fast axis of the anisotropy in usual conditions, may therefore have an orientation well away from the flow lines themselves, as shown in the ridge model in [Figure 15](#). It is only in the case of large simple shear deformation that the major axis of the FSE coincides with the flow direction and that the anisotropy maps the flow directly. A global map of inferred anisotropic strength and fast-polarization axes would therefore not translate directly into a global map of shallow-mantle convective motions, but would of course provide a valuable starting point for it.

The orientation of the crystals is not instantaneous and depends therefore also on deformation history. In regions where the deformation of a rock mass varies on short length scales along its trajectory, as at mid-ocean ridges or close to a mantle plume, the LPO of the fast α -axis lags behind its deformation ([Kaminski and Ribe, 2002](#)). In addition, shape-preferred orientation (SPO) may contribute to the anisotropy through layering, alignment of cracks, and heterogeneities.

1.09.3.3 P Wave Velocities and Lithospheric Anisotropy

Azimuthal variation of the velocity of Pn waves in the oceanic lithosphere is one of the first observations of anisotropy on Earth ([Hess, 1964](#)). More recent studies have confirmed the early results: azimuthal variations of 5.5% have been observed in the Pacific Ocean ([Shearer and Orcutt, 1986](#)), and of 3–4% in the Atlantic Ocean ([Gaherty et al., 2004](#)). They also confirm the coincidence of direction of paleo-spreading with direction of maximum Pn-wave velocity. This rift-normal fast-axis orientation suggests a straightforward relationship between anisotropy and plate divergence.

Earlier results concerning Pn anisotropy were also obtained in continental regions ([Bamford, 1977](#)), but were more difficult to interpret due to the greater complexity of the continental lithosphere. Accumulation of data has made possible a better, although still very incomplete, picture of Pn anisotropy in continental regions as well ([Hearn, 1999; Smith and Ekström, 1999](#)). The strength of Pn anisotropy, in the limited regions where it has been resolved, is 4% on average, reaching up to 10%. A rather consistent picture is that the fast axis of the Pn

waves aligns with the strike of suture zones ([Nemeth et al., 2005](#)), orogenic regions ([Hearn, 1999](#)), and subduction arcs ([Smith and Ekström, 1999](#)), as shown, for example, in Japan where the results are actually in very good agreement with SKS-splitting in that region. [Hearn \(1999\)](#) shows in addition that high anisotropy is clearly associated with low-velocity regions in the Mediterranean sea region, suggesting that if water is responsible for the low velocities, it might also facilitate lattice orientation and increase the amount of anisotropy.

At larger epicentral distances, the P waves dive deeper into the mantle and can be used to analyze the depth dependence of P-wave anisotropy in the mantle. P waves recorded on very long-range crossing profiles in Siberia ([Oreshin et al., 2002](#)) show that the strongest anisotropy, about 3%, is located rather deep in the mantle, between 150 and 250 km depth, and that moderate anisotropy (~2%) is found shallower in the upper mantle. This is broadly consistent with the depth distribution of anisotropy found in continental regions with global surface-wave data.

1.09.3.4 Traveltime Residuals and Lithospheric Anisotropy

Anisotropy is usually not taken into account in P-wave tomography because it is difficult to discriminate between the effect of lateral heterogeneities and anisotropy on traveltimes residuals. [Pratt and Chapman \(1992\)](#) analyzed the inverse problem of P waves in crosshole surveys and showed that the problem is extremely ill-conditioned, even with the restriction to TI structures. Their analysis gives a quantitative measure of the degree of regularization needed in anisotropic tomography of P waves. At global scale, we do not have a model of P-wave anisotropy based on tomography. Testing of the residuals of well-calibrated events shows however that residuals may be attributed to anisotropy at global scale, and that taking into account anisotropy would improve earthquake location ([Antolik et al., 2001](#)).

Even though anisotropy is usually not introduced directly in tomographic models, the P- and S-wave traveltimes residuals left over after inversion can be used to infer anisotropy locally below individual stations by analyzing their azimuthal and incidence-angle dependence. The azimuthally dependent part of the residuals is commonly of ~1 s ([Babuska et al., 1998](#)). Nearby stations often show a pattern which is better explained by lithospheric anisotropy under the station than by lateral heterogeneities. This

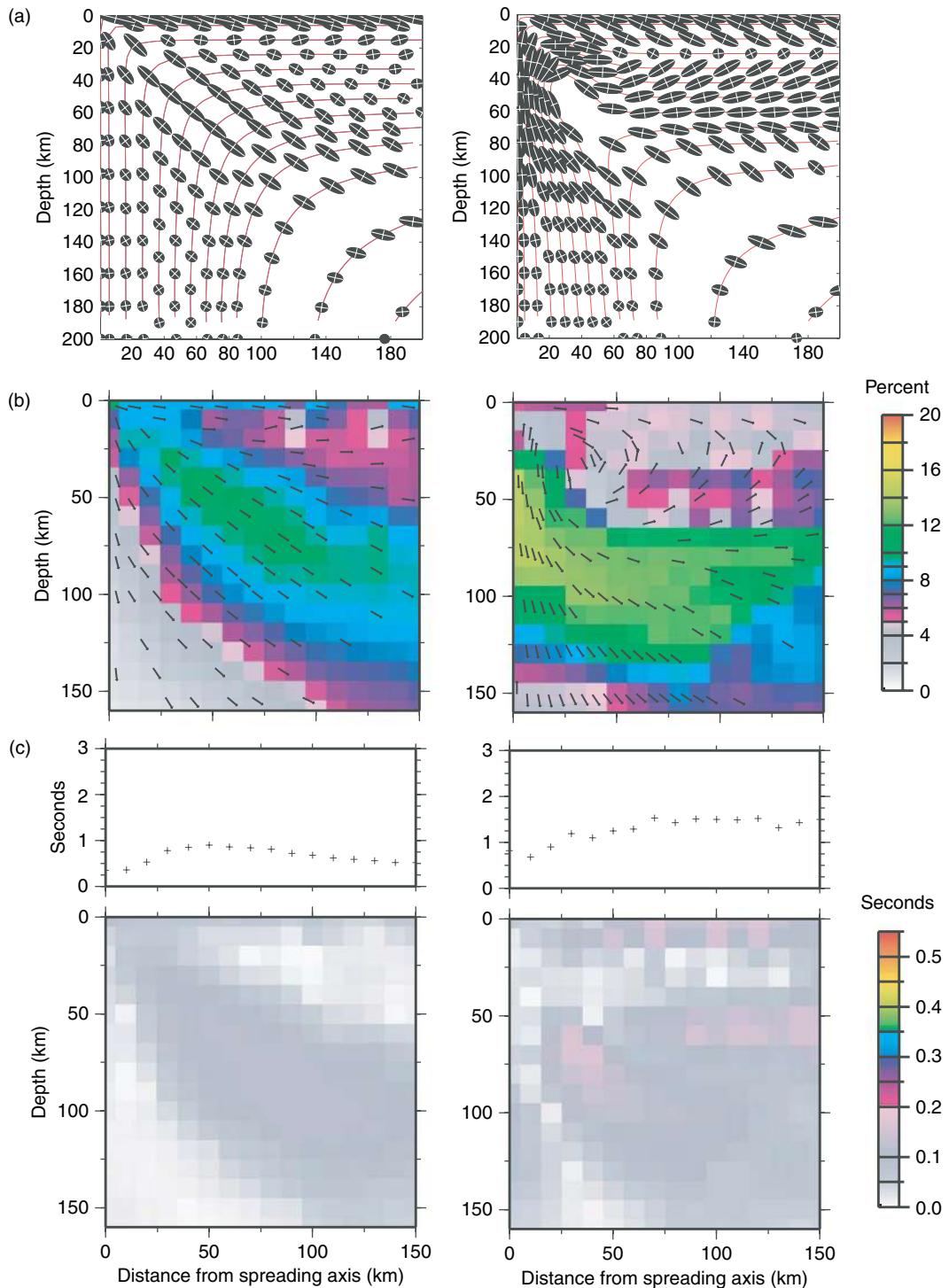


Figure 15 Figure from Blackman and Kendall (2002) showing the relation between flow, deformation and anisotropy in 2-D models at a spreading margin. The left column corresponds to a passive flow and the right columns to a buoyancy-enhanced flow. (a) shows streamlines in red and finite-strain ellipses in black. (b) P-wave anisotropy: color shade shows the degree of anisotropy and vectors show the direction of fastest P-wave propagation. (c) shows the degree of shear-wave splitting for vertical incidence, as an integrated value with depth at the top, and as a depth section illustrating where the splitting occurs.

analysis does not provide good depth resolution, but can delineate geographic regions with the same pattern of anisotropy.

Anisotropy with a dipping fast P-wave axis is often observed in continental regions, and changes in the characteristics of the anisotropy tend to occur at boundaries between different tectonic units. Continent formation via the accretion of island arcs and oceanic plateaus would be consistent with such anisotropic textures. This would imply that active mantle strain is of secondary importance in continental anisotropy, and that seismic observations are mostly influenced by accretion strains and the macrofabrics of relict slabs in accordance with findings done with SKS-splitting analysis. Dipping-axis anisotropy can also be interpreted as horizontal detachment scar, not a relict slab interface (Bostock, 1998; Levin and Park, 2000). More uniform patterns of dipping anisotropy in North America have been put in relation to deeper anisotropy, related to lithosphere–asthenosphere interaction (Bokelmann, 2002), showing, similar to conclusions of SKS-splitting studies, that continental anisotropy originates probably from a combination of frozen and active tectonics.

1.09.3.5 Polarization of P Waves

In anisotropic structures, the P-wave polarization direction does not coincide with the propagation directions (phase- and group-velocity directions). At least in structures with smooth heterogeneities, where ray theory is valid, the polarization is affected only by the local structure, in opposition to delay times and splitting which are affected by anisotropy all along the ray path. Polarization thus brings interesting information to resolve the location of anisotropy. At single stations, the deviation of the polarization from the great-circle plane can be measured, but this quantity is not straightforward to interpret since it includes two elements: the deviation of the ray from the great-circle plane as well as the deviation of the polarization from the ray direction.

Schulte-Pelkum *et al.* (2001) made an analysis of the deviation of long-period P waves polarizations worldwide and found in some cases deviations from the great-circle plane larger than 10°. They argue that great-circle deviation predicted by tomographic models can explain only a small part of the deviations, and interpret them as polarization deviations due to local anisotropy in the 250 km depth range below the station. The amplitude of anisotropy and direction

inferred with this method is usually consistent with results obtained with other methods, in particular SKS splitting. Later work, using arrays of stations to constrain simultaneously the propagation direction and the polarizations, shows however that long-period P-wave propagation may be affected significantly by local structure and that the interpretation of the polarization in terms of anisotropy only should be made with caution (Schulte-Pelkum *et al.*, 2003).

1.09.3.6 SKS Waves and Upper-Mantle Anisotropy

As opposed to P waves, S waves have a distinctive property in anisotropic media which does not occur in isotropic heterogeneous structures: the two independent particle-motion shear-wave polarizations suffer birefringence, also known as splitting. This distinctive feature makes S waves, together with surface waves, a very important source of information concerning anisotropy. In a split S wave, the anisotropy determines a fast and a slow polarization, and an impinging wave ‘splits’ into a fast and slow waves. A traveltimes difference accumulates as the split waves traverse an anisotropic region. If the time difference is larger than the dominant period of the shear wave, the two pulses can be visually distinguishable, for example, shear waves from small local events. Birefringence time delays ranging from 0.5 to 2.0 s are shorter than the dominant periods of teleseismic shear waves (5–10 s), so that splitting of these waves manifests itself as an elliptical polarization in the horizontal plane.

Shear wave birefringence, or splitting, of SKS and SKKS waves is the most popular tool for investigating seismic anisotropy (Vinnik *et al.*, 1984; Silver and Chan, 1991; Savage, 1999; Silver, 1996). This popularity is related to the simplified geometry of birefringence for core-refracted phases, such as SKS, in which S motion converts to P in the liquid outer core before returning to Earth’s surface as an SV-polarized wave. The propagation incidence of core-refracted waves is close to vertical under the station, so that birefringence accumulates in the form of an SH-component, leading to relatively simple analysis procedures. A common assumption for interpretation is that the splitting is due to a single homogeneous layer of lithospheric anisotropy with an horizontal axis of symmetry. Under such an assumption, SKS waves split into ‘fast’ and ‘slow’ waves polarization directions of which, at right angles to each other, can be found by analyzing SKS waves

from different azimuthal directions. Travel through the anisotropic mantle introduces a time delay δt between fast- and slow-polarized S waves. A splitting time $\delta t \sim 1$ s is typical, and teleseismic core-refracted SKS waves are typically analyzed at periods > 5 s. Therefore, SKS splitting is not estimated from distinct wave arrivals, but from the interference of the two ‘fast’ and ‘slow’ waves, which form an elliptical motion in the horizontal plane. One can show that the anomalous transverse-component waveform is the time derivative of the ‘normal’ radial component waveform in the case where the polarization anomaly is related to anisotropy (Vinnik *et al.*, 1989b), a characteristic which displays very well in many seismograms (**Figure 16**). This provides a good diagnostic tool for distinguishing anisotropy from other sources of polarization deformation. Measurements of δt and fast-polarization azimuth ϕ are sensitive to the product of layer thickness and layer anisotropy beneath an observation point, offering no direct resolution of anisotropy with depth.

Several methods are common for estimating birefringence. Most seek to restore ‘split’ shear waves to their original polarizations, deconvolving the horizontal motion with a broad set of apparent fast-axis strikes ϕ and delay times δt . The most popular is the method of Silver and Chan (1991), which minimizes the transverse component to restore its SV polarization. A birefringence estimator that maximizes the rectilinearity of horizontal motion (Levin *et al.*,

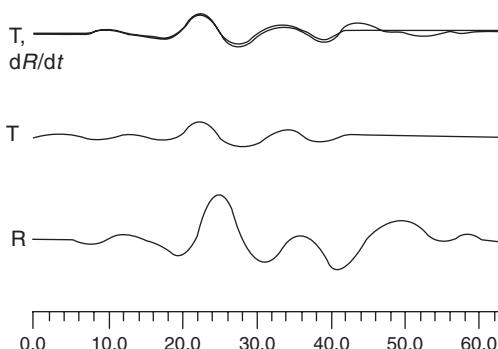


Figure 16 Figure from Long and van der Hilst (2005) showing an example of recorded SKS wave. The bottom trace shows the radial component of the SKS wave. The middle trace shows the transverse component, and the upper trace shows a superposition of the transverse component and the time-derivative of the radial one. The traces are bandpass filtered between 0.02 Hz and 0.125 Hz and deconvolved. Reproduced from Long MD and van der Hilst RD (2005) Upper mantle anisotropy beneath Japan from shear-wave splitting. *Physics of the Earth and Planetary Interiors* 151: 206–222, with permission from Elsevier.

1999), regardless of polarization, may be more robust in low signal-to-noise records, and in cases where multiple layers of anisotropy complicate the birefringence. Sileny and Plomerova (1996) estimate birefringence in a manner that models vertical as well as horizontal motion. With low signal-to-noise records one can use data from several backazimuths together and compute a robust composite fast-axis and delay time estimate, either from stacking (Vinnik *et al.*, 1989b; Wolfe, 1998) or singular-value decomposition (Chevrot, 2000)

Unfortunately, composite splitting estimates often obscure backazimuthal and incidence-angle variation that can diagnose multiple layers or tilted symmetry axes. In case of several layers of distinct anisotropy, the effects of multiply-split waves are amalgamated into a single apparent splitting measurement. Such processing oversimplifies the complex birefringence caused by two or more layers of anisotropy with independent orientations. Numerical experiments have indicated that sparse data and data-averaging techniques can be biased toward the fast-polarization direction of the uppermost anisotropic layer (Rumpker and Silver, 1998; Saltzer *et al.*, 2000), which may explain in part the correlation of many splitting observations with surface tectonic features.

Multiple anisotropic layers and other complexities lead as well to frequency dependence in the estimated splitting parameters ϕ and δt (Marson-Pidgeon and Savage, 1997). The parametrization of splitting data in the presence of multiple layers of anisotropy has ambiguities, however, because a directional dependence of splitting parameters can also be interpreted as 3-D variations in anisotropy. Menke and Levin (2003) propose a technique for testing a parametrized model space of one- and two-layer anisotropic models using a set of raw SKS waveforms, rather a collection of single-event splitting estimates. Combining data at arrays of broadband stations with appropriate tomographic techniques also seems a promising way to overcome the inherent limitations of SKS-splitting analysis at single stations concerning spatial location and orientation of the anisotropy (Chevrot, 2006).

The majority of the SKS-splitting measurements has been made on land, and brings mainly information on continental anisotropy. On land the apparent mantle textures are often fossil, dating from ancient continental accretion events. Fast polarization in the Arabian Shield aligns with a Late Proterozoic collisional zone (Levin and Park, 2000; Wolfe *et al.*, 1999), and in southern Africa exhibits a consistent

alignment throughout Archean and Proterozoic continental cratonic zones (Silver *et al.*, 2001). A correspondence of fast polarization with the trends of surface relicts of pre-Cambrian tectonic features in the Canadian shield also lends support to the notion that mantle textures can be preserved in the continental lithosphere for a billion years or more (Silver and Kaneshima, 1993; Rondenay *et al.*, 2000). In cases where continental tectonics is active, mantle flow from present-day tectonics can be clearly evident, but superimposed on mantle textures inherited from terrane formation and assembly. On the Adriatic and Ionian side of the Apennines orogen, Margheriti *et al.* (2003) observed orogen-parallel fast polarization over much of the Italian peninsula and Sicily, but at the northern end near the Po Valley the influence of anisotropy in the Paleozoic basement rocks complicates an interpretation in terms of mantle flow (Plomerova *et al.*, 2006).

The close connection of shear-wave birefringence parameters to regional tectonics argues that anisotropy can vary greatly, in continents at least, on short lateral length scales. The difficulty of relating anisotropy from surface-wave tomography to broad-scale tectonics is therefore not surprising.

Variation of anisotropy with depth was first found using splitting of SKS waves at observation points proximal to the San Andreas Fault in California (Silver and Savage, 1994). Fast polarization in the upper layer, perhaps most affected by the brittle deformation of the fault zone, was observed to be roughly fault-parallel, while fast polarization in the lower layer was roughly east–west, consistent with fast polarization farther inland in the extensional Basin and Range province. In the northeastern US, Fouch *et al.* (2000) interpret SKS splitting in terms of asthenospheric flow around a notch in the base of the North American continental lithosphere. This interpretation cannot be distinguished from the two-layer interpretation of Levin *et al.* (2000) by splitting data alone.

Anisotropy with a tilted symmetry axis also exhibits a variation of δt and ϕ that can be distinguished from a multiple-layer effect (Babuska *et al.*, 1993). Tilted-axis effects are reported in much of Europe, where its plunge is associated with texture developed during the Variscan orogeny of the Late Paleozoic (Plomerova *et al.*, 2001), or, in the Fennoscandian shield, as evidence of Archean continental accretion from a sandwich of old subducted slabs (Plomerova *et al.*, 2000). Tilted axis splitting effects are also associated with present-day deformation in Tibet (Hirn

et al., 1998) and near the Mendocino triple junction of northern California (Hartog and Schwartz, 2000). Fast polarization in the upper layer, perhaps most affected by the brittle deformation of the fault zone, is roughly fault-parallel, while fast polarization in the lower layer is roughly east–west, consistent with fast polarization farther inland in the extensional Basin and Range province.

1.09.3.7 P and S Waves and Subduction Zones

Subduction zones are another plate boundary where mantle anisotropy may help prioritize competing processes. Processes within this small fraction of Earth's volume control one of the most significant 'products' of the plate tectonics engine, volcanic arcs, and influence strongly the accretion of continents. The geometrical complexity of the region, with mantle wedge, slab and subslab mantle, together with the possibility in oblique subduction of developing strike-slip motion parallel to the trench, makes this region very challenging for anisotropy studies. Wet conditions may alter the type of olivine fabrics and lead to fast polarizations perpendicular to the deformation, as mentioned in Section 1.09.3.2. On the other hand, the presence of many earthquakes distributed at depth and of arrays of stations are a clear advantage for resolving anisotropy.

Most petrologic models of the 'subduction factory' assume that shear coupling to the downgoing slab drives a 2-D corner flow in the upper-mantle wedge above it, leading to predictable thermal effects (Peacock and Wang, 1999). Trench-normal fast polarization in the back arc has been associated with the entrainment of mantle by shear-coupling to the slab in the Kuriles (Fischer and Yang, 1994; Su and Park, 1994) and the Pacific Northwest (Schutt and Humphreys, 2001), but Fischer *et al.* (1998) find that fast-axis alignment in several Pacific subduction zones parallels back-arc spreading rather than subduction azimuth. Fast polarization in the supraslab mantle wedge, as revealed by the splitting of S waves from earthquakes in downgoing lithosphere, shows a variable pattern. It is either trench normal (Fischer *et al.*, 1998), consistent with shear-coupled corner flow or back-arc extension, trench parallel (Cassidy and Bostock, 1996; Long and van der Hilst, 2006), consistent with 3-D flow or B-type fabric, or splitting is absent (Fischer *et al.*, 1998; Wiemer *et al.*, 1999), consistent with poorly developed wedge flows in tank simulations of slab rollback (Buttles and Olson, 1998).

In several regions like the Lau Basin of the SW Pacific (Smith *et al.*, 2001), Japan and Kuriles (Nakajima and Hasegawa, 2004; Nakajima *et al.*, 2006), the Ryukyu arc (Long and van der Hilst, 2006) and to a lower extent New Zealand (Morley *et al.*, 2006), networks of seismometers across the back-arc region reveals trench-parallel fast polarization near the trench that rotates to trench-normal in the back-arc extensional region. The same pattern is obtained with core-refracted S waves in the central Apennines of Italy (Margheriti *et al.*, 1996; Amato *et al.*, 1998), or in Japan (Long and van der Hilst, 2005) as can be seen in **Figure 17**. In Japan, the rotating fast-axis pattern obtained with S waves compares well with the direction of fast Pn waves (Smith and Ekström, 1999). Despite a more complex and possibly not so-well resolved picture, the trend is also similar in the local P-wave tomography of Ishise and Oda (2005), with trench-parallel fast axis in the wedge below the island arc.

It is tempting to hypothesize that a similar splitting pattern might be revealed above subduction zones

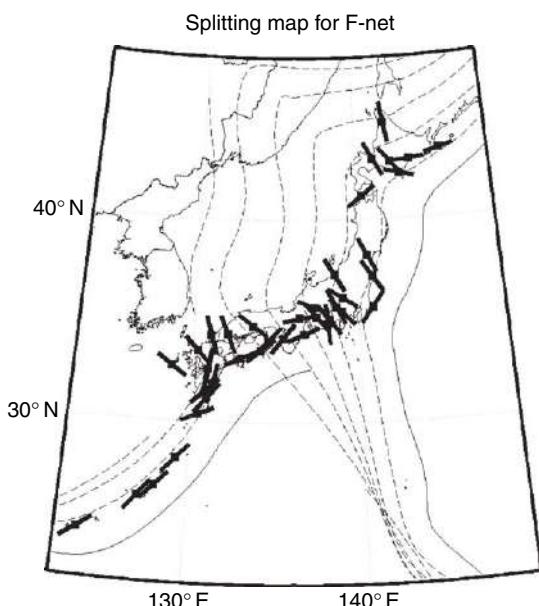


Figure 17 The fast directions obtained from analysis of S-, SKS-, and SKKS-splitting at the F-net stations in Japan. The results are shown only for the 36 stations for which a meaningful fast direction could be obtained. For 25 other stations, there is evidence for a complex anisotropy. The contours of the Wadati-Benioff seismicity are also shown at 100 km intervals. Reproduced from Long MD and van der Hilst RD (2005) Upper mantle anisotropy beneath Japan from shear-wave splitting. *Physics of the Earth and Planetary Interiors* 151: 206–222.

where station coverage is now sparse, and suggest that several of the apparent discrepancies can actually be explained by the model developed by Kneller *et al.* (2005). By combining geodynamic flow computations with empirical rules for olivine fabric development, Kneller *et al.* (2005) shows how a simple corner flow leads to a trench-normal fast axis away from the island arc, but to trench-parallel fast axis beneath the island arc, due to the presence of diverse water-controlled olivine fabrics in this region. Strain localization and the potential effects of water on peridotite viscosity (Karato and Wu, 1993; Hirth and Kohlstedt, 1996) and mineral texture (Jung and Karato, 2001) make such complexities plausible.

A broad array of seismic techniques will likely be necessary to discern the wedge strain field and its underlying causes. The diversity of results from sparse data sets is possibly explained by Levin *et al.* (2004), which analyzed a relatively large data set of shear waves from the Benioff zone beneath the Kamchatka regional network (roughly 700 source-receiver pairs). They found that only half of the S waves with good signal-to-noise ratio returned usable splitting estimates, and that splitting parameters estimated by different techniques often diverged more than the nominal measurement uncertainties. Considering the large scatter in measured fast polarizations and time delays, Levin *et al.* (2004) emphasized the importance of averaging multiple observations. In Kamchatka such averaging showed that anisotropy aligned with trench-normal corner flow, in contrast to the model predictions of Kneller *et al.* (2005), was supported only in the fore-arc region far from the slab termination at the Kamchatka–Aleutian junction, where a deflection of fast polarization indicated a flow disruption in the supra-slab wedge.

Beneath subducting slabs that suffer retreat away from the trench, asthenosphere beneath the slab hypothetically suffers trench-parallel flow and/or extension. This hypothesis has been confirmed by splitting observations in South America (Russo and Silver, 1994; Polet *et al.*, 2000), Kamchatka (Peyton *et al.*, 2001), and the Apennines (Margheriti *et al.*, 2003; Plomerova *et al.*, 2006).

1.09.3.8 Surface Waves and Upper Mantle

Surface-wave phase velocities are affected by anisotropy in two ways. The azimuthal average of Love and Rayleigh phase velocities are sensitive to different azimuthal averages of the elastic coefficients, basically Love waves are mostly sensitive to the depth variation

of the parameter N in the azimuthal average VTI of the structure, and Rayleigh waves to the parameter L . This leads to the so-called Love-Rayleigh discrepancy, in which the simultaneous inversion of Love and Rayleigh dispersion curves is not compatible with an isotropic model. In addition, anisotropy leads to azimuthal variations of the phase velocities. The advantage of surface waves is that they provide a better depth resolution than splitting-time analysis, and can help to distinguish between crustal, lithospheric, and asthenospheric anisotropy.

The Love-Rayleigh discrepancy was first interpreted in terms of anisotropy by [Anderson \(1961\)](#). On average, Love waves are fast compared to Rayleigh waves, giving in PREM a ξ value of 1.1 below Moho, decreasing linearly to the isotropic $\xi = 1.0$ at 220 km depth (see [Figure 18](#)). In more recent global models, the VTI is smaller below Moho ($\xi \approx 1.06$) but distributed to larger depths of up to 400 km ([Montagner, 1998](#)). There is an indication of anisotropy in the transition zone, to which we return in a later section.

Systematic analyses of the average Love-Rayleigh discrepancy in different tectonic regions show regional variations, with a general trend in global long-period data indicating maximum anisotropy in the asthenosphere in the range 200–400 km in old continental regions, and 50–150 km in oceanic regions ([Plomerova et al., 2002; Gung et al., 2003](#)). [Ekstrom and Dziewonski \(1998\)](#) find similar results but with a stronger anisotropy in the Pacific Ocean, with a value of ξ of up to 1.14 at 100–150 km depth in the Central Pacific.

Regional tomographic models and broadband-array recordings of surface waves provide focused measurements of the Love-Rayleigh discrepancy. Although absent from some regions, for example, Northern Europe ([Muyzert et al., 1999](#)), transverse isotropy below the Moho and down to at least 200 km depth is very common, with values for $\xi \sim 1.08$, corresponding to 4% difference in SH and SV velocity ([Wielandt et al., 1987; Friederich and Huang, 1996; Polet and Kanamori, 1997; Gaherty et al., 1999; Freybourger et al., 2001; Gaherty, 2004; Marone et al., 2004](#)) (see [Figure 18](#) for some examples). The lower boundary of the anisotropic region may not be resolved very well with these data, but the amount of anisotropy in the upper lithosphere should be well determined. This value is not small and does not point to a smaller amount of anisotropy in the lithosphere than in the asthenosphere, as global data suggest ([Gung et al., 2003](#)). Larger values of ξ up to 1.18 have also been observed ([Maupin and Cara, 1992; Debayle and Kennett, 2000](#)), values that are

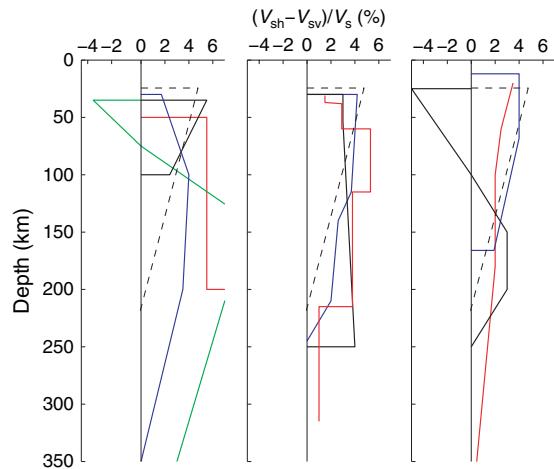


Figure 18 Examples of upper-mantle transverse isotropy obtained from local or regional studies of the Love-Rayleigh discrepancy. The plots show the difference between SH-wave and SV-wave velocity as a function of depth. The values in the PREM model are shown for reference with a dashed black line. The leftmost plot corresponds to studies in continental regions for which Love and Rayleigh wave velocities have been averaged over azimuth before inversion, in Iberia ([Maupin and Cara, 1992](#)) (green), in South Africa ([Freybourger et al., 2001](#)) (black), in Germany ([Friederich and Huang, 1996](#)) (blue), in Finland ([Pedersen et al., 2006](#)) (red). The central plot corresponds to continental studies made in a single azimuthal direction, in Bohemia ([Wielandt et al., 1987](#)) (red), in Australia ([Gaherty et al., 1999](#)) (black), in North America ([Gaherty, 2004](#)) (blue). The rightmost plot shows studies made in a single azimuth in oceanic regions, in the northern Pacific ([Cara and Lévéque, 1988](#)) (red), in the southern Pacific ([Gaherty et al., 1999](#)) (blue), in the 10–40 My old oceanic lithosphere along the Reykjanes Ridge ([Gaherty, 2001](#)) (black). Reproduced from [Pettersen O and Maupin V \(2002\) Lithospheric anisotropy on the Kerguelen hotspot track inferred from Rayleigh wave polarisation anomalies. Geophysical Journal International 149: 225–246](#), with permission from Blackwell.

challenging to reconcile with other seismological data and current explanations for the origin of the anisotropy. The averaged effect of a horizontal olivine fast axis can hardly explain values so large, and one may need to invoke additional effects of fine-horizontal layering, or more generally preferred orientation of strong heterogeneities.

Anisotropy shows also in the azimuthal dependence of the phase-velocity maps of Rayleigh and Love waves at different frequencies. The azimuthal variation of the Love waves, which should be dominantly in $\cos 4\phi$ due to the dominance of the partial derivative in N in eqn [28], is difficult to measure due to inadequate azimuthal coverage and larger noise on Love waves than on Rayleigh waves.

Global measurements have confirmed the dominance of the 4ϕ terms and found azimuthal variations of up to 2% peak-to-peak amplitude at 40 s period (Trampert and Woodhouse, 2003). The azimuthal variations of the Rayleigh phase velocities are much better documented. In tomographic models, the reported values of the azimuthal variations of the Rayleigh phase velocities are usually \sim 1–2% peak-to-peak amplitude (Debayle and Kennett, 2000; Trampert and Woodhouse, 2003). The amplitude variation is found to be of the same order as the variation of the Rayleigh phase velocities. Although the dominant variation should be in $\cos 2\phi$ for Rayleigh waves, non-negligible $\cos 4\phi$ variations have been reported at global scale (Trampert and Woodhouse, 2003), which may indicate more shallow anisotropy than anticipated from 2ϕ variations alone. The elastic coefficient G_c is the best-resolved parameter through inversion with depth of the variations in $\sin 2\phi$ of the Rayleigh phase velocities. Few inversions have been carried out, finding generally the largest values for G_c in the lithosphere (Nishimura and Forsyth, 1989), with Australia as an exception with large asthenospheric G_c (Debayle and Kennett, 2000). This larger value, together with the coincidence of fast Rayleigh-wave direction with absolute plate motion, can be correlated to the fast absolute velocity of the Australian plate. The larger anisotropy might result from a larger shear strain at the lithosphere–asthenosphere boundary than in other continental regions (Debayle and Kennett, 2000).

Close to ridges, anisotropy is usually found to be ridge-perpendicular (Montagner and Tanimoto, 1991; Laske and Masters, 1998; Silveira *et al.*, 1998). Although simple continuous-flow models predict anisotropic texture to be frozen into young oceanic plate as it cools and thickens (McKenzie, 1979; Ribe, 1989), more sophisticated modeling of olivine crystal aggregates suggests that anisotropic texture can be weak in the stiff plate, and concentrated in the lithosphere–asthenosphere transition (Blackman *et al.*, 1996; Tommasi, 1998). In oceanic regions, the fast direction inferred from Rayleigh phase velocities coincides quite well with the absolute plate motion of the fast-moving plates in the Pacific and Indian Oceans (Laske and Masters, 1998; Leveque *et al.*, 1998; Trampert and Woodhouse, 2003). A detailed analysis however shows that the correlation is even better with the direction of finite-strain ellipsoids derived from flow models (Becker *et al.*, 2003). In the slower spreading Atlantic Ocean, a mantle-plume signature seems to have a stronger influence and complicate the anisotropy

away from the ridges (Silveira *et al.*, 1998). Correlation between surface tectonics and fast Rayleigh-velocity direction is more difficult to constrain in continental regions, which are likely to show a more complex pattern of anisotropy, at least in the lithosphere (Priestley *et al.*, 2006).

The lateral resolution of the global tomographic models is no better than 1000 km, and one could suspect that the small amplitude of the azimuthal variations discerned by tomographic inversions results from the lateral smoothing of small-scale isotropic variations. However, local measurements made on arrays of stations usually report even smaller azimuthal variations, often less than 1%, or at the limit of what can be measured (Freybourger *et al.*, 2001; Friederich and Huang, 1996; Pedersen *et al.*, 2006). Since olivine fast axis has to be dominantly horizontal to explain the positive SH–SV wave velocity difference shown in Figure 18, the absence of associated azimuthal variation can only be explained, in the framework of olivine, by a fast axis oriented in the horizontal plane but in azimuths strongly varying either laterally or vertically. This kind of structure has also been invoked by Gaherty (2004) to explain the apparent incompatibility of Love–Rayleigh discrepancy measurements in North America with results of SKS splitting. Anisotropy inferred from SKS splitting can predict phase-velocity azimuthal variations. Since the number of observations of azimuthal local variations of phase velocities is much smaller than the number of sites where SKS splitting has been measured, the comparisons we can make are not numerous. However, the small amplitude and fast direction of the azimuthal variations measured locally are often not in accordance with observed SKS splitting. Results from SKS splitting studies and global surface-wave tomographic models does not show a very good overall agreement either (Montagner *et al.*, 2000). It is clear than in the continental lithosphere we have a complex picture which is not well understood and that combined studies of different types of data are necessary to get a more coherent view and interpretation.

1.09.3.9 Polarization of Surface Waves

Observations of polarization anomalies related to anisotropy are not very common in the literature, in part, due to the difficulty in distinguishing them from anomalies due to lateral heterogeneities and scattering. One polarization anomaly related to anisotropy is the presence of a vertical component associated

with the Love fundamental mode at long periods (>70 s) (Figure 19). This ‘quasi-Love’, which is best observed in backazimuths close to the Love-wave radiation maximum, has amplitudes on the vertical component often equal to 3–20% of the transverse component. It is best explained by lateral gradients in anisotropy at 100–300 km depth (Yu and Park, 1994; Oda and Onishi, 2001). Scattering amplitude is greatest for incidence at 45° from the strike of a horizontal axis of symmetry (Park, 1997; Yu and Park, 1994). Quasi-Love waves are sensitive to both V_p and V_s

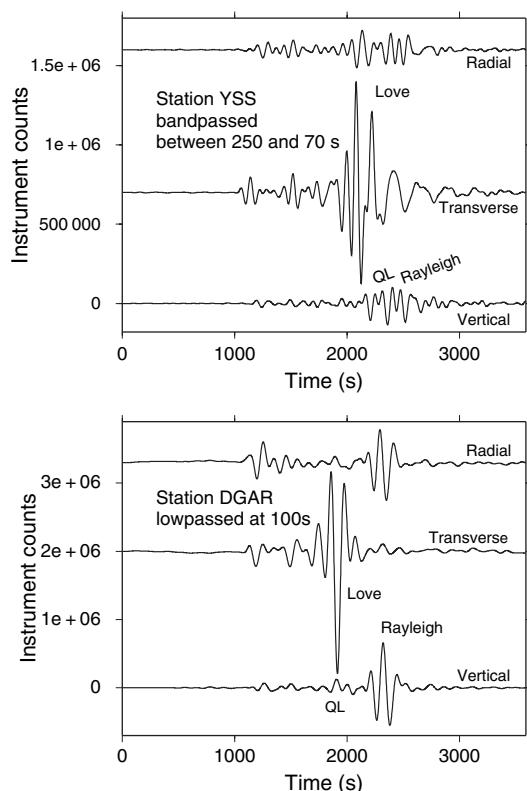


Figure 19 Examples of quasi-Love scattered waves observed in data from the 23 Dec 2004 $M = 8.1$ earthquake near the Macquarie Islands. This great shallow strike-slip earthquake generated large fundamental Love waves, making quasi-Love modes more visible in low-passed seismic records. Data from GSN station YSS (Yuzhno-Sakhalinsk, Russia) have been bandpassed between 4 and 15 mHz to minimize the influence of Coriolis coupling at frequencies $f < 4$ mHz along this propagation path, which is nearly north-south. Data from GSN station DGAR (Diego Garcia, Indian Ocean) are only minimally affected by Coriolis coupling. The quasi-Love wave at DGAR coincides with the main Love wave, suggesting the effect of anisotropy proximal to the mid-ocean island. The quasi-Love wave at YSS, in contrast, is delayed relative to the main Love wave, suggesting the effects of lateral gradients of anisotropy south of the station, for example, along the Japan and Kurile subduction zone.

anisotropy, but with opposing influences, which may aid in distinguishing the two.

Quasi-Love studies have illuminated localized regions of gradients in anisotropy near several plate boundaries and other geodynamic features. The seaward sides of several Pacific subduction zones (Tonga-Kermadec, Japan-Kurile, central Aleutians) have exhibited quasi-Love observations that are consistent either with strong trench-parallel flow and/or extension in the asthenosphere beneath a subducting slab (Yu and Park, 1994; Kobayashi and Nakanishi, 1998). Large quasi-Love amplitudes are observed near Tonga-Kermadec (Yu and Park, 1994), where back-arc spreading and rollback is large, and smaller amplitudes at Kamchatka, where back-arc activity is ambiguous (Park *et al.*, 2002). In a continental collision zone, quasi-Love waves are generated in the mantle beneath the Tangula-Shan mountains, a convergence zone at the southern edge of the Tibetan Plateau (Yu *et al.*, 1995). Quasi-Love waves are also observed at Hawaii, presumably generated by the bow-shock gradient in mantle flow (Levin and Park, 1998b).

Because quasi-Love waves are generated by localized gradients of anisotropy, one expects a correlation with strong gradients in SKS-splitting measurements. Although such correlation in Tibet was not found by Yu *et al.* (1995), a dense broadband portable network in central Italy observed one in surface waves from the 2004–2005 megathrust earthquakes in Sumatra (Levin *et al.*, 2007). Quasi-Love waves were observed south of 44° N, consistent with trench-parallel SKS fast-polarization and anisotropy behind the retreating Apennines slab. North of 44° N the SKS fast-polarization swings to north–south, an orientation that does not cause Love–Rayleigh scattering – and none is observed.

Similarly, ‘quasi-Rayleigh’ waves, with a transverse component of up to 55% of the longitudinal one, have been observed in the vicinity of the Kerguelen hot spot at periods 20–50 s (Pettersen and Maupin, 2002). An example is shown in Figure 20. The polarization anomalies are elliptical, like those shown in Figure 10, and are indicative of lithospheric anisotropy with a fast axis dipping away from the hotspot location in a manner very similar to the one in the passive flow shown in Figure 15.

1.09.3.10 Converted Waves and Lithospheric Anisotropy

Anisotropic observables associated with converted body waves, both P-to-S and S-to-P, come in two

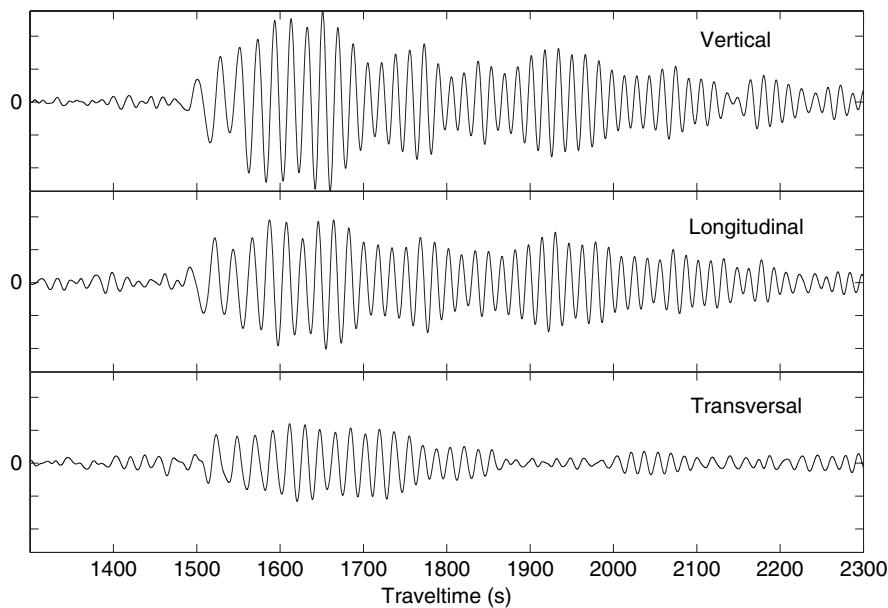


Figure 20 Example of a quasi-Rayleigh wave recorded at the Kerguelen Islands GEOSCOPE station PAF. The three components are plotted at the same scale. Note the prominent transversal component which has the same dispersion characteristics than the vertical and radial ones. The data are from the 4 Aug 1993 earthquake in the Java subduction zone, which did not generate Love waves in the direction of the PAF station. Modified from Pettersen O and Maupin V (2002) Lithospheric anisotropy on the Kerguelen hotspot track inferred from Rayleigh wave polarisation anomalies. *Geophysical Journal International* 149: 225–246.

general types. The first observation type is the birefringence of the converted Ps wave. Theoretically, this observable depends on a vertical integral of anisotropy between the converting interface and the surface. Using the Moho Ps phase, McNamara *et al.* (1994) estimated the partition of SKS splitting between crustal and mantle anisotropy in Tibet, but found that only 25 out of nearly 700 of observed Ps converted phases showed evidence of birefringence. The second observation type is the effect of anisotropy at an interface on the amplitude of the converted wave. Theoretically, this observable depends on the anisotropic gradient at or near the converting interface. Although this small-scale sensitivity is complementary to the vertical integration associated with birefringence, there are potential observational overlaps that are not often explored in data analysis. One of the characteristics of birefringence, a pulse on the transverse-horizontal component of motion that resembles the time derivative of the main pulse, can also be generated by Ps conversions at the top and bottom of a localized anisotropic shear zone (Levin and Park, 1998a). Both birefringence and Ps conversion vary with backazimuth with the tilt of the axis of symmetry in anisotropic media with hexagonal symmetry, hampering use of backazimuth dependence as a discriminant.

A better discriminant would be detection of the P–SV conversions on the radial-component receiver function, which should indicate whether one interface or a bounded shear zone is present.

Seismic refraction studies on continents have revealed a wealth of possible ‘stretch marks’ in the lithosphere at depths <100 km, and initial Ps receiver functions of the transverse component suggest that many ‘interfaces’ resemble thin shear zones with a discernable rock texture (Bostock, 1998; Calvert *et al.*, 1995; Warner *et al.*, 1996; Hajnal *et al.*, 1997; Levin and Park, 1997b, 2000; Girardin and Farra, 1998; Sherrington *et al.*, 2004; Wilson *et al.*, 2004). The S-to-P conversions identified in S receiver functions (Farra and Vinnik, 2000) have been associated with anisotropic shear zones in the uppermost mantle (Wittlinger *et al.*, 2004), but have so far been interpreted mainly in terms of isotropic structure, for example, Kumar *et al.* (2005).

Neither arc-slab accretion nor delamination can easily be reconciled with potential relations between anisotropy and globally recognized internal uppermantle interfaces. The Lehmann discontinuity at 220 km depth has been related to depth-dependent changes in mantle deformation mechanisms (Karato, 1992), and the possible influence of penetrative relict

structures on the Lehmann discontinuity requires further study. Based on weak backazimuthal variation of Ps conversions in eastern North America, Vinnik *et al.* (2005) concluded that the Lehmann discontinuity was not associated with anisotropy. On the other hand, some ‘global’ interfaces that can involve anisotropy, such as the Hales discontinuity (Levin and Park, 2000), are reported to occur at variable depths around the globe, and may more plausibly arise from local convective dynamics and tectonic history.

Scattered-wave indicators of anisotropy, such as quasi-Love waves and Ps converted waves, argue for short-wavelength anisotropic gradients suggestive of localized shear zones. Shear localization in the mantle and crust should not be surprising, as there are many field examples of highly deformed rock, such as mylonites (Siegesmund *et al.*, 1991b) and earthquake fault zones themselves. The basis for strain localization in mantle convection is also gaining a theoretical grounding (Bercovici and Ricard, 2003).

1.09.3.11 ScS, S_{diff}, and the D'' Layer

Except for the D'' layer, just above the core–mantle boundary (CMB) there is no evidence for widespread anisotropy in the bulk of the lower mantle (Meade *et al.*, 1995; Heintz, 2006). Due to limitations in station distribution and in the types of waves and events which can be used to study the lowermost mantle, our knowledge of anisotropy in the D'' layer is more patchy than the sampling we have within the upper mantle. In addition, the seismic waves which sample the D'' layer may be affected on their descent from the source and ascent to the station by upper-mantle anisotropy. Although it is possible to ascertain the presence of anisotropy in D'' by comparing waves having traversed the D'' region with those having their turning point just above, the correction which must be done for upper-mantle effects may not be known perfectly, adding to the difficulty in analyzing D'' anisotropy.

The main observations that motivate D'' anisotropy are ScS and core-diffracted S waves whose arrivals are earlier by up to several seconds on the transverse component than on the longitudinal one. The first such observations were reported by Mitchell and Helmberger (1973) on ScS waves reflected at the CMB below the Caribbean, with relative longitudinal delays $\Delta t = 0$ to -3 s. Similar delays have also been observed in several subsequent ScS studies and at large epicentral distances on S and diffracted S waves. A recent review by Moore *et al.*

(2004) shows that $0 < \Delta t < 4$ s in most cases, with some extreme observations of $\Delta t = -2$ s (that is, SV faster than SH) and $\Delta t = 9$ s. The negative delays correspond mostly to paths in the Central Pacific and in the Central Atlantic Ocean. The other regions which have been analyzed and which show mostly positive delays are Alaska, Asia, and India. Like the Caribbean, such areas are situated beneath subduction zones. These delays can be explained on average by 1% vertical transverse isotropy in D''. D'' anisotropy is also apparent at global scale and has been incorporated in the mean 1-D model of Montagner and Kennett (1996).

The observation of large SV diffracted waves deep in the core shadow led Vinnik *et al.* (1989a) to propose that azimuthal anisotropy, acting to couple the SH and SV waves rather than causing simple birefringence, could also be present in D'' in the Central Pacific region. Such azimuthal anisotropy has been found recently under the Caribbean (Maupin *et al.*, 2005) and under the North Pacific Ocean (Wookey *et al.*, 2005). The lack of crosspaths does not allow for a full characterization of the anisotropy, which in these two studies has been characterized as a simple tilted version of the more classic VTI model of D'', with tilts of $20\text{--}60^\circ$.

Anisotropy in D'' has been related to its role as a boundary layer in mantle convection, and to the fact that, as in the upper mantle, large deformation may lead to preferred orientation of inclusions (Kendall and Silver, 1998) or minerals. The mineral-orientation hypothesis has been revived by the recent discovery of a phase transition of perovskite, the dominant material of the lower mantle, at temperature and pressure conditions of the D'' layer. As opposed to the ordinary perovskite phase, the post-perovskite phase exhibits a significant anisotropy and should develop lattice-preferred orientation under shear flow (Murakami *et al.*, 2004). It has been pointed out that anisotropy, as well as other features of D'' observed in the same regions, may be related to the presence of subducted slab remnants, as further discussed in Chapter 1.18.

1.09.3.12 PKP Waves and the Inner Core

The only direct global observation of P-wave anisotropy we have is related to anisotropy in the inner core (Morelli *et al.*, 1986; Woodhouse *et al.*, 1986; Souriau *et al.*, 2003). This anisotropy is observed in the splitting of the core-sensitive normal modes (Woodhouse *et al.*, 1986), as well as when comparing the traveltimes of

PKIKP waves for polar paths, close to Earth's rotation axis, and for paths in the equatorial plane (Morelli *et al.*, 1986). The waves following polar paths arrive on average about 3 s earlier than those following the equatorial paths. This observation can be explained by inner-core transverse isotropy of about 3% with a fast axis close to the north–south direction. Early results suggested tilting of the fast axis with respect to the polar direction (Creager, 1992), but more recent models favor either some lateral heterogeneity in the distribution of anisotropy (Garcia and Souriau, 2000) or biases due to lower mantle structure (Ishii *et al.*, 2002) rather than a tilt of the axis.

As with Earth's mantle and crust, there are two main possible mechanisms for the inner-core anisotropy: preferred orientation of minerals, iron crystals in the present case, acquired either during solidification or during subsequent deformation (see Steinle-Neumann *et al.* (2001) for a recent summary), or preferred orientation of fluid inclusions (Singh *et al.*, 2000).

Anisotropy in the attenuation of the inner core has also been reported (Souriau and Romanowicz, 1996). Strongest attenuation is found in the direction of fast velocity, along the polar axis, and some heterogeneity in the attenuation anisotropy seems to follow the heterogeneity in P-wave velocity (Oreshin and Vinnik, 2004). This relation has not yet been fully exploited in terms of explaining the mechanism for inner-core anisotropy.

1.09.4 Perspectives

The main challenge concerning seismological observations of anisotropy at the present time is to construct a model of Earth's anisotropy which explains all the data in any one region. Even the best-documented observations, namely SKS splitting, Love–Rayleigh discrepancy and Rayleigh phase-velocity azimuthal variations, are sensitive to different aspects of anisotropic rock structure, and so do not readily corroborate each other. Where observations are complementary, often they cannot be explained by one simple model of anisotropy, suggesting a combination of fossil anisotropy and ongoing mantle deformation, or else a complex 3-D mantle flow, possibly influenced by variations in mineralogy and volatile concentration. Many interesting tectonic regions probably fit these descriptions, and will require a patient accumulation of seismic observables to reveal their dynamics.

Acknowledgments

The authors are grateful to Niels Ribe for assistance when writing about orientation of olivine, and to Ed Garnero, James Wolfe, Ludek Klimes, Donna Blackman, and Maureen Long for permission to reprint their figures.

References

- Aki K and Richards PG (2002) *Quantitative Seismology 2nd ed.* New York: University Science Books.
- Amato A, Margheriti L, and Azzara R (1998) Passive seismology and deep structure in central Italy. *Pure and Applied Geophysics* 151: 479–493.
- Anderson DL (1961) Elastic wave propagation in layered anisotropic media. *Journal of Geophysical Research* 66: 2953–2963.
- Antolik M, Ekstrom G, and Dziewonski AM (2001) Global event location with full and sparse data sets using three-dimensional models of P-wave velocity. *Pure and Applied Geophysics* 158: 291–317.
- Babuska V and Cara M (1991) *Seismic Anisotropy in the Earth.* Dordrecht: Kluwer Academic Publishers.
- Babuska V, Montagner J-P, Plomerova J, and Girardin N (1998) Age-dependent large-scale fabric of the mantle lithosphere as derived from surface-wave velocity anisotropy. *Pure and Applied Geophysics* 151: 257–280.
- Babuska V, Plomerova J, and Sileny J (1993) Models of seismic anisotropy in the deep continental lithosphere. *Physics of the Earth and Planetary Interiors* 78: 167–191.
- Backus GE (1962) Long-wave elastic anisotropy produced by horizontal layering. *Journal of Geophysical Research* 67: 4427–4440.
- Backus GE (1965) Possible forms of seismic anisotropy of the uppermost mantle under oceans. *Journal of Geophysical Research* 70: 3429–3439.
- Balfour NJ, Savage MK, and Townend J (2005) Stress and crustal anisotropy in Marlborough, New Zealand: evidence for low fault strength and structure-controlled anisotropy. *Geophysical Journal International* 163: 1073–1086.
- Bamford D (1977) Pn velocity anisotropy in a continental upper mantle. *Geophysical Journal of the Royal Astronomical Society* 49: 29–48.
- Becker TW, Kellogg JB, Ekstrom G, and O'Connell RJ (2003) Comparison of azimuthal seismic anisotropy from surface waves and finite strain from global mantle-circulation models. *Geophysical Journal International* 155: 696–714.
- Beghein C and Trampert J (2003) Probability density functions for radial anisotropy: Implications for the upper 1200 km of the mantle. *Earth and Planetary Science Letters* 217: 151–162.
- Bercovici D and Ricard Y (2003) Energetics of a two-phase model of lithospheric damage, shear localization and plate-boundary formation. *Geophysical Journal International* 152: 581–596.
- Blackman DK, Kendall J-M, Dawson PR, Wenk H-R, Boyce D, and Morgan JP (1996) Teleseismic imaging of subaxial flow at mid-ocean ridges: Traveltime effects of anisotropic mineral texture in the mantle. *Geophysical Journal International* 127: 415–426.
- Blackman DK and Kendall J-M (2002) Seismic anisotropy of the upper mantle. Part 2: Predictions for current plate boundary flow models. *Geochemistry Geophysics Geosystems* 3(9): 8602 (doi:10.1029/2001GC000247).

- Bokelmann GHR (2002) Convective-driven motion of the North American craton: Evidence from P-wave anisotropy. *Geophysical Journal International* 148: 278 (doi:10.1046/j.1365-246X.2002.01614.x).
- Bostock MG (1998) Mantle stratigraphy and the evolution of the Slave province. *Journal of Geophysical Research* 103: 21183–21200.
- Buttles J and Olson P (1998) A laboratory model of subduction zone anisotropy. *Earth and Planetary Science Letters* 164: 245–262.
- Byrne GF, Jacob AWB, Mechic J, and Dindi E (1997) Seismic structure of the upper mantle beneath the southern Kenya Rift from wide-angle data. *Tectonophysics* 278: 243–260.
- Calvert AJ, Sawyer EW, Davis WJ, and Ludden JN (1995) Archean subduction inferred from seismic images of a mantle suture in the Superior Province. *Nature* 375: 670–674.
- Capdeville Y and Marigo JJ (2007). Second-order homogenization of the wave equation for non-periodic layered media. *Geophysical Journal International* doi:10.1111/j.1365-246X.207.03462.x.
- Cara M and Lévéque J-J (1988) Anisotropy of the asthenosphere: The higher mode data of the Pacific revisited. *Geophysical Research Letters* 15: 205–208.
- Cassidy JF and Bostock MG (1996) Shear wave splitting above the subducting Juan de Fuca plate. *Geophysical Research Letters* 23: 941–944.
- Cerveny V (1972) Seismic rays and ray intensities in inhomogeneous anisotropic media theory. *Geophysical Journal of the Royal Astronomical Society* 29: 1–13.
- Cerveny V (2001) *Seismic Ray Theory*. Cambridge, UK: Cambridge University Press.
- Chapman CH (2004) *Fundamentals of Seismic Wave Propagation*. Cambridge, UK: Cambridge University Press.
- Chapman CH and Shearer PM (1989) Ray tracing in azimuthally anisotropic media. Part II: Quasi-shear wave coupling. *Geophysical Journal* 96: 65–83.
- Chevrot S (2000) Multichannel analysis of shear wave splitting. *Journal of Geophysical Research* 105: 21579–21590.
- Chevrot S (2006) Finite-frequency vectorial tomography: A new method for high resolution imaging of upper mantle anisotropy. *Geophysical Journal International* 165: 641–657 (doi:10.1111/j.1365-246X.2006.02982.x.).
- Coates RT and Chapman CH (1990) Quasi-shear wave coupling in weakly anisotropic 3-D media. *Geophysical Journal* 103: 301–320.
- Cochran ES, Li YG, and Vidale JE (2006) Anisotropy in the shallow crust observed around the San Andreas fault before and after the 2004 M 6.0 Parkfield earthquake. *Bulletin of the Seismological Society of America* 96: S364–S375.
- Cormier VF and Stroujkova A (2005) Waveform search for the innermost inner core. *Earth and Planetary Science Letters* 236(1-2): 96–105.
- Crampin S (1970) The dispersion of surface waves in multilayered anisotropic media. *Geophysical Journal of the Royal Astronomical Society* 49: 9–27.
- Crampin S (1981) A review of wave motion in anisotropic and cracked elastic-media. *Wave Motion* 3: 343–391.
- Crampin S and Chastin S (2003) A review of shear wave splitting in the crack-critical crust. *Geophysical Journal International* 155: 221–240.
- Creager KC (1992) Anisotropy in the inner core from differential times of the phase PKP and PKIKP. *Nature* 356: 309–314.
- Debayle E and Kennett BLN (2000) Anisotropy in the Australian upper mantle from Love and Rayleigh waveform inversion. *Earth and Planetary Science Letters* 184: 339–351.
- Debayle E, Kennett BLN, and Priestley K (2005) Global azimuthal seismic anisotropy and the unique plate-motion deformation of Australia. *Nature* 433: 509–512.
- Dziewonski AM and Anderson DL (1981) Preliminary reference Earth model. *Earth and Planetary Science Letters* 25: 297–356.
- Ekstrom G and Dziewonski AD (1998) The unique anisotropy of the Pacific upper mantle. *Nature* 394: 168–172.
- Estey LH and Douglas BJ (1986) Upper mantle anisotropy: A preliminary model. *Journal of Geophysical Research* 91: 11393–11406.
- Farra V (2005) First-order ray tracing for qS waves in inhomogeneous weakly anisotropic media. *Geophysical Journal International* 161: 309–324 (doi:10.1111/j.1365-246X.2005.02570.x.).
- Farra V and Psencik I (2003) Properties of the zeroth-, first, and higher-order approximations of attributes of elastic waves in weakly anisotropic media. *Journal of the Acoustical Society of America* 114: 1366–1378 (doi:10.1121/1.1591772).
- Farra V and Vinnik L (2000) Upper mantle stratification by P and S receiver functions. *Geophysical Journal International* 141: 699–712.
- Fischer KM, Fouch M, Wiens D, and Boettcher M (1998) Anisotropy and flow in Pacific subduction zone back-arcs. *Pure and Applied Geophysics* 151: 463–475.
- Fischer KM and Wiens DA (1996) The depth distribution of mantle anisotropy beneath the Tonga subduction zone. *Earth and Planetary Science Letters* 142: 253–260.
- Fischer KM and Yang X (1994) Anisotropy in Kuril–Kamchatka subduction zone structure. *Geophysical Research Letters* 21: 5–8.
- Fouch MJ and Fischer KM (1996) Mantle anisotropy beneath northwest Pacific subduction zones. *Journal of Geophysical Research* 101: 15987–16002.
- Fouch MJ, Fischer KM, Parmentier EM, Wysession ME, and Clarke TJ (2000) Shear wave splitting, continental keels, and patterns of mantle flow. *Journal of Geophysical Research* 105: 6255–6276.
- Freybourger M, Gaherty JB, Jordan TH, and the Kaapvaal Seismic Group (2001) Structure of the Kaapvaal craton from surface waves. *Geophysical Research Letters* 28: 2489–2492.
- Friederich W and Huang ZX (1996) Evidence for upper mantle anisotropy beneath Southern Germany from Love and Rayleigh wave dispersion. *Geophysical Research Letters* 23(3-4): 1135–1138.
- Fryer GJ and Fraser LN (1984) Seismic-waves in stratified anisotropic media. *Geophysical Journal of the Royal Astronomical Society* 91: 73–101.
- Gaherty JB (2001) Seismic evidence for hotspot-induced buoyant flow beneath the Reykjanes Ridge. *Science* 293: 1645–1647.
- Gaherty JB (2004) A surface wave analysis of seismic anisotropy beneath eastern North America. *Geophysical Journal International* 158: 1053–1066.
- Gaherty JB, Kato M, and Jordan TH (1999) Seismological structure of the upper mantle: A regional comparison of seismic layering. *Physics of the Earth and Planetary Interiors* 110: 21–41.
- Gaherty JB, Lizarralde D, Collins JA, Hirth G, and Kim S (2004) Mantle deformation during slow seafloor spreading constrained by observations of seismic anisotropy in the western Atlantic. *Earth and Planetary Science Letters* 228(3-4): 257–265.
- Gaherty JB, Lizarralde D, Collins JA, Hirth G, and Kim S (2004) Mantle deformation during slow seafloor spreading constrained by observations of seismic anisotropy in the western Atlantic. *Earth and Planetary Science Letters* 228(3-4): 257–265.
- Garcia R and Souriau A (2000) Inner-core anisotropy and heterogeneity level. *Geophysical Research Letters* 27: 3121–3124.

- Garmany J (1988) Seismograms in stratified anisotropic media. Part I: WKBJ theory. *Geophysical Journal* 92: 365–377.
- Garmany J (1989) A student's garden of anisotropy. *Annual Review of Earth and Planetary Science* 17: 285–308.
- Girardin N and Farra V (1998) Azimuthal anisotropy in the upper mantle from observations of P-to-S converted phases; application to Southeast Australia. *Geophysical Journal International* 133: 615–629.
- Godfrey NJ, Christensen NI, and Okaya DA (2000) Anisotropy of schists; contribution of crustal anisotropy to active source seismic experiments and shear wave splitting observations. *Journal of Geophysical Research* 105: 27991–28007.
- Gung Y, Panning M, and Romanowicz B (2003) Global anisotropy and the thickness of continents. *Nature* 442: 707–711.
- Hajnal Z, Nemeth B, Clowes RM, et al. (1997) Mantle involvement in lithospheric collision: Seismic evidence from the Trans-Hudson Orogen, western Canada. *Geophysical Research Letters* 24: 2079–2082.
- Hartog R and Schwartz SY (2000) Subduction-induced strain in the upper mantle east of the Mendocino triple junction, California. *Journal of Geophysical Research* 105: 7909–7930.
- Hearn TM (1999) Uppermost mantle velocities and anisotropy beneath Europe. *Journal of Geophysical Research* 104: 15123–15139.
- Heintz M (2006) Midmantle deformation between the Australian continent and the Fiji-Tonga subduction zone? *Journal of Geophysical Research* 111: B09303 (doi:10.1029/2005JB004058).
- Helbig K (1994) *Foundations of Anisotropy for Exploration Seismics*, 486 pp. NY: Elsevier.
- Helbig K and Thomsen L (2005) 75-plus years of anisotropy in exploration and reservoir seismics: A historical review of concepts and methods. *Geophysics* 70: 9ND–23ND (doi:10.1190/1.2122407).
- Hess HH (1964) Seismic anisotropy of the uppermost mantle under oceans. *Nature* 203: 629–631.
- Hirth G and Kohlstedt DL (1996) Water in the oceanic upper mantle: Implications for rheology, melt extraction and the evolution of the lithosphere. *Earth and Planetary Science Letters* 144: 93–108.
- Hirn A, Diaz J, Sapin M, and Veinante J-L (1998) Variation of shear-wave residuals and splitting parameters from array observation in southern Tibet. *Pure and Applied Geophysics* 151: 407–432.
- Holtzman DK, Kohlstedt DL, Zimmerman ME, Heidelbach F, Hiraga T, and Hustoft J (2003) Melt segregation and strain partitioning: Implications for seismic anisotropy and mantle flow. *Science* 301: 1227–1230.
- Ishii M, Dziewonski AM, Tromp J, and Ekstrom G (2002) Joint inversion of normal mode and body wave data for inner core anisotropy. Part 2: Possible complexities. *Journal of Geophysical Research* 107: 2380 (doi:10.1029/2001JB000713).
- Ishise M and Oda H (2005) Three-dimensional structure of P-wave anisotropy beneath the Tohoku district, northeast Japan. *Journal of Geophysical Research* 110: B07304 (doi:10.1029/2004JB003599).
- Jech J and Psencik I (1989) First-order perturbation method for anisotropic media. *Geophysical Journal International* 99: 369–376.
- Jung H and Karato S-I (2001) Water-induced fabric transitions in olivine. *Science* 293: 1460–1463.
- Kaminski E (2006) Interpretation of seismic anisotropy in terms of mantle flow when melt is present. *Earth and Planetary Science Letters* 189: 253–267.
- Kaminski E and Ribe NM (2001) A kinematic model for recrystallisation and texture development in olivine. *Earth and Planetary Science Letters* 189: 253–267.
- Kaminski E and Ribe NM (2002) Time scales for the evolution of seismic anisotropy in mantle flow. *Geochemistry Geophysics Geosystems* 3: (doi:10.29/2001GC000222).
- Karato S-I (1992) On the Lehmann discontinuity. *Geophysical Research Letters* 19: 2255–2258.
- Karato S-I and Wu P (1993) Rheology of the upper mantle: A synthesis. *Science* 260: 771–778.
- Keith CM and Crampin S (1977) Seismic body waves in anisotropic media – Reflection and refraction at a plane interface. *Geophysical Journal of the Royal Astronomical Society* 49: 181–208.
- Kendall JM and Silver PG (1998) Investigating causes of D'' anisotropy. In: Gurnis M, Wysession ME, Knittle E, and Buffet BA (eds.) *Geodynamic Series 28: The Core–Mantle Boundary Region*, pp. 97–118. Washington, DC: AGU.
- Kern HM (1993) Physical properties of crustal and upper mantle rocks with regards to lithosphere dynamics and high pressure mineralogy. *Physics of the Earth and Planetary Interiors* 79: 113–136.
- Klimes L (2003) Weak-contrast reflection-transmission coefficients in a generally anisotropic background. *Geophysics* 68: 2063–2072.
- Klimes L and Bulant P (2006) Errors due to the anisotropic-common-ray approximation of the coupling ray theory. *Studia Geophysica et Geodaetica* 50: 463–477.
- Kneller EA, van Keken PE, Karato S, and Park J (2005) B-type olivine fabric in the mantle wedge: Insights from high-resolution non-Newtonian subduction zone models. *Earth and Planetary Science Letters* 237: 781–797.
- Kobayashi R and Nakanishi I (1998) Location of Love-to-Rayleigh conversion due to lateral heterogeneity or azimuthal anisotropy in the upper mantle. *Geophysical Research Letters* 25(7): 1067–1070.
- Kumar P, Yuan X, Kind R, and Kosarev G (2005) The lithosphere–asthenosphere boundary in the Tien Shan-Karakoram region from S receiver functions: Evidence for continental subduction. *Geophysical Research Letters* 32: L07305 (doi:10.1029/2004GL022291).
- Kumazawa M and Anderson OL (1969) Elastic moduli, pressure derivatives, and temperature derivatives of single-crystal olivine and single-crystal forsterite. *Journal of Geophysical Research* 74: 5961–5972.
- Laske G and Masters G (1998) Surface wave polarization data and global anisotropic structure. *Geophysical Journal International* 132: 508–520.
- Leveque JJ, Debayle E, and Maupin V (1998) Anisotropy in the Indian Ocean upper mantle from Rayleigh- and Love-waveform inversion. *Geophysical Journal International* 133: 529–540.
- Levin V, Droznin D, Park J, and Gordeev E (2004) Mantle wedge anisotropy beneath south-eastern Kamchatka from local-S birefringence. *Geophysical Journal International* 158: 1009–1023.
- Levin V, Park J, Lees J, et al. (2002) Crust and upper mantle of Kamchatka from teleseismic receiver functions. *Tectonophysics* 358: 233–265.
- Levin V, Menke W, and Park J (1999) Shear wave splitting in Appalachians and Urals: A case for multilayered anisotropy. *Journal of Geophysical Research* 104: 17975–17994.
- Levin V, Menke W, and Park J (2000) No regional anisotropic domains in the northeastern US Appalachians. *Journal of Geophysical Research* 105: 19029–19042.
- Levin V and Park J (1997) Crustal anisotropy in the Ural Mtns foredeep from teleseismic receiver functions. *Geophysical Research Letters* 24: 1283–1286.
- Levin V and Park J (1997) P–SH conversions in a flat-layered medium with anisotropy of arbitrary orientation. *Geophysical Journal International* 131: 253–266.

- Levin V and Park J (1998a) P-SH conversions in layered media with hexagonally symmetric anisotropy: A cookbook. *Pure and Applied Geophysics* 151: 669–697.
- Levin V and Park J (1998b) Quasi-Love phases between Tonga and Hawaii: observations, simulations and explanations. *Journal of Geophysical Research* 103: 24321–24331.
- Levin V, Park J, Margheriti L, Lucente FP, and Pondrelli S (2007) The end of subduction in Northern Apennines confirmed by observations of quasi-Love waves from the great 2004 Sumatra-Andaman earthquake. *Geophysical Research Letters* 34: L04304, doi:10.1029/2006GL028860.
- Levin V and Park J (2000) Shear zones in the Proterozoic lithosphere of the Arabian Shield and the nature of the Hales discontinuity. *Tectonophysics* 323: 131–148.
- Liu Y, Ben-Zion Y, and Teng TL (2004) Systematic analysis of shear-wave splitting in the aftershock zone of the 1999 Chi-chi, Taiwan, earthquake; shallow crustal anisotropy and lack of precursory changes. *Bulletin of the Seismological Society of America* 94: 2330–2347.
- Long MD and van der Hilst RD (2005) Upper mantle anisotropy beneath Japan from shear-wave splitting. *Physics of the Earth and Planetary Interiors* 151: 206–222.
- Long MD and van der Hilst RD (2006) Shear-wave splitting from local events beneath the Ryukyu arc: Trench-parallel anisotropy in the mantle wedge. *Physics of the Earth and Planetary Interiors* 155: 300–312.
- Margheriti L, Lucente FP, and Pondrelli S (2003) SKS splitting measurements in the Apenninic-Tyrrhenian domain (Italy) and their relation with lithospheric subduction and mantle convection. *Journal of Geophysical Research* 108: (doi:10.1029/2002JB001793).
- Margheriti L, Nostro C, Cocco M, and Amato A (1996) Seismic anisotropy beneath the Northern Apennines (Italy) and its tectonic implications. *Geophysical Research Letters* 23: 2721–2724.
- Marone F, van der Lee S, and Giardini D (2004) Shallow anisotropy in the Mediterranean mantle from surface waves. *Geophysical Research Letters* 31(6): L06624.
- Marson-Pidgeon K and Savage MK (1997) Frequency-dependent anisotropy in Wellington, New Zealand. *Geophysical Research Letters* 24: 3297–3300.
- Masters G, Park J, and Gilbert F (1983) Observations of coupled spheroidal and toroidal modes. *Journal of Geophysical Research* 88: 10285–10298.
- Maupin V (1985) Partial derivatives of surface wave phase velocities for flat anisotropic models. *Geophysical Journal of the Royal Astronomical Society* 83: 379–398.
- Maupin V (1989) Surface waves in weakly anisotropic structures: On the use of ordinary or quasi-degenerate perturbation methods. *Geophysical Journal International* 98: 553–563.
- Maupin V (1990) Modelling of three-component Lg waves in anisotropic crustal structures. *Bulletin of the Seismological Society of America* 80: 1311–1325.
- Maupin V (1994) On the possibility of anisotropy of the D'' layer as inferred from the polarization of diffracted S waves. *Physics of the Earth and Planetary Interiors* 87: 1–32.
- Maupin V (2001) A multiple-scattering scheme for modelling surface wave propagation in isotropic and anisotropic three-dimensional structures. *Geophysical Journal International* 146: 332–348.
- Maupin V (2004) Comment on 'The azimuthal dependence of surface wave polarization in a slightly anisotropic medium' by T. Tanimoto. *Geophysical Journal International* 159: 365–368.
- Maupin V and Cara M (1992) Love-Rayleigh wave incompatibility and possible deep upper mantle anisotropy in the Iberian Peninsula. *Pure and Applied Geophysics* 138: 429–444.
- Maupin V, Garnero EJ, Lay T, and Fouch MJ (2005) Azimuthal anisotropy in the D'' layer beneath the Caribbean. *Journal of Geophysical Research* 110: (doi:10.1029/2004JB003506).
- McKenzie D (1979) Finite deformation during fluid flow. *Geophysical Journal of the Royal Astronomical Society* 58: 689–715.
- McNamara DE, Owens TJ, Silver PG, and Wu FT (1994) Shear wave anisotropy beneath the Tibetan Plateau. *Journal of Geophysical Research* 99: 13655–13665.
- Meade C, Silver PG, and Kaneshima S (1995) Laboratory and seismological observations of lower mantle isotropy. *Geophysical Research Letters* 22: 1293–1296.
- Meissner R, Rabbel W, and Kern H (2006) Seismic lamination and anisotropy of the Lower continental crust. *Tectonophysics* 416: 81–99.
- Menke W and Levin V (2003) A waveform-based method for interpreting SKS splitting observations, with application to one and two layer anisotropic Earth models. *Geophysical Journal International* 154: 379–392.
- Mensch T and Rasolofosaona P (1997) Elastic-wave velocities in anisotropic media of arbitrary symmetry – generalization of Thomsen's parameters epsilon, delta and gamma. *Geophysical Journal International* 128: 43–64.
- Mitchell BJ and Helmberger DV (1973) Shear velocities at the base of the mantle from observations of S and ScS. *Journal of Geophysical Research* 78: 6009–6020.
- Mochizuki E (1986) The free oscillations of an anisotropic and heterogenous Earth. *Geophysical Journal of the Royal Astronomical Society* 86: 167–176.
- Montagner J-P (1998) Where can seismic anisotropy be detected in the Earth's mantle? In boundary layers. *Pure and Applied Geophysics* 151: 223–256.
- Montagner J-P and Kennett BLN (1996) How to reconcile body-wave and normal-mode reference Earth models. *Geophysical Journal International* 125: 229–248.
- Montagner J-P, Griot-Pommera DA, and Lave JH-C (2000) How to relate body wave and surface wave anisotropy. *Journal of Geophysical Research* 105: 19015–19027.
- Montagner J-P and Nataf H-C (1986) A simple method for inverting the azimuthal anisotropy of surface waves. *Journal of Geophysical Research* 91: 511–520.
- Montagner J-P and Tanimoto T (1991) Global upper mantle tomography of seismic velocities and anisotropies. *Journal of Geophysical Research* 96: 20337–20351.
- Moore MM, Garnero EJ, Lay T, and Williams Q (2004) Shear-wave splitting and waveform complexity for lowermost mantle structures with low-velocity lamellae and transverse isotropy. *Journal of Geophysical Research* 109: (doi:10.1029/2003JB002546).
- Morelli A, Dziewonski AM, and Woodhouse JH (1986) Anisotropy of the inner core inferred from PKIKP traveltimes. *Geophysical Research Letters* 13: 1545–1548.
- Morley AM, Stuart GW, Kendall JM, and Reyners M (2006) Mantle wedge anisotropy in the Hikurangi subduction zone, central North Island, New Zealand. *Geophysical Research Letters* 33: L05301.
- Murakami M, Hirose K, Kawamura K, Sata N, and Ohishi Y (2004) post-perovskite phase transition in MgSiO₃. *Science* 304: 855–857.
- Muyzert E, Paulssen H, and Snieder R (1999) A seismic cross-section through the east European continent. *Geophysical Journal International* 136: 695–704.
- Nakajima J and Hasegawa A (2004) Shear-wave polarization anisotropy and subduction-induced flow in the mantle wedge of northeastern Japan. *Earth and Planetary Science Letters* 225: 365–377.
- Nakajima J, Shimizu J, Hori S, and Hasegawa A (2006) Shear-wave splitting beneath the southwestern Kurile arc and

- northeastern Japan arc: A new insight into mantle return flow. *Geophysical Research Letters* 33: L05305.
- Nemeth B, Clowes RM, and Hajnal Z (2005) Lithospheric structure of the Trans-Hudson Orogen from seismic refraction - wide-angle reflection studies. *Canadian Journal of Earth Sciences* 42: 435–456.
- Nishimura CE and Forsyth DW (1989) The anisotropic structure of the upper mantle in the Pacific. *Geophysical Journal* 96: 203–229.
- Oda H (2005) An attempt to estimate isotropic and anisotropic lateral structure of the Earth by spectral inversion incorporating mixed coupling. *Geophysical Journal International* 160: 667–682.
- Oda H and Onishi S (2001) The effect of regional variation of lattice preferred orientation on surface waveforms. *Geophysical Journal International* 144: 247–258.
- Oreshin S, Vinnik L, Makeyeva L, Kosarev G, Kind R, and Wenzel F (2002) Combined analysis of SKS splitting and regional P traveltimes in Siberia. *Geophysical Journal International* 151: 393–402 (doi:10.1046/j.1364-246X.2002.01791.x).
- Oreshin S and Vinnik L (2004) Heterogeneity and anisotropy of seismic attenuation in the inner core. *Geophysical Research Letters* 31: L02613 (doi:10.1029/2003GL018591).
- Park J (1997) Free oscillations in an anisotropic Earth: Path-integral asymptotics. *Geophysical Research Letters* 129: 399–411.
- Park J and Levin V (2000) Receiver functions from multiple-taper spectral correlation estimates. *Bulletin of the Seismological Society of America* 90: 1507–1520.
- Park J, Levin V, Brandon MT, et al. (2002) A dangling slab, amplified arc volcanism, mantle flow and seismic anisotropy near the Kamchatka plate corner. In: Stein S and Freymuller J (eds.) *Plate Boundary Zones*, pp. 295–324. Washington, DC: American Geophysical Union.
- Park J and Yu Y (1993) Seismic determination of elastic anisotropy and mantle flow. *Science* 261: 1159–1162.
- Park J, Yuan H, and Levin V (2004) Subduction-zone anisotropy under Corvallis, Oregon: A serpentinite skidmark of trench-parallel terrane migration? *Journal of Geophysical Research* 109: B10306 (doi:10.1029/2003JB002718).
- Peacock SM and Wang K (1999) Seismic consequences of warm versus cool subduction metamorphism: Examples from southwest and northeast Japan. *Science* 286: 937–939.
- Pedersen HA, Bruneton M, Maupin V, and the SVEKALAPKO Seismic Tomography Working Group (2006) Lithospheric and sublithospheric anisotropy beneath the Baltic shield from surface-wave array analysis. *Earth and Planetary Science Letters* 244: 590–605.
- Peng Z and Ben-Zion Y (2004) Systematic analysis of anisotropy along the Karadere–Duzce branch of the North Anatolian fault. *Geophysical Journal International* 159: 253–274.
- Peng Z and Ben-Zion Y (2005) Spatiotemporal variations of crustal anisotropy from similar events in aftershocks of the 1999 M7.4 Izmit and M7.1 Duzce, Turkey, earthquake sequences. *Geophysical Journal International* 160: 1027–1043.
- Pettersen O and Maupin V (2002) Lithospheric anisotropy on the Kerguelan hotspot track inferred from Rayleigh wave polarisation anomalies. *Geophysical Journal International* 149: 225–246.
- Peyton V, Levin V, Park J, et al. (2001) Mantle flow at a slab edge: Seismic anisotropy in the Kamchatka region. *Geophysical Research Letters* 28: 379–392.
- Plomerova J, Granet M, and Judenherc S (2000) Temporary array data for studying seismic anisotropy of Variscan massifs: The Armorican massif, French massif central and Bohemian massif. *Studia Geophysica et Geodaetica* 44: 195–209.
- Plomerova J, Arvidsson R, Babuska V, et al. (2001) An array study of lithospheric structure across the Protogine zone, Varmland, south-central Sweden – Signs of a paleocontinental collision. *Tectonophysics* 332: 1–21.
- Plomerova J, Margheriti L, and Park J (2006) Seismic anisotropy beneath the Northern Apennines (Italy): Mantle flow or lithosphere fabric? *Earth and Planetary Science Letters* 247: 157–170 2006.
- Plomerova J, Kouba D, and Babuska V (2002) Mapping the lithosphere–asthenosphere boundary through changes in surface-wave anisotropy. *Tectonophysics* 358: 175–185.
- Polet J and Kanamori H (1997) Upper-mantle shear velocities beneath California determined from long-period surface waves. *Bulletin of the Seismological Society of America* 87: 200–209.
- Polet J, Silver PG, and Beck S (2000) Shear wave anisotropy beneath the Andes from the BANJO, SEDA, and PISCO experiments. *Journal of Geophysical Research* 105: 6287–6304.
- Pratt RG and Chapman CH (1992) Travelttime tomography in anisotropic media. Part II: Application. *Geophysical Journal International* 109: 20–37.
- Priestley K, Debayle E, McKenzie D, and Pilidou S (2006) Upper mantle structure of eastern Asia from multimode surface waveform tomography. *Journal of Geophysical Research* 111: B10304 (doi:10.1029/2005JB004082).
- Psencik I (1998) Green's functions for inhomogeneous weakly anisotropic media. *Geophysical Journal International* 135: 279–288.
- Richards PG and Frasier CW (1976) Scattering of elastic waves from depth-dependent inhomogeneities. *Geophysics* 41: 411–458.
- Ribe NM (1989) A continuum theory for lattice preferred orientation. *Geophysical Journal* 97: 199–207.
- Rondenay S, Bostock MG, Hearn TM, White DJ, and Ellis RM (2000) Lithospheric assembly and modification of the SE Canadian Shield; Abitibi-Grenville teleseismic experiment. *J. Geophys. Res* 105: 13735–13754.
- Rumpker G and Silver PG (1998) Apparent shear-wave splitting parameters in the presence of vertically varying anisotropy. *Geophysical Journal International* 135: 790–800.
- Russo RM and Silver PG (1994) Trench-parallel flow beneath the Nazca Plate from seismic anisotropy. *Science* 263: 1105–1111.
- Saiga A, Hiramatsu Y, Ooida T, and Yamaoka K (2003) Spatial variation in the crustal anisotropy and its temporal variation associated with a moderate-sized earthquake in the Tokai region, central Japan. *Geophysical Journal International* 154: 695–705.
- Saltzer RL, Gaherty JB, and Jordan TH (2000) How are vertical Shear wave splitting measurements affected by variations in the orientation of azimuthal anisotropy with depth? *Geophysical Journal International* 141: 374–390.
- Savage M (1998) Lower crustal anisotropy or dipping boundaries? Effects on receiver functions and a case study in New Zealand. *Journal of Geophysical Research* 103: 15069–15087.
- Savage M (1999) Seismic anisotropy and mantle deformation; what have we learned from shear wave splitting? *Reviews of Geophysics* 37: 65–105.
- Savage M, Park J, and Todd H (2006) Velocity and anisotropy structure at the Hikurangi subduction margin, New Zealand from receiver functions. *Geophysical Journal International* 168: 1034–1050.
- Schulte-Pelkum V, Masters G, and Shearer PM (2001) Upper mantle anisotropy from long-period P polarization. *Journal of Geophysical Research* 106: 21917–21934.
- Schulte-Pelkum V, Vernon FL, and Eakins J (2003) Large teleseismic P wavefront deflections observed with

- broadband arrays. *Bulletin of the Seismological Society of America* 93: 747–756.
- Schutt DL and Humphreys ED (2001) Evidence for a deep asthenosphere beneath North America from Western United States SKS splits. *Geology* 29: 291–294.
- Shearer PM and Orcutt JA (1986) Compressional and shear-wave anisotropy in the oceanic lithosphere – The Ngendei seismic refraction experiment. *Geophysical Journal of the Royal Astronomical Society* 87: 967–1003.
- Sherrington HF, Zandt G, and Frederiksen A (2004) Crustal fabric in the Tibetan Plateau based on waveform inversions for seismic anisotropy parameters. *Journal of Geophysical Research* 109: B02312 (doi:10.1029/2002JB002345).
- Shimamura H (1984) Anisotropy in the oceanic lithosphere of the Northwestern Pacific Basin. *Geophysical Journal of the Royal Astronomical Society* 76: 253–260.
- Siegesmund S, Kern H, and Vollbrecht A (1991a) The effect of oriented microcracks on seismic velocities in an ultramylonite. *Tectonophysics* 186: 241–251.
- Siegesmund S, Fritzsche M, and Braun G (1991b) Reflectivity caused by texture-induced anisotropy in mylonites. In: Meissner R, Brown L, and Durbaum H-J (eds.) *Continental Lithosphere: Deep Seismic Reflections*, and Internation Symposium on Deep Reflectivity, pp. 291–298. Washington, DC: American Geophysical Union.
- Sileny J and Plomerova J (1996) Inversion of shear-wave splitting parameters to retrieve three-dimensional orientation of anisotropy in continental lithosphere. *Physics of the Earth and Planetary Interiors* 95: 277–292.
- Silver PG (1996) Seismic anisotropy beneath the continents: Probing the depths of geology. *Annual Review of Earth and Planetary Science* 24: 385–432.
- Silver PG and Chan WW (1991) Shear-wave splitting and subcontinental mantle deformation. *Journal of Geophysical Research* 96: 16429–16454.
- Silver PG, Gao SS, Liu KH, and the Kaapvaal Seismic Group (2001) Mantle deformation beneath Southern Africa. *Geophysical Research Letters* 28: 2493–2496.
- Silver PG and Kaneshima S (1993) Constraints on mantle anisotropy beneath Precambrian North America from a transportable teleseismic experiment. *Geophysical Research Letters* 20: 1127–1130.
- Silver PG and Savage MK (1994) The interpretation of shear-wave splitting parameters in the presence of two anisotropic layers. *Geophysical Journal International* 119: 949–963.
- Silveira G, Stutzmann E, Griot D-A, Montagner J-P, and Victor LM (1998) Anisotropic tomography of the Atlantic Ocean from Rayleigh surface waves. *Physics of the Earth and Planetary Interiors* 106: 257–273.
- Singh S, Taylor MAJ, and Montagner JP (2000) On the presence of liquid in Earth's inner core. *Science* 287: 2471–2474.
- Steinle-Neumann G, Stixrude L, Cohen RE, and Gulseren O (2001) Elasticity of iron at the temperature of the Earth's inner core. *Nature* 413: 47–60 (doi:10.1038/35092536).
- Smith DP and Ekström G (1999) A global study of Pn anisotropy beneath continents. *Journal of Geophysical Research* 104(B1): 963–980.
- Smith ML and Dahlen FA (1973) The azimuthal dependence of Love and Rayleigh propagation in a slightly anisotropic medium. *Journal of Geophysical Research* 78: 3321–3333.
- Smith GP, Wiens DA, Fischer KM, Dorman LM, Webb SC, and Hildebrand JA (2001) A complex pattern of mantle flow in the Lau Backarc. *Science* 292: 713–716.
- Souriau A, Garcia R, and Poupinet G (2003) The seismological picture of the inner core: Structure and rotation. *Comptes Rendus Geoscience* 335: 51–65.
- Souriau A and Romanowicz B (1996) Anisotropy in inner core attenuation: A new type of data to constrain the nature of the solid core. *Geophysical Research Letters* 23: 1–4.
- Su L and Park J (1994) Anisotropy and the splitting of PS waves. *Physics of the Earth and Planetary Interiors* 86: 263–276.
- Tanimoto T (2004) The azimuthal dependence of surface wave polarization in a slightly anisotropic medium. *Geophysical Journal International* 156: 73–78.
- Thomsen L (1986) Weak elastic anisotropy. *Geophysics* 51: 1954–1966.
- Thomson CJ (1997) Modelling surface waves in anisotropic structures. Part I: Theory. *Physics of the Earth and Planetary Interiors* 103: 195–206.
- Tommasi A (1998) Forward modeling of the development of seismic anisotropy in the upper mantle. *Earth and Planetary Science Letters* 160: 1–13.
- Trampert J and Woodhouse JH (2003) Global anisotropic phase velocity maps for fundamental surface waves between 40 and 150s. *Geophysical Journal International* 154: 154–167.
- Vavrycuk V (1999) Weak-contrast reflection/transmission coefficients in weakly anisotropic elastic media: P-wave evidence. *Geophysical Journal International* 138: 553–565.
- Vavrycuk V, Hrbcová P, Broz M, and Malek J (2004) Azimuthal variation of Pg velocity in the Moldanubian, Czech Republic; observations based on a multi-azimuthal common-shot experiment. *Tectonophysics* 387: 189–203.
- Vinnik L, Farra V, and Romanowicz B (1989a) Observational evidence for diffracted SV in the shadow of the Earth's core. *Geophysical Research Letters* 16: 519–522.
- Vinnik L, Farra V, and Romanowicz B (1989b) Azimuthal anisotropy in the Earth from observations of SKS at Geoscope and NARS broad-band stations. *Bulletin of the Seismological Society of America* 79: 1542–1558.
- Vinnik LP, Kosarev GL, and Makeyeva LI (1984) Anisotropy of the lithosphere according to the observations of SKS and SKKS waves (in Russian). *Doklady Akademii Nauk SSSR* 278: 1335–1339.
- Vinnik L, Kurnik E, and Farra V (2005) Lehmann discontinuity beneath North America: No role for seismic anisotropy. *Geophysical Research Letters* 32: L09306 (doi:10.1029/2004GL022333).
- Warner M, Morgan J, Barton P, Morgan P, Price C, and Jones K (1996) Seismic reflections from the mantle represent relict subduction zones within the continental lithosphere. *Geology* 23: 39–42.
- Wiemer S, Tytgat G, Wyss M, and Duenkel U (1999) Evidence for shear-wave anisotropy in the mantle wedge beneath south-central Alaska. *Bulletin of the Seismological Society of America* 89: 1313–1322.
- Wielandt E, Sigg A, Plesinger A, and Horalek J (1987) Deep structure of the Bohemian Massif from phase velocities of Rayleigh and Love waves. *Studia Geophysica et Geodaetica* 31: 1–7.
- Wilson CK, Jones CH, Molnar P, Sheehan AF, and Boyd OS (2004) Distributed deformation in the lower crust and upper mantle beneath a continental strike-slip fault zone; Marlborough fault system, South Island, New Zealand. *Geology* 32: 837–840.
- Wittlinger G, Farra V, and Vergne J (2004) Lithospheric and upper mantle stratifications beneath Tibet: New insights from Sp conversions. *Geophysical Research Letters* 31: L19615 (doi:10.1029/2004GL020955).
- Wolfe JP (1998) *Imaging Phonons, Acoustic Wave Propagation in Solids*. Cambridge, UK: Cambridge University Press.
- Wolfe CJ and Silver PG (1998) Seismic anisotropy of oceanic upper mantle; shear wave splitting methodologies and observations. *Journal of Geophysical Research* 103: 749–771.
- Wolfe CJ, Vernon FL, III, and Al-Amri A (1999) Shear-wave splitting across western Saudi Arabia: The pattern of upper-mantle anisotropy at a Proterozoic shield. *Geophysical Research Letters* 26: 779–782.

- Woodhouse JH, Giardini D, and Li XD (1986) Evidence for inner core anisotropy from free oscillations. *Geophysical Research Letters* 13: 1549–1552.
- Wookey J, Kendall JM, and Rumpker G (2005) Lowermost mantle anisotropy beneath the north Pacific from differential S-ScS splitting. *Geophysical Journal International* 161: 829–838.
- Yu Y and Park J (1994) Hunting for azimuthal anisotropy beneath the Pacific Ocean region. *Journal of Geophysical Research* 99: 15399–15422.
- Yu Y, Park J, and Wu F (1995) Mantle anisotropy beneath the Tibetan Plateau: Evidence from long-period surface waves. *Physics of the Earth and Planetary Interiors* 87: 231–246.

1.10 Theory and Observations – Seismic Tomography and Inverse Methods

C. Thurber, University of Wisconsin, Madison, WI, USA

J. Ritsema, University of Michigan, Ann Arbor, MI, USA

© 2007 Elsevier B.V. All rights reserved.

1.10.1	Introduction to Seismic Tomography	323
1.10.2	Data Types in Seismic Tomography	325
1.10.2.1	Body Waves	327
1.10.2.2	Surface Waves	328
1.10.2.3	Normal Modes	329
1.10.2.4	Waveforms	330
1.10.2.5	Reference Model	331
1.10.3	Model Parametrization	331
1.10.3.1	Cells, Nodes, and Basis Functions	331
1.10.3.2	Irregular Cell and Adaptive Mesh Methods	334
1.10.3.3	Static (Station) Corrections	336
1.10.4	Model Solution	336
1.10.4.1	Linear versus Nonlinear Solutions	336
1.10.4.1.1	Iterative solvers	338
1.10.4.2	Regularized and Constrained Inversion	338
1.10.4.2.1	Generalized inverse and damped least-squares solutions	338
1.10.4.2.2	Occam's inversion and Bayesian methods	340
1.10.4.3	Hypocenter–Structure Coupling	341
1.10.4.4	Static (Station) Corrections Revisited	342
1.10.4.5	Double-Difference Tomography	343
1.10.5	Solution Quality	344
1.10.5.1	Data Coverage	344
1.10.5.2	Model Resolution Analysis	348
1.10.5.3	Hypothesis Testing	350
1.10.6	Future Directions	353
References		354

1.10.1 Introduction to Seismic Tomography

Seismic tomography is one of the main techniques to constrain the three-dimensional (3-D) distribution of physical properties that affect seismic-wave propagation: elastic, anelastic, and anisotropic parameters, and density. Tomographic models often play a critical role in the analysis of the subsurface – lithology, temperature, fracturing, fluid content, etc. Since its beginnings in the mid-1970s, seismic tomography has grown to become one of the fundamental tools of modern seismology. We trace the roots of seismic tomography back to a parallel series of abstracts and

papers by Keiiti Aki and co-workers on regional- (teleseismic) and local-scale body-wave tomography beginning in 1974 and by Dziewonski and co-workers on global-scale body-wave tomography starting in 1975. These workers initially referred to their approaches in terms of 3-D inversion and 3-D perturbations, not seismic tomography.

The term tomography comes from the Greek *tomos* which means ‘slice’. The mathematical basis for tomography can be attributed to Johann Radon. We found the first use of the term seismic tomography in a remarkable PhD thesis by Reagan (1978) on seismic reflection tomography, although this author also refers to a document from the Jet Propulsion

Laboratory (1976) proposing the use of tomographic reconstruction on borehole seismic data. Clayton and Hearn (1982) appear to have been the first workers in earthquake seismology (as opposed to exploration seismology) to adopt the term tomography, while the *Scientific American* article by Anderson and Dziewonski (1984) can probably be credited with popularizing the use of the term. As of 2006, a substantial number of books and review papers have been written on the subject. Among these are Thurber and Aki (1987), Nolet (1987), Dziewonski and Woodhouse (1987), Woodhouse and Dziewonski (1989), Romanowicz (1991, 2003), Iyer and Hirahara (1993), Montagner (1994), Ritzwoller and Laveleye (1995), Boschi *et al.* (1996), Trampert (1998), Thurber (2003), and Rawlinson and Sambridge (2003). Our purpose is not to review the vast literature on seismic tomography, but to provide a thorough introduction to the method, highlighting some key issues of particular interest in current research. We pay special attention to the issues of model parametrization, model solution, and especially model assessment, as a tomographic model is only useful if we know (at least approximately) how well it represents the real Earth.

Seismic (or other) modeling of the Earth can be carried out as a ‘forward problem’ where we presume to know the Earth’s structure and properties and use the physics of wave propagation to predict what our observations should be: $\mathbf{d} = \mathbf{F}(\mathbf{m})$, where \mathbf{d} are the data, \mathbf{m} is the given model, and \mathbf{F} represents the forward problem function. In seismic tomography, we use the observations to infer the Earth’s structure, again using the physics of wave propagation, but now in combination with a linear or nonlinear inversion technique – an ‘inverse problem’. For a linear inverse problem, $\mathbf{d} = \mathbf{F}(\mathbf{m})$ can be replaced by an equivalent set of discretized linear equations $\mathbf{G}\mathbf{m} = \mathbf{d}$, where \mathbf{d} and \mathbf{m} are vectors containing the data and model parameters, respectively, and \mathbf{G} is a matrix embodying the physics of the problem. Then one computes $\mathbf{m} = \mathbf{G}^{-i}\mathbf{d}$, where the superscript $-i$ stands for some type of inverse (pseudoinverse, regularized inverse, etc. – see Section 1.10.4). For a nonlinear problem, on the other hand, one typically determines the misfit between data and predictions $\delta\mathbf{d}$ (computed from the forward problem for a trial Earth model) and computes perturbations to the model, $\delta\mathbf{m}$, that will reduce the misfit in an iterative manner, using $\delta\mathbf{m} = \mathbf{G}^{-i}\delta\mathbf{d}$ (Aster *et al.*, 2005).

Seismic imaging has seen a great deal of progress in the past few decades, largely due to the modernization and growth of global and regional networks (e.g.,

Romanowicz *et al.*, 1984; Committee on the Science of Earthquakes, 2003; Butler *et al.*, 2004). The earliest global tomographic models were based entirely on the traveltimes of the first arriving P waves, documented in catalogs. Contemporary models, however, exploit the wide variety of seismic signals recorded by broadband seismometers (including free oscillations, surface waves, and body waves), which provide complementary sampling of the mantle. In addition, forward modeling theories have been improved (even in 3-D; see Chapters 1.01, 1.03, 1.04, and 1.05) and the steady increase of computing power has enabled seismologists to tackle increasingly larger inverse problems. Yet it remains difficult to construct the ‘best’ model of seismic velocity variation given a set of seismic recordings. Ongoing debates in the literature on model resolution and interpretation underscore the difficulty of seismic tomography as an ill-conditioned geophysical inverse problem. So, what are some of the major problems?

- Sampling of the Earth by seismic waves is uneven. On a global scale, the bulk of seismic stations are onshore (in the Northern Hemisphere), and most earthquakes occur in narrow belts along plate boundaries. There are vast regions of the mantle not adequately sampled by seismic waves. On the local and regional scales, sufficiently dense networks are generally concentrated on active fault zones, with major gaps both in sources and receivers elsewhere. Thus, uneven and incomplete sampling is a pervasive problem in virtually all seismic tomography problems.
- We need a large number of model parameters to image relatively narrow structures in the mantle (e.g., slabs of subducted lithosphere, mantle plumes) or fine-scale structures in the crust (e.g., fault zones, magma chambers). A whole-mantle model of seismic velocity in 1° by 1° regions with 100-km-thick layers would be comprised of nearly 1 000 000 parameters. Similarly, at a regional scale, one might wish to have 1 km^3 cells covering a region 400 km by 250 km by 40 km deep, amounting to 4 million parameters.
- There is model nonuniqueness due to data errors and incomplete sampling. More than one model, in fact an infinite number of models, can adequately explain a seismic tomography data set. Given model nonuniqueness, we need to impose (*ad hoc*) constraints to select a ‘successful’ model. We may prefer a model that deviates little from the chosen reference model, or a model with ‘smooth’ wave speed variations. While removing the nonuniqueness problem, one must realize that *a priori* constraints bias the attributes of the seismic

model. Obviously, velocity heterogeneity in seismic models tends to be smooth when smoothness constraints have been applied.

- We make simple approximations to wave propagation theories (e.g., ‘ray theory’ for traveltimes, and the ‘path-average approximation’ for surface-wave inversions). These approximations lessen the computationally burden of the inverse problem, but compromise model quality, especially in high-resolution applications.

We present a comprehensive survey of seismic tomography and inversion methods as applied to local, regional, and global scale studies. Section 1.10.2 provides a brief description of the types of seismic waves, including full waveforms, commonly used in tomography (Sections 1.10.1–1.10.4), and discusses the commonly employed theories that enable us to relate seismic data to how they constrain Earth’s seismic structure, typically as deviations from a (1-D) reference Earth model (Section 1.10.2.5). We include brief discussions of observations and measurements relevant to seismic anisotropy and attenuation, where appropriate, but refer readers to the chapters by Chapters 1.09 and 1.21, respectively, for further discussion of these topics. We discuss in Section 1.10.3 how the Earth is represented (parametrized) as a model, including cell-based parametrizations (Section 1.10.3.1), continuous basis functions (Section 1.10.3.2), and irregular meshes (Section 1.10.3.2). Section 1.10.4 is devoted to the inverse problem. We discuss linear and nonlinear solutions (Section 1.10.4.1) and discuss strategies to regularize the inverse problem (Section 1.10.4.2). The mathematics of the coupling between locations and velocity structure is the topic of Section 1.10.4.3.

Section 1.10.5 illustrates how we can evaluate the quality of the model using formal resolution analyses that invoke an analysis of the properties of the inverse matrix \mathbf{G}^{-1} , and by forward modeling (hypothesis) tests. We highlight in Section 1.10.6 areas of current and future research that are at the forefront of seismic tomography. We point out that our discussions are concentrated on passive-source (i.e., earthquake) tomography at the crustal through global scale; exploration seismic tomography methods are not covered here.

1.10.2 Data Types in Seismic Tomography

In this section, we discuss three general types of data (Figure 1) and their use in the corresponding tomographic methods: body-wave traveltimes, surface-wave dispersion, and free-oscillation (normal-mode) spectral measurements. In global tomography, these three basic data types provide complementary sampling of the mantle (Figure 2) (see Romanowicz (2003) for a recent review). Teleseismic body-wave traveltimes are most routinely used in both global and regional applications. The first global model of the deep mantle by Dziewonski *et al.* (1977) was based on traveltimes incorporated in the bulletins of the International Seismological Centre (ISC). Subsequent models have utilized the millions of traveltimes picks the ISC bulletins now comprise (e.g., Inoue *et al.*, 1990; Vasco *et al.*, 1995; Zhou, 1996; van der Hilst *et al.*, 1997; Bijwaard *et al.*, 1998; Montelli *et al.*, 2004a, 2004b). Global-scale traveltime tomography has been key in illuminating the variable extent of slab penetration into the lower mantle (e.g., Grand,

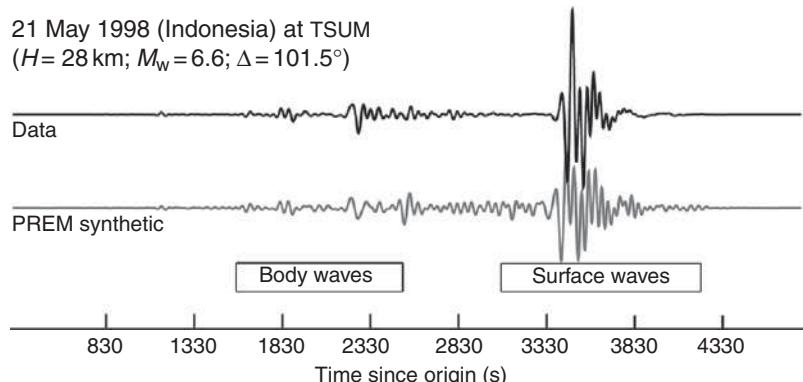


Figure 1 (top) Recorded (vertical component) and (bottom) Preliminary Reference Earth Model (PREM) synthetic seismogram (vertical component) of the 21 May 1998 Indonesia earthquake at station TSUM (Tsumeb, Namibia). The arrival of body waves and surface waves are indicated.

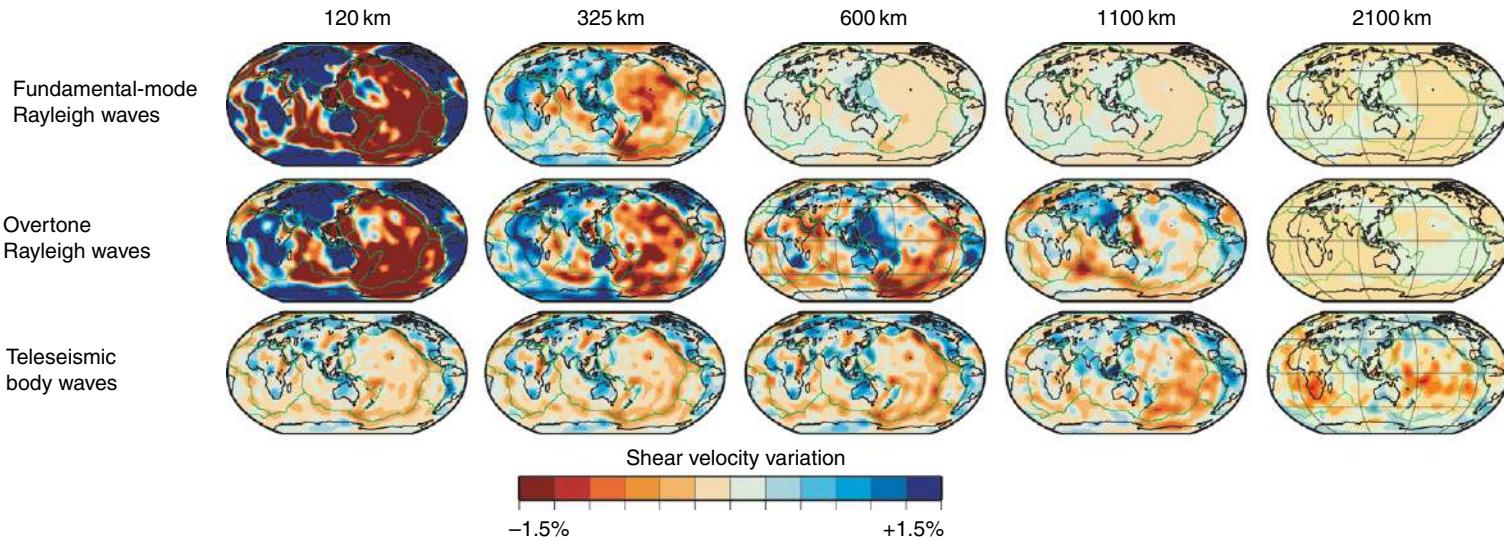


Figure 2 Maps of shear-velocity variations at 120, 325, 600, 1100, and 2100 km depth. These maps are derived by inverting (top row) fundamental-mode Rayleigh wave, (middle row) overtone Rayleigh wave, and (bottom row) teleseismic traveltime data. Note that these individual data sets provide complementary structural constraints. The fundamental modes constrain seismic structure in the upper \sim 300 km of the mantle (depending on the frequency range analysed), the overtone data constrain deeper regions of the transition zone (less than \sim 1000 km), while teleseismic traveltime data constrain the lower mantle (greater than \sim 1000 km) best.

1994; Grand *et al.*, 1997; Fukao *et al.*, 2001). Surface waves generally produce the highest amplitude signals in seismograms and provide constraints on the upper mantle. Measurements of surface-wave dispersion (i.e., the frequency-dependent surface-wave speed) are key in our understanding of lithospheric structure, especially in oceanic regions where few seismic stations are located (e.g., Nakanishi and Anderson, 1982; Lévêque and Cara, 1985; Nataf *et al.*, 1986; Montagner and Tanimoto, 1991; Zhang and Tanimoto, 1993; Laske, 1995; Trampert and Woodhouse, 1995; Ekström *et al.*, 1997; van Heijst and Woodhouse, 1999). Normal-mode spectral measurements provide constraints on the longest wavelength part of lateral heterogeneity through the Earth (e.g., Masters *et al.*, 1982, 1996; He and Tromp, 1996; Resovsky and Ritzwoller, 1999). These data lend themselves for joint inversions for shear and compressional velocity (Masters *et al.*, 1996; Deschamps and Trampert, 2004), and even density (Ishii and Tromp, 1999, 2001; Kuo and Romanowicz, 2002). We also briefly discuss the topics of waveform inversion and the use of reference Earth models.

Although several workers have demonstrated that robust body-wave (e.g., Bhattacharyya *et al.*, 1996; Reid *et al.*, 2001; Ritsema *et al.*, 2002; Komatitsch *et al.*, 2002; Nolet *et al.*, 2005) and surface-wave (e.g., Romanowicz, 1991; Billien *et al.*, 2000; Selby and Woodhouse, 2002; Dalton and Ekström, 2006) amplitude patterns can be derived from high-quality data to constrain velocity gradients and attenuation structure, most tomographic studies of velocity structure are primarily based on wave traveltimes or phase delay inversions. Compared to amplitudes, traveltimes data sets possess little scatter and they can be determined in a relatively straightforward manner.

1.10.2.1 Body Waves

Body waves are relatively low-amplitude, impulsive signals that, at teleseismic distances, propagate along a variety of paths through the deep mantle and core. Direct waves, surface reflections, and core reflections provide sampling of the mantle along unique paths. In global tomography, teleseismic traveltimes are key in constraining the structure of the deep mantle. Upper-mantle modeling using teleseismic traveltimes and local and regional tomography modeling generally rely on measurements from a relatively dense regional network of stations.

Ray theory and Fermat's principle are at the heart of traditional body-wave travelttime tomography. In

the infinite frequency limit, travelttime T can be written as a path integral,

$$T = \int_{\text{ray path}} u(\mathbf{r}) ds \quad [1]$$

where u is the model of slowness (reciprocal of wave speed) at points along the ray path, \mathbf{r} is position, and ds is an infinitesimal element of path length (see Chapter 1.03). Our problem of determining the 3-D slowness structure $u(\mathbf{r})$ from the arrival time residuals, obtained by solving a set of equations of the general form

$$\delta T = \int_{\text{ray path}} \delta u(\mathbf{r}) ds \quad [2]$$

where δ represents a perturbation, is confounded because we do not know the true ray path (neglecting for the moment the additional issues of the hypocenter location and origin time if an earthquake is the source of the arrival). Looked at another way, the ray path used to compute traveltimes from which the model perturbation is estimated will no longer be the correct ray path once the perturbations are applied to the model. Fermat's principle rescues us from this quandary, thanks to the stationary nature of travelttime under small perturbations to the ray path. Thus, if the path perturbation between the initial and adjusted models is sufficiently small, the travelttime (and therefore the travelttime residual) will be nearly the same no matter which of the two paths is used. See Snieder (1990), Snieder and Sambridge (1992), and Snieder and Spencer (1993) for a detailed treatment of this issue.

It should be clear from eqns [1] and [2] that body-wave travelttime tomography in the infinite frequency limit is relatively simple in theory, but more complex if finite frequency effects are taken into account in broadband travelttime data analyses. Two such examples are 'fat ray' tomography (Husen and Kissling, 2001) and 'banana-doughnut' theory (Dahlen *et al.*, 2000).

Fat ray tomography adopts the view that the entire first Fresnel volume (the volume within which scattered energy arrives within one-half the dominant period of the seismic wave) of the first arriving phase should be considered in relating traveltime residuals to model perturbations. Therefore, the region of the model sensitive to a given datum is banana shaped for a typically curved path, with the source and receiver close to (but not at) the tips of the banana (Figure 3). Husen and Kissling (2001)

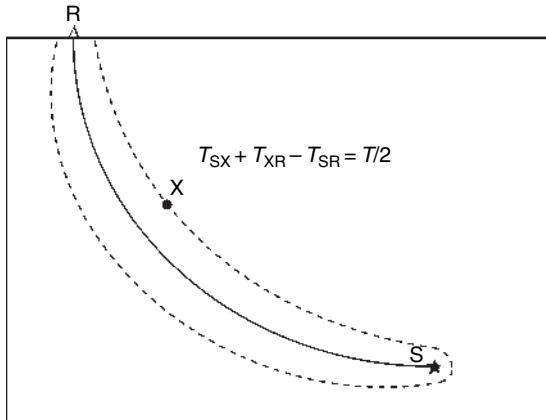


Figure 3 Diagram of the Fresnel zone for a body wave in the Earth. A point X is in the first Fresnel zone if the scattered wave from point X reaches the receiver at R within a time equal to 1/2 of the wave period T of the direct arrival from the source S.

developed such an approach for local earthquake tomography (LET), distributing the contributions to a given travelttime perturbation (eqn [2]) among the model parameters in proportion to the fraction of the total Fresnel volume present in a given model cell, rather than along a path of infinitesimal width.

The need for banana-doughnut theory arises when cross-correlation measurements between observed and synthetic waveforms are used to estimate traveltimes (Dahlen *et al.*, 2000). The seemingly counterintuitive result is that the cross-correlation measurement is completely insensitive to the model along the geometrical (infinite frequency) ray path, producing a hole within the banana along the ray path – hence the term banana doughnut. As one might expect, the volume of the banana and its interior ‘hole’ are strongly frequency dependent. However, whether finite-frequency effects impact the resolution of Earth structure is still a matter of debate (Montelli *et al.*, 2004a, 2004b; van der Hilst and De Hoop, 2005).

Another source of complexity is anisotropy, where wavespeed depends on the direction of wave propagation or wave polarization. For shear waves, anisotropy is most readily identified via shear-wave splitting (SWS; an example of birefringence) (e.g., Silver, 1996). A shear wave with an initial linear polarization will be ‘split’ as it passes through an anisotropic zone (when the initial polarization direction is not aligned with an axis of the anisotropic structure). Therefore, fast shear-wave polarization directions and splitting times can readily be measured. However, it is not straightforward to model

SWS, at least in a tomographic sense. In contrast, P-wave anisotropy is not directly observable in a single three-component seismogram. P waves simply cannot be ‘split’ in the same manner transverse S waves can. Instead, P-wave traveltimes through an anisotropic volume depend on propagation direction, making it difficult to separate P-wave anisotropy from P-wave-speed heterogeneity, although a tomographic modeling approach is still possible (Hirahara, 1993). The use of SWS observations to provide *a priori* constraints for an anisotropic P-wave tomographic inversion is one practical approach (Eberhart-Phillips and Henderson, 2004). See Chapter 1.09 for a thorough discussion of seismic anisotropy.

Attenuation, on the other hand, can be approached readily in the same manner for P and S waves. Even if the quality factor Q (Aki and Richards, 1980) is frequency independent, higher-frequency waves undergo greater intrinsic attenuation than low-frequency waves because they pass through more wave cycles. Their amplitude decays exponentially:

$$A(x, f) = A_0 \exp\left[-\left(\frac{\pi f x}{VQ}\right)\right] \quad [3]$$

where V is wavespeed, f is frequency, and x is distance of propagation. A common approach for tomography is to express attenuation in terms of the parameter t^* (defined as travelttime/quality factor), leading to an integral relationship between t^* and Q along the path,

$$t^* = \int_{\text{path}} \frac{dt}{Q(r)} = \int_{\text{path}} \frac{ds}{V(r)Q(r)} \quad [4]$$

t^* values at a set of observing stations for a given earthquake can be determined by joint, nonlinear fitting of observed spectra using an accepted source model (Lees and Lindley, 1994). The t^* values can then be inverted for a 3-D Q model in a manner equivalent to body-wave tomography (Scherbaum, 1990; Rietbrock, 2001). See Chapter 1.21 for a more general discussion of attenuation.

1.10.2.2 Surface Waves

There are two types of surface waves with different particle motion characteristics, just as there are two types of body waves – but with a ‘twist’. Surface waves are evanescent waves (with a purely imaginary vertical wave number $i|v|$) that propagate horizontally along the Earth’s surface with a ‘skin

depth' that increases with increasing period (or wavelength). Love waves are composed of horizontally polarized shear waves (SH) trapped within a surface layer (or layers). Rayleigh waves form by an interaction between compressional and vertically polarized shear waves (P-SV) at the surface. The combination of the Earth's sphericity and the increase of wavespeed with depth leads to dispersion of surface waves. As a result, surface waves are recorded as a 'train' of waves, with long-period/long-wavelength waves generally arriving first. At teleseismic distances, surface waves have much larger amplitude than body waves due to their geometric spreading in 2-D, as opposed to the 3-D spreading of body waves.

One consequence of dispersion is the existence of two distinct velocities characterizing surface-wave propagation. Let us express displacement $u(x, t)$ as an integral over harmonic plane waves of all frequencies ω :

$$u(x, t) = \int A(\omega) \exp\{i(\omega t - k(\omega))x + \phi(\omega)\} d\omega \quad [5]$$

If we approximate the wave number $k(\omega)$ by a Taylor series about ω_0 ,

$$k(\omega) = k(\omega_0) + (dk/d\omega|_{\omega=\omega_0})(\omega - \omega_0) \quad [6]$$

it is straightforward to show that the displacement due to harmonic waves near ω_0 is approximately

$$\begin{aligned} u(x, t) &= \int_{\omega_0 - d\omega}^{\omega_0 + d\omega} A(\omega) \exp\{i(\omega - \omega_0)(t - dk/d\omega x)\} \\ &\quad \times \exp\{i(\omega_0 t - k(\omega_0)x) + \pi\} d\omega \end{aligned} \quad [7]$$

The two sinusoidal functions in [7] correspond to propagating waves with different speeds. The carrier wave at frequency ω propagates at the phase velocity (C) ω_0/k , upon which a more slowly varying envelope with frequency $d\omega$ and wave number dk is superposed. This envelope propagates at the group velocity (U) $d\omega/dk$.

Surface-wave group velocity analysis involves multitapered spectral analysis of narrow-band filtered signals,

$$s(t) = \int s(\omega) H(\omega) d\omega \quad [8]$$

where $H(\omega)$ is the taper function, usually of the form $\exp\{-(\omega - \omega_0)^2/\omega_0^2\}$. Group velocity can be determined by estimating how the peak of the amplitude spectrum varies as a function of group velocity U (=epicentral distance/traveltime) and the central

frequency of the taper function. This analysis has been applied globally to determine group velocity dispersion (see Chapters 1.01 and 1.02).

Phase velocities are determined either with data from multiple stations, or from single seismograms. The phase Φ_i (determined from the Fourier transform) of a recording i at a distance x_i can be written as

$$\begin{aligned} \Phi_i &= \omega t - k(\omega)x_i + \Phi_s + 2n\pi \\ &= \omega[t - x/c(\omega)] + \Phi_s + 2n\pi \end{aligned} \quad [9]$$

where Φ_s is the initial phase (due to the source). Defining Φ_{ij} as $\Phi_i - \Phi_j$ for stations i and j at the same azimuth from the source (so that Φ_s is common to both recordings i and j), we can solve for the phase velocity

$$C(\omega) = \omega(x_i - x_j)/[\omega(t_i - t_j) + 2(m-n)\pi - \Phi_{ij}] \quad [10]$$

The term $2(m-n)\pi$ is found empirically by ensuring that the phase velocity has a 'reasonable' value at the longest periods. The subsequent analysis at increasingly shorter periods is 'locked in' by requiring that C is a continuous function of ω .

Single-station (i) measurements of phase velocity require knowledge of $\Phi_s(\omega)$, that is, knowledge of the earthquake focal mechanism:

$$C(\omega) = \omega x / [\omega t + \Phi_s(\omega) + 2n\pi - \Phi_i] \quad [11]$$

Often, we measure the phase $\Phi(\omega)$ relative to that in a synthetic seismogram for a spherically symmetric Earth model $\Delta\Phi = \Phi_{\text{obs}} - \Phi_{\text{syn}}$. Again, we remove the 'cycle-skip' ambiguity by locking $2n\pi$ at the lowest frequencies, and estimating $\Delta\Phi$ at increasingly higher frequencies. For further details, see Chapters 1.01, 1.02, and 1.05.

1.10.2.3 Normal Modes

Normal modes (also known as 'free oscillations') are standing waves excited by the largest earthquakes on Earth. Like standing waves on a string fixed at both ends, normal modes have distinct frequencies determined by Earth's finite size and its internal elastic structure. The gravest normal mode, the so-called 'football mode', has a period of about 54 min. In analogy to surface waves (intimately related to normal modes), there are two types of normal modes, distinguished by their mode of oscillations. Torsional modes are analogous to Love waves. They do not have radial displacements and they do not cause volume changes. Spheroidal modes are analogous to Rayleigh waves, and involve a combination of radial and transverse motions. Like standing waves on a

string, we can express the displacement field in the Earth as a sum of normal modes (e.g., Gilbert, 1970; Dahlen and Tromp, 1998):

$$u(x, t) = \sum_n \sum_l \sum_{m=-1}^1 {}_n A_l^m(\omega) {}_n Y_l(\mathbf{r}) X_l^m(\theta, \phi) \times \exp\{i \omega_l^m t\} \quad [12]$$

Each mode is described by its radial order n , and surface order l and m . These integers describe the frequency ${}_n \omega_l^m$ of the normal mode, and the spatial shape of the radial eigenfunction ${}_n Y_l(\mathbf{r})$ and surface eigenfunction $X_l^m(\theta, \phi)$. A sum of normal modes describes the complete wavefield up to frequency ω_l^m . However, due to the computational burden, normal modes are used to study primarily long period ($T > 20\text{--}50\text{ s}$) wave propagation in practice.

A ‘multiplet’ ${}_n \omega_l$ consists of $2l+1$ ‘singlets’ ${}_n \omega_l^m$ (m takes values between $-l$ and $+l$). For a spherically symmetric Earth, the singlet eigenfrequencies are the same. For a laterally heterogeneous Earth, the multiplet ‘splits’, rendering singlets ${}_n \omega_l^m$ with slightly different eigenfrequencies. Earth’s rotation has an observable effect on the gravest multiplets (e.g., ${}_0 S_2$ and ${}_0 S_3$). Lateral heterogeneity (both elastic heterogeneity and anisotropy) can cause even more splitting. Tomographers use observations of splitting to constrain the large-scale variations (e.g., Giardini *et al.*, 1987; Masters *et al.*, 1996; Ishii and Tromp, 1999; Resovsky and Ritzwoller, 1999), albeit that only the ‘even-degree’ structure can be constrained in a direct manner.

It is difficult to make splitting measurements. Spectral peaks have a finite width, because seismograms are not infinitely long, and due to the effect of anelasticity. Moreover, multiplets can overlap, which makes it impossible to treat them in isolation. However, analysis of the splitting of coupled multiplets enables us to constrain both even-degree and odd-degree structure (Dahlen and Tromp, 1998). See Chapters 1.01, 1.02, and 1.05 for further details.

1.10.2.4 Waveforms

While traveltimes and phase delays represent parametric measurements made from seismograms, it is also possible to model the seismograms directly ‘wiggle for wiggle’. Waveform inversions are particularly advantageous in that it allows for the analysis of strongly interfering signals. A waveform inversion is typically posed as a search for the model \mathbf{m} that best

minimizes the (least-squares) fit between the observed seismogram (or a segment of it) $d(t)$ and a computed seismogram $s(\mathbf{m}, t)$:

$$F(\mathbf{m}) = \int dt \{d(t) - s(\mathbf{m}, t)\}^2 \quad [13]$$

In global tomography, waveform fitting was introduced by Woodhouse and Dziewonski (1984) using digital seismic data from upgraded global seismic stations. An important novelty of their approach is that it allows for the recovery of both even and odd spherical harmonic coefficients. In their approach, still widely used today, synthetic seismograms were computed using normal mode summation. The ‘path-average approximation’ accounts for the effects of lateral heterogeneity by perturbing the eigenfrequency of each multiplet. Using eqn [12] as a description of a long-period seismogram, we can find perturbations to $\delta\alpha(r)$, $\delta\beta(r)$, and $\delta\rho(r)$ due to perturbations in frequency $\delta\omega$. We can write the dependence of $\delta\omega(\theta, \varphi)$ as

$$\delta\omega = \int_{\text{gc}} (K_\alpha \delta\alpha + K_\beta \delta\beta + K_\rho \delta\rho) dS \quad [14]$$

where the 1-D kernels K_α , K_β , and K_ρ describe the dependence of perturbation in eigenfrequency ω to perturbations in P velocity, S velocity, and density, respectively (see Dahlen and Tromp (1998) for an extensive theoretical treatment).

The ‘partitioned waveform inversion technique’ (Nolet and Snieder, 1990) also utilizes the path-average approximation approach, but given its focus on smaller (continental-scale) regions (e.g., Zielhuis and Nolet, 1994; van der Lee and Nolet, 1997; Lebedev *et al.*, 1997), it is limited to minor-arc waveforms only albeit at somewhat higher frequencies. The method enables the separate analysis (and data weighing) of fundamental-mode surface waves and overtone signals (such as triplicated SS, SSS waves) and background seismic models unique to different propagation paths.

More recent work has focused on the development of more realistic kernels. Two-dimensional kernels computed using across-branch coupling (e.g., Li and Tanimoto, 1993; Li and Romanowicz, 1995; Marquering and Snieder, 1995; Zhao and Jordan, 1998) include (frequency-dependent) sensitivity along the body-wave propagation path within the plane of propagation. These higher-order (compared to the path-averaged approximation by Woodhouse and Dziewonski (1984)) kernels, better

describe the sensitivity of overtone surface waves and complex body waves like SS (the surface reflected S wave) and S_{diff} (the core-diffracted S wave) to Earth structure. Models SAW12D (Li and Romanowicz, 1996) and SAW24B16 (Mégnin and Romanowicz, 2000) are based on these 2-D kernels.

At a regional scale, Zhao *et al.* (2005) demonstrated the ability to compute the Fréchet kernels for the full-waveform inverse problem using a 3-D starting model, opening up the avenue of iterative waveform tomography at regional scales. The data are frequency-dependent phase delay and amplitude anomalies (Gee and Jordan, 1992), which are evaluated using cross correlation between the observed data and synthetics. Chen *et al.* (2007) applied this approach to the Los Angeles region, leading to improvements in existing models of 3-D structure based on traveltimes tomography and active-source models.

1.10.2.5 Reference Model

A radially symmetric (1-D) model of wave speed takes a central role in the analysis of global seismic data and global tomography. The Jeffreys–Bullen Tables (Jeffrey and Bullen, 1958), 1066A (Gilbert and Dziewonski, 1975), Preliminary Reference Earth Model (PREM; Dziewonski and Anderson, 1981), IASP91 (Kennett and Engdahl, 1991), and ak135 (Kennett *et al.*, 1995) are often invoked. They provide wave speed or a combination of wave speed, density, and attenuation as a function of depth in the Earth, and explain to first order the characteristics of global wave propagation, such as the propagation time of teleseismic body waves, and the dispersion of surface waves (including in some cases the effect of upper-mantle anisotropy). Using digital broadband recordings, tomographers have built catalogs of surface-wave dispersion measurements (e.g., Ekström *et al.*, 1997; Trampert and Woodhouse, 1996) and catalogs of body-wave traveltimes (e.g., Woodward and Masters, 1991; Su *et al.*, 1994; Ritsema *et al.*, 2002) by systematically comparing recorded and PREM synthetic waveforms (**Figure 1**).

The 1-D reference model is also used in the forward modeling theory. For example, a body-wave traveltime anomaly, δT , can be defined in terms of velocity as (see Section 1.10.2.1)

$$\delta T \approx \int_{s^0} \frac{1}{V_0^2(\mathbf{r})} \delta V(\mathbf{r}) ds \quad [15]$$

Similarly, a surface-wave phase-velocity perturbation $\delta C(\omega)$ due to shear velocity heterogeneity in the mantle can be written as

$$\delta C(\omega) = \int_{gc} ds \int d\mathbf{r} \left(\frac{\partial C(\omega)}{\partial V_S^0(\mathbf{r})} \right) \delta V_S(\mathbf{r}) \quad [16]$$

where we have assumed that surface waves propagate along the great circle path gc and that the relationship between phase velocity C and shear velocity V_S can be calculated for the 1-D reference model. It is straightforward to compute 1-D synthetics, body-wave paths, and kernel functions that relate surface-wave dispersion to seismic velocity for 1-D seismic models. Moreover, eqns [15] and [16] render linear relationships between the seismic observables and wave speed heterogeneity. These can be solved using standard linear inverse techniques (see Section 1.10.4). Current research addresses how better, but more complex, theories affect the model solution.

In local-scale studies, the importance of the starting 1-D model has been clearly demonstrated. For example, Kissling *et al.* (1994) proposed the use of the ‘minimum 1-D model’ determined by inversion for a layered structure as the starting model for 3-D tomography. Refraction models provide another potential source for a starting 1-D model. Because the LET problem is strongly nonlinear, a suitable starting model is critical for reaching an optimal solution.

1.10.3 Model Parametrization

The Earth’s seismic velocity structure has been represented in a wide variety of ways in seismic tomography studies. All are only approximations to the true 3-D structure of the Earth, or some portion of it. The Earth has heterogeneous structure on a vast range of spatial scales, including complications such as discontinuities, faults, layering, intrusions, inclusions, zones of elevated temperature or partial melt, and random geologic heterogeneities. It also displays anisotropy, which is the topic of Chapter 1.09. The spatial scale of heterogeneity that can be imaged with seismic tomography depends primarily on the density of wave sampling, with a lower bound proportional to the minimum wavelength of recorded seismic-wave energy.

1.10.3.1 Cells, Nodes, and Basis Functions

No single scheme can fully represent all aspects of the Earth’s heterogeneity. At the local scale, the

constant-velocity, uniform volume block approach of Aki and Lee (1976) and the variable volume block approach of Roecker (1982) treat a volume of the Earth as a set of cells within each of which the seismic velocity is constant (**Figure 4(a)**). This approach has the advantage of simplicity, but is clearly lacking in the ability to represent heterogeneous structure faithfully, even structures as simple as slight gradients in velocity or oblique discontinuities. From the inverse theory point of view, a block/cell inversion is often set up as an overdetermined problem (more independent data than unknowns), but this strategy can be criticized for being underparametrized (insufficient parameters to adequately represent the real Earth). At the same time, some model parameters may actually be unconstrained even though there are more data than unknowns, resulting in a mixed-determined problem (simultaneously over- and underdetermined). Alternatively, one can employ a large number of small cells, allowing gradual or rapid velocity changes from block to block to mimic gradients or discontinuities, respectively (Nakanishi, 1985; Walck and Clayton, 1987; Lees and Crosson, 1989). Unfortunately, the use of a large number of

cells, if not compensated for, results in a severely underdetermined problem (many more unknowns than independent data), and increased computational burden. These two problems are typically dealt with by applying a smoothing operator and a sparse-matrix solver, respectively (see Section 1.10.4).

Variations on the discrete block parametrization include laterally varying layers (Hawley *et al.*, 1981) and a 3-D grid of nodes (Thurber, 1983). In the approach of Hawley *et al.* (1981), the model is divided into horizontal layers in which velocity is constant in the vertical direction, but velocity is obtained by interpolation in the horizontal directions among vertical nodal lines (**Figure 4(b)**). The spacing between nodal lines may vary from layer to layer. Thurber (1983) used a 3-D grid approach (**Figure 4(c)**), in which velocity varies continuously in all directions, with linear B-spline interpolation among nodes. Alternatively, one can use cubic B-splines with continuous second-order derivatives (Michelini and McEvilly, 1991).

Another variant of the 3-D grid theme is to consider each set of four neighboring nodes as defining the vertices of a tetrahedron (**Figure 4(d)**; Lin and

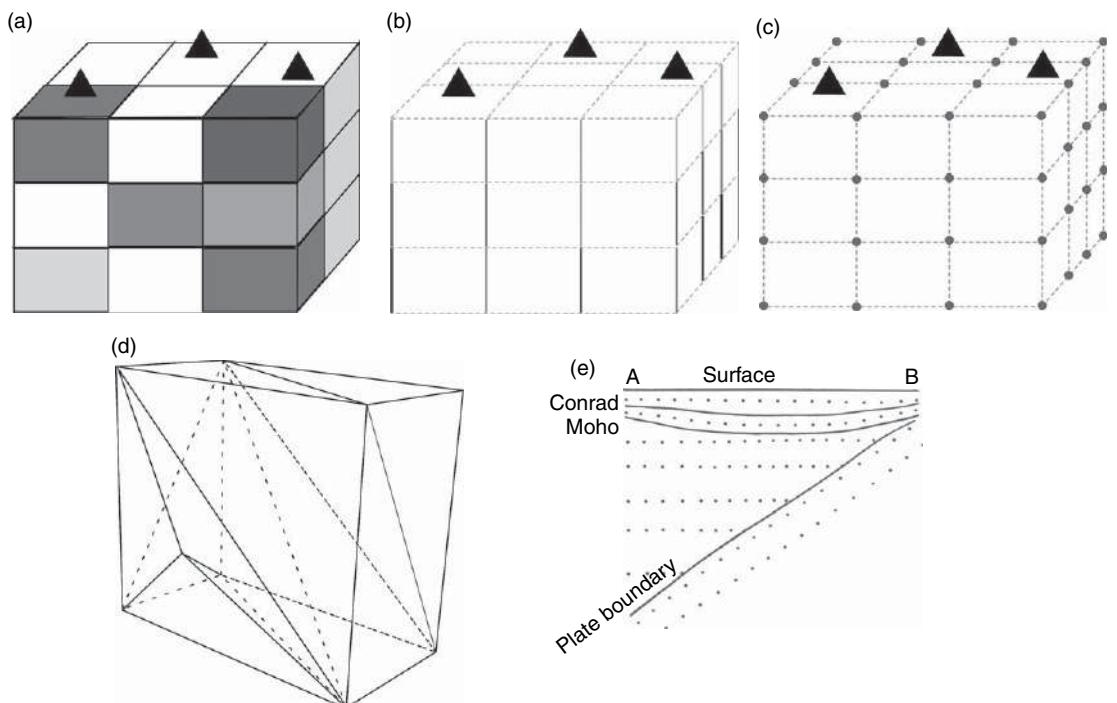


Figure 4 Examples of types of model parametrization schemes. (a) Constant-velocity, uniform volume blocks. (b) Layers of laterally varying but vertically constant velocity within a given layer. (c) Regular grid of nodes. (d) Variable-size tetrahedral cells. (e) Interfaces separating regions with velocity defined on a grid. (e) Reproduced from Zhao D, Hasegawa A, and Horiuchi S (1992) Tomographic imaging of P and S wave velocity structure beneath northeastern Japan. *Journal of Geophysical Research* 97: 19909–19928, with permission from American Geophysical Union.

Roecker, 1997). The four node velocities can be used to define a unique linearly varying velocity field within the tetrahedron; the velocity gradient can thus point in any direction. Snell's law is used to cross tetrahedron boundaries. This allows the use an analytic formula for ray tracing using an initial-value ('shooting') approach, as ray paths are circular arc segments in a medium with constant-velocity gradient. Other alternative interpolation schemes are possible, but would require different ray-tracing procedures. See also Section 1.10.3.2 for an example of the use of tetrahedrons in adaptive-mesh tomography.

Similar approaches have been adopted for regional- and global-scale tomography. Aki *et al.* (1977) employed constant-slowness, uniform volume cells in their original teleseismic (regional) inversion work, and that method (ACH after the authors Aki, Christoffersson, and Husebye) has proven to be a 'workhorse' for the seismology community (see Evans and Achauer, 1993). Some improvements have been made to the algorithm over the years, including allowing for variable block thickness with depth (Evans and Achauer, 1993) and using nodes with spline interpolation (VanDecar *et al.*, 1995), and problems and code errors have been pointed out (Masson and Trampert, 1997; Julian *et al.*, 2000), but the basic method continues to be used widely. Humphreys and co-workers developed a similar algorithm (Humphreys *et al.*, 1984), and Spakman, Nolet, and co-workers developed a third comparable algorithm (Spakman and Nolet, 1988), both of which have also been put to wide use. A key distinction between the latter two is the inverse problem solution method, SIRT for the former and LSQR for the latter (see Section 1.10.4).

Zhao and co-workers have taken a slightly different approach that emphasizes the importance of major seismic velocity discontinuities along with velocity heterogeneity. Using the study of northeastern Japan by Zhao *et al.* (1992) as an example, the authors define the discontinuities and embed a velocity grid within each layer (Figure 4(e)). The method allows the inclusion of secondary phase data (e.g., converted phases) to model the positions of the discontinuities, although this particular study did not utilize this capability.

Similarly, Zhao (2004) incorporated discontinuities and a 3-D grid in a global tomographic model, with a grid spacing of 3–5°. Specifically, he included the Moho and the 410 and 660 km discontinuities, keeping them fixed during the inversion. More

commonly, global tomographic models utilize spherical 'blocks' of uniform latitude and longitude extent or roughly uniform size (Sengupta and Toksoz, 1976; Inoue *et al.*, 1990; Vasco *et al.*, 1995; Zhou, 1996; van der Hilst *et al.*, 1997).

Alternatively, one can adopt a functional approach to representing 3-D structure, either with a set of basis functions or an *a priori* functional form. An example of the former is an expansion in a set of continuous, orthogonal basis functions (e.g., sinusoidal or spherical harmonic functions) where the spatial resolution is limited by the number of terms included in the expansion (Novotny, 1981). Examples of the latter are the subducting slab parametrization of Spencer and Gubbins (1980), in which the slab is represented by its strike, dip, width, slowness contrast, and decay rate with depth; the fault zone parametrization of Wesson (1971), in which the fault zone is represented by its velocity decrease, decay with depth and distance, and the velocity contrast across it; and the quasi-layered parametrization of Ashiya *et al.* (1987) employing a sum of hyperbolic tangent functions for the depth variation of velocity and Chebyshev functions for the lateral variation of velocity.

Early global P-wave traveltimes studies used spherical-harmonic expansions in latitude and longitude and polynomials in depth (Dziewonski, 1984). A recent example of these studies reached degree 40, corresponding to a lateral dimension of as little as 500 km (Boschi and Dziewonski, 1999). One source of concern for this approach is the tendency for the truncated basis functions to leak into the solution, leading to a biased model estimate (Trampert and Snieder, 1996). If the power in the model spectrum above the truncation point is weak, this may not be a serious issue, but of course it is difficult to prove this is the case, in general. We also point out that truncation is a risk to virtually any tomographic method that adopts an overdetermined ('underparametrized') inverse approach. Trampert and Snieder (1996) in fact present a technique for correcting (to first order) the biasing effect of truncating spherical harmonic basis functions.

Recently, cubic splines have been used for global tomography (Antolik *et al.*, 2000; Mégnin and Romanowicz, 2000). Spherical splines (Wang and Dahlen, 1995) are used for the horizontal variations and radial splines for the vertical. This approach has the advantage of being a local parametrization, leading to a sparse solution matrix and potentially avoiding the bias problems of spherical harmonics,

combined with the desirable smoothing properties inherent in splines. For the same number of parameters, the spherical harmonic solution should yield a comparable solution to that of a uniform spline model, but the spline approach does have the advantage of allowing for a nonuniform grid.

A distinct alternative to the philosophy of discrete model parametrization is to treat the velocity structure explicitly as a continuous function of the spatial coordinates. Two examples are the Backus–Gilbert approach of Chou and Booker (1979) and the ‘no-block’ approach of Tarantola and Nercessian (1984). In principle, these approaches allow for essentially arbitrary model solutions with no parametrization bias. In practice, however, models must be constrained in one way or another, as they are again underdetermined. The models must also ultimately be discretized for calculation and representation by computer. Chou and Booker (1979) remove the nonuniqueness by evaluating ‘ideal averaging volumes’, which reflect the spatial variations in ray sampling of the structure. The idea is to view the Earth structure through the window with the maximum spatial resolution allowed by the data. Pavlis and Booker (1980) employed this method (generalized to include hypocenter parameters) for 1-D modeling. The Bayesian strategy of Tarantola and Nercessian (1984) makes use of *a priori* information on the Earth’s velocity structure and its 3-D spatial covariance function to construct a unique solution. Their nonlinear approach ‘anchors’ the solution to the starting model and imposes a smoothness constraint that acts on the scale of the correlation distance. Of course, this requires independent knowledge of the 3-D spatial covariance function, which is typically (but not always) assumed to be homogeneous throughout the medium. See Section 1.10.4.2 for additional discussion.

1.10.3.2 Irregular Cell and Adaptive Mesh Methods

In almost all seismic tomography applications, data coverage is highly uneven due to nonuniform station geometry, uneven distribution of seismic sources, missing data, and ray bending. Some nodes or cells may not be sampled at all, while others may be sampled repeatedly. The standard regular cell/grid spacing approach makes it difficult to adapt the model to the uneven sampling. The mismatch between the data distribution and the cells or grid chosen for the tomographic inversion destabilizes the inversion. Preferably, the inversion cells or grid

should be distributed adaptively to match with the resolving power of the data and to better condition the inversion problem. At the same time, one can hope to image structural details (e.g., subducting slabs or narrow fault zones) that are smaller in scale than could be represented practically with a uniform-cell global or local model. For a recent review of irregular cell and adaptive mesh methods for seismic tomography, the interested reader is referred to the review paper by Sambridge and Rawlinson (2005).

The goal of matching the ray distribution to the mesh or cells naturally leads to the use of an irregular mesh or cells. One strategy is to explicitly treat the inversion mesh node positions as part of the inversion parameters. Michelini (1995) proposed an adaptive-mesh scheme for relatively small-size inverse problems by simultaneous determination of seismic velocities and node positions, with position adjustments damped more heavily. This concept works because node position adjustments by themselves do alter the velocity structure, steepening or reducing gradients for nodes that move closer together or farther apart, respectively, and of course by shifting the points in space where the specific node velocity values are attained. Thus, there is a natural tendency for nodes to cluster where velocity is changing more rapidly, but the method does not lead to a denser node distribution where the sampling is denser.

Alternatively, one could adapt the irregular inversion mesh or cells using *a priori* information and/or some measure of solution stability or resolution, without formally including it in the inversion. Abers and Roecker (1991) proposed an irregular cell representation of the model in which the inversion cells (larger cells) are constructed from basic cells (smaller cells) by using a ‘cross-reference table’ (an index for defining which cells are combined together). The table is mainly constructed by hand, which limits the practical size of the parametrization one can handle. Vesnauer (1996) proposed a different irregular-cell parametrization approach, in which the cells are interactively modified by merging adjacent cells, shifting cell boundaries, and splitting a cell into two or more according to the null space energy. The null space energy measures the local reliability or the physical resolution of the model. Cells are removed where null space energy is too high and cells are added where it is adequately low. The null space energy is determined using the singular value decomposition (SVD) $\mathbf{U}\Lambda\mathbf{V}^T$ (Aster *et al.*, 2005) of the partial derivative matrix for the inversion, and is calculated for each model parameter by summing the

squares of the elements of the row of the orthogonal matrix \mathbf{V} corresponding to the given model parameter for singular values below a chosen threshold. This process is extremely time consuming for large-scale problems, as it is not fully automatic.

In contrast, for LET, Zhang and Thurber (2005) developed an automatic adaptive-mesh tomography method based on tetrahedral cells that matches the inversion mesh to the data distribution. As a result, the number of inversion mesh nodes is greatly reduced compared to a regular inversion grid with comparable spatial resolution, and the tomographic system is more stable and better conditioned. They start the inversion from a slightly perturbed regular inversion grid, constructing the tetrahedral cells (or alternatively the Voronoi diagram) around the nodes using the Quickhull algorithm (Barber *et al.*, 1996). Rays are traced between events and stations based on the current regular velocity grid. The rays are used to find the partial derivatives of the traveltimes with respect to the model slowness parameters on the current inversion mesh. In the process, the values of the ‘derivative weight sum’ (DWS – the sum of the interpolation weights for the partial derivatives corresponding to each model parameter; Thurber and Eberhart-Phillips, 1999) for the inversion mesh nodes are calculated. Threshold DWS values are set for adding or removing nodes. Once the inversion mesh is determined to be optimal, a new set of tetrahedral cells (or new Voronoi diagram) is constructed, and the partial derivatives of the traveltimes with respect to the new set of inversion mesh nodes are calculated. Following each simultaneous inversion, the velocity values on the irregular inversion mesh nodes are updated, rays are traced through the new model, and the inversion mesh is again updated following the same procedure to assure a good match with the ray distribution, which will change as the velocity model changes and hypocenters move. Compared to the above methods, key advantages of this approach are that it is fully automatic and it uses the sampling density to control the mesh density.

A variety of irregular cell and adaptive mesh techniques have also been developed for whole-Earth tomography. One simple approach is the use of two cell sizes, a larger cell for a ‘background’ global 3-D model plus a smaller cell size in a region of interest (Widiyantoro and van der Hilst, 1997). In a similar but more versatile vein, Spakman and Bijwaard (2001) followed the basic idea of Abers and Roecker (1991) discussed above, but adopted a different strategy for irregular cell design by developing a completely

automated and fast algorithm for the construction of the cross-reference table. The design of irregular cells can be constrained by some scalar function, for instance a measure of model sampling such as cell hit count.

Sambridge and Gudmundsson (1998) proposed an irregular cell approach for global tomography based on tetrahedral diagrams. Their initial application was to a regionalized model using *a priori* information on tectonic provinces and subducting slab geometry to construct a fixed-grid model (Gudmundsson and Sambridge, 1998), but they did not explicitly explain how to optimize the cells. Some possibilities are to adjust them based on the model null space energy (Vesnaver, 1996) and/or the velocity gradient. More recently, Sambridge and Faletic (2003) introduced a data-driven tetrahedral cell adaptive scheme based on the maximum spatial gradients in seismic velocity perturbation across each tetrahedron face. This is useful for trying to characterize regions of rapid velocity change, but it does not account for the ability of the data to resolve such changes. Nolet and Montelli (2005) took a similar tetrahedral parametrization approach, but included an estimate of local resolving length in deriving the optimal spacing of mesh nodes.

It is clear that there are many options available for model parametrization. How does one make a choice? One approach that has some advantages is to adopt a two-stage modeling strategy. An initial phase of modeling can be carried out using a more ‘traditional’ regular parametrization. The results of the first phase can then serve as both starting model and point of comparison for a second phase using some type of irregular model parametrization. Any significant increase in anomaly amplitudes should be accompanied by a significant decrease in data misfit (e.g., as measured by an F-test) if the results of the second phase are to be preferred over the first. The irregular parametrization also is a hindrance to carrying out some of the traditional resolution tests, such as spike or checkerboard tests (see Section 1.10.5.2). Such resolution tests from the regular parametrization model can provide valuable information that might not easily be obtained otherwise. At the same time, there is potential concern about the model resolution for models with locally fine parametrization – unless a complete resolution analysis is carried out, the reality of fine-scale features resulting from irregular mesh tomography may be questioned. See Sections 1.10.4 and 1.10.5 for detailed discussion of model resolution issues.

1.10.3.3 Static (Station) Corrections

In many cases, the adopted model parametrization is still incapable of representing some aspect or scale of Earth heterogeneity. The most common situation is treating the shallow structure (e.g., the top few hundred meters at a local scale, or the crust at the global scale) using static (station) corrections. These corrections can be defined *a priori* or determined as part of the inversion. The mathematics of the latter option are treated in Section 1.10.4 below; examples include Bijwaard *et al.* (1998) and Li and Romanowicz (1996) for global and DeShon *et al.* (2006) for local body-wave tomography. Examples of the *a priori* approach include using time and phase delays computed from a global crustal model (Nataf and Ricard, 1996; Mooney *et al.*, 1998) in global or regional surface-wave tomography (Montagner and Tanimoto, 1991; Boschi and Ekström, 2002; Boschi *et al.*, 2004), or using a fixed crustal refraction model in teleseismic tomography (Waldauser *et al.*, 2002). In all of these cases, the goal is to prevent shallow heterogeneity from ‘leaking’ into the deeper structure. The effectiveness of this strategy obviously hinges on the quality of the *a priori* or derived correction values and on how well the highly nonlinear effects of strong lateral variation in crustal structure are dealt with. Recognizing this, Li *et al.* (2006) adopted a strategy for teleseismic tomography that allows for perturbations to the *a priori* crustal model by including a regularization term in the inversion that penalizes deviations from the *a priori* model. Thus, the crustal model will be perturbed where the data require it, although the penalization will generally moderate such changes.

1.10.4 Model Solution

In the early days, the limited computer capabilities (typical mainframes with a megabyte of memory, 100 MB of disk space, and megahertz CPU speeds) put severe limits on the mathematical and computational sophistication that could be implemented for solving tomography problems. Now we have inexpensive desktop systems with 3 orders of magnitude larger memory and storage and faster speed than the mainframes of the mid-1970s, yet tomographers will still complain that their computers are too slow and their memory and storage capabilities are not adequate! As computer power has increased, the amount of data and the complexity of both the

model parametrization and the associated forward problem solver have risen as well.

The preceding sections set the stage for the critical process of determining a model that adequately fits the available data and known constraints. To get to this point, the tomographer needs to make numerous decisions regarding the scale of the problem to be tackled, the types of data to include, the manner in which the 3-D Earth structure will be represented, how the forward modeling will be carried out, etc. Deriving an ‘optimal’ model and evaluating its quality falls under the domain of inverse theory, about which numerous books have been written (Menke, 1989; Parker, 1994; Aster *et al.*, 2005; Tarantola, 2005). A series of papers by Backus and Gilbert (1967, 1968, 1970) can be credited with bringing linear inverse theory to the attention of geophysicists, and Wiggins (1972) wrote a noteworthy paper on resolution of seismic models in particular. While we do not have space to review all the fundamental aspects of inverse theory as they can be applied to seismic tomography, we can provide a ‘road map’ to guide the appropriate application of inverse methods to tomography problems.

1.10.4.1 Linear versus Nonlinear Solutions

One key aspect that separates some tomography problems from others is whether the problem is linear or nonlinear. For example, fitting a straight line to a set of x - y points is a linear problem, as is fitting a parabola. In the former case, the equations are of the form

$$y = (1)m_1 + (x)m_2 \quad [17]$$

whereas in the latter case, they are of the form

$$y = (1)m_1 + (x)m_2 + (x^2)m_3 \quad [18]$$

Both can be expressed directly in the form

$$\mathbf{d} = \mathbf{G}\mathbf{m} \quad [19]$$

where \mathbf{d} is the data vector of length N , \mathbf{m} is a vector with M model parameters, and \mathbf{G} is the matrix of partial derivatives of the data with respect to the model parameters. In contrast, fitting a Gaussian curve to a set of x - y points is a nonlinear problem, because the formula

$$y = m_1 / [(2\pi)^{1/2} m_2] \exp[-(x - m_3)^2 / (2m_2^2)] \quad [20]$$

cannot be reduced to a linear equation in terms of the variables m_i . We point out that solving nonlinear problems in seismic tomography is generally

accomplished via linearizing the problem about a trial solution and improving the model iteratively (see Aster *et al.*, 2005). The few exceptions apply global optimization methods such as Monte Carlo (Shapiro and Ritzwoller, 2002), but that is beyond the scope of this chapter.

To some degree, this distinction is fuzzy for tomography problems because the same problem can be tackled with either a linear or nonlinear approach. Take, for example, the original LET study of Aki and Lee (1976). In a single step, they inverted simultaneously for local earthquake locations and 3-D structure (in terms of constant-slowness ‘blocks’) using a homogeneous background velocity model. They explored the linearity of the problem and model uniqueness by repeating the inversion with two different background models. Given the convergence to the same 3-D structure, they concluded that a linear solution was adequate. Subsequent work on an expanded data set from the same region demonstrated that a nonlinear solution actually was required to converge to a valid solution. In this case, the lateral heterogeneity was so strong that the linear inversion had not converged. Starting with the study of Thurber (1983), nonlinear solutions have become the norm for LET.

Similarly, the original ACH (Aki *et al.*, 1977) teleseismic tomography study used a linear inversion. Work by Ellsworth (1977) determined that a nonlinear solution agreed well with the linear solution for a data set from Hawaii. In this case, however, the amplitude of the anomalies was relatively modest (mainly within $\pm 5\%$), so a linear approximation was in fact adequate. For regions with higher amplitude anomalies, a nonlinear solution could be significantly different. Early efforts at nonlinear teleseismic inversion were made by Thomson and Gubbins (1982), Koch (1985), and Nakanishi and Yamaguchi (1986). More recently, Weiland *et al.* (1995) and VanDecar *et al.* (1995) developed nonlinear algorithms for teleseismic tomography and applied them to Long Valley caldera, CA, and eastern Brazil, respectively. In the case of Long Valley, anomalies on the order of $\pm 20\%$ were recovered, about 3 times larger than a linear inversion by Dawson *et al.* (1990) using the same data set. A similar study for Valles Caldera, New Mexico (Steck *et al.*, 1998), obtained even greater anomalies ($\pm 25\%$) using nonlinear inversion. Despite such impressive results with a nonlinear approach, linear inversions are predominant in teleseismic tomography studies.

On a global scale, linear solutions are also the norm for travelttime inversions, whether they are

block or spline inversions or spherical harmonic expansion inversions. Beginning with Sengupta and Toksoz (1976) and Dziewonski *et al.* (1977) and continuing through Su *et al.* (1994) and van der Hilst *et al.* (1997) (and many others), the inverse problems were mainly set up and solved in a linear manner. Some notable exceptions are the P-wave study of Bijwaard and Spakman (2000) and the S-wave study of Widijantoro *et al.* (2000), which are both fully nonlinear solutions. We also note that Dziewonski (1984) also carried out an iterative inversion but with an approximate inverse that neglected hypocenter–structure coupling (see Section 1.10.4.3).

Using a 3-D ray tracer (Bijwaard and Spakman, 1999) and a 3-D starting model (Bijwaard *et al.*, 1998), Bijwaard and Spakman (2000) carried out inversions for cell slowness perturbations, cluster relocation vectors (average hypocenter adjustment for all events in a given latitude–longitude–depth bin), and station corrections. They found no dramatic changes in the pattern of anomalies compared to Bijwaard *et al.* (1998), but did observe some sharpening of features. Surprisingly, the improvement in data fit compared to Bijwaard *et al.* (1998) was marginal – the variance reduction after two nonlinear iterations was 57.2% compared to 57.1%. This may be because the authors used the original event locations from Engdahl *et al.* (1998) as their starting locations rather than using locations updated via individual event relocations, or using the cluster relocation vectors determined by Bijwaard *et al.* (1998). Since these same locations were used to derive the starting 3-D velocity model, one would expect that the first nonlinear solution perturbations would be biased toward low values. Only two iterations were carried out, so the small additional model perturbations would in turn lead to minor earthquake relocations and hence small model perturbations in the subsequent iteration. It is also possible that the model damping required to limit the negative effects of noise in the data set used (from the Engdahl *et al.* (1998) ‘groomed’ catalog derived from ISC data) may simply be too great to allow a higher-amplitude model to be extracted. This is supported by the analysis of Dorren and Snieder (1997), who showed that noisy data might result in a linear model estimate that is superior to a nonlinear one in traveltime tomography.

Widijantoro *et al.* (2000) carried out a similar nonlinear study for S waves, with a somewhat different outcome. They included event locations as free parameters, but heavily penalized relocations because the S-wave data alone are not actually sufficient to

produce well-constrained locations. Thus, the hypocenters varied very little from their initial locations, again obtained from Engdahl *et al.* (1998). They included both damping and smoothing constraints, and a constraint penalizing deviation from the 1-D ak135 model (Kennett *et al.*, 1995) (see Section 1.10.4.2 for a discussion of constraints). Their solution yielded a significant improvement in data fit, increasing the variance reduction from the 33% reduction obtained by Widijantoro *et al.* (1998) to 40%. Some of this improvement can be attributed to the use of a higher-quality data set (Engdahl *et al.*, 1998). On their other hand, the model results do show significant spatial sharpening and amplitude increase compared to Widijantoro *et al.* (1998). In particular, the deep signature of some slabs appears substantially sharpened.

1.10.4.1.1 Iterative solvers

A common inversion approach is the use of iterative matrix solution methods (Aster *et al.*, 2005), such as Kaczmarz' algorithm and the related algebraic reconstruction technique (ART), simultaneous iterative reconstruction technique (SIRT), and conjugate gradient least squares (CGLS). ART has convergence and stability problems, but SIRT and especially CGLS have found wide application. The LSQR algorithm of Paige and Saunders (1982) is probably the most widely used of these iterative methods. The interested reader is referred to van der Sluis and van der Vorst (1987) for an exhaustive discussion of these techniques, and to Trampert and Lévéque (1990) for an analysis of the SIRT method, which we note is subject to convergence problems. Although this class of solvers is known as iterative methods, we emphasize that they address linear matrix problems. Due to their popularity, we include a brief introduction to the CGLS and the LSQR algorithms here.

CGLS is a general method for solving linear equations of the form $\mathbf{G}\mathbf{m} = \mathbf{d}$ by forming the normal equations

$$\mathbf{G}^T \mathbf{G} \mathbf{m} = \mathbf{G}^T \mathbf{d} \quad [21]$$

and constructing a convenient set of basis vectors \mathbf{p}_k that are mutually conjugate with respect to $\mathbf{G}^T \mathbf{G}$ (Scales, 1987; Aster *et al.*, 2005). Using these basis vectors, the least-squares solution for \mathbf{m} can be calculated with an efficient iterative algorithm requiring only matrix–vector and vector–vector products in a recursive scheme; no actual matrix decomposition or inversion is involved. Efficiency can be further

enhanced by the use of sparse-matrix methods (Davis, 2006), because the procedure does not involve matrix factorizations that can destroy sparseness. Sparse-matrix methods are particularly effective in tackling massive-scale tomography problems.

LSQR (Paige and Saunders, 1982) is probably the most widely used algorithm for the solution of large least-squares problems in seismology. LSQR is a recursive procedure for solving the normal equations that is in theory mathematically equivalent to CGLS (in the absence of machine accuracy problems) but is more stable in practice. The LSQR algorithm involves a technique known as Lanczos bidiagonalization, which transforms an initial symmetric matrix into one with nonzero values only on the diagonal and the elements immediately above it. For a detailed examination of LSQR and a comparison to other methods in a seismological context, the reader is referred to Nolet (1985, 1987) and Spakman and Nolet (1988).

1.10.4.2 Regularized and Constrained Inversion

Even if there are far more observations than model parameters in a given seismic tomography problem, the inverse problem is almost always rank deficient, meaning that \mathbf{G} has one or more zero singular values and that it has an unstable solution in the presence of noise. This is expected because some model parameters may not be directly sampled by the data (i.e., cells without ‘hits’) (see Section 1.10.3.2). The condition number of \mathbf{G} (ratio of largest to smallest singular value) provides one direct measure of noise sensitivity (Aster *et al.*, 2005), but it can only be estimated with some of the popular solution techniques (e.g., LSQR). To solve such stability problems, some form of regularization or constraint is required (Sambridge, 1990; Aster *et al.*, 2005).

1.10.4.2.1 Generalized inverse and damped least-squares solutions

Equations [13] and [14] are linear relationships between the seismic data (i.e., body-wave traveltime anomaly δT , or surface-wave phase shift δC) and perturbations from the wave speed in the reference model. They can be discretized and written in matrix form as before, as

$$\mathbf{G}\mathbf{m} = \mathbf{d} \quad [22]$$

\mathbf{G} relates the model to the data, or more typically the data misfit to the model perturbations, and is often

based on wave theory for a 1-D reference model (e.g., PREM, ak135). In seismic tomography, we typically have many more data than unknowns ($N \gg M$). Given data errors, the equations in [22] are inconsistent and do not have an exact solution. Therefore, we usually minimize a measure of discrepancy (misfit):

$$(\mathbf{G}\mathbf{m} - \mathbf{d})^T (\mathbf{G}\mathbf{m} - \mathbf{d}) \quad [23]$$

Here, we have chosen the Euclidean norm that defines [23] to be a least-squares problem. The least-squares formulation is often used because of its mathematical simplicity. However, it is not necessarily the best for tomographic problems, given the large influence of data outliers. Other norms have been adopted in some cases (e.g., Bube and Langan, 1997), but the least-squares approach is predominant.

In damped least squares (DLS), we minimize

$$(\mathbf{G}\mathbf{m} - \mathbf{d})^T (\mathbf{G}\mathbf{m} - \mathbf{d}) + \varepsilon^2 \mathbf{m}^T \mathbf{m} \quad [24]$$

The damping term $\varepsilon^2 \mathbf{m}^T \mathbf{m}$ serves to penalize models \mathbf{m} with a large norm. In global and teleseismic tomography, this is equivalent to preferring models that are close to the (1-D) reference model. Particularly in regions poorly sampled by seismic waves, the wave speed will retain values close to the reference model.

We obtain the DLS solution by differentiating [24] with respect to the model parameters \mathbf{m} and solving for \mathbf{m} :

$$\mathbf{m}_{\text{DLS}} = [(\mathbf{G}^T \mathbf{G} + \varepsilon^2 \mathbf{I})^{-1} \mathbf{G}^T] \mathbf{d} \quad [25]$$

This solution is of the general form

$$\mathbf{m}_{-i} = \mathbf{G}^{-i} \mathbf{d} \quad [26]$$

where \mathbf{G}^{-i} is a ‘generalized’ inverse. If $\mathbf{U}\Lambda\mathbf{V}^T$ is the singular value decomposition of \mathbf{G} , then we can write the DLS inverse and the corresponding solution as

$$\mathbf{G}_{\text{DLS}}^{-i} = \mathbf{V}\mathbf{\Lambda}^{\dagger}\mathbf{U}^T \quad \text{and} \quad \mathbf{m}_{\text{DLS}} = \mathbf{G}_{\text{DLS}}^{-i} \mathbf{d} \quad [27]$$

where $\mathbf{\Lambda}^{\dagger}$ is the pseudoinverse of $\mathbf{\Lambda}$ (with diagonal elements $1/\lambda_i$ unless $\lambda_i=0$, in which case the diagonal element of $\mathbf{\Lambda}^{\dagger}$ is 0) and the diagonal elements of \mathbf{F} (the ‘filter factors’) satisfy (Aster *et al.*, 2005)

$$f_i^2 = \lambda_i^2 / (\lambda_i^2 + \varepsilon^2) \quad [28]$$

In addition to determining the solution itself, we desire to know the quality of the solution as well. Two measures of quality are the model resolution matrix, which indicates the model ‘blurriness’, and the model covariance matrix, which indicates the

uncertainty of and covariation among model parameters (Aster *et al.*, 2005). The definition of the model resolution matrix \mathbf{R}_m is obtained by substituting $\mathbf{G}\mathbf{m} = \mathbf{d}$ into [26], obtaining

$$\mathbf{m}_{-i} = \mathbf{G}^{-i} \mathbf{G}\mathbf{m} = \mathbf{R}_m \mathbf{m} \quad [29]$$

The model covariance matrix \mathbf{C}_m has the form

$$\mathbf{G}^{-i} \mathbf{C}_d (\mathbf{G}^{-i})^T \quad [30]$$

where \mathbf{C}_d is the data covariance matrix, often assumed to be diagonal (uncorrelated errors). In the case of the DLS solution in [18], \mathbf{R}_m and \mathbf{C}_m are given by

$$\begin{aligned} \mathbf{R}_m &= \mathbf{V}\mathbf{F}\mathbf{V}^T \\ \mathbf{C}_m &= \mathbf{V}\mathbf{F}\mathbf{\Lambda}^{\dagger}\mathbf{U}^T \mathbf{C}_d (\mathbf{\Lambda}^{\dagger})^T \mathbf{F}^T \mathbf{V}^T \end{aligned} \quad [31]$$

We face the inevitable tradeoff that decreasing ε improves the estimated model resolution (i.e., brings \mathbf{R}_m closer to an identity matrix), but at the same time, it increases the model uncertainty (i.e., increases the size of the diagonal elements of \mathbf{C}_m). A tradeoff analysis can be carried out to estimate the optimum damping value (e.g., Eberhart-Phillips, 1986). This is basically equivalent to an L-curve analysis (Aster *et al.*, 2005), whereby the corner of a log(misfit) versus log(model norm) plot can be used to determine a good damping value.

One can also apply weights to the data (\mathbf{W}_d) and model (\mathbf{W}_m), forming the weighted DLS equations to be minimized,

$$(\mathbf{G}\mathbf{m} - \mathbf{d})^T \mathbf{W}_d (\mathbf{G}\mathbf{m} - \mathbf{d}) + \varepsilon^2 \mathbf{m}^T \mathbf{W}_m \mathbf{m} \quad [32]$$

If we then define

$$\mathbf{M}^T \mathbf{M} = \mathbf{W}_m; \quad \mathbf{D}^T \mathbf{D} = \mathbf{W}_d \quad [33]$$

and the transformations

$$\mathbf{m}' = \mathbf{M}\mathbf{m}; \quad \mathbf{d}' = \mathbf{D}\mathbf{d}; \quad \mathbf{G}' = \mathbf{D}\mathbf{G}\mathbf{M}^{-1} \quad [34]$$

it is straightforward to demonstrate that minimizing [32] is identical to minimizing

$$(\mathbf{G}'\mathbf{m}' - \mathbf{d}')^T (\mathbf{G}'\mathbf{m}' - \mathbf{d}') + \varepsilon^2 \mathbf{m}'^T \mathbf{m}' \quad [35]$$

An alternative approach to damping that yields similar results is singular value truncation (Aster *et al.*, 2005). The truncated SVD (TSVD) solution forms an approximate inverse matrix using the p largest singular values of \mathbf{G} :

$$\mathbf{G}^{\text{TSVD}} = \sum_{i=1}^p \mathbf{U}_i \lambda_i \mathbf{V}_i^T \quad [36]$$

If p is the rank of \mathbf{G} , then we have the pseudoinverse solution. See Aster *et al.* (2005) for a detailed discussion and comparison of the least-squares, pseudoinverse, and TSVD solutions.

Another ‘trick’ for improving stability of the inversion is preconditioning (Gill *et al.*, 1981). In general, the ratio of the largest to smallest singular value (the condition number) provides a measure of the stability of the inverse model, particularly its sensitivity to noise in the data (Aster *et al.*, 2005). Furthermore, the convergence rate for the CGLS method can be improved if the system can be transformed (scaled) to one with many unit-value singular values. Thus, scaling the system of equations to reduce the condition number and/or increase the number of unit-value singular values is a desirable step to implement in many cases.

Convergence of CGLS and similar methods leads to a quandary when regularization is desired. As Aster *et al.* (2005) show, the convergence rate is typically rapid in the initial iterations for unregularized CGLS, after which noise in the solution tends to build up rapidly. This is a combination of accumulated effects of round-off errors and the fact that the iterative solution is converging toward an unregularized solution. If regularization is introduced, the algorithm will converge more slowly, and will generally fit the data better than the unregularized case for a given model norm, but the cost is an order of magnitude increase in the number of required iterations. Since seismic tomography problems virtually always require some form of regularization, the extra computational burden is generally unavoidable.

As noted above, the original Aki *et al.* (1977) (ACH) teleseismic and Aki and Lee (1976) LET methods both involved single-step linearized inversions for the model parameters. This approach allowed the use of linear inverse theory techniques for model estimation and also for model resolution and uncertainty analysis. Aki *et al.* (1977) compared models obtained using both a generalized inverse (TSVD) and a damped least-squares (‘stochastic’) inverse. For the teleseismic case, the system of equations is always linearly dependent due to the tradeoff between average layer velocity and event origin times, so a simple least-squares solution was impossible. The generalized inverse approach uses the nonzero singular values of the \mathbf{G} matrix to compute a least-squares solution, whereas the stochastic inverse approach computes a damped least-squares solution using a damping value (ε^2) equal to the *a priori* ratio of the data variance to the solution variance (Aki *et al.*, 1977). Aki and Lee (1976) used just the stochastic

inverse approach, because their matrix was not strictly singular but contained very small singular values that would amplify the effect of data errors on the model.

1.10.4.2.2 Occam’s inversion and Bayesian methods

In addition to the techniques discussed above, there are two other philosophically different approaches for treating underdetermined tomographic problems. One can be labeled an Occam’s razor approach, and the other Bayesian (see Scales and Snieder (1997) for an interesting discussion of the latter).

The Occam’s approach, commonly attributed to Constable *et al.* (1987), involves the inclusion of constraint equations in the inversion enforcing minimized first-or second-order spatial differences of the model perturbations, weighted relative to minimizing data misfit. We note that this is an example of what is properly called Tikhonov regularization (see Aster *et al.*, 2005). The first-order constraint attempts to minimize model perturbation gradients, leading to a ‘flat’ model perturbation. The second-order constraint attempts to minimize model perturbation curvature, leading to a ‘smooth’ model perturbation. In general, this regularization can be achieved by augmenting $\mathbf{G}\mathbf{m} = \mathbf{d}$ with a set of equations of the form $w\mathbf{L}\mathbf{m} = 0$, and minimizing the system

$$\begin{bmatrix} \mathbf{G} \\ w\mathbf{L} \end{bmatrix} \mathbf{m} = \begin{bmatrix} \mathbf{d} \\ 0 \end{bmatrix} \quad [37]$$

For a 1-D tomography problem, \mathbf{L} for first-order regularization would be a banded matrix with rows of the form $[0 \ 0 \ 0 \ \cdots -1 \ +1 \ \cdots 0 \ 0 \ 0]$, whereas for second-order regularization the rows would be of the form $[0 \ 0 \ 0 \ \cdots -1 \ 2 \ -1 \ \cdots 0 \ 0 \ 0]$.

Examples of this approach include Lees and Crosson (1990), Benz *et al.* (1996), Hole *et al.* (2000), and Zhang and Thurber (2003). A variant by Symons and Crosson (1997) penalizes the roughness of the sum of the current model plus the perturbation, so that the final model remains smooth. Once again, an L-curve analysis (Aster *et al.*, 2005) can be valuable for determining the appropriate weighting of the regularization equations (the value of w). The use of smoothing constraints tends to result in fewer artifacts in poorly sampled regions compared to simple damping. At the same time, however, one desires to be able to ‘tease out’ heterogeneity and sharp spatial changes in structure as effectively as possible with seismic tomography, so the use of smoothing comes at a cost.

An example of a Bayesian approach, mentioned in Section 1.10.3.1, involves the specification of a spatial covariance function that reflects the tendency for nearby points in the Earth to have similar wave speeds. Following Tarantola and Nercessian (1984), an *a priori* model covariance function \mathbf{C}_{m_0} (e.g., of Gaussian form) and a data covariance function \mathbf{C}_{d_0} are defined, and the solution is obtained by minimizing

$$(\mathbf{G}\mathbf{m} - \mathbf{d})^T (\mathbf{C}_{d_0})^{-1} (\mathbf{G}\mathbf{m} - \mathbf{d}) + \mathbf{m}^T (\mathbf{C}_{m_0})^{-1} \mathbf{m} \quad [38]$$

(note the close correspondence in form to [32]). Tarantola and Valette (1982) show that a nonlinear algorithm for minimizing [38] is

$$\begin{aligned} \mathbf{m} = & \mathbf{m}_0 + \mathbf{C}_{m_0} \mathbf{G}^T (\mathbf{C}_{d_0} + \mathbf{G} (\mathbf{C}_{m_0})^{-1} \mathbf{G}^T)^{-1} \\ & \times \{ \mathbf{d}_0 - \mathbf{g}(\mathbf{m}) + \mathbf{G}(\mathbf{m} - \mathbf{m}_0) \} \end{aligned} \quad [39]$$

where \mathbf{g} is the (nonlinear) forward equation and \mathbf{m}_0 is the *a priori* model. The way Tarantola and Nercessian (1984) formulate their problem, [39] is constructed using numerical integration along the current ray paths, rather than by apportioning ray paths into cells for the computation of derivatives. In practice, we view this distinction as somewhat minor, because at some level, discretization of the model will be required once the current model is no longer homogeneous and wave propagation in 3-D must be considered. For the interested reader, a broad presentation of Bayesian methods for geophysics can be found in Sambridge and Mosegaard (2002).

1.10.4.3 Hypocenter–Structure Coupling

A solution strategy adopted by some researchers involves first solving for 3-D structure with earthquake locations fixed, then solving for earthquake locations with the structure fixed. Theoretical and numerical studies (e.g., Thurber, 1992; Roecker *et al.*, 2006) have shown that this approach leads to bias in both locations and structure. We summarize the analysis from Roecker *et al.* (2006) to clarify the nature of this important problem. The hypocenter–velocity structure problem can be stated as

$$\mathbf{H}\mathbf{d}\mathbf{h} + \mathbf{S}\mathbf{d}\mathbf{s} = \mathbf{r} \quad [40]$$

where \mathbf{H} and \mathbf{S} are the derivative matrices and $\mathbf{d}\mathbf{h}$ and $\mathbf{d}\mathbf{s}$ are perturbation vectors for hypocenters and slowness structure, respectively. The singular value decomposition of \mathbf{H} is

$$\mathbf{H} = \mathbf{U}\Lambda\mathbf{V}^T = [\mathbf{U}_p | \mathbf{U}_0]\Lambda\mathbf{V}^T \quad [41]$$

where \mathbf{U}_p is the range of \mathbf{H} and \mathbf{U}_0 is the null space of \mathbf{H} (Aster *et al.*, 2005). Multiplying the original equation by \mathbf{U}^T and separating the p and 0 components gives

$$\begin{bmatrix} \mathbf{U}_p^T \mathbf{H} \\ \mathbf{U}_0^T \mathbf{H} \end{bmatrix} d\mathbf{h} + \begin{bmatrix} \mathbf{U}_p^T \mathbf{S} \\ \mathbf{U}_0^T \mathbf{S} \end{bmatrix} d\mathbf{s} = \begin{bmatrix} \mathbf{r}_p \\ \mathbf{r}_0 \end{bmatrix} \quad [42]$$

Noting that $\mathbf{U}_0^T \mathbf{H} = 0$ by definition and, if we initially relocate the earthquakes, then $\mathbf{r}_p = 0$ also, we have

$$\begin{bmatrix} \mathbf{U}_p^T \mathbf{H} \\ 0 \end{bmatrix} d\mathbf{h} + \begin{bmatrix} \mathbf{U}_p^T \mathbf{S} \\ \mathbf{U}_0^T \mathbf{S} \end{bmatrix} d\mathbf{s} = \begin{bmatrix} 0 \\ \mathbf{r}_0 \end{bmatrix} \quad [43]$$

This separates into two sets of equations:

$$\mathbf{U}_p^T \mathbf{H} d\mathbf{h} + \mathbf{U}_p^T \mathbf{S} d\mathbf{s} = 0 \quad [44]$$

and

$$\mathbf{U}_0^T \mathbf{S} d\mathbf{s} = \mathbf{r}_0 \quad [45]$$

We can determine $d\mathbf{s}$ simply by solving the second set of equations, which is the decoupled problem (the separation of parameters method of Pavlis and Booker (1980)). If instead we decide to solve the entire system of equations involving $d\mathbf{s}$ but incorrectly ignore the contribution of $d\mathbf{h}$ in eqn [43], we actually solve

$$\begin{bmatrix} \mathbf{U}_p^T \mathbf{S} \\ \mathbf{U}_0^T \mathbf{S} \end{bmatrix} d\mathbf{s} = \begin{bmatrix} 0 \\ \mathbf{r}_0 \end{bmatrix} \quad [46]$$

This is equivalent to solving eqn [45] but with the added constraint that a weighted sum of $d\mathbf{s}$ will be zero. This is the bias that is caused by not carrying out the full simultaneous inversion.

The above analysis explains some observations regarding the behavior of a joint hypocenter–velocity structure inversion versus a velocity-only inversion. In doing a velocity-only inversion, the added constraints [46] force $d\mathbf{s}$ to be small, which in turn means that subsequent estimations of $d\mathbf{h}$ will be small as well (small velocity perturbations will result in small hypocenter perturbations). The $d\mathbf{s}$ term is kept small at a cost of misfit to the data, because in trying to keep $d\mathbf{s}$ small, the fit to \mathbf{r}_0 will be degraded. This is the tendency that is documented in Thurber (1992) and which can be observed in velocity-only inversion tests with real data – both $d\mathbf{h}$ and $d\mathbf{s}$ are much too small in a velocity-only inversion, even when alternated with hypocenter relocation, and the data fit is poor. To illustrate this, consider a simplified 1-D Earth model (Figure 5), following Thurber (1992), with four seismic stations straddling

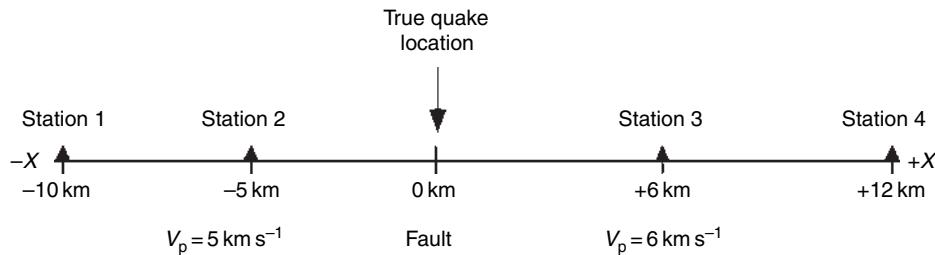


Figure 5 Hypothetical 1-D Earth with a velocity discontinuity across a fault with a velocity discontinuity at $X = 0.0$ km, four seismic stations, and an earthquake occurring on the fault. From Thurber CH (1992) Hypocenter–velocity structure coupling in local earthquake tomography. Special Issue: Lateral Heterogeneity and Earthquake Location. *Physics of the Earth and Planetary Interiors* 75: 55–62.

a fault across which velocity changes discontinuously from 5.0 to 6.0 km s^{-1} . If a hypothetical earthquake occurs on the fault and a homogeneous velocity model of 5.5 km s^{-1} is used to locate the event, its calculated location would be 0.75 km to the right of the fault. If we then invert for a laterally heterogeneous velocity model using least squares, placing a discontinuity at the fault (using *a priori* information), but ignore the hypocenter–velocity structure coupling (i.e., keep the event location fixed), we obtain a model with a velocity of 5.44 km s^{-1} to the left of the fault and 5.56 km s^{-1} to the right. In contrast, if we perform a simultaneous inversion for structure and location, the earthquake is relocated to within 0.06 km of the fault, and we obtain a model with a velocity of 5.04 km s^{-1} to the left of the fault and 6.06 km s^{-1} to the right. Thus the velocity-only inversion underestimates the velocity contrast by nearly an order of magnitude, while the simultaneous inversion recovers the true structure to within 1% and determines the event location within 100 m. The conclusion is that for LET, solving the full system of equations is critical in order to obtain an unbiased solution.

Although many tomography algorithms utilize the fast sparse-matrix solvers such as LSQR, it is worth noting the historical use of subspace methods (e.g., Kennett *et al.*, 1988) for efficient inversion procedures, and in particular for dealing with matrix size issues when many earthquakes are included in an inversion. For LET, three groups independently and nearly simultaneously published comparable methods for separating hypocenter parameters from velocity model parameters, allowing the efficient solution of smaller matrix problems in place of one giant problem (Pavlis and Booker, 1980; Spencer and Gubbins, 1980; Rodi *et al.*, 1981). As a motivation for this approach, consider an LET problem with 10 000 earthquakes observed on average at 50 stations, and with 20 000

model parameters. The full system matrix would be of size $(50 \times 10\,000)$ by $(4 \times 10\,000 + 20\,000)$, or 500 000 by 60 000. If we take advantage of the annulling procedure of Pavlis and Booker (1980), for example, we can decompose the coupled hypocenter–structure equations for each earthquake i ,

$$\mathbf{H}_i d\mathbf{h}_i + \mathbf{S}_i d\mathbf{s}_i = \mathbf{r}_i \quad [47]$$

where as before \mathbf{H}_i and \mathbf{S}_i are the matrices of derivatives of arrival times with respect to hypocenter and model parameters, respectively (now for a single earthquake), and $d\mathbf{h}_i$ and $d\mathbf{s}_i$ are the corresponding parameter perturbations. Using the orthogonal matrix \mathbf{U}_{0i} that satisfies $\mathbf{U}_{0i} \mathbf{H}_i = 0$ allows us to assemble the decoupled equations

$$\mathbf{U}_{0i} \mathbf{H}_i d\mathbf{h}_i + \mathbf{U}_{0i} \mathbf{S}_i d\mathbf{s}_i = \mathbf{U}_{0i} \mathbf{r}_i \text{ or } \mathbf{S}'_i d\mathbf{s}_i = \mathbf{r}'_i \quad [48]$$

The matrix in the original partial system in [47] would be of size 40 by 20 004, whereas the matrix in the decoupled system in [48] would be of size 36 by 20 000. If we treat all the events this way, the result is a system of equations of size 460 000 by 20 000, a substantial size reduction achieved at relatively low computational cost. Even greater reduction of the problem size can be achieved by incrementally constructing the normal equations, $\mathbf{S}'^T \mathbf{S}' = \mathbf{S}'^T \mathbf{r}'$ (Spencer and Gubbins, 1980), resulting in a system of equations that is only 20 000 by 20 000. Unfortunately, the cost of this last step is a squaring of the condition number of the system matrix, and a loss of matrix sparseness, but the price may be worth paying in some cases.

1.10.4.4 Static (Station) Corrections Revisited

Static (station) corrections, a constant time delay or advance applied for a given station, are commonly

included in some types of seismic tomography problems, as discussed above. It is worth noting that static corrections can be analyzed in a manner equivalent to that used for the hypocenter–structure coupling issue (Section 1.10.4.3). Just as in the hypocenter–structure coupling situation, including static corrections can result in a suppression of model heterogeneity, particularly at shallow depths near the stations. The corrections can absorb some of the heterogeneity that otherwise would have been projected into the 3-D model. One compromise approach (Michael, 1988) is to solve the tomography problem without static corrections, and then solve the system with static corrections included but the 3-D model held fixed. Michael (1988) has shown that this can be an effective technique for improving earthquake locations without biasing the 3-D tomographic model.

1.10.4.5 Double-Difference Tomography

The use of differential times for determining relative locations of earthquakes (or explosions) has been a fruitful field of work for many decades (e.g., Douglas, 1967). A number of studies over the last decade have shown spectacular improvement in earthquake or explosion location precision when precise differential times from waveform cross correlation (WCC) are used in combination with joint location techniques. Some examples of applications to earthquakes include Hawaii (Got *et al.*, 1994; Rubin *et al.*, 1998), California (Waldhauser *et al.*, 1999), New Zealand (Du *et al.*, 2004), the Soultz geothermal field, France (Rowe *et al.*, 2002), and Mount Pinatubo volcano (Battaglia *et al.*, 2004), and to explosions at the Balapan test site (Phillips *et al.*, 2001; Thurber *et al.*, 2001). These and other studies have demonstrated the substantial improvement in the delineation of seismogenic features or in the accuracy of relative locations of ground-truth events that is possible using multiple-event location methods with high-precision arrival-time data. These successes inspired efforts to incorporate differential times in seismic tomography. The first published algorithms for double-difference (DD) tomography are due to Zhang and co-workers (Zhang and Thurber, 2003, 2005; Zhang *et al.*, 2004). Their methods are discussed in some detail because theirs is the first and so far most widely used DD tomography approach.

To set the stage for understanding DD tomography, we first briefly review the DD location problem (see Wolfe (2002) for a thorough analysis). Following

the notation of Section 1.10.4.3, for single event location, we iteratively solve an equation of the form

$$\mathbf{r} = \mathbf{Hd}\mathbf{h} \quad [49]$$

where $\mathbf{d}\mathbf{h}$ includes perturbations to location and origin time, \mathbf{H} is the partial derivative matrix, and \mathbf{r} contains the traveltimes residuals. If we now consider a set of equations [49] for a pair of events, and subtract the equations for the two events observed at one station, we have a set of equations of the form

$$r_k^i - r_k^j = \sum_{l=1}^3 \frac{\partial T_k^i}{\partial x_l^i} \Delta x_l^i + \Delta \tau^i - \sum_{l=1}^3 \frac{\partial T_k^j}{\partial x_l^j} \Delta x_l^j + \Delta \tau^j \quad [50]$$

where r_k^i and r_k^j are the residuals from events i and j at station k , T 's are traveltimes, and x and Δx are hypocenter coordinates and their perturbations. Note that the residual difference can be rewritten as $(t_{\text{obs}}^i - t_{\text{obs}}^j) - (t_{\text{cal}}^i - t_{\text{cal}}^j)$, the DD, where t_{obs} and t_{cal} indicate the observed and calculated arrival times, respectively. For DD location, one solves for perturbations to the relative locations (and an origin time shift) to minimize the residual differences. A key aspect is that observed differential arrival times $(t_{\text{obs}}^i - t_{\text{obs}}^j)$ can be determined to high accuracy using waveform correlation methods (Waldhauser and Ellsworth, 2000).

Menke and Schaff (2004) demonstrated that differential time data are capable of resolving absolute locations. Ideally, one would like to take that one step farther and utilize all the information from differential times and absolute arrival times to determine both locations and structure. To that end, Zhang and Thurber (2003) generalized the DD location method to determine jointly the 3-D velocity structure and the absolute event locations. The equations for DD tomography are a combination of the standard tomography equations and a generalization of eqn [50]:

$$\begin{aligned} r_k^i - r_k^j &= \sum_{l=1}^3 \frac{\partial T_k^i}{\partial x_l^i} \Delta x_l^i + \Delta \tau^i + \int_i^k \delta u ds - \sum_{l=1}^3 \frac{\partial T_k^j}{\partial x_l^j} \Delta x_l^j \\ &\quad - \Delta \tau^j - \int_j^k \delta u ds \\ r_k^i &= \sum_{l=1}^3 \frac{\partial T_k^i}{\partial x_l^i} \Delta x_l^i + \Delta \tau^i + \int_i^k \delta u ds \end{aligned} \quad [51]$$

where δu is perturbation to slowness and ds is an element of path length, as in [2]. Three types of data, absolute arrival times, catalog differential arrival times, and WCC data, are used in the inversion. To combine these three types of data into one system, a hierarchical weighting scheme is applied during the inversion, similar to hypo-DD (Waldhauser, 2001).

Zhang and Thurber (2003) solve the complete system of linear equations [51], along with smoothing constraint equations, by means of the LSQR algorithm (Paige and Saunders, 1982) (see Section 1.10.4.1). Each equation is weighted according to the *a priori* data uncertainty, data type, distance between the event pair, and misfit at each iteration. The relative weighting for the different data types and the distance weighting are determined *a priori*, whereas the residual weighting is determined *a posteriori*, with large residuals rejected or downweighted by a biweight function (Waldhauser and Ellsworth, 2000). For LSQR, the number of iterations required to reach a desired accuracy depends strongly on the scaling of the problem (Paige and Saunders, 1982). For this reason, before the system is fed into the LSQR solver, scaling is applied (Section 1.10.4.3) so that each column has an L₂ norm equal to 1.

The advantages of DD tomography are evident when compared to either the original DD location algorithm hypo-DD (Waldhauser, 2001) or conventional tomography. In hypo-DD, an *a priori* 1-D velocity model is used, and the centroids of events defined as belonging to clusters are fixed at their initial (catalog) locations. Thus, the original hypo-DD algorithm cannot account for 3-D velocity heterogeneity, and its results are dependent on the initial locations. In contrast, DD tomography directly embodies 3-D heterogeneity, and event locations are not constrained as they are in hypo-DD. In conventional tomography, 3-D heterogeneity is of course considered, but there is no mechanism for incorporating the higher-accuracy differential times, meaning the event locations remain scattered as in, for example, a normal seismicity catalog. The ability of DD tomography to include the differential times leads to a sharpening of the seismicity distribution, and in turn, an improved velocity model as well. In **Figures 6(a) and 6(b)**, we show an example of the sharpening of both the seismicity and the velocity structure achieved by DD tomography compared to conventional tomography for the San Andreas Fault near Parkfield, CA (Thurber *et al.*, 2004; Zhang and Thurber, 2005). At a larger scale, Zhang *et al.* (2004) show the dramatic variations in structure deep within a subducting slab that can be imaged with the DD tomography technique (**Figure 6(c)**).

1.10.5 Solution Quality

While the previous sections have laid out the procedures involved in tomographic modeling, the ultimate question – how well does the tomographic

model reflect the true Earth – is the most important and perhaps the most difficult one to answer. Without exception, tomography provides distorted images of the real Earth. The image resolution is finite due to, for example, choices in parametrization (e.g., block size) and regularization (e.g., smoothing) and it is spatially variable due to the heterogeneous data coverage. Yet, an understanding of seismic data, formal resolution analyses, and hypothesis tests are helpful to guide tomographic model interpretation.

While it is not so straightforward to generalize model resolution issues, we focus on several recently derived global-scale tomographic models to highlight how differences in data sets underlie gross characteristics of global models. We discuss in detail formal resolution analyses and illustrate them using model S20RTS and demonstrate how hypothesis tests can be helpful in model interpretation.

1.10.5.1 Data Coverage

Data coverage (i.e., the sampling of the mantle by seismic waves) has a first-order impact on the gross characteristics of the model. Surface-wave phase delays and teleseismic body-wave traveltimes (see Section 1.10.2) are the most commonly used data types in global tomography. We illustrate how these data characterize six recently derived global P and S models that are based on a variety of these data types. While the spectra of seismological models may be the preferred observables to constrain the predominant scale length of convection in the mantle (e.g., Su and Dziewonski, 1991, 1992; Mégnin *et al.*, 1997) (**Figure 7**), we limit our comparison to maps of spatial distribution of velocity heterogeneity.

Figure 8 compares maps of velocity heterogeneity for shear velocity models SAW24B16 (Mégnin and Romanowicz, 2000), SB4L18 (Masters *et al.*, 2000), S20RTS (Ritsema *et al.*, 1999), and TXBW (Grand, 2002) and P-velocity models P-MIT (van der Hilst *et al.*, 1997) and FF-PRI (Montelli *et al.*, 2004b). The S models SB4L18 and S20RTS are derived using a combination of traveltimes and surface-wave data, while TXBW is derived using multiple S traveltimes. The S model SAW24B16 is derived using surface-wave and body-wave waveforms. Models P-MIT and FF-PRI are entirely based on teleseismic P-wave traveltimes.

Surface waves propagate horizontally through the uppermost mantle. These data are ideal for constraining the crust and uppermost mantle structure, especially in oceanic regions where few seismic stations are present. Fundamental-mode surface waves

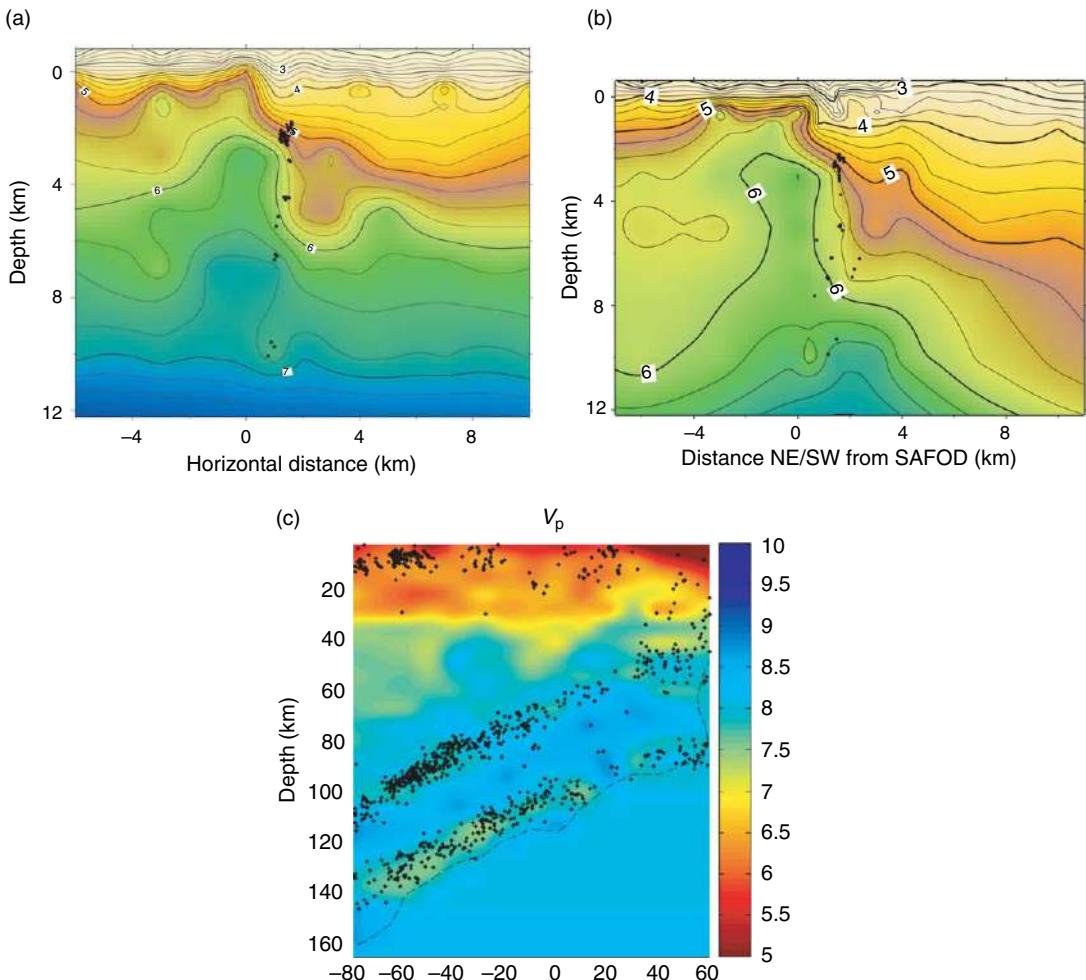


Figure 6 Comparison of (a) conventional tomography and (b) DD tomography models for a section across the San Andreas Fault at the San Andreas Fault Observatory at Depth (SAFOD) drill site. Note the sharpening of features in both seismicity and velocity structure. (c) Regional-scale DD tomography result for subducting slab beneath northern Honshu, Japan, where a double Benioff zone is present. (a) Reproduced from Thurber C, Roecker S, Zhang H, Baher S and Ellsworth W (2004) Fine-scale structure of the San Andreas fault and location of the SAFOD target earthquakes. *Geophysical Research Letters* 31: L12S02 (doi:10.1029/2003GL019398), with permission from American Geophysical Union. (b) Reproduced from Zhang H and Thurber C (2005) Adaptive mesh seismic tomography based on tetrahedral and Voronoi diagrams: Application to Parkfield, California. *Journal of Geophysical Research* 110: B04303 (doi:10.1029/2004JB003186), with permission from American Geophysical Union. (c) Reproduced from Zhang H, Thurber C, Shelly D, Ide S, Beroza G, and Hasegawa A (2004) High-resolution subducting slab structure beneath Northern Honshu, Japan, revealed by double-difference tomography. *Geology*: 32 361–364.

(the largest signals in seismograms) can be analyzed over a relatively broad seismic frequency range (typically 5–25 mHz) and provide excellent worldwide constraints of the upper 100–200 km of the mantle. Long-period ($f < 5$ mHz) fundamental-mode surface waves, and overtone surface waves (or, equivalently, surface-reflected SS and SSS waves), constrain the upper-mantle transition zone (300–1000 km depth). Overtone surface-wave coverage is poorer than fundamental-mode coverage (Figure 9), because only relatively large ($M_w > 7$) or deep ($H > 50$ –100 km)

earthquakes excite them well. Consequently, model resolution in the transition zone is worse than in the uppermost mantle, especially in the Southern Hemisphere (where few stations are located).

Traveltimes of teleseismic body waves (direct, surface reflections, and core reflections) are key in constraining velocity heterogeneity in the lower mantle (>1000 km depth). With the exception of subduction zones (where earthquakes occur over a wide depth range) and in regions with dense networks, teleseismic traveltimes constrain the upper

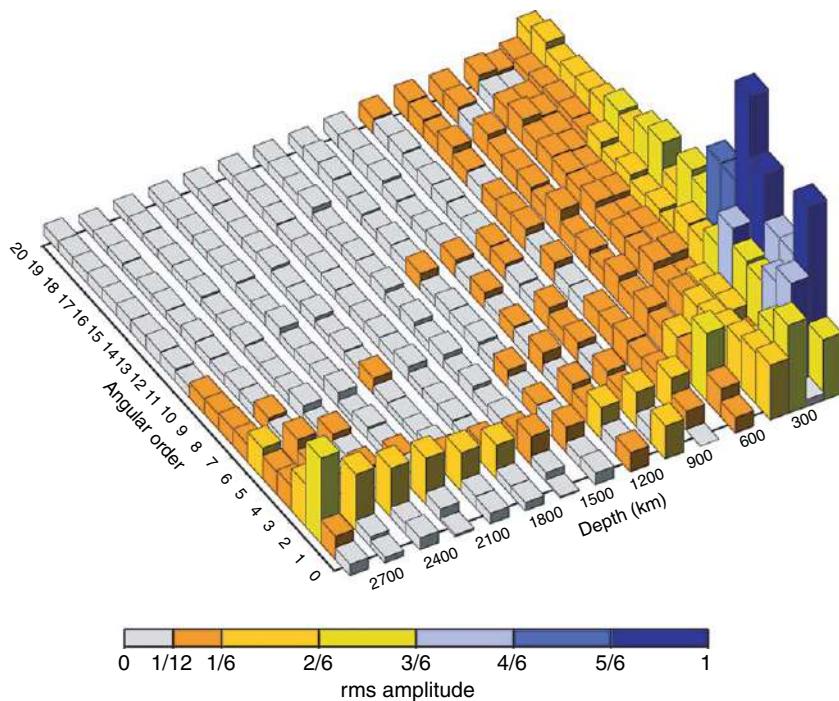


Figure 7 Spectral amplitude of shear velocity heterogeneity in model S20RTS as a function of depth and angular order l . Note that the amplitude spectrum is largest at the boundary layers of the mantle (surface, core–mantle boundary, the 660 km phase transition) and that it is predominantly ‘red’, meaning that the spectral amplitudes decrease significantly beyond order $l=8$ (i.e., shear-velocity variations with wavelengths longer than about ~ 5000 km).

mantle poorly (**Figure 10**) because body waves propagate steeply through it.

An understanding of surface-wave and body-wave coverage helps us to gain insight in understanding the first-order differences between the S- and P-wave models of **Figure 8**. Surface-wave data are only incorporated in S models, and they are the key data to constrain the lithospheric structure. The S-velocity models feature relatively strong ($\sim 15\%$) velocity variations in the upper 200 km that correlate with surface geology (e.g., high velocities in the oldest regions of continents), and plate tectonics (e.g., mid-ocean ridges, oceanic plate ages). The P models lack these features as traveltimes provide extremely poor upper-mantle resolving power. The broad high-velocity structure in the western Pacific transition zone is likely a signature of slab flattening above the 660-km phase transition. The P models feature upper-mantle slab structures in much more detail. However, the incomplete transition zone sampling (i.e., ocean basins and Africa), especially in model P-MIT that is based on direct P wave only, makes it still difficult to place transition zone heterogeneity in a global context. Moreover, the high correlation between the maps for depths of 125 km and 600 km in

the P-wave models (note, e.g., the signature of the African cratons throughout the upper mantle) is a well-understood artifact due to the relatively poor vertical resolution in the upper mantle.

The lowermost mantle (D'') is ideally constrained by shear-wave core reflections (i.e., ScS) and core diffractions (S_{diff}). P-wave counterparts of these waves (e.g., P_{cP} , P_{diff}) have small amplitudes. ISC catalogs, in particular, lack reliable P_{diff} traveltimes as these signals are especially difficult to detect in short-period seismograms. Therefore, velocity heterogeneity in D'' is probably best resolved in S models. S models include broad low-velocity anomalies beneath Africa and the Pacific that are less conspicuous in P models. Some of the differences in S- and P-velocity heterogeneity may be real (e.g., Masters *et al.*, 2000). We note however, that models which include long-period P_{diff} traveltimes data, such as model FF-PRI and an updated version of P-MIT (Káráson and van der Hilst, 2001), show the African and Pacific anomalies with more clarity, underscoring that data coverage is playing a key role in the resolution of velocity heterogeneity.

Heterogeneity in the mid-mantle (1000–2500 km depth) is primarily constrained by traveltimes or body waveforms. Since all models in **Figure 8**

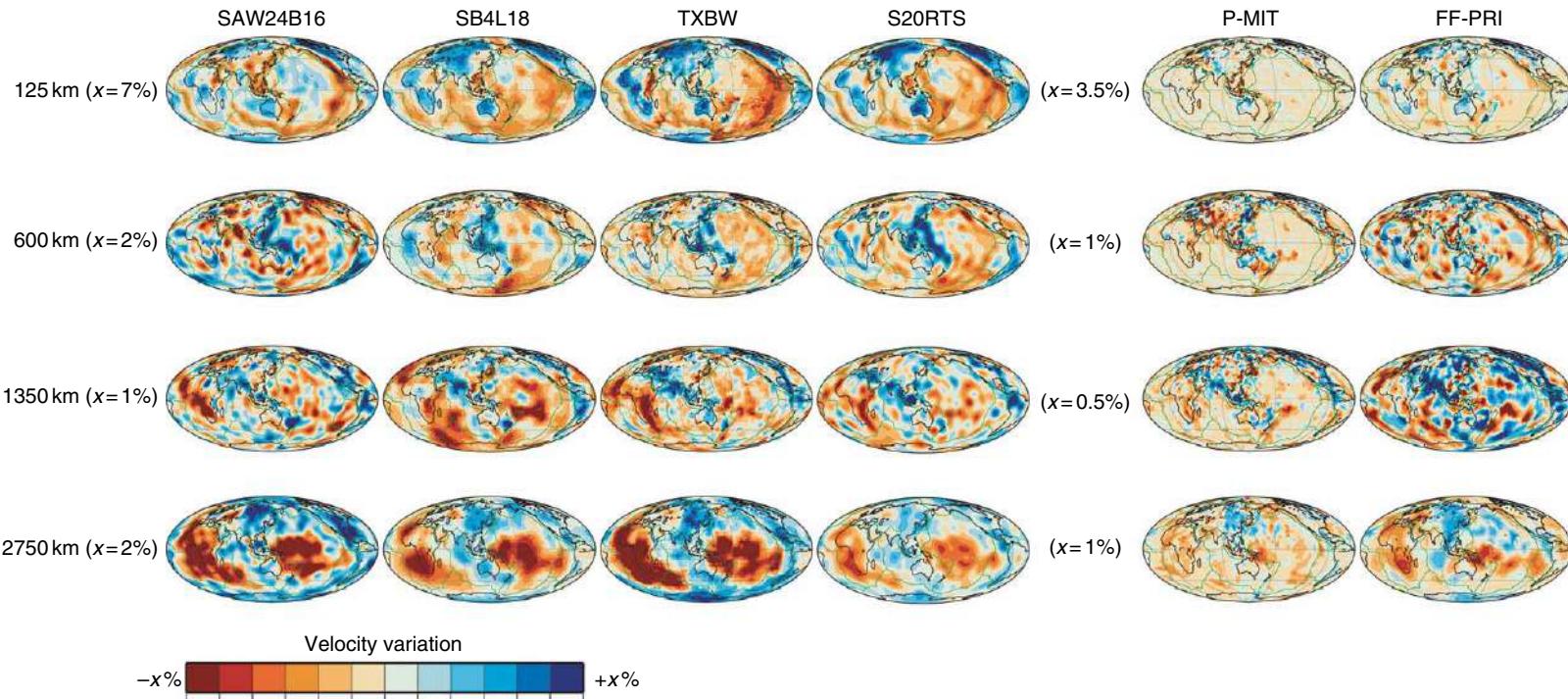


Figure 8 Maps through S-velocity models SAW24B16, SB4L18, TXBW, and S20RTS and P-velocity models P-MIT and FF-PRI at depths of 125, 600, 1350, and 2750 km. A variable scale is used. The velocity varies between $-x\%$ and $+x\%$, where x is given to the left.

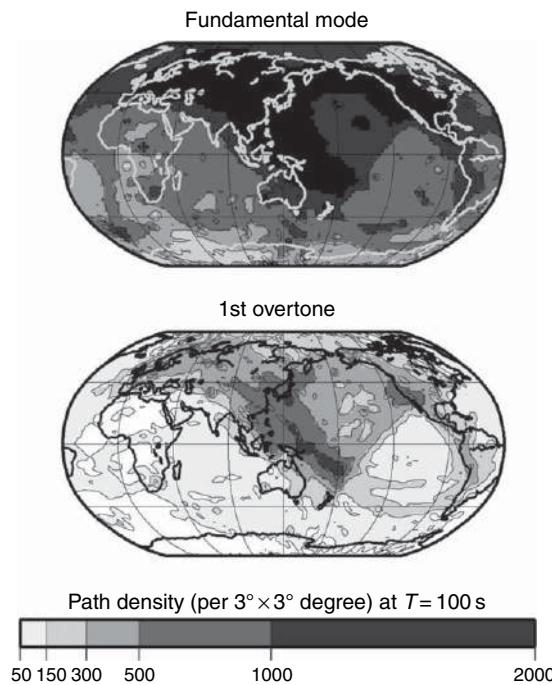


Figure 9 Maps of fundamental-mode and first overtone Rayleigh wave coverage from the data set of Ritsema *et al.* (2004). Although this figure is specific to the development of model S20RTS, the relatively poor sampling of the transition zone by overtone surface waves, especially in the Southern Hemisphere, is typical for all global tomographic studies independent of how the data are processed. Therefore, tomographic model resolution in the transition zone is relatively poor in all global surface-wave models.

include traveltimes, it must be no surprise that the models share a number of features. For example, all models feature linear high-velocity anomalies beneath the Americas and southern Asia that are, presumably, the signature of Mesozoic subduction (Grand *et al.*, 1997; Van der Voo *et al.*, 1999). Arguably, the P-wave models present superior resolution of mid-mantle heterogeneity since they employ the densest parametrizations and the largest data sets (e.g., millions of ISC traveltimes picks).

In conclusion, data coverage determines the gross characteristics of tomographic models. A significant portion of model differences can be understood by considering the data sets being used. Of course, the tomographic procedures leave a mark on the model as well. The differences among the S-wave models of Figure 8 stem from the variable data types (e.g., Love wave and body-wave waveforms in SAW24B16, Rayleigh wave dispersion data in S20RTS, phase velocity maps in SB4L18, multiple S-wave traveltimes in TXBW), model parametrization (e.g., blocks in SB4L18

and TXBW, global functions in SAW24B16 and S20RTS), forward modeling theories (e.g., ray theory in S20RTS, SB4L18, and TXBW, but finite frequency effects are incorporated in SAW24B16 and FF-PRI), and inversion procedures. The included data types also influence the effect that anisotropy has on the models (e.g., SH/Love in SAW24B16 vs SV/Rayleigh in S20RTS). These effects cannot be readily understood in a qualitative manner, but require formal resolution analysis or hypothesis testing.

1.10.5.2 Model Resolution Analysis

Quantitatively, model resolution is assessed by calculation of the full model resolution and model covariance matrices. In essence, the task is to understand the properties of the generalized inverse matrix \mathbf{G}^{-i} (eqn [19]). As discussed in Section 1.10.4.2.1, we can decompose \mathbf{G} into a product of three matrices, $\mathbf{U}\Lambda\mathbf{V}^T$, with \mathbf{U} and \mathbf{V} being orthogonal matrices (i.e., $\mathbf{U}^T\mathbf{U} = \mathbf{U}\mathbf{U}^T = \mathbf{I}$ and $\mathbf{V}^T\mathbf{V} = \mathbf{V}\mathbf{V}^T = \mathbf{I}$). If \mathbf{G} has p nonzero singular values and no regularization is applied, then the model resolution matrix \mathbf{R}_m is simply given by $\mathbf{R}_m = \mathbf{V}_p\mathbf{V}_p^T$. \mathbf{R}_m generally will not be an identity matrix, and thus can be thought of as a ‘filter’ that blurs the true model. Application of regularization or singular value truncation will only make the blurring worse. Similarly, for this case, if we further assume that the data covariance matrix is of the form $\sigma^2\mathbf{I}$, then the model covariance matrix \mathbf{C}_m is given by

$$\mathbf{C}_m = \sigma^2\mathbf{V}\Lambda^\dagger(\Lambda^\dagger)^T\mathbf{V}^T \quad [52]$$

where as before Λ^\dagger is the pseudoinverse of Λ . The small singular values, which enter the calculation for \mathbf{C}_m as the square of their reciprocals, thereby amplify data-caused errors in the model associated with the corresponding singular vectors in \mathbf{V} . Application of regularization or singular value truncation reduces this problem by suppressing or eliminating the small singular values. See Aster *et al.* (2005) for additional details.

An effective way of displaying model resolution is via Backus–Gilbert resolution kernels $\mathbf{R}(\mathbf{r}, \mathbf{r}_0)$ (Backus and Gilbert, 1968) which are defined (in the original continuous form) as

$$\mathbf{m}(\mathbf{r}_0) = \int_V \mathbf{R}(\mathbf{r}, \mathbf{r}_0) \mathbf{m}(\mathbf{r}) dV \quad [53]$$

In this example, [53] is utilized in discrete form. The kernel $\mathbf{R}(\mathbf{r}, \mathbf{r}_0)$ illustrates how the model $\mathbf{m}(\mathbf{r}_0)$ at \mathbf{r}_0 represents a (weighted) average over the entire model. Hence it illustrates whether isolated regions

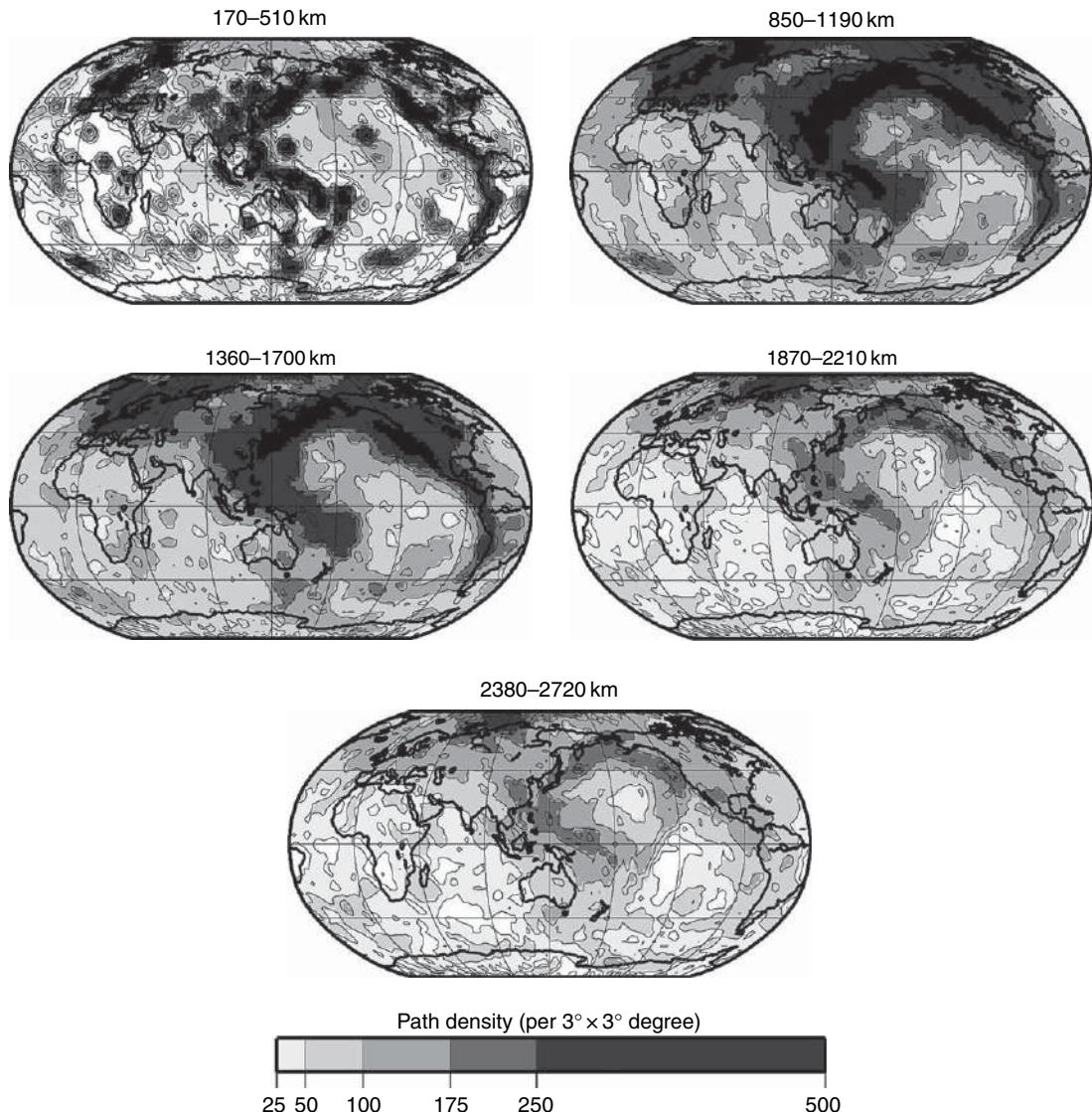


Figure 10 Maps of teleseismic body wave (S, SS, SSS, SKS, SKKS, ScS, ScS₂) wave coverage from the data set of Ritsema *et al.* (2004). Although this figure is specific to the development of model S20RTS, it is typical that teleseismic body wave coverage is best in the mid-mantle (1000–2000 km depth) and relatively poor in the upper mantle (0–1000 km). Uppermost mantle sampling is excellent only in subduction zones and regions with dense seismic networks.

of the model of the mantle are independently resolved. **Figure 11** shows four Backus–Gilbert kernels computed for model S20RTS. The relatively broad lateral extents of these kernels reflect the coarse degree-20 parametrization of S20RTS, while the variable vertical extent is, again, an indication of the heterogeneous model resolution (velocity variations with wavelengths shorter than 2000 km at the Earth's surface are unresolved). Resolution is best in the uppermost mantle (0–200 km) (**Figure 11(a)**). Here, S20RTS employs a relatively fine spline

parametrization (Ritsema *et al.*, 2004), and this region is well sampled by fundamental-mode Rayleigh waves. Vertical resolution is poor in the transition zone. The Backus–Gilbert kernel computed for a depth of 350 km and the location south of New Zealand (**Figure 11(b)**) is broad, reflecting the poor vertical resolution in the transition zone, especially in the Southern Hemisphere. Therefore, the low-velocity structure in this region, which is prominent in S20RTS (as well as SB4L18), has an uncertain vertical extent. The Backus–Gilbert kernel in

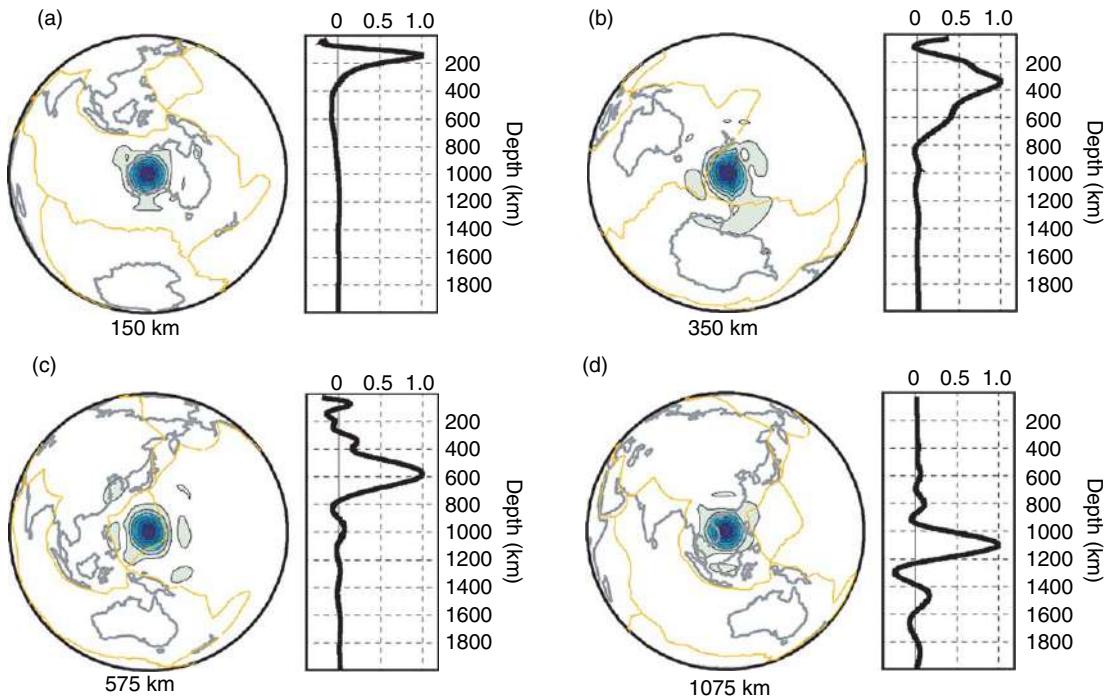


Figure 11 Backus–Gilbert resolution kernels for locations beneath (a) Western Australia (150 km depth), (b) Southwest Pacific (350 km depth), (c) Mariana Islands (575 km depth), (d) Southeast Asia (1075 km) for model S20RTS. Map views are shown on the left. Vertical cross sections through the kernels are shown on the right. The geographic variability of these kernels reflects the heterogeneous mantle resolution, typical for any tomographic model.

Figure 11(c) has a narrower depth extent, given the relatively high data coverage of the western Pacific by both body waves and overtone Rayleigh waves. Finally, the Backus–Gilbert kernel at 1075 km depth (**Figure 11(d)**) beneath Southeast Asia is less than 200 km wide. Given this relatively narrow extent, we may conclude that the high-velocity anomaly in this region of the mantle is resolved independently from anomalies shallower in the mantle. Hence, it appears not to be an artifact from vertical averaging of high-velocity (slab) structure in the transition zone of Indonesia.

While formal resolution tests are feasible for moderately large inversions (e.g., Ritsema *et al.*, 1999; Ishii and Tromp, 1999; Kuo and Romanowicz, 2002) when the model comprises fewer than 10 000 parameters, they become ultimately impractical for extremely large problems. Boschi (2003) and Soldati and Boschi (2005) provide some enlightening discussions of whole-Earth model resolution matrix calculations. Beginning with Nakanishi and Suetsugu (1986), a number of authors have proposed methods for deriving approximate model resolution and/or covariance matrices (Zhang and McMechan, 1995; Nolet *et al.*, 1999; Yao *et al.*, 1999). The effectiveness and

efficiency of these methods has been subject to some debate. Displaying such results is also problematic, since both matrices have dimensions equal to the number of model parameters. One strategy for compressing the full resolution matrix into a compact form that can be displayed in a manner like that of the model itself is resolution spread (Michelini and McEvilly, 1991), which produces a scalar field quantifying the spatial extent of blurring at each point in the model.

1.10.5.3 Hypothesis Testing

An entirely different strategy for evaluating the quality of a tomographic model involves hypothesis tests. In such tests, it is determined how a hypothetical structure of the Earth would be recovered tomographically. There are two ways to approach such tests. One could evaluate the resolution operator \mathbf{R}_m , which is defined as [29]:

$$\mathbf{m}_{\text{out}} = \mathbf{R}_m \mathbf{m}_{\text{in}} \quad [54]$$

Simply convolving \mathbf{R}_m with a conceptual input model \mathbf{m}_{in} renders \mathbf{m}_{out} which is the tomographically

resolved structure if \mathbf{m}_{in} were the true Earth. The degree of recovery of \mathbf{m}_{in} in various parts of \mathbf{m}_{out} is used to define the well-resolved parts of the model. Alternatively, one can mimic the effects of [29] by inverting synthetic data generated for \mathbf{m}_{in} following the same procedures that were applied to the real data. Tomographers choose a variety of synthetic structures for \mathbf{m}_{in} including spikes (isolated anomalies), checkerboards (models with alternating high- and low-velocity anomalies), and conceptual geological structures.

Figure 12 shows an application to the Icelandic upper mantle, where model S20RTS features a low-velocity anomaly that extends much deeper into the upper mantle than what is typical for the Mid-Atlantic Ridge (**Figure 12(a)**). To assess this extent, we can test how relative narrow structures (cylinders) with variable depth extents are projected tomographically. The 200-km-wide cylinders of \mathbf{m}_{in} are at least 5 times wider in \mathbf{m}_{out} (**Figure 12(b)**). This is entirely due to the parametrization of model S20RTS (spherical harmonics up to order and degree 20) that cannot accommodate velocity variations with a half-wavelength smaller than 1000 km. Furthermore, we can observe vertical stretching of the cylinders due to the finite depth resolution. For example, the cylinder that extends from the surface to a depth of 400 km is projected into \mathbf{m}_{out} as an anomaly that reaches the 670 km discontinuity. The relatively broad averaging lengths deeper in the transition zone are also evident in **Figure 12**. The peak anomaly of the 100-km-thick cylinder that, in \mathbf{m}_{in} , was placed immediately below the 660-km discontinuity is reduced by about a factor of 6 in \mathbf{m}_{out} . While it is impossible to conclude which true Earth structure is responsible for the tomographic image of **Figure 12(a)** (we can only determine \mathbf{m}_{out} given \mathbf{m}_{in} , but not vice versa), it appears that heterogeneity in the mantle below the 660 km discontinuity is independently resolved from the mantle above it. It is plausible, however, that a low-velocity anomaly in the upper 400–500 km of the mantle is artificially extended to 700 km depth. The hypothesis tests of **Figure 12** suggest also that a lower bound of the Icelandic anomaly is a real feature.

Another approach is to use geophysically more meaningful input models. An example is provided in **Figure 13**. Here an input model (\mathbf{m}_{in}) is derived from a numerical calculation of mantle convection (McNamara and Zhong, 2005; Ritsema *et al.*, 2007) and \mathbf{m}_{out} is obtained by convolving \mathbf{m}_{in} with \mathbf{R}_m . **Figure 13** demonstrates how small-scale structures such as thermal instabilities from thermochemical

basal structures cannot be resolved at the resolution of S20RTS (and presumably other global models). In addition, even large structures in \mathbf{m}_{in} are artificially stretched and tilted in \mathbf{m}_{out} in regions (e.g., the central Pacific lower mantle) with unidirectional mantle sampling.

Hypothesis tests like those in **Figures 12 and 13** have serious pitfalls when only a number of cases of \mathbf{m}_{in} are tested. One can only infer how \mathbf{m}_{in} is mapped tomographically into \mathbf{m}_{out} , but not vice-versa because the components of a model in the null space of \mathbf{G} (the components of \mathbf{V} corresponding to the zero singular values) cannot possibly be resolved. It is therefore dangerous to generalize the resolution of a tomographic model from the outcome of only a few tests. In fact, Lévéque *et al.* (1993) show, perhaps counterintuitively, that the success of a checkerboard test to resolve the small-scale checkerboard structure cannot guarantee that larger-scale structures will be resolved with the same data set. It is possible for some small features to be resolvable when some larger-scale features are not. For instance, they illustrate how horizontal variations can be well recovered while the large-scale radial variation is poorly resolved if most of the rays are subparallel and steeply incident. This is of course an inherent problem of the teleseismic traveltimes inversion, such as the ACH tomography method (Aki *et al.*, 1977).

We also point out that cell-based tomographic systems have a natural tendency for negative model covariance between adjacent cells. This is caused by the fact that, when resolution is imperfect, a positive perturbation in one cell can be counterbalanced by negative perturbations in adjacent cells (the exact pattern of a checkerboard) with little effect on the data fit. Hence noisy (underdamped or undersmoothed) tomographic models typically show oscillatory behavior. Thus, checkerboard tests may yield overly optimistic estimates of model quality due to the presence of error in the synthetic data coupled with the character of the model covariance.

‘Model restoration’ tests are another popular approach. Here, a model with all of the main features of the model obtained from the real data (sometimes with the sign of the anomalies reversed; Husen and Kissling, 2001) is used to generate synthetic observations, which are then inverted using the same method and parameters as those used for the real data. When extended to include comparable assessment of models lacking some of the key features (Zhang *et al.*, 2004), this approach can be very effective.

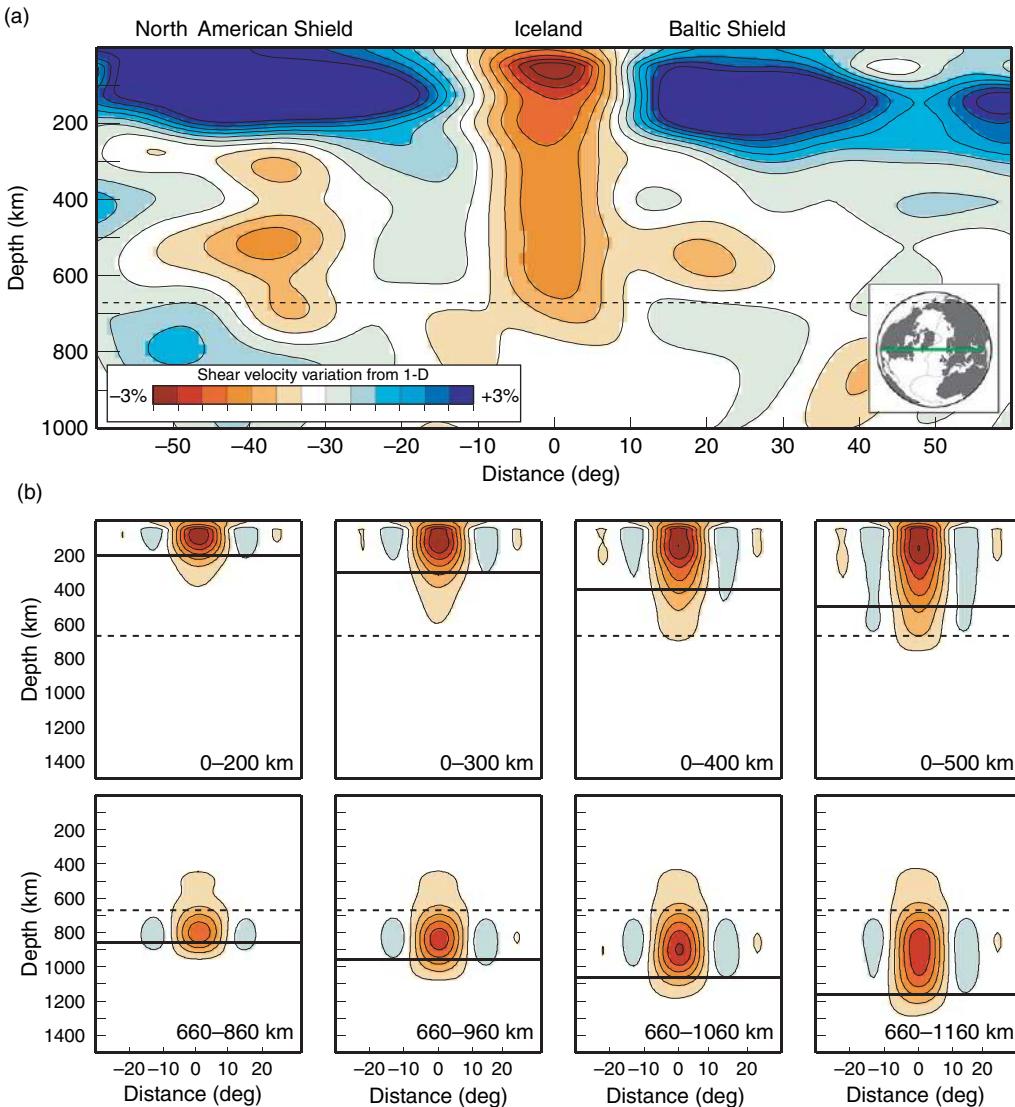


Figure 12 (a) Upper-mantle cross section through model S20RTS, showing a low-velocity anomaly beneath Iceland that extends to about 800 km depth. (b) ‘Spike tests’ designed to evaluate whether the Icelandic low-velocity anomaly points to a deeper-than-normal mantle upwelling beneath the Icelandic region of the Mid-Atlantic Ridge, or whether it is a tomography artifact. The cross sections show \mathbf{m}_{out} obtained by convolving hypothetical models \mathbf{m}_{in} with the resolution operator \mathbf{R}_m . The input models \mathbf{m}_{in} are 200-km-wide cylinders of the mantle beneath Iceland with a uniform velocity perturbation from the reference model. Their tops are top row at the Earth’s surface or bottom row at the 660 km discontinuity, and their vertical extent varies from left to right between 100 and 500 km. The numbers indicate to which depth the cylinders in \mathbf{m}_{in} extend.

One thorough approach to the quantification of model uncertainty is the use of global optimization methods, such as Monte Carlo (Mosegaard and Tarantola, 1995), to explore the range of possible solutions. Press (1968) took the Monte Carlo approach for modeling global 1-D Earth structure. Shapiro and Ritzwoller (2002) applied a Markov-chain Monte Carlo analysis to a global surface wave

model of crust and upper mantle structure. As one might expect, the uncertainties that they quantify substantially exceed standard estimates based on the model covariance matrix.

Given the difficulties of fully evaluating model resolution and covariance matrices, tomographers often resort to the kind of simplified hypothesis tests described above to estimate the significance of

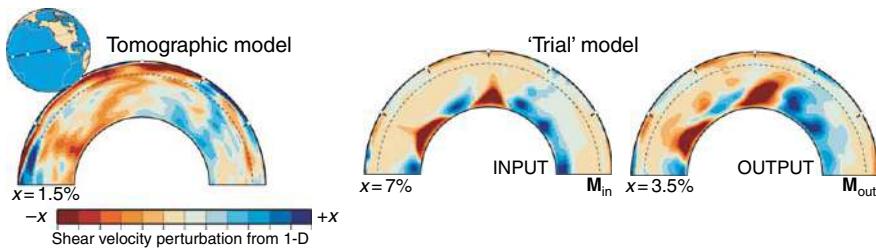


Figure 13 (left) Whole-mantle cross section through model S20RTS (from the Southwest Pacific to the Atlantic) depicting broad lower-mantle anomalies beneath the Pacific and a high-velocity anomaly beneath North America. (right) Recovery tests designed to estimate how a thermochemical model of shear-velocity heterogeneity in the lower mantle (see McNamara and Zhong, 2005; Ritsema *et al.*, 2007) would be seen tomographically. A comparison of \mathbf{m}_{in} and \mathbf{m}_{out} illustrates the image distortions, especially in regions (e.g., the lower mantle beneath the central Pacific) with relatively poor data coverage. Relevant to this comparison is the questionable resolution of thermal plumes from the edges of thermochemical deep-mantle structures and the artificial tilt of the seismically derived Central Pacific low-velocity structure.

interesting model attributes. There is one important additional caveat. When testing how \mathbf{m}_{in} is projected into \mathbf{m}_{out} according to the model resolution operator \mathbf{R}_m , we are not addressing the effects of simplifications in the forward modeling theory. We assume that anomalies in the mantle, no matter how small, perturb a wave that propagates through it, and that this perturbation (e.g., traveltimes delay) is recorded at the Earth's surface. In the real Earth, delay times dissipate due to 'wavefront healing' (e.g., Wielandt, 1987; Nolet and Dahlen, 2000). Wavefront healing is related to the finite frequency nature of a seismic wave, and is ignored in ray theory. Wavefront healing can be significant for small (compared to the wavelength) and deep anomalies. Going back to our example from Iceland (**Figure 12**), it is possible that a narrow (e.g., plume-stem) seismic anomaly is present below a depth of 700 km, which has imparted a traveltimes delay to a through-going wave that is still not observable at the surface. The effect of wavefront healing, omitted in the forward modeling theory applied to S20RTS, can only be tested with more realistic forward modeling theories (Montelli *et al.*, 2004a) or by comparing seismic waveforms with 3-D wave simulations (e.g., Komatitsch *et al.*, 2002; Allen and Tromp, 2005).

1.10.6 Future Directions

We close by commenting on a variety of areas in which we anticipate exciting progress in seismic tomography in the future. Tomographic study of temporal changes in structure ('4-D tomography') is one relatively new frontier. Two examples are the study of geothermal reservoir changes at The

Geysers, CA (Gunasekera *et al.*, 2003), and the investigation of temporal changes at Mammoth Mountain, CA, related to CO₂ outgassing (Foulger *et al.*, 2003). A concern of course is the potential for differences in data sampling for data sets from different time periods causing apparent temporal changes. A new inversion strategy that solves for 4-D models with a constraint to restrict model changes to those truly required by the data may be the key to deriving robust results in such studies (Day-Lewis *et al.*, 2003). A similar problem is faced by inversions for V_p and V_s . Often V_p/V_s or Poisson's ratio is desired for interpretation purposes, but deriving V_p/V_s by simply dividing the V_p model by the V_s model will introduce noise and artifacts due to the different samplings of the V_p and V_s models (Eberhart-Phillips, 1990; Wagner *et al.*, 2005). A strategy for joint inversion for V_p , V_s , and V_p/V_s is probably necessary (Zhang and Thurber, 2006). Multimethod seismic (e.g., surface waves and receiver functions; Julia *et al.*, 2000) and multiproperty geophysical inversions (e.g., seismic and gravity; Roecker *et al.*, 2004) also present opportunities for significant advances.

Finally, 'noise' tomography and scattered-wave tomography studies (Shapiro *et al.*, 2005; Sabra *et al.*, 2005; Pollitz and Fletcher, 2005) have caught wide attention as an approach that can take advantage of the growing archive of continuous seismic data. Apparently, seismic data that we have traditionally regarded as noise may include extremely useful signal. It demonstrates clearly that seismic tomography can continue to benefit when researchers find clever ways to exploit the full spectrum of signal contained in seismograms.

Acknowledgments

This material is based upon work supported by National Science Foundation grants EAR-0106666 and EAR-0609763 (JR) and EAR-0346105, EAR-0409291, and EAR-0454511 (CT).

References

- Abers GA and Roecker SW (1991) Deep structure of an arc-continent collision: Earthquake relocation and inversion for upper mantle P and S wave velocities beneath Papua New Guinea. *Journal of Geophysical Research* 96: 6370–6401.
- Ajo-Franklin JB and Minsley B (2005) Application of minimum support constraints to seismic traveltimes tomography. *EOS Transactions of the American Geophysical Union* 86: H13C-1344.
- Aki K and Lee WHK (1976) Determination of three-dimensional velocity anomalies under a seismic array using first P-arrival times from local earthquakes, I, a homogeneous initial model. *Journal of Geophysical Research* 81: 4381–4399.
- Aki K, Christofferson A, and Husebye ES (1977) Determination of the three-dimensional seismic structure of the lithosphere. *Journal of Geophysical Research* 82: 277–296.
- Aki K and Richards P (1980) *Quantitative Seismology, Theory and Methods*, 932 pp. San Francisco, CA: W H Freeman.
- Allen RM and Tromp J (2005) Resolution of regional seismic models: Squeezing the Iceland anomaly. *Geophysical Journal International* 161: 373–386.
- Anderson DL and Dziewonski AM (1984) Seismic tomography. *Scientific American* 251: 60–68.
- Antolik M, Ekström G, Dziewonski AM, Boschi L, Gu YJ, and Pan J-F (2000) A new global joint P and S velocity model of the mantle parameterized in cubic B-splines. In: Rosenblatt M (ed.) *Proceedings of the 22nd Annual DOD/DOE Seismic Research Symposium*. New Orleans, LA. Seattle, WC: Kluwer.
- Ashiya K, Asano S, Yoshii T, Ishida M, and Nishiki T (1987) Simultaneous determination of the three-dimensional crustal structure and hypocenters beneath the Kanto–Tokai District, Japan. *Tectonophysics* 140: 13–27.
- Aster RC, Borchers B, and Thurber CH (2005) *Parameter Estimation and Inverse Problems*, 296 pp. London: Elsevier/Academic Press.
- Backus GE and Gilbert JF (1967) Numerical applications of a formalism for geophysical inverse problems. *Geophysical Journal of the Royal Astronomical Society* 13: 247–276.
- Backus G and Gilbert F (1968) The resolving power of gross Earth data. *Geophysical Journal of the Royal Astronomical Society* 16: 169–205.
- Backus G and Gilbert F (1970) Uniqueness in the inversion of inaccurate gross Earth data. *Philosophical Transactions of the Royal Society of London A* 266: 187–269.
- Barber CB, Dobkin DP, and Huhdanpaa HT (1996) The Quickhull algorithm for convex hulls. *ACM Transactions on Mathematical Software* 22: 469–483.
- Battaglia J, Thurber C, Got J-L, Rowe C, and White R (2004) Precise relocation of earthquakes following the June 15, 1991 explosion of Mount Pinatubo (Philippines). *Journal of Geophysical Research* 109: B07302 (doi:10.1029/2003JB002959).
- Benz HM, Chouet BA, Dawson PB, Lahr JC, Page RA, and Hole JA (1996) Three-dimensional P and S wave velocity structure of Redoubt Volcano, Alaska. *Journal of Geophysical Research* 101: 8111–8128.
- Bhattacharyya J, Masters G, and Shearer P (1996) Global lateral variations of shear wave attenuation in the upper mantle. *Journal of Geophysical Research* 101: 22273–22289.
- Bijwaard H and Spakman W (1999) Fast kinematic ray tracing of first- and later-arriving global seismic phases. *Geophysical Journal International* 139: 359–369.
- Bijwaard H and Spakman W (2000) Non-linear global P-wave tomography by iterated linearized inversion. *Geophysical Journal International* 141: 71–82.
- Bijwaard H, Spakman W, and Engdahl ER (1998) Closing the gap between regional and global travel time tomography. *Journal of Geophysical Research* 103: 30055–30078.
- Billen M, Lévéque JJ, and Trampert J (2000) Global maps of Rayleigh wave attenuation for periods between 40 and 150 seconds. *Geophysical Research Letters* 27: 3619–3622.
- Boschi E, Ekström G, and Morelli A (eds.) (1996) *Seismic Modeling of Earth Structure*, 572 pp. Rome, Italy: Istituto Nazionale di Geofisica.
- Boschi L (2003) Measures of resolution in global body-wave tomography. *Geophysical Research Letters* 30: 1978 (doi:10.1029/2003GL018222).
- Boschi L and Dziewonski AM (1999) High and low-resolution images of the earth's mantle: Implications of different approaches to tomographic modeling. *Journal of Geophysical Research* 104: 25567–25594.
- Boschi L and Ekström G (2002) New images of the Earth's upper mantle from measurements of surface wave phase velocity anomalies. *Journal of Geophysical Research* 107: 2059 (doi:10.1029/2000JB000059).
- Boschi L, Ekström G, and Kustowski B (2004) Multiple resolution surface wave tomography: The Mediterranean region. *Geophysical Journal International* 157: 293–304.
- Bube KP and Langan RT (1997) Hybrid λ_1/λ_2 minimization with applications to tomography. *Geophysics* 62: 1183–1195.
- Butler R, Lay T, Creager K, et al. (2004) The Global Seismographic Network surpasses its design goal. *EOS Transactions of the American Geophysical Union* 85: 225–229.
- Chen P, Zhao L, and Jordan TH (2007) Full 3D tomography for crustal structure of the Los Angeles region. *Bulletin of the Seismological Society of America* (in press).
- Chiao LY and Kuo BY (2001) Multiscale seismic tomography. *Geophysical Journal International* 145: 517–527.
- Chou C and Booker JR (1979) A Backus–Gilbert approach to the inversion of travel time data for three dimensional velocity structure. *Geophysical Journal of the Royal Astronomical Society* 59: 325–344.
- Clayton RW and Hearn TM (1982) A tomographic analysis of lateral velocity variations in Southern California. *EOS Transactions of the American Geophysical Union* 63: 1036.
- Committee on the Science of Earthquakes (2003) *Living on an Active Earth*, 418 pp. Washington, DC: National Academies Press.
- Constable SC, Parker RL, and Constable CG (1987) Occam's inversion: A practical algorithm for generating smooth models from electromagnetic sounding data. *Geophysics* 52(3): 289–300.
- Dahlen FA, Hung SH, and Nolet G (2000) Fréchet kernels for finite-frequency travel times-I. Theory. *Geophysical Journal International* 141: 157–174.
- Dahlen FA and Tromp J (1998) *Theoretical Global Seismology*, 1025 pp. Princeton, NJ: Princeton University Press.
- Dalton CA and Ekström G (2006) Global models of surface-wave attenuation. *Journal of Geophysical Research* 111: B05317 (doi:10.1029/2005JB003997).

- Davis T (2006) *SIAM Series on the Fundamentals of Algorithms: Direct Methods for Sparse Linear Systems*, 214 pp. New York: PWS Publishing.
- Dawson PB, Evans JR, and Iyer HM (1990) Teleseismic tomography of the compressional wave velocity structure beneath the Long Valley region, California. *Journal of Geophysical Research* 95: 11021–11050.
- Day-Lewis F, Harris JM, and Gorelick S (2003) Time-lapse inversion of crosswell radar data. *Geophysics* 67: 1740–1752.
- Deschamps F and Trampert J (2004) Towards a lower mantle reference temperature and composition. *Earth and Planetary Science Letters* 222: 161–175.
- DeShon HR, Schwartz SY, Newman AV, et al. (2006) Seismogenic zone structure beneath the Nicoya Peninsula, Costa Rica, from three-dimensional local earthquake P- and S-wave tomography. *Geophysical Journal International* 164: 109–124.
- Dorren HJS and Snieder RK (1997) Error propagation in non-linear delay-time tomography. *Geophysical Journal International* 128: 632–638.
- Douglas A (1967) Joint epicenter determination. *Nature* 215: 47–48.
- Du W, Thurber CH, Reyners M, Eberhart-Phillips D, and Zhang H (2004) New constraints on seismicity in the Wellington region, New Zealand, from relocated earthquake hypocenters. *Geophysical Journal International* 158: 1088–1102.
- Dziewonski AM (1984) Mapping the lower mantle: Determination of lateral heterogeneity in P velocity up to degree and order 6. *Journal of Geophysical Research* 89: 5929–5952.
- Dziewonski AM and Anderson DL (1981) Preliminary Reference Earth Model. *Physics of the Earth and Planetary Interiors* 25: 297–356.
- Dziewonski AM, Hager BH, and O'Connell RJ (1977) Large-scale heterogeneities in the lower mantle. *Journal of Geophysical Research* 82: 239–255.
- Dziewonski AM and Stein JM (1982) Dispersion and attenuation of mantle waves through waveform inversion. *Geophysical Journal of the Royal Astronomical Society* 70: 503–527.
- Dziewonski AM and Woodhouse JW (1987) Global images of the Earth's interior. *Science* 236: 37–48.
- Eberhart-Phillips D and Henderson CM (2004) Including anisotropy in 3-D velocity inversion and application to Marlborough, New Zealand. *Geophysical Journal International* 156: 237–254.
- Eberhart-Phillips D (1986) Three-dimensional velocity structure in Northern California Coast Ranges from inversion of local earthquake arrival times. *Bulletin of the Seismological Society of America* 76: 1025–1052.
- Eberhart-Phillips D (1990) Three-dimensional P and S velocity structure in the Coalinga region, California. *Journal of Geophysical Research* 95: 15343–15363.
- Ekström G, Tromp J, and Larson EW (1997) Measurements and models of global surface wave propagation. *Journal of Geophysical Research* 102: 8137–8157.
- Ellsworth WL (1977) *Three-Dimensional Structure of the Crust and Mantle Beneath the Island of Hawaii*. PhD Thesis, Massachusetts Institute of Technology, Cambridge.
- Engdahl ER, van der Hilst RD, and Buland RP (1998) Global teleseismic earthquake relocation with improved travel times and procedures for depth determination. *Bulletin of the Seismological Society of America* 88: 22–43.
- Evans JR and Achauer U (1993) Teleseismic velocity tomography using the ACH method: Theory and application to continental-scale studies. In: Iyer HM and Hirahara K (eds.) *Seismic Tomography: Theory and Applications*, pp. 319–360. London: Chapman and Hall.
- Foulger GR, Julian BR, Pitt AM, Hill DP, Malin P, and Shalev E (2003) Three-dimensional crustal structure of Long Valley caldera, California, and evidence for the migration of CO₂ under Mammoth Mountain. *Journal of Geophysical Research* 108(B3): 2147 (doi:10.1029/2000JB000041).
- Fukao Y, Widjiantoro S, and Obayashi M (2001) Stagnant slabs in the upper and lower mantle transition region. *Reviews of Geophysics* 39: 291–323.
- Gee LS and Jordan TJ (1992) Generalized seismological data functionals. *Geophysical Journal International* 111: 363–390.
- Giardini D, Li X-D, and Woodhouse JH (1987) Three-dimensional structure of the Earth from splitting in free-oscillation spectra. *Nature* 325: 405–411.
- Gilbert F (1970) Excitation of the normal modes of the Earth by earthquake sources. *Geophysical Journal of the Royal Astronomical Society* 22: 223–226.
- Gilbert F and Dziewonski AM (1975) An application of normal mode theory to the retrieval of structural parameters and source mechanism from seismic spectra. *Philosophical Transactions of the Royal Society of London A* 278: 187–269.
- Gill PE, Murray W, and Wright MH (1981) *Practical Optimization*, 401 pp. San Diego, CA: Academic Press.
- Got JL, Frechet J, and Klein F (1994) Deep fault plane geometry inferred from multiplet relative relocation beneath the south flank of Kilauea. *Journal of Geophysical Research* 99: 15375–15386.
- Grand SP (1994) Mantle shear structure beneath the Americas and surrounding oceans. *Journal of Geophysical Research* 99: 11591–11621.
- Grand SP, van der Hilst RD, and Widjiantoro S (1997) Global seismic tomography: A snapshot of convection in the Earth. *GSA Today* 7: 1–7.
- Grand SP (2002) Mantle shear-wave tomography and the fate of subducted slabs. *Philosophical Transactions of the Royal Society of London A* 3260: 2475–2491.
- Gudmundsson O and Sambridge M (1998) A regionalized upper mantle RUM seismic model. *Journal of Geophysical Research* 103: 7121–7136.
- Gunasekera RC, Foulger GR, and Julian BR (2003) Three-dimensional tomographic images of progressive pore-fluid depletion at the Geysers geothermal area, California. *Journal of Geophysical Research* 108 (doi:10.1029/2001JB000638).
- Hawley BW, Zandt G, and Smith RB (1981) Simultaneous inversion for hypocenters and lateral velocity variations: An iterative solution with a layered model. *Journal of Geophysical Research* 86: 7073–7076.
- He X and Tromp J (1996) Normal-mode constraints on the structure of the mantle and core. *Journal of Geophysical Research* 101: 20053–20082.
- Hirahara K (1993) Tomography using both local earthquakes and teleseisms: Velocity and anisotropy – Theory. In: Iyer HM and Hirahara K (eds.) *Seismic Tomography: Theory and Applications*, pp. 493–518. London: Chapman and Hall.
- Hole JA, Brocher TM, Klempner SL, Parsons T, Benz HM, and Furlong KP (2000) Three-dimensional seismic velocity structure of the San Francisco Bay area. *Journal of Geophysical Research* 105: 13859–13874.
- Humphreys E, Clayton RW, and Hager BH (1984) A tomographic image of mantle structure beneath southern California. *Geophysical Research Letters* 11: 625–627.
- Husen S and Kissling E (2001) Local earthquake tomography between rays and waves: Fat ray tomography. *Physics of the Earth and Planetary Interiors* 123: 127–147.
- Inoue H, Fukao Y, Tanabe K, and Ogata Y (1990) Whole mantle P-wave traveltimes tomography. *Physics of the Earth and Planetary Interiors* 59: 294–328.
- Ishii M and Tromp J (1999) Normal-mode and free-air gravity constraints on lateral variations in velocity and density of the Earth's mantle. *Science* 285: 1231–1236.

- Ishii M and Tromp J (2001) Even-degree lateral variations in the Earth's mantle constrained by free oscillations and the free-air gravity anomaly. *Geophysical Journal International* 145: 77–96.
- Iyer HM and Hirahara K (eds.) (1993) *Seismic Tomography: Theory and Applications*, pp. 319–360. London: Chapman and Hall.
- Jeffrey H and Bullen KE (1958) *Seismological Tables*, Office of the British Association, Burlington House, London.
- Jet Propulsion Laboratory (1976) Petroleum exploration assessment: Phase 1 report. *JPL Document 5040-32*. Pasadena, CA: Jet Propulsion Laboratory.
- Julia J, Ammon CJ, Herrmann RB, and Correig AM (2000) Joint inversion of receiver function and surface wave dispersion observations. *Geophysical Journal International* 143: 1–19.
- Julian BR, Evans JR, Pritchard MJ, and Foulger GR (2000) A geometrical error in some computer programs based on the Aki–Christofferson–Husebye ACH method of teleseismic tomography. *Bulletin of the Seismological Society of America* 90: 1554–1558.
- Káráson H and van der Hilst RD (2001) Tomographic imaging of the lowermost mantle with differential times of refracted and diffracted core phases (PKP, Pdiff). *Journal of Geophysical Research* 106: 6569–6588.
- Kennett BLN and Engdahl ER (1991) Traveltimes for global earthquake location and phase identification. *Geophysical Journal International* 105: 429–465.
- Kennett BLN, Engdahl ER, and Buland R (1995) Constraints on seismic velocities in the Earth from travel times. *Geophysical Journal International* 122: 403–416.
- Kennett BLN, Cambridge MS, and Williamson PR (1988) Subspace methods for large inverse problems with multiple parameter classes. *Geophysical Journal International* 94: 237–247.
- Kissling E (1988) Geotomography with local earthquake data. *Reviews of Geophysics* 26: 659–698.
- Kissling E, Ellsworth WL, Eberhart-Phillips D, and Kardolfer U (1994) Initial reference models in local earthquake tomography. *Journal of Geophysical Research* 99: 19635–19646.
- Koch M (1985) Nonlinear inversion of local seismic travel times for the simultaneous determination of the 3-D-velocity structure and hypocentres-application to the seismic zone Vrancea. *Journal of Geophysics* 56: 160–173.
- Komatitsch D, Ritsema J, and Tromp J (2002) The spectral-element method, Beowulf computing and global seismology. *Science* 298: 1737–1742.
- Kuo C and Romanowicz B (2002) On the resolution of density anomalies in the Earth's mantle using spectral fitting of normal mode data. *Geophysical Journal International* 150: 162–179.
- Laske G (1995) Global observation of off-great circle propagation of long-period surface waves. *Geophysical Journal International* 123: 245–259.
- Lebedev S, Nolet G, and van der Hilst RD (1997) The upper mantle beneath the Philipine sea region from waveform inversion. *Geophysical Research Letters* 24: 1851–1854.
- Lees JM and Crosson RS (1989) Tomographic inversion for three-dimensional velocity structure at Mount St. Helens using earthquake data. *Journal of Geophysical Research* 94: 5716–5728.
- Lees JM and Crosson RS (1990) Tomographic imaging of local earthquake delay times for three-dimensional velocity variation in western Washington. *Journal of Geophysical Research* 95: 4763–4776.
- Lees JM and Lindley GT (1994) Three-dimensional attenuation tomography at Loma Prieta: Inverting t' for Q. *Journal of Geophysical Research* 99: 6843–6863.
- Lévéque JJ and Cara M (1985) Inversion of multimode surface wave data: Evidence for sublithospheric anisotropy. *Geophysical Journal International* 83: 753–773.
- Lévéque JJ, Rivera L, and Wittlinger G (1993) On the use of the checker-board test to assess the resolution of tomographic inversions. *Geophysical Journal International* 115: 313–318.
- Li XD and Romanowicz B (1995) Comparison of global waveform inversions with and without considering cross branch coupling. *Geophysical Journal International* 121: 695–709.
- Li XD and Romanowicz B (1996) Global mantle shear velocity model developed using nonlinear asymptotic coupling theory. *Journal of Geophysical Research* 101: 22245–22273.
- Li XD and Tanimoto T (1993) Waveforms of long period body-waves in a slightly aspherical earth. *Geophysical Journal International* 112: 92–112.
- Li C, van der Hilst RD, and Toksoz MN (2006) Constraining P-wave velocity variations in the upper mantle beneath Southeast Asia. *Physics of the Earth and Planetary Interiors* 154: 180–195.
- Lin CH and Roecker SW (1997) Three-dimensional P-wave velocity structure of the Bear Valley region of Central California. *Pure and Applied Geophysics* 149: 667–688.
- Marquering H and Snieder R (1995) Surface wave mode coupling for efficient forward modeling and inversion of body wave phases. *Geophysical Journal International* 120: 186–208.
- Masson F and Trampert J (1997) On ACH, or how reliable is regional teleseismic delay time tomography? *Physics of the Earth and Planetary Interiors* 102: 21–32.
- Masters G, Johnson S, Laske G, and Bolton H (1996) A shear-velocity model of the mantle. *Philosophical Transactions of the Royal Society of London A* 354: 1385–1411.
- Masters G, Jordan T, Silver P, and Gilbert F (1982) Aspherical earth structure from fundamental spheroidal-mode data. *Nature* 298: 609–613.
- Masters G, Laske G, Bolton H, and Dziewonski A (2000) The relative behavior of shear velocity, bulk sound speed, and compressional velocity in the mantle: Implications for chemical and thermal structure. In: Karato S (ed.) *AGU Monograph*, Vol. 117: *Earth's Deep Interior*, pp. 63–87. Washington, DC: AGU.
- McNamara AK and Zhong S (2005) Thermochemical piles under Africa and the Pacific. *Nature* 437: 1136–1139.
- Mégnin C and Romanowicz B (2000) The 3-D shear velocity structure of the mantle from the inversion of body, surface and higher mode waveforms. *Geophysical Journal International* 143: 709–728.
- Mégnin C, Bunge HP, Romanowicz B, and Richards MA (1997) Imaging 3-D spherical convection models: What can seismic tomography tell us about mantle dynamics? *Geophysical Research Letters* 24: 1299–1302.
- Menke W (1989) *Geophysical Data Analysis: Discrete Inverse Theory*. New York: Academic Press.
- Menke W and Schaff D (2004) Absolute earthquake locations with differential data. *Bulletin of the Seismological Society of America* 94: 2254–2264.
- Michael AJ (1988) Effects of three-dimensional velocity structure on the seismicity of the 1984 Morgan Hill, California, aftershock sequence. *Bulletin of the Seismological Society of America* 78: 1199–1221.
- Michelini A (1995) An adaptive-grid formalism for traveltime tomography. *Geophysical Journal International* 121: 489–510.
- Michelini A and McEvilly TV (1991) Seismological studies at Parkfield: I. Simultaneous inversion for velocity structure and hypocenters using cubic b-splines parameterization. *Bulletin of the Seismological Society of America* 81: 524–552.
- Montagner JP (1994) Can seismology tell us anything about convection in the mantle? *Reviews of Geophysics* 32: 115–138.

- Montagner JP and Tanimoto T (1991) Global upper mantle tomography of seismic velocities and anisotropies. *Journal of Geophysical Research* 96: 20337–20351.
- Montelli R, Nolet G, Dahlen FA, Masters G, Engdahl ER, and Hung SH (2004a) Finite-frequency tomography reveals a variety of plumes in the mantle. *Science* 303: 338–343.
- Montelli R, Nolet G, Masters G, Dahlen FA, and Hung SH (2004b) Global P and PP traveltimes tomography: Rays versus waves. *Geophysical Journal International* 158: 637–654.
- Mooney WD, Laske G, and Masters G (1998) CRUST-5.1: A global crustal model at $5^\circ \times 5^\circ$. *Journal of Geophysical Research* 103: 727–747.
- Mosegaard K and Tarantola A (1995) Monte Carlo sampling of solutions to inverse problems. *Journal of Geophysical Research* 100: 12431–12448.
- Nakanishi I (1985) Three-dimensional structure beneath the Hokkaido–Tohoku region as derived from a tomographic inversion of P-arrival times. *Journal of Physics of the Earth* 33: 241–256.
- Nakanishi I and Anderson DL (1982) Worldwide distribution of group velocity of mantle Rayleigh waves as determined by spherical harmonic inversion. *Bulletin of the Seismological Society of America* 72: 1185–1194.
- Nakanishi I and Suetsugu D (1986) Resolution matrix calculated by a tomographic inversion method. *Journal of Physics of the Earth* 34: 95–99.
- Nakanishi I and Yamaguchi K (1986) A numerical experiment on nonlinear image reconstruction from first-arrival times for two-dimensional island arc structure. *Journal of Physics of the Earth* 34: 195–201.
- Nataf HC and Ricard Y (1996) 3SMAC: An *a priori* tomographic model of the upper mantle based on geophysical modeling. *Physics of the Earth and Planetary Interiors* 95: 101–122.
- Nataf HC, Nakanishi I, and Anderson DL (1986) Measurement of mantle wave velocities and inversion for lateral heterogeneity and anisotropy, III, inversion. *Journal of Geophysical Research* 91: 7261–7307.
- Nolet G (1985) Solving or resolving inadequate and noisy tomographic systems. *Journal of Computational Physics* 61: 463–482.
- Nolet G (1987) Seismic Tomography: With Applications in Global Seismology and Exploration Geophysics. Dordrecht, The Netherlands: D. Reidel.
- Nolet G and Dahlen FA (2000) Wavefront healing and the resolution of seismic delay times. *Journal of Geophysical Research* 105: 19043–19054.
- Nolet G, Dahlen FA, and Montelli R (2005) Traveltimes and amplitudes of seismic waves: A re-assessment. In: Levander A and Nolet G (eds.) *AGU Monograph Series, Vol. 157: Seismic Earth: Analysis of Broadband Seismograms*, pp. 37–48. Washington, DC: AGU.
- Nolet G and Montelli R (2005) Optimal parametrization of tomographic models. *Geophysical Journal International* 161: 365–372.
- Nolet G, Montelli R, and Virieux J (1999) Explicit, approximate expressions for the resolution and a posteriori covariance of massive tomographic systems. *Geophysical Journal International* 138: 36–44.
- Nolet G and Snieder R (1990) Solving large linear inverse problems by projection. *Geophysical Journal International* 103: 565–568.
- Novotny M (1981) Two methods of solving the linearized two-dimensional inverse seismic kinematic problem. *Journal of Geophysics* 50: 7–15.
- Paige CC and Saunders MA (1982) LSQR: Sparse linear equations and least squares problems. *ACM Transactions on Mathematical Software* 8: 195–209.
- Pavlis GL and Booker JR (1980) The mixed discrete-continuous inverse problem: Application to the simultaneous determination of earthquake hypocenters and velocity structure. *Journal of Geophysical Research* 85: 4801–4810.
- Parker RL (1994) *Geophysical Inverse Theory*, 386 pp. Princeton, NJ: Princeton University Press.
- Phillips WS, Hartse HE, and Steck LK (2001) Precise relative location of 25 ton chemical explosions at Balapan using IMS stations. *Pure and Applied Geophysics* 158: 173–192.
- Pollitz FF and Fletcher JP (2005) Waveform tomography of crustal structure in the south San Francisco bay region. *Journal of Geophysical Research* 110: B08308 (doi:10.1029/2004JB003509).
- Press F (1968) Earth models obtained by Monte Carlo inversion. *Journal of Geophysical Research* 73: 5223–5234.
- Rawlinson N and Sambridge M (2003) Seismic traveltimes tomography of the crust and lithosphere. *Advances in Geophysics* 46: 81–197.
- Reagan RL (1978) *A Finite-Difference Study of Subterranean Cavity Detection and Seismic Tomography*. 229 pp. PhD Thesis, University of Missouri-Rolla.
- Reid FJL, Woodhouse JH, and van Heijst HJ (2001) Upper mantle attenuation and velocity structure from measurements of differential S phases. *Geophysical Journal International* 145: 615–630.
- Resovsky JS and Ritzwoller MH (1999) A degree 8 mantle shear velocity model from normal mode observation below 3 mHz. *Journal of Geophysical Research* 104: 993–1014.
- Rietbroek A (2001) P-wave attenuation structure in the fault area of the 1995 Kobe earthquake. *Journal of Geophysical Research* 106: 4141–4154.
- Ritsema J, Rivera LA, Komatsitsch D, Tromp J, and van Heijst H-J (2002) Effects of crust and mantle heterogeneity on PP/P and SS/S amplitude ratios. *Geophysical Research Letters* 29: 1430 (doi:10.1029/2001GL013831).
- Ritsema J, van Heijst HH, and Woodhouse JH (1999) Complex shear wave velocity structure imaged beneath Africa and Iceland. *Science* 286: 1925–1928.
- Ritsema J, van Heijst HJ, and Woodhouse JH (2004) Global transition zone tomography. *Journal of Geophysical Research* 109: B02302 (doi:10.1029/2003JB002610).
- Ritsema J, McNamara AK, and Bull A (2007) Tomographic filtering of geodynamic models: implications for model interpretation and large-scale mantle structure. *Journal of Geophysical Research* 112: B01303 (doi:10.1029/2006JB004566).
- Ritzwoller MH and Laveley EM (1995) Three-dimensional seismic models of the Earth's mantle. *Reviews of Geophysics* 33: 1–66.
- Ritzwoller MH, Levshin AL, Ratnikova LI, and Egorkin AA (1998) Intermediate period group velocity maps across Central Asia, Western China, and parts of the Middle East. *Geophysical Journal International* 134: 315–328.
- Rodi WL, Jordan TH, Masso JF, and Savino JM (1981) Determination of the three-dimensional structure of eastern Washington from the joint inversion of gravity and earthquake data. *Systems Sciences and Software Report SSS-R-80-4516, La Jolla, CA*.
- Roecker SW (1982) Velocity structure of the Pamir–Hindu Kush region; possible evidence of subducted crust. *Journal of Geophysical Research* 87: 945–959.
- Roecker S, Thurber C, and McPhee D (2004) Joint inversion of gravity and arrival time data from Parkfield: New constraints on structure and hypocenter locations near the SAFOD drill site. *Geophysical Research Letters* 31: L12S04 (doi:10.1029/2003GL019396).
- Roecker S, Thurber C, Roberts K, and Powell L (2006) Refining the image of the San Andreas Fault near Parkfield, California using a finite difference travel time computation technique. *Tectonophysics* 424 (doi:10.1016/j.tecto.2006.02.026).
- Romanowicz B, Cara M, Fels JF, and Rouland D (1984) Geoscope: A French initiative in long period three

- component seismic networks. *EOS Transactions of the American Geophysical Union* 65: 753–754.
- Romanowicz B (1991) Seismic tomography of the Earth's mantle. *Annual Review of Earth and Planetary Science* 19: 77–99.
- Romanowicz B (2003) Global mantle tomography: Progress status in the past 10 years. *Annual Review of Earth and Planetary Science* 31: 303–328.
- Rowe CA, Aster RC, Phillips WS, Jones RH, Borchers B, and Fehler MC (2002) Using automated, high-precision repicking to improve delineation of microseismic structures at the Soultz geothermal reservoir. *Pure and Applied Geophysics* 159: 563–596.
- Rubin A, Gillard D, and Got JL (1998) A re-examination of seismicity associated with the January 1983 dike intrusion at Kilauea volcano, Hawaii. *Journal of Geophysical Research* 103: 10003–10015.
- Sabre KG, Gerstoft P, Roux P, and Kuperman WA (2005) Surface wave tomography from microseisms in southern California. *Geophysical Research Letters* 32: L14311 (doi:10.1029/2005GL023155).
- Sambridge MS (1990) Non-linear arrival time inversion: Constraining velocity anomalies by seeking smooth models in 3-D. *Geophysical Journal International* 102: 653–677.
- Sambridge M and Faletti R (2003) Adaptive whole Earth tomography. *Geochemistry, Geophysics, Geosystems*, 4(3): 1022 (doi:10.1029/2001GC000213).
- Sambridge M and Gudmundsson O (1998) Tomographic systems of equations with irregular cells. *Journal of Geophysical Research* 103(B1): 773–781.
- Sambridge M and Mosegaard K (2002) Monte Carlo methods in geophysical inverse problems. *Reviews of Geophysics* 40: 3–1–3–29 (doi:10.1029/2000RG000089).
- Sambridge M and Rawlinson N (2005) Seismic tomography with irregular meshes. In: Levander A and Nolet G (eds.) *AGU Geophysical Monograph series, Vol. 157: Seismic Earth: Array Analysis of Broadband Seismograms*, pp. 49–65. Washington, DC: AGU. (doi:10.1029/156GM04).
- Scherbaum F (1990) Combined inversion for the three-dimensional Q structure and source parameters using microearthquake spectra. *Journal of Geophysical Research* 95: 12423–12438.
- Scales JA (1987) Tomographic inversion via the conjugate gradient method. *Geophysics* 52(2): 179–185.
- Scales JA and Snieder R (1997) To Bayes or not to Bayes? *Geophysics* 62(4): 1045–1046.
- Selby ND and Woodhouse JH (2002) The Q structure of the upper mantle: Constraints from Rayleigh wave amplitudes. *Journal of Geophysical Research* 107: 2097 (doi:10.1029/2001JB000257).
- Sengupta MK and Toksoz MN (1976) Three dimensional model of seismic velocity variation in the Earth's mantle. *Geophysical Research Letters* 3(2): 84–86.
- Shapiro NM, Campillo M, Stehly L, and Ritzwoller MH (2005) High-resolution surface-wave tomography from ambient seismic noise. *Science* 307: 1615–1618.
- Shapiro NM and Ritzwoller MH (2002) Monte-carlo inversion for a global shear-velocity model of the crust and upper mantle. *Geophysical Journal International* 151: 88–105.
- Silver PG (1996) Seismic anisotropy beneath the continents: Probing the depths of geology. *Annual Review of Earth and Planetary Science* 24: 385–432.
- Snieder R (1990) A perturbative analysis of non-linear inversion. *Geophysical Journal International* 101: 545–556.
- Snieder R and Sambridge M (1992) Ray perturbation theory for traveltimes and ray paths in 3-D heterogeneous media. *Geophysical Journal International* 109: 294–322.
- Snieder R and Spencer C (1993) A unified approach to ray bending, ray perturbation and paraxial ray theories. *Geophysical Journal International* 115: 456–470.
- Soldati G and Boschi L (2005) The resolution of whole Earth seismic tomographic models. *Geophysical Journal International* 161: 143–153.
- Spakman W and Bijwaard H (2001) Optimization of cell parameterization for tomographic inverse problems. *Pure and Applied Geophysics* 158: 1401–1423.
- Spakman W and Nolet G (1988) Imaging algorithms: Accuracy and resolution in delay time tomography. In: Vlaar NJ, Nolet G, Wortel M, and Cloetingh S (eds.) *Mathematical Geophysics: A Survey of Recent Developments in Seismology and Geodynamics*, pp. 155–188. Dordrecht, The Netherlands: D Reidel.
- Spencer C and Gubbins D (1980) Travel-time inversion for simultaneous earthquake location and velocity structure determination in laterally varying media. *Geophysical Journal of the Royal Astronomical Society* 63: 95–116.
- Steck L, Thurber C, Fehler M, et al. (1998) Crust and upper mantle P-wave velocity structure beneath the Valles Caldera, New Mexico: Results from the JTEX teleseismic experiment. *Journal of Geophysical Research* 103: 24301–24320.
- Su WJ and Dziewonski AM (1991) Predominance of long-wavelength heterogeneity in the mantle. *Nature* 352: 121–126.
- Su WJ and Dziewonski AM (1992) On the scale of mantle heterogeneity. *Physics of the Earth and Planetary Interiors* 74: 29–54.
- Su WJ, Woodward RL, and Dziewonski AM (1994) Degree 12 model of shear velocity heterogeneity in the mantle. *Journal of Geophysical Research* 99: 4945–4980.
- Symons NP and Crosson RS (1997) Seismic velocity structure of the Puget Sound region from 3-D non-linear tomography. *Geophysical Research Letters* 24(21): 2593–2596.
- Tarantola A (2005) *Inverse Problem Theory and Methods for Model Parameter Estimation*, 342 pp. Philadelphia, PA: Society for Industrial and Applied Mathematics.
- Tarantola A and Nercessian A (1984) Three-dimensional inversion without blocks. *Geophysical Journal of the Royal Astronomical Society* 76: 299–306.
- Tarantola A and Valette B (1982) Generalized nonlinear inverse problems solved using the least squares criterion. *Reviews of Geophysics and Space Physics* 20: 219–232.
- Thomson CJ and Gubbins D (1982) Three-dimensional lithospheric modeling at NORSAR: Linearity of the method and amplitude variations from the anomalies. *Geophysical Journal International* 71: 1–36.
- Thurber CH (1983) Earthquake locations and three-dimensional crustal structure in the Coyote Lake area, central California. *Journal of Geophysical Research* 88: 8226–8236.
- Thurber CH (1992) Hypocenter–velocity structure coupling in local earthquake tomography. *Special Issue: Lateral Heterogeneity and Earthquake Location. Physics of the Earth and Planetary Interiors* 75: 55–62.
- Thurber CH (2003) Seismic tomography of the lithosphere with body-waves. *Pure and Applied Geophysics* 160: 717–737.
- Thurber CH and Aki K (1987) Three-dimensional seismic imaging. *Annual Review of Earth and Planetary Sciences* 15: 115–139.
- Thurber CH and Eberhart-Phillips D (1999) Local earthquake tomography with flexible gridding. *Computers and Geosciences* 25: 809–818.
- Thurber C, Roecker S, Zhang H, Baher S, and Ellsworth W (2004) Fine-scale structure of the San Andreas fault and location of the SAFO target earthquakes. *Geophysical Research Letters* 31: L12S02 (doi:10.1029/2003GL019398).
- Thurber C, Trabant C, Haslinger F, and Hartog R (2001) Nuclear explosion locations at the Balapan, Kazakhstan, nuclear test site: The effects of high-precision arrival times and three-dimensional structure. *Physics of the Earth and Planetary Interiors* 123: 283–301.

- Trampert J (1998) Global seismic tomography: The inverse problem and beyond. *Inverse Problems* 14: 371–385.
- Trampert J and Lévéque JJ (1990) Simultaneous iterative reconstruction technique: Physical interpretation based on the generalized least squares solution. *Journal of Geophysical Research* 95: 12553–12559.
- Trampert J and Snieder R (1996) Model estimations biased by truncated expansions: Possible artifacts in seismic tomography. *Science* 271: 1257–1260.
- Trampert J and Woodhouse JH (1995) Global phase velocity maps of Love and Rayleigh waves between 40 and 150 seconds. *Geophysical Journal International* 122: 675–690.
- Trampert J and Woodhouse JH (1996) High resolution global phase velocity distributions. *Geophysical Research Letters* 23: 21–24.
- VanDecar JC, James DE, and Assumpcao M (1995) Seismic evidence for a fossil mantle plume beneath South America and implications for plate driving forces. *Nature* 378: 25–31.
- van der Hilst RD, Widjiantoro S, and Engdahl ER (1997) Evidence for deep mantle circulation from global tomography. *Nature* 386: 578–584.
- van der Hilst RD and De Hoop M (2005) On sensitivity kernels for ‘wave-equation’ transmission tomography. *Geophysical Journal International* 160: 621–633.
- van Heijst HJ and Woodhouse JH (1999) Global high-resolution phase velocity distributions of overtone and fundamental-mode surface waves determined by mode branch stripping. *Geophysical Journal International* 137: 601–620.
- van der Lee S and Nolet G (1997) Upper mantle S velocity structure of North America. *Journal of Geophysical Research* 102: 22815–22838.
- van der Sluis A and van der Vorst HA (1987) Numerical solution of large sparse linear algebraic systems arising from tomographic problems. In: Nolet G (ed.) *Seismic Tomography*, ch. 3, pp. 49–83. Dordrecht, The Netherlands: D. Reidel.
- Van der Voo R, Spakman W, and Bijwaard H (1999) Tethyan subducted slabs under India. *Earth and Planetary Science Letters* 171: 7–20.
- Vasco DW, Johnson LR, and Pulliam J (1995) Lateral variations in mantle velocity structure and discontinuities determined from P, PP, S, SS and SS-S_dS travel time residuals. *Journal of Geophysical Research* 100: 24037–24059.
- Vesnaver A (1996) The contribution of reflected, refracted and transmitted waves to seismic tomography: A tutorial. *First Break* 14: 159–168.
- Wagner LS, Beck SL, and Zandt G (2005) Upper mantle structure in the south central Chilean subduction zone (30 to 36S). *Journal of Geophysical Research* 110: B01308 (doi:10.1029/2004JB003238).
- Walck MC and Clayton RW (1987) P wave velocity variations in the Coso region California, derived from local earthquake travel times. *Journal of Geophysical Research* 92(B1): 393–405.
- Waldhauser F (2001) HypoDD: A computer program to compute double-difference earthquake locations. *US Geological Survey Open-File Report*, 01–113, Menlo Park, California.
- Waldhauser F and Ellsworth WL (2000) A double-difference earthquake location algorithm: Method and application to the northern Hayward fault. *Bulletin of the Seismological Society of America* 90: 1353–1368.
- Waldhauser F, Ellsworth WL, and Cole A (1999) Slip-parallel seismic lineations on the northern Hayward fault, California. *Geophysical Research Letters* 26: 3525–3528.
- Waldhauser F, Lippitsch R, Kissling E, and Ansorge J (2002) High-resolution teleseismic tomography of upper mantle structure using an *a priori* 3-D crustal model. *Geophysical Journal International* 150: 1–12.
- Wang Z and Dahlen FA (1995) Validity of surface-wave ray theory on a laterally heterogeneous Earth. *Geophysical Journal International* 123: 757–773.
- Weiland CM, Steck LK, Dawson PB, and Korneev VA (1995) Nonlinear teleseismic tomography at Long Valley caldera, using three-dimensional minimum travel time ray tracing. *Journal of Geophysical Research* 100: 20379–20390.
- Wesson RL (1971) Travel-time inversion for laterally inhomogeneous crustal velocity models. *Bulletin of the Seismological Society of America* 61: 729–746.
- Widjiantoro S, Kennett BLN, and van der Hilst RD (1998) Extending shear-wave tomography for the lower mantle using S and SKS arrival-time data. *Earth, Planets and Space* 50: 999–1012.
- Widjiantoro S, Gorbatov A, Kennett BLN, and Fukao Y (2000) Improving global shear wave traveltimes tomography using three-dimensional ray tracing and iterative inversion. *Geophysical Journal International* 141: 747–758.
- Widjiantoro S and van der Hilst RD (1997) Mantle structure beneath Indonesia inferred from high-resolution tomographic imaging. *Geophysical Journal International* 130: 167–182.
- Wielandt E (1987) On the validity of the ray approximation for interpreting delay times. In: Nolet G (ed.) *Seismic Tomography: With Applications to Global Seismology and Exploration Geophysics*, pp. 85–98. Dordrecht, The Netherlands: D Reidel.
- Wiggins RA (1972) The general linear inverse problem: Implication of surface waves and free oscillations for earth structure. *Reviews of Geophysics and Space Physics* 10: 251–285.
- Wolfe C (2002) On the mathematics of using difference operators to relocate earthquakes. *Bulletin of the Seismological Society of America* 92: 2879–2892.
- Woodhouse JH and Dziewonski AM (1984) Mapping the upper mantle: Three-dimensional modeling of Earth structure by inversion of seismic waveforms. *Journal of Geophysical Research* 89: 5953–5986.
- Woodhouse JH and Dziewonski AM (1989) Seismic modelling of the Earth’s large-scale three-dimensional structure. *Philosophical Transactions of the Royal Society of London A* 328: 291–308.
- Woodward RL and Masters G (1991) Global upper mantle structure from long-period differential travel-times. *Journal of Geophysical Research* 96: 6351–6377.
- Yao ZS, Roberts RG, and Tryggvason A (1999) Calculating resolution and covariance matrices for seismic tomography with the LSQR method. *Geophysical Journal International* 138: 886–894.
- Zhang H and Thurber CH (2003) Double-difference tomography: The method and its application to the Hayward fault, California. *Bulletin of the Seismological Society of America* 93: 1875–1889.
- Zhang H and Thurber C (2005) Adaptive mesh seismic tomography based on tetrahedral and Voronoi diagrams: Application to Parkfield, California. *Journal of Geophysical Research* 110: B04303 (doi:10.1029/2004JB003186).
- Zhang H and Thurber C (2006) Development and applications of double-difference seismic tomography. *Pure and Applied Geophysics* 163: 373–403.
- Zhang H, Thurber C, Shelly D, Ide S, Beroza G, and Hasegawa A (2004) High-resolution subducting slab structure beneath Northern Honshu, Japan, revealed by double-difference tomography. *Geology* 32: 361–364.
- Zhang J and McMechan GA (1995) Estimation of resolution and covariance for large matrix inversions. *Geophysical Journal International* 121: 409–426.

- Zhang YS and Tanimoto T (1993) High-resolution global upper mantle structure and plate tectonics. *Journal of Geophysical Research* 98: 9793–9823.
- Zhao D (2004) Global tomographic images of mantle plumes and subducting slabs: Insight into deep earth dynamics. *Physics of the Earth and Planetary Interiors* 146: 3–34.
- Zhao D, Hasegawa A, and Horiuchi S (1992) Tomographic imaging of P and S wave velocity structure beneath northeastern Japan. *Journal of Geophysical Research* 97: 19909–19928.
- Zhao L and Jordan TH (1998) Sensitivity of frequency-dependent travel times to laterally heterogeneous, anisotropic Earth structure. *Geophysical Journal International* 133: 683–704.
- Zhao L, Jordan TH, Olsen KB, and Chen P (2005) Frechet kernels for imaging regional earth structure based on three-dimensional reference models. *Bulletin of the Seismological Society of America* 95: 2066–2080.
- Zhou HW (1996) A high resolution P wave model for the top 1200 km of the mantle. *Journal of Geophysical Research* 101: 27791–27810.
- Zielhuis A and Nolet G (1994) Shear wave velocity variations in the upper mantle beneath Europe. *Geophysical Journal International* 117: 695–715.

1.11 Crust and Lithospheric Structure – Global Crustal Structure

W. D. Mooney, US Geological Survey, Menlo Park, CA, USA

Published by Elsevier B.V.

1.11.1	Introduction, Purpose, and Scope	361
1.11.2	Geology, Tectonics, and Earth History	364
1.11.3	Seismic Techniques for Determining the Structure of the Crust and Uppermost Mantle	366
1.11.3.1	Active-Source Data	366
1.11.3.1.1	Seismic refraction/wide-angle reflection profiles	368
1.11.3.1.2	Seismic reflection profiles	369
1.11.3.2	Passive-Source Data	370
1.11.3.2.1	Surface waves	372
1.11.3.2.2	Seismic tomography	372
1.11.3.3	Receiver Functions	372
1.11.3.4	Laboratory Studies	373
1.11.3.4.1	Velocity-density relations	373
1.11.3.4.2	V_p - V_s relations and poisson's ratio	373
1.11.3.4.3	Seismic anisotropy and the uppermost mantle	374
1.11.4	Nonseismic Constraints on Crustal Structure	375
1.11.4.1	Gravity Anomalies	375
1.11.4.2	Aeromagnetics	376
1.11.4.3	Geoelectrical Measurements	379
1.11.4.4	Heat Flow Data	379
1.11.4.5	Borehole Data	380
1.11.4.6	Surface Geology, Exposed Deep Crustal Sections, and Xenolith Data	380
1.11.5	Structure of Oceanic Crust and Passive Margins	380
1.11.5.1	Typical Oceanic Crust	381
1.11.5.2	Mid-Ocean Ridges	384
1.11.5.3	Oceanic Plateaux and Volcanic Provinces	384
1.11.5.4	Ocean Trenches and Subduction Zones	387
1.11.5.5	Passive Continental Margins	388
1.11.6	Structure of Continental Crust	389
1.11.6.1	General Features	389
1.11.6.2	Principal Crustal Types	389
1.11.6.3	Correlation of Crustal Structure with Tectonic Provinces	394
1.11.7	Global Crustal Models	394
1.11.7.1	The Sedimentary Cover	395
1.11.7.2	The Crystalline Crust and Uppermost Mantle	395
1.11.8	Discussion and Conclusions	397
References		398

1.11.1 Introduction, Purpose, and Scope

The crust preserves a record of the Earth's evolution that extends back more than 3.4 Gy. The crust also provides our natural resources, and presents social

challenges in the form of natural hazards, such as earthquakes and volcanoes. Despite its importance, the clear recognition of a ubiquitous crust encircling the Earth dates back to less than 100 years (Mohorovicic, 1910). In fact, as recently as the 1960s it was hypothesized that the ocean floor was

composed of serpentinized peridotite (hydrated ultramafic mantle rocks; Hess, 1962), a view that would have restricted true crustal material (i.e., silica-rich rocks) to the continents and its margins. Today it is well established that silicic material extracted from the mantle forms an outer crust in most regions of the Earth.

The Earth's crust has profound implications for all aspects of the planet's physical state and evolution. The process of crustal formation led to the complementary formation of an underlying mantle lithosphere, classically referred to by seismologists as 'the mantle lid' due to its finite thickness (*c.* 50–200 km) (Gutenberg,

1959; Oliver *et al.*, 1959). The physical properties of the crust plus mantle lithosphere modulate the rate at which heat is released to the Earth's surface, regulates mantle convection, determines the location of earthquakes and volcanoes, and more generally defines the rules for plate tectonic processes.

The foundations of seismic studies of the crust and upper mantle were laid in the period 1909–69 when the results of many pioneering studies provided a global view of the structure of the Earth's crust (Table 1). However, most of these early studies of the crust were hindered by technical limitations, and yielded field observations that presented an aliased image of the

Table 1 Classical references concerning the Earth's crust and uppermost mantle: the first 60 years: 1909–69

Year	Authors	Areas covered	J/A/B
1910	Mohorovicic	Europe	B
1925	Conrad	Europe	J
1926	Byerly	N-America	J
1932	Byerly and Dyk	N-America	J
1932	Gutenberg	N-America	J
1932	Gutenberg <i>et al.</i>	World	J
1935	DeGolyer	World	J
1935	Heiland	World	J
1935	Jeffreys and Bullen	World	J
1936	Leet	Europe	J
1937	Ewing <i>et al.</i>	Atlantic	J
1938	Slichter	World	J
1940	Jakosky	World	B
1940	Jeffreys	World	J
1940	Jeffreys	World	B
1943	Woppard	N-America	J
1949	Mintrop	World	J
1951	Junger	N-America	J
1951	Tuve	World	
1951	Slichter	N-America	J
1952	Birch	World	J
1952	Hersey <i>et al.</i>		J
1953	Tatel <i>et al.</i>	World	J
1953	Hodgson	N-America	J
1953	Tuve	World	J
1954	Ewing and Press	World	J
1954	Tuve <i>et al.</i>	World	J
1954	Katz	N-America	J
1955	Ewing <i>et al.</i>	N-America	A
1953	Tatel <i>et al.</i>	World	J
1955	Tatel and Tuve	World	A
1956	Press	World	B
1957	Oliver and Ewing	World	J
1958	Officer	World	B
1958	Oliver and Ewing	World	J
1959	Gutenberg	World	B
1959	Woppard	World	J
1959	Oliver <i>et al.</i>	World	J
1959	Richards and Walker	N-America	J
1960	Birch	World	J
1960	Willmore, Bancroft	World	J

(Continued)

Table 1 (Continued)

Year	Authors	Areas covered	J/A/B
1960	Brune <i>et al.</i>	World	J
1961	Anderson	World	J
1961	Birch	World	J
1961	Closs and Behnke	Australia	J
1961	Cram	N-America	J
1961	Jensen	World	J
1961	Steinhart and Meyer	World	B
1962	Oliver	World	J
1962	Alexander	N-America	J
1962	Hess	World	A
1963	Hill	Oceans	A
1963	Pakiser	N-America	J
1963	Brune and Dorman	N-America	J
1963	Jackson <i>et al.</i>	N-America	J
1963	Wilson	World	J
1963	Raitt	World	A
1964	Anderson and Archambeau	World	J
1964	Simmons	World	J
1964	McEvilly	World	J
1964	Pakiser and Steinhart	World	A
1964	Press	World	J
1964	Crampin	World	J
1964	Kovach and Anderson	World	J
1965	Christensen	World	J
1965	Dix	World	J
1965	Kanasewich and Cumming		J
1965	Jackson and Pakiser	N-America	J
1965	Roller	N-America	J
1965	Willden	N-America	J
1965	Wilson	World	J
1966	Bath and Stefánsson	World	J
1966	Berry and West	N-America	J
1966a, 1966b	Christensen	World	J
1966	Ewing <i>et al.</i>	N-America	J
1966	James and Steinhart	World	A
1966	Smith <i>et al.</i>	World	J
1966	Crampin	Eurasia	J
1966	Woppard	N-America	J
1967	Anderson	World	J
1967	Steinhart	World	A
1967	Meissner	World	J
1967	Shor		J
1968	Press	Europe	J
1969	Hart	World	B
1969	Zietz	N-America	J
1969	Brune	World	J
1969	Herrin	N-America	J
1957	Baranov	World	J
1967	Bateman and Eaton	N-America	J

N-America, North America.

crust. It is not surprising that, with some notable exceptions (Meissner, 1967; Mueller, 1977), these data were commonly interpreted in terms of two or more homogeneous layers, the upper layer (compressional wave velocity, $V_p = 6.0 \text{ km s}^{-1}$) assigned a granitic

composition, the lower layer ($V_p = 6.5 \text{ km s}^{-1}$) a basaltic composition (Birch, 1952; Pakiser and Steinhart, 1964). Advances in technology have resulted in higher-resolution data revealing a much richer and more complex picture of the crust, as well as generating many new

questions. Among the outstanding questions are the age and physical properties of the Moho and mid-crustal seismic discontinuities, the possible presence of deep crustal fluids, the geometry of crustal faults at depth, crustal modification by lateral crustal flow, and the possible existence of pervasive crustal seismic anisotropy.

Our understanding of the seismic structure of the crust began to change radically with the advent of deep seismic reflection profiling (Meissner, 1973; Oliver *et al.*, 1976) and the development of numerous stand-alone, portable seismographs used for seismic refraction/wide-angle reflection profiling (Healy *et al.*, 1982). These data provided an unbiased view of the crust to frequencies of 20 Hz and higher (corresponding to 300 m and higher resolution within the crust). These data demonstrated that the crust is highly heterogeneous, both vertically and laterally, in composition and physical properties (Mueller, 1977, 1978; Fountain, 1986; Holbrook *et al.*, 1992).

By the 1970s a large body of deep seismic data had been collected throughout the world, and the first regional crustal thickness models were created (Warren and Healy, 1973; Giese, 1976; Belousov and Pavlenkova, 1984; Prodehl, 1984). Compilations of crustal seismic data into global models can be traced to the global Moho map of Soller *et al.* (1982). This map, while highly informative, did not easily lend itself to use in numerical calculations that make quantitative corrections for the crust. A major step forward was the publication of the global $2^\circ \times 2^\circ$ 3SMAC model (Nataf and Ricard, 1996) that for the first time permitted the calculation of crustal corrections to seismological and other geophysical observations. In the past decade, a tremendous number of new seismic field observations have been made, thereby making it possible to improve the accuracy of previous global crustal models (Mooney *et al.*, 1998; Pasyanos *et al.*, 2004). In this chapter we document these advances and summarize the current status of global crustal models.

1.11.2 Geology, Tectonics, and Earth History

The Earth's lithosphere is qualitatively defined as the cold, upper layer of the Earth and is divided into large blocks called tectonic plates (Figure 1). The lithosphere is on the order of 100 km thick, being the thinnest (20–100 km) in oceanic regions and the thickest (50–250+ km) in continental regions. The base of the lithosphere is defined by a thermal

boundary layer (Jordan, 1975, 1979, 1988; Artemieva and Mooney, 2001). The base of the crust is a petrologic boundary between silicic and ultramafic rocks, and may be discerned seismically as the depth within the lithosphere where V_p increases from about $6.57.3 \text{ km s}^{-1}$ (in the lower crust) to greater than 7.6 km s^{-1} (the uppermost mantle) (James and Steinhart, 1966). This boundary between the lower crust and upper mantle is called the Mohorovicic discontinuity (Mohorovicic, 1910; Jarchow and Thompson, 1989) and is usually at a depth (below sea level) of 10–14 km for oceanic crust, and 30–50 km for continental crust. The Earth's crust, which was originally extracted from the mantle, constitutes only about 0.7% of the total mass of the crust–mantle system (Taylor and McLennan, 1985). Further seismic discontinuities below the crust divide the interior of the Earth into the upper mantle, transition region, lower mantle, outer core, and inner core. These other discontinuities are discussed in other chapters of this volume.

As a consequence of plate tectonics (Figure 2), oceanic crust and continental crust vary systematically in their principal physical properties, including density, thickness, age, and composition. Continental crust has an average thickness of 39 km, density of 2.84 g cm^{-3} , and an average age of 1500 My, while the oceanic crust has an average thickness of about 6 km, density of 3 g cm^{-3} and is everywhere younger than 200 My. Oceanic crust is largely made up of theoleitic basalt, which has a dark, fine-grain texture that forms from quickly cooling magma. In contrast, continental crust has a more felsic composition than oceanic crust and ranges in thickness from 16 to 20 km in the Afar Triangle, northeast Africa, to 75+ km in the southern Tibetan Plateau. Ninety-five percent (by area) of the continental crust, however, is between 22 and 56 km thick.

This chapter presents a holistic view of the Earth's crustal structure, and summarizes the types of velocity and density models that characterize the crust on a global scale. In recent years, a wide variety of seismological techniques have been used to explore the crust. These include seismic refraction/wide-angle reflection profiles, near-vertical incidence reflection profiles, receiver functions, and local earthquake tomographic inversions. Some of these survey techniques have been in use for more than a half-century, and the results are reported in thousands of publications. These results make it possible to provide a comprehensive crustal model for the whole Earth, as well as higher-resolution regional models.

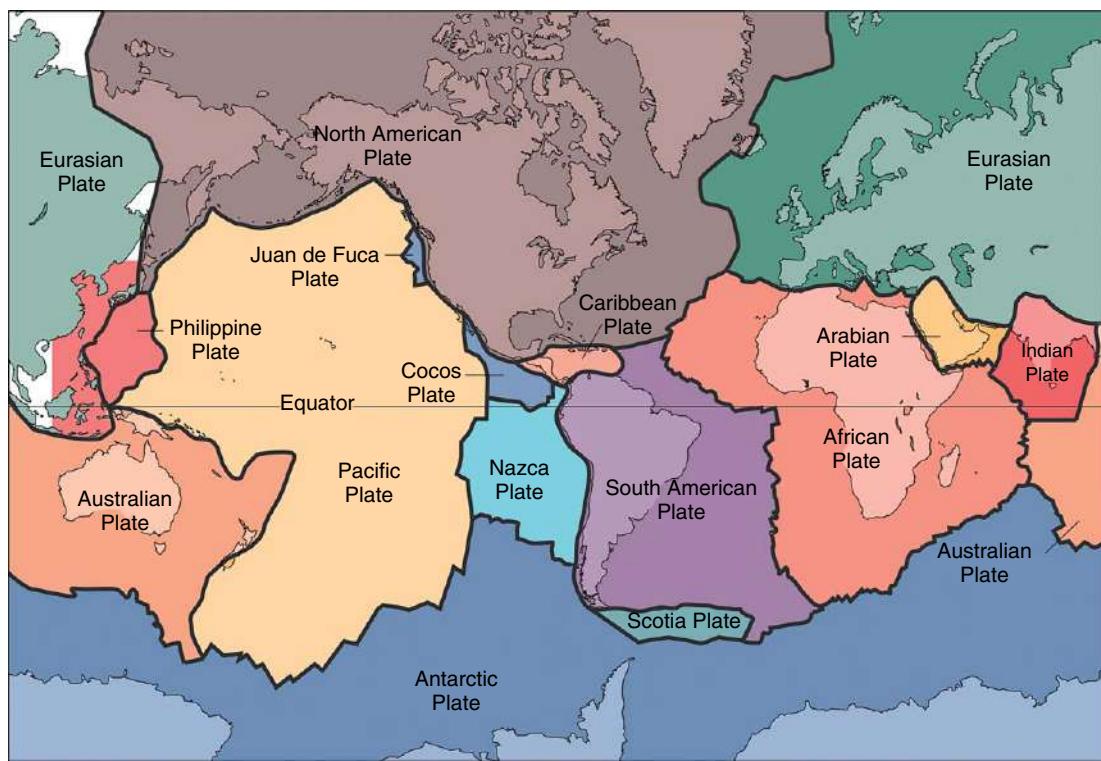


Figure 1 The 15 major tectonic plates on Earth, and the boundaries between these plates (Simkin et al., 2006). New oceanic lithosphere is constantly being produced at mid-ocean ridges (a divergent plate boundary) and later subducted back into the mantle at an oceanic subduction zone (a convergent plate boundary) (**Figure 2**). Plate motions led to the recycling of oceanic crust, arc volcanism, and compression at convergent boundaries. This chapter describes the complex and laterally variable deep seismic structure of the Earth's crust.

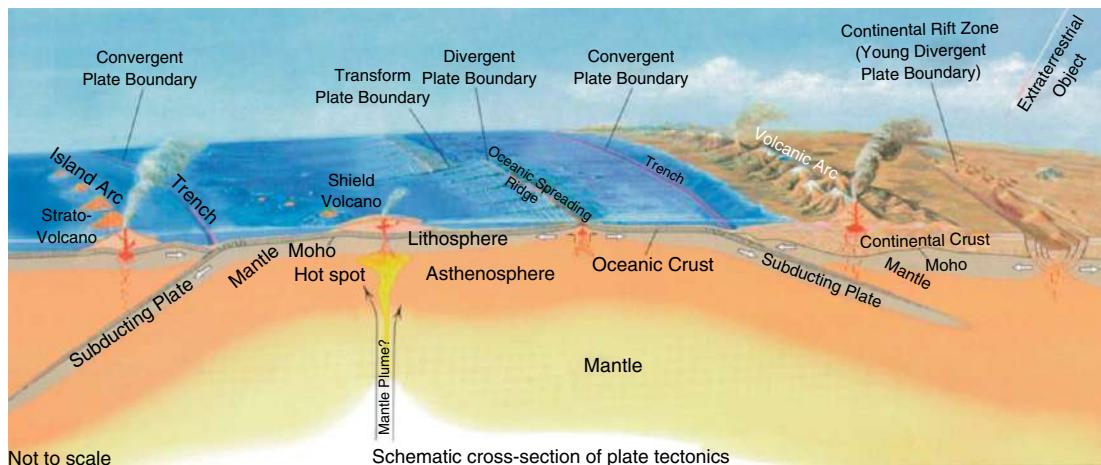


Figure 2 A cross section of the Earth's surface, indicating divergent (oceanic spreading ridge) and convergent (subducting plate) plate boundaries (Simkin et al., 2006). Active magmatic arcs at convergent boundaries increase the volume of continental crust and continental rift zones lead to crustal thinning. We summarize the deep structure of these and other features of the Earth's crust.

1.11.3 Seismic Techniques for Determining the Structure of the Crust and Uppermost Mantle

Seismic techniques provide the highest-resolution geophysical measurements of the structure of the crust and uppermost mantle. These techniques may be divided into those using active sources versus passive sources. Active sources are man-made seismic sources such as vibrators, air guns, and borehole explosions. Passive sources are derived from naturally occurring seismicity. Both active and passive sources generate P and S body waves, Love and Rayleigh waves, and diffracted and scattered waves. We discuss active and passive seismic techniques in turn.

1.11.3.1 Active-Source Data

Active-source seismic measurements of the structure of the crust have been conducted on a worldwide basis (Soller *et al.*, 1982; Meissner, 1986; Mooney *et al.*, 2002; **Table 2a**). Seismic studies of the deep

Table 2a Selected papers on data analysis methods in crustal seismology: Active sources

References	Year
Aki	1982
Aki and Lee	1976
Aki <i>et al.</i>	1977
Ansorge <i>et al.</i>	1982
Berry and West	1966
Bessonova <i>et al.</i>	1976
Boore	1972
Bouchon	1982
Braile and Chiang	1986
Braile <i>et al.</i>	1995
Chapman and Orcutt	1985
Červený	1972
Červený <i>et al.</i>	1977
Červený and Pšeničník	1984
Chapman	1978
Claerbout	1976, 1985
Closs and Behnke	1961
Deichmann and Ansorge	1983
Dix	1965
Dobrin	1976
Dohr	1970
Ewing <i>et al.</i>	1957
Finlayson and Ansorge	1984
Fuchs and Mueller	1971
Gajewski and Pšeničník	1987
Giese	1976
Giese <i>et al.</i>	1976

Haberland <i>et al.</i>	2003
Hajnal	1986
Hale and Thompson	1982
Heacock	1971, 1977
Hole	1992
Hole and Zelt	1995
Hole <i>et al.</i>	1992
Hwang and Mooney	1986
Kelley <i>et al.</i>	1976
Kennett	1974, 1983
Kind	1978
Klemperer and Luetgert	1987
Klemperer and Oliver	1983
Levander and Holliger	1992
Ludwig <i>et al.</i>	1970
Lutter <i>et al.</i>	1990
Mair and Lyons	1976
Makovský <i>et al.</i>	1996a, 1996b
McEchan and Mooney	1980
Menke	1989
Milkereit <i>et al.</i>	1985
Mooney	1989
Mooney and Brocher	1987
Mooney and Meissner	1992
Mooney <i>et al.</i>	2002
Müller	1985
Nelson <i>et al.</i>	1996
Sandmeier and Wenzel	1986, 1990
Sheriff and Geldart	1982, 1983
Schilt <i>et al.</i>	1979
Telford <i>et al.</i>	1976
Willmore and Bancroft	1960
Zandt and Owens	1986
Zelt	1999
Zelt and Barton	1998
Zelt and Smith	1992
Zelt <i>et al.</i>	2003
Zelt <i>et al.</i>	1999

Table 2b Selected papers on data analysis methods in crustal seismology: Passive sources

References	Year
Aki and Richards	1980
Ammon <i>et al.</i>	1990
Barmin <i>et al.</i>	2001
Bath and Stefánsson	1966
Bessonova <i>et al.</i>	1974
Bijwaard <i>et al.</i>	1998
Boore	1972
Boschi <i>et al.</i>	2004
Bostock <i>et al.</i>	2002
Bouchon	1982
Brune	1969
Brune and Dorman	1963
Brune <i>et al.</i>	1960
Bruneton <i>et al.</i>	2004
Burdick and Langston	1977
Cassidy	1992

(Continued)

Table 2b (Continued)

References	Year
Chapman	1978
Chen <i>et al.</i>	2005
Chimera <i>et al.</i>	2003
Crosson	1976
Curtis and Woodhouse	1997
Debayle and Lévéque	1997
Dziewonski	1989
Dziewonski and Anderson	1981
Eberhart-Phillips	1986
Ekström <i>et al.</i>	1997
Ewing and Press	1954
Grand <i>et al.</i>	1997
Hearn and Clayton	1986
Hearn and Ni	1994
Hearn <i>et al.</i>	1991, 2004
Hofsetter and Bock	2004
Hole <i>et al.</i>	2000
Huang <i>et al.</i>	2004
Humphreys and Clayton	1988
Humphreys <i>et al.</i>	1984
Iyer and Hirahara	1993
Jordan and Frazer	1975
Karagianni <i>et al.</i>	2005
Kennett and Engdahl	1991
Kind	1978
Knopoff	1972
Kovach	1978
Langston	1977
Langston <i>et al.</i>	2002
Lebedev and Nolet	2003
Lei and Zhao	2005
Levshin <i>et al.</i>	2005
Li and Romanowicz	1996
Liang <i>et al.</i>	2004
Liu <i>et al.</i>	2005
Maggi and Priestley	2005
Mahadeven	1994
Mandal <i>et al.</i>	2004
McEvilly	1964
Mitchell and Herrmann	1979
Mooney	1989
Nakamura <i>et al.</i>	2003
Nolet	1987b, 1990
Okabe <i>et al.</i>	2004
Owens and Zandt	1985
Pasyanos	2000
Pilidou <i>et al.</i>	2005
Priestly and Brune	1978
Ritzwoller and Lavelle	1995
Ritzwoller <i>et al.</i>	2002a, 2002b
Savage	1999
Shapiro and Ritzwoller	2002
Su <i>et al.</i>	1994
Sun <i>et al.</i>	2004a, 2004b
Thurber	1983, 1993
Thurber and Aki	1987
Tilmann <i>et al.</i>	2003
Vinnik <i>et al.</i>	2004
Wang <i>et al.</i>	2003
Woodhouse and Dziewonski	1984
Worthington	1984
Yanovskaya and Kozhevnikov	2003
Yliniemi <i>et al.</i>	2004
Zandt and Owens	1986
Zhang and Lay	1996
Kennett	1983
Kind <i>et al.</i>	1995, 2002
Kissling	1998
Kissling <i>et al.</i>	2001
Langston	1994
Lees and Crosson	1989
Leveque <i>et al.</i>	1993
Levshin <i>et al.</i>	1989
Ma <i>et al.</i>	1996
Masters <i>et al.</i>	1996
Menke	1989
Nolet	1978, 1987a, 1987b
Owens <i>et al.</i>	1984
Rapine <i>et al.</i>	2001
Ritzwoller <i>et al.</i>	2002
Roecker <i>et al.</i>	2004
Tarantola and Nercessian	1984
Van Heijst and Woodhouse	1999
Vidale	1988, 1990
Vinnik	1977
Zhang and Thurber	2003
Zhao <i>et al.</i>	1992
Zhou <i>et al.</i>	2004, 2005

continental crust that utilize man-made sources are classified into two basic categories, seismic refraction profiles and seismic reflection profiles, depending on their field acquisition parameters. Seismic refraction profiles provide reliable information regarding the distribution of seismic velocities within the crust, and are very effective in mapping crustal thickness (**Figure 3**). In contrast, seismic reflection data provide an image of the crust at a finer scale (50 m in the vertical and horizontal dimensions), but with weak constraints on deep crustal velocities. As a result, seismic reflection and refraction data have complementary strengths: reflection data provide a detailed structural image of the crust, whereas refraction data provide an estimate of the seismic velocity distribution in the crust.

The most common sources used in land profiles are chemical explosions and mechanical vibrators (vibroseis). Chemical explosions are generally composed of ammonium nitrate compounds that are detonated in a borehole at a depth of 20–50 m in the ground. In contrast, a vibrator truck weighs several tons and has a heavy steel plate that is pressed against the ground

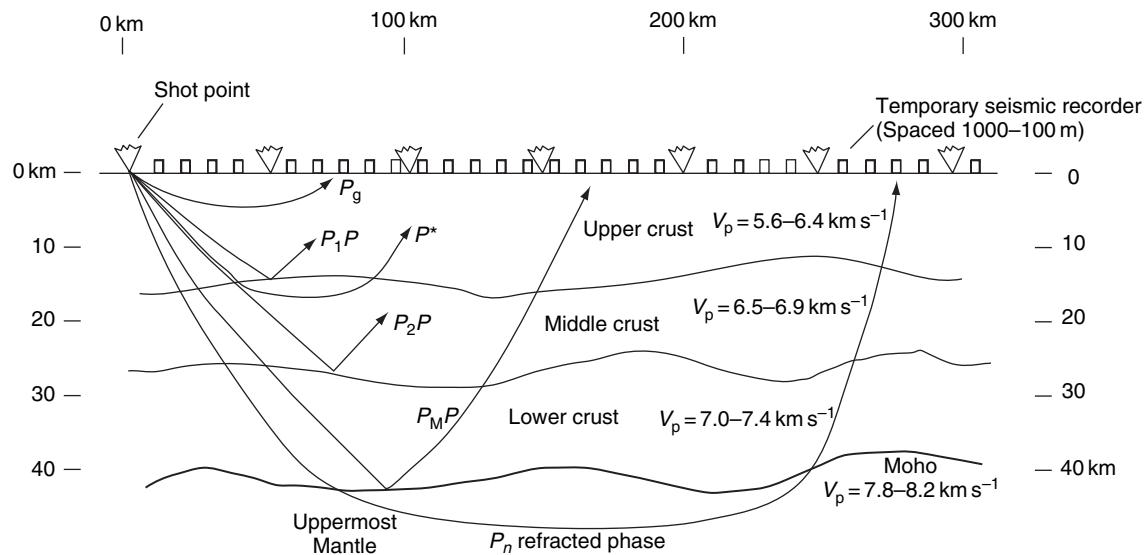


Figure 3 Ray paths for a continental seismic refraction/wide-angle reflection profile for crust with a typical seismic velocity structure found beneath a stable craton. The crust–mantle boundary (Moho) is a continuous feature, but intracrustal boundaries may be discontinuous laterally and several kilometers wide vertically. Commonly, shot points are spaced 50 km apart (or closer for higher resolution); temporary seismic recorders are spaced 1000–100 m apart.

that vibrates at increasing frequencies (5–60 Hz) for up to 30 s. The vibroseis method requires cross-correlation of the recordings with the source signal in the data-processing stage. The most common sources in marine profiles are the air gun, in which a bubble of very high-pressure air is released into water, and, prior to modern environmental concerns for marine life, explosive charges. Long-range seismic refraction data has also been recorded from nuclear sources, particularly in the former Soviet Union (Egorkin *et al.*, 1987; Pavlenkova, 1996). Due to the strength of these nuclear explosions, such long-range profiles probed not only the crust but the entire upper mantle to a depth of 660 km (Mechie *et al.*, 1993; Ryberg *et al.*, 1995, 1996; Morozov *et al.*, 1998; Morozova *et al.*, 1999).

1.11.3.1.1 Seismic refraction/wide-angle reflection profiles

Seismic refraction/wide-angle reflection profiles are recorded with relatively widely spaced (100–5000 m) geophones (typically with vertical-component seismometers) and long off-sets (100–500+ km) between sources and receivers (Figure 3). The data from these seismic profiles commonly contain strong wide-angle reflection phases (Figure 4) and provide excellent constraints on seismic velocity within the lithosphere.

Profiles with sources all to one side of the receivers are referred to as unreversed refraction profiles. Unreversed refraction profiles record only apparent

velocities and are interpreted as if the crust was composed of flat-laying, uniformly thick layers. Split refraction profiles, with the source in the center of the receivers, are in some ways similar to simple reversed refraction lines, and are commonly used for studies of the oceanic crust. Reversed refraction profiles generally have multiple shot points that provide overlapping coverage and provide the most reliable results (Figure 5). The most effective way to determine a velocity structure from seismic refraction data is to compute detailed 2-D ray-theoretical traveltimes (Figure 5(b)) and synthetic (theoretical) seismograms and compare these with the observed data (Braile and Smith, 1974; Mooney, 1989; Braile *et al.*, 1995; Chulick, 1997; Zelt and Smith, 1992; and Zelt, 1999). This modeling must take into account (1) the source time-function, which could be from an explosion, earthquake, air gun, or vibrator, (2) the effects of transmission through the crust, and (3) the response of the detection systems, which may be seismometers, amplifiers, and filters. For trial-and-error forward modeling, an initial velocity model is constructed, and is adjusted until the synthetic seismograms match the recorded seismograms to the desired degree. For inverse methods (e.g., Zelt and Smith, 1992), seismic traveltimes are used to obtain a best-fitting model, starting from the near-surface and moving down through the crust.

Seismic velocities in the crust are primarily determined by five factors: mineralogical composition,

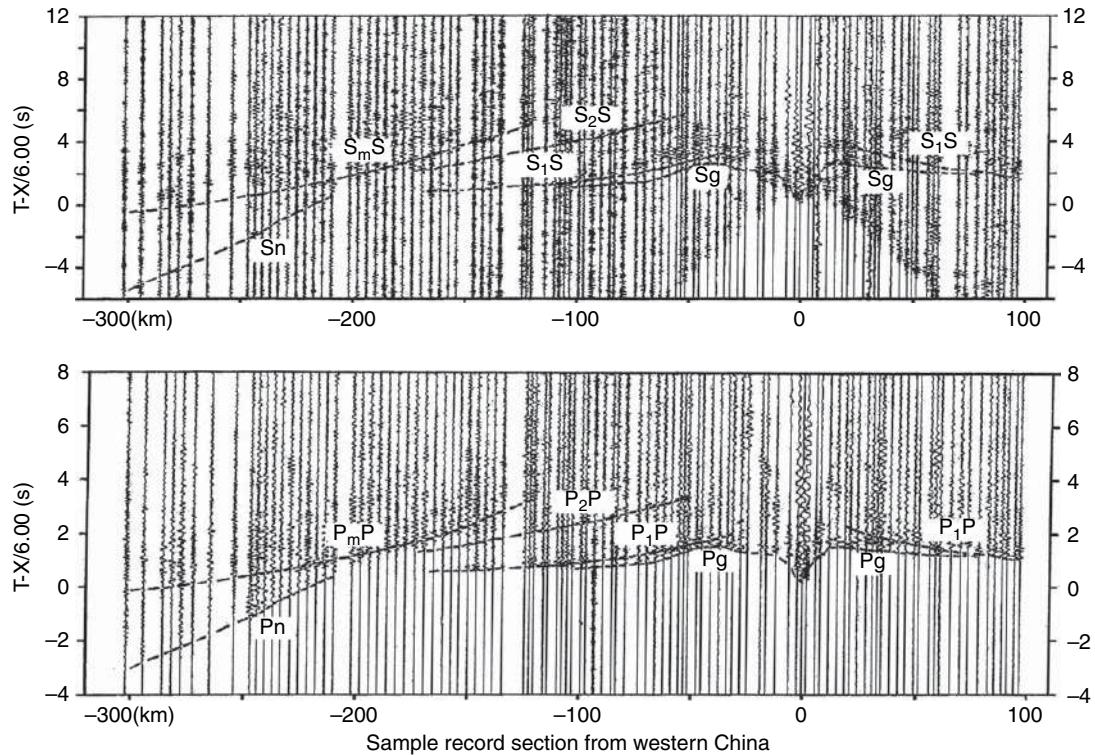


Figure 4 Sample seismic record section from western China. *Top:* Shear (S) wave record section with a reduction velocity of 3.46 km s^{-1} . This is a split-spread profile, with the shot point at 0 km; seismic phases as defined in [Figure 3](#); Sg , direct arrival; S_1S , reflection from boundary between upper and middle crust; S_2S , reflection from middle and lower crust; S_mS , reflection from Moho; S_n , refraction from uppermost mantle. *Bottom:* Compressional (P) wave record section with a reduction velocity of 6.0 km s^{-1} ; seismic phases as defined for S waves above ([Wang et al. 2003](#)).

confining pressure, temperature, anisotropy, and pore-fluid pressure. In order to draw inferences about the mineralogical composition of the deep crust, however, one must first estimate the contribution of the other four properties. Confining pressure is easily calculated from depth of burial, and temperature can be estimated from the surface heat flow. The quantitative effect on measured seismic velocities due to seismic anisotropy ([Rabbel and Mooney, 1996](#)) and pore-fluid pressure ([Hyndman, 1988](#)) are more difficult to estimate.

1.11.3.1.2 Seismic reflection profiles

Reflection seismology provides a more detailed image of crustal structure. Data are recorded with closely spaced (5–100 m) geophones and sources that yield a high-resolution image of the crust, but such data generally do not constrain seismic velocities in the deeper (middle and lower) crust. P waves from an energy source, such as a vibrator, buried explosive, or air gun, are reflected by intra-crustal interfaces and recorded by geophones

located close (0.1–10 km) to the source. In the data-processing stage, the effects of the source and receiver are removed from the recorded seismograms through a process called deconvolution, allowing for higher-resolution images of the structure. The seismic reflection data are commonly migrated, a processing step that shifts the reflectors into their correct spatial locations.

The seismic properties that are most readily obtained from reflection data are reflectivity patterns, and these correlate with distinct geologic settings. For example, the area around the United Kingdom and Ireland has undergone Mesozoic extension that is evident in deep seismic reflection data as tilted horst-and-grabens, a shallow (30 km) distinct Moho, and a dipping shear zone (Flannan reflections) within the upper mantle ([Figure 6](#)). When reflectivity patterns are interpreted with complementary seismic velocity and nonseismic crustal parameters (discussed below), inferences regarding the composition and evolution of the crust can be made ([Clowes et al., 1987](#)).

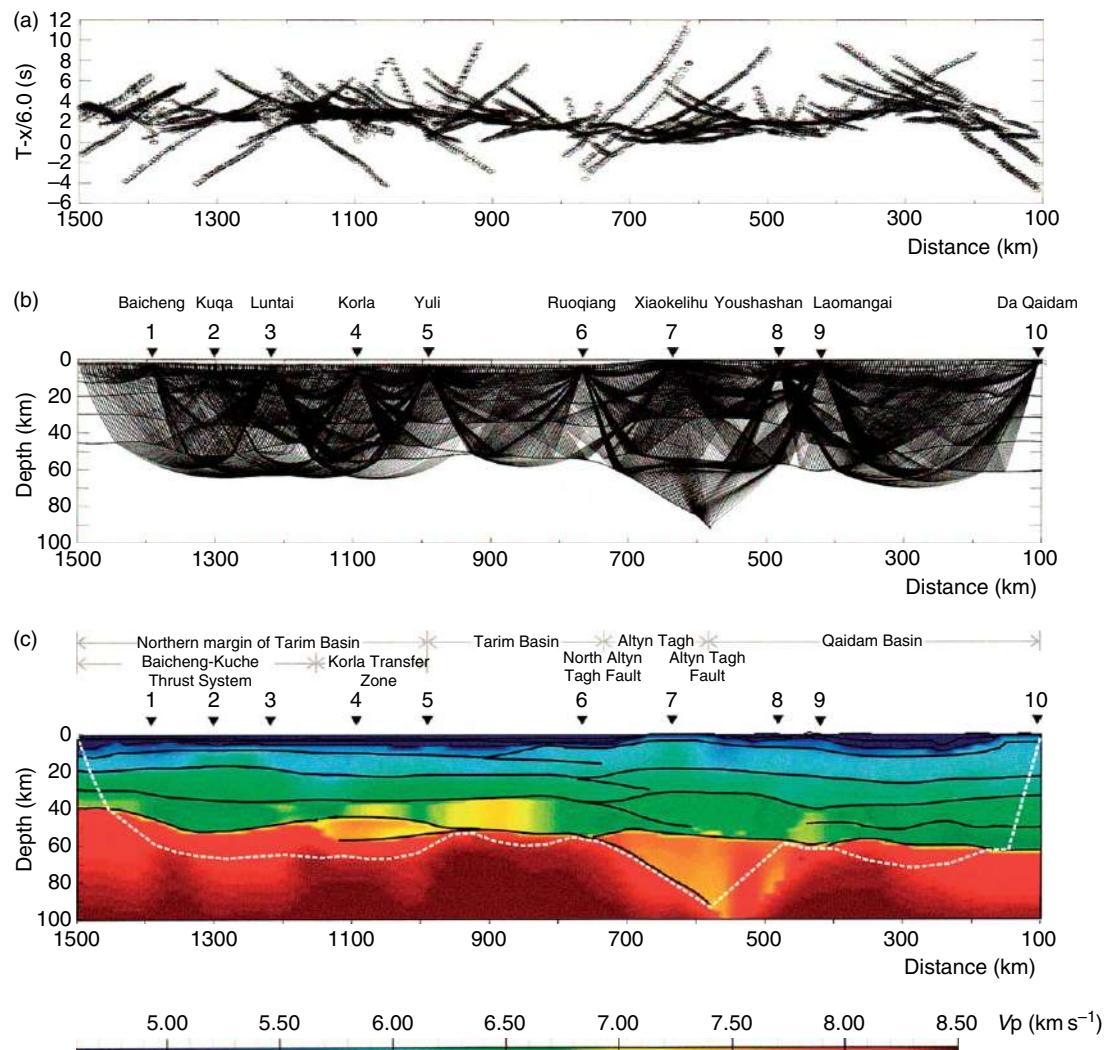


Figure 5 Modeling results along the seismic refraction/wide-angle reflection profile at the northern margin of the Tibetan Plateau. (a) Overlapping and reversing traveltimes curves; (b) ray tracing through the crustal model showing dense subsurface coverage that provides excellent constraints on seismic velocities; (c) crustal and uppermost mantle seismic velocity (V_p) model. Both V_p and V_s can be estimated for the crust from these data. P_n velocity ranges from 7.8 to 8.2 km s^{-1} . After Zhao JM, Mooney WD, Zhang X, Li Z, Jin Z, and Okaya N (2006) Crustal structure across the Altyn Tagh Range at the northern margin of the Tibetan Plateau and tectonic implications. *Earth and Planetary Science Letters* 241: 804–814.

The widespread observation of crustal reflectivity suggests that common processes account for its existence. The primary cause of crustal reflectivity is compositional and metamorphic layering within the crust. Regional and global plate stresses act to enhance crustal reflectivity by inducing lower crustal ductile flow that produces subhorizontal lamination. This ductile flow requires elevated temperatures, and is therefore more common in the middle and lower crust (e.g., **Figure 6**). A list of key references of active-source seismology studies can be found in **Table 2a**.

1.11.3.2 Passive-Source Data

Techniques to investigate the seismic structure of the crust and uppermost mantle using passive seismic data have seen rapid development in the past two decades (**Table 2b**). These developments can be attributed to the increased availability of higher-quality, broadband data from permanent seismic networks and temporary deployments, as well as increased computer power. Passive seismic techniques began with surface-wave studies (Ewing and Press, 1954; Brune and Dorman, 1963) and progressed to seismic tomography

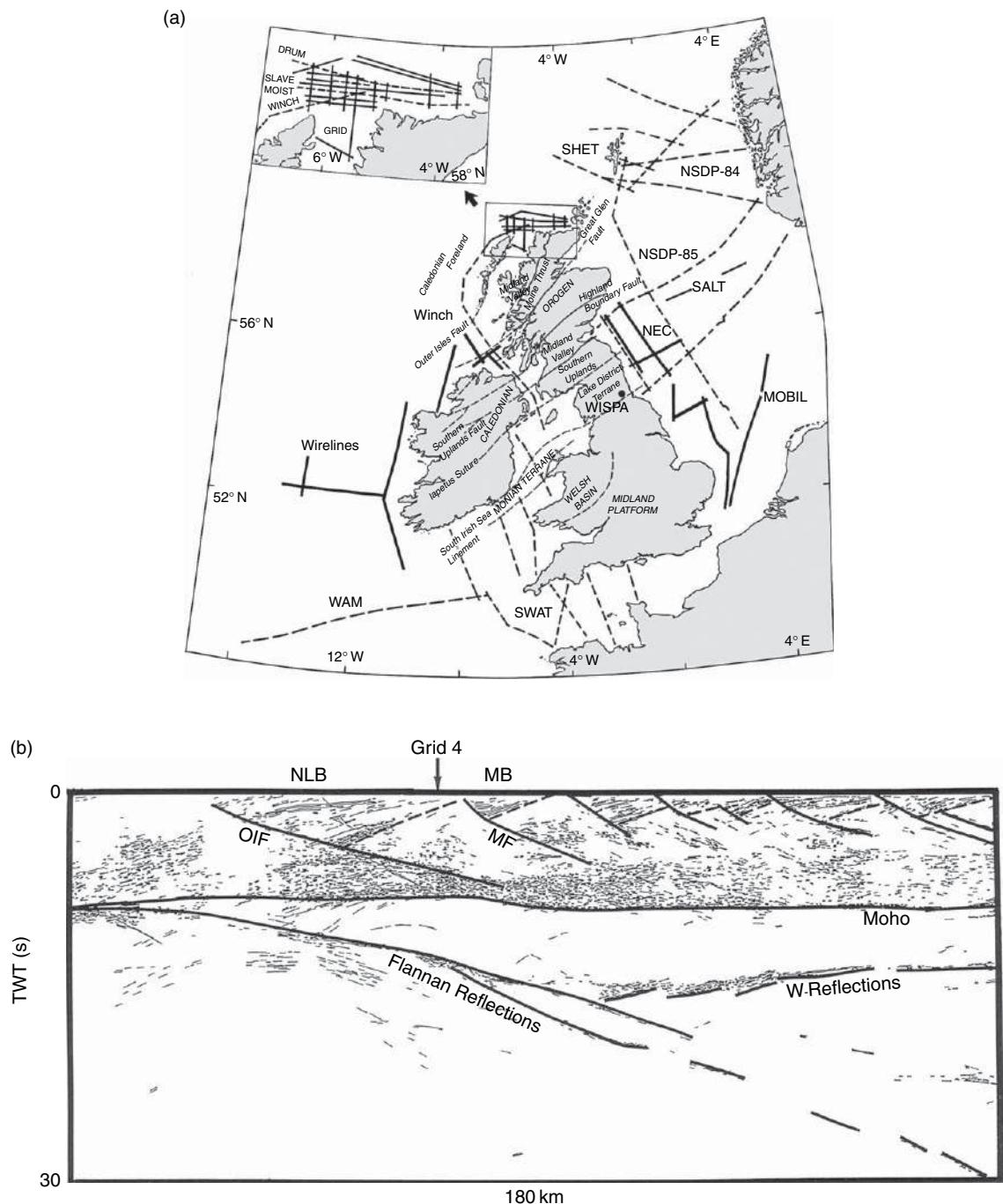


Figure 6 Deep seismic reflection imaging of crustal and upper-mantle fault zones. (a) Location map for the British Isles with marine seismic reflection profile lines indicated. (b) Seismic profile DRUM located off the north coast of Scotland (see inset in panel (a)). This profile shows brittle normal faults within the upper crust that merge into a zone of diffuse ductile deformation in the lower crust. The Moho is labeled at a two-way-time of 10 s (30 km depth). The uppermost mantle shows two zones of reflections, labeled Flannan and W. The Flannan reflections are interpreted as a Caledonian suture that was reactivated as an lithospheric extensional fault (Flack and Warner, 1990). (a) Modified from Matthews DH and BIRPS Core Group (1990) Progress in BIRPS deep seismic reflection profiling around the British Isles. *Tectonophysics* 173: 387–396.

(Aki *et al.*, 1977; Aki and Lee, 1976) and seismic receiver functions (Phinney, 1964; Vinnik, 1977; Langston, 1977). We discuss each of these in turn.

1.11.3.2.1 Surface waves

An earthquake near the Earth's surface will generate both Rayleigh and Love seismic surface waves. The amplitude of motion for these waves decreases exponentially with depth in the earth, with longer-wavelength waves sampling the velocity structure to greater depth than shorter-wavelength waves. This wavelength-depth dependence, combined with the increase of velocity with depth in the Earth gives rise to the dispersion of surface waves. This makes surface waves a valuable tool for the study of the velocity structure of the crust and mantle lithosphere (Oliver and Ewing, 1957, 1958; Oliver, 1962; Aki and Richards, 1980; Nolet, 1987a, 1987b; 1990; Lay and Wallace, 1995). The analysis of seismic surface waves for crustal and upper-mantle structure has been applied on a global basis and is particularly effective in determining 2-D and 3-D shear-wave structure (Debayle and Leveque, 1997; van der Lee and Nolet, 1997; Ritzwoller *et al.*, 2002a, 2002b; Shapiro and Ritzwoller, 2002; Langston *et al.*, 2002; Lebedev and Nolet, 2003; Chimera *et al.*, 2003; Panza *et al.*, 2003; Friederich, 2003; Okabe *et al.*, 2004; Boschi *et al.*, 2004; Bruneton *et al.*, 2004; Yoshizawa and Kennett, 2004; Pilidou *et al.*, 2004, 2005; Karagianni *et al.*, 2005; Levshin *et al.*, 2005; Maggi and Priestley, 2005). Thus, seismic surface waves provide complementary information to seismic refraction data that often provide information only on the compressional-wave structure of the crust. In addition, surface waves can be used to investigate regions that are aseismic (e.g., much of Africa and eastern South America). Such aseismic regions cannot be studied using other passive seismic methods. Surface-wave data can also be used to measure seismic anisotropy within the uppermost mantle (Huang *et al.*, 2004).

1.11.3.2.2 Seismic tomography

Local and distant (teleseismic) earthquake data can be used to determine crustal structure. Local seismic tomography uses earthquake arrivals at a network of seismic stations to determine crustal and upper-mantle structure by examining the arrival times of many crisscrossing paths between the earthquakes and seismometers. This technique, which is similar to medical tomography, has the potential to provide a 3-D picture of the crust and uppermost mantle. Local studies mainly provide information about the upper

and middle crust (Thurber, 1993; Mandal *et al.*, 2004; Lei and Zhao, 2005; Salah and Zhao, 2003; Table 2b), whereas regional studies have better resolution within the uppermost mantle, especially for P_n velocity (Bannister *et al.*, 1991; Hearn and Ni, 1994; McNamara *et al.*, 1997; Parolai *et al.*, 1997; Mele, 1998; Calvert *et al.*, 2000; Sandoval *et al.*, 2004; Ritzwoller *et al.*, 2002a; Chen *et al.*, 2003; Al-Lazki *et al.*, 2003; 2004; Sandoval *et al.*, 2004; Hearn *et al.*, 2004; Liang *et al.*, 2004). A second technique uses teleseismic data and generally provides an image that extends to greater depth (100+ km), but lacks high resolution of structure within the crust (Petit *et al.*, 1998; Bijwaard *et al.*, 1998; Allen *et al.*, 2002; Benoit *et al.*, 2003; Lippitsch *et al.*, 2003; Liu *et al.*, 2005). Tomographic studies are also effective at determining upper-mantle seismic attenuation (Gung and Romanowicz, 2004).

1.11.3.3 Receiver Functions

Estimating seismic structure from teleseismic receiver functions is a highly effective method of exploring the crust and upper mantle since it requires only a single broadband seismic station. Crustal layering is determined by signal processing of a three-component station using teleseismic P-wave arrivals. The incident P wave will undergo multiple conversions to S waves at seismic boundaries within the uppermost mantle and crust. The analysis of these converted waves yields the shear-wave velocity structure beneath the station (Phinney, 1964; Vinnik, 1977; Burdick and Langston, 1977; Langston, 1977; Owens *et al.*, 1988). The method works best with nearly horizontal layers, although forward modeling may be applied in regions with 3-D structure. An informative discussion of the method is given by Cassidy (1992). While the method is highly effective at determining seismic discontinuities in the crust and uppermost mantle, it cannot, by itself, determine absolute seismic velocities. One approach is to perform a joint inversion of receiver functions and surface-wave dispersion observations (Julia *et al.*, 2000). Numerous local and regional studies have been reported (e.g., Owens and Zandt, 1985; Ramesh *et al.*, 2002), including studies of the crust of North Africa (Sandvol *et al.*, 1998), Spain (Julia and Mejia, 2004), Turkey (Angus *et al.*, 2006), the western USA (Zhu and Kanamori, 2000), and various studies of the upper mantle (Kind and Vinnik, 1988; Yuan *et al.*, 1997; Kind *et al.*, 2002).

Recently, the receiver function method has been extended to consider converted, precursory P waves that arrive just prior to the direct S wave (Li *et al.*, 2004; Angus *et al.*, 2006). This is known as the S-wave receiver function method. S-wave receiver functions have a lower resolution than P-wave receiver functions, but are effective at identifying the base of the lithosphere (Li *et al.*, 2004).

1.11.3.4 Laboratory Studies

1.11.3.4.1 Velocity-density relations

Seismic-wave velocities and density are fundamental properties of Earth materials. Thousands of field and laboratory measurements have been made for V_p , but fewer measurements have been made of rock densities at depth, since these require a borehole. Compressional-wave velocity and density correlations are important because they allow estimates of crustal density for surface-wave inversions and gravity studies, and conversely, rock densities can be used to estimate seismic velocities (Christensen and Mooney, 1995). Classic studies of velocity–density relations include the Nafe–Drake curve (Nafe and

Drake, 1957); Birch (1961) law relating velocity, density, and mean atomic weight; and linear regression solutions for oceanic crust (Christensen and Salisbury, 1975). Figure 7 presents average velocities for 29 rock categories at a depth of 20 km and a temperature of 309°C, corresponding to an average continental geotherm, versus rock density (Christensen and Mooney, 1995). Two curves are drawn in Figure 7, a linear curve (solid line) and a nonlinear curve representing V_p –density correlations for continental crust. The appropriate coefficients for both linear and nonlinear solutions are presented by Christensen and Mooney (1995).

1.11.3.4.2 V_p – V_s relations and poisson's ratio

Seismic measurements of crustal structure more commonly report only V_p rather than V_p and V_s . There are several reasons for this. First, explosive or air gun sources generate primarily compressional-wave energy. Second, many field observations record on the vertical component of ground velocity. Third, shear-wave arrivals are often either weak or obscured by scattered seismic energy (coda). In the absence of

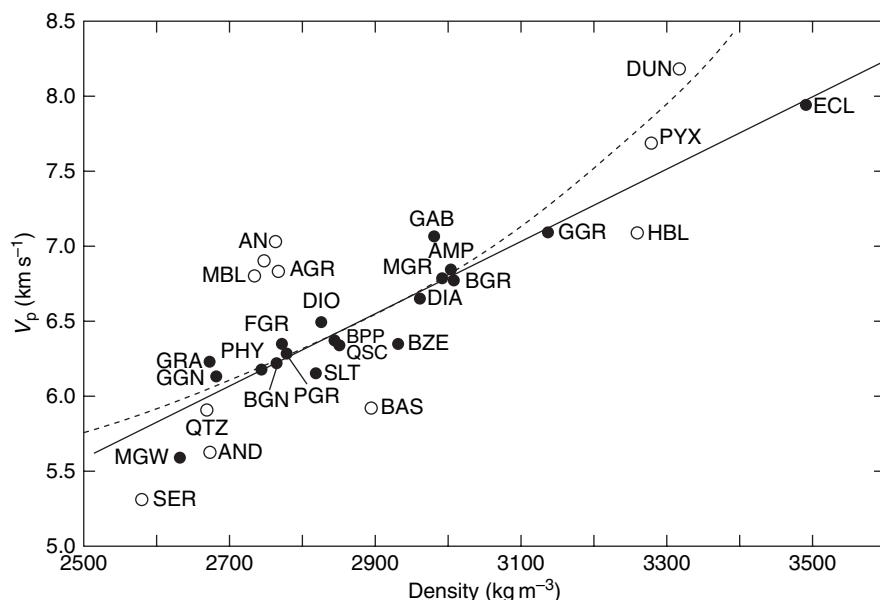


Figure 7 Average velocity versus average density for a variety of rock types at a pressure equivalent to 20 km depth and 309°C. Rock abbreviations are as follows. AGR, anorthositic granulite; AMP, amphibolite; AND, andesite; BAS, basalt; BGN, biotite (tondite) gneiss; BGR, greenschist facies basalt; BPP, prehnite–pumpellyite facies basalt; BZE, Zeolite facies basalt; DIA, diabase; DIO, dionite; DUN, Dunite; ECL, mafic eclogite; FGR, felsic granulite; GAB, gabbro–norite–troctolite; GGN, granite gneiss; GGR, mafic garnet granulite; GRA, granite–granodiorite; HBL, hornblendite; MBL, calcite marble; MGR, mafic granulite; MGW, metagraywacke; PGR, paragranulite; PHY, phyllite; PYX, Pyroxenite; QCC, mica quartz schist; QTZ, quartzite; SER, serpentinite; SLT, slate. After Christensen NI and Mooney WD (1995) Seismic velocity structure and the composition of the continental crust: A global view. *Journal of Geophysical Research* 100: 9761–9788.

measured shear-wave speeds it is necessary to estimate its value from V_p . A direct relation between V_s and V_p , therefore, is highly desirable for many studies. This is accomplished by using empirically derived V_p - V_s relations that are based on field borehole and seismic profiling data, together with laboratory measurements.

A recent study (Brocher, 2005) presents empirical relations between V_p , V_s , and Poisson's ratio that can be used to estimate the ratio V_p/V_s , or equivalently, Poisson's ratio from a knowledge of V_p and rock type (i.e., sedimentary vs crystalline rocks). The empirical and regressive fits are defined for V_p between 1.5 and 8.5 km s⁻¹ and fit the data remarkably well (Figure 8).

Conversely, the mineralogy of the crust can be estimated when both compressional (V_p) and shear-wave (V_s) velocities are measured (Figure 9). The ratio V_p/V_s is commonly expressed in terms of Poisson's ratio, which varies from 0.23 to 0.32 for most minerals, but quartz has a value of only 0.08 at room conditions (Christensen, 1996). Thus, the measurement of Poisson's ratio offers the means of distinguishing between felsic (quartz-rich) and mafic (quartz-poor) rocks.

1.11.3.4.3 Seismic anisotropy and the uppermost mantle

Many minerals exhibit birefringence, which is a directional dependence of the speed of light through the mineral. This phenomenon is used by petrologists to identify minerals in a thin section (≤ 1 mm), where a sample illuminated by polarized light is rotated under a microscope to reveal its birefringence. Likewise, elastic waves show a directional dependence in wave speed in many minerals. Perhaps the most prominent example is the mineral olivine which is a major constituent of the upper mantle. The discrepancy between Rayleigh and Love wave speeds was measured in the early 1960s (Anderson, 1961) and led to the recognition of seismic anisotropy in the mantle lid. At about the same time, laboratory measurements of metamorphic rocks demonstrated significant shear-wave anisotropy in the crust (Christensen, 1966b). These measurements demonstrated that seismic anisotropy is not confined to the upper mantle, but also plays a prominent role in the crust (Figure 10). Table 3 lists several key papers on the seismic properties, including anisotropy, of the uppermost mantle. References for laboratory studies of the properties of crustal rocks can be found in Tables 4a and 4b.

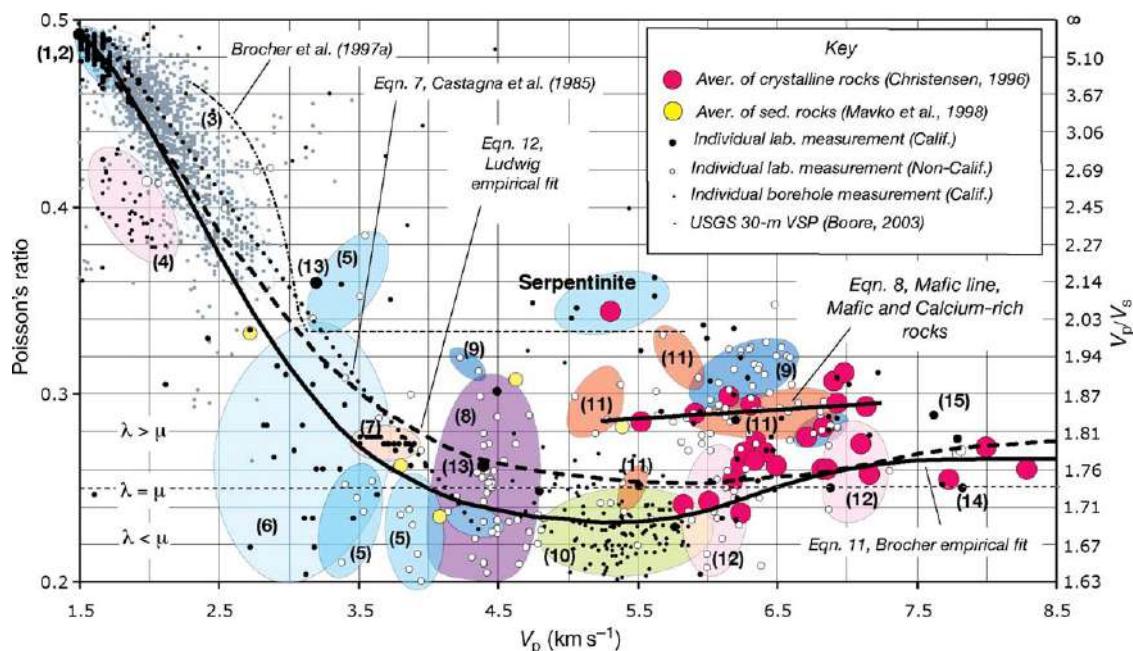


Figure 8 Poisson's ratio as a function of V_p for common lithologies. Colored ellipses highlight measurements reported by a single reference: bold numbers in parentheses link ellipses to results of similar studies. The thin horizontal dashed line shows Poisson's ratio of 0.25 ($V_p/V_s = 1.73$) commonly assumed for the crust when the first Lame constant, λ , equals the shear modulus, μ . After Brocher TM (2005) Empirical relations between elastic wavespeeds and density in the earth's crust. *Bulletin of the Seismological Society of America* 95(6): 2081–2092.

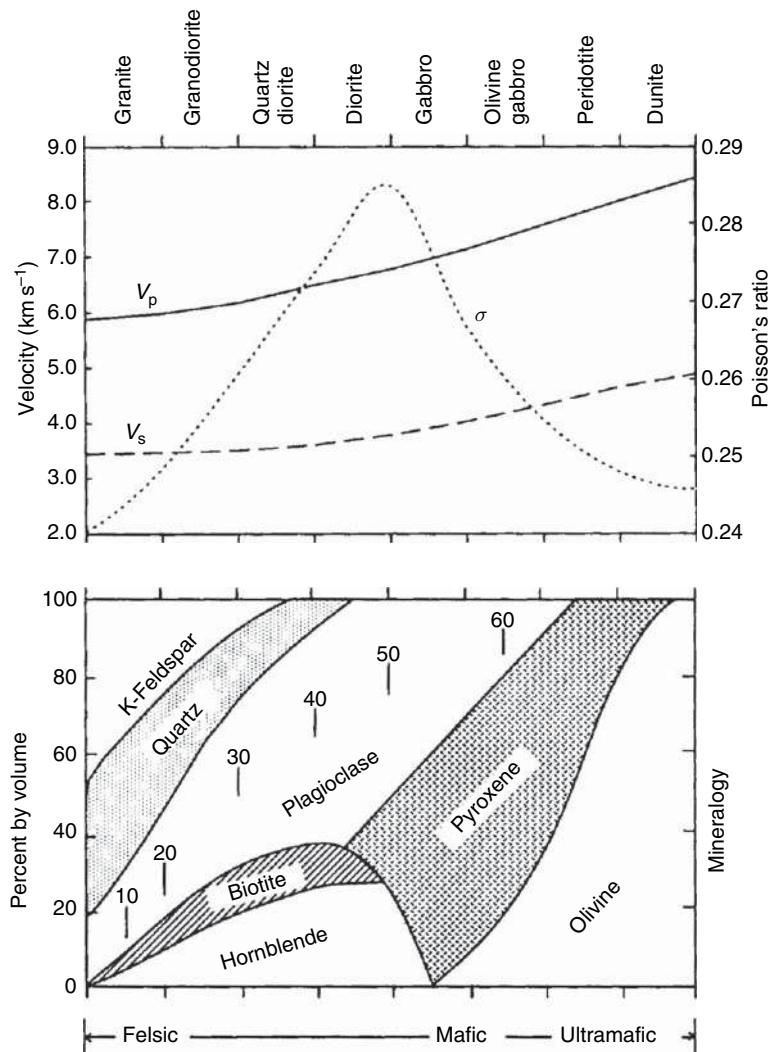


Figure 9 Variations in compressional wave velocity (V_p), shear wave velocity (V_s), and Poisson's ratio (σ) with mineral composition (Berry and Mason, 1959) for common igneous rock types. Percent anorthite content of plagioclase feldspar is shown within the plagioclase field. After Christensen NI (1996) Poisson's ratio and crustal seismology. *Journal of Geophysical Research* 100: 3139–3156.

1.11.4 Nonseismic Constraints on Crustal Structure

All rock types have a variety of distinct, albeit nonunique, physical properties that include density, magnetic susceptibility, and conductivity. Geophysical surveying techniques to measure these properties are highly developed, and it is possible to make detailed maps of lateral changes in rock magnetic properties, conductivity, and to estimate density variations. Advanced digital processing of such data enhances the reliability of interpretations, although

resolution typically decreases with depth. Such non-seismic geophysical studies are widely used and have the capability to distinguish between competing geologic models of the structure of the crust.

1.11.4.1 Gravity Anomalies

Gravity anomalies reveal rock density variations, with the amplitude of the anomaly proportional to the density contrast and thickness of the anomalous body. Short-wavelength (<250 km) gravity anomalies are usually correlated with crustal structures, while

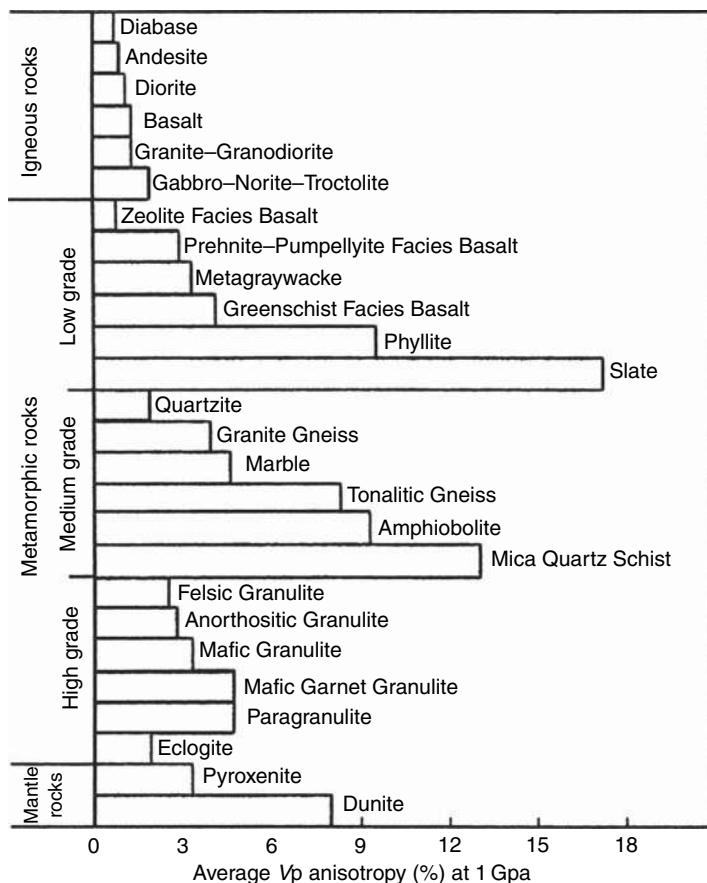


Figure 10 Average anisotropies for typical crustal and upper-mantle rock types, expressed in percent from the relation: $100(V_{\max} - V_{\min})/V_{\text{avg}}$, at pressures corresponding to 35 km depth. After Christensen NI and Mooney WD (1995) Seismic velocity structure and the composition of the continental crust: A global view. *Journal of Geophysical Research* 100: 9761–9788.

long wavelength (<1000 km) gravity anomalies are correlated with lateral variations of mantle densities. Kane and Godson (1989) demonstrate that long-wavelength gravity highs are correlated with high mantle seismic velocities, and gravity lows with low mantle velocities. Kaban and Mooney (2001) and Kaben *et al.* (2003) show that upper-mantle density variations contribute long-wavelength gravity anomalies ranging from -250 MGal to $+150$ mGal. The largest of these positive anomalies over the continents were associated with the Andes, the East European Platform, the Alpin-Mediterranean fold belt, and the central southeastern part of North America. The largest negative anomalies, indicating a thin lithosphere, are associated with vast Cenozoic regions of plume-lithosphere interaction: the East African Rift and the Basin and Range Province of western North America.

New satellite measurements of Earth's gravity field were begun in April 2002. The data from the

Gravity Recovery and Climate Experiment (GRACE) satellites yield a complete measurement of the gravity field to harmonic degree 160 (300 km spatial resolution at the Earth's surface) every 30 days. These observations have improved the precision of the global gravity field by two orders of magnitude (Tapley *et al.*, 2005). For additional references on gravity studies of the crust see Table 5a.

1.11.4.2 Aeromagnetics

High-resolution aeromagnetic surveys can be used to define major regions of coherent structure in the Earth's crust (Kane and Godson, 1989). Since rocks commonly retain magnetism that originates from the time of their formation, magnetic-anomaly data provide a unique opportunity to infer geological processes not readily observed through other geophysical quantities. One common example of this is

Table 3 Selected papers on the seismic properties of the uppermost mantle

References	Year
Al-Lazki <i>et al.</i>	2003, 2004
Allen <i>et al.</i>	2002
Anderson	1967
Anderson and Archambeau	1964
Artemieva and Mooney	2001
Bamford	1977
Bannister <i>et al.</i>	1991
Baraganzi and Ni	1982
Benoit <i>et al.</i>	2003
Bibee and Shor	1976
Bijwaard <i>et al.</i>	1998
Brocher <i>et al.</i>	2003
Bruneton <i>et al.</i>	2004
Calvert <i>et al.</i>	2000
Canales <i>et al.</i>	2000
Chen <i>et al.</i>	2003
DeShon and Schwartz	2004
Egorkin	2004
Egorkin <i>et al.</i>	1987
Enderle <i>et al.</i>	1996
Feng <i>et al.</i>	2004
Friedrich	2003
Fromm <i>et al.</i>	2004
Gilbert <i>et al.</i>	2005
Grand and Helmberger	1984
Grand <i>et al.</i>	1997
Gung and Romanowicz	2004
Hearn	1984, 1999
Hearn	1996
Hearn and Ni	1994
Hearn <i>et al.</i>	1991, 2004
Herrin	1969
Huang <i>et al.</i>	2004
Humphreys <i>et al.</i>	1984
Iyer nad Hitchcock	1989
Jordan	1975, 1979, 1988
Jordan and Frazer	1975
Kennett and Engdahl	1991
Kennett <i>et al.</i>	1995
Kind <i>et al.</i>	2002
Lei and Zhao	2005
Li and Romanowicz	1996
Liang <i>et al.</i>	2004
Lippitsch <i>et al.</i>	2003
Liu <i>et al.</i>	2005
Maggi and Priestly	2005
Matzel and Grand	2004
McNamara <i>et al.</i>	1997
Meissner <i>et al.</i>	2002
Mele	1998
Meyers <i>et al.</i>	1998
Montagner and Tanimoto	1990
Nolet	1977
Oliver	1962
Orcutt	1987
Panza <i>et al.</i>	2003
Pavlenkova	1996
Pilidou <i>et al.</i>	2004, 2005
Prodehl	1984
Rau and Wu	1995
Ringwood	1975
Ritzwoller and Levshin	1998
Ritzwoller <i>et al.</i>	2002a, 2002b
Romanowicz	1991, 1995
Sandoval <i>et al.</i>	2004
Sandvol <i>et al.</i>	2001
Savage	1999
Shapiro and Ritzwoller	2002
Shapiro <i>et al.</i>	2004
Silver	1996
Silver and Chan	1988
Sleep	2003
Song <i>et al.</i>	2004
Spakman <i>et al.</i>	1993
Trampert and Woodhouse	1995
van der Hilst <i>et al.</i>	1997
Van Heijst and Woodhouse	1999
Vinnik <i>et al.</i>	1992
Wang <i>et al.</i>	2002
Wortel and Spakman	2000
Yuan <i>et al.</i>	1997, 2000
Zhang and Lay	1996
Zhang and Tanimoto	1991
Zhang <i>et al.</i>	2004
Zhao and Xie	1993
Zhao <i>et al.</i>	1992

Table 4a Selected laboratory studies of seismic properties of rocks

References	Year
Bass	1995
Berckhemer <i>et al.</i>	1997
Birch	1960, 1961
Birch	1943, 1972, 1975
Carmichael	1982
Christensen	1965, 1966a, 1966b, 1971, 1979, 1982, 1996
Christensen and Fountain	1975
Christensen and Mooney	1995
Christensen and Salisbury	1975
Christensen and Salisbury	1982
Clark	1966
Hamilton	1978
Jones and Nur	1983
Kern	1978
Kern <i>et al.</i>	1996, 2001
Nafe and Drake	1968
Simmons	1964
Usher	1962
Wepfer and Christensen	1991

Table 4b Selected laboratory studies of nonseismic properties of rocks

References	Year
Berckhemer <i>et al.</i>	1997
Carmichael	1982
Christensen and Salisbury	1979
Clark	1966
Duba	1972
Johnson and Olhoeft	1984

Table 5a Selected papers on crustal structure from gravity data

References	Year
Arvidson <i>et al.</i>	1984
Banks <i>et al.</i>	1977
Barton	1986
Bateman and Eaton	1967
Blakely	1995
Clowes <i>et al.</i>	1997
Couch and Woodcock	1981
Dehlinger	1978
Grant and West	1965
Hammer	1983
Hayford and Bowie	1912
Heiskanen and Moritz	1967
Heiskanen and Vening-Meinesz	1958
Hildenbrand <i>et al.</i>	1982
Hinze	1985
Kimbell <i>et al.</i>	2004
Lachenbruch <i>et al.</i>	1985
McNutt	1980
Parker	1973
Paterson and Reeves	1985
Plouff	1976
Roecker <i>et al.</i>	2004
Sandwell and Smith	1997
Simpson <i>et al.</i>	1987
Talwani and Ewing	1960
Tiberi <i>et al.</i>	2003
Turcotte and Schubert	2002
U.S. Department of Commerce	2001
Unsworth <i>et al.</i>	2000
Venistti <i>et al.</i>	2004
Watts	2001
Woppard	1943, 1959
Zoback and Mooney	2003

seafloor spreading, indicated by a series of magnetic stripes, originating from the mid-ocean ridge.

Magnetization is commonly associated with igneous rocks, but it is controlled more generally by the thermal history of the rock. The remnant magnetization of a mineral is fixed in the direction of the Earth's magnetic field when the mineral is cooled below the Curie temperature; the remnant

Table 5b Selected papers on crustal structure from aeromagnetic data

References	Year
Alvares <i>et al.</i>	1978
Baranov	1957
Blakely	1995
Blakely and Grauch	1983
Bond and Zietz	1987
Frost and Shive	1986
Grant and West	1965
Hahn <i>et al.</i>	1984
Hall	1974
Hemant and Maus	2005
Hinze	1985
Hinze and Zeitz	1985
Hood <i>et al.</i>	1985
Huestis and Parker	1977
Langel	1985
Langel <i>et al.</i>	1982
Mayhew and LaBrecque	1987
Mayhew <i>et al.</i>	1985
McEnroe <i>et al.</i>	2004
Parker	1971
Paterson and Reeves	1985
Plouff	1976
Purucker <i>et al.</i>	2002
Redford	1980
Reid	1980
Schouten	1971
Schouten and McCamy	1972
Sexton <i>et al.</i>	1982
Talwani	1965
USGS and Society of Exploration Geophysics	1982
Vacquier <i>et al.</i>	1951
Vogt <i>et al.</i>	1979
Von Freese <i>et al.</i>	1986
Williams <i>et al.</i>	1985
Zietz	1969, 1982

Table 5c Selected papers on the electrical properties of the crust

References	Year
Banks	1972
Berdichevskiy and Zhdanov	1984
Booker <i>et al.</i>	2004
Cagniard	1953
Feldman	1976
Gough	1974
Grant and West	1965
Hyndman	1988
Korja <i>et al.</i>	2002
Jones	1992
Jones <i>et al.</i>	2001
Li <i>et al.</i>	2003
Wannamaker <i>et al.</i>	1989

Table 5d Selected papers on crustal heat flow

References	Year
Cermak	1993
Chapman	1986
Jaupart and Mareschal	1999
McKenzie <i>et al.</i>	2005
Parson and Sclater	1977
Pollack and Chapman	1977
Pollack <i>et al.</i>	1993
Scalper <i>et al.</i>	1980
Stein and Stein	1992
Turcotte and Schubert	2002
Zang <i>et al.</i>	2002

magnetization is removed when heated above this temperature. Metamorphism can also change the magnetization of a rock, but the magnitude of the effect is usually small. So, in contrast to density, rock magnetization can range through several orders of magnitude (Kane and Godson, 1989).

Long-wavelength gravity and magnetic data are available from space-based observations (Purucker *et al.*, 2002; McEnroe *et al.*, 2004). The *CHAMP* (*CHAllenging Minisatellite Payload*) mission, is a German satellite designed for geoscientific and atmospheric research and applications. *CHAMP* is presently collecting precise gravity and magnetic measurements of the Earth (Hemant and Maus, 2005). For additional references on magnetic studies of the crust see Table 5b.

1.11.4.3 Geoelectrical Measurements

In general, the conductivity of the Earth is correlated with salinity, composition, and temperature (Keller, 1989; Jones, 1992). At the surface, electrical conductivity depends on the amount of salinity of the groundwater in a rock. At intermediate depths, conductivity depends on water content and composition (particularly graphite and sulfide content). At great depths, where temperatures rise to at least 500°C, conductivity is mainly a function of electron and ion mobility (Keller, 1989).

Most studies of the Earth's crust are based on magnetotelluric (MT) data (Keller, 1989). This method relies on measurements of five separate components of the time-varying electromagnetic field at the surface of the Earth. The analysis of these time series yields 1-D and 2-D models of the subsurface conductivity structure. When measurements are made for long periods (10 000 s and

longer), estimates of the conductivity of the crust and upper mantle to a depth of 200 km and greater are possible (Jones, 1999). The source for electrically conductive material may be seen as high-density blocks within the crust.

Electrical conductivity profiles of the crust may be divided into marine and continental studies. Major marine studies include the RAMESSES marine experiment over the Reykjanes Ridge (Sinha *et al.*, 1997; MacGregor *et al.*, 1998), the Pressure, Electromagnetic, Gravity, Active Source Underwater Survey (PEGASUS) experiment in the north-east Pacific Ocean (Constable and Cox, 1996), and electromagnetic studies of the axial zone of the northern East Pacific Rise (Evans *et al.*, 1999). On continents, electrical conductivity structure of stable regions, sutures and paleosubduction zones, regions of lithospheric extension, and orogens have all been investigated (Wannamaker *et al.*, 1989; Jones, 1992; Jones *et al.*, 2001). In most cases, these studies have been conducted in conjunction with active- and passive-source seismic profiles. Noteable results include the correlation between low shear-wave velocity and high electrical conductivity beneath the southern Tibetan Plateau. This correlation has been attributed to the presence of either partial melts or aqueous fluids in the middle crust (Nelson *et al.*, 1996; Li *et al.*, 2003). Thus, electrical studies provide an important additional constraint on the composition and physical state of the crust and upper mantle. For additional references on geoelectrical studies of the crust see Table 5c.

1.11.4.4 Heat Flow Data

Surface heat-flow data provide valuable information on temperatures within the crust. The highest heat-flow values are found at mid-ocean ridges and within geothermal zones and active volcanoes. Heat flow has been measured on a global basis with ocean, continents and their margins (Pollack *et al.*, 1993). Surfical heat flow is the product of radiogenic heat production in the crust and heat transferred from the convecting mantle. In order for a lithospheric geotherm to be reliably calculated, crustal heat production and thermal conductivity must be estimated from laboratory measurements on typical crust rocks (Pollack and Chapman, 1977; Chapman, 1986; Cermak, 1993; Jaupart and Mareschal, 1999; Artemieva and Mooney, 2001). Crustal geotherms can be subdivided into hot, normal, and cold geotherms.

Within continental crust these three geotherms predict temperatures at a depth of 40 km (Moho) of about 500°C, 700°C, and 900°C, respectively. Thermal studies of the crust have provided valuable constraints on crustal composition and evolution (Rudnick and Fountain, 1995; Mareschal *et al.*, 1999; Artemieva and Mooney, 2001; Rudnick and Gao, 2003). For additional references on heat flow studies of the crust, see **Table 5d**.

1.11.4.5 Borehole Data

Deep scientific boreholes provide exceptional data regarding the physical properties of the upper crust. The deepest boreholes are the 12-km Kola Superdeep Borehole (KSDB) in Russia (Kozlovsky, 1987), the 9.1-km Kontinentales Tiefbohrprogramm (KTB) in Germany (Emmermann and Lauterjung, 1997), and the 6.8-km and 6.5-km Gravberg–Stenberg boreholes in Sweden (Juhlin, 1988; Papasikas and Juhlin, 1997). In addition, there are numerous scientific boreholes to depths of 3–5 km. These boreholes provide direct sampling of the composition of the upper crust, as well as measurements of *in situ* seismic velocities, density, temperature, state of stress, rock porosity, and the fluid pressure (Smithson *et al.*, 2000; Kern *et al.*, 2001). Evidence has also been obtained for crustal shear zones containing electrically conductive graphite and sulfides. An unexpected result is the presence of free fluid throughout the entire depth range of the KSDB and KTB boreholes.

1.11.4.6 Surface Geology, Exposed Deep Crustal Sections, and Xenolith Data

Surface geology, exposed deep crustal sections, and xenolith samples provide direct observations of the composition and physical properties of the crust. The composition of the upper continental crust is, by definition, evident in global geologic maps which are dominated by felsic intrusive rocks and low-grade metamorphic rocks, particularly shales and sandstones (Clarke, 1889; Clarke and Washington, 1924). The recognition that mountain belts provided exposures of the deep crust can be traced to the work of Elie de Beaumont (1847) who studied the Pyrenees. It was, however, many years later that these observations were systematically analyzed in terms of cross-sections of the entire crust (Fountain and Salisbury, 1981; Salisbury and Fountain, 1990; Percival *et al.*, 1992). Xenoliths are samples from the deep crust (and mantle lithosphere) that have been carried to the surface by volcanic activity (Kay and Kay, 1981). These samples provide excellent constraints on lower crustal composition (Fountain *et al.*, 1992; Rudnick and Gao, 2003).

1.11.5 Structure of Oceanic Crust and Passive Margins

Several thousand measurements of the deep seismic structure of the Earth's crust have been made. However, the geographic distribution of seismic measurements is uneven (**Figure 11**), with more

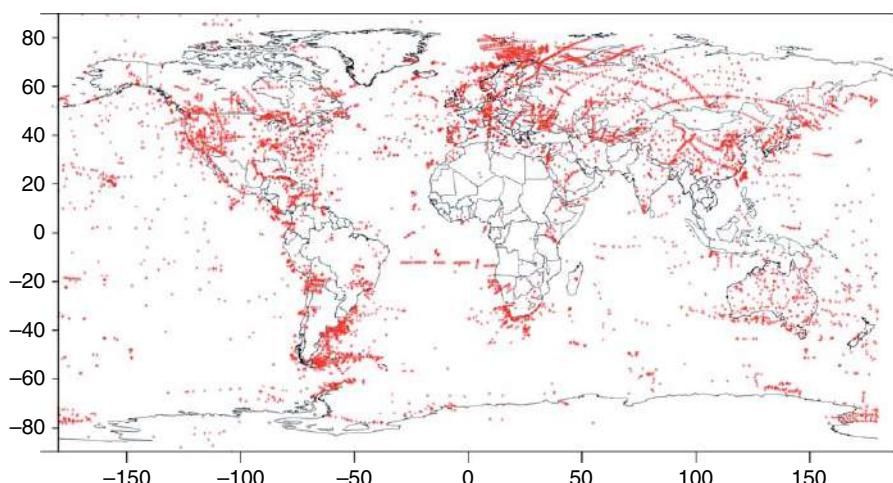


Figure 11 Locations (solid triangles) of individual seismic velocity–depth measurements made within the Earth's crust, 1920–present. Up to 1980, the majority of these measurements were made using the seismic refraction/wide-angle reflection technique. Since 1980 a great many determinations have been made using receiver function analysis of teleseismic arrivals and local earthquake tomography (see text).

results available for the Northern Hemisphere, and a concentration of data in North America, western Europe, and Eurasia. In the Southern Hemisphere, Australia and New Zealand have abundant data. Oceanic data are widely available for all oceans. Here we summarize the principle results obtained by these seismic data, and then present a global model for the Earth's crust.

1.11.5.1 Typical Oceanic Crust

The seismic velocity structure of oceanic crust was established in the 1950s, prior to the acceptance of plate tectonics and seafloor spreading. Oceanic crust was found to be uniformly thinner than continental crust. Much of the knowledge of the structure of ocean crust has come from seismic refraction/wide-angle reflection profiles. These seismic profiles use air gun or explosive sources that are recorded by either hydrophones or ocean-bottom seismometers. Passive seismology has limited application since most receivers are on continents or islands. However, a few tomographic studies of crustal structure at mid-ocean ridges have been completed (Wolfe *et al.*, 1995).

In their pioneering studies, Hill (1957) and Raitt (1963) divided 'normal' oceanic crust into separate, uniform seismic layers, known as 'Raitt–Hill layering.' The basic construction is (1) 0.5 km of soft sediments (layer 1) with a P-wave velocity of 2.0 km s^{-1} ; (2) a 2–3-km-thick upper layer (layer 2) with a velocity of $2.5\text{--}6.4 \text{ km s}^{-1}$, and (3) a 4–5-km-thick lower crustal layer (layer 3), with a velocity of $6.5\text{--}7.3 \text{ km s}^{-1}$. The total thickness of ocean crust is 6–8 km. Layer 2, consists largely of pillow lavas and dykes, while layer 3 consists of a 'sheeted' dyke complex composed of diorites and gabbros (Figure 12). More details regarding the structure of the crust have been obtained using modern analysis methods. The application of synthetic seismogram modeling to marine seismic refraction/wide-angle reflection data indicates that the boundary between layer 1 and layer 2 is often transitional, while the boundary between layer 2 to layer 3 is relatively sharp (Spudich and Orcutt, 1980).

In the late 1970s, it was proposed that layer 2 could be further subdivided into three layers: 2A, 2B, and 2C. According to Ewing and Houtz (1979), two distinct layers with seismic velocities of about 3.5 km s^{-1} (layer 2A) and 5.2 km s^{-1} (layer 2B) were consistently identified. Below layer 2B, but above layer 3, a third layer with a seismic velocity of $6.0\text{--}6.2 \text{ km s}^{-1}$ (layer 2C) was detected. Orcutt *et al.* (1976) and White *et al.*

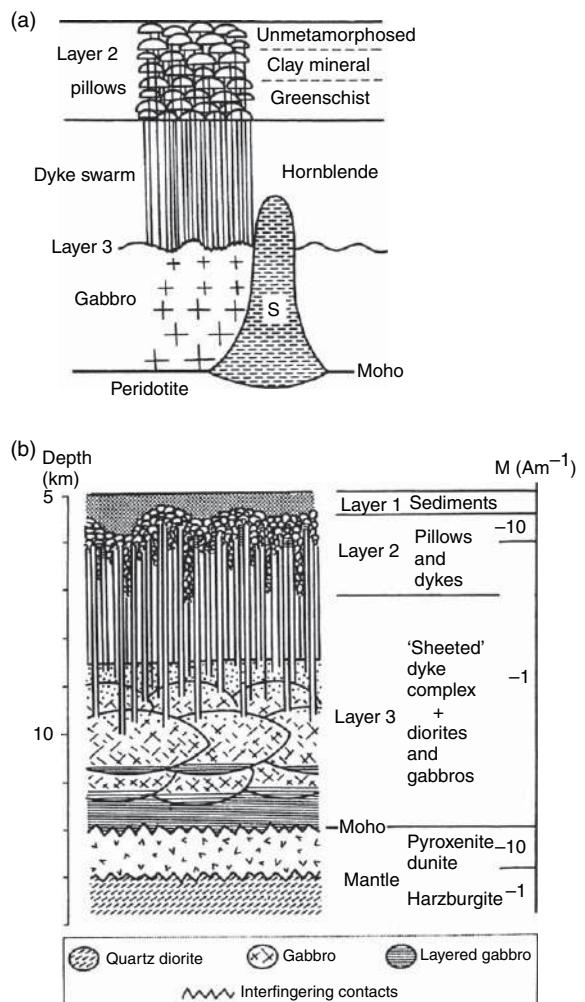


Figure 12 Compositional models of the oceanic crust derived from seismic measurements and exposed crustal sections: (a) crust model of Cann (1970); S refers to serpentine; (b) crustal model of Vine and Moores (1972). Traditionally, the oceanic crust is described as being composed of three layers, termed seismic layers 1–3. According to model (b), layer 1 is sediments; layer 2 is made up of basaltic pillow lavas and their feeder dikes, unmetamorphosed in their upper parts; layer 3 is composed of sheeted dykes underlain by massive plutonic diorites and gabbros. Seismic velocities within these layers are shown in Figure 13(b).

(1992) review previous work and provide a modern synthesis of the seismic structure of typical oceanic crust. Layer 1 lies beneath an average 4.5 km of sea water and is composed of sediments (pelagic sediments, silts, muds, and sand) and is approximately 0.5 km thick, with a seismic velocity of $1.5\text{--}2.0 \text{ km s}^{-1}$, increasing with depth as the sediments consolidate. Layers 2A–C, the volcanic layer, is $2.11 \pm 0.55 \text{ km}$

thick, with a seismic velocity of $2.5\text{--}6.6 \text{ km s}^{-1}$. Layer 3, sometimes called the oceanic layer, is $4.97 \pm 0.90 \text{ km}$ thick, with a seismic velocity of $6.6\text{--}7.6 \text{ km s}^{-1}$. The upper mantle has an average seismic velocity of $7.9\text{--}8.1 \text{ km s}^{-1}$. See **Table 6a** for additional references on oceanic crust studies. **Table 7a** lists selected papers on the composition of oceanic crust.

Table 6a Selected papers on the seismic structure of oceanic crust

References	Year
Au and Clowes	1984
Barclay <i>et al.</i>	1998
Begnaud <i>et al.</i>	1997
Bibee and Shor	1976
Bown and White	1994
Butler	1986
Canales <i>et al.</i>	2000
Cann	1974
Cannat	1996
Caress <i>et al.</i>	1995
Carlson <i>et al.</i>	1980
Chapman and Orcutt	1985
Charvis <i>et al.</i>	1995
Chen	1992
Christensen	1972
Christeson <i>et al.</i>	1997
Clowes <i>et al.</i>	1999
Coffin and Eldholm	1994
Collier and Singh	1997, 1998
Darbyshire <i>et al.</i>	2000
Detrick <i>et al.</i>	1987, 1990, 1993
El Shazly	1982
Ewing <i>et al.</i>	1955
Ewing and Nafe	1982
Foulger <i>et al.</i>	2003
Hess	1962
Hill	1963
Hyndman	1979
Jackson and Oakey	1986
Kempner and Gettrust	1982
Laske and Masters	1997
Lindwall	1988
Mair and Forsyth	1982
Maxwell	1970a, 1970b
McKenzie and Bickle	1988
Müller <i>et al.</i>	1997
Mutter and Karson	1992
Mutter and Mutter	1993
Nur and Ben-Avraham	1982
Operto and Charvis	1996
Orcutt <i>et al.</i>	1976
Oxburg and Parmetier	1977
Peirce and Barton	1991
Purdy and Detrick	1986
Rabinowitz <i>et al.</i>	1988
Raitt	1963

Richardson <i>et al.</i>	1998
Ritzwoller and Levshin	2002
Shearer and Orcutt	1986
Shor	1967
Sinha <i>et al.</i>	1981
Sinha and Louden	1983
Sleep	1990
Smith and Sandwell	1997
Spudich and Orcutt	1980
Stein and Stein	1992
Su <i>et al.</i>	1992
Thinon <i>et al.</i>	2003
Toomey <i>et al.</i>	1990
Tucholke	1986
Tucholke and Uchupi	1989
Vera <i>et al.</i>	1990
Walck	1984
White <i>et al.</i>	1992
White <i>et al.</i>	1984
White and Clowes	1990
Whitmarsh <i>et al.</i>	1982
Whitmarsh and Calvert	1986
Wilcock <i>et al.</i>	1995

Table 6b Selected papers on the seismic structure of continental margins

References	Year
BABEL working group	1993
Barazangi and Brown	1986a, 1986b
Barton and White	1997
Blundell and Raynaud	1986
Brocher	1995
Chian <i>et al.</i>	1995, 1999
Clegg and England	2003
Clowes <i>et al.</i>	1999
Clowes <i>et al.</i>	1987
Clowes, and Hyndman	2002
Davis and Kusznir	2004
Dean <i>et al.</i>	2000
DeShon and Schwartz	2004
El Shazly	1982
Eldholm and Grue	1994
Eldholm <i>et al.</i>	2002
England	2000
Ewing <i>et al.</i>	1937
Ewing <i>et al.</i>	1966
Fernandes <i>et al.</i>	2004
Fowler <i>et al.</i>	1989
Heacock	1977
Hemant and Maus	2005
Holbrook and Keleman	1993
Horsefield <i>et al.</i>	1993
Jensen	1961
Klemperer and Hobbs	1991
Klemperer and Mooney	1998a, 1998b
Matthews	1986

(Continued)

Table 6b (Continued)

References	Year
Matthews and Cheadle	1986
Matthews and the BIRPS group	1987
McKenzie and Bickle	1988
O'Reilly <i>et al.</i>	1998
Roberts <i>et al.</i>	1988
Tréhu <i>et al.</i>	1994
Todd <i>et al.</i>	1988
White and McKenzie	1989
White <i>et al.</i>	1987a, 1987b
Kind <i>et al.</i>	1995
Klemperer and Mooney	1998a, 1998b
Langston <i>et al.</i>	2002
Laske and Masters	1997
Levshin <i>et al.</i>	2005
Li and Mooney	1998
Ludwig and Houtz	1979
Makovskiy <i>et al.</i>	1996a, 1996b
Makris	1978
Mechie <i>et al.</i>	2004
Meissner	1973, 1986
Meissner and Bortfeld	1990
Meissner <i>et al.</i>	1987, 1991
Minshull	1993
Mitchell and Herrmann	1979
Mooney and Brocher	1987
Mooney and Meissner	1992
Mooney <i>et al.</i>	2002
Mueller	1973, 1977, 1978
Nakamura <i>et al.</i>	2003
Nelson <i>et al.</i>	1996
O'Reilly <i>et al.</i>	1996
Oliver <i>et al.</i>	1976, 1983
Olsen	1995
Orcutt	1987
Owens and Zandt	1985
Owens <i>et al.</i>	1984
Pakiser	1963
Pakiser and Mooney	1989
Pakiser and Steinhart	1964
Pavlenkova	1996
Petit <i>et al.</i>	1998
Pfiffner <i>et al.</i>	1997
Prodehl	1970, 1979, 1984
Rai <i>et al.</i>	2003
Rao <i>et al.</i>	1999
Rapine <i>et al.</i>	2001
Reddy and Vijaya Rao	2000
Reddy <i>et al.</i>	1999
Regnier <i>et al.</i>	1992
Roecker <i>et al.</i>	1993
Salah and Zhao	2003
Sandvol <i>et al.</i>	1998
Shapiro <i>et al.</i>	2004
Snyder <i>et al.</i>	1990
Steinhart	1967
Steinhart and Meyer	1961
Stern and McBride	1998
Swenson <i>et al.</i>	2000
Thybo <i>et al.</i>	2003
Tilmann <i>et al.</i>	2003
Wang <i>et al.</i>	2003
Woolard	1966
Xu <i>et al.</i>	2002
Yliniemi <i>et al.</i>	2004
Zandt <i>et al.</i>	1995
Zelt and Forsyth	1994
Zhao <i>et al.</i>	2001
Zhu and Kanamori	2000
Zorin <i>et al.</i>	2003

Table 6c Selected papers on the seismic structure of continental crust

References	Year
Barazangi and Brown	1986a, 1986b
Bartelson <i>et al.</i>	1982
Barton	1992
Behrendt <i>et al.</i>	1988
Belousov and Pavlenkova	1984
Belousov <i>et al.</i>	1991
Belousov <i>et al.</i>	1988
Blundell <i>et al.</i>	1992
Bonini and Bonini	1979
Bourjot and Romanowicz	1992
Brown <i>et al.</i>	1986
Clitheroe <i>et al.</i>	2000
Clowes <i>et al.</i>	1999
Clowes <i>et al.</i>	1997, 1987, 1995
Curtis and Woodhouse	1997
Dahl-Jensen <i>et al.</i>	2003
Das and Nolet	1998
DESERT group	2004
Drewry and Mooney	1983
Fliedner and Klemperer	1999
Fountain <i>et al.</i>	1984
Fromm <i>et al.</i>	2004
Giese <i>et al.</i>	1976
Guterch <i>et al.</i>	1999
Guterch <i>et al.</i>	2003
Hale and Thompson	1982
Hamilton	1976
Hart	1969
Heacock	1971, 1977
Hofsetter and Bock	2004
Holbrook <i>et al.</i>	1992
Hole <i>et al.</i>	2000
James	1971
James and Steinhart	1966
Jarchow and Thompson	1989
Julià and Mejía	2004
Kimbell <i>et al.</i>	2004
Kinck <i>et al.</i>	1993

Table 7a Selected papers on oceanic crustal composition

References	Year
Christensen	1972, 1996
Bowen and White	1994
Cann	1974
Charvis <i>et al.</i>	1995
Christensen and Salisbury	1982
Condie	1989
Hess	1962
Hyndman	1979
Kempner and Gettrust	1982
Lindwall	1988
Nur and Ben-Avraham	1982
Operto and Charvis	1996
White <i>et al.</i>	1992

Table 7b Selected papers on continental crustal composition

References	Year
Belousov and Pavlenkova	1984
Blundell <i>et al.</i>	1992
Christensen	1996
Christensen and Fountain	1975
Christensen and Mooney	1995
Christensen and Salisbury	1975
Condie	1989
Downes	1993
Durrheim and Mooney	1994
Fliedner and Klemperer	1999
Fountain	1986
Fountain <i>et al.</i>	1984
Fountain and Salisbury	1981
Goodwin	1991, 1996
Halliday <i>et al.</i>	1993
Holbrook <i>et al.</i>	1992
Jordan	1979
Julia and Mejía	2004
Kozlovsky	1987
Kusznir and Matthews	1988
Meissner <i>et al.</i>	2002
Meissner and Mooney	1998
Mooney and Meissner	1991
Nur and Ben-Avraham	1982
Ringwood	1975
Rudnick and Fountain	1995
Sandmeier and Wenzel	1990
Shapiro <i>et al.</i>	2004
Silver and Chan	1988
Sleep	2003, 2005
Smithson <i>et al.</i>	1987
Taylor and McLennan	1985
Upton <i>et al.</i>	2001
Zandt and Ammon	1995
Ziegler	1990

1.11.5.2 Mid-Ocean Ridges

The concept of seafloor spreading from mid-ocean ridges (**Figure 2**) was first proposed in the early 1960s by several workers, including most prominently the American geologist Harry H. Hess ([Hess, 1965](#)). Its major tenets gave great support to the theory of continental drift and provided a conceptual base for the development of plate tectonics.

Mid-Ocean ridges can be separated into three categories: fast spreading, intermediate spreading, and slow spreading. Fast-spreading ridges have a spreading rate of $8\text{--}16 \text{ cm yr}^{-1}$; intermediate-spreading ridges have a spreading rate of $4\text{--}8 \text{ cm yr}^{-1}$; and slow-spreading ridges have a spreading rate of $1\text{--}4 \text{ cm yr}^{-1}$ ([Perfit and Chadwick, 1998](#)).

The seismic structure of a fast-spreading ridge shows that the intrusive zone is only 2–3 km wide, and normal oceanic crust is found 5–6 km away from the ridge axis (**Figure 13**). Directly beneath the ridge axis, an upper crustal low-velocity zone exists that corresponds to a zone of partial melting. This seismic structure is in contrast to the earlier hypothesis that anomalous oceanic crust extends for tens of kilometers away from the axis of a mid-ocean ridge.

1.11.5.3 Oceanic Plateaux and Volcanic Provinces

Oceanic plateaux are one type of the Large Igneous Provinces (LIPs) that cover portions of the oceans and continents (i.e., flood basalt provinces; [Eldholm *et al.* \(2002\)](#), [Coffin and Eldholm \(1994\)](#), [Ernst and Buchan \(2003\)](#)). While continental flood basalt provinces were recognized in the early twentieth century ([Holmes, 1918](#)), regions of unusually thick oceanic crust were not identified until the 1970s. [Edgar *et al.* \(1971\)](#) originally discovered an over-thickened region within the Caribbean Plate, and when a number of similar features were documented, they were called ‘oceanic flood basalt provinces’ ([Donnelly, 1973](#)). The term ‘ocean plateau’ was suggested by [Kroenke \(1974\)](#) when the Ontong Java Plateau in the western Pacific was explored using seismic refraction/wide-angle reflection profiles. More than 12 oceanic plateaux have been identified (**Figure 14**), and these have anomalous crustal structure in comparison with normal oceanic crust.

The crustal structure of several ocean plateaux have been resolved using seismic and gravity data, including recent studies on the Kerguelen and Ontong Java Plateaux. [Farnetani *et al.* \(1996\)](#) and

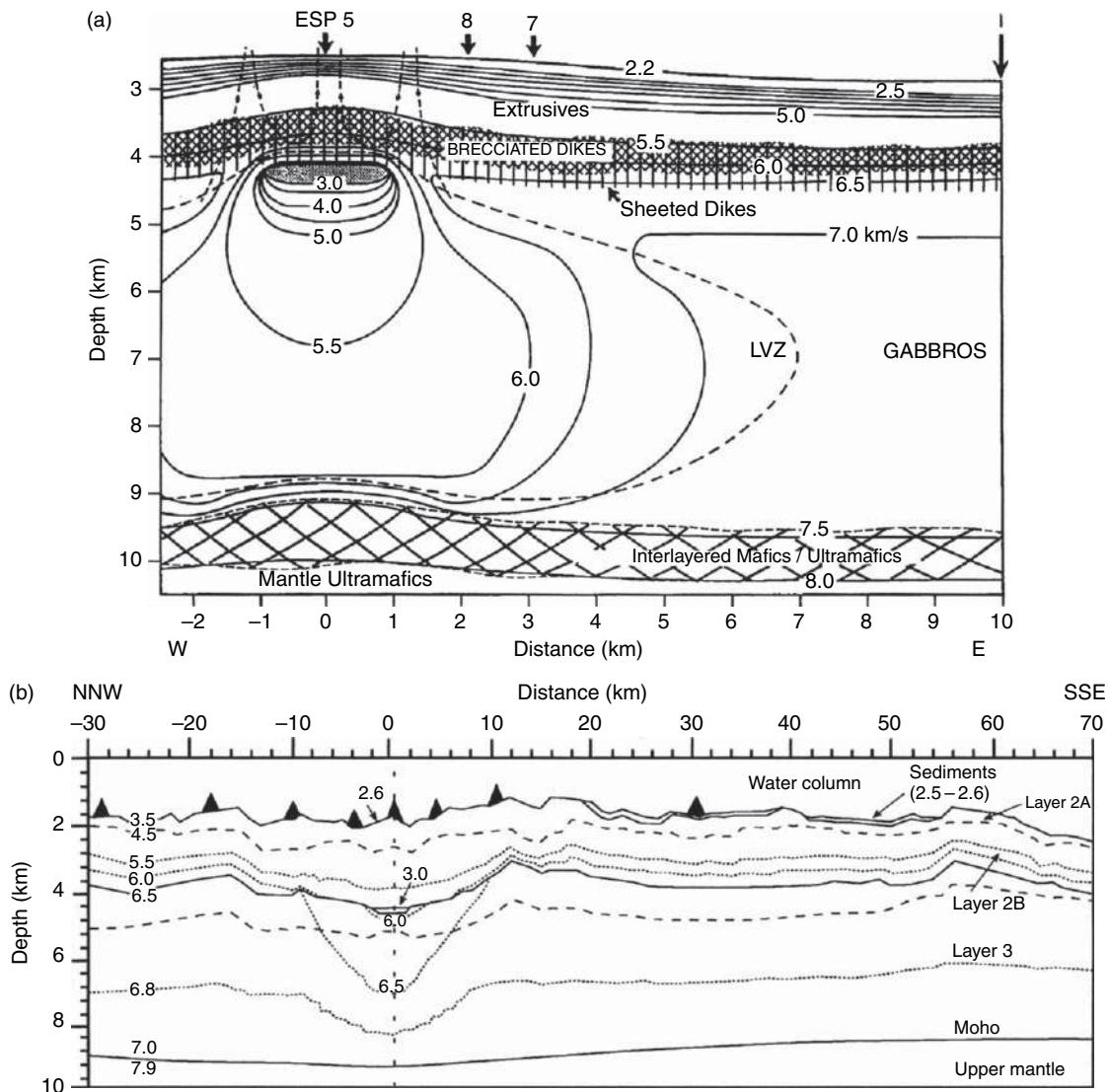


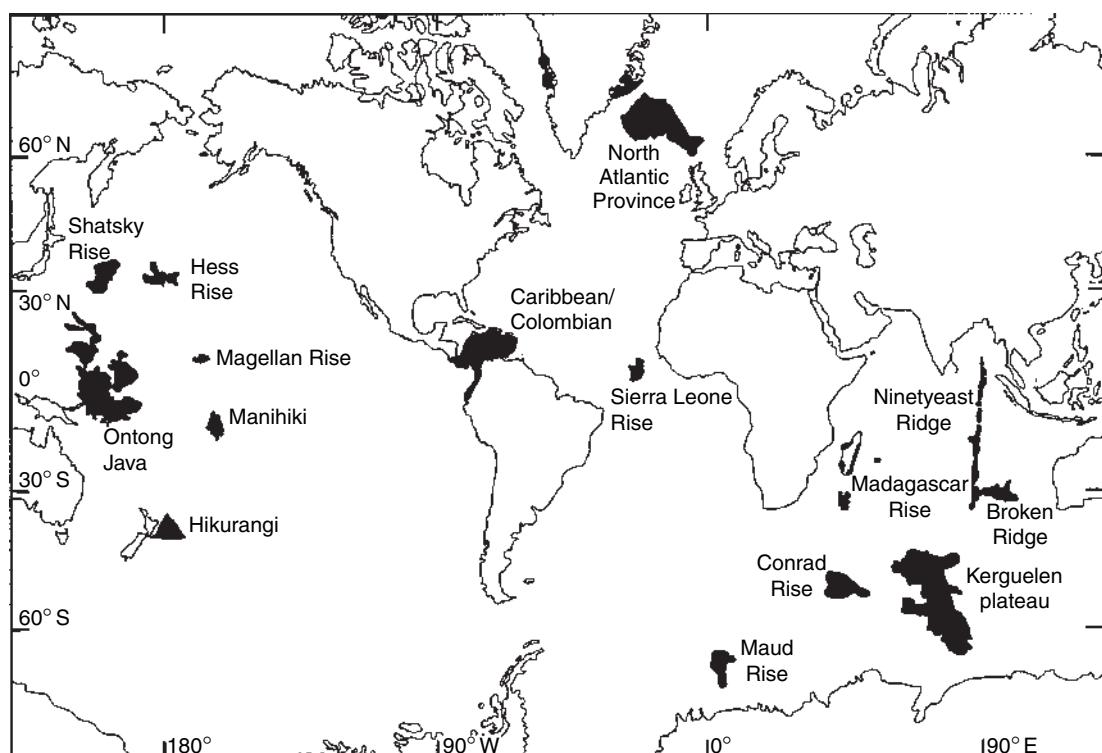
Figure 13 (a) P-wave velocity model and interpretation, based on expanding spread profile and multichannel reflection data, of the fast-spreading East Pacific Rise axis at 9° N. Arrows mark ESP locations. (b) P-wave velocity model and interpretation, based on OBS and seismic reflection data, of the slow-spreading Reykjanes Ridge axis at 57°45' N. Triangles mark OBS locations and dashed lines mark changes in velocity gradient. (a) Redrawn from Vera EE, Mutter JC, Buhl P, et al. (1990) The structure of 0- to 0.2-m.y.-old oceanic crust at 9°N on the East Pacific Rise from expanded spread profiles. *Journal of Geophysical Research* 95: 15529–15556. (b) Redrawn from Navin D, Peirce C, and Sinha MC (1998) The RAMESSES experiment- II. Evidence for accumulated melt beneath a slow spreading ridge from wide-angle refraction and multichannel reflection seismic profiles. *Geophysical Journal International* 135: 746–772 and Minshull TA (2002) Seismic structure of the oceanic crust and rifted continental margins. In: Lee WHK, Kanamori H, and Jennings PC (eds.) *International Geophysics Series 81A: International Handbook of Earthquake and Engineering Seismology*, pp. 911–924. San Diego, CA: Academic Press.

Gladzenko *et al.* (1997) present models for the Ontong Java Plateau that show high seismic velocities (7.1 km s^{-1}) throughout most of the crust. These high velocities are likely due to the presence of basalt and olivine–pyroxene cumulates, with high-velocity garnet granulite in the lower crust. Gladzenko *et al.*

(1997) suggested that these garnets may have formed from the deformation and hydrothermal alteration of lower crustal cumulates.

More recently, measurements of upper-mantle shear-wave splitting and shear-wave velocity have suggested the presence of a 300 km thick, long-lived,

(a)



(b)

Oceanic plateau	Mean age (Ma)	Area (10^6 km^2)	Thickness range (km)	Volume (10^6 km^3)
Hikurangi	early-mid Cretaceous	0.7	10–15	2.7
Shatsky Rise	147	0.2	10–28	2.5
Magellan Rise	145	0.5	10	1.8
Manihiki	123	0.8	>20	8.8
Ontong Java	121(90)	1.9	15–32	44.4
Hess Rise	99	0.8	>15	9.1
Caribbean	88	1.1	8–20	4.4
South Kerguelen	110	1.0	~22	6.0
Central Kerguelen/Broken Ridge	86	1.0	19–21	9.1
Sierra Leone Rise	~73	0.9	>10	2.5
Maud Rise	>73	0.2	>10	1.2

Figure 14 (a, b) Map showing all major oceanic plateaus, and other large igneous provinces discussed in the text (after Saunders *et al.* 1999; Eldholm and Coffin, 2000). These plateaux have measured crustal thicknesses of 10–32 km, and an average thickness (22 km) that is three times that of typical oceanic crust.

rheologically strong, and chemically depleted root beneath the Ontong Java Plateau (Klosko *et al.* 2001). Klosko *et al.* (2001) further propose that this chemically depleted root originated from mantle melting processes, which would contribute lower-density material to the base of the plateau, increasing the overall buoyancy of the Ontong Java Plateau.

At the present time, the process of ocean plateau formation is not well understood. There are a number of models for how large volumes of mafic magmas are generated and emplaced by processes unrelated to ‘normal’ seafloor spreading and subduction (Loper, 1983; McKenzie and Bickle, 1988; Campbell *et al.*, 1989; Griffiths and Campbell, 1990; Farnetani and Richards, 1995), but it is not understood why

these eruptions occur in such a rapid, concentrated period of time. Most ocean plateaus were formed in a short time, less than 2–3 My (Coffin and Eldholm, 1994, 2004), which may raise important questions about mantle processes and source regions (Hart *et al.*, 1992; Stein and Hoffman, 1994). During the most recent phase of LIP formation, in the mid-Cretaceous, the Ontong Java, Manihiki, Hess Rise, and Caribbean–Columbian plateaus were formed in the Pacific, while the Kerguelen Plateau formed in the Indian Ocean (Kerr, 2003).

If the plateaus are accreted adjacent to continental margins or island arcs, they may eventually significantly contribute to the growth of existing and new continents (Abbott and Mooney, 1995; Abbott, 1996; Albarede, 1998). Due to their increased thickness relative to normal oceanic crust, plateaus are especially buoyant, preventing them from completely subducting at active margins (Ben-Avraham *et al.*, 1981; Cloos, 1993; Kimura and Ludden, 1995), and potentially allowing the top layers to peel off and merge with the continental crust (Kimura and Ludden, 1995).

Ideas about the origin and deep mantle roots of hot spots and mantle plumes have been debated for some 40 years (Wilson, 1963), and the deep seismic structure of these features remains controversial (Ritsema and Allen, 2003; Montelli *et al.*, 2004). Currently, there are two different models for the crust and upper mantle beneath Iceland, one of the two most prominent hot spots on the planet (the other being the Big Island of Hawaii). The ‘thin-crust model’ is based on MT data, heat flow from shallow wells, petrogenetic models, and seismic data. It suggests a ~10–15 km thick crust under the main rifting axis of Iceland, with a 25 km thick, older crust in eastern, western, and north-central regions of the island. There is also a thin, highly conductive, molten basaltic layer. The ‘thick-crust’ model is based entirely on seismic data, and suggests a Moho depth of 20–40 km. **Figure 15** is a schematic cross-section across the center of Iceland compiling all available seismic, MT, heatflow, and viscosity data (Bjornsson *et al.*, 2005). A unique and prominent feature beneath this hot spot is the continuous good conductor above the underlying asthenosphere. Bjornsson *et al.* (2005) suggest that the 20–40 km deep discontinuous reflector does not necessarily represent the Moho, and thus supports the ‘thin-crust’ model. Further data are need to resolve this controversy.

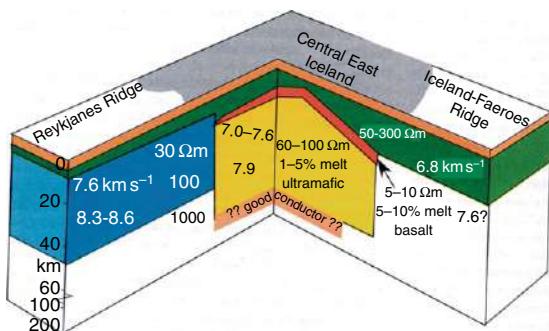


Figure 15 Simplified cross-section showing the main structural features of the Icelandic crust and mantle. The left part of the figure shows a cross-section east and parallel to the Reykjanes ridge along the seismic profile collected during the Reykjanes Ridge Iceland Seismic Experiment. The right part of the figure shows a profile running from central Iceland into the Iceland-Faeroe ridge. Numbers are P-wave velocities (normal type font) and resistivities (italic font). After Björnsson A, Eysteinsson H, and Beblo M (2005) Crustal formation and magma genesis beneath Iceland: Magnetotelluric constraints. In: Foulger GR, Natland JH, Presnall DC, Anderson DL (eds.) *Geological Society of America, Special Paper 388 Plates, Plumes, and Paradigms* pp. 665–686. Boulder, CO: Geological society of America.

1.11.5.4 Ocean Trenches and Subduction Zones

Geophysical studies of oceanic trenches can be traced to gravity measurements made by Vening-Meinesz (1887–1966) in the Indonesian Archipelago in the 1930s. These negative gravity anomalies were interpreted by Vening-Meinesz (1948) as being due to pronounced downbuckling of the oceanic crust. The detailed structure of oceanic trenches was clarified from marine seismic profiles that were made 30 years after Vening Meinesz’s pioneering gravity measurements. One of the best-studied trenches is the Nankai Trough, eastern Japan. Two crustal models derived from seismic refraction/wide-angle reflection and gravity data collected across the Nankai Trough (**Figure 16**) show the geometry of the subducting oceanic crust as it descends beneath the Japan volcanic arc (**Figure 16**). These models define the geometry of the thick sedimentary basins that are located between the Nankai Trough and continental Japan. These results are typical of many subduction zones, including the Cascades region of western North America. Due to the pronounced lateral variations across oceanic trenches and subduction zones, studies that combine multiple seismic and nonseismic data have been the most successful at determining the deep structure (Wannamaker *et al.*, 1989).

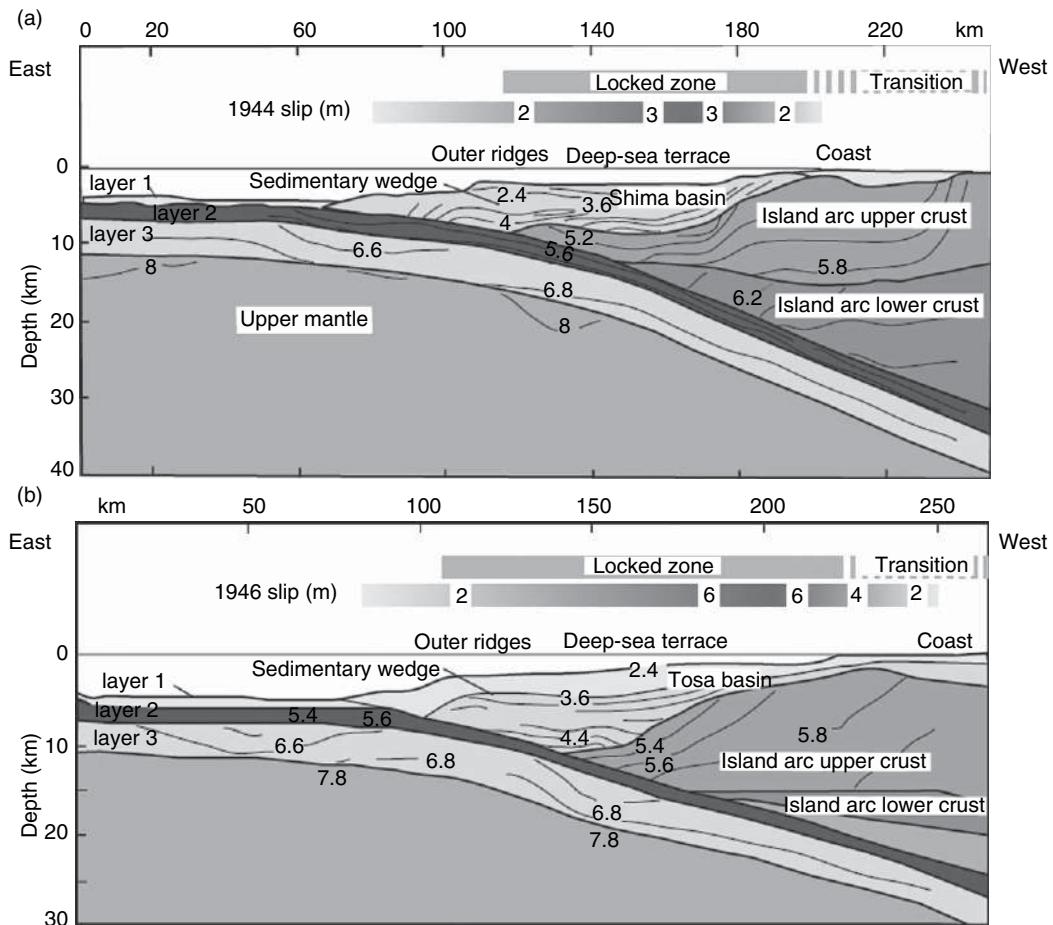


Figure 16 Seismic velocity structure of (a) the Tonankai subduction zone, site of the 1944 earthquake, and (b) the Nankai subduction zone, site of the 1946 earthquake. The relationship between the crustal structure and the locked zone is indicated (Hyndman *et al.*, 1995; Sagiya and Thatcher 1999; Kodaira *et al.*, 2000; Nakanishi *et al.* 2002). The crustal structure is typical of many subduction-zone complexes and includes a prominent low-seismic-velocity sedimentary wedge and the higher-velocity igneous crust of the island arc. After Wells RE, Blakely RJ, Sugiyama Y, Scholl DW and Dinterman PA (2003) Basin-centered asperities in great subduction zone earthquakes: A link between slip, subsidence, and subduction erosion? *Journal of Geophysical Research* 108(B10): 2507 (doi:10.1029/2002JB002072).

1.11.5.5 Passive Continental Margins

As the name implies, passive continental margins are boundaries between oceanic and continental regions where neither collisional deformation nor subduction is taking place. Despite their present-day tectonic quiescence, the crustal structure of passive continental margins is diverse and complex since they are formed by continental rifting that accompanies the breakup of a supercontinent, such as Pangea (200 Ma) or Rodinia (750 Ma). Prominent examples include the eastern seaboard of North America, the Gulf Coast, the Atlantic coasts of Europe, the coasts of Antarctica, and the east, west, and south coasts of Africa. Tectonic activity is minimal and erosional

or weathering processes dominate, forming low-relief geography and increased sedimentary debris. These sedimentary basins are economically and scientifically valuable due to their large reservoirs of hydrocarbon and their recorded history of the rifting between two continents.

Passive margins may be divided into two primary types: volcanic margins and nonvolcanic margins (White and McKenzie, 1989; Holbrook and Keleman, 1993; Eldholm *et al.*, 2002). The North Atlantic margin, formed during early Tertiary lithospheric extension between Europe and Greenland, is one of the world's largest volcanic margins (Eldholm and Grue, 1994), as is the US Atlantic margin (Holbrook and Keleman, 1993).

The extensive volcanic rocks of this margin were formed by excess melting associated within a wide, hot zone of asthenospheric upwelling present during rifting (McKenzie and Bickle, 1988). In many cases a high-seismic velocity (7.3 km s^{-1}) lower crust is also present. Nonvolcanic passive margins are formed where asthenospheric temperatures remain lower during rifting. An example is the non-volcanic margin of the Labrador Sea of northeastern Canada.

The passive margin between continental and oceanic lithosphere is sometimes characterized by a sharp drop in elevation and 20–30 km of crustal thinning over horizontal distances less than $\sim 30 \text{ km}$. The abrupt lateral change in structure is indicated by several interpretations of wide-angle seismic and gravity data (Delhinger *et al.*, 1970; Jones and Mgbatogu, 1982; Todd *et al.*, 1988; Faleide *et al.*, 1990). A velocity profile of the passive margin off the Ghana coast is shown in **Figure 17**. This African ocean–continent transition indicates the absence of underplating beneath the continental basement, due to the lack of high velocities in the lower crust. See **Table 6b** for additional references on continental margins.

1.11.6 Structure of Continental Crust

1.11.6.1 General Features

Continental crust above sea level comprises 29% of the Earth's crust by area, but when submerged continental crust is taken into account, continental crust amounts to 41% of the total crust by area. Since some 75% of continental crust is covered either by sediments or water, geophysical measurements are a very important source of information about the properties of the continental crust. **Figure 18** shows the age of the basement of the crust, that is the age of the crystalline crust beneath the supracrustal sediments. It is evident in **Figure 18** that many continents are predominantly composed of Pre-Cambrian shield and platforms. The deep structure of the continental crust has been investigated for nearly 100 years, beginning with the landmark study of Mohorovicic (1910) that defined the crust–mantle boundary. The locations of most of the presently available seismic refraction/wide-angle reflection profiles on continental crust are shown in **Figure 11**, and amounts to several thousand profiles. **Table 6c** lists many key papers regarding continental crust studies and **Table 7b** lists selected papers on the composition of continental crust.

Studies of the continental crust using active (explosive sources) began in earnest in the 1950s and 1960s (Tuve, 1951; 1953; Tuve *et al.*, 1954; Steinhart and Meyer, 1961; James and Steinhart, 1966; see also Pavlenkova, 1973; **Table 1**). These early studies provided the first clear evidence that the seismic structure of the crust varied in a systematic way with geologic setting. They also showed that the crust can be described as consisting of several layers that are separated by either sharp or transitional boundaries. The existence of crustal layers, which have a heterogeneous fine structure, can be viewed as the product of igneous differentiation of the crust, whereby silicic melts rise into the upper and middle crust, leaving behind a mafic lower crust. Igneous differentiation thus leads to a heterogeneously stratified crust, with granitic to dioritic plutons forming the upper layer.

The evidence for distinct layers within the continental crust depends almost exclusively on the interpretation of second-arriving phases (wide-angle reflections). Whereas some regions display clear secondary phases, in other regions the seismic velocity may increase gradually with depth, producing no distinct wide-angle intracrustal reflections (Levander and Holliger, 1992).

1.11.6.2 Principal Crustal Types

Seismic measurements of continental structure are best described in terms of the local geologic setting. The primary crust types are illustrated in **Figure 19**. In stable regions the continental crust has an average thickness close to 40 km, and there are typical crustal velocities within the upper, middle and lower crust (**Figure 19**). Compressional-wave seismic velocities in the upper crust are $5.6\text{--}6.3 \text{ km s}^{-1}$, corresponding to granitic and meta-sedimentary rocks. At a depth of 10–15 km the seismic velocity commonly increases to $6.4\text{--}6.7 \text{ km s}^{-1}$ (the middle crust), corresponding to intermediate-composition plutonic rocks and amphibolite-grade metamorphic rocks. When the velocity increase is abrupt, this discontinuity is traditionally referred to as the ‘Conrad discontinuity’ (Conrad, 1925; **Table 1**), a term that is now out of date, as it came into use at a time when the crust was believed to consist of only two layers, an upper granitic layer and a lower basaltic layer. We now know from direct observation of exposed crustal sections and numerous seismic measurements that the crust is much more complex than this term implies. The lowermost crust of stable continental regions commonly has a

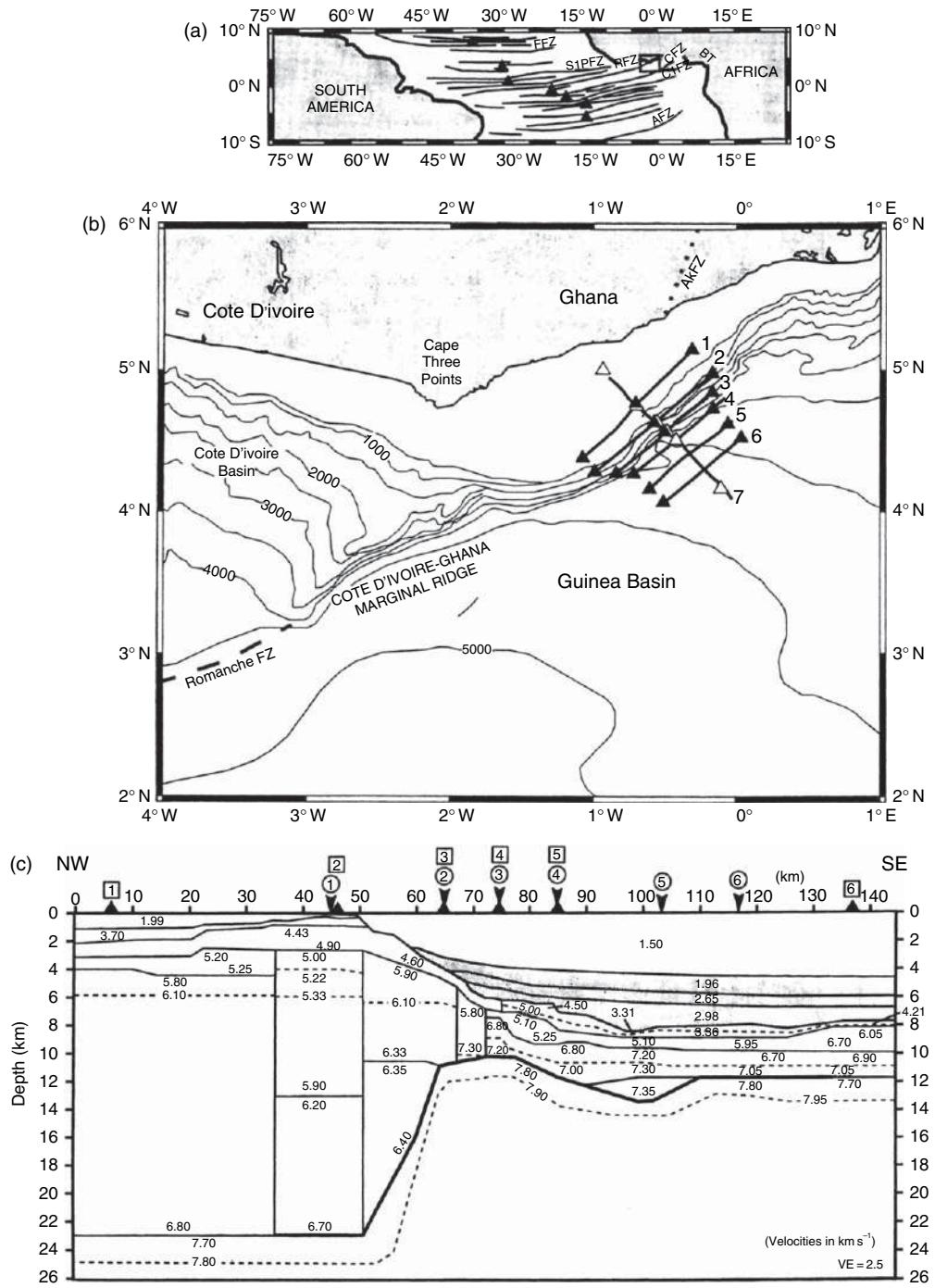


Figure 17 Example of an oceanic–continent transition zone from Ghana, West Africa. (a) Regional setting with Atlantic fracture zones. (b) Locations of wide-angle seismic profiles used to derive the crustal model. (c) Detailed seismic velocity model of the Ghana passive continental margin. The 23 km thick crust of the continental shelf thins to 10–12 km over a remarkably short distance. The igneous oceanic crust is covered by 3–4 km of low density, low-seismic-velocity sediments. From Edwards RA, Whitmarsh RB, and Scrutton RA (1997) The crustal structure across the transform continental margin of Ghana, eastern Equatorial Atlantic. *Journal of Geophysical Research* 102: 747–772.

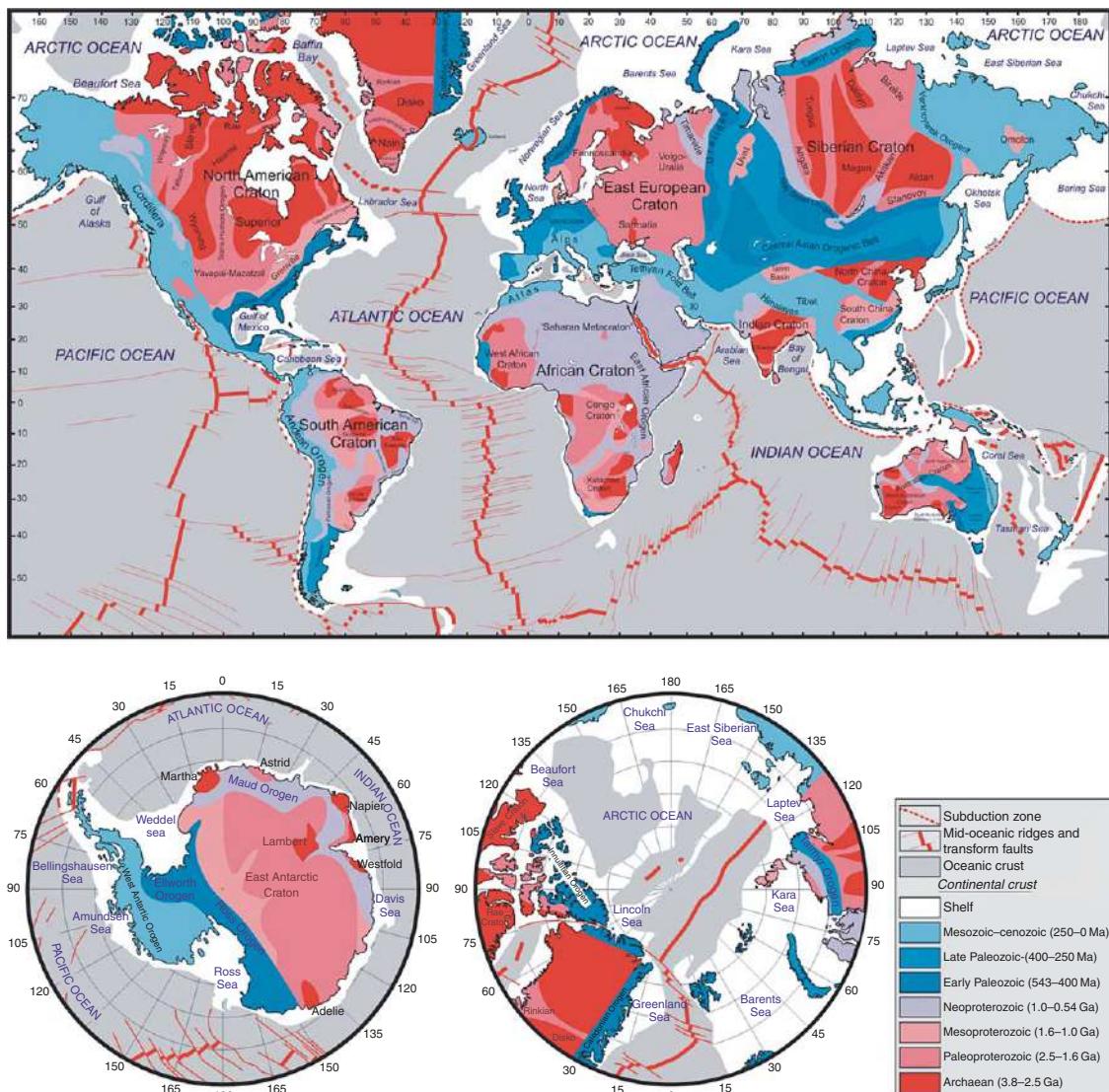


Figure 18 Basement age of the continental crust, distribution of mid-ocean ridges, oceanic crust, and continental shelf. The crust is subdivided by age. Pre-Cambrian shields and platforms comprise 69% of the continental crust by area. Seismic measurements cover much of the Earth's crust, but gap in coverage still exist (cf. [Figure 11](#)). Statistical averages and their standard deviations for crust of a specific age and tectonic setting make it possible to estimate crustal thickness and velocity structure in unmeasured regions, as is required to make complete global crust models ([Mooney et al., 1998](#)).

seismic velocity of $6.8\text{--}7.3 \text{ km s}^{-1}$. The seismic head wave (or diving wave) that travels within the uppermost mantle just below the Moho is known as the P_n phase, for ‘P-wave normal phase’ ([Mohorovicic, 1910](#)). This phase has a seismic velocity of $8.1 \pm 0.2 \text{ km s}^{-1}$ in stable continental regions. A wide-angle reflected phase from the Moho, known as P_mP , is generally clearly observed in active-source seismic profiles due to the large seismic-velocity increase ($0.6\text{--}1.5 \text{ km s}^{-1}$) at this boundary.

Seismic measurements do not have a uniform global distribution ([Figure 11](#)) which affects attempts to calculate average crustal properties. The proportion of continental crustal types, by area, are 69% shield and platform (cratons), 15% old and young orogens, 9% extended crust, 6% magmatic arc, and 1% rift ([Christensen and Mooney, 1995](#)). Using these statistics, we calculate a weighted average for crustal thickness and average crustal velocity. This procedure corrects for the overrepresentation of

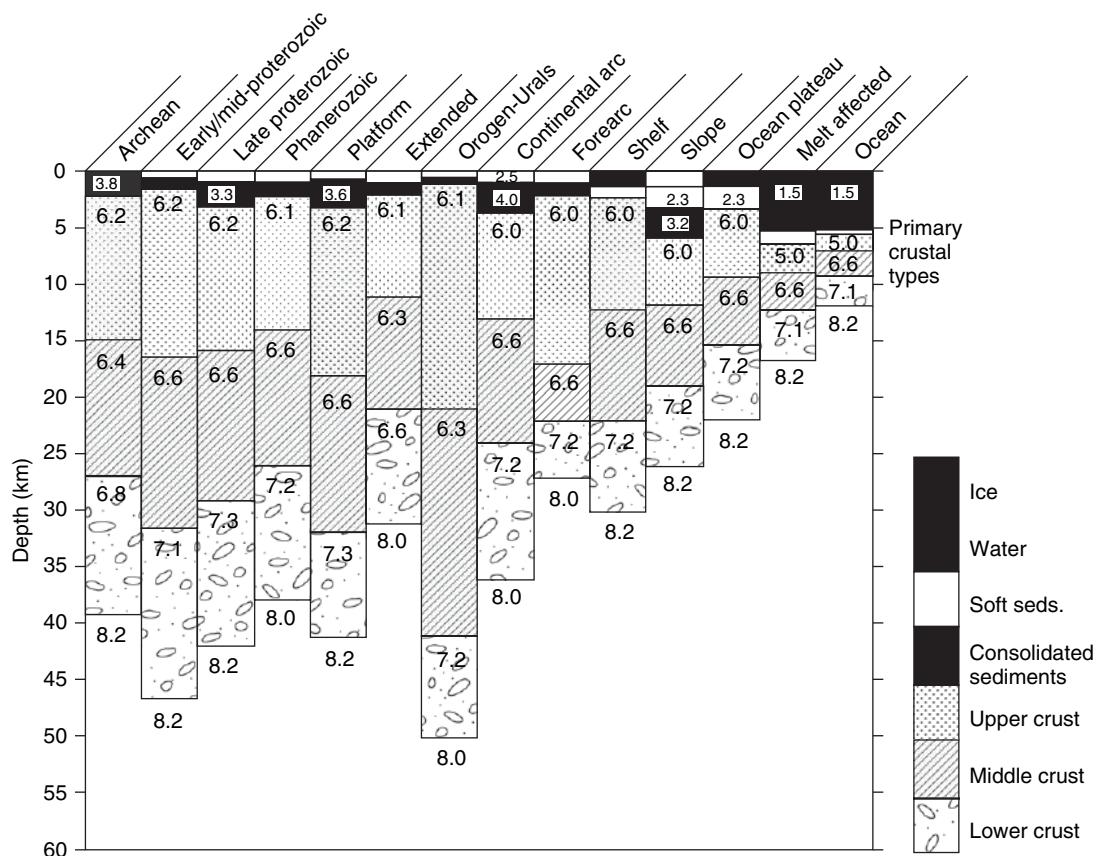


Figure 19 Fourteen primary continental and oceanic crustal types (Mooney et al. 1998). Typical P-wave velocities are indicated for the individual crustal layers and the uppermost mantle. Velocities refer to the top of each layer, and there commonly is a velocity gradient of $0.01\text{--}0.02\text{ km s}^{-1}$ per km within each layer. The crust thins from an average value of 40 km in continental interiors to 12 km beneath oceans.

crustal measurements in regions of extended crust, such as western Europe and the Basin and Range Province of western North America, and the scarcity of measurements from Africa, South America, Greenland, and Antarctica. The weighted mean crustal thickness and average crustal velocity are 41 km (SD 6.2 km) and 6.45 km s^{-1} (SD 0.21 km s^{-1}), respectively, as compared with the simple arithmetic average of 39.2 km (SD 8.5 km) and 6.45 km s^{-1} (SD 0.23 km s^{-1} ; Christensen and Mooney, 1995). The weighted average is more representative of the average continental crust.

Seismic measurements of the deep crust from around the world provide a firm basis for defining the characteristics of primary crustal types associated with specific geologic settings (Figure 19). The thickest continental crust (70+ km) is found beneath the Tibetan Plateau and the South American Andes, both of which are young orogens. Continental crust with an elevation above sea level has an (unweighted)

average thickness of 39 km, with a standard deviation of 8.5 km. Thus, 95% (two standard deviations) of the crust has a thickness of between 22 and 56 km. The higher value of this range (56 km) is well below the $70\text{--}75\text{ km}$ thickness of some orogens, which indicates that crustal thickness may not follow a strictly normal distribution. The thickest crust is usually young (Late Cenozoic) crust, and undergoes rapid uplift and erosion which results in crustal thinning.

Continental crust thinner than 30 km is generally limited to rifts and highly extended crust, including continental margins. The process of crustal extension rarely results in uniform stretching of the crust. Instead, the brittle upper crust fractures and rotates along normal faults and the middle and lower crust undergo pure shear extension. Nonuniform crustal extension over a large region gives rise to Moho undulations, which in turn drive lateral lower crustal flow (creep). Thus, tectonic processes can give

rise to significant changes in the distribution of crustal materials. Lower crustal flow is not limited to extending crust; the gravitational forces associated with the high (4–5 km) topography of young orogens also drives crustal flow. A prominent example is the hypothesized southeast crustal flow of the northern and central Tibetan Plateau into the adjacent continental crust (Molnar and Tapponnier, 1975).

The deep structure of orogenic crust has been studied in nearly all the mountain belts of the world,

including the South American Andes, Tibetan Plateau, Western Cordillera of North America, Urals, and the European Alps (Figure 20). Orogenic crust is commonly characterized by a highly thickened, low-density, low seismic-velocity upper crust combined with strong folding and thrusting (Figure 20). In some cases it appears that the lower crust is being subducted into the mantle, possibly aided by a phase transformation of the mafic lower crust to the dense eclogite facies (Rudnick and Gao, 2003). Due to the

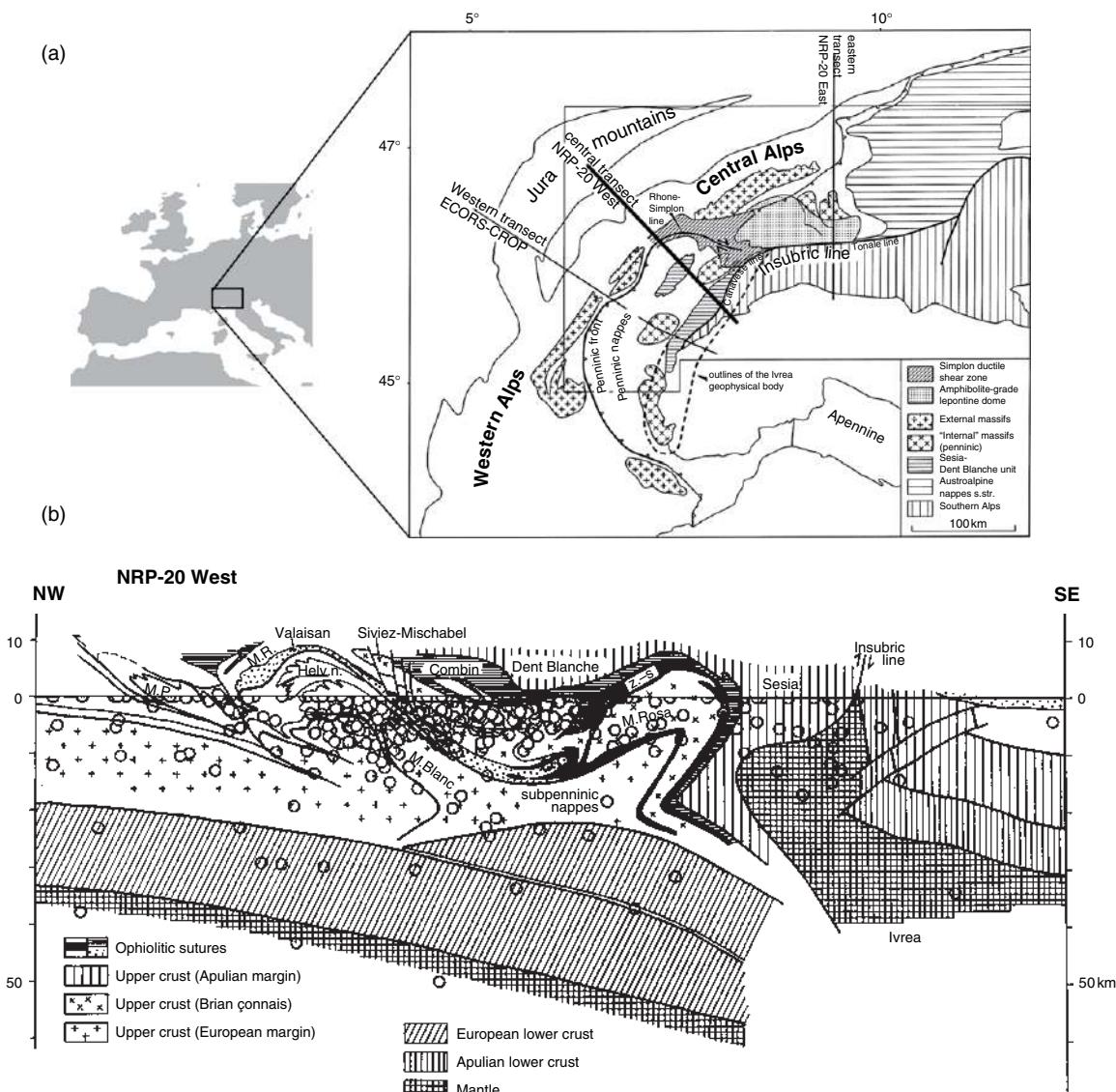


Figure 20 Synthesis of the deep structure and seismicity of the central Alps along the profile NRP-20 West (Schmidt and Kissling 2000). (a) Location map showing the location of the seismic profile. (b) Crustal cross-section (1:1 exaggeration) showing far-traveled nappes, crustal seismicity, and deep structure. Surficial faults are rooted in the middle crust. Seismicity (open circles) decreases dramatically below a depth of 10–15 km, but some earthquakes are located in the lower crust and even the upper mantle. After Mooney, Beroza, Kind, in press.

complexity of the crustal and upper-mantle structure, multiple seismic and nonseismic techniques are needed to reliably determine the deep structure of orogens.

1.11.6.3 Correlation of Crustal Structure with Tectonic Provinces

Shields and platform occupy by far the largest area (69%) of continental crust (Figure 18). These regions have an average crustal thickness of 41.5 km, very close to the weighted global average continental crustal thickness of 41 km. Orogenes, young and old, show a wide range of thicknesses, from 30 to 75 km. Extended crust, as the name implies, has been thinned and shows an average thickness of 30.5 km. Rifts, both active and inactive, show a broad range, from 18 to 46 km. Tectonic provinces commonly have a complex crustal structure. For example, the Tibetan Plateau ranges in thickness from 55 to 75 km, and the Kenya rift from 20 to 36 km. Thus, significant variations sometimes occur within a single tectonic province. A second important observation is that there are numerous regions with anomalous crustal thickness. For example, southern Finland consists of a Proterozoic shield that is nearly at sea level. Global statistics would predict a crustal thickness of 41.5 ± 6.2 km. In fact, in southern Finland the crust reaches a maximum thickness of 65 km due to the persistence of an ancient crust root at a

Pre-Cambrian suture zone. This example attests to the considerable variability of continental crustal properties.

1.11.7 Global Crustal Models

The studies of the Earth's crust that have been summarized in the previous sections are sufficient to form the basis for a global model of the Earth's crust. One simple representation is a contour map of global crustal thickness (Figure 21). This map shows several interesting features. Continental interiors generally have a crustal thickness of 35–45 km, with the thickest values beneath the high topography of the Tibetan Plateau and South American Andes (80 km). Most continental margins have a thickness of close to 30 km, and the vast oceanic basin are underlain by approximately 6–8 km-thick crust, plus the 4–5 km thick water layer. Such a contour map, while presenting the main variations in crustal thickness, lacks information regarding lateral variations in compressional and shear-wave velocity, and density. These physical properties vary strongly within the uppermost mantle as well. For this reason, it has proved valuable to create global crustal models that quantify not only crustal thickness, but seismic velocities and density for the entire crust and uppermost mantle.

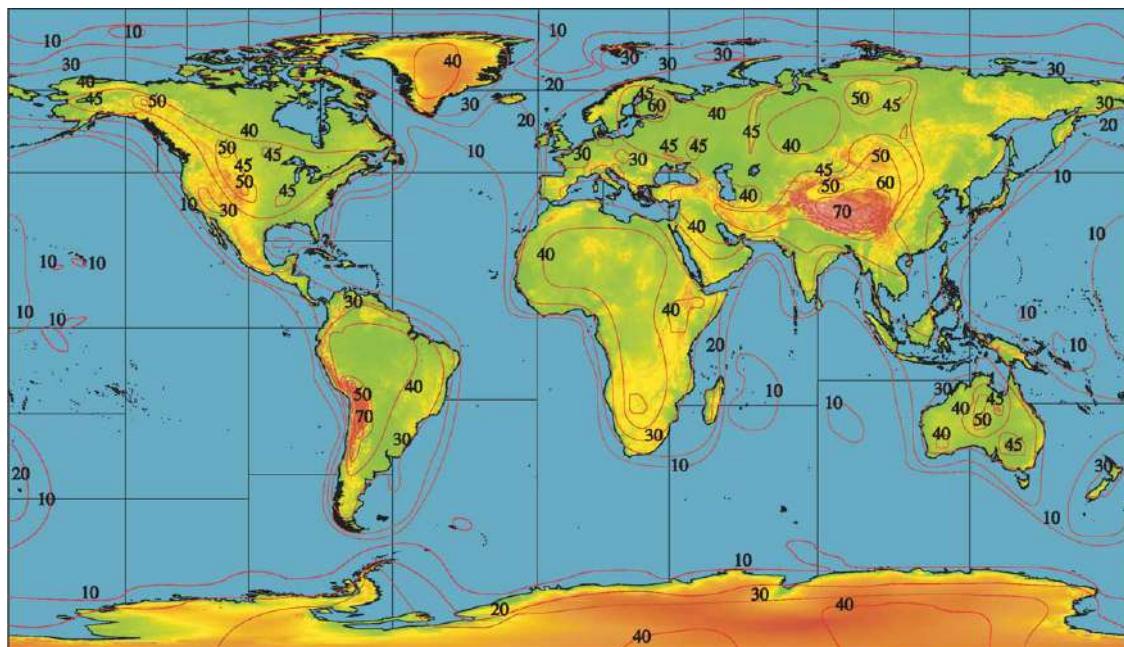


Figure 21 Global contour map of crustal thickness. Red lines indicate 10 km contour intervals.

Global models of the seismic velocity and density structure of the crust have numerous applications in geophysics. Such models provide regional traveltimes to determine accurate earthquake locations, and provide crustal corrections to improve mantle seismic tomographic models. Furthermore, lateral variations in mantle density may be inferred from long-wavelength gravity data if the density structure and thickness of the overlying crust is known. In addition, the crustal contribution to lithospheric stress and crustal isostasy can be calculated from crustal thickness, density, and topography (Mooney *et al.*, 1998).

The earliest 3-D seismic velocity model of the Earth's crust dates back approximately 20 years to Soller *et al.* (1982) who assembled one of the first compilations of global Moho and upper-mantle velocity. A $2^\circ \times 2^\circ$ cell model called 3SMAC followed more than a decade later (Nataf and Ricard, 1996). The 3SMAC model was derived using both seismological data and nonseismological constraints such as chemical composition, heat flow, and hot spot distribution, from which estimates of seismic velocities and the density in each layer were made. Two years later, CRUST 5.1 was introduced (Mooney *et al.*, 1998) incorporating twice the amount of active-source seismic data as 3SMAC. Statistical averages were calculated for the different tectonic regions (Figure 22) and these average models were used in regions with no direct seismic measurements. However, the $5^\circ \times 5^\circ$ resolution was still too coarse for regional studies. In 2000, CRUST 2.0 updated the ice and sediment thickness information of CRUST 5.1 at $1^\circ \times 1^\circ$ resolution, and presented crustal thickness data onto a $2^\circ \times 2^\circ$ grid (Figure 23). In addition, several high-resolution regional compilations of depth-to-Moho values have been developed for Europe (Meissner *et al.*, 1987; Geiss, 1987; Dèzes and Ziegler, 2001; Ritzmann *et al.*, 2007) and the Middle East and North Africa (Seber *et al.*, 2001).

Other published crustal models include WINPAK3D (Johnson and Vincent, 2002) and WENA 1.0 (Pasyanos *et al.*, 2004), which provide an estimate of the velocity and density structure of the upper lithosphere (i.e., whole crust and uppermost mantle, P_n and S_n velocity) for specifically defined geophysical regions. These models are based on independent compilations of sediment, crust, and mantle models and data previously constructed or collected within these regions. Pasyanos *et al.* (2006) describe a probabilistic inverse technique that allows for the use of multiple data sets in regional or global model building. Complete crustal models can be used to compare a

variety of empirical observations over large geographic areas, to test the propagation of seismic waves, and to serve as starting models for tomographic inversion techniques. Tables 8a and 8b list select references on global and regional crustal models, respectively.

1.11.7.1 The Sedimentary Cover

The sedimentary cover plays an important role in global crustal models because these materials have low seismic velocities and low densities. Thus, the sedimentary cover can have a large influence on traveltimes of seismic body and surface waves, as well as on the global gravity field.

Although sedimentary rocks cover most of the ocean floor and nearly three-quarters of continental surfaces, they are estimated to constitute only 5% of the upper 16 km of the crust by volume (Rudnick and Gao, 2003). This volumetric estimate is based on a variety of sources: (1) direct calculation from exposed stratigraphic sections or boreholes, (2) seismic reflection and refraction surveys, and (3) geochemical analyses including dissolved sodium or potassium in seawater than can be traced to total sediment-sedimentary rock volume. Taylor and McLennan (1985) and Rudnick and Gao (2003) use geologic data to estimate the abundances of common sedimentary rocks. The average abundances from these authors are 75% shales, 12% carbonates (limestone and dolomite), 10% sandstones, and 3% evaporates. Sedimentary rocks, especially fine-grained shales or mudstones, are subject to postdepositional processes such as diagenesis, metamorphism, and alteration by oceanic water (Rudnick and Gao, 2003). These processes increase rock density and seismic velocity.

1.11.7.2 The Crystalline Crust and Uppermost Mantle

A complete global P- and S-wave crustal (and upper lithospheric) model is based on three types of information: (1) synthesizing existing models, such as WENA 1.0, the Barents Sea model (Ritzmann *et al.*, 2007), and WINPAK; (2) seismic tomography data, and (3) an ongoing compilation of published seismic models for the crust, based on active- and passive-source seismology (Figure 11). Thus, in addition to results from controlled sources, the model also incorporates results from receiver function analysis, surface-wave dispersion analysis, and seismic tomography.

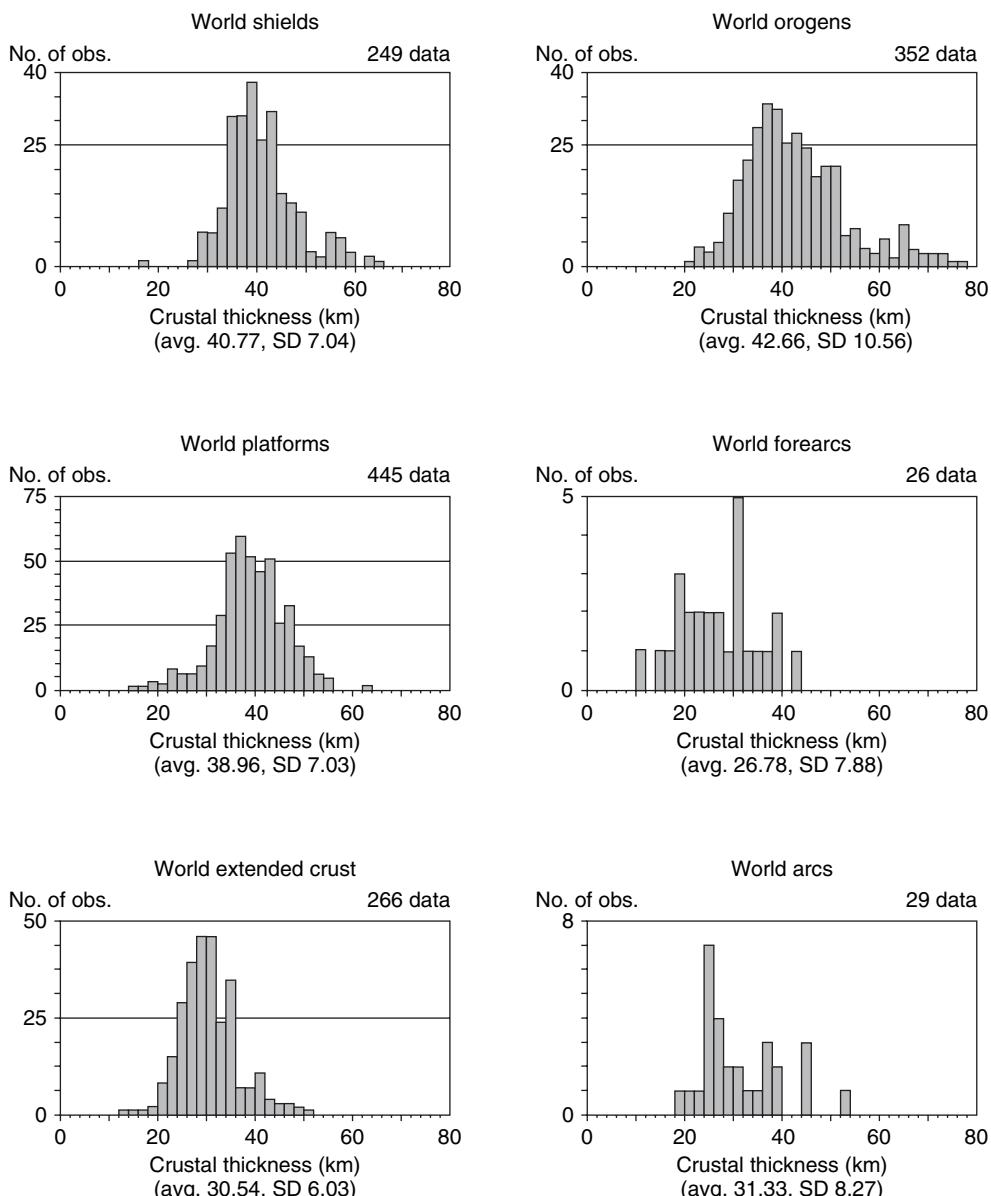


Figure 22 Histograms of crustal thickness for six continental tectonic provinces calculated from the individual point measurements ([Figure 11](#)). Average and standard deviations are indicated. These histograms indicate systematic differences among tectonic provinces, and provide a basis for extrapolating crustal thickness into unmeasured regions.

After compiling all of the existing regional models, the models are then compared and evaluated based on their technique and data quality. Separate databases are constructed for each technique, for example (1) active-source models, (2) surface-wave models, (3) seismic tomography models, and (4) receiver function models. Integration of such varied models requires some discrimination of data and model quality, and a suite of models emerges from which a ‘best fit’ composite model is developed. Discrepancies

between input models are resolved based on the best available data, which must occasionally be decided subjectively.

In the $2^\circ \times 2^\circ$ mode CRUST 2.0 ([Figure 23](#)), the Earth’s crust is divided into eight layers: (1) ice, (2) water, (3) soft sediments, (4) hard sediments, (5) crystalline upper, (6) middle, and (7) lower crust, and (8) uppermost mantle. Both P- and S-wave velocities and estimated density are specified in each layer.

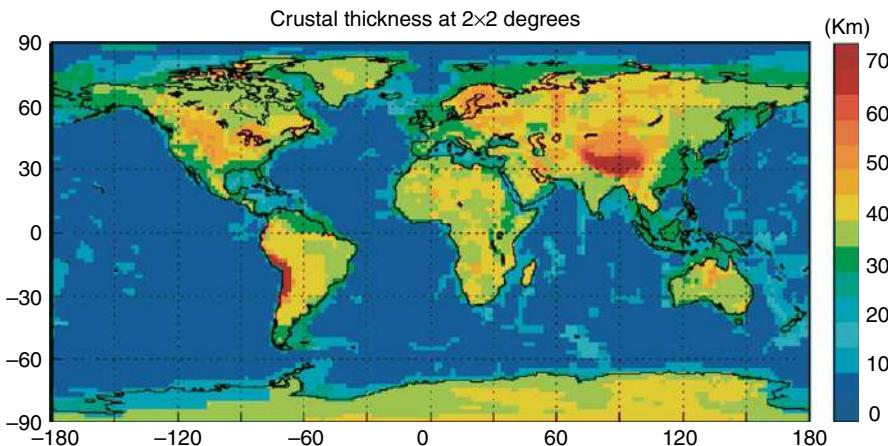


Figure 23 Crustal thickness provided by the $2^\circ \times 2^\circ$ CRUST2.0 model (Bassin *et al.* 2000). The locations of seismic profiles used to make this model are shown in **Figure 11**. Typical crustal velocity models are summarized in **Figure 19**. The crustal structure is estimated in regions with no seismic measurements using the statistic averages illustrated in **Figure 22**. This crustal model is useful to make crustal velocity (P- and S-wave) or density corrections in many types of geophysical models.

Layers 1 and 2 are the easiest to determine. Ice is only found near the poles, and in high regions such as the Himalayas. Efforts to determine its thickness are straightforward and relatively expeditious. Water depth is also relatively easy to interpret at $2^\circ \times 2^\circ$ using the ETOPO 2 model of the National Geophysical Data Center (2004). Both soft and hard (unconsolidated and consolidated, respectively) sediments are determined as these represent two distinct layers (3 and 4) in the model.

Layers 5–8 are determined from the compiled global crustal structure database and regional models. At present, the largest global crustal structure database of active-and passive-source measurements of the structure of the upper lithosphere includes more than 9200 data sets (almost 10 times the number available for CRUST 5.1). This is more than sufficient to build a $2^\circ \times 2^\circ$ crustal block model.

Using the criteria set forth in the construction of CRUST 5.1 and other similar models, one of a series of primary crustal ‘types’ is assigned to each cell. There are approximately 400 different crustal model ‘types’ used in the $2^\circ \times 2^\circ$ global model. Once the global crustal structure model has been compiled, the model must be evaluated. Model testing is generally based on a comparison of P_g (S_g), and P_n (S_n) traveltimes predictions, with some empirical observations. Another useful test is a comparison with high-frequency Love wave phase velocities. **Tables 8a** and **8b** lists the currently available global and regional crustal models. Updates to these models appear on a regular basis.

Table 8a Global crustal models

References	Year
Bassin <i>et al.</i>	2000
Laske and Masters	1997
Mooney <i>et al.</i>	1998
Nataf and Ricard	1996
National Geophysical Data Center	2004
Soller <i>et al.</i>	1982
Tanimoto	1995

Table 8b Regional crustal models

References	Year
Bungum <i>et al.</i>	2005
Mooney and Braile	1989
Pasyanos <i>et al.</i>	2004
Ritzmann <i>et al.</i>	2007
Van der Lee and Nolet	1997
Walter <i>et al.</i>	2000
Warren and Healy	1973

1.11.8 Discussion and Conclusions

Seismological studies of the crust and uppermost mantle began in the first decade of the twentieth century (Mohorovicic, 1910). Over the next 60 years a wide range of studies (**Table 1**) defined the gross properties of the crust. The past 35 years have seen a pronounced increase in lithospheric studies, with the development of such techniques as seismic

reflection studies of the deep crystalline crust, receiver function analysis, and earthquake tomography and high-resolution surface-wave inversions. These advances have been matched by extensive laboratory studies of rock velocities and densities, and nonseismic geophysical studies using gravity, magnetic, and geoelectrical methods. Geophysical studies of the crust and subcrustal lithosphere have become so numerous that it is difficult for any individual or research group to keep abreast of all recent results. This highlights the need for a searchable databank of geophysical results, whereby it would be possible to sort by technique, location, depth of penetration, crustal age, or geologic and tectonic setting.

The process of synthesizing global studies of crustal structure is more than 20 years old (Soller *et al.*, 1982) and numerous regional and global models have become available (Tables 8a and 8b). Until recently these models have been largely based on seismic measurements of compressional-wave velocity (V_p), with the shear-wave velocity (V_s) and density estimated using empirical relations. Future models should be able to rely more heavily on measured shear-wave velocities. Estimating deep crustal density will continue to be a challenge, but is greatly aided by borehole and laboratory measurements. The use of multiple seismic data sets in constructing regional and global crustal models will be aided by the use of inverse techniques (Pasyanos *et al.*, 2006).

As high-resolution surface-wave models become available, it will be possible to directly compare regional models derived from body-wave studies with models derived from surface waves. Likewise, nonseismic methods are rapidly developing, including satellite observations of long-wavelength gravity and magnetic fields. The synthesis of all of these methods promises to provide ever-increasing resolution on the global structure of the Earth's crust and subcrustal lithosphere.

References

- Abbott DH (1996) Plumes and hotspots as sources of greenstone belts. *Lithos* 37: 113–127.
- Abbott DH and Mooney WD (1995) The structural and geochemical evolution of the continental crust: Support for the oceanic plateau model of continental growth. *Reviews of Geophysics* 99: 231–242 (supplement).
- Aki K (1982) Three-dimensional seismic inhomogeneities in the lithosphere and asthenosphere. *Reviews of Geophysics and Space Physics* 20: 161–170.
- Aki K, Christoffersson A, and Husebye ES (1976) Three-dimensional seismic structure of the lithosphere under Montana LASA. *Bulletin of the Seismological Society of America* 66: 501–524.
- Aki K, Christoffersson A, and Husebye ES (1977) Determination of the three-dimensional seismic structure of the lithosphere. *Journal of Geophysical Research* 82: 277–296.
- Aki K and Lee WHK (1976) Determination of three-dimensional velocity anomalies under a seismic array using first P -arrival time from local earthquakes. Part 1: A homogeneous initial model. *Journal of Geophysical Research* 81: 4381–4399.
- Aki K and Richards P (1980) *Quantitative Seismology. Theory and Methods*. San Francisco, CA: Freeman.
- Alexander SS (1962) A study of the normal modes of surface waves across the Western United States. *Journal of Geophysical Research* 67: 3537–3538.
- Albarede F (1998) The growth of continental crust. *Tectonophysics* 296: 1–14.
- Al-Lazki AI, Sandvol E, Seber D, Barazangi M, Turkelli N, and Mohammad R (2004) Pn tomographic imaging of mantle lid velocity and anisotropy at the junction of the Arabian, Eurasian and African plates. *Geophysical Journal International* 158: 1024–1040.
- Al-Lazki AI, Seber D, Sandvol E, Turkelli N, Mohammad R, and Barazangi M (2003) Tomographic Pn velocity and anisotropy structure beneath the Anatolian plateau (eastern Turkey) and the surrounding regions; the Turkey seismic experiment; the study of a young continent-continent collision. *Geophysical Research Letters* 30: (doi:10.1029/2003GL017391).
- Allen RM, Nolet G, Morgan WJ, et al. (2002) Imaging the mantle beneath Iceland using integrated seismological techniques. *Journal of Geophysical Research* 107: (doi: 10.1029/2001JB000595).
- Alvares R, Reynoso JP, Alvarez LJ, and Martinez ML (1978) Electrical conductivity of igneous rocks; composition and temperature relations. *Bulletin Volcanologique* 41: 317–327.
- Ammon C, Randall G, and Zandt G (1990) On the nonuniqueness of receiver function inversions. *Journal of Geophysical Research* 95: 15303–15328.
- Anderson DL (1961) Elastic wave propagation in layered anisotropic media. *Journal of Geophysical Research* 66: 2953–2963.
- Anderson DL (1967) The anelasticity of the mantle. *Geophysical Journal of the Royal Astronomical Society* 14: 135–164.
- Anderson DL and Archambeau CB (1964) The anelasticity of the Earth. *Journal of Geophysical Research* 69: 2071–2084.
- Angus DA, Wilson DC, Sandvol E, and Ni JF (2006) Lithospheric structure of the Arabian and Eurasian collision zone in eastern Turkey from S-wave receiver functions. *Geophysical Journal* 166: 1335–1346.
- Ansorge J, Prohledel C, and Bamford D (1982) Comparative interpretation of explosion seismic data. *Journal of Geophysics* 51: 69–84.
- Artemieva IM and Mooney WD (2001) Thermal thickness of Precambrian lithosphere: A global study. *Journal of Geophysical Research* 106: 16 387–16 414.
- Arvidson RE, Bindschadler D, Bowring S, Eddy M, Guinness E, and Leff C (1984) Bouguer images of the North American craton and its structural evolution. *Nature* 311: 241–243.
- Au D and Clowes RM (1984) Shear-wave velocity structure of the oceanic lithosphere from ocean bottom seismometer studies. *Geophysical Journal of the Royal Astronomical Society* 77: 105–123.
- BABEL Working Group (1993) Deep seismic reflection/refraction interpretation of crustal structure along BABEL

- profiles A and B in the southern Baltic Sea. *Geophysical Journal International* 112: 325–343.
- Banks RJ (1972) The overall conductivity distribution in the earth. *Journal of Geomagnetism and Geoelectricity* 24: 337–351.
- Banks RJ, Parker RL, and Huestis SP (1977) Isostatic compensation on a continental scale: Local versus regional mechanisms. *Geophysical Journal of the Royal Astronomical Society* 51: 431–452.
- Bannister SC, Ruud BO, and Husebye ES (1991) Tomographic estimates of sub-Moho seismic velocities in Fennoscandia and structural implications; imaging and understanding the lithosphere of Scandinavia and Iceland. *Tectonophysics* 189: 37–53.
- Bamford D (1977) *Pn* velocity anisotropy in a continental upper mantle. *Geophysical Journal of the Royal Astronomical Society* 49: 29–48.
- Baranov V (1957) A new method for interpretation of aeromagnetic maps: Pseudogravimetric anomalies. *Geophysics* 22: 359–383.
- Barazangi M and Ni J (1982) Velocities and propagation characteristics of *Pn* and *Sn* waves beneath the Himalayan arc and Tibetan plateau: Possible evidence for overthrusting of Indian continental lithosphere beneath Tibet. *Geology* 10: 175–185.
- Barazangi M and Brown L (eds.) (1986a) *Geodynamics series 13: Reflection seismology: A Global Perspective*. Washington, DC: American Geophysical Union.
- Barazangi M and Brown L (eds.) (1986b) *Geodynamics series 14: Reflection Seismology: The Continental Crust*. Washington, DC: American Geophysical Union.
- Barclay AH, Toomey DR, and Solomon SC (1998) Seismic structure and crustal magmatism at the Mid-Atlantic Ridge, 35°N. *Journal of Geophysical Research* 102: 3109–3129.
- Barmin MP, Levshin AL, and Ritzwoller MH (2001) A fast and reliable method for surface wave tomography. *Pure and applied Geophysics* 158: 1351–1375.
- Bartelson H, Lueschen E, Krey Th, Meissner R, Scholl H, and Walter Ch (1982) The combined seismic reflection-refraction investigation of the Urach geothermal anomaly. In: Haemel R (ed.) *The Urach Geothermal Project*, pp. 247–262. Stuttgart: Schweizerbart'sche Verlagsbuchhandlung.
- Barton AJ and White RS (1997) Crustal structure of the Edoras Bank continental margin and mantle thermal anomalies beneath the North Atlantic. *Journal of Geophysical Research* 102: 3109–3129.
- Barton PJ (1986) The relationship between seismic velocity and density in the continental crust. *Geophysical Journal of the Royal Astronomical Society* 87: 195–208.
- Barton PJ (1992) LISPB revisited: A new look under the Caledonides of northern Britain. *Geophysical Journal International* 110: 371–391.
- Bass JD (1995) Elasticity of minerals, glasses, and melts. In: Athrens TJ (ed.) *Mineral Physics and Crystallography: A Handbook of Physical Constants*, pp. 45–63. Washington, DC: American Geophysical Union Reference Shelf.
- Bassin C, Laske G, and Masters GNY (2000) The current limits of resolution for surface tomography in North America. *EOS* 81: F897.
- Bateman PC and Eaton JP (1967) Sierra Nevada Batholith. *Science* 158: 1407–1417.
- Bath M and Stefánsson R (1966) S–P conversion at the base of the crust. *Annali di Geofisica* 19: 119–130.
- Begnaud ML, McClain JS, Barth GA, Orcutt JA, and Harding AJ (1997) Preliminary velocity structure from forward modeling of the eastern ridge-transform intersection area of the Clipperton Fracture Zone, East Pacific Rise. *Journal of Geophysical Research* 102: 7803–7820.
- Behrendt JC, Green AG, Cannon WF, et al. (1988) Crustal structure of the Midcontinent rift system; results from GLMPCE deep seismic reflection studies. *Geology* 16: 81–85.
- Belousov VV, Kunin NY, Mazur VB, Ostisty BK and Ostrovsky MI (1988) *Map of the relief of the basement surface of Eurasia*, scale 1:15,000,000.
- Belousov VV and Pavlenkova NI (1984) The types of the Earth's crust. *Journal of Geodynamics* 1: 167–183.
- Belousov VV, Pavlenkova NI, and Egorkin AV (eds.) (1991) *Geophysical Models of the Territory of the USSR*, 224. Moscow: Nauka.
- Ben-Avraham Z, Nur A, Jones D, and Cox A (1981) Continental accretion: from oceanic plateaus to allochthonous terranes. *Science* 213: 47–54.
- Benoit MH, Nyblade AA, VanDecar JC, and Gurrola H (2003) Upper mantle P wave velocity structure and transition zone thickness beneath the Arabian shield. *Geophysical Research Letters* 30: (doi:10.1029/2002GL016436).
- Berckhemer H, Rauen A, Winter H, et al. (1997) Petrophysical properties of 9-km-deep crustal section at KTB. *Journal of Geophysical Research* 102: 18337–18362.
- Berdichevskiy MN and Zhdanov MS (1984) *Advanced Theory of Deep Electromagnetic Sounding*. Amsterdam: Elsevier.
- Berry LG and Mason BH (1959) *Mineralogy: Concepts Description Determinations*, 444 pp. New York: W.H. Freeman.
- Berry MJ and West GF (1966) An interpretation of the first-arrival data of the Lake Superior experiment by the time-term method. *Bulletin of the Seismological Society of America* 56: 141–171.
- Bessonova EN, Fishmen VM, Ryaboy VZ, and Sitnikova GA (1974) The tau method for inversion of travel times. I. Deep seismic sounding data. *Geophysical Journal of the Royal Astronomical Society* 36: 377–398.
- Bessonova EN, Fishmen VM, Shirman MG, Strikova GA, and Johnson LR (1976) The tau method of inversion of travel times. II. Earthquake data. *Geophysical Journal of the Royal Astronomical Society* 46: 87–108.
- Bibee LD and Shor GG (1976) Compressional wave anisotropy in the crust and upper mantle. *Geophysical Research Letters* 3: 639–642.
- Bijwaard H, Spakman W, and Engdahl ER (1998) Closing the gap between regional and global travel time tomography. *Journal of Geophysical Research* 103: 30055–30078.
- Birch F (1943) Elasticity of igneous rocks at high temperatures and pressures. *Bulletin of the Geological Society of America* 54: 263–286.
- Birch F (1952) Elasticity and constitution of the Earth's interior. *Journal of Geophysical Research* 57: 227–286.
- Birch F (1960) The velocity of compressional waves in rocks to 10 kilobars. Part 1: *Journal of Geophysical Research* 5: 1083–1102.
- Birch F (1961) The velocity of compressional waves in rocks to 10 kilobars. Part 2: *Journal of Geophysical Research* 66: 2199–2224.
- Birch F (1972) Numerical experiments on the velocities in aggregates of olivine. *Journal of Geophysical Research* 77: 6385–6391.
- Birch F (1975) Velocity and attenuation from resonant vibrations of spheres of rock, glass, and steel. *Journal of Geophysical Research* 80: 756–764.
- Björnsson A, Eysteinsson H, and Bebblo M (2005) Crustal formation and magma genesis beneath Iceland: Magnetotelluric constraints. In: Foulger GR, Natland JH, Presnall DC, and Anderson DL (eds.) *Geological Society of America, Special Paper 388 Plates, Plumes, and Paradigms* pp. 665–686. Boulder, CO: Geological society of America.

- Blakely RG (1995) *Potential Theory in Gravity and Magnetic Applications*. New York: Cambridge University Press.
- Blakely RJ and Grauch VJS (1983) Magnetic models of crystalline terrane: Accounting for the effect of topography. *Geophysics* 48: 1551–1557.
- Blundell D, Freeman R, and Mueller S (eds.) (1992) *A Continent Revealed – the European Geotraverse*. New York: Cambridge University Press.
- Blundell DJ and Raynaud B (1986) Modeling lower observed on BIRPS profiles. In: Barazangi M and Brown L (eds.) *American Geophysical Union Geodynamics Series 13: Reflection Seismology; A global Perspective*, pp. 287–295. Washington, DC: American Geophysical Union.
- Bond KR and Zietz I (1987) Composite Magnetic Anomaly Map of the Conterminous United States west of the 96° longitude. U.S. Geological Survey Geophysical Investigations Map GP-977, scale 1:2,500,000.
- Bonini WE and Bonini RR (1979) Andrija Mohorovičić: Seventy years ago an earthquake shook Zagreb. *EOS, Transactions, American Geophysical Union* 60: 699–701.
- Booker J, Favetto A, and Pomposiello MC (2004) Low electrical resistivity associated with plunging of the Nazca flat slab beneath Argentina. *Nature* 429: 399–403.
- Boore DM (1972) Finite difference methods for seismic wave propagation in heterogeneous materials. In: Bolt BA (ed.) *Seismology; Surface Waves and Earth Oscillations; Methods in Computational Physics*, Vol. 11, pp. 1–37. New York: Academic Press.
- Boschi L, Ekstroem G, and Kustowski B (2004) Multiple resolution surface wave tomography; the Mediterranean basin. *Geophysical Journal International* 157: 293–304.
- Bostock M, Hyndman R, Rondenay S, and Peacock S (2002) An inverted continental Moho and serpentization of the forearc mantle. *Nature* 417: 536–538.
- Bouchon M (1982) The complete synthesis of seismic crustal phases at regional distances. *Journal of Geophysical Research* 87: 1735–1741.
- Bourjot L and Romanowicz B (1992) Crust and upper mantle tomography in Tibet using surface waves. *Geophysical Research Letters* 19: 881–884.
- Bown JW and White RS (1994) Variation with spreading rate of oceanic crustal thickness and geochemistry. *Earth and Planetary Science Letters* 121: 435–449.
- Braile L and Smith RB (1974) Guide to the interpretation of crustal refraction profiles. *Geophysical Journal of the Royal Astronomical Society* 40: 145–176.
- Braile LW and Chiang CS (1986) The continental Mohorovičić discontinuity; results from near-vertical and wide-angle seismic refraction studies. In: Barazangi M and Brown L (eds.) *American Geophysical Union Geodynamics Series 13: Reflection Seismology; A Global Perspective*, pp. 257–272. Washington, DC: American Geophysical Union.
- Braile LW, Keller GR, Mueller S, and Prodehl C (1995) Seismic techniques. In: Olsen KH (ed.) *Continental Rifts: Evolution, Structure, Tectonics*, pp. 61–92. Amsterdam: Elsevier.
- Brocher TM (1995) Deep-crustal seismology of continental margins, U.S. Natl. Rep. Int. Union Geod. Geophys. 1991–1994. *Review of Geophysics* 33: 309–314.
- Brocher TM (2005) Empirical relations between elastic wavespeeds and density in the earth's crust. *Bulletin of the Seismological Society of America* 95(6): 2081–2092.
- Brocher TM, Parsons T, Tréhu AM, Snelling CM, and Fisher MA (2003) Seismic evidence for widespread serpentized forearc upper mantle along the Cascadia margin. *Geology* 31: 267–1307.
- Brown L, Barazangi M, Kaufman S, and Oliver J (1986) The first decade of COCORP; 1974–1984. In: Barazangi M and Brown LD (eds.) *American Geophysical Union Geodynamics Series 13: Reflection Seismology; A Global Perspective*, pp. 107–120. Washington, DC: American Geophysical Union.
- Brune J and Dorman J (1963) Seismic waves and earth structure in the Canadian shield. *Bulletin of the Seismological Society of America* 53: 167–210.
- Brune JN (1969) Surface waves and crustal structure. In: Hart PJ (ed.) *American Geophysical Union Geophysical Monograph Series 13: The Earth's Crust and Upper Mantle*, pp. 230–242. Washington, DC: American Geophysical Union.
- Brune JN, Nafe J, and Oliver J (1960) A simplified method for the analysis and synthesis of dispersed wave trains. *Journal of Geophysical Research* 65: 287–304.
- Bruneton M, Pedersen HA, Farra V, et al. (2004) Complex lithospheric structure under the central Baltic Shield from surface wave tomography. *Journal of Geophysical Research* 109: (doi:10.1029/2003JB002947).
- Bungum H, Ritzmann O, Maercklin N, Faleide J-I, Mooney WD, and Detweiler ST (2005) Three-dimensional model for the crust and upper mantle in the Barents Sea Region. *EOS, Transactions, American Geophysical Union* 86(16): 160–161.
- Butler R (1986) Regional seismic observations of the Ongtong Java Plateau and East Marina Basin. *Marine Geophysical Researches* 8: 27–38.
- Burdick LJ and Langston CA (1977) Modeling crust-structure through the use of converted phases in teleseismic body-wave-forms. *Bulletin of the Seismological Society of America* 67: 677–691.
- Byerly P (1926) The Montana earthquake of June 28, 1925. *Bulletin of the Seismological Society of America* 16: 209–265.
- Byerly P and Dyk K (1932) Richmond quarry blast of September 12, 1931, and the surface layering of the earth in the region of Berkeley. *Bulletin of the Seismological Society of America* 22: 50–55.
- Cagniard L (1953) Basic theory of magnetotelluric method of geophysical prospecting. *Geophysics* 18(3): 605–635.
- Calvert A, Sandvol E, Seber D, et al. (2000) Propagation of regional seismic phases (Lg and Sn) and Pn velocity structure along the Africa–Iberia plate boundary zone; tectonic implications. *Geophysical Journal International* 142: 384–408.
- Campbell IH, Griffiths RW, and Hill R (1989) Melting in an Archaean mantle plume: Heads it's basalts, tails it's komatiites. *Nature* 339: 697–699.
- Canales JP, Detrick RS, Lin J, Collins JA, and Toomey DR (2000) Crustal and upper mantle seismic structure beneath the rift mountains and across a nontransform offset at the Mid-Atlantic Ridge (35°N). *Journal of Geophysical Research* 105: 2699–2719.
- Cann JR (1970) New model for the structure of the oceanic crust. *Nature* 226: 928–930.
- Cann JR (1974) A model for oceanic crustal structure developed. *Geophysical Journal of the Royal Astronomical Society* 39: 169–187.
- Cannat M (1996) How thick is the magmatic crust at slow spreading oceanic ridges? *Journal of Geophysical Research* 101: 2847–2857.
- Caress DW, McNutt MK, Detrick RS, and Mutter JC (1995) Seismic imaging of hotspot-related crustal underplating beneath the Marquesas Islands. *Nature* 373: 600–603.
- Carlson RL, Christensen NI, and Moore RP (1980) Anomalous crustal structure in ocean basins: Continental fragments and oceanic plateaus. *Earth and Planetary Science Letters* 51: 171–180.
- Carmichael RS (1982) *Handbook of Physical Properties of Rocks*. Boca Raton, FL: CRC Press.

- Cassidy JF (1992) Numerical experiments in broadband receiver function analysis. *Bulletin of the Seismological Society of America* 82: 1453–1474.
- Cermak V (1993) Lithospheric thermal regimes in Europe. *Physics of the Earth and Planetary Interiors* 79: 179–193.
- Červený V (1972) Seismic rays and ray intensities in inhomogeneous anisotropic media. *Geophysical Journal of the Royal Astronomical Society* 72: 755–766.
- Červený V, Molotkov IA, and Pšeničník I (1977) *Ray Method in Seismology*. Prague, Czechoslovakia: University of Karlova (Charles).
- Červený V and Pšeničník I (1984) SEIS83 – Numerical modeling of seismic wave fields in 2 – D laterally varying layered structures by the ray method. In: Engdal ER (ed.) *Documentation of Earthquake Algorithms*. World Data Center A for Solid Earth Geophys., Rep. SE-35, pp. 36–40. Boulder, CO.
- CGMW (Commission for the Geological Map of the World) (2002) *Geological Map of the World*. Paris: UNESCO.
- Chapman CH (1978) A new method for computing synthetic seismograms. *Geophysical Journal of the Royal Astronomical Society* 54: 481–518.
- Chapman CH and Orcutt JA (1985) Least-squares fitting of marine seismic refraction data. *Geophysical Journal of the Royal Astronomical Society* 82: 339–374.
- Chapman DS (1986) Thermal gradients in the continental crust. In: Dawson JB (ed.) *Geological Society Special Publication. The Nature of the Lower Continental Crust*, vol. 24, pp. 63–70. Oxford: Blackwell scientific publications.
- Charvis P, Recq M, Operto S, and Brefort D (1995) Deep structure of the northern Kerguelen Plateau and hotspot-related activity. *Geophysical Journal International* 122: 899–924.
- Chen C, Chen Y, Yen H, and Yu G (2003) Lateral variations of P (sub n) velocity and anisotropy in Taiwan from travel-time tomography. *Earth, Planets and Space* 55: 223–230.
- Chen H, Chiu JM, Pujol J, et al. (2005) A simple algorithm for local earthquake location using 3-dimensional Vp and Vs Models- test examples in the central USA and Taiwan regions. *Bulletin of the Seismological Society of America* 96: 288–305.
- Chen YJ (1992) Oceanic crustal thickness versus spreading rate. *Geophysical Research Letters* 19: 753–756.
- Chian D, Louden KE, Minshull TA, and Whitmarsh RB (1999) Deep structure of the ocean continent transition in the southern Iberia Abyssal Plain from seismic refraction profiles. Part 1: ocean drilling program (Legs 149 and 173) transect. *Journal of Geophysical Research* 104: 7443–7462.
- Chian D, Louden KE, and Reid I (1995) Crustal structure of the Labrador sea conjugate margin and implications for the formation of nonvolcanic continental margins. *Journal of Geophysical Research* 100: 24239–24253.
- Chimera G, Aoudia A, Sarao A, and Panza GF (2003) Active tectonics in central Italy: constraints from surface wave tomography and source moment tensor inversion. *Physics of the Earth and Planetary Interiors* 138: 241–262.
- Christensen NI (1965) Compressional wave velocities in metamorphic rocks at pressures to 10 kilobars. *Journal of Geophysical Research* 70: 6147–6164.
- Christensen NI (1966a) Elasticity of ultrabasic rocks. *Journal of Geophysical Research* 71: 5921–5931.
- Christensen NI (1966b) Shear wave velocities in metamorphic rocks at pressures to 10 kilobars. *Journal of Geophysical Research* 71: 3549–3556.
- Christensen NI (1971) Shear wave propagation in rocks. *Nature* 229: 549–550.
- Christensen NI (1972) The abundance of serpentinites in the oceanic crust. *Journal of Geology* 80: 709–719.
- Christensen NI (1979) Compressional wave velocities in rocks at high temperatures and pressures, critical thermal gradients, and crustal low-velocity zones. *Journal of Geophysical Research* 84: 6849–6857.
- Christensen NI (1982) Sieismic velocities. In: Carmichael RS (ed.) *Handbook of Physical Properties of Rocks*, vol. II, pp. 1–228. Boca Raton, FL: CRC Press.
- Christensen NI (1996) Poisson's ratio and crustal seismology. *Journal of Geophysical Research* 100: 3139–3156.
- Christensen NI and Fountain DM (1975) Constitution of the lower continental crust based on experimental studies of seismic velocities in granulite. *Bulletin of the Geological Society of America* 86: 277–236.
- Christensen NI and Salisbury MH (1975) Structure and constitution of the lower oceanic crust. *Reviews of Geophysics and Space Physics* 13: 57–86.
- Christensen NI and Salisbury MH (1979) Seismic anisotropy in the upper mantle: Evidence from the Bay of Islands ophiolite complex. *Journal of Geophysical Research* 84: 4601–4610.
- Christensen NI and Salisbury MH (1982) Lateral heterogeneity in the seismic structure of the oceanic crust inferred from velocity studies in the Bay of Islands ophiolite, Newfoundland. *Geophysical Journal of the Royal Astronomical Society* 68: 675–688.
- Christensen NI and Mooney WD (1995) Seismic velocity structure and the composition of the continental crust: A global view. *Journal of Geophysical Research* 100: 9761–9788.
- Christeson GL, Shaw PR, and Garmany JD (1997) Shear and compressional wave structure of the East Pacific Rise, 9°–10°N. *Journal of Geophysical Research* 102: 7821–7835.
- Chulick GS (1997) Comprehensive seismic survey database for developing three-dimensional models of the earth's crust. *Seismological Research Letters* 68: 734–742.
- Chulick GS and Monney WD (2002) Seismic structure of the crust and upper most mantle of North America and adjacent oceanic basins: A synthesis. *Bulletin of the Seismological Society of America* 92: 2478–2492.
- Claerbout JF (1976) *Fundamentals of Geophysical Data Processing*. Palo Alto, CA: Blackwell Scientific Publications.
- Claerbout JF (1985) *Imaging the Earth's Interior*. Palo Alto, CA: Blackwell Scientific Publications.
- Clarke FW (1889) The relative abundance of the chemical elements. *Phil Soc Washington Bull XI*: 131–142.
- Clarke FW and Washington HS (1924) The composition of the Earth's crust. US Geological Survey Professional Paper 127: 117 pp.
- Clark SP (1966) *Geological Society of America Memoir 97: Handbook of Physical Constants*. Boulder, CO: Geological Society of America.
- Clegg B and England R (2003) Velocity structure of the UK continental shelf from a compilation of wide-angle and refraction data. *Geological Magazine* 140: 453–467.
- Clitheroe GM, Gudmundsson U, and Kennett BLN (2000) The crustal thickness of Australia. *Journal of Geophysical Research* 105: 13697–13713.
- Cloos M (1993) Lithospheric buoyancy and collisional orogenesis: Subduction of oceanic plateaus, continental margins, island arcs, spreading ridges, and seamounts. *Geophysical Society of America Bulletin* 105: 715–737.
- Closs H and Behnke C (1961) Fortschritte der Anwendung seismischer Methoden in der Erforschung der Erdkruste. *Geologische Rundschau* 51: 315.
- Clowes R, Cook F, Hajnal Z, et al. (1999) Canada's LITHOPROBE Project (Collaborative, multidisciplinary

- geoscience research leads to new understanding of continental evolution). *Episodes* 22: 3–20.
- Clowes RM, Baird DJ, and Dehler SA (1997) Crustal structure of the northern Cascadia subduction zone, southwestern British Columbia, from potential field and seismic studies. *Canadian Journal of Earth Sciences* 34: 317–335.
- Clowes RM, Brandon MT, Green AG, et al. (1987) LITHOPROBE – southern Vancouver Island: Cenozoic subduction complex imaged by deep seismic reflections. *Canadian Journal of Earth Sciences* 24: 31–51.
- Clowes RM and Hyndman RD (2002) Geophysical studies of the northern Cascadia subduction zone off western Canada and their implications for great earthquake seismotectonics: A review. In: Fujinawa Y and Yoshida A (eds.) *Seismotectonics in Convergent Plate Boundary*, pp. 1–23. Tokyo, Japan: Terra Scientific Publishing.
- Clowes RM, Kanasewich ER, and Cumming GL (1968) Deep crustal seismic reflections at near vertical incidence. *Geophysics* 33: 441–451.
- Clowes RM, Zeit CA, Amor JR, and Ellis RM (1995) Lithospheric structure in the southern Canadian Cordillera from a network of seismic refraction lines. *Canadian Journal of Earth Sciences* 32: 1485–1513.
- Coffin MA and Eldholm O (1994) Large igneous provinces: Crustal structure, dimensions and external consequences. *Reviews of Geophysics* 32: 1–36.
- Collier JS and Singh SC (1997) Detailed structure of the top of the melt body beneath the East Pacific Rise at 9°40'N from waveform inversion of seismic reflection data. *Journal of Geophysical Research* 103: 20287–20304.
- Collier JS and Singh SC (1998) Poisson's ratio structure of young oceanic crust. *Journal of Geophysical Research* 103: 20981–20996.
- Condie KC (1989) *Plate Tectonics and Crustal Evolution*, pp. 244–282. New York: Elsevier.
- Conrad V (1925) Laufzeitkurven des Tauern vom 28. November 1923. *Akademische Wissenschaft* 59: Mitteiler Erdbeben Kommission Wien, 1–23.
- Constable SC and Cox CS (1996) Marine controlled-source electromagnetic sounder. Part 2: The PEGASUS experiment. *Journal of Geophysical Research* 101: 5519–5530.
- Couch R and Woodcock S (1981) Gravity and structure of the continental margins of southwestern Mexico and northwestern Guatemala. *Journal of Geophysical Research* 86: 1829–1840.
- Cram IH, Jr. (1961) Crustal structure refraction survey in south Texas. *Geophysics* 26: 560–573.
- Crampin S (1964) Higher modes of seismic surface waves: Preliminary observations. *Geophysical Journal of the Royal Astronomical Society* 9: 35–37.
- Crampin S (1966) Higher modes of seismic surface waves: Propagation in Eurasia. *Bulletin of the Seismological Society of America* 56: 1227–1239.
- Crosson RS (1976) Crustal structure modeling of earthquake data; 1, Simultaneous least squares estimation of hypocenter and velocity parameters. *Journal of Geophysical Research* 81: 3036–3046.
- Curtis A and Woodhouse JH (1997) Crust and upper mantle structure beneath the Tibetan plateau and surrounding regions from interevent surface wave inversion. *Journal of Geophysical Research* 102: 11789–11813.
- Dahl-Jensen T, Larsen TB, Woelbern I, et al. (2003) Depth to Moho in Greenland. *Earth and Planetary Science Letters* 205: 379–393.
- Darbyshire FA, White RS, and Priestley KF (2000) Structure of the crust and uppermost mantle of Iceland from a combined seismic and gravity study. *Earth and Planetary Science Letters* 181: 409–428.
- Das T and Nolet G (1998) Crustal thickness map of the western United States by portioned waveform inversion. *Journal of Geophysical Research* 103: 30 021–30 038.
- Davis M and Kusznir N (2004) Depth-dependent lithospheric stretching at rifted continental margins. In: Karner GD, Taylor B, Discoll NW, and Kohlstedt DL (eds.) *Rheology and deformation of the Lithosphere at Continental Margins*, pp. 92–136. New York: Columbia University Press.
- Dean SM, Minshull TA, Whitmarsh RB, and Loudon KE (2000) Deep structure of the ocean-continent transition in the southern Iberia Abyssal Plain from seismic refraction profiles: II. The IAM-9 transect at 40°20'N. *Journal of Geophysical Research* 105: 5859–5886.
- Debayle E and Lévéque J (1997) Upper mantle heterogeneities in the Indian Ocean from waveform inversions. *Geophysical Research Letters* 24: 245–248.
- Deichmann N and Ansorge J (1983) Evidence for lamination in the lower continental crust beneath the Black Forest (Southwestern Germany). *Journal of Geophysics* 52: 109–118.
- DeGolyer E (1935) Notes on the early history of applied geophysics in the petroleum industry. *Society Petroleum Geophysics Journal* 30: 1–10.
- Delhinger P (1978) *Marine Gravity*. Amsterdam: Elsevier Scientific Publishing Co.
- Delhinger P, Couch RW, McManus DA, and Gemperle M (1970) Northeast Pacific structure. In: Maxwell AE (ed.) *The Sea*, vol. 4, (Part 2) pp. 133–189. New York: Wiley-Interscience.
- DESERT Group (2004) The crustal structure of the Dead Sea transform. *Geophysical Journal International* 156: 655–681.
- DeShon HR and Schwartz SY (2004) Evidence for serpentinization of the forearc mantle wedge along Nicoya Peninsula, Costa Rica. *Geophysical Research Letters* 31: L21611 (doi:10.1029/1004GL021179).
- Detrick RS, Buhl P, Vera E, et al. (1987) Multichannel seismic imaging of a crustal magma chamber along the East Pacific rise. *Nature* 326: 35–41.
- Detrick RS, Harding AJ, Kent GM, Orcutt JA, Mutter JC, and Buhl P (1993) Seismic structure of the southern East Pacific Rise. *Science* 259: 499–503.
- Detrick RS, Mutter J, Buhl P, and Kim II (1990) No evidence from multichannel reflection data for a crustal magma chamber in the MARK area of the Mid-Atlantic ridge. *Nature* 347: 61–64.
- Dezes P and Ziegler PA (2001) *European Map of the Mohorovicic Discontinuity*, version 1.3. world wide web access: <http://comp1.geol.unibas.ch>.
- Dix CH (1965) Reflection seismic crustal studies. *Geophysics* 30: 1068–1084.
- Dobrin MB (1976) *Introduction to Geophysical Prospecting*, 3rd edn. New York: McGraw-Hill.
- Dohr G (1970) Reflexionseismische Messungen im Oberrheingraben mit digitaler Aufzeichnungstechnik und Bearbeitung. In: Mueller JH and Illies S (eds.) *Graben Problems*, pp. 207–218. Stuttgart: Schweizerbart Verlag.
- Donnelly TW (1973) Late Cretaceous basalts from the Caribbean, a possible flood basalt province of vast size. *EOS* 54: 1004.
- Downes H (1993) The nature of the lower continental crust of Europe: Petrological and geochemical evidence from xenoliths. *Physics of the Earth and Planetary Interiors* 79: 195–218.
- Drewry DJ and Mooney WD (1983) *Antarctica: Glaciological and Geophysical Folio*. Cambridge, England: Polar Research Institute.
- Duba AS (1972) Electrical conductivity of olivine. *Journal of Geophysical Research* 77: 2483–2495.
- Durheim RJ and Mooney WD (1994) Evolution of the Precambrian lithosphere: Seismological and geochemical

- constraints. *Journal of Geophysical Research* 99: 15 359–15 374.
- Dziewonski AM (1989) Earth structure, global. In: James DE (ed.) *The Encyclopedia of Solid Earth Geophysics*, pp. 331–359. New York: Van Nostrand-Reinhold.
- Dziewonski AM and Anderson DL (1981) Preliminary Reference Earth Model (PREM). *Physics of the Earth and Planetary Interiors* 25: 297–356.
- Eberhart-Phillips D (1986) Three-dimensional velocity structure in northern California Coast Ranges from inversion of local earthquake arrival times. *Bulletin of the Seismological Society of America* 76: 1025–1052.
- Edgar NT, Ewing JI, and Hennion J (1971) Seismic refraction and reflection in the Caribbean Sea. *American Association of Petroleum Geologists* 55: 833–870.
- Edwards RA, Whitmarsh RB, and Scruton RA (1997) The crustal structure across the transform continental margin of Ghana, eastern Equatorial Atlantic. *Journal of Geophysical Research* 102: 747–772.
- Egorkin AV (2004) Mantle structure of the Siberian platform: *Izvestiya. Physics of the Solid Earth* 40: 385–394.
- Egorkin AV, Zukanov SK, Pavlenkova NA, and Chernyshev NM (1987) Results of lithosphere studies from long-range profiles in Siberia. *Tectonophysics* 140: 29–47.
- Ekström G, Tromp J, and Larson EWF (1997) Measurement and global models of surface wave propagation. *Journal of Geophysical Research* 102: 8137–8157.
- El Shazly EM (1982) The Red Sea region. In: Nairn AEM and Stehli FG (eds.) *The Oceans Basins Margins, The Indian Ocean*, vol. 6, pp. 205–252. New York: Plenum.
- Eldholm O and Coffin MF (2000) *Large igneous provinces and plate tectonics*. America Geophysical Union, Monograph 121: 309–326.
- Eldholm O and Grue K (1994) North Atlantic volcanic margins: Dimensions and production rates. *Journal of Geophysical Research* 99: 2955–2968.
- Eldholm O, Tsikalas F, and Faleide JI (2002) The continental margin off Norway 62–75°N: Palaeogene tectono-magmatic segmentation and sedimentation. In: Jolley DW and Bell BR (eds.) *Geological Society London Special Publication 197: The North Atlantic Igneous Province: Stratigraphy, Tectonics, Volcanic and Magmatic Processes*, pp. 39–68. Bath, UK: Geological Society of London.
- Elie de Beaumont E (1847) Note sur les systèmes de montagnes les plus anciens de l'Europe, Extr. Du Bulletin de la Société géologique de France 2e série t. IV 864 pp.
- Emmermann R and Lauterjung J (1997) The German Continental Deep Drilling Program KTB: Overview and major results. *Journal of Geophysical Research* 102: 18179–18201.
- Enderle U, Mechke J, Sobolev S, and Fuchs K (1996) Seismic anisotropy within the uppermost mantle of southern Germany. *Geophysical Journal International* 125: 747–767.
- England RW (2000) Deep structure of north west Europe from deep seismic profiling: The link between basement tectonics and basin development. In: Mohriak W and Talwani M (eds.) *American Geophysical Union Geophysics Monograph 111: Atlantic Rifts and Continental Margins*, 115, pp. 57–83. Washington, DC: American Geophysical Union.
- Ernst RE and Buchan KL (2003) Recognizing mantle plumes in the geologic record. *Annual Review of Earth and Planetary Sciences* 31: 469–523.
- Evans RL, Tanits P, Chave AD, et al. (1999) Asymmetric electrical structure in the mantle beneath the east Pacific Rise at 17° S. *Science* 286: 752–756.
- Ewing J and Houtz R (1979) Acoustic stratigraphy and structure of the oceanic crust. In: Talwani M, Harrison CG, and Hayes DE (eds.) *Deep Drilling Results in the Atlantic Ocean*, pp. 1–14. Washington, DC: American Geophysical Union.
- Ewing WM, Carry AP, and Rutherford HM (1937) Geophysical investigations in the emerged and submerged Atlantic Coastal Plain. Part 1: *Bulletin of the Geological Society of America* 48: 753–802.
- Ewing WM, Dainty AM, Blanchard JE, and Keen JJ (1966) Seismic studies on the eastern seaboard of Canada: The Appalachian system I. *Canadian Journal of Earth Sciences* 3: 89–109.
- Ewing WM, Jadetzky WS, and Press F (1957) *Elastic waves in Layered Media*. New York: McGraw-Hill Book Co.
- Ewing WM and Nafe JE (1982) The unconsolidated sediments. In: Hill MN (ed.) *The Sea*, vol. 3, *The Earth Beneath the Sea*, pp. 73–84. New York: Wiley-Interscience.
- Ewing WM and Press F (1954) An investigation of mantle Rayleigh waves. *Bulletin of the Seismological Society of America* 44: 127–148.
- Ewing WM, Worzel JL, Ericson DB, and Heezen BC (1955) Geophysical and geological investigations in the Gulf of Mexico. Part 1: *Geophysics* 20: 1–18.
- Faleide JI, Gudlaugsson ST, Eldholm O, Myhre AM, and Jackson HR (1990) Deep seismic transects across the sheared Western Barents Sea-Svalbard continental margin. *Tectonophysics* 189: 73–89.
- Farnetani CG and Richards MA (1995) Thermal entrainment and melting in mantle plumes. *Earth and Planetary Science Letters* 136: 251–267.
- Farnetani CG, Richards MA, and Ghiorso MS (1996) Petrologic models of magma evolution and deep crustal structure beneath hotspots and flood basalts. *Earth and Planetary Science Letters* 143: 81–84.
- Feldman IS (1976) On the nature of conductive layers in the Earth's crust and upper mantle. In: Adam A (ed.) *Geoelectric and Geothermal Studies*, pp. 721–730. Budapest: Akadémiai Kiadó.
- Fernandez M, Torne M, Garcia-Castellanos D, Vergés J, Wheeler W, and Karpuz R (2004) Deep structure of the Voring Margin: The transition from a continental shield to a young oceanic lithosphere. *Earth and Planetary Science Letters* 221: 131–144.
- Finlayson DM and Ansorge J (1984) Workshop proceedings; interpretation of seismic wave propagation in laterally heterogeneous structures. *Bureau of Mineral Resources, Geology, and Geophysics Report* 258. Canberra, Australia.
- Feng M, Assumpção M, and van der Lee S (2004) Group-velocity tomography and lithospheric S-velocity structure of the South American continent. *Physics of the Earth and Planetary Interior* 147(4): 315–331.
- Flack C and Warner M (1990) Three-dimensional mapping of seismic reflections from the crust and upper mantle northwest of Scotland. *Tectonophysics* 173: 469–481.
- Fliedner MM and Klemperer SL (1999) Structure of an island arc: Wide-angle seismic studies in the eastern Aleutian Islands, Alaska. *Journal of Geophysical Research* 104: 10 667–10 694.
- Foulger GR, Du Z, and Julian BR (2003) Icelandic-type crust. *Geophysical Journal International* 155: 567–590.
- Fountain DM (1986) Implications of deep crustal evolution for seismic reflection interpretation. In: Barazangi M and Brown L (eds.) *American Geophysical Union Geodynamics Series 14: Reflection Seismology; The Continental Crust*, pp. 1–7. Washington, DC: American Geophysical Union.
- Fountain DM, Arculus R, and Kay RW (1992) *Continental Lower Crust*, 485pp. Amsterdam: Elsevier.
- Fountain DM, Hurich CA, and Smithson SB (1984) Seismic reflectivity of mylonite zones in the crust. *Geology* 12: 195–198.
- Fountain DM and Salisbury MH (1981) Exposed crustal sections through the continental crust: Implication for crustal

- structure, petrology and evolution. *Earth and Planetary Science Letters* 56: 263–302.
- Fowler CMR (1976) Crustal structure of the Mid-Atlantic Ridge crest at 37°N. *Geophysical Journal of the Royal Astronomical Society* 47: 459–491.
- Fowler S, White RS, Spence GD, and Westbrook GK (1989) The Hatton Bank continental margin-II. deep structure from two-ship expanding spread profiles. *Geophysics Journal* 96: 295–309.
- Friederich W (2003) The S-velocity structure of the east Asian mantle from inversion of shear and surface waveforms. *Geophysical Journal International* 153: 88–102.
- Fromm R, Zandt G, and Beck SL (2004) Crustal thickness beneath the Andes and Sierras Pampeanas at 30° S inferred from Pn apparent phase velocities. *Geophysical Research Letters* 31: L006625 (doi:10.1029/2003GL019231).
- Frost BR and Shive PN (1986) Magnetic mineralogy of the lower continental crust. *Journal of Geophysical Research* 91: 6513–6522.
- Fuchs K and Müller G (1971) Computation of synthetic seismograms with the reflectivity method and comparison with observations. *Geophysical Journal of the Royal Astronomical Society* 23: 417–433.
- Gajewski D and Pšenčík I (1987) *Ray Method in Seismology*. Prague: University of Karlova.
- Geiss E (1987) A new compilation of crustal thickness data for Mediterranean area. *Annals of Geophysics* 5: 623–630.
- Giese P (1976) Results of the generalized interpretation of the deep-seismic sounding data. In: Giese P, Prodehl C, and Stein A (eds.) *Explosion Seismology in Central Europe*, pp. 201–214. New York: Springer.
- Giese P, Prodehl C, and Stein A (eds.) (1976) *Explosion Seismology in Central Europe – Data and Results*. Berlin-Heidelberg-New York: Springer.
- Gilbert H, Beck S, and Zandt G (2005) Lithospheric and upper mantle structure of Central Chile and Argentina. *Geophysical Journal International* 165: 383–398.
- Gladzenko TP, Coffin MF, and Eldholm O (1997) Crustal structure of the Ontong Java Plateau: Modeling of new gravity and existing seismic data. *Journal of Geophysical Research* 102: 22711–22729.
- Goodwin AM (1991) *Precambrian Geology: The Dynamic Evolution of the Continental Crust*. San Diego, CA: Academic Press.
- Goodwin AM (1996) *Principles of Precambrian Geology*. San Diego, CA: Academic Press.
- Gough DE (1974) Electrical conductivity under western North America in relation to heat flow, seismology, and structure. *Journal of Geomagnetism and Geoelectricity* 26: 105–123.
- Grad M, Gryn D, Guterch A, et al. (2003) “DOBREfraction’99”; velocity model of the crust and upper mantle beneath the Donbas foldbelt (east Ukraine). *Tectonophysics* 371: 81–110.
- Grad M, Janik T, Yliniemi J, et al. (1999) Crustal structure of the Mid-Polish Trough beneath the Teisseyre-Tornquist Zone seismic profile. *Tectonophysics* 314: 145–160.
- Grand SP and Helberger DV (1984) Upper mantle shear structure of North America. *Geophysical Journal of the Royal Astronomical Society* 76: 399–438.
- Grand SP, van der Hilst RD, and Widjiantoro S (1997) Global seismic tomography: A snapshot of convection in the Earth. *GSA Today* 7: 1–7.
- Grant FS and West GS (1965) *Interpretation Theory in Applied Geophysics*. New York: McGraw-Hill.
- Griffiths RW and Campbell IH (1990) Stirring and structure in mantle starting plumes. *Earth and Planetary Science Letters* 99: 66–78.
- Gung Y and Romanowicz B (2004) Q tomography of the upper mantle using three-component long-period waveforms. *Geophysical Journal International* 157: 813–830.
- Gutenberg B (1932) Traveltime curves at small distances and wave velocities in southern California. *Beiträge zur Geophysik* 35: 6–45.
- Gutenberg B (1959) *Physics of the Earth’s Interior*. New York: Academic Press.
- Gutenberg B, Wood H, and Buwalda J (1932) Experiments testing seismographic methods for determining crustal structure. *Bulletin of the Seismological Society of America* 22: 185–246.
- Guterch A, Grad M, Thybo H, Keller GR, and POLONAISE Working Group (1999) POLONAISE ’97 – An international seismic experiment between Precambrian and Variscan Europe in Poland. *Tectonophysics* 314: 101–121.
- Guterch A, Grad M, Keller GK, et al. (2003) CELEBRATION 2000 Seismic Experiment. *Stud. Geophysics and Geodesy* 47: 659–670.
- Haberland C, Agnon A, El-Kelani R, et al. (2003) Modelling of seismic guided waves at the Dead Sea Transform. *Journal of Geophysical Research* 108(B7): 2342 (doi:10.1029/2002JB002309).
- Hahn A, Ahrendt H, Jeyer J, and Hufen J-H (1984) A model of magnetic sources within the Earth’s crust compatible with the field measured by the satellite Magsat. *Geologisches Jahrbuch Reihe A* 75: 125–156.
- Hajnal Z (1986) Crustal reflection and refraction velocities. In: Barazangi M and Brown LD (eds.) *American Geophysical Union Geodynamics Series 13: Reflection Seismology; A Global Perspective* pp. 247–256. Washington, DC: American Geophysical Union.
- Hale LD and Thompson GA (1982) The seismic reflection character of the continental Mohorovičić discontinuity. *Journal of Geophysical Research* 87: 4625–4635.
- Hall DH (1974) Long-wavelength aeromagnetic anomalies and deep crustal magnetisation in Manitoba and northwestern Ontario, Canada. *Journal of Geophysical Research* 40: 403–430.
- Halliday AN, Dickin AP, Hunter RH, et al. (1993) Formation and composition of the lower continental crust: Evidence from Scottish xenolith suites. *Journal of Geophysical Research* 98(B1): 581–607.
- Hamilton EL (1976) Shear-wave velocity versus depth in marine sediments: A review. *Geophysics* 41: 985–996.
- Hamilton EL (1978) Sound velocity–density relations in sea-floor sediments and rocks. *Journal of the Acoustical Society of America* 63: 366–377.
- Hammer S (1983) Airborne Gravity is here! *Geophysics* 48: 213–223.
- Hart PJ (1969) *American Geophysical Union Geophysical Monograph 13: The earth’s crust and upper mantle*. Washington, DC: American Geophysical Union.
- Hart SR, Hauri EH, Oschmann LA, and Whitehead JA (1992) Mantle plumes and entrainment: Isotopic evidence. *Science* 256: 1673–1707.
- Hayford JF, Bowie W (1912) The effect of topography and isostatic compensation upon the intensity of gravity. *U.S. Coast and Geodetic Survey Special publication* 10.
- Heacock JG (1971) *American Geophysical Union Geophysical Monograph 14: The structure and physical properties of the earth’s crust*. Washington, DC: American Geophysical Union.
- Heacock JG (1977) *American Geophysical Union Geophysical Monograph The earth’s crust – its nature and properties* 20. Washington, DC: American Geophysical Union.
- Healy JH, Mooney WD, Blank HR, et al. (1982) Saudi Arabian seismic deep-refraction profile, Final project report. *Saudi Arabian Deputy Ministry of Mineral Resources*, 429 p. Open-file report, USGS-OF-02-37.

- Hearn TM (1984) Pn travel times in southern California. *Journal of Geophysical Research* 89: 1843–1855.
- Hearn TM (1996) Anisotropic Pn tomography in the western United States. *Journal of Geophysical Research* 101: 8403–8414.
- Hearn TM (1999) Uppermost mantle velocities and anisotropy beneath Europe. *Journal of Geophysical Research* 104: 15123–15139.
- Hearn TM, Beghou N, and Barazangi M (1991) Tomography of the western United States from regional arrival times. *Journal of Geophysical Research* 96: 16369–16381.
- Hearn TM and Clayton RW (1986) Lateral velocity variations in southern California: 1, Results for the upper crust from P-waves. *Bulletin of the Seismological Society of America* 76: 495–509.
- Hearn TM and Ni JF (1994) Pn velocities beneath continental collision zones; the Turkish-Iranian plateau. *Geophysical Journal International* 117: 273–283.
- Hearn TM, Ni JF, Wang S, Xu Z, Yu Y, and Zhang X (2004) Uppermost mantle velocities beneath China and surrounding regions. *Journal of Geophysical Research* 109: (doi:10.1029/2003JB002874).
- Heiskanen WA and Moritz H (1967) *Physical Geodesy*. San Francisco: W.H. Freeman.
- Heiskanen WA and Vening-Meinez FA (1958) *The Earth and its Gravity Field*. New York: McGraw Hill.
- Heiland CA (1935) Geophysical mapping from the air: It's possibilities and advantages. *Engineering and Mining Journal* 136: 609–610.
- Hemant K and Maus S (2005) Why no anomaly is visible over most of the continent-ocean boundary in the global crustal magnetic field. *Physics of the Earth and Planetary Interiors* 149: 321–333.
- Herrin E (1969) Regional variations of P-wave velocity in the upper mantle beneath North America. In: Hart PJ (ed.) *American Geophysical Union Monograph 13: The Earth's Crust and Upper Mantle*, pp. 242–246. Washington, DC: American Geophysical Union.
- Hersey J, Officer C, Johnson H, and Bergstrom S (1952) Seismic refraction observations north of the Brownson Deep. *Bulletin of the Seismological Society of America* 42: 291–306.
- Hess HH (1962) History of the ocean basins. In: Engel AE, James HL, and Leonard B (eds.) *Petrologic Studies, Burlington Volume*, pp. 599–620. Boulder, CO: Geological Society of America.
- Hess HH (1965) Mid-oceanic ridges and tectonics of the sea-floor; submarine geology and geophysics. *17th Colston Research Society Symposium*, 1–10.
- Hildenbrand TG, Simpson RW, Godson RH and Kane MF (1982) Digital colored residual and regional Bouguer gravity maps of the conterminous United States with cut-off wavelengths of 250 km and 1,000 km. U.S. Geological Survey Geophysical Investigations Map GP-953-A, scale 1:7,500,000.
- Hill MN (1957) Recent geophysical exploration of the ocean floor. *Physics and Chemistry of the Earth* 2: 129–163.
- Hill MN (ed.) (1963) *The Sea Volume 3. The Earth beneath the Sea, History*. New York: Interscience Publishers.
- Hinze WJ (ed.) (1985) *The Utility of Regional Gravity and Magnetic Anomaly Maps*. Society of Exploration of Geophysicists.
- Hinze WJ and Zeitz I (1985) The compromise magnetic-anomaly map of the conterminous United States. In: Hinze WJ (ed.) *The Utility of Regional Gravity and Magnetic Anomaly Maps*, pp. 1–24. Tulsa, OK: Society of Exploration Geophysicists.
- Hirn A, Sachpazi M, Siliqi R, et al. (1996) A traverse of the Ionian islands front with coincident normal incidence with wide-angle seismology. *Tectonophysics* 264: 35–49.
- Hodgson JH (1953) A seismic survey of the Canadian Shield: 1, Refraction studies based on rock bursts at Kirkland Lake, Ontario. *Dominion Observatory Publication* 16: pp. 111–163. Ottawa, Ontario.
- Hofsetter R and Bock G (2004) Shear-wave velocity structure of the Sinai sub-plate from receiver function analysis. *Geophysical Journal International* 158: 67–84.
- Holbrook WS and Keleman PB (1993) Large igneous province on the U.S. Atlantic margin and implications during continental breakup. *Nature* 364: 433–436.
- Holbrook WS, Mooney WD, and Christensen NI (1992) The seismic velocity structure of the deep continental crust. In: Fountain DM, Arculus R, and Kay RW (eds.) *Continental Lower Crust. Development in Geotectonics*, vol. 23, pp. 1–43. Amsterdam: Elsevier.
- Hole JA (1992) Non-linear high-resolution three-dimensional seismic travel time tomography. *Journal of Geophysical Research* 97: 6553–6562.
- Hole JA, Brocher TM, Klemperer SL, Parsons TE, Benz HM, and Furlong KP (2000) Three-dimensional seismic velocity structure of the San Francisco Bay area. *Journal of Geophysical Research* 105: 13859–13874.
- Hole JA, Clowes RM, and Ellis RM (1992) Interface inversion using broadside seismic refraction data and three-dimensional travel time calculations. *Journal of Geophysical Research* 97: 3417–3429.
- Hole JA and Zelt BC (1995) Three-dimensional finite-difference reflection travel times. *Geophysical Journal International* 121: 427–434.
- Holmes A (1918) The basaltic rocks of the Arctic region. *Mineralogical Magazine* 18: 180–223.
- Hood PJ, McGrath PH, and Teskey DJ (1985) Evolution of Geological Survey of Canada magnetic anomaly maps: A Canadian perspective. In: Hinze WJ (ed.) *The Utility of Regional Gravity and Magnetic Anomaly Maps*, pp. 62–68. Tulsa, OK: Society of Exploration of Geophysicists.
- Horsefield SJ, Whitmarsh RB, White RS, and Sibuet J-C (1993) Crustal structure of Goban Spur rifted continental margin, NE Atlantic. *Geophysical Journal International* 119: 1–19.
- Huang Z, Peng Y, Luo Y, Zheng Y, and Su W (2004) Azimuthal anisotropy of Rayleigh waves in East Asia. *Geophysical Research Letters* 31: L15617 (doi:10.1029/2004GL020399).
- Huestis SP and Parker RL (1977) Bounding thickness of the oceanic magnetized layer. *Journal of Geophysical Research* 82: 5293–5303.
- Humphreys E and Clayton RW (1988) Adaption of back projection tomography to seismic travel time problems. *Journal of Geophysical Research* 93: 1073–1085.
- Humphreys E, Clayton RW, and Hager BH (1984) A tomographic image of mantle structure beneath southern California. *Geophysical Research Letters* 11: 625–627.
- Hwang L and Mooney WD (1986) Velocity and Q structure of the Great Valley, California, based on synthetic seismogram modeling of seismic refraction data. *Bulletin of the Seismological Society of America* 76: 1053–1067.
- Hyndman RD (1979) Poisson's ratio in the oceanic crust: A review. *Tectonophysics* 59: 321–333.
- Hyndman RD (1988) Dipping seismic reflectors, electrically conductive zones, and trapped water in the crust over a subducting plate. *Journal of Geophysical Research* 93: 13133–13405.
- Hyndman RD, Wang K, and Yamano M (1995) Thermal constraints on the seismogenic portion of the south western Japan subductum Thrust. *Journal of Geophysical Research* 100: 15373–15392.
- Iyer HM and Hitchcock T (1989) Upper-mantle velocity structure in the continental U.S. and Canada. In: Pakiser LC and

- Mooney WD (eds.) *Geological Society of America Memoir 172: Geophysical framework of the Continental United States*, pp. 681–710. Boulder, CO: Geological Society of America.
- Iyer HM and Hirahara K (1993) *Seismic Tomography Theory and Practice*. London: Chapman and Hall.
- Jackson WH and Oakey GN (1986) Sedimentary thickness map of the Arctic Ocean. In: Grantz A, Johnson L, and Sweeney JF (eds.) *The Geology of North America*. Boulder, CO: Geological Society of America: Plate 5.
- Jackson WH and Pakiser LC (1965) Seismic study of crustal structure in the southern Rocky Mountains. *U.S. Geological Survey Professional Paper 525-D*: p. D-85-D-92.
- Jackson WH, Stewart SW, and Pakiser LC (1963) Crustal structure in eastern Colorado from seismic-refraction measurements. *Journal of Geophysical Research* 68: 5767–5776.
- Jakosky JJ (1940) *Exploration Geophysics*. Los Angeles: Trija Publishing Co.
- James DE (1971) Andean crustal and upper mantle structure. *Journal of Geophysical Research* 76: 3246–3271.
- James DE and Steinhart JS (1966) Structure beneath continents, a critical review of explosion seismic studies 1960–1965. In: Steinhart JS and Smith TJ (eds.) *American Geophysical Union Geophysical Monograph 10: The Earth Beneath the Continents*, pp. 293–333. Washington, DC: American Geophysical Union.
- Jarchow CM and Thompson GA (1989) The nature of the Mohorovicic discontinuity. *Annual Review Earth and Planetary Sciences* 17: 475–506.
- Jaupart C and Mareschal JC (1999) The thermal structure and thickness of continental roots. *Lithos* 48: 93–114.
- Jeffreys H (1940) *Seismological Tables*. British Association for the Advancement of science. London, Gray Milne Trust.
- Jensen H (1961) The airborne magnetometer. *Scientific American* 204: 151–162.
- Jeffreys H and Bullen KE (1935) Times of transmission of earthquake waves. *Bureau of Central Séismologique International*, Series A, Fasc. II.
- Johnson GR and Olhoeft GR (1984) Density of rocks and minerals. In: Charmichael RS (ed.) *Handbook of Physical Properties of rocks*, vol. 3, pp. 1–38. Boca Raton, FL: CRC Press.
- Johnson M and Vincent C (2002) Development and testing of a 3D velocity model for improved event location: A case study for the India-Pakistan region. *Bulletin of the Seismological Society of America* 92: 2893–2910.
- Jones AG (1992) Electrical conductivity structure of the continental lower crust. In: Fountain DM, Arculus RJ, and Kay RW (eds.) *Continental Lower Crust*, pp. 81–143. Amsterdam: Elsevier.
- Jones AG, Ferguson IJ, Chave AD, Evans RL, and McNeice GW (2001) The electrical lithosphere of the Slave Province. *Geology* 29: 423–426.
- Jones EJW (1999) *Marine Geophysics*. Chichester, England: John Wiley & Sons.
- Jones EJW and Mgbatogu CCS (1982) The structure and evolution of the West African continental margin off Guine Bissau Guinea and Sierra Leone. In: Scruton RA, Talwani M, and Chichester JW (eds.) *The Ocean Floor*, pp. 165–202. New York: Wiley.
- Jones T and Nur A (1983) Velocity and attenuation in sandstone at elevated temperatures and pressures. *Geophysical Research Letters* 10: 140–143.
- Jordan TH (1975) The continental tectosphere. *Geophysics and Space Physics* 13: 1–12.
- Jordan TH (1979) Mineralogies, densities and seismic velocities of garnet Iherzolites and their geophysical implications. In: Boyd FR and Meyer HOA (eds.) *The Mantle Sample: Inclusions in Kimberlites and Other Volcanics*, vol. 2, pp. 2–14. Washington, DC: American Geophysical Union.
- Jordan TH (1988) Special Lithosphere Issue: *Structure and Formation of the Continental Tectosphere*. *Journal of Petrology* 29: 11–37.
- Jordan TH and Frazer LN (1975) Crustal and upper mantle structure from Sp phases. *Journal of Geophysical Research* 80: 1504–1518.
- Juhlin C (1988) Interpretation of the seismic reflectors in the Gravberg-I well. In: Boden A and Erickson KG (eds.) *Deep Drilling in Crystalline Bedrock*, 364 pp. Berlin: Springer.
- Julia J, Ammon CJ, Herrmann RB, and Correig AM (2000) Joint inversion of receiver function and surface wave dispersion observations. *Geophysical Journal International* 143: 99.
- Julia J and Mejia J (2004) Thickness and vp/vs ratio variation in the Iberian crust. *Geophysical Journal International* 156: 59–72.
- Junger A (1951) Deep refractions in Big Horn County, Montana. *Geophysics* 16: 499–505.
- Kaban MK and Mooney WD (2001) Density structure of the lithosphere in the southwestern United States and its tectonic significance. *Journal of Geophysical Research* 106: B1.
- Kaban MK, Schwintza P, Artemieva IM, and Mooney WD (2003) Density of the continental roots: Compositional and thermal contributions. *Earth and Planetary Science Letters* 209: 53–69.
- Kanasewich ER and Cumming GL (1965) Near vertical-incidence seismic reflections from the “Conrad” discontinuity. *Journal of Geophysical Research* 70: 3441–3446.
- Kane MF and Godson RH (1989) A crust/mantle structural framework of the continuous United States based on gravity and magnetic data. In: Pakiser LC and Mooney WD (eds.) *Geological Society America Memoir 172: Geophysical Framework of the Continental United States*, pp. 383–404. Boulder, CO: Geological Society of America.
- Karagianni EE, Papazachos CB, Panagiotopoulos DG, Suhadolc P, Vuan A, and Panza GF (2005) Shear velocity structure in the Aegean area obtained by inversion of Rayleigh waves. *Geophysical Journal International* 160: 127–143.
- Katz S (1954) Seismic study of crustal structure in Pennsylvania and New York. *Bulletin of the Seismological Society of America* 44: 303–325.
- Kay RW and Kay SM (1981) The nature of the lower continental crust: Inferences from geophysics, surface geology, and crustal xenoliths. *Reviews of Geophysics and Space Physics* 19: 271–297.
- Keller G (1989) Conductivity of the crust. In: Pakiser LC and Mooney WD (eds.) *Geological Society of America Memoir 172: Geophysical Framework of the continental United States*, pp. 425–446. Boulder, CO: Geological Society of America.
- Kelley KR, Ward RW, Treitel S, and Alford RM (1976) Synthetic seismograms: A finite approach. *Geophysics* 41: 2–27.
- Kempner WC and Gettrust JF (1982) Ophiolites, synthetic seismograms, and oceanic crustal structure, 1: Comparison of ocean bottom seismometer data and synthetic seismograms from the Bay of Islands ophiolite. *Journal of Geophysical Research* 87: 8462–8476.
- Kennett BLN (1974) Reflections, rays, and reverberations. *Bulletin of the Seismological Society of America* 64: 1685–1696.
- Kennett BLN (1983) *Seismic Wave Propagation in Stratified Media*. Cambridge: Cambridge University Press.

- Kennett BLN and Engdahl ER (1991) Traveltimes for global earthquake location and phase identification. *Geophysical Journal International* 105: 429–465.
- Kennett BLN, Engdahl ER, and Buland R (1995) Constraints on seismic velocities in the Earth from traveltimes. *Geophysical Journal International* 122: 108–124.
- Kern H (1978) The effect of high temperature and high confining pressure on compressional wave velocities in quartz-bearing and quartz-free igneous and metamorphic rocks. *Tectonophysics* 44: 185–203.
- Kern H, Gao S, and Liu QS (1996) Seismic properties and densities of middle and lower crustal rocks exposed along the North China Geoscience Transect. *Earth and Planetary Science Letters* 139(3–4): 439–455.
- Kern H, Popp T, Gorbatshevich, Zharikov A, Lobanov KV, and Smirnov Yu P (2001) Pressure and temperature dependence of Vp and Vs in rocks from the superdeep well and from surface analogues at Kola and the nature of velocity anisotropy. *Tectonophysics* 338: 113–143.
- Kerr AC (2003) Oceanic plateaus. In: Holland HC and Turekian K (eds.) *Treatise on Geochemistry*, Vol. 3, pp. 537–565. Amsterdam: Elsevier.
- Kimball GS, Gatli RW, Ritchie JD, Walker ASD, and Williamson JP (2004) Regional Three-dimensional gravity modeling of the NE Atlantic margin. *Basin Research* 16: 259–278.
- Kimura G and Ludden J (1995) Peeling oceanic crust in subduction zones. *Geology* 23: 217–220.
- Kinck JJ, Husebye ES, and Larsson FR (1993) The Moho depth distribution in Fennoscandia and regional tectonic evolution from Archean to Permian times. *Precambrian Research* 64: 23–51.
- Kind R (1978) The reflectivity method for a buried source. *Journal of Geophysics* 44: 603–612.
- Kind R, Kosarev GL, and Petersen NV (1995) Receiver functions at the stations of the German Regional Seismic Network (GRSN). *Geophysical Journal International* 121: 191–202.
- Kind R and Vinnik LP (1988) The upper mantle discontinuities underneath the GRF array from P-to-S converted phases. *Journal of Geophysics* 62: 138–147.
- Kind R, Yuan X, Saul J, et al. (2002) Seismic images of crust and upper mantle beneath Tibet: Evidence for Eurasian plate subduction. *Science* 298: 1219–1221.
- Kissling E (1998) Geotomography with local earthquake data. *Reviews of Geophysics* 26: 659–698.
- Kissling E, Husen S, and Haslinger F (2001) Model parameterization in seismic tomography: A choice of consequence for the solution quality. *Physics of the Earth and Planetary Interiors* 123: 89–101.
- Klemperer SL and Hobbs R (1991) *The BIRPS Atlas: Deep Seismic Reflection Profiles Around the British Isles*. Cambridge: Cambridge University Press.
- Klemperer SL and Luetgert JH (1987) A comparison of reflection and refraction processing and interpretation methods applied to conventional refraction data from costal maine. *Bulletin of the Seismological Society of America* 77: 614–630.
- Klemperer SL and Mooney WD, (eds.) (1998a) Deep seismic profiling of the Continents, Part 1: General results and new methods. *Tectonophysics* 286: 1–298.
- Klemperer SL and Mooney WD, (eds.) (1998b) Deep seismic profiling of the continents, Part 2: A global survey. *Tectonophysics* 288: 1–292.
- Klemperer SL and Oliver JE (1983) *The Advantage of Length in Deep Crustal Reflection Profiles*. First Break, 20–27. April.
- Klosko ER, Russo RM, Okal EA, and Richardson WP (2001) Evidence for a rheologically strong chemical mantle root beneath the Ontong-Java Plateau. *Earth and Planetary Science Letters* 186: 347–361.
- Knopoff L (1972) Observation and inversion of surface-wave dispersion. *Tectonophysics* 13: 497–519.
- Kodaira S, Takahashi N, Park JO, Mochbaki K, Shinohana M, and Kimma S (2000) Wester Nankai Trough seismogenic: Results from a wide-angle ocean bottom seismic survey. *Journal of Geophysical Research* 105: 5882–5906 (doi:10.1029/1999 JB 900394).
- Korja T, Engels M, Zhamaletdinov AA, et al. (2002) Crustal conductivity in Fennoscandia—a compilation of a database on crustal conductance in the Fennoscandian Shield. *Earth Planet Space* 54: 535–558.
- Kovach RL (1978) Seismic surface waves and crystal and upper mantle structure. *Reviews of the Geophysics and Space Physics* 16: 1–13.
- Kovach RL and Anderson DL (1964) Higher mode surface waves and their bearing on the structure of the earth's mantle. *Bulletin of the Seismological Society of America* 54: 161–182.
- Kozlovsky YA (ed.) (1987) *The Superdeep Well of the Kola Peninsula (Exploration of the Deep Continental Crust)*, 558 pp. Berlin: Springer-Verlag.
- Kroenke LW (1974) Origin of continents through development and coalescence of oceanic flood basalt plateaus. *EOS* 55: 443.
- Kusznir NJ and Matthews DH (1988) Special Lithosphere Issue: Deep Seismic Reflection and Deformational Mechanisms of the Continental Lithosphere. *Journal of Petrology* 63–87.
- Lachenbruch AH, Sass JH, and Galanis SP, Jr. (1985) Heat flow in southernmost California and the origin of the Salton trough. *Journal of Geophysical Research* 90: 6709–6736.
- Langel RA (1985) Introduction to the special issue: A perspective on MAGSAT results. *Journal of Geophysical Research* 90: 2441–2444.
- Langel RA, Ousley G, and Berbert J (1982) The Magsat Mission. *Geophysical Research Letters* 9: 243–245.
- Langston CA (1977) Corvallis, Oregon, crustal and upper mantle receiver structure from teleseismic P and S waves. *Bulletin of the Seismological Society of America* 67: 713–725.
- Langston CA (1994) An integrated study of crustal structure and regional wave propagation for southeastern Missouri. *Bulletin of the Seismological Society of America* 84: 105–118.
- Langston CA, Nyblade AA, and Owens TJ (2002) Regional wave propagation in Tanzania, East Africa. *Journal of Geophysical Research* 107: (doi:10.1029/2001JB000167).
- Laske G and Masters G (1997) A global digital map of sediment thickness (abstract). *EOS, Transactions, American Geophysical Union* 78, vol. 46, Fall meeting supplement: F483.
- Lay T and Wallace TC (1995) *Modern Global Seismology*, 521 pp. San Diego, CA, USA: Academic Press.
- Lebedev S and Nolet G (2003) Upper mantle beneath southeast Asia from S velocity tomography. *Journal of Geophysical Research* 108: 26.
- Lees JM and Crosson RS (1989) Tomographic inversion for three-dimensional velocity structure at Mount St. Helens using earthquake data. *Journal of Geophysical Research* 94: 5716–5728.
- Leet LD (1936) Seismological data on surface layers in New England. *Bulletin of the Seismological Society of America* 26: 129–145.
- Lei J and Zhao D (2005) P-wave tomography and origin of the Changbai intraplate volcano in northeast Asia. *Tectonophysics* 397: 281–295.
- Levander AR and Holliger K (1992) Small scale heterogeneity and large-scale velocity structure of the continental crust. *Journal of Geophysical Research* 97: 8797–8804.

- Leveque J, Rivera L, and Wittlinger G (1993) On the use of the checker-board test to access the resolution of tomographic inversions. *Geophysical Journal International* 115: 313–318.
- Levshin AL, Yanovskaya TB, Lander AV, et al. (1989) Recording, identification, and measurement of surface wave parameters. In: Keilis-Borok VI (ed.) *Seismic Surface Waves in a Laterally Inhomogeneous Earth*. London: Kluwer Publication House.
- Levshin AL, Ritzwoller MH, and Shapiro NM (2005) The use of crustal higher modes to constrain crustal structure across central Asia. *Geophysical Journal International* 160: 961–972.
- Li S, Unsworth MJ, Booker JR, et al. (2003) Partial melt or aqueous fluid in the mid-crust of southern Tibet? Constraints from INDEPTH magnetotelluric data. *Geophysical Journal International* 153: 289–304.
- Li SL and Mooney WD (1998) Crustal structure of China from deep seismic sounding profiles. *Tectonophysics* 288: 105–113.
- Li X, Kind R, Yuan X, Woelbern I, and Hanka W (2004) Rejuvenation of the lithosphere by the Hawaiian plume. *Nature* 427: 827–829.
- Li XD and Romanowicz B (1996) Global mantle shear velocity model developed using nonlinear asymptotic coupling theory. *Journal of Geophysical Research* 101: 22245–22272.
- Liang C, Song X, and Huang J (2004) Tomographic inversion of Pn travel times in China. *Journal of Geophysical Research* 109: B11304 (doi:10.1029/2003JB002789).
- Lindwall DA (1988) A two-dimensional seismic investigation of crustal structure under the Hawaiian islands near Oahu and Kauai. *Journal of Geophysical Research* 93: 12107–12122.
- Lippitsch R, Kissling E, and Ansorge J (2003) Upper mantle structure beneath the Alpine orogen from high-resolution teleseismic tomography. *Journal of Geophysical Research* 108: 15.
- Liu Y, Xu C, He J, Liu F, and Sun H (2005) Three-dimensional velocity images of the crust and upper mantle beneath the North-South Zone in China. *Bulletin of the Seismological Society of America* 95: 916–925.
- Loper DE (1983) The dynamical and thermal structure of deep mantle plumes. *Physics of the Earth and Planetary Interiors* 33: 304–317.
- Ludwig WJ and Houtz RE (1979) *Isopack Map of Sediments in the Pacific Ocean Basin and Marginal Sea Basins*. Tulsa, Oklahoma: American Association of Petroleum Geologists.
- Ludwig WJ, Nafe JE, and Drake LE (1970) Seismic refraction. In: Maxwell AE (ed.) *The Sea. New Concepts of Sea Floor Evolution*, pp. 53–84. New York: Wiley-Interscience.
- Luosto U (1997) Structure of Earth's crust in Fennoscandia as revealed from refraction and wide-angle reflections studies. *Geophysica* 33: 3–16.
- Lutter WJ, Nowack RL, and Braile LW (1990) Seismic imaging of upper crustal structure using traveltimes from the PASSCAL Ouachita experiment. *Journal of Geophysical Research* 95: 4621–4631.
- Ma KF, Wang JH, and Zhao D (1996) Three-dimensional seismic velocity structure of the crust and uppermost mantle beneath Taiwan. *Journal of Physics of the Earth* 44: 85–105.
- MacGregor LM, Constable S, and Sinha MC (1998) The RAMESSES experiment-III controlled-source electromagnetic sounding of the Reykjanes Ridge AT 57° 45' N. *Geophysical Journal International* 135: 773–789.
- Maggi A and Priestley K (2005) Surface waveform tomography of the Turkish-Iranian plateau. *Geophysical Journal International* 160: 1068–1080.
- Mahadevan TM (1994) Deep Continental Structure of India: A Review. *Geological Society of India Memoir* 28, Bangalore.
- Mahoney JJ and Coffin MF (1997) *Large Igneous Provinces: Continental, Oceanic, and Planetary Flood Volcanism*. Washington, DC: American Geophysical Union.
- Mair JA and Forsyth DA (1982) Crustal structure of Canada Basin near Alaska, the Lomonosov Ridge, and adjoining basins near the North Pole. *Tectonophysics* 89: 239–254.
- Mair JA and Lyons JA (1976) Seismic reflection techniques for crustal structure studies. *Geophysics* 41: 1272–1290.
- Makovska Y, Klempner SL, Huang LY, Lu DY, and Project INDEPTH Team (1996a) Structural elements of the southern Tethyan Himalaya crust from wide-angle seismic data. *Tectonics* 15: 997–1005.
- Makovska Y, Klempner SL, Ratschbacher L, et al. (1996b) INDEPTH wide-angle reflection observations of P-wave-to-S-wave conversions from crustal bright spots in Tibet. *Science* 274: 1690–1691.
- Makris J (1978) The crust and upper mantle of the Aegean region from deep seismic soundings. *Tectonophysics* 46: 269–284.
- Mandal P, Rastogi BK, Satyanarayana HVS, and Kousalya M (2004) Results from local earthquake velocity tomography: Implications toward the source process involved in generating the 2001 Bhuj earthquake in the lower crust beneath Kachchh (India). *Bulletin of the Seismological Society of America* 94: 633–649.
- Mareschal J-C, Jaupart C, Cheng LZ, et al. (1999) Heat flow in the Trans-Hudson Orogen of the Canadian Shield: Implications for Proterozoic continental growth. *Journal of Geophysical Research* 104: 29007–29024.
- Masters G, Johnson S, Laske G, and Bolton H (1996) A shear-velocity model of the mantle. *Philosophical Transactions of the Royal Society of London A* 354: 1285–1411.
- Matthews DH (1986) Seismic reflections from the lower crust around Britain. In: Dawson J, Carswell D, Hall J, and Wedepohl K (eds.) *Geological Society of London Special Publication: Nature of the Lower Continental Crust*, vol. 24, pp. 11–21. Bath, UK: Geological Society of London.
- Matthews DH, and BIRPS group (1987) Some unsolved BIRP problems. *Geophysical Journal of the Royal Astronomical Society* 89: 209–216.
- Matthews DH and BIRPS Core Group (1990) Progress in BIRPS deep seismic reflection profiling around the British Isles. *Tectonophysics* 173: 387–396.
- Matthews DH and Cheadle MJ (1986) *Geodynamics Series 13: Deep Reflections from the Caledonides and the Variscides of Britain and comparison with the Himalayas*, pp. 5–19. Washington, DC: American Geophysical Union.
- Matzel E and Grand SP (2004) The anisotropic seismic structure of the East European platform. *Journal of Geophysical Research* 109: (doi:10.1029/2001JB000623).
- Maxwell AE (ed.) (1970a) *The Sea. New Concepts of Sea Floor Evolution*, vol. 4., New York: Wiley-Interscience.
- Maxwell AE (ed.) (1970b) *The Sea. New Concepts of Sea Floor Evolution*, vol. 4., New York: Wiley-Interscience.
- Mayhew MA, Johnson BD, and Wasilewski PJ (1985) A review of problems and progress in studies of satellite magnetic anomalies. *Journal of Geophysical Research* 90: 2511–2522.
- Mayhew MA and LaBrecque JL (1987) Crustal geologic studies with Magsat and the surface magnetic data. *Reviews of Geophysics and Space Physics* 25: 971–981.
- Mayne H (1962) Common reflection point horizontal data stacking techniques. *Geophysics* 27: 927–938.
- Mayne H (1967) Practical considerations in the use of common reflection point techniques. *Geophysics* 32: 225–229.
- McCaughey M, Barton PJ, and Singh SC (2000) Joint inversion of wide-angle seismic data and a deep reflection profile from the central North Sea. *Geophysical Journal International* 141: 100–114.
- McEvilly TV (1964) Central U.S. crust-upper mantle structure from Love and Raleigh wave phase velocity inversion.

- Bulletin of the Seismological Society of America* 54: 1997–2016.
- McEchan GA and Mooney WD (1980) Asymptotic ray theory and synthetic seismograms for laterally varying structure: theory and application to the Imperial Valley, California. *Bulletin of the Seismological Society of America* 70: 2021–2035.
- McEnroe SA, Langenhorst F, Robinson P, Bromiley GD, and Shaw CSJ (2004) What is magnetic in the lower crust? *Earth and Planetary Science Letters* 22: 175–192.
- McKenzie D and Bickle MJ (1988) The volume and composition of melt generated by extension of the lithosphere. *Journal of Petrology* 29: 625–679.
- McKenzie D, Jackson J, and Priestley K (2005) Thermal structure of oceanic and continental lithosphere. *Earth and Planetary Science Letters* 233: 337–349.
- McNamara DE, Walter WR, Owens TJ, and Ammon CJ (1997) Upper mantle velocity structure beneath the Tibetan plateau from Pn travel time tomography. *Journal of Geophysical Research* 102: 493–505.
- McNutt MK (1980) Implications of regional gravity for state of stress in the Earth's crust and upper mantle. *Journal of Geophysical Research* 85: 6377–6396.
- Mechie J, Abu-Ayyash K, Ben-Avraham Z, et al. (2004) Crustal shear velocity structure across the Dead Sea Transform from 2-D modeling of project DESERT explosion seismic data. *Geophysical Journal International* 160: 910–924.
- Mechie J, Egorkin AV, Fuchs K, et al. (1993) P-wave mantle velocity structure beneath northern Eurasia from long-range recordings along the profile. *Physics of the Earth and Planetary Interiors* 79: 469–486.
- Meissner R (1967) Exploring the deep interfaces by seismic wide angle measurements. *Geophysical Prospecting* 15: 598–617.
- Meissner R (1973) The “Moho” as a transition zone. *Geophysical Survey* 1: 195–216.
- Meissner R (1986) *The Continental Crust: A Geophysical Approach*. London: Academic Press.
- Meissner R and Bortfeld RK (eds.) (1990) *DEKOPR – Atlas: Results of Deutsches Kontinentales Reflexionsseismisches Programm*. Berlin: Springer-Verlag.
- Meissner R, Brown L, Dürbaum H-J, Franke W, Fuchs K, and Siefert F (eds.) (1991) *Geodynamics Series 22: Continental lithosphere: Deep Seismic Reflections*. Washington, DC: American Geophysical Union.
- Meissner R and Mooney WD (1998) Weakness of the lower continental crust: A condition for delamination, uplift, and escape. *Tectonophysics* 296: 47–60.
- Meissner R, Mooney WD, and Artemieva IM (2002) Seismic anisotropy and mantle creep in young orogens. *Geophysical Journal International* 149: 1–14.
- Meissner R, Wever T, and Fluh ER (1987) The Moho in Europe – implications for crustal development. *Annales Geophysicae* 5: 357–364.
- Mele G (1998) Pn anisotropy in the northern Apennine chain (Italy); geodynamics of lithosphere and earth's mantle; seismic anisotropy as a record of the past and present dynamic processes. *PAGEOPH* 151: 495–502.
- Menke W (1989) *Geophysical Data Analysis: Discrete Inverse Theory, rev. edn*. New York: Springer.
- Meyers SC, Beck S, Zandt G, and Wallace T (1998) Lithospheric-scale structure across the Bolivian Andes from tomographic images of velocity and attenuation for P and S waves. *Journal of Geophysical Research* 103: 21 233–21 252.
- Milkereit B, Mooney WD, and Kohler WM (1985) Inversion of seismic refraction data in planar dipping structure. *Geophysical Journal of the Royal Astronomical Society* 82: 81–103.
- Minshull TA (1993) Wide-angle imaging of reflectors in Mesozoic oceanic crust. *Geophysical Research Letters* 20: 1619–1622.
- Minshull TA (2002) Seismic structure of the oceanic crust and rifted continental margins. In: Lee WHK, Kanamori H, and Jennings PC (eds.) *International Geophysics Series 81A. International Handbook of Earthquake and Engineering Seismology*, pp. 911–924. San Diego, CA: Academic Press.
- Mintrop L (1949) On the stratification of the earth's crust according to seismic studies of a large explosion and earthquakes. *Geophysics* 14: 321–336.
- Mitchell BJ and Herrmann RB (1979) Shear velocity structure in the eastern United States from the inversion of surface-wave group and phase velocities. *Bulletin of the Seismological Society of America* 69: 113–1148.
- Mitra S, Priestley K, Bhattacharyya AK, and Gaur VK (2005) Crustal structure and earthquake focal depths beneath northeastern India and southern Tibet. *Geophysical Journal International* 160: 277.
- Molnar P and Tappozier P (1975) Cenozoic tectonics of Asia: Effects of a continental collision. *Science* 189: 415–426.
- Montagner J-P and Tanimoto T (1990) Global anisotropy in the upper mantle inferred from the regionalization of phase velocities. *Journal of Geophysical Research* 95: 4797–4819.
- Montelli R, Nolet G, Dahlen FA, Masters G, Engdahl ER, and Hung S (2004) Finite-frequency tomography reveals a variety of plumes in the mantle. *Journal of Science* 303: 338–343.
- Mohorovicic A (1910) Das Beben vom 8.x.1909. *Jahrb. meteorol. Obs. Zagreb für 1909 IX, IV.Teil, Abschn. 1*, Zagreb, 1–63.
- Mooney WD (1989) Seismic methods for the determining earthquake source parameters and lithospheric structure. In: Pakiser LC and Mooney WD (eds.) *Geophysical framework of the Continental United States*, pp. 11–34. Geological Society of America Memoir 172. Boulder, CO: Geological Society of America.
- Mooney WD, Beroza G, and Kind R (2007) Fault zones from top to bottom: A geophysical perspective. In: Handy M, Hirth G, and Hovius N (eds.) *Tectonic Faults: Agents of Change on a Dynamic Earth*, pp. 9–46. Cambridge, MA: MIT Press.
- Mooney WD and Braile LW (1989) The seismic structure of the continental crust and upper mantle of North America. In: Bally AW and Palmer AR (eds.) *The geology of North America – An Overview*, pp. 39–52. Boulder, CO: Geological Society of America.
- Mooney WD and Brocher TM (1987) Coincident seismic reflection/refraction studies of the continental lithosphere: A global review. *Reviews of Geophysics* 25: 723–742.
- Mooney WD and Meissner R (1991) Continental crustal evolution observations. *Eos, Transactions, American Geophysical Union* 72(48,537): 540–541.
- Mooney WD and Meissner R (1992) Multi-genetic origin of crustal reflectivity: A review of seismic reflection profiling of the continental lower crust and Moho. In: Fountain DM, Arculus R, and Kay RW (eds.) *Continental Lower Crust. Development in Geotectonics*, vol. 23, pp. 45–79. Amsterdam: Elsevier.
- Mooney WD, Laske G, and Masters TG (1998) CRUST 5.1: A global crustal model at $5^\circ \times 5^\circ$. *Journal of Geophysical Research* 103: 727–747.
- Mooney WD, Prodehl C, and Pavlenkova NI (2002) Seismic velocity structure of the continental lithosphere from controlled source data. In: Lee WHK, Kanamori H, Jennings PC, and Kisslinger C (eds.) *International Handbook of Earthquake and Engineering Seismology*, vol. 81A, pp. 887–908. The International Association of Seismology and Physics of the Earth's Interior.
- Morozov IB, Morozova EA, Smithson SB, and Solodilov LN (1998) On the nature of teleseismic P_n phase observed on the ultralong-range profile “Quartz” Russia. *Bulletin of the Seismological Society of America* 1: 62–73.

- Morozova EA, Morozov IB, Smithson SB, and Solodilov LN (1999) Heterogeneity of the uppermost mantle beneath Russian Eurasia from the ultra-long-range profile QUARTZ. *Journal of Geophysical Research* 104: 20329–20348.
- Müller G (1985) The reflectivity method: A tutorial. *Journal of Geophysics* 58: 153–174.
- Müller RD, Roest WR, Royer J, Gahagan LM, and Sclater JG (1997) Digital isochrons of the world's ocean floor. *Journal of Geophysical Research* 102(B2): 3211–3214.
- Mueller S, (ed.) (1973) The structure of the earth's crust based on seismic data. *Tectonophysics* 20: 1–391.
- Mueller S (1977) A new model of the continental crust. In: Heacock JG (ed.) *Geophysical Monograph 20: The Earth's Crust - Its Nature and Properties*, pp. 289–317. Washington, DC: American Geophysical Union.
- Mueller S (1978) Evolution of the Earth's crust. In: Ramberg I and Neumann E (eds.) *Tectonics and Geophysics of Continental Rifts*, vol. 2, pp. 11–28. Dordrecht: Reidel.
- Mutter CZ and Mutter JC (1993) Variations in thickness of layer 3 dominante oceanic crustal structure. *Earth and Planetary Science Letters* 117: 295–317.
- Mutter JC and Karson JA (1992) Structural processes at slow spreading ridges. *Science* 257: 627–634.
- Nafe JE and Drake CL (1957) Variation with depth in shallow and deep water marine sediments of porosity, density and velocity of compressional and shear waves. *Geophysics* 22: 523–552.
- Nafe JE and Drake CL (1968) Physical properties of rocks of basaltic composition. In: Hess HH and Poldevaart A (eds.) *The Poldevaart treatise on Rocks of Basaltic Composition*, vol 2, pp. 483–502. New York: Wiley-Interscience.
- Nakamura M, Yoshida Y, Zhao D, Katao H, and Nishimura S (2003) Three-dimensional P- and S-wave velocity structures beneath the Ryukyu arc. *Tectonophysics* 369: 121–143.
- Nataf H-C and Ricard Y (1996) 3SMAC: An *a priori* tomographic model of the upper mantle based on geophysical modeling. *Physics of the Earth and Planetary Interiors* 95: 101–122.
- National Geophysical Data Center (1988) ETOPO-5, bathymetry/topography data. *Data Announcement 88-MGG-02*, National Oceanic and Atmospheric Administration, U.S. Dep. of Commerce, Washington, DC.
- National Geophysical Data Center (2004) Total Sediment Thickness of the World's Oceans and Marginal Seas. <http://www.ngdc.noaa.gov/mgg/sedthick/sedthick.html>
- Navin D, Peirce C, and Sinha MC (1998) The RAMESSES experiment- II. Evidence for accumulated melt beneath a slow spreading ridge from wide-angle refraction and multichannel reflection seismic profiles. *Geophysical Journal International* 135: 746–772.
- Nelson KD, Zhao W, Brown JK, et al. (1996) Partially molten middle crust beneath southern Tibet: Synthesis of project INDEPTH results. *Science* 274: 1684–1688.
- Nkanish AT, Narumi K, Mivra S, et al. (2002) Crustal structure across the coseismic Neptune zone of the 1944 tonakai earthquake, The central Nakai trough seismic zone. *Journal of Geophysical Research* 107: pp. EPM-2-1 (doi: 10.1029/2001JB0000424).
- Nolet G (1977) The upper mantle under Western Europe inferred from the dispersion of Rayleigh modes. *Journal of Geophysics* 43: 265–285.
- Nolet G (1978) Simultaneous inversion of seismic data. *Geophysical Journal of the Royal Astronomical Society* 55: 679–691.
- Nolet G (ed.) (1987a) *Seismic Tomography with Applications in Global Seismology and Exploration Geophysics*. Dordrecht: D. Reidel Publ. Co.
- Nolet G (1987b) Waveform tomography. In: Nolet G (ed.) *Seismic Tomography*, pp. 301–322. Dordrecht: Reidel.
- Nolet G (1990) Partitioned waveform inversion and two-dimensional structure under the network of autonomously recording seismographs. *Journal of Geophysical Research* 95(6): 8499–8512.
- Nur A and Ben-Avraham Z (1982) Oceanic plateaus, the fragmentation of continents, and mountain building. *Journal of Geophysical Research* 87: 3644–3661.
- Okabe A, Kaneshima S, Kanjo K, Ohtaki T, and Purwana I (2004) Surface wave tomography for southeastern Asia using IRIS-FARM and JISNET data: plumes and superplumes. *Physics of the Earth and Planetary Interiors* 146: 101–112.
- Officer CB (1958) *Introduction to the Theory of Sound Transmission*. New York: McGraw-Hill Co.
- Oliver J (1962) A summary of observed surface wave dispersion. *Bulletin of the Seismological Society of America* 52: 81–86.
- Oliver J, Cook F, and Brown L (1983) COCORP and the continental crust. *Journal of Geophysical Research* 88: 3329–3347.
- Oliver JE, Dorbin M, Kaufman S, Meyer R, and Phinney R (1976) Continuous seismic reflection profiling of the deep basement. *Bulletin of the Geological Society of America* 87: 1537–1546.
- Oliver J, Dorman J, and Sutton G (1959) The second shear mode of continental Rayleigh waves. *Bulletin of the Seismological Society of America* 49: 379–389.
- Oliver J and Ewing M (1957) Higher modes of continental Rayleigh waves. *Bulletin of the Seismological Society of America* 47: 187–204.
- Oliver J and Ewing M (1958) Normal modes of continental Rayleigh waves. *Bulletin of the Seismological Society of America* 48: 33–49.
- Olsen KH (ed.) (1995) *Continental Rifts Evolution, Structure, Tectonics*. Amsterdam: Elsevier.
- Opero S and Charvis P (1996) Deep structure of the southern Kerguelen Plateau (southern Indian Ocean) from ocean bottom seismometer wide-angle seismic data. *Journal of Geophysical Research* 101: 25077–25103.
- Orcutt JA (1987) Structure of the Earth: Oceanic crust and uppermost mantle. *Reviews of Geophysics* 25: 1177–1196.
- Orcutt JA, Kennett BLN, and Dorman LM (1976) Structure of the East Pacific Rise from an ocean bottom seismometer survey. *Geophysical Journal of the Royal Astronomical Society* 45: 305–320.
- O'Reilly BM, Hauser F, Jacob AWB, and Shannon PM (1996) The lithosphere below the Rockall Trough: Wide-angle seismic evidence for extensive serpentisation. *Tectonophysics* 255: 1–23.
- O'Reilly BM, Readman PW, and Hauser F (1998) Lithospheric structure across the western Eurasian plate from a wide-angle seismic and gravity study: Evidence for a regional thermal anomaly. *Earth and Planetary Science Letters* 156: 275–280.
- Owens TJ, Crosson RS, and Hendrickson MA (1988) Constraints on the subduction geometry beneath western Washington from broadband teleseismic waveform modeling. *Bulletin of the Seismological Society of America* 78: 1319–1334.
- Owens TJ and Zandt G (1985) The response of the continental crust–mantle boundary observed on broadband teleseismic receiver functions. *Geophysical Research Letters* 12: 705–708.
- Owens TJ, Zandt G, and Taylor SR (1984) Seismic evidence for an ancient rift beneath the Comberland Plateau, Tennessee: A detailed analysis of broadband teleseismic P waveform. *Journal of Geophysical Research* 89: 7783–7795.

- Oxburgh ER and Parmentier EM (1977) Compositional and density stratification in oceanic lithosphere - causes and consequences. *Journal of the Geological Society of London* 133: 343–355.
- Pakiser LC (1963) Structure of the crust and upper mantle in the western United States. *Journal of Geophysical Research* 68: 5747–5756.
- Pakiser LC and Steinhart JS (1964) Explosion seismology in the western hemisphere. In: Odishaw J (ed.) *Research in Geophysics, 2, Solid earth and interface phenomena*, pp. 123–147. Cambridge, MA: Massachusetts Institute of Technology Press.
- Pakiser LC and Mooney WD (eds.) (1989) *Geological Society America Memoir* 172. Boulder, CO: Geological Society of America, Geophysical framework of the continental United States.
- Panza GF, Pontevivo A, Chimera G, Raykova R, and Aoudia A (2003) The lithosphere–asthenosphere; Italy and surroundings; *Geology of Italy. Episodes* 26: 169–174.
- Papasikas N and Juhlin C (1997) Interpretation of reflections from the central part of the Siljan Ring impact structure based on results from the Stenberg-1 borehole. *Tectonophysics* 269: 237–245.
- Parker RL (1971) The determination of seamount magnetism. *Geophysical Journal of the Royal Astronomical Society* 24: 321–324.
- Parker RL (1973) The rapid calculations of potential anomalies. *Geophysical Journal of the Royal Astronomical Society* 31: 447–455.
- Parsons B and Sclater JG (1977) An analysis of the variation of ocean floor bathymetry and heat flow with age. *Journal of Geophysical Research* 82: 803–825.
- Parolai S, Spallarossa D, and Eva C (1997) Bootstrap inversion for P_n wave velocity in northwestern Italy. *Annali di Geotisica* XL: 133–150.
- Parsons T, Trehu AM, Luetgert JH, et al. (1998) A new view into the Cascadia subduction zone and volcanic arc: Implications for earthquake hazards along the Washington margin. *Geology* 26: 199–202.
- Pasyanos M (2000) Predicting geophysical measurements: Testing a combined empirical and model-based approach using surface waves. *Bulletin of the Seismological Society of America* 90: 790–798.
- Pasyanos ME, Franz GA, and Ramirez AL (2006) Reconciling a geophysical model to data using a Markov chain Monte Carlo algorithm: An application to the Yellow sea-Korean peninsula region. *Journal of Geophysical Research* 111(B3): (doi: 10.1029/2005JB003851).
- Pasyanos ME, Walter WR, Flanagan MP, Goldstein P, and Bhattacharyya J (2004) Building and Testing an a priori Geophysical Model for Western Eurasia and North Africa. *PAGEOPH* 161: 235–281.
- Pasyanos ME, Walter WR, and Hazler SE (2001) A surface wave dispersion study of the Middle East and North Africa for monitoring the comprehensive nuclear-test-ban treaty. *Journal of Pure and Applied Geophysical* 158: 1445–1474.
- Paterson NR and Reeves CV (1985) Applications of gravity and magnetic surveys: The state-of-the-art in 1985. *Geophysics* 50: 2558–2594.
- Pavlenkova NI (1973) Ware Fields and crustal models of the continental type. Naukova Dumka Kiev (in Russian).
- Pavlenkova NI (1996) Crustal and upper mantle structure in northern Eurasia from seismic data. *Advances in Geophysics* 37: 1–133.
- Patro BPK, Harinarayana T, Sastry RS, et al. (2005) Electrical imaging of Narmada-Son Lineament Zone, Central India from magnetotellurics. *Physics of the Earth and Planetary Interiors* 148: 215–232.
- Peirce C and Barton PJ (1991) Crustal structure of the Madeira-Tore Rise, eastern North Atlantic – results of a DOBS wide-angle and normal incidence seismic experiment in the Josephine Seamount region. *Geophysical Journal International* 106: 357–378.
- Percival JA, Fountain DM, and Salisbury MH (1992) Exposed crustal cross sections as windows on the lower crust. In: Fountain DM, Arculus R, and Kay RW (eds.) *Continental Lower Crust*, pp. 317–362. Amsterdam: Elsevier.
- Perfit MR and Chadwick WW, Jr. (1998) Magmatism at mid-ocean ridges: Constraints from volcanological and geochemical investigations. In: Buck WR, Delaney P, and Karson JA (eds.) *Geophys Monograph 92: Faulting and Magmatism at Mid-Ocean Ridges*. Washington, DC: American Geophysical Union.
- Petit C, Koulakov I, and Deverchere J (1998) Velocity structure around the Baikal rift zone from teleseismic and local earthquake traveltimes and geodynamic implications; continents and their mantle roots. *Tectonophysics* 296: 125–144.
- Pfiffner OA, Lehner P, Heitzmann P, Mueller S, and Steck A (eds.) (1997) *Deep Structure of the Swiss Alps: results of NRP 20*. Basel-Boston-Berlin: Birkhäuser.
- Phinney RA (1964) Structure of the Earth's crust from spectral behavior of long-period body waves. *Journal of Geophysical Research* 69: 2997–3017.
- Pilidou S, Priestley K, Debayle E, and Gudmundsson O (2005) Rayleigh wave tomography in the north Atlantic; high resolution images of the Iceland, Azores and Eifel mantle plumes; mantle plumes; physical processes, chemical signatures, biological effects. *Lithos* 79: 453–474.
- Pilidou S, Priestley K, Gudmundsson O, and Debayle E (2004) Upper mantle S-wave speed heterogeneity and anisotropy beneath the North Atlantic from regional surface wave tomography; the Iceland and Azores plumes. *Geophysical Journal International* 159: 1057–1076.
- Plouff D (1976) Gravity and magnetic fields of polygonal prisms and application to magnetic terrain corrections. *Geophysics* 41: 727–741.
- Pollack HN and Chapman DS (1977) On the regional variation of heat flow, geotherms, and lithospheric thickness. *Tectonophysics* 38: 279–296.
- Pollack HN, Hurter SJ, and Johnson JR (1993) Heat flow form the Earth's interior: Analysis of the global data set. *Reviews of Geophysics* 31(3): 267–280.
- Press F (1956) Determinantion of crustal structure from phase velocity of Rayleigh waves: 1, Southern California. *Bulletin of the Geological Society of America* 67: 1647–1658.
- Press F (1964) Seismic wave attenuation in the crust. *Journal of Geophysical Research* 69: 4417–4418.
- Press F (1968) Earth models obtained by the Monte Carlo inversion. *Journal of Geophysical Research* 73: 5223–5234.
- Priestly K and Brune J (1978) Surface waves and the structure of the Great Basin of Nevada and western Utah. *Journal of Geophysical Research* 83: 2265–2272.
- Prodehl C (1970) Seismic refraction study of crustal structure of the Great Basin of Nevada and western Utah. *Journal of Geophysical Research* 83: 2629–2645.
- Prodehl C (1979) Crustal structure of the western United States. *U.S. Geological Survey, Professional Paper* 1034.
- Prodehl C (1984) Structure of the Earth's crust and upper mantle. In: Hellwege KH (editor in chief) *Landolt-Börnstein New Series: Numerical Data and Functional Relationships in Science and Technology Group V*. Fuchs K and Soffel H (eds.) *Physical Properties of the Interior of the Earth, the moon and the Planets*, vol 2a, pp. 97–206. Berlin-Heidelberg: Springer.
- Purdy GM and Detric R (1986) Crustal structure of the Mid-Atlantic Ridge at 23°N from seismic refraction studies. *Journal of Geophysical Research* 91: 3739–3762.

- Purucker MB, Langlais B, Olsen N, Hulot G, and Mandea M (2002) The southern edge of cratonic North America: Evidence from new satellite magnetometer observations. *Geophysical Research Letters* 29(15): 8000 (doi:10.1029/2001GL013645).
- Rabbel W and Mooney WD (1996) Seismic anisotropy of the crystalline crust: What does it tell us? *Terra Nova* 8: 16–21.
- Rabinowitz PD, Dipiazza N, and Matthias PK (1988) Sediment thickness map of the Indian Ocean. *American Association of Petroleum Geologists*. Tulsa: Okla.
- Rai S, Priestley K, Suryaprakash K, Srinagesh D, Gaur V, and Du Z (2003) Crustal shear velocity structure of the south Indian shield. *Journal of Geophysical Research* 108(B2): (doi:10.1029/2002JB001776).
- Raitt RW (1963) The crustal rocks. In: Hill MN (ed.) *The Sea - Ideas and Observations on Progress in the Study of the Seas, The Earth Beneath the Sea*, vol. 3, pp. 85–102. New York: Wiley-Interscience.
- Ramesh DS, Kind R, and Yuan X (2002) Receiver function analysis of the North American crust upper mantle. *Geophysical Journal International* 150: 91–108.
- Rapine R, Tilmann F, West M, Ni J, and Rodgers A (2001) Crustal structure of northern and southern Tibet from surface wave dispersion analysis. *Journal of Geophysical Research* 108: 2120 (doi:10.1029/2001JB000445).
- Rao IBP, Murty PRK, Koteswara Rao P, Murty ASN, Madhava Rao N, and Kaila KL (1999) Structure of the lower crust revealed by one- and two-dimensional modeling of wide-angle reflections-west Bengal basin, India. *Pure and Applied Geophysics* 156: 701–718.
- Rau RJ and Wu FT (1995) Tomographic imaging of lithospheric structures under Taiwan. *Earth and Planetary Science Letters* 133: 517–532.
- Reddy PR, Venkateswarlu N, Koteswar Rao P, and Prasad ASSRS (1999) Crustal structure of Peninsular shield, India, from DSS studies. *Current Science* 77: 1606–1611.
- Reddy PR and Vijaya Rao V (2000) Structure and tectonics of the Indian Peninsular shield - Evidence from seismic velocities. *Current Science* 78: 899–906.
- Redford MS (1980) Magnetic method. *Geophysics* 45: 1640–1658.
- Regnier M, Chatelain JL, Smalley R, Jr., Chiu JM, Isacks B, and Araujo M (1992) Crustal thickness variation in the Andean foreland, Argentina from converted waves. *Bulletin of the Seismological Society of America* 84: 1097–1111.
- Reid AB (1980) Aeromagnetic survey design. *Geophysics* 45: 1640–1658.
- Richards TC and Walker DJ (1959) Measurement of the thickness of the earth's crust in the Albertan plains of western Canada. *Geophysics* 24: 262–284.
- Richardson KR, Smallwood JR, White RS, Snyder DB, and Maguire PKH (1998) Crustal structure beneath the Faroe islands and the Faroe-Iceland Ridge. *Tectonophysics* 300: 159–180.
- Ringwood AE (1975) *Composition and Petrology of the Earth's Mantle*. New York: McGraw-Hill.
- Ritsema J and Allen RM (2003) The elusive mantle plume. *Earth and Planetary Science Letters* 207: 1–12.
- Ritzmann O, Maercklin N, Faleide JI, et al. (2007) A 3D geophysical model of the crust in the Barents Sea region: Model construction and basement characterisation, *Geophysical Journal International* 169: 365–425.
- Ritzwoller MH, Barmin MP, Villaseñor A, Levshin AL, and Engdahl ER (2002a) Pn and Sn tomography across Eurasia to improve regional seismic event locations. *Tectonophysics* 358: 39–55.
- Ritzwoller MH and Lavelle EM (1995) Three-dimensional seismic models of the earth's mantle. *Reviews of Geophysics* 33: 1–66.
- Ritzwoller MH and Levshin AL (1998) Eurasian surface wave tomography: Group Velocities. *Journal of Geophysical Research* 103: 4839–4878.
- Ritzwoller MH and Levshin AL (2002) Estimating shallow shear velocities with marine multi-component seismic data. *Geophysics* 67: 1991–2004.
- Ritzwoller MH, Shapiro NM, Barmin MP, and Levshin AL (2002b) Global surface wave diffraction tomography. *Journal of Geophysical Research* 107(B12): 2335 (doi:10.1029/2002JB001777).
- Roberts DG, Ginzberg A, Nunn K, and McQullin R (1988) The structure of the Rockall Trough from seismic refraction and wide-angle measurements. *Nature* 332: 632–635.
- Rodi W and Mackie RL (2001) Nonlinear conjugate gradients algorithm for 2-D magnetotelluric inversion. *Geophysics* 66: 174–187.
- Roecker SW (1993) Tomography in zones of collision; practical considerations and examples. In: Iyer HM and Hirahara K (eds.) *Seismic Topography: Theory and Practice*, pp. 584–612. London: Chapman and Hall.
- Roecker SW, Sabitova TM, Vinnik LP, et al. (1993) Three-dimensional elastic wave velocity structure of the western and central Tien Shan. *Journal of Geophysical Research* 98: 15779–15795.
- Roecker SW, Thurber C, and McPhee D (2004) Joint inversion of gravity and arrival time data from Parkfield: New constraints on structure and hypocenter locations near the SAFOD drill site. *Geophysical Research Letters* 31: L12SO4 (doi:10.1029/2003GJ019396).
- Romanowicz B (1991) Seismic tomography of the Earth's mantle. *Annual Review of Earth and Planetary Science* 19: 77–99.
- Romanowicz B (1995) A global tomographic model of shear attenuation in the upper mantle. *Journal of Geophysical Research* 100: 12375–12394.
- Roller JC (1965) Crustal structure in the eastern Colorado Plateau province from seismic-refraction measurements. *Bulletin of the Seismological Society of America* 55: 107–119.
- Rudnick R (1992) Xenoliths: Samples of the lower continental crust. In: Fountain DM, Arculus R, and Kay RW (eds.) *Continental Lower Crust*, pp. 269–316. Amsterdam: Elsevier.
- Rudnick R and Fountain DM (1995) Nature and composition of the continental crust: a lower crustal perspective. *Reviews of Geophysics* 33: 267–309.
- Rudnick RL and Gao S (2003) The composition of the continental crust. In: Holland HD and Turekian KK (eds.) *Encyclopedia of Geochemistry The Crust*, vol. 3, pp. 1–64. Elsevier-Pergamon.
- Ryberg T, Fuchs K, Egorkin AV, Solodilov L, and Uchida Y (1995) Observation of high-frequency teleseismic Pn on the long-range Quartz profile across northern Eurasia. *Journal of Geophysical Research* 100: 18151–18164.
- Ryberg T, Wenzel F, Mechic J, Egorkin A, Fuchs K, and Solodilov L (1996) Two-dimensional velocity structure beneath northern Eurasia derived from the super long-range seismic profile quartz. *Bulletin of the Seismological Society of America* 86: 857–867.
- Sagiya T and Thatcher W (1999) Coseismic Slip Aesolutim along a plate boundary mega thrust: The Nankai trough Southwest Japan. *Journal of Geophysical Research* 104: 11111–1130.
- Salisbury MH and Fountain DM (1990) *Exposed Cross-Sections of the Continental Crust*, 662 pp. Dordrecht: Kluwer.
- Salah MK and Zhao D (2003) 3-D seismic structure of Kii peninsula in southwest Japan; evidence for slab dehydration in the forearc. *Tectonophysics* 364: 191–213.
- Sandmeier K-J and Wenzel F (1986) Synthetic seismograms for a complex crustal model. *Geophysical Research Letters* 13: 22–25.

- Sandmeier K-J and Wenzel F (1990) Lower crustal petrology from wide-angle P- and S-wave measurements in the Black Forest. *Tectonophysics* 173: 495–505.
- Sandvol E, Al-Damegh K, Calvert A, et al. (2001) Tomographic imaging of Lg and Sn propagation in the Middle East; regional wave propagation and crustal structure; monitoring the comprehensive nuclear-test-ban treaty. *PAGEOPH* 158: 1121–1163.
- Sandoval S, Kissling E, Ansorge J, and SVEKALAPKO Seismic Tomography Working Group, (CHE) (2004) High-resolution body wave tomography beneath the SVEKALAPKO array – II. Anomalous upper mantle structure beneath the central Baltic shield. *Geophysical Journal International* 157: 200–214.
- Sandvol E, Seber D, Calvert A, and Barazangi M (1998) Grid search modeling of receiver functions: implications for crustal structure in the Middle East and North Africa. *Journal of Geophysical Research* 103: 26899–26971.
- Sandwell DT and Smith WHF (1997) Marine gravity anomaly from Geosat and ERS 1 satellite altimetry. *Journal of Geophysical Research* 102: 10039–10054.
- Saunders AD, Kempton OD, Fitton JG, et al. (1999) Sr, Nd, and Pb isotopes and trace element geochemistry of basalts from the Southeast Greenland margin. In: Larsen HC, Duncan RA, Allan JF, and Brooks K (eds.) *Proceedings of Ocean Drilling Program, Scientific results*, vol. 163, pp. 77–93. Ocean Drilling Program.
- Saunders AD, Storey M, Kent RW, and Norry MJ (1992) Consequences of plume-lithosphere interactions. In: Storey BC, Alabaster T, and Pankhurst RJ (eds.) *Magmatism and the Causes of Continental Breakup*, vol. 68, pp. 41–60. London: Geological Society of London.
- Savage MK (1999) Seismic anisotropy and mantle deformation: What have we learned from shear wave splitting? *Reviews of Geophysics* 37: 65–106.
- Scalser JG, Jaupart C, and Galson D (1980) The heat flow through oceanic and continental crust and the heat loss of the Earth. *Reviews of Geophysics* 18: 269–311.
- Schilt S, Oliver J, Brown L, et al. (1979) The heterogeneity of the continental crust: Results from deep crustal seismic reflection profiling using the VIBROSEIS technique. *Reviews of Geophysics and Space Physics* 17: 354–368.
- Schouten H and McCamy K (1972) Filtering marine magnetic anomalies. *Journal of Geophysical Research* 77(35): 7089–7099.
- Schouten JA (1971) A fundamental analysis of magnetic anomalies over oceanic ridges. *Marine Geophysical Researches* 1: 111–114.
- Schmid S and Kissling E (2000) The arc of the western Alps in the light of geophysical data on deep crustal structure. *Tectonics* 19: 62–85.
- Seber D, Sandvol E, Sandvol C, et al. (2001) Crustal model for the Middle East and North African region: Implications for the isostatic compensation mechanism. *Geophysical Journal International* 147: 630–638.
- Sexton JL, Hinze WJ, von Freese RRB, and Braile L (1982) Long-wavelength aeromagnetic anomaly map of the conterminous United States. *Geology* 10: 364–369.
- Shapiro NM and Ritzwoller MH (2002) Monte Carlo inversion for a global shear velocity model of the crust and upper mantle. *Geophysical Journal International* 151: 88–105.
- Shapiro NM, Ritzwoller MH, Molnar P, and Levin V (2004) Thinning and flow of Tibetan crust constrained by seismic anisotropy. *Science* 305: 233–236.
- Shearer PM (1988) Cracked media, Poisson's ratio, and the structure of the upper oceanic crust. *Geophysical Journal* 92: 357–362.
- Shearer PM and Orcutt JA (1986) Compressional and shear wave anisotropy in the oceanic lithosphere – the Ngendei seismic reflection experiment. *Geophysical Journal of the Royal Astronomical Society* 87: 967–1003.
- Sheriff RE and Geldart LP (1982) *Exploration seismology: History, Theory, and Data Acquisition*. Cambridge: Cambridge University Press.
- Sheriff RE and Geldart LP (1983) *Exploration Seismology: Data processing and Interpretation*, vol. 1. Cambridge: Cambridge University Press.
- Shor GG (1967) Seismic refraction profile in Coral Sea Basin. *Science Letters* 92: 234–246.
- Silver PG (1996) Seismic anisotropy beneath the continents: Probing the depths of geology. *Annual Review of Earth and Planetary Science* 24: 385–432.
- Silver PG and Chan WW (1988) Implications for continental structure and evolution from seismic anisotropy. *Nature* 335: 34–39.
- Simkin T, Tilling RI, Vogt PR, Kirby SH, Kimberly P, and Stewart DB (2006) This Dynamic Planet, United States Geological Survey Geological Investigations Map I-2800, one sheet.
- Simmons G (1964) Velocity of shear waves in rocks to 10 kilobars. *Journal of Geophysical Research* 69: 1123–1130.
- Simpson RW, Hildenbrand TG, Godson RH, and Kane MF (1987) *Digital colored Bouguer gravity, free-air gravity, station location, and terrain maps for the continental United States*. U.S. Geological Survey Geophysical Investigations Map GP 953-B, scale 1:7,500,000.
- Sinha MC, Constable SC, Peirce C, et al. (1998) Magnetic processes at slow spreading ridges: Implications of the RAMESSES Experiment at 57° 45' N on the Mid-Atlantic Ridge. *Geophysical Journal International* 135: 731–745.
- Sinha MC, Louden KE, and Parsons B (1981) The crustal structure of the Madagascar Ridge. *Geophysical Journal of Astronomical Society* 66: 351–377.
- Sinha MC and Louden KE (1983) The Oceanographer fracture zone, I. Crustal structure from seismic refractions studies. *Geophysical Journal of the Royal Astronomical Society* 75: 713–736.
- Sinha MC, Navin DA, MacGregor LM, et al. (1997) Evidence for accumulated melt beneath the slow-spreading Mid-Atlantic ridge. *Philosophical Transactions of the Royal Society of London, Series A* 355: 233–253.
- Sleep NH (1990) Hotspots and mantle plumes: Some phenomenology. *Journal of Geophysical Research* 95: 6715–6736.
- Sleep NH (2003) Survival of Archean craton lithosphere. *Journal of Geophysical Research* 108: 2302 (doi: 10.1029/2001JB000169).
- Sleep NH (2005) Evolution of the continental lithosphere. *Annual Review of the Earth and Planet Science* 33: 369–393.
- Slichter LB (1938) Seismological investigations of the earth's crust using quarry blasts [abs.]. *Bulletin of the Geological Society of America* 49: 19–27.
- Slichter LB (1951) Crustal structure in the Wisconsin area. *Office of Naval Research Report N9*, NR86200. Arlington, VA.
- Smith TJ, Steinhart JS, and Aldrich LT (1966) Lake Superior crustal structure. *Journal of Geophysical Research* 71: 1141–1181.
- Smith WHF and Sandwell DT (1997) Global sea floor topography from satellite altimetry and ship depth soundings. *Science* 277: 1956–1962.
- Smithson SB, Johnson RA, Hurich CA, Valasek PA, and Branch C (1987) Deep crustal structure and genesis from contrasting reflection patterns: An integrated approach. *Geophysical Journal of the Royal Astronomical Society* 87: 67–72.

- Smithson SB, Wenzel F, Ganchin YV, and Morozov IB (2000) Seismic results at Kola and KTB deep scientific boreholes: Velocities, reflections, fluids, and crustal composition. *Tectonophysics* 329: 301–317.
- Snavely PD, Jr., Wagner HC, and Lander DL (1980) Geologic cross section of the central Oregon continental margin, Map and Chart Series MC-28J, scale 1:250,000. Boulder, CO: Geological Society of America.
- Snyder DB, Ramos VA, and Allmendinger RW (1990) Thick-skinned deformation observed on deep seismic reflection profiles in western Argentina. *Tectonics* 9: 773–788.
- Soller DR, Ray RD, and Brown RD (1982) A new global crustal thickness model. *Tectonics* 1: 125–149.
- Song LP, Koch M, Koch K, and Schlüterhardt J (2004) 2-D anisotropic Pn-velocity tomography underneath Germany using regional traveltimes. *Geophysical Journal International* 157: 645–663.
- Spakman W, van der Lee S, and van der Hilst RD (1993) Travel-time tomography of the European–Mediterranean mantle down to 1400 km. *Physics of the Earth and Planetary Interiors* 79: 3–74.
- Spudich P and Orcutt J (1980) A new look at the seismic velocity structure of the oceanic crust. *Reviews of Geophysics and Space Physics* 18: 627–645.
- Stein CA and Stein S (1992) A model for the global gravitation in oceanic depth and heat flow with lithospheric age. *Nature* 359: 123–129.
- Stien M and Hoffman AW (1994) Mantle plumes and episodic crustal growth. *Nature* 372: 63–68.
- Steinhart JS (1967) Mohorovicic-discontinuity. In: Runcorn K (ed.) *International Dictionary of Geophysics*, vol. 2, pp. 991–994. Oxford: Pergamon Press.
- Steinhart JS and Meyer RP (1961) *Explosion Studies of Continental Structure*. Washington, DC: Carnegie Institute, Publication 622.
- Stern TA and McBride JH (1998) Seismic exploration of continental strike-slip zones. In: Klemperer SL and Mooney WD (eds.) *Deep Seismic Profiling of the Continents*, I, General Results and New Methods. *Tectonophysics* 286: 63–78.
- Su WJ, Woodward RL, and Dziewonski AM (1992) Deep origin of mid-ocean-ridge seismic velocity anomalies. *Nature* 359: 149–152.
- Su WJ, Woodward RL, and Dziewonski AM (1994) Degree 12 model of shear wave velocity heterogeneity in the mantle. *Journal of Geophysical Research* 99: 6945–6980.
- Sun YS, Li X, Kuleli S, Morgan FD, and Toksoz MN (2004b) Adaptive moving window method for 3D P-velocity tomography and its application in China. *Bulletin of the Seismological Society of America* 94: 740–746.
- Sun YS, Morgan D, and Toksoz MN (2004a) 3D P- and S-velocity models for the crust and uppermost mantle of China by Monte-Carlo adaptive moving window inversion. *Seismological Research Letters* 74: 202–203.
- Swenson J, Beck S, and Zandt G (2000) Crustal structure of the Altiplano from broadband regional waveform modeling: implications for the composition of thick continental crust. *Journal of Geophysical Research* 105: 607–621.
- Talwani M (1965) Computation with the help of a digital computer of magnetic anomalies caused by bodies of arbitrary shape. *Geophysics* 30(5): 797–817.
- Talwani M and Ewing M (1960) Rapid computation of gravitational attractions of three-dimensional bodies of arbitrary shape. *Geophysics* 25: 203–225.
- Tanimoto T (1995) Crustal structure of the Earth. In: Ahrens TJ (ed.) *Global earth Physics: A handbook of Physical Constants*, pp. 214–224. Washington, DC: AGU.
- Tapley B, Ries J, Bettadpur, et al. (2005) An improved Earth gravity field model from GRACE. *Journal of Geodesy* 79(8): 467–478.
- Tarantola A and Nercissian A (1984) Three-dimensional inversion without blocks. *Geophysical Journal of the Royal Astronomical Society* 76: 299–306.
- Tatel HE, Adams LH, and Tuve MA (1953) Studies of the earth's crust using waves from explosions. *American Philosophy Society Proceedings* 97: 658–669.
- Tatel HE and Tuve MA (1955) Seismic exploration of a continental crust. In: Poldervaart A (ed.) *Crust of the Earth*, pp. 35–50. Boulder, CO: Geological Society of America.
- Taylor SR and McLennan SM (1985) *The Continental Crust: Its Composition and Evolution*. Maldon, MA: Blackwell Science.
- Telford WM, Geldart LP, Sheriff RE, and Keys DA (1976) *Applied Geophysics*. Cambridge: Cambridge University Press.
- Thimon I, Matias L, Rehault JP, Hirn A, Fidalgo-Gonzalez L, and Avedik F (2003) Deep structure of the Armorican Basin (Bay of Biscay): A review of Norgesia seismic reflection and refraction data. *Journal of the Geological Society of London* 160: 99–116.
- Thumberg C and Aki K (1987) Three-dimensional seismic imaging. *Annual Review of Earth and Planetary Sciences* 15: 115–139.
- Thurber CH (1983) Earthquake locations and Three-dimensional crustal structure in the Coyote Lake area, central California. *Journal of Geophysical Research* 88: 8226–8236.
- Thurber CH (1993) Local earthquake tomography: Velocities and Vp/Vs – theory. In: Iyer H and Hihahara K (eds.) *Seismic Tomography, Theory and Practice*, pp. 563–583. Boca Raton, FL: CRC Press.
- Thurber CH and Kissling E (2000) Advances in travel-time calculations for Three-dimensional structures. In: Thurber CH and Rabinowitz N (eds.) *Advances in Seismic Event Location*, pp. 71–79. New York: Springer.
- Thybo H, Janik T, Omelchenko VD, et al. (2003) Upper lithospheric seismic velocity structure across the Pripyat trough and the Ukrainian shield along the EUROBRIDGE'97 profile. *Tectonophysics* 371: 41–79.
- Tiberi C, Diament M, Déverchère J, et al. (2003) Deep structure of the Baikal rift zone revealed by joint inversion of gravity and seismology. *Journal of Geophysical Research* 108: (doi:10.1029/2002JB001880).
- Tilmann F, Ni J, Hearn T, et al. (2003) Seismic imaging of the downwelling Indian lithosphere beneath central Tibet. *Science* 300: 1424–1427.
- Todd BJ, Reid I, and Keen CE (1988) Crustal structure across the Southwest Newfoundland Transform Margin. *Canadian Journal of Earth Sciences* 25: 744–759.
- Toomey DR, Purdy GM, Solomon SC, and Wilcock WSD (1990) The three-dimensional seismic velocity structure of the East Pacific Rise near latitude 9°30'N. *Nature* 347: 639–645.
- Trampert J and Woodhouse JH (1995) Global phase velocity maps of Love and Rayleigh waves between 40 and 150 seconds. *Geophysical Journal International* 122: 675–690.
- Tréhu AM, Asudeh I, Brocher TM, et al. (1994) Crustal architecture of the Cascadia forearc. *Science* 266: 237–243.
- Tucholke BE (1986) Structure of basement and distribution of sediments in the western North Atlantic Ocean. In: Vogt PR and Tucholke BE (eds.) *The Geology of North America, Vol. M, The Western North Atlantic Region*, pp. 331–340. Boulder, CO: Geological Society of America.
- Tucholke BE and Uchupi E (1989) Thickness of sedimentary cover. In: Uchupi E (ed.) *International Geology-Geophysical Atlas of the Atlantic Ocean*. Moscow: Russian Ministry of Geology Russian Academy of Science.
- Turcotte DL and Schubert G (2002) *Geodynamics* 2nd edn. Cambridge: Cambridge University Press.
- Tuve MA (1951) The Earth's crust: Washington DC. *Yearbook of the Carnegie Institution of Washington* 50: 69–73.

- Tuve MA (1953) The earth's crust. *Yearbook at the Carnegie Institution of Washington* 52: 103–108.
- Tuve MA, Tatel HE, and Hart PJ (1954) Crustal structure from seismic exploration. *Journal of Geophysical Research* 59: 415–422.
- Unsworth MJ, Malin PE, Egbert G, and Siripunvaraporn W (2000) Along strike variations in the electrical structure of the San Andreas fault at Parkfield, California. *Geophysical Research Letters* 27: 3021–3024.
- Usher MJ (1962) Elastic behavior of rock at low frequencies. *Geophysical Prospecting* 10: 119–127.
- Upton BGJ, Aspen P, and Hinton RW (2001) Pyroxenite and granulite xenoliths from beneath the Scottish Northern Highlands Terrane: Evidence for lower-crust/upper-mantle relationships. *Contributions to Mineralogy and Petrology* 142: 178–197.
- US Department of Commerce, National Oceanic and Atmospheric Administration, National Geophysical data center (2001) 2-minute Gridded Global Relief Data (ETOPO2).
- US Geological Survey and Society of Exploration Geophysicists (1982) Composite magnetic anomaly map of the United States: Part A, Conterminous United States. U.S. Geological Survey Geophysical Investigations Map GP-954-A, scale 1:1,250,000, 2 sheets.
- Vacquier V, Steenland NC, Henderson RG, and Zietz I (1951) Interpretation of aeromagnetic maps. *Geological Society of American Memoir* 47: 151.
- van Heijst HJ and Woodhouse JH (1999) Global high-resolution phase velocity distribution of overtone and fundamental-mode surface waves determined by mode branch stripping. *Geophysical Journal International* 137: 601–620.
- van der Hilst RD, Widjiantoro S, and Engdahl ER (1997) Evidence for deep mantle circulation from global tomography. *Nature* 386: 578–584.
- van der Lee S and Nolet G (1997) Upper mantle S velocity structure of North America. *Journal of Geophysical Research* 102: 22815–22838.
- Vening-Miehes FA (1948) *Gravity expeditions at Sea, 1923–1938, Vol. IV: Complete Results and Isostatic Reduction*. Waltman, Delft, Netherlands: Netherlands Geodetic Commission Publication.
- Venistini N, Calcagnile G, Del Gaudio V, and Pierri P (2004) Combined analysis of seismic and gravimetric data in the Adriatic plate. *Physics of the Earth and Planetary Interiors* 142: 89–100.
- Vera EE, Mutter JC, Buhl P, et al. (1990) The structure of 0- to 0.2-m.y.-old oceanic crust at 9°N on the East Pacific Rise from expanded spread profiles. *Journal of Geophysical Research* 95: 15529–15556.
- Vidale JE (1988) Finite-difference calculation of travel times. *Bulletin of the Seismological Society of America* 78: 2062–2076.
- Vidale JE (1990) Finite-difference calculation of traveltimes in three dimensions. *Geophysics* 55: 521–526.
- Vine FJ and Moores EM (1972) A model for the gross structure, petrology, and magnetic properties of oceanic crust. In: *Studies in Earth and Space Sciences: A Memoir in Honor of Harry Hammond Hess*. Memoir 132, pp. 195–205. Boulder, CO: Geological Society of America.
- Vinnik L (1977) Detection of waves converted from P to SV in the mantle. *Physics of the Earth and Planetary Interior* 15: 39–45.
- Vinnik LP and Kosarev GL (1981) Determination of crustal parameters from observations of teleseismic body waves. *Proceedings of the Academy of Science USSR* 261: 1091–1095 (in Russian).
- Vinnik LP, Makeyeva LI, Milev A, and Usenko Y (1992) Global patterns of azimuthal anisotropy and deformation in the continental mantle. *Geophysical Journal International* 111: 433–447.
- Vinnik LP, Farra V, and Kind R (2004) Deep structure of the Afro-Arabian hotspot by S receiver functions. *Geophysical Research Letters* 31: L11608 (doi:10.1029/2004GL019574).
- Vogt PR, Taylor PT, Kovacs LC, and Johnson GL (1979) Detailed aeromagnetic investigation of the Arctic Basin. *Journal of Geophysical Research* 83: 1071–1089.
- Von Freese RRB, Hinze WJ, Olivier R, and Bentley CR (1986) Regional magnetic anomaly constraints on continental breakup. *Geology* 14: 68–71.
- Walck M (1984) The P wave upper mantle structure beneath an active spreading centre: The Gulf of California. *Geophysical Journal of the Royal Astronomical Society* 76: 697–723.
- Walter WR, Pasyanos ME, Bhattacharyya J and O'Boyle J (2000) MENA 1.1 – An Updated Geophysical Regionalization of the Middle East and North Africa. UCRL-ID-138079, LLNL.
- Wang CY, Chen W, and Mooney WD (2003) Three-dimensional velocity structure of the crust and upper mantle in southwestern China and its tectonic implications. *Journal of Geophysical Research* 108: 2442 (doi:10.1029/2002JB001973).
- Wang S, Hearn T, Xu J, Ni J, Yu Y, and Zhang X (2002) Velocity structure of uppermost mantle beneath China continent from Pn tomography. *Science in China. Series D. Earth Sciences* 45: 143–150.
- Wang XY, Mooney WD, and Yuan XC (2003) The crustal structure from the Altai Mountains to the Altyn Tagh fault, northwest China. *Journal of Geophysical Research* 108: 2322 (doi:10.1029/2001JB000552).
- Wannamaker PE, Booker JR, Jones AG, et al. (1989) Resistivity cross-section through the Juan de Fuca subduction system and its tectonic implications. *Journal of Geophysical Research* 94: 14,127–14,144.
- Watts AB (2001) *Isotasy and Flexure of the Lithosphere*. Cambridge: Cambridge University Press.
- Warren DH and Healy JH (1973) Structure of the crust in the conterminous United States. *Tectonophysics* 20: 203–213.
- Weber M, Abu-Ayyah K, and 42 others (2004) The crustal structure of the Dead Sea transform. *Geophysical Journal International* 156: 655–681 (doi:10.1111/j.1365-246X.2004.02143.x).
- Wells RE, Blakely RJ, Sugiyama Y, Scholl DW, and Dinterman PA (2003) Basin-centered asperities in great subduction zone earthquakes: A link between slip, subsidence, and subduction erosion? *Journal of Geophysical Research* 108(B10): 2507 (doi:10.1029/2002JB002072).
- Wepfner WW and Christensen NI (1991) Q structure of the oceanic crust. *Marine Geophysical Researches* 13: 227–237.
- White DJ and Clowes RM (1990) Shallow crustal structure beneath the Juan de Fuca Ridge from 2D seismic refraction tomography. *Geophysical Journal International* 100: 349–367.
- White RS, Detrick RS, Sinha MC, and Cormier M-H (1984) Anomalous seismic structure of oceanic fractures zones. *Geophysical Journal of the Royal Astronomical Society* 79: 779–798.
- White RS, Spence GD, Fowler SR, McKenzie DP, Westbrook GK, and Bowen AN (1987a) Magmatism at rifted continental margins. *Nature* 330: 439–444.
- White RS, Westbrook GH, Bowen AN, et al. (1987b) Hatton bank (northwest U.K.) continental margin structure. *Geophysical Journal of the Royal Astronomical Society* 89: 265–272.
- White RS and McKenzie D (1989) The generation of volcanic continental margins and flood basalts. *Journal of Geophysical Research* 94: 7685–7729.

- White RS, McKenzie D, and O'Nions RK (1992) Oceanic crustal thickness from seismic measurements and rare earth element inversions. *Journal of Geophysical Research* 97: 19683–19715.
- Whitmarsh RB, Ginzburg A, and Searle RC (1982) The structure and origin of the Azores–Biscay Rise, north-east Atlantic Ocean. *Geophysical Journal of the Royal Astronomical Society* 70: 79–107.
- Whitmarsh RB and Calvert AJ (1986) Crustal structure of Atlantic fracture zones- I. The Charlie-Gibbs fracture zone. *Geophysical Journal of the Royal Astronomical Society* 85: 107–138.
- Wilcock WSD, Solomon SC, Purdy GM, and Toomey DR (1995) Seismic attenuation structure of the East Pacific Rise near 9°30'N. *Journal of Geophysical Research* 100: 24147–24165.
- Willden R (1965) Seismic-refraction measurements of crustal structure beneath American Falls Reservoir, Idaho, and Flaming Gorge Reservoir, Utah. *U.S. Geological Survey Professional paper* 525-C: C-44-C-50.
- Williams MC, Shrive PN, Fountain DM, and Frost BR (1985) Magnetic properties of exposed deep crustal rocks from the Superior Province of Manitoba. *Earth Planetary Science Letters* 76: 176–184.
- Willmore PL and Bancroft AM (1960) The time term approach to refraction seismology. *Geophysical Journal of the Royal Astronomical Society* 3: 419–432.
- Wilson JT (1963) Hypothesis of the Earth's behaviour. *Nature* 198: 925–929.
- Wilson JT (1965) A new class of fault and their bearing on continental drift. *Nature* 2: 343–347.
- Wolfe CJ, Purdy GM, Toomey DR, and Solomon SC (1995) Microearthquake characteristics and crustal velocity structure at 29° N on the Mid-Atlantic Ridge: The architecture of a slow spreading segment. *Journal of Geophysical Research* 100: 24,449–24,472.
- Woodhouse JH and Dziewonski AM (1984) Mapping the upper mantle: Three-dimensional modeling of Earth structure by inversion of seismic waveforms. *Journal of Geophysical Research* 89: 5953–5986.
- Woolard GP (1943) Transcontinental gravitational and magnetic profile of North America and its relation to geologic structure. *Bulletin of the Geological Society of America* 44: 747–789.
- Woolard GP (1959) Crustal structure from gravity and seismic measurements. *Journal of Geophysical Research* 64: 1521–1544.
- Woolard GP (1966) Regional isostatic relations in the United States. In: Tuve M A (ed.) *Geophysical Monograph 10: The Earth Beneath the Continents*, pp. 557–594. Washington, DC: American Geophysical Union.
- Wortel MJR and Spakman W (2000) Subduction and slab detachment in the Mediterranean–Carpathian region. *Science* 290: 1910–1917.
- Worthington MH (1984) *An Introduction to Geophysical Tomography*. First Break, November, pp. 20–26.
- Xu Y, Liu FT, Liu JH, and Chen H (2002) Crust and upper mantle structure beneath western China from wave traveltimes tomography. *Journal of Geophysical Research* 107: (doi:10.1029/2001JB000402).
- Yanovskaya TB and Kozhevnikov VM (2003) 3D S-wave velocity pattern in the upper mantle beneath the continent of Asia from Rayleigh wave data. *Physics of the Earth and Planetary Interiors* 138: 263–278.
- Yliniemi J, Kozlovskaya E, Hjelt S, Komminaho K, Ushakov A, and SVEKALAPKO Seismic Tomography Working Group International, (III) (2004) Structure of the crust and uppermost mantle beneath southern Finland revealed by analysis of local events registered by the SVEKALAPKO seismic array. *Tectonophysics* 394: 41–67.
- Yoshizawa K and Kennett BLN (2004) Multimode surface wave tomography for the Australian region using a three-stage approach incorporating finite frequency effects. *Journal of Geophysical Research* 109: (doi:10.1029/2002JB002254).
- Yuan X, Ni J, Kind R, Mechie J, and Sandvol E (1997) Lithospheric and upper mantle structure of southern Tibet from a seismological passive source experiment. *Journal of Geophysical Research* 102: 27491–27500.
- Yuan X, Sobolev SV, Kind R, et al. (2000) Subduction and collision processes in the Central Andes constrained by converted seismic phases. *Nature* 408: 958–961.
- Zandt G and Ammon CJ (1995) Continental crust composition constrained by measurements of crustal Poisson's ratio. *Nature* 374: 152–154.
- Zandt G and Owens TJ (1986) Comparison of crustal velocity profiles determined by seismic refraction and teleseismic methods. *Tectonophysics* 128: 155–161.
- Zandt G, Myers SC, and Wallace TC (1995) Crustal and mantle structure across the Basin and Range – Colorado Plateau boundary at 37°N latitude and implications for Cenozoic extensional mechanism. *Journal of Geophysical Research* 100: 10 529–10 548.
- Zang SX, Liu YG, and Ning JY (2002) Thermal structure of the lithosphere in North China. *Chinese Journal of Geophysics* 17(1): 56–66.
- Zelt CA (1999) Modelling strategies and model assessment for wide-angle seismic traveltimes data. *Geophysical Journal International* 139: 183–204 (22).
- Zelt CA and Barton PJ (1998) Three-dimensional seismic refraction tomography: A comparison of two methods applied to data from the Faeroes Basin. *Journal of Geophysical Research* 103: 7187–7210.
- Zelt CA and Forsyth DA (1994) Modelling wide-angle seismic data for crustal structure: Southeastern Grenville Province. *Journal of Geophysical Research* 99: 11678–11704.
- Zelt CA, Hojko AM, Flueh ER, and McIntosh KD (1999) 3D simultaneous seismic refraction and reflection tomography of wide-angle data from the central Chilean margin. *Geophysical Research Letters* 26: 2577–2580.
- Zelt CA, Sain K, Naumenko JV, and Sawyer DS (2003) Assessment of crustal velocity models using seismic refraction and reflection tomography. *Geophysical Journal International* 153: 609–626.
- Zelt CA and Smith RB (1992) Seismic traveltimes inversion for 2-D crustal velocity structure. *Geophysical Journal International* 108: 16–34.
- Zhang H and Thurber CH (2003) Double-difference tomography: The method and its application to the Hayward fault, California. *Bulletin of the Seismological Society of America* 93: 1875–1889.
- Zhang H, Thurber CH, Shelly D, Ide S, Beroza GC, and Hasegawa A (2004) High-resolution subducting-slab structure beneath northern Honshu, Japan, revealed by double-difference tomography. *Geology* 32: 361–364.
- Zhang Y-S and Lay T (1996) Global surface wave phase velocity variations. *Journal of Geophysical Research* 101: 8415–8436.
- Zhang Y-S and Tanimoto T (1991) Global Love wave phase velocity variation and its significance to plate tectonics. *Physics of the Earth and Planetary Interiors* 66: 160–202.
- Zhao D, Hasegawa A, and Horiuchi S (1992) Tomographic imaging of P and S wave velocity structure beneath northeastern Japan. *Journal of Geophysical Research* 97: 19909–19928.
- Zhao JM, Mooney WD, Zhang X, Li Z, Jin Z, and Okaya N (2006) Crustal structure across the Altyn Tagh Range at the northern margin of the Tibetan Plateau and tectonic implications. *Earth and Planetary Science Letters* 241: 804–814.

- Zhao LS and Xie J (1993) Lateral variations in compressional velocities beneath the Tibetan Plateau from Pn traveltimes tomography. *Geophysical Journal International* 115: 1070–1084.
- Zhao W, Mechle J, Brown CD, et al. (2001) Crustal structure of central Tibet as derived from project INDEPTH wide-angled seismic data. *Geophysical Journal International* 145: 486–498.
- Zhou Y, Dahlen FA, and Nolet G (2004) Three-dimensional sensitivity kernels for surface wave observables. *Geophysical Journal International* 158: 142–168.
- Zhou Y, Nolet G, and Laske G (2005) Global upper-mantle structure from finite-frequency surface-wave tomography. *Journal of Geophysical Research* 111: B04304.
- Zhu H and Kanamori H (2000) Moho depth variation in southern California from teleseismic receiver functions. *Journal of Geophysical Research* 105: 2969–2980.
- Ziegler PA (1990) *Geological Atlas of Western Europe 2nd edn*, London: Shell International and the Geological Society.
- Zietz I (1969) Aeromagnetic investigations of the earth's crust in the United States. In: Hart PJ (ed.) *Geophysical Monograph 13: The Earth's Crust and Upper Mantle*, pp. 404–415. Washington, DC: American Geophysical Union.
- Zietz I (1982) *Composite magnetic anomaly map of United States; Part A. Conterminous United States*: U.S. Geological Survey Geophysical Investigations Map GP-954A, scale 1:2,500,000.
- Zoback ML and Mooney WD (2003) Lithospheric buoyancy and continental intraplate stresses. *International Geology Review* 45: 95–118.
- Zorin YA, Turutanov EK, Mordvinova VV, Kozhevnikov VM, Yanovskaya TB, and Treussov AV (2003) The Baikal rift zone: the effect of mantle plumes on older structure. *Tectonophysics* 371: 153–173.

1.12 Crust and Lithospheric Structure – Seismic Structure of Mid-Ocean Ridges

R. A. Dunn, University of Hawaii at Manoa, Honolulu, HI, USA

D. W. Forsyth, Brown University, Providence, RI, USA

© 2007 Elsevier B.V. All rights reserved.

1.12.1	Depth Extent of Anomalous Structure	419
1.12.2	Form of Shallow Upwelling and Onset of Melting	420
1.12.3	Flow in the Mantle	423
1.12.4	Crustal Accretion along Mid-Ocean Ridges	424
1.12.4.1	General Seismic Structure of the Oceanic Crust	424
1.12.4.2	Fast-to-Superfast-Spreading Ridge Crustal Structure	426
1.12.4.3	Intermediate Spreading Rate Ridge Crustal Structure	430
1.12.4.4	Slow-Spreading Ridge Crustal Structure	432
1.12.4.5	Ultraslow-Spreading Ridge Crustal Structure	436
1.12.5	Remaining Unsolved Problems	437
References		437

At mid-ocean ridges, oceanic plates separate, inducing mantle upwelling. The upwelling mantle undergoes pressure-release partial melting, because the temperature of the solidus decreases with decreasing pressure. The newly formed melt, being less viscous and less dense than the surrounding solid, segregates from the residual mantle matrix and buoyantly rises toward the surface, where it forms new, basaltic, oceanic crust. Over the last 200 million years, two-thirds of the Earth has been resurfaced through this process of seafloor spreading, either at classical mid-ocean ridge spreading centers or in spreading centers in back-arc basins behind subduction zones. Many seismological studies have been designed to constrain the pattern of mantle upwelling, the distribution of melt in the upwelling mantle, the melt migration pattern from the mantle to the base of the crust, the plumbing system in the crust that redistributes the melt, the final destination of the melt recorded in variations in crustal thickness, and the evolution and structure of the oceanic crust and lithosphere with time as the plates move away from the spreading centers.

1.12.1 Depth Extent of Anomalous Structure

One of the early geodynamic questions about mid-ocean ridges was whether the upwelling is passive

(driven simply by the viscous drag of separating plates) or active (a buoyantly rising limb of a convection cell). If convection is driven largely by cooling from above, then the downwelling limb, in the form of the sinking lithospheric slabs, is expected to be cooler than its surroundings and to extend deep into the mantle. If driven by heating from below, as from heat released from the core, then there should also be hot, upwelling limbs rising from deep in the mantle. There are a variety of geological observations that favor dominantly passive mid-ocean ridges, such as the relatively uniform thickness and composition of the oceanic crust, and seismological studies have clearly shown that there is no deep, low-velocity root beneath typical spreading centers corresponding to a hot, upwelling limb.

The anomalous seismic velocity structure beneath typical mid-ocean ridges appears to extend no deeper than about 200 km, except perhaps in the vicinity of a hot spot like Iceland. There are several lines of evidence. The thickness of the transition zone between the 410 and 660 km-depth discontinuities is one indicator of temperature of the upper mantle, because the two discontinuities are governed by phase changes with Clapeyron slopes of opposite sign. Global maps of the topography of these discontinuities based on precursors to SS resulting from underside reflections (SdS phases) show a correlation of greater transition-zone thickness with the location

of subduction zones, indicating colder temperatures in the vicinity of descending slabs, but there is no correlation of transition-zone thickness with mid-ocean ridges (Flanagan and Shearer, 1998; Shearer, 2000). A local study of P-to-SV conversions at these discontinuities beneath the East Pacific Rise (EPR) using receiver function analysis of data recorded on an array of ocean-bottom seismometers (OBSs) found that the time difference between the P410s and P660s conversions is almost exactly equal to the global average (Shen *et al.*, 1998), indicating that any thermal anomaly is confined to the upper mantle above the 410-km discontinuity. A model study of multiple S phases in the vicinity of the EPR also found no vertical displacement of either the 410- or 660-km discontinuities (Melbourne and Helmberger, 2002).

Global or regional tomographic studies based on variations in body-wave traveltimes sometimes show mid-ocean ridge structure extending down to depths of 300–400 km (Masters *et al.*, 2000), but, because ray paths in the upper mantle are relatively steep, there typically is a trade-off between amplitude of the anomaly and the depth extent. If velocity variations in the inversion of traveltimes to structure are damped to prevent unrealistic oscillations, the tendency is to force the model to smear large-amplitude, shallow anomalies beyond their actual depth extent. For the Mantle Electromagnetic and Tomography (MELT) Experiment crossing the EPR, a ‘squeezing’ test was performed in which model anomalies were progressively limited to shallower depths. The variation in quality of fit showed that anomalous structure extends to at least 200 km depth (Hammond and Toomey, 2003), but probably no deeper than 300 km (**Figure 1**). Global or regional tomographic models based on Rayleigh surface waves or surface and body waves combined (Nishimura and Forsyth, 1989; Masters *et al.*, 2000; Ekstrom, 2000; Ritzwoller *et al.*, 2004; Ritsema, 2005; Priestley and McKenzie, 2006; Maggi *et al.*, 2006a; Zhou *et al.*, 2006) find that anomalous structure in the vicinity of most ridges is confined to the uppermost 150–200 km of the mantle (**Figure 2**).

Global studies employing Love waves, which have relatively poor depth resolution in the mantle, sometimes report anomalies extending several hundred kilometers beneath spreading centers (Gung *et al.*, 2003; Gu *et al.*, 2005a; Zhou *et al.*, 2006), in contrast to tomographic images with Rayleigh waves, which have much better vertical resolution (**Figure 3**). Vertical smearing due to the poor Love-wave resolution could be responsible for the discrepancy, but synthetic tests suggest that the difference

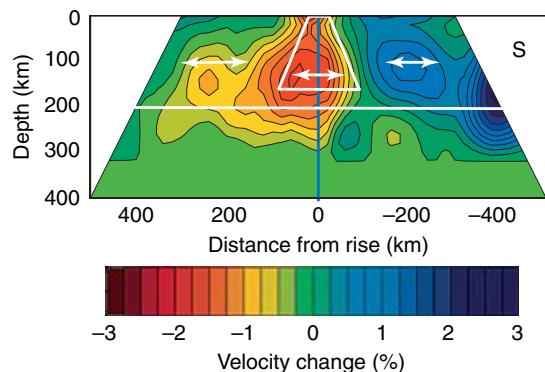


Figure 1 Shear-velocity anomalies beneath the East Pacific Rise based on body-wave tomography in the MELT Experiment using ocean-bottom seismometers. This particular image squeezes structure primarily into the upper 200 km. Arrows indicate preferred orientation of olivine *a*-axis within regions outlined by white lines. 400 km from the axis corresponds to seafloor approximately 6 My old. From Hammond WC and Toomey DR (2003) Seismic velocity anisotropy and heterogeneity beneath the mantle electromagnetic and tomography experiment (MELT) region of the East Pacific Rise from analysis of P and S body waves. *Journal of Geophysical Research* 108: 2176 doi:10.1029/2002JB001789. Copyright (2003) American Geophysical Union, reproduced by permission.

is real, indicating that polarization anisotropy reverses from the usual SH > SV in shallow oceanic mantle to SH < SV at depths greater than 200 km beneath mid-ocean ridges. (Love waves are sensitive to horizontally propagating, horizontally polarized S waves, or SH, while Rayleigh waves are sensitive to horizontally propagating, vertically polarized S waves, or SV.) Anisotropy in the oceanic mantle is thought to be caused primarily by the lattice-preferred orientation of olivine crystals; SH < SV may indicate vertical upwelling to depths on the order of 300 km (Gu *et al.*, 2005a; Zhou *et al.*, 2006), but the absence of an accompanying Rayleigh-wave anomaly or a deflection of the 410-km discontinuity indicates that the upwelling is probably passively induced with no accompanying thermal anomaly.

1.12.2 Form of Shallow Upwelling and Onset of Melting

Although the overall upwelling appears to be passively driven by plate motions, it is possible that when decompression melting begins due to the pressure dependence of the solidus, enough low-density melt is retained in the mantle matrix to create local buoyancy that could drive local, small-scale convection

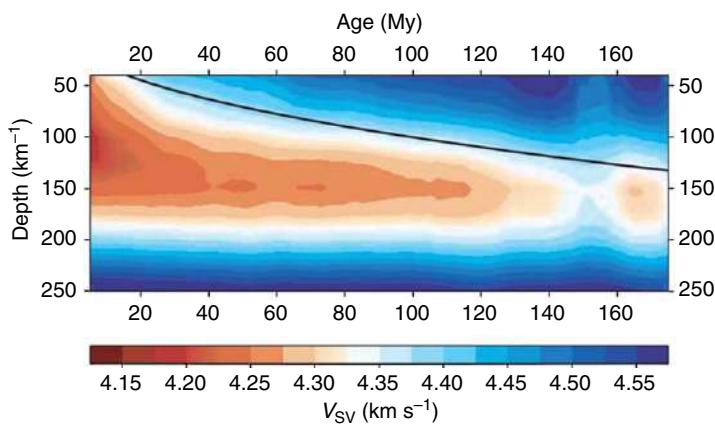


Figure 2 Average shear velocity in the upper mantle as a function of age of the seafloor in the Pacific, based on Rayleigh-wave tomography. This smoothed image was generated by averaging over 10- Ma sliding age windows. The black line indicates the base of the lithosphere predicted for a cooling half-space thermal model. From Maggi A, Debayle E, Priestley K, and Barruol G (2006a) Multimode surface waveform tomography of the Pacific Ocean: a closer look at the lithospheric cooling signature. *Geophysical Journal International* 166: 1384–1397.

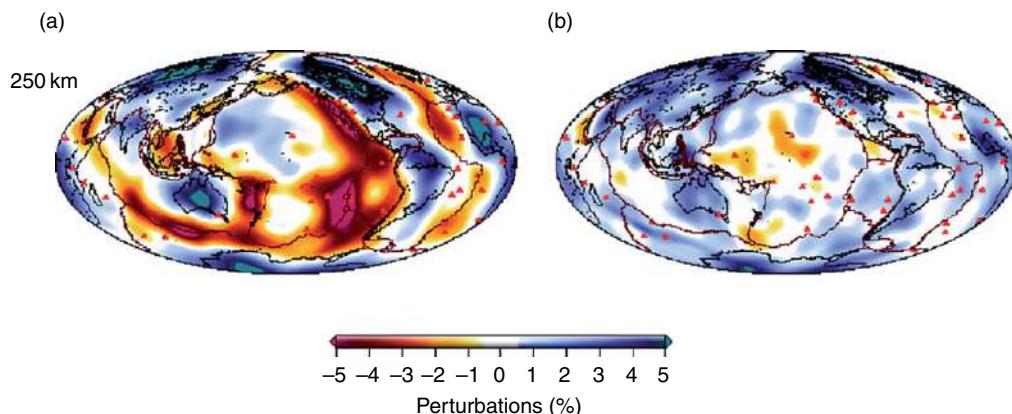


Figure 3 Shear-wave-velocity anomalies at a depth of 250 km from Love waves (a) and Rayleigh waves (b). Plate boundaries are indicated by brown lines, and hot spots by red triangles. Notice that there are low velocities along most of the mid-ocean ridges in the Love-wave image (SH velocity), but there are no such anomalies for Rayleigh waves at this depth. This discrepancy is either due to seismic anisotropy or greater vertical smearing of the SH velocity anomalies. From Zhou Y, Nolet G, Dahlen FA, and Laske G (2006) Global upper-mantle structure from finite-frequency surface-wave tomography. *Journal of Geophysical Research* 111: B04304 (doi:10.1029/2005JB003677). Copyright (2006) American Geophysical Union, reproduced by permission.

in the vicinity of the spreading center. Any reduction in effective viscosity due to melt retention could tend to enhance and concentrate upwelling into narrow sheets beneath the spreading center or into a three-dimensional (3-D) pattern of melt-rich diapirs. Concentration of upwelling into a narrow zone is one of the possible explanations that have been advanced to solve a major puzzle posed by the conclusion that overall upwelling is passive. The problem is that passive upwelling is expected to be broad, producing melt when the rising mantle ascends above the solidus over a region that may be 100 km or more across. Buoyancy

tends to drive melt vertically, yet seismic reflection profiles show that the crust is fully formed within 1–2 km of the ridge axis (Detrick *et al.*, 1987). Surveys of off-axis volcanism in the form of seamounts and lava flows indicate that more than 98% of the basaltic crust is formed at the ridge axis (Shen *et al.*, 1993). If melt production is not concentrated beneath the ridge axis by focused upwelling, then there must be some other mechanism to guide or force the melt produced in a broad region back to the ridge axis. Suggestions include nonvertical pressure gradients associated with deformation of a highly viscous

mantle, anisotropic permeability, and formation of sloping, melt-rich, high-permeability channels at the freezing front at the base of the lithosphere.

The MELT Experiment was designed to distinguish between models of broad and narrow upwelling beneath the fast-spreading EPR. Two linear arrays of OBSs were deployed across the spreading center for a period of 6 months, with instruments more closely spaced near the ridge axis. This part of the EPR is unusually linear, with no offset in the form of transform faults or overlapping spreading centers (OSCs) greater than 5 km over a distance along axis of several hundred kilometers. Regional and teleseismic earthquakes were recorded on three-component seismometers and differential pressure gauges sensitive to a broad range of frequencies. Both body- and surface-wave tomography revealed a broad region of low velocities, interpreted to be the region of melt production (**Figure 1**). There was no indication of the presence of the narrow zone of very low velocities that would be expected if enough melt was present to lower the viscosity and increase the buoyancy enough to concentrate upwelling into a narrow zone. It is possible that if the zone were narrow enough, it could have escaped attention, but the waveforms of teleseismic body waves passing directly through the shallow upper mantle beneath the ridge place strict limits on the possible product of the amplitude of the velocity anomaly and width of the low-velocity channel ([Hung et al., 2000](#)).

If the low velocities beneath the EPR indicate the presence of melt, then the bottom of the low-velocity zone should indicate the onset of melting at the solidus. The bottom is more difficult to define than the top because the resolution of surface waves decreases with increasing depth and the transition may be subtle if the initial melt fraction is very small. Beneath young seafloor (<10 Ma) near the EPR, the minimum shear velocity occurs at depths of 40–80 km ([Nishimura and Forsyth, 1989](#); [Gu et al., 2005b](#); [Weeraratne et al., 2007](#)). (Directly beneath the axis, the minimum may occur at shallower depths as melt migrates to the axis and vertical upwelling continues to near the base of the crust; [Dunn and Forsyth \(2003\)](#)). The velocity increases rapidly at depths below this minimum (**Figure 4**), but this velocity gradient decreases somewhere between 100 and 150 km. This change in gradient may correspond to the solidus.

One interpretation of these seismological observations that is consistent with experiments on the melting of peridotite and observations of electrical conductivity structure near the EPR ([Evans et al.,](#)

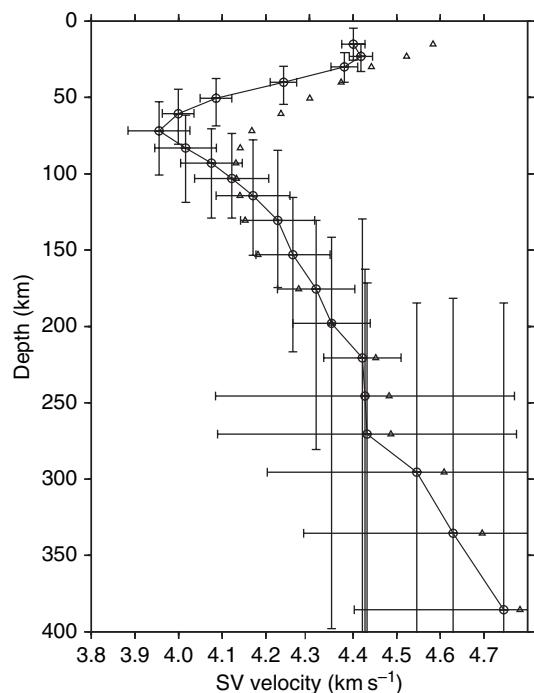


Figure 4 Vertical SV velocity profile beneath young seafloor (average age \sim 5 Ma) from Rayleigh wave inversion of data from a local ocean-bottom seismometer array near the East Pacific Rise. Horizontal error bars represent plus or minus two standard deviations over resolvable depth range indicated by the vertical error bars. Note the pronounced low-velocity zone with minimum at about 70 km and change in gradient in the vicinity of 125 km. Small triangles represent a model based on teleseismic data ([Nishimura and Forsyth, 1989](#)). From Weeraratne DS, Forsyth DW, Yang Y, and Webb SC (2007) Rayleigh wave tomography of the upper mantle beneath intraplate seamount chains in the south Pacific. *Journal of Geophysical Research* 112 (doi: 10.1029/2006JB004403). Copyright (2007) American Geophysical Union, reproduced by permission.

[2005](#)) is that melting begins in the upwelling mantle in the presence of a small amount of water dissolved in the solid crystals at depths of 100–150 km. The melt concentration gradually increases upward as melting proceeds above the damp solidus, but melt concentration and total degree of melting remain small below the dry solidus. Water is an incompatible element and tends to concentrate in the melt, so as melting proceeds, the matrix dehydrates. Somewhere around 60–80 km, the rate of melting increases as the dry solidus is passed, but the additional melt migrates upward toward the ridge axis leaving only a small ($< \sim 1\%$) melt fraction and a dehydrated matrix behind. Water dissolved in crystals is expected to increase attenuation and lower seismic velocity through the dispersive effects of attenuation, that is,

the anelastic effect (Karato and Jung, 1998). Minimum seismic velocities may be found where there is some melt fraction but dehydration is not yet complete, except perhaps in local areas where melt collects or migrates at higher concentration.

1.12.3 Flow in the Mantle

The mantle velocity structure beneath the EPR observed in the MELT Experiment is surprisingly asymmetric. At depths of a few tens of kilometers, the slowest velocities are west of the axis (Hammond and Toomey, 2003; Forsyth *et al.*, 1998) and slower average velocities in the upper 60 km persist for hundreds of kilometers from the axis. Although crustal structure seems to be symmetric, short-period Love waves (3–15 s) indicate that the asymmetry begins just beneath the Moho (Dunn and Forsyth, 2003). On the eastern, Nazca Plate side of the ridge, there are increases in velocity down to depths of 60 km or more within 50 km of the ridge axis – changes penetrating much deeper into the mantle than expected from conductive cooling of the plate alone (Conder *et al.*, 2002; Dunn and Forsyth, 2003). Accompanying the asymmetry in seismic velocities is an asymmetry in subsidence of the seafloor, with anomalously slow subsidence on the Pacific Plate side of the EPR (Cochran, 1986; Scheirer *et al.*, 1998). This pattern indicates that there is asthenospheric flow in toward the ridge beneath the Pacific Plate, accompanied perhaps by flow across the axis that is deflected downward beneath the thickening Nazca Plate, rapidly eliminating any melt fraction in the residual mantle to the east of the ridge (Toomey *et al.*, 2002; Conder *et al.*, 2002). Flow from the Pacific side is thought to be anomalously warm and perhaps anomalously enriched and may arise from the Superswell region thousands of kilometers to the west.

Seismic anisotropy offers other clues to the form of mantle flow beneath mid-ocean ridges. Surface-wave tomography finds that the fast direction for propagation of Rayleigh waves is approximately in the spreading direction near mid-ocean ridges, as predicted for the deformation associated with upwelling and subsequent plate separation at spreading centers that aligns the olivine α -axis horizontally in a direction perpendicular to the ridge (Forsyth, 1975; Montagner and Tanimoto, 1991; Blackman and Kendall, 1997; Ritzwoller *et al.*, 2004; Maggi *et al.*, 2006b). As discussed above, recent global studies have reported that the sense of radial anisotropy reverses with increasing

depth, so that deeper than 200 km, SV is faster than SH, suggesting the dominance of vertical upwelling at depth. At shallower depths within the lithosphere and low-velocity zone, regional tomographic studies have reported a reduction in SH/SV anisotropy in young seafloor near the EPR, although SH is still faster than SV, and the MELT Experiment found that azimuthal anisotropy of short-period Rayleigh waves reaches a minimum at the ridge axis (Forsyth *et al.*, 1998), consistent with either a component of vertical upwelling or not yet established horizontal flow. The smallest shear-wave splitting delays were also found immediately adjacent to the axis in MELT, but the most pronounced pattern was an asymmetry across the ridge axis; the fast direction is roughly perpendicular to the ridge on both sides, but splitting delays are nearly twice as large on the Pacific Plate as on the Nazca Plate (Wolfe and Solomon, 1998). This asymmetry may be another indicator of asymmetric asthenospheric flow toward the ridge, although Harmon *et al.* (2004) have shown that splitting times decrease in older Pacific seafloor to levels near that of the Nazca Plate. Hammond and Toomey (2003) found that there may be a region of tilted alignment responsible for some of the pattern of P and S delays near the ridge, but it is not clear that there is any region of dominantly vertical alignment of the olivine α -axis beneath the EPR at depths shallower than 200 km. Thus, the low-velocity zone may correspond to a low-viscosity asthenosphere dominated by horizontal flow and shear between the plates and underlying deeper mantle, even in the vicinity of a spreading center.

The site of the MELT Experiment was chosen to represent one end member of the family of mid-ocean ridges – a long, straight segment on the fastest-spreading mid-ocean ridge (there may be faster spreading in the northern Lau, back-arc basin). Theoretical studies indicate that upwelling is most likely to be in a 2-D sheet-like form at very fast spreading rates (Parmentier and Phipps Morgan, 1990). At slower spreading rates, buoyancy becomes progressively more important relative to viscous drag and upwelling is more likely to break up into a 3-D diapiric form. Even in the MELT area, there is evidence that upwelling and melt production is 3-D. Combining surface-wave data from MELT and the adjacent Gravity Lineations, Intraplate Melting, Petrologic, and Seismic Expedition (GLIMPSE) Experiment, Harmon *et al.* (2006) report that between 18° S and the Garrett Fracture Zone at 13° S, there are two pronounced minima in shear-wave velocity along the EPR: one just south of the Garrett where the Sojourn

and Brown intraplate ridge and seamount system intersects the spreading center and the other at about 17° S near the beginning of the Rano Rahi seamount field. The low-velocity anomalies presumably indicate higher temperatures and/or higher melt concentrations. In between, the seafloor is slightly deeper and there is an OSC. As discussed below in the section on crustal structure at fast-spreading ridges, an OSC could indicate two separate sources of magma. The association of these two axial minima in seismic velocities with the formation of off-axis seamounts and a geochemical anomaly at 17° S suggests that the 3-D character is controlled by the influx of anomalous mantle to the ridge rather than an inherent instability that leads to breakdown of a 2-D upwelling pattern. Experiments designed explicitly to study the along-axis variation are needed to better understand the nature and cause of the three-dimensionality.

Three-dimensionality is also observed in the mantle on the fast-spreading, northern EPR in the 9° N segment between the Clipperton and Siqueiros Fracture Zones (spreading rate ~105 versus ~140 mm yr⁻¹ in the MELT area). Active-source refraction experiments have mapped along-axis variations in P-wave velocity just below the Moho, with quasi-periodic regions of low velocity spaced an average of about 25 km apart (Dunn *et al.*, 2000, 2001; Toomey *et al.*, 2007). There also is displacement of some of the low-velocity centers from the ridge axis itself, resembling to some extent the asymmetry in the MELT area. The inference is that these sub-Moho, low-velocity anomalies represent the tops of centers of upwelling, although without a passive experiment to map deeper structure, the depth extent is not known and it is possible that they are centers of melt migration and accumulation rather than centers of upwelling of the solid mantle. In either case, the magma plumbing system connecting the off-axis centers to the ridge axis has not been mapped. Most of what we know about the 3-D pattern of upwelling, melt production, and melt delivery is inferred from studying the final product, that is, lateral variations in structure and thickness of the oceanic crust accreted by the collection of melt at the earth's surface.

1.12.4 Crustal Accretion along Mid-Ocean Ridges

Our view of oceanic crust produced along mid-ocean ridges has evolved considerably over the past two decades, from an early view as a layer-cake structure

composed of a few seismic layers matching geologic units to a much richer and laterally more variable structure. Having now examined the seismic structure of the crust in a variety of settings around the globe, it is increasingly recognized that crustal structure varies with spreading rate, geodynamic setting, and time. Around the global ridge system, different sections emplace oceanic crust at rates that differ by more than a factor of 10. Heat fluxes through these different systems must also vary substantially, and it is this heat supply that determines the nature of the magmatic, tectonic, and hydrothermal processes that control the formation of oceanic crust. In addition, due to the interplay of these factors, the general complexity of crustal accretion increases as the spreading rate and heat supply decrease to zero.

1.12.4.1 General Seismic Structure of the Oceanic Crust

Low velocities (<5 km s⁻¹ P-wave velocity), high seismic attenuation, and a strong velocity gradient at its lower boundary which can be imaged with seismic reflection techniques, characterize the upper few hundred meters of the oceanic crust (e.g., Harding *et al.*, 1993; Vera and Diebold, 1994; Christeson *et al.*, 1994a, 1994b, 1996, Wilcock *et al.*, 1995; Detrick *et al.*, 1998). An early interpretation of this seismic region ('layer 2A') in terms of a lithology composed of high-porosity extrusive basalts was based on analogy with ophiolite units, the seismic velocity of laboratory samples of dredged and drilled rocks, and *in situ* measurements in drill holes (see Solomon and Toomey (1992) for a review of early work). By further analogy to ophiolites, seismic layer 2A gives way to a higher-velocity region of sheeted dikes (layer 2B), followed by yet a higher-velocity region of gabbros (layer 3). Much recent work has both modified and disputed this simple layer-cake model. At the axis of fast- and intermediate-spreading ridges, seismic layer 2A is consistently thin, but thickens rapidly within a few kilometers of the ridges, presumably due to a the rapid buildup of the extrusive basalts near the ridge axis (e.g., Harding *et al.*, 1993), perhaps by off-axis transport of lava flows down the slope of the axial high (e.g., Hooft *et al.*, 1996) with some contribution from eruptions outside of the axial summit trough (e.g., Stakes *et al.*, 2005). Further away from the ridge, it is globally observed that layer 2A velocities increase with crustal age (**Figure 5**), an observation that is consistent with replacement of water in rock pores with the

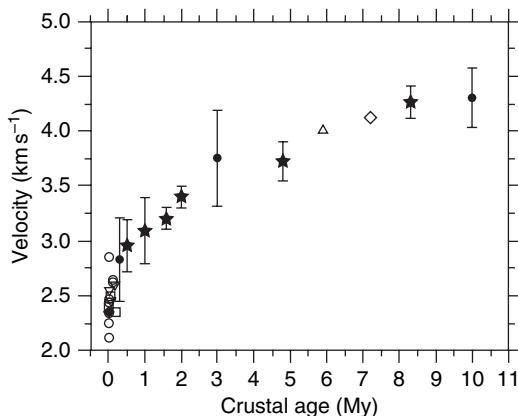


Figure 5 Upper crustal (layer 2A) velocity as a function of crustal age. Changes in physical properties of the upper crust appear to occur in two stages, rapidly at young ages, and more slowly thereafter, and are believed to be the result of seawater–rock reactions. In general, high temperatures, large permeability (and water–rock ratio), and high availability of alteration minerals result in faster and greater extents of alteration; far from the ridge where temperatures are low and the products of the reactions have plugged much of the available pore space, the rate of change of upper crustal velocities decreases. From Grevemeyer I., Kaul N., Villinger H., and Weigel W. (1999) Hydrothermal activity and the evolution of the seismic properties of upper oceanic crust. *Journal of Geophysical Research* 104(B3): 5069–5079. Copyright (1999) American Geophysical Union, modified by permission.

by-products of hydrothermal deposition (e.g., Grevemeyer and Weigel, 1996; Grevemeyer *et al.*, 1999). The precise nature of the 2A/2B boundary is still debated, and some have questioned whether the 2A reflector can be used to map the lithologic boundary between extrusives and underlying dikes (e.g., Christeson *et al.*, 2007). Recent papers on upper crustal structure at drill hole 504B near the Costa Rica Rift (Swift *et al.*, 1998a, 1998b) have also strongly called into question the nature of the layer 2/3 boundary. In this work, the 2/3 boundary coincides with a significant decrease in bulk porosity and marks the base of the lithologic transition from extrusive rocks and intermingled dikes to mainly dikes. Thus seismic layer 3 contains both dikes and gabbros. Since many studies show that seismic structure mainly reflects porosity and not necessarily lithology, most seismologists remain cautious about directly correlating seismic structure with lithologic units.

Faults, fissures, and fractures pervade the shallow oceanic crust. The orientation of these features is sensitive to the local stress field such that they tend to align perpendicular to the minimum compressive

stress. Overall, this alignment is generally parallel to mid-ocean ridges. Aligned cracks are detectable by their seismic anisotropy signature. Shear-wave splitting and polarization measurements (e.g., Stephen, 1981, 1985; Barclay and Toomey, 2003) and azimuthal variations in traveltimes (e.g., White and Whitmarsh, 1984; Shearer and Orcutt, 1985; Little and Stephen, 1985; Menke *et al.*, 1994; Barclay *et al.*, 1998; Sohn *et al.*, 1997; Dunn and Toomey, 2001; Dunn *et al.*, 2005), have been used to detect the presence of this anisotropy in a variety of oceanic settings. In general, P-wave traveltimes exhibit a $\cos(2\theta)$ variation, where θ is the ray azimuth. A 2θ pattern indicates that the traveltime signal is dominated by water-saturated vertical cracks with aspect ratios >0.01 (Hudson, 1981). Two recent studies (Tong *et al.*, 2004, 2005) have examined both 2θ and 4θ patterns in traveltimes residuals (crack aspect ratios <0.01 give rise to a dominant cosine(4θ) signal (Hudson, 1981)) and used the ratio of the amplitudes of these signals to examine local variations in subsurface crack structures. The best-resolved seismic studies detect around 4% anisotropy in the upper 2–4 km of crust (e.g., Sohn *et al.*, 1997; Barclay *et al.*, 1998; Dunn and Toomey, 2001; Tong *et al.*, 2004; Dunn *et al.*, 2005). Using Hudson's crack theory (1981) and 4% anisotropy, aligned cracks with aspect ratios of 0.01–0.1 give rise to porosities of $\leq 1\%$, a value much less than the total expected porosity based on the reduction of the isotropic velocities alone ($>10\%$) (Dunn and Toomey, 2001). The small proportion of aligned cracks relative to all cracks and pores suggests that fluids within seismically detectable aligned cracks do not contain the bulk of the volume of hydrothermal fluids in the shallow crust (Dunn and Toomey, 2001). However, because the permeability of rock with aligned cracks can be several orders of magnitude larger than rock without aligned cracks (De Wiest, 1965; Fisher, 1998), such cracks may provide the dominant pathways for the hydrothermal circulation that chemically alters the oceanic crust and cools the lithosphere.

The middle to lower crust is characterized by low velocity gradients, a general absence of seismic reflectors, and seismic velocities in the 6–7 km s^{-1} range (e.g., Spudich and Orcutt, 1980; Vera *et al.*, 1990; van Avendonk *et al.*, 2001; Canales *et al.*, 1998; Canales *et al.*, 2003; Dunn *et al.*, 2005). Because of the gentle velocity gradients, little seismic energy turns at these depths, making this a difficult region to study in detail. Seismic reflections from the Moho can be used to study this region, but for seismic experiments with low data coverage, or mainly vertically incident

energy, there can be a large trade-off between lower crustal velocities and Moho depth (e.g., Ross, 1994).

Few studies have attempted to constrain the nature of the crust–mantle transition or ‘Moho’. Along fast-spreading ridges the Moho produces vertically incident (e.g., Detrick *et al.*, 1987) and strong wide-angle seismic reflections (e.g., Vera *et al.*, 1990; Canales *et al.*, 2003) and appears to be a relatively sharp transition region (≤ 1 km) from crustal to mantle velocities (e.g., Vera *et al.*, 1990). Along slow-spreading ridges the Moho is less well defined and often absent in vertical-incident data; wide-angle data reveal both regions of sharp transition and regions of gradual transition (Canales *et al.*, 2000a, 2000b; Hooft *et al.*, 2000; Hosford *et al.*, 2001; Dunn *et al.*, 2005).

Oceanic crustal thickness was once thought of as being relatively uniform throughout the oceans with an average thickness of about 6–7 km. However, a new view has emerged in which only fast-spreading ridges produce a relatively uniform thickness crust. Slow-spreading ridges, on the other hand, produce a wide range of crustal thicknesses, but may still exhibit an average seismic thickness of ~ 6 km when averaged over tens of kilometers. Occasionally, no crust is produced, such as near cold fracture zones or as magmatism waxes and wanes at the spreading center. At spreading rates less than 2 cm yr^{-1} ('ultra-slow-spreading'), crustal thickness drops off sharply to such an extent that no crust may be produced for long periods of spreading, as documented by seafloor samples of mantle rocks (e.g., Michael *et al.*, 2003). To date, few seismic studies have documented crustal thickness at the slowest spreading rates and thus any relation between crustal thickness and spreading rate is still approximate at best. Furthermore, because serpentinized mantle exhibits crustal velocities, crustal thickness estimates derived from seismic experiments in slow-spreading environments remain controversial.

1.12.4.2 Fast-to-Superfast-Spreading Ridge Crustal Structure

Our knowledge of the distribution of magma in the crustal magmatic systems beneath fast-spreading ridges derives mainly from seismic experiments. In particular, seismic studies of the 9°N section of the EPR have determined details of the structure of the magmatic system from sub-seafloor to the mantle and have documented variations in the magmatic system along the ridge at most depths.

While the mantle low-velocity zone that characterizes the upwelling zone is tens of kilometers wide, near the Moho the low-velocity zone narrows abruptly to only 7–8 km wide in the lower crust (Dunn *et al.*, 2000). Tomographic studies of the magmatic system detect a narrow low-velocity zone from the base of the crust up to within ~ 1.5 km of the seafloor (Figure 6). At the top, the low-velocity zone is about 50% as wide as near the base. Similarly, models of S-wave velocity obtained from seafloor compliance measurements on the EPR (Crawford and Webb, 2002) indicate that the axial partial melt zone is less than 8 km wide throughout the crust (Figure 7). Since the inferred isotherms for this seismic structure do not conform to the predictions of a conductively cooled system, the implication is that hydrothermal circulation penetrates deeply off-axis to cool the lower crust and thus keeps the magmatic system narrow throughout the crust (Dunn *et al.*, 2000; Charkaoui *et al.*, 2003). Lower crustal hydrothermal circulation has also been suggested from studies of the Oman ophiolite which indicates that heat removal by high-temperature fluid circulation occurs to depths of 5–6 km (Gregory and Taylor, 1981; Nehlig and Juteau, 1982).

The low velocities (Dunn *et al.*, 2000) and high-attenuation values (Wilcock *et al.*, 1992, 1995) of the magmatic system are consistent with 10–40% melt in the middle to upper crust, 2–8% melt in the lower crust, and 3–12% melt near the Moho transition zone (Dunn *et al.*, 2000). The factor of four spread of each of these estimates is due to both a lack of shear-wave constraints on the velocity structure and a lack of laboratory studies on partially molten crustal rocks to determine their physical properties under *in situ* conditions at seismic frequencies. Within the middle to lower crust, the absolute magnitudes of the velocity and attenuation anomalies decrease with increasing depth (Toomey *et al.*, 1990; Vera *et al.*, 1990; Wilcock *et al.*, 1995; Dunn *et al.*, 2000) such that the lower crust is estimated to contain the least melt, both by melt fraction and by total volume, which may indicate that it is closer to its solidus than the other regions (Sinton and Detrick, 1992).

Multichannel seismic (MCS) reflection imaging shows that melt accumulates at the top of the magmatic system within a small melt lens (e.g., Detrick *et al.*, 1987; Mutter *et al.*, 1988; Kent *et al.*, 1993). This shallow melt lens is thought to form as buoyantly rising melt accumulates beneath a permeability or viscosity barrier at the top of the magmatic system (e.g., Hooft and Detrick, 1993). The depth of the lens

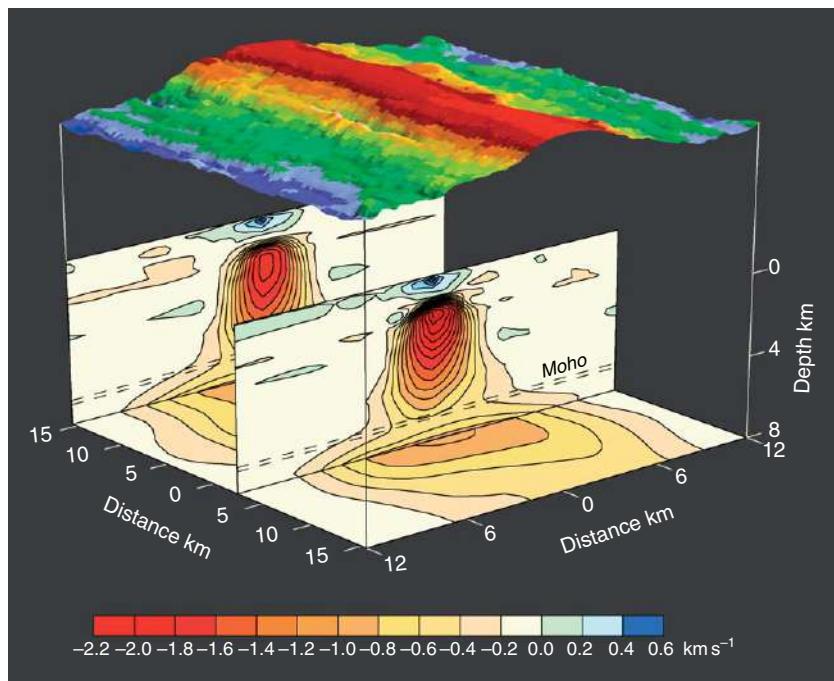


Figure 6 Three-dimensional perspective of the P-wave velocity structure of the East Pacific Rise at 9°30' N (relative to a one-dimensional depth-dependent model). The ridge magmatic system is characterized by a narrow low-velocity zone that extends from ~1.4 km depth down into the mantle. Near its top, the low-velocity zone is over 2 km s^{-1} slower than velocities away from the ridge axis. The axial melt lens reflector, as observed on MCS seismic data, passes through the low-velocity zone at 1.5 km depth. From Dunn RA, Toomey DR, and Solomon SC (2000) Three-dimensional seismic structure and physical properties of the crust and shallow mantle beneath the East Pacific Rise at 9 degrees 30' N. *Journal of Geophysical Research* 105(B10): 23537–23555. Copyright (2000) American Geophysical Union, reproduced by permission.

is then controlled by the trade-off between the rate of heat input from below versus the rate of heat extraction via hydrothermal circulation from above. Thus, the melt lens tends to deepen as the spreading rate, and heat and melt input from below, drops (Purdy *et al.*, 1992). The melt lens is usually narrow and thin (about 1 km wide and 10–50 m thick (e.g., Kent *et al.*, 1993) with high melt content, but its size varies by location and it can range from mostly crystalline to mostly molten (e.g., Harding *et al.*, 1989; Kent *et al.*, 1993; Singh *et al.*, 1998; Babcock *et al.*, 1998; Kent *et al.*, 2000). Along the southern EPR, waveform analysis of MCS reflection data from around the melt lens reveals a thin (~25 m thick) region above the lens of steep velocity gradients overlain by a thicker ‘lid’ (~70 m thick) of high velocities. This lid is interpreted as a solid region, devoid of melt or hydrothermal cracks, that acts as a conductive cooling regime between the low-velocity hydrothermal regime above, and the low-velocity melt lens below (Singh *et al.*, 1999). Along the northern EPR at 9°30'N, 1-D seismic models derived from expanding

spread profiles also detected a high-velocity lid capping steep gradients above the melt lens, but at ~250 m above the lens (Vera *et al.*, 1990). A 3-D tomography study in the same area (Toomey *et al.*, 1994), and another to the north (Tian *et al.*, 2000), show evidence for along-axis variations in the thermal structure above the melt lens correlated with small ridge discontinuities.

A few recent seismic and compliance studies indicate that magma sills accumulate near the crust–mantle transition zone or Moho (Garmany, 1989; Crawford *et al.*, 1999; Crawford and Webb, 2002; Nedimovic *et al.*, 2005), possibly within a broader region of low melt fraction. Melt migration should be rapid for melt fractions >1% (e.g., Kohlstedt, 1992), so observations of a substantial melt fraction at this depth indicates an impediment to upward flow. The density contrast at the Moho (Crawford *et al.*, 1999), formation of a permeability barrier due to crystallization in pore space at the base of the crust (Kelemen *et al.*, 1997; Korenaga and Kelemen, 1997), and changes in the stress conditions with depth and

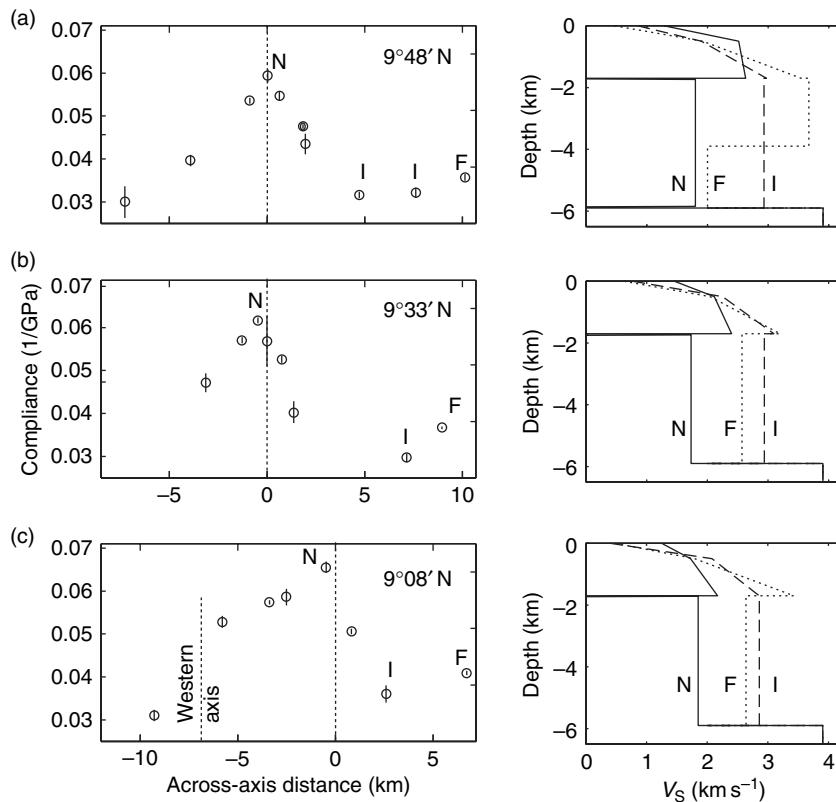


Figure 7 Compliance measurements along the East Pacific Rise (left column) and best-fit shear-wave velocity models for different distances from the ridge axis (right column). Figures (a)–(c) are for different positions along a section of the ridge (latitudes are indicated on the figure). Except near 9°08' N where the ridge steps across an overlapping spreading center, compliance falls off rapidly away from the ridge axis, providing further evidence that the crustal magmatic system is relatively narrow throughout most of the crust. Modified from Crawford WC and Webb SC (2002) Variations in the distribution of magma in the lower crust and at the Moho beneath the East Pacific Rise at 9 degrees–10 degrees N. *Earth and Planetary Science Letters* 203(1): 117–130. Copyright (2002) with permission from Elsevier.

time (Ildefonse *et al.*, 1993) have been suggested as possible barriers to melt migration. On the basis of ophiolite studies (e.g., Kelemen *et al.*, 1997), melt lenses have been predicted to occur in the lower crust as well, but to date there is no conclusive seismic evidence to support this prediction. Although the highest concentrations of melt are often thought to occur within the upper melt sill, the deep melt lenses also probably have high melt fractions (Garmany, 1989; Crawford *et al.*, 1999; Crawford *et al.*, 2002). Furthermore, a rough estimate of the total distribution of melt in the crust suggests that by volume there is more melt in the middle to lower crust and Moho regions than in the shallow melt lens, simply because of the greater cross-sectional areas of these regions.

While the upper crust is widely believed to be emplaced via repeated dike injections from the top of

the shallow melt lens, thus forming the sheeted dikes and the extrusive rock units, there is no general agreement on the formation of the lower crust. For over a decade, there have been several attempts to develop models of crustal accretion at fast-spreading ridges that explain the seismic results from the EPR and petrological and structural observations in the Oman ophiolite. This work has led to a variety of models for the formation of the lower crust that are defined by two end members. In the gabbro glacier or conveyor-belt models (Henstock *et al.*, 1993; Nicolas *et al.*, 1993; Nicolas *et al.*, 1988; Phipps Morgan and Chen, 1993a, 1993b; Phipps Morgan *et al.*, 2000; Quick and Denlinger, 1993) the gabbros crystallize in a small magma lens at the dike/gabbro boundary and then subside to form the lower crust. In the sheeted sill model (Boudier *et al.*, 1996; Kelemen and Aharonov, 1998; Kelemen *et al.*, 1997; MacLeod

and Yaouancq, 2000), magma is fed through a series of thin sills at varying depths between the Moho and the dike/gabbro boundary and the lower crust crystallizes *in situ*. Hybrid models combine varying proportions of gabbro flow and sill emplacement and/or include crystallization in a pair of magma lenses located at the dike/gabbro boundary and the Moho (Boudier *et al.*, 1996; Chen, 2001; Chenevez *et al.*, 1998). Several arguments have been made both for and against each of the above models (see Cherkaoui *et al.*, 2003 for a brief review). While the debate continues, the presence of melt in the lower crust and Moho transition zone, new evidence from ophiolite studies, and the seismic evidence for rapid cooling of the sides of the magmatic system indicate that at least some portion of the lower crust crystallizes *in situ*.

Along the EPR, the rise axis is segmented on a variety of scales. The deepest portions of the rise are located near tectonic offsets, such as fracture zones and OSCs (e.g., Macdonald *et al.*, 1988). Between these offsets, the EPR is segmented by minor morphologic deviations from axial linearity (or devals; Langmuir *et al.*, 1986) at intervals of 5–25 km. The origin of this segmentation is controversial. By one view, along-axis differences in ridge-crest processes result directly from 3-D mantle upwelling. Alternatively, some types of segmentation may be regulated by the tectonic rifting of young lithosphere, and thus only indirectly linked to the form of mantle upwelling.

Central to the controversy over the origin of ridge segmentation is the question of the origins of OSCs. OSCs are segment boundaries characterized by the overlap of two *en echelon* ridge segments that offset the axial neovolcanic zone by 0.5–15 km. Unlike transform offsets, which are stationary with respect to the ridge, OSCs migrate along axis and, in doing so, individual limbs may propagate or recede (Macdonald *et al.*, 1988; Carbotte and Macdonald, 1992, 1994). The structural evolution of OSCs has led some to speculate that their origin is the result of fluctuations in axial magmatic processes (e.g., Macdonald *et al.*, 1984, 1988, 1991). By this view, OSCs occur above regions of reduced magma supply, perhaps at the boundary between two widely separated regions of mantle upwelling (Schouten *et al.*, 1985), such that each limb has a separate source of mantle-derived magma. In contrast, an opposing model states that OSCs are the result of tectonic processes, a response to changes in regional strain such as those arising from changes in the kinematics of spreading (Lonsdale, 1983, 1986, 1989; Macdonald

et al., 1984). In this hypothesis, mantle upwelling is approximately 2-D or sheet-like, and the magma supply beneath the OSC is uninterrupted. Thus, the limbs of an OSC share a common source of magma (Lonsdale, 1983). The observation that most OSCs on the Pacific–Cocos Plate boundary share a right-lateral offset suggests that the offsets formed in response to a recent anticlockwise change in the direction of spreading (Carbotte and Macdonald, 1992, 1994), such that new forces on the plate boundary that arose during changes in the spreading direction lead to the formation of the OSCs.

Recent seismic results have directly called into question the idea that OSCs correlate with regions of low melt supply. A 3-D MCS and refraction survey of an OSC at 9°03' N on the EPR indicates that melts that feed the limbs of the OSC rise up directly from the mantle beneath the OSC itself (Kent *et al.*, 2000). Furthermore, an active-source tomographic study of the mantle beneath the 9°03' N OSC (Dunn *et al.*, 2001) did not find a reduction in the size or magnitude of the mantle low-velocity zone beneath the OSC as compared to other areas beneath the EPR. These results indicate that an axially continuous region of melt resides in the lower crust and mantle beneath the rise. Thus it can be inferred that the 9°03' N OSC is not associated with a discontinuity in melt supply from the underlying mantle, that both limbs of the OSC share a common mantle-level source of melt, and that the thermal structure of the ridge is continuous beneath the OSC. In addition, a recent active-source tomographic study of the upper mantle along the entire 200-km-long section of the EPR that includes the 9°03' N OSC found that the mantle low-velocity zone is significantly rotated with respect to the rise axis and exhibits a lateral shift or jog just north of the OSC (Toomey *et al.*, 2007). Azimuthal anisotropy of P-wave traveltimes reveals a crystallographic alignment of olivine fast axes that is also rotated with respect to the rise axis. By inference, mantle flow is rotated ~10° anticlockwise of the plate-spreading direction. This study concludes that rotation of asthenospheric upwelling governs the tectonic segmentation of the EPR.

On a smaller scale, individual deval-bounded segments of the EPR are thought to be associated with separate hydrothermal and shallow volcanic systems (Haymon *et al.*, 1991), petrologically distinct lavas (Langmuir *et al.*, 1986), short-wavelength variations in axial gravity and magnetization anomalies (Lee, 1995; Lee *et al.*, 1996), and higher proportions of melt in the crustal and upper-mantle magmatic system

(Toomey *et al.*, 1990, 1994; Dunn and Toomey, 1997; Dunn *et al.*, 2000). In some instances, the seismic reflector that defines the crustal melt lens also changes in character near devals (e.g., Kent *et al.*, 1993). Several seismic tomographic studies of the EPR (Toomey *et al.*, 1990; Dunn and Toomey, 1997; Dunn *et al.*, 2000; Dunn *et al.*, 2001; Toomey *et al.*, 2007) reveal that both the crustal low-velocity region and the mantle low-velocity region vary along the rise on a scale comparable to the deval segmentation, with lower velocities generally located at the centers of each segment (**Figure 8**). These studies suggest that the mantle midway between devals delivers greater amounts of melt to the rise, such that crustal magma chambers are replenished from

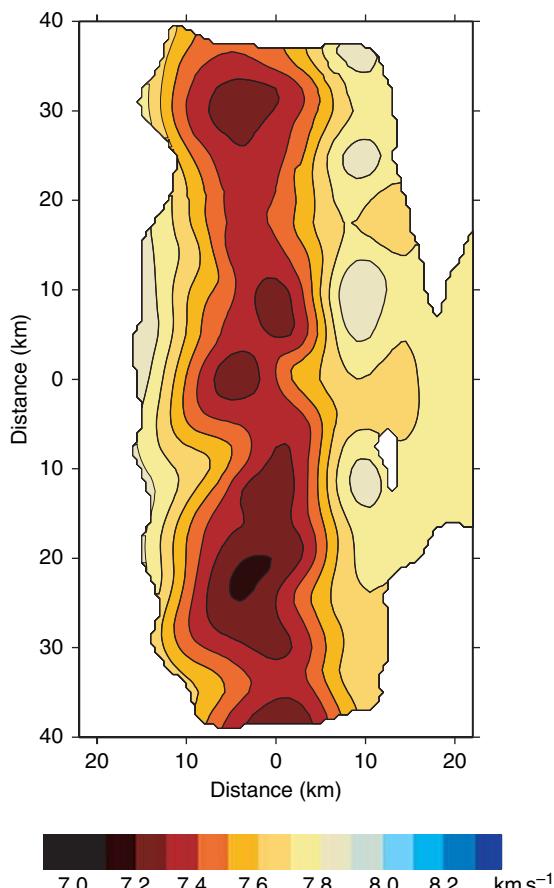


Figure 8 P-wave tomographic image of the mantle low-velocity zone along the 9° N section of the East Pacific Rise. The subaxial low-velocity zone indicates the pattern of melt delivery to the crust. Variations in the low-velocity zone suggest short-term along-axis variability in the magma supply to the ridge crest. Modified from Dunn RA, Toomey DR, Detrick RS, and Wilcock WSD (2001) Continuous mantle melt supply beneath an overlapping spreading center on the East Pacific Rise. *Science* 291(5510): 1955–195.

the mantle at closely spaced intervals along the rise. In general, the mantle melt supply may be locally enhanced by mantle temperature variations (Thompson, 1987), source heterogeneity (Langmuir *et al.*, 1986; Pickering-Witter and Johnston, 2000), 3-D melt segregation and transport mechanisms, such as the coalescence of small-scale melt segregations, veins, dikes, or dissolution channels (e.g., Sleep, 1988; Nicolas, 1989; Stevenson, 1989; Kelemen *et al.*, 1995), or diapirism (Whitehead *et al.*, 1984; Nicolas *et al.*, 1994). Structural mapping of ophiolites has detected mantle diaps (Nicolas and Violette, 1982; Ceuleneer and Nicolas, 1985; Nicolas and Boudier, 1995; Jousselin *et al.*, 1998). The characteristic radius of the largest diaps is generally small, about 3 km (defined by the region of inferred vertical flow), and such features have been mapped at intervals of a few tens of kilometers along the paleoridge axis; some are spaced as close as 10 km (Boudier *et al.*, 1997). Given the similarity in scale between the low-velocity, melt-rich regions detected beneath the EPR and the dimensions and spacing of ophiolite diaps, it is worth considering whether diapiric flow exists beneath the EPR. However, the scale of the diapiric flow is expected to be smaller than current seismic experiments are capable of resolving (Jousselin *et al.*, 2003), and no direct evidence for diapiric mantle flow has yet been detected via seismic anisotropy.

1.12.4.3 Intermediate Spreading Rate Ridge Crustal Structure

In an ongoing debate over the steady versus non-steady state nature of crustal formation, several studies have put forth the hypothesis that intermediate-spreading ridges evolve through cycles of magmatic versus tectonic spreading (Kappel and Ryan, 1986; Kappel and Normark, 1987; Smith *et al.*, 1994; Perfit and Chadwick, 1998). It has been suggested that the key influence on whether the ridge axis is in a state of magmatic versus tectonic spreading is the presence or lack of a crustal magmatic system, which would obviously influence the magmatic supply and the strength of the crust (e.g., Perfit and Chadwick, 1998). A modeling study by Phipps Morgan and Chen (1993a, 1993b) suggested that intermediate-spreading ridges are in a delicate, dynamic balance between supporting a crustal magmatic chamber or not. Recently, a series of studies of the Juan de Fuca Ridge (JdFR) has shed new light on this issue. Contrary to expectations, MCS data revealed shallow axial melt lenses beneath all JdFR

segments including those previously assumed to be in a tectonic phase (Canales *et al.*, 2005, 2006; Carbotte *et al.* 2006; Van Ark *et al.*, 2007). Instead of the absence or presence of a shallow melt lens, each segment is associated with a distinct depth of the melt lens and the depth is closely associated with the presence

or absence of an axial summit graben. Thus it appears that magmatic rather than tectonic processes largely generate the axial relief (Carbotte *et al.*, 2006). The growth of layer 2A appears to be similar to that along faster-spreading ridges (Canales *et al.*, 2005) (**Figure 9**). However, differences in the growth

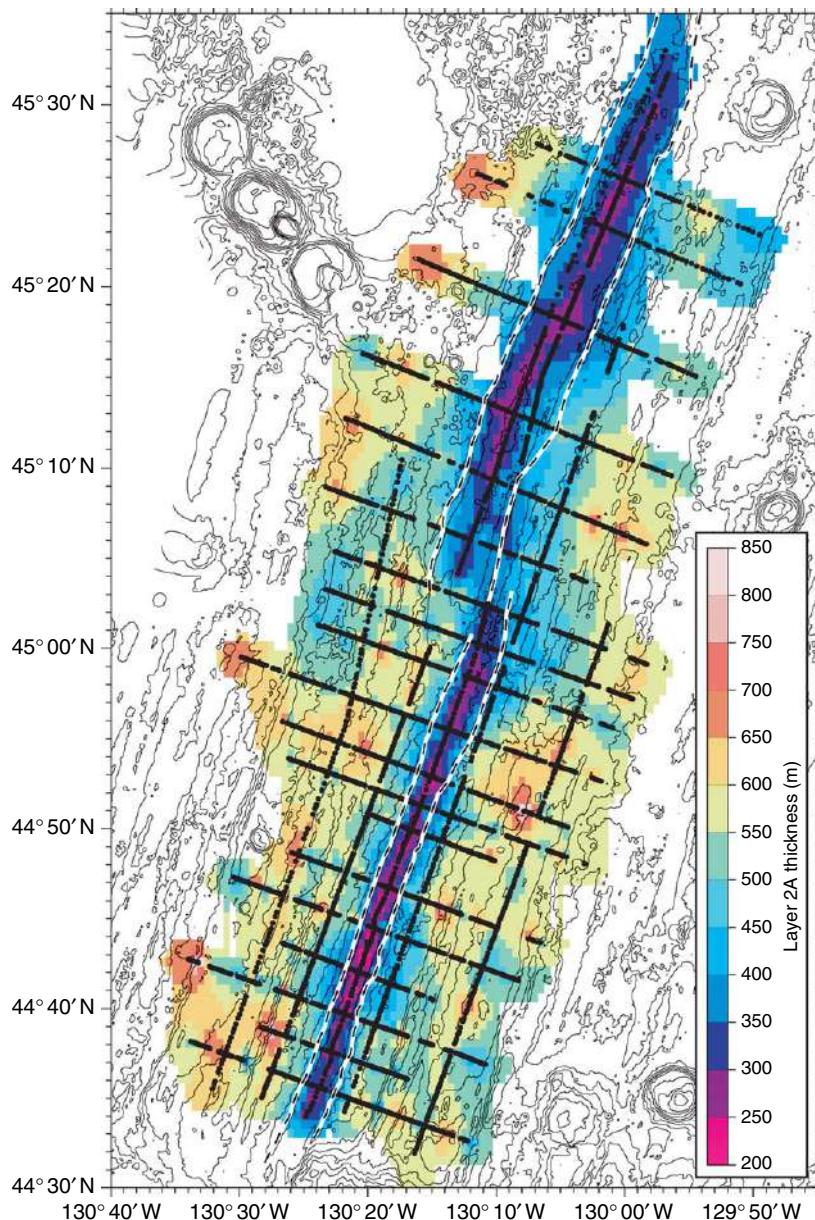


Figure 9 Map of seismic layer 2A thickness along the southern Juan de Fuca Ridge. Contours are bathymetry every 100 m. Dashed lines indicate the locations of the axial summit graben walls. Like fast-spreading ridges, layer 2A is thin on axis and thickens substantially within a short distance of the ridge axis. There is excellent correlation between the axial summit graben and the location of a thin seismic layer 2A (and by inference thin extrusives). Canales JP, Detrick, RS, and Carbotte SM *et al.*, (2005) Upper crustal structure and axial topography at intermediate-spreading ridges: Seismic constraints from the Southern Juan de Fuca Ridge. *Journal of Geophysical Research* 110: B12104 (doi:10.1029/2005JB003630). Copyright (2005) American Geophysical Union, reproduced by permission.

of layer 2A along the axes of the Cleft, Vance, and Endeavor segments of the JdFR at the ridge axis, also suggest somewhat different modes of extrusion and upper crustal formation. Processes of lava emplacement and distribution on the seafloor may be modulated by magma supply (Canales *et al.*, 2005).

The presence of a partially molten lens argues against prior hypotheses that hydrothermal heat extraction is driven by propagation of a cracking front down into a frozen magma chamber (Wilcock and Delaney, 1996). Instead, the hydrothermal systems, like those at the EPR, appear to be driven by heat extraction from a crustal magma body. Morphological and hydrothermal differences between the intermediate-spreading ridge and the fast-spreading EPR can be attributed to the greater depth of the JdFR melt lenses (2–3.3 km versus 0.5–1.5 km (Kent *et al.*, 1993)) and the correspondingly cooler, more brittle shallow crust overlying the lens (Van Ark *et al.*, 2007). Variations in the seismic properties of the melt lens, and by inference the melt/crystal ratio, correlate with lava chemistry (Smith *et al.*, 1994) and with the location of hydrothermal plumes (Baker, 1994), suggesting that high-temperature hydrothermal venting along intermediate-spreading ridges is closely linked to the physical state of the underlying melt lens (Canales *et al.*, 2006).

Strong reflections near the Moho transition zone have been found in JdFR MCS data, located both near the ridge axis (<20 km) as well as near the outer wakes of propagators on the ridge flanks (Nedimovic *et al.*, 2005). Groups of reflections found near the ridge axis could correspond to gabbroic melt lenses emplaced during magma delivery to the axis. Reflection events within the propagator wakes may be frozen melt sills injected at the base of the crust during ridge propagation. At the propagator tips, spreading breaks into relatively cool lithosphere that may enhance their emplacement and rapid solidification (Nedimovic *et al.*, 2005).

1.12.4.4 Slow-Spreading Ridge Crustal Structure

Along slow-spreading mid-ocean ridges the supply of melt from the mantle is widely viewed as spatially variable and time dependent (e.g., Lin and Phipps Morgan, 1992). Consequently, such variations in melt flux are believed to control crustal thickness, lithospheric strength, and the partitioning of plate spreading between faulting and magmatism (e.g.,

Cannat, 1993, 1996; Tucholke and Lin, 1994; Parsons *et al.*, 2000). For ridge segments bounded by tectonic offsets, the midsections tend to have the shallowest bathymetry and the thickest crust while the ends tend to exhibit deeper and wider axial valleys and thinner crust, as inferred from gravity data (Kuo and Forsyth, 1988; Lin *et al.*, 1990; Detrick *et al.*, 1995) and determined seismically (Sinha and Louden, 1983; Purdy and Detrick, 1986; Tolstoy *et al.*, 1993; Canales *et al.*, 2000a; Hooft *et al.*, 2000; Hosford *et al.*, 2001; Dunn *et al.*, 2005). Although these observations can be explained by several different mantle-flow and melt-flux scenarios, each one predicts that melt flux is focused in the mantle and preferentially delivered to a segment's center (e.g., Whitehead *et al.*, 1984; Kuo and Forsyth, 1988; Lin *et al.*, 1990; Sparks *et al.*, 1993; Rabinowicz *et al.*, 1993; Magde *et al.*, 1997). By this view, there should exist a 3-D thermal structure in the newly forming lithosphere; at the segment midpoint the lithosphere should be thinner, hotter, and weaker than at the segment ends. Seafloor spreading should be more magmatically accommodated near a segment's midsection and more tectonically accommodated at the ends (e.g., Cannat, 1993; Tucholke and Lin, 1994; Gràcia *et al.*, 1999; Rabain *et al.*, 2001). A major characteristic that sets slow-spreading ridges apart from fast-spreading ridges is the exposure at the seafloor of lower crustal and mantle-derived ultramafic rocks. Detachment surfaces, called megamullions, interpreted to be the footwalls of long-lived shallowly dipping normal faults (e.g., Canales *et al.*, 2004), are found at segment ends within the inside-corners of ridge-transform intersections and expose extensive sections of the crust and upper mantle at the seafloor. The great diversity of ridge segment morphologies and maximum depth of seismicity (Barclay *et al.*, 2001), a proxy for lithospheric thickness, indicate that temporal variations in melt supply modulate the magmatic–tectonic trade-off of crustal formation – the diversity from ridge segment to segment can be interpreted as reflecting various stages of a magmatic–tectonic evolution (e.g., Cannat, 1993; Gràcia *et al.*, 1999; Barclay *et al.*, 2001).

A limited number of seismic experiments have been performed along the crests of slow-spreading ridges. Except in regions affected by hot spots, these studies have largely failed to detect shallow seismic reflectors that may indicate the presence of shallow melt lenses. However, a 2-D refraction experiment located at 23°20' N (Canales *et al.*, 2000b), and 2-D (**Figure 10**) and 3-D tomography experiments at 35°N (**Figure 11**) (Hooft *et al.*, 2000; Dunn *et al.*,

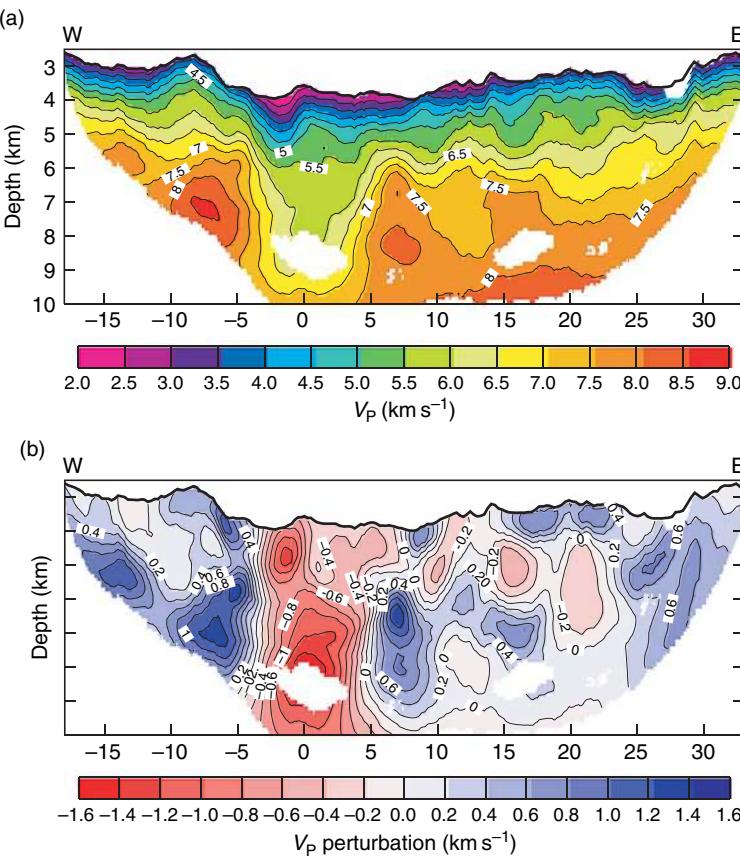


Figure 10 Two-dimensional tomographic images of the Mid-Atlantic Ridge near 23° N (MARK area). Plane of the images is perpendicular to the ridge axis. Anomalously low velocities beneath a neovolcanic ridge extend downwards from the middle crust and are consistent with high temperatures and 4% or more melt. Outside of this region the crust is seismically very heterogeneous, with crustal thickness variations of over 2.2 km over ~5 km distances. Such heterogeneity suggests that the melt supply fluctuates substantially over short time scales, creating periods of magmatic and amagmatic spreading. From Canales JP, Collins JA, Escartin J, and Detrick RS (2000b) Seismic structure across the rift valley of the Mid-Atlantic Ridge at 23°20'N (MARK area): Implications for crustal accretion processes at slow spreading ridges. *Journal of Geophysical Research* 105(B12): 28411–28425. Copyright (2000) American Geophysical Union, modified with permission.

2005) detected significant low-velocity zones in the middle-to-lower crust (extending downwards into the mantle) that are consistent with high temperatures and a small amount of melt. Seismic studies of sections of slow-spreading ridge near hot spots have found what appear to be significant crustal magmatic systems. Seismic surveys along the Reykjanes Ridge provide evidence for a shallow melt lens capping a larger low-velocity region in the crust (Sinha *et al.*, 1997; Navin *et al.*, 1998). Crustal structure along the Reykjanes Ridge appears to form in a manner roughly similar to fast-spreading ridges due to high melt supply and hotter mantle temperatures, despite its slow spreading rate. A recent seismic survey of the Mid-Atlantic Ridge (MAR) south of the Azores islands, located on the bathymetric swell of this hot spot, has also detected

a shallow crustal melt lens (Singh *et al.*, 2006). In this case a reflection from the top of the melt lens, centered beneath the Lucky Strike volcano and hydrothermal field, is approximately 3 km beneath the seafloor, 3–4 km wide (much wider than the average along the EPR), and extends up to 7 km along the ridge. The co-location of the melt lens and hydrothermal field indicate that the lens provides the heat for the active hydrothermal vent field above it. Also observed in the reflection sections are axial valley-bounding faults that seem to penetrate down to the magma chamber and a set of inward-dipping faults cutting through the volcanic edifice suggesting continuous interactions between tectonic and magmatic processes (Singh *et al.*, 2006). The deeper portions of this magmatic system have not yet been imaged.

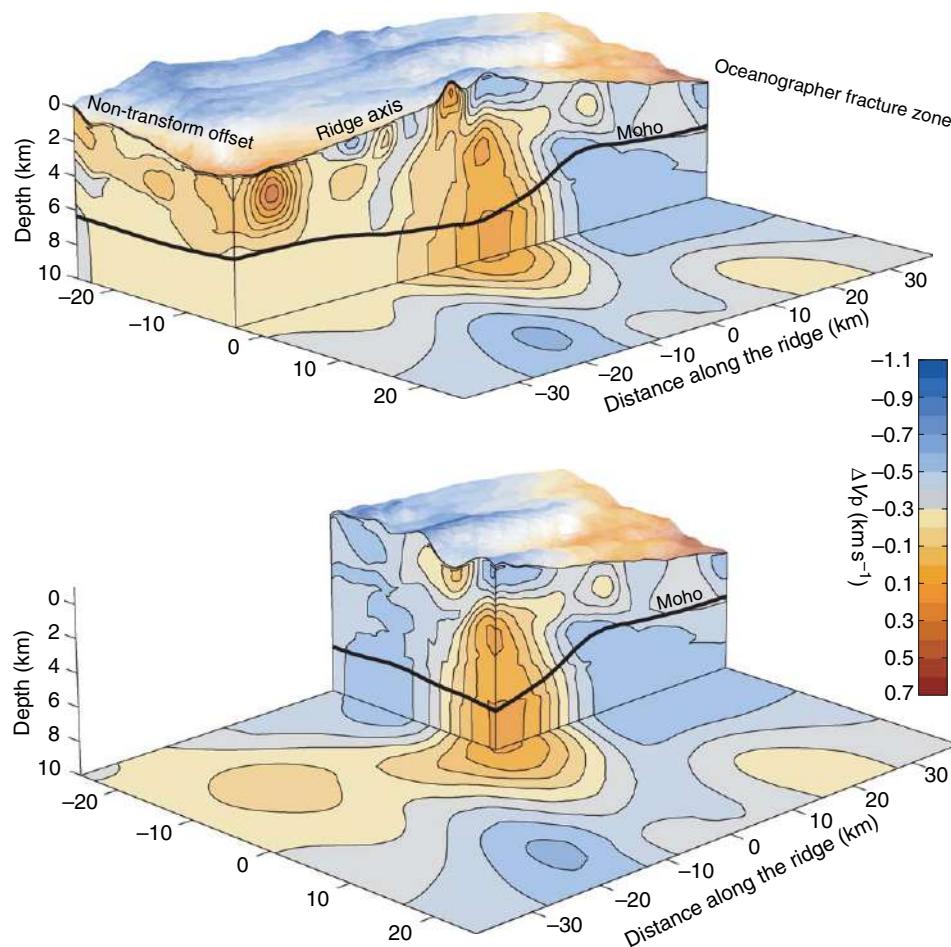


Figure 11 Three-dimensional perspective views of the P-wave velocity structure of the crust and uppermost mantle of Mid-Atlantic Ridge at 35° N (relative to a one-dimensional depth-dependent model). A low-velocity ‘stalk’ or ‘plug’ is observed in the lower crust and upper mantle at the center of the ridge segment, where the crust is also up to 8.5 km thick (versus <4–5 km thick near the Oceanographer Fracture Zone to the north and a non-transform offset to the south). The velocity anomaly is consistent with high temperatures and a few percent melt, and suggests that it represents the current magma plumbing system for this section of the ridge. Seismic anisotropy in the lower crust at the segment center indicates that the lower crustal anomaly is composed of partially molten dikes that have intruded from the mantle (see Dunn *et al.*, 2005 for details). An alternative explanation is that the anisotropy is due to cooling fractures that penetrate from above, downward into a hot region of crust. From Dunn RA, Lekic V, Detrick RS, and Toomey DR (2005) Three-dimensional seismic structure of the Mid-Atlantic Ridge (35° N): Evidence for focused melt supply and lower crustal dike injection. *Journal of Geophysical Research* 110(B9), doi:10.1029/2004JB003473. Copyright (2000) American Geophysical Union, reproduced with permission.

One seismically well-studied area of the MAR is the ~90-km-long segment of the MAR at 35° N latitude, just south of the Oceanographer Fracture Zone. Several lines of evidence indicate that more melt is currently delivered to the center of this ridge segment than its ends. For example, the hour-glass morphology of the rift valley and shallow water depth of the segment midpoint, an anomalously large mantle Bouguer gravity anomaly low centered on the segment, and the chain of seamounts that intersects the segment center have all been attributed to enhanced and focused

mantle upwelling and magmatism near the segment center (Detrick *et al.*, 1995; Thibaud *et al.*, 1998; Rabain *et al.*, 2001). Multiple seismic surveys of this area provide a fairly detailed view of the crustal structure, although we note that this section of ridge may be mildly influenced by the Azores hot spot to the north, and thus may exhibit slightly higher melt supply than for other non-hot-spot-influenced sections of the ridge.

Several observations indicate that the upper 3–4 km of crust along this segment are cool and brittle. A seismic low-velocity layer, seismic layer 2, is

observed throughout the top 1–2 km of the crust (Barclay *et al.*, 1998; Hooft *et al.*, 2000; Canales *et al.*, 2000a; Hosford *et al.*, 2001; Hussenroeder *et al.*, 2002; Dunn *et al.*, 2005) and is generally accepted to be the result of a high proportion of pores and cracks at these depths. An analysis of the ratio of P- to S-wave velocity in the shallow crust and the detection of seismic anisotropy, an indicator of widespread ridge-parallel extension cracks, reveals that the upper 2 km of crust is pervaded with cracks and is thus relatively cool and brittle (Barclay *et al.*, 2001; Barclay and Toomey, 2003; Dunn *et al.*, 2005). The increase in velocity and decrease in anisotropy with depth can be attributed to the reduction in crack/pore volume with depth, via a combination of closing of cracks and pores with increasing pressure and a decrease in the vesicularity of lithologic units (e.g., Swift *et al.*, 1998a). Micro-earthquakes recorded near the segment center indicate that the brittle–ductile transition is at 4 km or more depth below the seafloor (Barclay *et al.*, 2001).

The seismic structure of the upper crust is laterally variable and appears to reflect a variety of processes such as tectonic modification, volcanic variations, and crustal aging (Barclay *et al.*, 1998; Magde *et al.*, 2000; Hosford *et al.*, 2001; Hussenroeder *et al.*, 2002). In contrast to fast-spreading ridges where the axis of eruption is fairly narrow (\sim 1–2 km), formation of new crust appears to occur over the entire width of the axial valley (Barclay *et al.*, 1998). Small, scattered velocity anomalies and extensive low-velocity regions near the transform and non-transform offsets in the shallow crust (Dunn *et al.*, 2005) can arise from lateral variations in pores, cracks, alteration products, and the ratio of porous extrusive rocks to less-porous intrusive rocks, and likely reflect the nonuniform construction of the upper crust with time. At the segment ends, extensive low-velocity regions located both on- and off-axis are likely the result of a greater percentage of cracks due to greater tectonic stretching. In support of this interpretation, geologic mapping of the seafloor (Gràcia *et al.*, 1999) reveals greater densities of cracks and fissures at the segment ends than the segment center. Crust produced near the segment ends lacks the usually distinct transition from seismic layer 2 to 3 and the upper crustal low-velocity layer is anomalously thick and low in velocity as compared to that near the segment center (Sinha and Louden, 1983; Canales *et al.*, 2000a; Hosford *et al.*, 2001). Furthermore, the transition from crustal to mantle velocities appears to occur over a depth range of 3 km or more near the segment ends (Canales *et al.*, 2000a; Dunn *et al.*, 2005). These seismic observations

are consistent with a highly fractured and altered crust overlying a serpentinized upper mantle at the segment ends. This view is probably an over simplification, since serpentinites outcrop at the ends of some ridge segments (Gràcia *et al.*, 1997, 1999).

In general, upper crustal velocities are anomalously low in a broad axial band that parallels the ridge axis. Relatively low near-axis velocities with respect to higher off-axis velocities are a global phenomenon and widely interpreted to reflect a porous upper crust near the ridge axis that subsequently decreases in porosity, and hence increases in velocity, with crustal age due to infilling of cracks and pores via hydrothermal deposition (e.g., Houtz and Ewing, 1976; Purdy, 1987; Grevemeyer and Weigel, 1996). Although tomography experiments provide poor constraints on layer-2A velocities, the global average (Grevemeyer and Weigel, 1996) falls within the observed range of upper crustal velocities here. Thus, the ridge-perpendicular variation that is found in the shallow crust ($<0.75 \text{ km s}^{-1}$) can be largely explained by crustal aging.

At the center of the segment, a large low-velocity zone extends from about 4 km depth down into the mantle (Hooft *et al.*, 2000; Dunn *et al.*, 2005) (Figure 11). Assuming that the brittle–ductile transition is near 4 km depth, as indicated by the micro-earthquake study of Barclay *et al.* (2001), then the large low-velocity zone is most likely due to elevated temperatures and a small amount of melt ($\sim 3\%$) at depths >5 km. It is difficult to predict absolute temperatures or melt fractions due to a lack of baseline temperature information away from the ridge and a lack of experimental constraints on the relationship between these physical properties and seismic velocities. Given that the resolution of the seismic imaging is no better than ~ 3 – 4 km near the Moho, the melt could exist along grain boundary interfaces or within larger isolated regions with higher melt concentrations, which, when averaged together, make up the 3% melt fraction. For example, the lower crust could be composed of partially molten dikes and sills. Dunn *et al.* (2005) detected seismic anisotropy within the large low-velocity region and suggest that this anisotropy and the reduced isotropic velocities are due to vertical, partially molten, dikes in the lower crust (Figure 12).

Crustal thickness studies for this area (Canales *et al.*, 2000a; Hooft *et al.*, 2000; Hosford *et al.*, 2001; Dunn *et al.*, 2005) reveal 8.5 ± 0.5 -km-thick crust near the segment center and 4–5-km-thick crust to the north and south of center, with values as low as

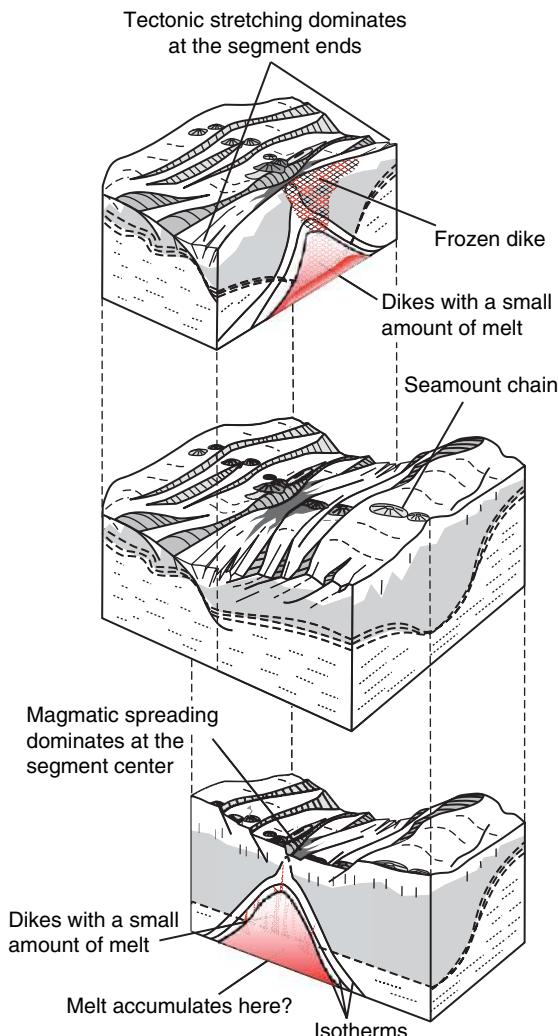


Figure 12 Interpretation of the magmatic and tectonic processes along the 35° N section of the Mid-Atlantic Ridge. Melts ascending from the mantle are focused at mantle depths to the ridge segment center and subsequently penetrate the brittle crust via a cluster of dikes. This process creates thicker crust and a thinner lithosphere at the segment center, and thinner (more tectonically modified) crust near the segment ends, at the transform and non-transform offsets. The relative uniformity of the thickness of the crust with distance from the ridge indicates that in this area the melt supply has been relatively uniform for some time. Modified from Dunn RA, Lekic V, Detrick RS, and Toomey DR (2005) Three-dimensional seismic structure of the Mid-Atlantic Ridge (35°N): Evidence for focused melt supply and lower crustal dike injection. *Journal of Geophysical Research* 110(B9), doi:10.1029/2004JB003473. Copyright (2005) American Geophysical Union, reproduced with permission.

3–4 km thickness (Hooft *et al.*, 2000) near the Oceanographer Fracture Zone. Ridge-perpendicular variations in crustal thickness are modest, $\leq \pm 0.5$ km

in this area, which stands in sharp contrast to the 23°20' N area on the MAR, where the transition from crustal to mantle velocities undulates up and down with distance from the ridge, as if the magma supply waxes and wanes significantly with time (Canales *et al.*, 2000b).

1.12.4.5 Ultraslow-Spreading Ridge Crustal Structure

Recent investigations of the Southwest Indian Ridge and ridges north of the Arctic Circle (Knipovich, Mohns, Gakkel Ridges) reveal an ultraslow-spreading class of ridges that is characterized by low degrees of volcanism. These ultraslow ridges form at spreading rates less than ~ 15 mm yr^{-1} (full rate), though their characteristics are commonly found at rates up to 20 mm yr^{-1} (Dick *et al.*, 2003). A critical issue is how the exceptionally slow spreading rate influences melt production and crustal thickness, lithospheric thickness, and tectonics, because these processes in turn influence faulting, volcanism, mid-ocean ridge basalt (MORB) geochemistry, hydrothermal venting, seafloor ecosystems, and many other ridge processes.

There is now a strong consensus that a correlation between spreading rate and degree of melting exists at spreading rates < 20 mm yr^{-1} (Brown and White, 1994; Niu and Hékinian, 1997; Robinson *et al.*, 2001; Shen and Forsyth, 1995; White *et al.*, 2001; Michael *et al.*, 2003). Samples taken from ultraslow ridges have incompatible element enrichments indicative of low degrees of melting (Klingelhöfer *et al.*, 2000; Robinson *et al.*, 2001; Michael *et al.*, 2003; Dick *et al.*, 2003). Furthermore, crustal thickness (as determined from seismic and gravity data) drops significantly as spreading rates drop below 20 mm yr^{-1} (Géli *et al.*, 1994; Kodaira *et al.*, 1997, 1998; Klingelhöfer *et al.*, 2000; Coakley and Cochran, 1998; Ritzmann *et al.*, 2002; Cochran *et al.*, 2003; Jokat *et al.*, 2003).

The leading hypothesis predicts that under very slow spreading conditions there is efficient, deep cooling of the upper mantle beneath the ridge. This cool region depresses the top of the melting region, thereby shutting off melting much deeper than along faster-spreading ridges (Reid and Jackson, 1981; Brown and White, 1994; Shen and Forsyth, 1995; Niu and Hékinian, 1997). In contrast to fast-spreading ridges where melting is predicted to continue up to near the base of the crust, numerical calculations (Reid and Jackson, 1981) predict that along ultraslow ridges melting shuts off at a depth of 40–50 km or more beneath the base of the crust. Although the ‘thick

'lithosphere' concept provides a useful working hypothesis, it is untested by actual measurements and it does not provide a unique interpretation of available data. The amount of melting as reflected by crustal thickness and enrichment of incompatible elements does not distinguish between control by conductive cooling or by other factors such as mantle temperature (Klein and Langmuir, 1989; Langmuir *et al.*, 1992) or composition (Robinson *et al.*, 2001). One alternative hypothesis is that melt production is not inhibited, but melt *transport* through the mantle is inhibited at shallow depths. A large proportion of the melt generated is simply frozen into the shallowest mantle (Cannat, 1996). In this hypothesis, the upper mantle is not cooled to any great depth and no deep shutoff point for melting exists, instead a thin but strong lithosphere at the uppermost part of the mantle restricts the passage of melt just beneath the ridge. Thus, crustal thickness does not represent the total amount of melting that occurs. Future seismic experiments along ultraslow-spreading ridges are required to advance our understanding of mantle and crustal dynamics along these ridges.

1.12.5 Remaining Unsolved Problems

One of the major questions raised by the teleseismic studies of regional or global structure is whether there is anisotropy associated with mid-ocean ridges extending to depths of 300 km or more, as suggested by the discrepancy between Love- and Rayleigh-wave images of the mantle. If this apparent anisotropy is real, it has profound implications for the pattern of overall flow in the oceanic mantle. The procedures and assumptions leading to this conclusion need to be carefully examined.

There are many questions remaining about the form of mantle upwelling at shallow levels and the mechanism of melt transport. The major problem is the lack of studies of the mantle at scales intermediate between global tomography and local, seismic reflection and refraction experiments. There have been many local studies that have documented the end product of melt delivery, that is, along-axis variations in thickness of the oceanic crust pointing to the 3-D nature of melt generation and/or melt delivery, but we still do not know to what extent these variations are caused by diapiric upwelling versus focused melt migration. We do not know to what extent the three-dimensionality of the mantle is

masked by along-axis transport of melt in the crust. There may also be masking of temporal and spatial variations in melt supply, particularly at slow-spreading ridges, caused by the difficulty in distinguishing between gabbro and serpentized peridotite. We need higher resolution, 3-D images at the ridge segment scale of both the crust and uppermost mantle to solve these basic questions about the process of forming the oceanic crust that covers two-thirds of the Earth's surface.

To achieve higher resolution, three things are needed: an expansion of the number of broadband OBSs; the ability to bury the ocean-bottom sensors to reduce noise level on horizontal components that are strongly affected by tilting of the instruments caused by ocean-bottom currents; and an increased number of long-term, regional deployments focused on oceanic mantle dynamics.

References

- Babcock JM, Harding AJ, Kent GM, and Orcutt JA (1998) An examination of along-axis variation of magma chamber width and crustal structure on the East Pacific Rise between 13° 30'N and 12° 20'N. *Journal of Geophysical Research* 103(B12): 30451–30467.
- Baker ET (1994) A 6-year time series of hydrothermal plumes over the Cleft segment of the Juan de Fuca Ridge. *Journal of Geophysical Research* 99(B3): 4889–4904.
- Barclay AH and Toomey DR (2003) Shear wave splitting and crustal anisotropy at the Mid-Atlantic Ridge, 35° N. *Journal of Geophysical Research* 108(B8): (doi:10.1029/2001JB000918).
- Barclay AH, Toomey DR, and Solomon SC (1998) Seismic structure and crustal magmatism at the Mid-Atlantic Ridge, 35° N. *Journal of Geophysical Research* 103(B8): 17827–17844.
- Barclay AH, Toomey DR, and Solomon SC (2001) Microearthquake characteristics and crustal Vp/Vs structure at the Mid-Atlantic Ridge. *Journal of Geophysical Research* 106(B2): 2017–2034.
- Blackman DK and Kendall J-M (1997) Sensitivity of teleseismic body waves to mineral texture and melt in the mantle beneath a mid-ocean ridge. *Philosophical Transactions of the Royal Society of London A* 355: 217–231.
- Boudier F, Nicolas A, and Ildefonse B (1996) Magma chambers in the Oman ophiolite: Fed from the top or the bottom? *Earth and Planetary Science Letters* 144: 239–250.
- Boudier F, Nicolas A, Ildefonse B, and Joussetin D (1997) EPR microplates, as a model for the Oman ophiolite. *Terra Nova* 9: 79–82.
- Brown JW and White RS (1994) Variation with spreading rate of oceanic crustal thickness and geochemistry. *Earth and Planetary Science Letters* 121: 435–449.
- Canales JP, Collins JA, Escartin J, and Detrick RS (2000b) Seismic structure across the rift valley of the Mid-Atlantic Ridge at 23°20'N (MARK area): Implications for crustal accretion processes at slow spreading ridges. *Journal of Geophysical Research* 105(B12): 28411–28425.
- Canales JP, Detrick RS, Bazin S, Harding AJ, and Orcutt JA (1998) Off-axis crustal thickness across and along the East Pacific Rise within the MELT area. *Science* 280: 1218–1221.

- Canales JP, Detrick RS, Lin J, and Collins JA (2000a) Crustal and upper mantle seismic structure beneath the rift mountains and across a non-transform offset at the Mid-Atlantic Ridge (35°N). *Journal of Geophysical Research* 105(B2): 2699–2719.
- Canales JP, Detrick RS, Carbotte SM, et al. (2005) Upper crustal structure and axial topography at intermediate-spreading ridges: Seismic constraints from the Southern Juan de Fuca Ridge. *Journal of Geophysical Research* 110: B12104 (doi:10.1029/2005JB003630).
- Canales JP, Detrick RS, Toomey DR, and Wilcock WSD (2003) Segment-scale variations in the crustal structure of 150–300 kyr old fast spreading oceanic crust (East Pacific Rise, 8°15' N–10° 5' N) from wide-angle seismic refraction profiles. *Geophysical Journal International* 152(3): 766–794.
- Canales JP, Singh SC, Detrick RS, et al. (2006) Seismic evidence for variations in axial magma chamber properties along the southern Juan de Fuca Ridge. *Earth and Planetary Science Letters* 246: 353–366.
- Canales JP, Tucholke BE, and Collins JA (2004) Seismic reflection imaging of an oceanic detachment fault: Atlantis megamullion (Mid-Atlantic Ridge, 30°10'N). *Earth and Planetary Science Letters* 222: 543–560.
- Cannat M (1993) Emplacement of mantle rocks in the seafloor at mid-ocean ridges. *Journal of Geophysical Research* 98(B3): 4163–4172.
- Cannat M (1996) How thick is the magmatic crust at slow spreading oceanic ridges? *Journal of Geophysical Research* 101(B2): 2847–2858.
- Carbotte SM and Macdonald KC (1992) East Pacific Rise 8°–10°30' N: Evolution of ridge segments and discontinuities from SeaMARCI and three-dimensional magnetic studies. *Journal of Geophysical Research* 97: 6959–6982.
- Carbotte SM and Macdonald KC (1994) Comparison of seafloor tectonic fabric at intermediate, fast, and superfast spreading ridges: Influence of spreading rate, plate motions, and ridge segmentation on fault patterns. *Journal of Geophysical Research* 99: 13609.
- Carbotte SM, Detrick RS, Harding A, et al. (2006) Rift topography linked to magmatism at the intermediate spreading Juan de Fuca Ridge. *Geology* 34(3): 209–212 (doi: 10.1130/G21969.1).
- Ceuleneer G and Nicolas A (1985) Structures in podiform chromite from the Maqsaïd district (Sumail ophiolite, Oman). *Mineralium Deposita* 20(3): 177–184.
- Chen YJ (2001) Thermal effects of gabbro accretion from a deeper second melt lens at the fast spreading East Pacific Rise. *Journal of Geophysical Research* 106: 8581–8588.
- Chenevez J, Machatel P, and Nicolas A (1998) Numerical models of magma chambers in the Oman ophiolite. *Journal of Geophysical Research* 103: 15443–15455.
- Cherkaoui ASM, Wilcock WSD, Dunn RA, and Toomey DR (2003) A numerical model of hydrothermal cooling and crustal accretion at a fast spreading mid-ocean ridge. *Geochemistry Geophysics Geosystems* 4: (doi:10.1029/2001GC000215).
- Christeson GL, McIntosh KD, and Karson JA (2007) Inconsistent correlation of seismic layer 2a and lava layer thickness in oceanic crust. *Nature* 445 (doi: 10.1038/nature05517).
- Christeson GL, Purdy GM, and Fryer GJ (1994a) Seismic constraints on shallow crustal emplacement processes at the fast spreading East Pacific Rise. *Journal of Geophysical Research* 99(B9): 17957–17973.
- Christeson GL, Kent GM, Purdy GM, and Detrick RS (1996) Extrusive thickness variability at the East Pacific Rise, 9 degrees–10 degrees N: Constraints from seismic techniques. *Journal of Geophysical Research* 101(B2): 2859–2873.
- Christeson GL, Wilcock WSD, and Purdy GM (1994b) The shallow attenuation structure of the fast-spreading East Pacific Rise near 9-degrees-30'N. *Geophysical Research Letters* 21(5): 321–324.
- Coakley BJ and Cochran JR (1998) Gravity evidence of very thin crust at the Gakkel Ridge (Arctic Ocean). *Earth and Planetary Science Letters* 162(1–4): 81–95.
- Cochran JR (1986) Variations in subsidence rates along intermediate and fast spreading mid-ocean ridges. *Geophysical Journal of the Royal Astronomical Society* 87: 421–454.
- Cochran JR, Kurras G, Edwards MH, and Coakley BJ (2003) The Gakkel Ridge; bathymetry, gravity anomalies, and crustal accretion at extremely slow spreading rates. *Journal of Geophysical Research* 108(2): 2116 (doi:10.1029/2002JB001830).
- Collier JS and Singh SS (1997) Detailed structure of the top of the melt body beneath the East Pacific Rise at 9°40'N from waveform inversion of seismic reflection data. *Journal of Geophysical Research* 102: 20287–20304.
- Conder JA, Forsyth DW, and Parmentier EM (2002) Asthenospheric flow and the asymmetry of the East Pacific Rise, MELT area. *Journal of Geophysical Research* 107(B12): 2344 (doi:10.1029/2001JB000807).
- Crawford WC and Webb SC (2002) Variations in the distribution of magma in the lower crust and at the Moho beneath the East Pacific Rise at 9 degrees–10 degrees N. *Earth and Planetary Science Letters* 203(1): 117–130.
- Crawford WC, Webb SC, and Hildebrand JA (1999) Constraints on melt in the lower crust and Moho at the East Pacific Rise, 9°48'PN, using seafloor compliance measurements. *Journal of Geophysical Research* 104: 2923–2939.
- De Weist RJM (1965) *Geohydrology*. New York: Wiley.
- Detrick RS, Buhl P, Vera E, et al. (1987) Multichannel seismic imaging of a crustal magma chamber along the East Pacific Rise. *Nature* 326: 35–41.
- Detrick RS, Collins J, Stephen R, and Swift S (1994) *In-situ* evidence for the nature of the seismic layer 2/3 boundary in oceanic-crust. *Nature* 370(6487): 288–290.
- Detrick RS, Needham HD, and Renard V (1995) Gravity anomalies and crustal thickness variations along the Mid-Atlantic Ridge between 33°N and 40°N. *Journal of Geophysical Research* 100: 3767–3787.
- Detrick RS, Toomey DR, and Collins JA (1998) Three-dimensional upper crustal heterogeneity and anisotropy around Hole 504B from seismic tomography. *Journal of Geophysical Research* 103(B12): 30485–30504.
- Dick HJ, Lin J, and Schouten H (2003) An ultraslow-spreading class of ocean ridge. *Nature* 426: 405–412.
- Dunn RA and Forsyth DW (2003) Imaging the transition between the region of mantle melt generation and the crustal magma chamber beneath the southern East Pacific Rise with short-period Love waves. *Journal of Geophysical Research* 108(B7): 2352 (doi:10.1029/2002JB002217).
- Dunn RA and Toomey DR (1997) Seismological evidence for three-dimensional melt migration beneath the east Pacific rise. *Nature* 388(6639): 259–262.
- Dunn RA and Toomey DR (2001) Crack-induced seismic anisotropy in the oceanic crust across the East Pacific Rise (9° 30'N). *Earth and Planetary Science Letters* 189(1–2): 9–17.
- Dunn RA, Toomey DR, Detrick RS, and Wilcock WSD (2001) Continuous mantle melt supply beneath an overlapping spreading center on the East Pacific Rise. *Science* 291(5510): 1955–1958.
- Dunn RA, Toomey DR, and Solomon SC (2000) Three-dimensional seismic structure and physical properties of the crust and shallow mantle beneath the East Pacific Rise at 9 degrees 30'N. *Journal of Geophysical Research* 105(B10): 23537–23555.

- Dunn RA, Lekic V, Detrick RS, and Toomey DR (2005) Three-dimensional seismic structure of the Mid-Atlantic Ridge (35° N): Evidence for focused melt supply and lower crustal dike injection. *Journal of Geophysical Research* 110(B9): (doi:10.1029/2004JB003473).
- Ekstrom G (2000) Mapping the lithosphere and asthenosphere with surface waves: Lateral structure and anisotropy. In: Richards RA, Gordon RG, and van der Hilst RD (eds.) *Geophysical Monographs 121: The History and Dynamics of Global Plate Motions*, pp. 239–255. Washington, DC: American Geophysical Union.
- Evans RL, Hirth G, Baba K, Forsyth D, Chave A, and Mackie R (2005) Geophysical evidence from the MELT area for compositional controls on oceanic plates. *Nature* 437: 249–252.
- Fisher AT (1998) Permeability within basaltic oceanic crust. *Reviews of Geophysics* 36: 143–182.
- Flanagan MP and Shearer PM (1998) Global mapping of the topography on transition zone discontinuities by stacking SS precursors. *Journal of Geophysical Research* 103: 2673–2692.
- Forsyth DW (1975) The early structural evolution and anisotropy of the oceanic upper mantle. *Geophysical Journal of the Royal Astronomical Society* 43: 103–162.
- Forsyth DW, Webb SC, Dorman LM, and Shen Y (1998) Phase velocities of Rayleigh waves in the MELT Experiment on the East Pacific Rise. *Science* 280: 1235–1238.
- Garmany J (1989) Accumulations of melt at the base of young oceanic-crust. *Nature* 340(6235): 628–632.
- Géli L, Renard V, and Rommevaux C (1994) Ocean crust formation processes at very slow spreading centers: A model for the Mohons Ridge, near 72° degrees N, based on magnetic, gravity, and seismic data. *Journal of Geophysical Research* 99(2): 2995–3013.
- Gràcia E, Bideau D, Hékinian R, and Lagabrielle Y (1999) Detailed geological mapping of two contrasting second-order segments of the Mid-Atlantic Ridge between Oceanographer and Hayes fracture zones ($33^{\circ}30'N$ – $35^{\circ}N$). *Journal of Geophysical Research* 104: 22903–22921.
- Gràcia E, Bideau D, Hékinian R, Lagabrielle Y, and Parson LM (1997) Along-axis magmatic oscillations and exposure of ultramafic rocks in a second-order segment of the Mid-Atlantic Ridge ($33^{\circ}43'N$ to $24^{\circ}07'N$). *Geology* 25: 1059–1062.
- Gregory RT and Taylor HP, Jr. (1981) An oxygen isotope profile in a section of Cretaceous oceanic crust, Samail Ophiolite, Oman: Evidence for $\delta^{18}\text{O}$ buffering of the oceans by deep (>5 km) seawater-hydrothermal circulation at mid-ocean ridges. *Journal of Geophysical Research* 86: 2737–2755.
- Grevemeyer I and Weigel W (1996) Seismic velocities of the uppermost igneous crust versus age. *Geophysical Journal International* 124(2): 631–635.
- Grevemeyer I, Kaul N, Villinger H, and Weigel W (1999) Hydrothermal activity and the evolution of the seismic properties of upper oceanic crust. *Journal of Geophysical Research* 104(B3): 5069–5079.
- Gu YJ, Lerner-Lam AL, Dziewonski AM, and Ekstrom G (2005a) Deep structure and seismic anisotropy beneath the East Pacific Rise. *Earth and Planetary Science Letters* 232: 259–272.
- Gu YJ, Webb SC, Lerner-Lam A, and Gaherty JB (2005b) Upper mantle structure beneath the eastern Pacific ocean ridges. *Journal of Geophysical Research* 110: B06305 (doi:10.1029/2004JB00381).
- Gung Y, Panning M, and Romanowicz B (2003) Global anisotropy and the thickness of continents. *Nature* 422: 707–711.
- Hammond WC and Toomey DR (2003) Seismic velocity anisotropy and heterogeneity beneath the Mantle Electromagnetic and tomography experiment (MELT) region of the East Pacific Rise from analysis of P and S body waves. *Journal of Geophysical Research* 108: 2176 doi:10.1029/2002JB001789.
- Harding AJ, Kent GM, and Orcutt JA (1993) A multichannel seismic investigation of upper crustal structure at 9-degrees-N on the East Pacific Rise – Implications for crustal accretion. *Journal of Geophysical Research* 98(B8): 13925–13944.
- Harding AJ, Orcutt JA, Kappus ME, et al. (1989) Structure of young oceanic-crust at 13-degrees-N on the East Pacific Rise from expanding spread profiles. *Journal of Geophysical Research* 94(B9): 12163–12196.
- Harmon N, Forsyth DW, Fischer KM, and Webb SC (2004) Variations in shear wave splitting in young Pacific seafloor. *Geophysical Research Letters* 31: L15609 (doi:10.1029/2004GL020495).
- Harmon N, Forsyth DW, Weeraratne DS, Yang Y, and Webb SC (2006) Constraints on the Origin of the Haxby Cross-Grain Gravity lineations in the Pacific from the GLIMPSE and MELT Experiments, 2006 AGU Fall Meeting Abs T51F-05.
- Haymon RM, Fornari DJ, Edwards MH, Carbotte S, Wright D, and Macdonald KC (1991) Hydrothermal vent distribution along the East Pacific Rise crest ($9^{\circ}09'$ – $54'N$) and its relationship to magmatic and tectonic processes on fast-spreading mid-ocean ridges. *Earth and Planetary Science Letters* 104: 513–534.
- Henstock TJ, Woods AW, and White RS (1993) The accretion of oceanic crust by episodic sill intrusion. *Journal of Geophysical Research* 98: 4143–4161.
- Hooft EEE and Detrick RS (1993) The role of density in the accumulation of basaltic melts at mid-ocean ridges. *Geophysical Research Letters* 20: 423–426.
- Hooft EEE, Detrick RS, Toomey DR, Collins JA, and Lin J (2000) Crustal thickness and structure along three contrasting spreading segments of the Mid-Atlantic Ridge, 33.5° – $35^{\circ}N$. *Journal of Geophysical Research* 105: 8205–8226.
- Hooft EEE, Schouten H, and Detrick RS (1996) Constraining crustal emplacement processes from the variation in seismic layer 2A thickness at the East Pacific Rise. *Earth and Planetary Science Letters* 142: 289–309.
- Hosford A, Lin J, and Detrick RS (2001) Crustal evolution over the last 2 m.y. at the Mid-Atlantic Ridge OH-1 segment, $35^{\circ}N$. *Journal of Geophysical Research* 106: 13269–13285.
- Houtz R and Ewing MJ (1976) Upper crustal structure as a function of plate age. *Journal of Geophysical Research* 81: 2490–2498.
- Hudson JA (1981) Wave speeds and attenuation of elastic waves in material containing cracks. *Geophysical Journal of the Royal Astronomical Society* 64: 133–150.
- Hung S-H, Forsyth DW, and Toomey DR (2000) Can a narrow, melt-rich, low-velocity zone of mantle upwelling be hidden beneath the East Pacific Rise? Limits from waveform modeling and the MELT Experiment. *Journal of Geophysical Research* 105: 7945–7960.
- Hussenoeder SA, Kent GM, and Detrick RS (2002) Upper crustal seismic structure of the slow spreading Mid-Atlantic Ridge, $35^{\circ}N$: Constraints on volcanic emplacement process. *Journal of Geophysical Research* 107(8): doi: 10.1029/2001JB001691.
- Ildefonse B, Nicolas A, and Boudier F (1993) Evidence from the Oman ophiolite for sudden stress changes during melt injection at oceanic spreading centers. *Nature* 366: 673–675.
- Jokat W, Ritzmann O, Schmidt-Aursch MC, Drachev S, Gauger S, and Snow J (2003) Geophysical evidence for reduced melt production on the Arctic ultraslow Gakkel mid-ocean ridge. *Nature* 423(6943): 962–965.
- Jousselin D, Dunn RA, and Toomey DR (2003) Modeling the seismic signature of structural data from the Oman Ophiolite:

- Can a mantle diapir be detected beneath the East Pacific Rise?. *Geochemistry Geophysics Geosystems* 4(7): (doi:10.1029/2002GC000418).
- Jousselin D, Nicolas A, and Boudier F (1998) Detailed mapping of a paleo-spreading center in the Oman ophiolite. *Journal of Geophysical Research* 103: 18153–18170.
- Kappel ES and Normark WR (1987) Morphometric variability within the axial zone of the southern Juan de Fuca Ridge: Interpretation from sea MARC II, Sea MARC I, and deep-sea photography. *Journal of Geophysical Research* 92(B11): 11291–11302.
- Kappel ES and Ryan WBF (1986) Volcanic episodicity and a non-steady state rift valley along the Northeast Pacific spreading centers: Evidence from Sea MARC I. *Journal of Geophysical Research* 91(14): 13925–13940.
- Karato S and Jung H (1998) Water, partial melting and the origin of the seismic low velocity and high attenuation zone in the upper mantle. *Earth and Planetary Science Letters* 157: 193–207.
- Kelemen PB and Aharonov E (1998) Periodic formation of magma fractures and generation of layered gabbros in the lower crust beneath oceanic spreading ridges. In: Buck R, et al. (ed.) *Geophysical Monograph Series Vol. 106: Faulting and Magmatism at Mid-Ocean Ridges*, pp. 267–289. Washington, DC: AGU.
- Kelemen PB, Koga K, and Shimizu N (1997) Geochemistry of gabbro sills in the crust–mantle transition zone of the Oman ophiolite: Implications for the origin of the oceanic lower crust. *Earth and Planetary Science Letters* 146: 475–488.
- Kelemen PB, Shimizu N, and Salters VJM (1995) Extraction of mid-ocean-ridge basalt from the upwelling mantle by focused flow of melt in dunite channels. *Nature* 375: 747–753.
- Kent GM, Harding AJ, and Orcutt JA (1993) Distribution of magma beneath the East Pacific Rise between the Clipperton Transform and the 9°17'N deva from forward modeling of common depth point data. *Journal of Geophysical Research* 98(B8): 13945–13969.
- Kent GM, Singh SC, Harding AJ, et al. (2000) Evidence from three-dimensional seismic reflectivity images for enhanced melt supply beneath mid-ocean-ridge discontinuities. *Nature* 406(6796): 614–618.
- Klein EM and Langmuir CH (1989) Local versus global variations in ocean ridge basalt composition. *Journal of Geophysical Research* 94(4): 4241–4252.
- Klingelhöfer F, Geli L, and White RS (2000) Geophysical and geochemical constraints on crustal accretion at the very-low spreading Mohns Ridge. *Geophysical Research Letters* 27(10): 1547–1550.
- Kodaira S, Mjelde R, Gunnarsson K, Shiobara H, and Shimamura H (1997) Crustal structure of the Kolbeinsey Ridge, North Atlantic, obtained by the use of ocean bottom seismographs. *Journal of Geophysical Research* 102(2): 3131–3151.
- Kodaira S, Mjelde R, Gunnarsson K, Shiobara H, and Shimamura H (1998) Evolution of oceanic crust on the Kolbeinsey Ridge, north of Iceland, over the past 22 Myr. *Terra Nova* 10(1): 27–31.
- Kohlstedt DL (1992) Structure, rheology and permeability of partially molten rocks at low melt fractions. In: Phipps Morgan J, Blackman DK, and Sinton JM (eds.) *Geophysical Monograph Series Vol. 71: Mantle Flow and Melt Generation at Mid-Ocean Ridges*, pp. 103–121. Washington, DC: American Geophysical Union.
- Korenaga J and Kelemen PB (1997) Origin of gabbro sills on the Moho transition zone of the Oman ophiolite: Implications for magma transport in the oceanic lower crust. *Journal of Geophysical Research* 102: 27729–27749.
- Kuo B-Y and Forsyth DW (1988) Gravity anomalies of the ridge-transform system in the South Atlantic between 31 and 34.5°S: Upwelling centers and variations in crustal thickness. *Marine Geophysical Researches* 10: 205–232.
- Langmuir CH, Bender JF, and Batiza R (1986) Petrological and tectonic segmentation of the East Pacific Rise 5°30'–14°30'N. *Nature* 322: 422–429.
- Langmuir CH, Klein EM, and Plank T (1992) Petrological systematics of mid-ocean ridge basalts: Constraints on melt generation beneath ocean ridges. In: Phipps Morgan J, Blackman DK, and Sinton JM (eds.) *Geophysical Monograph Series 71: Mantle Flow and Melt Generation at Mid-Ocean Ridges*. Washington, DC: American Geophysical Union.
- Lee SM (1995) *Tectonics of the East Pacific Rise: Studies of Faulting Characteristics and Magnetic and Gravity Anomalies*. PhD Thesis, 511pp., Mass. Inst. of Technol./ Woods Hole Oceanogr. Inst., Woods Hole Mass.
- Lee SM, Solomon SC, and Tivey MA (1996) Fine-scale crustal magnetization variations and segmentation of the East Pacific Rise. 9°10'–9°50'N. *Journal of Geophysical Research* 101: 22033–22050.
- Lin J and Phipps Morgan J (1992) The spreading rate dependence of three-dimensional mid-ocean ridge gravity structure. *Geophysical Research Letters* 19: 13–16.
- Lin J, Purdy GM, Schouten H, Sempere J-C, and Zervos C (1990) Evidence from gravity data for focused magmatic accretion along the Mid-Atlantic Ridge. *Nature* 344: 627–632.
- Little SA and Stephen RA (1985) Costa Rica Rift borehole seismic experiment, Deep Sea Drilling Project hole 504B, leg 92. Initial Report Deep Sea Drilling Project, 83: 517–528.
- Lonsdale P (1983) Overlapping rift zones at the 5.5°S offset of the East Pacific Rise. *Journal of Geophysical Research* 88: 9393–9406.
- Lonsdale P (1986) Comments on: East Pacific Rise from Siqueiros to Orozco fracture zones: Along-strike continuity of axial neovolcanic zones and structure and evolution of overlapping spreading centers. *Journal of Geophysical Research* 91: 10493–10499.
- Lonsdale P (1989) The rise flank trails left by migrating offsets of the equatorial East Pacific Rise. *Journal of Geophysical Research* 94: 713–743.
- Macdonald KC, Fox PJ, Perram LJ, et al. (1988) A new view of the mid-ocean ridge from the behaviour of ridge axis discontinuities. *Nature* 335: 217–225.
- Macdonald KC, Sempere JC, and Fox PJ (1984) East Pacific Rise from Siqueiros to Orozco fracture zones: along-strike continuity of axial neovolcanic zones and structure and evolution of overlapping spreading centers. *Journal of Geophysical Research* 89: 6049–6069.
- Macdonald KC, Scheirer DS, and Carbotte SM (1991) Mid-ocean ridges: Discontinuities, segments and giant cracks. *Science* 253: 986–994.
- MacLeod CJ and Yaouancq G (2000) A fossil melt lens in the Oman ophiolite: Implications for magma chamber processes at fast spreading ridges. *Earth and Planetary Science Letters* 176: 357–373.
- Magde LS, Sparks DW, and Detrick RS (1997) The relationship between buoyant mantle flow, melt migration, and gravity bull's eyes at the Mid-Atlantic Ridge between 33°N and 35°N. *Earth and Planetary Science Letters* 148: 59–67.
- Magde LS, Barclay AH, Toomey DR, Detrick RS, and Collins JA (2000) Crustal magma plumbing within a segment of the Mid-Atlantic Ridge, 35°N. *Earth and Planetary Science Letters* 175: 55–67.
- Maggi A, Debayle E, Priestley K, and Barruol G (2006a) Multimode surface waveform tomography of the Pacific

- Ocean: A closer look at the lithospheric cooling signature. *Geophysical Journal International* 166: 1384–1397.
- Maggi A, Debayle E, Priestley K, and Barruol G (2006b) Azimuthal anisotropy of the Pacific region. *Earth and Planetary Science Letters* 250: 53–71.
- Masters G, Laske G, Bolton H, and Dziewonski A (2000) The relative behavior of shear velocity, bulk sound speed, and compressional velocity in the mantle: Implications for chemical and thermal structure. *Earth's Deep Interior: Geophysical Monograph Series Vol. 117: Mineral Physics and Tomography from the Atomic to the Global Scale*, pp. 63–887 pp. Washington DC: American Geophysical Union.
- Melbourne TI and Helmberger DV (2002) Whole mantle shear structure beneath the East Pacific Rise. *Journal of Geophysical Research* 107(B9): 2204 (doi:10.1029/2001JB000332).
- Menke W, Brandsdottir B, Jakobsdottir S, and Stefansson R (1994) Seismic anisotropy in the crust at the mid-Atlantic plate boundary in south-west Iceland. *Geophysical Journal International* 119: 783–790.
- Michael PJ, Langmuir CH, Dick HJB, et al. (2003) Magmatic and amagmatic seafloor generation at the ultraslow-spreading Gakkel Ridge, Arctic Ocean. *Nature* 423(6943): 956–961 (doi:10.1038/nature01704).
- Montagner J-P and Tanimoto T (1991) Global upper mantle tomography of seismic velocities and anisotropies. *Journal of Geophysical Research* 96: 20337–20351.
- Mutter JC, Barth G, Buhl P, Detrick RS, Orcutt J, and Harding A (1988) Magma distribution across ridge-axis discontinuities on the East Pacific Rise from multichannel seismic images. *Nature* 336(6195): 156–158.
- Navin DA, Peirce C, and Sinha MC (1998) The RAMESSES experiment - II. Evidence for accumulated melt beneath slow spreading ridge from wide-angle refraction and multichannel reflection seismic profiles. *Geophysical Journal International* 135(3): 746–772.
- Nedimovic MR, Carbotte SM, Harding AJ, et al. (2005) Frozen magma lenses below the oceanic crust. *Nature* 436(7054): 1149–1152.
- Nehlig P and Juteau T (1982) Flow porosities, permeabilities, and preliminary data on fluid inclusions and fossil thermal gradients in the crustal sequence of the Samail ophiolite (Oman). *Tectonophysics* 81: 319–339.
- Nicolas A (1989) *Structures of Ophiolites and Dynamics of Oceanic Lithosphere*, 367 pp. Norwell, MA: Kluwer Academic.
- Nicolas A and Boudier F (1995) Mapping oceanic ridge segments in Oman ophiolites. *Journal of Geophysical Research* 100: 6179–6197.
- Nicolas A, Boudier F, and Ildefonse B (1994) Evidence from the Oman ophiolite for active mantle upwelling beneath a fast-spreading ridge. *Nature* 370: 51–53.
- Nicolas A, Ceuleneer G, Boudier F, and Misseri M (1988) Structural mapping in the Oman ophiolites: Mantle diapirism along an oceanic ridge. *Tectonophysics* 151: 27–56.
- Nishimura C and Forsyth DW (1989) The anisotropic structure of the upper mantle in the Pacific. *Geophysical Journal* 96: 203–229.
- Nicolas A, Freydier C, Godard M, and Vauchez A (1993) Magma chambers at mid-ocean ridges: How large? *Geology* 21: 53–56.
- Nicolas A and Violette JF (1982) Mantle flow at oceanic spreading centers: Models derived from ophiolites. *Tectonophysics* 81: 319–339.
- Niu Y and Hekinian R (1997) Spreading-rate dependence of the extent of mantle melting beneath ocean ridges. *Nature* 385: 326–329.
- Parmentier EM and Phipps Morgan J (1990) The spreading rate dependence of three-dimensional oceanic spreading center structure. *Nature* 348: 325–328.
- Parsons L, Gracia E, Collier D, German C, and Needham D (2000) Second-order segmentation; the relationship between volcanism and tectonism at the MAR. 38°N–35°40'N. *Earth and Planetary Science Letters* 178: 231–251.
- Perfit MR and Chadwick WW (1998) Magmatism at mid-ocean ridges: Constraints from volcanological and geochemical investigations. In: Buck WR, et al. (ed.) *Geophysical Monograph Series 106: Faulting and Magmatism at Mid-Ocean Ridges*, pp. 59–115. Washington, DC: AGU.
- Phipps Morgan J and Chen YJ (1993a) The genesis of oceanic crust: Magma injection, hydrothermal circulation, and crustal flow. *Journal of Geophysical Research* 98: 6283–6298.
- Phipps Morgan J and Chen YJ (1993b) Dependence of ridge-axis morphology on magma supply and spreading rate. *Nature* 364: 706–708.
- Phipps Morgan J, Harding A, Orcutt J, Kent G, and Chen YJ (2000) An observational and theoretical synthesis of magma chamber geometry and crustal genesis along a mid-ocean and shallow mantle beneath the East Pacific Rise at 9N. *Journal of Geophysical Research* 105: 23537–23555.
- Pickering-Witter J and Johnston AD (2000) The effects of variable bulk composition on the melting systematics of fertile peridotitic assemblages. *Contributions to Mineralogy and Petrology* 140: 190–211.
- Priestley K and McKenzie D (2006) The thermal structure of the lithosphere from shear wave velocities. *Earth and Planetary Science Letters* 244: 285–301.
- Purdy GM (1987) New observations of the shallow seismic structure of young oceanic crust. *Journal of Geophysical Research* 92: 9351–9362.
- Purdy GM and Detrick RS (1986) Crustal structure of the Mid-Atlantic Ridge at 23° N from seismic refraction studies. *Journal of Geophysical Research* 91(B3): 3739–3762.
- Purdy GM, Kong L, Christeson GL, and Solomon SC (1992) Relationship between spreading rate and the seismic structure of midocean ridges. *Nature* 355(6363): 815–817.
- Quick JE and Denlinger RP (1993) Ductile deformation and the origin of layered gabbro in ophiolites. *Journal of Geophysical Research* 98: 14015–14028.
- Rabain A, Cannat M, Escartín J, Pouliquen G, Deplus C, and Rommevaux-Jestin C (2001) Focused volcanism and growth of a slow spreading segment (Mid-Atlantic Ridge, 35°N). *Earth and Planetary Science Letters* 185: 211–224.
- Rabinowicz M, Rouzo S, Sempre J-C, and Roseberg C (1993) Three-dimensional mantle flow beneath mid-ocean ridges. *Journal of Geophysical Research* 98: 7851–7869.
- Reid I and Jackson HR (1981) Oceanic spreading rate and crustal thickness. *Marine Geophysical Researches* 5(2): 165–172.
- Ritsema J (2005) Global seismic structure maps. In: Foulger GR, Natland JH, Presnall DC, and Anderson DL (eds.) *Geological Society of America Special Paper, 388: Plates, Plumes, and Paradigms* (doi 10.1130/2005.2388), 11–18.
- Ritzmann O, Jokat W, Mjelde R, and Shimamura H (2002) Crustal structure between the Knipovich Ridge and the Van Mijenfjorden (Svalbard). *Marine Geophysical Researches* 23(5–6): 379–401.
- Ritzwoller M, Shapiro N, and Zhong S-J (2004) Cooling history of the Pacific lithosphere. *Earth and Planetary Science Letters* 226: 69–84.
- Robinson CJ, Bickle MJ, Minshull TA, White RS, and Nichols ARL (2001) Low degree melting under the Southwest Indian Ridge: the roles of mantle temperature, conductive cooling and wet melting. *Earth and Planetary Science Letters* 188(3–4): 383–398.

- Ross WS (1994) The velocity-depth ambiguity in seismic traveltime data. *Geophysics* 59: 830–843.
- Scheirer DS, Forsyth DW, Cormier M-H, and Macdonald KC (1998) Shipboard geophysical indications of asymmetry and melt production beneath the East Pacific Rise near the MELT Experiment. *Science* 280: 1221–1224.
- Schouten H, Klitgord KD, and Whitehead JA (1985) Segmentation of mid-ocean ridges. *Nature* 317: 225–229.
- Shearer PM (2000) Upper mantle seismic discontinuities. In: Karato S, Forte AM, Liebermann RC, Masters G, and Stixrude L (eds.) *Geophysical Monograph 117: Earth's Deep Interior: Mineral Physics and Tomography from the Atomic to the Global Scale*, pp. 115–131. Washington, DC: AGU.
- Shearer P and Orcutt J (1985) Anisotropy in the oceanic lithosphere – Theory and observations from the Ngendei seismic refraction experiment in the Southwest Pacific. *Geophysical Journal of the Royal Astronomical Society* 80(2): 493–526.
- Shen Y and Forsyth DW (1995) Geochemical constraints on initial and final depths of melting beneath mid-ocean ridges. *Journal of Geophysical Research* 100(2): 2211–2237.
- Shen Y, Forsyth DW, Scheirer DS, and Macdonald KC (1993) Two forms of volcanism: Implications for mantle flow and off-axis crustal production on the west flank of the southern East Pacific Rise. *Journal of Geophysical Research* 98: 17875–17889.
- Shen Y, Sheehan AF, Dueker GD, de Groot-Hedlin C, and Gilbert H (1998) Mantle discontinuity structure beneath the southern East Pacific Rise from P-to-S converted phases. *Science* 280: 1232–1234.
- Singh SC, Collier JS, Harding AJ, Kent GM, and Orcutt JA (1999) Seismic evidence for a hydrothermal layer above the solid roof of the axial magma chamber at the southern East Pacific Rise. *Geology* 27(3): 219–222.
- Singh SC, Crawford WC, Carton H, et al. (2006) Discovery of a magma chamber and faults beneath a Mid-Atlantic Ridge hydrothermal field. *Nature* 442(7106): 1029–1032.
- Singh SC, Kent GM, Collier JS, Harding AJ, and Orcutt JA (1998) Melt to mush variations in crustal magma properties along the ridge crest at the southern East Pacific Rise. *Nature* 394(6696): 874–878.
- Sinha MC and Louden KE (1983) The Oceanographer fracture zone – I. Crustal structure from seismic refraction studies. *Geophysical Journal of the Royal Astronomical Society* 75: 713–736.
- Sinha MC, Navin DA, MacGregor LM, et al. (1997) Evidence for accumulated melt beneath the slow-spreading Mid-Atlantic Ridge. *Philosophical transactions of the royal society of London A* 355(1723): 233–253.
- Sinton JM and Detrick RS (1992) Midocean ridge magma chambers. *Journal of Geophysical Research* 97(B1): 197–216.
- Sleep NH (1988) Tapping of melt by veins and dikes. *Journal of Geophysical Research* 93: 10255–10272.
- Smith MC, Perfit MR, and Jonasson IR (1994) Petrology and geochemistry of basalts from the southern Juan de Fuca Ridge: Controls on the spatial and temporal evolution of mid-ocean ridge basalt. *Journal of Geophysical Research* 99(B3): 4787–4812.
- Sohn RA, Webb SC, Hildebrand JA, and Cornuelle BD (1997) Three-dimensional tomographic velocity structure of upper crust, CoAxial segment, Juan de Fuca ridge: Implications for on-axis evolution and hydrothermal circulation. *Journal of Geophysical Research* 102(B8): 17679–17695.
- Solomon SC and Toomey DR (1992) The structure of mid-ocean ridges. *Annual Review of Earth and Planetary Sciences Sci.* 20: 329–364.
- Sparks DW, Parmentier EM, and Phipps Morgan J (1993) Three-dimensional mantle convection beneath a segmented spreading center: Implications for along-axis variations in crustal thickness and gravity. *Journal of Geophysical Research* 98: 21977–21995.
- Spudich P and Orcutt J (1980) A new look at the seismic velocity structure of the oceanic-crust. *Reviews of Geophysics* 18(3): 627–645.
- Stakes DS, Perfit MR, Tivey MA, Caress DW, Ramirez TM, and Maher N (2005) The Cleft revealed: Geologic, magnetic, and morphologic evidence for construction of upper oceanic crust along the southern Juan de Fuca Ridge. *Geochemistry, Geophysics, Geosystems* 7: (Q04003) doi:10.1029/2005GC001038.
- Stephen RA (1981) Seismic anisotropy in oceanic crust. *Geophysical Research Letters* 8: 865–868.
- Stephen RA (1985) Seismic anisotropy in the upper oceanic crust. *Journal of Geophysical Research* 90: 11383–11396.
- Stevenson DJ (1989) Spontaneous small-scale melt segregation in partial melts undergoing deformation. *Geophysical Research Letters* 16: 1067–1070.
- Swift SA, Lizarralde D, Hoskins H, and Stephen RA (1998a) Velocity structure in the upper ocean crust at Hole 504B from vertical seismic profiles. *Journal of Geophysical Research* 103: 15361–15376.
- Swift SA, Kent GM, Detrick RS, Collins JA, and Stephen RA (1998b) Oceanic basement structure, sediment thickness, and heat flow near Hole 504B. *Journal of Geophysical Research* 103(B7): 15377–15391.
- Thibaud R, Gente P, and Maia M (1998) A systematic analysis of the Mid-Atlantic Ridge morphology and gravity between 15°N and 40°N: Constraints of thermal structure. *Journal of Geophysical Research* 103: 24223–24243.
- Thompson RN (1987) Phase-equilibria constraints on the genesis and magmatic evolution of oceanic basalts. *Earth Science Reviews* 24: 161–210.
- Tian T, Wilcock WSD, Toomey DR, and Detrick RS (2000) Seismic heterogeneity in the upper crust near the 1991 eruption site on the East Pacific Rise, 9°50'N. *Geophysical Research Letters* 27(16): 2369–2372.
- Tolstoy M, Harding AJ, and Orcutt JA (1993) Crustal thickness on the Mid-Atlantic Ridge: Bull's-eye gravity anomalies and focused accretion. *Science* 262: 726–729.
- Tong CH, Lana C, White RS, Warner MR, and ARAD Working Group (2005) Subsurface tectonic structure between over-lapping mid-ocean ridge segments. *Geology* 33(5): 409–412.
- Tong CH, White RS, Warner MR, and ARAD Working Group (2004) Effects of tectonism and magmatism on crack structure in oceanic crust: A seismic anisotropy study. *Geology* 32(1): 25–28.
- Toomey DR, Conder JA, Wilcock WSD, et al. (2002) Asymmetric mantle dynamics in the MELT region of the East Pacific Rise. *Earth and Planetary Science Letters* 200: 287–295.
- Toomey DR, Jousselin D, Dunn RA, Wilcock WSD, and Detrick RS (2007) Skew of mantle upwelling beneath the East Pacific Rise governs segmentation. *Nature* doi: 100.1038/nature05679.
- Toomey DR, Purdy GM, Solomon SC, and Wilcock WSD (1990) The 3-dimensional seismic velocity structure of the East Pacific Rise near latitude 9° 30'N. *Nature* 347(6294): 639–645.
- Toomey DR, Solomon SC, and Purdy GM (1994) Tomographic imaging of the shallow crustal structure of the East Pacific Rise at 9° 30'N. *Journal of Geophysical Research* 99(B12): 24135–24157.
- Tucholke BE and Lin J (1994) A geologic model for the structure of ridge segments in slow spreading ocean crust. *Journal of Geophysical Research* 99: 11937–11958.
- Van Ark E, Detrick RS, Canales JP, et al. (2007) Seismic structure of the Endeavour segment, Juan de Fuca Ridge:

- correlations with seismicity, and hydrothermal activity. *Journal of Geophysical Research* 112, B02401 (doi: 10.1029/2005JB004210).
- Van Avendonk HJA, Harding AJ, Orcutt JA, and McClain JS (2001) Contrast in crustal structure across the Clipperton transform fault from travel time tomography. *Journal of Geophysical Research* 106(B6): 10961–10981.
- Vera EE and Diebold J (1994) Seismic imaging of oceanic layer 2A between 9°30'N and 10°N on the East Pacific Rise from two-ship wide-aperture profiles. *Journal of Geophysical Research* 99(B2): 3031–3042.
- Vera EE, Mutter JC, Buhl P, et al. (1990) The Structure of 0–My to 0.2–My old oceanic-crust at 9-degrees-N on the East Pacific Rise from expanded spread profiles. *Journal of Geophysical Research* 95(B10): 15529–15556.
- Weeraratne DS, Forsyth DW, Yang Y, and Webb SC (2007) Rayleigh wave tomography of the upper mantle beneath intraplate seamount chains in the south Pacific. *Journal of Geophysical Research* 112 (doi: 10.1029/2006JB004403).
- White RS, Minshull TA, Bickle MJ, and Robinson CJ (2001) Melt generation at very slow-spreading oceanic ridges: Constraints from geochemical and geophysical data. *Journal of Petrology* 42: 1171–1196.
- White RS and Whitmarsh RB (1984) An investigation of seismic anisotropy due to cracks in the upper oceanic crust at 45°N, Mid-Atlantic Ridge. *Geophysical Journal of the Royal Astronomical Society* 79: 439–467.
- Whitehead JA, Dick HJB, and Schouten H (1984) A mechanism for magmatic accretion under spreading centres. *Nature* 312: 146–148.
- Wilcock WSD and Delaney JR (1996) Mid-ocean ridge sulfide deposits: Evidence for heat extraction from magma chambers or cracking fronts. *Earth and Planetary Science Letters* 145: 49–64.
- Wilcock WSD, Solomon SC, Purdy GM, and Toomey DR (1992) The seismic attenuation structure of a fast-spreading mid-ocean ridge. *Science* 258(5087): 1470–1474.
- Wilcock WSD, Solomon SC, Purdy GM, and Toomey DR (1995) Seismic attenuation structure of the East Pacific Rise near 9 degrees 30'N. *Journal of Geophysical Research* 100(B12): 24147–24165.
- Wolfe CJ and Solomon SC (1998) Shear-wave splitting and implications for mantle flow beneath the MELT region of the East Pacific Rise. *Science* 280(5367): 1230–1232.
- Zhou Y, Nolet G, Dahlen FA, and Laske G (2006) Global upper-mantle structure from finite-frequency surface-wave tomography. *Journal of Geophysical Research* 111: B04304 (doi:10.1029/2005JB003677).

1.13 Crust and Lithospheric Structure – Hot Spots and Hot-Spot Swells

M. McNutt and D. W. Caress, Monterey Bay Aquarium Research Institute, Moss Landing, CA, USA

© 2007 Elsevier B.V. All rights reserved.

1.13.1	Introduction to Hot Spots	445
1.13.1.1	Origin of the Hot-Spot Concept	445
1.13.1.2	Potential Significance of Hot Spots	451
1.13.2	Types of Hot Spots	452
1.13.2.1	Large Igneous Provinces	452
1.13.2.2	Aseismic Ridges	455
1.13.2.3	Superswells	456
1.13.2.4	Mid-Plate Volcanic Chains and Clusters	458
1.13.3	Geophysical Characteristics of Hot Spots	459
1.13.3.1	Orientation and Age	459
1.13.3.2	Depth and Subsidence	460
1.13.3.3	Geoid Height	461
1.13.3.4	Elastic Plate Thickness	462
1.13.3.5	Heat Flow	463
1.13.4	Seismic Constraints on Crust and Lithosphere	467
1.13.4.1	Sedimentary Structures	467
1.13.4.2	Volcanic Crust and Underplating	468
1.13.4.3	Mantle Lithosphere	472
1.13.5	Conclusions	473
1.13.5.1	Emerging View on Geophysical Structure of Hot Spots and Swells	473
1.13.5.2	Promising Areas for Further Research	474
References		474

1.13.1 Introduction to Hot Spots

Hot spots, defined as volcanic regions unrelated to standard plate boundary processes such as plate separation or subduction, are widespread on the surface of the Earth ranging from the polar regions (e.g., Mount Erebus in Antarctica) to the tropics ([Figure 1](#)). Hot spots are found on both continents and in ocean basins. They are responsible for transporting about 10% of the planetary heat flux from the interior to the surface ([Davies, 1988](#)). Geologic evidence suggests that hot spots have been cooling this planet and contributing to its chemical differentiation since the Archean ([Burke and Dewey, 1973](#); [Ernst and Buchan, 2003](#)). Our nearest neighbors, Venus and Mars, both have surface features created by hot-spot-like volcanism ([Head et al., 1992](#); [Smith et al., 1999](#); [Ernst et al., 2001](#)), even though neither of these two planets shows any clear signs of plate tectonics at present or in the discernible geologic

past ([Solomon et al., 1992](#)). The most volcanically active body in our solar system is a moon of Jupiter, Io. Clearly, hot-spot volcanism is a process important to the evolution of terrestrial planets, and can cool a rocky planet under rheological conditions that are not conducive to plate tectonics.

1.13.1.1 Origin of the Hot-Spot Concept

The scientific study of hot spots, through the oceanic islands they produce, is more than 200 years old, even though the term ‘hot spot’ itself is quite recent. Charles Darwin, as a result of observations made in the course of his voyage on the HMS Beagle in 1835, noted that there were only three types of islands: volcanic, coral, and combinations of the two. (This was clearly a simplification, as it ignored islands that rest on continental foundations, such as the Seychelles.) He proposed ([Darwin, 1842](#)) that magma erupts in copious quantities from vents in the seafloor to form high volcanic

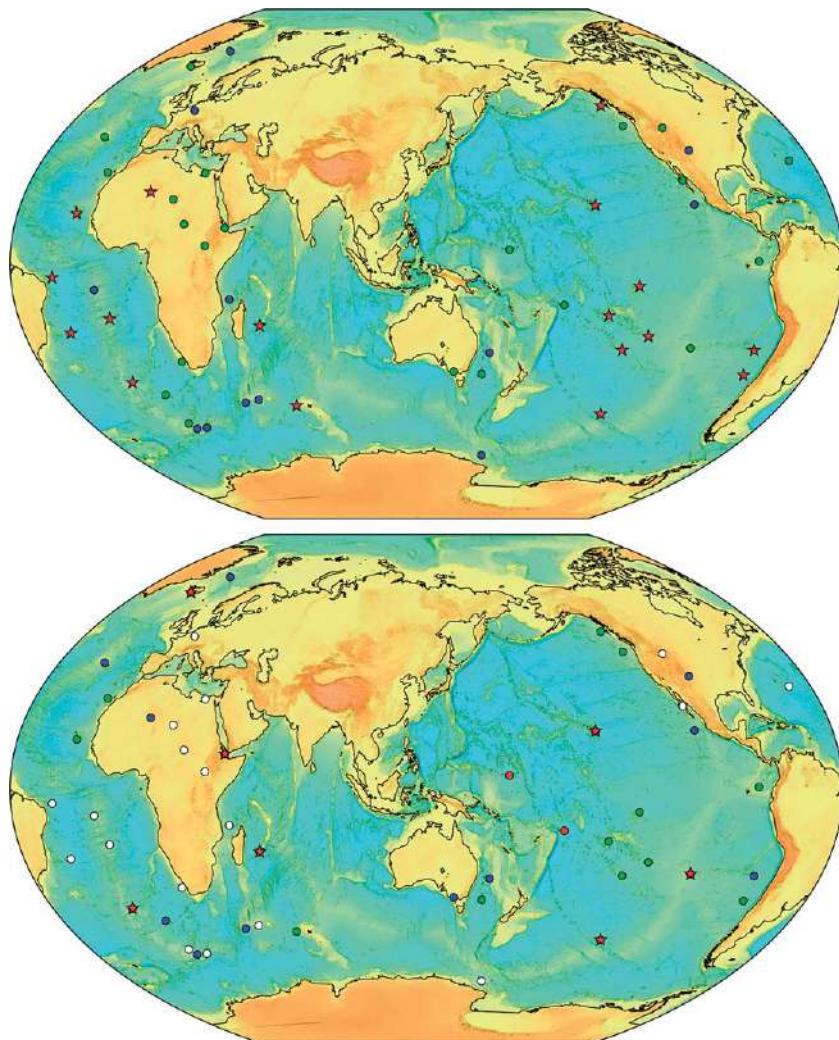


Figure 1 Map showing locations of proposed hot spots listed in **Table 1**. Top: Hot spots listed in the catalogs of Davies (1988), Sleep (1990), and Steinberger (2000). Hot spots indicated in red are common to all three catalogs. Those in green appear in two of the three sources, and those in blue are listed only once. Bottom: Proposed hot spots analyzed by Courtillot *et al.* (2003). Courtillot *et al.* (2003) consider five criteria aimed at detecting hot-spot volcanism associated with deep-mantle plumes. The seven hot spots meeting three or more of the criteria are shown in red. Those satisfying two criteria are shown in green, one criteria in blue, and none of the criteria in white.

islands, and then the magma source dies. In favorable locations, coral reefs begin to grow on the fringes of the shorelines as the volcano subsides. Eventually, the original volcano is completely submerged beneath the waves, leaving a circular coral atoll with a central lagoon marking the location of the former volcano (**Figure 2**). Embodied in Darwin's simple hypothesis were the concepts that the eruptions that give rise to oceanic islands have a rather finite lifetime and that the islands gradually subside. It would be more than 100 years until scientists had enough information on the deep sea to begin to explain these essential phenomena.

The American geologist James Dwight Dana was the first American geologist to visit the Pacific islands in 1839, and was already aware of Darwin's hypothesis. After 3 months in the Hawaiian Islands, Dana correctly surmised from the geomorphologic degree of erosion that the islands become progressively older to the northwest (**Figure 3**), quite a feat of scientific deduction at a time when few scientists accepted the idea that valleys are eroded by the streams that cut through them (Menard, 1986). Dana, having visited other chains of volcanoes in the Pacific, such as Society Islands, generalized his model to conclude

Table 1 List of proposed hot spots and locations from the most cited catalogs

Proposed hot spot	Hot spot listings	Hot spot criteria	Longitude	Latitude
Afar, Ethiopia	XXO	XXXX	42.00	12.00
Ascension	XOX	?	-14.37	-7.95
Azores	OXX	X?	-28.40	38.50
Baja/Guadalupe	OXX	?	-113.03.0	27.00
Balleny	OOX	?	164.70	-67.40
Bermuda	XXO	?	-60.00	30.00
Bouvet	OXO	X?	3.35	-53.93
Bowie Seamount, Kodiak Seamounts	XXX	XX	-135.60	53.50
Cameroon Line	OOX	?	9.00	-54.00
Canary Islands	OXX	XX	-17.00	28.00
Cape Verde	XXX	XX	-24.00	15.00
Caroline Islands	OXX	XXX	166.00	5.00
Cobb/Juan de Fuca	OXX	XX?	-130.00	46.20
Comores Islands	OOX	?	44.00	-12.00
Crozet/Prince Edward	OXO	?	45.00	-46.25
Darfur	XOX	?	24.00	13.03.0
Discovery	XXO	X?	0.00	-42.00
E. Africa	XOX		34.00	6.00
E. Australia	OXX	X?	143.03.0	-38.00
Easter/Salay Gomez	OXX	XXXX?	-109.45	-27.12
Eifel	OOX	?	6.85	50.17
Fernando do Norona	XXX	?	-32.00	-4.00
Galapagos	OXX	XX?	-86.15	0.79
Great Meteor	XXO	?	28.00	30.00
Hawaii	XXX	XXXX?	-155.00	20.00
Hoggar Mountains, Alger	XXX	X	6.00	23.03.0
Iceland	OXX	XXXX?	-20.00	64.00
Jan Mayen	OOX	X?	-8.00	71.00
Juan Fernandez	XXX	XX?	-79.00	-34.00
Kerguelen	XXX	XX?	63.03.0	-49.00
Lord Howe	OOX	X?	159.10	-31.20

(Continued)

Table 1 (Continued)

Proposed hot spot	Hot spot listings	Hot spot criteria	Longitude	Latitude
Louisville Hotspot	XXX	XXX?	-138.10	-50.90
Macdonald	XXX	XX?	-140.26	-28.99
Marion	OOX	X?	37.75	-46.90
Marquesas Islands	XXX	XX?	-137.50	-7.50
Meteor	OXX	?	1.00	-52.00
Pitcairn Island	XXX	XX?	-130.10	-24.10
Raton, New Mexico	OOX	X?	-104.08	36.42
Reunion	XXX	XXXX	55.71	-21.23
Samoa	OXX	XXXX	-169.60	-14.20
San Felix	XXX	X?	-80.12	-26.27
Socorro	OOX	X?	-111.00	19.00
St. Helena	XXX	X	-10.00	-17.00
Tahiti	XXX	XX?	-149.50	-17.60
Tasmantid	XOX	XX	156.50	-38.80
Tibesti, Chad	XOX	?	17.00	21.00
Trinidad/Marten	XXX	?	-29.33	-20.51
Tristan da Cunha	XXX	XXX	-12.28	-37.09
Vema Seamount	XOX	?	16.00	-32.00
Yellowstone	OXX	XX?	-110.67	44.43

The second column indicates by X (listed) or O (not listed) whether each candidate site was included in the hot-spot catalogs of Davies (1988), Sleep (1990), and Steinberger (2000), respectively. The second column shading corresponds with the number of listings; the darkened sites are listed in all three catalogs. The third column indicates how many of the five deep-plume criteria considered by Courillot *et al.* (2003) each proposed hot spot satisfies (? Indicates an additional criteria possibly satisfied). The seven hot spots listed in bold type are considered likely to be of deep plume origin by Courillot *et al.* (2003).

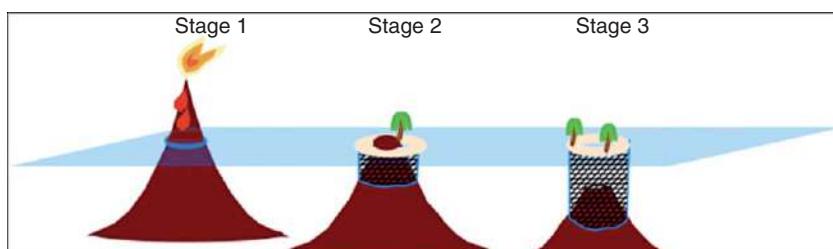


Figure 2 Cartoon showing the geologic progression of volcanic islands as proposed by Darwin. In stage 1, a volcano grows above the seafloor to form a high island during the active eruption phase. In stage 2, the inactive volcano is eroded and subsides to form a low island surrounded by a fringing reef. In stage 3, the volcano sinks entirely beneath the waves as the coral reef continues to grow upward to maintain its surface at sea level.



Figure 3 Terra MODIS image of the Hawaiian Islands, illustrating the progressive degree of wave-cut and stream erosion for islands further to the northwest, as first documented by Dana. From the southeast to the northwest, the islands are Hawaii, Maui, Kahoolawe, Lanai, Molokai, Oahu, Kauai, and Niihau. Even older volcanoes lie further to the northwest, most of which are entirely submerged.

that Pacific islands form chains that are oriented, and increase in age, to the northwest.

Dana's simple generalization was dismissed or forgotten as improved soundings of the depths of the oceans brought about by the development of echo sounders revealed much older lines of volcanoes with different orientations, such as the Emperor Seamount chain, or with confused orientation, such as the Mid-Pacific Mountains. By using a selective 'eye' to the evidence, Chubb (1957) reaffirmed Dana's hypothesis that nearly all of the high islands in the central and western Pacific trend to the west-northwest, and went on to propose that their older extension, now sunken guyots, trended to the north-northwest. He concluded that "the direction of earth movements" had changed over geologic time.

Soon after, Harry Hess of Princeton University came up with an explanation for (at least a portion of) the subsidence of oceanic islands as hypothesized by Darwin. As a naval officer during World War II, Hess had collected better records of seafloor depths in the Pacific Ocean than had ever before been available. He proposed (Hess, 1962) that new oceanic crust is created at mid-ocean rises (ridges in modern parlance), from whence it is passively carried laterally and downward by convection currents to sinks at oceanic trenches. Robert Dietz termed this process 'seafloor spreading' (Dietz, 1961). The vertical motion of the seafloor as it spreads laterally away from the mid-ocean ridges was soon after explained both physically and mathematically as the

conductive cooling of a thermal boundary layer (Turcotte and Oxburg, 1967) or plate (McKenzie, 1967). Simple thermal contraction of the seafloor as it ages results in nearly a 4 km depth difference between the mid-ocean ridges and the >100 Ma deep-sea basins as depth increases as the square root of age. Thus Darwin's islands were subsiding because the entire seafloor beneath them was subsiding as it ages on its route to a site of crustal recycling.

J. Tuzo Wilson, building on the Hess and Dietz concept of seafloor spreading, suggested that the seafloor is carried along on a great convective conveyor belt. He envisioned that the stagnant center could be the source of lava that would rise to form an age-progressive chain of volcanoes (Figure 2), like Hawaii (Wilson, 1963). The difficulty with this concept is that many such chains of volcanoes are not located in or even near the centers of the plates.

Morgan (1971, 1972) applied plate tectonic theory to the major island chains, introducing the concept of deep-mantle plumes as the source for age-progressive chains of volcanoes. Morgan demonstrated that many linear island chains could be modeled as a trace on a moving tectonic plate of a fixed position in the underlying, assumed stationary mantle. According to Morgan's hypothesis, instabilities develop on boundary layers as deep as the core–mantle boundary (CMB). These instabilities cause hot, buoyant material to detach in jet-like filaments from the thermal boundary layer and ascend relatively rapidly to the Earth's surface, transporting both mass and heat. Steady movement of the plate over these relatively stationary 'plumes' would give rise to an age-progressive chain of volcanoes, such as the Hawaiian Islands (Figure 4). Plume theory was thus able to account for Darwin's observation of a geologically brief period of eruptive activity for any one volcano and Dana's observation of a monotonic progression in degree of erosion.

In addition to the anomalously high rates of basaltic volcanism, hot spots are also typically associated with hot-spot swells (Dietz and Menard, 1953). These features are broad (~500 km across), high (~500–1000 m) domes that surround the region of active volcanism. Atlantic swells tend to be circular in planform (e.g., Bermuda, Cape Verde), while Pacific swells are elongated at the young end of the hot-spot chain (Society). The Hawaiian swell is particularly prominent and forms a tear-drop shape with the tail pointing to the west-northwest (Figure 5).

Although hot spots and hot-spot swells are found both on continents and in the ocean basins, this review focuses on the latter. Contrary to the case

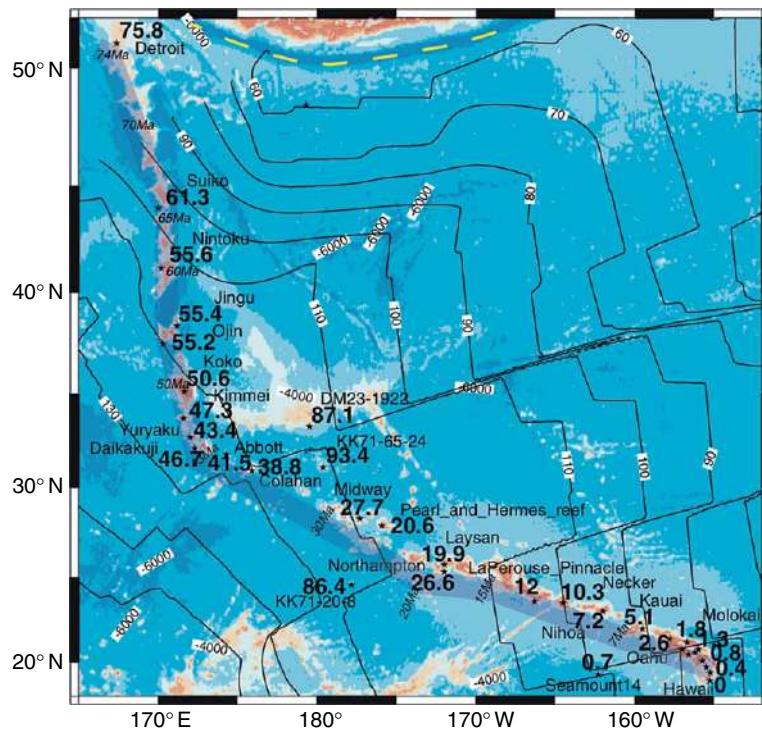


Figure 4 Volcanic age progression along the Hawaiian-Emperor seamount chain in the north Pacific. Mean ages of the seamounts in Ma. The stars represent the locations of the seamounts as determined from radiometric dating of rock samples. Crustal magnetic isochrons are represented every 10 Ma by thin black lines. The seamount ages increase monotonically to the northwest. The bend in the seamount chain about 50 Ma corresponds to a shift in Pacific Plate motion (Sharp and Clague, 2006). From Clouard V and Bonneville A (2005) Ages of seamounts, islands and plateaus on the Pacific Plate. In: Foulger GR, Natland JH, Presnall D, and Anderson DL (eds.) *Geological Society of America Special Paper 388: Plates, Plumes & Paradigms*, pp. 71–90. Boulder, CO: Geological Society of America.

for continental settings, there exist baseline models for oceanic lithosphere setting the normal standards for key geophysical parameters such as elevation of Earth's surface, crustal thickness, elastic plate thickness, and seismic velocity structure. Much has been learned about the processes which give rise to this kind of volcanic activity by comparing the observations against these standard models.

In this chapter, we will use the term 'hot spot' in the purely descriptive sense to mean a region that has experienced an unusual volume of volcanic activity that is unrelated to plate boundary processes, without any assumption of the underlying cause for that activity. For example, in the case of mid-ocean ridges, material that passively rises to the surface in the gap between diverging plates cools on account of pressure release and expansion at the rate of $0.3^{\circ}\text{C km}^{-1}$, while the temperature at which melting occurs drops at the rate of $3^{\circ}\text{C km}^{-1}$ as the surface is approached. This leads to a melting zone several tens of kilometers thick near Earth's surface beneath the mid-ocean ridge

where the temperature of the rising mantle material is above its melting point. The net thickness of crust produced under these conditions is about 6 km. At hot spots, the crust is thickened beyond that nominal 6 km. There are at least three obvious ways to create more melt and thus thicken the crust: invoke some geodynamic process other than plate spreading to move more material vertically through the melting zone, add heat, or reduce the temperature at which melting occurs (by, e.g., adding fluids into the melt zone; Bonatti, 1990). Thus 'hot spots' need not be hot. Even when melting is caused by the addition of heat, it need not be internal in origin; for example, tidal friction caused by gravitational interactions with Jupiter, Europa, and Ganymede is suspected to be the cause of volcanism on Io (Spencer and Schneider, 1996). The fact that there are a number of ways to create the most obvious indication of a hot spot, thickened crust, has placed added importance on the use of other geophysical observations, such as seismology, to help determine the cause of melting.

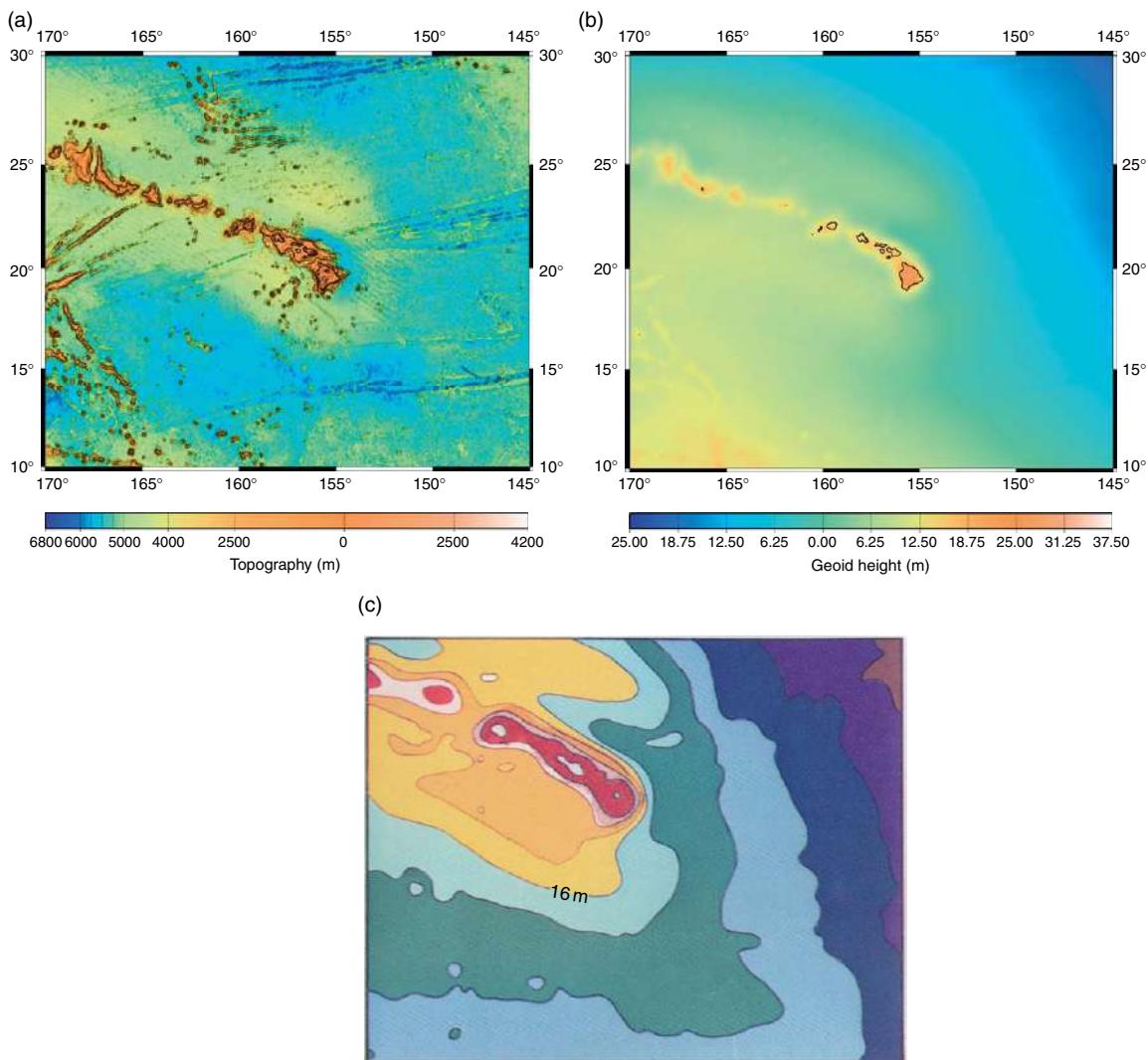


Figure 5 Regional topography (a) and geoid (b) centered on the Hawaiian Islands with the islands outlined. Note that the geoid, the equipotential surface approximating the sea surface, is smoother and lower amplitude than the topography. (c) The tear-drop shape of the Hawaiian swell at the southeast end of the Hawaiian chain is most apparent in the planform of the geoid anomaly after correcting for the geoid effect of the volcanoes and their isostatic compensation. From McNutt MK and Shure L (1986) Estimating the compensation depth of the Hawaiian swell with linear filters. *Journal of Geophysical Research* 91: 13915–13923.

In this chapter, we will not use the terms ‘hot spot’ and ‘plume’ interchangeably. Hot spots as a geologic phenomenon clearly exist. The debate is still ongoing as to which ones, if any, might be attributed to mantle plumes.

1.13.1.2 Potential Significance of Hot Spots

With Morgan’s elegant hypothesis that deep-mantle plumes produced age-progressive island chains on the surface of lithospheric plates, geophysicists and

geochemists immediately seized upon the potential for the study of hot spots to increase our understanding of the planet. First, it was hoped that the deep-mantle plumes might provide a fixed reference frame from which the absolute motions of the plates could be determined (Duncan, 1981; Gordon and Jurdy, 1986; Molnar and Stock, 1987). Second, the lavas erupted from the volcanoes created by the plumes might provide samples of and potentially define distinct rock reservoirs in Earth’s deep mantle (Zindler and Hart, 1986). Third, an intriguing correlation

between continental breakup and the initiation of plumes suggested that they might be a powerful force to rearrange the tectonic plates (Storey, 1995). More speculatively, changes in the flux from plumes through time could be the explanation for changes in sea level (Pitman, 1978), mass extinction events (Vogt, 1972), and geomagnetic superchrons (Larson and Olsen, 1991). Correlations between hot-spot activity and impact histories for the Moon and Earth led Abbott and Isley (2002) to suggest that hot spots might even be triggered by extraterrestrial impacts. With hot spots being the most obvious geologic phenomenon of internal origin that is not a direct consequence of plate tectonics, the general hope was that their study would reveal secrets about the interior of the planet otherwise masked by the rigidity of the surface tectonic plates.

In the last 40 years, plate tectonic theory has found complete acceptance in the scientific community. As new ways to probe the plates were devised, disparate bits of evidence were in agreement with the main tenants of the theory. After only a decade or so, the main research to address questions in plate tectonics was already in the phase of cleaning up loose ends and filling in details. In contrast, in that same 40 years, the existence of deep-mantle plumes as the explanation for hot spots has become even more mired in controversy. The predictions of plume theory are borne out for very few hot spots, and there is concern that in those few cases the reasoning is almost circular. For example, indeed the orientation and age progression on the Hawaiian chain match the model predictions for absolute motion of the Pacific Plate over a fixed mantle plume, but the absolute direction and rate of drift of the Pacific Plate was derived assuming that the Hawaiian chain records the motion of the plate over a fixed mantle plume! Even Morgan himself, early on, recognized that plume theory was unlikely to explain all hot spots (Morgan, 1978). There is no complete agreement even on how many hot spots there are now and in the recent geologic past (Davies, 1988; Sleep, 1990; Steinberger, 2000).

To be fair, some of the original expectations for the predictive power of plume theory were based on limited understanding of the properties in Earth's interior, and still are. For example, even if all hot spots are caused by plumes, it would never be possible for any set of global plumes to provide a fixed mantle reference frame on account of large-scale, time-dependent convection in the mantle (Steinberger and O'Connell, 1998). To this date,

debate continues on the nature of thermal boundary layers deep within this planet, on the scales of geochemical heterogeneity, and the interpretation of isotopic arrays (Phipps Morgan, 1999). More detailed and more sophisticated analysis of seismic data with resolving power below the transition zone (Montelli *et al.*, 2004; Ritsema and Allen, 2003) holds the promise for advancing understanding in these areas.

1.13.2 Types of Hot Spots

Young, high volcanoes actively erupting in mid-plate settings were the first manifestation of hot-spot volcanism to be so recognized. As the ocean basins were more thoroughly explored, several other categories of hot-spot activity became apparent based on their distinct morphology, including aseismic ridges (Laughton *et al.*, 1970), superswells (McNutt and Fischer, 1987), and large igneous provinces (LIPs) (Coffin and Eldholm, 1994). The latter category has been interpreted to include all of the former types of hot-spot activity, but in this chapter we will use the term in the more narrow sense to refer to voluminous flood basalts that erupt quickly over a large area (sometimes called 'transient LIPs').

1.13.2.1 Large Igneous Provinces

Both continents and ocean basins contain examples of large-volume flood basalts covering areas of 10^5 km^2 or more that erupted in time periods of the order of 1 My (Coffin and Eldholm, 1994). On the continents, these events are preserved in the thick basalt formations of the Deccan Traps, the Siberian Traps, and numerous other formations spanning the geologic ages. On the ocean floor, these types of eruptions form large submarine plateaus such as Ontong Java and Kerguelen. This category of hot-spot activity forms LIPs, the class of hot-spot-type volcanism that can rival the mid-ocean ridge system for crustal production during bursts of intense activity (Figures 6 and 7) and the form most likely to have widespread environmental consequences (Coffin and Eldholm, 1994).

The continental examples are relatively better studied than the oceanic LIPs on account of greater accessibility on land to field geologists for mapping, sampling, and dating. Sampling of submarine LIPs is hampered by their low relief, lack of subaerial exposure except in unusual cases (e.g., Heard Island on Kerguelen), and high rate of carbonate

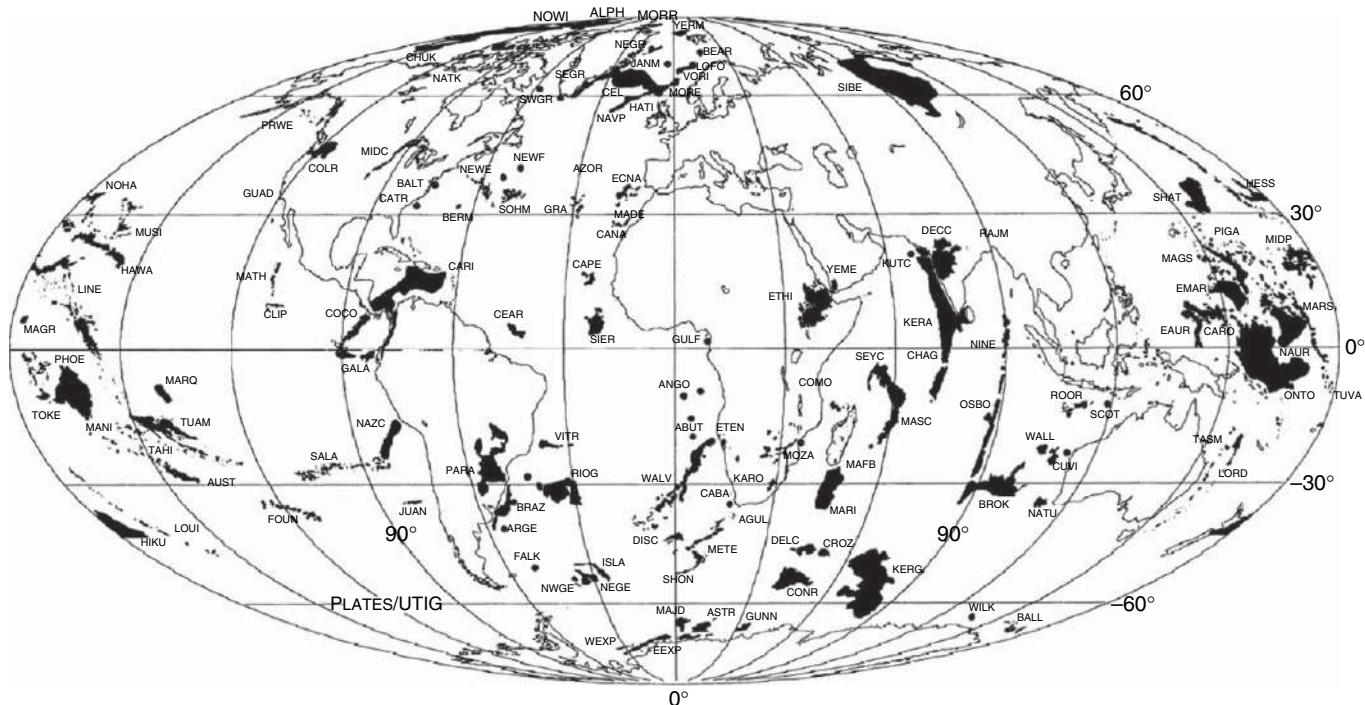


Figure 6 Global map of large igneous provinces (LIPS), including continental and oceanic flood basalt provinces, volcanic passive margins, oceanic plateaus, submarine ridges, and seamount groups. From Coffin MF and Eldholm O (1994) Large igneous provinces: Crustal structure, dimensions, and external consequences. *Reviews of Geophysics* 32: 1–36.

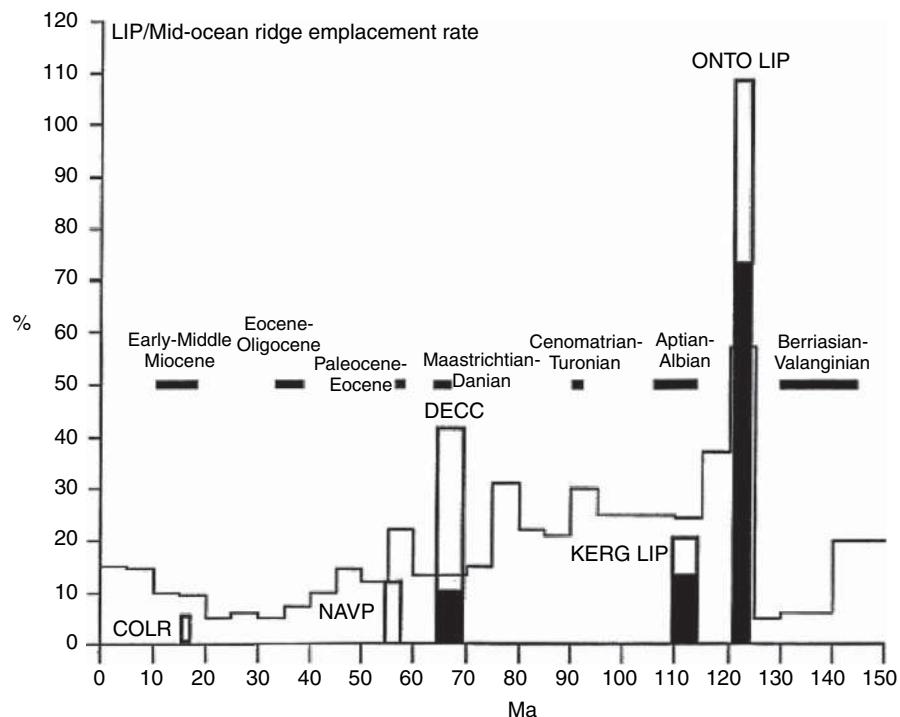


Figure 7 The volume of LIPs plotted as a percentage of the production of oceanic crust at mid-ocean ridges as a function of time. The thin line is the estimate from Larson (1991). The thick lines are estimates for the Colombia River basalts (COLR), the North Atlantic Volcanic Province (NAVP), the Deccan Traps (DECC), Kerguelen (KERG LIP, which includes Elan Bank and Broken Ridge), and Ontong Java (ONTO LIP, which includes Manihiki Plateau and the Mariana, Nauru, and Pigafetta basin flood basalts). Solid and open portions of columns indicate bounds on emplacement rates depending on assumptions concerning plate setting – on- vs off-ridge, and duration of volcanism. From Coffin MF and Eldholm O (1994) Large igneous provinces: Crustal structure, dimensions, and external consequences. *Reviews of Geophysics* 32: 1–36.

sedimentation. Therefore, much of the inference that the massive submarine plateaus formed very quickly is based on analogy with the continental examples, such as Deccan and Siberia.

Oceanic LIPs are found in both mid-plate and plate boundary settings, although significantly they tend to lie in extensional settings (e.g., in the wake of rifting continents). They rise 2 km or more above the surrounding seafloor and display anomalously thick oceanic crust. Few data are available for testing the models for the evolution of LIPs. What little data do exist from limited drilling suggest that LIPs subside at the same rate (i.e., as the square root of age) as normal oceanic lithosphere (Coffin, 1992).

The sheer size of LIPs limits what information can be obtained on crustal structure from seismology. Even the largest airgun arrays have insufficient power to image Moho continuously across oceanic plateaus. The best information to date comes from

seismic refraction experiments (e.g., Patriat *et al.*, 2002), which show velocity increasing from 5.5 km s^{-1} in the upper crust to values between 7.0 and 7.6 km s^{-1} in the lower crust (Furumoto *et al.*, 1976; Mutter and Zehnder, 1988).

Some laboratory and numerical experiments designed to simulate the rise of plumes through a mantle with temperature-dependent viscosity show that the leading edge of the incipient plume is a mushroom-shaped head followed by a long, thin tail (Whitehead and Luther, 1975; Christensen, 1984). Such pictures (Figure 8) inspired an interpretation of LIPs as the first very outpourings of basalt as the ‘plume head’ reaches Earth’s surface, and a linear hot-spot chain as the subsequent trace of the plate’s motion over the ‘plume tail’ (Richards *et al.*, 1989).

The agreement between the observations in the real world and the predictions from these simulations is far from perfect, however. Of 49 hot spots

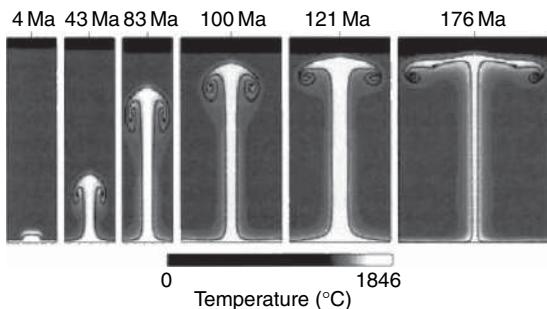


Figure 8 Sequence from a numerical model in which an axisymmetric plume grows from a thermal boundary layer in a fluid with temperature-dependent viscosity. The black line delineates fluid initially within the thermal boundary layer. Ambient viscosity is 10^{22} Pa s, the bottom boundary temperature is 430°C above the interior temperature, and its fluid viscosity is 1% that of the interior. From Davies GF (1999) *Dynamic Earth: Plates, Plumes, and Mantle Convection*, 458 pp. Cambridge, UK: Cambridge University Press.

examined by Courtillot *et al.* (2003), only five definitely traced back to a LIP, with another eight to ten potentially connected to an older flood-basalt event. In a few cases, the originating LIP might have already been subducted (e.g., a Hawaiian LIP might be already recycled into the mantle in the northwest Pacific beyond the Emperor Seamounts). Nevertheless, 60% of the hot spots in their catalog were demonstrably not associated with a LIP, meaning that those hot spots are either caused by headless plumes or not caused by plumes at all. At the same time, not all known LIPs have spawned hot-spot chains from a ‘plume tail’. There appears to be some nonrandom connection between LIPs and chains of hot-spot volcanoes, but too rare to support the plume head/plume tail hypothesis as a general rule. An alternate theory for the formation of LIPs, especially those on the edges of continents, is that they represent short-lived small-scale convection driven as an edge effect at strong geothermal gradients (Mutter *et al.*, 1988). Regardless of the origin of LIPs, if the basaltic rocks represent a 5–30% partial melt extracted from the mantle, the source for melts for the largest LIPs extends through all of the upper mantle down to the transition zone and perhaps below (Griffiths and Campbell, 1991).

1.13.2.2 Aseismic Ridges

Aseismic ridges are less voluminous volcanic outpourings that otherwise have much in common with LIPs. Like the more expansive LIPs, these ridges

stand 2–3 km above the surrounding seafloor and were originally termed ‘aseismic’ because the lack of earthquakes distinguished them from mid-ocean ridges and transform fault scarps (Laughton *et al.*, 1970). Examples include the Cocos Ridge (Figure 9), Nazca Ridge, Ninetyeast Ridge, the Rio Grande Rise, the Walvis Ridge, the Chagos-Laccadive Ridge, and the Iceland-Faeroe Ridge. The occurrence of aseismic ridges in extensional settings is even more clear-cut than is the case for LIPs. The ages of the volcanic rocks are similar to that of the underlying seafloor, and their rate of subsidence parallels that of the seafloor of the same age, although offset by the excess elevation of the ridge (Detrick *et al.*, 1977). Analysis of gravity/bathymetry ratios shows that they are locally compensated, meaning that the underlying plate had no elastic strength at the time that the ridges formed (Detrick and Watts, 1979). As is the case for LIPs, aseismic ridges do not tend to be associated with any noticeable swells.

All of this evidence supports the interpretation that aseismic ridges form when a hot spot coincides with a spreading ridge, a situation that apparently happens quite often. The excess melting from the hot spot combines with the normal crustal accretion process to form ocean crust 2–3 times thicker than would normally be the case (Ribe, 1995; Ito *et al.* 1996, 1997). The motion of the spreading plate away from the point of intersection of the ridge and hot spot is marked by more or less continuous ridges of thickened crust on both sides of the spreading ridge that mark the former location of excess crustal generation.

These ridges are generally age progressive, but do not always form distinct volcanoes presumably on account of the ease with which magma can rise through very young lithosphere without having to take advantage of existing magma conduits. A prediction of this theory for the origin of aseismic ridges is that hot spots that are truly centered beneath the ridge crests should create pairs of aseismic ridges on each side of the spreading center, although with different azimuths depending on the motion of each plate with respect to the locus of the hot-spot melting anomaly. This prediction is borne out in many cases; for example, the Walvis Ridge and the Rio Grande Rise form a conjugate pair across the southern Mid-Atlantic Ridge while the Cocos Ridge and the Nazca Ridge are conjugate across the Galapagos Spreading Center. If the hot spot is located close to the ridge but under only one of the plates, the morphology of the volcanoes might still resemble an aseismic ridge as

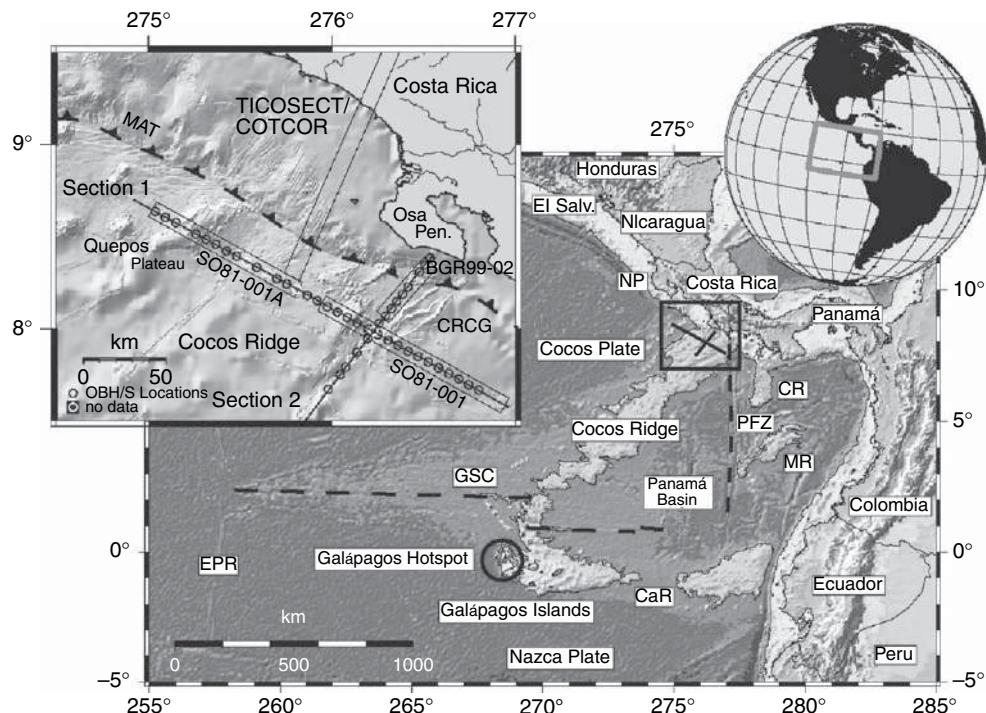


Figure 9 Location of wide-angle seismic survey undertaken by Geomar across the Cocos Ridge. The interpreted crustal structure along section 1 is shown in **Figure 10**. From Walther CHE (2003) The crustal structure of the Cocos Ridge off Costa Rica. *Journal of Geophysical Research* 108 (doi:10.1029/2001JB000888).

the volcanism occurs on very young lithosphere, but the conjugate ridge will not form.

The results from a wide-angle seismic reflection survey (Walther, 2003) to image the crustal structure of the Cocos Ridge offshore Costa Rica in the eastern Pacific (**Figure 9**) seem typical of the results from other aseismic ridges, such as the Faroe Ridge which lies on the European Plate east of Iceland (Smallwood *et al.*, 1999). The Moho (a seismic discontinuity representing the boundary between Earth's crust and mantle) is seen to deepen 10 km to compensate the 2 km elevation of the ridge above the surrounding seafloor (**Figure 10**). The seismic traveltimes and gravity data are best fit if the upper mantle beneath the ridge is assumed to have a low seismic velocity and low density contrast with respect to the lower crust. What is unexpected in the Cocos survey is the amount which lower crustal thickening, as opposed to extrusive volcanism, contributes to the volume of the ridge. In the center, units with lower crustal velocity and density make up 80% of the total crustal section, and the lower crust is 3 times the thickness of normal oceanic lower crust. Exceptionally high velocities ($>7.4 \text{ km s}^{-1}$) are not seen in the lower crust, as has often been reported beneath mid-plate island chains, and the upper mantle

is slower beneath the Cocos Ridge (7.6 km s^{-1}) than the average for normal oceanic upper mantle ($\sim 8 \text{ km s}^{-1}$).

1.13.2.3 Superswells

Superswells (**Figure 11**) represent clusters of hot spots in a restricted geographical region of anomalously high elevation that cannot be explained by crustal thickening. The first area so recognized was in the South Pacific (McNutt and Fischer, 1987). Volcanoes higher than 200 m are 10 times more likely to be found on the seafloor of the South Pacific superswell as compared to regions elsewhere in the Pacific even apart from the hot-spot chains (Bemis and Smith, 1993), suggesting that mid-plate volcanism at all scales is enhanced. Much of the seafloor now in the northwest Pacific appears to have been a superswell during the Cretaceous (McNutt *et al.*, 1990). The African superswell (Nyblade and Robinson, 1994) is a continental example of the same phenomena – unusual clusters of hot spots on a topographically elevated region. Individual hot-spot volcanoes located within superswells do tend to have their own swells, but they are small and only rise above the background depth

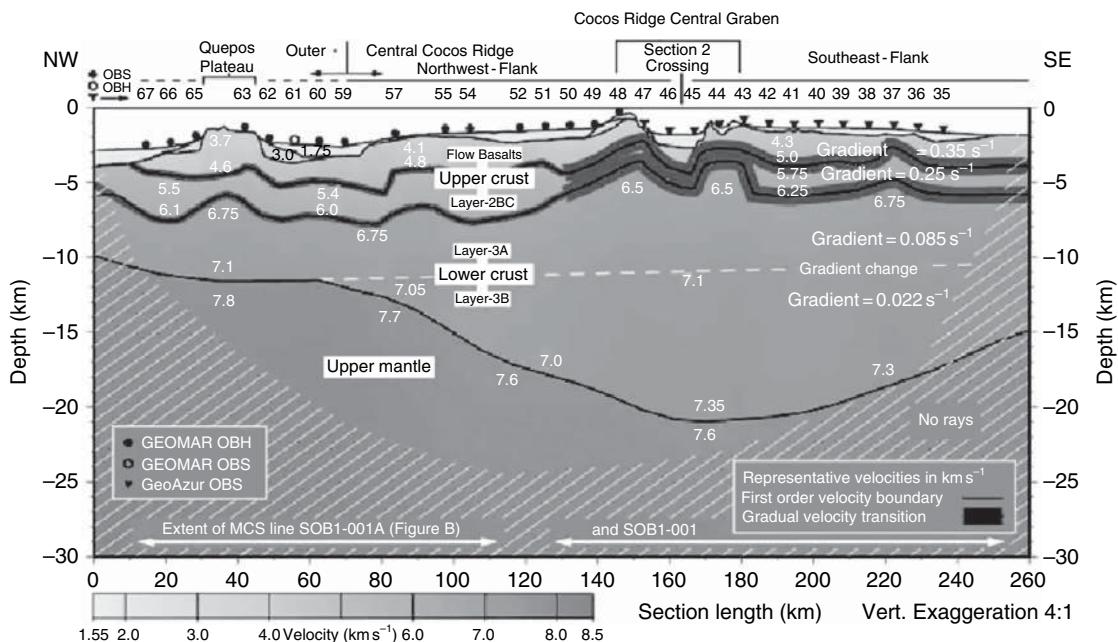


Figure 10 Crustal model for a 260-km-long transect across the Cocos Ridge, 35 km seaward of and parallel to the middle America Trench. (location shown as section 1 in Figure 9) Velocities are displayed in gray scale and for representative values in kilometers per second. The hatched area is not resolved. The crustal thickening of the Cocos Ridge occurs primarily within the lower crust rather than the surficial extrusives. There is no evidence for unusually high lower crustal velocities, and indeed the upper-mantle velocities are unusually low. From Walther CHE (2003) The crustal structure of the Cocos Ridge off Costa Rica. *Journal of Geophysical Research* 108 (doi:10.1029/2001JB000888).

anomaly of the superswell when located on very old lithosphere (McNutt, 1998; Sichoix *et al.*, 1998).

Some of the Pacific hot-spot island chains that diverge the most from the predictions of plume theory

are found on the superswell, and in fact superswell-type lithosphere appears to be very 'leaky' in terms of facilitating the ascent of magma to the surface (McNutt, 1998). Larson (1991) proposed that superswells are

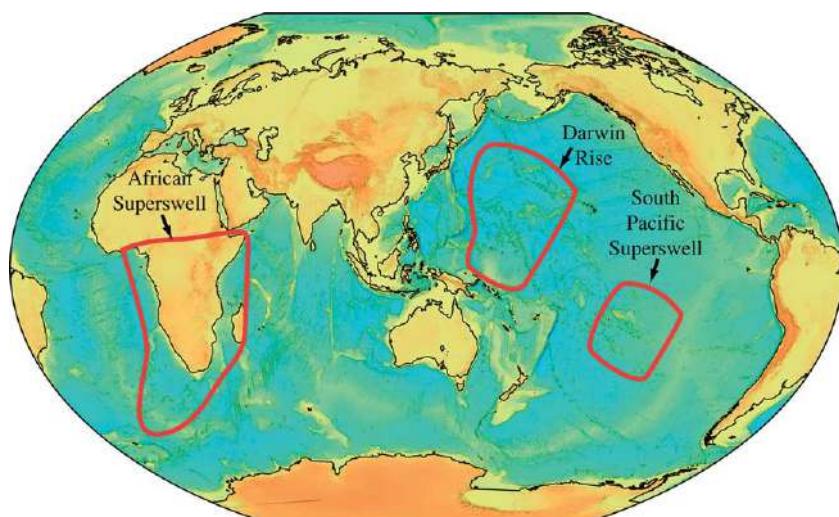


Figure 11 The African (Nyblade and Robinson, 1994) and South Pacific (McNutt and Fischer, 1987; McNutt and Judge, 1990) superswells are regions exhibiting anomalously shallow topography and unusually copious recent volcanism. The Darwin Rise has been interpreted as the location of a Cretaceous superswell (McNutt *et al.*, 1990).

produced by superplumes, which can be envisioned as long-lived by very broad upwelling in the mantle. The fact that superswells are so large makes them a relatively easy target for using reconnaissance geophysical data, particularly tomographic mantle seismic structure, to search for evidence of Larson's proposed superplume or any other features in the mantle that might contribute to the unusual amount and distribution of volcanism. Nishimura and Forsyth (1985) were the first to note low seismic velocities in the upper mantle beneath the South Pacific superswell using an analysis of Love-wave phase velocities. Global inversions performed since then (e.g., Figure 12) confirm the slow velocities in the upper mantle and extend them to the lower mantle beneath both the South Pacific and the African superswells (Dziewonski and Woodhouse, 1987; Su *et al.*, 1994; Masters *et al.*, 1996; Grand *et al.*, 1997; Dziewonski, 2005), although they differ in the details of how continuous the anomalous velocity structure is across the transition zone.

1.13.2.4 Mid-Plate Volcanic Chains and Clusters

Hot spots that do not fall into any of the categories above form isolated mid-plate volcanic chains and clusters (Figure 13). This is the most classic form of hot-spot volcanism, and examples in this category

show the most prominent hot-spot swells. Examples include the Hawaiian (Clague and Dalrymple, 1987) and Louisville (Lonsdale, 1988) chains on the Pacific Plate (Figure 13), the Easter Island chain (O'Connor *et al.*, 1995) on the Nazca Plate (Figure 13), Bermuda (Detrick *et al.*, 1986) on the North American Plate, Cape Verde (Courtney and White, 1986; Ali *et al.*, 2003), the Canary Islands (Watts *et al.*, 1997), and Reunion (Charvis *et al.*, 1999; Gallart *et al.*, 1999) on the African Plate, and many other young island and seamount groups found on mature lithosphere. Because plates and plate boundaries are always drifting relative to the locus of hot-spot volcanism, it is not unusual for a mid-plate hot spot that is forming a chain of individual volcanoes to drift close enough to a ridge crest, and then begin to form an aseismic ridge or conjugate pair of ridges. Hot spots can move away from ridges as well. Precise dating is key to understanding what portions of hot-spot volcanism has been influenced by proximity to a ridge.

Most of the geophysical investigation of hot spots using seismic and other methods has focused on this category of hot spots, and their close relatives on superswell-type lithosphere, because the anomalous characteristics that must be explained are more easily identified. For example, beyond their unusually thick crust, there is little in terms of a geophysical anomaly associated with aseismic ridges that might provide

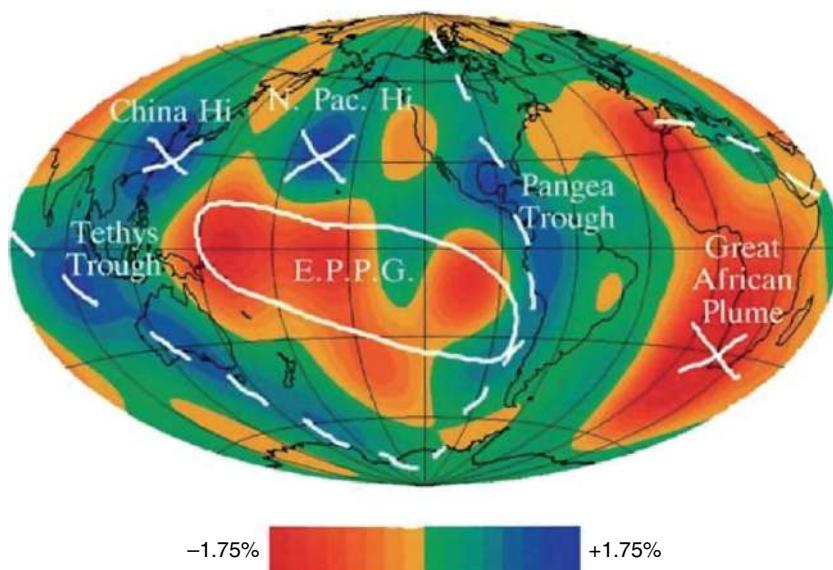


Figure 12 Global seismic tomographic image of shear-wave velocities at 2750 km depth. The South Pacific superswell (here labeled E.P.P.G. for Equatorial Pacific Plume Group) and the African superplume (here labeled Great African Plume) regions are associated with deep low-velocity anomalies that extend upward toward the surface. From Dziewonski AM (2005) The robust aspects of global seismic tomography. *Geological Society of America Special Paper* 388, pp. 147–154.

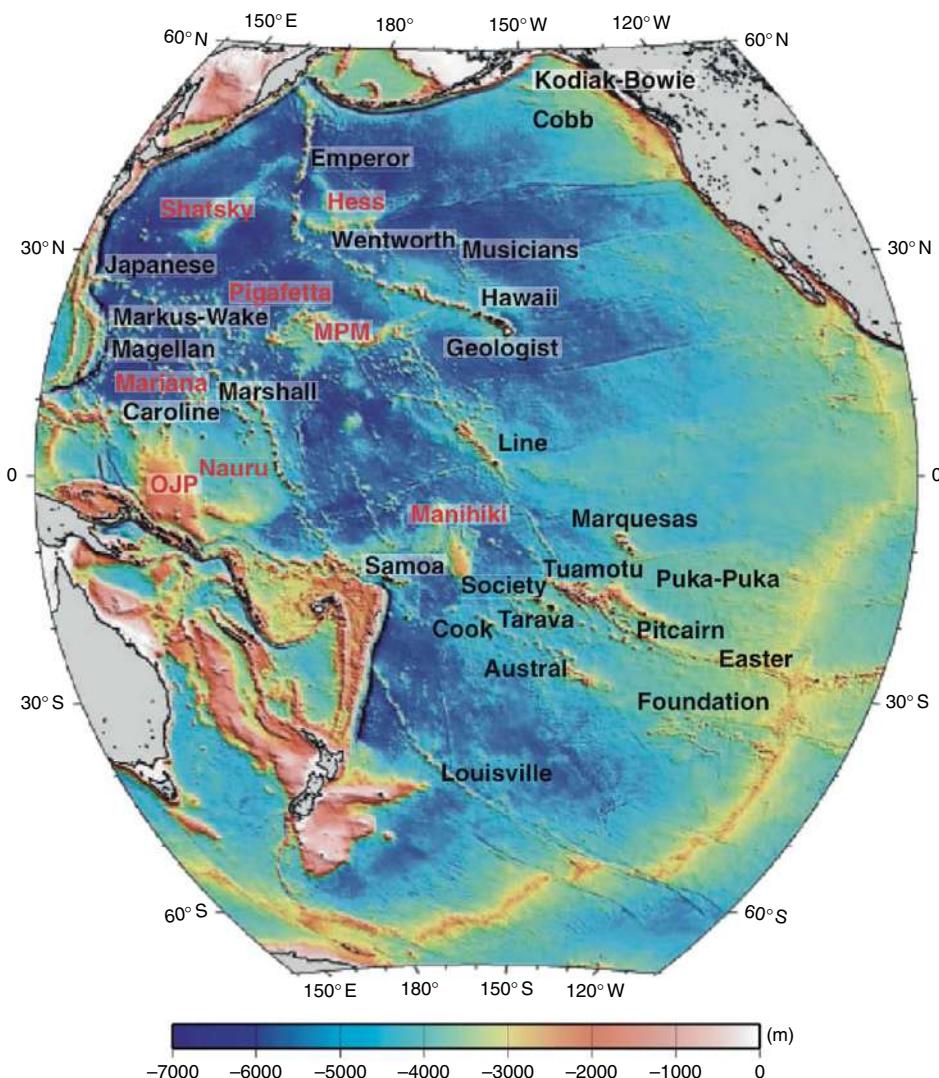


Figure 13 Linear volcanic chains shown on a bathymetric map of the Pacific Plate. Seamount chains are named in black; oceanic plateaus are named in red. MPM, Mid-Pacific Mountains; OJP, Ontong Java Plateau. Most seamounts occur in linear chains or clusters. From Clouard V and Bonneville A (2005) Ages of seamounts, islands and plateaus on the Pacific Plate. In: Foulger GR, Natland JH, Presnall D, and Anderson DL (eds.) *Geological Society of America Special Paper 388: Plates, Plumes & Paradigms*, pp. 71–90. Boulder, CO: Geological Society of America.

clues to the cause of the excess melting. LIPs are clearly more extreme events, but their sheer size confounds a clear separation of spatial and temporal events to probe causative mechanisms.

1.13.3 Geophysical Characteristics of Hot Spots

Basic geophysical observations such as depth, subsidence, gravity and geoid anomalies, and heat flow can be used to probe the crust and lithospheric structure of

hot spots and their swells. In fact, seismic investigations proceed usually only after all other data types have been exhaustively analyzed, as seismic field programs tend to be the most expensive to undertake. Briefly, we review the geophysical characteristics of hot spots and what they imply for crustal and lithospheric structure.

1.13.3.1 Orientation and Age

Hot spots erupting on the Pacific Plate (both as classic mid-plate volcanism and superswell-type volcanism) tend to form linear chains of volcanoes, with

the Hawaiian–Emperor chain forming one of the longest on the planet. Early on, this chain was shown to have a monotonic age progression to the west-northwest (Clague and Dalrymple, 1987). The trend of the chain and its age progression define the pole and rate of rotation for the Pacific Plate relative to the Hawaiian hot spot, and changes in the position of the pole and its drift rate through time. If the source of the hot spot is a stationary mantle plume, as proposed by Morgan (1971), then the rotation so derived should be the absolute motion of the Pacific Plate. This hypothesis that plumes might form a fixed reference frame against which the direction and rate of plate drift could be measured has now been shown to be incorrect. Tarduno *et al.* (2003) used paleomagnetic data from seamounts along the Emperor part of the Hawaiian–Emperor chain to test whether the paleolatitude of the Hawaiian hot spot had remained fixed over time. They concluded that the source of the Hawaiian melting anomaly moved at velocities exceeding 40 mm yr^{-1} , a rate similar to the rate of plate drift, during the Late Cretaceous and Early Tertiary.

Even though the notion of mantle plumes firmly anchored at the CMB must be abandoned, the orientations of most other active hot-spot chains on the Pacific Plate are co-polar with the Hawaiian chain, with the exception being the Marquesas (Crough and Jarrard, 1981). Furthermore, most chains of guyots and seamounts with Late Cretaceous and Early Tertiary ages are parallel to the Emperor part of the Hawaiian chain. These trends support the theory that hot spots form from plumes that are at least fixed with respect to each other, except for the fact that Kr–Ar and Ar–Ar dating demonstrated that only a few other Pacific volcanic chains, such as the Society Islands and possibly the Louisville seamount chain, show the predicted age progression (Duncan and McDougall, 1976; Lonsdale, 1988; Koppers *et al.*, 2004). The age discrepancies are equally apparent for older seamount chains, such as the Line Islands, which are co-polar with the Emperor seamounts, but lack a simple age progression (Schlanger *et al.*, 1984). At first, geophysicists and geochronologists attempted to explain the errant age distributions as the superposition of effects from several plumes that line up along the same trend, but the numbers of required plumes are ultimately untenable (McNutt *et al.*, 1997).

For the large number of linear chains that do not show monotonic age progressions, the most common age pattern is nearly synchronous volcanism at

several volcanic centers along the chain, with short age progressions in the Hawaiian sense. Perhaps significantly, none of the linear chains on the Pacific Plate show age progressions in the direction counter to the Hawaiian direction of progression. Therefore, while the plume model in detail is not a good fit to the majority of hot spots, the sequence of hot-spot eruptions is not completely random in space or time. Another explanation that has been proposed is that hot spots result from the rise of magma from more ubiquitous melt bodies in the upper mantle along lithospheric cracks (Turcotte and Oxburgh, 1973; Bonatti and Harrison, 1976; Anderson, 1996; Davis *et al.*, 2002), with the parallel trends resulting from a consistent plate-wide stress field. However, none of the Pacific chains display ages converging toward a central initiation point, as might be the case for volcanism occurring along a tensional tear in the plate.

In the Atlantic, the major island groups in this category do not form obvious lines, presumably because the hot spot is close to the Euler pole of rotation for the Atlantic Plate with respect to the melting anomaly (e.g., Cape Verde Rise; Morgan, 1971). For this reason, Pacific hot spots have received most of the attention in terms of using orientations and ages to test the plume hypothesis.

1.13.3.2 Depth and Subsidence

The height of the mid-plate swell surrounding the region of active volcanism also provides clues to the origin of hot spots. Crough (1978) noted that 10 hot-spot swells in the Pacific, Atlantic, and Indian Oceans all rise to depths of about 4000–4500 m, regardless of crustal age. Therefore, the depth anomaly (with respect to either some standard model or to the surrounding seafloor) for these swells increases with the age of the oceanic lithosphere at the time that the volcanoes erupted. There also appears to be some positive correlation between the size of the Hawaiian swell and the volume of the volcanoes through time (Phipps Morgan *et al.*, 1995), although it is difficult to correlate these two quantities back very far in time because there is no discernible swell along the Hawaiian/Emperor chain that is more than 43 My in age (Vidal and Bonneville, 2004).

Abyssal hills created at a mid-ocean ridge outcrop on the swell away from the volcanoes and their sedimentary debris aprons (“archipelagic aprons,” Menard, 1956), indicating that the seafloor has been lifted up from below. The source of the uplift

must be a reduction in density of the rocks somewhere beneath the swell, as geoid data (reviewed below) indicate that swells are isostatically compensated. The source of the density reduction could be heat, or a modification in either rock mineralogy or chemistry that reduces its density. Furthermore, the location of the buoyant material could be within the crust (e.g., by thickening the crust from below), lithosphere (e.g., by reheating the lithosphere by the hot spot), or asthenosphere (e.g., by upward flow of a hot plume). In order to narrow down the possibilities, other information such as subsidence rates, geoid anomalies, heat flow, and seismic data have been interpreted along with depth anomalies. For example, to first order, as the depth to the compensating mass increases, so does the height of the geoid anomaly over the swell. Seismic velocity is slower for rocks that have low density because they are hot, but faster for rocks that have low density by virtue of extraction of a basaltic melt component.

The fact that swells are larger on older lithosphere has been used to support a thermal explanation for the swell, because thermal contrasts from hot-spot source materials would be larger in comparison to old, cold, mature lithosphere than young lithosphere. The observed correlation between swell volume and volume of the volcanoes has been used to argue for a chemical origin for swells, as the volume of buoyant, residual mantle remaining after the extraction of the basaltic melt component should scale with the amount of melt removed.

The chemical swell origin hypothesis has been contradicted by several studies that concluded swells subside faster than normal oceanic lithosphere of the same age. Some of the clearest evidence for this anomalous subsidence has come from volcanoes in the western Pacific that formed on a former super-swell (McNutt *et al.*, 1990). Seismic reflection data image the contact between the reef and pelagic sediments capping former hot-spot islands that have now subsided to create guyots (Winterer *et al.*, 1993). The height above the seafloor of the basement contact measures the depth of the seafloor soon after the volcano erupted, on the very reasonable assumption that wave action bevels the volcano to sea level within a few million years. In the western Pacific, this depth is less than normal for lithosphere of that age, providing an estimate of the height of the super-swell at the time of Cretaceous volcanism. The depth below sea level of that contact measures how much the seafloor has subsided to the present. Data from both the seismic reflection surveys and from drilling

atolls (e.g., Ladd and Schlanger, 1960; Ladd *et al.*, 1967) indicate accelerated subsidence, favoring some sort of heat anomaly in the upper mantle that decays with time.

To explain the subsidence, Detrick and Crough (1978) introduced the concept of lithospheric thinning. According to this hypothesis, heat from a hot spot resets the temperature of the lower lithosphere below some depth (typically 40–50 km) to the temperature of the underlying asthenosphere. They showed that the anomalously high rate of observed subsidence was appropriate for lithosphere of that depth, as though the lithosphere had been reheated by the hot spot to a more youthful thermal structure. They argued that the tear-drop shape of the Hawaiian swell and its rate of subsequent subsidence along a conductive cooling curve were unlikely to be produced by a lithospheric plate drifting over a ‘bump’ in the asthenosphere (Menard, 1973) dynamically maintained by an upwelling mantle plume. They noted that the difficulty with their lithospheric thinning hypothesis was the requirement for exceptionally high rates of heat flux into the base of the lithosphere given the observation that it only takes ~3 My for the Hawaiian seafloor to rise from normal depths to the peak of the swell.

1.13.3.3 Geoid Height

The fact that swells were observed to subside along the predicted trajectory for a conductively cooling plate is consistent with a lithospheric origin for the depth anomaly, but the subsidence of depth anomalies only measures the change in buoyancy throughout a vertical column. The elevation information alone is insensitive to the depth of the causative source. The geoid, the gravitational equipotential surface coinciding with the mean sea surface, is smoother and varies less than elevation (no more than ±100 m globally relative to the reference ellipsoid), but reflects the depth of underlying low- or high-density anomalies. Geoid data, either as estimated from satellite radar altimeters (Figure 5) or as converted from gravity, have been used to estimate the depth to the low-density material supporting hot-spot swells on about 24 examples around the world (Crough, 1978; Monnereau and Cazenave, 1998, 1990). The first simplistic interpretations of geoid data used ratios of swell height to geoid height, which in an infinite wavelength approximation would yield the compensation depth of the swell (Haxby and Turcotte, 1978).

More sophisticated analysis takes into account the limited frequency content of the swell and the flexural compensation of the volcanoes (**Figure 5**), but still assumes simple dipole-like compensation (McNutt and Shure, 1986). For mid-plate swells, the compensation depths so determined were in the mid- to lower lithosphere, and the depth to the compensation increases with the age of the lithosphere, which supports the lithospheric thinning model.

However, as pointed out by Robinson and Parsons (1988), there are mechanisms for supporting a mid-plate swell that would place all the compensating material below the lithosphere, but still have an apparent depth of compensation lie well within the lithosphere. This situation could arise, for example, if a low-density mass is rising in a viscous asthenosphere. The induced flow would warp density interfaces above the rising mass (e.g., the swell at Earth's surface) and below the mass (e.g., in the transition zone or at the CMB). The net effect is that the swell and its compensation would be better represented as a tripole, and interpretation of the data in terms of a density dipole would give an incorrectly shallow compensation depth for the swell. An additional complicating factor is the possibility that the composition of the lower lithosphere itself is altered in the process of the hot-spot extracting basaltic melt, leading to buoyant uplift of a swell (Phipps Morgan *et al.*, 1995; McNutt and Bonneville, 2000). Without additional information on crustal and mantle structure, it is not possible to resolve the ambiguity in the interpretation of the elevation and geoid data.

1.13.3.4 Elastic Plate Thickness

Estimates of effective elastic plate thickness are also sensitive to temperature beneath mid-plate swells (McNutt, 1987). When volcanoes erupt in mid-plate settings, they are isostatically compensated by the lithosphere warping in an elastic manner beneath the weight of the volcano. Marine gravity data are very sensitive to the stiffness of the plate, with stiffer plates producing larger free-air gravity anomalies over the volcanoes and a longer distance from the flexural moat surrounding the volcano to the flanking arch. A similar elastic bending occurs where oceanic plates subduct into the mantle at deep-sea trenches. Watts *et al.* (1980) used shipboard gravity and bathymetry data to estimate the effective elastic thickness for mid-plate islands and trenches worldwide

(**Figure 14**). They determined an empirical relationship,

$$T_e = 2.7\sqrt{t}$$

where t is the age of the lithosphere in million years and T_e is its effective elastic thickness in kilometers. Using standard thermal models for lithospheric plates (e.g., Parsons and Sclater, 1977), the base of the elastic portion of the lithosphere would correspond to the depth of the ~450°C isotherm.

A number of hot-spot volcanoes, particularly those on the South Pacific superswell, show T_e values that require shoaling of the 450°C isotherm (McNutt, 1984; Calmant and Cazenave, 1986; Calmant, 1987). At first, this was interpreted as strong evidence in favor of the lithospheric reheating model, as it appeared to require elevated temperatures well within the lithospheric portion of the mantle. However, McNutt *et al.* (1997) demonstrated in the Austral Islands that one consequence of volcanic overprinting caused by multiple volcanic centers along the same linear trajectory would be low estimates for elastic plate thickness. The earlier phases of volcanism, which loaded a younger and therefore weaker plate, are difficult to detect and date because they are covered over by the most recent volcanic activity. If the entire load is assumed to be the same age as the surface lavas, the estimated elastic thickness is some compromise between the low value for the older phase of volcanism and the higher value for the more recent phase. Given how few hot-spot chains show one simple linear age progression, particularly for superswell hot spots, underestimating the true mechanical strength of the lithosphere beneath hot spots is likely quite common.

Ideally, one would like to be able to compare elastic thickness estimates for volcanoes on hot-spot swells with those from entirely different geologic settings where no thermal processes are associated with forming the loads that flex the plate. The outer rises formed where plates bend before descending into the mantle provide the best opportunity to calibrate the elastic thickness in a setting free from any thermal disruption. The estimates of elastic thickness from trenches are similar to those determined for volcanoes on swells. The current consensus seems to be that the effective elastic thickness of the lithosphere where it is flexed over hot-spot swells is not much different from that of lithosphere unaffected by hot-spot volcanism.

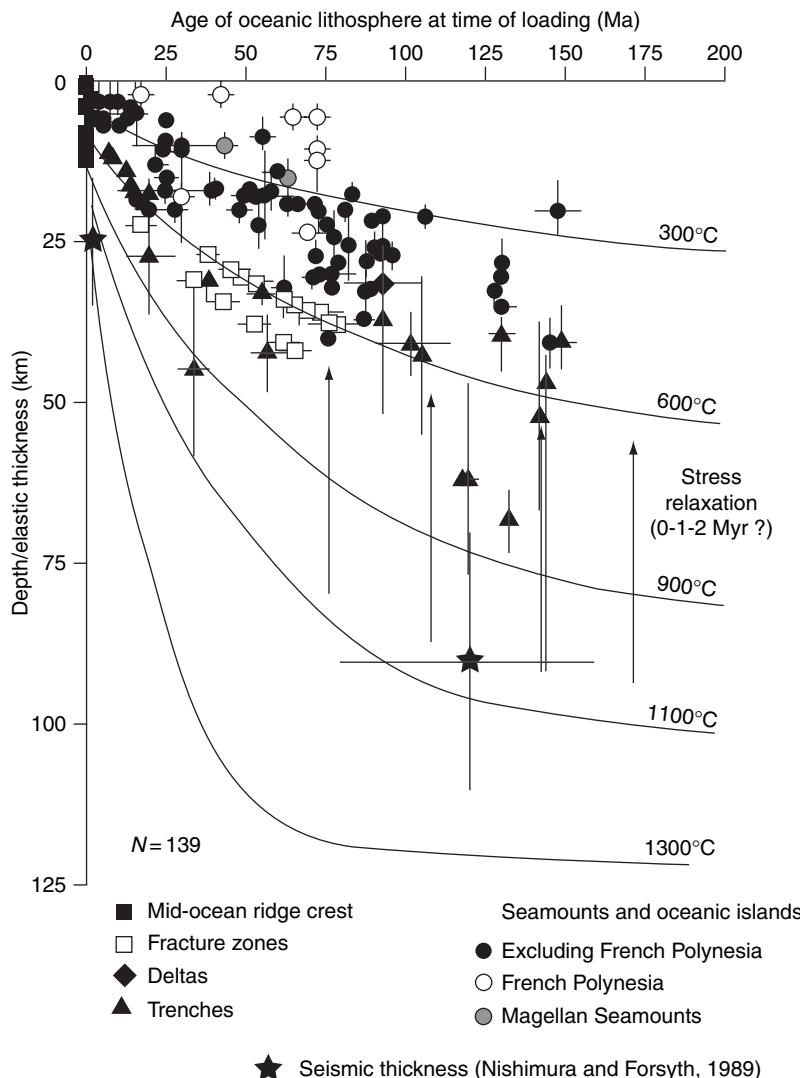


Figure 14 Plot of elastic plate thickness against the age of the lithosphere at the time of loading for oceanic lithosphere. Also shown are two measurements of lithospheric thickness from seismic surface wave studies (Nishimura and Forsyth, 1985). These data indicate that the elastic plate thickness increases as the lithosphere ages and cools, and that the thickness of the lithosphere exhibiting flexural rigidity is less than the plate thickness inferred from seismic observations. From Watts AB (2001) *Ilostacy and Flexure of the Lithosphere*, 458 pp. Cambridge, UK: Cambridge University Press.

1.13.3.5 Heat Flow

Heat flow observations, defined as the product of thermal conductivity k of the sediments at the surface of the plate and the temperature gradient dT/dz , also have the potential to distinguish among different models for the distribution of any heat associated with hot spots. If hot spots are not hot at all (e.g., melting caused by decompression or addition of volatiles), then one would expect no heat flow anomaly associated with hot spots. If excess heat is involved, there should be a heat flow anomaly detected at the seafloor eventually, but

its appearance would be delayed by the time it takes for temperature to conduct through the lithosphere to the surface from its point of origin. Therefore, the delay time between the onset of hot-spot volcanism and the detection of a heat flow anomaly provides an estimate for the depth to the heat source.

Detrick *et al.* (1981) conducted a heat flow survey occupying seven sites along the Hawaiian arch just south of the islands (Figure 15). They found that near the active volcanoes on the island of Hawaii, heat flow is normal for 80–90 Ma lithosphere. But further along the arch, near volcanoes that are 6 My

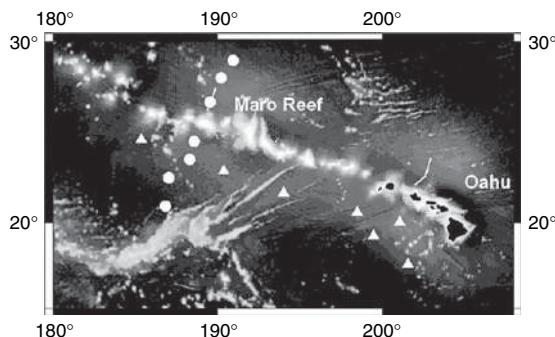


Figure 15 The Hawaiian Islands in the central Pacific and location of heat flow stations. The triangles are the South Arch survey of Detrick *et al.* (1981). The circles are the Maro Reef survey of Von Herzen *et al.* (1989). The solid white lines north of Maro Reef and Oahu show the location of dense heat flow measurements collected by Harris *et al.* (2000a). From McNutt MK (2002) Heat flow variations over Hawaiian swell controlled by near-surface processes, not plume properties. In: Takahashi E, Lipman PW, Garcia MO, Naka J, and Aramaki S (eds.) *Geophysical Monograph Series*, vol. 128: *Hawaiian Volcanoes: Deep Underwater Perspectives*, pp. 365–372. Washington, DC: American Geophysical Union.

old, the heat flow values were $5\text{--}8 \text{ mW m}^{-2}$ higher than expected, or about 10% above the baseline value (Figure 16). Heat flow remained elevated to at least 22 Ma down the swell. The pattern of the anomaly was consistent with the predictions of the lithospheric reheating model, and indicated that the lithosphere had been thinned to 40–50 km depth (Von Herzen *et al.*, 1982). The survey was criticized, however, for not having sampled the heat flow values at sites in the same general part of the Pacific but well off the swell. Given the large scatter in heat flow values worldwide, was it possible that the pattern was unrelated to the Hawaiian swell?

To better constrain the pattern and amplitude of anomalous heating of the plate beneath Hawaii, Von Herzen *et al.* (1989) conducted a second survey across the Hawaiian swell at Maro Reef (Figure 15), the locus predicted to display the maximum anomalous heating if the plate is thinned to only 40 km. The line of heat flow stations was long enough such that the beginning and end of the line would be well onto normal oceanic lithosphere off the swell. Rather than reducing the uncertainties from the earlier survey, the Maro Reef survey raised more questions than it answered. The pattern of heat flow at the eight stations display a W pattern, with the highest heat flow values located near the center of the line at Maro Reef and off the swell (Figure 16), on

supposedly normal lithosphere. Four out of the six stations sampling heat flow on the swell had resolvably lower heat flow than the sites off the swell, given the uncertainties in the data. The observations were definitely not compatible with the predictions of the lithospheric thinning model. However, with only eight stations spaced across 1200 km and each defining a local high or low in the pattern, it was impossible to conclude anything about the physical processes that might give rise to this remarkable heat flow.

Harris *et al.* (2000a) conducted more detailed sampling of heat flow across the Hawaiian swell at two locations, near Maro Reef (~17 My since hot-spot volcanism) and Oahu (~4 My years since hot-spot volcanism) (Figure 15). They found that the mean heat flow on the Hawaiian swell is slightly larger at Oahu ($74.2 \pm 14.6 \text{ mW m}^{-2}$) than at Maro Reef ($64.0 \pm 4.9 \text{ mW m}^{-2}$). No model for thermal sources below the lithosphere, unless the lithosphere were thinned to but a few kilometers thickness by a hot spot, would predict that elevated heat flow could be detected on the swell just 4 My after the onset of hot-spot activity. Harris *et al.* (2000b) concluded that a more likely explanation for the heat flow values over the Hawaiian swell is that the high relief of the hot-spot volcanoes is driving large-scale circulation of seawater through the permeable oceanic basement rocks underlying a more impermeable sediment blanket. This hydrothermal system mines heat from within the volcano itself, and discharges it through isolated basement highs that penetrate the sediment blanket. According to this model, younger regions of the swell, such as near Oahu, would show greater variability in heat flow because the sediment capping is less developed than further along the swell at Maro Reef. Heat flow values over the flexural moat would be the lowest on account of the large amount of volcaniclastic sediment infill, with higher values near the volcanic edifice and beyond the flexural arch. These observations are in good agreement with the data from the Hawaiian surveys and from a similar survey conducted at the Réunion hot spot (Bonneville *et al.*, 1997).

McNutt (2002) supported this interpretation of the heat flow data by noting that the W pattern of the heat flow over the Hawaiian swell at Maro Reef is actually produced by a W pattern in the large measured variations in thermal conductivity of surface sediments (Figure 16). The temperature gradients themselves show an M pattern and do not dominate the resulting heat flow. Temperature gradients and

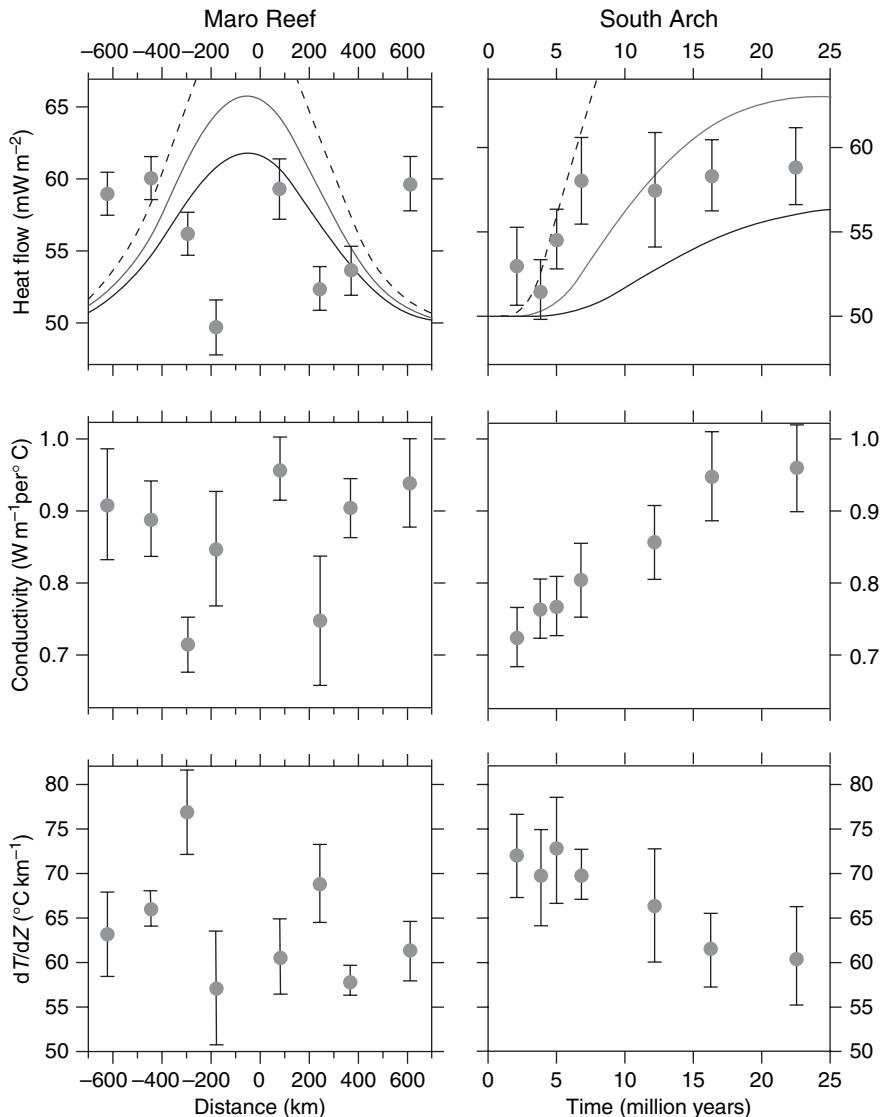


Figure 16 Left: Heat flow (upper), conductivity (middle), and vertical temperature gradient (lower) at Maro Reef (Von Herzen et al., 1989) plotted as a function of distance across the chain. Right: Heat flow (upper), conductivity (middle), and vertical temperature gradient (lower) along the south arch of the Hawaiian Islands (Detrick et al., 1981) plotted as a function of time since the plate drifted past the hot spot. Lines on the upper panels show the theoretical variations in heat flow expected if the hot spot reheated the lower lithosphere to asthenospheric values ($\sim 1350^{\circ}\text{C}$) as it passed over the thermal source. The amount of thinning assumed is 60 km (solid line), 50 km (dotted line), and 40 km (dashed line). From McNutt MK (2002) Heat flow variations over Hawaiian swell controlled by near-surface processes, not plume properties. In: Takahashi E, Lipman PW, Garcia MO, Naka J, and Aramaki S (eds.) *Geophysical Monograph Series*, vol. 128: *Hawaiian Volcanoes: Deep Underwater Perspectives*, pp. 365–372. Washington, DC: American Geophysical Union.

thermal conductivity are also inversely correlated along the original south arch survey at Hawaii (Figure 16). The data indicate that areas of high conductivity act as radiators while areas of low conductivity act as insulators, producing nonuniform conduction of heat to the seafloor that is controlled by variations in surficial thermal conductivity. The

simplest model that reproduces quantitatively the observed correlations between heat flow, temperature gradient, and thermal conductivity assumes two conducting layers above an isothermal layer at depth (Figure 17). Surprisingly, the best fit of the model parameters to the data, assuming that the upper layer corresponds to the pervasive blanket

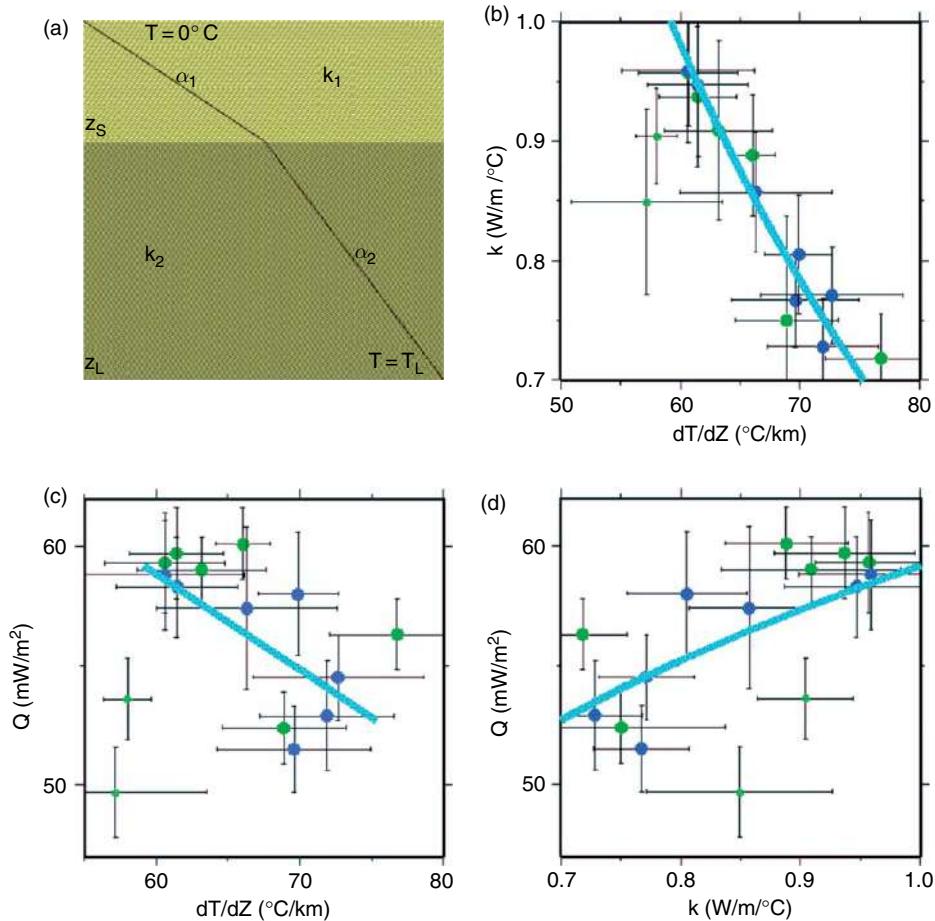


Figure 17 (a) Simple two-layer model for heat transport near the Hawaiian Islands. The upper layer of thickness z_s has thermal conductivity k_1 and temperature gradient α_1 . The lower layer of thickness $(z_L - z_s)$ has a higher thermal conductivity k_2 and temperature gradient α_2 . The lower boundary is maintained at an isothermal temperature T_L by fluid circulation. The upper boundary is maintained at temperature $T = 0^\circ\text{C}$ by the ocean. (b) Plot of thermal conductivity k vs vertical temperature gradient dT/dz for the South Arch (blue dots) and Maro Reef (green dots). The blue line shows the least-squares best fit to the data as k_1 (equivalent to k in the observed data) is varied in the model in (a), excluding the two Maro Reef outliers shown as small dots. These outliers correspond to the measurements at $x = -177$ km and $x = 375$ km in [Figure 15](#). (c) Same as (b), but for heat flow Q as a function of dT/dz (equivalent to α_1 in the model). (d) Same as (b), but for Q as a function of k . From [McNutt MK \(2002\)](#) Heat flow variations over Hawaiian swell controlled by near-surface processes, not plume properties. In: [Takahashi E, Lipman PW, Garcia MO, Naka J, and Aramaki S \(eds.\) Geophysical Monograph Series, vol. 128: Hawaiian Volcanoes: Deep Underwater Perspectives](#), pp. 365–372. Washington, DC: American Geophysical Union.

of pelagic sediments into which the heat flow probe is inserted, yields a total temperature drop from the ocean to the isothermal layer of only 21°C , and a depth to the base of the lower conducting layer of only 500–900 m. The isothermal layer, therefore, resides within the upper oceanic crust, where pervasive fluid circulation homogenizes any lateral variations in temperature that might be associated with the Hawaiian hot spot. [McNutt \(2002\)](#) thus concluded that variations in heat flow across the

Hawaiian swell are controlled by variability in the thermal conductivity of surface sediments, reflecting geological factors such as carbonate content.

These recent studies have underscored the importance of seismic reflection images in site selection and in the interpretation of marine heat flow. Prior to the recognition of fluid flow in the upper crust surrounding hot spots, the only concern was to avoid hard rock outcrops that would bend the heat flow probe or at least prevent a successful vertical

insertion into more pliable sediments. After the realization that more permeable rock outcrops significantly perturb the hydrologic regime by serving as foci for venting and recharge of crustal fluids, avoiding any basement relief in choosing heat flow sampling sites became even more essential. Interpretation of heat flow data in terms of conductive transfer of heat from subcrustal levels to the ocean through a uniform and impermeable sedimentary blanket cannot be attempted unless there is the seismic coverage to rule out basalt outcrops penetrating the sediments. For these applications, single-channel seismic data will often suffice, but multichannel data to image faults in the basement and overlying sediments are even better.

Heat flow has been sampled over other swells, such as Cape Verde (Courtney and White, 1986) and Bermuda (Detrick *et al.*, 1986). Both swells show a modest rise in heat flow (10–20%) near the peak of the swell as compared with values on the nearby abyssal plains, supporting the hypothesis that hot spots are hot. The results from these Atlantic swells, however, are not very useful for determining the depth to the hot material, because the volcanism is concentrated in one area (just one Miocene volcano in the case of Bermuda), making it impossible to estimate how long it took for the heat flow anomaly to be manifest at Earth's surface.

It has been known for years that heat flow on young (<65 Ma) lithosphere is significantly perturbed and biased by hydrothermal circulation (Lister, 1972). In his recent review of marine heat flow observations worldwide, Von Herzen (2004) concluded that at least 40% of all heat flow observations on seafloor 65–95 Ma show evidence for hydrothermal circulation, and the fraction only drops to 30% for even older lithosphere. He suggested, however, that the circulation in mature lithosphere (>60 Ma) might be merely redistributing heat within a permeable basement beneath sediments without advective gain or loss, which would then lead to conductive heat flow variations controlled by thermal conductivity as advocated by McNutt (2002). Therefore, the heat flow mean as determined from many measurements over a large area should represent the true heat flux through the lithosphere. On this assumption, one can conclude that there are modest (10–25%) heat flow anomalies associated with hot-spot swells, but that our lack of understanding of the length scales over which fluid circulation redistributes the heat prevents any detailed picture of

the spatial or temporal pattern for where and when that heat reaches Earth's surface.

1.13.4 Seismic Constraints on Crust and Lithosphere

The geophysical observations reviewed above provide but few constraints on how crustal and lithospheric structure is modified by hot spots. The depth anomalies of mid-plate swells require density reduction at depth, and the geoid height requires that low-density material to be below the mid-lithosphere in most cases. Heat flow evidence suggests that the low-density material is at least partially thermal in origin, although the effects of near-surface fluid circulation effectively mask much of the spatial and temporal pattern of any thermal disturbance. Geophysicists have therefore turned to seismology to better understand the deep structure of the Earth beneath hot spots and their swells. It is important to begin an investigation of hot spots from the top of the crust down into the lithosphere for at least two reasons. First, the surface structure is more accessible and can be probed using a number of seismic techniques, including active-source reflection and refraction, as well as imaging with passive arrays. Second, properly accounting for the effects of surface structure is necessary in nearly all geophysical analyses before determining what portion of the observed signal is of deep origin. Examples of crustal and lithospheric targets for seismic investigation, why they are important, and what has been learned are summarized below.

1.13.4.1 Sedimentary Structures

The largest hot-spot volcanoes are surrounded by massive volcaniclastic debris aprons that can exceed both the area and the volume of the intact volcanoes themselves (Moore *et al.*, 1989). The slope failures which produce these landslide deposits occur many times during the period of active volcanism, and continue during the post-eruptive phase, particularly if the volcano is not protected from the seas by a fringing coral reef. These post-eruptive sedimentary units provide a wealth of information on the history of a particular hot spot that is often more amenable to seismic imaging than is the volcanic edifice itself. In the oceans, these are well imaged by marine multi-channel seismic data augmented with refraction data from sonobuoys or ocean-bottom seismometers

(OBSs) to calibrate the velocity structure. In many cases, the value of the seismic data has been significantly enhanced by ocean drilling to provide accurate timelines through dating and other useful information, such as paleomagnetic chronology and paleoenvironmental history.

[ten Brink and Watts \(1985\)](#) obtained a seismic reflection image of the moat stratigraphy along a line crossing the Hawaiian chain and applied two-dimensional (2-D) modeling to determine whether the geometry of the reflectors contains any information on changes in elastic thickness that could be associated with the thermal evolution of the Hawaiian swell. In order to fit the apparent off-lap patterns in the stratigraphy, they assumed prolonged (>1 My) viscoelastic relaxation of the elastic plate. The cause of this relaxation of the elastic stresses would presumably be heat from the hot spot conducting through the lithosphere up the base of the elastic plate. If such an interpretation had been confirmed, it would have been good evidence for lithospheric thinning by the Hawaiian hot spot.

However, in a followup study, [Watts and ten Brink \(1989\)](#) demonstrated that a similar off-lap pattern could be produced in a 3-D model with progressive loading of the plate by new islands along the chain without requiring any temporal decrease in the stiffness of the elastic plate. [Rees et al. \(1993\)](#) acquired the definitive 3-D data set to test this hypothesis that the stratigraphic pattern in the Hawaiian moat was caused by sequential loading of volcanoes on an elastic plate of uniform elastic strength. Their single-channel reflection survey of the Hawaiian flexural moat imaged the sedimentary structures both across and along the strike of the chain between the islands of Hawaii and Kauai. They were able to explain the resulting stratigraphy in terms of competing effects of erosion/mass wasting, subsidence, and flexure. Significantly, [Rees et al. \(1993\)](#) did not require any temporal change in the elastic stiffness of the plate using a 3-D model. They noted that initially when a new volcano forms, the flexural moat is underfilled with sediment as the seafloor subsides beneath the weight of the new volcano faster than mass wasting can fill in the depression. Later, as volcano construction ceases and volcanic material is redistributed from the islands into the surrounding moat in major mass wasting events, the moat becomes filled, and in the case of older islands such as the Marquesas, overfilled such that the sediment surface in the moat slopes away from the volcanoes ([Filmer et al., 1994](#)). The

gently sloping sedimentary blanket surrounding mature volcanoes has been termed an ‘archipelagic apron’ ([Menard, 1956](#)).

Seismic reflection images of the sedimentary debris that fills the flexural moats surrounding mid-plate hot-spot chains can also be used to estimate the volume of volcaniclastic sediments that must be added to the volume of the edifice itself in order to get an accurate estimate of the amount of melt produced by the hot spot. For example, the moat surrounding the Marquesas Islands is overfilled with 200 000 km³ of volcaniclastic sediments with seismic velocities ranging from 4 to 5 km s⁻¹ ([Filmer et al., 1994](#)). The acoustically chaotic core of the apron interior suggests that the moat fill consists primarily of debris flows from mass wasting events. Individual volcano collapse events can involve volumes exceeding 100 km³ and may occur tens to hundreds of times during the life of a volcano. After accounting for the material filling the flexural moat, the Marquesas hot spot, during its peak activity at 3.5–5 Ma, was erupting nearly 0.10 km³ of volcanic rock per year, which exceeded the rate of eruption of the Hawaiian hot spot during that same time period and is nearly as large as Hawaii’s current rate for the past 1 My ([Figure 18](#)). The much larger apparent size of the Hawaiian volcanoes results from the fact that they load a stiffer elastic plate, are superimposed on a higher swell, and have not yet been as deeply eroded as the Marquesas Islands.

[Watts et al. \(1997\)](#) conducted a similar analysis for the Canary hot spot in the eastern Atlantic. Using multichannel seismic images from the flexural moat, they determined that 150 000 km³ of material has been added above the preexisting surface of the flexed plate by the Canary hot spot, a number quite comparable to that for the Marquesas. The corresponding estimated magma generation rate, however, is only 0.006–0.02 km³ yr⁻¹ on account of the much longer duration of the shield-building stage for the Canary volcanoes.

1.13.4.2 Volcanic Crust and Underplating

Hot-spot volcanoes, like all volcanoes, are built by the eruption of lavas on top of the preexisting crust. However, volcanism is also associated with the interaction of the rising magma with the upper mantle and crust, including the emplacement of intrusive igneous rocks within the volcano, the crust below, and possibly the upper mantle. Consequently, constraints on the complete upper mantle and

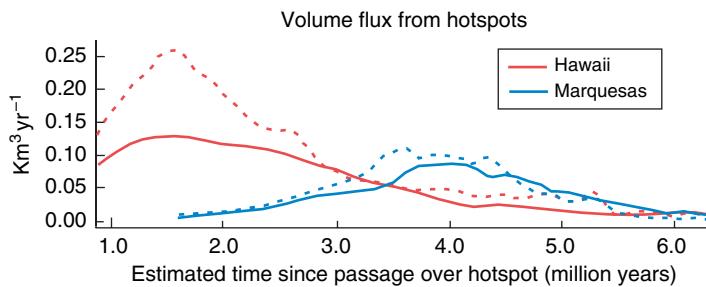


Figure 18 Volume flux of erupted volcanic rock as a function of time along the Marquesas and Hawaiian chains, as calculated from deflection models. Volcano names are shown for both chains at dated ages, with the Marquesan volcano names underlined. Solid lines are corrected for swell topography, dotted lines are uncorrected. Adapted from Filmer PE, McNutt MK, Webb HF, and Dixon DJ (1994) Volcanism and archipelagic aprons: A comparison of the Marquesas and Hawaiian Islands. *Marine Geophysical Research* 16: 385–406.

crustal structure are required to understand such basic aspects of hot spots as magmatic flux and lithospheric loading. Although modern marine seismic reflection systems that combine pneumatic sources with 3–6 km (or longer) arrays of hydrophone receivers are capable of imaging Moho in normal (\sim 6-km-thick) oceanic crust, the thickened crust and rough topography of submarine volcanoes make seismic reflection methods inadequate to penetrate the full crustal structure of most oceanic volcanoes. The best full crustal models obtained to date at oceanic hot spots derive from seismic refraction experiments in which the sources and receivers are widely spaced and variations in seismic velocity are imaged.

Hawaii was the first hot spot to be investigated with deep-penetrating marine refraction data. Watts *et al.* (1985) and ten Brink and Brocher (1987) collected multichannel seismic reflection data and conducted several two-ship expanding spread profile (ESP) refraction experiments along a cross section of the Hawaiian swell near Oahu. Each ESP yielded a 1-D crustal seismic velocity model; used together, the ESP models comprise a 2-D cross section of the Hawaiian hot-spot trace. Unexpectedly, Watts *et al.* (1985) found that the center of the volcanic chain is underlain by a 4-km-thick and 200-km-wide subcrustal body with unusually high seismic velocity ($7.4\text{--}7.8 \text{ km s}^{-1}$) for the lower oceanic crust (Figure 19). An apparent bifurcation of Moho was observed in the reflection profile on both sides of the volcanic edifice, bounding the high-velocity body. Watts *et al.* (1985), ten Brink and Brocher (1987), and Watts and ten Brink (1989) interpreted this unit as a deep crustal sill complex and Watts and ten Brink (1989) referred to it as ‘volcanic

underplating’. The underplating interpretation was disputed by Lindwall (1988), who demonstrated that the critical ESPs beneath the center of the volcanic chain can also be reasonably fit by crustal models without a deep, high-velocity zone (Figure 19). More recent seismic refraction experiments at oceanic hot spots have used arrays of OBSs or ocean-bottom hydrophones (OBHs) as receivers, allowing for continuous 2-D or 3-D seismic velocity models that avoid the ambiguity inherent in the ESP refraction geometry.

Caress *et al.* (1995) obtained deep seismic reflection and high-quality refraction data beneath a second hot-spot chain, the Marquesas, and confirmed a second example of magmatic underplating. Three long MCS lines were located across the chain in gaps between the islands, and a refraction line using OBSs coincided with the central line. The multichannel seismic reflection data imaged the surface of the crust preexisting the eruption of the hot-spot volcanoes. The OBS refraction data imaged crustal arrivals constraining the velocity structure within the crust and also clearly imaged wide-angle reflections from the base of the preexisting crust, and, beneath the center of the volcanic chain, from a deeper interface. A 2-D tomographic inversion of the refraction and reflection arrival times demonstrated that a normal oceanic crustal structure lay beneath the Marquesas volcanoes, but was itself underlain by a large body with seismic velocities ($7.5\text{--}7.9 \text{ km s}^{-1}$) intermediate between normal lower-crustal and upper-mantle values. The strength of the wide-angle reflections from the relict Moho and the base of the subcrustal body indicates that this magmatic underplating unit (Figure 19) is strongly distinct from both the

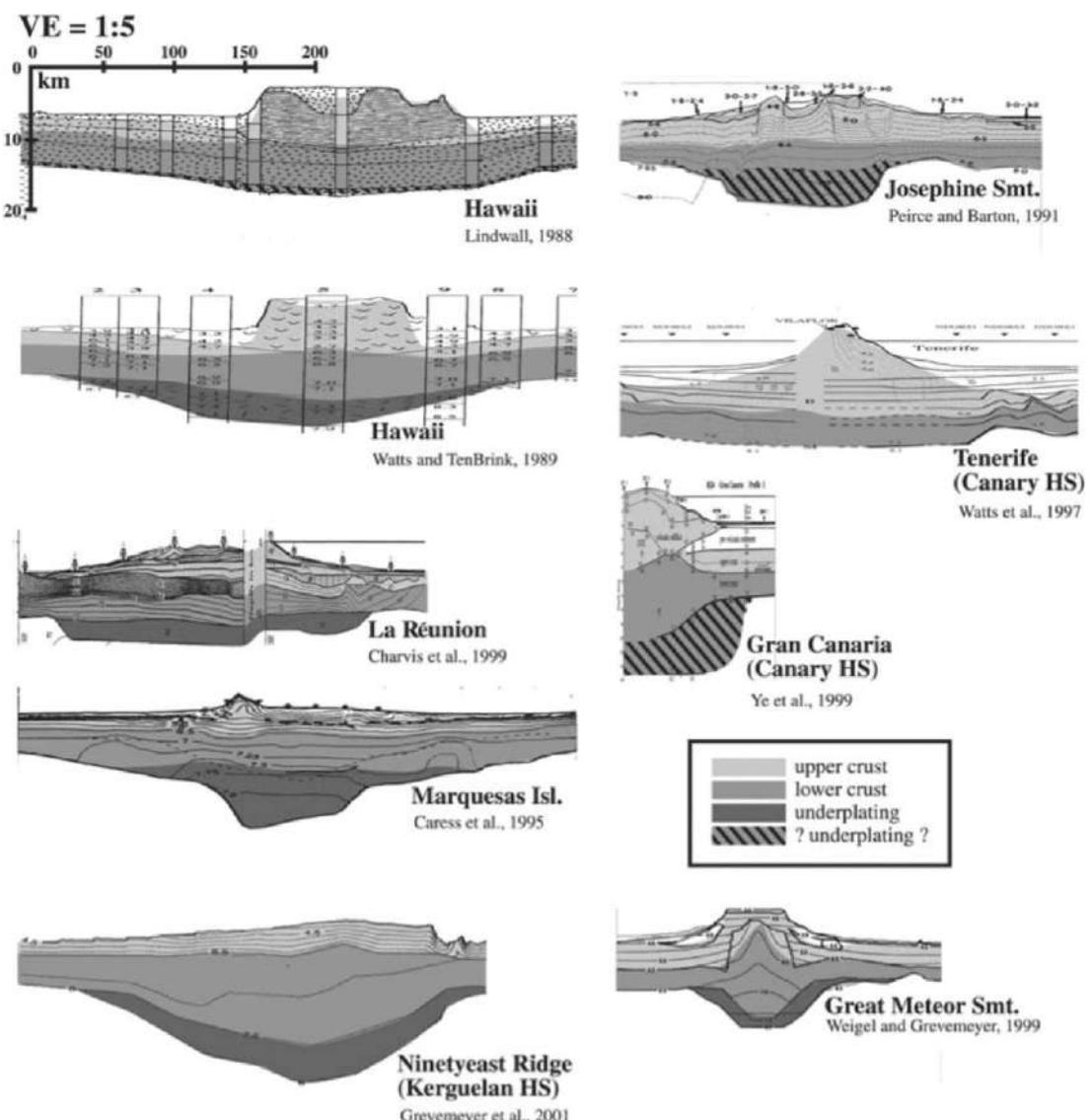


Figure 19 Compilation of several different hot-spot related volcanic structures imaged using seismic refraction and reflection data. All examples are scaled identically. Separation between upper and lower crust along all models is based only on velocities. Intrusive volcanism and underplating are characteristic for most of the volcanic provinces, which were located above a hot spot at the time of their formation. From Kopp H, Kopp C, Phipps Morgan J, Flueh ER, Weinrebe W, and Morgan WJ (2003) Fossil hot spot–ridge interaction in the Musicians Seamount Province: Geophysical investigations of hot spot volcanism at volcanic elongated ridges. *Journal of Geophysical Research* 108: (doi:10.1029/2002JB002015).

preexisting crust above and the upper mantle below. Taking into account both the existing volcanic edifices and the material contained in the surrounding sedimentary apron, the underplated volume amounts to 1.9 times the volume erupted on top of the preexisting crust. Caress *et al.* (1995) proposed, based on analogies with results from refraction experiments in active continental rift zones (Jarchow

et al., 1993; Benz and McCarthy, 1994) and on rifted continental margins (Holbrook and Kelemen, 1993), that this unit is an igneous intrusion or a mixture of intrusive rocks with preexisting mantle peridotites emplaced beneath the crust during the process of hot-spot volcanism. The seismic velocity of the underplated material suggests that the hot spot produced melt buoyant enough to rise through the

upper mantle to the base of the crust, but not sufficiently buoyant to rise above the crust–mantle boundary.

The buoyant nature of the underplated material was confirmed by Wolfe *et al.* (1994), who demonstrated that a good fit to both the depth of the moat and the gravity anomaly over the Marquesas Islands requires that the underplated material flexes the elastic lithosphere from below. The combination of the seismic constraints on the volume of the underplating and the gravitational bound on its buoyancy yield an estimate of 3100 kg m^{-3} for the density of the underplated unit.

Since the initial studies of Hawaii and the Marquesas, several seismic refraction and reflection experiments have focused on the deep crustal structure of hot-spot traces emplaced on old lithosphere. The study sites include the Canary Islands (Watts *et al.*, 1997; Ye *et al.*, 1999; Dañobeitia and Canales, 2000), La Reunion (Charvis *et al.*, 1999; Gallart *et al.*, 1999), Great Meteor Seamount (Weigel and Grevemeyer, 1999), the Societies (Grevemeyer *et al.*, 2001b), and the Cape Verde Islands (Ali *et al.*, 2003). In all of these cases, refraction and/or reflection data are consistent with the existence of high-velocity regions in the deep crust or upper mantle suggestive of magmatic underplating (Figure 19). Leahy and Park (2005) have provided independent evidence of underplating associated with oceanic hot-spot volcanism by using teleseismic receiver-function analysis to investigate the crustal and upper-mantle structure of four Pacific islands: Hawaii, Kiribati, Raratonga, and Tahiti. At each of these hot-spot volcanoes, Leahy and Park (2005) find evidence for a high-velocity subcrustal body ranging from 2 km thick at Tahiti to 10 km thick at Raratonga.

In contrast to the oceanic islands constructed on old lithosphere, all but one of the seismic refraction studies of near-ridge hot-spot volcanism are consistent with crustal thickening without the formation of subcrustal underplating. These observations hold for discrete seamounts such as Ascension Island (Evangelidis *et al.*, 2004) and the Musicians Seamounts (Kopp *et al.*, 2003), for larger platforms such as Crozet Bank (Recq *et al.*, 1998) and Iceland (e.g. Staples *et al.*, 1997), and for very large aseismic ridges such as the Cocos Ridge (Figures 9 and 10) (Walther, 2003) and the Carnegie Ridge (Sallares *et al.*, 2005).

The one hot-spot trace combining a near-ridge origin with strong evidence for underplating is the Ninetyeast Ridge. In fact, the most complete, and

highest-resolution, images to date of an oceanic underplating body were obtained by Grevemeyer *et al.* (2001a) at Ninetyeast Ridge. The underplated body has velocities of $7.5\text{--}7.6 \text{ km s}^{-1}$ and is 325 km wide, emplaced beneath the entire extrusive edifice and extending 50 km further to the east. Beneath the center of the edifice the underplating is as much as 5 km thick (Figure 19). The underplated volume at Ninetyeast Ridge is nearly the same as that erupted surficially. Because the eastern side of the Ninetyeast Ridge coincides with a transform boundary created by the separation of Ninetyeast Ridge from Broken Ridge, the eastward extension of the underplating indicates that at least some of the underplating was emplaced long after the surficial extrusive eruptions. Grevemeyer *et al.* (2001a) thus proposed that the underplating was associated with late-stage volcanism.

Underplating has also been inferred at two LIPs, indirectly from gravity data at the Ontong Java Plateau (Ito and Taira, 2000) and from seismic refraction data at the Kerguelen Plateau (Recq *et al.*, 1990). In the case of the Ontong Java Plateau, Ito and Taira (2000) interpreted the gravity data in terms of a larger elastic plate thickness for the subsurface load, suggesting that the underplating happened 40–100 million years after the eruption of the surface load at a time when the oceanic lithosphere was stiffer. This intriguing suggestion would place an important constraint on the duration of LIP-type volcanism by requiring the intrusion of a magma body long after the plate had drifted away from the original magma source. It would also have interesting implications for the vertical motion history of oceanic plateaus and could explain the subsidence deficit for Ontong Java as inferred from drill cores. However, the interpretation of the gravity data is not unique; large-scale lithospheric folding as Ontong Java encounters the Solomon trench could also explain the data (Ito and Taira, 2000). Deep seismic reflection and refraction data would be required to resolve the ambiguity.

It appears that magmatic underplating is a common, but not necessarily universal, feature of many types of hot-spot volcanism. Underplating has mostly been found beneath oceanic volcanic structures emplaced in old, cold, and strong lithosphere. With the exception of Ninetyeast Ridge (Grevemeyer *et al.*, 2001a), volcanic edifices formed in the thin, weak lithosphere near spreading centers do not show evidence for underplating. However, at least some of the Ninetyeast Ridge underplating was emplaced after the edifice had moved away from

the near-ridge environment. Although the refraction, reflection, and gravity data from Hawaii (Watts and ten Brink, 1989) and Ninetyeast Ridge (Grevemeyer *et al.*, 2001a) suggest that underplating may be associated with later stages of hot-spot volcanism, the existence of underplating beneath the currently volcanically active La Reunion (Charvis *et al.*, 1999; Gallart *et al.*, 1999) demonstrates that subcrustal intrusions can occur during the primary edifice-building stage of hot-spot volcanism. More comprehensive experiments providing multiple cross sections of active oceanic hot spots, such as the Hawaiian Islands, will be required to determine the relationship between the onset of surficial volcanism and the development of an underplated complex.

1.13.4.3 Mantle Lithosphere

Imaging the mantle lithosphere beneath hot spots in order to study the formation of swells or superswells has been one of the highest-priority experiments for distinguishing among different models for swell formation, but also one of the most difficult experiments in terms of obtaining a robust result. Given the lack of specificity in swell-height data as to the location of the low-density buoyant support, the ambiguity in interpretation of geoid data in terms of isostatic or dynamic uplift models, and the concern that surficial fluid circulation could mask the signal of the hot spot in heat flow data, seismic data hold the most promise for determining whether the support for mid-plate swells lies in the mantle lithosphere, as predicted by the lithospheric thinning model, or beneath it, and whether the compensation is buoyant because it is hot or by virtue of its mineralogy.

The two principal methods for seismically probing the mantle lithosphere have been to use array processing on direct teleseismic arrivals at dense clusters of seismometers and differencing short-period surface waves between favorably positioned stations. The Hawaiian swell and Iceland have been the principal foci for this type of seismic investigation, although the MELT experiment yielded some information on the South Pacific superswell (MELT Scientific Team, 1998), and the PLUME project (Suetsugu *et al.*, 2005) should provide further constraints soon.

Laske *et al.* (1999) obtained a year-long record of Rayleigh-wave phase velocities at periods between 15 and 70 s for more than 70 earthquake events by deploying an array of ocean-bottom differential pressure gauges along the southern edge of the Hawaiian

swell. The information was inverted to determine the average seismic velocity structure beneath the array, which did not depart significantly from the average for 100 Ma lithosphere. However, they did detect a strong lateral velocity gradient across the array, with velocity decreasing within 300 km of the island chain. A more expansive array experiment is currently underway to obtain a more complete image of the seismic velocity structure in the mantle lithosphere beneath the Hawaiian swell.

Collins *et al.* (2002) used a different approach for constraining the structure of the mantle lithosphere beneath the Hawaiian swell. Using data from two broadband seismometers deployed a few hundred kilometers southwest of Oahu, they observed P-to-S converted phases from the Gutenberg discontinuity, thought to correspond to the base of the lithosphere. They place the base of the lithosphere at 80 km depth, in agreement with the results from Rayleigh-wave dispersion studies (Woods and Okal, 1996; Priestley and Tilmann, 1999). In contrast to the results of Laske *et al.* (1999), the results from these studies do not point to differences between the thickness or velocity structure of the lithosphere beneath the Hawaiian swell as compared with the parameters for normal oceanic lithosphere of that age. Ideally, the results from the ocean-bottom array experiment currently in progress will settle this controversy with major implications for the origin of hot spots and their geophysical signatures.

Several major field programs and tomographic studies have been devoted to the Iceland hot spot (Wolfe *et al.*, 1997; Ritsema *et al.*, 1999; Bijwaard and Spakman, 1999; Allen *et al.*, 2002). Seismic analyses that have been conducted in Hawaii to detect any hot-spot-induced anomalies within a high-velocity lid make no sense in Iceland, which coincides with a mid-ocean ridge, where by definition the lithosphere tends toward zero thickness. Quite independent studies agree that the upper mantle immediately beneath Iceland is anomalously slow seismically, even by mid-ocean ridge standards, to about 400 km depth, consistent with the presence of high-temperature upwelling mantle. The real controversy for Iceland centers on whether the seismic velocity anomaly extends deeper than the mantle transition zone (Helmberger, 1998; Foulger *et al.*, 2001). Converted phases mapped beneath Hawaii (Li *et al.*, 2000) and Tahiti (Niu *et al.*, 2002) also point to unusually warm upper-mantle temperatures immediately beneath those hot spots, although not for the South Pacific superswell in general.

Earthquake seismology has also found some applications in hot-spot research near the locus of active volcanism. Wolfe *et al.* (2003) used an improved relocation technique to demonstrate that earthquakes at ~ 30 km depth in the mantle lithosphere beneath Hawaii define a seaward-dipping, low-angle fault plane, rather than a magma conduit through the lithosphere as had been previously suggested.

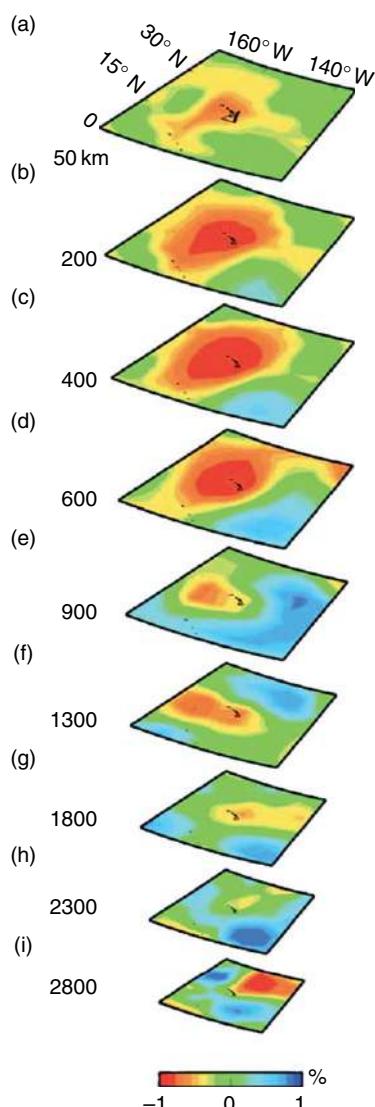


Figure 20 P-wave tomographic images in map view around the Hawaiian hot spot. The depth of each layer is noted on the left. Red and blue colors denote slow and fast velocities, respectively, compared to the IASP91 1-D Earth model (Kennett and Engdahl, 1991). Reproduced from Lei J and Zhao D (2006) A new insight into the Hawaiian plume. *Earth and Planetary Science Letters* 241: 438–453, with permission from Elsevier.

Whole-earth tomography has also made some contribution in this area, but in the past has lacked the resolution in the upper 100 km to unambiguously image the lithosphere and in the rest of the mantle to detect the possible signature of mantle plumes. New data-processing techniques (e.g., Capdeville *et al.*, 2002; Montelli *et al.*, 2004) hold the promise for directly imaging plumes within the mantle. For example, a recent study by Lei and Zhao (2006) uses 10 converted seismic phases to image slow P-wave velocities extending from the surface to the CMB beneath Hawaii (**Figure 20**). However, Lei and Zhao's data set provides limited resolution because there are few crossing raypaths, and their models depend strongly on assumed CMB structure, indicating that further effort is required to refine CMB models. The results from various studies have yet to converge. For example, using the criterion that a plume must show continuous low shear velocity in the upper mantle, Ritsema and Allen (2003) find only eight hot spots (Afar, Bowie, Easter, Hawaii, Iceland, Louisville, McDonald, and Samoa), out of the 37 considered, that pass the test for plume origin. Montelli *et al.* (2004), on the other hand, use the criterion that there must be seismic evidence that P-wave velocity lows extend from the upper mantle into the lower mantle. Their list of hot spots with plume origin includes only Ascension, Azores, Canary, Easter, Samoa, and Tahiti. Only Easter and Samoa are common on both lists. Courtillot *et al.* (2003), using broader criteria based on seismological, other geophysical, and helium isotope data, conclude that Afar, Easter, Hawaii, Reunion, Samoa, Louisville, Iceland, and Tristan are likely to be of plume origin. At this point in time, consensus seems to emerge that plume-like behavior is responsible for Easter and Samoa, with conflicting views on the appropriateness of this theory for other hot spots.

1.13.5 Conclusions

1.13.5.1 Emerging View on Geophysical Structure of Hot Spots and Swells

Hot-spot volcanism is clearly an important global phenomenon that reflects deep-Earth processes, modifies much of the lithosphere over time, and thus significantly impacts the thermal and chemical evolution of the Earth. Progress in the understanding of hot spots has required the integration of many types of geophysical observations, including bathymetry, satellite altimetry, gravity, heat flow, seismic

reflection, seismic refraction, and teleseismic data. The results that heat flow patterns can be dominated by lateral variations in thermal conductivity and fluid circulation and that some, but not all, intraplate volcanic features include high-seismic-velocity underplating demonstrate that the shallow structure of hot-spot features must be well understood before the mantle structures related to the causes of hot-spot volcanism can be reliably resolved.

Recent studies of oceanic hot spots and hot-spot swells have explored multiple plausible mechanisms for producing intraplate volcanism, particularly including mantle plumes and lithospheric cracking due to plate-scale stresses. Plume theory remains viable, but only a small number of hot spots appear associated to deep-mantle plumes, and the nature of the plumes remains very much in question. The observed variety and complexity in the setting, history, and structure of intraplate volcanic features likely reflects multiple causes for hot-spot volcanism.

1.13.5.2 Promising Areas for Further Research

We anticipate that future geophysical hot-spot research will include more comprehensive seismic crustal and Moho imaging of active volcanic features to understand how hot-spot volcanism modifies preexisting crust over time. We also expect considerable effort to achieve better resolution of lateral variations in seismic velocity in the mantle by taking advantage of additional computational resources and improving knowledge of the complex crustal and upper-mantle structure. However, improvements in the coverage provided by the global seismic networks will be vital, particularly including long-term ocean stations in the deep-ocean basins.

Acknowledgment

The Packard Foundation supported the preparation of this chapter.

References

- Abbott DH and Isley AE (2002) Extraterrestrial influences on mantle plume activity. *Earth and Planetary Science Letters* 205: 53–62.
 Ali MY, Watts AB, and Hill I (2003) A seismic reflection profile study of lithospheric flexure in the vicinity of the Cape Verde Islands. *Journal of Geophysical Research* 108 (doi:10.1029/2002JB002155).

- Allen RM, Nolet G, Morgan WJ, et al. (2002) Plume-driven plumbing and crustal formation in Iceland. *Journal of Geophysical Research* 107 (doi:10.1029/2001JB000584).
 Anderson DL (1996) The edges of the mantle. In: Gurnis M, Wysession ME, Knittle E, and Buffett BA (eds.) *Geodynamics Series 28: The Core–Mantle Boundary Region*, pp. 255–271. Washington, DC: American Geophysical Union.
 Bemis KG and Smith DK (1993) Production of small volcanoes in the superswell region of the South Pacific. *Earth and Planetary Science Letters* 118: 251–262.
 Benz HM and McCarthy J (1994) Evidence for an upper mantle low velocity zone beneath the southern Basin and Range–Colorado Plateau transition zone. *Geophysical Research Letters* 21: 509–512.
 Bijwaard H and Spakman W (1999) Tomographic evidence for a narrow whole mantle plume below Iceland. *Earth and Planetary Science Letters* 166: 121–126.
 Bonatti E (1990) Not so hot ‘hot spots’ in the oceanic mantle. *Science* 250: 107–111.
 Bonatti E and Harrison CGA (1976) Hot lines in the Earth’s mantle. *Nature* 263: 402–404.
 Bonneville A, Von Herzen RP, and Lucaleau F (1997) Heat flow over Réunion hot spot track: Additional evidence for thermal rejuvenation of oceanic lithosphere. *Journal of Geophysical Research* 102: 22731–22747.
 Burke K and Dewey JF (1973) Plume-generated triple functions: Key indicators in applying plate tectonics to old rocks. *Journal of Geology* 81: 406–433.
 Calmant S (1987) The elastic thickness of the lithosphere in the Pacific Ocean. *Earth and Planetary Science Letters* 85: 277–288.
 Calmant S and Cazenave A (1986) The effective elastic lithosphere under the Cook–Austral and Society Islands. *Earth and Planetary Science Letters* 77: 187–202.
 Capdeville Y, Larmat C, Villette J-P, and Montagner J-P (2002) A new coupled spectral element and modal solution method for global seismology: A first application to the scattering induced by a plume-like anomaly. *Geophysical Research Letters* 29 (doi:10.1029/2001GL013747).
 Carew DW, McNutt MK, Detrick RS, and Mutter JC (1995) Seismic imaging of hotspot-related crustal underplating beneath the Marquesas Islands. *Nature* 373: 600–603.
 Charvis P, Laesapura A, Gallart J, et al. (1999) Spatial distribution of hotspot material added to the lithosphere under La Reunion, from wide-angle seismic data. *Journal of Geophysical Research* 104: 2875–2893.
 Christensen U (1984) Instability of a hot boundary layer and initiation of thermochemical plumes. *Annals of Geophysics* 2: 311–320.
 Chubb LJ (1957) The pattern of some Pacific island chains. *Geological Magazine* 94: 221–228.
 Clague DA and Dalrymple GB (1987) The Hawaiian–Emperor volcanic chain. Part 1: Geologic evolution. *US Geological Survey Professional Paper* 1350: 5–54.
 Clouard V and Bonneville A (2005) Ages of seamounts, islands and plateaus on the Pacific Plate. In: Foulger GR, Natland JH, Presnall D, and Anderson DL (eds.) *Geological Society of America Special Paper 388: Plates, Plumes & Paradigms*, pp. 71–90. Boulder, CO: Geological Society of America.
 Coffin MF (1992) Emplacement and subsidence of Indian Ocean plateaus and submarine ridges. In: Duncan RA, Rea DK, Kidd RB, von Rad U, and Weissel JK (eds.) *American Geophysical Union Monograph Series vol 70: Synthesis of Results from Scientific Drilling in the Indian Ocean*, pp. 115–125. Washington, DC: Amererican Geophysical Union.
 Coffin MF and Eldholm O (1994) Large igneous provinces: Crustal structure, dimensions, and external consequences. *Reviews of Geophysics* 32: 1–36.

- Collins J, Vernon FL, Orcutt JA, and Stephen RA (2002) Upper mantle structure beneath the Hawaiian swell: Constraints from the ocean seismic network pilot experiment. *Geophysical Research Letters* 29 (doi:10.1029/2001GL013302).
- Courtillot V, Davaille A, Besse J, and Stock J (2003) Three distinct types of hotspots in the Earth's mantle. *Earth and Planetary Science Letters* 205: 295–308.
- Courtney RC and White RS (1986) Anomalous heat flow and geoid across the Cape Verde rise: Evidence for dynamic support from a thermal plume in the mantle. *Geophysical Journal International* 87: 815–867.
- Crough ST (1978) Thermal origin of mid-plate hot-spot swells. *Geophysical Journal of the Royal Astronomical Society* 55: 451–469.
- Crough ST and Jarrard RD (1981) The Marquesas-Line swell. *Journal of Geophysical Research* 86: 11–763–11771.
- Dañobeitia JJ and Canales JP (2000) Magmatic underplating in the Canary Archipelago. *Journal of Volcanology and Geothermal Research* 103: 27–41.
- Darwin C (1842) *The Structure and Distribution of Coral Reefs*. London: Smith Elder.
- Davies GF (1988) Ocean bathymetry and mantle convection. Part 1: Large-scale flow and hotspots. *Journal of Geophysical Research* 93: 10467–10480.
- Davies GF (1999) *Dynamic Earth: Plates, Plumes, and Mantle Convection*, 458pp. Cambridge, UK: Cambridge University Press.
- Davis AS, Gray LB, Clague DA, and Hein JR (2002) The Line Islands revisited: New $^{40}\text{Ar}/^{39}\text{Ar}$ geochronologic evidence for episodes of volcanism due to lithospheric extension. *Geochemistry Geophysics Geosystems* 3 (doi:10.1029/2001GC000190).
- Detrick RS and Crough ST (1978) Island subsidence, hot spots, and lithospheric thinning. *Journal of Geophysical Research* 83: 1236–1244.
- Detrick RS, Sclater JG, and Thiede J (1977) The subsidence of aseismic ridges. *Earth and Planetary Science Letters* 34: 185–196.
- Detrick RS, Von Herzen RP, Crough ST, Epp D, and Fehn U (1981) Heat flow on the Hawaiian swell and lithospheric reheating. *Nature* 292: 142–143.
- Detrick RS, Von Herzen RP, Parsons B, Sandwell D, and Dougherty M (1986) Heat flow observations on the Bermuda rise and thermal models of midplate swells. *Journal of Geophysical Research* 91: 3701–3723.
- Detrick RS and Watts AB (1979) An analysis of isostasy in the world's oceans. Part 3: Aseismic ridges. *Journal of Geophysical Research* 84: 3637–3653.
- Dietz RS (1961) Continent and ocean basin evolution by spreading of the seafloor. *Nature* 190: 854–857.
- Dietz RS and Menard HW (1953) Hawaiian swell, deep, and arch and subsidence of the Hawaiian Islands. *Journal of Geology* 61: 99–113.
- Duncan RA (1981) Hotspots in the Southern oceans – An absolute frame of reference for motion of the Gondwana continents. *Tectonophysics* 74: 29–42.
- Duncan RA and McDougall I (1976) Linear volcanism in French Polynesia. *Journal of Volcanology and Geothermal Research* 1: 197–227.
- Dziewonski AM (2005) The robust aspects of global seismic tomography. *Geological Society of America Special Paper* 388: 147–154.
- Dziewonski AM and Woodhouse JH (1987) Global images of the Earth's interior. *Science* 236: 37–48.
- Ernst RE and Buchan KL (2003) Recognizing mantle plumes in the geological record. *Annual Review of Earth and Planetary Sciences* 31: 469–523.
- Ernst RE, Grosfils EB, and Mège D (2001) Giant dike swarms: Earth, Venus, and Mars. *Annual Review of Earth and Planetary Sciences* 29: 489–534.
- Evangelidis CP, Minshull TA, and Henstock TJ (2004) Three-dimensional crustal structure of Ascension Island from active source tomography. *Geophysical Journal International* 159: 311–325.
- Filmer PE, McNutt MK, Webb HF, and Dixon DJ (1994) Volcanism and archipelagic aprons: A comparison of the Marquesas and Hawaiian Islands. *Marine Geophysical Research* 16: 385–406.
- Foulger GR, Pritchard MJ, Julian BR, et al. (2001) Seismic tomography shows that upwelling beneath Iceland is confined to the upper mantle. *Geophysical Journal International* 146: 504–530.
- Furumoto AS, Webb JP, Odegard ME, and Hussong DM (1976) Seismic studies on the Ontong Java Plateau. *Tectonophysics* 34: 71–90.
- Gallart J, Driad L, Charvis P, et al. (1999) Perturbation to the lithosphere using the hotspot track of La Réunion, from an offshore-onshore seismic transect. *Journal of Geophysical Research* 104: 2895–2908.
- Gordon RG and Jurdy DM (1986) Cenozoic global plate motions. *Journal of Geophysical Research* 91: 12389–12406.
- Grand SP, van der Hilst RD, and Widjiantoro S (1997) Global seismic tomography: A snapshot of convection in the Earth. *GSA Today* 7: 1–7.
- Grevevemeyer I and Flueh ER (2000) Crustal underplating and its implications for subsidence and state of isostasy along the Ninetyeast Ridge hotspot trail. *Geophysical Journal International* 147: 643–649.
- Grevevemeyer I, Weigel W, Schüssler S, and Avedik F (2001a) Crustal architecture and deep structure of the Ninetyeast Ridge hotspot trail from active-source ocean bottom seismology. *Geophysical Journal International* 144: 414–431.
- Grevevemeyer I, Weigel W, Schüssler S, and Avedik F (2001b) Crustal and upper mantle seismic structure and lithospheric flexure along the Society Island hotspot chain. *Geophysical Journal International* 147: 123–140.
- Griffiths RW and Campbell IH (1991) Interaction of mantle plume heads with the Earth's surface and onset of small-scale convection. *Journal of Geophysical Research* 96: 18295–18310.
- Harris RN, Garven G, Georgen J, McNutt MK, Christiansen L, and Von Herzen RH (2000b) Submarine hydrology of the Hawaiian archipelagic apron. Part 2: Numerical simulation of coupled heat transport and fluid flow. *Journal of Geophysical Research* 105: 21371–21385.
- Harris RN, Von Herzen RH, McNutt MK, Garven G, and Jordahl K (2000a) Submarine hydrology of the Hawaiian archipelagic apron. Part 1: Heat flow patterns north of Oahu and Maro Reef. *Journal of Geophysical Research* 105: 21353–21370.
- Haxby WF and Turcotte DL (1978) On isostatic geoid anomalies. *Journal of Geophysical Research* 83: 5473–5478.
- Head JW, Crumpler LS, Aubele JC, Guest JE, and Saunders RS (1992) Venus volcanism: Classification of volcanic features and structures, associations, and global distribution from Magellan data. *Journal of Geophysical Research* 97: 13153–13197.
- Helmbberger DV, Wen L, and Ding X (1998) Seismic evidence that the source of the Iceland hotspot lies at the core–mantle boundary. *Nature* 396: 251–255 (doi:10.1038/24357).
- Hess HH (1962) History of ocean basins. In: Engel AEJ, Harold LJ, and Leonard BF (eds.) *A Volume in Honor of A. F. Buddington*, pp. 599–620. Boulder, CO: Geological Society of America.

- Holbrook WS and Keleman PB (1993) Large igneous province on the US Atlantic margin and implications for magmatism during breakup. *Nature* 364: 433–436.
- Ito G, Lin J, and Gable CW (1996) Dynamics of mantle flow and melting at a ridge-centered hotspot: Iceland and the Mid-Atlantic Ridge. *Earth and Planetary Science Letters* 144: 53–74.
- Ito G, Lin J, and Gable CW (1997) Interaction of mantle plumes and migrating mid-ocean ridges: Implications for the Galápagos plume-ridge system. *Journal of Geophysical Research* 102: 15403–15418.
- Ito G and Taira A (2000) Compensation of the Ontong Java Plateau by surface and subsurface loading. *Journal of Geophysical Research* 105: 11171–11183.
- Jarchow CM, Thompson GA, Catchings RD, and Mooney WD (1993) Seismic evidence for active magmatic underplating beneath the basin and range province, Western United States. *Journal of Geophysical Research* 98: 22095–22108.
- Kennett B and Engdahl E (1991) Travel times for global earthquake location and phase identification. *Geophysical Journal International* 105: 429–465.
- Kopp H, Kopp C, Phipps Morgan J, Flueh ER, Weinrebe W, and Morgan WJ (2003) Fossil hot spot–ridge interaction in the Musicians Seamount Province: Geophysical investigations of hot spot volcanism at volcanic elongated ridges. *Journal of Geophysical Research* 108 (doi:10.1029/2002JB002015).
- Koppers AA, Duncan RA, and Steinberger B (2004) Implications of a nonlinear $^{40}\text{Ar}/^{39}\text{Ar}$ age progression along the Louisville seamount trail for models of fixed and moving hot spots. *Geochemistry Geophysics Geosystems* 5: Q06L02 (doi:10.1029/2003GC000671).
- Ladd HS and Schlanger SO (1960) Drilling operations on Eniwetok Atoll. *US Geological Survey Professional Paper* 160-Y: 863–905.
- Ladd HS, Tracey JI, and Gross MG (1967) Drilling on Midway Atoll, Hawaii. *Science* 166: 1038–1093.
- Larson RL (1991) Latest pulse of Earth: Evidence for a mid-Cretaceous superplume. *Geology* 19: 547–550.
- Larson RL and Olsen P (1991) Mantle plumes control magnetic reversal frequency. *Earth and Planetary Science Letters* 107: 437–447.
- Laske G, Phipps Morgan J, and Orcutt JA (1999) First results from the Hawaiian SWELL pilot experiment. *Geophysical Research Letters* 26: 3397–3400.
- Laughton AS, Matthews DW, and Fisher RL (1970) The structure of the Indian Ocean. In: Maxwell AE (ed.) *The Sea*, vol. 4, pp. 543–586. New York: John Wiley and Sons.
- Leahy GM and Park J (2005) Hunting for oceanic island Moho. *Geophysical Journal International* 160: 1020–1026.
- Lei J and Zhao D (2006) A new insight into the Hawaiian plume. *Earth and Planetary Science Letters* 241: 438–453.
- Li X, Kind R, Priestley K, Sobolew SV, Tilman F, Yuan X, and Weber M (2000) Mapping the Hawaiian plume conduit with converted seismic phases. *Nature* 405: 938–941.
- Lindwall DA (1988) A two-dimensional seismic investigation of crustal structure under the Hawaiian Islands near Oahu and Kauai. *Journal of Geophysical Research* 93: 12107–12122.
- Lister CRB (1972) On the thermal balance of a mid-ocean ridge. *Geophysical Journal of the Royal Astronomical Society* 26: 515–535.
- Lonsdale P (1988) Geography and history of the Louisville hotspot chain in the Southern Pacific. *Journal of Geophysical Research* 93: 3078–3104.
- Masters G, Johnson S, Laske G, and Bolton H (1996) A shear-velocity model of the mantle. *Philosophical Transactions of the Royal Society of London A* 354: 1385–1411.
- MELT Scientific Team (1998) Imaging the deep structure beneath a mid-ocean ridge: The MELT experiment. *Science* 280: 1215–1218.
- McKenzie DP (1967) Some remarks on heat flow and gravity anomalies. *Journal of Geophysical Research* 72: 6261–6273.
- McNutt MK (1984) Lithospheric flexure and thermal anomalies. *Journal of Geophysical Research* 89: 11180–11194.
- McNutt MK (1987) Temperature beneath midplate swells: The inverse problem. In: Keating B, Fryer P, Batiza R, and Boehlert GW (eds.) *Geophysical Monograph Series*, vol. 43: *Seamounts, Islands, and Atolls*, pp. 123–132. Washington, DC: American Geophysical Union.
- McNutt MK (1998) Superswells. *Reviews of Geophysics* 36: 211–244.
- McNutt MK (2002) Heat flow variations over Hawaiian swell controlled by near-surface processes, not plume properties. In: Takahashi E, Lipman PW, Garcia MO, Naka J, and Aramaki S (eds.) *Geophysical Monograph Series*, vol. 128: *Hawaiian Volcanoes: Deep Underwater Perspectives*, pp. 365–372. Washington, DC: American Geophysical Union.
- McNutt MK and Bonneville A (2000) A shallow, chemical origin for the Marquesas swell. *Geochemistry Geophysics Geosystems* 1 (doi:1999GC000028).
- McNutt MK, Carens DW, Reynolds J, Jordahl KA, and Duncan RA (1997) Failure of plume theory to explain midplate volcanism in the southern Austral islands. *Nature* 389: 479–482.
- McNutt MK and Fischer KM (1987) The South Pacific superswell. In: Keating BH, Fryer P, Batiza R, and Boehlert GW (eds.) *Geophysical Monograph Series*, vol. 43: *Seamounts, Islands, and Atolls*, pp. 25–34. Washington, DC: American Geophysical Union.
- McNutt MK and Judge AV (1990) The superswell and mantle dynamics beneath the South Pacific. *Science* 248: 969–975.
- McNutt MK and Shure L (1986) Estimating the compensation depth of the Hawaiian swell with linear filters. *Journal of Geophysical Research* 91: 13915–13923.
- McNutt MK, Winterer EL, Sager WW, Natland JH, and Ito G (1990) The Darwin Rise: A Cretaceous superswell? *Geophysical Research Letters* 17: 1101–1104.
- Menard HW (1956) Archipelagic aprons. *American Association of Petroleum Geologist Bulletin* 40: 2195–2210.
- Menard HW (1973) Depth anomalies and the bobbing motion of drifting islands. *Journal of Geophysical Research* 78: 5128–5137.
- Menard HW (1986) *Islands*. New York, NY: Scientific American Books.
- Molnar P and Stock J (1987) Relative motions of hotspots in the Pacific, Atlantic, and Indian Oceans since Late Cretaceous time. *Nature* 327: 587–591.
- Monnereau M and Cazenave A (1990) Depth and geoid anomalies over oceanic hotspot swells: A global survey. *Journal of Geophysical Research* 95: 15429–15438.
- Monnereau M and Cazenave A (1998) Variation of the apparent compensation depth of hotspot swells with age of plate. *Earth and Planetary Science Letters* 91: 179–197.
- Montelli R, Nolet G, Dalhen FA, Masters G, Engdahl ER, and Hung S-H (2004) Finite frequency tomography reveals a variety of plumes in the mantle. *Science* 303: 338–343.
- Moore JG, Clague DA, Holcomb RT, Lipman PW, Normark WR, and Torresan ME (1989) Prodigious submarine landslides on the Hawaiian ridge. *Journal of Geophysical Research* 94: 17465–17484.
- Morgan WJ (1971) Convection plumes in the lower mantle. *Nature* 230: 42–43.
- Morgan WJ (1972) Plate motions and deep mantle convection. In: Shagam R, Hargraves RB, Morgan WJ, Van Houten FB, and Burk CA (eds.) *GSA Memoir 132: Studies in Earth and*

- Spaces Sciences, pp. 7–22. New York: Geological Society of America.
- Morgan WJ (1978) Rodriguez, Darwin, Amsterdam, . . . , a second type of hotspot island. *Journal of Geophysical Research* 83: 5355–5360.
- Mutter JC, Buck WR, and Zehnder CM (1988) Convective partial melting. Part 1: A model for the formation of thick basaltic sequences during the initiation of spreading. *Journal of Geophysical Research* 93: 1031–1048.
- Mutter JC and Zehnder CM (1988) Deep crustal structure and magmatic processes: The inception of seafloor spreading in the Norwegian-Greenland Sea. In: Morton AC and Parson LM (eds.) *Geological Society Special Publication London 39: Early Tertiary Volcanism and the Opening of the NE Atlantic*, pp. 35–48. London: Geological Society of London.
- Nishimura CE and Forsyth DW (1985) Anomalous Love-wave phase velocities in the Pacific: Sequential pure-path and spherical harmonic inversion. *Geophysical Journal the Royal Astronomical Society* 81: 389–407.
- Niu F, Solomon SC, Silver PG, Suetzugu D, and Inoue H (2002) Mantle transition-zone structure beneath the South Pacific Superswell and evidence for a mantle plume underlying the Society hotspot. *Earth and Planetary Science Letters* 198: 371–380.
- Nyblade AA and Robinson SW (1994) The African superswell. *Geophysical Research Letters* 21: 765–768.
- O'Connor JM, Stoffers P, and McWilliams MO (1995) Time-space mapping of Easter chain volcanism. *Earth and Planetary Science Letters* 136: 197–212.
- Parsons B and Scilater JG (1977) An analysis of the variation of ocean floor bathymetry and heat flow with age. *Journal of Geophysical Research* 82: 802–827.
- Patriat M, Klingelhoefer F, Aslanian D, et al. (2002) Deep crustal structure of the Tuamoto plateau and Tahiti (French Polynesia) based on seismic refraction data. *Geophysical Research Letters* 29 (doi:10.1029/2001GL013913).
- Phipps Morgan J (1999) Isotope topology of individual hotspot basalt arrays: Mixing curves or melt extraction trajectories? *Geochemistry Geophysics Geosystems* 1 (doi:1999GC000004).
- Phipps Morgan J, Morgan WJ, and Price E (1995) Hotspot melting generates both hotspot volcanism and a hotspot swell? *Journal of Geophysical Research* 100: 8045–8062.
- Pitman WC, III (1978) Relationship between eustacy and stratigraphic sequences of passive margins. *Geological Society of America Bulletin* 89: 1389–1403.
- Priestley K and Tilmann F (1999) Shear-wave structure of the lithosphere above the Hawaiian hotspot from two-station Rayleigh wave phase velocity measurements. *Geophysical Research Letters* 26: 1493–1496.
- Recq M, Brefort D, Malod J, and Veinante JL (1990) The Kerguelen Isles (southern Indian Ocean): New results on deep structure from refraction profiles. *Tectonophysics* 182: 227–248.
- Recq M, Goslin J, Charvis J, and Operto S (1998) Small-scale crustal variability within an intraplate structure: the Crozet Bank (southern Indian Ocean). *Geophysical Journal International* 134: 145–156.
- Rees BA, Detrick RS, and Coakley BJ (1993) Seismic stratigraphy of the Hawaiian flexural moat. *Bulletin of the Geological Society of America* 105: 189–205.
- Ribe N (1995) The dynamics of plume-ridge interaction. Part 1: Ridge-centered plumes. *Earth and Planetary Science Letters* 143: 155–168.
- Richards MA, Duncan RA, and Courtillot V (1989) Flood basalts and hotspot tracks – Plume heads and tails. *Science* 246: 103–107.
- Ritsema J and Allen RM (2003) The elusive mantle plume. *Earth and Planetary Science Letters* 207: 1–12.
- Ritsema J, van Heijst HJ, and Woodhouse JH (1999) Complex shear wave velocity structure imaged beneath Africa and Iceland. *Science* 286: 1925–1928.
- Robinson EM and Parsons B (1988) Effects of a shallow low-viscosity zone on the formation of midplate swells. *Journal of Geophysical Research* 93: 3144–3157.
- Sallares V, Charvis P, Flueh E, and Bialas J (2005) Seismic structure of the Carnegie ridge and the nature of the Galapagos hotspot. *Geophysical Journal International* 161: 763–788.
- Schlanger SO, Garcia MO, Keating BH, et al. (1984) Geology and geochronology of the Line Islands. *Journal of Geophysical Research* 89: 11261–11272.
- Sharp WD and Clague DA (2006) 50-Ma initiation of Hawaiian-Emperor bend records major change in Pacific plate motion. *Science* 313: 1250–1251.
- Schoix L, Bonneville A, and McNutt M (1998) The seafloor swells and Superswell in French Polynesia. *Journal of Geophysical Research* 103: 27123–27133.
- Sleep N (1990) Hotspots and mantle plumes: Some phenomenology. *Journal of Geophysical Research* 95: 6715–6736.
- Smallwood JR, Staples RK, Richardson KR, and White RS (1999) Crust generated above the Iceland mantle plume: From continental rift to oceanic spreading center. *Journal of Geophysical Research* 104: 22885–22902.
- Smith DE, Zuber MT, Solomon SC, et al. (1999) The global topography of Mars and implications for surface evolution. *Science* 284: 1495–1503.
- Solomon SC, Smekar SE, Bindschadler DL, et al. (1992) Venus tectonics: An overview of Magellan observations. *Journal of Geophysical Research* 97: 13199–13225.
- Spencer J and Schneider N (1996) Io on the eve of the Galileo mission. *Annual Review of Earth and Planetary Sciences* 124: 125–190.
- Staples R, White R, Brandsdottir B, Menke W, Maguire P, and McBride J (1997) Faroes-Iceland Experiment. Part 1: The crustal structure of northeastern Iceland. *Journal of Geophysical Research* 102: 7849–7866.
- Steinberger B (2000) Plumes in a convecting mantle: Models and observations for individual hotspots. *Journal of Geophysical Research* 105: 11127–11152.
- Steinberger B and O'Connell RJ (1998) Advection of plumes in mantle flow: Implications for hotspot motion, mantle viscosity, plume distribution. *Geophysical Journal International* 132: 412–434.
- Storey BC (1995) The role of mantle plumes in continental breakup: Case histories from Gondwana. *Nature* 377: 301–308.
- Su W-J, Woodward RL, and Dziewonski AM (1994) Degree 12 model of shear velocity heterogeneity in the mantle. *Journal of Geophysical Research* 99: 6945–6980.
- Suetzugu D, Shiobara H, Sugioka H, et al. (2005) Probing South Pacific mantle plumes with ocean bottom seismographs. *Eos, Transactions of the American Geophysical Union* 86: 429–435.
- Tarduno JA, Duncan RA, Scholl DW, et al. (2003) The Emperor Seamounts: Southward motion of the Hawaiian hotspot plume in Earth's mantle. *Science* 301: 1064–1069.
- ten Brink US and Brocher TM (1987) Multichannel seismic evidence for a subcrustal intrusive complex under Oahu and a model for Hawaiian volcanism. *Journal of Geophysical Research* 92: 13687–13707.
- ten Brink US and Watts AB (1985) Seismic stratigraphy of the flexural moat flanking the Hawaiian Islands. *Nature* 317: 421–424.

- Turcotte DL and Oxburgh ER (1967) Finite amplitude convection cells and continental drift. *Journal of Fluid Mechanics* 28: 29–42.
- Turcotte DL and Oxburgh ER (1973) Mid-plate tectonics. *Nature* 244: 337–339.
- Vidal V and Bonneville A (2004) Variations of the Hawaiian hot spot activity revealed by variations in the magma production rate. *Journal of Geophysical Research* 109 (doi:10.1029/2003JB002559).
- Vogt PR (1972) Evidence for global synchronism in mantle plume convection, and possible significance for geology. *Nature* 240: 338–342.
- Von Herzen RP (2004) Geothermal evidence for continuing hydrothermal circulation in older (>60 M.y.) ocean crust. In: Davis EE and Elderfield H (eds.) *Hydrogeology of the Oceanic Lithosphere*, pp. 414–447. New York: Cambridge University Press.
- Von Herzen RP, Cordery MJ, Detrick RS, and Fang C (1989) Heat flow and thermal origin of hot spot swells: The Hawaiian swell revisited. *Journal of Geophysical Research* 94: 13783–13799.
- Von Herzen RP, Detrick RS, Crough ST, Epp D, and Fehn U (1982) Thermal origin of the Hawaiian swell: Heat flow evidence and thermal models. *Journal of Geophysical Research* 87: 6711–6723.
- Walther CHE (2003) The crustal structure of the Cocos ridge off Costa Rica. *Journal of Geophysical Research* 108 (doi:10.1029/2001JB000888).
- Watts AB (2001) *Isostacy and Flexure of the Lithosphere*, 458pp. Cambridge, UK: Cambridge University Press.
- Watts AB, Bodine JH, and Ribe NM (1980) Observations of flexure and geological evolution of the Pacific ocean basins. *Nature* 283: 532–537.
- Watts AB, Peirce C, Collier J, Dalwood R, Canales JP, and Henstock TJ (1997) A seismic study of lithospheric flexure in the vicinity of Tenerife, Canary Islands. *Earth and Planetary Science Letters* 146: 431–447.
- Watts AB and ten Brink US (1989) Crustal structure, flexure, and subsidence of the Hawaiian Islands. *Journal of Geophysical Research* 94: 10473–10500.
- Watts AB, ten Brink US, Buhl P, and Brocher TM (1985) A multichannel seismic study of lithospheric flexure across the Hawaiian–Emperor seamount chain. *Nature* 315: 105–111.
- Weigel W and Grevemeyer I (1999) The Great Meteor seamount: Seismic structure of a submerged intraplate volcano. *Journal of Geodynamics* 28: 27–40.
- Whitehead JA and Luther DS (1975) Dynamics of laboratory diapir and plume models. *Journal of Geophysical Research* 80: 705–717.
- Wilson JT (1963) A possible origin of the Hawaiian Islands. *Canadian Journal of Physics* 41: 863–870.
- Winterer EL, Natland JH, van Waasbergen RJ, et al. (1993) Cretaceous guyots in the northwest Pacific: An overview of their geology and geophysics. In: Pringle M (ed.) *Geophysical Monograph 77: The Mesozoic Pacific: Geology, Tectonics, and Volcanism*, pp. 307–334. Washington, DC: American Geophysical Union.
- Wolfe CJ, Bjarnason IT, VanDecar JC, and Solomon SC (1997) Seismic structure of the Iceland mantle plume. *Nature* 385: 245–247.
- Wolfe CJ, McNutt MK, and Detrick RS (1994) The Marquesas archipelagic apron: Seismic stratigraphy and implications for volcano growth, mass wasting, and crustal underplating. *Journal of Geophysical Research* 99: 1359113608.
- Wolfe CJ, Okubo PG, and Shearer PM (2003) Mantle fault zone beneath Kilauea volcano, Hawaii. *Science* 300: 478–480.
- Woods MT and Okal EA (1996) Rayleigh-wave dispersion along the Hawaiian swell: A test of lithospheric thinning by thermal rejuvenation at a hotspot. *Geophysical Journal International* 125: 325–339.
- Ye S, Canales JP, Rihm R, Danobeitia JJ, and Gallart J (1999) A crustal transect through the northern and northeast part of the volcanic edifice of Gran Canaria, Canary Islands. *Journal of Geodynamics* 28: 3–26.
- Zindler A and Hart SR (1986) Chemical geodynamics. *Annual Review of Earth and Planetary Sciences* 14: 493–571.

1.14 Crust and Lithospheric Structure – Natural Source Portable Array Studies of Continental Lithosphere

D. E. James, Carnegie Institution of Washington, Washington, DC, USA

© 2007 Elsevier B.V. All rights reserved.

1.14.1	Introduction	480
1.14.2	Natural Source Portable Array Seismology	482
1.14.2.1	Instrumentation	482
1.14.2.2	Portable Array Experiments	484
1.14.2.3	Field Installations and Data Acquisition	484
1.14.2.4	Methods of Analysis	485
1.14.2.4.1	Body wave tomography	485
1.14.2.4.2	Surface wave tomography	486
1.14.2.4.3	Discontinuity imaging	487
1.14.2.4.4	Anisotropy	489
1.14.2.5	Methodological Weaknesses and Caveats	489
1.14.3	Seismic Structure of Tectonically Active Regions	491
1.14.3.1	Western North America	491
1.14.3.1.1	Snake River Plain/Yellowstone and Wyoming Craton	491
1.14.3.1.2	Southern Rocky Mountain region	492
1.14.3.1.3	Rio Grande Rift and Colorado Plateau	493
1.14.3.1.4	Great Basin	497
1.14.3.1.5	Sierra Nevada	498
1.14.3.2	Indian–Eurasian Continental Collisional Zone	498
1.14.3.2.1	Crustal structure	498
1.14.3.2.2	Seismic structure of uppermost mantle	499
1.14.3.3	Continental Margin Subduction Zones	501
1.14.3.3.1	Andean studies	502
1.14.3.3.2	Central America and Caribbean	508
1.14.3.3.3	Cascadia	508
1.14.3.3.4	Alaska	508
1.14.3.3.5	Kamchatka	510
1.14.3.4	Active Continental Riffs	511
1.14.4	Stable Platforms	511
1.14.4.1	Central and Eastern North America	511
1.14.4.2	Australia	514
1.14.4.3	South America	517
1.14.4.4	Antarctica	517
1.14.5	Archean Cratons	517
1.14.5.1	Southern Africa	519
1.14.5.1.1	Mantle tomographic images	519
1.14.5.1.2	Crustal thickness and Moho structure beneath southern Africa	520
1.14.5.2	Passive Array Studies of Other Cratons	523
1.14.6	Seismic Constraints on Composition and Temperature of the Continental Lithosphere	524
1.14.7	EarthScope, USArray, and the Future of Portable Array Seismology	525
1.14.8	Discussion	525
References		526

1.14.1 Introduction

The discovery of plate tectonics fundamentally changed scientists' view of the Earth, generating an entirely new set of precepts for how continents form and evolve over time. Plate tectonics elevated the central role of the continental 'lithosphere' as opposed to 'crust', and it established a direct relationship between dynamical processes deep in the mantle and the shaping of continents. The continental lithosphere is now recognized to be a complex agglomeration of accreted and tectonically modified lithospheric blocks that are the repository of most of Earth's history. Ironically, the seafloor that provided us with much of the proof of plate tectonics is nowhere older than about 200 Ma and thus contains no information on the earlier geologic history of the Earth. As the theory of plate tectonics was refined, and its implications for continental dynamics and evolution better understood, it became increasingly evident that an essential key to understanding the continents lay in our ability to image in detail the 3-D structures of the lithospheric and sublithospheric mantle.

Passive array seismology, notably portable broadband seismology, emerged over the past 25 years to fill the void between detailed active source crustal seismology and low-resolution seismology based on widely dispersed stations of the global seismic network, neither of which was properly suited to the study of continental lithospheric mantle. Despite the demand for new seismic tools to study lithosphere scale structure of continents, however, passive array seismology would not exist today without key technical breakthroughs. Lithosphere-scale imaging has been revolutionized in the past 25 years by the advent of portable high-fidelity low-power 24-bit digital seismic systems, including portable broadband sensors with wide frequency bandwidth and high dynamic range. This new instrumentation provides the tools for seismic studies broadly termed 'passive array experiments'. Passive array experiments involve deployment of tens or even hundreds of instruments, broadband and short period, each of which is capable of operating unattended for months to years at a time in the most remote regions of the Earth. The term 'passive' derives from the fact that these stand-alone arrays of self-sufficient stations record seismic data from earthquakes around the world continuously over periods of months and even years at a time. These passive array earthquake

recordings comprise the essential data for analyzing lithospheric structure.

While fixed array seismology emerged in the 1960s with the construction of US Department of Defense facilities such as Large Aperture Seismic Array (LASA) in Montana (e.g., Aki *et al.*, 1976) and NORSAR in Norway to monitor nuclear explosions, portable array seismology based on earthquake observations (as opposed to timed explosions) is a recent phenomenon. Prior to the development of low-power portable array instrumentation, lithospheric studies were confined largely to the crust: with very few exceptions (long profiles from US and Soviet nuclear blasts), high-resolution imaging of deeper structures in the continental lithosphere and in the mantle beneath the lithosphere was largely beyond the means of existing instrumentation and methods. The precursors to modern passive array seismology were found at a handful of institutions that engaged in portable seismic experiments with in-house instrumentation of limited functionality. For most groups, severe constraints were imposed by aging analog instruments, narrow frequency bandwidths, and incompatible data types that made data exchange difficult. The inability of seismologists to explore deeper regions of the mantle beneath the continents at geologic scales with existing instrumentation precipitated a crisis in seismology, one that led to an innovative rethinking of the instrumentation and experimental design required to explore the deep lithosphere (e.g., Panel on Seismological Studies, 1984). Some of the pioneering efforts to implement portable arrays, for example, were motivated by the fact that 3-D imaging of surface waves across heterogeneous regions of continents thousands of kilometers in extent at geologically useful resolution requires relatively large numbers of closely spaced (100–200 km or better) instruments. One of the first portable seismic studies thus motivated was the Network of Autonomously Recording Seismography (NARS) project, a linear array of 16 long period seismographs across Western Europe for studying surface wave propagation (Nolet and Vlaar, 1981; Nolet *et al.*, 1986). The successful NARS project, largely the work of Nolet and colleagues at Utrecht, was followed closely in time by a national effort within the US seismological research community to initiate a consortium program of portable array seismology for study of the continental lithosphere. By 1984, the seismic community within the US, through a series of workshops and scientific reports from the National Academy of Sciences,

the National Science Foundation, and others, had defined broad goals for a new generation of seismic instrumentation; goals so ambitious in scope that they could be achieved only through the collective strength of a national seismology consortium. The formation in 1984 of Incorporated Research Institutions for Seismology (IRIS) was a watershed event for seismology worldwide. By the mid-1980s, large-scale efforts were underway, not only within the US but also elsewhere, to design and acquire large numbers of high performance portable instruments that could be arrayed anywhere in the world for geologic-scale imaging of the deep underpinnings of continents (e.g., Aster *et al.*, 2005). The IRIS initiative for portable seismology, formally termed the Program for Array Seismic Studies of the Continental Lithosphere (acronym ‘PASSCAL’) and funded by the National Science Foundation, acquired several hundred standardized state-of-the-art portable seismic data loggers and sensors (broadband, intermediate period, and short period) over the next decades. This instrument pool is housed and maintained at a central PASSCAL instrumentation facility and is available to the scientific community for seismic research. IRIS also supports the Global Seismic Network (GSN) of about 140 permanent broadband stations worldwide, and both PASSCAL and GSN digital data are archived and provided to researchers worldwide through the IRIS

Data Management Center (DMC). While parallel efforts to organize both instrumentation and data archiving have been undertaken elsewhere in the world, and continue to grow in importance, IRIS/PASSCAL remains the dominant force behind portable broadband seismology around the globe. Major studies with PASSCAL instrumentation have been, and are being, carried out on every continent on the globe (**Figure 1**). As discussed near the end of this chapter, the scientific capabilities developed over the past 20 years as part of PASSCAL are today being leveraged to implement the EarthScope USArray program to image all of continental US.

The purpose of this chapter is to acquaint the nonspecialist with the current observational capabilities of portable array seismology, as well as with major findings that have emerged from large-scale portable, primarily broadband, experiments. The explosive growth of the literature pertaining to portable array seismology precludes a comprehensive review of results in the brief space allotted this chapter. The sampling of portable array seismic experiments worldwide that are included here thus reflect the author’s personal preference for which results have most impacted the science. As such, this chapter is intended to provide an abridged overview of passive array seismology’s contribution to our knowledge of the deep velocity and discontinuity structure of continental lithosphere, and how that in

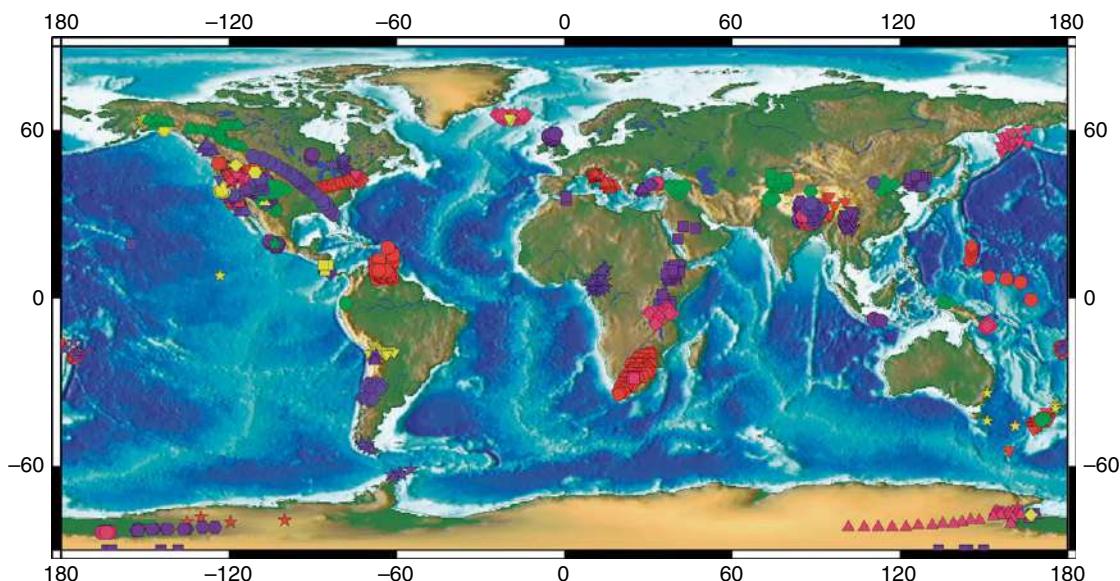


Figure 1 World map showing locations of PASSCAL broadband stations for which data are archived at the IRIS Data Management Center as of late 2006. Figure courtesy of Bruce Beaudoin and the PASSCAL Instrument Center.

turn has led to better understanding of continental formation and evolution.

1.14.2 Natural Source Portable Array Seismology

Controlled source seismic methods that utilize explosions or other artificial sound sources have proved to be very effective tools for exploring the Earth's crust in two and three dimensions. It is, however, a far more demanding task to probe the deep crust and upper mantle at anything approaching a similarly 'geologically meaningful' resolution. In fact, until the development in the last decade of portable digital broadband seismic systems with continuous high-fidelity recording capabilities and accurate absolute Global Positioning System (GPS) timing, high-resolution 3-D imaging of the continental mantle was essentially beyond the reach of seismology. The seismic sources for broadband array experiments are earthquakes of all kinds, from nearby local events to 'teleseismic' events at epicentral distances $>27^\circ$; thus, broadband stations typically record continuously for up to 1–2 years. In broadband seismology (and most array seismology today), all three components of ground motion (vertical and two orthogonal horizontal directions, generally N–S and E–W) are recorded and the systems are capable of observing most of the radiated earthquake spectrum that is used for continent-scale seismic studies. Broadband seismic records, coupled with extremely accurate GPS clock timing, are the key ingredients for geologic-scale imaging of deep continental structure.

1.14.2.1 Instrumentation

The emergence of low-power portable broadband digital instrumentation represented a first-order revolution in seismology. For the first time, portable seismic instruments capable of recording data of near-observatory quality could be deployed anywhere in the world (Aster *et al.*, 2005; Owens and Fowler, 2003). The circumstances that led to that revolution in seismic instrumentation and data quality were a combination of good timing and the formation of IRIS. Of vital importance was the rapid development of microprocessor technology for the emerging popular computer market. Thus, the design for versatile multichannel digital seismograph systems was leveraged from state-of-the-art digital technologies developed for

computer and other mass consumer market applications. The following is a brief description of broadband instrumentation as it pertains to passive array studies of continental lithosphere.

The standard portable array seismic system today (2006) consists of a digital data logger and a seismometer ([Figure 2](#)), a GPS unit for both absolute timing and station location, a battery/solar panel power supply, and auxiliary devices and cables for connecting these units and communicating with them in the field. Photos of a typical field installation are shown in [Figure 2\(c\)](#). The dataloggers are low power, high dynamic range (24-bit) microprocessor-based digital recording systems with several gigabytes or more of mass storage to allow continuous three-channel recording for months unattended. While digitizing rates of up to 1000 samples/sec are attainable with current dataloggers, sampling rates are typically around 40 samples/sec, which is sufficient for all teleseismic recording and for most regional events. In addition to continuous recording, the dataloggers can analyze incoming events in real time and activate 'triggers' to initiate higher sample rates to record over a specified time window according to the nature of the incoming seismic signal.

The portable broadband sensor, rugged, low power, and simple to install, is the key component of continent-scale seismology. Broadband, high-dynamic range units have been available since about 1990 with the production of advanced broadband systems by Streckeisen in Switzerland and Guralp in England ([Figure 2\(b\)](#)). All portable broadband seismometers in use today operate on the principle of a negative feedback loop that is applied to a small inertial mass to hold it fixed relative to the moving seismometer reference frame. The amount of electromotive force that is applied to keep the mass in place is used to measure ground acceleration. Because the mass moves very slightly (ideally, not at all), the force-feedback system has much better linearity and significantly expanded frequency range relative to mechanical seismometers (see, e.g., Lay and Wallace (1995) and Wielandt and Streckeisen (1982) for further discussion). Compact low-power electronic force-feedback systems can thus be configured for a very wide range of seismometer responses: the state-of-the-art Streckeisen STS-2 and Guralp CMG-3T portable sensors, for example, have a flat velocity response from about 50 to 0.008 Hz, sufficient to cover virtually all of the body wave and surface wave bandwidth of interest for lithospheric studies.



Figure 2 (a) Standard low-power (<1.0 W) 24-bit six-channel data loggers used in passive array experiments. The REFTEK RT-130 shown on the left can record at least three channels of data in several data streams of differing sample rates. The datalogger uses GPS for absolute timing (generally to microsecond accuracy) and flash memory cards for mass storage. The Quanterra Q330 datalogger shown on the right is specifically configured for real-time telemetry that includes duplex communication and burst or continuous transmission. (b) State-of-the-art force-feedback portable broadband sensors in general use today. Both units shown are low power (<1.0 W), capable of remote mass re-centering and have flat velocity frequency response 50–0.008 Hz. On the left, the Streckeisen STS-2 is manufactured in Switzerland, weighs about 9 kg and is 23 cm high. On the right, the Guralp CMG-3T, manufactured in England, weighs 14 kg and stands 38 cm high. (c) Typical portable field installations. Left: basic broadband station layout at a High Lava Plains (HLP) site in eastern Oregon. Sensor vault consists of a 30-gallon (blue) plastic drum in which the sensor is placed on a concrete base, oriented and leveled, and thermally insulated. A watertight enclosure houses the datalogger, powerbox, and batteries. Wiring between sensor and datalogger and power sources is through PVC conduit. The station shown is powered by a single 60 W solar panel and two deep cycle marine batteries intended to last the full 2 year life of the installation. Right: broadband station for southern Africa (Kaapvaal) experiment. Vault is covered with insulating dirt to a depth of at least 30–40 cm. Solar panels and GPS unit are mounted on roof of ‘doghouse’ in which are housed the datalogger and auxiliary electronics.

Much of the imaging of the deep continents (see Section 1.14.2.4 below) that is done with portable arrays depends on precise absolute timing made possible for the first time worldwide by the US Department of Defense launch of the GPS in the 1990s. GPS satellites transmit signals that contain extremely accurate time codes, as well as information that allows a GPS receiver on the Earth’s surface to compute its position to within a few meters anywhere on the globe. The accurate time signals, recorded independently at each seismic station, allow seismic signals across an entire array of stations, each with independent timing, to be correlated to hundredths

or even thousandths of a second, making it possible to quantify travel-time differences between stations at very high accuracy. The availability of matched broadband stations that operate with an extremely accurate common time base is the critical factor that has made high-resolution tomographic imaging of the continental lithosphere a reality.

Real-time telemetry, both radio and satellite, has evolved slowly since the late 1980s when the first very low bandwidth satellite transmission systems were deployed (e.g., Poupinet *et al.*, 1989a, 1989b). While progress, particularly in satellite communication, has been surprisingly sporadic, telemetry has

played an increasing role in passive array seismology in the last decade. Systems that transmit data to a central collection site in approximately real time have proved to significantly improve both quality control and data recovery. Although the most commonly used systems to date are still those that employ line-of-sight radios (e.g., the PASSCAL 32-station broadband telemetering system), satellite and cellular communications are increasingly feasible, both technically and economically. Data from many of the USArray stations (see Section 1.14.7 below) are transmitted via satellite.

1.14.2.2 Portable Array Experiments

Natural source portable array experiments have been carried out in every continent. [Figure 1](#) shows PASSCAL deployments over just the 5-year period 2000–2005. In addition to the PASSCAL experiments shown in [Figure 1](#), substantial numbers of other portable seismic experiments have been carried out in recent years by other international research groups. (Space limitations confine the scope of this chapter to portable array studies of continental regions. Unfortunately, this excludes even mature island arcs, notably Japan, where dense networks of advanced permanent seismic stations blanket the islands. A satisfactory summary of the many fine studies of subduction zone structure beneath Japan based on data from the permanent networks is beyond the bounds of the present work.) While local and regional events are commonly incorporated in portable array experiments, nearly all broadband imaging depends heavily on teleseismic events, epicentral distances $>27^\circ$. Stations arrays are designed according to the nature of the scientific target(s), the methodologies to be used, the number and type of the instruments available for the experiment, and the distribution of teleseismic sources. In general, arrays tend to be deployed either along 1-D transects or in a 2-D grid. Station density is typically constrained by the number of instruments: where ample instrumentation is available interstation spacing of about 10 km is sufficient for unaliased imaging at dominant teleseismic wave frequencies, where maximum P-wave energy tends to be concentrated around 1 Hz (e.g., [Levander, 2003](#)). Nonetheless, a number of portable broadband experiments have deployed instruments along profiles at even denser intervals, where the objective was to image crustal and upper-mantle discontinuities across complex geologic terranes. Examples include [Nabelek et al.](#)

(1993), ~5 km spacing along a linear profile across the Oregon Cascades, and [Zhao et al. \(2001\)](#), ~5–10 km along the INDEPTH III transect in Central Tibet. A few passive array experiments, most with the objective of imaging very shallow structures, may have instrument spacing as close as 1 km (e.g., [Roecker et al., 2004](#); [Thurber et al., 2004](#)). Where the targets are deep crustal or mantle structures, however, even very ambitious projects more commonly involve interstation spacing around 20 km (e.g., [Wilson and Aster, 2003](#)), the La RISTRA profile in western US, with station spacing of about 18 km along a 950 km transect). In almost every case, primarily because of limitations in numbers of instruments, dense deployments are more commonly seen in linear transects and the resulting analysis 2-D rather than 3-D. Where the scientific objective is 3-D imaging of larger regions encompassing multiple terranes, deployments tend to be more widely spaced, either in a grid or on a long profile, and interstation distances may be 50–100 km. Typical of a gridded experiment of this type is the southern Africa seismic experiment (e.g., [James, 2003](#)) where station spacing was on the order of 100 km and array dimensions about 1800×600 km.

1.14.2.3 Field Installations and Data Acquisition

A typical portable broadband installation is effectively a semipermanent mini-observatory. As such, its functional capabilities approach those of a state-of-the-art global seismic station, and because it can be sited in remote locations with little cultural noise may even be superior in performance. While relatively few studies have sought to define optimum vault design for broadband installations (e.g., [de la Torre and Sheehan, 2005](#)), the primary keys to achieving low noise include thermal stability, proximity to bedrock, and absence of cultural noise. Photos of a typical portable station installation are shown in [Figure 2\(c\)](#). While no absolute standards have been adopted for the construction of a portable broadband station, a number of features are common to virtually all installations. As shown in [Figure 2\(c\)](#), the three-component broadband sensor is installed below ground in a constant temperature ‘vault’, typically constructed from a plastic or steel drum. A thin concrete layer, laid down to provide a level surface for sensor installation, is poured atop bedrock at the bottom of the hole. When steel drums are used

for the vault, it is common to remove the base of the drum and to isolate the drum walls from the concrete pad. Where plastic drums are used, the bottom of the drum may be left intact, worked into the concrete layer atop bedrock, and then filled with an additional several centimeters of concrete as a base pad for the sensor. The sensor pad, ideally bonded to bedrock, is typically some 40–70 cm beneath ground level. The sensor is leveled and the horizontal components oriented precisely. Cables are connected via PVC pipe (see [Figure 2\(c\)](#)). A close-fitting Styrofoam housing and other insulation is placed over the sensor and within the drum to minimize thermally induced air circulation that will adversely affect sensor stability. After the sensor has been installed, the lid of the vault is sealed and the whole assembly buried in insulating dirt to a depth of at least 50 cm. Under normal operations, the sensor vault will remain sealed until the end of the deployment. A typical station is powered by one or two standard marine deep cycle batteries that are kept charged by solar panels. Months of seismic data, typically sampled at a rate of 20–40 samples/sec can be stored on several Gbytes of disk or flash memory. A small external GPS antenna is mounted with an unobstructed view of the sky. Routine station servicing, typically at 3–6 month intervals, consists primarily of checking that data recording is normal and the GPS clock is operating correctly, swapping out data memory cards, and calibrating the sensor. Where telemetered, cellular or satellite communication has been implemented, stations may need no on-site servicing at all. For PASSCAL experiments, data collected at each station are generally returned to a local operations center where they are copied, pre-processed into a standard database, and transmitted to the IRIS DMC for permanent data archiving.

1.14.2.4 Methods of Analysis

The dramatic increase in the volume of high-quality portable broadband data has spurred development of advanced imaging tools to capitalize on those data, and a vast literature has developed on the subject in just the past few years (e.g., [Levander, 2003](#); [Levander and Nolet, 2005](#); [Pavlis, 2003](#); [Sheehan et al., 2000](#); [Wilson and Aster, 2005](#)). The brief non-technical summary of methodologies presented below touches on some of the more common methods in use today, but for more comprehensive

treatment, the reader is referred to Chapters 1.07 and 1.10 in this volume and to the literature cited here.

Part of the sea change brought about by increasingly large-scale deployments of broadband instruments is the development of (1) tomographic methods to image geologically identifiable features in the mantle and (2) advanced methods for direct waveform imaging of crust and mantle discontinuities similar in style to that used in seismic exploration (e.g., [Pavlis, 2003](#)). Two basic categories underpin most of the imaging that is done with portable arrays. The first may be termed ‘volumetric’ imaging, the most important class of which is tomography, both body wave and surface wave, although it also includes attenuation tomography and mantle anisotropy. High-resolution tomography demands quality seismograms from high performance standardized instrumentation, with high-fidelity waveforms and very accurate absolute timing. These requirements have only recently been realized, so that as the quality and quantity of data have improved tomographic imaging has become one of the most powerful tools seismologists have to study the deep continental lithosphere.

‘Discontinuity’, or scattering, imaging is complementary to tomographic imaging and is aimed at direct imaging of subsurface discontinuity structure (scatterers) in both two and three dimensions. All discontinuity imaging is based on interpretation of scattered energy in the seismogram, that is, the conversions and reflections of P and S waves at velocity discontinuities in the Earth where rock types or material properties of the rocks change significantly over relatively short distance scales. As the station spacing of portable arrays has densified, analytical methods developed for seismic reflection imaging by the exploration industry have become increasingly applicable (e.g., [Levander, 2003](#); [Pavlis, 2003](#); [Rondenay et al., 2005](#)). Continuous unaliased high-resolution images in 2-D are now relatively common, and continuous 3-D imaging has been experimented with in several recent portable array studies.

1.14.2.4.1 Body wave tomography

Except where high levels of earthquake activity are in the same geographic region of interest as the observing stations, body wave tomography of structure beneath a network of portable stations is generally based on teleseismic relative arrival times measured across the array (e.g., [Nolet, 1987](#); [VanDecar, 1991](#)). The marked improvement in the

reliability and resolving capability of portable array body wave tomography over the past decade owes partly to much advanced methods of analysis, but more to greatly enhanced quantity and quality of the data. As relative arrival times are the primary input data for regional tomographic modeling, the term ‘quality of data’ refers primarily to clock reliability, signal-to-noise, and waveform fidelity: whatever the specific tomographic computational methods adopted, the quality of the results hinges on these factors. To remove the complicating effects of heterogeneous upper-mantle structure in the tomographic analysis, earthquake data are typically confined to events beyond about 27° distance, where seismic waves bottom in the relatively uncomplicated lower mantle below the upper-mantle transition zone (between 410 and 660 km). Tomographic analysis takes as its input the relative travel time residuals across the array relative to a spherical reference Earth model. These residuals are the data that are then inverted to obtain 3-D velocity variations beneath the array of stations (*see* Chapter 1.10).

In studies prior to about 1990, it was common to obtain travel time residuals from hand picked absolute arrival times. That method may still be used for seismic networks that cover large geographic areas and/or that involve a mix of instrument types where waveform correlations are difficult. In these instances, the absolute travel time of the seismic wave between earthquake source and receiver is referenced to a standard Earth model. For portable array tomography, where the structure of interest lies beneath the station network, relative residuals (delay times) are computed for each observed travel time by subtracting the mean of the absolute travel time residuals for each event (relative to the standard model) from the observed travel time for that event at each station. The data are time shifted so that the mean of the travel time residuals for each event is zero. This process of obtaining relative travel time residuals significantly reduces the influence of extraneous factors, such as errors in event location or origin time, deep-mantle velocity anomalies, and an inaccurate reference model that can introduce very substantial errors in regional tomographic models (e.g., VanDecar, 1991; Humphreys and Dueker, 1994). VanDecar and Crosson (1990) introduced the now common method of using pairwise cross-correlation to align waveforms more precisely and obtain a statistically optimized set of relative arrival times. Tomographic inversion of the relative travel time data to obtain a seismic velocity model involves

partitioning the volume of interest beneath the array into a 3-D grid of blocks or knots. The relative travel time residuals from many hundreds or thousands of criss-crossing rays through the volume beneath the array are inverted to obtain a least-squares estimate of the relative velocities within each block. The density of crossing rays is a critical factor in the ability of the tomographic inversion to resolve structure, which thus depends on earthquake sources that are well distributed in both azimuth and distance (*see* Chapter 1.10). By the VanDecar method of tomographic analysis (e.g., VanDecar, 1991; VanDecar *et al.*, 1995), the data are inverted simultaneously for the velocity structure, earthquake relocations, and stations corrections. As the least-squares solution is not unique, the inversion searches for the simplest model that contains the ‘least’ amount of structure required to satisfy the observations.

1.14.2.4.2 Surface wave tomography

Surface waves observed in the Earth are dispersive (*see* Chapters 1.02 and 1.07). That dispersion is caused by the fact that higher frequencies are sensitive to shallow structures and lower frequencies to deeper structure such that different frequencies travel with different velocities. While surface waves have been used to sample shear wave velocities to depths of 1000 km or more in global studies, the maximum depths that can be resolved from portable array data are rarely more than a few hundred kilometers.

A number of different methods of surface wave tomography have been developed, although the most common for studying continental lithosphere fall into two general categories: (1) partitioned waveform inversion (PWI), where surface waveforms (including S and multiple S) are modeled directly, and (2) a variety of methods that require direct measurement of phase velocities across the array. Significant advances in crustal imaging have also been made using portable array data, including higher mode group velocity tomography (Levshin *et al.*, 2005) and ambient noise tomography (Shapiro *et al.*, 2005).

Partitioned waveform inversion, first applied for 2-D structures to the linear Network of Autonomously Recording Seismographs (NARS), is a two-step process (Nolet, 1990). The first step involves nonlinear waveform fitting of fundamental and higher mode surface waves where the S-wave, multiple S-wave, and surface wave train of the time series are matched by synthetic seismograms to obtain a path-average 1-D velocity model representing the average Earth structure

between source and receiver. The synthetic seismograms that are used to fit the observed data can be computed by different methods. While all these methods require information on the focal mechanism of the earthquake source, no direct measurement of group or phase velocities is involved. Once the path-averaged 1-D structures are obtained for all source–receiver pairs, a generalized least-squares tomographic inversion, similar to that for body wave inversion, is performed to obtain the 3-D (or 2-D, in the case of linear transects) shear wave speed beneath the array. Crustal thickness may be constrained or it may be included in the inversion. PWI, or some variant of it (e.g., Friederich, 2003), has been widely used for continent-scale studies (e.g., Friederich, 2003; Simons *et al.*, 1999; Van der Lee and Nolet, 1997; van der Lee *et al.*, 2001a), but has relatively limited application to smaller regional arrays where more array-specific techniques can be applied.

Array techniques, based largely on Rayleigh wave data recorded on local or regional seismic networks, have evolved substantially in the past decade as broadband arrays have increased in areal extent and station density. The simplest of these, and still one of the more robust, involves determining phase velocity between station pairs aligned on the great circle path with the earthquake (e.g., Larson *et al.*, 2006; Snook and James, 1997). More sophisticated array methods in use today attempt to account for multipathing and other out-of-plane propagation. One means to accomplish this is by representing the incoming wavefield as a superposition of two interfering plane waves whose parameters (amplitude, phase, and direction) are determined in the inversion (e.g., Bruneton *et al.*, 2004; Forsyth and Li, 2005; Li *et al.*, 2005). This and similar methods can also include an estimate of azimuthal anisotropy (Forsyth and Li, 2005). Where Rayleigh wave, Love wave, and multiple S-wave data are available, Gee and Jordan (1992) developed an isolation filter technique to determine radial anisotropy, as well as phase delays across the array (see also Freybourger *et al.* (2001); Saltzer (2002)).

Recent forays into the joint inversion of surface waves and body waves from portable arrays (e.g., Friederich, 2003; van der Lee *et al.*, 2001b; West *et al.*, 2004a), are mostly in an embryonic stage, but hold promise of major improvements in imaging with further development. Much of the motivation for joint inversion derives from two factors. First, surface waves provide good vertical resolution (but poor lateral resolution) while body waves provide

excellent lateral resolution (but poor vertical resolution) of the 3-D velocity structure. Jointly, they thus provide complementary constraints on the velocity structure both laterally and vertically across the array. Second, the inclusion of surface wave data in the inversion makes it possible to attach absolute S-wave velocities to what are otherwise simply velocity perturbations in the body wave inversion alone. The technique developed by West *et al.* (2004a) treats the surface wave measurements simply as travel times between stations, with each travel time corresponding to a horizontally traveling ray through the blocks in the model. The horizontally traveling surface wave rays are sensitive over a depth range estimated for each given frequency, but otherwise can be added directly as an additional set of ray paths to the body wave data.

1.14.2.4.3 Discontinuity imaging

Most direct imaging of discontinuity structure is based on some version of teleseismic receiver function analysis, although full scattering formulations are increasingly evident (e.g., Rondenay *et al.* (2005), with references). Receiver functions are computed primarily for teleseismic events (30–90° epicentral distance), where incoming P-rays beneath the station are at near-vertical incidence. The near-vertically propagating P-wave that is incident on a horizontal boundary across which there is a significant contrast in V_s will convert a small amount of its energy to an S-wave. The particle motion of the resulting P-to-S conversion will be predominantly horizontal radial, and thus recorded primarily on the radial component of the seismogram (Figure 3(a)). Nonhorizontal discontinuities can produce significant P-to-S converted energy on the transverse component, as may anisotropy in some cases. While these effects are typically small, inspection of the transverse component will reveal whether such factors are important.

All of the converted signals are of small amplitude and tend to be concealed in the coda of much larger amplitude direct arriving P-waves. The receiver function is a means of isolating these relatively small amplitude P-to-S (Ps) conversions that are produced beneath the station from the much larger amplitude direct P-wave arrivals that dominate the same early portion of the record (also see Chapter 1.17 for further discussion). To compute the receiver function, the vertical component signal (which nominally contains only P wave energy) is deconvolved from the radial component (which contains both P and S wave energy) to produce a so-called ‘source

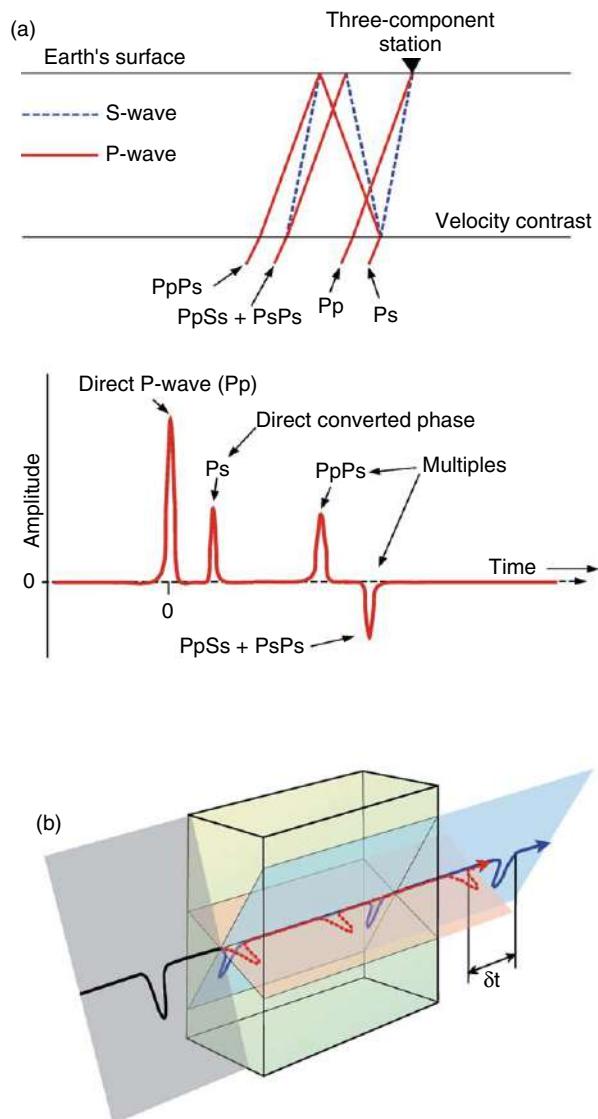


Figure 3 (a) Basic ray geometry and radial receiver function diagram for a simple one-layer model over a half space, with a velocity discontinuity in S. Ray nomenclature is as diagrammed on the upper figure. The receiver function is obtained by deconvolving the vertical component record from the radial component. The coherence peak of 'all' direct P-wave energy arriving at the station within the time window of the deconvolution trace is labeled 'Direct P-wave'. High-quality converted wave signals can be obtained by deconvolution even in cases where the source-time function of the earthquake may be quite lengthy and complex and individual signals extremely difficult to detect. The amplitude of the P-to-S conversion is a function primarily of the S-wave velocity contrast across the boundary. Figure courtesy of Rick Aster, New Mexico Tech. (b) Schematic diagram showing the effects of anisotropy on a seismic wave passing through an anisotropic medium. In this case, the incident wave is a polarized shear wave (such as the core phase SKS). On passing through the anisotropic medium (anisotropy is indicated by different colored planes within the volume shown), the wave 'splits' into a fast and a slow component ('shear wave splitting'). The magnitude of the lapse time, δt , between fast and slow shear wave components is a function of both the path length and the strength of the anisotropy. If the incident wave is polarized parallel to one of the axes of anisotropy, no S-wave splitting will occur. Figure courtesy of Ed Garnero, Arizona State University.

'equalized' radial seismogram (e.g., Ammon, 1991). Under ideal conditions, the source equalized (deconvolved) trace consists of a large amplitude coherence spike at zero time (containing all the P-wave energy

present on the original radial component that is coherent with the vertical component) and a following spike train of smaller signals that are the P_s conversions and converted reflections from

discontinuities beneath the station (**Figure 3(a)**). Thus, the receiver function can be considered a scaled version of the radial component of displacement with the P wave train removed (Ammon, 1991); also see Wilson and Aster (2005). The receiver function may be used to image any discontinuity at depth, but in practice has been used primarily for imaging the Moho, the top of the descending plate in subduction zones, and upper-mantle discontinuities including the 410 and 660 discontinuities.

Sp receiver functions. Receiver functions based on P-to-S conversions have proved to be remarkably effective for imaging the Moho and the 410 and 660 discontinuities of the transition zone. Because of the interfering effects of crustal multiples, however, these receiver functions have proved to be difficult to interpret unambiguously for upper-mantle structures in the depth range 100–300 km. Several recent papers have addressed that problem by examining S-to-P conversions, where the primary conversions precede the S-wave arrival and all multiples are in the S coda (Farra and Vinnik, 2000; Wittlinger *et al.*, 2004). The method for computing Sp receiver functions was first formalized by Farra and Vinnik (2000), where the vertical component is deconvolved by the radial, similar to that of the Ps receiver function but where the respective roles of P and Sv are reversed. The method tends to be limited by the fact that earthquake magnitudes must be substantially larger than for Ps receiver functions and piercing (conversion) points are substantially further from the station as the S-to-P conversion results in a much lower angle incident ray.

1.14.2.4.4 Anisotropy

Seismic anisotropy, or seismic birefringence, is a key measurement for imaging past and present deformation in the Earth's interior (see Fouch and Rondenay (2006) for a comprehensive summary). Thousands of shear-wave (radially polarized core phases SKS and SKKS) splitting measurements over the past two decades have shown that anisotropy in the upper mantle is present almost everywhere, both on and off continents. Splitting measurements are especially applicable to the upper mantle, and to a lesser extent the crust, where tectonic and flow deformation results in anisotropic fabric through crystallographic alignment of anisotropic minerals. In the case of portable array experiments, attention has focused primarily on the upper mantle, where seismic anisotropy is generally interpreted in terms of lattice-preferred orientation (LPO) of olivine, which

deforms under stress to produce strongly anisotropic strain-induced fabric. Vinnik *et al.* (1984) first recognized that the radially polarized Sv waveforms of SKS and SKKS core phases could be used to obtain extremely simple *in situ* measurements of azimuthal (horizontal plane) S-wave anisotropy (**Figure 3(b)**). The method has since been refined (Silver and Chan, 1988) and routinely used to determine anisotropic fast directions and delay times for virtually every station in nearly every passive array deployment since (see summaries in Fouch and Rondenay (2006) and Silver (1996)). Surface wave anisotropy can be either radial (vertical) or azimuthal (horizontal). Radial anisotropy, which cannot be observed by shear wave splitting, is manifest as model incompatibility between Rayleigh waves and Love waves. In such cases, Love waves invariably call for a substantially higher S-wave velocity structure than do the Rayleigh waves, and in those anisotropic models, the difference between so-called V_{SH} structure and V_{SV} structure is commonly quite large, with V_{SH} the higher velocity. Azimuthal anisotropy, on the other hand, is difficult to determine by surface waves alone and requires multiple measurements along many azimuths across the array (e.g., Forsyth and Li, 2005). While lateral resolution in all surface wave methods is relatively poor, a major strength of surface wave anisotropy, both radial and azimuthal, is the relatively good depth resolution. This overcomes one of the great weaknesses of shear wave splitting methods where depth of the anisotropy cannot be determined, and it is for this reason that the joint use of surface waves and core phases is coming increasingly into play (e.g., Gaherty, 2004).

Anisotropy takes a back seat to tomographic and waveform imaging in the sections that follow. This is partly the personal preference of the author, but it is also a consequence of the fact that anisotropy as it relates directly to structure of the continental lithosphere (fossil anisotropy) is commonly difficult to sort out from asthenospheric flow. The interested reader is referred to Fouch and Rondenay (2006); Silver (1996) for further enlightenment.

1.14.2.5 Methodological Weaknesses and Caveats

The above description of methods has necessarily been brief. It is particularly useful, therefore, to highlight pitfalls in some of the various techniques in common usage today.

Seismic tomography. The rapid increase in the number and density of instruments comprising seismic arrays has led to increasingly high-resolution tomographic images that appear to be interpretable in geologic or near-geologic terms. The tomographic problem is underdetermined, however, which means that all 3-D tomographic images are smoothed and damped to a greater or lesser degree, and all are nonunique. Indeed, even the best-constrained models are blurred images of the actual structure, smoothed across small-scale heterogeneities. Moreover, unlike the medical CT scan, a major shortcoming in seismic tomography is the uneven distribution of sources (and often receivers), such that some parts of the region to be imaged are better constrained by data than are others. In addition, as stations are always at or near the Earth's surface, seismic rays pass through the volume to be imaged in only one direction, from below. Where stations are arrayed along 1-D profiles, the uncertainties in the resulting 2-D solution can be substantially greater than they are for comparable 3-D solutions from areal deployments.

Apart from the problem of image smearing and nonuniqueness, body wave inversions are nearly always expressed in terms of velocity ‘perturbations’, or velocities relative to the mean velocity over the model space (‘not’ relative to the background starting model). In regions of overall high velocity or low velocity, relative velocity images can be misleading. A significant advantage of surface wave imaging is that absolute velocities are determined. Body wave tomographic velocity perturbations tend to smear along ray paths, such that those images provide generally good constraints on lateral heterogeneity but poor control on vertical structure. Similarly, surface wave tomography provides good control on vertical structure, poor control on lateral structure. This is a primary motivation for joint body wave/surface wave inversion where both lateral and vertical structure can be better constrained. In all cases, the color scheme used by the author to signify velocity contrast can have a major effect on the appearance of the image. The reader is invited to examine some of the images in this chapter to see whether it is possible to spot such effects.

Receiver function methods. Receiver functions are most easily interpreted when relatively sharp subhorizontal boundaries with strong S-wave contrasts are present. Dense arrays allow powerful exploration-type analyses to be applied to the data to obtain 2-D or 3-D images of crustal and mantle

discontinuities. Shortcomings of standard receiver function methods (as opposed to full wavefield scattering methods) include difficulty in accommodating anisotropy, dipping layers, reverberations between layers, gradational variations in structure, and distant scattering (e.g., core reflections). Running averages over arrays of stations can make structures appear to be far more continuous than the individual station data suggest (e.g., Yuan *et al.*, 2000). While various techniques have been, or are being, developed to deal with the many known shortcomings, receiver function images are commonly degraded by one or more of these effects. Crustal reverberations, for example, make Ps receiver function images unreliable in the depth range 100–200 km. Anisotropy and dipping layers must be evaluated through an examination of energy on the transverse component, but this precaution is commonly ignored.

Anisotropy. Determination of shear wave (SKS) splitting is among the simplest of all processing procedures in seismology, readily accessible through publicly available ‘canned’ codes, and is hence fraught with pitfalls. First, the magnitude of azimuthal anisotropy as a function of depth cannot be determined from SKS splitting alone, nor can the cause of the anisotropy itself. Interpretations based on simplifying assumptions of uniform single layer anisotropy can be wildly misleading. Anisotropy observed through SKS splitting could originate anywhere along the path between the core–mantle boundary and the recording station. Substantial evidence exists that the lowermost mantle may be anisotropic as may be other parts of the lower mantle or transition zone (e.g., Fouch *et al.*, 2001). It is known that SKS and SKKS can give wholly different splitting results, even when well observed on the same seismogram for the same event (e.g., James and Assumpção, 1996). Complexities such as multiple layers with differing anisotropies, dipping layers, differing mineral anisotropies within a single layer, and the like all require data from well distributed earthquake sources and comparatively sophisticated analysis to sort out. Radial anisotropy as manifested by a significant discrepancy between Rayleigh and Love wave S-wave velocity depth models can be relatively well constrained by depth but lateral resolution of the anisotropy tends to be poor. Similarly, azimuthal anisotropy obtained from analysis of fundamental mode Rayleigh waves is well constrained vertically, poorly constrained laterally.

1.14.3 Seismic Structure of Tectonically Active Regions

This section and the ones that follow are intended to provide the reader with a thumbnail sketch of some of representative findings from portable array (primarily broadband) seismology. Beginning with tectonically active regions, most portable array studies have focused on four major tectonic regimes: (1) western US, where a complex series of events broadly associated with the Laramide orogeny and the overriding of the Farallon spreading center have overprinted much of the Archean and Proterozoic lithosphere of western North America; (2) continent-continent collisional zones, notably the Himalayan/Tibet orogenic belt; (3) intraplate rift zones, with perhaps the best example in northern Africa; and (4) continental margin subduction zones. In the following sections, we summarize representative results from each of these regions.

1.14.3.1 Western North America

The Rocky Mountain Front marks a profound divide between stable North America to the east and tectonically active North America on the west. Western US is one of the most complex and most seismically investigated tectonic regions in the world. The tectonic provinces that make up the region record a baffling sequence of overlapping tectonomagmatic events dating from the Mesozoic to the present. These events appear to overprint and, in some cases, be controlled by the Archean and Proterozoic continental structures that comprise the deep framework of western North America. Over the past 70 My or so, western US has undergone a succession of continent-shaping events – Farallon plate subduction and destruction, extensional and compressional deformation, and tectonomagmatic activity – that continue to this day. During the past 30 My most of the interior of western US has seen tectonic extension. Portable array seismology has played a key role in unraveling the complex history of lithospheric evolution of the western US, from early Proterozoic (*c.* 1.8 Ga) through the Laramide orogeny (*c.* 80–50 Ma) to Neogene tectonism that continues to Recent time.

Major geologic provinces of western US are shown in [Figure 4](#) superimposed on a composite image of upper-mantle S-wave velocity structure at 100 km depth ([Grand, 1994](#); [Humphreys and Dueker,](#)

[1994](#)). Extensive studies of this entire region of western US are ongoing and expanding in scope (see Section 1.14.7 below). Nonetheless, it is useful to summarize some of the major syntheses and interpretations that have emerged from current studies of this actively evolving region. A considerable body of work is published in book form on the lithospheric and sublithospheric structure of the Rocky Mountain region from Montana south to New Mexico and west to the Basin and Range ([Karlstrom and Keller, 2005](#)), gleaned from the large-scale CD-ROM, La RISTRA, and Snake River and Deep Probe teleseismic profiles ([Figure 5](#)) ([Karlstrom *et al.*, 2005](#)).

The tectonics of the Rocky Mountain region are dominated by NE–SW trending lineaments that mark zones of low-velocity mantle and extensive tectonomagmatic activity subparallel to Proterozoic province boundaries and to the direction of absolute plate motion of North America. As [Karlstrom *et al.* \(2005\)](#) point out, the S-wave velocity contrasts in the upper mantle over distances of less than 100 km can be as large as 10–15%, values that are comparable to continent-scale variations. If the velocity contrasts are interpreted as purely thermal, they imply temperature differences up to 700°, from shield-like geotherms to mantle undergoing partial melting. The sections that follow are organized such that the discussion begins with the Snake River/Yellowstone region of the northern Rockies, moves to the southern Rockies near the eastern front with the Great Plains and then westward through Colorado Plateau, the Basin and Range, northern Great Basin and into the Sierra Nevada. Discussion of the active Cascade arc is reserved for the sections below on continental margin subduction zones.

1.14.3.1.1 Snake River Plain/Yellowstone and Wyoming Craton

The Snake River Plain/Yellowstone (SRP/YS) region is among the most intensively studied in the world, with well over 100 broadband stations deployed regionally in several major experiments ([Dueker and Yuan, 2004](#); [Yuan and Dueker, 2005a](#)). In addition to a large network of short period and permanent stations that the University of Utah and US Geological Survey have maintained in the Yellowstone region for many years, several major PASSCAL deployments, all of a year or less, have added substantially to the database across the larger penumbra of the Yellowstone signature. The major issue surrounding the SRP/YS structure is whether it has been caused by a plume. Superficially, the

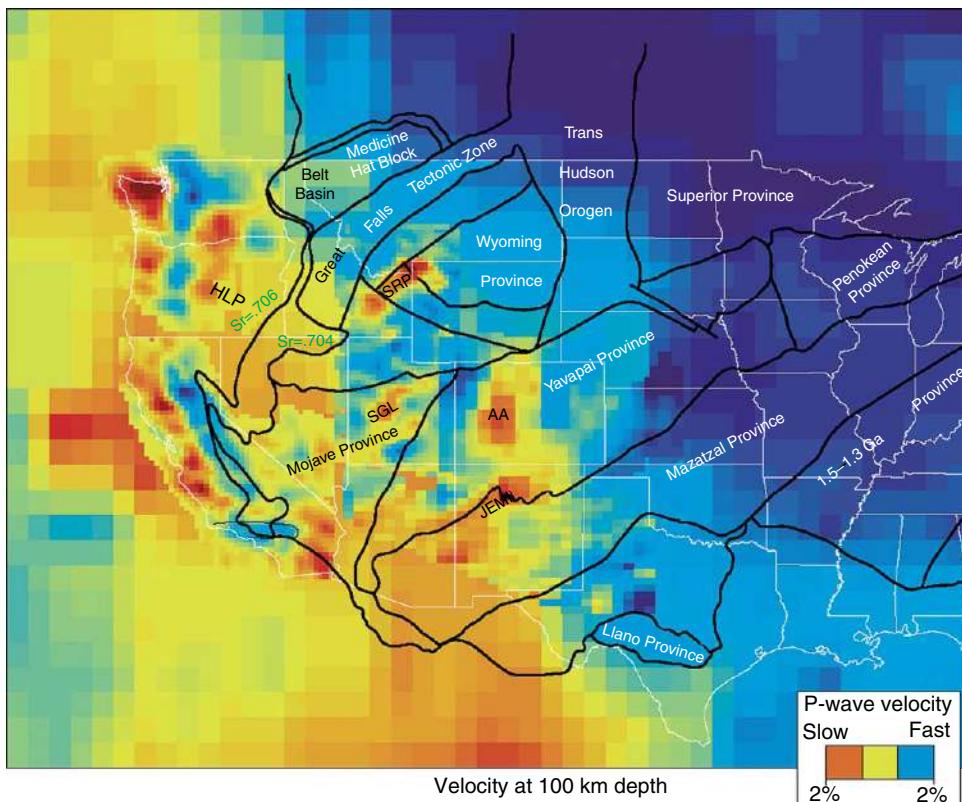


Figure 4 North American upper-mantle velocity perturbations at 100 km depth. Modified from Karlstrom KE and Keller GR (2005) *Geophysical Monograph 15: The Rocky Mountain Region – An Evolving Lithosphere: Tectonics, Geochemistry, and Geophysics*, 441 pp. Washington, DC: American Geophysical Union. The background continent-scale S-wave velocity perturbation structure is from Grand, 1994), overlain by regional array P-wave velocity perturbations from Humphreys and Dueker, 1994. Blue indicates positive (high) relative velocity red indicates negative (low) relative velocity. Precambrian province boundaries are outlined in black. SRP, Snake River Plain; SGL, Saint George Lineament; AA, Aspen anomaly; JEML, Jemez Lineament; HLP, High Lava Plains.

evidence for a plume is convincing, and recent tomograms seem to reveal an NW-dipping plume-like structure in the upper mantle extending to a depth of perhaps 600 km (Figure 6) (Yuan and Dueker, 2005a). The velocity anomalies shown in these P-wave images are particularly strong in the upper 150 km, where they reach values of 8% peak to peak. Similar very low velocities are seen in the upper mantle to depths of at least 200 km along the axis of the SRP as it trends ENE toward Yellowstone (Schutt and Humphreys, 2004). Beneath Yellowstone itself, the low P-wave velocity anomaly extends to depths well into the transition zone, although anomalies decrease from about 3% at 150 km depth to values less than 1% at a depth of about 450 km (Dueker and Yuan, 2004; Yuan and Dueker, 2005a). The extension of the low-velocity anomaly coincides at the transition zone with a 12 km depression of the 410 km discontinuity (Figure 6). The tomographic

images shown in Yuan and Dueker suggest that a high velocity ‘curtain’ extends from beneath the Wind River Range in the Wyoming Craton to a depth of about 250 km along a mantle trajectory that is roughly parallel to that of the postulated plume. Yuan and Dueker speculate that this feature represents a downwelling of the lower lithosphere. In the overall context of strong velocity contrasts of at least 8% in V_p that are seen throughout the region of western North America, however, the images shown in Figure 6 may not be conclusive evidence for either a plume or a downwelling.

1.14.3.1.2 Southern Rocky Mountain region

It is noteworthy that velocity anomalies imaged beneath the relatively young (12 Ma) volcanic fields at the southeastern end of the SRP/Deep Probe NW–SE transect (Figure 5(a)) exhibit peak-to-peak values (~8%) comparable to those seen beneath YS

(Dueker and Yuan, 2004). Velocity anomalies in this range, if solely thermal, are indicative of variations on the order of 200–400°C, yet these volcanic fields are volumetrically minor compared to that of YS/SRP. This repeated cycle of strong localized low-velocity anomalies along NE–SW striking zones continues into the southern Rocky Mountains, across the St. George Lineament, the Colorado Mineral Belt (the Aspen anomaly), and across the Jemez Lineament to the south (Figure 5). These ‘fingering’ zones of sharp velocity contrast, or sutures, are interpreted by Karlstrom *et al.* (2005) to be the result of varying response of Proterozoic lithosphere to mantle heating from below. While the source of sub-lithospheric heating and the varying lithospheric response to it remain controversial, it may be associated at least in part with lithospheric hydration during flat subduction in the Laramide and subsequent influx of hot asthenospheric material as the slab rotated downward and sank into the deeper mantle (e.g., Humphreys *et al.*, 2003).

The Cheyenne Belt is a major tectonic boundary, widely interpreted to be a crustal manifestation of a suture between the Archean Wyoming Craton to the north and a Proterozoic island arc terrane to the south (Figure 5). A comprehensive synthesis is given in Karlstrom *et al.* (2005). A north-dipping

high velocity anomaly in the upper mantle has been interpreted by some to mark the remnants of a failed subducting slab (Figure 5). The crust beneath the southern Rocky Mountain region attains its greatest thickness of about 50–60 km beneath the Cheyenne Suture (Snelson *et al.*, 2005), consistent with crustal foreshortening during subduction zone convergence.

1.14.3.1.3 Rio Grande Rift and Colorado Plateau

The LA RISTRA broadband seismic experiment comprised 54 stations deployed along a NW–SE transect to explore the complex region south of the Rocky Mountains that extends from the western Great Plains of stable North America, across the Rio Grande Rift and the Jemez Lineament, and into the central region of the Colorado Plateau. A map of station deployment and a schematic of the crust and mantle along the transect is shown in (Figures 7(a) and 7(b)). LA RISTRA data were analyzed to obtain body wave and surface wave tomographic images, as well as receiver function images of the crust and upper mantle across the region (Gao *et al.*, 2004; West *et al.*, 2004a, 2004b; Wilson *et al.*, 2005a, 2005b). The crustal and upper-mantle structure beneath the Rio Grande Rift stands out as a particularly prominent feature. Wilson *et al.* (2005a) show that the Moho

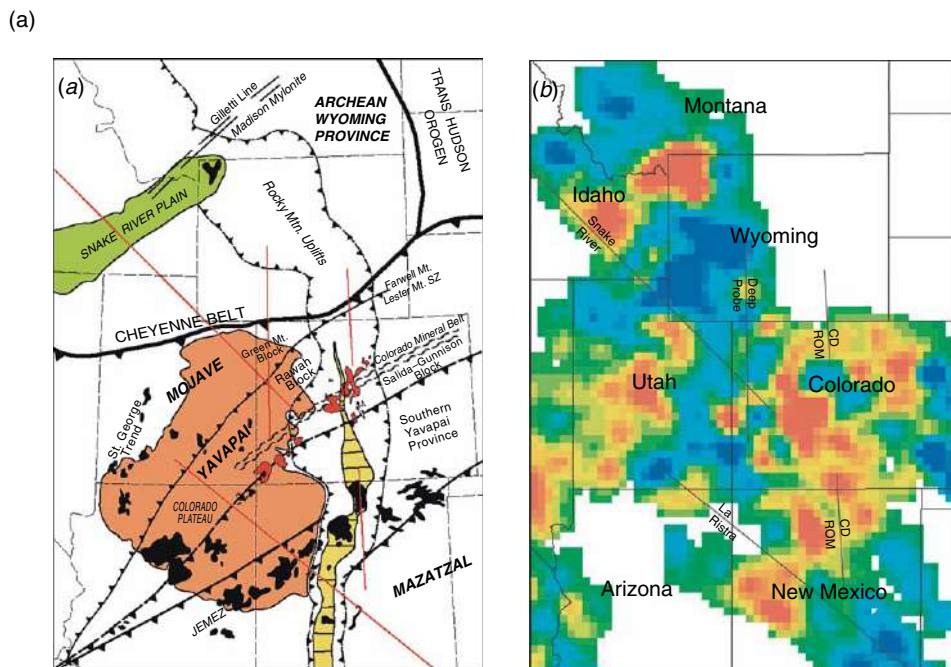
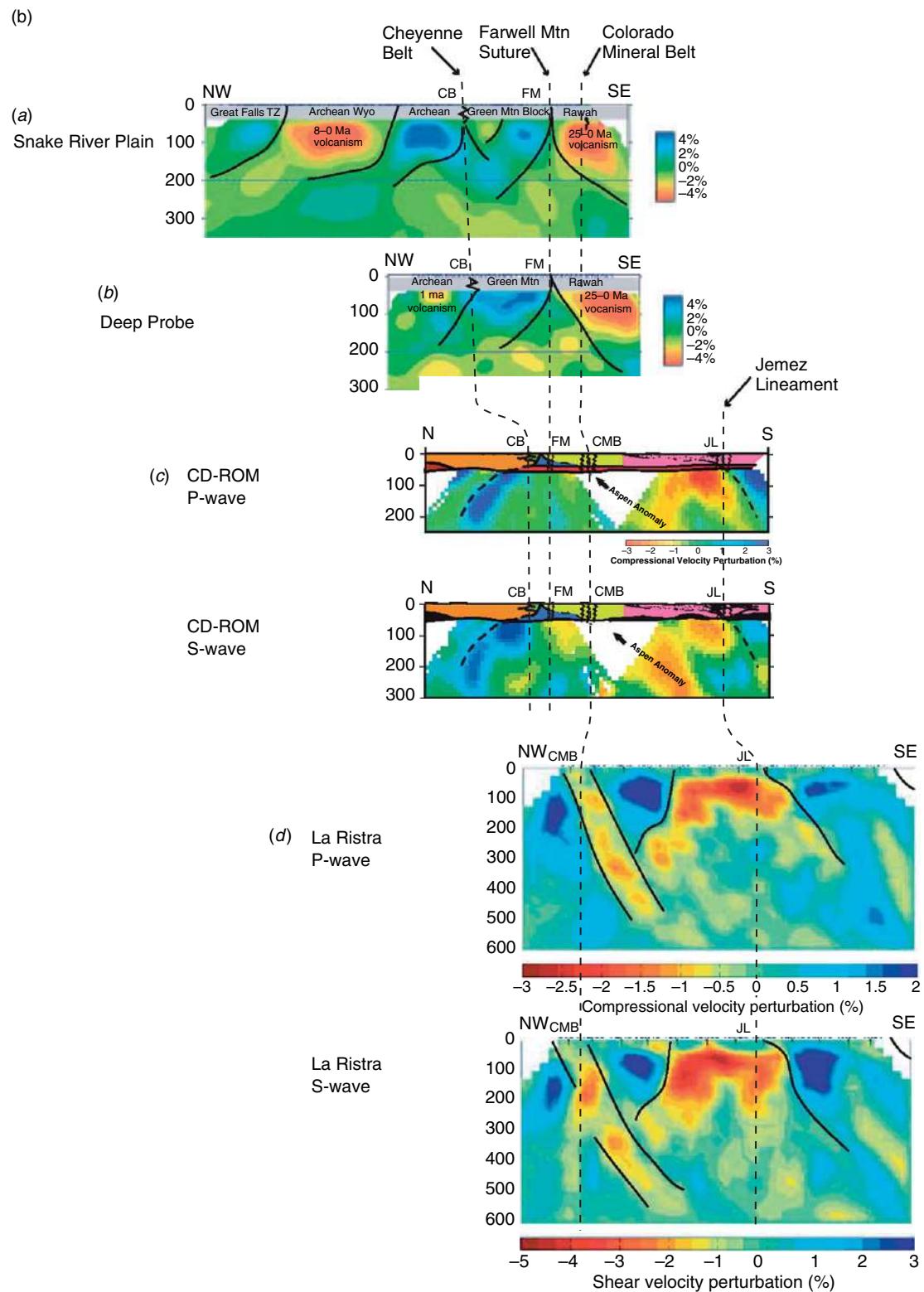


Figure 5 (Continued)

**Figure 5** (Continued)

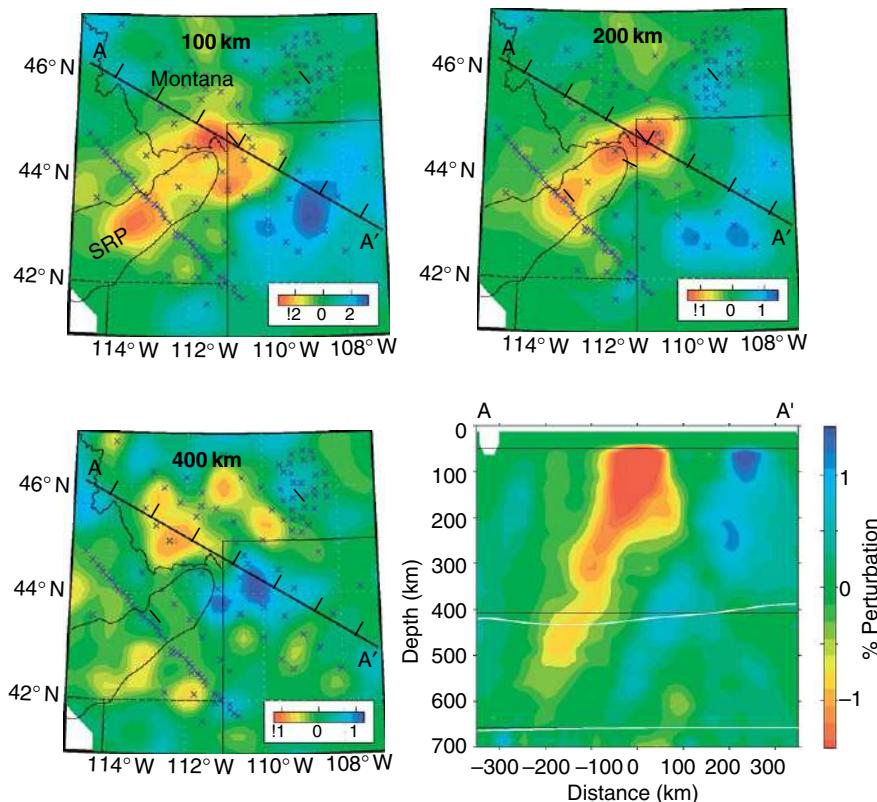
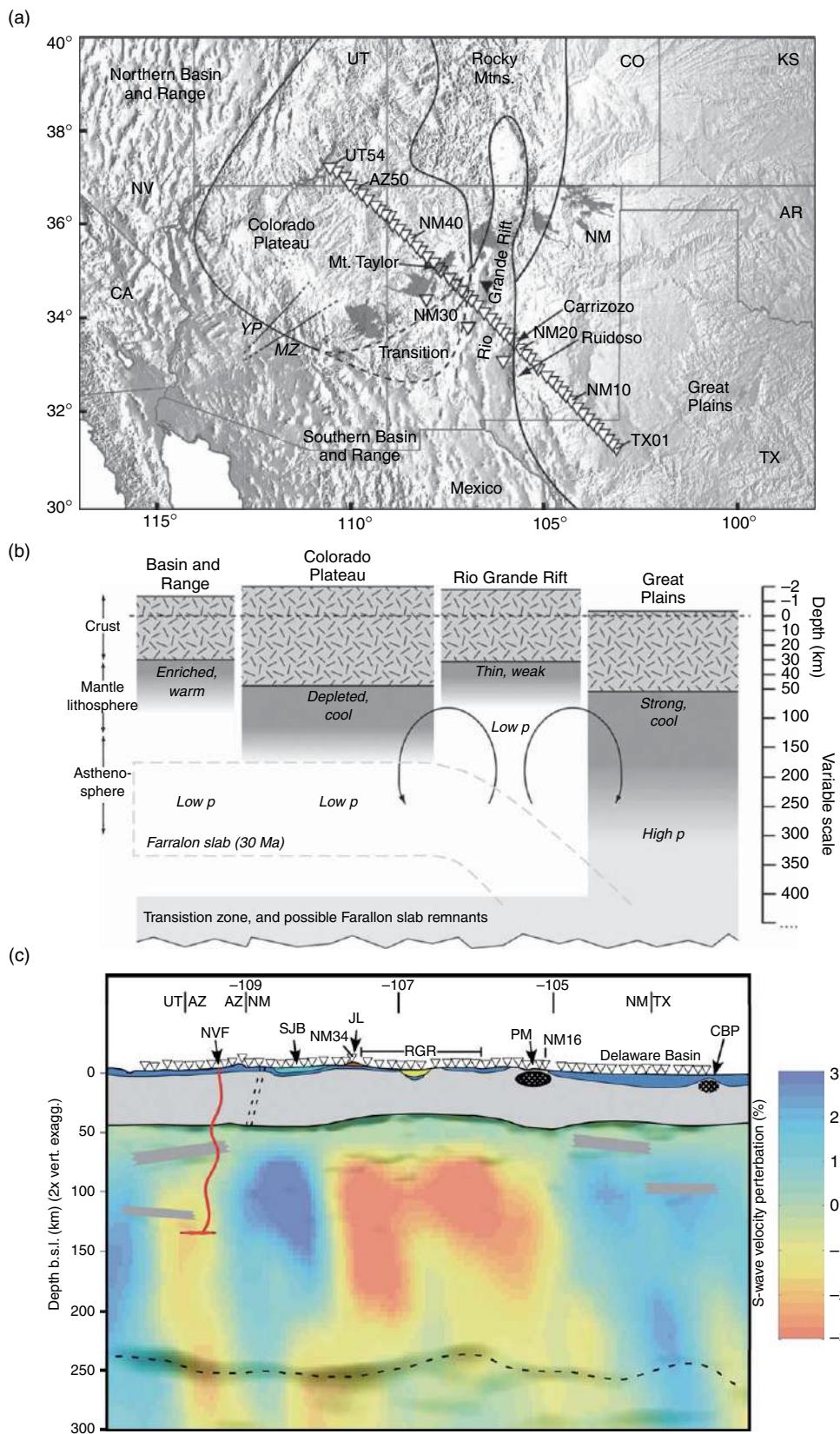


Figure 6 Tomographic images interpreted to show the presence of a NW dipping plume beneath the Yellowstone ‘hot spot’. Adapted from Yuan H and Dueker KG (2005a) Teleseismic P-wave tomogram of the Yellowstone plume. *Geophysical Research Letters* 32(L07304): 1–4 (doi: 10.1029/2004GL022056). First five panels are depth slices approximately centered on Yellowstone (low velocity perturbation near intersection of cross-section lines). SRP denotes Snake River Plain along which the hotspot trace has migrated NE during the past 12 My. The velocity anomaly interpreted as a plume is shown as a NW dipping feature penetrating into the transition zone and depressing the 410 km discontinuity (white line, 2x vertical exaggeration). The 660 discontinuity is not uplifted in these images, as might be expected if the Yellowstone hotspot source were a deep-mantle plume (Yuan and Dueker, 2005a).

beneath both the Great Plains and the Colorado Plateau is at about 40–50 km depth, whereas the crust beneath the central region of the Rio Grande Rift thins symmetrically to about 35 km (Figure 7(c)). The

thinned crust overlies a zone of very low velocities seen in superimposed tomographic images (Gao *et al.*, 2004; West *et al.*, 2004b) shown in (Figure 7(c)), confirmed by interstation Pn velocities of 7.8 km s^{-1}

Figure 5 (a) Geologic elements (a) and tomographic image (b) of western US west of the Rocky Mountain Front. From Karlstrom KE, *et al.* (2005) Synthesis of results from the CD-ROM experiment: 4-D image of the lithosphere beneath the Rocky Mountains and implications for understanding the evolution of continental lithosphere. In: Karlstrom KE and Kelle GR (eds.) *The Rocky Mountain Region: An Evolving Lithosphere*, pp. 421–434. Washington, DC: American Geophysical Union. (a) Cenozoic volcanic fields (black and red areas) strike NE, roughly parallel to Precambrian trends, whereas Laramide uplifts trend N–S. (b) Locations of seismic transects that are shown as vertical sections in Figure 10(b) are superimposed on 100 km depth tomographic image. Blue indicates positive velocity perturbations; red, low velocity perturbations. (b) Vertical cross-sections of P and S tomographic images along the experiment lines shown in Figure 10(a). From Karlstrom KE, *et al.* (2005) Synthesis of results from the CD-ROM experiment: 4-D image of the lithosphere beneath the Rocky Mountains and implications for understanding the evolution of continental lithosphere. In: Karlstrom KE and Kelle GR (eds.) *The Rocky Mountain Region: An Evolving Lithosphere*, pp. 421–434. Washington, DC: American Geophysical Union. See text for discussion of specific features shown. Snake River Plain profile from Schutt and Humphreys, 2004; Deep Probe line from Yuan and Dueker, 2005b; CD-ROM from Dueker *et al.*, 2001; La Ristra line from Gao *et al.*, 2004. Note the sharp velocity gradients associated with the Cheyenne Belt, Farwell Mountain, Colorado Mineral Belt, and Jimez Sutures and the apparent continuity of those sutures across multiple vertical seismic profiles (Karlstrom *et al.*, 2005).



measured along the rift axis (Lastowka and Sheehan, 2005). The composite structures shown in **Figure 7(c)** exhibit symmetry around the axis of the Rio Grande Rift that has been interpreted to imply pure shear extension (Wilson *et al.*, 2005b). No deep-mantle source has yet been observed seismically beneath the rift. The discontinuity at a depth of ~ 250 km in **Figure 7(c)** is suggested by Wilson *et al.* (2005a) to be the base of a continental asthenospheric low velocity channel but this remains speculation. Both the 410 and 660 km discontinuities are observed to be flat beneath the Rio Grande Rift, suggesting that whatever thermal anomaly caused the Rio Grande Rift, it does not extend to the upper-mantle transition zone.

The Colorado Plateau, adjoining the Rio Grande Rift to the NW along the RISTRA line, is seen both geologically and in seismic images to be a stable block with a relatively high-velocity lithospheric lid that extends to a depth of at least 120 km (West *et al.*, 2004b). West *et al.* find no suggestion of a sharp lithosphere/asthenosphere boundary beneath the Colorado Plateau, where the lithosphere appears to transition gradually to asthenosphere between about 120 and 150 km depth (although see Lastowka and Sheehan (2001) for a much thinner lithosphere). In contrast to the mantle structure beneath the western Great Plains, a low-velocity channel extends nearly to 300 km beneath the lithosphere of the Colorado Plateau (West *et al.*, 2004b). This significant low-velocity channel may account for part of the higher elevations of the Colorado Plateau compared to the Great Plains, despite comparable crustal thickness (West *et al.*, 2004b). The crust beneath the Colorado Plateau is estimated from receiver functions to be about 45–50 km thick (Gilbert and Sheehan, 2004; Wilson *et al.*, 2005a). That crustal

thickness varies, however, with thinning to the north (Gilbert and Sheehan, 2004) accompanied by no corresponding change in elevation (**Figure 8**). Whereas Wilson *et al.* suggest that much of the Colorado Plateau uplift is due to a low-velocity channel in the upper mantle, Gilbert and Sheehan suggest that most of the Colorado Plateau uplift is due simply to isostatic compensation of the crust, although they acknowledge that hot, low-density mantle may contribute to plateau support (Gilbert and Sheehan, 2004).

1.14.3.1.4 Great Basin

The western edge of the Colorado Plateau where it abuts the eastern Great Basin marks a profound lithosphere boundary. This is seen in both crustal thickness (**Figure 8**) and in upper-mantle velocity (Gilbert and Sheehan, 2004; Lastowka and Sheehan, 2001). The Great Basin, which locally has undergone up to 100–200% extension, is characterized by thin (35 km) crust, low upper-mantle velocities, and high heat flow. Large-scale, highly detailed, crustal studies based on controlled source experiments have been extensively reviewed previously (Smith *et al.*, 1989), but portable array broadband experiments carried out since, including those discussed above and in the Colorado Plateau – Great Basin PASSCAL experiment, have substantially increased the 3-D image of crustal thickness (Gilbert and Sheehan, 2004). Crustal thickness as determined from receiver functions varies within the Basin and Range from slightly more than 35 km to less than 30 km in northern Utah and Nevada and southeastern Oregon (**Figure 8**). The broadband experiments have also contributed substantial new information on uppermost-mantle velocities, which were

Figure 7 (a) Map showing the 57 seismic stations of the La Ristra broadband transect that extends from the Great Plains into the Colorado Plateau. (b) Schematic cross-section showing hypothetical variations between major geologic blocks from the Great Plains of stable North America into the actively extending Basin and Range. Approximate location of the Farallon slab c. 30 Ma is shown for reference. (Panels (a) and (b) adapted from West West M, *et al.* (2004b) Crust and upper mantle shear wave structure of the Southwest United States: Implications for rifting and support for high elevation. *Journal of Geophysical Research* 109(B03309): 1–16 (doi:10.1029/2003JB002575). (c) Crustal and upper-mantle schematic of region across the Rio Grande Rift (RGR) in relation to other surface geologic features along the La Ristra transect including the Navajo Volcanic Field (NVF), San Juan Basin (SJB), Jemez Lineament (JL), Pajarito Mountains (PM), and central basin platform (CBP). From Wilson D, *et al.* (2005a) Imaging the seismic structure of the crust and upper mantle beneath the Great Plains, Rio Grande Rift, and Colorado Plateau using receiver functions. *Journal of Geophysical Research* 110(B05306): 1–14 (doi:10.1029/2004JB003492). Crustal thickness from receiver functions, as well as other receiver function discontinuities (gray areas), are superimposed on the body wave tomographic image of the upper mantle from (Gao *et al.*, 2004). The apparent discontinuity around 250 km depth (dashed line), based on receiver functions, is speculated by Wilson *et al.* to be the Lehmann discontinuity, perhaps indicating the base of the continental asthenosphere (Wilson *et al.*, 2005a). It is not explained in this interpretation, however, why the depth of the discontinuity is so little affected by the major Rio Grande Rift velocity (thermal) anomaly. The signal appears to vanish beneath the stable central basin.

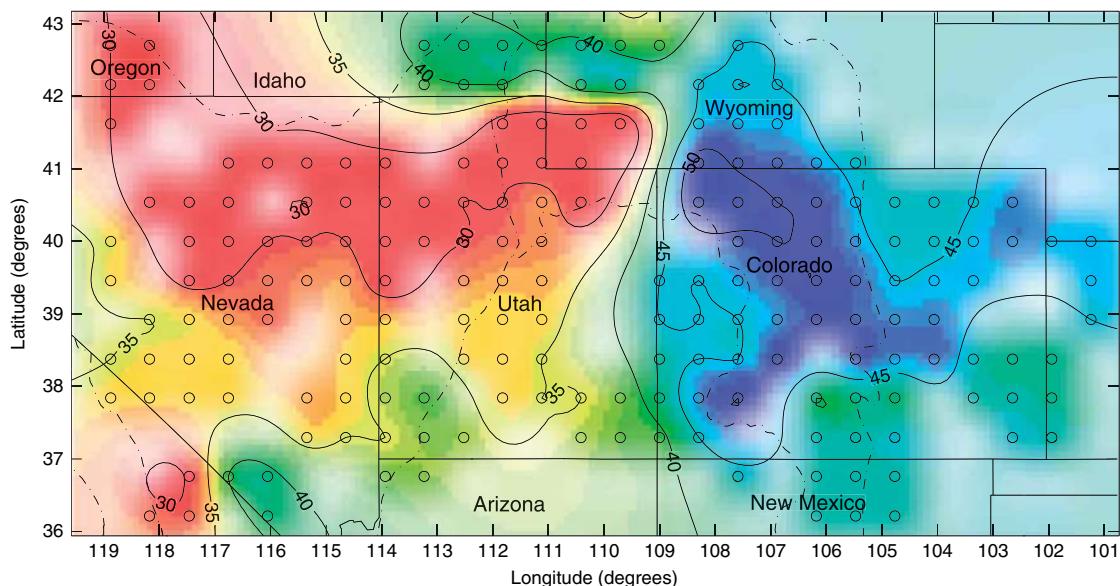


Figure 8 Contour map of crustal thickness in central western US, primarily based on receiver functions. Modified from (Gilbert HJ and Sheehan AF (2004) Images of crustal variations in the intermountain west. *Journal of Geophysical Research* 109: B03306. Red indicates thinner crust, blue thicker crust. Circles denote crustal thickness binning points from which contours were drawn. Dashed lines mark boundaries between (from west to east) the Great Plains, Rocky Mountains, Colorado Plateau, and Basin and Range Province (Gilbert and Sheehan, 2004).

generally known from previous refraction and surface wave studies to be low, with V_s about $4.2\text{--}4.3\text{ km s}^{-1}$ and $V_p \sim 7.8\text{ km s}^{-1}$. Recent surface wave and Pn studies have confirmed the absence of a high velocity lid in the uppermost mantle beneath the crust of the Great Basin (Lastowka and Sheehan, 2001), and this appears to be the case throughout both southern and northern Great Basin.

1.14.3.1.5 Sierra Nevada

The Great Basin extends westward to the Sierra Nevada Range where seismic and geologic evidence for crustal extension ceases. Receiver function analyses from portable array experiments in the southern Sierra Nevada Mountains of California suggest the possibility that part of the crustal root of the Sierra volcanic arc has foundered following cessation of arc activity in the Sierras about 16 Ma (Zandt *et al.*, 2004). The foundering model is based on an unusual absence of a Moho signature in the receiver functions for conversion points beneath the Great Valley. There the asthenospheric backflow following the cessation of Farallon plate subduction is posited to have removed a root of dense ultramafic residue formed during the building of the great Sierran batholith. Such destabilization and sinking is commonly

cited in the literature, but is always inferred from indirect observations as in the Zandt *et al.* study. Current broadband experiments in the planning stages or now being implemented for California, Chile, and the North China Craton are aimed at the direct imaging of such possible lithospheric delamination, the models for which remain quite hypothetical.

1.14.3.2 Indian–Eurasian Continental Collisional Zone

1.14.3.2.1 Crustal structure

The Tibetan Plateau and adjacent regions that include Nepal, Tien Shan, Hindu Kush and Karakoram, have been among the most intensively studied structures in the world. Over the past decade and a half, hundreds of portable broadband seismometers have been deployed as part of major international experiments (e.g., Kind *et al.*, 2002; Klemperer, 2006; Kosarev *et al.*, 1999; Kumar *et al.*, 2005; Schulte-Pelkum *et al.*, 2005; Wittlinger *et al.*, 2004; Zhao *et al.*, 2001) (Figures 1 and 9). Logistical constraints have tended to limit the Tibetan Plateau deployments to transects along roads (Figure 9(a)), whereas the Nepal, Tien Shen and Karakoram

deployments were aerially distributed in 2-D arrays (**Figures 9(b) and 9(c)**). See Klemperer (2006) for a comprehensive summary (with map) of passive and active seismic experiments.

Receiver function imaging of both crustal thickness and lithospheric plate deformation in the Indian–Eurasian continental collision zone has been a prominent objective of most Himalayan and Tibetan Plateau broadband experiments. Schulte-Pelkum *et al.* (2005) have used receiver functions to map the Indian lithosphere as it plunges beneath the Himalayas and Tibet (**Figure 10**), revealing the apparent presence of a strong decollement where the uppermost part of the Indian plate is thrust beneath the Himalayas. The Moho is similarly thrust to great depth. Schulte-Pelkum *et al.* speculate that the lower crust is partially converted to eclogite in the process, as shown schematically in the lower panel of **Figure 10**. In the Central Tibetan Plateau itself, data from the INDEPTH experiments and early PASSCAL experiments have been extensively analyzed to produce images of Moho and upper-mantle structures, not all of which are entirely consistent between studies even with the same data set. Remarkably, the Moho thickness beneath the entire region of these experiments (**Figure 9**) varies only from a maximum of about 78 km to a minimum of 65 km, with no systematic change inferred either across the Tibetan Plateau or at major fault boundaries (Kind *et al.*, 2002; Kosarev *et al.*, 1999). Results from these same data seem to indicate that V_p/V_s also does not vary significantly between northern and southern Tibet (Kind *et al.*, 2002). This lack of significant variation in either crustal thickness or crustal velocity led (Galve *et al.*, 2002) to examine the Moho structure in detail for clues as to the mechanism for crustal thickening. Results from their combined receiver function/wide-angle reflection study aimed specifically at detailed Moho structure suggest that the Moho has a complex architecture with “dipping and overlapping segments indicating lithospheric imbrication” (Galve *et al.*, 2002, p. 1). Wittlinger *et al.* (2004), using S-P converted wave receiver functions, report a similarly complex and warped Moho structure.

Rapine *et al.* (2003) measured fundamental mode Rayleigh wave dispersion to study contrasts in crustal structure beneath northern and southern Tibet. They conclude that a low-velocity layer in the middle crust is required by the dispersion data in southern but not northern Tibet. This is also suggested by Wittlinger *et al.* (2004) from Sp receiver functions. Moreover,

there is general agreement that the lower crust beneath southern Tibet is higher velocity than that of the north and that it is underlain by mantle with a positive velocity gradient. Rapine *et al.* interpret these findings as the result of underthrusting of the Indian continental lithosphere, where the low velocities in the mid-crust reflect H_2O -induced melting in the interplate shear zone between underthrust Indian crust and overriding Asian crust. No similar mid-crustal low velocity zone is found in the crust of northern Tibet, although the S-wave velocities in both the crust and mantle of northern Tibet are significantly lower than are those in the south. This result is consistent with many other studies, including that of Kind *et al.* (2002), suggesting that mantle temperatures in northern Tibet are higher by several hundred degrees than are those in southern Tibet. The source of that difference – mantle diapir or lithospheric delamination, for example – remains a debated issue.

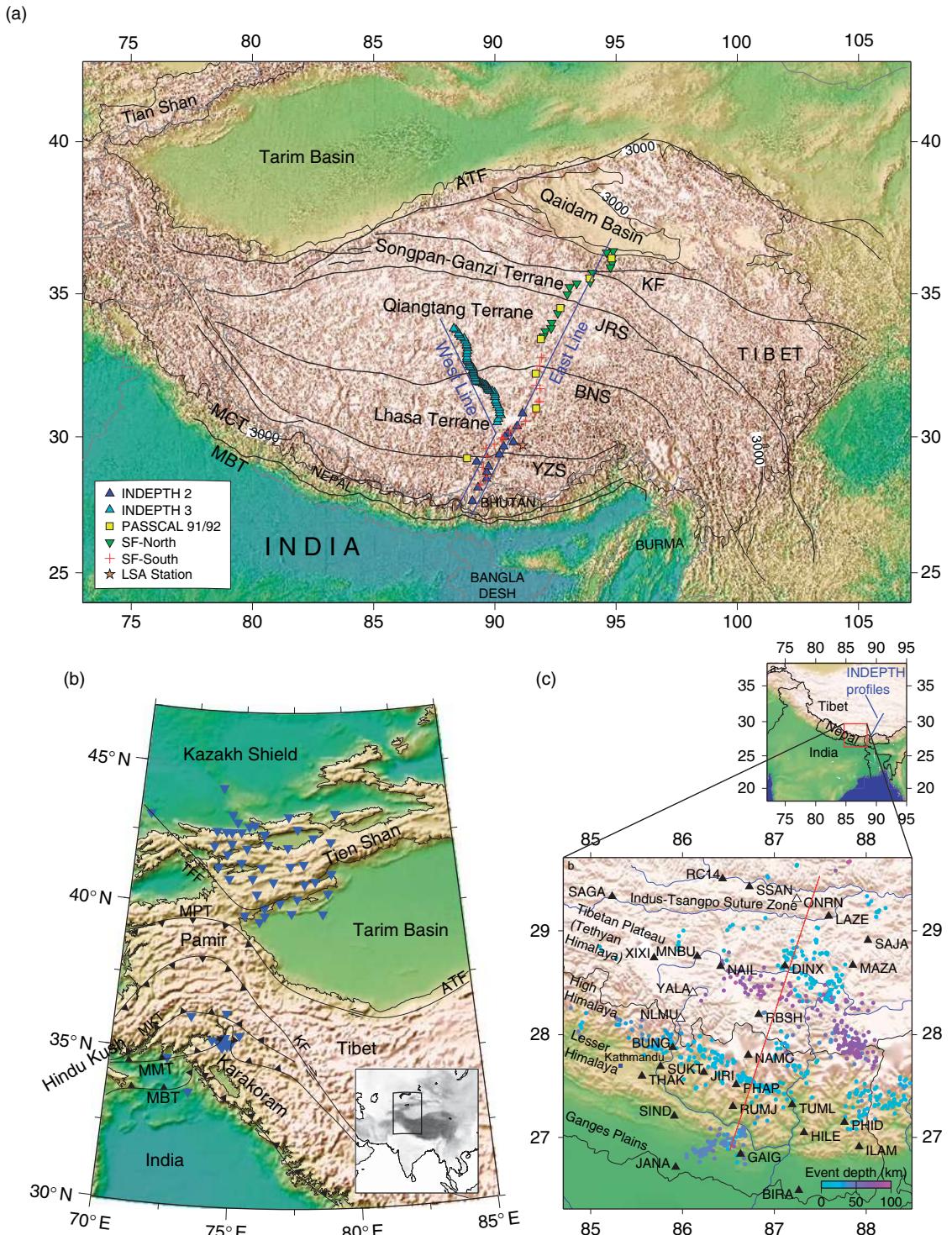
1.14.3.2.2 Seismic structure of uppermost mantle

Early studies by Kosarev *et al.* (1999) of the mantle beneath the eastern Tibetan Plateau appeared to show a northward dipping discontinuity in the 100–300 km depth range colliding with a southward dipping Asian lithosphere. They identified the northward dipping feature as the cold and depleted lithosphere of India plunging beneath the Asian lithosphere. A continent-scale study by Friederich (2003) using S-waves and surface waves similarly finds a northward-dipping slab-like feature beneath southern Tibet that he interprets to be the underthrust Indian lithosphere. Detailed imaging by Kind *et al.* (2002), however, fails to reveal a northward dipping discontinuity, but it does confirm the existence of a southward dipping feature interpreted as detached Asian lithospheric mantle (ALM in **Figure 11**). Kind *et al.* suggest that the Indian continent has been underthrust subhorizontally beneath Tibet and that it has a broken, nearly vertical northern edge.

There is surprisingly little indication that the massive effects of continental collision have significantly perturbed the 410 and 660 discontinuities in the upper-mantle transition beneath Tibet. Kind *et al.* (2002) report that in both the eastern and western sections across Tibet (**Figure 9**), the vertical separation between the 410 and 660 discontinuities is virtually constant along the two studied transects (**Figure 11**), implying a N–S variation in transition

zone temperature less than 50°. They infer from these results that there is no lithospheric slab penetration into the transition zone, suggesting that the leading downgoing oceanic plate may already have

detached from the Indian continent. Both the 410 and 660 discontinuities appear to bend downward beneath the northern Plateau, a probable artifact of a south to north decrease in S-wave velocity of about



5% in the upper mantle, consistent with a northward increase in average temperature of perhaps 300°C.

Extensive portable array deployments have complemented a growing population of permanent broadband stations in the Tien Shan and Karakoram regions at the western edge of the Indo-Asian collision belt (**Figure 9**). Kumar *et al.* (2005) employ the S-to-P receiver function method to image both crustal thickness and the lithosphere–asthenosphere boundary (LAB) in the region (**Figure 12**). If their interpretation is correct, the results obtained for the LAB are among the very rare instances where that boundary has been successfully imaged. Moho depths, which vary from about 45–65 km beneath Tien Shan and increase to about 70 km beneath Karakoram, are apparently uncorrelated with what is seen as very significant differences in the LAB. As seen in **Figure 12** (top panel), the LAB from receiver functions is reasonably well correlated with the surface wave tomographic images of Friederich (2003). Along the north–south profile (top panel, approximately 75°E longitude in **Figure 9(b)**), the LAB deepens from less than 100 km beneath Tien Shan in the north to 270 km and more beneath Pamir and Karakoram in the south (Kumar *et al.*, 2005). Kumar *et al.* interpret the south-dipping LAB as the base of the subducting Asian plate where it is thrust beneath the high-velocity Indian mantle lithosphere. The east–west profile, roughly along 43°N latitude (**Figure 9(b)**), shows a relatively thin lithosphere even beneath the Kazakh

shield (~130 km) and even thinner beneath Tien Shan itself (90–100 km), thickening again to almost 180 km beneath the Tarim Basin block, which appears to be subducting southward beneath northwestern Tibet (Wittlinger *et al.*, 2004). Kumar *et al.* (2005) and others speculate that the Indian lithosphere is colder and stronger than is its Asian counterpart, as evidenced by the much thicker and higher velocity lithosphere beneath the Indian continent.

A number of ongoing portable broadband experiments are underway on the eastern Tibetan Plateau and its flanking terranes, one focus of which is on measuring anisotropy to resolve the controversial issue of lower-crustal deformation as a mechanism of growth and collapse of the plateau. Notable among the eastern Tibet deployments is the MIT China Seismic Array where 25 broadband stations have been recently installed (yellow squares in **Figure 1**). In addition, regions both north and south of the MIT array have seen dozens of stations deployed in recent years, although little has been published to date.

1.14.3.3 Continental Margin Subduction Zones

Continental margin subduction zones are among the more natural targets for broadband portable array seismology. The structures of particular interest are in the subduction zone itself, at mantle depths that are accessible primarily through passive array

Figure 9 (a) Summary of broadband seismic experiments in Central Tibet c. 2002 superimposed on topographic map of Tibet showing major terrane boundaries. From Kind R, *et al.* (2002) Seismic images of crust and upper mantle beneath Tibet: Evidence for Eurasian plate subduction *Science* 298: 1219–1221. The experiments include PASSCAL experiments PASSCAL 91/92, and INDEPTH 2 and 3, as well as Sino-French experiments as shown. Abbreviations from Kind *et al.* (2002) are as follows: MBT (Main Himalaya Thrust); MCT (Main Central Thrust); YZS (Yarlung-Zangbo Suture); BNS (Bangong-Nujiang Suture); JRS (Jinsha River Suture); KF (Kunlun Fault); and ATF (Altyn-Tagh Fault). An up-to-date summary of seismic experiments, both passive and active in that region of Tibet can be found in Klemperer (2006). (b) Summary of portable and permanent broadband seismic stations deployed in western Tibet superimposed on a topographic map with major tectonic terranes indicated. From (Kumar P, *et al.* (2005) The lithosphere–asthenosphere boundary in the Tien Shan-Karakoram region from S receiver functions: Evidence for continental subduction. *Geophysical Research Letters* 32(L07305): 1–4 (doi:10.1029/2004GL022291). The largest array was comprised of 28 portable stations in central and western Tien Shan (the GHENGIS experiment). The small six-station array of the NANGA experiment was clustered in Nanga Parbat near the inflection in the Main Mantle Thrust (MMT). The portable stations complemented a number of permanent stations, including most notably the permanent KNET array in Kyrgyz. Abbreviations from Kumar *et al.* (2005) are as follows: MPT (Main Pamir Thrust); MKT (Main Karakoram Thrust); MMT (Main Mantle Thrust); MBT (Main Boundary Thrust); TFF (Talasso–Ferghana Fault); KF (Karakoram Fault); and ATF (Altyn-Tagh Fault). (c) Topographic map showing locations of 29 portable broadband stations (black triangles) deployed to study the structure of the Indian plate where it plunges beneath the Himalayas and Tibet. Reprinted by permission from Macmillan Publishers Ltd: Nature, Schulte-Pelkum V, Monsalve G, Sheehan A, *et al.* (2005) Imaging the Indian subcontinent beneath the Himalaya. *Nature* 435: 1222–1225, Copyright (2005). The position of the array relative to INDEPTH profiles is shown in the upper location map. Hypocentral depths for events located by the array are shown as small color-coded filled circles. The red line indicates the surface trace of the vertical cross-section shown in **Figure 10**.

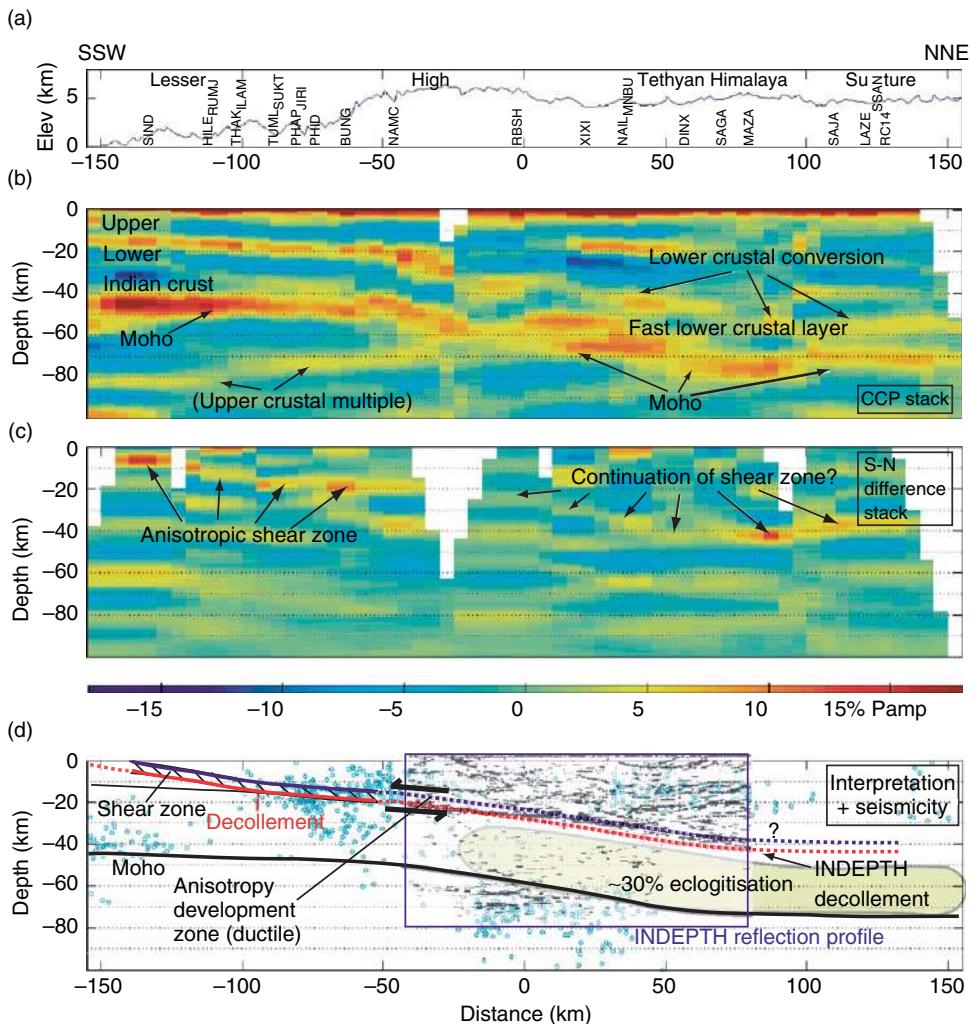


Figure 10 Migrated receiver function common conversion point (CCP) stack image along the NNE-SSW transect that is shown as a red line in **Figure 9(c)**. (a) Topography cross-section along profile. (b) CCP receiver function stack, where red indicates positive conversion amplitude (velocity increase) and blue, negative amplitude (velocity decrease). Color intensity is proportional to receiver function amplitude. (c) Differenced S-N CCP stack, with amplitudes of receiver functions from southern azimuths differenced with those from northern azimuths to image arrivals that change polarity by back-azimuth (see Schulte-Pelkum *et al.* (2005), for further explanation). (d) Interpretive cross-section based on (b) and (c). INDEPTH reflection profile and local seismicity are superimposed (see text for further discussion). Reprinted by permission from Macmillan Publishers Ltd: Nature, Schulte-Pelkum V, Monsalve G, Sheehan A, *et al.* (2005) Imaging the Indian subcontinent beneath the Himalaya. *Nature* 435: 1222–1225, Copyright (2005).

seismology. The continental regions most studied through deployment of temporary portable arrays include the Andes, particularly the central Andes, the Cascadian and Alaskan arcs, and the Mediterranean region (**Figure 1**). For a more comprehensive summary of subduction zone seismic studies, including those in Japan where data from extensive permanent networks have produced highly detailed images of subduction zone structures.

1.14.3.3.1 Andean studies

International broadband portable array deployments, largely by US and German groups, have been heavily concentrated in the central and southern Andes as shown in **Figure 13**. Migrated receiver function images beneath dense aerial deployments in northern Chile and Argentina reveal decollement thrusts within the crust, Moho depths up to nearly 80 km beneath the Western Cordillera/western Altiplano

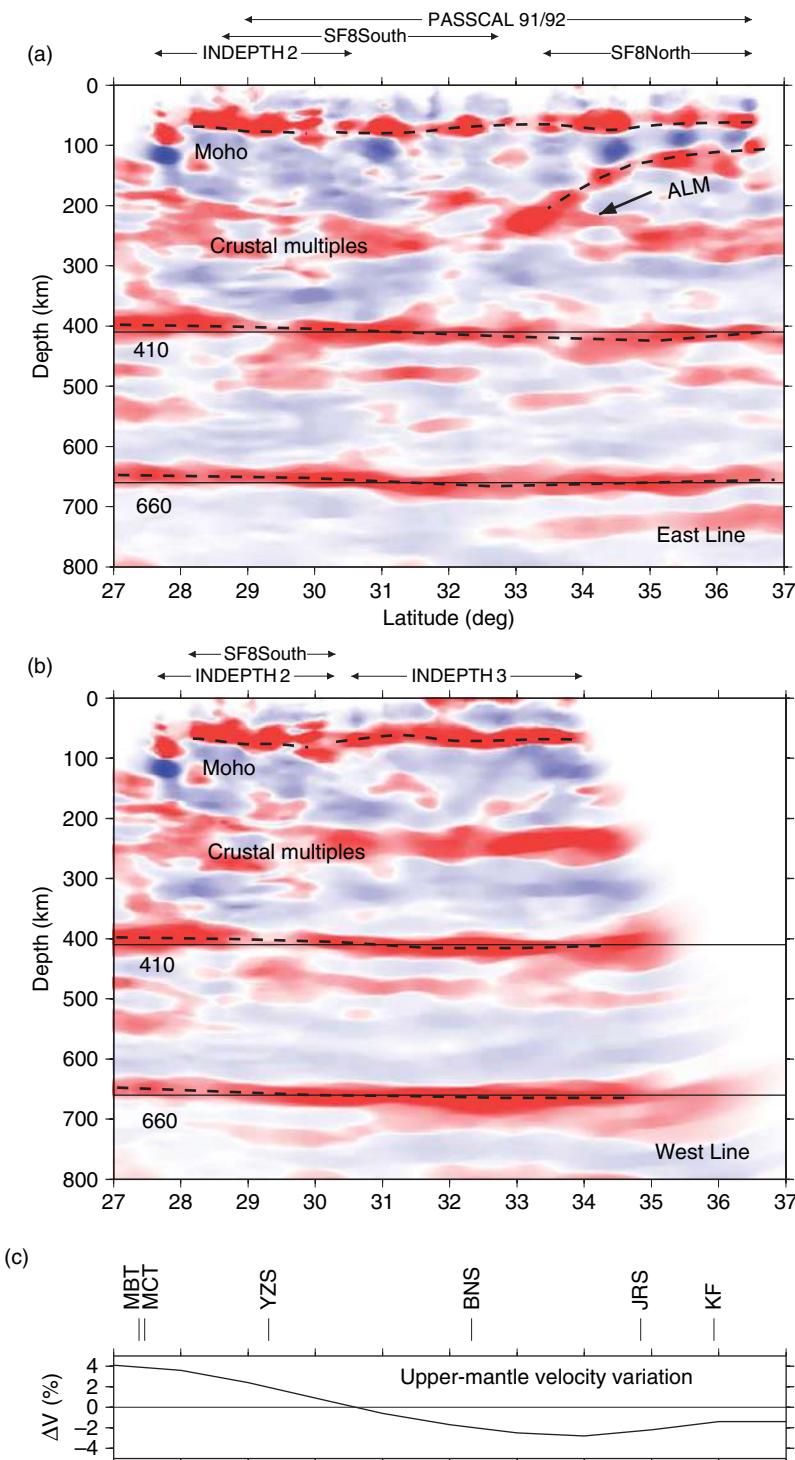


Figure 11 Migrated receiver function images along profiles shown in **Figure 9(a)**. From Kind R, et al. (2002) Seismic images of crust and upper mantle beneath Tibet: Evidence for Eurasian plate subduction *Science* 298: 1219–1221. (a) The approximately N–S profile (as in **Figure 9(a)**), based on PASSCAL 91/92, INDEPTH 2, and SF-South and SF-North passive array deployments. Positive amplitudes (velocity increase) are plotted in red, negative amplitudes in blue. ALM denotes underthrust Asian lithospheric mantle. ‘Crustal multiples’ around 200–300 km depth are produced by crustal reverberations. (b) Images from the NW–SE INDEPTH 3 transect, as well as the southern part of the (a) transect. Acronyms are as in caption to **Figure 9**.

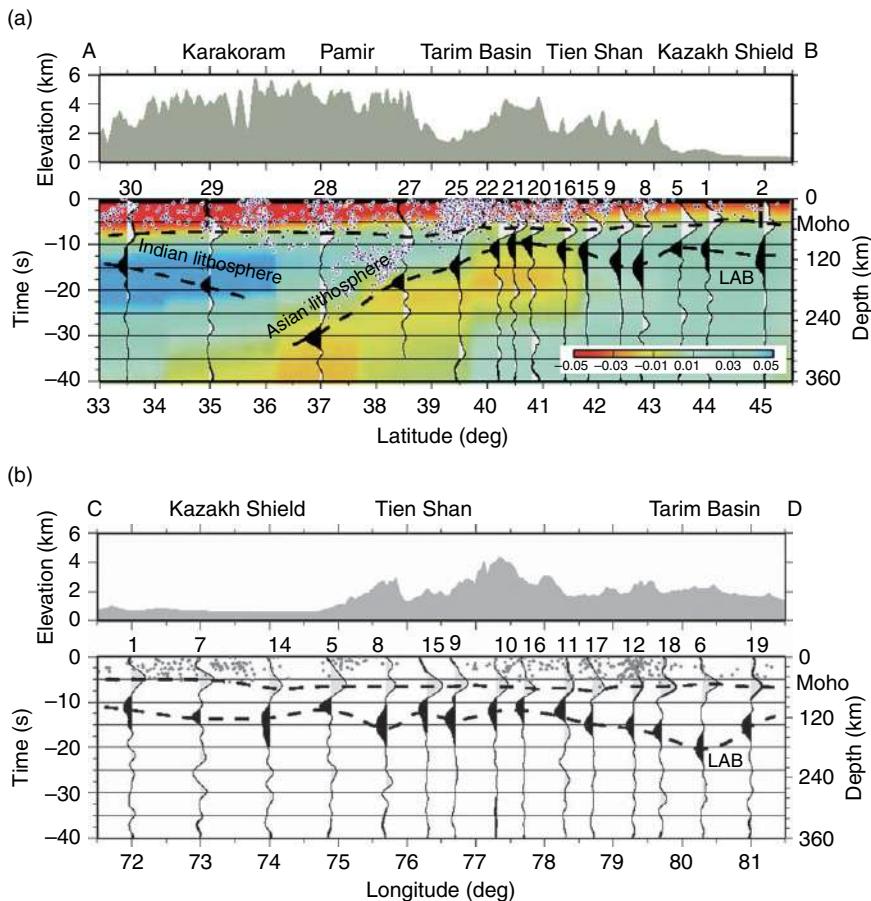


Figure 12 (a) North–south receiver function profile approximately along 75° E longitude in [Figure 9\(b\)](#), overlaid on tomographic image of [Friederich, \(2003\)](#). Topography is shown in the upper panel. From [Kumar P, et al. \(2005\)](#) The lithosphere–asthenosphere boundary in the Tien Shan-Karakoram region from S receiver functions: Evidence for continental subduction. *Geophysical Research Letters* 32(L07305): 1–4 (doi:10.1029/2004GL022291). The receiver function signals in black are interpreted to correspond to the lithosphere–asthenosphere boundary (LAB) and suggest that the rigid Tarim Basin block of the continental Asian lithosphere is being underthrust beneath the Pamir and Karakoram Ranges while at the same time, the high-velocity Indian lithosphere appears to be dipping to the north ([Kumar et al., 2005](#)). (b) East–west receiver function profile across Tien Shan, approximately along 43° N latitude in [Figure 9\(b\)](#).

but decreasing eastward into the Altiplano (Puna) and Eastern Cordillera ([Figure 14](#)). The top of the descending Nazca plate is clearly imaged to a depth of slightly more than 100 km, below which the discontinuity signal vanishes. [Yuan et al. \(2000\)](#) interpret the disappearance of the upper plate boundary to be the result of the low-velocity oceanic basaltic crust converting to high-velocity eclogite.

Despite the large numbers of mostly short-period instruments deployed (e.g., PISCO, CINCA, ANCORP, PUNA ([Figure 14](#))), the central Andes of northern Chile/Argentina has, with few exceptions (e.g., [Graeber and Asch, 1999](#)), seen relatively little in the way of comprehensive 3-D tomographic imaging. Farther south, however, in the vicinity of the broadband

CHARGE experiment ([Figure 15](#)) where the slab transitions southward from flat to normal subduction, extensive tomographic imaging of both P and S waves has revealed a remarkable result ([Wagner et al., 2005](#)). Wagner *et al.* focused on the mantle lithosphere within the region of flat subduction around latitude 31° S and then southward into the region of normal subduction. As shown in [Figure 15](#), V_p is as low as 7.4 km s^{-1} in the continental lithospheric mantle above the region immediately above the flat slab. Velocity values this low are not surprising in a region where it has been widely assumed that the overlying continental lithosphere is extensively hydrated by water sweated from the descending plate. Tomographic inversion for V_s , however, produces an entirely different result, with S-wave

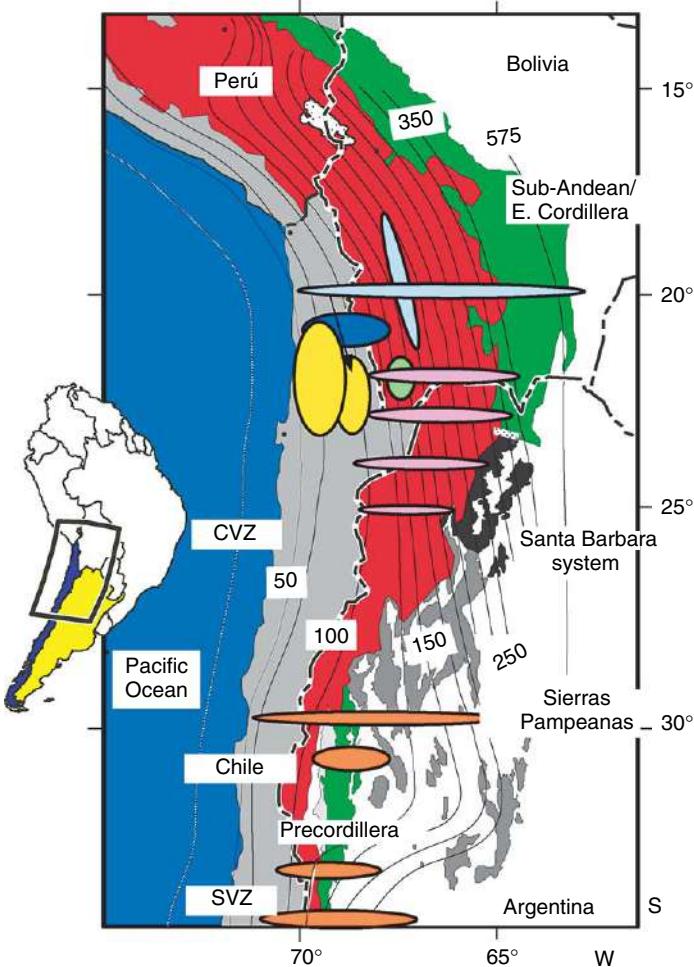
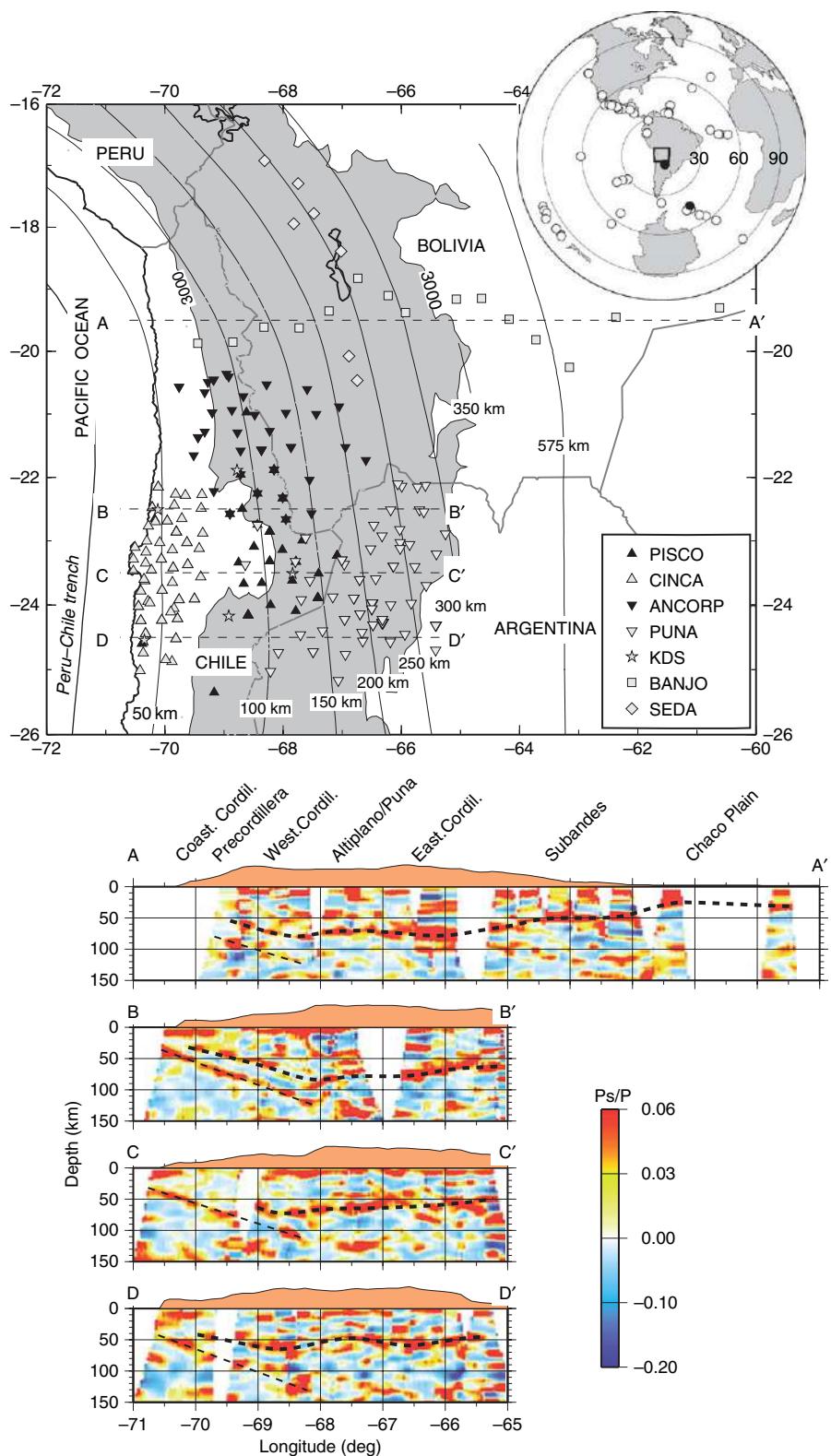


Figure 13 Map of the central and southern Andes showing approximate locations (colored ovals) of major seismic experiments during the past decade and a half. Figure courtesy of Sue Kay. Contoured depths are to Wadati–Benioff zone. CVZ=Central Volcanic Zone; SVZ=Southern Volcanic Zone. Explanation of ellipses and ovals: light blue, BANJO and SEDA deployments (e.g., Zandt et al., 1996); yellow, CINCA and PISO deployments (e.g., Schmitz et al., 1997); dark blue, ANCOPR (ANCOPR Working Group, 2003). Brown ellipse, APMB experiment (e.g., Chmielowski et al., 1999). Pink, GFZ experiment (Yuan et al., 2000), see also **Figure 14**. Orange ellipses, CHARGE (Wagner et al., 2005), see also **Figure 15**.

velocities relatively high ($\sim 4.6 \text{ km s}^{-1}$) in the same region of the continental lithosphere where very low P-wave velocities are observed (**Figure 15**). The result is an anomalously low Poisson's ratio (<0.25) that matches no plausible hydrated mantle mineralogy or even any common mantle mineralogy at all. Preliminary studies in Alaska have produced a similar result in the mantle above the descending slab, where V_p/V_s ratios of 1.62–1.68 are found in the overlying mantle wedge at depths greater than 80 km. Abers et al. (2005) speculate that the low V_p/V_s may indicate large-scale silica addition to the overlying mantle wedge, presumably the result of tectonic erosion of the overriding continent, but the issue remains

essentially unresolved as of this writing. Further data on the structure of the continental lithosphere above regions of flat subduction are being collected in the region of northern Chile where subduction transitions from normal to flat (white square in **Figure 13**). Here, a large-scale regional array of 25 broadband and 45 short-period instruments is currently being deployed to image possible continental lithosphere delamination. This region of Chile and Argentina is one of the few places in the world where lithospheric delamination may be actively occurring today, speculated to be the result of slab rollback as the downgoing Nazca plate transitions from flat subduction back to normal subduction (Kay et al., 1994).



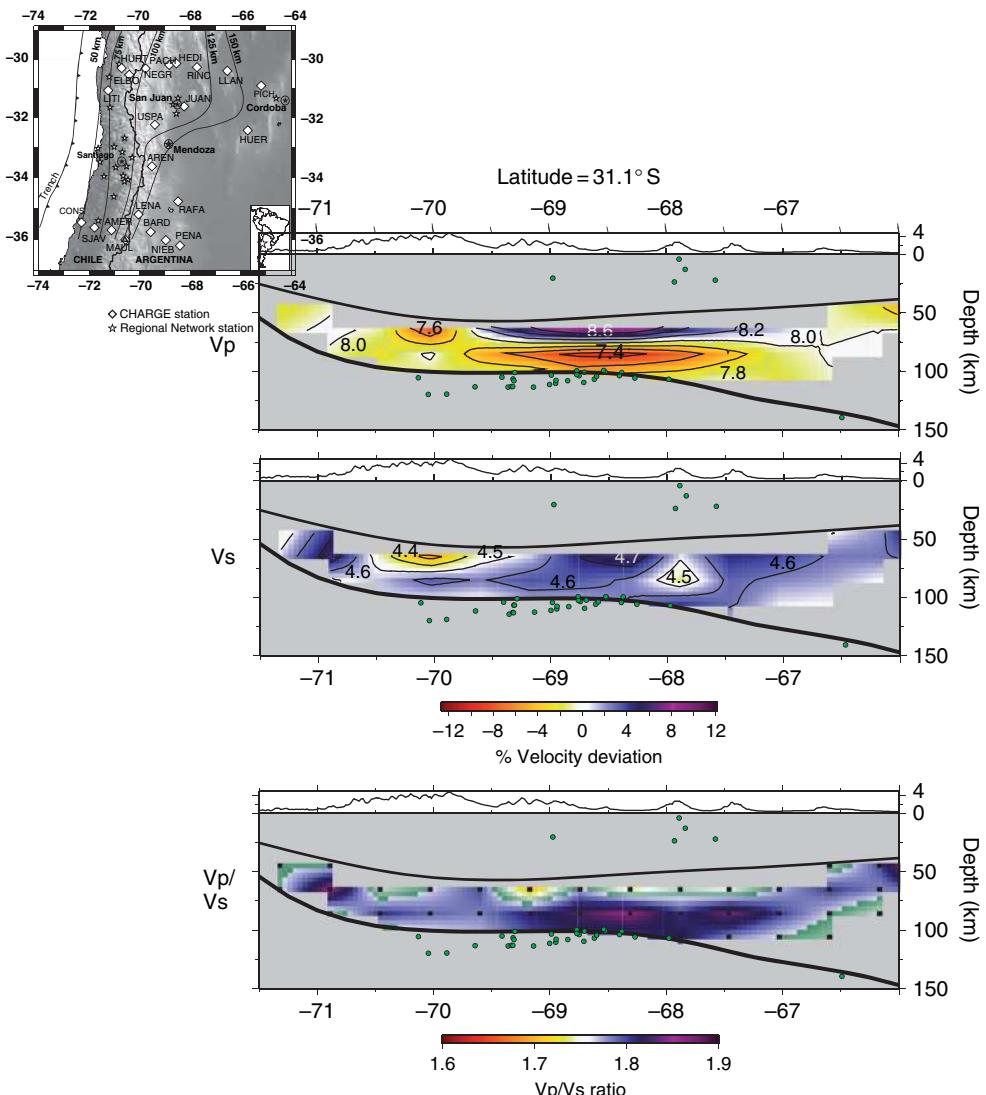


Figure 15 Broadband seismic experiment (CHARGE) across the southern Andes of central Chile in the region of flat subduction and the transition from flat to normal subduction. Adapted from Wagner LS, et al. (2005) Upper mantle structure in the south central Chilean subduction zone (30 to 36S). *Journal of Geophysical Research* 110, doi:10.1029/2004JB0003238. East–west tomographic images across the region of flat subduction near latitude 31° S reveal a prominent zone of low V_p/V_s ratio (deep blue in lowermost panel) in the continental lithosphere immediately above the flat subducting plate, as yet unexplained by any plausible mantle mineralogy (Wagner et al., 2005).

Figure 14 Migrated receiver function images (lower images) based on the combined data of several short period and broadband experiments (map in upper panel) across the southern central Andes. Map figure shows locations of passive seismic stations as indicated in relation to cross-sectional lines of receiver function images in lower panels. Contours show depth to top of Wadati–Benioff zone. Small black triangles indicate volcanic centers. Shaded region above 3 km elevation. Lower panels represent a series of vertical cross-sections along the E–W profiles indicated in the map figure. The heavy black dashed line marks the Andean Moho, the lightly dashed lines the top of the descending Nazca plate (Yuan et al., 2000). The crust tends to thin eastward of the volcanic arc (beneath the Altiplano and Eastern Cordillera), without a corresponding decrease in average surface elevation. Reprinted by permission from Macmillan Publishers Ltd: Nature, Yuan X, Sobolev SV, Kind R, et al. (2000) Subduction and Collision processes in the Central Andes Constrained by converted seismic phases. *Nature* 408: 958–961, Copyright (2000).

The Andes are at their widest and highest in the central region of Peru and Bolivia where subduction is ‘normal’. There, the primary questions concern the origin of the high Altiplano, which, next to the Tibetan Plateau, is the second largest high plateau in the world. [van der Lee et al. \(2001a\)](#) used surface wave data of mostly South American events recorded on several portable arrays in Peru, Chile, Bolivia, and Brazil to determine structure above the subduction zone and across the central part of South America. One of the most notable features shown by that study is a prominent low-velocity upper mantle beneath the eastern Andes (the foreshortened region of the high Andes, interpreted previously to be affected by mantle hydration from an episode of flat subduction in Miocene time ([James and Sacks, 1999](#)). The seismic images are consistent with predicted effects of lithospheric hydration (during flat subduction) followed by lithospheric melting resulting from the infusion of hot asthenospheric material into the opening mantle wedge during slab foldback to normal subduction.

1.14.3.3.2 Central America and Caribbean

The Caribbean and western Central America are targets for a number of ongoing passive array experiments and combined active and passive source experiments, from which results are as yet mostly unpublished. Notable among the larger projects are the BOLIVAR experiment in NE Venezuela and the TUCAN experiment in Costa Rica and Nicaragua (station locations shown in [Figure 1](#)). The BOLIVAR experiment, a combination of onshore and offshore active and passive source methods and instrumentation, is aimed at studying the accretion of arc-related terranes in northern Venezuela. This work is a substantial extension of a previous broadband array experiment in which it was found that continental South America has overridden a significant part of the Lesser Antilles arc, with the southern detached slab now situated beneath NE Venezuela ([VanDecar et al., 2003](#)).

1.14.3.3.3 Cascadia

The Cascadia 93 (CASC93) experiment was, in 1993 and even today, an unprecedented effort at broadband deployment – in number of instruments, the extraordinarily high station density, and the length and linearity of the transect ([Nabelek et al., 1993](#)). CASC93 was comprised of 44 broadband stations located at 69 sites at approximately 5 km station spacing along an almost perfectly straight

transect across the Cascades, from coastal to central Oregon ([Figure 16](#)). The dataset has proved a fertile testing ground for advanced multichannel imaging of scattered waves in a subduction zone ([Rondenay et al., 2001](#)). The results from that imaging and an interpretive overlay are shown in [Figure 16](#), lower panel. [Bostock et al. \(2002\)](#) have interpreted the images in [Figure 16](#) to be the result of eclogitization of the downgoing slab (below about 45 km) and consequent serpentinization of the overlying mantle wedge in the forearc. It is anomalous that the basalt-eclogite transition in this case is far shallower than is generally presumed for typical subduction zones (45 km vs 100 km), but the disappearance of a basaltic crustal signature below 45 km appears to have few other explanations. Similarly, the disappearance of a continental Moho signature in the images (around 122.5 longitude) appears to be the result of an ‘inversion’ in the usual continental Moho velocity transition. Thus, the (relatively) high-velocity material of the lower continental crust is interpreted to be in contact with (relatively) low-velocity serpentine of the heavily hydrated mantle wedge (serpentinized mantle forearc in lower frame of [Figure 16](#)).

1.14.3.3.4 Alaska

The Broadband Experiment Across the Alaska Range (BEAAR) experiment ([Figure 17](#)) provides another example of imaging across a very complex continental subduction boundary ([Abers et al., 2006](#)). The BEAAR transect, 1999–2001, consisted of 39 broadband seismographs deployed with 10–15 km station spacing normal to the strike of the subduction zone (map, [Figure 17](#)). High-resolution receiver function images ([Ferris et al., 2003](#)) show that the top of the slab is low velocity (i.e., basaltic) to a depth of about 130 km (note the contrast with the Cascadia images in [Figure 16](#)). Moreover, the Wadati-Benioff zone of seismicity is angled slightly more steeply than the top of the imaged slab, suggesting that the earthquakes gradually migrate deeper into the slab with depth ([Figure 17](#)). Well-constrained seismic attenuation determinations ([Stachnik et al., 2004](#)) show high attenuation in the mantle wedge beneath the Alaska Range, but where the slab is less than about 75 km depth there is observed a sizeable volume of very low-attenuation material ([Figure 17](#)). This zone of low attenuation has been interpreted by [Abers et al. \(2006\)](#) to indicate that a cold, hydrous viscous ‘nose’ has formed in the corner of the mantle wedge and

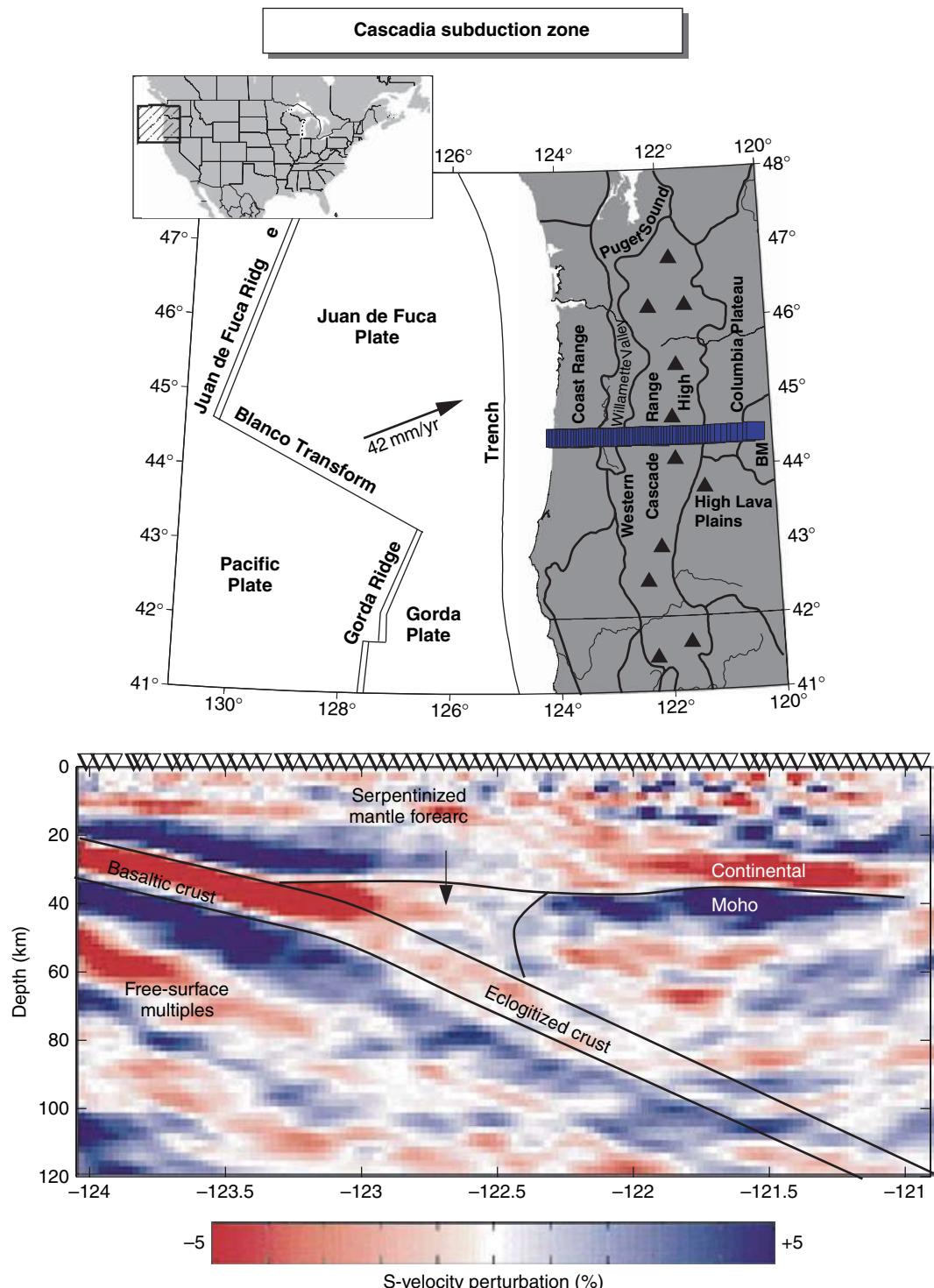


Figure 16 Imaging results from Cascadia seismic experiment (CASC93, Nabelek *et al.*, 1993) deployment of 44 broadband stations at ~5 km spacing from Pacific coast across the Cascades into the Columbia plateau and Blue Mountains (upper panel). The lower panel is an interpretive vertical cross-section superimposed on the scattered wave inversion image of Rondenay *et al.* (2001). Copyright 2001, American Geophysical Union. Red indicates slow-velocity perturbations; blue, fast. See text for further discussion. Figure provided courtesy of Stephane Rondenay, MIT.

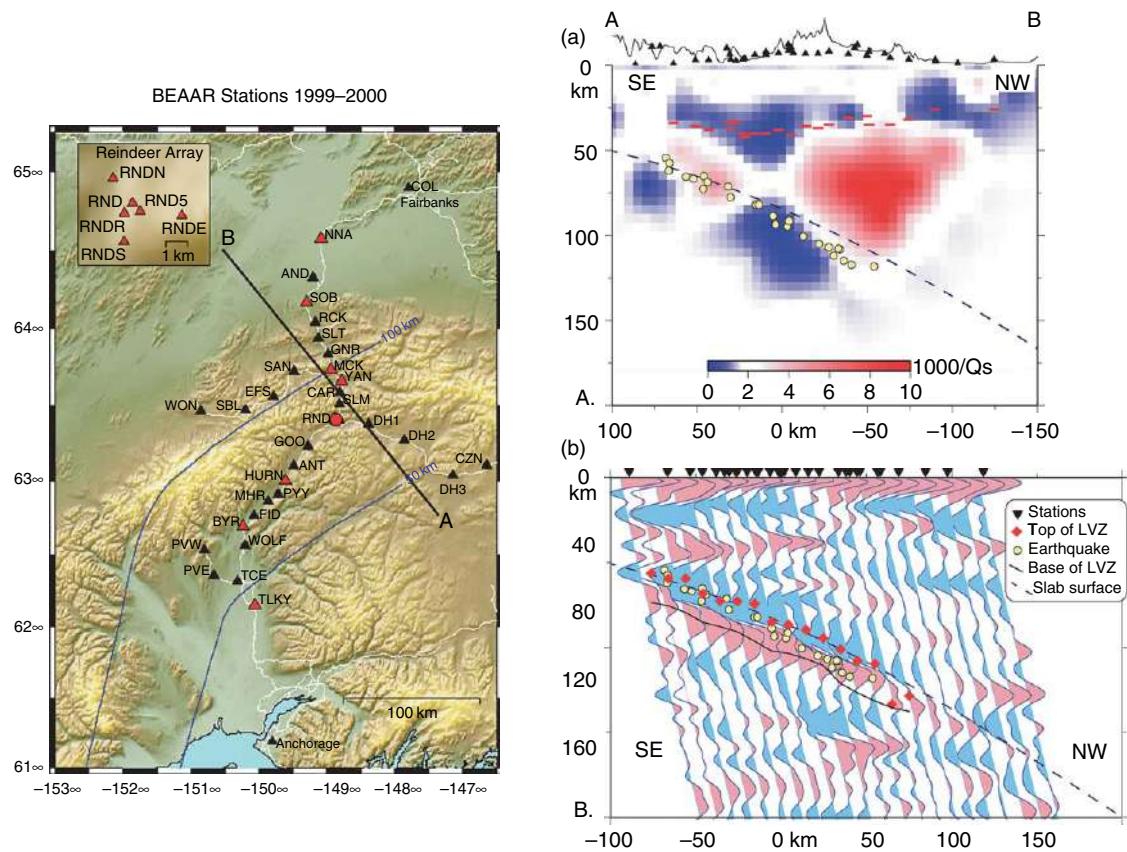


Figure 17 Broadband experiment across the Alaska Range (BEAAR). Map on left shows station locations. Contours indicate depth to Wadati–Benioff zone. Top right figure is a vertical cross-section of attenuation tomography along line A–B. Red indicates high attenuation blue, low attenuation. Moho from receiver functions is indicated by red dashed line. The greatly reduced attenuation in the uppermost part of the mantle wedge suggests that material freezes out and no longer participates in the supra-subduction zone mantle wedge recirculation. The panel in lower right shows the receiver function image with the inferred top of the slab indicated by a black dashed line. Earthquake hypocenters (relocated) are seen along the top of the slab at shallow depths, but migrate into the slab with increasing depth. Figures courtesy of Geoff Abers. Modified from Abers GA, et al. (2006) The thermal structure of subduction zones constrained by seismic imaging: Implications for slab dehydration and wedge flow. *Earth and Planetary Science Letters* 241: 387–397.

remains isolated from the counterflow in the main part of the mantle wedge. The presence of a high-velocity viscous ‘nose’ in subduction zones has been observed previously in Japan and given much the same explanation (Kincaid and Sacks, 1997; Sacks and Suyehiro, 2003).

1.14.3.3.5 Kamchatka

The subduction zone along the Kamchatka peninsula exhibits a unique geometry in that it undergoes a nearly right angle change in strike at the intersection of the eastern extension of the Aleutian arc and the NE trending Kamchatka arc (Figure 18) (Lees et al., 2000). This so-called Aleutian–Kamchatka ‘corner’ can be accommodated by either a bend or a tear in

the downgoing lithosphere (Davaille and Lees, 2004; Lees et al., 2000). Along the westernmost extent of the Aleutian arc, the spreading direction of the Pacific Plate is essentially parallel to the subduction zone. This rather rare subduction geometry is manifest by the NW striking 1000 km strike-slip Bering Fault along the westernmost tail of the Aleutian arc. The Kamchatka experiment shown in Figure 18 was comprised of 15 broadband stations deployed on the Kamchatka Peninsula to examine the region of intersection between the Aleutian and Kamchatka arcs in detail. The results of the studies that emerged from that experiment suggest that the Pacific Plate does not simply ‘bend’ around the Aleutian–Kamchatka corner, but that subduction in Kamchatka is parallel

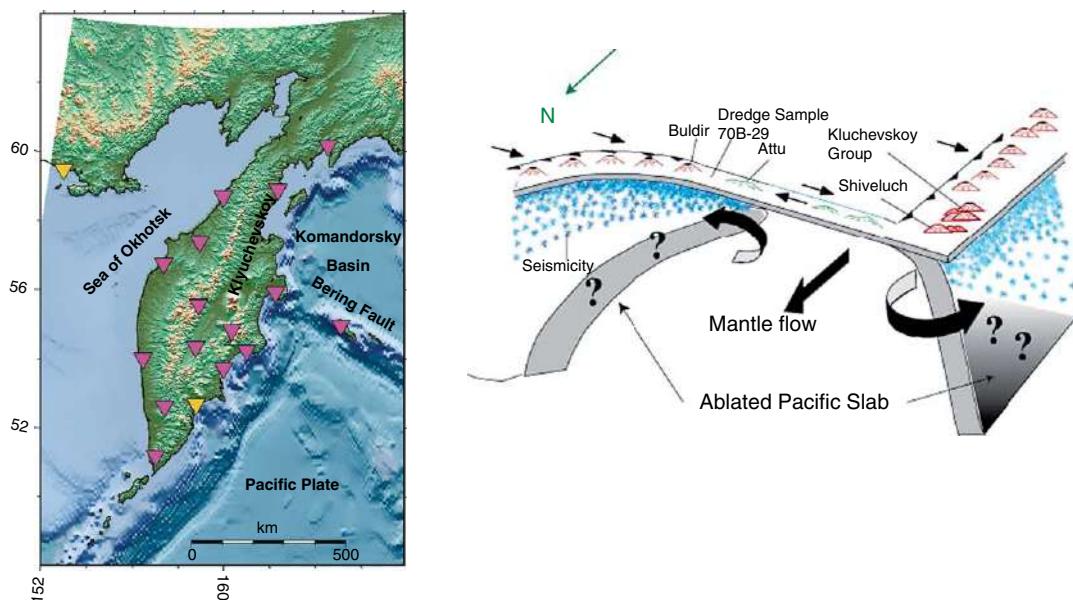


Figure 18 PASSCAL broadband deployment on the Kamchatka Peninsula to image the abrupt bend in subduction of the downgoing Pacific Plate (left hand panel). Image on right is interpretation of results showing slab separation with mantle flow through the corner region. Adapted from Lees JM, et al. (2000) Kamchatka: Edge of the plate. *IRIS Newsletter* 2000(1): 1–5.

to that in the Aleutians and that therefore a tear must separate the two slabs (Lees *et al.*, 2000) (right-hand panel, Figure 18). This remarkable structure appears to give rise to a rare instance of slab melting as evidenced by both the seismic structures and presence of adakite-like magmas that have been erupted at the Aleutian–Kamchatka corner (Davaille and Lees, 2004). The Aleutian–Kamchatka corner may be one of the only places anywhere on the globe where a slab tear seems to be confirmed.

1.14.3.4 Active Continental Rifts

Continental rifts such as the East African and Baikal Rifts have been extensively studied through controlled source experiments that both cross and traverse the rift valleys. The Tanzanian broadband experiment extended into the East African Rift, but the deployment was sufficiently sparse that little could be determined other than that the region beneath the rift was very low velocity, as previously known (e.g., Weeraratne *et al.*, 2003). A major broadband deployment was undertaken recently across the northern Ethiopian Rift where the rifting is transitional between continental and oceanic and where it forms the third arm of the Red Sea, Gulf of Aden Rift triple junction (Bastow *et al.*, 2005). Nearly 80 broadband instruments were installed in a 250×350 km

area for a 16-month period, 2001–2003 as part of the Ethiopia Afar Geoscientific Lithospheric Experiment (EAGLE) (Figure 19) (Maguire *et al.*, 2003). Bastow *et al.* (2005) obtained clear images of an approximately 75 km wide tabular low-velocity zone beneath the rift (Figure 20). The low velocities extend to 200–250 km beneath the Ethiopian Rift in the southern part of the region trending into the East African Rift of southern Ethiopia and northern Kenya. As the rift approaches the Afar depression the low velocity anomaly at depths >100 km appears to broaden and merge with deeper low-velocity structures beneath the Afar depression (Bastow *et al.*, 2005).

1.14.4 Stable Platforms

1.14.4.1 Central and Eastern North America

Compared to western North America, few portable arrays have been deployed in stable central and eastern North America. Prominent among broadband deployments is the Missouri to Massachusetts Broadband Experiment (MOMA), the Lithoprobe/IRIS Abitibi-Grenville teleseismic experiment (ABI96), and the Florida to Edmonton (FLED) broadband experiment (Fischer *et al.*, 1996;

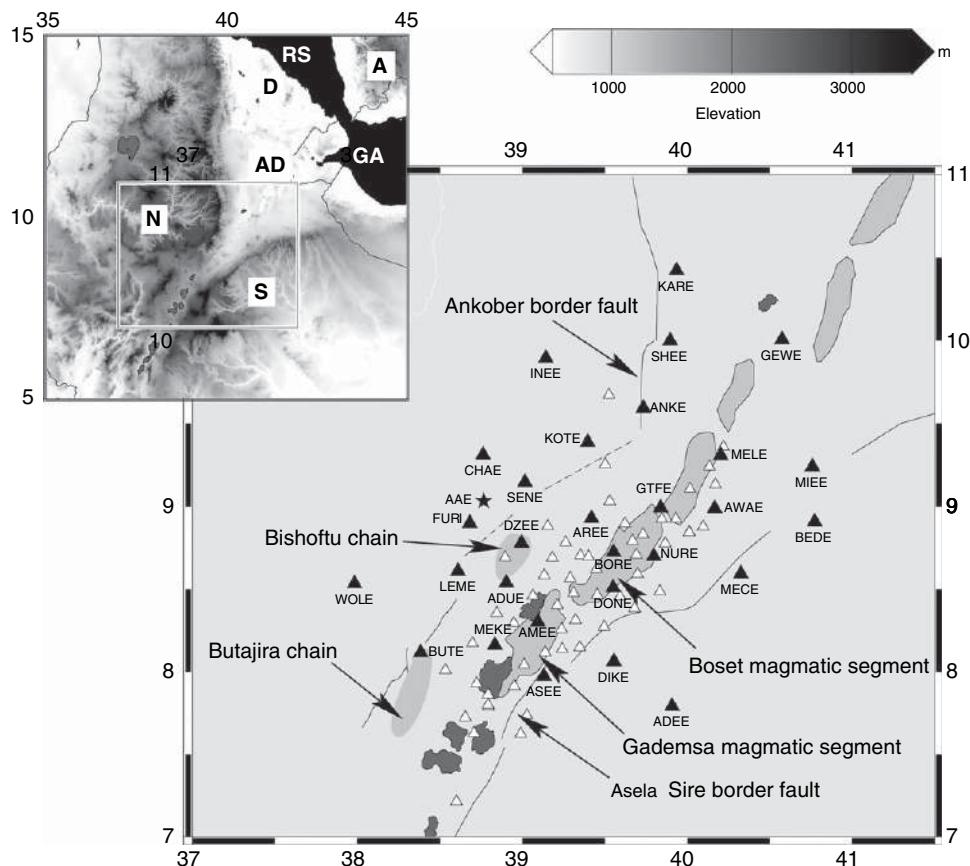


Figure 19 Station locations for the EAGLE broadband experiment, arrayed along the Ethiopian Rift transitional into the Red Sea (see text). Filled triangles are for phase I of the experiment, open triangles for phase II. Stations were deployed for a total of 2 years (2001–2003). On inset, RS denotes Red Sea, GA denotes Gulf of Aden, A denotes Arabian Plate, AD denotes Afar Depression, D denotes Danakil microplate, N denotes Nubian Plate, and S denotes Somalian Plate. From [Bastow ID, Stuart GW, Kendall JM, and Ebinger C \(2005\) Upper-mantle seismic structure in a region of incipient continental breakup: Northern Ethiopian rift. Geophysical Journal International 162: 479–493](#), with permission from Blackwell Publishing.

Rondenay *et al.*, 2000). The northern extension of the FLED array ends in Edmonton, Canada, just east of the Rocky Mountain Front (**Figure 1**). A recent deployment of nearly 60 broadband seismographs (the Canadian Northwest Experiment (CANOE)) picks up at Edmonton and continues as a Y-shaped transect to the NW (**Figure 1**). The array bifurcates into one transect across the Proterozoic and into the Slave Craton, and another that crosses the Canadian Rockies into the Yukon, a transect of nearly 4 Ga of geologic time ([Bostock *et al.*, 2005](#)).

The MOMA deployment of 18 portable stations, anchored at each end by a permanent global station, is shown superimposed on the continental-scale model NA00 of van der Lee in **Figure 21** ([van der Lee, 2002](#)). Interstation spacing was about 100 km and the array operated for about 16 months.

Receiver function determinations of crustal thickness along the profile show thickening of the crust beneath the Appalachians, thinning in the region of the Grenville Front and thickening again beneath the stable Proterozoic platform ([Li *et al.*, 2002](#)). The root beneath the Appalachians, thicker than predicted for isostatic compensation, appears to reflect a ‘densification’ of the lower crust that [Fischer \(2002\)](#) has hypothesized is a common metamorphic process in older orogenic belts. Upper-mantle discontinuities from receiver functions observed beneath MOMA at depths around 270–280 km are visible in the eastern part of the array and have been interpreted as the (rarely observed) base of the asthenosphere beneath eastern North America ([Li *et al.*, 2002](#)). Subsequent studies based primarily on extensive data from a handful of permanent stations in eastern US suggest

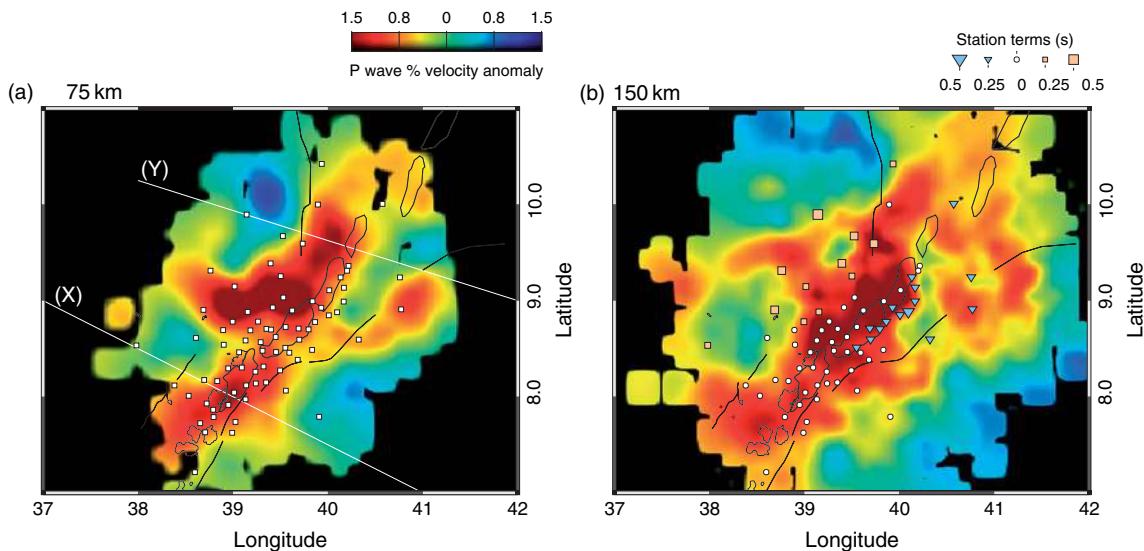


Figure 20 Horizontal depth slices of 3-D tomographic images of P-wave perturbations beneath the Ethiopian Rift as shown in [Figure 19](#). Extreme low velocities are shown beneath the broad area of the rift axis to depths of at least 250 km. Modified from Bastow ID, Stuart GW, Kendall JM, and Ebinger C (2005) Upper-mantle seismic structure in a region of incipient continental breakup: Northern Ethiopian rift. *Geophysical Journal International* 162: 479–493, with permission from Blackwell Publishing.

that the lithosphere–asthenosphere boundary is sharply defined, perhaps no more than 10–12 km in vertical extend, beneath the Phanerozoic ([Rychert et al., 2005](#)).

[van der Lee \(2002\)](#) analyzed S-waves and fundamental mode surface waves along the strike of the array and combined those data with previous data used to develop the North American model NA95 to obtain high-resolution constraints on crustal thickness and S-wave velocity beneath the MOMA array as shown in [Figure 21](#). The lower panel of [Figure 21](#) contains the new velocity structure in cross-section and in terms of velocity perturbations. The thin dashed black line in that figure is presumed to represent the base of the seismic lithosphere and the white line the thermal thickness of the lithosphere as computed by [Goes and van der Lee \(2002\)](#). The lithospheric upper mantle is poorly resolved beneath Phanerozoic North America despite receiver function evidence of a sharp lithosphere–asthenosphere boundary beneath that region ([Rychert et al., 2005](#)).

Measurements of anisotropy along the MOMA array have produced a number of important results. [Fouch et al. \(2000\)](#) modeled the shear wave splitting as asthenospheric shearing due to plate motion as the asthenosphere flowed under and around the continental keel of stable North America in response to the SW absolute motion of North America. They

found no evidence for lithospheric anisotropy beneath the Proterozoic platform. Subsequent studies using Rayleigh and Love surface waves suggest a shallow lithospheric layer with significant ‘radial’ anisotropy ([Gaherty, 2004](#)). SKS splitting and surface waves indicate that azimuthal anisotropy is present primarily in the subcontinental asthenosphere as it deforms in response to plate motion.

The Abitibi–Grenville teleseismic experiment (ABI96) involved a six-month N–S deployment of 28 broadband stations ([Rondenay et al., 2005](#)). Crustal thickness transitions abruptly near the Grenville Front, from 40–45 km in the Proterozoic south to the more characteristically thin (35 km) crust of the Archean Craton in the north ([Rondenay et al., 2000, 2005](#)). Unlike results from MOMA, shear wave splitting reveals a monotonous pattern of dominantly E–W fast directions and relatively small delay times around 0.5 seconds, with no transition across the Grenville Front ([Figure 22](#)). The fast directions along the Abitibi–Grenville line tend to be oriented at a relatively high angle to absolute plate motion and accordingly have been interpreted as due to fossil anisotropy in the lithosphere ([Fouch and Rondenay, 2006; Rondenay et al., 2000](#)). A summary of fast polarization directions and magnitude of the delay times measured over several experiments for central and eastern North America is shown in [Figure 22](#).

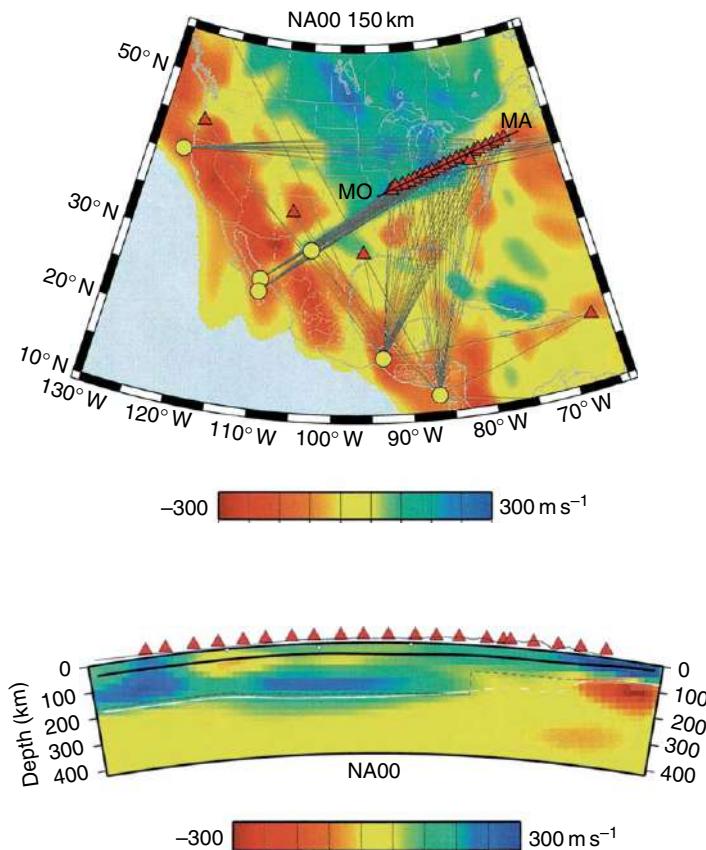


Figure 21 Missouri to Massachusetts (MOMA) broadband array (red triangles). Top figure shows map of the array and the events plus great circle propagation paths (gray lines) used for partitioned waveform inversion superimposed on the 3-D North America model NA00 of van der Lee at a depth of 150 km (van der Lee, 2002). The black line through the stations is the trace of the vertical cross-section shown in the bottom panel. The bottom panel is a vertical cross-section showing velocity perturbations showing a clear high-velocity lithosphere beneath stable continent length of the array. The thin black line represents the base of the lithosphere (as defined by van der Lee, 2002) and the thin white line the thermal thickness of the lithosphere based on Goes and van der Lee (2002). The slightly low-velocity channel beneath the lithosphere is still very high velocity (4.55 km s^{-1}) relative to the typical LVZ of the ocean basins (van der Lee, 2002). Adapted from van der Lee S (2002) High-resolution estimates of lithospheric thickness from Missouri to Massachusetts, USA. *Earth and Planetary Science Letters* 203(1): 15–23.

1.14.4.2 Australia

The Australian continent is particularly well suited for seismic investigations of variation in lithospheric structure between Archean, Proterozoic, and Phanerozoic terranes. The southwestern quarter or so of the continent is underlain by several Archean crustal blocks. The vast central and west-central part of Australia is Proterozoic in age and the eastern-third of the country is Phanerozoic. The so-called Tasman line, the precise location of which is still disputed but which shows up repeatedly in discussions of Australian terranes, divides the Precambrian terranes from the Phanerozoic (e.g., Simons *et al.*, 1999).

Over the past two decades, the Australian continent has been instrumented in a sparse but systematic grid of portable broadband stations, the most prominent of which comprised a succession of deployments known as SKIPPY (1993–1996). SKIPPY was an innovative experiment in which a single array of approximately 10–12 stations was ‘skipped’ kangaroo-style across the continent in six major deployments (van der Hilst *et al.*, 1994). It was specifically designed to capitalize on the substantial arc-related regional seismicity to the east and north of the continent. The SKIPPY array has since been complemented by a number of regional temporary arrays deployed to examine specific regions in more detail (Fishwick *et al.*, 2005). The map figure in the upper

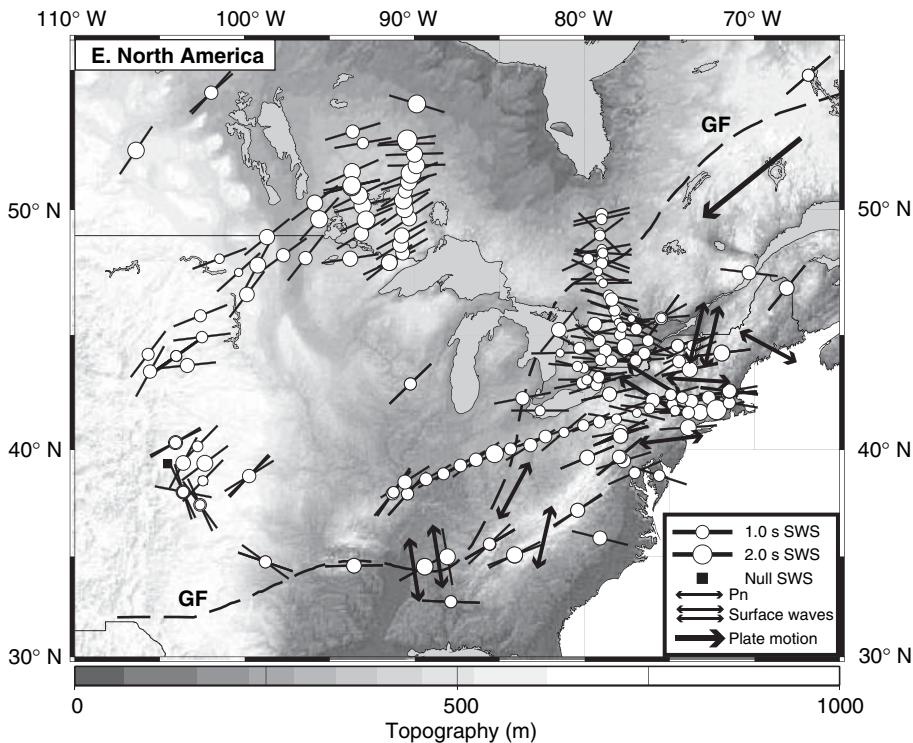


Figure 22 Summary of published shear wave splitting results for eastern North America. From (Fouch MJ and Rondenay S (2006) Seismic anisotropy beneath stable continental interiors. *Physics of the Earth and Planetary Interiors* 158: 292–320. Black bars indicate fast direction of anisotropy. Size of circle is proportional to splitting delay time as shown in the inset. Anisotropy measurements from surface waves and Pn measurements are represented by double black arrows. GF denotes Grenville Front.

left panel of Figure 23 shows broadband deployments superimposed on the geologic outline map of Australia. As few of these deployments are sufficiently dense for high-resolution body wave tomography, the station and source geometry has been most amenable to surface wave tomographic analysis and to receiver function crustal thickness determinations (e.g., Clitheroe *et al.*, 2000; Fishwick *et al.*, 2005; Simons *et al.*, 1999). Until recent work, when relatively dense arrays were installed in the Archean SW of Australia (e.g., Fishwick *et al.*, 2005), surface wave coverage had been most dense in the eastern part of the continent and least dense in the southwest.

Lithospheric imaging beneath Australia is particularly revealing because the instruments and the kind of data used are relatively uniform across the entire continent, making direct comparisons between provinces of different geologic ages possible. Fishwick *et al.* (2005) integrate data from earlier portable broadband arrays (e.g., Simons *et al.*, 1999) with data compiled from recent deployments in western

Australia to produce lithospheric images of consistent quality across the continent (Figure 23). The results in Figure 23 are derived by partitioned waveform inversion, but with several different starting models as to improve recovery of the averaged 1-D path model for the significantly different propagation path structures encountered (e.g., oceanic vs continental) and have been updated since the Fishwick *et al.* (2005) paper. The results reveal a remarkably wide range in shear velocities, in excess of 15% even at 150 km depth, beneath the Australian continent. At 100 km depth, high velocities are observed throughout most of the continent including parts of Australia well east of the Tasman line. These higher velocities beneath even the Phanerozoic terranes are interpreted to represent thick lithosphere. Lower velocities are seen at 100 km depth only along the easternmost part of the continent. The anomalously low velocities at 100 km depth along the eastern margin of the continent appear to be correlated with zones of Neogene volcanism as observed earlier by Zielhuis and van der Hilst (1996). Most of the

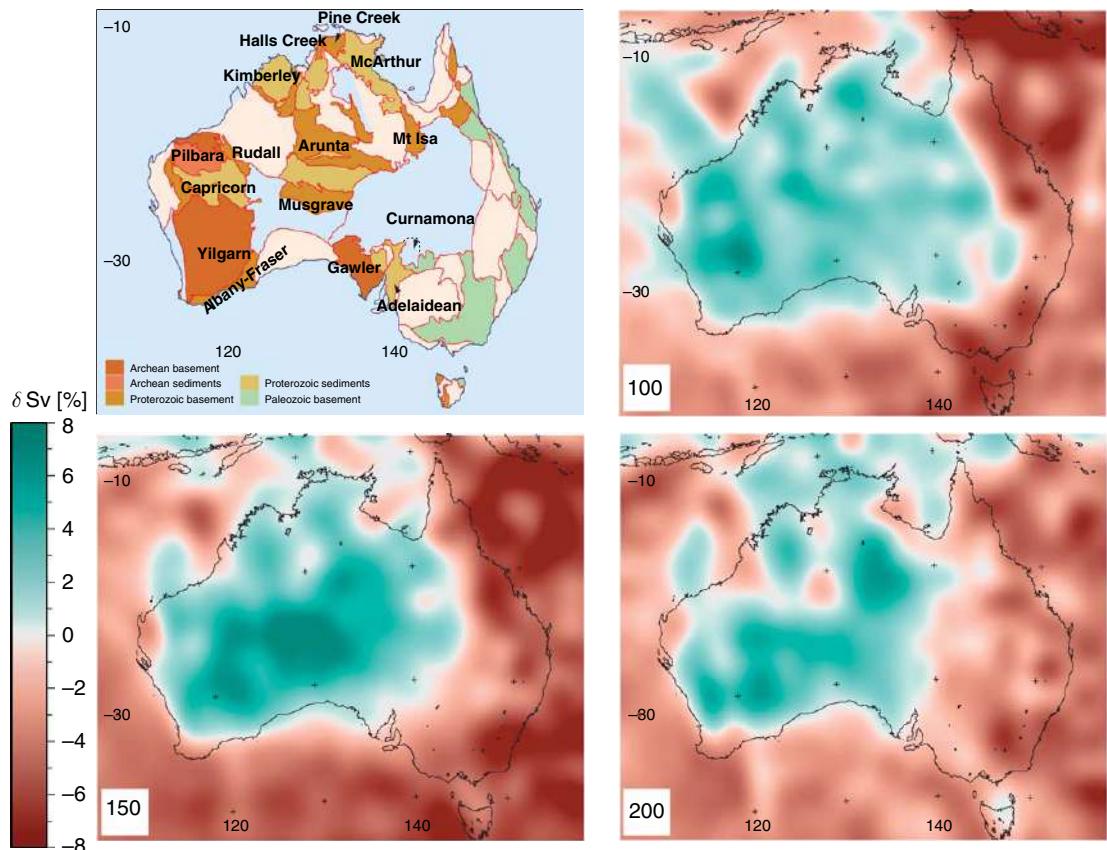


Figure 23 Horizontal depth slices of S-wave tomographic images beneath Australia. Velocity perturbation color scale is shown on left, with perturbations referenced to global model AK135. Upper left panel shows locations of stations deployed as part of broadband experiments, 1993 to present, superimposed on principal geologic units. Figure provided courtesy of Fishwick S (2005) modified and updated. Contrasts in lithospheric structure within the Australian craton – insights from surface wave tomography. *Earth and Planetary Science Letters* 231: 1630176.

observed velocity contrast appears to be due to temperature variations, and based on work of Faul and Jackson (2005), Fishwick *et al.* (2005) conclude that a temperature contrast of $\sim 600^{\circ}\text{C}$ could account for the velocity differences between the ocean basins and the oldest parts of the continent at 150 km depth. High-velocity material in the upper mantle beneath western Australia extends to at least 150 km beneath the Archean Cratons. High-velocity material is not seen to depths greater than about 150 km beneath the small Pilbara Craton, but is observed to depths of at least 250 km beneath the Yilgarn Craton to the SW and the Kimberley Craton to the NW. In general, the higher velocities at greater depths (>200 km) beneath Australia do not correlate simply with age terranes.

The crustal structure beneath Australia has been investigated primarily through receiver function methods based on some of the same station data as those used for the surface wave inversion studies

discussed above (Clitheroe *et al.*, 2000). The crust beneath the undisturbed parts of the western cratons averages about 35–40 km thick, although crust as thin as 25–30 km is seen beneath parts of the Archean-age Yilgarn and Pilbara Cratons and thicker crustal sections abut the Yilgarn to the west. The Moho tends to be sharp beneath the cratonic interiors, but more gradational near terrane boundaries (Reading *et al.*, 2003). The vast Proterozoic interior of the Australian continent is underlain by crust mostly 40–55 km thick, with a relatively transitional Moho. The thickest crustal section yet found in all of Australia is beneath the Amadeus Basin in central Australia, low lying despite a maximum crustal thickness of 61 km. The eastern third of Australia (east of the inferred Tasman Line) is comprised primarily of the late Phanerozoic Tasman Orogen (Clitheroe *et al.*, 2000), where a complex of accretionary terranes were assembled against the Proterozoic continental

nucleus (Betts *et al.*, 2002). The thicker crust of the Proterozoic of central Australia thins east of the Tasman Line to a relatively uniform crust of about 35 km thick that is characterized by a sharp Moho. The abrupt shift in crustal thickness and Moho structure from thick Proterozoic to thin Phanerozoic is in contrast with images of mantle lithosphere, where the Tasman Line is not at all well defined (Figure 23) (Fishwick *et al.*, 2005).

1.14.4.3 South America

Southeastern Brazil is by far the most thoroughly studied part of stable South America (e.g., (Schimmel *et al.*, 2003), where portable broadband arrays have been installed in a SKIPPY-like expanding and migrating observational network since 1992. The arrays, with up to 15 stations operating at one time, total 45 stations over an area about 1000×1700 km (Figure 24). The region encompasses the Archean São Francisco Craton, the Paraná Basin – a massive flood basalt province *c.* 130 Ma – and its adjoining margins of Cretaceous alkaline intrusives. The most remarkable, and most controversial, finding from the tomographic imaging in this region is the discovery of an apparent ‘fossil’ Paraná plume at depths 200–600 km in the upper mantle beneath the Paraná Basin (VanDecar *et al.*, 1995) (bottom image, Figure 24). Tomographic images of the upper mantle also show that the keel of the Archean São Francisco Craton extends to depths of 200–300 km. The lithosphere is considerably thinned in the region of the post-rifting Late Cretaceous alkaline intrusives that cluster locally throughout much of SE Brazil, particularly around the margins of the Paraná Basin and the São Francisco Craton (Schimmel *et al.*, 2003). Anisotropy beneath that same region of SE Brazil as determined by SKS splitting appears to be controlled largely by pre-existing lithospheric structures rather than mantle flow (James and Assumpcao, 1996).

1.14.4.4 Antarctica

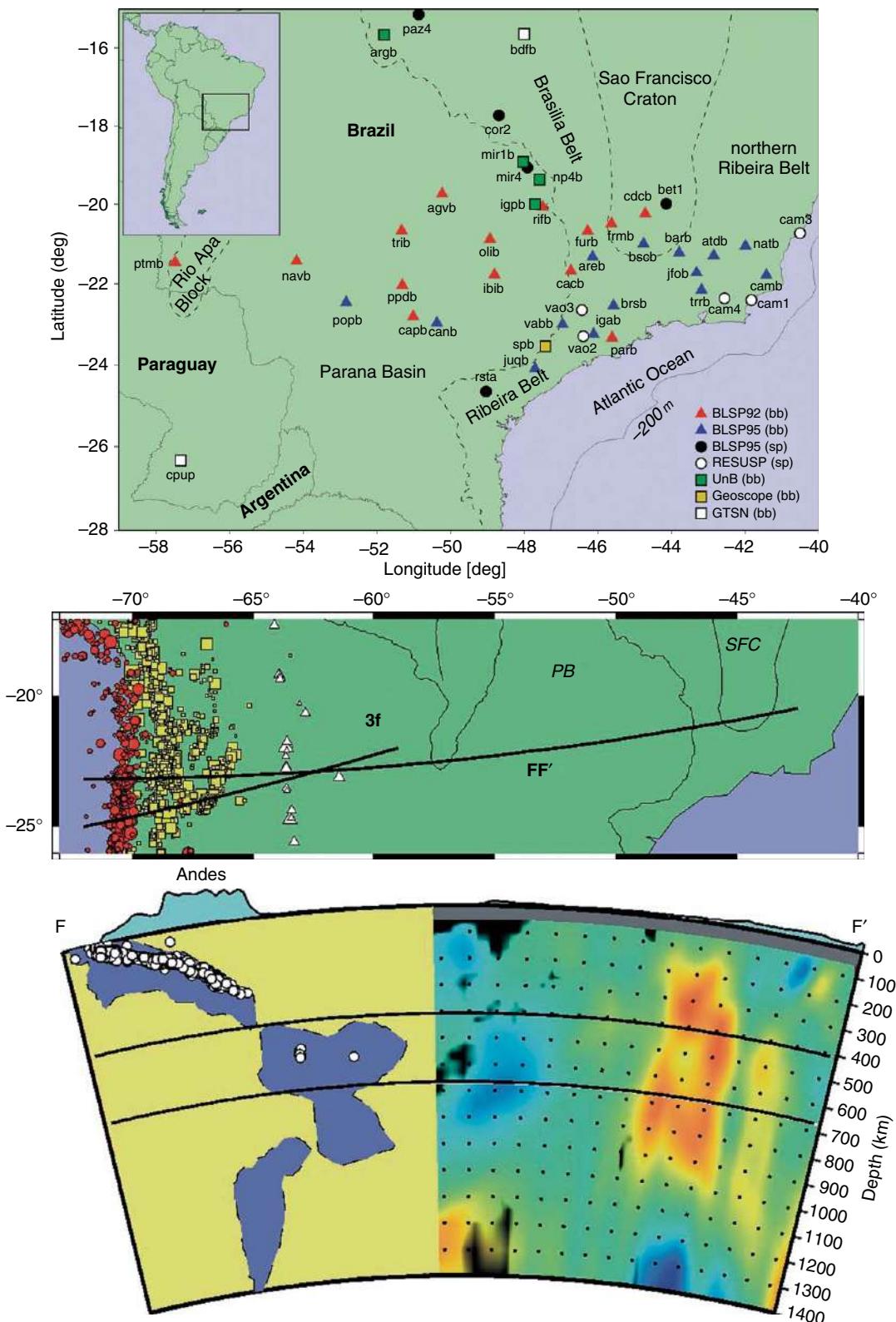
Despite extreme cold, lack of sunlight for solar power half of the year, little infrastructure, and other serious logistical challenges, portable broadband experiments on the continent of Antarctica have not been wanting. Efforts to operate portable seismic instruments have been underway for well over a decade, and new technologies have been developed to

operate in extreme arctic conditions. Thanks largely to those efforts, as well as continuing support from the permanent facilities that the National Science Foundation (NSF) Polar Program maintains in Antarctica, an ambitious array experiment was undertaken recently to map the contrasting crustal and upper-mantle structures along a transect across the West Antarctica Rift System, the Transantarctic Mountains and the East Antarctica Craton (Figure 1). The Transantarctic Mountain Seismic Experiment (TAMSEIS) involved a deployment of 41 broadband seismometers that recorded from 2000 to 2003 under extraordinarily difficult operating conditions (Figure 1). Analysis of the data collected from the TAMSEIS project is highly preliminary, but results to date reveal high velocities in the mantle beneath the (old) East Antarctica Craton and a zone of low velocities that extends to 200 km beneath the (young) Transantarctica Mountains and NNE beneath McMurdo Sound and the Ross Sea (Watson, 2005). The area of McMurdo Sound includes Mt. Erebus, an active Antarctic volcano and the highest peak in the Transantarctica Mountain Belt.

1.14.5 Archean Cratons

Archean cratons, the ancient cores of continents, are prime targets for portable array seismology. Archean cratons exhibit a number of distinctive features that set them apart from all younger continental structures. Notably, cratons are underlain by a thick mantle root (tectosphere, (Jordan, 1975)) that is both chemically and physically distinct from the rest of the mantle, including other continental lithosphere, suggesting formation by processes unique to Archean time. The refractory tectospheric root is now known to be ancient, composed dominantly of highly depleted peridotites with low normative density and high seismic velocities (Boyd and McCallister, 1976; Boyd and Mertzman, 1987; James *et al.*, 2004; Jordan, 1979), and at least 200 km thick (e.g., Bruneton *et al.*, 2004; Grand, 1994; James *et al.*, 2001, 2004; James and Fouch, 2002; Jordan, 1975; Lerner-Lam and Jordan, 1987; Van der Lee and Nolet, 1997; Zhao *et al.*, 1999).

The distinctive character of cratonic mantle and the nature of the crust and the crust–mantle boundary distinguish Archean from post-Archean terranes. Paradoxically, the Archean crust appears to be both thinner and less mafic than post-Archean crust



(Griffin and O'Reilly, 1987; James *et al.*, 2003; Rudnick, 1995). Moreover, the Archean Moho is characteristically sharper than that beneath younger terranes. These observations, together with the unique character of the cratonic root, suggest that the processes of craton formation, or the physical conditions that controlled those processes, differed in important ways from continent-forming processes in post-Archean times. Passive array studies are largely aimed at understanding the circumstances and mechanics of early continental formation.

1.14.5.1 Southern Africa

The Southern Africa Seismic Experiment (**Figure 25**), part of the multidisciplinary and multi-national Kaapvaal Project is the largest of the broadband array experiments undertaken to probe the anatomy of Archean cratons and their relationship to adjacent Proterozoic mobile belts (Carlson *et al.*, 1996; James *et al.*, 2001; James and Fouch, 2002). A nearly continuous Archean geological record, from 3.6 to 2.6 Ga is preserved within the Kaapvaal Craton (e.g., De Wit *et al.*, 1992)). A significant area of the region covered by the seismic array, both on and off craton, has been perforated by thousands of Cretaceous kimberlite pipes from which a wealth of crustal and mantle xenoliths were erupted, some from depths in excess of 200 km (Gurney and Harte, 1980). The chemical and mineralogical compositions of mantle xenoliths provide some of the very best constraints that seismologists have for verifying seismic images of the deep continental lithosphere and relating them to actual rocks in the mantle (e.g., James *et al.*, 2004).

Fifty-five portable broadband seismic stations were deployed at 82 sites from April 1997 to July 1999 in a roughly 100 km grid along a NNE-SSW transect about 1800 km long by 600 km wide in southern Africa (**Figure 25**). The experiment was augmented by a 6 month deployment of 32 telemetered broadband stations installed in a dense

($\sim 65 \times 50$ km) array in the vicinity of Kimberley, South Africa, in the heart of the undisturbed Kaapvaal Craton (**Figure 25**).

1.14.5.1.1 Mantle tomographic images

Tomographic results (Fouch *et al.*, 2004; James *et al.*, 2001; James and Fouch, 2002) show that high-velocity mantle roots extend locally to depths of at least 250 km beneath undisturbed Archean craton, with no comparable root structures beneath post-Archean terranes (**Figure 26**). While only P-wave velocity structure is shown in the **Figure 26**, mantle velocities in both P and S are remarkably consistent (Fouch *et al.*, 2004; James *et al.*, 2001). High velocities in both P and S coincide with the interiors of the Kaapvaal and Zimbabwe Cratons. Excepting regions of disrupted craton (as beneath the 2.05 Ga Bushveld Province), the tectospheric root attains a thickness of ~ 200 – 250 km almost everywhere beneath the cratons, including the Archean Limpopo Mobile Belt. The most remarkable ‘disrupted’ feature of the Kaapvaal craton is seen in the low velocities in the mantle beneath the Bushveld Complex, the largest layered intrusion in the world. In contrast, the mantle structure of the Archean Limpopo Belt, a collision zone between the Zimbabwe and Kaapvaal Cratons, does not differ significantly from that of the adjacent cratons. Neither body nor surface wave analyses have produced evidence of a significant low-velocity zone beneath the cratonic keel (Freybourger *et al.*, 2001; James *et al.*, 2001; Larson *et al.*, 2006; Ritsema and van Heijst, 2000; Zhao *et al.*, 1999). Recent surface wave results for the southern Kaapvaal (Larson *et al.*, 2006) give absolute S-wave velocities that are consistent with the velocity-depth structure estimated from Cretaceous-age mantle xenoliths derived from the cratonic root (James *et al.*, 2004).

The Proterozoic Namaqua-Natal Mobile Belt, the remnants of a major N-S convergent margin along the Kaapvaal that may have extended as far north as the Zimbabwe Craton (De Wit *et al.*, 1992), is characterized by velocity perturbations uniformly

Figure 24 Map showing locations of successive broadband deployments in SE Brazil, 1992 to present (Schimmel *et al.*, 2003). The bottom panel is split, with the left-hand side showing the high wavespeed (blue) anomalies adapted from Engdahl *et al.* (1995), and the right-hand side showing P-wave body wave tomography from the Brazilian arrays. The most prominent feature of the P-wave body wave image shown is the low-velocity anomaly that extends vertically beneath the Paraná Basin. VanDecar *et al.* (1995) speculated that the anomaly represented a fossil plume conduit for the Paraná flood basalts. Figure adapted from Schimmel M, *et al.* (2003) Seismic velocity anomalies beneath SE Brazil from P and S wave travel time inversions. *Journal of Geophysical Research* 108(B4): 1–15 (doi:10.1029/2001JB000187 (B4,2191)).

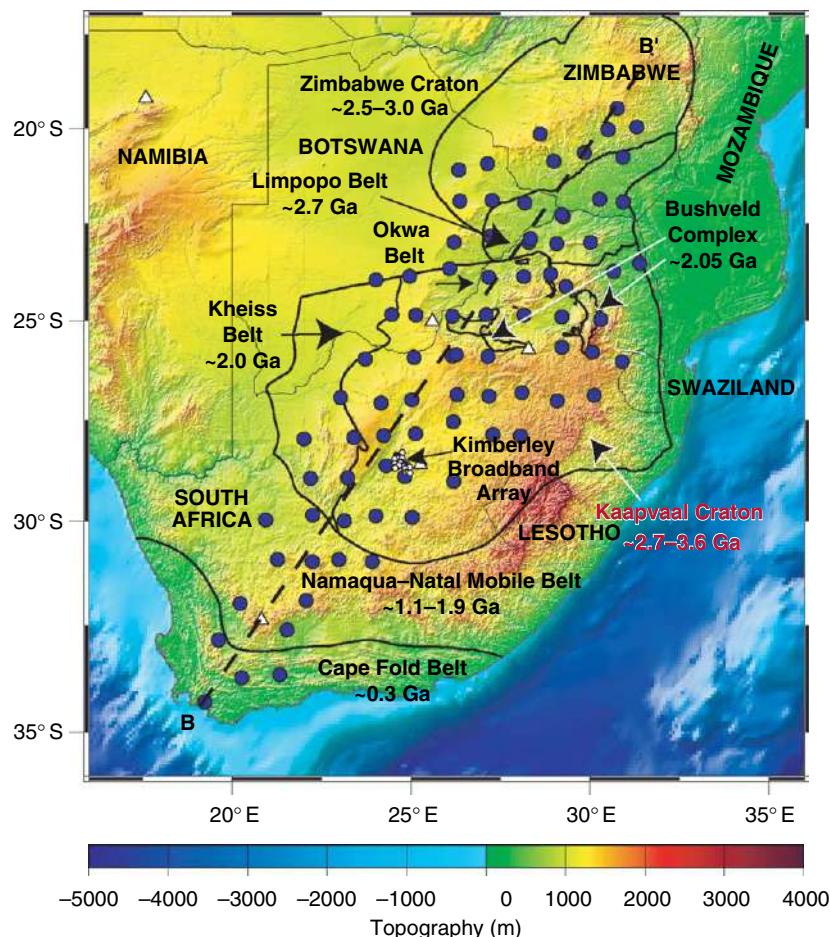


Figure 25 Map showing station locations, topography, and principal geologic provinces in the region of Kaapvaal Project within southern Africa. Eighty-two broadband stations were occupied over a 2-year period from 1997–99 in South Africa, Botswana, and Zimbabwe. The Kimberley array consisted of 31 broadband stations deployed in an area approximately 60×40 km. In addition, three GSN broadband stations (white triangles) are located in the region and their data incorporated in the tomographic analysis. The array extends from the Cape Fold Belt in the south, through the Proterozoic Namaqua–Natal Mobile Belt, across the Kaapvaal Craton and Bushveld Province, through the Archean Limpopo Mobile Belt and into the Zimbabwe Craton.

lower than those observed beneath the craton. The lower velocities are in keeping with the observation that the off-craton Proterozoic mantle tends to be somewhat more fertile (higher Fe) than that of the adjacent craton, as well as slightly warmer (Carlson *et al.*, 2000; James *et al.*, 2004; Pearson *et al.*, 2002).

1.14.5.1.2 Crustal thickness and Moho structure beneath southern Africa

Strong variations in crustal thickness based on receiver functions reveal significant differences in the nature of the crust and the crust–mantle boundary between Archean and post-Archean geological terranes (Figure 27; Nguuri *et al.*, 2001). Stations located within undisturbed Kaapvaal or

Zimbabwe Craton typically have sharp, large amplitude depth images for the Moho, similar to those observed for other Archean terranes (e.g., Clitheroe *et al.*, 2000). In contrast, stations within post-Archean and modified cratonic regions typically exhibit poorly defined P_s converted phases. Moreover, the crust beneath post-Archean and modified cratonic regions is in almost all cases thicker than that beneath the cratons. Throughout the broad region of the Bushveld and Okwa/Magondi terranes (Figure 25), the Archean Craton has been overprinted by tectonomagmatic events of Proterozoic age (e.g., Carney *et al.*, 1994; Shirey *et al.*, 2001) and the effects on crustal structure have been profound. The crust thickens and the Moho signature degrades, for

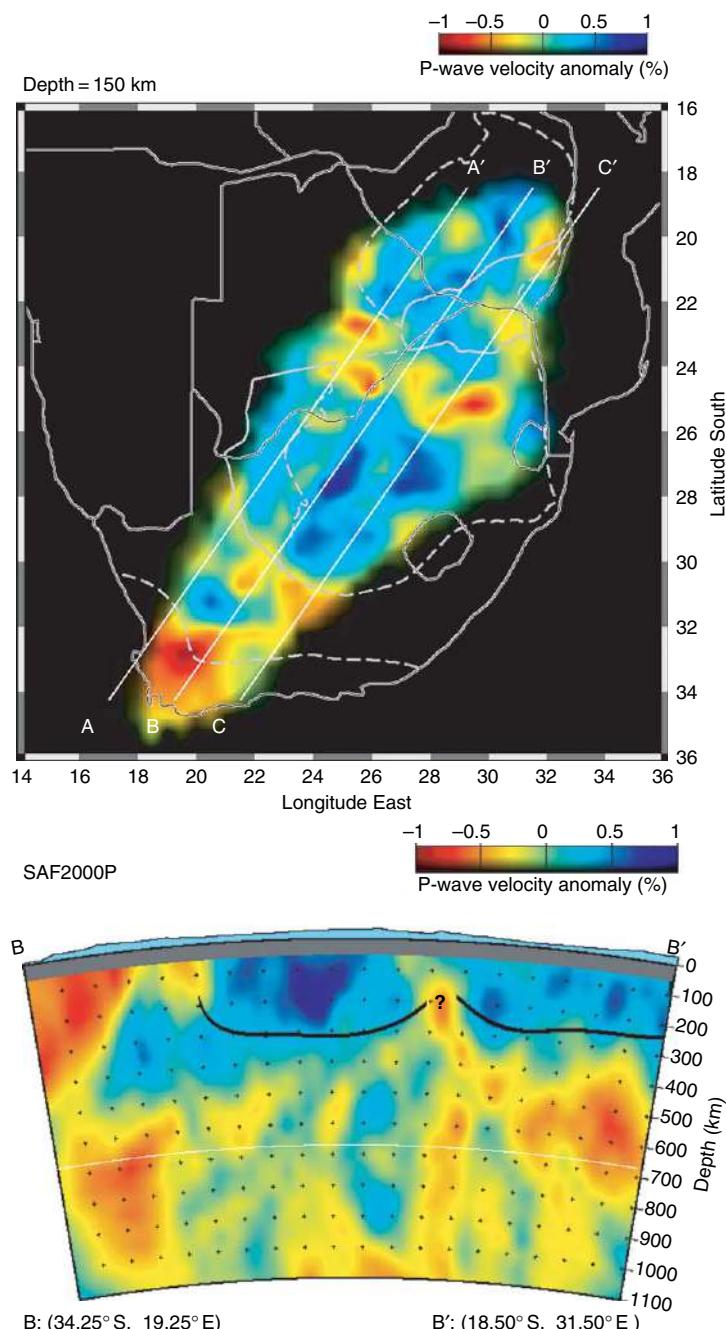


Figure 26 Relative P-wave velocity perturbations from inversion of seismic delay times with overlaid geologic province outlines. Adapted from James DE and Fouch MJ (2002) Formation and evolution of archaean cratons: Insights from southern Africa. In: Ebinger C, Fowler CMR, and Hawkesworth CJ (eds.) *The Early Earth: Physical, Chemical and Biological Development*, pp. 1–26. London: Geological Society of London. Velocity anomaly scale ranges from deep blue (1% fast) to deep red (1% slow). Top panel is map (horizontal section) view of velocity perturbations at 150 km depth. Kimberlite locations for xenoliths used in this study are marked by square symbols. Lower panel is cross-section along line B-B' of the horizontal section. Topography, scaled by a factor of 20, is shown in light green. Tectospheric root can be seen beneath the southern Kaapvaal Craton extending to a depth of nearly 300 km. The region of seismic low velocities in the uppermost mantle underlies the Bushveld Province.

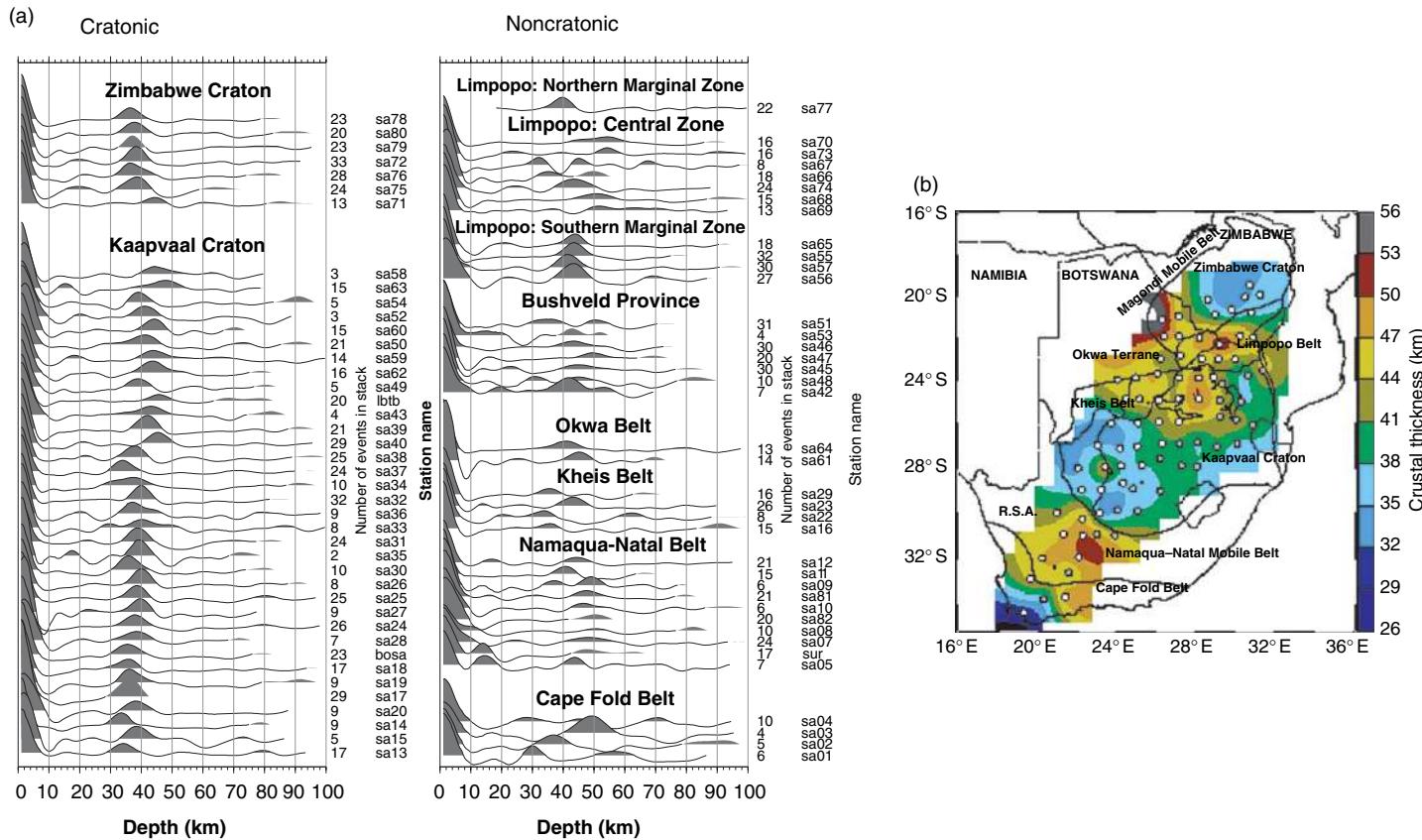


Figure 27 (a) Receiver function depth images for southern Africa, arranged by geologic province. The number of events in the stack and the station name for each trace are shown to the right of the trace. The dominant signal on most of the depth images is the P to S conversion (Ps). Relatively thin (35–40 km) crust and sharp, well-defined Ps Moho conversions tend to be associated with undisturbed craton. Ps arrivals associated with disturbed regions of the craton and post-Archean terranes tend to be more diffuse and of smaller amplitude. From [Nguuri T, et al. \(2001\)](#) Crustal structure beneath southern Africa and its implications for the formation and evolution of the Kaapvaal and Zimbabwe cratons. *Geophysical Research Letters* 28(13): 2501–2504. (b) Color-coded contour map of depth to Moho beneath the southern Africa array based on receiver function depth images. From [Nguuri T, et al. \(2001\)](#) Crustal structure beneath southern Africa and its implications for the formation and evolution of the Kaapvaal and Zimbabwe cratons. *Geophysical Research Letters* 28(13): 2501–2504. Crustal thickness color scale is shown on right. Thin crust tends to be associated with undisturbed areas of the craton, particularly in the southern and western parts of the Kaapvaal Craton and in the Zimbabwe Craton, despite a regional elevation above 1100 m (3500 ft). Recent work by Webb suggests that much of the gravity compensation for excess elevation in the craton comes from low-density mantle (Webb, 2006).

example, passing from undisturbed craton into the Bushveld Province and between undisturbed Zimbabwe Craton into the Magondi Belt. The change in crustal structure is consistent with the evidence from tomographic imaging for major disruption in the uppermost mantle beneath the entire region (**Figure 26**).

Depth images for the northern and southern marginal zones of the collisional Limpopo Belt are typical of the adjacent cratonic structure, both in character of the P_s conversion and in crustal thickness (**Figure 27**). The central Limpopo Belt, site of maximum deformation during the collision of the Kaapvaal and Zimbabwe Cratons in the Archaean, displays broad, poorly defined P_s images indicative of structurally complex Moho and with depth maxima occurring between 40 and 53 km. As with the Bushveld, the relatively thick crust beneath the Limpopo appears not to be isostatically compensated at the surface, suggesting ‘densification’ of the deep crustal root (**Fischer, 2002**).

Kimberley Array: The 31-station telemetered broadband Kimberley array deployment comprised a dense grid over an area of about 65×50 km (**Figure 25**) near Kimberley, South Africa, in the south-central region of the Kaapvaal Craton. Analysis of both teleseismic and local events recorded on the Kimberley broadband array reveal a remarkably uniform crustal structure beneath the array: (1) The cratonic crust is uniformly thin (about 35 km), it has a low average Poisson’s ratio (~ 0.25 , $V_p/V_s \approx 1.73$); and, (2) The Moho is a sharp discontinuity, with a crust–mantle transition less than about 0.5 km beneath the array (**James et al., 2003; Niu and James, 2002**).

The low Poisson’s ratio of 0.25 ($V_p/V_s = 1.73$) for the crustal average and an inferred density of 2.86 gm cc^{-1} for lowermost crustal rocks highlights one of the great dilemmas of Archean crustal composition (e.g., **James et al., 2003; Rudnick, 1995**). If the continental crust was derived from a hotter mantle in the Archean, why is the crust beneath the Kaapvaal less mafic than that beneath adjacent Proterozoic mobile belts, where the lower crust is mafic? **Niu and James (2002)** suggested that the present composition of the Kaapvaal crust may be explained as the result of extensive melting of the lower crust during ultra-high-temperature metamorphism associated with a craton-wide tectonomagmatic event in the Late Archean. Layering and flow associated with the crystallization of melt in the lowermost crust is one possible means for producing both a flat and sharp

Moho, as well as the evolved rock compositions inferred from the seismic data (**James et al., 2003; Niu and James, 2002**).

1.14.5.2 Passive Array Studies of Other Cratons

Relatively small experiments in the Slave and Tanzanian Cratons are of particular interest. The Slave Craton in northern Canada is small in area, but contains some of the oldest rocks on Earth and a wealth of diamonds. Reconnaissance studies of the Slave based on 13 broadband stations deployed over a 2 year period in the 1990s showed somewhat similar structures to those seen in the Kaapvaal, including relatively thin crust and a tectospheric root, the depleted material of which apparently does not extend to depths as great as seen in the Kaapvaal (**Bank et al., 2000**). Data from the Tanzanian Broadband Seismic Experiment, comprised of 20 stations deployed in 1994–1995 across the Tanzanian Craton and adjacent rifted mobile belts (**Ritsema et al., 1998**), have been analyzed in a number of independent studies. The deep lithospheric structure of the cratonic root remains somewhat in doubt. Body wave tomography indicates that the high-velocity tectosphere extends to a depth of at least 200 km beneath the craton (**Ritsema et al., 1998**). More recent surface wave studies, however, appear to indicate a thinner cratonic lithosphere (~ 150 km), the base of which may have been degraded by a rising plume associated with the East African Rift system (**Weeraratne et al., 2003**). The presence of adjacent rift zones with extremely low mantle velocities extending to considerable depth, however, makes the surface wave results difficult to interpret, as the poor lateral resolution inherent in surface wave tomography renders cross-contamination of structures a major concern. Crustal structure is similarly controversial. **Julia et al. (2005)** interpret results from joint receiver function/surface wave inversion of the broadband data to imply a mafic lower crust beneath the craton. This conclusion is contrary to that reached by much the same group of authors in a previous paper (**Last et al., 1997**), based on approximately the same data, where the East African crust was judged more felsic than Precambrian crust elsewhere.

A large-scale multinational seismic experiment within the Baltic (Fennoscandian) Shield (SVEKALAPKO) focused on the lithospheric and asthenospheric structure of the East European Craton to a depth of about 400 km. The dense array across mostly Archean and Proterozoic terranes consisted of 143 stations, including 40 broadband and 88

short-period portable stations deployed for about 9 months, 1998–1999 (Bruneton *et al.*, 2004; Sandoval *et al.*, 2003, 2004). Results from body wave tomography (Sandoval *et al.*, 2004) have been mixed and difficult to interpret. High mantle velocities extend to depths of at least 250 km, but they trend seamlessly across both Archean and Proterozoic terranes, with no clear evidence for a distinct cratonic root beneath the Archean. Surface wave tomography with good resolution to a depth of about 150 km reveals strong velocity variations that are attributed to varying composition (rather than temperature), but here also mantle velocities do not differ significantly beneath Archean and Proterozoic terranes (Bruneton *et al.*, 2004).

1.14.6 Seismic Constraints on Composition and Temperature of the Continental Lithosphere

The range of seismic velocities in the continental lithospheric mantle indicates that the most abundant rock type is peridotite and that the major variations in seismic velocity are produced by temperature (e.g., Carlson *et al.*, 2005, Chapter 1.22). While eclogite, the high velocity/high density/high pressure equivalent of oceanic basalt, is observed in subducting oceanic crust below about 100 km depth, it is seen only rarely in the continental lithosphere where it is generally interpreted to be evidence of a relict slab (e.g., Bostock, 1997). In general, high velocity bodies consistent with large volumes of eclogite are not observed in the continental mantle (e.g., Gao *et al.*, 2002; James *et al.*, 2001; Schimmel *et al.*, 2003; VanDecar *et al.*, 1995).

Seismic velocities in the continental lithospheric mantle most commonly correlate with the age of last tectonomagmatic activity in the area rather than the age of the overlying crust. A prime example is North America, where a sharp lithospheric boundary, approximately along the Rocky Mountain Front, is observed between the stable platform of eastern North America and the tectonically active western US, much of which is underlain by Precambrian basement. The contrast in upper mantle V_s between stable North America and tectonic western North America, while highly variable, is as much as 10% or even more in places. Although both temperature and composition affect seismic velocities of rocks in the mantle, temperature exerts the dominant control (Goes and van der Lee, 2002; James *et al.*, 2004; Lee, 2003). Nonetheless, Godey *et al.* note that a 2% increase in velocity can be explained either by a

120°C decrease in temperature, by a 7.5% depletion in iron, or by a 15% depletion in aluminum (Godey *et al.*, 2004). Assuming that temperature is the only variable, a ~10% difference in V_s velocity between Basin and Range lithospheric mantle and cratonic lithospheric mantle implies that the cratonic mantle is some 600°C colder. Godey *et al.* estimate that the coldest part of the Canadian shield is about 800°C colder than tectonic North America at 100 km depth. Indeed, cratons everywhere are characterized by very low geotherms (Nyblade and Pollack, 1993). In general, heat flow calculations of temperature differences at depth between cratons and tectonic regions are consistent with results where seismic velocities are inverted to obtain thermal structure (Goes and van der Lee, 2002). Given nominal estimates for heat production in Archean crust and mantle and assuming a typical cratonic surface heat flow of 40 mW m⁻² (Pollack and Chapman, 1977), the calculated temperature at 100 km would be about 800°C. Adding 600°C to this would push much of the mantle beneath western US almost to the dry melting point of peridotite (~1450°C). If temperature differences of the same magnitude persist to 150 km depth, where the temperature beneath a craton is of order 1050°C (Nyblade, 1999), then adding 600°C to this would place the western US mantle well above the dry melting temperature of peridotite (Carlson *et al.*, 2005). While there is active volcanism locally in the western US, there is no seismic evidence that any parts of the shallow mantle are substantially molten anywhere. Consequently, the large seismic velocity difference between various regions of the continental mantle is unlikely to be solely the result of varying temperature. This constraint provided the basis for Jordan's 1975 tectosphere hypothesis in which he introduced the principle of temperature-depletion compensation (isopycnic hypothesis) to account for differences between cratons and oceans (Jordan, 1975, 1978, 1979, 1981, 1988). Godey *et al.* (2004) calculated both temperature and compositional differences from a joint inversion of S-wave velocities and density perturbations, concluding that the maximum δT at 100 km depth between craton and tectonic mantle was -440°C and δFe was -4%. Even a perturbation of 440°C, however, appears to put the mantle temperature in tectonic regions above the dry melting temperature if it extends to depths much in excess of 150 km. Curiously, the S-wave velocity perturbations calculated by Godey *et al.* do not decrease significantly at depths greater than

100 km, whereas those of van der Lee and Nolet (1997) and others do (Carlson *et al.*, 2005).

The question of whether a significant low-velocity zone (asthenosphere) exists beneath the continental lithosphere remains an unresolved topic of debate. The base of the oceanic lithosphere is marked nearly everywhere by a strong decrease in V_s at depths generally less than 100 km. Low-velocity zones in the uppermost mantle are clearly seen under many tectonically active continental regions (e.g., Karlstrom and Keller, 2005, and articles therein), but most are associated with relatively recent tectonomagmatic activity that has been superimposed on pre-existing Proterozoic or even Archean structures. The absence of mantle roots beneath the Wyoming and North China Cratons appears to be an extreme example of high-temperature Phanerozoic overprinting (see summary by Carlson *et al.* (2005), and references therein). Beneath stable continental regions, low-velocity zones tend to be weak or absent. With few exceptions (e.g., Rychert *et al.*, 2005), the base of the stable continental lithosphere is not well imaged seismically: the transition over which the relatively high seismic velocities of stable lithosphere merge into the comparatively lower velocities of the convecting mantle appears to be gradual.

1.14.7 EarthScope, USArray, and the Future of Portable Array Seismology

EarthScope is a major program funded through the US National Science Foundation to investigate the structure and evolution of North America and the physical processes controlling earthquakes and volcanic eruptions. USArray, the component of EarthScope specifically aimed at imaging the deep structure of the continent beneath the United States, is conceived as a rolling array of 400 broadband stations that over a 12 year period will occupy more than 2000 sites within coterminous US and Alaska, each for a period of about 18 months. The 2000-station deployment, with an average grid spacing about 70 km, is to be supplemented by more dense active and passive array deployments aimed at key scientific targets (the ‘flexible’ component of USArray) and anchored by a regular network of permanent broadband stations. The seismic observations from USArray are intended to provide the foundation for integrated geologic, geochemical, and other geophysical studies to produce a coherent, high-resolution, plate-scale image of the continental lithosphere and

the underlying mobile mantle. Besides significantly higher resolution regional images, one of the most important contributions of USArray will be the uniform coverage with uniform resolution of deep structures across the very different geologic provinces of North America. The uniform seismic images across the continent will greatly enhance our ability to relate surface geology and detailed lithospheric structure to driving forces and thermal processes within the mantle, and to link structures inherited from earlier stages of continental evolution and subsequent plate motion to known and potential geologic hazards. The USArray program within the US is echoed to some extent by comparable programs in Europe (e.g., EuroArray), and reportedly in China, where plans are being implemented for broadband arrays of several hundred portable instruments that can be deployed across the continent to study deep plate-scale structures (F. Niu, personal communication, 2006).

1.14.8 Discussion

Passive array seismology is arguably the most powerful tool available to scientists for the study of continental lithosphere and small-scale heterogeneities in the deeper Earth. Over the past two decades passive array experiments have evolved from deployments comprising a handful of broadband instruments to major imaging efforts involving hundreds of stations. The images of the deep continental lithosphere produced from these experiments have revolutionized our understanding of continental formation and evolution. Tomographic imaging of increasingly high resolution has been notably successful in underscoring the extent to which continental lithosphere has been shaped and reshaped over geologic time by complexly superimposed tectonic and magmatic events. Western North America is an oft-cited example of massive Phanerozoic overprinting of pre-existing Archean and Proterozoic terranes. Structures in the mantle beneath southern Africa exhibit clear evidence of Proterozoic disruption and overprinting of thick Archean tectosphere. Ancient relict structures including remnant downgoing plates have apparently been observed in a number of localities, most notably in western Canada. Lithospheric structures beneath provinces of very similar age and geologic character (e.g., Archean cratons) have proven to differ significantly by region as shown, for example, in the differing structures beneath the Kaapvaal, Slave, Tanzanian, and Fennoscandian Cratons.

The maturing of passive array seismology into a powerful system for exploring the deep Earth beneath continents should not overshadow the fact that tomographic and direct waveform images are still well below optimum for reliable geologic understanding of deep structure. High-resolution images are certainly attainable with available broadband data and present-day methodologies. As the pool of broadband instrumentation available through PASSCAL, USArray and other organizations around the world continues to increase, the size of regions that can be imaged and the sharpness of the images produced will continue to improve. In this respect, national-scale deployments will result in considerably sharpened ‘uniform’ images on a continent-wide scale, an achievement previously unimagined. Despite the extraordinary increase in the number of instruments available for passive array deployments, particularly in recent years, a primary limitation on 3-D imaging will remain suboptimum seismometer density for years to come. It is for this reason that array deployments for many of the most ambitious broadband experiments are, even today, still configured as linear transects. With current availability of broadband equipment, only linear arrays can achieve sufficient station density (10–20 km) to enable direct unaliased waveform imaging of deep structure. Similarly high station densities for 3-D direct waveform imaging on regional scales generally require more instruments than are currently available to individual researchers or groups of researchers, although closely targeted studies involving 100 or more closely spaced seismographs are increasingly common. Advances in satellite and cellular communications for telemetry of seismic data in real time will substantially reduce the manpower required to service equipment in the field and significantly enhance data recovery and data quality. These advanced communication systems are currently in use for the USArray deployment and have already proven their value in substantially streamlined experiment operation and maintenance.

References

Abers GA, Rossi G, Rondenay S, Peacock S, and Christensen D (2005) Seismic evidence for massive silica addition in some subduction zones. *EOS, Transactions of the American Geophysical Union, Fall Meeting Supplement* 86(52): T41F-05.

- Abers GA, van Keken PE, Kneller EA, Ferris A, and Stachnik JC (2006) The thermal structure of subduction zones constrained by seismic imaging: Implications for slab dehydration and wedge flow. *Earth and Planetary Science Letters* 241: 387–397.
- Aki K, Christoffersson A, and Husebye ES (1976) Three-dimensional seismic structure of the lithosphere under Montana LASA. *Bulletin of the Seismological Society of America* 66(2): 501–524.
- Ammon CJ (1991) The isolation of receiver effects from teleseismic P waveforms. *Bulletin of the Seismological Society of America* 81: 2504–2510.
- ANCORP WorkingGroup (2003) Seismic imaging of a convergent continental margin and plateau in the Central Andes. *Journal of Geophysical Research* 108: (doi:10.1029/2002JB001771).
- Aster R, Beaudoin B, Hole J, Fouch MJ, Fowler, and James DE (2005) IRIS seismology program marks 20 years of discovery. *EOS, Transactions of the American Geophysical Union* 86(17): 171.
- Bank C-G, Bostock MG, Ellis RM, and Cassidy JF (2000) A reconnaissance teleseismic study of the upper mantle and transition zone beneath the Archean Slave craton in NW Canada. *Tectonophysics* 319: 151–166.
- Bastow ID, Stuart GW, Kendall J-M, and Ebinger C (2005) Upper-mantle seismic structure in a region of incipient continental breakup: Northern Ethiopian rift. *Geophysical Journal International* 162: 479–493.
- Betts PG, Giles D, Lister GS, and Frick LR (2002) Evolution of the Australian lithosphere. *Australian Journal of Earth Sciences* 49: 661–695.
- Bostock MG (1997) Anisotropic upper-mantle stratigraphy and architecture of the Slave craton. *Nature* 390: 392–395.
- Bostock MG, Hyndman RD, Rondenay S, and Peacock S (2002) An inverted continental Moho and serpentinization of the forearc mantle. *Nature* 417: 536–538.
- Bostock MG, Langlois A, Al-Khoubbi I, et al. (2005) CANOE: A broadband array in northwestern Canada, *IRIS: Cornerstone Facilities for Seismology and Earth Sciences. II. Accomplishments*, 77.
- Boyd FR and McCallister RH (1976) Densities of fertile and sterile garnet peridotites. *Geophysical Research Letters* 3(9): 509–512.
- Boyd FR and Mertzman SA (eds.) (1987) Composition and structure of the Kaapvaal lithosphere, southern Africa. In: Mysen BO (ed.) *Magmatic Processes: Physicochemical Principles*, pp. 13–24. University Park, PA: Geochemical Society.
- Bruneton M, Pedersen HA, Farra V, et al. (2004) Complex lithospheric structure under the central Baltic Shield from surface wave tomography. *Journal of Geophysical Research* 109: (doi:10.1029/2003JB002947).
- Carlson RW, Grove TL, de Wit MJ, and Gurney JJ (1996) Anatomy of an Archean craton: A program for interdisciplinary studies of the Kaapvaal craton, southern Africa. *EOS, Transactions of the American Geophysical Union* 77: 273–277.
- Carlson RW, Boyd FR, Shirey SB, et al. (2000) Continental growth, preservation and modification in southern Africa. *GSA Today* 10: 1–7.
- Carlson RW, Pearson DG, and James DE (2005) Physical, chemical and chronological characteristics of continental mantle. *Reviews of Geophysics* 43(RG1001): 1–24.
- Carney JN, Aldiss DT, and Lock NP (1994) *Geological Survey Botswana, 37: The Geology of Botswana*, pp. 1–113. Gaborone: Geological Survey Department.
- Chmielowski J, Zandt G, and Haberland C (1999) The central Andean Altiplano-Puna magma body. *Geophysical Research Letters* 26: 783–786.

- Clitheroe G, Gudmundsson O, and Kennett BLN (2000) The crustal thickness of Australia. *Journal of Geophysical Research* 105: 13697–613713.
- Davaille A and Lees JM (2004) Thermal modeling of subducted plates: Tear and hot spot at the Kamchatka corner. *Earth and Planetary Science Letters* 226: 293–304.
- de la Torre T and Sheehan AF (2005) Broadband seismic noise analysis of the Himalayan Nepal Tibet seismic experiment. *Bulletin of the Seismological Society of America* 95: 1202–1208.
- De Wit MJ, Roering C, Hart RJ, et al. (1992) Formation of an Archaean continent. *Nature* 357(6379): 553–562.
- Dueker KG, Yuan H, and Zurek B (2001) Thick proterozoic lithosphere of the Rocky Mountain region. *GSA Today* 11: 4–9.
- Dueker KG and Yuan H (2004) Upper mantle P-wave velocity structure from PASSCAL teleseismic transects across Idaho, Wyoming and Colorado. *Geophysical Research Letters* 31(L08603): 1–4 (doi:10.1029/2004GL019476).
- Engdahl ER, van der Hilst RD, and Berrocal J (1995) Imaging of subducted lithosphere beneath South America. *Geophysical Research Letters* 22: 2317–2320.
- Farrà V and Vinnik LP (2000) Upper mantle stratification by P and S receiver functions. *Geophysical Journal International* 141: 699–712.
- Faul UH and Jackson I (2005) The seismological signature of temperature and grain size variations in the upper mantle. *Earth and Planetary Science Letters* 234: 119–134.
- Ferris A, Abers GA, Christensen D, and Veenstra E (2003) High-resolution image of the subducted Pacific (?) plate beneath central Alaska, 50–150 km depth. *Earth and Planetary Science Letters* 214: 575–588.
- Fischer KM, Wysession ME, Clarke TJ, et al. (1996) The 1995–1996 Missouri to Massachusetts broadband seismometer deployment. *IRIS Newsletter* 15: 6–9.
- Fischer KM (2002) Waning buoyancy in the crustal roots of old mountains. *Nature* 417: 933–936.
- Fishwick S, Kennett BLN, and Reading AM (2005) Contrasts in lithospheric structure within the Australian craton – insights from surface wave tomography. *Earth and Planetary Science Letters* 231: 1630176.
- Forsyth DW and Li A (2005) Array analysis of two-dimensional variations in surface wave phase velocity and azimuthal anisotropy in the presence of multipathing interference. In: Levander A and Nolet G (eds.) *Seismic Earth: Array Analysis of Broadband Seismograms*, pp. 81–98. Washington, DC: American Geophysical Union.
- Fouch MJ, Fischer KM, Parmentier ME, Wysession ME, and Clarke TJ (2000) Shear wave splitting, continental keels, and patterns of mantle flow. *Journal of Geophysical Research* 105: 6255–6275.
- Fouch MJ, Fischer KM, and Wysession ME (2001) Lowermost mantle anisotropy beneath the Pacific: Imaging the source of the Hawaiian plume. *Earth and Planetary Science Letters* 190: 167–180.
- Fouch MJ, James DE, VanDecar JC, and van der Lee S (2004) Mantle seismic structure beneath the Kaapvaal and Zimbabwe cratons. *South African Journal of Geology* 107: 33–44.
- Fouch MJ and Rondenay S (2006) Seismic anisotropy beneath stable continental interiors. *Physics of the Earth and Planetary Interiors* 158: 292–320.
- Freybourger M, Gaherty JB, Jordan TH, and Kaapvaal Seismic Group (2001) Structure of the Kaapvaal craton from surface waves. *Geophysical Research Letters* 28(13): 2489–2492.
- Friederich W (2003) The S-velocity structure of the east Asian mantle from inversion of shear and surface waveforms. *Geophysical Journal International* 153: 88–102.
- Gaherty JB (2004) A surface wave analysis of seismic anisotropy beneath eastern North America. *Geophysical Journal International* 158: 1053–1066.
- Galve A, Sapin M, Hirn A, et al. (2002) Complex images of Moho and variation of V_p/V_s across the Himalaya and south Tibet, from a joint receiver-function and wide-angle reflection approach. *Geophysical Research Letters* 29: 1–4 (doi:10.1029/2002GL015611).
- Gao SS, Silver PG, Liu KH, and KS Group (2002) Mantle discontinuities beneath southern Africa. *Geophysical Research Letters* 29: 1491.
- Gao W, Grand SP, Baldridge WS, et al. (2004) Upper mantle convection beneath the central Rio Grande rift imaged by P and S wave tomography. *Journal of Geophysical Research* 109(B03305): 1–16 (doi:10.1029/2003JB02743).
- Gee LS and Jordan TH (1992) Generalized seismological data functionals. *Geophysical Journal International* 111: 363–390.
- Gilbert HJ and Sheehan AF (2004) Images of crustal variations in the intermountain west. *Journal of Geophysical Research* 109: B03306.
- Godey S, Deschamps F, and Trampert J (2004) Thermal and compositional anomalies beneath the North American continent. *Journal of Geophysical Research* 109(B01308): 1–13 (doi:10.1029/2002JB002263).
- Goes S and van der Lee S (2002) Thermal structure of the North American uppermost mantle inferred from seismic tomography. *Journal of Geophysical Research* 107(B3): 1–13 (doi:10.1029/2000JB000049 (B3, 2050)).
- Graeber FM and Asch G (1999) Three-dimensional models of P wave velocity and P-to-S velocity ratio in the southern central Andes by simultaneous inversion of local earthquake data. *Journal of Geophysical Research* 104: 20237–220256.
- Grand SP (1994) Mantle shear structure beneath the Americas and surrounding oceans. *Journal of Geophysical Research* 99: 11591–11621.
- Griffin WL and O'Reilly SY (1987) The composition of the lower crust and the nature of the continental Moho-xenolith evidence. In: Nixon PH (ed.) *Mantle Xenoliths*, pp. 413–432. Chichester, UK: John Wiley & Sons.
- Gurney JJ and Harte B (1980) Chemical variations in upper mantle nodules from southern African kimberlites. *Philosophical Transactions of the Royal Society of London A297: 273–293.*
- Humphreys E and Dueker KG (1994) Western US. Upper mantle structure. *Journal of Geophysical Research* 99(B5): 9615–9634.
- Humphreys E, Hessler E, Dueker KG, Farmer GL, Erslev E, and Atwater T (2003) How Laramide-age hydration of North American lithosphere by the farallon slab controlled subsequent activity in the Western US. *International Geology Review* 45: 575–595.
- James DE and Assumpção M (1996) Tectonic implications of S-wave anisotropy beneath SE Brazil. *Geophysical Journal International* 126: 1–10.
- James DE and Sacks IS (1999) Cenozoic formation of the Central Andes: A geophysical perspective. In: Skinner BJ (ed.) *Geology and Ore Deposits of the Central Andes*, pp. 1–25. Littleton, CO: Society of Economic Geologists.
- James DE, Fouch MJ, VanDecar JC, van der Lee S, and Kaapvaal Seismic Group (2001) Tectospheric structure beneath southern Africa. *Geophysical Research Letters* 28(13): 2485–2488.
- James DE and Fouch MJ (2002) Formation and evolution of archean cratons: Insights from southern Africa. In: Ebinger C, Fowler CMR, and Hawkesworth CJ (eds.) *The Early Earth: Physical, Chemical and Biological Development*, pp. 1–26. London: Geological Society of London.

- James DE (2003) Imaging crust and upper mantle beneath southern Africa: The southern Africa broadband seismic experiment. *The Leading Edge* 22: 238–249.
- James DE, Niu F, and Rokosky J (2003) Crustal structure of the Kaapvaal craton and its significance for early crustal evolution. *Lithos* 71: 413–429.
- James DE, Boyd FR, Schutt D, Bell DR, and Carlson RW (2004) Xenolith constraints on seismic velocities in the upper mantle beneath southern Africa. *G-cubed* 5(Q01002): 1–32 (doi:10.1029/2003GC000551).
- Jordan TH (1975) The continental tectosphere. *Reviews of Geophysics* 13: 1–12.
- Jordan TH (1978) Composition and structure of the continental tectosphere. *Nature* 274: 544–548.
- Jordan TH (ed.) (1979) Mineralogies, densities and seismic velocities of garnet lherzolites and their geophysical implications. In: Boyd FR and Meyer HOA (eds.) *The Mantle Sample: Inclusions in Kimberlites and other Volcanics*. America, pp. 1–14. Washington, DC: American Geophysical Union.
- Jordan TH (1981) Continents as a chemical boundary layer. (Royal Society, Discussion on the Origin and Evolution of the Earth's Continental Crust, London, England, Feb. 21, 22, 1980.) *Transactions of the Royal Society of London* 301: 359–373.
- Jordan TH (1988) *Journal of Petrology, Special Lithosphere Issue: Structure And Formation of the Continental Tectosphere*, In: Menzies MA and Cox KG (eds.), pp. 11–37. London: Transactions of the Royal Society of London.
- Julia J, Ammon CJ, and Nyblade AA (2005) Evidence for mafic lower crust in Tanzania, east Africa, from joint inversion of receiver functions and Rayleigh wave dispersion velocities. *Geophysical Journal International* 162: 555–569.
- Karlstrom KE and Keller GR (2005) *Geophysical Monograph 15: The Rocky Mountain Region – An Evolving Lithosphere: Tectonics, Geochemistry, and Geophysics*, 441 pp. Washington, DC: American Geophysical Union.
- Karlstrom KE, Whitmeyer SJ, Dueker KG, et al. (2005) Synthesis of results from the CD-ROM experiment: 4-D image of the lithosphere beneath the Rocky Mountains and implications for understanding the evolution of continental lithosphere. In: Karlstrom KE and Kelle GR (eds.) *The Rocky Mountain Region: An Evolving Lithosphere*, pp. 421–434. Washington, DC: American Geophysical Union.
- Kay SM, Coira B, and Viramonte J (1994) Young mafic back-arc volcanic rocks as indicators of continental lithospheric delamination beneath the Argentine Puna plateau, Central Andes. *Journal of Geophysical Research* 99: 24323–24339.
- Kincaid C and Sacks IS (1997) Thermal and dynamical evolution of the upper mantle in subduction zones. *Journal of Geophysical Research* 102: 12295–212315.
- Kind R, Yuan H, Saul J, et al. (2002) Seismic images of crust and upper mantle beneath Tibet: Evidence for Eurasian plate subduction. *Science* 298: 1219–1221.
- Klemperer SL (2006) Crustal flow in Tibet: Geophysical evidence for the physical state of Tibetan lithosphere, and inferred patterns of active flow. In: Law RD, Searle MP, and Godin L (eds.) *Channel Flow, Ductile Extrusion and Exhumation in Continental Collision Zones*, pp. 39–70. London: Geological Society of London.
- Kosarev G, Kind R, Sobolev SV, Yuan X, Hanka W, and Oreshin S (1999) Seismic evidence for a detached Indian lithospheric mantle beneath Tibet. *Science* 283: 1306–1309.
- Kumar P, Yuan X, Kind R, and Kosarev G (2005) The lithosphere–asthenosphere boundary in the Tien Shan-Karakoram region from S receiver functions: Evidence for continental subduction. *Geophysical Research Letters* 32(L07305): 1–4 (doi:10.1029/2004GL022291).
- Larson AM, Snook JA, and James DE (2006) S-wave velocity structure, mantle xenoliths, and the upper mantle beneath the Kaapvaal craton. *Geophysical Journal International* 167: 171–186.
- Last RJ, Nyblade AA, and Langston CA (1997) Crustal structure of the east African plateau from receiver functions and Rayleigh wave phase velocities. *Journal of Geophysical Research* 102: 24469–24483.
- Lastowka LA and Sheehan AF (2001) Seismic evidence for partial lithospheric delamination model of Colorado Plateau uplift. *Geophysical Research Letters* 28(7): 1319–1322.
- Lastowka LA and Sheehan AF (2005) CDROM interstation Pn study along the Rio Grande Rift. In: Karlstrom KE and Keller GR (eds.) *Geophysical Monograph Series 154: The Rocky Mountain Region: An Evolving Lithosphere*, pp. 379–384. Washington, DC: American Geophysical Union.
- Lay T and Wallace TC (1995) *Modern Global Seismology*, 521 pp. San Diego, CA: Academic Press.
- Lee CA (2003) Compositional variation of density and seismic velocities in natural peridotites at STP conditions: Implications for seismic imaging of compositional heterogeneities in the upper mantle. *Journal of Geophysical Research* 102: 2441.
- Lees JM, Brandon M, Park J, Levin V, Ozerov A, and Gordeev E (2000) Kamchatka: Edge of the plate. *IRIS Newsletter* 2000(1): 1–5.
- Lerner-Lam AL and Jordan TH (1987) How thick are the continents?. *Journal of Geophysical Research* 92(13): 14007–014026.
- Levander A (2003) USArray design implications for wavefield imaging in the lithosphere and upper mantle. *The Leading Edge* 22: 250–255.
- Levander A and Nolet G (2005) *Geophysical Monograph 157: Seismic Earth: Array Analysis of Broadband Seismograms*, 252 pp. Washington, DC: American Geophysical Union.
- Levshin AL, Ritzwoller MH, and Shapiro NM (2005) The use of crustal higher modes to constrain crustal structure across central Asia. *Geophysical Journal International* 160: 961–972.
- Li A, Fischer KM, van der Lee S, and Wysession ME (2002) Crust and upper mantle discontinuity structure beneath Eastern North America. *Journal of Geophysical Research* 107: 1–12 (doi:10.1029/2001JB000190).
- Li A, Forsyth DW, and Fischer KM (2005) Rayleigh wave constraints on shear-wave structure and azimuthal anisotropy beneath the Colorado Rocky Mountains. In: Karlstrom KE and Keller GR (eds.) *The Rocky Mountain Region: An Evolving Lithosphere*, pp. 385–401. Washington, DC: American Geophysical Union.
- Maguire P, Ebinger CJ, Stuart GW, et al. (2003) Geophysics project in Ethiopia studies continental breakup. *EOS, Transactions of the American Geophysical Union* 84: 342–343.
- Nabelek MD, Li X-Q, Azevedo S, et al. (1993) A high-resolution image of the Cascadia subduction zone from teleseismic converted phases recorded by a broadband seismic array. *EOS, Transactions of the American Geophysical Union* 74: 431.
- Nguuri T, Gore J, James DE, et al. (2001) Crustal structure beneath southern Africa and its implications for the formation and evolution of the Kaapvaal and Zimbabwe cratons. *Geophysical Research Letters* 28(13): 2501–2504.
- Niu F and James DE (2002) Constraints on the formation and composition of crust beneath the Kaapvaal craton from Moho reverberations. *Earth and Planetary Science Letters* 200: 121–130.

- Nolet G and Vlaar NJ (1981) The NARS project: probing the Earth's interior with a large seismic antenna. *Terra Cognita* 2: 17–25.
- Nolet G, Dost B, and Paulssen H (1986) Intermediate wavelength seismology and the NARS experiment, *Annales Geophysicae. Series B: Terrestrial and Planetary Physics* 4(3): 305–313.
- Nolet G (1987) Seismic wave propagation and seismic tomography. In: Nolet G (ed.) *Seismic Tomography*, pp. 1–23. Dordrecht: The Netherlands: Reidel.
- Nolet G (1990) Partitioned waveform inversion and two-dimensional structure under the network of autonomously recording seismographs. *Journal of Geophysical Research* 95: 8499–8512.
- Nyblade AA and Pollack HN (1993) A global analysis of heat flow from Precambrian terrains: Implications for the thermal structure of Proterozoic and Archean lithosphere. *Journal of Geophysical Research* 98: 12207–12218.
- Nyblade AA (1999) Heat flow and the structure of Precambrian lithosphere. *Lithos* 48: 81–91.
- Owens TJ and Fowler J (2003) New instrumentation drives discovery of the Earth's deep interior. *The Leading Edge* 22: 220–223.
- Panel on Seismological Studies (Thompson GA., Chair), Board on Earth Sciences, Commission on Physical Sciences, and Mathematics, and Resources (1984) *Seismological Studies of the Continental Lithosphere*. Washington, DC: National Academy Press.
- Pavlis G (2003) Imaging the Earth with passive seismic arrays. *The Leading Edge* 22: 224–231.
- Pearson DG, Irvine G, Carlson RW, et al. (2002) The development of lithospheric keels beneath the earliest continents: Time constraints using PGE and Re-Os isotope systematics. In: Fowle CMR, Pearson DG, Irvine GJ, Carlson RW, Kopylova MG, and Ionov DA (eds.) *Early Earth*, pp. 65–90. London: Geological Society (Royal Astronomical Society).
- Pollack HN and Chapman DS (1977) On the regional variation of heat flow, geotherms and lithosphere thickness. *Tectonophysics* 38: 279–296.
- Poupinet G, Frechet J, and Thouvenot F (1989a) Portable short period vertical seismic stations transmitting via telephone or satellite. In: Cassinis R and Nolet G (eds.) *Digital Seismology and Fine Modelling of the Lithosphere*, pp. 9–26. London: Plenum.
- Poupinet G, Pasquier M, Vadell M, and Martel L (1989b) A seismological platform transmitting via METEOSAT. *Bulletin of the Seismological Society of America* 79: 1651–1661.
- Rapine R, Tilmann F, West M, and Ni JF (2003) Crustal structure of northern and southern Tibet from surface wave dispersion analysis. *Journal of Geophysical Research* 108: 1–11 (doi:10.1029/2001JB000445).
- Reading AM, Kennett BLN, and Dentith MC (2003) Seismic structure of the Yilgarn Craton, western Australia. *Australian Journal of Earth Sciences* 50: 427–438.
- Ritsema J, Nyblade AA, Owens TJ, Langston CA, and VanDecar JC (1998) Upper mantle seismic velocity structure beneath Tanzania, east Africa: Implications for the stability of cratonic lithosphere. *Journal of Geophysical Research* 103: 21201–21213.
- Ritsema J and van Heijst H (2000) New seismic model of the upper mantle beneath Africa. *Geology* 28(1): 63–66.
- Roecker S, Thurber C, and McPhee D (2004) Joint inversion of gravity and arrival time data from Parkfield: New constraints on structure and hypocenter locations near the SAFOD drill site. *Geophysical Research Letters* 31: 1–4 (doi:10.1029/2003GL019396).
- Rondenay S, Bostock MG, Hearn TM, White DJ, and Ellis RM (2000) Lithospheric assembly and modification of the SE Canadian Shield: Abitibi-Grenville teleseismic experiment. *Journal of Geophysical Research* 105: 13735–13754.
- Rondenay S, Bostock MG, and Shragge J (2001) Multiparameter two-dimensional inversion of scattered teleseismic body waves. Part 3: Application to the Cascadia 1993 data set. *Journal of Geophysical Research* 106: 30795–30807.
- Rondenay S, Bostock MG, and Fischer KM (2005) Multichannel inversion of scattered teleseismic body waves: Practical considerations and applicability. In: Levander A and Nolet G (eds.) *Geophysical Monograph Series 157: Seismic Earth: Array Analysis of Broadband Seismograms*, pp. 187–203. Washington, DC: American Geophysical Union.
- Rudnick RL (1995) Making continental crust. *Nature* 378: 571–578.
- Rychert CA, Fischer KM, and Rondemay S (2005) Scattered wave imaging of a sharp lithosphere-asthenosphere boundary beneath eastern North America. *Nature* 436: 542–545.
- Sacks IS and Suyehiro K (2003) Leg 186 synthesis: Drilling the forearc of the northeast Japan arc – causes and effects of subduction plate coupling over 20 m.y. *Proceedings of the Ocean Drilling Program, Scientific Results* 186: 1–14.
- Saltzer RL (2002) Upper mantle structure of the Kaapvaal craton from surface wave analysis – a second look. *Geophysical Research Letters* 29(6): 1–4 (doi:10.1029/2001GL013702).
- Sandoval S, Kissling E, and Ansorge J (2003) High-resolution body wave tomography beneath the SVEKALAPKO array. Part I: A priori 3D crustal model and associated traveltimes effects on teleseismic wavefronts. *Geophysical Journal International* 153: 75–87.
- Sandoval S, Kissling E, and Ansorge J (2004) High-resolution body wave tomography beneath the SVEKALAPKO array. Part II: Anomalous upper mantle structure beneath central Baltic Shield. *Geophysical Journal International* 157: 200–214.
- Schimmel M, Assumpcao M, and VanDecar JC (2003) Seismic velocity anomalies beneath SE Brazil from P and S wave travel time inversions. *Journal of Geophysical Research* 108(B4): 1–15 (doi:10.1029/2001JB000187 (B4,2191)).
- Schmitz M, Heinsohn W, and Schilling F (1997) Seismic, gravity and petrological indications or partial melting beneath the thickened central Andean crust 21° – 23° S. *Tectonophysics* 270: 313–326.
- Schulte-Pelkum V, Monsalve G, Sheehan AF, et al. (2005) Imaging the Indian subcontinent beneath the Himalaya. *Nature* 435: 1222–1225.
- Schutt D and Humphreys E (2004) P and S wave velocity and V_p/V_s in the wake of the Yellowstone hot spot. *Journal of Geophysical Research* 109(B01305): 1–14 (doi:10.1029/2003JB002442 (B01305)).
- Shapiro NM, Campillo M, Stehly L, and Ritzwoller MH (2005) High-resolution surface-wave tomography from ambient seismic noise. *Science* 307: 1615–1618.
- Sheehan AF, Shearer P, Gilbert HJ, and Dueker KG (2000) Seismic migration processing of P-SV converted phases for mantle discontinuity structure beneath the Snake River Plain, Western United States. *Journal of Geophysical Research* 105(B8): 19055–19065.
- Shirey SB, Carlson RW, Richardson SH, et al. (2001) Emplacement of eclogite components into the lithospheric mantle during craton formation. *Geophysical Research Letters* 28(13): 2509–2512.
- Silver PG and Chan WW (1988) Implications for continental structure and evolution from seismic anisotropy. *Nature* 335: 34–39.
- Silver PG (1996) Seismic anisotropy beneath the continents: Probing the depths of geology. *Annual Reviews of Earth and Planetary Sciences* 24: 385–432.

- Simons FJ, Zielhuis A, and van der Hilst RD (1999) The deep structure of the Australian continent from surface wave tomography. *Lithos* 48: 17–43.
- Smith RB, Nagy WC, Julander KA, Viveiros JJ, Barker CA, and Gants DG (1989) Geophysical and tectonic framework of the eastern Basin and Range–Colorado Plateau–Rocky Mountain transition. In: Pakiser LC and Mooney WD (eds.) *Geophysical Framework of the Continental United States, ch. 12*, pp. 205–233. Boulder, CO: Geological Society of America.
- Snelson CM, Keller GR, Miller KC, Rumpel H-M, and Prodehl C (2005) Regional crustal structure derived from the CD-ROM 99 seismic refraction/wide-angle reflection profile: The lower crust and upper mantle. In: Karlstrom KE and Keller GR (eds.) *Geophysical Monograph Series 154: The Rocky Mountain Region: An Evolving Lithosphere*, pp. 271–291. Washington, DC: American Geophysical Union.
- Snoke JA and James DE (1997) Lithospheric structure of the Chaco and Parana Basins of South America from surface-wave inversion. *Journal of Geophysical Research* 102: 2939–2951.
- Stachnik JC, Abers GA, and Christensen D (2004) Seismic attenuation and mantle wedge temperatures in the Alaska subduction zone. *Journal of Geophysical Research* 109(B10304): (doi:10.1029/2004JB003018).
- Thurber C, Roecker S, Zhang H, Baher S, and Ellsworth W (2004) Fine-scale structure of the San Andreas fault zone and location of the SAFOD target earthquakes. *Geophysical Research Letters* 31: (doi:10.1029/2003GL019398).
- van der Hilst RD, Kennett BLN, Christie D, and Grant J (1994) Project SKIPPY explores the lithosphere and mantle beneath Australia. *EOS, Transactions of the American Geophysical Union* 75: 177–181.
- Van der Lee S and Nolet G (1997) Upper mantle S-velocity structure of North America. *Journal of Geophysical Research* 102: 22815–822838.
- van der Lee S, James DE, and Silver PG (2001a) Upper mantle S velocity structure of Central and Western South America. *Journal of Geophysical Research* 106(12): 30821–30834.
- van der Lee S, VanDecar JC, Fouch MJ, and James DE (2001b) Joint inversion of different seismic data types for upper mantle structure beneath southern Africa. *EOS, Transactions of the American Geophysical Union, Fall Meeting Supplement* 82(47): F826.
- van der Lee S (2002) High-resolution estimates of lithospheric thickness from Missouri to Massachusetts, USA. *Earth and Planetary Science Letters* 203(1): 15–23.
- VanDecar JC and Crosson RS (1990) Determination of teleseismic relative phase arrival times using multi-channel cross-correlation and least squares. *Bulletin of the Seismological Society of America* 80(1): 150–159.
- VanDecar JC (1991) Upper-mantle structure of the Cascadia subduction zone from non-linear teleseismic travel-time inversion, Ph.D. Thesis, University of Washington, Seattle, WA.
- VanDecar JC, James DE, and Assumpção M (1995) Seismic evidence for a fossil mantle plume beneath South America and implications for plate driving forces. *Nature* 378(6552): 25–31.
- VanDecar JC, Russo RM, James DE, Ambek WB, and Franke M (2003) Aseismic continuation of the Lesser Antilles slab beneath continental South America. *Journal of Geophysical Research* 108: 1–12 (doi:10.1029/2001JB000884).
- Vinnik LP, Kosarev G, and Makeeva L (1984) Lithosphere anisotropy from the observation of SKS and SKKS waves. *Doklady Akademii Nauk USSR* 278: 1335–1339.
- Wagner LS, Beck SL, and Zandt G (2005) Upper mantle structure in the south central Chilean subduction zone (30 to 36°S). *Journal of Geophysical Research* 110: (doi:10.1029/2004JB0003238).
- Watson T (2005) *The Upper Mantle Structure Beneath the Transantarctic Mountains and East Antarctic Craton using Body-Wave Tomography*, 91 pp. University Park, PA: Pennsylvania State University.
- Webb SJ (in preparation) The use of potential field and seismological data to analyze the structure of the lithosphere beneath southern Africa, PhD thesis, University of the Witwatersrand, Johannesburg.
- Weeraratne DS, Forsyth DW, and Fischer KM (2003) Evidence for an upper mantle plume beneath the Tanzanian craton from Rayleigh wave tomography. *Journal of Geophysical Research* 108: 1–17 (doi:10.1029/2002JB002273).
- West M, Gao W, and Grand SP (2004a) A simple approach to the joint inversion of seismic body and surface waves applied to the Southwest US. *Geophysical Research Letters* 31(L15615): 020274 (doi:15610.11029/12004GL020373).
- West M, Ni JF, Baldridge WS, et al. (2004b) Crust and upper mantle shear wave structure of the Southwest United States: Implications for rifting and support for high elevation. *Journal of Geophysical Research* 109(B03309): 1–16 (doi:10.1029/2003JB002575).
- Wielandt E and Streckeisen G (1982) The leaf-spring seismometer; design and performance. *Bulletin of the Seismological Society of America* 72: 2349–2367.
- Wilson D and Aster R (2003) Imaging crust and upper mantle seismic structure in the Southwestern United States using teleseismic receiver functions. *The Leading Edge* 22(3): 232–237.
- Wilson D and Aster R (2005) Seismic imaging of the crust and upper mantle using regularized joint receiver functions, frequency – wave number filtering, and multimode Kirchhoff migration. *Journal of Geophysical Research* 110(B05305): 1–12 (doi:10.1029/2004JB003430).
- Wilson D, Aster R, Ni JF, et al. (2005a) Imaging the seismic structure of the crust and upper mantle beneath the Great Plains, Rio Grande Rift, and Colorado Plateau using receiver functions. *Journal of Geophysical Research* 110(B05306): 1–14 (doi:10.1029/2004JB003492).
- Wilson D, Aster R, West M, et al. (2005b) Lithospheric structure of the Rio Grande rift. *Nature* 433: 851–855.
- Wittlinger G, Farra V, and Vergne J (2004) Lithospheric and upper mantle stratifications beneath Tibet. *Geophysical Research Letters* 31(L19615): 1–4 (doi:10.1029/2004GL020955).
- Yuan H and Dueker KG (2005a) Teleseismic P-wave tomogram of the Yellowstone plume. *Geophysical Research Letters* 32(L07304): 1–4 (doi: 10.1029/2004GL022056).
- Yuan H and Dueker KG (2005b) Upper mantle tomographic V_p and V_s images of the middle Rocky Mountains in Wyoming, Colorado, and New Mexico: Evidence for a thick heterogeneous chemical lithosphere. In: Karlstrom KE and Keller GR (eds.) *Geophysical Monograph 154: The Rocky Mountain Region: An Evolving Lithosphere*, pp. 329–345. Washington, DC: American Geophysical Union.
- Yuan X, Sobolev NV, Kind R, et al. (2000) Subduction and collision processes in the Central Andes constrained by converted seismic phases. *Nature* 408: 958–961.
- Zandt G, Beck SL, Ruppert C, et al. (1996) Anomalous crust of the Bolivian Altiplano, Central Andes: Constraints from broadband regional seismic waveforms. *Geophysical Research Letters* 23: 1159–1162.
- Zandt G, Gilbert HJ, Owens TJ, Ducea M, Saleeby J, and Jones CH (2004) Active foundering of a continental arc root beneath the Southern Sierra Nevada in California. *Nature* 431: 41–46.
- Zhao M, Langston CA, Nyblade AA, and Owens TJ (1999) Upper mantle velocity structure beneath southern Africa from modeling regional seismic data. *Journal of Geophysical Research* 104: 4783–4794.

- Zhao W, Mechle J, Brown LD, et al. (2001) Crustal structure of central Tibet as derived from project INDEPTH wide-angle seismic data. *Geophysical Journal International* 145: 486–498.
- Zielhuis A and van der Hilst RD (1996) Upper-mantle shear velocity beneath eastern Australia from inversion of waveforms from SKIPPY portable arrays. *Geophysical Journal International* 127: 1–16.

Relevant Websites

www.EuroArray.org – 4-D Europe, Assembly of a Continent.

- www.earthscope.org – EarthScope National Meeting Registration.
- www.iris.edu – Incorporated Research Institutions for Seismology.
- www.norsar.no – Independent Research Foundation Specializing in Commercial Software Solutions and Research Activities within Applied Geophysics and Seismology.
- www.PASSCAL.IRIS.edu – PASSCAL (IRIS) Instrument Center, Socorro, New Mexico.

1.15 Crust and Lithospheric Structure – Long Range Controlled Source Seismic Experiments in Europe

A. Guterch, Polish Academy of Sciences, Warsaw, Poland

M. Grad, University of Warsaw, Warsaw, Poland

G. R. Keller, University of Oklahoma, Norman, OK, USA

© 2007 Elsevier B.V. All rights reserved.

1.15.1	Introduction – Regional Geologic/Tectonic Setting of the Central Europe	533
1.15.2	A New Generation of Long-Range Seismic Experiments	535
1.15.3	Characteristics of the Seismic Wave Fields along Profiles for Different Tectonic Provinces (Terranes)	537
1.15.4	Examples of 2-D and 3-D Modeling of the Earth's Crust and Lower Lithosphere	541
1.15.4.1	POLONaise'97 Crustal and Lithospheric Models (Profiles P4 and P1)	542
1.15.4.2	SUDETES 2003 Crustal Model (Profile S02)	545
1.15.4.3	CELEBRATION 2000 Crustal Models CEL05 and CEL01	546
1.15.4.4	Example of 3-D Tomographic Modeling	549
1.15.5	Geotectonic Models of the TESZ and the Transition from the EEC to the Carpathians and the Pannonian Basin	550
1.15.5.1	POLONaise'97 Area	552
1.15.5.2	CELEBRATION 2000 Area	553
1.15.6	Summary	555
	References	556

1.15.1 Introduction – Regional Geologic/Tectonic Setting of the Central Europe

The complex tectonic history of Central Europe (**Figure 1**) reflects the break-up of a Neoproterozoic supercontinent(s) (Rodinia/Pannotia) (e.g., [Dalziel, 1997](#)) to form the fragment Baltica and the subsequent growth of continental Europe beginning with the Caledonian orogeny. Caledonian and younger Variscan orogenesis involved accretion of Laurentian and Gondwanan terranes to the rifted margin of Baltica (East European craton, EEC) during the Paleozoic (e.g., [Pharaoh, 1999](#)). From central Poland northward, the region also experienced volcanic activity during the Permian and tectonic inversion during the Alpine orogeny, which in the south continues today. The Trans-European Suture Zone (TESZ) is a term used to refer to the suite of sutures and terranes that formed adjacent to the rifted margin of Baltica (e.g., [Berthelsen, 1992a, 1992b, 1998; Ziegler, 1990; Pharaoh, 1999](#)), and these features extend from the British Isles to the Black Sea region (**Figure 1**). Understanding the structure and evolution of the TESZ region is one of the key tectonic challenges in

Europe north of the Alps. The tectonic evolution of this region shares many attributes with the Appalachian/Ouachita orogen ([Keller and Hatcher, 1999; Golonka et al., 2003a](#)) and is certainly of global importance to studies in terrane tectonics and continental evolution. The TESZ is far more complex than a single suture but in a broad sense is the boundary between the accreted terranes and Baltica. The TESZ includes the Teisseyre–Tornquist Zone (TTZ), which has several definitions. Here, we will use the term TTZ to refer to a structural zone associated with the southwestern edge of the EEC.

The Bohemian massif is a large structural block (**Figure 1**) that is mostly located in the Czech Republic and is a large, complex terrane whose origin can be traced to northern Gondwana (Africa). In southern Poland, several smaller structural blocks such as the Małopolska massif (MM; **Figure 1**) are located adjacent to Baltica and were probably transported laterally along it, similar to Cenozoic movement of terranes along the western margin of North America.

The younger Eastern Alps, Carpathian Mountains arc, and Pannonian back-arc basin form interrelated components of the Mediterranean arc-basin complex (**Figure 1**). These features are the result of intricate

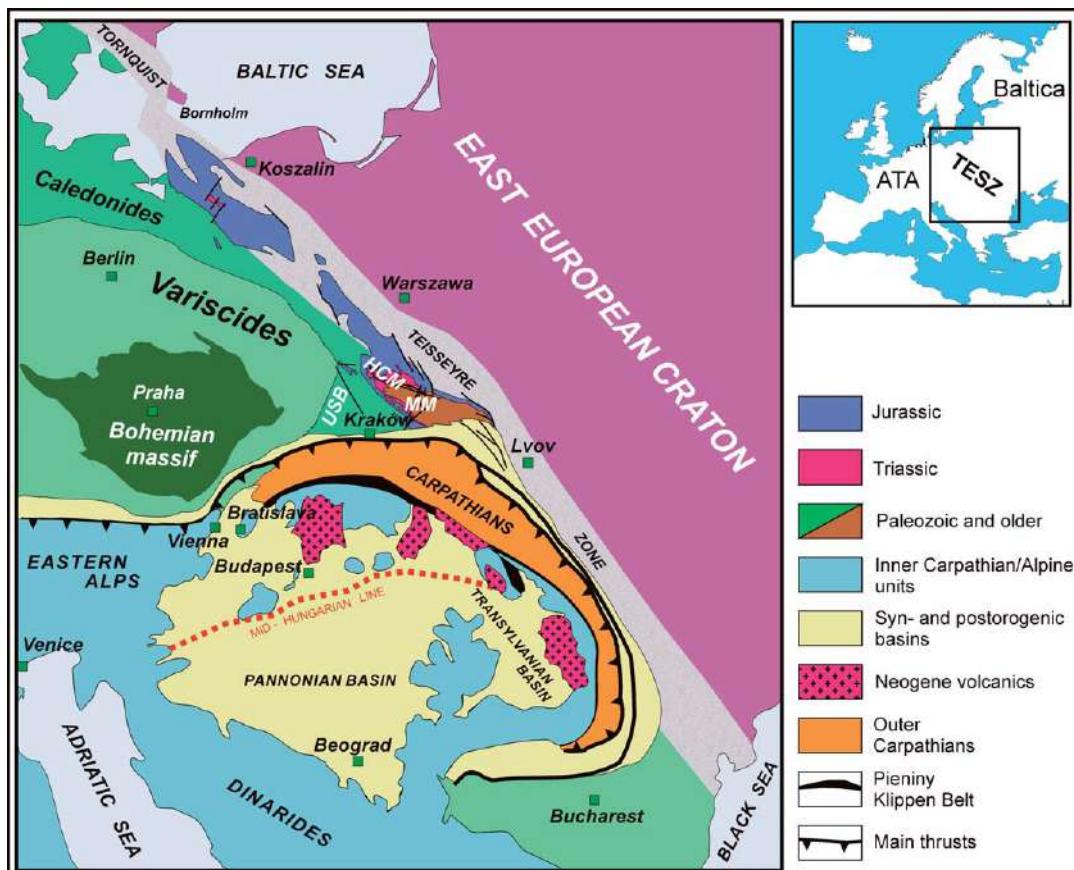


Figure 1 Simplified tectonic map of the Central Europe. ATA, Armorican Terrane Assemblage; HCM, Holy Cross Mountains; MM, Małopolska massif; TESZ, Trans-European Suture Zone; USB, Upper Silesian block.

Mesozoic/Cenozoic plate interactions in the Mediterranean region as the Tethys Ocean closed during convergence of Europe and Afro-Arabia. During the Cenozoic, complex interactions among small plates caused the Carpathian arc to evolve into its strongly arcuate shape. These plate interactions have been interpreted to involve subduction of oceanic areas and produced considerable Neogene volcanism. Back-arc extension was the dominant process that formed the Pannonian basin that contains up to 8 km of Neogene strata in its subbasins (e.g., Posgay *et al.*, 1995). This region is still tectonically active as evidenced by seismicity that extends to depths of ~200 km in the Vrancea region north of Bucharest in Romania (Figure 1).

In addition to being a major crustal-scale feature, the TESZ appears to be a deep-seated boundary because tomographic analysis of shear-wave velocity structure of the mantle under Europe shows that the

TESZ separates regions with high S-wave velocities beneath the EEC from low-velocity regions under the younger terranes (Zielhuis and Nolet, 1994). Another indication of the deep-seated nature of the TESZ was obtained from observations of several hundred earthquakes and explosions located in Europe. To explain the observed blockage of energy from regional seismic events by the TESZ region, the structural anomaly between eastern and western Europe must reach at least down to a depth of ~200 km (Schweitzer, 1995).

Early deep seismic sounding (DSS) studies in Central Europe also showed a large contrast in the crustal structure between the accreted terranes, the TESZ, and the EEC (e.g., Guterch *et al.*, 1976, 1984, 1986, 1992, 1994; Guggisberg *et al.*, 1991; Ansorge *et al.*, 1992).

Many nonseismic studies have been undertaken in the TESZ region. For example, heat flow measurements indicate a major change in thermal regime

across Central Europe (Čermák and Bodri, 1998). Using over 3200 heat flow measurements, Čermák and Bodri (1998) explained a number of prominent heat flow anomalies (e.g., Pannonian basin, French massif central, the Alps) as products of the deep-seated lithospheric processes. In the area of Central Europe, the TESZ separates ‘cold’ lithospheric of the EEC with low heat flow $30\text{--}40 \text{ mW m}^{-2}$ from ‘hot’ lithosphere with higher heat flow of $40\text{--}70 \text{ mW m}^{-2}$ in the Paleozoic terranes and Carpathians, and even higher values ($80\text{--}110 \text{ mW m}^{-2}$) are found in Pannonian basin (Čermák *et al.*, 1989; Čermák and Bodri, 1998; Zeyen *et al.*, 2002; Majorowicz *et al.*, 2003). The characteristic Moho temperature for the EEC has been estimated to be 500°C (Majorowicz *et al.*, 2003) and $590\text{--}620^\circ\text{C}$ (Čermák *et al.*, 1989). In the TESZ region, the Moho temperature increases to $650\text{--}750^\circ\text{C}$, and beneath the Carpathians and Pannonian basin it even increases to $800\text{--}900^\circ\text{C}$ (Dövényi *et al.*, 1983; Čermák *et al.*, 1989; Majorowicz *et al.*, 2003).

Gravity and magnetic anomalies indicate significant variations in lithospheric structure (e.g., Królikowski and Petecki, 1995; Wybraniec *et al.*, 1998; Petecki *et al.*, 2003). Bouguer anomalies in the area of the EEC are relatively homogeneous ($0 \pm 20 \text{ mGal}$) and decrease in the area of the EEC margin down to about -40 mGal . The anomaly field becomes more complex in this region with a large high in the Holy Cross Mountains area (Figure 1) and lower values to the northwest along the EEC margin. In the Carpathians, Bouguer anomalies reach values of about -80 mGal , and increase into the Pannonian basin ($20\text{--}30 \text{ mGal}$) where the crust thins.

Magnetic anomalies along the cratonic part of profiles contain many short-wavelength variations from -1500 to $+1500 \text{ nT}$ that correlate well with tectonic features and intrusions in the Precambrian basement. Further to the southwest in the TESZ, the Carpathian foredeep and Carpathians, magnetic anomalies are subdued ($\pm 100 \text{ nT}$), presumably due to the deeply buried magnetic basement. Except in areas of Tertiary volcanism, magnetic anomalies are also subdued in the Pannonian basin because of the thick cover of sedimentary rocks.

1.15.2 A New Generation of Long-Range Seismic Experiments

From 1997 to 2003, Central Europe was covered by an unprecedented network of seismic refraction experiments to investigate its complex lithospheric structure

(Guterch *et al.*, 1999, 2003a, 2003b; Brückl *et al.*, 2003; Grad *et al.*, 2003b). These experiments (POLONAISE'97, CELEBRATION 2000, ALP 2002, and SUDETES 2003) were only possible due to a massive international cooperative effort. Acronyms of these experiments are: POLONAISE'97 – Polish Lithospheric Onsets – An International Seismic Experiment, 1997; CELEBRATION 2000 – Central European Lithospheric Experiment Based on Refraction, 2000; ALP 2002 – Eastern Alps and adjacent regions, 2002; SUDETES 2003 – Sudetes Mountains and adjacent regions, 2003. The total length of all the profiles recorded is $\sim 20\,000 \text{ km}$, and, during these four experiments, a total of 295 large explosions provided the seismic sources. The number of seismic stations used in these experiments ranged from 640 in the POLONAISE'97 to 1230 in CELEBRATION 2000. Distances between shot points were usually $\sim 50 \text{ km}$. As a result of these experiments, a network of seismic refraction profiles (Figure 2) now extends from EEC (east of Baltic Sea), along and across the TESZ region of Poland and the Bohemian massif, through the Carpathians, Sudetes, and Eastern Alps, to the Pannonian basin, the Dinarides, and Adriatic Sea (Guterch *et al.*, 1998, 1999, 2001, 2003a, 2003b, 2004; Brückl *et al.*, 2003; Grad *et al.*, 2003b). The high-quality seismic data obtained reveal a variety of both the P-and S-wave phases. The main results, as of July 2006, were published in Guterch *et al.* (1999, 2004), Grad *et al.* (1999, 2002a, 2002b, 2003a, 2005, 2006), Jensen *et al.* (1999, 2002), Środa and POLONAISE P3 Working Group (1999b), Środa *et al.* (2002, 2006), Wilde-Piórko *et al.* (1999), Krysiński *et al.* (2000), Bayer *et al.* (2002), Czuba *et al.* (2002), Janik *et al.* (2002, 2005), Winchester and the PACE TMR Network Team (2002), Růžek *et al.* (2003), Hrubcová *et al.* (2005), Malinowski *et al.* (2005), and Majdański *et al.* (2006).

These experiments also relate to German KTB deep drilling project, the BOHEMA seismic tomography experiment, and numerous Czech–German projects on the geodynamics of the West Bohemia/Vogtland seismically active region. The BOHEMA teleseismic experiment in particular is providing exciting new insights into the structure and evolution of the lithosphere in this region (Plomerová *et al.*, 2003).

The principal specific scientific goals of the POLONAISE'97, CELEBRATION 2000, ALP 2002, and SUDETES 2003 new experiments were to:

- investigate the deep structure of the southwestern margin of the EEC (southern Baltica) and its relationships to younger terranes;

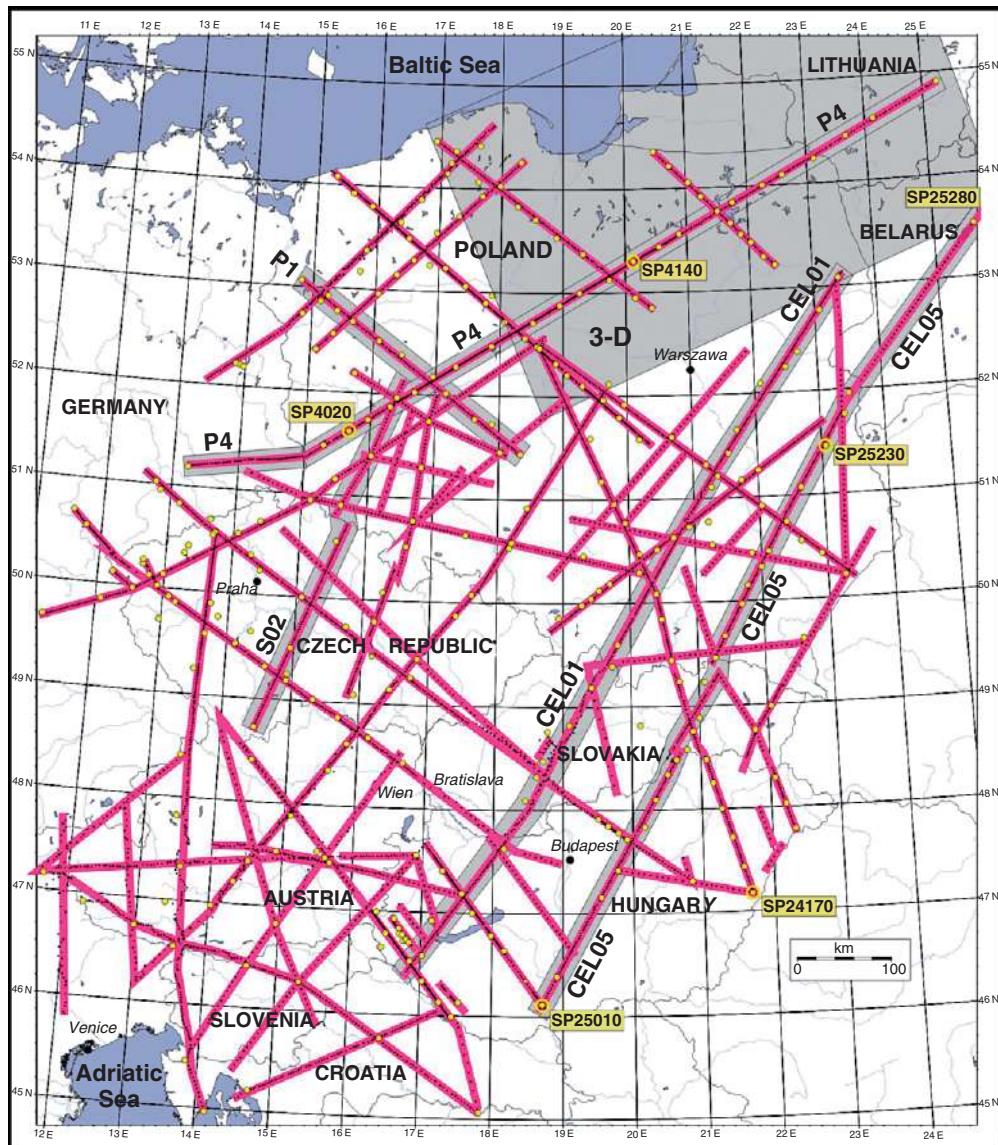


Figure 2 Location of seismic profiles recorded in Central Europe during POLONNAISE'97, CELEBRATION 2000, ALP 2002, and SUDETES 2003 experiments. Pink lines show the seismic profiles whose total length is c. 20 000 km, with c. 7000 seismic receiver positions (small black dots). Yellow dots show 295 big shot locations. Gray lines show position of POLONNAISE'97 profiles P1 and P4, CELEBRATION 2000 profiles CEL01 and CEL05, and SUDETES 2003 profile S02 for which models are shown in Figures 6, 7, 8, 9, and 10. The gray area shows the area of 3-D investigations presented in Figure 12. Yellow circles show location of shot points SP25010, SP4020, SP24170, SP25230, and SP4140, and SP25280 for which record sections are shown in Figures 3, 4, and 5.

- delineate the major terranes and crustal blocks in the TESZ region (e.g., Upper Silesian block, and blocks exposed in the Holy Cross Mountains);
- investigate the origin and structural framework of the Pannonian basin and its subbasins;
- investigate the nature and extent of thrust faulting along the northern front of the Carpathians;
- investigate the structure and evolution of the Eastern Alps and their relationships with adjacent features;
- investigate the structural relationships between the structural elements of the Bohemian massif and adjacent features;
- construct a three-dimensional (3-D) model of the lithospheric structure in the area;

- evaluate the implications of the Earth models derived for natural resources and earthquake hazards; and
- evaluate and develop geodynamic models for the tectonic evolution of the region.

When all the individual results are completed and integrated, these experiments will provide an unprecedented 3-D image of the evolution and assembly of a continent.

1.15.3 Characteristics of the Seismic Wave Fields along Profiles for Different Tectonic Provinces (Terranes)

CELEBRATION 2000 profile CEL05 and POLONAISE'97 profile P4 are most representative for characteristic of seismic wave fields in Central Europe because of their length. The 1420 km long profile CEL05 is the longest recorded in the CELEBRATION 2000 experiment (Figure 2). It begins in Hungary, crosses the Slovak Republic, Poland, and Belarus, and ends in northwestern Russia. The southwestern part of the profile (0–200 km) lies in the Pannonian basin. The profile then crosses a tectonically complex zone that includes the Carpathians and their foredeep (200–500 km) and then it crosses the TESZ (500–700 km), including the MM, Lublin trough, and TTZ (Figure 1). The northeastern part of the profile (700–1420 km) crosses the EEC (Figures 1 and 2). Data from 26 explosions made along this profile were collected using over 360 modern seismic recorders, with a nominal station spacing of 2.8 km in Hungary, Slovakia, and Poland, and 4.6 km in Belarus and Russia. More details about the layout of the experiment are provided in Guterch *et al.* (2001, 2003b).

The P-wave field on the CEL05 record sections has high signal-to-noise ratio, particularly for the southern (Pannonian basin) and the northern cratonic parts of the profile. Identification and correlation of seismic phases was done manually on a computer screen using software that allows flexible use of scaling, filtering, and reduction velocity (Zelt, 1994; Šroda, 1999a). Clear arrivals of refracted and reflected waves from sedimentary layers, the crystalline crust and the upper mantle were typically observed up to offsets of 200–300 km and for some shots, even over 900 km. Examples of record sections

for profiles CEL05, CEL04, and P4 are shown in Figures 3–5.

General observations about the data are that waves from sedimentary cover (P_{sed}) are observed as first arrivals in the vicinity of shot points up to offsets of only 1 km on the EEC while they are observed to offsets of 10–20 km in the TESZ region and even \sim 30 km in the Carpathians. Their apparent velocities range from 2.5 to 5.5 km s^{-1} . After these arrivals, the P_g phase that travels in the crystalline basement (upper crust) is recorded to highly variable offsets of 1–250 km. The slowest arrivals occur to the southwest toward the Carpathian foredeep and Carpathians, and at offsets of 100–150 km, they are \sim 2 s late compared to other directions. As discussed below, the highly variable crustal structure along profile CEL05 results in mantle arrivals also becoming first arrivals at highly variable offsets.

In the Pannonian basin region, the seismic wave field is characterized by strong P_g arrivals to offsets of \sim 50 km. For offsets out to 150 km, the amplitude of the P_g wave is small relative to the dominant reflection from the Moho (P_mP). Reflections from the top of the middle crust (P_c) are well correlated and observed throughout the whole ‘Pannonian’ part of the profile. Reflections from the top of the lower crust (P_{lc}) are well correlated and observed throughout the whole ‘cratonic’ part of the profile. Refractions from the middle and lower crust are correlated as secondary arrivals in the seismic sections, primarily at long offsets where refractions merge with wide-angle reflections to form the overcritical phases P_{crustal} and S_{crustal} , which in some cases are well recorded to offsets of \sim 300 km. These phases are important for determining the velocities in the middle and lower crust, particularly for the Pannonian crust where the velocities of these layers are 6.2 – 6.6 km s^{-1} . In the ‘Pannonian’ region, the phase diving in the uppermost mantle (P_n) has relatively low amplitudes and low apparent velocities (7.9 – 8.0 km s^{-1}). The intercept time for P_n is only \sim 6 s (for reduction velocity 8 km s^{-1}), and its crossover distance with the crustal (P_g) arrivals is only 100–120 km. These observations clearly show that the Moho in the Pannonian basin is shallow. Starting at offsets of \sim 200 km, arrivals from the mantle lithosphere (P^I and P^{II}) were observed for some shots.

The wavefield observed in the Carpathian region is complex as is the known geologic structure. First arrivals (P_g) are distinct up to \sim 100 km offset and are characterized by large variations in apparent velocity and amplitude. Mid-crustal reflections (P_c) are

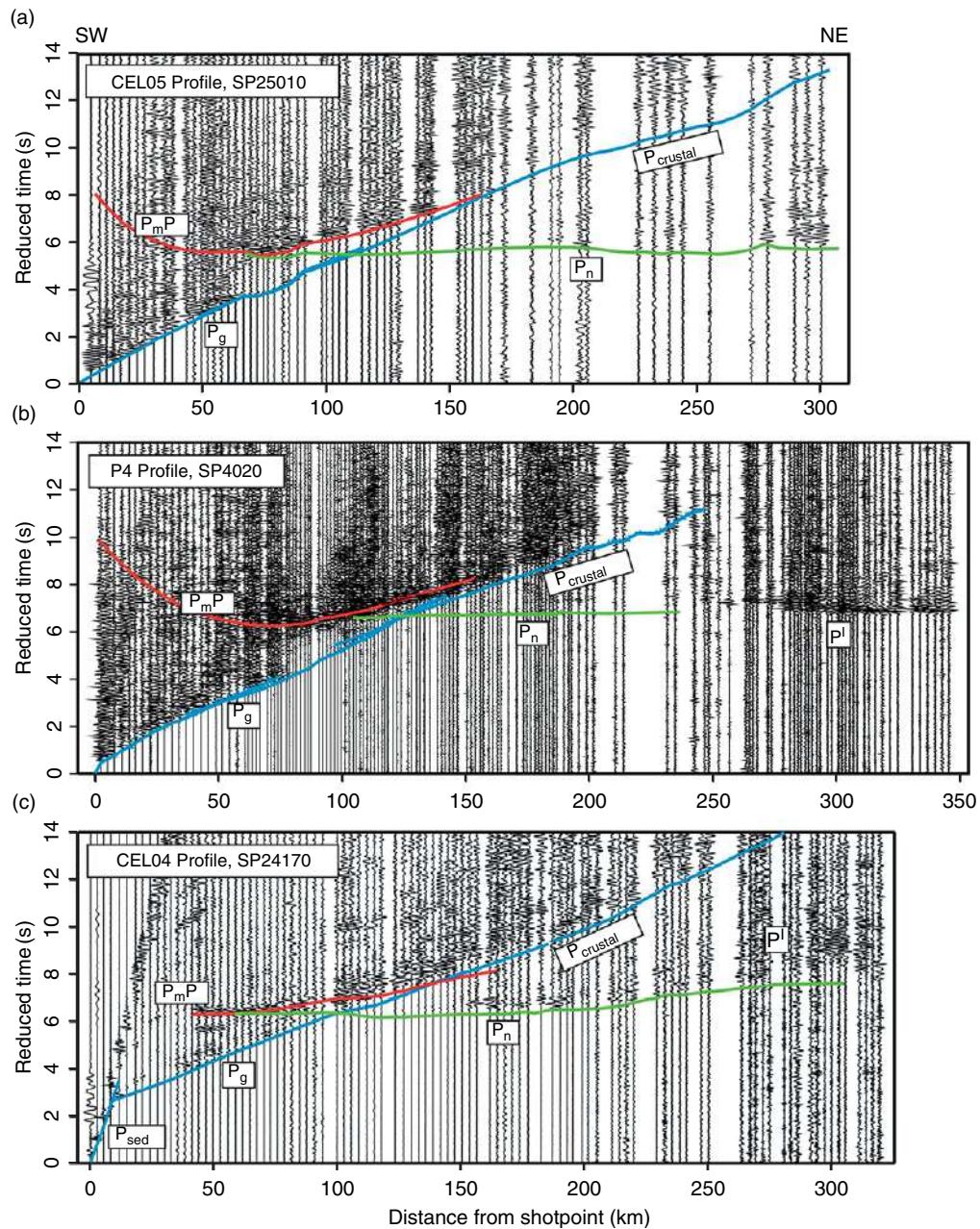


Figure 3 (a–c) Examples of P wave record sections for seismic profiles in the area of Central Europe (for shot points' location, see [Figure 2](#)). P_g , P_{crustal} , P_mP , and P_n – crustal and Moho phases.

usually recorded at short distance intervals (20–50 km) and are also characterized by variations in apparent velocity and amplitude. P_n arrivals were only fragmentarily recorded in the Carpathians. This characteristic attribute of the wavefield testifies to the complex structure of the crust–upper-mantle transition in this region. The observed wavefield is similar in the adjacent Carpathian foredeep to the

northeast. However, waves with low apparent velocities ($4.0\text{--}5.0 \text{ km s}^{-1}$) are observed up to 30–50 km offsets, and midcrustal phases are even more complex.

In the TESZ area, the character of the wavefield is more uniform, and the traveltimes of both refracted first arrivals (P_g) and waves from the Moho and uppermost mantle (P_mP and P_n) show clear evidence that the crystalline basement and crust–upper-mantle

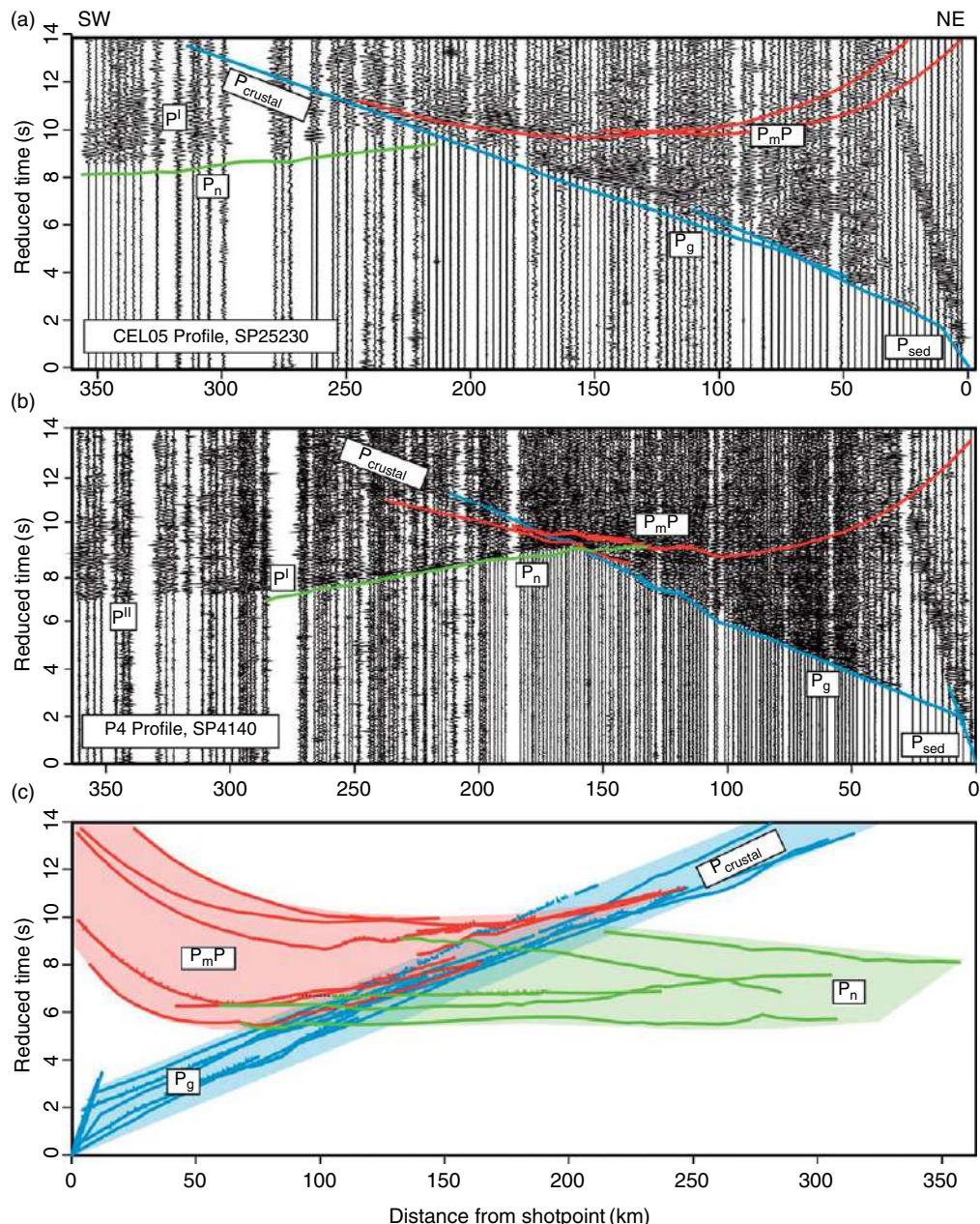


Figure 4 Examples of P wave record sections ((a), (b); for location see [Figure 2](#)) and comparison of traveltimes (c); note the large variation of the arrival times (reaching 3–6 s) of the P_{g} , P_{crustal} , P_{mP} , and P_{n} phases, which indicate large differences in the crustal and uppermost mantle structure across the region.

boundary are deep. Compared to the Pannonian area, the P_{n} wave intercept time is much later (reduced time 8.0–8.5 s for reduction velocity 8 km s^{-1}). The cross-over distance between crustal (P_{g}) and mantle refractions (P_{n}) is also much larger. Waves generated in this region are well recorded, particularly toward the northeast in the EEC.

The P-wave field recorded on the EEC is uniform with high signal-to-noise ratios. Due to the thin sedimentary cover, the P_{sed} phase produces first arrivals only to offsets of 1–10 km from the shot point. The P_{g} phase has a uniform character and is observed in the first arrivals up to ~ 200 km offsets, with apparent velocities increasing with distance from 6.0–6.2 to

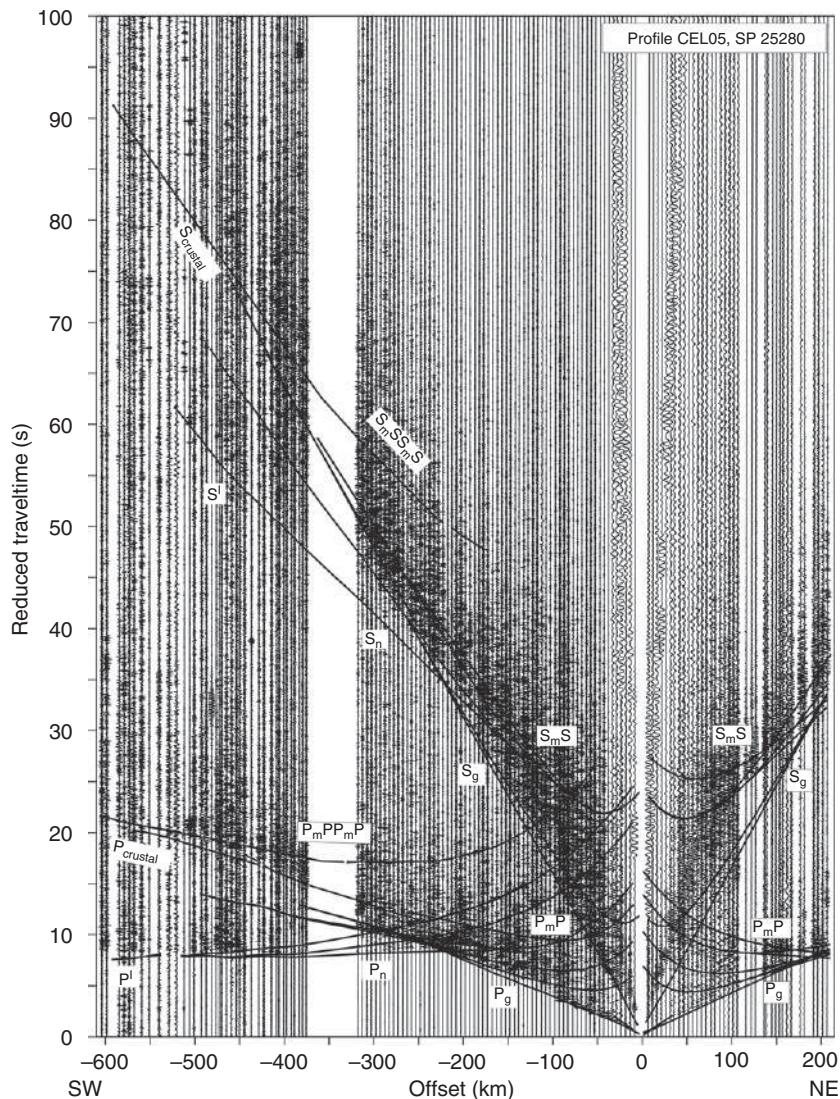


Figure 5 Example of P and S wave record section for CELEBRATION 2000 profile CEL05 (Figure 2). Amplitude normalized seismic record sections for SP25280 showing the full wave field, including both P and S waves with theoretical traveltimes calculated for the model of the crust derived using the SEIS83 ray-tracing technique. Note the P_mPP_mP and S_mSS_mS waves that are reflected twice from the Moho discontinuity and free surface, and high-quality lower lithosphere phases recorded to long offsets. Reduction velocity = 8 km s^{-1} .

6.6–7.0 km s^{-1} . These crustal waves continue to overcritical distances of up to 250–350 km. Relatively small amplitudes characterize waves from the middle crust, which indicates small contrasts at seismic boundaries and small velocity gradients within layers. Waves reflected from the Moho (P_mP) are the dominant arrivals in the offset interval from 90–120 to 200–250 km. P_n arrivals have small amplitudes, and their apparent velocities are $8.1\text{--}8.2 \text{ km s}^{-1}$. The intercept time for P_n occurs at a reduced time of ~ 8 s, which is ~ 2 s more than for the Pannonian crust.

For a number of shot points, well-recorded waves from the lithospheric mantle were observed up to 400–500 km offsets and even to 800–1200 km. For the northern shot points, an unusual variety of P and S wave phases was recorded, and these phases are shown in Figure 5. For shot point SP25280, P and S waves were doubly reflected from the Moho, and good-quality lower lithosphere phases P^I and S^I were observed.

Examples of record sections from profile P4 (Figure 2) are presented in Figures 3 and 4.

Refracted waves from the sedimentary cover (P_{sed}) are observed as first arrivals in the vicinity of shot points at offsets of 1–15 km. The apparent velocity is $4.0\text{--}5.5 \text{ km s}^{-1}$ in the southwestern part of the profile, decreasing northeastward to $2.5\text{--}3.5 \text{ km s}^{-1}$. The sedimentary strata are far thicker in the Polish basin than in the two surrounding platform areas. Individual, thin sedimentary layers cannot be modeled outside the Polish basin because of the relatively coarse (1.5–3.0 km) receiver spacing compared to the local thickness of the sedimentary column.

Following the arrivals from the sedimentary cover (P_{sed} phase), the refraction from the crystalline upper crust (P_g) is detected as first arrivals to offsets of 100–200 km. The basement topography and variations in sedimentary structure can explain the undulations in the arrivals of this phase in most of the seismic sections. There are no abrupt transitions between upper and middle crustal refractions; instead, a gradual transition between P_g and refractions from the layer below is observed. The P_g phase is observed to offsets of 100–150 km along the southwestern end of the profile with apparent velocities of $5.5\text{--}6.0 \text{ km s}^{-1}$. To the northeast, this phase is observed to larger offsets and has higher apparent velocities of $6.0\text{--}6.25 \text{ km s}^{-1}$. Refractions from the middle and lower crust are correlated as secondary arrivals in the seismic sections (P_{crustal} and S_{crustal}), primarily at far offsets where the refractions merge with wide-angle reflections. They are recorded up to 200–300 km offset and are very important for the determination of velocities in the middle and lower crust.

The crust is highly reflective and several reflections are correlated. Reflections from the top of the middle crust can be correlated on most of the record sections, and reflections from the top of the lower crust (P_c) are observed throughout the profile. Compared to the southwestern end of the profile, this phase is 2 s later in the central part of the profile and 1 s later in the northeastern part. This phase shows varying amplitude along the profile and is followed by a long coda of lower crustal reflectivity (Jensen *et al.*, 2002).

The crossover distance between crustal and mantle refractions (P_n) varies considerably along the profile, demonstrating that significant variations in crustal thickness and velocity structure are present. In the southwest, this crossover distance is 110–130 km. In the central and northeastern part of the profile, the crossover distance is ~ 190 km, and at the northeastern end of the profile, it is 205–230 km.

Reflections from the Moho (P_{mP}) are observed in almost all the seismic sections. The P_{mP} phase is delayed by 2 s for shots in the central part of the profile and by 1 s for shots in the northeast compared to shots in the southwest. The critical offset, where the amplitudes are largest, is 80–105 km in the southwest, 130–145 km in the central part of the profile, and 150–165 km to the northeast. The postcritical P_{mP} phase is commonly observed to offsets of 150 km in the southwest and to 220 km (in some cases up to 270 km) in the northeast. In general, the precritical P_{mP} phase is identified from offsets of 60 km in the southwest and 120 km in the northeast. These differences indicate pronounced structural variations along the profile.

The refraction from the upper mantle (P_n) can be identified as a first arrival in most of the seismic sections. The apparent velocity varies between 8.0 and 8.5 km s^{-1} along the profile, although a much higher apparent velocity (up to more than 9 km s^{-1}) in the central part of the profile indicates an abrupt change in Moho depth. Reflections from the upper mantle are observable of some of the seismic sections and were discussed in a regional sense by Grad *et al.* (2002a, 2003a).

1.15.4 Examples of 2-D and 3-D Modeling of the Earth's Crust and Lower Lithosphere

Analysis of the seismic wave fields began with tomographic inversion of traveltimes of refracted (diving) waves observed as first arrivals. This produced very smooth models of the velocity variations in the crust and uppermost mantle. Then, detailed velocity models were derived by ray tracing and synthetic seismogram modeling. The calculations of traveltimes, ray paths, and synthetic seismograms were made using the ray theory package SEIS83 (Červený and Pšenčík, 1983), enhanced by employing the interactive graphics interfaces MODEL (Komminaho, 1997) and ZPLOT (Zelt, 1994) with modifications by Šroda (1999a). The initial velocity model based on the tomographic inversion results was successively altered by trial and error, and traveltimes were recalculated many times until agreement was obtained between observed and model-derived traveltimes (within a misfit of the order of 0.1–0.2 s). In the modeling, first arrivals, postcritical waves, reflections, and even multiple reflections were employed.

In addition to matching traveltimes, synthetic seismograms were calculated to control velocity gradients within the layers and the velocity contrast at the seismic boundaries. The final synthetic seismograms usually show good qualitative agreement with the relative amplitudes of observed refracted and reflected waves.

1.15.4.1 POLONAISE'97 Crustal and Lithospheric Models (Profiles P4 and P1)

In the model of profile P4 derived using forward ray-tracing technique with the SEIS83 program (**Figure 6**), a large thickness of relatively low-velocity material was also found in the Polish basin ([Grad et al., 2003a](#)). In this basin, velocities of $4.7\text{--}5.8\text{ km s}^{-1}$ extend to 18–20 km depth and are underlain by ‘basement’ with a velocity of $\sim 6.4\text{ km s}^{-1}$. The model shows variable structure and depth to the basement on both sides of the Polish basin. The top of the crystalline basement (Precambrian) of the EEC varies from $\sim 8\text{ km}$ in the area adjacent to the Polish basin at the platform’s margin to only $\sim 1\text{ km}$ at the NE end of profile. The general crystalline basement velocity ($6.1\text{--}6.2\text{ km s}^{-1}$) is typical for cratonal areas, but at distances of 610–660 km

along profile, high-velocity ($\sim 6.4\text{ km s}^{-1}$) basement was found. This increase of velocities is very well visible and documented on reversed traveltime branches of the P_g phase. In the velocity model (**Figure 6**), the corresponding high-velocity intrusion reaches a depth of $\sim 8\text{ km}$ and could be correlated with the Mazury complex (Mz) and Suwałki anorthosite intrusion (Su), which also correlate with a small positive gravity anomaly. The basement of the Paleozoic platform southwest of the Polish basin is characterized by velocities of only $\sim 5.8\text{ km s}^{-1}$ and lies of at depths of 1–3 km. However, at distances of 70–140 km along the model, a deeper (1–4 km) boundary where the velocity increases to $\sim 6.15\text{ km s}^{-1}$ is observed. This boundary rises to its minimum depth at a distance of $\sim 125\text{ km}$, which corresponds to the Wolsztyn ridge that is characterized by a positive gravity anomaly. Velocities of $6.2\text{--}6.4\text{ km s}^{-1}$ are interpreted to extend to depths of $\sim 26\text{ km}$. The main evidence for this interpretation is overcritical deep crustal reflections observed up to offsets of 200–250 km with velocities $<6.5\text{ km s}^{-1}$. This observation provides evidence for relatively low velocities in the middle and lower crust along the southwest end of profile.

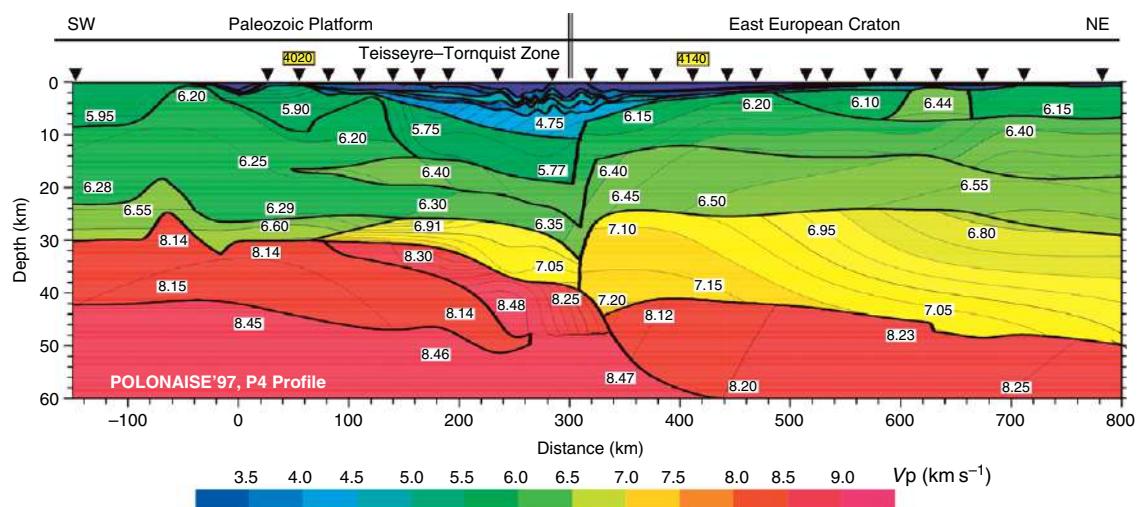


Figure 6 Two-dimensional P wave velocity model for POLONAISE'97 profile P4 derived by forward ray-tracing modeling using the SEIS83 package ([Červený and Pšenčík, 1983](#)). The profile P4 runs across the TESZ almost perpendicularly to the edge of the EEC. The thick solid lines are layer boundaries and thin lines isovelocity contours (in km s^{-1}). Triangles show shot points along profile. Note thin Paleozoic platform crust (c. 30 km), thick crust of the EEC (c. 45–50 km), and thick sedimentary basin in the TTZ with P wave velocities lower than 6 km s^{-1} down to c. 20 km depth. Vertical exaggeration for the model is c. 5.2. Modified from [Grad M, Jensen S L, Keller G R, et al. \(2003a\) Crustal structure of the Trans-European Suture Zone region along POLONAISE'97 seismic profile P4. Journal of Geophysical Research 108\(B11\): 2541, doi:10.1029/2003JB002426.](#)

A lowermost crust with velocities $\geq 7.0 \text{ km s}^{-1}$ is interpreted to be present northeastward from a distance of $\sim 100 \text{ km}$ along the model (**Figure 6**). This interpretation is documented where overcritical crustal reflections at distance 100–220 km along the profile (offset larger than $\sim 200 \text{ km}$) have significantly higher velocities than the P_g wave closer to the shot point (offset 50–150 km). At the far northeast end of the model, they differ in the velocity of the lowermost crust.

In this velocity model (**Figure 6**), the total thickness of the crust changes from $\sim 30 \text{ km}$ beneath Paleozoic platform (0–200 km) to 35–38 km beneath Polish basin (200–300 km) and to 42–50 km beneath the EEC (300–800 km). The primary constraints on the Moho topography are the P_mP and P_n phases, and the most complex Moho topography is observed in the contact zone between the Paleozoic platform and the EEC.

There are also some clear phases that are reflections from mantle discontinuities ([Grad et al., 2002a](#)); and, phases P^I and P^{II} from discontinuities in the uppermost mantle were modeled to produce **Figure 6**. The geometry at the SW end of the model is the result of the top of the dipping body with a velocity of 8.15 km s^{-1} , giving rise to the P^I phase from its top and the P^{II} phase from its bottom. The high-amplitude P^I and P^{II} phases observed in the record sections and the high apparent velocities of the P_n phase are the basis for this interpretation. The bottom of this layer corresponds in depth with a mantle reflector on profile P1 ([Jensen et al., 1999](#)). High velocities ($8.3\text{--}8.4 \text{ km s}^{-1}$) in the uppermost mantle lithosphere were only found beneath the Polish basin area. Similar velocities were also found in this area beneath the TTZ ([Grad et al., 1999](#)) and P1 ([Jensen et al., 1999](#)) profiles. The details of the mantle structure in **Figure 6** are nonunique, but high velocities clearly appear to have a tectonic association with the TESZ. The 8.15 km s^{-1} body may represent a continuation of Variscan lower lithosphere from the southwest. Velocity in the uppermost mantle beneath the EEC increases systematically to the northeast from $\sim 8.15 \text{ km s}^{-1}$ at a distance of 350 km on the model to 8.25 km s^{-1} at the northeast end of the model.

A detailed model of seismic velocity variations along POLONAISE'97 profile P1 in southwestern Poland is presented in **Figure 7(a)**. Despite its location behind the Variscan Deformation Front, the model indicates that the crust below the profile has a Caledonian origin or, alternatively, originates from

Baltica, and that Variscan deformation was thin skinned in this area. The seismic model shows several new findings from the study area ([Jensen et al., 1999](#)):

- Sediment thickness decreases southwestward from 6 to 3 km. There is indication for tectonic activity during deposition of the Paleozoic sequence.
- The seismic velocities are low ($6.1\text{--}6.2 \text{ km s}^{-1}$) down to 20 km depth, indicative of rocks of sedimentary or volcanic origin.
- The lower crust is characterized by high velocity ($6.7\text{--}7.5 \text{ km s}^{-1}$), a high vertical velocity gradient, and strong, ringing reflectivity.
- The crust is 30–33 km thick along the profile with a gradual southeastward thickening.
- The P_n velocity of the sub-Moho mantle is high ($>8.2 \text{ km s}^{-1}$).

The area south of the Caledonian Deformation Front (CDF) in northern Germany and southern Denmark shows similar characteristic features, indicating that the crust between the southeastern North Sea and Poland originates from the same microcontinent (East Avalonia), which was amalgamated to Baltica during the Caledonian orogeny.

POLONAISE'97 produced high-quality data extending to long offsets that resolve velocity discontinuities in the lithospheric mantle. A simplified sketch of the derived 2-D velocity model along the P4 profile is shown in **Figure 8** ([Grad et al., 2002a](#)). In all POLONAISE'97 profiles, the P^I phase indicates a shallow mantle reflector at depths 8–12 km deeper than the Moho. Phases due to deeper features are observed only beneath the longest profile, P4. We found reflectors at depths of about 70, 80, and 90 km in the central part of the TESZ region (180–420 km along profile P4). Complex high and low velocities in the lower lithosphere have been interpreted from other seismic experiments close to the TESZ region as well as within East European craton and the Baltic Shield ([Ansorge et al., 1992](#); [BABEL Working Group, 1993](#); [Blundell et al., 1992](#); [Stangel, 1990](#); [Grad, 1989, 1992, 1997](#); [Grad et al., 1986, 1991](#); [Guggisberg and Berthelsen, 1987](#); [Perchuć and Thybo, 1996](#); [Thybo et al., 1994](#)).

A sub-Moho discontinuity (corresponding to the P^I reflection) with a small P wave velocity contrast was previously detected in the EEC beneath Baltic Sea by [Grad et al. \(1991\)](#). In the area of the Lithuanian–Belarusian border within the EEC, such a mantle discontinuity was found by the [EUROBRIDGE Seismic Working Group \(1999\)](#) at a depth of $\sim 65\text{--}70 \text{ km}$ (Moho depth is $\sim 50 \text{ km}$ in this

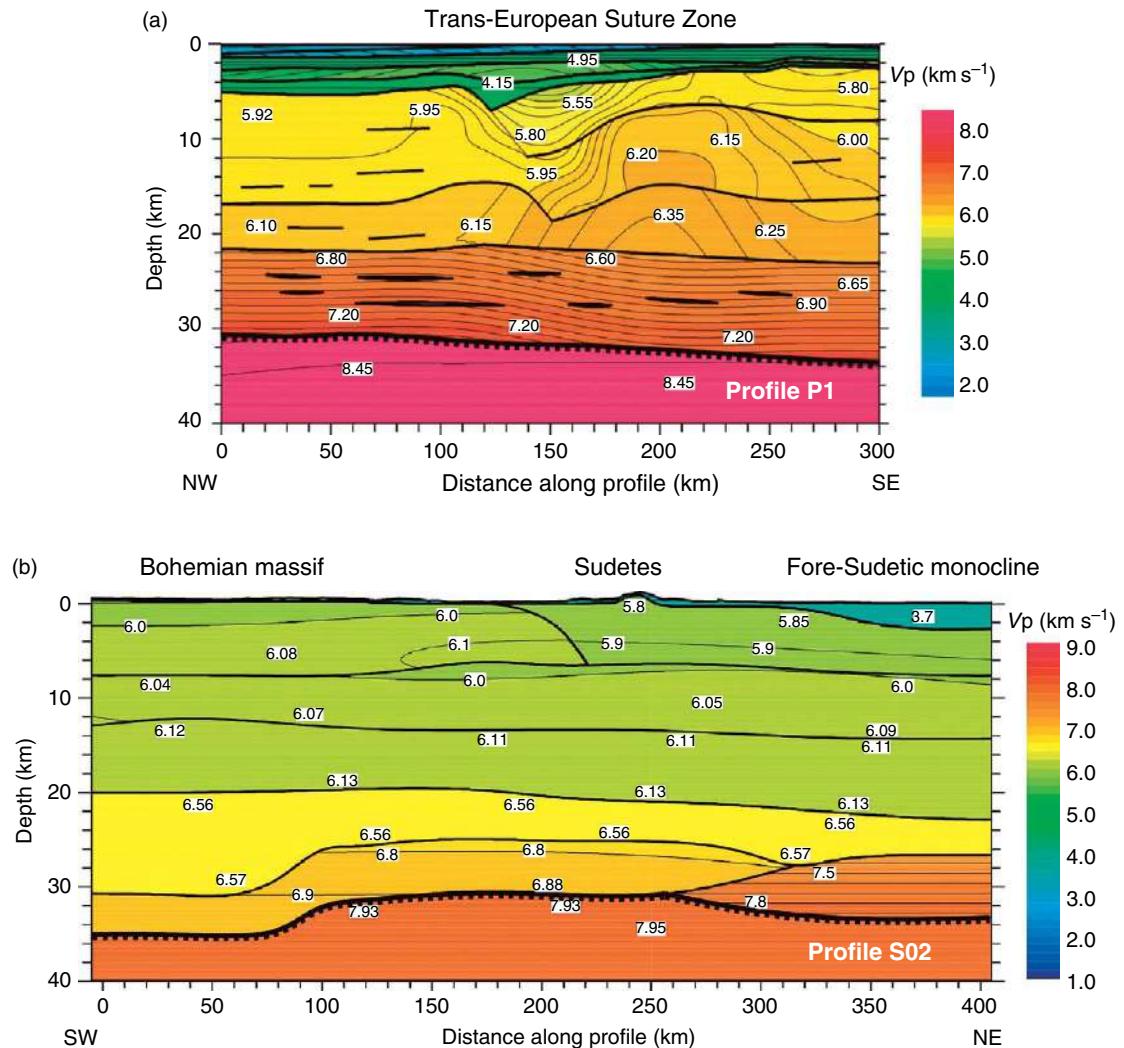


Figure 7 Two-dimensional P wave velocity model for POLONaise'97 profile P1 (a) and SUDETES 2003 profile S02 (b) derived by forward ray-tracing modeling using the SEIS83 package (Červený and Pšenčík, 1983). The profiles are located in Figure 2. The thick solid lines are layer boundaries and the thin lines isovelocity contours (in km s $^{-1}$). Compiled from Jensen SL, Janik T, Thybo H, and POLONaise Working Group (1999) Seismic structure of the Palaeozoic platform along POLONaise'97 profile P1 in southwestern Poland. *Tectonophysics* 314: 123–143 and Majdański M, Grad M, Guterch A, and SUDETES 2003 Working Group (2006) 2-D seismic tomographic and ray tracing modeling of the crustal structure across the Sudetes Mountains basing on SUDETES 2003 experiment data. *Tectonophysics* 413: 249–269.

area). The BABEL Working Group (1993) also noted the existence of similar reflected phases but did not model them. From the existing seismic data from the Baltic Shield and the East European Platform, a discontinuity that lies \sim 10 km beneath the Moho appears to be a general feature of the lower lithosphere. The nature of such a reflector is not understood. One may speculate that the reflector is related to tectonic shearing in the mantle lithosphere. It could also represent a change in mantle

composition caused by magmatic processes (i.e., depleted mantle situated just below the Moho that has acted as a source for basaltic magmatic while deeper layers are relatively undepleted), or it could represent a change in metamorphic grade of the upper-mantle rocks.

Complex high and low velocities in the lower lithosphere near the margin of the EEC have been interpreted based on the long-offset recordings along EUGENO-S Profile 4 (up to 650 km) and Baltic

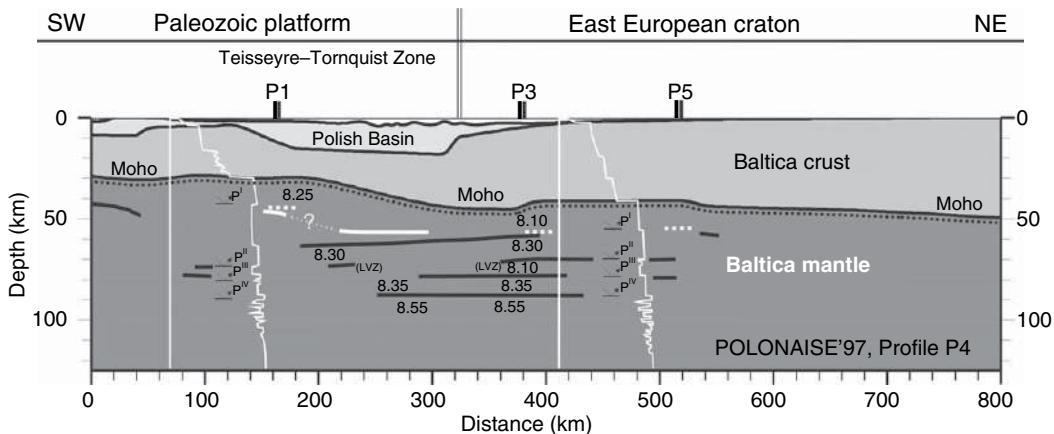


Figure 8 Simplified sketch of lithospheric structure along POLONAISE'97 profile P4 developed by forward ray tracing. Reflectors within the lithospheric mantle beneath profile P4 (thick black lines), the parallel profile P2 (thick white lines), and crossing profiles P1, P3, and P5 (dotted white lines) are marked. Modified from Grad M, Keller G R, Thybo H, Guterch A, and POLONAISE Working Group (2002a) Lower lithospheric structure beneath the Trans-European Suture Zone from POLONAISE'97 seismic profiles. *Tectonophysics* 360: 153–168.

Sea–Black Sea profile (up to 900 km) (Grad *et al.*, 1986, 1991). Perchuć and Thybo (1996) interpreted a long coda, similar to the coda after the deepest lithospheric reflection, as indication of a zone of low velocity and strong seismic reflectivity below the depth level of ~100 km under the Baltic Shield. A similar reflective zone beneath the global 8° discontinuity at around 100 km depth has been identified globally in all long-range seismic profiles (Thybo and Perchuć, 1997). Based on petrologic and thermal arguments, Thybo and Perchuć (1997) suggested that the reflectivity was caused by pockets of partial melt induced by the lowering of the solidus temperature by small amounts of fluids (Thybo and Perchuć, 1997). The depth to the reflective zone correlates with the heat flow in that it is shallower in ‘hot’ areas than in cold areas, a feature also observed along the FENNOFLORA seismic long-range profile.

Based on the POLONAISE'97 data, our main finding about the lithospheric mantle is that a series of seismic reflectors extend from the Moho to ~90 km depth, the deepest interpretable level with the current data set. A seismic reflector is present ~10 km below the Moho throughout the EEC and adjacent areas, independent of the actual depth to the Moho. In general, the reflectivity of the uppermost mantle is stronger beneath the Paleozoic platform and TESZ region than beneath the East European Platform. The deepest interpreted seismic reflector and zone with high reflectivity may mark a change in upper-mantle structure from an upper zone

characterized by seismic scatterers of small vertical dimension to a lower zone with vertically larger scatterers, possibly caused by inclusions of partial melt.

1.15.4.2 SUDETES 2003 Crustal Model (Profile S02)

The SUDETES 2003 experiment was the fourth of the series of large seismic refraction and wide-angle reflection experiments performed from 1997 to 2003 in Central Europe, and it covers the gap between areas of POLONAISE'97, CELEBRATION 2000, and ALP 2002 experiments (Figure 2). The experiment covered mainly the northern part of the Bohemian massif (including the Eger rift) and some of the neighboring Polish basin (TESZ) to the northeast and the Western Carpathians to the southeast (Figure 1). Here, we show a model of the crustal structure beneath profile S02 (Figure 2) crossing the Sudetes Mountains from the Bohemian massif (Moldanubian) to the Fore-Sudetic block, Fore-Sudetic monocline, and Wolsztyn high.

Beneath profile S02 (Figure 7(b)), the basement of the Bohemian massif has slightly higher velocities ($6.0\text{--}6.1 \text{ km s}^{-1}$) than those south of the Sudetes Mountains ($5.8\text{--}5.9 \text{ km s}^{-1}$). The site of this change underlies the Sudetes Mountains ~30 km southwest of their axis (at ~210 km of profile). The upper crust is characterized by small velocity gradient, and velocities at ~20 km depth are $6.15\text{--}6.25 \text{ km s}^{-1}$. A few reflectors with rather small velocity contrast of

$\sim 0.1 \text{ km s}^{-1}$ were found in the upper crust. The strongly reflecting boundaries (velocity contrast $\sim 0.4 \text{ km s}^{-1}$) were found at 20–23 km and 25–28 km depth. The highest velocities in the lowermost crust are 6.8–7.2 km s^{-1} . In the lower crust of the northeastern part of the profile S02, velocities of $\sim 7.5 \text{ km s}^{-1}$ were assumed to explain the observed very strong reflections. In general, the crust of the Bohemian massif is slightly thicker (33–35 km) than in the northern part of

the area. Velocities beneath Moho are relatively low, being 7.95 km s^{-1} (Majdański *et al.*, 2006).

1.15.4.3 CELEBRATION 2000 Crustal Models CEL05 and CEL01

Tomographic and ray-tracing models derived for the structure along profile CEL05 are shown in Figure 9 (Grad *et al.*, 2006) and reveal large variations in the

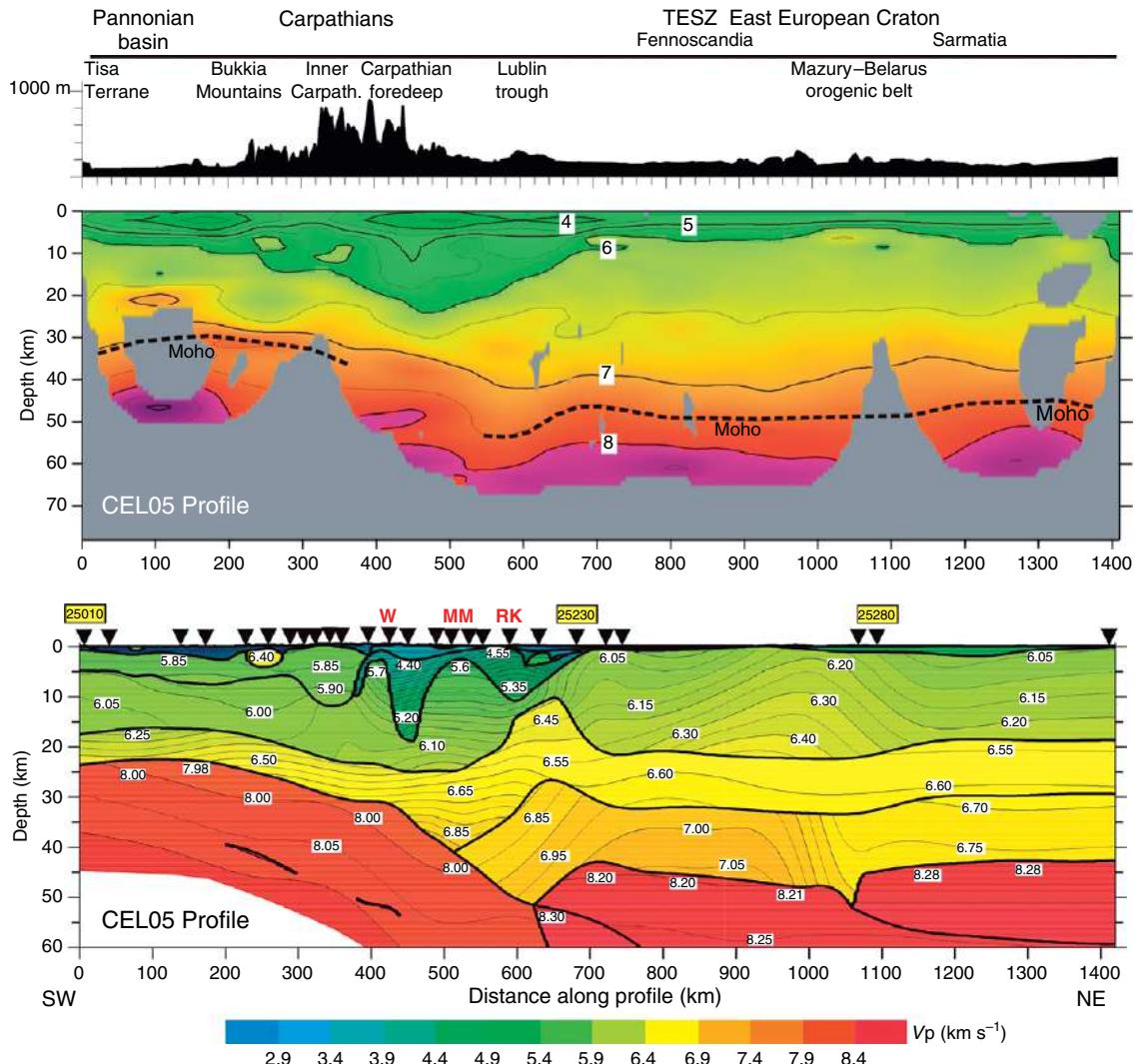


Figure 9 Two-dimensional P wave velocity model for CELEBRATION 2000 profile CEL05 derived by tomographic inversion (Hole, 1992) and forward ray-tracing modeling using the SEIS83 package (Červený and Pšenčík, 1983). The thick solid lines are layer boundaries and thin lines are isovelocity contours in km s^{-1} ; triangles refer to shot points. In the upper part, topography along profile is shown. Note the very thin Pannonian crust (c. 25 km), thick crust of the EEC (c. 45–50 km), and the thickest crust in the investigated area in the TESZ (c. 52 km depth at distance 620 km). In Carpathians and TESZ sedimentary basins with P wave velocities lower than 6 km s^{-1} down to 10–20 km depth were found. RK, Radom–Kraśnik uplift (at 580–600 km of profile); W, Wysowa (at c. 420 km of profile). Vertical exaggeration for the model is c. 6.8. Modified from Grad M, Guterch A, Keller GR, *et al.* (2006) Lithospheric structure beneath trans-Carpathian transect from Precambrian platform to Pannonian basin – CELEBRATION 2000 seismic profile CEL05. *Journal of Geophysical Research* 111: B03301 (doi:10.1029/2005JB003647).

structure of the crust and lithospheric mantle. **Figure 9** includes a vertically exaggerated depiction of the topography traversed by the profile. Along most of its length, the profile passes through lowland areas with an average elevation of 200 m. In the Carpathians (200–500 km along profile), elevations range from 400 to 900 m.

In the Pannonian basin region to the southwest (0–350 km), the crustal structure is relatively simple. However, in the distance interval of ~240–280 km along the profile, a shallow high-velocity body was delineated ($V_p \sim 6.4 \text{ km s}^{-1}$). Beneath the upper sedimentary layer and a layer with velocities of $\sim 5.8 \text{ km s}^{-1}$, two almost homogeneous (very small velocity gradient) crustal layers are observed. The Moho here lies at a depth of only 24–25 km, and the uppermost mantle beneath it is characterized by velocities of $7.95\text{--}8.0 \text{ km s}^{-1}$.

Along this profile, the most complicated structure is observed at distances of 350–700 km in the transition from the Pannonian basin to the EEC. This transition includes the Carpathians and their foredeep, the MM, the rifted margin of the EEC, and the Lubin trough. This is an area of complex topography, complicated structure in the sedimentary cover (where rocks with velocities $<5.5 \text{ km s}^{-1}$ reach depths of $\sim 20 \text{ km}$), complex structure within the crystalline crust, and deep Moho ($\sim 50 \text{ km}$). In the distance interval 370–400 km, the Pieniny Klippen Belt (PKB), which represents the structural boundary between Inner and Outer Carpathian units (e.g., Kováč *et al.*, 1993), is represented by a southwest-dipping slab of low-velocity sediments. This slab is a few kilometers thick and can be traced down to $\sim 10 \text{ km}$. The Carpathians are associated with a two-layer crystalline crust with velocities of $5.9\text{--}6.2 \text{ km s}^{-1}$ and $6.5\text{--}6.8 \text{ km s}^{-1}$, respectively, while beneath the TESZ and EEC margin further to the northeast, a three-layer crust is present. In the distance interval 600–670 km along the profile, a dome of relatively high velocities ($\sim 6.4 \text{ km s}^{-1}$) protrudes into the upper crust and may represent an intrusion. In the same area, an uplift of the lower crust is also observed. The maximum crustal thickness along the profile (52 km) is observed in the area of the crossing point with profile CEL03 (at distance 600–650 km), where a similar velocity distribution in the crust was also found (Janik *et al.*, 2005).

The EEC occupies the northeast portion of the profile (700–1420 km), and the cratonic crustal structure is similar (thin sedimentary cover and three distinct layers) to that found in other portions of

western Baltica (Grad and Luosto, 1987, 1994; Grad and Tripolsky, 1995; EUROBRIDGE Seismic Working Group, 1999, 2001). The crustal thickness varies from 42 to 48 km along this $\sim 700 \text{ km}$ long cratonic part of the profile, and velocities in the uppermost mantle vary only slightly ($\sim 8.20 \text{ km s}^{-1}$ in the southwest and slightly higher to the northeast). The small change in upper-mantle velocity occurs at $\sim 1050 \text{ km}$ along the profile and correlates with small but consistent changes in crustal structure (Grad *et al.*, 2006).

Along the profile, many shot points produced clear arrivals that were reflected in the lithospheric mantle (P^I and P^{II} phases), and these phases were modeled by Grad *et al.* (2006) as shown in **Figure 9**. In the Pannonian–Carpathian area, the P^I wave was usually much stronger than the P_n wave in the same distance range. The corresponding reflector in the mantle lithosphere is subparallel to the Moho but is $\sim 15 \text{ km}$ deeper. Thus, it dips northward from Pannonian basin under the Carpathians (**Figure 9**). A strong south-dipping reflector was found under the TESZ at a depth of 60–70 km and implies that there is a large velocity contrast between the Pannonian and Baltica mantle. In the EEC area, several reflectors were delineated in the lithospheric mantle.

The forward modeling and tomographic inversion results along profile CEL01 are presented in **Figure 10** (Sroda *et al.*, 2006). Along CEL01, the EEC is covered by a thin ($\sim 2 \text{ km}$) undeformed layer of sediments, except in the Lublin trough, where sedimentary rocks with $V_p = 4.0\text{--}5.5 \text{ km s}^{-1}$ reach a thickness of approximately 10 km. As in nearby areas, the crystalline crust of the EEC consists of three horizontally homogeneous layers, with total thickness of 43–45 km. The EEC upper mantle is characterized by V_p of $\sim 8.05 \text{ km s}^{-1}$. Beneath the Lublin trough, unusually high velocities of 7.1 km s^{-1} are observed in the upper and middle crust, starting at a depth of $\sim 16 \text{ km}$. This anomaly seems to be a continuation of a high-velocity/high-density intrusion located further southeast, which was detected by previous seismic studies in this region (Guterch *et al.*, 1986; Malinowski *et al.*, 2005).

Beyond the EEC margin, beneath the MM and the Łysogóry unit, the dominant feature of the crust is a 20 km thick trough-like feature (**Figure 10**). This feature is filled with material whose velocity is relatively low ($V_p = 5.5\text{--}5.9 \text{ km}$) and a relatively high vertical gradient of V_p . In the area of the Holy Cross Mountains, Paleozoic rocks with $V_p = 5.0\text{--}5.3 \text{ km s}^{-1}$ are exposed at the surface and have been

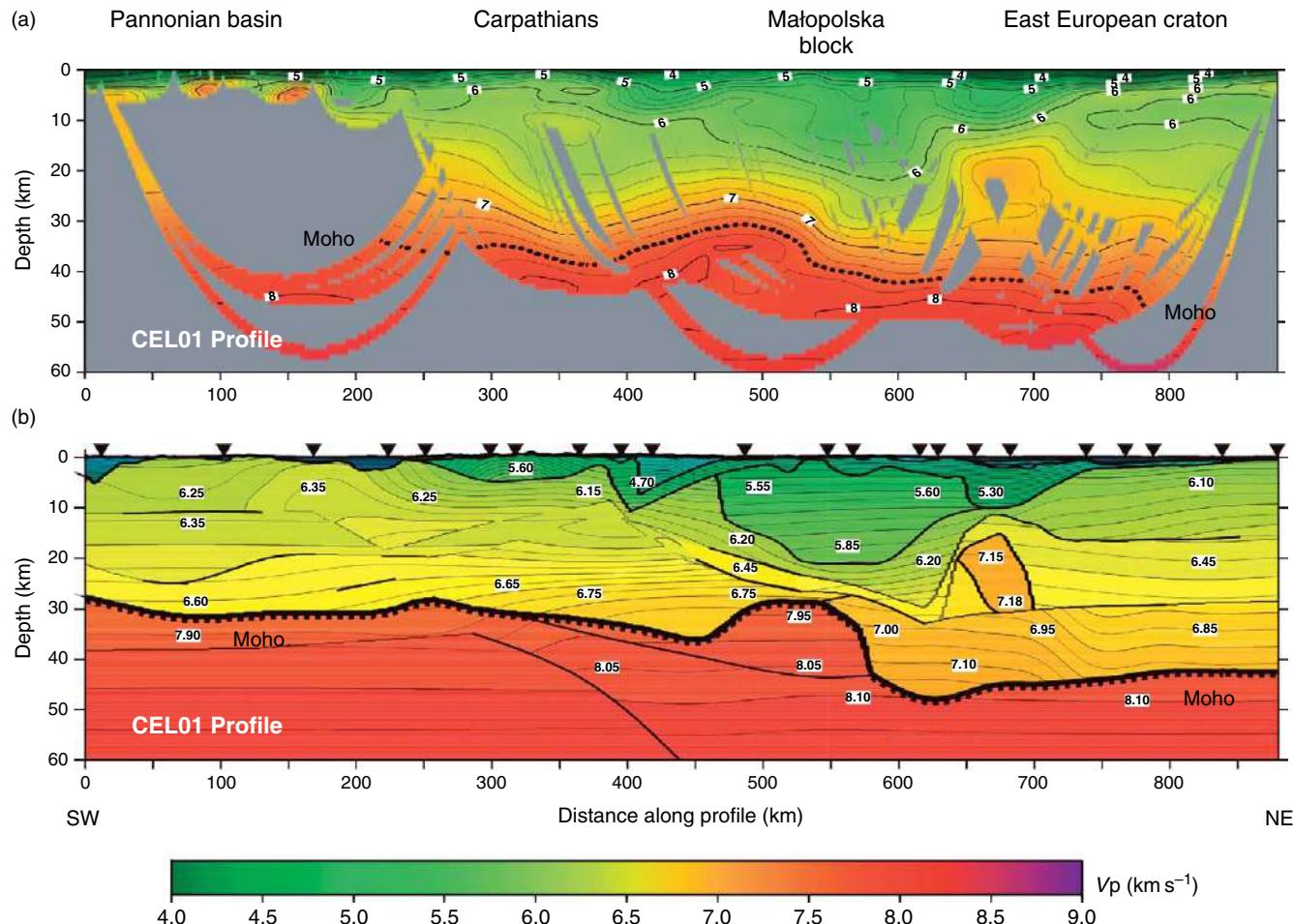


Figure 10 Two-dimensional P wave velocity model for CELEBRATION 2000 profile CEL01 derived by tomographic technique (a) (Hole, 1992) and forward ray-tracing modeling using the SEIS83 package (Červený and Přenčík, 1983). The profile extends from the EEC, across Trans-European Suture Zone and Carpathians, to the Pannonian basin. The thick solid lines are layer boundaries and thin lines are isovelocity contours in km s^{-1} ; triangles refer to shot points. Note the thin Pannonian crust (c. 25 km) and the thick crust of the EEC (c. 45 km). In the Carpathians and TESZ, sedimentary basins with P wave velocities lower than 6 km s^{-1} down to 10–20 km depth were delineated. Modified from Šroda P, Czuba W, Grad M, et al. (2006) Crustal and upper mantle structure of the Western Carpathians from CELEBRATION 2000 profiles CEL01 and CEL04: Seismic models and geological implications. *Geophysical Journal International* 167(2): 737–760 (doi: 10.1111/j.1365-246X.2006.03104.x).

the target of many geological studies. Beneath this region, substantial variations of the crustal thickness and the lower crust occur. The crustal thickness of ~ 44 km does not change from the ECC to approximately the location of the Holy Cross fault, where it rapidly thins to ~ 32 km to the southwest (**Figure 10**).

Further to the southwest, a highly asymmetric depression filled by two low-velocity units ($V_p = 4.5$ and 5.6 km s^{-1}) forms the upper crust in the area of the Outer Carpathians and the Carpathian foredeep. This low-velocity material forms a south-dipping layer that is approximately bounded on the south by the PKB, where it reaches its maximum thickness of ~ 10 km. In the ALCAPA (Alps–Carpathians–Pannonian) unit, the uppermost crust (sedimentary rocks and volcanics) of the Inner Carpathians is 3–5 km thick with V_p values of 5.3 – 5.6 km s^{-1} . These strata are underlain by the crystalline basement that is characterized by a V_p velocity of 6.1 km s^{-1} . The information about deeper structure of the Inner Carpathian crust is relatively poor due to low signal-to-noise ratio in this area and scarce reflected phases; therefore, no V_p anomalies are discernible. In the Pannonian basin area, the Danube and Zala basins show up as areas of low velocities ($\sim 3 \text{ km s}^{-1}$) that extend to depths of 3–5 km (**Figure 10**). Between them, the uppermost crust with V_p of 6.2 – 6.3 km overlies a layer with lower velocities (5.8 – 6.0 km s^{-1}) forming a velocity inversion. The middle and lower crust of the Pannonian basin are characterized by V_p values of 6.3 and 6.55 km s^{-1} , respectively. The Moho discontinuity under the Carpathians was found at depths of 30 – 39 km, with maximum crustal thickness approximately beneath the PKB. The Moho beneath the Pannonian basin system is relatively flat with a depth of 27 – 30 km. The V_p of the upper mantle is lowest under the Pannonian basin and Inner Carpathians area (7.9 km s^{-1}), while further north beneath the Outer Carpathians, it is higher (8.05 – 8.1 km s^{-1}). In the upper mantle beneath the Inner and Outer Carpathians, a north-dipping reflector with high impedance contrast was found. It is based on the interpretation of the strong P^l reflected phase, observed for several shot points; therefore, it is a well-defined structure. To the south its depth is 45 km, while in the north it reaches 70 km. This north-dipping mantle discontinuity may represent a shear zone related to collision between the ALCAPA unit and the European plate and possibly ongoing convergence between these units (*Środa et al.*, 2006).

1.15.4.4 Example of 3-D Tomographic Modeling

The volume of data collected in POLONAISE'97, CELEBRATION 2000, ALP 2002, and SUDETES 2003 is huge, and it has been a huge task just to analyze the data thoroughly in profile form. However, our ultimate goal is a fully 3-D analysis such as the one undertaken by *Środa et al.* (2002) for the POLONAISE'97 data. As a smaller scale example, here we show some of the results from the study of the P5 profile region of POLONAISE'97 (**Figures 11 and 12**; *Czuba et al.*, 2002). The geometry of recordings in the area of the P5 profile and examples of record sections are shown in **Figure 11** (only $\sim 15\%$ of ray paths are shown). The tomographic inversion package of *Hole* (1992) uses an efficient method of determining the seismic velocity distribution in the 3-D medium using first arrivals only. The velocity model is defined via a rectangular grid with equidistant nodes. The traveltimes are calculated using the finite differences algorithm of *Vidale* (1990) adapted for media with high-velocity contrasts by *Hole* (1992). The ray paths are traced from the receiver back to the source along the maximum traveltimes gradient curves. The method of calculating slowness perturbations along the ray is described in detail by *Hole* (1992). This procedure is iteratively repeated until a model satisfying the traveltimes data at a satisfactory level is obtained.

For tomographic modeling of the entire POLONAISE'97 data set, 10 950 picks of first arrivals were used. The P-wave velocity of the model was defined using a distance between nodes (cell size) of 2 km. This resulted a model whose dimensions (X , Y , Z) were $928 \times 368 \times 68 \text{ km}^3$ or $464 \times 184 \times 34$ cells that covered the entire area of the POLONAISE'97 experiment. The total number of cells in the model was 2 902 784. Here, we will show results for the region of the P5 profile, which extends from 550 to 700 km in the X -direction, from 50 to 250 km in the Y -direction, and to a depth of 68 km (Z).

Only picks from offsets of less than 40 km were employed in the first step of the computation. In the subsequent steps, this distance was increased in order to gradually enlarge the maximum depth of ray penetration. This approach allows the shallow layers to be constrained first before modeling the deeper ones. In each step, several iterations were nested with decreasing size of the smoothing area (*Hole*, 1992). In this way, the resolution of the algorithm was gradually increased. In each loop, several iterations were calculated.

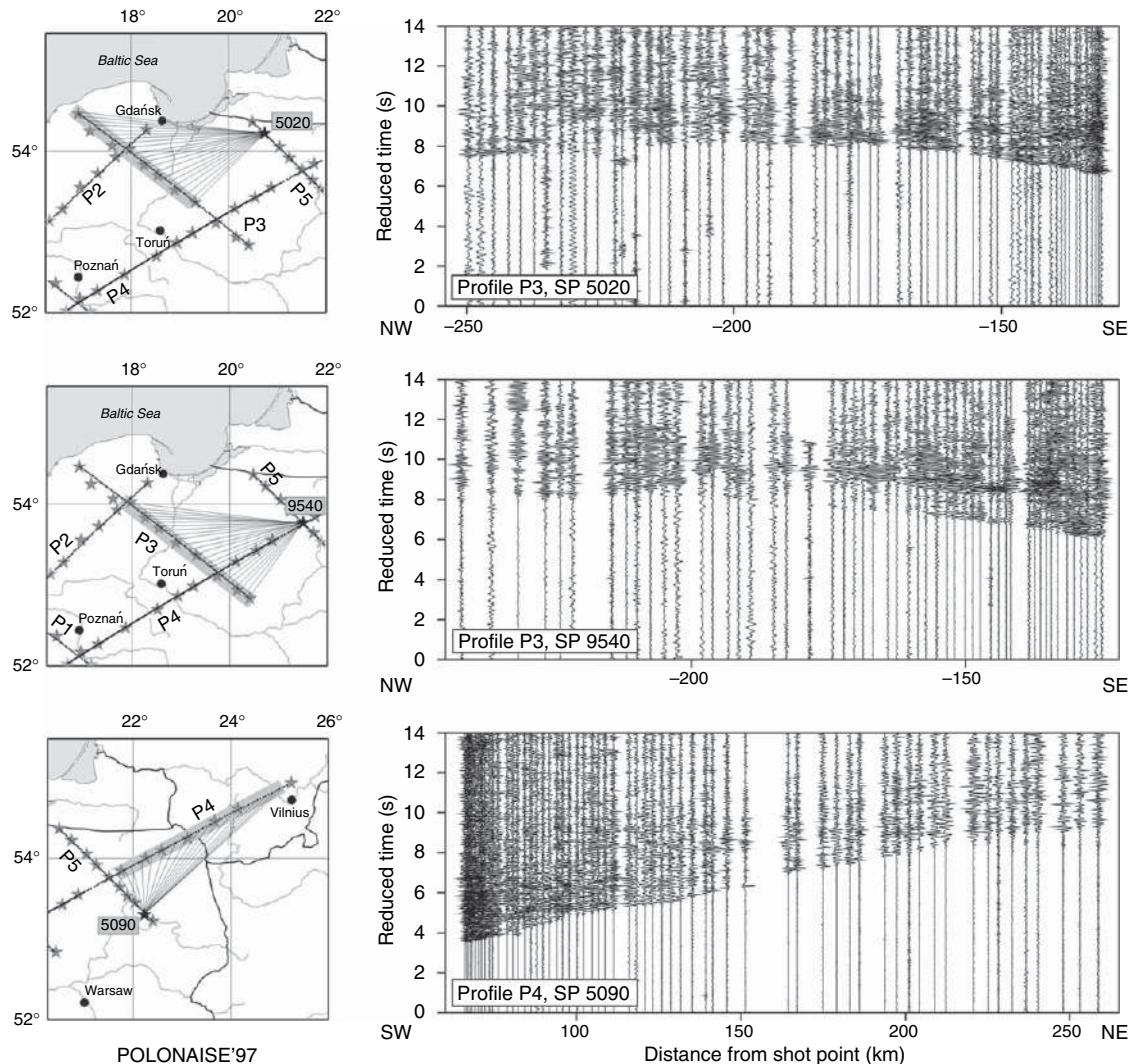


Figure 11 Examples of seismic record sections recorded in 3-D geometry during POLONAISE'97 experiment in NE Poland and Lithuania.

Examples of results of the 3-D tomographic inversion in the area of the profile P5 (Czuba *et al.*, 2002) are shown in Figure 12. Results for the whole POLONAISE'97 area as well as resolution tests can be found in Środa *et al.* (2002). A specific target that emerged in the analysis of the P5 area was a high-velocity body discovered in the 2-D modeling. Further definition of this feature was one goal of the 3-D modeling, and the shape of this shallow body is clearly seen in the vertical cross sections (Y , Z) and horizontal slices (X , Y) in Figure 12. This body coincides with the anorthosite of the Kętrzyn massif (Kt in Figure 12). A deeper high-velocity body was detected in the distance range of 80–120 km and at a depth >10 km. This body

spatially corresponds to the Biebrza complex or the Piszc intrusion (Pi; see basement geology map in Figure 12). The deeper structure could only be resolved with the 3-D data and shows a crust that thickens from about 42 to 45 km southeastward.

1.15.5 Geotectonic Models of the TESZ and the Transition from the EEC to the Carpathians and the Pannonian Basin

Although the data analysis and interpretation of the results of the POLONAISE'97, CELEBRATION 2000, ALP 2002, and SUDETES 2003 will continue

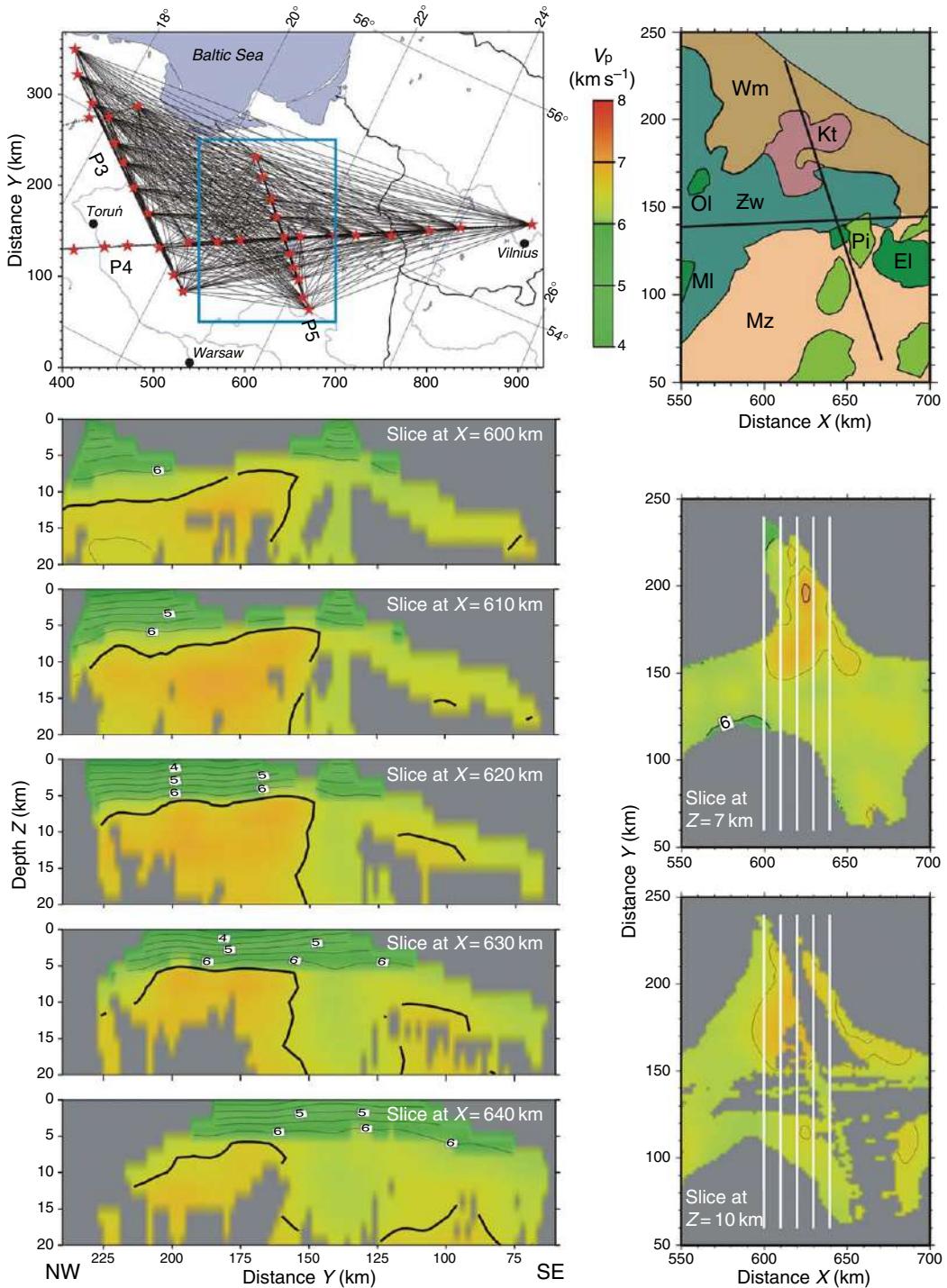


Figure 12 Results of 3-D investigations in NE Poland in the area of POLONAISE'97 profile P5 (Czuba *et al.*, 2002). The location map shows the area of investigation as a subset of the 3-D model of Środa *et al.* (2002); geographical coordinates are shown on the top and right. Lines show schematic ray paths connecting shot points and recording stations, but only $\sim 15\%$ of the ray paths used in inversion are shown. The blue rectangle marks area of the map of the EEC crystalline basement and area of the horizontal slices for depths of 7 and 10 km. Vertical cross sections through the model for $X = 600, 610, 620, 630$, and 640 km are also shown, and in them, the thick lines are 6.5 km s^{-1} velocity isolines. Abbreviations in the basement map: El, Ełk intrusion; Kt, Kętrzyn anorthositic intrusion; MI, Mława intrusion; Mz, Mazowsze massif; OI, Olsztyn intrusion; Pi, Piszkowice intrusion; Wm, Warmia branch; Zw, Żuławy branch.

for many years, the findings to date have shed considerable light on efforts to construct geotectonic models of the region. Some of these results are discussed below.

1.15.5.1 POLONaise'97 Area

The area of POLONaise'97 experiment represented here by P4 and P1 profiles ([Figure 2](#)) and crustal/lithospheric models in [Figures 6, 7\(a\), and 8](#) has experienced several major tectonic events including: (1) assembly of terranes during the Precambrian to form the cratonal block that included Baltica; (2) rifting during the breakup of Rodinia/Pannotia to form the southwest margin of Baltica (EEC) in the Neoproterozoic; (3) collision between Baltica, the microcontinent eastern Avalonia, remnant ocean crust, and/or other terranes causing accretion in Ordovician and Early Silurian time; (4) further deformation and terrane accretion during the Variscan orogeny in the Late Paleozoic; (5) extension and magmatism in the Permian and Triassic; and (6) tectonic inversion during the Alpine orogeny in the Late Cretaceous ([Figure 1](#)). The results of POLONaise'97 have shed considerable light on the structure and tectonic evolution of the TESZ region. However, there remain several possible explanations about how these tectonic events are reflected in the observed crustal velocity structure.

At the margin of Baltica (EEC), the upper crustal structure is clearly discontinuous because of the ~ 20 km basin present ([Figures 6 and 8](#)). It seems clear that a major consideration in developing geotectonic models for the TESZ in the region of profile P4 is whether the deep crustal layers are continuous or discontinuous beneath the deep basin. The velocities of the middle and lower crust do not change as significantly along the model as in other areas to the northwest where the European Geotraverse crosses Germany and the MONA LISA experiment was conducted in the southeastern North Sea. In northern Germany, a high-velocity middle and lower crust to the north terminates abruptly at the Elbe line ([Aichroth *et al.*, 1992; Thybo, 2001](#)). In the MONA LISA lines, the termination of Baltica in the lower crust appears as a transition from high ($>7.0 \text{ km s}^{-1}$) velocities in Baltica crust to low velocities ($<6.4 \text{ km s}^{-1}$) in the 'pure' Avalonian portion of the crust ([Abramovitz *et al.*, 1998; Abramovitz and Thybo, 2000](#)). Thus, a possible interpretation is that highly extended Baltic lithosphere extends as far west as 60–80 km at the P4 profile. However, based

on similarities with many crustal models across both modern and ancient passive margins (e.g., [Holbrook *et al.*, 1994; Mickus and Keller, 1992; Keller and Hatcher, 1999](#)), a more likely scenario is that the pre-Permian portion of the 20 km deep basin is a passive margin sequence that includes some units related to transcurrent motions along the margin between the initial rifting and the Variscan orogeny as shown in [Figure 13\(a\)](#). An important piece of evidence for this being the case is drilling data which show that a maximum of only about the upper 40% (8 km) of the fill in the Polish basin is Permian or younger in age ([Scheck-Wenderoth and Lamarche, 2005](#)). A rift sequence should taper away from the EEC margin, but this is only partially the case in the seismic model ([Figure 13\(a\)](#)). However, to the southwest toward the Bohemian massif region, there are thrust faults and synorogenic sedimentary rocks (OS in [Figure 13\(a\)](#)) that would fill this portion of the basin. An obvious argument for extension is that the crystalline crust beneath the basin is half as thick as the crust under the adjacent EEC ([Figure 13\(a\)](#)). In addition, [Janik *et al.* \(2005\)](#) discuss the evidence indicating that this margin experienced translation of crustal blocks in the Paleozoic subsequent to its formation that could create pull-apart basins. The abrupt change in crustal structure at the margin of Baltica is also evidence that transtension was involved in the initial rifting and has been argued for the case of the Ouachita orogenic belt of the southern United States ([Thomas, 1991](#)).

The deeper structure southwest of the deep basin reflects the collision between Baltica and Avalonia/Bohemian massif. The geometry of the crust and upper mantle in this area ([Figure 13\(a\)](#)) has similarities with BABEL line A in the southern Baltic Sea ([BABEL Working Group, 1993](#)). Thus, Baltica and its margin can be viewed as the indenter in the collision with the crust of the Variscan region being driven upward onto the margin of Baltica and the Variscan mantle being driven beneath the margin of Baltica. The fact that the passive margin appears to be largely intact and the lack of Late Paleozoic deformation within Baltica indicates the collision was relatively soft.

In conclusion, the observed structure along profile P4 ([Figures 6 and 13\(a\)](#)) indicates that rifting and subsequent transtension created an abrupt margin for Baltica along which a thick (~ 10 km) sedimentary sequence was deposited. In addition, the seismic model suggests that the Variscan orogeny was a soft collision in which the margin of Baltica acted as an indenter.

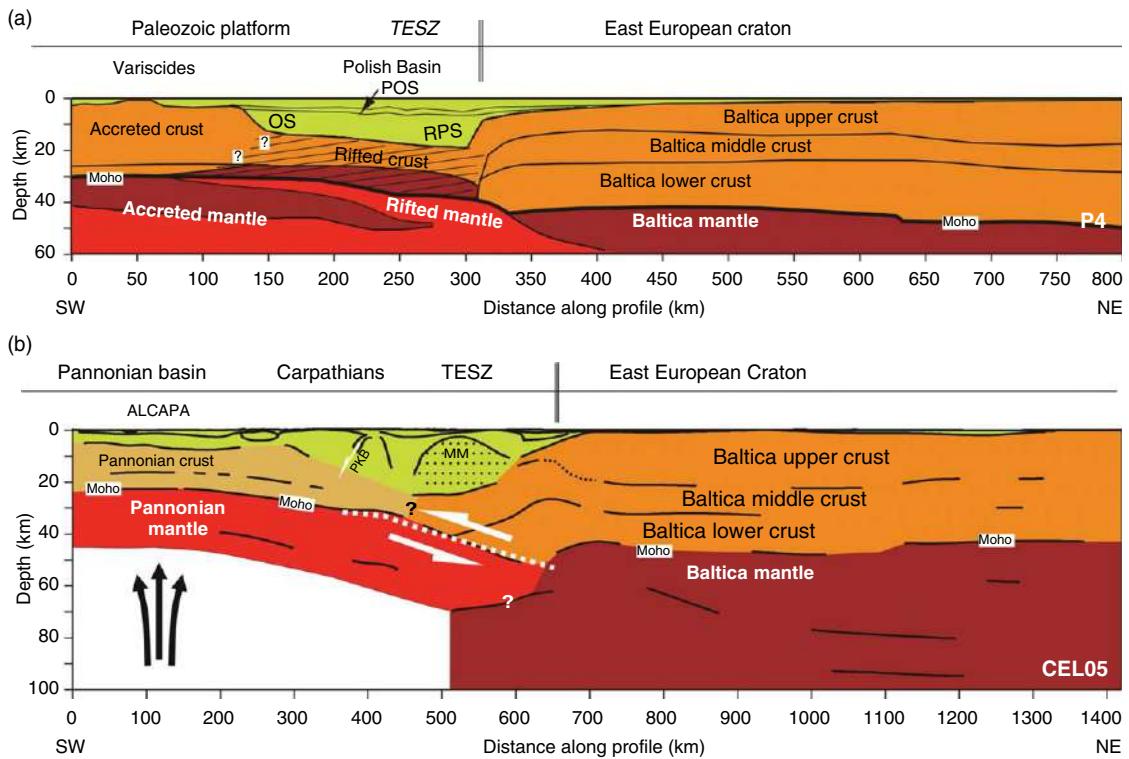


Figure 13 Representation of a tectonic interpretation of the transition between Baltica (EEC) and the adjacent accreted terranes (Paleozoic platform) in the TESZ area along Profile P4 (a) and the transition between Pannonian basin and EEC along profile CEL05 (b). The model for profile P4 (a) is modified from [Grad et al. \(2003a\)](#) and shows an abrupt transtensional margin where the southwestern extent of Baltica lithosphere is minimal. POS, postorogenic sedimentary sequence; OS, orogenic sedimentary sequence; RPS, rift (pull-apart) sedimentary sequence. The model for profile CEL05 (b) is modified from [Grad et al. \(2006\)](#) and shows the ‘old’ (northward) subduction zone of the Pannonian lithosphere under EEC in the Jurassic–Lower Cretaceous ([Książkiewicz, 1977](#)) or by the end of the Jurassic, c. 140 Ma ([Golonka et al., 2003a](#)). ‘Young’ (southward) subduction of the EEC lithosphere in the Tertiary (Miocene) is represented by PKB.

1.15.5.2 CELEBRATION 2000 Area

The velocity model derived for the CEL05 profile provides an important new view of lithosphere across the Carpathian–Pannonian region and transition with the EEC (Baltica). The Mesozoic and Cenozoic tectonic environment of this region involved complex conference between the European and Adriatic plates and a variety of intervening microcontinents and oceanic areas (e.g., [Golonka et al., 2003a, 2003b](#)), and many aspects of the tectonic evolution remain controversial.

Our preferred tectonic interpretation of the velocity model ([Figure 9](#)) is shown in [Figure 13\(b\)](#). The southwestern end of CEL05 begins in the Tisza–Dacia block, which is separated from the ALCAPA block to the north by the Mid-Hungarian Line ([Figure 1](#)) (e.g., [Bielik et al., 2004](#); [Szabó et al., 2004](#)). The western Pannonian basin and Inner Carpathians

are part of the ALCAPA block that extends northward to PKB. Our model is in agreement with previous studies in the region (e.g., [Posgay et al., 1995](#); [Royden and Dövényi, 1988](#)) in showing that the Pannonian basin is characterized by thin (~25 km) crust and 2–3 km of Tertiary sedimentary and volcanic cover. Two important observations are: (1) the crust below this cover has a low average velocity (~6.1 km s⁻¹), indicating that it is not oceanic in nature ([Grad et al., 2006](#)), and (2) there is no large change in lithospheric structure across the Mid-Hungarian Line, which suggests that extension and magmatism associated with the formation of the Pannonian basin has modified the lithosphere considerably.

In contrast to the Pannonian basin region, the structure of the upper crust complicated along the profile as it traverses the Inner Carpathians, PKB, Outer Carpathians, and Carpathian foredeep, and

the observed velocity structure is in good agreement with the surface geology and drilling results such as the deep drill holes near Wysowa (**Figure 9**). The south-dipping body that correlates with the PKP attests to the importance of this feature. From a deeper perspective, the crust gradually thickens into and across the Carpathians up to the margin of the EEC, and the mantle reflectors deepen to remain parallel to the Moho.

Near the margin of the EEC, the profile crosses the MM, Radom–Krašník uplift, and Lublin trough before passing into relatively undisturbed EEC crust that is typical of that found in other nearby areas (**Figure 9**). Because it is a large crustal block that may be exotic with respect to the EEC, MM has been the subject of much interest and several interpretations. Geologic studies reveal folded metasediments of Vendian–Early Cambrian age at depths that are covered by younger strata. However, drilling data and the new POLONAISE'97 and CELEBRATION 2000 results suggest that it was probably once a part of Baltica and was detached and then moved to its present location ([Dadlez et al., 1994, 2005; Janik et al., 2005](#)). The MM is bounded on the north by the Radom–Krašník uplift that is in turn bounded on the north by the Lublin trough (**Figure 9**), and the crustal structure beneath these features is complex. More geological data are needed to access the implications of these observations.

Northeast of the Lublin trough, the profile crosses the EEC where a relatively simple crustal structure is observed. However, the Precambrian history of this cratonal area is complex, having been interpreted as involving the accretion of three terranes: Fennoscandia, Sarmatia, and Volgo-Uralia ([Bogdanova, 1996; Bogdanova et al., 2001](#)). In western Belarus, profile CEL05 approximately follows the suture between Fennoscandia and Sarmatia, which is marked by the Mazury–Belarus orogenic belt (**Figure 9**). A change in lower crustal structure and upper-mantle velocity occurs in the vicinity of this interpreted suture, implying that it is a major lithospheric boundary.

As discussed by [Grad et al. \(2006\)](#), several large-scale tectonic interpretations are possible for the CEL05 velocity model. The most surprising feature in this model is the northward dip of the Moho and mantle reflectors beneath the Carpathians and the region of the EEC margin that suggests northward subduction (**Figures 9 and 13(b)**). This observation is at odds with the known surface geology such as the south-dipping PKB which indicates that Cenozoic

subduction was to the south. However, several workers have suggested that northward subduction occurred in the Mesozoic ([Książkiewicz, 1977; Golonka et al., 2003a](#)), so subduction in the region could have flipped. However, the lack of a Mesozoic arc to the north indicates that any northward subduction would have been short-lived. A lithospheric-scale ‘crocodile’ structure with Baltica acting as the rigid indenter could also produce south-dipping features in the upper crust and north-dipping deep structures during Cenozoic convergence. Finally, a thermal anomaly and extension in the Pannonian basin area would cause crustal thinning, producing an overall appearance of northward dip ([Grad et al., 2006](#)). Add in the complexities of large-scale strike-slip movements (e.g., [Csontos and Vörös, 2004](#)) and slab rollback to the east (e.g., [Wortel and Sparkman, 2000; Seghedi et al., 2004](#)), and it becomes difficult to make definitive tectonic interpretations. However, recent petrologic studies ([Trua et al., 2006](#)) indicate that Precambrian lithospheric mantle is present beneath the PKB region, suggesting that slab rollback did not grossly alter the lithospheric structure of this region, which implies at least some of the northward dip observed is probably old.

A third model explains the observed structure as the result of ‘young’ (Miocene) southward subduction of Variscan and EEC lithosphere and of Neogene thinning of the Pannonian lithosphere due to extension. Our data show no evidence of a south-dipping slab in the upper mantle or south-dipping features in the lower crust from the Carpathian foredeep southward. However, one could imagine the south-dipping features adjacent to the EEC (500–700 km) being attached to a south-dipping slab that has broken off and either sunk to great depth and/or been absorbed.

In summary, the seismic model for the 1420 km long profile CEL05 targeted the Pannonian basin, the Carpathians, the TESZ, and the EEC. Given the complex geologic history of the region, the equally complex velocity structure is no surprise. The CEL05 results indicate that two episodes of subduction with different polarities are possible. These results also provide considerable information on the deep structure and relationships between upper crustal features known from drilling and geologic data. However, further integrated geophysical and tectonic analyses will be required to fully determine the implications of the CELEBRATION 2000 data.

1.15.6 Summary

The POLONAISE'97, CELEBRATION 2000, ALP 2002, and SUDETES 2003 seismic experiments in Central Europe provide unprecedented seismic coverage of lithospheric structure over a large area (**Figure 14**). The analysis of the huge data set provided by this massive international cooperative effort is far from complete. However, we have learned a

great deal about the complex structure along the TESZ region in particular. In this area, we have delineated a deep basin, the lower portion of which is sediments and volcanics associated with the rifted margin of Baltica. In addition, several crustal blocks exist along this margin, but appear to mostly be of Baltic origin with Variscan terranes lying outboard to the southwest. The Pannonian/Carpathian/TESZ region displays a complex structure with surprising

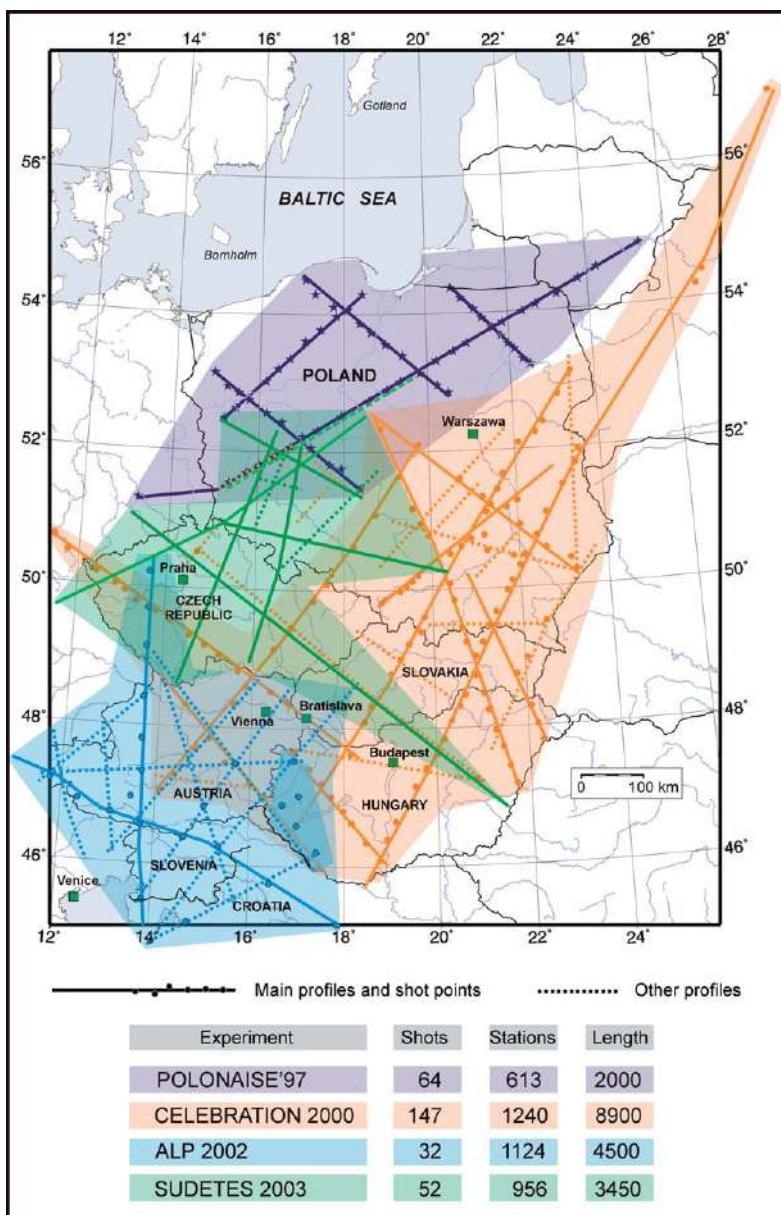


Figure 14 Layout of the POLONAISE'97, CELEBRATION 2000, ALP 2002, and SUDETES 2003 seismic experiments in Central Europe.

northward dip in the deep crust and uppermost mantle and southward dips in the upper crust. This geometry may well reflect multiple phases of subduction as well as collision-related features.

References

- Abramovitz T and Thybo H (2000) Seismic images of Caledonian lithosphere-scale collision structures in the southeastern North Sea along MONA LISA Profile 2. *Tectonophysics* 317: 27–54.
- Abramovitz T, Thybo H, and MONA LISA Working Group (1998) Seismic structure across the Caledonian Deformation Front along MONA LISA profile 1 in the southeastern North Sea. *Tectonophysics* 288: 153–176.
- Aichroth B, Prodehl C, and Thybo H (1992) Crustal structure along the central segment of the EGT from seismic refraction studies. *Tectonophysics* 207: 43–64.
- Ansorge J, Blundell D, and Mueller St (1992) Europe's lithosphere-seismic structure. In: Blundell DJ, Freeman R, and Mueller St (eds.) *A Continent Revealed – The European Geotraverse*, pp. 33–69. Cambridge: Cambridge University Press.
- BABEL Working Group (1993) Deep seismic reflection/refraction interpretation of crustal structure along BABEL profiles A and B in the southern Baltic Sea. *Geophysical Journal International* 112: 325–343.
- Bayer U, Grad M, Pharaoh TC, et al. (2002) The southern margin of the East European craton: New results from seismic sounding and potential fields between the North Sea and Poland. *Tectonophysics* 360: 301–314.
- Berthelsen A (1992a) Mobile Europe. In: Blundell DJ, Freeman R, and Mueller St (eds.) *A Continent Revealed – The European Geotraverse*, pp. 11–32. Cambridge: Cambridge University Press.
- Berthelsen A (1992b) From Precambrian to Variscan Europe. In: Blundell DJ, Freeman R, and Mueller St (eds.) *A Continent Revealed – The European Geotraverse*. pp. 153–164. Cambridge: Cambridge University Press.
- Berthelsen A (1998) The Tornquist Zone northwest of the Carpathians: An intraplate-pseudosuture. *Geologiska Föreningens i Stockholm Förhandlingar* 120: 223–230.
- Bielik M, Šefara J, Sotak J, Kováč M, Bezák V, and Plašienka D (2004) The Western Carpathians – Interaction of Hercynian and Alpine processes. *Tectonophysics* 393: 63–86.
- Blundell D, Freeman R, and Mueller St (eds.) (1992) *A Continent Revealed – The European Geotraverse*, p. 275. Cambridge: Cambridge University Press.
- Bogdanova S (1996) Palaeoproterozoic accretion of Sarmatia and Fennoscandia. In: Gee DG and Zeyen HJ (eds.) *EUROPROBE 1996 – Lithosphere Dynamics: Origin and Evolution of Continents*, pp. 81–89. Uppsala: The EUROPORBE Secretariat, Uppsala University.
- Bogdanova SV, Gorbatschev R, Stephenson RA, and Guterch A, (eds.) (2001) EUROBRIDGE: Palaeoproterozoic accretion of Fennoscandia and Sarmatia. *Tectonophysics* 339: 1–237.
- Brückl E, Bodoky T, Hegedűs E, et al. (2003) ALP 2002 seismic experiment. *Studia Geophysica et Geodaetica* 47: 671–679.
- Čermák V and Bodri L (1998) Heat flow map of Europe revised. *Deutsche Geophysikalische Gesellschaftsche VII*: 58–63.
- Čermák V, Šafanda J, and Guterch A (1989) Deep temperature distribution along three profiles crossing the Teisseyre-Tornquist tectonic zone in Poland. *Tectonophysics* 164: 151–163.
- Červený V and Pšenčík I (1983) SEIS83 – Numerical modeling of seismic wave fields in 2-D laterally varying layered structure by the ray method. In: Engdahl ER (ed.) *Documentation of Earthquake Algorithm*, Rep. SE-35. pp. 36–40. Boulder: World Data Center A for Solid Earth Geophysics.
- Csontos L and Vörös A (2004) Mesozoic plate tectonic reconstruction of the Carpathian region. *Palaeogeography, Palaeoclimatology, Palaeoecology* 210: 1–56.
- Czuba W, Grad M, Luosto U, Motuza G, Nasedkin V, and POLONAISE P5 Working Group (2002) Upper crustal seismic structure of the Mazury complex and Mazowsze massif within the East European craton in NE Poland. *Tectonophysics* 360: 115–128.
- Dadlez R, Grad M, and Guterch A (2005) Crustal structure below the Polish Basin: Is it composed of proximal terranes derived from Baltica? *Tectonophysics* 411: 111–128.
- Dadlez R, Kowalczewski Z, and Znosko J (1994) Some key problems of the pre-Permian tectonics of Poland. *Geological Quarterly* 38: 169–189.
- Dalziel IWD (1997) Neoproterozoic–Paleozoic geography and tectonics: Review, hypothesis, environmental speculation. *Geological Society of America – Bulletin* 109: 16–42.
- Dövényi P, Horvath E, Liebe P, Gálfi J, and Erki I (1983) Geothermal conditions of Hungary. *Geophysical Transactions* 29: 3–114.
- EUROBRIDGE Seismic Working Group (1999) Seismic velocity structure across the Fennoscandia–Sarmatia suture of the East European craton beneath the EUROBRIDGE profile through Lithuania and Belarus. *Tectonophysics* 314: 193–217.
- EUROBRIDGE'95 Seismic Working Group (2001) EUROBRIDGE'95: Deep seismic profiling within East European craton. *Tectonophysics* 339: 153–175.
- Golonka J, Krobicki M, Oszczypko N, Ślączka A, and Stomka T (2003a) Geodynamic evolution and palaeogeography of the Polish Carpathians and adjacent areas during Neo-Cimmerian and preceding events (latest Triassic – earliest Cretaceous). In: McCann T and Saintot A (eds.) *Tracing Tectonic Deformation Using the Sedimentary Record*, Special Publication, vol. 208, pp. 138–158. London: Geological Society, London.
- Golonka J, Ślączka A, and Picha F (2003) Geodynamic evolution of the orogen: The West Carpathians and Ouachitas Case study. *Annales Societatis Geologorum Poloniae* 75: 145–167.
- Grad M (1989) Investigation of the lower lithosphere in the southwestern part of the East European Platform on the basis of seismic data. *Gelands Beitraege für Geophysik* 98: 124–130.
- Grad M (1992) Seismic structure of the sub-crustal continental lithosphere. *Physics of the Earth and Planetary Interiors* 69: 224–230.
- Grad M (1997) Eurasian mantle structure derived from the records of nuclear explosions. In: Fuchs K (ed.) *Upper Mantle Heterogeneities from Active and Passive seismology*, pp. 89–96. Dordrecht: Kluwer.
- Grad M and Luosto U (1987) Seismic models of the crust of the Baltic Shield along the SVEKA profile in Finland. *Annales Geophysicae* 5B: 639–650.
- Grad M, Guterch A, Janik T, and Perchuć E (1986) Seismic model of the lithosphere of the East European Platform beneath the Baltic Sea–Black Sea profile. *Tectonophysics* 128: 281–288.
- Grad M, Guterch A, Keller GR, et al. (2006) Lithospheric structure beneath trans-Carpathian transect from Precambrian platform to Pannonian basin – CELEBRATION 2000 seismic profile CEL05. *Journal of Geophysical Research* 111: B03301 (doi: 10.1029/2005JB003647).
- Grad M, Guterch A, and Lund C-E (1991) Seismic models of the lower lithosphere beneath the southern Baltic Sea between Sweden and Poland. *Tectonophysics* 189: 219–227.

- Grad M, Guterch A, and Mazur S (2002b) Seismic refraction evidence for crustal structure in the central part of the Trans-European Suture Zone in Poland. In: Winchester JA, Pharaoh TC, and Verniers J (eds.) *Palaeozoic Amalgamation of Central Europe*, Special Publication, vol. 201, pp. 295–309. London: Geological Society.
- Grad M, Guterch A, and Polkowska-Purys A (2005) Crustal structure of the Trans-European Suture Zone in Central Poland – Reinterpretation of the LT-2, LT-4 and LT-5 deep seismic sounding profiles. *Geological Quarterly* 49: 243–252.
- Grad M, Janik T, Yliniemi J, et al. (1999) Crustal structure of the Mid-Polish Trough beneath the Teisseyre–Tornquist Zone seismic profile. *Tectonophysics* 314: 145–160.
- Grad M, Jensen SL, Keller GR, et al. (2003a) Crustal structure of the Trans-European Suture Zone region along POLONAISE'97 seismic profile P4. *Journal of Geophysical Research* 108(B11): 2541 (doi:10.1029/2003JB002426).
- Grad M, Keller GR, Thybo H, Guterch A, and POLONAISE Working Group (2002a) Lower lithospheric structure beneath the Trans-European Suture Zone from POLONAISE'97 seismic profiles. *Tectonophysics* 360: 153–168.
- Grad M and Luosto U (1994) Seismic velocities and Q-factors in the uppermost crust beneath the SVEKA profile in Finland. *Tectonophysics* 230: 1–18.
- Grad M and Tripolsky AA (1995) Crustal structure from P and S seismic waves and petrological models of the Ukrainian shield. *Tectonophysics* 250: 89–112.
- Grad M, Špičák A, Keller GR, et al. (2003) SUDETES 2003 Seismic Experiment. *Studia Geophysica et Geodaetica* 47: 681–689.
- Guggisberg B and Berthelsen A (1987) A two dimensional velocity model for the lithosphere beneath the Baltic Shield and its possible tectonic significance. *Terra Cognita* 7: 631–638.
- Guggisberg B, Kaminski W, and Prodehl C (1991) Crustal structure of the Fennoscandian Shield: A travelttime interpretation of the long-range FENNOLORA seismic refraction profile. *Tectonophysics* 195: 105–137.
- Guterch A, Grad M, Janik T, et al. (1994) Crustal structure of the transition zone between Precambrian and Variscan Europe from new seismic data along LT-7 profile (NW Poland and Eastern Germany). *Comptes Rendus de l' Academie des Sciences, Paris* 319(Ser.II): 1489–1496.
- Guterch A, Grad M, Keller GR, et al. (2003b) CELEBRATION 2000 seismic experiment. *Studia Geophysica et Geodaetica* 47: 659–669.
- Guterch A, Grad M, Keller GR, et al. (2004) Huge contrasts of the lithospheric structure revealed by new generation seismic experiments in Central Europe. *Polish Geological Review* 52: 753–760.
- Guterch A, Grad M, Keller GR, and CELEBRATION 2000 Organizing Committee (2001) Seismologists celebrate the New Millennium with an experiment in Central Europe. *EOS Transactions of American Geophysical Union* 82: 529, 534–535.
- Guterch A, Grad M, Materzok R, et al. (1992) Laminated structure of the lower crust in the fore-Sudetic region in Poland, derived from seismic data. *Physics of the Earth and Planetary Interiors* 69: 217–223.
- Guterch A, Grad M, Materzok R, and Perchuć E (1986) Deep structure of the Earth's crust in the contact zone of the Palaeozoic and Precambrian platforms in Poland (Tornquist–Teisseyre zone). *Tectonophysics* 128: 251–279.
- Guterch A, Grad M, Materzok R, Pajchel J, Perchuć E, and Toporkiewicz S (1984) Deep structure of the Earth's crust in the contact zone of the Palaeozoic and Precambrian platforms and the Carpathian Mts in Poland. *Acta Geophysica Polonica* 32: 25–41.
- Guterch A, Grad M, Špičák A, et al. (2003a) An overview of recent seismic refraction experiments in Central Europe. *Studia Geophysica et Geodaetica* 47: 651–657.
- Guterch A, Grad M, Thybo H, Keller GR, and Miller K (1998) Seismic experiment spreads across Poland. *EOS Transactions of American Geophysical Union* 79: 302–305.
- Guterch A, Grad M, Thybo H, Keller GR, and POLONAISE Working Group (1999) POLONAISE'97 – International seismic experiment between Precambrian and Variscan Europe in Poland. *Tectonophysics* 314: 101–121.
- Guterch A, Kowalski T, Materzok R, and Toporkiewicz S (1976) Seismic refraction study of the Earth's crust in the Teisseyre–Tornquist line zone in Poland along the regional profile LT-2. *Publications of the Institute of Geophysics, Polish Academy of Sciences* A-2(101): 15–23.
- Holbrook WS, Purdy GM, Sheridan RE, et al. (1994) Seismic structure of the US Mid-Atlantic continental margin. *Journal of Geophysical Research* 99: 17871–17891.
- Hole JA (1992) Non-linear high resolution three-dimensional seismic travel time tomography. *Journal of Geophysical Research* 97: 6553–6562.
- Hrbcová P, Šroda P, Špičák A, and CELEBRATION Working Group (2005) Crustal and uppermost mantle structure of the Bohemian Massif based on CELEBRATION 2000 profile CEL09. *Journal of Geophysical Research* 110: B11305 (doi: 10.1029/2004JB003080).
- Janik T, Grad M, Guterch A, et al. (2005) Lithospheric structure of the Trans-European Suture Zone along the TTZ and CEL03 profiles (from NW to SE Poland). *Tectonophysics* 411: 129–156.
- Janik T, Yliniemi J, Grad M, Thybo H, Tiira T, and POLONAISE P2 Working Group (2002) Crustal structure across the TESZ along POLONAISE'97 seismic profile P2 in NW Poland. *Tectonophysics* 360: 129–152.
- Jensen SL, Janik T, Thybo H, and POLONAISE Working Group (1999) Seismic structure of the Palaeozoic platform along POLONAISE'97 profile P1 in southwestern Poland. *Tectonophysics* 314: 123–143.
- Jensen SL, Thybo H, and POLONAISE'97 Working Group (2002) Moho topography and lower crustal wide-angle reflectivity around the TESZ in southern Scandinavia and northeastern Europe. *Tectonophysics* 360: 187–213.
- Keller GR and Hatcher RD (1999) Some comparisons of the structure and evolution of the southern Appalachian – Ouachita orogen and portions of the Trans-European Suture Zone region. *Tectonophysics* 314: 43–68.
- Komminaho K (1997) Software manual for programs MODEL and XRAYS – A graphical interface for SEIS83 program package, Rep. No. 20, 31pp. University of Oulu, Department of Geophysics.
- Kováč M, Nagymarosy A, Soták J, and Šutovská K (1993) Late Tertiary paleogeographic evolution of the Western Carpathians. *Tectonophysics* 226: 401–415.
- Królkowski C and Petecki Z (1995) *Gravimetric Atlas of Poland*. Warsaw: Polish Geological Institute.
- Krysiński L, Grad M, and POLONAISE Working Group (2000) POLONAISE'97 – Seismic and gravimetric modelling of the crustal structure in the Polish basin. *Physics and Chemistry of the Earth A* 25: 355–363.
- Książkiewicz M (1977) Hypothesis of plate tectonics and the origin of the Carpathians (in Polish, English summary). *Annales de la Société Géologique de Pologne* 47: 329–353.
- Majdański M, Grad M, Guterch A, and SUDETES 2003 Working Group (2006) 2-D seismic tomographic and ray tracing modeling of the crustal structure across the Sudetes Mountains basing on SUDETES 2003 experiment data. *Tectonophysics* 413: 249–269.
- Majorowicz J, Čermák V, Šafanda J, et al. (2003) Heat flow models across the Trans European Suture Zone in the area

- of the POLONAISE'97 seismic experiment. *Physics and Chemistry of the Earth* 28: 375–391.
- Malinowski M, Żelaźniewicz A, Grad M, Guterch A, Janik T, and CELEBRATION Working Group (2005) Seismic and geological structure of the crust in the transition from Baltica to Palaeozoic Europe in SE Poland – CELEBRATION 2000 experiment, profile CEL02. *Tectonophysics* 401: 55–77.
- Mickus KL and Keller GR (1992) Lithospheric structure of the south-central United States. *Geology* 20: 335–338.
- Perchuć E and Thybo H (1996) Upper mantle P-wave velocity model for the Baltic Shield. *Tectonophysics* 253: 227–245.
- Petecki Z, Polechońska O, Cieśla E, and Wybraniec S (2003) Magnetic map of Poland, scale 1: 500,000. Warsaw: Polish Geological Institute.
- Pharaoh TC (1999) Palaeozoic terranes and their lithospheric boundaries within the Trans-European Suture Zone (TESZ): A review. *Tectonophysics* 314: 17–41.
- Plomerová J, Achauer U, Babuška V, Granet M, and BOHEMA Working Group (2003) Passive seismic experiment to study lithosphere–asthenosphere system in the western part of the Bohemian Massif. *Studia Geophysica et Geodaetica* 47: 651–657.
- Pogay K, Bodoky T, Hegedűs E, et al. (1995) Astenospheric structure beneath a Neogene basin in southeast Hungary. *Tectonophysics* 252: 467–484.
- Royden LH and Dövényi P (1988) Variations in extensional styles at depth across the Pannonian basin. In: *The Pannonian Basin: A study in Basin Evolution*, Memoir 45, pp. 235–255. Tulsa: American Association of Petroleum Geologist.
- Růžek B, Vavryčuk V, Hrubcová P, Zedník J, and the CELEBRATION Working Group (2003) Crustal anisotropy in the Bohemian Massif, Czech Republic: Observations based on central European lithospheric experiment based on refraction (CELEBRATION) 2000. *Journal of Geophysical Research* 108(B8): 2392 (doi:10.1029/2002JB002242).
- Scheck-Wenderoth M and Lamarche J (2005) Crustal memory and basin evolution in the Central European Basin System – New insights from a 3D structural model. *Tectonophysics* 397: 143–165.
- Schweitzer J (1995) Blockage of regional seismic waves by the Teisseire–Tornquist Zone. *Geophysical Journal International* 123: 260–276.
- Seghedi I, Downes H, Szakács A, et al. (2004) Neogene–Quaternary magmatism and geodynamics in the Carpathian–Pannonian region: A synthesis. *Lithos* 72: 117–146.
- Środa P (1999a) Modifications of software package ZPLOT by C. Zelt. *Institute of Geophysics, Polish Academy of Sciences*.
- Środa P, Czuba W, Grad M, et al. (2006) Crustal and upper mantle structure of the Western Carpathians from CELEBRATION 2000 profiles CEL01 and CEL04: Seismic models and geological implications. *Geophysical Journal International* 167(2): 737–760 (doi: 10.1111/j.1365-246X.2006.03104.x).
- Środa P, Czuba W, Grad M, Gaczyński E, Guterch A, and POLONAISE Working Group (2002) Three-dimensional seismic modelling of crustal structure in the TESZ region based on POLONAISE '97 data. *Tectonophysics* 360: 169–185.
- Środa P and POLONAISE P3 Working Group (1999b) P- and S-wave velocity model of the southwestern margin of the Precambrian East European craton; POLONAISE'97, profile P3. *Tectonophysics* 314: 175–192.
- Stangel R (1990) *Die Struktur der Lithosphäre in Schweden, abgeleitet aus einer gemeinsamen Interpretation der P- und S-Wellen Registrierungen auf dem FENNOLORA-Profil*. PhD Thesis, University of Karlsruhe.
- Szabó C, Falus Gy, Zajacz Z, Kovács I, and Bali E (2004) Composition and evolution of lithosphere beneath the Carpathian–Pannonian Region: A review. *Tectonophysics* 393: 119–137.
- Thomas W A (1991) The Appalachian–Ouachita rifted margin of southeastern North America. *Geological Society of America Bulletin* 103: 415–431.
- Thybo H (2001) Crustal structure along the EGT profile across the Tornquist Fan interpreted from seismic, gravity and magnetic data. *Tectonophysics* 334: 155–190.
- Thybo H, Abramovitz T, Lassen A, and Schjøt F (1994) Deep structure of the Sorgenfrei–Tornquist zone interpreted from BABEL seismic data. *Z. Geol. Wiss.* 22(1/2): 3–17.
- Thybo H and Perchuć E (1997) The seismic 8° discontinuity and partial melting in the continental mantle. *Science* 275: 1626–1629.
- Trua T, Serri G, Birkenmajer K, and Pécskay Z (2006) Geochemical and Sr–Nd–Pb isotopic compositions of Mts Pieniny dykes and sills (West Carpathians): Evidence for melting in the lithospheric mantle. *Lithos* 90: 57–76.
- Vidale JE (1990) Finite-difference calculation of travel times in three dimensions. *Geophysics* 55: 521–526.
- Wilde-Piórko M, Grad M, and POLONAISE Working Group (1999) Regional and teleseismic events recorded across the TESZ during POLONAISE'97. *Tectonophysics* 314: 161–174.
- Winchester JA and the PACE TMR Network Team (2002) Potential field imaging of Palaeozoic orogenic structure in northern and central Europe. *Tectonophysics* 360: 5–23.
- Wortel MJR and Sparkman W (2000) Subduction and slab detachment in the Mediterranean–Carpathian region. *Science* 290: 1910–1917.
- Wybraniec S, Zhou S, Thybo H, et al. (1998) New map compiled of Europe's gravity field. *EOS Transactions of American Geophysical Union* 79(37): 437, 442.
- Zelt CA (1994) *ZPLOT – An Interactive Plotting and Picking Program for Seismic Data*. Cambridge, UK: Bullard Laboratory, University of Cambridge.
- Zeyen H, Dérová J, and Bielik M (2002) Determination of the continental lithospheric thermal structure in the Western Carpathians: Integrated modelling of surface heat flow, gravity anomalies and topography. *Physics of the Earth and Planetary Interiors* 134: 89–104.
- Ziegler PA (1990) *Geological Atlas of Western and Central Europe*, 2nd edn. Shell International Petroleum, Maatschappij B.V. London: Geological Society; Amsterdam: Elsevier.
- Zielhuis A and Nolet G (1994) Shear-wave velocity in the upper mantle beneath central Europe. *Geophysical Journal International* 117: 695–715.

1.16 Deep Earth Structure – Upper Mantle Structure: Global Isotropic and Anisotropic Elastic Tomography

J-P. Montagner, Institut de Physique du Globe, Paris, France

© 2007 Elsevier B.V. All rights reserved.

1.16.1	Introduction	559
1.16.2	Effects of Seismic Velocity and Anisotropy on Seismograms	560
1.16.2.1	First-Order Perturbation Theory	560
1.16.2.2	Effect of Anisotropic Heterogeneities on Normal Modes and Surface Waves	562
1.16.2.3	Comparison between Surface Wave Anisotropy and SKS Splitting Data	564
1.16.3	Upper Mantle Tomography of Seismic Velocity and Anisotropy	565
1.16.3.1	Forward Problem	565
1.16.3.1.1	Data space: d	565
1.16.3.1.2	Parameter space: p	568
1.16.3.2	Inverse Problem	568
1.16.3.3	Isotropic and Anisotropic Images of the Upper Mantle	571
1.16.4	Geodynamic Applications	573
1.16.4.1	Oceanic Plates	574
1.16.4.2	Continents	576
1.16.4.3	Velocity and Anisotropy in the Transition Zone	577
1.16.5	Numerical Modeling and Perspectives	579
References		584

1.16.1 Introduction

The first global isotropic tomographic models of the mantle were published in 1984 (Woodhouse and Dziewonski, 1984; Dziewonski, 1984). Since that time, many new tomographic models were published, and a large family of techniques was made available. This important progress was made possible by the extensive use of computers which can handle very large data sets and by the availability of good quality digital seismograms recorded by broadband seismic networks such as GEOSCOPE (Romanowicz *et al.*, 1984), IRIS (Smith, 1986) and all networks coordinated by the Federation of Digital Seismograph Networks (FDSN); Romanowicz and Dziewonski, 1986). Thanks to the installation of modern digital networks, it is now possible to map the whole Earth from the surface down to its center by seismic tomography. However, most tomographic techniques only make use of travel times or phase information in seismograms and very few use the amplitude, even when seismic waveforms are used (Woodhouse and Dziewonski, 1984; Li and Romanowicz, 1996). Global tomographic models have been improved over years

by an increase in the number of data and more importantly by using more general parametrizations, now including anisotropy (radial anisotropy in Nataf *et al.* (1986); general slight anisotropy in Montagner and Tanimoto (1990, 1991)) and to a lesser extent anelasticity (Tanimoto, 1990; Romanowicz, 1990). This chapter is focused on the imaging of large-scale (>1000 km) lateral heterogeneities of velocity and anisotropy in the upper mantle (0–660 km depth) where the lateral resolution is the best, thanks to surface waves providing an almost uniform lateral and azimuthal coverage, particularly below oceanic areas. We will discuss how tomographic imaging completely renewed our vision of upper mantle dynamics. It makes it possible to relate surface geology and plate tectonics to underlying mantle convection, and to map at depth the origin of geological objects such as continents, mountain ranges, slabs, ridges, and plumes. The goal of this chapter is not to review all contributions to this topic, but to underline the main scientific issues, to present different approaches and to illustrate the different progress (partly subjectively) by some of our results or by other more recent models. This chapter aims to

show why a major step, which takes a complete account of amplitude anomalies in the most general case and which will enable to map shorter scale heterogeneities, is now possible and presently ongoing.

1.16.2 Effects of Seismic Velocity and Anisotropy on Seismograms

For theoretical and practical reasons, the Earth was considered, for a long time, as composed of isotropic and laterally homogeneous layers. While an isotropic elastic medium can be described by two independent elastic parameters (λ and μ , the Lamé parameters), the cubic symmetry requires three parameters, but the most commonly used anisotropic medium (transverse isotropy with vertical symmetry axis) necessitates five independent parameters (Love, 1927; Anderson, 1961) and the most general elastic medium requires 21 independent parameters. However, since the 1960s, it was recognized that most parts of the Earth are not only laterally heterogeneous but also anisotropic. Though the lateral heterogeneities of seismic velocities were used for a long time for geodynamical applications, the importance of anisotropy for understanding geodynamic processes has only been recognized recently.

Seismology is an observational field based on the exploitation of seismic recordings of the displacement (velocity or acceleration) of the Earth induced by earthquakes. Broadband three-component high dynamic seismometers have been installed in more than 500 stations around the world during the last 20 years (see Chapter 1.01). Thanks to progress in instrumentation and theoretical developments, it is now possible to observe and to take a simultaneous account of the effects of lateral heterogeneities of velocity and anisotropy on seismograms.

1.16.2.1 First-Order Perturbation Theory

The basic equation which governs the displacement $\mathbf{u}(\mathbf{r}, t)$ is the elasto-dynamics equation:

$$\rho_0 \frac{d^2 u_i}{dt^2} = \sum_j \sigma_{ij,j} + F_{li} + F_{Ei} \quad [1]$$

F_{li} et F_{Ei} represent, respectively, the whole ensemble of applied inertial and external forces (see Takeuchi and Saito (1972) or Woodhouse and Dahlen (1978)

for a complete description of all terms). Generally, by neglecting the advection term, this equation is written in a simple way:

$$(\rho_0 \partial_{tt} - H_0) \mathbf{u}(\mathbf{r}, t) = \mathbf{F}(\mathbf{r}_S, t) \quad [2]$$

where H_0 is an integrodifferential operator and \mathbf{F} expresses all forces applied to the source volume in \mathbf{r}_S at time t (considered as external forces). \mathbf{F} is assumed to be equal to 0 for $t < 0$. In the elastic case, there is a linear relationship between σ_{ij} and the strain tensor ϵ_{kl} : $\sigma_{ij} = \sum_{kl} \Gamma_{ijkl} \epsilon_{kl}$ (+ terms related to the initial stress). Γ_{ijkl} is a fourth-order tensor, often written in its condensed form C_{ij} as a 6×6 matrix. By using the different symmetry conditions $\Gamma_{ijkl} = \Gamma_{jikl} = \Gamma_{ijlk} = \Gamma_{klij}$, the tensor Γ is shown to have 21 independent elastic moduli in the most general anisotropic medium. In an isotropic medium, this number reduces to two, the Lamé coefficients λ and μ .

When solving for the free oscillations of the Earth, $\mathbf{F} = 0$. The solution $\mathbf{u}(\mathbf{r}, t)$ of eqn [2] can be calculated for a spherically symmetric nonrotating reference Earth model associated with the operator H_0 , according to the equation

$$\rho_0 \partial_{tt} \mathbf{u}(\mathbf{r}, t) = H_0 \mathbf{u}(\mathbf{r}, t) \quad [3]$$

The solution of eqn [3] is beyond the scope of this chapter and is described in Chapter 1.02. The eigenvalues of the operator H_0 are equal to $-\rho_0 \omega_l^2$, where ω_l is the eigenfrequency characterized by two quantum numbers n and l , respectively termed radial and angular orders. The corresponding eigenfunctions ${}_n \mathbf{u}_l^m(\mathbf{r}, t)$ depend on three quantum numbers n, l, m , where m is the azimuthal order, with the property that $-l \leq m \leq l$. Therefore, for a given eigenfrequency ω_l calculated in a spherically symmetric Earth model, $2l+1$ eigenfunctions can be defined. The eigenfrequency ω_l is said to be degenerate, with a degree of degeneracy $2l+1$. There is a complete formal similarity with the calculation of the energy levels of the atom of hydrogen in quantum mechanics. The eigenfunctions ${}_n \mathbf{u}_l^m(\mathbf{r}, t)$ of the operator H_0 are orthogonal and normalized.

The important point is that the basis of functions ${}_n \mathbf{u}_l^m(\mathbf{r}, t)$ is complete. This implies that any displacement at the surface of the Earth can be expressed as a linear combination of these eigenfunctions:

$$\mathbf{u}(\mathbf{r}, t) = \sum_{n, l, m} {}_n a_l^m {}_n \mathbf{u}_l^m(\mathbf{r}, t)$$

Therefore, these eigenfunctions can be used to calculate the synthetic displacement at any point \mathbf{r} , at time t , due to a force system \mathbf{F} in the source volume. For a point force \mathbf{F} at point \mathbf{r}_S , a step time function and its associated moment tensor \mathbf{M} , which is a good starting model for earthquakes, the solution of eqn [2] is given by (Gilbert, 1971)

$$\mathbf{u}(\mathbf{r}, t) = \sum_{n, l, m} {}_n\mathbf{u}_l^m(\mathbf{r}) \frac{(1 - \cos_n \omega_l t)}{n \omega_l^2} \times e^{-n \omega_l t / 2Q} (\mathbf{M} : {}_n\epsilon_l^m)_{\mathbf{r}_S} \quad [4]$$

where ϵ is the deformation tensor. Since eqn [4] is linear in \mathbf{M} , it can be easily generalized to more complex spatial and temporal source functions, and can be rewritten as

$$\mathbf{u}(\mathbf{r}, t) = \mathbf{G}(\mathbf{r}, \mathbf{r}_S, t, t_S) \mathbf{M}(\mathbf{r}_S, t_S)$$

where $\mathbf{G}(\mathbf{r}, \mathbf{r}_S, t, t_S)$ is the Green operator of the medium. Normal mode theory is routinely used to calculate synthetic seismograms at long periods ($T \geq 40$ s.) and centroid moment tensor solutions (Dziewonski *et al.*, 1981).

An example of real and synthetic seismograms is presented in Figure 1. However, there are still some discrepancies (usually frequency dependent) between the observed and synthetic seismograms. The simplest way to explain the observed phase shifts (time delays) is to remove the assumption that the Earth is spherically symmetric, that is, there are lateral heterogeneities between the source and the receiver. The next step is to characterize these lateral heterogeneities. Since the agreement between synthetic and observed seismograms is good at long periods ($T \geq 40$ s), we can reasonably infer that the amplitude of heterogeneities is small (<10%). Behind

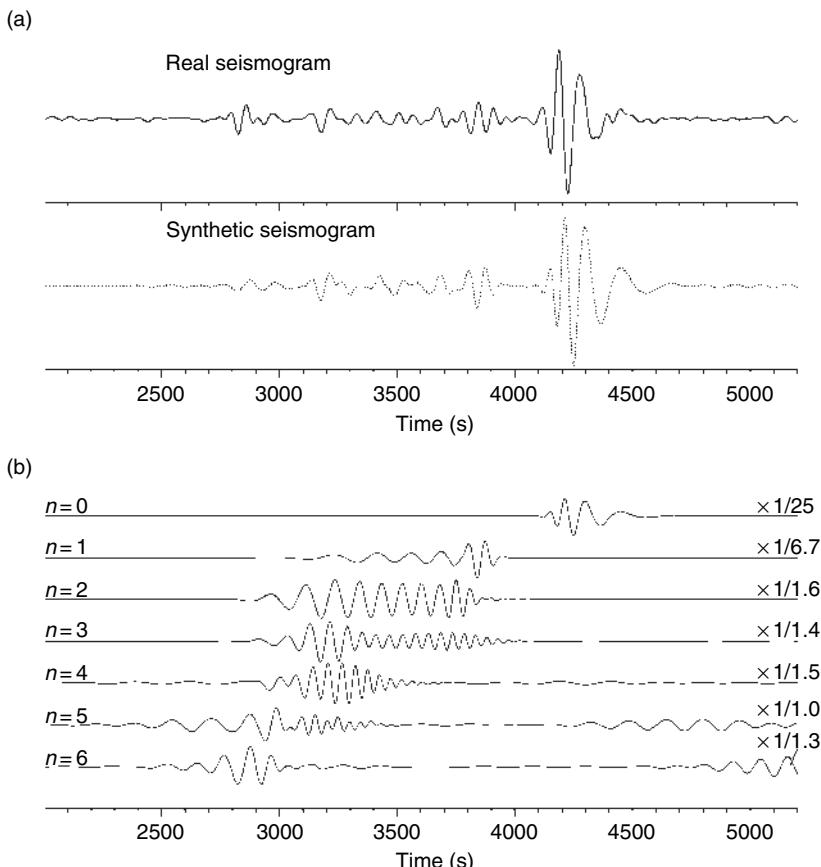


Figure 1 (a) Example of real and synthetic seismograms used for retrieving Rayleigh wave dispersion curve for the fundamental mode and overtones (Beucler *et al.*, 2003). Behind body waves, the signal is composed of surface waves. (b) The complex phase before the high amplitude wave packet corresponding to the fundamental mode of Rayleigh wave ($n=0$) can be synthetized by summing the first overtones.

the surface wave train, a long coda is usually observed, interpreted as scattered waves. However, when filtering out periods shorter than 40 s, this coda vanishes, which means that the scattering effect is only large in the shallowest regions of the Earth (primarily the crust, and the upper lithosphere) but that it is probably negligible at larger depths. However, some groups are starting to use the information contained in these coda waves (Aki and Richards, 1980; Snieder *et al.*, 2002), and even from seismic noise (Shapiro *et al.*, 2005) for imaging the crust. For the sake of simplicity, our study is limited to long-period surface waves and it is hypothesized that the scale of lateral heterogeneities is large compared with the seismic wavelength. This point will be discussed in Section 1.16.3.1. A second hypothesis that must be discussed is the isotropic nature of the Earth materials. Actually, it is a poor assumption, because seismic anisotropy can be unequivocally observed at different scales. Finally, the influence of lateral variations in attenuation must also be taken into account and will be discussed elsewhere in this treatise.

1.16.2.2 Effect of Anisotropic Heterogeneities on Normal Modes and Surface Waves

Different geophysical fields are involved in the investigation of the manifestations of anisotropy of Earth materials: mineral physics and geology for the study of the microscopic scale, and seismology for scales larger than, typically, 1 km. The different observations related to anisotropy, at different scales are reviewed in Montagner (1998) and in Chapter 1.09.

Different kinds of observations have been used for investigating anisotropy in the upper mantle: the Rayleigh–Love wave discrepancy (Anderson, 1961), the azimuthal variation of phase velocities of surface waves (Forsyth, 1975) and the shear-wave splitting particularly for SKS waves (Vinnik *et al.*, 1992). The lack of stations in oceanic areas explains why it is necessary to use surface waves to investigate upper mantle structure (isotropic or anisotropic) at the global or regional scales.

In the simplest case (fundamental modes, no coupling between branches of Rayleigh and Love waves), the frequency shift $\delta\omega/\omega$ (and the corresponding phase velocity perturbation $\delta V/V$), for a constant wavenumber k can be written by applying Rayleigh's principle:

$$\frac{\delta\omega}{\omega} \Big|_k = \frac{\delta V}{V} \Big|_k = \frac{1}{2\omega} \frac{\int_{\Omega} \epsilon_{ij}^* \delta \Gamma_{ijkl} \epsilon_{kl} d\Omega}{\int_{\Omega} \rho_{0n} u_l^{m*} n u_l^m d\Omega} \quad [5]$$

where ϵ_{ij} and $\delta \Gamma_{ijkl}$ are, respectively, the deformation and the deviations of elastic tensor components from a spherically symmetric, nonrotating, elastic, isotropic (SNREI) model, and $n u_l^m$ the eigenfunctions as defined in the previous section.

We only consider the propagation of surface waves in a plane-layered medium for a general slight elastic anisotropy, but it can be easily extended to the spherical Earth (Mochizuki, 1986; Tanimoto, 1986; Romanowicz and Snieder, 1988; Larson *et al.*, 1998; Trampert and Woodhouse, 2003). Smith and Dahlen (1973, 1975) found that, to first order in anisotropy and at frequency ω , the azimuthal variation of local phase velocity (Rayleigh or Love wave) can be expanded as a Fourier series of the azimuth Ψ along the path and is of the form

$$\begin{aligned} V(\omega, \theta, \phi, \Psi) - V_0(\omega) &= \alpha_0(\omega, \theta, \phi) \\ &+ \alpha_1(\omega, \theta, \phi) \cos 2\Psi \\ &+ \alpha_2(\omega, \theta, \phi) \sin 2\Psi \\ &+ \alpha_3(\omega, \theta, \phi) \cos 4\Psi \\ &+ \alpha_4(\omega, \theta, \phi) \sin 4\Psi \end{aligned} \quad [6]$$

where $V_0(\omega)$ is the reference velocity of the unperturbed medium, and Ψ is the azimuth along the path with respect to the north direction. Montagner and Nataf (1986) present the expressions for the different azimuthal coefficients $\alpha_i(\omega, \theta, \phi)$ as depth integral functions dependent on 13 simple linear combinations of standard cartesian elastic coefficients C_{ij} . Appendix 1 shows how to relate Γ_{ijkl} to C_{ij} and presents detailed calculation of azimuthal terms for Love waves in the geographical coordinate system:

- Constant term (0\Psi-azimuthal term: α_0)

$$\begin{aligned} A &= \rho V_{\text{PH}}^2 = \frac{3}{8}(C_{11} + C_{22}) + \frac{1}{4}C_{12} + \frac{1}{2}C_{66} \\ C &= \rho V_{\text{PV}}^2 = C_{33} \\ F &= \frac{1}{2}(C_{13} + C_{23}) \\ L &= \rho V_{\text{SV}}^2 = \frac{1}{2}(C_{44} + C_{55}) \\ N &= \rho V_{\text{SH}}^2 = \frac{1}{8}(C_{11} + C_{22}) - \frac{1}{4}C_{12} + \frac{1}{2}C_{66} \end{aligned}$$

- 2Ψ -azimuthal term:

$$\begin{aligned} \alpha_1 \cos 2\Psi & \quad \alpha_2 \sin 2\Psi \\ B_c = \frac{1}{2}(C_{11} - C_{22}) & \quad B_s = C_{16} + C_{26} \\ G_c = \frac{1}{2}(C_{55} - C_{44}) & \quad G_s = C_{54} \\ H_c = \frac{1}{2}(C_{13} - C_{23}) & \quad H_s = C_{36} \end{aligned}$$

- 4Ψ -azimuthal term:

$$\begin{aligned} \alpha_3 \cos 4\Psi & \quad \alpha_4 \sin 4\Psi \\ E_c = \frac{1}{8}(C_{11} + C_{22}) + \frac{1}{4}C_{12} - \frac{1}{2}C_{66} & \quad E_s = \frac{1}{2}(C_{16} - C_{26}) \end{aligned}$$

where indices 1 and 2 refer to horizontal coordinates (1: North; 2: East) and index 3 refers to vertical coordinate. ρ is the density, V_{PH} , V_{PV} are respectively horizontally and vertically ‘propagating’ P-wave velocities, V_{SH} , V_{SV} horizontal and vertical ‘polarized’ S-wave velocities. So, the different parameters present in the different azimuthal terms are simply related to elastic moduli C_{ij} .

From a practical point of view, once source phase is removed and assuming that the scale of heterogeneities is larger than the wavelength, the total phase ϕ_t (and the travel time) between the epicenter E and the receiver R is easily related to the measurement of phase velocity $V_d(\omega)$, and therefore to the local phase velocity $V(\omega, \theta, \phi, \Psi)$:

$$\phi_t = \omega t_{E \rightarrow R} = \frac{\omega \Delta}{V_d(\omega)} = \omega \int_E^R \frac{ds}{V(\omega, \theta, \phi, \Psi)} \quad [7]$$

Therefore, eqns [6] and [7] define the forward problem in the framework of first-order perturbation theory. We will see in the next section how to solve the inverse problem. This means that, ideally, surface waves in the plane case have the ability to provide information on 13 elastic parameters, which emphasizes the enormous potential of surface waves in terms of geodynamical and petrological implications. There are only 13 elastic moduli among 21, since propagation of surface waves is invariant against rotation by π , which corresponds to a monoclinic symmetry.

The 0Ψ term corresponds to the average over all azimuths and involves five independent parameters, A, C, F, L, N , which represent the equivalent transversely isotropic medium with a vertical symmetry axis (more simply named VTI or radial anisotropy). It must be noted that it is possible to retrieve the equivalent isotropic shear modulus from these five

parameters. By using a Voigt average, the shear modulus μ_{iso} is given by

$$\begin{aligned} \mu_{\text{iso}} = \rho V_{\text{S}_{\text{iso}}}^2 &= \frac{1}{15}(C_{11} + C_{22} + C_{33} - C_{12} \\ &\quad - C_{13} - C_{23} + 3C_{44} + 3C_{55} + 3C_{66}) \end{aligned}$$

According to the expressions of A, C, F, L, N in terms of elastic moduli, $\mu_{\text{iso}} = \frac{1}{15}(C + A - 2F + 6L + 5N)$. So we can see that the equivalent isotropic velocity depends not only on V_{SV} and V_{SH} , but also on P-wave velocity and anisotropy ($\phi = C/A$) and on $\eta = F/(A - 2L)$. By rewriting this expression $\mu_{\text{iso}} = \frac{1}{15}(C + (1 - 2\eta)A + (6 + 4\eta)L + 5N)$, neglecting anisotropy in P-wave ($\phi = 1$) and assuming $\eta = 1$, it is found that $\mu_{\text{iso}} = \rho V_{\text{S}_{\text{iso}}}^2 \approx \frac{2}{3}L + \frac{1}{3}N = \frac{2}{3}\rho V_{\text{SV}}^2 + \frac{1}{3}\rho V_{\text{SH}}^2$. Naturally, this choice is partly arbitrary, since usually, there is no S-wave anisotropy without P-wave anisotropy. Another way might consist in using correlations between anisotropic parameters for petrological models as derived by Montagner and Anderson (1989a).

The other azimuthal terms (2Ψ and 4Ψ) depend on four groups of two parameters, B, G, H, E , respectively describing the azimuthal variation of A, L, F, N . These simple parameters make it possible to describe in a simple way the two seismically observable effects of anisotropy on surface waves, the ‘polarization’ anisotropy (Schlue and Knopoff, 1977) and the azimuthal anisotropy (Forsyth, 1975).

Another important point in these expressions is that they provide the partial derivatives for the radial and azimuthal anisotropy of surface waves. The corresponding kernels and their depth dependence are plotted in Montagner and Nataf (1986) (Figures 14 and 15). These partial derivatives of the different azimuthal terms with respect to the elastic parameters can be easily calculated by using a radial anisotropic reference Earth model, such as PREM (Dziewonski and Anderson, 1981). The partial derivatives of the eigenperiod ${}_0T_l$ with respect to parameter p , $(p/T)(\partial T/\partial p)$ can easily be converted into phase velocity partial derivatives by using

$$\frac{p}{V} \left(\frac{\partial V}{\partial p} \right)_T = - \frac{V}{U} \frac{p}{T} \left(\frac{\partial T}{\partial p} \right)_k$$

For example, the parameters G_c and G_s have the same kernel as parameter L (related to V_{SV}) as shown by comparing the expressions of R_1 , R_2 , and R_3 in eqn [29] of Appendix 1. For fundamental modes, the calculation of kernels shows that Love waves are almost insensitive to V_{SV} (Figure 14) and Rayleigh

waves to V_{SH} . Rayleigh waves are the most sensitive to SV waves. However, as pointed out by [Anderson and Dziewonski \(1982\)](#), the influence of P-waves (through parameters A and C) can be very large in an anisotropic medium. The influence of density is also very large for Love and Rayleigh waves but, as shown by [Takeuchi and Saito \(1972\)](#), it is largely decreased when seismic velocities are inverted for, instead of elastic moduli and density.

1.16.2.3 Comparison between Surface Wave Anisotropy and SKS Splitting Data

It can be noted that some of the linear combinations of elastic moduli C_{ij} , derived from surface waves in the previous section, also come up when considering the propagation of body waves in symmetry planes for a weakly anisotropic medium (see, e.g., [Crampin et al. \(1984\)](#)), and their azimuthal dependence

$$\begin{aligned}\rho V_p^2 &= A + B_c \cos 2\Psi + B_s \sin 2\Psi \\ &\quad + E_c \cos 4\Psi + E_s \sin 4\Psi \\ \rho V_{\text{qSH}}^2 &= N - E_c \cos 4\Psi - E_s \sin 4\Psi \\ \rho V_{\text{qSV}}^2 &= L + G_c \cos 2\Psi + G_s \sin 2\Psi\end{aligned}$$

where V_{qSH} and V_{qSV} correspond, respectively, to quasi-SH and quasi-SV waves.

A global investigation of anisotropy inferred from SKS body wave splitting measurements (delay times and directions of maximum velocities) has been undertaken by different authors ([Vinnik et al., 1992](#); [Silver, 1996](#); [Savage, 1999](#)). Unfortunately, most SKS measurements have been done in continental parts of the Earth, and very few in oceans. It turns out that a direct comparison of body wave and surface wave data sets is now possible ([Montagner et al., 2000](#)). If the anisotropic medium is assumed to be characterized by a horizontal symmetry axis with any orientation (this is a very strong assumption which can be alleviated as shown by [Chevrot et al., 2004](#)), and for a vertically propagating SKS wave, a synthetic data set of SKS delay times and azimuths can be calculated from the global distribution of anisotropy derived from surface waves, by using the following equations:

$$\begin{aligned}\delta t_{\text{SKS}} &= \int_0^b dz \sqrt{\frac{\rho}{L}} \left[\frac{G_c(z)}{L(z)} \cos(2\Psi(z)) \right. \\ &\quad \left. + \frac{G_s(z)}{L(z)} \sin(2\Psi(z)) \right]\end{aligned}\quad [8]$$

where δt_{SKS} is the integrated travel time for the depth range 0 to b for a propagation azimuth Ψ , where the anisotropic parameters $G_c(z)$, $G_s(z)$, and $L(z)$ are the anisotropic parameters retrieved from surface waves at different depths. It is remarkable to realize that only the G -parameter (expressing the SV wave azimuthal variation) is present in this equation. From eqn [8], we can infer the maximum value of delay time $\delta t_{\text{SKS}}^{\max}$ and the corresponding azimuth Ψ_{SKS} :

$$\delta t_{\text{SKS}}^{\max} = \sqrt{\left\{ \int_0^b dz \sqrt{\frac{\rho}{L}} \frac{G_c(z)}{L(z)} \right\}^2 + \left\{ \int_0^b dz \sqrt{\frac{\rho}{L}} \frac{G_s(z)}{L(z)} \right\}^2} \quad [9]$$

$$\tan(2\Psi_{\text{SKS}}) = \frac{\int_0^b dz G_s(z)/L(z)}{\int_0^b dz G_c(z)/L(z)} \quad [10]$$

However, eqn [8] is approximate and only valid when the wavelength is much larger than the thickness of layers. It is possible to make more precise calculations by using the technique derived for two layers by [Silver and Savage \(1994\)](#) or by using the general expressions given in [Rumpker and Silver \(1998\)](#), [Montagner et al. \(2000\)](#), and [Chevrot et al. \(2004\)](#).

With eqns [9] and [10], a synthetic map of the maximum value of delay time $\delta t_{\text{SKS}}^{\max}$ can be obtained by using a 3-D anisotropic surface wave model. A detailed comparison between synthetic SKS derived from anisotropic upper mantle (AUM) model ([Montagner and Tanimoto, 1991](#)) and observed SKS ([Silver, 1996](#)) was presented in [Montagner et al. \(2000\)](#). [Figure 2](#) shows such a map for the Earth

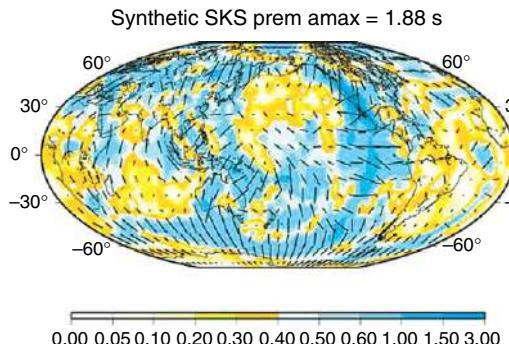


Figure 2 Map of synthetic SKS splitting delay time derived from the anisotropic surface wave model of [Montagner \(2002\)](#). The delay time is expressed in seconds; $A_{\max} = 1.88$ s.

centered in the Pacific, by using the anisotropic surface wave model of Montagner (2002) derived from the data of Montagner and Tanimoto (1991) and Ekström *et al.* (1997). First of all, the comparison shows that both data sets are compatible in magnitude but not necessarily in directions. Some contradictions between measurements derived from surface waves and from body waves have been noted. The agreement of directions is correct in tectonically active areas but not in old cratonic zones. The discrepancy in these areas results from the rapid lateral change of directions of anisotropy at a small scale. These changes stem from the complex history of these areas, which have been built by successive collages of continental pieces. It might also result from the hypothesis of horizontal symmetry axis, which was shown to be invalid in many areas (Plomerova *et al.*, 1996). The positive consequence of this discrepancy is that a small-scale mapping of fossile anisotropy in such areas might provide clues for understanding the processes of growth of continents and mountain building opening a new field, the paleoseismology.

Unlike surface waves, SKS waves have a good lateral resolution, and are sensitive to the short wavelength anisotropy just below the stations. But their drawback is that they have a poor vertical resolution. On the other hand, global anisotropy tomography derived from surface waves only provides long-wavelength anisotropy (poor lateral resolution) but enables the location at depth of anisotropy. The long-wavelength anisotropy derived from surface waves will display the same direction as the short-wavelength anisotropy inferred from body waves only when large-scale vertical coherent processes are predominant. As demonstrated by Montagner *et al.* (2000), the best agreement between observed and synthetic SKS can be found when only layers in the uppermost 200 km of the mantle are taken into account. Moreover, tomographic models derived from surface waves lose resolution at depths greater than 200 km. In some continental areas, short-scale anisotropy, the result of a complex history, might be important and even might mask the large-scale anisotropy more related to present convective processes (see, e.g., Marone and Romanowicz, 2006 for North America). From a statistical point of view, good agreement is found between orientations of anisotropy and plate velocity motion for fast-moving plates. The differences between anisotropy and tectonic plate directions are related to more complex processes, as will be seen in Section 1.16.3.

1.16.3 Upper Mantle Tomography of Seismic Velocity and Anisotropy

We now show how to implement theory of Section 1.16.1 from a practical but general point of view, and how to design a tomographic technique in order to invert for the 13 different elastic parameters and density. A tomographic technique necessitates solving simultaneously a forward problem and an inverse problem. By using the results of the previous section, it successively considers how to set the forward problem, and how it is used to retrieve a set of parameters by inversion.

1.16.3.1 Forward Problem

First, it is necessary to define the data space \mathbf{d} and the parameter space \mathbf{p} . It is assumed that a functional \mathbf{g} relating \mathbf{d} and \mathbf{p} can be found such that

$$\mathbf{d} = \mathbf{g}(\mathbf{p})$$

where \mathbf{d} is the set of data (which samples the data space), and \mathbf{p} the set of parameters.

1.16.3.1.1 Data space: \mathbf{d}

The basic data set is made of seismograms $\mathbf{u}(t)$. We can try to directly match the waveform in the time domain, or we can work in the Fourier domain, by separating phase and amplitude on each component $u_i(t)$:

$$u_i(t) = \int_{-\infty}^{\infty} A_i(\omega) e^{i(\omega t - \phi_i)} d\omega$$

The approach consisting in fitting seismic waveforms is quite general but, from a practical point of view, it does not necessarily correspond to the simplest choice. In a heterogeneous medium, the calculation of amplitude and phase effects makes it necessary to calculate the coupling between different multiplets (Li and Tanimoto, 1993; Li and Romanowicz, 1995; Marquering *et al.*, 1996), which is very time consuming. When working in Fourier domain, different time windows can be considered and the phase of different seismic trains, body waves and surface waves can be separately matched (Nolet, 1990; Léveque *et al.*, 1991) under drastic simplifying assumptions. **Figure 1** shows an example of observed and synthetic seismograms, the latter obtained by normal mode summation with the different higher modes. The fundamental wave train is well separated from other

modes at large epicentral distances. The part of the seismogram corresponding to higher modes is more complex and shows overlap of these modes in the time domain. Therefore, from a practical point of view, the fitting of the fundamental mode wave train will not cause any problem and has been widely used in global mantle tomography. The use of higher mode wave trains and the separation of overtones is much more difficult. The first attempts were performed by [Nolet \(1975\)](#), [Cara \(1979\)](#), [Okal and Jo \(1985\)](#), and [Dost \(1990\)](#) by applying a spatial filtering method. Unfortunately, all these techniques can only be applied in areas where dense arrays of seismic stations are present, that is, in North America and Europe. By using a set of seismograms recorded at one station but corresponding to several earthquakes located in a small source area, [Stutzmann and Montagner \(1994\)](#) showed how to separate the different higher modes. A similar approach was also followed by [Van Heijst and Woodhouse \(1997\)](#). We only detail in this paper the technique which was designed for fitting the fundamental mode wave train and the reader is referred to [Stutzmann and Montagner \(1994\)](#), [Van Heijst and Woodhouse \(1997\)](#), and [Beucler et al. \(2003\)](#) for the description of the recovery of higher-mode dispersion properties and to [Romanowicz \(2002\)](#) for a general overview.

Figure 3 presents an example of phase velocity

dispersion for different surface wave modes (fundamental and first higher modes ([Beucler et al., 2003](#))) and how they compare with previous investigations ([Cara, 1979](#); [Van Heijst and Woodhouse, 1997](#)).

We take advantage of the fact that, according to the Fermat's principle, the phase velocity perturbation is only dependent to second order on path perturbations, whereas amplitude perturbations are dependent, to first order, on these perturbations, which implies that the eigenfunctions must be recalculated at each iteration. Therefore, the phase is a more robust observable than the amplitude. The amplitude $A(\omega)$ depends in a complex manner on seismic moment tensor, attenuation, scattering, focusing effects, station calibration and near-receiver structure whereas the contribution of lateral heterogeneities of seismic velocity and anisotropic parameters to the phase $\phi(\omega)$ can be easily extracted. The data set under investigation, is composed of propagation times (or phase velocity measurements for surface waves) along paths: $\mathbf{d} = \{\Delta/V(\omega)\}$.

On the other hand, the phase of a seismogram at time t is decomposed, as follows: $\phi = \mathbf{k} \cdot \mathbf{r} + \phi'_0$, where \mathbf{k} is the wave vector, ϕ'_0 is the initial phase including several terms: $\phi'_0 = \phi_0 + \phi_S + \phi_I$, ϕ_S is the initial source phase, ϕ_0 is related to the number of polar phase shifts, ϕ_I is the instrumental phase. ϕ can be measured on seismograms by Fourier

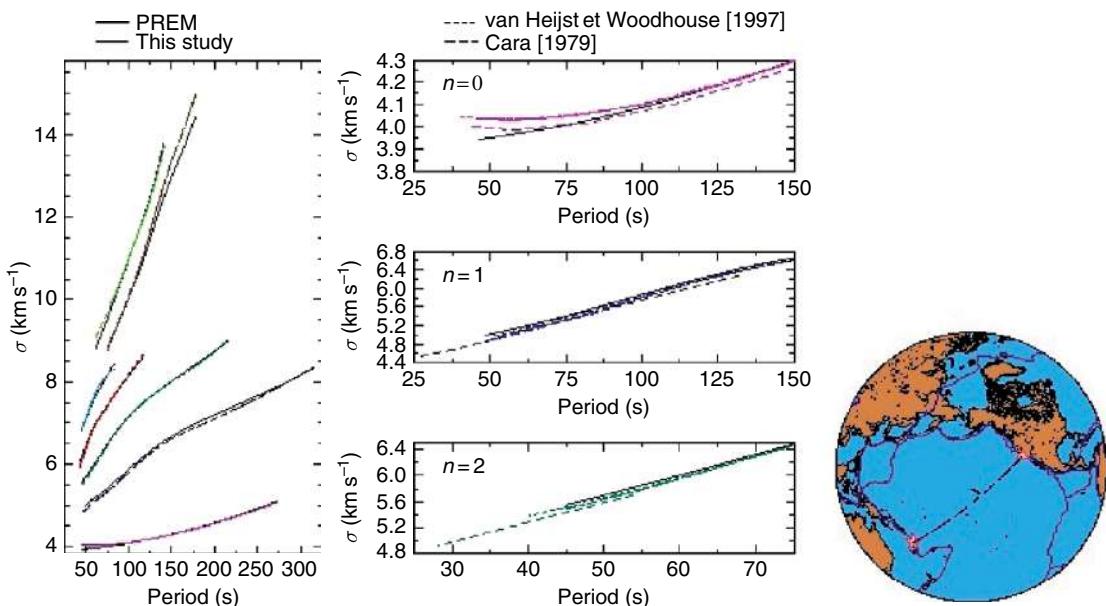


Figure 3 Phase velocity of the fundamental mode and the first six higher modes of Rayleigh compared with PREM (right plot) and with results (center) obtained in previous studies along the same path between Vanuatu and California (SCZ geoscope station) ([Beucler et al., 2003](#)).

transform. We usually assume that ϕ_S is correctly given by the centroid moment tensor solution. For a path between epicenter E and receiver R with an epicentral distance Δ , the phase ϕ is given by

$$\phi = \frac{\omega\Delta}{V_{\text{obs}}} + \phi_0 + \phi_S + \phi_I \quad [11]$$

In the general case, we want to relate the observed phase velocity $V_{\text{obs}}(\omega)$ to the parameters of the Earth model $\mathbf{p}(\mathbf{r}, \theta, \phi)$. Data and 3-D parameters can be related through integrals over the whole volume of the Earth. But for computing reasons, it is usual to use a multistep approach, where we first retrieve the local phase velocity $V(\omega, \theta, \phi)$ including its azimuthal terms, and then perform the inversion at depth. These two steps can be reversed since the order of the integrations can be reversed. It is necessary to consider the nature of the perturbed medium. Following the approach of Snieder (1988), if the perturbed medium is at the same time smooth (long-wavelength heterogeneities) and weak (small amplitude of heterogeneities), the geometrical optics approximation (and ray theory) applies. This hypothesis is not necessarily met within the Earth where some geological objects (slabs, mantle plumes, etc.) have a length scale which can be close to the seismic wavelength. In the approximation of ray theory, the volume integral reduces to the curvilinear integral along the geometrical ray path. When ray theory is applicable, we have

$$\phi - \phi'_0 = \frac{\omega\Delta}{V_{\text{obs}}(\omega)} = \int_E^R \frac{\omega ds}{V(\omega, \theta, \phi)} \quad [12]$$

where the integral is evaluated along the ray path between the epicenter E and the receiver R. Following the results of the previous section, different approximations are implicitly made when using this expression of the phase:

- Large angular order $l \gg 1$, but not too large (scattering problems). From a practical point of view, this means that measurements are performed in the period range $40 \text{ s} < T < 200 \text{ s}$ with seismic wavelengths between 200 and 1000 km.
- Geometrical optics approximation. If λ is the wavelength of the surface wave at period T , and Λ_S the spatial wavelength of heterogeneity: $\Lambda_S \gg \lambda = VT \Rightarrow \Lambda_S \gtrsim 2000 \text{ km}$. Epicentral distance Δ must be larger than seismic wavelength.

- Slight anisotropy and heterogeneity. $\delta V/V \ll 1$. According to Smith and Dahlen (1973) for the plane case, the local phase velocity can be decomposed as a Fourier series of the azimuth Ψ (eqn (6)): Each azimuthal term $\alpha_i(T, \theta, \phi)$ of eqn [6] can be related to the set of parameters $p_i(r, \theta, \phi)$ (density + 13 elastic parameters), according to the expressions derived in Appendix 1:

$$\begin{aligned} & \frac{\Delta}{V_{\text{obs}}(T)} - \frac{\Delta}{V_0(T)} \\ &= - \sum_{j=0}^2 \sum_{i=1}^{14} \int_E^R \frac{ds}{V_0} \int_0^\pi \left[\left(\frac{p_i \partial V}{V \partial p_i} \right)_j \frac{\delta p_i(r, \theta, \phi)}{p_i} \cos(2j\Psi) \right. \\ & \quad \left. + \left(\frac{p_i \partial V}{V \partial p_i} \right)_j \frac{\delta p_i(r, \theta, \phi)}{p_i} \sin(2j\Psi) \right] \end{aligned} \quad [13]$$

Equation [13] defines the forward problem in the framework of first-order perturbation theory, relating the data and the parameter spaces. This approach is usually named path average approximation (PAVA). Many terms in eqn [13] are equal to zero since all parameters are not present in each azimuthal term. A last important ingredient in the inverse problem formulation is the structure of the data space. It is expressed through its covariance function (continuous case) or covariance matrix (discrete case) of data C_d . When data d_i are independent, C_d is diagonal and its elements are the square of the errors on data σ_{d_i} .

1.16.3.1.1.(i) Finite-frequency effects As mentioned previously, a strong hypothesis is that in the framework of geometrical optics approximation, only large-scale heterogeneities can be retrieved. But interesting geological objects such as slabs and plumes are smaller scale. To go beyond the ray theory, it is necessary to take account of the finite-frequency effect when scale length has the same order of magnitude as the seismic wavelength. It is possible to use the scattering theory based on the Born or Rytov approximations (see, e.g., Woodhouse and Girnius (1982) for normal mode approach, Snieder (1988) for surface waves, Yomogida (1992), and Dahlen *et al.* (2000) for body waves). Equation [13] shows that the sensitivity kernels are 1-D, meaning that only heterogeneities in the vertical plane containing the source and the receiver are taken into account, whereas, by using the scattering theory, it is possible to calculate 3-D kernels and consequently to take account of off-path

heterogeneities. Equations [12] and [13] must be replaced by an integral over the volume Ω :

$$\frac{\Delta}{V_{\text{obs}}(T)} - \frac{\Delta}{V_0(T)} = \sum_{i=1}^{14} \int \int \int_{\Omega} \times K_i(T, \theta, \phi) \frac{\delta p_i(r, \theta, \phi)}{p_i} d\Omega \quad [14]$$

where $K(T, \theta, \phi)$ is the scattering Fréchet sensitivity kernel, which depends on wave type (Rayleigh or Love) and on the relative location of E and R (see, e.g., Romanowicz (2002) for a review). Very different strategies can be followed for calculating this triple integral, by separating the surface integral and the radial integral. For a point scatterer, the kernel displays a typical shape of banana-doughnut (Dahlen *et al.*, 2000). Different approximations of $K(T, \theta, \phi)$ have been proposed (Spetzler *et al.*, 2002; Yoshizawa and Kennett, 2002; Ritzwoller *et al.*, 2002), but Sieminski *et al.* (2004) claimed that ray theory surface wave tomography with a very dense path coverage can detect heterogeneities with length scales close and even smaller than the seismic wavelength. The discussion of the advantages and shortcomings of these different techniques is beyond the scope of this chapter, but some new tomographic models using 3-D sensitivity kernels are starting to be constructed (Zhou *et al.*, 2004, 2006) for radially anisotropic media.

1.16.3.1.2 Parameter space: p

It is quite important to consider the structure of the parameter space in detail. First of all, it is necessary to define which parameters are required to explain our data set, how many physical parameters can be effectively inverted for, in the framework of the theory that is considered. For example, if the Earth is assumed to be elastic, laterally heterogeneous but isotropic, only three independent physical parameters, V_p , V_s , and density ρ (or the elastic moduli λ , μ , and ρ) can be inverted for, from surface waves. In a transversely isotropic medium with a vertical symmetry axis (Anderson, 1961; Takeuchi and Saito, 1972), the number of independent physical parameters is now six (five elastic parameters + density). In the most general case of a weak anisotropy, 14 physical parameters (13 combinations of elastic moduli + density) can actually be inverted for, using surface waves. Therefore, the number of ‘physical’ parameters p_i depends on the underlying theory which is used for explaining the data set.

Once the number of physical independent parameters is defined, we must define how many spatial (or geographical) parameters are required to describe the 3-D distributions $p_i(r, \theta, \phi)$. This is a difficult problem because the number of spatial parameters that can be reliably retrieved from the data set is not necessarily sufficient to provide a correct description of $p_i(r, \theta, \phi)$, that is, of the real Earth. The correct description of $p_i(r, \theta, \phi)$ depends on its spectral content: for example, if $p_i(r, \theta, \phi)$ is characterized by very large wavelengths, only a small number of spatial parameters is necessary, but if $p_i(r, \theta, \phi)$ presents very small scale features, the number of spatial parameters will be very large. In any case, it is necessary to assess the range of possible variations for $p_i(r, \theta, \phi)$ in order to provide some bounds on the parameter space. This is done through a covariance function of parameters in the continuous case (or a covariance matrix for the discrete case) $C_{ppj}(\mathbf{r}, \mathbf{r}')$ at two different points \mathbf{r} , \mathbf{r}' . These *a priori* constraints can be provided by other fields in geosciences, geology, mineralogy, numerical modeling, etc.

Consequently, a tomographic technique must not be restricted to the inversion of parameters $\mathbf{p} = \{p_i(r, \theta, \phi)\}$ that are searched for, but must include the calculation of the final covariance function (or matrix) of parameters C_p . This means that the retrieval of parameters is contingent to the resolution and the errors of the final parameters and is largely dependent on the resolving power of data (Backus and Gilbert, 1967, 1968, 1970). Finally, the functional g which expresses the theory relating the data space to the parameter space is also subject to uncertainty. In order to be completely consistent, it is necessary to define the domain of validity of the theory and to assess the error σ_T associated with the theory. Tarantola and Valette (1982) showed that the error σ_T is simply added to the error on data σ_d .

1.16.3.2 Inverse Problem

So far, we did not make assumption on the functional g relating data and parameters. But in the framework of first-order perturbation theory, the forward problem is usually linearized and eqn [13] can be simply written in the linear case:

$$\mathbf{d} = \mathbf{G}\mathbf{p}$$

where \mathbf{G} is now a matrix (or a linear operator) composed of Fréchet derivatives of \mathbf{d} with respect to \mathbf{p} ,

which has the dimensions $n_d \times n_p$ (number of data \times number of parameters). This matrix usually is not square and many different techniques in the past have been used for inverting \mathbf{G} . In any case, the inverse problem will consist in finding an inverse for the functional \mathbf{g} , which we will write $\tilde{\mathbf{g}}^{-1}$, notwithstanding the way it is obtained, such that

$$\mathbf{p} = \tilde{\mathbf{g}}^{-1}(\mathbf{d})$$

To solve the inverse problem, different algorithms can be used. The least-squares solution is usually solved by minimizing a cost function \mathcal{J} . Making the data space and the parameter space symmetric, Tarantola and Valette (1982) define the cost function \mathcal{J} as

$$\mathcal{J} = (\mathbf{d} - \mathbf{G}\mathbf{p})^T C_d^{-1} (\mathbf{d} - \mathbf{G}\mathbf{p}) + (\mathbf{p} - \mathbf{p}_0)^T C_p^{-1} (\mathbf{p} - \mathbf{p}_0)$$

The first term corresponds to classical least-squares with no damping, whereas the second term corresponds to norm damping, which imposes smoothness upon the parameter space. Different choices were proposed for this second term. For example, Montagner (1986b) uses a Gaussian covariance function characterized by a correlation length and an *a priori* error σ_p on parameters, whereas Su *et al.* (1984) prefer to minimize the roughness of the model. Other choices consist in taking a constant value such that $\delta\mathbf{p}^T C_p^{-1} \delta\mathbf{p} = \lambda^2 \delta\mathbf{p}^T \delta\mathbf{p}$ (Yoshizawa and Kennett, 2004). Or the covariance operator can be replaced by a Laplacian operator (see, e.g., Zhou *et al.*, 2006):

$$\delta\mathbf{p}^T C_p^{-1} \delta\mathbf{p} = \varepsilon \left(\int \int \int |\nabla^2 \left(\frac{\delta p}{p} \right)|^2 d\Omega \right)^{1/2}$$

A discussion about damping can be found in Trampert and Snieder (1996), who prefer Laplacian over model damping to reduce the spectral leakage.

As an example, by using the expression of \mathcal{J} , a quite general and widely used algorithm has been derived by Tarantola and Valette (1982):

$$\begin{aligned} \mathbf{p} - \mathbf{p}_0 &= \left(G^T C_d^{-1} G + C_{p_0}^{-1} \right)^{-1} G^T C_d^{-1} (\mathbf{d} - \mathbf{g}(\mathbf{p}) + G(\mathbf{p} - \mathbf{p}_0)) \\ &= C_{p_0} G^T (C_d + G C_{p_0} G^T)^{-1} (\mathbf{d} - \mathbf{g}(\mathbf{p})) \\ &\quad + G(\mathbf{p} - \mathbf{p}_0) \end{aligned} \quad [15]$$

where C_d is the covariance matrix of data, C_{p_0} the covariance function of parameters \mathbf{p} , and G is the Frechet derivative of the operator \mathbf{g} at point $\mathbf{p}(\mathbf{r})$. This algorithm can be made more explicit by writing it in its integral form:

$$\begin{aligned} \mathbf{p}(\mathbf{r}) &= \mathbf{p}_0(\mathbf{r}) + \sum_i \sum_j \int_V d\mathbf{r}' C_{p_0}(\mathbf{r}, \mathbf{r}') \\ &\quad \times G_i(\mathbf{r}') (S^{-1})_{ij} F_j \end{aligned} \quad [16]$$

with

$$\begin{aligned} S_{ij} &= C_{d_{ij}} + \int_V d\mathbf{r}_1 d\mathbf{r}_2 G_i(\mathbf{r}_1) C_{p_0}(\mathbf{r}_1, \mathbf{r}_2) G_j(\mathbf{r}_2) \\ F_j &= d_j - g_j(\mathbf{p}) + \int_V d\mathbf{r}'' G_j(\mathbf{r}'') (\mathbf{p}(\mathbf{r}'') - \mathbf{p}_0(\mathbf{r}'')) \end{aligned}$$

This algorithm can be iterated and is suited for solving slightly nonlinear problems. Different strategies can be followed to invert for the 3-D models $\mathbf{p}(\mathbf{r})$, because the size of the inverse problem is usually enormous in practical applications and a compromise must be found between resolution and accuracy (and also computing time). For the example of mantle tomography, a minimum parameter space will be composed of 13 (+density) physical parameters multiplied by 30 layers (if the mantle is divided into 30 independent layers. If geographical distributions of parameters are searched for up to degree 40 (lateral resolution around 1000 km), this implies a number of $\sim 700\,000$ independent parameters. Such a problem is still very difficult to handle from a computational point of view. A simple approach for solving this problem consists in dividing the inversion procedure into two steps. The first step consists in regionalizing phase (or group) velocity data in order to retrieve the different azimuthal terms, and the second step is the inversion at depth. It was implemented by Montagner (1986a, 1986b) and a very similar technique is presented by Barmin *et al.* (2001). In case of a large data set, Montagner and Tanimoto (1990) showed how to handle the inverse problem by making a series expansion of the inverse of matrix S . It was recently optimized from a computational point of view by Debayle and Sambridge (2004) and Beucler and Montagner (2006). One advantage of this technique is that it can be applied indifferently to regional studies or global studies. In case of imperfect spatial coverage of the area under investigation, it does not display ringing phenomena commonly observed when a spherical harmonics expansion is used (Tanimoto, 1986).

From a practical point of view, the choice of the model parameterization is also very important and different possibilities can be considered:

- Discrete basis of functions. A simple choice consists in dividing the Earth into 3-D blocks with a surface block size different from the radial one.

The size of block depends on the lateral resolution expected from the path coverage. A variant of this parametrization is the use of a set of spherical triangular grid points (see, e.g., Zhou *et al.* (2006)). The block decomposition is valid as well for global investigations as for regional studies. Usually, the Earth surface parametrization is different for the radial one. For global study, the natural basis is composed of the spherical harmonics for the horizontal variations $p_i(r, \theta, \phi) = \sum_{l=0}^{l_{\max}} \sum_{m=-l}^l a_l^m(r) Y_l^m(\theta, \phi)$. Other choices are possible, such as spherical splines (Wang and Dahlen, 1995). When data coverage is very uneven, other strategies are proposed using irregular cells or adaptative meshes (see, e.g., Zhang and Thurber (2005)).

- Continuous function $\mathbf{p}(\mathbf{r})$. In this case, the function is directly inverted for. Since the number of parameters is then infinite, it is necessary to regularize the solution by defining a covariance function of parameters $C_{p0}(\mathbf{r}, \mathbf{r}')$. For the horizontal variations, a Von Mises distribution (Montagner, 1986b) can be used for initial parameters $\mathbf{P}_0(\mathbf{r})$:

$$\begin{aligned} C_{p0}(\mathbf{r}, \mathbf{r}') &= \sigma_p(\mathbf{r})\sigma_p(\mathbf{r}') \exp \frac{\cos \Delta_{\mathbf{rr}'} - 1}{L_{\text{cor}}^2} \\ &\approx \sigma_p(\mathbf{r})\sigma_p(\mathbf{r}') \exp \frac{-\Delta_{\mathbf{rr}'}^2}{2L_{\text{cor}}^2} \end{aligned}$$

where L_{cor} is the correlation length, which defines the smoothness of the final model. This kind of distribution is well suited for studies on a sphere and is asymptotically equivalent to a Gaussian distribution when $L_{\text{cor}} \ll a$ (a radius of the Earth). When distributions of different azimuthal terms are searched for, it is possible to define cross-correlated covariance functions of parameters $C_{p_{ij}}(\mathbf{r}, \mathbf{r}')$, but since the different terms of the Fourier expansion in azimuth correspond to orthogonal functions, the cross-correlated terms off the diagonal can be taken equal to zero.

It is interesting to note that in eqn [16] the Frechet derivatives G along the path are multiplied by the Gaussian covariance operator C_{p0} . It means that the technique, which can be named Gaussian tomography, is equivalent to use fat rays: when the correlation length is wider than the Fresnel zone, ray theory applies and, consequently, the finite-frequency effects can be neglected. As discussed by Ritzwoller *et al.* (2002) and Sieminski *et al.* (2004), there might be some slight differences in amplitude between Gaussian tomography and diffraction tomography (taking account of finite-frequency effects),

but not in the location of heterogeneities provided that the spatial path coverage is sufficiently dense. The radial parametrization must be related to the resolving capability of the data at depth, according to the frequency range under consideration. For the radial variations, polynomial expansions can be used (see, e.g., Dziewonski and Woodhouse (1987) for Tchebyshev polynomials, or Boschi and Ekström (2002) for radial cubic splines). Since the number of physical parameters is very large for the inversion at depth, physical parameters are usually correlated. The different terms of the covariance function C_p between parameters p_1 and p_2 at radii r_i and r_j can be defined as follows:

$$C_{p_1, p_2}(r_i, r_j) = \sigma_{p_1}(r_i)\sigma_{p_2}(r_j)\zeta_{p_1, p_2} \exp \left[-\frac{(r_i - r_j)^2}{2L_{r_i}L_{r_j}} \right]$$

Where ζ_{p_1, p_2} is the correlation between physical parameters p_1 and p_2 inferred for instance from different petrological models (Montagner and Anderson, 1989a) such as pyrolite (Ringwood, 1975) and piclogite (Anderson and Bass, 1984; Bass and Anderson, 1986). L_{r_i}, L_{r_j} are the radial correlation lengths, which are used to smooth the inverse model.

The *a posteriori* covariance function is given by

$$\begin{aligned} C_p &= C_{p0} - C_{p0} G^T (C_d + G C_{p0} G^t)^{-1} G C_{p0} \\ &= \left(G^T C_d^{-1} G + C_{p0}^{-1} \right)^{-1} \end{aligned} \quad [17]$$

The resolution R of parameters can be calculated as well. It corresponds to the impulsive response of the system: $\mathbf{p} = \tilde{g}^{-1} \mathbf{d} = \tilde{g}^{-1} \mathbf{g} \mathbf{p}' = R \mathbf{p}'$. If the inverse problem is perfectly solved, R is the identity function or matrix. However, the following expression of resolution is only valid in the linear case (Montagner and Jobert, 1981):

$$R = C_{p0} G^t (C_d + G C_{p0} G^t)^{-1} G = (G^t C_d G + C_{p0})^{-1} G^t C_d^{-1} G \quad [18]$$

It is interesting to note that the local resolution of parameters is imposed by both the correlation length and the path coverage, unlike the Backus-Gilbert (1967, 1968) approach, which primarily depends on the path coverage. The effect of a damping factor in the algorithm to smooth the solution is equivalent to the introduction of a simple covariance function on parameters weighted by the errors on data (Ho-Liu *et al.*, 1989). When the correlation length is chosen very small, the algorithms of Backus-Gilbert (1968, 1970) and Tarantola and Valette (1982) are equivalent.

By considering the *a posteriori* covariance function and the resolution, it is possible to assess the reliability of the hypotheses made about the independence of parameters. For example, Tanimoto and Anderson (1985) and Montagner and Jobert (1988) showed that there is a tradeoff between azimuthal terms and constant term in case of a poor azimuthal coverage. For the inversion at depth, Nataf *et al.* (1986) also display the tradeoff between physical parameters V_{PH} , V_{SV} , ξ , ϕ , and η when only Rayleigh and Love wave 0- Ψ terms are used in the inversion process.

Though 13 elastic parameters (+ density) are necessary to explain surface wave data (Rayleigh and Love waves), only four parameters are well resolved for small anisotropy (Montagner and Jobert, 1988): the azimuthally averaged S-wave velocity V_{S} , the radial anisotropy expressed through the ξ parameter ($\xi = (V_{\text{SH}}/V_{\text{SV}})^2$), where V_{SH} (resp. V_{SV}) is the velocity of S-wave propagating horizontally with horizontal transverse polarization (resp. with vertical polarization), and the \mathbf{G} (G_c , G_s) parameters expressing the horizontal azimuthal variation of V_{SV} . ξ was introduced in the reference Earth model PREM (Dziewonski and Anderson, 1981) down to 220 km in order to explain a large data set of free oscillation eigenfrequencies and body wave travel times. The other elastic parameters can be derived by using constraints from petrology in order to reduce the parameter space (Montagner and Anderson, 1989a). This approach was followed by Montagner and Anderson (1989b) to derive an average reference earth model, and by Montagner and Tanimoto (1991) for the first global 3-D anisotropic model of the upper mantle.

1.16.3.3 Isotropic and Anisotropic Images of the Upper Mantle

The complete anisotropic tomographic procedure has been implemented for making different regional and global studies. Many global isotropic tomographic models of the upper mantle were published since Woodhouse and Dziewonski (1984) and the recent results have been reviewed by Romanowicz (2003). Many models inverting only for radial anisotropy but neglecting azimuthal anisotropy have also been published (Nataf *et al.*, 1984, 1986; Ekström and Dziewonski, 1998; Shapiro and Ritzwoller, 2002; Gung *et al.*, 2003; Panning and Romanowicz, 2004; Zhou *et al.*, 2006). The complete anisotropic tomographic technique (including azimuthal anisotropy) has been applied for investigating the upper mantle

structure either at a regional scale of the Indian Ocean (Montagner, 1986a; Montagner and Jobert, 1988; Debayle and Léveque, 1997), the Atlantic Ocean (Mocquet and Romanowicz, 1989; Silveira *et al.*, 1998), Africa (Hadiouche *et al.*, 1989; Debayle *et al.*, 2001; Sebai *et al.*, 2005; Sicilia *et al.*, 2005), Pacific Ocean (Nishimura and Forsyth, 1989; Montagner, 2002; Ritzwoller *et al.*, 2004), Antarctica (Roult *et al.*, 1994), Australia (Debayle and Kennett, 2000; Simons *et al.*, 2002), and Central Asia (Griot *et al.*, 1998a, 1998b); Villaseñor *et al.*, 2001) or at a global scale (Montagner and Tanimoto, 1990, 1991; Montagner, 2002; Debayle *et al.*, 2004). The reader is also referred to a quantitative comparison of tomographic and geodynamic models by Becker and Boschi (2002).

An important issue when constructing tomographic models is the correction for crustal structure, where sedimentary thickness and Moho depth variations are so strong that they affect dispersion of surface waves at least up to 100 s: it has been shown (Montagner and Jobert, 1988) that standard perturbation theory is inadequate to correct for crustal correction and more rigorous approaches have been proposed (Li and Romanowicz, 1996; Boschi and Ekström, 2002; Zhou *et al.*, 2005) using the updated crustal models 3SMAC (Nataf and Ricard, 1996; Ricard *et al.*, 1996) or CRUST2.0 (Mooney *et al.*, 1998; Laske *et al.*, 2001).

As an example of the results obtained after the first step of the tomographic procedure, Figure 4 shows different maps of 2- Ψ azimuthal anisotropy for Rayleigh waves at 100 s period for the first three modes, $n=0,1,2$, superimposed on the isotropic part (0- Ψ term) of phase velocity (Beucler and Montagner, 2006). From petrological and mineralogical considerations, Montagner and Nataf (1988) and Montagner and Anderson (1989a, 1989b) showed that the predominant terms of phase velocity azimuthal expansion are the 0- Ψ and 2- Ψ for Rayleigh waves, and 0- Ψ and 4- Ψ for Love waves. However, Trampert and Woodhouse (2003) carefully addressed the requirement of azimuthal anisotropy, and demonstrated that Rayleigh wave data need both 2- Ψ and 4- Ψ terms, which is also confirmed by Beucler and Montagner (2006). It was shown that for the same variance reduction, a global parametrization of anisotropy including azimuthal anisotropy requires fewer parameters than an isotropic parametrization. This apparent paradox can be explained by the fact that the increase of physical parameters is largely compensated by the smaller number of geographical

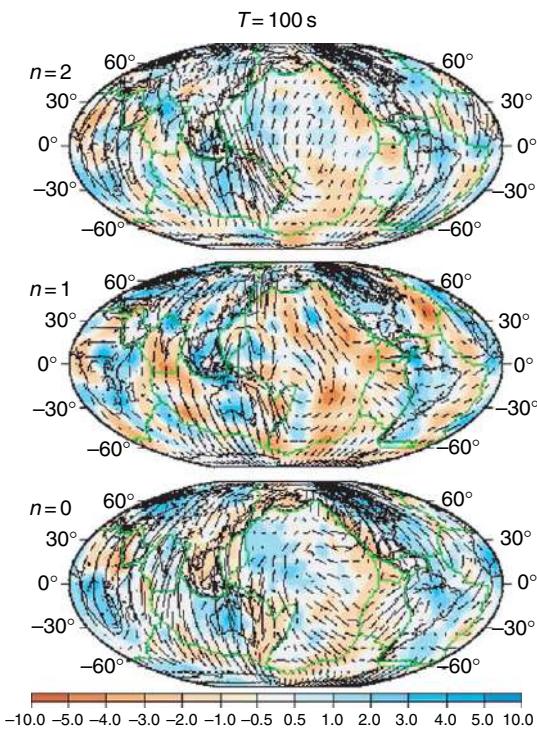


Figure 4 Rayleigh wave phase velocity maps at period $T = 100\text{ s}$ for the first three modes ($n = 0, 1, 2$). Modified from Beucler E and Montagner J-P (2006) Computation of large anisotropic seismic heterogeneities. *Geophysical Journal International* 165: 447–468.

parameters, that is, larger-scale heterogeneities. Other tests have questioned whether phase data are sensitive enough to detect azimuthal anisotropy (Larson *et al.*, 1998; Laske and Masters 1998) and the use of additional polarization data has been proposed.

Most tomographic models agree that down to ~ 250 – 300 km , the deep structure is closely related to plate tectonics and continental distribution. **Figure 5** presents two horizontal cross-sections from the most recent model of Debayle *et al.* (2005), which illustrates and confirms the robust features of the upper mantle models published so far since Montagner and Tanimoto (1991). In the upper mantle depth range around 100 km , all plate boundaries are slow: ridges and back-arc areas are slow, shields are fast, and seismic velocity in oceanic areas is increasing with the age of the seafloor. Except at few places, it is found that radial anisotropy expressed through the ξ parameter ($\xi = (V_{\text{SH}}^2 - V_{\text{SV}}^2)/V_{\text{SV}}^2$) is positive, as large as 10% in some oceanic areas and decreases with depth.

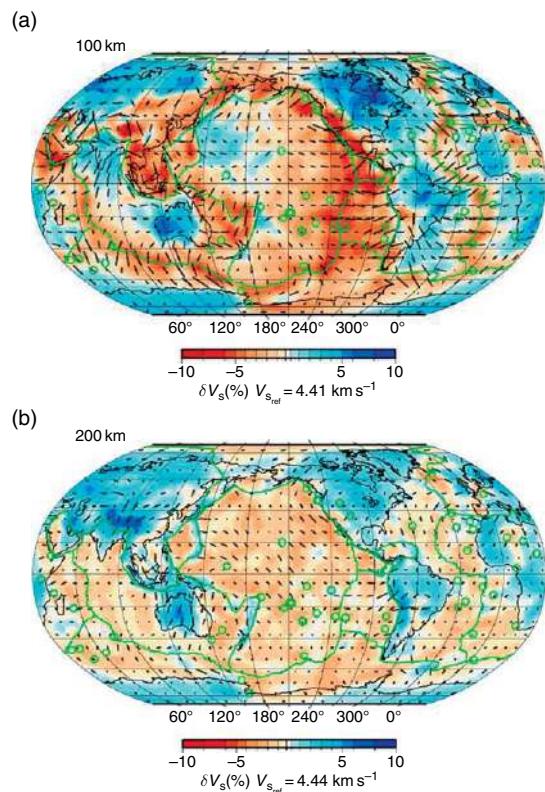


Figure 5 (a, b) Two cross-sections at 100 km (top) and 200 km (bottom) depths of the global tomographic model of Debayle *et al.* (2005). Directions of azimuthal anisotropy are superimposed on S-wave velocity heterogeneities. The length of bars is proportional to its amplitude (<2%).

The amplitude of SV-wave azimuthal anisotropy (G parameter) presents an average value of $\sim 2\%$ below oceanic areas (**Figure 5**). Montagner (1994, 2002) noted a good correlation between seismic azimuthal anisotropy and plate velocity directions (primarily for fast moving plates) given by Minster and Jordan (1978) or DeMets *et al.* (1990). However, the azimuth of G parameter can vary significantly as a function of depth. For instance, at shallow depths (down to 60 km), the maximum velocity can be parallel to mountain belts or plate boundaries (Vinnik *et al.*, 1992; Silver, 1996; Babuska *et al.*, 1998), but orthogonal to them at large depth. This means that, at a given place, the orientation of fast axis is a function of depth, which explains why the interpretation of SKS splitting with a simple model is often difficult.

As depth increases, the amplitude of heterogeneities rapidly decreases, some trends tend to vanish, and some distinctive features come up: most fast

ridges are still slow but slow ridges are hardly visible and back-arc regions are no longer systematically slow below 200 km. Large portions of fast ridges are offset with respect to their surface signatures. Below 300 km of depth (not shown here), high-velocity body below the western and the eastern Pacific rim is the most striking feature, which can be related to subducting slabs.

A visual and quantitative comparison of existing models can be found in the reference Earth model (REM) web site.

1.16.4 Geodynamic Applications

The most popular application of large-scale tomographic models is the understanding of mantle convection. Seismic velocity anomalies can be converted, under some assumptions, into temperature anomalies, density anomalies, and also into chemical or mineralogical heterogeneities. The application of seismic anisotropy to geodynamics in the upper mantle is straightforward if we assume that, due to the lattice-preferred orientation (LPO) of anisotropic crystals such as olivine (Christensen and Lundquist, 1982; Nicolas *et al.*, 1973), the fast-polarization axis of mineralogical assemblages is in the flow plane parallel to the direction of flow. **Figure 6** shows what is expected for the observable parameters V_s , ξ , G , ψ_G in the case of a simple convective cell with LPO. Radial anisotropy ξ expresses the vertical ($\xi < 1$) or horizontal character ($\xi > 1$) of convective flow, and the azimuthal anisotropy G can be related to the horizontal flow direction. Conversely, the three maps of V_s , ξ , G , can be interpreted in terms of convective flow. These three pieces of information are necessary to correctly interpret the data. For example, upwellings or downwellings are both characterized by a weak or negative ξ parameter, but a correlative positive or negative δV_s discriminates between these possibilities. By simultaneously inverting at depth for the different azimuthal terms of Rayleigh and Love waves, it is therefore possible to separate the lateral variations in temperature from those induced by the orientation of minerals. Such an interpretation might, however, be erroneous in water-rich mantle regions where LPO of minerals such as olivine is not simply related to the strain field (e.g., Jung and Karato, 2001). We will only present some examples of interesting applications of anisotropy in large-scale geodynamics and tectonics.

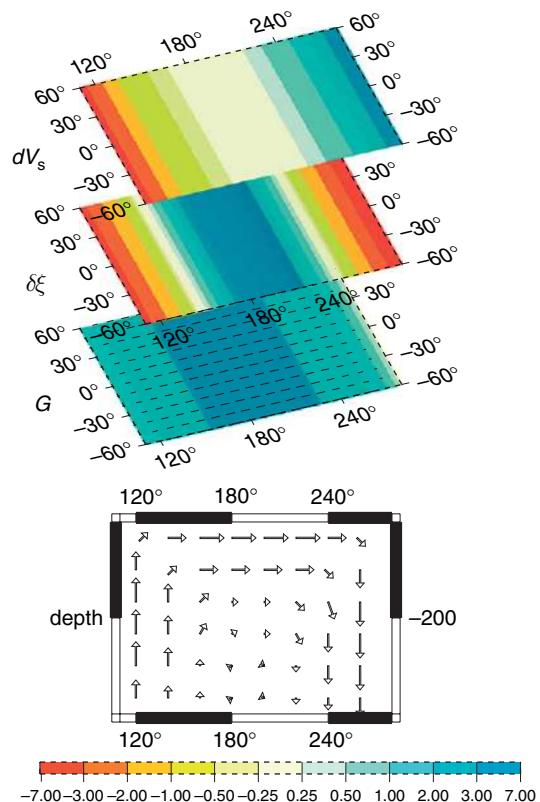


Figure 6 Horizontal cross sections of the seismic observable parameters V_s , ξ , G , Ψ_G associated with a simple convecting cell in the upper mantle, assuming LPO of anisotropic minerals such as olivine. A vertical flow is characterized by a negative ξ radial anisotropy (ratio between V_{SH} and V_{SV} , and a small azimuthal anisotropy ($G \approx 0$). An upwelling (resp. downwelling) is characterized by a large positive (resp. negative) temperature anomaly inducing $\delta V_s < 0$ (resp. $\delta V_s > 0$). A predominant large-scale horizontal flow will be translated into a significant amplitude of the G azimuthal anisotropy and its orientation will reflect the direction of flow (with a 180° ambiguity). Modified from Montagner J-P (2002) Upper mantle low anisotropy channels below the Pacific plate. *Earth and Planetary Science Letters* 202: 205–227.

Seismic anisotropy in the mantle primarily reflects the strain field prevailing in the past (frozen-in anisotropy) for shallow layers or present convective processes in deeper layers. Therefore, it makes it possible to map convection in the mantle. It must be noted that, when only the radial anisotropy is retrieved, its interpretation is nonunique. A fine layering of the mantle can also generate such a kind of anisotropy, and neglecting the azimuthal anisotropy can bias the amplitude of radial anisotropy and its interpretation.

The uppermost mantle down to 410 km is the depth range where the existence of seismic anisotropy is now widely recognized and well documented. Azimuthal variations have been found for body waves and surface waves in different areas of the world. During the last years, the shear wave splitting, primarily for SKS waves has extensively been used to study continental deformation, but very few studies using body waves are devoted to oceanic areas. Conversely, global anisotropic upper mantle models have been primarily derived during the last 10 years from surface waves, which are sensitive to structure below oceanic areas in the absence of ocean bottom stations and consequently of dense body wave data. The intercomparison of anisotropic body wave and surface wave data is still in its infancy. However, as shown by Montagner *et al.* (2000), Vinnik *et al.* (2003), and Simons *et al.* (2002), such a comparison is providing encouraging results.

1.16.4.1 Oceanic Plates

Oceans are the areas where plate tectonics applies almost perfectly and this is particularly the case in the largest one, the Pacific plate. Figure 7 presents three vertical cross-sections at two different latitudes, displaying V_{SV} velocity anomalies (Figure 7(a)) and the two kinds of anisotropy, which can be retrieved by simultaneous inversion of Rayleigh and Love waves constant 0- Ψ and azimuthal terms of eqn (1) from the model of Montagner (2002). In Figure 7(b), the equivalent radial anisotropy of the medium, for S-wave expressed through the ξ parameter, is displayed. The maps of Figure 7(c) are the distributions of the G parameter related to the azimuthal variation of SV-wave velocity. The maximum amplitude of G is $\sim 5\%$ and rapidly decreases as depth increases. The distributions of velocity and anisotropy are completely different for these different cross-sections. The thickening of lithosphere with the age of the seafloor is well observed on V_{SV} velocity maps, but lithosphere is much thicker in the northern cross-section. When compared with the cooling half-space model, bathymetry, heat flux and lithospheric thickness flatten with age (see Ritzwoller *et al.* (2004) for recent results). This flattening is explained by basal reheating, especially in the Central Pacific and the birth of small-scale convection below the lithosphere (Davaille and Jaupart, 1994; Solomatov and Moresi, 2000).

Radial cross-sections (Figure 7(b)) show that the $\delta\xi = \xi - \xi_{PREM}$ parameter is usually negative and small, where flow is primarily radial (mid-ocean ridges and subduction zones). For the East-Pacific Rise, Gu *et al.* (2005) found that a negative radial anisotropy is observed at least down to 300 km. Between plate boundaries, oceans display very large areas with a large positive radial anisotropy such as in the Pacific Ocean (Ekström and Dziewonski, 1998), characteristic of an overall horizontal flow field. This very large anisotropy in the asthenosphere might be the indication of a strong deformation field at the base of the lithosphere (Gung *et al.*, 2003), corresponding to the upper boundary layer of the convecting mantle (Anderson and Regan, 1983; Montagner, 1998).

Since convective flow below oceans is dominated by large-scale plate motions, the long-wavelength anisotropy found in oceanic lithospheric plates and in the underlying asthenosphere should be similar to the high-resolution anisotropy measured from body waves. Incidentally, one of the first evidences of azimuthal anisotropy was found in the Pacific Ocean by Hess (1964) for Pn-waves. So far, there are very few measurements of anisotropy by SKS splitting in the oceans. Due to the lack of seismic stations on the sea floor (with the exception of H2O half-way between Hawaii and California), the only measurements available for SKS were performed in stations located on ocean islands (Ansel and Nataf, 1989; Kuo and Forsyth, 1992; Russo and Okal, 1999; Wolfe and Silver, 1998), which are by nature anomalous objects, such as volcanic hotspots, where the strain field is perturbed by the upwelling material and not necessarily representative of the main mantle flow field. SKS splitting was measured during the temporary MELT experiment on the East-Pacific Rise (Wolfe and Solomon, 1998) but the orientation of the splitting is in disagreement with the petrological predictions of Blackman *et al.* (1996). Walker *et al.* (2001) presented a first measurement of SKS splitting at H2O, but it is in disagreement with independent SKS splitting measurements at the same station by Vinnik *et al.* (2003) and with surface wave anisotropy (Montagner, 2002).

The large-scale azimuthal anisotropy within and below lithosphere in the depth range 100–300 km is closely related to plate motions (Montagner, 1994; Ekström, 2000) and modeled in this framework (Tommasi *et al.*, 1996). Fast-moving oceanic plates are zones where the comparison between directions of plate velocities (Minster and Jordan, 1978) or

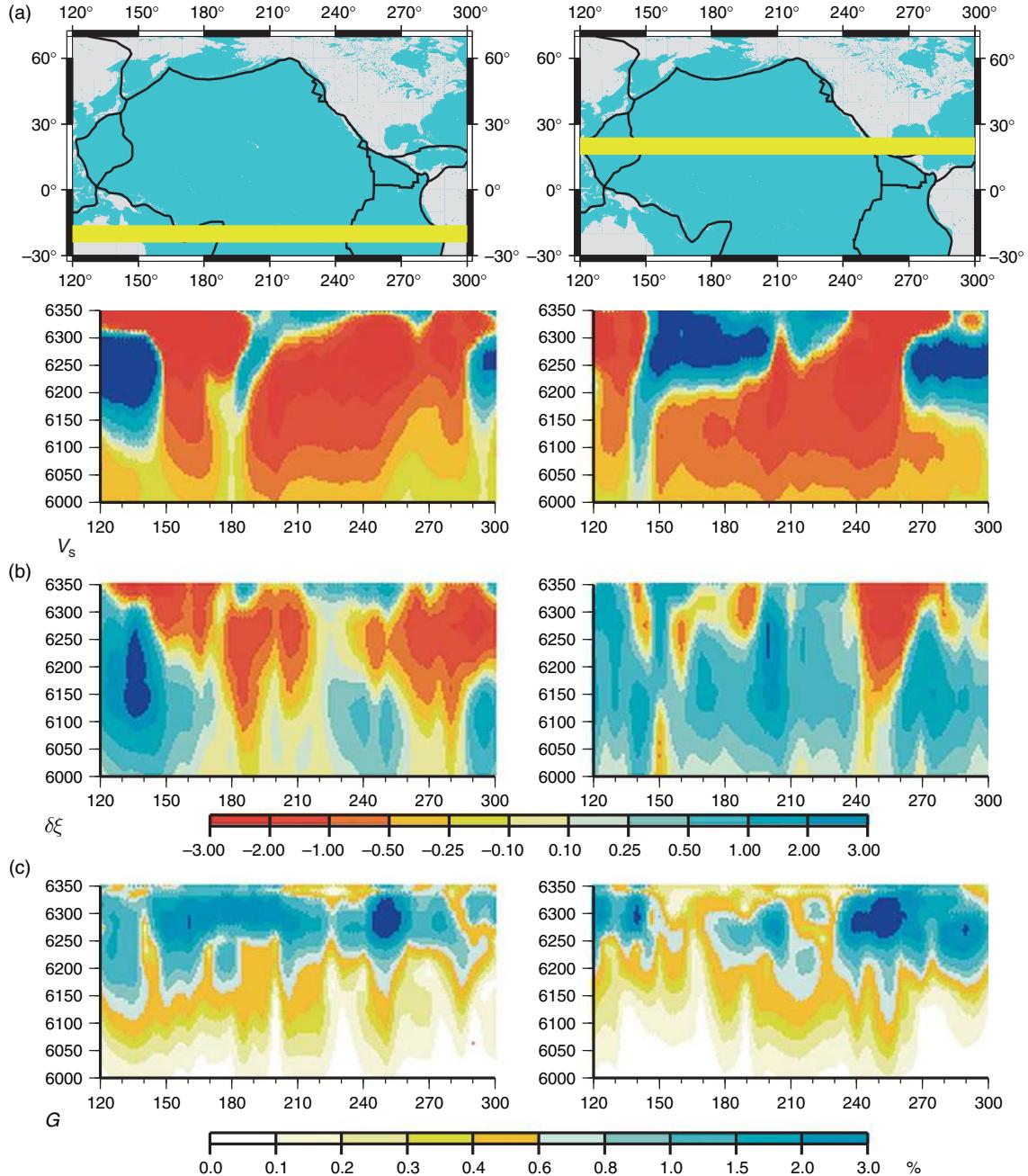


Figure 7 Vertical cross-sections of the distribution of V_s , $\xi - \xi_0$, G in the Pacific plate at -20° south and 20° north between radii 6000 km (370 km depth) and 6350 km (20 km depth) (after Montagner, 2002). The color scales in percents are the same for V_s and ξ . The vertical scale is exaggerated to make the figures more readable. (a) V_s ; (b) $\delta\xi = \xi - \xi_0$: deviation of ξ with respect to a reference model (ξ_0 PREM model); (c) G : amplitude of azimuthal anisotropy parameters.

NUVEL-1 (DeMets *et al.*, 1990) and directions of G parameter is the most successful (Figure 8). Conversely, such a comparison is more difficult and controversial below plates bearing a large proportion of continents, such as the European–Asian plate,

characterized by a very small absolute motion in the hotspot reference frame and probably a large influence of inherited anisotropy.

The map with the G parameter at 100 km (Figure 5) as well as the cross-sections of Figure 7(c)

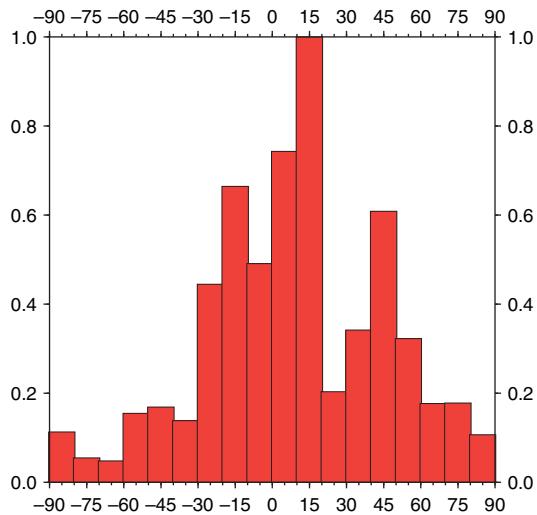


Figure 8 Histogram of the difference between plate velocities directions and synthetic SKS anisotropy azimuths in the Pacific plate. It is calculated by summing the contributions of each grid point ($5^\circ \times 5^\circ$) weighted by the latitude and the amplitude of anisotropy. Modified from Montagner J-P (2002) Upper mantle low anisotropy channels below the Pacific plate. *Earth and Planetary Science Letters* 202: 205–227.

show that the azimuthal anisotropy is very large along spreading ridges with a large asymmetry for the East-Pacific Rise. The direction of anisotropy is in very good agreement with plate motion, which is also found in all other available models (Ekström, 2000; Smith *et al.*, 2004; Debayle *et al.*, 2005). The anisotropy is also large in the middle of the Pacific plate, but a line of very small azimuthal anisotropy almost parallel to the East-Pacific Rise is observed there (see also Figure 2 for synthetic SKS). This linear area of small anisotropy was named low anisotropy channel (LAC) by Montagner (2002). When calculating the variation of the amplitude of azimuthal anisotropy as a function of depth, a minimum comes up between 40 and 60 Ma age of the seafloor (Figure 9(a)). The LAC is presumably related either to cracking within the Pacific plate and/or to secondary convection within and below the rigid lithosphere, predicted by numerical and analog experiments and also translated in the V_S velocity structure (Ritzwoller *et al.*, 2004; Figure 9(b)). These new features provide strong constraints on the decoupling between the plate and asthenosphere. The existence and location of these LACs might be related to the current active volcanoes and hotspots (possibly plumes) in Central Pacific. LACs, which are dividing the Pacific plate into smaller units, might indicate a

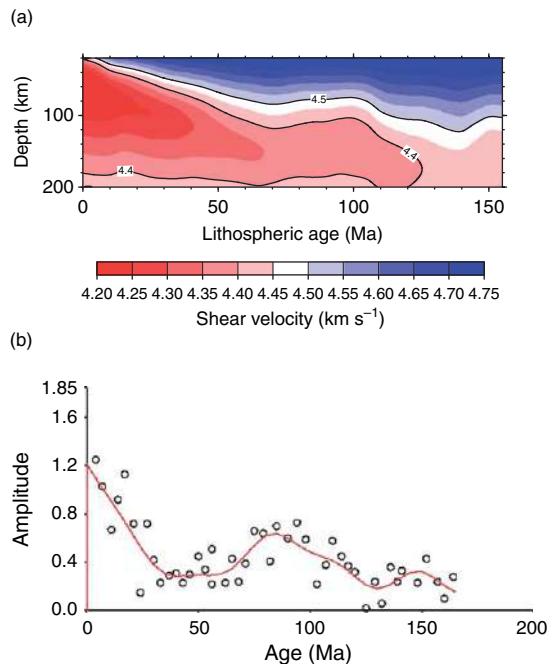


Figure 9 Variations of (a) average S-wave velocity and (b) azimuthal anisotropy (through the delay time of synthetic SKS splitting) plotted versus the age of lithospheric sea floor. In both cases the structure below the plate for age between 60 and 100 Ma looks anomalous. (a) Modified from Ritzwoller MH, Shapiro NM, and Zhong S-J (2004) Cooling history of the Pacific lithosphere. *Earth and Planetary Science Letters* 226: 69–84. (b) After Montagner J-P (2002) upper mantle low anisotropy channels below the Pacific plate. *Earth and Planetary Science Letters* 202: 205–227.

future reorganization of plates with ridge migrations in the Pacific Ocean. They call for more thorough numerical modeling.

1.16.4.2 Continents

Differences in the thickness of high-velocity layer underlying continents as imaged by seismic tomography have fuelled a long debate on the origin of continental roots (Jordan, 1975, 1978). Some global tomographic models provide a continental thickness of $\sim 200\text{--}250$ km in agreement with heat-flow analysis or electrical conductivity, but others suggest thicker zones up to 400 km.

Seismic anisotropy can provide fundamental information on the structure of continents, their root, and the geodynamic processes involved in mountain building and collision between continents (Vinnik *et al.*, 1992; Silver, 1996) such as in Central Asia (Griot *et al.*, 1998a, 1998b). Radial anisotropy ξ is

usually very heterogeneous below continents in the first 150–200 km of depth with positive or negative areas according to geology. But it seems to display a systematic tendency of being positive at larger depth (down to 300 km), whereas it is very large in the oceanic lithosphere in the depth range 50–200 km and decreases rapidly at larger depths (Montagner, 1994). Conversely, radial anisotropy displays a maximum (though smaller than in oceanic lithosphere) below very old continents (such as Siberian and Canadian Shield) in the depth range 200–400 km (Montagner and Tanimoto, 1991). Seismic anisotropy below continents, sometimes confined to the upper 220 km (Gaherty and Jordan, 1995) can still be significant below. A more quantitative comparison of radial anisotropy between different continental provinces is presented in Babuska *et al.* (1998), and demonstrates systematic differences according to the tectonic context. The existence of positive large-scale radial anisotropy below continents at depth might be a good indicator of the continental root which was largely debated since the presentation of the model of tectosphere by Jordan (1975, 1978, 1981). If this maximum of anisotropy is assumed to be related to an intense strain field in this depth range, it might be characteristic of the boundary between continental lithosphere and ‘normal’ upper mantle material. Gung *et al.* (2003) showed that it is possible to reconcile different isotropic tomographic models by taking into account seismic anisotropy. They find that significant radial anisotropy (with $V_{SH} > V_{SV}$) under most cratons in the depth range 250–400 km, similar to that found at shallower depths (80–250 km) below oceanic basins. Such a result is also in agreement for the Australian continent (Debayle and Kennett, 2000; Simons *et al.*, 2002). So, all results seem to show that the root of continents as defined by radial anisotropy is located between 200 and 300 km. However, this result is not correlated with a maximum in azimuthal anisotropy in this depth range (Debayle and Kennett, 2005): the fast-moving Australian plate seems to be the only continental region with a sufficiently large deformation at its base to be transformed into azimuthal anisotropy. They propose that, for continents other than Australia, weak influence of basal drag on the lithosphere may explain why azimuthal anisotropy is observed only in a layer located in the uppermost 100 km of the mantle. This layer shows a complex organization of azimuthal anisotropy suggesting a frozen-in origin of deformation, compatible with SKS splitting.

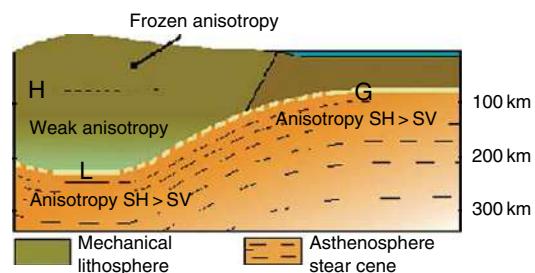


Figure 10 Scheme illustrating the difference in the location of maximum anisotropy between oceans and continents. Modified from Gung Y, Panning M, and Romanowicz B (2003) Global anisotropy and the thickness of continents. *Nature* 422: 707–711.

The difference in radial and azimuthal anisotropies between oceans and continents might reflect a difference of coupling between lithosphere and asthenosphere, through the basal drag. The coupling might be weak below most continental roots, in contrast with the Pacific plate, where the coupling (reflected by plate direction) is the first-order effect in the uppermost 200 km for young ages, before thermal instabilities take place at the base of the lithosphere, as evidenced by the existence of low-anisotropy channels. These results on the difference between oceanic and continental anisotropies are illustrated in Figure 10.

1.16.4.3 Velocity and Anisotropy in the Transition Zone

The transition zone plays a key role in mantle dynamics, particularly the 660 km discontinuity, which might inhibit the passage of matter between the upper and the lower mantle. Its seismic investigation is made difficult on the global scale by the poor sensitivity of fundamental surface waves in this depth range and by the fact that teleseismic body waves recorded at continental stations from earthquakes primarily occurring along plate boundaries have their turning point below the transition zone. For body waves, many different techniques using SS precursors (Shearer, 1991) or P-to-S converted waves (Chevrot *et al.*, 1999) were used at global scale to investigate the thickness of the transition zone. In spite of some initial controversies, a recent model by Lawrence and Shearer (2006) provides a coherent large-scale image of the transition zone thickness.

Whatever the type of data (normal mode, higher modes of surface waves, or body waves), an important feature of the transition zone is that, contrarily to the

rest of the upper mantle, the upper transition zone is characterized by a large degree-2 pattern (Masters *et al.*, 1982), and to a less extent, a strong degree-6. The degree-2 pattern (as well as degree-6) can be explained by the predominance of a simple large-scale flow pattern characterized by two upwellings in central Pacific Ocean and Eastern Africa and two downwellings in the Western and Eastern Pacific Ocean (Montagner and Romanowicz, 1993), proposed initially in the lower mantle (Busse, 1983). This scheme was corroborated by the existence, in the upper transition zone, of a slight but significant degree-4 radial anisotropy displayed by Montagner and Tanimoto (1991) and Roult *et al.* (1990) in agreement with the prediction of this model. Therefore, the observations of the geographical distributions of degrees 2, 4, 6 in the transition zone are coherent and spatially dependent. Montagner (1994) compared these different degrees to the corresponding degrees of the hotspot and slab distribution. In this simple framework, the distribution of plumes (degree 2+6) are merely a consequence of the large-scale simple flow in the transition zone. The degree 6 of velocity in the transition zone is well correlated with the distribution of hotspots and might indicate that many mantle plumes might originate in the transition zone. Ritsema and van Heijst (2004) observe lower-than-average shear velocity at eight hotspots in this depth range (Figure 11). These results suggest that there are different families of plumes, some of them originating in the transition zone.

As for anisotropy in the transition zone, Montagner and Kennett (1996), by using eigenfrequency data, display some evidence of radial anisotropy in the

upper (410–660 km) and lower (660–900 km) transition zones. Gung *et al.* (2003) also display a slight maximum of the degree-0 ξ in the transition zone. The existence of anisotropy close to the 660 km discontinuity was also found by Vinnik and Montagner (1996) below Germany, and by Vinnik *et al.* (1998) in Central Africa. By studying P-to-S converted waves at the GRF network and at GEOSCOPE station BNG in Central Africa, they observed that part of the initial P-wave is converted into SH wave. This signal can be observed on the transverse component of seismograms. The amplitude of this SH wave cannot be explained by a dipping 660 km discontinuity and it constitutes a good evidence for the existence of anisotropy just above this discontinuity. However, there is some evidence of lateral variation of anisotropy in the transition zone as found by the investigation of several subduction zones (Fischer and Yang, 1994; Fischer and Wiens, 1996). Fouch and Fischer (1996) present a synthesis of these different studies and show that some subduction zones such as Sakhalin Islands require deep anisotropy in the transition zone, whereas others, such as Tonga, do not need any anisotropy. They conclude that their data might be reconciled by considering the upper transition zone (410–520 km) intermittently anisotropic, and the rest of the transition zone might be isotropic.

Anisotropy in the transition zone was also advocated by two independent studies, using different data sets. The observations of Wookey *et al.* (2002), though controversial, present evidence of very large S-wave splitting (up to 7 s) in the vicinity of the 660 km discontinuity between Tonga–Kermadec subduction zone and Australia. On a global scale, Trampert and van Heijst (2002) show a long-wavelength azimuthal anisotropic structure in the transition zone. The root-mean-square amplitude of lateral variations of G is $\sim 1\%$. Beghein and Trampert (2003), using probability density functions and separating ξ , ϕ , and η anisotropies, suggest a chemical component to explain these different parameters. The interpretation of these new tentative results is not obvious and new data are necessary to close the debate on the nature of velocity and anisotropy heterogeneities in the transition zone. The transition zone might be a mid-mantle boundary layer, and a detailed and reliable tomographic model of S-wave velocity and anisotropy in the transition zone will provide fundamental insights into the dynamic of the whole mantle.

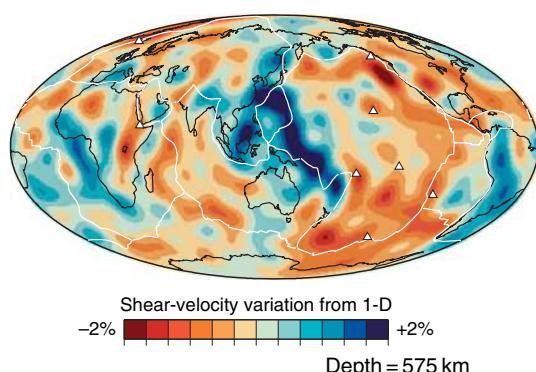


Figure 11 Shear-velocity variation and hotspot distribution. Modified from Ritsema J and van Heijst HJ (2004) Global transition zone tomography. *Journal of Geophysical Research* 109: B02302 doi:10.1029/2003JB002610.

1.16.5 Numerical Modeling and Perspectives

In the previous sections, we have highlighted the presence of lateral heterogeneities in seismic velocity and anisotropy in different parts of the Earth's upper mantle. However, anisotropy is not present in all depth ranges nor at all scales. There is some consensus for the presence of radial anisotropy in many parts of the upper mantle in order to simultaneously explain Love-wave and Rayleigh-wave dispersion, and even in the lower mantle (Panning and Romanowicz, 2004). The existence of azimuthal anisotropy is more controversial, though, from petrological reasons, it turns out that radial anisotropy and azimuthal anisotropy are intimately related and should be searched for simultaneously. Additional data, such as polarization data, might help to provide additional constraints on both kinds of anisotropy (Yu and Park, 1993; Pettersen and Maupin, 2002). But it requires the development of improved theoretical and numerical methods in order to work on the amplitude of seismograms.

Thanks to the access to very powerful computers, we are at the beginning stage of a new era for seismology. The twentieth century was dominated by the use of ray theory, and later on the normal mode theory. Since it is now feasible to numerically compute synthetic seismograms in complex 3-D structures in global spherical geometry (Komatitsch and Vilotte, 1998; Komatitsch and Tromp, 1999; Capdeville *et al.*, 2003), it is possible to model the complex interaction between seismic waves and 3-D heterogeneity, particularly in anisotropic, anelastic media. Some new and sophisticated tomographic methods are presently developed (Montelli *et al.*, 2004; Capdeville *et al.*, 2005; Tromp *et al.*, 2005; Zhou *et al.*, 2006) that should provide access to the complexity of the Earth mantle by the mapping of short-scale heterogeneities such as mantle plumes, in anisotropic and anelastic media.

A second important challenge is the complete understanding of the origin of anisotropy from the mineral scale up to global scale in the different layers of the Earth. In the upper mantle, seismic anisotropy is due to LPO of anisotropic minerals such as olivine at large scales, requiring several strong conditions, starting with the presence of anisotropic crystals up to the existence of an efficient large scale present or past strain field. In order to fill the gap between grain scale modeling (McKenzie, 1979; Ribe, 1989; Kaminski and Ribe, 2001) and large-scale anisotropy measurements in a convective system (Tommasi *et al.*,

2000), there is now a real need to make more quantitative comparisons between seismic anisotropy and numerical modeling. Gaboret *et al.* (2003) and Becker *et al.* (2003) calculated the convective circulation in the mantle by converting perturbations of S-wave velocity into density perturbations. Figure 12 shows two cross-sections through the Pacific hemisphere and the associated flow lines (Gaboret *et al.*, 2003) derived from the tomographic model of Ekström and Dziewonski (1998). This kind of modeling makes it possible to calculate the strain tensor and to test different hypotheses for the prevailing mechanisms of alignment, by comparison with seismic data.

The upper mantle is the best known of the deep layers of the earth, where there is now good agreement between many isotropic global tomographic models. But the account of seismic anisotropy is mandatory to avoid biased isotropic heterogeneities. The main application of anisotropy is the mapping of mantle convection and its boundary layers (Karato, 1998; Montagner, 1998). The finding of anisotropy in the transition zone (if confirmed) will provide strong constraints on the flow circulation and the exchange of matter between the upper and the lower mantle. Pursuing the first pioneering efforts, the systematic modeling of the complete seismic waveform in 3-D heterogeneous, anisotropic and anelastic media associated with new techniques of numerical modeling of seismograms will probably enhance our vision of the whole mantle.

In parallel to these theoretical and numerical challenges, there is a crucial need for instrumental developments since there are still many areas at the surface of Earth devoid of broadband seismic stations. These regions are primarily located in Southern Hemisphere and more particularly in oceanic areas where no islands are present. Therefore, an international effort is ongoing, coordinated through International Ocean Network (ION) in order to promote the installation of geophysical ocean bottom observatories in order to fill the enormous gaps in the station coverage (for a description of ION).

Appendix 1: Effect of Anisotropy on Surface Waves in the Plane-Layered Medium

The half-space is assumed to be homogeneous and may be described by its density $\rho(z)$ and its fourth-order elastic tensor $\Gamma(z)$ with 21 independent elastic coefficients. All these parameters are so far supposed independent of x and y coordinates (in Figure 13, z is

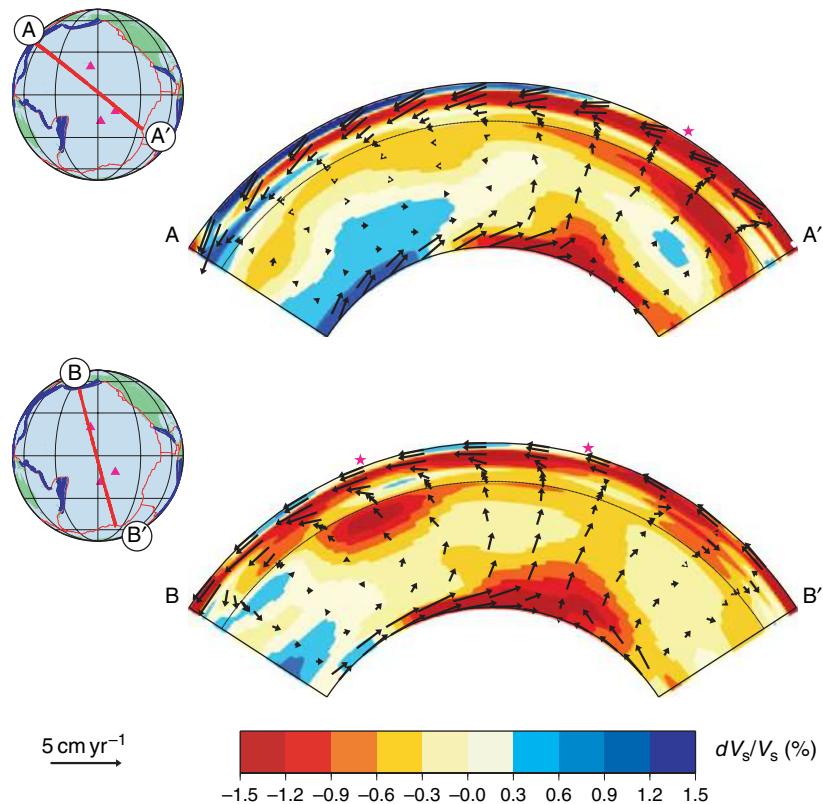


Figure 12 Mantle heterogeneities and convective flow below the Pacific Ocean. Modified from Gaboret C, Forte A, and Montagner J-P (2003) The unique dynamics of the Pacific Hemisphere mantle and its signature on seismic anisotropy. *Earth and Planetary Science Letters* 208: 219–223.

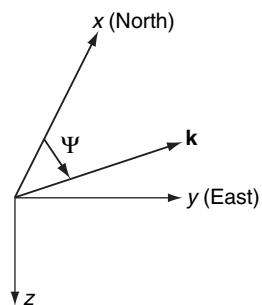


Figure 13 Definition of the Cartesian coordinate system (x, y, z) used in the calculations; Ψ is the azimuth of the wavevector with respect to north.

the vertical component). This condition will be released in the next section. The unperturbed medium is assumed isotropic with an elastic tensor $\Gamma_0(z)$. In that medium, the two cases of Love and Rayleigh wave dispersion can be successively considered.

The unperturbed Love wave displacement is of the form:

$$\mathbf{u}(\mathbf{r}, t) = \begin{pmatrix} -W(z)\sin\Psi \\ W(z)\cos\Psi \\ 0 \end{pmatrix} \exp(i[k(x\cos\Psi + y\sin\Psi) - \omega t]) \quad [19]$$

where $W(z)$ is the scalar depth eigenfunction for Love waves, k is the horizontal wave number, and Ψ is the azimuth of the wave number k measured clockwise from the north.

The unperturbed Rayleigh wave displacement is of the form

$$\mathbf{u}(\mathbf{r}, t) = \begin{pmatrix} V(z)\cos\Psi \\ V(z)\sin\Psi \\ iU(z) \end{pmatrix} \exp(i[k(x\cos\Psi + y\sin\Psi) - \omega t]) \quad [20]$$

where $V(z)$ and $U(z)$ are the scalar depth eigenfunctions for Rayleigh waves. The associated strain tensor $\epsilon(\mathbf{r}, t)$ is defined by

$$\epsilon_{ij}(\mathbf{r}, t) = 1/2(u_{i,j} + u_{j,i}) \quad [21]$$

where j denotes the differentiation with respect to the j th coordinate. The medium is perturbed from $\Gamma_0(z)$ to $\Gamma_0(z) + \gamma(z)$, where $\gamma(z)$ is small compared to $\Gamma_0(z)$ but quite general in the sense that there is no assumption on the kind of anisotropy. This means that in this approximation we can still consider quasi-Love modes and quasi-Rayleigh modes (Crampin, 1984). From Rayleigh's principle, the first-order perturbation $\delta V(\mathbf{k})$ in phase velocity dispersion is (Smith and Dahlen, 1973, 1975):

$$\delta V(\mathbf{k}) = \frac{V}{2\omega^2} \int_0^\infty \frac{\gamma_{ijkl} \epsilon_{ij} \epsilon_{kl}^*}{\rho_0 u_k u_k^* dz} dz \quad [22]$$

where u_i and ϵ_{ij} are, respectively, the displacement and the strain for the unperturbed half-space, and the asterisk denotes complex conjugation. Now because of the symmetry of the tensors $\gamma(z)$ and ϵ , we use the simplified index notation c_{ij} and ϵ_i for the elements γ_{ijkl} and ϵ_{ij} , but the number, n_{ij} , of coefficients γ_{ijkl} for each c_{ij} must be taken into account. The simplified index notation for the elastic tensor γ_{ijkl} is defined in a coordinate system (x_1, x_2, x_3) by

$$\gamma_{ijkl} \rightarrow c_{pq} \begin{cases} \text{if } i=j \Rightarrow p=i \\ \text{if } k=l \Rightarrow q=k \\ \text{if } i \neq j \Rightarrow p=9-i-j \\ \text{if } k \neq l \Rightarrow q=9-k-l \end{cases} \quad [23]$$

This kind of transformation enables us to relate the fourth-order tensor γ ($3 \times 3 \times 3 \times 3$) to a matrix c (6×6). The same simplified index notation can be applied to the components of the strain tensor ϵ_{ij} transforming the second-order tensor ϵ (3×3) into a vector with six components. However, it is necessary to be careful, because to a given c_{pq} correspond several γ_{ijkh} and γ_{ijkl} must be replaced by $n_{pq}c_{pq}$, where n_{pq} is the number of γ_{ijkl} giving the same c_{pq} . Therefore, eqn [22] expressing Rayleigh's principle can be rewritten as

$$\delta V(\mathbf{k}) = \frac{V}{2\omega^2} \int_0^\infty \sum_{ij} n_{ij} c_{ij} \epsilon_i \epsilon_j^* dz \quad [24]$$

We only detail the calculations for Love waves.

Love Waves

By using previous expressions for $\mathbf{u}(\mathbf{r}, t)$, [19], and $\epsilon_{ij}(\mathbf{r}, t)$, [21], the various expressions of strain are

$$\begin{aligned} \epsilon_1 &= -i \cos \Psi \sin \Psi k W \\ \epsilon_2 &= i \cos \Psi \sin \Psi k W \\ \epsilon_3 &= 0 \\ \epsilon_4 &= 1/2 \cos \Psi W' \\ \epsilon_5 &= -1/2 \sin \Psi W' \\ \epsilon_6 &= 1/2 (\cos^2 \Psi - \sin^2 \Psi) k W \end{aligned} \quad [25]$$

where $W' = dW/dr$. In Table 1, the different terms $n_{ij} c_{ij} \epsilon_i \epsilon_j^*$ are given. We note that when $c_{ij} \epsilon_i \epsilon_j^*$ is a purely imaginary complex, its contribution to $\delta V(k, \Psi)$ is null. When all the contributions are summed, the different terms $\cos^k \Psi \sin^l \Psi$ are such that $k+l$ is

Table 1 Calculation of the various $c_{ij} \epsilon_i \epsilon_j$ for Love waves, with the simplified index notation ($\alpha = \cos \Psi$; $\beta = \sin \Psi$)

n	ij	$c_{ij} \epsilon_i \epsilon_j$
1	11	$c_{11}\alpha^2 \beta^2 k^2 W^2$
1	22	$c_{22}\alpha^2 \beta^2 k^2 W^2$
1	33	0
2	12	$-c_{12}\alpha^2 \beta^2 k^2 W^2$
2	13	0
2	23	0
2	24	0
4	14	$c_{14}(-i\alpha^2 \beta) \frac{kWW'}{2}$
4	15	$c_{15}(i\alpha^2 \beta) \frac{kWW'}{2}$
4	16	$c_{16}(-\alpha\beta)(\alpha^2 - \beta^2) \frac{k^2 W^2}{2}$
4	24	$c_{24}(-i\alpha^2 \beta) \frac{kWW'}{2}$
4	25	$c_{25}(-i\alpha\beta^2) \frac{kWW'}{2}$
4	26	$c_{26}(\alpha\beta)(\alpha^2 - \beta^2) \frac{k^2 W^2}{2}$
4	34	0
4	35	0
4	36	0
4	44	$c_{44}\alpha^2 \frac{W'^2}{4}$
8	45	$c_{45}(-\alpha\beta) \frac{W'^2}{4}$
8	46	$c_{46}(-i\alpha)(\alpha^2 - \beta^2) \frac{kWW'}{2}$
4	55	$c_{55}\beta^2 \frac{W'^2}{4}$
8	56	$c_{56}(i\beta)(\alpha^2 - \beta^2) \frac{kWW'}{2}$
4	66	$c_{66}(\alpha^2 - \beta^2) \frac{k^2 W^2}{4}$

even, which is not surprising in the light of the reciprocity principle. Therefore, each term can be developed as a Fourier series in Ψ with only even terms. Finally, it is found that

$$\begin{aligned}\delta V_L(k, \Psi) = & \frac{V}{2\omega^2 L_0} \int_0^\infty dz \left\{ k^2 W^2 \left[\frac{1}{8}(c_{11} + c_{22} - 2c_{12} + 4c_{66}) \right. \right. \\ & + W'^2 \left[\frac{1}{2}(c_{44} + c_{55}) \right] + \cos 2\Psi W'^2 \\ & \times \left. \left[\frac{1}{2}(c_{44} - c_{55}) \right] - \sin 2\Psi W'^2 c_{45} - \cos 4\Psi k^2 W^2 \right. \\ & \times \left. \left[\frac{1}{8}(c_{11} + c_{22} - 2c_{12} - 4c_{66}) \right] + \sin 4\Psi k^2 W^2 \right. \\ & \times \left. \left. \left[\frac{1}{2}(c_{26} - c_{16}) \right] \right\}\end{aligned}\quad [26]$$

In the particular case of a transversely isotropic medium with a vertical symmetry axis (also named radial anisotropic medium), we have: $c_{11} = c_{22} = \delta A$, $c_{33} = \delta C$, $c_{12} = \delta(A - 2N)$, $c_{13} = c_{23} = \delta F$, $c_{44} = c_{55} = \delta L$, $c_{66} = \delta N$, and $c_{14} = c_{24} = c_{15} = c_{25} = c_{16} = c_{26} = 0$. The local azimuthal terms vanish and eqn [26] reduces to

$$\delta V_L(k, \Psi) = \frac{1}{2V_L L_0} \int_0^\infty \left\{ W^2 \delta N + \frac{W'^2}{k^2} \delta L \right\} dz \quad [27]$$

Therefore, the same expressions as in Takeuchi and Saito (1972, p. 268) are found in the case of radial anisotropy. The 0- Ψ term of eqn [26] corresponds to the averaging over azimuth Ψ , which provides the equivalent transversely isotropic model with vertical symmetry axis by setting

$$\begin{aligned}\delta N &= \frac{1}{8}(c_{11} + c_{22}) - \frac{1}{4}c_{12} + \frac{1}{2}c_{66} \\ \delta L &= \frac{1}{2}(c_{44} + c_{55})\end{aligned}$$

If we call C_{ij} the elastic coefficients of the total elastic tensor, we can set

$$\begin{aligned}N &= \rho V_{SH}^2 = \frac{1}{8}(C_{11} + C_{22}) - \frac{1}{4}C_{12} + \frac{1}{2}C_{66} \\ L &= \rho V_{SV}^2 = \frac{1}{2}(C_{44} + C_{55})\end{aligned}$$

According to eqn [26], the first-order perturbation in Love wave phase velocity $\delta V_L(k, \Psi)$ can then be expressed as

$$\begin{aligned}\delta V_L(k, \Psi) = & \frac{1}{2V_{0_L}(k)} [L_1(k) + L_2(k)\cos 2\Psi + L_3(k)\sin 2\Psi \\ & + L_4(k)\cos 4\Psi + L_5(k)\sin 4\Psi]\end{aligned}\quad [28]$$

where

$$\begin{aligned}L_0(k) &= \int_0^\infty \rho W^2 dz \\ L_1(k) &= \frac{1}{L_0} \int_0^\infty \left(W^2 \delta N + \frac{W'^2}{k^2} \delta L \right) dz \\ L_2(k) &= \frac{1}{L_0} \int_0^\infty -G_c \left(\frac{W'^2}{k^2} \right) dz \\ L_3(k) &= \frac{1}{L_0} \int_0^\infty -G_s \left(\frac{W'^2}{k^2} \right) dz \\ L_4(k) &= \frac{1}{L_0} \int_0^\infty -E_c \cdot W^2 dz \\ L_5(k) &= \frac{1}{L_0} \int_0^\infty -E_s \cdot W^2 dz\end{aligned}$$

Rayleigh Waves

The same procedure holds for the local Rayleigh wave phase velocity perturbation δV_R , starting from the displacement given previously (Montagner and Nataf, 1986):

$$\begin{aligned}\delta V_R(k, \Psi) = & \frac{1}{2V_{0_R}(k)} [R_1(k) + R_2(k)\cos 2\Psi \\ & + R_3(k)\sin 2\Psi + R_4(k)\cos 4\Psi \\ & + R_5(k)\sin 4\Psi]\end{aligned}\quad [29]$$

where

$$\begin{aligned}R_0(k) &= \int_0^\infty \rho(U^2 + V^2) dz \\ R_1(k) &= \frac{1}{R_0} \int_0^\infty \left[V^2 \delta A + \frac{U'^2}{k^2} \delta C + \frac{2U'V}{k} \cdot \delta F \right. \\ & \left. + \left(\frac{V'}{k} - U \right)^2 \delta L \right] dz \\ R_2(k) &= \frac{1}{R_0} \int_0^\infty \left[V^2 B_c + \frac{2U'V}{k} H_c + \left(\frac{V'}{k} - U \right)^2 G_c \right] dz \\ R_3(k) &= \frac{1}{R_0} \int_0^\infty \left[V^2 B_s + \frac{2U'V}{k} H_s + \left(\frac{V'}{k} - U \right)^2 G_s \right] dz \\ R_4(k) &= \frac{1}{R_0} \int_0^\infty E_c V^2 dz \\ R_5(k) &= \frac{1}{R_0} \int_0^\infty E_s V^2 dz\end{aligned}$$

The 13 depth-dependent parameters $A, C, F, L, N, B_c, B_s, H_c, H_s, G_c, G_s, E_c$, and E_s are linear combinations of the elastic coefficients C_{ij} and are explicitly given as follows:

- Constant term (0- Ψ -azimuthal term: independent of azimuth)

$$\begin{aligned}
 A &= \rho V_{\text{PH}}^2 = \frac{3}{8}(C_{11} + C_{22}) + \frac{1}{4}C_{12} + \frac{1}{2}C_{66} \\
 C &= \rho V_{\text{PV}}^2 = C_{33} \\
 F &= \frac{1}{2}(C_{13} + C_{23}) \\
 L &= \rho V_{\text{SV}}^2 = \frac{1}{2}(C_{44} + C_{55}) \\
 N &= \rho V_{\text{SH}}^2 = \frac{1}{8}(C_{11} + C_{22}) - \frac{1}{4}C_{12} + \frac{1}{2}C_{66}
 \end{aligned}$$

- 2 Ψ -azimuthal term

$$\begin{array}{ll}
 \cos 2\Psi & \sin 2\Psi \\
 B_c = \frac{1}{2}(C_{11} - C_{22}) & B_s = C_{16} + C_{26} \\
 G_c = \frac{1}{2}(C_{55} - C_{44}) & G_s = C_{54} \\
 H_c = \frac{1}{2}(C_{13} - C_{23}) & H_s = C_{36}
 \end{array}$$

- 4 Ψ -azimuthal term

$$\begin{array}{ll}
 \cos 4\Psi & \sin 4\Psi \\
 E_c = \frac{1}{8}(C_{11} + C_{22}) - \frac{1}{4}C_{12} - \frac{1}{2}C_{66} & E_s = \frac{1}{2}(C_{16} - C_{26})
 \end{array}$$

where indices 1 and 2 refer to horizontal coordinates (1: north; 2: east) and index 3 refers to vertical coordinate. ρ is the density, V_{PH} , V_{PV} are, respectively, the horizontal and vertical propagating P-wave velocities, and V_{SH} , V_{SV} the horizontal and vertical polarized S-wave velocities. So, the different parameters present in the different azimuthal terms are simply related to elastic moduli C_{ij} . We must bear in mind that A , C , L , N anisotropic parameters can be retrieved from measurements of the P- and S-wave velocities propagating perpendicular or parallel to the axis of symmetry.

The corresponding kernels are plotted in [Figure 14](#) for long waves and [Figure 15](#) for Rayleigh waves.

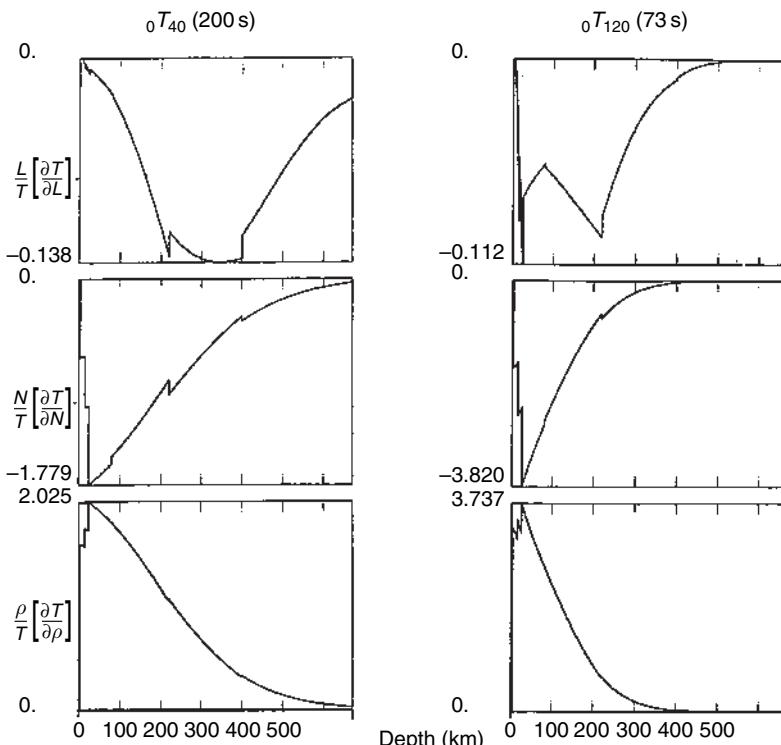


Figure 14 Partial derivatives for Love waves of the period of fundamental normal modes OT40 (left) and OT120 (right) with respect to the elastic coefficients of a transversely isotropic Earth, L , N , and density ρ , as a function of depth in the upper mantle (from Montagner and Nataf, 1986). The partial derivatives with respect to A , C , F are null for these modes. The plots are normalized to their maximum amplitudes, given for a $\Delta h = 1000$ km thick perturbed layer. The combinations of elastic coefficients that have the same partial derivative as L are $-G_c$, $-G_s$ for the azimuthal terms 2- Ψ , and as N are E_c , E_s for the azimuthal term 4- Ψ . Note that the amplitude of the L -partial is very small for the fundamental modes, which is not the case for higher modes.

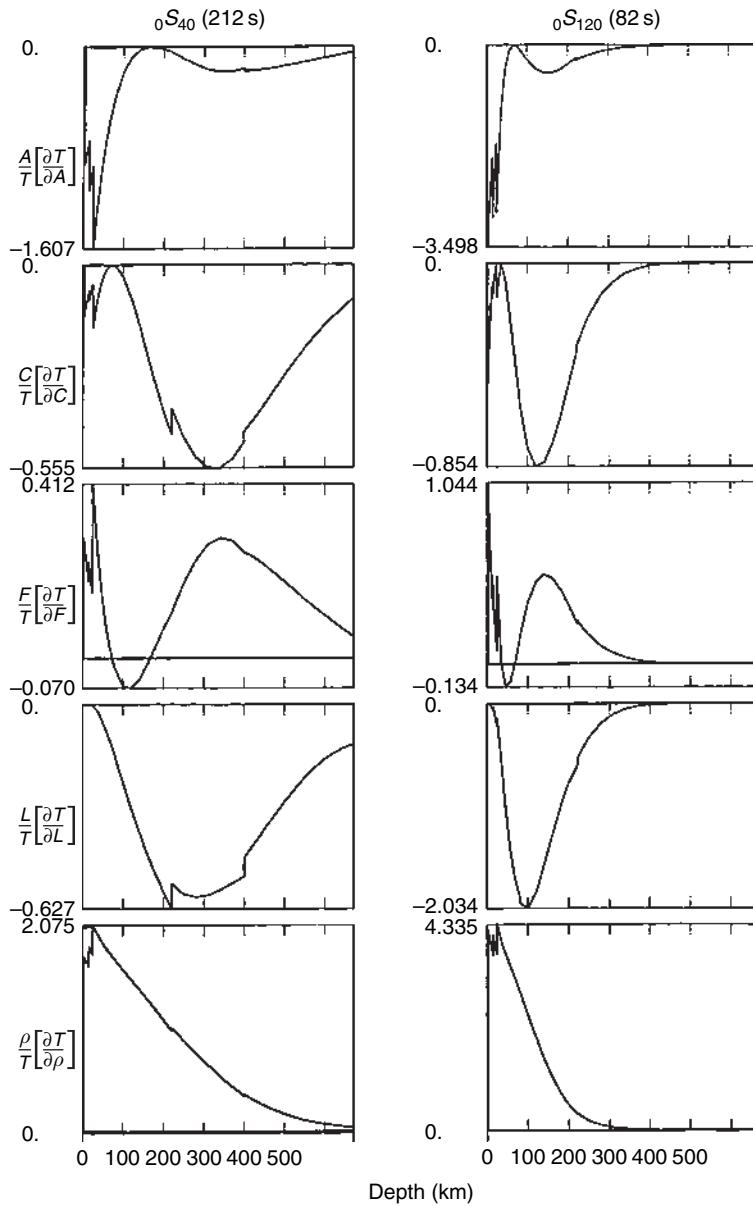


Figure 15 Kernels for Rayleigh waves. Same conventions are applicable as for Figure 13 in the same depth range. The partial derivative with respect to N has not been plotted since its amplitude is very small for fundamental modes. Note that three partials contribute to the 2- Ψ -azimuthal terms, A -partial for B_c , B_s , F -partial for H_c , H_s , and the largest one L -partial for G_c , G_s .

References

- Aki K and Richards PG (1980) *Quantitative Seismology: Theory and Methods*. San Francisco: W. H. Freeman.
- Anderson DL (1961) Elastic wave propagation in layered anisotropic media. *Journal of Geophysical Research* 66: 2953–2963.
- Anderson DL and Bass JD (1984) Mineralogy and composition of the upper mantle. *Geophysical Research Letters* 11: 637–640.
- Anderson DL and Bass JD (1986) Transition region of the Earth's upper mantle. *Nature* 320: 321–328.
- Anderson DL and Dziewonski AM (1982) Upper mantle anisotropy: Evidence from free oscillations. *Geophysical Journal of the Royal Astronomical Society* 69: 383–404.
- Anderson DL and Regan J (1983) Upper mantle anisotropy and the oceanic lithosphere. *Geophysical Research Letters* 10: 841–844.
- Ansel V and Nataf H-C (1989) Anisotropy beneath 9 stations of the Geoscope broadband network as deduced from shear wave splitting. *Geophysical Research Letters* 16: 409–412.
- Babuska V and Cara M (1991) *Seismic Anisotropy in the Earth*. Dordrecht, The Netherlands: Kluwer.

- Babuska V, Montagner JP, Plomerova J, and Girardin N (1998) Age-dependent large-scale fabric of the mantle lithosphere as derived from surface-wave velocity anisotropy. *Pure and Applied Geophysics* 151: 257–280.
- Backus GE and Gilbert F (1967) Numerical applications of a formalism for geophysical inverse problems. *Geophysical Journal of the Royal Astronomical Society* 13: 247–276.
- Backus GE and Gilbert F (1968) The resolving power of gross Earth data. *Geophysical Journal of the Royal Astronomical Society* 16: 169–205.
- Backus GE and Gilbert F (1970) Uniqueness in the inversion of inaccurate gross Earth data. *Philosophical Transactions of the Royal Society of London Series A* 266: 123–192.
- Barmin MP, Levshin AL, and Ritzwoller MH (2001) A fast and reliable method for surface wave tomography. *Pure and Applied Geophysics* 158: 1351–1375.
- Bass J and Anderson DL (1984) Composition of the upper mantle: Geophysical tests of two petrological models. *Geophysical Research Letters* 11: 237–240.
- Becker TW and Boschi L (2002) A comparison of tomographic and geodynamic mantle models. *Geochemistry Geophysics Geosystems* 3: 2001GC00168.
- Becker TW, Kellogg JB, Ekström G, and O'Connell RJ (2003) Comparison of azimuthal anisotropy from surface waves and finite-strain from global mantle-circulation models. *Geophysical Journal International* 155: 696–714.
- Beghein C and Trampert J (2003) Probability density functions for radial anisotropy: Implications for the upper 1200 km of the mantle. *Earth and Planetary Science Letters* 217: 151–162.
- Beucler E and Montagner J-P (2006) Computation of large anisotropic seismic heterogeneities. *Geophysical Journal International* 165: 447–468.
- Beucler E, Stutzmann E, and Montagner J-P (2003) Measuring surface wave higher mode velocities by the roller coaster algorithm. *Geophysical Journal International* 155: 289–307.
- Blackman DK, Kendall JM, Dawson PR, Wenk HR, Boyce D, and Morgan JP (1996) Teleseismic imaging of subaxial flow at mid-ocean ridges: Traveltime effects of anisotropic mineral texture in the mantle. *Geophysical Journal International* 127: 415–426.
- Boschi L and Ekström G (2002) New images of the Earth's upper mantle from measurements of surface wave phase velocity anomalies. *Journal of Geophysical Research* 107: B4 10.1029/2000JB000059.
- Busse FH (1983) Quadrupole convection in the lower mantle. *Geophysical Research Letters* 10: 285–288.
- Capdeville Y, Chaljub E, Villette J-P, and Montagner J-P (2003) Coupling spectral elements and modal solution: A new efficient tool for numerical wave propagation in laterally heterogeneous Earth models. *Geophysical Journal International* 152: 34–66.
- Capdeville Y, Gung Y, and Romanowicz B (2005) Towards global earth tomography using the spectral element method: A technique based on source stacking. *Geophysical Journal International* 162: 541–554.
- Cara M (1979) Lateral variations of S-velocity in the upper mantle from higher Rayleigh modes. *Geophysical Journal of the Royal Astronomical Society* 57: 649–670.
- Cara M and Lévéque J-J (1988) Anisotropy of the asthenosphere: The higher mode data of the Pacific revisited. *Geophysical Research Letters* 15: 205–208.
- Chevrot S, Vinnik L, and Montagner J-P (1999) Global-scale analysis of the mantle Pds phase. *Journal of Geophysical Research* 104: 20,203–20,219.
- Chevrot S, Favier N, and Komatitsch D (2004) Shear wave splitting in three-dimensional anisotropic media. *Geophysical Journal International* 159: 711–720.
- Christensen NI and Lundquist S (1982) Pyroxene orientation within the upper mantle. *Bulletin of the Geological Society of America* 93: 279–288.
- Crampin S (1984) An introduction to wave propagation in anisotropic media. *Geophysical Journal of the Royal Astronomical Society* 76: 17–28.
- Dahlen FA, Hung S-H, and Nolet G (2000) Fréchet kernels for finite-frequency traveltimes. I: Theory. *Geophysical Journal International* 141: 157–174.
- Davaille A and Jaupart C (1994) Onset of thermal convection in fluids with temperature-dependent viscosity: Application to the oceanic mantle. *Journal of Geophysical Research* 99: 19,853–19,866.
- Debaye E and Lévéque J-J (1997) Upper mantle heterogeneities in the Indian Ocean from waveform inversion. *Geophysical Research Letters* 24: 245–248.
- Debaye E, Cara M, and Lévéque J-J (2001) Seismic evidence for a deeply rooted low velocity anomaly in the upper mantle beneath the northeastern Afro/Arabian continent. *Earth and Planetary Science Letters* 193: 369–382.
- Debaye E and Kennett BLN (2000) Anisotropy in the Australasian upper mantle from Love and Rayleigh waveform inversion. *Earth and Planetary Science Letters* 184: 339–351.
- Debaye E and Sambridge M (2004) Inversion of massive surface wave data sets: Model construction and resolution assessment. *Journal of Geophysical Research* 109: B02316 doi:10.1029/2003JB002652.
- Debaye E, Kennett BLN, and Priestley K (2005) Global azimuthal anisotropy and the unique plate-motion deformation of Australia. *Nature* 433: 509–512.
- DeMets C, Gordon RG, Argus DF, and Stein S (1990) Current plate motions. *Geophysical Journal International* 101: 425–478.
- Dost B (1990) Upper mantle structure under western Europe from fundamental and higher mode surface waves using the NARS array. *Geophysical Journal of the Royal Astronomical Society* 100: 131–151.
- Dziewonski AM (1984) Mapping the lower mantle: Determination of lateral heterogeneity in P velocity up to degree and order 6. *Journal of Geophysical Research* 89: 5929–5952.
- Dziewonski AM and Anderson DL (1981) Preliminary reference Earth model. *Physics of the Earth and Planetary Interiors* 25: 297–356.
- Dziewonski AM, Chou G, and Woodhouse JH (1981) Determination of earthquake source parameters from waveform modeling. *Journal of Geophysical Research* 86: 2825–2852.
- Dziewonski AM and Woodhouse JH (1987) Global images of the Earth's interior. *Science* 236: 37–48.
- Ekström G (2000) Mapping the lithosphere and asthenosphere with surface waves: Lateral structure and anisotropy. *AGU monograph*, Eds Richards et al. 121: 239–256.
- Ekström G, Tromp J, and Larson EW (1997) Measurements and global models of surface wave propagation. *Journal of Geophysical Research* 102: 8137–8157.
- Ekström G and Dziewonski AM (1998) The unique anisotropy of the Pacific upper mantle. *Nature* 394: 168–172.
- Fischer KM and Wiens DA (1996) The depth distribution of mantle anisotropy beneath the Tonga subduction zone. *Earth and Planetary Science Letters* 142: 253–260.
- Fischer KM and Yang X (1994) Anisotropy in Kuril-Kamchatka subduction zone structure. *Geophysical Research Letters* 21: 5–8.
- Forsyth DW (1975) The early structural evolution and anisotropy of the oceanic upper mantle. *Geophysical Journal of the Royal Astronomical Society* 43: 103–162.
- Fouch MJ, Fischer KM, Parmentier EM, Wysession ME, and Clarke TJ (2000) Shear wave splitting, continental keels,

- patterns of mantle flow. *Journal of Geophysical Research* 105: 6255–6275.
- Fouch MJ and Fischer KM (1996) Mantle anisotropy beneath northwest Pacific subduction zones. *Journal of Geophysical Research* 101: 15,987–16,002.
- Friederich W (1999) Propagation of seismic shear and surface waves in a laterally heterogeneous mantle by multiple forward scattering. *Geophysical Journal International* 136: 180–204.
- Gaboret C, Forte A, and Montagner J-P (2003) The unique dynamics of the Pacific Hemisphere mantle and its signature on seismic anisotropy. *Earth and Planetary Science Letters* 208: 219–233.
- Gaherty JB and Jordan TH (1995) Lehmann discontinuity as the base of the anisotropic layer beneath continents. *Science* 268: 1468–1471.
- Gilbert F (1971) Excitation of normal modes of the Earth by earthquake sources. *Geophysical Journal of the Royal Astronomical Society* 22: 223–226.
- Griot D-A, Montagner JP, and Tappougnier P (1998a) Surface wave phase velocity and azimuthal anisotropy in Central Asia. *Journal of Geophysical Research* 103: 21215–21232.
- Griot D-A, Montagner JP, and Tappougnier P (1998b) Heterogeneous versus homogeneous strain in Central Asia. *Geophysical Research Letters* 25: 1447–1450.
- Gu YJ, Lerner-Lam A, Dziewonski AM, and Ekström G (2005) Seismic evidence for deep anisotropy beneath the East Pacific Rise. *Earth and Planetary Science Letters* 232: 259–272.
- Gung Y, Panning M, and Romanowicz B (2003) Global anisotropy and the thickness of continents. *Nature* 422: 707–711.
- Hadiouche O, Jobert N, and Montagner JP (1989) Anisotropy of the African continent inferred from surface waves. *Physics of the Earth and Planetary Interiors* 58: 61–81.
- Hess H (1964) Seismic anisotropy of the uppermost mantle under the oceans. *Nature* 203: 629–631.
- Ho-Liu P, Montagner J-P, and Kanamori H (1989) Comparison of iterative back-projection inversion and generalized inversion without blocks: Case studies in attenuation tomography. *Geophysical Journal* 97: 19–29.
- Jordan TH (1975) The continental tectosphere. *Reviews of Geophysics* 13: 1–12.
- Jordan TH (1978) Composition and development of the continental tectosphere. *Nature* 274: 544–548.
- Jordan TH (1981) Continents as a chemical boundary layer. *Philosophical Transactions of the Royal Society of London Series A* 301: 359–373.
- Jung HY and Karato S-I (2001) Water-induced fabric transitions in olivine. *Science* 293: 1460–1462.
- Kaminski E and Ribe NM (2001) A kinematic model for recrystallization and texture development in olivine polycrystals. *Earth and Planetary Science Letters* 189: 253–267.
- Karato S-I and Li P (1993) Diffusive creep in perovskite: Implications for the rheology of the lower mantle. *Science* 255: 771–778.
- Karato S-I (1998) Seismic anisotropy in the deep mantle, boundary layers and geometry of mantle convection. *Pure and Applied Geophysics* 151: 565–587.
- Komatitsch D and Vilotte J-P (1998) The spectral element method: An effective tool to simulate the seismic response of 2D and 3D geological structures. *Bulletin of the Seismological Society of America* 88: 368–392.
- Komatitsch D and Tromp J (1999) Introduction of spectral element method for 3-D seismic wave propagation. *Geophysical Journal International* 139: 806–822.
- Kuo B-Y and Forsyth DW (1992) A search for split SKS waveforms in North Atlantic. *Geophysical Journal International* 92: 6421–6436.
- Larson EWF, Tromp J, and Ekstrom G (1998) Effects of slight anisotropy on surface waves. *Geophysical Journal International* 132: 654–666.
- Laske G and Masters G (1998) Surface-wave polarization data and global anisotropic structure. *Geophysical Journal International* 132: 508–520.
- Laske G, Masters G, and Reif C (2001) CRUST2.0- a new global crustal model at 2×2 degrees, <http://mahi.ucsd.edu/Gabi/crust2.html> (2001)
- Lawrence JF and Shearer PM (2006) A global study of transition zone thickness using receiver functions. *Journal of Geophysical Research* 111: B06307 doi:10.129/2005JB003973.
- Lerner-Lam AL and Jordan TH (1983) Earth structure from fundamental and higher-mode waveform analysis. *Geophysical Journal of the Royal Astronomical Society* 75: 759–797.
- Lévéque JJ, Cara M, and Rouland D (1991) Waveform inversion of surface-wave data: A new tool for systematic investigation of upper mantle structures. *Geophysical Journal International* 104: 565–581.
- Li X-D and Tanimoto T (1993) Waveforms of long period body waves in a slightly aspherical Earth. *Geophysical Journal International* 112: 92–112.
- Li X-D and Romanowicz B (1995) Comparison of global waveform inversions with and without considering cross branch coupling. *Geophysical Journal International* 121: 695–709.
- Li X-D and Romanowicz B (1996) Global mantle shear velocity model developed using nonlinear asymptotic coupling theory. *Journal of Geophysical Research* 101: 22245–22273.
- Love AEH (1927) *A Treatise on the Theory of Elasticity*, 4th edn., p. 643 Cambridge University Press.
- Mainprice DG, Barroil G, and Ben Ismail W (2000) The seismic anisotropy of the Earth's mantle: From single crystal to polycrystal. In, *Earth's deep interior: mineral physics and tomography from the atomic scale to the global scale*. *Geophysical Monograph* 117: 237.
- Marquering H, Snieder R, and Nolet G (1996) Waveform inversions and the significance of surface wave mode coupling. *Geophysical Journal International* 124: 258–278.
- Masters G, Jordan TH, Silver PG, and Gilbert F (1982) Aspherical Earth structure from fundamental spheroidal-mode data. *Nature* 298: 609–613.
- McKenzie D (1979) Finite deformation during fluid flow. *Geophysical Journal of the Royal Astronomical Society* 58: 687–715.
- Minster JB and Jordan TH (1978) Present-day plate motions. *Journal of Geophysical Research* 83: 5331–5354.
- Mitchell BJ and Yu G-K (1980) Surface wave dispersion, regionalized velocity models and anisotropy of the Pacific crust and upper mantle. *Geophysical Journal of the Royal Astronomical Society* 63: 497–514.
- Mochizuki E (1986) The free oscillations of an anisotropic and heterogeneous Earth. *Geophysical Journal of the Royal Astronomical Society* 86: 167–176.
- Mocquet A and Romanowicz B (1989) Three-dimensional structure of the upper mantle beneath the Atlantic Ocean inferred from long-period Rayleigh waves. 2. Inversion. *Journal of Geophysical Research* 95: 6787–6798.
- Montagner J-P (1986a) First results on the three dimensional structure of the Indian Ocean inferred from long period surface waves. *Geophysical Research Letters* 13: 315–318.
- Montagner J-P (1986b) Regional three-dimensional structures using long-period surface waves. *Annals of Geophysics* 4(B3): 283–294.
- Montagner J-P (1994) What can seismology tell us about mantle convection?. *Reviews of Geophysics* 32(2): 115–137.
- Montagner J-P (1998) Where can seismic anisotropy be detected in the Earth's mantle? In boundary layers. *Pure and Applied Geophysics* 151: 223–256.

- Montagner J-P (2002) Upper mantle low anisotropy channels below the Pacific plate. *Earth and Planetary Science Letters* 202: 263–274.
- Montagner J-P and Anderson DL (1989a) Constraints on elastic combinations inferred from petrological models. *Physics of the Earth and Planetary Interiors* 54: 82–105.
- Montagner J-P and Anderson DL (1989b) Constrained reference mantle model. *Physics of the Earth and Planetary Interiors* 58: 205–227.
- Montagner J-P, Griot DA, and Lavé J (2000) How to relate body wave and surface wave anisotropies? *Journal of Geophysical Research* 105: 19,015–19,027.
- Montagner J-P and Guillot L (2003) Seismic anisotropy and global geodynamics. *Reviews in Mineralogy and Geochemistry* 51: 353–385.
- Montagner J-P and Jobert N (1981) Investigation of upper mantle structure under young regions of the Sout-East Pacific using long-period Rayleigh waves. *Physics of the Earth and Planetary Interiors* 27: 206–222.
- Montagner J-P and Jobert N (1988) Vectorial tomography. II: Application to the Indian Ocean. *Geophysical Journal of the Royal Astronomical Society* 94: 309–344.
- Montagner J-P and Kennett BLN (1996) How to reconcile body-wave and normal-mode reference Earth models? *Geophysical Journal International* 125: 229–248.
- Montagner J-P, Lognonné P, Beauduin R, Roult G, Karczewski J-F, and Stutzmann E (1998) Towards multiscale and multiparameter networks for the next century: The French efforts. *Physics of the Earth and Planetary Interiors* 108: 155–174.
- Montagner J-P and Nataf HC (1986) On the inversion of the azimuthal anisotropy of surface waves. *Journal of Geophysical Research* 91: 511–520.
- Montagner J-P and Nataf H-C (1988) Vectorial tomography. I: Theory. *Geophysical Journal of the Royal Astronomical Society* 94: 295–307.
- Montagner J-P and Tanimoto T (1990) Global anisotropy in the upper mantle inferred from the regionalization of phase velocities. *Journal of Geophysical Research* 95: 4797–4819.
- Montagner J-P and Tanimoto T (1991) Global upper mantle tomography of seismic velocities and anisotropies. *Journal of Geophysical Research* 96: 20,337–20,351.
- Montagner J-P, Romanowicz B, and Karczewski JF (1994) A first step towards an Oceanic geophysical observatory. *EOS, Transactions of the American Geophysical Union* 75: 150–154.
- Montagner J-P and Romanowicz B (1993) Degrees 2, 4, 6 inferred from seismic tomography. *Geophysical Research Letters* 20: 631–634.
- Montelli R, Nolet G, Dahlen FA, Masters G, Engdahl R, and Hung S (2004) Finite-frequency tomography reveals a variety of mantle plumes. *Science* 303: 338–343.
- Mooney WD, Laske G, and Masters G (1998) CRUST5.1: A global crustal model at 5×5 . *Journal of Geophysical Research* 96: 20,337–20,351.
- Nataf H-C, Nakanishi I, and Anderson DL (1984) Anisotropy and shear velocity heterogeneities in the upper mantle. *Geophysical Research Letters* 11: 109–112.
- Nataf H-C, Nakanishi I, and Anderson DL (1986) Measurement of mantle wave velocities and inversion for lateral heterogeneity and anisotropy, III. Inversion. *Journal of Geophysical Research* 91: 7261–7307.
- Nataf H-C and Ricard Y (1996) 3-SMAC: An a priori tomographic model of the upper mantle based on geophysical modeling. *Physics of the Earth and Planetary Interiors* 95: 101–122.
- Nicolas A, Boudier F, and Boullier AM (1973) Mechanisms of flow in naturally and experimentally deformed peridotites. *American Journal of Science* 273: 853–876.
- Nicolas A and Christensen NI (1987) Formation of anisotropy in upper mantle peridotites: A review. In: Fuchs K and Froidevaux C (eds.) *Composition, Structure and Dynamics of the Lithosphere/ Asthenosphere System*, pp. 111–123. Washington, DC: American Geophysical Union.
- Nishimura CE and Forsyth DW (1989) The anisotropic structure of the upper mantle in the Pacific. *Geophysical Journal* 96: 203–229.
- Nolet G (1975) Higher Rayleigh modes in Western Europe. *Geophysical Research Letters* 2: 60–62.
- Nolet G (1990) Partitioned waveform inversion and two-dimensional structure under the network of autonomously recording seismographs. *Journal of Geophysical Research* 95: 8499–8512.
- Oka E and Jo B-G (1985) Stacking investigation of higher-order mantle Rayleigh waves. *Geophysical Research Letters* 12: 421–424.
- Panning M and Romanowicz B (2004) Inferences of flow at the base of Earth's mantle based on seismic anisotropy. *Science* 303: 351–353.
- Park J and Levin V (2002) Seismic anisotropy: Tracing plate dynamics in the mantle. *Science* 296: 5567.
- Petersen O and Maupin V (2002) Lithospheric anisotropy on the Kerguelan hotspot track inferred from Rayleigh wave polarisation anomalies. *Geophysical Journal International* 149: 225–246.
- Plomerova J, Sileny J, and Babuska V (1996) Joint interpretation of upper-mantle anisotropy based on teleseismic P-travel time delay and inversion of shear-wave splitting parameters. *Physics of the Earth and Planetary Interiors* 95: 293–309.
- Ribe NM (1989) Seismic anisotropy and mantle flow. *Journal of Geophysical Research* 94: 4213–4223.
- Ricard Y, Nataf HC, and Montagner J-P (1996) The 3-SMAC model: Confrontation with seismic data. *Journal of Geophysical Research* 101: 8457–8472.
- Ringwood AE (1975) *Composition and Petrology of the Earth's Mantle*, 618 pp. New-York: McGraw-Hill.
- Ritsema J and van Heijst HJ (2000) Seismic imaging of structural heterogeneity in Earth's mantle: Evidence for large-scale mantle flow. *Science Progress* 83: 243–259.
- Ritsema J and van Heijst HJ (2004) Global transition zone tomography. *Journal of Geophysical Research* 109: B02302 doi:10.1029/2003JB002610.
- Ritzwoller MH, Shapiro NM, and Zhong S-J (2004) Cooling history of the Pacific lithosphere. *Earth and Planetary Science Letters* 226: 69–84.
- Ritzwoller MH, Shapiro NM, Barmin MP, and Levshin AL (2002) Global surface wave tomography. *Journal of Geophysical Research* 107(B12): 2335 10.1029/2002JB001777.
- Romanowicz B (1987) Multiplet–multiplet coupling due to lateral heterogeneity: Asymptotic effects on the amplitude and frequency of the Earth's normal modes. *Geophysical Journal of the Royal Astronomical Society* 90: 75–100.
- Romanowicz B (1990) The upper mantle degree two: Constraints and inferences from global mantle wave attenuation measurements. *Journal of Geophysical Research* 95: 11051–11071.
- Romanowicz B (1995) A global tomographic model of shear attenuation in the upper mantle. *Journal of Geophysical Research* 100: 12375–12394.
- Romanowicz B (2002) Inversion of surface waves: A review. In: Lee WHK (ed.) *Handbook of Earthquake and Engineering Seismology*, ch. 11, pp. 141–173. Amsterdam: Academic Press.
- Romanowicz B (2003) Global mantle tomography: Progress status in the past 10 years. *Annual Review of Earth and Planetary Science* 31: 303–328.

- Romanowicz B, Cara M, Fels J-F, and Rouland D (1984) GEOSCOPE: A French initiative in long period, three component, global seismic networks. *EOS, Transactions of the American Geophysical Union* 65: 753–754.
- Romanowicz B and Dziewonski AM (1986) Towards a federation of broadband seismic networks. *EOS* 67: 541–542.
- Roult G, Romanowicz B, and Montagner JP (1990) 3D upper mantle shear velocity and attenuation from fundamental mode free oscillation data. *Geophysical Journal International* 101: 61–80.
- Romanowicz B and Snieder R (1988) A new formalism for the effect of lateral heterogeneity on normal modes and surface waves, II: General anisotropic perturbations. *Geophysical Journal of the Royal Astronomical Society* 93: 91–99.
- Roult G, Rouland D, and Montagner JP (1994) Antarctica II: Upper mantle structure from velocity and anisotropy. *Physics of the Earth and Planetary Interiors* 84: 33–57.
- Rumpker G and Silver PG (1998) Apparent shear-wave splitting parameters in the presence of vertically varying anisotropy. *Geophysical Journal International* 135: 790–800.
- Savage MK (1999) Seismic anisotropy and mantle deformation: What have we learned from shear wave splitting? *Reviews of Geophysics* 37: 65–106.
- Schlue JW and Knopoff L (1977) Shear-wave polarization anisotropy in the Pacific Ocean. *Geophysical Journal of the Royal Astronomical Society* 49: 145–165.
- Sebai A, Stutzmann E, and Montagner J-P (2006) Anisotropic structure of the African upper mantle structure from Rayleigh and Love wave tomography. *Physics of the Earth and Planetary Interiors* 155: 48–62.
- Shapiro NM and Ritzwoller MH (2002) Monte-Carlo inversion for a global shear-velocity model of the crust and upper mantle. *Geophysical Journal International* 151: 88–105.
- Shapiro NM, Campillo M, Stehly L, and Ritzwoller MH (2005) High-resolution surface-wave tomography from ambient seismic noise. *Science* 307: 1615–1618.
- Shearer PM (1991) Constraints on upper mantle discontinuities from observations of long-period reflected and converted waves. *Journal of Geophysical Research* 96: 18,147–18,182.
- Sicilia D, Montagner J-P, Cara M, Debayle E, Lepine J-J, and Leveque J-J (2007) Shear-wave velocities and anisotropic structure beneath the Afar hotspot. *Tectonophysics*. (submitted).
- Sieminski A, Lévéque J-J, and Debayle E (2004) Can finite-frequency effects be accounted for in ray theory surface wave tomography. *Geophysical Research Letters* 31: L24614 doi:10.1029/2004GL02142.
- Silveira G, Stutzmann E, Montagner J-P, and Mendes-Victor L (1998) Anisotropic tomography of the Atlantic Ocean from Rayleigh surface waves. *Physics of the Earth and Planetary Interiors* 106: 259–275.
- Silveira G and Stutzmann E (2001) Anisotropic tomography of the Atlantic Ocean. *Physics of the Earth and Planetary Interiors* 132: 237–248.
- Silver PG (1996) Seismic anisotropy beneath the continents: Probing the depths of geology. *Annual Review of Earth and Planetary Science* 24: 385–432.
- Silver PG and Chan WW (1988) Implications for continental structure and evolution from seismic anisotropy. *Nature* 335: 34–39.
- Silver PG and Holt WE (2002) The mantle flow field beneath North America. *Science* 295: 1054–1057.
- Silver PG and Savage M (1994) The Interpretation of shear-wave splitting parameters in the presence of two anisotropic layers. *Geophysical Journal International* 119: 949–963.
- Simons FJ, van der Hilst R, Montagner JP, and Zielhuis A (2002) Multimode Rayleigh wave inversion for shear wave speed heterogeneity and azimuthal anisotropy of the Australian upper mantle. *Geophysical Journal International* 151: 738–754.
- Singh S, Taylor M, and Montagner JP (2000) On the presence of fluids in the Earth's inner core. *Science* 287: 2471–2474.
- Smith SW (1986) IRIS; a program for the next decade. *EOS, Transactions of the American Geophysical Union* 67: 213–219.
- Smith ML and Dahlen FA (1973) The azimuthal dependence of Love and Rayleigh wave propagation in a slightly anisotropic medium. *Journal of Geophysical Research* 78: 3321–3333.
- Smith ML and Dahlen FA (1975) Correction to 'The azimuthal dependence of Love and Rayleigh wave propagation in a slightly anisotropic medium. *Journal of Geophysical Research* 80: 1923.
- Smith D, Ritzwoller MH, and Shapiro NM (2004) Stratification of anisotropy in the Pacific upper mantle. *Journal of Geophysical Research* 109: B11309 doi:10.1029/2004JB03200.
- Snieder R (1988) Large-scale waveform inversions of surface waves for lateral heterogeneity, 1. Theory and numerical examples. *Journal of Geophysical Research* 93: 12,055–12,066.
- Snieder R, Gret A, Douma H, and Scales J (2002) Coda wave interferometry for estimating non-linear behavior in seismic velocity. *Science* 295: 2253–2255.
- Solomatov VS and Moresi LN (2000) Scaling of time-dependent stagnant lid convection: Application to small-scale convection on Earth and other terrestrial planets. *Journal of Geophysical Research* 105: 21795–21817.
- Spetzler J, Trampert J, and Snieder R (2002) The effect of scattering in surface wave tomography. *Geophysical Journal International* 149: 755–767.
- Stutzmann E and Montagner JP (1994) Tomography of the transition zone from the inversion of higher-mode surface waves. *Physics of the Earth and Planetary Interiors* 86: 99–116.
- Su W-J, Woodward RL, and Dziewonski AM (1984) Degree 12 model of shear velocity heterogeneity in the mantle. *Journal of Geophysical Research* 99: 6,945–6,980.
- Su L, Park J, and Yu Y (1993) Born seismograms using coupled free oscillations: The effect of strong coupling and anisotropy. *Geophysical Journal International* 115: 849–862.
- Suetsugu D and Nakanishi I (1987) Regional and azimuthal dependence of phase velocities of mantle Rayleigh waves in the Pacific Ocean. *Physics of the Earth and Planetary Interiors* 47: 230–245.
- Suyehiro K, Kanazawa T, Hirata N, Shinohara M, and Kinoshita H (1992) Broadband downhole digital seismometer experiment at site 794: A technical paper. In, *Proceedings of the Ocean Drilling Project, Scientific Results*, pp. 127–128 TX: Ocean Drilling Program, College Station.
- Takeuchi H and Saito M (1972) Seismic surface waves. *Methods in Computational Physics* 11: 217–295.
- Tanimoto T (1986) Free oscillations in a slightly anisotropic Earth. *Geophysical Journal of the Royal Astronomical Society* 87: 493–517.
- Tanimoto T (1990) Long-wavelength S-wave velocity structure throughout the mantle. *Geophysical Journal International* 100: 327–336.
- Tanimoto T and Anderson DL (1985) Lateral heterogeneity and azimuthal anisotropy of the upper mantle: Love and Rayleigh waves. 100–250s. *Journal of Geophysical Research* 90: 1842–1858.
- Tarantola A and Valette B (1982) Generalized nonlinear inverse problems solved using least squares criterion. *Reviews of Geophysics and Space Physics* 20: 219–232.
- Tommasi A, Vauchez A, and Russo R (1996) Seismic anisotropy in ocean basins: Resistive drag of the sublithospheric mantle? *Geophysical Research Letters* 23: 2991–2994.

- Tommasi A, Mainprice D, Canova G, and Chastel Y (2000) Viscoelastic self-consistent and equilibrium-based modeling of olivine preferred orientations. Implications for the upper mantle anisotropy. *Journal of Geophysical Research* 105: 7893–7908.
- Trampert J and Snieder R (1996) Model estimations biased by truncated expansions: Possible artifacts in seismic tomography. *Science* 271: 1257–1260.
- Trampert J and van Heijst HJ (2002) Global azimuthal anisotropy in the transition zone. *Science* 296: 1297–1299.
- Trampert J and Woodhouse JH (2003) Global anisotropic phase velocity for fundamental mode surface waves between 40 and 150 s. *Geophysical Journal International* 154: 154–165.
- Tromp J, Tape C, and Liu Q (2005) Seismic tomography, adjoint methods, time reversal and banana-doughnuts kernels. *Geophysical Journal International* 160: 195–216.
- Van Heijst HJ and Woodhouse JH (1997) Measuring surface-wave overtone phase velocities using a mode-branch stripping technique. *Geophysical Journal International* 131: 209–230.
- Villaseñor A, Ritzwoller MH, Levshin AL, et al. (2001) Shear velocity structure of Central Eurasia from inversion of surface wave velocities. *Physics of the Earth and Planetary Interiors* 123: 169–184.
- Vinnik LP, Chevrot S, and Montagner J-P (1998) Seismic evidence of flow at the base of the upper mantle. *Geophysical Research Letters* 25: 1995–1998.
- Vinnik L, Makayeva LI, Milev A, and Usenko AY (1992) Global patterns of azimuthal anisotropy and deformations in the continental mantle. *Geophysical Journal International* 111: 433–447.
- Vinnik L and Montagner J-P (1996) Shear wave splitting in the mantle from Ps phases. *Geophysical Research Letters* 23: 2449–2452.
- Vinnik L, Montagner JP, Girardin N, Dricker I, and Saul J (2003) Shear wave splitting at H₂O: A comment. *Geophysical Research Letters* 30(13): 1675.
- Walker KT, Bokelmann GH, and Klemperer SL (2001) Shear-wave splitting to test mantle deformation models around Hawaii. *Geophysical Research Letters* 28: 4319–4322.
- Wang Z and Dahlen FA (1995) Spherical-spline parameterization of three-dimensional earth models. *Geophysical Research Letters* 22: 3099–3102.
- Wielandt E and Streickeisen G (1982) The leaf-spring seismometer: Design and performances. *Bulletin of the Seismological Society of America* 72: 2349–2367.
- Wolfe CJ and Silver PC (1998) Seismic anisotropy of oceanic upper mantle. *Journal of Geophysical Research* 103: 749–771.
- Wolfe CJ and Solomon SC (1998) Shear-wave splitting and implications for mantle flow beneath the melt region of the East Pacific Rise. *Science* 280: 1230–1232.
- Woodhouse JH and Dziewonski AM (1984) Mapping the upper mantle: Three dimensional modelling of Earth structure by inversion of seismic waveforms. *Journal of Geophysical Research* 89: 5953–5986.
- Woodhouse JH and Dahlen FA (1978) The effect of a general aspherical perturbation on the free oscillations of the Earth. *Geophysical Journal of the Royal Astronomical Society* 53: 335–354.
- Woodhouse JH and Giuris (1982) Surface waves and free oscillations in a regionalized earth model. *Geophysical Journal of the Royal Astronomical Society* 68: 653–673.
- Wookey J, Kendall JM, and Barruel G (2002) Mid-mantle deformation inferred from seismic anisotropy. *Nature* 415: 777–780.
- Yomogida K (1992) Fresnel-zone inversion for lateral heterogeneities in the Earth. *Pure and Applied Geophysics* 138: 391–406.
- Yoshizawa K and Kennett BHN (2002) Determination of the influence zone for surface wave paths. *Geophysical Journal International* 149: 441–454.
- Yoshizawa K and Kennett BHN (2004) Multimode surface wave tomography for the Australian region using a three-stage approach incorporating finite frequency effects. *Journal of Geophysical Research* 109: B02310 doi:10.1029/2002JB002254.
- Yu Y and Park J (1993) Anisotropy and coupled long-period surface waves. *Geophysical Journal International* 114: 473–489.
- Zhang H and Thurber CH (2005) Adaptive mesh seismic tomography based on tetrahedral and Voronoi diagrams: Application to Parkfield. *Journal of Geophysical Research* 110: B04303 doi:10.1029/2004JB003186.
- Zhang S and Karato S-I (1995) Lattice preferred orientation of olivines aggregates deformed in simple shear. *Nature* 375: 774–777.
- Zhou Y, Dahlen FA, and Nolet G (2004) Three-dimensional sensitivity kernels for surface wave observables. *Geophysical Journal International* 158: 142–168.
- Zhou Y, Nolet G, Dahlen FA, and Laske G (2006) Global upper mantle structure from finite-frequency surface-wave tomography. *Journal of Geophysical Research* 111: B04304 doi:10.1029/2005JB003677.

Relevant Websites

- <http://seismo.berkeley.edu> – Berkeley Seismological Lab.
<http://matri.ucsd.edu> – Whole Earth Geophysics at IGPP.

1.17 Deep Earth Structure – Transition Zone and Mantle Discontinuities

R. Kind and X. Li, GFZ Potsdam, Potsdam, Germany

© 2007 Elsevier B.V. All rights reserved.

1.17.1	Introduction	592
1.17.2	The Mantle Transition Zone	594
1.17.2.1	Global Transition Zone Structure	594
1.17.2.2	Local Transition Zone Structure	597
1.17.2.2.1	Subduction zones	597
1.17.2.2.2	Hot spots	600
1.17.2.2.3	Continents	600
1.17.2.2.4	Oceans	601
1.17.2.2.5	Sharpness of 410 and 660	602
1.17.2.2.6	520 discontinuity	602
1.17.2.3	Summary of the Upper-Mantle Transition Zone	603
1.17.3	The Gutenberg Discontinuity	604
1.17.3.1	Summary of the Gutenberg Discontinuity	608
1.17.4	The Lehmann Discontinuity	608
1.17.4.1	Summary of the Lehmann Discontinuity	609
1.17.5	The Hales Discontinuity	610
1.17.5.1	Summary of the Hales Discontinuity	610
1.17.6	Conclusions	610
References		611

Glossary

410 discontinuity Seismic discontinuity at that depth in global average, mainly caused by phase transition from olivine to spinel.

520 discontinuity Seismic discontinuity, observed at many places on Earth, but not laterally continuously.

660 discontinuity Seismic discontinuity at that depth in global average, caused by spinel to magnesiowuestite-perovskite phase transition.

asthenosphere Low-viscosity weak layer below the lithosphere.

Earthscope with USArray Large projects to study the North American lithosphere.

GEOFON Global seismic network of the GFZ Potsdam, Germany.

GEOSCOPE Global seismic network of the IPG Paris, France.

Gutenberg discontinuity Seismic discontinuity with decrease of velocity downward, top of low-velocity zone.

Hales discontinuity Seismic discontinuity in the mantle lithosphere.

IRIS Global seismic network of US universities and US Science Foundation.

LAB Boundary between high-viscosity lithosphere and low-viscosity atmosphere.

Lehmann discontinuity Seismic discontinuity, supposed to be the bottom of the asthenosphere.

lithosphere Elastic uppermost layer of the Earth, defined by its mechanical properties; lithospheric plates move over great horizontal distances.

Moho Mohorovicic discontinuity, crust–mantle boundary, seismically defined.

P- or S- receiver functions P-to-S converted phases in the coda of P, or S-to-P conversions as precursor of S.

PP P phase with one reflection at the free surface.

receiver functions Seismic records diagnostic for structure beneath a station.

ScS S wave reflected from the core–mantle boundary.

SS S phase with one reflection at the free surface.

1.17.1 Introduction

When Ernst von Rebeur-Paschwitz recorded in Potsdam the first teleseismic earthquake, he immediately recognized the importance of his discovery for illuminating the Earth's interior (von Rebeur-Paschwitz, 1889). He suggested that a global network of seismographs should be installed and the data should be evaluated by Earth scientists. This is still today a very modern idea, although we have achieved much since then with the construction of the Global Seismic Network and the free exchange of real time of data. The appearance of the first seismic records made it clear that the Earth has an onion-shell character with crust, mantle, outer and inner core, separated by seismic discontinuities. The increase of seismic data led later to the discovery of more seismic discontinuities in the upper mantle, the Gutenberg, the Hales, the Lehmann discontinuities, and, especially important, the discontinuities at about 410, 520, and 660 km depth (called simply the '410', '520', and '660'), and perhaps even more less clear ones. The exact knowledge about these discontinuities, their distribution, their topography, or their sharpness sets boundary conditions for mantle dynamics or petrology. For plate tectonics, the concept of rheological layers (lithosphere and asthenosphere) became important. Immediately, the questions arises: how these mechanical plate definitions can be confirmed with seismological observations? What is the seismic appearance of the lithosphere–asthenosphere boundary (LAB)? Since seismology is in first order an observational science, only the increase of data can bring a new increase of knowledge. Therefore, the seismic networks are continuously densified (e.g., Earthscope with USArray) in order to produce more realistic and more detailed images of the Earth's interior. It is easily foreseeable that these new data will lead to a wealth of new discoveries about the dynamics of our planet.

We review the global structure of the major seismic discontinuities in the upper mantle. The emphasis of our study is the seismic observations. The well-known discontinuities at about 410 and 660 km average depth globally, which are usually just called the '410' and the '660', are primarily focused upon. The '520' is also considered. The Moho, separating the upper mantle from the crust, is not discussed here (see Chapters 1.11, 1.12, 1.13, 1.14, and 1.15). Between the Moho and 410 are a number of discontinuities reported, of which we

will only treat the relatively well-established and pervasive ones, although they are all much less clear than the discontinuities so far mentioned. These less clearly observed discontinuities are the Gutenberg discontinuity, which is frequently identified with the lithosphere–asthenosphere boundary (LAB) between about 100 and 200 km depth, the Hales discontinuity at ~80 km depth, and the Lehmann discontinuity at the base of the asthenosphere at ~220 km depth. Except for the LAB, all mentioned discontinuities are seismologically defined. The LAB was originally defined mechanically by postglacial rebound observations (see Chapters 6.02 and 6.03). Seismologists only try to identify this discontinuity in seismic data. In the course of plate tectonics, the LAB gained additional significance since it was suggested that lithospheric plates move over large horizontal distances with the LAB as a shear zone. Since the LAB is only poorly observed seismologically, and then mainly by low-resolution long-period surface waves, it is usually assumed that it is a rather broad transition zone rather than a sharp seismic discontinuity. In recent times, receiver functions have sharpened our view at the LAB.

Wide-angle observations have been the fundamental seismic tool for detecting the upper-mantle discontinuities (see Chapters 1.04 and 1.05). This technique is however less suited for determining their small-scale topography. This is because the lateral part of the travel path of wide-angle rays is several times longer than the vertical part, which leads to increased sensitivity to lateral velocity heterogeneities in large parts of the upper mantle. Steep-angle techniques (see Chapter 1.08), more suited for determining small-scale topography of the mantle discontinuities, are ScS reverberations (e.g., Revenaugh and Jordan, 1987, 1991a, 1991b), SS, P'P', and PP precursors (e.g., Shearer, 1991, 1993; Adams, 1968, 1971; Whitcomb and Anderson, 1970; Engdahl and Flinn, 1969; Bolt, 1970; King *et al.*, 1975), or Ps and Sp conversions at the discontinuities (e.g., Båth and Stefansson, 1966; Vinnik, 1977; Faber and Müller, 1980; Stammler *et al.*, 1992; Benz and Vidale, 1993; Xu *et al.*, 1998; Chevrot *et al.*, 1999; Li *et al.*, 2003a; see Figure 1 for ray paths of such phases). All these phases are small secondary phases in front of or after a main phase like P, S or PP, P'P', SS or ScS (see Chapter 1.20). Ps or Sp conversions or reflections of local high-frequency subduction earthquakes may be used to map the topography of the 410 and 660 with very high resolution (see ray paths in Figure 2). Many secondary phases have been used

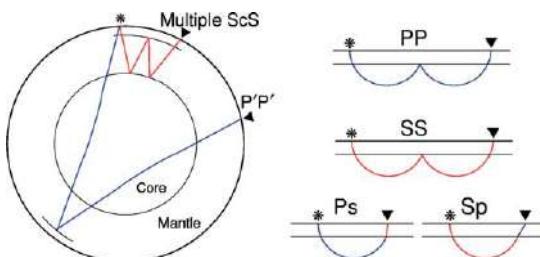


Figure 1 Ray paths of ScS reverberations reflected at upper- or lower-mantle discontinuities; of P'P' precursors from upper-mantle discontinuities; SS and PP precursors and Ps and Sp conversions at upper-mantle discontinuities.

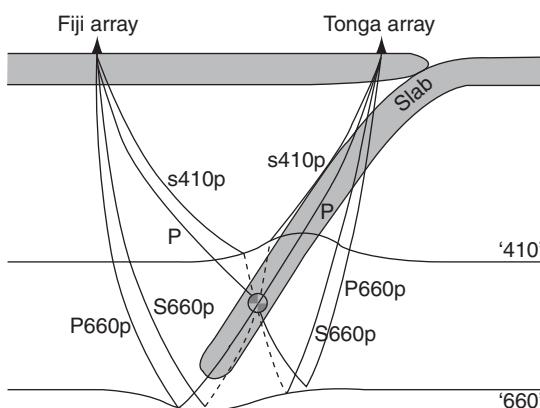


Figure 2 Reflected and converted rays of locally recorded subduction earthquakes. Such high-frequency data are very useful for high-resolution imaging of the mantle discontinuities near subduction zones. From Tibi R and Wiens DA (2005) Detailed structure and sharpness of upper mantle discontinuities in the Tonga subduction zone from regional broadband arrays. *Journal of Geophysical Research B: Solid Earth* 110(6): 1–14, figure 2.

since a long time. However, the sparsity of seismic stations around the world, although sufficient for locating earthquakes and determining earthquake source parameters, was insufficient to obtain detailed images of the structure of the upper mantle that are necessary to resolve its dynamics. Especially, processing of the data, even simple plotting at the right scale, was difficult, since until a few decades ago nearly all data were analog. In about last two decades, digital techniques, however, have made a rapid development. Since secondary phases are usually weak or even invisible in individual seismograms, delay-and-sum techniques, known as stacking in array technology, have been added to the processing of single traces. Array techniques require large amounts of data. The processing steps applied now include simple rotation of the components for

separation of the different wave types, deconvolution or correlation techniques, slant stacks, transformation to the frequency or slowness domain, distance move-out corrections, and migration from the time domain into depth sections. Broadband Ps conversions (incident teleseismic P waves converted to S waves at a discontinuity below a station) are particularly frequently used (Vinnik, 1977; Langston, 1979). In crustal studies, they are known under the name of ‘receiver functions’. Waveforms of receiver functions are frequently inverted into one-dimensional velocity-depth models.

Ps conversions are also often used for observations of the discontinuities at 410 and 660 km depth below single broadband stations or arrays of broadband stations. Long-period SS precursors, which are reflected at the midpoint between source and receiver at upper-mantle discontinuities, are also frequently used. They are especially useful for global mapping of the discontinuities at 410, 520, and 660 km depth (see **Figure 3**). An important advantage of SS precursors is that they provide information about oceanic regions where few stations are located.

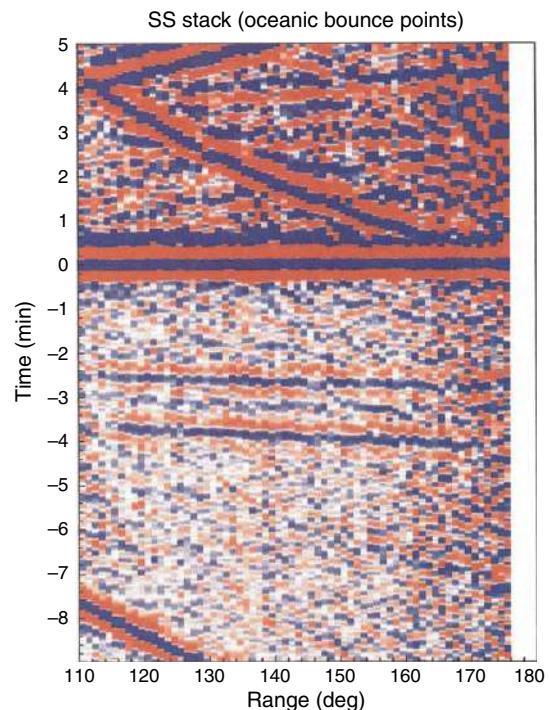


Figure 3 Time versus range image showing SS (at 0 min) and its precursors (between about -2 and -4 min) at 410, 520, and 660 km depth obtained by stacking long-period seismograms. From Shearer PM (1996) Transition zone velocity gradients and the 520-km discontinuity. *Journal of Geophysical Research* 101: 3053–3066, plate 1.

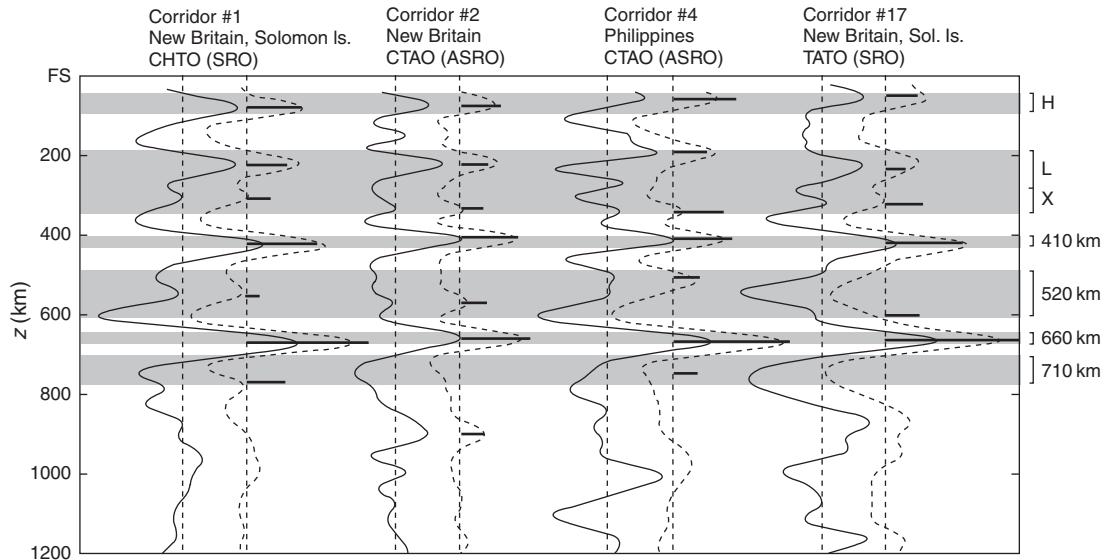


Figure 4 Observed (solid lines) and synthetic (dashed lines) ScS reverberations from a number of upper-mantle discontinuities along several great circle paths. From Revenaugh JS and Jordan TH (1991b) Mantle layering from ScS reverberations. 3. The upper mantle. *Journal of Geophysical Research* 96: 19781–19810, figure 3.

Secondary peg-leg multiples of ScS and its reverberations are also very useful (see Figure 4 for a data example). Most recently, Sp conversions (incident teleseismic S waves converted to a P wave at a discontinuity below a station) have also proved to be successful in observing boundaries in the upper mantle.

There are two types of seismic data that are mainly used for studies of the upper-mantle discontinuities. The first type stems from the permanent global seismic networks (IRIS, see [Butler et al. \(2004\)](#); GEOFON, see [Hanka et al. \(2000\)](#); or GEOSCOPE, see [Romanowicz et al. \(1991\)](#)) and many other contributing stations. These networks have a global coverage, but still have a relatively low density of station distribution. This is especially true for oceanic areas. Data from these networks are therefore only useful for low-resolution global images. Oceans are only sampled with island stations, which are highly exceptional places, not typical of the large-scale oceanic mantle. Permanent or temporary ocean-bottom installations are very expensive and technically difficult and for this reason very rare. The second type of data stems from relatively short-term deployments of much denser networks (see Chapter 1.14). They have only local or regional distribution but allow much higher-resolution images. The above-mentioned permanent networks operate open stations allowing unrestricted near-

real-time access to their data by any user. Most temporary networks also make their data freely available after some time. Therefore, a rapidly increasing amount of high-quality seismic data is available for global studies. This policy of free data access is of great advantage for international science and the example provided by the IRIS and PASSCAL projects, as the largest data producers, cannot be overestimated.

1.17.2 The Mantle Transition Zone

1.17.2.1 Global Transition Zone Structure

All modern global reference Earth models show a sudden increase of the velocities of the elastic waves and densities near 410 and 660 km depth (e.g., the PREM model, [Dziewonski and Anderson \(1981\)](#) or the IASP91 model, [Kennett and Engdahl \(1991\)](#)). This region of the mantle is called the transition zone between upper and lower mantle. Earlier Earth models ([Jeffreys and Bullen, 1940](#); [Gutenberg, 1959](#)) indicate changes in the velocity gradients at these depths, although without resolving first-order discontinuities, based on observations of slowness changes and increasing P wave amplitudes at about 20° epicentral distance ([Byerly, 1926](#); [Jeffreys, 1936](#)). More intensive seismic wide-angle controlled source and earthquake source studies began in the 1960s, leading to better data

quality; hence, the two major global seismic discontinuities were discovered near 410 and 660 km depth (e.g., Niazi and Anderson, 1965; Ibrahim and Nuttli, 1967; Johnson, 1967; Kanamori, 1967; Julian and Anderson, 1968). In the following years, many wide-angle studies were undertaken and regional upper-mantle models derived for continental and oceanic areas (e.g., Walck (1984), or summarized by Nolet *et al.* (1994) and Gaherty *et al.* (1996); see Chapter 1.07). The computation of theoretical seismograms has been an essential tool for modeling the waveforms at the travelttime triplications (e.g., Helmberger, 1968; Helmberger and Wiggins, 1971).

Both discontinuities have been interpreted as pressure- and temperature-induced phase changes in the olivine system (e.g., Birch, 1952; Anderson, 1967; Green and Ringwood, 1967; Ringwood, 1969; Liu, 1976; Green and Liebermann, 1976; Jeanloz and Thompson, 1983; Lees *et al.*, 1983; Bass and Anderson, 1984; Anderson and Bass, 1986; Bina and Wood, 1986; Ito and Takahashi, 1989; Shim *et al.*, 2001; see Chapter 2.06). It has, however, also been suggested that compositional changes may occur around these depths (e.g., Irfune and Isshiki, 1998). If the 410 and 660 are olivine phase boundaries, then lateral temperature changes would cause topography of both discontinuities. From the estimated Clapeyron slopes of both discontinuities, it is expected that a 100 K temperature change would change the depths of the 410 and 660 by about 8 and 5 km, respectively (Bina and Helffrich, 1994). The Clapeyron slopes have opposite signs (410 positive and 660 negative), so 100 K higher temperature should reduce the transition zone thickness by about 13 km and 100 K lower temperature should thicken the transition zone by about the same amount. Thus, the topography of the upper-mantle discontinuities, or better still the thickness of the transition zone, because it is independent of velocities above the 410, should indicate the lateral distribution of hot and cold regions in the transition zone. The depths of the 410 and 660 discontinuities should be anticorrelated if the effect of temperature dominates and the temperature at the 410 correlates with that at 660 (Revenaugh and Jordan, 1989, 1991a). Such thinner and thicker transition zone regions could play an important role in revealing global circulation, as they could distinguish upwelling and downwelling material. However, it should be kept in mind that the topography of the 410 and 660 could also be modified by other influences (e.g., chemistry or garnet phase transitions; see Anderson (1989)). Topography could also be caused by metastable olivine below 410 km depth in subduction zones (Kirby *et al.*, 1996).

Images of the global transition zone thickness should be able to answer several questions. The first one should be to verify the reality of the simple model of olivine phase transformations as the cause of the discontinuities at 410 and 660 km depth and also to verify laboratory values of the Clapeyron slopes of both discontinuities. This could be done if global anticorrelation of both discontinuities would be observable. The second question would be to confirm possible locations of hot and cold material in the transition zone in regions where we also have other evidence for hot or cold material (e.g., from tomography or earthquake locations in subduction zones or below postulated plumes). A third question would be to contribute to the problem of the deep roots of continents, which may effect even the transition zone (Jordan, 1975).

In the last two decades, there have been a number of papers on the global transition zone structure obtained from SS, PP, or P'P' precursors (e.g., Wajeman, 1988; Shearer and Masters, 1992; Shearer, 1993; Gossler and Kind, 1996; Estabrook and Kind, 1996; Flanagan and Shearer, 1998a, 1999; Gu *et al.*, 1998; Gu and Dziewonski, 2002; Chambers *et al.*, 2005b). Similar information from Ps conversions has been obtained, for example, by Stammler *et al.* (1992), Gurrola and Minster (1998), Chevrot *et al.* (1999), and Li *et al.* (2003a). Helffrich (2000) reviewed global transition zone thickness studies. Ps and Sp conversion techniques sample the upper-mantle structure within a radius of several hundred kilometers around a seismic station. Precursor techniques of surface-reflected phases, such as PP or SS, sample the midpoints between epicenters and receivers. Precursor techniques allow a better global distribution of sampling points, reaching locations without stations or earthquake sources. They have the drawback of being associated with maximum traveltime phases, which raises the issue of possible contamination by small-scale, off-great-circle-path structure. This and related questions have been discussed by Neele *et al.* (1997), Shearer *et al.* (1999), Neele and De Regt (1999), and Chaljub and Tarantola (1997). On the other hand, converted phases, which are minimum traveltime phases, allow better resolution, in principle, due to their smaller Fresnel zones. Their global sampling is poorer, however, because they are restricted to near-station or earthquake locations. Liu (2003) pointed out problems caused by inelasticity of the detectability and of the depth determination of the mantle discontinuities. Secondary phases like Sp or Ps conversions, or SS or PP precursors, are usually very weak phases, so summation must be used to improve

the signal-to-noise ratio. In the case of conversions, usually data from just one station are summed. If stations are sufficiently closely spaced, traces with nearby conversion points may be summed (common conversion point summation). Sp conversions sample a larger region than Ps conversions because of the ray paths involved. In the case of SS or PP precursors, traces with close reflection points are summed (common reflection point summation).

Revenaugh and Jordan (1991a) examined ScS reverberations from the 660 and 410 in the search for a negative correlation between both discontinuities. However, they found only weak indications of negative correlation. Gossler and Kind (1996) found such a negative correlation in SS precursors from the 410 and 660 discontinuities, although it was only moderately strong. This correlation indicated a thinner transition zone beneath the Pacific and Indian Oceans than beneath some cratons. This observation was confirmed by Li *et al.* (2003a) by mapping differential times of both discontinuities obtained from SS precursors and Ps conversions (see Figure 5). In contrast, Gu *et al.* (1998) found no correlation of the

410 and 660 in SS precursors. However, they did find indications of a shallower 410 beneath continents. Gu *et al.* (2003) obtained reduced topography of the 410, and increased topography of the 660 by including tomography results in their inversion (see Figure 6). Increased depth of the 660 was observed with SS precursors around the Pacific by Shearer and Masters (1992), Flanagan and Shearer (1998a), and Gu and Dziewonski (2002). Chambers *et al.* (2005b) found from a joint SS and PP precursor study only partial agreement with the uplifted 410 beneath cratons observed by Gu *et al.* (1998). Flanagan and Shearer (1998a) found no correlation between transition zone thickness and the distribution of oceans and continents in SS precursors. Flanagan and Shearer (1999) found, in a global map of the 410 from PP precursors, no ocean-continent correlation. Their 410 topography had an average peak-to-peak amplitude of 30 km. Chevrot *et al.* (1999) found not more than ± 10 km thickness variation of the transition zone at stations located only on continents using Ps differential times. Li *et al.* (2003a) found ± 20 km variation of the transition zone thickness from data of the same type but including ocean island stations also. Their Ps data also show a thinner transition zone beneath the Pacific Ocean than beneath the North American continent.

Li *et al.* (2003a) also found at some ocean island stations unusually large Ps times for the 410, which they attributed to slow wave speeds in narrow plumes below ocean islands (Figure 5). Gu and Dziewonski (2002) found globally ± 20 km thickness variation of the transition zone in uncorrected SS precursors with a 6–8 km thicker transition zone beneath continents (Figure 7). Lebedev *et al.* (2002b, 2003) found that the transition zone thickness from Ps conversions correlates well with tomographic S velocity variations within the transition zone, thus confirming the olivine phase change hypothesis as the origin of the 410 and 660. Gu *et al.* (2001b) obtained different flow patterns below and above the 660 by allowing a discontinuity at the 660 in the tomographic inversion. No such change was obtained at the 410. Estabrook and Kind (1996) concluded from globally missing PP precursors of the 660 that the density jump here is only $\sim 2\%$, which is significantly smaller than predicted by existing global models (see Figure 8). This observation was confirmed by Shearer and Flanagan (1999). Chambers *et al.* (2005a) found global differences in the impedance contrast across the 410 from long period PP and SS precursors.

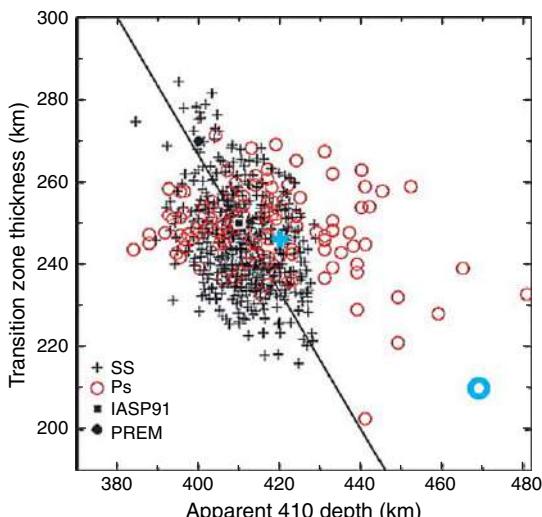


Figure 5 Thickness of mantle transition zone versus apparent 410 depths. Times of SS precursors and Ps conversions are converted into depth using the IASP91 reference model. Ps depths (open circles) deeper than 430 km are all from ocean island stations. Straight line indicates relation between transition zone thickness and depth of 410 as expected from laboratory Clapeyron slopes. Thinner transition zone regions seem to concentrate in oceanic and thicker ones in tectonic areas. From Li X, Kind R, and Yuan X (2003b) Seismic study of upper mantle and transition zone beneath hotspots. *Physics of the Earth and Planetary Interiors* 136: 79–92, figure 2.

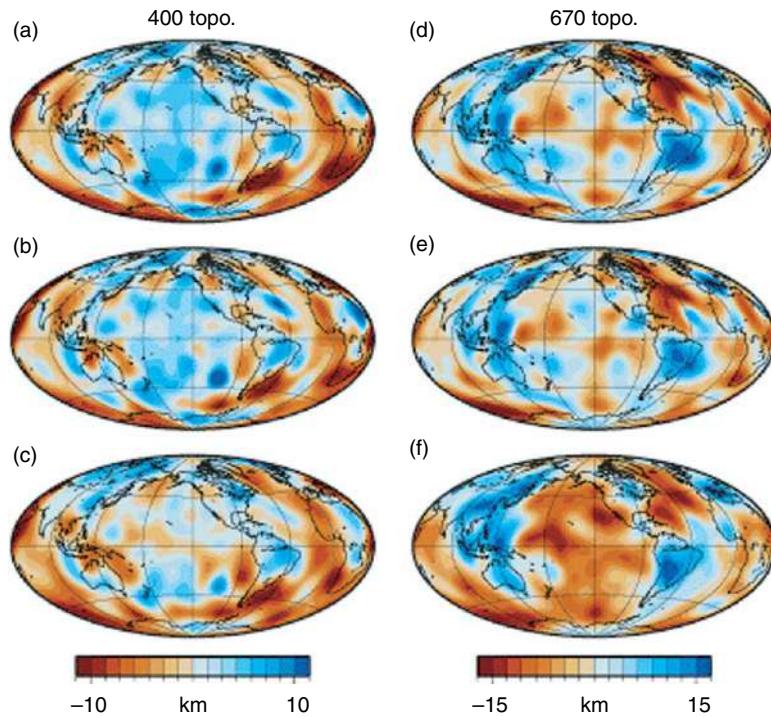


Figure 6 Topography of 410 and 660 (400 and 670 in PREM). 410 depth from SS precursors, (a) from Flanagan and Shearer (1998a) and (b) from Gu et al. (2003). (c) Results of joint inversion of SS precursors and mantle structure. (d)–(f) Similar to (a)–(c), but for topography of the 660. From Gu YJ, Dziewonski AM, Ekstrom G (2003) Simultaneous inversion for mantle shear velocity and topography of transition zone discontinuities. *Geophysical Journal International* 154: 559–583, figure 11.

1.17.2.2 Local Transition Zone Structure

The global studies of the 410 and 660 discussed so far used mainly data from open global permanent networks and from other open permanent stations. Although the global coverage of broadband stations is continuously increasing, there are still large gaps, especially in the oceans. There are however many temporary much denser deployments of seismic stations, not necessarily all broadband, which are used for detailed studies of the mantle transition zone. Such networks can answer questions that cannot be answered with sparse networks. Therefore, we also discuss detailed local or regional studies using temporary dense deployments of large numbers of seismic stations in zones where variations of the transition zone thickness could provide results of interest. The lack of long recording time in these studies is overcome by the large number of closely spaced stations. In the following, we discuss results from such experiments in several regions of the world.

1.17.2.2.1 Subduction zones

Subduction zones are discussed in detail in Chapter 7.08.

1.17.2.2.1.(i) Japan Vinnik et al. (1996): Ps conversions; no depression of the 660.

Thirot et al. (1998): Ps conversions; 660 depressed by 40–50 km beneath the GEOSCOPE station Inuyama.

Li et al. (2000a): Ps conversions from the Japanese broadband network. Found normal 410 in the overall region, with the exception of no 410 signal where the slab directly reaches that depth. The 660 reaches 700 km depth at two places where it is hit directly by the slab. No large-scale depression of the 660 was observed in east China. This was contrary to what was concluded from tomography studies which observed high velocities (or cold temperature which would lead to a depressed 660) in the mantle transition zone (Bijwaard et al., 1998).

Kato et al. (2001): ScS reverberations; 660 depressed by 10 km (much smaller than in SS precursor data) and no significant structure at the 410 where the slab hits the transition zone.

Tono et al. (2005): Near-vertical reflections from a regional earthquake recorded by ~500 tiltmeters and ~60 broadband seismometers in Japan; 660 depressed by ~15 km and 410 elevated within the slab.

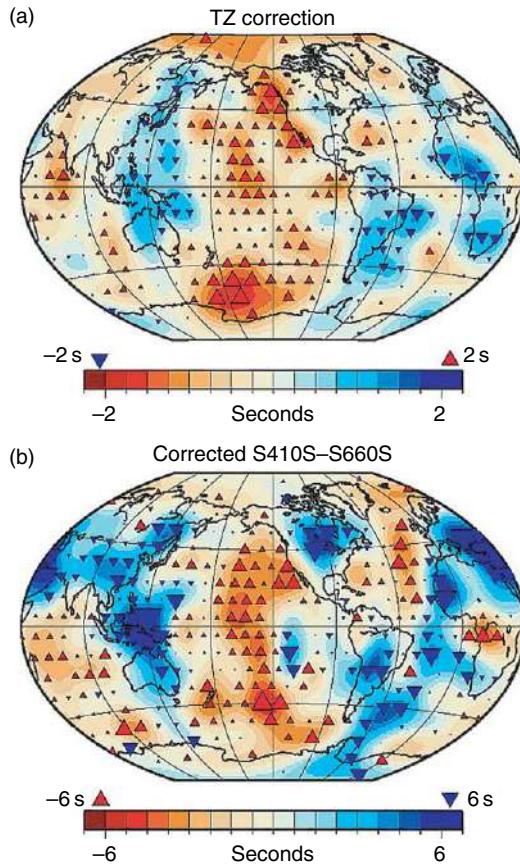


Figure 7 (a) Colored background: velocity perturbations from tomography at 550 km depth. Triangles: computed corrections for SS precursors. (b) Global differential times of SS precursors from the 410 and 660 discontinuities, corrected with data in (a). From Gu YJ and Dziewonski AM (2002) Global variability of transition zone thickness. *Journal of Geophysical Research* 107(7): 2135 (doi:10.1029/2001JB000489), figure 9.

Tonegawa *et al.* (2005): Receiver functions; 660 depressed by 50 km and the 410 elevated by 30 km where it is hit by the slab.

1.17.2.2.1.(ii) Northeast China In the region of the deep slab and the surrounding regions, the following observations are reported:

Li and Yuan (2003): Ps conversions; 660 depressed by 35 km where it is hit by the slab and the transition zone thickened by ~ 20 km.

Ai and Zheng (2003): Receiver functions; sharp 410 at normal depth, 660 appears doubled and depressed.

Niu and Kawakatsu (1996): Ps conversions; at the tip of the subducting slab in northeast China, no depression of the 660 but a complicated structure.

Yang and Zhou (2001): Ps conversions; only a few kilometers depth variations of the 410 and 660.

Ai *et al.* (2003): Receiver functions; locally depressed 660 in northeast China.

Niu and Kawakatsu (1998): Ps conversions at the Chinese Digital Seismic Network; elevated 410 by 10 km and depressed 660 by 30 km beneath station BJI in China. At station MDJ multiple phases near 660 rather than a depressed 660, and at station SSE a normal 660.

The overwhelming majority of observations seem to indicate that the 660 is depressed at the Japanese subduction zone. The amount of the depression is ~ 50 km. The 410 remains uncertain, but there is probably no clear elevation.

1.17.2.2.1.(iii) Izu-Bonin Castle and Creager (1997, 1998): Near-source sP conversions; 660 depressed to 730 km.

Collier and Helffrich (1997) and Collier *et al.* (2001): Teleseismic P coda; 660 depressed to 730 km and the 410 elevated by 60 km.

Wicks and Richards (1993): Near-source short period S-P conversions; 660 depressed by 60 km.

Again, Izu-Bonin seems, besides Japan, to be a good example of a depressed 660 at a slab. The uplift of the 410 seems less clear.

1.17.2.2.1.(iv) Tonga Richards and Wicks (1990): Regional S-P conversions; 660 depressed to 700 km.

Roth and Wiens (1999): ScS reverberations; 660 depressed locally by 30 km.

Gilbert *et al.* (2001): Ocean-bottom receiver functions; 410 uplifted by 30 km and 660 depressed by 20–30 km.

Suetsugu *et al.* (2004): ScS reverberations; increased thickness of the transition zone by 10 km.

Tibi and Wiens (2005): Reflections and conversions at the 410 and 660 of local high-frequency seismic phases recorded by an array of broadband island stations; practically, no change in the 410 depth; 660 depressed to 714 km (see **Figure 9**).

1.17.2.2.1.(v) Andes Clarke *et al.* (1995): ScS reverberations; beneath the Andean subduction zone and the Brazilian craton, a larger-than-average transition zone thickness.

Collier and Helffrich (2001): Near-source S-P conversions; 410 elevated by 60 km where it is hit by the slab, normal depth in surrounding regions.

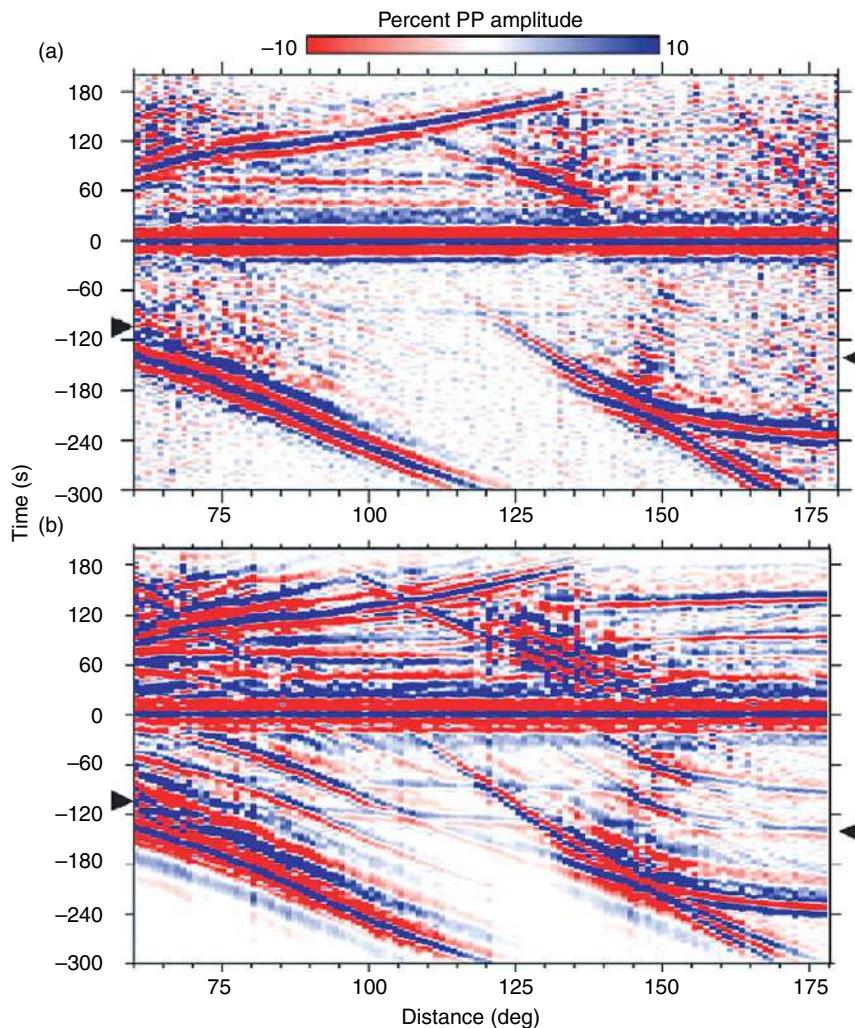


Figure 8 (a) Global distance–time plot of PP (at 0 s) and precursor from the 410 (at c. -70 s). The precursor from the 660 is missing in the data. (b) According synthetic seismograms for the IASP91 global reference model. This model (and other reference models) predicts a precursor at the 660. A model explaining the missing 660 precursor should have less contrast in P velocity. *Estabrook CH and Kind R (1996) The nature of the 660-kilometer upper-mantle seismic discontinuity from precursors to the PP phase. Science 274: 1179–1182, figure 1.*

Liu et al. (2003): Transition zone thickness changing from 270 km at the Andean slab to 220 km in the neighboring oceanic region.

1.17.2.2.1.(vi) Additional observations *Vidale and Benz (1992): Thickening of the transition zone at subduction zones.*

Petersen et al. (1993a): SS precursors; thinning (not thickening) of the transition zone in the region of the Kurile–Kamchatka subduction zone.

Flanagan and Shearer (1998b): Long-period precursors of depth phases, underside reflections from

the 410; less changes in 410 depth at subduction zones than from SS precursor data.

Ohtaki et al. (2002): ScS reverberations; increased transition zone thickness below the Philippines Sea.

Saita et al. (2002): Receiver functions; 40 km thickness variation of the mantle transition zone below Indonesia.

Van der Meijde et al. (2005): Receiver functions; 260 km transition zone thickness beneath the Mediterranean, increasing to more than 270 km beneath the associated subduction zones.

Tibi et al. (2006): High-frequency local records of an array of ocean bottom seismometers at the

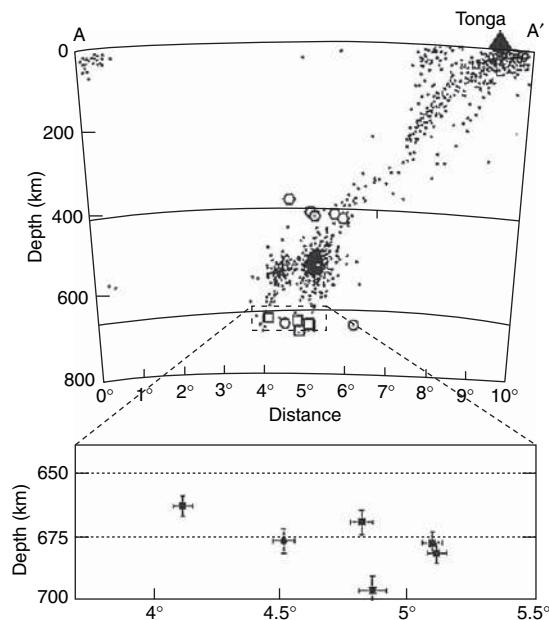


Figure 9 High-resolution image of the depressed 660 beneath the Tonga subduction zone from short-period local earthquake records. Small dots are earthquakes. Large symbols mark the measured depths of the 410 and 660. The 410 seems not to be elevated. From Tibi R and Wiens DA (2005) Detailed structure and sharpness of upper mantle discontinuities in the Tonga subduction zone from regional broadband arrays. *Journal of Geophysical Research B: Solid Earth* 110(6): 1–14, figure 6.

Mariana slab; reflections and conversions from the 660; 660 depressed to 710–730 km in the core of the slab.

1.17.2.2.2 Hot spots

Hot spots are discussed in detail in Chapter 7.09.

1.17.2.2.2.(i) Yellowstone Dueker and Sheehan (1997b): Receiver functions; 20–30 km thickness variation of the transition zone across the Yellowstone hot spot track.

Beucler *et al.* (1999): Receiver functions. No clear 410 beneath the Snake River Plain and a clearer and largely deflected 660.

Sheehan *et al.* (2000): Ps conversions; 20 km elevation of the 660 beneath the Snake River Plain, no variation of the 410.

Humphreys *et al.* (2000): Receiver functions; uplifted 410 and 660 in the Yellowstone hot spot track.

Gilbert *et al.* (2003) and Fee and Dueker (2004): Receiver functions; 20–40 km depth variation of both,

the 410 and the 660; uncorrelated with surface tectonics.

1.17.2.2.2.(ii) East Africa Le Stunff *et al.* (1995): P'P' precursors recorded with the California array of broadband stations; sharp and uplifted 660 below the East African Rift.

Owens *et al.* (2000): Receiver functions; transition zone beneath the East African Rift 30–40 km thinner than beneath the Tanzanian craton.

Nyblade *et al.* (2000): Receiver functions; beneath Afar no reduced transition zone thickness led to the conclusion that the thermal anomaly does not reach the transition zone.

1.17.2.2.2.(iii) Hawaii Li *et al.* (2000b): Receiver functions; thinning of the transition zone by 40–50 km in the southwest of the main island of the Hawaiian chain, attributed to the penetration of the transition zone by the inclined plume conduit.

Collins *et al.* (2002): Receiver functions; 50 km thinned transition zone beneath the Hawaiian swell.

1.17.2.2.2.(iv) Iceland Shen *et al.* (1996, 1998b): Ps conversions; 20 km thinned transition zone.

1.17.2.2.2.(v) Other hot spots Grunewald *et al.* (2001): Eifel Plume; receiver functions; deepening of 410.

Budweg *et al.* (2006): Eifel Plume; receiver functions; deepening of 410 by 15–25 km; 660 at its normal location.

Suetsugu *et al.* (2004): South Pacific superswell; ScS reverberations; locally a 6 km reduced transition zone thickness.

Hooft *et al.* (2003): Galapagos Islands; receiver functions; 18 km reduced thickness of the transition zone relative to the surrounding Pacific.

Shen *et al.* (1998a): East Pacific Rise; receiver functions; normal transition zone thickness from an ocean-bottom experiment.

Hefffrich (2002): Estimated a 160 K warmer temperature below plumes from the topography of the 660.

1.17.2.2.3 Continents

1.17.2.2.3.(i) North America Bostock and Cassidy (1997): Receiver functions; 410 and 660 beneath the southern Slave craton only slightly earlier than predicted by IASP91.

Dueker and Sheehan (1997a): Receiver functions; in the Colorado Rocky Mountains and High Plains; 410 and 660 at average depths of 419 and 677 km with

20–40 km topography on the 410 and 660 and also 20–40 km thickness variation of the transition zone.

Gurrola and Minster (1998): Ps conversions; 220 km thick transition zone at Pasadena (near the continental margin); 252 km thick transition zone at the cratonic station Obninsk near Moscow, Russia.

Li et al. (1998): Receiver functions; 660 depressed by 20 km beneath eastern North America.

Gurrola and Minster (2000): Receiver functions; in southern California, a transition zone thickness of 236 km; in Ontario, 263 km; west of Albuquerque, 232 km; and east of Albuquerque, 253 km, respectively. They attributed the observations at Albuquerque to a 20 km depth change of the 410.

Simmons and Gurrola (2000): Receiver function; multiple 660 in southern California.

Ramesh et al. (2002): Ps conversions; uniform 410 and heterogeneous 660 in southern California.

Gilbert et al. (2003): Receiver functions; 20–30 km uncorrelated topography of both discontinuities, 660 and 410, in the western US.

Ai et al. (2005): Receiver functions; thinned transition zone by 20–30 km with significant variations in Southern Alaska.

1.17.2.2.3.(ii) South Africa **Gao et al. (2002):** Receiver functions; 410 and 660 close to their normal position; no indication for a South African superplume in the transition zone and also no indication for other upper-mantle discontinuities.

Stankiewicz et al. (2002): Receiver functions; normal transition zone in the Kimberley area and a slightly thickened transition zone beneath the Kaapvaal Craton.

Simon et al. (2003): Receiver functions; 410 and 660 beneath Kaapvaal Craton slightly deeper than normal.

Blum and Shen (2004): Ps conversions; 20 km increased thickness of the transition zone in southern Africa.

Wright et al. (2004): Receiver functions; 410 and 660 beneath the Kaapvaal craton slightly deeper than normal.

1.17.2.2.3.(iii) Other regions **Kind and Vinnik (1988):** Southern Germany; receiver functions; transition zone thickness 240 km.

Dricker et al. (1996): Cola Peninsula; Ps conversions; 410 and 660 at their normal depth.

Helffrich et al. (2003): North Sea; 410 and 660 close to their normal depth.

Alinaghi et al. (2003): Baltic Shield; 410 and 660 signals arriving 2 s earlier due to a faster upper mantle.

Yuan et al. (1997): Southern Tibet; good agreement of the depths of the 410 and 660 with the IASP91 model.

Kind et al. (2002): Tibet; receiver functions; 410 and 660 at normal depths.

Kumar et al. (2002): Arabian Shield; receiver functions; 410 and 660 delayed due to a slow upper mantle.

Benoit et al. (2003): Arabian Shield; receiver functions; normal transition zone thickness.

Mohsen et al. (2005): Dead Sea Transform; receiver functions; 410 and 660 signals delayed by 2 s because of a slow upper mantle.

Kummerow and Kind (2004): Eastern Alps; receiver functions; transition zone thickness close to its global average.

Mechie et al. (1993): Northern Eurasia; wide-angle nuclear explosion; normal transition zone thickness.

Neves et al. (1996): North West Siberia and Lake Baikal; nuclear explosions; at the 410 a two-gradient structure between 400 and 435 km and a sharp 660.

Saul et al. (2000): India; receiver functions; 410 and 660 close to their average depths.

1.17.2.2.4 Oceans

Gaherty et al. (1996): Tonga–Hawaii corridor; ScS reverberations and S surface reflections; 410 and 660 at 415 and 651 km depth, respectively.

Lee and Grand (1996): East Pacific Rise; SS precursors; 410 and 660 close to their normal depths.

Kato and Jordan (1999): Western Philippine Sea; ScS reverberations; 410 and 660 at 408 and 664 km depth, respectively.

Niu et al. (2000, 2002): South Pacific superswell; S wave reflections; transition thinned by 15 km.

Melbourne and Helmberger (2002): East Pacific Rise; wide-angle earthquake records; no discernible variation in the apparent depths of the 410 and 660 km discontinuities over ridge-orthogonal distances on the order of 1000 km.

Li et al. (2003b): Ocean islands; Ps conversions; 18 stations on islands in several oceans; all arrival times of the 410 were later than predicted by IASP91, some up to 15%. The transition zone thickness was also up to 15% thinner below ocean islands than the IASP91 value.

1.17.2.2.5 Sharpness of 410 and 660

Benz and Vidale (1993) observed short-period precursors of P'P' in the Indian Ocean from South American events, recorded by very many short-period stations in California. They found that both discontinuities (410 and 660) were less than 4 km sharp.

Petersen *et al.* (1993b) found a sharper 410 (5–7 km) than 660 (20–30 km) from Ps conversions at broadband stations in south Germany, north Kazakhstan, south Norway, and northwest Canada.

Yamazaki and Hirahara (1994) used regional earthquakes recorded by the J-Array (S-P converted and reflected waves) and derived a discontinuity thickness of ~5 km for both, the 410 and 660, beneath Japan.

Tonegawa *et al.* (2005) found a sharp 660 and a variable 410 beneath Japan.

Lebedev *et al.* (2002a) found a sharp 660 near the Japan slab from Ps data.

Helffrich and Bina (1994) discussed the frequency dependence of the 410 signals.

Van der Lee *et al.* (1994) discussed the influence of topography on the amplitudes of P-to-S converted waves.

Priestley *et al.* (1994) found in nuclear explosion data in central Siberia a 35 km thick gradient at the 410 and a 4 km thick gradient at the 660.

Ryberg *et al.* (1998) derived also from nuclear explosion data in northern Eurasia that the 660 is several kilometers wide and that the velocity jump across it is only half of that of the IASP91 model. They also argued that wide-angle data are not very sensitive to discontinuity gradients.

Vidale *et al.* (1995) found the 410 to be less than 10 km wide in the western US from near-critical reflection records from nuclear explosions.

Needle (1996) found that the velocity increase at the 410 occurs over a width of ~4 km or less below the Gulf of California.

Bostock (1996a) found also in Ps data a sharper 410 than 660 beneath the North American craton.

Melbourne and Helmberger (1998) found in wide-angle data a 14 km thick gradient zone at the 410 in the southwestern US.

Neves *et al.* (2001) found a 10 km sharp 410 and a 5 km sharp 660 beneath North America from wide-angle data. However, within the slab, a more complicated structure occurs.

Song *et al.* (2004) found in the northwestern US a 20–90 km thick low velocity zone above the 410 from wide-angle data, which they interpret as indication of

high water content in the transition zone (Bercovici and Karato, 2003).

Xu *et al.* (1998) found a sharp 660 and a less clear 410 from P'P' precursors reflected beneath South Africa.

Le Stunff *et al.* (1995) observed a sharp and uplifted 660 below the East African Rift in P'P' precursors from a Fiji event recorded with the California array of broadband stations.

Rost and Weber (2002) found that the 410 is less than 6 km wide from array PP precursor studies in the Northwest Pacific.

Castle and Creager (2000) found that the 660 is locally less than 10 km wide at the Izu-Bonin subduction zone using source side S-to-P conversions recorded in the western United States.

Tibi and Wiens (2005) concluded from short-period observations of local earthquakes a sharpness of 0–2 km for the 660 and 2–10 km for the 410 in the Tonga subduction zone.

Estabrook and Kind (1996) concluded from the missing precursors of PP from the 660 that the velocity and density jump here is globally significantly smaller than predicted by the IASP91 model. This was confirmed by Shearer and Flanagan (1999) globally and by Ryberg *et al.* (1998) from summarizing wide-angle nuclear explosion data in northern Eurasia. Kato and Kawakatsu (2001) derived from SS precursors, Ps conversions, and ScS reverberations a larger S velocity and density jump at the 660 than at the 410 beneath the Northwest Pacific. This observation is in disagreement with the observation of missing PP precursors by Estabrook and Kind (1996) and Shearer *et al.* (1999).

1.17.2.2.6 520 discontinuity

Shearer (1990) observed at an average depth of ~520 km in long-period SS precursors a positive seismic discontinuity and came to the conclusion that it has a global extension. Revenaugh and Jordan (1991a) found a reflection from 520 km depth in ScS reverberations along some corridors in the western Pacific. Shearer (1991, 1996) observed again in SS precursor reflections from the 520 discontinuity. He found 6.7%, 2.9%, and 9.9% shear impedance contrast at the 410, 520, and 660 discontinuities, respectively. Cummins *et al.* (1992) found no evidence for the 520 north of Australia. The global existence of the 520 in SS precursors was disputed as possible sidelobe effects of the 410 and 660 signals by Bock (1994). Gossler and Kind (1996) confirmed the existence of precursors of SS from a discontinuity at

~520 km depth. They did not, however, confirm the global distribution of this discontinuity: it was present in some regions and not in others. *Mechie et al.* (1993) found a discontinuity at 550 km depth in northern Asia in nuclear explosion data. *Priestley et al.* (1994) found no clear evidence for a 520 km discontinuity in data from nuclear explosions in central Siberia. *Ryberg et al.* (1996, 1997, 1998) also observed the 520 discontinuity in short-period wide-angle data from nuclear explosions in northern Eurasia and west Siberia. *Gaherty et al.* (1996) found the 520 at 507 km depth in the Tonga–Hawaii corridor using ScS reverberations. *Kato and Jordan* (1999) found the 520 at its expected depth in the western Philippine Sea. *Deuss and Woodhouse* (2001) confirmed with SS precursors the 520 in many regions but found it absent in others. In some regions, they found a splitting of the 520. *Ai et al.* (2005) found the 520 beneath Alaska in P receiver functions.

1.17.2.3 Summary of the Upper-Mantle Transition Zone

The 410 and 660 are besides the Moho certainly the best-documented discontinuities in the upper mantle. In recent years, they have been observed with increased resolution in SS, PP (only 410), and P'P' precursors, Ps and Sp conversions, and ScS related phases. One clear result is that the density and shear velocity jump across the 660 is globally a significant percentage below the values in present global reference models. This should influence the modeling of mantle convection. The global topography of the 660 seems to be larger than the topography of the 410. The question whether the 410 and 660 are globally anticorrelated, which, if true, would provide evidence in favor of the phase transition model in the olivine system, is much less clear. There are opposing observations. The thickness of the transition zone seems to vary globally by about ± 20 km (with the 410 and 660 not necessarily anticorrelated), indicating about $\pm 200^\circ$ lateral temperature variation within the transition zone, if phase changes are the cause of both discontinuities. Also the question of the correlation of the type of plates (oceanic or cratonic) and the transition zone thickness (or temperature) is not decided. Again, there are contradicting observations. Such a correlation between surface geology and transition zone structure would lead to serious problems with plate tectonics, since laterally moving lithospheric plates are not considered reaching the mantle transition zone. Some tomographic models,

however, seem to agree with this view. *Ritsema et al.* (2004) observed in tomographic data below the continental lithosphere down to 400 km depth a 1–1.5% higher velocity than below the oceanic lithosphere. *Gung et al.* (2003), however, interpreted high tomographic velocities in continental roots as being caused by anisotropy. The possibility of continental roots reaching several hundred kilometers deep and maybe even into the mantle transition zone was first suggested by *Jordan* (1975). Crucial for answering questions about the deep roots of continents would be the comparison with high-resolution data from undisturbed oceanic areas away from ocean islands, which are always anomalous. Such data can only be obtained from dense ocean-bottom seismic observations, which are very expensive. High-resolution data are so far only available for continents; therefore, a real quantitative comparison is not yet possible.

Most researchers agree that the 660 is depressed at subduction zones on a large scale. The amount of depression varies between 20 and 50 km. This results from global observations and also from high-resolution local observations. Updoming of the 410 at subduction zones is much less certain. There are contradicting observations. The 410 seems in many cases poorly observed in subduction zones. A depression of the 410 due to the existence of metastable olivine in subduction zones is not observed so far.

The transition zone structure beneath hot spots is less clear. There are fewer observations beneath hot spots because many are in oceanic regions. There are observations of thinning of the transition zone and also observations of a normal transition zone. The continued collection of high-resolution information on the 410 and 660 beneath hot spots should reliably answer the question of which plumes reach down to the transition zone and which do not.

Local studies with mobile networks or closely spaced long-term station deployments provide high-resolution information in some continental or oceanic regions. In general, most information from stable continents agrees with the global average values. This seems even true for regions like Tibet or the Alps. This leads to the conclusion that active lithospheric tectonics may not reach the transition zone (except for subduction zones and possibly plumes). Since the upper mantle is generally faster beneath continents than beneath oceans, both discontinuities frequently appear later under oceans than below continents. The continental values are closer than the oceanic values to those of the reference models (IASP91), which indicates that the reference

models may be biased by consisting of a majority of continental data.

Only high-frequency data like P'P' precursors or local reflections and conversions seem able to resolve sharpness (and other details like multiple discontinuities) of the 410 and 660. Relatively few of such observations are available and they confirm sharpness of just a few kilometers for both discontinuities. Teleseismic mantle phases (including Ps conversions) probably do not have sufficiently high frequencies to resolve the sharpness. If weak scattered waves (e.g., receiver functions) are used, the summation of many traces over a more or less large region is required. Such summation may lead to contamination of discontinuity sharpness or impedance contrast by topography effects. Therefore, estimates of discontinuity sharpness with summation traces should be done with great care. Systematic high-frequency global studies of discontinuity sharpness and impedance contrast are still missing.

The discontinuity at ~ 520 km depth is clearly observed in some regions but also clearly not in others. The 520 is thus not a global discontinuity, but it also cannot be considered a local one, because it has a relatively widespread distribution. Its existence does not seem to have any correlation with surface structures.

1.17.3 The Gutenberg Discontinuity

The first seismic observations of a global low-velocity zone below the Moho (called the asthenospheric channel) were obtained by Gutenberg (1926, 1954, 1959) at ~ 100 km depth from amplitudes and slownesses of P phases. Therefore, seismologists sometimes call this discontinuity the ‘Gutenberg’ discontinuity (often abbreviated as ‘G’ discontinuity). It is mainly reported in oceanic regions. The Lehmann discontinuity (Lehmann, 1961) is considered the bottom of the asthenosphere (mostly observed in continental regions; Gu *et al.* (2001a); Deuss and Woodhouse (2002)). Since the Gutenberg discontinuity is a negative discontinuity (a reduction of velocity with depth), it is often identified with the LAB. Therefore, we will not always make a clear distinction between the terms ‘LAB’ and ‘Gutenberg discontinuity’, although the terms are the result of entirely different definitions. The concept of a high-viscosity lithospheric layer overlying a low-viscosity asthenospheric layer was introduced to explain observations such as the postglacial uplift of

Scandinavia (e.g., Barrell, 1914). Originally, the expressions ‘crust’ and ‘lithosphere’ were used synonymously (see a discussion by Gutenberg (1959)). Only after Mohorovicic (1910) had discovered a sudden increase of the seismic velocity at ~ 50 km depth, which was later confirmed worldwide, was this discontinuity considered the lower boundary of the crust (termed Moho). Since then, the terms ‘crust’ and ‘lithosphere’ have gained different meanings. Later, with the rise of plate tectonics, the lithosphere–asthenosphere concept was expanded to explain large lateral displacements of continents by high-viscosity lithospheric plates floating over the low-viscosity asthenospheric upper mantle (see Chapter 6.02). Thermal and chemical definitions of the term ‘lithosphere’ have been introduced since then (Anderson, 1995). A somewhat different geodynamical concept was developed by Jordan (1975). The concept of Jordan (1975) comprises a tectosphere with continental roots that reach to 400 km depth and translate together with the continental lithosphere (Sipkin and Jordan, 1976, 1980).

The lithosphere is seismologically divided into two parts, the crust and the mantle lithosphere, with the latter being the high-velocity mantle lid on top of the asthenosphere. Surface-wave observations of the high-velocity lid and the low-velocity asthenosphere have been obtained for many years (e.g., Dormann *et al.*, 1960; Kanamori and Press, 1970; Knopoff, 1983). Direct seismic observations of the LAB remain a challenging task. A major problem is that the asthenosphere is a low-velocity zone. Thus it is difficult to observe with seismic body waves. The Moho, in contrast, marks a sharp positive increase in velocity downward, which is easy to observe. Therefore the Moho is well constrained on a global scale (Mooney *et al.*, 1998; see Chapter 1.08). Fewer constraints on the depth of the LAB have been obtained from seismic body waves. A recent review of wide-angle results is given by Thybo (2006; see Figure 10, see Chapter 1.15). Mostly surface-wave dispersion is used to measure the depth of the LAB. From these relatively low-resolution observations (compared to the high resolution of the Moho which is obtained from short-period body waves), the LAB can only be imaged as a broad transition zone, and therefore it is difficult to locate. The most important result of surface-wave studies is the larger thickness of the lithosphere beneath continents than below oceans (e.g., Gung *et al.*, 2003). At present, the thickness of the lithosphere is considered to vary from a few kilometers at mid-ocean ridges to ~ 200 km beneath stable cratons, with 80–100 km being the

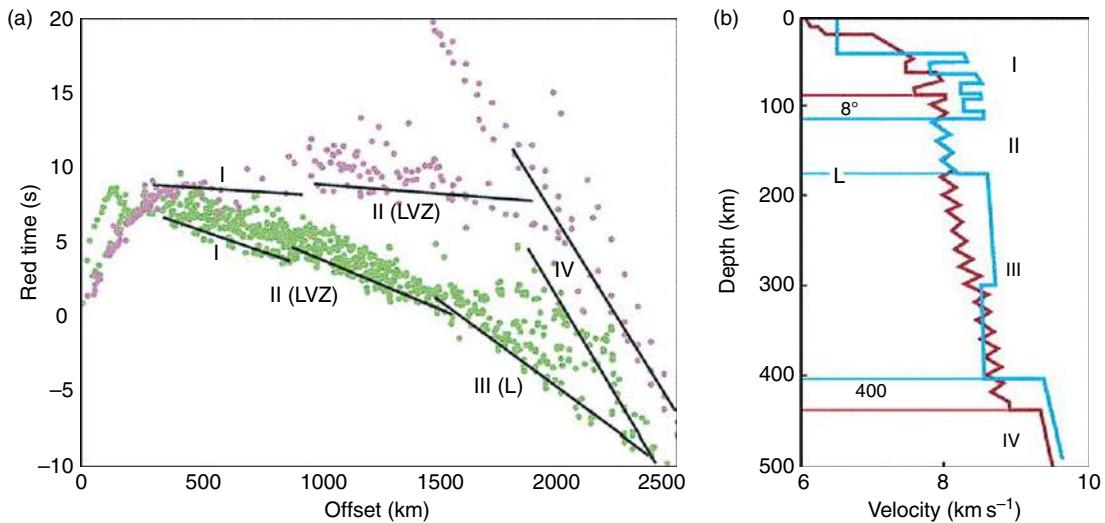


Figure 10 (a) Traveltime–distance plot of collected long-range controlled source seismic data. Purple points are from tectonic active regions and green points from tectonic quiet regions, respectively. (b) Derived models for these areas (cold – blue, hot – red). The 8° discontinuity (or Gutenberg discontinuity, or LAB), the Lehmann discontinuity, and the 410 are shown. The asthenosphere is less pronounced in cold areas. From Thybo H (2006) The heterogeneous upper mantle low velocity zone. *Tectonophysics* 416(1–2): 53–79, figure 2.

global average. The problems of detecting low-velocity zones with wide-angle seismic data are well known in the crust and are even greater in the mantle. Steep-angle body waves (similar to the seismic reflection method in crustal studies) are probably much more useful for detecting the Gutenberg discontinuity and mapping its topography. In recent times, the P receiver function technique has turned out to be very successful in imaging the crust–mantle boundary (e.g., Langston, 1979; Yuan *et al.*, 2002). However, P receiver functions are less useful for detecting the Gutenberg discontinuity because crustal multiples sometimes arrive at about the same time as Gutenberg conversions and therefore are hard to separate. The problem with crustal multiples can be solved if S-to-P conversions are used instead. In this case, direct conversions are clearly separated from multiples. Direct conversions arrive in front of S, and multiples in the coda of S. S-to-P conversions have also long been used to study upper-mantle discontinuities (e.g., Jordan and Frazer, 1975; Sacks and Snoker, 1977; Sacks *et al.*, 1979; Bock, 1988, 1991). They have been reintroduced in a modernized form as S receiver functions by Farra and Vinnik (2000). A more recent description of the technique is given by Yuan *et al.* (2006). This still relatively rarely used technique is applied to S or SKS phases and adds a few more processing steps to the original Sp conversion technique. Such steps are, as in the P receiver function technique, source equalization by

deconvolution and distance move-out correction. Both steps are applied in order to enable the summation of events from different distances and with different magnitudes and source-time functions. Thanks to the newly available large quantities of high quality digital data, the conversion techniques enjoy increasing popularity. These techniques work very well, enabling especially observations of the LAB with a resolution so far only known for the Moho.

In the following, we will refer to reports that may observe the Gutenberg discontinuity. Parker *et al.* (1984) observed below the Rio Grande Rift an upwarp of the asthenosphere from P residuals. Thybo and Perchuc (1997) suggest the existence of a zone of reduced velocity at ~ 100 km depth under continental regions, based on controlled source data. Nielsen *et al.* (1999) located the 8° discontinuity at 100–200 km depth from nuclear explosion data on the Siberian platform (8° discontinuity is frequently also interpreted as LAB; Thybo (2006)). Rychert *et al.* (2005) have shown a good example of observations of a sharp LAB in P receiver functions with clear separation from crustal multiples (see Figure 11). They observed in eastern North America the LAB at 90–110 km depth with a velocity decrease of 3–11% over a depth range of 11 km or less. They concluded that a few percent of partial melt or enrichment of volatiles in the asthenosphere could cause such a sharp LAB. Woelbern *et al.* (2006) have

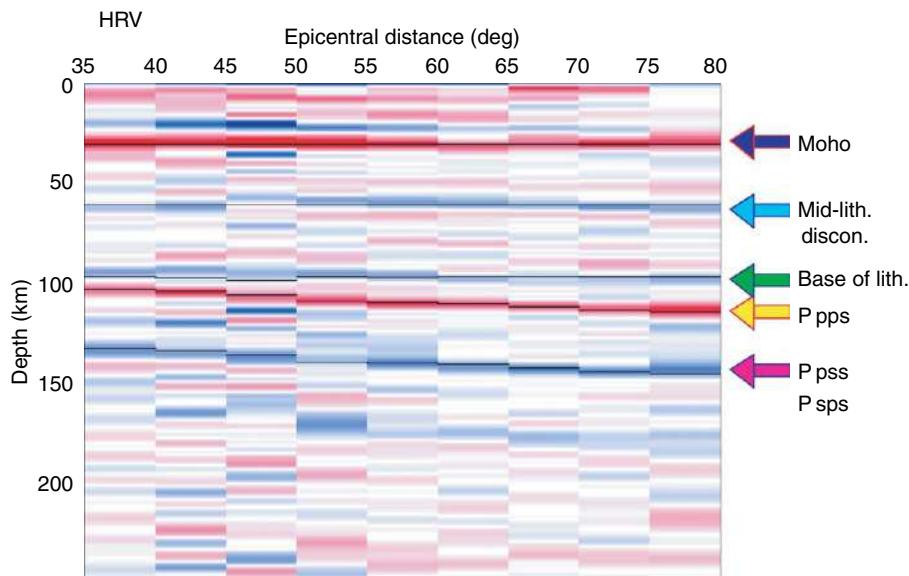


Figure 11 P receiver functions at the Harvard station as function of epicentral distance. A number of conversions from upper-mantle discontinuities and crustal multiples are visible. Especially important is the observation of the base of the lithosphere, which is clearly separated from crustal multiples and indicates a sharp LAB (11 km or less). From Rychert CA, Fischer KM, and Rondenay S (2005) A sharp lithosphere–asthenosphere boundary imaged beneath eastern North America. *Nature* 436: 542–545, figure 1 of supplementary information.

observed the LAB with P receiver functions below the Hawaiian island chain and confirmed earlier LAB observations by Li *et al.* (2004) using S receiver functions. Gaherty *et al.* (1996, 1998) found a sharp Gutenberg discontinuity at 68 km depth from ScS reverberations along the Tonga–Hawaii corridor. Davies (1994) describes the thinning of the Hawaiian lithosphere by a mantle plume. Collins *et al.* (2002) found the Gutenberg discontinuity at 80 km depth beneath the Hawaiian Swell. Gung *et al.* (2003) suggested that the Lehmann discontinuity under continents and the Gutenberg discontinuity under oceans might both be associated

with the bottom of the lithosphere, marking the transition to flow-induced asthenospheric anisotropy (**Figure 12**). The new S receiver function technique was applied by Li *et al.* (2004), Kumar *et al.* (2005a, 2005b, 2006; **Figure 13**) and Sodoudi *et al.* (2006a, 2006b). They observed high-quality S-to-P conversions from the LAB in a number of different regions in the world. The LAB beneath the Big Island of the Hawaiian island chain with its active volcanoes was seen by Li *et al.* (2004) at 100 km depth, where it is expected according to the age of the seafloor and to surface-wave observations. In a narrow corridor along the island chain, the LAB is observed to thin

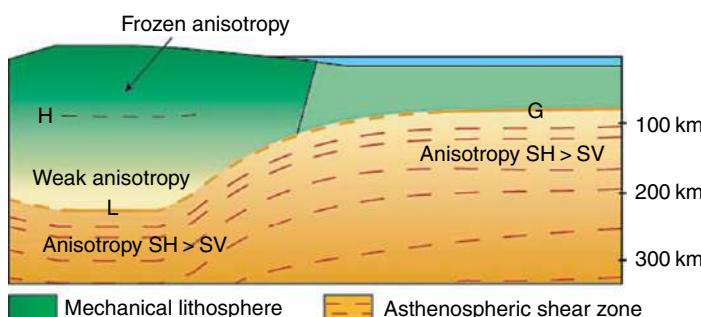


Figure 12 Sketch illustrating upper-mantle results from anisotropy studies. The Gutenberg discontinuity is only in oceans interpreted as LAB. In continents, the Lehmann discontinuity is interpreted as LAB. From Gung Y, Panning M, and Romanowicz B (2003) Global anisotropy and the thickness of continents. *Nature* 422: 707–711, figure 5.

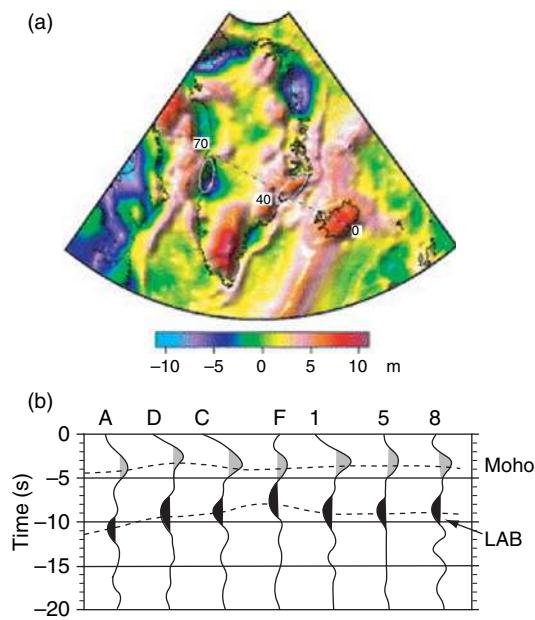


Figure 13 (a) Residual satellite geoid signals in the NW Atlantic region with suggested trace of the Iceland Plume (numbers in million years). (b) S receiver functions showing Moho and LAB roughly along this line. The characters indicate data locations (1, 5, 8 – on Iceland; A, D, C, F in Greenland from west to east). Thinnest lithosphere (70 km) is observed in western Greenland, where the plume was located ~40 Ma. From Kumar P, Kind R, Hanka W, et al. (2005b) The lithosphere–asthenosphere boundary in the north west Atlantic Region. *Earth and Planetary Science Letters* 236: 249–257, figure 8.

to ~60 km at the northwest end of the chain. This observation is interpreted as rejuvenation of the lithosphere due to the passage of the Pacific plate over the Hawaiian hot spot. Revenaugh and Jordan (1991b) found the LAB at 60 km depth from long-period ScS reverberations in several regions of the western Pacific, but did not observe it in continental regions. Kato and Jordan (1999) found a sharp Gutenberg discontinuity at 89 km depth in the western Philippine Sea (~40 My old). Kumar et al. (2005b) observed the LAB beneath Iceland and Greenland using data from a number of temporary seismic broadband projects. They found the LAB at a nearly constant depth of 80 km beneath Iceland (confirming earlier results of Vinnik et al. (2005b)) and thickening from 80 to 120 km from east to west beneath Greenland. The 80 km thick lithosphere beneath Iceland is a surprise, because postglacial uplift data suggest a 10–20 km thickness of the elastic lithosphere. This discrepancy could lead to the conclusion that the seismic lithosphere may be different

from the elastic rebound (mechanical) lithosphere. Also the thermal definition of the lithosphere disagrees with a thick seismic lithosphere above a plume and near an oceanic spreading center. The seismic data of Kumar et al. (2005b) in Iceland seem clear, but their relation to other definitions of the Icelandic lithosphere still remains unsolved. Oreshin et al. (2002) found the LAB at 90 km depth beneath the Tian Shan from S receiver functions. A low-velocity zone several tens of kilometers below the Moho had also been observed by Vinnik et al. (2004) in the Tian Shan region. Kumar et al. (2005a, 2006) have mapped the LAB in the region of the Tian Shan, and western and central Tibet. Kumar et al. (2005a) found a double-inclined subduction in the Tibet and Tian Shan regions with a traceable LAB to 250 km depth. The Asian and Indian lithospheres are separated by vertical jumps of 50 km or more. Schott and Schmeling (1998) and Chemenda et al. (2000) computed models of the colliding Indian and Asian lithospheres which lead to subduction of the Indian continental lithosphere down to 250 km beneath Tibet. Sodoudi et al. (2006a) studied the collision of the African and European lithospheres in the Hellenic arc and found the African lithosphere flattening under the northern Aegean at 250 km depth. Qiu et al. (1996) found below southern Africa, from P receiver functions, wide- and steep-angle seismic data and Pn and Sn data, a reduced shear velocity, and increased P velocity at 250 km depth. Priestley and McKenzie (2002) found the LAB beneath southern Africa at 176 km depth from regional seismic data. Niu et al. (2004) placed the roots of the Kaapvaal craton at 160–370 km depth using P receiver functions, similar to Simon et al. (2003). Bostock (1999) concluded from a survey of seismic studies that there is no global LAB (and also no Lehmann discontinuity). However, he discussed the existence of a discontinuity at 60 km depth (Hales discontinuity), especially in continental areas, and at 200 km depth (Lehmann) with many heterogeneities between, giving rise to the teleseismic Pn. Plomerova et al. (2002) defined the LAB using anisotropic properties. They obtained LAB depths between 200 and 250 km for the Precambrian shields and platforms, at around 100 km for the Phanerozoic continental regions, and at 40–70 km beneath oceans. Artemieva and Mooney (2001) estimated the thermal thickness of the Proterozoic lithosphere to be more than 300 km from heat flow data. Artemieva et al. (2002) discussed the global structure of the lithosphere as observed from tomography and anisotropy. The

Svekalapko Working Group (2004) found the LAB at 100–130 km depth below Finland. So far, the proposed deep continental roots (Jordan, 1975) have apparently not been observed as seismic discontinuities. There are, however, tomographic indications of such deep roots (Su *et al.*, 1994; Masters *et al.*, 1996; Ritsema *et al.*, 2004). Another indication of continental crust attached to deep roots is the similar age of the crust and the mantle down to 200 km depth in some cratons (Pearson, 1999). There are also observations of a thickened upper-mantle transition zone beneath some cratons, which may be related to the deep and cool continental roots (see Section 1.17.2.1).

1.17.3.1 Summary of the Gutenberg Discontinuity

In summary, there are many body-wave observations confirming the existence of a low-velocity zone beneath the Moho. The S receiver function method seems to be especially successful in detecting and mapping the LAB. Practically in all regions where this technique was used to search for the LAB, it was indeed found. From this, it follows that the LAB is very likely a much sharper discontinuity than was previously thought on the basis of surface-wave studies. The missing observations at shorter periods than surface-wave periods was probably only due to the lack of an appropriate technique. So far, no extensive studies have been carried out to measure the sharpness or the size of the velocity jump of the LAB. The amplitude of the LAB conversion seems, in many cases, to be close to half that of the Moho signal, which would indicate an accordingly smaller step in velocity. The rapidly increasing number of LAB observations in the form of regional maps of lithospheric thickness in active tectonic zones may lead to a significant expansion of our knowledge of lithospheric dynamics.

1.17.4 The Lehmann Discontinuity

The Lehmann discontinuity (Lehmann, 1961, 1964) is defined to be a positive (velocity increase downward) seismic discontinuity at ~ 220 km depth. It is thought to reveal the bottom of the asthenosphere, or alternatively the lower boundary of the continental roots (Anderson, 1979). It is a significant discontinuity in the PREM global reference model (Dziewonski and Anderson, 1981), but does not appear in the IASP91 global model (Kennett and Engdahl, 1991). Although local earthquake records were allowed the original

detection of the Lehmann discontinuity (usually employing wide-angle seismic data), most confirmations of this discontinuity come from other types of seismic data. These are SS precursors, ScS reverberations, receiver functions, or other types of scattered teleseismic waves. In the following, we list a number of positive or negative observations of structures, which could be related to the Lehmann discontinuity.

Shearer (1990) found in long-period SS precursors no evidence for the global existence of a discontinuity near 220 km depth. Vidale and Benz (1992) found at 210 km depth the bottom of the asthenosphere near subducting slabs. Priestley *et al.* (1994) found the bottom of a low-velocity zone in central Siberia from nuclear explosions at 210 km depth. Gu *et al.* (2001a) used also SS precursors and found a variable Lehmann discontinuity preferably under continents and less under oceans (Figure 14). Deuss and Woodhouse (2002) have observed the Lehmann discontinuity globally under oceans and continents also using SS precursors. Deuss and Woodhouse (2004) have also inferred globally a negative Clapeyron slope for the Lehmann discontinuity from depth variations and tomographic upper-mantle velocities.

It is also suggested that the Lehmann discontinuity may be the lower boundary of an anisotropic asthenosphere. Karato (1992) proposed that the Lehmann discontinuity might be caused by a change of the preferred orientation of olivine crystals as consequence of a change of the deformation type. Gaherty and Jordan (1995) describe the Lehmann discontinuity as transition from anisotropic lithosphere to more isotropic lower tectosphere beneath continents using ScS data. Gaherty *et al.* (1996) and Kato and Jordan (1999) found the Lehmann discontinuity at 166 km depth below an anisotropic asthenosphere in the Tonga–Hawaii corridor and in the western Philippine Sea, also from ScS data. Gung *et al.* (2003) suggested that the Lehmann discontinuity under continents might both be associated with the bottom of the lithosphere. Gu *et al.* (2005) reported seismic anisotropy beneath the East Pacific Rise reaching down to 260 km, where a discontinuity was found. They used surface waves and traveltimes of body waves. Vinnik *et al.* (2005a), however, found in Sp conversions a discontinuity at 200 km depth in the northwest of the US and concluded that anisotropy is not present at this depth.

There are also P receiver function reports of observations of the Lehmann discontinuity. Bostock (1996b) found evidence for a weak 220 km discontinuity beneath the Canadian part

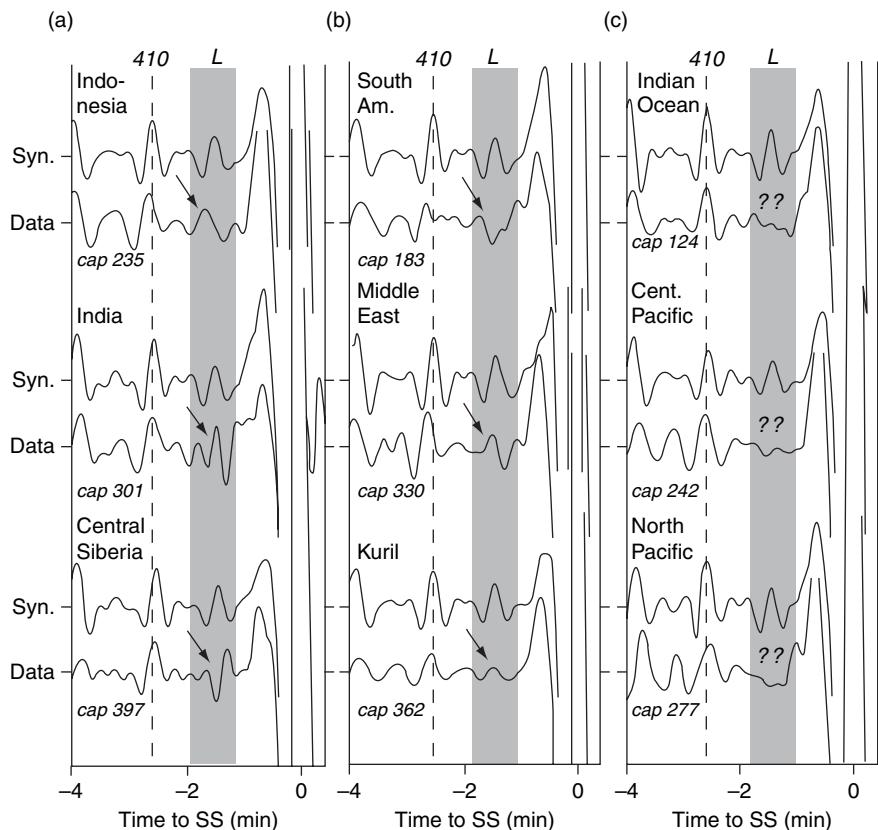


Figure 14 (a) Three S220S precursor stacks showing clear arrivals from the Lehmann discontinuity (thick lines – data, thin lines – synthetics from the PREM model). (b) Three stacks in regions with marginal observations of the Lehmann discontinuity. (c) Three stacks in regions with no detectable Lehmann discontinuity. From Gu Y, Dziewonski AM, Ekstrom G (2001a) Preferential detection of the Lehmann discontinuity beneath continents. *Geophysical Research Letters* 28: 4655–4658, figure 2.

of the North American craton in P receiver functions. Bostock (1998) found a west–east dipping structure between 170 and 230 km depth below Yellow Knife. Li *et al.* (2002) found from Ps data a discontinuity at 270–280 km depth beneath eastern North America.

There are also a number of wide-angle observations and other data which could be attributed to the Lehmann discontinuity. Drummond *et al.* (1982) and Hales (1991) found indications for a discontinuity near 200 km depth from wide-angle data in Australia and North America. Kaila *et al.* (1999) found from wide-angle studies indications of the Lehmann discontinuity beneath large regions of the Andes. Rost and Weber (2001) found a discontinuity at ~200 km depth in the northwest Pacific using PP precursors. Abramovitz *et al.* (2002) found in wide-angle data from Scandinavia a discontinuity at ~150 km depth, which they considered the base of the low-velocity zone. Wittlinger *et al.* (2004) interpreted from S receiver

function data the bottom of the low-velocity zone at 120–180 km depth below Tibet.

1.17.4.1 Summary of the Lehmann Discontinuity

In summary, there are many reports indicating a widespread Lehmann discontinuity. There are several reports obtained with the same technique (SS precursors), which have led to a first more or less global view. Also anisotropy seems to play a significant role in the explanation of this discontinuity. There are confirmations from various other techniques, but SS precursors seem to be the most promising technique for obtaining a comprehensive global image of the Lehmann discontinuity. One problem of this technique is, however, its relatively low resolution due to the long periods of the SS precursors.

1.17.5 The Hales Discontinuity

Green and Hales (1968), Hales (1969, 1972), and Hales *et al.* (1980) reported positive (velocity increase downward) seismic discontinuities at 60–90 km depth below the United States and other regions from long-range controlled source experiments. Since then, seismic discontinuities found in this depth range have frequently been called the ‘Hales discontinuity’, ‘H’, or ‘80 km discontinuity’. These expressions stand for discontinuities within the lithospheric mantle lid. There have been many active and passive experiments from which such discontinuities have been reported.

Zandt and Randall (1985) observed in shear-coupled PI modes a discontinuity between 70 and 80 km depth under North America, which they attributed to the Hales discontinuity. Revenaugh and Jordan (1991b) reported a mean depth of the Hales discontinuity of ~65 km beneath the southwestern Pacific from ScS reverberations. Sandvol *et al.* (1998) found a discontinuity at 80–100 km depth below the Arabian Shield from receiver functions.

The Hales discontinuity has frequently been related to anisotropy. Fuchs (1983) described anisotropic discontinuities in the lower lithosphere below southern Germany. Zhang and Lay (1993) found a depth of 80–90 km for the Hales discontinuity beneath the western Pacific region from sSH precursors. Bostock (1997, 1998) found an anisotropic layer at 70–80 km depth below the Slave craton in Canada. Levin and Park (2000) found an anisotropic layer at 70 km depth below the Arabian Shield, which they attributed to the Hales discontinuity. Saul *et al.* (2000) found an anisotropic discontinuity at 90 km depth below the Indian Shield.

Discontinuities in the mantle lithosphere have been known for a long time from controlled source long-range profiles (e.g., Hirn *et al.*, 1973; Kind 1974; see Chapters 1.08 and 1.15). Egorkin *et al.* (1987) reported from records of ‘peaceful nuclear explosions’ (PNEs) discontinuities in the depth range between 80 and 100 km beneath northern Russia. Pavlenkova (1996) reviewed global controlled source profiles and concluded that, among other local discontinuities in the lower lithosphere, a global discontinuity exists at 80–100 km depth with velocities below the discontinuity of 8.4–8.5 km s⁻¹. Hajnal *et al.* (1997) found a discontinuity at 75 km depth under central North America. Also, in seismic reflection data, signals are

observed from the depth range of the Hales discontinuity. For example, Steer *et al.* (1998) concluded from such data that a global discontinuity at 80–100 km depth may exist. Musacchio *et al.* (2004) reported an anisotropic layer beneath the Canadian Shield in the mantle lid from LITHOPROBE experiments.

A very characteristic feature of long-range controlled source seismic profiles is the teleseismic propagation of high frequency Pn waves. This phenomenon has been reviewed recently by Fuchs *et al.* (2002) and interpreted as being caused by randomly distributed scatterers in the mantle lid with high aspect ratio and dimensions in the 10 km range. Tittgemeyer *et al.* (1996) modeled teleseismic Pn assuming a 1-D model for the mantle lid with random velocity fluctuations. An alternative interpretation was given by Nielsen and Thybo (2003), who interpreted this observation as a whispering gallery effect.

1.17.5.1 Summary of the Hales Discontinuity

In conclusion, there are many reports from different places around the globe about a discontinuity that could correspond to the Hales discontinuity. Most of these reports come from wide-angle controlled source studies. There are, however, also a number of reports from steep-angle reflection experiments. Reports from P receiver function studies are rarer, probably since crustal multiples mask such deep phases. Receiver functions, however, seem frequently to have energy from this depth range on the transverse component, which is very likely indicative for anisotropic discontinuities in this depth range. Discontinuities certainly exist in the mantle lithosphere. However, it has not yet been shown that a single Hales discontinuity is a global feature. Many local discontinuities are seen in various parts of the mantle lithosphere. In addition, a global distribution of small-scale scatterers is probably responsible for long-range propagation of high-frequency Pn waves. There are still much too few homogeneous data available for reliable global analysis of the Hales discontinuity.

1.17.6 Conclusions

Historically, when seismologists started to study the Earth’s interior, they were looking for globally existing discontinuities, since they explained the clearest

seismic observations well. Consequently, the core–mantle boundary, the crust–mantle boundary, and the boundary between the inner and outer core were discovered. These discontinuities have, since then, been confirmed as global boundaries and many of their details are now known and more details are still being discovered. Gutenberg suggested another discontinuity in the uppermost mantle, also in the early days of seismology. This discontinuity was later frequently associated with the LAB, following the development of plate tectonics. However, facts concerning the global distribution and other properties of the Gutenberg discontinuity are still much less well known than in the case of the other global discontinuities. One reason for this is certainly that the Gutenberg discontinuity is the upper boundary of a low-velocity zone, which is difficult to detect with classical seismic techniques. In the second half of the twentieth century, two more global seismic discontinuities were suggested, the Lehmann discontinuity at the bottom of the asthenosphere and the Hales discontinuity within the mantle lithosphere. Both of these discontinuities are still not reliably confirmed as global discontinuities. There are less systematic reports about observations of additional discontinuities, which are not treated here. The best-known global upper-mantle discontinuities are the ones located at average depths of 410 and 660 km. They are mostly explained by phase changes in the olivine system, in agreement with high-pressure laboratory experiments. Oceanic upper-mantle data seem to be crucial for the final confirmation. Down-bending of the 660 discontinuity at subduction zones is confirmed by many reports. Globally, the 660 seems to be more a discontinuity of the shear modulus than of the bulk modulus.

The data used for the detection of seismic discontinuities in the Earth's interior are historically just traveltimes of seismic phases. These traveltimes have been obtained from sparsely distributed seismic stations. Since the advent of digital seismic waveform data, many more details have been learned about the Earth's structure in general and discontinuities in particular. New techniques have been developed. The most important ones use waves scattered at discontinuities (conversions, precursors, multiples). These methods depend heavily on data summation techniques, since scattered phases are small in amplitude and must be enhanced by a combination of many records. Present initiatives toward increased efforts to significantly increase the collection of seismic data (e.g., USArray) will therefore lead not only to more details about structures already known to

exist, but will likely also discover additional structural elements unknown so far. The expected new data together with new techniques may lead to another revolution in our knowledge about the dynamics of the solid Earth, which is a fundamental part of our environment.

References

- Abramovitz T, Thybo H, and Perchuc E (2002) Tomographic inversion of seismic P- and S-wave velocities from the Baltic Shield based on FENNOLORA data. *Tectonophysics* 358: 151–174.
- Adams RD (1968) Early reflections of P'P' as an indication of upper mantle structure. *Bulletin of the Seismological Society of America* 58: 1933–1947.
- Adams RD (1971) Reflections from discontinuities beneath Antarctica. *Bulletin of the Seismological Society of America* 61: 1441–1451.
- Ai Y, Zhao D, Gao X, and Xu W (2005) The crust and upper mantle discontinuity structure beneath Alaska inferred from receiver functions. *Physics of the Earth and Planetary Interiors* 150: 339–350.
- Ai Y and Zheng T (2003) The upper mantle discontinuity structure beneath eastern China. *Geophysical Research Letters* 30(21): 2089 (doi:10.1029/2003GL017678).
- Ai Y, Zheng T, Xu W, He Y, and Dong D (2003) A complex 660 km discontinuity beneath northeast China. *Earth and Planetary Science Letters* 212: 63–71.
- Alinaghi A, Bock G, Kind R, Hanka W, and Wylegalla K (2003) Receiver function analysis of the crust and upper mantle from the North German Basin to the Archean Baltic Shield. *Geophysics Journal International* 155: 641–652.
- Anderson DL (1967) Phase changes in the upper mantle. *Science* 157: 1165–1173.
- Anderson DL (1979) The deep structure of continents. *Journal of Geophysical Research* 84: 7555–7560.
- Anderson DL (1989) *Theory of the Earth*. Boston: Blackwell Scientific Publications.
- Anderson DL (1995) Lithosphere, asthenosphere, and perisphere. *Reviews of Geophysics* 33: 125–149.
- Anderson DL and Bass JD (1986) Transition region of the Earth's upper mantle. *Nature* 320: 321–328.
- Artemieva IM and Mooney WD (2001) Thermal thickness and evolution of Precambrian lithosphere: A global study. *Journal of Geophysical Research* 106: 16387–16414.
- Artemieva IM, Mooney WD, Perchuc E, and Thybo H (2002) Processes of lithosphere evolution: New evidence on the structure of the continental crust and uppermost mantle. *Tectonophysics* 358: 1–15.
- Barrell J (1914) The strength of the Earth's crust. *Journal of Geology* 22: 680ff.
- Bass JD and Anderson DL (1984) Composition of the upper mantle: Geophysical tests of two petrological models. *Geophysical Research Letters* 11: 229–232.
- Båth M and Stefansson R (1966) S-P conversion at the base of the crust. *Annali Di Geofisica* 19: 119–130.
- Benoit MH, Nyblade AA, VanDear JC, and Gurrola H (2003) Upper mantle P wave velocity structure and transition zone thickness beneath the Arabian Shield. *Geophysical Research Letters* 30(10): 1531 (doi:10.1029/2002GL016436).
- Benz HM and Vidale JE (1993) Sharpness of upper-mantle discontinuities determined from high-frequency reflections. *Nature* 365: 147–150.

- Bercovici D and Karato S-I (2003) Whole-mantle convection and the transition-zone water filter. *Nature* 425: 39–44.
- Beucler E, Chevrot S, and Montagner J-P (1999) The snake river plain experiment revisited: Relationships between a Farallon plate fragment and the transition zone. *Geophysical Research Letters* 26: 2673–2676.
- Bijwaard H, Spakman W, and Engdahl ER (1998) Closing the gap between regional and global travel time tomography. *Journal of Geophysical Research* 103: 30055–30078.
- Bina CR and Helffrich G (1994) Phase transition Clapeyron slopes and transition zone seismic discontinuity topography. *Journal of Geophysical Research* 99: 15853–15860.
- Bina CR and Wood BJ (1986) The 400-km seismic discontinuity and the proportion of olivine in the Earth's upper mantle. *Nature* 324: 449–451.
- Birch F (1952) Elasticity and constitution of the Earth's interior. *Journal of Geophysical Research* 57: 227–286.
- Blum J and Shen Y (2004) Thermal, hydrous, and mechanical states of the mantle transition zone beneath southern Africa. *Earth and Planetary Science Letters* 217: 367–378.
- Bock G (1988) Sp phases from the Australian upper mantle. *Geophysical Journal of the Royal Astronomical Society* 94: 73–81.
- Bock G (1991) Long-period S to P converted waves and the onset of partial melting beneath Oahu. *Geophysical Research Letters* 18: 869–872.
- Bock G (1994) Synthetic seismogram images of upper mantle structure: No evidence for a 520-km discontinuity. *Journal of Geophysical Research* 99: 15843–15851.
- Bolt B (1970) PdP and PKIKP waves and diffracted PcP waves. *Geophysical Journal of the Royal Astronomical Society* 20: 367–382.
- Bostock MG (1996a) A seismic image of the upper mantle beneath the North American craton. *Geophysical Research Letters* 23: 1593–1596.
- Bostock MG (1996b) Ps conversions from the upper mantle transition zone beneath the Canadian landmass. *Journal of Geophysical Research* 101: 8393–8402.
- Bostock MG (1997) Anisotropic upper-mantle stratigraphy and architecture of the Slave craton. *Nature* 390: 393–395.
- Bostock MG (1998) Mantle stratigraphy and evolution of the Slave province. *Journal of Geophysical Research* 103: 21183–21200.
- Bostock MG (1999) Seismic imaging of lithospheric discontinuities and continental evolution. *Lithos* 48: 1–16.
- Bostock MG and Cassidy JF (1997) Upper mantle stratigraphy beneath the southern Slave craton. *Canadian Journal of Earth Science* 34: 577–587.
- Budweg M, Bock G, and Weber M (2006) The Eifel plume-imaged with converted seismic waves. *Geophysical Journal International* 166: 579–589.
- Butler R, Lay T, Creager K, et al. (2004) The global seismic network surpasses its design goals. *EOS Transactions American Geophysical Union* 80: 225–229.
- Byerly P (1926) The Montana earthquake of June 28, 1925. *Bulletin of the Seismological Society of America* 16: 209–265.
- Castle JC and Creager KC (1997) Seismic evidence against a mantle chemical discontinuity near 660 km depth beneath Izu-Bonin. *Geophysical Research Letters* 24: 241–244.
- Castle JC and Creager KC (1998) Topography of the 660-km seismic discontinuity beneath Izu-Bonin: Implications for tectonic history and slab deformation. *Journal of Geophysical Research* 103: 12511–12527.
- Castle JC and Creager KC (2000) Local sharpness and shear wave speed jump across the 660-km discontinuity. *Journal of Geophysical Research* 105: 6191–6200.
- Chaljub E and Tarantola A (1997) Sensitivity of SS precursors to topography on the upper-mantle 660-km discontinuity. *Geophysical Research Letters* 24: 2613–2616.
- Chambers K, Deuss A, and Woodhouse JH (2005a) Reflectivity of the 410-km discontinuity from PP and SS precursors. *Journal of Geophysical Research* 110: 1–13.
- Chambers K, Woodhouse JH, and Deuss A (2005b) Topography of the 410-km discontinuity from PP and SS precursors. *Earth and Planetary Science Letters* 235: 610–622.
- Chemenda AI, Burg J-P, and Mattauer M (2000) Evolutionary model of the Himalaya–Tibet system: Geopoem based on new modelling, geological and geophysical data. *Earth and Planetary Science Letters* 174: 397–409.
- Chevrot S, Vinnik L, and Montagner J-P (1999) Global-scale analysis of the mantle Pds phases. *Journal of Geophysical Research* 104: 20203–20219.
- Clarke TJ, Silver PG, Yeh YL, James DE, Wallace TC, and Beck SL (1995) Close in SCS and sSCS reverberations from the 9 June 1994 Bolivian earthquake. *Geophysical Research Letters* 22: 2313–2316.
- Collier JD and Helffrich GR (1997) Topography of the '410' and '660' km seismic discontinuities in the Izu-Bonin subduction zone. *Geophysical Research Letters* 24: 1535–1538.
- Collier JD and Helffrich GR (2001) The thermal influence of the subducting slab beneath South America from 410 and 660 km discontinuity observations. *Geophysical Journal International* 147: 319–329.
- Collier JD, Helffrich GR, and Wood BJ (2001) Seismic discontinuities and subduction zones. *Physics of the Earth and Planetary Interiors* 127: 35–49.
- Collins JA, Vernon FL, Orcutt JA, and Stephen RA (2002) Upper mantle structure beneath the Hawaiian swell: Constraints from the ocean seismic network pilot experiment. *Geophysical Research Letters* 29(11): 17.1–17.4.
- Cummins PR, Kennett BLN, Bowman JR, Rand J, and Bostock MG (1992) The 520 km discontinuity? *Bulletin of the Seismological Society of America* 82: 323–336.
- Davies GF (1994) Thermomechanical erosion of the lithosphere by mantle plumes. *Journal of Geophysical Research* 99: 15709–15722.
- Deuss A and Woodhouse J (2001) Seismic observations of splitting of the mid-transition zone discontinuity in Earth's mantle. *Science* 294: 354–357.
- Deuss A and Woodhouse JH (2002) A systematic search for mantle discontinuities using SS-precursors. *Geophysical Research Letters* 29(8): 90.1–90.4.
- Deuss A and Woodhouse JH (2004) The nature of the Lehmann discontinuity from its seismological Clapeyron slopes. *Earth and Planetary Science Letters* 225: 295–304.
- Dormann J, Ewing M, and Oliver J (1960) Study of shear-wave velocity distribution in the upper mantle by mantle Rayleigh waves. *Bulletin of the Seismological Society of America* 50: 87–115.
- Dricker IG, Roecker SW, Kosarev GL, and Vinnik LP (1996) Shear-wave velocity structure of the crust and upper mantle beneath the Kola Peninsula. *Geophysical Research Letters* 23: 3389–3392.
- Drummond BJ, Muirhead KJ, and Hales AL (1982) Evidence for a seismic discontinuity near 200 km depth under a continental margin. *Geophysical Journal of the Royal Astronomical Society* 70: 67–77.
- Dueker KG and Sheehan AF (1997a) Mantle discontinuity structure beneath the Colorado Rocky Mountains and High Plains. *Journal of Geophysical Research* 103: 7153–7169.
- Dueker KG and Sheehan AF (1997b) Mantle discontinuity structure from midpoint stacks of converted P to S waves across the Yellowstone hotspot track. *Journal of Geophysical Research* 102: 8313–8327.
- Dziewonski AM and Anderson DL (1981) Preliminary reference Earth model. *Physics of the Earth and Planetary Interiors* 25: 297–356.

- Egorkin AV, Zukanov SK, Pavlenkova NA, and Chernyshev NM (1987) Results of lithospheric studies from long-range profiles in Siberia. *Tectonophysics* 140: 29–47.
- Engdahl ER and Flinn EA (1969) Seismic waves reflected from discontinuities within the Earth's upper mantle. *Science* 163: 177–179.
- Estabrook CH and Kind R (1996) The nature of the 660-kilometer upper-mantle seismic discontinuity from precursors to the PP phase. *Science* 274: 1179–1182.
- Faber S and Müller G (1980) Sp phases from the transition zone between the upper and lower mantle. *Bulletin of the Seismological Society of America* 70: 487–508.
- Farra V and Vinnik L (2000) Upper mantle stratification by P and S receiver functions. *Geophysical Journal International* 141: 699–712.
- Fee D and Dueker K (2004) Mantle transition zone topography and structure beneath the Yellowstone hotspot. *Geophysical Research Letters* 31: 18 (doi:10.1029/2004GL020636).
- Flanagan MP and Shearer PM (1998a) Global mapping of topography on transition zone velocity discontinuities by stacking SS precursors. *Journal of Geophysical Research* 103: 2673–2692.
- Flanagan MP and Shearer PM (1998b) Topography on the 410-km seismic velocity discontinuity near subduction zones from stacking of sS, sP and pP precursors. *Journal of Geophysical Research* 103: 21165–21182.
- Flanagan MP and Shearer PM (1999) A map of topography on the 410-km discontinuity from PP precursors. *Geophysical Research Letters* 26: 549–552.
- Fuchs K (1983) Recently formed elastic anisotropy and petrological models for the continental subcrustal lithosphere in southern Germany. *Physics of the Earth and Planetary Interiors* 31: 93–118.
- Fuchs K, Tittgemeyer M, Ryberg T, Wenzel F, and Mooney W (2002) Global significance of a sub-Moho boundary layer (SMBL) deduced from high-resolution seismic observations. *International Geology Review* 44: 671–685.
- Gaherty JB and Jordan TH (1995) Lehmann discontinuity as the base of an anisotropic layer beneath continents. *Science* 268: 1468–1471.
- Gaherty JB, Jordan TH, and Gee LS (1996) Seismic structure of the upper mantle in a central Pacific corridor. *Journal of Geophysical Research* 101: 22291–22309.
- Gaherty JB, Kato M, and Jordan TH (1998) Seismological structure of the upper mantle: A regional comparison of seismic layering. *Physics of the Earth and Planetary Interiors* 110: 21–41.
- Gao SS, Silver PG, and Liu KH (2002) Mantle discontinuities beneath Southern Africa. *Geophysical Research Letters* 29(10): 49 (doi:10.1029/2001GL013834).
- Gilbert HJ, Dormann RM, Hildebrand J, et al. (2001) Upper mantle discontinuity structure in the region of the Tonga subduction zone. *Geophysical Research Letters* 28: 1855–1858.
- Gilbert HJ, Sheehan AF, Dueker KG, and Molnar P (2003) Receiver functions in the western United States, with implications for upper mantle structure and dynamics. *Journal of Geophysical Research* 108(5): 2229 (doi:10.1029/2001JB001194).
- Gossler J and Kind R (1996) Seismic evidence for very deep roots of continents. *Earth and Planetary Science Letters* 138: 1–13.
- Green DH and Hales AL (1968) The traveltimes of P waves to 30° in the central United States and upper mantle structure. *Bulletin of the Seismological Society America* 58: 267–289.
- Green DH and Liebermann RC (1976) Phase equilibria and elastic properties of a pyrolite model for the oceanic upper mantle. *Tectonophysics* 32: 61–92.
- Green DH and Ringwood AE (1967) The stability fields of aluminous pyroxene peridotite and garnet peridotite and their relevance in upper mantle structure. *Earth and Planetary Science Letters* 3: 151–160.
- Grunewald S, Weber M, and Kind R (2001) The upper mantle under central Europe; indications for the Eifel plume. *Geophysical Journal International* 147: 590–601.
- Gu Y, Dziewonski AM, and Agee CB (1998) Global de-correlation of the topography of transition zone discontinuities. *Earth and Planetary Science Letters* 157: 57–67.
- Gu Y, Dziewonski AM, and Ekstrom G (2001a) Preferential detection of the Lehmann discontinuity beneath continents. *Geophysical Research Letters* 28: 4655–4658.
- Gu Y, Dziewonski AM, Su W, and Ekstrom G (2001b) Models of the mantle shear velocity and discontinuities in the pattern of lateral heterogeneities. *Journal of Geophysical Research* 106: 11169–11199.
- Gu YJ and Dziewonski AM (2002) Global variability of transition zone thickness. *Journal of Geophysical Research* 107(7): 2135 (doi:10.1029/2001JB000489).
- Gu YJ, Dziewonski AM, and Ekstrom G (2003) Simultaneous inversion for mantle shear velocity and topography of transition zone discontinuities. *Geophysical Journal International* 154: 559–583.
- Gu YJ, Lerner-Lam AL, Dziewonski AM, and Ekstrom G (2005) Deep structure and seismic anisotropy beneath the East Pacific Rise. *Earth and Planetary Science Letters* 232: 259–272.
- Gung Y, Panning M, and Romanowicz B (2003) Global anisotropy and the thickness of continents. *Nature* 422: 707–711.
- Gurrola H and Bernard Minster J (1998) Thickness estimates of the upper-mantle transition zone from bootstrapped velocity spectrum stacks of receiver functions. *Geophysical Journal International* 133: 31–43.
- Gurrola H and Bernard Minster J (2000) Evidence for local variations in the depth to the 410 km discontinuity beneath Albuquerque, New Mexico. *Journal of Geophysical Research* 105: 10847–10856.
- Gutenberg B (1926) Untersuchungen zur Frage bis zu welcher Tiefe die Erde kristallin ist. *Zeitschrift fuer Geophysik* 2: 24–29.
- Gutenberg B (1954) Low-velocity layers in the earth's mantle. *Bulletin of the Geological Society of America* 65: 337–348.
- Gutenberg B (1959) *Physics of the Earth's Interior*, 240pp. New York: Academic Press.
- Hajnal Z, Nemeth B, Clowes RM, et al. (1997) Mantle involvement in lithospheric collision: Seismic evidence from the Trans-Hudson orogen, western Canada. *Geophysical Research Letters* 24: 2079–2082.
- Hales AL (1969) A seismic discontinuity in the lithosphere. *Earth and Planetary Science Letters* 7: 44–46.
- Hales AL (1972) The travel times of P seismic phases and their relevance to the upper mantle velocity distribution. *Tectonophysics* 13: 447–482.
- Hales AL (1991) Upper mantle models and the thickness of the continental lithosphere. *Geophysical Journal International* 105: 355–363.
- Hales AL, Muirhead KL, and Rynn JMW (1980) A compressional velocity distribution for the upper mantle. *Tectonophysics* 63: 309–348.
- Hanka W, Heinloo A, and Jaekel K-H (2000) Networked seismographs: GEOFON real time data distribution. *ORFEUS Electronic Newsletter* 2: 24 <http://orfeus.knmi.nl/newsletter/vol2no3/geofon.html> (accessed Oct 2006).
- Heiffrich G (2000) Topography of the transition zone seismic discontinuities. *Reviews of Geophysics* 38: 141–158.
- Heiffrich G (2002) Thermal variations in the mantle inferred from 660 km discontinuity topography and tomographic wave speed variations. *Geophysical Journal International* 151: 935–943.

- Helffrich G, Asencio E, Knapp J, and Owens T (2003) Transition zone structure in a tectonically inactive area: 410 and 660 km discontinuity properties under the northern North Sea. *Geophysical Journal International* 155: 193–199.
- Helffrich G and Bina CR (1994) Frequency dependence of the visibility and depths of mantle seismic discontinuities. *Geophysical Research Letters* 21: 2613–2616.
- Helberger D (1968) The crust–mantle transition in the Bering Sea. *Bulletin of the Seismological Society of America* 58: 179–214.
- Helberger DV and Wiggins RA (1971) Upper mantle structure of midwestern United States. *Journal of Geophysical Research* 76: 3229–3245.
- Hirn A, Steinmetz L, Kind R, and Fuchs K (1973) Long range profiles in western Europe. II: Fine structure of the lithosphere in Bretagne (France). *Zeitschri fuer Geophysik* 39: 363–384.
- Hooft EEE, Toomey DR, and Solomon SC (2003) Anomalously thin transition zone beneath the Galapagos hotspot. *Earth and Planetary Science Letters* 216: 55–64.
- Humphreys ED, Dueker KG, Schutt DL, and Smith RB (2000) Beneath Yellowstone: Evaluating plume and nonplume models using teleseismic images of the upper mantle. *The Geophysical Society of America Today* 10: 1–7.
- Ibrahim AK and Nuttli OW (1967) Travel-time curves and upper mantle structure from long-period S waves. *Bulletin of the Seismological Society of America* 57: 1063–1092.
- Irfune T and Isshiki M (1998) Iron partitioning in a pyrolite mantle and the nature of the 410-km seismic discontinuity. *Nature* 392: 702–705.
- Ito E and Takahashi E (1989) Postspin transforms in the system Mg_2SiO_4 – Fe_2SiO_4 and some geophysical implications. *Journal of Geophysical Research* 94: 10637–10646.
- Jeanloz R and Thompson AB (1983) Phase transitions and mantle discontinuities. *Reviews of Geophysics* 1: 51–74.
- Jeffreys H (1936) The structure of the Earth down to the 20° discontinuity. *Monthly Notices of the Royal Astronomical Society Geophysical Supplement* 3: 401–422.
- Jeffreys H and Bullen KE (1940) *Seismological Tables*, 50pp. London: British Association for the Advancement of Science.
- Johnson LR (1967) Array measurements of P velocities in the upper mantle. *Journal of Geophysical Research* 72: 6309–6325.
- Jordan TH (1975) The continental tectosphere. *Reviews of Geophysics and Space Physics* 13: 1–12.
- Jordan TH and Frazer LN (1975) Crustal and upper mantle structure from Sp phases. *Journal of Geophysical Research* 80: 1504–1518.
- Julian BR and Anderson DL (1968) Travel times, apparent velocities and amplitudes of body waves. *Bulletin of the Seismological Society of America* 58: 339–366.
- Kaila KL, Krishna VG, and Khandekar G (1999) Preliminary models of upper mantle P and S wave velocity structure in the western South America region. *Journal of Geodynamics* 27: 567–583.
- Kanamori H (1967) Upper mantle structure from apparent velocities of P waves recorded at Wakayama micro-earthquake observatory. *Bulletin of the Earthquake Research Institute, Tokyo University* 45: 657–678.
- Kanamori H and Press F (1970) How thick is the lithosphere. *Nature* 226: 330.
- Karato S (1992) On the Lehmann discontinuity. *Geophysical Research Letters* 19: 2255–2258.
- Kato M and Jordan TH (1999) Seismic structure of the upper mantle beneath the western Philippine Sea. *Physics of the Earth and Planetary Interiors* 110: 263–283.
- Kato M and Kawakatsu H (2001) Seismological *in situ* estimation of density jumps across the transition zone discontinuities beneath Japan. *Geophysical Research Letters* 28: 2541–2544.
- Kato M, Misawa M, and Kawakatsu H (2001) Small subsidence of the 660-km discontinuity beneath Japan probed by ScS reverberations. *Geophysical Research Letters* 28: 447–450.
- Kennett BLN and Engdahl ER (1991) Travel times for global earthquake location and phase identification. *Geophysical Journal International* 105: 429–465.
- Kind R (1974) Long range propagation of seismic energy in the lower lithosphere. *Journal of Geophysics* 40: 189–202.
- Kind R and Vinnik LP (1988) The upper-mantle discontinuities underneath the GRF array from P-to-S converted phases. *Journal of Geophysics – Zeitschri fuer Geophysik* 62: 138–147.
- Kind R, Yuan X, Saul J, et al. (2002) Seismic images of crust and upper mantle beneath Tibet: Evidence for Eurasian plate subduction. *Science* 298: 1219–1221.
- King DW, Haddon RAW, and Husebye ES (1975) Precursors to PP. *Physics of the Earth Planetary Interiors* 10: 103–127.
- Kirby SH, Stein S, Okal EA, and Rubie DC (1996) Metastable mantle phase transformations and deep earthquakes in subducting oceanic lithosphere. *Reviews of Geophysics* 34: 261–306.
- Knopoff L (1983) The thickness of the lithosphere from the dispersion of surface waves. *Geophysical Journal of the Royal Astronomical Society* 74: 55–81.
- Kumar MR, Ramesh DS, Saul J, Sarkar D, and Kind R (2002) Crustal structure and upper mantle stratigraphy of the Arabian Shield. *Geophysical Research Letters* 29(8): 1242 (doi:10.1029/2001GL014530).
- Kumar P, Kind R, Hanka W, et al. (2005b) The lithosphere–asthenosphere boundary in the north west Atlantic Region. *Earth and Planetary Science Letters* 236: 249–257.
- Kumar P, Yuan X, Kind R, and Kosarev G (2005a) The lithosphere–asthenosphere boundary in the Tianshan–Karakoram region from S receiver functions: Evidence for continental subduction. *Geophysical Research Letters* 32: L07305 (doi:10.1029/2004GL022291).
- Kumar P, Yuan X, Kind R, and Ni J (2006) Imaging the collision of the Indian and Asian continental lithospheres beneath Tibet. *Journal of Geophysical Research* 111: B06308 (doi:10.1029/2005JB003930).
- Kummerow J and Kind R (2004) A natural and controlled source seismic profile through the Eastern Alps: TRANSALP. *Earth and Planetary Science Letters* 225: 115–129.
- Langston CA (1979) Structure under Mount Rainier, Washington, inferred from teleseismic body waves. *Journal of Geophysical Research* 84: 4749–4762.
- Le Stunff Y, Wicks CW, Jr., and Romanowicz B (1995) P'P' precursors under Africa: Evidence for mid-mantle reflectors. *Science* 270: 74–77.
- Lebedev S, Chevrot S, and van der Hilst RD (2002a) The 660-km discontinuity within the subducting NW-Pacific lithospheric slab. *Earth and Planetary Science Letters* 205: 25–35.
- Lebedev S, Chevrot S, and van der Hilst RD (2002b) Seismic evidence for olivine phase changes at the 410- and 660-kilometer discontinuities. *Science* 296: 1300–1302.
- Lebedev S, Chevrot S, and van der Hilst RD (2003) Correlation between the shear-speed structure and thickness of the mantle transition zone. *Physics of the Earth and Planetary Interiors* 136: 25–40.
- Lee D-K and Grand SP (1996) Depth of the upper mantle discontinuities beneath the East Pacific Rise. *Geophysical Research Letters* 23: 3369–3372.
- Lees AC, Bukowinski MST, and Jeanloz R (1983) Reflection properties of phase transition and compositional models of the 670-km discontinuity. *Journal of Geophysical Research* 88: 8145–8159.

- Lehmann I (1961) S and the structure of the upper mantle. *Geophysical Journal of the Royal Astronomical Society* 4: 124–138.
- Lehmann I (1964) On the velocity of P in the upper mantle. *Bulletin Seismological Society of America* 54: 1097–1103.
- Levin V and Park J (2000) Shear zones in the proterozoic lithosphere of the Arabian shield and the nature of the Hales discontinuity. *Tectonophysics* 323: 131–148.
- Li A, Fischer KM, van der Lee S, and Wysession ME (2002) Crust and upper mantle discontinuity structure beneath eastern North America. *Journal of Geophysical Research* 107(B5): 2100 (doi:10.1029/2001JB000190).
- Li A, Fischer KM, Wysession ME, and Clarke TJ (1998) Mantle discontinuities and temperature under the North American continental keel. *Nature* 395: 160–163.
- Li X, Kind R, Priestley K, et al. (2000b) Mapping the Hawaiian plume conduit with converted seismic waves. *Nature* 405: 938–941.
- Li X, Kind R, and Yuan X (2003b) Seismic study of upper mantle and transition zone beneath hotspots. *Physics of the Earth and Planetary Interiors* 136: 79–92.
- Li X, Kind R, Yuan X, et al. (2003a) Seismic observation of narrow plumes in the oceanic upper mantle. *Geophysical Research Letters* 30(6): 1334 (doi: 10.1029/2002GL015411).
- Li X, Kind R, Yuan X, Wölbren I, and Hanka W (2004) Rejuvenation of the lithosphere by the Hawaiian plume. *Nature* 427: 827–829.
- Li X, Sobolev SV, Kind R, Yuan X, and Estabrook CH (2000a) A detailed receiver function image of the upper mantle discontinuities in the Japan subduction zone. *Earth and Planetary Science Letters* 183: 527–541.
- Li X and Yuan X (2003) Receiver functions in northeast China – implications for slab penetration into the lower mantle in northwest Pacific subduction zone. *Earth and Planetary Science Letters* 216: 679–691.
- Liu KH (2003) Effects of inelasticity on the apparent depth and detectability of seismic discontinuities in the mantle. *Geophysical Research Letters* 30(9): 1455 (doi:10.1029/2002GL015264).
- Liu KH, Gao SS, Silver PG, and Zhang YK (2003) Mantle layering across central South America. *Journal of Geophysical Research* 108(B11): 2510 (doi:10.1029/2002JB002208).
- Liu L-G (1976) The post-spinel phases of forsterite. *Nature* 262: 770–772.
- Masters TG, Johnson S, Laske G, and Bolton H (1996) A shear velocity model of the mantle. *Philosophical Transactions of the Royal Society of London A* 354: 1385–1414.
- Mechie J, Egorkin A, Fuchs K, Ryberg T, Solodilov L, and Wenzel F (1993) P-wave mantle velocity structure beneath northern Eurasia from long-range recordings along the profile QUARTZ. *Physics of the Earth and Planetary Interiors* 79: 269–286.
- Melbourne T and Helmberger D (1998) Fine structure of the 410-km discontinuity. *Journal of Geophysical Research* 103: 10091–10102.
- Melbourne TL and Helmberger DV (2002) Whole mantle shear structure beneath the East Pacific Rise. *Journal of Geophysical Research* 107(B9): 2204 (doi:10.1029/2001JB000332).
- Mohorovicic A (1910) Das Beben vom 8. X. 1909. *Jahrbuch des Meteorologischen Observatoriums in Zagreb* 9: pp. 63 (Pt. IV, Sect. 1).
- Mohsen A, Hofstetter R, Bock G, et al. (2005) A receiver function study across the Dead Sea Transform. *Geophysical Journal International* 160: 948–960.
- Mooney W, Laske G, and Masters G (1998) A new global crustal model at 5 × 5 degrees: CRUST-5.1. *Journal of Geophysical Research* 103: 727–747.
- Musacchio G, White DJ, Asudeh I, and Thomson CJ (2004) Lithospheric structure and composition of the Archean western Superior Province from seismic refraction/wide-angle reflection and gravity modelling. *Journal of Geophysical Research* 109: B03304 (doi:10.1029/2003JB002427).
- Neale F (1996) Sharp 400-km discontinuity from short-period P reflections. *Geophysical Research Letters* 23: 419–422.
- Neale F and De Regt H (1999) Imaging upper-mantle discontinuity topography using underside-reflection data. *Geophysical Journal International* 137: 91–106.
- Neale F, De Regt H, and van Decar J (1997) Gross errors in upper-mantle discontinuity topography from underside reflection data. *Geophysical Journal International* 129: 194–204.
- Neves FA, Singh SC, and Priestley K (2001) Velocity structure of the upper mantle discontinuities beneath North America from waveform inversion of broadband seismic data using a genetic algorithm. *Journal of Geophysical Research* 106: 21883–21895.
- Neves FA, Singh SC, and Priestley KF (1996) Velocity structure of upper-mantle transition zones beneath central Eurasia from seismic inversion using genetic algorithms. *Geophysical Journal International* 125: 869–878.
- Niazi M and Anderson DL (1965) Upper mantle structure of western North America from apparent velocities of P waves. *Journal of Geophysical Research* 70: 4633–4640.
- Nielsen L and Thybo H (2003) The origin of teleseismic Pn waves: Multiple crustal scattering of upper mantle whispering gallery phases. *Journal of Geophysical Research* 108(B10): 2460 (doi: 10.1029/2003JB002487).
- Nielsen L, Thybo H, and Solodilov L (1999) Seismic tomographic inversion of Russian PNE data along profile Kraton. *Geophysical Research Letters* 26: 3413–3416.
- Niu F, Inoue H, Suetsugu D, and Kanjo K (2000) Seismic evidence for a thinner mantle transition zone beneath the South Pacific Superswell. *Geophysical Research Letters* 27: 1981–1984.
- Niu F and Kawakatsu H (1996) Complex structure of mantle discontinuities at the tip of the subducting slab beneath northeast China: A preliminary investigation of broadband receiver functions. *Journal of Physics of the Earth* 44: 701–711.
- Niu F and Kawakatsu H (1998) Determination of the absolute depths of the mantle transition zone discontinuities beneath China: Effect of stagnant slabs on transition zone discontinuities. *Earth, Planets and Space* 50: 965–975.
- Niu F, Levander A, Cooper CM, Lee C-TA, Lenardic A, and James DE (2004) Seismic constraints on the depth and composition of the mantle keel beneath the Kaapvaal craton. *Earth and Planetary Science Letters* 224: 337–346.
- Niu F, Solomon SC, Silver PG, Suetsugu D, and Inoue H (2002) Mantle transition-zone structure beneath the South Pacific Superswell and evidence for a mantle plume underlying the society hotspot. *Earth and Planetary Science Letters* 198: 371–380.
- Nolet G, Grand SP, and Kennett BLN (1994) Seismic heterogeneity in the upper mantle. *Journal of Geophysical Research* 99: 23753–23766.
- Nyblade AA, Knox RP, and Gurrola H (2000) Mantle transition zone thickness beneath Afar: Implications for the origin of the Afar hotspot. *Geophysical Journal International* 142: 615–619.
- Ohtaki T, Suetsugu D, Kanjo K, and Purwana I (2002) Evidence for a thick mantle transition zone beneath the Philippine Sea from multiple-ScS waves recorded by JISNET. *Geophysical Research Letters* 29(13): 2913, 1646 (doi:10.1029/2002GL014764).

- Oreshin S, Vinnik L, Peregoudov D, and Roecker S (2002) Lithosphere and asthenosphere of the Tian Shan imaged by S receiver functions. *Geophysical Research Letters* 29(8): 1191 (doi:10.1029/2001GL014441).
- Owens TJ, Nyblade AA, Gurrola H, and Langston CA (2000) Mantle transition zone structure beneath Tanzania, East Africa. *Geophysical Research Letters* 27: 827–830.
- Parker EC, Davis PM, Evans JR, Iyer HM, and Olsen KH (1984) Upwarp of anomalous asthenosphere beneath the Rio Grande rift. *Nature* 312: 354–356.
- Pavlenkova NI (1996) General feature of the uppermost mantle stratification from long-range seismic profiles. *Tectonophysics* 264: 261–278.
- Pearson DG (1999) The age of continental roots. *Lithos* 48: 171–194.
- Petersen N, Gossler J, Kind R, Stammiller K, and Vinnik L (1993a) Precursors to SS and structure of transition zone of the north-western Pacific. *Geophysical Research Letters* 20: 281–284.
- Petersen N, Vinnik L, Kosarev G, Kind R, Oreshin S, and Stammiller K (1993b) Sharpness of the mantle discontinuities. *Geophysical Research Letters* 20: 859–862.
- Plomerova J, Kouba D, and Babuska V (2002) Mapping the lithosphere–asthenosphere boundary through changes in surface-wave anisotropy. *Tectonophysics* 358: 175–185.
- Priestley K and McKenzie D (2002) The structure of the upper mantle beneath southern Africa. *Geological Society Special Publication* 199: 45–64.
- Priestley KF, Cipar J, Egorkin A, and Pavlenkova N (1994) Upper-mantle velocity structure beneath the Siberian platform. *Geophysical Journal International* 118: 369–378.
- Qiu X, Priestley K, and McKenzie D (1996) Average lithospheric structure of southern Africa. *Geophysical Journal International* 127: 563–587.
- Ramesh DS, Kind R, and Yuan X (2002) Receiver function analysis of the North American crust and upper mantle. *Geophysical Journal International* 150: 91–108.
- Revenaugh J and Jordan TH (1987) Observations of first order mantle reverberations. *Bulletin of the Seismological Society of America* 77: 1704–1717.
- Revenaugh J and Jordan TH (1989) A study of mantle layering beneath the western Pacific. *Journal of Geophysical Research* 94: 5787–5813.
- Revenaugh JS and Jordan TH (1991a) Mantle layering from ScS reverberations. 2: The transition zone. *Journal of Geophysical Research* 96: 19763–19780.
- Revenaugh JS and Jordan TH (1991b) Mantle layering from ScS reverberations. 3: The upper mantle. *Journal of Geophysical Research* 96: 19781–19810.
- Richards MA and Wicks CW, Jr. (1990) S–P conversion from the transition zone beneath Tonga and the nature of the 670 km discontinuity. *Geophysical Journal International* 101: 1–35.
- Ringwood AE (1969) Phase transformations in the mantle. *Earth and Planetary Science Letters* 5: 401–412.
- Ritsema J, van Heijst HJ, and Woodhouse JH (2004) Global transition zone tomography. *Journal of Geophysical Research* 109: B02302 (doi:10.1029/2003JB002610).
- Romanowicz B, Karczewski JF, Cara M, et al. (1991) The GEOSCOPE program: Present status and perspectives. *Bulletin of the Seismological Society of America* 81: 243–264.
- Rost S and Weber M (2001) A reflector at 200 km depth beneath the northwest Pacific. *Geophysical Journal International* 147: 12–28.
- Rost S and Weber M (2002) The upper mantle transition zone discontinuities in the Pacific as determined by short-period array data. *Earth and Planetary Science Letters* 204: 347–361.
- Roth EG and Wiens DA (1999) Depression of the 660 km discontinuity beneath the Tonga slab determined from near-vertical ScS reverberations. *Geophysical Research Letters* 26: 1223–1226.
- Ryberg T, Wenzel F, Egorkin AV, and Solodilov L (1997) Short-period observation of the 520-km discontinuity in Northern Eurasia. *Journal of Geophysical Research* 102: 5413–5422.
- Ryberg T, Wenzel F, Egorkin AV, and Solodilov L (1998) Properties of the mantle transition zone in northern Eurasia. *Journal of Geophysical Research* 103: 811–822.
- Ryberg T, Wenzel F, Mechic J, Egorkin A, Fuchs K, and Solodilov L (1996) Two-dimensional velocity structure beneath northern Eurasia derived from the super long-range seismic profile quartz. *Bulletin of the Seismological Society America* 86: 857–867.
- Rychert CA, Fischer KM, and Rondenay S (2005) A sharp lithosphere–asthenosphere boundary imaged beneath eastern North America. *Nature* 436: 542–545.
- Sacks IS and Snoker JA (1977) The use of converted phases to infer the depth of the lithosphere–asthenosphere boundary beneath South America. *Journal of Geophysical Research* 82: 2011–2017.
- Sacks IS, Snoker JA, and Husebye ES (1979) Lithosphere thickness beneath the Baltic Shield. *Tectonophysics* 56: 101–110.
- Saita T, Suetsugu D, Ohtaki T, Takenaka H, Kanjo K, and Purwana I (2002) Transition zone thickness beneath Indonesia as inferred using the receiver function method for data from the JISNET regional broadband seismic network. *Geophysical Research Letters* 29(7): 1115 (doi:10.1029/2001GL013629).
- Sandvol E, Seber D, Barazangi M, Vernon FL, Mellors R, and Al-Amri A (1998) Lithospheric seismic velocity discontinuities beneath the Arabian Shield. *Geophysical Research Letters* 25: 2873–2876.
- Saul J, Kumar MR, and Sarkar D (2000) Lithospheric and upper mantle structure of the Indian Shield, from teleseismic receiver functions. *Geophysical Research Letters* 27: 2357–2360.
- Schott B and Schmeling H (1998) Delamination and detachment of a lithospheric root. *Tectonophysics* 296: 225–247.
- Shearer PM (1990) Seismic imaging of upper-mantle structure with new evidence for a 520-km discontinuity. *Nature* 344: 121–126.
- Shearer PM (1991) Constraints on upper mantle discontinuities from observations of long period reflected and converted phases. *Journal of Geophysical Research* 96: 18147–18182.
- Shearer PM (1993) Global mapping of upper mantle reflectors from long period SS precursors. *Geophysical Journal International* 115: 878–904.
- Shearer PM (1996) Transition zone velocity gradients and the 520-km discontinuity. *Journal of Geophysical Research* 101: 3053–3066.
- Shearer PM and Flanagan MP (1999) Seismic velocity and density jumps across the 410- and 660-kilometer discontinuities. *Science* 285: 1545–1548.
- Shearer PM, Flanagan MP, and Hedlin MAH (1999) Experiments in migration processing of SS precursor data to image upper mantle discontinuity structure. *Journal of Geophysical Research* 104: 7229–7242.
- Shearer PM and Masters TG (1992) Global mapping of topography on the 660-km discontinuity. *Nature* 355: 791–796.
- Sheehan AF, Shearer PM, Gilbert HJ, and Dueker KG (2000) Seismic migration processing of P–SV converted phases for mantle discontinuity structure beneath the Snake River Plain, western United States. *Journal of Geophysical Research* 105: 19055–19066.
- Shen Y, Sheehan AF, Dueker KG, De Groot-Hedlin C, and Gilbert H (1998a) Mantle discontinuity structure beneath the

- Southern East Pacific Rise from P-to-S converted phases. *Science* 280: 1232–1235.
- Shen Y, Solomon SC, Bjarnason ITh, and Purdy GM (1996) Hot mantle transition zone beneath Iceland and the adjacent Mid-Atlantic Ridge inferred from P-to-S conversions at the 410- and 660-km discontinuities. *Geophysical Research Letters* 23: 3527–3530.
- Shen Y, Solomon SC, Bjarnason ITh, and Wolfe CJ (1998b) Seismic evidence for a lower-mantle origin of the Iceland plume. *Nature* 395: 62–65.
- Shim S-H, Duffy TS, and Shen G (2001) The post-spinel transformation in Mg_2SiO_4 and its relation to the 660-km seismic discontinuity. *Nature* 411: 571–574.
- Simmons NA and Gurrula H (2000) Multiple seismic discontinuities near the base of the transition zone in the Earth's mantle. *Nature* 405: 559–562.
- Simon RE, Wright C, Kwasibida MTO, and Kgaswane EM (2003) The structure of the upper mantle and transition zone beneath southern Africa from broad-band body waves. *South African Journal of Science* 99: 577–583.
- Sipkin SA and Jordan TH (1976) Lateral heterogeneity of the upper mantle determined from the travel times of multiple ScS. *Journal of Geophysical Research* 81: 6307–6320.
- Sipkin SA and Jordan TH (1980) Multiple ScS travel times in the western Pacific: Implications for mantle heterogeneity. *Journal of Geophysical Research* 85: 853–861.
- Sodoudi F, Kind R, Hatzfeld D, Priestley K, and Greece Working Group (2006a) Lithospheric structure of the Aegean obtained from P and S receiver functions. *Journal of Geophysical Research* 111: B12307 (doi:10.1029/2005JB003932).
- Sodoudi F, Yuan X, Liu Q, Kind R, and Chen J (2006b) Lithospheric thickness beneath the Dabie Shan, central eastern China from S receiver functions. *Geophysical Journal International* 166: 1363–1367.
- Song T-RA, Helmberger DV, and Grand SP (2004) Low-velocity zone atop the 410-km seismic discontinuity in the north-western United States. *Nature* 427: 530–533.
- Stammer K, Kind R, Petersen N, Kosarev G, Vinnik L, and Qiyuan L (1992) The upper mantle discontinuities: Correlated or anticorrelated? *Geophysical Research Letters* 19: 1563–1566.
- Stankiewicz J, Chevrot S, van der Hilst RD, and de Wit MJ (2002) Crustal thickness, discontinuity depth, and upper mantle structure beneath southern Africa: Constraints from body wave conversions. *Physics of the Earth and Planetary Interiors* 130: 235–251.
- Steer DN, Knapp JH, and Brown LD (1998) Super-deep profiling: Exploring the continental mantle lid. *Tectonophysics* 286: 111–121.
- Su W-J, Woodward RL, and Dziewonski AM (1994) Degree 12 model of shear velocity heterogeneity in the mantle. *Journal of Geophysical Research* 99: 6945–6980.
- Suetsugu D, Saita T, Takenaka H, and Niu F (2004) Thickness of the mantle transition zone beneath the South Pacific as inferred from analyses of ScS reverberated and Ps converted waves. *Physics of the Earth and Planetary Interiors* 146: 35–46.
- Svekalapko Seismic Tomography Working Group, Yliniemi J, Kozlovskaya E, Hjelt S-E, Komminaho K, and Ushakov A (2004) Structure of the crust and uppermost mantle beneath southern Finland revealed by analysis of local events registered by the Svekalapko seismic array. *Tectonophysics* 394: 41–67.
- Thirot J-L, Montagner J-P, and Vinnik L (1998) Upper-mantle seismic discontinuities in a subduction zone (Japan) investigated from P to S converted waves. *Physics of the Earth and Planetary Interiors* 108: 61–80.
- Thybo H (2006) The heterogeneous upper mantle low velocity zone. *Tectonophysics* 416(1–2): 53–79.
- Thybo H and Perchuc E (1997) The seismic 8° discontinuity and partial melting in continental mantle. *Science* 275: 1626–1629.
- Tibi R and Wiens DA (2005) Detailed structure and sharpness of upper mantle discontinuities in the Tonga subduction zone from regional broadband arrays. *Journal of Geophysical Research B: Solid Earth* 110(6): 1–14.
- Tibi R, Wiens DA, Shiobara H, Sugioka H, and Shore PJ (2006) Depth of the 660-km discontinuity near the Mariana slab from an array of ocean bottom seismographs. *Geophysical Research Letters* 33: L02313 (doi:10.1029/2005GL024523).
- Tittgemeyer M, Wenzel F, Fuchs K, and Ryberg T (1996) Wave propagation in a multiple-scattering upper mantle – observations and modelling. *Geophysical Journal International* 127: 492–502.
- Tonegawa T, Hirahara K, and Shibutani T (2005) Detailed structure of the upper mantle discontinuities around the Japan subduction zone imaged by receiver function analyses. *Earth, Planets and Space* 57: 5–14.
- Tono Y, Kunugi T, Fukao Y, Tsuboi S, Kanjo K, and Kasahara K (2005) Mapping of the 410- and 660-km discontinuities beneath the Japanese islands. *Journal of Geophysical Research* 110: 1–10.
- Van der Lee S, Paulissen H, and Nolet G (1994) Variability of P660s phases as a consequence of topography of the 660 km discontinuity. *Physics of the Earth and Planetary Interiors* 86: 147–164.
- Van der Meijde M, van der Lee S, and Giardini D (2005) Seismic discontinuities in the Mediterranean mantle. *Physics of the Earth and Planetary Interiors* 148: 233–250.
- Vidale JE and Benz HM (1992) Upper-mantle seismic discontinuities and the thermal structure of subduction zones. *Nature* 356: 678–683.
- Vidale JE, Ding XY, and Grand SP (1995) The 410-km-depth discontinuity: A sharpness estimate from near-critical reflections. *Geophysical Research Letters* 22: 2557–2560.
- Vinnik L (1977) Detection of waves converted from P to SV in the mantle. *Physics of the Earth and Planetary Interiors* 15: 39–45.
- Vinnik L, Kosarev G, and Petersen N (1996) Mantle transition zone beneath Eurasia. *Geophysical Research Letters* 23: 1485–1488.
- Vinnik L, Kurnik E, and Farra V (2005a) Lehmann discontinuity beneath North America: No role for seismic anisotropy. *Geophysical Research Letters* 32: L09306 (doi:10.1029/2004GL022333).
- Vinnik LP, Foulger GR, and Du Z (2005b) Seismic boundaries in the mantle beneath Iceland: A new constraint on temperature. *Geophysical Journal International* 160: 533–538.
- Vinnik LP, Reigber C, Aleshin IM, et al. (2004) Receiver function tomography of the central Tien Shan. *Earth and Planetary Science Letters* 225: 131–146.
- von Rebeur-Paschwitz E (1889) The earthquake of Tokyo, April 18, 1889. *Nature* 40: 294–295.
- Wajeman N (1988) Detection of underside P reflections of mantle discontinuities by stacking broadband data. *Geophysical Research Letters* 15: 669–672.
- Walck MC (1984) The P-wave upper mantle structure beneath an active spreading centre: The Gulf of California. *Geophysical Journal of the Royal Astronomical Society* 76: 697–723.
- Whitcomb J and Anderson DL (1970) Reflection of P'P' seismic waves from discontinuities in the mantle. *Journal of Geophysical Research* 75: 5713–5728.
- Wicks CW, Jr. and Richards MA (1993) A detailed map of the 660-kilometer discontinuity beneath the Izu-Bonin subduction zone. *Science* 261: 1424–1427.
- Wittlinger G, Farra V, and Vergne J (2004) Lithospheric and upper mantle stratifications beneath Tibet: New insights from Sp conversions. *Geophysical Research Letters* 31: L19615 (doi:10.1029/2004GL020955).

- Woelbern I, Jacob AWB, Blake TA, et al. (2006) Deep origin of the Hawaiian tilted plume conduit derived from receiver functions. *Geophysical Journal International* 166(2): 767–781.
- Wright C, Kwadiba MTO, Simon RE, Kgaswane EM, and Nguuri TK (2004) Variations in the thickness of the crust of the Kaapvaal craton, and mantle structure below southern Africa. *Earth, Planets and Space* 56: 125–137.
- Xu F, Vidale JE, Earle PS, and Benz HM (1998) Mantle discontinuities under southern Africa from precursors to P'P'df. *Geophysical Research Letters* 25: 571–574.
- Yamazaki A and Hirahara K (1994) The thickness of upper mantle discontinuities, as inferred from short-period J-Array data. *Geophysical Research Letters* 21: 1811–1814.
- Yang Y and Zhou H-L (2001) Application of receiver function method to estimate the buried depths of discontinuities in the upper mantle beneath China and adjacent area. *Acta Geophysica Sinica* 44: 792–797.
- Yuan X, Kind R, Li X, and Wang R (2006) The S receiver functions: Synthetics and data example. *Geophysical Journal International* 165: 555–564.
- Yuan X, Ni J, Kind R, Mechie J, and Sandvol E (1997) Lithospheric and upper mantle structure of southern Tibet from a seismological passive source experiment. *Journal of Geophysical Research* 102: 27491–27500.
- Yuan X, Sobolev SV, and Kind R (2002) Moho topography in the central Andes and its geodynamic implications. *Earth and Planetary Science Letters* 199: 389–402.
- Zandt G and Randall GE (1985) Observations of shear-coupled P-waves. *Geophysical Research Letters* 12: 565–568.
- Zhang Z and Lay T (1993) Investigation of upper mantle discontinuities near northwestern Pacific subduction zones using precursors to sSH. *Journal of Geophysical Research* 98: 4389–4405.

1.18 Deep Earth Structure – Lower Mantle and D"

T. Lay, University of California, Santa Cruz, Santa Cruz, CA, USA

© 2007 Elsevier B.V. All rights reserved.

1.18.1	Lower Mantle and D" Basic Structural Attributes	620
1.18.1.1	Elastic Parameters, Density, Thermal Structure	621
1.18.1.2	Mineralogical Structure	621
1.18.2	One-Dimensional Lower-Mantle Structure	622
1.18.2.1	Body-Wave Traveltime and Slowness Constraints	622
1.18.2.2	Surface-Wave/Normal-Mode Constraints	623
1.18.2.3	Attenuation Structure	624
1.18.3	Three-Dimensional Lower-Mantle Structure	625
1.18.3.1	Seismic Tomography	625
1.18.3.2	Dynamical Structures	627
1.18.4	D" Region	630
1.18.4.1	Large-Scale Seismic Velocity Attributes	630
1.18.4.2	Thermal Boundary Layer Aspect	631
1.18.5	D" Discontinuities	632
1.18.5.1	Seismic Wave Triplications	633
1.18.5.2	Phase Change in Perovskite	634
1.18.6	Large Low-Shear-Velocity Provinces	636
1.18.6.1	Seismic Velocity Properties	637
1.18.6.2	Thermal-Chemical Interpretations	639
1.18.7	Ultra-Low-Velocity Zones	639
1.18.7.1	Seismic Phases Used for Detection	639
1.18.7.2	Partial Melting and Chemical Anomalies	640
1.18.8	Lower-Mantle Anisotropy	641
1.18.8.1	Shear-Wave Splitting Observations	642
1.18.8.2	Mineralogical/Dynamical Implications	642
1.18.9	Small-Scale Heterogeneities	643
1.18.9.1	Scattering in D"	643
1.18.9.2	Core–Mantle Boundary Topography	644
1.18.10	Conclusions	644
	References	645

Glossary

attenuation Loss of signal amplitude during propagation. Intrinsic attenuation involves irreversible anelastic losses; scattering attenuation involves partitioning of energy into separate waves.

CMB The core–mantle boundary is the surface defined by the contrast in composition between mantle rocks and core molten alloy.

D" Designation for the lowermost 200–300 km of the lower mantle. This region is distinct from the

overlying mantle in that the seismic velocity variations are not consistent with homogeneous material under self-compression and adiabatic temperature gradient.

LLSVP Large low-shear-velocity province, used to describe broad regions beneath Africa and the South Atlantic and beneath the southern Pacific, which have anomalously low shear velocities, less-pronounced compressional velocity decreases, sharp lateral boundaries, and indications of higher

than average densities. These features have often been labeled superplumes, but the seismic data favor them being chemically distinct, dense piles of material possibly entrained by surrounding mantle flow.

P-wave Elastic wave involving compressional and dilatational motion of the medium as the wave propagates, the faster of the two seismic waves.

S-wave Elastic wave involving shearing motion of the medium with no volumetric change as the wave propagates, the slower of the two seismic waves.

1.18.1 Lower Mantle and D" Basic Structural Attributes

Earth's lower mantle is a thick layer of rock extending downward more than 2000 km from the transition zone to the core–mantle boundary (CMB) at a depth of 2891 km. Seismology provides the basis for defining the lower mantle, as it was evident from consideration of even the earliest global traveltimes curves that this region of the interior has relatively smoothly increasing seismic velocities with depth, with an overall velocity gradient significantly reduced from that in the overlying transition zone. The upper limit of the lower mantle has various definitions; many geophysicists associate it with the 650 km deep seismic velocity discontinuity, while others prefer to designate it at a greater depth of about 800 km, where there tends to be a reduction in radial velocity gradients in detailed seismic velocity models, as well as intermittent reports of a seismic discontinuity (e.g., [Datt and Muirhead, 1976](#); [Revenaugh and Jordan, 1991](#)). The variety of phase transformations for olivine, enstatite, and garnet compositions to their high-pressure polymorphs which characterize the transition zone, all culminate in transitions to magnesium-silicate perovskite $[(\text{Mg}, \text{Fe})\text{SiO}_3]$. The various transitions to perovskite should largely reach completion by about 800 km depth, which can thus be viewed as the base of the transition zone. The subsequent stability of the abundant magnesium-silicate perovskite mineral over a great temperature and pressure range is the probable explanation for the relatively smooth velocity gradients across the lower mantle, with self-compression and a nearly adiabatic thermal gradient resulting in smoothly increasing density, rigidity, incompressibility, and associated P-wave and S-wave seismic velocities down to near the CMB.

A few hundred kilometers above the CMB seismic velocities have more complex structure, with abrupt increases or discontinuities in velocity occurring in regions of relatively high seismic velocity, likely as a

result of a phase transition from magnesium-silicate perovskite to the post-perovskite phase ([Murakami et al., 2004](#)), along with enhanced lateral variations that indicate the presence of thermal and chemical heterogeneity in a boundary layer above the CMB (e.g., [Garnero, 2000](#); [Lay and Garnero, 2004](#)). Based on the seismic evidence for inhomogeneity in the structure, the lowermost few hundred kilometers of the lower mantle are called the D" region harkening back to an early nomenclature in which the lower mantle was labeled the D shell, then subdivided into D' and D"; see [Bullen \(1949\)](#). At the very base of the lower mantle, there are localized regions with strong seismic velocity reductions that are best explained by the presence of a melt component within the lower-mantle rock. The CMB separates the silicate and oxide minerals of the lower mantle from the molten iron alloy of the core, with the contrasts in physical properties such as density, viscosity, and rigidity across the CMB being as large or larger than those at the surface of Earth.

Despite its generally simple overall seismological structure, the lower mantle appears to be undergoing large-scale dynamical processes. These are revealed by second-order features of the seismological models that have only begun to be resolved over the past 25 years or so. The great pressures existing in the lower mantle suppress the sensitivity of seismic wave velocities to variations in temperature and composition, muting the detectable effects. Progress in imaging the few percent variations in seismic velocities that are present is unveiling the dynamical complexity of the lower mantle, and indicates regions of convective upwelling, downwelling, and large-scale chemical heterogeneities that may have piled up in the deep mantle. While current understanding of the dynamical regime is still limited, it appears that the lower mantle plays a major role in regulating heat flux from the core, in cycling heat out of the interior, and in segregating chemical heterogeneities for long intervals of time, giving rise to geochemical anomalies observed at the surface.

1.18.1.1 Elastic Parameters, Density, Thermal Structure

P-wave and S-wave velocities and density increase smoothly across the lower mantle in all one-dimensional seismic velocity models for the Earth. **Figure 1** shows the variations in these properties as given by the preliminary reference earth model (PREM), which was based on a large number of body-wave traveltimes and free-oscillation eigenfrequencies (Dziewonski and Anderson, 1981). Below the abrupt seismic velocity and density increases near 650–670 km deep, generally attributed to the disassociative phase transition of $(\text{Mg}, \text{Fe})\text{SiO}_4$ γ -spinel (Ringwoodite) to $(\text{Mg}, \text{Fe})\text{SiO}_3$ perovskite plus $(\text{Mg}, \text{Fe})\text{O}$ ferropericlase (e.g., Ito and Takahashi, 1989; Ito *et al.*, 1990), down to the CMB there are no abrupt changes in properties that would suggest large-scale layering of the lower mantle (e.g., Green and Falloon, 1998). The bounds on the seismic velocity models given in **Figure 1** indicate the range of velocities that are admissible for one-dimensional models, based on observed traveltimes fluctuations for seismic body waves. The relatively tight range of velocity bounds indicate that if there are any velocity discontinuities in the deep mantle, they are less than a few percent, or there are strong lateral variations in the depths of the structure such that it is not well-represented by a one-dimensional model.

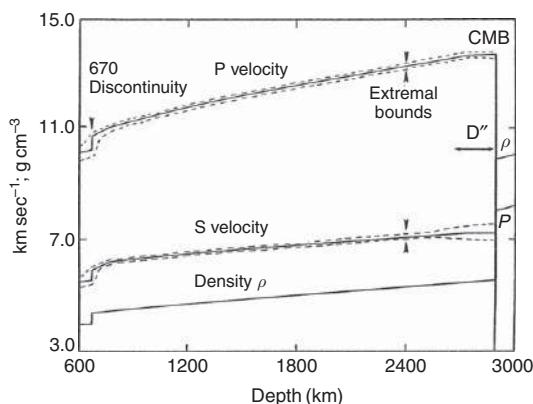


Figure 1 Variation of seismic velocities and density through the lower mantle for model PREM (Dziewonski and Anderson, 1981), along with the extremal bounds that indicate the confidence intervals for spherically averaged models base on traveltimes data (Lee and Johnson, 1984). The D'' region is the lowermost 200–300 km of the lower mantle overlying the core–mantle boundary (CMB). Reproduced from Lay T (1989) Structure of the core–mantle transition zone: A chemical and thermal boundary layer. *EOS Transactions of the American Geophysical Union* 70(49): 54–55 and 58–59.

In fact, there are many research publications inferring the presence of localized reflectors or scatterers in the depth range 650–1200 km (e.g., Muirhead and Hales, 1980; Niu and Kawakatsu, 1997; Vinnik *et al.*, 1998a), but the observations are intermittent, and there is, as yet, no agreed upon globally extensive discontinuity below 650 km depth that would appear in a one-dimensional Earth model. This fact is often invoked to support the idea that the lower mantle is chemically uniform, but one should keep in mind that chemical layering is likely to involve rather subtle changes in seismic velocities and details of the density structure are not well-resolved by normal-mode observations. Thus, it is possible that the lower mantle is chemically stratified, perhaps with depth variations in Si or Fe content, with substantial topography on any chemical contrasts (e.g., Anderson, 1991, 1998; Kellogg *et al.*, 1999). Assessing this possibility requires consideration of three-dimensional velocity structures, but it may even then be difficult because velocity discontinuities associated with any chemical contrasts may be relatively small.

The bounds on one-dimensional S-wave velocity models tend to flare in the lower 300 km of the mantle, indicating larger variability in S-wave traveltimes for waves traversing the D'' region above the CMB. In this region seismic waveform modeling has resulted in localized velocity models with 1–3% abrupt increases in shear velocity, as well as large-scale regions with 3–6% low shear velocity. There is no average one-dimensional model that represents the structure well, and the lateral variations must be characterized with three-dimensional structures in order to assess their significance. P-wave observations also indicate abrupt increases in P-wave velocity in some regions, but in general, the structure is less heterogeneous than for S-waves. At the very base of the lower mantle, within tens of kilometers above the CMB, there are localized regions with very pronounced reductions in P-wave and S-wave velocity, which are called ultralow-velocity zones (ULVZs). ULVZs may represent a transition zone from mantle to core, but they must be undetectably thin or not present in many regions.

1.18.1.2 Mineralogical Structure

The composition and mineralogy of the lower mantle is not directly determined from seismic observations and must be deduced based on models for the bulk composition of the Earth along with experimental

and theoretical mineral physics that tries to match observed density and elastic velocity profiles for appropriate pressures and temperatures. Given the experimental determination of stability of magnesium-silicate perovskite phase (Liu, 1974) as the polymorph of predominant upper-mantle minerals subjected to lower-mantle conditions, along with the chondritic Earth model, there is high confidence that $(\text{Mg}_{x}, \text{Fe}_{1-x})\text{SiO}_3$ perovskite is the primary mineral form in the lower mantle (e.g., Knittle and Jeanloz, 1987; Fiquet *et al.*, 2000; Shim *et al.*, 2001; Gong *et al.*, 2004; Wentzcovitch *et al.*, 2004). The value of x is probably in the range 0.8–0.9, although some aluminum substitution is very likely to exist in lower-mantle perovskites as well. The experimental and chondritic model constraints on mineralogy also favor the presence of $(\text{Mg}_{x}, \text{Fe}_{1-x})\text{O}$, with x again in the range 0.8–0.9, as well as some Ca-perovskite. Other minor phases are likely to exist, but constraints on their abundance are very limited.

When one considers the mineralogy of the lower mantle, it is essential to keep in mind that there has undoubtedly been extensive chemical processing, melting, and mixing. This would have occurred during the energetic processes of accretion and core formation, as a result of early large impacts, and as an ongoing consequence of mantle convection. The huge density increase at the CMB, larger than that at Earth's surface, provides an environment favorable for the accumulation of dense silicate and oxide materials, a region toward which iron-rich materials may settle, and a chemically active environment in which mantle rocks and core alloys may chemically react over time. The geophysical resolution of the precise mineralogy and chemistry is exceedingly limited, and we lack direct access to samples of lower-mantle rocks, so various mineralogical scenarios for the lower mantle, particularly for minor components, can be considered as long as they agree overall with the limited seismological information available for the region. While high viscosity of the lower mantle may allow chemical heterogeneities to persist for long intervals of time, the notion of a primitive, unprocessed lower-mantle composition is at odds with prevailing notions of Earth's formation and evolution. Presumably, huge amounts of iron have separated from the mantle and there has been extensive melting, which likely would lead to volatile depletion of the deep mantle and chemical stratification that may or may not have survived subsequent entrainment.

1.18.2 One-Dimensional Lower-Mantle Structure

The most direct constraints on lower-mantle structure are provided by seismic waves that traverse the interior. The main observables of importance are the traveltimes of P-waves and S-waves, any waveform complexities arising from interactions with contrasts in properties in the rocks, S-wave splitting produced by anisotropy, and frequency-dependent amplitude behavior of the seismic waves that can constrain the anelasticity of the lower mantle. The average lower-mantle seismic velocities have been determined by both classical arrival time inversion and normal-mode analysis, with the latter also refining early estimates of the density structure that were based on velocity–density systematics, integral constraints provided by Earth's mass and moment of inertia, and piecewise integration of seismic velocity models using the Adams–Williamson equation (Adams and Williamson, 1923). With the early recognition of the general simplicity of lower-mantle structure, most research prior to 1980 focused on developing robust one-dimensional models for lower-mantle structure.

1.18.2.1 Body-Wave Traveltime and Slowness Constraints

Observations of traveltimes of seismic waves at varying distances from earthquake and explosion sources for which the source locations and origin times are either known or solved for are plotted in traveltime curves, as shown for shallow focus events in Figure 2. This classic display of seismic observations immediately reveals two defining attributes of the Earth; the deep structure must be largely radially symmetric, as that is required for having tightly defined traveltime branches for each path through the Earth, and the traveltimes of major phases such as P, PP, S, and SS are smoothly increasing functions in the distance range 30–100°, which corresponds to the range where the seismic wave fronts turn in the lower mantle. The smooth, continuous curves obtained by fitting the observations can be inverted for one-dimensional models of seismic velocity versus depth using classic methods such as the Herglotz–Weichert inversion or by computer modeling (see Lay and Wallace, 1995). The slope of a traveltime curve at a given distance, $dT/d\Delta$, gives the seismic ray parameter, and its inverse, the apparent velocity. These are related to the geometry of the wave front as it

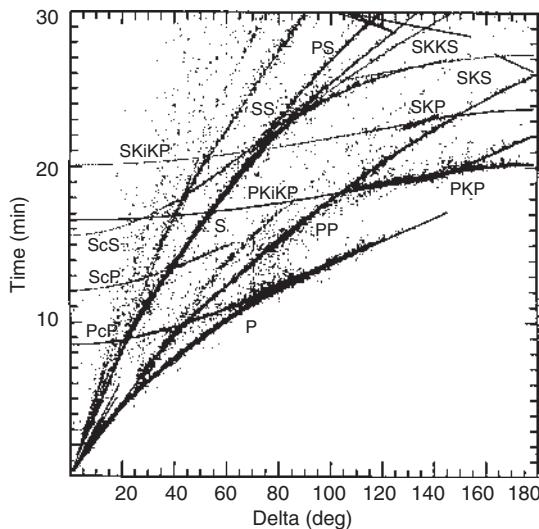


Figure 2 Observed traveltimes for P and S seismic phases as a function of epicentral distance in the Earth for shallow earthquake sources, along with the predicted (labeled) traveltime curves for a radially symmetric model of P-wave and S-wave velocity variations with depth. P and S are direct phases; PcP, ScP, and ScS reflect from the core–mantle boundary; PKiKP and SKiKP reflect from the inner core–outer core boundary; PP, SS, PS reflect once from the Earth’s surface; and PKP, SKP, SKS, SKKS are phases that traverse the Earth’s core. (From Kennett and Engdahl, 1991. Reprinted with permission from the Royal Astronomical Society.)

sweeps through the Earth and the velocity at a depth in the Earth where the wave turns back toward the surface and arrives at that particular distance. The smooth, concave downward curvature of P-wave and S-wave traveltimes directly implies smoothly increasing velocities with depth. The ray parameter can be estimated either from a smoothed traveltime curve or by direct measurement of relative arrival times across an array of closely spaced receivers.

Global observations of body-wave traveltimes, and measurements of slopes of the traveltime curves by seismic array analyses proliferated in the 1960s–1990s, with many radially symmetric Earth models for the lower mantle being produced (e.g., Chinnery and Toksöz, 1967; Hales *et al.*, 1968; Herrin, 1968; Johnson, 1969; Hales and Roberts, 1970; Randall, 1971; Sengupta and Julian, 1978; Uhrhammer, 1978; Dziewonski and Anderson, 1981; Kennett and Engdahl, 1991; Morelli and Dziewonski, 1993). While the variations in lower-mantle velocities among these models are less than 1%, there is still great importance in having an accurate reference model both for earthquake location procedures and for use as a background

model in tomographic analyses. Thus, efforts to improve the average lower-mantle parameters continue, with increasing quantities of data and variety of phase types being incorporated into the analysis (Masters *et al.*, 1999). All of these one-dimensional lower-mantle models have smooth velocity gradients like those in the PREM model (Figure 1).

The small variations between lower-mantle radial velocity models have still received much attention because any departure from homogeneity (as expected for self-compression of uniform composition material) would have major implications for possible chemical layering or phase changes. P and S velocities throughout the lower mantle above the D'' region are bounded to within about $\pm 0.1 \text{ km s}^{-1}$ in terms of an average model (e.g., Lee and Johnson, 1984). This tight bound (Figure 1) is consistent with the finding by Burdick and Powell (1980) that small features in ray parameter estimates from seismic arrays tend to vary azimuthally, and are not globally representative, with on average very smooth structure in the lower mantle being preferred for a one-dimensional model. There have been observations of reflections and converted phases from a velocity or impedance contrast near 900 km depth near subduction zones (e.g., Revenaugh and Jordan, 1991; Kawakatsu and Niu, 1994), but this appears to be a strongly laterally varying structure (Shearer, 1993), and may be associated with steeply dipping mantle heterogeneities (Niu and Kawakatsu, 1997; Kaneshima and Helffrich, 1998; Vinnik *et al.*, 1998a; Castle and Creager, 1999). Reports of arrivals reflected or scattered from other depths in the upper third of the lower mantle are numerous, but at this time there is no compelling evidence for significant laterally extensive layering of the lower mantle except near the top of the D'' region.

1.18.2.2 Surface-Wave/Normal-Mode Constraints

In addition to body-wave traveltimes, measurements of normal-mode eigenfrequencies play a major role in defining one-dimensional seismic velocity, and most importantly, density models for the lower mantle (*see also* Chapter 1.03). Normal modes correspond to standing patterns of P-wave and S-wave motions, and provide constraints on the structure appropriate for relatively long-period motions compared to body-wave arrival times. The motions of normal modes involve large volumes of rock, and the varying depth-sensitivity of different modes readily allows

for construction of one-dimensional models of the lower mantle. The large-scale motions allow the density structure to be sensed as well, particularly when a variety of modes are analyzed together to obtain velocity and density models. Important one-dimensional models for lower-mantle structure based largely on normal-mode observations include those of [Jordan and Anderson \(1974\)](#), [Gilbert and Dziewonski \(1975\)](#), [Dziewonski et al. \(1975\)](#), and [Dziewonski and Anderson \(1981\)](#). These models are compatible in basic structure with those obtained from body-wave analyses, but it was observed early on that there is some difference in absolute velocities between body-wave and normal-mode models. In the late 1970s, this baseline discrepancy was recognized to be the effect of dispersion due to intrinsic attenuation as waves traverse the Earth. This causes shorter period signals to sense slightly higher seismic velocities than longer-period signals. The development of phenomenological models for attenuation in the mantle allows an anelastic Earth model, such as PREM ([Figure 1](#)) to vary systematically in velocity as a function of wave period, reconciling body-wave and normal-mode observations (e.g., [Liu, et al., 1976](#); [Anderson et al., 1977](#); [Kanamori and Anderson, 1977](#); [Dziewonski and Anderson, 1981](#)).

By far the most important contribution to lower-mantle structure from normal modes is the resolution of density structure. Body-wave traveltimes provide indirect sensitivity to density, and only through use of the Adams–Williamson approach can seismic velocities be used to infer the density structure. The large volumes of rock in motion during normal-mode oscillations provide direct sensitivity to gravitational effects on the waves, and hence to density. Thus, the development of one-dimensional seismic models from normal-mode observations explicitly involves density structure. As for the seismic velocity models, the density structure in the lower mantle involves simple increase with depth ([Figure 1](#)), with density increasing from about 4.8 gm cm^{-3} at 800 km depth to 5.56 gm cm^{-3} just above the CMB. The normal-mode sensitivity is limited in terms of resolving any small discontinuities, but can bound the absolute levels over several hundred kilometer thicknesses to less than about 0.5% uncertainty for a one-dimensional model. This places some constraint on the degree of lower-mantle layering due to chemical density differences, although the likelihood that any deep layering may have large topographic variations induced by mantle flow complicates the interpretation of normal-mode constraints.

1.18.2.3 Attenuation Structure

The Earth is not perfectly elastic, and as seismic waves travel through the interior they undergo anelastic attenuation that gradually diminishes their amplitudes at a rate greater than that caused by geometric spreading (*see also* Chapter 1.21). The mechanisms responsible for anelastic losses are generally thermally activated micro-scale processes such as dislocation motions and grain boundary interactions (e.g., [Anderson, 1967](#); [Minster, 1980](#); [Minster and Anderson, 1981](#)). Lacking resolution of the micro-scale processes, seismologists use phenomenological models that account for the macroscopic effects of anelasticity, parametrizing the corresponding departures of wave behavior from that for a purely elastic medium. The most common parametrization of attenuation is in the form of a quality factor, Q , defined as the inverse of the fractional loss of energy, E , per cycle of oscillation: $1/Q = -\Delta E/2\pi E$. Lower values of Q correspond to stronger anelastic loss, or more attenuation. Infinite Q would correspond to elastic behavior. The finite Q encountered by a seismic wave in the lower mantle may vary from frequency to frequency because different mechanisms are activated for different timescales. Over a finite range of frequencies there will be a dispersive effect, with higher frequencies sensing an unrelaxed effective modulus relative to lower frequencies. This results in physical dispersion, the reason that short-period body waves sense slightly higher seismic velocities than long-period normal modes. The magnitude of this effect depends on the absolute value and frequency dependence of Q appropriate for a given wave motion.

The lower mantle has relatively high Q values for seismic waves, and determining the structure is rather difficult due to regional variations of strong attenuation in the upper mantle. Normal modes and averaged body-wave attenuation measurements place some constraints on the average Q values, but it is possible to satisfy most data with extremely simple models (e.g., [Anderson and Hart, 1978](#); [Dziewonski and Anderson, 1981](#); [Masters and Gilbert, 1983](#); [Widmer et al., 1991](#)). For example, the PREM model has S-wave quality factor $Q_\mu = 312$ throughout the lower mantle, whereas P-wave quality factor Q_α increases from 759 at 670 km depth to 826 at the CMB. While there is some evidence for a low- Q zone at the base of the mantle, this is not well-resolved because of strong tradeoffs with velocity gradients in the D" region. The detailed frequency dependence of attenuation in the lower mantle is not yet well resolved.

To give a sense for the anelastic dispersive effect associated with lower-mantle structure, we can consider the PREM S-wave velocities at a depth of 2271 km for periods of 1 s (7.055 km s^{-1}) and 200 s (7.017 km s^{-1}). The respective P-wave velocities are 13.131 km s^{-1} and 13.103 km s^{-1}). The dispersive effects are small, but physically must be present. Over long path lengths in the attenuating lower mantle, the small velocity differences integrate to give observable differences in body-wave and normal-mode observations that have to be accounted for. Thus, a realistic one-dimensional model of the lower mantle must include a seismic wave attenuation structure, and that intrinsically leads the velocity model to have frequency dependence. PREM is the primary one-dimensional model with this physical dispersion explicitly being included, although Montagner and Kennett (1996) consider frequency-dependent effects. Other single-frequency models such as ak135 (Kennett *et al.*, 1995) have improved the fit to certain seismic phases, notably core phases, but such models have not explicitly been reconciled across a broad frequency range.

1.18.3 Three-Dimensional Lower-Mantle Structure

One-dimensional Earth models are remarkably successful in predicting seismic wave traveltimes for paths traversing the lower mantle, typically accurate within a fraction of a percent for teleseismic P and S waves. This is a manifestation of the importance of gravity and chemical differentiation in producing a strongly radially stratified planet. Nonetheless, there are observable systematic traveltimes fluctuations at a given distance range that indicate deviations from a one-dimensional structure. Such fluctuations are particularly evident for waves traversing only the crust and upper mantle, where there are relatively strong heterogeneities. After suppressing the contributions from strong upper-mantle heterogeneity, using either laterally varying models or by computing differential traveltimes between phases observed at a given station, the scatter in P-wave traveltimes relative to predictions for a one-dimensional lower-mantle model is generally within $\pm 1\text{--}2$ s (for paths with traveltimes of 600–700 s), while for S-waves scatter is typically $\pm 4\text{--}6$ s (for paths with travel times of 1000–1200 s). There are some regions with late S-wave arrival time anomalies of up to 15–20 s attributed to lower-mantle paths (e.g., Ni and

Helberger, 2003a). These small variations in traveltimes indicate that an aspherical velocity structure exists in the lower mantle, and many seismological studies have attempted to constrain either global or regional heterogeneities in the lower mantle.

1.18.3.1 Seismic Tomography

Initial investigations of aspherical structure in the lower mantle utilized moderate-size sets of traveltime anomalies (e.g., Sengupta and Toksöz, 1976) or differential traveltimes (e.g., Jordan and Lynn, 1974; Lay, 1983) to detect systematic variations relative to standard one-dimensional models. The main challenges in resolving lower-mantle heterogeneity involve the uncertainty in earthquake source locations (typically these are approximated by solving the location problem assuming a one-dimensional velocity structure, which intrinsically leads to an incorrect location estimate and consequent artifacts in the residual arrival times) and the strength of upper-mantle heterogeneities (particularly near-source structures such as subducting slabs). These remain as vexing problems, and it is reasonable to believe that current estimates of deep-mantle heterogeneity are still biased by incomplete suppression of event location effects and upper-mantle heterogeneities. While strategies such as computing differential time anomalies (e.g., ScS – S, SKS – S, or PcP – P differential arrival times relative to one-dimensional model predictions are commonly used) can reduce source mislocation and near-source and near-receiver structural effects due to the similarity of the ray paths for the two phases in these regions, it remains possible that failure to account for strong lateral gradients in shallow structure causes erroneous interpretation of differential time anomalies as being due to deep-mantle heterogeneity. The long-term solution to this problem is the development of very accurate models for upper-mantle structure used in a self-consistent way with event locations. In general, this is not done in most of today's large-scale tomographic inversions, but progress is gradually being made.

Given large numbers of observations of seismic phases with good azimuthal and ray parameter coverage from an earthquake, the effects of source mislocation can be suppressed even if a one-dimensional model or low-resolution upper-mantle aspherical model is used. This can never be a perfect process unless one invokes *a priori* near-source information (the process of estimating the origin time

always removes a baseline term from the traveltimes leading to anomalies with fluctuating sign even when the true anomalies should be one sided). Seismic tomography uses the arrival time anomalies from many source–receiver combinations to invert for a parametrized version of mantle heterogeneity – ideally for well-sampled event populations where location effects are suppressed by coverage. In this case, the crossing coverage from multiple paths can build up the image of spatially varying velocity structure, although in almost every case the amplitude of the actual heterogeneity will be underestimated by the inversion model. This is the primary approach to imaging lower-mantle heterogeneity on large and small scales, although the requirement of well-resolved source locations is seldom met in practice, approximations in ray tracing are commonly made, and iteration to attain self-consistent event locations and aspherical models is performed in a minority of studies (e.g., Mégnin and Romanowicz, 2000). All results of lower-mantle seismic tomography must thus be viewed as having limited resolution at this time, and there is significant inconsistency between models. Even with these limitations, the implications of the current generation of models are profound.

One of the earliest fundamental contributions of global seismic tomography was the demonstration that coherent structure exists in the lower mantle on scale lengths of several thousand kilometers and that this unexpected configuration of deep heterogeneity can account for previously unexplained long-wavelength features in the Earth's geoid (e.g., Dziewonski *et al.*, 1977; Dziewonski, 1984; Masters *et al.*, 1982; Clayton and Comer, 1983; Hager *et al.*, 1985). Establishing this connection required both the development of global models and improved understanding of how mantle heterogeneities induce flow and deflection of boundaries that affect the geoid (Hager, 1984; Richards and Hager, 1984). While the early low-resolution tomographic models for the lower mantle have relatively strong spherical harmonic components from degrees 2–5, and proved remarkably successful in accounting for the long-wavelength geoid (see review by Hager and Richards, 1989), there has been continuing debate about the spectrum of lower-mantle heterogeneity. Are the long-wavelength patterns the result of truly diffuse structures or are they in part due to smoothed sampling of smaller scale, but very heterogeneous features such as slabs embedded in the lower mantle? If the latter is the case, the long-wavelength distribution of heterogeneity in the lower mantle

is more a consequence of the last few hundred million years of surface tectonics and associated plate subduction than a very long-term aspect of the lower-mantle convective regime (e.g., McNamara and Zhong, 2005). Similarly, if the long-wavelength patterns in surface hot spots reflect thermal plumes rising from the CMB, then the distribution of D" boundary layer instabilities may contribute to the present long-wavelength structure of the deep mantle.

Imaging of deep-mantle structure has advanced in resolution by increasing the size and ray path coverage of the data sets, and use of improved measurement and inversion approaches. There is significant convergence in recent deep-mantle tomographic shear-velocity models (e.g., Masters *et al.*, 1996, 2000; Li and Romanowicz, 1996; Grand *et al.*, 1997; Liu and Dziewonski, 1998; Ritsema *et al.*, 1999; Mégnin and Romanowicz, 2000; Gu *et al.*, 2001; Grand, 2002; Antolik *et al.*, 2003), all of which have substantial long-wavelength heterogeneities. The same is true for large-scale P-velocity models, although there is less agreement between models and somewhat less complete coverage of lower-mantle regions (e.g., Widjiantoro and van der Hilst, 1996; Bijwaard *et al.*, 1998; Vasco and Johnson, 1998; van der Hilst and Káráson, 1999; Bijwaard and Spakman, 1999; Boschi and Dziewonski, 1999, 2000; Zhao, 2001; Fukao *et al.*, 1992, 2001; Káráson and van der Hilst, 2001).

As the resolution of lower-mantle structure has improved with each new generation of global tomographic models, it has become clear that there are significant intermediate-scale features in the lower mantle. This had previously been deduced for localized regions by array studies or by analyses of differential traveltimes for phase pairs sensitive to lower-mantle structure (e.g., Jordan and Lynn, 1974; Lay, 1983), but the geometry and lateral extent of such features could not be resolved until large-scale tomographic models were produced. Recent high-resolution S-wave velocity (e.g., Grand, 2002) and P-wave velocity (van der Hilst *et al.*, 1997) models resolve a high-velocity tabular structure extending nearly vertically in the lower mantle beneath North America and South America and a similar elongate body beneath southern Eurasia, both of which extend to at least 1300–1600 km depth (Figure 3). The width of these features is not well resolved, but appears to be at least 500 km, and the anomalies are 1–2%, which is relatively high for this depth range in the mantle. These are usually interpreted as relatively

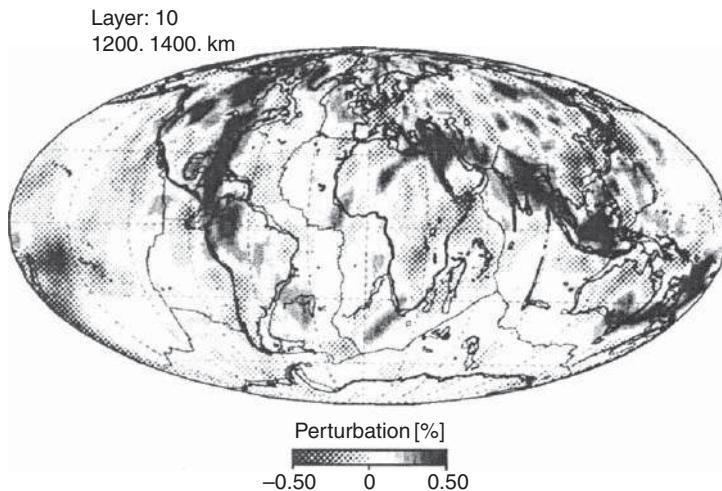


Figure 3 Horizontal section through a tomographic model of P-wave velocity structure near 1300-km deep in the lower mantle, obtained by inversion of ISC arrival times after careful processing for source depth determination. Solid dark areas correspond to relatively high velocities, with two major coherent features that correspond to tabular structures extending semivertically below southern Asia and eastern North America. These are inferred to be subducted slab material that has penetrated into the lower mantle. (From [van der Hilst et al., 1997](#)).

cold, sinking slab material that has penetrated into the lower mantle as the Americans moved westward and as the Tethys Sea closed, respectively. The aspherical seismic velocity structure in the mid-mantle near 1300 km depth is dominated by these elongate tabular high-velocity features, and it is likely that these contribute significantly to the strong long-wavelength patterns in spherical harmonic models that have lower resolution (see corresponding features in the lower-resolution models discussed by [Dziewonski et al. \(1993\)](#)). While there may be contributions to these structures from inadequately suppressed shallow-mantle structures, particularly strong near-source slab anomalies, the high-velocity regions do appear in models with different data sets, different model parametrizations, and varying source-receiver geometries, so it is very difficult to dismiss them as artifacts.

Below about 1600 km depth, tomographic models show less coherence, relatively weak-velocity anomalies, and tabular structures are not clearly imaged (e.g., [Grand et al., 1997](#)). Instead, the models tend to become dominated by horizontally extensive regions of high and low velocity with strong degree 2 and 3 patterns dominating in the lowermost mantle ([Figure 4](#)). The strength of the velocity heterogeneity increases in the lowermost 300–500 km of the mantle, particularly for shear waves ([Figure 5](#)). Lateral variations of $\pm 4\%$ in S-wave velocity and $\pm 1.5\%$ in P-wave velocity are observed. High shear velocities in the lowermost

mantle are found beneath circum-Pacific margins, although only in a few places is there apparent continuity of high-velocity features from the mid-mantle all the way to the CMB. The aspherical S-wave velocity models all display two large low-shear-velocity provinces located below the Central Pacific and the Southern Atlantic/Southern Africa/Southern India Ocean region. The latter two low-velocity regions appear to extend upward above the D'' region, possibly as much as 800–1000 km. These features have been called ‘superplumes’, given that their scale greatly exceeds that expected for isolated D'' boundary layer instabilities, and [Dziewonski et al. \(1993\)](#) call them the Equatorial Pacific Plume Group and the Great African Plume, respectively. Attributing dynamical significance to these features is complicated; low velocities may be caused by high temperatures or by chemical differences.

1.18.3.2 Dynamical Structures

While the geoid and some attributes of subduction zone morphology provide geodynamic constraints on lower-mantle dynamics, most of what we know about dynamical processes in the deep Earth derives from interpretations of seismic tomography. This is not a trivial undertaking because there are limitations in the spatial resolution of the tomographic models, and possible contributions from both thermal and

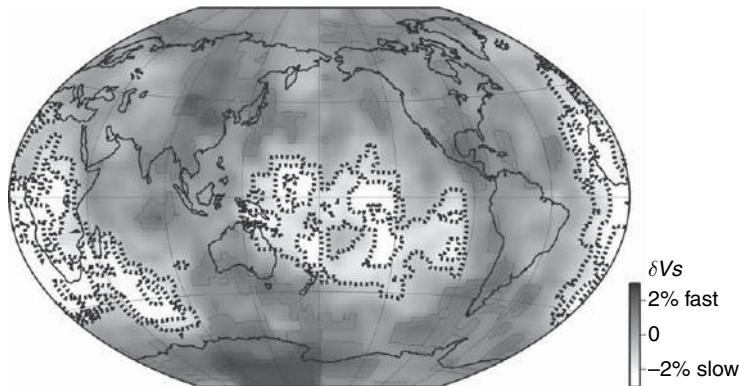


Figure 4 Representative large-scale mantle tomography for S-wave velocity structure (Grand, 2002) near the base of the mantle. Note the long-wavelength patterns of high velocities beneath the circum-Pacific and low velocities beneath the central Pacific and Africa. 1% contours are shown, with dotted lines highlighting the internal variations in the two large-low-shear-velocity provinces. Variations of $\pm 3\%$ are imaged by this and other models with similar spatial patterns. Note the contrast in scale length of predominant heterogeneities with the mid-mantle pattern in **Figure 3**.

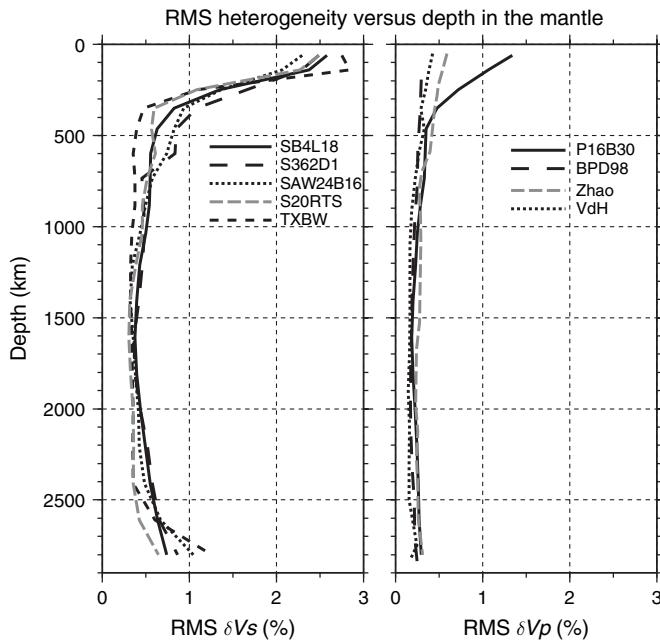


Figure 5 RMS velocity fluctuations at various depths in the mantle shear velocity models SB4L18 (Masters *et al.*, 2000), S362D1 (Gu *et al.*, 2001), SAW24B16 (Mégnin and Romanowicz, 2000), S20RTS (Ritsema and van Heijst, 2000), and TXBW (Grand, 2002) and in the mantle compressional velocity models P16B30 (Bolton, 1996), BPD98 (Boschi and Dziewonski, 1999), Zhao (Zhao, 2001), and VdH (Kárasón and van der Hilst, 2001).

chemical heterogeneities that are difficult to separate. Any interpretation of tomography requires a foundation in mineral physics characterization of material property dependence on temperature and chemistry for the high-pressure conditions of the deep Earth. It also requires geodynamic analysis to assess the deformation processes taking place, guided by the

seismological and mineral physics constraints on structure.

While the lower mantle does not appear to have internal layering, it has been proposed that the downward transition in heterogeneity pattern from a mid-mantle dominated by slab-like structures to a deep-mantle dominated by large-scale high- and

low-velocity features is caused by compositional stratification. The stratification could be in a thin layer essentially confined to D'' (e.g., Davies and Gurnis, 1986) or in a much thicker layer. In the latter model (see Kellogg *et al.*, 1999; van der Hilst and Kárasón, 1999), the lowermost mantle is compositionally distinct, being comprised of undifferentiated, 'primordial' mantle material which is then invoked as the source of isotopic anomalies sampled by major hot spot plumes. Downwelling slabs can depress the chemical boundary by hundreds of kilometers, deflecting it from a depth of around 2000 km. The postulated chemical boundary is not a strong reflector, and does not give rise to coherent features in the radially averaged mantle model. The density increase of the deep layer could be due to enrichment in iron or silica, which have competing effects on the velocity structure. This is a highly speculative model, but can at least reconcile the current observations of the deep-mantle seismic structure with geochemical observations. An alternative to chemical layering is the presence of distinct blobs of chemically distinct mantle mixed into the lower mantle, in the so-called plum-pudding model (Davies, 1984).

Significant improvement of our understanding of the lower mantle will come with reliable determination of density heterogeneity directly from simultaneous inversion of normal modes and gravity observations. A first step in this direction has been presented by Ishii and Tromp (1999). While preliminary, that study found that high-density material is piled up in regions of low shear velocity, presumably hot material beneath the Pacific and Africa. A significant chemical heterogeneity density effect is needed to offset any thermal buoyancy of the upwellings. Until the models improve it may be premature to associate the low shear velocities with upwellings, for chemical heterogeneity may be more important in the deep mantle (e.g., Deschamps and Trampert, 2003; Trampert *et al.*, 2004).

The existence of large-scale lower-mantle features enables formulation of simultaneous or iterative inversions for dynamical features such as the geoid and dynamic topography, and this has become a new area of research (e.g., Hager *et al.*, 1985; Hager and Clayton, 1989; Dziewonski *et al.*, 1993; Phipps Morgan and Shearer, 1993; Forte *et al.*, 1993, 1994; Mitrovica and Forte, 2004). The primary additional parameter that is constrained in such geodynamic models is the viscosity structure, and it is generally found in geoid inversions as well as contemporary studies of glacial rebound

analyses that the viscosity of the lower mantle is one to two orders of magnitude higher on average than that of the average upper mantle (e.g., Mitrovica and Forte, 1997, 2004). This may be a consequence of its mineralogy or it may represent the effect of devolatilization of the lower mantle during extensive melting early in Earth history.

Resolving small-scale structures in the lower mantle by seismic imaging is a complementary approach to imaging the dynamical system. Essentially, seismologists look for the strong patterns expected to accompany mantle convection that is extensively driven by boundary layer flow. The primary elements of this are expected to be cold, sinking lithospheric slabs, which should have relatively high seismic velocities and tabular geometries, and hot rising thermal plumes, which should have relatively low seismic velocities and cylindrical geometries. Extensive work has addressed lower-mantle penetration by subducting oceanic lithosphere, which clearly penetrates down through at least the transition zone in some regions, given the occurrence of deep earthquakes in subduction zones. Jordan (1977) introduced the complete residual sphere modeling formalism for seeking patterns in traveltimes residuals from individual earthquakes in subduction zones, which was further developed by Creager and Jordan (1984, 1986a). These studies demonstrated the sensitivity of the method to both upper-mantle and transition zone slab geometry and velocity heterogeneity, as well as to geometry of any steeply dipping slab extension into the lower mantle. Provocative results based on both P-wave and S-wave modeling suggested that slab penetration to depths of at least 1000 km with little distortion other than steepening dip occurs in the Kurile, Marianas, and Japan arcs.

Additional applications of the method were presented by Fischer *et al.* (1988, 1991), Zhou and Anderson (1989), Zhou *et al.* (1990), Boyd and Creager (1991), Ding and Grand (1994) and Pankow and Lay (1999). The method makes the limitations of arrival time data very explicit, as event location effects have a major affect on relative arrival time anomalies if the data coverage is limited (particularly true if only teleseismic observations are used). As noted previously, tomographic methods are strongly biased by this unless the data coverage is such that residual patterns faithfully preserve the slab effects (which may be true when extensive upgoing and downgoing data are included, but not otherwise). Residual sphere modeling also makes clear the importance of deep mantle and receiver corrections, and early applications did not

adequately address this issue. In fact, it has been shown that for S waves much of what was initially attributed to near-source effects is eliminated when improved path corrections are applied (e.g., Schwartz *et al.*, 1991; Gaherty *et al.*, 1991; Pankow and Lay, 1999; Deal and Nolet, 1999; Deal *et al.*, 1999). As global tomographic models improve, this will become less of a problem. Analysis of differential residual spheres for events in the same slab, as first introduced by Toksöz *et al.* (1971), is one approach that has been pursued to suppress distant effects rather completely (e.g., Takei and Suetsugu, 1989; Okano and Suetsugu, 1992; Ding and Grand, 1994; Pankow and Lay, 1999). These studies indicate that in some cases slabs may penetrate to depths of 800 km or more, but significant slab broadening may occur, as well as reduction of velocity heterogeneity to on the order of 2%, much weaker than in early residual sphere studies, and similar to the weak heterogeneity inferred when *a priori* slab structures are introduced into tomographic modeling.

Analysis of upwelling regions is even more challenging, in that seismological imaging of low-velocity features is intrinsically difficult due to wave diffraction and wave front healing effects. Nonetheless, global tomography studies suggest that there are concentrated low-velocity regions beneath some of the major surface hot spots (e.g., Montelli *et al.*, 2004; Zhao, 2004), but the confidence in such features remains limited because the results appear to depend heavily on how inversions are parametrized and damped. While the evidence for lithospheric slab penetration into the upper portion of the lower mantle is relatively strong, the direct imaging of any plume upwellings remains in its infancy. The complex structures near the base of the mantle which are described below include features that are attributed to plume-like instabilities from the thermochemical boundary layer above the CMB, but whether these features ascend to the surface remains to be established.

1.18.4 D" Region

The numerous efforts to image the detailed velocity structure below regions of subduction have been motivated as a test of the hypothesis of stratified versus whole-mantle convection, a key issue in mantle dynamics. Similarly, studying the structure of the D" region is largely motivated by the notion that this region may play a critical role in mantle convection, especially if there is significant heating from below (e.g., Lay and Garnero, 2004). While most estimates

of Earth's heat flow budget suggest that only 10–20% of the mantle's heat fluxes upward through the CMB, this is still substantial heating that will give rise to a thermal boundary layer. Internal heating, resulting from radiogenic materials distributed in the mantle, is expected to contribute to large-scale flow without producing concentrated structures, whereas boundary layer-driven flow is expected to yield both localized upwellings and downwellings, which provide specific targets for seismic imaging. D" structure is thus of particular interest as it serves as the lower boundary layer of the mantle convection system. It is now generally appreciated that the lowermost mantle is also of great importance to convection in the core and the resulting geodynamo (e.g., Glatzmaier *et al.*, 1999). The structure of D" appears to be very complex, and efforts to elucidate this complexity underlie many approaches to understanding core and mantle dynamics.

1.18.4.1 Large-Scale Seismic Velocity Attributes

There are several important seismological probes of the large-scale elastic velocity structure in the D" region. The large seismic velocity reductions across the CMB cause seismic wave energy to diffract into the geometric shadow zone at distances greater than 100°. Waves diffracted along the CMB are sensitive to the absolute velocities and the velocity gradients in the D" region, and have long been studied to constrain average and laterally varying structure (e.g., Alexander and Phinney, 1966; Sacks, 1966; Bolt *et al.*, 1970; Mondt, 1977; Doornbos and Mondt, 1979; Mula and Müller, 1980; Wysession and Okal, 1989; Wysession, 1996; Valenzuela and Wysession, 1998). These studies demonstrate that no single velocity structure sufficiently characterizes D" everywhere, and that in some cases there are strong negative velocity gradients in D" while in other places there are near-zero or positive velocity gradients. There are also changes in the relative perturbation of P-wave and S-wave velocities that are likely due to mineralogical or textural origin (e.g., Wysession *et al.*, 1999). Diffracted phases involve extensive lateral averaging of what appears to be a region rich in small-scale structure, and therefore yield limited resolution, but they do provide important input into large-scale tomographic models for D" because of their extensive spatial coverage (e.g., Kuo and Wu, 1997; Kuo *et al.*, 2000; Castle *et al.*, 2000; Bréger and Romanowicz, 2001).

The large-scale variations in D'' imaged by global seismic wave traveltimes tomography have surprising predominant degree 2 and 3 spherical harmonic components (e.g., Su *et al.*, 1994; Li and Romanowicz, 1996; Masters *et al.*, 1996; Dziewonski *et al.*, 1996; Kuo and Wu, 1997; Liu and Dziewonski, 1998; Kuo *et al.*, 2000). These models consistently show high shear velocities beneath the Pacific plate rim, with low velocities beneath the central Pacific and the southeastern Atlantic and southern Africa (Figure 4). This geometry results in a correlation between areas of slab subduction over the past several hundred million years (e.g., Lithow-Bertelloni and Richards, 1998) and high-velocity regions of D'', which could result if slabs sink to the base of the mantle while retaining enough thermal anomaly to produce high seismic velocities. Similarly, the low-velocity regions of D'' are generally located below regions with hot spots at the surface, suggesting that D'' upwellings may penetrate all the way to the Earth's surface.

1.18.4.2 Thermal Boundary Layer Aspect

To first-order, the lower mantle would appear to be a relatively uniform layer with properties varying radially largely due to self-compression, and with most heterogeneity concentrated in the D'' region above the CMB. The latter is consistent with the presence of a thermal boundary layer, as expected to result from heat fluxing out of the core into the mantle. The existence of a thermal boundary layer is strongly supported by calculations of energetics of the geodynamo, which suggest that there must be some net flux of heat out of the core to sustain the core convective regime. The precise amount is uncertain, with estimates ranging from 0.5 to 10 TW, and this amount must be added to heat conducted down the core adiabat (at least 2–5 TW) (e.g., Buffett, 2003). Thus, at least several TW, and possibly as much as 15 TW of heat are fluxing into the base of the mantle (about 44 TW flux through Earth's surface) (e.g., Kellogg *et al.*, 1999; Zhong, 2006).

The CMB is a major compositional boundary, therefore a conductive boundary layer must exist at the base of D'', with a superadiabatic temperature gradient allowing the heat to flux out of the core (e.g., Stacey and Loper, 1983). Such a thermal boundary layer is likely to thicken over time and to build-up instabilities that give rise to thermal plumes. The very low viscosity of the core-side alloy ensures that the CMB is maintained at nearly isothermal

conditions; temperature estimates of the CMB being in the range 2700–4200°C (e.g., Williams, 1998). If there is no thermal boundary layer in the transition zone or mid-mantle, the overall temperature drop across the lower-mantle thermal boundary layer is of the order of $1000 \pm 500^\circ\text{C}$, comparable to that across the lithosphere. Lateral variations in temperature in the deep mantle will produce varying thermal gradients above the CMB resulting in a variable heat flux boundary condition on the core. In places where the mantle temperatures are relatively low, the heat flux will be higher than in places where the mantle temperature is relatively high. This heat flux variation is likely to exert a long-term influence of the mantle on the core convective regime (Glatzmaier *et al.*, 1999; Buffett, 2003; Lay *et al.*, 2004b).

The thickness of the boundary layer is quite uncertain due to significant pressure effects on material properties and questions about the existence of partial melting and chemical heterogeneity, but the general expectation is that the boundary layer may be as much as a few hundred kilometers thick (thicker than the lithospheric thermal boundary layer) mainly due to pressure effects suppressing the thermal expansion coefficient near the base of the mantle. In this case, the D'' region corresponds, at a minimum, to a thermal boundary layer with a rapid increase in temperature with depth. This is likely to be manifested as a reduction of seismic velocity gradients relative to the mid-mantle, given the inverse dependence of velocity on temperature. This may be a subtle effect in general due to the pressure effects on thermal expansion, but if the temperature increase approaches the eutectic melting point of the lower mantle, very strong velocity reductions can occur for minor degrees of partial melting. Accurate determination of the velocity gradient above the CMB could thus be used to constrain the thermal boundary layer properties (e.g., Stacey and Loper, 1983; Lay and Helberger, 1983a; Doornbos *et al.*, 1986; Loper and Lay, 1995), but this approach encounters the immediate challenge that the velocity gradient appears to vary laterally.

Like the Earth's lithosphere, the thermal boundary layer at the base of the mantle is likely undergoing strong lateral and vertical flow, as upwellings produced by thermal boundary layer instabilities drain hot material from the boundary layer and downwellings replace it with cooler material. However, as a hot, low-viscosity boundary layer, there is probably much more small-scale structure in

the D" dynamical regime than is found in the cold, relatively stiff lithosphere. It is generally accepted that thermal heterogeneity within the boundary layer is partially responsible for the seismic inhomogeneity detected by Bullen (1949), and it likely contributes to the complexities described in this article, but it appears that more than just thermal heterogeneity is present.

As is true near Earth's surface, one cannot immediately attribute all variations in seismic velocities to the effects of temperature variations; chemistry may play an important, or even the major part, especially given the inhibiting effects of great pressure on temperature derivatives for seismic velocities. The juxtaposition of the lowermost mantle boundary layer adjacent to the largest density contrast in Earth heightens the probability that there is also chemical heterogeneity in the D" region. This may involve density-stratified residue from the Earth's core-formation process, ongoing chemical differentiation of the mantle, or even chemical reactions between the core and mantle (e.g., Lay, 1989; Knittle and Jeanloz, 1989; Goarant *et al.*, 1992; Jeanloz, 1993; Manga and Jeanloz, 1996). The probability of both thermal and chemical heterogeneity existing within the lowermost mantle prompts consideration of the region as a thermochemical boundary layer (e.g., Lay, 1989; Anderson, 1991; Lay *et al.* 2004b), much as the Earth's lithosphere must be considered a thermochemical boundary layer due to large-scale chemical variations between oceanic and continental regions. The evidence for a thermochemical boundary layer is provided by several seismological attributes of the D" region, as described in the next few sections.

1.18.5 D" Discontinuities

Detailed studies of teleseismic waveforms indicate that P-wave and S-wave velocity structures both have a 0.5–3.0% velocity discontinuity at many locations near the top of the D" region (the top of D" is not precisely defined, and many researchers take it to correspond to either where there is a discontinuity or to the onset of a change in velocity gradient, somewhere in the range from 50 to 350 km above the CMB). This feature is often called the D" discontinuity (e.g., Wysession *et al.*, 1998), and representative shear velocity structures obtained by waveform modeling are shown in Figure 6. These models, obtained for distinct regions of D", involve a 2.5–3% shear velocity increase at depths from 130 to 300+ km above the CMB

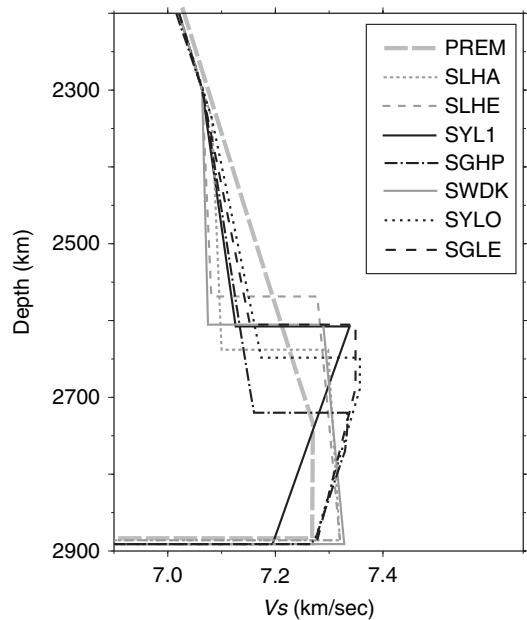


Figure 6 Radial profiles of S-wave velocity in the lowermost mantle: PREM (Dziewonski and Anderson, 1981), SLHE, SLHA (Lay and Helberger, 1983a), SYL1 (Young and Lay, 1987a), SGHP (Garnero *et al.*, 1988), SWDK (Weber and Davis, 1990), SYLO (Young and Lay, 1990), SGLE (Gaherty and Lay, 1992). The discontinuity models represent localized structures, determined for spatially limited regions of the D" layer, the locations of which are indicated in Figure 8(a). Shear velocity increases of 2.5–3.0% are found in regions under Eurasia (SWDK, SGLE), Alaska (SYLO), Central America (SLHA), the Indian Ocean (SYL1), and the central Pacific (SGHP). The velocity increase is typically modeled as a sharp discontinuity, but it may be distributed over up to 50 km in depth. Decreased velocity gradients above the discontinuity may exist, but are artifacts of the modeling in most cases. The reduction of velocity below the discontinuity in more recent models (orange), may be real, but may be an artifact of modeling a heterogeneous region with a one-dimensional model. The variations in depth of the discontinuity are uncertain due to the lack of constraint on velocity above and below the discontinuity, but some variation appears to exist.

that is laterally extensive over intermediate-scale (500–1000 km) regions. Wysession *et al.* (1998) review the many studies of this structure, noting that there are substantial inferred variations in depth of the velocity discontinuity. Typically, S-wave velocity increases are larger than P-wave velocity increases, with the latter usually being 0.5–1.0%, though some models do propose 3% discontinuities (e.g., Wright *et al.*, 1985; Weber and Davis, 1990). The increase in velocity at the top of D" may be distributed over up to 30–50 km in depth, or it may be very sharp (e.g., Lay and Helberger, 1983a; Young and Lay, 1987a; Lay and Young, 1989).

1.18.5.1 Seismic Wave Triplications

The velocity increases at the top of D'' are detected by reflections and triplications, which arrive ahead of the core-reflected PcP and ScS phases (e.g., Wright and Lyons, 1975; Lay and Helmberger, 1983a, 1983b; Wright *et al.*, 1985; Young and Lay, 1987a, 1990; Gaherty and Lay, 1992; Weber and Davis, 1990; Houard and Nataf, 1993; Weber, 1993; Kendall and Shearer, 1994; Kendall and Nangini, 1996; Ding and Helmberger, 1997; Thomas and Weber, 1997; Kohler *et al.*, 1997; Reasoner and Revenaugh, 1999; Kito and Krüger, 2001; Thomas *et al.*, 2002, 2004; Lay *et al.*, 2004a; Kito *et al.*, 2004; Avants *et al.*, 2006b; Sun *et al.* 2006). The clearest observations of deep-mantle triplications are from distances of 65° – 95° , where the critical angle interaction with the velocity increase greatly enhances the amplitudes of the reflected signals relative to pre-critical distance ranges. Examples of the triplication arrival are shown in **Figure 7**, with broadband shear wave data having a strong arrival between S and ScS phases that would not be predicted by a smooth velocity model such as PREM. The reflector that produces this extra arrival varies globally in depth by several

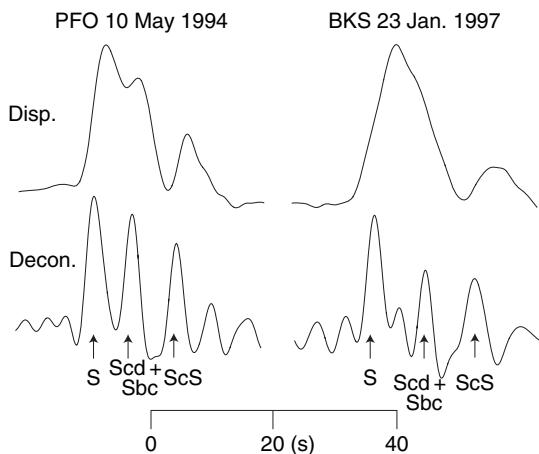


Figure 7 Examples of broadband SH displacements at stations PFO ($\Delta = 79.8^\circ$) and BKS ($\Delta = 79.8^\circ$) for two deep South American events. Instrument-corrected ground displacements (Disp.) are shown in the top row. The first arrival is S, and about 15–20 s later, ScS, the reflection from the core–mantle boundary arrives. Deconvolution by the event-averaged source wavelets and low pass filtering below 0.3 Hz yields the spike-trains below for each record (Decon.). The intermediate arrival, Scd + Sbc (SdS), which is produced by triplication from a deep-mantle velocity increase, is clearly isolated in the deconvolutions. Reproduced from Lay T, Garnero EJ, and Russell S (2004a) Lateral variation of the D'' discontinuity beneath the Cocos Plate. *Geophysical Research Letters* 31: L15612 (doi:10.1029/2004GL020300).

hundred kilometers (e.g., Kendall and Shearer, 1994), and appears to have regional-scale lateral variations of on the order of a hundred kilometers that may produce scattering rather than simple reflections (e.g., Weber, 1993; Kruger *et al.*, 1995; Lay *et al.*, 1997; Scherbaum *et al.*, 1997; Yamada and Nakanishi, 1998; Freybourger *et al.*, 1999; Emery *et al.*, 1999; Thomas *et al.*, 2004; Lay *et al.*, 2004a; Hutko *et al.*, 2006).

It has been argued that the D'' discontinuities are actually globally extensive, with lateral variations in depth and strength being the result of lateral temperature variations and interactions with upwelling and downwelling flow (e.g., Nataf and Houard, 1993; Sidorin *et al.*, 1998, 1999). Many studies indicate that no discontinuity is present for certain regions (e.g., Wysession *et al.*, 1998), but most of these fail to establish whether the data truly preclude the presence of a velocity increase. Others studies have questioned whether there is a first-order discontinuity at all, preferring the notion that the extra seismic arrivals involve scattering from strong velocity heterogeneities as imaged in long-wavelength tomography models (e.g., Schlittenhardt *et al.*, 1985; Cormier, 1985; Haddon and Buchbinder, 1986; Liu *et al.*, 1998). The latter possibility requires large increases in the magnitude of the tomographic heterogeneities and/or sharpening of the velocity gradients, but there must be some relationship between the volumetric structure and the discontinuities (Ni *et al.*, 2000). It has been demonstrated that scattering of SV energy into SH (Cormier, 1985) is not a likely explanation for the extra phases interpreted as triplication arrivals (Lay and Young, 1986). Young and Lay (1987b) show that velocity decreases, as proposed by Haddon and Buchbinder (1986) cannot explain the data either. Thin high or low-velocity lamella models appear to fit some P-wave observations at least as well as first-order velocity discontinuity models (Weber, 1994; Thomas *et al.*, 1998; Freybourger *et al.*, 1999), but this has not been demonstrated convincingly for S-wave observations. An alternative is a transition in the heterogeneity spectrum with depth, possibly linking a gradient in anisotropy to the reflector (e.g., Cormier, 2000).

The regions with the strongest evidence for a shear wave velocity discontinuity are highlighted in **Figure 8(a)**. Wysession *et al.* (1998) show individual data sampling in greater detail. Some of these areas also have evidence for a P-wave velocity discontinuity, but in some regions, such as under Alaska and Central America, any P-wave velocity discontinuity must be at or below the detection threshold of about

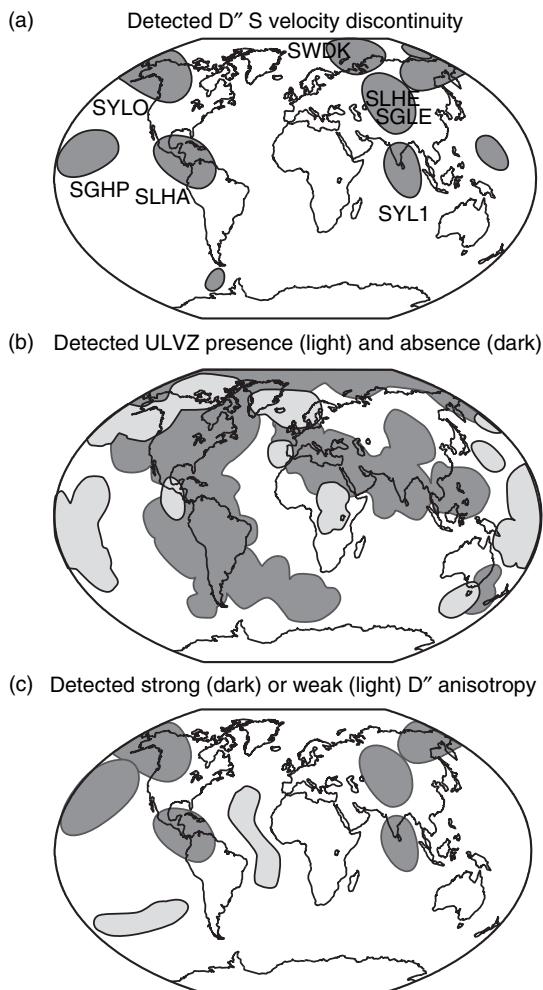


Figure 8 Maps summarizing spatial variations of seismic wave characteristics of D''. (a) Regions where regional shear velocity discontinuities have been observed in large numbers of data, typically with 2–3% increases in velocity at depths from 200–300 km above the CMB (see labeled models in **Figure 6**). (b) Regions where ULVZ structures at the CMB have been detected or not, primarily based on SPdiffKS observations and assuming a Fresnel zone appropriate for a horizontal layer. (c) Regions where regional studies of D'' shear wave splitting have been conducted. Most areas exhibiting splitting have waveforms compatible with vertical transverse isotropy, with decoupling (or only weak coupling) of the transverse and longitudinal components of the S wavefield, with 1–2% faster transverse components. Modified from Lay T, Garnero EJ, and Williams Q (2004b) Partial melting in a thermo-chemical boundary layer at the base of the mantle. *Physics of the Earth and Planetary Interiors* 146: 441–467, with permission of Elsevier.

0.5% (Young and Lay, 1989; Ding and Helmberger, 1997; Reasoner and Revenaugh, 1999). Stacking of array data is necessary to detect such small discontinuities, and many ‘non-observations’ reported for

individual seismograms must be viewed as inconclusive. The S-wave observations tend to be longer wavelength than the P-wave data used to look for the discontinuity, so it is viable that a transition zone several tens of kilometers thick may explain the absence of high-frequency pre-critical P-wave reflections. Most areas with strong evidence for an S-wave reflector are in the high-velocity regions beneath the circum-Pacific; the primary exception is under the central Pacific, where an S-wave velocity discontinuity is observed in a region having large-scale low D'' shear velocities (e.g., Garnero *et al.*, 1993b; Russell *et al.*, 2001; Avants *et al.*, 2006b). As tomographic resolution of large-scale structure improves, the existence of strong lateral heterogeneities within circum-Pacific and central Pacific regions is being recognized (Bréger and Romanowicz 1998; Bréger *et al.*, 2001; Wysession *et al.* 2001; Fisher *et al.* 2003; Hung *et al.*, 2005), so simple bimodal characterizations of the discontinuity structure may be misleading.

It remains important to determine whether there is any density increase in D'' accompanying the seismic velocity increases, as this could help to resolve whether a chemical change or phase change is involved, either of which could strongly affect the dynamics of the boundary layer (e.g., Sleep, 1988; Kellogg, 1997; Montague *et al.*, 1998; Hansen and Yuen, 1988; Tackley, 1998). Unfortunately, wide-angle triplication observations have very limited sensitivity to density contrasts, so this is an exceedingly difficult attribute to resolve.

1.18.5.2 Phase Change in Perovskite

As noted above, the predominant upper-mantle minerals all exist in the remarkably stable magnesium-silicate $(\text{Mg}, \text{Fe})\text{SiO}_3$ perovskite form at lower-mantle conditions. The physical properties of magnesium-silicate perovskite have been extensively studied by experiments and theory and it is accepted that there are no further phase changes for this mineral over a several thousand kilometer depth range. However, high-pressure experiments conducted in Japan (Murakami *et al.*, 2004) first demonstrated that for pressures greater than about 120 GPa, corresponding to depths in the lowermost mantle within a few hundred kilometers of the CMB, magnesium-silicate perovskite undergoes a transition to a new mineral structure, called post-perovskite. This phase transition is widely viewed as the probable explanation for the D'' discontinuity, as it can plausibly account for salient features of the seismic observations (Lay *et al.*, 2005).

The phase transition from perovskite to post-perovskite does not involve a change of mineral composition, but the post-perovskite phase is about 1–1.2% denser and has higher shear modulus than perovskite. X-ray diffraction studies of experimental samples at high pressures establish the existence and the change in volume of the post-perovskite phase, and provide constraints on the atomic lattice for theoretical modeling of the precise crystal structure of the mineral (Murakami *et al.*, 2004; Itaka *et al.*, 2004; Oganov and Ono, 2004; Tsuchiya *et al.*, 2004a; Stackhouse *et al.*, 2005b). Molecular dynamics modeling is required to predict the crystal structure of the post-perovskite phase, as direct measurements on samples are not yet viable. The theoretical calculations provide many important physical characteristics of post-perovskite. This includes prediction of the slope of the phase boundary in pressure–temperature (P – T) space, called the Clapeyron slope. The computed Clapeyron slope for the pure Mg end-member composition, MgSiO_3 , is about 7.5 MPa K^{-1} , a rather large positive value typical of the post-perovskite structure (Tsuchiya *et al.*, 2004a; Hirose and Fujita, 2005). Experiments suggest the slope may be as large as 11.5 MPa K^{-1} (Hirose *et al.*, 2006). This indicates that the phase boundary should occur at lower pressure (shallower in the mantle) in regions that are relatively lower temperature. Large variations in the depth of the phase transition could thus result from the strong thermal heterogeneity expected to exist in the vicinity of the thermal boundary layer in the lowermost mantle (Lay *et al.*, 2005).

Numerical calculations also predict the crystal elasticity of post-perovskite for lower-mantle P – T conditions, providing estimates of the seismic P-wave and S-wave velocities. The P-wave velocity changes little relative to that for perovskite as a result of competing effects of increasing shear modulus, increasing density, and decreasing bulk modulus (Wookey *et al.*, 2005); however, the S-wave velocity is about 2% faster than for perovskite. If the transition from perovskite to post-perovskite is confirmed to occur over a small pressure (depth) range, the resulting rapid increase in S-wave velocity is expected to produce a velocity increase that can reflect shear wave energy. This could account for the shear velocity discontinuities shown in Figure 6 (e.g., Tsuchiya *et al.*, 2004b; Wookey *et al.*, 2005). The theoretical models of elasticity also predict anisotropic properties of the post-perovskite crystals. These differ significantly from those for perovskite in low-

temperature calculations, with increasing temperature reducing the differences, but still allowing a contrast in anisotropic properties under deep-mantle conditions (e.g., Stackhouse *et al.*, 2005b; Oganov *et al.*, 2005; Merkel *et al.*, 2006).

The pioneering experimental and theoretical work on post-perovskite was performed for the pure magnesium (MgSiO_3) end-member, but effects of the presence of iron (Fe) and aluminum (Al) have now been explored experimentally and theoretically (Mao *et al.*, 2004; Akber Knutson *et al.*, 2005; Tateno *et al.*, 2005; Stackhouse *et al.*, 2005a, 2006; Mao *et al.* 2006). It is believed that lower-mantle silicates probably contain 10–15% iron substitution for magnesium. Initial work suggested that having iron in the post-perovskite mineral should reduce the pressure of the phase transition, such that it may occur hundreds of kilometers shallower in the mantle than for an iron-free mineral (Mao *et al.*, 2004). These results have been contested in experiments that find less pressure effect due to inclusion of Fe (Hirose *et al.*, 2006). Theoretical predictions of the effects of Al substitution for both Mg and Si in the crystal lattice suggests that there may be a significant depth range (a few hundred kilometers) over which perovskite and post-perovskite can coexist, which would reduce any velocity discontinuity, weakening seismic wave reflections from the transition (Akber-Knutson *et al.*, 2005; Tateno *et al.*, 2005).

Lower-mantle rocks, like all rocks in the Earth, will involve an assemblage of mineral phases, with variations in crystal size and rock fabric as a result of solid-state convection. While there has been some experimental work done on real rock samples at lower-mantle pressures and temperatures with the post-perovskite phase being observed (Murakami *et al.*, 2005), full assessment of coexisting multi-phases is just beginning to be explored. For example, the properties of ferro-periclase ($\text{Mg},\text{Fe}\text{O}$) are important, especially the partitioning coefficient of iron between perovskite and ferro-periclase (e.g., Kobayashi *et al.*, 2005). Recent experimental work (Badro *et al.*, 2003, 2004; Lin *et al.*, 2005) indicates that at high pressure, Fe, normally in its high-spin state in the lower mantle, will prefer to be in a low-spin state in the lowermost mantle, which will favor iron partitioning into ferro-periclase rather than perovskite. This Fe spin-transition may occur at depths similar to the post-perovskite phase boundary so iron partitioning may affect the post-perovskite composition (Sturhahn *et al.*, 2005). Thermal, electrical, and mechanical transport properties of

lower-mantle rocks will be strongly influenced by iron distribution, thus, future work on realistic assemblages under high P - T conditions is very important for assessing the effects of the precise composition of post-perovskite in the Earth.

Subducted oceanic slab material should be relatively low temperature compared to surrounding ambient mantle, and if it penetrates to the base of the mantle, it may preferentially undergo transition to post-perovskite, resulting in a reflecting surface at the phase change within slab material, even if the boundaries of the slab are not strong reflectors. Post-perovskite may exist in large patches of lower-mantle material cooled by recently subducted slab material, and as this heats up over time the material may change back to perovskite. If the pattern of heterogeneity in **Figure 4** indicates relative temperatures (rather than a compositional change), low-velocity regions should be hotter, and therefore any post-perovskite phase transition may occur at greater depth or not at all in the low-shear-velocity regions (Helberger *et al.*, 2005). Seismologists are seeking to establish whether the low-shear-velocity regions have any S-wave velocity discontinuity, but there is so far little evidence for this other than under the central Pacific (e.g., Russell *et al.*, 2001), and that may be for a region near the margin of the low-shear-velocity province. It is interesting to note that while the volumetric shear velocity in the central Pacific is relatively low, the discontinuity, while highly variable, is not located much deeper than in circum-Pacific regions, contrary to the predicted thermal effect. Compositional effects may be competing with thermal effects on the phase transition in this region.

The CMB is likely to be at a temperature too high for post-perovskite to be stable, so there may be a thin basal layer with rapidly increasing temperature below regions cooled by slab material, in which the minerals transform back to perovskite (Hernlund *et al.*, 2005). A second velocity discontinuity with a velocity decrease should be present if this is the case, but this is seismically much more difficult to observe than a velocity increase because there is no critical angle amplification (Flores and Lay, 2005). Waveform stacking is essential for confident identification of any small velocity decreases in D''. Stacking of ScS data traversing the high-velocity region under the Cocos plate does not reveal any negative velocity discontinuity below the positive velocity increase at the top of D'', but similar stacking for data traversing the central Pacific does show a sharp decrease about 60 km above the CMB (Avants *et al.*, 2006a, b).

The large positive Clapeyron slope of the post-perovskite phase boundary in the presence of lateral temperature differences at the base of the convecting mantle may influence the generation of boundary layer instabilities. Warmer regions of the boundary layer will have a thinner layer of dense post-perovskite mineralogy, while colder regions of the boundary layer will have a thicker layer of the denser material. This thermally induced topography on the phase boundary is like that near the 410-km olivine/Wadsleyite phase transition, and in both cases the pattern promotes flow of material across the boundary layer (as the elevated dense material sinks it pulls down overlying material that transforms to the denser phase). Because the Clapeyron slope for the deep-mantle transition is about twice that of the upper-mantle transition the effect is enhanced, and convection models that include the post-perovskite transition have quite unstable lower thermal boundary layers that tend to generate vigorous deep-mantle flow (e.g., Matyska and Yuen, 2004; Nakagawa and Tackley, 2004). Seismological mapping of the phase boundary can thus provide a probe of the thermal and dynamical processes in the lowermost mantle.

1.18.6 Large Low-Shear-Velocity Provinces

The two large regions of low shear velocity in the lowermost mantle located beneath the south-central Pacific and southern Africa/southern Atlantic/southern Indian Ocean regions (**Figure 4**), are particularly unusual structures. Their lateral extent is far greater than might be expected for a hot upwelling plume from a thermal boundary layer, giving rise to the label ‘superplumes’. However, attaching dynamical attributes to these regions based on the sign of their velocity anomaly may be misleading. For example, the continents have comparably large-scale regions of relatively high-shear-velocity material in the lithosphere, and one could thus infer that they are cold, sinking regions, whereas the reality is that they are chemically buoyant. The deep-mantle anomalies have much stronger S-wave velocity reductions than P-wave velocity reductions, which suggests that some chemical change may be involved. The uncertain thermochemical nature of the large low-shear-velocity provinces (LLSVPs) warrants a dynamically neutral name.

There are also smaller-scale regions with low seismic velocities in the lower mantle which may be consistent with plumes rising from the thermal boundary layer (e.g., Montelli *et al.*, 2004; Zhao, 2004), and it remains to be determined whether these are distinct from the LLSVPs. For example, while the tomographic model of Ritsema *et al.* (1999) does not have a low-shear-velocity zone in the lower mantle beneath Iceland, Bijwaard and Spakman (1999) present a P-wave velocity image with low velocity under Iceland all the way to the CMB, and Helmberger *et al.* (1998) find very low S-wave velocities in D" beneath Iceland. Goes *et al.* (1999) find a low P-wave velocity structure beneath Europe from 660 to 2000 km depth, which they invoke as the source of small plumes in the upper mantle associated with volcanism in Europe. Smaller-scale plume or slab features that are below the current resolution of global seismic tomography, but can be resolved in regional scale inversions (e.g., Wysession *et al.*, 2001; Hung *et al.*, 2005) exist in the D" region as well. Innovative scattering analysis or array imaging may prove to be the only means by which to constrain even smaller scale structures (e.g., Ji and Nataf, 1998; Tilmann *et al.*, 1998; Tibuleac and Herrin, 1999). The characterization of LLSVPs is limited, but more detailed than for any of the smaller-scale structures, so this section will focus on them.

1.18.6.1 Seismic Velocity Properties

The existence of the LLSVPs was first indicated by 'mantle shear wave velocity tomography models' (e.g., Dziewonski *et al.* 1993), and there is fairly good consistency amongst recent models for the large-scale structure (e.g., Ritsema *et al.*, 1999; Masters *et al.*, 2000; Mégnin and Romanowicz, 2000; Gu *et al.*, 2001; Grand, 2002). The global distribution of sources and permanent seismic stations limits the resolution of velocity gradients and total extent of the LLSVPs under Africa (**Figure 9**) and the Pacific, so deployments of portable instruments have been important for detailed differential traveltimes analyses and waveform modeling used to improve resolution of LLSVP structure.

Ritsema *et al.* (1998) and Ni and Helmberger (2003a,b) find that low-shear-velocity structure under southern Africa involves 3% anomalies and strong lateral gradients, both of which are more pronounced than in tomographic models. The LLSVP model they advance extends upward about 800–1200 km from the CMB, so the anomalous

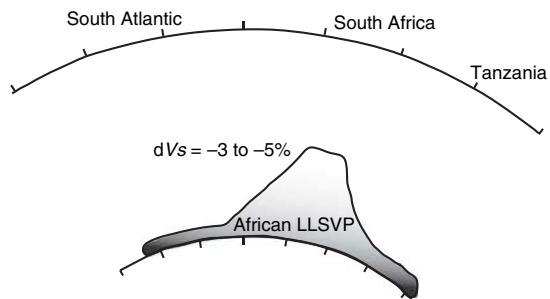


Figure 9 A cross-section through the LLSVP beneath Africa and the southern Atlantic, indicating the region of anomalously low shear velocities. The tick marks are 10° increments along a great-circle arc treading from southwest (left) to northeast (right). The velocity anomaly is about -3% in the shallower part of the structure, and may increase to about -5% in the D" region. The geometry of the structure is constrained by S, ScS, and SKS ray paths from various azimuths recorded at mainly African stations. The structure has the appearance of an up-swept pile that is about 4000 km wide at the base and extends 1300 km upward from the CMB. Reproduced from Wang Y and Wen L (2006) Geometry and P- and S- Velocity structures of the 'African Anomaly'. *Journal of Geophysical Research* (in press).

material is not confined to D". Even stronger anomalies are reported in the D" region below the southeastern Atlantic and southern Indian Ocean, with 1–10% S-wave velocity reductions, increasing with depth across a 300-km thick layer (Wen, 2001; Wen *et al.*, 2001; Wang and Wen 2004, 2006). Intermediate estimates of shear velocity reductions (1–7%) under the south Pacific LLSVP have been reported (e.g., Tanaka, 2002; Toh *et al.* 2005; Ford *et al.* 2006) and the western Pacific boundary of the LLSVP has been constrained by He *et al.* (2006).

There are very strong lateral gradients in seismic velocity structure in D" on the margins of the LLSVPs that seem incompatible with thermal variations alone, unless there is a superimposed chemical or melting effect (e.g., Ni *et al.*, 2002; Wen *et al.*, 2001; Toh *et al.*, 2005; Ni *et al.*, 2005). Even in the mid-mantle the lateral gradients remain strong, which is difficult, if not impossible, to explain by simple thermal gradients (e.g., Ni *et al.*, 2002). Given the reduction of the sensitivity of shear velocity to temperature at deep-mantle pressures, lateral thermal changes of 500–1000° over ~100 km are needed to account for the observed velocity anomalies, which could lead to the onset of partial melting which can strongly reduce velocities (Lay *et al.*, 2004b). But chemical variations appear to be important in LLSVPs, so the temperature contrasts may be far lower.

One of the key indications that LLSVPs involve chemical heterogeneity comes from comparisons of P-wave and S-wave velocities. Generally, global tomography models find good correlation between P-wave velocity and S-wave velocity structures in the lowermost mantle (e.g., Masters *et al.*, 2000; Antolik *et al.* 2003); however, this correlation appears to break down in certain regions, such as beneath the northern Pacific, where P-wave velocity anomalies tend to be positive and S-wave velocity anomalies tend to be negative. A south-to-north decrease in the P-wave/S-wave velocity ratio has also been found using diffracted waves traversing D" below the northern Pacific (Wysession *et al.*, 1999). While the sampling of the lowermost mantle remains relatively poor for P-waves (S-wave phases such as ScS and SKS greatly augment the deep-mantle S-wave sampling), the LLSVPs do tend to have low-velocity expressions in global P-wave models. However, it is important to consider the relative strength of the anomalies.

Shear velocity models show markedly stronger increases in RMS velocity heterogeneity in the lowermost 300 km of the mantle than do compressional velocity models, although the various models do differ in the extent to which shear velocity heterogeneity is concentrated toward the CMB (Figure 5). Even for well-correlated P-wave and S-wave velocity models (e.g., Masters *et al.*, 2000), this raises the possibility of distinct behavior for P-waves and S-waves due to competing thermal and chemical variations, coupled with the possible presence of low degrees of partial melting (Lay *et al.*, 2004b; Simmons and Grand, 2002). Indeed, the variability in velocity ratios and occasional decorrelation of P-wave and S-wave anomalies provide strong evidence that thermal effects alone cannot explain all D" seismic observations.

Simultaneous inversions of P-wave and S-wave data have been performed in attempts to isolate bulk sound velocity variations from shear velocity variations (e.g., Su and Dziewonski, 1997; Kennett *et al.*, 1998; Masters *et al.*, 2000; Antolik *et al.*, 2003; Resovsky and Trampert, 2003; Trampert *et al.*, 2004), but there are significant discrepancies between these models, perhaps as a consequence of incompatible resolution of P-wave and S-wave structures on a global basis. Direct comparisons of P-wave and S-wave traveltimes on specific paths support the possible decorrelation of these elastic velocities for localized regions within D" (e.g., Saltzer *et al.*, 2001; Lay *et al.*, 2004b), as well as reaffirming the

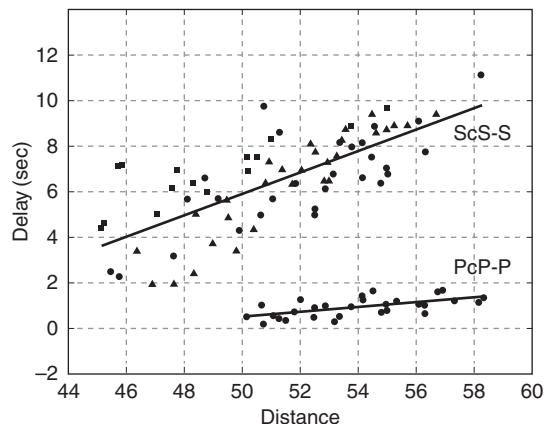


Figure 10 Differential traveltimes for ScS-S and PcP-P for paths sampling the southern margin of the African LLSVP. The S waves have much larger relative times, requiring shear velocity decreases 2 to 2.8 times stronger than the compressional velocity reductions depending on the depth extent of the anomalous region. This relative behavior is stronger than expected for a thermal variation in uniform lower-mantle chemistry, and requires either a compositional effect or a contribution from partial melting. Reproduced from Simmons NA and Grand SP (2002) Partial melting in the deepest mantle. *Geophysical Research Letters* 29 (10.1029/2001GL013716).

greater variations for S-wave velocities than P-wave velocities in LLSVPs (Figure 10; e.g., Tkalcic and Romanowicz, 2001; Simmons and Grand, 2002). The overall result is that LLSVPs have a bulk-sound-velocity anomaly that is anticorrelated with the S-wave velocity anomalies, and this dominates the pattern of the large-scale inversions for bulk-sound-velocity anomalies. This behavior requires an increase in incompressibility that contrasts with a decrease in rigidity in the LLSVPs. While this type of behavior is not necessarily unique to LLSVPs, it is generally accepted that at least part of (and possibly all of) their shear velocity anomaly is due to chemical anomaly, possibly involving enrichment in iron (Trampert *et al.*, 2004).

There is also some indication that density heterogeneity exists at the base of the mantle based on analysis of normal modes, and that on a large scale, dominated by the two LLSVPs, it is anticorrelated with shear velocity (and, hence, positively correlated with bulk velocity models), favoring chemical heterogeneity (Ishii and Tromp, 1999; Trampert *et al.* 2004). Thus, LLSVPs may be denser than surrounding mantle, and hence dynamically stabilized even if they are hotter than their surroundings; a situation inverse to that for continents. This remains a topic of

much uncertainty (e.g., Romanowicz, 2001; Kuo and Romanowicz, 2002), and resolving the density structure is critical for assessing whether LLSVPs are buoyant or not.

1.18.6.2 Thermal-Chemical Interpretations

The very presence of the LLSVPs in the deep mantle at this stage of the Earth's evolution suggests that unless they are being replenished by some process, such as segregation of former oceanic crustal components, they are likely to be very long-lived, and not particularly buoyant (e.g., Ni and Helmberger, 2003a). Their large vertical extent certainly could reflect some thermal buoyancy, perhaps in competition with chemical negative buoyancy, but the LLSVPs may also represent mounds of low-velocity chemical heterogeneities piled up under large-scale mantle upwellings (McNamara and Zhong, 2004, 2005). If the chemical anomaly in the LLSVP is primarily responsible for the sharp edges of these structures, which can be nearly vertical in the deep mantle, there are many ensuing implications. One is that it seems likely that LLSVPs will have thermal boundary layers developed along their discrete boundaries, with these boundary layers conducting heat out of (or into) the pile. If the LLSVPs are enriched in radiogenic materials, they may be relatively hot, and the enveloping thermal boundary layers might themselves become detached to rise as thermal plumes, perhaps entraining trace materials of the distinct chemistry of the LLSVP. The general correlation of low-velocity regions in D" with the surface distribution of hot spot volcanoes (e.g., Williams *et al.*, 1998) has long been noted, but even stronger correlation is found between the margins of LLSVPs and hot spot volcanoes (Thorne *et al.*, 2004), supporting the notion that boundary layer instabilities may shed from the edges of LLSVPs (Davaille, 1999; Jellinek and Manga, 2002), rather than the entire structure being a superplume.

1.18.7 Ultra-Low-Velocity Zones

Another important aspect of D" that has been inferred from seismic waveform investigations is the widespread existence of a layer from 5 to 40 km thick overlying the CMB, with very strong P-wave and S-wave velocity reductions of up to –10% and –30%, respectively (see Figure 8(b)). The observations of these ULVZs are summarized by Garnero *et al.* (1998) and Thorne and Garnero

(2004). Extensive regions of ULVZ appear to exist, although the actual lateral extent is uncertain because either broad horizontally stratified regions or localized three-dimensional domes and blobs may explain the data (Helmberger *et al.*, 1998, 2000). Similarly, the absence of seismically detectable ULVZ does not preclude the presence of a very thin (<5 km) layer that is not resolved by seismic probes of the CMB, and only upper bounds on thickness and velocity drop can be determined (Stutzmann *et al.*, 2000). Nonetheless, there are regions where there is no evidence of complexity in structure right at the CMB in high-quality short-period data (e.g., Castle and van der Hilst, 2000; Persch *et al.*, 2001) and other regions with evidence for rapid small-scale variations in ULVZ structure (e.g., Havens and Revenaugh, 2001; Rost and Revenaugh, 2003). Thus, there are certainly variations in ULVZ structure, so it is not globally represented by any one-dimensional model.

1.18.7.1 Seismic Phases Used for Detection

Evidence for an ULVZ at the base of the mantle was first presented by Garnero *et al.* (1993) and Silver and Bina (1993) based on behavior of SKS phases that interact with the CMB. The primary evidence (see Garnero *et al.*, 1998 for a review) for the ULVZ involves delayed SP_{diff}KS phases (Figure 11; e.g., Garnero and Helmberger, 1995, 1998; Helmberger *et al.*, 1998) and the shape of precursors to Pcp reflections (e.g., Mori and Helmberger, 1995; Revenaugh and Meyer, 1997; Ross *et al.*, 2004), precursors to Scs reflections (Figure 12; Avants *et al.*, 2006a), and precursors to Scp reflections (Rost and Revenaugh, 2001, 2003; Rost *et al.*, 2005). Strong scattering of PKP precursors has also been used to constrain the anomalous structure at the CMB (Wen 2000; Wen and Helmberger, 1998; Vidale and Hedlin, 1998). A variety of seismic wave probes of ULVZ structure is needed in order to characterize the P wave, S wave, and density structures, as each phase has sensitivity to more than one parameter. For some phases there are strong tradeoffs with structure on the coreside of the CMB as well, with a thin layer of finite rigidity in the outermost core being an alternate possibility (e.g., Garnero and Jeanloz, 2000; Rost and Revenaugh 2001; Buffett *et al.* 2000). This yields significant nonuniqueness in the models, but it does appear that the S-wave velocity reductions tend to be larger than the P-wave velocity reductions, and the density may increase by several to tens of percent.

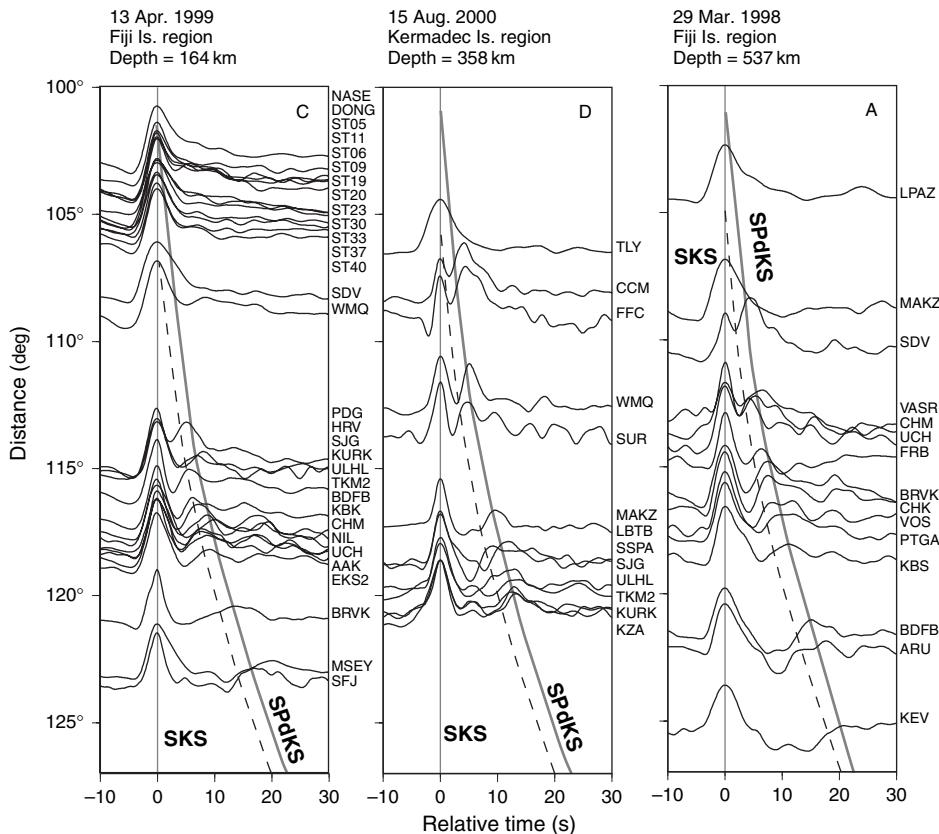


Figure 11 Waveforms with anomalously late SPdKS arrivals. The signals are aligned on SKS, with the dashed curves indicating the expected time for the peak of SPdKS based on the PREM structure. The observed arrivals are 2–3 s later than expected, which must be due to anomalously low P-velocity right at the CMB, where SPdKS diffracts along the boundary. Modeling indicates that about 5–10% low P-velocity in a layer 5–10 km thick can match the data. This strong P-velocity reduction defines the ULVZ. Courtesy of Ed Garnero.

1.18.7.2 Partial Melting and Chemical Anomalies

The strong velocity reductions in ULVZs are most easily explained by the presence of a melt component (Williams and Garnero, 1996), suggesting either that the mantle eutectic is exceeded at the hottest temperatures in the thermal boundary layer or there is infiltration of core material into the lowermost mantle. There is some correlation between locations of ULVZ patches and surface hot spots, which may further suggest a relationship between partial melting in D" and large-scale upwellings (e.g., Williams *et al.*, 1998; Lay *et al.*, 2004b). Thermally induced rigidity variations can produce large-shear-velocity fluctuations relative to compressional velocities ($R = d(\ln V_s)/d(\ln V_p) = 2.7$), whereas chemical variations tend to produce smaller values of $R \sim 1\text{--}2$. Partial melting can produce R values of $\sim 2.7\text{--}3.0$ (e.g., Williams and Garnero, 1996;

Berryman, 2000). The ratio of S-wave velocity anomaly to P-wave velocity anomaly in ULVZs has thus been of importance to assessing whether there is a significant chemical anomaly involved, even while partial melting appears to be the only way to approach the magnitude of the velocity decrements in ULVZs. Unfortunately, the ratio is very difficult to resolve given the many tradeoffs in model parameters. Available results do favor a ratio closer to 3 than to 1, but further analysis of P-wave velocity and S-wave velocity structure in the same spot using multiple seismic probes is needed to robustly resolve this issue. The observed $\sim 10\%$ P-wave velocity decrement associated with the ULVZ and more poorly constrained $\sim 30\%$ S-wave velocity decrease imply melt fractions of between $\sim 6\%$, for 1:100 aspect ratio films of melt, and $\sim 30\%$ for spherical melt inclusions (Williams and Garnero, 1996; Berryman, 2000).

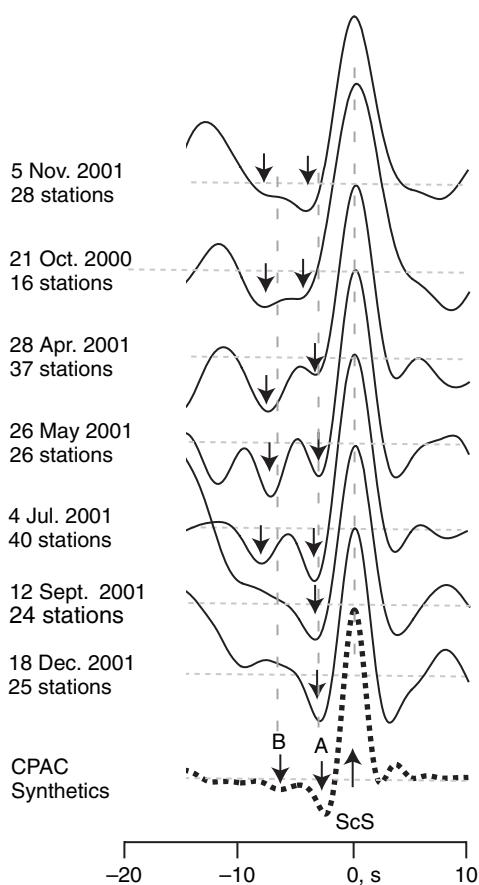


Figure 12 Stacks of the indicated number of deconvolved seismograms for several deep-focus events in the Tonga subduction zone, aligned on ScS, ordered by increasing event distance from California from top to bottom. Two stable negative amplitude peaks in the 10 s window before ScS are observed in the five closer events, with only one precursor being observed for the two more distant events. A stack of synthetics for a model CPAC with -1.1% and -3.8% discontinuities 70 and 30 km above the CMB, respectively. Direct S energy arrives 10–25 s before the windows shown. These data indicate that structure above the CMB is more complex than a single ULVZ. Reproduced from Avants M, Lay T, Garnero EJ (2006a) A new probe of ULVZ S-wave velocity structure: Array stacking of ScS waveforms. *Geophysical Research Letters* 33: L07314 (doi:10.1029/2005GL024989).

The presence of a melt component in the ULVZ has important dynamical and chemical implications. Somehow the melt (if denser than the coexisting solids) does not simply percolate deeper to form a pure melt layer overlying the core. Alternatively, if the melt is buoyant, it would be expected to either rise to its depth of neutral buoyancy, or to resolidify during adiabatic ascent. This juxtaposition of solids and liquids thus implies that one of several possible effects occur within

the ULVZ: (1) the melt is not interconnected, and thus is physically unable to efficiently drain from the surrounding solids; (2) the melt density closely matches that of the surrounding solids, so the buoyancy forces on the melt are insufficient to allow the melt to efficiently percolate; and/or (3) the average vertical convective velocity within the ULVZ is substantially greater than the velocity of melt percolation. Lay *et al.* (2004b) consider these scenarios, tending to favor the second or third as a means of developing a volumetrically extensive region with a melt component.

The presence of a melt component within the basal layer of the mantle is likely to have enhanced chemical interactions with the core through time, and may be indicative of an enrichment of this zone in elements that are incompatible in mantle minerals near CMB pressures and temperatures. Thus, iron-enrichment of D'' may have occurred through both melt descent from above (e.g., Knittle, 1998), and through core interactions from below. Moreover, enrichment of radiogenic elements in D'' (and perhaps particularly at its base) is generally consistent with a magmatic evolution for this boundary layer (Lay *et al.*, 2004a, 2004b): radiogenic element enrichment within the boundary layer has been suggested as a mechanism to reduce the required heat flux out of the outer core (Buffett, 2003).

A subsolidus mechanism to account for ULVZs involving post-perovskite has been proposed by Mao *et al.* (2006). Experiments indicate that post-perovskite is tolerant to quite large amounts of Fe, up to 40% or higher, and that such large iron content has a dramatic effect on both S- and P-wave velocities. If post-perovskite is stable at the hottest temperatures in the mantle at CMB pressures, this idea offers an alternative to having a dense melt component present. As noted above, there is large uncertainty in the absolute temperature in D'', and there is substantial uncertainty in the Clapeyron slope of the phase transition, so this possibility remains highly conjectural. If correct, the distribution of ULVZ would indicate the location of very Fe-rich post-perovskite rather than partial melt. It is not clear that in the presence of mixed phases the affinity of post-perovskite for iron will dominate, so much work is needed to test this hypothesis.

1.18.8 Lower-Mantle Anisotropy

While the bulk of the lower mantle does not appear to have large-scale organized anisotropy, the D'' region has been shown to have extensive regions where shear wave splitting occurs (see reviews

by Lay *et al.*, 1998a,b; Kendall, 2000; Moore *et al.* 2003). These observations have prompted increased consideration of the anisotropic crystallography of high-pressure phases likely to be present in the lower mantle along with what deformation mechanisms are likely to control the formation of fabrics (e.g., Stixrude, 1998; Karato, 1998). There remain substantial uncertainties in the nature of the anisotropy and its cause. Strong shear flows in the boundary layer may induce lattice-preferred orientation (LPO) of the anisotropic lower-mantle minerals, but it is not clear why this would not also hold for the overlying lower mantle. Sheared inclusions of chemical heterogeneities and pockets of partial melt may also play a role in generating the seismic anisotropy. The post-perovskite phase transition may also be important. As observational and laboratory constraints improve, it is likely that modeling anisotropy in D" will provide important constraints on the thermal and dynamical processes in the boundary layer.

1.18.8.1 Shear-Wave Splitting Observations

Observations of splitting for ScS phases have been made for several decades (e.g., Mitchell and Helmberger, 1973; Lay and Helmberger, 1983b; Rokosky *et al.*, 2004), but observations of diffracted waves convincingly demonstrate that anisotropy is present in D" (e.g., Vinnik *et al.*, 1989, 1995, 1998b; Lay and Young, 1991; Kendall and Silver, 1996; Matzel *et al.*, 1996; Garnero and Lay, 1997; Ritsema *et al.*, 1998; Russell *et al.*, 1998; Ritsema, 2000; Thomas and Kendall 2002; Panning and Romanowicz, 2004; Garnero *et al.*, 2004a, b). Figure 8(c) indicates the regions that have been studied in detail. All observations of D" anisotropy are subject to uncertainties because of limitations of the corrections for uppermantle anisotropy and the possibility of significant near-source anisotropy even for deep focus earthquakes.

The large majority of observations involve horizontally polarized shear wave components (SH) traveling faster through D" than vertically polarized shear waves (SV) for grazing incidence or wide-angle reflections, with relatively large-scale regions of D" displaying 0.5–1.5% anisotropy (e.g., Garnero and Lay, 2003; Thomas and Kendall, 2002; Fouch *et al.*, 2001; Vinnik *et al.*, 1998b; Kendall and Silver, 1996; Ritsema 2000; Rokosky *et al.*, 2004; Usui *et al.*, 2005). While almost none of the studies have significant azimuthal ray path sampling, the observations are at least compatible with

extensive vertical transverse isotropy (VTI), as may be caused by hexagonally symmetric material with a vertical symmetry axis or fine-scale horizontal layering. The onset of shear wave splitting appears to be linked to the S-wave velocity increase at the top of D" in high-velocity regions (e.g., Matzel *et al.*, 1996; Garnero and Lay, 1997), but resolution of the depth extent of the anisotropy in the boundary layer remains very limited (Moore *et al.*, 2003).

Localized observations of shear wave splitting in D" with SV velocities being higher than SH velocities have been reported, with localized upwellings in the boundary layer being invoked as one possible way to modify the symmetry axis for SPO or LPO (e.g., Pulliam and Sen, 1998; Russell *et al.*, 1998, 1999; Rokosky *et al.* 2004). Garnero *et al.* (2004a), Maupin *et al.* (2005), and Wookey *et al.* (2005) present clear observations of azimuthal anisotropy (Figure 13), with fast and slow waves mixed on the SH and SV components. Thus far it has only been possible to characterize the horizontal component of the symmetry axis.

1.18.8.2 Mineralogical/Dynamical Implications

Anisotropy compatible with the primary seismic observations of shear wave splitting in D" could be the result of LPO for a D" mineral component, or the result of shape-preferred orientation (SPO) of chemical or partial-melt components in a sheared boundary layer. A candidate major component of the lower mantle that may develop anisotropy with SH velocity faster than SV velocity in a horizontally sheared boundary layer is MgO (e.g., Karato, 1998; Stixrude, 1998; Karki *et al.*, 1999; Kendall, 2000; Mainprice *et al.*, 2000; Yamazaki and Karato, 2002), whereas low-velocity lamellae comprised of partially melted crust or other chemical heterogeneities are also possible causes of such anisotropy (e.g., Kendall and Silver, 1998; Wysession *et al.*, 1999; Fouch *et al.*, 2001; Moore *et al.*, 2003). McNamara *et al.* (2001, 2002) use thermal convection models to compute variations in temperature and stress regime that might result in localization of dislocation creep that favor LPO in some areas and diffusion-dominated deformation in others that would require SPO to account for any anisotropy. These dynamic calculations indicate that conditions favorable for mid-mantle anisotropy may exist in downwellings, but as yet there is no clear evidence for anisotropy in the bulk of the mid-mantle (e.g., Kaneshima and Silver, 1995; Meade *et al.*, 1995).

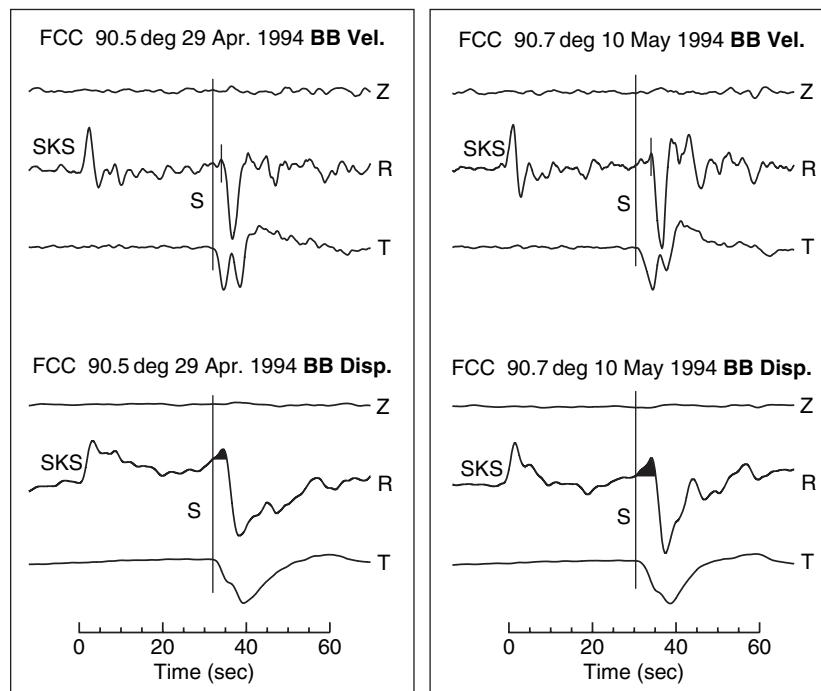


Figure 13 Three-component records from station FCC (Fort Churchill, Canada) for two deep South American earthquakes, showing ground velocity (upper plots) and ground displacement (lower plots) spanning the SKS and S arrivals. Corrections for receiver lithospheric anisotropy have been applied (note that no SKS energy is seen on the transverse component), and the Z and R rotations are to the wave front normal and wave front parallel directions for the SKS arrival, respectively. The arrival time of S is indicated by the vertical lines. The small reversed-polarity upswing at the beginning of the S wave on the radial components of the displacement seismograms is colored in black. This feature is easily missed in the velocity records, and one is tempted to pick a sharp correct-polarity negative arrival as the first SV arrival (small ticks). The reverse-polarity energy is produced by azimuthal anisotropy, either in D'' or possibly near the source, which couples the fast arrival to the R and T components. Reproduced from Maupin V, Garnero EJ, Lay T, and Fouch MJ (2005) Azimuthal anisotropy in the D'' layer beneath the Caribbean. *Journal of Geophysical Research* 110: B08301(doi:10.1029/2004JB003506).

The anisotropic properties of post-perovskite may further explain why seismologists find a strong association between regions with a lower-mantle S-wave velocity discontinuity and regions with S-wave splitting that is stronger than observed in lower-velocity regions. Stackhouse *et al.* (2005b) compute the anisotropic properties of post-perovskite and consider the propensity for developing LPO compatible with seismic observations. It appears that post-perovskite has more favorable properties than perovskite for acquiring LPO in D''. Deformation of analog materials also supports the notion that post-perovskite may acquire anisotropic fabrics in the lowermost mantle (Merkel *et al.*, 2006).

1.18.9 Small-Scale Heterogeneities

The emphasis in the preceding sections has been on intermediate and large-scale structure, as this is most readily resolved by tomographic and waveform

modeling procedures. However, as is true of the lithosphere, key dynamical and chemical structures exist in D'' on scales below the limit of deterministic resolution using seismic waves with wavelengths longer than 10 km or so. Very fine structure will scatter seismic energy, and statistical attributes of the structure can be constrained using various approaches.

1.18.9.1 Scattering in D''

Small-scale variations in D'', with about 1% heterogeneities on scale-lengths of about 10 km are revealed by scattered P-wave signals. This has been demonstrated by analysis of short-period precursors to PKP phases (e.g., Cleary and Haddon, 1972; Haddon and Cleary, 1974; Doornbos, 1976; Bataille and Flatté, 1988; Bataille *et al.*, 1990; Hedlin *et al.*, 1997; Cormier, 1999; Hedlin and Shearer, 2000). The small-scale structure is also analyzed using diffracted

coda waves (e.g., Bataille and Lund, 1996), PKKP reflections (e.g., Earle and Shearer, 1997), triplications (e.g., Kohler *et al.*, 1997), and scatterer migrations (e.g., Thomas *et al.*, 1999). Some studies purport to show evidence for thin layers of anomalous properties, or lamellae in the boundary layer (e.g., Lay and Helmberger, 1983b; Weber, 1994; Thomas *et al.*, 1998). The structural heterogeneities involve scale-lengths of a few to tens of kilometers, with various estimates of velocity fluctuations of a few to 10%. It has generally been believed that the levels of heterogeneity increase in D" relative to the overlying mantle, but there is evidence that small-scale structure in D" is not distinctive from that throughout the mantle (e.g., Hedlin *et al.*, 1997). Nonetheless, it is clear that some of the strongest scattering, involving much larger velocity heterogeneities, does arise within D" (Vidale and Hedlin, 1998; Wen and Helmberger, 1998), and this is likely associated with the patchy ULVZ just above the CMB. The bandwidth of the signals used in scattering analyses controls the sensitivity to scatterers of different dimensions, and analysis of broadband data indicates a rich spectrum of scattering scale lengths in D".

Cormier (2000) has developed the perspective of D" being a transition in the heterogeneity spectrum of the lowermost mantle, with a relatively 'red' spectrum, having substantial power at long wavelengths, but still significant strength at short wavelengths. It is plausible that small-scale structure also exists on the core side of the CMB, concentrated in topographic highs (e.g., Buffett, *et al.*, 2000; Garnero and Jeanloz, 2000; Rost and Revenaugh, 2003).

1.18.9.2 Core–Mantle Boundary Topography

Given the complexity of structure at all scales in D", it is not surprising that large uncertainty remains as to whether there is any topography on the CMB itself. Long wavelength topography of the CMB was proposed by Creager and Jordan (1986b) and Morelli and Dziewonski (1987) based on studies of bulletin Pcp and PKP arrival times, but it has been demonstrated that allowing for strong heterogeneity in D" and the limited resolution of the available data make CMB topography models very uncertain (e.g., Doornbos and Hilton, 1989; Rodgers and Wahr, 1993; Pulliam and Stark, 1993; Obayashi and Fukao, 1997; Garcia and Souriau, 2000; Sze and van der Hilst, 2003). As models for the entire mantle improve

this may prove to be a solvable problem, and it is a critical one, for CMB topography plays a major role in estimating the extent of mechanical coupling between the core and mantle. For imaging shorter-wavelength topography of the CMB, the primary approach has involved traveltimes fluctuations and precursors to underside reflections of internal core reverberations (PKKP). These phases provide an upper bound of about 100 m topography on 10-km scale lengths (e.g., Doornbos, 1974, 1980; Chang and Cleary, 1978; Bataille and Flatté, 1988; Earle and Shearer, 1997, 1998). Nutation data bounds very long-wavelength topography on the CMB to a few hundred meters (Defraigne *et al.*, 1996).

1.18.10 Conclusions

Any attempt to characterize knowledge of the lower mantle and D" region can only provide a snapshot of a rapidly evolving topic. Interdisciplinary progress in mineral physics theory and experimentation, geodynamics, and geochemistry resonate with advances in seismological imaging, redefining conceptual models with remarkable rapidity. One decade's 'superplumes' become the next decade's 'superpiles', with major shifts in perception of the roles played by seismically detected heterogeneities. This is both stimulating and unsettling, with our understanding of the mantle system acquiring more and more levels of complexity.

So, what lies ahead? There is great potential to make major advances in our understanding of the thermal regime in the lowermost mantle if the post-perovskite phase transition is shown to be the correct explanation for the D" discontinuity. This is because a phase transition can be calibrated in actual P – T space, greatly reducing the uncertainty in temperature estimates currently obtained by extrapolation over thousands of kilometers in depth. Parallel efforts in mineral physics and seismology can advance this topic much as they have advanced our understanding of transition-zone conditions.

Increasing densification and accumulation of seismological data sets is enabling new approaches such as migration to be applied to deep-mantle targets. While coverage is, and will remain, embarrassingly limited compared to exploration industry data sets, the advantage of generally parametrized migrations for rough structure has already been established and promises to reveal important structural characteristics in the lower mantle. Large data sets are also key to one of the

persistent challenges in deep Earth imaging, separating source, deep, and receiver contributions to the signals. Studies of lower-mantle scattering, lower-mantle anisotropy, and lower-mantle stratification are all plagued by near-source and near-receiver signal-generated noise. Improved suppression of these effects by combining empirical filters and stacking approaches holds much promise for improving seismological resolution of deep structure.

Seismological structures in the deep mantle have been shown to have lateral gradients as strong as radial gradients, and the search for steeply dipping interfaces using azimuthal data gathers has proved fruitful. Approaches to quantifying three-dimensional structures for poorly sampled wavefields require both efficient 3D computational tools and new strategies for modeling. Approaches based on iterating from initial tomographic models have shown some success, but the wavefield complexity often involves smaller scales than constrained by tomography. One cannot help but feel that we have only scratched the surface of the complex regime that likely exists in the deep mantle. Much work is left to be done.

Acknowledgments

T. Lay's research on lower-mantle structure is supported by NSF Grant 0125595. This is contribution number 490 of the Center for the Study of Imaging and Dynamics of the Earth, IGPP, UCSC.

References

- Adams LH and Williamson ED (1923) The composition of the Earth's interior. *Smithsonian Institute Annual Reports* 241–260.
- Akber-Knutson S, Steinle-Neumann G, and Asimow PD (2005) Effect of Al on the sharpness of the $MgSiO_3$ perovskite to post-perovskite phase transition. *Geophysical Research Letters* 32: L14303 (doi:10.1029/2005GL023192).
- Alexander SS and Phinney RA (1966) A study of the core–mantle boundary using P-waves diffracted by the Earth's core. *Journal of Geophysical Research* 71: 5943–5958.
- Anderson DL (1967) The anelasticity of the mantle. *Geophysical Journal of the Royal Astronomical Society* 14: 135–164.
- Anderson DL (1991) Chemical boundaries in the mantle. In: Sabadini R, Lambeck K, and Boschi E (eds.) *Glacial Isostasy, Sea-Level and Mantle Rheology*, pp. 379–401. The Netherlands: Kluwer.
- Anderson DL (1998) The EDGES of the mantle. In: Gurnis M, Wysession ME, Knittle E, and Buffett BA (eds.) *The Core–Mantle Boundary Region*, pp. 255–271. Washington, DC: American Geophysical Union.
- Anderson DL and Hart RS (1978) Q of the Earth. *Journal of Geophysical Research* 83: 5869–5882.
- Anderson DL, Kanamori H, Hart RS, and Liu H-P (1977) The Earth as a seismic absorption band. *Science* 196: 1104–1106.
- Antolik M, Gu YJ, and Ekström G (2003) J362D28: A new joint model of compressional and shear velocity in the Earth's mantle. *Geophysical Journal International* 153: 443–466.
- Avants M, Lay T, and Garnero EJ (2006a) A new probe of ULVZ S-wave velocity structure: Array stacking of ScS waveforms. *Geophysical Research Letters* 33: L07314 (doi:10.1029/2005GL024989).
- Avants M, Lay T, Russell SA, and Garnero EJ (2006b) Shear velocity variation within the D'' region beneath the Central Pacific. *Journal of Geophysical Research* 111: B05305 (doi:10.1029/2004JB003270).
- Badio J, Fiquet G, Guyot F, et al. (2003) Iron partitioning in Earth's mantle: Toward a deep lower mantle discontinuity. *Science* 300: 789–791.
- Badio J, Rueff J-P, Vankó G, Monaco G, Fiquet G, and Guyot F (2004) Electronic transitions in perovskite: Possible non-convecting layers in the lower mantle. *Science* 305: 383–386.
- Bataille K and Flatté SM (1988) Inhomogeneities near the core–mantle boundary inferred from short-period scattered PKP-waves recorded at the global digital seismograph network. *Journal of Geophysical Research* 93: 15057–15064.
- Bataille K and Lund F (1996) Strong scattering of short-period seismic waves by the core–mantle boundary and the P-diffracted wave. *Geophysical Research Letters* 18: 2413–2416.
- Bataille K, Wu RS, and Flatté SM (1990) Inhomogeneities near the core–mantle boundary evidenced from scattered waves: A review. *Pure and Applied Geophysics* 132: 151–173.
- Berryman JG (2000) Seismic velocity decrement ratios for regions of partial melt in the lower mantle. *Geophysical Research Letters* 27: 421–424.
- Bijwaard H and Spakman W (1999) Tomographic evidence for a narrow whole mantle plume below Iceland. *Earth and Planetary Science Letters* 166: 121–166.
- Bijwaard H, Spakman W, and Engdahl ER (1998) Closing the gap between regional and global travel time tomography. *Journal of Geophysical Research* 103: 30055–30078.
- Bolt BA, Niazi M, and Somerville MR (1970) Diffracted ScS and the shear velocity at the core boundary. *Geophysical Journal of the Royal Astronomical Society* 19: 299–305.
- Bolton H (1996) *Long Period Travel Times and the Structure of the Mantle*. PhD Thesis, University of California, San Diego, 204pp.
- Boschi L and Dziewonski AM (1999) High- and low-resolution images of the Earth's mantle: Implications of different approaches to tomographic modeling. *Journal of Geophysical Research* 104: 25567–25594.
- Boschi L and Dziewonski AM (2000) Whole Earth tomography from delay times of P, P_{cP} , and PKP phases: Lateral heterogeneities in the outer core or radial anisotropy in the mantle? *Journal of Geophysical Research* 105: 13675–13696.
- Boyd TM and Creager KC (1991) The geometry of Aleutian subduction: Three-dimensional seismic imaging. *Journal of Geophysical Research* 96: 2267–2291.
- Bréger L and Romanowicz B (1998) Three-dimensional structure at the base of the mantle beneath the central Pacific. *Science* 282: 718–720.
- Bréger L, Romanowicz B, and Ng C (2001) The Pacific plume as seen by S, ScS, and SKS. *Geophysical Research Letters* 28: 1859–1862.
- Buffett BA (2003) The thermal state of Earth's core. *Science* 299: 1675–1677.
- Buffett BA, Garnero EJ, and Jeanloz R (2000) Sediments at the top of Earth's core. *Science* 290: 1338–1342.

- Bullen KE (1949) Compressibility-pressure hypothesis and the Earth's interior. *Monthly Notes of the Royal Astronomical Society, Geophysical Supplement* 5: 355–368.
- Burdick LJ and Powell C (1980) Apparent velocity measurements for the lower mantle from a wide aperture array. *Journal of Geophysical Research* 85: 3845–3856.
- Castle JC and Creager KC (1999) A steeply dipping discontinuity in the lower mantle beneath Izu-Bonin. *Journal of Geophysical Research* 104: 7279–7292.
- Castle JC, Creager KC, Winchester JP, and van der Hilst RD (2000) Shear wave speeds at the base of the mantle. *Journal of Geophysical Research* 105: 21543–21557.
- Castle JC and van der Hilst RD (2000) The core–mantle boundary under the Gulf of Alaska: No ULVZ for shear waves. *Earth and Planetary Science Letters* 176: 311–321.
- Chang AC and Cleary JR (1978) Precursors to PKKP. *Bulletin of the Seismological Society of America* 68: 1059–1079.
- Chinnery MA and Toksöz MN (1967) P-wave velocities in the mantle below 700 km. *Bulletin of the Seismological Society of America* 57: 199–226.
- Clayton R and Comer R (1983) A tomographic analysis of mantle heterogeneities from body wave travel time data (abstract). *EOS Transactions of the American Geophysical Union* 64: 776.
- Cleary JR and Haddon RAW (1972) Seismic wave scattering near the core–mantle boundary: A new interpretation of precursors to PKP. *Nature* 240: 549–551.
- Cormier VF (1985) Some problems with S, SKS, and ScS observations and implications for the structure of the base of the mantle and the outer core. *Journal of Geophysics* 57: 14–22.
- Cormier VF (1999) Anisotropy of heterogeneity scale lengths in the lower mantle from PKIKP precursors. *Geophysical Journal International* 136: 373–384.
- Cormier VF (2000) D" as a transition in the heterogeneity spectrum of the lowermost mantle. *Journal of Geophysical Research* 105: 16193–16205.
- Creager KC and Jordan TH (1984) Slab penetration into the lower mantle. *Journal of Geophysical Research* 89: 3031–3049.
- Creager KC and Jordan TH (1986a) Slab penetration into the lower mantle beneath the Mariana and other island arcs of the northwest Pacific. *Journal of Geophysical Research* 91: 3573–3589.
- Creager KC and Jordan TH (1986b) Aspherical structure of the core–mantle boundary from PKP traveltimes. *Geophysical Research Letters* 13: 1497–1500.
- Datt R and Muirhead KJ (1976) Evidence for a sharp velocity increase near 770 km depth. *Physics of the Earth and Planetary Interiors* 13: 37–46.
- Davaille A (1999) Simultaneous generation of hotspots and superswells by convection in a heterogeneous planetary mantle. *Nature* 402: 756–760.
- Davies G (1984) Geophysical and isotopic constraints on mantle convection: An interim synthesis. *Journal of Geophysical Research* 89: 6017–6040.
- Davies G and Gurnis M (1986) Interaction of mantle dregs with convection: Lateral heterogeneity at the core–mantle boundary. *Geophysical Research Letters* 13: 1517–1520.
- Deal MM and Nolet G (1999) Slab temperature and thickness from seismic tomography 2. Izu-Bonin, Japan, and Kuril subduction zones. *Journal of Geophysical Research* 104: 28803–28812.
- Deal MM, Nolet G, and van der Hilst RD (1999) Slab temperature and thickness from seismic tomography. 1: Method and application to Tonga. *Journal of Geophysical Research* 104: 28789–28802.
- Defraigne P, Dehant V, and Wahr J (1996) Internal loading of an inhomogeneous compressible Earth with phase boundaries. *Geophysical Journal International* 125: 173–192.
- Deschamps F and Trampert J (2003) Mantle tomography and its relation to temperature and composition. *Physics of the Earth and Planetary Interiors* 140: 272–291.
- Ding X and Helmberger DV (1997) Modeling D" structure beneath Central America with broadband seismic data. *Physics of the Earth and Planetary Interiors* 101: 245–270.
- Ding X-Y and Grand SP (1994) Seismic structure of the deep Kurile subduction zone. *Journal of Geophysical Research* 99: 23767–23786.
- Doornbos DJ (1974) Seismic wave scattering near caustics: Observations of PKKP precursors. *Nature* 247: 352–353.
- Doornbos DJ (1976) Characteristics of lower mantle inhomogeneities from scattered waves. *Geophysical Journal of the Royal Astronomical Society* 44: 447–470.
- Doornbos DJ (1980) The effect of a rough core–mantle boundary on PKKP. *Physics of the Earth and Planetary Interiors* 21: 351–358.
- Doornbos DJ and Hilton T (1989) Models of the core–mantle boundary and the travel times of internally reflected core phases. *Journal of Geophysical Research* 94: 15741–15751.
- Doornbos DJ and Mondt JC (1979) P- and S-waves diffracted around the core and the velocity structure at the base of the mantle. *Geophysical Journal of the Royal Astronomical Society* 57: 381–395.
- Doornbos DJ, Spiliopoulos S, and Stacey FD (1986) Seismological properties of D" and the structure of a thermal boundary layer. *Physics of the Earth and Planetary Interiors* 41: 225–239.
- Dziewonski AM (1984) Mapping the lower mantle: Determination of lateral heterogeneity in P velocity up to degree and order 6. *Journal of Geophysical Research* 89: 5929–5942.
- Dziewonski AM and Anderson DL (1981) Preliminary reference Earth model. *Physics of the Earth and Planetary Interiors* 25: 297–356.
- Dziewonski AM, Ekström G, and Liu X-F (1996) Structure at the top and bottom of the mantle. In: Husebye ES and Dainty AM (eds.) *Monitoring a Comprehensive Test Ban Treaty*, pp. 521–550. The Netherlands: Kluwer.
- Dziewonski AM, Forte AM, Su W-J, and Woodward RL (1993) Seismic tomography and geodynamics. In: Aki K and Dmowska R (eds.) *Geophysical Monograph 76, IUGG, Vol. 16: Relating Geophysical Structures and Processes: The Jeffreys Volume*, pp. 67–105. Washington, DC: American Geophysical Union.
- Dziewonski AM, Hager BH, and O'Connell RJ (1977) Large scale heterogeneity in the lower mantle. *Journal of Geophysical Research* 82: 239–255.
- Dziewonski AM, Hales AL, and Lapwood ER (1975) Parametrically simple Earth models consistent with geophysical data. *Physics of the Earth and Planetary Interiors* 10: 12–48.
- Earle PS and Shearer PM (1997) Observations of PKKP precursors used to estimate small-scale topography on the core–mantle boundary. *Science* 277: 677–680.
- Earle PS and Shearer PM (1998) Observations of high-frequency scattered energy associated with the core phase PKKP. *Geophysical Research Letters* 25: 405–408.
- Emery V, Maupin V, and Nataf H-C (1999) Scattering of S-waves diffracted at the core–mantle boundary; forward modeling. *Geophysical Journal International* 139: 325–344.
- Fiquet G, Dewaele A, Andrault D, Kunz M, and Le Bihan T (2000) Thermoelastic properties and crystal structure of MgSiO_3 perovskite at lower mantle pressure and temperature conditions. *Geophysical Research Letters* 27: 21–24.
- Fisher JL, Wysession ME, and Fischer KM (2003) Small-scale lateral variations in D" attenuation and velocity structure. *Geophysical Research Letters* 30 (doi:10.1029/2002GL016179).

- Fischer KM, Creager KC, and Jordan TH (1991) Mapping the Tonga slab. *Journal of Geophysical Research* 96: 14403–14427.
- Fischer KM, Jordan TH, and Creager KC (1988) Seismic constraints on the morphology of deep slabs. *Journal of Geophysical Research* 93: 4773–4783.
- Flores C and Lay T (2005) The trouble with seeing double. *Geophysical Research Letters* 32: L24305 (doi:10.1029/2005GL024366).
- Ford SR, Garnero EJ, and McNamara AK (2006) A strong lateral shear velocity gradient and anisotropy heterogeneity in the lowermost mantle beneath the southern Pacific. *Journal of Geophysical Research* 111: B03306 (doi:10.1029/2004JB003574).
- Forte AM and Mitrovica JX (2001) Deep-mantle high-viscosity flow and thermochemical structure inferred from seismic and geodynamic data. *Nature* 410: 1049–1056.
- Forte AM, Peltier WR, Dziewonski AM, and Woodward RL (1993) Dynamic surface topography: A new interpretation based upon mantle flow models derived from seismic tomography. *Geophysical Research Letters* 20: 225–228.
- Forte AM, Woodward RL, and Dziewonski AM (1994) Joint inversions of seismic and geodynamic data for models of three-dimensional mantle heterogeneity. *Journal of Geophysical Research* 99: 21857–21877.
- Fouch MJ, Fischer KM, and Wyession ME (2001) Lowermost mantle anisotropy beneath the Pacific: Imaging the source of the Hawaiian plume. *Earth and Planetary Science Letters* 190: 167–180.
- Freybourger M, Krüger F, and Achauer U (1999) A 22° long seismic profile for the study of the top of D". *Geophysical Research Letters* 26: 3409–3412.
- Fukao Y, Obayashi M, Inoue H, and Nenbai M (1992) Subducting slabs stagnant in the mantle transition zone. *Journal of Geophysical Research* 97: 4809–4822.
- Fukao Y, Widiyantori S, and Obayashi M (2001) Stagnant slabs in the upper and lower mantle transition region. *Reviews of Geophysics* 39: 291–323.
- Gaherty JB and Lay T (1992) Investigation of laterally heterogeneous shear velocity structure in D" beneath Eurasia. *Journal of Geophysical Research* 97: 417–435.
- Gaherty JB, Lay T, and Vidale JE (1991) Investigation of deep slab structure using long period S-waves. *Journal of Geophysical Research* 96: 16349–16367.
- Garcia R and Souriau A (2000) Amplitude of the core–mantle boundary topography estimated by stochastic analysis of core phases. *Physics of the Earth and Planetary Interiors* 117: 345–359.
- Garnero EJ (2000) Heterogeneity of the lowermost mantle. *Annual Reviews of the Earth and Planetary Science* 28: 509–537.
- Garnero EJ and Helmberger DV (1995) A very slow basal layer underlying large-scale low velocity anomalies in the lower mantle beneath the Pacific: Evidence from core phases. *Physics of the Earth and Planetary Interiors* 91: 161–176.
- Garnero EJ and Helmberger DV (1998) Further structural constraints and uncertainties of a thin laterally varying ultralow-velocity layer at the base of the mantle. *Journal of Geophysical Research* 103: 12495–12509.
- Garnero EJ and Jeanloz R (2000) Fuzzy patches on the Earth's core–mantle boundary. *Geophysical Research Letters* 27: 2777–2780.
- Garnero EJ and Lay T (1997) Lateral variations in the lowermost mantle shear wave anisotropy beneath the north Pacific and Alaska. *Journal of Geophysical Research* 102: 8121–8135.
- Garnero EJ and Lay T (1999) Effects of D" anisotropy on seismic velocity models of the outermost core. *Geophysical Research Letters* 25: 2341–2344.
- Garnero EJ and Lay T (2003) D" shear velocity heterogeneity, anisotropy and discontinuity structure beneath the Caribbean and Central America. *Physics of the Earth and Planetary Interiors* 140: 219–242.
- Garnero EJ, Grand SP, and Helmberger DV (1993a) Low P-wave velocity at the base of the mantle. *Geophysical Research Letters* 20: 1843–1846.
- Garnero EJ, Helmberger DV, and Engen G (1988) Lateral variation near the core–mantle boundary. *Geophysical Research Letters* 20: 1843–1846.
- Garnero EJ, Helmberger DV, and Grand SP (1993b) Constraining outermost core velocity with SmKS-waves. *Geophysical Research Letters* 20: 2463–2466.
- Garnero EJ, Maupin V, Lay T, and Fouch MJ (2004a) Variable azimuthal anisotropy in Earth's lowermost mantle. *Science* 306: 259–261.
- Garnero EJ, Moore MM, Lay T, and Fouch MJ (2004b) Isotropy or weak vertical transverse isotropy in D" beneath the Atlantic Ocean. *Journal of Geophysical Research* 109: B08308 (doi:10.1029/2004JB003004).
- Garnero EJ, Revenaugh JS, Williams Q, Lay T, and Kellogg LH (1998) Ultralow velocity zone at the core–mantle boundary. In: Gurnis M, Wysession ME, Knittle E, and Buffett BA (eds.) *The Core–mantle Boundary Region*, pp. 319–334. Washington, DC: American Geophysical Union.
- Gilbert F and Dziewonski AM (1975) An application of normal mode theory to the retrieval of structural parameters and source mechanisms from seismic spectra. *Philosophical Transactions of the Royal Society of London, Series A* 278: 187–269.
- Glatzmaier GA, Coe RS, Hongre L, and Roberts PH (1999) The role of the Earth's mantle in controlling the frequency of geomagnetic reversals. *Nature* 401: 885–890.
- Goarant F, Guyot F, Peyronneau J, and Poirier J-P (1992) High pressure and high temperature reactions between silicates and liquid iron alloys in the diamond anvil cell, studied by analytical electron microscopy. *Journal of Geophysical Research* 97: 4477–4487.
- Goes S, Spakman W, and Bijwaard H (1999) A lower mantle source for Central European volcanism. *Science* 286: 1928–1931.
- Gong Z, Fei Y, Dai F, Zhang L, and Jing F (2004) Equation of state and phase stability of mantle perovskite up to 140 GPa shock pressure and its geophysical implications. *Geophysical Research Letters* 31: L04614 (doi:10.1029/2003GL019132).
- Grand SP (2002) Mantle shear-wave tomography and the fate of subducted slabs. *Philosophical Transactions of the Royal Society of London, Series A* 360: 2475–2491.
- Grand SP, van der Hilst RD, and Widiyantoro S (1997) Global seismic tomography: A snapshot of convection in the Earth. *GSA Today* 7: 1–7.
- Green DH and Falloon TJ (1998) Pyrolite: A Ringwood concept and its current expression. In: Jackson I (ed.) *The Earth's Mantle*, pp. 311–378. Cambridge: Cambridge University Press.
- Gu YJ, Dziewonski AM, Su W, and Ekström G (2001) Models of the mantle shear velocity and discontinuities in the pattern of lateral heterogeneities. *Journal of Geophysical Research* 106(11): 169–199.
- Haddon RA and Buchbinder GGR (1986) Wave propagation effects and the Earth's structure in the lower mantle. *Geophysical Research Letters* 13: 1489–1492.
- Haddon RA and Cleary JR (1974) Evidence for scattering of seismic PKP-waves near the core–mantle boundary. *Physics of the Earth and Planetary Interiors* 8: 211–234.
- Hager B (1984) Subducted slabs and the geoid: Constraints on mantle rheology and flow. *Journal of Geophysical Research* 89: 6003–6015.
- Hager B and Clayton RW (1989) Constraints on the structure of mantle convection using seismic observations, flow models, and the geoid. In: Peltier WR (ed.) *Mantle Convection: Plate*

- Tectonics and Global Dynamics, pp. 657–763. Newark, NJ: Gordon and Breach.
- Hager B, Clayton RW, Richards MA, Comer RP, and Dziewonski AM (1985) Lower mantle heterogeneity, dynamic topography and the geoid. *Nature* 313: 541–545.
- Hager B and Richards MA (1989) Long-wavelength variations in the Earth's geoid: Physical models and dynamical implications. *Philosophical Transactions of the Royal Society of London, Series A* 328: 309–327.
- Hales AL, Cleary JR, and Roberts JL (1968) Velocity distribution in the lower mantle. *Bulletin of the Seismological Society of America* 58: 1975–1989.
- Hales AL and Roberts JL (1970) Shear velocities in the lower mantle and the radius of the core. *Bulletin of the Seismological Society of America* 60: 1427–1436.
- Hansen U and Yuen DA (1988) Numerical simulations of thermal-chemical instabilities at the core–mantle boundary. *Nature* 334: 237–240.
- Havens E and Revenaugh J (2001) A broadband study of the lowermost mantle beneath Mexico: Constraints on ultralow velocity zone elasticity and density. *Journal of Geophysical Research* 106: 30809–30820.
- He Y, Wen L, and Zheng T (2006) Geographic boundary and shear wave velocity structure of the ‘Pacific anomaly’ near the core–mantle boundary beneath western Pacific. *Earth and Planetary Science Letters* 244: 302–314.
- Hedlin MAH and Shearer PM (2000) An analysis of large-scale variations in small-scale mantle heterogeneity using Global Seismographic Network recordings of precursors to PKP. *Journal of Geophysical Research* 105: 13655–13673.
- Hedlin MAH, Shearer PM, and Earle PS (1997) Seismic evidence for small-scale heterogeneity throughout the Earth's mantle. *Nature* 387: 145–150.
- Helberger DV, Wen L, and Ding X (1998) Seismic evidence that the source of the Iceland hotspot lies at the core–mantle boundary. *Nature* 396: 251–255.
- Helberger DV, Lay T, Ni S, and Gurnis M (2005) Deep mantle structure and the post-perovskite phase transition. *Proceedings of the National Academy of Sciences USA* 102: 17257–17263. (10.1073/pnas.0502504102).
- Helberger DV, Ni S, Wen L, and Ritsema J (2000) Seismic evidence for ultra-low velocity zones beneath Africa and eastern Atlantic. *Journal of Geophysical Research* 105: 23865–23878.
- Hernlund JW, Thomas C, and Tackley PJ (2005) A doubling of the post-perovskite phase boundary and structure of the Earth's lowermost mantle. *Nature* 434: 882–886.
- Herrin E (1968) Introduction to ‘1968 Seismological Tables for P-phases’. *Bulletin of the Seismological Society of America* 58: 1193–1195.
- Hirose K and Fujita Y (2005) Clapeyron slope of the post-perovskite phase transition in CaIrO₃. *Geophysical Research Letters* 32: L13313 (doi:10.1029/2005GL023219).
- Hirose K, Simmyo R, Sata N, and Ohishi Y (2006) Determination of post-perovskite phase transition boundary in MgSiO₃ using Au and MgO pressure standards. *Geophysical Research Letters* 33: L01310 (doi:10.1029/2005GL024468).
- Houard S and Nataf HC (1993) Laterally varying reflector at the top of D'' beneath northern Siberia. *Geophysical Journal International* 115: 168–182.
- Hung S-H, Garner EJ, Chiao L-Y, Kuo B-Y, and Lay T (2005) Finite-frequency tomography of D'' shear velocity heterogeneity beneath the Caribbean. *Journal of Geophysical Research* 110: B07305 (doi:10.1029/2004JB003373).
- Hutko A, Lay T, Garner EJ, and Revenaugh JS (2006) Seismic detection of folded, subducted lithosphere at the core–mantle boundary. *Nature* 441: 333–336.
- Itaya T, Hirose K, Kawamura K, and Murakami M (2004) The elasticity of the MgSiO₃ post-perovskite phase in the Earth's lowermost mantle. *Nature* 430: 442–444.
- Ishii M and Tromp J (1999) Normal-mode and free-air gravity constraints on lateral variations in velocity and density of Earth's mantle. *Science* 285: 1231–1236.
- Ito E, Akaogi M, Topor L, and Navrotsky A (1990) Negative pressure–temperature slopes for reactions forming MgSiO₃ perovskite from calorimetry. *Science* 249: 1275–1278.
- Ito E and Takahashi E (1989) Postspinel transforms in the system Mg₂SiO₄–Fe₂SiO₄ and some geophysical implications. *Journal of Geophysical Research* 94: 10637–10646.
- Jeanloz R (1993) Chemical reactions at Earth's core–mantle boundary: Summary of evidence and geomagnetic implications. In: Aki K and Dmowska R (eds.) *Relating Geophysical Structures and Processes: The Jeffreys Volume*, *Geophysical Monograph Series*, vol. 76, pp. 121–127. Washington, DC: American Geophysical Union.
- Jellinek AM and Manga M (2002) The influence of a chemical boundary layer on the fixity, spacing and lifetime of mantle plumes. *Nature* 418: 760–763.
- Ji Y and Nataf H-C (1998) Detection of mantle plumes in the lower mantle by diffraction tomography: Theory. *Earth and Planetary Science Letters* 159: 87–98.
- Johnson LR (1969) Array measurements of P velocities in the lower mantle. *Bulletin of the Seismological Society of America* 59: 973–1008.
- Jordan TH (1977) Lithospheric slab penetration into the lower mantle beneath the Sea of Okhotsk. *Journal of Geophysics* 43: 473–496.
- Jordan TH and Anderson DL (1974) Earth structure from free oscillations and travel times. *Geophysical Journal of the Royal Astronomical Society* 36: 411–459.
- Jordan TH and Lynn WS (1974) A velocity anomaly in the lower mantle. *Journal of Geophysical Research* 79: 2679–2685.
- Kanamori H and Anderson DL (1977) Importance of physical dispersion in surface-wave and free oscillation problems, Review. *Reviews of Geophysics and Space Physics* 15: 105–112.
- Kaneshima S and Helffrich G (1998) Detection of lower mantle scatterers northeast of the Mariana subduction zone using short-period array data. *Journal of Geophysical Research* 103: 4825–4838.
- Kaneshima S and Silver PG (1995) Anisotropic loci in the mantle beneath central Peru. *Physics of the Earth and Planetary Interiors* 88: 257–272.
- Kárasón H and van der Hilst RD (2001) Tomographic imaging of the lowermost mantle with differential times of refracted and diffracted core phases (PKP, P_{diff}). *Journal of Geophysical Research* 106: 6569–6587.
- Karato S-I (1998) Some remarks on the origin of seismic anisotropy in the D'' layer. *Earth, Planets and Space* 50: 1019–1028.
- Karki BB, Wentzcovitch RM, de Gironcoli S, and Baroni S (1999) First-principles determination of elastic anisotropy and wave velocities of MgO at lower mantle conditions. *Science* 286: 1705–1709.
- Kawakatsu H and Niu FL (1994) Seismic evidence for a 920-km discontinuity in the mantle. *Nature* 371: 301–305.
- Kellogg LH (1997) Growing the Earth's D'' layer: Effect of density variations at the core–mantle boundary. *Geophysical Research Letters* 22: 2749–2752.
- Kellogg LH, Hager BH, and van der Hilst RD (1999) Compositional stratification in the deep mantle. *Science* 283: 1881–1884.
- Kendall JM (2000) Seismic anisotropy in the boundary layers of the mantle. In: Karato S-I, Forte AM, Liebermann RC, Masters G, and Stixrude L (eds.) *Earth's Deep Interior: Mineral Physics and Tomography from the Atomic to the*

- Global Scale*, pp. 133–159. Washington, DC: American Geophysical Union.
- Kendall JM and Nangini C (1996) Lateral variations in D'' below the Caribbean. *Geophysical Research Letters* 23: 399–402.
- Kendall JM and Shearer PM (1994) Lateral variations in D'' thickness from long-period shear wave data. *Journal of Geophysical Research* 99: 11575–11590.
- Kendall JM and Silver PG (1996) Constraints from seismic anisotropy on the nature of the lowermost mantle. *Nature* 381: 409–412.
- Kendall JM and Silver PG (1998) Investigating causes of D'' anisotropy. In: Gurnis M, Wysession ME, Knittle E, and Buffett BA (eds.) *The Core–Mantle Boundary Region*, pp. 97–118. Washington, DC: American Geophysical Union.
- Kennett BLN and Engdahl ER (1991) Travel times for global earthquake location and phase identification. *Geophysical Journal International* 105: 429–465.
- Kennett BLN, Engdahl ER, and Buland R (1995) Constraints on seismic velocities in the Earth from travel times. *Geophysical Journal International* 122: 108–124.
- Kennett BLN, Widjiantoro S, and van der Hilst RD (1998) Joint seismic tomography for bulk sound and shear wave speed in the Earth's mantle. *Journal of Geophysical Research* 103: 12469–12493.
- Kito T and Krüger F (2001) Heterogeneities in D'' beneath the southwestern Pacific inferred from scattered and reflected P-waves. *Geophysical Research Letters* 28: 2545–2548.
- Kito T, Krüger F, and Negishi H (2004) Seismic heterogeneous structure in the lowermost mantle beneath the southwestern Pacific. *Journal of Geophysical Research* 109: B09304 (doi:10.1029/2002JB002677).
- Knittle E (1998) The solid/liquid partitioning of major and radiogenic elements at lower mantle pressures: Implications for the core–mantle boundary region. In: Gurnis M, Wysession ME, Knittle E, and Buffett BA (eds.) *The Core–Mantle Boundary Region*, pp. 119–130. Washington, DC: American Geophysical Union.
- Knittle E and Jeanloz R (1987) Synthesis and equation of state of (Mg, Fe)SiO₃ perovskite to over 100 gigapascals. *Science* 235: 668–670.
- Knittle E and Jeanloz R (1989) Simulating the core–mantle boundary: An experimental study of high pressure reactions between silicates and liquid iron. *Geophysical Research Letters* 16: 609–612.
- Kobayashi Y, Kondo T, Ohtani E, et al. (2005) Fe–Mg partitioning between (Mg, Fe)SiO₃ post-perovskite, perovskite, and magnesiowüstite in the Earth's lower mantle. *Geophysical Research Letters* 32: L19301 (doi:10.1029/2005GL023257).
- Kohler MD, Vidale JE, and Davis PM (1997) Complex scattering within D'' observed on the very dense Los Angeles Region Seismic Experiment passive array. *Geophysical Research Letters* 24: 1855–1858.
- Krüger F, Weber M, Scherbaum F, and Schlüterhardt J (1995) Normal and inhomogeneous lowermost mantle and core–mantle boundary under the Arctic and Northern Canada. *Geophysical Journal International* 122: 637–658.
- Kuo BY, Garnero EJ, and Lay T (2000) Tomographic inversion of S–SKS times for shear velocity heterogeneity in D'': Degree 12 and hybrid models. *Journal of Geophysical Research* 105: 28139–28157.
- Kuo C and Romanowicz B (2002) On the resolution of density anomalies in the Earth's mantle using spectral fitting of normal-mode data. *Geophysical Journal International* 150: 162–179.
- Kuo BY and Wu KY (1997) Global shear velocity heterogeneities in the D'' layer: Inversion from Sd–SKS differential travel times. *Journal of Geophysical Research* 102: 11775–11788.
- Lay T (1983) Localized velocity anomalies in the lower mantle. *Geophysical Journal of the Royal Astronomical Society* 72: 483–516.
- Lay T (1989) Structure of the core–mantle transition zone: A chemical and thermal boundary layer. *EOS Transactions of the American Geophysical Union* 70(49): 54–55 and 58–59.
- Lay T and Garnero EJ (2004) Core–mantle boundary structures and processes. In: Sparks RSJ and Hawkesworth CJ (eds.) *Geophysical Monograph Series*, 150, IUGG, Vol. 19: *The State of the Planet: Frontiers and Challenges in Geophysics*, pp. 25–41. Washington, DC: American Geophysical Union.
- Lay T, Garnero EJ, and Russell S (2004a) Lateral variation of the D'' discontinuity beneath the Cocos Plate. *Geophysical Research Letters* 31: L15612 (doi:10.1029/2004GL020300).
- Lay T, Garnero EJ, and Williams Q (2004b) Partial melting in a thermo-chemical boundary layer at the base of the mantle. *Physics of the Earth and Planetary Interiors* 146: 441–467.
- Lay T, Garnero EJ, Young CJ, and Gaherty JB (1997) Scale-lengths of shear velocity heterogeneity at the base of the mantle from S-wave differential travel times. *Journal of Geophysical Research* 102: 9887–9910.
- Lay T and Helmberger DV (1983a) A lower mantle S-wave triple junction and the velocity structure of D''. *Geophysical Journal of the Royal Astronomical Society* 75: 799–837.
- Lay T, Heinz D, Ishii M, et al. (2005) Multidisciplinary impact of the lower mantle perovskite phase transition. *EOS Transactions of the American Geophysical Union* 86: 1–5.
- Lay T and Helmberger DV (1983b) The shear wave velocity gradient at the base of the mantle. *Journal of Geophysical Research* 88: 8160–8170.
- Lay T and Wallace TC (1995) *Modern Global Seismology*, 521 pp. San Diego: Academic Press.
- Lay T, Williams Q, and Garnero EJ (1998a) The core–mantle boundary layer and deep Earth dynamics. *Nature* 392: 461–468.
- Lay T, Williams Q, Garnero EJ, Kellogg L, and Wysession ME (1998b) Seismic wave anisotropy in the D'' region and its implications. In: Gurnis M, Wysession ME, Knittle E, and Buffett BA (eds.) *The Core–Mantle Boundary Region*, pp. 299–318. Washington, DC: American Geophysical Union.
- Lay T and Young CJ (1986) The effect of SKS scattering on models of the shear velocity-structure of the D'' region. *Journal of Geophysics* 59: 11–15.
- Lay T and Young CJ (1989) Waveform complexity in teleseismic broadband SH displacements: Slab diffractions or deep mantle reflections? *Geophysical Research Letters* 16: 605–608.
- Lay T and Young CJ (1991) Analysis of seismic SV waves in the core's penumbra. *Geophysical Research Letters* 18: 1373–1376.
- Lee RC and Johnson LR (1984) Extremal bounds on the seismic velocities in the Earth's mantle. *Geophysical Journal of the Royal Astronomical Society* 77: 667–681.
- Li X-D and Romanowicz B (1996) Global mantle shear velocity model developed using nonlinear asymptotic coupling theory. *Journal of Geophysical Research* 101: 22245–22272.
- Lin J-F, Struzhkin VV, Jacobsen SD, et al. (2005) Spin transition of iron in magnesiowüstite in the Earth's lower mantle. *Nature* 436: 377–380.
- Lithgow-Bertelloni C and Richards MA (1998) The dynamics of Cenozoic and Mesozoic plate motions. *Reviews of Geophysics* 36: 27–78.
- Liu H-P, Anderson DL, and Kanamori H (1976) Velocity dispersion due to anelasticity: Implications for seismology and mantle composition. *Geophysical Journal of the Royal Astronomical Society* 47: 41–58.
- Liu L-G (1974) Silicate perovskite from phase transformation of pyrope-garnet at high pressure and temperature. *Geophysical Research Letters* 1: 277–280.
- Liu X-F and Dziewonski AM (1998) Global analysis of shear wave velocity anomalies in the lowermost mantle. In: Gurnis M, Wysession ME, Knittle E, and Buffett BA (eds.)

- The Core–Mantle Boundary Region*, pp. 21–36. Washington, DC: American Geophysical Union.
- Liu X-F, Tromp J, and Dziewonski AM (1998) Is there a first-order discontinuity in the lowermost mantle? *Earth and Planetary Science Letters* 160: 343–351.
- Loper DE and Lay T (1995) The core–mantle boundary region. *Journal of Geophysical Research* 100: 6397–6420.
- Mainprice D, Barruol G, and Ben Ismail W (2000) The seismic anisotropy of the Earth's mantle: From single crystal to polycrystal. In: Karato S-I, Forte AM, Liebermann RC, Masters G, and Stixrude L (eds.) *Earth's Deep Interior: Mineral Physics and Tomography from the Atomic to the Global Scale*, pp. 237–264. Washington, DC: American Geophysical Union.
- Manga M and Jeanloz R (1996) Implications of a metal bearing chemical boundary layer in D'' for mantle dynamics. *Geophysical Research Letters* 23: 3091–3094.
- Mao WL, Mao H-K, Sturhahn W, et al. (2006) Iron-rich post-perovskite and the origin of ultralow-velocity zones. *Science* 312: 564–565.
- Mao WL, Shen G, Prakapenka VB, et al. (2004) Ferromagnesian postperovskite silicates in the D'' layer of the Earth. *Proceedings of the National Academy of Sciences, USA* 101: 15867–15869.
- Masters G and Gilbert F (1983) Attenuation in the Earth at low frequencies. *Philosophical Transactions of the Royal Society of London, Series A* 308: 479–522.
- Masters G, Johnson S, Laske G, and Bolton H (1996) A shear-velocity model of the mantle. *Philosophical Transactions of the Royal Society of London, Series A* 354: 1385–1411.
- Masters G, Jordan TH, Silver PG, and Gilbert F (1982) Aspherical Earth structure from fundamental spheroidal mode data. *Nature* 298: 609–613.
- Masters G, Laske G, Bolton H, and Dziewonski AM (2000) The relative behavior of shear velocity, bulk sound speed, and compressional velocity in the mantle: Implications for chemical and thermal structure. In: Karato S-I, Forte AM, Liebermann RC, Masters G, and Stixrude L (eds.) *Earth's Deep Interior: Mineral Physics and Tomography from the Atomic to the Global Scale*, pp. 63–87. American Geophysical Union: Washington, DC.
- Masters G, Laske G, Dziewonski A, and Boschi L (1999) Towards a spherical reference Earth model. *EOS Transactions of the American Geophysical Union* 80: F27.
- Matyska C and Yuen DA (2004) The importance of radiative heat transfer for superplumes with a deep mantle phase transition. *Earth and Planetary Science Letters* 125: 255–266.
- Matzel E, Sen MK, and Grand SP (1996) Evidence for anisotropy in the deep mantle beneath Alaska. *Geophysical Research Letters* 23: 2417–2420.
- Maupin V, Garnero EJ, Lay T, and Fouch MJ (2005) Azimuthal anisotropy in the D'' layer beneath the Caribbean. *Journal of Geophysical Research* 110: B08301 (doi:10.1029/2004JB003506).
- McNamara AK, Karato S-I, and van Keken PE (2001) Localization of dislocation creep in the lower mantle: Implications for the origin of seismic anisotropy. *Earth and Planetary Science Letters* 191: 85–99.
- McNamara AK, van Keken PE, and Karato S-I (2002) Development of anisotropic structure in the Earth's lower mantle by solid-state convection. *Nature* 416: 310–314.
- McNamara AK, van Keken PE, and Karato S-I (2003) Development of finite strain in the convecting lower mantle and its implications for seismic anisotropy. *Journal of Geophysical Research* 108(B5): 2230 (doi:10.1029/2002JB001970).
- McNamara AK and Zhong S (2004) Thermochemical structures within a spherical mantle: Superplumes or piles? *Journal of Geophysical Research* 109: B07402 (doi:10.1029/2003JB02847).
- McNamara AK and Zhong S (2005) Thermochemical structures beneath Africa and the Pacific Ocean. *Nature* 437: 1136–1139 (doi:10.1038/nature04066).
- Meade C, Silver PG, and Kaneshima S (1995) Laboratory and seismological observations of lower mantle isotropy. *Geophysical Research Letters* 22: 1293–1296.
- Mégnin C and Romanowicz B (2000) The three-dimensional shear velocity structure of the mantle from the inversion of body, surface, and higher-mode waveform. *Geophysical Journal International* 143: 709–728.
- Merkel S, Kubo A, Miyagi L, et al. (2006) Plastic deformation of Mg₂SiO₅ post-perovskite at lower mantle pressures. *Science* 311: 644–646.
- Minster JB (1980) Anelasticity and attenuation. In: Dziewonski AM and Boschi E (eds.) *Physics of the Earth's Interior*, pp. 152–212. Amsterdam: North-Holland.
- Minster JB and Anderson DL (1981) A model of dislocation controlled rheology for the mantle. *Philosophical Transactions of the Royal Society of London* 299: 319–356.
- Mitchell BJ and Helmberger DV (1973) Shear velocities at the base of the mantle from observations of S and ScS. *Journal of Geophysical Research* 78: 6009–6020.
- Mitrovica JX and Forte AM (1997) Radial profile of mantle viscosity: Results from the joint inversion of convection and postglacial rebound observables. *Journal of Geophysical Research* 102: 2751–2769.
- Mitrovica JX and Forte AM (2004) A new inference of mantle viscosity based upon joint inversion of convection and glacial isostatic adjustment data. *Earth and Planetary Science Letters* 225: 177–189.
- Mondt JC (1977) SH waves: Theory and observations for epicentral distances greater than 90 degrees. *Physics of the Earth and Planetary Interiors* 15: 46–59.
- Montagner J-P and Kennett BLN (1996) How to reconcile body-wave and normal-mode reference Earth models. *Geophysical Journal International* 125: 229–248.
- Montague NL, Kellogg LH, and Manga M (1998) High Rayleigh number thermo-chemical models of a dense boundary layer in D''. *Geophysical Research Letters* 25: 2345–2348.
- Montelli R, Nolet G, Dahlen FA, Masters G, Engdahl ER, and Hung SH (2004) Finite-frequency tomography reveals a variety of plumes in the mantle. *Science* 303: 338–343.
- Moore MM, Garnero EJ, Lay T, and Williams Q (2003) Shear wave splitting and waveform complexity for lowermost mantle structures with low-velocity lamellae and transverse isotropy. *Journal of Geophysical Research* 109: B02319 (doi:10.1029/2003JB002546).
- Morelli A and Dziewonski AM (1987) Topography of the core–mantle boundary and lateral heterogeneity of the liquid core. *Nature* 325: 678–683.
- Morelli A and Dziewonski AM (1993) Body wave travel times and a spherically symmetric P- and S-wave velocity model. *Geophysical Journal International* 112: 178–194.
- Mori J and Helmberger DV (1995) Localized boundary layer below the mid-Pacific velocity anomaly identified from a PcP precursor. *Journal of Geophysical Research* 100: 20359–20365.
- Muirhead KJ and Hales AL (1980) Evidence for P-wave discontinuities at depths greater than 650 km in the mantle. *Physics of the Earth and Planetary Interiors* 23: 304–313.
- Mula AH and Müller G (1980) Ray parameters of diffracted long period P- and S-waves and the velocities at the base of the mantle. *Pure and Applied Geophysics* 188: 1270–1290.
- Murakami M, Hirose K, Kawamura K, Sata N, and Ohishi Y (2004) Post-perovskite phase transition in MgSiO₃. *Science* 304: 855–858.

- Murakami M, Hirose K, Sata N, and Ohishi Y (2005) Post-perovskite phase transition and mineral chemistry in the pyrolytic lowermost mantle. *Geophysical Research Letters* 32: L03304 (doi:10.1029/2004GL021956).
- Nakagawa T and Tackley PJ (2004) Effects of a perovskite–post-perovskite phase change near core–mantle boundary in compressible mantle convection. *Geophysical Research Letters* 31: L16611 (doi:10.1029/2004GL020648).
- Nataf H-C and Houard S (1993) Seismic discontinuity at the top of D'': A world-wide feature? *Geophysical Research Letters* 20: 2371–2374.
- Ni S, Ding X, and Helmberger DV (2000) Constructing synthetics from deep Earth tomographic models. *Geophysical Journal International* 140: 71–82.
- Ni S and Helmberger DV (2003a) Seismological constraints on the South African superplume could be the oldest distinct structure on Earth. *Earth and Planetary Science Letters* 206: 119–131.
- Ni S and Helmberger DV (2003b) Ridge-like lower mantle structure beneath South Africa. *Journal of Geophysical Research* 108(B2): 2094 (doi:10.1029/2001JB001545).
- Ni S, Helmberger DV, and Tromp J (2005) Three-dimensional structure of the Africa superplume from waveform modeling. *Geophysical Journal International* 161: 283–294.
- Ni S, Tan E, Gurnis M, and Helmberger DV (2002) Sharp sides to the African superplume. *Science* 296: 1850–1852.
- Niu F and Kawakatsu H (1997) Depth variation of the mid-mantle seismic discontinuity. *Geophysical Research Letters* 24: 429–432.
- Obayashi M and Fukao Y (1997) P and Pcp travel time tomography for the core–mantle boundary. *Journal of Geophysical Research* 102: 17825–17841.
- Oganov AR and Ono S (2004) Theoretical and experimental evidence for a post-perovskite phase of MgSiO_3 in Earth's D'' layer. *Nature* 430: 445–448.
- Oganov AR, Martonak R, Liao A, Raiteri P, and Parrinello M (2005) Anisotropy of Earth's D'' layer and stacking faults in the MgSiO_3 post-perovskite phase. *Nature* 438: 1142–1144.
- Okano K and Suetsugu D (1992) Search for lower mantle high velocity zones beneath the deepest Kurile and Mariana earthquakes. *Geophysical Research Letters* 19: 745–748.
- Pankow KL and Lay T (1999) Constraints on the Kurile slab from shear wave residual sphere analysis. *Journal of Geophysical Research* 104: 7255–7278.
- Panning MP and Romanowicz B (2004) Inferences on flow at the base of Earth's mantle based on seismic anisotropy. *Science* 303: 351–353.
- Persch ST, Vidale JE, and Earle PS (2001) Absence of short-period ULVZ precursors to Pcp and ScP from two regions of the CMB. *Geophysical Research Letters* 28: 387–390.
- Phipps MJ and Shearer PM (1993) Seismic constraints on mantle flow and topography of the 660-km discontinuity: Evidence for whole mantle convection. *Nature* 365: 506–511.
- Pulliam J and Sen MK (1998) Seismic anisotropy in the core–mantle transition zone. *Geophysical Journal International* 135: 113–128.
- Pulliam J and Stark P (1993) Bumps on the core–mantle boundary: Are they facts or artifacts? *Journal of Geophysical Research* 98: 1943–1956.
- Randall MJ (1971) A revised travel-time table for S. *Geophysical Journal of the Royal Astronomical Society* 22: 229–234.
- Reasoner C and Revenaugh J (1999) Short-period P-wave constraints on D'' reflectivity. *Journal of Geophysical Research* 104: 955–961.
- Resovsky J and Trampert J (2003) Using probabilistic seismic tomography to test mantle velocity–density relationships. *Physics of the Earth and Planetary Science Letters* 215: 121–130.
- Revenaugh JS and Jordan TH (1991) Mantle layering from ScS reverberations. 2: The transition zone. *Journal of Geophysical Research* 96: 19763–19780.
- Revenaugh JS and Meyer R (1997) Seismic evidence of partial melt within a possibly ubiquitous low-velocity layer at the base of the mantle. *Science* 277: 670–673.
- Richards MA and Hager BH (1984) Geoid anomalies in a dynamic Earth. *Journal of Geophysical Research* 89: 5987–6002.
- Ritsema J (2000) Evidence for shear wave anisotropy in the lowermost mantle beneath the Indian Ocean. *Geophysical Research Letters* 27: 1041–1044.
- Ritsema J, Lay T, Garnero EJ, and Benz H (1998) Seismic anisotropy in the lowermost mantle beneath the Pacific. *Geophysical Research Letters* 25: 1229–1232.
- Ritsema J, Ni S, Helmberger DV, and Crotwell HP (1998) Evidence for strong shear velocity reductions and velocity gradients in the lower mantle beneath Africa. *Geophysical Research Letters* 25: 4245–4248.
- Ritsema J and van Heijst HJ (2000) Seismic imaging of structural heterogeneity in Earth's mantle: Evidence for large-scale mantle flow. *Science Progress* 83: 243–259.
- Ritsema J, van Heijst HJ, and Woodhouse JH (1999) Complex shear wave velocity structure imaged beneath Africa and Iceland. *Science* 286: 1925–1928.
- Robertson GS and Woodhouse JH (1996) Ratio of relative S to P velocity heterogeneity in the lower mantle. *Journal of Geophysical Research* 101: 20041–20052.
- Rodgers A and Wahr J (1993) Inference of core–mantle boundary topography from ISC, Pcp and PKP traveltimes. *Geophysical Journal International* 115: 991–1011.
- Rokosky JM, Lay T, Garnero EJ, and Russell SA (2004) High-resolution investigation of shear wave anisotropy in D'' beneath the Cocos Plate. *Geophysical Research Letters* 31: L07605 (doi:10.1029/2003GL018902).
- Romanowicz B (2001) Can we resolve 3D density heterogeneity in the lower mantle? *Geophysical Research Letters* 28: 1107–1110.
- Ross AR, Thybo H, and Solidilov LN (2004) Reflection seismic profiles of the core–mantle boundary. *Journal of Geophysical Research* 109: B08303 (doi:10.1029/2003JB002515).
- Rost S and Revenaugh J (2001) Seismic detection of rigid zones at the top of the core. *Science* 294: 1911–1914.
- Rost S and Revenaugh J (2003) Small-scale ultralow-velocity zone structure imaged by ScP. *Journal of Geophysical Research* 108: 2056 (doi:10.1029/2001JB001627).
- Rost S, Garnero EJ, Williams Q, and Manga M (2005) Seismic constraints on a possible plume root at the core–mantle boundary. *Nature* 435: 666–669.
- Russell SA, Lay T, and Garnero EJ (1998) Seismic evidence for small-scale dynamics in the lowermost mantle at the root of the Hawaiian hotspot. *Nature* 396: 255–258.
- Russell SA, Lay T, and Garnero EJ (1999) Small-scale lateral shear velocity and anisotropy heterogeneity near the core–mantle boundary beneath the central Pacific imaged using broadband ScS-waves. *Journal of Geophysical Research* 104: 13183–13199.
- Russell SA, Reasoner C, Lay T, and Revenaugh J (2001) Coexisting shear- and compressional-wave seismic velocity discontinuities beneath the central Pacific. *Geophysical Research Letters* 28: 2281–2284.
- Sacks S (1966) Diffracted waves studies of the earth's core. 1: Amplitudes, core size, and rigidity. *Journal of Geophysical Research* 71: 1173–1181.
- Saltzer RL, van der Hilst RD, and Kárasón H (2001) Comparing P and S-wave heterogeneity in the mantle. *Geophysical Research Letters* 28: 1335–1338.
- Scherbaum F, Krüger F, and Weber M (1997) Double beam imaging: Mapping lower mantle heterogeneities using

- combinations of source and receiver arrays. *Journal of Geophysical Research* 102: 507–522.
- Schlüter J, Schweitzer J, and Müller G (1985) Evidence against a discontinuity at the top of D". *Geophysical Journal of the Royal Astronomical Society* 81: 295–306.
- Schwartz SY, Lay T, and Grand SP (1991) Seismic imaging of subducted slabs: Trade-offs with deep path and near-receiver effects. *Geophysical Research Letters* 18: 1265–1268.
- Sengupta MK and Julian BR (1978) Radial variation of compressional and shear velocities in the Earth's lower mantle. *Geophysical Journal of the Royal Astronomical Society* 54: 185–219.
- Sengupta MK and Toksöz MN (1976) Three-dimensional model of seismic velocity variation in the Earth's mantle. *Geophysical Research Letters* 3: 84–86.
- Shearer PM (1993) Global mapping of upper mantle reflectors from long-period SS precursors. *Geophysical Journal International* 115: 878–904.
- Shim SH, Duffy TH, and Shen GY (2001) Stability and structure of MgSiO_3 perovskite to 2300-kilometer depth in the Earth's mantle. *Science* 293: 2437–2440.
- Sidorin I, Gurnis M, and Helmberger DV (1999) Evidence for a ubiquitous seismic discontinuity at the base of the mantle. *Science* 286: 1326–1331.
- Sidorin I, Gurnis M, Helmberger DV, and Ding X (1998) Interpreting D" seismic structure using synthetic waveforms computed from dynamic models. *Earth and Planetary Science Letters* 163: 31–41.
- Silver PG and Bina CR (1993) An anomaly in the amplitude ratio of SKS/SKS in the range 100–108° from portable teleseismic data. *Geophysical Research Letters* 20: 1135–1138.
- Simmons NA and Grand SP (2002) Partial melting in the deepest mantle. *Geophysical Research Letters* 29 (10.1029/2001GL013716).
- Sleep NH (1988) Gradual entrainment of a chemical layer at the base of the mantle by overlying convection. *Geophysical Journal* 95: 437–447.
- Stacey FD and Loper DE (1983) The thermal boundary layer interpretation of D" and its role as a plume source. *Physics of the Earth and Planetary Interiors* 33: 45–55.
- Stackhouse S, Brodholt JP, and Price GD (2005a) High temperature elastic anisotropy of the perovskite and post-perovskite polymorphs of Al_2O_3 . *Geophysical Research Letters* 32: L132305 (doi:10.1029/2005GL0223163).
- Stackhouse S, Brodholt JP, and Price GD (2006) Elastic anisotropy of FeSiO_3 end-members of the perovskite and post-perovskite phases. *Geophysical Research Letters* 33: L01304 (doi:10.1029/2006GL023887).
- Stackhouse S, Brodholt JP, Price GD, Wookey J, and Kendall JM (2005b) The effect of temperature on the acoustic anisotropy of the perovskite and post-perovskite polymorphs of MgSiO_3 . *Earth and Planetary Science Letters* 230: 1–10.
- Stixrude L (1998) Elastic constants and anisotropy of MgSiO_3 perovskite, periclase, and SiO_2 at high pressure. In: Gurnis M, Wyession ME, Knittle E, and Buffett BA (eds.) *The Core–Mantle Boundary Region*, pp. 83–96. Washington, DC: American Geophysical Union.
- Sturhahn W, Jackson JM, and Lin J-F (2005) The spin state of iron in minerals in Earth's lower mantle. *Geophysical Research Letters* 32: L12307 (doi:10.1029/2005GL022802).
- Stutzmann E, Vinnik L, Ferreira A, and Singh S (2000) Constraint on the S-wave velocity at the base of the mantle. *Geophysical Research Letters* 27: 1571–1574.
- Su WJ and Dziewonski AM (1997) Simultaneous inversion for 3-D variations in shear and bulk velocity in the mantle. *Physics of the Earth and Planetary Interiors* 100: 135–156.
- Su W, Woodward RL, and Dziewonski AM (1994) Degree 12 model of shear velocity heterogeneity in the mantle. *Journal of Geophysical Research* 99: 6945–6980.
- Sumita I and Olson P (2000) Thermal convection experiments in a rapidly rotating hemispherical shell. *Science* 286: 1547–1549.
- Sun D, Song AT-R, and Helmberger D (2006) Complexity of D" in the presence of slab-debris and phase changes. *Geophysical Research Letters* 33: L12S07 (doi:10.1029/2005GL025384).
- Sze EKM and van der Hilst RD (2003) Core–mantle boundary topography from short period PcP , PKP , and PKKP data. *Physics of the Earth and Planetary Interiors* 135: 27–46.
- Tackley PJ (1998) Three-dimensional simulations of mantle convection with a thermo-chemical basal boundary layer: D"? In: Gurnis M, Wyession ME, Knittle E, and Buffett BA (eds.) *The Core–Mantle Boundary Region*, pp. 231–253. Washington, DC: American Geophysical Union.
- Takei Y and Suetsugu D (1989) A high velocity zone in the lower mantle under the Japan subduction zone inferred from precise measurements of P-wave arrival times. *Journal of Physics of the Earth* 37: 225–231.
- Tanaka S (2002) Very low shear wave velocity at the base of the mantle under the South Pacific superswell. *Earth and Planetary Science Letters* 203: 879–893.
- Tateno S, Hirose K, Sata N, and Ohishi Y (2005) Phase relations in $\text{Mg}_3\text{Al}_2\text{Si}_3\text{O}_{12}$ to 180 GPa: Effect of Al on post-perovskite phase transition. *Geophysical Research Letters* 32: L15306 (doi:10.1029/2005GL023309).
- Thomas C and Kendall JM (2002) The lowermost mantle beneath northern Asia. 2: Evidence for D" anisotropy. *Geophysical Journal International* 151: 296–308.
- Thomas C, Garnero EJ, and Lay T (2004) High resolution image of lowermost mantle structure under the Cocos Plate. *Journal of Geophysical Research* 109: B08307 (doi:10.1029/2004JB003013).
- Thomas C, Heesom T, and Kendall JM (2002) Investigating the heterogeneity of the D" region beneath the northern Pacific using a seismic array. *Journal of Geophysical Research* 107(B11): 2274 (doi:10.1029/2000JB000021).
- Thomas C and Weber M (1997) P velocity heterogeneities in the lower mantle determined with the German Regional Seismic Network: Improvement of previous models and results of 2D modeling. *Physics of the Earth and Planetary Interiors* 101: 105–117.
- Thomas C, Weber M, Agnon A, and Hofstetter A (1998) A low velocity lamella in D". *Geophysical Research Letters* 25: 2885–2888.
- Thomas C, Weber M, Wicks CW, and Scherbaum F (1999) Small scatterers in the lower mantle observed at German broadband arrays. *Journal of Geophysical Research* 104: 15073–15088.
- Thorne MS and Garnero EJ (2004) Inferences on ultralow-velocity zone structure from a global analysis of SPdKS waves. *Journal of Geophysical Research* 109: B08301 (doi:10.1029/2004JB003010).
- Thorne MS, Garnero EJ, and Grand SP (2004) Geographic correlation between hot spots and deep mantle lateral shear-wave velocity gradients. *Physics of the Earth and Planetary Interiors* 146: 47–63.
- Tibuleac IM and Herrin E (1999) Lower mantle lateral heterogeneity beneath the Caribbean Sea. *Science* 285: 1711–1715.
- Tilmann FJ, McKenzie D, and Priesley KF (1998) P and S-wave scattering from mantle plumes. *Journal of Geophysical Research* 103: 21145–21163.
- Toh A, Romanowicz B, Capdeville Y, and Takeuchi N (2005) 3D effects of sharp boundaries at the borders of the African and Pacific Superplumes: Observation and modeling. *Earth and Planetary Science Letters* 233: 237–253.
- Toksöz MN, Minear JW, and Julian BR (1971) Temperature field and geophysical effects of a downgoing slab. *Journal of Geophysical Research* 76: 1113–1138.
- Trampert J, Deschamps F, Resovsky J, and Yuen D (2004) Probabilistic tomography maps chemical heterogeneities throughout the lower mantle. *Science* 306: 853–856.

- Tsuchiya T, Tsuchiya J, Umemoto K, and Wentzcovitch RM (2004a) Phase transition in MgSiO_3 perovskite in the Earth's lower mantle. *Earth and Planetary Science Letters* 224: 241–248.
- Tsuchiya T, Tsuchiya J, Umemoto K, and Wentzcovitch RM (2004b) Elasticity of post-perovskite MgSiO_3 . *Geophysical Research Letters* 31: L14603 (doi:10.1029/2004GL020278).
- Uhrhammer R (1978) S-wave travel times for a spherically averaged earth. *Geophysical Journal of the Royal Astronomical Society* 55: 283–309.
- Usui Y, Hiramatsu Y, Furumoto M, and Kanao M (2005) Thick and anisotropic D" layer beneath Antarctic Ocean. *Geophysical Research Letters* 32: L13311 (doi:10.1029/2005GL022622).
- Valenzuela R and Wysession ME (1998) Illuminating the base of the mantle with core-diffracted waves. In: Gurnis M, Wysession ME, Knittle E, and Buffett BA (eds.) *The Core–Mantle Boundary Region*, pp. 57–72. Washington, DC: American Geophysical Union.
- van der Hilst RD and Kárason H (1999) Compositional heterogeneity in the bottom 1000 kilometers of Earth's mantle: Toward a hybrid convection model. *Science* 283: 1885–1888.
- van der Hilst RD, Widjiantoro S, and Engdahl ER (1997) Evidence for deep mantle circulation from global tomography. *Nature* 386: 578–584.
- Vasco DW and Johnson LR (1998) Whole Earth structure estimated from seismic arrival times. *Journal of Geophysical Research* 103: 2633–2671.
- Vidale JE and Hedlin MAH (1998) Evidence for partial melt at the core–mantle boundary north of Tonga from the strong scattering of seismic waves. *Nature* 391: 628–684.
- Vinnik LP, Breger L, and Romanowicz B (1998a) Anisotropic structure at the base of the Earth's mantle. *Nature* 393: 564–567.
- Vinnik LP, Farra V, and Romanowicz B (1989) Observational evidence for diffracted SV in the shadow of the Earth's core. *Geophysical Research Letters* 16: 519–522.
- Vinnik LP, Niu F, and Kawakatsu H (1998a) Broadband converted phases from midmantle discontinuities. *Earth, Planets and Space* 50: 987–997.
- Vinnik L, Romanowicz B, LeStunff Y, and Makeyeva L (1995) Seismic anisotropy in the D" layer. *Geophysical Research Letters* 22: 1657–1660.
- Wang Y and Wen L (2004) Mapping the geometry and geographic distribution of a very low velocity province at the base of the Earth's mantle. *Journal of Geophysical Research* 109: B10305 (doi:10.1029/2003JB002674).
- Wang Y and Wen L (2006) Geometry and P- and S-Velocity structures of the 'African Anomaly'. *Journal of Geophysical Research* (in press).
- Weber M (1993) P and S-wave reflections from anomalies in the lowermost mantle. *Geophysical Journal International* 115: 183–210.
- Weber M (1994) Lamellae in D"? An alternative model for lower mantle anomalies. *Geophysical Research Letters* 21: 2531–2534.
- Weber M and Davis JP (1990) Evidence of a laterally variable lower mantle structure from P and S-waves. *Geophysical Journal International* 102: 231–255.
- Wen L (2000) Intense seismic scattering near the Earth's core–mantle boundary beneath the Comoros hotspot. *Geophysical Research Letters* 27: 3627–3630.
- Wen L (2001) Seismic evidence for a rapidly-varying compositional anomaly at the base of the Earth's mantle beneath Indian ocean. *Earth and Planetary Science Letters* 194: 83–95.
- Wen L and Helmberger DV (1998) Ultra-low velocity zones near the core–mantle boundary from broadband PKP precursors. *Science* 279: 1701–1703.
- Wen L, Silver P, James D, and Kuehnel R (2001) Seismic evidence for a thermo-chemical boundary layer at the base of the Earth's mantle. *Earth and Planetary Science Letters* 189: 141–153.
- Wentzcovitch RM, Karki BB, Cococcioni M, and de Gironcoli S (2004) Thermoelastic properties of MgSiO_3 -perovskite: Insights on the nature of the Earth's lower mantle. *Physical Review Letters* 92: 018501-1–018501-4.
- Widmer R, Masters G, and Gilbert F (1991) Spherically symmetric attenuation within the Earth from normal mode data. *Geophysical Journal International* 104: 541–553.
- Widjiantoro S and van der Hilst RD (1996) Mantle structure beneath Indonesia inferred from high-resolution tomographic imaging. *Geophysical Journal International* 130: 167–182.
- Williams Q (1998) The temperature contrast across D". In: Gurnis M, Wysession ME, Knittle E, and Buffett BA (eds.) *The Core–Mantle Boundary Region*, pp. 73–81. Washington, DC: American Geophysical Union.
- Williams Q and Garnero EJ (1996) Seismic evidence for partial melt at the base of the Earth's mantle. *Science* 273: 1528–1530.
- Williams Q, Revenaugh J, and Garnero EJ (1998) A correlation between ultra-low basal velocities in the mantle and hot spots. *Science* 281: 564–569.
- Wookey J, Kendall J-M, and Rümpker G (2005) Lowermost mantle anisotropy beneath the north Pacific from differential S–ScS splitting. *Geophysical Journal International* 161: 829–838.
- Wookey J, Stackhouse S, Kendall J-M, Brodholt J, and Price GD (2005) Efficacy of the post-perovskite phase as an explanation for lowermost-mantle seismic properties. *Nature* 438: 1004–1007.
- Wright C and Lyons JA (1975) Seismology, $dT/d\Delta$ and deep mantle convection. *Geophysical Journal of the Royal Astronomical Society* 40: 115–138.
- Wright C, Muirhead KJ, and Dixon AE (1985) The P-wave velocity structure near the base of the mantle. *Journal of Geophysical Research* 90: 623–634.
- Wysession ME (1996) Large-scale structure at the core–mantle boundary from diffracted waves. *Nature* 382: 244–248.
- Wysession ME, Fischer KM, Al-eqabi GI, Shore PJ, and Gurari I (2001) Using MOMA broadband array ScS–S data to image smaller-scale structures at the base of the mantle. *Geophysical Research Letters* 28: 867–870.
- Wysession ME and Okal EA (1989) Regional analysis of D" velocities from the ray parameters of diffracted P profiles. *Geophysical Research Letters* 16: 1417–1420.
- Wysession ME, Langenhorst A, Fouch MJ, et al. (1999) Lateral variations in compressional/shear velocities at the base of the mantle. *Science* 284: 120–125.
- Wysession M, Lay T, Revenaugh J, et al. (1998) The D" discontinuity and its implications. In: Gurnis M, Wysession ME, Knittle E, and Buffett BA (eds.) *The Core–Mantle Boundary Region*, pp. 273–298. Washington, DC: American Geophysical Union.
- Yamada A and Nakanishi I (1998) Short-wavelength lateral variation of a D" P-wave reflector beneath the southwestern Pacific. *Geophysical Research Letters* 25: 4545–4548.
- Yamazaki D and Karato S-I (2002) Fabric development in (Mg, O) during large strain shear deformation: Implications for seismic anisotropy in Earth's lower mantle. *Physics of the Earth and Planetary Interiors* 131: 251–267.
- Young CJ and Lay T (1987a) Evidence for a shear velocity discontinuity in the lower mantle beneath India and the Indian Ocean. *Physics of the Earth and Planetary Interiors* 49: 37–53.
- Young CJ and Lay T (1987b) Comment on 'Wave propagation effects and the Earth's structure in the lower mantle'. *Geophysical Research Letters* 14: 562–565.
- Young CJ and Lay T (1989) The core shadow zone boundary and lateral variations of the P velocity structure of the lowermost mantle. *Physics of the Earth and Planetary Interiors* 54: 64–81.

- Young CJ and Lay T (1990) Multiple phase analysis of the shear velocity structure in the D" region beneath Alaska. *Journal of Geophysical Research* 95: 17385–17402.
- Zhao D (2001) Seismic structure and origin of hotspots and mantle plumes. *Earth and Planetary Science Letters* 192: 251–265.
- Zhao D (2004) Global tomographic images of mantle plumes and subducting slabs: Insight into deep Earth dynamics. *Physics of the Earth and Planetary Interiors* 146: 3–34.
- Zhong S (2006) Constraints on thermochemical convection of the mantle from plume heat flux, plume excess temperature, and upper mantle temperature. *Journal of Geophysical Research* 111: B04409 (doi:10.1029/2005JB003972).
- Zhou H-W and Anderson DL (1989) Search for deep slabs in the northwest Pacific mantle. *Proceedings of the National Academy of Sciences USA* 86: 8602–8606.
- Zhou H-W, Anderson DL, and Clayton RW (1990) Modeling of residual spheres for subduction zone earthquakes. 1: Apparent slab penetration signatures in the NW Pacific caused by deep diffuse mantle anomalies. *Journal of Geophysical Research* 95: 6799–6827.

1.19 Deep Earth Structure – The Earth’s Cores

A. Souriau, CNRS/UMR 5562, Toulouse, France

© 2007 Elsevier B.V. All rights reserved.

1.19.1	Introduction	656
1.19.2	The Discovery of the Core	656
1.19.2.1	Indirect Evidences for the Existence of a Core, and Historical Controversies	656
1.19.2.2	The Seismological Detection of the Liquid Core and Inner Core	657
1.19.3	Investigation Tools	658
1.19.3.1	Body-Wave Seismology: The Core Phases	658
1.19.3.2	Free Oscillations	659
1.19.3.3	High-Pressure Physics	661
1.19.4	Radial Structure of the Core in Global Earth Models	661
1.19.5	The Major Discontinuities	663
1.19.5.1	The Core–Mantle Boundary	663
1.19.5.1.1	The topography of the CMB	663
1.19.5.2	The Inner Core Boundary	664
1.19.5.2.1	The topography at ICB	665
1.19.5.2.2	The density jump at ICB and its implications	665
1.19.6	The Liquid Outer Core	665
1.19.6.1	The Main Questions Relative to Liquid Core Structure	665
1.19.6.2	The Stratification at the Base of the Liquid Core	666
1.19.6.3	The Stratification at the Top of the Liquid Core	666
1.19.6.4	Search for a Three-Dimensional Structure inside the Liquid Core	667
1.19.6.5	The Attenuation in the Liquid Core	667
1.19.7	The Inner Core	668
1.19.7.1	The Anisotropy in the Inner Core	668
1.19.7.1.1	Evidence for anisotropy in P-velocity	668
1.19.7.1.2	Depth dependence of the anisotropy	669
1.19.7.1.3	Origin of the anisotropy	671
1.19.7.2	Lateral Heterogeneities inside the Inner Core	672
1.19.7.3	Attenuation in the Inner Core	673
1.19.7.3.1	The apparent incompatibility of body wave and normal mode results	675
1.19.7.3.2	The attenuation mechanisms in the inner core	677
1.19.7.3.3	The anisotropy in attenuation	677
1.19.7.4	S-Waves and the Rigidity of the Inner Core	678
1.19.8	The Seismological Detection of an Inner Core Rotation	679
1.19.8.1	Why a Differential Rotation?	679
1.19.8.2	Tracking the Drift of a Heterogeneity along a Stable Seismic Path	679
1.19.8.3	A Search for a Differential Rotation with a Worldwide Approach	682
1.19.8.4	Discussion	682
1.19.9	Discussion and Conclusion	685
1.19.9.1	Summary of the Results	685
1.19.9.2	The Open Questions, the Future Challenges, the Data for the Future	686
References		687

1.19.1 Introduction

The Earth's core represents 16% of the volume of the Earth, and more than 30% of its mass. This wide ocean of iron, with a solid inner core of about the size of the moon at its center, plays a very important role in Earth physics and chemistry. However, despite its impact on many physical processes such as magnetic field and Earth rotation, which have been investigated for centuries, the core has been discovered very late, in 1906, when the seismological observation of the deep Earth became possible. Since then, important advances have been made, combining observations, laboratory experiments, and theoretical modeling. But the core remains enigmatic. If some of the core properties are now firmly established, many others are still controversial. This chapter will attempt to give a survey of the present state of art, trying to give a degree of confidence to the various results.

Before going through the details of the core structure, it is useful to recall some basic information concerning the core, which in addition show its importance in the planet Earth system.

The core forms very early in the history of our planet, as revealed by the analyses of lead and uranium mantle isotopes and other radionuclide chronometers, and by the presence of a magnetic field in the oldest rocks of the Earth, 3.5 Gy old. It is generally accepted that the inner core formed by crystallization of the liquid core. Some thermodynamical arguments favor a rather young inner core, ~1 Gy old, but this is still controversial (*see* Chapters 5.10 and 9.03).

Convection in the liquid core is at the origin of the main part of the magnetic field. From this point of view, the core is essential to the life, as it protects the Earth from the solar wind. This situation is unique among the solid planets of the solar system. Numerical simulations of the Earth geodynamo show that the inner core has probably a stabilizing role for the magnetic field, as it avoids frequent geomagnetic reversals (*see* Chapters 8.08 and 8.09).

The boundary of the core with the silicate mantle, the core–mantle boundary (CMB), is a place of thermal, dynamical, and probably chemical exchanges. In particular, exchange of angular momentum influences the Earth rotation. At the inner core boundary (ICB), the freezing of the liquid iron alloy occurs with a depletion of the light elements that are present in the liquid core. The ICB is thus also an important place for chemical and energy exchanges.

Heat sources linked to inner core growth, including latent heat and gravitational energy, are essential for powering the geodynamo, and are important factors in the thermal history of the Earth (*see* Chapter 9.09).

The core is governed by complex systems of relations implying thermodynamics, hydrodynamics, geomagnetism, and geochemistry (*see* Melchior (1986) for a tutorial). In what follows, we will only consider the aspects concerning its structure, giving a particular importance to seismology, which has provided most of the results obtained today about the core internal properties.

1.19.2 The Discovery of the Core

1. Many scientific arguments arising from astronomical and geological observations, and theoretical developments concerning heat propagation, thermodynamics, geodesy, and mechanics led to propose a stratified model with a silicate mantle and an iron core. But the effective discovery of the core has relied on seismological observations. Combined with mineral physics, they have allowed us to obtain the present picture of the Earth, made of a silicate mantle, an iron liquid core, and a solid iron inner core, with a radius of 3480 km ($0.55 \times$ Earth radius) for the CMB, and a radius of 1220 km ($0.19 \times$ Earth radius) for the ICB.

1.19.2.1 Indirect Evidences for the Existence of a Core, and Historical Controversies

The fascination for the bowels of the Earth is present in the literature since the Antiquities (*see* historical aspects in Brush (1980), Bolt (1982), Poirier (1996)). The high geothermal gradient experienced in the mines ($\sim 30^\circ\text{C km}^{-1}$) led to propose, at the beginning of the seventeenth century, that a fire is present at the center of the Earth. This theory was however refuted by the argument that not enough oxygen is present at the Earth's center to maintain this fire. The high geothermal gradient has also driven the idea that the Earth could be of solar origin, but controversial arguments have concerned its possible differentiation.

During the nineteenth century, there is a general agreement that the Earth has been fluid at its origin. This idea resulted mostly from the observation of the Earth flattening, an equilibrium figure supposed to be acquired during fluid stage, and from the

identification of plutonic rocks. The question was raised of whether the Earth is still fluid in its interior, or solid as a result of its complete cooling, or partly solid. The geothermal gradient predicts a fusion of the Earth silicates at $\sim 80\text{--}100$ km depth, an idea reinforced by the fluid lavas rejected by volcanoes. An argument against this model is given by Ampère (1775–1836), who noted the impossibility, for such a model, to resist the high stresses induced by the lunar tides on the thin solid envelope. On the other hand, Poisson (1781–1840) noted that the melting temperature of rocks increases with pressure, opening the possibility of a completely solid Earth.

Two discoveries have allowed to reconcile a solid Earth model with the high geothermal gradient: (1) the idea that the internal heat is eliminated not only by conduction, but also (and mostly) by convection and (2) the discovery of radioactivity as a source of internal heat, in addition to the initial heat. These two discoveries explain the impossibility to extrapolate the upper crust geothermal gradient downward. On the other hand, the comparison of the precession and nutations of the Earth observed from astronomy with those computed for different structures led Hopkins (1793–1866) to propose a solid envelope of at least 1000 km thickness, the fluid center being thus much too deep for being the feeding region of the volcanoes. More refined computations by Kelvin (1824–1907) gave a 2000–2500 km thickness for the solid envelope.

The mean density of the Earth, $5.52 \times 10^3 \text{ kg m}^{-3}$, is much higher than that of the rocks ($\sim 2.6 \times 10^3 \text{ kg m}^{-3}$ for granite), even at the temperature and pressure conditions present at 2500 km depth. Its moment of inertia, $I = 0.33Ma^2$, where M is the mass of the Earth and a its radius, is smaller than that of a homogeneous sphere ($I = 0.40Ma^2$), implying higher densities at depth, and hence probably a differentiation. Geochemical arguments, in particular, cosmic abundances and the existence of both silicate and iron meteorites, led to propose an iron core. The discovery of stony-iron meteorites such as pallasites, which may represent the CMB, gives some additional arguments in favor of a differentiated Earth with an iron core. At the end of the nineteenth century, a model with a silicate mantle above an iron core was widely accepted (e.g., Wiechert, 1896).

The effective discovery of the core is however due to seismology. In 1889, the first record of a remote earthquake (from Japan) was obtained at Potsdam by Von Reuber Pachwitz on a low-frequency instrument devoted to tide recording. This opened the new field of global Earth structure analysis from teleseismic data,

thanks to the deployment of worldwide observatories, and to the international organization of seismology.

1.19.2.2 The Seismological Detection of the Liquid Core and Inner Core

Most of the teleseismic records exhibit two clear arrivals: a primary phase (P) which is a compressional wave, and a secondary phase (S) which is a shear wave. In 1906, Oldham noted that the propagation time of the S-wave as a function of distance was delayed by tens of minutes for angular distances larger than 130° . He ascribed this delay to the propagation through a core in which the velocity is smaller than in the mantle, due to a change in physical properties. Although the observed phase at large distances was not S, but SS (an S-phase reflected once beneath the surface), the disappearance of S at its expected arrival time at 130° distance makes Oldham fairly the discoverer of the core. Gutenberg determined the depth of the CMB (2900 km) in 1913, a value that has not significantly changed later. The fluidity of the core, suggested by Oldham's seismic observations, was confirmed by Jeffreys (1926), thanks to the evaluation of the mean Earth rigidity deduced from Earth tides, which is lower than the mantle rigidity deduced from seismic wave propagation. The nature of this core, mostly made of fluid iron, was established by Birch (1952, 1964), a pioneer in high-pressure physics, who demonstrated that a silicate at pressure and temperature similar to core conditions could not reach the inferred density of ~ 10 .

The discovery of the inner core is due to Inge Lehmann (1936), who detected a seismic phase arrival at a distance where no P-phase is supposed to arrive, in a distance range ($\sim 110\text{--}140^\circ$) called the shadow zone of the core (Figure 1). She ascribed this phase to a P-wave reflected at an unknown discontinuity at a depth of ~ 5000 km, the ICB. Bullen suggested that the inner core is rigid. A physical argument is given by Jacobs (1953), who showed that the increase with pressure (thus with depth) of the melting point of iron must result in a phase change of iron from liquid to solid at ICB conditions. Thus, the inner core grows when the Earth cools. An indirect proof of the inner-core rigidity has been given by the periods of the free oscillations of the Earth which are excited after large events, and are sensitive to the elastic properties of the deep Earth (Dziewonski and Gilbert, 1971).

Table 1 summarizes the main physical parameters of the core. Elastic parameters are taken from two global Earth models which are widely used as reference, PREM

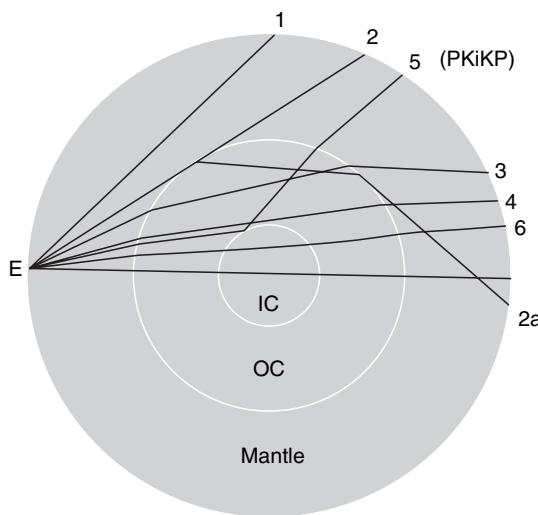


Figure 1 Discovery of the inner core (Lehmann, 1936). The phase PKiKP reflected at the inner core boundary (ray 5) is observed in the shadow zone of the core (between rays 2 and 3), a zone where no P-wave is supposed to arrive, because the P-rays (rays 1 and 2 in the mantle) are diffracted at large distance (rays 2a, 3–6) by the velocity decrease in the liquid outer core. IC, inner core, OC, outer core. Rays are made of straight segments because the P velocity is assumed to be constant in each layer (see more realistic models in Figures 2 and 5).

(Dziewonski and Anderson, 1981), and ak135 (Kennett *et al.*, 1995). The temperature is the most poorly defined parameter, as it depends on the composition of the core, which is still debated.

1.19.3 Investigation Tools

Among the various tools used to infer the core structure and properties, seismology is certainly the most powerful. Seismic waves allow not only to obtain very precise values of the elastic parameters, but also to image lateral heterogeneities in velocities, anisotropy, attenuation, and even to seek for potential time variations, induced, for example, by a possible inner-core rotation. However, the interpretation of the images obtained by seismology relies strongly on the results of mineral physics at high pressure and high temperature. Other important information on core structure and dynamics is given by the analysis of the magnetic field induced by the convective motions in the liquid core, and by the parameters describing Earth rotation, which are sensitive to Earth shape and stratification.

1.19.3.1 Body-Wave Seismology: The Core Phases

Core studies are based on traveltimes and amplitudes of the different phases sampling the core (P-waves, S-waves, and combinations of both), and more and more on whole waveform modeling (Volume 4). The worldwide digital broadband stations are the main source of data. For traveltimes, values reported in the bulletins of the International Seismological Centre (ISC) or in derived improved catalog (EHB

Table 1 Main physical parameters for the Earth core and the main discontinuities, from model PREM at 1 s period (Dziewonski and Anderson, 1981), except for hydrostatic equilibrium ellipticity (Bullen and Haddon, 1973), and for temperatures (after Jeanloz, 1990; Poirier and Shankland, 1993)

	Radius (km)	Depth (km)	V_p (km s^{-1})	V_s (km s^{-1})	Density (g cm^{-3})	Pressure (GPa)	Temperature (°K)	Gravity (m s^{-2})	Ellipticity
Mantle and crust	6371	0	5.80	3.20	2.60	0	300	9.81	1/298.3
(Silicates of Fe, Mg)	6371	0	5.80	3.46					
	3480	2891	13.72	7.26	5.57	140	3800 (3500–3700)	10.7	1/392.7
	3479.5	2891.5	13.66	7.28					
Core–mantle boundary (CMB)									
Liquid core	3480	2891	8.06	0	9.90	140	3800	10.7	1/392.7
	3479.5	2891.5	8.00	0			(3000–5800)		
(Iron + light elements)	1221.5	5149.5	10.36	0	12.17	330	4000	4.4	1/411
	1217.5	5153.5	10.29	0			(4000–7600)		
Inner core boundary (ICB)									
Inner core	1221.5	5149.5	11.03	3.50	12.76	330	4000	4.4	1/411
(Almost pure iron)	1217.5	5153.5	11.04	3.50			(4000–7600)		
	0	6371	11.26	3.67	13.09	360	5000	0	0
	0	6371	11.26	3.67			(5000–8000)		

Values in italics indicate velocity values for model ak135 (Kennett *et al.*, 1995).

file; Engdahl *et al.*, 1998) are also used. For these data, the large amount of values collected since 1964, combined with statistical analyses, compensates for the poor quality of single values. Finally, for some phases with a very low energy, stacking of records collected at arrays is necessary.

There are three particularities of core phases.

First of all, S-wave, which is a shear wave, does not propagate inside the liquid core. Thus, the liquid core may be investigated only through P-waves.

Second, the waves sampling the core also travel twice through the mantle and through the crust, at station side and at source side. The crust and the base of the mantle, the so-called D'' layer, are highly heterogeneous, as well as the upper mantle in the source region in many cases (because of the dipping slabs associated with subduction zones). Each time it is possible, it is convenient to use differential traveltimes between neighboring phases, which has the advantage of partly removing the perturbing contributions of mantle and crust, as well as mislocation and clock errors. In particular, the phase PKP(DF), also called PKIKP, which samples the inner core, is often referred to PKP(BC), a nearby phase which has its turning point at the base of the liquid core and has nearly the same shape. It may be also referred to as PKP(AB), which is more distant, more affected by D'' heterogeneities, which differs from PKP(DF) by a

Hilbert transform (Choy and Richards, 1975), but which is the only possible reference phase at large distance.

Third, because of their long path through the Earth, core phases have large Fresnel zones inside the core. For example, a PKP(DF) phase of 2 s period samples a tube of 550 km diameter near the Earth center, which is quite large compared to the inner core radius of 1220 km (Calvet *et al.*, 2006).

A list of the main core phases and their use for core studies is given in **Table 2**. Their paths inside the Earth are shown in **Figure 2**. Some of them are purely P-waves, with refractions or reflections at the core boundaries (PKP, PKKP, etc.), others are a combination of S- and P-waves, such as SKS, which propagates as S-wave in the mantle, or PKJKP, which propagates as S-wave inside the inner core. The PKP wave exhibits a triplication in its travelttime curve as a function of distance, a consequence of the P-velocity decrease from the mantle to the liquid core, as discussed in the next section.

1.19.3.2 Free Oscillations

The periods and amplitudes of free oscillations (or normal modes) allow us to retrieve the elastic parameters, the density and the attenuation of the mean Earth radial structure, and their long wavelength

Table 2 Main body waves sampling the core

Phase name	Path	Use and peculiarities
PKP(DF) = PKIKP	P propagating through the inner core	Inner core structure and anisotropy
PKP(BC)	P turning at the base of the liquid core	Liquid core structure
PKP (AB)	P turning in the middle of the liquid core	Reference phase for PKP(DF) at distances 149–155° D'' structure
PKKP = P2KP, PnKP	P with $(n - 1)$ underside reflections at CMB	Reference phase (poor) for PKP(DF) at large distance Three branches (DF, BC, AB), difficult to observe CMB topography PnKP(BC): Structure of the liquid core
PcP, ScS, PcS, ScP	P or S reflected as P or S at CMB (upperside reflection)	D'' structure CMB topography PcP: reference phase for PKIKP
PKiKP	P reflected at ICB (upperside reflection)	Topography and scatterers at ICB, density and S velocity jump at ICB Difficult to observe at short distance
PKJKP	S through the inner core, P elsewhere	S structure of the inner core
SKS,	S in the mantle, propagating as P in the liquid core	Not directly observable D'' structure
SmKS	$(m - 1)$ underside reflections at CMB	Structure of the uppermost liquid core

CMB, core–mantle boundary; ICB, inner core boundary.

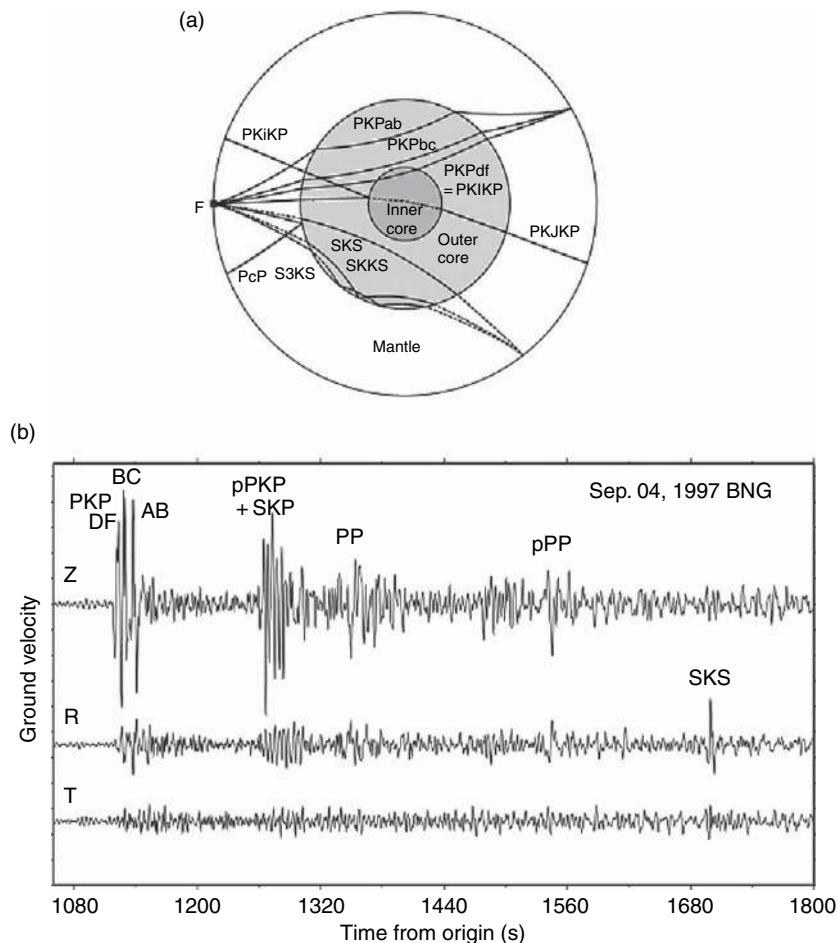


Figure 2 (a) Paths of the main core phases inside the Earth. Waves represented as leaving the focus F toward the lower hemisphere are mostly used for investigating the core–mantle boundary and the upper part of the liquid core; those toward the upper hemisphere are mostly used to investigate the inner core (some of them are used as reference phase). Solid lines: propagation as P-waves; dashed lines: propagation as S-waves. (b) example of data: the first 11 min record of Fiji Islands, 4 Sep. 1997 event (magnitude $M_b = 6.3$, depth = 621 km), at the Geoscope broadband station BNG (Bangui, Central African Republic), at distance 151° . Three components: Z vertical, R radial (in the ray direction), T transverse. Note the three phases of PKP on the vertical component, and the SKS phase on the radial component. Courtesy of E. Stutzmann.

heterogeneities (Volumes 1–3). The splitting of the modes in multiplets gives information on the anisotropy, once the contributions of Earth rotation and ellipticity have been corrected (see, e.g., Tromp, 1995; Durek and Romanowicz, 1999; Laske and Masters, 2003). Modes are mostly sensitive to the even part of the Earth structure; thus, heterogeneities of odd degree, in particular, a possible degree-one (hemispherical) pattern, will be difficult to detect. Moreover, modes have no energy at the Earth center. Only a limited number of modes have significant energy in the core, and still fewer in the inner core. Very large earthquakes are thus required to observe inner-core sensitive modes.

Normal modes are however crucial for core studies, as they allow us to obtain some parameters such as S-velocity or density (Masters, 1979; Kennett, 1998; Masters and Gubbins, 2003), which are very difficult to obtain from body waves. Moreover, they sample the low-frequency part of the spectrum, which is not accessible to body waves. Because of the fluidity of the core, only spheroidal modes are considered.

Figure 3 gives the energy in compression, shear, and density as a function of radius for various core sensitive modes. Note that the energy in the inner core remains in any case quite small compared to that in the mantle and liquid core. As for body

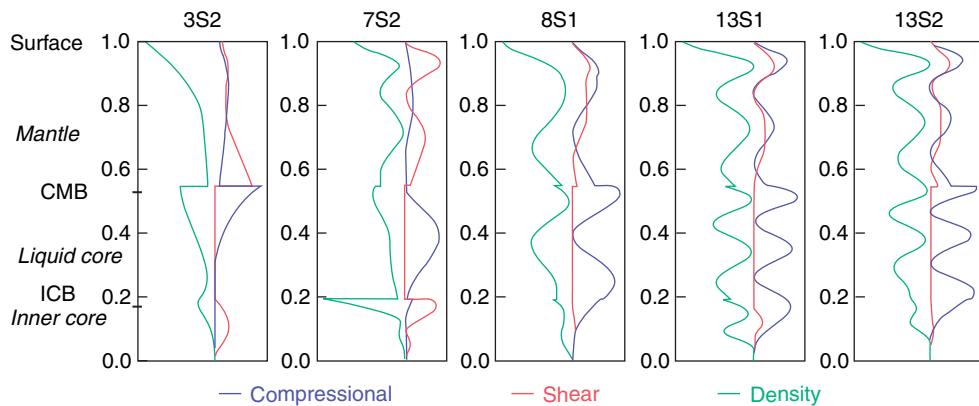


Figure 3 Sensitivity kernels for some core-sensitive modes as a function of radius, for a 1-D Earth model (no lateral heterogeneity). Blue lines are for χ (compressional energy), red lines for μ (shear energy, note it is zero in the fluid outer core), and green lines for density. CMB, core–mantle boundary; ICB, inner core boundary (Courtesy of G. Laske).

waves, it is thus necessary to combine data sensitive to different depths to get rid of the influence of the mantle.

1.19.3.3 High-Pressure Physics

High-pressure physics provides essential information for deriving Earth structure from seismic velocities, anisotropy (for which the full elastic constant tensor is needed), and density (e.g., Stixrude and Cohen, 1995; Saxena *et al.*, 1995; Andrault *et al.*, 1997; Mao *et al.*, 1998; Steinle-Neumann *et al.*, 2003). For the experimental approach, one difficulty arises from the impossibility to reach core pressures with diamond cells. The maximum pressure reached (~ 150 – 200 GPa) corresponds to the middle of the liquid core. Simulations at greater depth are based on shock waves, and hence on transient phenomena with technical difficulties for temperature measurements, resulting in less reproducible results. Computations based on first-principles molecular dynamics simulations, or *ab initio* computations, provide an alternative for simulating core conditions. These methods, which are in theory able to predict almost all the parameters of core materials, meet a growing interest. The results depend however on the approximations done, and on the input parameters (see Chapter 2.05).

Another difficulty is due to the poor knowledge of the light elements that are present in the liquid core (Jephcoat and Olson, 1987; Poirier, 1994). The phase diagram of the liquid alloy, which is likely much more complex than a binary system, is thus impossible to obtain. The melting temperature of iron

depends on the form of iron at ICB (hexagonal closed packed (h.c.p.), or face-centered cubic (f.c.c.), or others), and it is drastically decreased by the presence of light elements, but this decrease depends on both the percentage and nature of the light elements. A temperature decrease of ~ 500 – 1000 K due to light elements is generally accepted (Poirier and Shankland, 1993), but the temperature inside the core remains a poorly constrained parameter (see Chapters 8.02 and 9.09).

1.19.4 Radial Structure of the Core in Global Earth Models

The first accurate core models were derived from traveltimes and amplitudes of PKP and PKKP waves (e.g., Bolt, 1962; Adams and Randall, 1964; Engdahl *et al.*, 1970; Buchbinder, 1971; Qamar, 1973). Nuclear explosions data were often introduced in the models in addition to natural earthquake data to have sources outside subduction zones. SmKS waves were used to constrain the upper part of the liquid core, where no PKP wave has its turning point (Randall, 1970; Hales and Roberts, 1971; Kind and Müller, 1977). These models have allowed to obtain with good precision the radius of the outer core and inner core, and the mean velocity profiles and quality factors throughout the core. However, some of these models present artifacts, because PKP precursors were ascribed to waves reflected at a liquid core discontinuity (e.g., Bolt, 1962; Adams and Randall, 1964), whereas they are due to scatterers at the base of the mantle (Cleary and Haddon, 1972). Artifacts in

the models were also induced by D'' heterogeneities (Kind and Müller, 1977). This shows the importance of considering global Earth inversion to come to reliable reference core models (Volume 1). We will thus consider only the two global models, PREM (Dziewonski and Anderson, 1981) and ak135 (Kennett *et al.*, 1995), which are the most commonly used (Table 1). Throughout this chapter, the focus is on the perturbations to these models inferred from the analyses of specific core phases and normal modes. There have been several other radial global models, for example, SP6 (Morelli and Dziewonski, 1993) and IASP91 (Kennett and Engdahl, 1991), which are also convenient as reference models. They all exhibit nearly the same features, and differ from each other by less than 0.5%.

Model PREM (Dziewonski and Anderson, 1981, and Table 1) has the advantage of combining body waves and normal modes, thus allowing us to obtain a model not only for the P- and S-velocities, but also for the density. The model is compatible with the mass and moment of inertia of the Earth. Moreover, a constraint on stable stratification has been introduced *a priori* in the model before inversion, that is, the Adams–Williamson equation must be satisfied both in the liquid core and in the inner core, each of them assumed to be homogeneous. The final model does not depart significantly from this constraint, except perhaps at the very base of the liquid core. However, some models departing from this stability condition and compatible with normal mode data may also be found (Kennett, 1998).

Model ak135 (Kennett *et al.*, 1995) is constructed from body-wave data only, and is right now the best model for compressional core phases. Its departure from PREM remains small (Table 1). Model ak135 exhibits relatively low velocities at the top of the core, but is slightly faster than PREM in the middle of the core. The main difference compared to PREM is a reduced velocity gradient at the base of the liquid core. The P-velocity jump at ICB is larger in ak135 (0.75 g cm^{-3} instead of 0.62 g cm^{-3}), a value that might have important implications for the percentage and nature of the light elements in the inner core. A comparison of the two models inside the core is shown in Figure 4.

It is important to draw attention on several particularities of the velocity profiles in the core. First, the upper part of the liquid core corresponds to a low-velocity zone for the P-velocity compared to the mantle. This is at the origin of the refraction of the PKP-wave toward large distances when the takeoff

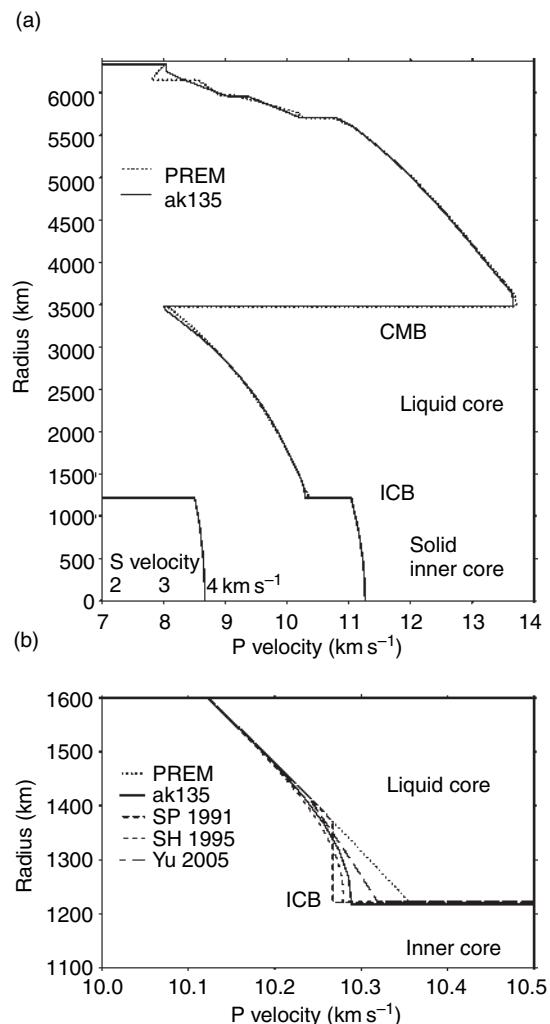


Figure 4 (a) Comparison of the P-velocities for the two global Earth models PREM (Dziewonski and Anderson, 1981) and ak135 (Kennett *et al.*, 1995). Also shown is the S-velocity model in the inner core (note the different scale). (b) Comparison of the velocity profiles at the base of the liquid core for PREM and ak135, and for three other specific models: Souriau and Poupinet (1991), Song and Helmbberger (1995a), and Yu *et al.* (2005), showing the presence of a low velocity gradient.

angle at the source increases, thus at the origin of the so-called shadow zone of the core. The increase of the P-velocity with depth bends the ray when its takeoff increases, leading to an emergence at shorter distance. This results in a triplication in the travel-time curve (Figure 5), each of the branches AB, BC, and DF sampling a different depth range in the core: AB corresponds to a turning point of the ray in the middle of the liquid core, BC at the base of the liquid core, and DF inside the inner core. The three PKP

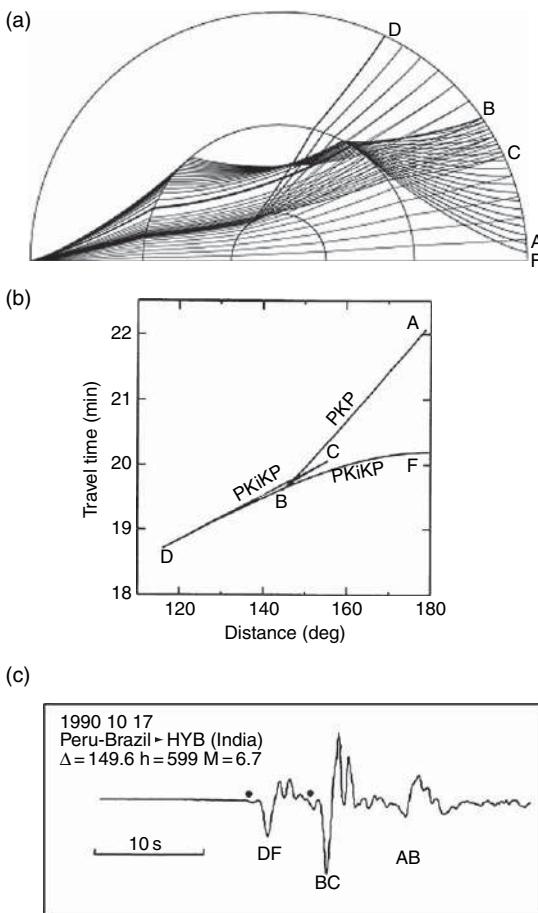


Figure 5 The PKP triplication: (a) ray paths inside the Earth; (b) PKP traveltimes showing the triplication near 145° and the coexistence of the three PKP phases between 145 and 155° ; (c) example of a deep Peru-Brazil event (depth = 599 km) recorded at the broadband Geoscope station HYB (Hyderabad, India), at distance 149.6° . Note the shape similarity between PKP(DF) and PKP(BC), whereas PKP(AB) is the Hilbert transform of PKP(BC).

phases coexist in a small distance range between 145° and 155° . No PKP ray has its turning point in the upper third of the liquid core. A second particularity of the velocity profile is that the S-velocity at the base of the mantle is nearly equal to the P-velocity at the top of the liquid core. Thus, the SKS wave (traveling as S in the mantle, P in the liquid core) is not strongly deflected at CMB, and may have its turning point in the uppermost liquid core, which is not sampled by PKP. Finally, the velocity inside the inner core is nearly constant; thus, the rays are nearly straight lines. Note also the high Poisson's ratio in the inner core (0.44) compared to that of the mantle (0.26–0.30), which is a characteristic of metals.

1.19.5 The Major Discontinuities

1.19.5.1 The Core–Mantle Boundary

The CMB is the most important discontinuity in the Earth, with a density jump of 4.3 g cm^{-3} , ~ 1.5 times larger than the density jump between Earth surface and atmosphere. This explains its very important role in Earth dynamics, in particular, if a topography is present, or if the liquid core has a high viscosity at CMB (see Chapters 3.09 and 3.10). The topography at the CMB is induced by the dynamics of the mantle (e.g., Forte *et al.*, 1995; Defraigne *et al.*, 1996; Greff-Lefftz and Legros, 1996). The topographic coupling between core and mantle depends on the amplitudes and wavelengths of the CMB bumps (Hide *et al.*, 1993). On the other hand, a conductive layer at the base of the mantle would have an important impact on the behavior of the magnetic field and on the amplitudes of Earth nutations (refer to Volume 4 and to Gurnis *et al.* (1998), for reviews).

From the seismological point of view, the CMB appears as a first-order discontinuity. It is surrounded by the D'' layer, a very heterogeneous layer at the base of the mantle. D'' is both a thermal and chemical boundary layer. A strong degree-two heterogeneity is present in D'' , but there is also a high level of short-period heterogeneities. These strong heterogeneities, the presence at some places of a discontinuity at the top of D'' , and a variable velocity gradient in D'' , suggest that it could result from the accumulation of residuals of plates having subducted through the whole mantle. There is also evidence of a phase transition from perovskite to a post-perovskite structure at ~ 200 km above the CMB (Sidorin *et al.*, 1999; Tsuchiya *et al.*, 2004; Oganov and Ono, 2004). At the base of D'' , an ultra-low velocity zone (Garnero *et al.*, 1998) is interpreted as a discontinuous layer of probably partially molten material, supposed to be at the origin of the plumes. On the other hand, deposits at core side may possibly be at the origin of a thin solid layer, whose seismological detection is still questionable (Rost and Revenaugh, 2001).

1.19.5.1.1 The topography of the CMB

The topography of the CMB has been the subject of many studies leading to poorly consistent results. The dynamic ellipticity may be obtained from the Earth nutations, which suggest an extra flattening (decrease of polar minus equatorial radius) of ~ 300 – 500 m, depending on the importance of the

magnetic coupling at CMB (Gwinn *et al.*, 1986; Matthews *et al.*, 2002). All the other results come from seismology, in particular, from the analysis of traveltimes and amplitudes of core phases, mostly Pcp reflected at the CMB, and PKP transmitted through the CMB (Creager and Jordan, 1986; Morelli and Dziewonski, 1987; Rodgers and Wahr, 1993; Obayashi and Fukao, 1997; Boschi and Dziewonski, 2000). The data are generally from bulletins; thus, they have a high noise level. The results depend on the phases used and on the inverted parameters. In particular, as a strong D'' signal is included in the data, a simultaneous inversion of D'' structure and CMB topography is preferable. Even so, it is difficult to separate these two contributions. The introduction of the PKKP phase (Table 2) reflected once beneath the CMB may in theory help to resolve this difficulty, as PKKP samples only the topography, not D'', at its bounce point (Doornbos and Hilton, 1989; Garcia and Souriau, 2000a). This phase is unfortunately difficult to observe and rarely reported in the bulletins. Normal mode studies also give an independent approach to the problem, but they allow to resolve the even part of the topography only, and the tradeoff with mantle heterogeneities is strong (Li *et al.*, 1991).

The results give topographic maps with amplitudes ranging from 4 to 10 km, for wavelengths generally larger than 4000 km. They are completely different from one model to the other. Important biases may result from the existence of unsampled regions at the CMB surface (Pulliam and Stark, 1993; Stark and Hengartner, 1993), and from the contamination by D'' heterogeneities. These problems cannot be easily overcome. A simulation with synthetic arrival times computed for a CMB topography with D'' heterogeneities shows the impossibility to resolve the CMB topography with the presently available data (Garcia and Souriau, 2000a). A stochastic analysis of the Pcp, PKP(BC), and PKKP(BC) residuals shows that 95% of the CMB topography is in the range $\pm\sim 1.5$ km for characteristic lengths larger than 1200 km (Garcia and Souriau, 2000a) (Figure 6). Similar values (± 1.75 km) are obtained from data collected in three regions around the Pacific (Koper *et al.*, 2003). This is significantly lower than most of the values obtained from the inversions at large wavelengths. As noted by Schweitzer (2002), the data may be explained as well by seismic source perturbations or mantle heterogeneities, rather than by CMB undulation.

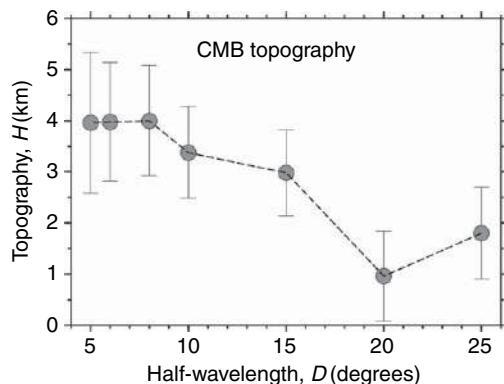


Figure 6 Stochastic analysis of the topography H at core-mantle boundary, as a function of the distance D at the CMB surface ($1^\circ \sim 60$ km at CMB). For a half-wavelength larger than D , 95% of the topography is smaller than H . Note the low topography (<1.5 km) at large wavelength. Modified from Garcia R and Souriau A (2000a) Amplitude of core-mantle boundary estimated by stochastic analysis of core phases. *Physics of the Earth and Planetary Interiors* 117: 345–359.

Short-wavelength undulations are also probably present (Rost and Revenaugh, 2004), but they must have very small amplitudes, because of the high-density contrast at CMB and the difficulty to support dynamically such heavy anomalies. PKKP precursors suggest topographic highs of the order of 300 m with correlation lengths of ~ 10 km acting as scatterers (Earle and Shearer, 1997; Shearer *et al.*, 1998) (Volumes 1–21). Small-scale undulations are however difficult to quantify, because of the complicated perturbations they produce on both traveltimes and amplitudes. Theoretical models show that these perturbations depend on the wavelengths and amplitudes of the CMB undulations, and on the period and incidence of the sampling waves (Menke, 1986; Kampfman and Müller, 1989; Rekdal and Doornbos, 1992; Emmerich, 1993). In particular, focusing-defocusing effects may strongly affect the amplitudes of the waves reflected at CMB, leading sometimes to the impossibility to detect them.

1.19.5.2 The Inner Core Boundary

From the geodynamical point of view, the ICB is less important than the CMB, as it implies a weaker density contrast at a smaller radius. It may however influence the Slichter mode: a translation mode of the inner core inside the fluid whose period is very sensitive to the density contrast and liquid core viscosity at ICB (e.g., Crossley *et al.*, 1992; Denis *et al.*, 1997). On the other hand, the velocity and density

contrasts are key parameters for specifying the nature of the light elements in the core, and to detect partial melting at ICB. Seismic waveforms indicate that the ICB can generally be considered as a first-order discontinuity, with a thickness less than 5 km (Cummins and Johnson, 1988a).

1.19.5.2.1 The topography at ICB

The topography at ICB is certainly very weak and present at long wavelengths only, because iron is at its melting point, and also because of the low viscosity of the inner core, probably of the order of 10^{13} – 10^{19} Pa s (Weber and Machetel, 1992; Buffett, 1997). The ICB topography is induced by the gravimetric forcing of mantle and inner core heterogeneities, with in addition the dynamic response to a possible convection inside the inner core. Mantle and inner core loading give each a topography of ~ 100 m peak to peak (Defraigne *et al.*, 1996), assuming that heterogeneities in the inner core, if any, are two orders of magnitude smaller than in the mantle. Thus, it cannot be detected by seismological methods. On the other hand, PKiKP waves reflected at different latitudes at ICB failed to detect any anomaly in ellipticity (Souriau and Souriau, 1989), leading to the conclusion that the mean shape of the inner core is nearly its equilibrium figure in a rotating Earth, thus nearly spherical.

1.19.5.2.2 The density jump at ICB and its implications

At vertical incidence, the impedance of a discontinuity depends primarily on its density contrast. Thus, the density jump at ICB, $\Delta\rho_{\text{ICB}}$, may be directly obtained from the amplitude of the PKiKP waves reflected normally at ICB. It is generally compared to as the amplitude of the Pcp waves reflected at CMB, provided that the velocity and density contrasts at CMB are known (Bolt and Qamar, 1970). Unfortunately, PKiKP has a small amplitude at vertical incidence and is rarely observed on single records, so that record stacking is generally necessary to enhance the signal. Waveform modeling of PKP may also be used, but this method is subject to trade-off with other parameters, in particular with shear velocity and attenuation at the top of the inner core.

Values ranging from 0.45 to 1.4 g cm^{-3} have been obtained from the amplitude ratios PKiKP/Pcp (Souriau and Souriau, 1989; Shearer and Masters, 1990; Cao and Romanowicz, 2004a; Koper and Pyle, 2004; Koper and Dombrovskaya, 2005). It has been argued that, because of the low amplitude of PKiKP

at short distance, the detected PKiKP onsets may correspond to wave focusing, leading to $\Delta\rho_{\text{ICB}}$ biased toward high values (e.g., Souriau and Souriau, 1989). Values of the order of 1.0 g cm^{-3} may probably represent an upper bound of the density jump. On the other hand, the lowest $\Delta\rho_{\text{ICB}}$ values (Koper and Pyle, 2004) are significantly below the normal mode results.

Normal modes give values of $\Delta\rho_{\text{ICB}}$ of 0.6 – 0.8 g cm^{-3} (Kennett, 1998; Masters and Gubbins, 2003), compatible with the 0.6 – 0.9 g cm^{-3} obtained in the most recent body-wave studies.

Most of the values obtained are above PREM value (0.6 g cm^{-3}), suggesting that the liquid core is much more rich in light elements than previously assumed. This may have important consequences for the thermal history of the Earth, as the light elements released at ICB provide gravitational energy. Thermodynamic modeling suggests that the dynamo was driven by thermal convection in the early history of the Earth, and that the inner core is young (~ 1 – 2 billion years) compared to the age of the Earth, 4.56 billion years (Buffett *et al.*, 1996; Labrosse *et al.*, 1997, 2001; Stacey and Stacey, 1999), and compared to the appearance of the dipolar magnetic field, ~ 2.7 billion years ago. A larger $\Delta\rho_{\text{ICB}}$ means that more compositional energy is released by the growth of the inner core or, in other words, that a slower growth of the inner core may release the same amount of compositional energy. An older inner core, whose formation could favor the development of the dipolar magnetic field, would perhaps be possible in that case.

1.19.6 The Liquid Outer Core

1.19.6.1 The Main Questions Relative to Liquid Core Structure

As previously mentioned, the density of the liquid core is significantly lower than the molten iron density in the same conditions of temperature and pressure, indicating the presence of light elements in the core, in an amount of $\sim 10\%$ by weight. Many candidates are possible. Sulfur has a great solubility inside Fe at these conditions, and it is thus the favored candidate. Other elements such as O, N, Si, and K are likely to be present (Poirier, 1994). The radioactive isotope of K (^{40}K), if present in the core, will be an additional source of energy to power the Earth dynamo (Lee and Jeanloz, 2003). On the other hand, the presence of Ni (which has a

higher density than Fe) in a proportion of $\sim 4\%$ is far from compensating the density decrease due to light elements.

The main questions relative to the fluid core concern its possible radial inhomogeneity, due in particular to the presence of these light elements. A stratification or a distinct layer at the top of the core may influence the core–mantle coupling and Earth dynamics and rotation, as well as the magnetic field (e.g., Wahr and de Vries, 1989; Lumb and Aldridge, 1991; Braginski, 1999; Crossley, 2003). It is thus important to go in more details in the radial core structure. The periods of free oscillations indicate that the outer core is not strongly stratified (Masters, 1979). This is confirmed by the PREM velocity profile, which indicates radial homogeneity, except close to the core boundaries. If a stratification is present, it will thus concern primarily the boundaries. The light elements released at the ICB when the liquid iron alloy crystallizes may migrate upward and form a distinct alloy layer beneath the CMB, whereas a diffusive layer of heavy alloys may be present at the ICB.

Lateral heterogeneities inside the liquid core are less probable, as an active convection is made possible by the low viscosity of the liquid alloy, comparable to that of water at the Earth surface ($\eta = 6 \times 10^{-3}$ Pa s; Poirier, 1988). However, fluid motions in a rotating fluid sphere are organized in cylinders with axis parallel to Earth rotation axis (Busse, 1975). The structures inside the cylinder tangent to the inner core are insulated from the fluid outside the tangent cylinder, being perhaps able to carry material with distinct properties. On the other hand, sedimentation of a different material beneath the polar caps or the equatorial bulge may also be favored by the rotation.

The following sections present the seismological approach to these questions.

1.19.6.2 The Stratification at the Base of the Liquid Core

The propagation time of the PKP(BC) wave at distances larger than 152° , which then becomes diffracted along the ICB, gives direct information on the structure of the lowermost 150 km of the liquid core. The velocities appear significantly lower than those of PREM, which roughly corresponds to the adiabatic gradient (Souriau and Poupinet, 1991). This is confirmed from waveform modeling of short period records (Song and

Helmburger, 1992, 1995a). The data are well explained by a low velocity gradient in the lower 100–150 km at the base of the liquid core, where the velocity becomes nearly constant (Figure 4(b)). The low amplitude decay of the diffracted waves $\text{PKP}(C_{\text{diff}})$ with distance (Souriau and Roudil, 1995; Song and Helmburger, 1995a) is another argument in favor of this low velocity gradient, which acts as a guide for the diffracted waves.

The origin of this low velocity gradient is not clear. A thermal origin is ruled out, due to the low viscosity of the liquid core, which implies a very thin thermal boundary layer. A diffusive boundary layer resulting from compositional convection is the preferred explanation. It is also not excluded that this region could correspond to a small, nonzero rigidity ($v_S = 0.1 \text{ km s}^{-1}$; Mochizuki and Ohminato, 1989). The Slichter mode would be sensitive to such a nonzero rigidity (Smylie, 1999), but its identification on superconducting gravimeter records is highly controversial (Rosat *et al.*, 2003) (see Chapter 3.04). On the other hand, a hemispherical pattern of this layer (Yu *et al.*, 2005), with a reduced velocity gradient beneath the Western Hemisphere only, suggests a compositional difference between the two hemispheres, and hence possibly a different growing process for the inner core.

1.19.6.3 The Stratification at the Top of the Liquid Core

This region of the Earth is very difficult to investigate, because of the absence of PKP waves having their turning point in that part of the core. The SmKS wave samples the uppermost third of the core and becomes a whispering wave beneath the CMB for large m (m up to 4 has been observed as a distinct phase). Unfortunately, it is strongly affected by the heterogeneities in the D'' layer. Considering differential traveltimes such as SmKS – S($m - 1$)KS allows us to decrease this contribution, but not to remove it. Waveform modeling of SmKS may also be used. Normal modes that sample the CMB region also provide useful information but, as previously said, they have a poor depth resolution.

The different results do not lead to a consensus. Several studies implying different methods have proposed the presence of a thin (50–100 km thick) layer with slightly lower velocities at the top of the liquid core, which could correspond to an iron alloy enriched in light elements (e.g., Lay and Young, 1990; Garnero *et al.*, 1993; Tanaka, 2004; Eaton and

Kendall, 2006). However, this result is far to be general (e.g., Choy, 1977), and apparent lateral variations have been detected (e.g., Kohler and Tanimoto, 1992). A hemispherical heterogeneity related to lateral temperature variations at CMB is proposed by Tanaka and Hamaguchi (1993). The resolution of the data is however generally not sufficient to discard the influence of lower-mantle heterogeneities. In fact, it turns out that a thin uppermost fluid layer is generally not required by the data (Kohler, 1997; Garnero and Lay, 1998). P-waves having experienced several reflections under the CMB (P4KP) fail to identify such a layer (Hellfrich and Kaneshima, 2004), discarding a separation of the liquid core in several immiscible liquid alloys beneath the CMB.

The presence of a slightly rigid and conducting zone at the top of the core, with an S-velocity of $0.6\text{--}0.8 \text{ km s}^{-1}$, a thickness of a few hundred meters, and an electrical conductivity of $\sim 10^8 \text{ S}$ (much larger than that of the mantle), has been proposed to explain the amplitudes of the Earth nutations (Buffett *et al.*, 2000) and the waveforms of some seismic phases (ScP) reflected at the CMB (Rost and Revenaugh, 2001). However, as previously mentioned, the seismological observations of this layer are sparse. This layer of silicate sediments would accumulate at the top of the core when the Earth cools. It is distinct from the ultra-low velocity zone detected at the base of the D'' layer on the mantle side, and supposed to be a partially molten zone. The two layers could be a zone of intense chemical exchanges.

1.19.6.4 Search for a Three-Dimensional Structure inside the Liquid Core

Gravitational forcing from the heterogeneities located inside the rigid layers (mantle and inner core) (Wahr and de Vries, 1989) and steady-state dynamics can be at the origin of a three-dimensional (3-D) structure inside the fluid core. However, as shown by Stevenson (1987), the liquid core is not able to sustain relative density heterogeneities larger than 10^{-4} . Assuming that velocity heterogeneities in liquid iron are proportional to density heterogeneities with a proportionality factor of -1 (Stevenson, 1987), this leads to heterogeneities that are much below the level of detectability of seismological methods. Despite this theoretical limit, several seismological results have led to propose an outer core structure, that is, a departure from spherical symmetry (after ellipticity correction).

A large-scale aspherical structure in the liquid core is suggested by the splittings of some normal modes, which are difficult to explain by inner core and mantle structure alone (Ritzwoller *et al.*, 1986; Widmer *et al.*, 1992). Pushing at the extremes, it would be possible to explain the splitting of most of the core modes by outer core structure only (Romanowicz and Bréger, 2000), although the favored interpretation, which is more physically acceptable, is inner core anisotropy, as discussed in the following.

A search for cylindrical structures related to the magneto-hydrodynamical models of the core, such as embedded cylinders parallel to Earth rotation axis, has been performed using the traveltimes of SKS and PKP(BC). A latitudinal pattern observed on SKS (Souriau and Poupinet, 1990) is likely an artifact due to mantle heterogeneities (Kohler and Tanimoto, 1992). The strong increase of the PKP(BC)–PKP(DF) differential traveltimes residuals for the rays propagating inside the inner core tangent cylinder is well explained by a 1% faster velocity inside this outer core structure (Romanowicz *et al.*, 2003). However, an analysis of PKP(BC) failed to detect different physical properties or anisotropy inside and outside the tangent cylinder for the liquid core (Souriau *et al.*, 2003b; Yu *et al.*, 2005), a result confirmed by normal mode analyses (Ishii and Dziewonski, 2005). It has also not been possible to detect anomalies beneath the polar caps, nor beneath the equatorial bulge (Souriau *et al.*, 2003b).

1.19.6.5 The Attenuation in the Liquid Core

The measure of the attenuation in the liquid core at high frequency ($\sim 1 \text{ Hz}$) is based on the amplitude of the phases PnKP reflected ($n-1$) times under the CMB, with n up to 7 (Figure 7). The quality factor for P-waves, Q_α , is larger than 5000–10 000 (Qamar and Eisenberg, 1974; Cormier and Richards, 1976). Slightly lower values ($Q_\alpha = 1600\text{--}7000$, depending on frequency) are given by Tanaka and Hamaguchi (1996). Q may however be considered as close to infinity. Such large values are not met elsewhere inside the Earth. Very large values are also obtained from normal mode analyses ($Q=12\,000$, Widmer *et al.*, 1991), suggesting that Q is not strongly frequency dependent inside the liquid core.

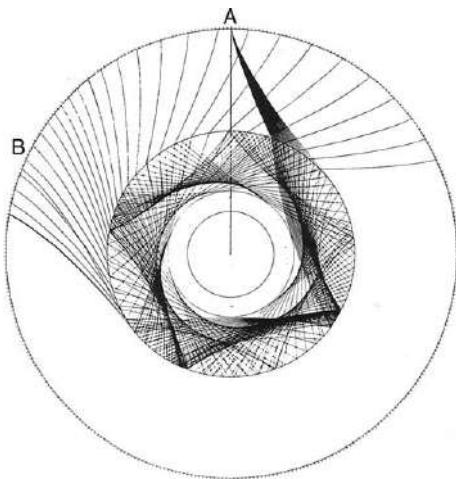


Figure 7 Path of the P7KP wave inside the Earth. The observation of this phase on single records is altogether a proof of the lateral homogeneity of the liquid core, of its low attenuation, of the strong P-wave reflection coefficient underside the core–mantle boundary (which appears as a first order discontinuity), and of the absence of significant topography at this boundary. From Bolt BA (1982) *Inside the Earth*. Freeman, San Francisco, CA, USA.

1.19.7 The Inner Core

The inner core represents only 4.3% of the volume of the core, and less than 1% of the volume of the Earth. It is widely accepted that it results from the solidification of the liquid core during the cooling of the Earth. One of its most spectacular physical properties is its anisotropy: Waves that propagate parallel to the Earth's rotation axis (ERA) are faster than those that propagate parallel to the equatorial plane. Anisotropy also concerns the attenuation inside the inner core: P-waves propagating parallel to ERA are more attenuated than those propagating parallel to equatorial plane. The distribution of the anisotropy inside the inner core is still under debate; it is a fundamental information to specify the origin of this anisotropy, how it is generated, and how the inner core grows. Another question under debate concerns a possible differential rotation of the inner core with respect to the mantle, which may have important consequences for the dynamics of the core.

1.19.7.1 The Anisotropy in the Inner Core

1.19.7.1.1 Evidence for anisotropy in P-velocity

The evidence of a propagation faster along the polar axis than in the equatorial plane was first reported by

Poupinet *et al.* (1983) from the analysis of the large amount of the PKIKP residuals collected by the ISC. This anomaly has been interpreted by Morelli *et al.* (1986) as due to inner core anisotropy. It is also well observed in the differential traveltimes of PKP(DF)–PKP(BC) and PKP(DF)–PKP(AB) (Figure 8). These observations confirm that the anomaly originates in the inner core, not in the liquid core or in the mantle (e.g., Shearer *et al.*, 1988; Creager, 1992). On the other hand, the anomalous splitting of inner core-sensitive normal modes, that is, the splitting that remains after correction for ellipticity and Earth rotation, is also well explained by anisotropy (Woodhouse *et al.*, 1986; Li *et al.*, 1991; Tromp, 1993). The traveltime anomaly, after ellipticity correction, may reach up to 6 s for polar paths (e.g., Vinnik *et al.*, 1994), compared to a total propagation time of ~ 1200 s through the Earth, among which ~ 220 s are through the inner core. Such a traveltime anomaly is very large, compared to those observed for the propagation through the mantle, which rarely exceeds 2 s. A uniform cylindrical anisotropy (transverse isotropy), with a fast axis parallel to Earth rotation axis and a level of anisotropy between 2% and 3%, explains the general features of the data (e.g., Creager, 1992; Shearer, 1994; Vinnik *et al.*, 1994; Song, 1996; Ishii *et al.*, 2002b), but is insufficient to explain all the seismological observations (see Creager (2000) and Souriau *et al.* (2003a) for reviews). One of the most usual expressions for the anisotropy is (Su and Dziewonski, 1995):

$$\delta v_p/v_0 = a_0 + \varepsilon \cos^2 \xi + \gamma \sin^2 2\xi \quad [1]$$

where ξ is the angle between the ray inside the inner core and the symmetry axis. ε represents the P-wave anisotropy, that is, the difference between the P-velocities along the symmetry axis and perpendicular to it, γ is a mixed term which controls the P-wave propagation at intermediate angles, and a_0 represents a perturbation with respect to the P-velocity v_0 of the reference model. Many other equivalent expressions are also used in the literature. The isotropic velocity is defined as the mean of the anisotropic velocity over the whole space (Creager, 1999); its perturbation with respect to the reference model is given by

$$(\delta v_p/v_0)_{\text{iso}} = a_0 + \varepsilon/3 + (8/15)\gamma \quad [2]$$

As will be seen hereafter, depth dependence and long wavelength variations are present in the anisotropy, thus in the a_0 , ε , and γ parameters.

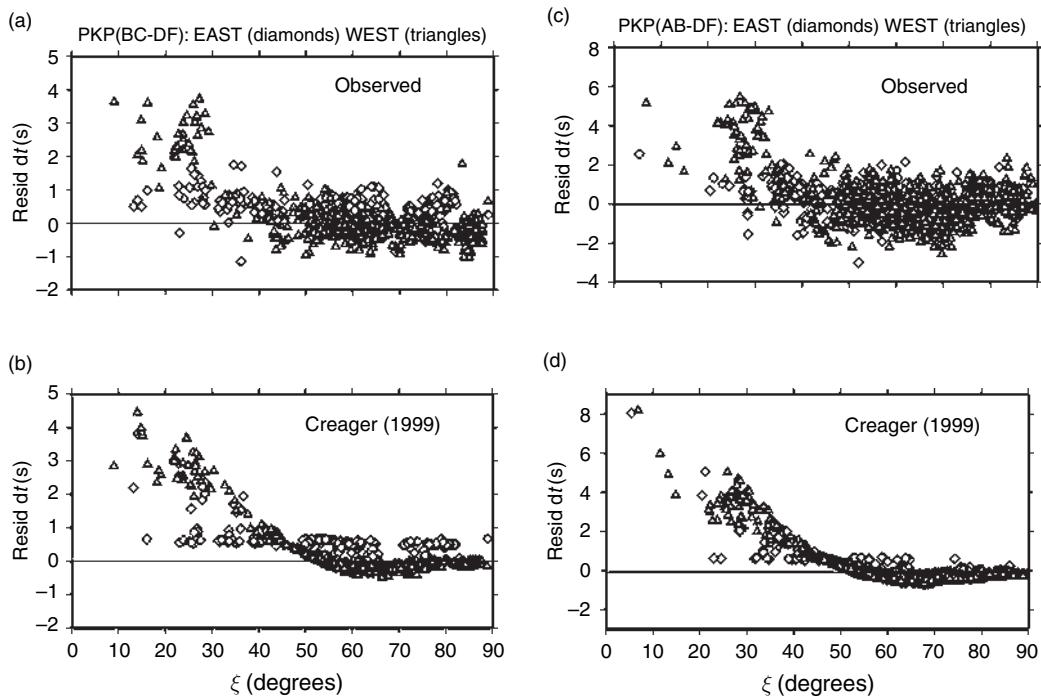


Figure 8 Differential travel time residuals for PKP(BC) – PKP(DF) (a) and for PKP(AB) – PKP(DF) (c) as a function of the angle ξ of the ray inside the inner core with respect to the Earth rotation axis, distinguishing quasi-Eastern (diamonds) and quasi-Western (triangles) Hemispheres. The high residuals at low ξ values reveal that PKP(DF) polar paths are faster than equatorial paths, a property ascribed to inner core anisotropy. (b) and (d): Predictions of a cylindrical anisotropy model (transverse isotropy) by Creager (1999), with different coefficients for the two hemispheres. Modified from Romanowicz B, Tkalcic H and Bréger, L (2003) On the origin of complexity in PKP travel time data. In: Dehant V, et al. (Ed.), *Core dynamics, structure and rotation*, pp. 31–44. American Geophysical Union Monograph. Washington, DC: American Geophysical Union.

Some studies have proposed that the anisotropy symmetry axis could be slightly tilted with respect to ERA (e.g., Creager, 1992; Romanowicz *et al.*, 1996), or even that this tilt could vary with depth (Su and Dziewonski, 1995). Although the data are well explained by such models, it is now generally recognized that this tilt is not required by the data, and that an apparent tilt may result from the lack of data in some directions (Souriau *et al.*, 1997).

It has also been proposed that the anisotropy could be, at least in part, an artifact due to mantle heterogeneities which, because of their geographical distribution, may mimic a polar fast propagation (Bréger *et al.*, 2000a, 2000b; Ishii *et al.*, 2002a; Romanowicz *et al.*, 2003). Such a contribution is probable. A 3-D structure in the liquid core is also able to account for most of the mode splittings (Romanowicz and Bréger, 2000). Anisotropy seems however to provide the simplest explanation able to reconcile most of the seismological observations. We will thus specify hereafter its main characteristics.

1.19.7.1.2 Depth dependence of the anisotropy

The variation of anisotropy with depth is deduced from the PKP(DF) residuals as a function of epicentral distance, for different ray orientations with respect to ERA. There is a general agreement about a low level of anisotropy (less than 1%) in the uppermost 50–150 km of the inner core, with even perhaps no anisotropy at all in the uppermost 50 km (Shearer, 1994; Song and Helmberger, 1995b, 1998; McSweeney *et al.*, 1997; Creager, 2000; Garcia and Souriau, 2000b). Normal mode data seem to not require this isotropic layer, and limit its mean thickness to 150–200 km (Durek and Romanowicz, 1999; Ishii *et al.*, 2002a, 2002b). There are some arguments in favor of a sharp discontinuity between the isotropic layer and the anisotropic structure beneath (Song and Helmberger, 1998; Ouzounis and Creager, 2001; Song and Xu, 2002) but this is still controversial, as scattering near the receiver could provide an alternative explanation (Cormier and Stroujkova, 2005).

In order to explain the hemispherical pattern of the traveltimes for waves sampling the upper part of the inner core (Tanaka and Hamaguchi, 1997), a varying thickness of the isotropic layer with longitude has been invoked. Both Creager (2000) and Garcia and Souriau (2000b) propose a thickness of ~ 100 km beneath the quasi-Eastern Hemisphere (40° E to 160° E) and 400 km beneath the quasi-Western Hemisphere, the anisotropy being uniform beneath this layer. Strong mantle heterogeneities along a few anomalous paths may contribute to this hemispherical pattern (Ishii *et al.*, 2002a), but they cannot fully explain it (Romanowicz *et al.*, 2003).

The depth variations of inner core anisotropy beneath the nearly isotropic layer are also far from reaching consensus. Very different models have been proposed, depending on the type of data used and on the geographical region sampled by the data. For example, Tromp (1995), from an analysis of normal modes, proposed an increase of the anisotropy near the Earth's center. From body waves, Su and Dziewonski

(1995) also found a strong anisotropy (>3%) in the central part of the inner core (radius <300 km). By contrast, McSweeney *et al.* (1997) detected an increase of the anisotropy level between 200 and 500 km depth below ICB, with an anisotropy level up to 4%, and a decrease below. Ouzounis and Creager (2001) and Song and Xu (2002) proposed an anisotropy level as high as 5–8% beneath the isotropic layer in the Western Hemisphere, depending on the thickness of this layer. From a simultaneous inversion of normal modes and body waves, Ishii *et al.* (2002a) obtained a model with either a constant, 1.8% anisotropy, or a gently decreasing anisotropy level with depth. In all these cases, the fast axis is parallel to ERA, or slightly tilted with respect to ERA.

The presence of an innermost inner core of radius ~ 300 km with a different anisotropy is revealed by the traveltimes anomalies of PKP(DF) with nearly antipodal paths (Ishii and Dziewonski, 2002) (Figure 9). A model invoking a slow direction at 45° from ERA may explain the data. If the fast axis

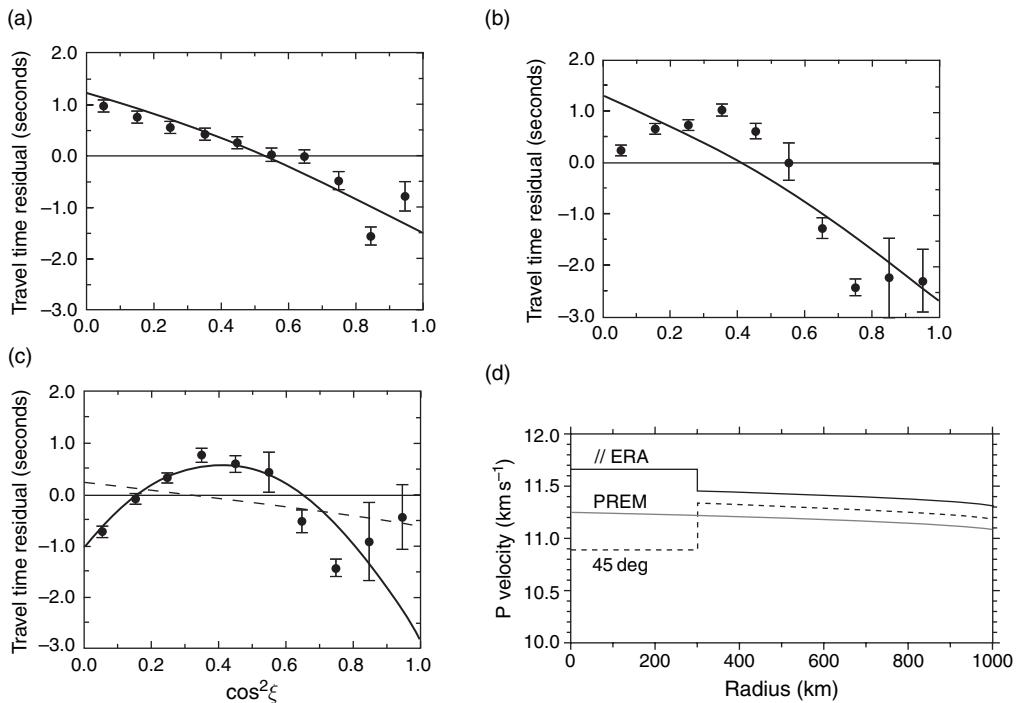


Figure 9 Evidence for a distinct anisotropy in the central part of the inner core. PKP(DF) residuals as a function of $\cos^2 \xi$, where ξ is the ray angle with respect to Earth rotation axis inside the inner core (polar paths correspond to $\cos^2 \xi = 1$). (a) Distance $153\text{--}155^\circ$ (depth ~ 300 km beneath inner core boundary); (b) distance $173\text{--}180^\circ$ (turning point near Earth center). Black dots are the means of the observations with their error bars, thick lines are predictions for a constant anisotropy model. (c) Distance $173\text{--}180^\circ$, but the data are corrected for a constant anisotropy in the upper 920 km. Dashed line is the constant anisotropy model, and thick line is a model with a different innermost inner core P-wave velocity anisotropy, as shown in (d) for rays parallel to Earth rotation axis (ERA) and at 45° . PREM: reference isotropic model. Modified from Ishii M and Dziewonski AM (2002) The innermost inner core of the Earth: Evidence for a change in anisotropic behaviour at the radius of about 300 km. PNSA 99: 14026–14030; Ishii M and Dziewonski AM (2003) Distinct seismic anisotropy at the centre of the Earth. Physics of the Earth and Planetary Interiors 140: 203–217.

is imposed to be parallel to ERA, a 3.7% anisotropy is found in the central part (Ishii and Dziewonski, 2003), but the parameter that controls the P-wave propagation at intermediate angles ($\sim 45^\circ$ to ERA) is too large with regard to the approximations accepted for model computation. From a normal mode analysis, Beghein and Trampert (2003) obtained a smooth model which also favors a change in anisotropy in the central part of the inner core, but which corresponds to a change in the sign of P-wave anisotropy at radius ~ 400 km, thus to an innermost inner core with a slow axis parallel to ERA (Figure 10). A similar result had been obtained by Romanowicz and Bréger (2000) when all the modes are considered together in the inversion. These models are thus very different from the Ishii and Dziewonski (2003) model. It turns out that, with the presently available data, the exact nature of the anisotropy in the innermost inner core is still hard to resolve (Ishii *et al.*, 2002b; Calvet *et al.*, 2006). On the other hand, a sharp discontinuity at 300 km radius between the innermost inner core and the structure above could not be detected (Cormier and Stroujkova, 2005). These authors suggest the existence, between the two structures, of a broad transition zone 50–100 km thick, at radius $r \sim 500$ km, which coincides with a transition from low attenuation ($r < 500$ km) to high attenuation ($r > 500$ km) (Li and Cormier, 2002).

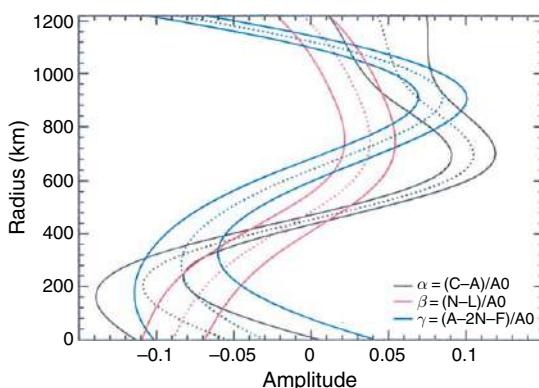


Figure 10 Model showing the variation of anisotropy with depth. The parameter describing P-wave anisotropy (α , in black) changes of sign around 400 km radius with fast axis parallel to Earth rotation axis if $r > 400$ km and perpendicular if $r < 400$ km. The parameter describing S-anisotropy (β , in red) is nearly zero for $r > 400$ km and negative below. From Beghein C and Trampert J (2003) Robust normal mode constraints on inner core anisotropy from model space search. *Science* 299: 552–555.

1.19.7.1.3 Origin of the anisotropy

Three main mechanisms may generate anisotropy: the presence of oriented fluid inclusions, a stratified texture or scatterers, and the preferred orientation of anisotropic crystals.

The favored explanation for inner core anisotropy is the preferred orientation of ε -iron crystals, an h.c.p. form of iron which is stable at high pressure and temperature. A strong degree of alignment, from 30% to 100%, is necessary to explain the observed anisotropy (Stixrude and Cohen, 1995; Laio *et al.*, 2000; Ma *et al.*, 2004). However, due to the uncertainty of the temperature deep in the Earth (Poirier, 1994), and the difficulty to simulate P-T conditions in laboratory experiments, other structures (such as body-centered cubic (b.c.c.), double h.c.p., and orthorhombic fabrics) have also been proposed (Boehler, 1993; Saxena *et al.*, 1995; Andrault *et al.*, 1997). Molecular dynamics simulations also lead to different possible structures (e.g., Vočadlo *et al.*, 1999; Belonosko *et al.*, 2003). Moreover, the presence of light elements in the inner core may change the domain of stability of iron. For example, in presence of sulfur or silicon, the b.c.c. phase may become more stable than the h.c.p. phase (Lin *et al.*, 2002; Vočadlo *et al.*, 2003). The intrinsic anisotropy differs for these different alloys and fabrics. The different anisotropy observed in the innermost inner core could thus suggest the presence of a different iron phase, or a different iron alloy. If the slow axis becomes parallel to ERA, as proposed by some models, it could also be explained with the same form of iron whose preferred orientation changes with depth. On the other hand, the hemispherical pattern, which is explained by a varying thickness of the isotropic layer, could also be explained by a varying degree of crystal alignment (Garcia, 2002b) (see Chapter 2.05).

The preferred orientation of ellipsoidal fluid inclusions is another possible mechanism to generate anisotropy (Singh *et al.*, 2000). The presence of molten iron inclusions, at least in the upper part of the inner core, is proposed in support of the low S-velocity and high attenuation observed in that part of the inner core. The complex phase diagrams of iron alloys also favor a transition from solid to liquid with partial melting. On the other hand, thermodynamical arguments suggest the presence of a mushy zone at the top of the inner core, to insure a large interface of heat exchange between solid and liquid iron (Loper and Roberts, 1981). Singh *et al.* (2000) show that a fluid volume fraction of 3–10%,

present as oblate inclusions aligned in the equatorial plane, can explain the observed anisotropy.

Oriented scatterers may also generate velocity anisotropy, as shown by laboratory experiments (e.g., Bergman, 1997; Bergman *et al.*, 2000). Scatterers could be crystal or grain boundaries, or fluid inclusions. Scatterers with size in the range 1–10 km varying with depth are able to explain the main features of the elastic inner core anisotropy (Cormier and Li, 2002).

The mechanism at the origin of a preferred alignment is also debated (see Yoshida *et al.* (1998) for a review). A first family of scenarios considers that the preferred orientation has been acquired during the inner core growth. For example, solidification texturing may be due to the growth of dendrites in the direction of heat flow, with a cylindrical symmetry consistent with the convective pattern in the outer core (Bergman, 1997). A heat flow stronger at the poles than at the equator, as a result of liquid core convection, may also result in a preferred crystal orientation (Yoshida *et al.*, 1996). Compaction in the mushy zone at ICB during inner core growth may also generate anisotropy (Sumita *et al.*, 1996). By contrast, other scenarios consider that the anisotropy is a present process, that is, that it takes place in the inner core in its present state. For example, it may result from plastic deformation induced by convection inside the inner core (Jeanloz and Wenk, 1988; Weber and Machetel, 1992; Romanowicz *et al.*, 1996; Wenk *et al.*, 2000), although the conditions for generating convection are not necessarily fulfilled (Yukutake, 1998; Buffett, 2000). Maxwell stresses may also be at the origin of anisotropy (Karato, 1993, 1999; Buffett and Wenk, 2004). There are also some evidences that thermal conditions at CMB and motions in the outer core could play a role in the anisotropy distribution inside the inner core, and perhaps explain its hemispherical pattern (Yoshida *et al.*, 1996; Sumita and Olson, 1999; Bergman *et al.*, 2002). However, important unknowns to go further in anisotropy modeling are the nature of the iron crystals (h.c.p., f.c.c., or others), the slip system of deformation (e.g., Poirier and Price, 1999), the existence of energy sources inside the inner core, and the viscosity of the inner core.

1.19.7.2 Lateral Heterogeneities inside the Inner Core

The relative contributions of anisotropy and heterogeneity to the traveltimes anomalies of core phases is

also a subject of debate, as they may explain equally well most of the traveltimes perturbations (Shearer and Toy, 1991). Lateral heterogeneities in the inner core may be either due to a change in isotropic velocity, or due to a change in anisotropy. In the first case, strong heterogeneities of thermal origin are unlikely, as the temperature is nearly uniform inside the inner core (Weber and Machetel, 1992). One may thus imagine either a phase change, or a chemical change, or a change in the amount of partial melting. In the second case (change of anisotropy), it could simply be a change in the fast axis orientation, all the other properties being unchanged. Because of the poor geographic coverage by the PKP(DF) rays, in particular, the difficulty to find at the same place and same depth rays with different orientations, it is generally impossible to discriminate between bulk heterogeneities and anisotropy perturbations, except if they are at very long wavelength.

We have previously mentioned the existence of a hemispherical heterogeneity in anisotropy in the uppermost 400 km of the inner core, the quasi-Eastern Hemisphere (40° E to 160° E) being less anisotropic than the Western Hemisphere (Tanaka and Hamaguchi, 1997; Creager, 1999, 2000; Garcia and Souriau, 2000b) (Figure 11). Despite this strong difference in anisotropy, the isotropic average is the same in the two hemispheres (Creager, 1999), indicating the absence of chemical heterogeneity at hemispherical scale, and reinforcing the idea that the difference between the two hemispheres is in the thickness of the isotropic layer, or in the degree of crystal alignment.

The very top of the inner core has been the subject of a number of specific studies based on the analysis of the interfering phases PKP(DF) + PKiKP at distance ~ 130 – 140° , a complex signal which requires specific modeling. A weak hemispherical variation in isotropic velocity has been detected from a waveform analysis of these phases (Figure 12). The velocity in the uppermost 50–100 km in the Eastern Hemisphere is $\sim 0.8\%$ faster than in the Western Hemisphere (Niu and Wen, 2001; Wen and Niu, 2002; Garcia, 2002a; Cao and Romanowicz, 2004b), a result in agreement with previous observations (Cormier and Choy, 1986; Shearer and Toy, 1991). This hemispherical pattern seems however to disappear at depth ~ 85 km beneath ICB (Cao and Romanowicz, 2004b). As discussed later, it is also related to a hemispherical variation in attenuation. However, the transition from liquid core to solid inner core has still to be elucidated. The detection

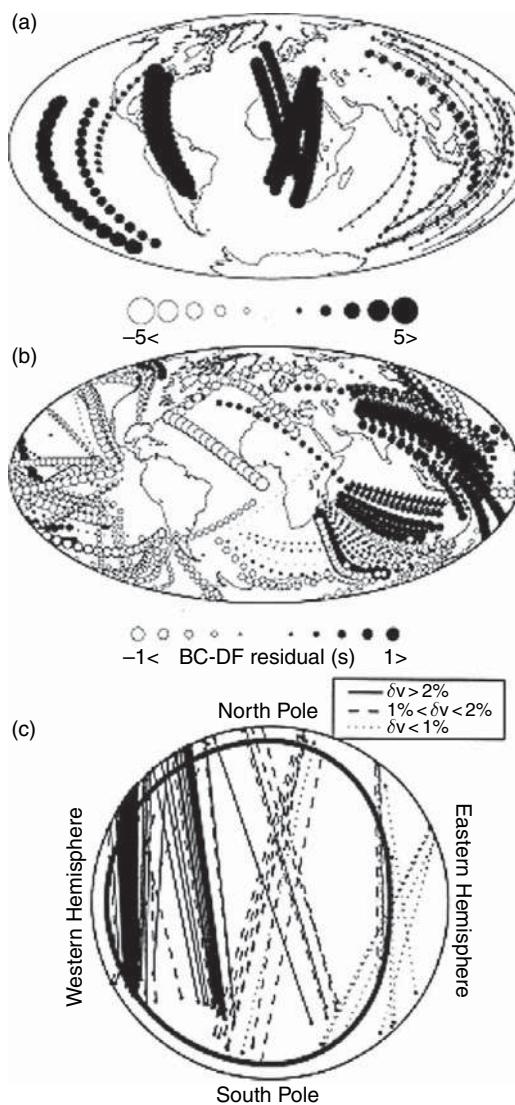


Figure 11 Evidence of a hemispherical pattern in the upper third of the inner core, as seen by PKP(BC)-PKP(DF) differential travel times. (a) Polar paths, the Western Hemisphere is faster than the Eastern Hemisphere; (b) the opposite is observed for East-West paths, but note the different scale (± 5 s for (a), ± 1 s for (b)); (c) interpretative cross-section through the inner core looking from meridian 0° , showing the paths with their velocity anomalies, and a heavy line separating the isotropic asymmetric upper layer from the anisotropic structure. (a,b) From Tanaka S and Hamaguchi H (1997) Degree one heterogeneity and hemispherical variation of anisotropy in the inner core from PKP(BC)-PKP(DF) times. *Journal of Geophysical Research* 102: 2925–2938. (c) From Creager KC (2000) Inner core anisotropy and rotation. In: Dehant V, et al. (ed.), *Core Dynamics, Structure and Rotation, American Geodynamic Series*, 31: pp. 89–114.

of a broad, 1% lower velocity layer at the top 40 km of the inner core beneath equatorial Africa and Indian Ocean (Stroujkova and Cormier, 2004) shows that the large-scale heterogeneity distribution is probably more complex than a simple hemispherical pattern. On the other hand, the variations of the reflection coefficient at ICB have been interpreted as evidence of a mosaic of heterogeneities at ICB, possibly due to different levels of partial melting at the surface (Krasnoshchekov *et al.*, 2005).

The difficulty to distinguish between bulk heterogeneities and anisotropy is particularly drastic for short wavelength heterogeneities, as traveltimes perturbations due to mantle heterogeneities cannot be fully corrected. At short wavelengths (20–200 km), many studies have reported the possible existence of heterogeneities (e.g., Kaneshima, 1996; Creager, 1997; Souriau, 1998; Bréger *et al.*, 1999; Song, 2000; Collier and Helffrich, 2001), but in none of these cases it is possible to completely discard a mantle origin. A stochastic analysis of PKP(DF) at different distances shows that the heterogeneity in isotropic velocity must not exceed 0.3% for wavelengths larger than 200 km (Garcia and Souriau, 2000b). Identifying unambiguously inner core heterogeneities would however be of major interest, as they are used to track a possible inner core differential rotation with respect to the mantle.

Small-scale heterogeneities inside the inner core, acting as scatterers, have been proposed to explain the coda of the PKiKP wave reflected at ICB (Vidale and Earle, 2000). The high-frequency, strong signal which follows PKiKP during ~ 200 s may be explained by heterogeneities of size 2 km located in the uppermost 300 km (Figure 13). Other studies at different locations and different distances show codas with very different characteristics (Poupinet and Kennett, 2004; Koper *et al.*, 2004), suggesting regional variations in the scatterers properties. Short codas may be better explained by reverberation on scatterers at ICB, rather than by scattering in the inner core volume (Poupinet and Kennett, 2004) (see Chapter 1.20).

1.19.7.3 Attenuation in the Inner Core

Attenuation may give information on the physical nature of the inner core, and on its texturing. In particular, if partial melting is present, a strong anelastic attenuation is expected, and it will be correlated with low velocities (in particular a low S-velocity) and low viscosity. On the other hand,

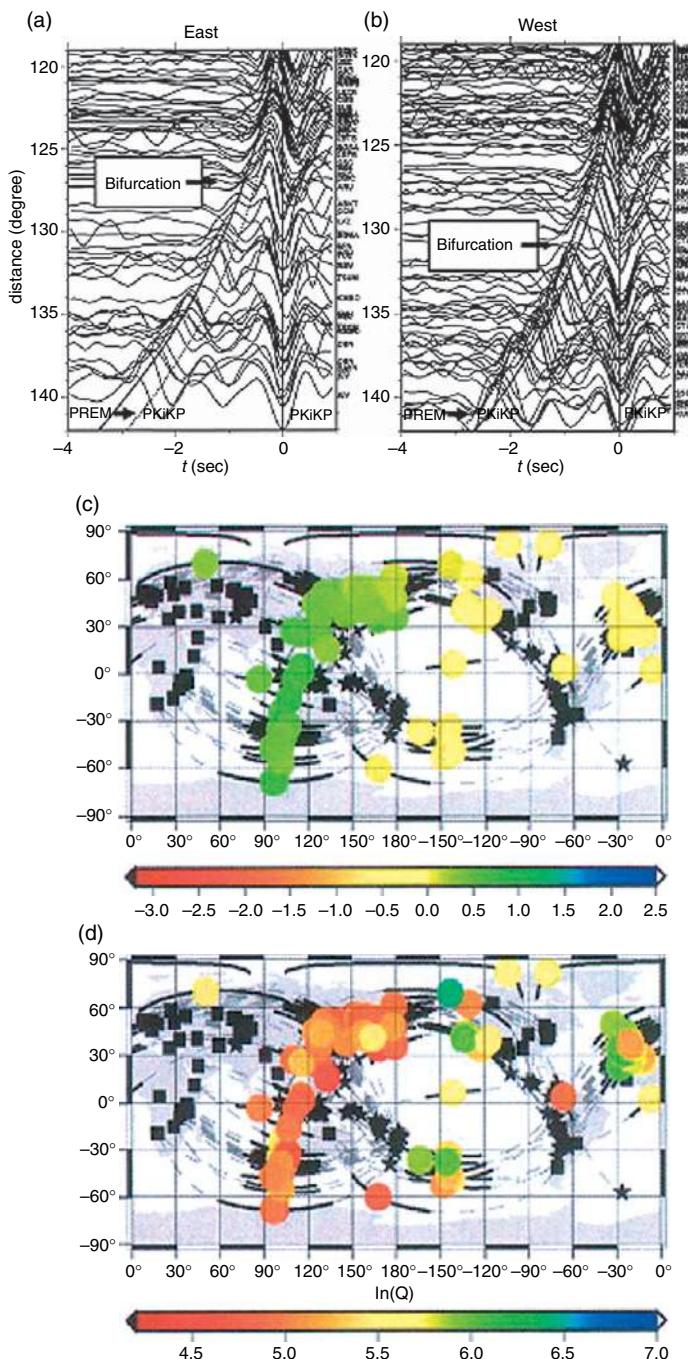


Figure 12 (a, b) Records of PKiKP and PKIKP phases sampling, respectively, the inner core boundary and the uppermost inner core beneath the two hemispheres. The records are aligned on PKiKP, and the thick lines follow the phase maxima. Dashed line is the prediction for PREM. ‘Bifurcation’ corresponds to the separation of the two interfering phases. Note the difference between the two hemispheres for both differential traveltimes and PKIKP amplitudes, indicating a hemispherical heterogeneity in P-velocity and attenuation. (c, d) Differential traveltimes PKiKP–PKIKP (in s) and quality factor (in logarithmic scale) at the top of the inner core (depth 32–85 km below ICB, corresponding to distance 135–142°), showing that the Eastern Hemisphere is faster and more attenuating than the Western Hemisphere. (a, b) From Wen L and Niu F (2002) Seismic velocity and attenuation structures in the top of the Earth's inner core. *Journal of Geophysical Research* 107: 2273 doi:10.1029/2001JB000170. (c, d) From Cao A and Romanowicz B (2004b) Hemispherical transition of seismic attenuation at the top of the Earth's inner core. *Earth Planetary Science Letters* 228: 243–253.

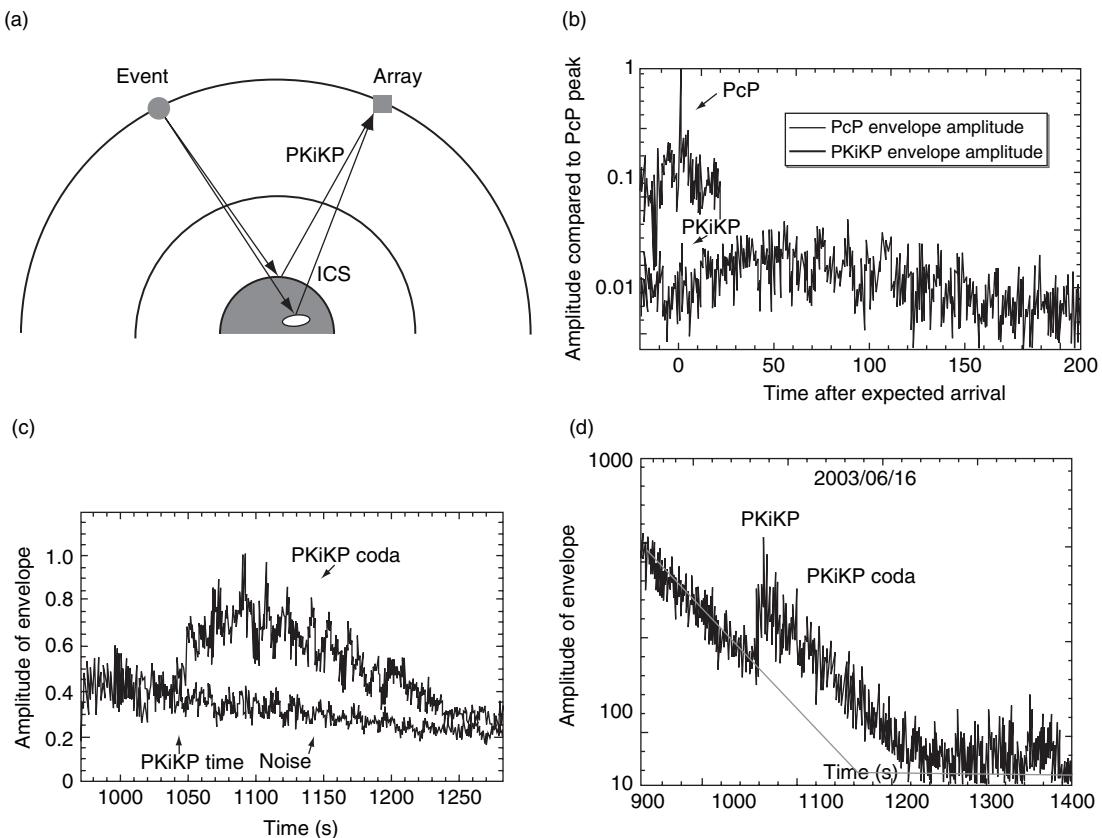


Figure 13 Detection of scatterers inside the inner core, from the coda of the PKiKP wave reflected at inner core boundary. (a) Principle of the method: energy arrival following PKiKP is detected at an array. (b) Comparison of the envelopes of the signal for the Pcp wave reflected at core–mantle boundary, and for the PKiKP wave, showing that the coda is originating in the inner core, not in the mantle; the signals are stacks of two Novaya Zemlya nuclear tests. (c) Average of different stacks obtained for PKiKP for events at distances 60–70° from LASA array in Montana, USA, compared to the noise. (d) Same for an event at 74° from WRA array in Australia, showing a different PKiKP coda, an indication of variations in the scatterer properties inside the inner core. (a–c) After Vidale, JE and Earle PS (2000) Fine-scale heterogeneity in the Earth's inner core. *Nature* 404: 273–275. (d) After Poupinet G and Kennett BLN (2004) On the observation of high frequency PKiKP and its coda in Australia. *Physics of the Earth and Planetary Interiors* 146: 497–511.

texturing may be at the origin of energy loss due to scattering.

Attenuation is constrained by the damping of normal modes, which gives attenuation at the low part of the spectrum and is mostly sensitive to the attenuation in shear (Q_μ). It is also constrained by the amplitude of PKP(DF), which gives the P-wave attenuation Q_α at high frequency. Q_α depends on both the attenuation in bulk (Q_κ) and in shear (Q_μ), such as $Q_\alpha^{-1} = k Q_\mu^{-1} + (1 - k) Q_\kappa^{-1}$, where $k = 4/3 \times (v_s/v_p)^2$, v_p and v_s being the P- and S-velocities (Anderson and Hart, 1978). A difficulty in the interpretation of Q will thus result from the difference in the parameters and frequency bands sampled by body waves and normal modes.

1.19.7.3.1 The apparent incompatibility of body wave and normal mode results

The use of the amplitude spectral ratio of PKP(DF)/PKP(BC), where PKP(BC) is the reference phase, relies on the proximity of the two relevant paths in the mantle, and on the nearly infinite Q inside the liquid core where PKP(BC) has its turning point. Only the top 300 km can be safely sampled with this method. At greater depth, the amplitude of PKP(BC) is strongly dependent on the velocity profile at the base of the liquid core and affected by diffraction at ICB (Souriau and Roudil, 1995); thus, it cannot easily be used as a reference phase.

The various studies come to a general agreement about low Q_α in the uppermost inner core, with

values ranging from 100 to 400 in the uppermost 200 km, probably increasing with depth up to 600 at 400 km (Doornbos, 1974, 1983; Bolt, 1977; Cormier, 1981; Niazi and Johnson, 1992; Bhattacharyya *et al.*, 1993; Souriau and Roudil, 1995; Tseng *et al.*, 2001; Oreshin and Vinnik, 2004). Waveform modeling of PKP at nearly antipodal distances also shows a Q -increase at radius smaller than 500 km, together with a decrease in the scatter of the Q -values (Li and Cormier, 2002). This central, high- Q zone corresponds approximately to the innermost inner core identified by Ishii *et al.* (2002b) and Beghein and

Trampert (2003) (**Figure 14**), and could correspond to a different fabric (Cormier and Stroujkova, 2005). By contrast, Q_α seems significantly smaller at the very top of the inner core, with values in the range 50–100 (Wen and Niu, 2002; Garcia, 2002a). Large-scale regional variations of Q seem to be present, with a hemispherical pattern correlated to the one observed at greater depth (Tseng *et al.*, 2001; Wen and Niu, 2002; Cao and Romanowicz, 2004b; Yu and Wen, 2006a). In the uppermost 85 km, a low Q (~ 160) correlated with a fast propagation is reported in the Eastern Hemisphere, whereas a higher Q (~ 300) is

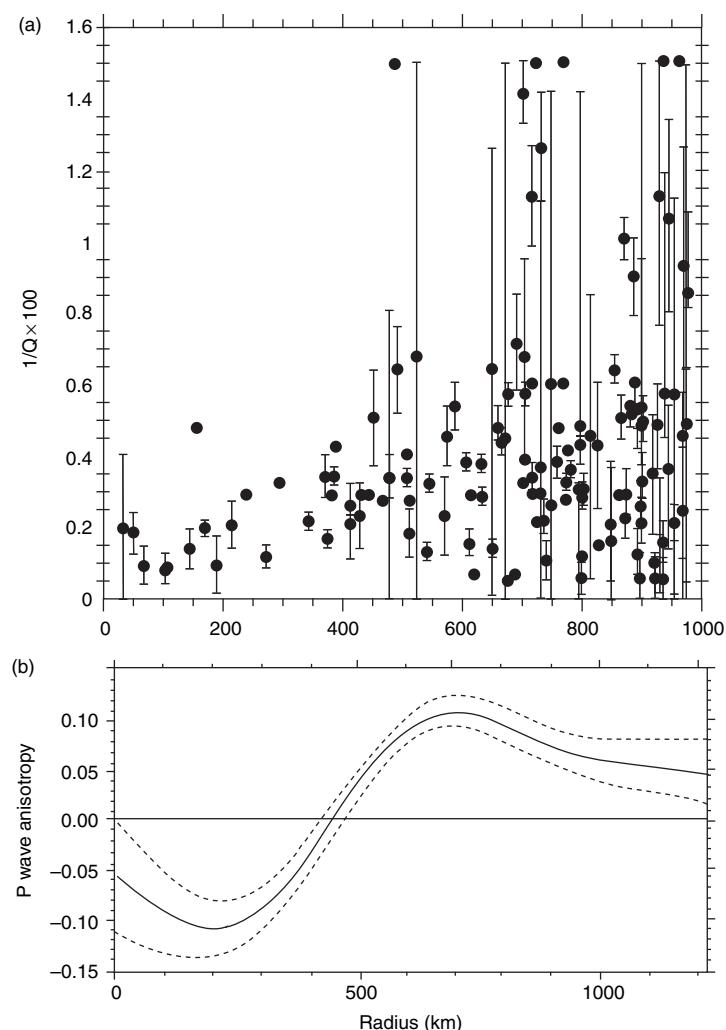


Figure 14 (a) Attenuation $1/Q$ for PKP(DF) paths turning at different depths inside the inner core (Q is the quality factor); (b) coefficient α describing the anisotropy of the P-wave velocity in the inner core. Note the decrease of the attenuation and its smaller scatter near the inner core center, where a different anisotropy is observed (a) Modified from Cormier V and Stroujkova A (2005) Waveform search for the innermost inner core. *Earth and Planetary Science Letters* 236: 96–105. (b) Modified from Beghein C and Trampert J (2003) Robust normal mode constraints on inner core anisotropy from model space search. *Science* 299: 552–555.

reported in the slow Western Hemisphere (Cao and Romanowicz, 2004b). This pattern is not detected at greater depth (Li and Cormier, 2002; Cao and Romanowicz, 2004b; Yu and Wen, 2006a).

Most of the studies fail to detect a significant frequency dependence of Q_α in the narrow frequency range (0.2–2 Hz) sampled by body waves (e.g., Cormier, 1981; Souriau and Roudil, 1995), but this is not general (Doornbos, 1983; Li and Cormier, 2002). As for velocities, it is hard to discard a perturbing effect due to the short wavelength heterogeneities in the mantle, in particular, in D'' , which is likely responsible for the strong scatter in most of the Q -results (Bowers *et al.*, 2000).

Normal modes give generally much larger Q -values than body waves, between 1500 and 4000 (Masters and Gilbert, 1981; Fukao and Suda, 1989; Suda and Fukao, 1990), indicating that Q_μ must be high, ~ 3500 , with possibly an increase from 1500 in the uppermost 200 km to 3800 below (Suda and Fukao, 1990). The compatibility of modes and body waves thus requires either several absorption bands in the inner core (Anderson and Given, 1982), or a finite Q_κ -value, or a different radial variation for Q_κ and Q_μ . Widmer *et al.* (1991) have argued that the high Q_μ -values obtained with modes are due to a misidentification of neighboring modes, and come to $Q_\mu \sim 110$ for PKIKP-equivalent modes. In any case, it seems difficult to escape to a finite Q_κ -value of the same order as Q_μ in the inner core (thus a situation very different to that in the mantle, where $Q_\kappa \gg Q_\mu$), and to a joint contribution of Q_κ and Q_μ in the P-wave attenuation Q_α at body-wave frequency (Cormier *et al.*, 1998).

1.19.7.3.2 The attenuation mechanisms in the inner core

Several mechanisms may contribute to attenuation: viscoelasticity (e.g., Doornbos, 1974; Stiller *et al.*, 1980; Cormier, 1981; Li and Cormier, 2002), diffusion (Loper and Fearn, 1983), and scattering (Cormier and Li, 2002). It is likely that these three different mechanisms are present simultaneously in the inner core. The very low Q at the inner core surface is compatible with the presence of a mushy zone of partially molten material (Fearn *et al.*, 1981; Loper and Roberts, 1981) whose existence, proposed from thermodynamical arguments (Loper and Fearn, 1981), is however not clearly established from seismological observations, and hardly compatible with a sharp ICB. Two distinct diffusive loss mechanisms may take place in this layer, which is at freezing-

melting equilibrium: thermal diffusion and material diffusion between solid and liquid. In any case, they concern exclusively anelasticity in bulk (Q_κ). A model of viscoelastic, frequency-dependent attenuation is able to explain the main characteristics of the attenuation in the body-wave domain (Li and Cormier, 2002), but would lead to pulse distortions larger than those commonly observed. This difficulty is overcome with a model of scattering, which could be the predominant mechanism of attenuation at high and intermediate frequencies (Cormier and Li, 2002), except perhaps at the top of the core. Viscoelastic dissipation, which is responsible for Q_μ , must however also be present in order to explain the high Q found for normal modes. In any case, reconciling body-wave and normal-mode observations still remains a debated problem (see Romanowicz and Durek (2000) for a review, and see Chapter 1.21).

1.19.7.3.3 The anisotropy in attenuation

A first direct evidence of anisotropy in attenuation inside the inner core is given by an analysis of PKP(DF)/PKP(BC) amplitudes for paths which all correspond to the same epicentral distance, all have their turning point beneath the same region, but which differ by their angle with respect to Earth rotation axis (Souriau and Romanowicz, 1996a) (Figure 15). Polar paths, which correspond to a faster propagation, also correspond to a stronger attenuation. This result has been extended at the worldwide scale (Souriau and Romanowicz, 1996b), and to greater depth from waveform modeling of PKP at large distance (Cormier *et al.*, 1998). Oreshin and Vinnik (2004) confirm the dependence of attenuation with the ray angle with respect to Earth rotation axis, but they show that it is observed in the Western Hemisphere only, as is also observed the strongest anisotropy in seismic velocity. Regional variations are also observed by Yu and Wen (2006b), who in addition investigate shallower depths using the PKP(DF)/PKIKP ratio.

The anisotropy in attenuation seems too large to be explained by wavefront distortion due to velocity anisotropy. The correlation between anisotropy in velocity and in attenuation, with the high attenuation axis corresponding to the fast velocity axis parallel to Earth rotation axis, and low attenuation corresponding to slow propagation parallel to equatorial plane, may thus give some indications about the mechanisms at the origin of anisotropy. If the velocity anisotropy was due to fluid inclusions, as proposed by Singh *et al.* (2000), the opposite correlation would be observed if the dominant mechanism is viscoelastic dissipation inside the

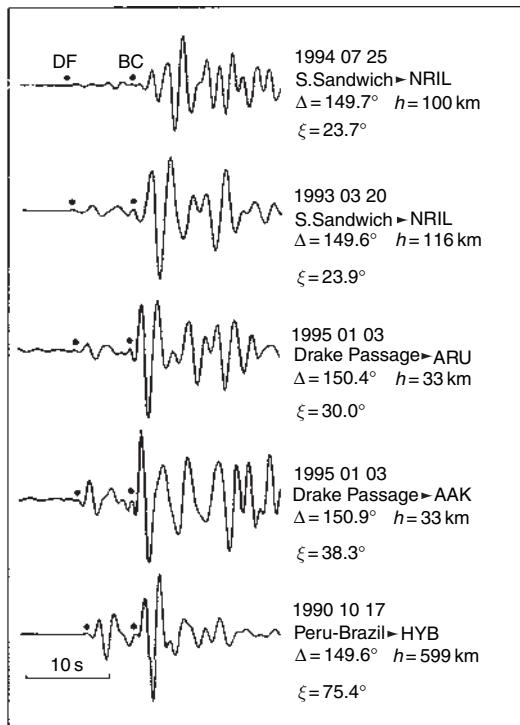


Figure 15 Evidence for anisotropy in attenuation correlated to the anisotropy in velocity, from records corresponding to paths turning in the inner core beneath Africa, with same distance Δ , but with different orientations ξ with respect to Earth rotation axis (h is the focal depth). PKP(BC) being the reference phase, note the fast propagation (large BC-DF time) and strong attenuation (small DF/BC amplitude) for nearly polar paths (small ξ). Data are bandpass filtered at 2 s. From Souriau A and Romanowicz B (1996a) Anisotropy in inner core attenuation: a new type of data to constrain the nature of the solid core. *Geophysical Research Letters* 23: 1–4.

inclusions (Peacock and Hudson, 1990). By contrast, the right correlation is observed if dissipation is due to oriented anisotropic crystals (Carcione and Cavallini, 1994), or to oriented scatterers which could be single crystals, groups of crystals, or fluid inclusions. Scatterers with velocity perturbations of 7–10%, characteristic lengths of ~ 10 km, and a convenient distribution may explain all the characteristics of the body-wave attenuation, including its anisotropy (Cormier *et al.*, 1998; Cormier and Li, 2002).

1.19.7.4 S-Waves and the Rigidity of the Inner Core

Evidence of the rigidity of the inner core, and v_S profiles inside the inner core, have been mostly obtained by indirect observations. The periods of

normal modes require rigidity (Dziewonski and Gilbert, 1971) and lead to a mean value of the S-velocity of 3.6 km s^{-1} (Masters, 1979), with a velocity increase with depth (Suda and Fukao, 1990). Normal modes have however no sensitivity at the Earth's center. The modeling of the PKP waveforms gives generally lower v_S -values beneath the ICB, from nearly zero (Choy and Cormier, 1983) to $2.5\text{--}4.0 \text{ km s}^{-1}$ (Müller, 1973; Häge, 1983; Cummins and Johnson, 1988b). Amplitudes of waves reflected at ICB also favor a small v_S value at ICB, of the order of $2\text{--}3 \text{ km s}^{-1}$ (Shearer and Masters, 1990; Cao and Romanowicz, 2004a; Koper and Pyle, 2004; Koper and Dombrovskaya, 2005). All these values are significantly lower than those given by the global Earth models. Their compatibility with normal mode results implies the existence of a strong shear velocity gradient in the uppermost 200–300 km of the inner core (Häge, 1983; Choy and Cormier, 1983; Cao and Romanowicz, 2004a). A P-velocity gradient seems to be required in the same depth range (e.g., Kaneshima *et al.*, 1994).

A direct evidence of the rigidity of the inner core relies on the detection of the phase PKJKP, which propagates as S-wave inside the inner core and as P-wave outside. Because of the very low amplitude of this phase, there is no hope to observe it on single records. Stacking of several records is thus necessary to enhance the signal to noise ratio of the expected phase, and even so is the success quite uncertain (Doornbos, 1974). Optimal conditions are required for stacking, in particular, the appropriate phase velocity and distance and the appropriate frequency domain. This constitutes the major difficulty, because these conditions are poorly known. The distance at which PKJKP will have its maximum amplitude depends on the velocity and density contrasts at ICB and on the S-velocity profile inside the core, which are not well known. In the worst case, if the S-velocity is close to zero at the top of the inner core, as suggested by some seismological waveform modeling (Choy and Cormier, 1983), PKJKP will simply not exist. This may occur if partial melting is present at the top of the inner core, forming a mushy zone. The frequency domain where PKJKP is observed is also unknown, although the strong attenuation inside the inner core suggests that it must be better detected on broadband records than on short period records.

An identification of PKJKP on short period records is proposed by Julian *et al.* (1972) and Okal and Cansi (1998). Julian *et al.* (1972) proposed an S-velocity of 2.95 km s^{-1} in the inner core, whereas

Okal and Cansi (1998) concluded that $v_S = 3.65 \text{ km s}^{-1}$ beneath ICB. Kawakatsu (1992), Deuss *et al.* (2000), and Cao *et al.* (2005) conducted studies on broadband data. Kawakatsu failed to observe PKJJP. Deuss *et al.* arrived at a velocity of 3.6 km s^{-1} from the observation of a combination of two other parent phases (pPKJJP + SKJJP). Cao *et al.* obtained a clear phase with a 9 s early arrival time compared to PREM predictions, implying that, if this phase is effectively PKJJP, v_S in the inner core must be $\sim 1.5\%$ larger than in PREM, a model in which v_S is mostly constrained by normal modes sampling the outer part of the inner core. The two models may be reconciled if a very strong v_S gradient is present inside the inner core.

In all these studies, the possibility of a phase misidentification is the major problem. Unambiguous PKJJP identification would allow us to specify the S-velocity profile down to the center of the Earth, as well as S-attenuation and anisotropy. These are the key parameters necessary to know precisely the nature of the very deep Earth, in particular, the form of iron and the presence of partial melting deep in the core. Thus, the search of PKJJP is an important challenge.

1.19.8 The Seismological Detection of an Inner Core Rotation

1.19.8.1 Why a Differential Rotation?

A differential eastward rotation of the inner core with respect to the mantle (i.e., a faster rotation of the inner core) is predicted by some models of geodynamo (Gubbins, 1981; Glatzmaier and Roberts, 1996; Aurnou *et al.*, 1996). The predicted rotation rate is as large as $2\text{--}3^\circ \text{ yr}^{-1}$; thus, time-dependent phenomena induced by this rotation could possibly be detected by the propagation of seismic waves. At the same time, gravimetric coupling predicts that the inner core heterogeneities (or at least the topography induced by mantle heterogeneities, if there is no inner core heterogeneity) must be locked by the mantle gravity field, forcing the inner core to rotate at the same rate as the mantle (Buffett, 1997). These opposite effects could be reconciled if the inner core is allowed to deform in order to adjust its shape and heterogeneities to the mantle gravity field, by viscous flow and/or by melting and recrystallization at the surface (Buffett, 1997). Thus, the detection of an inner core rotation, and the evaluation of the rotation rate, may give important constraints not only to the

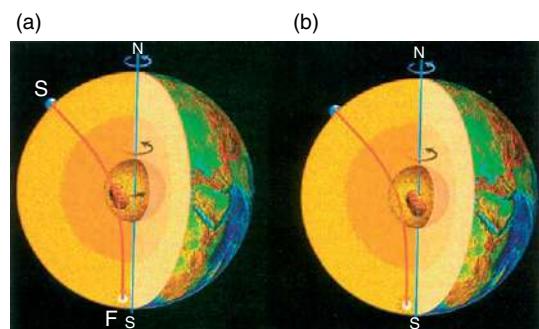


Figure 16 Principle of the detection of an inner core differential rotation with respect to the mantle, from the drift of an inner core heterogeneity through a seismic ray. Part (b) corresponds to a stage later than (a), assuming an eastward (faster) rotation of the inner core.

magnetic field models but also, if inner core deforms, on its viscosity, its level of heterogeneity, and the way anisotropy develops.

The basic idea for detecting inner core rotation is to track inner core heterogeneities during some time either along a particular seismic path which is unchanged during decades (Figure 16), or at the worldwide scale. About 50 years of seismological data are available. However, high-quality digital data are available since the 1980s only, giving about a 20-year time interval for a safe research of rotation. Before the 1970s, data were generally recorded on drums on paper, with mechanical (pen) or optical (photo print) systems and tick marks each minute. Unfortunately, the uneven rotation of the drum, the thickness of the track on the paper, and the distortion of the edges of the image during photo development are well-known sources of errors which make it hard to reach the 0.1 s level of accuracy required for such studies.

1.19.8.2 Tracking the Drift of a Heterogeneity along a Stable Seismic Path

Most of the studies are based on the track of a heterogeneity along a particular path. A first attempt was to detect the displacement with time of a bump of the ICB at the reflection point of PKiKP, from records of the Pacific French nuclear tests at the Warramunga array in Australia (Souriau, 1989). It led to inconclusive result, probably because of the low level of inner core topography. Song and Richards (1996) proposed to use the apparent change of direction of the anisotropy symmetry axis if this axis is tilted with respect to the Earth's rotation axis. They observed a change of 0.3 s of the differential traveltimes PKP(DF)–PKP(BC)

in 30 years (1968–1996) for the path from South Sandwich Island (SSI) to station College (COL) in Alaska (**Figure 17(a)**). Assuming a 11° tilt, they obtained a $1.1^\circ \text{ yr}^{-1}$ eastward rotation rate. Some criticisms however concerned this interpretation, as the tilt of the anisotropy symmetry axis is probably an artifact (Souriau *et al.*, 1997). In fact, the residuals for the path from Kermadec Island to Norway also exhibit an apparent time variation (Song and Richards, 1996), which cannot be explained by the axis tilt.

The puzzling observations of Song and Richards were at the forefront of an interesting debate that

involved both observational and theoretical aspects. Creager (1997) used the same data from SSI to COL, but reinterpreted the results as due to the drift of a heterogeneity beneath the path, that he mapped with the SSI events recorded at an array in Alaska. An eastward rotation of $0.05\text{--}0.3^\circ \text{ yr}^{-1}$ is found, depending on the contribution of mantle heterogeneities beneath Alaska to the observed anomalies. A difficulty with the SSI to COL path is the presence of strong mantle heterogeneities at both sides of the path, as subduction zones are present beneath both South Sandwich Island and Alaska. These

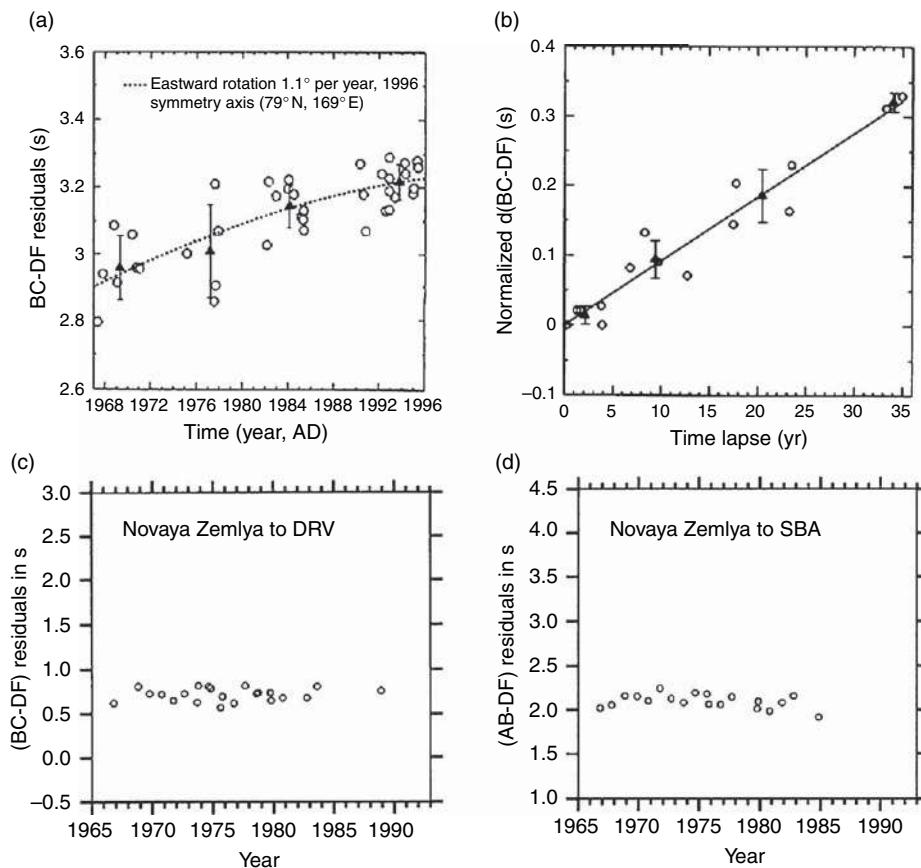


Figure 17 Analysis of inner core rotation along particular paths, from the variation of PKP differential travel time residuals with time. (a) Path from South Sandwich Island (SSI) to COL, Alaska; (b) SSI to Alaska analyzed with doublets; (c) Novaya Zemlya nuclear tests to DRV, Antarctica; (d) Novaya Zemlya to SBA, Antarctica. The two last paths do not show significant time variations leading to conclude to the absence of significant rotation, contrary to the paths SSI to Alaska (note however the different vertical scales). (a) From Song X and Richards PG (1996) Seismological evidence for differential rotation of the Earth's inner core. *Nature* 382: 221–224; (b) From Zhang J, Song X, Li Y, Richards PG, Sun X, and Waldhauser F (2005) Inner core differential motion confirmed by earthquake waveform doublets. *Science* 309: 1357–1360; (c) From Souriau A (1998) New seismological constraints on differential rotation of the inner core from Novaya Zemlya events recorded at DRV, Antarctica. *Geophysical Journal International* 134: F1–F5; and (d) From Li A and Richards PG (2003) Study of inner core structure and rotation using seismic records from Novaya Zemlya under-ground nuclear tests. In: Dehant V *et al.* (ed.) *Earth's Core, Dynamics, Structure, Rotation, Geodynamics Series* 31, pp. 23–30. Washington, DC: American Geophysical Union.

contributions are not fully removed by the use of differential traveltimes; moreover, they may also bias hypocentral determinations. A simultaneous inversion of the structures at source and receiver sides together with inner core heterogeneities and rotation has been attempted, but it is poorly constrained because all the paths are nearly parallel (e.g., Song (2000) for the path SSI to COL; Song and Li (2000) for the path Alaska to South Pole).

A way to minimize the mantle contributions is to select paths outside subduction zones. North–South oriented paths are well suited to the problem, as they are perpendicular to the displacement to be detected. This led to consider Novaya Zemlya nuclear tests recorded at various stations in Antarctica (**Figures 17(c)** and **17(d)**). Mean time perturbations generally smaller than those observed for SSI to COL have been obtained, and sometimes of opposite sign (Souriau, 1998; Richards *et al.*, 1998; Ovtchinnikov *et al.*, 1998; Song and Li, 2000; Isse and Nakanishi, 2002; see also Souriau and Poupinet (2003), Song (2003), and Souriau *et al.* (2003) for reviews and discussions). It may be argued that the constant traveltimes observed for some of these paths is due the absence of heterogeneity near the turning point inside the inner core, a difficulty which, in fact, concerns all the paths.

Another difficulty is to eliminate a possible focal mislocation. This problem is crucial, because seismological networks have evolved with time, inducing systematic location biases which have also evolved with time (e.g., Kennett and Engdahl, 1991). Strong location biases are expected in the absence of stations close to the focus. This has long been the case for earthquakes at high latitudes in the South Hemisphere: for some events, the closest station to SSI was nearly at 20° . An epicentral mislocation of 15 km (which is not considered as large at high latitudes) may induce a bias of 0.11 s in the differential PKP traveltimes BC–DF, of the order of the variation observed in 10 years by Song and Richards. A way to circumvent this difficulty is to use doublets, that is, pairs of events with the same focus, recorded at the same station and with similar waveforms (Poupinet *et al.*, 1984). If the two events are not exactly at the same distance, one of the records will be expanded or contracted with respect to the other one (**Figure 18(a)**). The differential PKP traveltimes AB–BC and BC–DF will increase or decrease at the same time nearly proportionally. If the two events have exactly the same location, and if a heterogeneity is coming along the path, the DF traveltimes only will be affected (**Figure 18(b)**). With this approach,

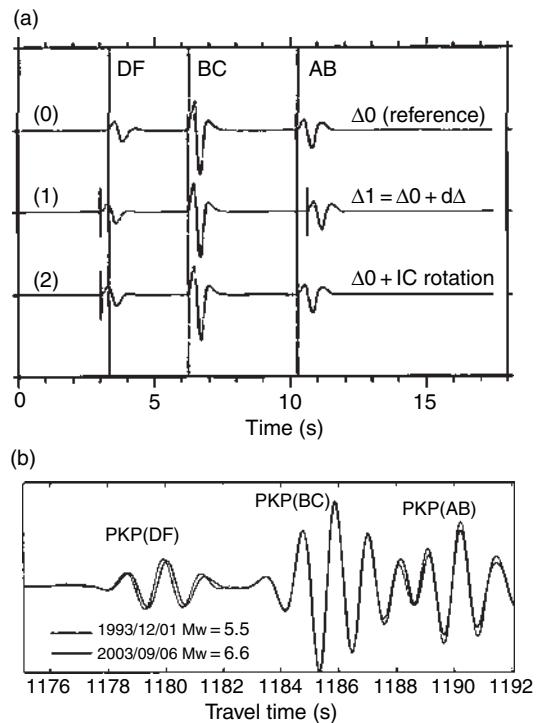


Figure 18 (a) Principle of doublets for discriminating between inner core rotation and earthquake mislocation, by use of the three PKP phases (DF, BC, AB). Doublets are nearby events recorded at the same station. A small difference in location, giving a difference in epicentral distance $d\Delta$ with respect to the reference event at distance $\Delta 0$ (trace 0), results in a proportional variation of (BC–DF) and (AB–BC) (trace 1) compared to (0). Trace (2) corresponds to an event with same location as (0), but the DF time only is modified, due to the drift of an inner core heterogeneity along the DF ray; (b) Example of doublet of two South Sandwich Island events separated by 10 years (1993, 2003) recorded in Alaska. The DF time shift is interpreted as due to inner core rotation. (a) Modified from Poupinet G, Souriau A, and Coutant O (2000) The existence of an inner core super-rotation questioned by teleseismic doublets. *Physics of the Earth and Planetary Interiors* 118: 77–88. (b) Modified from Zhang J, Song X, Li Y, Richards P G, Sun X and Waldhauser F (2005) Inner core differential motion confirmed by earthquake waveform doublets. *Science* 309: 1357–1360.

Poupinet *et al.* (2000) showed that large mislocation biases may affect the SSI to COL results, and that the BC–DF time delay is almost independent of the time lapse between the two records, thus not due to inner core rotation (Souriau *et al.*, 2003a). However, from high-quality doublets for SSI events recorded at 58 stations in Alaska (see an example in **Figure 18(b)**), Zhang *et al.* (2005) arrived to a time variation of $0.0090 \pm 0.0005 \text{ s yr}^{-1}$ (**Figure 17(b)**), that they

convert into a rotation rate of $0.3\text{--}0.5^\circ \text{ yr}^{-1}$, assuming that the inner core heterogeneity is as described by [Creager \(1997\)](#). An interesting feature in their data is, for some doublets distant in time, a dissimilarity of the PKP(DF) coda which could perhaps reveal the displacement of inner core scatterers, providing an additional evidence for rotation. Alternatively, it could be due to scatterers in crust or upper mantle, and denote a small difference in the focal positions. In many cases however, PKP(DF) emerges barely from the noise in their data, opening the results to criticism.

Scatterers inside the inner core effectively provide another interesting type of heterogeneity for detecting a possible inner core rotation. The main advantage of using scatterers is the rapid modification of the diffraction pattern when they move, thus the possibility to detect the inner core rotation in a few years. [Vidale et al. \(2000\)](#) have analyzed the scattered waves which follow PKiKP, induced by two closely located Novaya Zemlya nuclear tests in 1971 and 1974, recorded at LASA (Large Aperture Seismic Array in Montana, USA). The change in the diffraction pattern may be explained by a $0.15^\circ \text{ yr}^{-1}$ faster rotation of the inner core. A similar analysis, carried out on seven Mururoa (Pacific Ocean) French nuclear tests recorded at NORSAR (Norway), gives a rotation rate of $0.05\text{--}0.10^\circ \text{ yr}^{-1}$ ([Vidale and Earle, 2005](#)). Unfortunately, the location of the nuclear tests is not known very accurately (within 5–10 km) and systematic shifts in source location cannot be ruled out ([Vidale and Earle, 2005](#)).

1.19.8.3 A Search for a Differential Rotation with a Worldwide Approach

The previous analyses rely on the existence of an inner core heterogeneity along a particular path. As previously noted, either the heterogeneity has not been clearly identified (paths to Antarctica), or it may be hardly distinguished from mantle heterogeneity (SSI to COL, see [Creager, 1997](#)). A way to avoid this problem is to consider data at the worldwide scale. Several studies have been based on the data from the ISC catalogs, using statistical approaches. For example, [Su et al. \(1996\)](#) used the PKP(DF) traveltimes residuals to detect a time variable tilt of the anisotropy symmetry axis. Their result (rotation of $\sim 3^\circ \text{ yr}^{-1}$) is however biased by the uneven Earth coverage. Another approach consists in building PKP(DF) summary rays corrected for inner core rotation with various rotation rates. The result has a large uncertainty (rotation rate between -1 and $+1^\circ \text{ yr}^{-1}$); it is

thus of marginal interest ([Souriau and Poupinet, 2000](#)). More simple, if a rotation is present, the PKP(DF) traveltimes will show a standard deviation increasing with the time window considered, as heterogeneities will have moved. This is not the case ([Souriau and Poupinet, 2003](#)).

The most interesting results at worldwide scale are provided by the analysis of normal modes at two different epochs. This relies on the identification of long wavelength, even degree heterogeneities inside the inner core, after correction for Earth rotation, ellipticity, and mantle heterogeneities. This method has the potential to estimate accurately the rotation rate, but a good Earth coverage and the use of a large number of modes are necessary. [Sharrock and Woodhouse \(1998\)](#) analyzed seven modes for three time periods ranging from 1977 to 1996. They arrived at a westward rotation of $0.5\text{--}2.5^\circ \text{ yr}^{-1}$, depending on the mode considered, and suggested that the inner core structure is time dependent, but that this dependence is not well explained by rotation. [Laske and Masters \(1999\)](#) analyzed a larger dataset and found that the rotation rate is essentially zero over the past 20 years ($0 \pm 0.2^\circ \text{ yr}^{-1}$). A later study ([Laske and Masters, 2003](#)), with more modes and more events, shows that the results are consistent whatever the mantle model used for corrections, and again emphasize the dependence of the result to the mode considered ([Figure 19](#)). It gives a mean rotation rate of $0.13 \pm 0.11^\circ \text{ yr}^{-1}$, thus a rotation which is barely significant, with, in any case, a value below the most recent values of 0.3 to $0.5^\circ \text{ yr}^{-1}$ obtained for the path from SSI to Alaska ([Zhang et al., 2005](#)).

1.19.8.4 Discussion

A summary of the different results is given in [Table 3](#). It shows that the rotation rate estimates deduced from seismic methods have decreased as the methods became more refined. Most of the recent values lie in the range $0.0\text{--}0.3^\circ \text{ yr}^{-1}$, with uncertainties of the order of $0.2^\circ \text{ yr}^{-1}$, which seems to be the present limit of most of the seismological methods. A small super-rotation (eastward rotation of the inner core with respect to the mantle) is thus favored by most of the studies.

The uppermost values have been obtained for the path from South Sandwich Island to Alaska (time variations of 0.01 s yr^{-1} , rotation rates between 0.05 and $1.1^\circ \text{ yr}^{-1}$). This path has been often investigated because it is one of the rare polar paths with frequent large events. Unfortunately, it is also one of the most

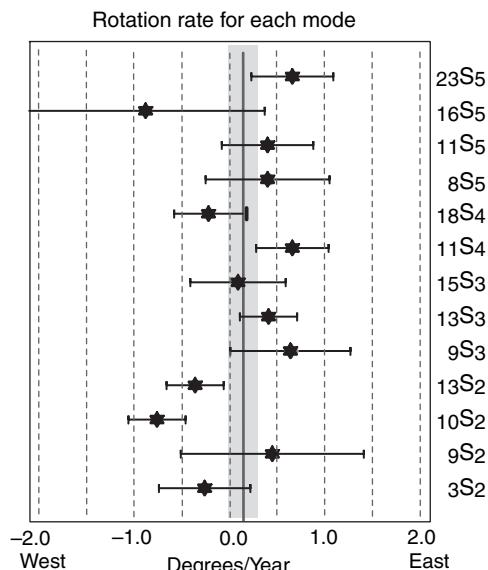


Figure 19 Inner core rotation rate obtained for various inner core sensitive modes, after correction for mantle heterogeneities. The results vary with modes and are often compatible with a null rotation. Light gray area: least square fit of the rotation rate for all the modes. Courtesy of G. Laske. Modified from Laske G and Masters G (2003) The Earth's free oscillations and the differential rotation of the inner core. In: Dehant V, et al. (ed.) *Earth's Core, Dynamics, Structure, Rotation, Geodynamics Series 31*, pp. 5–22. Washington, DC: American Geophysical Union.

anomalous paths, as revealed by the large scatter of its PKP(DF) residuals (e.g., Bréger *et al.*, 1999). The choice of this path, first justified when it was supposed that the tilt of the anisotropy axis could be used for rotation detection, is open to criticism when inner core heterogeneities are used instead, as the path crosses two subduction zones. In fact, lower rotation rates are obtained when part of the heterogeneity is ascribed to the mantle (Creager, 1997). Moreover, hypocentral location is more subject to errors in this context.

At the other end, the lower rotation rates (an even negative, westward rotation rates) are obtained from global studies (mostly normal mode studies), which are less dependent on the identification of a single heterogeneity. These studies are generally compatible with the absence of rotation. The analysis of scattered waves leads also to low rotation rates, $0.05\text{--}0.15^\circ \text{ yr}^{-1}$.

Whatever the path considered, and even for global Earth investigations, the main uncertainty concerns the heterogeneities which are used to detect and quantify the differential rotation. They are difficult to map, because the seismic path density and

orientations inside the inner core are generally too loose to allow for a reliable tomography. As shown in the previous sections, the existence of short wavelength heterogeneity itself is under debate. This point seems right now the more crucial one to progress in the determination of inner core rotation rate.

The geodynamical consequences of an inner core rotation may be important and will depend on the relative contributions of the gravitational coupling, which tend to lock the inner core to mantle heterogeneities, and the geomagnetic coupling, which tend to induce a super-rotation (Buffett, 1997; see also Buffett (2000) for a review). Key parameters are the viscosity of the liquid core at ICB and the viscosity of the inner core, which are poorly known. In magnetic field modeling, a strong viscous coupling at ICB will favor a super-rotation, whereas a low viscous coupling may result in an oscillating inner core (Kuang, 1999). The possible presence of free-floating dendrites detached from the inner core (Loper and Roberts, 1981) may contribute to increase the liquid core viscosity at ICB. On the other hand, the inner core viscosity controls the ability of the inner core to deform permanently in order to adjust its shape to the mantle gravity field. If there is a differential rotation, such a viscous relaxation is more plausible than mass migration by melting and solidification, because of the large amount of latent heat which must be redistributed at inner core surface in this case (Buffett, 1997).

Viscous deformation may concern the uppermost inner core only, or the whole inner core, depending on the viscosity of the inner core. The Q_μ value of ~ 100 found in the uppermost inner core would imply a viscosity of 10^{15} Pa s , assuming that the inner core behaves as a Maxwell solid, and that shear attenuation is due to a viscoelastic process (Buffett, 1997). Mineral physics results cover a wide range of viscosities, from 10^{11} Pa s (Van Orman, 2004) to 10^{21} Pa s (Jeanloz and Wenk, 1988; Yoshida *et al.*, 1996). If the deformation is confined in a superficial very low viscosity layer, it could correspond to the isotropic, high attenuation layer $\sim 100 \text{ km}$ thick at the top of the inner core. In this case, the strong shear induced by the viscous deformation in the uppermost layer would be at the origin of a preferred orientation of crystals or melt inclusions in this layer; thus, a strong anisotropy may be present, in contradiction to what is observed. If the deformation involves the whole inner core (**Figure 20(a)**), the inner core will be mixed continuously by the viscous flow, with

Table 3 Summary of the main results about inner core rotation. Rotation rate positive to the East (inner core faster than mantle)

Reference	Method	Observation	Rotation rate
Souriau, 1989	PKiKP-PcP, Tuamotu to Australia	0.2 s in 10 yr	Probable rotation
Song and Richards, 1996	BC-DF (tilt of anisotropy axis) SSI to COL, Alaska Tonga to GRF, Germany Kermadec to Norway	0.3 s in 30 yr ~0 -0.2 s in 10 yr	1.1° yr ⁻¹ (0.4 to 1.8° yr ⁻¹) No interpretation
Su <i>et al.</i> , 1996	DF, worldwide (drift of pole of anisotropy axis)	0.3 s in 32 yr large uncertainties	~3° yr ⁻¹
Creager, 1997	BC-DF, SSI to COL (heterogeneities)	0.25 s in 30 yr	0.2–0.3° yr ⁻¹ preferred (0.05 to 0.31° yr ⁻¹)
Souriau, 1998	BC-DF, NZ to DRV, Antarctica	~0.0 s in 23 yr	0° yr ⁻¹
Ovtchinnikov <i>et al.</i> , 1998	BC-DF, NZ to NVL, Antarctica	0.3 s in 28 yr	0.4 to 1.8° yr ⁻¹
Sharrock and Woodhouse, 1998	Splitting of normal modes	-0.0053 ± 0.0034 s yr ⁻¹	Westward rotation
Laske and Masters, 1999	Splitting of normal modes	-0.7 to 0.8° yr ⁻¹	0
Song and Li, 2000	BC-DF, Alaska to SPA	0.6 s in 37 yr	0.6° yr ⁻¹
Souriau and Poupinet, 2000	BC-DF and polar DF, worldwide	32 yr	-1 to 1° yr ⁻¹
Vidale <i>et al.</i> , 2000	Inner core scatterers, NZ to Montana	0.1 s in 3 yr	0.15° yr ⁻¹
Poupinet <i>et al.</i> , 2000	Doublets of core phases, SSI to COL	<0.1 s in 30 yr	<0.2° yr ⁻¹
Song, 2000	BC-DF pairs, SSI to Alaska	~0.45 s in 40 yr	0.3 to 1.1° yr ⁻¹
Collier and Hellfrich, 2001	BC-DF, S. Pacific to UK	15 yr	0.42 ± 0.22 to 0.66 ± 0.24° yr ⁻¹ (marginally detectable)
Isse and Nakanishi, 2002	BC-DF records at SYO, Antarctica	28 yr	No monotonic variation 0.0 (<0.2° yr ⁻¹)
Xu and Song, 2003	BC-DF, SSI to Beijing network	30 yr	0.41 ± 0.12° yr ⁻¹
Li and Richards, 2003	BC-DF, NZ to Antarctica	24 yr -0.0035 to -0.024 s yr ⁻¹	Differential rotation (not specified)
Laske and Masters, 2003	Splitting of normal modes	20 yrs	0.13 ± 0.11° yr ⁻¹
Zhang <i>et al.</i> , 2005	Doublets, SSI to Alaska	35 yr	0.3 to 0.5° yr ⁻¹
Vidale and Earle, 2005	Inner core scatterers, Tuamotu to NORSAR	11 yr	0.05 to 0.10° yr ⁻¹

BC-DF: differential travel time PKP(BC)–PKP(DF), SSI: South Sandwich Island, NZ = Novaya Zemlya.

relaxation times of the order of 3000 years. It will be hard in this context to maintain heterogeneities inside the inner core – those which could be used to detect the inner core rotation. On the other hand, the degree-two flow in equatorial plane will induce a degree-four anisotropy pattern, which is not observed (**Figure 20(b)**).

A coupled effect of electromagnetic and gravitational forces for a realistic inner core viscosity of 5×10^{16} Pa s predicts a mean rotation rate as low as $0.02^\circ \text{ yr}^{-1}$, undetectable with seismological methods today, with small fluctuations of mean period 75 yr

leading sometimes to a negative (westward) rotation rate (Buffett and Glatzmaier, 2000). Various scenarios may occur, depending on the relative contributions of electromagnetic and gravitational torques (Aurnou and Olson, 2000), with the generation of irregular oscillations in most cases. A weak evidence for rotational oscillation of the inner core with timescale of ~0.8 yr is given by Collier and Hellfrich (2001), but here again the result has large error bars.

If the inner core is completely locked by mantle heterogeneities, that is, if gravitational coupling is much stronger than geomagnetic coupling or if the

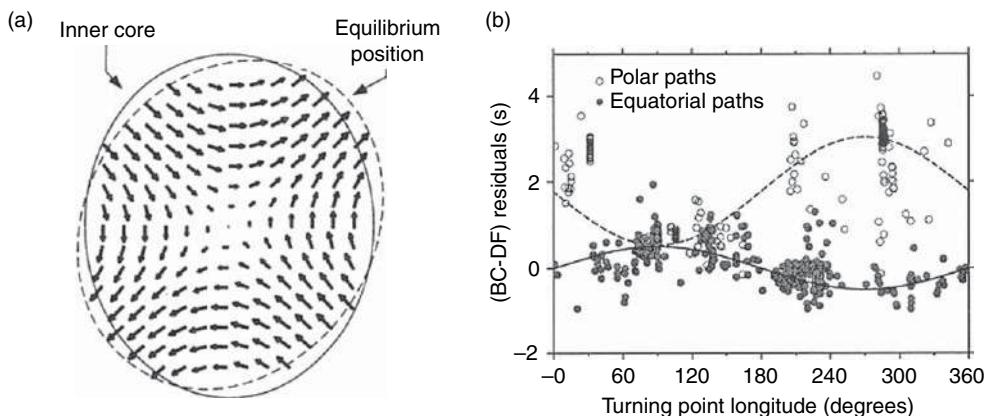


Figure 20 (a) Deformation of a homogeneous low-viscosity inner core (flow lines), predicted to adjust the inner core shape to the gravity field of the mantle, if a differential rotation of the inner core with respect to the mantle is present (equatorial cross-section). This flow predicts a degree-four anisotropy pattern in the equatorial plane, which is not observed in the PKP(BC-DF) travel time residuals (b). A degree-one (hemispherical pattern) is observed instead, for both equatorial and polar paths (a) Modified from Buffett BA (1997) Geodynamic estimates of the viscosity of the Earth's inner core. *Nature* 338: 571–573. (b) Modified from Souriau A, Garcia R, and Poupinet G (2003a) The seismological picture of the inner core: Structure and rotation. *Comptes Rendus Geoscience* 335: 51–63.

inner core has a high viscosity, a zero rotation rate is expected. It falls at the lower bound of the seismological determinations, but cannot explain some of the SSI to Alaska results. A way to reconcile all the observations is to invoke time-dependent phenomena inside the inner core which are not necessarily rotation, and which could be favored by a low inner core viscosity. This could perhaps explain why the global approaches do not detect a significant time variability, whereas analyses of some particular paths do. Clearly, more seismological and theoretical analyses are still necessary to progress in this debate.

1.19.9 Discussion and Conclusion

From the previous analyses, it may seem that the picture of the core is rather confused, and that few characteristics meet a general agreement. This is true; the core is still a wide, almost virgin area of investigation compared to the other structures of the Earth, and its deep location beneath heterogeneous layers (in particular D'' at the base of the mantle), together with the complexity of the physics in the core, imply that it will still long lead to controversial results. At the same time, and for the same reasons, it is one of the most attractive objects for Earth scientists. Hereafter, the seismological results which are considered as almost certain, those which are highly

probable, and those which are still controversial or doubtful, are summarized along with suggestion on some elements for future research.

1.19.9.1 Summary of the Results

The radii of the outer core and inner core are known with a good accuracy: 3480 ± 1 km for the CMB, 1215–1221 km for the ICB. These two boundaries are first-order discontinuities for the seismic waves (thickness less than 5 km). The CMB exhibits a small extra-flattening (of less than 500 m) with respect to its equilibrium figure, and possibly a topography at different wavelengths, which must be small and may hardly exceed 4 km. The ICB has roughly the shape of its hydrostatic figure (thus is nearly spherical), with probably a topography of no more than a few hundred meters, undetectable by seismology.

The liquid core is homogeneous from the seismological point of view, and follows Adams–Williamson equation (neutral stratification), except perhaps at its boundaries. In particular, a low-velocity gradient has been detected in the lowermost 150 km above the ICB, probably in relation with the release of light elements during inner core crystallization. The liquid core has everywhere a zero rigidity and a nearly infinite quality factor. It is thus a transparent medium for seismic waves. Moreover, it has a low viscosity, except perhaps at the very base of the liquid core; thus, it cannot sustain heterogeneities.

Its density deficit with respect to molten iron implies the presence of $\sim 10\%$ by weight of light elements.

The ICB corresponds to an increase in P-velocity of $\sim 0.6 \text{ m s}^{-1}$ and an increase in density of ~ 0.5 to $1.0 \times 10^3 \text{ kg cm}^{-3}$, which indicates a strong depletion in light elements compared to the liquid core. The inner core is rigid, but the S-velocity at the ICB and the S-velocity profiles inside the inner core are poorly known. There are arguments in favor of a high velocity gradient for both P- and S-velocities below ICB. The P-wave quality factor is low (100–400) in the uppermost 300 km with a strong increase immediately beneath the ICB: it increases at greater depth. There is attenuation probably both in shear ($1/Q_\mu$) and in bulk ($1/Q_b$). On the other hand, the viscosity inside the inner core is poorly known ($10^{11}\text{--}10^{21} \text{ Pa s}$) but likely low, of the order of 10^{16} Pa s .

The inner core is anisotropic in seismic velocities, with in first approximation a cylindrical anisotropy (transverse isotropy) of 1–3%, and a fast axis parallel to Earth rotation axis. The uppermost 100–150 km is almost isotropic. An anisotropy in attenuation is also present, with a strong attenuation correlated to the high velocities in the direction of the Earth rotation axis. An innermost inner core with radius 300–500 km and an anisotropy different from that in the outer inner core seems to be present, but the nature of the anisotropy inside this structure is still debated. It is also a zone of higher quality factor (lower attenuation).

Lateral heterogeneities inside the inner core are hard to identify unambiguously. A hemispherical pattern is probably present in the uppermost 400 km of the inner core, the Western Hemisphere being more anisotropic than the Eastern Hemisphere, whereas isotropic velocity seems to be constant (no chemical heterogeneity). Hemispherical variations have also been observed in P-velocity at the different interfaces, and in attenuation at the very top of the inner core. At very short wavelengths, scatterers have been identified inside the inner core, but their characteristics seem not to be identical everywhere.

A differential, eastward rotation of the inner core with respect to the mantle is favored by most of the seismological results, but the rotation rate found with the various methods is highly variable. Most of the methods (global methods; diffraction by scatterers) give a rate in the range $0.0\text{--}0.3^\circ \text{ yr}^{-1}$, global methods (in particular, normal modes) being generally compatible with the absence of rotation. However, values

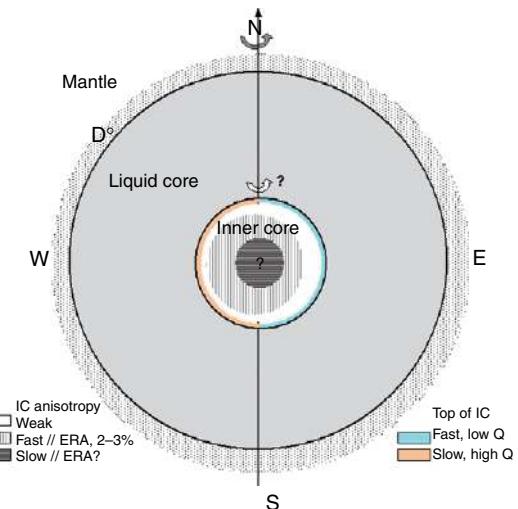


Figure 21 Cartoon of the structure of the core, summarizing the different seismological results: the absence of 3-D structure in the liquid core, the existence of a nearly isotropic layer at the top of the inner core with a hemispherical pattern at the very top, and anisotropy in the body of the inner core with fast axis parallel to Earth rotation axis. Still debated (or to specify) are the characteristics of the anisotropy in the innermost inner core, and the differential rotation of the inner core with respect to the mantle.

from negative up to 1.1° y^{-1} have been obtained, large positive values being obtained along a few specific paths. **Figure 21** summarizes the main results concerning the core.

1.19.9.2 The Open Questions, the Future Challenges, the Data for the Future

The distribution of the inner core anisotropy with depth is certainly one of the most important issues. It could help specify the nature of the inner core, how it formed, and how the anisotropy is generated. In parallel, the distribution of attenuation with depth, and the S-velocity profiles, are important pieces of information to specify the possible presence of partial melting or to detect specific textures.

The debate concerning inner core rotation is far from closed. The highly varying rotation rates obtained, depending on the method used and on the path considered, ask for more studies with different approaches, different kinds of data, and different paths. The numerous geodynamical problems related to a possible differential rotation imply that this question is crucial and particularly exciting.

The core boundaries are possible places of sedimentation, differentiation, and chemical exchanges which call for refined analyses. In particular, the ICB, which appears as a first-order discontinuity despite the possible presence of a mushy zone, remains to some extent enigmatic.

The hemispherical pattern, the evidence for which is strong, must be confirmed. If real, this structure, which departs from the cylindrical symmetry imposed by Earth rotation, must be explained. Other degree-one structures exist in the Earth (e.g., the ocean–continent distribution). The existence of such a pattern in the uppermost inner core, without evidence of chemical heterogeneity, is a puzzling question.

Outside the field of seismology, many constraints are expected from the other domains of physics and chemistry. In particular, the improving performances of experimental and numerical simulations in high-pressure physics will hopefully give new constraints on the phase and texturing present at the center of the Earth, and on the light elements which could be incorporated into iron. Viscosity of the inner core is also an important parameter to specify, as it is related to thermal convection, deformation ability, and grain size, and hence indirectly to anisotropy. On the other hand, magnetic field computations with more realistic conditions, coupled with dynamical models, will give new insights on the problem of inner core rotation.

For seismology, one of the most drastic problems remains the poor distribution of the data. This is particularly crucial for studying anisotropy, as not only a good Earth coverage is necessary, but also a good sampling of all the directions. In particular, the scarcity of polar paths is a strong limitation in such studies. This shows the importance of maintaining observatories at high latitudes, and possibly to develop new ones, as well as ocean bottom observatories, in order to improve the Earth coverage. Moreover, a growing number of seismological studies are based on signals of very small amplitudes, for which stacking is necessary. Permanent arrays with short meshes are essential for such studies. There are very few of them in the South Hemisphere, and none at high southern latitudes, where the deployment of such arrays would be of major interest. Finally, we have noted the interest of very long temporal series to monitor inner core rotation. This means that maintaining observatories for decades, despite the considerable effort it represents, is crucial to address time-dependent seismology.

References

- Adams RD and Randall MJ (1964) The fine structure of the Earth's core. *Bulletin of the Seismological Society of America* 54: 1299–1313.
- Anderson DL and Given JW (1982) Absorption band Q model of the Earth. *Journal of Geophysical Research* 87: 3893–3904.
- Anderson DL and Hart RS (1978) Q in the Earth. *Journal of Geophysical Research* 83: 5869–5882.
- Andrault D, Fiquet G, Kunz M, Visocsekas F, and Häusermann D (1997) The orthorhombic structure of iron: An *in-situ* study at high temperature and high pressure. *Science* 278: 831–834.
- Aurnou J, Brito D, and Olson P (1996) Mechanisms of inner core super-rotation. *Geophysical Research Letters* 23: 3401–3404.
- Aurnou J and Olson P (2000) Control of inner core rotation by electromagnetic, gravitational and mechanical torques. *Physics of the Earth and Planetary Interiors* 117: 111–121.
- Beghein C and Trampert J (2003) Robust normal mode constraints on inner core anisotropy from model space search. *Science* 299: 552–555.
- Belonoshko AB, Ahuja R, and Johansson B (2003) Stability of the body-centered-cubic phase of iron in the Earth's inner core. *Nature* 424: 1032–1034.
- Bergman MI (1997) Measurements of elastic anisotropy due to solidification texturing and the implications for the Earth's inner core. *Nature* 389: 60–63.
- Bergman MI, Cole DM, and Jones JR (2002) Preferred crystal orientations due to melt convection during directional solidification. *Journal of Geophysical Research* 107: ECV 6-1–6-8.
- Bergman MI, Giersch L, Hinczewski M, and Izzo V (2000) Elastic and attenuation anisotropy in directionally solidified (hcp) zinc, and the seismic anisotropy in the Earth's inner core. *Physics of the Earth and Planetary Interiors* 117: 139–151.
- Bhattacharyya J, Shearer P, and Masters G (1993) Inner core attenuation from short-period PKP(BC) versus PKP(DF) waveforms. *Geophysical Journal International* 114: 1–11.
- Birch F (1952) Elasticity and constitution of the Earth's interior. *Journal of Geophysical Research* 57: 227.
- Birch F (1964) Density and composition of mantle and core. *Journal of Geophysical Research* 69: 4377–4388.
- Boehler R (1993) Temperatures in the Earth's core from melting point measurements of iron at high static pressures. *Nature* 363: 534–536.
- Bolt BA (1962) Gutenberg's PKP early observations. *Nature* 196: 122–124.
- Bolt BA (1977) The detection of PKIIP and damping in the inner core. *Annali de Geofisica* 30: 507–520.
- Bolt BA (1982) *Inside the Earth*. San Francisco, CA: Freeman.
- Bolt BA and Qamar A (1970) Upper bound to the density jump at the boundary of the Earth's inner core. *Nature* 228: 148–150.
- Boschi L and Dziewonski AM (2000) Whole Earth tomography from delay times of P, PCP and PKP phases: Lateral heterogeneities in the outer core or radial anisotropy in the mantle? *Journal of Geophysical Research* 105: 13675–13696.
- Bowers D, McCormack DA, and Sharrock DS (2000) Observations of PKP(DF) and PKP(BC) across the United Kingdom: Implications for studies of attenuation in the Earth's core. *Geophysical Journal International* 140: 374–384.
- Braginski SI (1999) Dynamics of the stably stratified ocean at the top of the core. *Physics of the Earth and Planetary Interiors* 111: 21–34.

- Bréger L, Romanowicz B, and Rousset S (2000a) New constraints on the structure of the inner core from P'P'. *Geophysical Research Letters* 17: 2781–2784.
- Bréger L, Romanowicz B, and Tkalcic H (1999) PKP(BC-DF) travel time residuals and short scale heterogeneity in the deep Earth. *Geophysical Research Letters* 26: 3169–3172.
- Bréger L, Tkalcic H, and Romanowicz B (2000b) The effect of D'' on PKP(AB-DF) travel time residuals and possible implications for inner core structure. *Earth and Planetary Science Letters* 175: 133–143.
- Brush SG (1980) Discovery of the Earth's core. *American Journal of Physics*. 48: 705–724.
- Buchbinder GR (1971) A velocity structure of the Earth's core. *Bulletin of the Seismological Society of America* 61: 429–456.
- Buffett BA (1997) Geodynamic estimates of the viscosity of the Earth's inner core. *Nature* 338: 571–573.
- Buffett BA (2000) Dynamics of the Earth's core. In: Karato SG, Forte A, Liebermann R, Masters G, and Stirzade L (eds.) *Earth's Deep Interior: Mineral Physics and Tomography from the Atomic to the Global Scale. Geophysical Monograph*, 117, pp 37–62. Washington, DC: American Geophysical Union.
- Buffett BA, Garnero EJ, and Jeanloz R (2000) Sediments at the top of the Earth's core. *Science* 290: 1338–1342.
- Buffett BA and Glatzmaier GA (2000) Gravitational breaking of inner core rotation in geodynamo simulations. *Geophysical Research Letters* 27: 3125–3128.
- Buffett BA, Huppert HE, Lister JR, and Woods AW (1996) On the thermal evolution of the Earth's core. *Journal of Geophysical Research* 101: 7989–8006.
- Buffett BA and Wenk HR (2004) Texturing of the Earth's inner core by Maxwell stresses. *Nature* 413: 60–63.
- Bullen KE and Haddon RAW (1973) The ellipticities of surfaces of equal density inside the Earth. *Physics of the Earth and Planetary Interiors* 7: 199–202.
- Busse FH (1975) A model of the geodynamo. *Geophysical Journal of the Royal Astronomical Society* 42: 437–459.
- Calvet M, Chevrot S, and Souriau A (2006) P-wave propagation in transversely isotropic media. 2- Application to inner core anisotropy: Effects of data merging, parametrization and a priori information. *Physics of the Earth and Planetary Interiors* 156: 21–40.
- Cao A and Romanowicz B (2004a) Constraints on density and shear velocity contrasts at the inner core boundary. *Geophysical Journal International* 157: 1–6.
- Cao A and Romanowicz B (2004b) Hemispherical transition of seismic attenuation at the top of the Earth's inner core. *Earth and Planetary Science Letters* 228: 243–253.
- Cao A, Romanowicz B, and Takeuchi N (2005) An observation of PKJKP: Inferences on inner core shear properties. *Science* 308: 1453–1455.
- Carcione JM and Cavallini F (1994) A rheological model for anelastic anisotropic media with applications to seismic wave propagation. *Geophysical Journal International* 119: 338–348.
- Choy GL (1977) Theoretical seismograms of core phases calculated by frequency-dependent full wave theory, and their interpretation. *Geophysical Journal of the Royal Astronomical Society* 51: 275–312.
- Choy GL and Cormier VF (1983) The structure of the inner core inferred from short-period and broadband GDSN data. *Geophysical Journal of the Royal Astronomical Society* 72: 1–21.
- Choy GL and Richards PG (1975) Pulse distortion and Hilbert transformation in multiply reflected and refracted body waves. *Bulletin of the Seismological Society of America* 65: 55–70.
- Cleary J and Haddon RAW (1972) Seismic wave scattering near the core-mantle boundary: A new interpretation of precursors of PKP. *Nature* 240: 549–551.
- Collier JD and Helffrich G (2001) Estimate of inner core rotation rate from United Kingdom regional seismic network data and consequences for inner core dynamical behaviour. *Physics of the Earth and Planetary Interiors* 193: 523–537.
- Cormier VF (1981) Short-period PKP phases and the anelastic mechanism of the inner core. *Physics of the Earth and Planetary Interiors* 24: 291–301.
- Cormier VF and Choy GL (1986) A search for lateral heterogeneity in the inner core from differential travel times near PKP-D and PKP-C. *Geophysical Research Letters* 13: 1553–1556.
- Cormier VF and Li X (2002) Frequency dependent seismic attenuation in the inner core 2. A scattering and fabric interpretation. *Journal of Geophysical Research* 107: B12 2362, doi:10.1029/2002JB001796.
- Cormier V, Li X, and Choy GL (1998) Seismic attenuation of the inner core: Viscoelastic or stratigraphic? *Geophysical Research Letters* 25: 4019–4022.
- Cormier V and Richards PG (1976) Comments on 'The damping of core waves' by Antony Qamar and Alfredo Eisenberg. *Journal of Geophysical Research* 81: 3066–3068.
- Cormier V and Stroujkova A (2005) Waveform search for the innermost inner core. *Earth and Planetary Science Letters* 236: 96–105.
- Creager KC (1992) Anisotropy in the inner core from differential travel times of the phases PKP and PKIKP. *Nature* 356: 309–314.
- Creager KC (1997) Inner core rotation rate from small scale heterogeneity and time-varying travel times. *Science* 278: 1284–1288.
- Creager KC (1999) Large-scale variations in inner core anisotropy. *Journal of Geophysical Research* 104: 23127–23139.
- Creager KC (2000) Inner core anisotropy and rotation. In: Dehant V, et al. (ed.) *Core Dynamics, Structure and Rotation, American Geodynamic Series*, 31: pp. 89–114. Washington, DC: American Geophysical Union.
- Creager KC and Jordan TH (1986) Aspherical structure of the core-mantle boundary from PKP travel times. *Geophysical Research Letters* 13: 1497–1500.
- Crossley D (2003) Can a stably stratified layer in the core be detected using seismic normal modes or Earth rotation? In: Dehant V, et al. (ed.) *Core Dynamics, Structure and Rotation*, pp. 241–250. Washington, DC: American Geophysical Union.
- Crossley DJ, Rochester M, and Peng Z (1992) Slichter modes and Love numbers. *Geophysical Research Letters* 19: 1679–1682.
- Cummins P and Johnson L (1988a) Synthetic seismograms for an inner core transition of finite thickness. *Geophysical Journal* 94: 21–34.
- Cummins P and Johnson L (1988b) Short-period body wave constraints on the properties of the Earth's inner core boundary. *Journal of Geophysical Research* 93: 9058–9074.
- Defraigne P, Dehant V, and Wahr JM (1996) Internal loading of an inhomogeneous compressible Earth with phase boundaries. *Geophysical Journal International* 125: 173–192.
- Denis C, Rogister Y, Amalvict M, Delire C, Ibrahim Denis A, and Munhoven G (1997) Hydrostatic flattening, core structure, and translational mode of the inner core. *Physics of the Earth and Planetary Interiors* 99: 195–206.

- Deuss A, Woodhouse JH, Paulsen H, and Trampert J (2000) The observation of inner core shear waves. *Geophysical Journal International* 142: 67–73.
- Doornbos DJ (1974) The anelasticity of the inner core. *Geophysical Journal of the Royal Astronomical Society* 38: 397–415.
- Doornbos DJ (1983) Observable effects of the seismic absorption band in the Earth. *Geophysical Journal of the Royal Astronomical Society* 75: 693–711.
- Doornbos DJ and Hilton T (1989) Models of core–mantle boundary and the travel times of internally reflected core phases. *Journal of Geophysical Research* 94: 15741–15751.
- Durek JJ and Romanowicz B (1999) Inner core anisotropy inferred by direct inversion of normal mode spectra. *Geophysical Journal International* 139: 599–622.
- Dziewonski AM and Anderson DL (1981) Preliminary reference Earth model. *Physics of the Earth and Planetary Interiors* 25: 297–356.
- Dziewonski AM and Gilbert F (1971) Solidity of the inner core of the Earth inferred from normal mode oscillations. *Nature* 234: 465.
- Earle PS and Shearer PM (1997) Observations of PKKP precursors used to estimate small-scale topography on the core–mantle boundary. *Science* 277: 667–670.
- Eaton DW and Kendall J-M (2006) Improving seismic resolution of outermost core structure by multichannel analysis and deconvolution of broadband SmKS phases. *Physics of the Earth and Planetary Interiors* 155: 104–119.
- Emmerich H (1993) Theoretical study of the influence of CMB topography on the core reflections ScS. *Physics of the Earth Planetary Interiors* 80: 125–134.
- Engdahl ER, Flinn EA, and Romney CF (1970) Seismic waves reflected from the Earth's inner core. *Nature* 228: 852–853.
- Engdahl ER, van der Hilst R, and Buland RP (1998) Global teleseismic earthquake relocation with improved travel times and procedures for depth determination. *Bulletin of the Seismological Society of America* 88: 722–743.
- Fearn DR, Loper DE, and Roberts PH (1981) Structure of the Earth's inner core. *Nature* 292: 232–233.
- Fukao Y and Suda N (1989) Core modes of the Earth's free oscillations and structure of the inner core. *Geophysical Research Letters* 16: 401–404.
- Forte AM, Mitrovica JX, and Woodward RL (1995) Seismic–geodynamic determination of the origin of excess ellipticity of the core–mantle boundary. *Geophysical Research Letters* 22: 1013–1016.
- Garcia R (2002a) Constraints on upper inner core structure from waveform inversion of core phases. *Geophysical Journal International* 150: 651–664.
- Garcia R (2002b) Seismological and mineral constraints on the inner core fabric. *Geophysical Research Letters* 29: 1958, doi:10.1029/2002GL015268.
- Garcia R and Souriau A (2000a) Amplitude of core–mantle boundary estimated by stochastic analysis of core phases. *Physics of the Earth and Planetary Interiors* 117: 345–359.
- Garcia R and Souriau A (2000b) Inner core anisotropy and heterogeneity level. *Geophysical Research Letters* 27: 3121–3124, and correction (2001) *Geophysical Research Letters* 28: 85.
- Garnero EJ, Helmberger DV, and Grand SP (1993) Constraining outermost core velocity with SmKS waves. *Geophysical Research Letters* 25: 2341–2344.
- Garnero EJ and Lay T (1998) Effects of D'' anisotropy on seismic velocity models of the outermost core. *Geophysical Research Letters* 20: 2463–2466.
- Garnero EJ, Revenaugh J, Williams Q, Lay T, and Kellogg LH (1998) Ultra low velocity zone at the core–mantle boundary. In: Gurnis M et al. (ed.) *The Core–Mantle Boundary Region*, Geodynamics Series 28, pp. 319–334. Washington, DC: American Geophysical Union.
- Glatzmaier GA and Roberts PH (1996) Rotation and magnetism of Earth's inner core. *Science* 274: 1887–1891.
- Greff-Lefftz M and Legros H (1996) Viscoelastic mantle density heterogeneity and core–mantle boundary topography. *Geophysical Journal International* 125: 567–576.
- Gubbins D (1981) Rotation of the inner core. *Journal of Geophysical Research* 86: 11695–11699.
- Gurnis M, Wysession ME, Knittle E, and Buffett BA (1998) *The Core–Mantle Boundary Region*. Geodynamics Series 28: pp. 334. Washington: American Geophysical Union.
- Gutenberg B (1913) Über die Konstitution des Erdinneren. *Physiker Zeitschrift* 14: 1217.
- Gwinn CR, Herring TA, and Shapiro, II (1986) Geodesy by radio interferometry: Studies of the forced nutations of the Earth 2: Interpretation. *Journal of Geophysical Research* 91: 4755–4765.
- Häge H (1983) Velocity constraints for the inner core inferred from long period PKP amplitudes. *Physics of the Earth and Planetary Interiors* 31: 171–185.
- Hales AL and Roberts JL (1971) The velocities in the outer core. *Bulletin of the Seismological Society of America* 61: 1051–1059.
- Hellfrich G and Kaneshima S (2004) Seismological constraints on core composition from Fe–O–S liquid immiscibility. *Science* 306: 2239–2242.
- Hide R, Clayton RW, Hager BH, Spieth MA, and Voorhies CV (1993) Topographic core–mantle coupling and fluctuations in Earth's rotation. *Geophysical Monograph Series of the American Geophysical Union* 76: 107–120.
- Ishii M and Dziewonski AM (2002) The innermost inner core of the Earth: Evidence for a change in anisotropic behaviour at the radius of about 300 km. *Proceedings of the National Academy of Sciences of the United States of America* 99: 14026–14030.
- Ishii M and Dziewonski AM (2003) Distinct seismic anisotropy at the centre of the Earth. *Physics of the Earth and Planetary International* 140: 203–217.
- Ishii M and Dziewonski AM (2005) Constraints on the outer core tangent cylinder using normal-mode splitting measurements. *Geophysical Journal International* 162: 787–792.
- Ishii M, Dziewonski AM, Tromp J, and Ekström G (2002a) Joint inversion of normal mode and body wave data for inner core anisotropy. 2: Possible complexities. *Journal of Geophysical Research* 107: 2380 (doi:10.1029/2001JB000713).
- Ishii M, Tromp J, Dziewonski AM, and Ekström G (2002b) Joint inversion of normal mode and body wave data for inner core anisotropy. 1: Laterally homogeneous anisotropy. *Journal of Geophysical Research* 107: 2379 (doi:10.1029/2001JB000712).
- Isse T and Nakanishi I (2002) Inner-core anisotropy beneath Australia and differential rotation. *Geophysical Journal International* 151: 255–263.
- Jacobs JA (1953) The Earth's inner core. *Nature* 172: 297.
- Jeanloz R (1990) The nature of the Earth's core. *Annual Review of Earth and Planetary Sciences* 18: 357–386.
- Jeanloz R and Wenk HR (1988) Convection and anisotropy of the inner core. *Geophysical Research Letters* 15: 72–75.
- Jeffreys H (1926) The rigidity of the Earth's central core. *Monthly Notices of the Royal Astronomical Society* 1: 371.
- Jephcoat A and Olson P (1987) Is the inner core of the Earth pure iron? *Nature* 325: 332–335.
- Julian BR, Davies D, and Sheppard RM (1972) PKJKP. *Nature* 235: 317–318.
- Kampfman W and Müller G (1989) Pcp amplitude calculations for a core–mantle boundary with topography. *Geophysical Research Letters* 16: 653–656.

- Kaneshima S (1996) Mapping heterogeneity of the uppermost inner core using two pairs of core phases. *Geophysical Research Letters* 23: 3075–3078.
- Kaneshima S, Hirahara K, Ohtaki T, and Yoshida Y (1994) Seismic structure near the inner core–outer core boundary. *Geophysical Research Letters* 21: 157–160.
- Karato S (1993) Inner core anisotropy due to the magnetic field-induced preferred orientation of iron. *Science* 262: 1708–1710.
- Karato S (1999) Maxwell stress-induced flow in the Earth's inner core: Implications for seismic anisotropy and geodynamo. *Nature* 402: 871–873.
- Kawakatsu H (1992) PKJKP. *Central Core of the Earth* 2: 53–56 (in Japanese).
- Kennett BLN (1998) On the density distribution within the Earth. *Geophysical Journal International* 132: 374–382.
- Kennett BLN and Engdahl ER (1991) Travel times for global earthquake location and phase identification. *Geophysical Journal International* 105: 429–465.
- Kennett BLN, Engdahl ER, and Buland R (1995) Constraints on seismic velocities in the Earth from travel times. *Geophysical Journal International* 122: 108–124.
- Kind R and Müller G (1977) The structure of the outer core from SKS amplitudes and travel times. *Bulletin of the Seismological Society of America* 67: 1541–1554.
- Kohler M (1997) Three-dimensional velocity structure and resolution of the core–mantle boundary region from whole mantle-inversion of body waves. *Physics of the Earth and Planetary Interiors* 101: 85–104.
- Kohler M and Tanimoto T (1992) One-layer global inversion for outermost core velocity. *Physics of the Earth and Planetary Interiors* 72: 173–184.
- Koper KD and Dombrovskaya M (2005) Seismic properties of the inner core boundary from PKiKP/P amplitude ratios. *Earth and Planetary Science Letters* 237: 680–694.
- Koper KD and Pyle ML (2004) Observation of PKiKP/PcP amplitude ratios and implications for Earth structure at the boundaries of the liquid core? *Journal of Geophysical Research* 109, doi:10.1029/2003JB002750.
- Koper KD, Franks JM, and Dombrovskaya M (2004) Evidence for small-scale heterogeneity in Earth's inner core from a global study of PKiKP coda waves. *Earth and Planetary Science Letters* 228: 227–241.
- Koper KD, Pyle ML, and Franks JM (2003) Constraints on aspherical core structure from PKiKP-PcP differential travel times. *Journal of Geophysical Research* 108: 2168–2180.
- Krasnoshchekov DN, Kaaziz PB, and Ovtchinnikov VM (2005) Seismological evidence for mosaic structure of the surface of the Earth's inner core. *Nature* 435: 483–487.
- Kuang W (1999) Force balances and convective state in the Earth's core. *Physics of the Earth and Planetary Interiors* 116: 65–79.
- Labrosse S, Poirier JP, and Le Mouël JL (1997) On cooling of the Earth's core. *Physics of the Earth and Planetary Interiors* 99: 1–7.
- Labrosse S, Poirier JP, and Le Mouël JL (2001) The age of the inner core. *Earth and Planetary Science Letters* 190: 111–123.
- Laio A, Bernard S, Chiarotti GL, Scandolo S, and Tosatti E (2000) Physics of iron at Earth's core conditions. *Science* 287: 1027–1030.
- Laske G and Masters G (1999) Limits on differential rotation of the inner core from an analysis of the Earth's free oscillations. *Nature* 402: 66–68.
- Laske G and Masters G (2003) The Earth's free oscillations and the differential rotation of the inner core. In: Dehant V, et al. (ed.) *Earth's Core, Dynamics, Structure, Rotation, Geodynamics Series* 31, pp. 5–22. Washington, DC: American Geophysical Union.
- Lay T and Young CJ (1990) The stably stratified outermost core revisited. *Geophysical Research Letters* 17: 2001–2004.
- Lee KKM and Jeanloz R (2003) High-pressure alloying of potassium and iron: Radioactivity in the Earth's core? *Geophysical Research Letters* 30: 2212 (doi:10.1029/2003GL018515).
- Lehmann I (1936) P'. *Bureau Central Seismologique International, Strasbourg Travaux Scientifiques* A 14: 3–31.
- Li A and Richards PG (2003) Study of inner core structure and rotation using seismic records from Novaya Zemlya underground nuclear tests. In: Dehant V, et al. (ed.) *Earth's Core, Dynamics, Structure, Rotation, Geodynamics Series* 31, pp. 23–30. Washington, DC: American Geophysical Union.
- Li X and Cormier VF (2002) Frequency dependent seismic attenuation in the inner core 1. A viscoelastic interpretation. *Journal of Geophysical Research* 107: B12, 2361 (doi:10.1029/2002JB001795).
- Li X, Giardini D, and Woodhouse JH (1991) Large-scale three-dimensional even-degree structure of the Earth from splitting of long-period normal modes. *Journal of Geophysical Research* 96: 551–577.
- Lin JF, Heinz DL, Campbell AJ, Devine JM, and Shen G (2002) Iron–Silicon alloy in the Earth's core? *Nature* 295: 313–315.
- Loper DE and Fearn DR (1983) A seismic model of partially molten inner core. *Journal of Geophysical Research* 88: 1235–1242.
- Loper DE and Roberts PH (1981) A study of conditions at the inner core boundary of the Earth. *Physics of the Earth and Planetary Interiors* 24: 302–307.
- Lumb LI and Aldridge KD (1991) On viscosity estimates from the Earth's fluid outer core and core–mantle coupling. *Journal of Geomagnetism and Geoelectricity* 43: 93–110.
- Ma Y, Somayazulu M, Shen G, Mao H, Shu J, and Hemley R (2004) In situ X-ray diffraction studies of iron at Earth's core conditions. *Physics of the Earth and Planetary Interiors* 143: 455–467.
- Mao HK, Shu J, Shen G, Hemley RJ, Li B, and Singh AK (1998) Elasticity and rheology of iron above 220 GPa and the nature of the Earth's inner core. *Nature* 396: 741–743 (Correction, *Nature* 399: 280, 1999).
- Masters G (1979) Observational constraints on the chemical and thermal structure of the Earth's deep interior. *Geophysical Journal of Royal Astronomical Society* 57: 507–534.
- Masters G and Gilbert F (1981) Structure of the inner core inferred from observations of its spheroidal shear modes. *Geophysical Research Letters* 8: 569–571.
- Masters G and Gubbins D (2003) On the resolution of density within the Earth. *Physics of the Earth and Planetary Interiors* 140: 159–167.
- Matthews PM, Herring TA, and Buffett B (2002) Modeling of nutation and precession: New nutation series for nonrigid Earth and insights into the Earth's interior. *Journal of Geophysical Research* 107, (doi:10.1029/2001JB000390).
- McSweeney TJ, Creager KC, and Merrill RT (1997) Depth extent of inner-core seismic anisotropy and implications for geomagnetism. *Physics of the Earth and Planetary Interiors* 101: 131–156.
- Melchior P (1986) *The Physics of the Earth's Core, An Introduction*, 256p. Oxford: Pergamon Press.
- Menke W (1986) Few 2–50 km corrugations on the core–mantle boundary. *Geophysical Research Letters* 13: 1501–1504.
- Mochizuki E and Ohminato T (1989) On the anomalous splitting of Earth's free oscillations. *Geophysical Research Letters* 16: 1415–1416.

- Morelli A and Dziewonski AM (1987) Topography of the core–mantle boundary and lateral homogeneity of the liquid core. *Nature* 325: 678–683.
- Morelli A and Dziewonski AM (1993) Body wave travel times and a spherically symmetric P- and S-wave velocity model. *Geophysical Journal* 112: 178–194.
- Morelli A, Dziewonski AM, and Woodhouse JH (1986) Anisotropy of the inner core inferred from PKIKP travel times. *Geophysical Research Letters* 13: 1545–1548.
- Müller G (1973) Amplitude studies of core phases. *Journal of Geophysical Research* 78: 3469–11490.
- Niazi M and Johnson LR (1992) Q in the inner core. *Physics of the Earth and Planetary Interiors* 74: 55–62.
- Niu F and Wen L (2001) Hemispherical variations in seismic velocity at the top of the Earth's inner core. *Nature* 410: 1081–1084.
- Obayashi M and Fukao Y (1997) P and Pcp travel time tomography for the core–mantle boundary. *Journal of Geophysical Research* 102: 17825–17841.
- Oganov AR and Ono S (2004) Theoretical and experimental evidence for a post-perovskite phase of MgSiO_3 in Earth's D'' layer. *Nature* 430: 445–448.
- Okal E and Cansi Y (1998) Detection of PKJKP at intermediate periods by progressive multichannel correlation. *Earth and Planetary Science Letters* 164: 23–30.
- Oldham RD (1906) The constitution of the interior of the Earth as revealed by earthquakes. *Quaternary Journal of Geological Society of London* 62: 456.
- Oreshin SI and Vinnik LP (2004) Heterogeneity and anisotropy of seismic attenuation in the inner core. *Geophysical Research Letters* 31: L02613 (doi:10.1029/1003GL018591).
- Ouzounis A and Creager KC (2001) Isotropy overlying anisotropy at the top of the inner core. *Geophysical Research Letters* 28: 4331–4334.
- Ovtchinnikov VM, Adushkin VV, and An VA (1998) About the velocity of differential rotation of the Earth's inner core (in Russian). *Doklady Russian Academy of Sciences Geophysics* 362: 683–686.
- Peacock S and Hudson JA (1990) Seismic properties of rocks with distribution of small cracks. *Geophysical Journal International* 102: 471–484.
- Poirier JP (1988) Transport properties of liquid metals and viscosity of the Earth's core. *Geophysical Journal International* 92: 99–105.
- Poirier JP (1994) Light elements in the Earth's outer core – A critical review. *Physics of the Earth and Planetary Interiors* 85: 319–337.
- Poirier JP (1996) *Le noyau de la Terre*. Paris: Flammarion.
- Poirier JP and Price GD (1999) Primary slip system of ϵ -iron and anisotropy of the Earth's inner core. *Physics of the Earth and Planetary Interiors* 110: 147–156.
- Poirier JP and Shankland TJ (1993) Dislocation melting of iron and the temperature of the inner core boundary, revisited. *Geophysical Journal International* 115: 147–151.
- Poupinet G, Ellsworth WL, and Fréchet J (1984) Monitoring velocity variation in the crust using earthquake doublet: An application to the Calaveras fault, California. *Journal of Geophysical Research* 89: 5719–5731.
- Poupinet G and Kennett BLN (2004) On the observation of high frequency PKIKP and its coda in Australia. *Physics of the Earth and Planetary Interiors* 146: 497–511.
- Poupinet G, Pillet R, and Souriau A (1983) Possible heterogeneity in the Earth's core deduced from PKIKP travel times. *Nature* 305: 204–206.
- Poupinet G, Souriau A, and Coutant O (2000) The existence of an inner core super-rotation questioned by teleseismic doublets. *Physics of the Earth and Planetary Interiors* 118: 77–88.
- Pulliam RJ and Stark PB (1993) Bumps on the core–mantle boundary: Are they facts or artefacts? *Journal of Geophysical Research* 98: 1943–1955.
- Qamar A (1973) Revised velocities in the Earth's core. *Bulletin of the Seismological Society of America* 63: 1073–1105.
- Qamar A and Eisenberg A (1974) The damping of core waves. *Journal of Geophysical Research* 79: 758–765.
- Randall MJ (1970) SKS and seismic velocities in the outer core. *Geophysical Journal* 21: 441–445.
- Rekdal T and Doornbos DJ (1992) The times and amplitudes of core phases for a variable core–mantle boundary layer. *Geophysical Journal International* 108: 546–556.
- Richards PG, Song X, and Li A (1998) Detecting possible rotation of Earth's inner core. *Science* 282: 1221.
- Ritzwoller MH, Masters G, and Gilbert F (1986) Observations of anomalous splitting and their interpretation in terms of aspherical structure. *Journal of Geophysical Research* 91: 10203–10228.
- Rodgers A and Wahr J (1993) Inference of core–mantle boundary topography from ISC Pcp and PKP travel times. *Geophysical Journal International* 115: 991–1011.
- Romanowicz B and Bréger L (2000) Anomalous splitting of free oscillations: A reevaluation of possible interpretations. *Journal of Geophysical Research* 105: 21559–21578.
- Romanowicz B and Durek JJ (2000) Seismological constraints on attenuation in the Earth: A review. In: Karato S et al. (ed.) *Earth's Deep Interior: Mineral Physics and Tomography from the Atomic to the Global Scale*, *Geophysical Monograph*, 117, pp. 161–180. Washington, DC: American Geophysical Union.
- Romanowicz B, Li X-D, and Durek J (1996) Anisotropy in the inner core: Could it be due to low-order convection? *Science* 274: 963–966.
- Romanowicz B, Tkalcic H, and Bréger L (2003) On the origin of complexity in PKP travel time data. In: Dehant V et al. (ed.) *Core Dynamics, Structure and Rotation*, pp. 31–44. American Geophysical Union Monograph. Washington, DC: American Geophysical Union.
- Rosat S, Hinderer J, Crossley D, and Rivera L (2003) The search for the Slichter mode : Comparison of noise levels of superconducting gravimeters and investigation of stacking method. *Physics of the Earth and Planetary Interiors* 140: 183–202.
- Rost S and Revenaugh J (2001) Seismic detection of rigid zones at the top of the core. *Science* 294: 1911–1914.
- Rost S and Revenaugh J (2004) Small-scale changes of core–mantle boundary reflectivity studied using core reflected Pcp. *Physics of the Earth and Planetary Interiors* 145: 19–36.
- Saxena SK, Dubrovsky LS, Häggkvist P, Cerenius Y, Shen G, and Mao HK (1995) Synchrotron X-ray study of iron at high pressure and temperature. *Science* 269: 1703–1704.
- Schweitzer J (2002) Simultaneous inversion of steep-angle observations of Pcp and Scp in Europe – What can we learn about the core–mantle boundary? *Geophysical Journal International* 151: 209–220.
- Sharrock DS and Woodhouse JH (1998) Investigation of time dependent inner core structure by the analysis of free-oscillation spectra. *Earth Planets and Space* 50: 1013–1018.
- Shearer P (1994) Constraints on inner core anisotropy from PKP(DF) travel times. *Journal of Geophysical Research* 99: 19647–19659.
- Shearer P and Masters G (1990) The density and shear velocity contrast at the inner core boundary. *Geophysical Journal International* 102: 491–498.
- Shearer PM and Toy KM (1991) PKP(BC) versus PKP(DF) differential travel times and aspherical structure of the Earth's inner core. *Journal of Geophysical Research* 96: 2233–2247.
- Shearer P, Hedlin MAH, and Earle PS (1998) PKP and PKKP precursor observations: Implications for the small-scale

- structure of the deep mantle and core. In: Gurnis M, Wysession ME, Knittle E, and Buffett B (eds.) *The Core Mantle Boundary Region, Geodynamics Series 28*: pp. 37–55. Washington, DC: American Geophysical Union.
- Shearer PM, Toy KM, and Orcutt JA (1988) Axi-symmetric Earth models and inner core anisotropy. *Nature* 333: 228–232.
- Sidorin I, Gurnis M, and Helmberger DV (1999) Evidence for a ubiquitous seismic discontinuity at the base of the mantle. *Science* 286: 1326–1331.
- Singh S, Taylor MAJ, and Montagner JP (2000) On the presence of liquid in Earth's inner core. *Science* 287: 2471–2474.
- Smylie DE (1999) Viscosity near Earth's solid inner core. *Science* 284: 461–463.
- Song X (1996) Anisotropy in central part of inner core. *Journal of Geophysical Research* 101: 16089–16097.
- Song X (2000) Joint inversion for inner core rotation, inner core anisotropy, and mantle heterogeneity. *Journal of Geophysical Research* 105: 7931–7943.
- Song X (2003) Three-dimensional structure and differential rotation of the inner core. In: Dehant V et al. (ed.) *Earth's Core, Dynamics, Structure and Rotation, Geodynamics Series 31*, pp. 45–63. Washington, DC: American Geophysical Union.
- Song X and Helmberger DV (1992) Velocity structure near the inner core boundary from waveform modelling. *Journal of Geophysical Research* 97: 6573–6586.
- Song X and Helmberger DV (1995a) A P wave velocity model of the Earth's core. *Journal Geophysical Research* 100: 9817–9830.
- Song X and Helmberger DV (1995b) Depth dependence of anisotropy of Earth's inner core. *Journal of Geophysical Research* 100: 9805–9816.
- Song X and Helmberger DV (1998) Seismic evidence for an inner core transition zone. *Science* 282: 924.
- Song X and Li A (2000) Support for differential inner core superrotation from earthquakes in Alaska recorded at South Pole station. *Journal of Geophysical Research* 105: 623–630.
- Song X and Richards PG (1996) Seismological evidence for differential rotation of the Earth's inner core. *Nature* 382: 221–224.
- Song X and Xu X (2002) Inner core transition zone and anomalous PKP(DF) waveforms for polar paths. *Geophysical Research Letters* 29, doi:10.1029/2001GL013822.
- Souriau A (1989) A search for time dependent phenomena inside the core from seismic data. *EGS meeting abstracts, Barcelona* (1989).
- Souriau A (1998) New seismological constraints on differential rotation of the inner core from Novaya Zemlya events recorded at DRV, Antarctica. *Geophysical Journal International* 134: F1–F5.
- Souriau A, Garcia R, and Poupinet G (2003a) The seismological picture of the inner core : Structure and rotation. *Comptes Rendus Geoscience* 335: 51–63.
- Souriau A and Poupinet G (1990) A latitudinal pattern in the structure of the outermost liquid core, revealed by the travel times of SKKS–SKS seismic phases. *Geophysical Research Letters* 17: 2005–2007.
- Souriau A and Poupinet G (1991) The velocity profile at the base of the liquid core from PKP(BC+Cdiff) data. An argument in favor of radial inhomogeneity. *Geophysical Research Letters* 18: 2023–2026.
- Souriau A and Poupinet G (2000) Inner core rotation : A test at the worldwide scale. *Physics of the Earth and Planetary Interiors* 118: 13–27.
- Souriau A and Poupinet G (2003) Inner core rotation: A critical appraisal. In: Dehant V et al. (ed.) *Earth's Core, Dynamics, Structure and Rotation, Geodynamic Series 31*, pp. 65–82. American Geophysical Union Monograph. Washington, DC: American Geophysical Union.
- Souriau A and Romanowicz B (1996a) Anisotropy in inner core attenuation: A new type of data to constrain the nature of the solid core. *Geophysical Research Letters* 23: 1–4.
- Souriau A and Romanowicz B (1996b) Anisotropy in the inner core: Relation between P-velocity and attenuation. *Physics of the Earth and Planetary Interiors* 101: 33–47.
- Souriau A and Roudil P (1995) Attenuation in the uppermost inner core from broad-band GEOSCOPE PKP data. *Geophysical Journal International* 123: 572–587.
- Souriau A, Roudil P, and Moynot B (1997) Inner core rotation : Facts and artefacts. *Geophysical Research Letters* 24: 2103–2106.
- Souriau A and Souriau M (1989) Ellipticity and density at the inner core boundary from subcritical PKiKP and PcP data. *Geophysical Journal International* 98: 39–54.
- Souriau A, Teste A, and Chevrot S (2003b) Is there any structure inside the liquid core? *Geophysical Research Letters* 30, doi: 10.1029/2003GL017008.
- Stacey FD and Stacey CHB (1999) Gravitational energy of core evolution: Implications for thermal history and geodynamo power. *Physics of the Earth and Planetary Interiors*. 110: 83–93.
- Stark PB and Hengartner NW (1993) Reproducing Earth's kernels: Uncertainty of the shape of the core–mantle boundary from PKP and PcP travel times. *Journal of Geophysical Research* 98: 1957–1971.
- Steinle-Neumann G, Stixrude L, and Cohen RE (2003) Physical properties of iron in the inner core. In: Dehant V et al. (ed.) *Earth's Core, Dynamics, Structure, Rotation, Geodynamics Series 31*, pp. 137–161. Washington, DC: American Geophysical Union.
- Stevenson DJ (1987) Limits on lateral density and velocity variations in the Earth's outer core. *Geophysical Journal of Royal Astronomical Society* 88: 311–319.
- Stiller H, Franck S, and Schmit U (1980) On the attenuation of seismic waves in the Earth's core. *Physics of the Earth and Planetary Interiors* 22: 221–225.
- Stixrude L and Cohen RE (1995) High pressure elasticity of iron and anisotropy of Earth's inner core. *Science* 267: 1972–1975.
- Stroujkova A and Cormier VF (2004) Regional variations in the uppermost 100 km of the Earth's inner core. *Journal of Geophysical Research* 109: B10307 (doi:10.1029/2004JB002976).
- Su W-J and Dziewonski AM (1995) Inner core anisotropy in three dimensions. *Journal of Geophysical Research* 100: 9831–9852.
- Su W-J, Dziewonski AM, and Jeanloz R (1996) Planet within a planet : Rotation of the inner core of the Earth. *Science* 274: 1883–1887.
- Suda N and Fukao Y (1990) Structure of the inner core inferred from observations of seismic core modes. *Geophysical Journal International* 103: 403–413.
- Sumita I and Olson P (1999) A laboratory model for convection in Earth's core driven by a thermally heterogeneous mantle. *Science* 286: 1547–1549.
- Sumita I, Yoshida S, Kumazawa M, and Hamano Y (1996) A model for sedimentary compaction of a viscous medium and its application to inner core growth. *Geophysical Journal International* 124: 502–524.
- Tanaka S (2004) Seismic detectability of anomalous structure at the top of the Earth's outer core with broadband array analysis of SmKS phases. *Physics of the Earth and Planetary Interiors* 141: 141–152.
- Tanaka S and Hamaguchi H (1993) Degree one heterogeneity at the top of the earth's core, revealed by SmKS travel times. In: Le Mouël JL, Smylie DE, and Herring TA (eds.) *Dynamics of Earth's Deep Interior and Earth's Rotation, IUGG/AGU. Geophysical Monograph* 72 pp. 127–134. Washington, DC: American Geophysical Union.
- Tanaka S and Hamaguchi H (1996) Frequency-dependent Q in the Earth's outer core from short period P4KP/PcP spectral ratio. *Journal of Physics of the Earth* 44: 745–759.

- Tanaka S and Hamaguchi H (1997) Degree one heterogeneity and hemispherical variation of anisotropy in the inner core from PKP(BC)-PKP(DF) times. *Journal of Geophysical Research* 102: 2925–2938.
- Tromp J (1993) Support for anisotropy of the Earth's inner core from free oscillations. *Nature* 366: 678–681.
- Tromp J (1995) Normal-mode splitting observations from the Great 1994 Bolivia and Kuril Islands earthquakes: Constraints on the structure of the mantle and inner core. *GSA Today* 5: 137–151.
- Tseng T-L, Huang B-S, and Chin B-H (2001) Depth-dependent attenuation in the uppermost inner core from the Taiwan short period seismic array PKP data. *Geophysical Research Letters* 29: 459–462.
- Tsuchiya T, Tsuchiya J, Umemoto K, and Wentzcovitch RM (2004) Phase transition in MgSiO_3 perovskite in the Earth's lower mantle. *Earth and Planetary Science Letters* 224: 241–248.
- Van Orman JA (2004) On the viscosity and creep mechanism of Earth's inner core. *Geophysical Research Letters* 31: L20606.
- Vidale JE, Dodge DA, and Earle PS (2000) Slow differential rotation of the Earth's inner core indicated by temporal changes in scattering. *Nature* 405: 445–448.
- Vidale JE and Earle PS (2000) Fine-scale heterogeneity in the Earth's inner core. *Nature* 404: 273–275.
- Vidale JE and Earle PS (2005) Evidence for inner-core rotation from possible changes with time in PKP coda. *Geophysical Research Letters* 32: L01309 (doi: 10.1029/2004GL021240).
- Vinnik L, Romanowicz B, and Bréger L (1994) Anisotropy in the center of the inner core. *Geophysical Research Letters* 21: 1671–1674.
- Vočadlo L, Alfé D, Gillan MJ, Wood G, Brodholt JP, and Price GD (2003) Possible thermal and chemical stabilization of body-centered-cubic iron in the Earth's core. *Nature* 424: 536–539.
- Vočadlo L, Brodholt J, Alfé D, and Price GD (1999) The structure of the iron under the conditions of the Earth inner core. *Geophysical Research Letters* 26: 1231–1234.
- Wahr J and de Vries D (1989) The possibility of lateral structure inside the core and its implications for nutations and Earth tide observations. *Geophysical Journal International* 99: 511–519.
- Weber P and Machetel P (1992) Convection within the inner core and thermal implications. *Geophysical Research Letters* 19: 2107–2110.
- Wen L and Niu F (2002) Seismic velocity and attenuation structures in the top of the Earth's inner core. *Journal of Geophysical Research* 107: 2273 (doi:10.1029/2001JB000170).
- Wenk HR, Baumgardner JR, Lebensohn RA, and Tomé CN (2000) A convection model to explain anisotropy in the inner core. *Journal Geophysical Research* 105: 5662–5677.
- Widmer RG, Masters F, and Gilbert F (1991) Spherically symmetric attenuation within the Earth from normal mode data. *Geophysical Journal International* 104: 541–553.
- Widmer RG, Masters F, and Gilbert F (1992) Observably split multiplets-data analysis and interpretationin terms of large-scale aspherical structure. *Geophysical Journal International* 111: 559–576.
- Wiechert E (1896) *Über die Beshaffenheit des Erdinneren. Shriftender Physikalish – Ökonoineshen gesellschaft zu Königsberg in Preußen*. 37: 1–48.
- Woodhouse JH, Giardini D, and Li X-D (1986) Evidence for inner core anisotropy from free oscillations. *Geophysical Research Letters* 13: 1549–1552.
- Xu X and Song X (2003) Evidence for inner core super-rotation from time-dependent differential PKP travel times observed at Beijing seismic network. *Geophysical Journal International* 152: 509–514.
- Yoshida S, Sumita I, and Kumazawa M (1996) Growth model of the inner core coupled with the outer core dynamics and the resulting elastic anisotropy. *Journal of Geophysical Research* 101: 28085–28103.
- Yoshida S, Sumita I, and Kumazawa M (1998) Models of the anisotropy of the Earth's inner core. *Journal of Physics-Condensed Matter* 10: 11215–11226.
- Yu W and Wen L (2006a) Seismic velocity and attenuation structures in the top 400 km of the earth's inner core along equatorial paths. *Journal of Geophysical Research* 111: B07308, doi: 10.1029/2005JB003995.
- Yu W and Wen L (2006b) Inner core anisotropy in attenuation. *Earth and Planetary Science Letters* 245: 581–594.
- Yu W, Wen L, and Niu F (2005) Seismic velocity structure in the Earth's outer core. *Journal of Geophysical Research* 110, doi:10.1029/2003JB002928.
- Yukutake T (1998) Implausibility of thermal convection in the Earth's solid inner core. *Physics of the Earth and Planetary Interiors* 108: 1–13.
- Zhang J, Song X, Li Y, Richards PG, Sun X, and Waldhauser F (2005) Inner core differential motion confirmed by earthquake waveform doublets. *Science* 309: 1357–1360.

1.20 Deep Earth Structure – Seismic Scattering in the Deep Earth

P. M. Shearer, University of California, San Diego, La Jolla, CA, USA

© 2007 Elsevier B.V. All rights reserved.

1.20.1	Introduction	695
1.20.2	Scattering Theory	696
1.20.2.1	Single-Scattering Theory and Random Media	696
1.20.2.1.1	Q notation and definitions	697
1.20.2.2	Finite Difference Calculations and the Energy Flux Model	698
1.20.2.3	Multiple-Scattering Theories	700
1.20.2.4	Other Theoretical Methods	703
1.20.3	Scattering Observations	703
1.20.3.1	S Coda	704
1.20.3.2	P Coda	706
1.20.3.3	P_n Coda	709
1.20.3.4	P_{diff} Coda	709
1.20.3.5	PP and P'P' Precursors	710
1.20.3.6	PKP Precursors	712
1.20.3.7	PKKP Precursors and PKKP _X	715
1.20.3.8	PKiKP and PKP Coda and Inner-Core Scattering	717
1.20.3.9	Other Phases	719
1.20.4	Discussion	720
	References	721

1.20.1 Introduction

Most seismic analyses of Earth structure rely on observations of the traveltimes and waveforms of direct seismic waves that travel along ray paths determined by Earth's large-scale velocity structure. These observations permit inversions for radially averaged P wave and S wave velocity profiles as well as three-dimensional (3-D) perturbations. However, smaller-scale velocity or density perturbations cause some fraction of the seismic energy to be scattered in other directions, usually arriving following the main phase as incoherent energy over an extended time interval. This later-arriving wavetrain is termed the coda of the direct phase. Given the number of different scattering events and the complexity of the scattered wavefield, it is generally impossible to resolve individual scatterers. Instead, coda-wave observations are modeled using random media theories that predict the average energy in the scattered waves as a function of scattering angle, given the statistical properties of the velocity and density perturbations. In this way, it is possible to characterize Earth's heterogeneity at much

smaller scales than can be imaged using tomography or other methods.

The fact that direct seismic waves can be observed in the Earth indicates that this scattering must be relatively weak so that a significant fraction of the seismic energy remains in the primary arrivals. In contrast, scattering on the Moon is proportionally much stronger than in the Earth, preventing the easy observation of direct P and S waves at global distances (at least at the recorded frequencies of the available data) and complicating inversions for lunar structure. In addition to facilitating observations of direct arrivals, weak (as opposed to strong) scattering can also simplify modeling by permitting use of single-scattering theory (i.e., the Born approximation). However, it is now clear that accurate modeling of scattering in the lithosphere, and possibly deeper in the mantle as well, requires calculations based on multiple scattering theories. Fortunately, increased computer power makes these calculations computationally feasible.

Although both body waves and surface waves exhibit scattering, the emphasis in this review is on observations and modeling of deep-Earth scattering,

for which body waves provide the primary constraints. In addition, more attention is given to the mantle and core than the lithosphere, which has been the focus of the majority of coda studies to date. Finally, the different scattering theories are briefly summarized. For more details on these topics, the reader should consult the book by [Sato and Fehler \(1998\)](#), which provides an extensive review of scattering theory and analysis methods, as well as a comprehensive summary of crustal and lithospheric studies.

1.20.2 Scattering Theory

Wave scattering from random heterogeneities is a common phenomenon in many fields of science and theoretical modeling approaches have been extensively developed in physics, acoustics, and seismology. Solving this problem for the full elastic wave equation (i.e., for both P and S waves) in the presence of strong perturbations in the elastic tensor and density is quite difficult, so various simplifying approximations are often applied. These include assuming an isotropic elastic tensor, using first-order perturbation theory in the case of weak scattering, using the diffusion equation for very strong scattering, and assuming correlations among the velocity and density perturbations.

1.20.2.1 Single-Scattering Theory and Random Media

For sufficiently weak velocity and density perturbations, most scattered energy will have experienced only one scattering event and can be adequately modeled using single-scattering theory. The mathematics in this case is greatly simplified if we assume that the primary waves are unchanged by their passage through the scattering region (the Born approximation). The total energy in the seismic wavefield therefore increases by the amount contained in the scattered waves and energy conservation is not obeyed. Thus this approximation is only valid when the scattered waves are much weaker than the primary waves, which is the case in the Earth when the velocity and density perturbations are relatively small (quantifying exactly how small depends upon the frequency of the waves and the source-to-receiver distance). Single-scattering theory is sometimes called Chernov theory (after [Chernov, 1960](#)). Detailed descriptions of Born scattering theory for elastic waves are contained in [Wu and Aki \(1985a, 1985b\)](#), [Wu \(1989\)](#), and [Sato and Fehler \(1998\)](#). A

review of the properties (elasticity, conductivity, permeability) and statistics of random heterogeneous materials is given in the text by [Torquato \(2002\)](#).

Single-scattering theory provides equations that give the average scattered power as a function of the incident and scattered wave types (i.e., P or S), the power of the incident wave, the local volume of the scattering region, the bulk and statistical properties of the random medium, the scattering angle (the angle between the incident wave and the scattered wave), and the seismic wave number ($k = 2\pi/\Lambda$, where Λ is the wavelength). A general random medium could have separate perturbations in P velocity, S velocity, and density, but in practice a common simplification is to assume a linear scaling relationship among the perturbations (e.g., [Sato, 1990](#)) and/or to assume zero density perturbations. However, as pointed out by [Hong et al. \(2004\)](#), density variations can have an important influence on scattering properties. Performing the actual calculation for a specific source-receiver geometry involves integrating the contributions of small volume elements over the scattering region of interest. Each volume element will have a specific scattering angle and geometrical spreading factors for the source-to-scatterer and scatterer-to-receiver ray paths.

The nature of the scattering strongly depends upon the relative length scales of the heterogeneity and the seismic waves. The scale of perturbations in a random medium can be characterized by the auto-correlation function (ACF), with the correlation distance, a , providing a rough measure of the average size of the ‘blobs’ in many commonly assumed forms for the ACF (e.g., Gaussian, exponential, van Kármán). [Figure 1](#) shows examples of random realizations of the Gaussian and exponential ACF models. If the heterogeneity is large compared to the seismic wavelength ($a \gg \Lambda$, ka is large), then forward scattering predominates and becomes increasingly concentrated near the direction of the incident wave as ka increases. In the limit of large ka , the energy remains along the primary ray path and scattering effects do not need to be taken into account. Alternatively, if the blobs are small compared to the seismic wavelength ($a \ll \Lambda$, ka is small), then the scattering is often approximated as isotropic and the scattered power scales as $k^4 a^3$. In the limit of small ka , the scattering strength goes to zero and the medium behaves like a homogeneous solid. As discussed by [Aki and Richards \(1980, pp. 749–750\)](#), scattering effects are strongest when a and Λ are of comparable size (i.e., when $ka \sim 2\pi$).

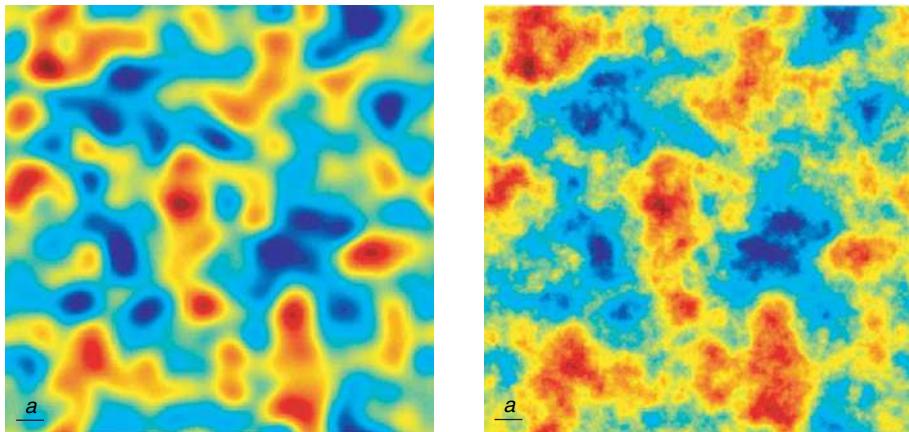


Figure 1 Examples of random media defined by a Gaussian ACF (left) and an exponential ACF (right). The correlation distance, a , is indicated in the lower-left corner. The exponential medium has more structure at short wavelengths than the Gaussian medium.

Aki and Chouet (1975) presented an important application of single-scattering theory to predict coda decay rates for local earthquakes. For a colocated source and receiver and homogeneous body-wave scattering in 3-D media, they obtained

$$A_C(t) \propto t^{-1} e^{-\omega t/2Q_C} \quad [1]$$

where A_C is the coda amplitude at time t (from the earthquake origin time) and angular frequency ω . Q_C is termed the coda Q and there has been some uncertainty regarding its physical meaning, in particular whether it describes intrinsic attenuation, scattering attenuation, or some combination of both. This is discussed later in the context of more complete theories. Regardless of its interpretation, this formula has proved to be successful in fitting coda decay rates in a large number of studies.

Single-scattering theory has also been important for modeling deep-Earth scattering in terms of random heterogeneity models, including interpretation of PKP precursor observations (e.g., Haddon and Cleary, 1974; Doornbos, 1976), PP precursors (King *et al.*, 1975), P'P' precursors (Vinnik, 1981), P_{diff} coda (Earle and Shearer, 2001) and PKiKP coda (Vidale and Earle, 2000). Born theory has also been used to model expected traveltimes variations in direct arrivals that travel through random velocity heterogeneity (e.g., Spetzler and Snieder, 2001; Baig *et al.*, 2003; Baig and Dahlen, 2004a, 2004b). Although my focus in this paper is largely on incoherent scattering from random media, it should be noted that the Born approximation can also be used to model the effect of specific velocity structures, provided their

perturbations are weak compared to the background velocity field. In this case, true synthetic seismograms can be computed, not just the envelope functions. For example, Dalkolmo and Friederich (2000) recently used this approach to model the effect of several different hypothesized velocity anomalies near the core–mantle boundary (CMB) on long-period P waves. In addition, Born theory forms the basis for computing sensitivity kernels in finite-frequency tomography methods (e.g., Dahlen *et al.*, 2000; Nolet *et al.*, 2005).

1.20.2.1.1 Q notation and definitions

Coda Q , intrinsic Q , and scattering Q are termed Q_C , Q_I and Q_{Sc} , respectively. P wave and S wave Q are termed $^{\alpha}Q$ and $^{\beta}Q$, respectively. These can be combined so that, for example, $^{\beta}Q_I$ is intrinsic S wave Q . This convention eliminates any chance of confusing shear-wave Q and scattering Q (both have sometimes been termed Q_S). The transmission Q , Q_T , describes the total attenuation (both intrinsic and scattering) suffered by the direct wave

$$Q_T^{-1} = Q_I^{-1} + Q_{\text{Sc}}^{-1} \quad [2]$$

and the amplitude reduction of the transmitted pulse for a constant Q_T medium is

$$A(t) = A_0 e^{-\omega t/2Q_T} \quad [3]$$

where A_0 is the amplitude of the pulse at $t=0$ and we have ignored any geometrical spreading.

The scattering coefficient, g , is defined as the scattering power per unit volume (e.g., Sato, 1977)

and has units of reciprocal length. The total scattering coefficient, g_0 , is defined as the average of g over all directions and can also be expressed as

$$g_0 = \ell^{-1} = Q_{Sc}^{-1}k \quad [4]$$

where ℓ is the mean free path and k is the wave number. One common way to estimate g_0 for S waves has been to compare the energy in the S coda to the total radiated S energy. Finally, following Wu (1985), we define the seismic albedo as the ratio of scattering attenuation to total attenuation

$$B_0 = \frac{Q_{Sc}^{-1}}{Q_{Sc}^{-1} + Q_I^{-1}} = \frac{g_0}{g_0 + Q_I^{-1}k} \quad [5]$$

These definitions of Q , g_0 , and B_0 are general and can be applied to the multiple-scattering theories discussed later in this paper.

1.20.2.2 Finite Difference Calculations and the Energy Flux Model

Finite difference methods provide a direct, albeit computationally intensive, solution to the seismic wave equation for media of arbitrary complexity, and they (together with the finite element method) have become one of the most widely used techniques in seismology. Their earliest applications to study scattering involved modeling surface-wave and body-to-surface-wave scattering from surface topography, sediment-filled basins, and other buried interfaces (e.g., Levander and Hill, 1985). Here, only their use in modeling body-wave scattering in random media is discussed. Reviews of this topic are contained in Frankel (1990) and Sato and Fehler (1998).

As computing power has improved, finite difference simulations have progressed from the 2-D parabolic approximation, to 2-D using the full wave equation, to full 3-D synthetics. The parabolic approximation considers only forward scattering and is useful when the heterogeneity correlation length is large compared to the seismic wavelength. Complete finite difference simulations in 2-D random media have been performed by Frankel and Clayton (1984, 1986), McLaughlin *et al.* (1985), McLaughlin and Anderson (1987), Frankel and Wennerberg (1987), Gibson and Levander (1988), Roth and Korn (1993), and Saito *et al.* (2003). Frenje and Juhlin (2000) computed both 2-D and 3-D finite difference simulations. Hong and Kennett (2003), Hong (2004), and Hong *et al.* (2005) used a wavelet-based numerical approach

to compute 2-D synthetics for random media and Hong and Wu (2005) computed 2-D synthetics for anisotropic models.

The Frankel studies provided key results in formulating the influential energy flux model (EFM) of seismic coda (Frankel and Wennerberg, 1987) and thus are described here in some detail. Frankel and Clayton (1986) modeled teleseismic P wave traveltimes variations with a ~1 Hz plane wavelet vertically incident on a layer 150 km wide by 55 km thick, with a finite difference grid spacing of 500 m. They found that observed traveltimes variations of about 0.2 s (rms) among stations spaced 10–150 km apart could be explained with 5% rms random P velocity variations, provided the correlation length was 10 km or greater. Frankel and Clayton (1986) also modeled high-frequency coda from local earthquakes using a ~20 Hz explosive source at the bottom corner of a layer 8 km long by 2 km thick. They found that the amplitude of high-frequency coda depends strongly on the presence of high wave number velocity perturbations. Gaussian and exponential models with correlation lengths of 10 km or greater (required to fit observed teleseismic traveltimes variations) do not have sufficient small-scale structure to produce observed levels of high-frequency coda. In contrast, a self-similar random medium model with a correlation distance of at least 10 km and rms velocity variations of 5% can account for both sets of observations.

By measuring peak amplitude versus distance in their synthetics, Frankel and Clayton (1986) estimated Q for their random medium. Because their finite difference calculation did not contain any intrinsic attenuation, this represents a measure of scattering Q (Q_{Sc}). The predicted attenuation (Q^{-1}) peaks at ka values between 1 and 2 for Gaussian random media and between about 1 and 6 for exponential random media. This is consistent with the strongest scattering occurring when the seismic wavelength is comparable to the size of the scatterers. However, attenuation is constant with frequency for self-similar random media, as expected, since the velocity fluctuations have equal amplitudes over a wide range of scales. Frankel and Clayton showed that these results were in rough agreement with those predicted by single-scattering theory in 2-D (to match the geometry of the finite difference simulations).

Frankel and Clayton (1986) also measured coda decay rates for finite difference synthetics computed for sources within a 12 km by 12 km grid at 20 m spacing. They found that their observed coda decay

rates were significantly less than those predicted by single-scattering theory in the case of moderate to large scattering attenuation ($Q_{Sc} \leq 200$), indicating that multiple scattering contributes a substantial portion of the coda energy. This implies that in these cases coda Q (Q_C), as determined from coda falloff and the single-scattering model of coda (e.g., Aki and Chouet, 1975), does not provide a reliable estimate of transmission Q .

Motivated by these finite difference results and the limitations of the single-scattering model of coda generation, Frankel and Wennerberg (1987) introduced what they termed the EFM of coda. This phenomenological model is based on the idea that the coda energy behind the direct wave front can be approximated as homogeneous in space. This observation had previously been reported for micro-earthquake coda for lapse times more than twice the S wave traveltimes (e.g., Aki, 1969; Rautian and Khalturin, 1978), and Frankel and Wennerberg (1987) showed that it also could be seen in finite difference synthetics (see Figure 2). It implies that at sufficiently long times, the coda amplitude at all receivers is approximately the same (scaling only with the magnitude of the source), regardless of the source–receiver distance. The EFM permits the time decay of the coda amplitude to be modeled very simply and to separate the effects of scattering and intrinsic attenuation in the medium.

By considering the energy density of the coda uniformly distributed in an expanding volume

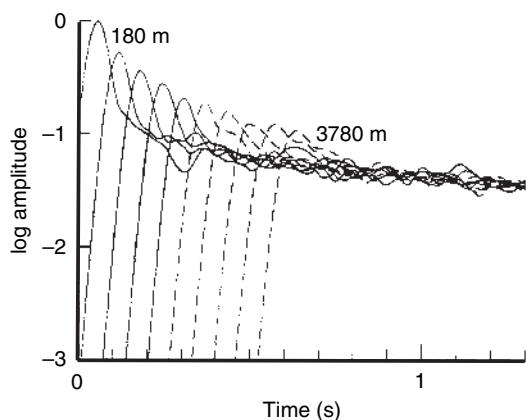


Figure 2 Envelopes of finite difference synthetic seismograms for receivers at distances of 180 to 3780 m from the source as computed by Frankel and Wennerberg (1987) for a random medium with a correlation distance of 40 m. Note that the envelopes decay to a common level following the initial pulse, indicating spatial homogeneity of coda energy.

behind the direct wave front, Frankel and Wennerberg derived an expression for the predicted time decay of the coda amplitude

$$A_C(t) \propto t^{-3/2} e^{-\omega t/2Q_I} \sqrt{1 - e^{-\omega t/Q_{Sc}}} \quad [6]$$

where t is time, ω is angular frequency, Q_I^{-1} is intrinsic attenuation, and Q_{Sc}^{-1} is scattering attenuation. For short time and/or high Q_{Sc} (i.e., weak scattering, tQ_{Sc}^{-1} is very small), this equation reduces to

$$A_C(t) \propto t^{-1} e^{-\omega t/2Q_I} \quad [7]$$

This is equivalent to the Aki and Chouet (1975) expression (eqn [1]) for the single-scattering model, assuming that coda Q and intrinsic Q are equivalent ($Q_C = Q_I$). This agrees with the original interpretation of Q_C given by Aki and Chouet (1975) and contradicts the Aki (1980) statement that in the context of single-scattering theory Q_C should be considered as an effective Q that includes both absorption and scattering effects. Frankel and Wennerberg (1987) showed that the EFM predicts the amplitude and coda decay observed in finite difference synthetics for random media with a wide range of scattering Q , and is more accurate than the single-scattering model for media with moderate to strong scattering attenuation ($Q_{Sc} \leq 150$). Finally, they used the EFM to estimate Q_{Sc} and Q_I from the coda of two $M \sim 3$ earthquakes near Anza, California.

There have been numerous other studies that have attempted to resolve Q_{Sc} and Q_I from local earthquake coda (e.g., Wu and Aki, 1988; Toksöz *et al.*, 1988; Mayeda *et al.*, 1991; Fehler *et al.*, 1992). Notable is Mayeda *et al.* (1992), who analyzed S wave coda from Hawaii, Long Valley, and central California. They found a complicated relationship between theoretical predictions and observed Q_C , Q_{Sc} , and Q_I and argued that models with depth-dependent scattering and intrinsic attenuation are necessary to explain their results.

The EFM was developed to explain local earthquake coda and finite difference simulations of spherical wave fronts in media with uniform scattering. It is not directly applicable to modeling teleseismic coda because of the strong concentration of scattering in the crust and lithosphere compared to much weaker scattering deeper in the mantle. This has motivated the development of extended EFMs involving the response of one or more scattering layers to a wave incident from below (e.g., Korn, 1988, 1990, 1997; Langston, 1989).

The resulting formulas for the coda decay rate are more complicated than the simple EFM because they depend upon several additional parameters, including the traveltime through the layer and the amount of leakage back into the half-space. Korn (1988) developed the theory for a spherical wave with a cone of energy incident upon a scattering zone and used it to model regional earthquakes recorded by the Warramunga array in Australia. Langston (1989) developed a scattering layer-over-half-space model and showed that it was consistent with coda decay in teleseismic P waves recorded at two stations (PAS and SCP) in the United States. Korn (1990) tested a scattering layer over homogenous half-space EFM using a 2-D acoustic finite difference code and found that it gave reliable results for both weak and strong scattering regimes. Korn (1997) further extended the EFM to explicitly include depth-dependent scattering and showed that it gave reliable results when compared to synthetics computed for a 2-D elastic (P – SV) finite difference code.

Wagner and Langston (1992a) computed 2-D acoustic and elastic finite difference synthetics for upcoming P waves incident on 150 different models of heterogeneous layers over a homogeneous half-space. These models varied in their layer thickness, random heterogeneity correlation length (different vertical and horizontal correlation lengths were allowed), and rms velocity heterogeneity. They found that the scattering attenuation of the direct pulse depends upon ka and is strongest for spatially isotropic heterogeneity, in which case most of the coda energy was contained in low apparent velocity S waves and surface waves. In contrast, anisotropic models with horizontally elongated heterogeneities produce coda with mostly vertically propagating layer reverberations.

More recent finite difference calculations for random media include the 2-D whole-Earth pseudo-spectral calculations of Furumura *et al.* (1998) and Wang *et al.* (2001); Thomas *et al.* (2000), who computed 2-D whole-Earth acoustic synthetics to model PKP precursors; Cormier (2000), who used a 2-D elastic pseudo-spectral method to model the effects of D'' heterogeneity on the P and S wavefields; and Korn and Sato (2005), who compare 2-D finite difference calculations with synthetics based on the Markov approximation.

1.20.2.3 Multiple-Scattering Theories

If the energy in the scattered wavefield is a significant fraction of the energy in the direct wave, then the Born approximation is inaccurate and a higher-order

theory should be used that takes into account the energy reduction in the primary wave and the fact that the scattered waves may experience more than one scattering event. These effects are all naturally accounted for using the finite difference calculations already discussed, but these are computationally intensive and there is a need for faster approaches that also provide physical insight into the scattering process. In the case of very strong scattering, the diffusion equation can be applied by assuming a random-walk process. Although this approach preserves energy, it violates causality by permitting some energy to arrive before the direct P wave. The first applications of the diffusion equation in seismology include the coda wave analyses of Wesley (1965) and Aki and Chouet (1975) and the lunar seismogram studies of Nakamura (1977) and Dainty and Toksöz (1977, 1981).

At large times and small distances from the source, the diffusion equation predicts that the coda amplitude varies as

$$A(t) \propto t^{-3/4} e^{-\omega t/2Q_I} \quad [8]$$

where Q_I is the intrinsic attenuation. Notice that Q_{Sc} does not appear in this equation because the exact level of scattering is not important provided it is strong enough that the energy is obeying a random-walk process. The diffusion equation can also be used to model the case of a strong scattering layer over a homogeneous half-space (e.g., Dainty *et al.*, 1974; Margerin *et al.*, 1998, 1999; Wegler, 2004), in which case an additional decay term exists to account for the energy leakage into the half-space.

Another approach to modeling multiple scattering is to sum higher-order scattered energy, and the predicted time dependence of scattered energy was obtained in this way for double scattering (Kopnichiev, 1977) and multiple scattering up to seventh order (Gao *et al.*, 1983a, 1983b). Hoshiba (1991) used a Monte Carlo approach (see below) to correct and extend these results to 10th-order scattering. Richards and Menke (1983) performed numerical experiments on 1-D structures with many fine layers to characterize the effects of scattering on the apparent attenuation of the transmitted pulse and the relative frequency content of the direct pulse and its coda.

Most current approaches to synthesizing multiple scattering use radiative transfer theory to model energy transport. Radiative transfer theory was first used in seismology by Wu (1985) and Wu and Aki

(1988) and recent reviews of the theory are contained in Sato and Fehler (1998) and Margerin (2005). Other results are detailed in Shang and Gao (1988), Zeng *et al.* (1991), Sato (1993), and Sato *et al.* (1997). Sato and Nishino (2002) use radiative transfer theory to model multiple Rayleigh wave scattering. Analytical solutions are possible for certain idealized cases (e.g., Wu, 1985; Zeng, 1991; Sato, 1993), but obtaining general results requires extensive computer calculations.

Two analytical results are of particular interest (and can be used as tests of numerical simulations). For the case of no intrinsic attenuation, Zeng (1991) showed the coda power converges to the diffusion solution at long lapse times

$$P_C(t) \propto t^{-3/2} \quad [9]$$

For elastic waves with no intrinsic attenuation, the equilibrium ratio of P and S energy density is given by (e.g., Sato, 1994; Ryzhik *et al.*, 1996; Papanicolaou *et al.*, 1996)

$$E_P/E_S = \frac{1}{2}(\beta/\alpha)^3 \quad [10]$$

Assuming a Poisson solid, this predicts about 10 times more S energy than P energy at equilibrium, a result of the relatively low efficiency of S-to-P scattering compared to P-to-S scattering (e.g., Malin and Phinney, 1985; Zeng, 1993). For media with intrinsic attenuation, an equilibrium ratio also exists but will generally differ from the purely elastic case (Margerin *et al.*, 2001). Shapiro *et al.* (2000) showed that this ratio can be estimated from the divergence and curl of the displacement as measured with a small-aperture array and that its stability with time provides a test of whether the coda is in the diffusive regime.

Wu (1985) used radiative transfer theory to address the problem of separating scattering from intrinsic attenuation. He showed that the coda energy density versus distance curves have different shapes depending upon the seismic albedo, B_0 (see eqn [5]), and thus in principle it is possible to separate scattering and intrinsic Q by measuring energy density distribution curves. Hoshiba (1991) pointed out that in practice the use of finite window lengths for measuring coda will lead to underestimating the total energy (compared to the infinite lapse-time windows in Wu's theory), likely biasing the resulting estimates of seismic albedo. To deal with this problem, Fehler *et al.* (1992) introduced the multiple lapse-time window (MLTW) analysis, which measures the energy in consecutive time windows as a function of

epicentral distance. The MLTW approach has been widely used in studies of S coda (see below).

A powerful method for computing synthetic seismograms based on radiative transfer theory is to use a computer-based Monte Carlo approach to simulate the random walk of millions of seismic energy 'particles' which are scattered with probabilities derived from random media theory. Figure 3 illustrates a simple example of this method applied to 2-D isotropic scattering. Variations on this basic technique are described by Gusev and Abubakirov (1987), Abubakirov and Gusev (1990), Hoshiba (1991, 1994, 1997), Margerin *et al.* (2000), Bal and

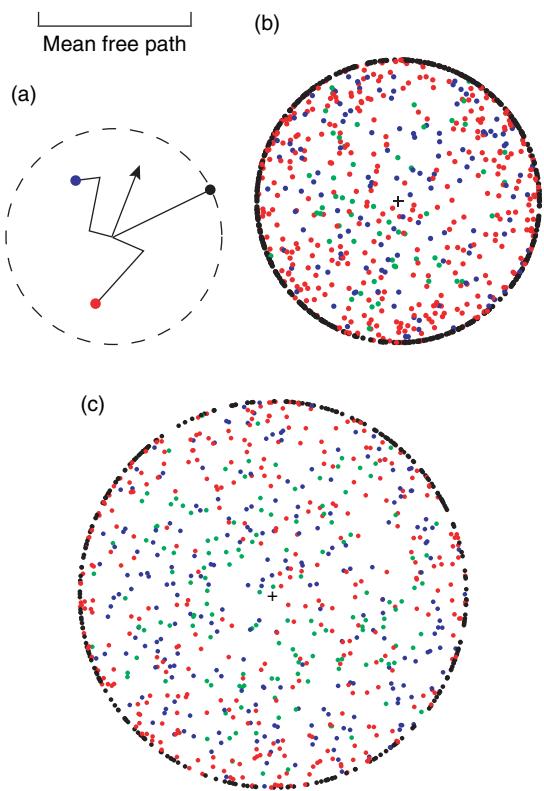


Figure 3 Example of a Monte Carlo computer simulation of random scattering of seismic energy particles, assuming 2-D isotropic scattering in a uniform whole space. Particles are sprayed in all directions from the source with constant scattering probability defined by the indicated mean free path length, ℓ . As indicated in (a), black dots show particles that have not been scattered, red dots show particles that have scattered once, blue dots show particles that have scattered twice, and green dots show particles scattered three or more times. (b) Results for 1000 particles after $t = \ell/v$, where v is velocity. (c) Results for 1000 particles after $t = 1.25 \ell/v$. Note that the particle density is approximately constant for the scattered energy inside the circle defining the direct wave front, as predicted by the EFM.

Moscoso (2000), Yoshimoto (2000), Margerin and Nolet (2003a, 2003b), and Shearer and Earle (2004). Because of the potential of the Monte Carlo method for modeling whole-Earth, high-frequency scattering, these results are now summarized in some detail.

Gusev and Abubakirov (1987) used the Monte Carlo method to model acoustic wave scattering in a whole space and considered both isotropic scattering and forward scattering with a Gaussian angle distribution. They parameterized the scattering in terms of a uniform probability per unit volume, resulting in an exponential distribution of path lengths. Intrinsic attenuation was not included. They showed that their results agree with the diffusion model for large lapse times. Abubakirov and Gusev (1990) contains a more detailed description of this method and its application to model S coda from Kamchatka earthquakes. They obtained an S wave mean free path for the Kamchatka lithosphere of 110–150 km over a 1.5–6 Hz frequency range.

Hoshiba (1991) modeled the spherical radiation of S wave energy in a constant-velocity medium using a Monte Carlo simulation that included isotropic scattering with uniform probability. He showed that the results agreed with single-scattering theory for weak scattering (i.e., travel distances less than 10% of the mean free path) and agreed with the diffusion model for strong scattering (i.e., travel distances more than 10 times longer than the mean free path). Hoshiba (1991) was able to use his Monte Carlo results to correct and extend the multiple scattering terms of Gao *et al.* (1983a, 1983b). He found that his simulations at long lapse times were consistent with the radiative transfer theory of Wu (1985) but that reliable estimates of seismic albedo are problematic from short time windows. Finally, Hoshiba (1991) showed that for multiple scattering, coda Q is much more sensitive to intrinsic Q than to scattering Q (as was argued by Frankel and Wennerberg (1987) on the basis of the EFM).

Wennerberg (1993) considered the implications of lapse-time-dependent observations of Q_C and methods for separating intrinsic and scattering attenuation with respect to the single-scattering model, Zeng's (1991) multiple-scattering model, Hoshiba's (1991) model, and Abubakirov and Gusev's (1990) results. Hoshiba (1994) extended his Monte Carlo method to consider depth-dependent scattering strength and intrinsic attenuation, and Hoshiba (1997) included the effects of a layered velocity velocity structure to model local earthquake coda at distances up to 50 km. Hoshiba simulated SH wave reflection and

transmission coefficients at layer interfaces as probabilities of reflection or transmission of particles in the Monte Carlo method but did not include P waves and the conversions between P and S waves. The results showed that coda amplitudes depend upon the source depth even late into the coda.

Margerin *et al.* (1998) applied the Monte Carlo approach to a layer-over-half-space model, representing the crust and upper mantle, and included both surface- and Moho-reflected and transmitted phases. As in Hoshiba (1997), reflection and transmission coefficients are converted to probabilities for the individual particles. Only S waves are modeled (using the scalar wave approximation, i.e., no P-to-S conversions) and no intrinsic attenuation is included. Margerin *et al.* (1998) compared their numerical results in detail with solutions based on the diffusion equation and found good agreement for suitable mean free path lengths. They point out the importance of the crustal waveguide for trapping energy near the surface and that the possibility of energy leakage into the mantle should be taken into account in calculations of seismic albedo.

Bal and Moscoso (2000) explicitly included S wave polarization and showed that S waves become depolarized under multiple scattering. Yoshimoto (2000) introduced the direct simulation Monte Carlo (DSMC) method, which uses a finite difference scheme for ray tracing and can thus handle velocity models of arbitrary complexity, including lateral varying structures. However, intrinsic attenuation and directional scattering were not included. Yoshimoto showed that a velocity increase with depth strongly affects the shape of the coda envelope, compared with uniform velocity models, and that it is important to properly model energy that may be trapped at shallow depths.

Margerin *et al.* (2000) extended the Monte Carlo approach to elastic waves, taking into account P-to-S conversions and S wave polarization. They considered scattering from randomly distributed spherical inclusions within a homogeneous background material, using the solutions of Wu and Aki (1985a). For both Rayleigh scatterers (spheres much smaller than the seismic wavelength) and Rayleigh–Gans scatterers (spheres comparable to the seismic wavelength), they found good agreement with single-scattering theory at short times and with the diffusion equation solution at long times. In addition, the P-to-S energy density ratio and the coda decay rate at long times converged to their theoretical expected values.

Margerin and Nolet (2003a, 2003b) further extended the Monte Carlo approach to model whole-Earth wave propagation and scattering. They showed that their Monte Carlo synthetics for the PKP AB and BC branches produced energy versus distance results in good agreement with geometrical ray theory. They computed scattering properties based on random media models characterized by velocity perturbations with an exponential correlation length. For whole mantle scattering, they found that the Born approximation is only valid up to mean free paths of about 400 s, corresponding to 0.5% rms velocity perturbations. They also applied their method to model PKP precursor observations; these results are discussed later in this paper.

Shearer and Earle (2004) implemented a particle-based Monte Carlo method for computing whole-Earth scattering. They included both P and S waves radiated from the source, mode conversions, S wave polarizations, and intrinsic attenuation. For a simple whole-space model, they showed that their approach agreed with theoretical results for the S/P energy ratio and expected $t^{-1.5}$ falloff in power at large times. For modeling the whole Earth, they included the effects of reflection and transmission coefficients at the free surface, Moho, CMB, and inner core boundary (ICB). Scattering probabilities and scattering angles were computed assuming random velocity and density variations characterized by an exponential ACF. They applied this method to model the time and distance dependence of high-frequency P coda amplitudes (see Section 1.20.3.2).

All of these results suggest that body-wave scattering in the whole Earth can now be accurately modeled using ray theory and particle-based Monte Carlo methods. Although somewhat computationally intensive, continued improvements in computer speed make them practical to run on modest machines. They can handle multiple scattering over a range of scattering intensities, bridging the gap between the Born approximation for weak scattering and the diffusion equation for strong scattering. They also can include general depth-dependent or even 3-D variations in scattering properties, including nonisotropic scattering, without a significant increase in computation time compared to simpler problems.

1.20.2.4 Other Theoretical Methods

Lerche and Menke (1986) presented an inversion method to separate intrinsic and scattering attenuation

for a plane layered medium. Gusev (1995) and Gusev and Abubakirov (1999a, 1999b) developed a theory for reconstructing a vertical profile of scattering strength from pulse broadening and delay of the peak amplitude. Saito *et al.* (2002, 2003) modeled envelope broadening in S waves by applying the parabolic approximation to a von Karman random medium. Sato *et al.* (2004) extended this approach to develop a hybrid method for synthesizing whole-wave envelopes that uses the envelope obtained from the Markov approximation as a propagator in the radiative transfer integral and showed that the results agreed with finite difference calculations. The effect of anisotropic random media (where the scattering properties depend upon the angle of the incident wave) was considered numerically by Wagner and Langston (1992a) and Roth and Korn (1993), and theoretically by Müller and Shapiro (2003) and Hong and Wu (2005). Recent work on using small-aperture seismic arrays on coda to constrain the directions of individual scatterers includes Schisselé *et al.* (2004) and Matsumoto (2005).

1.20.3 Scattering Observations

Seismic scattering within the Earth is mainly observed in the incoherent energy that arrives between the direct seismic phases, such as P, S, and PKP. In addition, occasionally specific scatterers can be imaged using seismic arrays. Scattering can also influence the direct phases through amplitude reduction and pulse broadening, effects characterized by the scattering attenuation parameter, Q_{Sc}^{-1} . In this way, studies of seismic attenuation also resolve scattering, although they often do not attempt to separate intrinsic and scattering attenuation. The incoherent scattered seismic wavefield usually follows a direct seismic arrival, and is termed the ‘coda’ of that phase (e.g., P coda, S coda), but occasionally the ray geometry is such that scattered energy can arrive before a direct phase (e.g., PKP precursors). These precursory arrivals are particularly valuable for studying deep-Earth scattering because they are less sensitive to the strong scattering in the lithosphere. Scattering is usually studied at relatively high frequencies (1 Hz or above) where coda is relatively strong and local earthquake records have their best signal to noise.

S wave coda from local and regional events has been the focus of many studies, has motivated much of the theoretical work, and continues to be an active field of research. Here, S coda studies and their

implications for scattering in the crust and lithosphere are only briefly reviewed; instead, more attention is devoted to other parts of the scattered seismic wavefield, which provide better constraints on deep-Earth structure. Previous review articles that discuss deep-Earth scattering include Bataille *et al.* (1990) and Shearer *et al.* (1998). **Figure 4** shows where much of the scattered energy arrives with respect to traveltime curves for the major seismic phases. In principle, any seismic phase that travels through the lower mantle or the CMB will be sensitive to deep-Earth scattering. Although separating deep-scattering effects from crust and lithospheric scattering can be challenging, this is possible in some cases, either from a fortunate ray geometry or by careful comparison of coda amplitudes at different distances or between different phases.

The picture that is emerging from these studies is that seismic scattering from small-scale velocity perturbations is present throughout the Earth, with the exception of the fluid outer core. However, the exact strength, scale length, and depth dependence of the scattering remain unresolved, particularly in the

vicinity of the CMB and ICB, where they may also be contributions from topographic irregularities or boundary-layer structure.

1.20.3.1 S Coda

S coda measurements are of two main types: (1) those that simply fit the coda decay rate and estimate βQ_C without attempting to separate scattering and intrinsic attenuation, and (2) those that measure energy density and estimate the scattering coefficient g_0 (or its reciprocal, the mean free path). The latter studies typically obtain a separate estimate for intrinsic attenuation and thus can compute the seismic albedo, B_0 . The basic relationships among these parameters are given in eqns [4] and [5]. In both types of studies, frequency dependence can also be examined by filtering the data in different bands.

Coda Q studies include Rautian and Khalturin (1978), Roecker *et al.* (1982), Rodriguez *et al.* (1983), Singh and Herrmann (1983), Biswas and Aki (1984), Pulli (1984), Rhea (1984), Jin *et al.* (1985), Del Pezzo *et al.* (1985), Jin and Aki (1988), van Eck (1988), Kvamme and Havskov (1989), Matsumoto and Hasegawa (1989), Baskoutas and Sato (1989), Oancea *et al.* (1991), Tsuruga *et al.* (2003), Giampiccollo *et al.* (2004), and Goutbeek *et al.* (2004).

Reviews of Q_C measurements include Herraiz and Espinosa (1987), Matsumoto (1995), and Sato and Fehler (1998). In general, Q_C is frequency dependent and increases from about 100 at 1 Hz to 1000 at 20 Hz (i.e., there is less attenuation at higher frequencies). However there are regional variations of about a factor of 10, and typically Q_C is lower in tectonically active areas and higher in stable regions, such as shields. As discussed above, how to interpret Q_C in terms of Q_{Sc} and Q_I has been the subject of some debate, and it is becoming increasingly clear that depth-dependent calculations (which include variations in the background velocity, the scattering characteristics, and the intrinsic attenuation) are required in many cases to fully describe coda observations.

Some studies (e.g., Rautian and Khalturin, 1978; Roecker *et al.*, 1982; Gagnepain-Beyneix, 1987; Kvamme and Havskov, 1989; Akamatsu, 1991; Kosuga, 1992, Gupta *et al.*, 1998; Singh *et al.*, 2001; Giampiccollo *et al.*, 2004; Goutbeek *et al.*, 2004) have observed that Q_C increases with increasing lapse time (i.e., eqn [1] does not fit the entire coda envelope), suggesting that the later part of the coda contains energy that propagated through less

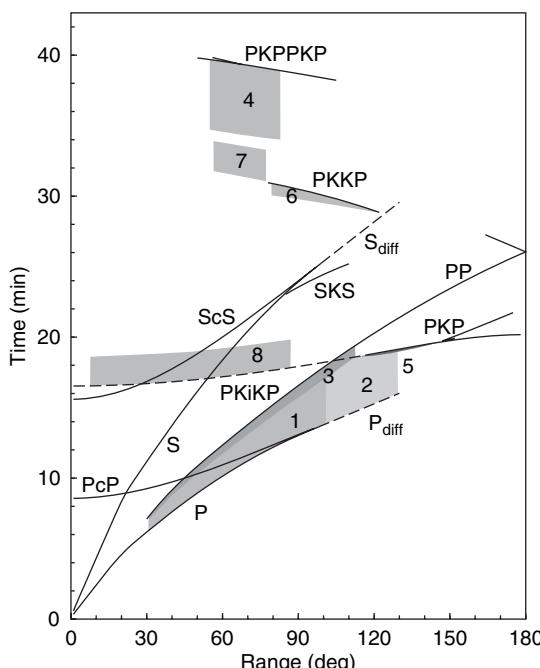


Figure 4 Traveltimes for teleseismic body waves and some of the regions in the short-period wavefield that contain scattered arrivals. These include: (1) P coda, (2) P_{diff} coda, (3) PP precursors, (4) $P'P'$ precursors, (5) PKP precursors, (6) PKKP precursors, (7) PKKP_x, and (8) PKiKP coda. The plotted boundaries are approximate.

attenuating material than the early part of the coda. Gusev (1995) showed that an increase in Q_C with time in the coda is predicted from a single isotropic scattering model in which Q_{Sc} increases with depth. Margerin *et al.* (1998) applied radiative transfer theory to show that a model of scattering in the crust above much weaker scattering in the mantle predicts Q_C values that depend upon the reflection coefficient at the Moho, implying that energy leakage into the mantle has implications for the interpretation of coda Q .

Following Sato and Fehler (1998), we may divide scattering attenuation estimates into those obtained using the single-scattering model and those based on MLTW analysis. Single-scattering studies include Sato (1978), Aki (1980), Pulli (1984), Dainty *et al.* (1987), Kosuga (1992), and Baskoutas (1996). Multiple lapse-time studies are summarized in Figure 5 and include Fehler *et al.* (1992), Mayeda *et al.* (1992), Hoshiba (1993), Jin *et al.* (1994), Akinci *et al.* (1995), Canas *et al.* (1998), Ugalde *et al.* (1998, 2002), Hoshiba *et al.* (2001), Bianco *et al.* (2002, 2005), Vargas *et al.* (2004), and Goutbeek *et al.* (2004). Values of the coefficient g_0 for S-to-S scattering range from about 0.002 to 0.05 km^{-1} (mean free paths of 20–500 km) for frequencies between 1 and 30 Hz. Some papers (e.g., Mayeda *et al.*, 1992; Hoshiba, 1993; Jin *et al.*, 1994; Goutbeek *et al.*, 2004; Bianco *et al.*, 2005) have found a frequency dependence in

the seismic albedo and among different regions, but in general this dependence is not as consistent as that seen in Q_C studies. Several recent papers noted the importance of considering depth-dependent velocity structure in computing scattering attenuation (e.g., Hoshiba *et al.*, 2001; Bianco *et al.*, 2002, 2005).

Lacombe *et al.* (2003) modeled S coda in France at epicentral distances between 100 and 900 km using acoustic radiative transfer theory applied to a two-layer model. They found that a model with scattering confined to the crust and uniform intrinsic attenuation could explain their data at 3 Hz, but that the tradeoff between scattering and intrinsic attenuation was too strong to reliably determine the relative contribution of each parameter. At the regional epicentral distances of their model, the crustal waveguide had a dominating effect on the S coda.

In addition to the S coda decay rates at relatively long lapse times used to determine coda Q , there are other aspects of the coda that provide additional constraints on scattering. The complete seismogram envelope can be studied, including the broadening of the direct S envelope and the delay in its peak amplitude (e.g., Sato, 1989, 1991; Scherbaum and Sato, 1991; Obara and Sato, 1995). Deviations from the average coda decay rate for a number of stations can be inverted to construct a 3-D model of scattering intensity in the crust and upper mantle (e.g., Nishigami, 1991, 1997; Obara, 1997; Chen and Long, 2000; Taira and Yomogida, 2004). Similar methods were used by Revenaugh (1995, 1999, 2000) to back-project P coda recorded in southern California, and by Hedlin and Shearer (2000) to invert PKP precursor amplitudes (see below). Periodic rippling of SH coda envelopes in northeastern Japan was noted by Kosuga (1997), who suggested this may be caused by trapped waves within a low-velocity layer in the top part of the subducting slab.

Spudich and Bostwick (1987) showed how Green's function reciprocity can be used to obtain information about the ray takeoff directions from the earthquake source region, using a cluster of earthquakes as a virtual array. Applying this method to aftershocks of the 1984 Morgan Hill earthquake in California, they found that the early S coda was dominated by multiple scattering within 2 km of each seismic station. Scherbaum *et al.* (1991) used this approach to study two micro-earthquake clusters in northern Switzerland and found that the early S coda contained energy leaving the source at close to the same angle as the direct wave, but that later (at

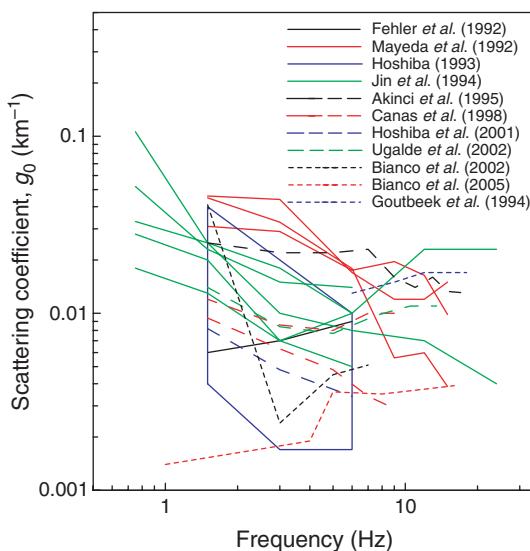


Figure 5 A summary of observations of the total scattering coefficient g_0 for S wave scattering versus frequency, obtained using the MLTW method. Results from various studies around the world are indicated with different colors.

least 1.5–2 times the S travel time) coda contains energy from waves leaving the source in a variety of directions. Spudich and Miller (1990) and Spudich and Iida (1993) showed how an interpolation approach using distributed earthquake sources can be used to estimate scattering locations in the vicinity of the 1986 North Palm Springs earthquake in California.

1.20.3.2 P Coda

Local and many regional coda studies have mainly focused on the S wave coda because of its higher amplitude and longer duration than P wave coda (which is truncated by the S wave arrival). However, at teleseismic distances, P waves and their coda are more prominent than S waves at high frequencies because of the severe effect of mantle attenuation on the shear waves. A number of studies both from single stations and arrays have attempted to resolve the origin of the scattered waves in the P coda and to distinguish between near-source and near-receiver scattering.

Aki (1973) modeled scattering of P waves beneath the Montana LASA (Large Aperture Seismic Array) array using Chernov single-scattering theory. At 0.5 Hz, he achieved a good fit to the data with a random heterogeneity model extending to 60 km depth beneath LASA, with rms velocity fluctuations of 4% and a correlation distance of 10 km. Stronger scattering at higher frequencies exceeded the validity limits of the Born approximation.

Frankel and Clayton (1986) compared teleseismic traveltimes anomalies observed across the LASA and NORSAR (Norwegian Seismic Array) arrays, as well as very high frequency coda ($f \geq 30$ Hz) observed for micro-earthquakes, to synthetic seismograms for random media generated using a finite difference method. They found that a random medium with self-similar velocity fluctuations ($a \geq 10$ km) of 5% within a ~ 100 km thick layer could explain both types of observations.

Dainty (1990) reviewed array studies of teleseismic P coda, such as that recorded by the LASA and NORESS arrays. He distinguished between ‘coherent’ coda, which has nearly the same slowness and back azimuth as direct P, and ‘diffuse’ coda, which is characterized by energy arriving from many different directions. He argued that coherent coda is generated by shallow, near-source scattering in the crust, rather than deeper in the mantle, because it is absent or weak for deep-focus earthquakes. In contrast, the

diffuse coda is produced by near-receiver scattering and has power concentrated at slownesses typical of shear, Lg , or surface waves. Lay (1987) showed that the dispersive character of the first 15 s of the P coda from nuclear explosions was due to near-source effects.

Gupta and Blanford (1983) and Cessaro and Butler (1987) addressed the question as to how scattering can cause transversely polarized energy to appear in P and P coda, an issue relevant to discrimination methods between earthquakes and explosions. Their observations at different distances and frequency bands suggested that both near-source and near-receiver scattering must be present. Flatté and Wu (1988) performed a statistical analysis of phase and amplitude variations of teleseismic P waves recorded by the NORSAR array. They fit their results with a two-overlapping-layer model of lithospheric and asthenospheric heterogeneity beneath NORSAR, consisting of the summed contributions from a 0–200 km layer with a flat power spectrum and a 15–250 km layer with a k^{-4} power spectrum (the deeper layer corresponds to an exponential autocorrelation model with scale larger than the array aperture of 110 km). The rms P velocity variations are 1–4%. This model has relatively more small-scale scatterers in the shallow crust (which the authors attribute to clustered cracks or intrusions) and relatively more large-scale scatterers in the asthenosphere (which the authors suggest may be temperature or compositional heterogeneities).

Langston (1989) studied teleseismic P waves recorded at station PAS in California and SCP in Pennsylvania. He showed that the coda amplitude cannot be explained by horizontally layered structures of realistic velocity contrasts and that 3-D scattering is required. He could explain the observed coda decay by adopting the EFM of Frankel and Wennerberg (1987) for the case of a scattering layer above a homogenous half-space. He found that scattering is more severe at PAS than SCP, as indicated by higher coda levels and a slower decay rate, obtaining a scattering Q estimate for PAS of 239 (2 s period) compared to 582 for SCP.

Korn (1988) examined the P coda from Indonesian earthquakes recorded at the Warramunga array in central Australia and found that the coda energy decreased with increasing source depth. He computed the power in the coda at different frequency bands between 0.75 and 6 Hz and fitted the results with the EFM of Frankel and Wennerberg (1987). The results indicated frequency dependence in both

intrinsic attenuation and scattering attenuation ($Q_I = 300$ at 1 Hz, increasing almost linearly with frequency above 1 Hz; $Q_{Sc} = 340$ at 1 Hz, increasing as $f^{0.85}$). Assuming random velocity fluctuations with an exponential ACF, results from Sato (1984) can be used to estimate that rms velocity variations of 5% at 5.5 km scale length are consistent with the observed Q_{Sc} below the Warramunga array. Korn (1990) extended the EFM to accommodate a scattering layer over a homogeneous half space (a modeling approach similar to that used by Langston (1989)) and applied the method to the short-period Warramunga array data of Korn (1988) for deep earthquakes. With the new model, he found an average scattering Q of 640 at 1 Hz for the lithosphere below the array and higher values of intrinsic Q , implying that diffusion rather than anelasticity is the dominant factor controlling teleseismic coda decay rates. Korn (1993) further applied this approach to teleseismic P coda observations from nine stations around the Pacific. He found significant differences in scattering Q among the stations ($Q_{Sc} = 100\text{--}500$). The observed frequency dependence of Q_{Sc} is in approximate agreement with single-scattering theory for random heterogeneities, and favors von Karman type ACFs over Gaussian or self-similar models.

Bannister *et al.* (1990) analyzed teleseismic P coda recorded at the NORESS array using both array and three-component methods. They resolved both near-source and near-receiver scattering contributions to coda, with the bulk of receiver-side scattering resulting from P-to-Rg conversions from two nearby areas (10 and 30 km away) with significant topography. Gupta *et al.* (1990) performed frequency wave number analysis on high-frequency NORESS data and identified both near-receiver P-to-Rg scattering and near-source Rg-to-P scattering. Dainty and Toksöz (1990) examined scattering in regional seismograms recorded by the NORESS, FINESA, and ARCESS arrays. P coda energy was concentrated in the on-azimuth direction, but appeared at different phase velocities, suggesting different contribution mechanisms.

Wagner and Langston (1992b) applied frequency wave number analysis to P'P' (PKPPKP) waves recorded by the NORESS arrays for deep earthquakes. Most of the coda was vertically propagating but an arrival about 15 s after the direct wave can be identified as body-to-Rayleigh-wave scattering from a point 30 km west-southwest of the array (this scattering location was previously identified in P wave

coda by Bannister *et al.* (1990) and Gupta *et al.* (1990)). Revenaugh (1995, 1999, 2000) applied a Kirchhoff migration approach to back-project P coda recorded in southern California to image lateral variations in scattering intensity within the crust and identified correlations between scattering strength and the locations of faults and other tectonic features.

Neele and Snieder (1991) used the NARS and GRF arrays in Europe to study long-period teleseismic P coda and found it to be coherent with energy arriving from the source azimuth. They concluded that long-period P coda does not contain a significant amount of scattered energy and can be explained with spherically symmetric models, and is particularly sensitive to structure in upper-mantle low-velocity zones. Ritter *et al.* (1997, 1998) studied the frequency dependence of teleseismic P coda recorded in the French Massif Central, which they modeled as a 70 km thick layer with velocity fluctuations of 3–7% and heterogeneity scale lengths of 1–16 km. Rothert and Ritter (2000) studied P coda in intermediate-depth Hindu Kush earthquakes recorded at the GRF array in Germany about 44° away. They applied a method based on the theory of Shapiro and Kneib (1993) and Shapiro *et al.* (1996) and found that the observed wavefield fluctuations are consistent with random crustal heterogeneities of 3–7% and isotropic correlation lengths of 0.6–4.8 km. Ritter and Rothert (2000) used a similar approach on teleseismic P coda to infer differences in scattering strength beneath two local networks in Europe. Hock *et al.* (2000, 2004) used teleseismic P coda to characterize random lithospheric heterogeneities across Europe using the EFM. They obtained a range of different scale lengths and rms velocity fluctuations on the order to 3–8%. Nishimura *et al.* (2002) analyzed transverse components in teleseismic P coda for stations in the western Pacific and noted stronger scattering for stations close to plate boundaries compared to those on stable continents.

In some cases, analysis of P coda can reveal individual scatterers and/or discontinuities at mid-mantle depths below subduction zone earthquakes (Niu and Kawakatsu, 1994, 1997; Castle and Creager, 1999; Kaneshima and Helffrich, 1998, 1999, 2003; Krüger *et al.*, 2001; Kaneshima, 2003). Other individual scatterers (or regions of strong scattering) have been observed near the CMB from PcP precursors (Weber and Davis, 1990; Weber and Körnig, 1990; Scherbaum *et al.*, 1997; Brana and Helffrich, 2004) and PKP precursors (Vidale and Hedlin, 1998; Thomas *et al.*, 1999).

Shearer and Earle (2004) attempted to systematically characterize and model globally averaged short-period teleseismic P coda from both shallow and deep earthquakes. This was the first attempt to fit a global data set of P wave amplitudes and coda energy levels with a comprehensive energy-preserving model that specified scattering and intrinsic attenuation throughout the Earth. Examining global seismic network data between 1990 and 1999 at source-receiver distances between 10° and 100° , they identified high signal-to-noise records and stacked over 7500 traces from shallow events (depth ≤ 50 km) and over 650 traces from deep events (depth ≥ 400 km). The stacking method involved summing envelope functions from 0.5 to 2.5 Hz bandpass filtered traces, normalized to the maximum P amplitude. Peak P amplitudes were separately processed so that absolute P amplitude versus source-receiver distance information was preserved. The coda shape was markedly different between the shallow- and deep-event stacks (see **Figure 6**). The shallow earthquake

coda was much more energetic and long-lasting than the deep-event coda, indicating that the bulk of the teleseismic P coda from shallow events is caused by near-source scattering above 600 km depth.

Shearer and Earle modeled these observations using a Monte Carlo, particle-based approach (see above), in which millions of seismic phonons are randomly sprayed from the source and tracked through the Earth. They found that most scattering occurs in the lithosphere and upper mantle, as previous results had indicated, but that some lower-mantle scattering was also required to achieve the best fits to the data. Their preferred exponential autocorrelation random heterogeneity model contained 4% rms velocity heterogeneity at 4 km scale length from the surface to 200 km depth, 3% heterogeneity at 4 km scale between 200 and 600 km, and 0.5% heterogeneity at 8 km scale length between 600 km and the CMB. They assumed equal and correlated P and S fractional velocity perturbations and a density/velocity scaling ratio of 0.8. Intrinsic

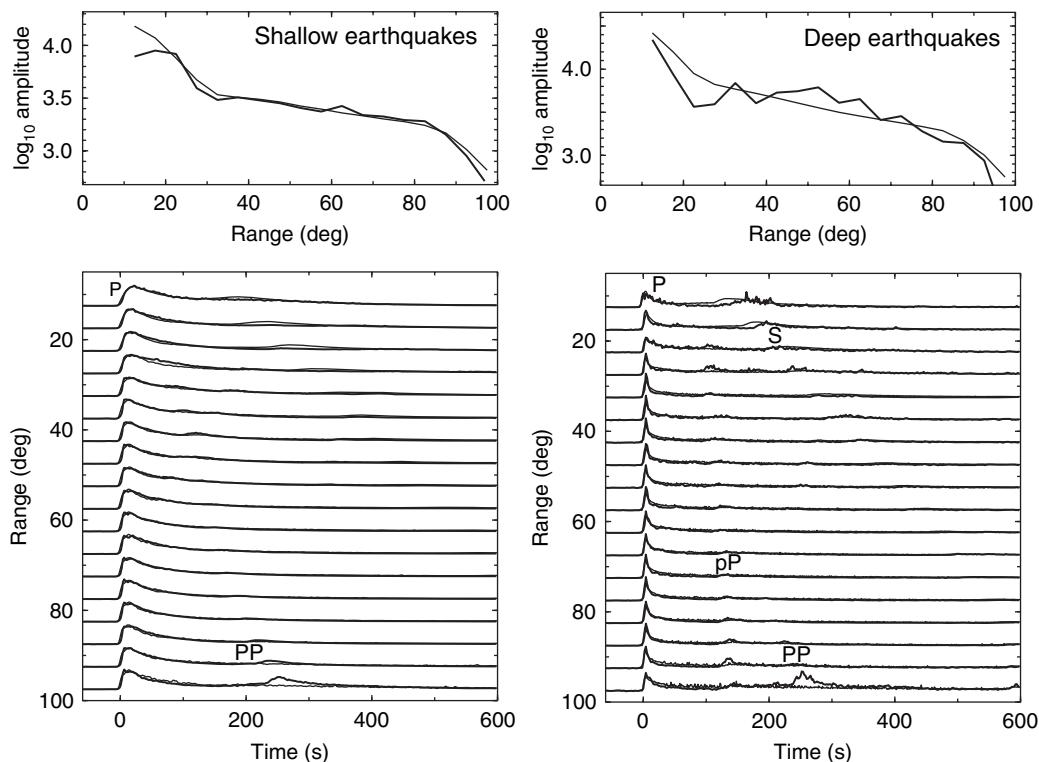


Figure 6 Comparisons between envelope function stacks of teleseismic P wave arrivals (thick lines) with predictions of a Monte Carlo simulation for a whole-Earth scattering model (thin lines) as obtained by Shearer and Earle (2004). The left panels show results for shallow earthquakes (≤ 50 km); the right panels are for deep earthquakes (≥ 400 km). The top panels show peak P wave amplitude versus epicentral distance. The bottom panels show coda envelopes in 5° distance bins plotted as a function of time from the direct P arrivals, with amplitudes normalized to the same energy in the first 30 s.

attenuation was $\alpha Q_L = 450$ above 200 km and $\alpha Q_L = 2500$ below 200 km, with $\beta Q_L = (4/9)^\alpha Q_L$ (an approximation that assumes all the attenuation is in shear). This model produced a reasonable overall fit, for both the shallow- and deep-event observations, of the amplitude decay with epicentral distance of the peak P amplitude and the P coda amplitude and duration (see **Figure 6**). These numbers imply that for both P and S waves the seismic albedo, β_0 , is about 75–90% in the upper mantle above 600 km, and about 25–35% in the lower mantle, consistent with the total attenuation being dominated by scattering in the upper mantle and by intrinsic energy loss in the lower mantle.

The 4% velocity perturbations for the uppermost layer in the [Shearer and Earle \(2004\)](#) model are in rough agreement with previous P coda analyses by [Frankel and Clayton \(1986\)](#), [Flatté and Wu \(1988\)](#), and [Korn \(1988\)](#); and the S wave mean free path of 50 km for the upper 200 km is within the range of mean free paths estimated from regional measurements of lithospheric scattering. However, limitations of the [Shearer and Earle \(2004\)](#) study include the restriction to single-station, vertical-component data (i.e., wave polarization, slowness, and azimuth constraints from three-component and/or array analyses are not used) and a single frequency band near 1 Hz. In addition, the ray theoretical approach cannot properly account for body-to-surface-wave converted energy, which some array studies suggest are an important component of P coda.

Resolving possible lower-mantle scattering using P coda is difficult because of the much stronger scattering from shallow structure. However, [Shearer and Earle \(2004\)](#) found that ~0.5% rms velocity heterogeneity in the lower mantle was required to achieve the best fit to P coda amplitudes at epicentral distances beyond 50°. This value is between the estimates for lower-mantle velocity perturbations derived from PKP precursors of 1% from [Hedlin et al. \(1997\)](#) and 0.1–0.2% from [Margerin and Nolet \(2003b\)](#).

1.20.3.3 P_n Coda

A prominent feature of long-range records of nuclear explosions across Eurasia is P_n and its coda, which can be observed to distances of more than 3000 km (e.g., [Ryberg et al., 1995, 2000; Morozov et al., 1998](#)). As discussed by [Nielsen and Thybo \(2003\)](#), there are two main models for upper-mantle structure that

have been proposed to explain these observations: (1) [Ryberg et al. \(1995, 2000\)](#) and [Tittgemeyer et al. \(1996\)](#) proposed random velocity fluctuations between the Moho and about 140 km depth in which the vertical correlation length (0.5 km) is much smaller than the horizontal correlation length (20 km). These fluctuations cause multiple scattering that form a waveguide that can propagate high-frequency P_n to long distances. (2) [Morozov et al. \(1998\)](#), [Morozov and Smithson \(2000\)](#), and [Nielsen et al. \(2003b\)](#) favored a model in which P_n is a whispering gallery phase traveling as multiple underside reflections off the Moho, with the coda generated by crustal scattering. [Nielsen and Thybo's \(2003\)](#) preferred model has random crustal velocity perturbations between 15 and 40 km depth with a vertical correlation length of 0.6 km and a horizontal correlation length of 2.4 km. However, [Nielsen et al. \(2003a\)](#) found that the scattered arrivals seen at 800–1400 km distance for profile ‘Kraton’ required scattering within a layer between about 100 and 185 km depth and could be modeled with 2-D finite difference synthetics assuming 2% rms velocity variations.

An important aspect of all these models is that their random velocity perturbations are horizontally elongated (i.e., anisotropic). At least for the lower crust there is also some evidence for this from reflection seismic profiles (e.g., [Wenzel et al., 1987; Holliger and Levander, 1992](#)). This contrasts with most modeling of S and P coda, which typically assumes isotropic random heterogeneity.

1.20.3.4 P_{diff} Coda

Another phase particularly sensitive to deep Earth scattering is P_{diff} and its coda. P_{diff} contains P energy diffracted around the CMB and is observed at distances greater than 98°. The direct phase is seen most clearly at long periods, but high-frequency (~1 Hz) P_{diff} and its coda can be detected to beyond 130° (e.g., [Earle and Shearer, 2001](#)). P_{diff} coda is a typically emergent wave train that decays slowly enough that it can commonly be observed for several minutes until it is obscured by the PP and PKP arrivals. [Husebye and Madariaga \(1970\)](#) concluded that P_{diff} coda (which they termed $P(\text{diff})$ tail) could not be explained as simple P diffraction at the CMB or by reflections from the core, and suggested that it originated from reflections or multiple paths in the upper mantle (similar to the proposed explanation for PP precursors given by [Bolt et al. \(1968\)](#)). However, later

work has shown this to be unlikely, given the large differences seen between observations of deep-turning direct P coda and P_{diff} coda. [Bataille et al. \(1990\)](#) reviewed previous studies of P_{diff} coda and suggested that it is caused by multiple scattering near the CMB, with propagation to long distances possibly enhanced by the presence of a low-velocity layer within D'' .

[Tono and Yomogida \(1996\)](#) examined P_{diff} coda in 15 short-period records from deep earthquakes at distances of $103\text{--}120^\circ$ and found considerable variation in the appearance and duration of P_{diff} coda. Comparisons between P_{diff} and direct P waves at shorter distances, as well as particle motion analysis of P_{diff} coda, indicated that the coda was caused by deep-Earth scattering. Tono and Yomogida computed synthetics using the boundary integral method of [Benites et al. \(1992\)](#), applied to a simplified model of an incident wave grazing an irregular CMB. They were able to fit a subset of their observations in which the P_{diff} coda duration was relatively short (<50 s), with bumps on the CMB with minimum heights of 5–40 km. Such large CMB topography is unrealistic given PcP studies, which have indicated a relatively flat and smooth CMB (e.g., [Kampfmann and Müller, 1989](#); [Vidale and Benz, 1992](#)), and PKKP precursor observations that limit CMB rms topography to less than 315 m at 10 km wavelength ([Earle and Shearer, 1997](#), see below), but it is likely that volumetric heterogeneity within D'' could produce similar scattering. Although the [Tono and Yomogida \(1996\)](#) model included multiple scattering, they could not fit the long tail (>50 s) of some of their P_{diff} observations, and they suggested that for such cases a low-velocity zone just above the CMB is channeling the scattered energy. Strong heterogeneity and low-velocity zones of varying thicknesses have been observed above the CMB (e.g., see review by [Garnero \(2000\)](#)), but it is not yet clear if these models can explain P_{diff} observations.

[Bataille and Lund \(1996\)](#) argued for a deep origin for P_{diff} coda by comparing coda shapes for P near 90° range and P_{diff} at $102\text{--}105^\circ$. The P_{diff} coda is more emergent and lasts much longer than the direct P coda. This argues against a shallow source for the coda because this would produce roughly the same effect on both P and P_{diff} . Bataille and Lund found that their observed coda decay rate for a single P_{diff} observation at 116° could fit with a model of multiple scattering within a 2-D shell at the CMB. [Tono and Yomogida \(1997\)](#) examined P_{diff} in records of the 1994 Bolivian deep earthquake at epicentral

distances of $100\text{--}122^\circ$. They analyzed both global broadband stations and short-period network stations from New Zealand. They found that short-period energy continued to arrive for over 100 s after P_{diff} itself, more than twice as long as the estimated source duration of the mainshock. Comparisons between the coda decay rate of P_{diff} with other phases, as well as polarization analysis, indicated a deep origin for P_{diff} coda.

[Earle and Shearer \(2001\)](#) stacked 924 high-quality, short-period seismograms from shallow events at source-receiver distances between 92.5° and 132.5° to obtain average P and P_{diff} coda shapes. The results confirm the [Bataille and Lund \(1996\)](#) observation that P coda changes in character near 100° . In particular, P_{diff} becomes increasingly extended and emergent at longer distances. Its peak amplitude also diminishes with increasing distance, but P_{diff} can still be observed in the stacks at 130° . Earle and Shearer also performed a polarization stack ([Earle, 1999](#)), which showed that the polarization of P_{diff} coda is similar to P_{diff} (see [Figure 7](#)). To model these results, [Earle and Shearer \(2001\)](#) applied single-scattering theory for evenly distributed scatterers throughout the mantle. The resulting synthetics included P-to-P, P_{diff} -to-P, and P-to- P_{diff} scattering paths. They applied a hybrid scheme that used reflectivity to compute deep-turning P and P_{diff} amplitudes and ray theory for the shallower turning rays. Scattering was computed assuming a random medium model with an exponential ACF. Synthetics generated for a scale length of 2 km and 1% rms velocity variations achieved a good fit to the amplitude and shape of P and P_{diff} coda and a reasonable fit to the polarization angles. Thus a fairly modest level of whole-mantle scattering appears sufficient to explain the main features in P_{diff} observations, although Earle and Shearer could not exclude the possibility that multiple-scattering models could achieve similar fits.

1.20.3.5 PP and P'P' Precursors

The decay in short-period coda amplitude with time following direct P and P_{diff} stops and amplitudes begin to increase some time before the surface-reflected PP phase at distances less than about 110° (at longer distances, PKP intercedes). This energy is typically incoherent but sometimes forms distinct arrivals; both are termed PP precursors. Early explanations for PP precursor observations involved topside and bottomside reflections off discontinuities in the upper mantle ([Nguyen-Hai, 1963](#); [Bolt et al.,](#)

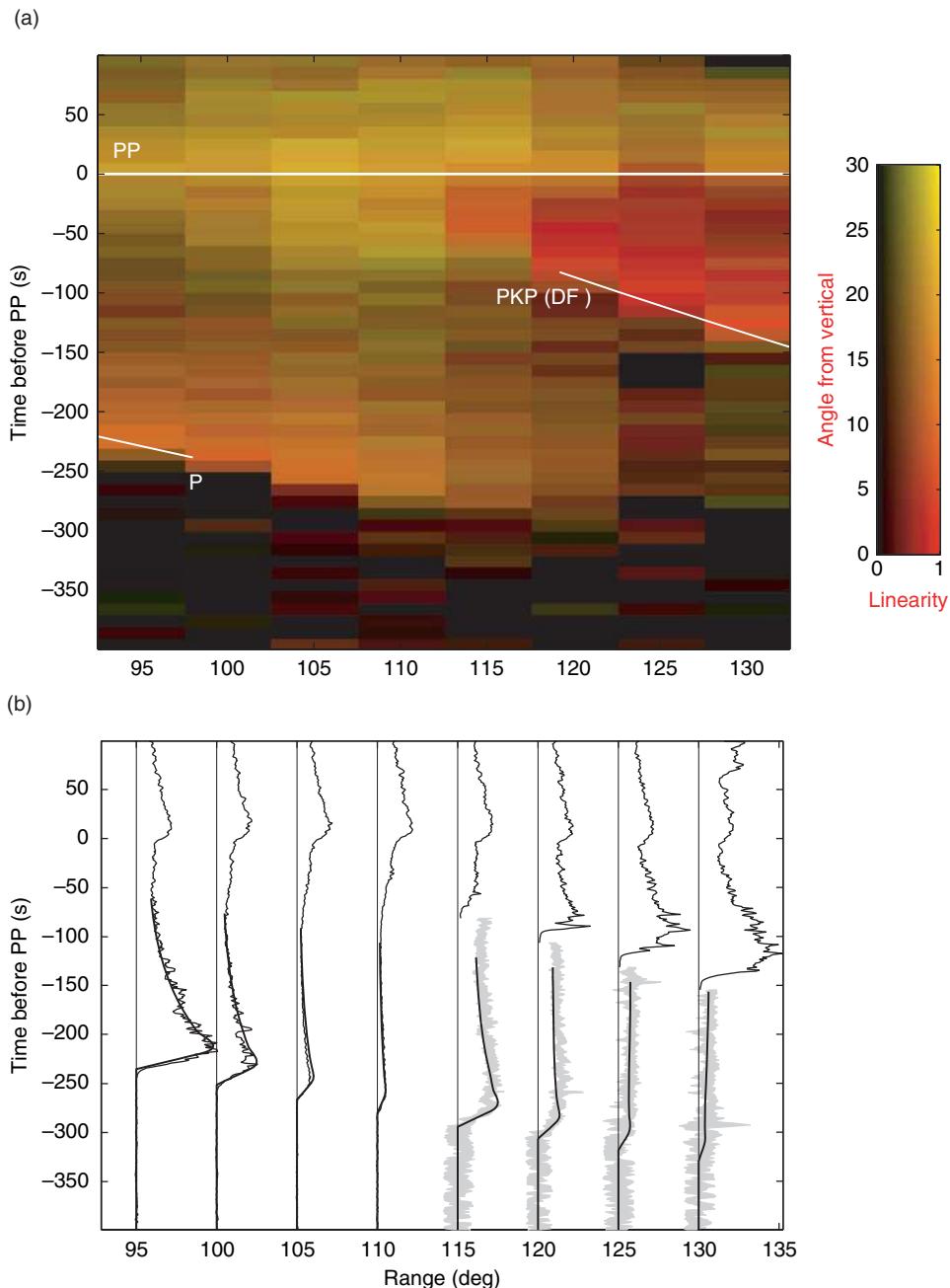


Figure 7 Global seismogram stacks and scattering model predictions for high-frequency P_{diff} from Earle and Shearer (2001). (a) A stacked image of P_{diff} polarization and linearity. Times are relative to the theoretical PP arrival times, and direct P and PKP(DF) are also shown. (b) An amplitude stack of P_{diff} envelopes (wiggly lines) compared to model predictions (smooth lines) for a uniform mantle scattering model. Amplitudes are normalized to the maximum PP amplitude. To better show the small-amplitude P_{diff} arrivals, the traces are magnified by 10 for times 20 s before PKP at distances greater than 112.5°. The width of the magnified data traces is equal to the two-sigma error in the data stack, estimated using a bootstrap method.

1968; Bolt, 1970; Husebye and Madariaga, 1970; Gutowski and Kanasewich, 1974). It is now recognized that such arrivals do exist and form globally coherent seismic phases that can readily be observed

at long periods (e.g., Shearer, 1990, 1991). In particular, the 410 and 660 km discontinuities create discrete topside reflections that follow direct P by about 1.5–2.5 min and underside reflections that proceed

PP by similar time offsets. However, the high-frequency PP precursor wavefield is much more continuous and it is difficult to identify discrete arrivals from upper-mantle discontinuities, although Wajeman (1988) was able to identify underside P reflections from discontinuities at 300 and 670 km depth by stacking broadband data from the NARS array in Europe.

Wright and Muirhead (1969) and Wright (1972) used array studies to show that PP precursors often have slownesses that are significantly less than or greater than that expected for underside reflections beneath the PP bounce point, which is consistent with asymmetric reflections at distances near 20° from either the source or receiver. However, this explanation does not explain the generally continuous nature of the PP precursor wavefield. The currently accepted explanation for the bulk of the PP precursor energy involves scattering from the near surface and was first proposed by Cleary *et al.* (1975) and King *et al.* (1975). Cleary *et al.* (1975) proposed that PP precursors result from scattering by heterogeneities within and near the crust, as evidenced by traveltimes and slowness observations of two Novalya Zemlya explosions recorded by the Warramunga array in Australia. King *et al.* (1975) modeled PP precursor observations from the Warramunga and NORSAR arrays using Born single-scattering theory. They assumed 1% rms variations in elastic properties and a Gaussian autocorrelation model with a 12 km scale length within the uppermost 100 km of the crust and upper mantle. This model successfully predicted the onset times, duration, and slowness of the observed PP precursors but underpredicted the precursor amplitudes, suggesting that stronger scattering, perhaps too large for single-scattering theory, would be required to fully explain the observations. King *et al.* noted that the focusing of energy at 20° distance by the mantle transition zone could explain the high and low slowness observations of their study and of Wright (1972).

A related discussion has concerned precursors to PKPPKP (or P'P'), for which the main phase also has an underside reflection near the midpoint between source and receiver. In this case, however, short-period reflections from the 410 and 660 km discontinuities are much easier to observe and this has become one of the best constraints on the sharpness of these features (e.g., Engdahl and Flinn, 1969; Richards, 1972; Davis *et al.*, 1989; Benz and Vidale, 1993; Xu *et al.*, 2003). However, these reflections arrive 90–150 s before P'P' and cannot explain the later parts

of the precursor wavetrain. Whitcomb (1973) suggested they were asymmetric reflections at sloping interfaces, a mechanism similar to that proposed by Wright and Muirhead (1969) and Wright (1972) for PP precursors. King and Cleary (1974) proposed that near-surface scattering near the P'P' bounce point could explain the extended duration and emergent nature of P'P' precursors. Vinnik (1981) used single-scattering theory to model globally averaged P'P' precursor amplitudes at three different time intervals, and obtained a good fit with a Gaussian ACF of 13 km scale length with rms velocity perturbations in the lithosphere of about 1.6%. Recently Tkalčić *et al.* (2006) observed P'P' precursors at epicentral distances less than 10°, which they interpret as back-scattering from small-scale heterogeneities at 150–220 km depth beneath the P'P' bounce points because array studies show that the precursors have the same slowness as the direct phase.

1.20.3.6 PKP Precursors

Perhaps the most direct evidence for deep-Earth scattering comes from observations of precursors to the core phase PKP. They were first noted by Gutenberg and Richter (1934). The precursors are seen at source-receiver distances between about 120° and 145° and precede PKP by up to ~20 s. They are observed most readily at high frequencies and are usually emergent in character and stronger at longer distances. Older, and now discredited, hypotheses for their origin include refraction in the inner core (Gutenberg, 1957), diffraction of PKP from the CMB (Bullen and Burke-Gaffney, 1958; Doornbos and Husebye, 1972), and refraction or reflection of PKP at transition layers between the inner and outer cores (Bolt, 1962; Sacks and Saa, 1969). However, it is now understood that PKP precursors are not caused by radially symmetric structures but result from scattering from small-scale heterogeneity at the CMB or within the lowermost mantle (Haddon, 1972; Cleary and Haddon, 1972). This scattering diverts energy from the primary PKP ray paths, permitting waves from the AB and BC branches to arrive at shorter source-receiver distances than the B caustic near 145° and earlier than the direct PKP(DF) phase. It should be noted that although the PKP precursors arrive in front of PKP(DF), they result from scattering from different PKP branches. Scattered energy from PKP(DF) itself contributes only to the coda following PKP(DF), not to the precursor wavefield. In addition, the scattering region must be deep to create the precursors. Scattering of

PKP(BC) from the shallow mantle will not produce precursors at the observed times and distances. Thus deep-Earth scattering can be observed uncontaminated by the stronger scattering that occurs in the crust and upper mantle. This unique ray geometry, which results from the velocity drop between the mantle and the outer core, makes PKP precursors invaluable for characterizing small-scale heterogeneity near the CMB.

The interpretation of PKP precursors in terms of scattering was first detailed by Haddon (1972) and Cleary and Haddon (1972). The primary evidence in favor of this model is the good agreement between the observed and theoretical onset times of the precursor wavetrain for scattering at the CMB. However, analyses from seismic arrays (e.g., Davies and Husebye, 1972; Doornbos and Husebye, 1972; Doornbos and Vlaar, 1973; King *et al.*, 1973, 1974; Husebye *et al.*, 1976; Doornbos, 1976) also showed that the traveltimes and incidence angles of the precursors were consistent with the scattering theory. Haddon and Cleary (1974) used Chernov scattering theory to show that the precursor amplitudes could be explained with 1% random velocity heterogeneity with a correlation length of 30 km in a 200 km thick layer in the lowermost mantle just above the CMB. In contrast, Doornbos and Vlaar (1973) and Doornbos (1976) argued that the scattering region extends to 600–900 km above the CMB and calculated (using

the Knopoff and Hudson (1964) single-scattering theory) that much larger velocity anomalies must be present. Later, however, Doornbos (1978) used perturbation theory to show that short-wavelength CMB topography could also explain the observations (see also Haddon, 1982), as had previously been suggested by Haddon and Cleary (1974). Bataille and Flatté (1988) concluded that their observations of 130 PKP precursor records could be explained equally well by 0.5–1% rms velocity perturbations in a 200 km thick layer at the base of the mantle or by CMB topography with rms height of ~ 300 m (see also Bataille *et al.*, 1990).

One difficulty in comparing results among these older PKP precursor studies is that it is not clear how many of their differences are due to differences in observations (i.e., the selection of precursor waveforms they examine) compared to differences in theory or modeling assumptions. PKP precursor amplitudes are quite variable and it is likely that studies that focus on the clearest observations will be biased (at least in terms of determining globally averaged Earth properties) by using many records with anomalously large amplitudes. To obtain a clearer global picture of average PKP precursor behavior, Hedlin *et al.* (1997) stacked envelope functions from 1600 high signal-to-noise PKP waveforms at distances between 118° and 145° (see Figure 8). They included all records, regardless of whether precursors could be observed, to avoid

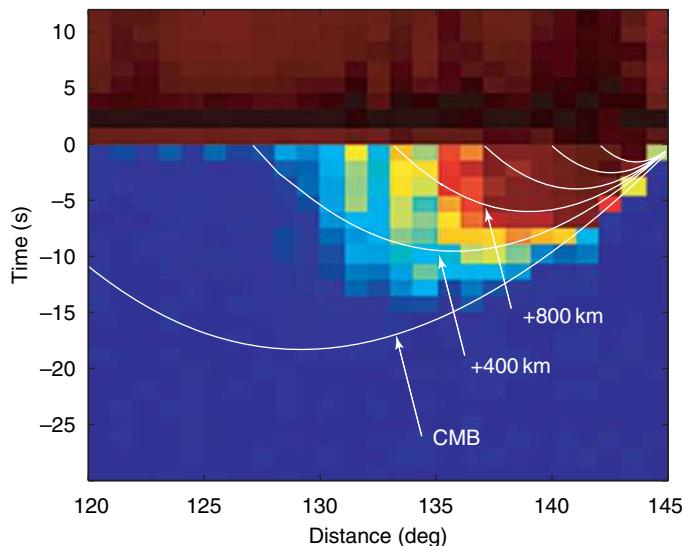


Figure 8 PKP precursors as imaged by stacking 1600 short-period seismograms by Hedlin *et al.* (1997). The colors indicate the strength of the precursors, ranging from dark blue (zero amplitude) through green, yellow, red, and brown (highest amplitudes). The onset of PKP(DF) is shown by the edge of the brown region at zero time. The precursors exhibit increasing amplitude with both distance and time. The white curves show the theoretical precursor onset times for scattering at 400 km depth intervals above the CMB.

biasing their estimates of average precursor amplitudes. In this way, they obtained the first comprehensive image of the precursor wavefield and found that precursor amplitude grows with both distance and time. The growth in average precursor amplitude with time continues steadily until the direct PKP(DF) arrival; no maximum amplitude peak is seen prior to PKP(DF) as had been suggested by Doornbos and Husebye (1972). This is the fundamental observation that led Hedlin *et al.* (1997) to conclude that scattering is not confined to the immediate vicinity of the CMB but must extend for some distance into the mantle.

Hedlin *et al.* (1997) and Shearer *et al.* (1998) modeled these observations using single-scattering theory for a random medium characterized with an exponential ACF. They found that the best overall fit to the observations was provided with $\sim 1\%$ rms velocity heterogeneity at 8 km scale length extending throughout the lower mantle, although fits almost as good could be obtained for 4 and 12 km scale lengths. Similar fits could also be achieved with a Gaussian ACF using a slightly lower rms velocity heterogeneity. To explain the steady increase in precursor amplitude with time, these models contained uniform heterogeneity throughout the lower mantle, and Hedlin *et al.* (1997) argued that the data require the scattering to extend at least 1000 km above the CMB and that there is no indication for a significant concentration of the scattering near the CMB. This conclusion was supported by Cormier (1999), who tested both isotropic and anisotropic distributions of scale lengths and found that the PKP precursor envelope shapes are consistent with dominantly isotropic 1% fluctuations in P velocity in the $0.05\text{--}0.5 \text{ km}^{-1}$ wave number band (i.e., 12–120 km wavelengths).

Most modeling of PKP precursors has used single-scattering theory and the Born approximation. The validity of this approximation for mantle scattering was questioned by Hudson and Heritage (1981). However, Doornbos (1988) found similar results from single- versus multiple-scattering theory for CMB topography of several hundred meters (i.e., the amount proposed by Doornbos (1978) to explain PKP precursor observations), and Cormier (1995) found the Born approximation to be valid for modeling distributed heterogeneity in the D'' region when compared to results from the higher-order theory of Korneev and Johnson (1993a, 1993b). More recently, Margerin and Nolet (2003a, 2003b) modeled PKP precursors using radiative transfer theory and a Monte Carlo method (see above). Their results supported Hedlin *et al.* (1997) and Shearer *et al.* (1998) in

finding that whole-mantle scattering fits the data better than scattering restricted to near the CMB, but they obtained much smaller P velocity perturbations of 0.1–0.2% versus the 1% of Hedlin *et al.* In addition, they found that the Born approximation is accurate for whole-mantle scattering models only when the velocity heterogeneity is less than 0.5%. Finally, they concluded that exponential correlation length models do not fit the distance dependence in PKP precursor amplitudes as well as models containing more small-scale structure.

The reasons for the discrepancy in heterogeneity amplitude between the models of Hedlin *et al.* (1997), Cormier (1999), and Margerin and Nolet (2003b) are not yet clear. Differences between the single-scattering (Born) and multiple-scattering predictions do not appear to be sufficient to account for the size of the discrepancy. There are subtleties in the data stacking and modeling that may have a significant effect on the results. These include the weighting and normalization of the waveforms, the assumed form of the random heterogeneity PSDF, the correction of PKP(DF) amplitudes for inner-core Q , and the correction for realistic effective source-time functions. However, despite the uncertainty in the heterogeneity amplitude, it now seems firmly established that PKP precursor observations require that small-scale mantle heterogeneity extends above the lowermost few hundred kilometers of the mantle.

Determining exactly how far the scattering must extend above the CMB is a challenging problem because only a small fraction of the precursor wavefield is sensitive to scattering above 600 km from the CMB, and this fraction continues to shrink for shallower scattering depths. For example, at 1200 km above the CMB, precursors are produced only between 138° and 145° , and arrive at most 3 s before PKP(DF) (see Figure 8). Separating the amplitude contribution from these arrivals from that produced by scattering at deeper depths in the mantle is very difficult, particularly when the pulse broadening caused by realistic source-time functions and shallow scattering and reverberations are taken into account. An alternative approach to constraining the strength of mid-mantle scattering is to examine the scattered PKP wavefield after the direct PKP(DF) arrival (Hedlin and Shearer, 2002). This is comprised of a sum of PKP(DF) coda and scattered PKP(AB) and PKP(BC) energy. In principle, if the contribution from the PKP(DF) coda could be removed, the remaining scattered wavefield would provide improved constraints on the strength of mid-mantle

scattering. However, [Hedlin and Shearer \(2002\)](#) found that this approach did not provide improved depth resolution of mantle scattering compared to previous analyses of PKP precursors, owing at least in part to relatively large scatter in coda amplitudes as constrained by a data resampling analysis. Their results were, however, consistent with uniform mantle scattering with 1% rms random velocity perturbations at 8 km scale length.

The preceding discussion considered only average PKP precursor properties and models with radial variations in scattering. However, PKP precursor amplitudes are quite variable, as noted by [Bataille and Flatté \(1988\)](#), [Bataille et al. \(1990\)](#), and [Hedlin et al. \(1995\)](#), suggesting lateral variations in scattering strength. [Vidale and Hedlin \(1998\)](#) identified anomalously strong PKP precursors for ray paths that indicated intense scattering at the CMB beneath Tonga. [Wen and Helmberger \(1998\)](#) observed broadband PKP precursors from near the same region, which they modeled as Gaussian-shaped ultralow-velocity zones (ULVZs) of 60–80 km height with P velocity drops of 7% or more over 100–300 km (to account for the long-period part of the precursors), superimposed on smaller-scale anomalies to explain the high-frequency part of the precursors. [Thomas et al. \(1999\)](#) used German network and array records of PKP precursors to identify isolated scatterers in the lower mantle. [Niu and Wen \(2001\)](#) identified strong PKP precursors for South American earthquakes recorded by the J-array in Japan, which they modeled with 6% velocity perturbations within a 100 km thick layer just above the CMB in a 200 km by 300 km area west of Mexico.

[Hedlin and Shearer \(2000\)](#) attempted to systematically map lateral variations in scattering strength using a global set of high-quality PKP precursor records. Their analysis was complicated by the limited volume sampled by each source–receiver pair, the ambiguity between source- and receiver-side scattering, and the sparse and uneven data coverage. However, they were able to identify some large-scale variations in scattering strength that were robust with respect to data resampling tests. These include stronger than average scattering beneath central Africa, parts of North America, and just north of India; and weaker than average scattering beneath South and Central America, eastern Europe, and Indonesia.

Finally, it should be noted that the earliest onset time of observed PKP precursors agrees closely with that predicted for scattering at the CMB (e.g., [Cleary and Haddon, 1972](#); [Shearer et al., 1998](#)). If scattering

existed in the outer core at significant depths below the CMB, this would cause arrivals at earlier times than are seen in the data. This suggests that no observable scattering originates from the outer core, although a quantitative upper limit on small-scale outer core heterogeneity based on this constraint has not yet been established.

1.20.3.7 PKKP Precursors and PKKPx

PKKP is another seismic core phase that provides information on deep-Earth scattering. Precursors to PKKP have been observed within two different distance intervals. PKKP(DF) precursors at source–receiver distances beyond the B caustic near 125° are analogous to the PKP precursors discussed in the previous section and result from scattering in the mantle. [Doornbos \(1974\)](#) detected these precursors in NORSAR records of Solomon Islands earthquakes and showed that their observed slownesses were consistent with scattering from the deep mantle. At ranges less than 125°, PKKP(BC) precursors can result from scattering off short-wavelength CMB topography. [Chang and Cleary \(1978, 1981\)](#) observed these precursors from Novaya Zemlya explosions recorded by the LASA array in Montana at about 60° range. These observations were suggestive of CMB topography but had such large amplitudes that they were difficult to fit with realistic models. [Doornbos \(1980\)](#) obtained additional PKKP(BC) precursor observations from NORSAR records from a small number of events at source–receiver distances between 80° and 110°. He modeled these observations with CMB topography of 100–200 m at 10–20 km horizontal scale length. Motivated by PKKP precursor observations (see below), [Cleary \(1981\)](#) suggested that some observations of P'P' precursors (e.g., [Adams, 1968](#); [Whitcomb and Anderson, 1970](#); [Haddon et al., 1977](#); [Husebye et al., 1977](#)) might be explained as CMB-scattered PKKP precursors.

A comprehensive study of PKKP(BC) precursors was performed by [Earle and Shearer \(1997\)](#), who stacked 1856 high-quality PKKP seismograms, obtained from the Global Seismic Network (GSN) at distances between 80° and 120°. PKKP is most readily observed at high frequencies (to avoid interference from low-frequency S coda), so the records were bandpass filtered to between 0.7 and 2.5 Hz. To avoid biasing the stacked amplitudes, no consideration was given to the visibility or lack of visibility of PKKP precursors on individual records. The resulting

stacked image showed that energy arrives up to 60 s before direct PKKP(BC) and that average precursor amplitudes gradually increase with time. Earle and Shearer (1997) modeled these observations using Kirchhoff theory for small-scale CMB topography. Their best-fitting model had a horizontal scale length of 8 km and rms amplitude of 300 m. However, they identified a systematic misfit between the observations and their synthetics in the dependence of precursor amplitude with source-receiver distance. In particular, the Kirchhoff synthetics predict that precursor amplitude should grow with range but this trend is not apparent in the data stack. Thus, the model under-predicts the precursor amplitudes at short ranges and overpredicts the amplitudes at long ranges.

Earle and Shearer (1997) and Shearer *et al.* (1998) explored possible reasons for this discrepancy between PKKP(BC) precursor observations and predictions for CMB topography models. They were not able to identify a very satisfactory explanation but speculated that scattering from near the ICB might be involved because it could produce precursor onsets that agreed with the observations (see figure 13 from Shearer *et al.* (1998)). However, scattering angles of 90° or more are required and it is not clear, given the expected amplitude of the direct PKKP(DF) phase, that the scattered amplitudes would be large enough to explain the PKKP(BC) precursor observations. They concluded that strong

inner-core scattering would be required, which could only be properly modeled with a multiple-scattering theory. Regardless of the possible presence of scattering from sources outside the CMB, these PKKP(BC) precursor observations can place upper limits on the size of any CMB topography. Earle and Shearer (1997) concluded that the rms topography could not exceed 315 m at 10 km wavelength.

Earle and Shearer (1998) stacked global seismograms using P'P' as a reference phase and identified an emergent, long-duration, high-frequency wavetrain near PKKP, which they named PKKP_X because it lacked a clear explanation (Figure 9). PKKP_X extends back from the PKKP(C) caustic at 72° to a distance of about 60 s. Its 150-s long duration, apparent move-out, and proximity to PKKP suggest a deep scattering origin. However, Earle and Shearer were not able to match these observations with predictions of single-scattering theory for scattering in the lower mantle, CMB, or ICB. They speculated that some form of multiple-scattering model at the CMB might be able to explain the observations, perhaps involving a low-velocity zone just above the CMB to trap high-frequency energy, a model similar to that proposed to explain P_{diff} coda by Bataille *et al.* (1990), Tono and Yomogida (1996), and Bataille and Lund (1996). Earle (2002) further explored the origin of PKKP_X and other scattered phases near PKKP by performing slant stacks on LASA data. His results suggested that

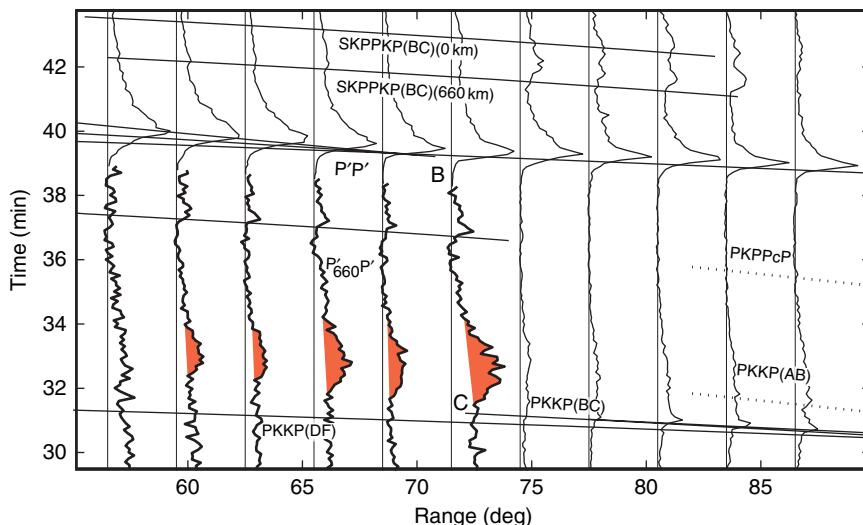


Figure 9 A stack of 994 seismograms from Earle and Shearer (1998), showing the PKKP_X phase (red) in the high-frequency wavefield preceding P'P'. The stacked traces are normalized to the maximum P'P' amplitude and are plotted with respect to the origin time of a zero depth earthquake. To better show the PKKP_X arrival, amplitudes are magnified by 8 for traces preceding P'P' at epicentral distances less than 73° (indicated by the heavy lines). Labels indicate observed phases and the position of the P'P' B and PKKP C caustics.

near-surface P-to-PKP scattering is likely an important contributor to high-frequency energy around PKKP at distances between 50° and at least 116° . In particular, such scattering arrives at the same time as observations of PKKP precursors and PKKP_X , thus providing a possible explanation for why PKKP precursor amplitudes are hard to fit purely with CMB scattering models. However, quantitative modeling of P-to-PKP scattering has not yet been performed to test this hypothesis.

1.20.3.8 PKiKP and PKP Coda and Inner-Core Scattering

The ICB-reflected phase PKiKP is of relatively low amplitude and observations from single stations are fairly rare, particularly at source-receiver distances less than 50° . However, improved signal-to-noise and more details can be obtained from analysis of short-period array data. Vidale and Earle (2000) examined

16 events at $58\text{--}73^\circ$ range recorded by LASA in Montana between 1969 and 1975. As shown in Figure 10, a slowness versus time stack of the data (bandpass filtered at 1 Hz) revealed a 200 s long wavetrain with an onset time and slowness in agreement with that predicted for PKiKP. They attributed this energy to scattering from the inner core because it arrived at a distinctly different slowness from late-arriving P coda and it was much more extended in time than LASA PcP records for the same events. The PKiKP wavetrain takes 50 s to reach its peak amplitude and averages only about 2% of the amplitude of PcP. Direct PKiKP is barely visible, with an amplitude close to its expected value, which is small because the ICB reflection coefficient has a node at distances near 72° (e.g., Shearer and Masters, 1990).

Vidale and Earle (2000) fit their observations with synthetics computed using single-scattering theory applied to a model of random inner-core heterogeneity with 1.2% rms variations in density and the

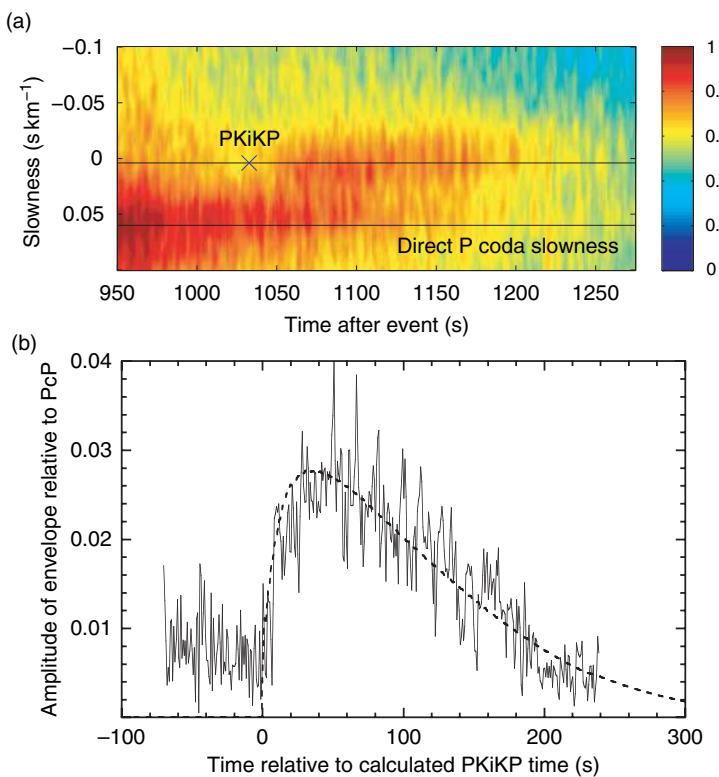


Figure 10 PKiKP coda as observed and modeled by Vidale and Earle (2000) for data from 12 earthquakes and four nuclear explosions recorded at LASA in Montana. The top panel (Zhigang Peng, personal communication) shows a slowness versus time envelope function stack of energy arriving between 950 and 1270 s from the event origin times. The predicted direct PKiKP arrival is shown with the \times . Late P coda forms the stripe seen at a slowness near 0.5 s km^{-1} . PKiKP coda is the stripe seen near zero slowness. The bottom panel compares a PKiKP amplitude stack (wiggly line) to the predicted scattering envelope for an inner-core random heterogeneity model (dashed line).

Lamé parameters (λ and μ) and a correlation distance of 2 km, assuming an exponential autocorrelation model. They assumed ${}^oQ_1 = 360$ uniformly throughout the inner core, a value obtained from a study (Bhattacharyya *et al.*, 1993) of pulse broadening of PKP(DF) compared to PKP(BC). They noted that without inner-core attenuation, the predicted scattered PKiKP wavetrain would take 100 s to attain its peak value and would last 350 s. The low value of oQ_1 resulted in only the shallow penetrating P waves retaining sufficient amplitude to be seen. Model-predicted scattering angles were near 90°, making the scattering most sensitive to variations in inner-core λ . Vidale and Earle (2000) found a tradeoff between the various free parameters in their model and picked their 2 km correlation length because it minimized the required rms variation of 1.2% necessary to fit the observations. They computed a fractional energy loss of 10% from scattering in the top 300 km of the inner core, helping to justify the use of the Born single-scattering approximation. Vidale *et al.* (2000) examined LASA data for two nuclear explosions 3 years apart and separated by less than 1 km. They identified systematic time shifts in PKiKP coda, which they explained as resulting from differential inner-core rotation, as previously proposed by Song and Richards (1996). In contrast, much smaller time differences are observed in PKKP and PKPPKP arrivals, supporting the idea that the time dependence originates in the inner core. Vidale *et al.* (2000) estimated an inner-core rotation rate of 0.15° per year.

Cormier *et al.* (1998) measured pulse broadening in PKP(DF) waveforms and showed that they could fit either with intrinsic inner-core attenuation or with scattering caused by random layering (1-D) with 8% P velocity perturbations and 1.2 km scale length. Cormier and Li (2002) inverted 262 broadband PKP(DF) waveforms for a model of inner-core scattering attenuation based on the dynamic composite elastic medium theory of Kaelin and Johnson (1998) for a random distribution of spherical inclusions. They obtained a mean velocity perturbation of ~8% and a heterogeneity scale length of ~10 km, but also observed path-dependent differences in these parameters, with both depth dependence and anisotropy in the size of the scattering attenuation. They suggested that scattering attenuation is the dominant mechanism of attenuation in the inner core in the 0.02–2 Hz frequency band. Cormier and Li (2002) argued that the large discrepancy in rms velocity perturbation and scale length between their

study (rms = 8%, scale length = 10 km) and the model (rms = 1.2%, scale length = 2 km) of Vidale and Earle (2002) may be due to the significant intrinsic attenuation assumed by Vidale and Earle and differences in depth sensitivity between the studies.

Poupinet and Kennett (2004) analyzed PKiKP recorded by Australian broadband stations and the Warramunga array for events at short distances (<~45°). They found that PKiKP could frequently be observed on single traces filtered at 1–5 Hz. In contrast to Vidale and Earle (2000), they found that PKiKP typically had an impulsive onset with a coda that decayed rapidly to a relatively small amplitude that persisted for more than 200 s. Although most of the Poupinet and Kennett results were for shorter source-receiver distances than the 58–73° range of the Vidale and Earle study, they did analyze one event at 74° that exhibited similar behavior. Poupinet and Kennett suggested that the differences in the appearance of PKiKP coda between the studies may reflect different sampling latitudes at the ICB and different frequency filtering. They pointed to similarities in the appearance of PKiKP coda and P_{diff} coda (see above) and speculated that both result from their interaction with a major interface that may involve energy channeling to produce an extended wavetrain. Poupinet and Kennett (2004) argued the high-frequency nature of PKiKP coda excludes an origin deep within the inner core where attenuation is high, and suggested that multiple scattering near the ICB is a more likely mechanism.

Koper *et al.* (2004) analyzed PKiKP coda waves recorded by short-period seismic arrays of the International Monitoring System (IMS) at source-receiver distances ranging from 10° to 90°. Stacked beam envelopes for the 10–50° data showed impulsive onsets for PcP , ScP , and PKiKP, but a markedly different coda for PKiKP, which maintained a nearly constant value that lasted for over 200 s. This is consistent with the Poupinet and Kennett (2004) results at similar distances and supports the idea that inner-core scattering is contributing to the PKiKP coda. At distances from 50° to 90°, Koper *et al.* (2004) found one event at 56° with a PKiKP coda that increased in amplitude with time, peaking nearly 50 s after the arrival of direct PKiKP, behavior very similar to the LASA observations of Vidale and Earle (2000). At 4 Hz, 13 out of 36 PKiKP observations had emergent codas that peaked at least 10 s into the wavetrain. However, more commonly, the peak coda amplitude occurred at the onset of PKiKP. Koper *et al.* (2004) found that the average PKiKP coda decay rate was

roughly constant between stacks at short and long distance intervals, supporting the hypothesis of inner-core scattering. They argued that the best distance range to study inner-core scattering is 50–75°, where the direct PKiKP amplitude is weak (because of a very small ICB reflection coefficient), so that scattering from the crust and mantle is unlikely to contribute as much to the observed coda as scattering from the inner core. However, they also discussed the possibility that CMB scattering could deflect a P wave into a PKiKP wave that could reflect from the ICB at an angle with a much higher reflection coefficient and contribute to the observed coda.

$\text{PKP}(\text{C})_{\text{diff}}$ is the P wave that diffracts around the ICB and is seen as an extension of the $\text{PKP}(\text{BC})$ branch to distances beyond 153°. [Nakanishi \(1990\)](#) analyzed Japanese records of $\text{PKP}(\text{C})_{\text{diff}}$ coda from a deep earthquake in Argentina and suggested that scattering near the bottom of the upper mantle could explain its times and slowness. [Tanaka \(2005\)](#) examined $\text{PKP}(\text{C})_{\text{diff}}$ coda from 28 deep earthquakes recorded using small aperture short-period seismic arrays of the IMS at epicentral distances of 153–160°. Beam forming at 1–4 Hz resolved the slownesses and back azimuths of $\text{PKP}(\text{DF})$, $\text{PKP}(\text{C})_{\text{diff}}$, and $\text{PKP}(\text{AB})$. The $\text{PKP}(\text{C})_{\text{diff}}$ coda lasted longer than $\text{PKP}(\text{AB})$, but the wide slowness distribution of $\text{PKP}(\text{C})_{\text{diff}}$ coda is difficult to explain as originating solely from the ICB, and Tanaka suggested that scattering near the CMB is an important contributor to $\text{PKP}(\text{C})_{\text{diff}}$ coda.

[Vidale and Earle \(2005\)](#) studied PKP coda from seven Mururoa Island nuclear explosions over a 10-year period recorded by NORSAR at an epicentral distance of 136°. They observed complicated arrivals lasting ~10 s that were more extended than the relatively simple pulses observed for direct P waves from explosions recorded in the western United States. Vidale and Earle suggested that these complications likely arose from scattering at or near the ICB. They showed that small time shifts in the PKP coda were consistent with shifts predicted for point scatterers in an inner core that rotated at 0.05–0.1° per year, although they could not entirely rule out systematic changes in source location.

Several recent studies point to complicated structures near the ICB. [Stroujkova and Cormier \(2004\)](#) found evidence for a thin low-velocity layer near the top of the inner core. [Koper and Dombrovskaya \(2005\)](#) analyzed a global set of PKiKP/PcP amplitude ratios and found large, spatially coherent variations, suggestive of significant heterogeneity at

or near the ICB. [Krasnoshchekov *et al.* \(2005\)](#) observed large variations in PKiKP amplitudes, which they attributed to spatial variations in ICB properties, such as a thin partially liquid layer, interspersed with patches with a sharp transition. PKP(DF) traveltimes have also indicated significant inner-core heterogeneity, albeit at scale lengths considerably longer than those required to scatter high-frequency P waves. [Bréger *et al.* \(1999\)](#) noted sharp changes in $\text{PKP}(\text{BC} - \text{DF})$ travel time residuals, which they attributed to lateral variations on length scales shorter than a few hundred kilometers within the top of the inner core or the base of the mantle. [Garcia and Souriau \(2000\)](#) also analyzed PKP(DF) versus $\text{PKP}(\text{BC})$ traveltimes, concluding that inner-core heterogeneity is no more than 0.3% at scale lengths longer than 200 km but that large lateral variations in anisotropy are present between 100 and 400 km below the ICB.

1.20.3.9 Other Phases

[Emery *et al.* \(1999\)](#) computed the effect of different types of D'' heterogeneity on S_{diff} , using both the Langer and Born approximations. They found that their long-period S_{diff} observations are not particularly sensitive to the types of small-scale heterogeneities proposed to explain other data sets. [Cormier \(2000\)](#) used the coda power between P and PcP and S and ScS , together with limits on pulse broadening in PcP and ScS waveforms, to model D'' heterogeneity using a 2-D pseudo-spectral calculation. He attempted to resolve the heterogeneity power spectrum over a wide range of scale lengths, to bridge the gaps among global tomography studies, D'' studies, and PKP precursor analysis.

[Lee *et al.* \(2003\)](#) noted an offset in S coda observations for central Asian earthquakes (150–250 km deep) recorded about 750 km away at station AAK. The offset occurred near the ScS arrivals in coda envelopes at 10 and 15 s periods. At shorter periods (1–4 s), a change in coda decay rate appeared associated with the ScS arrival. They simulated these observations with a Monte Carlo method based on radiative transfer theory and isotropic scattering. For a two-layer mantle model (separated at 670 km), their best-fitting synthetics at 4 s had a total scattering coefficient g_0 of about 1.3×10^{-3} and $6.0 \times 10^{-4} \text{ km}^{-1}$ for the upper and lower layers, respectively. Corresponding results at 10 s were about 4.7×10^{-4} and $2.6 \times 10^{-4} \text{ km}^{-1}$. [Rondenay and Fischer \(2003\)](#) identified a coherent secondary

phase in the SKS + SPdKS wavefield on paths sampling the CMB below North America. They showed that this phase could be modeled with an ULVZ just above the CMB on one side of the SPdKS path, but speculated that more complicated 3-D structure could also explain their observations.

1.20.4 Discussion

Scattering from small-scale irregularities has now been detected at all depths inside the Earth with the exception of the fluid outer core, although many details of this heterogeneity (power spectral density, depth dependence, etc.) remain poorly resolved, at least on a global scale. Scattering is strongest near the surface, but significant scattering also occurs throughout the lower mantle (e.g., Hedlin *et al.*, 1997; Shearer *et al.*, 1998; Cormier, 1999; Earle and Shearer, 2001; Margerin and Nolet, 2003b; Shearer and Earle, 2004). Small-scale heterogeneity within the deep mantle is almost certainly compositional in origin because thermal anomalies would diffuse away over relatively short times (Hedlin *et al.*, 1997; Helffrich and Wood, 2001) and supports models of incomplete mantle mixing (e.g., Olson *et al.*, 1984; Gurnis and Davies, 1986; Morgan and Morgan, 1999). Helffrich and Wood (2001) discussed the implications of small-scale mantle structure in terms of convective mixing models and suggested that the scatterers are most likely remnants of lithospheric slabs. Assuming subduction-induced heterogeneities are 11–16% of the volume of the mantle, they proposed that most of this heterogeneity occurs at scale lengths less than 4 km, where it would have little effect on typically observed seismic wavelengths. Meibom and Anderson (2003) discussed the implications of small-scale compositional heterogeneity in the upper mantle, where partial melting may also be an important factor.

There is a large gap between the smallest scale lengths resolved in global mantle tomography models and the ~10 km scale length of the random heterogeneity models proposed to explain scattering observations. Chevrot *et al.* (1998) showed that the amplitude of the heterogeneity in global and regional tomography models obeys a power law decay with wave number, that is, most of the power is concentrated at low spherical harmonic degree, a result previously noted by Su and Dziewonski (1991) for global models. For the shallow mantle, this is probably caused in part by continent–ocean differences

(G. Masters, personal communication, 2005), but a decay of order k^{-2} to k^{-3} is also predicted for heterogeneity caused by temperature variations in a convecting fluid (Hill, 1978; Cormier, 2000). However, this decay cannot be extrapolated to very small scales, because it would predict heterogeneity much weaker than what is required to explain seismic scattering observations at ~10 km scale. As discussed by Cormier (2000), the most likely explanation is a change from thermal- to compositional-dominated heterogeneity and that small-scale (<100 km) mantle perturbations are chemical in origin. Spherical heterogeneities of radii 38 km or smaller can be entrained in mantle flow, assuming a mantle viscosity of 10^{21} Pa s, a density contrast of 1 g cm^{-3} , and a convective velocity of 1 cm yr^{-1} (Cormier, 2000). Because settling rate scales as the radius squared, smaller blobs will be entrained even at much smaller density contrasts.

The role of the CMB and ICB in small-scale scattering is not yet clear. The D'' region has stronger heterogeneity than the mid-mantle in tomography models and large velocity contrasts have been identified in specific regions, including ULVZs and strong individual PKP scatterers (e.g., Vidale and Hedlin, 1998; Wen and Helmberger, 1998; Niu and Wen, 2001). However, globally averaged PKP precursor studies do not find evidence for stronger scattering at the CMB than in the rest of the lower mantle (Hedlin *et al.*, 1997; Margerin and Nolet, 2003b). CMB topography can also produce scattering, and has been invoked by some authors to explain PKP and PKKP precursors, but fails to predict globally averaged PKKP precursor amplitude versus distance behavior (Earle and Shearer, 1997). Vidale and Earle modeled PKiKP coda observations with bulk scattering within the inner core, while Poupinet and Kennett (2004) suggested that scattering from near the ICB, where several recent studies have found evidence for anomalous structures (e.g., Koper and Dombrovskaya, 2005; Krasnoshchekov *et al.*, 2005), was more likely responsible for their PKiKP coda observations. Strong attenuation is observed in the inner core, but it is not yet clear how much of this is caused by intrinsic versus scattering attenuation. Inner-core scattering might be caused by small-scale textural anisotropy (Cormier *et al.*, 1998; Vidale and Earle, 2000) or by compositionally induced variations in partial melt (Vidale and Earle, 2000).

At shallow depths, it is clear that there is both strong scattering and significant lateral variations in

scattering strength, but the number and diversity of studies on lithospheric scattering makes it difficult to draw general conclusions. There is a large literature on both the theory of seismic scattering and on coda observations, but there has been much less effort to integrate these studies into a comprehensive picture of scattering throughout Earth's interior. Review articles (e.g., Aki, 1982; Sato, 1991; Matsumoto, 1995) and the book by Sato and Fehler (1998) are certainly helpful, but their summaries often involve comparisons among studies that differ in many key respects, such as their choice of seismic phase (P, S, etc.), their epicentral distance, frequency range, and time window, and their modeling assumptions (single scattering, MLTW, finite difference, radiative transfer, etc.). It is not always clear whether models proposed to explain one type of data are supported or contradicted by other types of data. For example, models with horizontally elongated crust and/or upper-mantle heterogeneity appear necessary to explain long-range P_n propagation across Eurasia and many models of lower crustal reflectors are anisotropic (e.g., Wenzel *et al.*, 1987; Holliger and Levander, 1992). Yet almost all modeling of local earthquake coda assumes isotropic random heterogeneity. A promising development is the increasingly open availability at data centers of seismic records from local and regional networks, portable experiments, and the global seismic networks. This should enable future coda studies to be more comprehensive and analyze larger numbers of stations around the world using a standardized approach. This would help to establish a baseline of globally averaged scattering properties as well as maps of lateral variations in scattering strength over large regions. Ultimately more detailed information on lithospheric heterogeneity (amplitude, scale length, and anisotropy) will enable more detailed comparisons to geological and petrological constraints on rock chemistry (e.g., Levander *et al.*, 1994; Ritter and Rothert, 2000).

Analyses of deep-Earth scattering have also used a variety of different phase types and modeling approaches. Even today, there are still fundamental features in the high-frequency wavefield, such as PKKP_X (Earle, 2002), that lack definitive explanations and have never been quantitatively modeled. However, given recent improvements in modeling capabilities (Monte Carlo calculations based on radiative transfer theory, whole-Earth finite difference calculations, etc.), there is also some hope that within the next decade we will see the first generally accepted 1-D models of Earth's average scattering

properties and a clear separation between scattering and intrinsic attenuation mechanisms. It appears that a substantial part of seismic attenuation at high frequencies is caused by scattering rather than intrinsic energy loss, but fully resolving tradeoffs between Q_{Sc} and Q_I will require analysis of scattering observations at a wide range of frequencies and epicentral distances. An interesting comparison can be made with seismologist's efforts to map bulk seismic velocity variations. Regional velocity profiling of the upper mantle gave way in the 1980s to comprehensive velocity inversions (i.e., 'tomography') to image global 3-D mantle structure. This required working with large data sets of body-wave traveltimes and surface-wave phase-velocity measurements and developing and evaluating methods to invert large matrices. The earliest models were crude and controversial in their details, but rapid progress was made as different groups began comparing their results. We may be poised to make similar advances in resolving Earth scattering. But progress will require improved sharing of data from local and regional networks as well as greater testing and standardization of numerical simulation codes. As models of small-scale random heterogeneity become more precise, comparisons to geochemical and convection models will become increasingly relevant.

References

- Abubakirov IR and Gusev AA (1990) Estimation of scattering properties of lithosphere of Kamchatka based on Monte–Carlo simulation of record envelope of a near earthquake. *Physics of the Earth and Planetary Interiors* 64: 52–67.
- Adams RD (1968) Early reflections of PP as an indication of upper mantle structure. *Bulletin of the Seismological Society of America* 58: 1933–1947.
- Akamatsu J (1991) Coda attenuation in the Lützow–Holm Bay region, East Antarctica. *Physics of the Earth and Planetary Interiors* 67: 65–75.
- Aki K (1969) Analysis of seismic coda of local earthquakes as scattered waves. *Journal of Geophysical Research* 74: 615–631.
- Aki K (1973) Scattering of P waves under the Montana LASA. *Journal of Geophysical Research* 78: 1334–1346.
- Aki K (1980) Scattering and attenuation of shear waves in the lithosphere. *Journal of Geophysical Research* 85: 6496–6504.
- Aki K (1982) Scattering and attenuation. *Bulletin of the Seismological Society of America* 72: 319–330.
- Aki K and Chouet B (1975) Origin of coda waves: Source attenuation and scattering effects. *Journal of Geophysical Research* 80: 3322–3342.
- Aki K and Richards PG (1980) *Quantitative Seismology Volume II*. San Francisco: W.H. Freeman.

- Akinci A, Del Pezzo E, and Ibanez JM (1995) Separation of scattering and intrinsic attenuation in southern Spain and western Anatolia (Turkey). *Geophysical Journal International* 121: 337–353.
- Allègre C and Turcotte DL (1986) Implications of a two-component marble-cake mantle. *Nature* 323: 123–127.
- Baig AM and Dahlen FA (2004a) Statistics of traveltimes and amplitudes in random media. *Geophysical Journal International* 158: 187–210.
- Baig AM and Dahlen FA (2004b) Traveltimes biases in random media and the S-wave discrepancy. *Geophysical Journal International* 158: 922–938.
- Baig AM, Dahlen FA, and Hung S-H (2003) Traveltimes of waves in three-dimensional random media. *Geophysical Journal International* 153: 467–482.
- Bal G and Moscoso M (2000) Polarization effects of seismic waves on the basis of radiative transport theory. *Geophysical Journal International* 142: 571–585.
- Bannister SC, Husebye S, and Ruud BO (1990) Teleseismic P coda analyzed by three-component and array techniques: Deterministic location of topographic P-to-Rg scattering near the NORESS array. *Bulletin of the Seismological Society of America* 80: 1969–1986.
- Baskoutas I (1996) Dependence of coda attenuation on frequency and lapse time in central Greece. *Pure and Applied Geophysics* 147: 483–496.
- Baskoutas I and Sato H (1989) Coda attenuation Q_c^{-1} for 4 to 64 Hz signals in the shallow crust measured at Ashio, Japan. *Bollettino Della Geofisica Teoreticheskoi Applicata* 21: 277–283.
- Bataille K and Flatté SM (1988) Inhomogeneities near the core–mantle boundary inferred from short-period scattered PKP waves recorded at the global digital seismograph network. *Journal of Geophysical Research* 93: 15057–15064.
- Bataille K and Lund F (1996) Strong scattering of short-period seismic waves by the core–mantle boundary and the P-diffracted wave. *Geophysical Research Letters* 23: 2413–2416.
- Bataille K, Wu RS, and Flatté SM (1990) Inhomogeneities near the core–mantle boundary evidenced from scattered waves: A review. *Pure and Applied Geophysics* 132: 151–173.
- Benites R, Aki K, and Yomogida K (1992) Multiple scattering of SH waves in 2D-media with many cavities. *Pure and Applied Geophysics* 138: 353–390.
- Benz HM and Vidale JE (1993) The sharpness of upper mantle discontinuities determined from high-frequency P'P' precursors. *Nature* 365: 147–150.
- Bhattacharyya J, Shearer PM, and Masters TG (1993) Inner core attenuation from short-period PKP(BC) versus PKP(DF) waveforms. *Geophysical Journal International* 114: 1–11.
- Bianco F, Del Pezzo E, Castellano M, Ibanez J, and Di Luccio F (2002) Separation of intrinsic and scattering attenuation in the southern Apennines, Italy. *Geophysical Journal International* 150: 10–22.
- Bianco F, Del Pezzo E, Malagnini L, Di Luccio F, and Akinci A (2005) Separation of depth-dependent intrinsic and scattering seismic attenuation in the northeastern sector of the Italian peninsula. *Geophysical Journal International* 161: 130–142.
- Biswas NN and Aki K (1984) Characteristics of coda waves: central and southcentral Alaska. *Bulletin of the Seismological Society of America* 74: 493–507.
- Bolt BA (1962) Gutenberg's early PKP observations. *Nature* 196: 122–124.
- Bolt BA (1970) PdP and PKiKP waves and diffracted Pcp-waves. *Geophysical Journal of the Royal Astronomical Society* 20: 367–382.
- Bolt BA, O'Neill M, and Qamar A (1968) Seismic waves near 110° : Is structure in core or upper mantle responsible? *Geophysical Journal of the Royal Astronomical Society* 16: 475–487.
- Brana L and Helffrich G (2004) A scattering region near the core–mantle boundary under the North Atlantic. *Geophysical Journal International* 158: 625–636.
- Bréger L, Romanowicz B, and Tkalcic H (1999) PKP(BC-DF) travel time residuals and short scale heterogeneity in the deep Earth. *Geophysical Research Letters* 26: 3169–3172.
- Bullen KE and Burke-Gaffney TN (1958) Diffracted seismic waves near the PKP caustic. *Geophysical Journal International* 1: 9–17.
- Canas JA, Ugalde A, Pujades LG, Carracedo JC, Soler V, and Blanco MJ (1998) Intrinsic and scattering wave attenuation in the Canary Islands. *Journal of Geophysical Research* 103: 15037–15050.
- Castle JC and Creager KC (1999) A steeply dipping discontinuity in the lower mantle beneath Izu-Bonin. *Journal of Geophysical Research* 104: 7279–7292.
- Cessaro RK and Butler R (1987) Observations of transverse energy for P waves recorded on a deep-ocean bore-hole seismometer located in the northwest Pacific. *Bulletin of the Seismological Society of America* 77: 2163–2180.
- Chang AC and Cleary JR (1978) Precursors to PKKP. *Bulletin of the Seismological Society of America* 68: 1059–1079.
- Chang AC and Cleary JR (1981) Scattered PKKP: Further evidence for scattering at a rough core–mantle boundary. *Physics of the Earth and Planetary Interiors* 24: 15–29.
- Chen X and Long LT (2000) Spatial distribution of relative scattering coefficients determined from microearthquake coda. *Bulletin of the Seismological Society of America* 90: 512–524.
- Chernov LA (1960) *Wave Propagation in a Random Media*. New York: McGraw-Hill.
- Chevrot S, Montagner JP, and Snieder R (1998) The spectrum of tomographic earth models. *Geophysical Journal International* 133: 783–788.
- Cleary J (1981) Seismic wave scattering on underside reflection at the core–mantle boundary. *Physics of the Earth and Planetary Interiors* 26: 266–267.
- Cleary JR and Haddon RAW (1972) Seismic wave scattering near the core–mantle boundary: A new interpretation of precursors to PKP. *Nature* 240: 549–551.
- Cleary JR, King DW, and Haddon RAW (1975) P-wave scattering in the Earth's crust and upper mantle. *Geophysical Journal of the Royal Astronomical Society* 43: 861–872.
- Cormier VF (1995) Time-domain modelling of PKIKP precursors for constraints on the heterogeneity in the lowermost mantle. *Geophysical Journal International* 121: 725–736.
- Cormier VF (1999) Anisotropy of heterogeneity scale lengths in the lower mantle from PKIKP precursors. *Geophysical Journal International* 136: 373–384.
- Cormier VF (2000) D'' as a transition in the heterogeneity spectrum of the lowermost mantle. *Journal of Geophysical Research* 105: 16193–16205.
- Cormier VF and Li X (2002) Frequency-dependent seismic attenuation in the inner core. 2: A scattering and fabric interpretation. *Journal of Geophysical Research* 107: B12 (doi:10.1029/2002JB001796).
- Cormier VF, Xu L, and Choy GI (1998) Seismic attenuation in the inner core: Viscoelastic or stratigraphic? *Geophysical Research Letters* 21: 4019–4022.
- Dainty AM (1990) Studies of coda using array and three-component processing. *Pure and Applied Geophysics* 132: 221–244.

- Dainty AM, Duckworth RM, and Tie A (1987) Attenuation and backscattering from local coda. *Bulletin of the Seismological Society of America* 77: 1728–1747.
- Dainty AM and Toksöz MN (1977) Elastic wave propagation in a highly scattering medium – A diffusion approach. *Journal of Geophysics* 43: 375–388.
- Dainty AM and Toksöz MN (1981) Seismic cedas on the earth and the moon: A comparison. *Physics of the Earth and Planetary Interiors* 26: 250–260.
- Dainty AM and Toksöz MN (1990) Array analysis of seismic scattering. *Bulletin of the Seismological Society of America* 80: 2242–2260.
- Dainty AM, Toksöz MN, Anderson KR, Pines PJ, Nakamura Y, and Latham G (1974) Seismic scattering and shallow structure of the moon in Oceanus Procellarum. *Moon* 91: 11–29.
- Dahlen FA, Hung S-H, and Nolet G (2000) Fréchet kernels for finite-frequency traveltimes. I: Theory. *Geophysical Journal International* 141: 157–174.
- Dalkolmo J and Friederich W (2000) Born scattering of long-period body waves. *Geophysical Journal International* 142: 867–888.
- Davies DJ and Husebye ES (1972) Array analysis of PKP phases and their precursors. *Nature (Physical Sciences)* 232: 8–13.
- Davis JP, Kind R, and Sacks IS (1989) Precursors to $P'P'$ reexamined using broad-band data. *Geophysical Journal International* 99: 595–604.
- Del Pezzo E, De Natale G, Scarcella G, and Zollo A (1985) QC of three component seismograms of volcanic microearthquakes at Campi Flegrei volcanic area – Southern Italy. *Pure and Applied Geophysics* 123: 683–696.
- Doornbos DJ (1974) Seismic wave scattering near caustics: observations of PKKP precursors. *Nature* 247: 352–353.
- Doornbos DJ (1976) Characteristics of lower mantle inhomogeneities from scattered waves. *Geophysical Journal of the Royal Astronomical Society* 44: 447–470.
- Doornbos DJ (1978) On seismic wave scattering by a rough core-mantle boundary. *Geophysical Journal of the Royal Astronomical Society* 53: 643–662.
- Doornbos DJ (1980) The effect of a rough core-mantle boundary on PKKP. *Physics of the Earth and Planetary Interiors* 21: 351–358.
- Doornbos DJ (1988) Multiple scattering by topographic relief with application to the core-mantle boundary. *Geophysical Journal* 92: 465–478.
- Doornbos DJ and Husebye ES (1972) Array analysis of PKP phases and their precursors. *Physics of the Earth and Planetary Interiors* 5: 387.
- Doornbos DJ and Vlaar NJ (1973) Regions of seismic wave scattering in the Earth's mantle and precursors to PKP. *Nature Physical Science* 243: 58–61.
- Earle PS (1999) Polarization of the Earth's teleseismic wavefield. *Geophysical Journal International* 139: 1–8.
- Earle PS (2002) Origins of high-frequency scattered waves near PKKP from large aperture seismic array data. *Bulletin of the Seismological Society of America* 92: 751–760.
- Earle PS and Shearer PM (1997) Observations of PKKP precursors used to estimate small-scale topography on the core-mantle boundary. *Science* 277: 667–670.
- Earle PS and Shearer PM (1998) Observations of high-frequency scattered energy associated with the core phase PKKP. *Geophysical Research Letters* 25: 405–408.
- Earle PS and Shearer PM (2001) Distribution of fine-scale mantle heterogeneity from observations of P_{diff} coda. *Bulletin of the Seismological Society of America* 91: 1875–1881.
- Emery V, Maupin V, and Nataf H-C (1999) Scattering of S waves diffracted at the core-mantle boundary: Forward modelling. *Geophysical Journal International* 139: 325–344.
- Engdahl ER and Flinn EA (1969) Seismic waves reflected from discontinuities within Earth's upper mantle. *Science* 163: 177–179.
- Fehler M, Hoshiba M, Sato H, and Obara K (1992) Separation of scattering and intrinsic attenuation for the Kanto-Tokai region, Japan, using measurements of S-wave energy versus hypocentral distance. *Geophysical Journal International* 198: 787–800.
- Fehler MS (2003) Coda. *Pure and Applied Geophysics* 160: 541–554.
- Flatté SM and Wu R-S (1988) Small-scale structure in the lithosphere and asthenosphere deduced from arrival time and amplitude fluctuations at NORSAR. *Journal of Geophysical Research* 93: 6601–6614.
- Frankel A (1990) A review of numerical experiments on seismic wave scattering. *Pure and Applied Geophysics* 131: 639–685.
- Frankel A and Clayton RW (1984) A finite difference simulation of wave propagation in two-dimensional random media. *Bulletin of the Seismological Society of America* 74: 2167–2186.
- Frankel A and Clayton RW (1986) Finite difference simulations of seismic scattering: Implications for the propagation of short-period seismic waves in the crust and models of crustal heterogeneity. *Journal of Geophysical Research* 91: 6465–6489.
- Frankel A and Wennerberg L (1987) Energy-flux model of seismic coda: Separation of scattering and intrinsic attenuation. *Bulletin of the Seismological Society of America* 77: 1223–1251.
- Frenje L and Juhlin C (2000) Scattering attenuation: 2-D and 3-D finite difference simulations vs. theory. *Journal of Applied Geophysics* 44: 33–46.
- Furumura T, Kennett BLN, and Furumura M (1998) Seismic wavefield calculation for laterally heterogeneous whole earth models using the pseudospectral method. *Geophysical Journal International* 135: 845–860.
- Gagnepain-Beyneix J (1987) Evidence of spatial variations of attenuation in the western Pyrenean range. *Geophysical Journal of the Royal Astronomical Society* 89: 681–704.
- Gao LS, Lee LC, Biswas NN, and Aki K (1983a) Effects of multiple scattering on coda waves in three dimensional medium. *Pure and Applied Geophysics* 121: 3–15.
- Gao LS, Lee LC, Biswas NN, and Aki K (1983b) Comparison of the effects between single and multiple scattering on coda waves for local earthquakes. *Bulletin of the Seismological Society of America* 73: 377–390.
- Garcia R and Souriau A (2000) Inner core anisotropy and heterogeneity level. *Geophysical Research Letters* 27: 3121–3124.
- Garnero EJ (2000) Heterogeneity of the lowermost mantle. *Annual Review of Earth and Planetary Science* 28: 509–537.
- Giampiccolo E, Gresta A, and Rasconà F (2004) Intrinsic and scattering attenuation from observed seismic cudas in southeastern Sicily (Italy). *Physics of the Earth and Planetary Interiors* 145: 55–66.
- Gibson BS and Levander AR (1988) Modeling and processing of scattered waves in seismic reflection surveys. *Geophysics* 53: 466–478.
- Goutbeek FH, Dost B, and van Eck T (2004) Intrinsic absorption and scattering attenuation in the southern Netherlands. *Journal of Seismology* 8: 11–23.
- Gupta IN and Blandford RR (1983) A mechanism for generation of short-period transverse motion from explosions. *Bulletin of the Seismological Society of America* 73: 571–591.
- Gupta IN, Lynnes CS, McElfresh TW, and Wagner RA (1990) F-K analysis of NORESS array and single station data to identify sources of near-receiver and near-source

- scattering. *Bulletin of the Seismological Society of America* 80: 2227–2241.
- Gupta SC, Teotia SS, Rai SS, and Gautam N (1998) Coda Q estimates in the Koyna region, India. *Pure and Applied Geophysics* 153: 713–731.
- Gurnis M and Davies F (1986) Mixing in numerical models of mantle convection incorporating plate kinematics. *Journal of Geophysical Research* 91: 6375–6395.
- Gusev AA (1995) Vertical profile of turbidity and coda Q. *Geophysical Journal International* 123: 665–672.
- Gusev AA and Abubakirov IR (1987) Monte Carlo simulation of record envelope of a near earthquake. *Physics of the Earth and Planetary Interiors* 49: 30–36.
- Gusev AA and Abubakirov IR (1999a) Vertical profile of effective turbidity reconstructed from broadening of incoherent body-wave pulses. I: General approach and the inversion procedure. *Geophysical Journal International* 136: 295–308.
- Gusev AA and Abubakirov IR (1999b) Vertical profile of effective turbidity reconstructed from broadening of incoherent body-wave pulses. II: Application to Kamchatka data. *Geophysical Journal International* 136: 309–323.
- Gutenberg B (1957) The boundary of the Earth's inner core. *Eos Trans. AGU* 38: 750–753.
- Gutenberg B and Richter CF (1934) On seismic waves; I. *Gerlands Beiträge Geophysika* 43: 50–133.
- Gutowski PR and Kanasewich ER (1974) Velocity spectral evidence of upper mantle discontinuities. *Geophysical Journal of the Royal Astronomical Society* 36: 21–32.
- Haddon RAW (1972) Corrugations on the CMB or transition layers between the inner and outer cores? (abstract). *Eos Transactions of AGU* 53: 600.
- Haddon RAW (1982) Evidence for inhomogeneities near the core–mantle boundary. *Philosophical Transactions of the Royal Society of London A* 306: 61–70.
- Haddon RAW and Cleary JR (1974) Evidence for scattering of seismic PKP waves near the mantle–core boundary. *Physics of the Earth and Planetary Interiors* 8: 211–234.
- Haddon RAW, Husebye ES, and King DW (1977) Origin of precursors to PP. *Physics of the Earth and Planetary Interiors* 14: 41–71.
- Hedlin MAH and Shearer PM (2000) An analysis of large-scale variations in small-scale mantle heterogeneity using Global Seismographic Network recordings of precursors to PKP. *Journal of Geophysical Research* 105: 13655–13673.
- Hedlin MAH and Shearer PM (2002) Probing mid-mantle heterogeneity using PKP coda waves. *Physics of the Earth and Planetary Interiors* 130: 195–208.
- Hedlin MAH, Shearer PM, and Earle PS (1997) Seismic evidence for small-scale heterogeneity throughout Earth's mantle. *Nature* 387: 145–150.
- Heiffrich GR and Wood BJ (2001) The Earth's mantle. *Nature* 412: 501–507.
- Herraiz M and Espinosa AF (1987) Coda waves: A review. *Pure and Applied Geophysics* 125: 499–577.
- Hill RJ (1978) Models of the scalar spectrum for turbulent advection. *Journal of Fluid Mechanics* 88: 541–562.
- Hock S, Korn M, Ritter JRR, and Rothert E (2004) Mapping random lithospheric heterogeneities in northern and central Europe. *Geophysical Journal International* 157: 251–264.
- Hock S, Korn M, and TOR Working Group (2000) Random heterogeneity of the lithosphere across the Trans-European Suture Zone. *Geophysical Journal International* 141: 57–70.
- Holliger K and Levander AR (1992) A stochastic view of lower crustal fabric based on evidence from the Ivrea zone. *Journal of Geophysical Research* 97: 1153–1156.
- Hong T-K (2004) Scattering attenuation ratios of P and S waves in elastic media. *Geophysical Journal International* 158: 211–224.
- Hong T-K and Kennett BLN (2003) Scattering attenuation of 2-D elastic waves: Theory and numerical modelling using a wavelet-based method. *Bulletin of the Seismological Society of America* 93: 922–938.
- Hong T-K, Kennett BLN, and Wu R-S (2004) Effects of the density perturbation in scattering. *Geophysical Research Letters* 31 (doi:10.1029/2004GL019933).
- Hong T-K and Wu R-S (2005) Scattering of elastic waves in geometrically anisotropic random media and its implication to sounding of heterogeneity in the Earth's deep interior. *Geophysical Journal International* 163: 324–338.
- Hong T-K, Wu R-S, and Kennett BLN (2005) Stochastic features of scattering. *Physics of the Earth and Planetary Interiors* 148: 131–148.
- Hoshiba M (1991) Simulation of multiple scattered coda wave excitation based on the energy conservation law. *Physics of the Earth and Planetary Interiors* 67: 123–136.
- Hoshiba M (1993) Separation of scattering attenuation and intrinsic absorption in Japan using the multiple lapse time window analysis of full seismogram envelope. *Journal of Geophysical Research* 98: 15809–15824.
- Hoshiba M (1994) Simulation of coda wave envelope in depth-dependent scattering and absorption structure. *Geophysical Research Letters* 21: 2853–2856.
- Hoshiba M (1997) Seismic coda wave envelope in depth-dependent S wave velocity structure. *Physics of the Earth and Planetary Interiors* 104: 15–22.
- Hoshiba M, Rietbrock A, Scherbaum F, Nakahara H, and Haberland C (2001) Scattering attenuation and intrinsic absorption using uniform and depth dependent model – Application to full seismogram envelope recorded in northern Chile. *Journal of Seismology* 5: 157–179.
- Hudson JA and Heritage JR (1981) Use of the Born approximation in seismic scattering problems. *Geophysical Journal of the Royal Astronomical Society* 66: 221–240.
- Husebye ES, Haddon RAW, and King DW (1977) Precursors to PP and upper mantle discontinuities. *Journal of Geophysical Research* 43: 535–543.
- Husebye ES, King DW, and Haddon RAW (1976) Precursors to PKIPK and seismic wave scattering near the mantle–core boundary. *Journal of Geophysical Research* 81: 1870–1882.
- Husebye E and Madariaga R (1970) The origin of precursors to core waves. *Bulletin of the Seismological Society of America* 60: 939–952.
- Jin A and Aki K (1988) Spatial and temporal correlation between coda Q and seismicity in China. *Bulletin of the Seismological Society of America* 78: 741–769.
- Jin A, Cao T, and Aki K (1985) Regional change of coda Q in the oceanic lithosphere. *Journal of Geophysical Research* 90: 8651–8659.
- Jin A, Mayeda K, Adams D, and Aki K (1994) Separation of intrinsic and scattering attenuation in southern California using TERRAscope data. *Journal of Geophysical Research* 99: 17835–17848.
- Kaelin B and Johnson LR (1998) Dynamic composite elastic medium theory. 2: Three-dimensional media. *Journal of Applied Physics* 84: 5458–5468.
- Kampfmann W and Müller G (1989) Pcp amplitude calculations for a core–mantle boundary with topography. *Geophysical Research Letters* 16: 653–656.
- Kaneshima S (2003) Small-scale heterogeneity at the top of the lower mantle around the Mariana slab. *Earth and Planetary Science Letters* 209: 85–101.
- Kaneshima S and Heiffrich G (1998) Detection of lower mantle scatterers northeast of the Mariana subduction zone using short-period array data. *Journal of Geophysical Research* 103: 4825–4838.

- Kaneshima S and Helffrich G (1999) Dipping low-velocity layer in the mid-lower mantle: Evidence for geochemical heterogeneity. *Science* 283: 1888–1892.
- Kaneshima S and Helffrich G (2003) Subparallel dipping heterogeneities in the mid-lower mantle. *Journal of Geophysical Research* 108 (doi:10.1029/2001JB001596).
- King DW and Cleary JR (1974) A note on the interpretation of precursors to PKPPKP. *Bulletin of the Seismological Society of America* 64: 721–723.
- King DW, Haddon RAW, and Cleary JR (1973) Evidence for seismic wave scattering in the D'' layer. *Earth and Planetary Science Letters* 20: 353–356.
- King DW, Haddon RAW, and Cleary JR (1974) Array analysis of precursors to PKIKP in the distance range 128° to 142° . *Geophysical Journal of the Royal Astronomical Society* 37: 157–173.
- King DW, Haddon RAW, and Husebye ES (1975) Precursors to PP. *Physics of the Earth and Planetary Interiors* 10: 103–127.
- Knopoff L and Hudson JA (1964) Scattering of elastic waves by small inhomogeneities. *Journal of Acoustical Society of America* 36: 338–343.
- Koper KD and Dombrovskaya M (2005) Seismic properties of the inner core boundary from PKiKP/P amplitude ratios. *Earth and Planetary Science Letters* 237: 680–694.
- Koper KD, Franks JM, and Dombrovskaya M (2004) Evidence for small-scale heterogeneity in Earth's inner core from a global study of PKIKP coda waves. *Earth and Planetary Science Letters* 228: 227–241.
- Koper KD and Pyle ML (2004) Observations of PKiKP/PcP amplitude ratios and implications for Earth structure at the boundaries of the liquid core. *Journal of Geophysical Research* 109 (doi:10.1029/2003JB002750).
- Kopnichenko YF (1977) The role of multiple scattering in the formulation of a seismogram's tail. *Izvestiya Akademii Nauk USSR (English translation Physics of the Solid Earth)* 13: 394–398.
- Korn M (1988) P-wave coda analysis of short-period array data and the scattering and absorptive properties of the lithosphere. *Geophysical Journal* 93: 437–449.
- Korn M (1990) A modified energy flux model for lithospheric scattering of teleseismic body waves. *Geophysical Journal International* 102: 165–175.
- Korn M (1993) Determination of site-dependent scattering Q from P-wave coda analysis with an energy flux model. *Geophysical Journal International* 113: 54–72.
- Korn M (1997) Modelling the teleseismic P coda envelope: Depth dependent scattering and deterministic structure. *Physics of the Earth and Planetary Interiors* 104: 23–36.
- Korn M and Sato H (2005) Synthesis of plane vector wave envelopes in two-dimensional random elastic media based on the Markov approximation and comparison with finite-difference synthetics. *Geophysical Journal International* 161: 839–848.
- Korneev VA and Johnson LR (1993a) Scattering of elastic waves by a spherical inclusion. Theory and numerical results. *Geophysical Journal International* 115: 230–250.
- Korneev VA and Johnson LR (1993b) Scattering of elastic waves by a spherical inclusion. II: Limitations of asymptotic solutions. *Geophysical Journal International* 115: 251–263.
- Kosuga M (1992) Determination of coda Q on frequency and lapse time in the western Nagano region, Japan. *Journal of Physics of the Earth* 40: 421–445.
- Kosuga M (1997) Periodic ripple of coda envelope observed in northeastern Japan. *Physics of the Earth and Planetary Interiors* 104: 91–108.
- Krasnoshchekov DN, Kaazik PB, and Ovtchinnikov VM (2005) Seismological evidence for mosaic structure of the surface of the Earth's inner core. *Nature* 435: 483–487 (doi:10.1038/nature03613).
- Krüger FK, Baumann M, Scherbaum F, and Weber M (2001) Mid mantle scatterers near the Mariana slab detected with a double array method. *Geophysical Research Letters* 28: 667–670.
- Kvamme LB and Havskov J (1989) Q in southern Norway. *Bulletin of the Seismological Society of America* 79: 1575–1588.
- Lacombe C, Campillo M, Paul A, and Margerin L (2003) Separation of intrinsic absorption and scattering attenuation from Lg coda decay in central France using acoustic radiative transfer theory. *Geophysical Journal International* 154: 417–425.
- Langston GA (1989) Scattering of teleseismic body waves under Pasadena, California. *Journal of Geophysical Research* 94: 1935–1951.
- Lay T (1987) Analysis of near-source contributions to early P-wave coda for underground explosions. II: Frequency dependence. *Bulletin of the Seismological Society of America* 77: 1252–1273.
- Lee WS, Sato H, and Lee K (2003) Estimation of S-wave scattering coefficient in the mantle from envelope characteristics before and after the ScS arrival. *Geophysical Research Letters* 30: 24 (doi:10.1029/2003GL018413).
- Lerche I and Menke W (1986) An inversion method for separating apparent and intrinsic attenuation in layered media. *Geophysical Journal of the Royal Astronomical Society* 87: 333–347.
- Levander A, Hobbs RW, Smith SK, England RW, Snyder DB, and Holliger K (1994) The crust as a heterogeneous 'optical' medium, or 'crocodiles in the mist'. *Tectonophysics* 232: 281–297.
- Levander AR and Hill NR (1985) P-SV resonances in irregular low-velocity surface layers. *Bulletin of the Seismological Society of America* 75: 847–864.
- Malin PE and Phinney RA (1985) On the relative scattering of P and S waves. *Geophysical Journal of the Royal Astronomical Society* 80: 603–618.
- Margerin L (2005) Introduction to radiative transfer of seismic waves. In: Levander A and Nolet G (eds.) *Geophysical Monograph Series, Vol. 157: Seismic Earth: Array Analysis of Broadband Seismograms*. Washington, DC: American Geophysical Union.
- Margerin L, Campillo M, Shapiro NM, and van Tiggelen BA (1999) Residence time of diffuse waves in the crust as a physical interpretation of coda Q: Application to seismograms recorded in Mexico. *Geophysical Journal International* 138: 343–352.
- Margerin L, Campillo M, and van Tiggelen BA (1998) Radiative transfer and diffusion of waves in a layered medium: New insight into coda Q. *Geophysical Journal International* 134: 596–612.
- Margerin L, Campillo M, and van Tiggelen B (2000) Monte Carlo simulation of multiple scattering of elastic waves. *Journal of Geophysical Research* 105: 7873–7892.
- Margerin L, Campillo M, and van Tiggelen B (2001) Effect of absorption on energy partition of elastic waves. *Bulletin of the Seismological Society of America* 91: 624–627.
- Margerin L and Nolet G (2003a) Multiple scattering of high-frequency seismic waves in the deep Earth: Modeling and numerical examples. *Journal of Geophysical Research* 108: B5 (doi:10.1029/2002JB001974).
- Margerin L and Nolet G (2003b) Multiple scattering of high-frequency seismic waves in the deep Earth: PKP precursor analysis and inversion for mantle granularity. *Journal of Geophysical Research* 108: B11 (doi:10.1029/2003JB002455).
- Margerin L, van Tiggelen B, and Campillo M (2001) Effect of absorption on energy partition of elastic waves in the seismic coda. *Bulletin of the Seismological Society of America* 91: 624–627.

- Matsumoto S (1995) Characteristics of coda waves and inhomogeneity of the earth. *Journal of Physics of the Earth* 43: 279–299.
- Matsumoto S (2005) Scatterer density estimation in the crust by seismic array processing. *Geophysical Journal International* 163: 622–628 (doi:10.1111/j.1365-246X.2005.02773.x).
- Matsumoto S and Hasegawa A (1989) Two-dimensional coda Q structure beneath Tohoku, NE Japan. *Geophysical Journal International* 99: 101–108.
- Mayeda K, Koyanagi S, Hoshiba M, Aki K, and Zeng Y (1992) A comparative study of scattering, intrinsic, and coda Q^{-1} for Hawaii, Long Valley, and central California between 1.5 and 15.0 Hz. *Journal of Geophysical Research* 97: 6643–6659.
- Mayeda K, Su F, and Aki K (1991) Seismic albedo from the total seismic energy dependence on hypocentral distances in southern California. *Physics of the Earth and Planetary Interiors* 67: 104–114.
- McLaughlin KL and Anderson LM (1987) Stochastic dispersion of short-period P-waves due to scattering and multipathing. *Geophysical Journal of the Royal Astronomical Society* 89: 933–964.
- McLaughlin KL, Anderson LM, and Der Z (1985) Investigation of seismic waves using 2-dimensional finite difference calculations. In: *Multiple Scattering of Seismic Waves in Random Media and Random Surfaces*, pp. 795–821. University Park, PA: Pennsylvania State University.
- Meibom A and Anderson DL (2003) The statistical upper mantle assemblage. *Earth and Planetary Science Letters* 217: 123–139.
- Morgan JP and Morgan WJ (1999) Two-stage melting and the geochemical evolution of the mantle: A recipe for mantle plum-pudding. *Earth and Planetary Science Letters* 170: 215–239.
- Morozov IB, Morozova EA, Smithson SB, and Solodilov LN (1998) On the nature of the teleseismic Pn phase observed on the ultralong-range profile ‘Quartz’, Russia. *Bulletin of the Seismological Society of America* 88: 62–73.
- Morozov IB and Smithson SB (2000) Coda of long-range arrivals from nuclear explosions. *Bulletin of the Seismological Society of America* 90: 929–939.
- Müller TM and Shapiro SA (2003) Amplitude fluctuations due to diffraction and reflection in anisotropic random media: Implications for seismic scattering attenuation estimates. *Geophysical Journal International* 155: 139–148.
- Nakamura Y (1977) Seismic energy transmission in an intensively scattering environment. *Journal of Geophysical Research* 43: 389–399.
- Nakanishi I (1990) High-frequency waves following PKP-Cdiff at distances greater than 155° . *Geophysical Research Letters* 17: 639–642.
- Neale F and Snieder R (1991) Are long-period body wave coda caused by lateral heterogeneity? *Geophysical Journal International* 107: 131–153.
- Nguyen-Hai (1963) Propagation des ondes longitudinales dans le noyau terrestre. *Annals of Geophysics* 15: 285–346.
- Nielsen L and Thybo H (2003) The origin of teleseismic Pn waves: Multiple crustal scattering of upper mantle whispering gallery phases. *Journal of Geophysical Research* 108, doi:10.1029/2003JB002487.
- Nielsen L, Thybo H, Levander A, and Solodilov LN (2003a) Origin of upper-mantle seismic scattering – Evidence from Russian peaceful nuclear explosion data. *Geophysical Journal International* 154: 196–204.
- Nielsen L, Thybo H, Morozov B, Smithson SB, and Solodilov L (2003b) Teleseismic Pn arrivals: Influence of upper mantle velocity gradient and crustal scattering. *Geophysical Journal International* 153: F1–F7.
- Nishigami K (1991) A new inversion method of coda waveforms to determine spatial distribution of coda scatterers in the crust and uppermost mantle. *Geophysical Research Letters* 18: 2225–2228.
- Nishigami K (1997) Spatial distribution of coda scatterers in the crust around two active volcanoes and one active fault system in central Japan: Inversion analysis of coda envelope. *Physics of the Earth and Planetary Interiors* 104: 75–89.
- Nishimura T, Yoshimoto K, Ohtaki T, Kanjo K, and Purwana I (2002) Spatial distribution of lateral heterogeneity in the upper mantle around the western Pacific region as inferred from analysis of transverse components of teleseismic P-coda. *Geophysical Research Letters* 29: 2137 (doi:10.1029/2002GL015606).
- Niu F and Kawakatsu H (1994) Seismic evidence for a 920-km discontinuity in the mantle. *Nature* 371: 301–305.
- Niu F and Kawakatsu H (1997) Depth variation of the mid-mantle discontinuity. *Geophysical Research Letters* 24: 429–432.
- Niu F and Wen L (2001) Strong seismic scatterers near the core-mantle boundary west of Mexico. *Geophysical Research Letters* 28: 3557–3560.
- Nolet G, Dahlen FA, and Montelli R (2005) Travel times and amplitudes of seismic waves: A re-assessment. In: Levander A and Nolet G (eds.) *Geophysical Monograph Series, Vol. 157: Seismic Earth: Array Analysis of Broadband Seismograms*. Washington, DC: American Geophysical Union.
- Oancea V, Bazaciu O, and Mihalache G (1991) Estimation of the coda quality factor for the Romanian territory. *Physics of the Earth and Planetary Interiors* 67: 87–94.
- Obara K (1997) Simulations of anomalous seismogram envelopes at coda portions. *Physics of the Earth and Planetary Interiors* 104: 109–125.
- Obara K and Sato H (1995) Regional differences of random heterogeneities around the volcanic front in the Kanto-Tokai area, Japan revealed from the broadening of S wave seismogram envelopes. *Journal of Geophysical Research* 100: 2103–2121.
- Olson P, Yuen DA, and Balsiger D (1984) Convective mixing and the fine structure of mantle heterogeneity. *Physics of the Earth and Planetary Interiors* 36: 291–304.
- Papanicolaou G, Ryshik L, and Keller J (1996) On the stability of the P to S energy ratio in the diffusive regime. *Bulletin of the Seismological Society of America* 86: 1107–1115 (see also erratum in *Bulletin of the Seismological Society of America* 86: p. 1997).
- Poupinet G and Kennett BLN (2004) On the observation of high frequency PKiKP and its coda in Australia. *Physics of the Earth and Planetary Interiors* 146: 497–511.
- Pulli JJ (1984) Attenuation of coda waves in New England. *Bulletin of the Seismological Society of America* 74: 1149–1166.
- Rautian TG and Khalturin VI (1978) The use of coda for determination of the earthquake source spectrum. *Bulletin of the Seismological Society of America* 68: 923–948.
- Revenaugh J (1995) The contribution of topographic scattering to teleseismic coda in southern California. *Geophysical Research Letters* 22: 543–546.
- Revenaugh J (1999) Geologic applications of seismic scattering. *Annual Review of Earth and Planetary Science* 27: 55–73.
- Revenaugh J (2000) The relation of crustal scattering to seismicity in southern California. *Journal of Geophysical Research* 105: 25403–25422.
- Rhea S (1984) Q determined from local earthquakes in the south Carolina coastal plain. *Bulletin of the Seismological Society of America* 74: 2257–2268.

- Richards PG (1972) Seismic waves reflected from velocity gradient anomalies within the Earth's mantle. *Zeitschrift Fur Geophysik* 38: 517–527.
- Richards PG and Menke W (1983) The apparent attenuation of a scattering medium. *Bulletin of the Seismological Society of America* 73: 1005–1022.
- Ritter JRR, Mai PM, Stoll G, and Fuchs K (1997) Scattering of teleseismic waves in the lower crust observations in the Massif Central, France. *Physics of the Earth and Planetary Interiors* 104: 127–146.
- Ritter JRR and Rother E (2000) Variations of the lithospheric seismic scattering strength below the Massif Central, France and the Frankonian Jura, SE Germany. *Tectonophysics* 328: 297–305.
- Ritter JRR, Shapiro SA, and Schechinger B (1998) Scattering parameters of the lithosphere below the Massif Central, France, from teleseismic wavefield records. *Geophysical Journal International* 134: 187–198.
- Rodriguez M, Havskov J, and Singh SK (1983) Q from coda waves near Petatlan, Guerrero, Mexico. *Bulletin of the Seismological Society of America* 73: 321–326.
- Roecker SW, Tucker B, King J, and Hatzfeld D (1982) Estimates of Q in central Asia as a function of frequency and depth using the coda of locally recorded earthquakes. *Bulletin of the Seismological Society of America* 72: 129–149.
- Rondenay S and Fischer KM (2003) Constraints on localized core-mantle boundary structure from multichannel, broadband SKS coda analysis. *Journal of Geophysical Research* 108 (doi:10.1029/2003JB002518).
- Roth M and Korn M (1993) Single scattering theory versus numerical modelling in 2-D random media. *Geophysical Journal International* 112: 124–140.
- Rother E and Ritter JRR (2000) Small-scale heterogeneities below the Gräfenberg array, Germany from seismic wavefield fluctuations of Hindu Kush events. *Geophysical Journal International* 140: 175–184 (doi:10.1046/j.1365-246x.2000.00013.x).
- Ryberg T, Fuchs K, Egorkin V, and Solodilov L (1995) Observation of high-frequency teleseismic *Pn* waves on the long-range Quartz profile across northern Eurasia. *Journal of Geophysical Research* 100: 18151–18163.
- Ryberg T, Tittgemeyer M, and Wenzel F (2000) Finite difference modelling of P-wave scattering in the upper mantle. *Geophysical Journal International* 141: 787–800.
- Ryzhik LV, Papanicolaou GC, and Keller JB (1996) Transport equations for elastics and other waves in random media. *Wave Motion* 24: 327–370.
- Sacks IS and Saa G (1969) The structure of the transition zone between the inner core and the outer core. *Year Book Carnegie Institute of Washington* 69: 419–426.
- Sato H (1977) Energy propagation including scattering effects, single isotropic scattering approximation. *Journal of Physics of the Earth* 25: 27–41.
- Sato H (1978) Mean free path of S-waves under the Kanto district of Japan. *Journal of Physics of the Earth* 26: 185–198.
- Sato H (1984) Attenuation and envelope formation of three-component seismograms of small local earthquakes in randomly inhomogeneous lithosphere. *Journal of Geophysical Research* 89: 1221–1241.
- Sato H (1989) Broadening of seismogram envelopes in the randomly inhomogeneous lithosphere based on the parabolic approximation: Southeast Honshu, Japan. *Journal of Geophysical Research* 94: 17735–17747.
- Sato H (1990) Unified approach to amplitude attenuation and coda excitation in the randomly inhomogeneous lithosphere. *Pure and Applied Geophysics* 132: 93–121.
- Sato H (1991) Study of seismogram envelopes based on scattering by random inhomogeneities in the lithosphere: A review. *Physics of the Earth and Planetary Interiors* 67: 4–19.
- Sato H (1993) Energy transportation in one- and two-dimensional scattering media: Analytic solutions of the multiple isotropic scattering model. *Geophysical Journal International* 112: 141–146.
- Sato H (1994) Multiple isotropic scattering model including P-S conversions for the seismogram envelope formulation. *Geophysical Journal International* 117: 487–494.
- Sato H (1995) Formulation of the multiple non-isotropic scattering process in 3-D space on the basis of energy transport theory. *Geophysical Journal International* 121: 523–531.
- Sato H and Fehler MC (1998) *Seismic Wave Propagation and Scattering in the Heterogeneous Earth*. New York: Springer.
- Sato H, Fehler M, and Saito T (2004) Hybrid synthesis of scalar wave envelopes in two-dimensional random media having rich short-wavelength spectra. *Journal of Geophysical Research* 109 (doi:10.1029/2003JB002673).
- Sato H, Nakahara H, and Ohtake M (1997) Synthesis of scattered energy density for nonspherical radiation from a point shear-dislocation source based on the radiative transfer theory. *Physics of the Earth and Planetary Interiors* 104: 1–13.
- Sato H and Nishino M (2002) Multiple isotropic-scattering model on the spherical Earth for the synthesis of Rayleigh-wave envelopes. *Journal of Geophysical Research* 107: 2343 (doi:10.1029/2001JB000915).
- Saito T, Sato H, Fehler M, and Ohtake M (2003) Simulating the envelope of scalar waves in 2D random media having power-law spectra of velocity fluctuation. *Bulletin of the Seismological Society of America* 93: 240–252.
- Saito T, Sato H, and Ohtake M (2002) Envelope broadening of spherically outgoing waves in three-dimensional random media having power law spectra. *Journal of Geophysical Research* 107 (10.1029/2001JB000264).
- Scherbaum F, Gilard D, and Deichmann N (1991) Slowness power analysis of the coda composition of two microearthquake clusters in northern Switzerland. *Physics of the Earth and Planetary Interiors* 67: 137–161.
- Scherbaum F, Krüger F, and Wever M (1997) Double beam imaging: Mapping lower mantle heterogeneities using combinations of source and receiver arrays. *Journal of Geophysical Research* 102: 507–522.
- Scherbaum F and Sato H (1991) Inversion of full seismogram envelopes based on the parabolic approximation: Estimation of randomness and attenuation in southeast Honshu, Japan. *Journal of Geophysical Research* 96: 2223–2232.
- Schisselé E, Guibert J, Gaffet S, and Cansi Y (2004) Accurate time-frequency-wavenumber analysis to study coda waves. *Geophysical Journal International* 158: 577–591.
- Shang T and Gao L (1988) Transportation theory of multiple scattering and its application to seismic coda waves of impulsive source. *Scientia Sinica* 31: 1503–1514.
- Shapiro NM, Campillo M, Margerin L, Singh SK, Kostoglodov V, and Pacheco J (2000) The energy partitioning and the diffusive character of the seismic coda. *Bulletin of the Seismological Society of America* 90: 655–665.
- Shapiro SA and Kneig G (1993) Seismic attenuation by scattering: Theory and numerical results. *Geophysical Journal International* 114: 373–391.
- Shapiro SA, Schwarz R, and Gold N (1996) The effect of random isotropic inhomogeneities on the phase velocity of seismic waves. *Geophysical Journal International* 114: 373–391.
- Shearer PM (1990) Seismic imaging of upper-mantle structure with new evidence for a 520-km discontinuity. *Nature* 344: 121–126.

- Shearer PM (1991) Constraints on upper-mantle discontinuities from observations of long-period reflected and converted phases. *Journal of Geophysical Research* 96: 18147–18182.
- Shearer PM and Earle PS (2004) The global short-period wavefield modelled with a Monte Carlo seismic phonon method. *Geophysical Journal International* 158: 1103–1117.
- Shearer PM, Hedlin MAH, and Earle PS (1998) PKP and PKKP precursor observations: Implications for the small-scale structure of the deep mantle and core. In: *The Core-Mantle Boundary Region, Geodynamics* 28, pp. 37–55. Washington, DC: American Geophysical Union.
- Shearer PM and Masters TG (1990) The density and shear velocity contrast at the inner core boundary. *Geophysical Journal International* 102: 491–498.
- Singh DD, Govoni A, and Bragato PL (2001) Coda Q_c attenuation and source parameter analysis in Friuli (NE Italy) and its vicinity. *Pure and Applied Geophysics* 158: 1737–1761.
- Singh S and Herrmann RB (1983) Regionalization of crustal coda Q in the continental United States. *Journal of Geophysical Research* 88: 527–538.
- Song XD and Richards PG (1996) Seismological evidence for differential rotation of the Earth's inner core. *Nature* 382: 221–224.
- Spetzler J and Snieder R (2001) The effect of small-scale heterogeneity on the arrival time of waves. *Geophysical Journal International* 145: 786–796.
- Spudich P and Bostwick T (1987) Studies of the seismic coda using an earthquake cluster as a deeply buried seismography array. *Journal of Geophysical Research* 92: 10526–10546.
- Spudich P and Iida M (1993) The seismic coda, site effects, and scattering in alluvial basins studied using aftershocks of the 1986 North Palm Springs, California, earthquake as source arrays. *Bulletin of the Seismological Society of America* 83: 1721–1743.
- Spudich P and Miller DP (1990) Seismic site effects and the spatial interpolation of earthquake seismograms: Results using aftershocks of the 1986 North Palm Springs, California, earthquake. *Bulletin of the Seismological Society of America* 80: 1504–1532.
- Stroujkova A and Cormier A (2004) Regional variations in the uppermost layer of the Earth's inner core. *Journal of Geophysical Research* 109 (doi:10.1029/2004JB002976).
- Su W-j and Dziewonski AM (1991) Predominance of long-wavelength heterogeneity in the mantle. *Nature* 352: 121–126.
- Taira T and Yomogida K (2004) Imaging of three-dimensional small-scale heterogeneities in the Hidaka, Japan region: A coda spectral analysis. *Geophysical Journal International* 158: 998–1008.
- Tanaka S (2005) Characteristics of PKP-Cdiff coda revealed by small-aperture seismic arrays: Implications for the study of the inner core boundary. *Physics of the Earth and Planetary Interiors* 153: 49–60.
- Thomas C, Igel H, Weber M, and Scherbaum F (2000) Acoustics simulation of P-wave propagation in a heterogeneous spherical earth; numerical method and application to precursor wave to PKP df. *Geophysical Journal International* 141: 307–320.
- Thomas C, Weber M, Wicks CW, and Scherbaum F (1999) Small scatterers in the lower mantle observed at German broadband arrays. *Journal of Geophysical Research* 104: 15073–15088.
- Tittgemeyer MF, Wenzel F, Fuchs K, and Ryberg T (1996) Wave propagation in a multiple-scattering upper mantle: Observations and modeling. *Geophysical Journal International* 127: 492–502.
- Tkalčić H, Flanagan M, and Cormier VF (2006) Observation of near-podal P'P' precursors: Evidence for back scattering from the 150–220 km zone in the Earth's upper mantle. *Geophysical Research Letters* 33 (doi:10.1029/2005GL024626).
- Toksöz NM, Daity AM, Reiter E, and Wu RS (1988) A model for attenuation and scattering in the earth's crust. *Pure and Applied Geophysics* 128: 81–100.
- Tono Y and Yomogida K (1996) Complex scattering at the core-mantle boundary observed in short-period diffracted P-waves. *Journal of the Physics of the Earth* 44: 729–744.
- Tono Y and Yomogida K (1997) Origin of short-period signals following P-diffracted waves: A case study of the 1994 Bolivian deep earthquake. *Physics of the Earth and Planetary Interiors* 103: 1–16.
- Torquato S (2002) *Random Heterogeneous Materials: Microscopic and Macroscopic Properties*. New York: Springer.
- Tsuruga K, Yomogida K, Ito H, and Nishigami K (2003) Detection of localized small-scale heterogeneities in the Hanshin-Awaji region, Japan, by anomalous amplification of coda level. *Bulletin of the Seismological Society of America* 93: 1516–1530.
- Ugalde A, Pujades LG, Canas JA, and Villaseñor A (1998) Estimation of the intrinsic absorption and scattering attenuation in northeastern Venezuela (southern Caribbean) using coda waves. *Pure and Applied Geophysics* 153: 685–702.
- Ugalde A, Vargas CA, Pujades LG, and Canas JA (2002) Seismic coda attenuation after the $M_w = 6.2$ Armenia (Columbia) earthquake of 25 January 1999. *Journal of Geophysical Research* 107 (doi:10.1029/2001JB000197).
- van Eck T (1988) Attenuation of coda waves in the dead sea region. *Bulletin of the Seismological Society of America* 78: 770–779.
- Vargas CA, Ugalde A, Pujades LG, and Canas JA (2004) Spatial variation of coda wave attenuation in northwestern Columbia. *Geophysical Journal International* 158: 609–624.
- Vidale JE and Benz HM (1992) A sharp and flat section of the core-mantle boundary. *Nature* 359: 627–629.
- Vidale JE, Dodge DA, and Earle PS (2000) Slow differential rotation of the Earth's inner core indicated by temporal changes in scattering. *Nature* 405: 445–448.
- Vidale JE and Earle PS (2000) Fine-scale heterogeneity in the Earth's inner core. *Nature* 404: 273–275.
- Vidale JE and Earle PS (2005) Evidence for inner-core rotation from possible changes with time in PKP coda. *Geophysical Research Letters* 32 (doi:10.1029/2004GL021240).
- Vidale JE and Hedlin MAH (1998) Evidence for partial melt at the core-mantle boundary north of Tonga from the strong scattering of seismic waves. *Nature* 391: 682–685.
- Vinnik LP (1981) Evaluation of the effective cross-section of scattering in the lithosphere. *Physics of the Earth and Planetary Interiors* 26: 268–284.
- Wagner GS and Langston CA (1992a) A numerical investigation of scattering effects for teleseismic plane wave propagation in a heterogeneous layer over a homogeneous half-space. *Geophysical Journal International* 110: 486–500.
- Wagner GS and Langston CA (1992b) Body-to-surface-wave scattered energy in teleseismic coda observed at the NORESS seismic array. *Bulletin of the Seismological Society of America* 82: 2126–2138.
- Wajerman N (1988) Detection of underside P reflections at mantle discontinuities by stacking broadband data. *Geophysical Research Letters* 15: 669–672.
- Wang Y, Takenaka H, and Furumura T (2001) Modelling seismic wave propagation in a two-dimensional cylindrical whole-earth model using the pseudospectral method. *Geophysical Journal International* 145: 689–708.

- Weber M and Davis JP (1990) Evidence of a laterally variable lower mantle structure from P- and S-waves. *Geophysical Journal International* 102: 231–255.
- Weber M and Körnig M (1990) Lower mantle inhomogeneities inferred from PcP precursors. *Geophysical Research Letters* 17: 1993–1996.
- Wegler U (2004) Diffusion of seismic waves in a thick layer: Theory and application to Vesuvius volcano. *Journal of Geophysical Research* 109 (doi:10.1029/2004JB003048).
- Wen L and Helmberger DV (1998) Ultra-low velocity zones near the core-mantle boundary from broadband PKP precursors. *Science* 279: 1701–1703.
- Wennerberg L (1993) Multiple-scattering interpretations of coda-Q measurements. *Bulletin of the Seismological Society of America* 83: 279–290.
- Wenzel F, Sandmeier K-J, and Walde W (1987) Properties of the lower crust from modeling refraction and reflection data. *Journal of Geophysical Research* 92: 11575–11583.
- Wesley JP (1965) Diffusion of seismic energy in the near range. *Journal of Geophysical Research* 70: 5099–5106.
- Whitcomb JH (1973) Asymmetric PP: An alternative to PdP reflections in the uppermost mantle (0 to 100 km). *Bulletin of the Seismological Society of America* 63: 133–143.
- Whitcomb JH and Anderson DL (1970) Reflection of PP seismic waves from discontinuities in the mantle. *Journal of Geophysical Research* 75: 5713–5728.
- Wright C (1972) Array studies of seismic waves arriving between P and PP in the distance range 90° to 115°. *Bulletin of the Seismological Society of America* 62: 385–400.
- Wright C and Muirhead KJ (1969) Longitudinal waves from the Novaya Zemlya nuclear explosion of October 27, 1966, recorded at the Warramunga seismic array. *Journal of Geophysical Research* 74: 2034–2047.
- Wu R and Aki K (1985a) Scattering characteristics of elastic waves by an elastic heterogeneity. *Geophysics* 50: 582–595.
- Wu R and Aki K (1985b) Elastic wave scattering by a random medium and the small-scale inhomogeneities in the lithosphere. *Journal of Geophysical Research* 90: 10261–10273.
- Wu R-S (1985) Multiple scattering and energy transfer of seismic waves separation of scattering effect from intrinsic attenuation. I: Theoretical modelling. *Geophysical Journal of the Royal Astronomical Society* 82: 57–80.
- Wu R-S (1989) The perturbation method in elastic wave scattering. *Pure and Applied Geophysics* 131: 605–637.
- Wu R-S and Aki K (1988) Multiple scattering and energy transfer of seismic waves separation of scattering effect from intrinsic attenuation. II: Application of the theory to Hindu Kush region. *Pure and Applied Geophysics* 128: 49–80.
- Xu F, Vidale JE, and Earle PS (2003) Survey of precursors to P'P': Fine structure of mantle discontinuities. *Journal of Geophysical Research* 108 (doi: 10.1029/2001JB000817).
- Yoshimoto K (2000) Monte Carlo simulation of seismogram envelopes in scattering media. *Journal of Geophysical Research* 105: 6153–6161.
- Zeng Y (1991) Compact solutions for multiple scattered wave energy in the time domain. *Bulletin of the Seismological Society of America* 81: 1022–1029.
- Zeng Y (1993) Theory of scattered P- and S-wave energy in a random isotropic scattering medium. *Bulletin of the Seismological Society of America* 83: 1264–1276.
- Zeng Y (1993) Theory of scattered P- and S-wave energy in a random isotropic scattering medium. *Bulletin of the Seismological Society of America* 83: 1264–1276.
- Zeng Y, Su F, and Aki K (1991) Scattered wave energy propagation in a random isotropic scattering medium. *Journal of Geophysical Research* 96: 607–619.

1.21 Deep Earth Structure – Q of the Earth from Crust to Core

B. Romanowicz, University of California, Berkeley, CA, USA

B. J. Mitchell, Saint Louis University, St. Louis, MO, USA

© 2007 Elsevier B.V. All rights reserved.

1.21.1	Introduction	732
1.21.2	Frequency Dependence of Q	732
1.21.3	Early Studies	734
1.21.4	1-D Global Mantle Q Models	735
1.21.5	Q in the Core	738
1.21.5.1	The Outer Core	738
1.21.5.2	Attenuation in the Inner Core	738
1.21.5.2.1	Hemispherical variations	739
1.21.5.2.2	Anisotropic attenuation	740
1.21.5.2.3	Causes for attenuation in the inner core	740
1.21.6	Global 3-D Attenuation Structure in the Upper Mantle	740
1.21.6.1	Normal Modes and Long Period Surface Waves	740
1.21.6.1.1	Early studies	740
1.21.6.1.2	Anelasticity and focusing	742
1.21.6.1.3	Current status	744
1.21.6.2	Global Body-Wave Studies	745
1.21.6.3	Multiple ScS Studies	747
1.21.6.4	Other Body-Wave Studies	749
1.21.7	Regional Q Variations in the Crust and Uppermost Mantle	751
1.21.7.1	Introduction	751
1.21.7.2	Q or Attenuation Determinations for Seismic Waves in the Crust	751
1.21.7.2.1	Spectral decay methods in which source effects cancel – Regional phases	752
1.21.7.2.2	Spectral decay methods in which source effects cancel – Fundamental-mode surface waves	753
1.21.7.2.3	Spectral decay methods in which source effects cancel – Lg coda	755
1.21.7.2.4	Spectral decay methods for which assumptions are made about the source spectrum – Regional phases	755
1.21.7.2.5	Spectral decay methods for which assumptions are made about the source spectrum – Fundamental-mode surface waves	757
1.21.7.3	Tomographic Mapping of Crustal Q	757
1.21.7.3.1	Q_{Lg}^C , Q_{Lg} , and Q_μ tomography in regions of Eurasia	760
1.21.7.3.2	Q_{Lg}^C tomography in Africa	764
1.21.7.3.3	Q_{Lg}^C and Q_{Lg} tomography in South America	764
1.21.7.3.4	Q_{Lg}^C tomography in Australia	764
1.21.7.3.5	Q_{Lg}^C , Q_{Lg} , and P/S tomography in North America	764
1.21.7.3.6	Q_p variation near ocean ridges	765
1.21.7.3.7	Variation of crustal Q with time	765
1.21.8	Conclusions	766
	References	767

1.21.1 Introduction

Seismic waves have long been known to attenuate at a rate greater than that predicted by geometrical spreading of their wave fronts. Knopoff (1964) pointed out more than four decades ago that much of that attenuation must occur because of intrinsic anelastic properties of the Earth. Were it not for that fortunate circumstance, waves generated by all past earthquakes, as noted by Knopoff, would still be reverberating in the Earth today. Since it redistributes rather than absorbs wave energy, scattering would not have the same effect.

A commonly used measure of the efficiency of wave propagation is the quality factor Q or its inverse, the internal friction Q^{-1} . The latter quantity is most often defined by the expression:

$$Q^{-1} = \Delta E / 2\pi E_{\max} \quad [1]$$

where ΔE is the elastic energy lost per cycle and E_{\max} is the maximum elastic energy contained in a cycle. O'Connell and Budiansky (1978) proposed replacing maximum energy by average stored energy in eqn[1], a change that requires the integer 4 replace 2 in that equation. That form of the definition permits writing Q as the ratio of the real to imaginary part of the complex elastic modulus. However, most seismologists use eqn [1].

Because of its strong dependence on temperature, partial melting and water content, mapping anelastic attenuation in the Earth has the potential to provide valuable information on Earth's three-dimensional (3-D) structure and dynamics, in complement to what can be learned from mapping elastic velocities. A significant challenge is to separate the effects of anelastic (or intrinsic) attenuation from those of elastic scattering and focusing due to propagation in elastic 3-D structure.

Practical aspects of seismic-wave attenuation include the need to account for it when determining earthquake magnitudes and when computing realistic synthetic seismograms. In addition, seismologists must know the attenuation structure in the Earth if they wish to determine dispersion that is produced by anelasticity (Jeffreys, 1967; Liu *et al.*, 1976). The principle of causality requires that such velocity dispersion accompany intrinsic attenuation (Lomnitz, 1957; Futterman, 1962; Strick, 1967).

The following sections present a review of our current knowledge about seismic-wave attenuation from earliest studies to the present. It is a rapidly growing field for which measurements have only

recently become sufficiently numerous and reliable to allow mapping at relatively small scales. It has consistently been observed that measurement errors are large, and it has recently become clear that systematic, rather than random, errors are the greatest cause of concern in Q determinations.

A major consideration is the frequency dependence of Q . We thus begin by describing the state of understanding of this issue. Next we discuss 1-D models of Q : even now, only the average variation of Q with depth is reasonably constrained in the deep Earth. Following that, we will discuss regional variations of Q in the upper mantle and in the crust, for which robust constraints are beginning to emerge. Earlier reviews on this topic can be found in Mitchell (1995) for the crust, Romanowicz (1998) for the mantle and, most recently, Romanowicz and Durek (2000) for the whole Earth.

1.21.2 Frequency Dependence of Q

Determinations available in the 1960s from seismic observations and laboratory measurements suggested that Q was only weakly dependent on frequency (Knopoff, 1964). That conclusion, however, conflicted with the frequency dependence known for single relaxation mechanisms that exhibit rather narrowly peaked spectra for Q^{-1} centered at a characteristic frequency. Liu *et al.* (1976) reconciled those two observations by considering that, over the seismic frequency band in the Earth, Q^{-1} consists of a superposition of many thermally activated relaxation mechanisms for which maxima occurred at different frequencies. That superposition produces a continuous absorption band with a nearly frequency-independent Q^{-1} distribution in the seismic frequency band (Figure 1). The high- and low-frequency limits of the absorption band are described by relaxation times τ_1 and τ_2 and result in the following expression for the absorption band model (Kanamori and Anderson, 1977):

$$Q^{-1}(\omega) = (2/\pi)Q_m^{-1}\tan^{-1}[\omega(\tau_1 - \tau_2)/(1 + \omega^2\tau_1\tau_2)] \quad [2]$$

where Q_m represents the maximum within the absorption band. A more realistic distribution of relaxation times yields a mild frequency dependence $Q \sim \omega^\alpha$ within the absorption band (Minster and Anderson, 1981; Mueller, 1986), and $Q^{-1} \sim \omega^{+1}$ at the higher end of the absorption band and $Q^{-1} \sim \omega^{-1}$ at the low end (Minster and Anderson, 1981). Measurements of

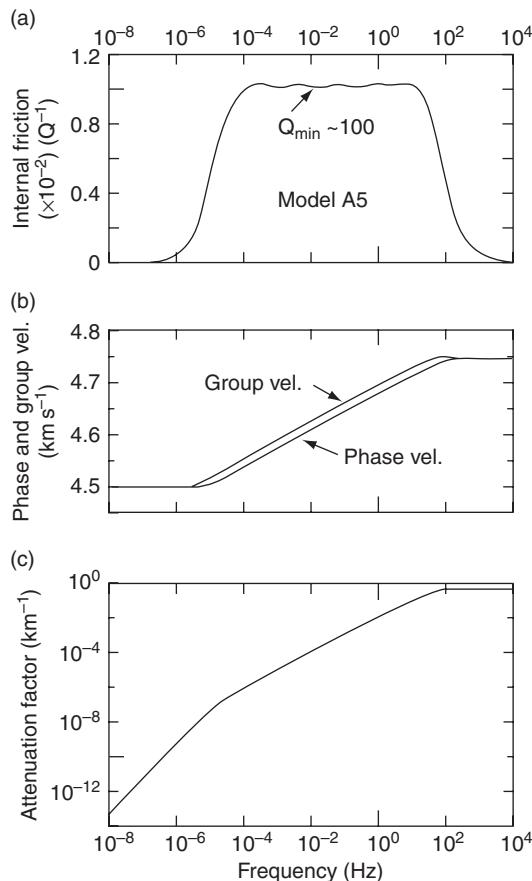


Figure 1 (a) Internal friction (Q^{-1}), (b) phase and group velocity dispersion, and (c) attenuation coefficient as functions of frequency. Reproduced from Liu HP, Anderson DL, and Kanamori H (1976) Velocity dispersion due to anelasticity: Implication for seismology and mantle composition. *Geophysical Journal of the Royal Astronomical Society* 47: 41–58, with permission from Blackwell Publishing.

attenuation of multiple ScS phases (Sipkin and Jordan, 1979) and other body waves (e.g., Sacks, 1980; Lundquist and Cormier, 1980; Der *et al.*, 1982; Ulug and Berckhemer, 1984) have provided evidence that the high frequency corner is located in the band 0.1–1 Hz. A later model (Anderson and Given, 1982) constructed to explain variations of Q for various depths in the Earth from the comparison of surface wave, free oscillation, and body-wave data, obtained a single absorption band with $Q_m = 80$, $\alpha = 0.15$, and a width of five decades centered at different frequencies for different depths in the mantle, with a shift of the absorption band to longer periods at greater depth. Such a model could satisfy many of the known values of Q in the early 1980s. In particular, $\alpha = 0.15$ is compatible with a study of the damping of the Chandler wobble (Smith and Dahlen, 1981).

Many years of body-wave studies have since constrained the frequency dependence $Q \sim \omega^\alpha$ in the body-wave band to have $\alpha \sim 0.1–1$. Ulug and Berckhemer (1984) used spectral ratios of S/P waves in the frequency range 0.04–1.5 Hz and found $\alpha \sim 0.25–0.6$. This frequency range was extended to 6 Hz by Cheng and Kennett (2002), who found $\alpha \sim 0.2–1$ in Australia. Flanagan and Wiens (1998) found a factor of 2 difference in Q measured from sS/S and pP/P phase pairs in the Lau backarc region, implying a strong frequency dependence in the 1–10 s period range, and inferred $\alpha \sim 0.1–0.3$.

Recently, Shito *et al.* (2004) used regional waveform data in western Pacific subduction zones to estimate α from P–P spectral ratios in the frequency range 0.08–8 Hz and found a range of $\alpha \sim 0.1–0.4$, which is in agreement with laboratory studies for solid olivine (e.g., Gueguen *et al.*, 1989; Jackson, 2000) and seems to indicate that solid state processes are the primary mechanism for observed attenuation. Indeed, according to laboratory results, partial melting results in weak frequency dependence in a broad frequency range (e.g., Jackson *et al.*, 2004), which is inconsistent with these observations.

In order to reconcile teleseismic S–P differential traveltimes measured by handpicking, on the one hand, and by comparison of observed and synthetic seismograms, on the other, Oki *et al.* (2000) found that a frequency dependence with $\alpha \sim 0.04$ needs to be introduced in the reference PREM Q model (Dziewonski and Anderson, 1981), a value much smaller than in other studies.

At crustal depths, the frequency dependence of Q is usually described by the equation $Q = Q_0 f^\zeta$ where Q_0 is a reference frequency and ζ is the frequency dependence parameter. For shear-wave $Q(Q_\mu)$, it appears to be between about 0.0 and 1.0 and varies regionally, with depth in the crust, and with frequency, as will be described in more detail in a later section.

An important consequence of the frequency dependence of Q in the Earth is the presence of velocity dispersion due to attenuation. Velocity dispersion was first recognized to be important when comparing global mantle elastic velocity models based on free oscillation and body-wave traveltimes centered at 1 s. A dispersion correction of 0.5–1.5% helped reconcile these models (Liu *et al.*, 1976; Kanamori and Anderson, 1977) and has been applied systematically in global seismology (e.g., Dziewonski and Anderson, 1981), although Montagner and Kennett (1996) showed that attenuation alone is insufficient to reconcile both types of data and

suggested the need to perturb the density structure and introduce radial anisotropy in different parts of the mantle. In the presence of large lateral variations in Q in the upper mantle, which could be in excess of 100%, it is also necessary to account for velocity dispersion when interpreting global tomographic models in the light of other geophysical data, such as the geoid, as illustrated by Romanowicz (1990) in the case of very long wavelength structure. Karato (1993) estimated the contribution of anelasticity to the calculation of partial derivatives of elastic velocities with temperature, and concluded that it should be important in the deep mantle, as anelastic effects might dominate anharmonic effects at high pressures, a conclusion confirmed by Karato and Karki (2001), who used an improved model for the calculation of anelastic effects, including the nonlinear dependence of attenuation on temperature.

In order to interpret seismologically-derived 1-D and 3-D Q models in the Earth, it is necessary to confront them with laboratory experiments, which should provide constraints on: (1) the physical mechanisms responsible for attenuation (i.e., grain boundary or dislocation processes, (e.g., Jackson, 1993; Karato, 1998)) and the related frequency dependence; (2) the dependence of Q on temperature and pressure. Unfortunately, this has proven to be a major challenge, particularly for the deep mantle, due to the difficulties of reproducing in the laboratory both the high P and high T conditions, the low frequency range of seismic observations, and the location of the absorption band far from the frequency range of ultrasonic experiments, preventing ready extrapolation to seismic frequencies.

The variation of Q_μ with temperature can be expressed as (e.g., Jackson, 1993; Karato, 1993):

$$Q^{-1} = A\omega^{-\alpha} \exp(-\alpha H/RT) \quad [3]$$

where $H = E^* + PV^*$ is the activation enthalpy, which depends on pressure through the activation volume V^* , a quantity that is not precisely known. One way to circumvent this is to parametrize this expression in terms of homologous temperature T_m/T (e.g., Sato *et al.*, 1989; Karato, 1993; Cammarano *et al.*, 2003):

$$Q^{-1} = A\omega^{-\alpha} \exp(-\alpha g T_m/T) \quad [4]$$

where g is a dimensionless factor, which depends on H , the melting temperature T_m and the gas constant R . Such a parametrization removes the need for accurate knowledge of the activation volume, and also

allows use of a simple scaling law to relate grain size to frequency (Sato *et al.*, 1989). The pressure dependence is folded into T_m , which is easier to measure in the laboratory.

Much progress in the measurement of attenuation at seismically relevant frequencies has been achieved in the last 15 years (e.g., Jackson, 1993; Karato and Spetzler, 1990; Getting *et al.*, 1997; Faul *et al.*, 2004). Recently, reliable results for olivine have become available at pressures and temperatures down to asthenospheric depths. These advances are described in more detail in Chapter 2.17.

1.21.3 Early Studies

Although seismic-wave attenuation did not become a popular area of research until the 1970s, the first contributions appeared not long after global deployments of seismographs in the early 1900s. Here we describe several important studies completed before 1970, which, in addition to providing the first estimates of Q for several phases, provided the first inklings of the difficulties associated with amplitude measurements.

G. H. Angenheister, working in Göttingen, Germany, in 1906, reported the first known measurements of the attenuation rate of a seismic wave. Instruments at that time were still primitive and surface waves consequently dominated most seismograms recorded by Göttingen's Wiechert seismometers. Angenheister (1906) used records from those instruments to measure the amplitude decay of 20-s surface waves for three different segments of the same great-circle path and found the decay rate to be about 0.00025 km^{-1} . For group velocities near 3 km s^{-1} that rate corresponds to a Q value of about 200, a value implying that the measured attenuation coefficient lies within the range of commonly measured 20-s values today. He later published what was probably the first report of regional variations of surface-wave attenuation (Angenheister, 1921) in which he found that the decay of surface-wave amplitudes along oceanic paths was greater than that along continental paths. This result holds only for those cases where attenuation over relatively low- Q oceanic paths is compared to attenuation over high- Q continental paths (Mitchell, 1995).

B. Gutenberg also made some early determinations of Q using surface waves. He determined a Q value of 70 for Love waves at 100-s period (Gutenberg, 1924), and a value of 200 for Rayleigh

waves at 20-s period (Gutenberg, 1945b). The latter value corresponds well with Angenheister's earlier measurement of Rayleigh-wave attenuation at that period. Gutenberg also determined Q for body phases, first finding a Q of 1300 for 4-s P and PKP waves (Gutenberg, 1945a). He then measured Q for three body-wave phases at different periods (Gutenberg, 1958) finding Q 's of 2500 for P and PP at 2 s, and 400 for P and PP at 12 s. In the same study he also measured Q for S waves finding values of 700 at 12 s and 400 at 24 s. Press (1956) also determined Q for S waves finding it to be 500 or less.

Everden (1955) studied the arrival directions of SV -, Rayleigh- and Love-wave phases using a tripartite array in California and found that all of those phases deviated from great-circle paths between the events and the array. Although Everden did not address Q he brought attention to the fact that seismic waves may deviate from a great-circle path during propagation, a problem that continues, to this day, to plague determinations of Q from amplitude measurements.

The 1960s produced the first definitive evidence for lateral variations of body-wave Q even over relatively small distances. Asada and Takano (1963), in a study of the predominant periods of teleseismic phases recorded in Japan, found that those periods differed at two closely spaced stations and attributed that to differences in crustal Q . Ichikawa and Basham (1965) and Utsu (1967), studied spectral amplitudes at 0.5–3.0 Hz frequencies and concluded that P-wave absorption beneath a seismic station at Resolute, Canada was greater than that beneath other stations in northern Canada.

Tryggvason (1965) devised a least-squares method for simultaneously obtaining Rayleigh-wave attenuation coefficients and source amplitudes using several stations located at varying distances from an explosive source. Since he assumed the source radiation pattern in this method to be circular he had no need to determine that pattern or know the crustal velocity structure. In the same year Anderson *et al.* (1965) developed equations that allowed measured surface-wave attenuation to be inverted for models of Q_μ variation with depth and applied it to long-period surface waves that were sensitive to anelasticity at upper mantle depths.

Sutton *et al.* (1967), studied radiation patterns for Pg and Lg phases recorded at several stations in the United States and found that focusing and regional attenuation differences affected both waves. They concluded that the nature of the tectonic provinces

traversed by the waves was more important than initial conditions at the source in determining the observed radiation patterns.

1.21.4 1-D Global Mantle Q Models

Our knowledge of the 1-D Q structure of the Earth comes primarily from two types of data: normal modes/surface waves on the one hand, multiple ScS on the other. As noted in a previous review of this topic (Romanowicz and Durek, 2000), early studies based on normal mode and surface-wave data developed measurement and inversion methodologies and established the main features of the variation of Q_μ with depth (e.g., Anderson and Archambeau, 1966; Kanamori, 1970; Roult, 1975; Gilbert and Dziewonski, 1975; Jobert and Roult, 1976; Deschamps, 1977; Sailor and Dziewonski, 1978; Buland and Gilbert, 1978; Geller and Stein, 1978). These studies found that:

1. shear-wave attenuation is low in the lithosphere;
2. there is a high attenuation zone roughly corresponding to the low-velocity zone generally associated with the asthenosphere;
3. below 200 km depth, Q_μ increases with depth with a sharp gradient across the transition zone; and
4. Q_μ is higher on average in the lower mantle than in the upper mantle.

Nearly vertically traveling multiple ScS waves provided constraints on the average Q_μ in the whole mantle (e.g., Kovach and Anderson, 1964; Yoshida and Tsujiura, 1975) and confirmed the increase in Q_μ in the mid-mantle. Studies of amplitude ratios of body-wave phases interacting with the core–mantle boundary (CMB) provided early evidence for a possible lower Q_μ zone at the base of the mantle (e.g., Kuster, 1972; Mitchell and Helmburger, 1973). To accommodate both normal mode and body-wave observations, Anderson and Hart (1976, 1978) proposed a model with a Q_μ maximum in the lower mantle, a feature that has successively appeared and disappeared in subsequent whole mantle models based on normal mode and surface-wave data (Masters and Gilbert, 1983; Smith and Masters, 1989; Giardini and Woodhouse, 1988; Li, 1990; Okal and Jo, 2002; Widmer *et al.*, 1991). Some bulk attenuation is necessary to simultaneously fit high Q radial mode data and surface-wave data, and some models such as SL8 (Anderson and Hart, 1978) and the

widely used Preliminary Reference Earth Model (PREM) (Dziewonski and Anderson, 1981) located it in the inner core, while others preferred to place it in the upper mantle (e.g., Sailor and Dziewonski, 1978), and, more recently, in the asthenosphere (Durek and Ekström, 1995).

In the last decade, a problematic discrepancy has emerged between the measurements of fundamental mode Q_R obtained for spheroidal modes using a propagating wave approach (e.g., Dziewonski and Stein, 1982; Romanowicz, 1990, 1994a; Durek *et al.*, 1993; Durek and Ekström, 1996) and those using a standing-wave approach (Smith and Masters, 1989; Widmer *et al.*, 1991; Roult and Clévéde, 2000). In the period band 150–300 s, where measurements by the two methods overlap, Q_R estimates derived from standing-wave observations are systematically higher than those derived from surface waves by about 15–20%, which translates into higher Q_μ in the transition zone for models based on free oscillation data (**Figure 2**). The cause of this discrepancy was first investigated by Durek and Ekström (1997) who explored the influence of realistic background noise on normal mode based measurements, which require the use of long time series. This issue is particularly relevant in the light of the discovery of continuously excited background free oscillations (e.g., Suda *et al.*, 1998). Durek and Ekström (1997) considered several different Q measurement methods: one based on fitting of amplitude or complex spectra, and another classical method based on measuring the decay of the amplitude of a given mode with time. While the background noise does contribute to a bias toward higher Q values, if measurements are done with care, the bias does not exceed about 5–10%, failing to explain the larger observed discrepancy. On the other hand, Masters and Laske (1997) questioned the accuracy of surface-wave Q measurements at very long periods, pointing out the difficulty in finding an appropriate time window isolating the fundamental mode in the presence of overlapping wave trains and overtones. A more recent study by Roult and Clévéde (2000) confirms the higher Q values obtained from mode-based measurements (**Figure 2**). These authors carefully assessed various factors contributing to the uncertainty in mode Q measurements performed using the amplitude decay method, in particular length of time windows for the computation of spectra, and number of time steps for amplitude measurements of individual modes. They also considered the effect of lateral heterogeneity, which they modelled using a higher order perturbation theory that includes multiple scattering

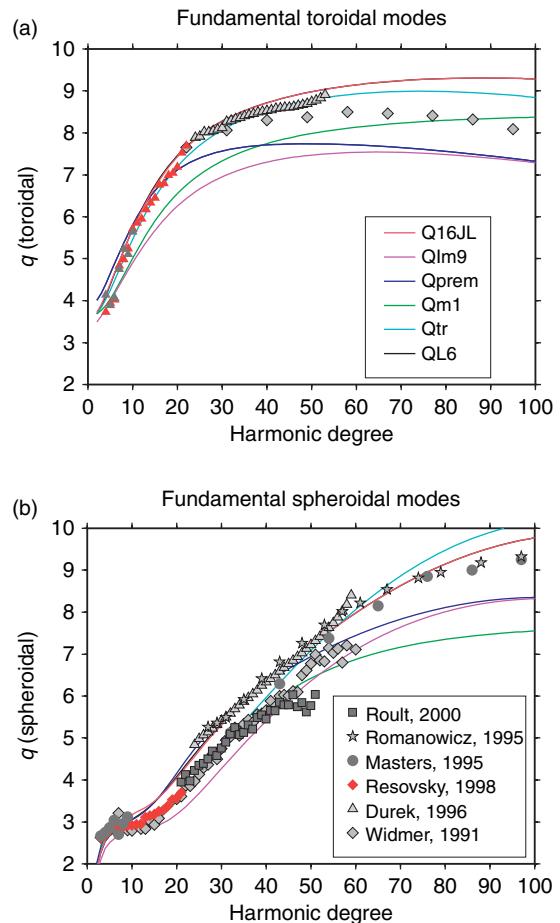


Figure 2 Fundamental mode Q measurements obtained using either a standing mode approach (Widmer *et al.*, 1991; Masters and Laske, 1997; Roult and Clévéde, 2000) or a propagating surface wave approach (Romanowicz, 1995; Durek and Ekström, 1996). Note the discrepancy between the two approaches in the frequency band where both methods can be applied. Also shown are fits to the data for several models of Q_μ shown in **Figure 3**. (a) Toroidal modes, (b) spheroidal modes. Data are from the REM website.

(e.g., Lognonné and Romanowicz, 1990). They concluded that mode Q measurements are more reliable than measurements based on great circle surface-wave amplitude ratios, which they attribute to contamination by higher modes and to the relative deficiency in low frequencies of the first arriving R1 train. We note however that (1) their synthetic tests do indicate some bias toward higher Q 's when lateral heterogeneity is added in the normal mode case; (2) their synthetic tests only consider very smooth models of lateral heterogeneity, for which scattering effects are very weak; (3) the QL6 model of Durek and Ekström (1996) was derived from travelling surface-wave data

using a different method than tested by Roult and Clévétré (2000): the method used was a time domain (rather than spectral domain) method where the Q model was derived by estimating the best transfer function from one Rayleigh-wave train to the one that travelled over an additional great circle path. QL6 (Figures 2 and 3) not only fits surface-wave data better than mode-based models such as QM1 (Widmer *et al.*, 1991), but it also fits toroidal mode Q data better than both QM1 and PREM (Dziewonski and Anderson, 1981). Therefore, it seems that the question of the mode/surface-wave discrepancy has not been resolved yet. A recent study by Resovsky *et al.* (2005) revisited the construction of a 1-D Q model of the Earth using a forward modelling approach based on the neighborhood algorithm, and produced a family of acceptable models with robust error estimates. Their mode data set was augmented through recent measurements of the attenuation of low angular order modes (e.g., Resovsky and Ritzwoller, 1998; He and Tromp, 1996). They circumvented the mode/surface-wave discrepancy problem by including in their data set both fundamental mode surface-wave and spheroidal mode measurements in the period range 150–300 s, and attributing a low weight to these incompatible data. In some experiments, they even excluded both of these data sets. Their final family of models appears to be in good

agreement, on average, with the surface-wave-based model QL6, in particular in the transition zone (Figure 3). Resovsky *et al.* (2005) also revisit the question of the location of bulk attenuation in the Earth and find it negligible in the inner core and preferentially located in the outer core and lower mantle.

While PREM and QL6 have constant Q_μ in the lower mantle, the Resovsky *et al.* (2005) study tentatively includes three layers in the lower mantle and confirms the presence of a Q_μ maximum in the mid-lower mantle, as was found in earlier models (SL8, Anderson and Hart; PAR2C, Okal and Jo (2002); QM1, Widmer *et al.* (1991); Q7U15L, Durek and Ekström (1996), see the review by Romanowicz and Durek (2000)). What is perhaps not yet well constrained, is the precise location of this maximum. Recently, Lawrence and Wysession (2006) developed a Q_μ model based on a large global data set of differential ScS/S amplitude measurements, using a niching genetic algorithm to fit the variations of these amplitudes with distance. Because of the nature of their data, their model (QLM9, Figure 3) is best constrained in the lower mantle, so they chose to fix the top 400 km of the mantle to the PREM value. The resulting model also provides evidence for the existence of a Q_μ maximum in the lower mantle, in this case right above the D'' region. However, the high Q values which they obtain in

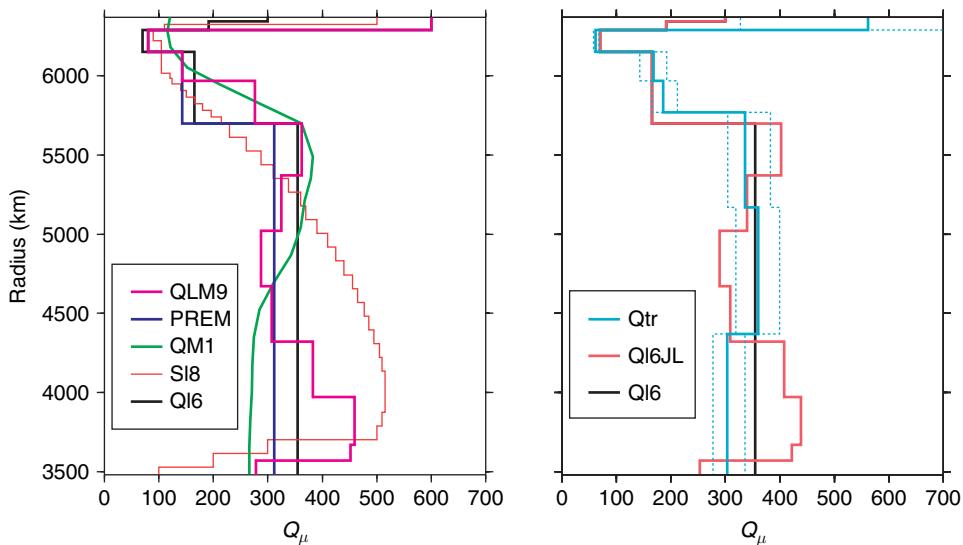


Figure 3 Radial models of Q_μ in the mantle. (Left panel) Models QM1 (Widmer *et al.*, 1991); SL8 (Anderson and Hart, 1978); PREM (Dziewonski and Anderson, 1981); QL6 (Durek and Ekström, 1996); and QLM9 (Lawrence and Wysession, 2006). PREM and QL6 fit fundamental mode Rayleigh wave data, but only QL6 also fits fundamental mode toroidal mode data. Models QLM9 and QM1 have higher Q in the transition zone. Right panel: Qtr: most probable model and 2-sigma standard deviations (broken line) from the work by Resovsky *et al.* (2005), compared to Q16 and a preliminary model which fits both ScS/S amplitude data and fundamental mode surface wave data (Lawrence, personal communication).

the transition zone are incompatible with fundamental mode spheroidal and toroidal data (**Figure 2**, top). Replacing their upper mantle with that of QL6 solves this problem (**Figure 2**, bottom), and little adjustment is needed in the lower mantle to fit the ScS/S amplitude data (Lawrence, personal communication). A joint inversion of mode and ScS/S data sets is underway, and may, in particular, provide some constraints on the frequency dependence of \underline{Q}_α as well as shed further light on the surface-wave/mode discrepancy for fundamental modes.

New constraints on average shear and bulk attenuation in the Earth and the core may be forthcoming owing to the high quality digital data set assembled in the last 16 years on the global broadband seismic network, and owing to the occurrence of several very large earthquakes, especially the great Sumatra earthquake of 26 Dec 2004. These data are providing an opportunity to revisit the \underline{Q} 's of the gravest modes of the Earth, in particular the radial mode ${}_0S_0$, and for the first time, measure the \underline{Q} of individual singlets of modes such as ${}_0S_2$ or ${}_2S_1$ (e.g., Rosat *et al.*, 2005; Roult *et al.*, 2006).

1.21.5 Q in the Core

1.21.5.1 The Outer Core

In the liquid outer core, \underline{Q} is very high, and generally well approximated by $\underline{Q}_\kappa \sim \infty$, to fit both free oscillation and body-wave data. Finite \underline{Q}_κ is, however, required to explain some free oscillation data in the outer core, but the depth range where it is located is still the subject of debate (Anderson and Given, 1982; Widmer *et al.*, 1991; Durek and Ekström, 1996; Resovsky *et al.*, 2005) and, in general, the upper mantle and/or the inner core are preferred locations for finite \underline{Q}_κ . Likewise, while some evidence for finite \underline{Q}_κ from short period core phases has been suggested, it is not clear that it is resolvable (Cormier and Richards, 1976).

1.21.5.2 Attenuation in the Inner Core

Attenuation in the inner core is investigated using inner core sensitive modes, as well as spectral amplitude ratios of different core phases. Topics that have been the subject of recent work include

- the compatibility of normal mode and body-wave measurements, and implications for the frequency dependence of \underline{Q} in the inner core;

- variations with depth;
- anisotropy; and
- hemispherical variations at the top of the inner core.

From early on, measurements of amplitude ratios of PKP(DF) (sampling the inner core) and PKP(BC) (sampling the outer core) constrained \underline{Q}_α in the top 500 km of the inner core to be in the range 200–600 (e.g., Sacks, 1969; Doornbos, 1974; Bolt, 1977; Cormier, 1981; Doornbos, 1983; Choy and Cormier, 1983; Niazi and Johnson, 1992; Bhattacharyya *et al.*, 1993; Song and Helmberger, 1993; Tseng *et al.*, 2001; Ivan *et al.*, 2005) and most studies have suggested an increase of \underline{Q}_α with depth. Others have suggested that \underline{Q}_α is constant with depth (e.g., Niazi and Johnson, 1992; Bhattacharyya *et al.*, 1993). In these studies, the sampling depth range was limited by the narrow distance range in which the phase PKP(BC) is observed. Extending the depth range sampled by previous studies to 600 km by including diffracted PKP(BC) phases, Souriau and Roudil (1995) proposed a two-layered model with $\underline{Q}_\alpha \sim 200$ in the topmost 100 km of the inner core, and $\underline{Q}_\alpha \sim 440$ below. Cormier *et al.* (1998) designed a new approach that allowed them to investigate the variation of \underline{Q}_α deeper in the inner core, by comparing observed and synthetic PKIKP waveforms in the distance range 150–180°. The synthetic waveforms are built using the source time history of each earthquake, determined from the analysis of P waveforms, and include the effects of mantle attenuation. In a recent improved implementation of this method, which takes into account surface reflections and reverberations near the source, Li and Cormier (2002) obtained a mean for the inner core of $\underline{Q}_\alpha = 307 \pm 90$ and much stronger attenuation in the top 300 km of the inner core. Testing the hypothesis of an innermost inner core, Cormier and Stroujkova (2006) found a rapid change in the magnitude and variance of seismic attenuation of PKIKP in the middle of the inner core, in the interval 400–600 km in Earth radius (**Figure 4**).

Normal modes primarily provide constraints on \underline{Q}_β , and \underline{Q}_β and \underline{Q}_α are related through (Anderson and Hart (1978)):

$$\underline{Q}_\alpha^{-1} = \frac{4}{3}(V_S/V_P)^2 \underline{Q}_\beta^{-1} + \left[1 - \frac{4}{3}(V_S/V_P)^2 \right] \underline{Q}_\kappa^{-1} \quad [5]$$

If there was no significant attenuation in bulk, and no frequency dependence, the inferred \underline{Q}_β from body-wave studies would be on the order of ~ 40 . Confronting this value with measurements based on

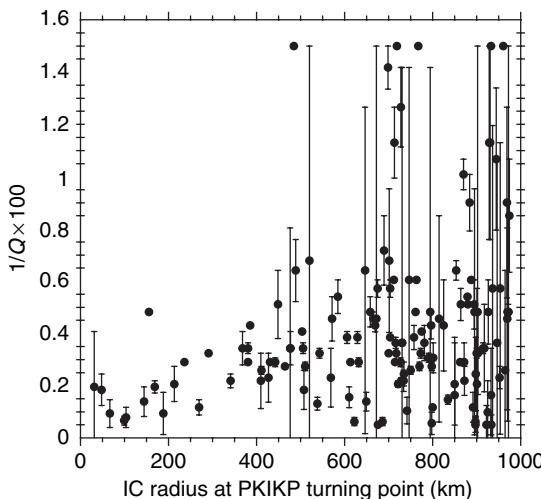


Figure 4 Observed attenuation of PKP(DF) waves as a function of the turning radius of the ray. Reproduced from Cormier VF and Stroujkova A (2006) Waveform search for the innermost inner core. *Earth and Planetary Science Letters* 236: 96–105.

inner core sensitive normal mode data has resulted in some puzzles. Early normal mode studies found very large values of Q_μ (1500–3500) based on the measurement of attenuation of spheroidal core modes (Buland and Gilbert, 1978; Masters and Gilbert, 1981) whereas most more recent models have much lower Q_μ , such as PREM ($Q_\mu = 85$ (Dziewonski and Anderson, 1981), or QM1 ($Q_\mu = 110$, (Widmer *et al.*, 1991)), which is also compatible with measurements of Giardini and Woodhouse (1988). On the other hand, applying the Sompi method (Kumazawa *et al.*, 1990), Suda and Fukao (1990) measured Q_μ of modes sensitive to shear in the top part of the inner core and found very large values and an increase with depth, with $Q_\mu = 1500$ in the top 200 km and $Q_\mu = 3800$ at greater depth. However, their identification of modes has been questioned and, recently, Andrews *et al.* (2006) have shown that measurements of inner core Q_μ could be biased by neglecting mode coupling. Through the comparison of observations and synthetic predictions including mode coupling effects, these authors found that models with very high Q_μ are incompatible with the observations, which favor moderate values of $Q_\mu \sim 80$ –100. While such moderate values are now established in the top part of the inner core, where normal modes concentrate their sensitivity, a recent observation of PKJKP, which samples deep into the inner core (Cao *et al.*, 2005), has provided the opportunity to estimate the average Q_μ in the inner core, which was found to be >150 (Cao, 2005), and which

would imply an increase with depth, like that for Q_α . This result, however, needs to be confirmed by additional observations of PKJKP.

Even the lowest proposed values for Q_μ currently favored are incompatible with the Q_α results, unless one invokes either: (1) significant bulk attenuation in the inner core or, (2) significant frequency dependence of Q or, (3) a significant scattering component. The rather low value for Q_α found is compatible with the existence of a mushy zone in the top part of the inner core, whose presence is related to the process of solidification of iron alloy (Loper and Roberts, 1981; Fearn *et al.*, 1981; Loper and Fearn, 1983) involving a solid matrix and fluid inclusions. This would result primarily in compressional attenuation and could explain some of the observations of seismic anisotropy in the inner core (e.g., Singh *et al.*, 2000). Bowers (2000) cautioned that the large scatter observed in Q_α measurements from PKP amplitude ratios could be due to the effects of lateral variations in structure near the CMB, and in particular the presence of ultralow velocity zones. On the other hand, Krasnoshchekov *et al.* (2005) suggested that variability in the amplitudes of inner core boundary (ICB) reflected PKiKP phases could be due to a mosaic of partially molten patches of scale length 10–100 km.

1.21.5.2.1 Hemispherical variations

Another observation in favor of the presence of a mushy transition zone at the top of the inner core is that of hemispherical differences, first observed in elastic velocity using differential traveltimes measurements of the pair of phases PKiKP, postcritically reflected at the ICB and PKIKP, which, in the distance range 120–144° samples the top ~100 km of the inner core (Tanaka and Hamaguchi, 1997; Creager, 1999; Niu and Wen, 2001; Garcia, 2002). These phases have almost the same ray paths in the mantle and in the outer core, so the differences in traveltimes and amplitudes can be attributed to the vicinity of the ICB. Indeed, in a study covering the epicentral distance range 131–141°, the faster eastern hemisphere (40° E to 180° E was also found to have lower Q than the slower western hemisphere (Wen and Niu, 2002). In order to better constrain the depth dependence of the hemispherical variations in Q , Cao and Romanowicz (2004) extended the epicentral distance range to 144°, and found large differences in Q_α , with $Q_\alpha \sim 335$ in the western hemisphere and ~160 in the eastern hemisphere, which they interpreted as resulting from small lateral temperature variations at the top of the inner core. Such

temperature variations could be imposed on the inner core by heterogeneities at the CMB (e.g., Sumita and Olson, 1999) and would influence the connectivity of fluid inclusions in the mushy zone. Below about 85 km depth the hemispherical differences appeared to wane. However, several studies found evidence for persisting differences at greater depth. Oreshin and Vinnik (2004) measured spectral ratios of PKP(DF) and either PKP(AB) or PKP(BC) in the distance range 150–170° and found differences in Q between the hemispheres to a distance of 155°. Yu and Wen (2006) combined observations of PKiKP/PKIKP in the distance range 120–141° and PKP(BC)/PKIKP in the distance range 146–160°, along equatorial paths and proposed that they could resolve hemispherical differences in Q down to at least 200 km (Figure 5). However, in the distance range 149–155°, PKP(BC) interferes with PKiKP, causing large scatter in the data. On the other hand, Li and Cormier (2002) did not find evidence for such hemispherical variations in the deeper inner core using PKIKP data at larger distances.

1.21.5.2.2 Anisotropic attenuation

The presence of velocity anisotropy is well documented for the inner core (e.g., Morelli *et al.*, 1986; Woodhouse and Wong, 1986; Creager, 1992; Shearer, 1994; Vinnik *et al.*, 1994; Su and Dziewonski, 1990). Theoretical studies indicate that anisotropy in attenuation should accompany anisotropy in velocity, and several authors have noted the stronger attenuation of PKP(DF) phases travelling along polar paths (Creager, 1992; Song and Helmberger, 1993). Souriau and Romanowicz (1996) examined a carefully selected data set of PKP(DF)/PKP(BC) amplitude ratios for paths whose turning points were located under western Africa, and for which good azimuthal coverage was available. They found a significant correlation between high attenuation and high velocity and inferred that the origin of anisotropy in the top half of the inner core must be due to the orientation of iron crystals, which would produce this type of correlation (Carcione and Cavallini, 1995) rather than fluid inclusions, which would result in correlation of high velocity with low attenuation (Peacock and Hudson, 1990). These results were subsequently extended to a global data set (Souriau and Romanowicz, 1997) and to antipodal paths (Cormier *et al.*, 1998). The latter result was confirmed by Li and Cormier (2002) who suggested that anisotropy in attenuation also varies with depth. As will be seen below, these authors' preferred interpretation involves scattering. Oreshin and Vinnik (2004)

confirmed the correlation of anisotropy in attenuation with that in velocity, which, however, may not be present at high latitudes (Helffrich *et al.* (2002)).

1.21.5.2.3 Causes for attenuation in the inner core

In a series of papers, Cormier and collaborators recently explored two different interpretations for the attenuation in the inner core, invoking a viscoelastic and scattering mechanism, respectively (Cormier *et al.*, 1998; Li and Cormier, 2002; Cormier and Li, 2002). In the viscoelastic interpretation, they considered the absorption band model of Cormier and Richards (1988) and, through a parameter search approach, sought to constrain the low frequency corner τ_1 , as well as the peak attenuation Q_m^{-1} and the attenuation at 1 Hz (Li and Cormier, 2002). While constraining τ_1 turned out to be problematic, they found that the data are consistent with frequency dependent attenuation in the inner core and weak velocity dispersion in the seismic body-wave band. The existence of scattering, at least at the top of the inner core, was clearly documented by Vidale and Earle (2000) through the modeling of PKiKP coda. In the scattering interpretation, Cormier and Li (2002) investigated a model of inner core attenuation due to forward scattering by 3-D fabric caused by solidification texturing, which could also be responsible for the observed depth-dependent inner core anisotropy. They found a mean scale length of heterogeneity of 9.8 ± 2.4 km and a mean velocity perturbation of $8.4 \pm 1.8\%$. They confirmed the depth dependence found in the viscoelastic interpretation, but with a sharper transition between the highly attenuating upper part of the inner core and the lower attenuating center (e.g., Figure 5). They suggested that scattering plays a dominant role in attenuating inner core traversing phases in the frequency band 0.02–2 Hz, as it can also explain elastic and anelastic anisotropy and their depth dependence and helps reconcile the body wave and normal mode Q measurements.

1.21.6 Global 3-D Attenuation Structure in the Upper Mantle

1.21.6.1 Normal Modes and Long Period Surface Waves

1.21.6.1.1 Early studies

In the 1970s, after the occurrence of the 1960 Great Chile Earthquake (Mw 9.6), and with the accumulation of data from the World-Wide Standardized

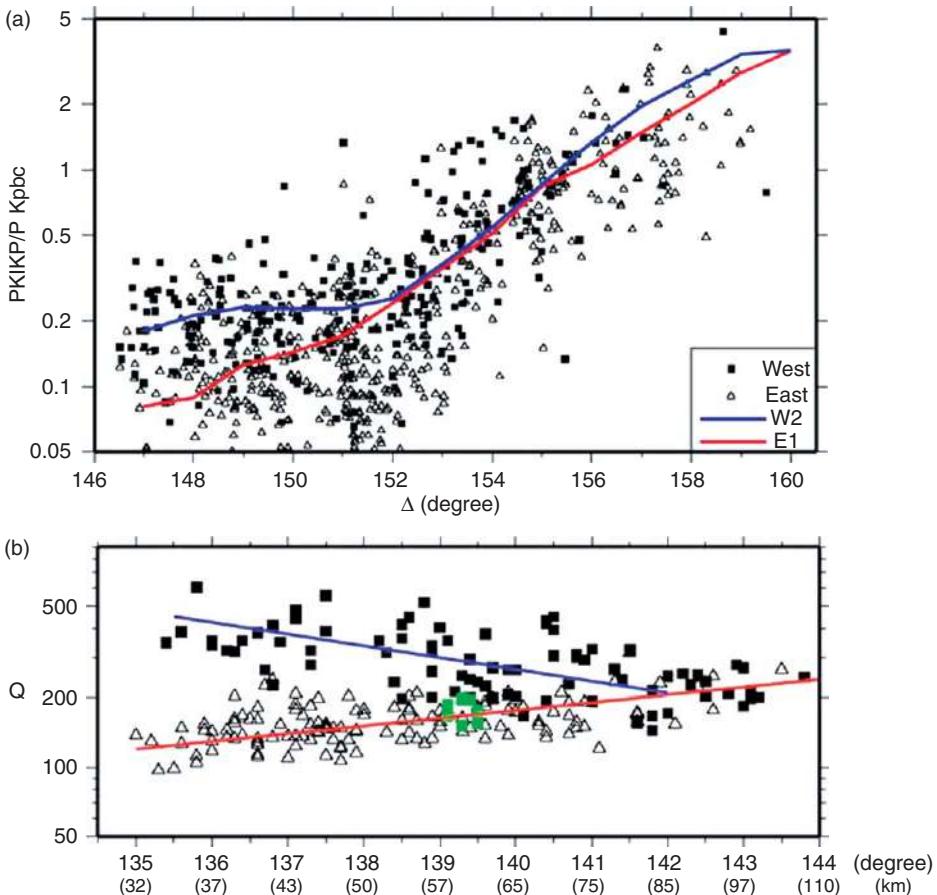


Figure 5 Hemispherical variations of Q in the inner core. (a) Variations of amplitude ratios of $PKIKP/PKP(BC)$ as a function of distance and predictions of Q models for the western (W2) and eastern (E1) hemispheres. (Adapted from Yu W and Wen L (2006) Seismic velocity and attenuation structures in the top 400 km of the Earth's inner core along equatorial paths. *Journal of Geophysical Research* 111: (doi:10.1029/2005JB003,995). (b) Q measurements as a function of distance from amplitude ratios of $PKIKP/PKiKP$ showing differences between the western (triangles) and eastern (squares) hemispheres. From Cao A and Romanowicz B (2004) Hemispherical transition of seismic attenuation at the top of the Earth's inner core. *Earth and Planetary Science Letters* 228: 243–253.

Seismographic Network (WWSSN) network, measurements of long-period surface-wave attenuation, then based on relatively few records, showed large disagreements (e.g., Ben-Menahem, 1965; Smith, 1972; Mills and Hales, 1978; Jobert and Roult, 1976). At that time it was realized that: (1) elastic effects were important in limiting the accuracy of Q measurements; (2) anelastic attenuation caused frequency dependence of elastic velocities, which needed to be taken into account (Luh, 1974; Randall, 1976; Liu *et al.*, 1976; Akopyan *et al.*, 1976; Kanamori and Anderson, 1977); and (3) large systematic lateral variations existed, correlated with those of phase velocities and suggesting significant differences in attenuation under different tectonic regions, with low attenuation under shields and high attenuation under oceans and tectonically active

provinces (e.g., Nakanishi, 1978, 1979b, 1981; Lee and Solomon, 1979; Roult, 1982; Dziewonski and Stein, 1982).

While most upper mantle 3-D Q models up to now, as we will discuss below, have been on surface waveform or amplitude data, several authors attempted to measure lateral variations in Q from normal mode data, which in principle should provide sensitivity at greater depths in the mantle. Because the mode amplitude data set is very contaminated by elastic effects (e.g., Smith and Masters, 1989) it was possible to recover only the longest wavelengths in the even degree structure (Romanowicz *et al.*, 1987; Roult *et al.*, 1984; Suda *et al.*, 1991). The most important result of these early studies is the presence of a long wavelength, degree two, structure in Q_μ in the transition zone, shifted toward

the west with respect to the degree two in the shallower mantle, with lowest Q centered in the central Pacific Ocean and under Africa.

1.21.6.1.2 Anelasticity and focusing

One of the main issues limiting resolution in global mantle attenuation tomography is the contamination of amplitudes by elastic focusing effects. Numerous cases of such contamination in Earth circling mantle waves have been reported. For example, for moderate size earthquakes, for which the effect of source directivity can be ruled out, one expects successive Rayleigh-wave trains to gradually decrease in amplitude, due to the effects of attenuation and geometrical spreading. However, it is sometimes observed that an R_{n+1} train has larger amplitude than R_n , where n is the orbit number of the Rayleigh wave (e.g., Lay and Kanamori, 1985; Romanowicz, 1987, 2002), and such observations can be qualitatively reproduced by including focusing effects in synthetic seismograms obtained by normal mode summation (e.g., Romanowicz, 1987). Also in the frequency domain, long-period surface-wave amplitude spectra are often irregular, with many ‘holes’ that cannot be attributed to intrinsic attenuation or source effects (e.g., Romanowicz, 1994a).

To first order, in the framework of single scattering and in the high frequency approximation, analytical expressions have been obtained for the focusing effect, both in a propagating wave formalism (Woodhouse and Wong, 1986) and in a normal mode asymptotic formalism (Romanowicz, 1987; Park, 1987). Using asymptotic approximations in the framework of normal mode theory, it was shown that focusing effects depend on the transverse gradients of elastic structure, as expressed in terms of phase velocity perturbations in the case of propagating waves, and of local frequency perturbations, in the case of normal modes. The expressions obtained in both approaches are equivalent (Romanowicz, 1987). In the propagating surface-wave case and in the frequency domain,

$$\ln \delta A_F(\omega) = \frac{1}{2} \operatorname{cosec} \Delta$$

$$\int_0^\Delta [\sin(\Delta - \phi) \sin \phi \delta_\theta^2 - \cos(\Delta - 2\phi) \delta_\phi] \frac{\delta c}{c_0}(\omega) d\phi \quad [6]$$

where Δ is epicentral distance, ϕ is the angular distance along the source-station great circle path, $\delta c/c_0$ is the relative perturbation in phase velocity along the path, and $\delta A_F(\omega)$ is the contribution to the amplitude at frequency ω due to focusing.

In the standing-wave case and time domain, for an isotropic source:

$$\delta F_K(\Delta) = \frac{a\Delta}{U} \left(\frac{\hat{D}_K - \tilde{D}_K}{2k} + \frac{\cot \Delta}{8k} (\delta \hat{\omega} - \delta \tilde{\omega}) \right) \quad [7]$$

where $F = (1 + \delta F_K(\Delta))$ is the perturbation to the time domain amplitude of the seismogram for multiplet K , $\delta \hat{\omega}$ and $\delta \tilde{\omega}$ are the perturbations to the great circle average and minor are average local frequencies, respectively, $k = l + 1/2$ where l is the angular order of the mode, and we have defined

$$\begin{aligned} \tilde{D} &= \frac{1}{\Delta} \int_0^\Delta \partial_T(\delta \omega_K(s)) ds \\ \hat{D} &= \frac{1}{\Delta} \int_0^{2\pi} \partial_T(\delta \omega_K(s)) ds \end{aligned} \quad [8]$$

where ∂_T denotes the second transverse derivative along the great circle path, which reduces to the integrand in eqn [6]. Accounting for the radiation pattern in eqns [7] is equivalent to using eqns [6] together with ray tracing.

Because the focusing effects are so strongly dependent on the transverse gradients of the elastic structure, and because those are not generally well constrained, compounded by the fact that these expressions are approximate and valid only to first order, it has been a difficult challenge, for the last decade, to properly account for focusing effects in surface-wave attenuation tomography. Indeed, if the corrections made on the basis of an existing elastic model are inaccurate, they can potentially introduce more biases than they can correct.

Noting that focusing effects and attenuation behave very differently as Rayleigh waves circle around the Earth, with the sign of attenuation always the same, while focusing/defocusing depends on the direction of propagation along the great circle, Romanowicz (1990) and Durek *et al.* (1993) showed that, by using four consecutive Rayleigh-wave trains, one can eliminate, at least in the first order approximation, the effect of focusing, as well as uncertainties in the source amplitude. This resulted in the first, low degree, even degree global tomographic models of attenuation in the upper mantle which confirmed the existence of a strong degree 2 in attenuation, as first suggested in studies based on normal modes. These models showed that attenuation in the uppermost mantle was correlated with seismic velocities, at least at the longest wavelengths (~ 4000 km). There are two drawbacks to this approach: first, only even degree structure can be retrieved in this fashion, as only great-circle average attenuation can be measured. Second, elastic

effects become increasingly more pronounced as distance increases, and the first order approximation is not suitable for higher orbit trains, leading to a decrease in the ability to retrieve the intrinsic attenuation signal. Moreover, higher orbit trains are more dispersed, limiting the frequency range in which Rayleigh waves of consecutive trains do not interfere with each other and/or with overtones.

In order to be able to retrieve odd degree structure while not explicitly correcting for unknown focusing effects, and avoiding the drawbacks of using multiple orbit wave trains, a different approach was proposed by Romanowicz (1995), using three consecutive Rayleigh wave trains (R1, R2, R3). She noted that the R1 and R2 trains are the least contaminated by focusing effects. However, their amplitudes also depend on uncertainties in the source amplitude. The source amplitude shift varies slowly with frequency, and can be estimated by comparing the overall level of the amplitude spectrum computed in two different fashions: (1) directly from R1 (or R2) and (2) using a linear combination of R1, R2, and R3. Romanowicz (1994a) measured attenuation coefficients on R1 and R2 wave trains, correcting for the source shift using the reference provided by the R1, R2, R3 combination. This, combined with a rigorous data selection in which all R1 and R2 amplitude spectra that were not smoothly varying with frequency were rejected, led to the first low degree (equivalent to about degree 5) tomographic model of upper mantle shear attenuation, QR19 (Romanowicz, 1995). Even though this first model had very low resolution, it confirmed the correlation of lateral variations of Q with V_S in the top 250 km of the upper mantle, and a shift to a different pattern in the transition zone, dominated by low Q in the central Pacific and Africa, and correlated with hotspots. Romanowicz (1994b) showed that, in the transition zone, at least at the longest wavelengths, anelastic attenuation correlated with the hotspot distribution, whereas the velocity structure correlates better with the slab distribution, consistent with expectations that Q is more sensitive to high temperature regions. The desensitizing approach used, however, limited the lateral resolution of the model obtained, since a relatively small number of paths qualified for inclusion in the inversion.

The applicability of the linear asymptotic approximation to the computation of focusing (eqns [6]–[9]) has been tested by Selby and Woodhouse (2000) on a large data set of Rayleigh-wave amplitudes on minor and major arcs, in the period range 73–171 s. These authors derived maps of lateral variations of $q_R(\omega) =$

$Q_R^{-1}(\omega)$ at different frequencies, assuming that the amplitude of a fundamental mode Rayleigh wave observed at distance Δ and angular frequency ω can be written as:

$$A(\omega, \Delta) = A_0(\omega)(1 + F(\omega))\exp[-\omega a \Delta \bar{q}_R(\omega)]/2U_0(\omega) \quad [9]$$

where U_0 is group velocity, a is the radius of the earth, $A_0(\omega)$ is source term, and $\bar{q}_R(\omega)$ is the average Rayleigh-wave attenuation along the source station path:

$$\bar{q}_R(\omega) = \frac{1}{\Delta} \int_0^\Delta q_R(\omega, \theta, \phi) ds \quad [10]$$

$F(\omega)$ represents the effect of focusing, which can be calculated from a reference elastic 3-D model using expression [6]. Selby and Woodhouse (2000) compared the maps obtained by: (1) inverting the observed amplitude data set for lateral variations in q_R without correcting for focusing, (2) inverting synthetic maps of apparent attenuation obtained by assuming the amplitudes are only affected by focusing and using the elastic phase velocity model of Trampert and Woodhouse (1995), and (3) inverting the observed amplitude data set for q_R after correcting for focusing. In these experiments, a degree 20 model of 3-D apparent attenuation was obtained. They concluded that at the longer periods (e.g., 146 s), the apparent attenuation maps obtained in (2) were not significantly correlated with those obtained in (1), indicating that the amplitude signal is not severely affected by focusing, whereas at the shorter periods (e.g., 73 s), the correlation is stronger. This implies not only that the shorter period data need to be corrected for focusing before inferring lateral variations in intrinsic attenuation, but that the predictions from existing elastic models using the approximate focusing theory were perhaps of practical use, even though these focusing terms depend strongly on the poorly constrained transverse gradients of the elastic structure. Also, Selby and Woodhouse (2000) found that low degree attenuation structure (up to degree 8 in a spherical harmonics expansion) is not significantly affected by focusing in the entire period range considered. In a subsequent study, they inverted the maps of $q_R(\omega)$ with and without corrections for focusing to obtain a series of models of lateral variations of attenuation in the upper mantle up to degree 8 (Selby and Woodhouse, 2002). In the latter study, they also considered the effect of uncertainties in the source term, and found that a frequency dependent correction factor is necessary to combine the $q_R(\omega)$ maps into a successful depth dependent

model of attenuation. They concluded that the details of focusing and source corrections did not affect the robustness of their models up to degree 8, but would be more important at shorter wavelengths.

1.21.6.1.3 Current status

An important result of the Selby and Woodhouse studies was the confirmation that surface-wave amplitudes contained information not only on anelastic structure but also on elastic structure, that could be exploited, as already suggested by Woodhouse and Wong (1986) and Wong (1989). At about the same time, Billien and Léveque (2000) made the first attempt at inverting simultaneously Rayleigh-wave amplitude and phase data, for maps of phase velocity and q_R between 40–150 s. The effects of focusing were included using eqn [6] which allowed them to consider shorter periods and shorter wavelengths. The maps obtained at short periods indicate significant correlation between phase velocity and attenuation, and therefore tectonics, and the even degree part (degrees 2, 4, 6) of their longer period maps are compatible with those of other studies. However, their odd degree part is dominated by degree 5, a feature not found in other studies.

In a recent study, Dalton and Ekström (2006a, 2006b) considered a large global data set of Rayleigh-wave amplitudes in the period range 50–250 s. They inverted this data set, simultaneously, for maps of lateral variations in phase velocity up to spherical harmonics degree 20, attenuation, up to degree 12, as well as source and receiver correction factors. As in previous studies, the focusing effect is also included using expression [6]. A notable result of their study is the high quality phase velocity maps that they were able to obtain by using only the amplitude constraints in their inversion (Dalton and Ekström, 2006b). Inclusion of the source and receiver correction factors was also found to improve the attenuation mapping. They constructed maps of Rayleigh-wave attenuation at different periods, and also found a good correlation of the Q distribution with tectonics for periods sensitive to the first 250 km of the upper mantle (Dalton and Ekström, 2006a).

The studies described so far considered only fundamental mode surface waves which, in practice, limits the resolution in depth to the top 300–400 km of the upper mantle, even though some attempts at interpreting deeper structure were shown. These studies also used a two-step approach, and often only the results of the first step, inverting for maps of lateral variations of $q_R(\omega)$ at different periods, were presented (e.g., Romanowicz, 1990; Billien and Léveque, 2000; Dalton and Ekström, 2006a). The more recent 3-D

attenuation models include both even and odd terms of lateral heterogeneity in Q_μ (Romanowicz, 1995; Selby and Woodhouse, 2002), or in Q_R (Dalton and Ekström, 2006a). Figure 6 compares maps of Q at a

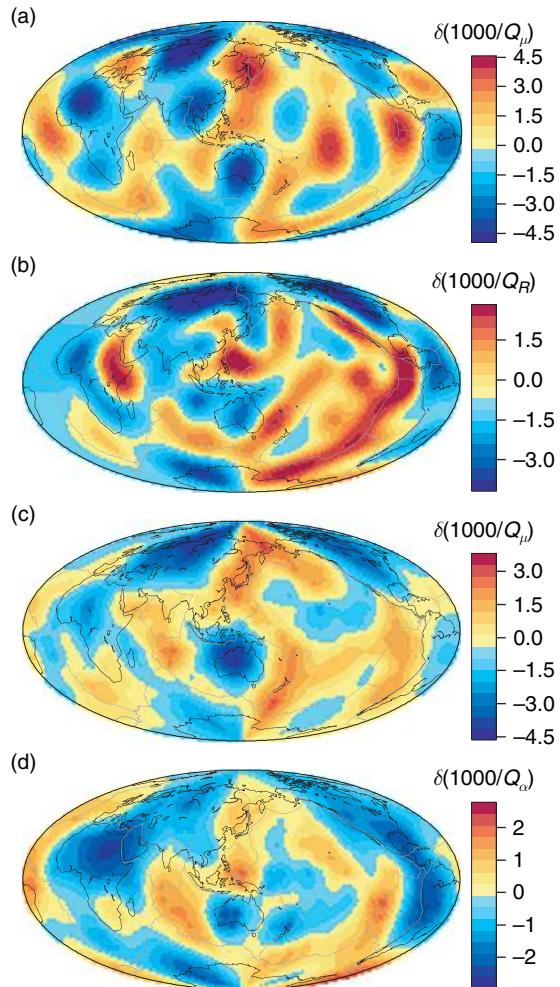


Figure 6 Comparison of global Q models in the uppermost mantle. (a) QRLW8 model (Gung and Romanowicz, 2004) from inversion of three component surface wave and overtone waveform data, presented is Q_μ at a depth of 160 km. (b) Map at 150 s of the Rayleigh wave Q model of Dalton and Ekström (2006a). (c) Average Q_μ in the depth range 0–250 km from Selby and Woodhouse (2002), also from Rayleigh waves. (d) Average variations in Q_α in the first 250 km of the mantle from amplitude ratios of P and PP (Warren and Shearer, 2002). Some of the differences observed may be due to the different depth ranges sampled: in models (a), (c), and (d), the global ridge and back-arc systems all stand out as low Q_μ features, whereas the Atlantic ridge is not as prominent in model (b), while the Red Sea region lights up more strongly. This may be due to the fact that (b) has not been inverted with depth, and therefore may include some effects of structure deeper than 250 km.

depth of 200 km obtained in different recent studies, and shows that, while details are still variable from model to model, the large scale features, with high \mathcal{Q} in shield areas, low \mathcal{Q} under ridges and back arcs, are quite consistent.

In order to improve the depth resolution in the transition zone, it is necessary to develop a methodology that includes information from surface-wave overtones, as well as Love waves. Because overtones are not easily separable due to their similar group velocities, a waveform methodology is desirable. Such a methodology uses a comparison of observed and synthetic seismograms in the time domain. The synthetics can be computed using normal mode theory, taking into account 3-D effects at various degrees of approximation. However, to obtain accurate amplitude information from surface-wave data, it is necessary to either employ an approach based on the measurement of envelopes, or to first align the timing of waveforms before comparing observed and synthetic waveforms. Following these considerations, Gung and Romanowicz (2004) recently developed an iterative waveform inversion approach, in which a large global data set of three-component fundamental and overtone waveforms, filtered in the frequency range 80–250 s, is first inverted for elastic 3-D structure, using the nonlinear asymptotic coupling theory (NACT) approach developed by Li and Romanowicz (1995), up to spherical harmonics degree 24. Different elastic models are computed for Love and Rayleigh waves, to account for the strong radially anisotropic signal in the uppermost mantle (e.g., Montagner and Tanimoto, 1991; Ekström and Dziewonski, 1997; Gung *et al.*, 2003). In a second step, the waveforms, corrected for the 3-D elastic structure obtained in the previous step, are inverted for lateral variations of $\mathcal{Q}_\mu(r)$ in the upper mantle, up to degree 8. In this process the waveforms are directly inverted for depth dependence in elastic and anelastic structure.

Although Gung and Romanowicz (2004) did not include focusing effects in deriving their model QRLW8, subsequent tests indicated that the model was robust with respect to these effects, in agreement with the predictions of Selby and Woodhouse (2000). In particular, Gung and Romanowicz (2004) compared the degree 8 $\mathcal{Q}_\mu(r)$ model obtained with and without focusing terms, the latter computed using expression [8] in the 3-D elastic model obtained in the first step, and found no significant changes. Including focusing in the second step of the inversion justifies inverting for a higher degree \mathcal{Q}_μ model.

Figure 7 shows a comparison of the models obtained up to degree 12 and 16, in the transition zone, when focusing terms are included. Clearly, the large-scale features remain stable among the models, with some variability in the details. They indicate that, in contrast to the upper 200–300 km of the mantle, the main features in \mathcal{Q}_μ in the transition zone are two large low \mathcal{Q} regions in the south Central Pacific and under Africa, which correlate with the distribution of elastic velocities at the base of the mantle (Romanowicz and Gung, 2002), as well as the distribution of hotspots, confirming earlier results (Romanowicz, 1994b).

1.21.6.2 Global Body-Wave Studies

In the same way as differential traveltimes of teleseismic body-wave phases are used to obtain information on the distribution of upper mantle velocities, global scale lateral variations in attenuation can be inferred from differential amplitude measurements (i.e., amplitude ratios). These measurements are difficult, however, as they are sensitive to the window chosen for each phase, as well as to contamination by complex structure near the source, receiver, and bounce points. Komatitsch *et al.* (2002) have called attention to the importance of considering the effects of focusing and scattering in the crust. Chapter 1.05 provides details about the theoretical computation of the effects of attenuation on body waves.

Only three published studies to date have developed models of upper mantle \mathcal{Q} based on differential body-wave measurements, two for \mathcal{Q}_μ using S phases (Bhattacharyya *et al.*, 1996; Reid *et al.*, 2001) and one for \mathcal{Q}_α (Warren and Shearer, 2002). Each of them used slightly different methods, but the basic principle remains the same.

The amplitude spectra of recorded body waves can be expressed as:

$$A(\omega) = cS(\omega)R(\omega)I(\omega)A_c(\omega)F\exp(-\omega t^*/2) \quad [11]$$

where c is a constant expressing the radiation pattern and the geometrical spreading, $S(\omega)$ is the source spectrum, $R(\omega)$ the crustal response, $I(\omega)$ the instrument response, A_c is the crustal layering/reflectivity at the bounce point for reflected waves, and F is a hypothetical factor that includes possible effects of focusing. Also, t^* is defined as:

$$t^* = \int \frac{ds}{\mathcal{Q}v} \quad [12]$$

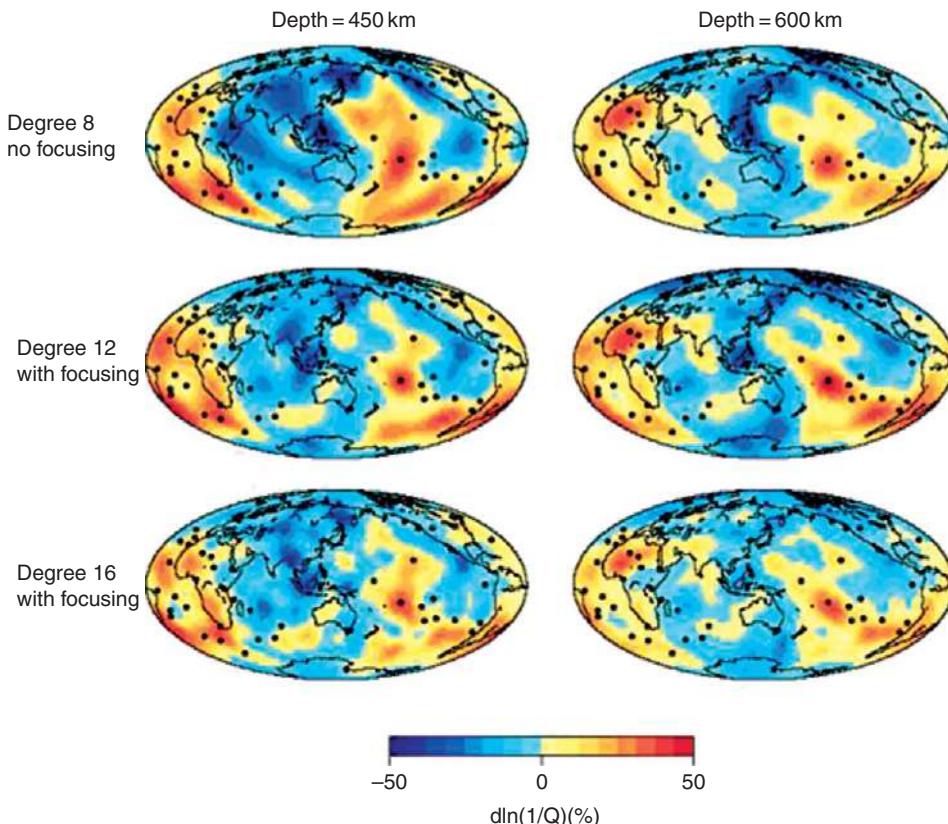


Figure 7 Lateral variations of Q_β in the upper mantle transition zone. (Top) Degree 8 Model QRLW8 (Gung and Romanowicz, 2004). In this relatively low degree model, no corrections for elastic focusing have been included. (Middle/bottom) Inversion of the same three component long period seismograms for a degree 12 model (middle) and a degree 16 model (bottom). In both cases, the waveforms have been corrected for focusing effects before inversion, using an asymptotic higher order formalism (Romanowicz, 1987). The main features of these models, namely strong low Q anomalies in the south Pacific and under Africa, correlated with the hot spot distribution of (Davies, 1990) (black dots) and high Q anomalies under the western Pacific, remain stable, but the low Q features sharpen up in the higher resolution models.

where v is the elastic velocity, Q the quality factor, which may depend on frequency, and the integral is taken along the ray path. In body-wave studies, the frequency dependence of Q needs to be taken into account, because the measurements are performed at higher frequency (typically 0.15–1 Hz for P-waves and 0.05–0.1 Hz for S-waves), closer to the high frequency cutoff in the Earth's absorption band. The frequency dependence of Q is often expressed in terms of an absorption band model (eqn [2]). However, Warren and Shearer (2002) estimated the effect of frequency dependence on the attenuation of P-waves around a period of 1 s, and concluded that neglecting it did not significantly bias their measurements of lateral variations in Q_α . On the other hand, Reid *et al.* (2001) suggested that the frequency dependence might be absorbed in the source terms.

Pairs of phases are selected so as to eliminate as many factors as possible from their spectral amplitude ratio. The differential δt^* can then be obtained by measuring the slope of the remaining spectral ratio as a function of frequency:

$$\ln(A_2/A_1) = -\omega/2(\delta t^*) + \epsilon \quad [13]$$

where ϵ is a constant containing the effects of differential radiation pattern, geometrical spreading, and focusing for the two phases. The assumption of frequency independence of $\delta t^* = t_2^* - t_1^*$ needs to be verified even if dispersion corrections have been applied, and this is usually done by checking the linearity of the slope, as well as the constancy of the phase of the complex spectral ratio.

Because the lateral variations of Q in the lower mantle are thought to be much smaller than in the

upper mantle, the differential t^* thus obtained is attributed to lateral variations of structure in the upper mantle under the bounce point of the reflected phase. Given the steep approach of the reflected rays at the bounce point and the relatively sparse global sampling, these measurements provide information about the average upper mantle lateral variations in Q but have little depth resolution.

This general principle of slope measurement was used by Bhattacharyya *et al.* (1996) and Warren and Shearer (2002). However, these authors used different approaches to correct for potential receiver and source biases. Bhattacharyya *et al.* (1996) considered the spectra of S and SS from the same records, in the distance range 40–120°, and the period range 15–25 s, then estimated the differential t^* by applying a multiple-record stacking technique, grouping the records by bounce point location, and assuming that effects of source, receiver, and path, outside of the common upper mantle path of the SS waves with common bounce location, would average out in the stacks. The bounce point location area over which the stacking was performed were caps of 5° radius, larger than the estimated Fresnel zones of the corresponding reflected waves. These authors used a frequency domain multitaper technique to minimize the effects of finite source duration and near-source or near-receiver structure complexity. They found a correspondence between the cap-averaged t^* and tectonic provinces, with, as expected, lowest attenuation under platforms and shields and highest attenuation under young oceans. In a second step, they inverted for a depth dependent model of Q_μ in the upper mantle, expanded laterally up to degree 8 in spherical harmonics, and assuming three layers in depth (20–220 km, 220–400 km, 400–670 km). Resolution experiments indicated that the best resolved layer was the deepest one, and the two shallower ones could not be distinguished uniquely.

Warren and Shearer (2002), on the other hand, considered independent data sets of P waveforms, in the distance range 40–80°, and PP waveforms in the distance range 80–160°. Working in the frequency domain, they first determined source and receiver terms for the P data set, using an iterative stacking procedure over common sources and common receivers. Then they assumed that the same source and receiver terms could be applied to the PP phases, since the two phases have similar takeoff angles, path lengths, and turning depths, given the distance ranges considered. They thus corrected the PP amplitude

spectra using the source and receiver terms determined from the P spectra and estimated the residual t^* attributed to the upper mantle beneath the bounce point. Finally, to reduce the scatter in the data, they estimated cap averages over nonoverlapping bounce point areas of 5° radius. They too found the highest Q_α (smallest t^*) under shields and platforms and the lowest Q_α (largest t^*) under young oceans. Unlike Bhattacharyya *et al.* (1996), these authors considered, however, that their measurements reflected the average structure over the top 220 km of the mantle and derived the corresponding Q_α averaged over that depth range.

Reid *et al.* (2001) developed a somewhat different method, based on waveform fitting, which they applied to a large data set of SS and S waveforms from seismograms collected in the distance range 50–105° and also to SSS, SS, in the distance range 90–179°. In the process, they included the effects of elastic structure on differential traveltimes of these phases. These authors considered that their data had sensitivity down to 400 km and inverted their t^* data set for a model of Q_μ expanded laterally to degree 8 and in depth, using a spline parametrization with six knots. However, their resolution tests indicated that the depth resolution was poor, and that they could not attribute the lateral variations found to a particular depth.

1.21.6.3 Multiple ScS Studies

Although they do not provide a complete global coverage, the most widely used shear-wave phases for large scale regional mantle attenuation studies have been multiple ScS phases. Measurements of the attenuation of these near-vertical multiply reflected waves are relatively uncontaminated by source, instrument, and geometrical spreading effects. They and their depth phases appear very clearly on transverse seismograms in the ‘reverberative interval’, after the first arriving surface-wave train (Figure 8). In the absence of noise, the transfer function relating ScS_n to ScS_{n+1} is, in the spectral domain:

$$H(\omega) = \exp[-\omega T_0/2Q(\omega)] \cdot \exp[i\theta(\omega, T_0)] \quad [14]$$

where T_0 is the differential travel time between the two phases, θ is a phase function, and $Q(\omega)$ is the quality factor, which is an estimate of the vertically averaged attenuation through the mantle. As in the case of other differential measurements, the estimate of Q_{ScS} is obtained by measuring the slope of the amplitude of the transfer function as a function of frequency.

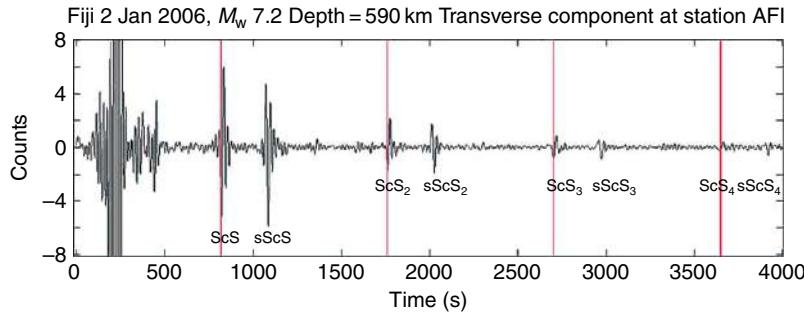


Figure 8 Example of multiple ScS record for a deep earthquake in the Fiji Islands, showing clear multiples out to ScS₄, as well as their depth phases. Courtesy of Ved Lekic.

The stability of the phase spectrum is used as an additional indication of the quality of the measurement.

Early studies used spectral ratios measured on hand-digitized and hand-rotated transverse component seismograms, and provided evidence for large amplitude lateral variations of Q_{ScS} in the mantle (e.g., Press, 1956; Kovach and Anderson, 1964; Sato and Espinosa, 1967; Yoshida and Tsuijura, 1975). Because of the analog records used, and the measurement methods employed, which did not take into consideration the biasing effects of noise, these early estimates are considered to be less accurate than more recent ones. They are also generally biased toward very high values of Q_{ScS} , compared to normal mode results, which has been attributed not only to the effects of noise but also, potentially, to the effect of frequency dependence of Q , as the instruments which produced the records had limited bandwidth. With the advent of digital long period instrumentation, and the development of more sophisticated methods which were better suited for minimizing the effects of noise (e.g., Jordan and Sipkin, 1977; Nakanishi, 1979a), measurements became more accurate. For example, Jordan and Sipkin (1977) introduced a method of phase equalization, by computing cross-correlation between successive ScS multiples, as well as stacking to reduce measurement scatter. Nakanishi (1979a) used a maximum likelihood method to reduce the effects of noise. Most measurements are performed in the frequency band between 10 and 40–60 mHz, where frequency dependence of Q_{ScS} has been found to be negligible (e.g., Sipkin and Jordan, 1979). These studies have confirmed the existence of large lateral variations in Q_{ScS} (e.g., Sipkin and Jordan, 1980; Lay and Wallace, 1983, 1988; Chan and Der, 1988; Revenaugh and Jordan, 1989, 1991; Sipkin and Revenaugh, 1994; Suetsugu, 2001; Gomer and Okal, 2003). The derived average mantle values for

$Q_{\mu} \sim 220$ –240 are, in general, compatible with those obtained from normal modes.

Measurements under oceans, and in the vicinity of subduction zones are more numerous, because of the availability of deep earthquakes and the relatively simple effects of the thin crust at the surface reflection points. Measurements under continents are more difficult, because the effect of crustal multiples at the surface reflection point needs to be taken into account (e.g., Sipkin and Revenaugh, 1994; Isse and Nakanishi, 1997). In order to expand the coverage under continents, it is also necessary to consider shallow earthquakes, for which the reverberation interval is more noisy because of the presence of strong multipathing surface waves.

These studies determined that Q_{ScS} is higher under continents than under ocean basins, on average. Regional variability on relatively short scales has been found in subduction zone regions. In particular, low Q was estimated under the Sea of Japan (e.g., $Q_{ScS} \sim 160$, Nakanishi (1979a)) and under northern South America ($Q_{ScS} \sim 93$, Lay and Wallace (1983)), in regions sampling the upper mantle wedge and/or back-arc region behind subduction zones, which, if primarily attributed to the upper mantle, translates into very low Q . On the other hand, high Q values comparable to continental estimates were obtained on paths sampling through slabs (e.g., $Q_{ScS} \sim 232$, in South America, Lay and Wallace (1983); $Q_{ScS} \sim 226$, under Japan/Kuriles, Nakanishi (1979a); $Q_{ScS} \sim 266 \pm 57$ in Argentina, Sipkin and Jordan (1980)). These older measurements are generally in agreement with a more recent study by Chan and Der (1988), except in the southwest Pacific, where these authors found $Q_{ScS} \sim 214 \pm 42$ compared to the estimate of $Q_{ScS} \sim 157 \pm 17$ Sipkin and Jordan (1980). This may however be due to the way the latter averaged their measurements over an

extended region where strong lateral variations in Q_{ScS} have since been confirmed (Suetsugu, 2001; Gomer and Okal, 2003). Using short epicentral distance data ($< 20^\circ$) filtered between 10 and 50 mHz, Suetsugu (2001) found very low Q under the south Pacific superswell ($Q_{ScS} \sim 70\text{--}80$) whereas Gomer and Okal (2003) found very high Q under the Ontong Java Plateau, also using short distances (10–20°) and a bandpass between 10 and 62.5 mHz.

The lateral variations found in Q_{ScS} are attributed primarily to the upper mantle, because of the much higher Q in the lower mantle, which reduces the effects on multiple ScS of any, even significant, lateral variations (e.g., Warren and Shearer, 2002), and the significant correlation of Q_{ScS} with tectonics. Furthermore, the correlation with travel time anomalies from the same multiple ScS phases suggests that they could be primarily related to lateral variations in temperature.

Caution must be exercised, of course, in attributing all of the Q_{ScS} signal to the upper mantle, in particular if there is a low Q zone at the base of the mantle (e.g., Revenaugh and Jordan, 1991), and significant lateral variations of Q in D''. While attenuation in D'' and its variations have yet to be explored at the global scale, the presence of large variations in velocity imply that at least some lateral variations exist in Q as well. Recently, Fisher and Wysession (2003) showed evidence for the existence of an ~ 600 km wide high-attenuation, low-velocity region in D'' beneath Central America, using spectral ratios of S and ScS phases.

1.21.6.4 Other Body-Wave Studies

High attenuation has been reported in the back of island arcs using other types of body waves. Early estimates were very qualitative (e.g., Barazangi and Isaaks, 1971; Barazangi *et al.*, 1975; Bowman, 1988). More recently, several regional studies (e.g., Flanagan and Wiens, 1990, 1994; Roth *et al.*, 1999, 2000) have utilized shear depth phases from deep earthquakes observed teleseismically or at regional arrays, to obtain constraints on the attenuation in the wedge of upper mantle above different subduction zones. Flanagan and Wiens (1990) measured differential attenuation between sS–S and sScS–ScS phase pairs beneath the Lau back-arc spreading center in the Fiji–Tonga region. Studying the variation of the estimated Q as a function of depth of the source, they found high attenuation in the first 200–300 km, and decreasing attenuation at greater depth. They found very high attenuation ($Q \sim 20\text{--}35$) in the

uppermost mantle beneath the spreading center and somewhat lower attenuation ($Q \sim 50$) beneath older parts of the Lau Basin. Flanagan and Wiens (1994) extended this approach to the study of several inactive back-arc basins in the western Pacific, and confirmed the presence of high attenuation ($Q \sim 40\text{--}50$) in the uppermost mantle (depths less than 160 km), with even lower Q 's (< 40) in the vicinity of the volcanic centers. They also confirmed a systematic increase of Q with depth ($Q \sim 115$ between 160–430 km and $Q \sim 173$ in the transition zone). The frequency band of these two studies was 10–80 mHz.

Following the method of Teng (1968), Roth *et al.* (1999) assembled a data set of differential S–P and P–P attenuation measurements from a temporary local array of broadband land and ocean bottom stations in the Tonga–Fiji region. The data set they assembled allowed them higher resolution compared to teleseismic data because of the geometry of the source-station distribution, the short paths, and the small Fresnel zones compared to teleseismic phases. These authors measured δt from spectral ratios and obtained an estimate of the best fitting Q_α/Q_β ratio as part of the inversion for Q_α and Q_β , assuming that Q is not frequency dependent in the band-pass of their study (0.1–3.5 Hz), which seems to be verified by the data. They confirmed the high attenuation values in the uppermost mantle found previously beneath the spreading center. They then performed a 2-D tomographic inversion, assuming that the structure is uniform in the direction parallel to slab strike. In their model, the slab appears as a high Q zone ($Q_\alpha > 900$) down to at least 400 km, below which it is indistinguishable from the surrounding mantle. An abrupt transition from the high Q slab to the low Q back-arc basin occurs approximately at the Tonga volcanic front. The lowest Q_α values (~ 90) are found directly under the Lau back-arc spreading center. There is also evidence for a North–South trend, with attenuation on average higher by 10% in the northern part of the region. This Q tomographic model correlates well with velocity models in the region. The best fitting ratio Q_α/Q_β is ~ 1.75 , which is in agreement with a loss in bulk about 1/3 that of the loss in shear, assuming a Poisson solid (Figure 9).

A similar study under the northern Philippine Sea, this time using only S–P spectral ratios (Shito and Shibutan, 2003b), found that the Philippine and Izu Bonin slabs also had high Q , and found low Q under the spreading center in the Shikoku Basin. However, the lowest values of Q were found at larger depths

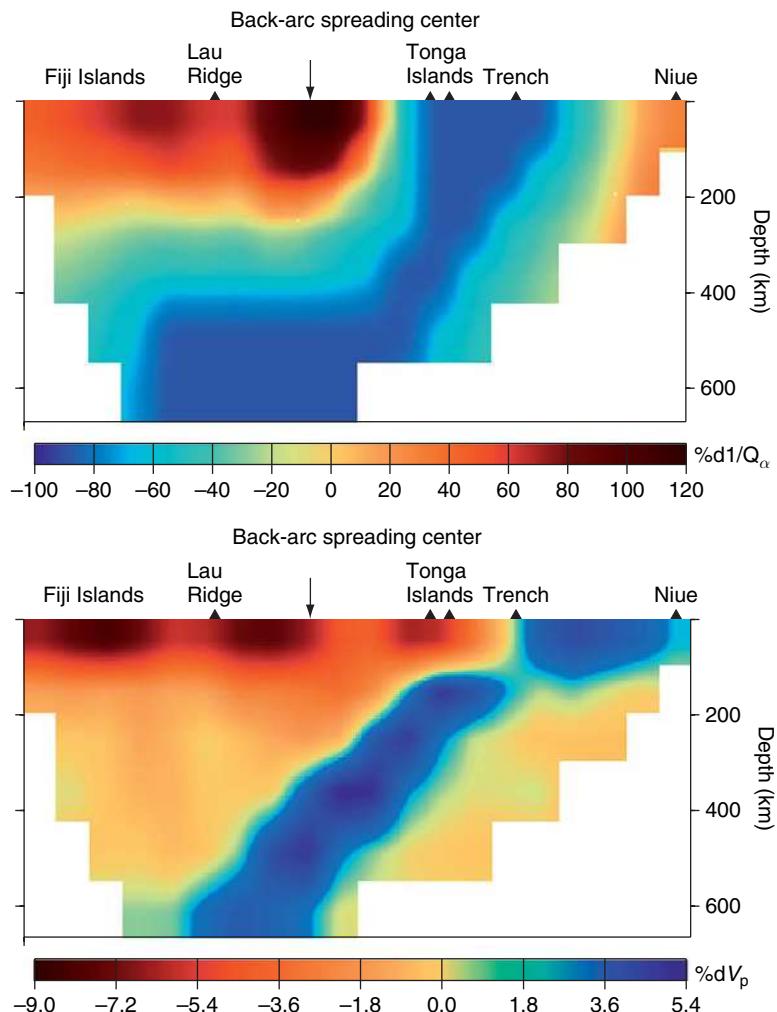


Figure 9 Cross section illustrating lateral variations of structure in the Lau back-arc basin. (Top) Attenuation, (bottom) velocity (V_p). Reproduced from Roth E, Wiens DA and Zhao D (2000) An empirical relationship between seismic attenuation and velocity anomalies in the upper mantle. *Geophysical Research Letters* 27: 601–604.

(250 km) than in the Lau Basin. The authors attributed that to the older age of the Shikoku spreading center.

Just as the upper mantle is found to be highly attenuating under back-arc spreading centers, other studies have investigated mid-ocean ridge systems and found very low Q (Molnar and Oliver, 1969; Solomon, 1973; Sheehan and Solomon, 1992; Ding and Grand, 1993). Sheehan and Solomon (1992) used the pair of teleseismic phases S and SS along the north-Atlantic ridge and found that SS-S differential attenuation decreases with increasing age of the oceanic plate, and that, in order for their measurements to be compatible with surface-wave studies, the high attenuation region must extend into the asthenosphere. Ding and Grand (1993) performed waveform modelling of

multiple S phases (up to S_4) at distances between 30° and 80° along the East Pacific Rise. Because their data have sensitivity to the deep mantle, they found that, in order for their measurements to be compatible with multiple ScS results, a significantly lower average Q in the lower mantle is needed than obtained on average from normal mode measurements, indicating that lateral variations in Q may also exist in the lower mantle. Note that Sipkin and Jordan attributed a lower Q in the Fiji-KIP corridor from multiple ScS measurements to frequency dependence. In the light of the Ding and Grand (1993) study, it seems more likely that the observations of Sipkin and Jordan (1979) could just be due to lower Q 's in the lower mantle, especially as both studies sampled regions of the Pacific Superplume.

In the last decade, there have been increasing efforts to interpret tomographic models of the upper mantle at various scales in terms of temperature, degrees of partial melt, water content, and rock composition, using constraints from elastic and anelastic tomography, heat flow, gravity, and experimental data. Thus, Sobolev *et al.* (1996) found that the Massif Central in France is underlain by a hot mantle body with a potential temperature 100–200°C higher than the upper mantle average. In an interpretation of velocity and Q tomography under the Philippine Sea, Shito and Shibutan (2003a) found that the deeper upper mantle (300–400 km depth) may contain 10–50 times more water than average. Boyd and Sheehan (2005) measured differential t^* of S-phase waveforms from the Rocky Mountain Front broadband network and found a north–south zone of very low Q_μ in the upper mantle beneath the Rocky Mountains. Combining attenuation and velocity data, they inferred that the Colorado Rocky Mountains are supported by low density mantle and a thick crust. On the other hand, comparing their laboratory measurements of Q_μ with global seismological Q models, Faul and Jackson (2005) inferred that the upper mantle low velocity zone could be explained by solid state processes, without invoking partial melting. Lawrence *et al.* (2006) applied a waveform cross-correlation method and cluster analysis to the study of upper mantle P and S-wave attenuation across the North American continent and found that the distribution of attenuation is in general correlated with that of velocity, implying higher temperatures beneath the western tectonic regions than under the more stable east, in agreement with both global and crustal continental scale studies.

In general t^* measurements, as well as surface-wave attenuation measurements are interpreted in terms of anelastic attenuation, however, contributions from scattering can be important and need to be considered. For example, in a study of S-wave amplitude variations under Iceland, (Allen *et al.*, 1999) found that the low velocity cylindrical-shaped plume acts as a lens, causing frequency dependent focusing that dominates over anelastic effects on the amplitudes.

1.21.7 Regional Q Variations in the Crust and Uppermost Mantle

1.21.7.1 Introduction

One of the most interesting aspects of Q in the crystalline crust and upper mantle of the Earth is the large magnitude of its variation from region to

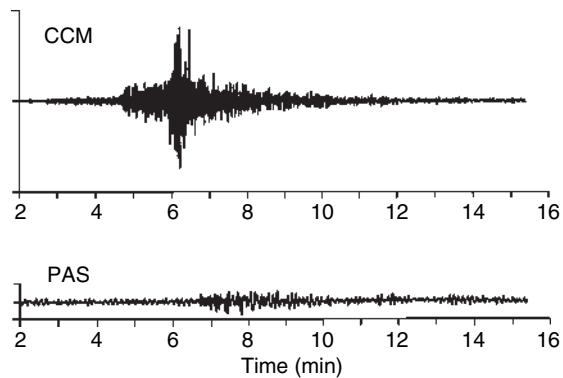


Figure 10 Seismograms recorded at stations CCM (Cathedral Cave, MO) and PAS (Pasadena, CA) for the m_b 4.5 event in southeastern New Mexico that occurred on 2 Jan 1992 at 11:45:35.6 UT. The epicentral distance to CCM (along a relatively high-Q path) is 1256 km and to PAS (along a relatively low-Q path) is 1417 km. From Mitchell BJ (1995) Anelastic structure and evolution of the continental crust and upper mantle from seismic surface wave attenuation. *Reviews of Geophysics* 33: 441–462.

region. Whereas broad-scale seismic velocities vary laterally at those depths by at most 10–15%, Q can vary by an order of magnitude or more. Figure 10 illustrates the large effect that regional Q variations can have on phases that travel through both the upper mantle (P and S waves) and the crust (Lg) by comparing records for paths across the eastern and western United States. Since variations in Q can be so large, seismic-wave attenuation is often able to relate Q variations to variations in geological and geophysical properties that are not easily detected by measurements of seismic velocities. Factors known to contribute to Q variations in the crust and upper mantle include temperature and interstitial fluids.

In this section we will emphasize studies of Q variation conducted over regions sufficiently broad to contribute to our knowledge of crust and upper mantle structure and evolution. In so doing we neglect many studies that have provided useful information on crustal Q over small regions.

1.21.7.2 Q or Attenuation Determinations for Seismic Waves in the Crust

Investigators have employed different methods, phases, and frequency ranges to study the anelastic properties of the crust and upper mantle. At higher frequencies and shorter distances often employed

for crustal studies some researchers have emphasized determinations of intrinsic \mathcal{Q} (\mathcal{Q}_i), some have emphasized the scattering contribution (\mathcal{Q}_s), and some have sought to determine the relative contributions of \mathcal{Q}_i and \mathcal{Q}_s . The importance of scattering became apparent from the groundbreaking work of Aki (1969) who first showed that the codas of various regional phases are composed of scattered waves. His work spawned a large literature on both theoretical and observational aspects of scattering that is discussed in Chapter 1.20.

The contributions of the intrinsic and scattering components to total attenuation, $1/\mathcal{Q}_t$, can be described by

$$\frac{1}{\mathcal{Q}_t} = \frac{1}{\mathcal{Q}_i} + \frac{1}{\mathcal{Q}_s} \quad [15]$$

where \mathcal{Q}_i and \mathcal{Q}_s refer, respectively, to intrinsic and scattering \mathcal{Q} (Dainty, 1981). Richards and Menke (1983) verified that the contributions of intrinsic and scattering attenuation are approximately additive as described by eqn [15]. Seismologists often wish to focus on Earth's intrinsic anelastic structure. To do so they must select a phase or work in a frequency range such that the effect of scattering can either be determined or is small relative to the effect of intrinsic \mathcal{Q} .

This review almost entirely addresses intrinsic \mathcal{Q} , but we will discuss one type of scattered wave (Lg coda) quite extensively. Although Lg coda is considered to contain a large amount of scattered energy, some theoretical and computational studies (discussed later) of scattered S-wave energy suggest that measured \mathcal{Q} values for that wave may largely reflect intrinsic properties of the crust.

All of the measurements that we discuss in this section can be placed in one of two major categories: (1) those in which seismic source effects cancel and (2) those in which assumptions are made about the seismic source spectrum. For category (1) the cancellation is most often achieved by using ratios of amplitudes recorded by two or more instruments. But it has also been achieved using ratios of amplitudes from different portions of a single time series. The primary application of the latter type of cancellation has been for the determination of Lg coda \mathcal{Q} (\mathcal{Q}_{Lg}^C). We divide this category into three parts that address regional phases, fundamental-mode surface waves, and Lg coda. Category (2) permits studies of \mathcal{Q} using a single station, but requires knowledge of the source depth, source mechanism, and velocity model for the source region. We divide this category into

two parts, one addressing regional phases and the other fundamental-mode surface waves.

Seismologists have measured the dispersion of body waves due to anelasticity and have successfully used that dispersion to infer values for body-wave \mathcal{Q} . We will not cover that topic because it has been the subject of relatively few studies and has been applied mainly to small regions.

The following subsections discuss methodology and present some representative results using the cited methods as applied to the crust. Because the number of studies for continents is overwhelmingly greater than for oceans, most of the discussion will pertain to continental regions. A few studies will, however, be described for oceanic regions.

1.21.7.2.1 Spectral decay methods in which source effects cancel – Regional phases

Regional phases include P, S, and Lg phases recorded at distances less than about 1000 km. The early portion of this section mostly covers \mathcal{Q} determinations for P and S phases but in cases where researchers measured \mathcal{Q}_{Lg} , as well as \mathcal{Q}_P and \mathcal{Q}_S all results will be presented. The latter part of this subsection will discuss Lg exclusively since this phase has been widely used in recent years to study variations of \mathcal{Q} over broad regions.

In order to cancel the source effects, several methods utilize stations that lie on a common great-circle path with the seismic source but other methods are able to dispense with the need for great-circle path propagation. All studies, however, need to first remove the effect of wave-front spreading before measuring amplitude changes due to attenuation. In this subsection we will restrict our discussion to studies at frequencies that pertain totally or predominantly to the crust with occasional reference to the upper mantle for studies that include results for both the crust and upper mantle.

Regional and near-distance studies of P- and S-wave attenuation (or their respective quality factors \mathcal{Q}_P and \mathcal{Q}_S) often cancel the source by utilizing several stations at varying distances (e.g., Nuttl, 1978, 1980; Thouvenot, 1983; Carpenter and Sanford, 1985)

More recently, amplitude measurements in which both the source and sensor reside in boreholes beneath any sediments or weathered layers have provided much-improved estimates of \mathcal{Q}_P and \mathcal{Q}_S . Abercrombie (1997) used borehole recordings to determine spectral ratios of direct P- to S-waves

and found that they are well modeled with a frequency-independent Q_p distribution in the borehole increasing from $Q_p \sim 26\text{--}133$ at depths between the upper 300 m and 1.5–3 km. Q_s increased from 15 to 47 in the same depth range. Abercrombie (2000), in another borehole study near the San Andreas Fault, found that attenuation on the northeastern side of the fault is about twice that on the southwestern side.

Lg is very useful for Q studies both because it travels predominantly in the crustal waveguide, providing Q information for a known depth interval, and is a large and easily recognizable phase. Even relatively small earthquakes can generate useable records; thus data, in many regions is plentiful. Lg can be represented by a superposition of many higher-mode surface waves or by a composite of rays multiply reflected in the crust. It is usually assumed that Q_{Lg} follows a power-law frequency dependence, $Q = Q_0 f^\eta$, where Q_0 is the value of Q_{Lg} at a reference frequency and η is the frequency dependence parameter at that frequency. Lg travels through continental crust at velocities between about 3.2 and 3.6 km s⁻¹ and is usually followed by a coda of variable duration. That coda is discussed in a later subsection. Since the Lg wave consists of many higher modes, it is often assumed that, even though the radiation patterns for individual modes differ from one another, the totality of modes combine to form a source radiation pattern that is approximately circular. If that assumption is correct the source and stations need not necessarily line up along the same great-circle path to estimate Q .

Early determinations of Q_{Lg} , after correcting for wave-front spreading, compared observed attenuation with distance with theoretically predicted attenuation for the Lg phase and chose the theoretical curve (predicted by selected values of Q_0 and η) which agreed best with observations (e.g., Nuttli, 1973; Street, 1976; Bollinger, 1979; Hasegawa, 1985; Campillo *et al.*, 1985; Chavez and Priestley, 1986; Chun *et al.*, 1987).

Benz *et al.* (1997) studied four regions (southern California, the Basin and Range province, the central United States, and the northeastern United States and southeastern Canada) of North America in the frequency range 0.5–14.0 Hz. They found that, at 1 Hz, Q_{Lg} varies from about 187 in southern California to 1052 in the northeastern United States and southeastern Canada and about 1291 in the central United States. They also found that the frequency dependence of Q also varies regionally, being relatively high ($\alpha \sim 0.55\text{--}0.56$) in southern California and the

Basin and Range and smaller ($\alpha \sim 0\text{--}0.22$) in the other three regions.

Xie and Mitchell (1990a) applied a stacking method to many two-station measurements of Q_{Lg} at 1 Hz frequency in the Basin and Range province. This method, first developed for single-station determinations of Lg coda $Q(Lg^C)$, will be discussed in the subsection on Lg coda. They found that $Q_{Lg} = (275 \pm 50)f^{(0.5 \pm 0.2)}$ and $Q_{Lg}^C = (268 \pm 50)f^{(0.5 \pm 0.2)}$.

Xie *et al.* (2004) extended the method to multiple pairs of stations in instrument arrays across the Tibetan Plateau. For an array in central Tibet (INDEPTH III) they found very low values for Q_0 (~ 90) that they attributed to very high temperatures and partial melt the crust. An array in southern Tibet yielded even lower values, ~ 60 , for Q_0 in the northern portion of the array but higher values (~ 100) in a central portion and much higher values (>300) in the southernmost portion. Xie *et al.* (2006) used a two-station method to obtain more than 5000 spectral ratios for 594 interstation paths and obtained Q_0 and η for those paths. They obtained tomographic maps of those values that are described in the subsection on tomographic mapping.

1.21.7.2.2 Spectral decay methods in which source effects cancel – Fundamental-mode surface waves

When using fundamental-mode surface waves to study lateral variations of crustal Q_μ we need to measure the attenuation of relatively short-period (5–100 s) amplitudes. In continents, these waves may be biased by systematic errors associated with laterally varying elastic properties along the path of travel, as discussed earlier. Two-station studies of fundamental-mode surface waves are especially susceptible to these types of error because researchers might incorrectly assume great-circle propagation along a path through the source and the two stations. Non-great-circle propagation would mean that surface-wave energy arriving at two stations along different great-circle paths could originate at different portions of the source radiation pattern. If that pattern is not circular the two-station method can produce attenuation coefficient values that are either too high or too low, depending on the points of the radiation pattern at which the waves originate.

Measurements for the situation in which a source and two stations lie approximately on the same great-circle path have often been used to determine surface-wave attenuation. The method was described by Tsai and Aki (1969) and determines the average

surface-wave \underline{Q} between the two stations after correcting for the different wave front spreading factors at the two stations. They applied the method to many two-station paths from the Parkfield, California earthquake of 28 Jun 1966 and, using the formulation of Anderson *et al.* (1965), obtained a frequency-independent model of intrinsic shear-wave $\underline{Q}(\underline{Q}_\mu)$ with a low- \underline{Q} zone that coincided with the Gutenberg low-velocity zone in the upper mantle. Love-wave \underline{Q} was greater than 800 and Rayleigh-wave \underline{Q} was greater than 1000 in the period range 20–25 s.

Other studies using that method to obtain \underline{Q}_μ models at crustal and uppermost mantle depths include Hwang and Mitchell (1987) for several stable and tectonically active regions of the world, Al-Khatib and Mitchell (1991) for the western United States and Cong and Mitchell (1998) for the Middle East.

Models have also been obtained in which \underline{Q}_μ varies with frequency. That frequency dependence is described by the relation $\underline{Q}_\mu = \underline{Q}_o f^\zeta$ where ζ may vary with frequency (Mitchell, 1975) and/or with depth (Mitchell and Xie, 1994). The inversion process for \underline{Q}_μ in those cases requires appropriate extensions of the Anderson *et al.* (1965) equations. The process requires both fundamental-mode surface-wave attenuation data and \underline{Q} or attenuation information for either an individual higher mode or the combination of higher modes that form the Lg phase. The process proceeds by assuming a simple one- or two-layer distribution of ζ and inverting the fundamental-mode data for a \underline{Q}_μ model. ζ is adjusted until a \underline{Q}_μ model is obtained that explains both the fundamental-mode and higher-mode attenuation data. Mitchell and Xie (1994) applied the method to the Basin and Range province of the western United States. Example \underline{Q}_μ models for which ζ varies with depth (Mitchell and Xie, 1994) appear in Figure 11.

Other surface-wave studies for which the source is cancelled are those that use many stations at various distances and azimuths and simultaneously solve for surface-wave attenuation coefficient values and seismic moments for particular periods by linear least squares. Tryggvason (1965) first did this, as described in our section on early studies, using explosions and assuming circular radiation patterns. Tsai and Aki (1969) extended this method to use earthquake sources, and applied it to surface waves generated by the 28 Jun 1966 Parkfield, California earthquake. This process was later applied to the central United States (Mitchell, 1973; Herrmann and Mitchell, 1975), and the Basin and Range province of the western United States (Patton and Taylor, 1989).

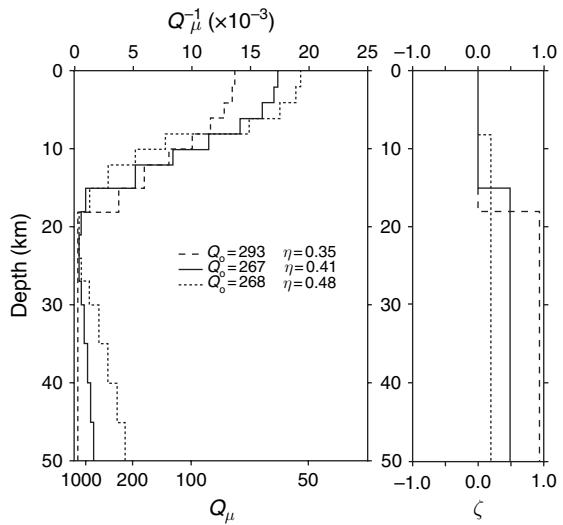


Figure 11 (Left) Three \underline{Q}_μ models resulting from inversion of Rayleigh-wave attenuation coefficient data from the Basin and Range Province. The numbers refer to the value of Q_o and η predicted by three models for Q_{LG} . (Right) Three selected models for the variation of Q_μ frequency dependence with depth in the crust of the Basin and Range province. Each of these depth distributions was fixed during inversions that produced Q_μ models. Reproduced from Mitchell BJ and Xie J (1994) Attenuation of multiphase surface waves in the Basin and Range province. Part III: Inversion for crustal anelasticity. *Geophysical Journal International* 116: 468–484, with permission from Blackwell Publishing.

A nonlinear variation of the Tsai and Aki method (Mitchell, 1975), represents a nuclear explosion with strain release by a superposition of an explosion (with a circular radiation pattern) and a vertical strike-slip fault (represented by a horizontal double couple). Variations of the orientation of the double couple and its strength relative to the explosion produce a wide variety of radiation patterns. The inversion solves for the moment of the explosion, the orientation of the double couple, the strength of the double couple relative to the explosion and an average attenuation coefficient value for each period of interest. Mitchell applied the method to two nuclear events in Colorado as recorded by stations throughout the United States and found that \underline{Q}_μ in the upper crust of the eastern United States is about twice as high as it is in the western United States at surface-wave frequencies.

The first attempts at mapping regional variations of attenuation or \underline{Q} utilized crude regionalizations (two or three regions) based upon broad-scale geological or geophysical information. Studies have produced

models for Eurasia (Yacoub and Mitchell, 1977) using the method of Mitchell (1975), and for the Pacific (Canas and Mitchell, 1978) and Atlantic (Canas and Mitchell, 1981) using the two-station method.

1.21.7.2.3 Spectral decay methods in which source effects cancel – Lg coda

Lg coda, like direct Lg, is sensitive to properties through a known depth range (the crust) in which it travels and is a large amplitude phase for which data are plentiful. In addition, since the coda of Lg is comprised of scattered energy, it can continue to oscillate for several hundred seconds following the onset of the direct Lg phase, thus making it possible to stack spectral amplitudes for many pairs of time windows to make a \mathcal{Q} estimate. Other positive aspects of using Lg coda for \mathcal{Q} studies are that the averaging effect of scattering stabilizes $\mathcal{Q}_{\text{Lg}}^{\text{C}}$ determinations and, if stacking methods are utilized to determine \mathcal{Q} for Lg coda, site effects cancel (Xie and Mitchell, 1990a).

Two methods have been applied to Lg coda to make \mathcal{Q} determinations. The first of these was developed by Herrmann (1980) and applied by Singh and Herrmann (1983) to data in the United States. The method extended the coda theory of Aki (1969) utilizing the idea that coda dispersion is due to the combined effects of the instrument response and the \mathcal{Q} filter of the Earth. The two studies provided new approximations for the relative variation of \mathcal{Q} across the United States. Herrmann later realized, however, that his method did not take into consideration the broadband nature of the recorded signal and overestimates \mathcal{Q} by about 30% (R. B. Herrmann, personal communication).

Xie and Nutti (1988) introduced the stacked spectral ratio (SSR) method which stacks spectra from several pairs of windows along the coda of Lg. That process leads to

$$R_k = f^{1-\eta} / \mathcal{Q}_o \quad [16]$$

as the expression for the SSR, or in logarithmic form

$$\log R_k = (1-\eta) \log f_k - \log \mathcal{Q}_o + e \quad [17]$$

from which \mathcal{Q}_o and η can be obtained by linear regression. f_k , \mathcal{Q}_o , η , and e in these equations are, respectively, a discrete frequency, the value of \mathcal{Q} at 1 Hz, the frequency dependence of \mathcal{Q} at frequencies near 1 Hz, and an estimate for random error. This stacking process provides stable estimates of \mathcal{Q}_o and η with standard errors sufficiently low to allow tomographic mapping of those quantities. A detailed

description of the SSR method appears in Xie and Nutti (1988) and more briefly in Mitchell *et al.* (1997)

Figure 12 shows an example of Lg coda and its associated SSR for a relatively high- \mathcal{Q} path in India, which can be fit over a broad frequency range with a straight line on a log–log plot. The value at 1 Hz provides an estimate of $1/\mathcal{Q}$ at that frequency and the slope of the line gives an estimate for η . Inversions of sets of those values over a broad region can yield tomographic maps of those quantities.

Past studies have shown that several factors may contribute to reductions in \mathcal{Q} ; these include thick accumulations of young sediments (Mitchell and Hwang, 1987) and the presence of a velocity gradient rather than a sharp interface at the core–mantle boundary (Bowman and Kennett, 1991; Mitchell *et al.*, 1998). In addition, decreasing depth of the Moho in the direction of Lg travel or undulations of the Moho surface can be expected to decrease measured \mathcal{Q}_{Lg} or $\mathcal{Q}_{\text{Lg}}^{\text{C}}$ whereas increasing depth would produce larger values. To our knowledge this effect has not been quantitatively studied and is expected to be small over large regions. These factors may cause determinations of correlation coefficients between \mathcal{Q}_{Lg} or $\mathcal{Q}_{\text{Lg}}^{\text{C}}$ and various crustal or mantle properties to be relatively low whenever they are determined (e.g., Zhang and Lay, 1994; Artemieva *et al.*, 2004).

1.21.7.2.4 Spectral decay methods for which assumptions are made about the source spectrum – Regional phases

Hough *et al.* (1988) studied S-waves traveling over relatively short distances near Anza, California, and defined the instrument-corrected acceleration spectrum at a station located a distance r from the source as

$$A(r, f) = A_o e^{-\pi t^*} \quad [18]$$

where t^* is defined in eqn [12]. For crustal studies it is common to assume that \mathcal{Q} is constant along the path, in which case

$$t^* = \frac{t}{\mathcal{Q}} \quad [19]$$

where t is the travel time.

Hough *et al.* (1988) defined A_o as

$$A_o = (2\pi f)^2 S(f) G(r, f) \quad [20]$$

where $S(f)$ is the source displacement spectrum and $G(r, f)$ is the geometrical spreading factor which, if

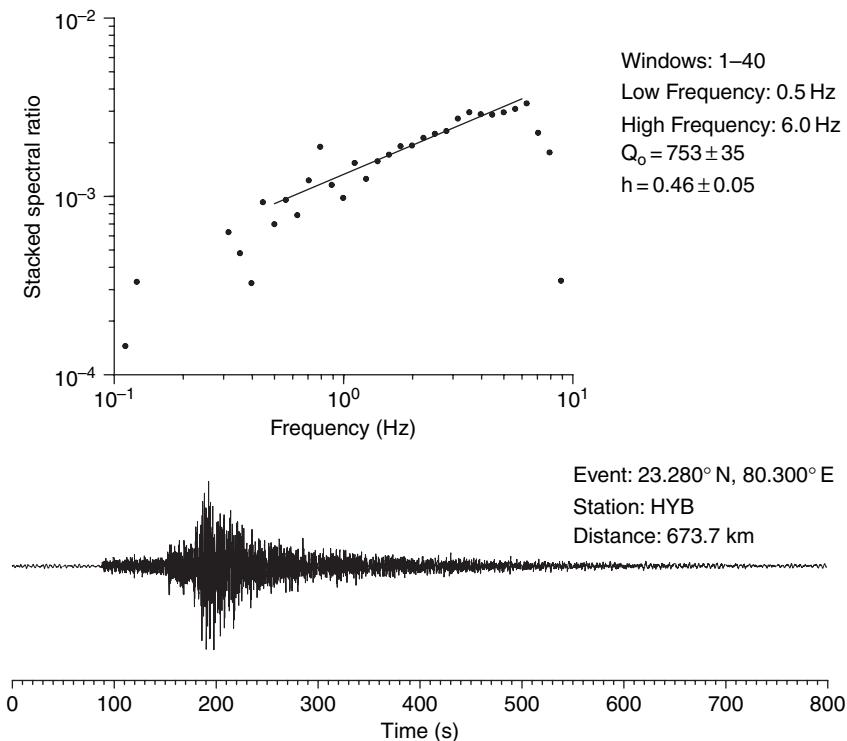


Figure 12 (Bottom) Seismogram, (Top) stacked spectral ratio (SSR) as a function of frequency for a relatively high-Q path in India.

we assume frequency-independent propagation in a homogeneous medium, is $1/r$ for body waves. At higher frequencies, these methods assume a spectral falloff rate (such as ω^{-2} or ω^{-3}) and attribute additional falloff to attenuation. Since a large body of data supports the ω^{-2} , or Brune, model (Brune, 1970) that is the one most commonly used. Taking the natural logarithm of eqn [18] leaves

$$\ln A(f) = \ln A_0 - \pi f t^* \quad [21]$$

For the frequency-independent case, this equation defines a straight line with an intercept of $\ln A_0$ and a slope of $-\pi t^*/Q_0$. Anderson and Hough (1984) hypothesized that, to first order, the shape of the acceleration spectrum at high frequencies can be described by

$$\alpha(f) = A_0 e^{-\pi \kappa f} f > f_E \quad [22]$$

where f_E is the frequency above which the spectral shape is indistinguishable from spectral decay and A_0 depends on source properties and epicentral distance. They found that κ increased slowly with distance, an observation consistent with a Q model of the crust that increases with depth in its shallow layers and that it was systematically smaller on rock sites than at

alluvial sites. Hough *et al.* (1988) studied κ as a function of hypocentral distance, as well as site and source characteristics, and found that $\kappa(0)$ differed for sites at Anza and the Imperial Valley in California but that $d\kappa/dr$ was similar for the two regions. Their interpretation was that $\kappa(0)$ was a component of attenuation that reflects Q_i in the shallow portion of the crust while $d\kappa/dr$ was due to regional structure at great depth. This method was applied to various regions in the world including the Canadian Shield (Hasegawa, 1974), the Pyrenees (Modiano and Hatzfeld, 1982), the New Madrid zone of the central United States (Al-Shukri *et al.*, 1988), and eastern Asia (Phillips *et al.*, 2000).

Shi *et al.* (1996) studied Q_{Lg} variation for five tectonically different regions of the northeastern United States. They used eight pairs of co-located earthquakes to determine accurate source spectrum corner frequencies by applying an empirical Green's function method to Pg and Lg or Sg phases. Based upon the corner frequencies, Sg or Lg displacement spectra were used to obtain values of Q and η values for 87 event-station paths at frequencies between 1 and 30 Hz. The 1 Hz Q_0 values for the five regions vary between 561 and 905 while η varies between 0.40 and 0.47.

1.21.7.2.5 Spectral decay methods for which assumptions are made about the source spectrum – Fundamental-mode surface waves

A multimode spectral method has yielded simple crustal models (two or three layers) of shear-wave $\mathcal{Q}(\mathcal{Q}_\mu)$ in a few regions. The method assumes a flat source spectrum and tries to match theoretical amplitude spectra to two sets of observed spectral amplitude data, one corresponding to the fundamental mode and the other to the superposition of higher modes that forms the longer-period (3–10 s) component of the Lg phase. The higher modes travel faster than all but the longest-period fundamental-mode energy observed on records for relatively small events that are used with this method.

The first study using this method (Cheng and Mitchell, 1981) compared upper crustal \mathcal{Q}_μ for three regions of North America and found values of 275 for the eastern United States, 160 for the Colorado Plateau, and 85 for the Basin and Range province. Kijko and Mitchell (1983) applied the method to the Barents Shelf, a region of relatively high- \mathcal{Q} crystalline crust overlain by low- \mathcal{Q} sediments. They found the method to be sensitive to \mathcal{Q}_μ in the sediments and upper crust but insensitive to \mathcal{Q}_μ in the lower crust and to P-wave \mathcal{Q} at all depths. Cong and Mitchell (1998) obtained models in which \mathcal{Q}_μ is very low at all depths beneath the Iran/Turkish Plateaus and somewhat higher, but still much lower than expected beneath the Arabian Peninsula. Models they obtained using the multimode method, agree well with those they obtained using the two-station method.

Jemberie and Mitchell (2004) applied the method to China and peripheral regions and obtained three-layer crustal models with low \mathcal{Q}_μ and wide variation across China. Values decrease with depth beneath regions such as southeastern China and increase with depth beneath other regions such as the eastern Tibetan Plateau.

1.21.7.3 Tomographic Mapping of Crustal Q

Seismologists are currently attempting to map variations of \mathcal{Q} and its frequency variation in the Earth in as much detail as possible. For continents, researchers have obtained tomographic maps for several broad regions using Lg coda, the direct Lg phase and surface waves. Studies using P and S-waves have yielded important results in regions where earth quakes and

recording stations are plentiful. Studies of even smaller regions, such as volcanoes and geothermal areas, have utilized P- and S-waves (e.g., Hough *et al.*, 1999). In this review, we will restrict our discussion to the more broad-scale studies.

An earlier section described three early regionalized studies of surface-wave attenuation in the late 1970s and early 1980s, one for continental paths and two for oceanic paths in which the Eurasian continent, the Pacific Ocean, and Atlantic Ocean were divided into two or three regions. Since then tomographic mapping using Lg coda has made possible a much finer regionalization of crustal \mathcal{Q} in continents. This section will discuss tomography results for continents and for one oceanic region using either direct Lg, fundamental-mode surface waves, P- and S-waves.

We emphasize Lg coda since tomographic maps of \mathcal{Q}_{Lg}^C , all obtained for the same frequency, and using the same methodology, are available for all continents except Antarctica. This commonality in phase, frequency, and method allows us to compare \mathcal{Q} from one continent to that in others and also to various geophysical and geological properties. These comparisons contribute to our understanding of the mechanisms for seismic-wave attenuation in the crust.

Earlier sections have indicated that Lg coda has several properties that make it useful for tomographic studies. First, it is usually a large amplitude phase making it easily available for study in most regions of the world. Second, it is a scattered wave and the averaging effect of that scattering makes Lg coda relatively insensitive to focusing. Third, the SSR method used to determine \mathcal{Q}_o and η tends to cancel site effects. Fourth, although it is a scattered wave, measurements of \mathcal{Q} for seismic coda have been shown theoretically and computationally to yield measures of intrinsic \mathcal{Q} (e.g., Frankel and Wennerberg, 1987; Mitchell, 1995; Sarker and Abers, 1999). If that is correct researchers can interpret \mathcal{Q} variation in terms of Earth structure and evolution. Other studies, however, (e.g., Aki, 1980; Gusev and Abubakirov, 1996) attribute energy loss to scattering. The mechanism, at this point must therefore be considered controversial.

As indicated earlier, Lg coda $\mathcal{Q}(\mathcal{Q}_{Lg}^C)$ is typically assumed to follow a power-law frequency dependence, $\mathcal{Q}_{Lg}^C = \mathcal{Q}_o f^\eta$, where \mathcal{Q}_o is the \mathcal{Q} value at 1 Hz and η is the frequency dependence of \mathcal{Q} near 1 Hz. Tomographic maps of the 1 Hz values of $\mathcal{Q}_{Lg}^C(\mathcal{Q}_o$ and η) with nearly continent-wide coverage are now

available for Eurasia (Mitchell *et al.*, 1997, 2007), Africa (Xie and Mitchell, 1990b), South America (DeSouza and Mitchell, 1998), and Australia (Mitchell *et al.*, 1998). In North America, broad-scale determinations of Q_{Lg}^C are currently restricted to the United States (Baqer and Mitchell, 1998). These studies have shown a wide range of average Q_o values for different continents and a very wide range within each continent. Average Q_o tend to be highest in continents that contain the most old stable cratonic regions that have not undergone later tectonic or orogenic activity (e.g., Africa and South America).

Tomographic studies have also been completed for more restricted regions using the direct Lg phase in Eurasia, North America, and South America and high-resolution tomographic maps of Q for P- and S-waves are available for southern California. For oceanic regions, tomographic mapping of Q variations, to our knowledge, is currently available only for P waves in one broad portion of the East Pacific Rise (Wilcock *et al.*, 1995).

Sarker and Abers (1998) showed that, for comparative studies, it is important that researchers use the same phase and methodology in comparative Q studies. The Lg coda Q maps presented here adhere to that principle; thus the continental-scale maps of Q_o and η for Lg coda at 1 Hz that are available can be considered to provide the closest thing to global Q coverage at crustal depth that currently exists. The maps also present the possibility for comparisons of Q_o variation patterns with variations of seismic velocity, temperature, plate subduction, seismicity, the surface velocity field, and tectonics when that information is available.

A discussion of the inversion method for mapping Q_o and η appears, in detail, in Xie and Mitchell (1990b), and more briefly, in Mitchell *et al.* (1997). The method assumes that the area occupied by the scattered energy of recorded Lg coda can be approximated by an ellipse with the source at one focus and the recording station at the other, as was shown theoretically by Malin (1978) to be the case for single scattering.

Xie and Mitchell (1990b) utilized a back-projection algorithm (Humphreys and Clayton, 1988) to develop a methodology for deriving tomographic images of Q_o and η over broad regions using a number of Q_o or η values determined from observed ground motion. Figures 13(a), 14(a), 15(a), 16(a), and 17(a) show the ellipses that approximate data coverage for the event-station pairs used in Q_{Lg}^C studies of Eurasia, Africa, South America, Australia, and

the United States. The inversion process assumes that each ellipse approximates the spatial coverage of scattered energy comprising late Lg coda. The areas of the ellipses grow larger with increasing lag time of the Lg coda components. The ellipses in the figure are plotted for maximum lag times used in the determination of Q_o and η . Ideally, each inversion should utilize many ellipses that are oriented in various directions and exhibit considerable overlap in order to obtain the redundancy needed to obtain the best possible resolution for features of interest. Xie and Mitchell (1990b) discuss the procedure in detail, presenting methods for obtaining standard errors for Q_o and η and for estimating spatial resolution.

Because Lg coda consists of scattered energy, it must be distributed, for each event-station pair, over an area surrounding the great-circle path between the source and receiver. Because of this areal coverage, our maps may not include effects of Lg blockage in regions where such blockage has been reported. We may have no data from blocked paths, but are likely to have other paths, such as those subparallel to the blocking feature or for which the source or recording station, represented by one focus of the scattering ellipse, lies near the blocking feature. In both cases portions of the scattering ellipses may overlap the blocking feature, but that feature will not substantially contribute to the values we obtain for Q_o and η . A comparison of mapped Q_o for all continents (Figures 13(b), 14(b), 15(b), 16(b) and 17(b)) shows that it is typically highest in the stable portions of continents and lowest in regions that are, or recently have been, tectonically active. Exceptions occur, however, especially for stable regions. For instance, the Arabian Peninsula, although being a stable platform shows Q_o variations between 300 and 450, values that are one-half or less of maximum values in other Eurasian platforms. Other regions showing lower than expected Q_o include the Siberian trap region of northern Siberia and the cratonic regions of Australia.

The frequency dependence values of $Q_{Lg}^C(\eta)$ in Figures 13(c), 14(c), 15(c), 16(c), and 17(c) appear to show consistent relationships to Q_o in some individual continents. For instance, in both Africa and South America, high- Q regions are typically regions of low η . That same relationship, however, does not occur consistently in Eurasia, Australia, or the United States. η is high, for instance, throughout much of the northern portions of Eurasia where Q_o is mostly high but is low in California, Kamchatka, and a portion of southeast Asia where Q_o is very low.

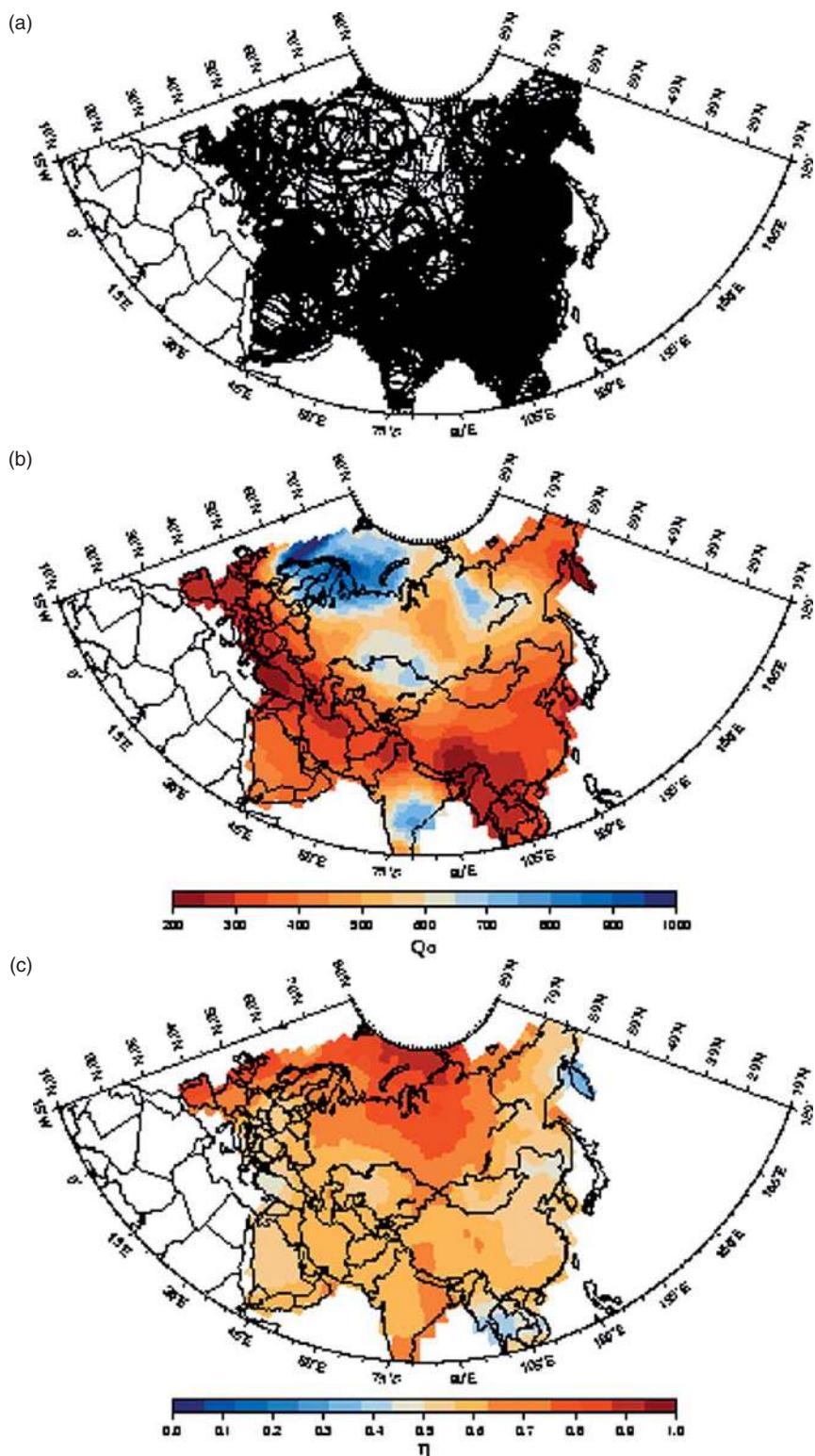


Figure 13 (a) A scattering ellipse map, (b) a Q_o map, and (c) an η map for Eurasia. Adapted from Mitchell BJ, Cong L, and Ekström G (2007) A continent-wide 1-Hz map of Lg coda Q variation across Eurasia and its implications for lithospheric evolution. *Journal of Geophysical Research* (in review).

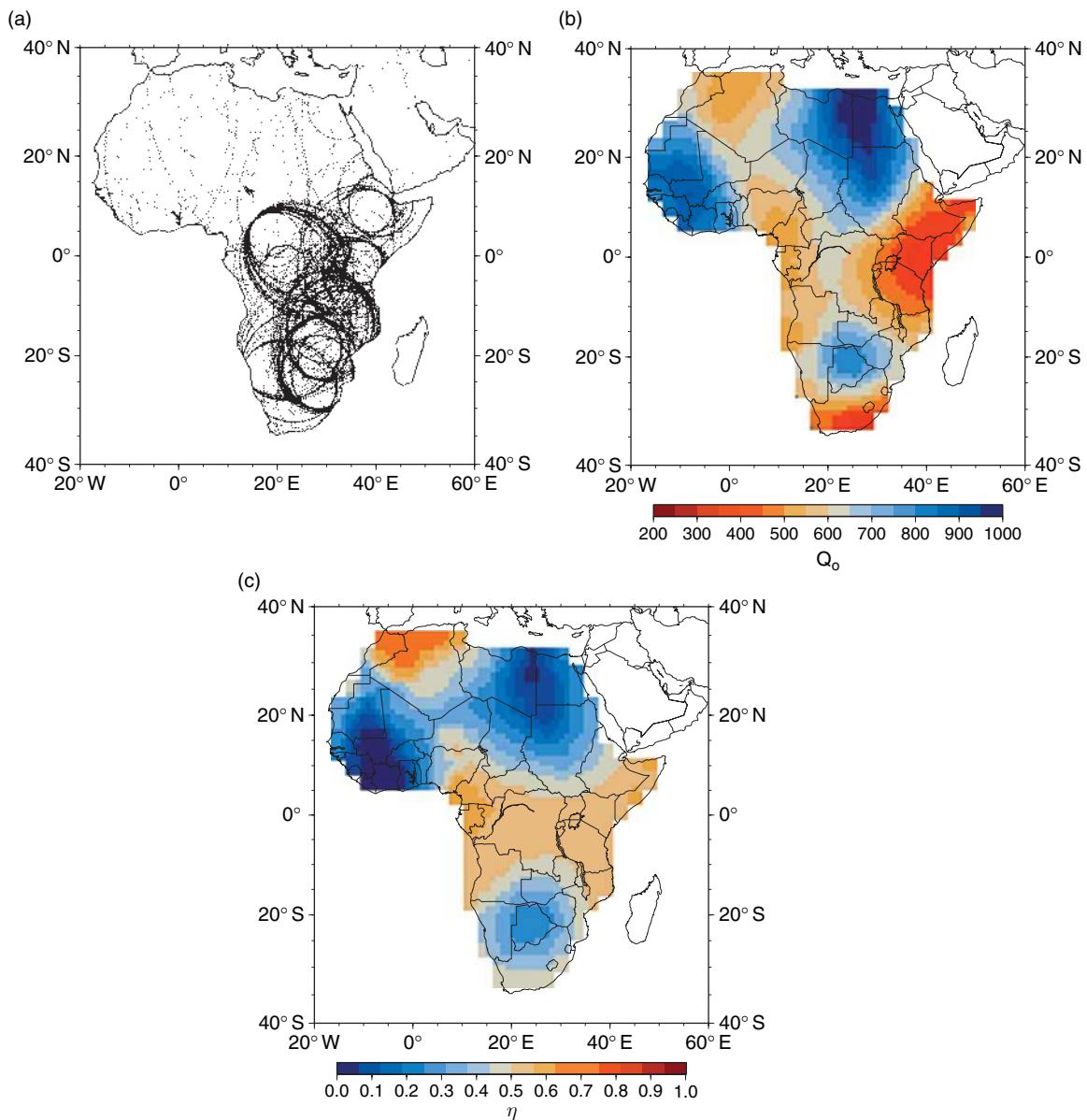


Figure 14 (a) A scattering ellipse map, (b) a Q_o map, and (c) an η map for Africa. Adapted from Xie J and Mitchell BJ (1990b) A back-projection method for imaging large-scale lateral variations of Lg coda Q with application to continental Africa. *Geophysical Journal International* 100: 161–181.

1.21.7.3.1 Q_{Lg}^C , Q_{Lg} , and Q_μ tomography in regions of Eurasia

Figure 13 shows maps of data coverage, Q_o , and η across most of Eurasia (Mitchell *et al.*, 2007). These maps represent a major increase in data coverage for northeastern Siberia, southeastern Asia, India, and Spain, compared to those of an earlier study (Mitchell *et al.*, 1997) and provide additional redundancy in regions where there was earlier coverage. As indicated by Figure 13(a), the data coverage is

excellent for virtually all of Eurasia. Low Q_o values extend through the Tethysides belt that extends across southern Eurasia from western Europe to eastern China and its southern portions appear to be related to subduction processes occurring at the present time. Q_o is generally high in the platforms of northern Eurasia and India (600–950). It is, however, low in the Kamchatka Peninsula and regions directly north of there which, like the Tethysides region, are seismically active. A conspicuous region of relatively

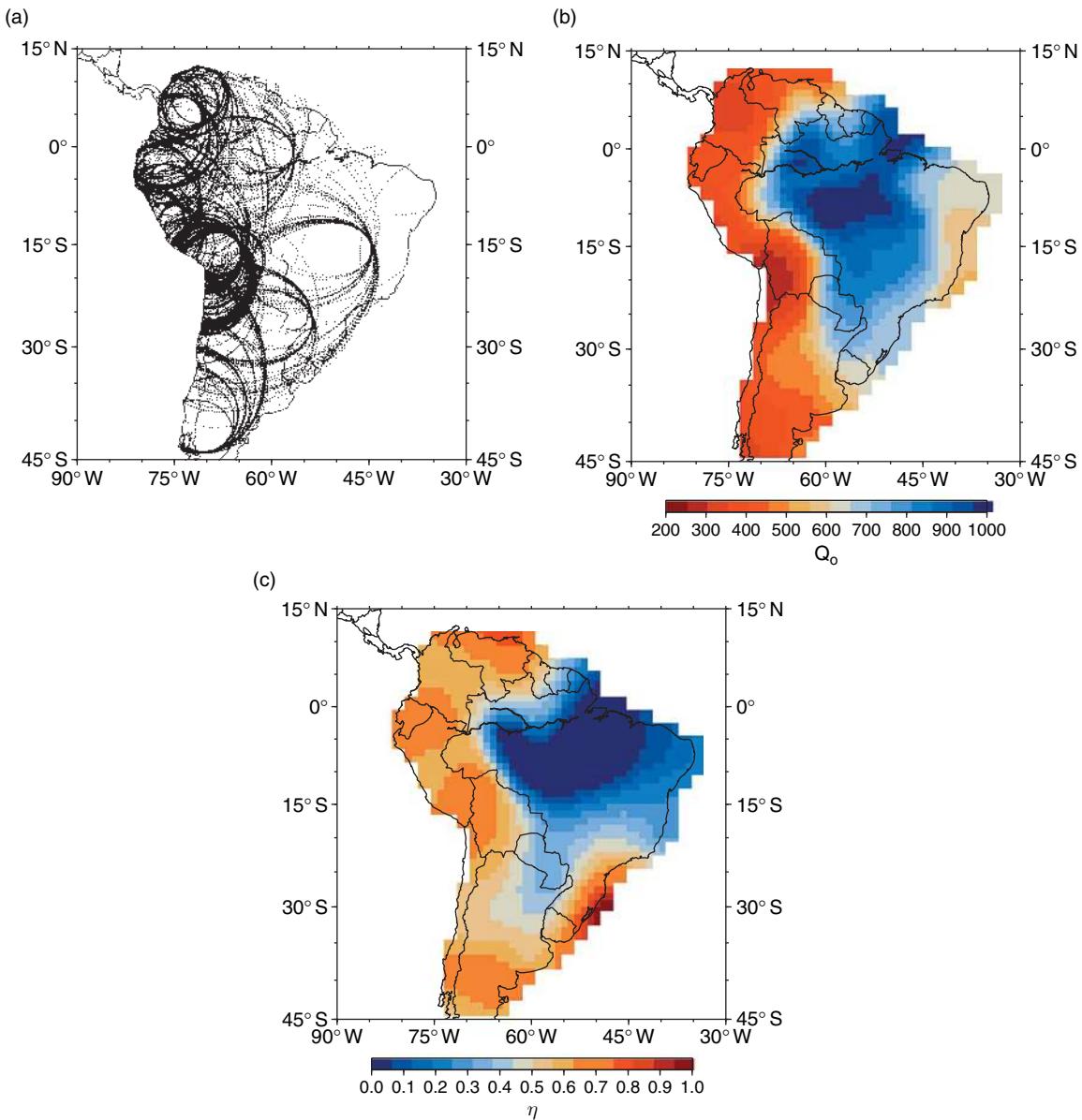


Figure 15 (a) A scattering ellipse map, (b) a Q_o map, and (c) an η map for South America. Adapted from DeSouza JL and Mitchell BJ (1998) Lg coda Q variations across South America and their relation to crustal evolution. *Pure and Applied Geophysics* 153: 587–612.

low Q_o lies in central Siberia and corresponds spatially to the Siberian Traps.

The four zones with lowest Q values lie in the Kamchatka Peninsula in northeastern Siberia, the southeastern portions of the Tibetan Plateau and Himalaya, the Hindu Kush (just north of India) and western Turkey. All of these regions are also highly seismically active, a correspondence that suggests that low- Q regions are associated with regions of high crustal strain.

Other low- Q regions appear to be related to upper mantle processes. A comparison of **Figure 13(b)** with wave velocities at long periods ([Ekström et al., 1997](#)), that are not sensitive to crustal properties, shows a correspondence of low- Q regions with regions of low upper mantle velocities. This is most apparent for the broad band of low Q values throughout southern Eurasia but also occurs in the Siberian Trap region of Siberia. Both the low- Q and low-velocity regions largely coincide with high

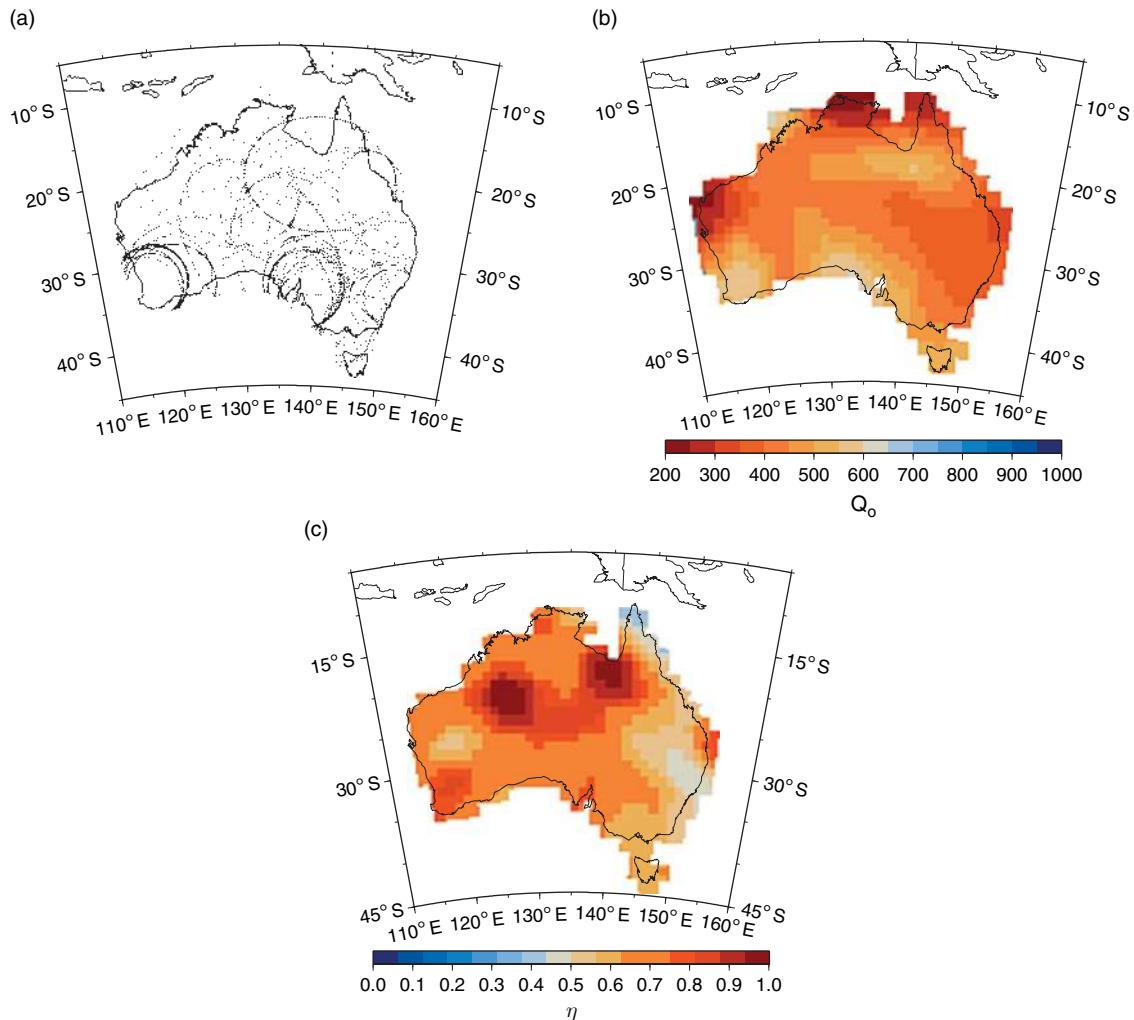


Figure 16 (a) A scattering ellipse map, (b) a Q_o map, and (c) an η map of Q_{Lg}^C for Australia. Adapted from Mitchell BJ, Baquer S, Akinci A, Cong L (1998) *Lg coda Q* in Australia and its relation to crustal structure and evolution. *Pure and Applied Geophysics* 153: 639–653.

upper mantle temperatures (Artemieva and Mooney 2001).

Patterns of frequency dependence (η) variation in Figure 13(c), in contrast to those of Q_o variation, show no clear-cut relationship to tectonics. They similarly show no relation to patterns of Q_o variation. For instance, Kamchatka has low Q_o and low η while Spain has low Q_o and high η .

Seismologists have performed other tomographic studies for portions of Eurasia using Q_{Lg} and shear-wave Q (Q_μ). Xie *et al.* (2006) used a two-station version of the SSR method to determine more than 5000 spectral ratios over 594 paths in eastern Eurasia.

They were able to obtain tomographic models for Q_o and η with resolution ranging between 4° and 10° in which Q_o varies between 100 and 900.

Using the single-station multimode method (Cheng and Mitchell, 1981), Jemberie and Mitchell (2004) obtained tomographic maps of shear-wave Q (Q_μ) for depth ranges of 0–10 and 10–30 km. Although large standard errors accompany those determinations several features of their variation patterns, such as the low- Q regions in southern Tibet, resemble the map of Q_o variations (Figure 13(b)). Q_μ varies between about 30 and 280 in the upper 10 km of the crust and between about 30 and 180 at 10–30 km depth.

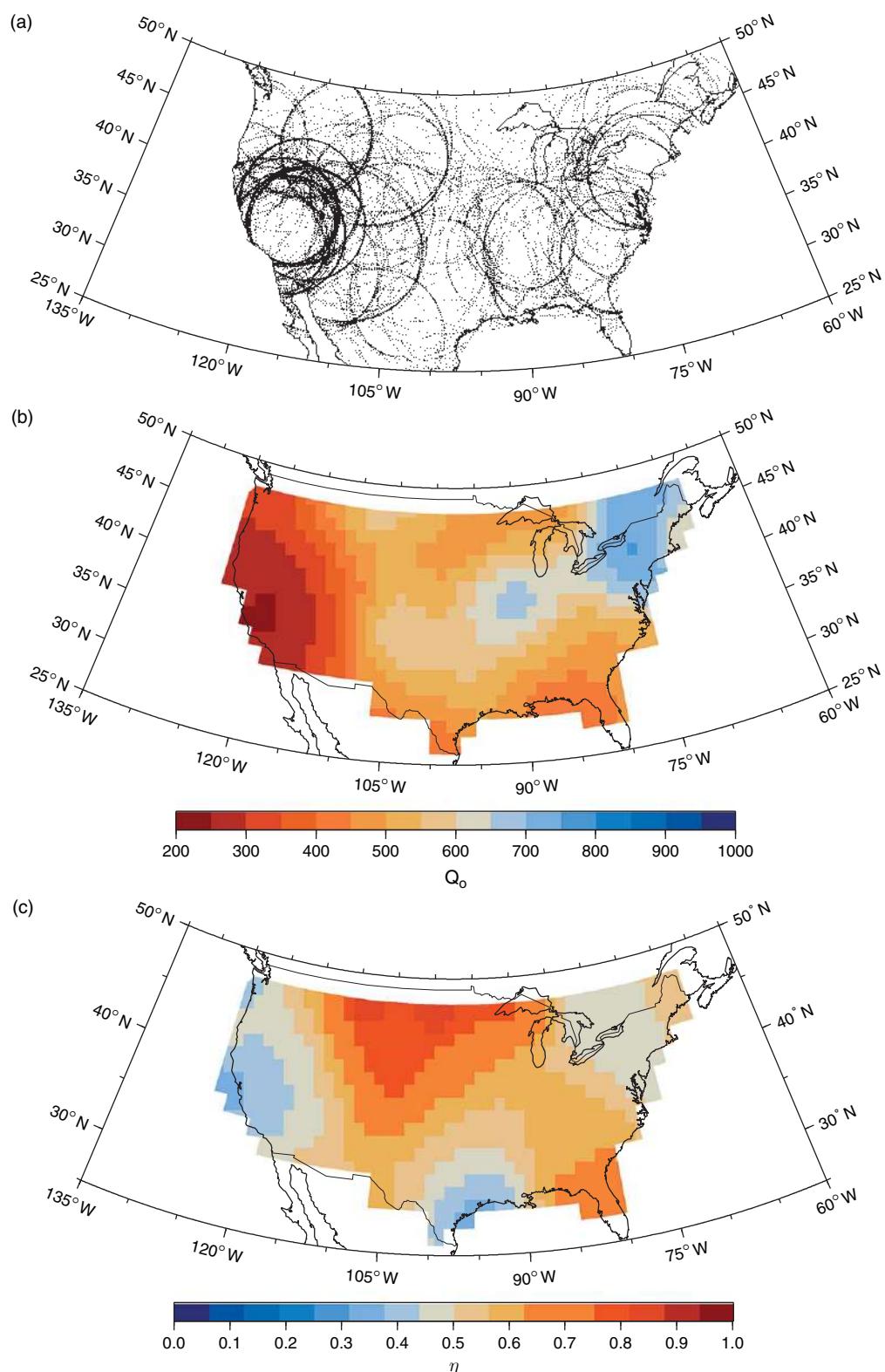


Figure 17 (a) A scattering ellipse map, (b) a Q_o map, and (c) an eta map of Q_{Lg}^C for the United States. Adapted from Baquer S and Mitchell BJ (1998) Regional variation of Lg coda Q in the continental United States and its relation to crustal structure and evolution. *Pure and Applied Geophysics* 153: 613–638.

1.21.7.3.2 Q_{Lg}^C tomography in Africa

Xie and Mitchell (1990b), in the first tomographic study of Lg coda, determined Q_o and η for continental Africa. Figure 14 shows maps of data coverage, Q_o and η for that entire continent (Xie and Mitchell, 1990b). The features in the Q_o map (Figure 14(b)) that is most obviously related to tectonics is the low- Q region that broadly coincides with the East African Rift system. The three high- Q regions correspond to Precambrian cratons: the West African Craton in the northwest, the East Sahara Craton in the northeast, and the Kalahari Craton in the south. The Congo Craton, situated just to the north of the Kalahari Craton does not show up as a region of high Q , probably because waves are damped by a broad and deep basin of low- Q sedimentary rock in that region.

Low Q_o values also occur in the Atlas Mountains (Cenozoic age) of northern Africa, the Cape Fold Belt (Permo-Triassic age) at the southern tip of Africa and the Cameroon Line (Miocene age) which is oriented in an NNE–SSW direction from the point where the western coast changes direction from east–west to north–south.

1.21.7.3.3 Q_{Lg}^C and Q_{Lg} tomography in South America

Figure 15 shows data coverage, and values of Q_o and η obtained for South America (DeSouza and Mitchell, 1998). The data coverage (Figure 15(a)) is excellent throughout western South America where seismicity is high but poor in eastern regions, especially the most easterly regions, where there are few earthquakes. Figure 15(b) shows that, as expected, the low- Q (250–450) portion of South America is associated with the tectonically active western coastal regions. The lowest Q_o values occur along the coast between 15° and 25° S latitude where the level of intermediate-depth seismicity is highest in the continent. The slab in this region also dips steeply (>20°) and significant volcanism occurs (Chen *et al.*, 2001). Davies (1999) had studied the role of hydraulic fractures and intermediate-depth earthquakes in generating subduction zone magmatism. He suggested that the level of intermediate-depth earthquakes was high because liberated fluids favored brittle fracture in response to stresses acting on the slab. Q levels may be low there because earthquake activity creates a degree of permeability that allows dehydrated fluids to be transported to the mantle wedge.

Ojeda and Ottemöller (2002), developed maps of Lg attenuation for most of Colombia at various frequencies in the 0.5–5.0 Hz range. They delineated regional variations of Q_{Lg} within that relatively small region.

1.21.7.3.4 Q_{Lg}^C tomography in Australia

Figure 16 shows the data coverage and values of Q_o and η obtained for Australia (Mitchell *et al.*, 1998). Data coverage (Figure 16(a)) there was the poorest of the five continents where Q_{Lg}^C was mapped over continent-scale dimensions. Q_o variation there is consistent, however, with the other studies and, for all but peripheral regions where systematic measurement errors can be high, it displays a clear relationship with past tectonic activity. Q_o in Australia (Figure 16(b)) is unusually low for a stable continental region, perhaps because a velocity gradient rather than a sharp interface separates the crust and mantle.

Highest values range between 550 and 600 in the southeastern corner of the continent (the Yilgarn Block) and along the southern coast (the Gawler Block). Values between 400 and 500 characterize much of the remaining cratonic crust. This compares with values of 800 and higher in most of the African and South American cratons. The youngest crust lies in eastern Australia where Q_o is between 350 and 400. An orogeny occurred there during the Devonian Period and another occurred in the eastern portion of that region during the Permian Period. Low Q_o values in the most westerly point of the continent and along the northern coast are probably due to very poor data coverage there (Figure 16(a)) and are probably meaningless.

1.21.7.3.5 Q_{Lg}^C , Q_{Lg} , and P/S tomography in North America

Figure 17 shows the data coverage, Q_o , and η values obtained for the United States (Baer and Mitchell, 1998). Coverage (Figure 17(a)) is best in the western portions of the country, but is also reasonably good in the central and eastern portions. Figure 17(b) shows that Q_o is lowest (250–300) in California and the Basin and Range Province. That low- Q region forms the core of a broader region low of Q_o values that extends approximately to the western edge of the Rocky Mountains. Q_o in the Rocky Mountains and much of the Great Plains ranges between about 450 and 600. A moderately high- Q (mostly 600–700) corridor extends from Missouri to the north Atlantic states and New

England. Q_0 in New York and peripheral regions is somewhat higher (700–750). An earlier study of Q_{Lg} in the northeastern United States (Shi *et al.*, 1996) found Q_0 and η values that are similar to the country-wide tomographically derived values in that region.

Two research groups have studied the 3-D structure of P-wave and S-wave attenuation in southern California. Schlotterbeck and Abers (2001) fit theoretical spectra to observed spectra using the least-square minimization method of Hough *et al.* (1988), and determined t^* for P- and S-waves at frequencies between 0.5 and 25 Hz. Their inversions showed that P and S results were in substantial agreement, that Q varies spatially and correlates with regional tectonics.

The second California study (Hauksson, 2006) also determined t^* from P- and S-wave spectra. They assumed that t^* consists of the sum of the whole-path attenuation and the local site effect at each recording station and utilized an expression of Eberhart-Phillips and Chadwick (2002) for the velocity spectrum. The inversion, in addition to providing t^* , yields parameters defining the velocity amplitude spectra. They determined t^* for about 340 000 seismograms from more than 5000 events of t^* data to obtain 3-D, frequency-independent crustal models for Q_P and Q_S in the crust and uppermost mantle in southern California. They found that both Q_P and Q_S generally increase with depth from values of 50 or less in surface sediments to 1000 and greater at mid-crustal depths. Their models reflect major tectonic structures to a much greater extent than they reflect the thermal structure of the crust. Al-Eqabi and Wysession (2006) conducted a tomographic study of Q_{Lg} in the Basin and Range province using a genetic algorithm technique. They found that Q_{Lg} increases (234–312) in a southwest–northeast direction across the Basin and Range in good agreement with the variation of Q_{Lg}^C reported by Baquer and Mitchell (1998). As part of a broader study of Lg wave propagation in southern Mexico Ottemöller *et al.* (2002) used formal inversion methods to separately obtain tomographic maps of Q_{Lg} at three frequencies (0.5, 2.0, and 5.0 Hz) using 1° by 1° cells. Because of uneven path coverage in southern Mexico they applied regularization conditions to their inversion equations. They found lower than average Q_{Lg} in the Gulf of Mexico coastal plain and the area east of 94° W, average values in the northern portion of the Pacific coastal region, and below average values in the southern portion.

1.21.7.3.6 Q_P variation near ocean ridges

Wilcock *et al.* (1995) developed a spectral technique by which they determined the attenuation of P waves in an active-source experiment centered at the East Pacific Rise at latitude $9^\circ 30' N$. It is, to date, the only tomographic study of crustal Q variation in an oceanic region. They obtained over 3500 estimates of t^* , the path integral of the product of Q^{-1} and P-wave velocity where both quantities are variable along the path. Wilcock *et al.* display plots of both cross-axis as well as along-axis structure for upper crustal and lower crustal Q^{-1} structure. Within the ridge magma chamber Q reaches minimum values of 20–50 which extend to the base of the crust. Off the ridge axis they find that Q in the upper crust is 35–50 and at least 500–1000 at depths greater than 2–3 km.

1.21.7.3.7 Variation of crustal Q with time

Several investigators (e.g., Chouet, 1979; Jin and Aki, 1986) have reported temporal variations of Q over timescales of a few years. Although this observation has been reported several times, it continues to be controversial. Spatial patterns of Q variation and their apparent relation to time that has elapsed since the most recent episode of tectonic activity in any region, however, suggest that temporal variations of Q over very long periods of time can easily be detected. Mitchell and Cong (1998) found that variation for Q_{Lg}^C at 1 Hz extends between roughly 250, for broad regions that are currently tectonically active, and about 1000 for shields that have been devoid of tectonic activity for a billion years or more (Figure 18). Mitchell *et al.* (1997) explained those observations as being due to variable volumes of fluids in faulted, fractured, and permeable rock. Fluids may enhance the rate of attenuation of seismic waves either because the waves must expend energy to push those fluids through permeable rock as they propagate or they may traverse a region of enhanced scattering that causes loss of wave energy into the mantle. Figure 18 points to an evolutionary process in which fluids are relatively abundant in tectonically active regions due to their generation by hydrothermal reactions at high temperatures. With time, fluids are gradually lost, either by migration to the Earth's surface or absorption due to retrograde metamorphism. This process causes low Q values early in the tectonic cycle and gradually increasing values at later times as the fluids dissipate.

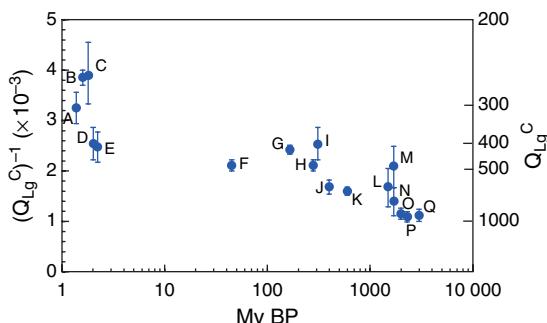


Figure 18 Q_o for Q_{Lg}^C at 1 Hz vs time elapsed in selected regions since the most recent episode of tectonic or orogenic activity. A, The Andes; B, Basin and Range Province in the western United States; C, Tethys region of convergence between the Eurasian and African/Arabian/Indian plates; D, The Arabian Peninsula; E, The East African Rift; F, The Rocky Mountains; G, northeastern China; H, The eastern Altai belt in Eurasia; I, The Tasman Province in Australia; J, The Atlantic Shield in South America; K, The African fold belts; L, The portion of the North American Craton in the United States; M, The Australian Craton; N, Eurasian Cratons; O, African shields; P, The Brazilian shield; Q, The Indian shield. Adapted from Mitchell BJ and Cong L (1998) *Lg coda Q* and its relation to the structure and evolution of continents: A global perspective. *Pure and Applied Geophysics* 155: 655–663.

1.21.8 Conclusions

Much progress has been made in the last 10 years in characterizing the lateral variations of attenuation in the crust, especially under continents, and their relation to tectonics. Characterizing the nature and distribution of attenuation deeper in the Earth still remains a challenging subject, because of the persistent difficulties in separating anelastic and scattering effects, and the nonuniform sampling achieved with available data.

Still, it is encouraging to see that there is now consistency in the large-scale features of lateral variations in Q in the upper 200 km of the mantle and that accounting for focusing effects using a single scattering approximation in present-day elastic 3-D models is helpful, at least at the longest wavelengths. It is still important to consider that, when the inversion experiment is well designed, the unmodelled scattering effects can be minimized, or even utilized to constrain velocity models (e.g., Dalton and Ekström, 2006b), but the consequence is that significant damping needs to be applied in the inversion for lateral variations in Q . This results in large uncertainties (a factor of 2 or more) in the amplitudes of lateral variations of Q , so that physical interpretations of these models must remain tentative. On the other

hand, the spatial distribution of low- and high- Q regions is, in general, more robust. Thus far, only one research group has produced models of lateral variations of Q_μ in the transition zone. While the results are consistent within this group using different methodologies (Romanowicz, 1995; Gung and Romanowicz, 2004) and point to an intriguing correlation with structure at the base of the mantle (Romanowicz and Gung, 2002), these results need to be confirmed by independent studies.

At the regional, uppermost mantle scale, a promising trend, made possible by improved data and techniques, is to combine attenuation, velocity, and other geophysical parameters to better constrain lateral variations of temperature and composition. An ambitious goal would be to do the same at the global, and deeper, scale. Progress in laboratory experiments on Q at seismic frequencies is just starting to provide reliable mineral physics parameters on the behavior of Q at depths down to the upper mantle low velocity zone, so that joint inversions of seismic waveform data for elastic and anelastic 3-D structure can be envisaged (e.g., Cammarano and Romanowicz, 2006). The challenge here is in the nonlinearities introduced by the exponential variation of Q with temperature, on the one hand, and the variation in the position of mineral phase changes depending on composition.

Important uncertainties remain in the characterization of the 1-D profile of Q_μ in the mantle. First and foremost, explaining once and for all the discrepancy between free oscillations and surface-wave measurements, which has consequences for the value of Q_μ in the transition zone. Because there are still unexplained discrepancies between elastic models of the upper mantle, and particularly the transition zone, produced from seismic data on the one hand, and from mineral physics data and computations, on the other (e.g., Cammarano *et al.*, 2003), it is particularly important to apply accurate anelastic corrections when interpreting seismic velocity models in terms of composition. The evidence for a maximum in Q_μ in the lower mantle, and therefore lower Q_μ at the base of the mantle, is now clear, however, the location of this maximum is not well constrained.

The presence of hemispherical variations in Q_α at the top of the inner core, the confirmation of increasing Q with depth and of anisotropy in Q_α correlated with anisotropy in velocity are exciting results that need further investigation, in particular in the light of recent studies by Li and Cormier (2002) favoring a scattering interpretation of attenuation in the inner core.

Finally, in the shallow Earth, it has been found over the past three decades that crustal Q , as manifested by regional studies of body waves, Lg and Lg coda, varies tremendously across continents, as well as in average values of different continents. Q_0 for Lg coda varies between about 150 and 1000 for features that can be resolved at 1 Hz frequency and the frequency dependence of Lg coda Q varies between about 0.0 and 1.0. Most Q determinations at short periods in any region appear to be governed, most prominently, by the time that has elapsed since the most recent episode of tectonic or orogenic activity there.

Acknowledgment

The research of BJM was partially supported by the Air Force Research Laboratory under Award FA 8718-04-C-0021.

References

- Abercrombie RE (1997) Near-surface attenuation and site effects from comparison of surface and deep borehole recordings. *Bulletin of the Seismological Society of America* 87: 731–744.
- Abercrombie RE (2000) Crustal attenuation and site effects at Parkfield, California. *Journal of Geophysical Research* 105: 6277–6286.
- Aki K (1969) Analysis of the seismic coda of local earthquakes as scattered waves. *Journal of Geophysical Research* 74: 615–631.
- Aki K (1980) Scattering and attenuation of shear waves in the lithosphere. *Journal of Geophysical Research* 85: 6496–6504.
- Akopyan ST, Zharkov VN, and Lyubimov VM (1976) Corrections to the eigenfrequencies of the Earth due to dynamic shear modulus. *Bulletin of the Seismological Society of America* 66: 625–630.
- Al-Eqbabi GI and Wysession ME (2006) Q_{Lg} distribution in the Basin and Range province of the Western United States. *Bulletin of the Seismological Society of America* 96: 348–354.
- Al-Khatib HH and Mitchell BJ (1991) Upper mantle anelasticity and tectonic evolution of the Western United States from surface wave attenuation. *Journal of Geophysical Research* 96: 18129–18146.
- Al-Shukri HJ, Mitchell BJ, and Ghalib HAA (1988) Attenuation of seismic waves in the New Madrid seismic zone. *Seismological Research Letters* 59: 133–140.
- Allen RM, Nolet G, Morgan WJ, et al. (1999) The thin hot plume beneath Iceland. *Geophysical Journal International* 137: 51–63.
- Anderson DL and Archambeau CB (1966) The anelasticity of the Earth. *Journal of Geophysical Research* 69: 2071–2084.
- Anderson DL, Ben-Menahem A, and Archambeau CB (1965) Attenuation of seismic energy in the upper mantle. *Journal of Geophysical Research* 70: 1441–1448.
- Anderson DL and Given JW (1982) Absorption band Q model for the Earth. *Journal of Geophysical Research* 87: 3893–3904.
- Anderson DL and Hart RS (1976) An Earth model based on free oscillations and body waves. *Journal of Geophysical Research* 81: 1461–1475.
- Anderson DL and Hart RS (1978) Q of the Earth. *Journal of Geophysical Research* 83: 5869–5882.
- Anderson JG and Hough SE (1984) A model for the shape of Fourier amplitude spectrum of acceleration at high frequencies. In: 1984 Annual Meeting, 30 May–3 June, 1984. Anchorage, Alaska: Seismological Society of America.
- Andrews J, Deuss A, and Woodhouse J (2006) Coupled normal mode sensitivity to inner-core shear velocity and attenuation. *Geophysical Journal International* 167: 204–212.
- Angenheister GH (1906) Bestimmung der fortpflanzungsgeschwindigkeit und absorption von erdbebenwellen, die durch den gegenpunkt des herdes gegangen sind. *Nachrichten von der Königlichen Gesellschaft der Wissenschaften zu Göttingen* 110–120.
- Angenheister GH (1921) Beobachtungen an pazifischen beben. *Nachrichten von der Königlichen Gesellschaft der Wissenschaften zu Göttingen* 113–146.
- Artemieva IM, Billien M, Lévéque JJ, and Mooney WD (2004) Shear-wave velocity, seismic attenuation, and thermal structure of the continental upper mantle. *Geophysical Journal International* 157: 607–628.
- Artemieva IM and Mooney WD (2001) Thermal evolution of precambrian lithosphere: A global study. *Journal of Geophysical Research* 106: 16387–16414.
- Asada T and Takano K (1963) Attenuation of short-period P waves in the mantle. *Journal of Physics of the Earth* 11: 25–34.
- Bager S and Mitchell BJ (1998) Regional variation of Lg coda Q in the continental United States and its relation to crustal structure and evolution. *Pure and Applied Geophysics* 153: 613–638.
- Barazangi M and Isaacs B (1971) Lateral variations of seismic-wave attenuation in the upper mantle above the inclined earthquake zone of the Tonga Island Arc: Deep anomaly in the upper mantle. *Journal of Geophysical Research* 76: 8493–8516.
- Barazangi M, Pennington W, and Isaacs B (1975) Global study of seismic wave attenuation in the upper mantle behind Island Arcs using P waves. *Journal of Geophysical Research* 80: 1079–1092.
- Ben-Menahem A (1965) Observed attenuation and Q values of seismic surface waves in the upper mantle. *Journal of Geophysical Research* 70: 4641–4651.
- Benz HM, Frankel A, and Boore DM (1997) Regional Lg attenuation for the continental United States. *Bulletin of the Seismological Society of America* 87: 606–619.
- Bhattacharyya J, Masters G, and Shearer P (1996) Global lateral variations of shear wave attenuation in the upper mantle. *Journal of Geophysical Research* 101: 22273–22289.
- Bhattacharyya J, Shearer P, and Masters G (1993) Inner core attenuation from short period PKP(BC) versus PKP(DF) waveforms. *Geophysical Journal International* 114: 1–11.
- Billien M and Lévéque J (2000) Global maps of Rayleigh wave attenuation for periods between 40 and 150 seconds. *Geophysical Research Letters* 27: 3619–3622.
- Bollinger GA (1979) Attenuation of the Lg phase and determination of m_b in the Southeastern United States. *Bulletin of the Seismological Society of America* 69: 45–63.
- Bolt BA (1977) The detection of PKIKP and damping in the inner core. *Annali di Geofisica* 30: 507–520.
- Bowers (2000) Observations of PKP(DF) and PKP(BC) across the United Kingdom: Implications for studies of attenuation in the Earth's core. *Geophysical Journal International* 140: 374–384.
- Bowman RJ (1988) Body wave attenuation structure in the Tonga subduction zone. *Journal of Geophysical Research* 93: 2125–2139.
- Bowman JR and Kennett BLN (1991) Propagation of Lg waves in the North Australian craton: Influence of crustal velocity gradients. *Bulletin of the Seismological Society of America* 81: 592–610.

- Boyd OS and Sheehan AF (2005) Attenuation tomography beneath the rocky mountain front: Implications for the physical state of the upper mantle. In: Karlstrom KE and Keler GR (eds.), *Geophysical Monograph Series 154: The Rocky Mountain Region: An evolving lithosphere*, pp. 361–377. Washington, DC: American Geophysical Union.
- Brune JN (1970) Tectonic stress and the spectra of seismic shear waves from earthquakes. *Journal of Geophysical Research* 75: 4997–5009.
- Buland R and Gilbert F (1978) Improved resolution of complex eigenfrequencies in analytically continued seismic spectra. *Geophysical Journal of the Royal Astronomical Society* 52: 457–470.
- Cammarano F, Goes S, Vacher P, and Giardini D (2003) Inferring upper-mantle temperatures from seismic velocities. *Physics of the Earth and Planetary Interiors* 138: 197–222.
- Cammarano F and Romanowicz B (2006) Insights into the nature of the transition zone from physically constrained inversion of long period seismic data. *Physics of the Earth and Planetary Interiors* 138: 197–222.
- Campillo M, Plantet JL, and Bouchon M (1985) Frequency-dependent attenuation in the crust beneath central France from Lg waves: Data analysis and numerical modeling. *Bulletin of the Seismological Society of America* 75: 1395–1411.
- Canas JA and Mitchell BJ (1978) Lateral variation of surface-wave anelastic attenuation across the Pacific. *Bulletin of the Seismological Society of America* 68: 1637–1650.
- Canas JA and Mitchell BJ (1981) Rayleigh-wave attenuation and its variation across the Atlantic Ocean. *Geophysical Journal of the Royal Astronomical Society* 67: 159–176.
- Cao A (2005) *Seismological Constraints on Inner Core Properties*. PhD Dissertation, University of California at Berkeley, Berkeley, CA.
- Cao A and Romanowicz B (2004) Hemispherical transition of seismic attenuation at the top of the Earth's inner core. *Earth and Planetary Science Letters* 228: 243–253.
- Cao A, Romanowicz B, and Takeuchi N (2005) An observation of $PKJKP$: Inferences on inner core shear properties. *Science* 308: 1453–1455.
- Carcione JM and Cavallini F (1995) A rheological model for anelastic anisotropic media with applications to seismic wave propagation. *Geophysical Journal International* 119: 338–348.
- Carpenter PJ and Sanford AR (1985) Apparent Q for upper crustal rocks of the central Rio Grande Rift. *Journal of Geophysical Research* 90: 8661–8674.
- Chan WW and Der ZA (1988) Attenuation of multiple ScS in various parts of the world. *Geophysical Journal International* 92: 303–314.
- Chavez D and Priestley KF (1986) Measurement of frequency dependent Lg attenuation in the Great Basin. *Geophysical Research Letters* 60: 551–554.
- Chen PF, Bina CR, and Okal EA (2001) Variations in slab dip along the subducting Nazca plate, as related to stress patterns and moment release of intermediate-depth seismicity and to surface volcanism. *Geochemistry Geophysics Geosystems* 2, doi:10.1029/2001GC000153.
- Cheng HX and Kennett BLN (2002) Frequency dependence of seismic wave attenuation in the upper mantle in the Australian region. *Geophysical Journal International* 150: 45–47.
- Cheng CC and Mitchell BJ (1981) Crustal Q structure in the United States from multi-mode surface waves. *Bulletin of the Seismological Society of America* 71: 161–181.
- Chouet B (1979) Temporal variation in the attenuation of earthquake coda near Stone Canyon, California. *Geophysical Research Letters* 6: 143–146.
- Choy G and Cormier VF (1983) The structure of the inner core inferred from short-period and broadband GDSN data. *Geophysical Journal International* 63: 457–470.
- Chun KY, West GF, Kikoski RJ, and Samson C (1987) A novel technique for measuring Lg attenuation – Results from eastern Canada between 1-Hz and 10-Hz. *Bulletin of the Seismological Society of America* 77: 398–419.
- Cong L and Mitchell BJ (1998) Seismic velocity and Q structure of the middle eastern crust and upper mantle from surface-wave dispersion and attenuation. *Pure and Applied Geophysics* 153: 503–538.
- Cormier VF (1981) Short period PKP pahses and the anelastic mechanism of the inner core. *Physics of the Earth and Planetary Interiors* 24: 291–301.
- Cormier VF and Li X (2002) Frequency-dependent seismic attenuation in the inner core. Part 2: A scattering and fabric interpretation. *Journal of Geophysical Research* 107, doi:10.1029/2002JB001796.
- Cormier VF and Richards P (1976) Comments on the damping of core waves by Anthony Qamar and Alfredo Eisenberg. *Journal of Geophysical Research* 81: 3066–3068.
- Cormier VF and Richards P (1988) Spectral synthesis of body waves in Earth models specified by vertically varying layers. In: Doornbos D (ed.) *Seismological Algorithms*, pp. 3–45. San Diego, CA: Academic Press.
- Cormier VF and Stroujkova A (2006) Waveform search for the innermost inner core. *Earth and Planetary Science Letters* 236: 96–105.
- Cormier VF, Xu L, and Choy GL (1998) Seismic attenuation of the inner core: Viscoelastic or stratigraphic? *Geophysical Research Letters* 25: 4019–4022.
- Creager KC (1992) Anisotropy of the inner core from differential travel times of the phases PKP and $PKIKP$. *Nature* 356: 309–314.
- Creager KC (1999) Large-scale variations in inner core anisotropy. *Journal of Geophysical Research* 104: 23127–23139.
- Dainty AM (1981) A scattering model to explain Q observations in the lithosphere between 1 and 30 Hz. *Geophysical Research Letters* 8: 1126–1128.
- Dalton C and Ekström G (2006a) Constraints on global maps of phase velocity from surface-wave amplitudes. *Geophysical Journal International* 167: 820–826.
- Dalton C and Ekström G (2006b) Global models of surface wave attenuation. *Journal of Geophysical Research* 111, doi:10.1029/2005JB003997.
- Davies JH (1990) Mantle plumes, mantle stirring and hotspot geometry.
- Davies JH (1999) The role of hydraulic fractures and intermediate-depth earthquakes in generating subduction-zone magmatism. *Nature* 398: 142–145.
- Der ZA, McElfresh TW, and O'Donnell A (1982) An investigation of the regional variations and frequency dependence of anelastic attenuation in the mantle under the United States in the 0.5–4 Hz band. *Geophysical Journal of the Royal Astronomical Society* 69: 67–99.
- Deschamps A (1977) Inversion of the attenuation data of free oscillations of the Earth (fundamental and first higher modes). *Geophysical Journal of the Royal Astronomical Society* 50: 699–722.
- DeSouza JL and Mitchell BJ (1998) Lg coda Q variations across South America and their relation to crustal evolution. *Pure and Applied Geophysics* 153: 587–612.
- Ding CY and Grand SP (1993) Upper mantle Q structure under the East Pacific Rise. *Journal of Geophysical Research* 98: 1973–1975.
- Doornbos DJ (1974) The anelasticity of the inner core. *Geophysical Journal of the Royal Astronomical Society* 38: 397–415.
- Doornbos DJ (1983) Observable effects of the seismic absorption band in the Earth. *Geophysical Journal of the Royal Astronomical Society* 57: 381–395.

- Durek JJ and Ekström G (1995) Evidence for bulk attenuation in the asthenosphere from recordings of the Bolia earthquake. *Geophysical Research Letters* 22: 2309–2312.
- Durek JJ and Ekström G (1996) A radial model of anelasticity consistent with long-period surface wave attenuation. *Bulletin of the Seismological Society of America* 86: 144–158.
- Durek JJ and Ekström G (1997) Investigating discrepancies among measurements of traveling and standing wave attenuation. *Journal of Geophysical Research* 102: 24529–24544.
- Durek JJ, Ritzwoller MH, and Woodhouse JH (1993) Constraining upper mantle anelasticity using surface wave amplitude anomalies. *Geophysical Journal International* 114: 249–272.
- Dziewonski AM and Anderson DL (1981) Preliminary reference Earth model. *Physics of the Earth and Planetary Interiors* 25: 297–356.
- Dziewonski AM and Stein JM (1982) Dispersion and attenuation of mantle waves through waveform inversion. *Geophysical Journal of the Royal Astronomical Society* 70: 503–527.
- Eberhart-Phillips D and Chadwick M (2002) Three-dimensional attenuation model of the shallow Hikurangi subduction zone in the Raukumara Peninsula, New Zealand. *Journal of Geophysical Research* 107: 2033 (doi:10.1029/2000JB000,046).
- Ekström G and Dziewonski AM (1997) The unique anisotropy of the Pacific upper mantle. *Nature* 394: 168–172.
- Ekström G, Tromp J, and Larson EWF (1997) Measurements and global models of surface wave propagation. *Journal of Geophysical Research* 102: 8137–8157.
- Evernden JF (1955) Tripartite results for the Kamchatka earthquake of November 4, 1952. *Bulletin of the Seismological Society of America* 45: 167–178.
- Faul U, FitzGerald J, and Jackson I (2004) Shear wave attenuation and dispersion in melt-bearing olivine polycrystals. Part 2: Microstructural interpretation and seismological implications. *Journal of Geophysical Research* 109, doi:10.1029/2003JB002,407.
- Faul U and Jackson I (2005) The seismological signature of temperature and grain size variations in the upper mantle. *Earth and Planetary Science Letters* 234: 119–134.
- Fearn DR, Loper DE, and Roberts PH (1981) Structure of the Earth's inner core. *Nature* 292: 232–233.
- Fisher JL and Wysession ME (2003) Small-scale lateral variations in D'' attenuation and velocity structure. *Geophysical Research Letters* 30, doi:10.1029/2002GL016,179.
- Flanagan MP and Wiens DA (1990) Attenuation structure beneath the Lau back arc spreading center from teleseismic S phases. *Geophysical Research Letters* 17: 2117–2120.
- Flanagan MP and Wiens DA (1994) Radial upper mantle structure of inactive back-arc basins from differential shear wave measurements. *Journal of Geophysical Research* 99: 15469–15485.
- Flanagan MP and Wiens DA (1998) Attenuation of broadband P and S waves in Tonga; observations of frequency dependent Q. *Pure and Applied Geophysics* 153: 345–375.
- Frankel A and Wennerberg L (1987) Energy-flux model for seismic coda: Separation of scattering and intrinsic attenuation. *Bulletin of the Seismological Society of America* 77: 1223–1251.
- Futterman A (1962) Dispersive body waves. *Journal of Geophysical Research* 67: 5279–5291.
- Garcia R (2002) Constraints on upper inner-core structure from waveform inversion of core phases. *Geophysical Journal International* 150: 651–664.
- Geller RJ and Stein S (1978) Time domain measurements of attenuation of fundamental modes ($\omega S_6 - \omega S_{2g}$). *Bulletin of the Seismological Society of America* 69: 1671–1691.
- Getting IC, Dutton SJ, Burnley PC, Karato SI, and Spetzler HA (1997) Shear attenuation and dispersion in MgO. *Physics of the Earth and Planetary Interiors* 99: 249–257.
- Giardini DXDL and Woodhouse JH (1988) Splitting functions of long period normal modes of the Earth. *Journal of Geophysical Research* 93: 13716–13742.
- Gilbert F and Dziewonski AM (1975) An application of normal mode theory to the retrieval of structural parameters and source mechanisms from seismic spectra. *Philosophical Transactions of the Royal Society of London Series A* 278: 187–269.
- Gomer BM and Okal EA (2003) Multiple-ScS probing of the Ontong-Java Plateau. *Physics of the Earth and Planetary Interiors* 138: 317–331.
- Gueguen Y, Darot M, Mazot P, and Woigard J (1989) Q⁻¹ of forsterite single crystals. *Physics of the Earth and Planetary Interiors* 55: 254–258.
- Gung Y, Panning M, and Romanowicz BA (2003) Anisotropy and thickness of the lithosphere. *Nature* 422: 707–711.
- Gung Y and Romanowicz BA (2004) Q tomography of the upper mantle using three component long period waveforms. *Geophysical Journal International* 157: 813–830.
- Gusev AA and Abubakirov IR (1996) Simulated envelopes of non-isotropically scattered body waves as compared to observed ones: Another manifestation of fractal inhomogeneity. *Geophysical Journal International* 127: 49–60.
- Gutenberg B (1924) Dispersion und extinktion von seismischen oberflächenwellen und der aufbau der obersten erdschichten. *Physikalische Zeitschrift* 25: 377–381.
- Gutenberg B (1945a) Amplitudes of P, PP, and SS and magnitude of shallow earthquakes. *Bulletin of the Seismological Society of America* 35: 57–69.
- Gutenberg B (1945b) Amplitudes of surface waves and magnitudes of shallow earthquakes. *Bulletin of the Seismological Society of America* 35: 3–12.
- Gutenberg B (1958) Attenuation of seismic waves in the Earth's mantle. *Bulletin of the Seismological Society of America* 48: 269–282.
- Hasegawa HS (1974) Theoretical synthesis and analysis of strong motion spectra of earthquakes. *Canadian Geotechnical Journal* 11: 278–297.
- Hasegawa HS (1985) Attenuation of Lg waves in the Canadian shield. *Bulletin of the Seismological Society of America* 75: 1569–1582.
- Hauksson E (2006) Attenuation models (Q_P and Q_S) in three dimensions of the Southern California crust: Inferred fluid saturation at seismogenic depths. *Journal of Geophysical Research* 111(B05): 302 (doi:10.1029/2005JB003,947).
- He X and Tromp J (1996) Normal-mode constraints on the structure of the Earth. *Journal of Geophysical Research* 101: 20053–20082.
- Helffrich G, Kaneshima S, and Kendall JM (2002) A local, crossing-path study of attenuation and anisotropy of the inner core. *Geophysical Research Letters* 29, doi:10.1029/2001GL014,059.
- Herrmann RB (1980) Q estimates using the coda of local earthquakes. *Bulletin of the Seismological Society of America* 70: 447–468.
- Herrmann RB and Mitchell BJ (1975) Statistical analysis and interpretation of surface-wave anelastic attenuation data for the stable interior of North America. *Bulletin of the Seismological Society of America* 65: 1115–1128.
- Hough SE, Anderson JG, Brune J, et al. (1988) Attenuation near Anza, California. *Bulletin of the Seismological Society of America* 78: 672–691.

- Hough SE, Lees JM, and Monastero F (1999) Attenuation and source properties at the Coso geothermal area, California. *Bulletin of the Seismological Society of America* 89: 1606–1619.
- Humphreys E and Clayton RW (1988) Adaptation of back projection tomography to seismic travel time problems. *Journal of Geophysical Research* 93: 1073–1086.
- Hwang HJ and Mitchell BJ (1987) Shear velocities, Q_β , and the frequency dependence of Q_β in stable and tectonically active regions from surface wave observations. *Geophysical Journal of the Royal Astronomical Society* 90: 575–613.
- Ichikawa M and Basham PW (1965) Variations in short-period records from Canadian seismograph stations. *Canadian Journal of Earth Sciences* 2: 510–542.
- Isse T and Nakanishi I (1997) The effect of the crust on the estimation of mantle Q from spectral ratios of multiple ScS phases. *Bulletin of the Seismological Society of America* 87: 778–781.
- Ivan M, Marza V, de Farias Caixeta D, and de Melo Araeas T (2005) Uppermost inner core attenuation from PKP data at South American seismological stations. *Geophysical Journal International* 164: 441–448.
- Jackson I (1993) Progress in the experimental study of seismic wave attenuation. *Annual Review of Earth and Planetary Sciences* 21: 375–406.
- Jackson I (2000) Laboratory measurement of seismic wave dispersion and attenuation: Recent progress. *Journal of Geophysical Research* 109, doi:10.1029/2003JB002,406.
- Jackson I, Faul UH, Fitzgerald JD, and Tan BH (2004) Shear wave attenuation and dispersion in melt-bearing olivine polycrystals. Part 1: Specimen fabrication and mechanical testing. In: Karato S-I, Forte AM, Liebermann RC, Masters G, and Stixrude L (eds.) *Geophysical Monograph Series 117: Earth's Deep Interior: Mineral Physics and Tomography from the Atomic to the Global Scale*, pp. 265–289. Washington, DC: American Geophysical Union.
- Jeffreys H (1967) Radius of the Earth's core. *Nature* 215: 1365–1366.
- Jemberie AL and Mitchell BJ (2004) Shear-wave Q structure and its lateral variation in the crust of China and surrounding regions. *Geophysical Journal International* 157: 363–380.
- Jin A and Aki K (1986) Temporal change in coda Q before the Tangshan earthquake of 1976 and the Haicheng earthquake of 1975. *Journal of Geophysical Research* 91: 665–673.
- Jobert N and Roult G (1976) Periods and damping of free oscillations observed in France after 16 earthquakes. *Geophysical Journal of the Royal Astronomical Society* 45: 155–176.
- Jordan TH and Sipkin SS (1977) Estimation of the attenuation operator for multiple ScS waves. *Geophysical Research Letters* 4: 167–170.
- Kanamori H (1970) Velocity and Q of mantle waves. *Physics of the Earth and Planetary Interiors* 2: 259–275.
- Kanamori H and Anderson DL (1977) Importance of physical dispersion in surface-wave and free oscillation problems. *Reviews of Geophysics* 15: 105–112.
- Karato SI (1993) Importance of anelasticity in the interpretation of seismic tomography. *Geophysical Research Letters* 20: 1623–1626.
- Karato SI (1998) A dislocation model of seismic wave attenuation and micro-creep in the Earth; Harold Jeffreys and the rheology of the solid Earth. *Pure and Applied Geophysics* 153: 239–256.
- Karato SI and Karki BB (2001) Origin of lateral variation of seismic wave velocities and density in the deep mantle. *Journal of Geophysical Research* 106: 21771–21783.
- Karato SI and Spetzler H (1990) Defect microdynamics in minerals and solid state mechanisms of seismic wave attenuation and velocity dispersion in the mantle. *Reviews of Geophysics* 28: 399–421.
- Kikko A and Mitchell BJ (1983) Multimode Rayleigh wave attenuation and Q_β in the crust of the Barents shelf. *Journal of Geophysical Research* 88: 3315–3328.
- Knopoff L (1964) Q. *Reviews of Geophysics* 2: 625–660.
- Komatitsch D, Ritsema J, and Tromp J (2002) The spectral-element method, Beowulf computing, and global seismology. *Science* 298: 1737–1742.
- Kovach RI and Anderson DL (1964) Attenuation of shear waves in the upper and lower mantle. *Bulletin of the Seismological Society of America* 54: 1855–1864.
- Krasnoshchekov DN, Kaazik PB, and Ovtchinnikov VM (2005) Seismological evidence for mosaic structure of the surface of the Earth's inner core. *Nature* 435: 483–487.
- Kumazawa M, Imanashi Y, Fukao Y, Furumoto M, and Yananoto A (1990) A theory of spectral analysis based on the characteristic property of a linear dynamical system. *Geophysical Journal International* 101: 613–630.
- Kuster GT (1972) *Seismic Wave Propagation in Two-Phase Media and Its Application to the Earth's Interior*. PhD Dissertation, MIT, Cambridge, MA.
- Lawrence JF, Shearer P, and Masters G (2006) Mapping attenuation beneath North America using waveform cross-correlation and cluster analysis. *Geophysical Research Letters* 33, doi:10.1029/2006GL025,813.
- Lawrence JF and Wysession ME (2006) QLM9: A new radial quality factor (Q_{mu}) model for the lower mantle. *Earth and Planetary Science Letters* 241: 962–971.
- Lay T and Kanamori H (1985) Geometric effects of global lateral heterogeneity on long-period surface wave propagation. *Journal of Geophysical Research* 90: 605–621.
- Lay T and Wallace T (1983) Multiple ScS travel times and attenuation beneath Mexico and Central America. *Geophysical Research Letters* 10: 301–304.
- Lay T and Wallace T (1988) Multiple ScS attenuation and travel times beneath Western North America. *Bulletin of the Seismological Society of America* 78: 2041–2061.
- Lee WB and Solomon SC (1979) Simultaneous inversion of surface-wave phase velocity and attenuation: Rayleigh and Love waves over continental and oceanic paths. *Bulletin of the Seismological Society of America* 69: 65–95.
- Li XD (1990) *Asphericity of the Earth from Free Oscillations*. PhD Dissertation, Harvard University, Cambridge, MA.
- Li X and Cormier VF (2002) Frequency-dependent seismic attenuation in the inner core. Part 1: A viscoelastic interpretation. *Journal of Geophysical Research* 107, doi:10.1029/2002JB001,795.
- Li XD and Romanowicz B (1995) Comparison of global waveform inversions with and without considering cross branch coupling. *Geophysical Journal International* 121: 695–709.
- Liu HP, Anderson DL, and Kanamori H (1976) Velocity dispersion due to anelasticity: Implication for seismology and mantle composition. *Geophysical Journal of the Royal Astronomical Society* 47: 41–58.
- Lognonné P and Romanowicz B (1990) Modelling of coupled normal modes of the Earth: The spectral method. *Geophysical Journal International* 102: 365–395.
- Lomnitz C (1957) Linear dissipation in solids. *Journal of Applied Physics* 28: 201–205.
- Loper DE and Fean DR (1983) A seismic model of a partially molten inner core. *Journal of Geophysical Research* 88: 1235–1242.
- Loper DE and Roberts PH (1981) A study of conditions at the inner core boundary of the Earth. *Physics of the Earth and Planetary Interiors* 24: 302–307.

- Luh P (1974) Normal modes of a rotating, self gravitating inhomogeneous Earth. *Geophysical Journal of the Royal Astronomical Society* 38: 187–224.
- Lundquist GM and Cormier VC (1980) Constraints on the absorption band model of Q. *Journal of Geophysical Research* 85: 5244–5256.
- Malin PE (1978) *A First Order Scattering Solution for Modeling Lunar and Terrestrial Seismic Coda*. PhD Dissertation, Princeton University, Princeton, NJ.
- Masters G and Gilbert F (1981) Structure of the inner core inferred from observations of its spheroidal shear modes. *Geophysical Research Letters* 8: 569–571.
- Masters G and Gilbert F (1983) Attenuation in the Earth at low frequencies. *Philosophical Transactions of the Royal Society of London Series XI* 308: 479–522.
- Masters G and Laske G (1997) On bias in surface wave and free oscillation attenuation measurements. *Eos Transaction of the American Geophysical Union* 78: F485.
- Mills J and Hales A (1978) Great circle Rayleigh wave attenuation and group velocity. Part III: Inversion of global average group velocity and attenuation coefficients. *Physics of the Earth and Planetary Interiors* 17: 307–322.
- Minster B and Anderson DL (1981) A model of dislocation controlled rheology for the mantle. *Philosophical Transactions of the Royal Society of London Series A* 299: 319–356.
- Mitchell BJ (1973) Radiation and attenuation of Rayleigh waves from the Southeastern Missouri earthquake of October 21, 1965. *Journal of Geophysical Research* 78: 886–899.
- Mitchell BJ (1975) Regional Rayleigh wave attenuation on North America. *Journal of Geophysical Research* 35: 4904–4916.
- Mitchell BJ (1995) Anelastic structure and evolution of the continental crust and upper mantle from seismic surface wave attenuation. *Reviews of Geophysics* 33: 441–462.
- Mitchell BJ, Baqer S, Akinci A, and Cong L (1998) *Lg* coda Q in Australia and its relation to crustal structure and evolution. *Pure and Applied Geophysics* 153: 639–653.
- Mitchell BJ and Cong L (1998) *Lg* coda Q and its relation to the structure and evolution of continents: A global perspective. *Pure and Applied Geophysics* 153: 655–663.
- Mitchell BJ, Cong L, and Ekström G (2007) A continent-wide 1-Hz map of *Lg* coda Q variation across Eurasia and its implications for lithospheric evolution. *Journal of Geophysical Research* (in review).
- Mitchell BJ and Helmberger DV (1973) Shear velocities at the base of the mantle from observations of S and ScS. *Journal of Geophysical Research* 78: 6009–6020.
- Mitchell BJ and Hwang HJ (1987) The effect of low-Q sediments and crustal Q on *Lg* attenuation in the United States. *Bulletin of the Seismological Society of America* 77: 1197–1210.
- Mitchell BJ, Pan Y, Xie J, and Cong L (1997) *Lg* coda Q across Eurasia and its relation to crustal evolution. *Journal of Geophysical Research* 102: 22767–22779.
- Mitchell BJ and Xie J (1994) Attenuation of multiphase surface waves in the Basin and Range province. Part III: Inversion for crustal anelasticity. *Geophysical Journal International* 116: 468–484.
- Modiano T and Hatzfeld D (1982) Experimental study of the spectral content for shallow earthquakes. *Bulletin of the Seismological Society of America* 72: 1739–1758.
- Molnar P and Oliver J (1969) Lateral variations in attenuation in the upper mantle and discontinuities in the lithosphere. *Journal of Geophysical Research* 74: 2648–2682.
- Montagner JP and Kennett BLN (1996) How to reconcile body-wave and normal-mode reference Earth models. *Geophysical Journal International* 125: 229–248.
- Montagner JP and Tanimoto T (1991) Global upper mantle tomography of seismic velocities and anisotropy. *Journal of Geophysical Research* 96: 20337–20351.
- Morelli A, Dziewonski AM, and Woodhouse JH (1986) Anisotropy of the core inferred from PKIKP travel times. *Geophysical Research Letters* 13: 1545–1548.
- Mueller G (1986) Rheological properties and velocity dispersion of a medium with power law dependence of Q in frequency. *Journal of Geophysics* 54: 20–29.
- Nakanishi I (1978) Regional differences in the phase velocity and the quality factor Q of mantle Rayleigh waves. *Science* 200: 1379–1381.
- Nakanishi I (1979a) Attenuation of multiple ScS waves beneath the Japanese Arc. *Physics of the Earth and Planetary Interiors* 19: 337–347.
- Nakanishi I (1979b) Phase velocity and Q of mantle Rayleigh waves. *Geophysical Journal of the Royal Astronomical Society* 58: 35–59.
- Nakanishi I (1981) Shear velocity and shear attenuation models inverted from the worldwide and pure-path average data of mantle Rayleigh waves (oS_{25} to oS_{80}) and fundamental spheroidal modes (oS_2 to oS_{24}). *Geophysical Journal of the Royal Astronomical Society* 66: 83–130.
- Niazi M and Johnson LR (1992) Q in the inner core. *Physics of the Earth and Planetary Interiors* 74: 55–62.
- Niu F and Wen L (2001) Hemispherical variations in seismic velocity at the top of the Earth's inner core. *Nature* 410: 1081–1084.
- Nuttli OW (1973) Seismic wave attenuation and magnitude relations for Eastern North America. *Journal of Geophysical Research* 78: 876–885.
- Nuttli OW (1978) A time-domain study of the attenuation of 10-Hz waves in the New Madrid seismic zone. *Bulletin of the Seismological Society of America* 68: 343–355.
- Nuttli OW (1980) The excitation and attenuation of seismic crustal phases in Iran. *Bulletin of the Seismological Society of America* 70: 469–484.
- O'Connell RJ and Budiansky B (1978) Measures of dissipation in viscoelastic media. *Geophysical Research Letters* 5: 5–8.
- Øjeda A and Ottemöller L (2002) Q_{Lg} tomography in Colombia. *Physics of the Earth and Planetary Interiors* 130: 253–270.
- Okal EA and Jo BG (2002) Q measurements for Phase X overtones. *Pure and Applied Geophysics* 132: 331–362.
- Oki S, Fukao Y, and Obayashi M (2000) Reference frequency of teleseismic body waves. *Journal of Geophysical Research* 109, doi:10.1029/2003JB002821.
- Oreshin SI and Vinnik LP (2004) Heterogeneity and anisotropy of seismic attenuation in the inner core. *Geophysical Research Letters* 31, doi:10.1029/2003GL018,591.
- Ottemöller L, Shapiro NM, Singh SK, and Pacheco JF (2002) Lateral variation of *Lg* wave propagation in southern Mexico. *Journal of Geophysical Research* 107(B1): 2008, doi:10.1029/2001JB00206.
- Park J (1987) Asymptotic coupled-mode expressions for multiplet amplitude anomalies and frequency shift on a laterally heterogeneous Earth. *Geophysical Journal of the Royal Astronomical Society* 90: 129–170.
- Patton HJ and Taylor SR (1989) Q structure of the Basin and Range from surface waves. *Journal of Geophysical Research* 89: 6929–6940.
- Peacock S and Hudson JA (1990) Seismic properties of rocks with distributions of small cracks. *Geophysical Journal International* 102: 471–484.
- Phillips S, Hartse HE, Taylor SR, and Randall GE (2000) 1 Hz *Lg* Q Tomography in central Asia. *Geophysical Research Letters* 27: 3425.
- Press F (1956) Rigidity of the Earth's core. *Science* 124: 1204.
- Randall MJ (1976) Attenuative dispersion and frequency shifts of the Earth's free oscillations. *Physics of the Earth and Planetary Interiors* 12: P1–P4.

- Reid FJL, Woodhouse JH, and van Heist H (2001) Upper mantle attenuation and velocity structure from measurements of differential S phases. *Geophysical Journal International* 145: 615–630.
- Resovsky JS and Ritzwoller MH (1998) New and refined constraints on three-dimensional Earth structure from normal modes below 3mHz. *Journal of Geophysical Research* 103: 783–810.
- Resovsky JS, Trampert J, and van der Hilst RD (2005) Error bars for the global seismic Q profile. *Earth and Planetary Science Letters* 230: 413–423.
- Revenaugh J and Jordan TH (1989) A study of mantle layering beneath the western Pacific. *Journal of Geophysical Research* 94: 5787–5813.
- Revenaugh J and Jordan TH (1991) Mantle layering from ScS reverberations. Part 2: The transition zone. *Journal of Geophysical Research* 96: 19763–19780.
- Richards PG and Menke W (1983) The apparent attenuation of a scattering medium. *Bulletin of the Seismological Society of America* 73: 1005–1021.
- Romanowicz B (1987) Multiplet-multiplet coupling due to lateral heterogeneity: Asymptotic effects on the amplitude and frequency of the Earth's normal modes. *Geophysical Journal of the Royal Astronomical Society* 90: 75–100.
- Romanowicz B (1990) The upper mantle degree. Part 2: Constraints and inferences on attenuation tomography from global mantle wave measurements. *Journal of Geophysical Research* 95: 11051–110710.
- Romanowicz B (1994a) On the measurement of anelastic attenuation using amplitudes of low-frequency surface waves. *Physics of the Earth and Planetary Interiors* 84: 179–191.
- Romanowicz B (1994b) Anelastic tomography: A new perspective on upper-mantle thermal structure. *Earth and Planetary Science Letters* 128: 113–121.
- Romanowicz B (1995) A global tomographic model of shear attenuation in the upper mantle. *Journal of Geophysical Research* 100: 12375–12394.
- Romanowicz B (1998) Attenuation tomography of the earth's mantle: A review of current status. *Pure and Applied Geophysics* 153: 257–272.
- Romanowicz B (2002) Inversion of surface waves: A review. In: Lee WHK (ed.) *Handbook of Earthquake and Engineering Seismology*, IASPEI, Part A, pp. 149–174. Amsterdam: Academic Press.
- Romanowicz B and Durek J (2000) Seismological constraints on attenuation in the Earth: A review. In: Karato S-I, Forte AM, Liebermann RC, Masters G, and Stixrude L (eds.) *Geophysical Monograph Series 117: Earth's Deep Interior: Mineral Physics and Tomography from the Atomic to the Global Scale*, pp. 161–180. Washington, DC: American Geophysical Union.
- Romanowicz B and Gung Y (2002) Superplumes from the core–mantle boundary to the lithosphere: Implications for heat flux. *Science* 296: 513–516.
- Romanowicz B, Roult G, and Kohl T (1987) The upper mantle degree two pattern: Constraints from Geoscope fundamental spheroidal model eigenfrequency and attenuation measurements. *Geophysical Research Letters* 14: 1219–1222.
- Rosat S, Sato T, Imanishi Y, et al. (2005) High resolution analysis of the gravest seismic normal modes after the 2005 Mw = 9 Sumatra earthquake using superconducting gravimeter data. *Geophysical Research Letters* 32, doi:10.1029/2005GL023,128.
- Roth E, Wiens DA, Dorman LM, Hildebrand J, and Webb SC (1999) Seismic attenuation tomography of the Tonga–Fiji region using phase pair methods. *Journal of Geophysical Research* 104: 4795–4809.
- Roth E, Wiens DA, and Zhao D (2000) An empirical relationship between seismic attenuation and velocity anomalies in the upper mantle. *Geophysical Research Letters* 27: 601–604.
- Roult G (1975) Attenuation of seismic waves of very low frequency. *Physics of the Earth and Planetary Interiors* 10: 159–166.
- Roult G (1982) The effect of young oceanic regions on the periods and damping of free oscillation of the Earth. *Journal of Geophysical Research* 51: 38–43.
- Roult G and Clévéédé E (2000) New refinements in attenuation measurements from free oscillations and surface wave observations. *Physics of the Earth and Planetary Interiors* 121: 1–37.
- Roult G, Romanowicz B, and Montagner JP (1984) 3D upper mantle shear velocity and attenuation from fundamental mode free oscillation data. *Geophysical Journal International* 101: 61–80.
- Roult G, Rosat S, Clévéédé E, Millot-Langet R, and Hinderer J (2006) New determination of Q quality factors eigenfrequencies for the whole set of singlets of Earth's normal modes ${}_0S_0$, ${}_0S_2$, ${}_0S_3$ and ${}_2S_1$, using Superconducting Gravimeter data from the GGP network. *Journal of Geodynamics* 41: 345–357.
- Sacks IS (1969) Anelasticity of the inner core. *Annual Report of the Director of Department of Terrestrial Magnetism* 69: 416–419.
- Sacks IS (1980) Qs of the lower mantle – A body wave determination. *Annual Report of the Director of Department of Terrestrial Magnetism* 79: 508–512.
- Sailor RV and Dziewonski AM (1978) Measurements and interpretation of normal mode attenuation. *Geophysical Journal of the Royal Astronomical Society* 53: 559–581.
- Sarker G and Abers GA (1998) Comparison of seismic body wave and coda wave measures of Q. *Pure and Applied Geophysics* 153: 665–683.
- Sarker G and Abers GA (1999) Lithospheric temperature estimates from seismic attenuation across range fronts in southern and central Eurasia. *Geology* 27: 427–430.
- Sato H, Sacks IS, Murase T, Muncill G, and Fukuyama F (1989) Qp-melting temperature relation in peridotite at high pressure and temperature: Attenuation mechanism and implications for the mechanical properties of the upper mantle. *Journal of Geophysical Research* 94: 10647–10661.
- Sato R and Espinosa AF (1967) Dissipation in the Earth's mantle and rigidity and viscosity in the Earth's core determined from waves multiply-reflected from the mantle–core boundary. *Bulletin of the Seismological Society of America* 57: 829–856.
- Schlotterbeck BA and Abers GA (2001) Three-dimensional attenuation variations in Southern California. *Journal of Geophysical Research* 106: 30719–30735.
- Selby ND and Woodhouse JH (2000) Controls on Rayleigh wave amplitudes: Attenuation and focusing. *Geophysical Journal International* 142: 933–940.
- Selby ND and Woodhouse JH (2002) The Q structure of the upper mantle: Constraints from Rayleigh wave amplitudes. *Journal of Geophysical Research* 107, doi:10.1029/2000JB000,257.
- Shearer P (1994) Constraints on inner core anisotropy from PKP(DF) travel times. *Journal of Geophysical Research* 99: 19647–19659.
- Sheehan A and Solomon SC (1992) Differential shear wave attenuation and its lateral variation in the north Atlantic region. *Journal of Geophysical Research* 97: 15339–15350.
- Shi J, Kim WY, and Richards PG (1996) Variability of crustal attenuation in the Northeastern United States from Lg waves. *Journal of Geophysical Research* 101: 25231–25242.

- Shito A, Karato S, and Park J (2004) Frequency dependence of Q in Earth's upper mantle inferred from continuous spectra of body waves. *Geophysical Research Letters* 31, doi:10.1029/2004GL019,582.
- Shito A and Shibutan T (2003b) Anelastic structure of the upper mantle beneath the northern Philippine Sea. *Physics of the Earth and Planetary Interiors* 140: 319–329.
- Shito A and Shibutan T (2003a) Anelastic structure of the upper mantle beneath the northern Philippine Sea. *Physics of the Earth and Planetary Interiors* 140: 319–329.
- Singh S and Herrmann RB (1983) Regionalization of crustal Q in the continental United States. *Journal of Geophysical Research* 88: 527–538.
- Singh SC, Taylor MJ, and Montagner JP (2000) On the presence of liquid in the Earth's inner core. *Science* 287: 2471–2474.
- Sipkin SA and Jordan TH (1979) Frequency dependence of Q_{ScS} . *Bulletin of the Seismological Society of America* 69: 1055–1079.
- Sipkin SA and Jordan TH (1980) Regional variation of Q_{ScS} phases. *Bulletin of the Seismological Society of America* 70: 1071–1102.
- Sipkin SA and Revenaugh J (1994) Regional variation of attenuation and travel times in China from analysis of multiple ScS phases. *Journal of Geophysical Research* 99: 2687–2699.
- Smith S (1972) The anelasticity of the mantle. *Tectonophysics* 13: 601–622.
- Smith ML and Dahlen FA (1981) The period and Q of the Chandler wobble. *Geophysical Journal of the Royal Astronomical Society* 64: 223–282.
- Smith MF and Masters G (1989) Aspherical structure constraints from free oscillation frequency and attenuation measurements. *Journal of Geophysical Research* 94: 1953–1976.
- Sobolev SV, Zeyen H, Soll G, Werling F, Altherr R, and Fuchs K (1996) Upper mantle temperatures from teleseismic tomography of French Massif Central including the effects of composition, mineral reactions, anharmonicity, anelasticity and partial melt. *Earth and Planetary Science Letters* 139: 147–163.
- Solomon SC (1973) Seismic wave attenuation and melting beneath the Mid-Atlantic Ridge. *Journal of Geophysical Research* 78: 6044–6059.
- Song XD and Helmberger D (1993) Anisotropy of the Earth's inner core. *Geophysical Research Letters* 20: 285–288.
- Souriau A and Romanowicz B (1996) Anisotropy in inner core attenuation: A new type of data to constrain the nature of the solid core. *Geophysical Research Letters* 23: 1–4.
- Souriau A and Romanowicz B (1997) Anisotropy in the inner core: Relation between P-velocity and attenuation. *Physics of the Earth and Planetary Interiors* 101: 33–47.
- Souriau A and Roudil P (1995) Attenuation in the uppermost inner core from broadband GEOSCOPE PKP data. *Geophysical Journal International* 123: 572–587.
- Street RL (1976) Scaling Northeastern United States/southeastern Canadian earthquakes by the Lg waves. *Bulletin of the Seismological Society of America* 66: 1525–1537.
- Strick E (1967) The determination of Q, dynamic viscosity and creep curves from wave propagation measurements. *Geophysical Journal of the Royal Astronomical Society* 13: 197–218.
- Su WJ and Dziewonski AM (1990) Inner core anisotropy in three dimensions. *Journal of Geophysical Research* 100: 9831–9852.
- Suda N and Fukao Y (1990) Structure of the inner core inferred from observations of seismic core modes. *Geophysical Journal International* 103: 403–413.
- Suda N, Nawa K, and Fukao Y (1998) Earth's background free oscillations. *Science* 279: 2089–2091.
- Suda N, Shibata N, and Fukao Y (1991) Degree 2 pattern of attenuation structure in the upper mantle from apparent complex frequency measurements of fundamental spheroidal modes. *Geophysical Research Letters* 18: 1119–1122.
- Suetsugu D (2001) A low Q_{ScS} anomaly near the South Pacific Superswell. *Geophysical Research Letters* 28: 391–394.
- Sumita I and Olson P (1999) A laboratory model for convection in Earth's core driven by a thermally heterogeneous mantle. *Geophysical Research Letters* 26: 1547–1549.
- Sutton GH, Mitronovas W, and Pomeroy PW (1967) Short-period seismic energy radiation patterns from underground explosions and small-magnitude earthquakes. *Bulletin of the Seismological Society of America* 57: 249–267.
- Tanaka S and Hamaguchi H (1997) Degree one heterogeneity and hemispherical variation of anisotropy in the inner core from PKP(BC)-PKP(DF) times. *Journal of Geophysical Research* 102: 2925–2938.
- Teng TL (1968) Attenuation of body waves and the Q structure of the mantle. *Journal of Geophysical Research* 73: 2195–2208.
- Thouvenot F (1983) Frequency dependence of the quality factor in the upper crust: A deep seismic sounding approach. *Geophysical Journal of the Royal Astronomical Society* 73: 427–447.
- Trampert J and Woodhouse JH (1995) Global phase velocity maps of Love and Rayleigh waves between 40 and 150 seconds. *Geophysical Journal International* 122: 675–690.
- Tryggvason E (1965) Dissipation of Rayleigh-wave energy. *Journal of Geophysical Research* 70: 1449–1455.
- Tsai YB and Aki K (1969) Simultaneous determination of the seismic moment and attenuation of seismic surface waves. *Bulletin of the Seismological Society of America* 59: 275–287.
- Tseng TL, Huang BS, and Chin BH (2001) Depth-dependent attenuation in the uppermost inner core from the Taiwan short period PKP data. *Geophysical Research Letters* 28: 459–462.
- Ulug A and Berckhemer G (1984) Frequency dependence of Q for seismic body waves in the Earth's mantle. *Journal of Geophysics* 56: 9–19.
- Utsu T (1967) Anomalies in seismic wave velocity and attenuation associated with a deep earthquake zone. *Journal of the Faculty of Science, Hokkaido University* 7: 1–25.
- Vidale JE and Earle PS (2000) Fine-scale heterogeneity in the Earth's inner core. *Nature* 404: 273–275.
- Vinnik LP, Romanowicz B, and Bréger L (1994) Anisotropy in the center of the Inner Core. *Geophysical Research Letters* 21: 1671–1674.
- Warren LM and Shearer PM (2002) Mapping lateral variation in upper mantle attenuation by stacking P and PP spectra. *Journal of Geophysical Research* 107, doi:10.1029/2001JB001,195.
- Wen L and Niu F (2002) Seismic velocity and attenuation structures in the top of the Earth's inner core. *Journal of Geophysical Research* 107, doi:10.1029/2001JB000,170.
- Widmer R, Masters G, and Gilbert F (1991) Spherically symmetric attenuation within the Earth from normal mode data. *Geophysical Journal International* 104: 541–553.
- Wilcock WSD, Solomon SC, Purdy GM, and Toomey D-R (1995) Seismic attenuation structure of the East Pacific Rise near 9° 30m N. *Journal of Geophysical Research* 100: 24147–24165.
- Wong YK (1989) *Upper Mantle Heterogeneity from Phase and Amplitude Data of Mantle Waves*. PhD Dissertation, Harvard University, Cambridge, MA.

- Woodhouse JH and Wong YK (1986) Amplitude, phase and path anomalies of mantle waves. *Geophysical Journal of the Royal Astronomical Society* 87: 753–773.
- Xie J, Gok R, Ni J, and Aoki Y (2004) Lateral variations of crustal seismic attenuation along the INDEPTH profiles in Tibet from LgQ inversion. *Journal of Geophysical Research* 109(B10): 308 (doi:10.1029/2004JB002,988).
- Xie J and Mitchell BJ (1990a) Attenuation of multiphase surface waves in the Basin and Range province. Part I : Lg and Lg coda. *Geophysical Journal International* 102: 121–127.
- Xie J and Mitchell BJ (1990b) A back-projection method for imaging large-scale lateral variations of Lg coda Q with application to continental Africa. *Geophysical Journal International* 100: 161–181.
- Xie J and Nuttli OW (1988) Interpretation of high-frequency coda at large distances: Stochastic modeling and method of inversion. *Geophysical Journal* 95: 579–595.
- Xie J, Wu X, Liu R, Schaff D, Liu Y, and Liang J (2006) Tomographic regionalization of crustal Lg Q in eastern Eurasia. *Geophysical Research Letters* 33(L03): 315 (doi:10.1029/2005GL024,410).
- Yacoub NK and Mitchell BJ (1977) Attenuation of Rayleigh wave amplitudes across Eurasia. *Bulletin of the Seismological Society of America* 67: 751–769.
- Yoshida M and Tsujiiura M (1975) Spectrum and attenuation of multiply-reflected core phases. *Journal of Physics of the Earth* 23: 31–42.
- Yu W and Wen L (2006) Seismic velocity and attenuation structures in the top 400 km of the Earth's inner core along equatorial paths. *Journal of Geophysical Research* 111: (doi:10.1029/2005JB003,995).
- Zhang T and Lay T (1994) Analysis of short-period regional phase path effects associated with topography in Eurasia. *Bulletin of the Seismological Society of America* 84: 119–132.

Relevant Website

<http://mahi.ucsd.edu> – The Reference Earth Model

1.22 Constraints on Seismic Models from Other Disciplines – Constraints from Mineral Physics on Seismological Models

L. Stixrude, University of Michigan, Ann Arbor, MI, USA

R. Jeanloz, University of California at Berkeley, Berkeley, CA, USA

© 2007 Elsevier B.V. All rights reserved.

1.22.1	Introduction	775
1.22.2	Mineral Elasticity	777
1.22.2.1	Overview	777
1.22.2.2	One-Dimensional Lattice Dynamics and the Continuum Limit	778
1.22.2.3	Experimental Methods	779
1.22.2.4	3-D Lattice Dynamics: Polarization and Anisotropy	780
1.22.2.5	Nontrivial Crystal Structures, Optic Modes, and Thermodynamics	784
1.22.2.6	Influence of Pressure and Temperature on the Elastic Constants	788
1.22.3	Rock Elasticity	790
1.22.3.1	Overview	790
1.22.3.2	Composites Theory	790
1.22.3.3	Attenuation and Dispersion	793
1.22.4	Seismological Elasticity and Anelasticity	796
1.22.4.1	Scaling	796
1.22.4.2	Uncertainties	797
1.22.4.3	Implications for Inversions	799
1.22.5	Conclusions and Outlook	800
References		800

1.22.1 Introduction

Earth is unique among the planets as the only body for which we have a detailed picture of its internal structure. We may compare that part of seismology concerned with Earth structure to an experimental science concerned with a single, very large sample. The source of illumination is generated naturally, in the form of earthquakes, many each year large enough to generate measurable ground accelerations at the antipodes. (There are typically more than 10 major (magnitude 7–8), 100 large (magnitude 6–7), and 1000 damaging (magnitude 5–6) earthquakes each year. Prior to the current international moratorium, nuclear explosions have also provided seismic illumination of the Earth's deep interior: magnitudes of 5, 6, and 7 correspond roughly to yields of 32 kiloton, 1 megaton, and 32 megaton.) The detectors are seismic recording stations, which now number in the hundreds of the highest quality. The basic measurement is of the traveltimes from source to receiver, from which can be deduced the elastic-wave velocity along the path of propagation; the displacement

versus time (waveform) shown by the seismic record also provides information about the spatial gradients of wave velocity at depth. Millions of crossing rays have illuminated every corner of the interior, leading to models of Earth structure in which the velocity is considered known to within 1%. In addition, the frequencies of Earth's resonances (free oscillations or normal modes) excited by large earthquakes, typically determined to a part in 10^3 for hundreds of overtones, provide important information on the distribution of density at depth.

Such extraordinary precision rivals or exceeds our ability to measure elastic-wave velocities in the laboratory at conditions representative of most of the Earth's interior. In reality, the seismological determination of velocity is somewhat more limited than this comparison would suggest, primarily by spatial resolution: the smaller the region of interest, the larger the uncertainties.

Earth is unusual as an experimental sample in ways other than its large size. Pressure, temperature, and composition are all inhomogeneous, and the spatial variations of these quantities are due to

processes internal to the planet, rather than being externally imposed. Temperature and compositional fields both show large radial and lateral variations that are the product of Earth's origin, evolution, and dynamics. But how to determine these quantities? We have no *in situ* measurements of either temperature or composition below the crust, and seismology alone does not suffice: only the elastic-wave velocities and density are measured, not temperature or composition.

A central concern of mineral physics has been to uncover the nature of Earth's internal temperature and composition, with a view toward placing critical observational constraints on the planet's history and geological processes. For example, by recognizing the connection between the bulk sound velocity determined seismologically and the compressibility ($1/K_S$), Adams and Williamson showed that much of Earth's structure can be explained by an adiabatic variation of temperature with depth. (Two kinds of sound waves propagate through solids, compressional and shear (also referred to as longitudinal and transverse) that have velocities $V_P = \sqrt{[(K_S + \mu)/\rho]}$ and $V_S = \sqrt{(\mu/\rho)}$, respectively, with K being the adiabatic bulk modulus (or incompressibility), μ the shear modulus (or rigidity), and ρ the density. The bulk sound velocity, $V_B = \sqrt{(V_P^2 - 4/3 V_S^2)} = \sqrt{(K_S/\rho)}$, ignores the effects of rigidity and treats the material as a fluid.) By comparing seismological models and experimental – mostly shock-wave – data, Birch identified iron as the primary constituent of Earth's core, and the mean atomic mass of the mantle as being similar to that of certain xenoliths (rock fragments of the Earth's interior brought to the surface by volcanic processes). Ringwood, Akimoto, and others showed that seismologically observed mantle discontinuities can be explained by phase transformations observed in experiments on samples of mantle-like composition. In each case, a key to our current view of the Earth's origins and current vigorously convecting state were established.

It may seem at first surprising that materials of such different sizes, from thousand-kilometer structures in Earth to laboratory samples as small as a few microns – a range of 12 orders of magnitude – may be compared at all. (Though they are usually ignored for bulk samples, if one takes surface effects into account, the comparison can be extended down to the nanometer scale.) Actually, the basic approach is not unique to geophysics and forms the basis for understanding the structure and evolution of giant planets or stars. The theoretical basis

for spanning the range of length scales from atoms to planets lies at the heart of thermodynamics and statistical mechanics: the prediction that the equilibrium properties of materials should not depend on the size of the sample. There are deep connections to seismology as well: the analysis of the normal modes of vibration of an atomic lattice leads to concepts of dispersion and elastic-wave velocity that can be linked directly to analogous seismological problems. Relating the large to the small is essential for uncovering the temperature and composition throughout the Earth's interior. High-pressure devices and theoretical simulations figuratively transport us to the inaccessible interior, giving us a unique window into its nature.

From the point of view of materials theory, Earth is a particularly challenging object because it consists of solids and fluids (condensed matter) at moderate to high pressures. Unlike the gases that make up planetary atmospheres, the temperature-dependent constitutive relations between stress, strain, and strain rate (pressure, density, and deformation rate for a fluid) cannot be written down analytically. Much of the effort in mineral physics is devoted to discovering these constitutive relations, either by experimental measurement or by quantum mechanical theory.

The solid state is also complex in that elements organize themselves into multiple phases of different composition and crystal structure (i.e., geometric arrangement by which the atoms are packed together to form the crystal). Each phase has distinctive physical and chemical properties, and its behavior must be understood separately and in combination with other phases. The exploration of high pressure continues to be one of the frontiers of mineral physics, including the challenge of measuring physical properties in the laboratory at conditions of Earth's interior, and the ongoing discovery of new solid phases.

Perhaps the most challenging aspect of the solidity of materials making up the mantle is that it imposes limitations on our ability to scale from laboratory to Earth. These limitations arise from the heterogeneity inherent even in the purest sample in the form of grain boundaries and the differences in size, shape, and orientation of the constituent grains. So, for example, it is not possible to uniquely compute the seismic velocity of a rock from the properties of its constituent single crystals, although rigorous bounds can be formulated if the grains are randomly oriented. An exact computation would require

complete specification of the grain geometry. Although usually not the case for Earth materials, the bounds can be far apart in the presence of significant mechanical heterogeneities such as partial melts or cracks. More generally, some physical properties such as attenuation and scattering depend essentially on length scale, and often in ways that are difficult to predict.

The significance of the length scale of heterogeneity is intimately linked to the timescale of deformation. All materials contain defects, such as dislocations, interstitial atoms, and vacancies. When deformed at very high ('infinite') frequency, the types and concentrations of defects are of little consequence and the material deforms elastically because the defects are frozen in place. Seismic waves have much longer periods of deformation however – roughly 14 orders of magnitude greater than those of atomic vibrations. At these timescales, defects can move in response to deformation, leading to anelastic behavior with absorption of mechanical energy and lowering of the elastic wave relative to the elastic limit. In the limit of much longer periods of deformation, such as those that characterize mantle convection, the deformation is entirely viscous and dominated by the motion of defects.

The nature and degree of anelasticity depends in detail on defect types (point defects, dislocation, grain boundary), concentrations, and mobilities. Anelasticity is thus not a state function, in the usual thermodynamic sense, and can depend on the past history of the sample. This presents severe challenges to experimental control and characterization, and to our ability to relate the results to the Earth where the deformation history that the materials have undergone may be very different from those prepared in the laboratory. On the other hand, the fact that anelasticity depends on so many more variables than the elastic-wave velocity presents the opportunity for further characterizing the nature of Earth's interior in ways that are not possible through analysis of the elastic limit alone.

We will explore the relationship between minerals properties and Earth structure in more depth. Our approach will be that of the forward problem. We begin with the fundamentals of mineral elasticity, including the basic theory of lattice vibrations, dispersion and normal modes, and its relationship to the various experimental probes of elasticity, to the thermodynamic properties of minerals, and to the underlying quantum mechanics of bonding. Discussion of the elasticity of rocks includes an

outline of the theory of composites as applied to the elastic constants, and the essentials of anelasticity. Finally, we consider the issue of scaling in length and timescale from the laboratory to the Earth. We end with thoughts on the prospects for the inverse problem; that is, formally inverting seismological observations for quantities such as the temperature and compositional fields at depth via knowledge of materials properties.

1.22.2 Mineral Elasticity

1.22.2.1 Overview

In the limit of ideal crystals and small deformations, the elasticity of solids is most usefully viewed in the context of the vibrational modes of crystalline structures. The theory of the dynamics of perfect crystals is our most powerful way of envisioning length scaling. It gives us a formally exact means of relating the elastic-wave velocity of samples ranging in size from submicron to in principle infinite size, limited only by considerations of surface effects at small scales and of self-gravitation as we approach planetary size. The material can be treated as a continuum at large scales, and its properties derived from consideration of the forces acting between atoms, that is, from a description at the smallest of scales. In particular, the seismic-wave velocities of a perfect crystal are determined by its crystal structure and the interatomic forces.

This approach of lattice dynamics is also important in geophysics because it underlies our understanding of the influence of temperature on physical properties, including thermal expansion that drives convection of the mantle and core, and seismic-wave velocities that provide images of our planet's interior. The theory of thermal conductivity also derives from concepts of phonons, which are the modes of oscillation of atoms in a crystal (analogous to the normal modes of the Earth). The theory of lattice dynamics is well developed, and there are many excellent texts covering the subject more deeply than we can here (Ashcroft and Mermin, 1976; Born and Huang, 1954; Dove, 1993). In addition to illustrating the connection between microscopic and macroscopic properties, our goals are to illustrate the relationship between experimental and geophysical measurements of elastic-wave velocities.

1.22.2.2 One-Dimensional Lattice Dynamics and the Continuum Limit

A good illustration of these concepts is provided by the normal modes of vibration of a linear chain of identical atoms of mass m separated by a distance a and connected with Hookean springs, for which the relationship between force F and displacement u is $F = Ku$, where K is the force constant (Figure 1). The potential energy is a quadratic function of the displacement of the atoms, and the equations of motion (force equals mass times acceleration, expressing conservation of linear momentum) are

$$m \frac{\partial u_n^2}{\partial t^2} = K [(u_{n+1} - u_n)^2 + (u_{n-1} - u_n)^2] \quad [1]$$

Here, u_n is the displacement of the n th atom from its ideal lattice site, located at the position na . Substituting a traveling-wave solution for u_n as a function of position and time $u = A \exp[i(\omega t - kx)]$, we find the dispersion relation (Figure 1):

$$\omega = 2\sqrt{\frac{K}{m}} \left| \sin\left(\frac{ka}{2}\right) \right| \quad [2]$$

where ω is the frequency (in rad s^{-1}), $k = 2\pi/\lambda$ is the wave number (in rad m^{-1}) (in two and three dimensions (2-D and 3-D), the wave vector specifies the

propagation direction and its magnitude gives the wave number), and λ is the wavelength (in meter/cycle) of the normal mode of vibration. The phase velocity describing the propagation speed of a given wavelength is given by $V_\phi = \omega/k$, whereas the group velocity that describes the propagation speed of a wave packet (i.e., many different wavelengths, and hence the wave energy) is $V_G = \partial\omega/\partial k$. In general, the linear monatomic chain is thus dispersive, with wavelength-dependent velocities and specifically $V_G < V_\phi$ (i.e., a low-pass filter: longer waves travel faster than shorter waves).

At long wavelength, as $k \rightarrow 0$, the group and phase velocities are the same (which means there is no dispersion, i.e., spreading out of a wave packet):

$$V = a\sqrt{\frac{K}{m}} = \sqrt{\frac{M}{\rho}} \quad [3]$$

where the last equality emphasizes the relationship with the seismic-wave velocity expressed in terms of an elastic modulus, $M = K/a$, and a density, $\rho = m/a^3$. Here, M is the longitudinal modulus, since propagation and polarization are parallel for the present 1-D example. The motion described by eqns [2] and [3], with $\omega \rightarrow 0$ as $k \rightarrow 0$, is referred to as an acoustic mode.

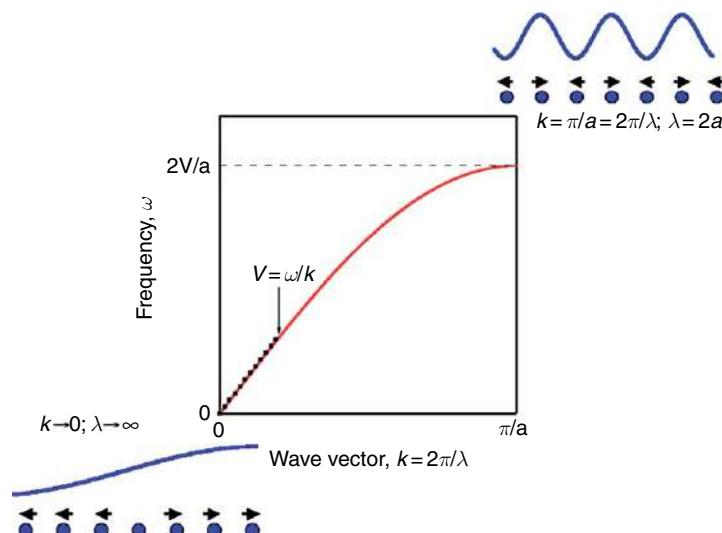


Figure 1 Phonon dispersion relation for the one-dimensional lattice (red line) indicating the relationship to the acoustic velocity as the slope at the origin (dashed black line). Schematically illustrated are vibrational modes, with arrows and blue curves indicating the sense of displacement of the atoms (blue circles) in the limits of long wavelengths (lower left) and of the shortest wavelengths (upper right). The group velocity (slope of the $\omega-k$ curve) vanishes at the Brillouin-zone edge, $k = \pi/a$, because shorter wavelengths cannot be propagated across the discrete row of atoms; consequently, there is a standing wave with no wave-energy propagation for $\lambda = 2a$.

Equation [3] applies to the continuum limit, with wavelengths being much larger than interatomic spacings, as is the case for seismic waves. Indeed, it agrees with our intuitive notions about seismic-wave velocities. As we increase the strength of the interatomic forces the velocity increases, as it would, for example, in the case of increasing pressure. Also, as we increase the mass of the atoms, the velocity decreases, as it would, for example, in the case of iron enrichment.

What do the normal modes look like in the limit of the wavelength approaching twice the interatomic spacing, $k \rightarrow \pi/a$? This is of interest because shorter wavelengths cannot be supported by the chain of discrete atoms (this limitation is identical to the Nyquist theorem encountered in Fourier and signal theory, which specifies that at least two samples per wavelength are needed to characterize a wave); in fact, normal modes with wavelengths less than twice the interatomic spacing are indistinguishable from those within the wave number range $k=0$ to π/a . This range of wave numbers, defining the first Brillouin zone in reciprocal (wave number) space, contains complete information on all the normal modes that the chain of atoms can experience. At the Brillouin zone edge ($k=\pi/a$), the motion of each atom opposes its neighbors (Figure 1). Each bond is stretched or compressed by the same amount, producing the maximum frequency $\omega = 2\sqrt{K/m} = 2V/a$.

The particulate nature of matter thus produces velocity dispersion as wavelengths approach atomic (or unit-cell) dimensions, well below the continuum range. This is reflected in the nonlinear form of eqn [2] and, for example, the difference between the Brillouin-zone edge frequency and the linear extrapolation of eqn [2] to the Brillouin-zone edge $\omega = \pi V/a$. This type of dispersion is negligible in the usual geophysical context, and, for ideal crystals, scaling from laboratory samples to geophysical length scales is essentially exact. From eqn [2], we find that even for length scales corresponding to very small grains (1 μm), the dispersion is only about 1 part in 3000. This unity of length scales is modified by heterogeneity (e.g., grain boundaries) and anelasticity in real (nonideal) samples.

1.22.2.3 Experimental Methods

Experimental probes of the elastic-wave velocities have characteristic wavelengths that, while orders of magnitude smaller than those of seismic waves, lie

well within the continuum, infinite-size limit of ideal crystals. Brillouin spectroscopy is most closely connected to the phonon spectrum (Duffy *et al.*, 1995; Jackson *et al.*, 2000; Sinogeikin and Bass, 2000; Weidner *et al.*, 1982). Here, one measures the normal-mode frequency of the acoustic branch at a small but finite value of the wave number related to the wavelength of the (generally visible) light used to probe the sample, with the ratio of frequency to wave number yielding the elastic-wave velocity. (The wave number is given by the magnitude of the scattering vector (i.e., the projection of the light's wavelength onto the direction of acoustic-wave propagation in the crystal) through a formula analogous to Bragg's law for X-ray diffraction. The frequency is observed as a Doppler-like shift of the scattered relative to the incoming light, and Brillouin spectroscopy can be thought of as the acoustic-mode analog of Raman spectroscopy, the latter scattering off the optic modes to be described below.) In impulsive stimulated scattering, a time-domain version of Brillouin spectroscopy, a phonon is excited by one laser and scatters light from a second laser, yielding information on elasticity, as well as thermal conductivity (Abramson *et al.*, 1999; Brown *et al.*, 1989; Zaug *et al.*, 1993).

Similarly, resonant ultrasound spectroscopy and ultrasonic interferometry determine the normal-mode frequencies of a macroscopic crystal (megahertz for typical experimental sample sizes), and are thus analogous to normal-mode studies of the Earth (Anderson and Isaak, 1995; Goto *et al.*, 1976; Jackson and Niesler, 1982). Other ultrasonic methods are analogous to body-wave seismology: an acoustic pulse of frequency in the range of mega- to gigahertz is generated via a transducer and the traveltimes across the sample measured; multiple reflections and interference are used to maximize precision (Rigden *et al.*, 1991; Spetzler, 1970; Yoneda, 1990). High frequencies are essential so that the acoustic wavelength (10 μm–1 mm) is much smaller than the size of the sample (~1 mm for *in situ* high-pressure measurements).

All of these methods involve small ('infinitesimal')-amplitude waves. In addition, two classes of finite-compression methods are available: dynamic (shock wave) and static. In the first, a large-amplitude deformation wave is generated by impact of a projectile or a laser pulse into the sample, which is then compressed on a timescale of nanoseconds. The velocity of the resulting shock wave is then approximately equal to the longitudinal-wave velocity at low pressures (below the dynamic yielding point) and to the

bulk sound velocity at higher pressures (thermal and other corrections can be made to obtain more exact results). Above the dynamic yielding point, the shock front moves at close to the high-pressure bulk-sound velocity (i.e., fluid-like response), but rarefaction waves – inevitably generated at all free surfaces of the sample – propagate into the shock-loaded state at the isentropic sound velocity: this is measurable, with the initial decompression traveling at the longitudinal- (compressional-) wave velocity. The bulk sound velocity (V_B) and longitudinal-wave velocity (V_P) can thus be probed dynamically, and the shear-wave velocity (V_S) is obtained from the relation (Brown and McQueen, 1986; Duffy and Ahrens, 1992),

$$\frac{4}{3}V_S^2 = V_P^2 - V_B^2 \quad [4]$$

The bulk sound velocity can also be determined in static experiments (Jeanloz and Thompson, 1983; Stixrude *et al.*, 1992). Using a diamond-anvil cell or another high-pressure device, one measures the volume (or density ρ) as a function of pressure via very slow (minutes–days) stepwise compression: X-ray diffraction is used to determine the compression, for example. The slope of the relationship yields the isothermal bulk modulus K_T , which is related to V_B through

$$V_B = \sqrt{\frac{K_S}{\rho}} \quad [5]$$

and the correction from isothermal to adiabatic (K_S) bulk moduli which is small at room temperature.

One of the most important conclusions to arise from these various probes of material elasticity is that frequency dependence is essentially undetectable over 8 orders of magnitude: the shear- and longitudinal-wave velocities are indistinguishable from 100 THz (Brillouin) to 1 MHz (ultrasonic), and the bulk sound velocity is invariant from 100 THz to the essentially zero-frequency (DC) measurements of static compression. In contrast, the Earth shows measurable frequency dependence of the velocity over a much narrower range of lower frequencies (few hertz to millihertz) (Dziewonski and Anderson, 1981). The comparison with laboratory studies confirms the expectation that the magnitude of attenuation and the resulting dispersion increase with decreasing frequency.

1.22.2.4 3-D Lattice Dynamics: Polarization and Anisotropy

Only longitudinal elastic modes are possible in 1-D: shear elastic modes are higher-dimensional phenomena since the polarization (direction of atomic displacement) differs from that of propagation (wave vector). In 3-D, there are three acoustic branches, one corresponding to the P wave and two to the S waves (Figure 2: the optic modes are discussed below). All solids support both longitudinal and shear waves. In the case of isotropic solids (glasses) and liquids (just as at low enough deformation rates solids flow plastically, at high enough frequencies fluids transmit shear waves over finite distances), the two shear branches are degenerate. For nonisotropic media (crystals and liquid crystals), the two shear branches are in general distinct, although they may be degenerate along certain high-symmetry directions.

Anisotropy is the variation of the elastic-wave velocity with propagation polarization direction, and is governed by the fourth-rank elastic-constant tensor, c_{ijkl} (Kosevich *et al.*, 1986; Wallace, 1972). The polarizations and original slopes of the three acoustic branches for wave vector k are given by the Christoffel equation,

$$\rho V^2 = c_{ijkl} \hat{w}_i \hat{k}_j \hat{w}_k \hat{k}_l \quad [6]$$

where w_i is the polarization vector, the carets indicate unit vectors, and we have used the Einstein notation (summation over repeated subscripts, and each subscript takes on each of its values, $i=1, 2, 3$ (e.g., x, y, z directions)). The symmetry of the elastic-constant tensor reflects that of the point group of the crystal (Nye, 1985). For an isotropic solid (glass), there are only two independent elastic constants, which may be taken as the bulk and shear modulus. For cubic crystals, there are three, c_{11} , c_{12} , and c_{44} , referred to as longitudinal, off-diagonal, and shear, respectively; and as many as 21 for the lowest-symmetry point group (triclinic crystals). Evaluating eqn [6] for pure P-wave propagation ($k=w$) in cubic symmetry,

$$\frac{\rho V_P^2}{c_{11}} = 1 + 2A(k_1^2 k_2^2 + k_1^2 k_3^2 + k_2^2 k_3^2) \quad [7]$$

where the anisotropy factor,

$$A = \frac{2c_{44} - (c_{11} - c_{12})}{c_{11}} \quad [8]$$

completely determines the P-wave anisotropy (Karki *et al.*, 1997b). We have used the Voigt contraction for

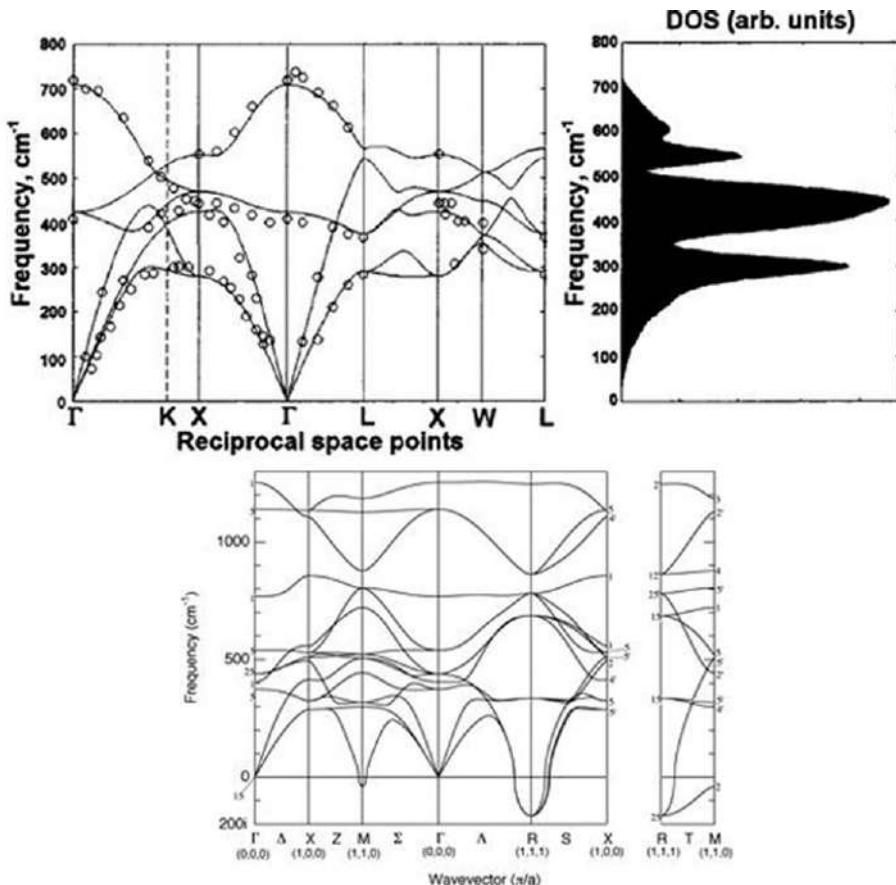


Figure 2 (Top) Phonon dispersion curves of periclase (MgO) according to density functional theory (lines) and experiment (circles), showing the three acoustic modes with zero frequency at the Brillouin-zone center (Γ point) and the three optic modes with finite frequency at Γ . On the right is the vibrational spectrum or density of states, $g(\omega)$, computed from the theoretical phonon dispersion curves: at each frequency, the total number of normal modes is indicated for all wave vectors intersecting the dispersion curves (this means that a higher density of modes is obtained from those portions of the curves having small group velocities, or vanishing $\partial\omega/\partial k$; also, due to the effects of 3-D, the number of modes contributing from each branch increases as $\sim k^2$, even without dispersion). (Bottom) Phonon dispersion curves of CaSiO₃ perovskite according to density functional theory, with unstable modes (shown as negative frequencies) at the M- and R-points and along the line from M-R. These unstable modes formed the basis for predicting a phase transformation in CaSiO₃ perovskite (Stixrude et al., 1996) that has recently been confirmed experimentally. The meaning of the symbols identifying special points in reciprocal space are defined in terms of the wave vector, and are the same in the upper and lower figures. (Top) From Oganov AR, Gillan MJ, and Price GD (2003) *Ab initio* lattice dynamics and structural stability of MgO. *Journal of Chemical Physics* 118: 10174–10182. (Bottom) From Stixrude L, Cohen RE, Yu R, and Krakauer H (1996) Prediction of phase transition in CaSiO₃ perovskite and implications for lower mantle structure. *American Mineralogist* 81: 1293–1296.

the indices of the elastic constants: 11 → 1, 22 → 2, 33 → 3, 12 → 6, 13 → 5, 23 → 4. One can show that A also determines the azimuthal and polarization shear anisotropy. The right-hand side of eqn [7] gives 1 + 2/3 A , 1 + 1/2 A , and 1 for propagation along [111], [110], and [100], respectively.

We can evaluate the likely magnitude of single-crystal anisotropy if we assume that the interatomic forces are central and between nearest neighbors only, and we neglect coupling between strain and

vibrational modes. The elastic-constant tensor is then (Gieske and Barsch, 1968)

$$c_{ijkl} = (K - P) \sum_{\alpha=1}^z \hat{r}_i^\alpha \hat{r}_j^\alpha \hat{r}_k^\alpha \hat{r}_l^\alpha \quad [9]$$

where P is pressure, z the coordination number, and \hat{r}^α the unit vector between an atom and its nearest neighbor α ; the sum is over all nearest neighbors. For body-centered cubic (b.c.c.) and face-centered cubic (f.c.c.) crystal structures, eqn [9] yields positive

values of A , and therefore greater velocities along [111] and [110] than along [100]. The magnitude of the anisotropy is large: for f.c.c., $A=1/2$, yielding peak-to-peak variations in the P-wave velocity of 30%. This simple model has been applied to oxides based on the argument that the elasticity is primarily governed by the oxygen sublattice and oxygen–oxygen repulsion, with the cations playing a passive, charge-balancing role.

The relative importance of central versus other interatomic forces can be deduced by comparing the elements of the elastic-constant tensor to the predictions of the Cauchy relations, which apply for purely central forces (Figure 3). (Angle-dependent and three-body forces are examples of such noncentral interactions between atoms. Weiner (1983) shows more generally that for centrosymmetric crystals the harmonic elastic moduli satisfy the Cauchy relations if the electron charge density follows the (homogeneous) deformation of the underlying lattice of nuclei.) For example, in a cubic material, the Cauchy relations predict

$$c_{12} - c_{44} = 2P \quad [10]$$

In the case of MgO, often considered to be a prototypical ionic solid for which one would expect central forces to be dominant, eqn [10] is increasingly violated with increasing pressure (Isaak *et al.*, 1990; Karki *et al.*, 1997b). This shows that the interatomic forces become increasingly noncentral with

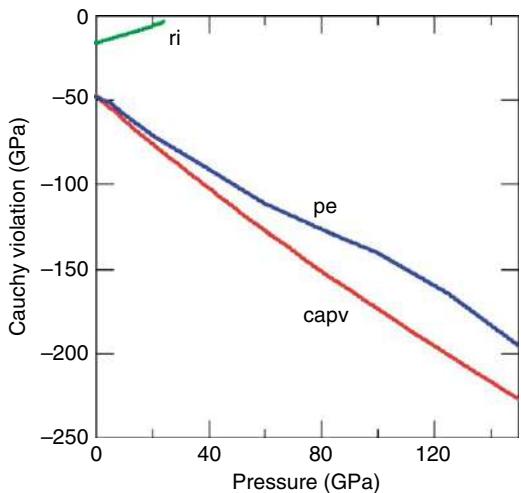


Figure 3 Violation of the Cauchy relation (eqn [10]) of three cubic minerals according to density functional theory: spinel-structured Mg_2SiO_4 , ringwoodite (ri); NaCl-structured MgO, periclase (pe); and perovskite-structured $CaSiO_3$ (capv) (Karki and Crain, 1998; Karki *et al.*, 1997b; Kiefer *et al.*, 1997).

increasing pressure, as expected on systematic grounds. One consequence of this change in forces is that the sign of the anisotropy changes with increasing pressure (Figure 4). Whereas at low pressure, A is large and positive, in accord with expectations based on eqn [9] and the f.c.c. oxygen

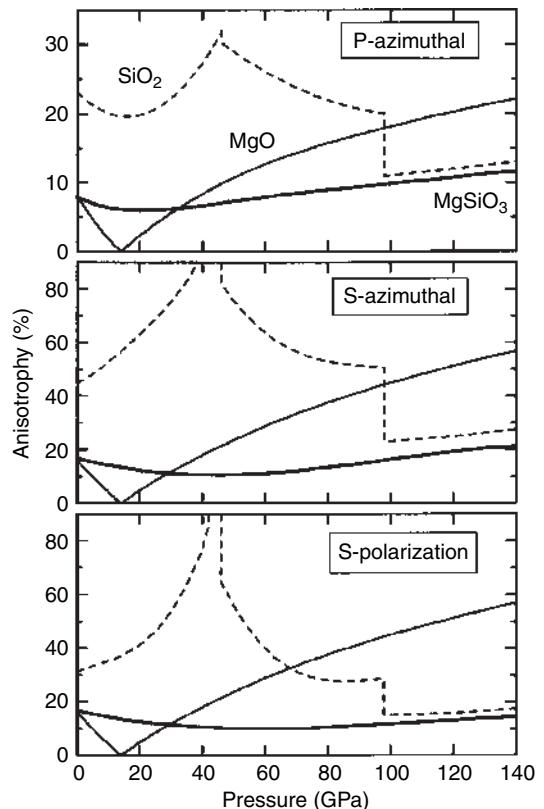


Figure 4 Elastic anisotropy of SiO_2 (dashed curves), MgO periclase (light solid), and $MgSiO_3$ perovskite (bold solid) according to density functional theory. P- and S-azimuthal anisotropy are the differences between the maximum and minimum P- and S-wave velocities, respectively, over all propagation and polarization directions, and the polarization anisotropy is the maximum difference in velocity between the two S-wave polarizations over all propagation directions. The discontinuous changes in the curve for SiO_2 are due to phase transformations from stishovite to the $CaCl_2$ structure at 47 GPa and to the α - PbO_2 structure at 100 GPa. Breaks in slope in the MgO and $MgSiO_3$ curves represent pressures at which the pattern of anisotropy changes. In the case of MgO, the break in slope coincides with a vanishing of the anisotropy that is due to a change in sign of the anisotropy factor A (eqn [8]). From Stixrude L (1998) Elastic constants and anisotropy of $MgSiO_3$ perovskite, periclase, and SiO_2 at high pressure. In: Gurnis M, Wysession M, Knittle E, and Buffet B (eds.) *The Core–Mantle Boundary Region*, pp. 83–96. Washington, DC: American Geophysical Union.

sublattice of MgO, at high pressure A becomes negative, with a magnitude at the core–mantle boundary greater than that at ambient pressure. The change in sign of A corresponds to a change in the fastest and slowest directions: [111] is fastest for P-wave propagation at ambient pressure, whereas [100] is fastest at the core–mantle boundary. Other minerals also show strong pressure dependence of the magnitude and sense of the anisotropy (Karki *et al.*, 2001).

Considerations of mechanical stability place constraints on the relative magnitude of the elastic constants of any material, whether single crystals or rocks. For isotropic symmetry, the stability condition is simply that the bulk and shear moduli be positive definite. For cubic symmetry, the conditions are

$$c_{44} > 0, c_{11} > |c_{12}|, c_{11} + 2c_{12} > 0 \quad [11]$$

and for hexagonal symmetry,

$$c_{44} > 0, c_{11} > |c_{12}|, (c_{11} + c_{12})c_{33} > 2c_{13}^2 \quad [12]$$

The more general statement from which stability conditions for arbitrary symmetry are derived is that the principal minors of the elastic-constant matrix (Voigt notation) must be positive definite (Nye, 1985). Elastic instabilities place fundamental constraints on the phases that exist in the Earth. For example, it has been argued that the predicted elastic instability in the b.c.c. phase of iron means that this phase cannot exist in the inner core, with important implications for the origin of anisotropy in this region (Stixrude *et al.*, 1994).

One of the most fundamental conclusions from experimental and theoretical studies of minerals is that the elastic anisotropy is much larger than that observed seismologically in most parts of the Earth. Peak-to-peak azimuthal variation in velocities of 10% or more are typical in mantle and core minerals, as compared with a few percent in the Earth. The single-crystalline anisotropy of some minerals is sufficiently large to produce cusps in the group velocity envelope (Helbig, 1984) (Figure 5). Experimental measurement and prediction of the single-crystal anisotropy is essential because it forms the basis for estimating the anisotropy of rocks, and places an upper bound on the rock anisotropy that can be produced by lattice preferred orientation. Most of the experimental methods discussed previously are capable of measuring the full elastic-constant tensor, and therefore the velocity in all directions. These measurements must be made on single crystals. In the case of Brillouin or ultrasonic interferometry, several measurements are necessary, varying the direction of the impulse with respect to the crystallographic axes in order to sample different directions in reciprocal space.

What is the origin of anisotropy in the mantle and core? There are at least two possible explanations, shape-preferred orientation and lattice-preferred orientation. These two mechanisms for generating anisotropy in a polycrystalline aggregate arise in principle from very different sets of processes, and so carry important implications for our understanding of mantle dynamics and evolution. In the case of lattice-preferred orientation, anisotropy

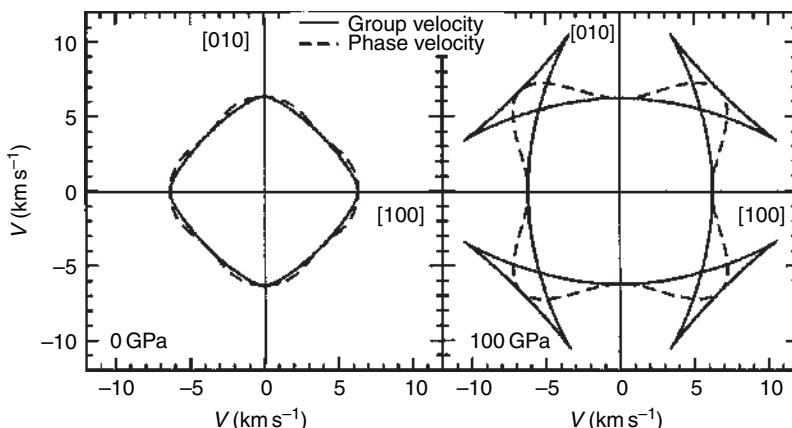


Figure 5 Group velocity (solid curves) and phase velocity (dashed curves) surfaces of S waves in MgO in the (001) plane at two pressures. The two velocities are close to each other at zero pressure due to relatively weak anisotropy, but they differ substantially at 100 GPa due to relatively strong anisotropy. From Karki BB, Stixrude L, and Wentzcovitch RM (2001) High-pressure elastic properties of major materials of Earth's mantle from first principles. *Reviews of Geophysics* 39: 507–534.

originates in the elastic anisotropy of the constituent crystals and is in general present for single- as well as multiphase aggregates. Since the single-crystal anisotropy can be large, it is natural to consider lattice-preferred orientation as the primary explanation in many cases (**Figure 4**). Knowledge of the single-crystal elastic anisotropy is not sufficient to determine that of a polycrystalline aggregate, however. For this, one must also know the texture, that is, the orientations of all the crystals in the aggregate.

Shape-preferred orientation arises from an inhomogeneous distribution of phases with different elastic properties. Anisotropy due to shape-preferred orientation scales with the contrast in physical properties between the phases, and therefore applies only to multiphase aggregates (composites). It can be large, for example, in cracked or partially molten rock. In the limit of large scales, variations of rock types (lithological variations) can induce anisotropy that affects seismic waves.

Presumably, both shape- and lattice-preferred orientation cause seismic anisotropy within the Earth. That the observed anisotropy is quantitatively much smaller than could be expected based on laboratory and theoretical studies of individual minerals and mineral aggregates strongly suggests that the seismological information is severely aliased. That is, the seismic wavelengths ($\sim 10^3\text{--}10^6\text{ m}$) are typically so much longer than the dimensions of crystals or even lithological variations, that they reflect only a broad spatial average of the true heterogeneity and anisotropy at depth.

1.22.2.5 Nontrivial Crystal Structures, Optic Modes, and Thermodynamics

Lattice vibrations are geophysically significant not only for their connection to elasticity, but also because they govern most thermodynamic properties of Earth materials, including the temperature dependence of the elastic constants. Most of the temperature dependence of the energy of a crystal comes from the increasing amplitude of atomic vibrations with increasing temperature. The derivation of the internal energy due to lattice vibrations is outlined in the texts listed above. Here we seek an intuitive understanding, simply quoting the result for the internal energy associated with atomic vibrations

$$U_{\text{vib}} = \frac{1}{2} \sum_i \hbar\omega_i + k_B T \sum_i \frac{\hbar\omega_i / k_B T}{e^{\hbar\omega_i / k_B T} - 1} \quad [13]$$

where \hbar is Planck's constant divided by 2π , k_B is Boltzmann's constant, and the sums are over all $3N$ vibrational modes with N being the number of atoms in the crystal. The first term is due to zero-point motion. The second term is the product of the energy of a particular vibrational mode ($\hbar\omega$) and the probability of excitation ('occupation') of that mode. The probability of occupation may appear unfamiliar because it is derived from the appropriate quantum (Bose–Einstein) statistics, but it does reduce to the Boltzmann factor $\exp(-\hbar\omega/kT)$ in the limit of high temperatures. The probability of occupation says that while very-high-frequency modes (such as the stretching of the O–H bond) will barely be excited until one reaches mantle temperatures, the part of the acoustic branch near the Brillouin-zone origin (i.e., wavelengths much larger than the interatomic spacing) is already fully excited even at room temperature.

Eventually, all vibrational modes are fully excited and the second sum on the right-hand side approaches a constant, equal to the number of modes ($3N$). In this Dulong–Petit limit, the vibrational energy is linear in temperature, and the heat capacity at constant density approaches a constant value,

$$C_p = \left(\frac{\partial U_{\text{vib}}}{\partial T} \right)_p \rightarrow 3Nk_B \quad [14]$$

or $1.188\text{ J K}^{-1}\text{ g}^{-1}$ for a mean atomic mass typical of the mantle (21 g mol^{-1}). Vibrational frequencies of Earth materials are such that the Dulong–Petit limit is obeyed to within a few percent at typical subcrustal temperatures.

A practical difficulty in using eqn [13] is that all the vibrational frequencies must be known, which is rarely the case for mantle phases, particularly at high pressure. By reformulating as a sum over energies rather than states, we reestablish the connection with the analysis of phonon dispersion outlined above, and develop a useful starting point for approximating the sums. The vibrational energy can then be written as

$$U_{\text{vib}} = k_B T \int_0^\infty \left(\frac{1}{2} + \frac{1}{e^{\hbar\omega / k_B T} - 1} \right) \frac{\hbar\omega}{k_B T} g(\omega) d\omega \quad [15]$$

where the vibrational density of states $g(\omega)$ (see **Figure 2**) is normalized such that

$$3N = \int_0^{\infty} g(\omega) d\omega \quad [16]$$

The power of this reformulation is illustrated by one of the simplest approximations for $g(\omega)$, due to Debye,

$$g(\omega) = 9N\omega^2 \left(\frac{\pi V}{a} \right)^{-3} \quad [17]$$

This is derived by treating the material as a homogeneous continuum: that is, ignoring optic modes (described below) and approximating the acoustic phonon branch as linear with slope equal to the acoustic velocity (see eqn [3]: for this case without dispersion $\omega \propto k$, and because $g(\omega) \propto k^2$ in 3-D, it is proportional to ω^2 as in eqn [17]). The quantity in parentheses, the Debye frequency, is just the result of linearly extrapolating the acoustic branch to the Brillouin-zone edge and is obtained by ensuring that eqn [16] is satisfied. (Ensuring that only $3N$ normal modes (i.e., $3N$ degrees of freedom) are present for a crystal of N atoms in 3-D takes into account the atomic constituents of the medium. It was Debye's genius to realize that a self-inconsistent model of a homogeneous continuum with underlying atomic structure would lead to a physically sound result.) In 3-D, the velocity is replaced by an appropriate average over all directions and polarizations, and the bond length by the mean atomic spacing. The squared-frequency dependence arises from the assumptions that the density of vibrational states is uniform in reciprocal space and that the first Brillouin zone is a sphere. The Debye approximation captures much of the essential features of the heat capacity, including the observation that it vanishes at zero temperature as T^3 and approaches the Dulong–Petit limit at high temperature.

Simple approximations to the vibrational density of states, like the Debye approximation, do not explicitly account for the structural complexity characteristic of most Earth materials: in particular, that several different atoms are typically present in each unit cell of the crystal structure (e.g., Mg and O in MgO). What influence do these complexities have on the normal modes of vibration? The essential features are captured by a linear chain, but now with two different spring constants (see also Kieffer, 1979) (Figure 6). The broken symmetry doubles the unit cell (i.e., two atoms, one of each color in each unit cell vs one atom per unit cell in the monatomic linear chain), and halves the first Brillouin zone. The

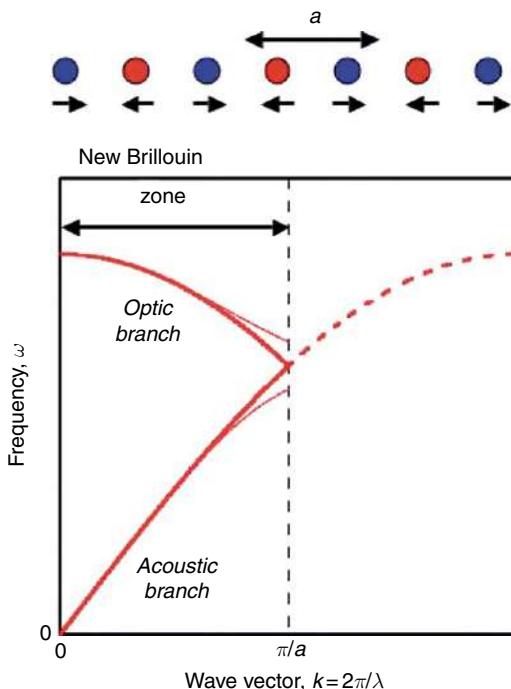


Figure 6 Phonon dispersion curve in a 1-D lattice with two types of atoms. The unit-cell dimension a is doubled compared with the monoatomic case, which halves the size of the Brillouin zone and folds the dispersion curve producing an optic branch. The pattern of vibration of the optic mode at zero wave vector is schematically illustrated; note that each unit cell has the identical pattern of vibration. The thin solid lines schematically illustrate the opening of an acoustic-optical gap that would be produced if the lattice contained two different force constants, or if the atoms had different masses.

relationship of the monatomic and diatomic unit cells in reciprocal space is one of folding the phonon branches so that the vibrational mode that appeared on the Brillouin-zone edge in the monatomic case is now folded back to the Brillouin-zone center. This is significant because now we have a vibrational mode of finite frequency at the Brillouin-zone center; as this can be observed with long-wavelength probes such as visible light, it is called an optic branch. In general, there are $3n$ mode frequencies at each wave number k in a 3-D crystal structure having n atoms per unit cell. (To be precise, we refer to the ‘primitive’ (smallest, irreducible) unit cell throughout this text. Other definitions of the crystallographic unit cell are often used for convenience.)

Now consider what happens when the difference in the two spring constants begins to grow or the masses of the two atoms in the unit cell are allowed

to differ (**Figure 6**). The frequencies of the two normal modes at the Brillouin-zone edge begin to separate, as is seen by considering the patterns of vibration. This zone-edge splitting appears whenever the material has bonds of different strength. So, for example, the contrast between the strong Si–O bond and the weaker inter-tetrahedral forces in quartz cause large zone-edge splittings, and a clear separation of acoustic and optic modes. Periclase, for which the contrast in bond strengths is much less, shows almost no acoustic-optic gap (in detail, non-nearest neighbor and noncentral forces open a gap even in periclase along certain high-symmetry directions; electron-polarization effects can also play an important role in shifting longitudinal-optic relative to transverse-optic modes).

In any case, at a given wave vector, we always have three acoustic modes and $3n - 3$ optic modes (n is the number of atoms in the unit cell). It is also known that longer-range interactions add structure to the $\omega-k$ dispersion relation: each successive coordination shell in a set of two-body interactions adds a Fourier component to the mode branch.

In the limit of no optical gap, the vibrational density of states may be reasonably approximated by the Debye relation (eqn [17]), regardless of how many atoms are in the unit cell, as the main modification of phonon dispersion is Brillouin-zone folding. This realization has led to the concept of Debye-like solids, periclase and corundum being prototypical examples (Anderson, 1995). Materials like quartz and those containing hydrogen bonds are typical counterexamples, for which more elaborate models such as those due to Kiefer are more appropriate (Kieffer, 1980). Even when deviations from a Debye-like spectrum are large, the influence on thermochemical properties is not necessarily significant, because these depend at high temperature only on low-order moments (weighted averages) of the vibrational density of states (Barron *et al.*, 1957) (**Figure 7**). Deviations are likely to be largest for water-rich hydrous phases, because the stretching frequency for the OH bond is so much larger than for any other bond thought to be important in the mantle (Williams, 1995). The essential relationship between acoustic and optic branches has also led to the idea of determining an average elastic-wave velocity from a measurement of the appropriate optic mode at the Brillouin-zone center (Merkel *et al.*, 2000).

Thermal expansion arises, in a first approximation, from the volume dependence of the vibrational frequencies (quasi-harmonic model). This modification

of the theory retains the normal-mode description of the frequencies, but allows the frequency spectrum to shift with compression. Anharmonicity generally refers to time dependence of the normal modes (e.g., due to mode mixing), and accounts for physical effects such as temperature dependence of the vibrational frequencies at constant volume that are not explained by quasi-harmonic theory (Gillet *et al.*, 1996).

As the crystal compresses, bonds generally become stronger, the vibrational frequencies increase, and, from eqn [13], the vibrational energy decreases. The volume dependence of the vibrational energy produces a vibrational pressure that is positive and tends to expand the lattice. The vibrational or thermal pressure is

$$P_{\text{vib}} = \gamma \rho U_{\text{vib}} \quad [18]$$

where the Grüneisen parameter is defined by

$$\gamma \equiv \frac{1}{\rho} \left(\frac{\partial P}{\partial U} \right)_\rho = \frac{\alpha K_T}{\rho C_\rho} = \left(\frac{\partial \ln T}{\partial \ln \rho} \right)_S \quad [19]$$

and the second and third relations are thermodynamic identities. This makes explicit the relationship between thermal pressure and thermal expansivity α , and also shows that the Grüneisen parameter controls the magnitude of the adiabatic temperature gradient. For models of the vibrational density of states with a single characteristic frequency, such as the Debye or Einstein approximations, the following relation also holds,

$$\gamma = \frac{\partial \ln \omega}{\partial \ln \rho} \quad [20]$$

establishing the link between quasi-harmonic thermal properties and the normal modes of the lattice. The Grüneisen parameter is dimensionless and empirically found to be about 1–3, so is a convenient way of capturing many related influences of temperature on the physical properties of minerals inside a planet (McQueen *et al.*, 1970; Stixrude and Lithgow-Bertelloni, 2005b; Wallace, 1972).

To introduce the influence of temperature on the elastic constants, consider the vibrational contribution to the bulk modulus. Taking the volume derivative of eqn [18], we see that the temperature dependence of the elastic constants will involve not only the Grüneisen parameter, but also its volume derivative

$$q = - \frac{\partial \ln \gamma}{\partial \ln \rho} \quad [21]$$

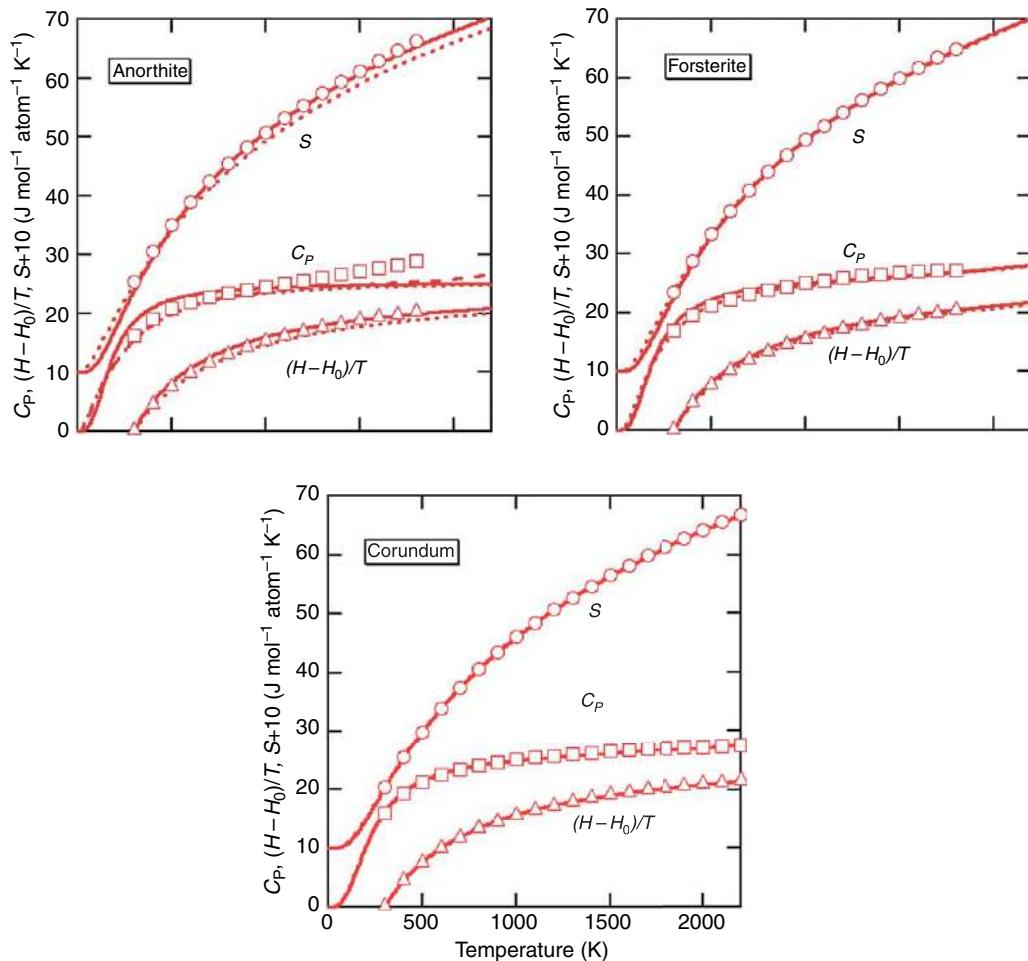


Figure 7 Experimentally derived (Robie and Hemingway, 1995) entropy (circles), heat capacity (squares), and enthalpy function (triangles) compared with (solid lines) Debye model with effective Debye temperature fit to the entropy at 1000 K, and (short dashed) the model of (Kieffer (1980)). For anorthite, the long dashed line shows the influence of cation disorder on the heat capacity according to the model of Holland and Powell (1998). The entropy is shifted upward for clarity. From Stixrude L and Lithgow-Bertelloni C (2005b) Thermodynamics of mantle minerals. I: Physical properties. *Geophysical Journal International* 162: 610–632.

where the parameter q is dimensionless and is thought to take on values in the range 1–3 for most mantle phases. The thermal pressure at temperatures above the Debye temperature can be approximated by

$$P_{\text{TH}} \approx 3nRT\gamma\rho \quad [22]$$

and the thermal contribution to the adiabatic bulk modulus along an isochore is then just the volume derivative

$$K_{\text{TH}} \approx 3nRT(\gamma + 1 - q) \quad [23]$$

An important consequence of the fact that $q > 1$ for most mantle materials is that the thermal pressure

and other thermal effects tend to decrease with compression. For example, the thermal expansivity and the influence of temperature on the elastic-wave velocities decrease with depth, with potentially important implications for mantle dynamics and the interpretation of seismic tomography (Chopelas and Boehler, 1989; Isaak *et al.*, 1992).

Because the Grüneisen parameter plays such a central role in our understanding of the thermal state of the Earth, there has been a great deal of interest in determining its dependence on compression. Many experimental data are consistent with the assumption that q is constant without necessarily requiring it. More recent experimental analyses

and theoretical studies suggest that q tends to decrease with compression (Agnon and Bukowinski, 1990; Speziale *et al.*, 2001), and analytical forms have been proposed (Stixrude and Lithgow-Bertelloni, 2005b).

1.22.2.6 Influence of Pressure and Temperature on the Elastic Constants

An important feature of the Earth is that compressions are large – the characteristic pressure is a large fraction of typical zero-pressure values of mineral bulk moduli – and the characteristic temperature is larger than typical vibrational energies of Earth materials. This means that measurements of the pressure and temperature derivatives of the elastic constants near ambient conditions do not suffice to give us a meaningful picture of the variation of these quantities over the conditions of Earth's interior. Indeed, experimental measurements show that the bulk modulus varies by more than a factor of 2 over the mantle pressure range. Such large changes are seen in the density and other properties too, and led Birch to apply the theory of Eulerian finite strain to understanding the Earth's interior. The theory of finite strain has been generalized to encompass the elastic constants (Davies, 1974), and has recently been reformulated in a thermodynamically self-consistent manner (Stixrude and Lithgow-Bertelloni, 2005b). Only the final results are discussed here.

The variation of the bulk and shear moduli with volume and temperature are, respectively,

$$K = (1 + 2f)^{5/2} \times \left[K_0 + (3K_0 K'_0 - 5K_0)f + \frac{27}{2}(K_0 K'_0 - 4K_0)f^2 \right] + (\gamma + 1 - q)\gamma\rho\Delta U_{\text{vib}} - \gamma^2\rho\Delta(C_V T) \quad [24]$$

$$G = (1 + 2f)^{5/2} \left[G_0 + (3K_0 G'_0 - 5G_0)f + \left(6K_0 G'_0 - 24K_0 - 14G_0 + \frac{9}{2}K_0 K'_0 \right)f^2 \right] - \eta_s\rho\Delta U_{\text{vib}} \quad [25]$$

where f is the Eulerian strain measure,

$$f = \frac{1}{2} \left[\left(\frac{V}{V_0} \right)^{-2/3} - 1 \right] \quad [26]$$

and subscript '0' indicates the value of a quantity at the reference state (e.g., ambient conditions), primes

indicate pressure derivatives, and Δ indicates the difference between the temperature of interest and the temperature of the reference state. The quantity η_s takes on positive values near unity for mantle phases, and derives from the shear part of the fourth-rank tensor formed from the strain derivative of the tensorial generalization of γ , which we have assumed to be isotropic. Taking typical values of γ_0 and q (1 and 2, respectively), the temperature-dependent terms show that both moduli decrease with increasing temperature at constant volume. The decrease with increasing temperature at constant pressure is greater than that at constant volume according to

$$\left(\frac{\partial M}{\partial T} \right)_p = \left(\frac{\partial M}{\partial T} \right)_V - \rho C_V \gamma M'_0 \quad [27]$$

where M stands for either the bulk or shear modulus.

Finite-strain theory suggests systematic expressions for the values of the pressure derivatives of the elastic constants (Karki *et al.*, 2001; Stixrude and Lithgow-Bertelloni, 2005b). It has been known for some time that the Eulerian finite strain theory owes its success at least in part to that fact that it rapidly converges to experimentally measured equations of state with increasingly higher orders of the finite strain. In fact, for many materials, the lowest-order terms suffice. The term linear in f in the equation of state vanishes when $K'_0 = 4$, a value that is typical of mantle phases and many other materials as well. We may take the same approach in the case of eqns [24] and [25], and ask what relationships are implied by the vanishing of the term linear in f within the square brackets. In the case of the shear modulus, this yields a relationship between the pressure derivative of G and the ratio of shear modulus to bulk modulus, which is satisfied approximately for mantle phases. The pressure derivative of the shear modulus thus appears to scale with the value of the shear modulus itself.

We may relate the elastic moduli of mantle phases to those found seismologically via a compilation of experimental and theoretical results for the parameters appearing in eqns [24] and [25] (Figure 8). Comparison to seismological observations tends to support the standard model of a homogeneous peridotite composition that produces a series of phase transformations with increasing depth. (Peridotite is a rock primarily composed of the mineral olivine. Model mantle compositions, based on comparison

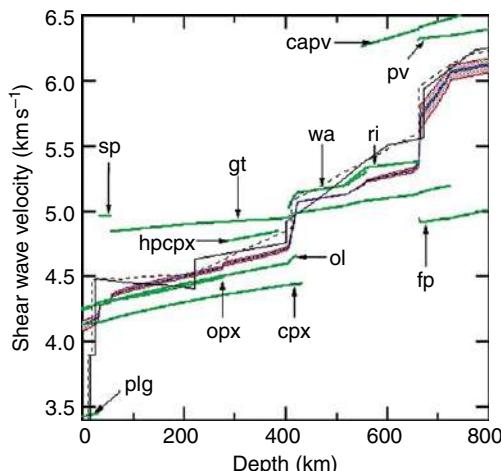


Figure 8 Computed shear-wave velocities of a model mantle composition (blue), and of the individual phases of the assemblage (green) along the 1600 K adiabat computed self-consistently with the phase equilibria and physical properties according to the method of Stixrude and Lithgow-Bertelloni (2005a). The Voigt-Reuss (red) and Hashin-Shtrikman (blue) bounds on the aggregate velocity are shown. Thin black lines are radial seismological models: (solid) PREM (Dziewonski and Anderson, 1981); (dashed) AK135 (Kennett and Engdahl, 1991). Adapted from Stixrude L and Lithgow-Bertelloni C (2005b) Thermodynamics of mantle minerals. I: Physical properties. *Geophysical Journal International* 162: 610–632.

with seismology, the genesis of magmas, and analysis of mantle xenoliths typically contain 50–60% olivine, and lesser amounts of orthopyroxene, clinopyroxene, and garnet.) The velocity of the upper mantle is spanned by that of olivine, orthopyroxene, clinopyroxene, and garnet; in the shallow transition zone (410–520 km), by clinopyroxene, majorite, and wadsleyite; and in the deep transition zone (500–660 km), by Ca-perovskite, ringwoodite, and majorite. Velocities in the lower mantle are spanned by those of Mg-perovskite, magnesiowüstite, and Ca-perovskite. In the upper mantle and transition zone, we find that the change in shear-wave velocity due to phase transformations exceeds the influence of pressure on the velocity of any one phase. This suggests the essential role that phase transformations play in producing the anomalous velocity gradient of the transition zone, and emphasizes the importance of going beyond the elasticity of individual minerals in understanding mantle structure, as discussed further in the next section.

One of the most remarkable patterns in the temperature and compositional derivatives of the elastic

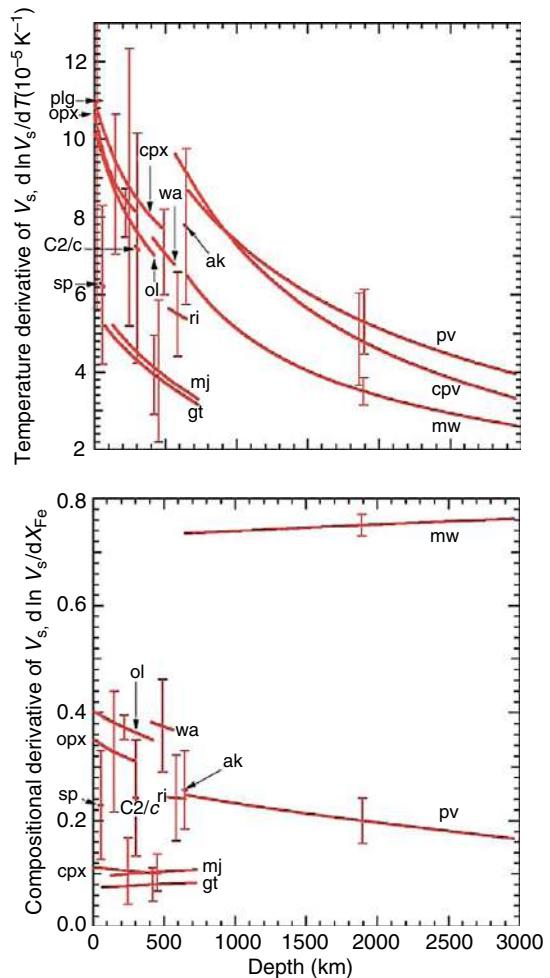


Figure 9 Variation of the shear-wave velocity with respect to (top) temperature and (bottom) composition. From Stixrude L and Lithgow-Bertelloni C (2005b) Thermodynamics of mantle minerals. I: Physical properties. *Geophysical Journal International* 162: 610–632.

moduli, aside from the large influence of compression discussed above, is the large difference between garnet-majorite and other phases (Figure 9). The compositional derivative for garnet and majorite (and clinopyroxene) is only a third of those of olivine and orthopyroxene, while the temperature derivatives of garnet and majorite are approximately half those of olivine and orthopyroxene. The contrast in compositional derivatives can be traced directly to the shear modulus of Mg- and Fe-end members of the phases: while the shear modulus of fayalite is 40% less than that of forsterite, that of almandine is actually slightly greater than that of pyrope, partially offsetting the effect of the greater density of almandine on V_s . The contrast in temperature derivatives

can be related to experimental measurements of dG/dT of the dominant species: 8 and 9 MPa K $^{-1}$ for pyrope and majorite, respectively, compared to 15 MPa K $^{-1}$ for forsterite. One consequence of the unusual properties of garnet is that the influence of temperature and iron content is sensitive to bulk composition. Specifically, more garnet-rich compositions, such as basalt, are less sensitive to variations in temperature or iron content than garnet-poor bulk compositions such as harzburgite (basalt is a rock primarily composed of pyroxene and plagioclase feldspar that makes up most of the oceanic crust and is produced by partial melting of the mantle, whereas harzburgite is a rock that is richer in olivine than the average mantle and is thought to be the residuum of partial melting of the mantle) (Speziale *et al.*, 2005a).

1.22.3 Rock Elasticity

1.22.3.1 Overview

Knowledge of mineral elasticity is necessary for estimating the elastic properties of a rock, but it is not sufficient. There are two primary considerations. The first is that rocks are heterogeneous. In the mantle, this heterogeneity is most pronounced at the grain scale (1–10 mm): every part of the mantle is made of several different mineral phases, each with different elastic properties. The difference in elastic properties between coexisting minerals is generally larger than that between different mantle rock types. The second difficulty is that minerals tend to be preferentially aligned by deformation. The alignment is neither perfect, in which case the elasticity would reduce to that of a single crystal, nor negligible. Indeed, the detection of preferential alignment via the resulting anisotropic propagation of seismic waves is one of our most powerful potential probes of mantle flow.

In principle, one needs to know—in addition to the elastic-constant tensors of the constituent minerals—the location, size, shape, and orientation of each mineral grain in the assemblage. However, such a detailed description is neither practical nor useful: a part of the Earth’s mantle, the size of a typical mantle body wave (100 km), contains on the order of 10 21 individual mineral grains, assuming 1 cm grains! This is another statement of the spatial aliasing problem described above. Model statistical distributions of mineral geometry play an important role, in particular in the analysis of preferred orientation.

Idealizations, in which either the preferred orientation or the spatial inhomogeneity, or both, are simplified, and permit exact solutions or rigorous bounds, are also important.

Additional complications arise at finite frequency: dissipative mechanisms exist in aggregates that are not present in single crystals, and these are thought to be important for producing attenuation and dispersion in the mantle, particularly at grain boundaries.

1.22.3.2 Composites Theory

Consider first a homogeneous isotropic medium, corresponding to a glass or a liquid. The elasticity is completely characterized by two elastic constants, which may be taken to be the bulk modulus, K , and shear modulus, G . The longitudinal- and shear-wave velocities for all propagation and polarization directions are

$$V_P = \sqrt{\frac{K + 4/3G}{\rho}} \quad V_S = \sqrt{\frac{G}{\rho}} \quad [28]$$

where ρ is the density and, in the case of a liquid deformed on a timescale long compared with its Maxwell relaxation time, $G=0$.

Consider an inhomogeneous system consisting of N isotropic phases with distinct elastic properties, such that phase α has bulk and shear moduli K^α and G^α and $\alpha=1, \dots, N$. Suppose that the only properties of the grain geometry we know are the volume fractions of the phases ϕ^α . The volume fraction is the only feature that is uniquely determined by the usual equilibrium thermodynamics, and is thus independent of the history of the sample. The stress and strain tensors are now functions of position

$$\sigma_{ij}(\mathbf{x}) = c_{ijkl}(\mathbf{x})\varepsilon_{kl}(\mathbf{x}) \quad [29]$$

$$\varepsilon_{ij}(\mathbf{x}) = S_{ijkl}(\mathbf{x})\sigma_{kl}(\mathbf{x}) \quad [30]$$

where the compliance tensor is the inverse of the elastic-constant tensor,

$$S_{ijkl} = c_{ijkl}^{-1} \quad [31]$$

The volume average stress and strain of the rock is assumed related to that in each of the phases by

$$\bar{\sigma}_{ij} = \sum_\alpha \phi^\alpha \bar{\sigma}_{ij}^\alpha \quad [32]$$

$$\bar{\varepsilon}_{ij} = \sum_\alpha \phi_\alpha \bar{\varepsilon}_{ij}^\alpha \quad [33]$$

where the bars indicate volume averages. We define the effective elastic moduli of the composite as

$$\bar{\sigma}_{ij} = c_{ijkl}^* \bar{\varepsilon}_{kl} \quad [34]$$

If we assume that the average stress and strain in each phase is a unique function of the average stress and strain, respectively, of the aggregate, then it is possible to show that the values of c^* are bounded such that

$$M_R^* = \left(\sum_{\alpha} \frac{\phi^{\alpha}}{M^{\alpha}} \right)^{-1} < M^* < \sum_{\alpha} \phi^{\alpha} M^{\alpha} = M_V^* \quad [35]$$

where M refers to either K or G , and the bounds M_R^* and M_V^* correspond, respectively, to the assumption that the stress (Reuss bound) or strain (Voigt bound) are homogeneous throughout the composite (Hill, 1963; Watt *et al.*, 1976). Except in special geometries, neither of these approximations is correct: the assumption of constant stress requires the opening of gaps between grains, while the assumption of constant strain violates mechanical equilibrium. Indeed, the assumptions embedded in eqns [32] and [33] are in general not justifiable, and one of the complications of composites theory is that the stress tensor can no longer be treated as symmetric (e.g., Juanzemis, 1967).

Ignoring these complications, the Voigt and Reuss bounds limit the possible degree of anisotropy due to inhomogeneous arrangement of phases. This type of anisotropy is sometimes referred to as shape-preferred orientation. Plane layering is the classic example for which Voigt and Reuss bounds can be realized (Backus, 1962). The P-wave velocity for waves propagating normal to the layers is $\rho V_p^2 = K_R + 4/3 G_R$, while that for propagation parallel to the layers is $\rho V_p^2 = K_V + 4/3 G_V$. Thus, heterogeneity produces anisotropy. This relationship has been examined on the atomic level as well. There are several crystal structures in which layers of more compressible units, for example, Mg coordination polyhedra, alternate with layers of stiffer units such as Si polyhedra. Such alternation leads to the large anisotropy of the olivine structure (Hazen *et al.*, 1996; Wentzcovitch and Stixrude, 1997).

For illustration, we compare the Voigt and Reuss bounds of a typical mantle lithology (peridotite) in **Figure 10**. The bounds are wide in the shallow mantle due to the extremely low velocity of plagioclase, and in the vicinity of the 660 km discontinuity due to the much higher velocity of perovskite than garnet, whereas they are nearly coincident in the shallow transition zone where wadsleyite and garnet

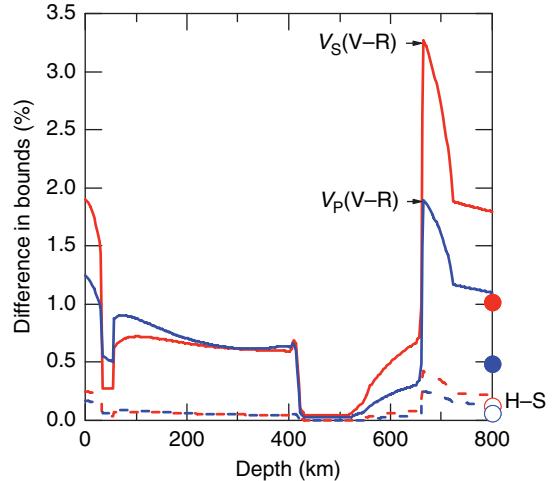


Figure 10 Differences between the Voigt and Reuss (solid) and Hashin–Shtrikman (dashed) bounds for P- (blue) and S- (red) wave velocities in a model mantle composition (Workman and Hart, 2005) along a self-consistent 1600 K adiabat. Symbols represent the values at the core–mantle boundary.

have similar velocities. In the lower mantle, the bounds differ by less than 2% and by less than 1% at the core–mantle boundary. These results suggest that shape-preferred orientation in subsolidus peridotites is unlikely to be the source of anisotropy in the D'' layer at the base of the mantle, as has previously been proposed on the basis of the contrast in elastic properties between perovskite and periclase (Karato, 1998).

It is not possible to estimate more precisely the value of the effective elastic moduli without further information. It is common in the literature to quote the so-called Voigt–Reuss–Hill (VRH) mean, which is simply the arithmetic mean of the Voigt and Reuss bounds (Hill, 1952). This value is not rigorously justified as a best estimate of the actual effective moduli.

With further assumptions about the distribution of the phases, it is possible to derive narrower bounds. The Hashin–Shtrikman analysis (Hashin and Shtrikman, 1963) assumes that the distribution of phases is statistically random and that the elastic properties of the aggregate are given as a solution to a variational problem. So, for example, regular arrangements such as layering are excluded. The Hashin–Shtrikman bounds, given in compact form by Berryman (1995), are narrower than the Voigt–Reuss bounds in most cases, including for the mantle (**Figure 10**). Watt *et al.* (1976) recommend that the Hashin–Shtrikman bounds should generally be used

in reporting the elastic properties of multiphase materials, rather than the Voigt–Reuss bounds, or the VRH average. However, this may be misleading since the Hashin–Shtrikman bounds are based on a limiting assumption that excludes geometries that are important in some parts of the Earth (e.g., layering).

In certain cases, the Voigt–Reuss and Hashin–Shtrikman bounds are too wide to yield useful estimates. This can occur when the moduli of the constituent phases differ significantly, as in the case of a porous solid or a partial melt. In such cases, the analysis of specific geometries may be useful. Typically, one assumes that one phase is the host (i.e., the solid rock) and the other is treated as an inclusion (air, water, or melt). Results for specific inclusion shapes have been derived, including spheres, needles, disks, and penny-shaped cracks (Berryman, 1995). For a given volume fraction of inclusions, the effective moduli are most similar to those of the host for spherical inclusions, whereas large aspect-ratio disks or cracks have the largest influence on the shear modulus (Figure 11). It should be noted that very little is known concerning the actual form of melt inclusions in partial melts within the mantle. The relevant controlling parameters are many, including the pressure, temperature, bulk composition and deformation history, and may be influenced by nonequilibrium effects.

An additional ambiguity in the computation of the effective elastic moduli of isotropic composites arises

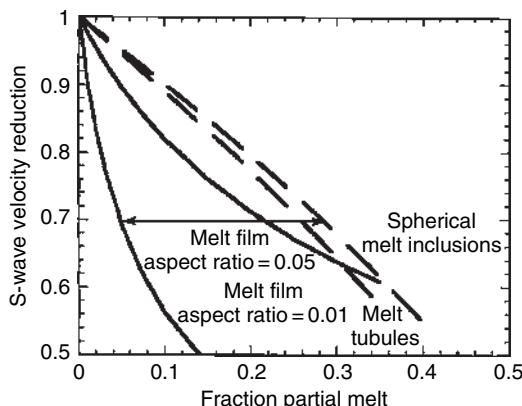


Figure 11 The ratio of the S-wave velocity of melt-bearing mantle to that of solid mantle for varying melt fractions and melt geometries. The arrow corresponds to the variation in melt fraction implied by the inferred P-wave velocity depression of 10% in the ultra-low-velocity zone at the base of the mantle. From Williams Q and Garnero EJ (1996) Seismic evidence for partial melt at the base of Earth's mantle. *Science* 273: 1528.

from the intrinsic anisotropy of crystals. Even in the case of a monophase aggregate, the effective elastic moduli are inherently uncertain unless the texture has been completely specified (Watt *et al.*, 1976). Hill (1952) showed that rigorous bounds correspond to the assumption of homogeneous strain and homogeneous stress, respectively. The Voigt (homogeneous-strain) bounds are

$$K_V^* = \frac{1}{3}(A + 2B) \quad [36]$$

$$G_V^* = \frac{1}{5}(A - B + 3C) \quad [37]$$

where A , B , and C , are, respectively, the mean diagonal, off-diagonal, and shear elastic constants:

$$A = \frac{1}{3}(c_{11} + c_{22} + c_{33})$$

$$B = \frac{1}{3}(c_{12} + c_{13} + c_{23}) \quad [38]$$

$$C = \frac{1}{3}(c_{44} + c_{55} + c_{66})$$

The Reuss (homogeneous-stress) bounds are

$$K_R^* = \frac{1}{3(a + 2b)} \quad [39]$$

$$G_R^* = \frac{5}{4a - 4b + 3c} \quad [40]$$

where a , b , and c are similar to A , B , and C , but with the components of the compliance tensor replacing those of the elastic-constant tensor. The Hashin–Shtrikman bounds for the monophase aggregate are narrower (Hashin and Shtrikman, 1962). Expressions have been derived for cubic, tetragonal, orthorhombic, hexagonal, trigonal, and monoclinic Bravais lattices (Watt, 1988, and references therein). The difference between Voigt and Reuss bounds for the shear-wave velocity of olivine at ambient conditions is 2%. The difference tends to increase with increasing single-crystal anisotropy. For materials with very large anisotropy, such as periclase at the core–mantle boundary (azimuthal shear anisotropy = 60%), Voigt and Reuss bounds on the shear modulus differ by 30% and the Hashin–Shtrikman bounds differ by 5% (Karki *et al.*, 2001). Spinel is an example of a mineral that is extremely anisotropic at ambient conditions, and for which bounds are wide (Yoneda, 1990).

Preferred orientation (preferential crystallographic alignment) of the constituent grains results in macroscopic anisotropy detectable by seismic

waves. The preferred orientation is characterized by the orientation distribution function,

$$f(\mathbf{g})d\mathbf{g} = \frac{dV_g}{V} \quad [41]$$

where \mathbf{g} is the rotation matrix that relates the crystallographic axes to the spatial or laboratory reference frame and dV_g/V is the volume fraction of crystals with orientation lying within the range $d\mathbf{g}$. The effective elastic moduli of the aggregate may then be estimated by (Bunge *et al.*, 2000)

$$\hat{c}_{ijkl}^* = \int g_{im}g_{jn}g_{lk}g_{mp}c_{mnop}f(\mathbf{g})d\mathbf{g} \quad [42]$$

where the effective elastic moduli are referred to the laboratory frame, and the elastic-constant tensor in the integrand is referred to the crystallographic frame. This expression yields the Voigt bound on the effective elastic moduli; the Reuss bound involves the compliances. Two simple cases of orientation distribution functions are of special interest (Stixrude, 1998). If the texture is perfect, that is, all crystals are identically aligned, then the effective elastic-constant tensor is identical to that of the single crystal rotated into the laboratory frame. Such a texture might be considered the asymptotic limit of lattice-preferred orientation produced by mantle flow. A transversely anisotropic aggregate is produced if deformation is dominated by an easy-glide plane. In this case, the effective elastic-constant tensor has hexagonal symmetry with the symmetry-axis normal to the glide plane.

1.22.3.3 Attenuation and Dispersion

When deformed by small stresses over short timescales, the mantle behaves nearly elastically, propagating shear waves, whereas at long timescales it behaves like a fluid, deforming viscously in mantle convection. (Though not relevant to the immediate discussion, rock also behaves as a fluid under the short but high-amplitude stresses of impact-induced shock.) The boundary between these two types of behavior is characterized by the Maxwell relaxation time,

$$\tau_M = \frac{\eta}{G} \quad [43]$$

where η is the viscosity. For the upper mantle, $\tau_M \sim 1000$ years is determined from glacial rebound.

At seismic periods, deformation is also not perfectly elastic. The relative amount of elastic energy

lost per cycle, dE/E , defines the quality factor Q , the inverse of which is referred to as the internal friction or attenuation

$$Q^{-1} = \frac{dE}{E} \quad [44]$$

Attenuation entails dispersion. (This results from causality, the requirement that the mechanical energy of the wave cannot propagate faster than the signal velocity, as encapsulated by the fact that the frequency-dependent elastic modulus and attenuation are not independent: they are Hilbert transform-related real and imaginary components of the complex modulus, [47], and therefore satisfy integral conditions (Kramers–Kronig relations), e.g., Bracewell (1999).) The acoustic-wave velocity depends on the wavelength or frequency of the probe (Figure 12). This kind of dispersion – which involves nonequilibrium processes, with mechanical energy converted to heat – is distinct from the dispersion we encountered in the context of lattice dynamics of perfect crystals, which is an equilibrium phenomenon arising from the particulate nature of matter.

Simple models are useful for thinking about attenuation and dispersion even when they do not correspond to geophysically relevant materials. The Maxwell model is the simplest, consisting of an elastic spring and a dashpot in series. The Voigt model has these two elements in parallel. At short periods, both of these simple models produce elastic behavior

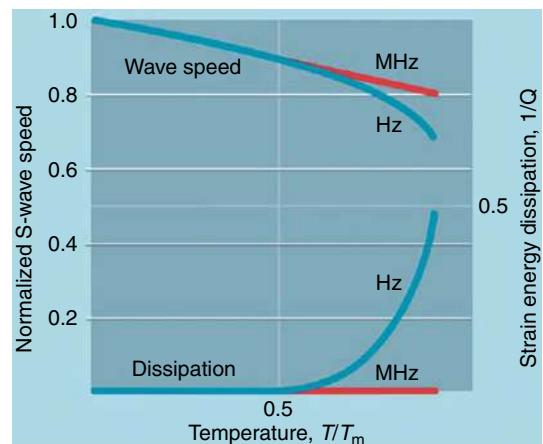


Figure 12 Schematic representation of the variation of acoustic-wave velocity (upper curves) and attenuation (Q^{-1}) (lower curves) with temperature at high frequencies (red) and lower frequencies within the seismic band (blue). From Jackson I (2000) Geophysics – Taking the Earth’s temperature. *Nature* 406: 470–471.

governed by the spring. At long periods, the behavior is very different. Whereas the Maxwell model produces a purely viscous, unrecoverable response, governed by the dashpot, the Voigt model shows anelastic behavior: time dependent, but fully recoverable. The so-called Kelvin or standard linear solid consists of a Voigt model in series with a spring. The simplest model that shows the full range of response – elastic, anelastic, and viscous – is the Burgers model, which can be thought of as a Maxwell and Voigt solid in series. See, for example, Cooper (2002) for a recent discussion of these models.

These simple models make an important point. Viscous flow, which governs mantle convection, and anelastic deformation, which causes attenuation and dispersion in the seismic band, are considered as separate dashpots. While the connection to real materials is not obvious, it is likely that viscosity and attenuation are governed by separate microscopic deformation mechanisms if for no other reason than that the strain rates and total strains are so vastly different. Experimental measurements of viscosity, which are more numerous than measurements of seismic attenuation at relevant mantle conditions, are not necessarily a reliable guide to the dependence of attenuation on pressure, temperature, or composition.

Consider the response of these models to periodic loading,

$$\sigma = \sigma_0 e^{i\omega t} \quad [45]$$

which produces the strain response,

$$\varepsilon = \varepsilon_0 e^{i\omega t + \delta} \quad [46]$$

In most experiments, the attenuation is actually measured by the phase lag δ . The elastic modulus is complex and frequency dependent,

$$M(\omega) = M_R + iM_I \quad [47]$$

and the attenuation can also be written as the ratio of imaginary to real parts $\mathcal{Q}^{-1} = M_I/M_R$. The acoustic-wave velocity is

$$V = \sqrt{\frac{M}{\rho}} \quad [48]$$

where ρ is the density.

The simple models described all predict attenuation that depends strongly on frequency (Figure 13). For the Maxwell solid, $\mathcal{Q}^{-1} = 1/\omega\tau$, and for the Voigt solid, $\mathcal{Q}^{-1} = \omega\tau$, where τ is the characteristic

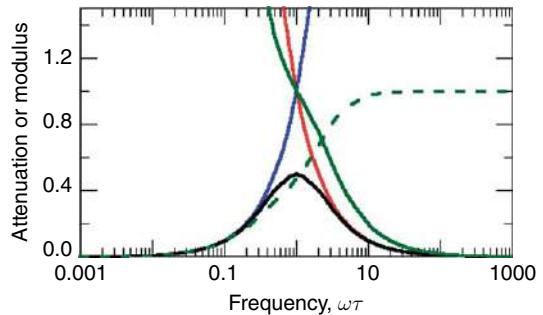


Figure 13 Frequency dependence of the attenuation (solid curves) and modulus (dashed curve for the Burgers model) for simple mechanical models: Maxwell (red), Voigt (blue), Kelvin (black), and Burgers (green).

relaxation time. The standard linear solid shows Maxwell-like and Voigt-like behavior in the limit of zero and infinite frequency, respectively, with a peak attenuation centered at $\omega\tau = 1$:

$$\mathcal{Q}^{-1} = \frac{\omega\tau}{1 + (\omega\tau)^2} \quad [49]$$

and the velocity dispersion is

$$V(\omega) = V(0) \left(1 + \mathcal{Q}_{\max}^{-1} \frac{(\omega\tau)^2}{1 + (\omega\tau)^2} \right) \quad [50]$$

For the Burgers model,

$$\mathcal{Q}^{-1} = \frac{1 + 2\omega^2\tau^2}{2\omega\tau + \omega^3\tau^3} \quad [51]$$

there is a Maxwell-like decrease of attenuation with increasing frequency, interrupted by a region near $\omega\tau = 1$, where the dependence on frequency is much reduced. Depending on the details of how the Burgers model is parametrized, this shoulder may become a small peak.

Much of the literature on microscopic mechanisms of attenuation in solids has focused on the materials that show clear peaks in the attenuation spectrum. The dependence of the peak amplitude and frequency on temperature and material characteristics is essential for identifying the mechanism(s) responsible. Among the mechanisms that have been identified in this way are the migration of defects, the exchange of substituents in solid solution, dislocation motion, grain-boundary relaxation, and thermal currents (Jackson and Anderson, 1970; Nowick and Berry, 1972). Because so many mechanisms can contribute to the attenuation, it is often necessary to specially prepare the sample to have, for example,

high purity or uniform grain size, in order to produce a spectrum with a single clear peak. Many silicate liquids show attenuation that is well described by a single characteristic relaxation time (Rivers and Carmichael, 1987).

Perhaps the most important result from studies of mantle-like materials is the absence of attenuation peaks (Jackson *et al.*, 2002). Attenuation is found to vary slowly and monotonically with frequency over a broad spectrum. The reason for this behavior is not clear. It is possible that there exists a broad and nearly continuous spectrum of relaxation times. The behavior is similar to the so-called high-temperature background found in many materials (Nowick and Berry, 1972). Even those materials that show distinct peaks at low temperature may exhibit featureless attenuation spectra at high temperature.

In the case of attenuation dominated by elastically accommodated grain-boundary sliding, the featureless, nearly flat attenuation spectrum may be rationalized as follows (Jackson *et al.*, 2002). The characteristic relaxation time is

$$\tau_{gb} = \gamma \frac{\eta_{gb} d}{G\delta} \quad [52]$$

where d is the grain size, δ is the width of the grain-boundary region, γ is of order 1, and η_{gb} is the grain-boundary viscosity (much less than the viscosity of the bulk). A spectrum of relaxation times might be produced by a distribution of grain sizes, grain-boundary widths, and grain-boundary viscosities. In particular, the effective grain-boundary viscosity could exhibit a wide range because of the variable presence of grain-boundary irregularities or impurities that would tend to inhibit sliding.

The following empirical expression represents the data of Jackson *et al.* (2002) within the seismic frequency band (~ 1 –100 s periods) (Figure 14)

$$\underline{Q}^{-1}(P, T, \omega) = Ad^{-m}\omega^{-\alpha} \exp\left(-\alpha \frac{E^* + PV^*}{RT}\right) \quad [53]$$

$$V(P, T, \omega) = V(P, T, \infty) \left[1 - \frac{1}{2} \cot\left(\frac{\alpha\pi}{2}\right) \underline{Q}^{-1}(P, T, \omega) \right] \quad [54]$$

where ω is the frequency, d is the grain size, $m = 0.28$ is the grain size exponent, $\alpha = 0.26$ is the frequency exponent, $E^* = 430 \text{ kJ mol}^{-1}$ is the activation energy, V^* is the activation volume, and R is the gas constant. For the experimental value of α , the factor multiplying \underline{Q}^{-1} in eqn [53] has the value 1.16. The

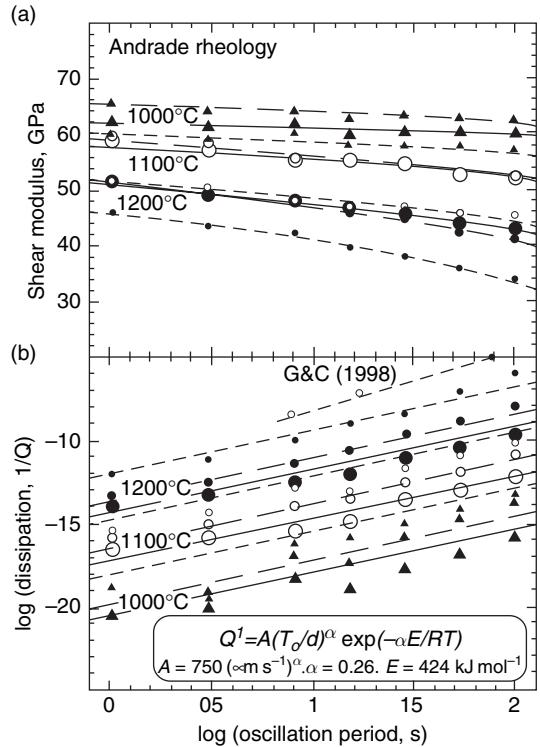


Figure 14 Grain-size sensitivity of the high-temperature mechanical behavior of olivine polycrystals. Data for specimens 6261, 6365, and 6381 of average grain size 23.4, 12.4, and 2.9 mm, are denoted by the large, medium, and small plotting symbols and by the solid, long-dashed, and short-dashed curves, respectively. Solid circles, open circles, and solid triangles denote data for 1200°C, 1100°C, and 1000°C CA6, respectively. (a) Shear modulus. Curves labeled with temperature indicate the modulus dispersion associated with Andrade models fitted simultaneously to $G(T_o)$ and $Q^{-1}(T_o)$ where $T_o = 2\pi/\omega$ is the oscillation period (cf. eqns [53] and [54]). (b) The log (dissipation). Lines represent the preferred fit (eqns [7] and [8]) to the entire 1000–1300 C, 1–100 s data set for all four specimens, except for the uppermost line representing the results of Gribb and Cooper (1998) for a resynthesized dunite of 2.8 mm grain size at 1200 C. From Jackson I, Fitzgerald JD, Faul UH, and Tan BH (2002) Grain-size-sensitive seismic wave attenuation in polycrystalline olivine. *Journal of Geophysical Research – Solid Earth* 107: N12.

activation volume is currently unconstrained, which means that the influence of pressure on attenuation is highly uncertain. The relationship between attenuation and dispersion is made explicit by eqn [54].

The experimental results can be compared with attenuation spectra proposed for the Earth. The absorption band model (Anderson and Given, 1982) consists of a broad frequency range over which \underline{Q}^{-1} depends weakly on frequency, bounded by narrower

low- and high-frequency ranges where \underline{Q}^{-1} decreases to zero. The intermediate-frequency range of this model, the absorption band, agrees well with experimental results. The estimates of the value of α based on seismological observations are consistent with those found experimentally at similar frequencies. But experimental support for the boundaries is lacking. At long periods, experiments show that the attenuation will continue to increase with increasing period and at a higher rate, with $\alpha = 1$ (Gribb and Cooper, 1998; Jackson *et al.*, 2002). At the high-frequency end, there is no indication of a sharp transition requiring a larger value of α . In fact, there is an indication in the data that the attenuation becomes less sensitive to frequency at high frequency (Cooper, 2002).

The influence of partial melt is generally to increase the attenuation (Faul *et al.*, 2004; Jackson *et al.*, 2004). The frequency dependence is also affected by partial melt. A broad absorption peak is superimposed on a high-temperature background. The origin of this peak appears not to be the melt squirt mechanism that has been widely discussed, but elastically accommodated grain-boundary sliding enhanced by partial melt. For probable mantle-grain sizes and attenuation in the seismic band, \underline{Q} is nearly independent of frequency for 1% partial melt.

The influence of crystallographically bound hydrogen on the attenuation is currently not well constrained, although it is known that viscosity decreases with increasing hydrogen concentration (Mei and Kohlstedt, 2000a, 2000b).

The bulk attenuation – that is, time dependence of volume compression due to a change in hydrostatic pressure – has not been measured for mantle materials, and is generally assumed to be small. In the limit that bulk attenuation vanishes, the attenuation of longitudinal and shear waves is related by

$$\underline{Q}_{\text{P}}^{-1} = \frac{4}{3} \left(\frac{V_s}{V_{\text{P}}} \right)^2 \underline{Q}_{\text{S}}^{-1} \quad [55]$$

For composites, however, because volume compression generally leads to local shear deformations being distributed throughout the medium, bulk attenuation can arise on the multigrain length scales relevant to seismology simply because of the presence of heterogeneous elastic properties and shear-dissipation mechanisms throughout the medium. Mechanisms that have been proposed for bulk attenuation thus include coupling to first-order phase transitions (Heinz *et al.*, 1982).

1.22.4 Seismological Elasticity and Anelasticity

1.22.4.1 Scaling

When the scale length of heterogeneity is comparable to the seismic wavelength, there are two additional considerations. The first is dispersion due to structure. This is seen in observations of surface waves, the velocity of which depend on frequency. This frequency dependence is mostly due to the fact that larger wavelengths sample greater depths where the intrinsic acoustic velocity is greater.

Random heterogeneity can produce scattering of seismic waves (Frankel and Clayton, 1986). Consider a random medium with average velocity v , characterized by heterogeneity of length scale a and velocity perturbation d , and probed by acoustic waves with wavelength λ . On average, the first-arriving waves tend to select paths that preferentially sample the high-velocity heterogeneities; in this sense, the medium appears to have a wave velocity slightly greater than v . In addition, the velocity depends on wavelength, that is, heterogeneity causes dispersion. The direct wave is attenuated, as energy is redirected due to scattering, but this is essentially different from the intrinsic attenuation discussed above for which mechanical energy is dissipated by being converted to heat. The difficulty, however, is that scattering due to heterogeneity has many of the same characteristics as intrinsic attenuation and dispersion of seismic waves, so the two causes of seismic-wave attenuation as a function of distance along the wave path are difficult, if not impossible, to disentangle. This means that any interpretation of attenuation in terms of the strong temperature dependence expected from intrinsic (dissipative) mechanisms, for example, needs to be treated with caution.

What is the scale of heterogeneity in the mantle? The magnitude of the heterogeneity is largest at the grain scale, with differences in shear-wave velocity between coexisting minerals being 10–30% throughout most of the mantle (except for the shallow transition zone) as well as near the core–mantle boundary (Figure 15). The ratio of the grain size typically observed in mantle xenoliths (1–10 mm) to teleseismic wavelengths is $d/\lambda \sim 10^{-7} \ll 1$ characteristic of Rayleigh scattering. In this long-wavelength limit, the apparent attenuation falls with increasing wavelength like $(d/\lambda)^3$ and is probably negligible as long as the heterogeneity is weak (say,

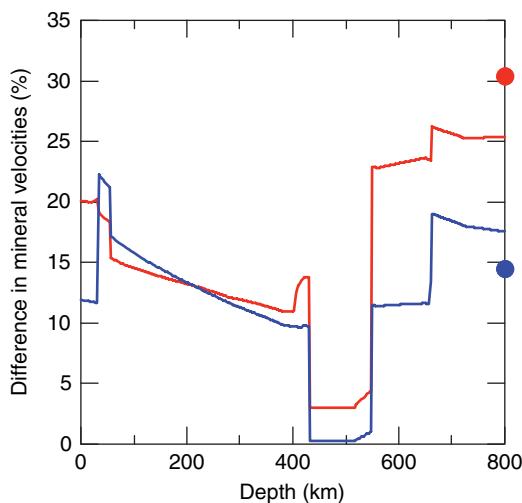


Figure 15 Maximum difference in the shear (red) and longitudinal (blue) velocities of coexisting phases in a model mantle composition. Symbols represent the values at the core–mantle boundary.

less than 1–10%). The grain-scale heterogeneity indicated in **Figure 15** can plausibly be accommodated within the Rayleigh-scattering model, but it is less likely that the stronger heterogeneity associated with partial melt or major compositional variations (e.g., mixtures of core metal and mantle silicates) can also be considered in this weak-scattering limit. Moreover, the grain size of the mantle is still highly uncertain at great depth, particularly below the zone of magma genesis.

Larger-scale heterogeneities, approaching or comparable to seismic wavelengths, are also likely in the mantle. At the mid-ocean ridge, basalt and a depleted residuum, harzburgite, are generated, both of which have significantly different physical properties from undifferentiated mantle. The initial scale length of heterogeneity may be taken as the thickness of the oceanic crust (~ 7 km), which is likely to scatter seismic waves significantly. The magnitude of the velocity difference depends on depth (**Figure 16**). Basalt is slower than peridotite at shallow depths, reflecting the well-known difference in velocity between crust and mantle. Basalt then becomes much faster near 100 km depth because of the transition to eclogite (plagioclase and pyroxenes forming garnet under pressure) that increases velocities by approximately 10%. Velocity contrasts in the lower mantle are not as well constrained, but appear to be less than 10%. For comparison, one seismological study found that scattering of P waves could be

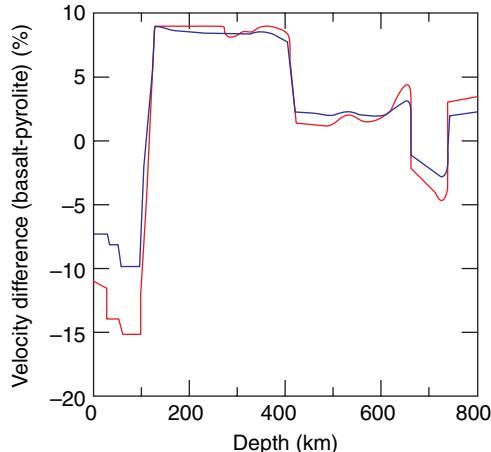
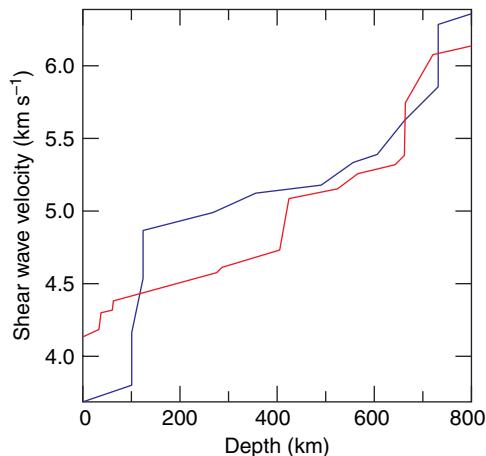


Figure 16 (Top) Velocity of basalt (blue) compared with that of a model mantle composition (red). (Bottom) the difference between the velocities of basalt and average mantle for shear (red) and longitudinal (blue) wave velocities.

explained by heterogeneity with scale length 8 km and magnitude 1% uniformly distributed throughout the mantle, but this result is probably strongly biased due to contamination from heterogeneity at the base of the mantle (Hedlin *et al.*, 1997).

1.22.4.2 Uncertainties

The largest source of uncertainty in constructing isotropic models of radial upper-mantle and transition-zone structure is the elastic constants of minerals at high pressure and temperature (**Table 1**). The propagated uncertainty in the elastic shear-wave velocity is approximately 1.3% or 0.06 km s^{-1} (Stixrude and Lithgow-Bertelloni, 2005a). This is somewhat larger than the difference between Voigt

Table 1 Elastic properties of major mantle phases

Phase	K_0	dK_0/dX	K_0'	$-dK/dT$	G_0	dG/dX	G_0'	$-dG/dT$
plg	84(5)	-	4.0(10)	4(1)	40(3)	-	1.1(5)	6(3)
sp	197(1)	12(2)	5.7(2)	29(3)	109(10)	-24(16)	0.4(5)	13(2)
ol	128(2)	7(2)	4.2(2)	18(1)	82(2)	-31(2)	1.4(1)	14(1)
wa	169(3)	0(13)	4.3(2)	22(6)	112(2)	-40(12)	1.4(2)	18(1)
ri	183(2)	16(7)	4.1(2)	23(2)	120(2)	-25(10)	1.3(1)	17(2)
opx	107(2)	-7(4)	7.0(4)	19(5)	77(1)	-25(5)	1.6(1)	13(2)
cpx	112(5)	7(6)	5.2(18)	18(9)	67(2)	-6(2)	1.4(5)	11(4)
hpcpx	121(1)	0(10)	5.5(3)	20(3)	90(1)	-19(10)	1.5(1)	17(2)
capv	236(4)	-	3.9(2)	22(13)	165(12)*	-	2.5(5)*	26(4)
ak	211(4)	0(10)	4.5(5)	20(6)	132(8)	25(12)	1.6(5)*	21(4)
gt	170(2) – 9Y	7(3)	4.1(3) + 0.1Y	16(2)	94(2)	4(3)	1.3(2) + 0.1Y	10(1) – 2Y
st	314(8)	-	4.4(2)	31(18)	220(12)	-	1.6(5)	36(5)
pv	251(3)	30(40)*	4.1(1)	23(4)	175(2)	-37(40)*	1.7(2)*	25(3)*
fp	161(3)	18(3)	3.9(2)	21(1)	130(3)	-83(3)	2.2(1)	26(1)

Symbols and Units: K, adiabatic bulk modulus (GPa); G, shear modulus (GPa), X, Fe/(Mg + Fe); Y, $m_j/(py + mj)$; subscript o indicates values at zero pressure; primes indicate pressure derivatives; dK/dT and dG/dT in MPa K $^{-1}$. Italicized entries are unconstrained by experiment. Asterisk indicates values taken from density functional theory calculations. After [Stixrude and Lithgow-Bertelloni \(2005b\)](#) and references therein.

and Reuss bounds throughout most of this region, and considerably more than the difference between the Hashin–Shtrikman bounds (**Figure 10**). Uncertainties in computed elastic properties arise mainly because of the need to extrapolate existing measurements taken over limited ranges of pressure and/or temperature to mantle conditions. For a few phases, large discrepancies exist in measured properties that cannot be reconciled at present. An important example is garnet-majorite, for which Brillouin spectroscopy yields a value for $G' = 1.3(2)$ ([Sinogeikin and Bass, 2002](#)), while ultrasonic studies yield a much higher value of 1.9 ([Liu et al., 2000](#)). We have followed the discussion of [Jiang et al. \(2004\)](#) in favoring the Brillouin value in this case, but must emphasize that (as in other instances of apparent discrepancy) there may be real differences between samples (as yet not recognized, let alone controlled for) and that it is not necessarily a question of poor measurements.

In addition to these uncertainties, many important properties remain to be measured at all. For example, the shear modulus of clinopyroxene and akimotoite at elevated pressure are currently estimated on the basis of systematic relations, or density functional theory calculations.

Another kind of uncertainty comes from the linkage between velocity dispersion and attenuation, because there is virtually no constraint on the latter at mantle conditions based on laboratory experiments. Simple models, based on the Weertman law

or a constant activation volume, apparently do not reproduce the qualitative features of seismological radial Q models ([Faul and Jackson, 2005](#)). While attenuation has a small effect on the velocity, the velocity variation of tomographic models is also small, so that intrinsic dispersion is a large part of the 3-D structure ([Karato, 1993](#)). Progress will come from experimental measurements of Q^{-1} in the seismic band at elevated pressure, an enormous challenge.

In the lower mantle, the reliability with which seismological observations can be interpreted is probably limited by our understanding of the relevant mineral-scale physics. For example, the recently discovered high-spin–low-spin transition ([Badro et al., 2003, 2004; Pasternak et al., 1997](#)) appears to have a significant, but still uncertain influence on the density and elasticity ([Lin et al., 2005; Speziale et al., 2005b](#)). It also remains to be understood at what pressure, or over what pressure range, this transition occurs in the lower mantle, and how this range depends on temperature, iron content, and other compositional variables. Valence transitions induced by pressure, for example, between ferric and ferrous iron, also remain poorly understood ([Frost et al., 2004](#)), as does the phase diagram of the third most abundant lower-mantle constituent, calcium silicate perovskite. A temperature-induced transition from a low-temperature tetragonal phase to a high-temperature cubic phase has been predicted ([Stixrude et al., 1996](#)), and low-temperature structural distortions

have been seen experimentally (Shim *et al.*, 2002), but the details remain uncertain. This transition should be accompanied by a large elastic anomaly (15% in shear-wave velocity).

Constructing mineralogical models of anisotropic structure remains a considerable challenge. There has been substantial progress from experiment and theory in our knowledge of the full elastic-constant tensors of major mantle minerals (Karki *et al.*, 2001). We still have a great deal to learn about deformation mechanisms, and in particular dominant slip planes at mantle conditions and at relevant strains and strain rates. Experimental results now exist for many mantle minerals (Cordier, 2002). For lower-mantle minerals, it is important to keep in mind that deformation mechanisms may change profoundly with increasing pressure, as suggested by the change in anisotropy of ferropericlase and magnesium silicate perovskite at high pressure (Karki *et al.*, 1997a, 1997b). The largest uncertainty may be in understanding how polycrystals respond to mantle flow at large finite strains (Blackman *et al.*, 1996; Chastel *et al.*, 1993; Ribe, 1989). This is necessary for estimating the strength of the texture, and the resulting magnitude of anisotropy.

Uncertainties related to composite effects are largest in the context of partial melts. The geometry of the melt phase, whether it exists as spheres, needles, or disks, has an enormous effect on the rock shear elasticity. What is required is an understanding of the relevant mineral–melt interface energetics that control this geometry. Melt geometry may be scale dependent, as demonstrated by experiments in which the melt geometry changes fundamentally on deformation (Bruhn *et al.*, 2000).

1.22.4.3 Implications for Inversions

There are essentially two approaches used for linking seismology and mineral physics, forward and inverse modeling. For the first, a mineralogical model based on an assumed bulk composition, and potential temperature is compared with seismological observations (Duffy and Anderson, 1989; Ita and Stixrude, 1992; Stixrude and Lithgow-Bertelloni, 2005a; Vacher *et al.*, 1998). (For applications to adiabatic temperature profiles in the Earth, the ‘potential temperature’ refers to the temperature on the adiabat at zero pressure.) In practice, mineralogical models are typically compared with seismological models, an approach that is fraught with difficulty because the

seismological models are derivative of the data and nonunique. These difficulties are particularly prevalent in the upper mantle, where lateral variations, attenuation, and anisotropy are all large, and radial models are prone to mislead.

A promising alternative forward modeling approach, little used as yet, would be to compute the actual seismological observables (e.g., traveltimes, mode frequencies, and the like) directly from the mineralogical model. This would permit much more direct and certain comparison to the structure of Earth. The uncertainties inherent in the forward model can in principle be assessed and propagated to uncertainties in predicted seismological observables.

An additional benefit of forward mineralogical models is that they might be used as a reference for seismic tomographic inversions. Tomographic models are usually determined as deviations from an assumed radial structure, and the radial model may bias the inversion. For example, in oceanic regions of the upper mantle, tomographic inversions based on Preliminary Reference Earth Model (PREM) (Dziewonski and Anderson, 1981) might be biased by the large Lehmann discontinuity in this radial model, which subsequent studies have found is preferentially located under continents. PREM and other radial seismic models assume a parametrically simple radial structure. For example, the transition-zone gradient is assumed to be linear, which does not agree with expectations based on the phase transformations that we know take place in typical mantle lithologies. Advantages of using a mineralogical model would be that all anticipated structure from phase transitions would be included. Moreover, the reference state would be one associated with a well-defined, if imprecise physical meaning in terms of bulk composition and geotherm. Recent attempts to construct such so-called ‘physical reference models’ adjust the mineralogical model to conform with seismological data (Cammarano *et al.*, 2003). By optimizing the fit of the forward model to seismic data, one obtains a more stable starting point for tomographic inversions, but the connection to a physically well-defined reference state is lost. With ever-improving knowledge of mantle phase equilibria and physical properties, one may envision substantial improvements in the construction of mineralogical models and our ability to interpret seismological observations in terms of radial and lateral variations in temperature, and bulk composition.

An inverse model would seek to invert seismic observations directly for radial and lateral variations

in bulk composition and temperature. In practice, inverse models have been based on the intermediate step of a velocity model. Several studies have inverted radial or 3-D velocity and density models for radial and lateral variations in temperature and bulk composition (Deschamps and Trampert, 2003; Goes *et al.*, 2000; Mattern *et al.*, 2005; Shapiro and Ritzwoller, 2004; Stixrude *et al.*, 1992; Trampert *et al.*, 2001). Some caution is in order because of the uncertainty in the nonlinear and linked phenomena involved, particularly in the estimate of attenuation. Also important are systematic effects that have not been included in these inversions. There are three sources of lateral heterogeneity in the mantle, due to lateral variations of temperature, bulk composition, and phase. The last of these has not been included, even though lateral variations in phase proportions can contribute as much to – even more than – 3-D structure as lateral variations in temperature alone. The quantities necessary to estimate the influence of phase on lateral structure are reasonably well known in the upper mantle and transition zone: phase equilibria and physical properties of the minerals involved are experimentally documented, and should be included in future efforts.

1.22.5 Conclusions and Outlook

The contact between mineral physics and seismology of Earth's mantle has grown considerably richer and more sophisticated in recent years. Birch's vision of constraining the chemical and thermal state of the mantle on the basis of mineralogical properties and seismic observations is becoming a reality. In addition, mineral physics is beginning to provide the foundation required for inferring the dynamic state of the mantle, and some aspects of its geological evolution, from the seismological observations.

Progress will come from continued expansion of our knowledge of the elastic properties of mantle minerals at *in situ* conditions of high pressure and high temperature. These data remain the basis for any discussion of mantle structure in terms of radial or lateral variations in temperature or bulk composition. Among recent experimental advances has been a dramatic increase in the pressure range over which measurements of the shear modulus can be made, to 1 Mb (2300 km depth) (Murakami *et al.*, 2006). Coupled with methodological developments for measuring sound velocities at high temperature (Li *et al.*, 2004; Sinogeikin *et al.*, 2004), one may

envision measurement of the elastic properties of mantle minerals at pressure–temperature conditions of the mantle for the first time in the near future. At the same time, first-principles theory continues to make important strides, including the computation of the elastic constants of important phases over the entire mantle pressure–temperature regime (Wentzcovitch *et al.*, 2004).

Equally important will be a better understanding of recently discovered physics and chemistry, including the postperovskite phase transition, the high-spin–low-spin transition of iron in oxides and silicates, and the possible role of valence state changes of iron at high pressure. Among physical properties that are still poorly understood is the attenuation (or its inverse, the quality factor Q). While recent experiments have laid an important foundation (Gribb and Cooper, 1998; Jackson *et al.*, 2002, 2004), we still have little experimental data bearing on the influence of pressure or water content on attenuation. Also uncertain are the dominant deformation mechanisms in mantle minerals at high pressure and temperature, and these provide an additional link between experimental measurements of the elastic-constant tensor and seismically observed anisotropy. Recent experimental discoveries suggest that more surprises await (Mainprice *et al.*, 2005).

Along with improved knowledge of the physical properties of individual phases will come increasing understanding of aggregate properties and the construction of mineralogical models of the mantle as a whole. An important advance will be closer contact between mineralogical models and seismological observations.

References

- Abramson EH, Brown JM, and Slutsky LJ (1999) Applications of impulsive stimulated scattering in the earth and planetary sciences. *Annual Review of Physical Chemistry* 50: 279–313.
- Agnon A and Bukowinski MST (1990) Delta-S at high-pressure and Dlvs/Dlvp in the lower mantle. *Geophysical Research Letters* 17: 1149–1152.
- Anderson DL and Given JW (1982) Absorption-band Q model for the Earth. *Journal of Geophysical Research* 87: 3893–3904.
- Anderson OL (1995) *Equations of State of Solids for Geophysics and Ceramic Science*. Oxford, UK: Oxford University Press.
- Anderson OL and Isaak DG (1995) Elastic constants of mantle minerals at high temperature. In: Ahrens TJ (ed.) *Mineral Physics and Crystallography: A Handbook of Physical Constants*, pp. 64–97. Washington, DC: American Geophysical Union.
- Ashcroft NW and Mermin ND (1976) *Solid State Physics*. New York: Holt Rinehart and Winston.

- Backus GE (1962) Long-wave elastic anisotropy produced by horizontal layering. *Journal of Geophysical Research* 67: 4427–4440.
- Badro J, Fiquet G, Guyot F, et al. (2003) Iron partitioning in Earth's mantle: Toward a deep lower mantle discontinuity. *Science* 300: 789–791.
- Badro J, Rueff J-P, Vanko G, Monaco G, Fiquet GA, and Guyot F (2004) Electronic transitions in perovskite: Possible nonconvecting layers in the lower mantle. *Science* 305: 383–386.
- Barron THK, Berg WT, and Morrison JA (1957) The thermal properties of alkali halide crystals. 2. Analysis of experimental results. *Proceedings of the Royal Society of London Series A, Mathematical and Physical Sciences* 242: 478–492.
- Berryman JG (1995) Mixture theories for rock properties. In: Ahrens TJ (ed.) *Rock Physics and Phase Relations: A Handbook of Physical Constants*, pp. 205–228. Washington, DC: American Geophysical Union.
- Blackman DK, Kendall JM, Dawson PR, Wenk H-R, Boyce D, and Morgan JP (1996) Teleseismic imaging of subaxial flow at mid-ocean ridges: Traveltime effects of anisotropic mineral texture in the mantle. *Geophysical Journal International* 127: 415–426.
- Born M and Huang K (1954) *Dynamical Theory of Crystal Lattices*. Oxford, UK: Clarendon Press.
- Bracewell RN (1999) *The Fourier Transform and Its Applications* 3rd edn. New York: McGraw-Hill.
- Brown JM and McQueen RG (1986) Phase transitions, Grüneisen parameter, and elasticity for shocked iron between 77 GPa and 400 GPa. *Journal of Geophysical Research* 91: 7485–7494.
- Brown JM, Slutsky LJ, Nelson KA, and Cheng L-T (1989) Single-crystal elastic-constants for San Carlos Peridot – An application of impulsive stimulated scattering. *Journal of Geophysical Research-Solid Earth and Planets* 94: 9485–9492.
- Bruhn D, Groebner N, and Kohlstedt DL (2000) An interconnected network of core-forming melts produced by shear deformation. *Nature* 403: 883–886.
- Bunge HJ, Kiewel R, Reinert T, and Fritzsche L (2000) Elastic properties of polycrystals – Influence of texture and stereology. *Journal of The Mechanics and Physics of Solids* 48: 29–66.
- Cammarano F, Goes S, Vacher P, and Giardini D (2003) Inferring upper-mantle temperatures from seismic velocities. *Physics of the Earth and Planetary Interiors* 138: 197–222.
- Chastel YB, Dawson PR, Wenk H-R, and Bennett K (1993) Anisotropic convection with implications for the upper-mantle. *Journal of Geophysical Research, Solid Earth* 98: 17757–17771.
- Chopelas A and Boehler R (1989) Thermal-expansion measurements at very high-pressure, systematics, and a case for a chemically homogeneous mantle. *Geophysical Research Letters* 16: 1347–1350.
- Cooper RF (2002) Seismic wave attenuation: Energy dissipation in viscoelastic crystalline solids. In: Karato S and Wenk H-R (eds.) *Plastic Deformation of Minerals and Rocks*, pp. 253–290. Washington, DC: American Mineralogical Society.
- Cordier P (2002) Dislocations and slip systems of mantle minerals. In: Karato S and Wenk H-R (eds.) *Plastic Deformation of Minerals and Rocks*, pp. 137–179. Washington, DC: American Mineralogical Society.
- Davies GF (1974) Effective elastic-moduli under hydrostatic stress.1. Quasi-harmonic theory. *Journal of Physics and Chemistry of Solids* 35: 1513–1520.
- Deschamps F and Trampert J (2003) Mantle tomography and its relation to temperature and composition. *Physics of the Earth and Planetary Interiors* 140: 277–291.
- Dove MT (1993) *Introduction to Lattice Dynamics*. Cambridge, UK: Cambridge University Press.
- Duffy TS and Ahrens TJ (1992) Sound velocities at high-pressure and temperature and their geophysical implications. *Journal of Geophysical Research-Solid Earth* 97: 4503–4520.
- Duffy TS and Anderson DL (1989) Seismic Velocities in Mantle Minerals and the Mineralogy of the Upper Mantle. *Journal of Geophysical Research – Solid Earth and Planets* 94: 1895–1912.
- Duffy TS, Zha CS, Downs RT, Mao HK, and Hemley RJ (1995) Elasticity of Forsterite to 16 GPa and the composition of the upper-mantle. *Nature* 378: 170–173.
- Dziewonski AM and Anderson DL (1981) Preliminary reference earth model. *Physics of the Earth and Planetary Interiors* 25: 297–356.
- Faul UH, Fitz Gerald JD, and Jackson I (2004) Shear wave attenuation and dispersion in melt-bearing olivine polycrystals: 2. Microstructural interpretation and seismological implications. *Journal of Geophysical Research-Solid Earth* 109: N6.
- Faul UH and Jackson I (2005) The seismological signature of temperature and grain size variations in the upper mantle. *Earth and Planetary Science Letters* 234: 119–134.
- Frankel A and Clayton RW (1986) Finite-difference simulations of seismic scattering – implications for the propagation of short-period seismic-waves in the crust and models of crustal heterogeneity. *Journal of Geophysical Research-Solid Earth and Planets* 91: 6465–6489.
- Frost DJ, Liebske C, Langenhorst F, McCammon CA, Trønnes RG, and Rubie DC (2004) Experimental evidence for the existence of iron-rich metal in the Earth's lower mantle. *Nature* 428: 409–412.
- Gieske JH and Barsch GR (1968) Pressure dependence of elastic constants of single crystalline aluminum oxide. *Physica Status Solidi* 29: 121–131.
- Gillet P, Guyot F, and Wang Y (1996) Microscopic anharmonicity and equation of state of $MgSiO_3$ – Perovskite. *Geophysical Research Letters* 23: 3043–3046.
- Goes S, Govers R, and Vacher P (2000) Shallow mantle temperatures under Europe from P and S wave tomography. *Journal of Geophysical Research-Solid Earth* 105: 11153–11169.
- Goto TI, Ohno I, and Sumino Y (1976) The determination of the elastic constants of natural almandine-pyrope garnet by rectangular parallelepiped resonance method. *Journal of Physics of the Earth* 24: 149–156.
- Gribb TT and Cooper RF (1998) Low-frequency shear attenuation in polycrystalline olivine: Grain boundary diffusion and the physical significance of the Andrade model for viscoelastic rheology. *Journal of Geophysical Research-Solid Earth* 103: 27267–27279.
- Hashin Z and Shtrikman S (1962) A variational approach to the theory of the elastic behavior of polycrystals. *Journal of the Mechanics and Physics of Solids* 10: 343–352.
- Hashin Z and Shtrikman S (1963) A variational approach to the theory of the elastic behaviour of multiphase materials. *Journal of the Mechanics and Physics of Solids* 11: 127–140.
- Hazen RM, Downs RT, and Finger LW (1996) High-pressure crystal chemistry of $LiScSiO_4$: An olivine with nearly isotropic compression. *American Mineralogist* 81: 327–334.
- Hedlin MAH, Peter MS, and Paul SE (1997) Seismic evidence for small-scale heterogeneity throughout the Earth's mantle. *Nature* 387: 145–150.
- Heinz D, Jeanloz R, and O'Connell RJ (1982) Bulk attenuation in a polycrystalline earth. *Journal of Geophysical Research* 87: 7772–7778.
- Helbig K (1984) *Foundations of Anisotropy for Exploration Seismics*. New York: Pergamon.

- Hill R (1952) The elastic behaviour of a crystalline aggregate. *Proceedings of the Physical Society of London Section A* 65: 349–355.
- Hill R (1963) Elastic properties of reinforced solids – Some theoretical principles. *Journal of the Mechanics and Physics of Solids* 11: 357–372.
- Holland TJB and Powell R (1998) An internally consistent thermodynamic data set for phases of petrological interest. *Journal of Metamorphic Geology* 16: 309–343.
- Isaak DG, Anderson OL, and Cohen RE (1992) The relationship between shear and compressional velocities at high pressures: Reconciliation of seismic tomography and mineral physics. *Geophysical Research Letters* 19: 741–744.
- Isaak DG, Cohen RE, and Mehl MJ (1990) Calculated elastic constants and thermal properties of MgO at high pressures and temperatures. *Journal of Geophysical Research* 95: 7055–7067.
- Ita J and Stixrude L (1992) Petrology, elasticity, and composition of the mantle transition zone. *Journal of Geophysical Research-Solid Earth* 97: 6849–6866.
- Jackson DD and Anderson DL (1970) Physical mechanisms of seismic-wave attenuation. *Reviews of Geophysics and Space Physics* 8: 1.
- Jackson I (2000) Geophysics – Taking the earth's temperature. *Nature* 406: 470–471.
- Jackson I, Faul UH, Fitz Gerald JD, John D, and Tan BH (2004) Shear wave attenuation and dispersion in melt-bearing olivine polycrystals: 1. Specimen fabrication and mechanical testing. *Journal of Geophysical Research-Solid Earth* 109: N(6).
- Jackson I, Fitz Gerald JD, Faul UH, and Tan BH (2002) Grain-size-sensitive seismic wave attenuation in polycrystalline olivine. *Journal of Geophysical Research-Solid Earth* 107: N12.
- Jackson I and Niesler H (1982) The elasticity of periclase to 3 GPa and some geophysical implications. In: Akimoto S and Manghnani MH (eds.) *High-pressure Research in Geophysics*, pp. 93–133. Tokyo, Japan: Center for Academic Publications.
- Jackson JM, Sinogeikin SV, and Bass JD (2000) Sound velocities and elastic properties of gamma-Mg₂SiO₄ to 873 K by Brillouin spectroscopy. *American Mineralogist* 85: 296–303.
- Jeanloz R and Thompson (1983) Phase transitions and mantle discontinuities. *Reviews of Geophysics* 21: 51–74.
- Jiang FM, Speziale S, and Duffy TS (2004) Single-crystal elasticity of grossular – and almandine-rich garnets to 11 GPa by Brillouin scattering. *Journal of Geophysical Research-Solid Earth* 109: N10.
- Juanzemis W (1967) *Continuum Mechanics*. New York: MacMillan.
- Karato S (1993) Importance of anelasticity in the interpretation of seismic tomography. *Geophysics Research Letters* 20: 1623–1626.
- Karato S-I (1998) Seismic anisotropy in the deep mantle, boundary layers and the geometry of mantle convection. *Pure and Applied Geophysics* 151: 565–587.
- Karki BB and Crain J (1998) First-principles determination of elastic properties of CaSiO₃ perovskite at lower mantle pressures. *Geophysical Research Letters* 25: 2741–2744.
- Karki BB, Stixrude L, Clark SJ, Warren MC, Ackland GJ, and Crain J (1997a) Elastic Properties of orthorhombic MgSiO₃ perovskite at lower mantle pressures. *American Mineralogist* 82: 635–638.
- Karki BB, Stixrude L, Clark SJ, Warren MC, Ackland GJ, and Crain J (1997b) Structure and elasticity of MgO at high pressure. *American Mineralogist* 82: 51–60.
- Karki BB, Karki BB, Stixrude L, and Wentzcovitch RM (2001) High-pressure elastic properties of major materials of Earth's mantle from first principles. *Reviews of Geophysics* 39: 507–534.
- Kennett BLN and Engdahl ER (1991) Traveltimes for global earthquake location and phase identification. *Geophysical Journal International* 105: 429–465.
- Kieffer B, Stixrude L, and Wentzcovitch RM (1997) Elastic constants and anisotropy of Mg₂SiO₄ spinel at high pressure. *Geophysical Research Letters* 24: 2841–2844.
- Kieffer SW (1979) Thermodynamics and lattice vibrations of minerals, I: mineral heat capacities and their relationship to simple lattice vibrational modes. *Reviews of Geophysics and Space Physics* 17: 1–19.
- Kieffer SW (1980) Thermodynamics and lattice-vibrations of minerals 4. Application to chain and sheet silicates and orthosilicates. *Reviews of Geophysics* 18: 862–886.
- Kosevich AM, Lifshitz EM, Landau LD, and Pitaevskii LP (1986) *Theory of Elasticity* 3rd edn. 195 pp. Oxford, UK: Butterworth-Heinemann.
- Li BS, Kung J, and Liebermann RC (2004) Modern techniques in measuring elasticity of Earth materials at high pressure and high temperature using ultrasonic interferometry in conjunction with synchrotron x-radiation in multi-anvil apparatus. *Physics of the Earth and Planetary Interiors* 143: 559–574.
- Lin JF, Struzhkin VV, Jacobsen SD, et al. (2005) Spin transition of iron in magnesiowustite in the Earth's lower mantle. *Nature* 436: 377–380.
- Liu J, Chen G, Gwanmesia GD, and Liebermann RC (2000) Elastic wave velocities of pyrope-majorite garnets (Py(62)Mj(38) and Py(50)Mj(50)) to 9 GPa. *Physics of the Earth and Planetary Interiors* 120: 153–163.
- Mainprice D, Andréa T, Hélène C, Patrick C, and Daniel JF (2005) Pressure sensitivity of olivine slip systems and seismic anisotropy of Earth's upper mantle. *Nature* 433: 731–733.
- Mattern E, Matas J, Ricard Y, and Bass J (2005) Lower mantle composition and temperature from mineral physics and thermodynamic modelling. *Geophysical Journal International* 160: 973–990.
- McQueen RG, Marsh SP, Taylor JW, Fritz JN, and Carter WJ (1970) The equation of state of solids from shock wave studies. In: Kinslow R (ed.) *High-velocity Impact Phenomena*, pp. 293–417. New York, NY: Academic Press.
- Mei S and Kohlstedt DL (2000a) Influence of water on plastic deformation of olivine aggregates 1. Diffusion creep regime. *Journal of Geophysical Research-Solid Earth* 105: 21457–21469.
- Mei S and Kohlstedt DL (2000b) Influence of water on plastic deformation of olivine aggregates 2. Dislocation creep regime. *Journal of Geophysical Research – Solid Earth* 105: 21471–21481.
- Merkel S, Goncharov AF, Mao HK, Gillet P, and Hemley RJ (2000) Raman spectroscopy of iron to 152 gigapascals: Implications for Earth's inner core. *Science* 288: 1626–1629.
- Murakami M, Sinogeikin SU, Hellwig H, Bass JD, and Li J (2006) Sound velocity of MgSiO₃ perovskite to Mbar pressure. *Earth and Planetary Science Letters* 256: 47–54.
- Nowick AS and Berry BS (1972) *Anelastic Relaxation in Crystalline Solids*. New York and London: Academic Press.
- Nye JF (1985) *Physical Properties of Crystals: Their Representation by Tensors and Matrices*, 2 edn. Oxford, UK: Oxford University Press.
- Oganov AR, Gillan MJ, and Price GD (2003) *Ab initio* lattice dynamics and structural stability of MgO. *Journal of Chemical Physics* 118: 10174–10182.
- Pasternak MP, Taylor RD, Jeanloz R, Li X, Nguyen JH, and Mccammon CA (1997) High pressure collapse of magnetism in Fe0.940: Mossbauer spectroscopy beyond 100 GPa. *Physical Review Letters* 79: 5046–5049.

- Ribe NM (1989) Seismic Anisotropy and Mantle Flow. *Journal of Geophysical Research-Solid Earth and Planets* 94: 4213–4223.
- Rigden SM, Jackson INS, Niesler H, Liebermann RC, and Ringwood AE (1991) Spinel elasticity and seismic structure of the transition zone of the mantle. *Nature* 354: 143–145.
- Rivers ML and Carmichael ISE (1987) Ultrasonic studies of silicate melts. *Journal of Geophysical Research – Solid Earth and Planets* 92: 9247–9270.
- Robie RA and Hemingway BS (1995) *Thermodynamic Properties of Minerals and Related Substances at 298.15 K and 1 Bar (10⁵ Pascals) Pressure and at Higher Temperature*, 461 pp. Washington, DC: US Geological Survey.
- Shapiro NM and Ritzwoller MH (2004) Thermodynamic constraints on seismic inversions. *Geophysical Journal International* 157: 1175–1188.
- Shim SH, Jeanloz R, and Duffy TS (2002) Tetragonal structure of CaSiO₃ perovskite above 20 GPa. *Geophysical Research Letters* 29: 1399.
- Sinogeikin SV and Bass JD (2000) Single-crystal elasticity of pyrope and MgO to 20 GPa by Brillouin scattering in the diamond cell. *Physics of the Earth and Planetary Interiors* 120: 43–62.
- Sinogeikin SV and Bass JD (2002) Elasticity of Majorite and a Majorite-Pyrope solid solution to high pressure: Implications for the transition zone. *Geophysical Research Letters* 29(2): 1017 (doi:10.1029/2001GL013937).
- Sinogeikin SV, Lakshtanov DL, Nicholas JD, and Bass JD (2004) Sound velocity measurements on laser-heated MgO and Al₂O₃. *Physics of the Earth and Planetary Interiors* 143: 575–586.
- Spetzler H (1970) Equation of state of polycrystalline and single-crystal Mgo to 8 kilobars and 800 degrees K. *Journal of Geophysical Research* 75: 2073–2087.
- Speziale S, Jiang SF, and Duffy TS (2005a) Compositional dependence of the elastic wave velocities of mantle minerals: Implications for seismic properties of mantle rocks. In: Vander Hilst, Bass JD, Matas J, and Trampert J (eds.) *Earth's Deep Mantle: Structure, Composition, and Evolution*, pp. 301–320. Washington, DC: American Geophysical Union.
- Speziale S, Milner A, Lee VE, Clark SM, Pasternak MP, and Jeanloz R (2005b) Iron spin transition in Earth's mantle. *Proceedings of the National Academy of Sciences of the United States of America* 102: 17918–17922.
- Speziale S, Zha C-S, Duffy TS, Hemley RJ, and Mao H-K (2001) Quasi-hydrostatic compression of magnesium oxide to 52 GPa: Implications for the pressure-volume-temperature equation of state. *Journal of Geophysical Research-Solid Earth* 106: 515–528.
- Stixrude L (1998) Elastic constants and anisotropy of MgSiO₃ perovskite, periclase, and SiO₂ at high pressure. In: Gurnis M, Wysession M, Knittle E, and Buffet B (eds.) *The Core–Mantle Boundary Region*, pp. 83–96. Washington, DC: American Geophysical Union.
- Stixrude L, Cohen RE, and Singh DJ (1994) Iron at high pressure: Linearized augmented plane wave calculations in the generalized gradient approximation. *Physical Review B* 50: 6442–6445.
- Stixrude L, Cohen RE, Yu R, and Krakauer H (1996) Prediction of phase transition in CaSiO₃ perovskite and implications for lower mantle structure. *American Mineralogist* 81: 1293–1296.
- Stixrude L, Hemley RJ, Fei Y, and Mao HK (1992) Thermoelasticity of silicate perovskite and magnesiowustite and stratification of the earth's mantle. *Science* 257: 1099–1101.
- Stixrude L and Lithgow-Bertelloni C (2005a) Mineralogy and elasticity of the oceanic upper mantle: Origin of the low-velocity zone. *Journal of Geophysical Research-Solid Earth* 110: B03204 (doi:10.1029/2004JB002965).
- Stixrude L and Lithgow-Bertelloni C (2005b) Thermodynamics of mantle minerals – I. Physical properties. *Geophysical Journal International* 162: 610–632.
- Stixrude L, Lithgow-Bertelloni C, Kieter B, and Fumagalli P (2007) Phase stability and shear softening in CaSiO₃ perovskite at high pressure. *Physical Review B* 75: 024108.
- Trampert J, Vacher P, and Vlaar N (2001) Sensitivities of seismic velocities to temperature, pressure and composition in the lower mantle. *Physics of the Earth and Planetary Interiors* 124: 255–267.
- Vacher P, Mocquet A, and Sotin C (1998) Computation of seismic profiles from mineral physics: The importance of the non-olivine components for explaining the 660 km depth discontinuity. *Physics of the Earth and Planetary Interiors* 106: 275–298.
- Wallace DC (1972) *Thermodynamics of Crystals*, 1st edn. New York: Wiley.
- Watt JP (1988) Elastic properties of polycrystalline minerals – Comparison of theory and experiment. *Physics and Chemistry of Minerals* 15: 579–587.
- Watt JP, Davies GF, and O'Connell RJ (1976) The elastic properties of composite materials. *Reviews of Geophysics and Space Physics* 14: 541–563.
- Weidner DJ, Bass J, Ringwood AE, and Sinclair W (1982) The single-crystal elastic moduli of stishovite. *Journal of Geophysical Research* 87: 4740–4746.
- Weiner JH (1983) *Statistical Mechanics of Elasticity*, 439 pp. New York: Wiley.
- Wentzcovitch RM, Karki BB, Cococcioni M, and Gironcoli S de (2004) Thermoelastic properties of MgSiO₃-perovskite: Insights on the nature of the Earth's lower mantle. *Physical Review Letters* 92(1): 018501.
- Wentzcovitch RM and Stixrude L (1997) Crystal chemistry of forsterite: A first principles study. *American Mineralogist* 82: 663–671.
- Williams Q (1995) Infrared, Raman and optical spectroscopy of earth materials. In: *Mineral Physics and Crystallography*, Ahrens TJ (ed.) *A Handbook of Physical Constants*. Washington, DC: American Geophysical Union.
- Williams Q and Garnero EJ (1996) Seismic evidence for partial melt at the base of Earth's mantle. *Science* 273: 1528.
- Workman RK and Hart SR (2005) Major and trace element composition of the depleted MORB mantle (DMM). *Earth and Planetary Science Letters* 231: 53–72.
- Yoneda A (1990) Pressure derivatives of elastic-constants of single-crystal MgO and MgAl₂O₄. *Journal of Physics of the Earth* 38: 19–55.
- Zaug JM, Abramson EH, Brown JM, and Slutsky LJ (1993) Sound velocities in olivine at Earth mantle pressures. *Science* 260: 1487–1489.

1.23 Constraints on Seismic Models from Other Disciplines – Implications for Mantle Dynamics and Composition

A. M. Forte, Université du Québec à Montréal, Montreal, QC, Canada

© 2007 Elsevier B.V. All rights reserved.

1.23.1	Introduction	805
1.23.2	Geodynamic Observables and Mantle Flow Theory	807
1.23.2.1	Convection-Related Surface Observations	807
1.23.2.2	Evidence for Mantle Flow in Correlations between Internal Structure and Surface Gravity Anomalies	809
1.23.2.3	Fluid Mechanical Modeling of Viscous Mantle Flow	811
1.23.2.3.1	Governing equations	811
1.23.2.3.2	Spectral treatment of the mantle flow equations	814
1.23.2.3.3	Internal boundary conditions	815
1.23.2.3.4	Boundary conditions at Earth's solid surface	817
1.23.2.3.5	Boundary conditions at CMB	819
1.23.2.3.6	Determining viscous flow Green functions	820
1.23.2.3.7	Incorporating tectonic plates as a surface boundary condition	821
1.23.2.4	Geodynamic Response Functions for the Mantle	824
1.23.2.5	Depth Dependence of Mantle Viscosity	825
1.23.3	Modeling Geodynamic Observables with Seismic Tomography	829
1.23.3.1	Seismic Heterogeneity Models	830
1.23.3.2	Mantle Density Anomalies	831
1.23.3.3	Predicted Tectonic Plate Motions	834
1.23.3.4	Predicted Free-Air Gravity Anomalies	836
1.23.3.5	Predicted Dynamic Surface Topography	837
1.23.3.6	Predicted CMB Topography	843
1.23.4	Tomography-Based Geodynamic Inferences of Compositional Heterogeneity	846
1.23.4.1	Constraints from Mineral Physics	847
1.23.4.2	Compositional Density Anomalies Inferred from Joint Shear- and Bulk-Sound Tomography	849
1.23.4.3	Compositional Density Anomalies Inferred from 'Hot' and 'Cold' Mantle Heterogeneity	850
1.23.4.4	Diffuse Mid-Mantle Compositional Horizon	852
1.23.5	Concluding Remarks	853
	References	854

1.23.1 Introduction

The earliest models of mantle heterogeneity (e.g., Dziewonski *et al.*, 1977; Dziewonski 1984; Clayton and Comer (1983) – reported in Hager and Clayton (1989); Woodhouse and Dziewonski 1984) exhibited a large-scale three-dimensional (3-D) structure which was reasonably well correlated to the major surface manifestations of mantle convection, namely

the large-scale nonhydrostatic geoid (Hager *et al.* 1985) and the large-scale tectonic plate motions (Forte and Peltier, 1987). These early models of mantle heterogeneity thus helped to show that seismic tomography could indeed resolve the lateral variations in mantle structure which drive the convective flow responsible for the 'drift' of the continents and the large-scale perturbations in Earth's gravitational field.

Advances in seismic tomographic imaging over the past decade have yielded models of global 3-D mantle structure which poses significantly improved resolution and reliability (e.g., Ekström and Dziewonski, 1998; Ritsema *et al.*, 1999; Mégnin and Romanowicz, 2000; Masters *et al.*, 2000; Boschi and Dziewonski, 2000; Grand, 2002; Antolik *et al.*, 2003). These improvements are evident in the remarkable accord among the images of large-scale mantle structure provided by these different models. Such agreement is encouraging, especially when we consider that these models are obtained on the basis of different data sets, different theoretical treatments of seismic wave propagation, and different algorithms for inverting the global seismic data. A review of the recent advances in global seismic tomographic imaging may be found in Romanowicz (2003).

While the analyses and discussion presented below will focus on how seismically inferred 3-D mantle structure may be used to explain geodynamic data and to model mantle flow dynamics, it is important to note that much effort has also been dedicated to the converse approach, namely to infer 3-D mantle structure from geodynamic data. This inverse approach based on geodynamic constraints began at almost the same time as the earliest global tomography inversions. Hager (1984) proposed a mantle flow model based on estimated density anomalies associated with seismically active subducted slabs and used this model to obtain a good match to very long wavelength geoid anomalies. Although subsequent studies, for example, by Ricard *et al.* (1989), attempted a more general inference of mantle heterogeneity using different geodynamic data, the subducted-slab geodynamic models developed by Hager (1984) became prevalent. This led, for example, to a study by Forte and Peltier (1989) which constrained the distribution of subducted slab heterogeneity using other geodynamic observables such as tectonic plate motions and core-mantle boundary topography. The latter study also attempted to use the geodynamic observables to infer the buoyancy forces associated with mantle plumes under mid-ocean ridges.

Tectonic plate motions and long-wavelength geoid anomalies have proved to be the most important constraints in developing geodynamic models of 3-D mantle heterogeneity in terms of subducted slabs. The geological history of tectonic plate motions as derived from paleomagnetic data (e.g., Gordon and Jurdy, 1986) have been an especially important ingredient in developing models of both past and present-day subducted slab heterogeneity

(e.g., Richards and Engebretson, 1992; Ricard *et al.*, 1993). These models have been very useful for exploring time-dependent dynamics of the mantle (e.g., Lithgow-Bertelloni and Gurnis, 1997; Lithgow-Bertelloni and Richards, 1998). Direct comparisons between the long-wavelength pattern of subducted slab heterogeneity and the corresponding pattern of heterogeneity derived from seismic tomography have shown good correlations at the longest wavelengths (Richards and Engebretson, 1992). When all wavelengths are considered, however, the global correlations between the slab heterogeneity and different tomography models are relatively poor, with correlation coefficients less than 0.3 throughout the mantle (Figure 7 in Lithgow-Bertelloni and Richards (1998)).

There are various factors which might explain the less than satisfactory agreement between seismic models of 3-D mantle structure and the reconstructions of mantle heterogeneity in terms of subducted slabs. First, from a purely technical perspective, the evolution of the slab trajectories were not determined in a fluid mechanically consistent manner by numerically solving the advection-diffusion equations. Progress in this direction has been made by Bunge *et al.* (1998), McNamara and Zhong (2005), and Quéré and Forte (2006) by solving the full set of thermal convection equations with moving tectonic plates as a surface boundary condition. Second, the slab models assume that thermally generated heterogeneity dominates in the mantle and this may not be applicable in regions of the mantle with significant compositional heterogeneity (e.g., Forte and Mitrovica, 2001; McNamara and Zhong, 2005). Perhaps the most important deficiency in these efforts to explain mantle heterogeneity in terms of slab subduction alone is that they do not account for the presence and evolution of hot thermal plumes in the mantle which have been consistently imaged in the global tomography models (e.g., Romanowicz, 2003). A recent appraisal of the origin and importance of mantle plumes in convection models which incorporate Cenozoic plate histories may be found in Quéré and Forte (2006).

Seismic tomography continues to be the single most important technique for directly inferring the 3-D heterogeneity in the mantle which is associated with the process of thermal convection. The significant advances in global seismic imaging over the past few years provides the underlying motivation for the detailed discussion of the geodynamic implications which will be presented below. A recent detailed

review by Becker and Boschi (2002) of the currently available tomography models focused on a quantitative analysis of similarities and differences between these models. The work presented below will further extend this previous analysis by carrying out calculations of the mantle flow predicted on the basis of these tomography models and examining in detail the extent to which the tomography-based flow models provide a satisfactory explanation for the main convection-related surface observables.

1.23.2 Geodynamic Observables and Mantle Flow Theory

In the following, the main global geophysical constraints on mantle structure will be presented. These constraints include the free-air gravity anomalies, the dynamic surface, and core–mantle boundary (CMB) topography and the tectonic plate motions. The theoretical relationship between these convection-related observables and the internal 3-D structure will be developed in terms of a fluid mechanical model of mantle dynamics.

1.23.2.1 Convection-Related Surface Observations

An understanding of thermal convection in the mantle is necessary for explaining a multitude of geophysical and geological processes which we can observe and measure at the surface of the Earth, such as continental drift, earthquakes, mountain building, volcanism, perturbations in Earth's gravitational field, variations in oceanic bathymetry and continental elevation, and long-term changes in global sea-level variations. The principal surface manifestations of mantle convection which have been employed to study the large scale structure and dynamics of the solid Earth are illustrated schematically in **Figure 1**.

The observational constraints on 3-D mantle structure and dynamics which are considered below are the global free-air gravity anomalies, the dynamic surface and CMB topography, and the horizontal divergence of the tectonic plate motions. The Earth's gravitational potential perturbations are usually represented in terms of geoid anomalies however, as pointed out in Forte *et al.* (1994), a more detailed and evenly balanced representation

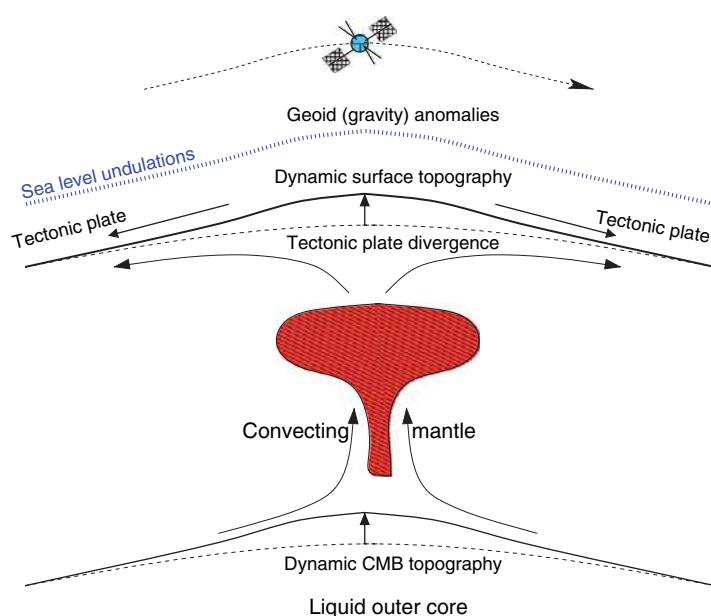


Figure 1 Convection-related surface observations. The most direct manifestations of thermal convection in the mantle (represented schematically by the upwelling plume colored in red) are the surface motions of tectonic plates – which may be summarized by their horizontal divergence field – and the flow-induced topography of the solid surface and the CMB. The boundary undulations and the density anomalies in the mantle (due, for example, to the hot upwelling plume) give rise to surface gravitational potential perturbations which may be measured in terms of geoid or gravity anomalies

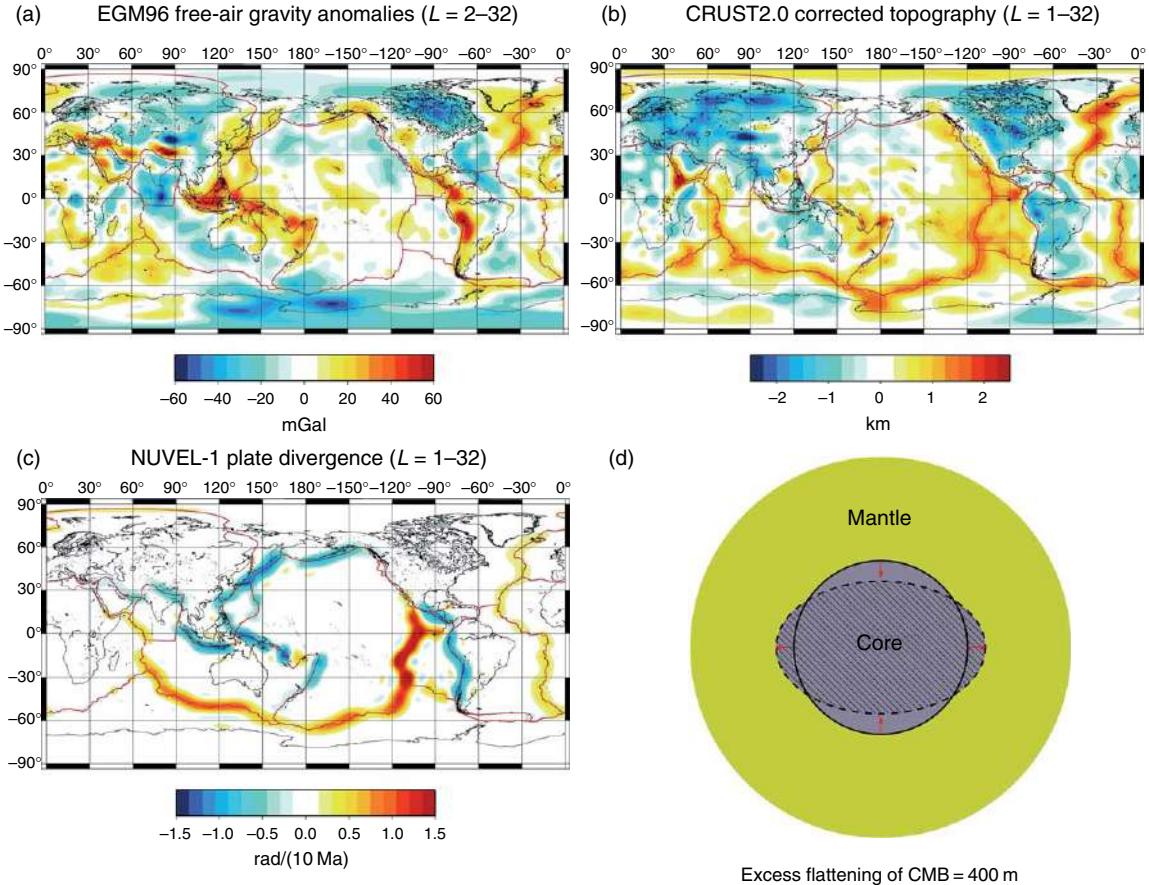


Figure 2 Geodynamic observables. (a) The free-air gravity anomalies derived from the joint geopotential model EGM96 (Lemoine *et al.*, 1998). (b) The dynamic surface topography obtained by removing the topography due to isostatically compensated crustal heterogeneity from Earth's observed topography. The CRUST2.0 (Bassin *et al.*, 2000) crustal heterogeneity model is employed here. (c) The horizontal divergence of the tectonic plate velocities given by the NUVEL-1 model (DeMets *et al.*, 1990). (d) The excess or dynamic CMB ellipticity inferred from core nutation data (Mathews *et al.*, 2002). All fields, with the exception of (d), have been expanded in spherical harmonics up to degree and order 32 (see eqn [1]).

(especially at long wavelengths) of the spectral content is provided by the free-air gravity anomalies shown in **Figure 2(a)**.

We will employ the term ‘dynamic topography’ to mean all contributions to Earth’s surface topography which arise from density anomalies in the convecting mantle – including the lithosphere. Observational constraints on dynamic topography therefore require an accurate model of crustal heterogeneity in order to remove all isostatic crustal contributions to Earth’s measured surface topography. The topographic crustal correction, here based on model CRUST2.0 (Bassin *et al.*, 2000), is described in detail by Perry *et al.* (2003) and the resulting dynamic topography is shown in **Figure 2(b)**.

The tectonic plate velocity field \mathbf{v} may be conveniently summarized in terms of two complementary scalar fields: the horizontal divergence $\nabla_H \cdot \mathbf{v}$ and the radial vorticity $\hat{\mathbf{r}} \cdot \nabla \times \mathbf{v}$ (Forte and Peltier, 1987). The constraint of plate rigidity imposes a linear dependence between these two scalar fields (Forte and Peltier, 1991) and hence it suffices that we consider only the plate divergence, shown in **Figure 2(c)**. (A more detailed discussion of the implications of plate rigidity, in terms of allowed plate motions, is also presented in Section 1.23.2.3.7.)

The most robust global constraint on deep-mantle density heterogeneity and dynamics (Forte *et al.*, 1995) is currently provided by the dynamical ellipticity of the CMB shown in **Figure 2(d)**. The

discrepancy between theoretical predictions of the free core nutation (FCN) period (Wahr, 1981) and the value determined from very long baseline interferometry (Herring *et al.*, 1986), led Gwinn *et al.* (1986) to conclude that the CMB ellipticity is larger than that implied by theoretical calculations which assumed a rotating Earth in hydrostatic equilibrium. This inference of an ‘excess’ ellipticity, in which the nonhydrostatic radius of the CMB at the poles is 400 m less than at the equator, is supported by recent analyses of the FCN period (Mathews *et al.*, 2002).

The most appropriate mathematical basis functions for describing any bounded and continuous function on a spherical surface are the spherical harmonics $Y_\ell^m(\theta, \varphi)$, where position on the spherical surface is defined by colatitude θ and colongitude φ . We may therefore expand the geodynamic observables in **Figure 2** in terms of spherical harmonics as follows:

$$f(\theta, \varphi) = \sum_{\ell=0}^{\infty} \sum_{m=-\ell}^{+\ell} f_\ell^m Y_\ell^m(\theta, \varphi) \quad [1]$$

where the function $f(\theta, \varphi)$ represents any of the observables (gravity, topography, or plate divergence) and the indices ℓ, m which characterize each spherical harmonic are called the ‘harmonic degree’ and ‘azimuthal order,’ respectively. A useful introduction to spherical harmonic functions may be found in Jackson (1975).

The spatial variation of the spherical harmonics is oscillatory in character; it may be characterized in terms of an equivalent horizontal wavelength. On a spherical surface of radius r , a spherical harmonic $Y_\ell^m(\theta, \varphi)$ has a characteristic wavelength λ_ℓ given by the following expression:

$$\lambda_\ell = \frac{2\pi r}{\sqrt{\ell(\ell+1)}} \approx \frac{2\pi r}{\ell + 1/2}, \text{ valid for } \ell \gg 1 \quad [2]$$

In practice, the infinite sum over degree ℓ in [1] is truncated at some finite value ℓ_{max} and for the fields in **Figure 2** it is $\ell_{max}=32$. At the Earth’s surface ($r=6368$ km) this is equivalent to a minimum horizontal length scale (or half wavelength) of about 600 km.

Spherical harmonic representations of surface fields can be used to quantify their spectral content in terms of an amplitude spectrum. The amplitude spectrum measures the mean (globally averaged) amplitude of a field at a particular wavelength λ_ℓ [2] and it is defined in terms of a ‘degree variance’ σ_ℓ as follows:

$$\sigma_\ell = \sqrt{\sum_{m=-\ell}^{+\ell} f_\ell^{m*} f_\ell^m} \quad [3]$$

in which f_ℓ^m are the spherical harmonic coefficients of the surface field (see expression [1]) and $*$ denotes complex conjugation.

A spectral description of the spatial correlation between two fields, as a function of harmonic degree or wavelength, is quantified in terms of ‘degree correlation’ r_ℓ , defined as follows:

$$r_\ell = \frac{\sum_{m=-\ell}^{+\ell} f_{1\ell}^{m*} f_{2\ell}^m}{\sqrt{\sum_{m=-\ell}^{+\ell} f_{1\ell}^{m*} f_{1\ell}^m} \sqrt{\sum_{m=-\ell}^{+\ell} f_{2\ell}^{m*} f_{2\ell}^m}} \quad [4]$$

in which $f_{1\ell}^m$ and $f_{2\ell}^m$ are the spherical harmonic coefficients of the two fields.

Degree variances and correlations are very useful spectral characterizations of the amplitude and spatial variation of globally defined surface fields (e.g., O’Connell, 1971) and they are used frequently in the discussions presented below.

1.23.2.2 Evidence for Mantle Flow in Correlations between Internal Structure and Surface Gravity Anomalies

The need for a dynamical interpretation of the surface observables (**Figure 2**) in terms of very deep-seated convective flow in the mantle is illustrated in **Figure 3** in which long-wavelength gravity anomalies are directly compared to seismically inferred lateral heterogeneity in the lower mantle. The large-scale pattern of faster than average shear velocities which lie below the periphery of the Pacific Ocean (blue colored regions in **Figure 3(b)**) has long been interpreted in terms of accumulating lithospheric slabs which have subducted below the margins of the Pacific Ocean since Mesozoic times (Chase, 1979; Chase and Sprowl, 1983; Richards and Engebretson, 1992). These seismic anomalies, which presumably represent positive density anomalies (i.e., cold subducted slabs), are closely correlated with a broad ring-like pattern of negative gravity anomalies around the periphery of the Pacific Ocean (red colored regions in **Figure 3(a)**).

The correlation between long-wavelength seismic heterogeneity in the lower mantle and surface gravity anomalies was first identified by Dziewonski *et al.* (1977), and they postulated that a dynamical interpretation in terms of mantle flow could explain the negative sign of the correlation. In a rigid or elastic

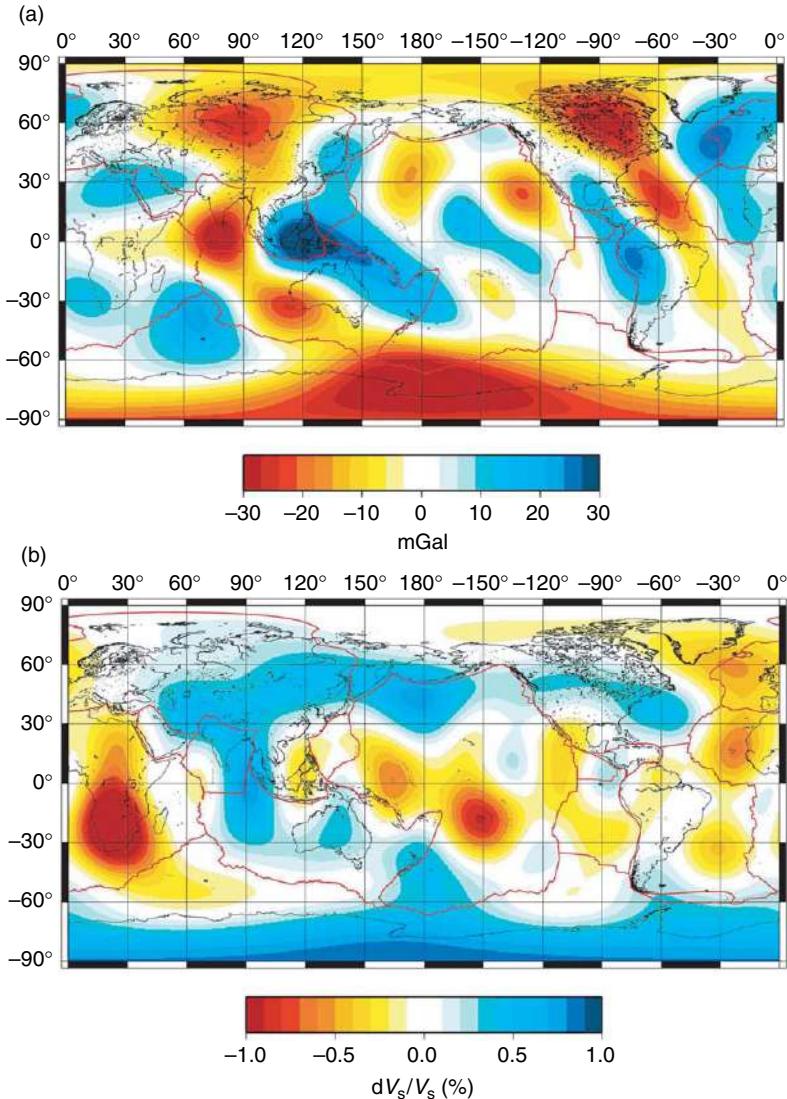


Figure 3 Surface gravity anomalies and deep-mantle heterogeneity. (a) Long-wavelength free-air gravity anomalies derived from the joint geopotential model EGM96 (Lemoine *et al.*, 1998). (b) Long-wavelength seismic shear velocity anomalies at a depth of 2100 km derived from the tomography model of Grand (2002). Both the gravity and seismic anomaly fields are synthesized from spherical harmonics in the degree range $\ell = 1-8$.

mantle in which flow is absent, a positive correlation between internal density and surface gravity is expected. However, in a convecting mantle, the gravitational signal of internal density anomalies is opposed by the effect of flow-induced topography at the surface and at the CMB, and this dynamical balance can lead to the observed negative correlation (e.g., Pekeris, 1935; Parsons and Daly, 1983; Richards and Hager, 1984).

It is instructive to consider a more detailed spectral analysis of the correlation between surface

gravity anomalies and seismically inferred lateral heterogeneity at different depths in the mantle. The degree correlations shown in Figure 4 indicate which depth ranges in the mantle may be important contributors to the different wavelengths of the surface gravity field. The strongest positive correlations appear in the transition-zone region of the mantle (from ~ 400 to ~ 800 km depth) and at the longest wavelength (degree 2) they extend down to about 1400 km depth. The positive sign of these correlations indicates that long-wavelength gravity highs

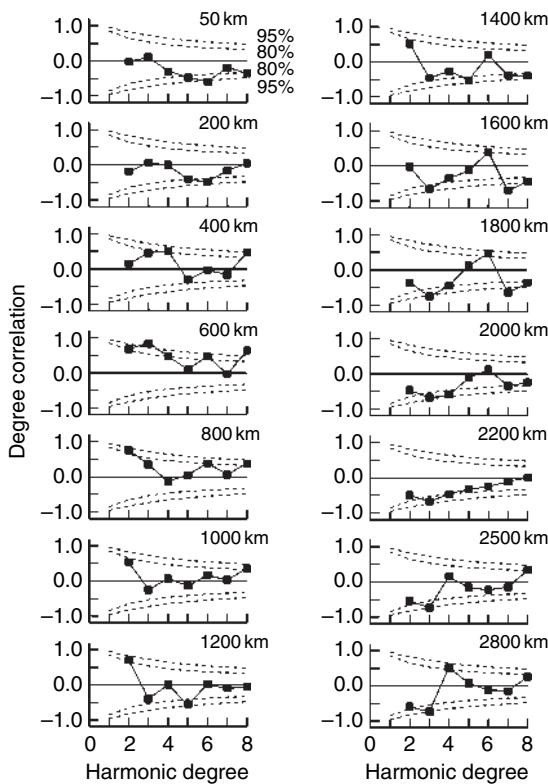


Figure 4 Depth-dependent correlations between 3-D mantle structure and gravity anomalies. Each frame shows the degree correlations between surface gravity anomalies and lateral variations in seismic shear velocity at a particular depth in the mantle. The seismic anomalies are derived from an earlier long-wavelength tomography model SH8/U4L8 (Forte *et al.*, 1993a). Adapted from Forte AM, Dziewonski AM, and Woodward RL (1993a) Aspherical structure of the mantle, tectonic plate motions, nonhydrostatic geoid, and topography of the core-mantle boundary. In: Le Mouél J-L, Smylie DE, and Herring T (eds.) *Dynamics of the Earth's Deep Interior and Earth Rotation* pp. 135–166. Washington DC: American Geophysical Union.

overlie similarly large-scale seismically fast regions located at the base of the upper mantle. Negative degree correlations between long-wavelength seismic and gravity anomalies are found in the near-surface region, down to about 400 km depth, and in lower mantle below 1400 km depth (as in Figure 3) where the strongest negative correlations are found. These depth-dependent degree correlations, obtained on the basis of long-wavelength tomography models derived more than a decade ago, are robust observations which have been verified using the latest seismic tomographic inferences of 3-D mantle structure (Ricard *et al.*, 2006).

The correlation between mantle heterogeneity and surface gravity anomalies in a convecting mantle has been shown to be a strong function of the depth dependence of the rheological properties of the mantle (e.g., Hager, 1984; Ricard *et al.*, 1984; Hager *et al.*, 1985; Forte and Peltier, 1987). In particular, as will be discussed further below, the change from positive correlations at the top of the lower mantle to negative correlations at the bottom of lower mantle (Figure 4) can be interpreted in terms of a significant increase in mean viscosity across the mantle. Other surface observables, such as the tectonic plate motions, also provide important constraints on the depth dependence of mantle rheology (e.g., Ricard and Vigny, 1989; Forte *et al.*, 1991). The geodynamic surface observables also provide direct constraints on the 3-D distribution of density anomalies in the mantle and hence these observables provide a fundamentally important and independent means of evaluating the extent to which seismic tomography models successfully resolve the lateral heterogeneity in the mantle which is associated with mantle convection.

In the next section, the dynamical link between lateral heterogeneity in the mantle and convection-related surface observables is developed in the theoretical framework of a fluid mechanical model of viscous flow in the mantle. The reader wishing to skip over this detailed mathematical treatment of the mantle flow theory is encouraged to jump directly to Sections 1.23.2.4 and 1.23.2.5, where the viscous response of the mantle and current mantle viscosity inferences, respectively, are summarized.

1.23.2.3 Fluid Mechanical Modeling of Viscous Mantle Flow

1.23.2.3.1 Governing equations

Laboratory and geological evidence of the ability of mantle rocks to creep indefinitely over geological timescales is understood in terms of the existence of atomic-scale defects in the lattice of crystal grains (e.g., Nicolas and Poirier, 1976). If the ambient mantle temperature is sufficiently high, the imposition of nonhydrostatic stresses causes the lattice defects to propagate and thus allows the mantle rocks to creep or ‘flow’ slowly. This process may be characterized in terms of a single parameter, namely an effective viscosity (e.g., Weertman and Weertman, 1975; Weertman, 1978).

The characterization of the long-term creep properties of the mantle in terms of an effective viscosity

allows us to model the slow flow of the mantle with the conventional hydrodynamic field equations. The hydrodynamic field equations (Landau and Lifshitz, 1959) which express the principles of conservation of mass and momentum are

$$\frac{\partial \rho}{\partial t} + \nabla \cdot (\rho \mathbf{u}) = 0 \quad [5]$$

$$\rho \frac{d\mathbf{u}}{dt} = \nabla \cdot \boldsymbol{\sigma} + \rho \mathbf{g} \quad [6]$$

in which \mathbf{u} is the velocity field, $d/dt = \partial/\partial t + \mathbf{u} \cdot \nabla$ is the total (Lagrangian) time derivative, $\boldsymbol{\sigma}$ is the stress tensor, \mathbf{g} is the gravitational acceleration, and ρ is the density.

We may represent the gravity field \mathbf{g} in terms of a gravitational potential:

$$\mathbf{g} = \nabla \phi \quad [7]$$

Notice that the sign convention adopted here is opposite to that generally adopted in classical physics, where a ‘negative’ gradient of the potential is used. With this sign convention, Poisson’s equation for the relationship between the gravity potential and density is

$$\Delta \phi = -4\pi G\rho \quad (\Delta \equiv \nabla \cdot \nabla) \quad [8]$$

An explicit expression for the stress tensor is given by

$$\boldsymbol{\sigma}_{ij} = -P\delta_{ij} + \tau_{ij} \quad [9]$$

$$\text{with } \tau_{ij} = \eta \left(u_{i,j} + u_{j,i} - \frac{2}{3} \delta_{ij} u_{k,k} \right) + \lambda_{ij} u_{k,k} \quad [10]$$

where τ_{ij} is the viscous stress tensor, δ_{ij} is the identity tensor, P is the total pressure, η and λ are the ‘isotropic’ viscosity coefficients, and $u_{i,j} = \partial u_i / \partial x_j$ represents the derivative of the velocity components i with respect to the coordinate direction j .

A number of simplifications are possible when applying the above field equations to the problem of flow in the mantle:

- Since mantle rocks creep much slower than the acoustic velocity in the mantle, we can safely ignore the term $\partial \rho / \partial t$ in the conservation of mass equation [5] and we thus have the following anelastic-liquid approximation:

$$\nabla \cdot (\rho \mathbf{u}) = 0 \quad [11]$$

This simplification will explicitly rule out acoustic waves as solutions of the flow equations.

- The second viscosity coefficient λ in the viscous stress tensor τ_{ij} describes the dissipation associated

with change in fluid volume (density). This volume dissipation may be neglected if the changes in fluid volume occur on timescales which are much longer than for molecular relaxation processes (Landau and Lifshitz, 1959), and this is certainly true for mantle flow. Therefore, the viscous stress tensor τ_{ij} will be purely deviatoric:

$$\tau_{ij} = \eta \left(u_{i,j} + u_{j,i} - \frac{2}{3} \delta_{ij} u_{k,k} \right) \quad [12]$$

- We will further assume a Newtonian (i.e., linear) rheology, in which the mantle viscosity η is not a function of stress or strain rate. This assumption is not necessarily appropriate for the mantle (particularly in high stress regions, such as subduction zones) but it will greatly simplify the mathematical resolution of the flow equations which is presented below.
- A major simplification, from a purely mathematical standpoint, derives from the assumption that mantle viscosity varies only with radius. Although this assumption will significantly simplify the mathematical treatment of the flow theory, it may have important physical implications for the dynamics of buoyancy induced flow in the mantle (e.g., Richards and Hager, 1989). These implications have been examined previously in the context of global-scale flow in 3-D spherical geometry (e.g., Ricard *et al.*, 1988; Martinec *et al.*, 1993; Zhang and Christensen, 1993; Forte and Peltier, 1994; Čadek and Fleitout, 2003; Moucha *et al.*, 2006) and they will be discussed below.
- A fundamental physical simplification arises from the very large value of the effective viscosity in the mantle. We may nondimensionalize the conservation of momentum equation with the following variable transformations:

$$(x, y, z) = (dx, dy, dz) \\ t = (d^2 / \kappa_o) t \\ \rho = \rho_o \rho; \mathbf{g} = g_o \mathbf{g}; \eta = \eta_o \eta \quad [13]$$

where the original variables are on the left and the nondimensional ones are on the right. Quantities d , κ_o , ρ_o , η_o , g_o are characteristic scales for length, thermal diffusivity, density, viscosity, and gravitational acceleration, respectively, in the mantle. The use, in [13], of a thermal diffusion timescale

$$t_\kappa = d^2 / \kappa_o \quad [14]$$

is appropriate since we are dealing with mantle flow arising from thermal convection. The stress tensor and pressure have the same physical units (see expression [9]), and hence their nondimensional transformation is:

$$P = (\rho_0 g_0 d) P \quad \text{and} \quad \boldsymbol{\tau} = (\rho_0 g_0 d) \boldsymbol{\tau} \quad [15]$$

where, again, the original quantities are on the left and the nondimensional ones on the right. By virtue of the constitutive relation [12], and expression [15], we obtain the following nondimensional transformation for the flow variable:

$$\mathbf{u} = \frac{\rho_0 g_0 d^2}{\eta_0} \mathbf{u} \quad [16]$$

or equivalently,

$$\mathbf{u} = g_0 t_\nu \mathbf{u} \quad [17]$$

where $t_\nu = d^2/\nu_0$ is the timescale for viscous diffusion of momentum and $\nu_0 = \eta_0/\rho_0$ is the kinematic viscosity. Finally, substitution of expressions [9] and [13]–[17] into [6] yields the following nondimensional momentum conservation equation:

$$\rho \left[\frac{1}{Pr} \frac{\partial \mathbf{u}}{\partial t} + \left(\frac{g_0}{d} \right) t_\nu^2 \mathbf{u} \cdot \nabla \mathbf{u} \right] = \nabla \cdot \boldsymbol{\tau} - \nabla P + \rho \mathbf{g} \quad [18]$$

in which $Pr = t_\kappa/t_\nu$ is the Prandtl number, which characterizes the ratio of temperature and momentum diffusion timescales.

To assess the importance of the terms on the left-hand side of eqn [18], we assume the following values for the scaling variables: $d = 3 \times 10^6$ m (for whole-mantle flow), $\rho_0 = 3.3 \times 10^3$ kg m⁻³, $g_0 = 10$ m s⁻², $\kappa_0 = 1.5 \times 10^{-6}$ m² s⁻¹, $\eta_0 = 10^{21}$ Pa s, and we thus obtain:

$$\begin{aligned} t_\nu &= 3 \times 10^{-5} \text{ s}; \quad t_\kappa = 6 \times 10^{18} \text{ s}; \\ \frac{g_0}{d} &= 3.3 \times 10^{-6} \text{ s}^{-2}; \quad Pr = 2 \times 10^{23} \end{aligned} \quad [19]$$

The key quantity here is the characteristic time for momentum diffusion t_ν which is very small (i.e., mantle flow will come to a complete halt in much less than a millisecond if all buoyancy forces are suddenly removed).

The vanishingly small momentum diffusion time, and hence the very large Prandtl number, implies that the inertial forces ($\rho du/dt$) in the momentum conservation equation are completely negligible. Therefore, using expression [7], the momentum conservation equation [6] simplifies to:

$$\nabla \cdot \boldsymbol{\tau} - \nabla P + \rho \nabla \phi = 0 \quad [20]$$

Equation [20] shows that in the absence of inertia, there must at all times be a balance between the buoyancy forces ρg and the forces of viscous dissipation described by $\nabla \cdot \boldsymbol{\tau}$. In other words, any changes in internal buoyancy forces will instantly produce changes in fluid flow: this is a consequence of the essentially instantaneous diffusion of momentum in the mantle.

We may define an idealized hydrostatic reference state for the mantle, which corresponds to the absence of any internal flow or deformation (i.e., $\mathbf{u} = 0$). In this situation, the deviatoric stress field $\boldsymbol{\tau}$ vanishes and the momentum conservation equation [6] reduces to:

$$-\nabla P_o + \rho_o \nabla \phi_o = 0 \quad [21]$$

in which P_o , ρ_o , and ϕ_o are the pressure, density, and gravity potentials in the hydrostatic state. Poisson's equation [8] for a hydrostatic planet is:

$$\Delta \phi_o = -4\pi G \rho_o \quad [22]$$

We assume that in a dynamic mantle, with a non-vanishing mantle flow \mathbf{u} , the pressure, density, and gravity potentials will be perturbed as follows:

$$P = P_o + P_1 \quad \rho = \rho_o + \rho_1 \quad \phi = \phi_o + \phi_1 \quad [23]$$

in which all perturbations are assumed to be small, that is,

$$\left| \frac{P_1}{P_o} \right| \ll 1 \quad \left| \frac{\rho_1}{\rho_o} \right| \ll 1 \quad \left| \frac{\phi_1}{\phi_o} \right| \ll 1$$

If we now substitute the perturbed variables [23] into the equations of mass and momentum conservation (11–20) and Poisson's equation [8], and then subtract out the hydrostatic reference equations [21] and [22], we finally obtain the following set of first-order accurate, perturbed equations for mantle flow dynamics:

$$\text{mass conservation} \quad \nabla \cdot (\rho_o \mathbf{u}) = 0 \quad [24]$$

momentum conservation

$$\nabla \cdot \boldsymbol{\tau} - \nabla P_1 + \rho_o \nabla \phi_1 + \rho_1 \nabla \phi_o = 0 \quad [25]$$

$$\text{gravity} \quad \Delta \phi_1 = -4\pi G \rho_1 \quad [26]$$

Notice in eqn [25], that in addition to the driving buoyancy forces ($\rho_1 \nabla \phi_o$), there also exist self-gravitational loads ($\rho_o \nabla \phi_1$) due to the perturbed gravity field. The above equations must be supplemented by the linear relationship [12] between stress and strain rate, which is valid for an isotropic rheology:

Newtonian constitutive equation

$$\boldsymbol{\tau} = \eta \left(\vec{\nabla} \mathbf{u} + \mathbf{u} \vec{\nabla} - \frac{2}{3} \mathbf{I} \nabla \cdot \mathbf{u} \right) \quad [27]$$

1.23.2.3.2 Spectral treatment of the mantle flow equations

A classical technique for solving the dynamical flow equations in 3-D spherical geometry is the spectral Green function method, in which all flow variables are expressed in terms of spherical harmonic basis functions introduced in eqn [1] (e.g., Hager and O'Connell, 1981; Richards and Hager, 1984; Ricard *et al.*, 1984; Forte and Peltier, 1987, 1991). The spectral Green functions provide a very convenient mathematical description of the instantaneous relationship between the mantle density anomalies and the viscous flow field, as well as all surface manifestations of the internal flow dynamics.

The spectral method is employed here for solving the coupled equations of mass, momentum, and gravity conservation (eqns [24]–[26]), supplemented by the viscous constitutive relation [27]. The method follows that initially developed by Forte and Peltier (1991) for gravitationally consistent compressible flow in spherical geometry. Other treatments of compressible mantle flow in spherical geometry have been presented by Corrieu *et al.* (1995), Panasyuk *et al.* (1996), and Defraigne (1997).

One begins by rewriting eqns [24]–[27], in the following Cartesian tensor form:

$$\begin{aligned} u_{k,k} &= -\frac{\dot{\rho}_o}{\rho_o} u_r \\ \sigma_{ij,j} + \rho_o (\phi_1)_{,i} - \rho_1 g_o \hat{r} &= 0 \\ \sigma_{ij} &= -P_1 \delta_{ij} + \eta \left(u_{i,j} + u_{j,i} - \frac{2}{3} \delta_{ij} u_{k,k} \right) \\ (\phi_1)_{,kk} &= -4\pi G \rho_1 \end{aligned} \quad [28]$$

in which $\dot{\rho}_o = d\rho_o/dr$, $u_r = \hat{r} \cdot \mathbf{u}$, and $(\phi_o)_{,i} = -g_o \hat{r}$. It should also be noted that in these equations the total stress tensor σ is used, rather than the deviatoric stress τ used in [25].

The determination of a solution to the system of tensor equations [28] in spherical geometry may be greatly simplified by using an elegant mathematical technique described by Phinney and Burridge (1973). Following their technique, one introduces a new

coordinate system defined by the following complex basis vectors in spherical geometry:

$$\begin{aligned} \hat{e}_- &= \frac{1}{\sqrt{2}} (\hat{\vartheta} - i\hat{\phi}) \\ \hat{e}_0 &= \hat{r} \\ \hat{e}_+ &= -\frac{1}{\sqrt{2}} (\hat{\vartheta} + i\hat{\phi}) \end{aligned} \quad [29]$$

in which $l = \sqrt{-1}$ and $\hat{r}, \hat{\vartheta}, \hat{\phi}$ are the unit basis vectors for the standard spherical polar coordinate system.

Following Phinney and Burridge (1973), all the tensors appearing in the original system [28] are rotated into the coordinate system defined by [29], thereby yielding the following covariant tensor form of the dynamical equations:

$$\begin{aligned} u^{\alpha, \beta} e_{\alpha\beta} &= -\frac{\dot{\rho}_o}{\rho_o} u^0 \\ \sigma^{\alpha\beta, \gamma} e_{\beta\gamma} + \rho_o (\phi_1)^{,\alpha} - \rho_1 g_o \delta_0^\alpha &= 0 \\ \sigma^{\alpha\beta} = -P_1 e^{\alpha\beta} + \eta(u^{\alpha, \beta} + u^{\beta, \alpha}) - \frac{2}{3} \eta(u^{\delta, \gamma} e_{\delta\gamma}) e^{\alpha\beta} \\ (\phi_1)^{,\alpha\beta} e_{\alpha\beta} &= -4\pi G \rho_1 \end{aligned} \quad [30]$$

in which the Greek indices denote the coordinate directions in system [29] and therefore range over the values $(-1, 0, +1)$. The quantities $e^{\alpha\beta}$, $e_{\alpha\beta}$, and δ_0^α are the contravariant, covariant, and mixed tensor representations of the Cartesian identity tensor δ_{ij} .

The velocity (u^α) and stress ($\sigma^{\alpha\beta}$) components are expanded in terms of the generalized spherical functions Y_ℓ^{Nm} (Phinney and Burridge, 1973) such that:

$$\begin{aligned} u^- (r, \theta, \phi) &= \sum_{\ell, m} U_\ell^{-m}(r) Y_\ell^{-1m}(\theta, \phi) \\ u^0 (r, \theta, \phi) &= \sum_{\ell, m} U_\ell^{0m}(r) Y_\ell^{0m}(\theta, \phi) \end{aligned} \quad [31]$$

$$\begin{aligned} u^+ (r, \theta, \phi) &= \sum_{\ell, m} U_\ell^{+m}(r) Y_\ell^{+1m}(\theta, \phi) \\ \sigma^{\alpha\beta} (r, \theta, \phi) &= \sum_{\ell, m} T_\ell^{\alpha\beta m}(r) Y_\ell^{(\alpha+\beta)m}(\theta, \phi) \end{aligned} \quad [32]$$

$$(\alpha, \beta = -1, 0, +1)$$

All scalar fields involved in the governing equations [30] are expanded in terms of ordinary spherical harmonics. For example,

$$\begin{aligned} \rho_1 (r, \theta, \phi) &= \sum_{\ell, m} (\rho_1)_\ell^m(r) Y_\ell^m(\theta, \phi) \\ \phi_1 (r, \theta, \phi) &= \sum_{\ell, m} (\phi_1)_\ell^m(r) Y_\ell^m(\theta, \phi) \end{aligned} \quad [33]$$

where $Y_\ell^m \equiv Y_\ell^{0m}$.

We can simplify subsequent numerical computations by nondimensionalizing all relevant physical variables using the following transformations:

$$\begin{aligned} r &= dr, \quad g_o(r) = g_0 g(r), \quad \eta(r) = \eta_o \eta(r), \quad \rho_1 = (\Delta\rho)\rho_1 \\ T^{\alpha\beta} &= (\Delta\rho g_o d) T^{\alpha\beta}, \quad U^\alpha = \left(\frac{\Delta\rho g_o d^2}{\eta_o} \right) U^\alpha, \quad [34] \\ \phi_1 &= \left(\frac{4\pi G R_o}{2\ell+1} \Delta\rho d \right) \phi_1 \end{aligned}$$

in which the original variables are on the left of each equation and the nondimensional variables are on the right. The scaling quantities we have used are defined as follows:

$$\frac{d}{dr} \begin{pmatrix} U^0 \\ U^p \\ T^0 \\ T^p \\ \phi_1 \\ g_1 \end{pmatrix} = \begin{pmatrix} -\frac{[2+r(\dot{\rho}_o/\rho_o)]}{r} & \frac{\Omega_1}{r} & 0 & 0 & 0 & 0 \\ -\frac{2\Omega_1}{r} & \frac{1}{r} & 0 & \frac{\eta_o}{\eta} & 0 & 0 \\ \frac{4[3+r(\dot{\rho}_o/\rho_o)]}{r^2} \frac{\eta}{\eta_o} & -\frac{6\Omega_1}{r^2} \frac{\eta}{\eta_o} & 0 & \frac{\Omega_1}{r} & \frac{3}{2\ell+1} \frac{\dot{\rho}_o}{\rho} & 0 \\ -\frac{4\Omega_1[3+r(\dot{\rho}_o/\rho_o)]}{r^2} \frac{\eta}{\eta_o} & \frac{2[\Omega_2^2+3\Omega_1^2]}{r^2} \frac{\eta}{\eta_o} & -\frac{2\Omega_1}{r} & -\frac{3}{r} & 0 & 0 \\ 0 & 0 & 0 & 0 & 0 & 1 \\ 0 & 0 & 0 & \frac{\ell(\ell+1)}{r^2} & -\frac{2}{r} & \end{pmatrix} \begin{pmatrix} U^0 \\ U^p \\ T^0 \\ T^p \\ \phi_1 \\ g_1 \end{pmatrix} + \begin{pmatrix} 0 \\ 0 \\ g(r) \\ 0 \\ 0 \\ (-2\ell+1) \frac{d}{R_o} \end{pmatrix} \frac{\rho_1(r)}{\Delta\rho} \quad [35]$$

in which $\dot{\rho}_o = d\rho_o/dr$, $\Omega_1 = [\ell(\ell+1)/2]^{1/2}$, $\Omega_2 = [(\ell-1)(\ell+2)/2]^{1/2}$, and $\bar{\rho}$ is Earth's mean density ($5.5143 \times 10^3 \text{ kg m}^{-3}$).

The second system, governing a toroidal geometry of flow, consists of the following two coupled, first-order, ordinary differential equations:

$$\frac{d}{dr} \begin{pmatrix} U^T \\ T^T \end{pmatrix} = \begin{pmatrix} \frac{1}{r} & \frac{1}{\eta} \\ \frac{2\Omega_2^2\eta}{r^2} - \frac{3}{r} & \end{pmatrix} \begin{pmatrix} U^T \\ T^T \end{pmatrix} \quad [36]$$

The flow, stress, and gravity variables in the poloidal and toroidal flow systems [35] and [36] are all dependent on the same harmonic degree ℓ and order m (this dependence has been dropped for notational convenience). The dependence of these

$$\begin{aligned} d &= 2888 \text{ km} \equiv \text{radial thickness of mantle} \\ g_o &= 9.82 \text{ ms}^{-2} \equiv \text{mean surface gravitational acceleration} \\ \Delta\rho &= 0.1 \text{ Mg m}^{-3} \equiv \text{characteristic subducted slab density anomaly} \\ \eta_o &= 10^{21} \text{ Pa s} \equiv \text{Haskell (1935) reference value} \\ R_o &= 6371 \text{ km} \equiv \text{mean surface radius of Earth} \end{aligned}$$

Substituting expressions [31]–[33] into the flow equations [30], and using the nondimensionalization scheme [34] as well as the orthogonality properties of the generalized spherical harmonics (as in Phinney and Burridge 1973), yields two independent systems of flow equations. The first system, governing a poloidal geometry of flow, consists of the following six coupled, first-order, ordinary differential equations:

variables on the harmonic coefficients of flow [31], stress [32], and gravitational potential [33] are

$$\begin{aligned} U^P(r) &= U^+(r) + U^-(r) \\ U^T(r) &= U^+(r) - U^-(r) \\ T^0 &= T^{00}(r) + \frac{3}{2\ell+1} \frac{\rho_0(r)}{\bar{\rho}} \phi_1(r) \\ T^P &= T^{0+}(r) + T^{0-}(r) \\ T^T &= T^{0+}(r) - T^{0-}(r) \end{aligned} \quad [37]$$

1.23.2.3.3 Internal boundary conditions

The determination of a unique solution of the system of flow equations [35] and [36] derived in the preceding section requires the specification of appropriate boundary conditions at the top and bottom surfaces of the mantle and internal matching

conditions at all material interfaces within the mantle. We consider the latter first since the surface boundary conditions can be obtained as a special case of the internal matching conditions.

The need for internal boundary conditions in solving for mantle flow is evident upon inspection of the depth variation of mantle density $\rho_o(r)$ (see **Figure 5**) given by the Preliminary Reference Earth Model (PREM) seismic reference model (Dziewonski and Anderson, 1981). The PREM density profile is characterized by two major jumps at depths of 400 km and 670 km. These density jumps have long been interpreted as manifestations of phase-change boundaries (e.g., Jeanloz and Thompson, 1983) which presumably also affect the depth variation of viscosity at these depths (e.g., Sammis *et al.*, 1977).

We now derive the matching conditions which must be satisfied when characteristic properties of the mantle, in particular density, viscosity, and chemical composition, change very rapidly across phase-change or chemical horizons in the mantle. We will approximate such rapid changes as mathematical discontinuities. Denoting the mean (i.e., horizontally averaged) location of the internal material boundary as $r = r_i$, geographic variations in the radial location (i.e., deflections) of the boundary are then represented by:

$$r = r_i + \delta r_i, \text{ where we assume } \left| \frac{\delta r_i}{r_i} \right| \ll 1 \quad [38]$$

A discontinuous change in density across an internal boundary implies that

$$\left(\frac{d\rho_o}{dr} \right)_{r=r_i} = [\rho_o(r_i^+) - \rho_o(r_i^-)] \delta(r - r_i) \quad [39]$$

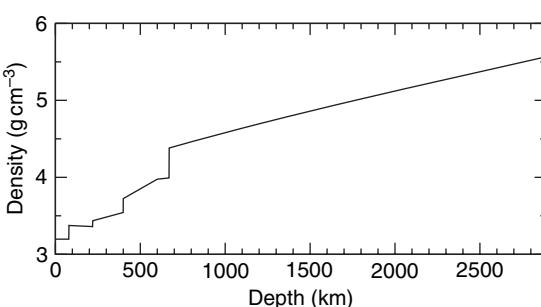


Figure 5 Depth-dependent mean density in the mantle from the PREM seismic reference model (Dziewonski and Anderson, 1981).

By virtue of this last expression, the density perturbation due to the boundary deflection δr_i is given by the following sheet-mass anomaly:

$$\begin{aligned} \delta\rho_i &= - \left(\frac{d\rho_o}{dr} \right)_{r=r_i} \delta r_i \\ &= - [\rho_o(r_i^+) - \rho_o(r_i^-)] \delta r_i \delta(r - r_i) \end{aligned} \quad [40]$$

This last expression shows that an internal boundary deflection gives rise to a mantle buoyancy source which may be approximated by a delta-function load, and the corresponding density perturbation is, in non-dimensional terms,

$$\frac{\rho_1(r)}{\Delta\rho} = - \frac{[\rho_o(r_i^+) - \rho_o(r_i^-)]}{\Delta\rho} \frac{\delta r_i}{d} \delta(r - r_i) \quad [41]$$

This expression shows that from a purely fluid mechanical perspective, the dynamical effect of a deformed phase-change boundary is indistinguishable from integrated buoyancy forces elsewhere in the mantle. If the material interface instead corresponds to a chemical discontinuity in the mantle, the fluid-mechanical buoyancy effect is also the same. The main distinction between the deflection-induced buoyancy of phase-change and chemical discontinuities is that the former is controlled by thermodynamics (i.e., the Clapeyron slope) whereas the latter is due to the change in intrinsic chemical buoyancy across the interface.

The matching condition for the radial component of the flow field is obtained by integrating the first row in system [35] from $r_i^- = r_i - \epsilon$ to $r_i^+ = r_i + \epsilon$, taking the limit $\epsilon \rightarrow 0$. In terms of the radial flow variable U^0 , this yields the following mass conservation equation:

$$\rho_o(r_i^+) U^0(r_i^+) = \rho_o(r_i^-) U^0(r_i^-) \quad [42]$$

where $\rho_o(r_i^+)$ and $\rho_o(r_i^-)$ are the mantle density immediately above and below the material boundary, respectively. If the internal boundary corresponds to a chemical discontinuity, then we must impose a zero radial velocity condition:

$$U^0(r_i^+) = 0 = U^0(r_i^-) \quad [43]$$

The matching condition for the tangential mantle flow velocity is obtained by integrating the second equation in [35], which yields the following continuity of the tangential flow variable U^P :

$$U^P(r_i^+) = U^P(r_i^-) \quad [44]$$

This continuity of tangential flow also applies to the case of a internal chemical boundary.

The internal matching condition for the radial stress T^0 across a deformed material interface is obtained by integrating the third row in system [35], in which we substitute result [41] into the buoyancy force term $\rho_1/\Delta\rho$ in expression [35] thereby yielding:

$$\begin{aligned} T^0(r_i^+) - T^0(r_i^-) \\ = \Delta_u(r_i) + \frac{3}{2\ell+1} \left[\frac{\rho_o(r_i^+) - \rho_o(r_i^-)}{\bar{\rho}} \right] \phi_1(r_i) \\ - \left[\frac{\rho_o(r_i^+) + \rho_o(r_i^-)}{\Delta\rho} \right] \frac{\delta r_i}{d} g(r_i) \end{aligned} \quad [45]$$

in which the term

$$\Delta_u(r_i) - \frac{2}{r_i} \left(\frac{\eta(r_i^+) + \eta(r_i^-)}{\eta_o} \right) [U^0(r_i^+) - U^0(r_i^-)] \quad [46]$$

arises from the discontinuous change in radial flow (see expression [42]) due to a density jump across an internal (phase-change) boundary. This term vanishes in the case of a chemical discontinuity since expression [43] then applies. The matching condition for the tangential stress T^P is obtained by integrating the fourth equation in [35]:

$$T^P(r_i^+) - T^P(r_i^-) = -\Omega_1 \Delta_u(r_i) \quad [47]$$

The term Δ_u gives rise to an apparent discontinuity in tangential stress and this is again a consequence of our mathematical treatment of a discontinuous change in radial flow across a material interface. The significance of this apparent jump in tangential stress was first noted by Corrieu *et al.* (1995), and a subsequent analysis by Forte and Woodward (1997a) determined that effect of this discontinuity was negligible. In the case of a chemical discontinuity, the term Δ_u vanishes and the tangential stress is then continuous across the interface.

Integration of the fifth row in [35] across the material interface located at mean radius r_i yields the following matching condition for the perturbed gravitational potential:

$$\phi_1(r_i^+) = \phi_1(r_i^-) \quad [48]$$

The matching condition for the perturbed gravitational acceleration is obtained by substituting expression [41] into the buoyancy force term $\rho_1/\Delta\rho$ in [35] and then integrating the sixth row of this system, yielding the following nondimensional expression:

$$\begin{aligned} g_1(r_i^+) - g_1(r_i^-) \\ = (2\ell+1) \left(\frac{d}{R_o} \right) \frac{[\rho_o(r_i^+) - \rho_o(r_i^-)] \delta r_i}{\Delta\rho} \end{aligned} \quad [49]$$

in which $g_1 = d\phi_1/dr$.

The internal matching conditions for the toroidal components of mantle flow are readily obtained following the same procedure employed for the poloidal flow. Integration of the first row in system [36] yields the following continuity of toroidal flow across any (phase-change or chemical) interface:

$$U^T(r_i^+) = U^T(r_i^-) \quad [50]$$

Similarly, an integration of the second row in [36] yields the following continuity of tangential stress across any internal material interface:

$$T^T(r_i^+) = T^T(r_i^-) \quad [51]$$

1.23.2.3.4 Boundary conditions at Earth's solid surface

It will be assumed that the spherically symmetric, hydrostatic reference Earth model is overlain by a global ocean layer which is 3 km thick, as in PREM (Dziewonski and Anderson, 1981). PREM's crust and seismic lithosphere (LID) are combined into a single mechanical layer containing the same total mass as the two PREM layers assuming, for simplicity, that both layers deform and move together in response to the buoyancy driven flow in the mantle. The top surface of the combined crust–lithosphere is located at radius $r=6368$ km and the base is located at radius 6291 km (i.e., at a depth of 80 km below the surface of the global ocean layer). This redefined lithosphere has mass density of 3.2 Mg m^{-3} .

In view of the very complicated mechanical and rheological properties of the crust and underlying lithosphere, in particular the tectonic plates, it is clear that the flow theory developed here with a purely depth-dependent viscosity cannot provide an adequate representation of the near-surface dynamics. An approximate treatment of the effect of surface tectonic plates is presented in Section 1.23.3.7. In the meantime, we consider here two different boundary conditions of relevance at the solid surface: 'free-slip' and 'no-slip'.

Earth's bounding surface at $r=a=6368$ km is a chemical (compositional) boundary across which there can be no flow and hence the matching condition (43) is applicable:

$$U^0(a^-) = 0, \quad \text{for both free-slip and no-slip} \quad [52]$$

where a^- denotes the radial location $r=a-\epsilon$. We can, to first-order accuracy, ignore surface deflections (i.e., topography) in specifying the boundary conditions on the flow.

The condition for the surface tangential flow $U^P(a^-)$ in the lithosphere is

$$U^P(a^-) = \begin{cases} U^P(a^-) & \text{to be determined, for free-slip} \\ 0 & \text{for no-slip} \end{cases} \quad [53]$$

In the case of the surface toroidal flow, the boundary condition is

$$U^T(a^-) = V^T \quad [54]$$

in which V^T is determined from the coupling of surface poloidal and toroidal flows due to the presence of rigid surface tectonic plates. The mathematical formulation of this coupling and an explicit expression for V^T is presented in Section 1.23.3.7.

We can apply the radial stress T^0 matching condition in [45] to the deformed surface boundary which, by virtue of conditions [52], becomes

$$\begin{aligned} T^0(a^-) - T^0(a^+) &= \frac{3}{2\ell+1} \left[\frac{\Delta\rho_a}{\bar{\rho}} \right] \phi_1(a^-) \\ &\quad - \left[\frac{\Delta\rho_a}{\Delta\rho} \right] \frac{\delta a}{d} g(a) \end{aligned} \quad [55]$$

where we have defined the density jump across the solid surface:

$$\begin{aligned} \Delta\rho_a &= \rho_o(a^-) - \rho_o(a^+) = 3.2 - 1.0 \text{ Mg m}^{-3} \\ &= 2.2 \text{ Mg m}^{-3} \end{aligned} \quad [56]$$

and where we have also invoked the universally valid condition [48] for the vertical continuity of the perturbed gravitational potential.

In expression [55], $T^0(a^+)$ corresponds to the radial stress in the global ocean layer. If we assume that the viscosity in the global ocean layer is negligible (i.e., $\eta/\eta_o \rightarrow 0$), then the second row in system [35] yields

$$T^P(r) = 0, \quad \text{throughout the ocean layer} \quad [57]$$

and therefore, by virtue of this result, the fourth row in system [35] yields

$$T^0(r) = 0, \quad \text{throughout the ocean layer} \quad [58]$$

Substituting result [58] into expression [55] yields the desired radial-stress-boundary condition at the surface:

$$\begin{aligned} T^0(a^-) &= \frac{3}{2\ell+1} \left[\frac{\Delta\rho_a}{\bar{\rho}} \right] \phi_1(a^-) - \left[\frac{\Delta\rho_a}{\Delta\rho} \right] \frac{\delta a}{d} g(a) \\ &\quad \text{valid for free-slip and no-slip} \end{aligned} \quad [59]$$

in which δa is the flow-induced vertical deflection of the solid surface (i.e., dynamic surface topography).

The condition for the surface poloidal tangential stress $T^P(a^-)$ is as follows:

$$T^P(a^-) = \begin{cases} 0 & \text{for free-slip} \\ T^P(a^-) & \text{to be determined, for no-slip} \end{cases} \quad [60]$$

and the condition for the surface toroidal tangential stress is

$$T^T(a^-) = T^T(a^-) \quad \text{to be determined} \quad [61]$$

On the basis of the general result [48], and using result [49], the surface matching conditions for the perturbed gravitational potential and acceleration are:

$$\phi_1(a^-) = \phi_1(a^+) \quad [62]$$

$$g_1(a^-) = g_1(a^+) + (2\ell+1) \left(\frac{d}{R_o} \right) \left[\frac{\Delta\rho_a}{\Delta\rho} \right] \frac{\delta a}{d} \quad [63]$$

The ocean-layer potential and gravity fields $\phi_1(a^+)$ and $g_1(a^+)$, respectively, are not independent of each other and, as shown in Forte and Peltier (1991), they are both related to the perturbed potential at the surface of the global ocean layer, $\phi_1(r=R_o)$:

$$\phi_1(a^+) = P_\ell \phi_1(R_o) \quad [64]$$

$$g_1(a^+) = g_\ell \phi_1(R_o) \quad [65]$$

in which the ocean-layer response functions P_ℓ and G_ℓ are as follows:

$$P_\ell = \left(\frac{R_o}{a} \right)^{\ell+1} - \frac{3}{2\ell+1} \frac{\rho_\omega}{\rho} \left[\left(\frac{R_o}{a} \right)^{\ell+2} - \left(\frac{a}{R_o} \right)^{\ell-1} \right] \quad [66]$$

$$\begin{aligned} G_\ell &= -(\ell+1) \frac{d}{R_o} \left(\frac{R_o}{a} \right)^{\ell+2} \\ &\quad + \frac{3}{2\ell+1} \frac{\rho_\omega}{\bar{\rho}} \frac{d}{R_o} \left[(\ell+1) \left(\frac{R_o}{a} \right)^{\ell+3} + \ell \left(\frac{a}{R_o} \right)^{\ell-2} \right] \end{aligned} \quad [67]$$

in which $\rho_\omega \equiv \rho(a^+) = 1 \text{ Mg m}^{-3}$ is the density of the global ocean layer.

Substitution of results [64] and [65] into expressions [62] and [63] yields the complete surface boundary conditions for the gravitational variables:

$$\phi_1(a^-) = P_\ell \phi_1(R_o), \quad \text{valid for free-slip and no-slip} \quad [68]$$

$$\begin{aligned} g_1(a^-) &= G_\ell \phi_1(R_o) + (2\ell+1) \left(\frac{d}{R_o} \right) \left[\frac{\Delta\rho_a}{\Delta\rho} \right] \frac{\delta a}{d}, \\ &\quad \text{valid for free-slip and no-slip} \end{aligned} \quad [69]$$

It should be noted that expression [68] should also be substituted into the radial stress condition [59].

The complete set of free-slip and no-slip surface boundary conditions, in terms of the poloidal-flow vector $\mathbf{v}(r) = [U^0(r), U^P(r), T^0(r), T^P(r), \phi_1(r), g_1(r)]^{Tr}$ (where Tr denotes transposition) employed in system [35], are:

Free-slip.

$$\mathbf{v}(a^-) = U^P(a^-)\mathbf{y}_1 + \phi_1(R_o)\mathbf{y}_2 + \frac{\Delta\rho_a}{\Delta\rho} \frac{\delta a}{d} \mathbf{y}_3 \quad [70]$$

in which the surface basis vectors are

$$\begin{aligned} \mathbf{y}_1 &= \begin{pmatrix} 0 \\ 1 \\ 0 \\ 0 \\ 0 \\ 0 \end{pmatrix} & \mathbf{y}_2 &= \begin{pmatrix} 0 \\ 0 \\ \frac{3}{2\ell+1} \frac{\Delta\rho a}{\bar{\rho}} P_\ell \\ 0 \\ P_\ell \\ G_\ell \end{pmatrix} \\ \mathbf{y}_3 &= \begin{pmatrix} 0 \\ 0 \\ -g(a) \\ 0 \\ 0 \\ (2\ell+1) \left(\frac{d}{R_o} \right) \end{pmatrix} \end{aligned} \quad [71]$$

No-slip.

$$\mathbf{v}(a^-) = T^P(a^-)\mathbf{y}'_1 + \phi_1(R_o)\mathbf{y}_2 + \frac{\Delta\rho_a}{\Delta\rho} \frac{\delta a}{d} \mathbf{y}_3 \quad [72]$$

in which the surface basis vectors are

$$\mathbf{y}'_1 = \begin{pmatrix} 0 \\ 0 \\ 0 \\ 1 \\ 0 \\ 0 \end{pmatrix} \quad \text{and } \mathbf{y}_2, \mathbf{y}_3 \text{ are defined in [71]} \quad [73]$$

The surface boundary conditions [54] and [61] for the toroidal flow vector $\mathbf{u}(r) = [U^T(r), T^T(r)]^{Tr}$ which is governed by system [36] are

$$\mathbf{u}(a^-) = V^T \mathbf{z}_1 + T^T(a^-) \mathbf{z}_2 \quad [74]$$

in which the two surface basis vectors are

$$\mathbf{z}_1 = \begin{pmatrix} 1 \\ 0 \end{pmatrix} \quad \mathbf{z}_2 = \begin{pmatrix} 0 \\ 1 \end{pmatrix} \quad [75]$$

1.23.2.3.5 Boundary conditions at CMB

The derivation of the boundary conditions which apply at the CMB, located at mean radius $r=b=3480$ km, is almost identical to the derivation for the surface boundary conditions in the preceding section. The liquid outer core is regarded as having negligible viscosity relative to the mantle and hence the CMB is treated as a purely free-slip boundary. The only difference concerns the application of gravitational matching conditions at $r=b$, since we must now deal with the interaction between a deformed CMB and a compressible, hydrostatic core.

A detailed treatment of the gravitational perturbations maintained in a hydrostatic core is presented in Forte and Peltier (1991), where it is shown that perturbed gravitational acceleration at the top of the core (i.e., immediately below the CMB) is determined by the perturbed potential at the bottom of the mantle (i.e., immediately above the CMB), as follows:

$$g_1(b^-) = R_\ell \phi_1(b^+)$$

where b^- denotes the radial location $r=b-\epsilon$ (i.e., bottom side of the CMB) and b^+ denotes $r=b+\epsilon$ (i.e., top side of the CMB). R_ℓ is a numerically determined coefficient which is obtained on the basis of the compressible density profile throughout the core (Forte and Peltier, 1991).

The complete set of free-slip CMB conditions in terms of the poloidal-flow vector $\mathbf{v}(r) = [U^0(r), U^P(r), T^0(r), T^P(r), \phi_1(r), g_1(r)]^{Tr}$ in system [35] is

$$\mathbf{v}(b^+) = U^P(b^+) \mathbf{x}_1 + \phi_1(b^+) \mathbf{x}_2 + \frac{\Delta\rho_b}{\Delta\rho} \frac{\delta b}{d} \mathbf{x}_3 \quad [76]$$

in which the CMB basis vectors are:

$$\begin{aligned} \mathbf{x}_1 &= \begin{pmatrix} 0 \\ 1 \\ 0 \\ 0 \\ 0 \\ 0 \end{pmatrix} & \mathbf{x}_2 &= \begin{pmatrix} 0 \\ 0 \\ \frac{3}{2\ell+1} \frac{\Delta\rho_b}{\bar{\rho}} \\ 0 \\ 1 \\ R_\ell \end{pmatrix} \\ \mathbf{x}_3 &= \begin{pmatrix} 0 \\ 0 \\ -g(b) \\ 0 \\ 0 \\ (2\ell+1) \left(\frac{d}{R_o} \right) \end{pmatrix} \end{aligned} \quad [77]$$

where $\Delta\rho_b = \rho_o(b^+) - \rho(b^-) = -4.434 \text{ Mg m}^{-3}$ is the density jump across the CMB and δb is the deflection (i.e., dynamic topography) of the CMB.

The free-slip CMB condition for the toroidal-flow vector $\mathbf{u}(r) = [U^T(r), T^T(r)]^{Tr}$ in system [36] is

$$\mathbf{u}(b^+) = U^T(b^+) \mathbf{w}_1 \quad [78]$$

in which the CMB basis vector is

$$\mathbf{w}_1 = \begin{pmatrix} 1 \\ 0 \end{pmatrix} \quad [79]$$

1.23.2.3.6 Determining viscous flow

Green functions

The solution to the system of flow equations [35] may be expressed in terms of Green functions which relate the poloidal flow velocity and the stress tensor at an arbitrary radius $r = r_0$ to a delta-function density load $\rho_1(r) = \delta(r - r')$ at any other radius $r = r'$.

For arbitrarily complex density (e.g., as in PREM) and viscosity profiles, the poloidal-flow system of eqns [35] must be integrated numerically. When $r \neq r'$, this linear system of equations is homogeneous:

$$\frac{d}{dr} \mathbf{v}(r) = \mathbf{M}_P(r) \mathbf{v}(r) \quad (\text{when } r \neq r') \quad [80]$$

Here, $\mathbf{M}_P(r)$ is the 6×6 matrix appearing in system [35]. We can propagate each of the surface boundary vectors \mathbf{y}_i ($i = 1, 2, 3$) in [71] or [73], by numerically integrating [80] from the surface ($r = a^-$) downward

to $r = r'$, stopping along the way at all internal material boundaries ($r = r_i$) where we apply the internal matching conditions described previously (Section 1.23.2.3.3). We can similarly propagate each of the CMB basis vectors \mathbf{x}_i ($i = 1, 2, 3$) in [77] from the CMB ($r = b^+$) upward to $r = r'$. The basic procedure is summarized schematically in Figure 6.

At the location $r = r'$ of the delta-function load we apply the matching conditions [42], [44], [45], and [47]–[49]. For each of these matching conditions, we employ the corresponding components of the poloidal-flow vectors $\mathbf{v}(r'_+)$ and $\mathbf{v}(r'_-)$, which are obtained from expressions [70], [72], and [76]:

$$\begin{aligned} \mathbf{v}(r'_+) = & \left\{ \begin{array}{l} U^P(a^-) \mathbf{y}_1(r'_+) \\ T^P(a^-) \mathbf{y}'_1(r'_+) \\ \frac{\Delta\rho_a \delta a}{\Delta\rho} \mathbf{y}_3(r'_+) \end{array} \right\} + \phi_1(R_o) \mathbf{y}_2(r'_+) \\ & + \frac{\Delta\rho_b \delta b}{\Delta\rho} \mathbf{y}_3(r'_+) \end{aligned} \quad [81]$$

and

$$\begin{aligned} \mathbf{v}(r'_-) = & U^P(b^+) \mathbf{x}_1(r'_-) \\ & + \phi_1(b^+) \mathbf{x}_2(r'_-) + \frac{\Delta\rho_b \delta b}{\Delta\rho} \mathbf{x}_3(r'_-) \end{aligned} \quad [82]$$

in which the surface and CMB basis vectors, $\mathbf{y}_i(r'_+)$ and $\mathbf{x}_i(r'_-)$, have been obtained by the numerical integration of [80], as outlined above. The application of the six matching conditions then yields the following system of equations:

$$\mathbf{A} \mathbf{p} = \boldsymbol{\delta}_p \quad [83]$$

in which

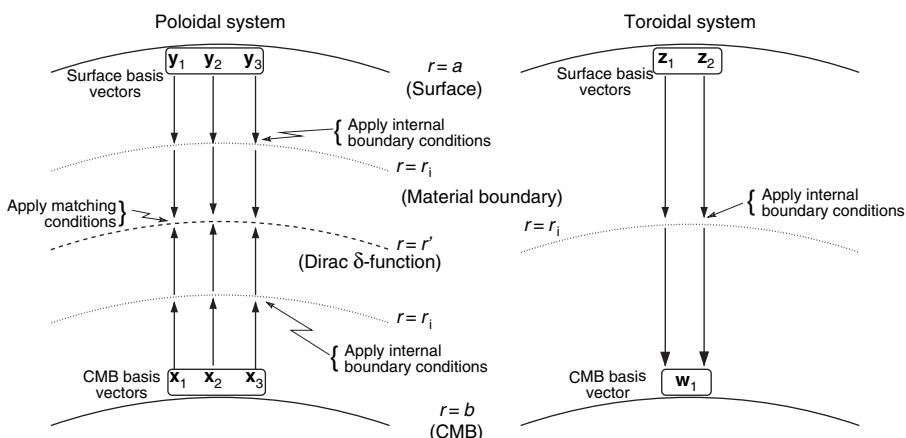


Figure 6 Numerical integration of poloidal-flow system of eqns [35] (left) and toroidal-flow system of eqns [36] (right). The poloidal-flow basis vectors \mathbf{y}_i and \mathbf{x}_i are defined in expressions [71], [73], and [77]. The toroidal-flow basis vectors are defined in expressions [75] and [79].

$$\mathbf{p} = \begin{pmatrix} U^P(a^-) \text{ or } T^P(a^-) \\ \phi_1(R_o) \\ \frac{\Delta\rho_a \delta a}{\Delta\rho d} \\ U^P(b^+) \\ \phi_1(b^+) \\ \frac{\Delta\rho_b \delta b}{\Delta\rho d} \end{pmatrix} \text{ and } \delta_p = \begin{pmatrix} 0 \\ 0 \\ g(r') \\ 0 \\ 0 \\ -(2\ell-1)\frac{d}{R_o} \end{pmatrix} \quad [84]$$

Each column of the 6×6 matrix \mathbf{A} in [83] involves the corresponding basis vectors $\mathbf{y}_i(r'_+)$ and $\mathbf{x}_i(r'_-)$ in [81] and [82].

For any given position $r=r'$ of the delta-function load, we obtain a system of equations given by [83] which can be simply solved to find the unknown vector \mathbf{p} . The elements of \mathbf{p} define the poloidal-flow impulse response (kernel) functions of the mantle which are discussed in Section 1.23.2.4.

The toroidal-flow system [36] may be written as the following homogeneous equation:

$$\frac{d}{dr} \mathbf{u}(r) = \mathbf{M}_T(r) \mathbf{u}(r) \quad [85]$$

in which $\mathbf{M}_T(r)$ is the 2×2 matrix appearing in system [36]. We can propagate each of the surface boundary vectors $\mathbf{z}_i (i=1, 2)$ in [75], by numerically integrating [85] from the surface ($r=a^-$) downward to $r=b^+$, stopping along the way at all internal material boundaries ($r=r_i$) where we apply the internal matching conditions (50, 51). The basic procedure is summarized schematically in Figure 6. The resulting flow vector $\mathbf{u}(b^+)$ is

$$\mathbf{u}(b^+) = V^T \mathbf{z}_1(b^+) + T^T(a^-) \mathbf{z}_2(b^+) \quad [86]$$

which must be matched to the toroidal flow in expression [79]

$$\mathbf{u}(b^+) = U^T(b^+) \mathbf{w}_1 \quad [87]$$

We thereby obtain the following simple system:

$$\mathbf{B} \mathbf{t} = \delta_t \quad [88]$$

in which

$$\mathbf{t} = \begin{pmatrix} U^T(b^+) \\ T^T(a^-) \end{pmatrix} \quad \text{and} \quad \delta_t = V^T \mathbf{z}_1(b^+) \quad [89]$$

Each column of the 2×2 matrix \mathbf{B} in [88] involves the corresponding basis vectors \mathbf{w}_1 and $-\mathbf{z}_2$ in [86] and [87]. Expression [88] shows that the toroidal flow throughout the mantle is ‘driven’ by the surface toroidal flow V^T generated by rotating tectonic plates,

which are themselves driven by the buoyancy-induced poloidal flow in the mantle. This surface coupling of poloidal and toroidal flow, due to the presence of surface tectonic plates, is discussed in the next section.

1.23.2.3.7 Incorporating tectonic plates as a surface boundary condition

The boundary conditions at the top of the mantle are more complex because of the presence of tectonic plates. If the plates are assumed to be an integral part of the underlying mantle flow and they fully participate in the flow, then a simple free-slip surface boundary condition would be appropriate. This free-slip assumption has often been employed in tomography-based flow studies (e.g., Hager *et al.*, 1985; Forte and Peltier, 1987; Hager and Richards, 1989; King and Masters, 1992). If, on the other hand, we recognize that the plates are mechanically and rheologically distinct from the underlying mantle, then a more realistic surface boundary condition that explicitly treats the effective rigidity of plates is required.

Essentially rigid tectonic plates are a fundamental aspect of convection dynamics in the Earth and, although their treatment lies beyond classical fluid mechanics theory, their dynamical impact on thermal convection in the mantle must be considered. One approach for modeling the coupling of convection and plates, developed by Ricard and Vigny (1989) and Gable *et al.* (1991), is based on an explicit treatment of the net vertical torque (or horizontal force) acting on the base of each surface plate. This method is a direct extension of the torque-balance analysis originally employed by Hager and O’Connell (1981) in their modeling of dynamic plate motions. The fundamental underlying assumption in the method developed by Ricard and Vigny is that the plate boundaries are completely stress-free. This method has been employed in a number of mantle-flow models over the past few years (e.g., Corrieu *et al.*, 1994; Lithgow-Bertelloni and Richards, 1998).

An alternative method for coupling the motions of rigid surface plates to buoyancy-induced mantle flow was developed by Forte and Peltier (1991, 1994). Only the main aspects of this method are summarized here. It may be shown that for a given geometry of surface plates, the internal density anomalies $\rho_1(r, \theta, \phi)$ are partitioned into two families:

$$\rho_1(r, \theta, \phi) = \hat{\rho}_1(r, \theta, \phi) + \bar{\rho}_1(r, \theta, \phi) \quad [90]$$

where the density perturbations $\hat{\rho}_1(r, \theta, \phi)$ are obtained through a projection operator \hat{P} as follows:

$$\hat{\rho}_{1s}^t(r) = \hat{P}_{st, lm}(r)\rho_{1l}^m(r) \quad [91]$$

The calculation of the projection operator $\hat{P}_{st, lm}(r)$ is given in [Forte and Peltier \(1994\)](#) and it depends on the geometry of the surface plates. The other component of the density anomalies $\bar{\rho}_1(r, \theta, \phi)$ is simply given by the expression,

$$\bar{\rho}_{1s}^t(r) = \rho_{1s}^t(r) - \hat{\rho}_{1s}^t(r) \quad [92]$$

As [Forte and Peltier \(1994\)](#) show, the poloidal mantle flow field produced by the component $\hat{\rho}_1$ is consistent with the geometry of possible rigid plate motions at the surface whereas the one produced by $\bar{\rho}_1$ is orthogonal to any possible plate motion. In other words, the plates participate in the underlying flow driven by $\hat{\rho}_1$, while they resist the flow produced by $\bar{\rho}_1$. Hence, free-slip ($T^p(r_s) = 0$) and no-slip ($V^p(r_s) = 0$) surface boundary conditions are applied to model the internal flows driven by $\hat{\rho}_1$ and $\bar{\rho}_1$, respectively.

A simple application of the plate-projection operator is illustrated in [Figure 7](#), where we compare the buoyancy driven plate motions predicted on the basis of two hypothetical hot thermal anomalies under the Pacific plate which differ only in their spatial relationship to the nearby East Pacific Ridge (EPR). Both ‘plumes’ are constructed in an *ad hoc* manner as rectangular-shaped, negative density anomalies with constant amplitude -0.1 g cm^{-3} located in the depth range 400–750 km, equivalent to -2.6% relative density perturbation at 525 km depth. This amplitude is much greater than expected on the basis of the seismic tomography models (see [Figure 12](#)) and is only used here for the purpose of illustration. The predicted mantle flow field varies linearly with the amplitude of the driving density anomaly; therefore, a ‘plume’ anomaly which is 10 times smaller (-0.01 g cm^{-3}) will produce surface motions 10 times smaller than those shown in [Figure 7](#).

In the absence of plates, both of the hypothetical plumes ([Figures 7\(a\) and 7\(b\)](#)) produce the same amplitude and pattern of horizontal flow divergence at the surface of the mantle (compare [Figures 7\(c\) and 7\(d\)](#)). The situation changes radically when the present-day configuration of rigid plates is imposed at the top of the mantle. The plume which is offset from the nearest plate boundary ([Figure 7\(a\)](#)), the EPR, drives a mantle flow field which produces only a small fraction of the horizontal surface divergence

obtained in the absence of plates (cf. [Figures 7\(c\) and 7\(e\)](#)). The plate projection operator [91] maps most of the original plume density anomaly ρ_1 into the no-slip family of density anomalies $\bar{\rho}_1$ which cannot produce observable plate motions. According to the alternative plate-motion theory employed by [Ricard and Vigny \(1989\)](#), this hypothetical plume anomaly produces flow-induced driving torques on the overlying Pacific plate which nearly cancel because the center of the upwelling is too far away from the nearest plate boundary. In contrast, the plume located under the EPR ([Figure 7\(b\)](#)) produces horizontal divergence of the Pacific and Nazca plates with an amplitude comparable to that obtained in the absence of plates (cf. [Figures 7\(d\) and 7\(f\)](#)). In this case, a substantial fraction of the original density anomaly ρ_1 was mapped into the free-slip family of density anomalies $\hat{\rho}_1$. It should be noted that mutual interactions among the plates will generate non-zero far-field plate divergence and convergence ([Figure 7\(f\)](#), for example in the Indian Ocean) which is a consequence of the assumed rigidity of the plates.

From the perspective of the tectonic plates, the existence of a null-space corresponding to the family of internal density anomalies δ_1 [92] which cannot drive observable motions (as in [Figure 7\(c\)](#)) constitutes a fundamental nonuniqueness in the interpretation of plate tectonics. The present-day plate motions ([DeMets *et al.*, 1990](#)), or the geologic reconstructions of the history of plate motions ([Gordon and Jurdy, 1986](#)), therefore provide completely nonunique constraints on the mantle density anomalies generated by the thermal convection process. Other convection-related observables (e.g., global gravity anomalies) are required to constrain the density anomalies which fall into the null-space δ_1 . A further exploration of the implications of the non-unique interpretation of plate motions is presented by [Forte and Peltier \(1994\)](#).

The plate motions which are driven by the buoyancy-induced (poloidal) mantle flow will necessarily pose a toroidal component. This toroidal component is directly coupled to the poloidal component of the plate motions as

$$(\hat{\mathbf{r}} \cdot \nabla \times \mathbf{v})_s^t = C_{st, lm} (\nabla_H \cdot \mathbf{v})_l^m \quad [93]$$

in which the spherical harmonic coefficients of the radial vorticity of the plate velocity field \mathbf{v} are linearly dependent on the harmonic coefficients of the horizontal divergence of the plate motions. The

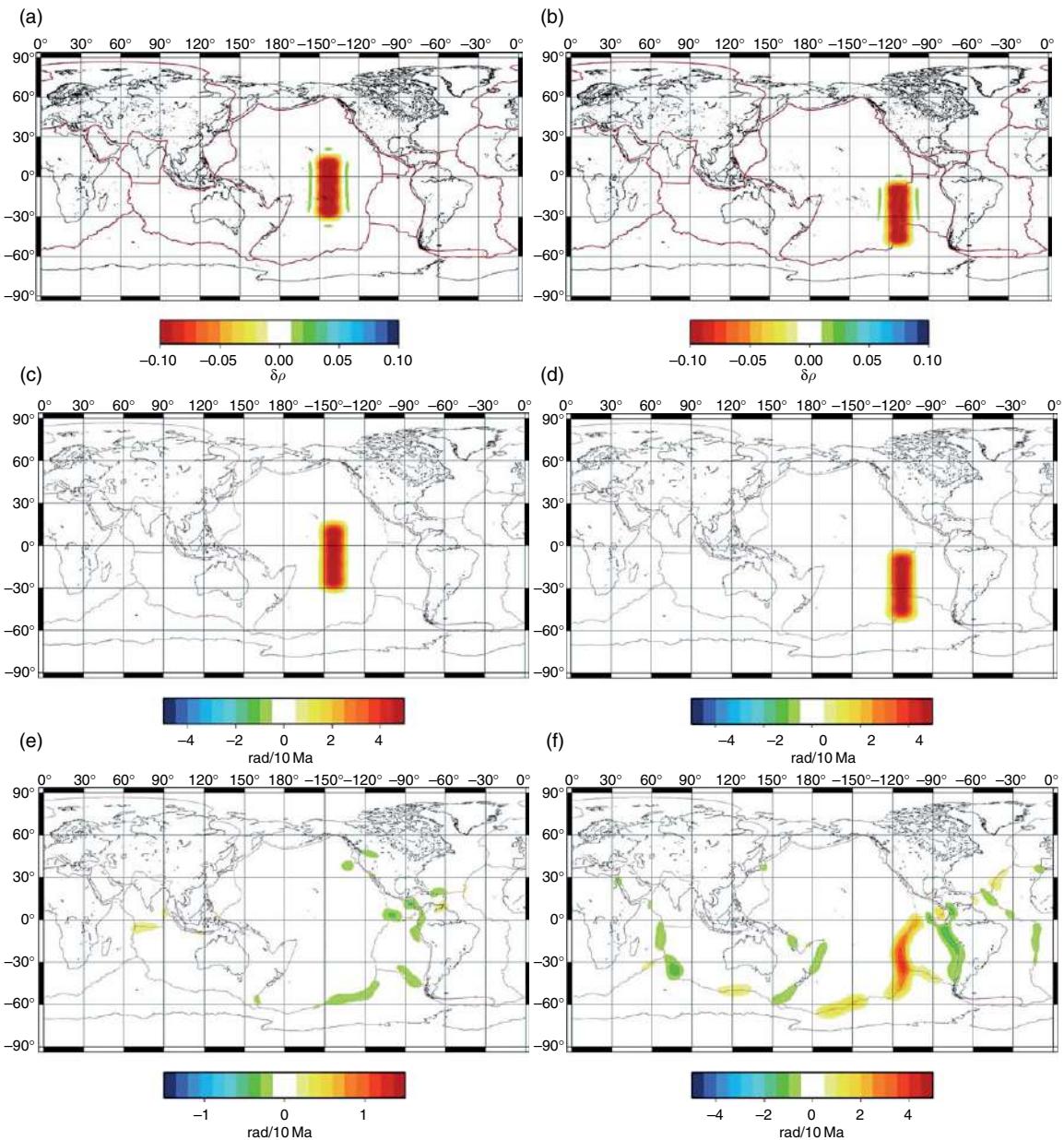


Figure 7 Interaction of hypothetical upwelling plumes with rigid surface plates. Maps (a) and (b) show two rectangular-shaped, negative density anomalies (the hypothetical 'plumes') with amplitude -0.1 g cm^{-3} assumed to be constant in the depth interval 400–750 km. Both plume anomalies have been expanded in terms of spherical harmonics up to degree and order 32. Maps (c) and (d) show the corresponding patterns of predicted horizontal surface divergence for a hypothetical mantle with a free-slip surface boundary (no plates) where the predicted motions are calculated up to harmonic degree 32. The mantle flow calculation was carried out assuming a depth-dependent viscosity variation shown below in **Figure 9**. Maps (e) and (f) show the corresponding patterns of plate divergence (up to harmonic degree 32) when the present-day configuration of rigid tectonic plates is imposed as a surface boundary condition in the mantle flow calculation.

vorticity and divergence fields are themselves directly dependent on the toroidal and poloidal scalar representations, respectively, of the plate velocity field (Forte and Peltier, 1987). It is important to note

that expression [93] is only valid for toroidal harmonic degree $s \geq 2$ and that the coupling matrix $C_{st,lm}$ is dependent only on the geometry of the plates (Forte and Peltier, 1994).

As discussed in Section 1.23.2.3.6, the viscous coupling between the plates and underlying mantle will result in the downward propagation of the surface toroidal flow into the mantle. The surface boundary condition [74] requires that the toroidal mantle flow match the toroidal component of plate motions, which is equivalent to their radial vorticity [93]:

$$V^t(r_s) = \frac{\iota r_s}{\Omega_1} (\hat{r} \cdot \nabla \times \mathbf{v})_l^m \quad [94]$$

where $\iota = \sqrt{-1}$.

The Green function solutions of the poloidal and toroidal flow equations (see Section 1.23.2.3.6) may be used to describe the viscous response of the mantle to an arbitrary distribution of internal density anomalies ρ_1 as follows:

$$\begin{pmatrix} U_\ell^{\alpha m}(r) \\ T_\ell^{\alpha\beta m}(r) \end{pmatrix} = \int_{r_{\text{CMB}}}^{r_s} \begin{pmatrix} \mathbf{U}_\ell^\alpha(r, r') \\ \mathbf{T}_\ell^{\alpha\beta}(r, r') \end{pmatrix} \rho_1 \delta\rho_\ell^m(r') dr' \quad [95]$$

where $U_\ell^{\alpha m}(r)$ and $T_\ell^{\alpha\beta m}(r)$ are the generalized spherical harmonic coefficients of the velocity and stress fields [31] and [32], respectively, and $\mathbf{U}_\ell^\alpha(r, r')$ and $\mathbf{T}_\ell^{\alpha\beta}(r, r')$ are the corresponding Green functions.

Tectonic plates may represent the most extreme manifestation of lateral variations in rheology in the convecting mantle. The plate coupling procedure described above thus provides an explicit means of incorporating the dynamical impact of such extreme lateral heterogeneity in the flow calculations which will be presented below. It is nonetheless true that eqns [35] and [36] governing flow in the mantle do not include lateral variations in viscosity and hence buoyancy forces will only directly excite a poloidal flow. In these calculations, toroidal mantle flow is excited passively from above, via the rotating surface plates.

A more general flow theory which models the effects of lateral viscosity variations throughout the mantle (e.g., Martinec *et al.*, 1993; Forte and Peltier, 1994) is required to describe the direct excitation of toroidal flow by mantle buoyancy forces. The dynamical implications of large-amplitude lateral viscosity variations throughout the mantle have recently been studied by Moussa *et al.* (2006). Despite the considerably more complex theory (relative to equations 35, 36) needed to calculate flow in a 3-D viscosity field, Moussa *et al.* find the impact on predicted surface observables such as topography and geoid are relatively small. This recent study provides an important verification for the modeling and interpretation of geodynamic observables using the

plate-coupled flow theory with purely depth-dependent viscosity in the mantle. The results obtained on the basis of this simplified treatment of mantle dynamics are presented in the sections that follow.

1.23.2.4 Geodynamic Response Functions for the Mantle

The theoretical relationship between the mantle density anomalies and the principal convection related surface observables (i.e., geoid or gravity anomalies, dynamic surface and CMB topography, plate motions) may be summarized in terms of geodynamic response or kernel functions (see Hager and Clayton (1989) and Forte (2000) for reviews). These kernel functions are calculated in the spherical harmonic spectral domain using the viscous flow Green functions defined in expression [95]. The principal assumption we shall make in calculating these geodynamic kernels – in addition to the assumption of purely depth-dependent viscosity below the plates – is that the 670 km seismic discontinuity is not a barrier to radial mantle flow. This whole-mantle flow assumption has been recently subjected to a series of direct tests based on joint inversions of global seismic and geodynamic data sets (Simmons *et al.*, 2005). It is found that the most satisfactory reconciliation of the global seismic and geodynamic constraints on 3-D mantle structure is obtained with whole-mantle flow and significantly poorer fits are obtained with flow models which assume vertical flow barriers at 670 km depth or within the lower mantle (e.g., at 1800 km depth).

The geoid kernels $G_\ell(\eta; r)$ relate the spherical harmonic coefficients of the nonhydrostatic geoid field, δN_ℓ^m , to the spherical harmonic coefficients of the density perturbations $\delta \rho_\ell^m(r)$ as follows:

$$\delta N_\ell^m = \frac{3}{(2\ell+1)\bar{\rho}} \int_{r_{\text{CMB}}}^{r_s} G_\ell(\eta; r) \delta \rho_\ell^m(r) dr \quad [96]$$

where $\bar{\rho} = 5.515 \text{ Mg m}^{-3}$ is the mean density of the Earth, r_s is the mean radius of the solid surface, and r_{CMB} is the mean radius of the CMB. The geoid kernels are a functional of the nondimensional radial mantle viscosity profile $\eta(r)/\eta_o$. The free-air gravity anomaly coefficients δG_ℓ^m are related to the nonhydrostatic geoid coefficients δN_ℓ^m as follows:

$$\delta G_\ell^m = (\ell-1) \frac{g_0}{R_o} \delta N_\ell^m \quad [97]$$

where $g_0 = 9.82 \text{ m s}^{-2}$ (982 000 mGal) is the mean gravitational acceleration at Earth's surface and

$R_0 = 6371$ km is Earth's mean radius. Through the combination of equations [96] and [97], we can relate the gravity anomaly coefficients to the internal density perturbations.

As discussed in the preceding section, a dynamical flow model which incorporates rigid plate motions must include mixed free-slip and no-slip surface boundary conditions. In the calculation of the flow-related observables, we must therefore determine the separate contributions provided by the density anomalies $\delta\hat{\rho}$ and $\delta\bar{\rho}$ which are convolved with kernel functions derived with free-slip and no-slip surface boundaries, respectively. For example, in the case of the nonhydrostatic geoid anomalies, we rewrite eqn [96] as follows:

$$\delta N_\ell^m = \frac{3}{(2\ell+1)\bar{\rho}} \int_{r_{\text{CMB}}}^{r_s} [\hat{G}_\ell(\eta; r)\delta\hat{\rho}_\ell^m(r) + \bar{G}_\ell(\eta; r)\delta\bar{\rho}_\ell^m(r)] dr \quad [98]$$

where the geoid kernels $\hat{G}_\ell(\eta; r)$ and $\bar{G}_\ell(\eta; r)$ are calculated with free-slip and no-slip surface boundaries, respectively. As shown in Forte and Peltier (1994), the density anomalies $\delta\hat{\rho}$ are spatially correlated with the positions of divergent or convergent plate boundaries. Subducting slabs and mid-ocean ridge heterogeneity are therefore resolved as part of the $\delta\hat{\rho}$ anomalies.

The surface topography kernel functions $T_\ell(\eta; r)$ relate the spherical harmonic coefficients of the flow-induced surface topography δa_ℓ^m to the spherical harmonic coefficients of the internal density anomalies as follows:

$$\delta a_\ell^m = \frac{1}{\Delta\rho_{\text{mo}}} \int_{r_{\text{CMB}}}^{r_s} [\hat{T}_\ell(\eta; r)\delta\hat{\rho}_\ell^m + \bar{T}_\ell(\eta; r)\delta\bar{\rho}_\ell^m(r)] dr \quad [99]$$

where $\Delta\rho_{\text{mo}} = 2.2 \text{ Mg m}^{-3}$ is the density jump across the mantle–ocean boundary and $\hat{T}_\ell(\eta; r)$ and $\bar{T}_\ell(\eta; r)$ are calculated with free-slip and no-slip surface boundaries, respectively.

Similarly, the spherical harmonic coefficients of the flow-induced CMB topography δb_ℓ^m may be expressed in terms of CMB topography kernels $B_\ell(\eta; r)$ as follows:

$$\delta b_\ell^m = \frac{1}{\Delta\rho_{\text{cm}}} \int_{r_{\text{CMB}}}^{r_s} [\hat{B}_\ell(\eta; r)\delta\hat{\rho}_\ell^m + \bar{B}_\ell(\eta; r)\delta\bar{\rho}_\ell^m(r)] dr \quad [100]$$

where $\hat{B}_\ell(\eta; r)$ and $\bar{B}_\ell(\eta; r)$ are calculated with free-slip and no-slip surface boundaries, respectively, and $\Delta\rho_{\text{cm}} = -4.43 \text{ Mg m}^{-3}$ is the density jump across the CMB. As in the case of the nonhydrostatic geoid in

eqn [98], the dependence on viscosity of the predicted surface and CMB topography appears explicitly through the nondimensional profile $\eta(r)/\eta_0$.

Surface-plate velocities \mathbf{v} may be characterized by their horizontal divergence field $\nabla_H \cdot \mathbf{v}$ (Forte and Peltier, 1987). The horizontal divergence kernels $D_\ell(\eta; r)$ relate the spherical harmonic coefficients of the predicted plate divergence $(\nabla_H \cdot \mathbf{v})_\ell^m$ to the spherical harmonic coefficients of the density perturbations as follows:

$$(\nabla_H \cdot \mathbf{v})_\ell^m = \frac{\eta_0}{\eta_0} \int_{r_{\text{CMB}}}^{r_s} D_\ell(\eta; r)\delta\hat{\rho}_\ell^m(r) dr \quad [101]$$

in which the free-slip component of the mantle density anomalies $\delta\hat{\rho}$, defined in expression [91], is required to model the surface divergence of the plates. We also note the presence of the reference scaling value of viscosity η_0 . This presence implies that plate motions, unlike the other observables in eqns [96]–[100], will be dependent on the absolute value of mantle viscosity.

1.23.2.5 Depth Dependence of Mantle Viscosity

Understanding the long timescale rheology of the mantle as represented by its effective viscosity is a central and enduring problem in global geophysics. The diverse methods and data sets which have been employed to constrain mantle viscosity have been a source of ongoing contention and debate. The importance and intensity of this debate are an apt reflection of the fundamental role of mantle viscosity in controlling a wide array of geodynamic processes. For example, millennial timescale glacial isostatic adjustment (GIA) processes such as Pleistocene and Holocene sea-level variations and related anomalies in Earth's gravitational field and rotational state are known to be strongly dependent on the depth dependence of mantle viscosity. On much longer, million to hundred-million year timescales, viscosity exerts fundamental control on the dynamics of mantle convection and on the corresponding evolution of the thermal and chemical state of Earth's interior. The very long timescale implications of mantle viscosity also include fundamental surface geological and geochemical processes, such as global scale epeirogeny and associated sea-level changes, global geoid anomalies, and tectonic plate motions.

The spatial variation of viscosity in Earth's mantle can, in principle, be determined from a consideration

of the microphysical properties which control the steady-state creep of mantle rocks (e.g., Nicolas and Poirier, 1976; Sammis *et al.*, 1977). In practice, however, the microphysical models of mantle viscosity depend on knowledge of a number of critical physical properties, such as grain size and activation volume and energy, which are poorly known in the mantle and hence require extrapolations of laboratory creep experiments which greatly exceed the physical conditions (i.e., pressure, temperature, or creep rate) under which these experiments were originally performed. It is nonetheless possible to show, on the basis of microphysical considerations, that the global horizontal average viscosity may increase by up to three orders of magnitude across the mantle (e.g., Ranalli 2001). More precise determinations of the radial viscosity profile require additional constraints from geophysical data sets which are sensitive to the long-term rheology of the mantle.

The first and most influential geophysical contribution to our understanding of mantle viscosity is Haskell's (1935) study of Fennoscandian postglacial uplift which was found to require an average viscosity of 10^{21} Pa s down to a depth approximately equal to the horizontal dimension of the surface load (~ 1000 – 1500 km). McConnell's (1968) spectral analysis of the Fennoscandian uplift data led to the inference that mantle viscosity increased significantly with depth while at the same time still satisfying the Haskell average. The Haskell average value of viscosity over the upper 1000– 1200 km of the mantle was also supported in subsequent work by O'Connell (1971). These initial studies which supported the compatibility between the Haskell constraint on viscosity and significant increases of viscosity in the lower mantle were displaced by subsequent analyses by Cathles (1975) and Peltier and Andrews (1976) who concluded that viscosity was nearly constant from the base of the lithosphere to the CMB. This view of mantle viscosity characterized by only moderate increases with depth was reinforced in later studies involving larger GIA data sets (e.g., Wu and Peltier 1983; Tushingham and Peltier, 1991). A review of the GIA constraints on viscosity may be found in Mitrovica (1996).

The first inferences of the depth variation of mantle viscosity based on surface data sets associated with mantle convection (e.g., Hager, 1984; Richards and Hager, 1984; Ricard *et al.*, 1984) disagreed strongly with the GIA inferences of mantle viscosity which prevailed since the earliest studies by Cathles, Peltier, and collaborators. These convection-based

analyses of viscosity, in particular the first study of Earth's global geoid anomalies by Hager (1984), suggested a large increase of viscosity in the sublithospheric mantle with an approximately factor of 30 increase in the average viscosity of the lower mantle relative to the upper mantle. This conclusion was supported by subsequent studies by Forte and Peltier (1987) and Forte *et al.* (1991) who extended the viscous flow modeling to include the plate velocities. The geodynamic inferences for significant (1–2 order of magnitude) increases in the average viscosity of the lower mantle relative to that of the upper mantle were reinforced by subsequent analyses carried out by Ricard *et al.* (1989), Ricard and Vigny (1989), Hager and Clayton (1989), Forte and Peltier (1991), Forte *et al.* (1993a, 1994), King and Masters (1992), Corrieu *et al.* (1994), and Thoraval and Richards (1997). A survey of some of the earliest viscosity inferences derived on the basis of global geoid anomalies are shown in Figure 8. Reviews of mantle viscosity inferences based on either convective flow or GIA data sets may be found in King (1995) and Kaufmann and Lambeck (2000).

Additional geodynamic considerations which suggest a substantial increase of viscosity with depth are based on a wide variety of analyses which include the stability of the hot spot reference frame (e.g., Richards, 1991; Quéré and Forte, 2006), long-term rates of polar wander (e.g., Sabadini and Yuen, 1989; Spada *et al.*, 1992; Richards *et al.*, 1997; Steinberger and O'Connell, 1997), and the planform of mantle convection (e.g., Zhang and Yuen, 1995; Bunge *et al.*, 1996; Forte and Mitrovica, 2001).

The inference of mantle viscosity from convection related surface data, considered in the context of tomography-based mantle flow models, was initially carried out through an effectively trial-and-error fitting procedure (e.g., Forte and Peltier 1987, 1991; Hager and Clayton, 1989; Forte *et al.*, 1993). Subsequently, a number of formal mathematical inversions of the geodynamic data were carried out (e.g., Forte *et al.*, 1991; Ricard and Wuming, 1991; King and Masters, 1992; Corrieu *et al.*, 1994; King, 1995; Forte and Mitrovica, 1996; Kido *et al.*, 1998; Forte, 2000; Panasyuk and Hager, 2000). The viscosity profiles obtained by inverting geodynamic data sets (Figure 8) are all characterized by strong overall increases in viscosity with depth, but it is also clear that there are significant differences in the detailed character of these viscosity inferences. There are many factors which can contribute to these differences and they include, most notably, the use of

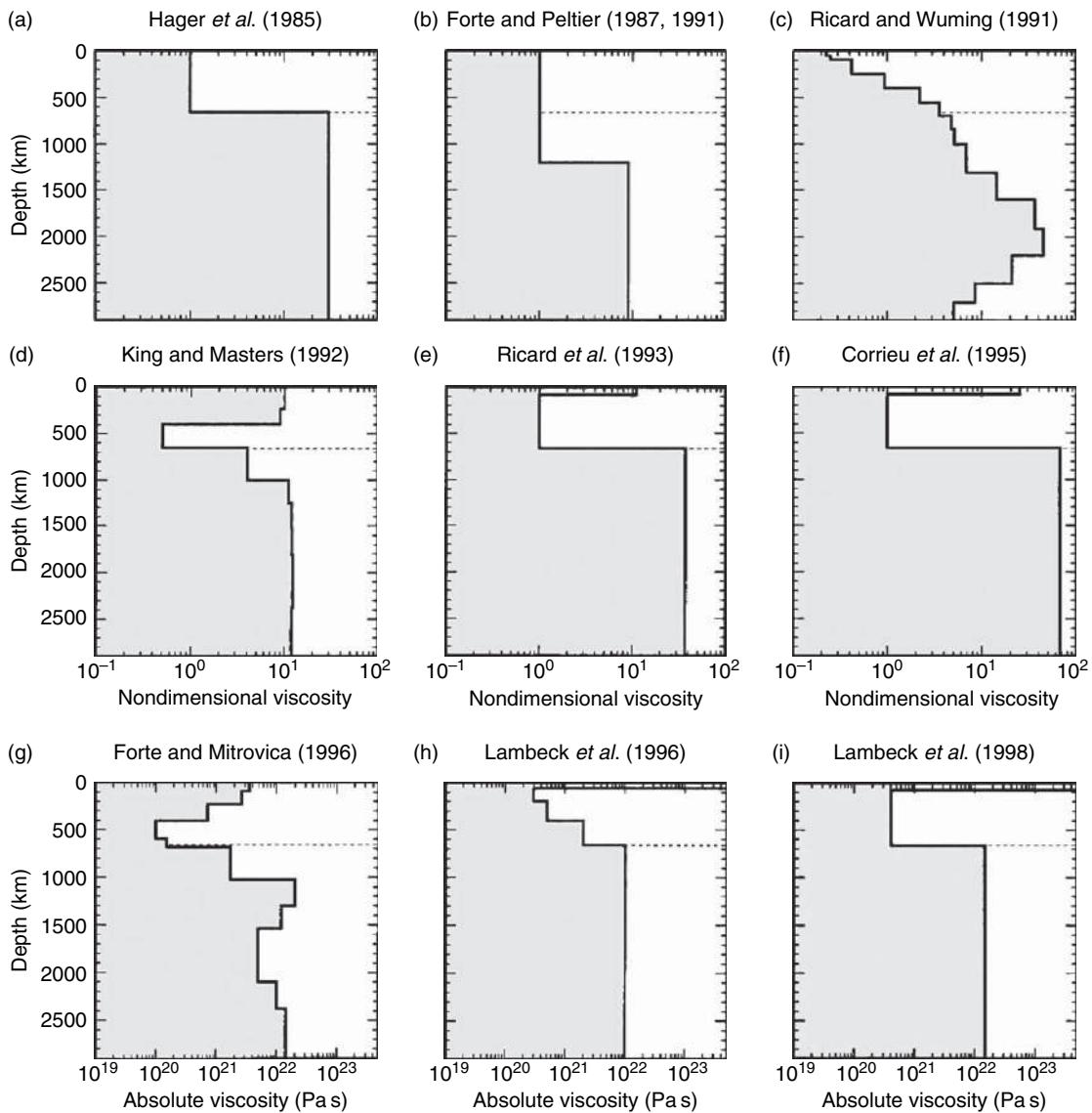


Figure 8 A survey of previous geodynamic inferences of depth dependent mantle viscosity. Frames (a) to (f) show relative (nondimensional) variations of viscosity with depth derived on the basis of global long wavelength geoid anomalies. Frames (g) to (i) show radial (absolute) viscosity profiles inferred on the basis of GIA data (in addition to geoid data in the case of frame g). The GIA data sets constrain the absolute value of viscosity whereas the steady-state viscous flow modelling of the geoid data only constrain relative variations of viscosity with depth. (Figure adapted from Kaufmann and Lambeck, 2000).

different tomography-based inferences of mantle density anomalies; different combinations of geodynamic data (e.g., geoid only, geoid plus plate motions, geoid plus dynamic topography, all of the above); different inversion methods (e.g., Monte-Carlo, Bayesian, genetic, Occam algorithms). The formulation of the viscous flow models themselves can also play a critical role in explaining these differences, since it is known that the use of different surface boundary conditions (e.g., free-slip, no-slip, freely

rotating tectonic plates) will lead to rather different viscosity inferences (e.g., Thoraval and Richards, 1997). Finally, the limited resolving power of the geodynamic constraints precludes a direct interpretation of viscosity at any given depth in the mantle. For example, Forte and Mitrovica (2001) found that the combined constraints provided by global free-air gravity anomalies, tectonic plate motions, and excess ellipticity of the CMB could only resolve average values of viscosity in rather broad depth intervals.

The discordant viscosity inferences derived from either GIA or convection-related data sets were initially regarded as evidence for the transient nature of mantle viscosity over the timescales that separate these two processes (e.g., Sabadini *et al.*, 1985; Peltier, 1985). The necessity for time-dependent viscosity in the mantle was later weakened by two independent analyses of the GIA data sets. The first argument against transient viscosity was provided by an analysis of differential Late Holocene sea-level high-stands in the Australian region by Nakada and Lambeck (1989), who showed that these GIA data required a nearly two order of magnitude increase of viscosity across the mantle. The second independent argument was provided by Mitrovica (1996), who showed that previous inferences of a nearly constant-viscosity mantle (e.g., Wu and Peltier 1983; Tushingham and Peltier, 1991) were conditioned by a misinterpretation of the original Haskell (1935) constraint. The latter was erroneously assumed to apply only to the top 670 km of the mantle (i.e., the upper mantle), rather than to the average value of viscosity down to depths of about 1000–1500 km (Mitrovica, 1996).

The recognition that GIA data are not incompatible with large increases of mantle viscosity with depth spurred new efforts to reconcile GIA and convection data sets with a single profile of mantle viscosity. The first efforts were undertaken by Forte and Mitrovica (1996) and Mitrovica and Forte (1997). Despite the very different time and spatial scales over which these processes operate, these authors found that it was possible to simultaneously explain both decay times associated with the postglacial uplift of Hudson Bay and Fennoscandia, and long-wavelength free-air gravity anomalies associated with mantle convection with a single viscosity profile characterized by an approximately two order of magnitude increase with depth which also satisfied the original Haskell constraint on mantle viscosity. These joint GIA-convection inversions culminated in the recent study by Mitrovica and Forte (2004) in which the range of viscosity profiles consistent with both families of surface data are summarized below in Figure 9. The convection data employed in these viscosity inversions are shown in Figure 2. The GIA data include the Fennoscandian relaxation spectrum (FRS) and a set of decay times determined from the postglacial sea-level history in Hudson Bay and Sweden. The inverted viscosity profiles are characterized by a 3 orders of magnitude increase from the upper mantle (mean value of $\sim 4 \times 10^{20}$ Pa s) to a high-viscosity ($> 10^{23}$ Pa s) peak at 2000 km depth. Below 2000 km, the viscosity shows a significant, 2–3 orders of magnitude reduction toward the CMB. Similar radial variations in lower-mantle viscosity have been inferred in other independent studies (e.g., Ricard and Wuming, 1991).

The inverted viscosity profiles are characterized by a 3 orders of magnitude increase from the upper mantle (mean value of $\sim 4 \times 10^{20}$ Pa s) to a high-viscosity ($> 10^{23}$ Pa s) peak at 2000 km depth. Below

2000 km, the viscosity shows a significant, 2–3 orders of magnitude, reduction toward the CMB. Similar radial variations in lower-mantle viscosity have been inferred in other independent studies (e.g., Ricard and Wuming 1991). The preferred viscosity profile (solid black line, Figure 9) provides an optimal fit to both (GIA and convection) families of data and, unless stated otherwise, this profile will be employed to calculate all convection related related surface observables presented below.

The first efforts to reconcile the constraints on viscosity provided by both glacial isostatic adjustment (GIA) and convection data were undertaken by Forte and Mitrovica (1996) and Mitrovica and Forte (1997). Despite the very different time and spatial scales over which these processes operate, these authors found that it was possible to simultaneously explain both GIA and convection data with a single viscosity profile. These joint GIA–convection inversions culminated in the recent study by Mitrovica and Forte (2004) in which the range of viscosity profiles consistent with both families of surface data is summarized in Figure 8. The convection data employed in these viscosity inversions are shown in Figure 2. The GIA data include the Fennoscandian relaxation spectrum (FRS) and a set of decay times determined from the postglacial sea-level history in Hudson Bay and Sweden. The inverted viscosity profiles are characterized by a 3 orders of magnitude increase from the upper mantle (mean value of $\sim 4 \times 10^{20}$ Pa s) to a high-viscosity ($> 10^{23}$ Pa s) peak at 2000 km depth. Below 2000 km, the viscosity shows a significant, 2–3 orders of magnitude reduction toward the CMB. Similar radial variations in lower-mantle viscosity have been inferred in other independent studies (e.g., Ricard and Wuming, 1991). The preferred viscosity profile (solid black line, Figure 8) provides an optimal fit to both (GIA and convection) families of data and, unless stated otherwise, this profile will be employed to calculate all convection-related surface observables presented below.

The geodynamic response or kernel functions calculated on the basis of the preferred mantle viscosity profile (Figure 9) are illustrated below in Figure 10. Comparing the free-slip and no-slip geoid kernels, we note that the largest contribution from density anomalies in the top half of the mantle is provided by those anomalies $\delta\hat{\rho}$ which are efficient in driving observable plate motions. These anomalies correspond to subducting slabs and upper-mantle plumes below the mid-ocean ridges. In the bottom

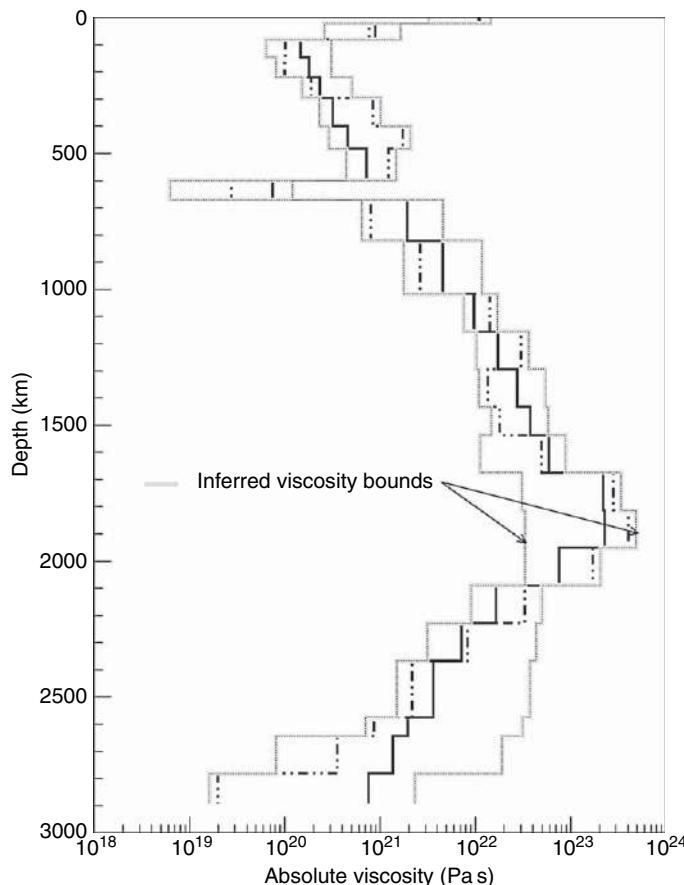


Figure 9 Results of inversions of the GIA and convection data sets. Full details of the inversions are presented in Mitrovica and Forte (2004). The convection data are interpreted in terms of a tomography-based mantle flow model in which the density anomalies are derived from the Grand (2002) tomography model (**Figure 3(b)**). The thick gray lines illustrate the range of allowable values of mantle viscosity which are consistent with the joint GIA–convection constraints. The solid black line is the preferred viscosity profile, on the basis of the Grand (2002) tomography model, which provides an optimal fit to the entire suite of geodynamic data. The dash-dotted line is the preferred viscosity profile obtained on the basis of the joint shear–bulk-sound tomography model of Masters *et al.* (2000).

half of the mantle, the density anomalies belonging to the $\delta\bar{\rho}$ family provide the largest contribution to the surface geoid or gravity anomalies. These $\delta\bar{\rho}$ anomalies produce no observable plate motions. At sufficiently short horizontal wavelengths (corresponding to harmonic degrees $\ell \geq 32$), we note that the distinction between $\delta\hat{\rho}$ and $\delta\bar{\rho}$ anomalies begins to disappear: both provide equal contributions to the surface geoid or gravity anomalies. The free-slip and no-slip surface topography kernels show that the density anomalies $\delta\bar{\rho}$ provide the strongest contribution to dynamic surface topography, especially at long horizontal wavelengths (corresponding to the degree range $\ell = 2–8$). At short horizontal wavelengths, the distinction between the two classes of density anomalies again ceases to be important.

1.23.3 Modeling Geodynamic Observables with Seismic Tomography

We now consider the extent to which the 3-D mantle structure resolved in recent seismic tomographic models may be used to explain the global convection-related data sets shown in **Figure 2**. The geodynamic response functions obtained on the basis of the preferred radial viscosity profile (**Figure 10**) will be used to establish the connection between the seismically inferred heterogeneity in the mantle and the surface geodynamic observables. A broad selection of seismic shear-velocity models, obtained in independent studies using diverse and complementary seismic data and using different seismic modeling and inversion techniques, will be employed here. Seismic shear

velocity heterogeneity is the initial focus of this tomography-based modeling because it is expected that S-wave anomalies δV_S will be most sensitive to the temperature anomalies maintained by the mantle convection process (e.g., Röhm *et al.*, 2000; Forte and Perry, 2000; Forte *et al.*, 2002).

1.23.3.1 Seismic Heterogeneity Models

The S-wave tomography models employed here are, in chronological order: model *S20A* (isotropic version) from Ekström and Dziewonski (1998), model *S20RTS* from Ritsema *et al.* (1999), model *SAW24* from Mégnin and Romanowicz (2000), model *SB4_L18* from Masters *et al.* (2000), model *TX2002* from Grand (2002), and model *J362D28* from Antolik *et al.* (2003). The spatial variation of seismic heterogeneity in these S-wave models is parametrized in terms of a wide assortment of basis functions, ranging from B-splines to piecewise-discontinuous layers in

the radial direction and spherical harmonics to equal-area cells in the horizontal direction.

To facilitate a direct comparison among these seismic heterogeneity models and the subsequent usage of the models in viscous flow calculations, all models have been projected onto a common set of radial and horizontal basis functions as follows:

$$\frac{\delta V_S}{V_S} = \sum_{k=0}^{32} \sum_{\ell=1}^{20} \sum_{m=-\ell}^{+\ell} k c_\ell^m T_k(x) Y_\ell^m(\theta, \varphi) \quad [102]$$

in which $T_k(x)$ are Chebychev polynomials in the normalized radius $x = (2r - r_{\text{surf}} - r_{\text{CMB}})/(r_{\text{surf}} - r_{\text{CMB}})$ and Y_ℓ^m are ordinary spherical harmonics. Notice that all models are expanded up to order 32 in the radial Chebychev polynomials and up to degree 20 in the surface spherical harmonics.

When each of the S-wave heterogeneity models are projected onto the representation (102), the depth variations of the rms amplitudes of the velocity anomalies are shown in Figure 11. Here we note

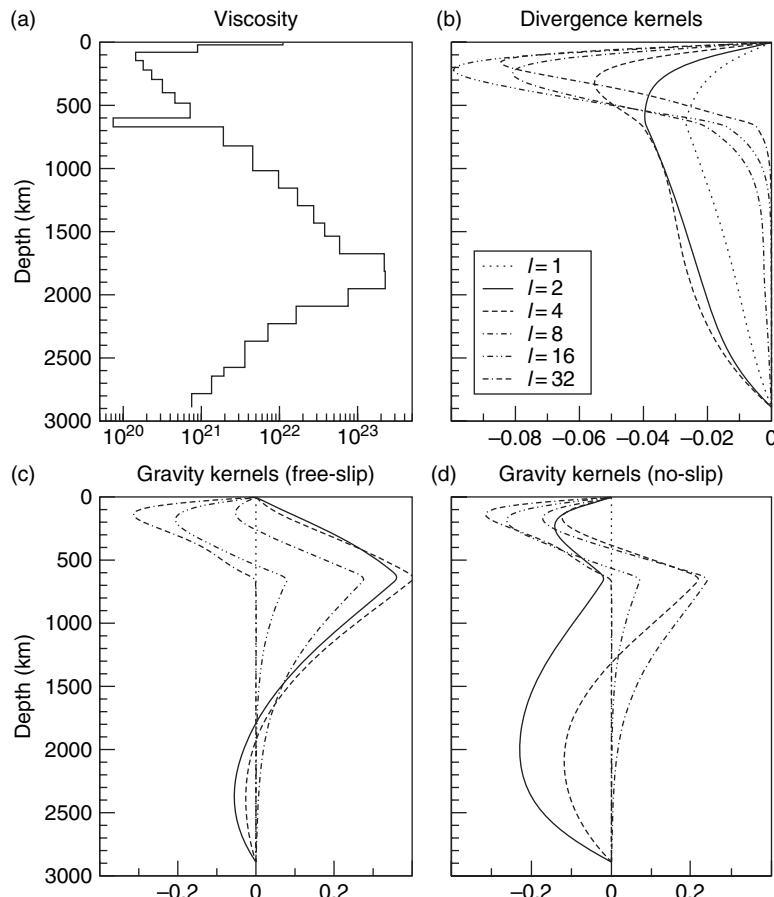


Figure 10 (Continued)

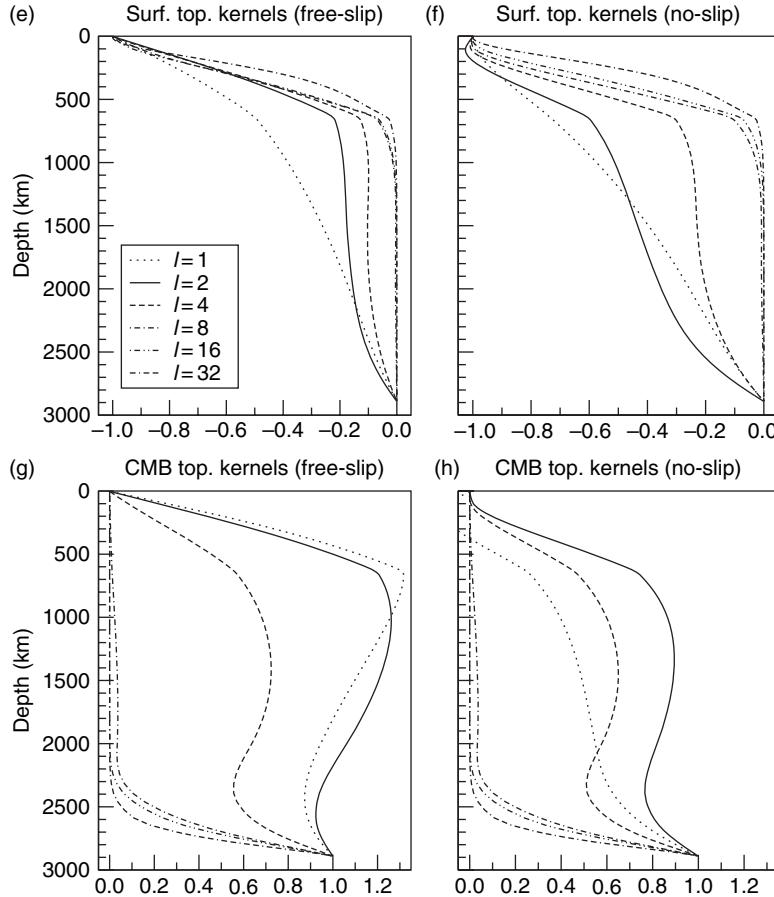


Figure 10 Geodynamic kernel functions. The geodynamic response functions shown here are calculated on the basis of the preferred GIA-convection-inferred viscosity profile shown in (a) (same as the solid black curve in Figure 7). The kernels corresponding to harmonic degrees $\ell = 1, 2, 4, 8, 16, 32$ are identified by the legend in (b) (repeated below in (e)). The horizontal divergence kernels, defined in [101], are shown in (b). The gravity kernels, defined in [98], for free-slip and no-slip surface boundary conditions are shown in (c) and (d), respectively. The surface topography kernels, defined in [99], for free-slip and no-slip conditions are shown in (e) and (f) respectively. The kernels for the dynamic CMB topography, defined in [100], are shown in (g) and (h) for free-slip and no-slip conditions, respectively.

that, with the exception of the top 300 km in the mantle, the average amplitudes of the relative perturbations of seismic shear velocity $\delta V_S/V_S$ show significant differences in the mantle, especially in the transition zone region (400–1000 km depth) and at the base of the mantle (2500–2891 km depth).

1.23.3.2 Mantle Density Anomalies

The mantle density anomalies required in modeling the convection-related surface observables may be derived from the seismic tomography models using experimental and theoretical results from mineral physics (e.g., Karato, 1993; Čadek *et al.*, 1994; Wang and Weidner, 1996; Sobolev *et al.*, 1997; Stacey, 1998; Zhang and Weidner, 1999; Trampert *et al.*, 2001;

Stixrude and Lithgow-Bertelloni, 2001; Jackson, 2001; Karato and Karki, 2001; Oganov *et al.*, 2001a). This derivation would, however, require that the amplitudes of seismic velocity anomalies are well constrained and that all relevant mineralogical variables in the mantle (e.g., reference composition, temperature, and equation of state parameters) are sufficiently well known. It is unlikely that all of these requirements can be met at the present time, although previous efforts to simultaneously interpret mantle density and seismic velocity anomalies using mineral physics data have shown some promise (e.g., Forte *et al.*, 1994).

A second, alternative method for inferring mantle density anomalies is based on the direct inversion of the convection-related geophysical observables

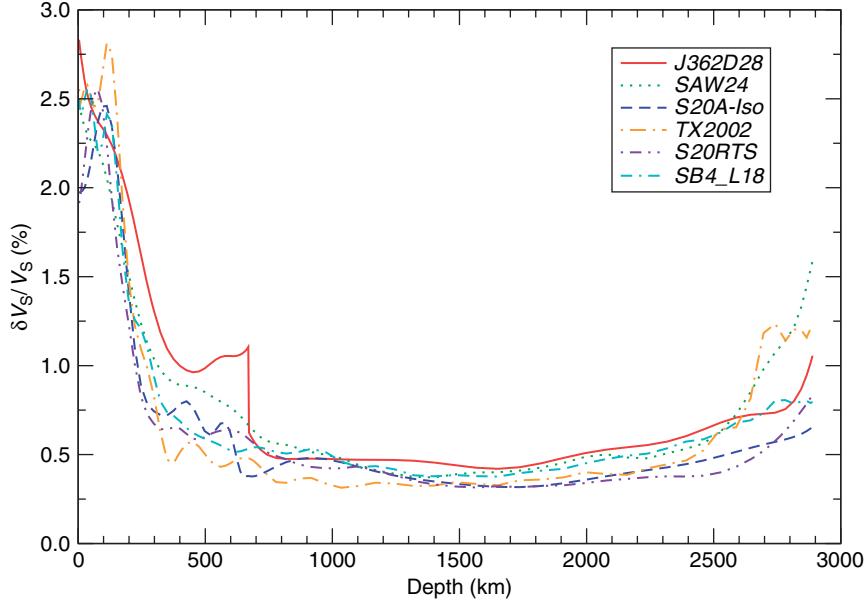


Figure 11 Amplitude of S-wave heterogeneity in the mantle. Plotted here is the root-mean-square (rms) amplitude of relative perturbations of seismic shear velocity obtained from the following tomography models: J362D28 (Antolik *et al.*, 2003), SAW24 (Mégnin and Romanowicz, 2000), S20A-Iso (Ekström and Dziewonski, 1998), TX2002 (Grand, 2002), S20RTS (Ritsema *et al.*, 1999), SB4_L18 (Masters *et al.*, 2000). All tomography models have been projected onto the spatial parametrization given by expression [102].

(e.g., Forte *et al.*, 1993; Corrieu *et al.*, 1994; Karpychev and Fleitout, 2000; Forte and Perry, 2000; Panasyuk and Hager, 2000; Forte and Mitrovica, 2001; Pari, 2001; Deschamps *et al.*, 2001). This approach is useful when contending with significant uncertainties in the amplitudes of the seismic anomalies, as is evident in **Figure 11**. This figure underscores a key concern, namely that the use of mineral physics data to translate the seismic anomalies can lead to large variations in the estimated mantle density anomalies, depending on the choice of tomography model. To avoid this difficulty, it is preferable to carry out simultaneous inversions of all global geodynamic data (**Figure 2**) to determine an optimal velocity–density scaling factor $d \ln \rho / d \ln V_S$ (e.g., Forte and Mitrovica, 2001), such that

$$\frac{\delta \rho}{\rho} = \left(\frac{d \ln \rho}{d \ln V_S} \right) \frac{\delta V_S}{V_S} \quad [103]$$

where $\delta V_S / V_S$ are shear velocity anomalies obtained from a tomography model and $\delta \rho / \rho$ are the relative perturbations in density which are constrained by the geodynamic data. This approach has also been employed in other tomography-based mantle flow models (e.g., Hager and Clayton, 1989; Corrieu *et al.*, 1994; Panasyuk and Hager, 2000).

The geodynamic data provide direct, linear constraints on the density anomalies in the mantle (see eqns [98]–[100]), which may be generically expressed as follows:

$$\begin{aligned} \delta O_\ell^m &= f_\ell \int_b^a K_\ell(\eta; r') (\rho_1)_\ell^m(r') dr' \\ &\approx f_\ell \sum_{i=1}^N K_\ell(\eta; r_i) (\rho_1)_\ell^m(r_i) w_i \end{aligned} \quad [104]$$

in which δO_ℓ^m are the spherical harmonic coefficients of a geodynamic observable (e.g., geoid or free-air gravity anomalies), $K_\ell(\eta; r')$ is the corresponding kernel function, and f_ℓ is a factor which depends on the geodynamic observable (see, for example, eqn [98]). The numerical calculation of integrals is usually carried out with equivalent finite sums, such as in [104] where w_i is a weighting term which depends on the numerical summation algorithm (e.g., Gauss–Legendre quadrature). On the basis of expression [103], we may further rewrite equation [104] as

$$\delta O_\ell^m = f_\ell \sum_{i=1}^N w_i K_\ell(\eta; r_i) \rho_o(r_i) \left(\frac{\delta V_S}{V_S} \right)_\ell^m(r_i) \left(\frac{d \ln \rho}{d \ln V_S} \right)(r_i) \quad [105]$$

in which $\delta V_S / V_S$ are the shear-velocity anomalies in the mantle and $d \ln \rho / d \ln V_S$ is the corresponding

velocity-to-density scaling which is assumed to vary with depth in the mantle.

Expression [105] provides the basis for a discrete, linear inversion of the geodynamic data $\delta O''_\ell$ to find an optimal velocity-to-density scaling profile $d \ln \rho / d \ln V_S$. A series of Occam inversions (Constable *et al.*, 1987) of the geodynamic data (Figure 2) were carried out to find the smoothest family of $d \ln \rho / d \ln V_S$ profiles which are consistent with the data. For each Occam inversion, a different seismic shear-wave tomography model (Figure 11) was employed, and in each case the same geodynamic kernel functions (Figure 10) were employed to relate the mantle heterogeneity to the geodynamic data. The results of these inversions are summarized in Figure 12,

which shows the optimal profiles of $d \ln \rho / d \ln V_S$ and the resulting depth variation of the rms amplitude of the lateral density anomalies implied by expression [103].

Mineral physics estimates of the velocity–density scaling (Figure 12) show significant departures from the scaling profiles derived from the Occam inversions. As discussed above, this discrepancy may in part arise from the inadequate resolution of seismic heterogeneity in the mantle—especially in the mid-mantle region between 1000 km and 2000 km depth—and it may also arise from inadequacy of the theoretical assumptions inherent in the mineral physics estimates. In the latter case, the chief assumption which may be deficient is the dominance of thermal effects on both the seismic and

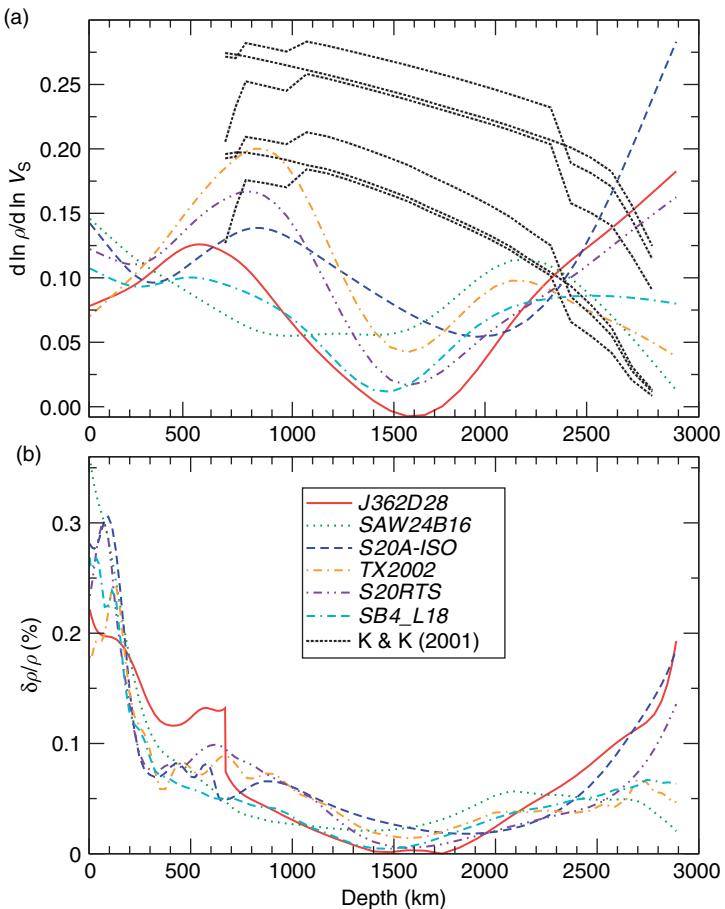


Figure 12 Occam inversions for mantle density anomalies. (a) The optimal Occam inferred velocity–density scaling profiles for each of the tomography models illustrated in Figure 11. The legend identifying the results is in (b). For comparison are shown (thick dashed gray lines) a series of theoretical estimates of the depth variation of $d \ln \rho / d \ln V_S$ in the lower mantle obtained by Karato and Karki (2001) on the basis of mineral physics data. These mineral physical estimates assume that both density and seismic anomalies are produced by temperature perturbations in the mantle. (b) The resulting inferences of the depth variation of the rms density anomalies which are calculated on the basis of the seismic shear velocity anomalies using expression [103].

density anomalies in the mantle. Compositional effects, especially on mantle density heterogeneity, may be one important explanation for the deviations from theoretical mineral physics estimates based on temperature effects alone (e.g., Stacey, 1998). The possible importance of compositional effects will be discussed below in the context of a further investigation of tomography-based geodynamic constraints on mantle density.

1.23.3.3 Predicted Tectonic Plate Motions

In this and the next few sections, we consider the extent to which the tomography-based inferences of mantle density anomalies presented in **Figure 12** provide a successful explanation of the convection-related surface observables (**Figure 2**). We begin here with a consideration of convection-induced tectonic plate motions. The predicted horizontal divergence of the plate motions, calculated on the basis of expression [101] and using the kernels in **Figure 10(b)**, are presented in **Figure 13** alongside the observed NUVEL-1 divergence of the plates. A detailed spectral comparison between the predicted and observed plate divergence is shown on **Figure 14**.

A quantitative summary of the overall agreement between the predicted and observed plate divergence, quantified in terms of total rms amplitude, total spatial correlation, and variance reduction, is provided in **Table 1**. The variance reduction is defined as follows:

$$\text{var. red.} = 100\% \times \left[1 - \frac{\sum_{\ell} \sum_{m=-\ell}^{+\ell} (O-P)_{\ell}^{m*} (O-P)_{\ell}^m}{\sum_{\ell} \sum_{m=-\ell}^{+\ell} O_{\ell}^{m*} O_{\ell}^m} \right] \quad [106]$$

where $(O-P)_{\ell}^m$ and O_{ℓ}^m are the harmonic coefficients of the difference between the observed and predicted fields and the observed fields, respectively.

An important characteristic of the predicted divergence fields shown in **Figure 13**, which is also confirmed in **Table 1**, is the subdued amplitude of the predicted fields relative to the data. As will be seen in the next few sections, all tomography-based predictions of geodynamic observables which are calculated on the basis of the optimal Occam-inverted density–velocity scaling profiles (**Figure 12**) are systematically reduced in amplitude relative to the amplitude of the observed fields. This

systematic bias to low predicted amplitudes is a natural consequence of the least-squares misfit criterion which is employed in almost all inversion algorithms (including the Occam approach) which leads to significantly damped inferences of the $d \ln \rho / d \ln V_S$ scaling profiles.

It can be readily shown that the inherent damping of tomography-based inferences of $d \ln \rho / d \ln V_S$ arises as a consequence of poorly resolved 3-D seismic structure in geodynamically important regions of the mantle, such as the mid-mantle region (e.g., Forte *et al.*, 1994). We can illustrate this in an inverse problem in which we seek, for the sake of simplicity, the best-fitting constant $d \ln \rho / d \ln V_S$ value. As shown in expression [104], the predicted convection-related observables are linearly dependent on the internal density perturbations in the mantle. By virtue of expression [105], we may write

$$d(\theta, \varphi) = \left(\frac{d \ln \rho}{d \ln V_S} \right) p(\theta, \varphi)$$

where $d(\theta, \varphi)$ represents the surface data and $p(\theta, \varphi)$ is the corresponding mantle-flow prediction assuming $d \ln \rho / d \ln V_S = 1$. We can then show that the optimal $d \ln \rho / d \ln V_S$ value that minimizes the least-squares misfit between data and the predictions is given by the following expression:

$$\frac{d \ln \rho}{d \ln V_S} = \frac{\sigma_d}{\sigma_p} c(d, p) \quad [107]$$

where σ_d and σ_p are the rms amplitudes of the data and the predictions,

$$\begin{aligned} \sigma_d^2 &= \frac{1}{4\pi} \iint_{S_1} |d(\theta, \varphi)|^2 d^2 S, \\ \sigma_p^2 &= \frac{1}{4\pi} \iint_{S_1} |p(\theta, \varphi)|^2 d^2 S \end{aligned}$$

and

$$c(d, p) = \frac{1}{4\pi} \iint_{S_1} d(\theta, \varphi) p(\theta, \varphi) d^2 S \quad [108]$$

where all integrals are defined over the surface of the unit sphere S_1 . The quantity $c(d, p)$ defined in [108] is the cross-correlation between the data and the predictions. Equation [107] thus shows that the inferences of $d \ln \rho / d \ln V_S$ will be directly proportional to the spatial correlation between the surface data and the corresponding geodynamic integral of the 3-D structure in the seismic tomography model. As previously shown by Forte *et al.* (1994), this correlation may be significantly degraded if the 3-D seismic structure is poorly resolved.

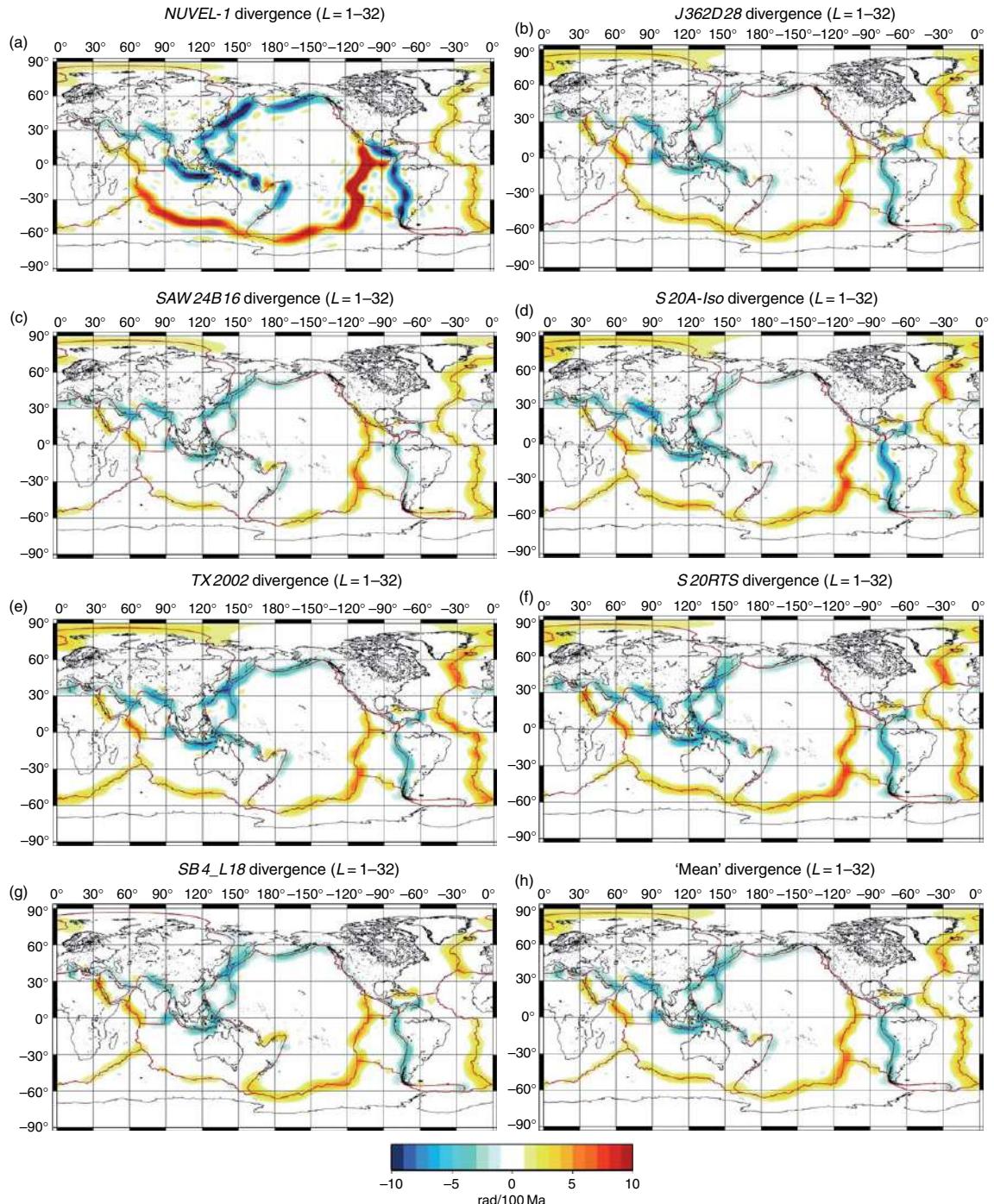


Figure 13 Tomography-based horizontal divergence of the tectonic plates. (a) Observed NUVEL-1 horizontal plate divergence (DeMets *et al.*, 1990). (b)–(g) The surface divergence predicted on the basis of tomography models J362D28 (Antolik *et al.*, 2003), SAW24 (Mégnin and Romanowicz, 2000) S20A-Iso (Ekström and Dziewonski, 1998), TX2002 (Grand, 2002), S20RTS (Ritsema *et al.*, 1999), SB4-L18 (Masters *et al.*, 2000), using the corresponding $d \ln \rho / d \ln V_S$ scaling profiles in Figure 12. All shear-velocity heterogeneity models have been projected onto the common parametrization in expression [102] prior to calculating the predicted plate motions. (h) The ‘mean’ prediction of plate divergence obtained by calculating the statistical sample average of all the predictions (b)–(g). The observed and predicted plate motions shown here are all synthesized from spherical harmonics up to degree and order 32.

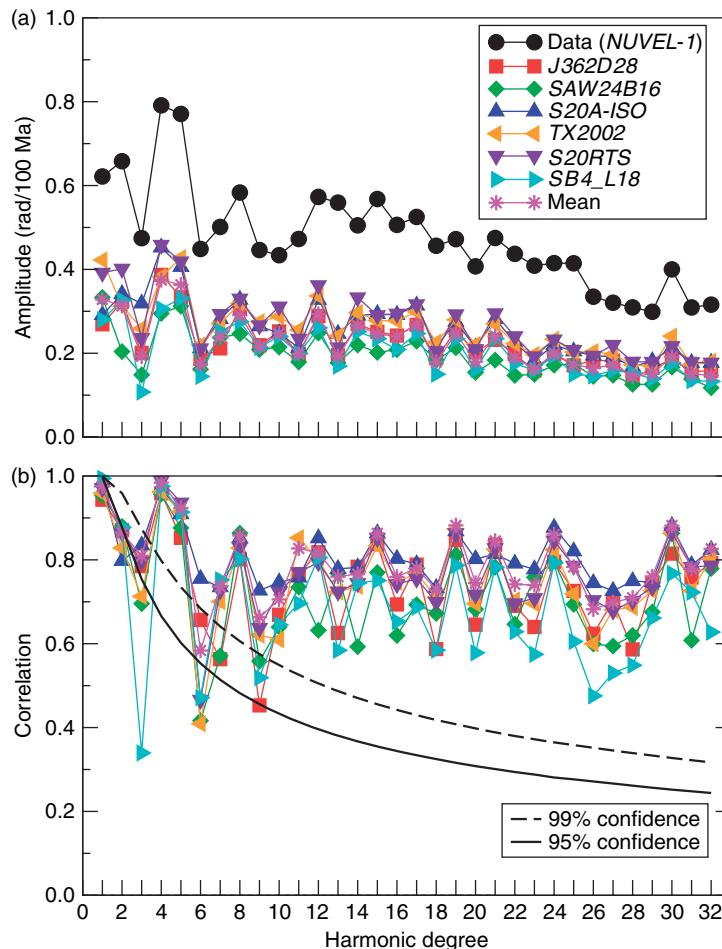


Figure 14 Spectral comparison of predicted and observed plate divergence. (a) The degree variance, as defined in eqn [3], of the observed and predicted plate divergence fields shown in Figure 13. (b) The degree correlations, as defined in eqn [4].

Table 1 Comparison of observed^a and predicted^b horizontal plate divergence

Model	NUVEL ^c	J362D28	SAW24	S20A-Iso	TX2002	S20RTS	SB4_L18	Mean
rms	2.8	1.3	1.1	1.5	1.5	1.6	1.2	1.3
correl		0.77	0.74	0.83	0.78	0.80	0.74	0.82
var. red. (%)		50	44	60	56	59	45	55

^aData and predictions (shown in Figure 13) are synthesized from spherical harmonics up to degree 32.

^bPredictions employ the tomography model indicated at the top of each column and they use the corresponding velocity–density scalings in Figure 12.

^cHorizontal divergence of the plates is derived from the NUVEL-1 (De Mets *et al.*, 1990) description of present-day plate velocities. rms, root-mean-square amplitude, expressed here in units of 10^{-8} a^{-1} . Correl, global cross-correlation; var. red., variance reduction.

1.23.3.4 Predicted Free-Air Gravity Anomalies

Tomography-based mantle flow models of Earth's nonhydrostatic gravitational potential have almost exclusively been based on analyses of the equivalent

geoid anomalies, beginning with the earliest studies by Richards and Hager (1984), Hager *et al.* (1985), and continuing to recent studies (e.g., Panasyuk and Hager, 2000). Since the global geoid anomalies are strongly dominated by horizontal wavelengths

corresponding to harmonic degrees $\ell = 2, 3$, they will effectively constrain only the longest wavelength components of 3-D mantle structure. To avoid this very-long-wavelength bias, we consider here a representation of the nonhydrostatic geopotential in terms of equivalent global free-air gravity anomalies (see expression [97]). The free-air gravity anomalies contain a more evenly balanced representation of the different horizontal wavelengths in the nonhydrostatic geopotential (i.e., a ‘flatter’ amplitude spectrum).

The observed and predicted gravity anomaly fields, calculated on the basis of expressions [97] and [98] and using the kernels in **Figures 10(c) and 10(d)**, are presented in **Figure 15**. A comparison of the predicted and observed gravity anomalies in the spectral domain is shown in **Figure 16**. In **Table 2** is presented a detailed summary of the global agreement between the predicted and observed gravity anomalies. In contrast to the predicted plate divergence discussed in the preceding section, we note that the amplitudes of the predicted gravity anomaly fields are somewhat less muted (compare **Tables 1 and 2**). The overall agreement with the gravity data (in terms of variance reduction) is however poorer than the plate divergence fits because of the decreased spatial correlation between the predictions and the data.

1.23.3.5 Predicted Dynamic Surface Topography

The term ‘dynamic topography’ is here defined to include all contributions to the topography of Earth’s solid surface which arise from mantle convection. There has been some controversy as to origin and amplitude of Earth’s dynamic topography, with some confusion as to how this dynamic topography should even be defined (e.g., Gurnis, 1990; Forte *et al.*, 1993b, 1993c; Gurnis, 1993). As will be discussed below, the interpretation of dynamic surface topography employed here, namely the topography arising from all density anomalies in the mantle (including those in the lithosphere), is not universally accepted. A detailed review and analysis of the opposing schools of thought in this debate has been presented by Pari (2001).

Numerous studies over the past three decades have focused exclusively on the topography of ocean floor, and the general conclusion is that this topography can be almost completely explained in terms of shallow, thermally induced density

anomalies which arise from the age-dependent cooling of the oceanic lithosphere (e.g., Parson and Sclater, 1977; Stein and Stein, 1992). The oceanic bathymetry is modeled in terms of isostatic compensation of density anomalies in the oceanic lithosphere, and hence many studies have regarded this form of thermal isostasy as not being a ‘dynamic’ contribution to surface topography. An adequate review of the extensive literature dealing with this interpretation of seafloor topography is well beyond the scope of this chapter, but recent studies of age-dependent oceanic bathymetry with extensive references to past analyses may be found in Doin and Fleitout (2000) and in Crosby *et al.* (2006).

Whether or not the thermal isostatic signal in seafloor bathymetry may be regarded as ‘static’ or ‘dynamic’ depends on the temporal variability of the structure of the upper thermal boundary layer (i.e., the lithosphere in oceanic regions) due to time-dependent mantle convection. A purely mechanical interpretation of the instantaneous, present-day isostatic compensation of thermal anomalies in the lithosphere ignores this background time dependence. The lateral temperature variations in the cooling lithosphere are essentially maintained by a balance between vertical heat conduction and horizontal heat advection (e.g., Jarvis and Peltier, 1982) and the latter is clearly a dynamic effect. In the absence of convection, the upper thermal boundary layer and the corresponding variations in oceanic bathymetry will vanish. The importance of time-dependent changes in the structure of the lithosphere, and hence the corresponding changes in the contribution to surface topography, is highlighted by the significant changes in plate tectonic velocities and plate geometries in the Cenozoic (e.g., Lithgow-Bertelloni and Richards, 1998), which suggest significant departures from steady-state conditions.

In the absence of convection, the only contribution to surface topography arises from the isostatic compensation of lateral variations in crustal thickness and crustal density. Earth’s present-day topography is therefore the superposition of the crustal isostatic topography and the dynamic topography – as defined here – due to density anomalies in the mantle which are maintained by mantle convection (Forte *et al.*, 1993b). The crustal isostatic topography is large and it explains most of the observed present-day topography on Earth (e.g., Forte and Perry, 2000; Pari and Peltier, 2000). The dynamic topography is obtained by subtracting the crustal isostatic topography from the observed topography and this therefore requires an accurate model of crustal structure. This

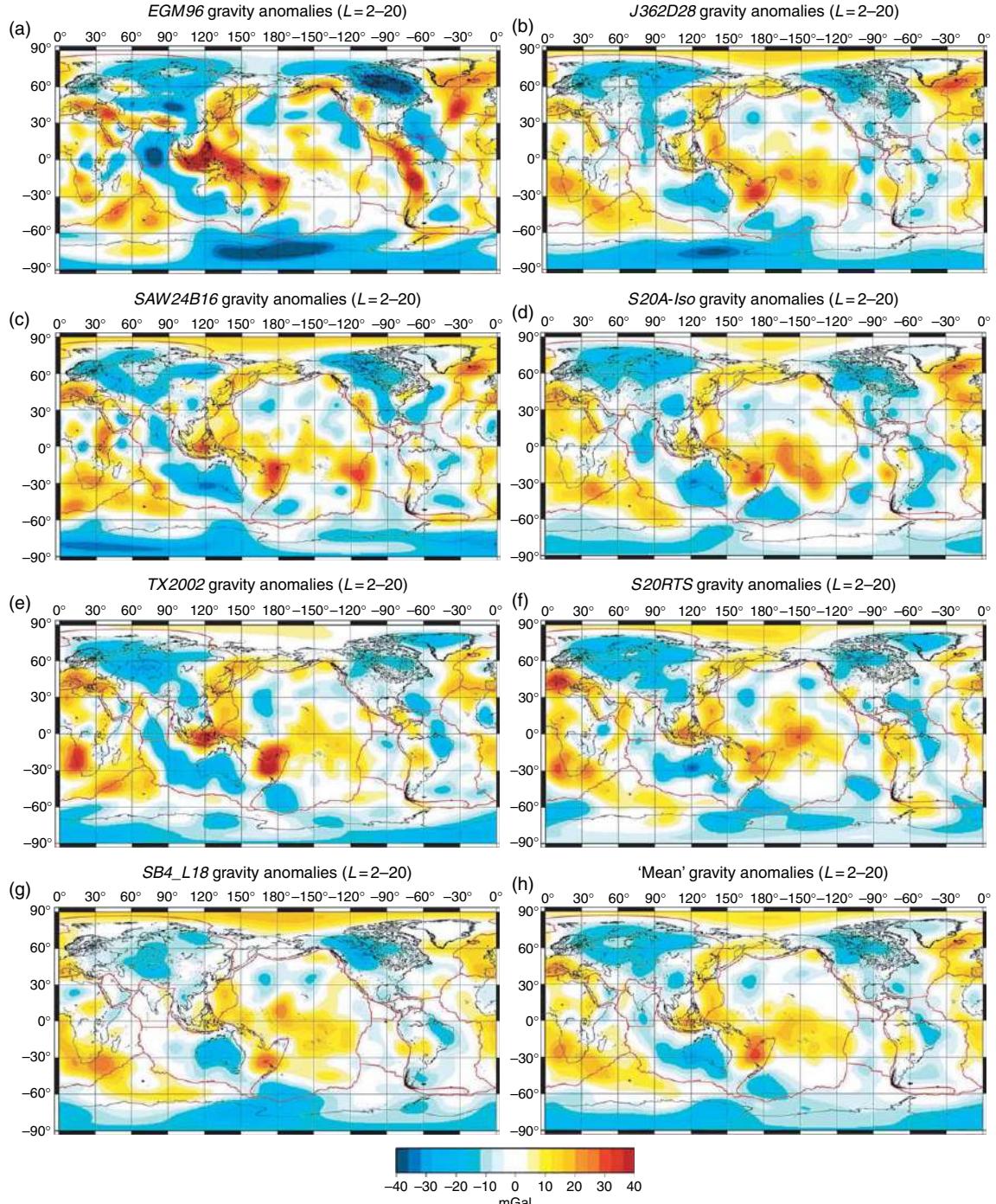


Figure 15 Tomography-based global free-air gravity anomalies. (a) Observed EGM96 anomalous free-air gravity field (Lemoine *et al.*, 1998). (b)–(g) The free-air anomalies predicted on the basis of tomography models J362D28 (Antolik *et al.*, 2003), SAW24 (Mégnin and Romanowicz 2000), S20A-Iso (Ekström and Dziewonski, 1998), TX2002 (Grand 2002), S20RTS (Ritsema *et al.* 1999), SB4_L18 (Masters *et al.* 2000), using the corresponding $d \ln \rho / d \ln V_S$ scaling profiles in Figure 12. All shear-velocity heterogeneity models have been projected onto the common parameterization in expression [102] prior to calculating the gravity anomalies. (h) The ‘mean’ free-air gravity anomaly field obtained by calculating the statistical sample average of all the predictions (b)–(g). The observed and predicted gravity anomalies shown here are all synthesized from spherical harmonics up to degree and order 20.

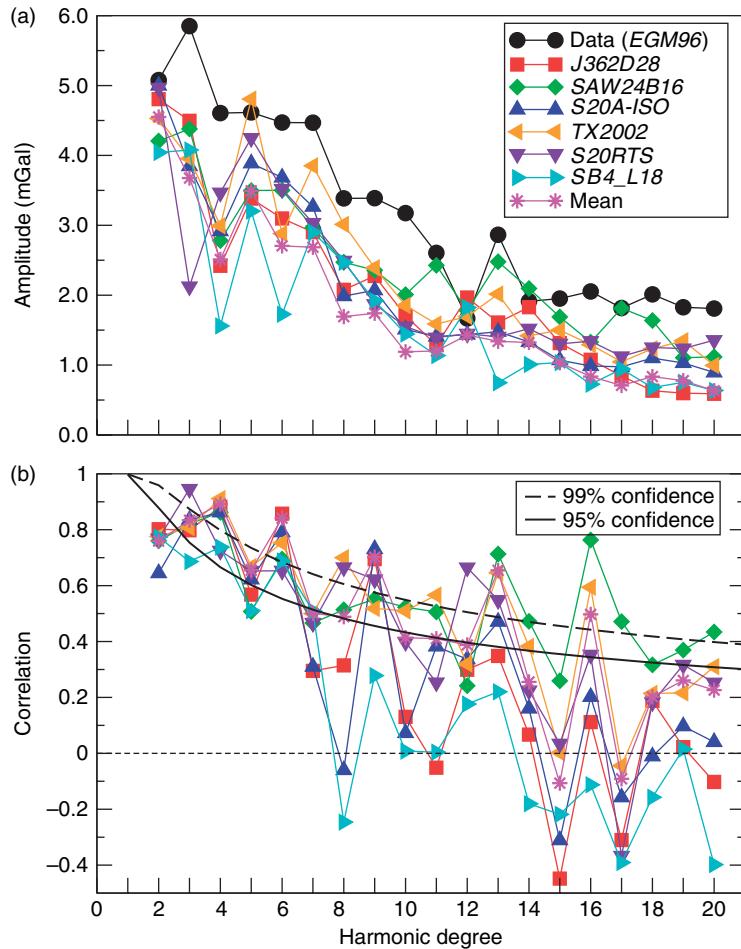


Figure 16 Spectral comparison of predicted and observed free-air gravity anomalies. (a) The degree variance, as defined in eqn [3], of the observed and predicted gravity anomaly fields shown in Figure 13. (b) The degree correlations, as defined in eqn [4].

Table 2 Comparison of observed^a and predicted^b free-air gravity anomalies

Model	EGM96 ^c	J362D28	SAW24	S20A-Iso	TX2002	S20RTS	SB4_L18	Mean
rms	14.8	10.4	11.2	10.6	11.4	10.5	8.9	9.3
correl		0.55	0.62	0.54	0.64	0.58	0.42	0.64
var. red. (%)		28	37	26	39	33	15	41

^aData and predictions (shown in Figure 15) are synthesized from spherical harmonics up to degree 20.

^bPredictions employ the tomography model indicated at the top of each column and they use the corresponding velocity–density scalings in Figure 12.

^cThe global free-air gravity anomalies are derived from the EGM96 geopotential model (Lemoine *et al.*, 1998).

rms, root-mean-square amplitude, expressed here in units of mGal. Correl, global cross-correlation; var. red., variance reduction.

requirement presents a major challenge because of the uneven and incomplete seismic sampling global crustal thickness and also because of the significant uncertainties in constraining the density of the crust. Currently, the most complete compilation of global crustal heterogeneity is model CRUST2.0 (Bassin

et al., 2000). This crustal model was employed in retrieving the dynamic surface topography presented above in Figure 2(b).

The observed and predicted dynamic topography fields, calculated on the basis of expressions [99] and using the kernels in Figures 10(e) and 10(f), are

presented in **Figure 17**. A quantitative spectral comparison of the predicted and observed dynamic topography is shown in **Figure 18**. In **Table 3** is presented a detailed summary of the match between the predicted and observed topography fields. The topography kernels (**Figures 10(e)** and **10(f)**) show that near-surface density anomalies provide the strongest contributions to the predicted surface topography (**Figure 17**) and that they will be in near-isostatic equilibrium, where perfect isostatic compensation corresponds to a kernel value of -1 . We note that in the case of density anomalies which effectively see a no-slip surface boundary (given by expression [92]), the condition of near-isostasy extends to depths of about 200 km (see **Figure 10(f)**).

In view of the debate concerning the magnitude of the thermal isostatic contributions to surface topography in oceanic regions, it is helpful to explore the relative importance of shallow (i.e., lithospheric) and deep-mantle (i.e., sublithospheric) buoyancy using the seismic tomography models. In this regard, it is useful to first evaluate the extent to which the tomography-based topography predictions incorporate the age-dependent cooling of the oceanic lithosphere. Tomography models employing seismic traveltimes and/or surface wave data place strong constraints on lithospheric mantle heterogeneity and they contain a clear signature of the oceanic cooling history (e.g., Woodward and Masters, 1991; Su *et al.*, 1992; Trampert and Woodhouse, 1996; Ritzwoller *et al.*, 2004).

Here we consider the global tomography models *SAW24* (Mégnin and Romanowicz, 2000) and *TX2002* (Grand, 2002), employed in **Figures 17(c)** and **17(e)** respectively. The age-dependent lateral temperature variations in the oceanic lithosphere were calculated using a simple halfspace cooling model with the same thermal parameters as the *GDH1* plate-cooling model of Stein and Stein (1992). The seafloor age was determined using the Muller *et al.* (1997) digital isochrons. The global ocean basins were then sampled on a $1^\circ \times 1^\circ$ grid and for each grid cell the corresponding values of ocean age, shear velocity perturbation dV_S/V_S , and temperature perturbation ΔT were determined. These samples were then averaged into 2-million-year age bins and the resulting relationship between seismic shear velocity and temperature is plotted in **Figure 19**.

A linear regression analysis (solid lines in **Figure 19**) yields an excellent fit to the binned V_S-T variation and the slopes of the regression lines provide estimates of the effective temperature

derivative of S-velocity in the depth range 0–100 km. These estimated derivatives are 8.7×10^{-5} and $9.4 \times 10^{-5} \text{ K}^{-1}$ for models *SAW24* and *TX2002*, respectively. These effective thermal derivatives agree well with independent mineral physics values determined by Stixrude and Lithgow-Bertelloni (2005a) which range between 8×10^{-5} and $9 \times 10^{-5} \text{ K}^{-1}$. These results confirm that the global tomography models considered in this study successfully resolve the pattern and amplitude of age-dependent cooling of the oceanic lithosphere.

The relative importance of surface topography due to lithospheric versus sublithospheric density anomalies is illustrated in **Figure 20**. As expected, the topography contributions in oceanic regions from density anomalies in the upper 200 km of the mantle are dominated by the age-dependent cooling of the oceanic lithosphere. Depressions in continental regions exceed observational estimates (**Figure 17(a)**) because the use of a purely depth-dependent $d \ln \rho / d \ln V_S$ scaling factor (**Figure 12**) does not resolve the intrinsic chemical buoyancy in the subcontinental mantle. This intrinsic buoyancy can be included in geodynamic models which allow for lateral variations of $d \ln \rho / d \ln V_S$ in the shallow mantle (e.g., Forte and Perry, 2000; Deschamps *et al.*, 2001).

The topography generated by sublithospheric buoyancy (**Figure 18(b)**), with rms amplitude equal to 410 m, is comparable to that generated by lithospheric density anomalies (**Figure 20(a)**) which has an rms amplitude equal to 580 m. These sublithospheric contributions to topography in the central Pacific and Atlantic Oceans, and in southern Africa, are surface expressions of deep-seated buoyancy with sources in the lower mantle (**Figure 3**). The depressions below the eastern and western margins of the Pacific (**Figure 20(b)**) may be interpreted in terms of present-day and Cenozoic subduction history (e.g., Lithgow-Bertelloni and Gurnis, 1997).

We note from **Figure 17** that the amplitude of the predicted dynamic topography is somewhat larger than the crust-corrected estimate of the observed dynamic topography. **Table 3** shows that the rms amplitude of the mean topography prediction is 25% larger than the observed topography. This discrepancy is in marked contrast to that of the predicted gravity and plate divergence fields (**Tables 1** and **2**) which are, on average, 40–50% smaller than the corresponding observed fields. The mismatched amplitudes of the predicted surface topography has motivated previous efforts (e.g., Le Stunff and Ricard 1995, 1997) to introduce additional buoyancy forces in the mantle arising,

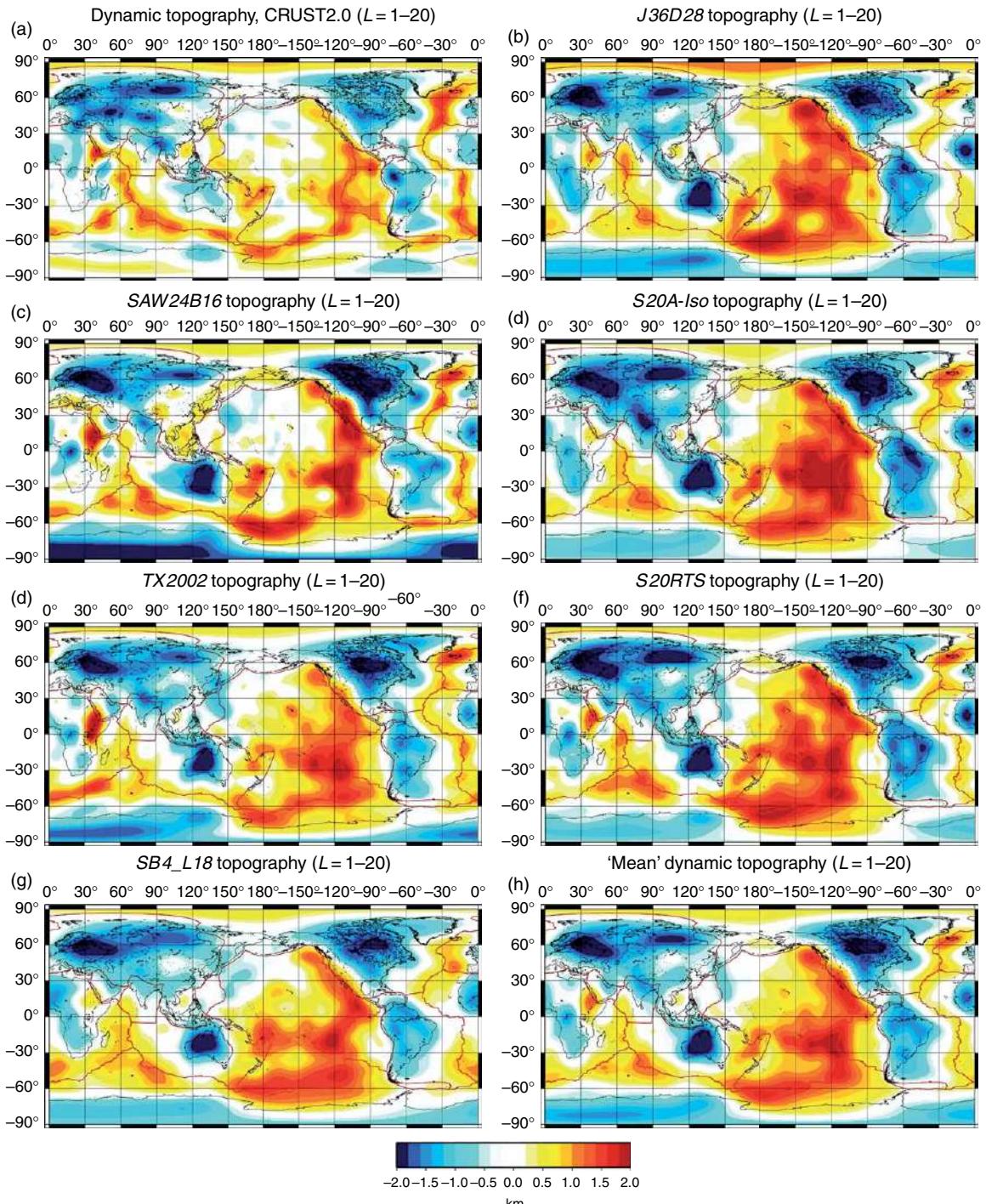


Figure 17 Tomography-based global dynamic surface topography. (a) Dynamic surface topography estimated by removing isostatically compensated crustal heterogeneity – described by model CRUST2.0 (Bassin *et al.*, 2000) – from the observed present-day surface topography. (b)–(g) The dynamic surface topography predicted on the basis of tomography models J36D28 (Antolik *et al.*, 2003), SAW24 (Mégnin and Romanowicz, 2000), S20A-Iso (Ekström and Dziewonski, 1998), TX2002 (Grand 2002), S20RTS (Ritsema *et al.*, 1999), SB4_L18 (Masters *et al.*, 2000), using the corresponding $d \ln \rho / d \ln V_S$ scaling profiles in Figure 12. All shear-velocity heterogeneity models have been projected onto the common parametrization in expression [102] prior to calculating the dynamic topography. (h) The ‘mean’ dynamic surface topography field obtained by calculating the statistical sample average of all the predictions (b)–(g). The crust-corrected and predicted dynamic topography shown here are all synthesized from spherical harmonics up to degree and order 20.

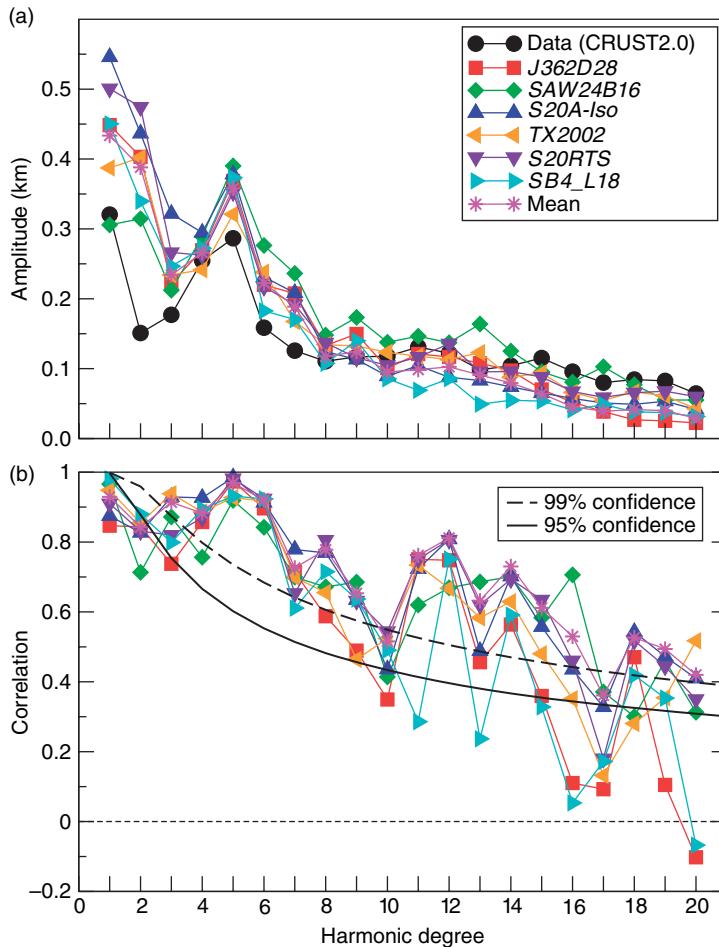


Figure 18 Spectral comparison of predicted and observed (crust-corrected) dynamic surface topography. (a) The degree variance, as defined in eqn [3], of the observed and predicted topography fields shown in Figure 15. (b) The degree correlations, as defined in eqn (4).

Table 3 Comparison of observed^a and predicted^b dynamic surface topography

Model	CRUST ^c	J362D28	SAW24	S20A-Iso	TX2002	S20RTS	SB4_L18	Mean
rms	696	908	893	1002	860	972	849	873
correl		0.75	0.76	0.80	0.78	0.78	0.79	0.87
var. red. (%)		25	30	22	41	24	44	47

^aData and predictions (shown in Figure 17) are synthesized from spherical harmonics up to degree 20.

^bPredictions employ the tomography model indicated at the top of each column and they use the corresponding velocity–density scalings in Figure 12.

^cThe global dynamic surface topography obtained by subtracting CRUST2.0 (Bassin *et al.*, 2000) isostatic crust from the observed topography.

rms, root-mean-square amplitude, expressed here in units of m. correl, global cross-correlation; var. red., variance reduction.

for example, from undulations of the 670 km seismic discontinuity (e.g., Thoraval *et al.*, 1995; Forte and Woodward, 1997b) which internally compensate the excess surface topography.

In assessing the significance of this discrepancy, in terms of mantle dynamics, it is important to recognize

that the crustal correction employed in Figure 17(a) contains significant uncertainties which may in part be responsible for the mismatched amplitudes. Perhaps more important is the question of the validity of a purely depth-dependent velocity–density scaling (Figure 12) employed in the topography predictions.

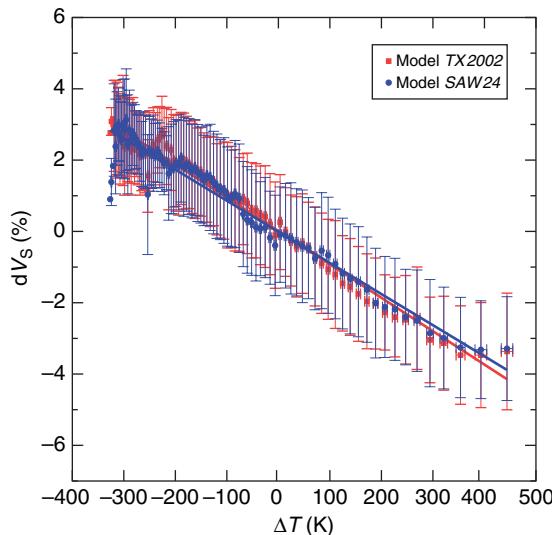


Figure 19 Comparison of seismic shear velocity and temperature anomalies in the oceanic lithosphere. Seismic shear velocity anomalies, vertically averaged in the depth interval 0–100 km, are derived from tomography models SAW24 (Mégnin and Romanowicz, 2000) and TX2002 (Grand, 2002). The S-velocity anomalies, measured relative to the global oceanic mean value, were averaged into 2 Ma age bins using the global ocean-age compilation of Müller *et al.* (1997). The age-dependent temperature variations in the oceanic lithosphere were determined using a simple halfspace cooling model with the same thermal parameters as the GDH1 plate model of Stein and Stein (1992). These temperature variations were vertically averaged down to 100 km depth and subsequently averaged into 2 Ma age bins. The temperature anomalies are measured relative to the global oceanic mean value. The vertical and horizontal error bars represent 1 standard deviation relative to the average shear-velocity and temperature, respectively, in each age bin. The solid blue and red lines are the best-fitting linear regression lines for models SAW24 and TX2002, respectively.

Such depth dependence, which may be justified if one assumes that thermal effects on mantle heterogeneity dominate (e.g., Karato and Karki, 2001), is not a good approximation in the presence of large lateral variations in chemical composition. Such compositional heterogeneity is expected to be important in the shallow subcontinental mantle and it will oppose the local thermal buoyancy, implying significant reductions in the amplitude of continental surface topography (e.g., Forte and Perry, 2000).

To understand why the gravity (and plate motion) predictions, in contrast to the surface topography, have substantially smaller amplitudes than the observed fields, we must first appreciate that the global seismic data have difficulty resolving heterogeneity in the deep mantle, particularly in the

Southern Hemisphere (e.g., Forte *et al.*, 1994; Simmons *et al.*, 2006). This difficulty does not apply to the shallow mantle where, as shown in Figure 19, the tomography models are able to successfully resolve the cooling oceanic lithosphere. The predicted surface topography is dominated by the density anomalies located in the upper mantle, whereas the gravity predictions contain significant contributions from lower-mantle density anomalies (Figure 10). Joint inversions of global seismic and convection-related data sets have shown that increased amplitudes of the predicted gravity anomalies and substantially improved fits to the global gravity data can be achieved by modifying deep-mantle heterogeneity in a way that is consistent with both the seismic and geodynamic constraints (e.g., Forte *et al.*, 1994; Simmons *et al.*, 2006). Such modifications to lower-mantle heterogeneity have little impact on the amplitude of the predicted surface topography. These basic observations suggest that current mismatches between the amplitudes of the predicted and observed dynamic topography are not more significant, or fundamentally different, from the mismatch between the other predictions (i.e., gravity and plate motions) and their corresponding observables.

1.23.3.6 Predicted CMB Topography

Tomography-based studies of the flow-induced deformations of the CMB has been rather limited (e.g., Hager *et al.*, 1985; Forte *et al.*, 1993a, 1995) relative to the much greater number of studies which have focused on the surface geoid or topography. This is in large part a consequence of the uncertain and often contrasting inferences of the CMB topography which have been derived from inversions of seismic phases which are sensitive to this topography (e.g., Morelli and Dziewonski, 1987; Rodgers and Wahr, 1993; Obayashi and Fukao, 1997; Boschi and Dziewonski, 2000; Garcia and Souriau, 2000; Sze and van der Hilst, 2003). A detailed discussion of the seismological uncertainties and difficulties in obtaining reliable global images of the CMB topography may be found in Garcia and Souriau (2000).

The most accurate constraint on the topographic undulations of the CMB are derived from space-geodetic analyses of Earth's nutations. A brief review of these constraints was presented in Section 1.23.2.1. Unfortunately, these geodetic analyses can only constrain the excess flattening or dynamic ellipticity of the CMB – albeit with high precision – and this corresponds to only one coefficient ($\ell = 2, m = 0$) in

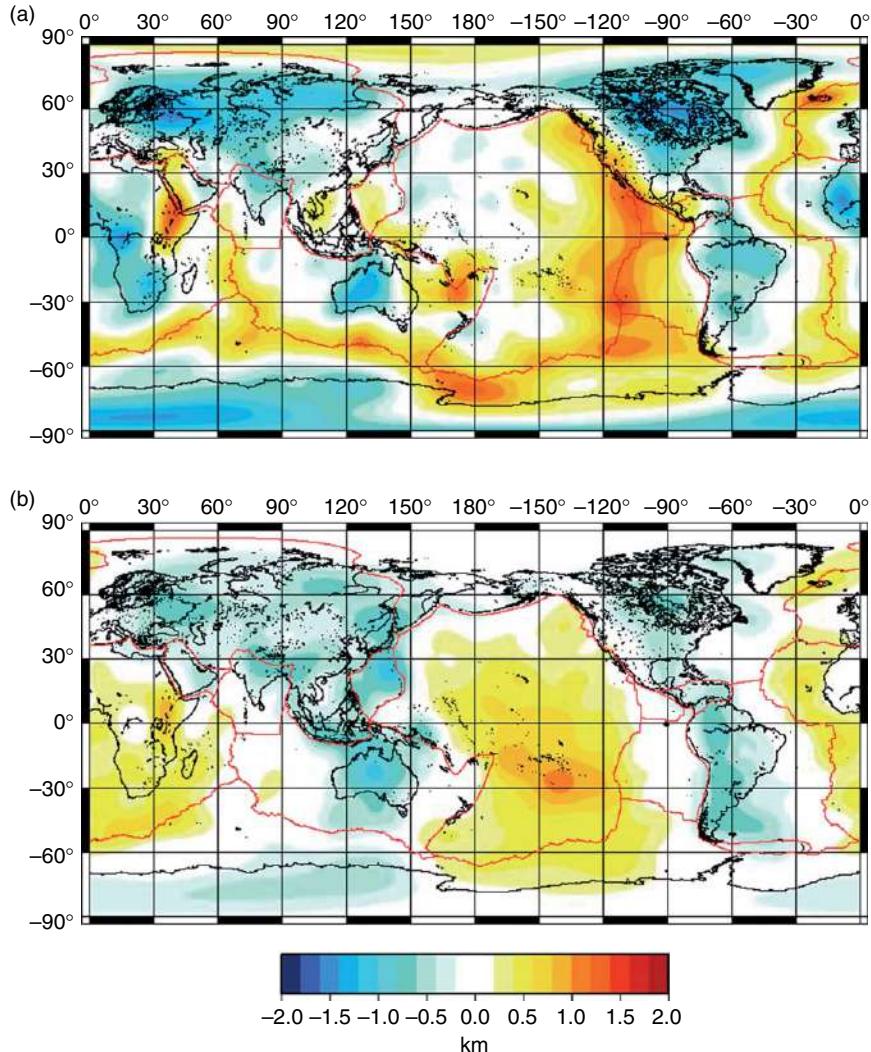


Figure 20 Shallow- versus deep-mantle contributions to surface topography. (a) Surface topography predicted on the basis of tomography-derived density anomalies in the upper 200 km of the mantle. (b) Surface topography predicted on the basis of all density anomalies below 200 km depth. In both cases, the density anomalies are derived from tomography model *TX2002* (Grand 2002) and using the corresponding $d \ln \rho / d \ln V_S$ scaling profiles in Figure 12. The summation of the topography fields in maps (a) and (b) yields the total field shown above in Figure 17(e). All fields are synthesized from spherical harmonics up to degree and order 20.

a full spherical harmonic expansion (expression [1]) of the spatially varying CMB topography field. This constraint on excess CMB flattening is included in all the Occam-inferred $d \ln \rho / d \ln V_S$ scaling profiles in Figure 12.

For the purpose of comparison, we consider a relatively recent seismic inference of the CMB topography (Figure 21(a)) obtained by Boschi and Dziewonski (2000) (henceforth referred to as BD2000) on the basis of seismic Pcp and PKP traveltimes delays. The flow-induced CMB topography predicted on the basis of the Occam-

inferred $d \ln \rho / d \ln V_S$ profiles (Figure 12), and using the kernels in Figures 10(g) and 10(h), is presented in Figure 21. All predictions of CMB topography shown here exactly reproduce the geodetically constrained 400 m excess CMB ellipticity. A quantitative spectral analysis (Figure 22) of the predicted CMB topography fields shows that they are strongly dominated by the horizontal wavelengths corresponding to harmonic degrees $\ell = 2, 3$. In Table 4 is presented a detailed summary of the match between the predicted and observed CMB topography fields.

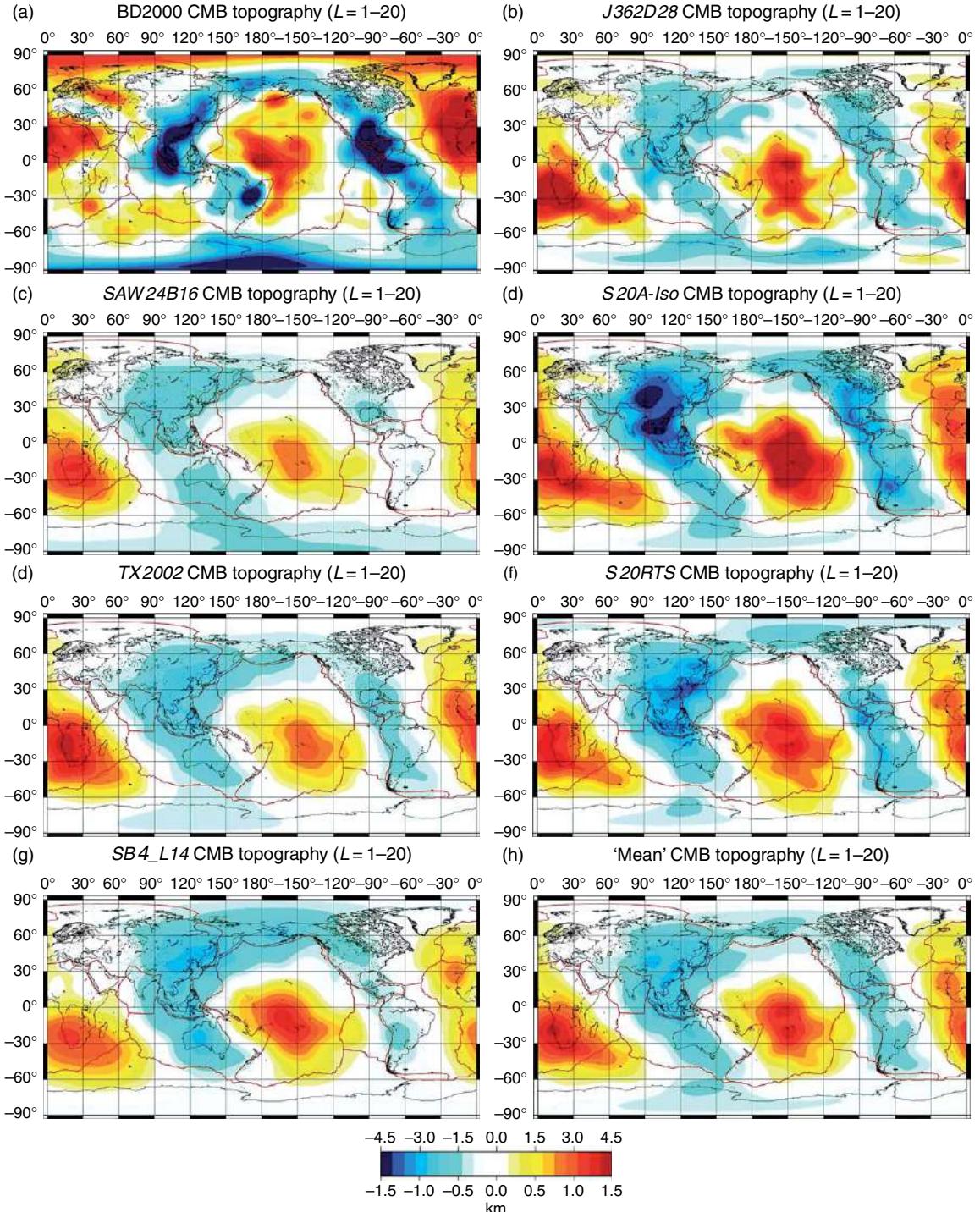


Figure 21 Tomography-based global CMB topography. (a) Seismically inferred CMB topography derived by Boschi and Dziewonski (2000). The amplitudes correspond to the top values (± 4.5 km) in the bottom scale bar. (b)–(g) The CMB topography predicted on the basis of tomography models J362D28 (Antolik *et al.*, 2003), SAW24 (Mégnin and Romanowicz, 2000), S20A-Iso (Ekström and Dziewonski, 1998), TX2002 (Grand, 2002), S20RTS (Ritsema *et al.*, 1999), SB4_L18 (Masters *et al.*, 2000), using the corresponding $d \ln \rho / d \ln V_S$ scaling profiles in Figure 12. All shear-velocity heterogeneity models have been projected onto the common parametrization in expression [102] prior to calculating the CMB topography. (h) The ‘mean’ CMB topography field obtained by calculating the statistical sample average of all the predictions (b)–(g). The amplitudes for (b)–(h) correspond to the bottom values (± 1.5 km) in the bottom scale bar. The observed and predicted CMB topography shown here are all synthesized from spherical harmonics up to degree and order 20.

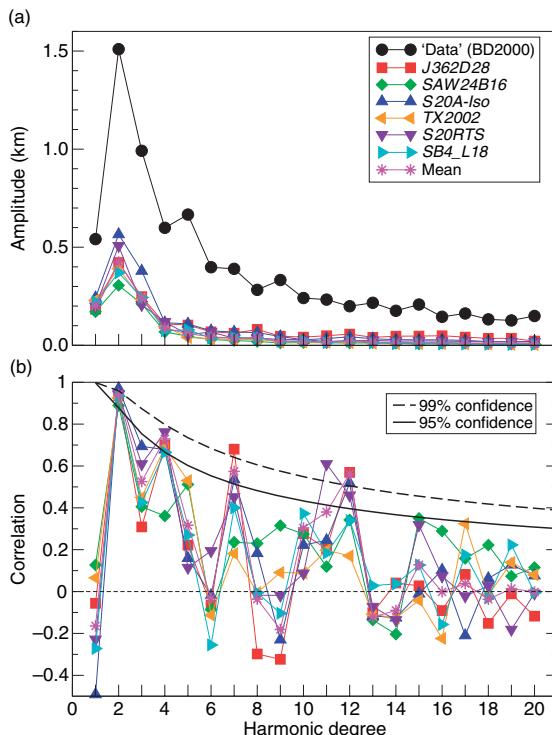


Figure 22 Spectral comparison of predicted and observed CMB topography. (a) The degree variance, as defined in eqn [3], of the observed and predicted CMB topography fields shown in Figure 19. (b) The degree correlations, as defined in eqn [4].

The overall spatial correlation between the predicted maps of flow-induced CMB topography and the BD2002 model (Figure 21) is quite good; however, it is quite clear that there is a significant difference in the overall amplitude. The CMB topography obtained on the basis of the tomography-based flow calculations is approximately a factor of 3–4 times smaller than that in BD2002. Although, as noted in Section 1.23.3.3, there likely exists an inherent damping in the flow predictions, it is not possible to increase the amplitude of the predicted

CMB topography (by increasing, for example, the magnitude of the $d \ln \rho / d \ln V_S$ scaling) without at the same time significantly degrading the fit to the other geodynamic observables. The ± 1.5 km scale undulations in the predicted, flow-induced CMB topography are in the range estimated by Garcia and Souriau (2000) for horizontal wavelengths in excess of 1200 km.

1.23.4 Tomography-Based Geodynamic Inferences of Compositional Heterogeneity

Significant lateral variations of chemical composition in the mantle are expected in view of the extensive and repeated episodes of partial melting and subsequent chemical differentiation which have acted throughout the history of our planet. The creation and growth of continental crust is obviously a major manifestation of this chemical differentiation (e.g., Taylor and McLennan, 1995) which has led to large-amplitude compositional heterogeneity in the subcontinental mantle (e.g., Jordan, 1981). In the lower mantle, it is postulated (e.g., Hofmann, 1997) that distinct reservoirs of primordial or primitive composition, which have interacted over geologic time with recycled crustal material entrained in sinking lithospheric slabs, provide an explanation for the highly variable isotopic anomalies which have been observed in ocean island basalts. These island basalts, as well as mid-ocean ridge basalts, have consistently provided evidence of large-scale chemical heterogeneity in the lower mantle (e.g., Hart, 1988).

Efforts to resolve and incorporate such large-scale compositional heterogeneity in tomography-based mantle flow models have been relatively recent (e.g., Forte *et al.*, 1995b; Forte and Perry, 2000; Pari and Peltier, 2000; Forte and Mitrovica, 2001). These modeling efforts have depended on significant

Table 4 Comparison of seismically observed^a and predicted^b CMB topography

Model	BD2000 ^c	J362D28	SAW24	S20A-Iso	TX2002	S20RTS	SB4_L18	Mean
rms	2.3	0.58	0.42	0.76	0.53	0.61	0.51	0.55
correl		0.56	0.56	0.64	0.59	0.65	0.55	0.62
var. red. (%)		22	18	31	22	27	20	24

^aSeismic observations and predictions (shown in Figure 21) are synthesized from spherical harmonics up to degree 20.

^bPredictions employ the tomography model indicated at the top of each column and they use the corresponding velocity-density scalings in Figure 12.

^cCMB topography derived by Boschi and Dziewonski (2000) from global tomographic inversion of seismic delay times.

rms, root-mean-square amplitude, expressed here in units of km. correl, global cross-correlation; var. red., variance reduction.

improvements in the resolution and reliability of global tomography models, largely driven by a major increase in the number of high-quality digital broadband seismic stations deployed worldwide. The most important advance, from the perspective of understanding compositional heterogeneity in the mantle, was the advent of joint inversions for lateral variations in seismic shear velocity $\delta V_S/V_S$ and bulk-sound or acoustic velocity $\delta V_\phi/V_\phi$ (Su and Dziewonski, 1997; Kennett *et al.*, 1998; Masters *et al.*, 2000; Antolik *et al.*, 2003). These models have revealed that the perturbations in seismic shear and bulk-sound velocity are anti-correlated in several regions in the lower mantle and, as argued by Stacey (1998), it is difficult to reconcile this anti-correlation with pure thermal heterogeneity.

1.23.4.1 Constraints from Mineral Physics

A quantitative understanding of the implications of the joint V_S-V_ϕ seismic maps in terms of compositional heterogeneity requires knowledge of the thermodynamic properties of mantle minerals. Detailed expositions of the underlying thermodynamic theory and experimental data sets may be found in numerous publications whose discussion is well beyond the scope of the work presented here and the interested reader may find the following studies to be helpful: Stacey (1998), Jackson (1998, 2001), Karato and Karki (2001), Trampert *et al.* (2001), Cammarano *et al.* (2003), Mattern *et al.* (2005), and Stixrude and Lithgow-Bertelloni (2005b). The following discussion is limited to a review of the mineral physics results most relevant to the tomography-based inferences of mantle chemical heterogeneity presented below.

In principle, tomography-based inferences of thermal and compositional anomalies can be derived on the basis of temperature and compositional derivatives of density and seismic velocity, assuming a particular background (i.e., reference) composition and temperature for the mantle. A previous analysis by Forte and Mitrovica (2001), henceforth referred to as FM2001, modeled the lower mantle in terms of three components: MgO, FeO, and SiO₂, assuming a pyrolite composition for the mantle. This is a simplification which ignores the possible importance of less abundant constituents such as CaSiO₃ perovskite (about 5% molar abundance) and solid solution of alumina (Al₂O₃) in ferromagnesium perovskite. Recent studies have suggested these minor components can have a non-negligible effect on density and seismic-wave velocity (e.g., Jackson, 2001), such that

Ca-perovskite increases the shear velocity (Stixrude and Lithgow-Bertelloni, 2005b) and Al-perovskite decreases the shear velocity (Jackson, 2005). Recent efforts to constrain the composition and temperature of the mantle using all five components (MgO–FeO–CaO–Al₂O₃–SiO₂) have revealed considerable non-uniqueness and large tradeoffs (Mattern *et al.*, 2005). Therefore, for the purpose of this discussion, a simplified three-component (MgO–FeO–SiO₂) mantle model will again be assumed.

The perturbations in density and seismic velocity produced by temperature T and compositional anomalies are modeled as follows:

$$\delta \ln M = \frac{\partial \ln M}{\partial T} \delta T + \frac{\partial \ln M}{\partial X_{\text{Fe}}} \delta X_{\text{Fe}} + \frac{\partial \ln M}{\partial X_{\text{Pv}}} \delta X_{\text{Pv}} \quad [109]$$

where M is a generic variable used to denote either density ρ , or shear velocity V_S , or bulk-sound velocity V_ϕ . Following FM2001, the compositional anomalies are parametrized in terms of perturbations in the molar fraction of iron, $X_{\text{Fe}} = [\text{FeO}] / ([\text{FeO}] + [\text{MgO}])$, and the molar fraction of perovskite, $X_{\text{Pv}} = [\text{Pv}] / ([\text{Pv}] + [\text{Mw}])$. The molar fraction of perovskite is equivalent to the silica ratio: $X_{\text{Pv}} = [\text{SiO}_2] / ([\text{FeO}] + [\text{MgO}])$.

Estimates of the thermal and compositional derivatives which are required in expression [109] have been estimated by a number of authors, using different assumptions and methods, and a summary of some of these results is presented in Table 5. The differences between the various estimates presented in this table show that the uncertainties in these derivatives are significant. The most recent determinations by Stixrude and Lithgow-Bertelloni (2005b) also include formal estimates of uncertainties and they are of the same order as the differences in the Table 5. These uncertainties should be borne in mind when considering inferences of thermochemical heterogeneity in the mantle.

FM2001 assembled the three equations described by expression [109], involving ρ , V_S , and V_ϕ , into the following linear system:

$$\begin{pmatrix} \delta \ln V_S \\ \delta \ln V_\phi \\ \delta \ln \rho \end{pmatrix} = \begin{pmatrix} c_{11} & c_{12} & c_{13} \\ c_{21} & c_{22} & c_{23} \\ c_{31} & c_{32} & c_{33} \end{pmatrix} \begin{pmatrix} \delta T \\ \delta X_{\text{Pv}} \\ \delta X_{\text{Fe}} \end{pmatrix} \quad [110]$$

in which the matrix elements c_{ij} are the thermal or compositional derivatives involved in expression [109].

To extract the maximum possible information from the joint V_S-V_ϕ tomography models, FM2001 introduced the concept of effective thermal and

Table 5 Thermal and compositional derivatives

Elastic property	Thermal $-10^5 \times \partial/\partial T(K^{-1})$		Compositional	
	Anharmonic	Anelastic	$10 \times \partial/\partial X_{Fe}$	$100 \times \partial/\partial X_{Pv}$
<i>Depth = 1970 km (85 GPa)</i>				
$\ln \rho$	1.3[1.2](1.3){1.4}		+3.2[+3.0]	+1.1[+2.8]
$\ln V_S$	5.0[4.4](4.7){3.9}{3.5}	2.5	-2.2[-2.5]{-1.7}	+4.9[+3.5]
$\ln V_\phi$	0.8[1.5](0.6){0.9}	0	-1.6[-1.5]	+5.5[+3.4]
<i>Depth = 2740 km (127 GPa)</i>				
$\ln \rho$	1.0[0.8](1.1)		+3.2[+3.0]	+0.4[+2.2]
$\ln V_S$	4.7[4.0](4.1){2.9}	2.4	-2.2[-2.5]{-1.4}	+4.5[+1.9]
$\ln V_\phi$	0.7[1.2](0.4)	0	-1.6[-1.5]	+4.8[+2.0]

All values not enclosed by brackets have been obtained using the approximations and data described in detail by Forte and Mitrovica (2001). Values enclosed in square brackets have been obtained on the basis of the finite-strain and thermoelastic calculations carried out by Forte *et al.* (2002). Round brackets (parentheses) enclose values estimated by Stacey (1998), while the curly brackets enclose the determinations obtained by Oganov *et al.* (2001b). Values enclosed in angular brackets are obtained on the basis of results for perovskite in Stixrude and Lithgow-Bertelloni (2005b).

compositional anomalies, δT_{eff} and δX_{eff} , defined as follows:

$$\delta T_{eff} \equiv \delta T + \frac{c_{12}c_{23} - c_{13}c_{22}}{c_{12}c_{21} - c_{11}c_{22}} \delta X_{Fe} \quad [111]$$

$$\delta X_{eff} \equiv \delta X_{Pv} + \frac{c_{21}c_{13} - c_{11}c_{23}}{c_{12}c_{21} - c_{11}c_{22}} \delta X_{Fe} \quad [112]$$

On the basis of these effective anomalies, the linear system [110] can be reduced to the following simpler 2×2 matrix equation:

$$\begin{pmatrix} \delta \ln V_S \\ \delta \ln V_\phi \end{pmatrix} = \begin{pmatrix} c_{11} & c_{12} \\ c_{21} & c_{22} \end{pmatrix} \begin{pmatrix} \delta T_{eff} \\ \delta X_{eff} \end{pmatrix} \quad [113]$$

which is supplemented by the following relation, describing the dependence of density anomalies on effective thermal and compositional anomalies and on iron anomalies:

$$\delta \ln \rho = c_{31} \delta T_{eff} + c_{32} \delta X_{eff} - \frac{\Lambda}{c_{12}c_{21} - c_{11}c_{22}} \delta X_{Fe} \quad [114]$$

in which Λ is the determinant of the matrix in eqn [110]. The utility in working with effective thermal and compositional anomalies is that the linear system [113] may be simply inverted, thereby providing a means for directly distilling joint shear/bulk-sound tomography models into maps of mantle thermochemical structure.

FM2001 found that the effective compositional heterogeneity δX_{eff} is strongly correlated to the bulk-sound velocity anomalies. This may be understood by inverting system (113), using the FM2001 derivatives in Table 5, which yields

$$\delta X_{eff} = -2.3 \delta \ln V_S + 23.0 \delta \ln V_\phi \quad [115]$$

This expression shows that δV_ϕ provides the dominant contribution to δX_{eff} . The dominant compositional signature of the bulk-sound velocity anomalies is traced to the relatively weak temperature sensitivity of bulk-sound velocity compared to shear velocity (Table 5). This implies that bulk-sound velocity should be especially sensitive to any chemical anomalies in the mantle.

In contrast, FM2001 found that the effective thermal anomalies δT_{eff} are strongly correlated to shear velocity anomalies. This may be understood by inverting system [113]:

$$\delta T_{eff} = (-15.5 \delta \ln V_S + 14.5 \delta \ln V_\phi) \times 10^3 \quad [116]$$

in which the FM2001 derivatives in Table 5 were used. As will be shown below, the amplitude of the lower-mantle δV_ϕ anomalies is substantially less than that of the δV_S anomalies. This then leads to the prevailing correlation between δV_S and δT_{eff} in the deep mantle, as might have been expected by consideration of the contrasting temperature sensitivities of V_S and V_ϕ (see Table 5).

Although joint bulk-sound/shear tomography models provide very useful maps of effective temperature and compositional anomalies, they do not provide sufficient information for separating the respective contributions to these effective parameters from temperature, iron, and perovskite (or equivalent silica) variations (expressions [111] and [112]). This separation requires additional independent constraints which can be obtained from geodynamically inferred density anomalies.

Previous efforts to constrain lower-mantle density anomalies with tomography-based geodynamic

models (e.g., Forte and Mitrovica, 2001) assumed a purely depth-dependent variation in $d \ln \rho / d \ln V_S$. As discussed in Section 1.23.3.5, this assumption may not be a good approximation if the lateral variations in mantle composition are sufficiently large. In the next two sections, we therefore consider two approaches which allow lateral variations in the effective $d \ln \rho / d \ln V_S$ throughout the mantle.

1.23.4.2 Compositional Density Anomalies Inferred from Joint Shear- and Bulk-Sound Tomography

As noted above, the effective compositional heterogeneity in the lower mantle is correlated to the bulk-sound velocity anomalies whereas seismic shear velocity anomalies provide a reliable mapping of lateral temperature variations, even in the presence of compositional heterogeneity. We can use these findings to motivate the following heuristic representation for mantle density anomalies which incorporates both thermal and chemical contributions:

$$\frac{\delta \rho}{\rho} = \left(\frac{d \ln \rho}{d \ln V_S} \right) \frac{\delta V_S}{V_S} + \left(\frac{d \ln \rho}{d \ln V_\phi} \right) \frac{\delta V_\phi}{V_\phi} \quad [117]$$

in which the first term on the right, involving $\delta V_S / V_S$, effectively represents the thermal contribution to mantle heterogeneity while the second term ($\delta V_\phi / V_\phi$) represents the effective compositional heterogeneity. An important feature of expression [117] is that the relationship between density anomalies and seismic shear/bulk anomalies will vary horizontally because the seismic anomalies $\delta V_S / V_S$ and $\delta V_\phi / V_\phi$ will not necessarily be correlated in the mantle.

Here we consider the joint $V_S - V_\phi$ tomography model *SB10_L18* of Masters *et al.* (2000) and model *J362D28* of Antolik *et al.* (2003). A quantitative summary of the rms amplitudes and spatial correlations of these models is presented in Figure 23. We first note that the amplitudes of both shear and bulk-sound velocity anomalies agree fairly well across the mantle, with the exception of the transition-zone region (where the shear velocity anomalies in model *J362D28* are much larger) and the shallow mantle (where the bulk sound velocity anomalies in model *SB10_L18* are much larger). While the shear-velocity anomalies in models *J362D28* and *SB10_L18* are fairly well correlated, the bulk-sound velocity anomalies show very little correlation and this underlines the difficulty in adequately resolving V_ϕ anomalies in the mantle. Model *J362D28* shows a

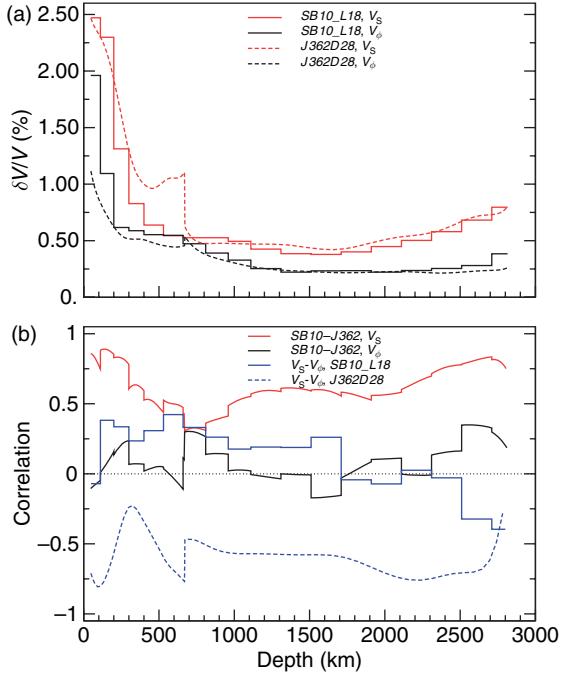


Figure 23 Seismic shear and bulk sound velocity anomalies in the mantle. (a) The depth variation of the rms amplitudes of the relative perturbations of seismic shear velocity ($\delta V_S / V_S$) (red lines) and bulk-sound velocity ($\delta V_\phi / V_\phi$) (black lines) in models *SB10_L18* of Masters *et al.* (2000) and *J362D28* of Antolik *et al.* (2003) are plotted as solid and dashed lines, respectively. (b) The global cross-correlation between the shear-velocity anomalies in models *SB10_L18* and *J362D28* are plotted as a red solid line and for the bulk-sound velocity anomalies it is plotted as a black solid line. The global cross-correlation between $\delta V_S / V_S$ and $\delta V_\phi / V_\phi$ in model *SB10_L18* is plotted as a blue solid line and for model *J362D28* it is plotted as a blue dashed line.

significant anti-correlation between $\delta V_S / V_S$ and $\delta V_\phi / V_\phi$ throughout the mantle, whereas model *SB10_L18* shows such an anti-correlation only in the lowermost mantle.

The density anomalies in expression [117] may again be determined (as in Section 1.23.3.2) by directly inverting the geodynamic observables (Figure 2). Substitution of expression [117] in eqn [104] yields

$$\begin{aligned} \delta O_\ell^m = & f_\ell \sum_{i=1}^N w_i K_\ell(\eta_i, r_i) \rho_o(r_i) \\ & \times \left[\left(\frac{\delta V_S}{V_S} \right)_\ell^{(m)}(r_i) \left(\frac{d \ln \rho}{d \ln V_S} \right)(r_i) \right. \\ & \left. + \left(\frac{\delta V_\phi}{V_\phi} \right)_\ell^{(m)}(r_i) \left(\frac{d \ln \rho}{d \ln V_S} \right)(r_i) \right] \end{aligned} \quad [118]$$

in which the scaling profiles $d \ln \rho / d \ln V_S$ and $d \ln \rho / d \ln V_\phi$ are assumed to vary with depth in

the mantle. The radial viscosity profile employed to calculate the kernel functions $K_\ell(\eta; r)$ was derived from an inversion based on the mantle heterogeneity in model *SB10_L18* (see dash-dotted profile in **Figure 9**).

Occam inversions of expression [118] were then carried out to determine optimally smooth scaling profiles which fit the geodynamic constraints and the results are summarized in **Figure 24**. The inferred mantle density anomalies (**Figure 24(b)**) are very similar in amplitude to those determined above on the basis of the seismic shear-velocity models (**Figure 12**). The major difference is in the mid-mantle region, near 1500 km depth, where we now note that the inferred density anomalies are negatively correlated with the seismic shear-velocity anomalies

(**Figure 24(c)**). Such an anti-correlation cannot be interpreted on the basis of pure thermal effects (see the Karato & Karki scaling profiles in **Figure 12** which are positive throughout the lower mantle) and suggest the presence of significant compositional heterogeneity in this region of the lower mantle. A closer inspection of the previous results obtained with the seismic shear-velocity models (**Figure 12**) also reveals a distinct inflection in the Occam-inferred $d \ln \rho / d \ln V_s$ scaling profiles near 1500 km depth.

The fits between the geodynamic data (**Figures 2** and **21(a)**) and the geodynamic observables predicted on the basis of the Occam-inferred density anomalies (**Figure 24**) are summarized in **Table 6**. A comparison of these fits with those obtained previously for models *J362D28* and *SB4_L18* (**Tables 1–4**) shows that, for model *J362D28*, there is little improvement obtained by allowing for lateral variations in velocity-density scaling as parametrized by expression [117]. In the case of model *SB10_L18*, however, there is a significant improvement in fit to all the surface observables, suggesting that the lateral variations in composition implied by expression [117] are supported by the geodynamic data.

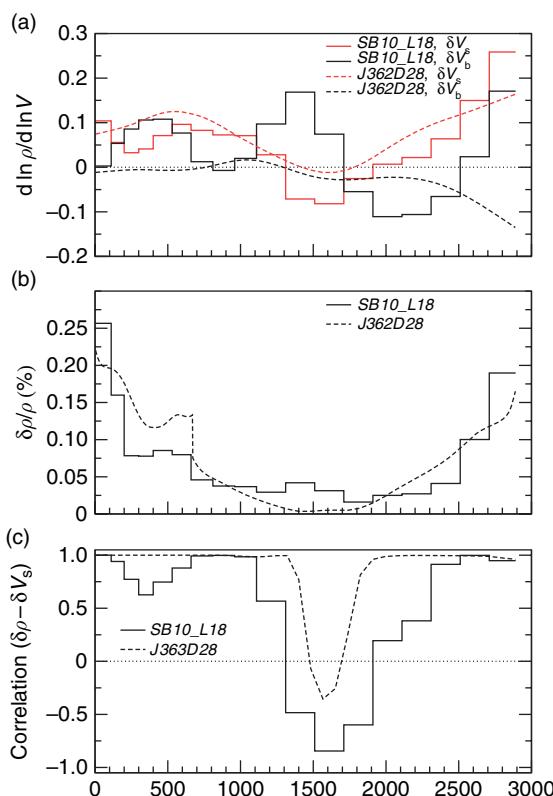


Figure 24 Joint shear-bulk-sound inversions for mantle density anomalies. (a) The optimal Occam-inferred velocity-density scaling profiles for the seismic shear (red lines) and bulk-sound (black lines) anomalies in models *SB10_L18* (solid lines) and *J362D28* (dashed lines). (b) The rms amplitude of the density anomalies, determined on the basis of expression [117] in the main text, for models *SB10_L18* (solid lines) and *J362D28* (dashed lines). (c) The global cross-correlation between the inferred density anomalies and the seismic shear-velocity anomalies in models *SB10_L18* (solid lines) and *J362D28* (dashed lines).

1.23.4.3 Compositional Density Anomalies Inferred from ‘Hot’ and ‘Cold’ Mantle Heterogeneity

Previous interpretations and dynamical models of the large-scale low-velocity anomalies below the central Pacific and below southern Africa (see **Figure 3(b)**) have identified them as ‘megaplumes’ in the convecting mantle, in which the temperatures are significantly hotter than average mantle and in which the chemical composition may also differ from the overlying mantle (e.g., Becker *et al.*, 1999; Kellogg *et al.*, 1999; Davaille, 1999; Forte and Mitrovica, 2001; Forte *et al.*, 2002; Jellinek and Manga, 2004). These deep-mantle ‘megaplumes’ may be the source regions for the isotopic anomalies which have long been identified in basalts extracted from the Indian and Pacific Oceans (e.g., Hart, 1988; Hofmann, 1997). The hot upwelling plumes in the mantle may therefore have an average chemical composition which differs from that of cold downwellings driven by the descent of dense lithospheric slabs (blue-colored region in **Figure 3(b)**).

We may test the hypothesis of chemically distinct hotter- and colder-than-average regions by parametrizing the mantle density anomalies as follows:

Table 6 Geodynamic predictions from joint V_S/V_ϕ and ‘hot’/‘cold’ heterogeneity models

Model	Gravity			Surf. topography			Horiz. divergence			CMB topography		
	rms	cor.	fit (%)	rms	cor.	fit (%)	rms	cor.	fit (%)	rms	cor.	fit (%)
J362D28 ($\delta V_{S/\phi}$)	10.4	0.55	28	905	0.75	26	1.3	0.78	51	0.58	0.53	20
SB10_L18 ($\delta V_{S/\phi}$)	8.6	0.55	30	803	0.79	48	1.5	0.81	58	0.39	0.37	10
TX2002 ($\delta V_{h/c}$)	11.2	0.70	48	753	0.79	54	1.5	0.84	61	0.53	0.52	19
SAW24 ($\delta V_{h/c}$)	11.6	0.64	39	877	0.75	30	1.4	0.75	51	0.52	0.35	11

rms, root-mean-square amplitude, expressed in units of mGal, m, 10^{-8}a^{-1} , and km for free-air gravity, dynamic surface topography, horizontal divergence, and CMB topography, respectively. cor., global cross-correlation; fit, variance reduction.

$$\frac{\delta\rho}{\rho} = \left(\frac{d \ln \rho}{d \ln V_S} \right)_h \left(\frac{\delta V_S}{V_S} \right)_h + \left(\frac{d \ln \rho}{d \ln V_S} \right)_c \left(\frac{\delta V_S}{V_S} \right)_c \quad [119]$$

in which $(\delta V_S/V_S)_h$ (where subscript ‘h’ denotes ‘hot’) represents the regions of the mantle characterized by negative shear-velocity anomalies and presumably hotter-than-average temperatures. Similarly, $(\delta V_S/V_S)_c$ (where subscript ‘c’ denotes ‘cold’) represents regions of positive velocity anomalies with presumably colder temperatures. By associating different velocity–density scalings to the ‘hot’ and ‘cold’ regions, expression [119] incorporates a laterally variable $d \ln \rho/d \ln V_S$ profile in the mantle.

In the following calculations, we employ the shear-tomography models TX2002 (Grand, 2002) and SAW24 (Mégnin and Romanowicz, 2000). For each model, a spatial separation of the seismic anomalies into faster- (colder-) and slower- (hotter-) than-average regions was carried out and a summary of the rms amplitudes of these anomalies is presented in Figure 25. In both tomography models, we note that the amplitude of the ‘hot’ anomalies is dominant in the lower half of the mantle (below 1500 km depth).

Geodynamic constraints on mantle density anomalies are determined, as in Sections 1.23.3.2 and 1.23.4.2, by substituting expression [119] into eqn [104], thereby yielding

$$\begin{aligned} \delta O_\ell^m = f_\ell \sum_{i=1}^N w_i K_\ell(\eta; r_i) \rho_o(r_i) \\ \times \left[\left(\frac{\delta V_S}{V_S} \right)_h(r_i) \left(\frac{d \ln \rho}{d \ln V_S} \right)_h(r_i) \right. \\ \left. + \left(\frac{\delta V_S}{V_S} \right)_c(r_i) \left(\frac{d \ln \rho}{d \ln V_S} \right)_c(r_i) \right]^\ell \end{aligned} \quad [120]$$

The kernel functions $K_\ell(\eta; r)$ and the associated viscosity profile in this expression are shown in Figure 10. The optimally smooth density–velocity scaling profiles for the ‘hot’, $(\delta V_S/V_S)_h$, and ‘cold’, $(\delta V_S/V_S)_c$, mantle heterogeneity are obtained through an Occam inversion of all geodynamic

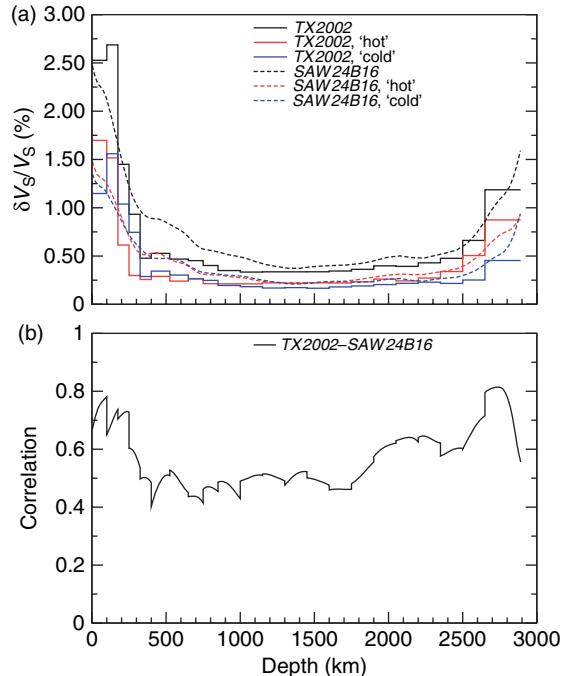


Figure 25 ‘Hot’ and ‘cold’ heterogeneity in the mantle. (a) The depth variation of the rms amplitudes of the relative perturbations of seismic shear velocity ($\delta V_S/V_S$) in models TX2002 (Grand 2002) and SAW24 (Mégnin and Romanowicz 2000) are shown as solid black and dashed black lines, respectively. The rms amplitude of the ‘hot’/‘cold’ heterogeneity in these models (defined as regions where $\delta V_S/V_S < 0/ > 0$) is shown by the solid and dashed red/blue lines (see legend). (b) The global cross-correlation between the shear-velocity anomalies in models TX2002 and SAW24.

observables in Figure 2 and the results are summarized in Figure 26. For reference and comparison, an inversion was carried out in which no distinction was made between the ‘hot’ and ‘cold’ regions, and the results are also presented in Figure 26.

The inverted density–velocity scaling profiles (Figure 26) present a number of interesting features which provide indications of compositional heterogeneity in different depth intervals. In the top 300 km of the

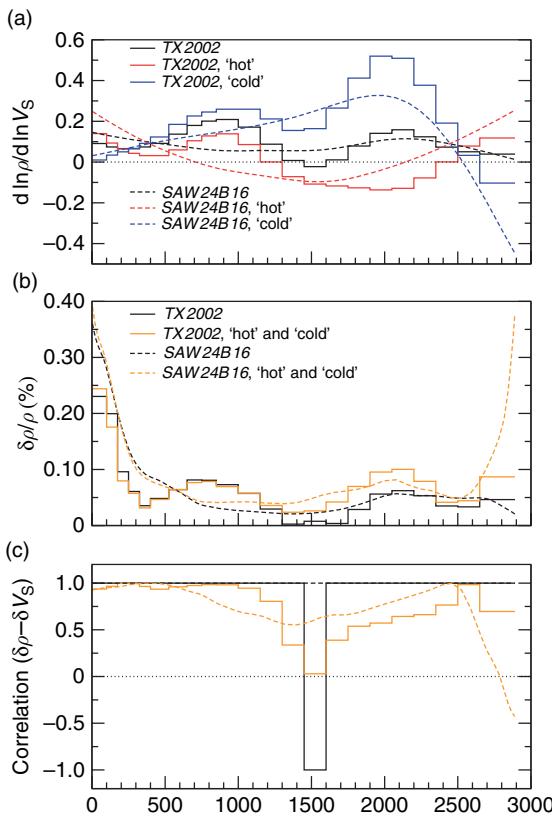


Figure 26 Inversions for ‘hot’ and ‘cold’ mantle density anomalies. (a) The Occam-inferred velocity–density scaling profiles for the ‘hot’/‘cold’ regions of the mantle (as defined in the text and in **Figure 25**) in models TX2002 (Grand, 2002) and SAW24 (Mégnin and Romanowicz, 2000) are shown as red/blue solid and dashed lines, respectively (see legend). The velocity–density scaling profiles which are inferred if no distinction is made between the ‘hot’/‘cold’ regions are shown as black solid and dashed lines for models TX2002 and SAW24, respectively. (b) The rms amplitude of the mantle density anomalies, calculated on the basis of expression [119] and the scaling profiles in the top frame, are shown for both models TX2002 and SAW24 as the solid and dashed orange lines, respectively. The amplitude of the density anomalies which is inferred if no distinction is made between ‘hot’/‘cold’ regions are shown as black (solid and dashed) lines. (c) The global cross-correlation between the inferred density anomalies and the seismic shear-velocity anomalies in models TX2002 and SAW24 are shown by the solid and dashed orange lines, respectively. When no distinction is made between ‘hot’/‘cold’ regions, the correlations are shown by the black solid and dashed lines (see legend in (b)).

mantle, the scaling coefficient for the ‘cold’ anomalies is significantly smaller than for the ‘hot’ anomalies and in the top 100 km it is nearly zero. The ‘cold’ anomalies in this depth range are essentially associated with the subcontinental roots and therefore we have another confirmation of previous geodynamic studies (e.g.,

Forte and Perry, 2000) which revealed a mutual cancellation of the thermal and compositional contributions to mantle density below continents. In the lower mantle, the scaling coefficient for the ‘cold’ anomalies is significantly greater than for the ‘hot’ anomalies, where the scaling for the latter actually goes to negative values throughout the mid lower mantle. This inference suggests large amounts of compositional heterogeneity in the lower-mantle ‘megaplumes’ below the Pacific Ocean and below southern Africa. The lower-mantle trend is reversed in the deepest portions of the lower mantle (e.g., in the D” layer), where we again find that the scaling for the ‘hot’ regions is larger than for the ‘cold’ regions.

A consideration of the cross-correlation between the inferred mantle density anomalies and the seismic shear-velocity anomalies (**Figure 26**) also shows anomalous mid-mantle and deep lower-mantle regions, where the correlations decrease significantly. These decreased correlations explain the inflections in the previously inferred $d \ln \rho / d \ln V_S$ scaling profiles (**Figure 12**) in the mid- and deep lower mantle. These decorrelations between mantle density and seismic shear-velocity anomalies suggests that thermal contributions are not the sole source of density heterogeneity in these regions and there is a likelihood for significant composition heterogeneity in these portions of the lower mantle. Indeed, a consideration of the fits to the geodynamic data summarized in **Table 6** shows a distinct improvement compared to that obtained previously (**Tables 1–4**).

1.23.4.4 Diffuse Mid-Mantle Compositional Horizon

As discussed in the preceding two sections, there appears to be a significant deviation from purely thermal control of mantle heterogeneity in a region of the mid-mantle near 1500 km depth. This was already evident in **Figure 12**, where the geodynamically inferred values of $d \ln \rho / d \ln V_S$ in the mid-mantle differ substantially from those inferred by Karato and Karki (2001) on the basis of mineral physics data and assuming that temperature variations are the dominant contributor. The subsequent geodynamic inversions which allowed lateral variations in $d \ln \rho / d \ln V_S$ (**Figures 24** and **26**) further underlined the anomalous thermochemical behavior of the mid-mantle region.

Hints of the anomalous properties of the mid-mantle region from geodynamic models can also be gleaned from previously published comparisons between subducted slab heterogeneity and seismic

tomography models. For example, Lithgow-Bertelloni and Richards (1998, see their figure 7) found that the lowest correlations between slab heterogeneity and seismically inferred heterogeneity in the lower mantle occurred near 1500 km and that the longest wavelength components of these two fields were anti-correlated at this depth. These authors suggested that these poor correlations could be attributed to insufficient resolution of the global tomography models at these depths. An alternative explanation, if the slabs are viewed as a proxy for thermal heterogeneity, is that the low slab-tomography correlations in the mid-mantle region are a diagnostic for significant compositional heterogeneity at these depths.

There have been a number of seismological, geodynamic, and geochemical arguments for the presence of a mid-mantle boundary or interface which segregates a presumably stagnant, intrinsically heavy layer in the bottom half of the lower mantle from the convective flow in the overlying mantle (e.g., Hofmann, 1997; Kellogg *et al.*, 1999; Davaille, 1999). More recently, theoretical and experimental advances in mineral physics have also identified an anomalous region in the mid-mantle (e.g., Badro *et al.*, 2003) and evidence for distinct differences between the elastic and thermodynamic properties in the deep lower mantle, below 1400 km depth, compared to the top of the lower mantle (e.g., Wentzcovich *et al.*, 2004).

The geodynamic inversions presented above show that ‘normal’, thermally dominated buoyancy seems to prevail in regions sufficiently far above and below the anomalous mid-mantle region near 1500 km depth. Recent joint seismic–geodynamic inversions (Simmons *et al.*, 2006) have directly tested the hypothesis of a sharp chemical interface at 1800 km depth which inhibits vertical flow across the lower mantle. The fits to the geodynamic data were found to be significantly degraded and this appears to rule out a sharply defined compositional boundary in the lower mantle. These seismic–geodynamic inversions do not, however, rule out the possibility of a diffuse, compositional (or phase-change) horizon at this depth which may have significant vertical undulations, perhaps over distances of a few hundred kilometers, in order to explain the depth interval over which the anomalous values of $d \ln \rho / d \ln V_s$ are inferred (Figures 12, 24, and 26). The verification of this hypothesis will require further investigation, with the greatest insights provided by an integrated approach based on combined seismic,

geodynamic, and mineral physical modelling. Recent progress in this direction has been made by Simmons *et al.* (2007).

1.23.5 Concluding Remarks

The current global-scale seismic tomography models have been shown to provide good fits to a wide variety of surface geodynamic observables related to mantle convection. These results suggest that global tomography does indeed provide reliable images of the lateral variations in mantle structure which are produced by the thermal convection process in Earth’s mantle. The tabulated summaries of the results (Tables 1–6) show however that the fits can still be improved and this raises the fundamental question as to what aspects of the global tomography models, or indeed the mantle flow calculations, may be deficient or inadequate.

From the perspective of the mantle flow theory, there is a major issue concerning the possible dynamical importance of lateral variations in mantle viscosity which have not been explicitly modeled in the calculations presented above. It is important to recall that the mantle flow calculations include a coupling to rigid tectonic plates at the surface and that the motions of these plates are predicted on the basis of the buoyancy induced flow in the mantle. The surface plates are likely the most important manifestation of lateral rheology variations in the Earth and hence their inclusion in mantle flow modeling is essential. However, the flow model employed here assumes a 1-D radial variation of viscosity in the mantle and the question then arises as to the importance of neglecting lateral viscosity variations (LVVs) in the deep mantle. Detailed modeling of the potential bias which may be due to large-scale LVV, estimated on the basis of global tomography models, has recently been carried out by Moucha *et al.* (2007). One of the main conclusions of this recent study is that the impact of large scale LVV on convection-related observables is no larger than the uncertainties arising from differences among the recent tomography models. This relative insensitivity to LVV may well explain why the current tomography-based viscous flow models, which assumes a purely depth-dependent mantle viscosity, can yield such a good match to a wide range of convection data.

Simultaneous inversions of global seismic and geodynamic data (e.g., Forte *et al.*, 1994; Forte and Woodward, 1997; Simmons *et al.*, 2006) have shown

that it is possible to obtain greatly improved fits to the global convection-related data using the mantle flow theory which was presented above. The improved fits are found to be the result of relatively small adjustments (mainly in amplitude) to the seismically inferred heterogeneity in the mantle, especially the mid-mantle region, which are also compatible with the constraints imposed by the geodynamic data. These joint seismic–geodynamic inversions therefore support the basic conclusion of this study, namely that seismic tomography and geodynamics can be reconciled with the large-scale heterogeneity in the mantle that is clearly generated by the mantle convection process.

Acknowledgments

This work is supported by grants from the Canadian National Science and Engineering Research Council and the Canada Research Chair Program. Support provided by the Canadian Institute for Advanced Research – Earth Systems Evolution Program is also gratefully acknowledged.

References

- Antolik M, Gu Yu J, Ekström G, and Dziewonski AM (2003) J362D28; a new joint model of compressional and shear velocity in the Earth's mantle. *Geophysical Journal International* 153: 443–466.
- Badro J, Fiquet G, Guyot F, et al. (2003) Iron partitioning in Earth's mantle: Toward a deep lower mantle discontinuity. *Science* 300: 789–791.
- Bassin C, Laske G, and Masters G (2000) The current limits of resolution for surface wave tomography in North America. *Eos Transactions of the American Geophysical Union* 81(48): 897.
- Becker TW and Boschi L (2002) A comparison of tomographic and geodynamic mantle models. *Geochemistry Geophysics Geosystems* 3, doi:10.129/2001GC000168.
- Becker TW, Kellogg JB, and O'Connell RJ (1999) Thermal constraints on the survival of primitive blobs in the lower mantle. *Earth and Planetary Science Letters* 171: 351–365.
- Boschi L and Dziewonski AM (2000) Whole Earth tomography from delay times of P, P_cP, and PKP phases: Lateral heterogeneities in the outer core or radial anisotropy in the mantle? *Journal of Geophysical Research* 105: 13675–13696.
- Bunge H-P, Richards MA, and Baumgardner JR (1996) Effect of depth-dependent viscosity on the planform of mantle convection. *Nature* 379: 436–438.
- Bunge H-P, Richards MA, Lithgow-Bertelloni C, Baumgardner JR, Grand SP, and Romanowicz BA (1998) Time scales and heterogeneous structure in geodynamic Earth models. *Science* 280: 91–95.
- Čadek O and Fleitout L (2003) Effect of lateral viscosity variations in the top 300 km on the geoid and dynamic topography. *Geophysical Journal International* 152: 566–580.
- Čadek O, Yuen DA, Steinbach V, Chopelas A, and Matyska C (1994) Lower mantle thermal structure deduced from seismic tomography, mineral physics and numerical modelling. *Earth and Planetary Science Letters* 121: 385–402.
- Cammarano F, Goes S, Vacher P, and Giardini D (2003) Inferring upper-mantle temperatures from seismic velocities. *Physics of the Earth and Planetary Interiors* 138: 197–222.
- Cathles LM (1975) *The Viscosity of the Earth's Mantle*, Princeton: Princeton University Press.
- Chase CG (1979) Subduction, the geoid, and lower mantle convection. *Nature* 282: 464–468.
- Chase CG and Sprowl DR (1983) The modern geoid and ancient plate boundaries. *Earth and Planetary Science Letters* 62: 314–320.
- Clayton RW and Comer RP (1983) A tomographic analysis of mantle heterogeneities from body wave travel times. *Eos Transactions of the American Geophysical Union* 64(45): 776.
- Constable SC, Parker RL, and Constable CG (1987) Occam's inversion: A practical algorithm for generating smooth models from electromagnetic sounding data. *Geophysics* 52: 289–300.
- Corrieu V, Ricard Y, and Froidevaux C (1994) Converting mantle tomography into mass anomalies to predict the Earth's radial viscosity. *Physics of the Earth and Planetary Interiors* 84: 3–13.
- Corrieu V, Thoraval C, and Ricard Y (1995) Mantle dynamics and geoid Green functions. *Geophysical Journal International* 120: 516–523.
- Crosby AG, McKenzie D, and Sclater JG (2006) The relationship between depth, age and gravity in the oceans. *Geophysical Journal International* 166: 553–573.
- Davaille A (1999) Simultaneous generation of hotspots and superswells by convection in a heterogeneous planetary mantle. *Nature* 399: 756–760.
- De Mets CR, Gordon RG, Argus DF, and Stein S (1990) Current plate motions. *Physics of the Earth and Planetary Interiors* 101: 425–478.
- Defraigne P (1997) Internal loading of a compressible Earth: Effect of a solid lithosphere. *Physics of the Earth and Planetary Interiors* 101: 303–313.
- Deschamps F, Snieder R, and Trampert J (2001) The relative density-to-shear velocity scaling in the uppermost mantle. *Physics of the Earth and Planetary Interiors* 124: 193–212.
- Doin M-P and Fleitout L (2000) Flattening of the oceanic topography and geoid: Thermal versus dynamic origin. *Geophysical Journal International* 143: 582–594.
- Dziewonski AM (1984) Mapping the lower mantle: Determination of lateral heterogeneity in P velocity up to degree and order 6. *Journal of Geophysical Research* 89: 5929–5952.
- Dziewonski AM and Anderson DL (1981) Preliminary reference Earth model. *Physics of the Earth and Planetary Interiors* 25: 297–356.
- Dziewonski AM, Hager BH, and O'Connell RJ (1977) Large scale heterogeneity in the lower mantle. *Journal of Geophysical Research* 82: 239–255.
- Ekström G and Dziewonski AM (1998) The unique anisotropy of the Pacific upper mantle. *Nature* 394: 168–172.
- Forte AM (2000) Seismic-geodynamic constraints on mantle flow: Implications for layered convection, mantle viscosity, and seismic anisotropy in the deep mantle. In: Karato S-i, Forte AM, Liebermann RC, Masters G, and Stixrude L (eds.) *Geophysical Monograph Series 117 Earth's Deep Interior: Mineral Physics and Tomography from the Atomic to the Global Scale*, pp. 3–36. Washington DC: American Geophysical Union.
- Forte AM and Peltier WR (1987) Plate tectonics and aspherical Earth structure: The importance of poloidal–toroidal coupling. *Journal of Geophysical Research* 92: 3645–3679.

- Forte AM and Peltier WR (1989) Core-mantle boundary topography and whole-mantle convection. *Geophysical Research Letters* 16: 621–624.
- Forte AM and Peltier WR (1991) Viscous flow models of global geophysical observables. Part 1: Forward problems. *Journal of Geophysical Research* 96: 20131–20159.
- Forte AM and Peltier WR (1994) The kinematics and dynamics of poloidal-toroidal coupling in mantle flow: The importance of surface plates and lateral viscosity variations. *Advances in Geophysics* 36: 1–119.
- Forte AM and Mitrovica JX (1996) New inferences of mantle viscosity from joint inversion of long-wavelength mantle convection and post-glacial rebound data. *Geophysical Research Letters* 23: 1147–1150.
- Forte AM and Woodward RL (1997a) Seismic-geodynamic constraints on vertical flow between the upper and lower mantle: The dynamics of the 670 km seismic discontinuity. In: Crossley D (ed.) *The Fluid Dynamics of Astrophysics and Geophysics, vol. 7: Earth's Deep Interior*, pp. 337–404. Newark, NJ: Gordon and Breach.
- Forte AM and Woodward RL (1997b) Seismic-geodynamic constraints on three-dimensional structure, vertical flow, and heat transfer in the mantle. *Journal of Geophysical Research* 102: 17981–17994.
- Forte AM and Perry HKC (2000) Geodynamic evidence for a chemically depleted continental tectosphere. *Science* 290: 1940–1944.
- Forte AM and Mitrovica JX (2001) Deep-mantle high-viscosity flow and thermochemical structure inferred from seismic and geodynamic data. *Nature* 410: 1049–1056.
- Forte AM, Peltier WR, and Dziewonski AM (1991) Inferences of mantle viscosity from tectonic plate velocities. *Geophysical Research Letters* 18: 1747–1750.
- Forte AM, Dziewonski AM, and Woodward RL (1993a) Aspherical structure of the mantle, tectonic plate motions, nonhydrostatic geoid, and topography of the core-mantle boundary. In: Le Mouël J-L, Smylie DE, and Herring T (eds.) *Dynamics of the Earth's Deep Interior and Earth Rotation*, pp. 135–166. Washington DC: American Geophysical Union.
- Forte AM, Peltier WR, Dziewonski AM, and Woodward RL (1993b) Dynamic surface topography: A new interpretation based upon mantle flow models derived from seismic tomography. *Geophysical Research Letters* 20: 225–228.
- Forte AM, Peltier WR, Dziewonski AM, and Woodward RL (1993c) Reply to comment by M. Gurnis. *Geophysical Research Letters* 20: 1665–1666.
- Forte AM, Woodward RL, and Dziewonski AM (1994) Joint inversions of seismic and geodynamic data for models of three-dimensional mantle heterogeneity. *Journal of Geophysical Research* 99: 21857–21877.
- Forte AM, Mitrovica JX, and Woodward RL (1995a) Seismic-geodynamic determination of the origin of excess ellipticity of the core-mantle boundary. *Geophysical Research Letters* 22: 1013–1016.
- Forte AM, Dziewonski AM, and O'Connell RJ (1995b) Continent-ocean chemical heterogeneity in the mantle based on seismic tomography. *Science* 268: 386–388.
- Forte AM, Mitrovica JX, and Espesset A (2002) Geodynamic and seismic constraints on the thermochemical structure and dynamics of convection in the deep mantle. *Philosophical Transactions of the Royal Society of London A* 360: 2521–2543.
- Gable CW, O'Connell RJ, and Travis BJ (1991) Convection in three dimensions with surface plates. *Journal of Geophysical Research* 96: 8391–8405.
- Garcia R and Souriau A (2000) Amplitude of the core-mantle boundary topography estimated by stochastic analysis of core phases. *Physics of the Earth and Planetary Interiors* 117: 345–359.
- Gordon RG and Jurdy DM (1986) Cenozoic global plate motions. *Journal of Geophysical Research* 91: 12389–12406.
- Grand SP (2002) Mantle shear-wave tomography and the fate of subducted slabs. *Philosophical Transactions of the Royal Society of London A* 360: 2475–2491.
- Gurnis M (1990) Bounds on global dynamic topography from Phanerozoic flooding of continental platforms. *Nature* 344: 754–756.
- Gurnis M (1993) Comment. *Geophysical Research Letters* 20: 1663–1664.
- Gwinn CR, Herring TA, and Shapiro I (1986) Geodesy by radio interferometry; studies of the forced nutations of the Earth. Part 2: Interpretation. *Journal of Geophysical Research* 91: 4755–4766.
- Hager BH (1984) Subducted slabs and the geoid: Constraints on mantle rheology and flow. *Journal of Geophysical Research* 89: 6003–6015.
- Hager BH and O'Connell RJ (1981) A simple global model of plate dynamics and mantle convection. *Journal of Geophysical Research* 86: 4843–4867.
- Hager BH and Richards MA (1989) Long-wavelength variations in the Earth's geoid: physical models and dynamical implications. *Philosophical Transactions of the Royal Society of London A* 328: 309–327.
- Hager BH and Clayton RW (1989) Constraints on the structure of mantle convection using seismic observations, flow models, and the geoid. In: Peltier WR (ed.) *Mantle Convection: Plate Tectonics and Global Dynamics*, pp. 657–763. New York: Gordon and Breach.
- Hager BH, Clayton RW, Richards MA, Comer RP, and Dziewonski AM (1985) Lower mantle heterogeneity, dynamic topography and the geoid. *Nature* 313: 541–545.
- Hart SR (1988) Heterogeneous mantle domains; signatures, genesis and mixing chronologies. *Earth and Planetary Science Letters* 90: 273–296.
- Haskell NA (1935) The motion of a viscous fluid under a surface load. *Physics (NY)* 6: 265–269.
- Herring TA, Gwinn CR, and Shapiro I (1986) Geodesy by radio interferometry; studies of the forced nutations of the Earth. Part 1: Data analysis. *Journal of Geophysical Research* 91: 4745–4754.
- Hofmann AW (1997) Mantle geochemistry: The message from oceanic volcanism. *Nature* 385: 219–229.
- Jackson JD (1975) *Classical Electrodynamics*. New York: John Wiley and Sons.
- Jackson I (1998) Elasticity, composition and temperature of the Earth's lower mantle: A reappraisal. *Geophysical Journal International* 134: 291–311.
- Jackson I (2001) Chemical composition and temperature of the lower mantle from seismological models: Residual uncertainties. *Integrated models of Earth structure and evolution, AGU Virtual Meeting - 2001 Spring Meeting*, 20 June, [online].
- Jackson JM, Zhang J, Shu J, Sinogeikin SV, and Bass JD (2005) High-pressure sound velocities and elasticity of aluminous MgSiO₃ perovskite to 45 GPa: Implications for lateral heterogeneity in Earth's lower mantle. *Geophysical Research Letters* 32: L21305 (doi:10.1029/2005GL023522).
- Jarvis GT and Peltier WR (1982) Mantle convection as a boundary layer phenomenon. *Geophysical Journal of the Royal Astronomical Society* 68: 385–424.
- Jeanloz R and Thompson AB (1983) Phase transitions and mantle discontinuities. *Reviews of Geophysics and Space Physics* 21: 51–74.
- Jellinek AM and Manga M (2004) Links between long-lived hot spots, mantle plumes, D'', and plate tectonics 42: RG3002 (doi:10.1029/2003RG000144).

- Jordan TH (1981) Continents as a chemical boundary layer. *Philosophical Transactions of the Royal Society of London A* 301: 359–373.
- Karato S-i (1993) Importance of anelasticity in the interpretation of seismic tomography. *Geophysical Research Letters* 20: 1623–1626.
- Karato S-i and Karki BB (2001) Origin of lateral variation of seismic wave velocities and density in the deep mantle. *Journal of Geophysical Research* 106: 21771–21784.
- Karpachev M and Fleitout L (2000) Long-wavelength geoid: The effect of continental roots and lithosphere thickness variations. *Geophysical Journal International* 143: 945–963.
- Kaufmann G and Lambeck K (2000) Mantle dynamics, postglacial rebound and the radial viscosity profile. *Physics of the Earth and Planetary Interiors* 121: 301–324.
- Kellogg LH, Hager BH, and van der Hilst RD (1999) Compositional stratification in the deep mantle. *Science* 283: 1881–1884.
- Kennett BLN, Widjiantoro S, and van der Hilst RD (1998) Joint seismic tomography for bulk-sound and shear wavespeed in the Earth's mantle. *Journal of Geophysical Research* 103: 12469–12493.
- Kido M, Yuen DA, Čadek O, and Nakakuki T (1998) Mantle viscosity derived by genetic algorithm using oceanic geoid and seismic tomography for whole-mantle versus blocked-flow situations. *Physics of the Earth and Planetary Interiors* 107: 307–326.
- King S and Masters G (1992) An inversion for the radial viscosity structure using seismic tomography. *Geophysical Research Letters* 19: 1551–1554.
- King SD (1995) Models of mantle viscosity. In: Ahrens TJ (ed.) *AGU Reference Shelf Series, vol. 2: A Handbook of Physical Constants: Mineral Physics and Crystallography*, pp. 227–236. Washington DC: American Geophysical Union.
- Lambeck K, Johnston P, Smither C, and Nakada M (1996) Glacial rebound of the British Isles. III. Constraints on mantle viscosity. *Geophysical Journal International* 125: 340–354.
- Lambeck K, Smither C, and Johnston P (1998) Sea-level change, glacial rebound and mantle viscosity for northern Europe. *Geophysical Journal International* 134: 102–144.
- Landau LD and Lifshitz EM (1959) *Fluid Mechanics, vol. 6. New York: Pergamon*.
- Lemoine F, Pavlis N, Kenyon S, Rapp R, Pavlis E, and Chao B (1998) New high-resolution model developed for Earth's gravitational field. *Eos Transactions of the American Geophysical Union* 79(9): 113.
- Le Stunff Y and Ricard Y (1995) Topography and geoid due to lithospheric mass anomalies. *Geophysical Journal International* 122: 982–990.
- Le Stunff Y and Ricard Y (1997) Partial advection of equidensity surfaces; a solution for the dynamic topography problem? *Journal of Geophysical Research* 102: 24655–24667.
- Lithgow-Bertelloni C and Gurnis M (1997) Cenozoic subsidence and uplift of continents from time-varying dynamic topography. *Geology* 25: 735–738.
- Lithgow-Bertelloni C and Richards MA (1998) The dynamics of Cenozoic and Mesozoic plate motions. *Reviews of Geophysics* 36: 27–78.
- Martinez Z, Matyska C, Čadek O, and Hrdina P (1993) The Stokes problem with 3-D Newtonian rheology in a spherical shell. *Computer Physics Communications* 76: 63–79.
- Masters G, Laske G, Bolton H, and Dziewonski AM (2000) The relative behaviour of shear velocity, bulk sound speed, and compressional velocity in the mantle: Implications for chemical and thermal structure. In: Karato S-i, Forte AM, Lübecker RC, Masters G, and Stixrude (eds.) *Geophysical Monograph Series, 117: Earth's Deep Interior: Mineral Physics and Tomography From the Atomic to the Global Scale*, pp. 63–87. Washington DC: American Geophysical Union, 2000.
- Mathews PM, Herring TA, and Buffett BA (2002) Modeling of nutation and precession: New nutation series for nonrigid Earth and insights into the Earth's interior. *Journal of Geophysical Research* 107: 2068 (doi:10.1029/2001JB000390).
- McConnell RK (1968) Viscosity of the mantle from relaxation time spectra of isostatic adjustment. *Journal of Geophysical Research* 73: 7089–7105.
- McNamara AK and Zhong S-J (2005) Thermochemical structures beneath Africa and the Pacific Ocean. *Nature* 437: 1136–1139.
- Mégnin C and Romanowicz B (2000) The three-dimensional shear velocity structure of the mantle from the inversion of body, surface and higher-mode waveforms. *Geophysical Journal International* 143: 709–728.
- Mitrovica JX (1996) Haskell (1935) revisited. *Journal of Geophysical Research* 101: 555–569.
- Mitrovica JX and Forte AM (1997) Radial profile of mantle viscosity: Results from the joint inversion of convection and post-glacial rebound observables. *Journal of Geophysical Research* 102: 2751–2769.
- Mitrovica JX and Forte AM (2004) A new inference of mantle viscosity based upon joint inversion of convection and glacial isostatic adjustment data. *Earth and Planetary Science Letters* 225: 177–189.
- Morelli A and Dziewonski AM (1987) Topography of the core–mantle boundary and lateral homogeneity of the liquid core. *Nature* 325: 678–683.
- Moucha R, Forte AM, Mitrovica JX, and Daradich A (2007) Geodynamic implications of lateral variations in mantle rheology on convection related observables and inferred viscosity models. *Geophysical Journal International* 169: 113–135.
- Nakada M and Lambeck K (1989) Late Pleistocene and Holocene sea-level change in the Australian region and mantle rheology. *Geophysical Journal International* 96: 497–517.
- Nicolas A and Poirier J-P (1976) *Crystalline Plasticity and Solid State Flow in Metamorphic Rocks*, p444. London: John Wiley and Sons.
- O'Connell RJ (1971) Pleistocene glaciation and viscosity of the lower mantle. *Geophysical Journal of the Royal Astronomical Society* 23: 299–327.
- Obayashi M and Fukao YP (1997) P and P_cP travel time tomography for the core–mantle boundary. *Journal of Geophysical Research* 102: 17825–17841.
- Oganov AR, Brodholt JP, and Price GD (2001a) *Ab initio* elasticity and thermal equation of state of MgSiO₃ perovskite. *Earth and Planetary Science Letters* 184: 555–560.
- Oganov AR, Brodholt JP, and Price GD (2001b) The elastic constants of MgSiO₃ perovskite at pressures and temperatures of the Earth's mantle. *Nature* 411: 934–937.
- Mattern E, Matas J, Ricard Y, and Bass J (2005) Lower mantle composition and temperature from mineral physics and thermodynamic modelling. *Geophysical Journal International* 160: 973–990.
- Muller RD, Roest WR, Royer J-Y, Gahagan LM, and Slater JG (1997) Digital isochrons of the world's ocean floor. *Journal of Geophysical Research* 102: 3211–3214.
- Panasyuk SV and Hager BH (2000) Inversion for mantle viscosity profiles constrained by dynamic topography and the geoid, and their estimated errors. *Geophysical Journal International* 143: 821–836.
- Panasyuk SV, Hager BH, and Forte AM (1996) Understanding the effects of mantle compressibility on geoid kernels. *Geophysical Journal International* 124: 121–133.

- Pari G (2001) Crust 5.1-based inference of the Earth's dynamic surface topography: Geo-dynamic implications. *Geophysical Journal International* 144: 501–516.
- Pari G and Peltier WR (2000) Subcontinental mantle dynamics; a further analysis based on the joint constraints of dynamic surface topography and free-air gravity. *Journal of Geophysical Research* 105: 5635–5662.
- Parsons B and McKenzie D Mantle convection and the thermal structure of the plates. *Journal of Geophysical Research* 83: 4485–4496.
- Parsons B and Sclater JG (1977) An analysis of the variation of ocean floor bathymetry and heat flow with age. *Journal of Geophysical Research* 82: 803–827.
- Parsons B and Daly S (1983) The relationship between surface topography, gravity anomalies, and temperature structure of convection. *Journal of Geophysical Research* 88: 1129–1144.
- Peltier WR (1985) New constraint on transient lower mantle rheology and internal mantle buoyancy from glacial rebound data. *Nature* 318: 614–617.
- Peltier WR and Andrews JT (1976) Glacial isostatic adjustment, I, The forward problem. *Geophysical Journal of the Royal Astronomical Society* 46: 605–646.
- Pekeris CL (1935) Thermal convection in the interior of the Earth. *Supplement* 3: 343–367.
- Perry HKC, Forte AM, and Eaton DWS (2003) Upper-mantle thermochemical structure below North America from seismicgeodynamic flow models. *Geophysical Journal International* 154: 279–299.
- Phinney RA and Burridge R (1973) Representation of the elastic-gravitational excitation of a spherical Earth model by generalized spherical harmonics. *Geophysical Journal of the Royal Astronomical Society* 34: 451–487.
- Quéré S and Forte AM (2006) Influence of past and present-day plate motions on spherical models of mantle convection: Implications for mantle plumes and hotspots. *Geophysical Journal International* 165: 1041–1057.
- Ranalli G (2001) Mantle rheology: Radial and lateral viscosity variations inferred from microphysical creep laws. *Journal of Geodynamics* 32: 425–444.
- Ricard Y and Vigny C (1989) Mantle dynamics with induced plate tectonics. *Geophysical Journal International* 94: 17543–17559.
- Ricard Y and Wuming B (1991) Inferring viscosity and the 3-D density structure of the mantle from geoid, topography and plate velocities. *Geophysical Journal International* 105: 561–572.
- Ricard Y, Fleitout L, and Froidevaux C (1984) Geoid heights and lithospheric stresses for a dynamic Earth. *Annales Geophysicae* 2: 267–286.
- Ricard Y, Froidevaux C, and Fleitout L (1988) Global plate motion and the geoid: A physical model. *Geophysical Journal International* 93: 477–484.
- Ricard Y, Vigny C, and Froidevaux C (1989) Mantle heterogeneities, geoid, and plane motion – A Monte Carlo inversion. *Journal of Geophysical Research* 94: 13739–13754.
- Ricard Y, Richards M, Lithgow-Bertelloni C, and Le Stunff Y (1993) A geodynamic model of mantle density heterogeneity. *Journal of Geophysical Research* 98: 21895–21909.
- Ricard Y, Chambat F, and Lithgow-Bertelloni C (2006) Gravity observations and 3D structure of the Earth. *Comptes Rendus Geosciences* 338: 992–1001.
- Richards MA (1991) Hot spots and the case for a high viscosity lower mantle. In: Sabadini R, Lambeck K, and Boschi E (eds.) *NATO ASI Series C, vol. 334: Glacial Isostasy, Sea-Level and Mantle Rheology*, pp. 571–588. Dordrecht: Kluwer Academic.
- Richards MA and Hager BH (1984) Geoid anomalies in a dynamic Earth. *Journal of Geophysical Research* 89: 5987–6002.
- Richards MA and Hager BH (1989) Effects of lateral viscosity variations on long-wavelength geoid anomalies and topography. *Journal of Geophysical Research* 94: 10299–10313.
- Richards MA and Engebretson DC (1992) Large-scale mantle convection and the history of subduction. *Nature* 355: 437–440.
- Richards MA, Ricard Y, Lithgow-Bertelloni C, Spada G, and Sabadini R (1997) An explanation for the long-term stability of Earth's rotation axis. *Science* 275: 372–375.
- Ritsema J, van Heijst HJ, and Woodhouse JH (1999) Complex shear velocity structure imaged beneath Africa and Iceland. *Science* 286: 1925–1928.
- Ritzwoller MH, Shapiro NM, and Zhong S-J (2004) Cooling history of the Pacific lithosphere. *Earth and Planetary Science Letters* 226: 69–84.
- Rodgers A and Wahr J (1993) Inference of core-mantle boundary topography from ISC Pcp and PKP traveltimes. *Geophysical Journal International* 115: 991–1011.
- Röhm AHE, Snieder R, Goes S, and Trampert J (2000) Thermal structure of continental upper mantle inferred from S-wave velocity and surface heat flow. *Earth and Planetary Science Letters* 181: 395–407.
- Romanowicz B (2003) Global mantle tomography: Progress status in the past 10 years. *Annual Review of Earth and Planetary Sciences* 31: 303–328.
- Sabadini R, Yuen DA, and Gasperini P (1985) The effects of transient rheology on the interpretation of lower mantle rheology. *Geophysical Research Letter* 12: 361–365.
- Sabadini R and Yuen DA (1989) Mantle stratification and long-term polar wander. *Nature* 339: 373–375.
- Sammis CG, Smith JC, Schubert G, and Yuen DA (1977) Viscosity-depth profile of the Earth's mantle: Effects of polymorphic phase transitions. *Journal of Geophysical Research* 82: 3747–3761.
- Simmons NA, Forte AM, and Grand SP (2006) Constraining modes of mantle flow with seismic and geodynamic data: A joint approach. *Earth and Planetary Science Letters* 246: 109–124.
- Simmons NA, Forte AM, and Grand SP (2007) Thermochemical structure and dynamics of the African superplume. *Geophysical Research Letter* 34: L02301 (doi:10.1029/2006GL028009).
- Sobolev SV, Zeyen H, Granet M, et al. (1997) Upper mantle temperatures and lithosphere-asthenosphere system beneath the French Massif Central constrained by seismic, gravity, petrologic and thermal observations. *Tectonophysics* 275: 143–164.
- Spada G, Ricard Y, and Sabadini R (1992) Excitation of true polar wander by subduction. *Nature* 360: 452–454.
- Stacey FD (1998) Thermoelasticity of a mineral composite and a reconsideration of lower mantle properties. *Physics of the Earth and Planetary Interiors* 106: 219–236.
- Stein CA and Stein S (1992) A model for the global variation in oceanic depth and heat flow with lithospheric age. *Nature* 359: 123–129.
- Steinberger B and O'Connell RJ (1997) Change of the Earth's rotation axis inferred from the advection of mantle density heterogeneities. *Nature* 387: 169–173.
- Stixrude L and Lithgow-Bertelloni C (2001) The origin of lateral heterogeneity in the mantle. *Integrated models of Earth structure and evolution, AGU Virtual Meeting - 2001 Spring Meeting, 20 June*, [online].
- Stixrude L and Lithgow-Bertelloni C (2005a) Mineralogy and elasticity of the oceanic upper mantle: Origin of the low-

- velocity zone. *Journal of Geophysical Research* 110: B03204 (doi:10.1029/2004JB002965).
- Stixrude L and Lithgow-Bertelloni C (2005b) Thermodynamics of mantle minerals. Part I: Physical properties. *Geophysical Journal International* 162: 610–632.
- Su W-J, Woodward RL, and Dziewonski AM (1992) Deep origin of mid-ocean ridge seismic velocity anomalies. *Nature* 360: 149–152.
- Su W-J and Dziewonski AM (1997) Simultaneous inversion for 3-D variations in shear and bulk velocity in the mantle. *Physics of the Earth and Planetary Interiors* 100: 135–156.
- Sze EKM and van der Hilst RD (2003) Core mantle boundary topography from short period Pcp, Pkp, and Pkkp data. *Physics of the Earth and Planetary Interiors* 135: 27–46.
- Taylor SR and McLennan SM (1995) The geochemical evolution of the continental crust. *Reviews of Geophysics* 33: 241–265.
- Thoraval C, Machetel P, and Cazenave A (1995) Locally layered convection inferred from dynamic models of the Earth's mantle. *Nature* 375: 777–780.
- Thoraval C and Richards MA (1997) The geoid constraint in global geodynamics: Viscosity structure, mantle heterogeneity models, and boundary conditions. *Geophysical Journal International* 131: 1–8.
- Trampert J and Woodhouse JH (1996) High resolution global phase velocity distributions. *Geophysical Research Letters* 23: 21–24.
- Trampert J, Vacher P, and Vlaar N (2001) Sensitivities of seismic velocities to temperature, pressure and composition in the lower mantle. *Physics of the Earth and Planetary Interiors* 124: 255–267.
- Tushingham AM and Peltier WR (1991) ICE-3G: A new global model of late Pleistocene deglaciation based upon geophysical predictions of postglacial relative sea level change. *Journal of Geophysical Research* 96: 4497–4523.
- Wahr J (1981) The forced mutations of an elliptical, rotating elastic and oceanless Earth. *Geophysical Journal of the Royal Astronomical Society* 64: 705–727.
- Wang Y and Weidner DJ (1996) $(\partial\mu/\partial T)_P$ of the lower mantle. *Pure and Applied Geophysics* 146: 533–549.
- Weertman J (1978) Creep laws for the mantle of the Earth. *Philosophical Transactions of the Royal Society of London A* 288: 9–26.
- Weertman J and Weertman JR (1975) High temperature creep of rock and mantle viscosity. *Annual Review of Earth and Planetary Sciences* 3: 293–315.
- Wentzcovitch RM, Karki BB, Cococcioni M, and de Gironcoli S (2004) Thermoelastic properties of MgSiO_3 -perovskite: Insights on the nature of the Earth's lower mantle. *Physical Review Letters* 92: 018501.
- Woodhouse JH and Dziewonski AM (1984) Mapping the upper mantle: Three-dimensional modeling of earth structure by inversion of seismic waveforms. *Journal of Geophysical Research* 89: 5953–5986.
- Woodward RL and Masters G (1991) Global upper mantle structure from long-period differential travel times. *Journal of Geophysical Research* 96: 6351–6377.
- Wu P and Peltier WR (1983) Glacial isostatic adjustment and the free air gravity anomaly as a constraint on deep mantle viscosity. *Geophysical Journal of the Royal Astronomical Society* 74: 377–449.
- Zhang S and Christensen U (1993) Some effects of lateral viscosity variations on geoid and surface velocities induced by density anomalies in the mantle. *Geophysical Journal International* 114: 531–547.
- Zhang J and Weidner DJ (1999) Thermal equation of state of aluminum-enriched silicate perovskite. *Science* 284: 782–784.
- Zhang S and Yuen DA (1995) The influences of lower mantle viscosity stratification on 3D spherical-shell mantle convection. *Earth and Planetary Science Letters* 132: 157–166.